XLV Symposium of the Optical Society of India

Conference on Optics, Photonics & Quantum Optics

COPaQ 2022

10-13 November 2022

ABSTRACTS

Organized by

Department of Physics

Indian Institute of Technology Roorkee

175 YEARS OF IIT ROORKEE Estd. 1847

COPaQ 2022

XLV Symposium of the Optical Society of India

Conference on Optics, Photonics & Quantum Optics

(10-13 November 2022)

ABSTRACTS

Organized by

Department of Physics

Indian Institute of Technology Roorkee

Contents

Selected Papers

Keynote Talk

Quantum Optical Routes to Realising Quantum Technology

Peter Knight
Blackett Laboratory, Imperial College, London SW72AZ, UK,
Quantum Metrology Institute, National Physical Laboratory
&
Chair of the UK National Quantum Technology Strategic Advisory Board for UKRI

p.knight@imperial.ac.uk

Abstract: My talk will explain how we exploit a hitherto largely unexplored *technology* capability enabled by some of the stranger aspects of quantum physics: quantum coherence and entanglement. These new capabilities include novel sensing, timing, imaging and computing. I will describe for the non-specialist the UK £1Bn investment to develop the next generation of quantum technologies.
Keywords: quantum imaging, quantum communications, timing, sensing, quantum computing

1. Introduction

We already live in a quantum enabled world, with devices powered by quantum science affecting our everyday life (lasers, telecoms, semiconductor chips and much more). But we are now poised to exploit a previously largely unexplored *technology* capability enabled by some of the stranger aspects of quantum physics: quantum coherence and entanglement [1]. These new capabilities include novel sensing, timing, imaging and computing. I will describe the UK £1Bn investment to develop the next generation of quantum technologies [2]. This new era of quantum technologies will transform economies in our maturing digital age and help to address society's challenges: advancing health care and environmental protection, achieving better land use, supporting financial services and communications, providing defence and security capabilities and providing extraordinary computing power. These technologies will create new global market opportunities and competitive advantage for those able to develop and exploit them.

Quantum computing, the area receiving most media attention, represents a unique opportunity due to its complexity and the challenges that quantum computing presents to modern encryption. All current public key encryption (which underpins internet security) is undermined by quantum computational power. Being quantum-ready requires researchers, companies and government to engage now to upskill and explore applications that could have a significant impact on industry and wider society.

Sensors are used in everyday technologies to detect motion, sound, and light. They range from the billions of low-cost motion sensors in mobile phones to high-end systems in healthcare and Earth observation. New quantum sensors offer a step change in performance: more sensitive, accurate and stable than current technology. Quantum science enables us to see through walls, around corners and through fog, unlocking new applications, feeding into sectors including aerospace, climate, construction, defence, energy, healthcare, security, transport and water.

2. References

[1] Blackett Review: The Quantum Age: technological opportunities." Government Office for Science, Available: https://www.gov.uk/government/publications/quantum-technologies-blackett-review;

[2] Peter Knight and Ian Walmsley 2019 *Quantum Sci. Technol.* **4** 040502

Plenary Talk

The Wonderful World of Random Lasers and Random Fiber Lasers

Anderson S. L. Gomes
Physics Department, Universidade Federal of Pernambuco, Recife, PE, 50670-901, Brazil.

Abstract: In this talk, I shall describe how Random lasers and Random Fiber Lasers have been developed over the last three decades, highlighting their developments and applications which range from biophotonics to statistical physics and complex systems.
Keywords: Random Lasers; Random Fiber Lasers; Optical Amplifiers; Sensors; Nanophotonics; Biophotonics; Complex Systems

1. Introduction

Random Lasers (RLs) are coherent light sources whose feedback mechanism relies on light scattering in a strongly scattering media in the presence of a gain medium, instead of a pair of fixed mirrors. Upon appropriate pumping, inversion population and amplification precede the optical feedback such as the gain overcomes the loss as in conventional lasers. As reviewed in [1], where most of the historical background and theoretical/experimental developments until June 2021 can be read, RLs, as well as Random Fiber Lasers (RFLs) have become an important tool for photonic studies. As light sources, RLs and RFLs have been demonstrated in all 1D, 2D and 3D configurations, and well characterized regarding threshold, line narrowing/emitted intensity versus excitation intensity, polarization, spatial and temporal coherence, photon statistics (which has been shown to be Poissonian) and operation in the continuous wave or pulsed regime. Regarding RL materials, as long as there is a suitable gain medium (dye, rare earth doped glasses and crystals, semiconductors, quantum dots, etc) and a scattering medium (which can be the same as the gain medium or external to it) a myriad of RLs/RFLs have been demonstrated [see ref. 1]. As for RFLs, even the Rayleigh scattering in a few kms fiber length is enough to provide optical feedback, and intrinsic Raman or Brillouin processes provide the gain for laser action. Flexible RLs in 2D have also been exploited using biomaterials as hosts, and of course RFLs (1D) are intrinsically flexible by nature. Regarding applications, RLs and RFLS have been exploited for speckle-free imaging, which is an important feature for diagnostic by imaging. A variety of sensing devices based on RLs/RFLs have been recently reviewed in [2], including biosensors, powder delivery rate sensor, dopamine detection, among others. In optical communications, RFLs optical amplifiers have been demonstrated to perform better than conventional optical fiber amplifiers, as reviewed in [1] and refs therein. Finally, RLs and RFLs have been exploited as a photonic platform to study, by analogy, turbulence, photonic spin glass, Lévy statistics, Floquet states and extreme events. The connection between photonic turbulence and spin glass behavior of light has shown to bridge the two subjects and, through experiments using RFLs, have been highlighted in connection with recently awarded 2021 Nobel Prize in Physics [3].

All these exciting features of the wonderful world of RLs and RFLs will be touched upon during this lecture.

2. References

[1] Anderson S.L. Gomes, André L. Moura, Cid B. de Araújo and Ernesto P. Raposo, (Review) Recent advances and applications of random lasers and random fiber lasers, Progress in Quantum Electronics 78, 100343 (2021).
[2] Atiqah Nabieha Azmi, Wan Zakiah Wan Ismail, Haslan Abu Hassan, Mohd Mahadi Halim, Norzaini Zainal, Otto L. Muskens and Wan MaryamWan Ahmad Kamil, Review of Open Cavity Random Lasers as Laser-Based Sensors, ACS Sens. 7, 914−928 (2022)
[3] A. S. L. Gomes, C. B. de Araújo, A. M. S. Macêdo, I. R. R. González, L. de S. Menezes, P. I. R. Pincheira, R. Kashyap, G. L. Vasconcelos and E. P. Raposo “Photonics bridges between turbulence and spin glass phenomena in the 2021 Nobel Prize in Physics,” Light: Science & Applications 11:104 (2022)

Semiconductor Nanostructures for Optoelectronics Applications

Chennupati Jagadish
Australian Research Council Centre of Excellence on Transformative Meta-Optical Systems, Research School of Physics, The Australian National University, Canberra, ACT 2600, AustraliaEmail: c.jagadish@ieee.org

Semiconductors have played an important role in the development of information and communications technology, solar cells, solid state lighting. Nanowires are considered as building blocks for the next generation electronics and optoelectronics. In this talk, I will present the results on optoelectronic devices such as lasers/LEDs, THz detectors, energy devices such as solar cells, photoelectrochemical (PEC) water splitting and Neuro-electrodes. Future prospects of the semiconductor nanowires will be discussed.

Professor Jagadish is a Distinguished Professor and Head of Semiconductor Optoelectronics and Nanotechnology Group in the Research School of Physics, Australian National University. Prof. Jagadish is the Editor-in-Chief of Applied Physics Reviews (IF:19.5), Editor of 2 book series and serves on editorial boards of 20 other journals. He has published more than 1000 research papers (730 journal papers), holds 7 US patents, co-authored a book, co-edited 15 books and edited 12 conference proceedings and 20 special issues of Journals. He is a fellow of 12 Science and Engineering Academies (US, UK, Australia, Europe, India) and 14 Professional Societies (IEEE, MRS, APS…). He received many awards including IEEE Pioneer Award in Nanotechnology, IEEE Photonics Society Engineering Achievement Award, OSA Nick Holonyak Award, IUMRS Somiya Award, UNESCO medal for his contributions to the development of nanoscience and nanotechnologies and Lyle medal from Australian Academy of Science for his contributions to Physics. He has received Australia's highest civilian honor, AC, Companion of the Order of Australia, for his contributions to physics and engineering, in particular nanotechnology. He is currently serving as the President of the Australian Academy of Science.

The High Intensity Laser Frontier

G. Ravindra Kumar
Tata Institute of Fundamental Research, Homi Bhabha Road, Colaba, Mumbai 400005
grk@tifr.res.in

Abstract: We discuss the advances made in generating ultrahigh light intensities using amplified femtosecond laser pulses and the extreme physical states that can be produced on a lab tabletop using these. These pulses are enabling experiments never envisaged before, in high energy density science, laboratory astrophysics, particle acceleration and bright x-ray and gamma ray emission.
Keywords: High energy density physics, Intense laser-matter interaction, Extreme nonlinear optics, Extreme states, table-top particle acceleration

Most of the universe exists in conditions that combine high material density with high temperature. In recent times, such extreme states of 'high energy density' have been studied in the laboratory focusing 'extreme light' namely, high peak power, ultrashort pulsed laser light to micron spatial scales. As laser technology climbs to higher powers, we can simulate such matter at ever increasing material densities coupled with high temperatures in lab experiments and learn more about the complex interactions and dynamics that take place in such environments. These experiments help understand condensed matter, plasma, astro, nuclear and particle physics all in one setting. At the same time, we can exploit the rich emissions of high energy photons and material particles from such matter to fashion novel, tabletop sources of radiation for a variety of applications in science, technology and medicine [1 and the references therein].

This talk will attempt to describe in a broad perspective, some of the science and applications of dense, hot matter, with reference to the research at TIFR – creation of gigantic magnetic pulses (100s of megagauss), ultrafast plasma dynamics, passage of relativistic electrons through dense, hot matter and its consequences in terms of MeV ion production, ultrafast hard x-ray emission *etc.* [2-8].

REFERENCES

[1] S.V. Bulanov *et al.*, *Plasma Physics Reports* **41**, 1 (2015)

[2] G. Chatterjee et al., *Phys. Rev. Lett.* **108**, 235005 (2012)

[3] M. Shaikh *et al.*, *Phys. Rev. Lett.* **120**, 065001 (2018)

[4] S. Mondal *et al.*, *Proc. Natl. Acad. Sci. (USA)* **109**, 8011 (2012)

[5] S. Mondal *et al.*, *Phys. Rev. Lett.* **105**, 105002 (2010)

[6] A. Adak *et al*., *Phys. Rev.Lett.* **114**, 115001 (2015)

[7] K. Jana *et al.*, *Phys. Rev. Res*. **3**, 033034 (2021); AIP Adv. **12**, 095112 (2022)

[8] G. Chatterjee *et al*., *Nat. Commun.* **8**,159709 (2017); A. Das et al., *Phys. Rev. Res.* **3**, 033405 (2021)

Metasurfaces: potential and challenges

Pierre Chavel[1] and Philippe Lalanne[2]

1 - Laboratoire Hubert Curien, Institut d'Optique, Université Jean-Monnet de Saint-Etienne, Centre national de la recherche scientifique, 18 rue du professeur Benoît Lauras, F 42000 Saint-Etienne

2 – Laboratoire Photonique, Numérique et Nanosciences, Institut d'Optique, Université de Bordeaux, Centre national de la recherche scientifique, rue François Mitterrand, F 33400 Talence

Corresponding authors: pierre.chavel@institutoptique.fr

Abstract: an ideal metasurface would be able to arbitrarily transform an incoming wavefront by nanostructuration of matter over a thickness negligible compared to the local wavelength. While such a goal remains elusive in its full generality, approaches compete to approach it. We compare recent achievements using plasmonic antennas, Huygens metasurfaces based on dielectric resonances, and waveguiding pillars in terms of flexibility, fabrication requirements, spectral behavior, spurious light and final thickness.

Keywords: nanophotonics, diffractive optics, metasurfaces

1. Introduction

A metasurface is supposed to bend light according to the so-called "generalized Snell's law", where the surface gradient of the phase "discontinuity" imparted on the incoming wave complements to the standard Snell's law. In fact, metasurfaces provide only approximate discontinuities, as they consist of thin layers of nanostructured material.

2. Theory

We interpret the generalized Snell's law in terms of the local periodicity of the nanostructure, evidencing the role of the grating law as the underlying principle of metasurfaces, at least when it comes to arbitrarily shape an incoming wavefront.

3. Implementations

We compare three main approaches to nanostructuring matter in metasurfaces:

1. Plasmonic nanoantennas: plasmons provide extremely sharp phase changes and reach record low thickness for a given phase modulation. They suffer some absorption and the competition of the desired diffracted wavefront with spurious terms.

2. Mie resonances, such as those involved in Huygens metasurfaces, enjoy the absence of absorption while still benefiting from resonance effects to minimize thickness.

3. Nanopillars designed as monomode waveguides avoid resonances for better light efficiency, and angular behaviour. The price to pay is that the minimal thickness for full wavefront control is not much smaller than the wavelength.

4. Conclusion

Arbitrary spectral control is still in infancy. For monochromatic operation, to a good extent, metasurfaces can nowadays be designed, fabricated and replicated for a wide variety of wavefront control functions deriving from such basic types as metalenses, metagratings and aberration control.

Invited Talk

Laser Induced Breakdown: A Versatile Tool

Alika Khare

Departmnet of Physics, Indian Institute of Technology Guwahati, Guwahati 781039Author affiliation and full e-mail: alika@iitg.ac.in

Abstract: Laser induced breakdown (LIB) is being viewed as a very versatile tool in present era. One of the salient features is its applicability in any kind of environment. In this system, a pulsed high power laser is focused on to the sample (solid, liquid or gas), the material in the focal region breaks down and furnishes a tiny transient plasma. The dynamics of such plasma is quite complex and therefore basic understanding of LIB is continuing to be very active field of research even after its realization way back 1965 besides its numerous applications. LIB can process any material with a great deal of precision. It can be used to grow the phototonic band gap material and for fine coating on optical components. It is also a source of high energy electron beam and X-rays. It is used to synthesis any kind of nanoparticles free from contamination which can be used as a template for SERS, antibacterial agent etc. The focus on the present talk is going to be on some of the applications of LIB to demonstrate its versatility and simplicity particularly in the field related to Optical Sciences.

Image Processing requirements for Electro-Optical Sensors

Ajay Kumar
Instruments Research & Development Establishment
Raipur Road,
Dehradun-248008
ajay@irde.drdo.in

Abstract:

Electro-Optical (EO) & Infra-Red (IR) Sensors are means to provide Imagery Intelligence (IMINT) with desired terminal effects and are becoming necessity in all "Strategic Defence Missions". EO/IR sensors are required for Reconnaissance, Surveillance and Target Acquisition (RSTA), Precision Guided Munitions (PGMs) as a part of Fire Control Systems, Missile Seekers, Warning & Counter Measure Systems from Ground, Sea & Air-Borne platforms. In recent years, various EO/IR Systems like Electro Optics Fire Control Systems for Naval Ships, Integrated Multi-Function Sight, Commander Thermal Sight for AFVs, Costal Surveillance and Laser designators have been designed & developed at IRDE. Gyro stabilized Long Range EO payload comprising of IR, Day CCD &Laser designator having ranges of the order of 40 km has also been realized for Air-borne applications. The paper highlights the technology growth profile and future trends in both cooled and uncooled IR imaging Systems. The cooled IR Sensors are operating either in MWIR (3-5 μm) or LWIR (8-12 μm) spectral bands. IRFPAs have been evolved from 320 x 256 to 640 x 512 pixels and now HD array formats of 1920 x 1536 pixels with pixel sizes down to 10 μm are in use. Attempts are being made for 4K x 4K detector with 05-10 μm pixels sizes with digital output. New materials like Type-II Super Lattice detector as an alternative to MCT/InSb have been realized & are undergoing testing. These high performance cooled MWIR/LWIR sensors can be deployed from high value platforms for long applications whereas LWIR uncooled sensors can be used for short range applications in micro UAV, Rifle sights and missile seekers. Efforts made by IRDE in the development of advanced IR systems using state-of-art detectors including the design of Hyper-Spectral Imaging will also be presented.

Performance of the these sensors are heavily dependent on the associated image processing. Active /Passive Imaging at the focal plane, new detector material operating at high temperature, dual color detector and advanced image processing will also be discussed. Need for Multi Spectral & Hyper-spectral payloads with Multi-Sensor Data Fusion (MSDF) capabilities required to achieve C4ISR capabilities for future war fighting & Decision Support Systems will be highlighted.

Relaxation Oscillation Suppression for a QCW TDFL Using Optical Feedback Amplifier Design

Vincent Akash Gomes[1,2,*], Sourav Das Chowdhury[1], Sajib Chowdhury[1,2], Shubhranil Maity[1,3] Atasi Pal[1,2]

1 CSIR-Central Glass & Ceramics Research Institute, Kolkata, 700032
2 Academy of Scientific & Innovative Research (AcSIR), Ghaziabad, Uttar Pradesh 201002
3 Department of Physics, Jadavpur University, Jadavpur, Kolkata 700032
**Corresponding Author: gomesvincent12@gmail.com*

Abstract: A thulium-doped fiber laser (TDFL) in all-fiber master oscillator power amplifier (MOPA) configuration operating in quasi-continuous wave (QCW) with suppressed relaxation oscillation peak at 1940 nm has been designed and characterized. A wavelength matched optical feedback mechanism has been adopted by using a low reflective fiber Bragg grating in the power amplifier to achieve the reduction of relaxation oscillation.
Keywords: Thulium Fiber Laser, Quasi-CW, Relaxation Oscillation, Fiber Laser, MOPA, Optical feedback.

1. Introduction

Operating wavelength in the range of 1900-2050 nm for thulium doped fiber laser (TDFL) finds its applications in remote sensing, atmospheric sensing, and tissue surgery [1]. TDFL at 1940 nm has proved its superiority as a surgical laser over clinical Ho:YAG laser at 2090 nm due to four times absorption coefficient in water [2]. In surgical laser-based applications, a certain high peak power is desirable [2]. To achieve that for quasi-continuous mode (QCW), amplification is an effective approach. However, major challenges in amplification are: inadvertent amplification of relaxation oscillation (RO) peak, added amplified spontaneous emission (ASE) and noise along with the master oscillator (MO) signal. Due to Shorter pulse width of RO peaks, it gains significant peak power after amplification which often can cause damage to the optical components. To reduce RO, Yin et al. in [3] proposed a method in which the rise time of the pump power is increased to reduce RO generation. In [4] a numerical simulation on bias-pump gain switched fiber laser is presented for suppressing chaotic RO generation in a gain switched fiber laser which allowed the use of higher power and longer duration of pump pulse. The presented work is on the design of an all-fiber-based master oscillator power amplifier (MOPA) incorporating a wavelength matched optical feedback (WMOF) to reduce RO generation in a QCW TDFL at 1940 nm.

2. Experimental Setup

The MO used was a in house designed TDFL system at 1940 nm with an output of 10 W under 793 nm pumping. The MO operated in continuous wave (CW) mode or in QCW modes by modulation of pump diodes. In conventional MOPA architecture, output of MO was spliced to isolator (ISO), which was spliced to signal port of a (6+1):1 pump signal combiner (PSC). Six pump laser diodes (PLD) of 15 W at 793 nm were used. Output of PSC was spliced to a 2 m long 10/130 µm N.A 0.15 double clad thulium doped (DC-TDF) fiber, whose length was optimized for good gain without intrinsic lasing in range of 1950-2100 nm, in the power amplifier (PA) and followed by cladding mode stripper (CMS), shown in fig.1(a). In modified design, a WMOF was realized by adding a low reflective (5% at 1940 nm, $\Delta\lambda$ at 3dB=0.5 nm) fiber Bragg grating (LR-FBG) after CMS of the PA while ISO was excluded, shown in fig.1(b). This supported the WMOF coupling between PA and MO, leaving remaining architecture same as conventional MOPA.

3. Results and Discussions

For QCW mode of the MO, the RO peaks appear at the starting edge of every pulse in the pulse train due to the occurrence of transient non-equilibrium condition of population inversion in the laser resonator cavity of MO just after the threshold of the resonator is crossed [5]. In case of the MOPA architecture, these RO peaks originating in the MO are amplified along with the pulses. For our experimental setup we measured the RO pulse width in the range of

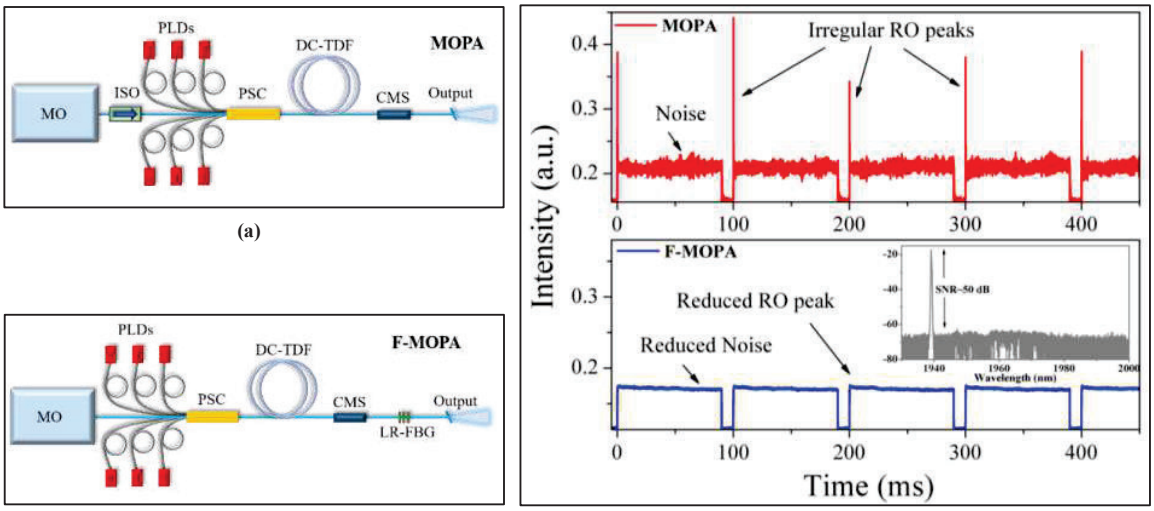

Fig. 1: (a) MOPA; (b) F-MOPA setup diagram; (c) Temporal comparison of MOPA & F-MOPA, inset: Spectral plot of F-MOPA

250-400 ns after MOPA. Such short duration with irregular amplitude can gain sudden instantaneous high peak power after amplification which can cause damage to the laser system. In our feedback MOPA (F-MOPA) architecture, the WMOF provided by LR-FBG in conjunction with the LR-FBG of the MO creates a weak CW signal in the PA, since PA was being continuously pumped. This CW light interacts with the MO due to the absence of the ISO. Interaction and reabsorption of the CW light in the MO gain fiber in the absence of pump light for QCW mode leads to generation of partial CW power in the MO. This eliminates the transient non-equilibrium condition of population inversion when transitioning from complete OFF to ON conditions in QCW mode, resulting in complete suppression of the RO in the MO itself. Partial CW condition is maintained in the F-MOPA system because of multi-cavity formation between the FBGs of MO and the LR-FBG of the PA. The reflectivity of the LR-FBG was selected at 5% to help extract majority of the power from the F-MOPA cavity and to prevent the CW power from overwhelming the intended QCW nature of the signal light.

As shown in fig.1(c), the RO peaks are completely suppressed when operated in 90% duty cycle mode of operation for pulse width of 90 ms in the F-MOPA in comparison to conventional MOPA. F-MOPA showed lower gain in comparison to conventional MOPA with 6 dB and 6.5 dB at 90% duty cycle respectively. Also, at a lower duty cycle of 20% F-MOPA showed a lower gain of 11.2 dB over 11.6 dB for MOPA with similar pump power. This reduction in gain is due to the fact that partial output signal power is being used for the optical feedback in the F-MOPA system. Another benefit of the new amplifier design proved to be reduced temporal intensity noise in the output of the F-MOPA system as shown in fig.1(c). Spectral plot of F-MOPA operating at 1940 nm is shown in inset of fig.1(c).

4. Conclusion

In conclusion, we present an all-fiber based modified MOPA for TDFL which experimentally demonstrated complete elimination of RO peaks in QCW mode of operation. Elimination of the RO peaks were achieved utilizing optical feedback by using a LR-FBG in the PA, which led to evolution of a CW power in the F-MOPA. This CW power eliminated the transition from complete OFF to complete ON condition which led to elimination of RO.

5. References

[1] Gregory D. Goodno, Lewis D. Book, and Joshua E. Rothenberg, "Low-phase-noise, single-frequency, single-mode 608 W thulium fiber amplifier," Opt. Lett. 34, 1204-1206 (2009)
[2] Taratkin, M., Kovalenko, A., Laukhtina, E. et al. "Ex vivo study of Ho:YAG and thulium fiber lasers for soft tissue surgery: which laser for which case?," Lasers Med Sci 37, 149–154 (2022).
[3] Jingchan Yin, Xiaosheng Xiao and Changxi Yang, "Dynamics and suppression of relaxation oscillation caused by stimulated Brillouin scattering in optical fiber," 2009 14th OptoElectronics and Communications Conference, 2009, pp. 1-2
[4 Fuyong Wang, "Stable pulse generation in a bias-pumped gain-switched fiber laser," J. Opt. Soc. Am. B 35, 231-236 (2018)
[5] Anthony E. Siegman, *LASERS* (University Science Books Sausalito, California 1986), Chap. 25

Challenges in Achieving Multi-kW Laser Sources Through Coherent Beam Combining

B. Srinivasan*, C. L. Linslal, V. Sankar, S. Maji, M. S. Sooraj, and D. Venkitesh
Department of Electrical Engineering, Indian Institute of Technology Madras, Chennai 600036 Tamil Nadu, India
**Email id: balajis@ee.iitm.ac.in*

Abstract: In this talk, we will discuss the key challenges that need to be overcome to achieve multi-kW laser sources through coherent beam combining. Such challenges include stimulated Brillouin scattering (SBS), the phase noise in the individual arms, the precise matching of length as well as polarization of the radiation in the individual arms, scaling to large (>100) number of sources, and the maintaining of coherence through atmospheric propagation.
Keywords: Coherent Beam Combining, Tiled Aperture, Phase Synchronization.

1. Motivation

Coherent combining of multiple fiber lasers is a promising technique to achieve high power (hundreds of kW) laser beams with good beam quality for several applications including directed energy, light detection and ranging (LIDAR), and material processing [1]. In coherent beam combining, light from a master oscillator is typically split into multiple arms, amplified independently, and interfered coherently to achieve high power levels. However, to achieve high beam combination efficiency the phase of the individual arms needs to be precisely controlled and sophisticated phase control techniques are used for correcting the accumulated phase noise in the array elements. A diffractive optical element in a filled aperture configuration or a collimator array in a tiled aperture configuration is used to realize the beam combination in a CBC system.

2. Challenges in Multi-kW CBC

A schematic diagram illustrating a typical CBC configuration is presented in Fig. 1. It consists of a narrow linewidth seed laser (coherence is controlled through an external phase modulator to mitigate any SBS from the high-power fiber amplifiers, FAs), whose output is split into N number of channels. The light radiation in the individual arms is amplified through multi-stage fiber amplifiers before being fed into a beam combining apparatus – either a diffractive beam combining element or a tiled aperture configuration. A key aspect of the coherent beam combining is the phase synchronization between the various arms, which is achieved through phase modulators in the individual arms controlled through a feedback circuit.

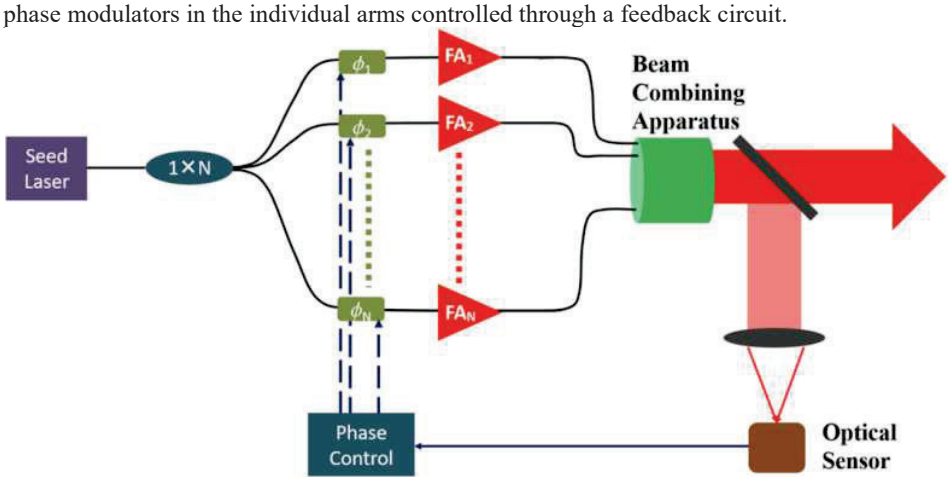

Fig 1. Schematic diagram of an N-channel coherent beam combination system

A CBC system generating 300 kW output power has recently been announced by Northrop Grumman. However, in order to achieve such high power levels, several key challenges need to be overcome. One such challenge is the mitigation of SBS in the high-power fiber amplifiers. This has been conventionally addressed by using noise/PRBS phase modulation of the seed laser output, but it has been recently reported that an optimized phase modulation waveform could potentially provide better results [3]. Phase noise control through the feedback loop is another key challenge, which is widely addressed using the Stochastic Parallel Gradient Descent (SPGD) algorithm. However, since the scalability of such an approach is questionable, Reinforcement Learning (RL) techniques have been explored recently. From the perspective of scalability, tiled aperture beam combining is mostly preferred but its efficiency is limited by the overlap of the tiled beams in the far field. This issue has been recently addressed by using a hybrid approach which involves overlap of the beams in the near field itself through an appropriate optical arrangement e.g. a pair of microlens arrays. Finally, the collection of tiled beams need to travel through the atmosphere and combine effectively at the target. This necessitates a target-in-the-loop configuration, which poses several engineering challenges. In this talk, we will discuss each of these challenges as well as the most promising approaches to overcome them, leading to multi-100 kW laser sources.

3. References

[1] C.L. Linslal, *et. al*. Challenges in coherent beam combining of high power fiber amplifiers: a review. ISSS J Micro Smart Syst 11, 277–293 (2022).
[2] P. Ayyaswamy, *et.al.*, "Data-Driven Modeling of Phase Noise Sources in Coherent Beam Combining," Laser Congress 2021, OSA Technical Digest.
[3] Y. Panbiharwala et al, “Stimulated Brillouin scattering mitigation using optimized phase modulation waveforms in high power narrow linewidth Yb-doped fiber amplifiers”, Opt Express 29,17183–17200 (2021)

HOLOGRAPHIC PRINCIPLE USING POYNTING'S THEOREM

C S Narayanamurthy
Applied and Adaptive Optics Laboratory, Department of Physics, Indian Institute of Space Science and Technology, Valiamala(PO), Trivandrum – 695547
Email : murthy@iist.ac.in

Abstract: A new approach to the explanation of holographic principle using the concept of Poynting's theorem is explained with examples. The interpretation for construction and reconstruction of wavefront is carried out for both parallel and perpendicular polarization of interfering beams in the recording plane.

Keywords: Poynting's theorem, holography, wavefront etc

1. Introduction

Holography is perhaps the best experimental discovery since the invention of lasers in 1961. Though the original concept of holography was conceptulated in 1948 by British scientist Denis Gabor[1,2], real experimental demonstration had to wait till the invention of lasers by Charles Hard Townes in 1960[3-5]. Unlike, photography, holography has two stages construction and reconstruction of wavefront scattered from the object. Initially we record the interference between object and reference beams conventionally on a recording plane and then we reconstruct using only the reference beam. In this paper we consider that incident object and reference beams having parallel and perpendicular polarization states with respect to incident recording plane and show the influence of imaging.

2. Parallel polarization states for object and reference beams

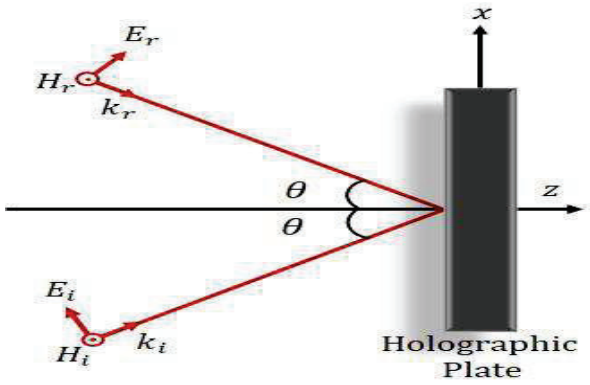

Fig.1

Fig.1 shows our first recording configuration with both object and reference beams have polarization states parallel to recording plane. We found that the after reconstruction the diffracted beams consisting of direct beams and object and its phase conjugate beams can be separated out by choosing reconstruction angular values. The final recording intensity in this case becomes,

$$I_h = (\tfrac{1}{2})\,\varepsilon_0 c\,[2E_0^2 \sin^2 2\theta] + 4E_0E_r \cos 2\theta \cos(\phi_0 - \phi_r)\, e^{-j\beta_1(x\sin\theta - z\cos\theta)} \quad (01)$$

3. Perpendicular polarization states for object and reference beams

In the second recording configuration we had incident object and reference beams with perpendicular polarization states with respect to recording planes. In this experimental geometry we found that the reconstructed direct beams which have to be removed for high efficient holograms are getting eliminated without additional requirements. In digital holographic reconstruction this problem is eliminated by choosing proper reconstructing beams.

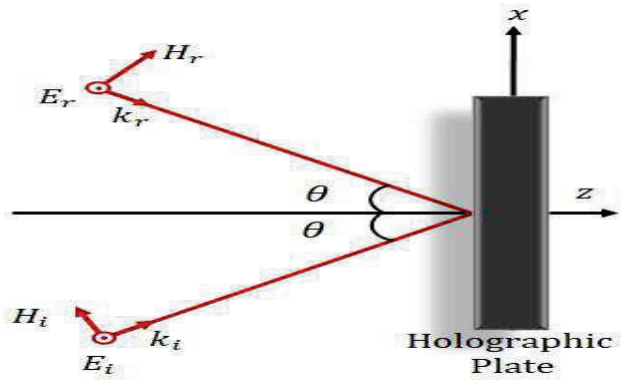

Fig.2

Final expression for perpendicular polarization state reduces to,

$$I_h = E_r^2(E_0\, e^{i\phi_0} + E_0^*\, e^{-i\phi_0}) \qquad (02)$$

4. Conclusion

We at the end demonstrate some experimental results to show the importance of this new approach to explain holographic reconstructions via Poynting's theorem.

5. References

[1] D. Gabor, "A new microscopic principle", Nature,161, 777-778 (1948).
[2] D. Gabor, "Microscopy by reconstructed wavefront", Proc. Royal Society A,197, 454-487 (1949).
[3] E. Leith and J. Upatnieks, "Reconstructed wavefronts and communication theory", JOSA, 52, 1123-1128 (1962).
[4] Y N Denisyuk, "Photographic reconstruction of the optical properties of an object in its own scattered field", Sov.Phys. Dokl,7:543, (1962).
[5] E. N. Leith and J. Upatnieks, " Wavefront Reconstruction with Continuous-Tone Objects," JOSA, 53, 1377 (1963).

Novel 1D photonic architectures for giant optical nonlinearities and strong electron-photon interactions

Jitendra Nath Acharyya and G. Vijaya Prakash*
Nanophotonics Lab, Department of Physics,
Indian Institute of Technology Delhi, New Delhi-110016, India
**E-mail address: prakash@physics.iitd.ac.in*

Abstract: Carefully designed one-dimensional (1D) photonic structures in the form of metal-dielectric (MD) multilayers and all-dielectric optical microcavities enable large spatial optical field confinement resulting into giant enhancement in third- and higher-order optical nonlinearities. The study of nonlinear optical interactions in such wavelength-order photonic architectures reveals the strong interaction between photonic modes and electronic state interactions with the spatial field distribution. The novel photonic architectures are the potential for future ultrafast photonic device applications.
Keywords: 1D photonic crystals, optical microcavity, Giant third-order optical nonlinearities, Ultrafast dynamics

1. Introduction

With the recent advances in ultrafast lasers, many immense applications have emerged in the recent past, that include material processing, textured fabrication, biophotonic, and defense applications. For such ultrafast lasers, the traditional optical systems are no longer viable and optical components require high-quality precise control over reflectivity/transmission, laser damage threshold, and tunable optical nonlinearities. Noble metals typically exhibit large nonlinear susceptibilities and incorporating metals into photonic structures gives rise to the additional advantages to harness extremely high nonlinearities and ultrafast dynamics. Thus, the study of laser-matter interactions with ultrafast laser pulses and related induced effects can provide a very interesting understanding of the underlying physics, which goes along with the optimization of required optical parameters to enhance the optical system performance. The present study demonstrates the third- and higher-order nonlinear optical properties and ultrafast dynamics in carefully designed metal-dielectric (MD) and all-dielectric wavelength-ordered 1D photonic structures in the form of distributed Bragg reflector (DBR) and optical microcavity. The studies are not limited to the controlled light propagation/inhibition for a selective domain of wavelengths, but rather, with precise control over electron-photon interactions in the linear and nonlinear regimes. On the other hand, the all-dielectric photonic structures exhibited enhanced electron-photon interactions exploiting the coupling of electronic states with photonic modes. The temporal dynamic evolution of photonic *minibands* of both sides of the photonic cavity mode is investigated for a better understanding of electron-photon interaction, which paves the way for many novel nonlinear, hybrid optoelectronic, and photonic device applications.

2. Results and Discussions

Here is the example of carefully crafted $(Ag/SiO_2)_n$ MD multilayered photonic structure exhibit a prominent photonic stop band in the visible region along with the transmission minibands on both sides of the stopband (Fig 1a). These photonic *minibands* are interesting due to the huge optical field confinement within the dielectric layer by the *coupled* Fabry–Pérot resonators of Ag-SiO_2-Ag. The transfer matrix simulations at *minibands* show the optimal optical field confinement within the structures (Fig.1a). The broad origin of giant nonlinearity is ascribed to the strong local cavity field enhanced metal inter-band transitions initiated by multiphoton absorption processes. The strong confinement of optical field and energy dissipation within these metal -dielectric coupled resonators is further evidenced by simulations. The giant multi-photon absorptive type nonlinearities with very high laser damage threshold (~50 GW/cm^2) from these composite transparent metals are potentially beneficial for novel nonlinear based extremely high power ultrafast laser applications [1]. The ultrafast temporal evolution of nonlinear absorption (Fig 1b) clearly demonstrates the electronic origin of the enhanced optical nonlinearity, which is further disentangled by the electron-electron and electron-phonon interactions involved during the energy relaxation process at picosecond time scales. Further, a phenomenological pulse propagation model is eventually employed incorporating the experimentally obtained nonlinear coefficients and invoking different nonlinear effects exhibited by the system, both in time and frequency domains [2].

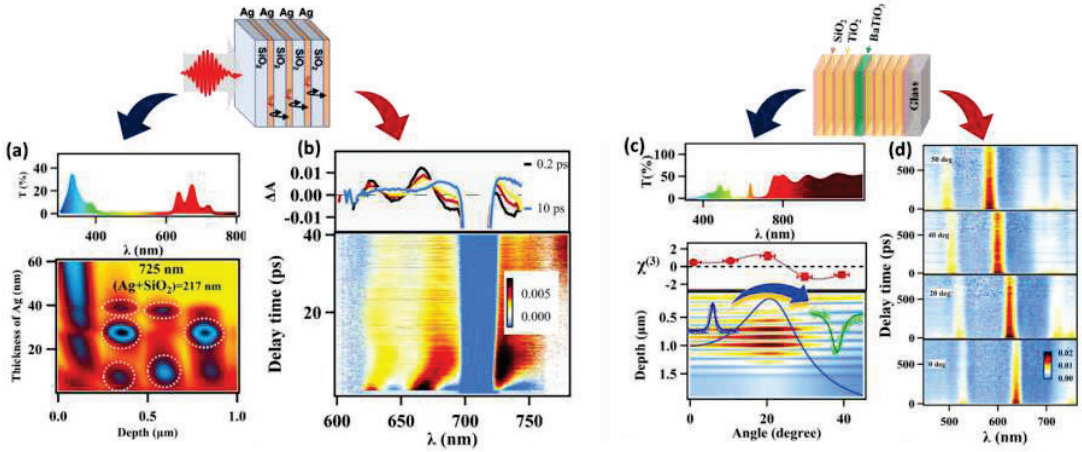

Fig. 1. (a) Linear transmission spectra and optical field confinement in $(Ag/SiO_2)_4$ metal-dielectric (MD) 1D structure (b) transient absorption dynamics results of MD 1DPC pumped at 350 nm (120 fs, 1 kHz). (c) transmission spectra of Bi_2O_3-based optical (SiO_2/TiO_2) microcavity. The strong nonlinear absorption switching from saturation of absorption (SA) to a reverse saturation of absorption (RSA) provided by the angle resolved electron-photon interactions. (d) The electron-photon interactions are also directly reflected in the angle resolved transient absorption (ΔA) temporal dynamics of the photonic cavity modes, excited at 350 nm laser excitation.

The temporal dynamic evolution of the photonic *minibands* in the 1D MD structure is illustrated in Fig. 1b using 350 nm (120 fs, 1 kHz) as the pump and broadband white light as the probe. The photonic minibands dynamics at the non-resonant spectral region are strongly influenced by strong electron-electron and electron-photon interactions. Another interesting 1D photonic architecture called optical microcavity is further studied to visualize the electron-photon interaction due to the strong optical field confinement as shown in Fig. 1c. The Bi_2O_3-based 1D optical microcavity exhibited a nonlinear absorption switching behavior from saturation of absorption (SA) to the reverse saturation of absorption (RSA) due to the variation of spatial optical fields and enormous coupling of laser photons with the cavity defect photonic mode and Bi_2O_3 electronic energy levels. The angle-tuned transient absorption studies reveal the strong excited stated absorption due to the presence of a large number of defect electronic energy levels of Bi_2O_3 strongly interacting with the photonic modes of the optical microcavity (Fig. 1d). The photonic mode density dependent pronounced two-/multi-photon absorptions are systematically analyzed with experiments and simulations [3,4].

3. Conclusion

In summary, the spatial optical field confinement and the ultrafast absorption dynamics, and the photonic-electronic state interaction are realized in 1D metal-dielectric 1DPC and all-dielectric optical microcavity. The large spatial optical field confinement results in a huge enhancement of the third- and higher-order optical nonlinearities of the structures. The transient absorption dynamics reveal the strong correlation between the interaction between photonic modes and the electronic energy states of the embedded material. The present study can pave the way to a better understanding of the optical nonlinearities and the ultrafast electron-photon interactions in such complex photonic structures.

4. References

[1] J. N. Acharyya, D. N. Rao, M. Adnan, C. Raghavendar, R. B. Gangineni, and G. Vijaya Prakash, “Giant optical nonlinearities of photonic minibands in metal–dielectric multilayers," Adv. Mater. Interfaces **7**, 2000035 (2020).

[2] J. N. Acharyya, A. K. Mishra, D. N. Rao, A. Kumar and G. Vijaya Prakash, "Ultrafast nonlinear pulse propagation dynamics in metal–dielectric periodic photonic architectures," Adv. Mater. Interfaces **8**, 2100757 (2021).

[3] J. N. Acharyya, D. N. Rao, R. B. Gangineni and G. Vijaya Prakash, "Effect of Photonic Cavity Interactions on Femtosecond Multiphoton Optical Nonlinear Absorptions from Bi_2O_3-Based One-Dimensional Photonic Crystal," ACS Photonics **9**, 2092–2100 (2022).

[4] J.N. Acharyya, D.N. Rao, R.B. Gangineni, and G.Vijaya Prakash, “Photonic Cavity-Mediated Tunable Ultrafast Absorption Dynamics in $BaTiO_3$-Based One-Dimensional Photonic Crystal,”ACS Appl. Elec. Mater. **3**, 1904-1911 (2021).

Liquid crystal and thermochromic tunable metamaterials for energy saving and photonic applications

Ibrahim Abdulhalim

Department of Electro-Optics and Photonics Engineering and the Ilse-Katz Center for Nanoscale Science and Technology, Ben-Gurion University of the Negev, Beer Sheva 84105, Israel

Abstract: Metamaterials allow building new miniature devices with superior properties such as achromatic flat lenses, smart windows and wide field of view waveplates. Liquid crystals possess strong electrooptic and thermooptic effect, can penetrate nano and micro holes, and therefore are ideal for making tunable metamaterial devices. Recently we have been studying several nano-micro structures tunable with liquid crystals for variety of applications such as tunable achromatic waveplates, tunable filters and smart windows. In this talk I will review our latest results on thermochromic and tunable liquid crystal metamaterials.

Tunable Terahertz Generation with Nanosecond Lasers and Active Terahertz Imaging

[#]Nimish Dixit, Ajay Mishra, Sudhir Khare and Ajay Kumar

Instruments R&D Establishment, Defence R & D Organization (DRDO)
Dehradun, Uttarakhnad, India
[#]ndixit.irde@gov.in

Abstract: In this paper, generation of THz radiation exploiting second order optical nonlinearity using nanosecond lasers as a pump source has been discussed. Two different techniques viz. terahertz parametric oscillator (TPO) and injection seeded terahertz parametric generation (is-TPG) have been employed for generating THz frequencies. Paper also presents the demonstration of detection of concealed metallic objects using THz frequencies paving the way for niche homeland security application.
Keywords: Terahertz generation, terahertz imaging, TPO, is-TPG

1. Introduction

THz frequencies, which lie between infrared and millimeter waveband (0.1 to 10 THz), have been referred to as 'THz Gap' for many years due to unavailability of sources and detectors. THz waves can transmit through most non-metallic materials such as paper, plastic, wood, cardboard etc. and are highly opaque to metals giving rise to possibility of detection of hidden metallic objects. THz waves have very low photon energies (4 meV @ 1 THz i.e. one million times weaker than x-ray photon) and therefore will not cause any harmful photoionization in biological tissues leading to biological and body scanning applications. THz technology has been at helm of affairs for past one decade or so and is still growing at a very rapid rate for applications in security and defence. The research on THz has been manifold, beginning with generation, detection, THz optics and its propagation into the atmosphere & materials.

2. Description

Although there are many optical methods of generation of THz, the generation of THz exploiting second order optical nonlinearity is one of the most suitable methods, which has the capability of providing substantial amount of power in a relatively compact size and at room temperature [1-4]. Femtosecond and picoseconds lasers use the process of optical rectification for generating THz. On the other hand, nanosecond lasers exploit difference frequency mixing, terahertz parametric oscillation (TPO) [1-2, 4] and Terahertz parametric generation (TPG) [1, 3] for frequency conversion into THz region. In present talk, we will discuss the nanosecond laser based tunable THz generation based on TPO and TPG. In both of these schemes, Lithium Niobate has been used as nonlinear parametric converter. This cristal utilizes a special non-collinear phase matching unlike conventional phase matching shemes.

THz frequencies can also be exploited for the detection of metallic objects hidden under clothing and packaging materials [5-7]. This is due to the fact that these frequencies have capability to penetrate all the common clothing and packing materials. In this paper, we will also deal with advances made towards metallic object detection in IRDE Dehradun. In this scheme, a quantum cascade laser (QCL) has been used as a source of THz photons and THz focal plane array (FPA) for the detection of reflected/transmitted THz frequencies from the object.

The knowledge and expertise gained from these activities can be exploited to develop a THz imaging system for airport scanning/crowd monitoring. In addition, this will also be helpful in developing a THz scanning system for detection of illicit drugs from the mails and packaging materials.

Acknowledgement

The authors would like to acknowledge Director, IRDE for his support and permission to present this work.

3. References

[1] K. Kawase, Jun-ichi Shikata and H. Ito, `Terahertz wave parametric source Topical Review'. *J. Phys. D: Appl. Phys.* **34,** R1-R14 (2001)

[2] Kodo Kawase, Yuichi Ogawa, Yuuki Watanabe "Non-destructive terahertz imaging of illicit drugs using spectral fingerprints", Optics *Express* **11**, No. 20 2549 (2003)

[3] S.Hayashi,1, K. Nawata, H. Sakai, T. Taira, H. Minamide and K. Kawase, `High-power, single-longitudinal-mode terahertz-wave generation pumped by a microchip Nd:YAG laser'. *Optics Express*, **20**, No. 3, 2881 (2012)

[4] H. Minamide, T. Ikari, and H. Ito, `Frequency-agile terahertz-wave parametric oscillator in a ring-cavity configuration'. *Review of Scientific Instruments*, **80**, 123104 (2009)

[5] Lee A W M *et al.*, "Real-time imaging using 4.3-THz Quantum Cascade Laser and a 320x240 microbolometer focal plane array," *IEEE Photon. Technol. Lett.*, **18**, 1415-1417 (2006)

[6] Lee A W M *et al.*, "Real-time terahertz imaging over a standoff distance (> 25 meters)," *Appl. Phys. Lett.*, **89**, 141125 (2006)

[7] M Linda *et al.*, "A micro-bolometer based THz imager," *Proc. of SPIE,* **7671**, 76710Z-1 (2010)

Stokes singularities

P. Senthilkumaran

Optics and Photonics Centre, Indian Institute of Technology Delhi. New Delhi 110 016.

psenthil@physics.iitd.ac.in,

Abstract: Stokes singularities occur in Stokes fields. The construction of Stokes fields and their properties and usefulness in the study of polarization singularities will be highlighted in this talk. Starting from the Stokes formalism in polarization optics, inhomogenous polarization distributions will be introduced. For inhomogenously polarized fields all the four Stokes parameters are defined by four distributions. Using these distributions, construction of different types of Stokes fields are presented. Mathematical definitions and singular nature of such singularities will be explained. One of the main uses of these fields is in the study of polarization singularities. Polarization singularities are explained using superposition of scalar field singularities namely phase singularities. Co-axial and non-coaxial superposition of scalar optical fields leading to the construction of polarization singularities will be explained. For every polarization distribution, there are three different Stokes fields possible. At the Stokes singularities, either the azimuth of the polarization ellipse or its handedness becomes indeterminate. Polarization and Poincare singularities are subset of Stokes singularities and they will be explained in this talk.

Generation and detection methods for Stokes singularities, introduction of new types of beams called Poincare beams will be dealt with. New topological constructs that are useful in dealing with Stokes singularities will be introduced. Degenerate Stokes index states, index conservation, helicity conservation and self healing of these singularities will be touched up on.

Keywords: Stokes parameters, Stokes fields, Stokes Singularities, Stokes phases, Poincare beams, Poincare singularities, Poincare spheres.

References

[1] I.Freund, A.I.Mokhun, M.S.Soskin, O.V.Angelsky and I.I. Mokhun, "Stokes singularity relations" Opt.lett., Vol.27, 545-547 (2002).
[2] Ruchi, P.Senthilkumaran and S.K.Pal, Phase singularities to polarization singularities, *Int. J. Optics*, Vol.2020, 2812803 (2020).
[3] Gauri Arora, Ruchi and P.Senthilkumaran, Hybrid order Poincare sphere for Stokes singularities, *Opt.lett.,* Vol.45, 5136-5139 (2020).
[4] Gauri Arora, S.Deepa, Saba N Khan and P.Senthilkumaran, "Detection of degenerate Stokes index states," *Scientific Reports*, 10: 20759 (2020).
[5] Sushanta Kumar Pal and P.Senthilkumaran, "Synthesis of Stokes singularities," *Opt.Lett*., Vol.44, 130-133 (2019).

Design and Fabrication of Meta-optics for Light Manipulation: Challenges and Prospects

Jerin Geogy George, Susan Thomas, and Shanti Bhattacharya
Department of Electrical Engineering, Indian Institute of Technology Madras, Chennai, India
shanti@ee.iitm.ac.in

Abstract: Meta-optics have been explored extensively in the past decade and have the potential to replace bulky refractive optics. These flat optical elements can also realise unique functionalities that are not possible using conventional optics. In this work, we discuss the design and fabrication of metasurfaces for light manipulation. The challenges in determining the 'meta-atom' geometries and accurately realising these structures through fabrication is presented. We also discuss using these metasurfaces for aberration correction in microlenses with the help of the design tool: ZEMAX.
Keywords: flat optics, meta-optics, dielectric metasurface, aberration correction, Zemax design

1. Meta-optics

Meta-optical elements are sub-wavelength scatterers arranged laterally to realise a desired functionality [1]. Compared to binary diffractive optical elements, meta-optical elements can provide higher efficiency as several phase levels can be realised inspite have structures of only one height. The sub-wavelength scatterers in these elements impart an abrupt phase shift to the incoming field. This phase shift can be varied by changing the lateral dimensions of the scatterers. By suitable arranging different 'meta-atom' geometries, a wavefront can be engineered or shaped. The first part in designing such elements is to create a lookup map of the meta-atoms with the imparted phase shift. Numerical simulation techniques like FEM/FDTD can be used for this purpose. For single wavelength applications, cylindrical pillars are the most commonly used geometry because of their simplicity and polarisation-independent nature [2]. The conventional approach while designing a metasurface for light manipulation is given below:

The designed metasurface is then fabricated using standard CMOS compatible processes. However, while these are well-established, there are many challenges in the design step as well as in the fabrication process, which are discussed next.

1.1. Limitations of the unit cell approximation

The popular design approach simulates meta-atoms with periodic boundary conditions to evaluate its electromagnetic (EM) response. This model assumes an infinite periodic structure and does not consider the spatial variation in the actual metasurface. Models that simulate meta-atoms as single isolated scatterers are also not accurate as they ignore the lateral scattering from neighbouring meta-atoms. A full-wave simulation of the entire metasurface can be done to obtain an accurate EM response, but it requires enormous computational power. The accuracy of the unit cell simulation is also dependent on the size of the meta-atoms. If the meta-atoms are well separated, then the lateral scattering from nearby cells can be ignored and the meta-atom can be considered an isolated scatterer. Meta-atoms that are closely spaced having local periodicity can be modeled with the periodic boundary condition [3].

1.2. The choice of meta-atom material: variations in the simulation and experiment data

The material for structuring the meta-atoms are chosen by considering its bulk optical parameters in the desired wavelength. Standard refractive index data imported or already available in the numerical simulation software are used while generating the meta-atom lookup map. The height of the meta-atoms are kept constant and the lateral dimensions are varied for generating the lookup map. This allows to complete the fabrication process with a single lithography step. A thin film of the chosen material with the designed thickness is coated on top of a substrate using a standard deposition technique. The meta-atom structure can then be defined by a substractive process. The material deposited during the fabrication process may have variations in the optical parameters compared to the simulated data. The deposition thickness may also have a tolerance, and there will be surface roughness. This will result in a slightly different EM response than the designed one.

The lookup map of the meta-atoms can be modified based on the optical parameters and thickness of the deposited material. A spectroscopic ellipsometer may be used for this purpose.

1.3. Challenges during patterning and post-processing

The most commonly used patterning technique for metasurface is e-beam lithography. The patterning is done by focusing accelerated electrons on a resist whose chemical properties change upon exposure. The patterns can then be developed using a suitable developer. E-beam lithography has excellent patterning accuracy, and while features less than 10 nm can be patterned, typical sizes are usually in the order of 100nm. The lateral resolution in e-beam lithography is mainly determined by the resist thickness and the e-beam acceleration voltage. Its' major drawback is its throughput compared to optical lithography.

Once the resist is patterned and developed, the next step is to transfer this pattern to the material. Pattern transfer techniques like lift-off/etching or both can be used for this purpose. Lift-off is normally done after metallisation and for proper lift-off, resist thickness should be much higher than the metal thickness. This limits the lateral resolution which can be achieved, as the greater the thickness of the resist, the lower the pattern resolution. Etching after metallisation or directly using resist as a mask for etching is used to define the meta-atoms. Mostly dry etching is employed as it has good anisotropy and selectivity. While wet etching causes undercuts, the sidewalls after dry etching will be corrugated [4]. This will cause undesired light scattering and deviation from predicted EM response.

Despite variations in the simulated and experimental results, metasurfaces are revolutionizing the field of optics. In the next section we discuss the use of metasurfaces for aberration correction in microlenses.

2. Aberration correction in microlenses using metasurfaces

Microlenses employed in miniaturized imaging systems such as microendoscopes suffer from optical aberrations leading to poor image quality. The conventional aberration-corrected lenses are complex in structure and challenging to realize due to their complicated phase profile. Such lenses are bulky and not suitable for endoscopic imaging systems. Metasurfaces is a flat optic solution to such optical designs with size constraints. Adding metasurface to an existing optical system imparts an additional change in the wavefront phase. The phase profile of this surface can be designed to correct the off-axis and on-axis aberrations simultaneously[5].

The optical system consisting of microlenses along with a phase element can be designed in ray tracing software such as Zemax Optic studio. The phase element is modeled as a binary optic surface in Zemax with a phase profile as given in the following equation,

$$\phi(\rho) = \sum_{i=1}^{N} a_i \left(\frac{\rho}{R}\right)^{2i}$$

where a_i is the phase coefficients, N is the number of radial polynomial coefficients, ρ is the radial aperture coordinate and R is the radius of the metasurface. The radial polynomials represent the variation in phase across the optical surface. The phase coefficients are set as variables to optimize for the best spot quality. The surface phase profile of the phase element is extracted for further design of the metasurface.

3. Conclusions

In this paper, the design and fabrication processes of meta-surfaces are discussed and means of optimising them for specific applications are presented.

4. References

[1] Brener, Igal, Sheng Liu, Isabelle Staude, Jason Valentine, and Christopher Holloway, eds. *Dielectric metamaterials: fundamentals, designs and applications*. Woodhead publishing, 2019.

[2] Dharmavarapu, Raghu, Soon Hock Ng, Fatima Eftekhari, Saulius Juodkazis, and Shanti Bhattacharya. "MetaOptics: Opensource software for designing metasurface optical element GDSII layouts." *Optics express* 28, no. 3 (2020): 3505-3516.

[3] Ciarella, Luca, et al. "Finite-Size and Illumination Conditions Effects in All-Dielectric Metasurfaces." *Electronics* 11.7 (2022): 1017

[4] Bazylenko, M. V., M. Gross, and M. Faith. "Effect of reactive ion etching–generated sidewall roughness on propagation loss of buried-channel silica waveguides." *Applied physics letters* 69, no. 15 (1996): 2178-2180.

[5] Yan Liu, "Metaobjective with submicrometer resolution for microendoscopes," Photonics Research 9:2, 106-115 (2021).

Next Generation Electro-optical Systems

Sudhir Khare
Instruments Research and Development Establishment, Dehradun 248008, India
email: sudhirkhare.irde@gov.in

Abstract
Electro-optical (EO) systems are true force multiplier as it allows the weapon and equipment's to be used effectively during day and night in fair and bad weather conditions. It is an emerging technology whichhas evolved in last 40 years. Infrared imagers has become favourite of military forces since World War-II and it performed exceptionally well during past few wars. The development in infrared imaging technologyimproves the imaging quality and finds the application in different area. In last few decades, the advancement in detector technologies i.e. sensitivity, smaller pixel with small coolersize makes infrared imager very compact in size, weight and power. The development in the infrared imaging technology changes the concept of conventional war. Infrared imagers are used almost in every platform from airborne to a small weapon system.

Keywords: Infrared Imaging, IDDCA, Image Processing, Hyper-spectral, Dual Color, Hot Detector

1. Introduction

IR radiation [1] was discovered originally in 1800 by Sir William Herschel, who is also famous for discovering the planet Uranus. It originates from the Latin word infra, which means below. That is, the IR band lies below the visual red light band. The electromagnetic spectrum is a range of all electromagnetic waves arranged according to frequency or wavelength. Infrared imaging system for terrestrial imaging applications have been confined to Medium Wave InraRed (MWIR 3-5 μm) and Long Wave InraRed (LWIR 3-5 μm 8-12 μm) spectral band [2] due to atmospheric absorption effects [3].Infrared imaging systems are finding wide range of applications as they work in truly passive manner, utilizes the target to background thermal contrast[4]. It allows the operator to see and acquire the targets in total darkness including adverse weather conditions (poor ambient light). It can give ranges for detection & recognition [5] of targets in day and night conditions. With the advancement in detector, optics and image processing technologies, infrared imagers are finding new areas of exploration. Today, there is a demand in the market for high resolution, more compact, low power and light weight EO systems with higher Field of View (FOV). All these market demands require further advancement in the detector, optical and image processing technologies. Market demands have always been a key factor in development of infrared imager.

Infrared imager's 1st generation started with the single element detector, single field of view system where two dimensional scanning is required which can be accomplished by either using a combination of two plane mirrors or going for one polygon scanner for azimuth scan & one plane mirror for elevation scan. Then, the 2nd generation of infrared imager with linear Focal Plane Array (FPA) detectors, only one dimensional scanning is required which can be accomplished by either rotating a polygon or by an oscillating mirror. Finally we arrive in the era of 3rd generation of infrared imager with high format Focal Plane Array (FPA) detectors and continuous zoom system. Current market demand needs very high format detectors viz. 640x512, 1280x1024, 1920x1536 with detector pitch of the order of 10 μm [6].

1.1 Advancement in IR detector technologies

Advancements in the IR detector technologies always governed the performance and application of infrared imaging system. Started with first generation single detector technology, now matured third generation FPA based technology detectors are available. With the increasing market demand for compact and low powered infrared imagers, advancement in the detector technologies [7] is still progressing. Latest trends in detector technologies is low pitch, high format, broad band high operating temperature detectors.Some of the detectors are as under.

(i) Low pitch and high format detector
(ii) High Operating Temperature Detector (HOT detector)
(iii) Type Two Super Lattice (T2SL) LWIR detector
(iv) Hybrid Dual-Color MWIR Detector
(v) Broadband IR Photon Detector

1.2 Trends in Infrared optics:

Infrared Optics module collects the radiations from the targets and form images on to the detector. The available optical materials which transmit infrared radiations are very limited. In IR region Silicon (Si), Germanium (Ge), Zinc Selenide (ZnSe) and Zinc Shulphide (ZnS) are the few common materials. ZnSe being a non RoHs complained materials, therefore,unfriendly material during processing. In LWIR spectral band, chalcogenide, Amorphous Materials Transmitting IR (AMTIR) are the new invention which helps in development of low cost infrared imager. Chalcogenide materials are cheaper than germanium and can be moulded in to lenses.

Optics design modeling software is now very matured and has ability to optimize complex and non-sequential optics. Before prototyping the optical systems, the detail analysis and simulation for different temperature ranges are possible. The modeling and simulation software reduces the cost, time and risk in R&D. The new optimization technique for Diffractive Optical Element (DOE) is helpful to reduce the optical components in the optics module for better performance.

1.3 Advanced Image Processing Techniques

With the advancement of detector technology, a compatible image processing technologies for high format and high frame rate is required. To cater for this high amount of real time data processing, FPGA based parallel processing technique is required. The performance of infrared imager can further be enhanced using advance image processing features like through fog imaging, real time turbulence correcting algorithms. Different spectral window have different advantage and disadvantages. Weighted image fusing technique provides high quality video in different weather and different time with the advantage of each spectral window. Image processing on FPA is the futuristic technique to reduce system noises and power consumption requirement. World over, researchers are working on following image processing algorithms to enhance the performance of infrared imagersin different environmental conditions:

(i) Automatic target recognition
(ii) Super-resolution
(iii) Panorama generation with change detection
(iv) Observation range enhancement in bad weather condition

2. Emerging Trends in development of EO Systems

Future EO systems would be designed towards being more compact, low power and low cost with improved observation capabilities like detection, and identification in difficult conditions (low contrast, camouflage etc.). The requirements are posing new challenges to infrared imaging technology, so today, only rely on radiation intensity is not enough, there is a need to exploit additional attributes of incoming radiation like spectral characteristics, polarisation etc.

(i) Long Range EO Systems
(ii) Omni-directional surveillance systems with unattended sensor network
(iii) Computational Imaging
(iv) High frame rate Infrared Imaging System
(v) Low cost infrared imager for IR seeker
(vi) Infra-Red search and track systems (IRST)
(vii) Dual color missile warning systems
(viii) Imaging based on Dual colour, Multispectral and Hyper-spectral Imager

3. References

[1] R. D. Hudson, *Infrared System Engineering*, (John Wiley & Sons, NY, 1969).
[2] G. C. Holst, *Electro-Optical Imaging System Performance*, (JCD Publishing, Third Edition, Florida), SPIE Optical Engineering Press, Bellingham, Washington, 2003, pp. 355-384.
[3] R. G. Driggers, M. H. Friedman, J. Nicholas, *Introduction to Infrared and Electro-Optical systems*, (Artech House, Boston, 2012).
[4] M. S. Seán, "Analysis of the relative merits of the 3-5 μm and the 8-12 μm spectral bands using detected thermal contrast," in Proceedings of SPIE 9485 on Thermal Infrared Applications XXXVII, 2015.
[5] S. Keßler, R. Gal, W. Wittenstein, "TRM4: Range performance model for electro-optical imaging systems." In Proceedings of the Infrared Imaging Systems: Design, Analysis, Modeling, and Testing XXVIII, Anaheim,CA, USA, 11–12,vol. 10178, pp. 2–12, 2017.
[6] A. Rogalski, "Recent progress in infrared detector technologies," Infrared Physics and Technology, **54**, 136-154 (2011).
[7] A. Karim, J. Y. Andersson, "Infrared detectors: Advances, challenges and new technologies," in Proceedings of IOP Conf. Series: Material Science and Engineering, vol. 51, pp. 1-8, 2013.
[8] P. C. Klipstein, et.al, "Type II Superlattice infrared detector technology at SCD", Journal of Electronic Materials, **47(10)**, 5725-5729 (2018).
[9] A. Kumar. S. Sarkar, R. P. Agarwal, "An adaptive image enhancement algorithm and real-time implementation for an infrared imaging system", in Proceedings of SPIE 5909, Application of Digital Image Processing XXVIII, 2005.
[10] J. Gao, W. Chenglin, L. Meiqin, "Robust Small Target Co-Detection from Airborne Infrared Image Sequences," Journal of Sensors, 17(10), 2242 (2017).

Carbon Dots as Sustainable Materials for UV Screener, Direct White Light Emitter, and Laser

Barun Kumar Barman,[1,2] and Tadaaki Nagao[2,3]

[1]*International Center for Materials Nanoarchitectonics (MANA), National Institute for Materials Science (NIMS), Tsukuba, Ibaraki 305-0044, Japan*

[3]*Department of Condensed Matter Physics Graduate School of Science, Hokkaido University, Kita-10 Nishi-8 Kita-ku, Sapporo 060-0810, Japan*

e-mail address: NAGAO.Tadaaki@nims.go.jp

Abstract: We summarize our recent study on the development of luminescent carbon dots (CDs) for UV and high-energy blue light screener, direct white light emitter, as well as laser. An example of chromaticity tuning of *single-component* white light emitter by controlling the dopant types is demonstrated. Some examples for applications by combining CDs with transparent matrix as well as a photonic cavity structure for a single longitudinal solid-sate blue laser will be presented.

Keywords: Carbon dots, UV screener, light emitting device, white light emitter, chromaticity, anomalous spontaneous emission, laser

1. Introduction

Carbon dot (CD) is a futuristic candidate for the rare-earth and toxic metal-free luminescent material [1,2]. The fluorescent CD has emerged as a new class of materials that are composed mainly of C, O, H which is completely metal-free and non-toxic. The emission property is tuned by the doping centre and surface functional groups leading to multi-coloured emission[1]. The systematic investigation of the N-doping centres and surface functional groups has provided a vital role of the emission property. The optimized synthetic strategy enabled us to tune the N doping sites and lead to the broadband emission, resulting in direct white light emission (WLE) in the entire visible spectra (400 to 750 nm). The decrease or increase of the N doped sites into the CDs led to the green to orange emission, respectively. The graphitic N creates mid-gap states within the HOMO-LUMO gap of the pristine CDs. As a result, the light absorption is red-shifted which gives rise to the low energy fluorescence in the visible spectrum. Identification of N sites reported in the literature have been mostly reported by X-ray Photoelectron Spectroscopy (XPS). Due to the lack of sufficient resolution in XPS, it is difficult to fully characterize the functional groups present in CDs because of the peak overlap. In that point of view solid-state nuclear magnetic resonance (SS-NMR), N NMR is a promising route to identify the local N sites due wide chemical shift range. Here, we combined N SS-NMR with XPS to evaluate the local N doping environment to understand the emission property of rationally designed NCDs to produces the direct WLE. As synthesized CDs show direct and ideal WLE both in solution and in solid forms with CIE coordinates value of (0.34, 0.36) and high colour rendering index (CRI 92) via controlling the doing sites. This study delivers vital guiding principles for synthesis of multicolor and WLE CDs by systematically controlling the N doping sites. Next, we also tried to enhance the light emission of CDs by combining with a planar microcavity structure with only one resonant mode coupled with the emission of the CDs and we observed amplified spontaneous emission and lasing. Our results will aid the detailed understanding of the CDs and their efficient solid-state emission towards development of completely rare-earth free lighting devices.

2. Results and Discussions

Carbon dots (CDs) were prepared by hydrothermal or solvothermal reaction between citric acid and various N-dopant sources in water or formamide (FA) medium, and systematic choice of precursors enables us to design desirable CDs [1,2]. Both cyan-emitting CDs (C-CDs) and white-emitting CDs (W-CDs) in DMSO solution show a light reddish appearance, while orange-emitting CDs (O-CDs) appear bright reddish in solution in daylight (Fig. 1a), and they exhibit cyan, white, and orange emission when excited at 365 nm (Fig. 1b). Interestingly, W-CDs display WLE via UV excitation and also display excitation-dependent FL, emitting intense cyan to red light during excitation from 400 to 600 nm (Fig. 1c). Similarly, these multicolor-emitting CDs show unusually broad UV-vis absorption bands (Fig. 1d), indicating the multiple electronic transitions. All of these CDs show sharp UV absorption at 215 nm due to π-π^* transitions. W-CDs exhibit a broad absorption band at around 350 nm, which is usually assigned to the transition of conjugated C=O and C=N. Another broad absorbance band was observed at 420 nm and a strong absorption band at 550 nm, as well as the absorbance band at 360 nm. This blue light absorption also originates from the transitions of the aromatic sp^2 system containing C=O and C=N bonding configurations. Absorption at 550 nm

can be attributed to the N-bonding configuration. These N-doping sites create mid-gap excitation between HOMO-LUMO energy gaps. Figure 1e shows the FL characterization results of C-, W-, and O-CD1s and their CIE chromaticity coordinates under UV (365 nm) excitation in DMSO solution. CIE coordinates of C-CD1, W-CD1, O-CD1 are (0.26, 0.34), (0.32, 0.34), and (0.44, 0.40), respectively (Fig. 1f), which shows flexible tunability of chromaticity of white light emission from "*cold*" to "*warm*."

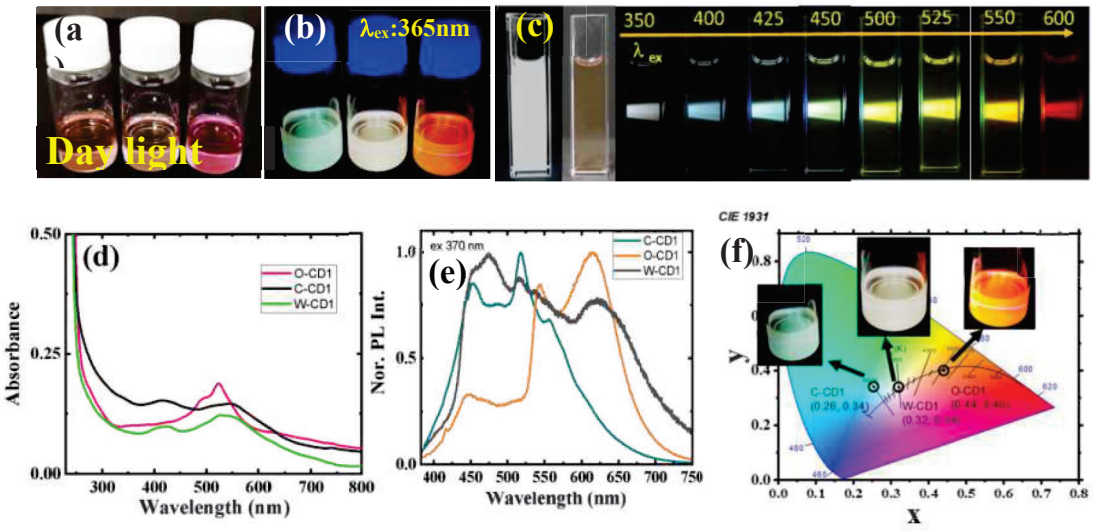

Fig. 1: (a and b) Photographs in daylight and UV of excited colloidal solutions of different types of CDs in DMSO solution. (c) Photographs of W-CD1s in DMSO solution captured under UV light (left), daylight (middle), and different excitation wavelengths from 350 nm to 600 nm (right).

We also prepared photonic planar microcavities formed by two distributed Bragg reflectors (DBR) that sandwiches CDs. Both sharp amplified spontaneous emission (ASE) and single-mode laser emission are achieved. These results contribute to the fundamental understanding of the structural and optical properties of CDs, and may pave the way towards the development of completely rare-earth-free light emitting devices among other photonic devices.

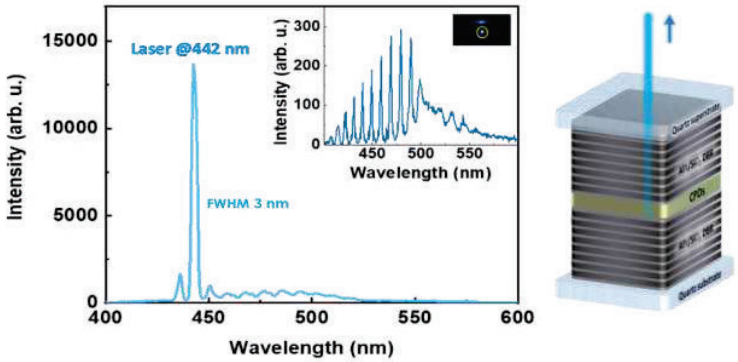

Fig. 2: Laser emission at a wavelength matching the maximum emission of CDs. Inset shows the Amplified Spontaneous Emission (ASE) of the DBR/CDs/DBR sample upon UV excitation as well as a photograph of the sample during the experiments.

[1] B. K. Barman *et al*, "Microcavity-Integrated Carbon Dots for Chromaticity-Switchable White light Emission," *ACS Sustainable Chemistry & Engineering,* accepted.

[2] B. K. Barman *et al*, "Transparent Hard Coatings with SiON-Encapsulated N-Doped Carbon Dots for Complete UV Blocking and White Light Emission," *ACS Applied Electronic Materials* **3** [9], 3761-3773(2021).

Silicon Nanophotonics for Space Laser Beam Pointing

Alessandro R. Santos[a,b], Willer G. Santos[a] and Vilson R. Almeida[a,c]
[a]*Aeronautics Institute of Technology, Sao Jose dos Campos, Brazil*
[b]*Brazilian Navy Coordination Study Center in Sao Paulo, Sao Paulo, Brazil*
[c]*Brazil University, Scientific and Technological Institute, Sao Paulo, Brazil*
vilsonra@ita.br

Abstract: Silicon nanophotonics is contributing to the development of devices with small dimensions and low energy consumption. In optical systems for space applications, whether in large or small satellites, the interest for integrated photonic devices is continuously increasing, specially for the communication subsystem, since it allows for the construction of an optical beam pointing system without moving parts, such as optical phased array antennas. We propose a silicon photonic integrated approach, including a non-resonant all-optical modulator topology based on thermos-optical effect, for achieving efficient space laser beam pointing functionality. Thermal and photonics computational simulation results are presented and discussed.
Keywords: all-optical modulator; silicon nanophotonics; thermo-optical effect; integrated photonics.

1. Introduction

Optical Phased Array (OPA) Antennas have been applied for Laser Beam Pointing in several applications and environments, being a promising candidate for space applications as well, considering silicon photonics based on silicon-on-insulator as its technological platform [1]. Optical phase modulators/shifters have been used in several nanophotonic devices used in quantum optics, optical neural networks and optical phased arrays. Among several types of phase modulation schemes in silicon photonics, the thermo-optical effect is the most used [2], usually with the use of metal plates powered by electrical energy, called heater, which convert energy into heat for attaining modulation results. In addition to heater, there are other ways to heating up the waveguide, such as by causing absorption of photons in the device material, which can be seen as an indirect all-optical modulation scheme. This method consists of controlling the propagation of light signal in the waveguide by means of a second beam of light applied to and absorbed by the waveguide material [3], leading to a high modulation speed and efficiency. Such an approach finds applications in remote or harsh environment sensing and communications, as well as for space systems, where it may be relevant for the communication subsystems of a CubeSat [4]. The waveguide geometry can significantly impact the device performance, and an Archimedean spiral structure can improve it. This geometry allows the phase modulator to attain a better performance as compared to straight waveguide modulators, since their compactness requires a much smaller heating surface area1. This paper presents our current and previous works in this research field [1,5], related to OPA based on Archimedean spiral waveguides as all-optical phase modulators driven by thermo-optical effect.

2. Design, Results and Analysis

Figure 1 schematically depicts a proposed architecture for an Optical Phased Array (OPA) Antenna applied for Laser Beam Pointing functionality, whereas Figure 2 schematically depicts the cross section and top view of an Archimedean spiral waveguide, used as a building block of optical phase modulation. In order to obtain high heat concentration and rapid heat dissipation, it was necessary to build a compact thermo-optical phase modulator with a small footprint and short total waveguide length [1,5]. We performed an iterative set of photonics and thermal computational simulations, intercalated with thermo-optical calculations, until we converged to the device topology, which allows to achieve an optical phase modulation amplitude of around π radians by applying realistic optical pump power levels. The optical phase variation (shift), $\Delta\phi$, is calculated by equation (1) [1,5].

$$\Delta\phi = \frac{2\pi}{\lambda}\frac{\partial n_{eff}}{\partial T}\Delta T.L \quad (1)$$

where $\Delta\phi$ is the optical phase shift, $\partial n_{eff}/\partial T$ is the thermo-optical coefficient, ΔT is the temperature variation, λ is the optical signal wavelength, and L is the total length of the spiral waveguide. From the iterative set of computational

simulations and calculations, we obtained the device footprint dimensions of 25 µm x 25 µm with a total length of the spiral waveguide of 360 µm; the waveguide core, made of Si, has a height (h_{core}) of 310 nm and two distinct widths (w_{guide}) of 0.5 µm and 0.6 µm, in each spiral arm direction (clockwise and counterclockwise, respectively), laterally separated by a distance between the core center of two subjacent waveguides (pitch) of 1.0 µm, which leads to a lateral SiO_2 gap of 450 nm. The choice of waveguides widths and pitch arose from preliminary optimization, taking into account several parameters of interest, such as: low propagation losses, low propagation coupling, compactness and efficient optical phase modulation.

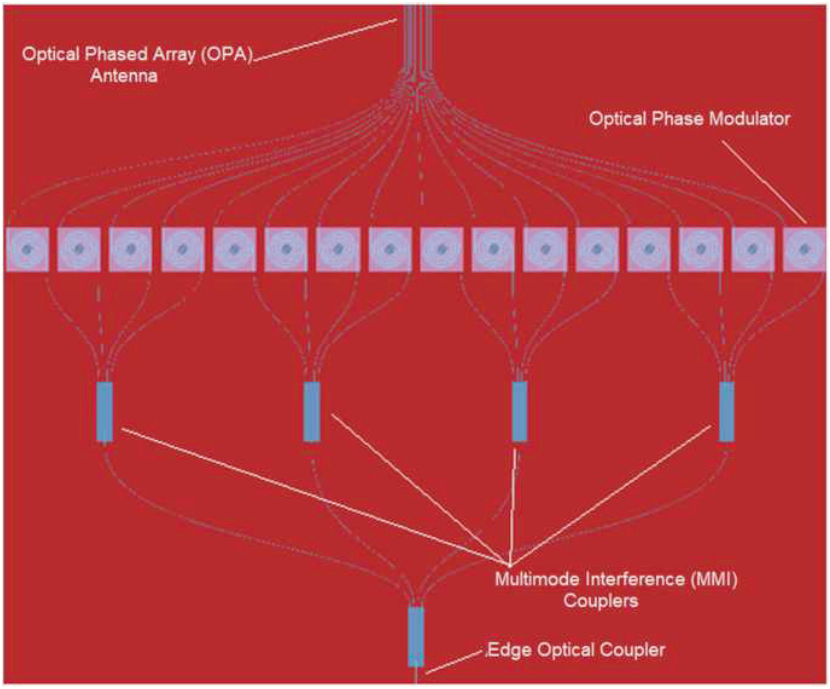

Fig. 1: Schematic of an Optical Phased Array (OPA) Antenna for Laser Beam Pointing.

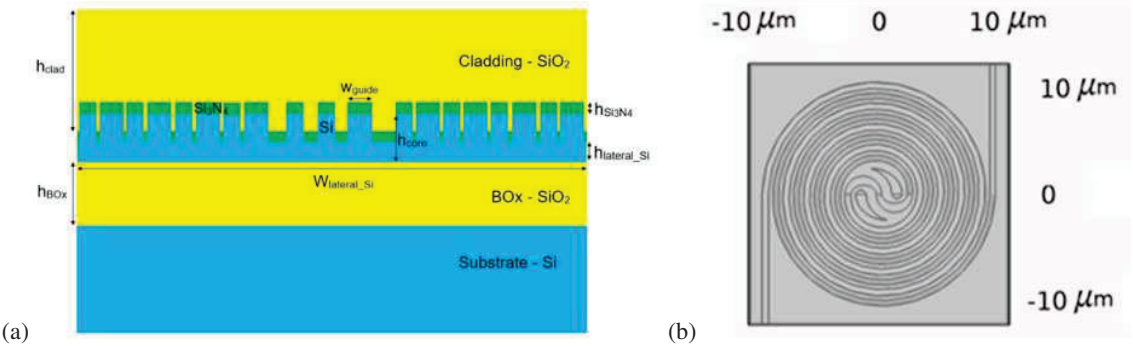

(a) (b)

Fig. 2: Schematic of an Archimedean spiral waveguide: (a) cross section and (b) top view [4,5].

Photonics computational simulations were performed with LUMERICAL software package and thermal computational simulations were carried out with COMSOL software package.

Optical heating is achieved by using visible or UV light as out-of-plane optical pump excitation (λ_p = 400 nm in this study), which is absorbed in Si core and lateral layers of the Archimedean spiral waveguide topology used as optical

phase modulators. Thermo-optical effect acts towards translating heat into optical phase modulation for optical signal carriers at C-band telecommunication wavelengths (around λ_s = 1550 nm).

We have assessed the effect of absorption of pump light by Si, by using the Transfer Method Matrix (TMM) approach; the absorption coefficient shows a peak for a 60 nm thickness of top Si_3N_4 layer, which provides an optical pump absorption rate of 88% in the waveguide core and 64% in the lateral Si layers.

The temperature distribution obtained from the simulation of stationary (steady state) heat condition mode is shown in Fig. 3, for out-of-plane optical pump excitation of P_p = 1 mW.

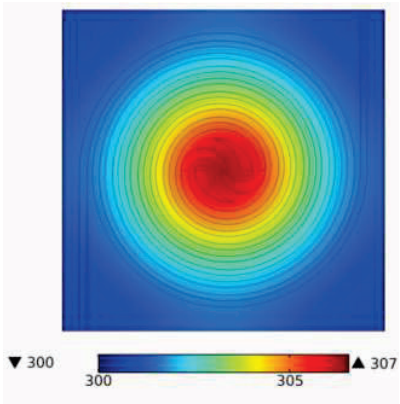

Fig. 3: Temperature distribution on the Archimedean spiral waveguide for P_p = 1 mW [1].

We observe a double temporal thermal response behavior, stemming from the fact that pump light is absorbed both by Si waveguide core and by other Si parts of the overall structure, with fast and slow thermal components showing approximate response times of only 1.4 and 10.3 μs, respectively. The steady state average temperature variation is 2.87 K. Figure 4 shows both transient and (asymptotically) steady state thermal behaviors.

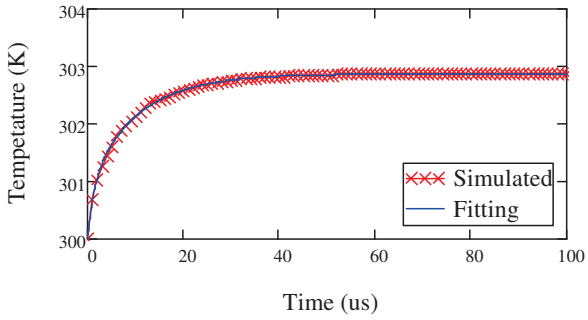

Fig. 4: Average temperature variation across the entire spiral waveguide - transient heat transfer [5].

The optical transmittance of the guided (signal) beam after propagating throughout each Archimedean spiral waveguide is found to be of 72%. This structure is still being optimized, and higher transmission efficiencies are foreseen.

From our photonics simulations, we estimate that an optical phase variation of $\Delta\phi = \pi$ in the optical signal will demand about P_p = 2.71 mW near λ_s = 1500 nm, and P_p = 2.90 mW near λ_s = 1550 nm. Comparing these results with state-of-the-art integrated optical phase modulators (phase shifters), shows that the power absorbed (or consumed) by this phase shifter, in order to attain $\Delta\phi = \pi$, is lower than those presented in references [6-9] and it is similar to the one in reference [2].

3. Conclusion

In summary, this work proposes an architecture for Optical Phased Array (OPA) Antennas related with Laser Beam Pointing functionality, based on silicon nanophotonics for compatibility with space applications; this approach includes an integrated thermo-optical phase shifter based on Archimedean spiral waveguide topology, and makes use of an all-optical modulation scheme, with out-of-plane optical pump excitation ($\lambda_p = 400$ nm) and guided optical signal (C-band) traveling inside the integrated spiral waveguide. Computational results show that such a compact device helps reduce the optical pump power consumption, allowing high non-optimized optical signal transmittance of 72%, and efficient optical signal phase shift; optical pump power below 3 mW was demanded for achieving optical signal phase shift of $\Delta\phi = \pi$ at wavelengths in the C-band. The proposed all-optical phase modulator has potential application in Optical Phased Array devices for space subsystems, remote or harsh environment sensors and communications, among others.

4. Acknowledgment

Vilson R. Almeida acknowledges Brazilian National Council for Scientific and Technological Development (CNPq) for research grants (306389/2021-5, 310855/2016-0 and 403031/2019-2).

5. References

[1] A. R. Santos, V. R. Almeida, and W. G. Santos, "Archimedean spiral waveguide as efficient all-optical phase modulator for space laser beam pointing", SPIE-OE **61**(8), 087102 (2022).
[2] H. Qiu *et al*., "Energy-efficient thermo-optic silicon phase shifter with well-balanced overall performance," Opt. Lett. **45**(17), 4806 (2020).
[3] V. R. Almeida *et al.*, "All-optical control of light on a silicon chip," Nature **431**(7012), 1081–1084 (2004).
[4] J. He *et al.*, "Review of Photonic Integrated Optical Phased Arrays for Space Optical Communication," IEEE Access **8**, 188284 (2020).
[5] A. R. Santos, W. G. Santos, and V. R. Almeida, "Archimedean spiral waveguide as a phase shifter for Optical Phased Arrays," in 2021 SBMO/IEEE MTT-S International Microwave and Optoelectronics Conference (IMOC), pp. 1–3 (2021).
[6] H. Nejadriahi *et al.* "Efficient and compact thermo-optic phase shifter in silicon-rich silicon nitride", Opt. Lett. **46**(18), 4646, (2021).
[7] S. Sabouri *et al.*, "Thermo Optical Phase Shifter with Low Thermal Crosstalk for SOI Strip Waveguide" IEEE Phot. J. **13**(2), 6600112 (2021).
[8] S. De*et al.*, "CMOS-Compatible Photonic Phase Shifters with Extremely Low Thermal Crosstalk Performance," J. Light. Technol. **39**(7), 2113–2122 (2021).
[9] J. Parra *et al.*, "Ultra-low loss hybrid ITO/Si thermo-optic phase shifter with optimized power consumption" Opt. Express **28**(7), 9393 (2020).

Random Laser Spectroscopy

Priyanka S. Choubey,[1] Renu Yadav,[2] Anirban Sarkar,[3] Shivakiran Bhaktha B.N.[1,2,*]

[1] *School of Nano-Science and Technology, Indian Institute of Technology Kharagpur, Kharagpur - 721302, India*

[2] *Department of Physics, Indian Institute of Technology Kharagpur, Kharagpur - 721302, India*

[3] *Department of Physics, National Institute of Technology Calicut, Kozhikode 673601, India*

[*]kiranbhaktha@phy.iitkgp.ac.in

Abstract: Random laser emission spectra strongly depend on the properties of the scatterers embedded gain media. Here, statistical analysis of random laser intensity fluctuations is presented in a dye-doped polymer thin film waveguide subjected to a constant heat treatment. The changes occurring in the density of the polymer thin film during the various stages of solvent evaporation are studied using the changes in the statistics of random laser emission intensities. The statistical analyses of the random laser emission intensity fluctuations help us to develop a novel spectroscopic tool to probe material properties.

Keywords: random laser, replica symmetry breaking, dye-doped polymer waveguides, photoluminescence spectroscopy

1. Introduction

Polymer based waveguides have attracted considerable attention over silicates as well as semiconductor-based technologies for the development of photonic devices due to their low-cost, ease of fabrication, low-temperature and low-pressure processing ability [1,2]. Polymer waveguides have great potential for the fabrication of all-optical devices as they are good host materials for organic dye molecules, and also due to their optical transparency in the visible as well as near infrared region. Incorporation of dye molecules in polymer waveguides has driven the development of solid-state dye lasers and optical amplifiers [3,4] leading to the growth of cost-effective photonic technologies.

Dye-doped polymers, though very attractive, also give rise to scattering of light due to inhomogeneities created by polymer density variations or dye aggregate formation. The phenomenon of random laser (RL) emission has been studied in the past in many optically active dye-doped polymer waveguides (DDPWs) [5,6]. Furthermore, in recent years, the ease of fabrication of DDPWs using spin-coating or dip-coating techniques have led to their interesting applications and mass production. In these devices, the evaporation of solvent can tailor the morphology of the film by creating polymer density fluctuations, and thus play a vital role in attaining desired optical quality. Hence, it is essential to understand the behavior of the DDPWs during the solvent evaporation process. However, there are scarce experimental tools available to track the formation of these microscopic inhomogeneities in real-time. Here, we propose RL as a probe to track microscopic changes in polymers via monitoring the statistics of RL emission intensity fluctuations and replica symmetry breaking (RSB) phase transitions [7]. The changes occurring at the microscopic level in the polymer due to the solvent evaporation process leads to fluctuations in DDPW RL emission intensities as shown in Fig. 1. The effect of microscopic changes, in the polymer thin film, on the RL modes are being studied in a controlled manner by selective excitation of the modes under various experimental configurations (scattering strengths, solvent evaporation rates and optical pump profile). The RL emission intensity statistics [8] is used to model the microscopic changes in the polymer thin film during the solvent evaporation process. This novel RL tool opens up a new avenue to RL spectroscopy that can monitor real-time microscopic changes in various materials.

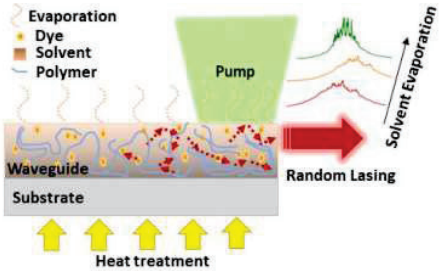

Fig. 1. Schematic representation of solvent-evaporation and corresponding changes in RL emission.

2. Experiments and Results

In this work, we study both wet (wet-DDPW) and heated thin films (HT-DDPW). The threshold characteristic of the HT-DDPW is shown in Fig. 2(a), with its lasing threshold at 0.01 mJ. The full width at half maximum (FWHM) of the emission spectrum is found to reduce drastically at the RL emission threshold. When the pump pulse energy exceeds the lasing threshold, discrete narrow

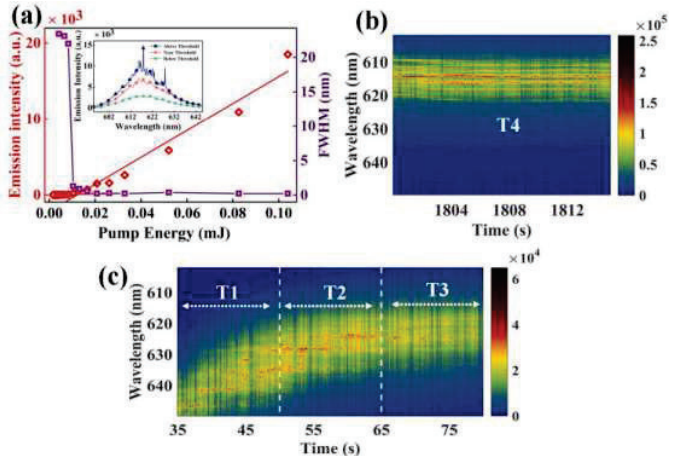

Fig. 2. (a) RL threshold plot for HT-DDPW. Insert shows the RL emission spectra recorded below and above the lasing threshold for HT-DDPW. RL emission spectra I(λ,t) recorded for the wet-DDPW in windows: (b) T4 (from 1800 to 1815 s) and (c) T1 (from 35 to 50 s), T2 (from 50 to 65 s) and T3 (from 65 to 80 s).

lasing peaks appear in the emission spectrum as shown in the insert of Fig. 2(a), which is a characteristic behaviour of a RL. Figure 2(b) shows the series of emission spectra recorded for HT-DDPW, referred to as window T4 (from 1800 to 1815 s). For the studies on wet-DDPW, a constant heating was maintained at 65 ˚C throughout the experiment. To ensure the observation of narrow lasing peaks throughout the duration of the experiment, an optimum incident pump pulse fluence was chosen. Single-pulse emission spectra I(λ,t) were recorded over a large number of pulses at a fixed pump energy as shown in Fig. 2(c). The series of recorded spectra were divided into several windows for analysis. In Fig. 2(c) three windows are considered, T1 (from 35 to 50 s), T2 (from 50 to 65 s) and T3 (from 65 to 80 s), of $\Delta T = 15$ s duration each (300 pulses), for the sake of statistical analysis. The choice of ΔT is based on the fact that the spectra change drastically during the initial 15 s, and change gradually in the next 15 s, before reaching a quasi-steady behaviour, as evident in Fig. 2(c). In windows T1 to T4, sharp peaks are observed in the emission spectra confirming the lasing behaviour of the wet-DDPW and HT-DDPW samples.

Overall, as the solvent dries from the wet-DDPW the random lasing characteristics evolve. A detailed discussion on the statistical properties of the lasing modes observed during the drying process of the wet thin film will be discussed in the conference. The modal interactions will be quantified in terms of correlation, survival function and RSB analysis.

3. References

[1] L. Sznitko, J. Mysliwiec and A. Miniewicz, "The role of polymers in random lasing," *J. Polym. Sci. Part B Polym. Phys.* **53,** 951–74 (2015).

[2] S. V. Frolov, Z. V. Vardeny, K. Yoshino, A. Zakhidov and R. H. Baughman, "Stimulated emission in high-gain organic media," *Phys. Rev. B* **59,** R5284–7 (1999).

[3] A. Costela, O. García, L. Cerdán, I. García-Moreno and R. Sastre, "Amplified spontaneous emission and optical gain measurements from pyrromethene 567-doped polymer waveguides and quasi-waveguides," *Opt. Express* **16,** 7023–36 (2008).

[4] T. Grossmann, S. Schleede, M. Hauser, M. B. Christiansen, C. Vannahme, C. Eschenbaum, S. Klinkhammer, T. Beck, J. Fuchs, G. U. Nienhaus, U. Lemmer, A. Kristensen, T. Mappes and H. Kalt, "Low-threshold conical microcavity dye lasers," *Appl. Phys. Lett.* **97,** 1–3 (2010).

[5] A. Tulek and Z. V. Vardeny, "Studies of random laser action in π-conjugated polymers," *J. Opt. A Pure Appl. Opt.* **12,** 024008 (2010).

[6] A. Sarkar, N. N. S. Ojha and B. N. S. Bhaktha, "Effect of photonic stop-band on the modes of a weakly scattering DCM-PVA waveguide random laser," *Appl. Phys. Lett.* **110,** 25110 (2017).

[7] A. Sarkar, B. N. Shivakiran Bhaktha and J. Andreasen, "Replica Symmetry Breaking in a Weakly Scattering Optofluidic Random Laser," *Sci. Rep.* **10,** 1–12 (2020).

[8] R. Uppu, A. K. Tiwari, and S. Mujumdar, "Identification of statistical regimes and crossovers in coherent random laser emission," *Opt. Lett.* **37**, 662 (2012).

Enhanced optical nonlinearities and SERS studies through photonic structures

Jitendra Nath Acharyya[a], R B Gangineni[b], G Vijaya Prakash[a] and D Narayana Rao[c]

[a]*Nanophotonics Lab, Department of Physics, Indian Institute of Technology Delhi, New Delhi-110016, India;*
[b]*Department of Physics, Pondicherry University, Puducherry-605014, India.*
[c]*School of Physics, University of Hyderabad, Hyderabad-500046, India.*
[c]*Email: dnrsp@uohyd.ac.in; narayanarao.desai@gmail.com*

Abstract: We will be presenting here our results on Surface Enhanced Raman Scattering (SERS) and enhanced nonlinearities with the photonic crystal structure, particularly in 1D photonic crystal configuration. The 1D photonic structure was prepared using SiO_2 and TiO_2 alternating layers. ZnO, Bi_2O_3 and $BaTiO_3$ are used as defect layers with a layer thickness of $\lambda/2$. We have also replaced the TiO_2 layer with Ag so that the new Fabry-Perot cavity forms as Ag-SiO_2-Ag, which induces huge optical field enhancement inside the SiO_2 layer. The giant optical nonlinearities observed and their application to record the SERS studies are demonstrated.

Keywords: Photonic crystals, Metal-dielectric photonic structures, Two-photon absorption

1. Introduction

The photonic cavity-mediated enhanced optical nonlinearity has become the frontier research area in optics and photonics as one tries obtain many nonlinear phenomena with very low power laser sources [1-4]. This demands novel photonic structures, where incident filed can create huge local fields within the medium so that the medium can exhibit higher order nonlinear phenomena. Many approaches have been implemented to harness the enhanced nonlinearity utilizing the ultrafast $\chi^{(3)}$ of nonlinear media sandwiched in various microcavities in strong and weak coupling regimes which play a pivotal role in ultrafast optics and quantum information processing. Incorporation of a defect in such periodic photonic architecture leads to slowing light propagation which further increases the electron-photon interaction time, thereby enhancing the optical nonlinearities. Use of the photonic crystal near the photonic band edge and the defect mode facilitate giant nonlinear enhancement due to the field localizations. Optimization of the nonlinear optical properties in photonic crystals and photonic waveguides can lead to next generation all-optical switch, modulator, optical beam steering, and advanced photonic devices. Apart from the photonic microcavity defect mode induced fascinating optical effects, differences in the photonic field confinement and the photon density of states in the air-band and dielectric-band extended to both sides of the fundamental photonic stopband are of particular importance. Much effort has been devoted towards integrating photonics with materials science to achieve ultrafast photonic devices. Photonic crystals with localized defect modes have entrenched a new platform to control and manipulate photons, invoking enhanced optical nonlinearity by an enormous photon confinement with large local field intensity [5,6]. High refractive index dielectric media with heavy metal oxides such as zinc oxide (ZnO), bismuth oxide (Bi_2O_3), barium titanate ($BaTiO_3$) often meet these requirements. They lead to unique optoelectronic properties, large third-order optical nonlinearity, high hyperpolarizability with ultrafast electronic response. Also, wide range of energy levels of these systems introduce abundant optical transitions in the UV-Vis region enabling enhanced light-matter interaction.

2. Results and Discussion

Here we demonstrate strong photon-electron nonlinear interactions and cavity-enhanced tunable third- and higher-order ultrafast optical nonlinearities in a 1D photonic crystal with these three as photonic defect layers. Ultrafast femtosecond laser probing has been utilized to evaluate the third- and higher-order optical nonlinearities over a broad spectral region from 350 nm to 1600 nm (~ 3.54 ev to 0.77 eV). Incorporating each of them as a defect layer within two SiO_2/TiO_2 Bragg mirrors gives rise to distinct and strong photonic eigenmode inside the photonic stopgap. The typical bandgaps of low and high refractive index layer, SiO_2 and TiO_2 are ~8.95 and 3.50 eV, respectively, with extended Urbach (defect) tails.

The spatial optical field confinement, detailed energy deposition, and the field distribution in each layer of the photonic structure are evident from the transfer matrix simulations (Fig. 1d). All the simulations are carried out using the transfer matrix method (TMM), utilizing the reported experimental optical constants (n, k) over a wide spectral region. From Fig. 1c, the spectral region extending from 540 to 730 nm is called the photonic stopband with the defect-induced cavity photonic mode at 637 nm. The spatial transverse electric and magnetic fields (|E|, |H|) at the cavity resonance (637 nm, $\theta = 0^{\circ}$) reveal that the defect cavity layer (Bi_2O_3) accommodates three transverse electric (TE) and two transverse magnetic (TM) modes, which supports strong photon confinement within the cavity (Fig. 1e).

The nonlinear optical interactions of electronic states of defect layer with the cavity mode and other photonic minibands are closely monitored by single femtosecond Gaussian laser beam propagation (Z-scan technique) for nonlinear absorption and nonlinear refraction over a wide spectral region. The experiments were performed utilizing femtosecond laser beam with laser parameters 120 fs, 1 kHz, 350-1600 nm.

The observed optical nonlinear absorption phenomena can be explained from the spatial optical field confinement within the microcavity. In case of 350 nm (~3.54 eV) excitation, the transmission field penetration is dominated by the band-to-band absorption of top DBR layers (SiO2 and TiO2) thus, and the beam attenuates within the first few top surface layers. Thus, the excitation produces one-photon (1PA) induced pronounced nonlinear absorption, which potentially invokes the higher-order excited state absorptions of SiO_2/TiO_2 layers. Whereas the optical field confinement observed for 800 nm suggests that the strong two-photon (2PA) induced effects are the observed dominating nonlinear absorption.

In case of the metal-dielectric photonic structures (Ag/SiO_2), where alternate stacks of Ag and SiO_2 demonstrates very large enhancement in the nonlinear properties SiO_2. We extracted the nonlinear absorption coefficients (β, γ, δ, and αeff) as a function of the laser intensity at 725 nm. The observed 2PA coefficient are found to be in the range of 0.7 to 2.38 $x10^3$ cm/GW. The nonlinear refraction behavior exhibits a valley-peak configuration in closed aperture Z-scan which indicates positive nonlinear refractive refraction due to electronic Kerr nonlinearity. The nonlinear refractive index n2 is found to be 1.26×10^{-11} cm^2/W at 725 nm. The observed optical nonlinearities in (Ag/SiO_2) structure is manifold is compared with the bulk Ag and SiO2. The broad origin of giant nonlinear absorption can be safely ascribed to Ag contribution of inter-band transition initiated by the 2PA and 3PA followed by strong multiphoton absorption processes.

3. Conclusions

Photonic cavity mediated orders of magnitude enhanced femtosecond laser induced optical nonlinearities are reported in 1D photonic crystal, where nonlinear material ZnO, Bi_2O_3 and $BaTiO_3$ are introduced as a defect layers. The unusual giant nonlinear absorption switching at the cavity resonance and several orders of magnitude enhanced optical nonlinearities provide new insights into the realizing new 1D, 2D, and 3D photonic structures. The results also rouse significant interest in potential nonlinear devices such as optical switches, optical limiters, and on-chip integrated ultrafast devices. We also show a giant optical nonlinearity in (Ag/SiO_2) photonic crystal structure as compared to bulk Ag and SiO_2 due to the enhancement of intrinsic nonlinearity of Ag by the coupled Fabry–Pérot resonators. The strong multi-photon absorption was also observed due to the strong field confinement effect in the coupled Fabry–Pérot resonators.

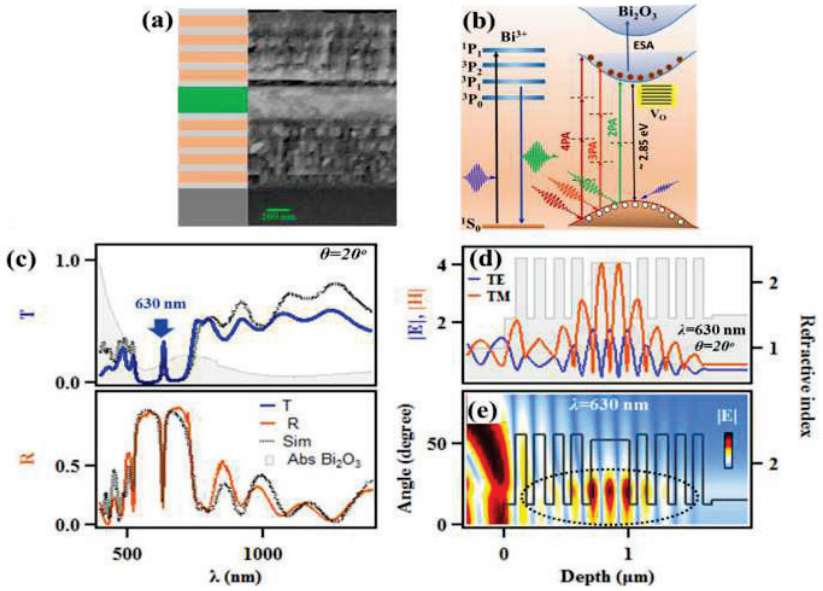

Fig. 1. (a) Schematic of Bi_2O_3 based optical microcavity composed of (SiO_2/TiO_2) Bragg mirrors and corresponding FESEM image. (b) Schematic representation of the energy levels of Bi_2O_3, (c) Experimental and TMM simulated transmission and reflection spectra of the optical microcavity (grey region represents the absorption spectra of pristine Bi_2O_3 film), (d) transverse spatial optical field (|E|, |H|) profiles for 637 nm (at θ=0°) (e) angle-resolved transverse electric field (|E|) spatial map at 637 nm. White lines are refractive index profiles.

4. References

[1] T. Baba, "*Slow light in photonic crystals*". Nat Photonics 2008, 2, (465-473).
[2] M. Notomi, "*Manipulating light with strongly modulated photonic crystals*", Rep. Prog. Phys. 2010, 73, 096501.
[3] P. M. Johnson, A. F. Koenderink, and W. L. Vos, "*Ultrafast switching of photonic density of states in photonic crystals*", Phys. Rev. B 2002, 66, 081102
[4] B. Y. Soon, J. W. Haus, M. Scalora, C. Sibilia, "*One-dimensional photonic crystal optical limiter*", Opt. Express 2003, 11, 2018
[5] J. N. Acharyya, N. R. Desai, R. B. Gangineni, and G. Vijaya Prakash, "Photonic cavity mediated tunable ultrafast absorption dynamics and nonlinearities in BaTiO3 based one-dimensional photonic crystal", ACS Appl. Electron. Mater. 2021, 4, (1904–1911).
[6] J. N. Acharyya, N. R. Desai, R. B. Gangineni, and G Vijaya Prakash, "*Effect of Photonic Cavity Interactions on Femtosecond Multiphoton Optical Nonlinear Absorptions from Bi2O3-Based One-Dimensional Photonic Crystal*", ACS Photonics, May 16, 2022; Vol 9, Issue 6, (2092-2100).

Non-Hermitian Optics: A New Paradigm

Amarendra K. Sarma
Department of Physics, Indian Institute of Technology Guwahati, Guwahati – 781039, India
Author e-mail address: aksarma@iitg.ac.in

In Quantum Mechanics, the Hamiltonian, H, describing a quantum system needs to be Hermitian, i.e. $H = H^{\dagger}$. This is because, the eigenvalues corresponding to a Hermitian Hamiltonian is always real; and eigenvalues are directly related to physically observable quantities in experiments. While the quantum mechanics we are familiar with is still quite successful, in 1998 Carl Bender and S. Boettcher [1] put forward a completely new perspective. They said that even non-Hermitian Hamiltonians could exhibit real eigen-spectra provided they obey the parity-time symmetry, resulting in the so-called parity-time symmetric quantum mechanics. This seemingly new quantum mechanics is not in conflict with the usual quantum mechanics, rather it is an extension of the conventional quantum mechanics into the complex domain [2]. This mathematical curiosity, however, influenced optical physics tremendously giving birth to a new paradigm called parity-time symmetric optics, and more generally non-Hermitian optics [3]. In fact, optical systems can provide a ground to realize the mathematical concepts of parity-time (PT) symmetry in the table-top experiments. In optics or photonics, PT symmetry has been readily established by judiciously incorporating balanced gain and loss in coupled system so that the refractive index profile plays the role of the complex potential. One of the most important characteristics of such systems is the presence of exceptional points (EP), at which they could exhibit abrupt phase transition [4].

In this talk, the author, after discussing the basic and key concepts, will give a short overview on the recent developments in this field. Finally, the author will present his own research endeavors in the area of non-Hermitian optics [5,6]. In particular, the author will discuss how tailoring higher-order exceptional points, it is possible enhance sensitivity of various seeming different devices [6].

[1] C. M. Bender and S. Boettcher, Real Spectra in Non-Hermitian Hamiltonians Having PT Symmetry, Phys. Rev. Lett. 80, 5243 (1998).
[2] A. K. Sarma, "Non-Hermitian Optics," arXiv:1810.10516 (2018).
[3] R. El-Ganainy, *et a*l., Non-Hermitian physics and PT symmetry, Nat. Phys. 14, 11 (2018).
[4] H. Hodaei *et al,* Enhanced sensitivity at higher-order exceptional points, Nature (London) 548, 187 (2017).
[5] S. Chakraborty and A. K. Sarma, Delayed sudden death of entanglement at exceptional points, Phys. Rev. A 100, 063846 (2019).
[6] A. Sahoo and A. K. Sarma, Two-way enhancement of sensitivity by tailoring higher-order exceptional points, Phys. Rev. A 106, 023508 (2022).

Study of modal gain characteristics of dual-annulus-core EDFA for space division multiplexing system

Ankita Gaur
Institute for Plasma Research, Gandhinagar-382428, Gujarat, India
ankitagaur.phy@gmail.com

Abstract: We propose dual-annulus-core EDFA for the amplification of five-mode-groups. The proposed fiber is studied with dual-annulus-core-doping and fundamental pumping. The refractive index profile of fiber is optimized in such a manner that it provides more than 25 dB amplification with less than 1 dB DMG.
Keywords: Optical communication, Erbium doped fiber amplifier, Space division multiplexing.

1. Introduction

Global internet traffic has increased dramatically in recent years. Majority of data transmission is supported by optical fiber network. With the existing technology based on single mode fiber (SMF), an issue of capacity crunch can be arisen soon due to Shannon limit of SMF. Space division multiplexing (SDM) is a breakthrough technology which promises to resolve of the issue of capacity crunch. It could provide a quantum leap in transmission carrying capacity by increasing data carrying channels using spatial domain of fiber. Few-mode fiber (FMF) is the most attractive approach of SDM technology. FMF supports restricted number of modes and these orthogonal modes of fiber (including degeneracy and polarisation) acts as the data carrying channels. The cost-effective FMF integration requires simultaneous amplification of all the signals through a single amplifier, therefore, the development of few-mode erbium doped fiber amplifier (FMEDFA) is essential. Gain equalization and number of modes scaling are two major challenges in designing of FMEDFA. Initially, a FMEDFA with uniform doping and multi-mode pump scheme was studied to minimize the DMG of two mode groups and fine tuning of the pump powers of the different pump modes helps in achieving less than ±0.5 dB DMG at 1530 nm signal wavelength [1]. A theoretically investigation of step-index-fiber with ring shaped erbium doping profile was reported for the gain equalization of LP_{01} and LP_{11} signal mode groups with 20 dB amplification and nearly 2 dB DMG over the C -band using fundamental mode pumping. The reduction in DMG was achieved by tuning of fiber length and pump power [2]. The modal gains and cross gain modulation of the three modes was investigated experimentally using ring-doped FM-EDFA [3]. In another study, it was reported that refractive index profile of FMEDFA play significant role in reducing the DMG. The comparative study showed that depressed-clad graded-index FMEDFA is superior to graded-index FMEDFA [4]. An elliptical core EDF was studied for the amplification of five non-degenerate modes (LP_{01}, LP_{11a}, LP_{11b}, LP_{21a} and LP_{21b}). The uplifting of degeneracy and the cross-talk reduction was also reported [5]. The optimum choice of pumping scheme is also necessary for DMG minimization. A mode-selective bi-directional pumping was used to achieve gain equalization of 6 spatial modes using ring doped FMEDFA [6]. A 6-mode EDFA along with mode-selective pumping using photonic lantern was studied to achieve nearly 28 dB modal gain with less than 2.9 dB DMG [7].

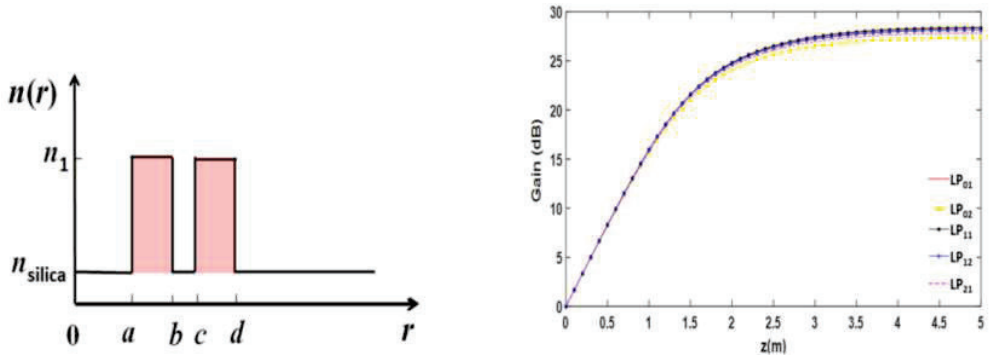

Fig. 1:(a) A schematic of refractive index profile of proposed fiber with dual core doping represented by shaded portion, (b) Variations of modal gains of signal mode groups with FM-EDF length.

2. Fiber Design and Gain Analysis

We consider a dual-annulus-core EDFA (as shown in Fig.1(a)) where the erbium doping profile is represented by the color shading in the both annulus core. The parameters used in the calculations are n_1=1.4594, a=4.4 μm, b=7.4 μm, c=8.4 μm and d=11.4 μm. The erbium doping concentration used is 1×10^{25}. The mode profiles of supported signal and pump modes of fiber and their effective indices are evaluated by using transfer matrix method [8]. The signal mode spacing greater than 4×10^{-4} is maintained to avoid any mode coupling due to macro -bending. The gain of five mode groups of proposed FM-EDF LP_{01}, LP_{02}, LP_{11}, LP_{12}, and LP_{21} are evaluated by using mathematical model given in Ref. [1]. The input power in every orientation and polarization of different signal mode groups used is 30 μW. The values of absorption and emission cross-section at the signal wavelength of 1530 nm used are 4.68×10^{-25} m^2 and 5.54×10^{-25} m^2, respectively. For pumping, the input pump power injected in the fundamental mode is 700 mW. The value of pump cross-section used in the calculation is 1.879×10^{-25} m^2.

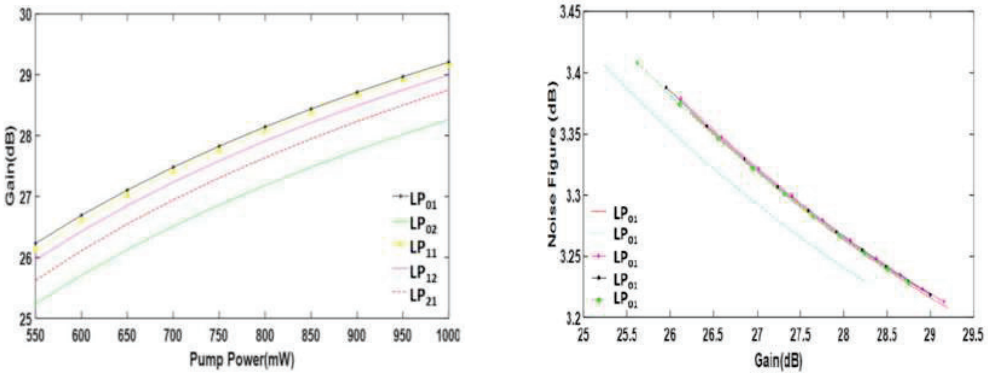

Fig. 2: (a) Variation of gains of signal mode groups with pump at signal wavelength of 1530 nm, (b) Variation of noise figure with the gains of signal mode groups.

Fig. 1(b) represents the variation of the modal gain of signal mode groups with FM-EDF length using dual-annulus-core doping at signal wavelength of 1530 nm. The results show more than 20 dB amplification of signal mode groups for the fiber length greater than 1.4 m and less than 1.1 dB DMG up to fiber length of 5m. The variations of gains of signal mode groups with pump power using dual-annulus-core-doping and fundamental pumping are shown in Fig. 2(a). Fig. 2(b) represents the variation of noise figure with gains of signal mode groups. The results show that for the fiber length of 3m, more than 25 dB amplification is achieved and DMG remain less than 1 dB for pump power variation from 550 mW to 1000 mW. It means any fluctuation in pump power would not affect DMG.

3. Conclusions

The proposed FM-EDF of fiber length 3 m is capable to provide more than 25 dB amplification of 16 modes of LP_{01}, LP_{11}, LP_{21}, LP_{02}, and LP_{12} mode groups at signal wavelength of 1530 nm. Less than 1 dB DMG is achieved using proposed fiber with fundamental mode pumping. This study would be useful for SDM optical communication system.

4. References

[4] N. Bai, E. Ip, T. Wang, and G. Li, "Multimode fiber amplifier with tunable modal gain using a reconfigurable multimode pump," Opt. Express **19**, 16601–16611, (2011).

[2] Q. Kang, E. L. Lim, Y. Jung, J. K. Sahu, F. Poletti, C. Baskiotis, and S. U. Alam and D. J. Richardson, "Accurate modal gain control in a multimode erbium doped fiber amplifier incorporating ring doping and a simple LP01 pump configuration," Opt. Express **20**, 20835-20843 (2012).

[3] Y. Jung, Q. Kang, V. A. J. M. Sleiffer, B. Inan, M. Kuschnerov, V. Veljanovski, B. Corbett, R. Winfield, Z. Li, P. S. Teh, A. Dhar, J. Sahu, F. Poletti, S. U. Alam, and D. J. Richardson, "Three mode Er3+ ring-doped fiber amplifier for mode-division multiplexed transmission," Opt. Express **21**, 10383-10392 (2013).

[4] D. Askarov, and J. M. Kahn, "Design of transmission fibers and doped fiber amplifiers for mode-division multiplexing," IEEE Photon. Technol. Lett. **24**, 1945-1948 (2012).

[5] J. B. Trinel, Y. Quiquempois, A. L. Rouge, G. L. Cocq, L. Garcia, J._F. Morizur, G. Labroille, and L. Bigot, "Amplification sharing of non-degenerate modes in an elliptical-core few-mode erbium-doped fiber," Opt. Express **24,** 4654-4661 (2016).

[6] Y. Jung, Q. Kang, J. K. Sahu, B. Corbett, J. O'Callagham, F. Poletti, S.-U. Alam, and D. J. Richardson "Reconfigurable modal gain control of a few-mode EDFA supporting six spatial modes," IEEE Photon. Technol. Lett. **26**, 1100-1103 (2014).

[7] G. L. Galmiche, Z. S. Eznaveh, J. E. A. Lopez, A. M. Velazquez Benitez, J. R. Asomoza, J. J. S. Mondragon, C. Gonnet, P. Sillard, G. Li, A. Schülzgen, C. M. Okonkwo, and R. A. Correa "Few-mode erbium-doped fiber amplifier with photonic lantern for pump spatial mode control," Opt. Lett. **41**, 2588- 2591 (2016).

[8] K. Morishita, "Numerical Analysis of Pulse Broadening in Graded index Optical Fibers," IEEE Transactions on Microwave Theory and Techniques **29**, 348 -352 (1981).

Digital Holographic Microscopy with Partially Spatially Coherent Laser Light:

10X times improved spatial phase sensitivity and space bandwidth product

Dalip Singh Mehta

Bio-photonics and Green-photonics Laboratory, Department of Physics, Indian Institute of Technology Delhi, Hauz-Khas, New Delhi-110016, India.

Coherent-noise free quantitative phase microscopy (QPM) with an order of magnitude improved spatial phase sensitivity, space-bandwidth product and high temporal phase stability is developed. The technique was utilized for sperm cells, macrophages, Liver sinusoidal endothelial cells, cancer cells and RBCs for precise QPM.

Quantitative phase microscopy (QPM) has recently become indispensable technology for label-free quantitative analysis of various biological cells and tissues, such as, sperm cells, macrophages, liver sinusoidal cells, and cancerous cells. QPM generates high contrast imaging of nearly transparent specimen using their intrinsic refractive index distribution without any exogenous contrast agents. The key parameters controlling measurement accuracy and capability of any QPM systems depends on its spatial and temporal phase sensitivity. The spatial phase sensitivity of QPM is governed by the coherence properties of light source and temporal stability depends on the optical configuration of QPM whether it is common-path or off-axis in nature. Most of QPM techniques utilize highly coherent light sources like lasers benefited by their remarkable properties, such as, high spatial and temporal coherence, and brightness. High spatio-temporal coherence leads to occurrence of speckle noise and spurious fringes leading to inhomogeneous illumination and poor spatial phase sensitivity. During the last few years, we have developed QPM systems using partially spatially coherent monochromatic (PSCM) light sources which guarantees high contrast interferograms over large field-of-view to increase space-bandwidth product of QPM system and demonstrated 10-fold improvement in spatial-phase sensitivity and phase measurement accuracy compared to coherent laser light. By means of using PSCM with common path configuration we could also achieve 10-fold temporal phase stability.

We have demonstrated advantages of PSCM based QPM in various bio-imaging applications; such as, successfully reconstructing complete structure including thin tail region (~ 100 nm) of the sperm cells and utilized deep neural network for it's classification under stressed conditions [1-10]. Quantitative assessment of morphology and sub-cellular changes in macrophages and trophoblasts during inflammation was also investigated [8]. These studies were further complemented by utilizing the power of artificial intelligence for classification of different cells (red blood cells, macrophages and placenta tissue samples) with improved space-bandwidth product and high-throughput spatially sensitive QPM. Thus, we believe that use of PSCM will push the limits of QPM system and increase its widespread penetration in the fields of bio-imaging, life sciences and material science.

References:

1. V. Singh, R. Joshi, S. Tayal, and D. S. Mehta, "Speckle-free common-path quantitative phase imaging with high temporal phase stability using a partially spatially coherent multi-spectral light source," Laser Physics Letters 16, 025601 (2019).

2. A. Butola, Sheetal Raosaheb Kanade, Sunil Bhatt, Vishesh Kumar Dubey, Anand Kumar, Azeem Ahmad, Dilip K Prasad, Paramasivam Senthilkumaran, Balpreet Singh Ahluwalia, Dalip Singh Mehta, "High space-bandwidth in quantitative phase imaging using partially spatially coherent digital holographic microscopy and a deep neural network, Optics Express 28, 36229 (2020).
3. Shilpa Tayal, Veena Singh, Tejinder Kaur, Neetu Singh, and Dalip Singh Mehta, Multi-modal biomicroscopic system for the characterization of MG63 osteosarcoma cell line with high spatial phase sensitivity and sub-pixel accuracy, Journal of Biophotonics (2021), e202100258.
4. Azeem Ahmad, Vishesh Dubey, Ankit Butola, Jean-Claude Tinguely, Balpreet Singh Ahluwalia, Dalip Singh Mehta, Sub-nanometer height sensitivity by phase shifting interference microscopy under environmental fluctuations, Optics Express 28 (7) 9340-9358 (2020).
5. A. Butola, D. Popova, D. K. Prasad, A. Ahmad, A. Habib, J. C. Tinguely, P. Basnet, G. Acharya, P. Senthilkumaran, Dalip Singh Mehtaand B. S. Ahluwalia, "High spatially sensitive quantitative phase imaging assisted with deep neural network for classification of human spermatozoa under stressed condition" Scientific Reports 10, 1(2020).
6. A. Ahmad, Vishesh Dubey, Nikhil Jayakumar, Anowarul Habib, Ankit Butola, Mona Nystad, Ganesh Acharya, Purusotam Basnet, Dalip Singh Mehta, Balpreet Singh Ahluwalia, "High-throughput spatial sensitive quantitative phase microscopy using low spatial and high temporal coherent illumination," Scientific Reports 11, 1 (2021).
7. Ankit Butola, David A Coucheron, Karolina Szafranska, Azeem Ahmad, Hong Mao, Jean-Claude Tinguely, Peter McCourt, Paramasivam Senthilkumaran, Dalip Singh Mehta, Krishna Agarwal, Balpreet Singh Ahluwalia, Multimodal on-chip nanoscopy and quantitative phase imaging reveals the nanoscale morphology of liver sinusoidal endothelial cells, PNAS-Proceedings of the National Academy of Sciences 118 (47) (2021), pp. e2115323118.
8. R. Singh, V. Dubey, D. Wolfson, A. Ahmad, A. Butola, G. Acharya, D. S. Mehta, P. Basnet, B. S. Ahluwalia , "Quantitative assessment of morphology and sub-cellular changes in macrophages and trophoblasts during inflammation" Biomedical Optics Express 11, 3733 (2020).
9. A. Ahmad, V. Dubey, A. Butola, B. S. Ahluwalia, D. S. Mehta, Highly temporal stable, wavelength-independent, and scalable field-of-view common-path quantitative phase microscope, Journal of Biomedical Optics 25 (11), 116501 (2020).
10. S.Tayal, V. Singh, T. Kaur, N. Singh, and D. S. Mehta, Simultaneous fluorescence and quantitative phase imaging of MG63 osteosarcoma cells to monitor morphological changes with time using partially spatially coherent light source, Methods and Applications in Fluorescence 8 (3), 035004 (2020).
11. Shilpa Tayal, Anuj Saxena, Veena Singh, Tejinder Kaur, Neetu Singh, Kedar Khare, Dalip Singh Mehta, Design and development of integrated TIRF and common-path quantitative phase microscopic health care system with high stability, Optics and Lasers in Engineering 155, 107057 (2022).
12. Azeem Ahmad, Tanmoy Mahanty, Vishesh Dubey, Ankit Butola, Balpreet Singh Ahluwalia, and Dalip Singh Mehta, Effect on the longitudinal coherence properties of pseudo thermal light source as a function of source size and temporal coherence, Optics Letters 44 (7), 1817-1820 (2019).

Image encryption through structured light

Praveen Kumar and Naveen K. Nishchal*
Department of Physics, Indian Institute of Technology Patna, Bihta, Patna 801 106, Bihar, India
**E-mail: nkn@iitp.ac.in*

Abstract: With the technological advancement enormous amount of information/data is being generated, stored, and disseminated, which requires efficient cryptosystem. Digital techniques of security are being further researched for improvement in terms of fast processing and robustness. Optical technologies for information security are being developed as an alternative tool with ultra-high speed. Further, desired light fields as structured beams are being considered for security applications by controlling the parameters amplitude, phase, and polarization. Image encryption through structured light has several features including intensity-based measurement that makes it suitable for storage and transmission. This paper reviews image encryption techniques employing controllable properties of light beam. © Author

Keywords: Structured light, Optical vortex, Orbital angular momentum, Image encryption

1. Introduction

Light fields having complex wavefront structures with spatial inhomogeneity give rise to unique features. One of the features is the formation of optical vortices [1]. Due to the spiral phase front of the optical field, optical vortex is created at the phase singularity, where phase becomes indeterminate and intensity is zero. Light beams with spiral phase front are expressed as $exp(il\varphi)$, which contain orbital angular momentum (OAM). The symbol φ and l denote the azimuthal angle and topological charge (TC), respectively. Theoretically, light beams can have more orthogonal modes associated with OAM than polarization, which makes optical vortices an attractive solution for optical communications, high-dimensional data encoding and processing [2].

With the pioneering work first reported in 1995, a large number of algorithms and architectures for optical image encryption have been proposed and implemented exploiting the inherent features of light [3,4]. Optical logic gates such as exclusive-OR operation which plays an important role in computing applications have been implemented through light field propagation and optical modulation. Though logic states are often expressed either by amplitude or polarization of light, the development of encryption approaches is obstructed by difficulty in high-dimensional encoding. Sincere efforts have been reported for improving the performance by expressing the logic variables through orthogonal bases of light such as OAM modes [5-7]. Various modes of OAM correspond to different orders of optical vortices assigned with integral azimuthal indices.

Optical cryptosystems are designed to prevent unauthorized information access during their distribution [3,8-11]. Polarization encoding is one of the preferred approaches [4]. It is performed with a pair of liquid crystal spatial light modulators (SLMs) for input arguments to modify the polarization. Further, encryption of quick-response (QR) codes has been demonstrated using this approach. Beyond polarization, optical vortices open up new possibilities to progress with enhanced degrees of freedom. Recent works have shown the formation of multiple vortices in an optical beam, commonly known as an optical vortex array [10,11]. Controlled realization of such array creates an opportunity to utilize the spatial degrees of freedom for parallel-processing of data using orthogonal states of light.

2. Theory

The approach of double-phase modulation of light has been implemented for two-dimensional exclusive OR operation through optical vortices. In the double-phase modulation method, the incident light is transmitted through two different phase masks, expressed as A and B. These masks are designed to create optical vortices in the light beam that transmits through it. Figure 1 depicts the illustration of two-dimensional exclusive OR operation using optical vortices for $|l| = 1$. Similarly for other TC values, the process can be followed.

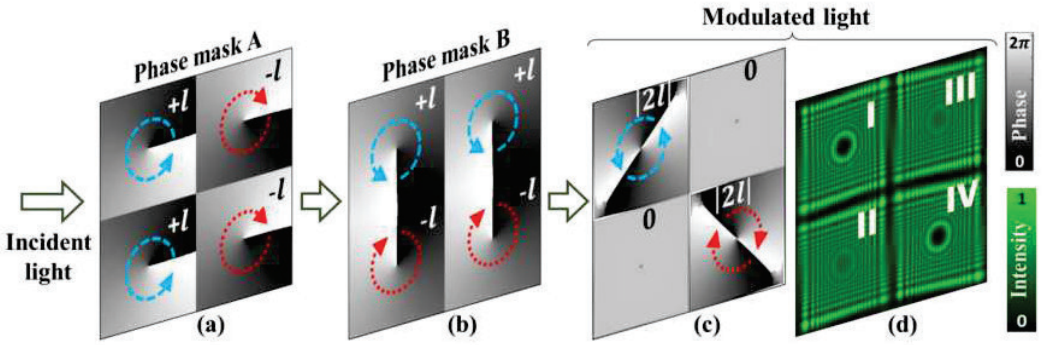

Fig. 1 Illustration of two-dimensional exclusive OR operation using optical vortices for $|l| = 1$ [Ref. 11].

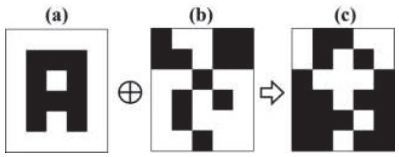

Fig. 2 Encryption using two-dimensional exclusive OR operation. (a) Input image, (b) key, and (c) encrypted image [Ref. 11].

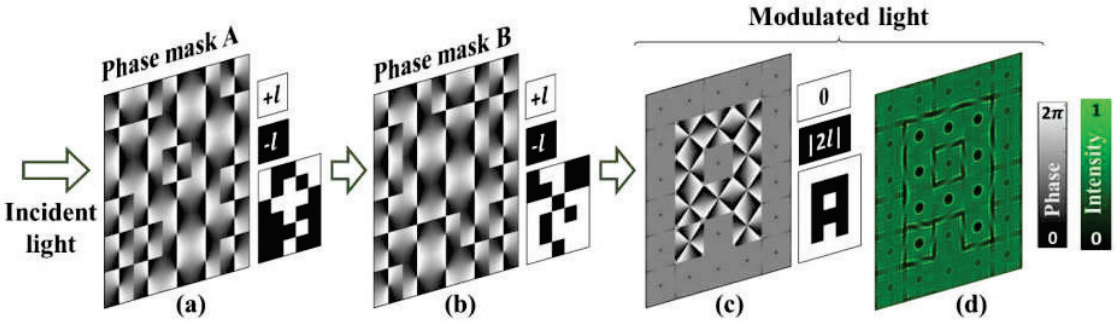

Fig. 3 Decryption through optical vortex array-based exclusive OR operation. (a) Encrypted image as a phase mask, (b) key as a phase mask, (c) exclusive OR-operated phase profile of modulated light, and (d) intensity profile [Ref. 11].

Figure 2 presents the encryption approach through exclusive OR operation and the decryption process is shown in Figs. 3(a-d). The decryption process can be carried out using exclusive OR operation with encrypted image and key phase mask as input. The input logic from each element of the encrypted image and key phase mask are encoded as azimuthal index $+l$ and $-l$ through phase masks [11].

3. Conclusion

The paper presents one of the aspects of structured light in the form of optical vortex array for image encryption and decryption. The presented method opens up new dimension in the field of optical security. Such schemes offer high level of security and can be suitable for practical systems.

Acknowledgement

The financial support from the Science and Engineering Research Board, Dept. of Science and Technology, Govt. of India through grant No. CRG/2021/001763 is duly acknowledged.

References

[1] H. Rubinsztein-Dunlop *et al*., "Roadmap on structured light," J. Opt. 19, 013001 (2017).
[2] A. M. Yao and M. J. Padgett, "Orbital angular momentum: origins, behavior and applications," Adv. Opt. Photon. 3, 161-204 (2011).
[3] N. K. Nishchal, *Optical Cryptosystems*, IOP Publs. Ltd., Bristol, UK (2019).
[4] A. AlFalou and C. Brosseau, "Dual encryption scheme of images using polarized light," Opt. Lett. 35, 2185-2187 (2010).
[5] X. Li, T. H. Lan, C. H. Tien, and M. Gu, "Three-dimensional orientation-unlimited polarization encryption by a single optically configured vectorial beam," Nat. Commun. **3**, 998 (2012).
[6] L. Liu, Y. Gao, and X. Liu, "High-dimensional vortex beam encoding/decoding for high-speed free-space optical communication," Opt. Commun. 452, 40-47 (2019).
[7] X. Fang, H. Ren, and M. Gu, "Orbital angular momentum holography for high-security encryption," Nat. Photonics 14, 102-108 (2020).
[8] P. Kumar, A. Fatima, and N. K. Nishchal, "Arbitrary vector beam encoding using single modulation for information security for information security applications," IEEE Photon. Technol. Lett. 33, 243-246 (2021).
[9] P. Kumar, N. K. Nishchal, and A. AlFalou, "Controllable Optical vortex array for image encoding," IEEE Photon. Technol. Lett. 34, 521-524 (2022).
[10] P. Kumar, N. K. Nishchal, and A. AlFalou, "Color image encryption using vectorial field through a compact optical set-up," J. Opt. 24, 064017 (2022).
[11] P. Kumar, N. K. Nishchal, T. Omatsu, and A. S. Rao, "Optical vortex array for two-dimensional exclusive-OR operation," Appl. Phys. B: Lasers Opt. 128, 98 (2022).

Topological Effects due to Reflection of Normally-incident Light Beam

Nirmal K. Viswanathan
School of Physics, University of Hyderabad, Hyderabad - 500046
Author e-mail address: nirmalsp@uohyd.ac.in

Abstract: A careful and closer relook into the simplest of the optical process, reflection of a normally-incident beam of light at a planar dielectric interface allows us to unravel a spate of novel and fundamentally significant topological optical effects with application potential. Theoretical, simulation and experimental results of our investigation will be presented.
Keywords: Spin-orbit interaction of light, Spin-Hall effect, Reflection, Polarization.

A beam of light from a typical laser is transversely confined and so has to be treated as a superposition of an infinite number of plane waves of differing propagation directions $(\bar{k})$, but can be of same frequency (ω) in the simplest case [1]. Since the electric $(\bar{E})$ and magnetic $(\bar{B})$ field vectors of the electromagnetic (EM) wave are perpendicular to $\bar{k}$, to maintain transversality, for propagating diverging or converging optical beams the projected fields and their behavior will be different from that of a plane wave. However, since optical beams were incorrectly assumed to be plane wave beams in several investigations, fundamentally significant topological optical effects with application potential were missed. With the emergence of understanding a beam of light and light-matter interactions in terms of *spin-orbit interaction* (SOI) [2], it is important that one takes an in-depth relook at the simplest of such interactions, reflection / refraction of a beam of light at / through a planar dielectric interface.

To this effect we carry out analysis of reflection of real optical beams at a planar dielectric interface by transforming each plane wave component and subsequently recombining them appropriately to obtain the correct forms of the complete reflected beam-field [3]. The spatial dispersion of Fresnel reflection coefficients comes into play in this context, giving rise to distorted complicated reflected field profiles due to polarization dependent angular dependence of the reflection amplitude. The resulting reflected intensity and field distribution are generally shifted from the geometrically expected positions, known as *Goos-Hanchen* (GH) shift and *Imbert-Fedorov* (IF) shift respectively for in and perpendicular to the central plane of incidence [4].

For the degenerate case when the central wavevector is normal to the dielectric interface, the inability to define the plane of incidence leads to the disappearance of the GH and IF shifts. However, the azimuthally symmetric variation of Fresnel coefficients combined with inhomogeneous polarization of incident non-planar beam leads to hitherto unexplored field profiles, which is understood in terms of *spin-orbit interaction* (SOI) in the beam-field [5,6]. In the process we have unified the fundamental EM reflection / transmission problem with the emerging understanding of SOI of light. This has enabled us to propose and demonstrate several topological optical phenomena including spin-to-orbital angular momentum conversion, spin-Hall effect of light [7, 8], singularity dynamics, all arising due to reflection of normally-incident light beam at a dielectric interface. Application potential of emerging understanding of light and light-matter interactions are just opening up. Our recent results in this area of research will be presented at the conference.

Acknowledgements

The author acknowledges SERB for continued financial support to this area of research. This abstract is a summary of several PhD students' research work and I acknowledge all of them in advancing and enriching this and related areas of research pursued in the group.

References

[1] B. E. A. Saleh and M. C. Teich, Fundamentals of Photonics, 2nd ed. (John Wiley & Sons, Inc., NJ, 2007)
[2] K. Y. Bliokh, F. J. Rodríguez-Fortu no, F. Nori, and A. V. Zayats, Nat. Photonics **9**, 796 (2015).
[3] A. Debnath and N. K. Viswanathan, J. Opt. Soc. Am. A **37**, 1971 (2020).
[4] K. Y. Bliokh and A. Aiello, J. Opt. **15**, 014001 (2013).
[5] A. Debnath and N. K. Viswanathan, Phys. Rev. A **103**, 013510 (2021).

[6] G. J. Gbur, Singular Optics (CRC Press, Taylor & Francis Group, LLC, FL, 2017).
[7] A. Debnath and N. K. Viswanathan, Phys. Rev. A **106**, 013522 (2022).
[8] U. Baishya, N. Kumar, and N. K. Viswanathan, Opt. Lett., **47**, 4479 (2022).

Tailoring the emission landscapes of NV centers in diamond

Rajesh V. Nair

Laboratory for Nano-scale Optics and Meta-materials (LaNOM), Department of Physics, Indian Institute of Technology Ropar, Rupnagar, Punjab 140001, India

E-mail: rvnair@iitrpr.ac.in

Abstract: We discuss the optical properties of quantum emitters like nitrogen-vacancy (NV) centers and devise the methods which can enhance their utility in various applications ranging from tailored emission, quantum sensing, and bio-imaging. We have utilized engineered photonic structures to control the spontaneous emission from an ensemble as well as few NV centers. We discuss spectral- and spatial-dependent emission enhancement of NV centers by engineering unique scattering pattern exhibited by the photonic structure. The indigenous developments of a confocal microscope to map the isolate single NV centers and their emission characteristics, at the level of single photons, would be discussed.

Keywords: Quantum emitter, NV centers, nanophotonics. Single photon emission

1. Introduction

The quest for generating on-demand deterministic single quantum of light from solid state emitters has refined the research into the spontaneous emission control, wherein a single photon is generated per excitation cycle. Consequently, single emitters like single quantum dots or the atomic defects in materials like diamond, silicon carbide, and two-dimensional (2D) materials are integrated to different types photonic structures. Tailoring the emission of such single emitter has profound applications in antennas, quantum photonics and spin physics. The recent surge in quantum photonics disseminates that nitrogen vacancy center (NV) in diamond is a promising single photon source even at room temperature. The excellent optical and spin properties of NV center make them very attractive for areas like quantum sensing, magnetometry, bio-markers, and sensors in harsh environments. The NV center is formed by a substitutional nitrogen atom adjacent to a carbon vacancy in the diamond lattice. The NV center emission is characterized by a zero phonon line (ZPL) at 637 nm, which is accompanied by a broad phonon induced sideband (PSB) emission up to 750 nm. Such PSB emission induces decoherence in the system with limited (1-2%) emission at the ZPL even at low temperatures. Hence, ZPL enhancement with simultaneous PSB inhibition is a sought-after-goal in the NV center based quantum technology. Several systems such as photonic cavities, plasmonic gap modes, waveguides, and high-index metasurfaces are proposed by the deterministically changing in the photon density of states through strong field confinement in these systems.

2. Results and discussion

The emission properties of diamonds that contains ensemble as well as few NV centers in both frequency as well as the time domain is studied. We introduce different types of photonic structures that can be used to tailor the emission properties of NV centers. The results are analysed using finite difference time domain methods and analytical calculations. The enhancement in the emission rate of single NV centers at the ZPL wavelength exploiting the Kerker condition using an all-dielectric metasurface is evoked. The Kerker condition with unidirectional scattering is originated due to the constructive interference between several multipoles which is elaborated using simulations as well as using analytical calculations. The Kerker condition induce strong field confinement with unidirectional scattering, which is used to tailor the emission rate of single quantum emitter through modifying the photon density of states. We have obtained an enhancement of 400 in the emission rate of a single NV center at ZPL wavelength with strong emission directivity. We will also discuss the development of confocal microscope to image the isolated NV centers and its emission properties in frequency and time domain at the level of single photon. The emission properties of NV center in nanodiamonds as well as in bulk diamonds would be elaborated.

3. References

[1] M. W. Doherty, N. B. Manson, P. Delaney, F. Jelezko, J. Wrachtrup, and L. C. Hollenberg, The nitrogen-vacancy colour centre in diamond, Physics Reports **528**, 1 (2013)
[2] Sachin Sharma and Rajesh V. Nair, "Nanophotonic control of the color center emission from nanodiamonds," Optics Letters **43**, 3989 (2018).
[3] Megha Khokhar, Sachin Sharma, Sudhir K. Saini, and Rajesh V. Nair, "Enhancing the spontaneous emission using the structural resonances of self-assembled monolayers", Journal of Optics **23**, 085004 (2021).
[4] Megha Khokhar, Faraz A. Inam, and Rajesh V. Nair, "Kerker condition for enhancing emission rate and directivity of single emitter coupled to dielectric metasurfaces", Advanced Optical Materials (In press 2022).

Asymmetric and nonreciprocal control of light with nonlinear dielectric metasurfaces

Sergey S. Kruk
Nonlinear Physics Center, Research School of Physics, Australian National University, Canberra ACT 2601 Australia
sergey.kruk@outlook.com

Abstract: We break the symmetry of light control at the nanoscale with magneto-electric coupling in nonlinear resonators. We integrate large quantities of such resonators into compact metasurface designs that demonstrate different and completely independent functionalities for the reversed direction of illumination
Keywords: Nanophotonics, nanofabrication, metasurfaces, metaphotonics, nonlinear optics, nonreciprocity.

Introduction

Over just a few years we have seen a tremendous progress of dielectric metasurfaces from fundamental concepts [1] to mass-fabricated consumer products. Passive and linear dielectric metasurfaces have started replacing conventional bulky optical components. One of the new frontiers of both fundamental and applied metasurface research is in nonlinear light-matter interactions rendered by nanoscale engineering. Nonlinearity offers a solution to a vital but largely unaddressed problem of contemporary optics and photonics: nonreciprocal optical response at the nanoscale. The 21st century photonics might depend on nanoscale nonreciprocal metasurfaces as much as the 20th century electronics depended on nanoscale nonreciprocal semiconductor diodes. A nonreciprocal system exhibits different received-transmitted field ratios when their sources and detectors are exchanged [see Fig. 1]. Such response requires breaking the Lorentz reciprocity theorem. Nonlinearity is one of only few fundamentally possible pathways to such behavior [2].

The talk will cover our latest experimental results on nonreciprocal one-way transmission of light and optical isolation with dielectric metasurfaces. The presentation will extend to nonlinearity-induced asymmetries with regards to the exchange of sources and detectors to parametric generation of light, including asymmetric images experimentally observed via a third-harmonic generation process [3].

Nonreciprocal propagation of light through nonlinear metasurfaces

We will discuss a a recent demonstration of a half-a-micron-thick nonlinear and nonreciprocal metasurface with one-way transmission over an extended spectral region (see Fig. 1). It operates at very low intensities of about 200 W/cm^2 of CW power, being in a striking contrast with Kerr-based nonlinear self-action devices in nanophotonics often requiring pulsed peak powers reaching and exceeding GW/cm^2

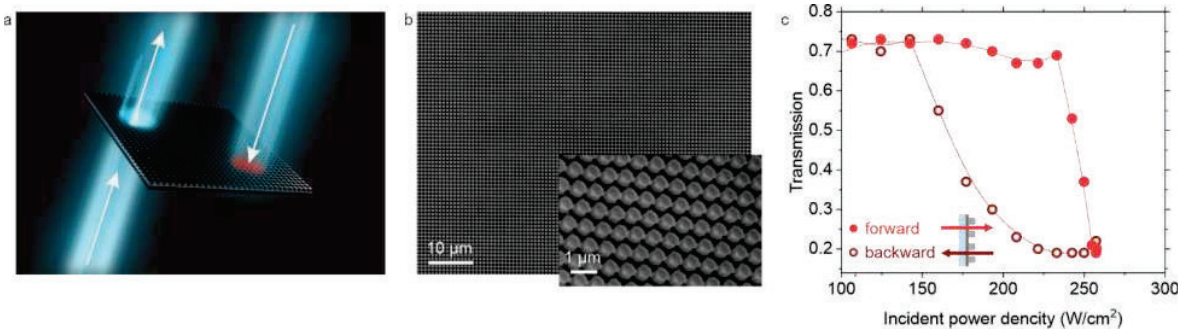

Fig. 1. Nonreciprocal transmission of light through a metasurface. (a) Concept image of one-way transmission through the metasurface. (b) Electron microscope image of the fabricated metasurface. (c) Experimental measurements of transmission for two opposite directions of illumination at 1450 nm wavelength. For power density around 200 W/cm^2, the metasurface demonstrates high contrast between forward and backward transmission.

Asymmetric parametric generation of images in nonlinear metasurfaces

In recent work [3], we demonstrated asymmetric parametric generation of light in nonlinear metasurfaces. We assembled the metasurfaces from a set of four dissimilar dielectric resonators. The resulting layouts were producing images in the visible spectral range on being illuminated by infrared radiation via a third-harmonic generation (THG) process. By design, the metasurfaces produced two different independent images for the opposite directions of illumination.

Each nanoresonator was a bi-layer cylinder made of silicon and silicon nitride materials. The resonators' response was dominated by two overlapping resonances: the electric dipole and the magnetic dipole Mie modes. The difference in the refractive indices between silicon and silicon nitride was inducing strong magneto-electric coupling leading to THG dependency on the direction of excitation. The following four types of resonators were developed: (i) a resonator producing bright THG for forward illumination and dark THG for backward illumination, (ii) dark for forward and bright for backward, (iii) bright for both forward and backward, (iv) dark for both forward and backward. The metasurfaces were fabricated with electron beam lithography and experimentally tested with a pulsed laser system at around 1.5 μm excitation wavelength.

As light was passing through the metasurface, an image of Australia could be seen, but when we flipped the metasurface and looked again, an image of the Sydney Opera House was visible. The demonstrated traffic control of light via asymmetry in parametric generation also points out the direction to self-induced nonlinear nonreciprocity in nanoscale optics that is expected to lead to numerous practical devices, including isolators, circulators, and directional power limiters.

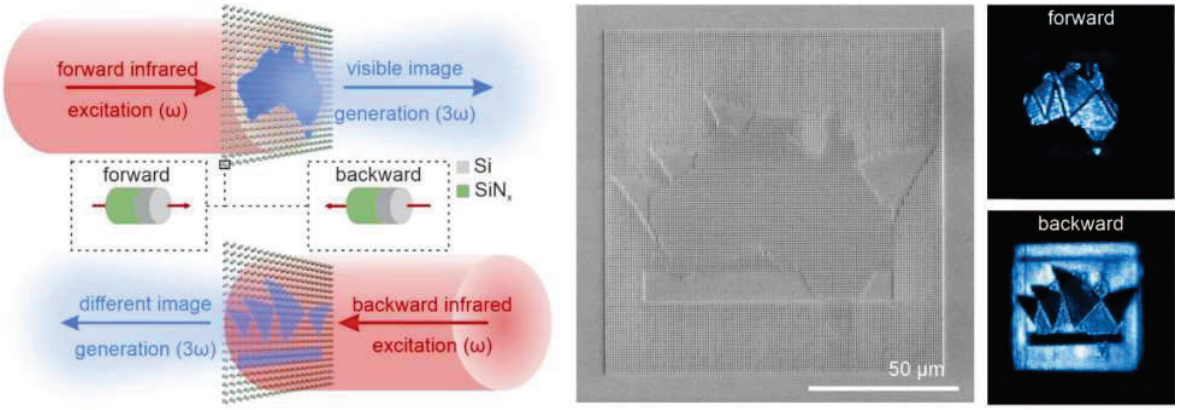

Fig. 2. Directional generation of images at the third-harmonic frequency with a dielectric metasurface. The metasurface is assembled from a set of asymmetric nanoresonators with strong magneto-electric coupling between the Mie modes leading to asymmetry in the nonlinear optical response. Middle: electron microscope image of a fabricated sample. Right: experimentally observed images at the third-harmonic frequency for both forward and backward illuminations.

Conclusions

We have observed high contrast between forward and backward transmission for the same level of the incident power with a metasurface of a subwavelength thickness via nonlinear self-action. We have demonstrated formation of independent images via nonlinear generation of the third harmonic frequency. These results pave the way to broadband nanoscale components for nonreciprocal and asymmetric control of light. Nonreciprocal passive flat optics will assist the advancement of optical communications, LiDAR machine vision, as well as photonic information processing, routing, and switching.

Acknowledgements

The authors acknowledge a support from the Australian Research Council (grants DE210100679 and DP210101292) and the EU Horizon 2020 Research and Innovation Program (grant 896735).

References

[1] S. Kruk and Y. S. Kivshar, "Functional meta-optics and nanophotonics governed by Mie resonances," ACS Photon., 4, 2638 (2017).
[2] C. Caloz et al., "Electromagnetic Nonreciprocity" Phys. Rev. Applied 10, 047001 (2018).
[3] S. Kruk et al., "Asymmetric parametric generation of images with nonlinear dielectric metasurfaces" Nature Photon. 16, 561–565 (2022).

Measurement of Complexity in Two-Dimensional, Open Anderson Localizing systems

Sandip Mondal[1], Kedar Khare[2], Martin Kamp[3], Sushil Mujumdar[1,*]

[1]*Nano-optics and Mesoscopic Optics Laboratory, Tata Institute of Fundamental Research, 1, Homi Bhabha Road, Mumbai, 400005, India*

[2]*Indian Institute of Technology Delhi, New Delhi 110016, India*

[3]*Lehrstuhl für Technische Physik, Universität Würzburg, 97074 Würzburg, Germany*

Author e-mail address: mujumdar@tifr.res.in

Abstract: Non-Hermiticity, introduced by open boundaries of a system, significantly modifies the eigenfunctions of the system and alters the transport properties. Due to non-Hermiticity, the orthogonality between the eigenmodes is lifted, and the real-valued wavefunctions become complex. In this work, we experimentally measure the complexity of such modes in a two-dimensional Anderson localizing system. An interferometric setup is employed to measure the complex wavefunctions for various levels of localization. A linear dependence is observed between the localization length and the complexity of the modes.

Keywords: Anderson Localization, Disorder, Complexity.

1. Introduction

In disordered systems, transport is hindered due to Anderson localization [1], which arises because of self-interference between the scattered wavelets. In a closed system, these localized states are static resonances, and the wavefunctions are completely real and static. However, in a realistic system, the open boundaries of the system introduce non-Hermiticity. This non-Hermiticity lifts the orthogonality between the eigenfunctions of the system, and the wavefunctions become complex and traveling. This stationarity of the wavefunctions is quantified by a parameter complexity [2,3], defined as, $q^2 = \langle\psi_i^2\rangle/\langle\psi_r^2\rangle$. The complexity is bounded between 0, for a completely localized wavefunction, and 1, for a traveling wave. As the localization increases, the extent of the modes decreases and thus coupling of the modes to the boundary. Therefore, it is expected that the openness will reduce with increasing localization. Thus, it is desirable to measure the complexity as a function of localization. Here, we study the complexity of two-dimensional Anderson localized modes in the optical domain. We employed an interferometer-based setup augmented with a phase extraction algorithm [4] to measure the complex wavefunctions. The phase distribution of extended modes exhibits a flat distribution, whereas the distribution for localized modes is peaked at 0 and π rads. Finally, a linear dependence with a unity slope is extracted in relation between the localization length and the complexity.

2. Results

For experimental measurements, we used samples with varying degrees of disorder [5]. For statistical consistency, a large number of configurations is used for each disorder. The dimensions of each sample are 20×20 μm^2. The experiment is performed in the near-infrared wavelengths ($\lambda \sim 1550$ nm). To measure the phase, three sets of data are recorded corresponding to the object beam (also referred to as the modes), reference beam, and the interference pattern. A measured Bloch mode in the periodic sample is shown in Fig. 1(a). The parallel wavefronts correspond to the standing wave formed because of the interference between the counter-propagating Bloch waves. Figure 1(b) shows the extracted phase for the mode in (a).

Next, we discuss the distribution of the phase. It is theoretically predicted that, for highly localized modes, the phase distribution is sharply peaked at 0 and π rads [3]. With decreasing localization, the distribution flattens out. Here we present the first experimental measurements of the same. Figure 1(c) and (d) show the measured phase distribution for two localization lengths. The data is averaged over a large number of modes to represent averaged behavior. It is clearly visible that, for a large localization length ($\xi = 0.95$ in (c)), the distribution is flat and when the localization is strong ($\xi = 0.60$ in (d)), the distribution is peaked at 0 and π rads, endorsing the theoretical predictions.

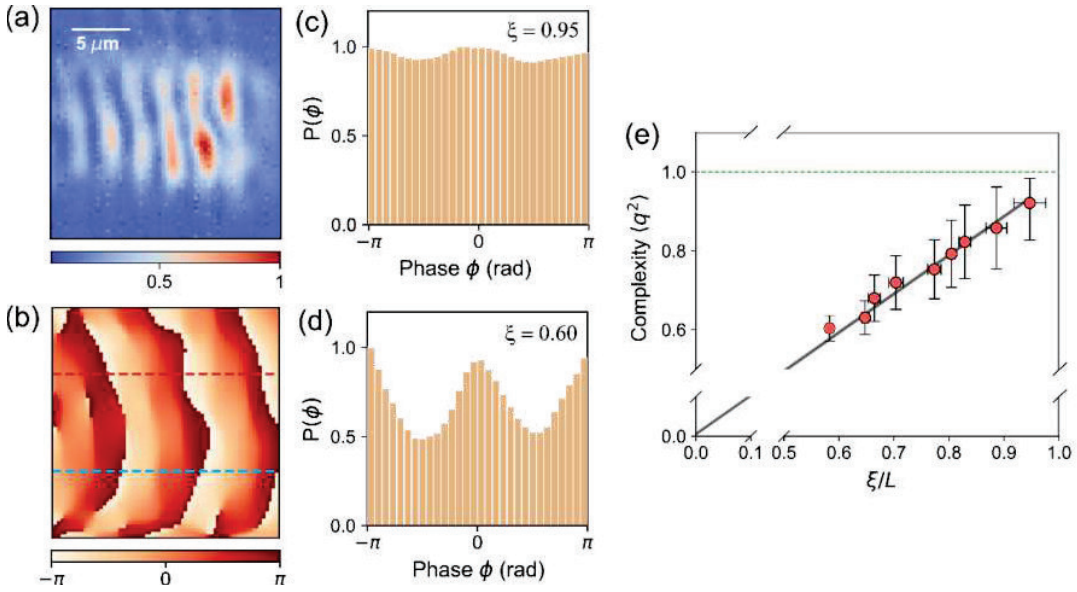

Fig. 1: (a) A measured Bloch mode. (b) Phase map for the mode as shown in (a). (c), (d) Phase distribution for two different localization lengths. (e) Complexity as a function of normalized localization length. The black line is a linear fit with a slope of 1.

Finally, we calculate the complexity as a function of localization length, as shown in Fig. 1(e). Evidently, a linear behavior is seen, and the best fit (black line) provides a slope of 1. To our knowledge, this simple but significant observation has never been reported in theory or experiments. The extrapolation of the fit intersects at to origin, endorsing the fact that for a completely localized wavefunction, the wavefunction will be real, and the complexity will be zero. These results reveal a hitherto unknown behavior of complex systems and provide an interesting direction for further examinations in particular relevance to nonstationary transport.

3. References

[1] P. W. Anderson, Phys. Rev. **109** (5), 14921505 (1958).
[2] P. W. Brouwer, Phys. Rev. E **68**, 046205 (2003).
[3] C. Vanneste, and P. Sebbah, Phys. Rev. A **79**, 041802(R) (2009).
[4] M. Singh and K. Khare, Opt. Lett. **41**, 4871-4874 (2016).
[5] R. Kumar, S. Mondal, M. Balasubrahmaniyam, M. Kamp and S. Mujumdar, Phys. Rev. B **102**, 220202(R) (2020).

Ultrafast Laser Induced Nanostructures: Physics and Sensing Applications

Venugopal Rao Soma

Advanced Centre of Research in High Energy Materials ***(ACRHEM),***
University of Hyderabad, Hyderabad 500046, Telangana, India.

e-mail: ***soma_venu@uohyd.ac.in*** *OR* ***somavenu@gmail.com***

Ultrafast laser ablation (ULA) of a variety of materials (semiconductors, metals, dielectrics, etc.) has reached a matured position with developments in the understanding of several underlying physical mechanisms at various timescales, varying from femtoseconds to milliseconds, and applications resulting from these interactions [1-5]. The process of ULA [using both picosecond (ps) and femtosecond (fs) laser pulses] can be performed in different media [vacuum, air, and liquids], ensuing in a variety of nanostructures on surfaces. Using femtosecond laser material processing, we created versatile nanostructures (inside the bulk/on surfaces) and nanomaterials (nanocolloids) of plasmonic materials such as silver (Ag), gold (Au), copper (Cu), alloys (Ag-Au, Au-Cu, Ag-Cu, etc.), and semiconductors such as Si and GaAs. We have been exploring the utility of such nanostructures for trace sensing of military-grade explosives (ammonium nitrate, picric acid, RDX, HMX, NTO, TNT, etc.) using the surface-enhanced Raman spectroscopy (SERS) technique [6-15]. We will present some of our recent results obtained using Ag/Au and GaAs.

Acknowledgments

DRDO is also acknowledged for support through ACRHEM [ERIP/ER/1501138/M/01/319/D (R&D)]. Venugopal Rao Soma also thanks the University of Hyderabad for support through the Institute of Eminence (IoE) project UOH/IOE/RC1/RC1-2016. The IoE grant was gotten through notification F11/9/2019-U3(A) from MHRD, India.

References

1. N.A. Inogamov, Y.V. Petrov, V.A. Khokhlov, V.V. Zhakhovskii, High Temperature **58(4),** 632-646 (2020).
2. D. Zhang, J. Liu, P. Li, Z. Tian, C. Liang, ChemNanoMat **3(8),** 512-533 (2017).
3. B. Gökce, M. Filipescu, S. Barcikowski, Appl. Surf. Sci. **513,** 145762 (2020).
4. D. Zhang, B. Gökce, S. Barcikowski, Chem. Rev. **117,** 3990–4103 (2017).
5. R. Stoian, J.-P. Colombier, Nanophotonics **9(16),** 4665–4688 (2020).
6. D. Banerjee, M. Akkanboina, S. Ghosh, V.R. Soma, Materials (MDPI) **15,** 4155 (2022).
7. A. Mangababu, R.S.P. Goud, C. Byram, J. Rathod, D. Banerjee, V.R. Soma, S.V.S.N. Rao, Appl. Surf. Sci., **589,** 152802 (2022).
8. K.R. Kumar, D. Banerjee, A. Mangababu, R.S.P. Goud, V.R. Soma**,** S.V.S. Nageswara Rao, J. Phys. D: Appl. Phys., **55,** 405103 (2022).
9. T.K. Naqvi, A. Bajpai, S.S.B. Moram, M.M. Kulkarni, A.M. Siddiqui, S. Venugopal Rao, P.K. Dwivedi, J. Hazard. Mater., **407,** 124353 (2021).
10. M.S.S. Bharathi, S. Abdul Kalam, B. Chandu, S. Hamad, S. Venugopal Rao, Anal. Chim. Acta, **1101,** 157-168 (2020).
11. T.K. Naqvi, M.S.S. Bharati, A.K. Srivastava, M.M. Kulkarni, A.M. Siddiqui, S. Venugopal Rao, P.K. Dwivedi, ACS Omega, **4,** 17691−17701 (2019).
12. B. Chandu, M.S.S. Bharathi, S. Venugopal Rao, J. Raman Spectros., **50,** 1103-1113 (2019).
13. B. Chandu, M.S.S. Bharathi, S. Venugopal Rao, Analyst, **144,** 2327–2336 (2019).
14. S. Hamad, M.S.S. Bharathi, G.K. Podagatlapalli, Y. Balaji, M.A. Mohiddon, S.V.S. Nageswara Rao, A.P. Pathak, S. Venugopal Rao, ACS Omega, **3(12),** 18420-18432 (2018).
15. S. Hamad, G.K. Podagatlapalli, M.A. Mohiddon, S. Venugopal Rao, Appl. Phys. Lett. **104**, 263104 (2014).

Liquid crystal based large mode area rib waveguide

U S Tripathi[a], Rajat Chauhan[b] and Vipul Rastogi[b,c]
[a]*Instrument Research & Development Establishment*
Dehradun 248008, Uttarakhand, India. email: ust.irde@gov.in
[b]*Department of Physics, Indian Institute of Technology Roorkee*
Roorkee 247667, Uttarakhand, India
[c]*Center for Photonics and Quantum Communication Technology, Indian Institute of Technology Roorkee*
Roorkee 247667, Uttarakhand, India

Abstract

Abstract: *In this paper, we propose a novel approach for the realization of liquid crystal (LC) core based large mode area rib waveguide whose modal characteristics can be electrically shaped over a wide range of wavelengths for single-mode operation. This is formed by creating a slight low refractive index in the rib region of large cross-section rib waveguide.*
Keywords: Liquid crystal, Large mode area waveguide, rib waveguide.

Introduction

Large mode area (LMA) waveguides with single mode operation have always been a matter of interest for applications in compact integrated optical devices with higher power handling capacity without non-linear effects. Conventional waveguides offer single-mode operation only in small core size, hence have low optical damage threshold. In this regard, the efforts have been made to achieve single-mode LMA waveguides for applications in high power sustainable integrated optical devices. Low contrast waveguides, leaky cladding waveguide, graded-index waveguide, large-core multi trench channel waveguides and shallow rib waveguide have been reported to enlarge the effective core dimension for effective single mode operation. However, in all the above reported waveguides, mode area is not very large than the conventional waveguides. In this paper, we propose a novel approach for the design of LC core based single mode LMA rib waveguide. This is achieved by creating an electrically controlled low refractive region in the LC rib region.

The proposed LC core rib structure is shown in figure 1, which follows the condition of refractive index such that $n_{cl} \leq n_s < n_c < n_{sl}$. In-plane switching configuration is considered to control the orientation of LC molecules. Alignment layer is used for vertical anchoring of LC molecules.

Threshold voltage of proposed structure is given by Eq. (1), this equation shows that V_{th} is inversely proportional to the cell gap of LC cell. We have considered the two regions in LC rib waveguide structure for refractive index of LC for TM mode in presence of electric filed. First region is the rib region where the waveguide height is d while second region is the slab region where the waveguide height is $(d\text{-}h)$.

Threshold voltage in the rib region V_{th1} is given by

$$V_{th1} = \pi(l/d)\left(\frac{k}{\varepsilon_0 \Delta\epsilon}\right)^{1/2} \quad (1)$$

and the threshold voltage in the slab region V_{th2} is written as

$$V_{th2} = \pi(l/(d-h))\left(\frac{k}{\varepsilon_0 \Delta\epsilon}\right)^{1/2} \quad (2)$$

Eqs. (1) and (2) show that the threshold voltage is smaller in the rib region than that in the slab region. Hence, in case of vertical alignment of LC molecules for TM mode, the refractive index of LC in the rib region is less than that in the slab region due to rotation of LC molecule for $V > V_{th1}, V_{th2}$. Value of applied voltage has been taken such that the refractive index n_c in rib

region follows the condition $\Delta n=n_{sl} - n_c < 0.0011$. The rib height d, width W, etch depth h and refractive index n_c ($\Delta n=n_{sl} - n_c < 0.0011$) has been optimized for single-mode operation at 1550 nm wavelength.

The modal characteristic of the rib waveguide has been simulated by using the finite difference mode (FDM) method for $W = 30$ µm, $d = 10$ µm and $h = 4$ µm. The simulated modal profile is shown in figure 2. We have obtained the mode area $A_{eff} \sim 282$ µm^2 with MFD ~ 40.7 µm in horizontal and 9.94 µm in vertical direction, respectively.

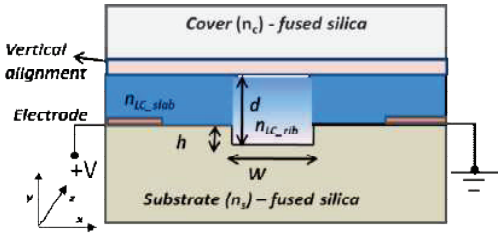

Figure 1: Schematic of LC core rib waveguide

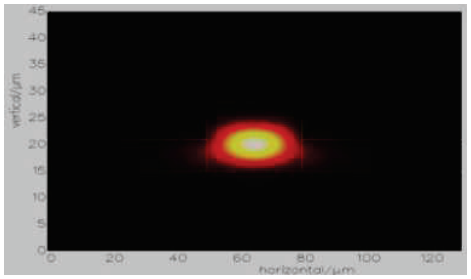

Figure 2: Mode profile of rib waveguide

We have shown the realization of large-mode-area single-mode waveguide in an electrically controlled LC rib waveguide structure. The proposed liquid-crystal-core rib waveguide has the possibility of cost-effective on-chip fabrication for tunable integrated optic devices.

References

[1] M. C. Oh, S. H. Cho, Y. O. Noh, H. J. Lee, J. J. Joo, and M. H. Lee, "Variable optical attenuator based on large-core single-mode polymer waveguide," IEEE Photon. Technol. Lett. 17, 678–680 (2005).

[2] A. Kumar, V. Rastogi, and K. S. Chiang, "Large-core single-mode channel waveguide based on geometrically shaped leaky cladding," Appl. Phys. B 90, 507–512 (2008).

[3] Than Singh Saini, Ajeet Kumar, and Ravindra Kumar Sinha, "Design and analysis of large-core multi trench channel waveguide for high-power application" Appl. Opt., 54, 6134–6139, (2015).

[4] S Pogossian, L Vescan and A Vonsovici, "The single mode condition for semiconductor rib waveguides with large cross-section", IEEE J. Lightwave Technol. 16, 1851-1853 (1998).

[5] U. S. Tripathi, and Vipul Rastogi, "Liquid Crystal Based Rib Waveguide," IEEE J. Lightwave Technol., Vol. 38, No. 15, 2020.

Plasmonic and all-dielectric metamaterials

Venu Gopal Achanta
CSIR-National Physical Laboratory, New Delhi 110012 India
(On lien from Tata Institute of Fundamental Research, Homi Bhabha Road, Mumbai 400005 India)
Author e-mail address:achanta@nplindia.org

Abstract: Metamaterials are designed materials with sub-wavelength constituents of either metal and dielectric or all-dielectrics. Due to their designer nature, they have unique properties that do not exist in naturally existing materials. Metamaterials are useful for modulating material properties like optical, electro-optical, and magneto-optical properties. They have important applications in light-matter interaction studies, photon emission, manipulation and detection, and sensors among others. In this talk, some of our recent results will be presented.
Keywords: Nanophotonics, perfect absorber, bound state in the continuum, reflectionless potential, all-dielectric metamaterials, metal-dielectric metamaterials

1. Introduction

Metamaterials could be realized with sub-wavelength featured metals and dielectrics. Thus, their response to electromagnetic radiation and their dispersion profiles can be studied from the effective medium theories. Metal and dielectric interfaces support surface plasmon polaritons and metal nanoparticle inclusions have localized plasmon resonances. Depending on the thickness of the dielectric, coupled plasmon modes contribute to the overall dispersion profile of the metamaterial. Metals have interband absorption in the visible wavelength regions, especially, gold. This leads to absorptive losses in plasmonic metamaterials. In spite of the losses, metamaterials based on metal-dielectric elements have numerous applications that are unique [1]. Some of the metamaterials demonstrated include periodic and aperiodic structures, perfect absorbers, and hyperbolic metamaterials, among others. Their applications are shown in modulating the optical, electro-optical, and magneto-optical properties, stealth applications, directional single photon emitters, etc. [2-4]. For different applications, one would need resonant structures with high-Q factors (eg. Sensors) or broadband-responsive materials (eg. Photovoltaics, light detectors).

Broadband response of metamaterials could be achieved in different ways. One way is to have random patterns which will be difficult to reproduce and also design for specific wavelength ranges. A second way is to have regular scattering elements arranged in quasi-periodic arrays or in periodic arrays but randomly distributed shapes. A periodic array with differently shaped elements has been demonstrated with the dimensions of different elements suitable for a specific wavelength region [5]. Plasmonic quasicrystals (PlQCs), air hole arrays conforming to 5-fold symmetry in the gold thin film have been demonstrated for a broadband plasmonic response. Linear and non-linear optical properties of PlQCs, plasmon dynamics in PlQCs, and plasmon-exciton coupling in these structures are interesting [6-9].

All-dielectric metamaterials with no metal constituents are useful for a lossless response. Such structures are recently being studied for the bound state in the continuum (BIC). BICs are of interest due to the possibility of achieving near-infinite high Q- factors and directional emission. In addition, the studies showed the vector nature of the BIC resonance and polarization-independent BICs [10]. These have an interesting application in the generation of single photons in orbital angular momentum states. Another interesting all-dielectric metamaterial is an optical reflectionless potential (ORP). This has been experimentally demonstrated a few years ago for broadband omnidirectional suppression of reflection [11]. Recently, the broadband negative group velocity dispersion property of ORPs and their application in efficiently coupling a 5fsec laser pulse to a medium to enhance the supercontinuum generation in the UV region [12].

In this talk, I will cover some of the challenges in realizing various metal-dielectric and all-dielectric metamaterials and demonstrate their applications.

2. References

[1] Venu Gopal Achanta, "Surface waves at metal-dielectric interfaces: Material Science perspective", Rev. Phys. **5**, 100041 (2020).

[2] A. Kala, F. A. Inam, S-A. Biehs, P. Vaity, Venu Gopal Achanta, “Hyperbolic metamaterial with quantum dots for enhanced emission and collection efficiencies”,Adv. Opt. Mater. 2000368 (2020).
[3] V. I. Belotelov, L. E. Kreilkamp, I. A. Akimov, A. N. Kalish, D. A. Bykov, S. Kasture, V. J. Yallapragada, Achanta Venu Gopal, A. M. Grishin, S. I. Khartsev, M. Nur-E-Alam, M. Vasiliev, L. L. Doskolovich, D. R. Yakovlev, K. Alameh, A. K. Zvezdin, and M. Bayer, “Plasmon-mediated magneto-optical transparency”, Nature Commun. 4:2128 (2013).
[4] Jitendra K. Pradhan, S. Anantha Ramakrishna, Bharathi Rajeswaran, Arun M. Umarji, Venu Gopal Achanta, Amit K. Agarwal, Amitava Ghosh, “High contrast switchability of VO2 based metamaterial absorbers with ITO ground plane”, Opt. Express 25, 9116 (2017).
[5] Arvind Nagarajan, Kumar Vivek, Manav Shah, Venu Gopal Achanta,and Giampiero Gerini, “A Broadband Plasmonic Metasurface Superabsorber at Optical Frequencies: Analytical Design Framework and Demonstration”, Adv. Opt. Mat. 1800253 (2018).
[6] Venu Gopal Achanta, “Plasmonic Quasicrystals”, Prog. Quant. Electron. 39, 1-23 (2015).
[7] Sachin Kasture, Ajith P R, V J Yallapragada, Raj Patil, Nikesh V. V., Gajendra Mulay, and Venu Gopal Achanta, “Plasmonic quasicrystals with broadband transmission enhancement”, Sci. Rep. 4, 5257 (2014).
[8] A. P. Ravishankar, V. J. Yallapragada, S. Kasture, A. Nagarajan, and V. G. Achanta, “Broadband linear and nonlinear optical response of plasmonic quasicrystals”, Opt. Comm. 366, 57-60 (2016).
[9] A. Kalish, R. S. Komarov, M. A. Kozhaev, V. G. Achanta, S. A. Dagesyan, A. N. Shaposhnikov, A. R. Prokopov, V. N. Berzhansky, A. K. Zvezdin, V. I. Belotelov, “Magnetoplasmonic quasicrystals: an approach for multiband magneto-optical response”, Optica 5, 617 (2018).
[10] P Vaity, H Gupta, A Kala, S Dutta Gupta, YS Kivshar, VR Tuz, VG Achanta, “Polarization-Independent Quasibound States in the Continuum”, Adv. Photon. Res., 2100144 (2022).
[11] L. V. Thekkekara, Achanta Venu Gopal, and S. Dutta Gupta, “Optical reflectionless potentials for broadband, omnidirectional antireflection”, Opt. Express 22, 17382 (2014).
[12] Pravin Vaity, Rishav Sagar, JA Dharmadhikari, AK Dharmadhikari, S Dutta Gupta, Venu Gopal Achanta, “Broadband negative group velocity dispersion in all-dielectric metamaterial and its role in supercontinuum generation”, Opt. Letts. 46 (2), 182-185 (2021).

High Dimensional Effects in Orbital Angular Momentum Entangled Photons

Yoko Miyamoto
Department of Engineering Science, The University of Electro-Communications
Institute for Advanced Science, The University of Electro-Communications
1-5-1 Chofugaoka, Chofu, Tokyo 182-8585 Japan
yoko.miyamoto@uec.ac.jp

Abstract: We have examined how experimental parameters can be tweaked to strengthen high dimensional effects of orbital angular momentum (OAM) entangled photons, and how the OAM spectrum may be quickly assessed with a tilted lens.
Keywords: optical orbital angular momentum, entanglement, astigmatism

1. Introduction

Photon pairs entangled in orbital angular momentum (OAM) are generally in states of high dimensional entanglement, that is, entanglement involving 3 or more bases for each photon. This is in contrast to polarization entanglement, where dimension is naturally limited to 2. While there are methods to evaluate this dimensionality [1], its effect can appear in unintended places. A typical example is the anharmonicity in the photon correlation signal obtained with the hologram shifting method [2,3]. This is due to the difficulty in designing superposition detections that accurately limit the number of bases involved [3,4], but it also means that experiments can be designed to enhance the high dimensional effects [5].

In designing such experiments a method to quickly evaluate the OAM spectrum of each photon can be useful. When the photons are not analyzed in proper pairs, each photon appears to be in an incoherent mixture of OAM states. By introducing astigmatism the OAM modes can be made to deform in a distinct manner [6,7], so that information may be gathered from their incoherent superpositions [8].

2. Anharmonicity in the Hologram Shifting Method

OAM entangled photon pairs can be analyzed by examining coincidence count rates when both photons are being detected in OAM superposition states. If the photons are entangled one sees high coincidence count rate for certain combinations of superposition states and a low coincidence count rate for certain combinations. When the detected superpositions involve just 2 bases for each photon, either through restrictions on the photon side or the detection side, the coincidence count rate shows a sinusoidal behavior when the relative phase between the two bases are scanned. However, if 3 or more bases are involved, the coincidence count rate can become anharmonic.

The hologram shifting method is based on a hologram that removes the rotating phase factor $\exp(\pm i\phi)$, where ϕ is the azimuthal angle around its center. This hologram converts an OAM ±1 beam to a Gaussian (OAM 0) beam when the hologram center is on the beams axis. The resulting Gaussian beam can be filtered through a single mode fiber and detected. When the hologram center is shifted from the beam axis, the hologram approximately converts a superposition of OAM bases 0 and ±1 to a Gaussian beam. However, this also introduces many excess modes to the detected states, resulting in an anharmonic behavior of the coincidence count rate with respect to the relative phase.

We have analyzed this behavior using the framework given in [3]. The anharmonic component is larger for the wider pump beam, owing to the larger OAM bandwidth for the generated photon pairs. Effective crystal length also affects this bandwidth. However, further analysis shows that for a given shift distance to beam width ratio there is an optimal pump beam width. Experiments are planned to compare this to the path interferometer method given in [4], where the detection scheme limits the number of bases involved for each photon to 2.

3. Orbital Angular Momentum Spectrum Analysis

Astigmatism can convert Laguerre-Gaussian modes and similar beams with well-defined azimuthal mode numbers into beams with Hermite-Gaussian-like intensity distributions. If the different modes are coherent with one another,

they interfere to create a new beam profile. However if the modes are mutually incoherent, the resulting profile is a simple sum of their intensities. Initial experiments performed with vector beams showed that this sum nature facilitates the OAM spectrum analysis. The vector beams are composed of two orthogonally polarized components with different OAM, and behave as incoherent mixtures when the polarization states are ignored.

More complex cases have been analyzed numerically. We have analyzed mixtures of up to 5 modes, and have shown that beams with similar complexity and different OAM components can be distinguished with the astigmatic method. In general interaction between rotation and astigmatism makes the beam structure more complex in one direction and less complex in another, which can be read out in the far field.

4. Summary

We have examined how experimental parameters can be tweaked to strengthen high dimensional effects, and how the OAM spectrum may be quickly assessed with a tilted lens. High dimensionality is an important feature of OAM entanglement and it is useful to know how they appear in and interact with the measurement system.

References

[1] R. Inoue, T. Yonehara, Y. Miyamoto, M. Koashi, and M. Kozuma, "Measuring qutrit-qutrit entanglement of orbital angular momentum states of an atomic ensemble and a photon," PRL **103**, 110503 (2009).

[2] B. Jack, A. M. Yao, J. Leach, J. Romero, S. Franke-Arnold, D. G. Ireland, S. M. Barnett, and M. J. Padgett, "Entanglement of arbitrary superpositions of modes within two-dimensional orbital angular momentum state spaces," PRA **81**, 043844 (2010).

[3] D. Kawase, Y. Miyamoto, M. Takeda, K. Sasaki, and S. Takeuchi, "Effect of high-dimensional entanglement of Laguerre-Gaussian modes in parametric downconversion," JOSA B **26**, 797-804 (2009).

[4] Y. Miyamoto, D. Kawase, M. Takeda, K. Sasaki, and S. Takeuchi, "Detection of superposition in the orbital angular momentum of photons without excess components and its application in the verification of non-classical correlation," J. Opt. **13**, 064027 (2011).

[5] Y. Miyamoto, S. Hayase, and Y. Sawa, "Parameter optimization for observation of high-dimensional effect in orbital angular momentum entanglement," in Optical Manipulation Conference, Vol. 10712 of Proceedings of SPIE (2018), 107120R.

[6] A. Wada, T. Ohtani, Y. Miyamoto, and M. Takeda, "Propagation analysis of Laguerre-Gaussian beam with astigmatism," JOSA A **22**, 2746-2755 (2005).

[7] P. Vaity, J. Banerji, and R. P. Singh, "Measuring the topological charge of an optical vortex by using a tilted convex lens," Phys. Lett. A **377**, 1154-1156 (2013).

[8] Y. Miyamoto and G. R. Salla, "Probing the orbital angular momentum spectrum of complex incoherent mixtures," in Light in Nature VII, Vol. 11099 of Proceedings of SPIE (2019), 1109905.

Adiabaticity in Optics: Analysis and Design of Photonic Lanterns

Anurag Sharma and Sugeet Sunder*
Optics and Photonics Center and Physics Department, Indian Institute of Technology Delhi, New Delhi - 110016
E-mail:asharma@iitd.ac.in
** Present address: Information Sciences Institute, University of Southern California, Arlington, VA (USA)*
E-mail: sugeet.research@gmail.com

Abstract: Adiabaticity is a concept used in quantum mechanics and translated to optics, it would imply that a waveguides changes so slowly that power in a mode remains in the same mode though shape of the waveguide or the mode may change drastically. This concept has been used to model propagation through photonic lanterns to transform field from *N*-single modes to *N* modes of a multimode waveguide. We discuss our work in this direction.
Keywords: Adiabatic transitions, photonic lanterns, propagation method, optical fibers

1. Introduction

In quantum mechanics, adiabaticity refer to a condition in which the Hamiltonian of a system changes so slowly that the eigenstate of the system remains the same locally and there is no transition to another state, though the initial and final Hamiltonians and the local eigenstates may be differ drastically[1]. In optics, this is applied to guided wave systems and would mean that the waveguide structure changes along its length so gradually that the local mode throughout remains the same, retaining all its power, though the shape of the waveguide and the field distribution of the mode may finally be very different from the ones at the initial position[2,3]. This concept has been used for designing tapers, directional couplers and beam shapers. One of the most interesting applications is the design of photonic lanterns. A photonic lantern is an optical fiber device, which is realized by adiabatic tapering of a bunch of *N*single mode fibers within a low index capillary to a final multimode structure which can support *N* modes. Photonic lanterns were developed for application in astrophotonics so that single mode like processingcould be used for light gathered through a multimode fiber [4]. Later these have found applications in space-division multiplexing and mode-division multiplexing [5,6]. Due to the requirement of very gradual variation such devices areof very large lengths and simulation studies on such three dimensionally varying long structures using conventional methods are computationally very intensive. Exploiting adiabaticity, we have developed an efficient propagation algorithm as well as a method for optimization of device lengths in adiabatically tapered photonic devices such as photonic lanterns. The algorithm and examples of its application will also be presented.

2. Propagation algorithm

A waveguide variation is said to be adiabatic, when the power launched into a certain mode remains unchangedin the same local mode, though the modalfield evolving through the varying waveguide may change its shape drastically. If we consider $|\varphi_m\rangle_0$ as an orthonormal set of super-modes at the beginning end, then the coupled input field $|\psi\rangle_0$ can be expressed mathematically as $|\psi\rangle_0 = \sum c_m|\varphi_m\rangle_0$, where c_m are the expansion coefficients which determine the fraction of power coupled into the m^{th} mode. Based on the adiabatic theorem, we now assert that the coefficients c_m remain constant as the modes evolvethrough the tapered structure. The field at any other point along the propagation direction would be [7]

$$|\psi\rangle_z = \sum c_m|\varphi_m\rangle_z \, e^{-\int_0^z i\beta_m(z)dz} \qquad (1)$$

where $\beta_m(z)$ are the propagation constants of the super-modes and these vary with *z*.The super modes at the point of interest need to be computed numerically and are denoted by $|\varphi_m\rangle_z$. The propagation constants can be described by smoothly varying non-linear functions obtained by fitting, and the integration in the exponential term in Eq.(1) can be performed to compute the accumulated phase for each mode. In this way we can obtain the propagated field. In order to implement this algorithm, we have to obtain modes at certain intervals which are mainly determined by the

variation of $\beta_m(z)$ which is usually very smooth and the z-intervals can be significantly larger than the ones required in usual propagation methods such as the FD methods. In a typical case, the interval could be several orders of magnitude larger, representing a staggering advantage in computational effort.

3. Optimizing Length

As mentioned above, photonic lanterns are very long devices, typically being 8 cm long for a 6-mode device and the length scales as square of the number of modes. Optimizing length is an important design exercise. The design has to ensure that coupling among various propagating modes is negligible or more specifically the coupling strength, suitably defined is kept below a certain small value. In a standard linear taper, the coupling is negligible at the beginning of the taper as the modes of the individual single mode fibers are well separated. The coupling gradually increases as the transverse size of the device reduces making mode field overlap. Finally at the multimode end, modes are orthogonal to each other and hence, there is no coupling among them. Thus, the taper can be made steep at the two ends and be kept gradual in the transition region. This would reduce the device length. A mathematically rigorous way for achieving this has been implemented using the Shortcuts-to-Adiabaticity protocol [8]. An example for optimizing a photonic lantern will be presented.

4. Summary

Using the concept of adiabaticity, we have developed an algorithm for wave propagation through unusually long devices such as photonic lanterns. Using this algorithm, we have also developed a procedure for optimizing the length of the device. Examples for propagation and for length optimization will be presented.

Acknowledgement: The work of Anurag Sharma was partially supported by a grant of JC Bose Fellowship by the SERB (Govt. of India).

[1] Max Born and Vladimir Fock,"Beweis des adiabatensatzes,"ZeitschriftfuerPhysik, 51(3-4):165-180(1928). doi: 10.1007/bf01343193.
[2] J. Love, "Spot size, adiabaticity and diffraction in tapered fibres," Electronics letters, vol. 23, no. 19, pp. 993–994 (1987).
[3] S. G. Johnson, P. Bienstman, M. Skorobogatiy, M. Ibanescu, E. Lidorikis, and J. Joannopoulos, "Adiabatic theorem and continuous coupled-mode theory for efficient taper transitions in photonic crystals," Phys. Rev. E 66, 066608(2002).
[4] S. G. Leon-Saval, T. Birks, J. Bland-Hawthorn, and M. Englund, "Multimode fiber devices with single-modeperformance," Optics letters, vol. 30, no. 19, pp. 2545–2547, 2005.
[5] N.K. Fontaine, R. Ryf, J. Bland-Hawthorn, and S.G. Leon-Saval, "Geometric requirements for photonic lanterns in space división multiplexing," Opt. Express 20, 27123–27132 (2012).
[6] T. Mizuno and Y. Miyamoto, "High-capacity dense space división multiplexing transmission," Opt. Fiber Technol. 35, 108–117 (2017).
[7] Sugeet Sunder and Anurag Sharma, "Adiabatic propagation algorithm for photonic lanterns," Optical Fiber Technology, vol. 57, p. 102219, 2020.
[8] Sugeet Sunder and Anurag Sharma, "Engineering Adiabaticity for efficient design of Photonic Lanterns,"IEEE Photonics Journal13, Art no. 2200113 (1-13) (2021).

Recent Results on High Power Fiber Laser Development Activity at RRCAT

B. N. Upadhyaya
Laser Electronics Division, Raja Ramanna Centre for Advanced Technology, Indore-452013, India
e-mail: bnand@rrcat.gov.in

Abstract: Monolithic fiber lasers are new generation of solid state lasers, which have now been well established for various industrial, medical and defence applications. In view of growing applications of fiber lasers, development of up to 1 kW of monolithic Yb-doped continuous wave (CW) fiber laser at 1080 nm, 50 W of Er-doped CW fiber laser at 1600 nm and more than 100 W of Tm-doped CW fiber laser at 1940 nm has been carried out at our Centre.
Keywords: Fiber laser, Yb-doped, Er-doped, Tm-doped fiber laser, Fiber Bragg grating.

1. Introduction

Fiber lasers offer several advantages over bulk solid-state lasers, which includes diffraction-limited beam quality, efficient heat dissipation due to large surface area to volume ratio, higher conversion efficiency, long life of maintenance free operation without any risk of misalignment due to in-built fiber Bragg grating mirrors. High power CW fiber lasers with multi-kW output power and nearly diffracted-limited beam quality have been reported by several researchers worldwide [1-3]. Generation of high power CW and pulsed output from fiber lasers is done by pumping with high power laser diodes and splicing the gain fiber with different fiber laser components together. Laser configurations used for generation of high output power from fiber lasers are: (a) oscillator configuration, (b) master oscillator power amplifier (MOPA) configuration, and (c) amplification of seed signal from laser diodes[4]. There are several technological challenges towards the development of high power fiber lasers. Selection of matched fiber laser components is critical for development of monolithic fiber laser systems. These components include selection of high power fiber coupled pump diode and its wavelength, pump combiner, doped fiber core and inner clad size, fiber Bragg grating mirrors, pump stripper and beam delivery fiber. Major challenges in development of high power fiber laser are minimization of splice loss, reliable recoating at different splice joints, removal of unabsorbed pump power, and efficient removal of heat load from thin polymer coated double-clad fibers. Several physical phenomena such as self-pulsing, fiber fuse effect, transverse mode instabilities, optical damage, photodarkening, and nonlinear effects such as stimulated Raman scattering (SRS), stimulated Brillouin scattering (SBS), self-phase modulation (SPM) and four wave mixing (FWM) pose limitations in the generation of high output power from fiber lasers [4].

2. Experimental Details and Results

At Raja Ramanna Centre for Advanced Technology (RRCAT), research and development on high power Yb-doped, Er-doped, Er:Yb co-doped and Tm-doped CW and pulsed fiber lasers is being pursued since past several years. We have performed development of up to 1 kW of single transverse mode monolithic Yb-doped CW fiber laser at 1080 nm. Figure 1(a) shows a schematic of in-house developed monolithic 1 kW single transverse mode Yb-doped CW fiber laser at 1080 nm and Fig. 1(b) variation of output power as a function of input pump power showing a slope efficiency of ~74.4%. An engineered version of 500 W of Yb-doped CW fiber laser based on indigenously developed fiber laser engine has also been developed for cutting, welding and laser additive manufacturing applications [5]. Further, Er-doped fiber (EDF) lasers emitting in the spectral range of 1500-1700 nm are attractive for many applications including free space communication, LIDAR, sensing, target illumination, etc. Generation of high output power from EDF laser is quite challenging due to higher quantum defect and lower allowable Er^{3+}-ion concentration in EDF to avoid clustering effects, which results in manufacturing of less efficient double-clad fibers. Out of the several approaches used to increase the laser efficiency near 1550 nm wavelength, the simplest and the most efficient approach is clad-pumping of EDFs with commercially available low cost 976 nm pump diodes. Development of 50 W of CW output power from an all-fiber Yb-free EDF laser using master oscillator power

amplifier (MOPA) configuration by pumping with 976 nm pump diodes with a slope efficiency of ~24% has also been carried out.

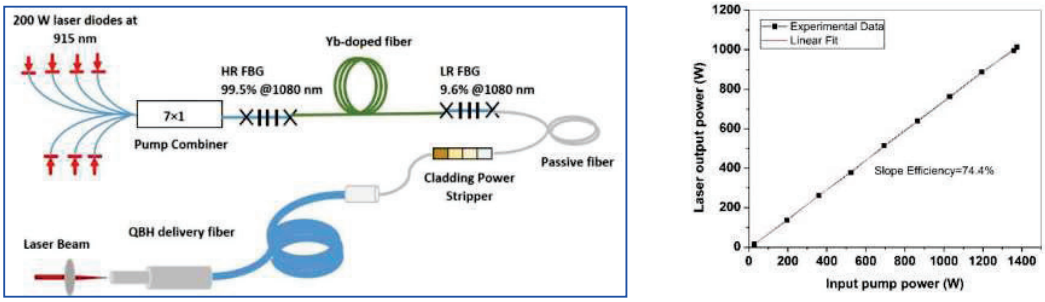

(a) *(b)*

Fig. 1: (a) Schematic of in-house developed monolithic 1 kW single transverse mode Yb-doped CW fiber laser, and (b) variation of laser output power vs input pump power.

Laser generation at 1940 nm wavelength is particularly important due to water absorption peak at 1940 nm and water being main constituent of biological tissues results in strong absorption and substantial heating of small areas of biological tissues. Thus, lasers at 1940 nm have become ideal source for surgical procedures since very precise cutting of biological tissues can be achieved and bleeding during the process of laser cutting is also suppressed by coagulation. Tm-doped fibers can be easily pumped using readily available 793 nm laser diodes, but due to higher quantum defect, theoretical limit for efficiency is ~41%. However, due to cross-relaxation process, two excited Tm-ions can be obtained for one pump photon and much higher efficiencies as compared to theoretical value can be achieved [6]. We have performed development of more than 100 W of CW output power at 1940 nm from an all-fiber oscillator configuration with an optical-to-optical conversion efficiency of ~45% [7]. Figure 2(a) shows a schematic of 100 W Tm-doped CW fiber laser at 1940 nm and Fig. 2(b) Tm-doped fiber laser spectrum at 100 W of CW output power showing a peak at 1940 nm. This talk will cover details of development of different high power CW fiber lasers at RRCAT along with challenges and limitations in these developments.

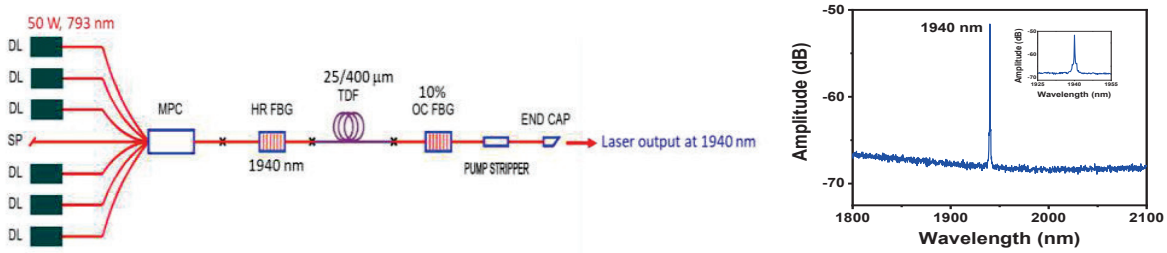

(a) *(b)*

Fig. 2: (a) Schematic of 100 W Tm-doped CW fiber laser at 1940 nm, and (b) Tm-doped fiber laser spectrum at 100 W of CW output power showing a peak at 1940 nm.

3. References

[1] URL: <http://www.ipgphotonics.com>.
[2] Wang et al., *Proc. of SPIE* 11260, Fiber Lasers XVII: Technology and systems, 1126022 (2020).
[3] Baolai Yang et al., "Monolithic fiber laser oscillator with record high power", Laser Phys. Lett., **15**, 075106 (2018).
[4] Michalis N. Zervas and Christophe A. Codemard, "High Power Fiber Lasers: A Review", IEEE J. of Selected Topics in Quantum. Electron., **20**, 0904123 (2014).
[5] Avdhesh Kumar et al., "Development of compact engineered 500 W of single transverse mode all-fiber Yb-doped CW fiber laser", Proceedings of *DAE-BRNS National Laser Symposium (NLS-29)*, 12-15 Feb. 2021, Indore, India.
[6] Peter F. Moulton et al., "Tm-Doped Fiber Lasers: Fundamentals and Power Scaling", IEEE J. of Selected Topics in Quantum. Electron., **15**, 85-92 (2009).
[7] Usha Chakravarty et al., "Generation of more than 100 W of CW output power from all-fiber Tm-doped fiber laser" Proceedings of DAE-BRNS National Laser Symposium NLS-29, Shri Vaishnav Vidyapeeth Vishwavidyalaya (SVVV), Indore, 12-15 Feb. 2021.

Tunable diode laser-based spectroscopy for robust in-field measurements of trace gases

Arup Lal Chakraborty
Electrical Engineering, Indian Institute of Technology Gandhinagar, Gandhinagar. 382055, Gujarat
arup@iitgn.ac.in

Abstract: High-sensitivity tunable diode laser absorption spectroscopy (TDLAS) is a powerful technique for trace gas sensing. Implementing the technique in outdoor conditions is especially challenging because there are multiple interfering gas species and the signals levels received by the photodetector fluctuates over time due to inevitable variations in the optical alignment. This talk will describe recent developments in wavelength modulation spectroscopy (WMS) techniques and present the performance of compact and portable measurement systems that have been deployed for in-field measurements in Gandhinagar and Ahmedabad.
Keywords: tunable diode laser spectroscopy, wavelength modulation spectroscopy, trace gas sensing, quantum cascade laser.

1. Introduction

The harmful environmental effects of the increasing levels of industrial emissions are widely acknowledged to be one of the most pressing issues. Unregulated emissions not only contribute to long-term global warming but also to serious impacts on the health of the citizens. This makes trace gas sensing is an important field of applied research. One of the main challenges in this kind of work is the need to develop compact portable systems that can perform high-sensitivity detection in the presence of environmental challenges such as the presence of multiple gases and opto-mechanical alignment issues. In-field measurement systems (as opposed to laboratory systems) must contend with the inevitable variations in the received light intensity, and operate without frequent recalibration. It is therefore necessary to adopt technology that can be used to develop systems that offer high sensitivity, high specificity, are robust, have low power requirements and are remotely controllable. Urban emissions are never localized. This implies that systems need to be compact and portable so that they can be deployed in transport networks in the cities and mounted on aerial systems to monitor the spatio-temporal distribution of emissions over large areas. This is where TDLAS using near-infrared and mid-infrared lasers has made its mark.

Tunable semiconductor lasers have been widely used for high-resolution near-infrared and mid-infrared absorption spectroscopy-based systems. In these TDLAS systems, the emission wavelength of a narrow linewidth distributed feedback (DFB) diode laser is tuned across an absorption line of a gas (several GHz) by applying a low-frequency ramp signal to the injection current. The spectral absorbance is recovered with a photodetector and the line shape is analyzed to extract the mole fraction, pressure and temperature of the gas. Wavelength modulation spectroscopy (WMS) [1] is a high-sensitivity version of TDLAS that uses an additional high-frequency sinusoidal modulation of the laser's injection current to bring out signals at various harmonics of the modulation frequency. The harmonic signal components are recovered for analysis using phase-sensitive lock-in detection. The various harmonics have specific forms and the gas parameters can be extracted from them as well. It is important to note that WMS measurements are not automatically calibration-free. Calibration-free WMS techniques have therefore received much attention [2]. This paper will present the results of in-field measurements using a recent calibration-free $R_{1f}/\Delta I_1$ WMS technique [3] that was used for reliable and accurate estimation of mole fraction over extended periods of time.

Two systems were deployed for in-field measurements of carbon dioxide and water vapour in Gandhinagar. The systems used a 10 mW mid-infrared 4320 nm quantum cascade laser (QCL) (Alpes Laser, HHL-513) and a 12 mW near infrared 1392 nm DFB (distributed feedback) laser (EP1392-5-DM-B01-FM. The carbon dioxide absorption line at 4319.30 nm with line strength 7.945 x 10^{-19} $cm^{-1}/(mol\ cm^2)$ and the absorption line at 1391.672 nm with line strength 5.984 x 10^{-22} $cm^{-1}/(mol\ cm^2)$ were selected to measure carbon dioxide and water vapour respectively. The dimension and weight of the system is 25.5 x 20.5 x 12.8 cm and 3.86 kg respectively. The water vapour system consumes 25.5 W. The detection limit for carbon dioxide (4.2 cm path length) was 0.18 ppm for an integration time of 42 s and for water vapour it was 32.6 ppm (10.3 cm path length) for an integration time of 68 s. A Raspberry Pi unit controlled data acquisition and signal processing, and also made the system remotely accessible over a wifi connection. The in-

field measurements could be monitored from the lab using this remote connection. The system was mounted on a vehicle and in-field measurements were carried out at fixed locations and with the vehicle moving in Gandhinagar. The time-resolution of the system iss 1.5 min and could be further improved. The systems showed excellent long-term stability and repeatability and are therefore suitable for long-term, time-resolved measurements in open and closed spaces.

2. References

[1] S. Schilt, L. Thevenaz, and P. Robert," Wavelength modulation spectroscopy: combined frequency and intensity laser modulation", *Applied Optics*, vol. *42*, no.33, pp. 6728-6738, 2003.

[2] Sun, X. Chao, R. Sur, C. S. Goldenstein, J. B. Jeffries and R. K. Hanson, "Analysis of calibration-free wavelength-scanned wavelength modulation spectroscopy for practical gas sensing using tunable diode lasers", *Measurement Science and Technology*, vol. *24*, no. 12, pp. 125203, 2013.

[4] A. Roy and A. L. Chakraborty, "Intensity modulation-normalized calibration-free 1f and 2f wavelength modulation spectroscopy", IEEE Sensors Journal, vol. 20, no. 21, pp. 12691-12701, 2020.

Robust phase retrieval with complexity guidance

Kedar Khare
Optics and Photonics Centre, Indian Institute of Technology Delhi, New Delhi 110016 INDIA
kedark@opc.iitd.ac.in

Abstract: We describe a novel methodology of complexity guided Fourier phase retrieval which is noise robust and provides a stagnation-free solution to the iterative phase retrieval problem. The complexity guidance concept will be introduced first followed by applications of such an algorithm for improving the solution for coherent X-ray scattering data.
Keywords: Fourier phase retrieval, coherent X-ray imaging, noise robust image reconstruction, inverse problems

1. Introduction

Iterative phase retrieval from noisy and incomplete Fourier intensity data continues to be a challenging inverse problem that is important for diverse applications in Optics, astronomy, and coherent scattering with X-rays. Phase retrieval algorithms typically use measured amplitude constraint in the Fourier domain and other constraints such as support, positivity or sparsity in the object domain. The application of constraints in the Fourier and object domains is however somewhat independent of each other. In this talk I will introduce a complexity parameter that is able to measure the expected degree of fluctuations in the phase retrieval solution directly from the raw Fourier intensity data. This complexity information can then be utilized as a guidance while applying the object domain constrains in a controlled manner to obtain solutions that are nearly free from the usual stagnation artifacts (e.g. the twin image or stripes). The complexity-guidance methodology is observed to be noise-robust in the sense that with increasing noise the phase retrieval solution degrades benignly. In particular, we examine the behavior of two popular algorithms - Hybrid Input Output (HIO) and Relaxed Averaged Alternating Reflections (RAAR) - from the complexity viewpoint and provide some new insights. The methodology will be illustrated with simulations as well as with Coherent X-ray diffraction data recorded at synchrotron facilities.

2. The complexity constraint and its application to Fourier phase retrieval problem

The Fourier phase retrieval problem aims to find, in general, a complex-valued solution $g(x,y)$ from its Fourier transform intensity $\left|G(f_x,f_y)\right|^2$ that is typically measured in the coherent scattering experiments. Typically a noisy version of this Fourier intensity is available in experiments with additional artifacts such as missing pixels due to detector defects as well as saturated (and hence unusable) pixels at the center of the Fourier space. Recovering a meaningful solution from such a data is a challenge. Solving this inverse problem is currently critical to scattering experiments at leading synchrotron facilities particularly for problems in structural biology. At present a number of age-old algorithms, e.g., Error Reduction, Hybrid Input-Output (HIO), Difference Map (DM) and Relaxed Averaged Alternating Reflections (RAAR) are being employed in these studies. Further with noisy data the currently used error criterion is not suitable as a low error solution may actually be overfitting the noise. The noisy incomplete data further implies that no solution that exactly satisfies the object domain and Fourier domain solution actually exists. This leads to a number of well-known stagnation artifacts and no uniform strategy to deal with this critical problem currently exists other than brute force averaging of hundreds of solutions. In recent works [1-3] we have introduced a novel complexity criterion that is possible to compute directly from the raw Fourier intensity data and can be used to control the application of image domain constraints during the phase retrieval iterations. The constraint provides a novel regularizing methodology to control the phase retrieval solution in a data dependent manner and is observed to provide artifact free solutions. The methodology additionally provides an independent criterion to evaluate the quality of phase retrieval solution particularly when the data is noisy.

3. References

[1] M. Butola, S. Rajora, K. Khare, "Phase retrieval with complexity guidance," JOSA A **36,** 202-211 (2019).
[2] M. Butola, S. Rajora, K. Khare, "Complexity guided Fourier phase retrieval from noisy data," JOSA A **38,** 488-497 (2021).
[3] M. Butola, S. Rajora, K. Khare, "Robust phase retrieval with complexity guidance for coherent X-ray imaging," (in review), arXiv preprint arXiv:2205.04094, (2022).

Magnetoplasmonic effects in physical mixtures of $CoFe_2O_4$-PVA water dispersion with Au and Ag nano-colloids

Lakshmi B[1] and Pramod Gopinath[1,2]*

[1]*International School of Photonics and* [2]*Inter University Centre for Nanomaterials and Devices, Cochin University of Science and Technology, Cochin-682022, India*
**pramod@cusat.ac.in*

Abstract: The talk highlights Magneto-optic Faraday rotation (MFR) studies carried out in cobalt ferrite ($CoFe_2O_4$) based liquid dispersions by incorporating plasmonic nanoparticles, using a custom-made measurement system operating at three different laser wavelengths of 405, 532 and 650 nm. For $CoFe_2O_4$-Ag based dispersions, an enhancement in rotation have been obtained for the wavelength of 650 nm due to the contribution from the trailing edge of plasmonic band of Ag to the region of lower absorption coefficients of $CoFe_2O_4$, whereas for $CoFe_2O_4$-Au based dispersions, an enhancement at 532 nm has been obtained corresponding to the plasmon resonance wavelength of Au.
Keywords: Magneto-optics, Faraday rotation, plasmonics, nanoparticles

1. Introduction

Magneto-optic Faraday rotation (MFR) studies form an interesting research domain, a subdivision of which may be considered as magnetoplasmonics where the effects due to the interaction of plasmonic nanoparticles (NP) with the magneto-optic properties of typical magnetic materials is investigated. In this report, MFR studies on $CoFe_2O_4$ nanoparticles have been studied with respect to inclusions of plasmonic components Au and Ag. Measurements have been performed with a custom-made MFR measurement system where three distinct laser sources are used, namely at 405, 532 and 650 nm. $CoFe_2O_4$ NP are dispersed in 2 wt% PVA (polyvinyl alcohol) - water medium and is mixed with separately synthesized Au and Ag nano-colloids in various concentration ratios. Measurements have been performed at different applied fields ranging from 200 to 5000 Oe.

2. Results and Discussions

Figure1 shows the MFR behavior of 2 different concentrations of $CoFe_2O_4$-PVA water dispersions along with the Langevin fits to the data. The MFR values show a saturation tendency consistent with the chain formation in them [1-3].

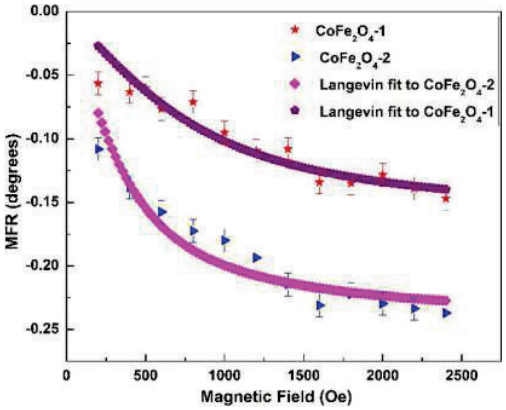

Fig.1. MFR of $CoFe_2O_4$-PVA water dispersions at two different concentrations.

Figure 2 represents the MFR behavior of a typical mixture of $CoFe_2O_4$ dispersion with Au nanocolloid at the laser wavelength of 532 nm. An enhancement in MFR values is clearly seen with increasing field [4]. It was noticed that the enhancement is obtained only for a typical concentration of $CoFe_2O_4$ and Au NP which could be confirming the plasmonic effect of Au that are at close proximity to $CoFe_2O_4$ NP. Fig.3. represents the MFR behavior of $CoFe_2O_4$ and $CoFe_2O_4$-Ag mixtures at the laser wavelength of 650 nm.

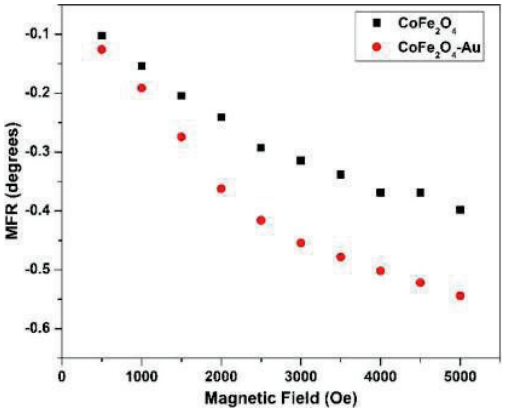

Fig.2. MFR of samples at 532 nm.

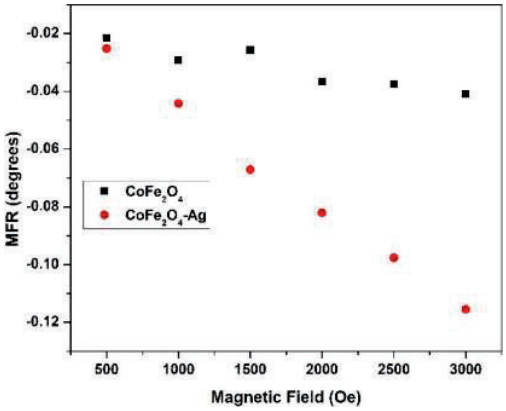

Fig.3. MFR of samples at 650 nm

The enhancement in MFR values in this case is seen at 650 nm, the wavelength at which the contribution to absorption coefficients by $CoFe_2O_4$ is substantially less. Though a plasmonic absorption for Ag is seen at around 425 nm, an enhancement in MFR is seen at the wavelength corresponding to the edge of plasmonic band of Ag. This is because at the plasmonic absorption wavelength of Ag, $CoFe_2O_4$ NP also show a substantial contribution due to the intense inter-band transitions typical of the ferrite material and hence an effect is not seen [5].

3. Conclusions

We have seen spectacular magnetoplasmonic effects in physical mixtures of $CoFe_2O_4$-PVA water medium with Au and Ag nano-colloids. Interesting effects are seen corresponding to plasmonic absorption bands at exactly the resonance wavelength as well as the plasmonic edge, corresponding to Au and Ag respectively. Intriguing dependence on concentration of the samples have also been seen with both the studied cases. The results point to excellent tunability of magnetoplasmonic effects in binary magnetoplasmonic mixtures.

4. References

[1] M. F. Rotacije, S. Küçükdermenci, D. Kutluay and Y. Avg Mater. Technol. **47,** 71-78 (2013).
[2] S. S. Nair, S. Rajesh, V. S. Abraham, M. R. Anantharaman and V. P. N. Nampoori J. Magn. Magn. Mater. **305,** 28–34 (2006).
[3] Narsetti H K, Wani W A, Navaratna N, Ramaswamy K, Patra D and Gopalan B 2021 J. Magn. Magn. Mater. **528** 167779
[4] M. Plasmonic, C. Shell, C.S. Levin, C. Hofmann, T.A. Ali, A.T. Kelly, E. Morosan, P. Nordlander, K.H. Whitmire and N.J. Halas, ACS Nano. 3 1379–1388 (2009).
[5] Y. Li, Q. Zhang, A. V. Nurmikko and S. Sun, Nano Lett. 5, 1689–1692 (2005).

Pilot-assisted light to see the invisible

Rakesh Kumar Singh
Laboratory of Information Photonics and Optical Metrology, Department of Physics, Indian Institute of Technology (Banaras Hindu University), Varanasi, 221005, Uttar Pradesh, India.
Author e-mail address: krakeshsingh.phy@iitbhu.ac.in

Abstract: Propagation of a laser beam through scatterer and atmospheric turbulence is a challenging task due to scrambling of the light and mode coupling. In spite of these challenges, propagation of laser beam through turbid media is desired in applications ranging from medicine to defense. Here, we discuss and demonstrate use of a pilot-assisted laser light to see the invisible and our recent contributions in this area.
Keywords: Laser, Information photonics, Speckle, Imaging

1. Introduction

Optical regime has attracted significant interests due to their ability to securely deliver information and in high data capacity. For instance, free space optical systems benefit from simultaneous recovering the two-dimension complex field, i.e., amplitude and phase information spatial distributions. However, presence of random scattering in the propagation channel severely affects the beam quality and scrambles it into space and time. For instance, atmospheric turbulence affects coherent detection and induces cross coupling with the undesired modes. Intermodal coupling and spatial scrambling of the light destroy the wavefront of the light and plays determinantal role in the information delivery and imaging. To enable imaging through the scattering, techniques such as adaptive optics, phase coupling, and transmission matrix have been proposed. These methods require measurement and compensation of the randomly scattered wavefront [1].
In this paper, we present and discuss an alternative method based on pilot assisted laser beam propagation for countering the path induced randomness for seeing the unseen. In contrast to the previously mentioned techniques, pilot-assisted approach is capable to cancel the randomness in a real time and also preserve the desired two-dimensional information. Specifically, we consider two orthogonal bases of this light where one of orthogonal polarization provides pilot-assistance to the other orthogonal polarization modes loaded with the information and both these beams collinearly launched through a scattering media.

2. Basic principle and implementation

Consider a transversely polarized coherent beam with orthogonal polarization bases x and y at z=0 plane as

$$E(\hat{r},t) = A_0(\hat{r},t)\, exp(\, i\psi(\hat{r},t))\hat{e}_x + A(t)\hat{e}_{y,} \qquad (1)$$

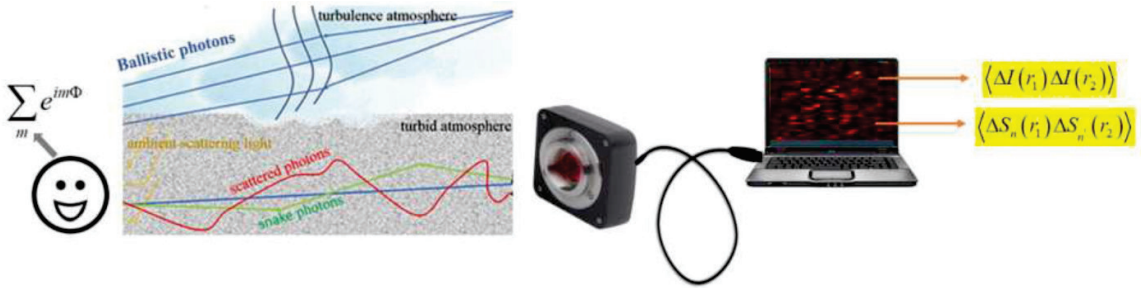

Fig. 1: Schematic representation of seeing target through scattering medium. Target is encoded into one of orthogonal polarization components and keeping another polarization component as a pilot beam

where $\hat{e}_x$ and $\hat{e}_y$ are horizontal and vertical polarization bases of the light respectively and $\hat{r}$ represents spatial position vector. $A_0(\hat{r},t)$, denotes the amplitude of the target beam and ψ is the phase structure. Other orthogonal basis with amplitude $A_0(t)$ works as a pilot beam. A monochromatic polarized light, represented by Eq. (1), propagates through

a random scattering medium and recorded at the observation plane as shown in Fig.1. Nature of the scattered photons through a random scattered is shown by a cartoon and given in detail in Ref [1]. Here, a target is considered to be composition of several orbital angular modes (OAM) represented by integer m.

3. Correlation methods to see the invisible

Recovery of the information of the target from the speckle pattern is possible by measuring the two-point intensity $\langle \Delta I(r_1) \Delta I(r_2) \rangle$ and polarization correlations $\langle \Delta S_n(r_1) \Delta S_n(r_2) \rangle$ as shown in right hand side of Fig.1. Here $I(r)$ represents intensity at a spatial position r and $S_n(r)$ represents the Stokes parameters (polarization) with $n = 0 - 3$. Phase recovery in the intensity correlation is possible by combining the Hanbury Brown-Twiss (HBT) approach with the holography [2-4]. In a recent development, we have also demonstrated use of a polarization correlation, i.e., the Stokes correlation to see through the diffuser [5-8]. Recovery of the information encoded into one of the orthogonal polarization components is demonstrated in Fig. 2 using the polarization correlation. Here, we consider a fractional vortex beam of topological charge l= -0.5 as a target. A complex field of the target is recovered from the speckle patterns and result is shown in Fig. 2. Recovered complex field can be projected on the spiral harmonics to determine composition of the OAM modes in the target, and using this method we found major contribution from integral charge m =[-1,0] in the experimentally reconstructed target. Some residual OAM modes may also arise in the decomposition process due to experimental limitations.

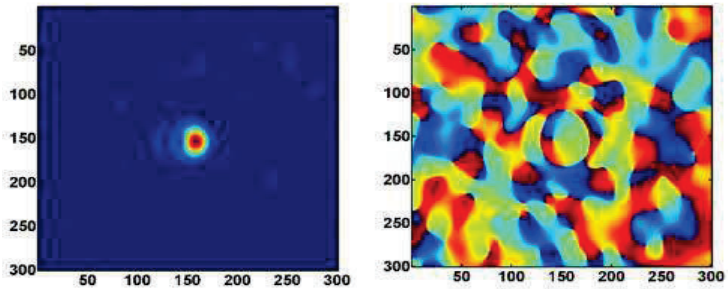

Fig. 2: Recovered complex field of vortex beam with l=-0.5 (a) amplitude (b) phase distribution

4. Conclusion

Idea of pilot-assisted light is discussed in the context of complex field imaging through random scattering medium. Such experimental strategy helps to counter and cancel the randomness of the propagation channels and helps to see through randomness and in the OAM decomposition.

5. Acknowledgment: Author acknowledges support from the SERB and CSIR in this work.

6. References

[1] R. Joseph, B. Hildon, A De, A. Vijayakumar, et.al.. "Roadmap on chaos-inspired imaging technologies (CI2-Tech)" Applied Physics B **128**, 1-26 (2022).
[2] R K Singh,Vinu R. V., A. M. Sharma, "Recovery of complex valued objects from two-point intensity correlation measurement," Applied Physics Letters, **104,** 111108(2014).
[3] L Chen, R. K. Singh, Z Chen, and J. Pu. "Phase shifting digital holography with the Hanbury Brown–Twiss approach." Optics Letters **45,** 212-215(2020).
[4] L. Chen., Z. Chen, R. K. Singh, Vinu, R. V., and J. Pu. "Increasing field of view and signal to noise ratio in the quantitative phase imaging with phase shifting holography based on the Hanbury Brown-Twiss approach" Optics and Lasers in Engineering **148,** 106771(2022).
[5] T. Sarkar, P. Reajmina , M. B. Maruthi, and R. K. Singh, Higher-order Stokes-parameter correlation to restore the twisted wave front propagating through a scattering medium. Phys. Rev A **104**, 013525/1-10 (2021).
[6] Tushar S.,Reajmina P., Maruthi M. B., and R. K. Singh,. "Measuring obscured OAM spectrum using Stokes fluctuations in a non-interferometric approach" Optics and Lasers in Engineering **155,** 107065/1-8(2022).
[7] T. Sarkar, P. Reajmina, M. B. Maruthi, and R. K. Singh, "Unscrambling OAM mode using digital phase-shifting in the Stokes fluctuations correlation" Opt. Lett. **46,** 5546-5549(2021).
[8] S. Tushar., V. Tiwari., S. Chandra., N. S. Bisht, and R. K. Singh "Holography with higher-order Stokes correlation." Phys. Rev. A **106**, 013508(2022).

Development of Fiber Optic Probes for Optical Coherence Tomography and applications in Clinical Diagnosis

Nijas Mohamed, Amandeep Singh, Renu John
Department of Biomedical Engineering, Indian Institute of Technology Hyderabad, Telangana-502285
renujohn@bme.iith.ac.in

Abstract: Optical coherence tomography (OCT) has emerged as a vital tool in bio-imaging. Being a non-invasive and real-time imaging technique, it offers many promising applications in the medical field. It has many intriguing medical uses as a non-invasive and real-time imaging method. The advancements in optical fiber technology have made it possible to design and develop miniature optical fiber probes for OCT. We report the design and fabrication of two different OCT probes for different clinical applications. A ball lens based optical fiber probe has been designed and developed for OCT assisted needle for guided epidural injections.
Keywords: Optical coherence tomography, Gastrointestinal cancer, Optical Biopsy, Epidural Injection.

1. Introduction

OCT, a low coherence interferometry imaging, is a derivative of the Michelson interferometer and was demonstrated for the first time in 1990 by Huang et al. at Massachusetts Institute of Technology (MIT) at Prof James Fujimoto's laboratory [1]. It was quickly discovered to be a valuable tool for retinal imaging. The field of OCT imaging is now much more diversified, with systems used in medical imaging, art restoration, non-destructive testing, thin-film analysis, and other applications. Real-time processing of OCT data is now possible thanks to advances in parallel computing and GPU architecture. Therefore, OCT rapidly evolves into a standard imaging modality [2], [3].

Low coherence sources like superluminescent diodes (SLD), wideband, or supercontinuum laser sources are used in OCT. This is since the lateral resolution and light bandwidth is inversely related [4]. A low spatial and temporal coherent source is ideal for a high-resolution OCT device and combining two or more SLDs with different emission bandwidths can result in extremely high bandwidths and ultra-high-resolution imaging. Broadband supercontinuum laser sources, on the other hand, are emerging as viable sources for OCT due to their massive emission bandwidths and better temporal coherence characteristic of laser sources. Figure 1 shows the schematic of an OCT system.

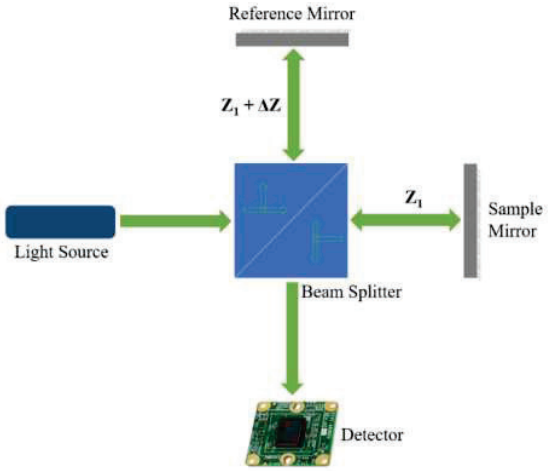

Figure 1. Basic OCT set up using Michelson Interferometer.

Time Domain OCT (TD-OCT) and Fourier Domain OCT (FD-OCT) are the primary imaging modalities used in OCT. The sample is placed in one of the arms of a balanced interferometer, and the interferogram is recorded with the help of a detector in TD-OCT. The refractive index variation in the depth profile of the sample is encoded in the interferogram, which will provide the variations in-depth, also known as an axial scan or A-Scan image. A lateral scan or B -scan can be formed by raster scanning several A-scans along with the sample. Because each B-scan is a cross-sectional image, a volumetric image of the sample can be obtained by stacking B-scans.

Although OCT has a wide range of applications, it used to be an expensive optical setup, which was one of its main drawbacks and is the crucial reason OCT is still not widely used in medical imaging. However, OCT systems' cost is decreasing as innovative technologies develop, such as fibre-based supercontinuum sources, fibre-based systems, integrated optical components, etc. Another issue is the OCT size of the OCT system. With the advent of small, fibre-based OCT devices [5], even this problem has an optimal solution. Developing integrated optical devices such as fibre mirrors, circulators, and other components is projected to reduce OCT system size further. OCT modules the size of a briefcase have previously been demonstrated, including a battery-operated source that makes the device portable [6].

For a long time, epidural injection has been one of several medical procedures utilised for anaesthesia and discomforts associated with radiculopathy. Epidural anaesthesia is one of the most common anaesthesia [7]. Epidural space is very small with a thickness, located between dura and ligamentum flavum. During insertion the needle must pass through several tissue layers: fat, supraspinous ligaments, interspinous ligaments, and ligamentum flavum carefully delineating the epidural space. Improper and insufficient visual feedback for guided insertion is a huge drawback as it can induce about 20% failure rate and can even cause irrevocable never damage [8]. Currently the success rate is entirely relied upon the expertise and experience of the surgeon [9]. The current practices for assessing the epidural space are LOR, or "Loss of resistance" due to saline and air and needle insertion under ultrasound guidance and fluoroscopy. However, confounding factors like myoglobin in muscle and carotenes in epidural fat may affect the quantification accuracy. Furthermore, whenever the needle's pressure changes the tissue's geometric layout, adjacent tissue layers can considerably impact spectroscopic results

We report the use of a Spectral Domain OCT system to detect malignancies in the Gastrointestinal tract. We demonstrate the application of OCT for the demarcation of tumours in stomach tissues and the identification of malignancies. Ex-vivo OCT imaging was performed on GI tract tissues surgically extracted from multiple cancer patients. These images provide pertinent information about the different stages of the disease progression in detail, and the diagnoses were later reaffirmed by comparing with results of gold standard histopathology. The advantages of OCT for cancer screening includes the direct, non-contact, label-free, subsurface imaging (2-3mm) at microscopic resolution, without any need to alter the tissue sample.

Further, we are demonstrating an epidural needle guided by OCT. The prime focus is to make a low-cost disposable probe for the system, which can help the clinicians accurately locate the epidural space. A ball lens probe is designed for the system as the entire probe can be made into 250 micrometres in thickness. The ball lens is fabricated to the fibre tip using a glass processing station. Later the probe is used to guide a needle through different tissue phantoms.

2. Experimental Methods

2.1 optical Biopsy

Tissue samples were surgically extracted from the patients who were diagnosed with a gastrointestinal tumour. The gastrectomy specimen was received with attached omentum altogether, measuring 30x22x4cms. One end of the stomach (distal resected end) was stapled, and the other end of the stomach was opened and everted. Then the specimen was immediately transferred into a normal saline medium to avoid tissue disintegration. The same was soon kept under SD-OCT for imaging. B scan imaging was performed over different positions of the specimen to identify different stages of the tumour. Then those positions were marked with India ink for easy identification during histopathology. The specimen is transferred into formaldehyde solution once the images are captured. After the imaging histopathology is performed and the results are compared with OCT images.

2.2 OCT Probe for Epidural Injection

A single-mode optical fibre with 125µm is used to fabricate the ball lens. The fibre tip is cleaned and cleaved first before loading it onto a glass processing station (Thorlabs GPX3400) for making the ball lens. The process is optimised over multiple iterations to obtain a ball lens diameter of 250 µm.

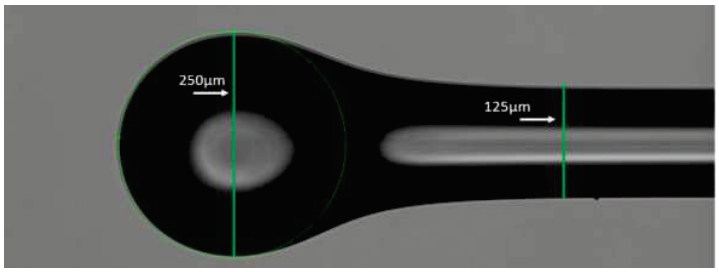

Figure 2. Microscopic image of the fabricated ball lens on a 125mm single-mode optical fibre.

The focal length of the ball lens is calculated to be around 200 micrometres from the centre of the prepared ball lens, and the same was confirmed later by the experiment.

A 21-gauge needle is used for the experiment, which falls in the usual range (18-22 gauge) for epidural injections. The ball lens is then attached to the needle with the help of an index matching optical adhesive (Norland, NOA-61) and fixed by UV curing. The UV curing time is so fixed that the bond formed is not very strong and will be easily removable. Here the biocompatibility of the glue does not matter much as we are working with tissue phantoms. A schematic of the ball lens and the needle probe is given below:

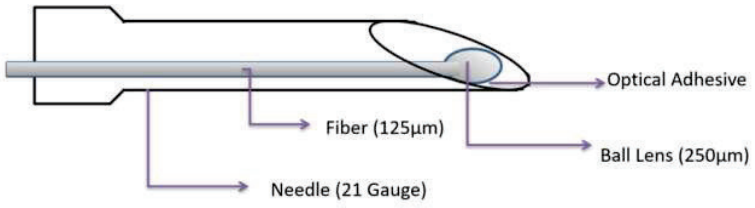

Figure 3. A schematic of the needle probe, with the ball lens attached to it using an optical adhesive.

3. Results

3.1 optical Biopsy

OCT images were captured and processed to analyze different stages of tumour in the obtained sample. These images were compared with the gold standard histopathology results to reassure the findings. Figure 4 shows the sample and the respective OCT and histopathology results.

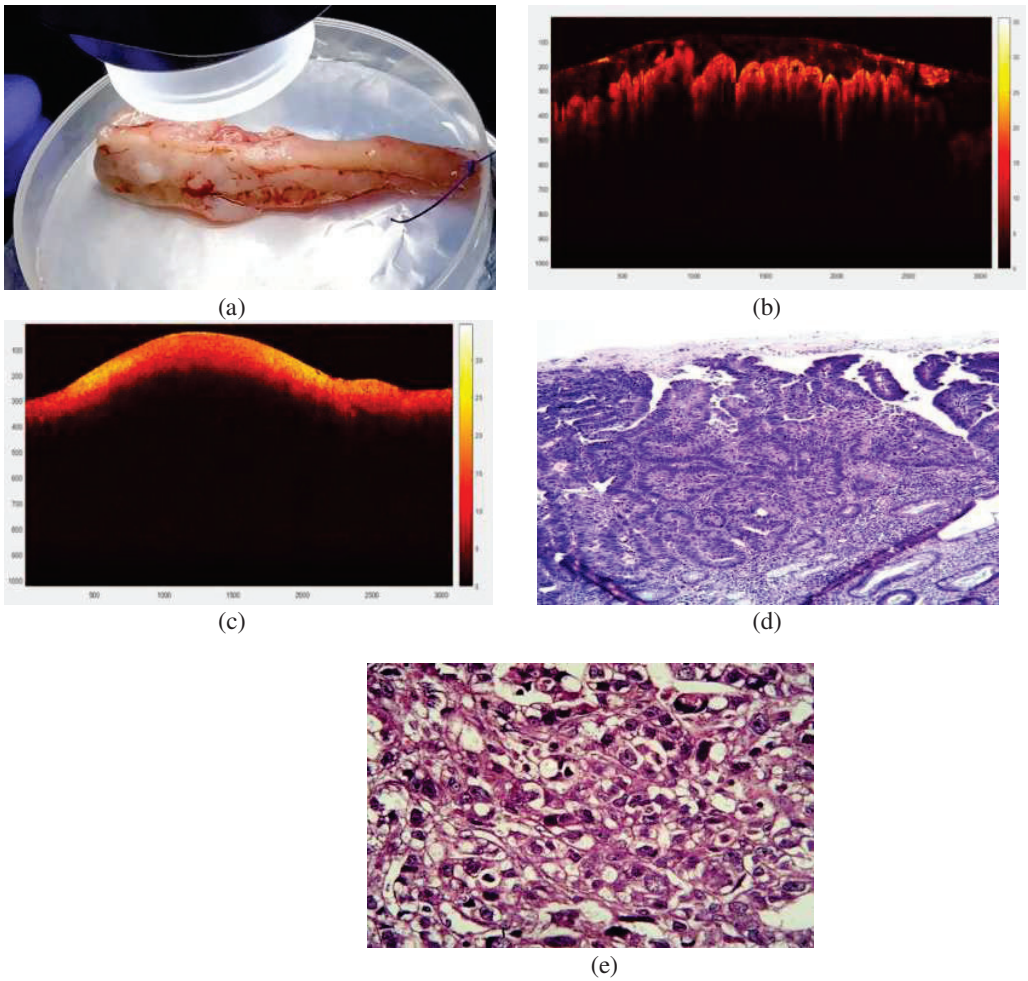

Figure 4. (a) GI sample (esophageal tumor tissue) cross-section where OCT is performed (b) OCT image of healthy GI tissue (c) OCT image of fully developed tumor (d) Histopathology result of normal tissue (e) Histopathology shows infiltrating tumor to the muscularis mucosa.

After comparing the OCT images and histopathology results, we were able to see that that the histopathology results confirm the OCT findings. The study reaffirms that the OCT can be used for detecting the gastrointestinal tumours in an early stage, as it able to clearly differentiate between normal, malignant, and marginally tumorous tissues. This can save a lot of time and effort as the OCT imaging can be done in-vivo compared to histopathology. Moreover, the system is real time and can be used for quick imaging.

3.2 OCT Probe for Epidural Injection

The OCT assisted needle probe was fabricated and inserted orthogonally into the tissue phantom. As the needle approaches the tissue phantom, the surface of the phantom layer becomes visible in the live time reconstruction in the LabVIEW programme. The probe was then slowly inserted further deep into the phantom through the layers, watching the display closely. The number of layers on the show was then matched with the number of layers prepared. A video record of the live reconstruction is given in video 1.

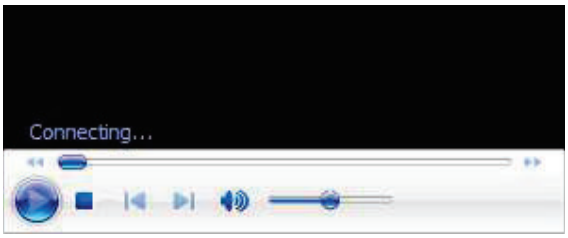

Video 1. The graphic user interfaces for the probe system for assisting the clinicians.

Here in the GUI, we can easily visualise the needle approaching the sample and the inner layers one by one. The number of layers identified with the system came out to be the same in multiple iterations throughout the trials, thus confirming the repeatability of the test. Also, we can see that the signal is entirely lost once the needle enters the dilute concentrate phantom, which mimics the epidural space while clearly showing the boundaries.

4. References

[1] J. G. Fujimoto, C. Pitris, S. A. Boppart, and M. E. Brezinski, "Optical coherence tomography: An emerging technology for biomedical imaging and optical biopsy," *Neoplasia*, vol. 2, no. 1–2. Nature Publishing Group, pp. 9–25, 2000. doi: 10.1038/sj.neo.7900071.

[2] X. Li, G. Shi, and Y. Zhang, "High-speed optical coherence tomography signal processing on GPU," *J. Phys. Conf. Ser.*, vol. 277, no. 1, pp. 0–7, 2011, doi: 10.1088/1742-6596/277/1/012019.

[3] Y. Jian, K. Wong, and M. V. Sarunic, "Graphics processing unit accelerated optical coherence tomography processing at megahertz axial scan rate and high resolution video rate volumetric rendering," *Journal of Biomedical Optics*, vol. 18, no. 02. p. 1, 2013. doi: 10.1117/1.jbo.18.2.026002.

[4] J. Fujimoto and E. Swanson, "The development, commercialization, and impact of optical coherence tomography," *Investig. Ophthalmol. Vis. Sci.*, vol. 57, no. 9, pp. OCT1–OCT13, 2016, doi: 10.1167/iovs.16-19963.

[5] J. M. Schmitt, A. Knuttel, M. Yadlowsky, and M. A. Eckhaus, "Optical-coherence tomography of a dense tissue: Statistics of attenuation and backscattering," *Phys. Med. Biol.*, vol. 39, no. 10, pp. 1705–1720, 1994, doi: 10.1088/0031-9155/39/10/013.

[6] S. Kim, M. Crose, W. Eldridge, B. Cox, W. Brown, and A. Wax, "Design and implementation of a low-cost, portable OCT system," *Biomed. Opt. Express*, vol. 9, no. 3, 2018, doi: 10.1364/BOE.9.001232.

[7] M. A. Huntoon and D. P. Martin, "Paralysis after transforaminal epidural injection and previous spinal surgery," *Reg. Anesth. Pain Med.*, vol. 29, no. 5, pp. 494–495, Sep. 2004, doi: 10.1016/j.rapm.2004.05.002.

[8] M. A. Huntoon and D. P. Martin, "Paralysis after transforaminal epidural injection and previous spinal surgery," *Reg. Anesth. Pain Med.*, vol. 29, no. 5, pp. 494–495, 2004, doi: 10.1016/j.rapm.2004.05.002.

[9] M. Y. Stitz and H. M. Sommer, "Accuracy of blind versus fluoroscopically guided caudal epidural injection," *Spine*, vol. 24, no. 13. pp. 1371–1376, 1999. doi: 10.1097/00007632-199907010-00016.

On the role of topology in parametric frequency-conversion experiments

Ritwick Das
School of Physical Sciences, National Institute of Science Education and Research, An OCC of Homi Bhabha National Institute, Bhubaneswar, Odisha-752050, India
Author e-mail address: ritwick.das@niser.ac.in

Abstract: We explore the topological aspects in a parametric frequency conversion experiments involving $\chi^{(2)}$ susceptibility. The experiment involve an ultrashort pulse frequency downconversion process in a 50-mm long periodically-poled $LiNbO_3$ crystal pumped by a 350 fs Yb-fiber laser delivering 350 fs pulses centered at 1030 nm wavelength. We show that the interaction dynamics could be explained using a pseudo-Hermitian Hamiltonian under no-pump depletion approximation. Subsequently, the phase-space trajectory allows us to obtain a geometric phase for the interaction which has verified through an experiment. In the experiment, we also show an experimental evidence of Stern-Gerlach-like splitting in mutual beams formed by a superposition of downconverted signal and idler modes.

Keywords: Nonlinear optics, frequency conversion, lithium niobate, topology

A large number of phenomenon observed in quantum mechanics such as Zeeman effect, Stern-Gerlach (SG) effect, spin-orbit coupling etc. are beyond the realm of optics owing to the absence of any interaction of photons or optical waves with the conventional magnetic field. However, a closer look at the coupled-wave formalism point towards a possible analogy with two-level atomic system which is coupled through an electromagnetic wave [1,2]. In fact, it could be shown that linear (coupled) as well as nonlinear optical systems could be modelled so as to have a dynamical evolution of modes resembling a system exhibiting *SU(2)* symmetry. Consequently, a few investigations show the the dynamical evolution of newly generated frequencies in an optical parametric process results in acquisition of a geometric phase which could modify the shape of such beams. The Hamiltonian for such systems is Herimitian and the newly generated frequency modes (signal and idler) constitute the eigenstates for the system. By projecting the state vectors on an equivalent Bloch sphere, it could be shown that the signal mode (or the idler mode) would necessarily acquire a geometric phase as the parametric interaction takes place along the propagation direction (z) [3]. In the present talk, I would discuss a theoretical formalism developed by us to show an equivalent SG-like splitting in a frequency down conversion process and experimentally validate the assertion by producing an suitable transverse gradient in an analogous magnetic field $\vec{B}$ through an in-homogeneous pump wavefront. The experimental results show SG-like splitting in an optical parametric generation (OPG) process using a long periodically-poled LN (PPLN) crystal and a pump laser exhibiting suitable spatial beam profile. The experimentally measured deviation angle for the mutual beam closely matches with the prediction from theoretical formalism using a Gaussian pump wavefront.

In the theoretical formalism, we express dynamical equations representing the frequency conversion process (in presence of a strong pump ω_p) *i.e.* $\omega_p = \omega_s + \omega_i$ as,

$$-j\frac{\partial}{\partial q_3}\begin{bmatrix}\tilde{A}_s^{\,*}\\ \tilde{A}_i\end{bmatrix} = \left(\frac{\tilde{p}_T^2}{2M} - \vec{\sigma}\,.\,\vec{B}\right)\begin{bmatrix}\tilde{A}_s^{\,*}\\ \tilde{A}_i\end{bmatrix} \quad \ldots \quad (1)$$

where $\tilde{A}_s$ and $\tilde{A}_i$ are complex field amplitudes of signal and idler beams respectively, $\tilde{p}_T^2 \equiv -\vec{\nabla}_T^2$, $M = \dfrac{\sigma_z + \xi 1}{m}$ is the equivalent *mass* operator, $\vec{\sigma} = [\sigma_x, \sigma_y, \sigma_z]$ is the triad representing Pauli's spin matrices and $q_3 = \sqrt{k_s k_i}z$ is the normalised coordinate along the propagation direction [1,4]. Here, $m = \dfrac{2\sqrt{k_s k_i}}{k_s + k_i}$, $\xi = \dfrac{k_s - k_i}{k_s + k_i}$ and 1 is an identity matrix. It is obvious to note that Eq. (1) resembles the Schrodinger's equation representing the dynamics of spin-1/2 particles in a magnetic field ($\vec{B}$) with 'time' (t) coordinate being replaced by 'space' (z) coordinate. In that case, Eq. (1) represents the spatial dynamics of *pseudo-spin* states $\omega_s$and ω_i in the z-basis i.e. the evolution of signal and idler waves along propagation direction in presence of an analogous magnetic field

$\vec{B} = j|\kappa|\left(-\sin\phi\hat{x} + \cos\phi\hat{y}\right) + \frac{\Delta\tilde{k}}{2}\hat{z}$ where $|\kappa| = \frac{4d_{eff}|A_p|}{n_s n_i}$ and $\Delta\tilde{k} = \frac{\Delta k}{\sqrt{k_s k_i}}$. It is worth noting that $\vec{B}$ exists in the parameter (or phase) space which is spanned by dynamical variables $\mathfrak{R}(\kappa)$, $\mathfrak{I}(\kappa)$ and Δk. Also, ϕ is the phase of pump envelope and could be geometrically interpreted as the azimuthal (in-plane) angle in the parameter space spanned by $\vec{B}$. Therefore, one-to-one analogy could be drawn between the evolution of signal and idler fields in a classical frequency conversion process (*i.e.* OPG) and that of a dynamical motion of particles with $\frac{\hbar}{2}$ intrinsic spin angular momentum in a conventional magnetic field (constituted by current). Further, the conversion efficiency of the OPG process could be ascertained by projecting the constituent *state*-vector on an equivalent *Bloch*-sphere [4]. In case the frequency down conversion process is quasi-phase-matched *i.e.* $\Delta k \approx 0$, the signal state (ω_s) and the idler state (ω_i) interacts only with the transverse components of analogous magnetic field ($\vec{B}$) field. In such a scenario, an optical equivalent of SG-effect could be conceptualized by introducing a spatial (x or y) variation in $\vec{B}_T$ (transverse component of analogous magnetic field) which would introduce a spatial separation between mutual beams ω_+ and ω_- which are symmetric and anti-symmetric superposition of beams (states) ω_s and ω_i. In analogy with quantum mechanical framework, the mutual beams ω_+ and ω_- are equivalent eigenstates of operators $\sigma_+ = \frac{\sigma_x + i\sigma_y}{\sqrt{2}}$ and $\sigma_- = \frac{\sigma_x - i\sigma_y}{\sqrt{2}}$ respectively and therefore, they exhibit interaction with $\vec{B}_T$.

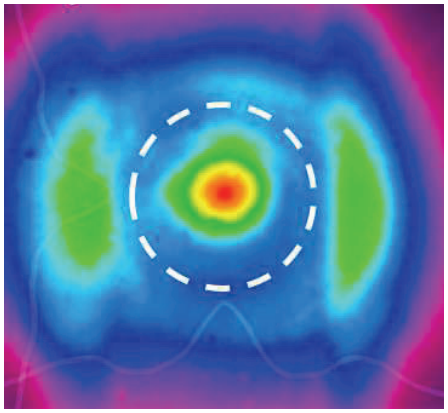

Fig. 1 Shows the spatial distribution of the mutual beam at pump power 2.71 W

The impact of such a spatial dependence of $\vec{B}_T(x, y)$ is investigated experimentally through a single-pass OPG set-up with a loosely focused ultrashort pulsed pump beam and *50-mm* long periodically-poled $LiNbO_3$ (PPLN) crystal. The recorded beam profile of the mutual beams ω_+ and ω_- at 2.1W pump power is shown in Fig. 1 which represents an asymmetric circular ring (marked using a dotted white-coloured curve) with two bright lobes (green colour-coded) along the *y*-axis. The asymmetry is essentially brought by a small shear in the pump beam along the *y*-axis which essentially brings in non-uniformity in the spatial dependence (along *y*) of pump beam. This asymmetrically distributed ring around the central bright lobe is formed by the mutual beam and essentially resembles a SG-like splitting where the radial (*x* or *y*) variation in the pump laser beam.

References:

[1] A. Karnieli and A. Arie, "All-optical stern-gerlach effect," Phys. Rev. Lett. 120, 053901 (2018).
[2] A. Karnieli, S. Tsesses, G. Bartal, and A. Arie, "Emulating spin transport with nonlinear optics, from high-order skyrmions to the topological hall effect," Nat. Commun. 12, 1092 (2021).
[3] A. Karnieli and A. Arie, "Frequency domain stern-gerlach effect for photonic qubits and qutrits," Optica, 5, 1297–1303 (2018).
[4] A. Mondal and R. Das, "Experimental evidence of pump-wavefront induced Stern-Gerlach-like splitting in optical parametric generators," Opt. Lett., 47, 3668-3671 (2022)

Single-molecule photonic techniques measure protein fluctuations in the critical ns-µs regime

Viky Vishvakarma, Arpan Dey, and Sudipta Maiti

Biophotonics Lab, Tata Institute of Fundamental Research, Homi Bhabha Road, Colaba, Mumbai 400005, INDIA

maiti@tifr.res.in

Abstract: Protein fluctuations in the ns-µs time scale report on drug binding, folding, and intermolecular interactions. Such information will be critical to address the challenges posed by toxic protein oligomers, which cause human diseases such as Alzheimer's and Type II diabetes. However, this time window is difficult to access with conventional techniques. We show that few-molecule Fluorescence Correlation Spectroscopy and single-molecule photobleaching methods, when combined, are capable of performing these measurements with extraordinary sensitivity. We have designed and constructed spectrometers and imaging instruments to perform these measurements. We show that they can unambiguously measure drug binding to toxic protein oligomers, and also measure their degree of insertion into lipid membranes. These new tools can provide new levers to tackle the intractable problems caused by the protein oligomers.

Keywords: Fluorescence correlation spectroscopy, single molecule photobleaching, protein fluctuations, biophotonics

[1] Arpan Dey, Vicky Vishvakarma, Anirban Das, Mamata Kallianpur, Simli Dey, Roshni Joseph and Sudipta Maiti, Single Molecule Measurements of the Accessibility of Molecular Surfaces, Front. Mol. Biosci., (2021) | https://doi.org/10.3389/fmolb.2021.745313

Bio-based waveguides as biosensors: a new paradigm in high-precision and flexible sensing of bio-analytes

Roshan Tiwari[1], Srayoshi Roy Chowdhury[2], Nirmalya Ghosh[1], Debasish Haldar[2], and **Ayan Banerjee**[1]

[1]Department of Physical Sciences, IISER Kolkata, Mohanpur, WB 741246
[2]Department of Chemical Sciences, IISER Kolkata, Mohanpur, WB 741246

Bioinspired waveguides have introduced a new paradigm in a large number of applications in photonics at small scales due to their microscopic size, and high flexibility and ease of fabrication [1]. A large body of work exists in deploying peptides as waveguides – with, typically, a laser source being used to excite transverse electromagnetic (TEM) modes inside such waveguides via total internal reflection (TIR), which occurs due to the higher refractive index of the peptides compared to their surroundings. Several applications – chiefly regarding transmission, distribution, modulation, and processing of optical signals in optical communication systems [1], optical switching [2], and also as light-focusing and light-polarizing elements below the diffraction limit [3] – all in a lab-on-a-chip environment. Understandably, such waveguides also hold substantial promise in the sensing of chemical and bio-analytes, from changes in their transmission due to the influence of the analytes.

In this talk, I will describe our recent efforts in this direction – where we fabricate waveguides around different bio-motifs, ranging from diphenyalanine (FF) derivatives to urea, and use them to detect very low concentrations (nM) of different bio-compatible dyes. Using FF, we develop waveguides in the shapes of rings, rods, and tubes of microscopic dimensions, and couple white light sources – both LED and a supercontinuum laser – into the structures. The broadband nature of the excitation source, coupled with the narrow linewidth of the waveguide TEM modes in rings and rods, lead to the observation of Fano resonances in the out-coupled light – which we deploy to determine μM concentrations of the Congo-red dye [4]. We then go on to employ FF tubes, developed from a slightly different derivative as compared to the first set of experiments (stepwise coupling of Boc-protected phenylalanine acid and phenylalanine methyl ester, followed by hydrolysis with 2N NaOH in methanol), and demonstrate that chromatic aberration – which is often considered a nuisance in precision optics – is actually a very useful tool to exploit in the coupling of white light into microscopic waveguides. The fact that a chromatically aberrated microscope objective lens spatially separates the constituent wavelengths of the white light (laser) source, allows us to couple in different wavelengths controllably into our waveguides, so that we obtain both higher Signal-to-noise and wavelength separation in the out-coupled spectra in the case of the aberrated lens in comparison to a corrected one [5]. We also demonstrate two different types of sensing mechanisms using different dyes – one (Congo Red), which absorbs at the wavelength emitted from the waveguides, and the other (Coumarin), which does not – but which we are able to detect by virtue of the refractive index contrast generated when the dye is introduced into the waveguides. However, the sensitivity is much higher for the dye which absorbs the waveguide emission wavelength (up to 10 nM), compared to a few mM for the dye which does not [4]. Finally, I shall describe our work in biosensing using tetragonal hollow waveguides developed out of Urea, where the closed ends of the waveguides allow the generation of longitudinal modes that have far higher quality factor (more than 2 orders of magnitude) compared to the transverse modes, when coupled once again with white light. Thus, we are able to achieve a very high dynamic range of close to 8 orders of magnitude for sensing the Congo Red dye (which absorbs the out-coupled light) with this strategy – using the damping of the longitudinal modes to detect low concentrations up to 1 nM – and that of the transverse modes to detect even 10 mM concentrations, for which the longitudinal modes disappear [6]. It is therefore clear that our work can lead to a new generation of waveguide-based biosensors that are high-sensitive yet flexible, increasing their scope of potential applications significantly.

References:

[1] Amir Handelman, Nadezda Lapshina, Boris Apter, and Gil Rosenman, Adv. Mater. 1705776 (2017).

[2] Amir Handelman, Igor Lapsker, Avi Jacob, and Alexander Laikhtman, Adv. Funct. Mater. 31, 2008183 (2020).
[3] Kilian Vogele et al., ACS Nano 10, 11377 (2016).
[4] Roshan Tiwari et al., J. Mater. Chem. C 8, 9663 (2020).
[5] Roshan Tiwari et al., J. Biophoton. e202200044 (2022).
[6] Roshan Tiwari et al., manuscript under preparation.

Towards robust quantum information processing with Femtosecond Spatiotemporal control

Debabrata Goswami
Department of Chemistry, Indian Institute of Technology Kanpur, Kanpur – 208016
dgoswami@iitk.ac.in

Abstract: Achieving controllable qubits that can be scaled is our quintessential goal. Instead of focusing on low-temperature qubits which need drastic environmental conditions, we focus on attaining experimental developments that work at room temperatures and can be scaled up. Towards this end, we have developed a methodology using ultrafast high repetition rate lasers to localize and isolate nanoscale objects in the liquid phase that does not require the low-temperature environments [1]. We have also demonstrated MHz femtosecond pulse shaping technology [2] that has the capability to simultaneously transfer information to optically immobilized nanoparticles for subsequent controlled operations. Thermal effects have played a significant role in such micro and nanoscale manipulation and control developments [3], and we have, in fact, additionally formulated a methodology to utilize this to our benefit by using thermal effects as additional control and measurement knobs [4]. A direct consequence of the proposed controlled qubit manipulations is that it enabled a simultaneous theoretical development to ascertain the level of success in qubit manipulations and interactions as demonstrated from our experimental results.
Keywords: Femtosecond pulse shaping; Pulsed optical tweezers; Femtosecond Thermal Lens

References

[1] D. Mondal, P. Mathur, and D. Goswami, "Precise control and measurement of solid– liquid interfacial temperature and viscosity using dual-beam femtosecond optical tweezers in the condensed phase", Phys. Chem. Chem. Phys. **18**(37), 25823-25830 (2016).
[2] S. Dinda, S. N. Bandyopadhyay, and D. Goswami, "Rapid Programmable Pulse Shaping of Femtosecond Pulses at MHz Repetition Rate", Optics Continuum **2**(4), 1386-1400 (2019).
[3] S. Singhal and D. Goswami, "Unraveling the molecular dependence of femtosecond laser-induced thermal lens spectroscopy in fluids", Analyst, **145**(3), 929-938 (2020).
[4] A. K. Rawat, S. Chakraborty, A. K. Mishra, and D. Goswami, "Unraveling Molecular Interactions in Binary Liquid Mixtures with Time-Resolved Thermal-Lens-Spectroscopy", Journal of Molecular Liquids, **336**, 116322 (2021).

A window into the brain: Advances in super-resolution microscopy

Juliet T. Gopinath[1,2] , Brendan Heffernan[2], Stephanie A. Meyer[3], Diego Restrepo[4], Mark E. Siemens[5], and Emily A. Gibson[3]

[1]Dept of Electrical, Computer and Energy Engineering University of Colorado Boulder, Boulder Colorado USA
[2]Department of Physics, University of Colorado Boulder 80309, USA
[3]Department of Bioengineering, University of Colorado Anschutz Medical Campus, Aurora, Colorado 80045, USA
[4]Department of Cell and Developmental Biology, University of Colorado Anschutz Medical Campus, Aurora, Colorado 80045, USA
[5]Department of Physics and Astronomy, University of Denver, Denver, Colorado 80210, USA
Juliet.gopinath@colorado.edu

Abstract: The brain is an incredibly complex organ; however, many structures cannot be seen with diffraction limited imaging. We focus on stimulated emission depletion microscopy (STED) as a promising super-resolution technique. We demonstrate fiber-coupled one and two-photon STED.

Keywords: super-resolution, microscopy, stimulated emission depletion microscopy, STED

The brain is an incredibly complex organ, with more than 86 billion neurons. Optogenetics has opened a window into the brain and provided an incredible tool for optical studies. However, many structures cannot be seen with diffraction limited imaging. For example, morphological changes in dendritic spines have been linked to memory formation, learning and Alzheimers. Study of sub-diffraction dynamics of neural nanostructures involved in learning and memory in a freely moving animal is a challenge.

There are very few methods that enable high resolution imaging with miniature microscopes suitable for freely moving animal recordings. One promising technique is stimulated emission depletion microscopy (STED) [1, 2] , which can provide an order of magnitude improvement in resolution compared with conventional diffraction-limited confocal microscopy. The technique is implemented using a fluorescence excitation laser beam (Gaussian) is overlapped with a donut-shaped depletion beam. The depletion beam wavelength is chosen to overlap with the tail of fluorescence emission and deplete the fluorescence, enabling a much smaller fluorescing spot than the illuminated area. Because no post-image computation is necessary, video rate speeds are accessible.

However, fiber coupled STED has remained elusive, due to challenges in propagating the Gaussian fluorescence excitation laser in combination with the donut-shaped depletion beam. Custom fiber with promising results has been demonstrated, but requires expensive manufacturing [3]. We present an innovative solution, which uses the higher order modes of polarization maintaining fiber to support the depletion beam, enabling bend-insensitive operation. We demonstrate one-photon STED with super-resolution imaging of HeLa cells [4] immunostained for tubulin (**Figure 1**) [5]. Additionally, by extending the technique to two-photon STED, imaging at greater depths possible, due to reduced scattering with longer wavelengths. Additionally, we demonstrate a two-photon (2P) fiber-coupled stimulated emission depletion microscope and show super-resolved images of mammalian cells [6].

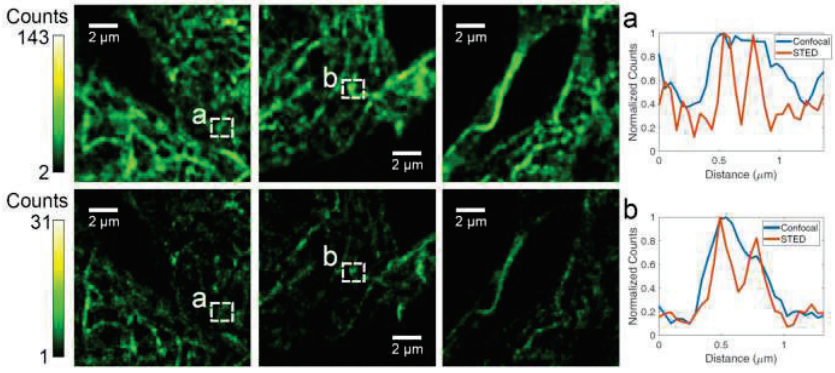

Figure 1. Images of HeLa cells immunostained for tubulin using Alexa 488. The images have been convolved with a Gaussian with a waist of 0.8 pixels (39 nm) for smoothing and the background was subtracted. The top row are confocal and the bottom row are STED images. Normalized linecuts of raw data are shown in (**a**) and (**b**), demonstrating at least a two-fold improvement in resolution. The pixel size is 48.8 nm and approximately 20 mW of STED and 6 μW of excitation power were used, measured before the objective. Figure reproduced from [5].

References

[1] S. W. Hell and J. Wichmann, "Breaking the diffraction resolution limit by stimulated emission: stimulated-emission-depletion fluorescence microscopy," *Opt Lett,* vol. 19, no. 11, pp. 780-2, Jun 1 1994.

[2] B. Harke, J. Keller, C. K. Ullal, V. Westphal, A. Schönle, and S. W. Hell, "Resolution scaling in STED microscopy," *Optics Express,* vol. 16, no. 6, pp. 4154-4162, 2008/03/17 2008.

[3] L. Yan, P. Kristensen, and S. Ramachandran, "Vortex fibers for STED microscopy," *APL Photonics,* vol. 4, p. 022903, 2019.

[4] Available: https://hela100.org/

[5] B. M. Heffernan, S. A. Meyer, D. Restrepo, M. E. Siemens, E. A. Gibson, and J. T. Gopinath, "A Fiber-Coupled Stimulated Emission Depletion Microscope for Bend-Insensitive Through-Fiber Imaging," *Scientific Reports,* vol. 9, no. 1, p. 11137, 2019/07/31 2019.

[6] B. M. Heffernan, P. S. Riley, O. D. Supekar, S. A. Meyer, D. Restrepo, M. E. Siemens, E. A. Gibson, and J. T. Gopinath, "Two-photon, fiber-coupled, super-resolution microscope for biological imaging," *APL Photonics,* vol. 7, no. 3, p. 036102, 2022/03/01 2022.

A Brief review of the In-house Developed Fiber Cantilever Deflection Device for Electric and Magnetic Field Sensing

Partha Roy Chaudhuri[1], Isha Sharma[1], Somarpita Prodhan[2]
[1]Department of Physics, Indian Institute of Technology Kharagpur-721302, India
[2]Optoelectronics Research Centre, University of Southampton, United Kingdom
[1]roycp@phy.iitkgp.ac.in

Abstract: Several designs and experimental demonstration of fiber-optic sensors based on fiber-cantilever beam-deflection are discussed here in a sequence of chronological developments in the context of devising magnetic and electric field sensing as well as determining the magnetization /polarization properties of the probe samples. A theoretical model to describe the behavior of the fiber cantilever deflection is worked out and implemented to predict and interpret the variety of experimental results obtained in our research.

Keywords: Fiber optic Sensor, Cantilever Beam Deflection, Weak Magnetic Field, Magnetization, Electric Field sensing

1. Introduction

Detection and precise measurement of magnetic and electric field have drawn huge research attention over the years devising various optical and nonoptical experiments [1–3]. In the recent years, research on fiber optic sensors has grown exponentially because of many unique advantages offered by fiber based interrogation systems. In this direction, we focused our research on designing all-optical fiber-cantilever beam deflection configuration and experimentally demonstrated sensing of low magnetic field. Using magnetic field sensing nanocomposite (optimized composition of cobalt doped nickel ferrite) coated on the tip of single-mode optical fiber forming the deflection cantilevers we performed a series of experiments and established the efficacy of our new experimental approach. As an initial step, a fiber double-slit type interferometer using coated fiber-cantilever-deflection is configured to sense the surrounding magnetic field by precisely measuring the changes in interference fringe-width. A theoretical platform is developed to model the cantilever deflection phenomenon that in turn yields the magnetization value of the probe sample. Next we refined the experiment by tracking the amplitude-modulation of propagating light through fiber-to-fiber coupling cantilever deflection-transmission arrangement which showed sensitivity increased further. In a chronological development modifying the setup to explore higher sensitivity, *etched* single-mode fiber cantilever, cascaded twin cantilever arrangement, Sagnac based path reversal gain-multiplication setup (figure 1) are tested which

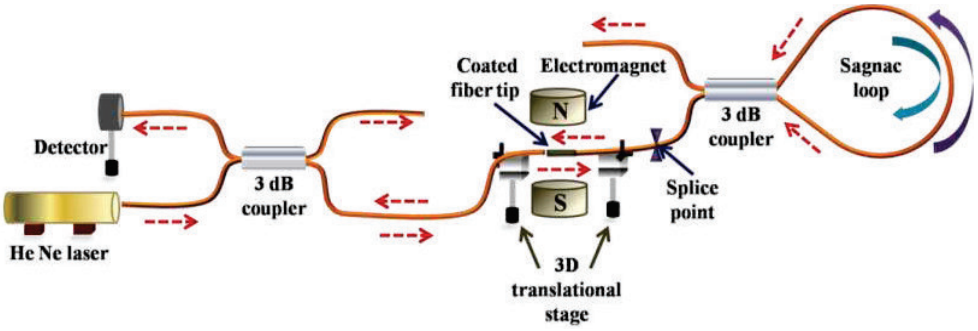

Fig.1: Schematic of Sagnac loop assisted cascaded cantilever configuration.

have shown marked improvements in performance in terms of low field sensing and determining the magnetization properties. In a series of experiments starting with single cantilever transmission, we could eventually achieve different cascaded systems to sense very low order (~ 1mT) magnetic field. Developed theoretical model fairly predicts experimentally obtained results. Magnetization of the probe sample is also obtained using the experimental results and theoretical formulation. We demonstrate that the scheme is capable of reproducing magnetization data obtained from high precision SQUID measurement [4].

Following the same principle, we then tested the same devise platform for sensing and measurement of electric field. Configuring cascaded twin fiber-deflection experiment we recorded a minimum detectable electric field as low as ~0.042 kV/cm reproducibly [5].

2. Cantilever Deflection Model

In a magnetic field (B), the Magnetization (M) of the sample is estimated from the torque (τ_m) relation,

$$\tau_m = V_m M \times B$$

where, the volume of magnetic particles is V_m. For fiber cantilever, torque experienced due to the external magnetic field is balanced by the internal bending moment (EI/R) of the fiber. E and I represent the elastic modulus and the geometrical moment of inertia of the cantilever substrate respectively. By equating these two, for the case of distributed torque acting over the coated length (b-a) of the fiber (figure 2(left)), deflection (Δ) can be expressed as

$$\Delta = \frac{V_m B M}{6EI}\ [2b(b+a) - a^2]$$

The estimated deflections of normal and etched fiber tips under different calibrated magnetic field are shown in figure 2(right). Using this defection we modeled the magnetic and electric field values and the corresponding magnetization/polarization data.

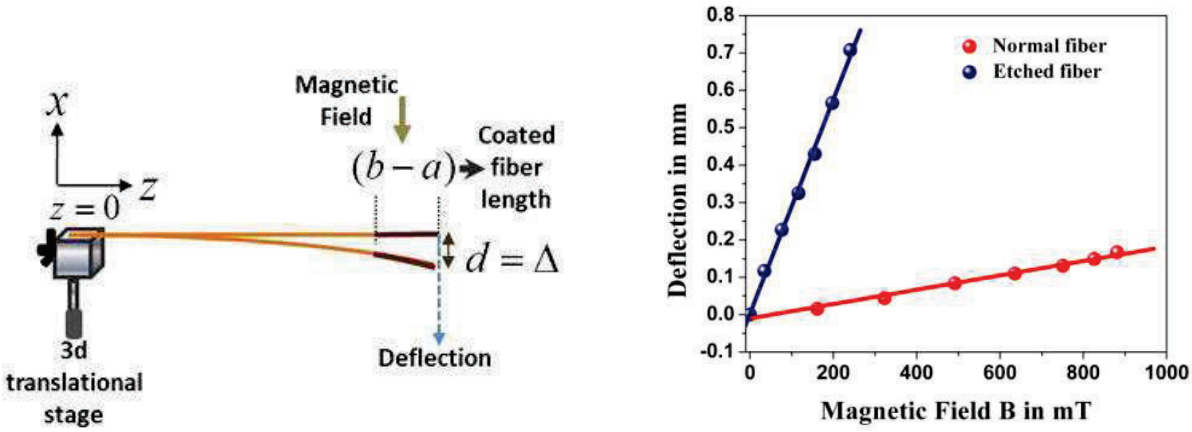

Fig. 2: Schematic of fiber bending due to surrounding field (left) and variation of deflection for normal and etched coated fiber cantilever configuration (right).

The details of the several experimental configurations and the results pertaining to these will be discussed. Notably, all the experimental arrangements are all-optical having minimum system complexities. The results reported are new and should be extremely useful towards understanding and designing fiber-based magnetic and electric field sensors for applications in industry, defense projects and mines.

3. References

[1] J.E. Lenz, "A review of magnetic sensors", Proc. IEEE **78 (6),** 973–989(1990).
[2] J. Lenz and A.S. Edelstein, "Magnetic sensors and their applications", IEEE Sens. **6,** 631–649(2006).
[3] L. Duvillaret, S. Rialland, J.-L. Coutaz, "Electro-optic sensors for electric field measurements", J. Optical Soc. Am. B **19**, 2704-2715(2002).
[4] S. Pradhan and P. Roy Chaudhuri, "Experimental demonstration of all-optical weak magnetic field detection using beam-deflection of single-mode fiber coated with cobalt-doped nickel ferrite nanoparticles", Appl. Optics **54(20)**, 6269-6276(2015).
[5] I. Sharma and P. Roy Chaudhuri, "A new approach to sensing low electric field using optical fibers' beam-deflection configuration with BiFe0.9Co0.1O3 nanoparticles as probe and determination of polarisation", Opt. Fib. Tech. **62**, 102472(2021).

Selected Paper

Design and computation of all-metal plasmonic perfect absorber for Vis-NIR radiation detection: design rule

Urvashi Solanki, P. Mandal
Department of Physics, Applied Science cluster, School of Engineering,
University of Petroleum and Energy Studies, Bidholi, Dehradun-248007
Author e-mail address: pmandal@ddn.upes.ac.in

Abstract: We report design and computation of all-metal based plasmonic perfect absorber in the visible to near-infrared (Vis-NIR) spectral regime. The perfect absorbing metasurface is designed using novel design concept which is validated through FDTD computations. The simplistic design rule is applied to achieve perfect absorption (100%) at pre-determined wavelengths for a variety of metasurfaces consisting of array of cylindrical grooves, cylinders, spheres, dimples. The present finding is useful in designing optical and optoelectronic devices.
Keywords: Perfect absorber, plasmonic metasurface, FDTD computation, design rule, Vis-NIR.

1. Introduction

Plasmonic perfect absorbers are optical metasurface devices that have attracted huge research interests owing to their wide spread applications in radiation detection, especially, solar cells, thermal imaging and detection, spectral funneling etc [1-3]. Plasmonic metamaterial absorbers use surface plasmons resonance at metal-dielectric interface to show characteristic absorption reaching to 100% in some specific cases which is greatly design specific fulfilling impedance matching condition [4-6]. Numerous literature reports are available on the single and multi band perfect absorption studied on a variety of plasmonic metasurfaces. However, complex structural configuration very often limits real fabrication and hence applications. Therefore, a simplistic design concept is essential that can reduce/eliminate complex processing steps and save manpower and capital cost. In the present report we have proposed a variety of plasmonic metasurfaces that are designed using simple design concept. Finite difference time domain (FDTD) computation is used to validate design concept and achieve 100% absorption at pre-determined wavelengths in the Vis-NIR regime.

2. Plasmonic Perfect Absorber Design and Computations

Plasmonic perfect absorbers are designed using a novel design concept. The absorber structures are shown in Fig.1. Metasurfaces consisting of square array of cylinders, cylindrical grooves, hemispheres and dimples. Ground gold layer thickness is 100 nm for cylinders and hemispheres, and 250 nm for cylindrical holes and dimples. Cylinder height (h) groove depth (h) are set as in Table-I. As per design concept, diameter D of cylinder (= 2P/3), grooves (= P/2), hemisphere (= P/2) and dimple (= P/2) is set (where, P = structural period). Height of cylinder is fixed at 50 nm and cylindrical groove depth is set to 200 nm for 500 nm period and 150 nm for all other periods. Gold (Au) metal is considered for all the studies to achieve surface plasmon resonance at the metal-air interface. Au has Lorentz-Drude dispersion with detailed parameters as can be found elsewhere [6]. Bottom supportive layer (made of SiO_2) is 200 nm thick and has constant refractive index of 1.5. A Gaussian modulated continuous wave is considered for FDTD study to realize broadband excitation. Absorption (A(λ)) spectrum is obtained from reflection (R(λ)) and transmission (T(λ)) spectra. Due to the thicker ground gold layer, transmission is expected to be negligible, hence, absorption can be obtained using the relation, A(λ) = 1-R(λ). Periodic boundary conditions are applied along X and

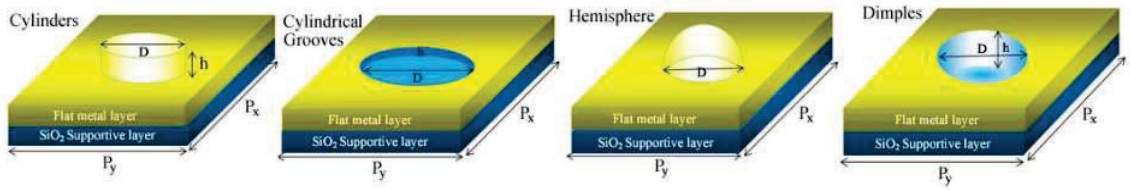

Fig. 1: Plasmonic perfect absorbers made of cylinders, cylindrical grooves, hemispheres and dimples (from left).

Y directions and anisotropic perfectly matched layer along Z direction. For converging results at least 5000 time steps are set. Mess size of less than 10 cells per λ along all the three directions (X, Y, and Z) are set [5, 6]. All the structures are computed for different periods (500 nm, 600 nm, 700 nm, 800 nm) as in Table-1.

3. Results and Discussions

Absorption spectra of the metasurfaces containing cylinders (a), cylindrical grooves (b), hemispheres (c) and dimples (d) are shown in the Fig.2. The metasurface containing square array of cylinders shows single resonant absorption at 646 nm, 700 nm, 775 nm and 890 nm for the structural period (P) of 500 nm, 600 nm, 700 nm and 800 nm, respectively. The strength of the absorption is ~100% except that for 800 nm period; for which it is ~95%. The full width at half maximum (FWHM) is broad (87 nm) for 500 nm period, although it is relatively narrow (<50 nm) for the metasurface having higher period. Similar absorption characteristics are observed for all the other structures as shown in the figure. Period and other structural parameters dependent resonant absorption and wavelength and are as summarized in Table-1. Surface plasmon resonance and fulfilling the impedance matching conditions result in 100% absorption in these structures.

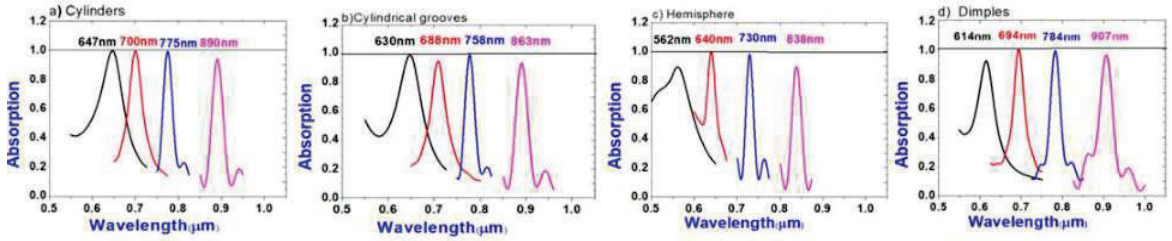

Fig. 2: Absorption spectra of plasmonic metasurface made of cylinders, cylindrical grooves, hemispheres and dimples (from left).

Table-1: Period (P), diameter (D), resonant wavelength (λ_{res}), absorption (%) of a) cylinders, b) cylindrical grooves, c) hemisphere, and d) dimples

P (nm)	D (nm)				Resonance wavelength, λ_{res}				Absorption (%)			
	a)	b)	c)	d)	a)	b)	c)	d)	a)	b)	c)	d)
500	333	250	250	250	647	630	562	614	***100***	***99.5***	90	92.4
600	400	300	300	300	700	688	640	694	***99.9***	95.2	***100***	***100***
700	467	350	350	350	775	758	730	784	***99.2***	***100***	***98.2***	***99.4***
800	533	400	400	400	890	863	838	907	94.4	94	90	96.7

4. Conclusions

In the current work, a simplistic design concept is applied to achieve Vis-NIR perfect absorbers. Absorbing metasurfaces are made of all-metal layers structured appropriately in the form of array of nanogrooves, nanocylinders, half sphere and dimples and placed on a flat gold ground plane. Our FDTD computations show that single band 100% absorption is achievable at tunable spectral frequency as per design rule. Furthermore, spectral resonant absorption can be tuned simply by changing array periods and other structural parameters set as per rule. The current work demonstrates appealing design concept for achieving all-metal layers based plasmonic perfect absorbers that have wide spread applications in plasmonic and photonic device integration.

5. References

[1] O. Shinpei, K. Masafumi, "Metal-insulator-metal-based plasmonic metamaterial absorbers at visible and infrared wavelengths: a review," Materials **11**, 458 (2018).

[2] G. Dayal, S. a. Ramakrishna, "Broadband infrared metamaterial absorber with visible transparency using ITO as ground plane," Optics express **22**, 15104-15110 (2014).

[3] G. Liu, X. Liu, J. Chen, Y. Li, L. Shi, G. Fu, Z. Liu, " Near-unity, full-spectrum, nanoscale solar absorbers and near-perfect blackbody emitters," Sol Energy Mater Sol Cells **190**, 20–9(2019).

[4] Z. Liu, G. Liu, G. Fu, X. Liu, Z. Huang, G. Gu, "All-metal meta-surfaces for narrowband light absorption and high performance sensing," J Phys D Appl. Phys **49**, 445104 (2016).

[5] U. Solanki, P. Mandal, "All-metal plasmonic metasurface at NIR wavelengths for optical absorption manipulation and refractive index sensing," Optik **260**, 169107 (2022). .

[6] P. Mandal, "Visible frequency plasmonic perfect absorber made of thin metal layer containing cylindrical grooves," Photonics and Nanostructures-Fundamentals and Application **31**, 66-70 (2018).

Delay Dependent Signal Pulse Manipulation by Control Airy Pulse

Deependra Singh Gaur, Ankit Purohit and Akhilesh Kumar Mishra
Department of Physics, Indian Institute of Technology Roorkee, Roorkee-247667 Uttarakhand India
akhilesh.mishra@ph.iitr.ac.in

Abstract: We numerically investigate the interaction between co-propagating signal and control pulses launched at different wavelengths in a medium. We show an efficiently controllable process that enables Airy control pulse to manipulate sech signal pulse in anomalous dispersion regime by tuning delay between signal and control pulses.
Keywords: Airy pulse, cross-phase modulation, accelerating soliton, nonlinearity, dispersion

1. Introduction

Nonlinear phenomena such as cross-phase modulation (XPM) play a vital role in light manipulation. Two pulses propagating at different wavelengths in a medium interact with each other via XPM and their temporal and spectral evolutions are thereby modify [1]. All optical switching, logic gates and pulse train generation in nonlinear medium are a few examples which manifest the significance of the XPM [2, 3]. In addition, soliton timing tuning by intermittent injection of cw light pulses also exploit XPM [4].

Recently, self-accelerating Airy pulses are introduced which are known for their better utility in supercontinuum generation, optical tweezing etc. [5,6]. The propagation dynamics of Airy pulses is explored in both linear and nonlinear domains [7,8]. Moreover, efficient manipulation of the signal pulse has been shown by using Airy pulse wherein XPM plays a significant role [9].

In this work, we use Airy pulse as control pulse for the manipulation of signal solitonic sech pulse. The signal pulse accelerates towards the leading edge for small negative time delay. This pulse acceleration can be manipulated by tuning the time delay between control and signal pulse.

2. Theoretical Model

We consider two pulses co-propagating in a nonlinear medium at different wavelengths. The propagation and interaction of such optical pulses can be modelled exploiting coupled nonlinear Schrödinger equation (CNLSE). The CNLSEs in their dimensionless form can be expressed as [1]

$$\frac{\partial A_1}{\partial z} = -\frac{i}{2} sgn(\beta_{21}) \frac{L_{NL1}}{L_{D1}} \frac{\partial^2 A_1}{\partial \tau^2} + i|A_1|^2 A_1 + 2i|A_2|A_1, \tag{1}$$

$$\frac{\partial A_2}{\partial z} = \delta \frac{L_{NL1}}{L_W} \frac{\partial A_2}{\partial \tau} - \frac{i}{2} sgn(\beta_{22}) \frac{L_{NL1}}{L_{D2}} \frac{\partial^2 A_2}{\partial \tau^2} + \frac{L_{NL1}}{L_{NL2}} [i|A_2|^2 A_2 + 2i|A_1|A_2], \tag{2}$$

where A_1 and A_2 denote the dimensionless pulse envelopes and T_0 represents the pulse width . $L_{D1} = T_0^2/|\beta_{21}|$ and $L_{D2} = T_0^2/|\beta_{22}|$ are the dispersion lengths corresponding to signal and control pulses respectively. Herein, β_{21} and β_{22} are the respective group-velocity dispersion (GVD) coefficients for signal and control pulses. $L_{NL1} = 1/\gamma_1 P_0$ and $L_{NL2} = 1/\gamma_2 P_0$ are the corresponding nonlinear lengths, wherein $\gamma_1$and γ_2 are respective nonlinear coefficients. The absolute difference between two frequencies is assumed to be small, $|\omega_1 - \omega_2| \ll \omega_1, \omega_2$, that leads to equal nonlinear coefficients i.e.$\gamma_1 = \gamma_2$. The walk-off length is represented as $L_W = T_0/|v_{g1}^{-1} - v_{g2}^{-1}|$, where $v_{g1}$and v_{g2} are the group velocities of the signal and control pulses, respectively. And, sgn and δ denotes the sign of GVD and sign of the difference in group velocities respectively. The functional forms of the signal and control pulse envelopes are assumed to be expressed, respectively, by

$$A_1 = \text{sech}\,(\tau - \tau_0) \tag{3}$$

$$A_2 = Ai(\tau)\exp\,(a\tau) \tag{4}$$

where a is truncation factor and the parameter τ_0 is the time delay of the signal solitonic pulse with respect to the control Airy pulse.

3. Numerical Results

In our simulation, we consider the same nonlinear lengths for both pulses and therefore $L_{NL1} = L_{NL2}$, while $L_{NL1}/L_{D1} = 1$. Moreover $\delta L_{NL1}/L_w = -1$ i.e. the group velocity of the control pulse is smaller than the signal pulse. The time delay $\tau_0 = -1$. The value of the truncation factor a is taken to be 0.1. The control Airy pulse creates a potential which is large for its main lobe. Therefore, the sign and numerical value of the time delay play a crucial role. If the signal pulse is in the vicinity of the Airy pulse main lobe, it sees strongest potential and the resultant acceleration will be maximum as shown in fig. 1 . On the other hand, the effect of potential is reduced for the large value of time delay. Therefore, signal pulse radiates dispersive waves as shown in fig. 1 (b).The temporal position of the signal solitonic sech pulse is also altered by delay between the two pulses. Insets in fig.1 shows the relative positions of the two pulses at the input for the two values of the input delay.

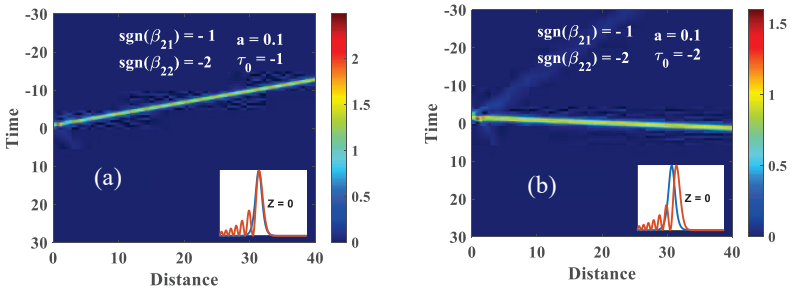

Fig. 1 Temporal evolution of the signal soliton in anomalous dispersion regime for delay (a) $\tau_0 = -1$ and (b) $\tau_0 = -2$. The input positions of the two pulses for the two delay values are shown in the insets.

4. Conclusion

In summary, we show that the dynamics of signal solitonic pulse can be manipulated by using the control Airy pulse and the soliton acceleration depends on the time delay between the pulses.

5. References

[1] G. P. Agrawal, P. L. Baldeck and R. R. Alfano, "Temporal and spectral effects of cross-phase modulation on copropagating ultrashort pulses in optical fibers" Phys. Rev. A **40**, 5063-5071 (1989).
[2] J. E. Sharping, M. Fiorentino, P. Kumar and R. S. Windeler, " All-optical switching based on cross-phase modulation in microstructure fiber" IEEE Photonics Technol. Lett. **14**, 77 (2002)
[3] A. Demircan and Sh. Amiranashvili, "Controlling light by light with an optical event horizon" Phys. Rev. Lett. **106**, 163901 (2011)
[4] Q-Han Park and H. J. Shin, "Parametric control of soliton light traffic by cw traffic light" Phys. Rev. Lett. **82**, 4432-4435 (1999)
[5] C. Ament, P. Polynkin and J. V. Moloney, "Supercontinuum generation with femtosecond self-healing Airy pulses" Phys. Rev. Lett. **107**, 243901 (2011).
[6] J. Baumgartl, M. Mazilu and K. Dholakia, "Optically mediated particle clearing using Airy wavepackets" Nat. Photonics **2**, 675-678 (2008)
[7] D. S. Gaur, A. Purohit and A. K. Mishra, "Soliton shedding from Airy pulses in a highly dispersive and nonlinear medium" JOSA B **38** 3729-3736 (2021)
[8] A. Purohit, D. S. Gaur and A. K. Mishra, "Dynamics of a chirped Airy pulses in a dispersive medium with higher-order nonlinearity" JOSA B 38 3608-3615 (2021)
[9] M. Goutsoulas, V. Paltoglou and N. K. Efremidis, "Cross-phase modulation mediated pulse control with Airy pulses in optical fibers" J. Opt. **19** 115505 (2017)

Photonic crystal based ultracompact All-optical OR gate

Jeevan Jot Singh
Ph.D. Student, Department of Electronics and Communication Engineering, Punjab Engineering College (Deemed to be University), Chandigarh, India
jeevanjotsingh.phdece@pec.edu.in
Dr. Divya Dhawan
Associate Professor, Department of Electronics and Communication Engineering, Punjab Engineering College (Deemed to be University), Chandigarh, India
divyadhawan@pec.ac.in
Dr. Neena Gupta
Professor, Department of Electronics and Communication Engineering, Punjab Engineering College (Deemed to be University), Chandigarh, India
neenagupta@pec.ac.in

Abstract: This paper proposes designing and implementing an All-Optical OR gate based on 2-D photonic crystal technology for the future promising optical computing technology. The proposed device operates on the interference principle and exhibits a unique combination of line defects and additional holes r1 and r2. It is arranged in a hexagonal lattice structure of air holes in the Si background. The logic gate is simulated using the Finite Difference Time Domain (FDTD) and Plane Wave expansion (PWE) tool. The contrast ratio (CR) achieved for the proposed OR gate is 21.17 dB. Moreover, it offers a response time of 0.193 ps and a bit rate of 5.18 Tb/s.
Keywords: Photonic crystal, line defect, point defect, FDTD, PWE, interference effect, OR gate

1. Introduction

As technology progresses, there is a growing need for optical computers due to their numerous advantages, such as being as fast as light, having no fan in fan out problem, and dissipating less heat than conventional electronic computers[1]. In recent years, essential components required for optical computing, such as linear waveguides, waveguide bends,spliters[2], and all-optical logic gates[1], have gained interest due to their applications in ultrafast information processing [1,3]and their ability to perform various logical operations in optical computing systems[4]. All-optical logic gates based on the interference phenomenon in the photonic crystals are the initial step toward realizing complex digital capabilities in an optical computer. These devices are compact and give fast processing speed compared to conventional devices on semiconductor platforms. On the other hand, earlier proposed techniques like the semiconductor optical amplifier (SOA)[5] and the nonlinear waveguides[6] suffer from disadvantages like the requirement of high input power, posing manufacturing issues, slow recovery time, polarization sensitivity, and the system's complexity. The most common phenomenon used in designing all-optical logic gates is 2D photonic crystals based on the interference effect because it has certain advantages like simpler design, requires no phase shifters, high contrast ratio (CR), and high bit rate (BR)[1].

In this paper, an All-optical OR gate is designed using the photonic crystal technology. The interference method is used to obtain the desired output, in which the input signals interact based on the phase shift applied to the input. For constructive interference, the phase difference between the input signals must be $2k\pi$ [where k=0,1,2,...] and a signal with a strong output is seen. In contrast, the destructive interference phase difference must be $(2k+1)\,\pi$ [where k=0,1,2,...] to generate a signal with low output intensity[1].

2. Results

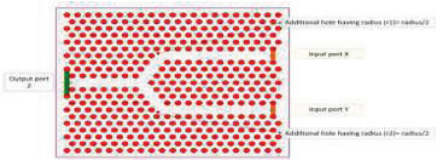

Fig. 1: Design of the proposed All-optical OR gate

Table 1: Variation of additional holes r1 and r2 and their effect on transmittance

Variation of the radius of additional holes r1 and r2		Transmittance at Output port Z
In terms of the radius of holes (r)	Values in decimal (μm)	
r/1	0.13	0.84 P_o
r/2	0.06	0.87 P_o
r/3	0.04	0.83 P_o
r/4	0.03	0.82 P_o

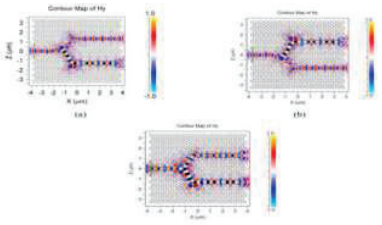

Fig. 2: The distribution of the electric field in the proposed OR gate for (a) X=0, Y=1; (b) X=1, Y=0 and (c) X=1, Y=1

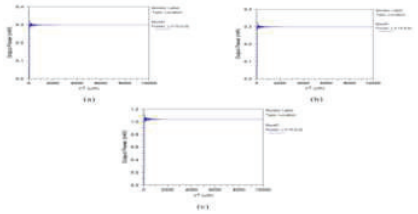

Fig. 3: Time evolving curve for the proposed OR gate for (a) X=0, Y=1; (b) X=1, Y=0 and (c) X=1, Y=1

Table 2: Summary of the proposed OR gate's performance with output Z measured in terms of input power Po

Input Ports		Logic Output	Output Y	Response time (ps)	Bit rate (Tb/s)
Port X	Port Y				
0	0	0	0	0.19	5.18
0	1	0	0.32 P_0		
1	0	0	0.32 P_0		
1	1	1	1.31 P_0		

3. References

[1] J. Jot Singh, D. Dhawan, and N. Gupta, "All-optical photonic crystal logic gates for optical computing: an extensive review," *Opt. Eng.*, vol. 59, no. 11, 2020.

[2] L. C. Yang, C. C. Huang, H. C. Huang, and S. L. Tsao, "A novel 1 × 2 optical power splitter with PBG structures on SOI substrate," *Optik (Stuttg).*, vol. 123, no. 4, pp. 306–309, 2012.

[3] D. Cotter *et al.*, "Nonlinear optics for high-speed digital information processing," *Science (80-.).*, vol. 286, no. 5444, pp. 1523–1528, 1999.

[4] Y. Suzuki, J. Shimada, and H. Yamashita, "High-Speed Optical-Optical Logic Gate For Optical Computers," *Electron. Lett.*, vol. 21, no. 4, pp. 161–162, 1985.

[5] C. Bintjas *et al.*, "All-Optical Packet Address and Payload Separation," vol. 14, no. 12, pp. 1728–1730, 2002.

[6] Y. D. Wu, "All-optical logic gates by using multibranch waveguide structure with localized optical nonlinearity," *IEEE J. Sel. Top. Quantum Electron.*, vol. 11, no. 2, pp. 307–312, 2005.C. Bintjas *et al.*, "20 Gb/s all-optical XOR with UNI gate," *IEEE Photonics Technol. Lett.*, vol. 12, no. 7, pp. 834–836, 2000.

Controlled shaping of high-order sinusoidal Laguerre-Gaussian laser modes

Hemant Kumar Meena, Brijesh Kumar Mishra, and #Brijesh Kumar Singh
Department of Physics, School of Physical Sciences, Central University of Rajasthan, Ajmer-305817, India
 # brijeshsingh@curaj.ac.in

Abstract: Here, we introduce a numerical method for controlled shaping of sinusoidal Laguerre-Gaussian (SLG) modes by redistributing the optical energy among the lobes. This modulation generates different structured modes by having all the lobes equally peak intense as well by transforming low intense lobes to high intense lobes and vice-versa.
Keywords: Laser modes, Sinusoidal Laguerre-Gaussian Beam, Fourier transform, and Phase mask.

1. Introduction

Electromagnetic waves consist of three important quantities i.e., angular momentum (spin angular momentum (SAM) & orbital angular momentum (OAM)), linear momentum, and energy. Generally, Laguerre-Gaussian beam (LGB) [1, 2] has a helical phase-front and have a fixed value of OAM. In the past days, much attention has been paid to generalize the characteristics of the LG beams which is the solutions of the free space paraxial Helmholtz equation in cylindrical-polar coordinates. LG modes with a sinusoidal amplitude dependency in azimuthal angle is known as sinusoidal Laguerre-Gaussian laser modes (SLG) [2]. SLG modes also exhibit the stable, shape invariant features like LG beam. The multiple lobes of high order sinusoidal Laguerre-Gaussian (SLG) laser modes differs in terms of shape, size, and non-uniform optical energy distribution. The normalized form of the complex amplitude of the SLG mode is given by following expression [2]

$$SLG_{p,l}(r,\phi,z) = \frac{2}{w(z)}\sqrt{\frac{2p!}{1+\delta_{0l}\pi(|l|+p)!}} \times e^{(i(2p+|l|+1)\Psi(z))}\left(\frac{\sqrt{2}r}{w(z)}\right)^{|l|} L_p^{(|l|)}\left(\frac{2r^2}{w(z)^2}\right) \times e^{\left(-ik\left(\frac{r^2}{2q(z)}\right)\right)}\begin{Bmatrix} sin\,(l\phi) \\ cos\,(l\phi) \end{Bmatrix} \quad (1)$$

Where, $p \geq 0$ is the radial mode index, l is the azimuthal mode index, Ψ corresponds to the Gouy phase and w is beam radius. $L_p^{|l|}$ is the associated Laguerre polynomial, and δ is the Kronecker delta. A complete set of sinusoidal outcomes involves of the functions as shown in Eq. (1) applying $\cos(l\phi)$ for $l \geq 0$ and $\sin(l\phi)$ if $l < 0$.

Since, all the lobes are not uniformly optical intense; they cannot be utilized simultaneously with equal efficiency in many applications such as optical tweezers and optical lithography, etc. [3, 4]. Therefore, we proposed a numerical method to equalize the optical intensity of each lobe of the SLG modes as well as controlled transfer of the optical energy from high intense lobes to the low intense lobes in the various modes of SLG beams by using an appropriate mask.

Method: To achieve the modulation of the optical energy among the lobes of the high-order sinusoidal Laguerre-Gaussian laser modes, we mathematically simulated computer-generated hologram (CGH) that involves of two sections with opposite binary phases and is given by [4, 5]

$$P(r) \propto \begin{cases} -1, & r \leq r_\pi \\ 1, & r_\pi \leq r \leq r_{max} \end{cases} \quad (2)$$

where, $r_\pi = \gamma(r_{max})$, $r_{max} = {}^{d}/_{2}$, d is the diameter of annular mask aperture. γ is a coefficient changes as $0 \leq \gamma \leq 1$ and r_π is the π phase shifted radial length. When the annular phase mask presented by Eq. (2) is illuminated with the input plane wave, output beam shaped at the focal plane is mathematically the Fourier transform of the modulated mask i.e., FT$\{P(r)\}$. By varying the values of the γ, optical energy is modulated from inner lobes to the outer lobes and vice-versa [5] of the higher-order SLG beams in a controlled fashion. The phase mask relates to the SLG beam from Eq. (1) is modulated by the proposed phase mask fabricated from Eq. (2) at the pupil plane of the Fourier transforming lens. By applying the Fourier transform of the modulated resultant phase mask at the pupil plane, we analyzed the modulation in the 2D intensity patterns of the SLG beams at the Fourier plane.

2. Result and Conclusion:

The SLG mode having uneven peak intensity arrangement among the various lobes of SLG_{12} mode. The phase masks associated Fourier transformed 2D transverse intensity patterns of SLG_{12} mode at Fourier plane and the 1D normalized intensity plots are given in first, second and third columns of the Fig.1, respectively. The complex 2D intensity profiles of the normal SLG_{12} mode shown in Fig.1(b) consists of eight lobes, out of which four inner lobes are maximum peak intense and other outer four lobes are low intense as it is confirmed from its 1D plot plotted along the horizontal axis (x-axis) shown in Fig. 1(c). The normal phase mask of SLG_{12} mode present in the Fig. 1(a) is modulated by annular mask given in Eq. (2) for the value $\gamma = 0.305$ and 0.335, as shown in Figs. 1(d) and 1(g), respectively. The corresponding Fourier transformed 2D transverse intensity patterns at the Fourier plane are shown in the Fig.1(e) and 1(h), respectively. We observed that for $\gamma = 0.305$, optical energy distribution shown in Fig. 1(b) is redistributed among the lobes in such a way that outer four low intense lobes converted to high intense lobes and four inner high intense lobes are converted to low intense lobes as the profile shown in Fig. 1(e). The modulated 2D intensity profile is just opposite to that of the normal profile of SLG_{12} mode shown in Fig.1(b). Further, for the $\gamma = 0.335$, all the eight lobes are converted to equally peak intense as shown in Fig. 1(h) and is further confirmed from its 1D plot shown in Fig.1(i). Plots shown in the blue color is corresponded to the normal profile of SLG_{12} mode also given in Fig. 1(f) and 1(i) for comparison purposes. Note that, in all the sub-figures (b, e & h), intensity profiles are normalized from 0 (black) to 1 (white) whereas phase maps (a, d & g), changes from 0 (black) to π (white). Scale bars in normal phase mask is also applicable for corresponding modulated phase mask of the Fig. (1). Scale bar implanted in the standard 2D intensity profile of SLG_{12} mode is valid for all the modulated 2D intensity profiles of the second column of Fig.1.

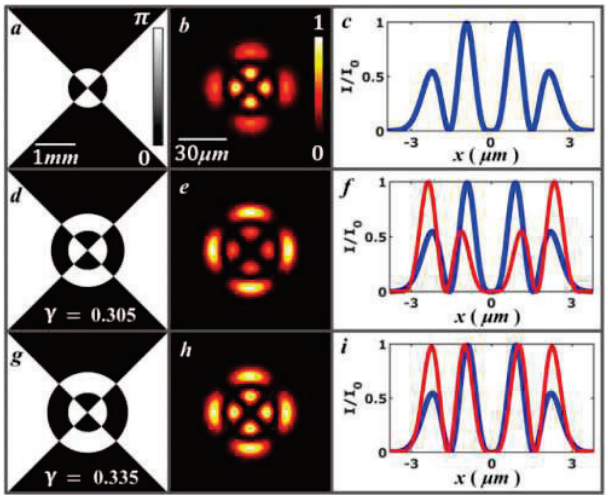

Fig. 1: First row is for normal while second row (for γ = 0.305), and third row (for γ = 0.335) are modulated SLG_{12} mode. First column (a, d, & g) corresponds to the phase maps, second column (b, e, & h) corresponds to Fourier transformed 2D intensity profiles of the first column while third column (c, f, & i) is 1D intensity plots along the horizontal axis of the second column2D profile, respectively.

In conclusion, the uneven intense lobes of the SLG_{12} modes transformed together into the evenly high energize lobes for a particular value of γ, in a controlled way. In this format, our method raises the number of high intense lobes in the modulated SLG_{12} beams. We visualize that such type of precise modulation of optical intensity of SLG_{12} mode may be selectively utilized in many applications like multiple particles trapping in optical tweezers and optical communications.

3. References

[1] M.W. Beijersbergen, L. Allen, H.E.L.O. van der Veen, J. P. Woerdman, "Astigmatic laser mode converters and transfer of orbital angular momentum Optics Communications, **96**(1-3), 123-132 (1993).

[2] P. Fulda, K. Kokeyama, S. Chelkowski, and A. Freise, "Experimental demonstration of higher-order Laguerre-Gauss mode interferometry," PHYSICAL REVIEW D **82**, 012001-7 (2010).

[3] B. K. Singh, R. Remez. Y. Tsur, A. Arie, "Super-Airy beam: self-accelerating beam with intensified main lobe," Opt. Lett. **40**, 4703-4706 (2015).

[4] B. K. Singh, H. Nagar, Y. Roichman, A. Arie, "Particle manipulation beyond the diffraction limit using structured super-oscillating light beams," Light: Sci. & Appl. **6**, e17050 (2017).

[5] H. K. Meena, and B. K. Singh, "Controlled modulation of optical energy in high order Hermite-Gaussian laser modes," Optik **232(**166560**),** 1-11 (2021).

Fast layer-based CGH generation for large matrix dimensions

Anuj Gupta*, Raj Kumar and Bhargab Das
CSIR-Central Scientific Instruments Organisation, Chandigarh - 160030
**Corresponding Author: anujgupta@csio.res.in*

Abstract: The generation of a computer generated hologram (CGH) involves intensive calculations making the display of object information hard to achieve. The object size, number of pixels, and resolution significantly affect the computational cost of CGH generation. Therefore, it becomes very important to optimize the CGH generation algorithm for large matrix dimensions in order to use it in several practical applications, such as holographic printers. This work includes the comparative analysis of CGH generation for various resolutions in two different programming languages, viz., MATLAB and Python.
Keywords: Computer-generated hologram; Holographic displays, Layer-based method.

1. Introduction

Holography represents the formation of a two dimensional complex pattern which contains the amplitude as well as the phase information of a three dimensional (3D) scene. This information is used to optically reconstruct the object from the recorded hologram. Computer generated hologram (CGH) is a hologram which can be generated by numerical methods even in the absence of any physical object [1]. CGH generation is very useful but it is a computationally expensive process. It involves the intensive calculations which depends upon several factors such as size of the modeled object, pixel size in the object plane, the resolution of the CGH or hologram plane etc. The huge computational cost which significantly increases with the increase in any of the above mentioned factors necessitates the optimization of the CGH generation process. This work is an effort to optimize the process of CGH generation for holographic displays at higher resolutions. The optimization of this process can be achieved by executing the working of hardware as well as software parts in synergy. In order to accelerate the process of CGH generation, several hardware accelerator platforms like CPU, GPU, FPGA etc. are used [2]. Along with this, algorithms should be designed in an optimized way to get the maximum output from the available sources. This work is an effort to work on the efficiency of the algorithm so as to speed up the process of CGH generation for higher resolutions.

2. Methodology

Point cloud based, polygon based, layer based, and light field method are the four major categories in which CGH generation is divided [3]. In the present work, the layer based method is implemented to generate the CGH. The method can also be called as plane based method because of the implementation of only a single plane in the algorithm. The pixel size and the number of pixels in the object plane significantly affect the execution time of the algorithm. The larger the resolution, the higher will be the execution time. We started with the lower resolution of 1024×1024 and generated the CGH for this. Subsequently, the resolution of the object model is increased to 2048×2048, 4096×4096 and 8192×8192. The pixel pitch is kept to be 6.4 μm, wavelength 632.8 nm and distance between object plane and CGH plane is $1m$.

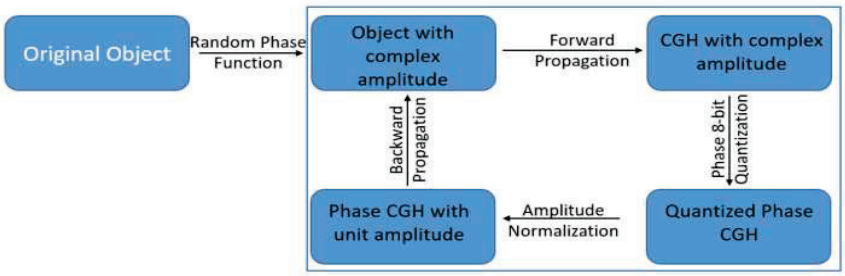

Fig. 1: Flow chart of the plane-based CGH generation with iterative beam propagation method

Initially, the original object is combined with a diffusive function implemented by a random phase pattern. Afterwards, the object plane is propagated in the forward direction using FFT based algorithm. The propagated field

is a complex amplitude function consisting of phase as well as amplitude information. In this CGH plane, the phase part is retained and amplitude part is reduced to unit value. Subsequently, phase of the CGH is 8-bit quantized. This unit amplitude phase-CGH is propagated back to the object plane wherein the amplitude information is replaced by the original object information. Multiple iterations are carried and the generated phase-CGH is used for both numerical and optical reconstruction.

3. Results and Discussion

Firstly, we developed a basic algorithm in MATLAB as well as in Python which generated a CGH using a plane based technique in a sequential manner. The implementation of underlying physics is cross verified by developing the algorithms for an object at a smaller resolution and reconstructing its output CGH numerically as well as optically. The resolution of generated CGH is matched with that of spatial light modulator (SLM) resolution viz. 1920×1080. This is achieved with the use of zero padding of the CGH. Subsequently, the phase CGH is quantized to 8 bit and loaded into the SLM in order to reconstruct the object optically. In addition to this, object models are also reconstructed numerically with the basic technique of backward propagation to the object plane. Fig. 2(a)-(c) shows the original object, corresponding computed CGH zero padded to match SLM resolution, and the numerically reconstructed result, respectively.

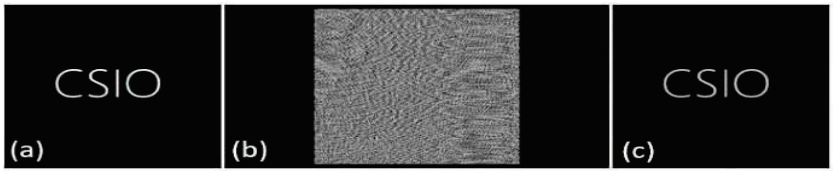

Fig. 2: (a) Original object of resolution 1024 × 1024, (b) CGH padded to SLM resolution of 1920 × 1080 (c) Numerically reconstructed result

Here, we have shown the results of only one model because the results in all the different simulation models are completely consistent with each other. After the successful benchmarking of the algorithm, the object models are run at higher resolutions and execution times for the same are observed.

Table 1: Execution time for different resolutions

Resolution Execution time	1024 × 1024	2048 × 2048	4096 × 4096	8192 × 8192
MATLAB	~ 3 seconds	~ 18 seconds	~ 1.2 minutes	~ 6.76 minutes
Python	~ 7 seconds	~ 24 seconds	~ 1.6 minutes	~ 7.06 minutes

The results of different resolutions of object model in this CGH generation by two different programming languages are compared in Table 1. It can be seen that MATLAB and Python produces the results almost at same speed for higher matrix dimensions. It is a computationally expensive process to generate CGH because of the involved intensive calculations. In the future work, we will further extend the algorithm to higher dimension and optimize the algorithm by parallelizing it or by using the available hardware accelerators like GPU.

4. Acknowledgement

Authors acknowledge CSIR, India for providing financial support under project number MLP2014. Authors thank Ms Pardeep Bhanot and Ms Monika Rani for their help.

5. References

[1]. E. Sahin, E. Stoykova, J. Makinen, and A. Gotchev, "Computer-generated holograms for 3D imaging: A survey", ACM Comput. Surv. **1**, 1 (2019)

[2]. Y. Wang, D. Dong, P.J. Christopher, A. Kadis, R. Mouthaan, F. Yang, and T.D. Wilkinson, "Hardware implementations of computer-generated holography: a review", Optical Engineering **59**, 1-30 (2020).

[3]. T. Shimobaba, D. Blinder, T. Birnbaum, I. Hoshi, H. Shiomi, P. Schelkens, and T. Ito, "Deep-Learning Computational Holography: A Review (Invited)", Frontiers in Photonics, **3**, [854391] (2022).

A tunable digital holographic microscope for quantitative imaging

Shivam Kumar Chaubey*, Mohit Rathor, Rakesh Kumar Singh
Information Photonics & Optical Metrology Laboratory, Department of Physics, Indian Institute of Technology (Banaras Hindu University), Varanasi - 221005, India
**e-mail address: shivamkumarchaubey.rs.phy21@itbhu.ac.in*

Abstract: We present and experimentally demonstrate application of a spatially resolved digital holographic microscope (DHM) for quantitative imaging. This is accomplished by making angular multiplexing using the Mach-Zehnder interferometer, which is embedded with a tunable triangular Sagnac interferometer in the reference arm. After calibration of our DHM with known samples, we present quantitative results for the Molybdenum Disulphide (MoS_2) and fibrous tissue.
Keywords: Digital holography, Microscopy, Quantitative imaging.

1. Introduction

Quantitative imaging is recognized as a useful technique in metrology for imaging, signaling, and nondestructive assessment of the inner structure. Quantitative imaging has been developed to provide a coherent framework for dealing with light-matter interaction [1]. Although it is difficult, quantitative imaging analysis is crucial and highly wanted in fields like biomedical optics, soft matter physics, chemistry, spectroscopy, etc. Sagnac interferometer and a 2D grating were recently combined in a recent experiment to provide a high-speed holographic approach in two-shot measurements that allows for the quantitative determination of the light field. In real-time imaging situations, the two-shot imaging approaches are incompatible for dynamic objects. In response to the increased need for a one-shot measurement, specifically, to handle dynamic objects, one-step measuring approaches are being developed [2]. For a single measurement, an off-axis holographic approach is shown that is implemented using pairs of coherent sources and 2D orthogonal gratings [3]. These gratings must be replaced since they cannot be adjusted to satisfy the varying carrier frequency requirements for various samples. In this work, we experimentally demonstrate an alternative spatially resolved single shot DHM technique. To solve the problems caused by spatial resolution in diverse anisotropic samples, we specifically developed a tunable carrier frequency source. This is accomplished by making angular multiplexing with the help of the Mach-Zehnder interferometer, which is outfitted with a triangular Sagnac interferometer in the reference arm.

2. Experimental set-up and results:

The experimental setup for DHM is shown in Figure 1. A half-wave plate (HWP) transforms vertically polarized He-Ne laser light into 45-degree linearly polarized light. Then, this light is spatially filtered and collimated by the spatial filter (SF) and lens L1. The collimated beam is then divided into two equal-intensity arms by the beam splitter BS1. In the object arm, light travels through the mirror (M1) and the sample plane is illuminated by the light field and imaged by a system made up of a 20x microscopic objective and lens L4. In the reference arm, the polarization beam splitter (PBS) divides the 45-degree polarized beam into two orthogonal, counterpropagating polarization components in the common path interferometer. The emergent orthogonally polarized components receive the necessary tilt by the mirrors M2 and M3. The carrier frequency of the reference (polarized) beam can be changed through the use of the angular multiplexed arm, as a result, tunability is emphasized in our experimental strategy. At BS2, the reference beam from the common-path interferometer interferes with the imaged object field, and at the observation plane (CCD camera), the interference between the object and reference fields results in a multiplexed interference pattern, which is represented as,

$$I = \left|O_x + R_x\right|^2 + \left|O_y + R_y\right|^2 \quad (1)$$

$$I = I_o(r) + \left[O_x R_x^* + O_y R_y^*\right] + \left[R_x O_x^* + R_y O_y^*\right] \quad (2)$$

Where O_x and O_y are the orthogonal X and Y components of the object beam while O_x^* and O_y^* are its conjugate term. Similarly, R_x and R_y are the orthogonal reference beam components, R_x^* and R_y^* are its conjugate terms, and $I_o(r)$ is the dc component. In general, an interferogram's spectrum consists of four Fourier spectra, two of which are the conjugate of the remaining two peaks excluding the central dc. By filtering the frequency spectra of the terms in the second square bracket of Eq (2), information about the amplitude and phase in the signal domain is retrieved.

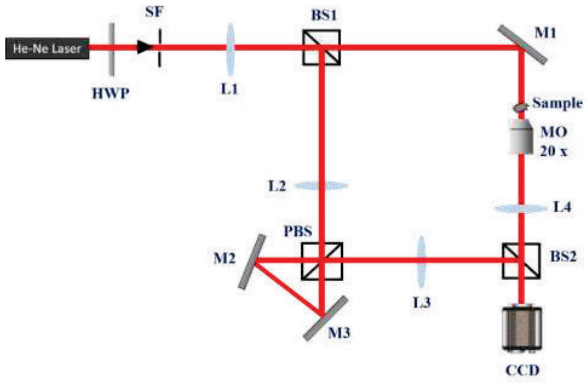

Figure. 1: Experimental setup for the tunable digital holographic microscope.

The experimental setup is first calibrated with known transparent samples (polarizer, half wave-plate, etc). These results are consistent with the theoretical values. A recorded interferogram for MoS_2 is shown in Fig. 2(a). Figure 2(f) clearly shows the two spectrums and two of their respective conjugate terms of the corresponding interferogram (Fig. 2(a)). Fig. 2(b)-2(e) shows the retrieved amplitude and phase distributions of the orthogonal X and Y components for MoS_2. Similarly, 2(g)-2(j) represent the amplitude and phase distributions of orthogonal X and Y components for fibrous tissue. From the experimental results, it is clear that both the samples are nearly polarization insensitive.

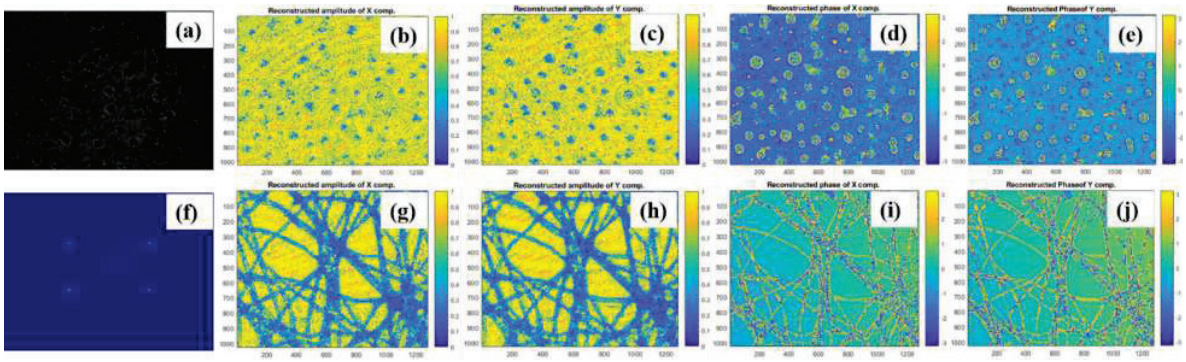

Figure. 2: (a) Holographic image of MoS_2 sample, (f) Frequency spectrum corresponding to 2(a). (b) and (c) are the amplitude of X and Y components for MoS_2, (d) and (e) are the corresponding phase. Similarly (g)-(j) are the amplitude and corresponding phase of X and Y components for fibrous tissue (MC-5, Thor lab).

3. Conclusion:

We have presented and experimentally demonstrated the use of a spatially resolved DHM for quantitative imaging. MoS_2 and Fibrous tissue (transparent sample) were tested as part of the experimental implementation. Both samples were nearly insensitive to polarization. A similar concept can be applied to reflecting type materials with a minor change in sample positioning. This DHM may have an immediate influence on the determination of the anisotropic properties of dynamic samples.

4. Funding:

The work is supported by the Department of Biotechnology (DBT) Grant No. BT/PR35587/MED/32/707/2019.

5. References

[1] D.K. Naik, R.K. Singh, H. Itou, M.M. Brundavanam, Y. Miyamoto, M. Takeda, "Single-shot full-field interferometric polarimeter with an integrated calibration scheme," *Opt Lett.* 37(**15**):3282-3284 (2012).
[2] M. M. Sreelal, R. V. Vinu, and R.K. Singh, "Jones matrix microscopy from a single-shot intensity measurement," *Opt. Lett*. **42**, 5194-5197 (2017).
[3] Xuan Liu, Yang Yang, Lu Han, and Cheng-Shan Guo, "Fiber-based lensless polarization holography for measuring Jones matrix parameters of polarization-sensitive materials," *Opt. Express.* **25**, 7288-7299 (2017).

Sensing performances of linearly tapered Gaussian apodized fiber Bragg gratings

Souryadipta Maiti, Vivek Singh*
Department of Physics, Institute of Science, Banaras Hindu University, Varanasi-221005, India
*Author e-mail address: souryaphysics1@gmail.com, viveks@bhu.ac.in**

Abstract: Sensing performance of linearly tapered fiber Bragg gratings is optimized in presence of Gaussian apodization and compared with tapered nonapodized gratings. Reflectivity equation obtained using standard coupled mode theory with the help of transfer matrix method. Also, reflectivity values plotted in logarithmic scale to see the sidelobe suppression ability. Reflectivity values, resonance peak position, full width at half maximum, sensitivities, detection accuracies, quality parameters, sidelobe levels tabulated and compared. Linearly tapered gaussian apodized fiber Bragg gratings show huge impact on sensing performances.
Keywords: Fiber Bragg grating, FWHM, Linear tapering, Sensitivity, Sidelobe level

1. Introduction

Nowadays fiber Bragg gratings (FBGs) based sensors drawn much attention for sensing of biological, physical, chemical parameters due to their specific properties like lightweight, long-term stability, linear output, miniature size, low cost of installation etc. [1,2]. FBGs have periodic refractive index (RI) variation of period few micrometers inside the fiber core of length few millimeters. Because of this periodic RI variation, when light enters into this waveguide all the reflected signals combined over a narrow length of wavelengths called reflection signal. This particular wavelength is called Bragg wavelength [3] and rest of the light construct out of phase condition and formed transmission signal. Thus, basic working principle based on multiple Bragg reflection condition. But the reflection signal consists of various sidelobes due to continuous changes at various boundaries. This sidelobes acts as noise and hampered sensing performances. So, it is mandatory to eliminate these sidelobes by properly using suitable apodization function [3]. Further, the survey of literature suggest that the tapering of fiber drastically improves sensing performance [4] of waveguide-based sensor. Such the tapering can be achieved by simply heating and stretching method in association with applying tension. Keeping these facts in mind a linearly tapered Gaussian apodized Bragg grating sensors is proposed and optimized for biosensing application. The obtained results are compared with linearly tapered unapodized Bragg grating sensor. In this work a linearly tapered core diameter (d_{core}) from 9μm to 3μm is considered in which 20 mm long grating is placed in a 30 mm long tapered cone with 5mm grating is placed in taper waist side as shown in Fig. 1. Core index (n_{core}) and cladding index (n_{clad}) of fiber Bragg grating is chosen 1.451 and 1.445 respectively with index modulation (Δn) 5×10^{-4} and grating period (Λ) 530nm.

2. Mathematical Formulation

The core refractive index of FBG along propagation direction (z) is given by [3]

$$n(z) = n_{core} + \Delta n \cos\left(\frac{2\pi z}{\Lambda}\right) \quad (1)$$

In case of tapered grating effective RI of the fundamental propagating mode related with core diameter is [4]

$$\frac{2\pi}{\lambda} d_{core}(z) \sqrt{(n_{core})^2 - n_{eff}^2(z)} - \frac{\pi}{2} = 2 \arccos \sqrt{\frac{n_{core}^2 - n_{eff}^2(z)}{n_{core}^2 - n_{clad}^2}} \quad (2)$$

Reflectivity equation derived from coupled mode equations with the help of transfer matrix approach.

$$R(\lambda) = |r(\lambda)|^2 = \left|\frac{T_{21}}{T_{11}}\right|^2 = \frac{k^{TFBG^2} \sin^2(\Upsilon^{TFBG} L)}{\Delta\beta^{TFBG^2} \sinh^2(\Upsilon^{TFBG} L) + k^{TFBG^2} \cosh^2(\Upsilon^{TFBG} L)} \quad (3)$$

where $\Upsilon_k^{TFBG} = \sqrt{k^{TFBG^2} - \Delta\beta^{TFBG^2}}$. Further, the performances of proposed sensor are optimised on the basis of their sensitivity, detection accuracy and quality parameter [3]. The sensitivity of sensor is defined as the change in sensing signal with respect to change in RI of sensing medium. Also, the detection accuracy (DA) is defined as the ratio of resonance wavelength with the full width at half maximum (FWHM) of the reflectance peak. Hence the quality parameter (Q) is simply written as the ratio of sensitivity with FWHM. To obtain the larger sensing performance of the sensor these parameters should be large.

3. Results and Discussion

To estimate the sensitivity of our proposed tapered Bragg grating the cladding refractive index is increased from *1.443* to *1.445* respectively and a graph between reflectance versus wavelength is plotted and shown in Fig. 2. To see the sidelobe suppression ability reflectivities, plot in logarithmic scale is also performed and shown in Fig. 3. The obtained sensing performance is tabulated in Table-1. It is clear from figures that the presence of Gaussian apodization reduces the reflectivity but the same time increases the sensitivity (525nm/RIU maximum) with large side lobe suppression ability -100.20dB. It is also noticed that the sensitivity 332.49nm/RIU obtained in tapered unapodized grating sensor is smaller with low side lobe suppression ability -1.68dB. Hence too many side lobes are appeared in tapered unapodized grating based sensor.

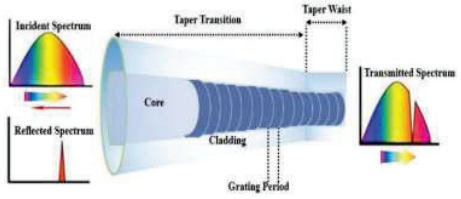

Fig. 1: Schematic diagram of linearly tapered Bragg grating sensor

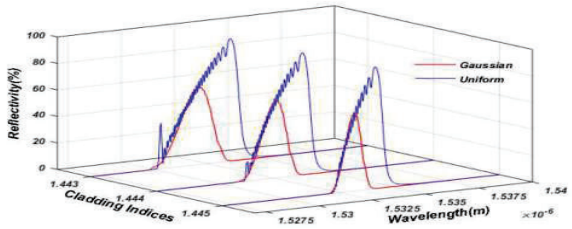

Fig. 2: Reflection spectrum of linearly tapered apodized fiber Bragg gratings

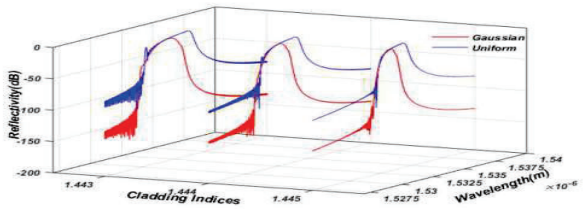

Fig. 3: Reflection spectrum in logarithmic scale of tapered apodized fiber Bragg gratings

Table 1: Performance of linearly tapered apodized fiber Bragg gratings

Apodization	Reflectivity (%)	Resonance Peak(μm)	FWHM (nm)	Sensitivity (nm/RIU)	DA	Q	Dominating Sidelobes (dB)
Gaussian	59.2196	1.5331925	0.8545		1794		-89.25
	58.5427	1.5326675	1.2734	525.00	1203	614	-100.20
	58.4831	1.53209	1.6631	577.49	921	453	-92.71
Uniform	91.8075	1.5341725	1.5814		970		-1.68
	92.1890	1.53384	2.0721	332.49	740	210	-1.49
	92.3174	1.5335425	2.4621	297.50	622	143	-1.43

4. Acknowledgement

The authors are thankful to DST-INSPIRE India, IoE BHU Grant No. 6031 for their financial supports.

5. References

[1] M. Liang, X. Fang, Y. Song, S. Li, N. Chen, and F. Zhang, "Research on Three-Dimensional Stress Monitoring Method of Surrounding Rock Based on FBG Sensing Technology," *Sensors*, vol. 22, no. 7, p. 2624, doi: 10.3390/s22072624 (2022).

[2] W. Zhang, L. Zhu, M. Dong, X. Lou, and F. Liu, "A temperature fiber sensor based on tapered fiber Bragg grating fabricated by femtosecond laser," *Appl. Sci.*, vol. 8, no. 12, doi: 10.3390/app8122616 (2018).

[3] S. Maiti and V. Singh, "Performance Analysis of Apodized Fiber Bragg Gratings for Sensing Applications," *Silicon*, vol. 14, no. 2, pp. 581–587, doi: 10.1007/s12633-020-00852-0 (2022).

[4] T. Osuch, K. Markowski, and K. Jędrzejewski, "Numerical model of tapered fiber Bragg gratings for comprehensive analysis and optimization of their sensing and strain-induced tunable dispersion properties," *Appl. Opt.*, vol. 54, no. 17, pp. 5525, doi: 10.1364/ao.54.005525 (2015).

Digital Holography with a Wollaston prism

***Mohit Rathor, Rakesh Kumar Singh**

Laboratory of Information Photonics and Optical Metrology, Department of Physics, Indian Institute of Technology (Banaras Hindu University) Varanasi, 221005, Uttar Pradesh, India

**Author e-mail address: mohitrathor.rs.phy21@itbhu.ac.in*

Abstract: A digital holographic (DH) imaging system design is based on a Wollaston prism to recover the complex information (i.e. amplitude and phase) of the object using the Fourier fringe analysis algorithm on the digitally recorded hologram. To make the experimental setup simple, a common path configuration based on a Wollaston prism is implemented. The performance of this system is experimentally tested and results are presented to show the performance of the technique.

Keywords: Digital holography, Phase imaging, Common-path configuration.

1. Introduction

The phase information of an object plays a crucial role to explain the features of the object. In a conventional imaging system, the image of the object recorded through a camera is unable to offer the phase information of the object. In order to record phase information of the light, holography is one of the interesting techniques due to its capability to record and reconstruct complex fields [1,2]. However, the major technical challenge in holography is the stability of experimental hologram recording techniques without a twin image problem[3]. To record the hologram different types of interferometer systems are used like the Michelson interferometer[4], Mach-Zehnder interferometer[5], etc. However, different path geometries of the beams in these interferometers make these designs susceptible to external vibrations. In this paper, we present a nearly common path interferometer for recording the hologram and use the digital algorithm for the reconstruction of the hologram. This design uses a Wollaston prism and interference of the orthogonal polarization components by a project approach.

2. Experimental Setup

Figure 1 shows a schematic configuration of the proposed common path, compact DH system based on the Wollaston prism (WP). A horizontally polarized beam from a He-Ne laser of wavelength 632.8nm (model No.: HNL150LB) converts into a diagonally polarized beam after passing through the half-wave plate (HWP), collimating this beam using spatially filter assembly with a lens L1. This collimated beam pierces into WP and breaks into two orthogonal linear polarization states with a small separation (1° beam separation Model No.:WPM10, Thorlab)

An object is placed in one of the transmitted beams from WP and this beam carries complex information about the object and is referred to as an object beam. The second orthogonal polarization component coming out of the WP is referred to as a reference beam. An imaging lens L2 (focal length, f=250mm) at 2f relay the light field, and a digital hologram are recorded at a distance of 2f from L2. The hologram is recorded by the complementary metal oxide semiconductor (CMOS) camera plane by introducing a polarizer P at an angle of 45° from the pass axis of the horizontal in front of the CMOS camera. The information of the complex object is encoded in that hologram. Now, the amplitude and phase information of the complex object can be reconstructed by analyzing the digitally recorded hologram with the help of the Fourier fringe analysis (FFA) algorithm[6].

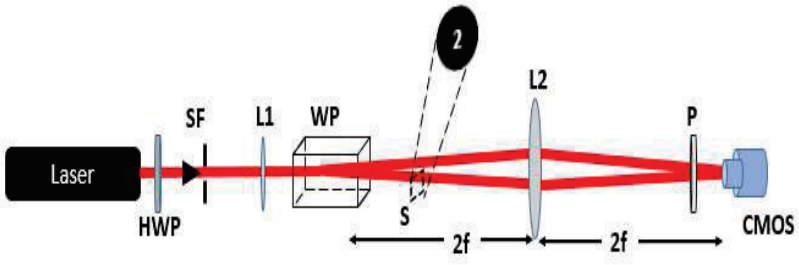

Fig.1: *A compact Experimental setup design for recording the digital hologram with the help of Wollaston prism. HWP is half wave plates, SF is spatial filter, L1 &L2 are lens, WP is Wollaston prism, S is sample, P is a polarizer, CMOS is the complementary metal oxide semiconductor camera.*

3. Result and discussion

Figure 2. (a) shows the digital hologram recorded at the CMOS camera plane. For recovering the object's complex information, we use the FFA algorithm on a digitally recorded hologram. As a result, the ±1 conjugate order of the spatial spectrum disengages from DC part in the frequency (Fourier) domain of the hologram as shown in figure 2 (b) with blocking the DC part. To reconstruct the holographic image of the sample, +1 or -1 order of the spatial spectra is filtered out and then the holographic image can be acquired by using the convolution method.

We use two objects, namely the transparency of "2" and "ψ" on the overhead projector (OHP) sheet in the experiment as shown earlier. Figure 2 (c) and (d) shows the amplitude and phase information of the reconstructed object **"ψ"** from the recorded hologram. Similarly, Figure 2 (e) and (f) show the amplitude and phase information of object **"2".**

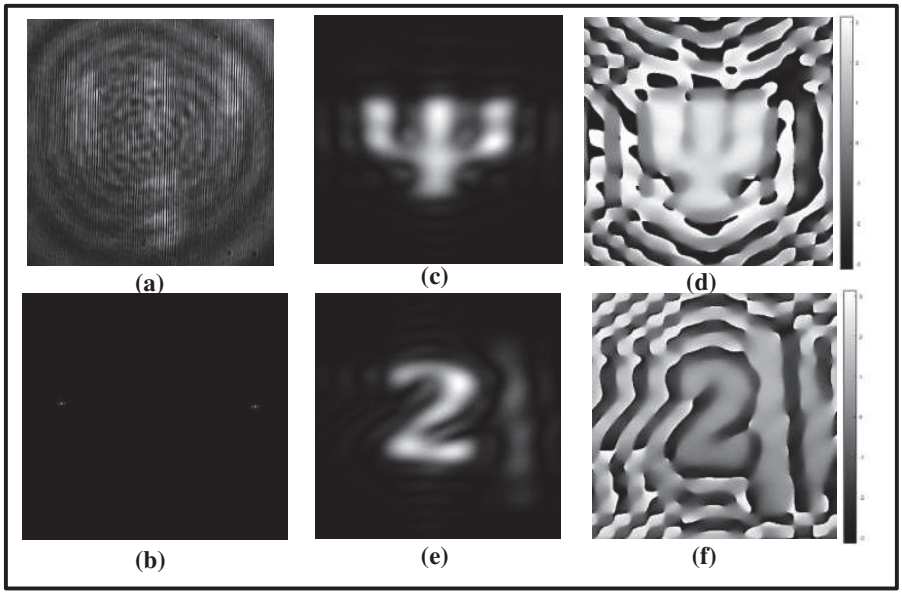

Fig.2: *a) Recorded hologram b) ±1 conjugate order of the spatial spectrum disengage from DC part in the frequency (Fourier) domain, c) & d) Recovered amplitude and phase of the object "ψ", e) & f) Recovered amplitude and phase of the object "2".*

4. Conclusion

In this paper, we present a simple and compact common path Digital holography imaging setup using a Wollaston prism which is more stable than other interferometry systems like the Michelson interferometer and Mach Zehnder interferometer. The feasibility of the proposed techniques is experimentally demonstrated for imaging.

5. Acknowledgement

Mohit Rathor would like to acknowledge the Council of Scientific and Industrial Research, India (CSIR India- Grant No.: 80 (0092) /20/EMR-II) for financial support.

6. References

[1] M. Liebling, T. Blu, and M. Unser, "hologram," vol. 21, no. 3, pp. 367–377, 2004.
[2] S. Grilli, P. Ferraro, S. De Nicola, A. Finizio, G. Pierattini, and R. Meucci, "Whole optical wavefields reconstruction by Digital Holography," *Opt. Express*, vol. 9, no. 6, p. 294, 2001, doi: 10.1364/oe.9.000294.
[3] "[Joseph_W_Goodman]_Introduction_to_Fourier_Optics.pdf."
[4] J. A. Pomarico, P. F. Molina, and C. D. Angelo, "Quantitative phase determination by using a Michelson interferometer," *Eur. J. Phys.*, vol. 28, no. 5, pp. 797–804, 2007, DOI: 10.1088/0143-0807/28/5/003.
[5] M. K. Kim, L. Yu, and C. J. Mann, "Interference techniques in digital holography," *J. Opt. A Pure Appl. Opt.*, vol. 8, no. 7, 2006, doi: 10.1088/1464-4258/8/7/S33.
[6] W. W. Macy, "Two-dimensional fringe-pattern analysis," vol. 22, no. 23, pp. 2–5, 1983.

Demonstration of fiber ring resonator with beam deflection transducer in the loop for sensing electric field

Isha Sharma, Mitali Sahu and Partha Roy Chaudhuri
Indian Institute of Technology, Kharagpur, West Bengal 721302
roycp@phy.iitkgp.ac.in

Abstract: We propose and demonstrate a modified direct coupled fiber ring resonator configuration for sensing the surrounding electric field. By introducing a fiber cantilever-deflection transducer within the ring loop, we performed experiments to investigate the resultant variation in resonance pattern on the application of an electric field. We successfully demonstrate a sensitivity of 0.06 kV/cm in the dynamic range of 0 – 0.90 kV/cm. The working of the cantilever based ring resonator system is theoretically for a clear understanding of our experimental findings.
Keywords: Fiber-optic sensor, fiber ring resonator, electric field sensor.

1. Introduction

In the past few years, the optical fiber ring resonator has emerged as a promising technology in sensing and device applications because of its practical and potential importance [1]. Fiber based ring resonators are very powerful regarding the sensitivity to the external perturbation impressed on the loop. When the light with the resonant wavelength propagates through the fiber loop, due to multiple round-trips, the light builds up in intensity as the consequence of constructive interference which results in a more significant response. Following the development, we integrated a fiber cantilever-deflection transducer in a direct coupled fiber ring resonator configuration for sensing the electric field. The transducer probe is the free end of the fiber forming the loop whose tip is coated with cobalt-modified bismuth ferrite nanoparticles forming a deflecting fiber cantilever details of which is reported in our previous work [2].

2. Experimental Details and Results

The schematic of the experimental setup is shown in Fig. 1. Light from the He-Ne laser source (632nm, 5mW) is cupled using a 40X microscopic objective into the input port (port 1) of a 3dB coupler (@ 632 nm). The tip of the coupled port (port 4) is coated with our electric probe material. The tip remains freely suspended like a cantilever and is placed head-on with respect to another input port (port 2) of the 3 dB coupler between two electric field plates using 3d translational stages, forming a direct-coupled fiber loop ring configuration. The output is recorded from the direct port (port 3), as shown in Fig. 1. While performing the experiment, the coated length of the fiber is 1±0.1 cm having a coating thickness of 0.32 mm, as optimized from our previously reported cantilever experiment. The circumference of the fiber ring (L) is kept 0.5 m.

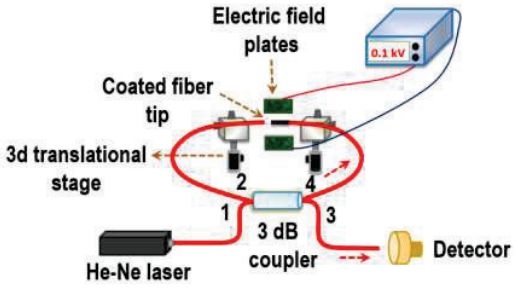

Fig. 1: Schematic of experimental set-up.

Initially, before applying the electric field, an off-set adjustment is performed to achieve the resonance condition. When an electric field is applied, the coated fiber tip deflects due to the induced polarization of our probe sample

resulting in a coupling misalignment between the head-on fiber tips giving an output power variation of 3dB coupler. We performed the experiment for different cantilever lengths, 3.0 cm and 2.8 cm, respectively, keeping the separation as 1 cm between the plates producing electric. The response curve of our cantilever modified fiber ring resonator configuration is shown in Fig 2. It is evident from the above experimentally obtained transmission characteristics that in the dynamic range of 0 - 0.90 kV/cm of an electric field, our modified scheme's sensitivity is high with a minimum electric field detection limit of 0.06 kV/cm.

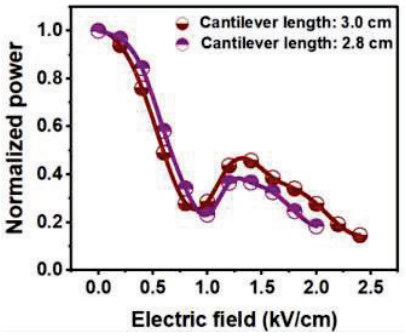

Fig. 2: Normalized output intensity variation with application of electric field.

2.1 Theoretical model

In our fiber ring loop experimental scheme, the modulation of the output power is associated with two different mechanisms: the periodic power variation pattern as a function of loop fiber length [4] and another is the exponential decay because of power coupling between two optical fibers. The output power variations of these two mechanisms and the resultant output power profile of our modified configuration are plotted in Fig. 3.

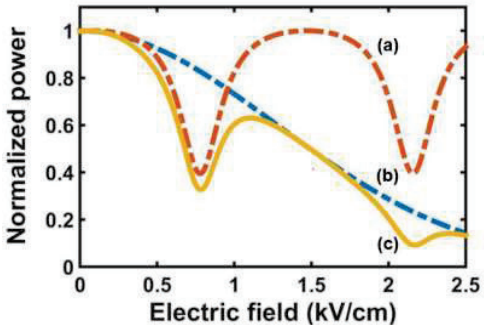

Fig. 3: (a) The resonance output intensity of fiber ring resonator (b) Transmitted coupled power variation of cantilever deflection configuration (c) Resultant output power profile of our modified fiber ring resonator.

From Fig. 3, it is evident that our theoretical model matches very well with our experimental findings (Fig.2).

3. Conclusion

In this article, we report our experimental analysis and findings pertaining to the transmission characteristics of direct-coupled fiber ring resonator containing a fiber cantilever beam-deflection transducer arrangement in loop for measuring electric field in the vicinity. We successfully demonstrate a minimum detectable electric field of 0.06 kV/cm preferably in the range of $0 - 0.90$ kV/cm. We developed a theoretical platform to understand the effect of cantilever modulation of circulating signal in the resonator loop. The sensitivity of our proposed electric field sensor can be further tuned by modifying the cantilever design and exploring more sensitive probe material.

4. References

[1] V. van, “Optical microring resonators: theory, techniques, and applications,” (CRC Press), 2016.
[2] I. Sharma and P. R. Chaudhuri, A new approach to sensing low electric field using optical fibers’ beam-deflection configuration with BiFe0.9Co0.1O3 nanoparticles as probe and determination of polarization, Opt Fiber Technol **62**, 102472(2021).
[3] F. Zheng, “Direct-coupling single-mode fiber ring resonator” JOSA A **33,** 1347-1355(1988).
[4] A. Ghatak, K. Thyagarajan, Introduction to Fiber Optics, (Cambridge University Press), Reprint 2011.

Robust edge states for Vis-IR frequency bands of 1D topological photonic crystal

Ankit Singh, Pramod Kumar, Akhilesh Tiwari
Spintronic and Metamaterial Laboratory, Modeling and Simulation Laboratory,
Department of Applied Sciences,
Indian Institute of Information Technology, Allahabad, 211015, India.
atiwari@iiita.ac.in , pkumar@iiita.ac.in

Abstract: In this manuscript, a one-dimensional photonic crystal (1D PhC) hetero-structure with inversion symmetry has been proposed and theoretically studied from visible to infra-red (IR) frequency range. The proposed hetero-structure has shown the robust resonant modes for each frequency bandgap. These resonant modes are characterized by the Zak phase (0 or π) and the opposite sign of reflection phase. This hetero-structure enhances the strong light–matter interaction and paves new explorations in topological photonics and opens up new applications in optics, photonics, and opto-electronics devices etc.
Keywords: 1D PhC hetero-structure, Edge states, Zak phase.

1. Introduction

Recently, research in topological photonics has attracted the attentions of many researchers because of its unique properties like topological protected edge and surface states [1,2]. They have applications in integrated optics, photonics, and optoelectronics devices, because of their robustness against any perturbations like back-scattering and immune to impurities and disorders. Topological protected states occur at the interface of two PhCs hetero-structure, which is equivalent to the quantum spin Hall effect and its topological protected edge conductance [3,4]. A strong localization throughout the frequency range is still very challenging with single optical devices. In this paper, a 1D PhC hetero-structure has been proposed and theoretically studied. This hetero-structure shows edge states for all the frequency bandgap and due to the topologically protected edge state, it provides a way to control strong light-matter interaction for the frequency range from UV to IR regions. The proposed structure may pave the way for new explorations in optics, photonics integrated circuits, industrial applications, etc. The analysis has been done with the help of Comsol multiphysics 5.4a and MATLAB software.

2. Results and discussion

2.1 Proposed Hetero- structure and Zak Phase

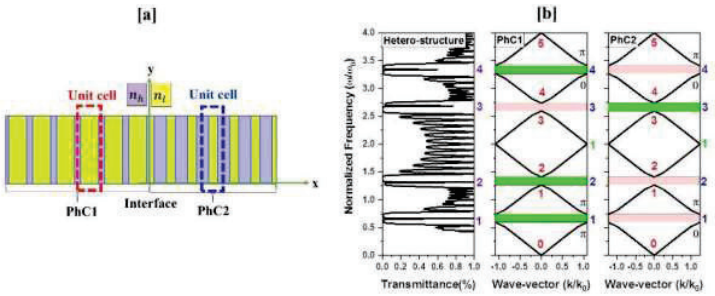

Fig. 1:(a) Schematic diagram of 1D PhC hetero-structure. PhC1 (PhC2) consists of six-unit cells $\frac{t_h}{2}t_l t_l \frac{t_h}{2}$ $\left(\frac{t_l}{2}t_h t_h \frac{t_l}{2}\right)$ ***of materials*** Ta_2O_5 $(n_h = 2.14)$ ***and*** SiO_2 $(n_l = 1.45)$ ***and thickness of high (low) refractive index layer*** $t_h = 245.32\ nm$ $(t_l = 362.02\ nm)$ ***(b) shows transmittance profile and dispersion diagrams of PhC1 and PhC2.***

Fig1 (a) shows the schematic diagram of the proposed hetero-structure. It consists of two PhCs, and their transmittance profile shows edge states for frequencies 94.25 THz, 187.61 THz, 383.63 THz and 476.94 THz and are shown in Fig1 (b) in magenta digits. The dispersion diagrams of proposed structure show six bands and four band-gaps as shown in

red and blue digits. All bands are characterized by Zak phase as $0 or\ \pi$ and are shown in Fig1(b) as black digits. It is calculated for periodic system with the help of the corresponding band structure and used to characterize the frequency inside the bandgap by considering the sign of the surface impedance. It is calculated from the following equation as

$$sgn\left[\xi^{(n)}\right] = (-1)^n(-1)^l exp\left(i\sum_{n=0}^{n-1}\theta_n^{Zak}\right) \quad (1)$$

Where θ_n^{Zak} is the Zak phage and n (l) is the number of bandgap (crossing). Crossing is occurred in between 3 and 4 bands. For each band-gap, the reflection phase may be obtained using eq.(1) as $\xi < 0$ and $\xi > 0$ which are shown in Fig.1(b) as the green and pink strips, respectively. The edge states occur for the opposite sign of surface impedance [5].

2.2 Topological Edge state

Fig. 2 shows topological edge states and their corresponding electric field norm. The dotted lines denote the fitting curve, which is symmetric under Lorentzian line shape. It means Lorentzian resonance has occurred in between the interface of PhC1 and PhC2 with transmittance 99.89%, 99.96%, 76.71 %, and 59.73% at resonant frequencies 94.25 THz, 187.61 THz, 383.63 THz, and 476.94 THz. The full width half maxima (FWHM) for each peak is 0.7121, 0.78014, 0.93447, and 1.06785. The quality factor is defined as the ratio of resonant frequency (RF) to FWHM i.e. $Q = RF/FWHM$. And for each topological edge mode, it is equal to 132.35, 240.48, 410.53, and 446.63 THz.

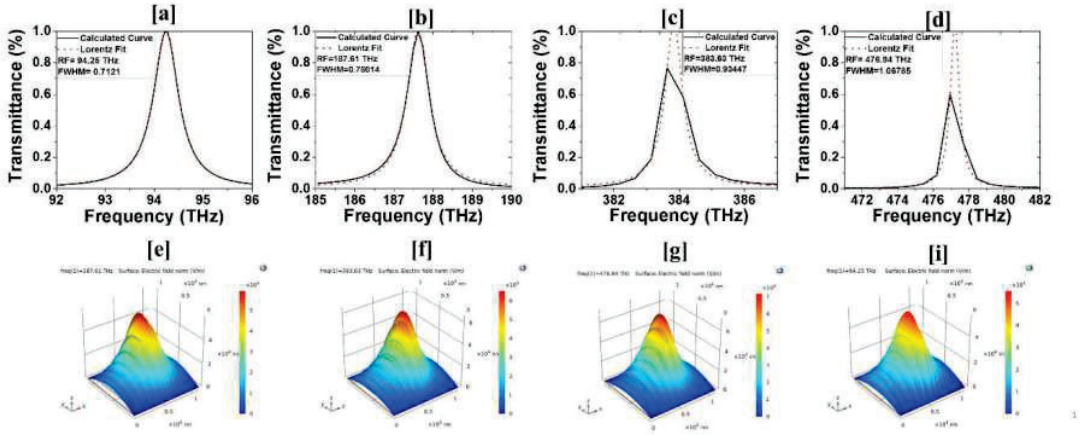

Fig. 2: Topological edge states at the frequency (a) 94.25 THz, (b) 187.61 THz, (c) 383.63 THz and (d) 476.94 THz and their electric field norm.

The RF is a sharp transmission peak, which is located at the interface between two PhCs, which can be shown by the electric field norm in Fig. 2 (e) (f) (g), and (h). These validate the presence of topological edge states.

3. Conclusion

In conclusion, a way to enhance the strong light-matter interaction throughout the frequency range has been discussed. The proposed hetero-structure has shown topological edge modes from visible to IR frequency range. This work may be helpful to develop novel application in the field of optics, photonic, and laser devices.

4. References

[1] A. Singh, A. Gupta, A. Tiwari & P. Kumar, "Heterogeneous integration of TiO2 epitaxial growth for one-dimensional photonic crystal: An experimental and theoretical analysis," Materials Today comm., 25, 101367 (2020).

[2] L. Lu, J. D. Joannopoulos, & M. Soljačić. "Topological photonics," *Nature Photonics*, *8*(11), 821–829 (2014).

[3] K. H. Choi, C. W. Ling, K. F. Lee, Y. H. Tsang, & Kin Hung Fung, "Simultaneous multi-frequency topological edge modes between one-dimensional photonic crystals," *Optics Letter* 41(7), 1644-1647 (2016).

[4] A. B. Khanikaev, S. H. Mousavi, W. K. Tse,, M. Kargarian, A. H. MacDonald & G. Shvets, "Photonic topological insulators," *Nature Materials*, *12*(3), 233–239 (2013).

[5] M. Xiao, Z. Q. Zhang, & C. T. Chan, "Surface Impedance and Bulk Band Geometric Phases in One-Dimensional Systems," *Physical Review X*, 4, 021017 (2014).

Improvement of electron bunch characteristics trapped within the wake bubble using upward plasma density ramp lengths in laser wakefield acceleration

Mohit Kumar[a], Hitendra Kumar Malik[b], Sandeep Kumar[c]
[a,b]PWAPA Laboratory, Department of Physics, IIT Delhi, New Delhi-110016, India
[c]Department of Physics, Manav Rachna University, Faridabad-121004, India
[a]mohitkushwaha8793@gmail.com, [b]hitendra.k.malik@gmail.com, [c]sandeepkumar@mru.edu.in

Abstract: Laser Wakefield acceleration (LWFA) is a method used for generating high-quality electron beams. These beams can be used further for the development of a compact X-ray source. In LWFA, the energy gain of the injected electron bunch inside the plasma bubble can be maximized by optimizing the parameters of the laser and the plasma density profile. In this work, we study the effect of different linear upward density ramp lengths on electron bunch energy gain (E), its charge (Q), and its normalized rms emittance in the x-y direction $(\epsilon_x - \epsilon_y)$ by using Fourier-Bessel particle-in-cell simulations (FBPIC). In our simulation, for the optimal parameters of the laser, we report 527.34 MeV energy gain in a 3.01 mm long plasma channel.
Keywords: Wake Bubble, Laser Wakefield acceleration, Emittance, X-ray Source

1. Introduction

Conventional particle accelerators used for particle acceleration are generally very expensive due to their large size. Laser-plasma-based particle accelerators are the next generation accelerators capable of producing extremely large accelerating gradients, roughly three orders of magnitude greater than the conventional RF accelerators [1] act with plasma. Because of the high inertia of stripped ions, the radial ponderomotive force of the laser pulse causes complete electron cavitation, forming a bubble behind the driver. The ion cavity is also known as the bubble or the blowout region [2]. To generate good quality electron bunches in LWFA, most experiments and theoretical studies are conducted in the blowout regime. This innovation has the potential to enable next-generation accelerators and compact radiation sources [3-6]. The quality and stability of the electron beam are one of the most important aspects of LWFA. Longitudinal and transverse electron-injection mechanisms control the energy gain and emittance of accelerated electron bunches [7-10]. This paper aims to investigate how an upward linear density ramp structure influences the energy gain of accelerated electrons in the bubble regime of LWFA by performing 2D-FBPIC simulations. In this work, we use a slightly modified density profile as described in [8], with the profile:

$$\frac{n^2}{n_0^2} = \begin{cases} H(z)z/L_r & if\ z \le L_r \\ 1 + H\left(b - |z - z_i|\ \alpha\ cos^2\left(\pi \frac{z-z_i}{2b}\right)\right) & if\ z \ge L_r, \end{cases} \quad (1)$$

Here, $H(z)$ is the Heavyside function, n_0^2 is the fraction of density plateau of the critical density $n_c = \omega^2 \epsilon_0 m_e / e^2$ with the laser frequency ω , L_r the initial ramp length of the plasma, z_i the position of the peak density with half-width b and relative amplitude α. A simulation box has the dimensions of $60 \times 60 \mu m$ in the longitudinal and radial directions. Consider the density of the plasma is $0.22 \times 10^{25}\ m^{-3}$ and plasma medium has a length of 5mm.

2. Simulation Results

2.1 Effect of Ramp length on electron bunch characteristics

Figure 1 shows the plasma density profile for different plasma ramp lengths. It is observed in all cases that the density profile increases linearly from 0 to n_e for $0 \le x \le Z_{ramp}$. The chosen normalized vector potential is $a_0 = 4.0$, and the waist of the laser

pulse is $w_0 = 11\ \mu m$, 800 nm is the laser wavelength. The laser is focused near the end of the ramp length in a 5 mm long plasma channel.

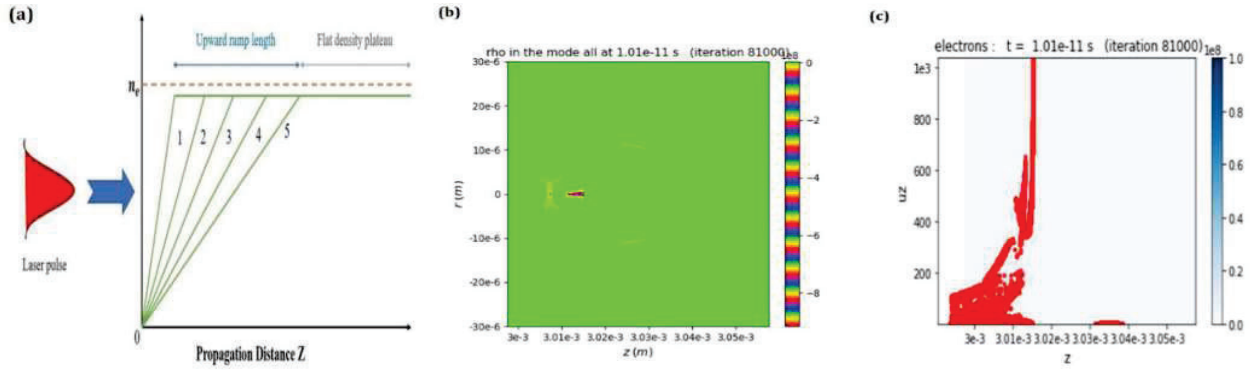

Fig.1. (a) *FBPIC simulation of linear-upward plasma density ramp lengths for five different cases:* (i) Z_{ramp} *= 20 μm,* (ii) Z_{ramp}*= 40 μm,* (iii) Z_{ramp}*= 60 μm,* (iv) Z_{ramp} *= 80 μm and (v)* Z_{ramp} *=100 μm.* ***(b)*** *2-D snapshot of injected electron bunch inside the bubble,* ***(c)*** *Maximum velocity of electron bunch along the z-direction in the case of density profile with linear upward movement with* Z_{ramp}*= 40 μm for* $a_0 = 4.0$ *at time t =* 1.01×10^{-11} *sec.*

In the LWFA method, we try to improve the energy gain, normalized rms emittance in the x-y direction $(\epsilon_x - \epsilon_y)$ and charge of the injected electron bunch inside the wake bubble. We find that the linear upward density ramp mainly changes the phase velocity of the wake bubble. These parameters change the dephasing length. An electron travels a certain distance before it is decelerated and this is called the dephasing length. Due to the linear upward density ramp length, the dephasing length is increasing and with the increase in the dephasing length, the electron bunch is accelerated a longer distance, so the electron bunch gains higher energy inside the wake bubble. The laser Wakefield acceleration scheme produces, $u_z = 1034$ in a plasma channel with a length of 3.01 mm and a corresponding energy gain is 527.34 MeV. A ramp length of longer values results in a greater energy gain for the electron bunch being injected. After that, the effect of different ramp lengths on the amount of the charge injected inside the bubble and normalized emittance in the x-y direction $(\epsilon_x - \epsilon_y)$ have been studied. Results show that if the value of the ramp length is increased then the value of the charge, trapped inside the bubble is also reduced. Because increasing the ramp length the bubble back phase velocity also increases so the value of charge trapped inside the bubble is reduced. A stable variation in normalized rms emittances $(\epsilon_x - \epsilon_y)$ was observed when ramp length was increased. The result indicated that the value of the emittance in the y-direction is smaller than the emittance in the x-direction.

3. References

[1] Esarey, Eric, C. B. Schroeder, and W. P. Leemans. "Physics of laser-driven plasma-based electron accelerators." *Reviews of modern physics* 81, no. 3 (2009): 1229.

[2] Pukhov, Alexancer, and Jürgen Meyer-ter-Vehn. "Laser wake field acceleration: the highly non-linear broken-wave regime." *Applied Physics B* 74, no. 4 (2002): 355-361.

[3] Nakajima, Kazuhisa. "Towards a table-top free-electron laser." *Nature physics* 4, no. 2 (2008): 92-93.

[4] Albert, Felicie, A. G. R. Thomas, S. P. D. Mangles, S. Banerjee, Sébastien Corde, Alessandro Flacco, Michael Litos et al. "Laser wakefield accelerator based light sources: potential applications and requirements." *Plasma Physics and Controlled Fusion* 56, no. 8 (2014): 084015.

[5] Malik, Hitendra K. *Laser-Matter Interaction for Radiation and Energy*. CRC Press, 2021.

[6] Malik, Hitendra K. "Generalized treatment of skew-cosh-Gaussian lasers for bifocal terahertz radiation." *Physics Letters A* 384, no. 15 (2020): 126304.

[7] Dawson, John M. "Nonlinear electron oscillations in a cold plasma." *Physical Review* 113, no. 2 (1959): 383.

[8] Faure, Jérôme, Yannick Glinec, A. Pukhov, S. Kiselev, S. Gordienko, E. Lefebvre, J-P. Rousseau, F. Burgy, and Victor Malka. "A laser–plasma accelerator producing monoenergetic electron beams." *Nature* 431, no. 7008 (2004): 541-544.

[9] Geddes, C. G. R., Cs Toth, J. Van Tilborg, E. Esarey, C. B. Schroeder, D. Bruhwiler, C. Nieter, J. Cary, and W. P. Leemans. "High-quality electron beams from a laser wakefield accelerator using plasma-channel guiding." *Nature* 431, no. 7008 (2004): 538-541.

[10] Tooley, M. P., B. Ersfeld, S. R. Yoffe, A. Noble, E. Brunetti, Z. M. Sheng, M. R. Islam, and D. A. Jaroszynski. "Towards attosecond high-energy electron bunches: Controlling self-injection in laser-wakefield accelerators through plasma-density modulation." *Physical Review Letters* 119, no. 4 (2017): 044801.

Near optimal emission enhancement from quantum-emitters embedded in dielectric pillars

Mohammed Ashahar Ahamad and Faraz Ahmed Inam
Department of Physics, Aligarh Muslim University, Aligarh, Uttar Pradesh 202002, India
faraz.inam@gmail.com

Abstract: Fluorescence-enhancement from quantum-emitters embedded-in high refractive-index micro-pillars has been limited to about an-order-of-magnitude. Using multi-polar electromagnetic-scattering and near-field plasmonic resonances, we report a hybrid resonator-antenna-scheme to achieve around three-orders-of-magnitude fluorescence-enhancement.

1. Introduction

In the last decade, micro and nano-pillars have been extensively fabricated out of the high refractive indexed bulk crystals for enhancing the fluorescence of quantum-emitters embedded in these host material, mainly diamond and silicon-carbide (SiC) [1,2]. However, in these dielectric high refractive-index pillars, the Purcell enhancement (or decay rate enhancement relative to the bulk substrate) is mainly restricted to around unity [2,3]. The fluorescence enhancement (FE) therefore results mainly due the enhancement of the collection efficiency (CE) for dipole emission inside these micro/nano-pillars instead of a bulk substrate. This limits the maximum FE observed from the pillars structures to around an order of magnitude [1–3].

For perpendicular dipoles (relative to the interface), the rates are significantly enhanced for dipole emission in the vicinity of the metallic surface [4] (Fig. 1a). The Purcell factor, F_p is the ratio of the decay rates near the Ag substrate to the decay rate in vacuum $\frac{\gamma_{Ag}}{\gamma_{vacuum}}$. To understand the physics of dipole emission inside the high indexed SiC pillar, we first analytically calculated the various multi-polar scattering cross-section for the case of a dielectric SiC and metallic Ag pillar. From Mie theory, the far-field scattering cross-section for an infinite cylinder placed in air, excited by an electromagnetic field is given by [5]:

$$Q_{scatt} = \frac{4}{x}\sum_{n=1}^{\infty}(|a_n|^2 + |b_n|^2). \tag{1}$$

Here, $x = ka$ is the size parameter with a being the cylinder's radius, and a_n and b_n being the electric and magnetic scattering coefficients. When the excitation field is in resonance with the modes of the cylinder, large amplification of the field amplitudes inside the cylinder is expected [6]. This will also result in the increase in the decay rates for dipole emission in the cylinder. The local electromagnetic density of states (LDOS) provided by the local electromagnetic environment around the dipole emitter is defined as [7]:

$$\rho(\omega, r) = \sum_{k,\sigma} |\hat{d}.\vec{E}_{k,\sigma}(r)|^2 \delta(\omega - \omega_{k,\sigma}). \tag{2}$$

The summation here is over all wave-vectors (k) and polarizations (σ). The decay rate will therefore be proportional to $|E|^2$ at the dipole's position. For the case of dipole emission within the SiC and in proximity of Ag cylinder (Fig. 1 b), the excitation field will correspond to the dipole's radiation field itself. In the present case, it corresponds to the nitrogen vacancy centre in SiC, $N_C V_{Si}$, whose emission is centered at 1300 nm [8]. The scattering cross-sections for a SiC is plotted in Fig. 1 (c). Here, clear resonance modes in the scattering cross-sections are observed, with the first major maximum observed for SiC cylinder diameter around 580 nm, somewhat lower than $\lambda/2$.

2. Results and Discussion

We vary the SiC/Ag cylinder diameter for various SiC pillar heights. The Ag cylinder height is initially fixed at 340 nm with the position of the vertical dipole (perpendicular to the SiC-Ag interface) fixed at a separation of 20 nm below the SiC cylinder's top surface. These results are presented in Fig. 2. In accordance with the resonance peaks in the scattering cross-section curve for SiC (Fig. 1c), sharp resonance peaks are observed in the relative decay rate ($\frac{\gamma}{\gamma_{bulk}}$) curve (Fig. 2b). As the SiC cylinder's height is increased, the resonance peak is observed to shift

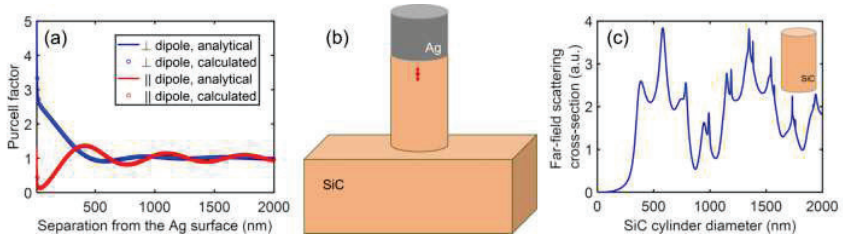

]

Fig. 1. (a) Purcell enhancement of the dipole emission near a metallic substrate for the case of horizontal or perpendicular dipole showing the analytical and computational methods. (b) Schematic of the diameter-matched pillar-antenna resonator design. (c) Multi-polar scattering cross-section for the case of a dielectric SiC pillar.

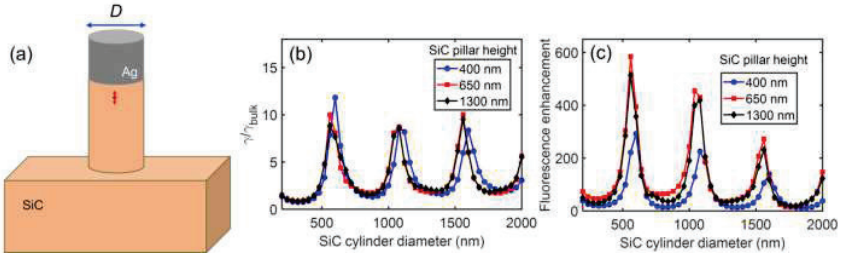

Fig. 2. (a) Schematic showing a dipole in the SiC cylinder at 20 nm from the Ag cylinder when varying the diameter of both cylinders. (b) Relative decay rate ($\frac{\gamma}{\gamma_{bulk}}$), (c) FE curves obtained by varying the SiC/Ag cylinder diameter for three SiC pillar heights. The Ag cylinder's height is fixed at 340 nm.

towards lower cylinder diameter (around 560 nm) and close to the observed first major maximum around 580 nm in the scattering cross-section curve for the case of an infinite SiC cylinder (Fig. 1c). Also, it can be clearly observed that the decay rate enhancement factor is much larger than the near unity factor observed for the case of a dielectric pillar [2, 3]. With an increase in the SiC cylinder's height more cylindrical modes are expected to become available for the dipole emitter to couple to, leading to an increase in the CE. Very large FE values around 600 are calculated around the first resonance peak for cylinder diameter around 560 nm (Fig. 2d).

References

1. T. M. Babinec, B. J. M. Hausmann, M. Khan, Y. Zhang, J. R. Maze, P. R. Hemmer, and M. Lončar, "A diamond nanowire single-photon source," Nat. Nanotechnol. **5**, 195–199 (2010).
2. S. Castelletto, A. S. Al Atem, F. A. Inam, H. J. von Bardeleben, S. Hameau, A. F. Almutairi, G. Guillot, S.-i. Sato, A. Boretti, and J. M. Bluet, "Deterministic placement of ultra-bright near-infrared color centers in arrays of silicon carbide micropillars," Beilstein J. Nanotechnol. **10**, 2383–2395 (2019).
3. S. W. Jeon, J. Lee, H. Jung, S. W. Han, Y. W. Cho, Y. S. Kim, H. T. Lim, Y. Kim, M. Niethammer, W. C. Lim, J. Song, S. Onoda, T. Ohshima, R. Reuter, A. Denisenko, J. Wrachtrup, and S. Y. Lee, "Bright Nitrogen-Vacancy Centers in Diamond Inverted Nanocones," ACS Photonics **7**, 2739–2747 (2020).
4. J. R. Lakowicz, "Radiative decay engineering 5: metal-enhanced fluorescence and plasmon emission," Anal. Biochem. **337**, 171–194 (2005).
5. F. Frezza, F. Mangini, and N. Tedeschi, "Introduction to electromagnetic scattering: tutorial," J. Opt. Soc. Am. A **35**, 163 (2018).
6. J. F. Owen, P. W. Barber, and R. K. Chang, "Internal electric field distributions of a dielectric cylinder at resonance wavelengths," Opt. Lett. **6**, 540 (1981).
7. F. A. Inam, T. Gaebel, C. Bradac, L. Stewart, M. J. Withford, J. M. Dawes, J. R. Rabeau, and M. J. Steel, "Modification of spontaneous emission from nanodiamond colour centres on a structured surface," New J. Phys. **13**, 073012 (2011).
8. S. Castelletto and A. Boretti, "Silicon carbide color centers for quantum applications," J. Physics; Photonics **2**, 022001 (2020).

Auxiliary-cavity and Quantum dot molecules assisted tunable multistability in a hybrid optomechanical system

Surabhi Yadav and Aranya B Bhattacherjee
Department of Physics, Birla Institute of Technology and Science, Pilani-Hyderabad Campus, Telangana-500078, India
Email: p20190049@hyderabad.bits-pilani.ac.in

Abstract: In this work, we theoretically study a hybrid cavity quantum electrodynamic (C-QED) system consisting of embedded quantum dot molecules (QDMs) in a photonic crystal cavity (PhC) coupled to an auxiliary cavity via a single optical mode waveguide. We investigate the optical response of multistability, which can be used in designing potential all-optical switches in quantum information processing. The results indicate that the proposed system exhibits either bistability or tristability that can be tuned and controlled, depending on the system parameters.

Keywords: Optomechanical system, Photonic crystal cavity, Quantum dot molecules, Optical response.

1. Introduction:

In the domain of C-QED, the interaction between quantum emitters and photons has gained considerable interest as it provides potential application in quantum information processing [1-2]. A self-assembled quantum dot system in PhC nanocavities [3] is an exciting platform for studying a solid-state C-QED system because of the strong light-matter interaction resulting from the cavities' strong optical confinement. In the past few years, significant progress has been seen in cavity optomechanics, both theoretically and experimentally. In an optomechanical system, light pressure on the mechanical oscillator (i.e., radiation pressure) alters the cavity's length, which modulates the cavity's optical intensity generating optomechanical nonlinearity. Some interesting phenomena in this field are optomechanically induced transparency (OMIT) [4], photon blockade [5], and optical bistability (OB) [6]. Quantum dot molecules, consisting of two semiconductor dots coupled with tunnelling, have recently received attention because of exciting phenomena in this new semiconductor structure. QDMs are assembled by self-assembly either through chemical synthesis or epitaxial growth [7].

2. Theoretical Model:

In this work, we consider a C-QED system, as shown in figure 1. The proposed model consists of primary PhC cavity "a" and N-three level QDMs directly driven by a strong pump laser and a weak probe field, which is embedded in the cavity. In addition, the primary cavity is coupled to an auxiliary cavity "c" with coupling strength "J." The pump field with frequency "ω_p" drives the primary cavity having frequency "ω_a" and the optical response of the system is probed by weak field with frequency "ω_c" and strength E_s.

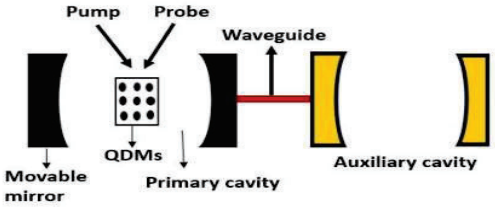

Figure 1: Schematic of the proposed C-QED system. The primary PhC has one movable mirror. The pump field with strength E_p directly excites the QDMs.

The coupling between the two cavities is described by the Hamiltonian, $H_{ac} = \hbar J(a^\dagger c + c^\dagger a)$ and $H_{free} = \hbar\omega_m b^\dagger b + \hbar\omega_a a^\dagger a + \hbar\omega_c c^\dagger c$ describes the free energies of the mechanical mode with ω_m as the frequency of the mechanical mode and the two optical modes. The tunnelling Hamiltonian between the energy level of the QDM is given by $H_T = \hbar T \sum_1^N(\sigma_{12}^\iota + \sigma_{21}^\iota)$ and the total energy of the QDM is, $H_{QDM} = \hbar\sum_1^N(\omega_{10}\sigma_{11}^\iota + \omega_{20}\sigma_{22}^\iota)$. The coupling between the QDMs excitons and the optical cavity mode is given by the Hamiltonian $H_{QDM,a} = \hbar g\sum_1^N(a\sigma_{10}^\iota + a^\dagger\sigma_{01}^\iota)$, where g is the coupling strength. The optomechanical interaction between the mechanical mode and the primary cavity is describe by the Hamiltonian, $H_{om} = -\hbar G a^\dagger a(b^\dagger + b)$, where G is the optomechanical coupling strength. Hamiltonian of the QDM coupled to the pump and probe field is written as, $H_{QDM,f} = -\mu E_p\sum_1^N(\sigma_{10}^\iota e^{(-\iota\omega_p)t} + \sigma_{01}^\iota e^{(\iota\omega_p)t}) - \mu E_s\sum_1^N(\sigma_{10}^\iota e^{(-\iota\omega_s)t} + \sigma_{01}^\iota e^{(\iota\omega_s)t})$, μ is the exciton's electric dipole moment. Working in the rotating frame of ω_p, the new Hamiltonian of the system is written as,

$$H = \hbar\Delta_a a^\dagger a + \hbar\Delta_c c^\dagger c + \hbar\omega_m b^\dagger b + \hbar(\Delta_1 A^\dagger A + \Delta_2 B^\dagger B) + \hbar J(a^\dagger c + c^\dagger a) + \hbar g_1(aA^\dagger + a^\dagger A) + \hbar T(A^\dagger B + B^\dagger A) - \hbar G a^\dagger a(b^\dagger + b) - \mu_N E_p(A^\dagger + A) - \mu_N E_s\left(A^\dagger e^{-\iota\delta t} + A e^{\iota\delta t}\right). \quad (1)$$

Here, $\Delta_a = \omega_a - \omega_p$, $\Delta_c = \omega_c - \omega_p$, $\Delta_j = \omega_{j0} - \omega_p (j = 1,2)$, $\delta = \omega_s - \omega_p$, $g_1 = g\sqrt{N}$, $\mu_N = \mu\sqrt{N}$ and A and B are the Holstein-Primakoff transformation. The system's dynamics are described by the following Heisenberg-Langevin equation,

$$\dot{a} = -\left[\kappa_a + \iota\left(\Delta_a - G(b^\dagger + b)\right)\right]a - \iota g_1 A - \iota J c + \sqrt{2\kappa_a}a_{in},$$

$$\dot{b} = -[\gamma_m + \iota\omega_m]b + \iota G a^\dagger a + \sqrt{2\gamma_m}\xi,$$

$$\dot{c} = -[\kappa_c + \iota\Delta_c]c - \iota J a + \sqrt{2\kappa_c}c_{in},$$

$$\dot{A} = -[\gamma_1 + \iota\Delta_1]A - \iota g_1 a - \iota T B + \frac{\mu_N E_p}{\hbar} + \frac{\mu_N E_s}{\hbar}e^{-\iota\delta t} + \sqrt{2\gamma_1}a_{in},$$

$$\dot{B} = -[\gamma_2 + \iota\Delta_2]B - \iota T A + \sqrt{2\gamma_2}a_{in}. \quad (2)$$

On simplifying the steady state solutions of eqn (2), we obtain the expression for the intracavity photon number $I_{as} = |a_s|^2$ and plot the following graphs.

3. Results:

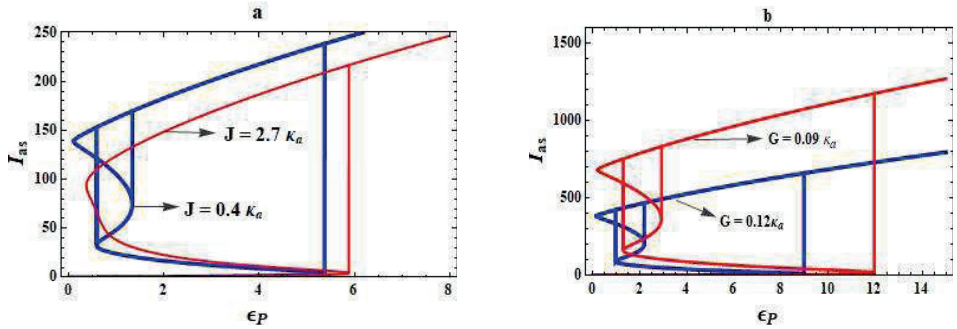

Figure 2: I_{as} vs ϵ_p/κ_a for (a) two optical cavities coupling strength (b) Optomechanical coupling strength. All parameters used are dimensionless w.r.t κ_a.

Figure 2(a) displays the plot of I_{as} as a function of $\epsilon_P = (\mu E_P)/\hbar$ for $J = 0.4\kappa_a$ and $J = 2.7\kappa_a$ where both plots show hysteresis curve. For $J = 0.4\kappa_a$ the plot shows a distinct tristable behaviour and $J = 2.7\kappa_a$ displays a single bistable curve. A high value of J shows that a large amount of energy is transferred to the auxiliary cavity, which reduces the optomechanical nonlinearity associated with the primary cavity. As a result, the tristable behaviour for low J changes to the bistable behaviour for high J. Also, the optical switching of $J = 0.4\kappa_a$ occurs at a low pump Rabi frequency compared to $J = 2.7\kappa_a$. Figure 2(b) plots the mean intracavity photon number I_{as} versus ϵ_P for two values of optomechanical coupling strength, $G = 0.09\kappa_a$, and $G = 0.12\kappa_a$ for cavity-pump detuning, $\Delta_a = 0.1\kappa_a$. As seen from the graph, tristability appears for both the G values, but for $G = 0.09\kappa_a$, tristability appears for a high intracavity photon number compared to $G = 0.12\kappa_a$. Also, the optical switching points appear at a lower value of ϵ_P for $G = 0.12\kappa_a$. Optimizing the necessary system variables makes an efficient transition from bistability to tristability feasible.

4. References:

1. C. Monroe, "Quantum information processing with atoms and photons", *Nature* **416**, 238–246 (2002).
2. A. Majumdar, M. Bajcsy, and J. Vučković, "Probing the ladder of dressed states and nonclassical light generation in quantum-dot–cavity QED," Phys. Rev. A **85**, 041801(2012).
3. T. Yoshie, A. Scherer, J. Hendrickson, G. Khitrova, H. M. Gibbs, G. Rupper, C. Ell, O. B. Shchekin, and D. G. Deppe, "Vacuum Rabi splitting with a single quantum dot in a photonic crystal nanocavity," Nature **432**, 200–203 (2004).
4. G. S. Agarwal and Sumei Huang, "Electromagnetically induced transparency in mechanical effects of light," Phys. Rev. A **81**, 041803 (2010).
5. V. Bhatt, S. Yadav, P. Jha and A. B. Bhattacherjee, "Photon Blockade in a coupled double quantum dot-nonlinear Optomechanical system," Phys. *Scr.* **96** 125108 (2021).
6. S. Yadav and A. B. Bhattacherjee, "Nonlinear optical response in coupled quantum wells optomechanical microcavity," Phys. *Scr.* **97** 015102 (2022).
7. L. Wang, A. Rastelli, S. Kiravittaya, M. Benyoucef, and O.G. Schmidt, "Self-Assembled Quantum Dot Molecules," Adv. Mater., 21 2601 (2009).

Theoretical study of Magneto-Optical Rotation and its coherent control in presence of Vector beam as coupling light

Rohit Kumar, Dixith Manchaiah and Raghavan K Easwaran
Department of Physics, Indian Institute of Technology Patna, Bihta, Patna, Bihar, India
raghavanke@iitp.ac.in, rohitkumar25121995@gmail.com

Abstract: In this study, we have theoretically obtained results for Magneto-Optical Rotation (MOR) and its coherent control by using vector beam of light as coupling source. Different modes on higher order Poincare sphere (HOPS) is taken and its effect on MOR is presented.
Keywords: MOR, HOPS, Vector beam.

1. Introduction

In the previous three decades, large class of physical phenomena is discovered on coherent interaction basis which is not possible in otherwise incoherent interaction. Some of the examples are - electromagnetically induced transparency (EIT) [1], coherent control of magneto-optical rotation (CCMOR) [2] etc. MOR is generally arises due to birefringence or dichroism induced by medium on the light propagation which leads to rotation of plane polarization of probing light. This birefringence or dichroism can be induced either by magnetic field which breaks the isotropy of space and/or by additional laser sources (CCMOR) which also controls the amount of rotation [3]. MOR has useful application in several areas such as laser frequency stabilization, magnetometry, polarization control etc. [4]. In present study, we have reported the coherent control of MOR by vector beam of light as coupling beam with and without presence of magnetic field.

2. Theoretical Model

A 4-level system figure (1) is considered for the study which can be found in real atomic system such as Rb by properly adjusting the frequency and polarization under consideration. Probe is linearly polarized light which can be thought of as linear combination of right circularly polarized (RCP) and left circularly polarized (LCP). From figure (1) it is clear that σ− component of the probe addresses the transition |4> to |3> while σ+ component drive the transition |4> to |2>.

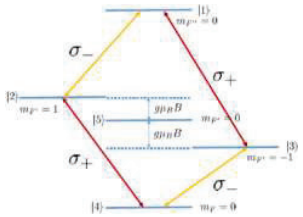

Fig. 1. Four level atomic system.

We have used coupling light as vector beam which is also can be thought of as superposition of RCP and LCP but the amount of contribution of RCP and LCP is not same as compared to linear polarization case. A magnetic field lift the degeneracy of middle state which is F' = 1 state into $m_{F'} = 1,0,-1$ states respectively. Since $m_{F'} = 0$ state is not connected with any light source so the system practically reduces to 4-level only.

2.1 Vector Beam

Vector beam is a special class of beam where polarization is not uniform throughout the transverse plane of propagation. It can be generated through orthogonal superposition of Laguerre-Gaussian(LG) modes. Best way to

visually represent this kind of beam is through HOPS. This is a two dimensional surface of sphere where the states can be represented as [5] –

$$\psi_{LG_p^{l_1,l_2}} = cos(\frac{\phi}{2})LG_p^{l_1}e^{i\frac{\theta}{2}}\hat{\mathbf{e}}_\mathbf{R} + sin(\frac{\phi}{2})LG_p^{l_2}e^{-i\frac{\theta}{2}}\hat{\mathbf{e}}_\mathbf{L} \quad (1)$$

Here θ and φ are azimuthal and polar coordinates in spherical coordinate. LG_{l1} and LG_{l2} are the Laguerre-Gaussian modes of light. $\hat{\mathbf{e}}_\mathbf{R}$ and $\hat{\mathbf{e}}_\mathbf{L}$ are unit polarization vector corresponding to RCP and LCP.

2.2 Time Evolution

Dynamics of the system described here is best captured by Liouville equation where decay is considered by phenomenological means. This equation can be solved analytically in steady state condition and coherence for the RCP and LCP component of the probe can be found as –

$$\rho_{42,43}^{\sigma_\pm} = \frac{\frac{i\gamma_2}{2}}{[\frac{\gamma_2}{2} + i(\delta_p \pm g\mu_B B)] + \frac{\Omega_{c,v_\mp}^2}{2(\gamma_3 - 2i(\delta_p + \delta_c))}} \quad (2)$$

Here δ_p and δ_c are probe and coupling light detuning. γ_2 and γ_3 are decay rates from intermediate and upper state. $\mathbf{\Omega}_{c,v\pm}$ are the Rabi frequencies for concerned transition. Polarization rotation angle for probe can be given as –

$$\Theta = \frac{\alpha L}{2}[Re(\rho_{43}^{\sigma_-}) - Re(\rho_{42}^{\sigma_+})] \quad (3)$$

Here α is absorption coefficient and L is interaction length for light and atom system.

3. Results and Conclusion

We have obtained rotation angle (3) as a function of probe field detuning with and without magnetic field. Rotation of probe polarization angle has strong dependence on polar angle φ on HOPS.

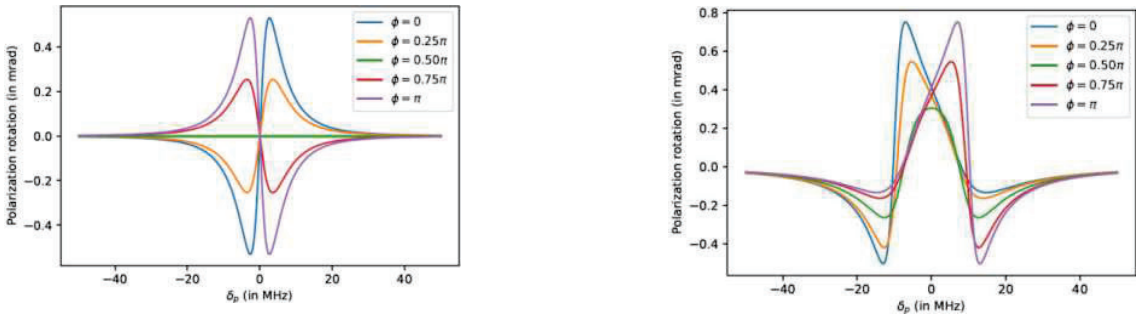

Fig. 2. Variation of rotation angle as a function of probe detuning for different value of polar angle φ (a) in absence and (b) in presence of magnetic field. Other parameters used are - $\gamma_2 = 6$MHz, $\gamma_3 = 11$MHz, $\delta_c = 0$.

In the absence of magnetic field (fig 2 (a)), intermediate state (fig 1) is degenerate and rotation is solely caused by different field strength for σ+ and σ− polarization component of vector beam. Maximum angle of rotation can be obtained for the case of $\varphi = 0$ and $\varphi = \pi$. These cases are extreme cases and in these situation vector beam behaves like a RCP and LCP respectively. On the other hand, minimum angle of rotation (in this case zero) can be obtained for $\varphi = 0.5\pi$ case which correspond to equal strength in both RCP and LCP component. In presence of magnetic field, lifted degeneracy accounts for additional rotation in figure (2 (b)). In this case even for $\varphi = 0.5\pi$ case we see a minimum rotation angle but not zero identically. This rotation is solely caused due to magnetic field. Also peak of the rotation curve is broader in this case. Other observation is same as the case with absence of magnetic field apart from slightly off detuned rotation. In conclusion, we have shown effect of vector coupling beam on MOR with different modes with and without presence of magnetic field and highlighted the rotation angle variation with controllable experimental parameters.

4. References

[1] M. Fleischhauer, A. Imamoglu, and J. P. Marangos, "Electromagnetically induced transparency: Optics in coherent media," Rev. modern physics 77, 633 (2005).

[2] A. K. Patnaik and G. Agarwal, "Laser field induced birefringence and enhancement of magneto-optical rotation," Opt. communications 179, 97–106 (2000).

[3] K. Pandey, A. Wasan, and V. Natarajan, "Coherent control of magneto-optic rotation," J. Phys. B: At. Mol. Opt. Phys. 41, 225503 (2008).

[4] V. V. Yashchuk, D. Budker, and J. R. Davis, "Laser frequency stabilization using linear magneto-optics," Rev. Sci. Instruments 71, 341–346 (2000).

[5] C. Rosales-Guzman, B. Ndagano, and A. Forbes, "A review of complex vector light fields and their applications," J. ´ Opt. 20, 123001 (2018).

Terahertz Characterization of Laser Scribed Graphene Oxide (GO) films

Shreeya Rane[a], Avinash Kothuru[b], Arun Jana[a], Sanket Goel[b], Dibakar Roy chowdhury[a]

[a]*Department of Physics, École Centrale School of Engineering, Mahindra University, Hyderabad, Telangana, India.*

[b]*MEMS, Microfluidics and Nanoelectronics (MMNE) Lab, Department of Electrical and Electronics Engineering, Birla Institute of Technology and Science (BITS)Pilani, Hyderabad Campus, Hyderabad, India.*

Email: shreeya20pphy007@mahindrauniversity.edu.in

Abstract: Graphene oxide films fabricated through laser scribed method on different flexible substrates have been studied using THz-TDS. It is observed that the surface inhomogeneity resulted from line-by-line irradiation of polyamide through laser leads to optical anisotropy in GO films. Additionally, it is noted that, within the broadband THz characterization frame, the wave guide resonance mode and Fabry Perot oscillations dominate THz transmissions.

Keywords: Terahertz, Graphene oxide, anisotropy

1. Introduction

Graphene oxide (GO) has been conventionally recognized as the precursor for the synthesis of graphene through thermal or chemical reduction. But in recent years GO itself has become a subject of interest due to its fascinating properties [1]. GO offers far greater versatility than graphene in terms of modifying its material characteristics through modification of the oxygen-containing functional groups. However, the applications of graphene oxide are limited due to the intrigue synthesis methods which must be carried out in well controlled environments. Recently, a simple approach of laser assisted synthesis of GO is proposed that do not require optimized environmental conditions, high cost equipments or post processing [2]. In this process, the GO films are fabricated by permulating the surface of polyimide sheets by irradiating it with focused CO2 laser in line by line scan method under ambient conditions.

On the other hand, Terahertz radiations are studied intensively due to its superiority in the fields of engineering, chemistry, material science and medicine, etc [3–6]. Although a lot of effort have been taken the THz technology still suffers from lack of material availability in this frequency regime. In this regard, we have studied the THz properties of GO films fabricated on flexible polyimide substrates. This study can be useful in realizing GO based terahertz flexible electronics that can push terahertz technology into innovative applications.

2. Result and discussion:

In this work, the graphene oxide films are fabricated on two distinct flexible substrates (Lamination and Kapton sheets). The optical microscope images of the fabricated samples are emphasized in inset of figure 1a and 1b for lamination and kapton substrate respectively, the yellow arrow illustrates the direction of laser scan. Here, it can be observed that the samples have miniature grooves (pink dashed line) developed between two adjacent laser scanning lines due to low lasing power at the edges of laser spot. This can also be confirmed by the scalloped edges formed at the film substrate interface.

The GO samples are further characterized using terahertz time domain spectroscopy (THz-TDS) in transmission configuration. The THz transmission is measured as a function of angle between the scanning lines and incident electric field polarization for various cases (0º,15º,45º,75º,90º). The measured THz transmission for GO films on lamination and kapton substrates are shown in figure 1a and 1b respectively. It is noticed that, with increase in angle between the scanning lines and polarization of incident electric field, the THz transmission is increased. This optical anisotropy is because of miniature groove formed during the line-by-line scribing of polyimide sheet that leads to spatial asymmetry in the GO films. Moreover, it is also noticed that the measured THz transmission is dominated by Fabry perot like oscillation with a sharp guided mode resonance [7] at around 1.7THz. Further optical properties of these GO films are extensively studied through parameter extraction using THz transmission [8].

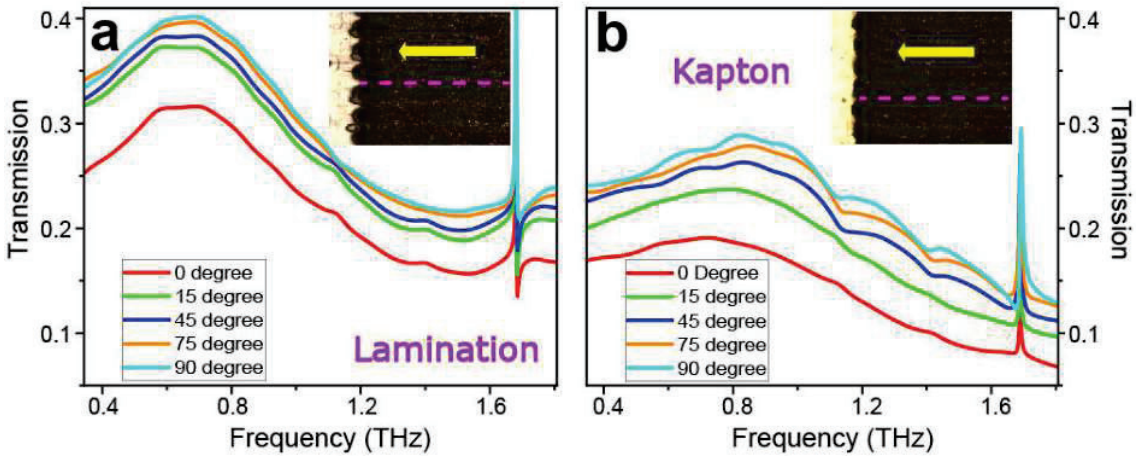

Fig 1: (a) and (b) Demonstrates the measured THz transmission through GO films fabricated on lamination and Kapton substrate respectively. The inset figure illustrates the optical microscope image of fabricated samples.

3. Conclusion:

In this study, THz-TDS is used to investigate the THz characteristics of GO films on lamination and Kapton substrate that are fabricated utilising laser irradiation techniques. It is observed that the optical anisotropy introduced by the laser scribing process is apprehend during THz transmission measurement by the THz-TDS technique. As a result of spatial unevenness occurred due to the line-by-line laser scan on polyimide, the THz transmission of the GO films varies depending on the angle between the scanning lines and polarization of incident electric field.

4. References:

[1] Wu J, Jia L, Zhang Y, Qu Y, Jia B and Moss D J, "Graphene Oxide for Integrated Photonics and Flat Optics," Advanced Materials **33** 2006415 (2021).

[2] Lin J, Peng Z, Liu Y, Ruiz-Zepeda F, Ye R, Samuel E L G, Yacaman M J, Yakobson B I and Tour J M, "Laser-induced porous graphene films from commercial polymers," Nature Communications **5** 5714 (2014).

[3] Kleine-Ostmann T and Nagatsuma T, "A Review on Terahertz Communications Research," Journal of Infrared, Millimeter, and Terahertz Waves **32** 143–71 (2011).

[4] Fischer B, Hoffmann M, Helm H, Modjesch G and Jepsen P U, "Chemical recognition in terahertz time-domain spectroscopy and imaging," Semiconductor Science and Technology **20** S246–53 (2005)

[5] Hangyo M, Tani M and Nagashima T, "Terahertz Time-Domain Spectroscopy of Solids: A Review," International Journal of Infrared and Millimeter Waves **26** 1661–90 (2005).

[6] Parrott E P J, Sun Y and Pickwell-MacPherson E, "Terahertz spectroscopy: Its future role in medical diagnoses" Journal of Molecular Structure **1006** 66–76 (2011).

[7] Fan S and Joannopoulos J D, "Analysis of guided resonances in photonic crystal slabs," Physical Review *B* **65** 235112 (2002).

[8] Rane S, Kothuru A, Jana A, Devi K M, Goel S, Prabhu S and Roy Chowdhury D, "Broadband terahertz characterization of graphene oxide films fabricated on flexible substrates," Optical Materials **125** 112045 (2022).

Interferometry with a light emitting diode

Akanksha Gautam,[1,*] Athira T S,[2] Dinesh N. Naik,[2] Rajeev Singh,[1] Rakesh Kumar Singh[1]
[1]*Laboratory of Information Photonics and Optical Metrology, Department of Physics, Indian Institute of Technology (Banaras Hindu University), Varanasi-221005, India*
[2]*Applied and Adaptive Optics Laboratory, Department of Physics, Indian Institute of Space Science and Technology, Thiruvananthapuram-695547, India*
**Author e-mail address: akankshagautam.rs.phy19@itbhu.ac.in*

Abstract: We have experimentally measured the complex spatial coherence function of a generic incoherent thermal source *i.e.* light emitting diode (LED) using a Sagnac radial shearing interferometer. Here, a very basic theory for incoherent light *i.e.* the van Cittert-Zernike theorem is used to connect the spatial coherence function with the source structure. The coherence is quantitatively measured in an experiment by measuring the fringe visibility from the interferograms and coherence function is analyzed using phase shifting technique.
Keywords: Coherence function, Interferometry, Fringe visibility, Phase shifting techniques.

1. Introduction

The coherent light sources such as lasers are a commonly used deterministic source with high coherence length and this helps to get interference using various interferometric geometries. Whereas, in case of purely incoherent sources like LED and broad band light sources all the points are acting as independent scatterers and also the coherence length of the source is very small. Therefore, interferometry with such light sources is a challenging task. In a coherent case and deterministic light, the field is the measurable quantity whereas the complex coherence function is a useful quantity for the light with many modes [1]. In an incoherent light, the interference can be achieved by the principle of incoherent light interferometry in which two copies of the incoming field is generated and interfere and here we present one such interferometer [2]. The interference is made possible between them when light coming from each independent point only interferes with its counterpart in its copy. Thus, the incoherent addition of the interference patterns results in fringes and on using phase shifting technique [3] and digitally analyzing it finally represents the complex coherence function of the source.

2. Principle

The principle is based on the van Cittert-Zernike theorem [1, 4] which connects the spatial coherence function with an incoherent source by a Fourier transform relation. The field coming from LED with spectral scattering density $\eta(\boldsymbol{r}, z; \lambda)$ gets Fourier transformed using a lens L having a focal length f. Variables r and z are transverse and longitudinal coordinates at the source and λ is the wavelength. The spatial coordinates at the Fourier plane are represented by $\hat{r}$ and $\hat{z}$ for transverse and longitudinal coordinates respectively. The coherence function at Fourier plane is represented by by

$$\Gamma(\hat{\boldsymbol{r}}_1, \hat{\boldsymbol{r}}_2, \hat{z}=0) = \frac{\kappa}{\lambda^2 f^2} \int \exp\left[-i(k_z(\hat{\boldsymbol{r}}_2;\lambda) - k_z(\hat{\boldsymbol{r}}_1;\lambda))z\right] \left\{ \int \eta(\boldsymbol{r}, z;\ \lambda)\, exp\left[-i\frac{2\pi}{\lambda f}\boldsymbol{r}.(\hat{\boldsymbol{r}}_2 - \hat{\boldsymbol{r}}_1)\right] d\boldsymbol{r} \right\} d\lambda \qquad (1)$$

where **κ** is a constant physical quantity having dimensions of length square and $k_z(\boldsymbol{r},\ \lambda) = (\frac{2\pi}{\lambda})\left[\sqrt{1 - \left(\frac{|\boldsymbol{r}|}{f}\right)^2}\right]$.

The integration over the wavelength λ is performed as the source is non-monochromatic having finite spectral bandwidth.

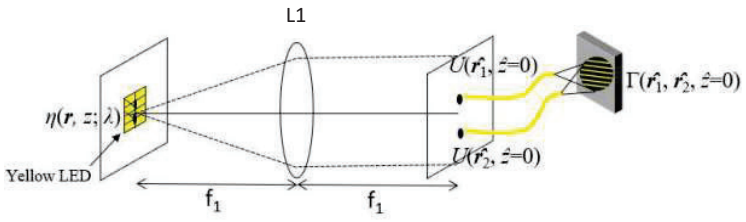

Fig.1 Geometry for performing Fourier transform of the LED

From Eq.(1) we can see that the mutual coherence function $\Gamma(\hat{\boldsymbol{r}}_2, \hat{\boldsymbol{r}}_1)$ measured is reduced to $\Gamma(\hat{\boldsymbol{r}}_2\text{-}\hat{\boldsymbol{r}}_1)$. To visualize the spatial coherence function of the field distribution, we need an interferometer which introduces a radial shear $\hat{\mathbf{r}}_2\text{-}\hat{\mathbf{r}}_1$. The Sagnac interferometer is very stable to external vibrations and we have used it to measure the coherence. Also, in one shot we can record the whole information using this Sagnac common path radial shearing interferometer with a telescopic lens system having two lenses with different focal lengths. The two counter propagating beams following common path were superposed at the output plane such that the wavefront of one beam is expanded and the other is contracted having magnifications α and α^{-1}, respectively. The radial shear introduced by the lens system in the Fourier domain is given by $\hat{\boldsymbol{r}}_2 - \hat{\boldsymbol{r}}_1 = (\alpha - \alpha^{-1})\,\hat{\boldsymbol{r}}$. Now we measure the mutual coherence function $\Gamma(\hat{\boldsymbol{r}}_1, \hat{\boldsymbol{r}}_2, \hat{z}=0)$ as $\Gamma(\alpha\hat{\boldsymbol{r}}_1, \alpha^{-1}\hat{\boldsymbol{r}}_2, \hat{z}=0)$.

3. Experimental Setup and Results

As shown in Fig. 1 the incoherent light field coming from yellow LED is Fourier transformed by lens L1 kept at its front focal length f_1 from LED. The field is now divided into two parts by a polarizing beam splitter (PBS) as shown in Fig. 2 and enters into a Sagnac interferometer made up of three plane mirrors M1, M2 and M3 and a telescopic lens system with lenses L2 and L3 having focal lengths f_2=12cm and f_3=12.5cm, respectively. The lens system with magnification $\alpha=f_3/f_2$ =1.041 set up by lenses L3 and L2 gives a radial shear between the two oppositely propagating beams. When the beams are brought back at the output plane, we observe the interference pattern formed by two radially sheared beams. To measure the complex coherence function, we use a polarization phase shifting technique for fringe analysis. This is realized by a combination of quarter wave plate (QWP) and a polarizer P. The incoming beams from two arms at the output of the interferometer have linear orthogonal polarizations so the QWP kept at 45° from its fast axis converts them into right-handed circularly polarized and left-handed circularly polarized beams, respectively. After QWP, we use a polarizer to get interference. Five interferograms are recorded in an interval of 0° to 360° by rotating polarizer. The interferograms were imaged using lens L4 with focal length f_4=15cm onto a CMOS camera such that the image size fits the aperture of the camera.

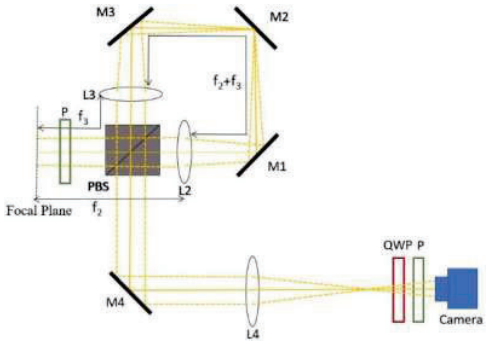

Fig.2 Experimental set up for recording the complex coherence function

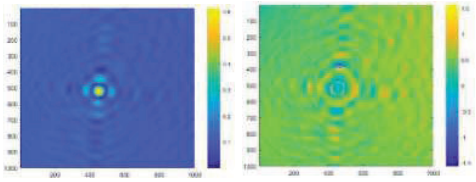

(a) (b)

Fig.3 Experimentally measured coherence function (a)modulus of complex coherence and (b) phase

The complex coherence function $\Gamma(\alpha\hat{\boldsymbol{r}}_1, \alpha^{-1}\hat{\boldsymbol{r}}_2, \hat{z}=0)$ is digitally reconstructed from the recorded interferograms and results are shown in Fig. 3.

4. Conclusion

In summary, we have designed a stable interferometric technique to measure the complex coherence function of an incoherent source. A Sagnac common path interferometer is used to introduce radial shearing using a telescopic lens system and estimate the far field complex coherence distribution of an incoherent source.

5. Acknowledgment

Akanksha Gautam would acknowledge scholarship from the DST-INSPIRE (IF180930).

6. References

[1] M. Born anld E. Wolf, "*Principles of Optics*," 4th ed. (Pergamon, London, 1970),
[2] D. N. Naik, T. Ezawa, R. K. Singh, Y. Miyamoto, and M. Takeda, *"Coherence holography by achromatic 3-D field correlation of generic thermal light with an imaging Sagnac shearing interferometer,"* Opt. Express 20(18), 19658–19669 (2012).
[3] D. N. Naik, T. Ezawa, Y. Miyamoto, and M. Takeda, *"Phase-shift coherence holography,"* Opt. Lett. 35(10), 1728–1730 (2010).
[4] J. W. Goodman, *"Statistical Optics,"* 1st ed. (Wiley, New York, 1985).

Progress Towards a Cold Atomic Vapor Based Entangled Photon Pair Source for use in Scalable Quantum Networks

Sumit Achar[1], Abhijit Kundu[1], Rashtrapriya Kumar Kapri[1] & Arijit Sharma[1,2]

[1]Department of Physics, Indian Institute of Technology Tirupati, Yerpedu-517619, Andhra Pradesh, India

[2]Center for Atomic, Molecular, and Optical Sciences and Technologies, Indian Institute of Technology Tirupati, Yerpedu-517619, Andhra Pradesh, India

Author e-mail address: ph21d502@iittp.ac.in, ph21d501@iittp.ac.in, rp.kapri@iittp.ac.in, arijit@iittp.ac.in

Abstract: The development of quantum communication protocols and technologies is key to a secure communication network. Entangled photons promise secured communication through the transfer of arbitrary quantum states. This paper discusses the development of an entangled photon pair source using a cold dilute atomic vapor of neutral rubidium atoms (^{87}Rb) in a 2D+ MOT (magneto-optical trap).

Keywords: Quantum Network, Spontaneous four-wave mixing, Entangled photon, MOT

1. Introduction

Classical communication networks are vulnerable to hacking, eavesdropping, spoofing, and other threats. Researchers have been working to create secure quantum networks comprised of interconnected quantum nodes using the superposition principle of quantum states, entanglement, and the no-cloning theorem [1]. Secure long-distance quantum communication and the realization of a quantum internet will be made possible by networked quantum nodes [Figure 1]. Such networked quantum nodes enable the secure transfer of information through a quantum channel using single-photon states (a.k.a. information) or by teleporting the information between two quantum nodes using a pair of entangled photons [2]. Entangled photons have been established spanning multiple degrees of freedom, such as time bins, polarization, orbital angular momentum, etc. Polarization entanglement has been studied extensively due to its robustness and the availability of very stable optical elements for controlling and detecting the polarization of single photons in the large-distance quantum network [3].

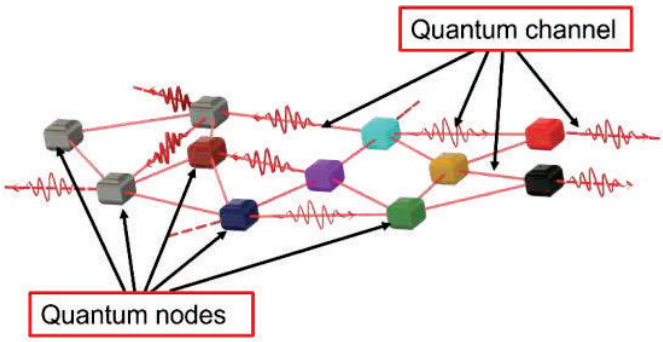

Fig. 1: Quantum network with different quantum nodes connected by high fidelity quantum channels

Entangled photons are generated mainly via two kinds of schemes. One is spontaneous parametric down-conversion (SPDC) in a nonlinear (periodically poled) crystal, and the other is spontaneous four-wave mixing (SFWM) based on a hot or cold atomic ensemble. Spontaneous Four-Wave Mixing (SFWM) is a third-order nonlinear process in which two pump photons are annihilated to create a pair of signal and idler photons whose wavelengths are governed by the energy and momentum conservation conditions. Signal and idler/probe photons are generated simultaneously. In the case of SPDC, it is possible to produce multi-mode biphotons with a linewidth of nearly 250 kHz [4], and currently, all the single-mode biphotons have linewidth larger than 1 MHz. However, in the case of laser-cooled atoms in the Electromagnetically Induced Transparency (EIT) based SFWM process, it is possible to generate single-mode biphotons with a linewidth of 50 kHz or even less [5].

At IIT Tirupati, we are developing an experiment to generate entangled photon pairs using a cold, dilute cloud of ^{87}Rb atoms prepared inside a 2D+ MOT and then applying a coupling and pump beam with 780 nm and 795 nm

respectively, along the length of the trapped cold, cloud. Subsequently, Stokes and anti-Stokes entangled pairs of photons will be generated from the trapped atomic cloud via the SFWM process [Figure 2(a)]. These entangled photon pairs can then be used for secure communication. The polarization state of the photon pairs can be characterized via Quantum State Tomography (QST) by detecting the individual photons in a combination of linear and circular polarization by introducing polarization filters (Including a quarter-wave plate, a half-wave plate, a polarizing beam splitter) along the path of signal and idler photons. In this article, the authors consider a simple four-level double Λ-type energy level diagram [Figure 2(b)] that illustrates the relevant pump, coupling, signal, and idler photons in the experiment.

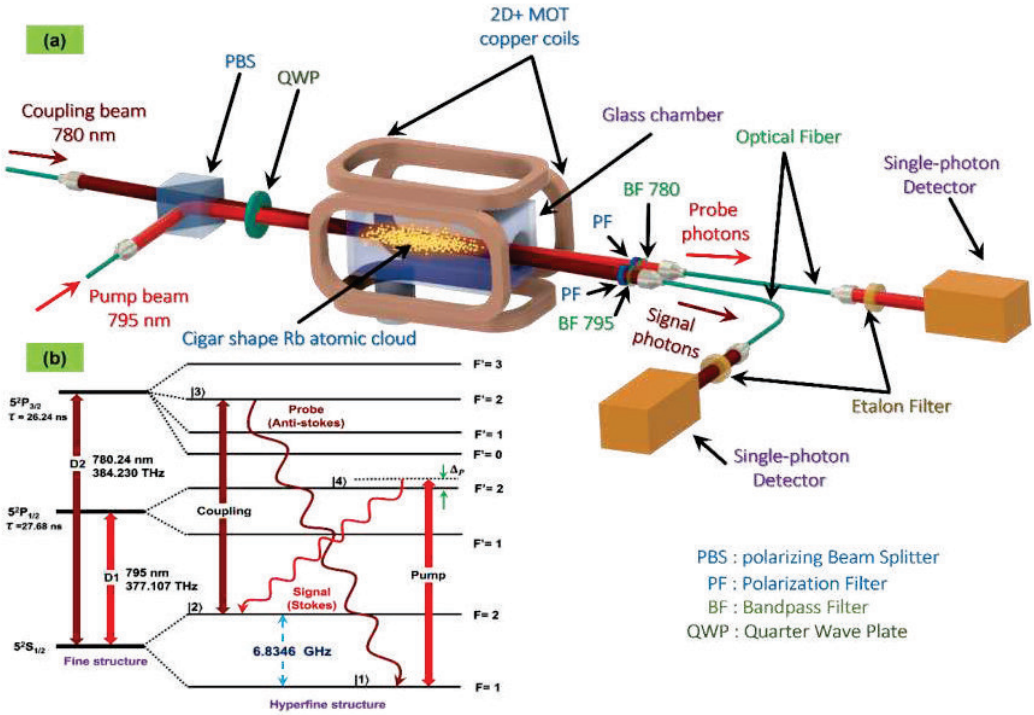

Fig. 2: (a) Schematic diagram for entangled photon pair generation from cold Rb atomic cloud. (b) Relevant energy level scheme for spontaneous Four-Wave Mixing in ^{87}Rb (bottom-left corner)

The development of another quantum node based on trapped ion inside an optical cavity is also in progress in our laboratory. Our long-term goal is to establish secure communication between these two quantum nodes.

We acknowledge financial support from CAMOST and CSIR (GoI) through a Junior Research Fellowship (JRF). R. K. Kapri gratefully acknowledges financial support from the I-Hub Quantum Technology Foundation, IISER Pune through the Chanakya Postdoctoral Fellowship. A. Kundu gratefully acknowledges financial support from IIT Tirupati. The authors acknowledge stimulating discussions with other scientists during the TAMIONS II Discussion Meeting supported and hosted by the International Center for Theoretical Sciences (ICTS) on 9-13 May 2022.

2. References

[1] H. J. Kimble, "The quantum internet", Nature, **453**, 1023-1030 (2008).
[2] X.-H. Bao, Y. Qian, J. Yang, H. Zhang, Z.-B. Chen, T. Yang, and J.-W. Pan, "Generation of narrowband polarization-entangled photon pairs for atomic quantum memories", Physical Review Letter, **101**, 190501.1-190501.4 (2008).
[3] B. G. Englert, C. Kurtsiefer and H. Weinfurter, "Universal unitary gate for single-photon two-qubit states", Physical Review A **63**, 032303.1-032303.10 (2001).
[4] S. Du, J. Wen and M. H. Rubin, " Narrowband biphoton generation near atomic resonance", Journal of Optical Society of America B, **25**, 98-108 (2008).
[5] Y.-S. Wang, K.-B. Li, C.-F. Chang, T.-W. Lin, Y.-F. Chen et al., "Temporally-ultralong biphotons with a linewidth of 50 kHz", arXiv:2205.13778 (2022).

Dependence of PT symmetry of a mutually coupled diode laser system on frequency detuning and coupling strength

Prachi*, S. Sivaprakasam
Department of Physics, Pondicherry University, Pondicherry,605014, India
**prachiphy16phd@gmail.com*

Abstract: We study a system of two semiconductor lasers coupled face to face where the field of one laser coupled to the field of the other but with a delay time. The corresponding eigenvalues are obtained theoretically for the field transformation matrix formulated using normalized Lang–Kobayashi rate equations. If the time delay between the lasers is varied, we find recurrence of PT symmetry regime and the transition to broken regime. Detuning frequency and coupling strength are found to have a systematic control over the occurrence of PT symmetry regime.
Keywords: Coupled semiconductor laser, PT symmetry, frequency detuning.

1. Introduction

Physical systems with non-hermitian Hamiltonian have been shown to be PT symmetric [1]. Optical systems proved to be one exciting area for studying the nature of PT symmetry [2, 3]. Study of PT symmetry acquired momentum in optical domain due to its possible applications in optical lattices, stable single mode operation of lasers, micro ring lasers, phonon laser, optical solitons and in semiconductor diode lasers [2-4]. In this work, a system of two diode lasers coupled face-to-face with a finite delay is investigated for the occurrence of PT symmetry, using normalized Lang–Kobayashi rate equations [5,6].

2. Theoretical model

A mutually coupled semiconductor diode laser system is investigated with a finite time delay between them and the corresponding rate equations are as follows:

$$\frac{dE_1(t)}{dt} = (1 + i\alpha)N_1(t)E_1(t) + i\Delta\omega E_1(t) + \kappa E_2(t-\tau)e^{-i\theta\tau} \quad (1a)$$

$$\frac{dE_2(t)}{dt} = (1 + i\alpha)N_2(t)E_2(t) + i\Delta\omega E_2(t) + \kappa E_1(t-\tau)e^{-i\theta\tau} \quad (1b)$$

$$T\frac{dN_{1,2}(t)}{dt} = J_{1,2} - N_{1,2}(t) - \left(1 + 2N_{1,2}(t)\right)\left|E_{1,2}(t)\right|^2 \quad (2)$$

where E_i and N_i represent the normalized complex electric field and normalized excess carrier densities respectively, $J_{1,2}$ are the pumping currents above threshold for Laser-1 and Laser-2 respectively. α is line width enhancement factor.τ is the delay time and κ is the mutual coupling strength between the two lasers. The laser oscillation frequencies are ω_1 and ω_2. Frequency detuning of the laser frequencies is $\Delta\omega=(\omega_1-\omega_2)$ and θ is average effective frequency for both the lasers which is defined as $\theta = (\omega_1+\omega_2)/2$.

3. Results and discussion

The rate equations are simplified to reduce the nonlinearity and the excess carrier densities are considered to be smaller near the threshold condition i.e. $N_{1,2}(t) \to 0$. The eigen value for the field transformation matrix obtained from equation 1 is shown below and the eigne value evolutions are shown in figure 1.

$$\lambda_{1,2} = \frac{2}{(1-\kappa^2\tau^2 e^{-i2\theta\tau})}\left[-\kappa^2\tau e^{-i2\theta\tau} \pm \kappa e^{-i\theta\tau}\sqrt{\left\{1 + \frac{\Delta\omega^2}{\kappa^2}(\tau^2 - 1)e^{i2\theta\tau}\right\}}\right] \quad (3)$$

The values of τ, for which real parts of eigen values are zero are marked as vertical line A in figure 1. Existence of PT symmetry is investigated as a function of frequency detuning at a constant time delay corresponding to the line A in figure 2 and the results are shown in figure 2. In figure 2, the real and imaginary parts of eigen values are shown as a function of frequency detuning for coupling strengths (a) $\kappa = 0.05$, (b) $\kappa = 0.10$ and (c) $\kappa = 0.15$. It can be seen that there is a range of $\Delta\omega$ for which real parts of eigen values are zero ($|\Delta\omega|<\kappa$) where as for other regime ($|\Delta\omega|>\kappa$) it is showing linear growth or decay. The vertical lines represent the transition of PT symmetry to broken regime.

In figure 3, the real and imaginary parts of eigen values are shown as a function of coupling strength (κ) at fixed detuning values as (a) 0.05, (b) 0.10 and (c) 0.15 respectively. It can be seen that the system exhibits PT symmetry for coupling constant greater than a critical value ($|\Delta\omega| = \kappa$) and the transition in indicated by vertical lines.

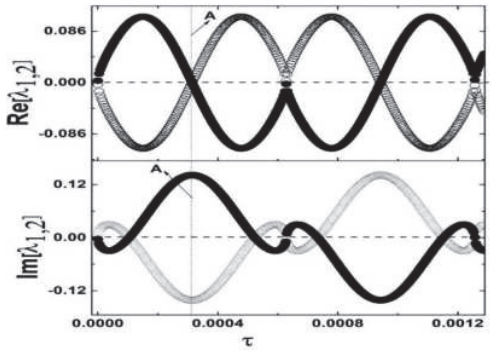

Figure 1. Eigen values as a function of delay time (τ) at a constant coupling coefficient (κ= 0.10) and at constant frequency detuning ($\Delta\omega$ = 0.10). The top panel has the real eigen values and bottom panels has the imaginary components of eigen values. Closed circles (open circles) represent first (second) eigen values

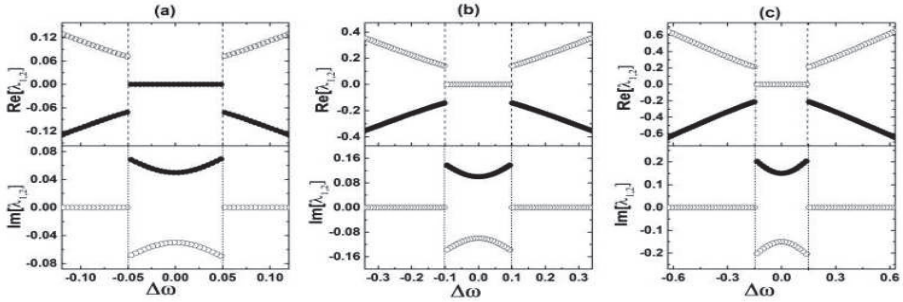

Figure.2. Eigen values as a function of detuning at a constant delay time (point A in figure 2) and at constant coupling coefficients(κ) as (a) 0.05, (b) 0.10, (c) 0.15.

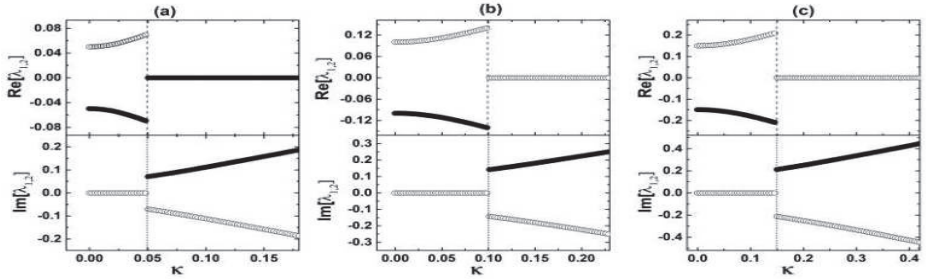

Figure 3. Eigen values as a function of coupling coefficient at a constant delay time (point A in figure 2)and at constant frequency detuning ($\Delta\omega$) as (a) 0.05, (b) 0.10, (c) 0.15

In conclusion, we have shown the existence of PT symmetry in system of mutually coupled diode lasers with a finite time delay between them. Also, we have shown the possibility of controlling the PT symmetric regime by controlling the laser operating parameters. These results bear the possibility in real life applications demanding fine control of PT symmetry. Futuristic work will be on investigating asymmetrically coupled diode lasers

4. References

[1] C. M. Bender, S. Boettcher, Real spectra in non-hermitian Hamiltonians having PT symmetry, *Phys. Rev. Lett.*, **80** (1997) 5243–5246.
[2] M. Bertolotti, PT symmetry in quantum and classical physics, *Contemp. Phys.*, **60** (2019) 196–197.
[3]C. E. Rüter, K. G. Makris, R. El-Ganainy, D. N. Christodoulides, M. Segev, D. Kip, Observation of parity–time symmetry in optics, *Nat. Phys*., **63** (2010) 192–195.
[4] A. Wilkey, J. Suelzer, Y. Joglekar and G. Vemuri, Parity–time symmetry in bidirectionally coupled semiconductor lasers. MDPI - *Photonics,* **6**, (2019) art. No. 122.
[5] J. S. Suelzer, Y. N. Joglekar, G. Vemuri, Parity-time symmetry breaking in optically coupled semiconductor lasers. *Proc. of SPIE*, **9920**, M1-M8, 2017, doi: 10.1117/12.2239487.

Multicolor emission of non-stoichiometric magnesium aluminate spinel

Prabhpreet Kaur and Suman Rani

Department of Physic, School of Sciences, Lovely Professional University, Punjab-14411, India

suman.rani@lpu.co.in

Abstract: Magnesium aluminate spinel ($Mg_xAl_{2y}O_4$, x:y=1:1/2,1:1 and 2:1/2), MAS had been synthesized by wet chemical route technique. The prepared sample were sintered in muffle furnace at 1100ºC. The cationic effect on the luminescent properties of Magnesium aluminate spinel(MAS) had been studied by varying the molar ratio of Mg to Al.as 1:1/2,1:1 and 2:1/2. All the prepared samples exhibit cubic structure . The crystallinity decreases with change in the stoichiometric ratio of Magnesium aluminate spinel i.e., as molar ratio of Mg to Al changes from1:2 to 1:1/2:1. The crystallite size of the sample with molar ratio 1:2, 1:1, and 2:1 is 33.03nm, 28.69nm, and 28.41nm, respectively. Fluorescence spectra show multicolours emission due to defect states in the energy bandgap arises due to non-stoichiometric MAS. These defect states are anionic, cationic, Schottky and interstitial [1,2]. Calculated CIE, CCT and CRI coordinates are close to ideal white light indicating the potential of the material for optoelectronic devices.

Keywords: Magnesium aluminate spinel, non-stoichiometric, Defect states and multicolours

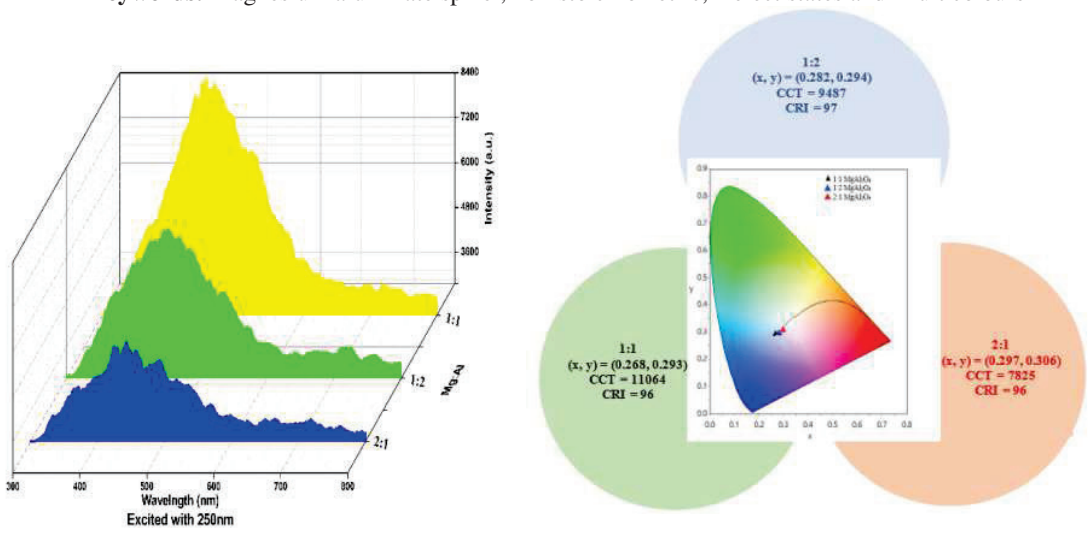

Highlights

1. MAS has broad emission spectra from 300 - 650 nm peaked at 450nm with 250 nm excitation. This broad spectra is due to presence of F and F^+ centers in the energy forbidden gap.
2. Non stoichiometric ratio of 1:1 (Mg: Al) has maximum spectral width in UV-visible region and high intensity as compared to other ratio including stoichiometric MAS(1:2) due to the the presence of more defect centers in it.
3. Prepared material is tested quantitively by calculating CIE,CCT and CRI parameters. The calculated parameters are very close to the ideal white light source.

References

[1] N. Pathak, P.S. Ghosh, S.K. Gupta, S. Mukherjee, R.M. Kadam, and A. Arya "An insight into the various defects-induced emission in MgAl2O4 and their tunability with phase behavior: combined experimental and theoretical approach," *The Journal of Physical Chemistry C* **120** 4016-4031 (2016).

[2] S.T. Murphy, C.A. Gilbert, R. Smith, T.E. Mitchell, and R.W. Grimes, "Non-stoichiometry in MgAl2O4 spinel," *Philosophical Magazine* **90** 1297-1305 (2010).

Theoretical study of lateral and depth resolution of reconstructed object from Computer Generated Hologram

Pardeep Bhanot[1,2], Sanjit K. Debnath[1,2,*], Bhargab Das[1,2], Raj Kumar[1,2]

[1]*Micro and Nano Optics Centre, CSIR-Central Scientific Instruments Organisation, Sector30C, Chandigarh, India-160030*

[2]*Academy of Scientific and Innovative Research (AcSIR), Ghaziabad 201002, India*

[*]*Corresponding author's email id: sanjit.debnath@csio.res.in*

Abstract: A Computer Generated Hologram (CGH) is formed by the complex addition of spherical waves emitted from each point in an object. The lateral and depth resolution of the reconstructed object from CGH is a function of the distance of object to the CGH plane and the dimensions of the CGH. In this work, we have studied the resolution (lateral and depth) of reconstructed object from CGH using Rayleigh criteria. A simulation study has been carried out to find the values of lateral and depth resolution followed by the optical reconstruction of the object.

Keywords: Computer Generated Hologram (CGH), Phase distribution, Lateral resolution, Depth resolution.

1. Introduction

A physical object is considered as a distribution of a large number of self illuminating point objects lying in the object space [1,2]. Each point object emits a spherical wave. These spherical waves propagate through the space and form a complex amplitude distribution in CGH plane. The resolution of the reconstructed object from this CGH is an important parameter for three dimensional holographic displays. Thus, we study the lateral and depth resolution of reconstructed object from CGH in this work. To determine the same, Rayleigh criteria has been used [3].

2. Theory

According to the Rayleigh criteria, two point objects are said to be just resolved when the intensity maximum of one point coincides with the intensity minimum of the other point. Two point objects are considered to be laterally resolved if the distance between them is as follows [4]:

$$r_{lateral} = \frac{\lambda}{2.NA} \qquad (1)$$

where λ is the wavelength, $NA = n\sin\theta = D/2z$ is the numerical aperture with 'n'=1 being the refractive index of the object space, θ is half angle of the cone of light falling on the CGH plane from the object, 'D' being the dimensions of the CGH plane and 'z' being the distance between the CGH plane and the object [5]. And two point objects are considered to be resolved in depth when the distance between them follows the following relation [4]:

$$r_{depth} = \frac{\lambda}{2.(NA)^2} \qquad (2)$$

3. Results and Discussion

An object model with dimensions 512×512 is considered for simulation study. The distance from the object plane to the CGH plane is taken to be 80 cm with pixel size of the CGH plane as 6.4 μm. Figure 1(a) shows two bars separated by 96 μm. Using this object, CGH is generated by Point based method [6].

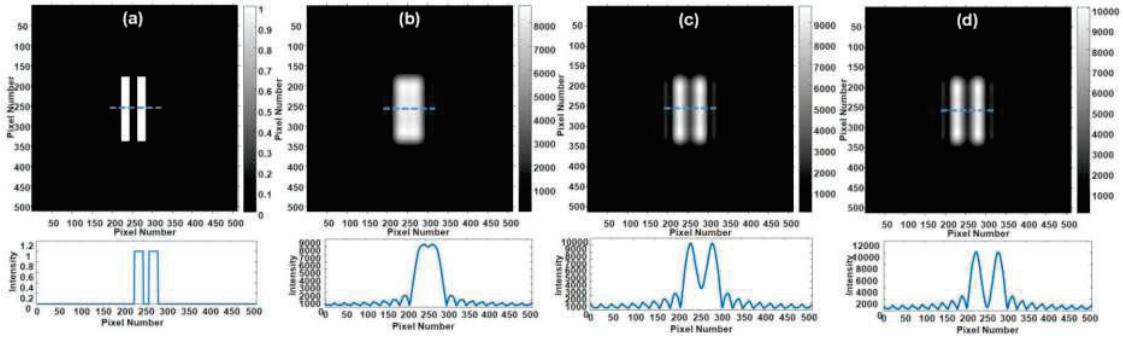

Fig. 1: (a) Object matrix, (b) Reconstructed object at $r_{lateral}$ = 96 μm,(c) Reconstructed object at $r_{lateral}$ =160 μm,(d) Reconstructed object at $r_{lateral}$ = 256μm

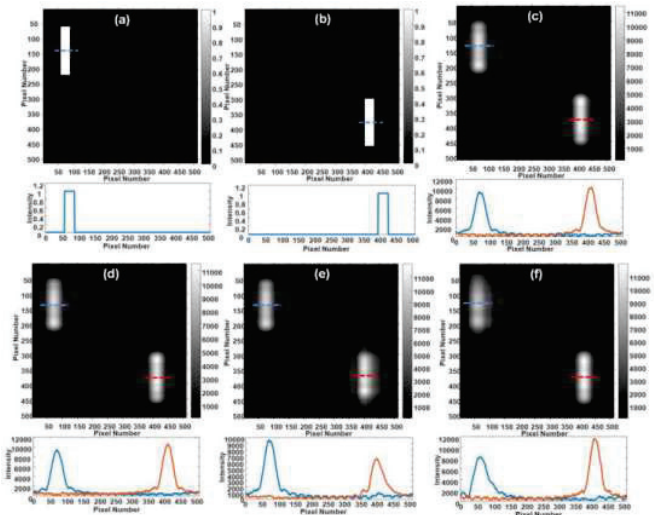

Fig. 2: (a),(b) Object matrix at different depths, (c),(d) Reconstructed object at r_{depth} = 10 mm, (e),(f) Reconstructed object at r_{depth} = 100mm

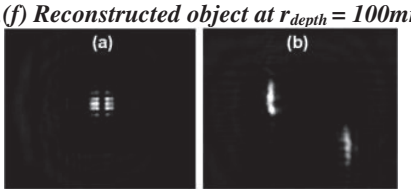

Fig. 3: Optical reconstruction of (a)Laterally resolved objects at $r_{lateral}$ =160 µm, (b) Longitudinally resolved objects at r_{depth} = 90mm

Using the CGH, the object is reconstructed by angular spectrum method [2] which is shown in Fig. 1(b). It can be seen from the corresponding line profile that two bars are not resolved as the lateral resolution in this condition is 155 µm which is calculated from Eq. (1). So, the distance between the bars is increased to 160 µm and 256 µm. And then, the reconstructed objects of the same are shown in Fig. 1(c) and 1(d) in which two bars are just resolved and well resolved respectively as the distance between them is more than the theoretical lateral resolution value. Thus, the simulation study is in agreement with the Eq. (1) of lateral resolution.

The depth resolution value using Eq. (2) is found to be 87 mm. To verify this, we consider two bars at different depth as shown in Fig. 2(a) and 2(b) separated by 10 mm longitudinally. The reconstructed objects are shown in Fig. 2(c) and 2(d). It can be seen that the intensity of both bars is almost equal. It indicates that the depth is not resolved. Hence, the longitudinal distance is now increased to 100 mm which is more than theoretical value of depth resolution. Fig. 2(e) and 2(f) show the reconstructed objects at respective depths. It can be observed that the top left bar is focused in Fig. 2(e) and the bottom right bar starts getting blurred as can be seen from the intensity profile below the figure. The same argument holds for Fig. 2(f). Thus, the simulation study verifies Eq. (2) of depth resolution.

Figure 3(a) and 3(b) shows the optical reconstruction of just resolved objects placed laterally at 160 µm and longitudinally at 90 mm respectively displayed in CMOS sensor. As can be observed from Fig. 3, the results recorded in CMOS are affected by the zero order diffraction pattern which is to be analyzed in future work.

4. References

[1] K. Matsushima, Introduction to Computer Holography: creating Computer-Generated Holograms as the Ultimate 3D Images (Springer, 2020).
[2] T.-C. Poon and J.-P. Liu, Introduction to Modern Digital Holography with MATLAB (Cambridge University, 2014).
[3] L. Rayleigh, "XII. On the manufacture and theory of diffraction-gratings," The London, Edinburgh, and Dublin Philosophical Magazine and Journal of Science, vol. 47, pp. 81-93, 1874.
[4] J. G. Sucerquia, W. Xu, S. K. Jericho, P. Klages, M. H. Jericho, and H. J. Kreuzer, "Digital in-line holographic microscopy". Applied Optics, 5(45), pp. 836 – 850, 2006.
[5] X. Hao, C. Kuang, Z. Gu, Y. Wang, S. Li, Y. Ku, Y. Li, J. Ge, and X. Liu, "From microscopy to nanoscopy via visible light," Light Sci Appl, vol. 2, e108, 2013.
[6] P.W.M. Tsang, T.C. Poon and Y.M. Wu, "Review of fast methods for point based computer generated holography". Photonics Research, 6(9), pp. 837 – 846, 2018.

Acknowledgement
Authors thank Dr. Anuj Gupta for fruitful discussions. Authors thank CSIR, India for providing financial support under project number MLP2014 to carry out this research work.

Ghost polarimetry

Manisha*, Akanksha Gautam, Rakesh Kumar Singh
Laboratory of Information Photonics and Optical Metrology, Department of Physics, Indian Institute of Technology (Banaras Hindu University), Varanasi, 221005, Uttar Pradesh, India.
Author e-mail address: manisha.rs.phy18@itbhu.ac.in*

Abstract: We propose and demonstrate a new scheme for ghost polarimetry based on Stokes correlations. Generalized Stokes parameters are derived from few combinations of Stokes fluctuation correlation. These generalized Stokes parameters are subjected to a phase retrieval algorithm for the complete recovery of object in ghost polarimetry. Results are presented for an object with incident diagonally polarized beam.
Keywords: Speckle, Ghost diffraction, Polarization.

1. Introduction

Ghost diffraction (GD) is an important diffraction imaging scheme that exploits correlation features of the scattered optical field. In contrast to traditional imaging methods, the Ghost diffraction (GD) & Ghost Imaging (GI) collect light coming from a transparency using a non-spatially resolved bucket detector. This information is spatially correlated with another random field with the object information measured with the help of an array of pixels detector. Initially it was demonstrated for a quantum mechanically entangled light beam. Later research revealed that GD and GI could also be performed with classically correlated light [1]. Most of the GD and GI techniques that are currently in use have been centered on obtaining information about the characteristics of the object, and not related with its polarization properties except some recent investigations. Polarization plays a very important role in imaging techniques for obtaining information beyond what is revealed by their spectral and intensity distributions. Recently few polarization-based techniques have been developed [2-4]. In polarimetric ghost imaging setups, the reflective intensity of objects is decomposed into different polarization intensity. However, most of such schemes recovers the polarization state for different polarization sensitive objects based on jones or Mueller matrix. In this paper, we propose and demonstrate yet another approach for ghost polarimetry by evaluating the Stokes fluctuations from Stokes parameters of an object with incident diagonally polarized beam. By making few combinations of different Stokes fluctuations, generalized Stokes parameters are measured. A phase retrieval algorithm is implemented for the full recovery of object. Wide range of applications of the scheme lies in medicine, remote sensing, biomedical imaging.

2. Theory and Methodology

For an incident light beam, the fluctuations of Stokes parameters are given by following,

$$\Delta S_p(u) = S_p(u) - \langle S_p(u) \rangle \tag{1}$$

where $S_p(u)$ are the Stokes parameters at observation plane with spatial point u and p=0,1,2,3. Parenthesis $\langle ... \rangle$ represents the ensemble average. A correlation between these Stokes parameters can be represented as,

$$C_{pq}(\Delta u) = \langle \Delta S_p(u_1) \Delta S_q(u_1 + \Delta u) \rangle \tag{2}$$

where p,q=0,1,2,3. u_1 and u_2 are two spatial points at the observation plane and $u_2 = u_1 + \Delta u$.

A diagonally polarized light beam is incident on the object, and four Stokes parameters i.e., S_0, S_1, S_2 and S_3 are measured. The Stokes fluctuations are calculated from two sets of Stokes parameters; one with the object information and other without any object information. A two-point Stokes parameters correlation between the same Stokes parameters is measured, and C_{00}, C_{11}, C_{22} and C_{33} are calculated. The elements of the Stokes fluctuation matrix can be given as [5,6]

$$C_{pq}(u_1, u_2) = \langle S_p(u_1) S_q(u_2) \rangle - \langle S_p(u_1) \rangle \langle S_q(u_2) \rangle \tag{3}$$

By utilizing Eq. 3 and making few combinations of Stokes fluctuations, generalized Stokes parameters are calculated. Two generalized Stokes parameters can be given as,

$$S_0(u_1, u_2) = C_{00} + C_{22} + C_{11} + C_{33} \quad (4)$$

$$S_1(u_1, u_2) = C_{00} + C_{22} - C_{11} - C_{33} \quad (5)$$

3. Results and Discussion

The Stokes fluctuations i.e. C_{00}, C_{11}, C_{22} and C_{33} are given in Fig1.Two generalized Stokes parameters that survived for the case of diagonally polarized incident beam, are shown in first row of Fig. 2.

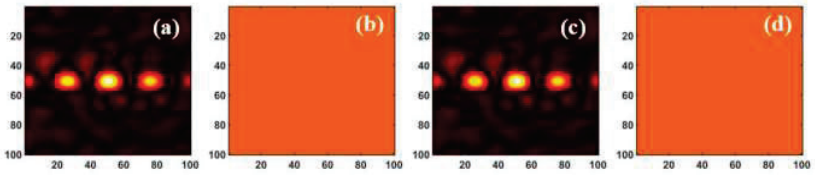

Fig. 1: Stokes fluctuations; (a-d) C_{00},C_{11},C_{22} and C_{33}.

A phase retrieval algorithm [7] by applying few constraints, is implemented to the generalized Stokes parameters and a reconstruction of object obtained with different polarization states, is shown in second row of Fig.2.

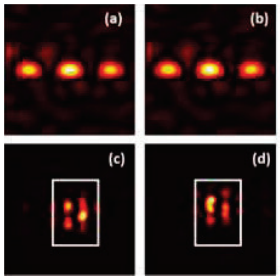

Fig. 2: Generalized Stokes parameters GS_0 and GS_2 (a) and (b). Retrieved object results;(c) and (d) for two parallel strips corresponding to (a) and (b).

4. Conclusion

We have proposed a technique for the ghost diffraction with the consideration of polarization. The technique uses generalized Stokes parameters derived from combinations of Stokes fluctuation and a phase receival algorithm. Results are presented for an object "two parallel strips" with different polarization states.

5. Acknowledgment:

Manisha acknowledges fellowship from the IIT (BHU). Akanksha Gautam would like to acknowledge support from DST-INSPIRE (IF-180930).

6. References

[1] Bennink, R. S., Bentley, S.L., and Boyd, R.W., "Two-Photon" Coincidence Imaging with a Classical Source, Phys. Rev. Lett. **89**, 113601(2002).

[2] Chirkin, A.S.,Gostev, P.P., Agapov, D.P., and Magnitskiy, S.A., "Ghost polarimetry: ghost imaging of polarization-sensitive objects" Laser Physics Letters **15**, 115404(2018).

[3] Shi, D., Hu, S., and Wang, Y., "Polarimetric ghost imaging" Opt. Lett. **39**, 1231-1234(2014).

[4] Kellock, H., Setälä, T., Friberg, A. T., and Shirai, T., "Polarimetry by classical ghost diffraction" Journal of Optics **16,** 055702(2014).

[5] Kuebel, D., and Visser, T. D., "Generalized hanbury brown-twiss effect for Stokes parameters" JOSA A **36**, 362-367(2019).

[6] Sarkar, T., Parvin, R., Brundavanam, M.M., and Singh, R.K., "Higher-order Stokes-parameter correlation to restore the twisted wave front propagating through a scattering medium". Physical Review A **104**, 013525(2021).

[7] Fienup, J.R., "Reconstruction of an object from the modulus of its Fourier transform" Opt. Lett. **3**, 27-29(1978).

One-dimensional gold nanoparticle photonic-plasmonic lattice for enhanced broadband optical absorption

[1#]Saurabh Pandey, [1]Shereena Joseph, [1,2]Joby Joseph
[1]Department of Physics, Indian Institute of Technology Delhi, New Delhi 110016, India
[2]Optics and Photonics Centre, Indian Institute of Technology Delhi, New Delhi 110016, India
 # sp839090@gmail.com

Abstract: The photonic-plasmonic resonating structures have gained substantial interest for solar energy conversion using light trapping through the supported photonic and plasmonic resonant modes. We have employed a sustainable, low-cost fabrication technique such as Laser interference lithography (LIL) and electrochemical deposition to construct a 1D plasmonic lattice, on an ITO waveguide that supports guided mode resonance (GMR), Rayleigh anomalies (RA), and broadband plasmonic mode. The multiple in-plane scattering of the incoming light through closed-packed nanoparticles within the groves together with various resonating states offers 20% enhanced absorption compared to the conventional metal bar grating structure.
Keywords: laser Interference lithography, Electrochemical deposition, guided-mode resonance, Plasmon resonance.

1. Introduction

Light-matter interaction can be boosted through subwavelength confinement, manifested through dielectric and plasmonic resonators[1]. Such architecture is credited with improved performance in diverse applications in Nano-photonics, biomedicine, and Nano-electronics**.** Furthermore, the radiative (scattering) and non-radiative (absorption) interaction of light with gold nanoparticles (Au-nps) are dependent on the size of the particles, whereas the smaller size nps promises a large absorption cross-section[2]. The higher absorption for an extended wavelength is the primary concern for photovoltaic and energy harvesting applications[3]. It has been demonstrated that the plasmonic absorption can further increase light trapping through photonic modes, which upsurges the light-matter interaction time and endorses significant absorption. The realization of such a structure should be cost-effective and easy to fabricate. Here we followed a large area fabrication technique in a single shot through top-down laser interference lithography[4] and bottom-up electrochemical deposition to realize photonic-plasmonic hybrid structures. The architecture supports various photonic and plasmonic modes in a broad spectrum.

2. Results and discussion:

Figure 1(a) represents the schematic diagram of considered structures, where the light diffracted at the grating can support the guided wave condition in the ITO waveguide and satisfies guided mode resonance conditions[1]. On the other hand, light diffracted at the grazing angle (cut-off diffracted order) shows RA under normal illumination is given by the relation $\lambda_{RA}=n_c\Lambda/m$, where n_c is the refractive index of the surrounding medium, Λ is the period, and m is the diffracted order. Here we considered the cover medium as water (n_c = 1.33), period and width of the structure were optimized as 550nm and 320nm, respectively, to exhibit resonances in the broad spectral region from 400nm-900nm. The desired structure was experimentally realized through a combination of laser interference lithography (LIL) and electrochemical deposition (ECD). The photoresist(PR) grating was fabricated using LIL, which acts as a template and working electrode (WE) for ECD. The ECD cell consists of the three-electrode system (Figure1(b)) and the electrolyte composed of tetrachloroauric(III) acid, buffer solution of sodium hydro-phosphate and citric acid, and potassium chloride. The pH value of the mixture solution is maintained as 4.2. The applied potential vs. Ag/AgCl demonstrates a sinusoidal potential on the ITO surface due to periodic non-conducting PR grating, where the potential strength near the edges of the grooves is rapidly varying and leads to the formation of nanoparticle clusters. In contrast, the particle size is comparatively smaller and uniform near the center of grating valleys, owing to the steady potential strength in that region.

A rigorous optimization process has been followed to obtain the required gold nanoparticle grating on the ITO layer; their resultant FESEM images are shown in Figure 1(c). Different size of Au-nps was achieved through varying the

ECD running time at a fixed voltage of -100mV resulting in the development of grating ridges with an average particle of size 39nm, 28 nm, and 22 nm, termed as S1, S2, and S3 with average size distribution as given in Figure 1(c). In particular, S3 illustrates highly dense nps formation along the grating line, while the density of nps in S1 and S2 is relatively less. For comparative studies of our designed structure, we have fabricated metal bar grating with identical parameters on the ITO waveguide using LIL followed by the deposition of 25 nm thick Au. Through the lift-off process, the desired metal bar photonic structure is obtained. The optical extinction (2-logT(%)) for normal incidence was estimated for different sizes of Au-nps grating and metal bar grating structures under TM polarization. The resulting extinction spectra are plotted in Figure 1(d), corresponding to samples S1, S2, and S3. The spectra reveal that the smaller size of the nanoparticle grating significantly enlarges the absorption cross-section. Further, Figure 1(e) represents the FDTD simulated and experimentally obtained optical extinction corresponding to metal bar grating and the optimized Au-nps grating with an average particle size of 22 nm. The electric field distribution(Figure1(f)) GMR, RA, and Plasmon resonance is depicted in Figure 1(f) to ensure the enhanced field confinement in the lattice plane close to the interface of the metal grating and cover region.

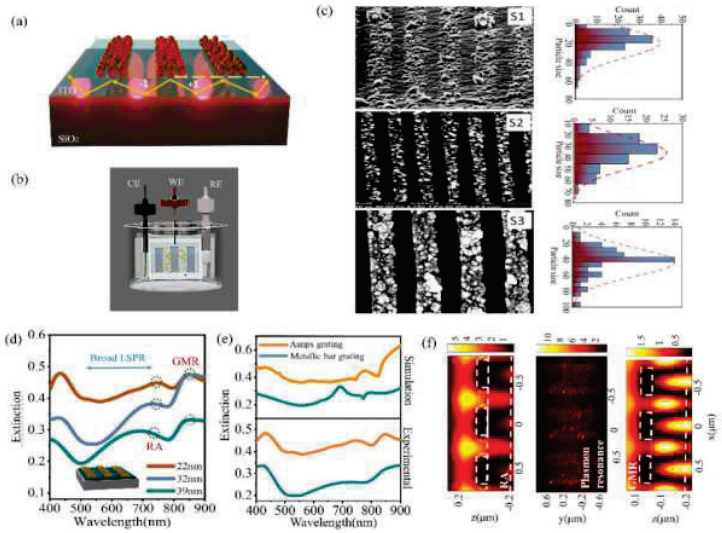

Figure 1: fabrication of 1D gold nanoparticle grating and its optical responses. (a) pictorial representation of photonic-plasmonic resonating structure, (b) electrodeposition cell with pt wire as counter electrode, Ag/AgCl as reference electrode and PR grating as a working electrode, (c) FESEM image corresponding to S1, S2 and S3 with their particle size distribution and,(d) their corresponding extinction spectrum, (e) simulated and experimentally obtained extinction spectra corresponding to Au-nps grating and metal bar grating, (f) Electric field distribution corresponding to GMR, RA and plasmonic resonance.

3. Conclusive Remarks

In summary, we have designed and fabricated a one-dimensional nps-grating hybrid structure for the excitation of various photonic and plasmonic modes. The investigation of the grating with ridges constituted from different sizes of nps demonstrates a size-dependent enhanced absorption compared to conventional metal bar one-dimensional plasmonic crystal. The proposed architecture can be effectively used for enhancing the performance of photovoltaic and energy harvesting-based devices.

4. References:

[1].S.Pandey, N.Baburaj, S.Joseph, J.Jospeh, "Resonant Optical Modes in Periodic Nanostructures," ISSS Journal of Micro and Smart Systems, 113–137, (2022).

[2]. Prashant K. Jain, Kyeong Seok Lee, Ivan H. El-Sayed, and Mostafa A. El-Sayed, "Calculated Absorption and Scattering Properties of Gold Nanoparticles of Different Size, Shape, and Composition," Applications in Biological Imaging and Biomedicine. J. Phys. Chem. B, 110, 7238–7248, (2006).

[3]. P.V. Karthik Yadav, B. Ajitha, Y. Ashok Kumar Reddy, Adem Sreedhar, "Recent Advances in Development of Nanostructured Photodetectors from Ultraviolet to Infrared Region," Chemosphere, 279, 1–6(2021).

[4]. S.Joseph, S.Sarkar, and J.Joseph, "Grating-Coupled Surface Plasmon-Polariton Sensing at a Flat Metal-Analyte Interface in a Hybrid-Configuration," ACS applied materials & interfaces, 12, 46519–46529 (2020).

Discriminating strain and temperature using fiber Bragg grating-PMMA fiber cavity based sensor

Jasjot Kaur Sahota
PhD research scholar, Punjab Engineering College (Deemed to be University), Chandigarh
jksahota91@gmail.com
Dr. Divya Dhawan
Associate Professor, Punjab Engineering College (Deemed to be University), Chandigarh
divyadhawan@pec.edu.in
Dr. Neena Gupta
Professor, Punjab Engineering College (Deemed to be University), Chandigarh
neenagupta@pec.ac.in

Abstract: In this paper, analysis of cascaded fiber Bragg grating with polymethylmethacrylate fiber cavity based sensor is proposed for discrimination of strain and temperature. Within the main reflection band, two spectral peaks are formed exhibiting linear variation in normalized peak difference with strain and temperature. Along with variation in normalized peak power difference, Bragg wavelength also changes linearly with strain and temperature. Coefficients of strain and temperature are obtained for the proposed method using matrix formulation. The results obtained for the proposed method is better than conventional method where silica cavity based cascaded FBGs are used for sensing.
Keywords: fiber Bragg grating, polymethylmethacrylate, strain sensor, temperature sensor

1. Introduction

Fiber Bragg gratings have gained immense popularity in field of sensing technology owing to inherent advantages such as distributed sensing, multiplexing capability, fast response, compactness, immune to electromagnetic field and anti-corrosive nature. Various physical parameters such as strain, temperature, humidity, pressure and refractive index can be measured using FBG in structural health monitoring, pharmaceutical, biomedical engineering, robotic engineering, defense and maritime applications. However, one long standing issue that needs to be addressed is temperature cross-sensitivity in FBG sensors. Recently, various sensor configurations have been presented for strain and temperature discrimination such as gratings inscribed in doped fiber [1], cascading FBG with PANDA fiber [2], using reverse indexed FBG[3], multimode interference effect [4], partially embedded chirped FBG [5], bimetal cantilever [6], few mode concept [7] etc. The shortcomings of such techniques are less durability, low range of operation, fragility, high cost and complex pre-processing. To circumvent these issues, a new technique has been proposed in which two similar FBGs made of silica glass are cascaded with PMMA cavity sandwiched between them.

2. Working principle of proposed method

The proposed method to discriminate strain and temperature works on the principle of Fabry Perot interferometer which is formed by two similar FBGs acting as mirrors. The reflection spectrum of the structure comprises of two peaks and is expressed by equation (1):

$$r_{fp}(\lambda)=C.r_g(\lambda).F(\phi) \quad (1)$$

where C is a constant, $r_g(\lambda)$ is the power of reflection spectrum and $F(\phi)$is the interference function of the cavity which is dependent on phase difference ($\phi(\lambda)$) between the light reflected by the two gratings. The interference function can be expressed by equation (2):

$$F(\lambda)=1+\cos(4\pi n_c L_c/\lambda) \quad (2)$$

where n_c is the effective refractive index of the cavity section and L_c is the cavity length. Variation caused in phase of cavity modulates the reflection spectrum of the structure. Such a structure having silica based cavity does not

contribute in discriminating strain and temperature thus the design is modified by using cavity of PMMA fiber as illustrated in Fig. 1. Due to different thermal expansion coefficient of silica fiber and PMMA fiber, linear variation in normalized peak difference and Bragg wavelength of reflection spectrum can be obtained. Using matrix formulation then temperature and strain can be measured.

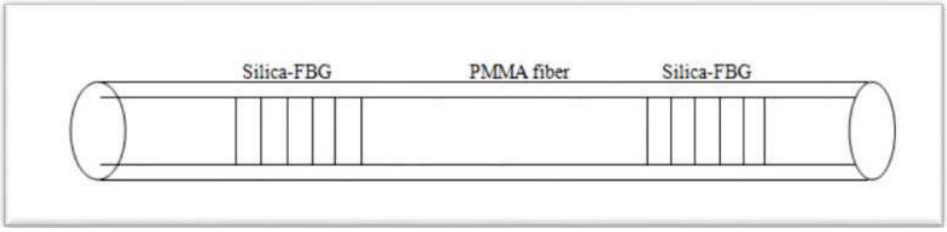

Fig. 1: Proposed design of cascaded FBG with PMMA cavity.

3. Results

Simulation results on RSoft GratingMod software as shown in Fig. 2 indicates variation in power of two peaks as well as shift in Bragg wavelength with increase of strain and temperature. Using matrix formulation, coefficient of strain and temperature are obtained as expressed by equation (3):

$$\begin{pmatrix} T \\ \varepsilon \end{pmatrix} = \begin{pmatrix} -0.56\times10^{-2} & 11.2 \\ -5.67\times10^{-4} & 1.14 \end{pmatrix}^{-1} \begin{pmatrix} M \\ \lambda_B \end{pmatrix} \quad (3)$$

Where M is normalized peak difference, λ_B is Bragg wavelength (nm), T is temperature (degree Celsius) and ε is strain (microstrain). The results obtained for the proposed method are better than conventional method of using silica cavity based cascaded FBG [8]. The results indicate high sensitivity to strain and low sensitivity to temperature making it potentially applicable in areas where dynamic temperature variation is involved.

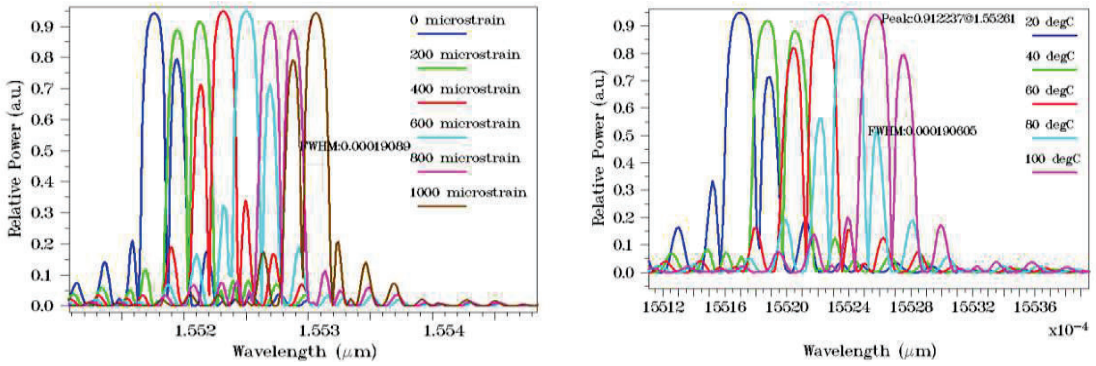

(a) *(b)*

Fig. 2: Reflection spectrum of proposed sensor with (a) strain variation and (b) temperature variation.

4. References

[1] U. Tiwari, K. Thyagarajan, and M. R. Shenoy, "Strain and temperature discrimination technique by use of a FBG written in erbium doped fiber," *Opt. - Int. J. Light Electron Opt.*, vol. 125, no. 1, pp. 235–237, 2014.

[2] Z. Ding, Z. Tan, Y. Gao, Y. Wu, and B. Yin, "Strain and Temperature Discrimination Using a Fiber Bragg Grating Concatenated with PANDA Polarization-Maintaining Fiber in a Fiber Loop Mirror," *Opt. - Int. J. Light Electron Opt.*, vol. 221, 2020.

[3] S. O. Park, B. W. Jang, Y. G. Lee, C. G. Kim, and C. Y. Park, "Simultaneous measurement of strain and temperature using a reverse index fiber Bragg grating sensor," *Meas. Sci. Technol.*, vol. 21, no. 035703, pp. 1–8, 2010.

[4] C. Li *et al.*, "Strain and temperature discrimination using a fiber Bragg grating and multimode interference effects," *Opt. Commun.*, vol. 343, pp. 6–9, 2015.

[5] S. Kim, S. Member, J. Kwon, S. Kim, and B. Lee, "Temperature-Independent Strain Sensor Using a Chirped Grating Partially Embedded in a Glass Tube," *IEEE Photonics Technol. Lett.*, vol. 12, no. 6, pp. 678–680, 2000.

[6] K. Tian, Y. Liu, and Q. Wang, "Temperature-independent fiber Bragg grating strain sensor using bimetal cantilever," *Opt. Fiber Technol.*, vol. 11, pp. 370–377, 2005.

[7] X. Gao *et al.*, "A dual-parameter fiber sensor based on few-mode fiber and fiber Bragg grating for strain and temperature sensing," *Opt. Commun.*, vol. 454, no. August 2019, p. 124441, 2020.

[8] Du, W., Tao, X. and Tam, H. 'Fiber Bragg Grating Cavity Sensor for Simultaneous Measurement of Strain and Temperature', *IEEE Photonics Technology Letters*, 11(1), pp. 105–107,1999.

An Integrated Quantum System for Conduction of Half Adder with Light.

Mir Nadim Sarfaraj* and Sourangshu Mukhopadhyay
Department of Physics, The University of Burdwan, Golapbag, Purba Bardhaman, West Bengal, India, 713104
Author e-mail Address: mirnadim222@gmail.com

Abstract: Light is already proved as a particle which maintain the quantum states in regards of its polarization, phase, frequency, etc. In last few years several approaches are proposed by the scientists and technologist, where different quantum logic operations are developed by using light as the carrier. In this connection, we have proposed a quantum qubit gate which is capable to perform the half adder operation in an integrated approach.

Keywords: Quantum half adder, Phase encoding, Qubits, Quantum logic gates.

1. Introduction

Quantum computing can provide a high speed, secured and noise-free communication. High speed and high degree of parallelism of Photons makes the computing a novel and useful approach with quantum system [1, 2]. Many authors have proposed various quantum circuits using the light as the signal carrier [3-7]. Pauli gates, their square roots, Phase shift gate, Toffoli gate, CNOT, etc. are some of the well-known quantum digital systems which can be used for quantum computing. These circuits are designed by using one or more encoding techniques like Phase encoding, frequency encoding, polarization encoding, etc [3-7].

In this paper, authors propose an integrated quantum system for conduction of half adder operation using light as the signal carrier. A classical half adder circuit consists of an XOR logic and an AND logic. The sum and carry are observed at the outputs of XOR and AND logic respectively. In this quantum presentation of half adder, both XOR and AND logic operations can be performed in a single circuit. The matrix form of the quantum half adder is developed by using input to output conversion and then an equivalent circuit is developed that can give the same operation physically. Phase encoding technique of light signal is used to design this quantum half adder circuit.

2. Development of the proper matrix for conduction of half adder

The input to output relation has been established for two input qubits along with a control bit. The overall input is taken as a 3-bit signal that is represented by an 8×3 matrix. The logic of half adder operation is chosen such that when the control bit is '1', the output will give the XOR gate operation and when the control bit is '0', the output will show the AND gate operation. So, the input to output relation will be as following –

$$\begin{bmatrix} a & b & c & d & e & f & g & h \\ i & j & k & l & m & n & p & q \\ r & s & t & u & v & w & x & y \\ a' & b' & c' & d' & e' & f' & g' & h' \\ i' & j' & k' & l' & m' & n' & p' & q' \\ r' & s' & t' & u' & v' & w' & x' & y' \\ a'' & b'' & c'' & d'' & e'' & f'' & g'' & h'' \\ i'' & j'' & k'' & l'' & m'' & n'' & p'' & q'' \end{bmatrix} \times \begin{bmatrix} 1 & 0 & 0 \\ 1 & 0 & 1 \\ 1 & 1 & 0 \\ 1 & 1 & 1 \\ 0 & 0 & 0 \\ 0 & 0 & 1 \\ 0 & 1 & 0 \\ 0 & 1 & 1 \end{bmatrix} = \begin{bmatrix} 1 & 0 & 0 \\ 1 & 0 & 1 \\ 1 & 0 & 1 \\ 1 & 0 & 0 \\ 0 & 0 & 0 \\ 0 & 0 & 0 \\ 0 & 0 & 0 \\ 0 & 0 & 1 \end{bmatrix} \quad (1)$$

Numerically solving the above equation, one can get the matrix for quantum half adder operation is an 8×8 square matrix which is written as –

$$\begin{bmatrix} 1 & 0 & 0 & 0 & 0 & 0 & 0 & 0 \\ 0 & 1 & 0 & 0 & 0 & 0 & 0 & 0 \\ 0 & 1 & 0 & 0 & 0 & 0 & 0 & 0 \\ 1 & 0 & 0 & 0 & 0 & 0 & 0 & 0 \\ 0 & 0 & 0 & 0 & 1 & 0 & 0 & 0 \\ 0 & 0 & 0 & 0 & 1 & 0 & 0 & 0 \\ 0 & 0 & 0 & 0 & 1 & 0 & 0 & 0 \\ 0 & 0 & 0 & 0 & 0 & 1 & 0 & 0 \end{bmatrix} \quad (2)$$

3. Implementation of half adder circuit using phase encoding of light

A circuit for quantum half adder can be designed by using phase encoding, frequency encoding, intensity encoding, etc. techniques. In our work, the phase encoding technique is used. Figure-1 is the schematic diagram of quantum half adder circuit. Here, A and B are two inputs and outputs are observed at O_1 and O_2. Developed circuit gives the similar operation as the matrix operation. The output shows classical XOR logic or quantum CNOT logic when the control bit is '1' and the output gives classical AND operation when the control bit is '0'.

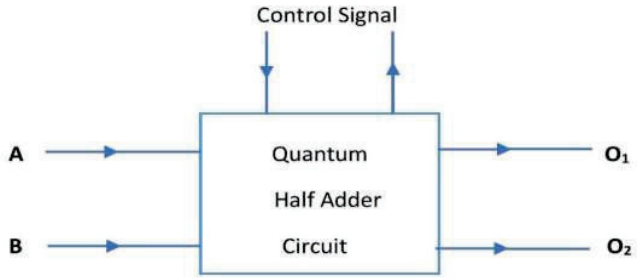

Fig.1: Block diagram of quantum half adder circuit.

4. Conclusions

The electro-optic Pockels cell has the well-known characteristic of changing the phase of the passing light being triggered by external biasing signal. In our proposed work the integrated half adder is implemented by the use of such Pockels cell which ensures the very fast speed of operation (beyond Gigahertz). As the phase of light exhibits the quantum nature, the whole operation supports the quantum treatment and for which the quantum state of the input signals is changed successfully by the gate operation as per requirement. In future we will develop the whole scheme of the above operation both physically and by simulation.

Acknowledgement

The authors acknowledge University Grants Commission (UGC), Govt. of India for extending a research fellowship to Mir Nadim Sarfaraj.

References

[1] S. Mukhopadhyay, Role of Optics in superfast information processing. *Indian J. Phys* **84(8),** 1069 (2010).

[2] A. Ghatak., K. Thyagarajan,'*Optical electronics*', New Delhi, India, Cambridge University Press, (2008).\

[3] B. Sarkar, S. Mukhopadhyay, all optical scheme for implementing an integrated Pauli's X, Y and Z quantum gates with optical switches. *J. Opt*. **46(2),** 143–148 (2017).

[4] S. Dey, S. Mukhopadhyay: 'Approach of implementing phase encoded quantum square root of NOT gate', *Electron. Lett.*, **53, (20)**, pp. 1375– 1377, (2017).

[5] M. Mandal, S. Mukhopadhyay, Photonic scheme for implementing quantum square root controlled Z gate using phase and intensity encoding of light, IET opto-electronics, Volume 15, pages-52-60. 2021.

[6] M. N. Sarfaraj, S. Mukhopadhyay, All-optical scheme for implementation of tristate Pauli-X, Y and Z quantum gates using phase encoding, *Optelectronics letters*, Vol 17, No. 12, (2021).

[7] M. N. Sarfaraj, S. Mukhopadhyay, Implementation of quantum optical tristate oscillators based on tristate Pauli-X, Y and Z gates by using joint encoding of phase and intensity, *Optelectronics letters*, Accepted for Publication.

Sensitivity of a metal-clad planar waveguide having PMN-0.38PT material under external potential

Rajiv Maurya, Vivek Singh*

Department of Physics, Institute of Science, Banaras Hindu University, Varanasi-221005, India

*Author e-mail address: rajivmaurya819@gmail.com, *viveks@bhu.ac.in*

Abstract: Sensing performance of a hollow prism coupled metal-clad planar waveguide having PMN-0.38PT material as an adlayer is estimated in the presence of various applied potential. The sensitivity of proposed structure is increased with the applied potential. The maximum obtained sensitivity of this structure is 313.40 degree/RIU at 40V in our considered applied potential range.

Keywords: Hollow prism, metal-clad planar waveguide, PMN-PT, potential variation, sensitivity.

1. Introduction

In recent years, planar optical waveguide sensors have received much attention due to its quick and accurate detection technique, simple fabrication, and adaptability as an optical component in integrated circuits [1]. The typical dielectric planar waveguide (WG) sensors, surface-plasmon resonance (SPR) and metal-clad planar waveguide (MCWG) sensors are some popular evanescent waves sensing technique-based sensor are widely used for various sensing applications [2–4]. These sensors work by detecting changes in refractive index (RI) that occur close to the sensing surface, or that occur within the probing depth that is also known as the evanescent field's penetration depth [5–6]. In terms of the number of modes propagation, detection accuracy, and tunability of evanescent wave penetration depth, The MCWG based sensors have proved their superiority over the SPR and typical dielectric WG based sensors [7]. Further, the sensitivity of the MCWG can be increased by utilizing graphene [8], switching to hollow prisms in place of solid coupling prisms [9] and using transition metal dichalcogenide (TMDC) materials [10]. In this connection some researcher used piezoelectric material to tune the performance of waveguide sensor [11].

So, in this communication, an attempt has been made to increase and dynamically tuned the sensitivity of MCWG using PMN-PT. The PMN-PT $(1\text{-}x)Pb(Mg_{1/3}Nb_{2/3}Nb_{2/3})O_3\text{-}xPbTiO_3$ is polycrystalline ceramics which have much better electromechanical coupling and piezoelectric properties. A single crystal of 0.62PMN-0.38PT is capable of generating a giant recoverable strain due to its reversible domain switching mechanism with quick response time, accurate control of displacement and small device size. These piezoelectric single crystals demonstrating a large electro strain have very good temperature stability in a wide temperature range from room temperature to 160°C. In addition to this, these piezoelectric materials are cost-effective and easy to manipulate, that is the reason for selecting this material instead of others.

2. Model and Structure

The proposed MCWG sensor is a five-layer planar waveguide structure as shown in Fig.1 which consist of a hallow prism substrate, very thin layer of metal, guided film region (Polyvinyl Chloride), an adlayer (PMN-PT) and cover (air). In this structure a thin silver metallic layer of thickness d_m is coated on a semi-infinite substrate of RI n_s. The metal layer is shielded by the coating of a film layer of refractive index n_F and thickness d_F. The film layer is covered by a thin layer of PMN-0.38PT ceramic of thickness d_a. The PMN-0.38PT is surrounded by air of RI n_c. To find thickness of guiding layer corresponding desired number of modes, its dispersion relation is derived [7, 10] and given as

$$2k_F d_F + \varphi_{SMF} + \varphi_{FAC} = 2m\pi \tag{1}$$

where m=0, 1…corresponding to mode of order 0th, 1st…so on. k_F, φ_{SMF} and φ_{FAC} is the respective wave vector of guiding layer, total phase shift of substrate-metal-guiding film and film-adlayer-air. Further, reflectance, R, of incident light is analyzed by relation $R = |r_{SMFAC}|^2$, where r_{SMFAC} is net reflection coefficient of proposed structure [10]. By using reflectance, the sensitivity (S) is calculated by relation $S = \frac{\Delta\theta_{res}}{\Delta n_s}$, where $\Delta\theta_{res}$ and Δn_s change in resonance angle and change in substrate RI, respectively.

3. Results

Proposed MCWG structure contains hallow prism substrate of RI n_s=1.330, metallic layer of silver having RI n_m=0.065+4i with thickness d_m=45nm, guiding film layer of PVC (Polyvinyl Chloride) having RI n_F=1.54 and PMN-0.38PTof RI n_a=2.6 with thickness d_a=20nm at operating wavelength λ_0=632.8nm. In addition, PMN-0.38PT has property of thickness variation with applied external field across its thickness which is given by expression $\Delta d_a = \frac{\alpha\lambda_0}{2n_a}$ where the variable α is associated with the strain of piezoelectric PMN-0.38PT single crystal that depends on the external electric field [11]. For

analyzing the performance of proposed MCWG sensor, the dispersion curve is plotted at operating wavelength 632.8nm and shown in Fig.2. The obtained cut-off film thickness is 173nm, 614nm, 1051nm for TE_0, TE_1, TE_2 respectively and 20nm, 451nm, 893nm for TM_0, TM_1, TM_2 respectively. For further analysis TE polarized mode is considered because of better detection accuracy than TM polarized mode. Therefore, TE_0 mode is used to plot reflectance curve by considering guiding layer thickness d_F=350nm which is shown in Fig.3. Using the reflectance of Fig. 3 the sensitivity of proposed sensor is calculated between n_s=1.330 and 1.335. Now by applying different external voltages onto two compliant electrodes on layer of PMN-0.38PT crystal, its thickness can be altered by squeezing and stretching. Table1 shows that difference in resonance angles increases on increasing potential difference across PMN-0.38PT layer. The maximum obtained sensitivity in the of proposed structure is 313.40 degree/RIU at 40V in our considered applied potential.

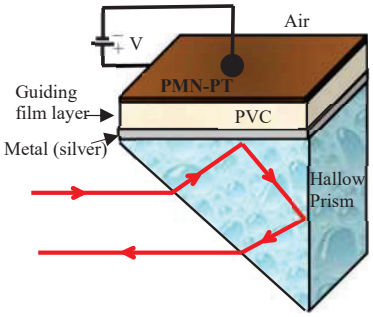

Fig.1: Schematic diagram of five-layer MCWG

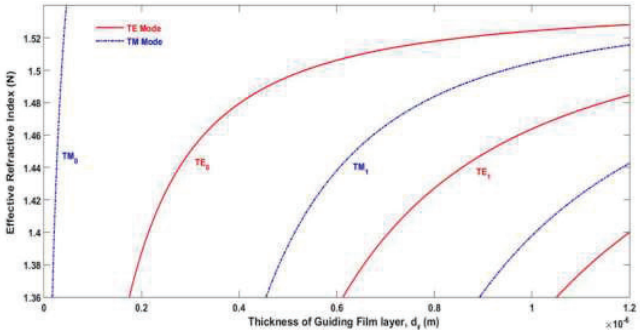

Fig.2: Dispersion curve of proposed MCWG

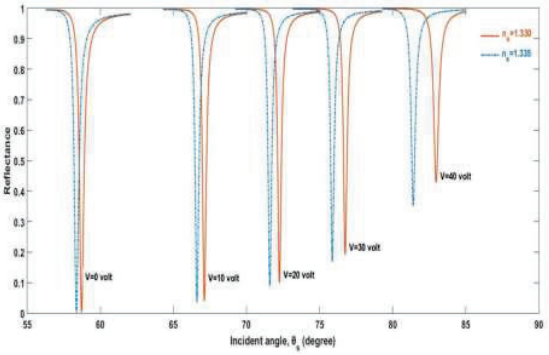

Fig. 3: Reflectance at different applied potential

Table 1: Variation of sensitivity with applied potential

Applied Potential (volt)	Difference in resonance angle $\Delta\theta_{res}$ (degree)	Sensitivity (degree/RIU)
0	0.35	70.36
5	0.43	85.83
10	0.50	100.72
15	0.58	115.62
20	0.66	131.78
25	0.75	150.92
30	0.88	176.58
35	1.09	217.61
40	1.57	313.41

4. Acknowledgments

The author RM is thankful to University Grant Commission, New Delhi for providing fellowship to pursue this work. We also acknowledge the support from Institutions of Eminence (IoE) BHU Grant scheme No. 6031.

5. References

[1] H. Mukundan, A.S. Anderson, W.K. Grace, K.M. Grace, N. Hartman, J.S. Martinez, B.I. Swanson, Waveguide-based biosensors for pathogen detection, Sensors. 9 (2009) 5783–5809.
[2] R.G. Heideman, G.J. Veldhuis, E.W.H. Jager, P. v Lambeck, B Fabrication and packaging of integrated chemo-optical sensors, 1996.
[3] N. Skivesen, R. Horvath, H.C. Pedersen, Multimode reverse-symmetry waveguide sensor for broad-range refractometry, 2003.
[4] G.C. Yadav, S. Prakash, G. Sharma, S. Kumar, V. Singh, Detection of kerosene adulteration in automobile fuel with a novel metal clad planar waveguide, Optics and Laser Technology. 119 (2019).
[5] W. Lukosz, Principles and sensitivities of integrated optical and surface plasmon sensors for direct affinity sensing and immunosensing, 1991.
[6] R. Horvath, H.C. Pedersen, N. Skivesen, D. Selmeczi, N.B. Larsen, Monitoring of living cell attachment and spreading using reverse symmetry waveguide sensing, Applied Physics Letters. 86 (2005) 1–3.
[7] N. Skivesen, R. Horvath, H.C. Pedersen, Optimization of metal-clad waveguide sensors, Sensors and Actuators, B: Chemical. 106 (2005) 668–676.
[8] G.C. Yadav, G. Sharma, S. Kumar, V. Singh, Performance study of metallic clad planar waveguide sensors in presence of graphene layer, Optik. 147 (2017) 366–372.
[9] G.C. Yadav, S. Prakash, G. Sharma, S. Kumar, V. Singh, Performance analysis of a liquid-filled glass prism-coupled metal-clad planar waveguide sensor, Applied Physics A: Materials Science and Processing. 124 (2018).
[10] R. Maurya, V. Mishra, V. Singh, Towards Sensing Performance of Metal Clad Planar Waveguide Sensor with Transition Metal Dichalcogenide Materials, Silicon. (2022).
[11] G. Sharma, S. Kumar, S. Prasad, V. Singh, Theoretical modelling of one dimensional photonic crystal based optical demultiplexer, Journal of Modern Optics. 63 (2016) 995–999

Single Image Dehazing Techniques for Vision Enhancement Applications

Prasenjit Praharaj[1, 2], Manoj Kumar Bhuyan[1, 2, #]
[1]*CSIR-Central Scientific Instruments Organisation, Chandigarh-160030*
[2]Academy of Scientific and Innovative Research, Ghaziabad, Uttar Pradesh- 201002
[#]*manoj.bhuyan@csio.res.in, manoj.femto@gmail.com*

Abstract: Degraded vision due to hazy environment is often a challenge for transportation and surveillance applications. Single image dehazing techniques are quite successful for vision enhancement although each technique works well with certain scattering and illumination conditions. Here, we developed an image dehazing technique based on histogram equalization and flat field correction that works well in a variety of environmental conditions.

Keywords: Image dehazing, Fog removal, Vision enhancement, Histogram equalization.

1. Introduction

The vision has been a challenging aspect of applications related to surveillance, traffic, driver-less transportation, object recognition etc. In particular, the degraded vision may be related to the loss of optical transparency of the environment by the presence of dust, sand, fog and rain. From a physics viewpoint, light incident on a micron and sub-micron size particles such as fog, aerosol gets absorbed as well as scattered depending on the nature of scattering particle and illumination conditions. Nevertheless, high-level scattering is detrimental to the vision through the medium – a long standing problem that many researchers are trying to address.

The earlier investigations in this domain were related to polarization based imaging. For instance, a series of images of a scene were recorded at different degrees of polarization and by establishing their correlation, image dehazing was performed [1]. Although the technique can dehaze images well, it suffers from the drawback related to the practical applications where the scene is dynamic. To deal with realistic situations, several dehazing methods involving single image instead of multiple images were also developed [2-6]. R. T. Tan [2] has developed a single image dehazing technique based on the fact that hazy image has lower contrast than the original scene; hence, local contrast of image may be maximized to suppress the haziness of the image. Indeed, visually contrasted images were obtained but with unrealistic color reproduction. R. Fattal [3] has also developed an image dehazing technique based on the assumption of local non-correlation between surface shading and light transmission. It has been observed that the technique works well under low dense fog and well-lit condition and fails in the conditions of high dense fog and poor ambient light condition. He et al. [4] have also developed an image dehazing technique, often referred as "dark channel prior (DCP)" based on the assumption that at least one color channel of a clear image has very low pixel intensity value, and hence pixel intensity of each color channel of the image can be recalibrated accordingly to dehaze the image. This technique is highly successful in dehazing the images recorded under well-lit and low-dense fog conditions, but fails for images recorded with insufficient airlight and high dense fog condition. The basis of the image dehazing techniques lies with Koschmieder's law, which is used for atmospheric haze image modeling:

$$I(x,y) = J(x,y)t(x,y) + A\big(1 - t(x,y)\big)$$

Where (x, y) is the pixel position, I (x, y) is the observed image intensity, J (x, y) is the image intensity in the absence of scattering medium such as fog. t (x, y) is the transmission coefficient of scattering medium, often expressed as follows: $t(x,y) = e^{-\beta d(x,y)}$, where β is the extinction co-efficient, and d (x, y) is depth of the scene for all pixels i.e. the thickness of the scattering medium. A is referred as "airlight" i.e. global environmental light.

Histogram equalization technique has also been exploited for single image dehazing [5]. For instance, Pizer et al. have successfully dehazed images but their technique often referred as "CLAHE" does not work for images with non-uniform scene radiance.

Here, we propose a hybrid single image dehazing technique based on "Histogram equalization followed by box-blur-filter based flat field correction". The following section presents the results of our hybrid approach along with the other standard single-image dehazing techniques for sake of comparison. The image processing involves images representing the outdoor images recorded under different fog and illumination conditions.

2. Results and Discussions

Through simulation, we have observed that our hybrid imaging technique (T4 row in Fig. 1) works at par with DCP (T1 row in Fig. 1) which normally works well at low fog, high-lit conditions. However, our method produces high quality images even under high dense, low-lit conditions and also in sandy environment, where other methods are poorly performing, as can be seen in Fig. 1. In particular, our technique can be applied for color reproduction and overall uniformity in hazy images over a wide range of environmental conditions.

Fig. 1: Image processing results .T1: Dark channel prior technique [4], T2: Fast visibility restoration technique [6], T3: Contrast limited adaptive histogram equalization technique [5], T4: Our Hybrid approach (Histogram equalization followed by flat field correction). PTI: Press Trust of India

Acknowledgement: Dr. Manoj Kumar Bhuyan and Mr. Prasenjit Praharaj acknowledge the financial support provided by DST-SERB through grant no. SRG/2020/001538.

3. References

[1] Y. Y. Schechner, S. G. Narasimhan and S. K. Nayar,"Instant dehazing of images using polarization," in Proceedings of the 2001 IEEE Computer Society Conference on Computer Vision and Pattern Recognition, *CVPR 2001*, 2001, pp. 325-332.
[2] R. T. Tan, "Visibility in bad weather from a single image," in IEEE Conference on Computer Vision and Pattern Recognition (CVPR), Vol. 1, (IEEE, Anchorage, 2008), pp. 1–8.
[3] R. Fattal, "Single image dehazing," in SIGGRAPH, Vol. 27, (New York, USA, 2008), pp. 72–1729.
[4] K. He, J. Sun, X. Tang, "Single image haze removal using dark channel prior," in IEEE Trans. Pattern Anal. Mach. Intell, Vol. 33(12), 2010 pp. 2341–2353.
[5] Pizer S. M., A.E.Philip, A. John D., C. Robert, G. Ari, G. Trey, Bart, (...), Karel, "Adaptive histogram equalization and its variations," in Computer vision, graphics, and image processing, Vol. 39(3), 1987, pp.355-368.
[6] J.-P. Tarel, N. Hautiere, "Fast visibility restoration from a single color or gray level Image," in IEEE International Conference on Computer Vision *(ICCV), vol. 1*. (IEEE, Kyoto, 2009), pp. 2201–2208.

Photoluminescence quenching due to reabsorption in carbon dots

Devan C M[1], Subhamoy Sahoo[1], Bijeesh M M[1],C. Vijayan[1] and Jayeeta Bhattacharyya [1]

Department of Physics, Indian Institute of Technology Madras, Chennai, 600036, India

Corresponding author: jayeeta@iitm.ac.in

Abstract: Emission quenching mechanisms in carbon dots (CDs) have been a topic of active research in recent times. Various processes like aggregation, energy transfers and carrier losses with change in concentration of CD solutions are investigated. We studied the effect of reabsorption in the emission properties of CDs. Reabsorption was identified as the dominant phenomenon contributing to the concentration quenching of PL emission in our CD samples. We discuss an experimental method to isolate reabsorption from other quenching mechanisms. Apart from a decrease in PL intensities with increase in CD concentration in solutions, reabsorption caused an apparent redshift in the PL spectra. We explained the origin of the shift using absorption spectra. Results from our transient PL measurements rule out aggregation effects and validate that the underlying mechanism is reabsorption.

Keywords: Carbon dots, photoluminescence quenching, Reabsorption.

1. Introduction

Carbon dots are carbon nanoparticles particles, having typical dimension ranging between a few nm to tens of nm. High emissivity in visible wavelength regime, tunability of emission wavelength, easy and cheap synthesis processes and non-toxic nature make them promising candidates for luminescence applications such as light emitting diode and bio-imaging[1-2]. Their emission properties are greatly influenced by the surface states attached to the carbon core, which can be modified by adding different dopant molecules in the synthesis process [3].

The emission properties of the carbon dots in solution is influenced by the concentration of the solution. Generally, photoluminescence (PL) increases initially with concentration, but further increase in concentration results in reduction of PL intensity due to various processes. Concentration quenching of PL in carbon dots was reported earlier, where the mechanism was primarily aggregation-induced quenching resulting from Forster resonance energy transfer or direct π-π stacking interactions [4]. Aggregation-induced quenching typically induces redshift in the PL spectrum [5].

In the present work, we systematically measured PL intensities of carbon dot solutions with increasing CD concentrations. Quenching of PL intensities and red shifts were observed. Using our experimental technique, we identified the mechanism responsible for the observed changes in the PL spectra of our samples. This paper discusses the experimental method used and the inference drawn from the measured data regarding effect of CD concentration on PL emission efficiency in CD solutions.

2. Results and Discussion

Carbon dots were synthesized by solvothermal method using citric acid as the carbon precursor and formamide as the nitrogen dopant. The as-synthesized carbon dot solution was then centrifuged and filtered. Photoluminescence emission of carbon dot solution was measured for different concentrations for the dilute solutions in ethanol. Initially we have observed a linear increase in PL intensity with the concentration of carbon dots. The enhancement in emission was due to the increase in the number of dots. Further increase in the carbon dot concentration caused the PL intensity to saturate and decrease eventually. We did not observe any considerable redshift in the PL spectrum with concentration, which suggests that aggregation effects do not play a role in the quenching. It has been reported that aggregation effects result in changes in lifetimes [5]. But in our case, time-resolved PL decay studies did not show any change in the lifetimes with increase in concentration. This observation also suggests that some other mechanism is responsible for the PL quenching. Reabsorption is another possible mechanism for concentration quenching, which results from the overlap between the absorption and emission spectra of carbon dots [6].

To understand the reabsorption in detail, we have designed an experiment. We have excited the sample with a 405 nm laser at varying depths and measured the emission spectrum at each depth. With the increase in excitation depth, the emitted light traverse a longer path length in the medium. Hence for higher depth, the emitted light encounters a more number of carbon dots and the strength of reabsorption will be high. As shown in **Figure1,** the emission intensity falls with an apparent redshift in PL spectrum with the depth. The redshift in the PL spectrum suggests that the reabsorption is dependent on the emission wavelength. To explain that, we have measured the absorbance spectrum for different concentration. We have found that the nature of absorbance spectrum of carbon dots gives rise to the apparent redshift. Also we have shown that we can reconstruct the shifted PL spectrum by considering the effect of reabsorption.

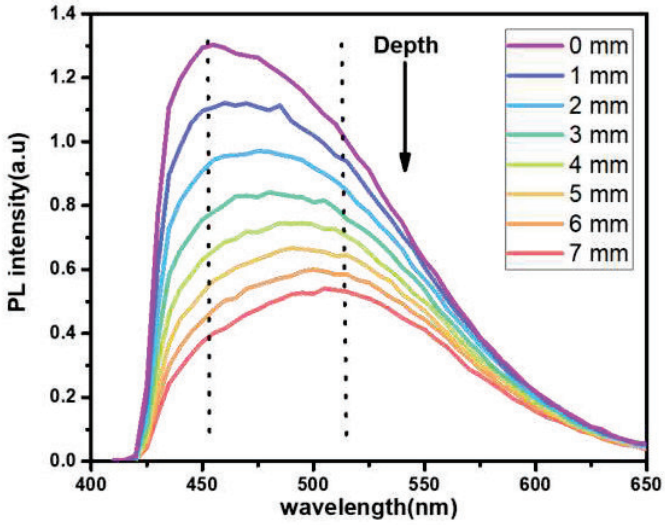

Fig.1. PL spectra of carbon dots for different excitation depth.

3. References

[1] Maria Semeniuk, Zhihui Yi, Vida Poursorkhabi, Jimi Tjong, Shaffiq Jaffer, Zheng-Hong Lu, and Mohini Sain "Future Perspectives and Review on Organic Carbon Dots in Electronic Applications", ACS Nano,13, 6224−6255 (2019).

[2] Junjun Liu, Rui Li, and Bai Yang," Carbon Dots: A New Type of Carbon-Based Nanomaterial with Wide Applications", ACS Cent. Sci., 6, 2179−2195 (2020).

[3] Sadat Anwar, Haizhen Ding, Mingsheng Xu, Xiaolong Hu, Zhenzhen Li, Jingmin Wang, Li Liu, Lei Jiang, Dong Wang, Chen Dong, Manqing Yan, Qiyang Wang, and Hong Bi," Recent Advances in Synthesis, Optical Properties, and Biomedical Applications of Carbon Dots", ACS Appl. Bio Mater., 2, 2317−2338 (2019).

[4] Hyo Jeong Yoo, Byeong Eun Kwak, and Do Hyun Kim," Self-Quenching Origin of Carbon Dots and the Guideline for Their Solid-State Luminescence", J. Phys. Chem. C, 123, 27124−27131 (2019).

[5] Hyo Jeong Yoo, Byeong Eun Kwak, Do Hyun Kim," Competition of the roles of π-conjugated domain between emission center and quenching origin in the photoluminescence of carbon dots depending on the interparticle separation", Carbon 183 560e570 (2021).

[6] Fanlin Zu, Fanyong Yan, Zhangjun Bai, Jinxia Xu, Yinyin Wangl Yicun Huang, Xuguang Zhou," The quenching of the fluorescence of carbon dots: A review on mechanisms and applications", Microchim Acta 184:1899–1914 (2017).

Crack Monitoring in Underground Mines Using All-Optical Techniques

Sarbojit Mukherjee,[1] Khanindra Pathak,[2] Shivakiran Bhaktha B.N.[3,*]

[1] *Advanced Technology Development Centre, Indian Institute of Technology Kharagpur, Kharagpur 721302, India*

[2] *Department of Mining Engineering, Indian Institute of Technology Kharagpur, Kharagpur 721302, India*

[3] *Department of Physics, Indian Institute of Technology Kharagpur, Kharagpur 721302, India*

* kiranbhaktha@phy.iitkgp.ac.in

Abstract: Excavation in underground mining causes geological stress and increases the possibility of rock movement and development of crack causing disasters in the coal mine such as roof fall, rock burst, coal, and gas outburst and loss of human lives. To monitor crack development and propagation, all-optical crack monitoring sensor can be used as it does not use electrical power at site hence it is explosion-proof and can be used in a hazardous environment Three different all-optical techniques to monitor crack namely polarization, diffraction and interferometric are proposed and discussed in this paper.

Keywords: optical strain sensing, interferometry, birefringence, diffraction, underground mines

1. Introduction

As the production capacity is increasing in underground mines, the excavation is becoming deeper. The geological stress increases the possibility of rock movement causing disasters in the mine such as roof fall, rock burst, coal, and gas outburst [1]. Geological failure and water in rush (roof collapse, rock falls, etc.) contribute to the highest number of accidents and equipment breakdowns resulting in revenue loss. Regular surveys are conducted by engineers to detect early signs of failures. Frequent underground surveys in remote areas are not possible and are risky due to unpredictable and harsh conditions. By using electrical and optical devices it is possible to remotely monitor a site from the mine surface. Electrical crack monitors such as vibrating wire type, piezoelectric type and resistive strain gauge type are used most commonly. But, they require complex signal processing and are required to be fire and explosion proof. Optical methods such as fiber Bragg gratings (FBG), micro and macro bending of fiber are also used, but suffers from limited range, high production and maintenance cost and attenuation of signal over long distance [2,3]. In this work, elastic polydimethylsiloxane (PDMS) membranes are used as strain sensors to monitor crack using diffraction, polarization and interferometric techniques.

2. Fabrication and experimental

PDMS membranes were fabricated using Sylgard™ 184 silicone elastomer kit procured from Dow. The base and the curing agent were mixed in a 10:1 ratio and spin-coated on a cleaned glass substrate and grating mask at 1000 rotations per minute (rpm) for 40 seconds, and then cured at 75 °C for 1 hour. The PDMS membranes with and without grating were then peeled off the substrate and suspended between two microscope glass slides, 20 mm apart, with the help of adhesive tapes. The PDMS membranes bond strongly with the adhesive tapes and do not slide over the glass substrates when pulled. The stress that is developed in various membranes without any structured surface, as a result of stretching them is studied using (i) interferometric and (ii) polarization-based techniques. For membranes with grating structures imprinted on them by soft-lithography technique, the periodicity of the grating varies on the application of stress, which can be characterized by (iii) optical diffraction experiments. CMOS camera was used in polarization and interferometric studies and in diffraction study a photodiode was used to study the displacement of first order diffraction with strain.

The PDMS membrane is fixed on sliding rails, anchored on both sides of the crack. As the crack widens the strain in the membrane increases which changes its birefringence properties [4]. Figure 1 shows the experimental schematic, photographs captured by the camera during the stretching process and the variation of intensity at a particular position of the membrane. In the interferometric technique the PDMS membrane is placed in one of the arms of a Michelson Interferometer (Fig. 2(a)). The interferogram and the phase variations occurring at a single point on the membrane are shown in Figs. 2(b) and (c), respectively.

In the diffraction setup as shown in Fig. 3(a), one of the optical fibers carries monochromatic light from the light source to the grating. The light from that fiber is collimated using a PDMS lens and falls onto the PDMS membrane imprinted with grating structures. The receiving optical fiber collects the transmitted 1st order diffraction light. The 1st order diffraction moves towards the central bright order as the periodicity reduces, as shown in Fig. 3(b). In Fig. 3(c), the schematic diagram of the proposed device is shown that can be economical and easier to implement and does not have the problem of electromagnetic interference like that of electrical crack monitoring device. Variation in intensity vs strain is mapped and the intensity signal can be easily carried to the surface using optical fiber and can be monitored using a simple photodiode. The details of the stress-map generated using the above mentioned three all-optical techniques will be presented during the conference and a comparative analysis will be presented.

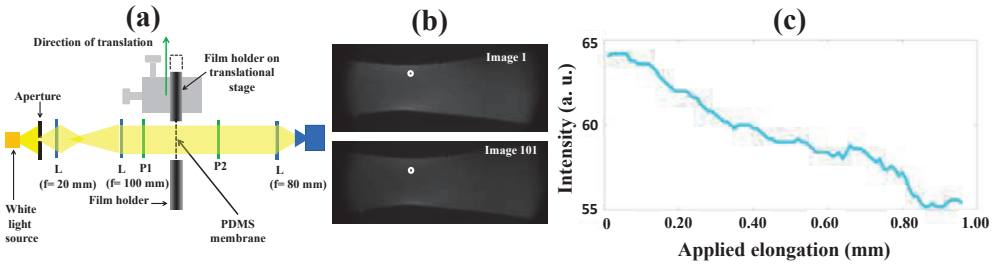

Fig. 1: (a) Polarization setup where L is biconvex lens, P is polarizer placed in cross position. (b) Optical images of the single point of the membrane as it is stretched, (c) intensity variation as membrane is stretched.

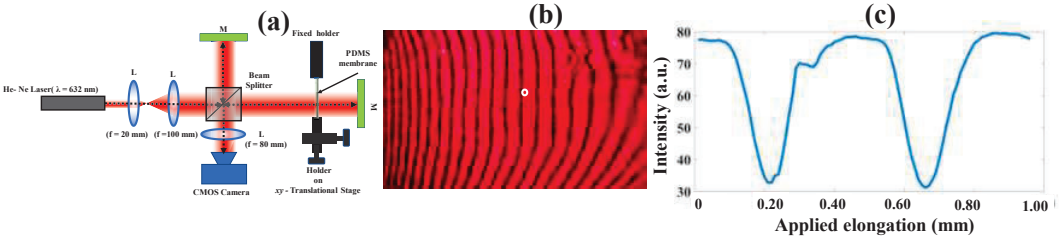

Fig. 2: (a) Interferometric setup where L is biconvex lens, M is mirror, (b) interferogram of the membrane, (c) intensity variation at appoint on the membrane as it is stretched.

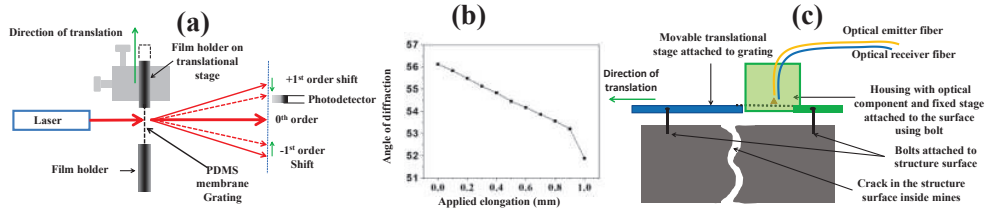

Fig. 3: (a) Diffraction setup, (b) diffraction angle vs elongation given to the membrane (c) proposed device.

3. References

[1] G. Molinda and C. Mark, "Ground failures in coal mines with weak roof," Electronic Journal of Geotechnical. Engineering, 15(F):547-588 (2010).
[2] Y. Yao, S. Tung, B Glisic, "Crack detection and characterization techniques—An overview," Structural Control Heath Monioring., 21, 1387–1413, (2014).
[3] S.K. Chaulya and G.M. Prasad, "Sensing and Monitoring Technologies for Mines and Hazardous Areas Monitoring and Prediction Technologies" Elsevier Inc, Amsterdam, Netherlands, 23- 24, (2016).
[4] Tarjányi, N., Turek, I., & Martinček, I. (2014). Effect of mechanical stress on optical properties of polydimethylsiloxane II - Birefringence. *Optical Materials*, *37*(C), 798–803. https://doi.org/10.1016/j.optmat.2014.09.010

Statistical analysis of specklegrams in a stress induced multimode fiber

Nikhil Vangety, Koustav Dey, Sourabh Roy*

Department of Physics, National Institute of Technology Warangal, 506004, Telangana, India.

*sroy@nitw.ac.in

Abstract: In this work, we have carried out the statistical response analysis of multimode fiber (MMF) specklegrams for different applied stress stimuli on the MMF. Specifically, we have quantitatively estimated the normalized first and second order radial moments as statistical parameters. The efficacy of these parameters is determined using performance metrics namely non-linearity, precision and correlation error. The comparison is made with the previously reported results which suggests the improvement in the performance.

Keywords: Multimode fiber, Specklegram, Statistical parameters, Performance metrics.

1. Introduction

A speckle pattern is a random granular pattern caused by the interference between the incident coherent light beams reflecting from the rough surface with relative optical phases. Fiber specklegrams are speckle patterns resulting from the interference between large numbers of guided modes accommodated in multimode optical fiber (MMF) upon interaction with coherent laser light. When a MMF is subjected to external stress, the specklegrams get reconfigured by the movement of certain bright regions (speckles), change in their shapes, and intensity levels [1]. This leads to the random pattern changes in the specklegrams with applied stresses. Due to the whole process being random, statistical parameters are employed which act as response characteristics to the applied stress stimuli. The statistical parameters known as first and second moments [2] as well as their normalized version [3] are efficient than the statistical parameters like image differencing, image correlation etc. when we consider the precision, accuracy and correlation error as performance metrics of the system. Moreover, there is no requirement for referencing the fiber, i.e., the knowledge about the initial status (zero stress condition) of the fiber for estimating the moments. In this paper, we have demonstrated a simple experiment for collecting the specklegrams for varied applied stresses. Further we have estimated the normalized first and second moments from each specklegrams. The performance metrics namely non-linearity, precision and correlation error which are compared with the previous results. We will use the term stress and weight interchangeably throughout the paper represented in kg units.

2. Experimental arrangement for data acquisition

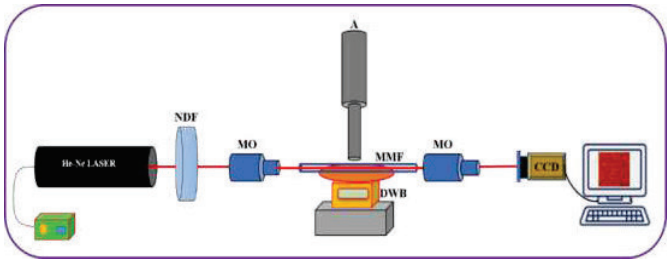

Fig. 1. Schematic of the experimental set-up. NDF: Neutral Density Filter, MO: Microscope Objective, DWB: Digital Weighing Balance, A: Actuator.

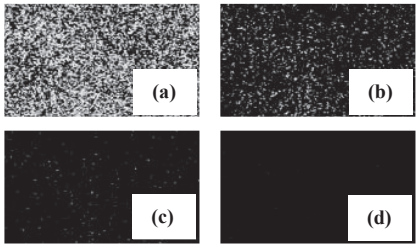

Fig. 2. Binary specklegram images at attenuation factors (a) 12.3 %, (b) 34.9 %, (c) 46.2 % and (d) 57.5 % of NDF.

Fig. 1 shows the experimental schematic diagram. A coherent light from He-Ne laser source (Thorlabs model: HNL020L, 632.38 nm, 2mW) is launched at different contrasts using the variable step neutral density filter (NDF, Thorlabs Model: NDC-50S-3M, attenuation factor: 12.3% - 91.2%) into the multi-mode fiber (MMF, core diameter 980 µm, 0.502 NA made from PMMA (poly-methyl methacrylate)) using Microscope objective (MO, 20X, 0.4 NA). The resultant specklegrams are captured into the computer system via CCD camera (Thorlabs model: DCU223C) focused through MO. Fig. 2 shows the binary images of specklegrams at different attenuation factors, where the bright white spots depicting the speckles. These binary images are converted from raw specklegram images using simple binary thresholding algorithm implemented in python program. The NDF position is fixed at least attenuation factor of 12.3% which corresponds to the maximum contrast of specklegram. Then, a controlled transverse weights in the range 0-3 kg in steps of 0.5 kg is applied using 12V DC Linear actuator (model: B098R82TCD) which is monitored

by Digital weighing balance and further captured into the computer system by CCD camera. The experiment is repeated for ten times under same conditions.

3. Results and Discussions

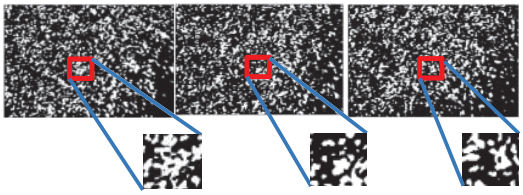

Fig. 3 left – right Binary specklegram images for 0 kg, 0.5 kg and 1 kg respectively at attenuation factor 12.3% of NDF.

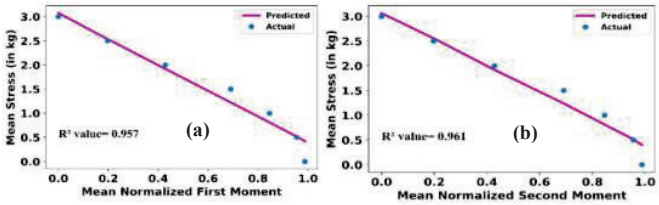

Fig. 4 Mean estimated stress vs **(a)** mean first and **(b)** mean second moments by linear regression.

The binary format of specklegrams corresponding to different weights at 12.3% NDF attenuation factor are shown in Fig. 3. The enlarged squared region shows the change in shape and size of the speckles with increase in stresses. For each specklegram, we have estimated the normalized first and second moment values [3]. Using linear regression, we have estimated the stresses by normalized first and second moments. Fig. 4 shows the variation of mean stresses with mean normalized first moment and mean normalized second moments. It is important to note that we have averaged these values over ten observations. A good agreement between actual and predicted stress is depicted in Fig. 4 with R^2 value of more than 0.95. We have also estimated the performance metrics namely precision, non-linearity defined in [2] as well as correlation error as mentioned in [4]. Table 1 shows the comparison between the previously reported results with our results. The lower precision value signifies the best repeatability and lower non-linearity value signify the best predictability of the stimulus-response system whereas the lower correlation error indicates the strong correlation between stress and moments. It signifies the improvement in the performance metrics of the system depicting the efficacy of the normalized moments as a response parameter.

Table 1: Comparison of performance metrics for various statistical parameters.

Statistical Parameter	Non-Linearity	Precision	Correlation Error	Reference
First Moment	3.3984	0.1547	-	
Second Moment	2.4970	0.1215	-	[2]
Center of mass (one fiber configuration)	-	10.6675	0.0806	
Center of mass (10 loop fiber configuration)	-	7.6933	0.1465	[4]
Normalized First Moment	0.1157	0.11917	0.032	
Normalized Second Moment	0.1105	0.11746	0.0297	Our results

4. Conclusions

To conclude in brief, we have demonstrated the effectiveness of the normalized first and second moments in terms of improvement performance metrics such as non-linearity, precision and correlation error. Authors believe that the statistical parameter namely normalized first and second might be useful for employing into Fiber specklegram sensors (FSSs) for stress sensing purpose when non-linearity, precision and correlation error is taken into account as vital performance metrics.

5. References

[1] Efendioglu, H. S., T. Yildirim and O. Toker. "Advanced image processing and artificial intelligence-based approaches to fiber optic statistical mode sensor design," Proc. SPIE **7982**, 1- 7 (2011).
[2] Hasan S. Efendioglu, et al., "New statistical features for the design of fiber optic statistical mode sensors," Optical Fiber Technology **19**, 279–284 (2013).
[3] N. Vangety, K. Dey and S. Roy, "Quality Factor Assessment of a Laser speckle pattern for Stress sensing in a Statistical Modal Sensors," in 2021 Asian Conference on Innovation in Technology (ASIANCON) (2021), pp. 1-6.
[4] Muhammed Burak Alver, Onur Toker, Kemal Fidanboylu, "Polar format statistical image processing based fiber optic pressure sensors," Proc. SPIE **9217**, 1- 7 (2014).

CNN-Powered Multicasting Optical Communication using Orbital Angular Momentum Beams

Purnesh Singh Badavath†, Venugopal Raskatla††, Vijay Kumar*
National Institute of Technology-Warangal, Warangal, Telangana, India-506004.
*Author e-mail address: bpurneshsingh@gmail.com†, venuraskatla@gmail.com††, vijay@nitw.ac.in**

Abstract: Orbital angular momentum (OAM) modes have addressed the bandwidth issues with high information capacity by employing mode-division-multiplexing. State-of-the-art terabits/sec speed was achieved by using OAM modes. By establishing OAM modes into multicasting communication channel applications, single channel advantages can be inculcated in multiple channels at the same time. In this work, we experimentally proved the feasibility of speckle-based one-to-three multicasting free-space optical communication. Demultiplexing of Laguerre-Gaussian (LG_{nm}) beams from its far-field speckle patterns have been performed through 2D Convolutional Neural Networks (CNN) with an average classification accuracy of >86%.
Keywords: Orbital angular momentum, Speckles, Laguerre-Gaussian Modes, Convolutional Neural Networks.

1. Introduction

Applications of OAM modes in free-space and fiber-based optical communication have marked its importance in the recent past [1]. Using OAM modes orthogonality property to encode information in mode-division-multiplexing with other degrees of freedom had a great impact on the increase of information capacity in the given bandwidth [2]. Taking the cutting-edge applications of OAM modes in increasing the spectral efficiency into account, speckle-based OAM demultiplexing through artificial Intelligence has been introduced to increase the classification accuracy [3]. Speckle-based free-space optical communication has already been performed in a single channel and proved to be robust in demultiplexing the encoded modes [4]. In this paper, we established a speckle-based one-to-three multicasting communication channel effectively and efficiently. The encoded $\boldsymbol{LG_{nm}}$ modes in the form of speckles have been demultiplexed by using Alexnet (a pre-trained CNN) and the trained network has achieved an average classification accuracy of $> \mathbf{86}\%$.

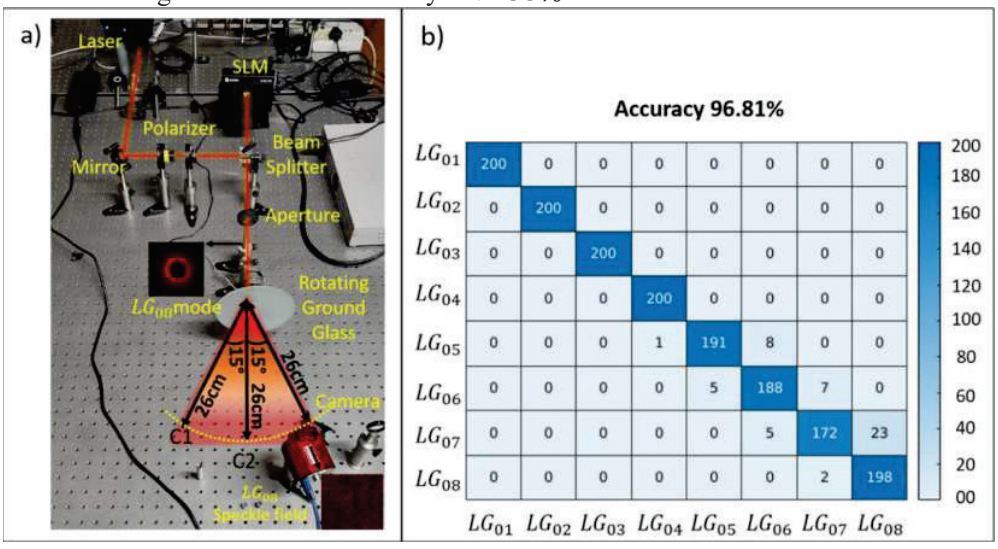

Fig. 1 a) Experimental setup for Speckle-based one-to-three free-space multicasting channel. b) Confusion matrix for the classification of channel C2 intensity speckle images.

2. Experimental Setup

A blazed hologram is projected on the spatial Light Modulator (SLM), which has been illuminated using a 3mW laser source. The required LG_{nm} mode is isolated by using an aperture and passed through rotating ground glass resulting in speckle far-field. It scatters the LG_{nm} mode to wider region analogs to broadcasting information in multiple directions. Rotating ground glass varies the intensity of the speckle pattern of a particular mode by preserving modal information in the ensemble of far-field speckle patterns of the respective LG_{nm} beams. Projected speckle patterns have been captured by a CMOS camera at three different positions over a radial distance of 26cm. The camera is kept along the beam axis (C2) and at an angle of 15° on either side (C1 & C3) from the beam axis as shown in Fig 1a. We have used $n = 0$ and $m = 1\ to\ 8$ to generate eight LG_{nm} beams to establish the multicasting communication channel. For each beam, 1000 intensity speckle images have been captured and each image has a size of 1200×1920 pixels.

3. CNN Architecture

We have performed transfer learning to classify the LG_{nm} modes through its intensity speckle images. To perform transfer learning, we have used Alexnet, a pre-trained CNN, which has been trained on a million images to classify 1000 regularly seen objects. As the network is pre-trained, it has already updated its weights and biases according to the 1000 classes for which it has trained. We modify the last classification layer according to the number of classes to classify eight beams. By training the Alexnet again for the required number of classes, it updates the weights and biases according to the trained data. Alexnet accepts images of size 227×227×3, we have resized the captured intensity speckle images accordingly and trained/tested the network on them. In the captured 1000 images for each class, 80% of the images are used to train the network, and 20% of images to test the trained network. The network has been trained for 30 epochs by using an Adam optimizer with a constant learning rate of value 0.0001. The network has achieved > 80%, 96%, and 84% classification accuracies for channels C1, C2, and C3 respectively. The confusion matrix for the classification of channel C2 has been shown in Fig 1b.

4. Results and Future Scope

We have successfully established a one-to-three multicast communication channel using LG_{nm} beams and achieved the average classification accuracy of $> 86\%$. The classification accuracy of the on-axis (C1) channel is higher than the off-axis (C1 and C2) channels, because of the gradual decrease of intensity and the increase in noise as we move away from the beam axis. Further classification accuracy can be improved by increasing the laser power and diffracting speckles in a wider region.

Such speckle-based OAM multicasting channels can be used to increase the information capacity in multiple channels at once by encoding the information in multiple degrees of freedom. Speckle-based multicasting would make the receiver free of precise alignment.

5. Acknowledgments

We acknowledge Prof. Nirmal K. V, University of Hyderabad for allowing us to use his lab facility and V. K. acknowledges SERB funding (SRG/2021/001375).

6. References

[1] G. Rademacher et al., "*Peta-bit-per-second optical communications system using a standard cladding diameter 15-mode fiber*," Nature Communications **12**, (2021).
[2] H. Huang et al., "*100 Tbit/s free-space data link enabled by three-dimensional multiplexing of orbital angular momentum, polarization, and wavelength*," Optic Letters **39**, 197 (2014).
[3] V. Raskatla et al., "*Speckle-based deep learning approach for classification of orbital angular momentum modes*," JOSA A **39**, 759 (2022).
[4] V. Raskatla and V. Kumar, "*Deep learning assisted OAM modes demultiplexing*", in Fifteenth Int. Conf. Correl. Opt., O. V. Angelsky, Ed., (SPIE, Chernivtsi, Ukraine, 2021).
[5] V. Raskatla, P. S. Badavath, and V. Kumar, "*Convolutional networks for speckle-based orbital angular momentum modes classification*," Optical Engineering, **61** (2022).
[6] V. Raskatla and V. Kumar, "*Deep Learning Assisted Classification of Noisy Laguerre Gaussian Modes*," in *Front. Opt. Laser Sci. 2021*, (OSA, Washington, DC, 2021).

Controlled generation of high-dimensional OAM entangled state without postselection

Suman Karan, Radhika Prasad, and Anand K. Jha
Department of Physics, Indian Institute of Technology Kanpur, Kanpur, UP 208016, India
karans@iitk.ac.in

Abstract: We propose and experimentally demonstrate a true postselection-free method for generating up to the 200-dimensional OAM entangled state with complete control over the shape of the OAM Schmidt spectrum, employing both phase matching adjustments and pump-shaping. We report the generation of Gaussian, rectangular and triangular spectra with high generation accuracy.
Keywords: Postselection-free, High-dimension, Orbital angular momentum, entanglement, Parametric down-conversion

1. Introduction

The high-dimensional photonic entangle state in orbital angular momentum (OAM) basis offers numerous advantages in entanglement-enabled quantum cryptography, communications, and metrology. Spontaneous parametric down-conversion (SPDC) is the most widely utilized method for generating entangled signal (s) and idler (i) photon pairs in OAM basis. From the conservation of OAM, one can write the two-photon state generated from SPDC in Schmidt decomposed form as $|\psi\rangle_{tp} = \sum S_l |l\rangle_s |-l\rangle_i$ for pump's OAM index $l_p = 0$, where S_l is called the OAM Schmidt spectrum. Control over the shape of S_l is paramount to harnessing the entanglement-enabled advantages of the two-photon state. For example, quantum key distribution protocols require a rectangular spectrum. Several attempts have been executed, but most existing techniques require a postselection process to obtain the desired shape of S_l. Moreover, the postselection approach diminishes the security benefits of the entangled state. Although a few specific strategies that do not require postselection have been proposed recently, these methods are demonstrated only up to a 5-dimensional state, and some of the very high-dimensional generation methods can only change the spectrum size without having any control over the shape. Therefore, a proper postselection-free method for generating a very high-dimensional OAM entangled state with the desired shape of S_l is required. Here we present a novel method to control the shape of the OAM Schmidt spectrum. Our scheme employs a coherent superposition of the radial modes p with $l_p = 0$ in the Laguerre Gaussian (LG) basis as the down-conversion pump field with non-collinear phase matching.

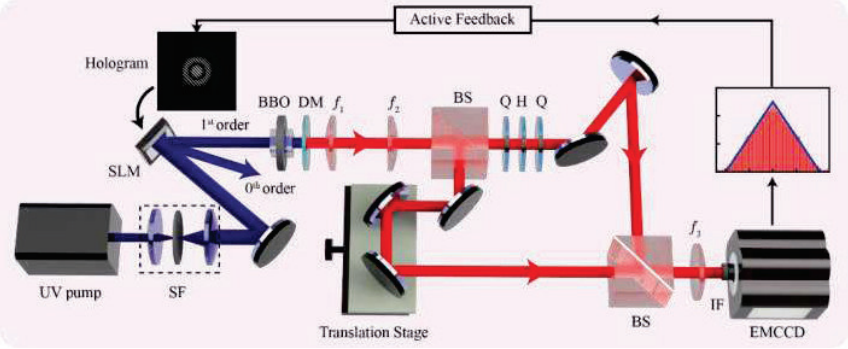

Fig. 1: Schematic of the experimental setup. SF: spatial filter, SLM: spatial light modulator, BBO: β-barium borate crystal, DM: dichroic mirror, BS: beam splitter, Q: quarter-wave plate, H: half-wave plate, IF: interference filter of central wavelength 810nm.

2. Theory

The two-photon OAM Schmidt spectrum S_l for the type-I SPDC process in transverse polar coordinate can be expressed as [1]

$$S_l = \frac{1}{4\pi^2}\int_0^\infty \rho_s\rho_i \left| \int_{-\pi}^{\pi} V(\rho_s,\rho_i,\phi_s,\phi_i)\,\Phi(\rho_s,\rho_i,\phi_s,\phi_i,\theta_p) e^{-il(\phi_s-\phi_i)} d\phi_s d\phi_i \right|^2 d\rho_s d\rho_i, \qquad (1)$$

where $V(\rho_s, \rho_i, \phi_s, \phi_i)$ is the pump field amplitude, $\Phi(\rho_s, \rho_i, \phi_s, \phi_i, \theta_p)$ is the phase matching function, and θ_p is the angle between the optic axis of the crystal and pump propagation direction. We use non-collinear phase matching, characterized by θ_p for the SPDC process. For the pump field; we express $V(\rho_s, \rho_i, \phi_s, \phi_i)$ as

$$V(\rho_s, \rho_i, \phi_s, \phi_i) = \sum_{p=0}^{N-1} \alpha_p LG_p^{l_p=0}(\rho_s, \rho_i, \phi_s, \phi_i), \qquad (2)$$

where α_p is the superposition coefficient corresponds to radial mode index p, N is the number of radial modes. In our method, we numerically optimize θ_p and α_p to generate a desired OAM Schmidt spectrum, and the generation accuracy is characterized by R^2 value. In the experiment, we measure S_l using an interferometric technique described in Ref. [2]. We further optimize α_p experimentally through active feedback to obtain the desired spectrum.

3. Results

Figure 1 depicts the experimental setup. We employ five radial mode superpositions as UV pump of wavelength 405nm and beam waist $w = 320$ mm. We use a BBO crystal of thickness $L = 15$ mm at $\theta_p = 28.71°$ and down-conversion wavelength equal to 810 nm. Experimentally obtained spectra are shown in Fig.2, together with the corresponding pump intensity profiles in the insets [3]. Fig 2 (a), (b) display experimentally generated Gaussian spectrum with a standard deviation of 20 and 30, respectively. Fig.2 (c), (d) shows the rectangular spectrum of widths of 100 and 150. The triangular shape of base widths 100 and 200 are shown in Fig.2 (e), (f), respectively. We calculate the entanglement of formation E_f, using the formula $E_f = -\sum S_l \log_2 S_l$ and confirm the presence of entanglement of the generated state [4]. We report the values of E_f and R^2 for all generated spectra in Fig. 2. We note that for the Gaussian and the triangular spectra, R^2 value is more than 97%, whereas, for the rectangular spectrum, the average R^2 value is around 84%.

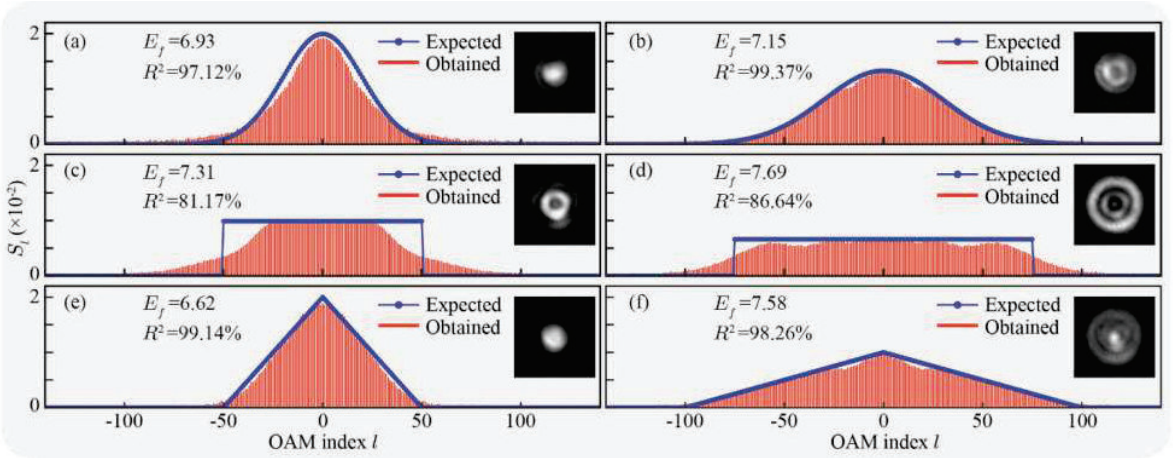

Fig. 2: Experimentally generated two-photon entangled OAM spectrum. Expected versus experimentally obtained (a)-(b) Gaussian, (c)-(d) rectangular, and (e)-(f) triangular spectrum of two distinct sizes in each. The associated pump intensity profiles are shown in the inset of each spectrum plot.

4. Conclusions

In conclusion, we have demonstrated a postselection-free method for generating up to 200-dimensional OAM entangled states with complete control over the spectrum's shape. We have reported the generation of Gaussian, rectangular and triangular spectra with outstanding generation accuracy and verified the entanglement of each generated spectrum. We expect this technique to be useful in high-dimensional quantum information applications while ensuring full security benefits.

5. References

[1] S. Karan, S. Aarav, H. Bharadhwaj, L. Taneja, A. De, G. Kulkarni, N. Meher, and A. K. Jha, "Phase matching in β-barium borate crystals for spontaneous parametric down-conversion," J. Opt. 22, 083501 (2020).

[2] G. Kulkarni, R. Sahu, O. S. Magaña-Loaiza, R. W. Boyd, and A. K. Jha, "Single-shot measurement of the orbital-angular-momentum spectrum of light," Nat. Commun. 8 (2017).

[3] S. Karan, R. Prasad, and A. K. Jha, "Postselection-free controlled generation of high-dimensional OAM entangled state," arXiv:2203.14799.

[4] C. K. Law and J. H. Eberly, "Analysis and interpretation of high transverse entanglement in optical parametric down conversion," Phys. Rev. Lett. 92, 127903 (2004).

Enhancement of angular displacement measurement sensitivity by modified SU(2)- type quantum interferometer

Karunesh Kumar Mishra[1,2], **Priyanka Sharma**[1], **Devendra Kumar Mishra**[1]
[1]*Department of Physics, Institute of Science, Banaras Hindu University, Varanasi-221005, India*
[2]*Extreme Light Infrastructure - Nuclear Physics (ELI-NP), 30 Reactorului Street, 077125 Romania*
mishrakarunesh321@gmail.com, priyashara2016@gmail.com, kndmishra@gmail.com

Abstract: In this paper, we investigate the angular displacement measurements using the homodyne detection method in a modified SU (2) Mach-Zehnder interferometer (MZI). Three parametric amplifiers are used (PAs). PA's role is to increase the number of photons and reduce shot noise. We also take into account quantum Fisher information (QFI) and derive expressions for two-parameter and single-parameter and corresponding quantum Cramer-Rao bounds (QCRB). We find that angular displacement sensitivity exceeds the standard quantum limit (SQL) or short-noise limit (SNL) and two-parameter QCRB and approaches the single parameter QCRB. Finally, we look into the impact of photon losses on sensitivity.
Keywords: Quantum metrology, Quantum Fisher Information, Coherent state, homodyne detection.

1. Introduction

Quantum metrology provides a means of circumventing practical constraints in sensing devices. An optical interferometer can be used to precisely measure the phase shift [1-3]. MZI is combined by beam splitters (BSs), which split the light beam into two arms and recombine the beam. MZI has two ports, one of which is normally injected by a coherent state. The MZI's sensitivity is limited by the quantum noise of the unused port. Caves proposed [4] that by using squeezed states at an unused port, the MZI's sensitivity is greatly improved and it overcomes the SQL; the same method is used in the Laser Interferometer Gravitational-wave Observatory (LIGO). Aside from measuring phase sensitivity, the measurement of angular rotation using an interferometer has recently gained popularity. In general, an optical beam can carry two types of angular momentum: orbital angular momentum (OAM) and spin angular momentum (SAM). SAM is concerned with light beam polarization, while OAM corresponds to the spiral wavefront or transverse angular phase of the light beam. OAM has gotten a lot of attention and played an important role in optical communication, optical imaging, quantum simulation, and particle manipulation [5]. Some interferometric configurations have recently been used to realize the precision measurement of angular displacements. Jha et al. [6] demonstrated that the sensitivity of angular displacement measurements can be increased to $1/2lN$ and $1/2l\sqrt{N}$ by using *N*-entangled and *N*-unentangled photons, respectively. We propose a modified SU (2) MZI and analyze the angular displacements measurements. The multiparameter quantum Cramer-Rao bound (QCRB) is derived using the method of quantum Fisher information matrix (QFIM).

2. Our Proposal

In our model, we use the two sets of PAs, which are kept beyond the second beam splitter, and one PA located in one arm is used for squeezing the shot noise and amplifying the internal photon number, spiral plates (SPPs) and Dove prisms (DPs) are located in the two arms of MZI, which is different from the usual MZI as shown in Fig.1. Here, we introduce coherent state $|\alpha>,\ \alpha = |\alpha|e^{i\theta_\alpha}$ in one port while vacuum state $|0>$ at other port of MZI. The SPPs are used to provide the OAM degree of freedom, in the other words we can say that the light which is passing with SPP canting OAM. The transformation of the topological charge from l to $-l$ is conducted by DP and it also creates a phase shift of $2l\theta$ to the optical field, where θ represents the rotation angle of the DP. Mirrors are denoted by M (1,2).

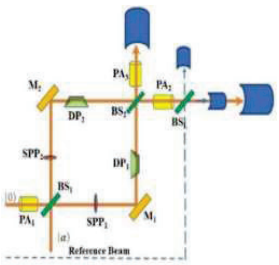

Figure 1 Schematic diagram of MZI setup.

2.1 Angular Displacement Estimation

We consider the most general situation, in which $\theta_d = \theta_2 - \theta_1$ and $\theta_s = \theta_2 + \theta_1$ are two the parameters. These types of situations can be handled by the multi-parameter quantum estimation theory approaches. The angular displacement estimation uncertainty bounds can be expressed by the quantum Cramer-Rao inequality [7] $\sum(\theta_2, \theta_1) \geq F^{-1}(\theta_2, \theta_1)$. The coefficients of Fisher-matrix can be calculated by $F_{ij} = 4\,Re(<\partial_i\psi_\theta|\partial_j\psi_\theta> - <\partial_i\psi_\theta|\psi_\theta><\partial_j\psi_\theta|\psi_\theta>)$. Here $|\psi_\theta>$ is state passing through DP and $|\partial_i\psi_\theta> = \partial|\psi_\theta>/\partial\theta_i$. Two-parameter QFI is define as, $F^{2p} = F_{dd} - F_{sd}F_{ds}/F_{ss}$ corresponding two-parameter QCRB imply $\Delta\theta_{QCRB} = 1/\sqrt{F^{2p}}$. Single parameter ($\theta_1 = 0$) QFI is define as, $F^i = 16l^2(<n_{b2}^2> - <n_{b2}>^2)$, corresponding single-parameter QCRB can be calculated as $\Delta\theta_{QCRB} = 1/\sqrt{F^i}$.

2.2 *Balanced Homodyne Detection Scheme*

The phase sensitivity of the setup can be obtained by the balanced homodyne detection scheme with straight forward calculation as,

$$\Delta^2\theta_{hom} = \frac{(|\alpha|^2\cosh 2r_2 + (1+2|\alpha|^2)\sinh r_2\cosh r_2 + \cosh 2r_2\sinh 2r_2)}{8|l\alpha(\cosh r_2 - \sinh r_2)|^2} - \frac{(\cosh 2r_2|\alpha|^2 - 1 - |\alpha|^2\sinh 2r_2 - 4l^2|\alpha|^2(\cosh r_2 - \sinh r_2)^2)}{16|l\alpha(\cosh r_2 - \sinh r_2)|^2}.$$

We observed from figure 2(a) that the angular displacement sensitivity of MZI overcome the short-noise- limit (SNL) and attain the two-parameter QCRB in low intensity regime. The transmission coefficient of beam splitter also plays a crucial role to enhance the sensitivity of MZI. We analysis the effect of internal loss (μ) and external loss (η) on the angular displacement sensitivity. The best sensitivity is obtained when both internal and external losses are taken into account. In figure 2(b) we can see that the optimum value of sensitivity in not depend on whatever the value of squeezing parameter r_2 of the second and third parametric amplifier.

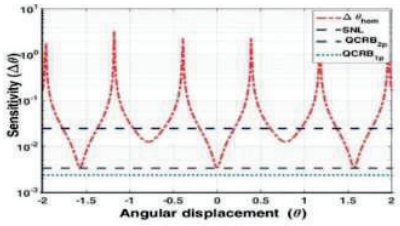

Figure 2(a) Variation of the angular displacement sensitivity Δθ & angular displacement.

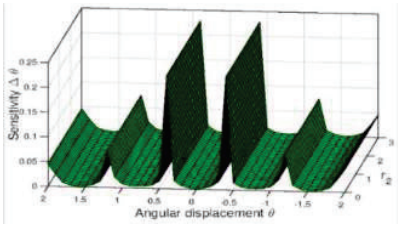

Figure 2(b) The effect of the squeezing parameter r_2 on the angular sensitivity.

3. Conclusions: We have examined the protocol based on angular displacement, which is based on the modified SU (2) MZI. For analysis of angular displacement sensitivity, we have utilized the homodyne detection approach. Additionally, we examine the single and two-parameter QCRB, which tells us, if we have a certain number of input resources, how much of a lower bound we can obtain through MZI. The internal and exterior losses of MZI play a crucial role in angular displacement sensitivity, we analyze both the losses and the fact that the angular displacement sensitivity of MZI reaches the QCRB value for a two-parameter. Outside the beam splitter, parametric amplifiers (PAs) have no effect on the optimal angular displacement sensitivity.

4. Acknowledgements: Authors acknowledge financial supports from SERB, New Delhi (**CRG/2021/005917**) and IoE Incentive grant of Banaras Hindu University, Varanasi.

5. References:

[1] B. T. Gard, C. You, D. K. Mishra *et al.*, *Nearly optimal measurement schemes in a noisy Mach-Zehnder interferometer with coherent and squeezed vacuum,* EPJ Quantum Technol. 4, 4 (2017).

[2] G. Shukla, K. K. Mishra, D. Yadav, R. K. Pandey, and D. K. Mishra, *Quantum-enhanced super-sensitivity of a Mach–Zehnder interferometer with superposition of Schrödinger's cat-like state and Fock-state as inputs using a two-channel detection,* J. Opt. Soc. Am. B 39, 59-68 (2022).

[3]. *G. Shukla, D. Salykina, G. Frascella, D. K. Mishra, M. V. Chekhova, and F. Ya. Khalili, Broadening the high sensitivity range of squeezing-assisted interferometers by means of two-channel detection,* Opt. Express 29, 95-104 (2021).

[4] C. M. Caves, *Quantum-mechanical noise in an interferometer* Phys. Rev. D 23, 1693 (1981).

[5] S. G. F Roux, and T. Konrad, *Implementing Quantum Walks Using Orbital Angular Momentum of Classical Light,* Phys. Rev. Lett. 110, 263602 (2013).

[6] A. K. Jha, G. S. Agarwal, and R. W. Boyd, *Supersensitive measurement of angular displacements using entangled photons,* Phys. Rev.A 83, 053829 (2011).

[7] M. D. Lang and C. M. Caves, *Optimal Quantum-Enhanced Interferometry Using a Laser Power Source*, Phys. Rev. Lett. 111, 173601 (2013).

Rotation of Coupled Optical Mode due to Spin-orbit Interaction

Anagha Sreedharan and Nirmal K. Viswanathan
School of Physics, University of Hyderabad, Hyderabad, Telangana – 500046, India
anaghakandoth@gmail.com

Abstract: The coupling of spin and orbital angular momentum degrees of freedom in the light beam and upon propagation through an anisotropic medium is of fundamental interest. The superposition of transverse and longitudinal optical field components in an anisotropic medium induces optical torque resulting in the rotation of optical mode and/or the state of polarization in the transverse plane. Here, we demonstrate the spin-polarized transverse optical mode rotation upon propagating through a tilted-rotated uniaxial crystal plate.

Keywords: Spin-orbit interaction, uniaxial crystal plate, transverse spin mode rotation.

1. Introduction

A paraxial or non-paraxial beam of light, carrying the intrinsic spin (S_I), intrinsic and extrinsic orbital ($O_{I/E}$) angular momentum (AM) degrees of freedom propagating in free space or an anisotropic medium, focusing/diverging has a wide variety of applications and is of fundamental interest as well [1]. Apart from the spatial separation of the spin and orbital AM components in a beam of light leading to the spin-Hall effect of light (SHEL) and orbital-Hall effect of light (OHEL), respectively, the study on the spin-orbit optical Hall effect [5] and spin-orbit mapping [6] is also reported recently. Rotating or shifting of the optical mode is one of the revelations of the coupling of different AM degrees of light [2 – 4]. Which further exploits the fundamental aspects of the spin-orbit (SO) interaction and to apply its various aspects.

2. Experimental details and Results

By propagating a paraxial beam of light through an elliptically birefringent crystal plate (XP), we bring forward a novel aspect due to SO coupling via simulation and experimental demonstration. We note that both the polarization ellipticity-ellipse orientation angle and the optical mode pattern rotate as a function of the tilt angle (θ) and the optic-axis (OA) orientation (ϕ) of the XP. The (θ, ϕ) degrees of freedom of the XP provides the necessary coupling between the transverse and longitudinal phase difference to the polarized light beam propagating through the crystal. This observation further establishes our recent report of a dislocation line threading the polarization interferometer, leading to the observation of spiral and saddle topological features, alternating with each other as a function of the phase difference between the crystal eigen modes [7]. The output beam field characteristics of the XP are comprehensible with the combination of longitudinal (in-plane) [8] and transverse (out-of-plane) [9] spin variations in the beam cross-section arising due to the simultaneous presence of linear and circular birefringence in the rotated-tilted XP.

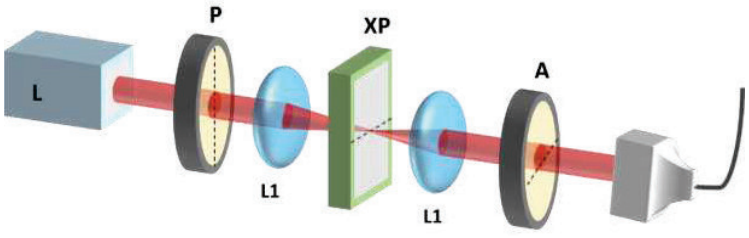

Figure 1. Schematic of the experimental setup

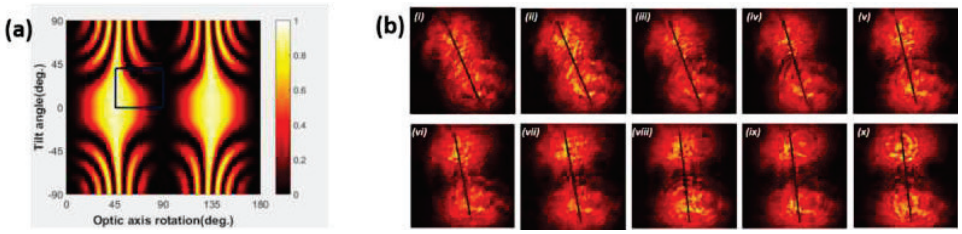

Figure 2 (a) XP tilt and OA rotation angle dependence on the output beam intensity, (b) Measured optical mode and polarization rotation

Figure 1 shows the schematic of the experimental setup used. It consists of a linearly polarized supercontinuum laser (SL) beam that is weakly focused and collimated by a lens pair (L1=7.5 cm-L2=5 cm). The XP is kept at the focus, and the output beam characteristics are measured using a CCD camera as a function of tilt angle (θ) and OA rotation angle (θ). Figure 2 (a) shows the simulation result of the output beam intensity as a function of (θ, ϕ) variation of the XP. The experiment corresponds to the region is marked with a blue rectangle in Fig. 1 (b). The results in Figure 2 (b) clearly show both the output mode rotation and the change in the polarization ellipticity-ellipse orientation angle in the output beam measured after the analyzer (A). The measured effects are further corroborated with simulation and experiment of the phase difference, polarization ellipticity-ellipse orientation, the Stokes parameters, and Stokes phase difference. The amount of phase difference accumulated in the output beam is further quantified via weak measurement [10]. The rotating mode-polarization structure can be understood from the optical torque introduced due to the interference of transverse and longitudinal optical fields in the rotated-tilted crystal plate [11].

3. Acknowledgments: The authors thank SERB for financial support in this area of research.

4. References

[1] K. Y. Bliokh, F. J. Rodríguez-Fortuño, F. Nori, and A. V. Zayats, Nat. Photonics 9, 796 (2015).
[2] V. S. Liberman and B. Y. Zel'dovich, Phys. Rev. A 46, 5199–5207 (1992).
[3] D. L. P. Vitullo, C. C. Leary, P. Gregg, R. A. Smith, D. V. Reddy, S. Ramachandran, and M. G. Raymer, Phys. Rev. Lett. 118, 083601 (2017).
[4] T. P. Chakravarthy, D. N. Naik and N. K. Viswanathan, J. Opt. 19, 105607 (2017).
[5] S. Fu, C. Guo, G. Liu, Y. Li, H. Yin, Z. Li and Z. Chen, Phys. Rev. Lett. 123, 243904 (2019).
[6] L. Fang, H. Wang, Y. Liang, H. Cao and J. Wang, Phys. Rev. Lett. 127, 233901 (2021).
[7] A. Sreedharan and N. K. Viswanathan Opt. Lett. 47, 770 (2022).
[8] N.W. M. Ritchie, J. G. Story, and R. G. Hulet, Phys. Rev. Lett. 66, 1107 (1991).
[9] K. Y. Bliokh, C. T. Samlan, C. Prajapati, G. Puentes, N. K. Viswanathan, and F. Nori, Optica 3, 1039 (2016).
[10] A. Sreedharan, and N.K. Viswanathan Opt. Lett. 47,3768 (2022).
[11] *El Ketara, M., Kobayashi, H. and Brasselet, E., 2021. Nature Photonics, 15(2), pp.121-124.*

Development of a Customized and Multi-Modal Polarizing Microscope for Imaging of Samples Ranging from Biological Specimens to Rock Specimens

Shibsankar Roy[1, 2, 3], Barnini Bhattacharya[2, 3], Rajdeep Das[1], Bijay Bal[4], Rajen Haldar[3] and Kuntal Ghosh[1, 2]

[1]Machine Intelligence Unit
Indian Statistical Institute,
203 B. T. Road Kolkata - 700 108, India
[2]Laboratory for Cognitive Systems and Cybernetics Research
Centre for Soft Computing Research
Indian Statistical Institute, Kolkata
[3]Department of Physiology
University of Calcutta
[4]Saha Institute of Nuclear Physics (Retired)

Abstract: Polarized light microscopy is a technique that enables imaging of specimens having birefringence property. However, there are certain constraints of the existing commercial polarizing microscopes like there is no option for variation of angles of either the analyzer or polarizer, only the sample stage can be rotated and has only two imaging modes – plane and cross. In this backdrop, a portable, low-cost, customized and multi-modal digital polarizing microscope has been constructed in the laboratory to study both, live plant tissue sections and geological rock specimens.

Keywords: *Alternanthera philoxeroides*, Rock Samples, Birefringence, Circular Polarization, Polarizing Microscope

1. Introduction

In the commercial polarizing microscopes, conventionally only two imaging modes are present, cross or plane polarized. Another limitation is that there is no provision for continuous variation of angles of either the analyzer or polarizer, only the sample stage can be rotated. Moreover, such commercial microscopes have high product cost, are quite larger in size and requires multiple objective lenses for varying the magnification. In this backdrop, a portable, low-cost, customized, and multi-modal digital polarizing microscope has been constructed in the laboratory (Fig. 1) to study both, live plant tissue sections and geological rock specimens. This microscope allows continuous angle variation through rotation of either the analyzer or the polarizer, with respect to each other and provides multiple modes of imaging in addition to the conventional plane and cross polarized modes. Along with this, by adding multiple attenuators images can be formed using this developed microscope. The lab-built polarizing microscope has been further employed in analyzing relevant properties and processes of the rock and plant-tissue samples under observation. In this microscope, the samples under observation are illuminated by means of transmission technique. The microscope can also be used to detect change in optical property of live plant tissue sections that have undergone any sort of biological perturbation like drying [1].

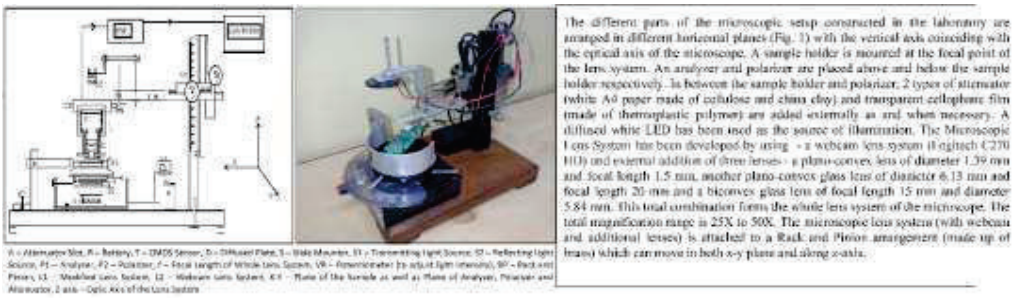

Fig. 1: Schematic and photographic images of the lab-built multi-modal polarizing microscope

1. Findings

In the present study, the multiple modes of imaging of the lab-built microscope are – i) Plane polarized ii) Cross polarized iii) Attenuated cross polarized (White sheet) and iv) Attenuated pseudo-color cross polarized (Transparent Cellophane sheets). The two types of specimens used in the present study are a cross-section of a dicot plant stem, *Alternanthera philoxeroides* and a thin section of rock.

Imaging of Plant-tissue cross section (Fig. 2): It has been found that under the cross-polarized mode the biologically relevant tissue structures become more conspicuous which are not that distinguishable under the plane polarized mode. Moreover, under the Attenuated pseudo-color mode the prominent tissue structures that were observed under the normal cross polarized mode appeared to be more differentiable owing to the development of pseudo-coloration of the background and tissue structures. In this mode the epidermis and cambium ring shows different color – epidermis shows whitish color and cambium ring shows yellowish-red color.

Imaging of Rock section (Fig. 2): In case of the cross-polarized mode the edges of the grains are prominent and it appears that some of the grains are selectively more intensified in comparison to their surrounding ones. In the attenuated pseudo-colored mode each of the grains of the specimen shows multiple colors (which are mixture of primary colors) and this facilitates identification of cracks and different geometrical shapes present in the crystals of the specimen. In addition, the inter-spaces between the rocks are markedly prominent.

The formation of pseudo-coloration of the specimen structures in presence of the transparent cellophane sheets is possibly due to the anisotropy and birefringence of the specimens [2]. It is known that under cross polarized mode, anisotropic materials show distinct bands of color, while isotropic materials do not show up at all. Moreover, the transparent cellophane sheets may probably also act as optical waveplates. Waveplates are transparent plates having a defined amount of birefringence [3]. They are sometimes also called "retardation plates" because they add or subtract a specified number of wavelengths to what is being viewed. As light travels through an anisotropic material, one of the rays will be slower than the other (i.e. "retarded") resulting in a difference in phase velocity of the light. The waveplates are used to modify the state of polarization of the light (linear to circular polarization).

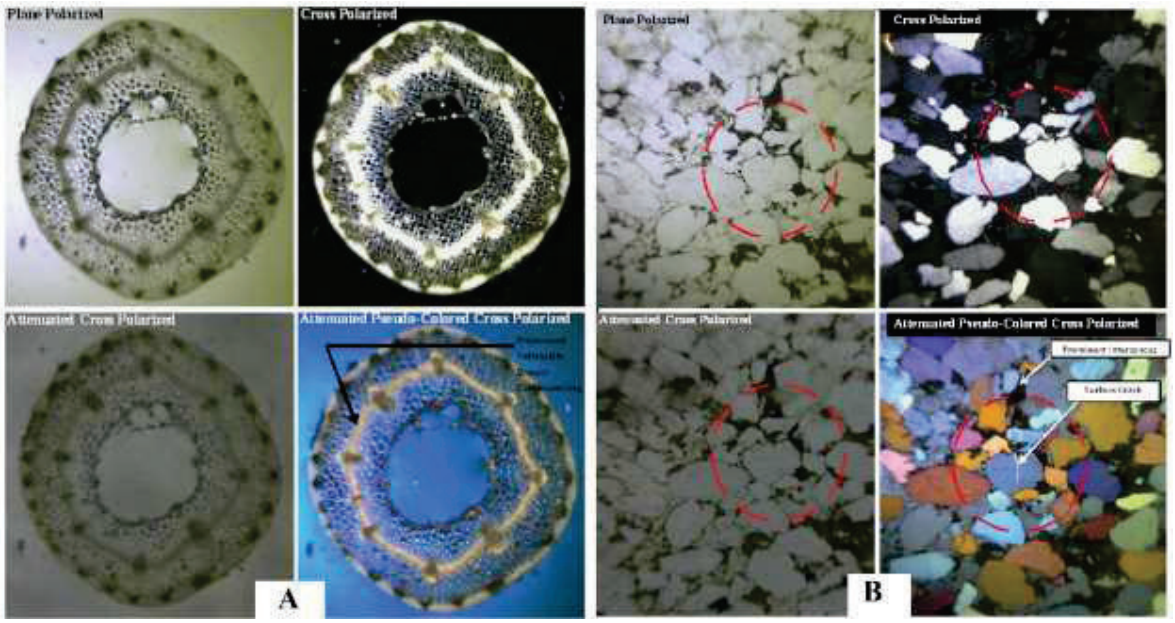

Fig. 2: Microphotographs of* A *– plant tissue section (25X magnification) and* B *– thin rock section (50X magnification) under the lab-built polarizing microscope

2. References

[1] Roy S, Bhattacharya B, Bal B and Ghosh K, "A microscopic study on scattering in tissue section of Alternanthera philoxeroides under polarized light", *Journal of Biosciences* **46**, 1-8 (2021).

[2] Frandsen AF, "*Polarized light microscopy"* (No. KSC-E-DAA-TN37401) (2016).

[3] Newton RH, Haffegee JP and Ho MW, "Polarized light microscopy of weakly birefringent biological specimens", *Journal of microscopy*, **180**, 127-130 (1995).

Figures

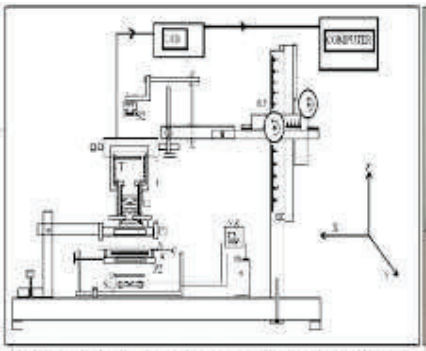

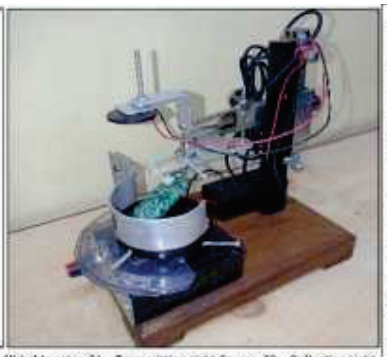

A – Attenuator Slot, B – Battery, T – CMOS Sensor, D – Diffused Plate, S – Slide Mounter, S1 – Transmitting Light Source, S2 – Reflecting Light Source, P1 – Analyzer, P2 – Polarizer, f – Focal Length of Whole Lens System, VR – Potentiometer (to adjust light intensity), RP – Rack and Pinion, L1 – Modified Lens System, L2 – Webcam Lens System, X-Y – Plane of the Sample as well as Plane of Analyzer, Polarizer and Attenuator, Z-axis – Optic Axis of the Lens System

The different parts of the microscopic setup constructed in the laboratory are arranged in different horizontal planes (Fig. 1) with the vertical axis coinciding with the optical axis of the microscope. A sample holder is mounted at the focal point of the lens system. An analyzer and polarizer are placed above and below the sample holder respectively. In between the sample holder and polarizer, 2 types of attenuator (white A4 paper made of cellulose and china clay) and transparent cellophane film (made of thermoplastic polymer) are added externally as and when necessary. A diffused white LED has been used as the source of illumination. The Microscopic Lens System has been developed by using - a webcam lens system (Logitech C270 HD) and external addition of three lenses - a plano-convex lens of diameter 1.39 mm and focal length 1.5 mm, another plano-convex glass lens of diameter 6.13 mm and focal length 20 mm and a biconvex glass lens of focal length 15 mm and diameter 5.84 mm. This total combination forms the whole lens system of the microscope. The total magnification range is 25X to 50X. The microscopic lens system (with webcam and additional lenses) is attached to a Rack and Pinion arrangement (made up of brass) which can move in both x-y plane and along z-axis.

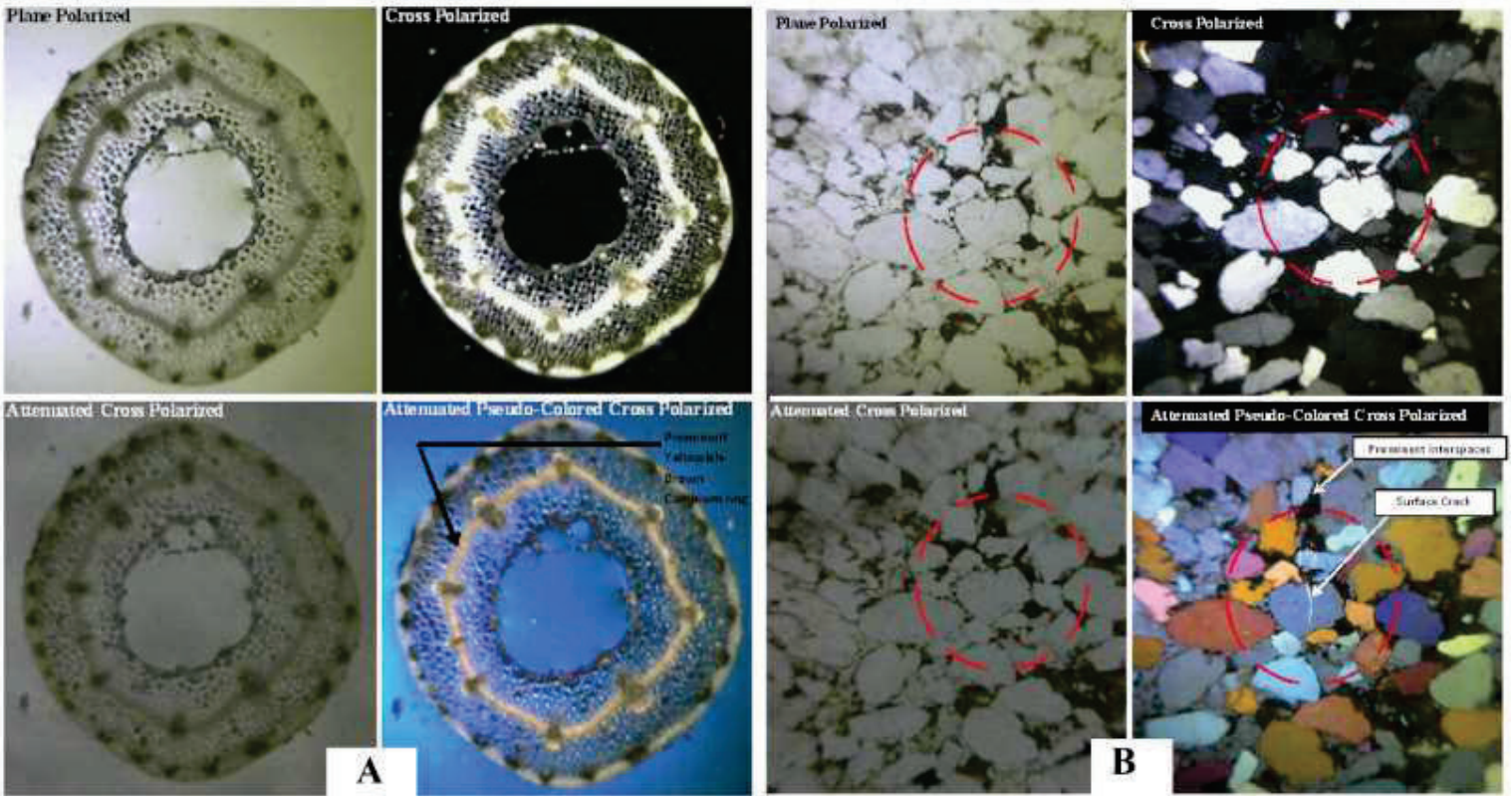

Light storage and retrieval in a hybrid cavity optomechanical system

Sabur A Barbhuiya*, and Aranya B Bhattacherjee

Department of Physics, Birla Institute of Technology and Science Pilani, Hyderabad Campus, Telangana-500078, India

**E-mail address: dsabur21@gmail.com*

Abstract: Quantum memory devices can store and retrieve photonic-qubit quantum states on-demand and are essential components for scalable quantum technologies. Here, we present a theoretical study of the storage and retrieval of light pulses in a double cavity optomechanical system coupled to a two-level system(TLS), based on electromagnetically induced transparency (EIT) phenomena. We also present the transduction of optical fields by tuning the cavity frequency with respect to the input Gaussian and super-Gaussian light pulses. The results obtained in this study are promising for practical applications in all-optical information processing systems.

Keywords: Cavity optomechanics, Qubit, Pulse propagation.

1.Introduction

The recent development of the cavity magnonic system provides a natural platform to engineer quantum sensors which is one of the main chachallenges in achieving high fidelity control and readout of the output probe pulse as well [1]. As a synchronizing tool in quantum information processing, on demand, the readout of a photonic qubit is a fundamental requirement for quantum memory [2]. In this paper, we show the potential to store the probe field in coherent vibrational phonons and how the probe field can be retrieved by applying the reading pulse at a later time. We expect that all optically controlled realization of input powers could be explored to build new tunable memory devices in quantum information networks

2. Model and Hamiltonian

We propose our model as a three-mode hybrid optomechanical system with one movable mirror with perfect reflectivity inserted between two fixed mirrors with the partial transmission. The mechanical membrane is linearly coupled to a TLS(qubit) via the Jaynes-cummings interaction. Thus the total Hamiltonian with respect to the control frequencies ω_L and ω_R can be written as,

$$H_{total} = \hbar(\omega_1 - \omega_L){c_1}^{\dagger}c_1 + \hbar(\omega_2 - \omega_R){c_2}^{\dagger}c_2 - \hbar g_1{c_1}^{\dagger}c_1\left(b^{\dagger} + b\right) + \hbar g_2{c_2}^{\dagger}c_2\left(b^{\dagger} + b\right) + \hbar\omega_m b^{\dagger}b + i\hbar\epsilon_L\left({c_1}^{\dagger} - c_1\right) + i\hbar\epsilon_R\left({c_2}^{\dagger} - c_2\right) + i\hbar\left({c_1}^{\dagger}{\epsilon_p}e^{-i\delta t} - c_1{\epsilon_p}^{*}e^{i\delta t}\right) + \frac{1}{2}\omega_q\sigma_z + \hbar g\left(b\sigma^{\dagger} + b^{\dagger}\sigma^{-}\right) \quad (1)$$

We describe the two optical modes by annihilation (creation) operators $c_{1,2}$ (${c_{1,2}}^{\dagger}$), while the mechanical mode is described by $b(b^{\dagger})$. Here, $\sigma^{-}, \sigma^{\dagger}$ and σ_z are the Pauli operators describing the TLS.

3. Results and discussions

We solve the propagation of the pump and probe numerically for our hybrid optomechanical system. For ϵ_L (t) and ϵ_p(t), we assume the Gaussian-shaped input pulse with the spectral half-width τ_L and τ_p [3, 4]. So,

$\epsilon_p(t) = \epsilon_p e^{\frac{-(t-t_{\omega r})^2}{2{\tau_p}^2}}$ and $\epsilon_L(t) = \epsilon_L e^{\frac{-(t-t_{\omega r})^2}{2{\tau_L}^2}} + \epsilon_L e^{\frac{-(t-t_{rd})^2}{2{\tau_L}^2}}$.

where $t_{\omega r}$ and t_{rd} are the central time of the writing and reading coupling lasers. We also assume that the width τ_L of the coupling laser is no less than the width τ_p of the probe pulse.

In figure 1(a), we show the Gaussian writing pulse is a combination of three modes: photon-phonon-exciton, which corresponds to the fact that the EIT window that produces during the transmission is small in width compared to the spectrum width of the probe pulse [5]. On increasing the width that is at τ_p = 0.3 in figure 1(b), it is shown that the spectrum that appears in the writing pulse has broader width, which is due to the coherence, $\omega_p - \omega_L = \omega_m$ i.e, the process converts probe pulse (photons in the optical field) into coherent phonons of the mechanical membrane. There is a significant difference in the lifetime of coherent phonos (typically in the order of ${\gamma_m}^{-1}$), which is far longer than the lifetime of the cavity (${\kappa_1}^{-1}$). The reading pulses can be used to retrieve probe pulses later (in less than ${\gamma_m}^{-1}$)[6].

Moreover, we consider the case P_R = 0.4 mW (power of the right control field) when the second cavity is red-detuned, as shown in figure 2(a,b). In this case, the optomechanical interaction in the left cavity is somewhat weakened by the right-hand coupling field because the radiation-pressure is partially counteracted due to weak probe power. Consequently, there are not enough Stokes output photons generated to contribute to a perfect destructive interference with incident probe photons. However, depending on the power employed to pump the second cavity, the anti-Stokes output may be comparable to the input probe pulse ϵ_p. Note that the outputs from the second cavity have frequencies $\omega_2 \pm \omega_m$, whereas the incident probe has a frequency of $\omega_p = \omega_2 + \omega_m \approx \omega_1$.

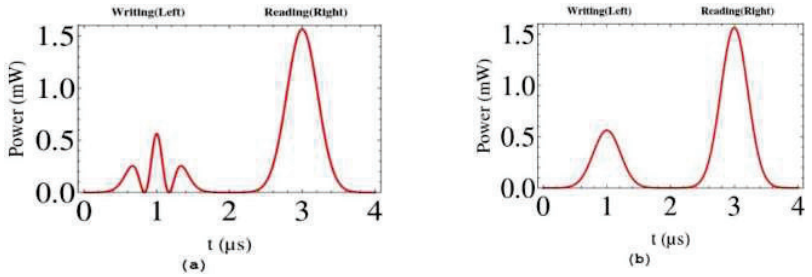

Figure 1: Storage and retrieval of Optical pulse in the output power $|\frac{2\kappa_1 c_{1+}(t)-\epsilon_p(t)}{\epsilon_p}|^2$ *of the respective writing and reading Gaussian probe pulse as a function of storage time (t) for the different values of width (a): at* $\tau_p = 0.15$ *and* $\epsilon_p = 0.8$*, (b): at* $\tau_p = 0.3$ *and* $\epsilon_p = 0.8$*.*

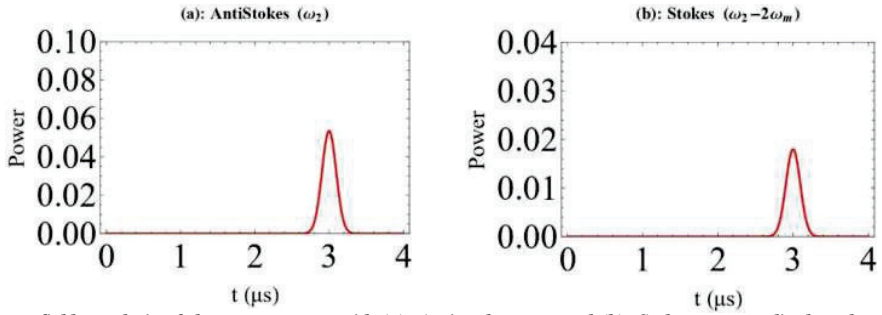

Figure 2: Quantum fields analysis of the output power with (a): Anti-stokes a_{2+}*, and (b): Stokes* a_{2-} *amplitudes when the reading cavity frequency at red detuned with the reading laser frequency* ω_R*.*

4. Conclusion

In summary, our result shows interesting phenomena that the probe field transmission could be attained in the hybrid system to store and retrieve the optical pulses. It may be worth noting that the transduction of the optical field showed different dynamics with different power. Flexible control of EIT should be important in quantum information networks to achieve photonic switching, routing, swapping, and entanglement.

5. References

[1] D. Quirion, S. Wolski, Y. Tabuchi , S. Kono, K. Usami, and Y. Nakamura, "Entanglement-based single-shot detection of a single magnon with a superconducting qubit," Science 367, 425-428 (2020).

[2] Chao L , T. Zhu, M. Su, Y. Ma, Z. Zhou , C Li and G. Guo, "On-Demand quantum storage of photonic qubits in an On-Chip waveguide," PRL. 125, 260504 (2020).

[3] Eyob A. Sete and H. Eleuch, "High-efficiency quantum state transfer and quantum memory using a mechanical oscillator, Physical review A 91, 032309 (2015).

[4] Pardeep Kumar, M. Bhattacharya, "Storage and retrieval of optical information in levitated cavityless optomechanics ," Quantum Information Science, Sensing, and Computation X 10660, (2018).

[5] Yan-Cheng Wei, Bo-Han Wu,Ya-Fen Hsiao,Pin-Ju Tsai and Ying-Cheng Chen,"Broadband coherent optical memory based on electromagnetically induced transparency," Physical review A 102, 063720 (2020).

[6] Yafei Wen, Pai Zhou, Zhongxiao Xu, Liang Yuan, Minjie Wang, Shengzhi Wang, Lirong Chen and Hai Wang,"Cavity enhanced and long-lived optical memories for two orthogonal polarizations in cold atoms," Optics express 28, 360-368 (2020).

Role of slow light effect in enhancing the nonlinear absorption of a 1D plasmonic-photonic crystal structure

Athulya Kadeprath Satheesan, Nikhil Puthiyapurayil, Chandrasekharan Keloth*
Laser and Nonlinear Optics Laboratory, Department of Physics, National Institute of Technology, Calicut-673601
Author e-mail address: csk@nitc.ac.in

Abstract: The suppression of group velocity at the photonic band edges can induce significant changes in the optical nonlinearity of a material. Herein, we explore the contribution of band-edge effect in the enhanced absorptive nonlinearity of an all-polymer Distributed Bragg Reflector with silver nanoparticles dispersed in its low index layers. Silver nanoparticles are synthesized by pulsed laser ablation in liquid method and the third order nonlinear optical properties are studied using standard z-scan technique. Moreover, the spectral tunability at the band edge can be exploited in the design and fabrication of low power, compact photonic devices.

Keywords: Photonic band edge, slow light, silver nanoparticle, nonlinear absorption, z-scan

Introduction

One-dimensional photonic crystals (1DPCs), commonly known as Distributed Bragg Reflectors (DBRs) are artificially designed periodic dielectric structures which can modify the propagation of electromagnetic waves through it. Their characteristic photonic band gap and the highly dispersive nature results in various interesting optical phenomena like strong field localization, negative refraction, slow light effects etc[1,2]. Out of these, slow light propagation inside the photonic band gap structures has gained considerable attention as controlling the speed of light is difficult to achieve using the conventional photonic technologies.

The group velocity of light gets greatly reduced at the band edges so that the photons have longer optical path to traverse through the material[3]. Consequently, growth of electromagnetic field can be witnessed at the band edges due to prolonged light-matter interaction time. This property can be made use in boosting up the nonlinear optical properties of materials. Unfortunately, most of the naturally occurring materials exhibit weak nonlinear response, thus requiring high input power for their practical applications. Thus, it is high time we find new materials with ultrafast response or enhance the nonlinearity of the existing materials using some physical or chemical mechanisms. Introduction of noble metal nanoparticles in the photonic crystal structures can increase the light-matter interaction through the combined effect of surface plasmon resonance and light localization[4]. Several plasmonic photonic configurations have been proposed which finds application in sensing, optical switching, optical fiber communication etc[5]. In this report, we utilize the band edge effect in a polymeric one-dimensional nonlinear photonic crystal (1D NLPC) to improve the nonlinear absorption of silver nanoparticles.

Experimental

Silver nanoparticles are prepared using the method of Pulsed Laser Ablation in Liquid (PLAL). PLAL is one of the easiest and cleanest method of nanoparticle synthesis as it is a one step process without any byproduct formation. In this technique, a silver metal target (>99.9%) of 1 mm thickness is placed inside a glass beaker containing 2 ml diacetone alcohol solvent. The target is placed at the focus of a 10 cm convex lens and is ablated with the second harmonic of a pulsed laser (Nd:YAG (1064 nm), 7 ns pulse duration and 10 Hz repetition rate). The ablation energy was set to be 30 mJ and carried out for 15 minutes.

For the fabrication of 1D NLPC, polyvinyl carbazole (PVK, n=1.68)) in chlorobenzene and silver doped cellulose acetate (Ag:CA, n=1.47) in diacetone alcohol were taken as the high and low index layers respectively. The solvents were chosen so as to prevent interpenetration to the adjacent layers. The thickness of the individual layers was optimized to get the lower photonic band edge around 532 nm. The final structure was realized by alternate spin coating of 10.5 bilayers of PVK and Ag:CA. Intermediate annealing was carried out to improve the optical quality of the overall structure.

Results and Discussion

The UV-Vis absorption spectrum of the synthesized solution shows a surface plasmon resonance (SPR) peak around 410 nm confirming the formation of silver nanoparticles (figure 1c inset). The intense heat and energy produced during the ablation results in the creation of a plasma plume eventually generating nanoparticles. The nanoparticles are incorporated in the alternate layers of the DBR and the transmittance spectrum of the final structure is shown in figure

1a. Experimentally we obtained the photonic band gap centered around 587 nm with the lower band edge at 540 nm. The structure also exhibited a minimum transmittance of 26%. Inorder to get maximum NLO contribution, the band edge should be located at 532 nm, which is the wavelength of the excitation source used for NLO studies. For this, we tuned the photonic band edge to coincide at 532 nm by carefully changing the angle of incidence and the angle was experimentally obtained as 16^0 (figure 1b).

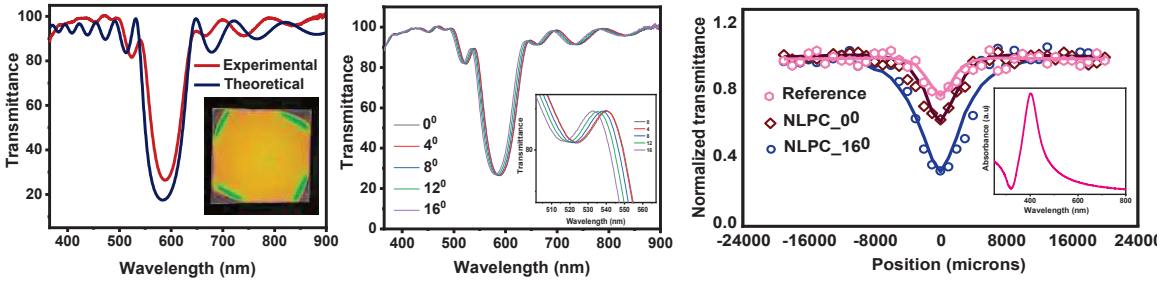

Figure 1(a) Experimental and theoretical transmittance spectra of the NLPC. Photographic image in the inset. (b) Angle tuning of the transmittance spectra. (c) Open aperture z-scan plot at 0.138 GW/cm^2 (absorbance spectrum of Ag nanoparticles in the inset)

The nonlinear absorption measurements of NLPC were carried out by open aperture (OA) Z-scan technique [6] using the same laser system used for PLAL but in single shot mode. Here the sample is translated along the direction of a tightly focused gaussian beam and the transmittance at each point is measured as a function of sample position. We used a single layer of Ag:CA and PVK having the same thickness as that of the NLPC structure as the reference. The OA plot reveals a decrease in transmittance at the focus indicating the reverse saturable absorption behavior of the sample (figure 1c). The best theoretical fit to the experimental data gives the effective nonlinear absorption coefficient value at 0.138 GW/cm^2 as 7.86×10^4 cm/GW for NLPC_16^0. The experiment was conducted at different input powers and it was found that the NLPC exhibited optimum nonlinear absorption at 16^0 compared to normal incidence and reference sample confirming the contribution of slow light effect at the band edge.

In our case, since the NLO material is doped in the lower refractive index layers, the electromagnetic energy concentrated at the high frequency PBE mode will grow in strength resulting in maximum field enhancement in these layers. The nonlinear absorptive behavior of bare silver nanoparticles is already well established and is mainly originating from the d-sp interband and sp-sp intraband transitions[7]. Hence the combined effect of plasmonic excitations and light localization at the band edges trigger the optical field concentration in the nonlinear layers of the NLPC leading to stronger nonlinearity at very small incident energies.

Conclusions

A one-dimensional polymeric nonlinear photonic crystal was fabricated with silver nanoparticles dispersed in the alternating layers. The structure was found to exhibit maximum nonlinear response at 16^0 angle of incidence where the photonic band edge exactly coincides with the excitation wavelength. Due to the enhanced light- matter interaction, the band-edge effect can be used to improve the efficiency of the nonlinear process by inducing nonlinearity at very small input powers.

References

[1] R.D.M. John D. Joannopoulos, Steven G. J, Joshua N. Winn, Photonic Crystals: Molding the Flow of Light (2nd. Ed.), 2008.
[2] E. Ozbay, B. Temelkuran, Photonic Crystals and Light Localization in the 21st Century (2001).
[3] Toshihiko Baba, Slow Light in Photonic Crystals, 2008.
[4] L. Sun, H. Lin, K.L. Kohlstedt, G.C. Schatz, C.A. Mirkin, Proc Natl Acad Sci U S A 115 (2018) 7242–7247.
[5] D.J.J. Hu, H.P. Ho, Advances in Optics and Photonics 9 (2017) 257.
[6] M. Sheik-Bahae, A.A. Said, T.H. Wei, D.J. Hagan, E.W. van Stryland, IEEE Journal of Quantum Electronics 26 (1990) 760–769.
[7] H.H. Mai, V.E. Kaydashev, V.K. Tikhomirov, E. Janssens, M. v. Shestakov, M. Meledina, S. Turner, G. van Tendeloo, V. v. Moshchalkov, P. Lievens, Journal of Physical Chemistry C 118 (2014) 15995–16002.

Numerical modelling of a Lyot filter-based all-fiber Mamyshev oscillator

Uttam Kumar Samanta[1,2*], Mukul Chandra Paul[1], Sourav Das Chowdhury[1]
[1]*Fiber Optics & Photonics division, CSIR-Central Glass & Ceramic Research Institute, Kolkata-700032, India*
[2]*Department of Physics, Jadavpur University, Kolkata-700032, India*
**Author e-mail address: uttamsamanta9@gmail.com*

Abstract: The viability of obtaining stable mode-locked pulses at 1.06 µm from a Mamyshev oscillator using a Gaussian filter and a wavelength-tunable Lyot filter has been studied aiming at an all-fiber cavity configuration. Intra-cavity pulse propagation and compressibility of the output pulse have also been investigated.

Keywords: Fiber laser, Mode-locked laser, Mamyshev Oscillator, Lyot filter.

1. Introduction:

The working principle of a Mamyshev oscillator relies on the technique of the Mamyshev regenerator proposed in 1998 [1]. SPM-induced spectral broadening of two concatenated regenerators is reshaped by two offset spectral filters giving rise to an effective stepwise saturable absorption effect. Although the technique has been implemented first by Rochette et. al. [2], the 'Mamayshev Oscillator' term was first coined after the work of Regelskis et.al in 2015 [3]. A Mamyshev oscillator consists of two coupled arms; each arm containing a signal amplifier that produces SPM-induced spectral broadening, followed by a spectral filter. In literature, diffraction gratings, temperature-controlled fiber Bragg gratings and thin film-based spectral filters have been implemented in various cavity architectures. In this work, the performance of a Mamyshev oscillator has been studied numerically where the combination of a Gaussian filter and a wavelength-tunable Lyot filter has been used for the first time as two spectral filters aiming at an all-fiber cavity design.

2. Schematic of the simulated cavity and filter properties:

To model the cavity architecture (Fig. 1(a)), nonlinear optical pulse propagation in optical fiber with and without gain has been simulated by solving the Ginzburg-Landau equation (GLE) [4]. The cavity consists of two arms, each arm consisting of one Yb-doped fiber amplifier with a gain fiber length of 1 meter, 90:10 splitter (10% port as the output), 2 meters long SMF and a spectral filter placed consecutively. The second-order group velocity dispersion and the nonlinear coefficient of the fibers are considered to be 22.7 x 10^{-3} ps^2/m and 5.1 /W-km respectively (matched with HI-1060 fiber). The design of a single-stage Lyot filter has been shown in Fig. 1(b) where a polarization-maintaining

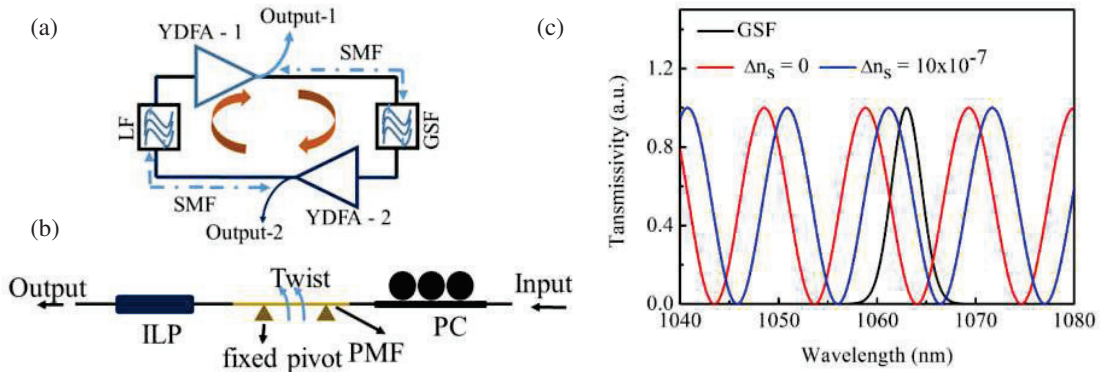

Figure 1: (a) Schematic of the cavity design YDFA: Yb-doped fiber amplifier; SMF: Single mode fiber GSF: Gaussian spectral filter; LF: Lyot filter; (b)Schematic of the LF, PC: polarization controller; ILP: In-line polarizer (c) Transmission curve of the LF for different effective birefringence

$$T(\theta,\lambda,\Delta n) = \frac{1}{2} * (1 + sin2\theta) * cos^2\left(\frac{\pi * \Delta n}{\lambda} L\right) \quad \text{Equation (1)}$$

fiber of a certain length is spliced between a fiber polarization controller and an in-line fiber polarizer. Equation 1 gives the spectral response of a Lyot filter [5]. Here λ is the operating wavelength, θ is the angle of polarization controller with the fast axis of the PMF, L is the length of the PMF and Δn is the effective birefringence [$\Delta n = \Delta n_{PM}\,(birefringence\ of\ the\ PMF, 4.5x10^{-4}) + \Delta n_S\,(stress - induced\ birefringence)$]. By introducing stress on the PMF, the effective birefringence can be changed which shifts the transmission curve. The transmission spectrum of the Lyot filter has been presented in Fig. 1(c) for different effective birefringence. The central wavelength of the Gaussian filter is fixed at 1063 nm with 3 nm FWHM.

3. Results & Discussions:

At a small signal value of 2.4 m^{-1} for both the amplifiers, a single pulse state has been achieved from background noise after 60 roundtrips even though for 2000 roundtrips the stability has been checked. Although the stable output has been obtained from both outputs, the smooth temporal profile has been obtained from output-2 only. Spectra and the temporal profile obtained from output -1 (output-2) and along with the associated chirp have been shown in Fig. 2(a) and Fig. 2(b) (Fig. 2(c) and Fig. 2(d),) respectively. The wrinkled shape of the spectra from output-1 is because of the interference of multi-wavelength transmission from LF which also degrades the pulse temporal shape as a result. The intra-cavity propagation of spectrum and pulse have been shown in Fig. 2(e) and Fig. 2(f) respectively from where the change of spectral and temporal shape throughout the cavity length can be observed. The 3-dB spectral width and pulse duration obtained from output-2 is 29.8 nm and 1.4 ps respectively. As the chirp profile is linear across the pulse, the pulse duration is easily compressible to 120 fs externally.

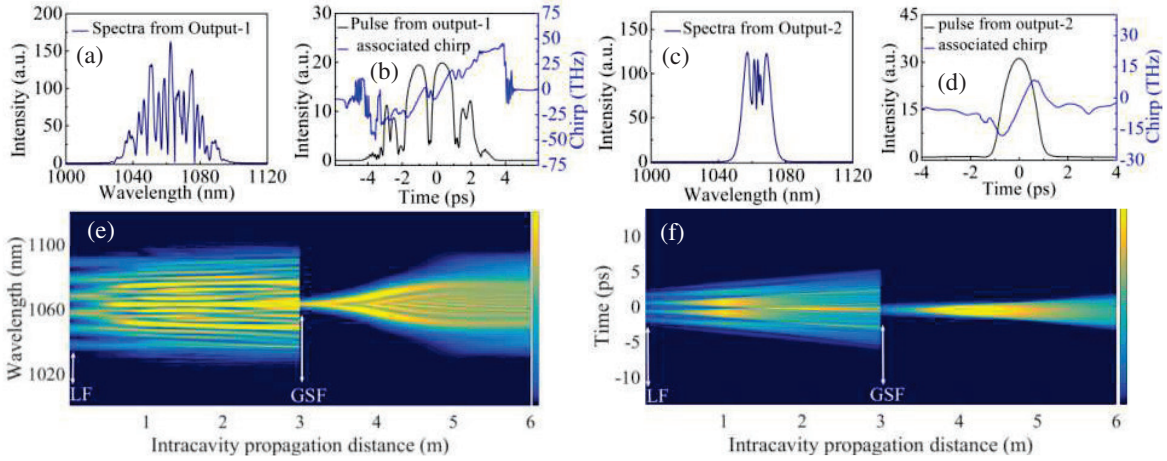

Figure 2: (a)spectra and (b) temporal intensity with associated chirp from output-1 (c)spectra and (d)temporal intensity with associated chirp from output-2. Intra-cavity propagation of (e) spectra and (f) pulse.

4. Conclusion:

A single stable pulse state has been achieved from the novel Mamyshev oscillator architecture and the study of pulse quality and actual pulse shape is ongoing to complete the theoretical model before designing the experiment.

5. References:

[1] P. V. Mamyshev, "All-optical data regeneration based on self-phase modulation effect". in 24th European Conference on Optical Communication. (Madrid, Spain,1998). Vol. 1. pp. 475–476.

[2] M. Rochette, L. R. Chen, K. Sun,& J. Hernandez-Cordero,."Multiwavelength and tunable self-pulsating fiber cavity based on regenerative SPM spectral broadening and filtering." IEEE Photonics Technology Letters **20.17** 1497-1499 (2008)

[3] K. Regelskis, J. Želudevičius, K. Viskontas, & G. Račiukaitis,"Ytterbium-doped fiber ultrashort pulse generator based on self-phase modulation and alternating spectral filtering." Optics letters **40.22** 5255-5258 (2015)

[4] B. D. Gupta, S. D. Chowdhury, D. Dhirhe, & M. Pal, "Intermittent events due to spectral filtering induced multi-pulsing instability in a mode-locked fiber laser." JOSA B **37.8** 2278-2286 (2020).

[5] Y. Zhu, Z. Cui, X. Sun, T. Shirahata, L. Jin, S. Yamashita, & S. Y. Set,"Fiber-based dynamically tunable Lyot filter for dual-wavelength and tunable single-wavelength mode-locking of fiber lasers." Optics Express **28.19** 27250-27257 (2020).

Random Lasing in a Dye Doped Thin Film: The Influence of Cavity Shape

Arindam Dey[a,*], Udit Chatterjee[b], Pathik Kumbhakar[a]
[a]*Nanoscience Laboratory, Department of Physics, NIT Durgapur, 713209, India.*
[b]*Laser Laboratory Department of Physics, The University of Burdwan, Burdwan, 713104, India.*
**Author e-mail address: arindamdeyphysics@gmail.com*

Abstract: Herein we report emission of visible random laser (RL) in R6G dye doped PVA film, under 532 nm Nd: YAG pulsed laser excitation. Spherical SiO_2 nanoparticles, dispersed in the prepared thin films, are found to play important role as passive scatterer for generation of efficient narrow band RL emission. Furthermore, for better confinement and to provide an additional feedback into the gain media, glass slides have been systematically included in one side and both side of thin film. It has been found that the introduction of glass slide has influenced significantly in the modification of lasing threshold of RL action.
Keywords: Random Lasing, SiO_2 nanospheres, PVA film, Waveguided feedback.

1. Introduction

Random lasers (RLs) are drawing a huge attention of researchers due to their various photonics applications [1-4]. However, the optical feedback in RL systems relies on disorder induced scattering events, unlike that in conventional lasers where reflections from finely aligned mirror arrangements provide the necessary optical feedback. In 1968, Letokhov *et al.* predicted that within an amplifying scattering medium, lasing action can take place due to diffusive transport of light, when the total gain surpasses the overall loss [2]. In that case, the intensity diverges and output spectra narrows down to a few nanometers. In a RL system, judiciously chosen gain/scatterer duo provide required optical amplification for achieving such lasing emission. RLs containing various dye solutions can be useful to tune the peak lasing emission (λ_p) as well as lowering the lasing threshold fluences (P_{in}). However, any external modification of a RL system may also influence its emission characteristics. In this regard, attachment of any external feedback system with the gain/scattering is an attractive way towards achieving tunable RL emission [3-4].

Here, a waveguide mediated RL system with spherical SiO_2 nanoparticles included in a luminescent laser dye, namely Rhodamine-6G (R6G) polymer thin films excited by nanosecond pulse laser is demonstrated. A tunable and low threshold RL system has been realized by the virtue of scalable, robust and simple mechanism of open cavity (X), half cavity (Y) and full cavity (Z) configurations. Furthermore, a comparative study of these cavity configurations with 400 nm SiO_2 as passive scatterer has been examined. Upon investigation, 5.7 nm wavelength tunability in λ_p of RL is observed with the lowest FWHM lying below 5 nm. In case of Z configuration with 400 nm SiO_2 as scattering centers shows the best result with narrow band RL emission at 585.7 nm with a RL threshold fluence value ($^{th}P_{in}$) of 1.59 mJ/cm^2. Furthermore, a reduction in amplified spontaneous emission (ASE) threshold and $^{th}P_{in}$ is attained as compared to those for X and Y configurations. The major reason behind this reduction and tunable RL emission is the multiple scattering of amplified light between randomly distributed SiO_2 particles within R6G films as well as the cavity configuration with those glass slides which gives additional feedback of light by internal reflections from their surfaces. The engineered RL system is shown to exhibit superior single modal RL emission with lesser threshold, compared to previously reported RL configurations with silica nanoparticles as scattering elements [5].

The developed RL system made of R6G dye added PVA film with silica nanoparticles as scattering elements in waveguide structure is a promising candidate for advanced photonics applications.

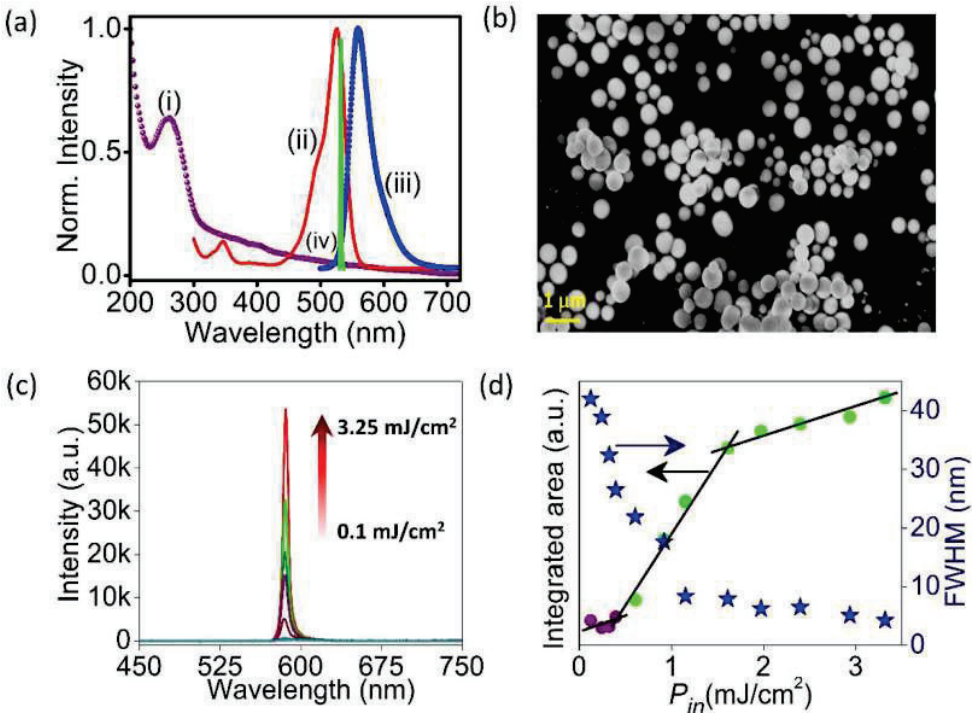

Fig. 1: (a) UV-Vis. absorption spectra of (i) SiO_2 nanospheres and (ii) Rhodamine 6G dye, (iii)PL emission spectra of Rhodamine 6G dye under 532 nm excitation, (iv) Spectra of 532 nm pump laser. (b) FESEM images of SiO_2 nanospheres, (c) RL emission spectra of a closed cavity configuration, under variable excitation fluences, (d) Variation of integrated area and FWHM with variable pump fluences.

Authors are very much thankful to Department of Science & Biotechnology, Govt. of West Bengal, (Ref. No. 332(Sanc.)/ST/P/S&T/16G-24/2018, dt. 06/03/2019) for providing the financial support. A. Dey acknowledges MoE, Govt. of India & NIT Durgapur for the maintenance fellowship. Also, authors like to thank Dr. S. Biswas and Dr A. Pramanik for their help.

2. References

[1] A. S. L. Gomes, A. L. Moura, C.B. de Araújo, E. P. Raposo, "Recent advances and applications of random lasers and random fiber lasers," Prog. Quantum. Electron. **78**, 100343 (2021).
[2] V.S. Letokhov, "Generation of light by a scattering medium with negative resonance absorption," Sov. Phys. JETP **26**, 835–840 (1968).
[2] A. Pramanik, S. Biswas, P. Kumbhakar, P. Kumbhakar, "External feedback assisted reduction of the lasing threshold of a continuous wave random laser in a dye doped polymer film and demonstration of speckle free imaging," J. Lumin. **230**, 117720 (2021).
[3] S. Biswas, P. Kumbhakar, "Continuous wave random lasing in naturally occurring biocompatible pigments and reduction of lasing threshold using triangular silver nanostructures as scattering media," Nanoscale **9**, 18812–18818 (2017).
[4] L. Ye, Y. Feng, C. Lu, G. Hu, Y. Cui, "Coherent random lasing from liquid waveguide gain layer containing silica nanoparticles," Laser Phys. Lett. **13**, 105002 (2016).

Analytical model of Band Rejection filter based on Multimode-Single mode-Multimode fiber concatenation structure

Protik Roy and Partha Roy Chaudhuri*
Department of Physics, Indian Institute of Technology Kharagpur, West Bengal, India
**Corresponding author : roycp@phy.iitkgp.ac.in*

Abstract: Here we propose a novel all-fiber band rejection filter utilizing multimode-single mode-multimode (M-S-M) concatenated structure. The proposed filter consists of two identical multimode fibers (MMFs) and a conventional single-mode fiber (SMF) of a very small length, which is spliced between the MMFs. Since there is a core diameter difference between MMF and SMF, an interference loss between core mode and cladding modes is observed. By systematically adjusting the fibers' parameters of the M-S-M configuration, we show the interference loss in the device can be utilized as a band rejection filter.
Keywords: Optical fiber filter, modal overlap, core and cladding mode, modal interference.

1. Theoretical Introduction

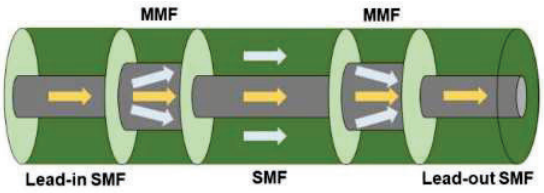

Fig. 1: Schematic of the proposed filter.

Fig. 1 shows the schematic of the proposed band rejection filter. The design incorporates a short SMF segment of length L, which is sandwiched between two conventional step-index MMFs [1]. Due to the core diameter difference at MMFs and SMF splicing junctions, when the light passes through the first MMF and falls into the central SMF, light couples from the core of the first MMF to the core as well as the cladding of the central SMF exciting the core modes and the cladding modes [2,3]. Any change in the medium of certain refractive index surrounding the central SMF cladding region modulates the way light is transmitted through the fiber. After traversing the central SMF, when combining in the last segment of the MMF, the core mode and the cladding mode of the central SMF interfere and the intensity of the interference can be expressed as,

$$I = I_1 + I_p + 2\sqrt{I_1 I_p}\cos\left(\frac{2\pi\Delta n_{eff}^{p} L}{\lambda}\right) \tag{1}$$

$$\Delta n_{eff}^{p} = n_{core} - n_{clad}^{p} \tag{2}$$

Where the corresponding intensities of the core mode and the pth order cladding mode are expressed as I_1 and I_p, respectively. The effective refractive indices of the core mode and the pth cladding mode are expressed as n_{core} and n_{clad}^{p}, respectively. For destructive interference, the difference in the phases between the core mode and the pth order cladding mode generally satisfies,

$$\frac{2\pi\Delta n_{eff}^{p} L}{\lambda_{dip}} = (2t+1)\pi\,, \qquad t = 0, 1, 2 \ldots \tag{3}$$

Thus, λ_{dip} can be calculated as,

$$\lambda_{dip} = \frac{2\Delta n_{eff}^{p} L}{(2m+1)} \tag{4}$$

Total transmission (T) of the proposed M-S-M structure will be then,

$$T = \frac{\int_0^\infty I \, rdr}{\int_0^\infty |E(r,0)|^2 rdr} \tag{5}$$

This interference loss in the device can be adjusted by varying fibers' parameters to reject any desirable wavelength band.

2. Results

Here, we analyze the performance of the concatenated M-S-M structure by changing fibers' parameters. By systematically adjusting the fibers' parameters of the M-S-M configuration, we show the interference loss in the device can be utilized as a band rejection filter. We have tabulated (Table 1) different fiber parameters used to tune transmission spectrum of the M-S-M device shown in figure 2.

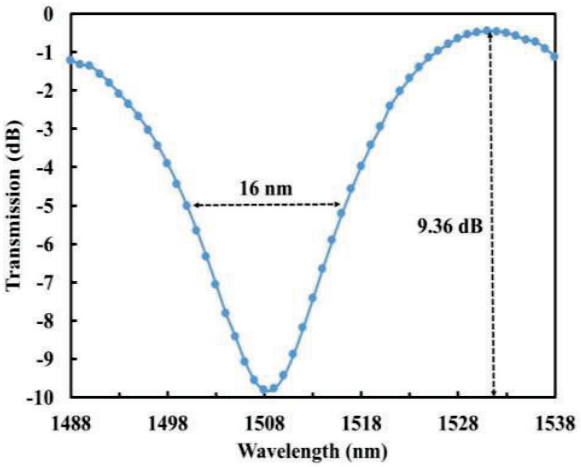

Fig. 2: Transmission spectrum of the proposed filter.

Table 1: Fibers' parameters with external medium RI 1.42

Fiber type (length)	Core/Clad RI	Core/Clad diameter (μm)	V number
SMF (4 mm)	1.4448-1.4441/ 1.4338-1.4331	6.4/120	2.4044-2.3227
MMF (2 mm)	1.4648-1.4641/ 1.4548-1.4541	24/100	8.6579-8.3638

In this infrared region, the M-S-M structure gives a band rejection filter. The full width at half minimum is computed to be ~16 nm for the M-S-M structure as shown in figure 2. An intensity loss of 9.36 dB is also observed.

Here, we perform a systematic analysis of the M-S-M fibers circuit that eventually can be used as a band rejection filter. The performance of the inline filter device at different operating wavelengths is presented, generated by simulation.

3. References

[1] T. Sun, Z. Liu, Y. Liu, *et al.* "All-fiber liquid-level sensor based on in-line msm fiber structure," Photonic Sens **11**, 291–297 (2021).
[2] S. N. Khan and P. Roy Chaudhuri, "Selective excitation of higher-order modes in etched gelatine-coated few-mode fiber and demonstration of high relative humidity measurement," J. Opt. Soc. Am. A 34, 122-132 (2017).
[3] P. Roy Chaudhuri and W. X. and C. Lu, "Scalar model and exact vectorial description for the design analysis of hollow optical fiber components," Opt. communications 228, 285–293 (2003).

Saturable nonlinearity effects on the modulational instability on Rogue waves

Satyabrata Sahu, P. Mohanraj and R. Sivakumar
Department of Physics, Pondicherry University, Puducherry- 14.
Author e-mail address: satyabrata1307@gmail.com

Abstract: In the current work, we examine the modulational instability (MI) and rogue wave excitation in coupled system with saturable coherent nonlinearity. Our intention is to study the role of coherent coupling nonlinearity in a saturable system for both normal and anomalous regimes. However, the results can be more helpful for the generation and manipulation of solitary and rogue waves in two core fiber systems.
Keywords: Rogue waves, Modulation instability, Nonlinear Schrodinger equation, Saturable nonlinearity, Coherent coupling nonlinearity.

1. Introduction

Even though discovered in the study of fluid dynamics, the Rough waves and modulation instability condition have been observed in the study of pulse propagation in optical fibers, and they are described by the nonlinear Schrodinger equation. In addition, it is found that modulation instability can also lead to the supercontinuum generation [1, 2]. Saturable nonlinearity (SNL) has piqued curiosity among the various types of nonlinear response in fibres due to its unique nonlinear features. When a system is subjected to high pump power operation, often above the medium's saturation threshold, the saturation of nonlinearity becomes a strong case [3-7]. In this work, will study the characteristics of modulational instability as well as the effect of saturable nonlinearity in coupled fibres and the interaction between SNL and coherent coupling strength.

2. Mathematical Model and Analysis

A coherently coupled nonlinear media can be described by the system of two dimensionless NLS (Nonlinear Schrodinger) based equation [8, 9]

$$\begin{aligned} &i\frac{\partial A}{\partial z}+\beta\frac{\partial^2 A}{\partial t^2}+\gamma_1\left[f\left(\Gamma|A|^2\right)\right]A+\gamma_2\left[f\left(\Gamma|B|^2\right)\right]A+\\ &\gamma_3\left(B^2A^*\right)=0\\ &i\frac{\partial B}{\partial z}+\beta\frac{\partial^2 B}{\partial t^2}+\gamma_1\left[f\left(\Gamma|B|^2\right)\right]B+\gamma_2\left[f\left(\Gamma|A|^2\right)\right]B+\\ &\gamma_3\left(A^2B^*\right)=0 \end{aligned} \qquad (1)$$

where, A and B are the envelopes of the waves, γ_1, γ_2 and γ_3 denotes the co-efficient of nonlinear, coherent an incoherent, respectively. The nonlinear saturation is taken in the form of

$$f\left(\Gamma|A|^2\right)=\frac{|A|^2}{1+\Gamma|A|^2} \qquad (2)$$

$$f\left(\Gamma|B|^2\right)=\frac{|B|^2}{1+\Gamma|B|^2} \qquad (3)$$

where Γ is the saturation parameter and it is connected with the saturation power P_{sat} by the relation $\Gamma^{-1}=P_{sat}$. Based on the above governing equations, we use the linear stability analysis to study the modulational instability and the results are presented.

3. Results and Discussion

Here, we discuss the role coherent coupling nonlinearity in the saturable absorption media in normal dispersion regime. Fig. 1 shows the different strength of nonlinear saturation effects on modulational instability with coherent coupling nonlinearity. We plotted MI gain spectrum as a function of perturbation frequency (Ω) and coherent coupling nonlinearity (γ_3) for normal ($\beta = 1$) dispersion regime. From the contour images, we observed MI gain spectrum with two symmetric side lobes, when coherent coupling strength above the threshold value ($\gamma_3 = -[\gamma_1 + \gamma_2]$) for normal dispersion regimes as shown in fig. 1(a). This kind of feature can observe in conventional nonlinear optical fiber without saturable nonlinearity. Further, we increase the nonlinear saturation strength like $\Gamma = 1$ the threshold value is decreased with increased MI gain spectrum as in Fig. 1(b). Next, Fig. 1(c) illustrates that the MI gain spectrum fully exceeds the threshold value of coherent coupling nonlinearity. These can be achieved only by using the saturable nonlinearity.

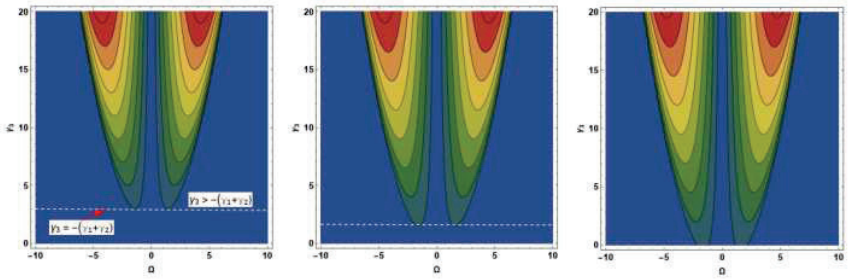

(a) $\Gamma = 0$ (b) $\Gamma = 1$ (c) $\Gamma = 2$

Fig. 1: Shows the strength of saturable nonlinearity on MI gain spectra as a function of perturbation frequency (Ω) and coherent coupling nonlinearity (γ_3) for normal dispersion regime. Other physical parameters are $\gamma_1 = 1$, $\gamma_2 = -2$ and $\beta = 1$.

4. Conclusions

We have investigated the characteristics of MI and rogue wave in normal dispersion regime with in and out phase continuous wave solutions. When the saturable nonlinearity exists in coupled fiber, the MI bands are induced with the help of large gain and bandwidth. However, when coupling and saturation effects combined together into coupled system, the MI scenario was different for different parameter setting.

References

1. J. M. Dudley, G. Genty, and S. Coen, "Supercontinuum generation in photonic crystal fiber," Rev. Mod. Phys., vol. 78, pp. 1135–1184, Oct. 2006.
2. J. M. Dudley, G. Genty, F. Dias, B. Kibler, and N. Akhmediev, "Modulation instability, Akhmediev Breathers and continuous wave supercontinuum generation," Opt. Express, vol. 17, pp. 21497–21508, Nov. 2009. Publisher: OSA.
3. A. K. Shafeeque Ali, K. Nithyanandan, K. Porsezian, and A. I. Maimistov, "Modulation instability in a triangular three-core coupler with a negative-index material channel," J. Opt., vol. 18, p. 035102, Mar. 2016.
4. W. J. Liu, M. L. Liu, B. Liu, R. G. Quhe, M. Lei, S. B. Fang, H. Teng, and Z. Y. Wei, "Nonlinear optical properties of MoS 2 -WS 2 heterostructure in fiber lasers," Opt. Express, vol. 27, p. 6689, Mar. 2019.
5. M. Liu, Y. Ouyang, H. Hou, W. Liu, and Z. Wei, "Q-switched fiber laser operating at 1.5 μm based on WTe2," Chin. Opt. Lett., vol. 17, p. 020006, Feb. 2019. Publisher: OSA.
6. M. Liu, W. Liu, and Z. Wei, "MoTe 2 Saturable Absorber With High Modulation Depth for Erbium-Doped Fiber Laser," J. Lightwave Technol., vol. 37, pp. 3100–3105, July 2019.
7. W. J. Liu, M. L. Liu, S. Lin, J. C. Liu, M. Lei, H. Wu, C. Q. Dai, and Z. Y. Wei, "Synthesis of high quality silver nanowires and their applications in ultrafast photonics," Opt. Express, vol. 27, p. 16440, June 2019.
8. H. Jia, B. Li, R. Yang, and J. Tian, "Diverse composite waves in coherently coupled inhomogeneous fiber systems with external potentials," Nonlinear Dyn, vol. 99, pp. 2987–2999, Mar. 2020.
9. W.-R. Sun and L. Liu, "Asymmetrical, rotational and ultra-high amplitude fundamental polarized optical rogue waves associated with the coherent coupling," Physics Letters A, vol. 391, p. 127132, Mar. 2021.

MIP fiber optic sensor for the detection of Tetrabromobisphenol-A in water samples

[1]Shivani Maurya, [1, #]Roli Verma
[1]Department of Physics, University of Lucknow, India
[#]roliverma10@gmail.com

Abstract: The rapid industrialization demands for time to time effective measures to regulate and meet environmental balance and compliance. We present an experimental study for the detection of a brominated flame retardant-Tetrabromobisphenol-A (TBBPA). It is one of the prime source of water and soil pollution. In the present study we have analyzed the performance of our fabricated optical fiber MIP based probe. It is found that our probe is capable of sensing minute concentration variation of the analyte from 10^{-1} M to 10^{-3} M with the total shift in resonance wavelength equals to 54 nm.
Keywords: Molecular Imprinted Polymer (MIP), Surface Plasmon Resonance (SPR), Tetrabromobisphenol-A (TBBPA), De-ionized (DI) water.

1. Introduction

TBBPA belongs to a brominated flame retardants (BFR's) family [1]. It is widely used in polymers such as epoxy, polycarbonate resins etc. TBBPA demand is primarily in electrical devices such as Printed Circuit Boards (PCB's), Integrated circuits plates and automotive parts. These electronic devices have complex recycling process. Therefore, its release into the environment and disturbance in ecosystem adds on in from all three forms water, soil and air pollution. To date, several studies revealed that its exposure is hazardous for both human and several other life creatures. As a result, it is necessary to detect TBBPA level in water bodies. Thus it is the need of an hour to pave an accurate reliable and cost-effective sensor which is sensitive to changes in chemical and biological parameters. Surface Plasmon Resonance (SPR) based optical sensor is one of the prominent techniques which fulfils all the above requirements and in addition provides label free and real time analysis. SPR technique opens broader prospect of research when it comes to detection of environmental parameters and bio molecular interactions. Surface Plasmon's (SP's) refers to the collective oscillations of free electron density present near the metal-dielectric interface. The SP's gets excited only by the TM wave (p-polarized light) when the momentum or the k-vector of the incident light matches with the momentum of the oscillating electron density. To excite the SP's and to meet the condition of resonance we make use of high index material [2]. The condition of resonance results in a dip in transmission at a particular value of wavelength. This specific dip position changes when there is change in analyte properties. This property of SPR dip makes it a highly sensitive sensing technique. In the present study we have made use of the MIP technique together with SPR to extract the advantages of the both in detecting TBBPA in water sample. MIP is a perfect and highly specific format of investigating the target molecule [2].

2. Methodology

The proposed sensor probes utilize spectral interrogation technique so we have made use of a polychromatic light source. The optical fiber is placed inside the flow cell in such a way that its one end receives maximum light from the source and transmits at the other end. The transmitted light is received by the spectrometer interfaced with a laptop having RSpec software for recording the SPR spectrum. The analyte of varying concentration were allowed over the sensing region through the inlet provided in the flow cell. The sensing surface was washed with DI after each and every SPR spectra reading was recorded so as to completely remove the left over TBBPA sample on it as well as to avoid any interference while taking the new readings. The experimental setup is shown in Fig. 1. Firstly, for the preparation of MIP the master solution was prepared by mixing Acrylamide (AM) /Bisacrylamide (BIS) in (19:1) and template molecule (40% of AM) in DI water and mixed thoroughly. Then the polymer matrix is prepared by taking appropriate amount of master solution, Phosphate buffer (pH 7), APS and TEMED in a cylindrical flask and diluted up to 10ml. Immediately, after this the silver coated fiber is dipped in it and kept in UV light for 4 hrs. After completion of polymerization process the fiber is taken out and washed with KOH/Methanol (1:9) to remove template molecules.

Finally it is rinsed with DI water properly and dried for 4 hrs before starting the characterization of probe. AM acts monomer, BIS is a cross-linker while APS is used as initiator while TEMED acts as catalyst for the reaction.

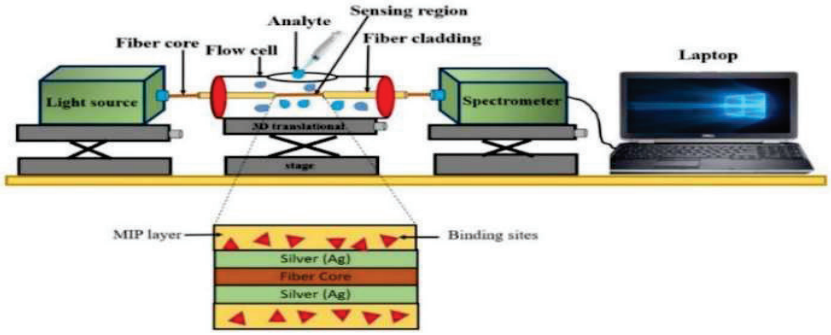

Fig. 1: Schematic of the experimental setup for the characterization of the fabricated probe.

3. Result & Discussion

For the characterization of the TBBPA MIP probe, solutions of different molar concentration ranging from 10^{-1} M to 10^{-3} M were poured in the flow cell one by one and the SPR curve for varying molar concentration of TBBPA were recorded and is shown in Fig. 2. The SPR spectra range is found to be in 600-1000nm. From the transmittance curve it is observed that the resonance dips for 0.1M, 0.01M and 0.001M occurred at 830 nm, 808 nm and 776 nm respectively. The shift occurs because as soon as the TBBPA molecule comes in the vicinity of the MIP layer the effective refractive of the sensing surface changes due to the binding of TBBPA molecules with its 'to-copy' recognition sites present on the MIP surface. These binding sites are active only for TBBPA, the template molecule, as these have captured the same shape and size and are specific in behaviour to template molecule. The rebinding process of TBBPA with its duplicated cavities leads to change in dielectric properties of the polymer matrix layer. Otherwise, absence of template molecules does not alter any change in dielectric properties of the polymer. Thus with increasing concentrations of TBBPA there is exponential increase in the SPR resonance wavelength which may get saturated at more concentrated solutions of TBBPA. Hence SPR response shows the red shift on varying concentrations from low to high as seen in Fig. 3. The total shift obtained for change in concentration of TBBPA from 10^{-1} M to 10^{-3} M is 54nm.

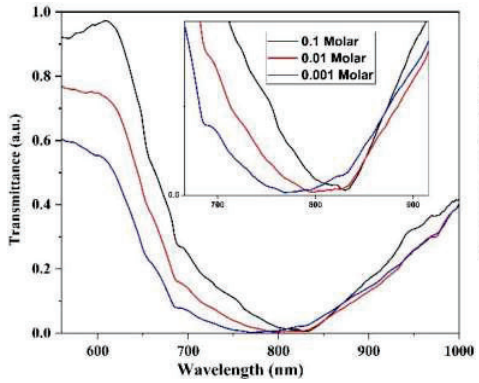

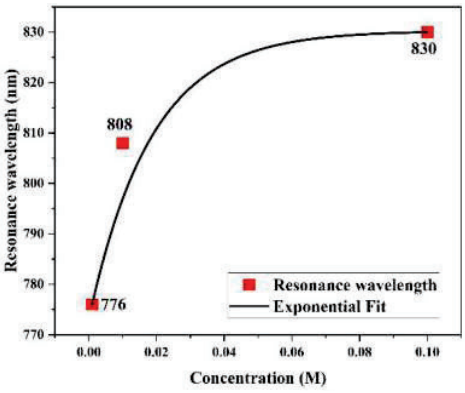

Fig. 2: SPR spectra for varying concentration of TBBPA. *Fig. 3: Variation of resonance wavelength with TBBPA concentration.*

In a nutshell, the proposed experimental study is providing a capable sensor for the detection of low concentrations of TBBPA. The proposed sensor has advantage of high selectivity, easy to handle, capable of remote sensing and online monitoring. The designed probe may find application in sensing TBBPA in e-waste in water.

Dr. Roli Verma is thankful to UGC for providing BSR-Start-up grant.

4. References

[1] B. Dan and Z. HUI, "A Novel Immunosorbent Assay for the Detection of Brominated Flanme Retardant Tetrabromobisphenol A," in Proc. of the Sixth Intl. Conf. Advances in Bio-Informatics, Bio-Technology and Environmental Engineering- ABBE, (Institute of Research Engineers and Doctors, USA, 2018),pp. 59–63.

[2] R. Verma and B. D. Gupta, "Optical fiber sensor for the detection of tetracycline using surface plasmon resonance and molecular imprinting," *Analyst*, **138**, no. **23**, pp. 7254–7263, (2013).

Pulse compression induced enhancement of second-harmonic generation in a silica nanowire

Seth Mathew V, Akhileshwar Mishra and Ravi Pant

Laboratory for Phoxonics and Nonlinear Optics in Nanostructures (PHONON Lab), School of Physics,Indian Institute of Science Education and Research (IISER) Thiruvananthapuram, Kerala, India

Author e-mail address: sethmathewv19@iisertvm.ac.in

Abstract: We achieve nearly two-fold increase in second-harmonic-generation (SHG) efficiency in a silica nanowire by optimizing pulse profile at a fixed pulse energy. For pulse energy ~580 pJ, we tune mode-locked pulse profile to enhance pulse compression and SHG.

Combs in Near-IR, visible and UV have multiple applications. For some of the applications like single photon spectroscopy in NIR (780 nm) [1], low power combs are desirable. These combs can be generated by frequency doubling an IR (1560 nm) comb using a nonlinear crystal. Ideally for a centro-symmetric medium like silica, $\chi^{(2)}$ is zero. However, material defects, symmetry breaking at the surface, and contribution from bulk multipoles can induce $\chi^{(2)}$ nonlinearity [2-4]. Thus, silica-based fibers can support generation of second harmonic (SHG) signals. It has been demonstrated earlier that a single silica nanowire can simultaneously generate SHG, THG and sixth harmonic [5]. The efficiency of the observed harmonics was however very small in this demonstration. Enhanced efficiency of harmonic generation will enable compact visible frequency combs for applications in photon-level spectroscopy and quantum optics. In [6], a loop resonator was used to enhance the SHG efficiency in a silica nanowire.

Here, we exploit pulse profile tailoring to achieve two-fold enhancement in the efficiency of SHG signal for a fixed pulse energy. We demonstrate that by controlling the input pulse parameter we can compress the pulse in the nano-fiber, which results in an increase in the efficiency of the SHG process by increasing the peak power inside the Nano-fiber. We fabricated an optical nanowire with a waist diameter of ~900 nm by tapering a standard telecom single mode fiber (Corning SMF-28e) using a Vytran glass processor. The fabricated nanowire has an up and down transition region of 16 mm on each side and a ~ 10 mm long central waist region. These tapers have a low loss (< 1.5 dB) and strong evanescent field to interact with surface nonlinearities. The nanowire is pumped with an Erbium fiber mode locked laser (MLL) with a repetition rate of 82 MHz and an average power of ~48 mW coming out of the taper. We generated different pulse profiles while keeping the pulse energy fixed by controlling the driving currents of the MLL.

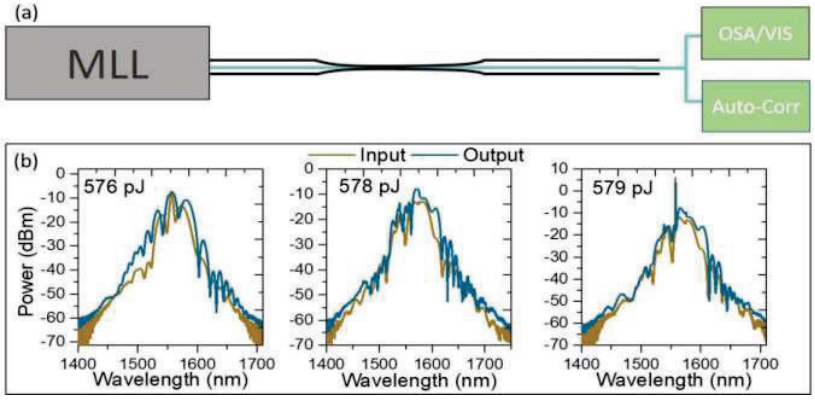

Fig 1:(a) Device setup for generation of the Second harmonic generation and characterization (MLL: Mode-locked laser, OSA/VIS: IR and visible spectrometer, Auto-Corr : Auto- Correlator for pulse characterization.(b) Input and output spectrum of the IR Pulses at similar pulse energies at but different pulse widths.

Figure 1(a) shows the schematic of the experimental setup used to study SHG in the silica nanowire. We use an IR spectrum analyzer to measure the input and output pulse spectra and a visible spectrometer for the measurement of the SHG signal. The input and output pulses are characterized using an auto-correlator. To study the pulse profile

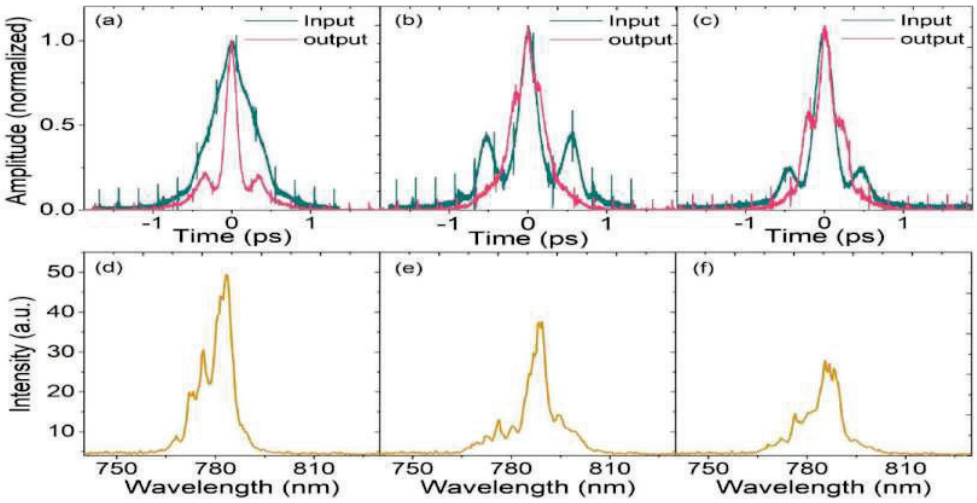

Fig. 2: Input and output pulses (a) 576 pJ, (b) 578 pJ, (c) 579 pJ pulse energies. (d-e) SHG spectra for 576 pJ, 578 pJ and 579 pJ respectively.

induced efficiency enhancement, we propagate pulses with similar pulse energies but different pulse profiles through the nanowire. Figure 1(b) shows the input (brown) and output (blue) optical spectrum of the IR pulses of similar pulse energies used in this study. Even though the pulse spectra shown in Fig. 1(b) correspond to input pulses of similar energy, the output pulse at 576 pJ pulse energy has the highest spectral broadening.

Figures 2 (a-c) show the pulses at the input and output of the silica nanowire. From Fig. 2(a) we note that the output pulse compresses by a factor of ~3, which in turn increases the peak power inside the nanowire by the same factor. The output pulse width in Figs. 2(b) and (c) either broaden or remain similar to the input pulse width. We also see that the ratio of the area under the curve for Fig. 2(d) to (e) is 1.35 and (d) to (f) is 1.7. This clearly shows that for the pulses of similar pulse energy, pulse parameters like chirp, pulse width and peak power plays a role in determining the behavior of the pulses inside the nanowire. Thus, control of these parameters can lead to higher efficiency of the SHG. Since the tapered fiber has a very large normal dispersion (1.1 ns/km-nm) [5], which is two orders of magnitude higher than the standard single mode fiber, a pulse with a negative chirp will undergo compression depending on the peak power and pulse width. As can be seen from Figs. 2 (a)-(c) we achieve compression only for Fig. 2(a), which in turn gives the best efficiency of SHG.

We have demonstrated SHG efficiency enhancement exploiting pulse profile tailoring of fixed energy input pulses. Tailoring the input pulse profile leads to higher pulse compression and thus larger peak power inside the nanowire. The larger peak power then enhances the efficiency of harmonic generation. We demonstrated a nearly two-fold increase in the SHG efficiency by controlling the pulse parameters for input pulses with an energy ~ 580 pJ. Since silica taper is capable of generating multiple harmonics [5], this technique can be used to simultaneously enhance the efficiency of the generated harmonics.

Acknowledgment:

We acknowledge financial support provided by Department of Science and Technology Science and Engineering Research Board through grant # CRG/000993/2019.References

References

[1] Picqué, Nathalie, and Theodor W. Hänsch. "Photon-level broadband spectroscopy and interferometry with two frequency combs." *Proceedings of the National Academy of Sciences* 117, no. 43 (2020): 26688-26691.

[2] R. W. Terhune and D. A. Weinberger, "Second-harmonic generation in fibers," J. Opt. Soc. Am. B **4**, 661-674 (1987)

[3] Dana Z. Anderson, Victor Mizrahi, and John E. Sipe, "Model for second-harmonic generation in glass optical fibers based on asymmetric photoelectron emission from defect sites," Opt. Lett. **16**, 796-798 (1991)

[4] Victor Mizrahi and J. E. Sipe, "Phenomenological treatment of surface second-harmonic generation," J. Opt. Soc. Am. B **5**, 660-667 (1988)

[5] Akhileshwar Mishra and Ravi Pant, "Deep UV to NIR frequency combs via cascaded harmonic generation in a silica nanowire using nanojoule pulse energies," Optica **8**, 1210-1217 (2021)

[6] Gouveia, M. A., Lee, T., Ismaeel, R., Ding, M., Broderick, N. G., Cordeiro, C. M., & Brambilla, G. (2013). Second harmonic generation and enhancement in microfibers and loop resonators. *Applied Physics Letters*, *102*(20), 201120.

[5] Author(s), "Title of paper," in Title of Proceedings, Name(s), ed(s)., Vol. XX of OSA Proceedings Series (Optical Society of America, Washington, D.C., 1900), pp. 00-00.

Fabrication of High-Q Dye-Doped Polymer Microdisc Resonators Using Electron Beam Lithography and Soft-Lithography

Subhajit Dutta,[1] R. Hemant Kumar,[1] Rabaya Basori,[2] Shivakiran Bhaktha B. N.[1,*]

[1] *Department of Physics, Indian Institute of Technology Kharagpur, Kharagpur 721302, India*

[2] *School of Nano Science and Technology, Indian Institute of Technology Kharagpur, Kharagpur 721302, India*

[*] *kiranbhaktha@phy.iitkgp.ac.in*

Abstract: Polymer microresonators are essential components for the realization of several photonic devices such as lasers, filters, sensors etc. Choosing polymer cavity over inorganic cavities has a great advantage of easy doping with dyes, plasmonics, quantam dots, rare-earth ions etc. Polymeric microspheres yield high quality factors, but are difficult to integrate on a chip using non-lithographic techniques. Here, we present fabrication of dye doped poly (methyl methacrylate) microdiscs using electron beam lithography on silica on silicon substrate. A comparative study on the morphological, optical and spectroscopic characteristics of these microdiscs will be presented with respect to the structures fabricated by soft-lithography.

Keywords: microresonators, whispering gallery modes, electron beam lithography, soft-lithography

1. Introduction

Optical microcavities such as microspheres, microdiscs, micro toroids etc., are fundamental elements in various optical systems because of its high-quality factor (Q) values, for example in sensing [1], lasing [2], and filtering [3]. Despite the very high Q values exhibited by microspheres, microdiscs are preferred when a higher integration degree is required to enhance compactness and mechanical robustness. Integrated microdiscs can be designed within complex photonic circuits using a simple planar substrate, more easily than microspheres [4]. The well-shaped microdiscs are ideal candidates to support whispering gallery modes (WGMs) via total internal reflection along the curved circumference. WGM microcavities with high Q, combined with large oscillator strength, gain materials are a perfect approach for the development of the low-threshold lasers [5]. Polymeric microcavities as hosts

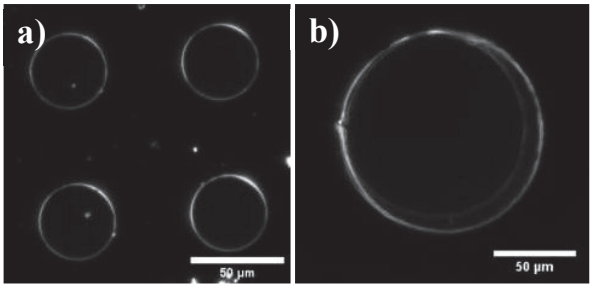

Fig. 1: Optical dark-field microscope images of the microdiscs fabricated by (a) EBL and (b) soft-lithography

for gain material are easy to dope with different dyes, involve low material costs and allow large scale fabrication. Dyes have been studied widely in various cavity geometries [6] and found to be a highly efficient gain material among other organic gain materials [7]. Dyes are suitable for direct integration into the polymeric host matrices such as poly (methyl methacrylate) (PMMA) [8]. Since PMMA is a positive resist for electron beam lithography (EBL), microdiscs can directly be fabricated on a substrate by patterning circles on it. Here, we report a comparative study on two attractive fabrication techniques, EBL and soft-lithography, that are used to fabricate dye-doped polymeric microdiscs.

2. Fabrication and Experimental

Among several dyes, pyrromethene has been chosen for its high absorbance at 532 nm and higher Stoke's shift [7]. To dope pyrromethene into PMMA matrices, solutions of pyrromethene-anisole and PMMA-anisole were prepared and then both were mixed to obtain the dye concentration of 13 µM/gm (pyrromethene/PMMA) in anisole. This concentration is found to give the

highest quantum yield [7]. The solution was spin coated on silica on silicon substrate at 1500 rpm for 1 minute. The thin film was then dried to get rid of the solvent and to obtain uniform dye-doped PMMA film. The masks for EBL were designed on NanoSuite software by Raith GmbH. The 2 × 2 array of microdiscs, each of diameter 40 μm, were fabricated on the pyrromethene doped PMMA thin film with dose of 500 μC/cm^2. The structures were later developed with a developer solution (volume ratio of MIBK: IPA = 1:3). Fig. 1(a) presents the dark-field optical microscope image of the microdiscs fabricated by EBL process which confirms the high optical quality of the surface. Soft-lithography technique which allows easy replication and mass-fabrication, has also been employed to fabricate dye-doped polymeric microdiscs [7]. Figure 1(b) shows the dark-field optical microscope image of the structure fabricated by soft-lithography.

.

In order to quantify the quality of the fabricated microdiscs photoluminescence technique has been employed. The dye-doped microdiscs were excited using the micro-photoluminescence setup shown in Fig. 2(a). Fig. 2(b) presents the lasing characteristics of microdiscs fabricated by soft-lithography, exhibiting high Q (~ 10^4) resonances. The morphological, optical and spectroscopic properties of the microdiscs fabricated by EBL and soft-lithography techniques will be discussed in the conference in detail.

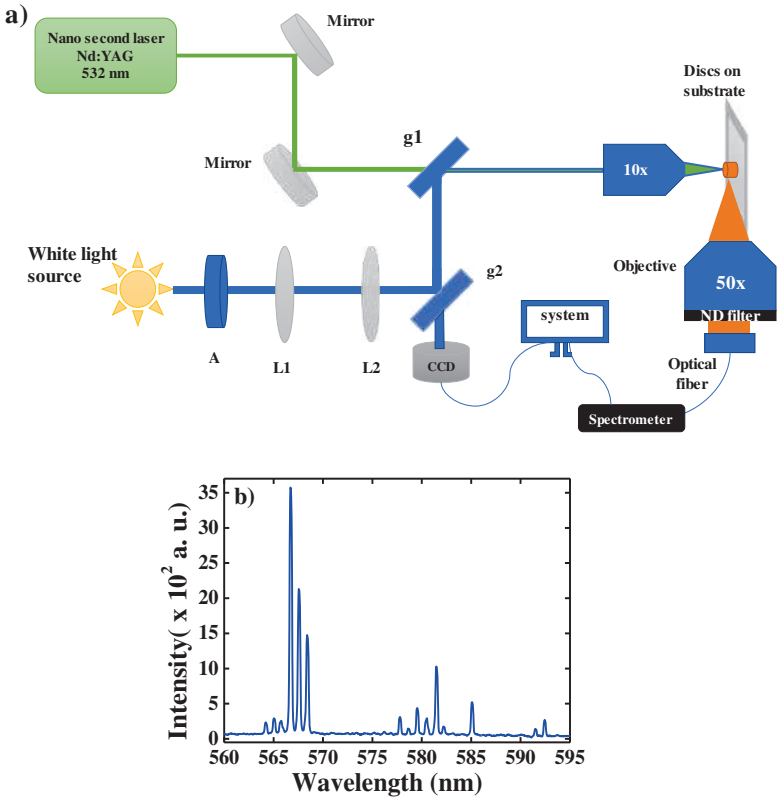

Fig. 2: (a) Micro-photoluminescence setup used to characterize the emission properties of microdiscs (L's are convex lens, A is aperture and g's are glass plates). (b) Lasing characteristics of the microdisc fabricated by soft-lithography.

3. References

[1] M. Kuwata-Gonokami, R. H. Jordan, A. Dodabalapur, H. E. Katz, M. L. Schilling, R. E. Slusher, and S. Ozawa, *Opt. Lett.* 20, 2093 (1995).
[2] P. Rabiei, W. H. Steier, C. Zhang, and L. R. Dalton, J. *Lightwave Technol. 20*, 1968 (2002).
[3] S. Cho and N. M. Jokerst, *IEEE Photonics Technol. Lett. 18*, 2096 (2006).
[4] T. Grossmann, M. Hauser, T. Beck, C. Gohn-Kreuz, M. Karl, H. Kalt, C. Vannahme, and T. Mappes, *Appl. Phys. Lett. 96*, 013303 (2010).
[5] A. Tulek, D. Akbulut, and M. Bayindir, *Appl. Phys. Lett. 94*, 203302 (2009).
[6] H.-J. Moon, Y.-T. Chough, J. B. Kim, K. An, J. Yi, and J. Lee, *Appl. Phys. Lett. 76*, 3679 (2000).
[7] Brijesh Kumar, Priyanka S. Choubey, and B.N. Shivakiran Bhaktha, *Eur. Phys. J. Spec. Top. 231*, 781–789(2022).
[8] A. Kurian, N. George, B. Paul, V. P. N. Nampoori, and C. P. G. Vallabhan, *Laser Chem. 20*, 99 (2002).

Sensitivity and Range Characterization of Optical Gyroscope using Controlled Rotation Stage

Reuben S Mathew[1]*, Athira T S[2], Dinesh N Naik[2], Harikrishnan P[2]

[1]*National Institute of Technology, Calicut, Kerala 673601, India*

[2]*Applied and Adaptive Optics Laboratory, Department of Physics, Indian Institute of Space Science and Technology, Thiruvananthapuram, Kerala 695547, India*

**Corresponding author: rbnsmathew@gmail.com*

Abstract: Optical gyroscopes are highly accurate and versatile instruments used to measure precise angular velocities of rotating bodies. Applications include inertial guidance of launch vehicles and missiles and orbit maintenance, disturbance detection and correction of modern satellites. This report gives the details of the design, realization and characterization of a highly accurate rotating experimental platform with high degree of controllability for testing optical gyroscopes. Further scope of study includes imaging of modes to check if they provide any extra information.

Keywords: Fiber optic gyroscope, inertial sensor, rotational stage.

1. Introduction

Gyroscopes are devices capable of measuring angular velocity. Mechanical gyroscopes consist of a rapidly spinning flywheel about an instantaneous axis which always passes through a fixed point. The flywheel persists to maintain its plane of rotation [1]. Optical gyroscopes use the interference of light and Sagnac effect to measure rotation. Optical gyroscopes have low energy consumption, low wear and tear, and high accuracy when compared to mechanical gyroscopes. When light travels along opposite directions in a closed path, and the area enclosed by the path is rotating, a phase change is produced between the two beams, giving rise to interference [2,3]. The phase difference is given by $\Delta\phi(r) = \frac{8\pi NA}{\lambda c}\Omega$ and the resulting intensity of the interfering light is given by $I \propto I_0 \cos^2(\Delta\phi(r))$ where N is the number of loops of fiber; A is the area enclosed by the fiber loop; c is the speed of light; Ω is the angular velocity along area vector axis; λ is the wavelength of the light; I_0 is the intensity of the light source.

2. Experiment

2.1. Design of rotation stage

The rotation stage was designed to rotate with controlled angular velocity. It has stable speed and provides high torque, with a maximum angular velocity of 1Hz. The setup as shown in figure 1(a) consists of a perforated optical breadboard attached to a motor; the motor is mounted below a plate; the plate being attached to the optical table using optical posts. The motor shaft will be attached to a flange using a key and supported by flange bearings. The optical breadboard is mounted to the flange. This setup is designed to maximize radial load supplied by the motor while minimizing the axial load exerted on the motor shaft. The rate of rotation will be actively measured using a tachometer, enabling fine tuning of angular velocity using the feedback received from the tachometer. The motor selected is a high torque NEMA34 stepper motor. The motor is driven with a stepper motor driver, driven using 24V. The motor speed and feedback mechanism are controlled using an Arduino Uno, with code written in C/C++. The tachometer consists of an IR distance sensor, which triggers once every rotation. The microcontroller measures the time interval between triggers, giving angular velocity. A knob is used to adjust the frequency, which is then shown on an OLED display.

2.2. Calibration of Fiber optic gyroscope.

A commercial, off-the-shelf fiber optic gyroscope from Skyhunt [4] as shown in figure 1(b) was used for the experiments. It consisted of an IR laser diode operating at a wavelength of 1.3 μm, which goes through a non-polarization maintaining fiber loop. A half wave plate is used to minimize the unwanted phase differences caused

by polarization mixing due to birefringence in the optical fiber cable. A photodiode measures the intensity of light received and outputs the value as a voltage, which is amplified by a simple op-amp, and read by a digital multimeter. The voltage will be proportional to the intensity. Measuring the intensity will provide the phase difference, and the angular velocity is computed. Multiple sets of experiments were conducted, and the data has shown similar tendencies. A constant factor $k= (8\pi NA)/(\lambda c)$ was used to contain the parameters of the gyroscopes such as area, number of loops and birefringence effects of optical fiber [5].

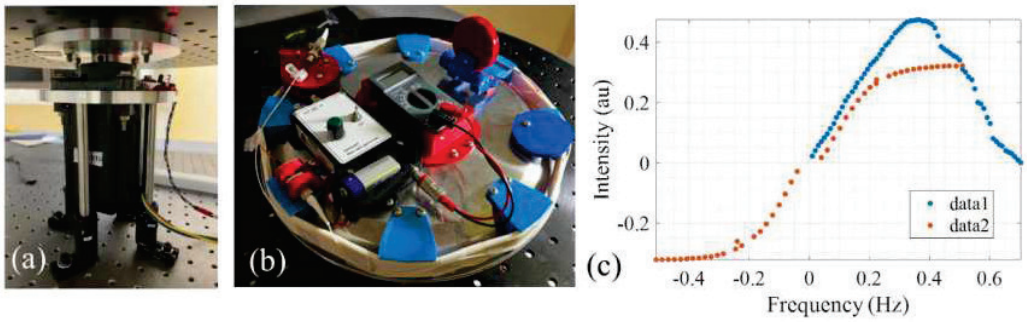

Figure 1(a) Rotation stage built in house (b) Commercially available FOG kit from Skyhunt (c) The calibration curves obtained

By rotating the FOG in the range of 0 to 0.7 Hz, we obtained a curve as shown as data1 in the figure 1 (c) hinting at sinusoidal modulation of intensity as a function of variation in rotation rate. By adjusting the polarization/ phase shift controller provided in the FOG, the operating range can be set to linear region of the variation. The data2 in figure 1 (c) also shows the intensity variation as the rotation of the FOG is reversed.

3. Conclusion

From the intensity vs. frequency plot as shown in figure 1 (c), by operating the gyroscope in its linear region the parameters linking the rotation rate to the phase shift, can be quantified from the slope of the curve. Further testing included 2D imaging of fiber modes using an IR camera to check if the modes obtained provide any extra information that is lost by an averaging photodiode. Unfortunately, the gyroscope was found to be very susceptible to changes in orientation and position of the fiber cable. The modes were very sensitive to even minute disturbances of the apparatus and proper imaging of modes was not possible with the current setup [5]. In the future, using more stable and robust fiber optic gyroscopes to image modes properly is planned.

4. Acknowledgement

We thank Dr. Priyadarshnam for the discussions and Small Satellites and Payloads Centre (SSPACE) for the support with FOG kit and related electronics.

5. References

[1] James B. Scarborough, *The Gyroscope Theory and Applications* (Interscience Publishers Ltd., London, 1958), Chap.3.
[2] Hervé C. Lefevre, *The Fiber-Optic Gyroscope* (Artech House, 2022), Chap.2.
[3] Frank L. Pedrotti, Leno M. Pedrotti, Leno S. Pedrotti, *Introduction to Optics* (Pearson, 2006), Chap.7.
[4] Doug Marett,"Single Mode Fiber Optic Sagnac Interferometer with Wireless Data Collection" https://vixra.org/pdf/1506.0002v1.pdf
[5] Ralph A. Bergh, H.C. Lefevre, Herbert J. Shaw, "An Overview of Fiber-Optic Gyroscope" Journal of light wave technology (1984)

Design and Development of Projection Optics for DMD Source to Replace The CRT Tube in Refractive Type Augmented Reality Display

Rahul Rohilla, [1] Vinod Mishra, [2] Vipan Kumar, [3] Harry Grag, 4[*]

Imaging avionics & Display system, CSIR-Central scientific instrument organization, sector30c, Chandigarh-160030, India
Academy of scientific and innovation research (Acsir) , Ghaziabad 201002 , India
Corresponding Author: rohilla.rahul24@gamil.com

Abstract: From many of decade application of augmented reality is used in form of refractive type head up display. Flight information is projected by an image source on partially coated combiner in front of the pilot line of sight. This partially coated combiner superimposed the virtual information on real see through view. In these system monochromatic CRT tube is used as an image source. Now high brightness source OLED, LCD and DMD are available that can replace the CRT tube. Replacement of the CRT tube with the same refractive optics with existed field of view is itself a challenging task. The work of this paper is to design & development of a projection optics for DMD source which can replace CRT tube in refractive type augmented reality display.

Key word: Refractive, On-axis, Augmented reality, optical design, projection optics, CRT tube, DMD.

1. Introduction

Augmented reality application is used in fighter aircraft in form of head up display [1,2]. In which the image is projected on partial coated combiner. This combiner superimposed the virtual information on real see through view. This application enhances the interface between pilot and aircraft which helps pilot to take the better decision at a high speed. Moreover, Size and field of view of such kind of augmented reality display is depend on the space available in cockpit.

1.1. Refractive type optical design

Refractive type augmented reality system in which both projection optics and combiner optics are on common optical axis as shown in figure 1.

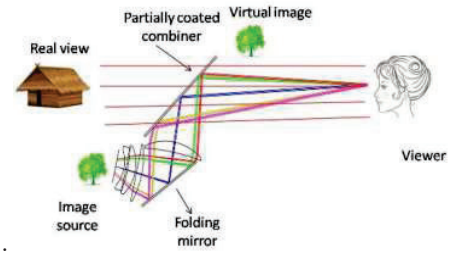

Fig1. Refractive type augmented reality display

These are F-1 pitzal type optical design, having the limited field of view depends on the source. Monochromatic CRT tube is used as an image source [3]. Replacement of CRT tube by Digital micro mirror device (DMD) without changing the refractive optics to maintain the existed field of view. A projection optics is designed for DMD to magnify the image from source size to CRT screen size.

2. Design method of projection optics

System is designed for Paraxial first order to evaluate the optical parameter of projection optics like magnification, focal length, entrance pupil diameter, screen size and projection distance. Paraxial optical design is optimized to minimize the third and higher order of optical aberration by using Zemax optic-studio. A ray diagram of the projection optics as shown in figure 2.

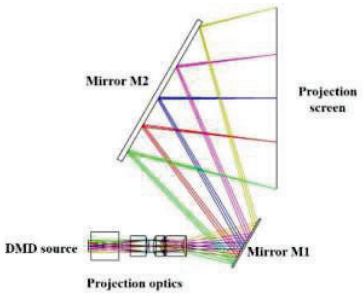

Fig 2. Ray diagram of projection optics from DMD source to projection screen

Diffraction limited Spot size is shown in figure 3 (a) and seidel aberration diagram of optimized projection optics design as shown in figure3 (b).

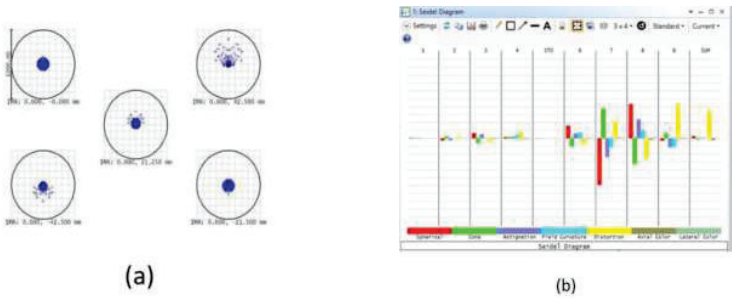

Fig 3.(a) diffrection limited spot size , (b) seidel aberration digram

References

[1] C.H.valiance, Marconi avionics Ltd, Rochester, "The approach to optical system design for aircraft head up display,"Uk (1983).

[2] Robert B, wood, mark A. thomes flight dynamic inc…, "Holographic head-up display combiners with optimal photometric efficiency and uniformity ,"Portland, 97224 (1990).

[3] Totan Chandra, b Sanjit K. Debnath, a, b* Shravana Kumar Rayagond, Dr. Vinod Karar, "Design of refractive Head-up display system using rotational symmetric aspheric optics," optik-international journal for light and electron optic. 131, 515-519 (2017).

Role of nonic saturation on Modulational instability in birefringent Kundu–Ekchaus equation.

Emonisha Rajamani[1], **P. Mohanraj**[1] **and R. Sivakumar**[1]

[1]*Department of Physics, Pondicherry University, Puducherry-605014, India.*

Author e-mail address: emophysics1312@gmail.com

Abstract: This paper investigates the nonic saturation effect on modulational instability (MI) in a coupled birefringent Kundu-Eckhaus (KE) model. Using standard linear stability analysis, we examine the instability characteristics in the KE system with self-phase modulation (SPM) and cross-phase modulation (XPM). In addition, we study the impact of both cubic and nonic saturation nonlinearity for small perturbation in both normal and anomalous dispersion regimes.

Keywords: Modulational Instability (MI), Nonic saturation effect, Kundu-Echkaus Model, Self-Phase Modulation (SPM), Cross Phase Modulation (XPM).

Introduction

The modification of optical properties of a system due to the interaction of light led to the exploration of Optics [1]. At high powers, the material properties can change rapidly, leading to nonlinear effects. Modulational Instability (MI) is one such nonlinear phenomenon. The MI is studied in diverse fields such as fluid dynamics, Nonlinear Optics, Plasma physics, etc. [2]. The nonlinear Schrodinger equation (NLSE) governs the dynamics of modulational instability [3]. The NLSE recognizes solitary waves through a conservative interaction between the abnormal group velocity dispersion (GVD) and self-centered Kerr nonlinearity [4–6]. Kundu – Eckhaus equation is a linearizable form of NLSE. The fourth term in the KE equation denotes the nonlinear Kerr effect, and the last term denotes the Raman Effect, which accounts for the self-frequency shift of waves [7]. Recently Yildirim has found that dark, bright and unique solitons are called the optical solitons of the coupled KE equation system [8, 9].

Saturable nonlinearity (SNL) has an upper limit for optically induced refractive index variation, beyond which the higher order susceptibility will saturate the nonlinear response of the medium [10]. However, we are discussing the modulation instability of the nonlinear optical wave in the KE equation by analyzing the stability of the nonlinear wave in KE models by altering the effects of self-phase modulation (SPM) and cross-phase modulation (XPM) with the adjustable effect of nonic saturable nonlinearity.

Theoretical Model

The dimensional shape of the KE equation for polarizing fibers is indicated by,

$$iQ_t + aQ_{xx} + b|Q|^8 Q + c(|Q|^2)_x Q = 0 \tag{1}$$

The parameters c and b are nonlinear cubic and nonic nonlinearity.

The above divides in two components as shown below for birefringent optical fibers [10].

$$iu\ + a_1 u_{xx} + (\alpha_1|u|^8 + \beta_1|u|^4|u|^4 + \gamma_1 v^8)u + R_1(|u|^2)_x u + S_1(|u|^2)_x u = 0 \tag{2}$$

$$iu_t + a_2 u_{xx} + (\alpha_2|u|^8 + \beta_2|u|^4|u|^4 + \gamma_2 v^8)u + R_2(|u|^2)_x u + S_2(|u|^2)_x u = 0 \tag{3}$$

Where, a_1 and a_2 are the dispersion group speed conditions and α_1, α_2, R_1, R_2 is the nonlinear term which reflects the SPM whereas β_1, β_2, γ_1, γ_2, S_1, and S_2 are the XPM terms. Nonlinear saturation model for KE equation is already available in the literature [11-13].

$$f(\Gamma|u,v|^2) = \frac{|u,v|^2}{1+\Gamma|u|^2}, f(\Gamma|u,v|^4) = \frac{|u,v|^4}{1+\Gamma|u|^4}\ and\ f(\Gamma|u,v|^8) = \frac{|u,v|^8}{1+\Gamma|u|^8} \tag{4}$$

Here, Γ represents for nonlinear saturation term.

We accept the general form solution

$$\Delta u, v = F_{1,2} e^{i(\mathrm{K}x - \Omega t)} + G_{1,2} e^{-i(\mathrm{K}x - \Omega t)} \tag{5}$$

The MI criterion for KE equation birefringent fiber can be defined as

$$g(\Omega) = \mathrm{Im}(\Omega) \tag{6}$$

Result and Discussion

In this section, we intend to study the role of nonlinear saturation on the MI gain spectrum in the KE equation with the adjustable SPM and XPM effects. The gain spectrum profile is shown in Figure as a function of Q and K. The results show that the SPM and XPM effects enormously change the stability/instability region without nonlinear saturation, as shown in Fig. 1(a). Fig. 1(b) indicates the MI gain spectrum of the KE equation with a nonlinear saturation effect. From the contour image, we observed dramatic changes in the stability/instability region in the Q=-20 to 20. Fig. 1(c) illustrates the anomalous dispersion regime; we observed two symmetric side lobes with nil propagation constant k=0. In the inclusion of the nonlinear saturation effect, we observed two nonconventional MI bands with large stability regions, as shown in Fig. 1(d). However, nonlinear saturation and SPM and XPM values strongly affect the MI gain profile. Finally, the nonlinear saturation can produce a new path to manipulate and generate solitary wave and ultrashort pulses in the KE model.

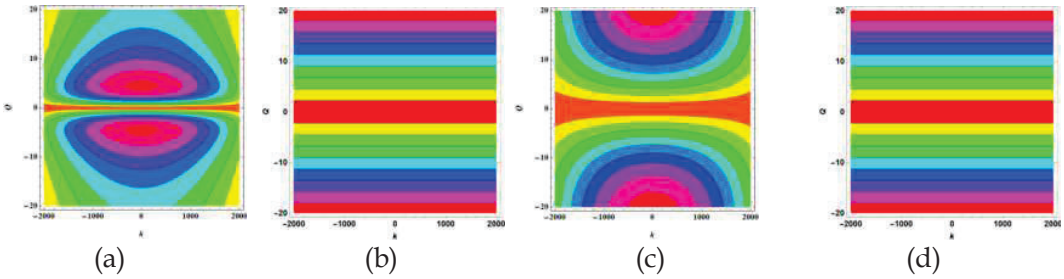

Figure 1: *Contour plot shows the stability and instability of MI in a birefringent fiber of KE equation in both normal (a-b) and anomalous dispersion (c-d). Other nonlinear parameters are* $u_0 = 0.2$, $v_0 = 5.8$, $a_{1,2} = 0.1$, $\eta_{1,2} = 1.2$, $\zeta_{1,2} = 1.2$, $r_{1,2} = 1$

Conclusion

In summary, we analyzed the KE equation's MI characteristics with a nonic nonlinear saturation effect. For a complete picture, we consider both dispersion regimes and comprehensively analyze the interplay between nonic and nonlinear saturation effects. Saturable nonlinearity strongly alters the MI criterion in the KE model. As a result, the results presented in this study, which highlight the interaction between nonlinear saturation and nonic nonlinear effects, could impact how well we grasp the dynamics of ultrashort pulse propagation in KE models.

References

1. Robert Boyd, *Nonlinear Optics*,3rd Edition - March 28, 2008
2. G. Agrawal, *Nonlinear fibre optics* (San Diego, 5th edition: Academic Press) (2012).
3. Boris I. Lembrikov, *Nonlinear Optics* - Novel Results in Theory and Applications, 2019
4. M. F. Saleh, W. Chang, J. C. Travers, P. S. J. Russell and F. Biancalana, *Phys. Rev. Lett.* **109** 113902 (2012).
5. A. Hasegawa, *Opt. Lett.* **9** 288–29 (1984).
6. K. Tai, A. Hasegawa and A. Tomita, **56** 135–138 (1986).
7. J. M. Dudley, G. Genty and S. Coen, *Rev. Mod. Phys.* **78** 1135–1184 (2006).
8. J. Vega-Guzman, A. Biswas, M.F. Mahmood, Q. Zhou, S. Khan, S.P. Moshokoa, Optik **181** 499–502 (2019).
9. Y. Yildirim, Optik **182** 393–399 (2019).
10. P. Mohanraj, Optik **245** 167687 (2021).
11. K. Nityanandan, R. Vasantha Jayakantha Raja, K. Porsezian, Modulation instability in twin-care fiber with the saturable nonlinear response and coupling coefficient dispersion, Phys. Rev. A 87 (2013) 043805
12. K. Nithyanandan, K. Porsezian, Observation of two state behavior in the instability spectra of saturable noninear media, Eur. Phys. J. 222 (2013) 821.
13. A. Kumar, T. Kurz, W. Lauterborn, Two-state bright solitons in doped fibers with saturating nonlinearity, Phys. Rev. E 53 (1996) 1166.

Development of frequency encoded tristate Pauli X-gate using SOA Dopped photonic Band Gap nanocrystalline structure

Ayan Dey* & Sourangshu Mukhopadhyay
Department of Physics, The University of Burdwan, Golapbag, Burdwan-713104, West Bengal, India
**Email id: ayandeybwn@gmail.com*

Abstract: The quantum Tristate Pauli-X gate can broadly be used due to its very fast speed of operation in order to THz order, very fast information processing rate, very strong noise-free communication and advantages to be used in the field of all-optical quantum computing. This Pauli X-gate is also important due to its inversion operation. In this proposed scheme, the quantum tristate Pauli-X logic gate have been constructed by nanocrystalline photonic band gap structure. The frequency encoding technique is used here to establish the logic of all-optical tristate Pauli X-gate towards the need of obtaining a three-input-three output inversion system.
Keywords: Semiconductor Optical Amplifier (SOA), Frequency encoding principle, Cross gain modulation (XGM)

1. Introduction

Tristate quantum logic gates have broadly been used in different fields of quantum computation and rapidly information processing controlling mechanism due to its very fast response time, very strong information handling capacity and very high-speed of operation of the system with low power [1-3]. In last few decades, various types of the quantum logic gates are developed by using Pockels and Kerr materials and based optical switches. All-optical Pauli X, Y and Z gates are designed by optical switches [4]. Also an all-optical integrated Pauli X, Y and Z gates designed by using 2D photonic crystal with the intensity and phase encoding techniques jointly was proposed by Paromita De et al [5]. All optical quantum logic gates are established by using phase, polarization, intensity and frequency encoding techniques. An all-optical reversible tristate Pauli X, Y and Z gates developed by electro-optic modulator using the phase encoding principle was suggested by M.N. Sarfaraj et al [6]. In this paper, all-optical tristate Pauli X- gate is developed by nanocrystalline photonic band gap structure using two SOAs with frequency encoding principle. This nanocrystalline structure based proposed scheme is supposed to perform the all-optical quantum tristate Pauli X-gate operation i.e., the path of two input signals are cross-exchanged to one another at the output, retaining the path of the middle input signal same. This nano-crystalline scheme-based all-optical tristate Pauli X-gate has individual characteristics of dealing with low power having the THz order speed of operation.

2. SOA as optical switch

Semiconductor Optical Amplifier (SOA) based optical switch is developed by using Gallium Arsenide (GaAs) which can perform optical non-linear operation successfully. Because of excess photo-excitation with high degree of carrier recombination, the refractive index of the medium changes, in such a way, so that the optical gain changes equivalently.

3. Photonic Band gap structure (PBG) as optical switch

All-optical tristate Pauli x-gate have been developed by using GaAs material based optical switch like SOA. The semiconductor material GaAs has higher carrier recombination capability and wide ranges of band gap which can used as optical switch. This proposed nanocrystalline photonic structured based scheme performs in a wide range of band gap (PBG) region for exhibiting the switching action.

4. Design of the proposed tristate Pauli X-gate with PhCs with SOA dopping

This proposed nanocrystalline photonic band gap structure based scheme has been established for performing of all-optical tristate Pauli x-gate operation. The output results are also verified with the possible combinations of input signals, so that this whole proposed scheme is universal in nature. In this proposed scheme, we used three input signals including A_0, A_1 and A_2 and three output channels including O_0, O_1 and O_2 respectively as shown in **Fig. 1**. This three input signals A_0, A_1 and A_2 are

encoded by three different frequencies of light ν_1, ν_2 and ν_3 respectively by using the technique of the frequency encoding principle for establishment the logic of an all-optical nanocrystalline photonic band gap structure based tristate Pauli X-gate.

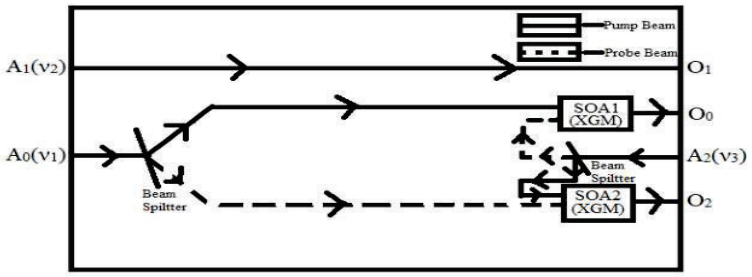

Fig. 1: Layout of an all-optical nanocrystalline photonic band gap structure based tristate Pauli X-gate.

5. Operation of the system

In this proposed scheme, the pump beam of input signal A_0 and the probe beam of input signal A_2 are passing into the SOA1. Due to the cross-gain modulation (XGM) type non-linearity of SOA, we get strongly amplified intense signal A_2 at the output O_0. The pump beam of input signal A_2 and the probe beam of input signal A_0 are passing into the SOA2. At the output O_2, we get strong amplified intense signal A_0. The input signal A_1 is directly carried at the output channel O_1 which is performed as the same logic of an all-optical tristate Pauli X-gate.

6. Simulation

This same proposed scheme of all-optical tristate Pauli X-gate can be developed by defect creation on nanocrystalline square lattice of 2D air photonic band gap crystals (PhCs) of GaAsInP rods and the simulation is conducted using Finite-Difference Time-Domain (FDTD) technique and Plane Wave Expansion (PWE) band solver parameter with two photonic crystals structure based SOAs (pc-SOA). One can observe the value of intensity of XGM process as proposed. The output results should be analyzed and verified by the above simulation experiment with the various combinations of input signals.

7. Conclusion

The proposed all-optical tristate Pauli X-gate scheme has been developed by nanocrystalline photonic band gap structure-based device using two SOAs and frequency encoding technique. This photonic crystals based scheme has a very speedy response time rate, low output power, very quick data storage capability.

8. Acknowledgement

The author acknowledge to the Govt. of West Bengal and Department of Physics, The University of Burdwan, for financial support.

9. References

[1] Seth Lloyd, "Almost Any Quantum Logic Gate is Universal", (Phys. Rev. Lett. 75, **346** – Published 10 July 1995).
[2] Anthony Mark Fox, Mark Fox, "Quantum optics: an introduction", (Oxford university press, 2006/4/27, 15).
[3] A. Ghatak and K. Thyagarajan, "Optical Electronics", (New Delhi: Cambridge University Press, 1989).
[4] Baishali Sarkar & Sourangshu Mukhopadhyay, "An all optical scheme for implementing an integrated Pauli's X, Y and Z quantum gates with optical switches", (Journal of Optics), **46**, 143-148 (2017).
[5] Paromita De,Sapana Ranwa,Sourangshu Mukhopadhyay, " Intensity and phase encoding for realization of integrated Pauli X, Y and Z gates using 2D photonic crystal", (Optics & Laser Technology), **152** (2022), 108141, https://doi.org/10.1016/j.optlastec.2022.108141.
[6] Mir Nadim Sarfaraj & Sourangshu Mukhopadhyay, "All-optical scheme for implementation of tri-state Pauli-X, Y and Z quantum gates using phase encoding", (Optoelectronics Letters), **17**, 746–750 (2021).

Consistency Study of Guided-Mode-Resonance Structures for Point-of-Care Applications

Pankaj K Sahoo, Kezheng Li, Thomas F Krauss
Photonics Research Group, School of Physics, Engineering and Technology, University of York, UK
pankaj.sahoo@york.ac.uk

Abstract: Guided mode resonance (GMR) structures are very promising for healthcare applications. Fabrication reproducibility is a key issue towards commercialization of the technology. Here, we have tested more than 50 samples in order to understand how to achieve high consistency. We find that ebeam focusing and baking temperature significantly affects the consistency of the resonance behavior of the GMR sensors.
Keywords: Guided Mode Resonance, Optical Sensor, Quality Consistency

1. Introduction

Guided-Mode-Resonance (GMR) structures consist of wavelength-scale gratings and they exhibit Fano resonances that are suitable for biosensing applications. One of the key advantages of GMR structures is that they are easily excited by out-of-plane illumination using simple collimated light sources, including LEDs [1]. This ease of coupling allows them to be used in low-cost devices, even by untrained personnel for point-of-care (POC) applications. However, a challenge for their implementation in many cases is that they require an external spectrometer as the read-out. This issue can be resolved by chirping the period or fill-factor of the GMR [2], which enables integration of the sensing and the readout function into the same structure. The idea of the chirped GMR approach is that it converts spectral information into spatial information that can be easily picked up by a simple camera, i.e., it exploits the imaging capability of the GMR. This technique has already been used to detect proteins with pg/ml-level sensitivities, and in a real clinical matrix, i.e., urine [3]. Taking this idea further, we aim to fabricate GMR structures for real POC applications. However, we have realized that the fabricated structures suffer from low consistency, with only 30% of structures achieving the target performance. The purpose of this report is to discuss the fabrication strategy of chirped GMR devices, and evaluate their performance consistency for biosensing applications.

2. Results and Discussion

The chirped GMR structures (schematic in Fig. 1a) used in this study have gratings with varying periodicity (Λ) between 426 nm and 434 nm. They are fabricated by electron beam lithography (EBL) on a silicon nitride (150 nm thick) coated glass substrate. The overall fabrication process involves (i) Sample Cleaning, (ii) Coating EBL resist (ARP13), (iii) ebeam Exposure, (iv) Resist development, and (v) Reactive Ion Etching (RIE). The SEM image (Fig. 1b) shows the chirping of the grating period with ridge thickness of 150 nm. Before fabrication, the structure parameters are optimized through FDTD modelling. The resonance of the fabricated samples is analyzed in a low-cost imaging setup as shown schematically in Fig. 1c. A LED source is filtered to 647 ± 1 nm wavelength and is collimated through a lens system. The sample is kept vertically with the grating side facing upward so that the analyte can be put on the surface of the sample which is then imaged through the reflected light by a CMOS camera (pixel size = 1.14 μm) at the sensor position. The obtained image looks like a bright bar that moves laterally as a function of the refractive index change. So, the position of this bar provides the readout for the chirped GMR sensor. Determination of the peak position is normally done by fitting the pixel intensity data with an appropriate mathematical function, such as a harmonic function or a Fano function. The shape of the fitted curve is characterized by FWHM and peak intensity [4] which determines the accuracy of the fitting results and in turn the accuracy of the readout and the limit of detection (LOD). In order to reduce the FWHM and enhance the peak intensity (as required for the biosensor) we start optimizing the following five parameters, namely film thickness, ebeam focusing, ebeam alignment, development time, and baking time, as they are directly linked with the resonance. The typical relationship of these parameters can be represented as a polygon (Fig. 1d), where the blue shade refers to the relationship among these parameters before optimization. Our aim is to optimize the fabrication process so that the blue shade approaches towards the optimized pink shade and ultimately towards the ideal case (black contour). Although every step in the GMR fabrication accounts for making the results consistent, we developed a strategy to converge our efforts as

described below. In the 1st step, the etch rate of SiN in the RIE machine is optimized for a simultaneous etching of four samples. In the 2nd step, the development time of the exposed samples after EBL is fixed to an optimized value (2 minutes in Xylene). In the 3rd step, the coating process is optimized to maintain a constant resist thickness (200nm). Our observation and analysis show that, out of the above five parameters the ebeam focusing and baking temperature significantly affects the consistency and that is why the differences in the blue and pink shades (Fig. 1(d)) is more for these two parameters. If the temperature of the hot plate is nonuniform and unstable (> ±3 °C), the shape of the resonant bar gets curved as shown in the left images of Fig. 1(e). On the other hand, a stable temperature within ±3 °C makes the bars straight as in the right images. The average value of the pixel intensity along the horizontal direction of the bars are fitted with the Fano line shape with respect to the pixel positions (vertical direction) of the camera. The FWHM and the pixel intensity are retrieved from the Fano fit and are compared in Fig. 1f. It can be observed that the resonance shape is broader, and the peak intensity is lower for the left patch of images. As discussed, the broader peak will reduce the fitting accuracy, whereas the lowered peak intensity reflects a lower signal to noise ratio (SNR), which reduces the LOD [4] and both are not beneficial for biosensing applications. Furthermore, the position of these bars on the sample surface is affected by the exposure condition of the focused ebeam which decides the grating ridge-width and thus the fill fraction of the gratings. The right patch of samples in Fig. 1(e) are fabricated with similar ebeam focusing condition and thus the bars are at the same positions on the sample surface unlike left patches. Using this optimized fabrication strategy, we fabricated and demonstrated the resonance behavior of 50 samples. The spread of FWHM before and after the optimization are compared in Fig. 1(g) which shows that the spread is narrowed down and the standard deviation (SD) of the measured values are reduced (3-4 times) after optimization.

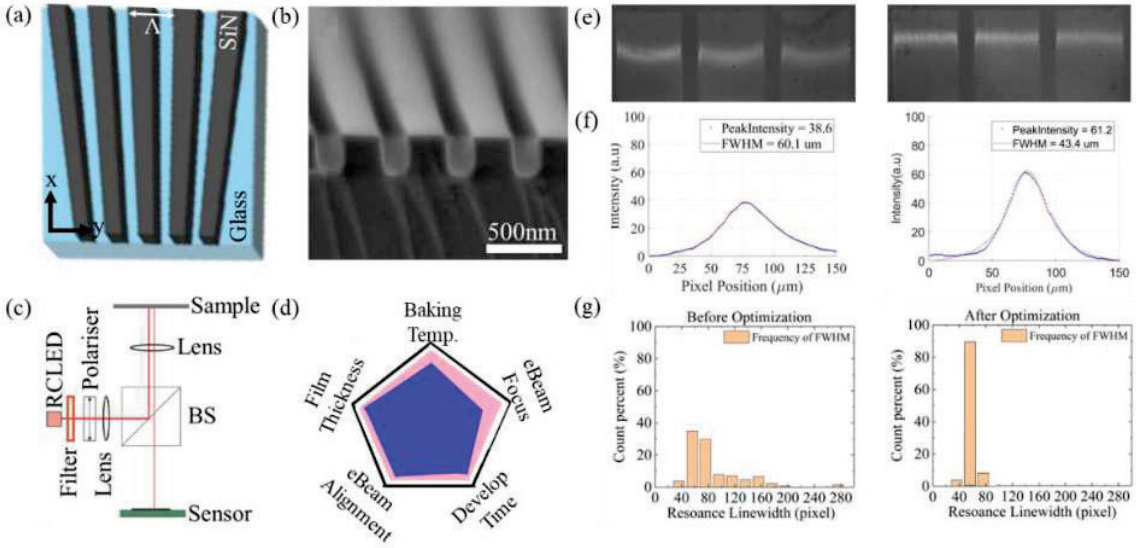

Fig. 1: (a) Schematic of the Chirped GMR structure, (b) SEM image of the fabricated gratings showing chirping of the grating lines (c) Schematic of the imaging set-up used as a biosensor, (d) Relationship of fabrication parameters, (e) Image of the resonance lines at 647 nm wavelength, where the left patches corresponds to an unstable baking temperature compared to the right patches. (f) Comparison of the FWHM and peak intensity for the two cases of resonant lines described in Fig (e). (g) Spread of FWHM before & after optimization.

In conclusion, it is found that the resonance of the chirped GMR is significantly affected by the baking temperature and ebeam focusing and it can be controlled to maintain consistent results among the fabricated GMR sensors. This analysis can pave the way for mass production of low cost POC devices based on chirped GMR structure showing consistent performance. Further development in the study with more detailed results will be communicated in future.

3. References

[1] A. Drayton, et al., Performance limitations of resonant refractive index sensors with low-cost components, Opt. Express 28, (2020).
[2] G. J. Triggs, et al., Chirped guided-mode resonance biosensor," Optica 4, 229-234 (2017).
[3] A. Kenaan, et al., Biosens. Bioelectron. 153, 112047 (2020).
[4] D. Conteduca, et al., ACS Photonics, 9, 5, 1757–1763 (2022).

Recovery of OAM modes from three-step phase-shifting

Amit Yadav[1*], Tushar Sarkar[1], Takamasa Suzuki[2] and Rakesh Kumar Singh[1]
[1]*Laboratory of Information Photonics and Optical Metrology, Department of Physics, Indian Institute of Technology (Banaras Hindu University), Varanasi, Uttar Pradesh, India*
[2]*Electrical and Electronic Engineering, Niigata University, Japan*
[*]*Author e-mail address: yadavamitupac@gmail.com*

Abstract: We present a technique to recover the Orbital Angular Momentum (OAM) modes from the coherent light that is scattered randomly. We also quantitatively measure the amplitude and phase structure from the incident random light. This idea is accomplished by the evaluation of correlation between two points Stokes fluctuations of incident light which helps in the recovery of complex polarization correlation function with three steps phase- shifting approach. The theoretical approach of the suggested method is discussed and simulation results are shown.
Keywords: Orbital Angular Momentum, Phase Imaging, Coherence.

1. Introduction

A light beam having orbital angular momentum is referred as vortex light and is characterized by exp($il\varphi$) [1], where l is the topological charge (TC) and φ is the azimuthal angle. Due to the eccentric features, the OAM beams exhibit a great potential for applications in numerous fields, ranging from optical metrology, optical communication, particle trapping and imaging. Different methods have been suggested for the purpose of TC detection and OAM mode sorting. However, the majority of these methods are capable to detect the OAM distribution of vortex beam in only free space or homogeneous media. Recently, a machine learning-based approach is demonstrated for recognition of vortex beams.

When the light beam propagates through scattering media, it influences the beam hence limits their use in practical applications such as optical metrology, remote sensing, and imaging. Due to the presence of scattering media such as foggy medium, wavefront of an incident coherent vortex beam gets distorted and generates the speckle patterns. Some significant methods have been developed to extract the information from speckle patterns [2]. We present a new technique to recover the OAM modes with the help of limited Stokes parameters (SPs). The first three SPs of the scattered field are used as the theoretical foundation for our method which involves three steps of phase-shifting in order to obtain the complex polarization correlation function (CPCF). The complex valued Fourier coefficient is provided by CPCF which is used in the extraction of incident vortex beam. The orthogonal helical mode projection of the retrieved CPCF is also used to explore the incident OAM modes.

2. Theoretical Model

Let us consider a polarized coherent light having two orthogonal polarization states i.e., *x* and *y* coaxially propagating along z-axis. The complex field of coherent polarized light at the transverse plane z=0 is given as,

$$E(\hat{r}) = e^{il\varphi}\hat{e}_x + B\,\hat{e}_y \tag{1}$$

Where exp($il\varphi$) represents the phase factor of the vortex beam and B is the amplitude of the plane wave. A light beam given in Eq. (1) passes through the scattering media and travels to the detection plane which is located at any random distance z by Fresnel diffraction formula. At any distance of z from the detecting plane the scattered field is given as

$$E_q(r) = \int E_q(\hat{r}) e^{i\delta(\hat{r})} g(r,\hat{r}) d\hat{r} \quad , \quad \text{q=(x,y)} \tag{2}$$

Where $g(r,\hat{r}) = \frac{-ik}{2\pi z}\exp\{\frac{ik}{2}[\frac{(r-\hat{r})^2}{z}]\}$ is a propagation kernel of wavenumber *k*. The position vector at the detector plane and source are denoted by r and r̂ respectively and the diffuser introduces a random phase $\delta(\hat{r})$. Pauli spin matrices are used to define the Stokes parameter of the scattered field as

$$S_n = E^T(\hat{r})\sigma^n E^*(\hat{r}), \qquad n \in (0,..3) \tag{3}$$

σ^0 is the identity matrix and σ^1, σ^2, σ^3 are the Pauli spin matrices of 2x2 order. The Stokes fluctuation around the mean value of SPs are given as

$$\Delta S_n(r) = S_n(r) - < S_n(r) > \quad (4)$$

where bracket < > represents ensemble average. Let us consider that the random light follows Gaussian statistics, the Gaussian moment theorem is used to illustrate the SPs fluctuations are correlated as

$$C_{nm}(r_1, r_2) = < \Delta S_n(r_1) \Delta S_m(r_2) > \quad n, m \in (0,...,3). \quad (5)$$

From above equation we calculate $C_{20}(r_1,r_2)$ and $C_{21}(r_1,r_2)$.The real part of the CPCF are obtain by adding $C_{20}(r_1,r_2)$ and $C_{21}(r_1,r_2)$.

$$C(\Delta r) = C_{20}(r_1, r_2) + C_{21}(r_1, r_2) \quad (6)$$

We combined Eq. (6) with three steps- phase shifting method [3] to obtain CPCF which is given below

$$C(\Delta r) = (2C_{Re}^{0}(\Delta r) - C_{Re}^{2\pi/3}(\Delta r) - C_{Re}^{4\pi/3}(\Delta r)) + \sqrt{3}i(C_{Re}^{2\pi/3}(\Delta r) - C_{Re}^{4\pi/3}(\Delta r)) \quad (7)$$

Where $C_{Re}^{4\pi/3}(\Delta r)$, $C_{Re}^{2\pi/3}(\ \Delta r)$ and $C_{Re}^{0}(\Delta r)$ indicate the real component of the CPCF with phase shift of $\frac{4\pi}{3}, \frac{2\pi}{3}, 0$ respectively. $C(\Delta r)$ is our required quantity and is utilized to recover the complex amplitude of the incident light.

3. OAM Analysis

To investigate the OAM modes of incoming vortex beam, project the CPCF onto the spiral harmonic exp(ilφ),where l represent the topological charge. We use angular Fourier transform to calculate coefficient A_m as

$$A_m(\Delta r) = \frac{1}{2\pi} \int_0^{2\pi} d\varphi e^{-il\varphi}\, C(\Delta r)$$

OAM power spectrum of the incident light is obtained by integrating $|A_m|^2$ with respect to radial coordinates.

$$P(l) = \frac{1}{S} \int_0^{\infty} dr\, r |A_m(\Delta r|^2 \quad (8)$$

where $S = \sum \int_0^{\infty} drr \mid A_m(\Delta r) \mid^2$ and P(l) represents the beam power and OAM power spectrum respectively.

4. Results and Discussion

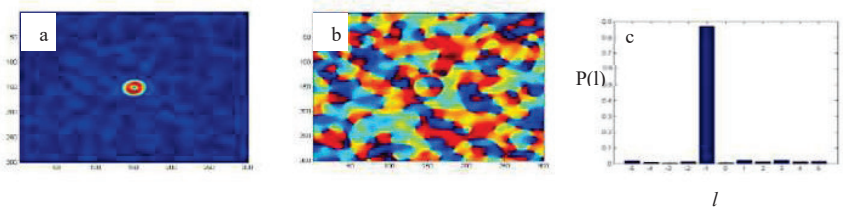

Fig. 1. (a), (b) and (c) represent amplitude, phase and OAM distribution of CPCF for l= -1

In Fig.1. (a) shows the amplitude of the CPCF, (b) is the phase distribution and shows helical phase structures in the CPCF for l= -1, and (c) shows the OAM distribution of topological charge l= -1.

5. Acknowledgement

Amit Yadav acknowledges University Grant Commission, India for financial support as Junior Research Fellowship.

6. Conclusions

We present a new method to recover the OAM modes with higher-order Stokes fluctuations correlation by using three step phase- shifting method. This technique is anticipated to be useful in optical metrology for detection of orientation and shape of the target.

7. References

[1] A. D'Errico, R.D'Amelio, B. Piccirillo, F. Cardano, and L. Marrucci, "Measuring the complex orbital angular momentum spectrum and spatial mode decomposition of structured light beams," Optica 4, 1350-1357 (2017)

[2] T. Sarkar, R. Parvin, M. M. Brundavanam, and R. K. Singh, "Higher-order Stokes-parameter correlation to restore the twisted wavefront propagating through a scattering medium", Phys. Rev. A, vol. 104, no. 1, pp. 013525, 2021.

[3] P. S. Huang and S. Zhang, "Fast three-step phase-shifting algorithm" Appl. Opt., vol. 45, no. 21, pp. 5086-5091, 2006.

Urea detection in milk using ZnO nanorods based fiber optic sensor

Jyoti, R.K.Verma*

Department of Physics, Central University of Rajasthan, NH-8 Bandarsindri, Ajmer 305817, India

**Corresponding Author e-mail address:* rkverma@curaj.ac.in

Abstract: The use of adulterants in milk is very common all over the world for financial benefits which can cause many health hazards as well as this is ethically wrong. The pathophysiological range of urea in the human body is 30 mM to 150 mM and if the amount of urea exceeds this limit in the human body then kidneys have to do extra work which might lead to the failure of kidneys and other health problems. A comparative study of enzymatic and nonenzymatic based sensors has been performed and it has been analyzed that the enzymatic sensor has 8-fold higher sensitivity than the nonenzymatic based sensor.

Keywords: Urea, ZnO nanorods, Fiber optic, Urease, Adulteration

1. Introduction

Milk is the key ingredient of our diet and has a sufficient amount of proteins, fat, vitamins, minerals, amino acid and carbohydrates for the growth of kids and adults [1-3]. A number of adulterants like water, urea, melamine, preservative, non-milk protein, vegetable fats, milk powder, whey protein and low-valued milk have been investigated in milk which reduces its nutritional level. Water and urea are the most common and cheap milk adulterants. Water in milk can be easily investigated by the lactometer but the solids present in milk cannot be identified by the lactometers. An enzyme-based sensor can be fabricated for the detection of urea in milk. To solve such a problem, a Urease coated ZnO nanorods-based sensor has been proposed in this work. Selectivity study, sensitivity, detection accuracy, LOD, LOQ and time response has been measured in this work.

To perform this experiment, we placed a urease-coated ZnO nanorods-based fiber optic probe in the flow cell and light has been incident from one end of the fiber, and the spectra were recorded from the other end of the fiber using a spectrometer as shown in figure 1. The peak wavelength has been measured for every sample poured into the flow cell and then the wavelength shift and sensitivity were calculated.

We synthesized two ZnO nanorods coated probes using a hydrothermal process and one of them was further coated with a urease layer on the ZnO nanorods. Using both the probes, a selectivity test was done and it has been investigated that the urease-coated probe has a 12 times higher shift in the peak wavelength than the ZnO nanorods coated probe. Afterward, using both the enzymatic and nonenzymatic probes, the peak wavelength shift in both cases was measured. Sensitivity is actually the ratio of peak wavelength shift and the change in concentration. In this experiment, we examined that the sensitivity in the urease-coated fiber optic probe was 8 times higher than the ZnO nanorods coated probe. This might be due to that when urea present in milk comes in the contact urease present on fiber then ammonia is produced and the refractive index of ammonia is higher [4]. So the resonance condition satisfies at a higher wavelength and large shift in wavelength occurs as shown in table 1.

Figure and table

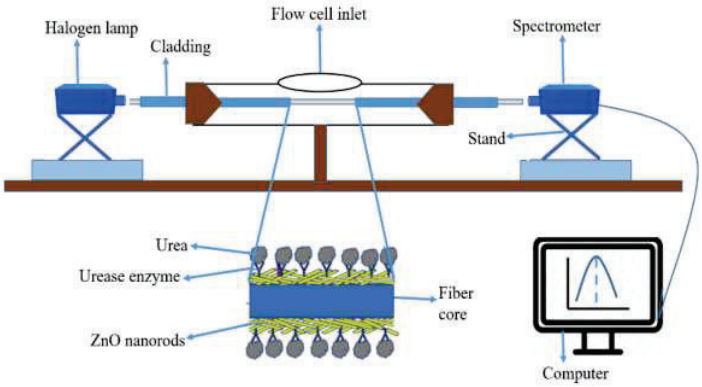

Fig. 1: ***Schematic diagram of the experimental setup used for urea detection.***

Table 1: Peak absorbance wavelength for ZnO nanorods coated probe and urease+ ZnO nanorods coated probe

Concentration (mM)	ZnO peak λ (nm)	Urease + ZnO peak λ (nm)
50	496.755	561.781
100	497.978	575.836
200	499.375	589.920
400	500.788	598.642
600	502.109	614.321
800	504.281	624.541

2. References

[1] Afzal Ali, M. S. Mahmood, Iftikhar Hussain, Masood Akhtar, "Adulteration and microbiological quality of milk (a review)," Pakistan Journal of Nutrition **10**, 1195-1202 (2011).
[2] Tomer Noyhouzer, Ron Kohen, Daniel Mandler, "A new approach for measuring the redox state and redox capacity in milk," Analytical Methods **1**, 93-99 (2009).
[3] Charlotte Neumann, Diane M. Harris, Lisa M. Rogers, "Contribution of animal source foods in improving diet quality and function in children in the developing world" Nutrition research **22**, 193-220 (2002).
[4] Syed M. Usman Ali, Zafar Hussain Ibupoto, Salah Salman, Omer Nur, Magnus Willander, Bengt Danielsson, "Selective determination of urea using urease immobilized on ZnO nanowires," Sensors and Actuators B: Chemical **160**, 637-643 (2011).

Comparative study: Relativistic Self-Focusing of Dark Hollow Gaussian beam in plasmas with different ramp density profiles

Subhajit Bhaskar[(a)], Hitendra K. Malik[(b)]

PWAPA Laboratory, Department of Physics, IIT Delhi, New Delhi-110016, India
[(a)]subhajit5995bhaskar@gmail.com
[(b)]hkmalik@physics.iitd.ac.in

Abstract: In this paper, we have performed a comparative investigation of the self-focusing phenomenon of Dark Hollow-Gaussian laser in an underdense cold plasma of different ramp density profiles. We have adopted the well-known WKB method to obtain the solution of the wave equation and then used the paraxial approximation in terms of the position of maximum intensity of the beam. We further observed the self-focusing for two distinct orders of the HG beam.

Keywords: Dark Hollow Gaussian beam, Relativistic and Ponderomotive nonlinearities, self-focusing, Density ramp

1. Introduction

The introduction of chirped pulse amplification (CPA) technique has led to rapid developments in ultrafast and ultra-intense laser technologies. The interaction of this high-intensity laser with plasmas has been the center of attraction for many researchers because of its applications in inertial confinement, particle acceleration, harmonic generation, etc. [1,2] Recently, the self-focusing phenomenon of the laser in plasma has proved its importance in producing ultraintense and divergenceless beam. Researchers have investigated the self-focusing phenomenon in an underdense plasma with relativistic and ponderomotive nonlinearities.[3,4] Though the literature was mainly focused on the propagation properties of Gaussian laser, there are few articles on vortex beams [5] and Dark Hollow-Gaussian beam (DHGB) [6,7] because of their applications in particle trapping and acceleration. Chaitanya, et al. have demonstrated their scheme of nonlinear generation of the HG beam [8]. As per our knowledge, there is no investigation on the self-focusing of HG laser beam in inhomogeneous plasmas. In this article, we have done a comparative study of the propagation properties and compression of the hollow Gaussian beam, $\vec{E} = E_0\,(r^2/2r_0^2)^l\ \exp(-r^2/r_0^2)\ exp(-i(\omega t - kz))\ (\hat{x} + i\,\hat{y})$ where l is the order of the beam, in an underdense and collision-less plasma under different ramp density profiles: (i) $n/n_0 = 1$ (homogeneous), (ii) $n/n_0 = \exp(\xi/d)$, (iii) $n/n_0 = \tan(\xi/d)$ and (iv) $n/n_0 = \exp(-(\xi - d/2)^2/d^2)$; where $\xi = z/R_d$ $(R_d = \text{Rayleigh length})$ is the normalized distance of propagation, and d is a dimensionless parameter which is adjustable.

2. Theory and Discussions

To study the propagation properties, we have considered the beam to be circularly polarized and is propagating in the Z-direction. The wave equation reads as $\nabla^2\vec{E} + \frac{\omega^2}{c^2}\epsilon\,\vec{\mathrm{E}} = 0$, where $\epsilon = 1 - \omega_{p0}^2(z)/\gamma\omega^2$ is the dielectric constant and $\gamma = (1 + a^2)^{\frac{1}{2}}$ is the relativistic factor with $a = e|\vec{E}|/m\omega c$ as normalized field amplitude.

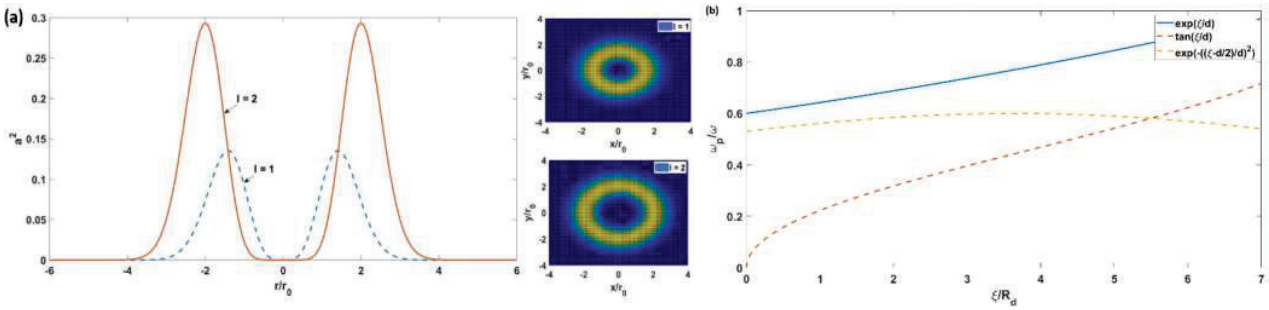

Fig. 1: (a) *The transverse profile of the normalized intensity of HG beam of order* $l = 1$ *and 2,* ***(b)*** *Ramp density profile for* $\omega_{p0}/\omega = 0.6$ *and* $d = 7.3$.

For, relativistic and ponderomotive nonlinearities the modified plasma density can be written as $n_e = n_0(z)\left[1 + \frac{c^2}{\omega_{p0}^2}(\nabla^2\gamma - (\nabla\gamma)^2/\gamma)\right]$. To solve the wave equation, we have adopted the WKB approximation method and obtained

$$2ik\frac{\partial A}{\partial z} = \nabla^2 A + \frac{\omega^2}{c^2}(\epsilon - \epsilon_0) \tag{1}$$

We considered the following ansatz: $$E(r,z)^2 = \left(\frac{E_0}{f(z)}\right)^2 \left(\frac{r^2}{2r_0^2 f(z)^2}\right)^{2l} \exp\left(-\frac{r^2}{r_0^2 f(z)^2}\right) \tag{2}$$

As, the intensity is maximum at $r = r_0 f\sqrt{2l}$, we can write $a^2 = \left(\frac{a_0}{2^l f}\right)^2 \left(\eta + \sqrt{2l}\right)^{4l} \exp\left(-\left(\eta + \sqrt{2l}\right)^2\right)$

where, $\eta = r/r_0 f - \sqrt{2l}$. In terms of the *eikonal* function $S(r,z)$, $A = A_0(r,z)\exp\left(-ikS(r,z)\right)$

where, $S = \frac{\left(\eta+\sqrt{2l}\right)^2}{2} r_0^2 f \frac{df}{dz} + \phi(z)$. Substituting this in eq.(2) we obtain the real and imaginary parts as

$$2\frac{\partial S}{\partial z} - 2\frac{\left(\eta+\sqrt{2l}\right)}{f}\frac{df}{dz}\frac{\partial S}{\partial \eta} + \frac{1}{r_0^2 f^2}\left(\frac{\partial S}{\partial \eta}\right)^2 = \frac{1}{k^2 A_0 r_0^2 f^2}\left(\frac{\partial^2 A_0}{\partial \eta^2} + \frac{1}{\eta+\sqrt{2l}}\frac{\partial A_0}{\partial \eta}\right) - \eta^2 \frac{\omega^2}{k^2 c^2}\epsilon_2 \tag{3}$$

$$\frac{\partial A_0^2}{\partial z} - \frac{\eta+\sqrt{2l}}{f}\frac{df}{dz}\frac{\partial A_0^2}{\partial \eta} + \frac{A_0^2}{r_0^2 f^2}\left(\frac{\partial^2 S}{\partial \eta^2} + \frac{1}{\eta+\sqrt{2l}}\frac{\partial S}{\partial \eta}\right) + \frac{1}{r_0^2 f^2}\frac{\partial A_0^2}{\partial \eta}\frac{\partial S}{\partial \eta} = 0 \tag{4}$$

The dielectric constant is written as, $\epsilon = \epsilon_0 - \eta^2\epsilon_2$. Using the relation of S in eq.(5) we obtain

$$\epsilon_0 f \frac{d^2 f}{d\xi^2} = \frac{4}{f^2} - \left(\frac{\omega^2 r_0^2}{c^2}\right)\epsilon_2 \tag{5}$$

$$\epsilon_0(z) = 1 - \frac{\omega_{p0}^2(z)/\omega^2}{\gamma_0} + \frac{c^2}{\omega^2 r_0^2 f^2}\frac{2a_{0l}^2/f^2}{\gamma_0^2},\ \epsilon_2 = \frac{\omega_{p0}^2(z)}{\omega^2}\frac{a_{0l}^2/f^2}{\gamma_0^3}\left[1 + \frac{c^2}{\omega_{p0}^2(z) r_0^2 f^2}\frac{12}{\gamma_0}\right],\ \gamma_0 = (1 + a_{0l}^2/f^2),\ a_{0l}^2 = a_0^2\, l^{2l}\exp(-2l).$$

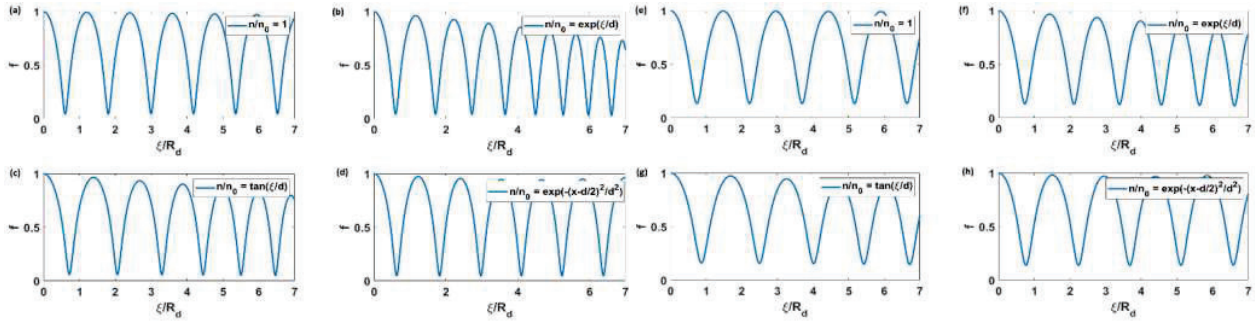

Fig. 2: *Variation of normalized beam width with propagation distance for four different background density profiles: (a),(e) homogeneous, (b),(f) exponential, (c),(g) tangential and (d),(h) Gaussian; and two different orders of the Hollow Gaussian beam:* $l = 1$ *for (a), (b),(c) & (d), and* $l = 2$ *for (e), (f), (g) and (h). Given:* $a_0^2 = 1, \frac{\omega_{p0}}{\omega} = 0.6, \frac{r_0\omega}{c} = 5, d = 7.3$.

Fig. 2 shows the self-focusing of Hollow Gaussian laser beam in the plasma medium for four distinct background density distributions and two different orders of the beam $l = 1$ and 2. It is clear that the self-focusing of the beam in a plasma with homogeneous and Gaussian ramp density profile are similar, and that in the plasmas of exponential and tangential ramp density profiles are more effective. We can see more compression of the beam in case of exponential density background than of tangential density background. On the other hand, the self-focusing of HG beam becomes less efficient for higher orders.

3. References

[1] Malik, Hitendra K. *Laser-Matter Interaction for Radiation and Energy*. CRC Press, 2021.

[2] Malik, Hitendra K., and Lalita Devi. "Relativistic self focusing and frequency shift of super-Gaussian laser beam in plasma." *Results in Physics* 17 (2020): 103070.

[3] Purohit, Gunjan, Ramesh Kumar Sharma, and Pradeep Kothiyal. "Relativistic-ponderomotive effect on the self-focusing of a high-intensity cosh-Gaussian laser beam in plasma: higher-order paraxial regime." *Journal of Optics* (2022): 1-9.

[4] Kovalev, V. F., and V. Yu Bychenkov. "Analytic theory of relativistic self-focusing for a Gaussian light beam entering a plasma: Renormalization-group approach." *Physical Review E* 99, no. 4 (2019): 043201.

[5] Dwivedi, M., Dhawan, R., Punia, S., & Malik, H. K. (2019, August). Relativistic self-focusing of Laguerre-Gaussian beam in an underdense plasma. In *AIP Conference Proceedings* (Vol. 2136, No. 1, p. 060006). AIP Publishing LLC.

[6] MIshra, Shikha, and Sanjay Kumar Mishra. "Focusing of dark hollow Gaussian electromagnetic beams in a plasma with relativistic-ponderomotive regime." *Progress In Electromagnetics Research B* 16 (2009): 291-309.

[7] Malik, Lohit. "Dark hollow lasers may be better candidates for holography." *Optics & Laser Technology* 132 (2020): 106485.

[8] Chaitanya, N. Apurv, M. V. Jabir, Jagannath Banerji, and Goutam Kumar Samanta. "Hollow Gaussian beam generation through nonlinear interaction of photons with orbital angular momentum." *Scientific Reports* 6, no. 1 (2016): 1-6.

Relaxation Oscillation Suppression for a QCW TDFL Using Optical Feedback Amplifier Design

Vincent Akash Gomes[1,2,*], Sourav Das Chowdhury[1], Sajib Chowdhury[1,2], Shubhranil Maity[1,3] Atasi Pal[1,2]

1 CSIR-Central Glass & Ceramics Research Institute, Kolkata, 700032
2 Academy of Scientific & Innovative Research (AcSIR), Ghaziabad, Uttar Pradesh 201002
3 Department of Physics, Jadavpur University, Jadavpur, Kolkata 700032
**Corresponding Author: gomesvincent12@gmail.com*

Abstract: A thulium-doped fiber laser (TDFL) in all-fiber master oscillator power amplifier (MOPA) configuration operating in quasi-continuous wave (QCW) with suppressed relaxation oscillation peak at 1940 nm has been designed and characterized. A wavelength matched optical feedback mechanism has been adopted by using a low reflective fiber Bragg grating in the power amplifier to achieve the reduction of relaxation oscillation.
Keywords: Thulium Fiber Laser, Quasi-CW, Relaxation Oscillation, Fiber Laser, MOPA, Optical feedback.

1. Introduction

Operating wavelength in the range of 1900-2050 nm for thulium doped fiber laser (TDFL) finds its applications in remote sensing, atmospheric sensing, and tissue surgery [1]. TDFL at 1940 nm has proved its superiority as a surgical laser over clinical Ho:YAG laser at 2090 nm due to four times absorption coefficient in water [2]. In surgical laser-based applications, a certain high peak power is desirable [2]. To achieve that for quasi-continuous mode (QCW), amplification is an effective approach. However, major challenges in amplification are: inadvertent amplification of relaxation oscillation (RO) peak, added amplified spontaneous emission (ASE) and noise along with the master oscillator (MO) signal. Due to Shorter pulse width of RO peaks, it gains significant peak power after amplification which often can cause damage to the optical components. To reduce RO, Yin et al. in [3] proposed a method in which the rise time of the pump power is increased to reduce RO generation. In [4] a numerical simulation on bias-pump gain switched fiber laser is presented for suppressing chaotic RO generation in a gain switched fiber laser which allowed the use of higher power and longer duration of pump pulse. The presented work is on the design of an all-fiber-based master oscillator power amplifier (MOPA) incorporating a wavelength matched optical feedback (WMOF) to reduce RO generation in a QCW TDFL at 1940 nm.

2. Experimental Setup

The MO used was a in house designed TDFL system at 1940 nm with an output of 10 W under 793 nm pumping. The MO operated in continuous wave (CW) mode or in QCW modes by modulation of pump diodes. In conventional MOPA architecture, output of MO was spliced to isolator (ISO), which was spliced to signal port of a (6+1):1 pump signal combiner (PSC). Six pump laser diodes (PLD) of 15 W at 793 nm were used. Output of PSC was spliced to a 2 m long 10/130 µm N.A 0.15 double clad thulium doped (DC-TDF) fiber, whose length was optimized for good gain without intrinsic lasing in range of 1950-2100 nm, in the power amplifier (PA) and followed by cladding mode stripper (CMS), shown in fig.1(a). In modified design, a WMOF was realized by adding a low reflective (5% at 1940 nm, $\Delta\lambda$ at 3dB=0.5 nm) fiber Bragg grating (LR-FBG) after CMS of the PA while ISO was excluded, shown in fig.1(b). This supported the WMOF coupling between PA and MO, leaving remaining architecture same as conventional MOPA.

3. Results and Discussions

For QCW mode of the MO, the RO peaks appear at the starting edge of every pulse in the pulse train due to the occurrence of transient non-equilibrium condition of population inversion in the laser resonator cavity of MO just after the threshold of the resonator is crossed [5]. In case of the MOPA architecture, these RO peaks originating in the MO are amplified along with the pulses. For our experimental setup we measured the RO pulse width in the range of

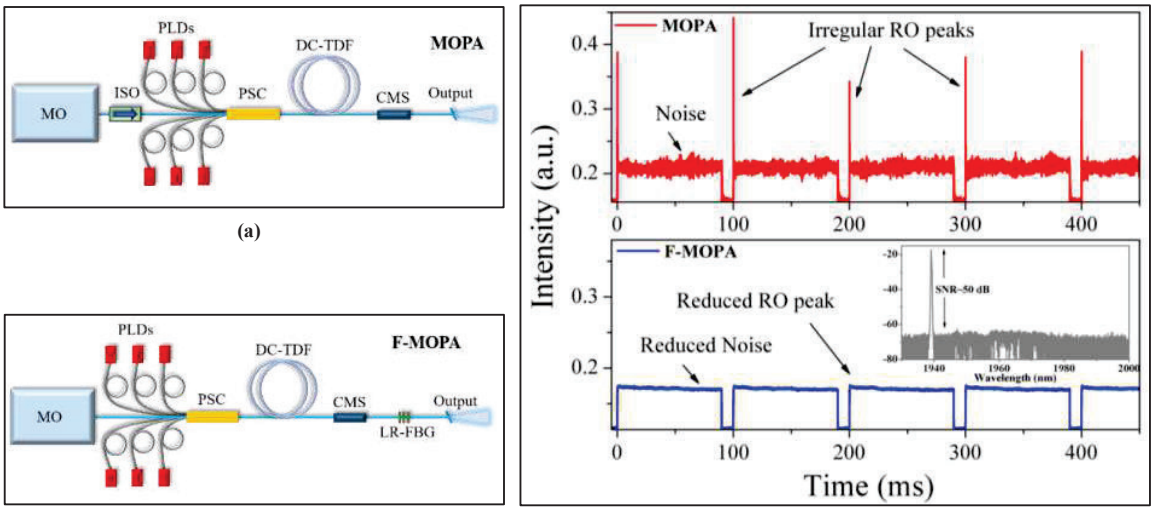

Fig. 1: (a) MOPA; (b) F-MOPA setup diagram; (c) Temporal comparison of MOPA & F-MOPA, inset: Spectral plot of F-MOPA

250-400 ns after MOPA. Such short duration with irregular amplitude can gain sudden instantaneous high peak power after amplification which can cause damage to the laser system. In our feedback MOPA (F-MOPA) architecture, the WMOF provided by LR-FBG in conjunction with the LR-FBG of the MO creates a weak CW signal in the PA, since PA was being continuously pumped. This CW light interacts with the MO due to the absence of the ISO. Interaction and reabsorption of the CW light in the MO gain fiber in the absence of pump light for QCW mode leads to generation of partial CW power in the MO. This eliminates the transient non-equilibrium condition of population inversion when transitioning from complete OFF to ON conditions in QCW mode, resulting in complete suppression of the RO in the MO itself. Partial CW condition is maintained in the F-MOPA system because of multi-cavity formation between the FBGs of MO and the LR-FBG of the PA. The reflectivity of the LR-FBG was selected at 5% to help extract majority of the power from the F-MOPA cavity and to prevent the CW power from overwhelming the intended QCW nature of the signal light.

As shown in fig.1(c), the RO peaks are completely suppressed when operated in 90% duty cycle mode of operation for pulse width of 90 ms in the F-MOPA in comparison to conventional MOPA. F-MOPA showed lower gain in comparison to conventional MOPA with 6 dB and 6.5 dB at 90% duty cycle respectively. Also, at a lower duty cycle of 20% F-MOPA showed a lower gain of 11.2 dB over 11.6 dB for MOPA with similar pump power. This reduction in gain is due to the fact that partial output signal power is being used for the optical feedback in the F-MOPA system. Another benefit of the new amplifier design proved to be reduced temporal intensity noise in the output of the F-MOPA system as shown in fig.1(c). Spectral plot of F-MOPA operating at 1940 nm is shown in inset of fig.1(c).

4. Conclusion

In conclusion, we present an all-fiber based modified MOPA for TDFL which experimentally demonstrated complete elimination of RO peaks in QCW mode of operation. Elimination of the RO peaks were achieved utilizing optical feedback by using a LR-FBG in the PA, which led to evolution of a CW power in the F-MOPA. This CW power eliminated the transition from complete OFF to complete ON condition which led to elimination of RO.

5. References

[1] Gregory D. Goodno, Lewis D. Book, and Joshua E. Rothenberg, "Low-phase-noise, single-frequency, single-mode 608 W thulium fiber amplifier," Opt. Lett. 34, 1204-1206 (2009)
[2] Taratkin, M., Kovalenko, A., Laukhtina, E. et al. "Ex vivo study of Ho:YAG and thulium fiber lasers for soft tissue surgery: which laser for which case?," Lasers Med Sci 37, 149–154 (2022).
[3] Jingchan Yin, Xiaosheng Xiao and Changxi Yang, "Dynamics and suppression of relaxation oscillation caused by stimulated Brillouin scattering in optical fiber," 2009 14th OptoElectronics and Communications Conference, 2009, pp. 1-2
[4 Fuyong Wang, "Stable pulse generation in a bias-pumped gain-switched fiber laser," J. Opt. Soc. Am. B 35, 231-236 (2018)
[5] Anthony E. Siegman, *LASERS* (University Science Books Sausalito, California 1986), Chap. 25

The QOM Toolbox – an object-oriented Python framework for cavity optomechanical systems

Sampreet Kalita and Amarendra Kumar Sarma
Department of Physics, Indian Institute of Technology Guwahati, Guwahati – 781039, India
Author e-mail address: sampreet@iitg.ac.in

Abstract: We present an open-source Python toolbox to simulate cavity optomechanical systems. Using an object-oriented programming paradigm, our toolbox allows its users to interface unique system-objects with its built-in methods, which analyze both stationary and dynamical properties. Its solvers are written to validate system stability, calculate classical and quantum properties, and study classical nonlinear dynamics and linearized quantum dynamics. Written in a modular architecture, our toolbox is highly scalable and can also be extended to simulate many-body systems. Additional benefits of the toolbox include automated loopers of system parameters, journal-inspired plotters for simulated results, and a graphical user interface.

Keywords: numerical library, linearized quantum dynamics, nonlinear classical dynamics, quantum optomechanics, toolbox

1. Introduction and Features

Cavity optomechanical systems [1] provide a versatile platform for the study of classical and quantum dynamics in the macroscopic domain. In the past decade, such systems have been extensively used to perform ultra-sensitive measurements by generation of nonclassical states, transduce information between different degrees of freedom through hybrid architectures, build novel schemes for communication and computation using quantum properties, etc. Typically, they can be modelled as a laser-driven cavity with a moveable end-mirror. The radiation pressure force exerted by the intracavity photons on the mechanically compliant mirror displaces the mirror and changes the cavity resonance frequency. This results in an optomechanical coupling which is inherently nonlinear and can be described by the interaction Hamiltonian $H_{int} = -\hbar g_0 a^\dagger a(b^\dagger + b)$, where a and b are the annihilation operators of the optical and mechanical modes and g_0 denotes the strength of optomechanical coupling. However, when the cavity is driven by a strong coherent field in the weak-coupling regime, the system can be safely expressed as a sum of classical amplitudes and quantum fluctuations around them such that the quantum dynamics can be approximated by a linearized description [2]. This approximation is utilized in most studies to estimate quantum signatures like squeezing, entanglement and synchronization, or to explore new measures to quantify quantum correlations. The calculation of such numerical measures relies on the zero-mean, delta-correlated nature of thermal fluctuations, which in turn results in deterministic second-order moments of the quantum fluctuation operators. An exact simulation of the quantum dynamics should otherwise take into account the stochastic nature of these quantum noises. To this end, Monte-Carlo methods are used to simulate single quantum trajectories, and then averaged over multiple runs [3].

The most popular framework used to simulate open quantum systems such as quantum optomechanical (QOM) systems is QuTiP. This open-source Python toolbox implements both the Lindblad master equation approach and Monte-Carlo methods. Other notable libraries featuring simulation of open quantum systems include Strawberry Fields (Python), QuantumOptics (Julia), scQubits (Python), OpenQuantumTools (Julia) and the Quantum Optics Toolbox (MATLAB). However, most numerical packages do not directly support linearized QOM systems, nor the calculation of nonlinear dynamical properties for many-body QOM systems in the semi-classical limit. We therefore present a generalized toolbox which incorporates (i) solvers for stationary and dynamical behaviour with estimation of multi-stability [1, 2] and dynamical stability [4], (ii) methods to detect nonlinear behaviour like fixed-point and limit-cycle oscillations [5], and (iii) methods to obtain classical and quantum signatures like synchronization [6] and entanglement [7] using both linearization approximations and stochastic approaches [3]. Together with these, our toolbox also features (i) automatable loopers that sweep through select system variables and output user-defined properties, (ii) highly configurable plotters that are templated for figures in academic journals, and (iii) a graphical user interface (GUI) to loop the variables, solve for measures and plot the results with a simple set of clicks. Backed by numerical libraries like NumPy and SciPy and featuring highly customizable visualizations offered by Matplotlib and Seaborn, the QOM toolbox is aimed as an alternative to writing explicit code and executing repetitive blocks.

2. Demonstration and Prospects

By simply defining methods such as the rates at which the classical modes change, the drift matrix of the quantum fluctuations and the initial values of the classical modes and correlations of the fluctuation quadratures as well as input noises, one can calculate a variety of classical and quantum properties using the toolbox's built-in methods. Fig. 1 demonstrates some quantum and classical properties obtained using its loopers, solvers and plotters for different systems. Our toolbox can also be used to study quantum electromechanical systems, quantum magnomechanical systems, Bose-Einstein condensate systems or other hybrid systems that can be described by a linearized Hamiltonian. Verified with more than a dozen published papers, the QOM toolbox provides a flexible set of resources to simulate a wide range of systems. In the future, we plan to integrate the toolbox's numerical backend to a web-based interface.

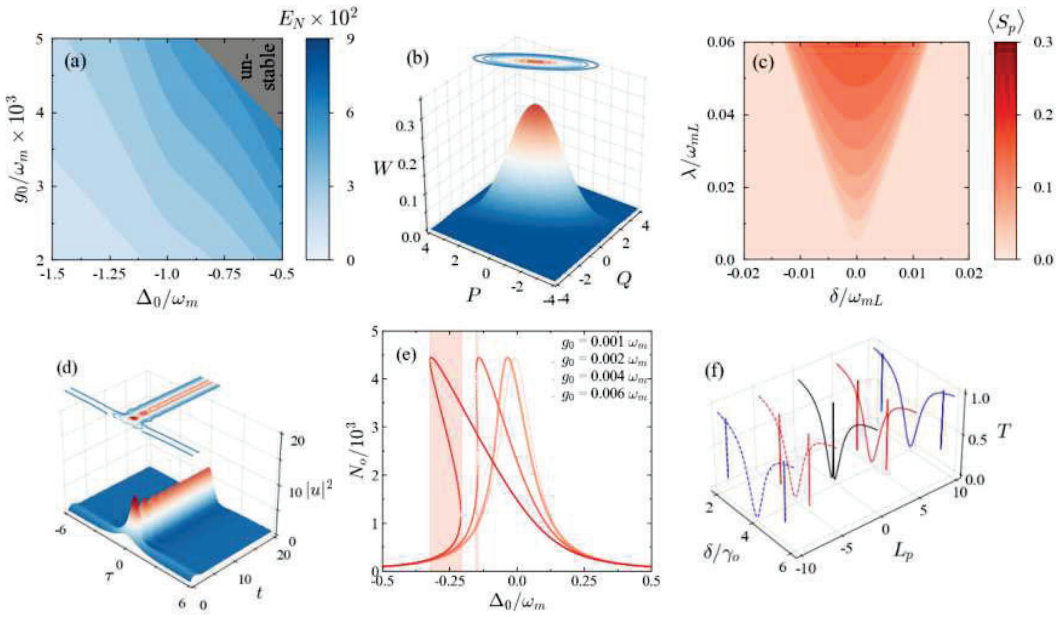

Fig. 1: (a) Stationary quantum entanglement (E_N) between the optical and mechanical modes of an end-mirror QOM system with variation in laser detuning (Δ_0) and optomechanical strength (g_0) normalized by the mechanical frequency (ω_m). The values are obtained using the `get_measure_stationary` method after stability-analysis using the `get_optical_stability_zones` method. (b) Wigner distribution (W) of the mechanical mode of a membrane-in-the-middle optomechanical cavity in the phase space of its fluctuation quadratures (Q, P) obtained using the `get_wigner_single_mode` method. (c) Averaged quantum phase synchronization ($\langle S_p \rangle$) between the mechanical modes of two optically coupled cavities with variation in coupling strength (λ) and mechanical frequency difference (δ) normalized by the frequency of the first mechanical oscillator (ω_{mL}). Here, the `get_measure_average` method is used. (d) Intensity profile ($|u|^2$) of a cavity soliton for fast (τ) and slow (t) times obtained with the `get_lle_dynamics` method. (e) Intracavity photon number (N_o) in an end-mirror QOM system with variation in the laser detuning for different values of optomechanical strength obtained using the `get_mean_optical_occupancies` method. (f) Optomechanically induced transparency (T) in a ring-BEC analogue of QOM system for different values of winding number (L_p) and probe detuning (δ) normalized by the optical decay (γ_o). The values are obtained by looping a user-defined function. All plots are obtained by using the `MPLPlotter` module of the toolbox.

[1] M. Aspelmeyer, T. J. Kippenberg and F. Marquardt, "Cavity optomechanics," Rev. Mod. Phys. **86,** 1391 (2014).
[2] W. P. Bowen and G. J. Milburn, *Quantum optomechanics* (Taylor & Francis, 1995), Chap. 2.
[3] F. E. van Dorsselaer and G. Nienhuis, "Quantum trajectories," J. Opt. B: Quantum Semiclass. Opt. **2**, R25 (2000).
[4] E. X. DeJesus and C. Kaufman, "Routh-Hurwitz criterion in the examination of eigenvalues of a system of nonlinear ordinary differential equations," Phys. Rev. A **35**, 5288 (1987).
[5] T. F. Roque, F. Marquardt and O. M. Yevtushenko, "Nonlinear dynamics of weakly dissipative optomechanical systems," New J. Phys. **22**, 013049 (2020).
[6] D. Vitali *et al.*, "Optomechanical entanglement between a moveable mirror and a cavity field," Phys. Rev. Lett. **98**, 030405 (2007).
[7] A. Mari *et al.*, "Measures of quantum synchronization in continuous variable systems," Phys. Rev. Lett. **111**, 103605 (2013).

Problem and Solution for holography

Surya Kumar Gautam[1], Dinesh N Naik[2]
[1]*National Physical Laboratory, (CSIR-NPL)*
New Delhi, Delhi 110012, India
[2]*Applied and Adaptive Optics Laboratory, Department of Physics, Indian Institute of Space Science and Technology (IIST), Trivandrum, Kerala 695547, India*
suryagautam89@gmail.com

Abstract: In this paper, we first present the problems associated with the phase shifting and off-axis holography techniques. Secondly, we proposed a method for solving these problems using slight off-axis holography geometry. For the validation, experimental results are provided.
Keywords: Holography, Edge point referencing, 3D complex object reconstruction, Common path, phase shifting.

1. Introduction

For 3-dimensional imaging, amplitude and phase both the parts of a complex object need to be recorded. Since camera is only sensitive to amplitude part of the field, phase part of the field is lost while imaging. Therefore, direct reconstruction of the 3D object from the amplitude information alone is difficult. In order to record both the parts a holography techniques is used. In the holography, an interference pattern or a hologram H is formed by overlapping object O and reference R fields with one another. Thus the hologram equation can be written as follow $H = |O|^2 + |R|^2 + OR^* + O^*R$ which contains four terms. From the four terms, our aim is to obtain the 3rd term which contains the object information. In order to remove other terms from the hologram, phase shifting holography (PSH) [1] and off-axis holography [2] techniques are used. In PSH multiple holograms $H(0), H\left(\frac{\pi}{2}\right), H(\pi), H(\frac{3\pi}{2})$ of a 3D object are recorded by varying the phase of the reference field in the following steps $0, \frac{\pi}{2}, \pi, \frac{3\pi}{2}$ respectively. From the recorded holograms, object information can then be solved by numerical processing. The main problems in this method are as follows 1) object should remain stable during the multiple recording, 2) if the phase of the reference field is not varying exactly as mentioned before, quality of reconstruction is degraded due to the presence of the other terms, 3) Additionally, due to the external vibration, reference and object field can vibrate independently from each other which results in introduction of extra phase and 4) phase shifting element is very costly. Whereas, in off-axis holography, object information can be obtained in a single shot; however, on the cost of low resolution. Therefore, in this paper we are proposing a common path slight off-axis geometry for recording the holograms by changing the intensity of the reference beam. By incorporating it, number of recordings can be reduced, and due to the common path setup external vibration effect can be reduced and since slight off-axis geometry is employed, resolution will be two-fold better compared to off-axis holography and costly element such as phase shifter can be avoided.

2. Experimental setup

To design a compact robust common path, slight off-axis geometry setup several optical components are arranged as shown in figure 1 (a). Setup consists of a coherent and collimated He-Ne laser, which emits light at a wavelength $\lambda = 632.8\, nm$ and a Sagnac interferometer (SI). SI consists of a polarizing beam splitter (PBS), two mirrors M1, M2 and two lenses L1, L2 each of them having focal length equal to $25\, cm$. In the setup, laser beam is first divided by the PBS into two beams: transmitted (horizontally polarized) and reflected (vertically polarized), as delineated by dotted and solid lines, respectively. Lens L1 focuses the beams inside and outside the triangle part of the Sagnac, and lens L2 is placed such that focused point of transmitted beam is collimated, while the focused point of reflected beam is imaged or converged at the center of the collimated beam. Now to shift the focused point or spot from the center to the edge of the illumination, the position of mirror M2 is shifted slightly along the direction perpendicular to its plane. The scattered fields resulting from the object illumination from the two orthogonally polarized beams interfere at the camera by placing a polarizer just before the camera.

3. Experimental results

According to the figures 1 (b-e) multiple holograms are recorded by varying the phase in steps $0, \frac{\pi}{2}, \pi, \frac{3\pi}{2}$ respectively, the reconstruction of amplitude and phase of the object are shown in figures 1 (f) and (g), respectively. In ideal case where phase of the reference field is varying exactly as mentioned before, in the reconstruction shown in figures 1 (f) and (g) only the portion located left side contained the object information should be present without the presence of the other terms. However, it is clear from the figures 1 (f) and (g) that a portion is still visible which is located at the right side containing the conjugate and inverted copy (twin copy) of the object, that confirmed the presence of the other terms. These terms are not completely removed from the reconstruction due to the error while phase shifting or due to the vibration. Since we are using the slight off-axis geometry, left and right portions are still separated from one another. Otherwise in purely in-line holography this effect will be severe where object and twin copy of the object overlapped completely with one another. Therefore, one should opt slight off-axis geometry.

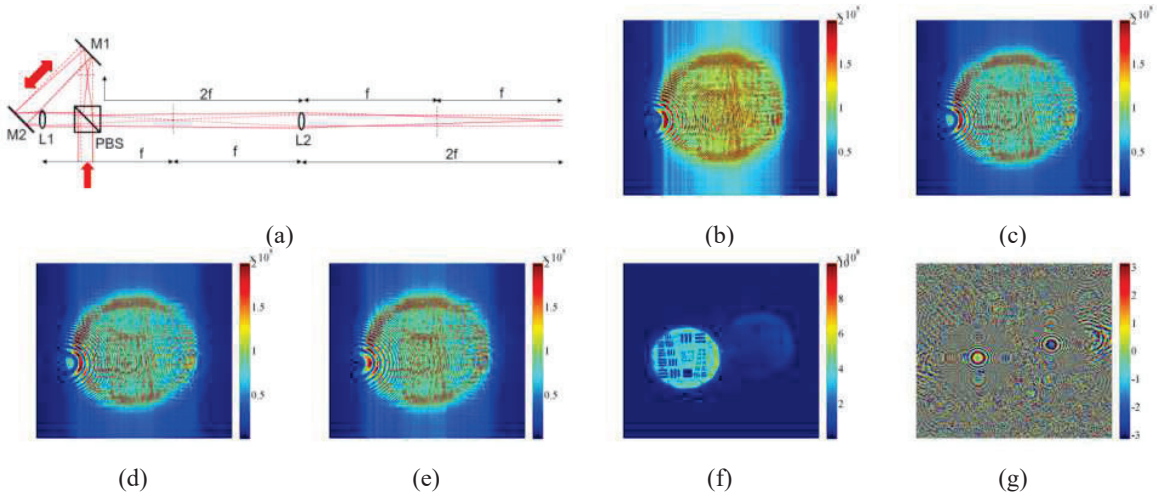

Fig. 1 (a) common path setup for recoding holograms, (b-e) holograms recorded at the phase steps of $0, \frac{\pi}{2}, \pi, \frac{3\pi}{2}$ respectively, (f) and (g) amplitude and phase of the complex object.

On the other hand, recording the holograms by changing the intensity of the reference beam is much easy which can be performed by placing a HWP and a polarizer before and after the Sagnac [3]. In this case only two holograms need to be recorded as shown in figures 2 (a) and (b). And the reconstruction of amplitude and phase of the object are shown in the figures 2 (c) and (d).

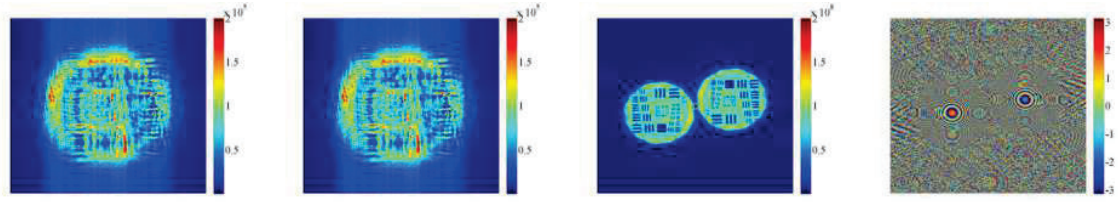

Fig.2 (a) and (b) Holograms recorded by varying the intensity of the reference beam, (c) and (d) amplitude and phase of the complex object.

4. References

[1] Ichirou Yamaguchi and Tong Zhang, "Phase-shifting digital holography," Opt. Lett. 22, 1268-1270 (1997).
[2] Emmett N. Leith and Juris Upatnieks, "Reconstructed Wavefronts and Communication Theory*," J. Opt. Soc. Am. 52, 1123-1130 (1962).
[3] Surya Kumar Gautam, R. Kumar Singh, C. S. Narayanamurthy, and D. N. Naik, "Reconstruction of complex-object using edge point referencing," J. Opt. 22, 055601 (2020).

Experimental Investigations in Cascaded Fiber System for Broadband Continuum Generation

Rudranil Chowdhury*,#, Mohd Rehan#, and Shailendra K. Varshney
FONQP group, Advance Photonics Lab, E & ECE Department, IIT Kharagpur, West Bengal-721302, India
**neel.ch05@iitkgp.ac.in*
#Authors contributed equally

Abstract: We present a cascaded fiber system (graded-index fiber and single-mode SMF28e fiber) which is pumped with 0.7ns Nd:YAG laser at 1064 nm wavelength. The cascaded fiber system require low input pump power to generate broadband continuum due to stimulated Raman scattering and intermodal four wave mixing processes. The proposed combination of fibers can find various applications, like optical coherence tomography.
Keywords: Cascaded Fiber System, Broadband Continuum Generation, Stimulated Raman scattering, Intermodal four wave mixing.

1. Introduction

The nonlinearity of the medium plays an important key role when it comes to the generation of new frequencies. The broadband continuum generation (BCG) is a collaboration of multiple nonlinear effects for example intermodal four wave mixing (IMFWM) and cascaded Raman scattering (CRS) where energy from the pump wavelength is transported to lower or higher wavelengths in the form of anti-stokes and stokes beam respectively [1, 2]. BCG gained popularity in the recent years for the applications in optical coherence tomography, optical frequency metrology, and gas sensing [3]. In this work, we have cascaded a fiber of larger effective mode area (graded-index fiber (GRIN)) to the smaller effective mode area one (single mode fiber (SMF28e)) to enhance the nonlinearity which inversely depends on the effective mode area of the medium [4]. We utilize the enhanced nonlinearity to generate the broadband continuum ranging from 600 nm – 1700 nm wavelengths at low average power (~3 mW).

2. Experimental Set up

The schematic of experimental set-up for the nonlinearity enhancement and BCG in a cascaded fiber system is shown in Fig. 1. Here, the passively mode-locked micro-chip Q-switched Nd:YAG laser (Teem Photonics Micro-chip series) with single-mode output, 770 ps duration, and 23 kHz repetition rate at 1064 nm wavelength is injected in the cascaded fiber system. The pump laser is routed using mirrors and is focused using 20X microscopic objective on the input end of 50 m long GRIN-MMF which is spliced with 50 m section of SMF28e. The spectral evolution is observed using optical spectrum analyzer (OSA) (Yokagawa, AQ6319) ranging from 600 nm to 1700 nm.

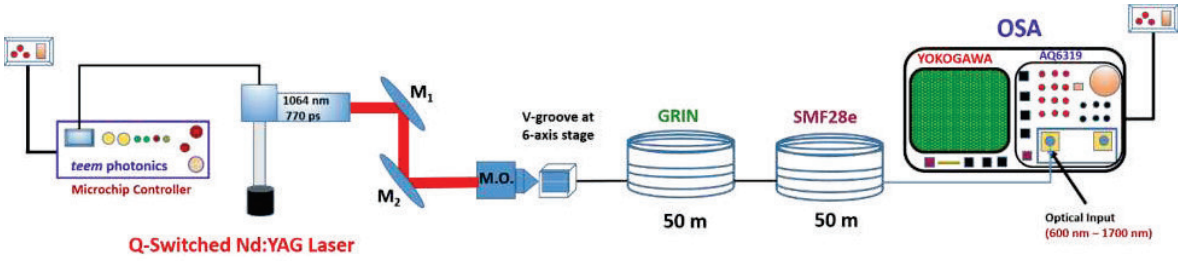

Fig. 1: Schematic of the experimental set-up for the nonlinearity enhancement and BCG in cascaded fiber system pumped at 1064 nm wavelength. Here, M_1, M_2: Silver Mirrors; M.O.: Microscopic Objective; GRIN: Graded-index fiber; SMF28e: Single mode fiber; OSA: Optical spectrum analyzer.

3. Result and discussion

The evolution of the spectral power with respect to wavelength in a proposed cascaded fiber system when coupled with the passively mode-locked micro-chip Q-switched Nd:YAG laser is shown in Fig. 2. The pump wavelength (λ_p) is 1064 nm, which is below the cutoff wavelength of both the fibers, facilitating multimode operation. We thus see prominent IMFWM peaks around 800 nm wavelength along with the prominent CRS on the right side of the pump, generating broadband continuum at the expense of a low average power of ~3 mW. Here, laser radiation travels from a large effective mode area (GRIN-MMF) to a smaller effective mode area (SMF28e), on doing so, nonlinearity is enhanced and hence generating new frequencies [4]. The increase in the number of stokes lines with gradual increase in average power which results in BCG, can be seen clearly.

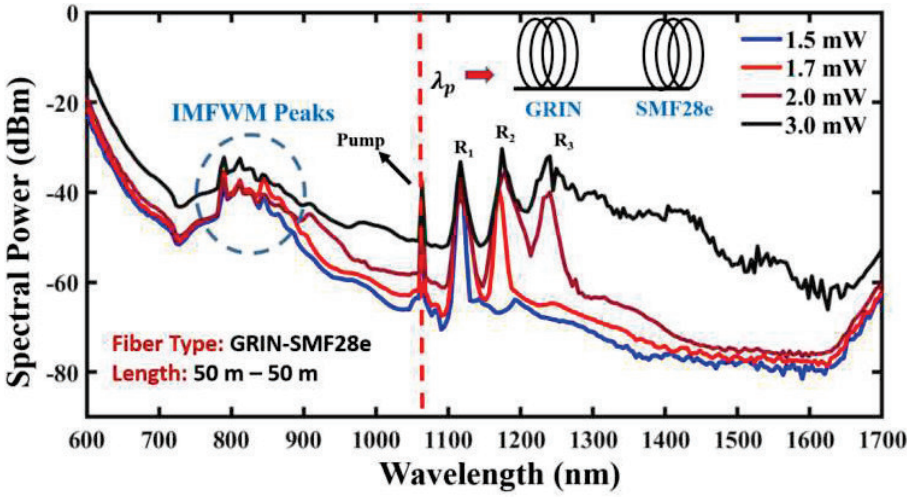

Fig. 2: Evolution of spectral power with respect to the wavelength in the proposed cascaded fiber system when coupled with the passively mode-locked micro-chip Q-switched Nd:YAG laser. R_1,R_2,R_3 are first,second and third Raman stoke respectively.

4. Conclusion

We experimentally demonstrated the nonlinearity enhancement in a cascaded fiber system and exploited it for the application of BCG mediated by CRS and IMFWM at low average power while pumping with passively Q-switched Nd: YAG at 1064 nm wavelength. The achieved broadband continuum can be useful in spectroscopy applications.

5. Acknowledgement

This work has been supported by the Department of Science and Technology (International Bilateral Cooperation Division) through an Indo-Korean project on “Development of Ultra-High Repetition Rate Soliton Light Source based on High Quality Optical Waveguide Resonator

6. References

[1] Mondal, Partha, Nitin Bhatia, Vishwatosh Mishra, Raktim Haldar, and Shailendra K. Varshney,"Cascaded Raman and intermodal four-wave mixing in conventional non-zero dispersion-shifted fiber for versatile ultra-broadband continuum generation" J. Light. Technol., **36,** 2351-2357(2018).

[2] A. Bendahmane, M. Conforti, O. Vanvincq, C. Mas Arabí, A. Mussot, and A. Kudlinski, "Origin of spontaneous wave mixing processes in multimode GRIN fibers," Opt. Express 29(19), 30822-30833 (2021).

[3] G. P. Agrawal, Nonlinear Fiber Optics, (Academic Press, Elsevier, 2013).

[4] Rehan, M., G. Kumar, V. Rastogi, D. A. Korobko, and A. A. Sysolyatin, "Compression of femtosecond pulses in a wide wavelength range using a large-mode-area tapered fiber" Laser Phy.,**29.2,**025104(2019).

Investigations on Thermal Sensitivity of PDMS Embedded FBG Sensor for Temperature Sensing Applications

Archana Thrikkaikuth Chalackal, Amal Chirayil Soman, Srijith Kanakambaran
Department of Electronics and Communication Engineering
Indian Institute of Information Technology, Design and Manufacturing, Kancheepuram
Chennai, Tamil-Nadu-600127, India
srijith@iiitdm.ac.in

Abstract: We present a comparative study of the temperature sensitivity of a Fiber Bragg Grating (FBG) embedded in a PDMS (Polydimethylsiloxane) block of dimensions 40 mm x10 mm x 5 mm through analytical calculation, simulations of thermal strain using COMSOL Multiphysics and temperature characterization experiments for a temperature range of 40 to 100°C. The sensitivity obtained are comparable with values 30.55 pm/°C, 31.2 pm/°C and 34.06 pm/°C respectively.
Keywords: FBG, Fiber Optic Sensors, temperature, thermal strain.

1. Motivation

Temperature sensing has numerous applications in industries, space application, agriculture, healthcare etc which demands high accuracy, sensitivity and ability to operate in harsh environments. For such applications, optical fiber based sensors are an attractive alternative to conventional sensors. Fiber Bragg Grating (FBG) sensors with the advantages of immunity to electromagnetic interference, compact structure and simple fabrication are suitable for temperature sensing but have low thermal sensitivity which can be improved using suitable host materials. Embedding FBG in PDMS improves temperature sensitivity due to the high thermal expansion coefficient of PDMS (300×10^{-6}/°C) and provides advantages of high thermal sensitivity, trouble-free fabrication, better durability and stability [1].

2. Background

FBG refers to periodic variations in the refractive index of the core of an optical fiber. When a broadband light is input to the FBG, a narrow band of wavelengths centered on Bragg wavelength (λ_B) is reflected, while all other wavelengths are transmitted. As shown in Equation (1), λ_B depends on effective refractive index (n_{eff}) and grating period (Λ).

$$\lambda_B = 2n_{eff}\Lambda \tag{1}$$

In the event of change in temperature and strain, n_{eff} and Λ changes causing a shift in the Bragg wavelength as shown in Equation (2):

$$\frac{\Delta\lambda_B}{\lambda_B} = (1 - P_e)\varepsilon + (\alpha + \zeta)\Delta T \tag{2}$$

where P_e is the photoelastic constant, ε is the strain induced, α is the thermal expansion coefficient, ζ is the thermo-optic coefficient and ΔT is the change in temperature.

3. Analysis and results

The variation in Bragg wavelength ($\Delta\lambda_B$) with temperature for a certain area of cross section A_p of the PDMS block is given by [2]:

$$\frac{\Delta\lambda_B}{\Delta T} = \lambda_B\left[\alpha_n + (1 - P_e)\left\{\alpha_f + (\alpha_{p-}\alpha_f)\frac{A_pE_p}{A_pE_p + A_fE_f}\right\}\right] \tag{3}$$

where λ_B is the Bragg wavelength of the embedded FBG, α_f and α_p are the thermal expansion coefficient of silica fiber (0.55×10^{-6}/°C) and PDMS (300×10^{-6}/°C) respectively, α_n is the thermo-optic coefficient of the silica fiber

(8.6×10^{-6}/°C), ΔT is the temperature variation, P_e (0.212) is the effective photoelastic coefficient, A_f is the area of cross section of the optical fiber and E_f (72 GPa) and E_p (870 kPa) are the Young's moduli of the fiber and PDMS respectively. The calculations were performed for the sample dimensions 40 mm x10 mm x 5 mm in the temperature range 40-100°C and the slope was found to be 30.55 pm/°C.

The thermal strains developed in the PDMS block were studied using COMSOL Multiphysics for temperature range of 40 to 100°C. The fiber (length 50 mm) is placed at depths 1.5, 2.5 and 3.5 mm. The model is shown in Fig 1(a).

(a) (b)

Fig. 1: (a) COMSOL model for PDMS embedded FBG (b) Bragg wavelength shift vs temperature

The bottom face of the PDMS block is assigned as fixed support and the probe is placed at the particular depth. The plot of $\Delta\lambda_B$ vs temperature is obtained using the curve fitting tool in MATLAB and is shown in Fig 1(b). The sensitivity is obtained as 27.08, 31.2 and 36.52 pm/°C for depths 1.5, 2.5 and 3.5 mm respectively. Due to the fixed support constraint at the base, strain at depth of 3.5 mm is higher than at 1.5 and 2.5 mm resulting in a higher value of sensitivity.

The experimental study is conducted for a PDMS block with fiber embedded at 2.5 mm depth prepared in-house using a suitable mould and following the process of mixing of reagents, dessication and curing in hot air oven at 100°C for 35 mins. The reflection spectrum of embedded FBG is shown in Fig 2(a). The temperature was varied from 40 to 100°C using a hot air oven and Bragg wavelength was monitored every 20 s using IMON 512 USB interrogator as shown in Fig 2(b). The wavelength shifts were plotted for five trials and is shown in Fig 2(c).

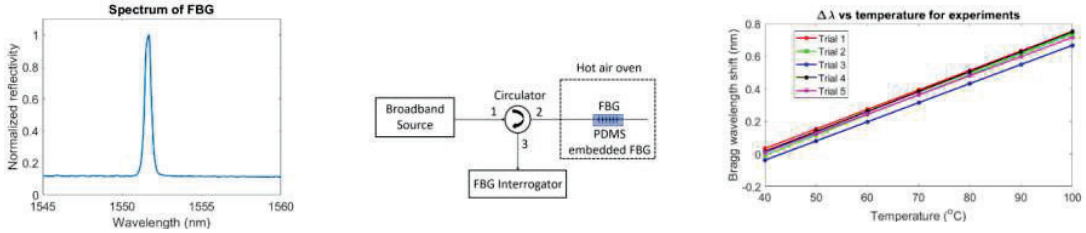

(a) (b) (c)

Fig. 2: (a) Spectrum of FBG (b) Setup for temperature characterization (c) Bragg wavelength shift vs temperature

The sensitivity obtained is 34.06±0.52 pm/°C which is in close agreement with those obtained from analytic and numerical studies.

4. Conclusions

The temperature sensitivity of a PDMS embedded FBG was investigated through analytical calculation, numerical simulations and experiments. The results are compared and are found to be in good agreement.

5. References

[1] C. Li, W. Yang, M. Wang, X. Yu, J. Fan, Y. Xiong, Y. Yang, and L. Li, "A review of coating materials used to improve the performance of optical fiber sensors," Sensors, vol. 20, no. 15, p. 4215, 2020

[2] C.-S. Park, K.-I. Joo, S.-W. Kang, and H.-R. Kim, "A pdms-coated optical fiber bragg grating sensor for enhancing temperature sensitivity," Journal of the Optical Society of Korea, vol. 15, no. 4, pp. 329–334, 2011

Low-loss $Ge_{1-x}Si_x$ alloy-based Rib Optical Waveguide for Sensing in Mid-Infrared Regime

Apoorv Sharma and Harshvardhan Kumar*

Department of Electronics and Communication Engineering, The LNM Institute of Information Technology, Jaipur 302031, Rajasthan, India

*harshvardhan.kumar@lnmiit.ac.in

Abstract: In mid-infrared (MIR) regime, group-IV photonics (GFP) is expected to provide significant advances in several areas including sensing, chip-scale spectroscopy, non-linear optics, and communications. In recent years, $Ge_{1-x}Si_x$ alloy has shown great potential for MIR applications and it can be used in the broadband spectral range from 2.48 to 12.4 µm. In this work, we propose a $Ge_{1-x}Si_x$ (x = 10%)-based novel rib optical waveguides for trace gas sensing at λ=4.5µm. Here, we optimize the rib waveguide structure based on theoretical models in order to achieve the minimum propagation loss. The proposed structure shows a propagation loss of 2.86 dB/cm and a confinement factor of 98.9% at λ=4.5µm. These results show that $Ge_{1-x}Si_x$ platforms pave the wave toward the demonstration of low-loss and compact optical waveguides for MIR sensing.

Keywords: Low-loss, mid-infrared, rib waveguide, Si photonics

1. Introduction

In recent decades, on-chip integrated silicon photonic platforms (Si photonics) have received remarkable research attention for the mid-infrared (MIR, 2-5µm) wavelength range due to their excellent electrical, optical properties, thermal, and compatibility with the complementary metal-oxide semiconductor (CMOS) technology[1]. MIR bands encompass absorption peaks for extensive trace gases such as CO, H_2O, CO_2, N_2O, NH_3, NO, and CH_4[2]. These trace gases show strong absorbance in MIR bands ($\lambda > 2.5\ \mu m$) due to their rotational and vibrational transitions. Chalcogenide glasses or III-V materials have a great impact on MIR technology. In addition, Si photonics have also been successfully implemented at near-infrared (NIR) and MIR bands, providing a reliable and high-volume platform that strengthens a standalone and mature technology that has been largely used now to develop on-chip integrated circuits[1]. Moreover, silicon-on-insulator (SOI) material provides key advantages because of the high refractive index contrast and the process compatibility with the current CMOS technology[3]. However, the conventional SOI waveguides are not suitable at MIR wavelength particularly in the spectral range of 2.6-2.9 µm and at λ > 3.6µm because of the buried SiO_2 layer[4]. The buried SiO_2 layer shows a strong and continuous optical absorption for $2.6\mu m < \lambda < 2.9\mu m$ and beyond $\lambda = 3.6\mu m$.

To circumvent this situation, alternative approaches such as the use of pedestal waveguide geometry[5] or suspended membranes[6] have been proposed to extend the operating wavelength of Si-based waveguides in MIR bands. Sapphire (Al_2O_3) provides a transmission window up to 5.5 um and has been recognized as an alternative material to SOI for MIR bands[7]. In addition, SiGe waveguides have also been considered a promising solution to take benefit from such a large transmission window of Ge. In recent years, few works on SiGe-on-Si waveguides have also been reported for MIR sensing applications (particularly beyond λ > 3.6µm)[8, 9]. The propagation loss of their devices at MIR bands was 4-8 dB/cm for double graded buffer[9] and 7-8 dB/cm for single graded buffer[8] on Si substrate. The propagation loss of SiGe waveguides can be further reduced by the implementation of waveguide engineering strategies and optimizing the device structure.

In this work, we demonstrate the $Ge_{1-x}Si_x$ (x = 10%)-on-sapphire rib optical waveguide with low propagation loss at λ=4.5µm. Additionally, we optimized the waveguide structure based on the theory in order to achieve low propagation loss and high confinement factor. Sapphire on SiO_2 substrate platform was considered to extend the transmission window up to 5.5 µm. This platform may have synergy with other Si photonics platforms to enable a novel low-loss waveguide structure for sensing in MIR bands.

2. Design Considerations and Characterization

The two-dimensional (2-D) cross-sectional schematic of the waveguide under consideration is shown in Fig. 1(a) and fundamental TE mode along with the optical confinement factor (OCF) is shown in Fig. 1(b) with different rib waveguide widths. The device was simulated using the commercially available multiphysics tool. The result shows that OCF increases with the increasing rib waveguide width. The refractive indices of the materials used in the proposed structure were taken from[10, 11]. The device structure was optimized by selecting the optimal aspect ratio of rib structure and it can be determined using the relation[12]; $(W/H) \leq \alpha + \left(r/\sqrt{1-r^2}\right)$; for $0.5 \leq r \leq 1.0$, where, W/H is the aspect ratio of rib waveguide width to the height, r is the slab height to the total height of the rib waveguide. The value of $\alpha = 0.3$ and $H = 2\mu m$ was considered in this work.

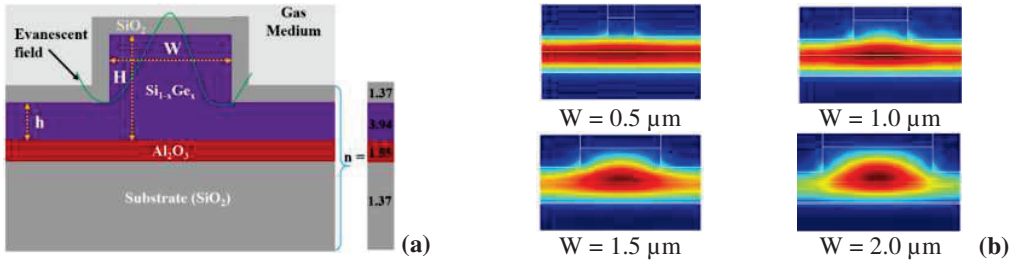

Fig. 1: (a) Cross-section schematic of the waveguide under consideration and (b) finite element method (FEM) simulated fundamental TE mode for different rib waveguide widths.

Next, the important metrics, the effective refractive index, and propagation loss were analyzed as a function of rib waveguide width [shown in Fig. 2(a-b)]. The propagation loss (in dB) of the waveguide was calculated using the relation; $\alpha = 10log_{10}(e) \times [4\pi Im(n_{eff})/\lambda]$, where, $Im(n_{eff})$ is the imaginary part of the effective refractive index and λ is the operating wavelength. The results show that n_{eff} increases, while α decreases with the increasing the rib waveguide width. Furthermore, the OCF and the overlap factor (η) were also calculated and the results are shown in Fig. 2(c-d). The OCF increases while the overlap factor decreases with the increasing rib waveguide width.

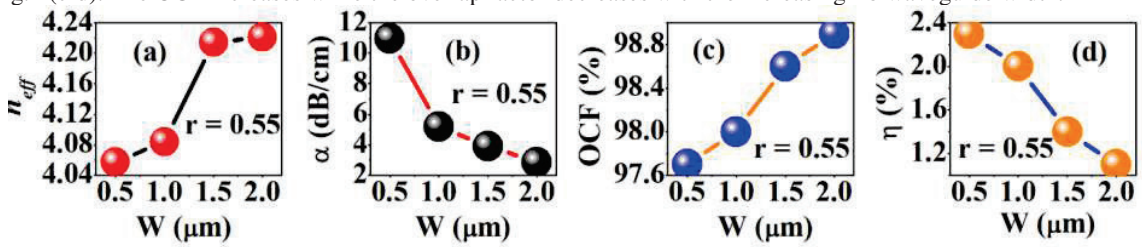

Fig. 2: (a) Calculated effective refractive index, (b) propagation loss, (c) OCF, and (d) overlap factor as a function of rib waveguide width.

In conclusion, we have investigated the $Ge_{1-x}Si_x$ waveguide at λ = 4500 nm by using the FEM mode solver. Several determination methods such as propagation loss, OCF, and overlap factor were used to provide the optimal width for determining the propagation conditions. The proposed waveguide exhibits a low loss of 2.86 dB/cm and confinement factor of ~98.9% at λ = 4500 nm. These results pave the way for designing the optimal low-loss waveguide for MIR applications.

3. References

[1].Lin H, Luo Z, Gu T, Kimerling LC, Wada K, Agarwal A, Hu J (2017) Mid-infrared integrated photonics on silicon: A perspective. Nanophotonics 7:393–420.

[2]. Siebert R, Müller J (2005) Infrared integrated optical evanescent field sensor for gas analysis: Part I: System design. Sensors Actuators, A Phys 119:138–149.

[3]. Kopp C, Bernabé S, Bakir B Ben, Fedeli JM, Orobtchouk R, Schrank F, Porte H, Zimmermann L, Tekin T (2011) Silicon photonic circuits: On-CMOS integration, fiber optical coupling, and packaging. IEEE J Sel Top Quantum Electron 17:498–509.

[4]. Soref RA, Emelett SJ, Buchwald WR (2006) Silicon waveguided components for the long-wave infrared region. J Opt A Pure Appl Opt 8:840–848.

[5]. Lin PT, Singh V, Hu J, Richardson K, Musgraves JD, Luzinov I, Hensley J, Kimerling LC, Agarwal A (2013) Chip-scale Mid-Infrared chemical sensors using air-clad pedestal silicon waveguides. Lab Chip 13:2161–2166.

[6]. Soler Penadés J, Alonso-Ramos C, Khokhar AZ, Nedeljkovic M, Boodhoo LA, Ortega-Moñux A, Molina-Fernández I, Cheben P, Mashanovich GZ (2014) Suspended SOI waveguide with sub-wavelength grating cladding for mid-infrared. Opt Lett 39:5661–5664.

[7]. Baehr-Jones T, Spott A, Ilic R, Spott A, Penkov B, Asher W, Hochberg M (2010) Silicon-on-sapphire integrated waveguides for the mid-infrared. Opt Express 18:12127–12135.

[8]. Liu Q, Ramirez JM, Vakarin V, Le Roux X, Ballabio A, Frigerio J, Chrastina D, Isella G, Bouville D, Vivien L, Ramos CA, Marris-Morini D (2018) Mid-infrared sensing between 52 and 66 µm wavelengths using Ge-rich SiGe waveguides [Invited]. Opt Mater Express 8:1305–1352.

[9]. Ramirez JM, Liu Q, Vakarin V, Frigerio J, Ballabio A, Le Roux X, Bouville D, Vivien L, Isella G, Marris-Morini D (2018) Graded SiGe waveguides with broadband low-loss propagation in the mid infrared. Opt Express 26:870–877. https://doi.org/10.1364/oe.26.000870

[10]. Kischkat J, Peters S, Gruska B, Semtsiv M, Chashnikova M, Klinkmüller M, Fedosenko O, MacHulik S, Aleksandrova A, Monastyrskyi G, Flores Y, Masselink WT (2012) Mid-infrared optical properties of thin films of aluminum oxide, titanium dioxide, silicon dioxide, aluminum nitride, and silicon nitride. Appl Opt 51:6789–6798.

[11]. Humlíček J, Röseler A, Zettler T, Kekoua MG, Khoutsishvili E V. (1992) Infrared refractive index of germanium–silicon alloy crystals. Appl Opt 31:90–94.

[12]. Soref RA, Schmidtchen J, Petermann K (1991) Large Single-Mode Rib Waveguides in GeSi-Si and Si-on-SiO2. IEEE J Quantum Electron 27:1971–1974.

Metal oxide-based optical coatings for spectral and angle selective optical response of surfaces

Sraboni Dey, J. Mitra

School of Physics, Indian Institute of Science Education and Research, Thiruvananthapuram-695551, India

E-mail: srabonidey20@iisertvm.ac.in

Abstract: Spectrally selective optical coatings absorb light in a desired spectral regime and reflect strongly elsewhere. Such coatings hold relevant applications in areas like radiative cooling, smart windows, solar energy conversion etc. Here, we discuss the development of a spectrally selective ultra-thin optical coating having average absorption of 90% over the entire visible regime up to a tunable cut-off wavelength λ_0 and has a reflectance of 80% at longer wavelengths. This has been developed using ultrathin, nanostructured coatings of indium tin oxide, an epsilon-near-zero material, supported by buried absorbing films on a commercially relevant substrate, stainless steel.

Keywords: spectrally selective, step-function, epsilon-near-zero

1. Introduction

Surface plasmons excited on nanostructures and thin films offers unique ways to influence and control light-matter interactions [1]. Degenerately doped, wide band gap metal oxides such as doped ZnO, indium tin oxide (ITO), doped CdO etc. have been utilized to develop innovative new functionalities replacing metals as plasmonic materials in NIR. This has been enabled by their large and controllable carrier density which also allows tuning of their plasma frequency and thus the dielectric to metallic transition wavelength, known as the epsilon near zero (ENZ) wavelength (λ_{ENZ}) [2]. A niche application of ENZ materials and their plasmonic properties is evidenced in the development of spectrally selective coatings, where the optical property of a reflecting metallic surface can be modified with the ability to selectively absorb light below a pre-defined wavelength and reflect at longer wavelengths. Coatings of such materials have potential applications in areas such as broadband absorbers, spectrally selective absorbers/emitters, etc [3]. The challenges being the overall complexity and thickness of the coatings along with the angular dependence of their spectral selectivity. Studies have been conducted where various methods are employed to control the absorption and emission of light from surfaces including photonic crystals [4], optical metamaterials [5], multilayer thin films [6], and nanostructures [7].

Here we demonstrate the evolution of spectrally selective optical properties on a ubiquitous substrate like stainless steel (SS) from visible to near IR through surface engineering. The surface engineering has been executed by coating a tri-layer thin film (ITO/Cr/Cr_2O_3) each of optimal thicknesses on stainless steel with an elementary periodic grating of ITO nanostructures of optimized dimensions over the coated substrate as shown in Fig 1a. Investigated from 400 – 4000 nm, the coated substrate shows high average absorption (~90%) over the entire visible up to a particular wavelength λ_0 beyond which the reflectivity becomes ~ 80%. In other words, the reflection coefficient is like a "step function" at that particular wavelength λ_0 (here ~1670 nm), which is an omnidirectional feature realized between 0° to 60°. Importantly, this λ_0 is tunable based on the selection of materials which has been showcased here through an ENZ material i.e. ITO in thin film as well as nanostructured form supported by the absorbing coating underneath.

2. Results and discussions

Designing of the spectrally selective system was conducted via finite element method calculations (COMSOL Multiphysics 5.3a). Fig1b. shows the spectral selective "step function" like response achieved on through performing surface engineering on bare SS. The high absorption over the entire visible spectrum till λ_0 is a manifestation of a buried Cr/Cr_2O_3 layer with its optimized thicknesses. However, the high reflectance (80%) beyond λ_0 arises from the high reflectivity of the ITO thin film with the periodic nanostructures. Importantly, the entire multilayer coating is < 150 nm in thickness, which is far smaller than the wavelength range of operation.

It was seen that the nanostructuring helped the coating to achieve a typical "step function" like reflectivity at λ_0 as shown in Fig 1b. which is a manifestation of the localized resonances happening in the vicinity of the nanostructures. These resonances result from strong near-field enhancements near the nanostructures thereby making the system nearly perfect absorptive at certain wavelengths. Also, this reflectivity holds not only at normal incidence

but also at oblique incidences until 60° as shown in Fig 1b. Thereby, the spectral response exhibits a wide angle behavior that would result in various applications.

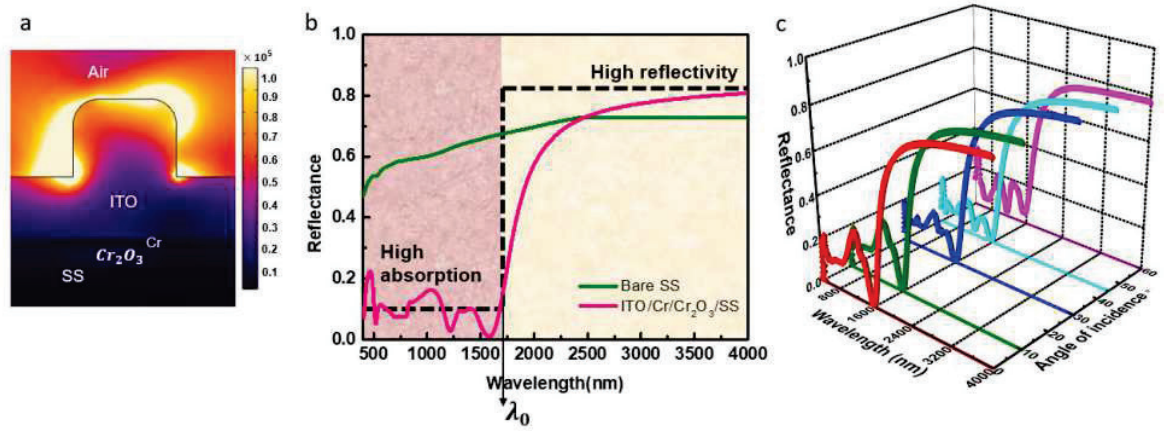

Fig. 1a. Magnitude of electric field (in V/m) variation across the system, b. Simulated reflectance spectra depicting the evolution of the spectrally selective response from bare SS, c. Reflectance plots from 0 to 60° angle of incidences

The roles played by the individual building blocks of this system and the reason behind choosing these material systems may be further comprehended via the power absorption calculations which have been depicted in Fig 2. The power absorption calculation performed for particular wavelengths from visible to IR exhibits the contribution of the underlying Cr/Cr_2O_3 coatings on stainless steel in bringing down the reflectivity to nearly 10% in the visible regime and also for ITO in playing the major role as the reflector in the near IR.

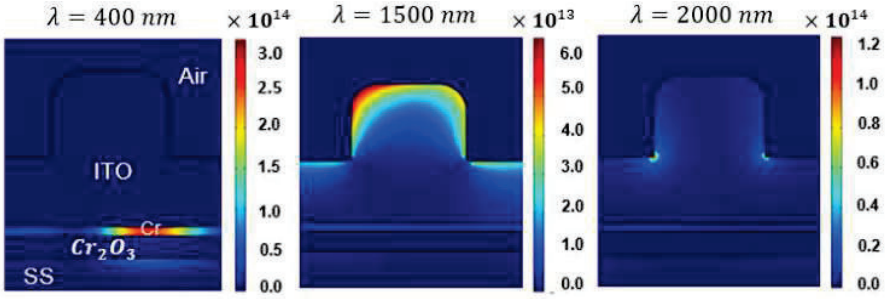

Fig. 2. Power absorption (in W/m^3) across different layers at different wavelengths (400nm, 1500 nm, 2000 nm)

Overall, the opportunistic deployment of the chosen materials in the right geometry and dimensions has proven to develop a unique response, which have later been verified through experimental realization of the same. Finally, we discuss the application potential of such coatings and scope of surface engineering in diversifying the functionalities.

3. References

[1] Halas, N. J. Plasmonics: An emerging field fostered by nano letters. *Nano Letters*, *10*(10), 3816–3822 (2010).

[2] Johns, Ben Puthoor, Navas Meleth Gopalakrishnan, Harikrishnan Mishra, Akhileshwar Pant, Ravi Mitra, J., *Journal of Applied Physics,* 127,043102(2020)

[3] Yoon, J., Zhou, M., Badsha, M. A., Kim, T. Y., Jun, Y. C., & Hwangbo, C. K. Broadband Epsilon-Near-Zero Perfect Absorption in the Near-Infrared. *Scientific Reports*, *5*, 1–8(2015).

[4] Rinnerbauer, V.; Lenert, A.; Bierman, D.M.; Yeng, Y.X.; Chan, W.R.; Geil, R.D.; Senkevich, J.J.; Joannopoulos, J.D.; Wang, E.N.; Solja˘ci´c, M. Metallic photonic crystal absorber-emitter for efficient spectral control in high-temperature solar thermophotovoltaics. Adv. Energy Mater. , 4, 1400334 (2014).

[5] Wang, H.; Sivan, V.P.; Mitchell, A.; Rosengarten, G.; Phelan, P.; Wang, L. Highly efficient selective metamaterial absorber for high-temperature solar thermal energy harvesting. Sol. Energy Mater. Sol. Cells, 137, 235–242(2015).

[6] Kecebas, M.A.; Menguc, M.P.; Kosar, A.; Sendur, K. Spectrally selective filter design for passive radiative cooling. JOSA B, 37, 1173–1182(2020).

[7] Gupta, M.C.; Carlson, D.E. Laser processing of materials for renewable energy applications. MRS Energy Sustain. 2, 285–310(2015)

Composite polarization vortices

Gauri Arora, and P. Senthilkumaran
Department of Physics, Indian Institute of Technology Delhi, Hauz Khas, New Delhi 110016, India
Optics and Photonics Center, Indian Institute of Technology Delhi, Hauz Khas, New Delhi 110016, India
Gauriarora02@gmail.com

Abstract: Composite phase vortices are formed due to coaxial/non-coaxial interference of two or more optical vortices. This article reports the creation of composite polarization vortices using non-coaxial superposition of two polarization vortices. It is found that the number and location of composite polarization singularities depend on the polarization singularity index of superposing beams, lateral separation between the two superposing beams, and the phase difference between them. Simulation results are presented.
Keywords: Optical vortices, spin-orbit beams, optical angular momentum

1. Introduction

Optical vortices can be created by superimposing three or more optical beams. Multiple beams containing phase vortices can be combined to generate optical vortex links, loops, and knots [1, 2]. In such a superposition, the resulting new vortices are known as composite phase vortices. These vortices can be created by either coaxial or non-coaxial superposition of LG type vortex beams. Polarization vortices are analogous to phase vortices in inhomogeneously polarized beams [3, 4]. These vector vortices can be expressed as superposition of orthogonally polarized phase vortices [5]. Polarization vortices can be located as points of phase vortices in the Stokes phase (ϕ_{12}) map [3] which is defined as $tan^{-1}\left(\frac{S_2}{S_1}\right)$. Here, S_1 and S_2 are normalized Stokes parameters.

This article reports the generation of composite polarization vortices by superposing two non-coaxial, collinear polarization singularities. The creation and annihilation of singularities during this process are analyzed in this article. It is observed that the location and number of such optical vortices in the resultant beam depends on mainly three factors: (a) the polarization singularity index of the superposing beams (b) phase difference between them, and (c) the lateral separation between the two polarization singular beams.

2. Theory

Resultant field due to superposition of two non-coaxial, collinear polarization singular beams can be mathematically expressed as:

$$\left|\psi_{l_2,m_2}^{l_1,m_1}\right> = a\left|\psi_{l_1,m_1}(r,\theta)\right> + bexp\,(i\phi)\left|\psi_{l_2,m_2}(r_s,\theta_s)\right> \qquad (1)$$

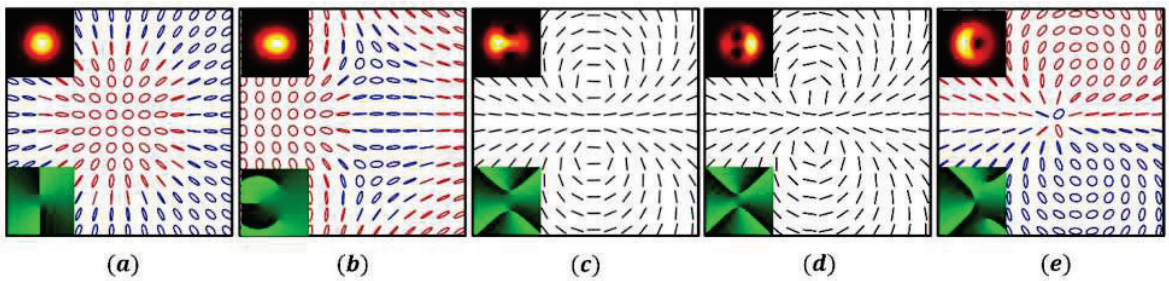

Fig. 1: Resultant polarization distributions due to superposition of two non-coaxial and collinear polarization singular beams. Various parameters in each case are: (a) $l_1 = 0, m_1 = 1;\ l_2 = 0, m_2 = 2, x_s = 0.28d, \phi = 0$ ***(b)*** $l_1 = 0, m_1 = 1;\ l_2 = 2, m_2 = 0, x_s = 0.14d, \phi = 0$ ***(c)*** $l_1 = -1, m_1 = 1;\ l_2 = -2, m_2 = 2, x_s = 0.84d, \phi = 0$ ***(d)*** $l_1 = -1, m_1 = 1;\ l_2 = -2, m_2 = 2, x_s = 0.28d, \phi = 0,$ ***(e)*** $l_1 = -1, m_1 = 1;\ l_2 = -2, m_2 = 2, x_s = 0.28d, \phi = \frac{\pi}{2}$. ***Respective intensity and Stokes phase*** ϕ_{12} ***distributions are shown as insets of each polarization distribution.*** x_s ***represents the amount of shear in x direction and*** d ***in terms of beam waist is*** $2w_0$.

Here, $|\psi_{l,m}(r,\theta)>$ represent a polarization singular beam composed of orthogonally circularly polarized phase vortices with topological charges l and m. Polarization singularity index is used to characterize polarization singular beams and is related to topological charges l and m as $m-l$. Variables a, b represent scaling factors, and ϕ denotes the phase difference between the two superposing beams. For simplicity, a and b in Eq. 1 are assumed to be equal. The other parameters in Eq. 1 are: $r=\sqrt{(x^2+y^2)}, r_s=\sqrt{((x-x_s)^2+y^2)}, \theta=tan^{-1}\left(\frac{y}{x}\right), and\ \theta=tan^{-1}\left(\frac{y}{x-x_s}\right)$. For this study, lateral shear is considered in x direction only.

3. Results and Discussion

The resultant beam in such superposition contains various polarization vortices depending on the type of superposing polarization singular beams as shown in Fig. 1. Five examples are shown in this figure. The resultant polarization distributions, intensity and Stokes phase distributions are depicted in the figure. The respective topological charges, amount of lateral shear, and the phase difference between the superposing beams are mentioned in the figure caption for each case. The number of singularities depend on the topological charges of the input beams (refer to Fig. 1 (a,b)). It can be seen that superposition of vector field polarization singularities can result in both vector and ellipse field composite polarization singularities (refer to Fig. $(c-e)$). Creation of new vortices is observed on varying the phase difference between the two superposing beams (refer to Fig. $(d-e)$).

4. Conclusions

In conclusion, the creation of composite polarization vortices using superposition of non-coaxial, collinear polarization singularities is studied. The factors that decide the number and location of composite vortices in the resultant beam are also examined. Polarization gradients present in these structured beams may be useful in optical manipulation and trapping of particles.

5. References

[1] J. Leach, M.R. Dennis, J. Courtial, M.J. Padgett, "Knotted threads of darkness," Nature **432**, 165 (2004).
[2] J.Leach, M.R.Dennis, J.Courtial, M.J.Padgett, "Vortex knots in light," New J. Phys. **7**, 1 (2005).
[2] I. Freund, A. I. Mokhun, M. S. Soskin, O. V. Angelsky, I. I. Mokhun, "Stokes singularity relations," Opt. Lett. **27**, 545 (2002).
[3] P. Senthilkumaran, Singularities in Physics and Engineering. 2053-2563 (IOP Publishing, 2018).
[4] Gauri Arora and P. Senthilkumaran, "Generation of Stokes singularities using polarization lateral shear interferometer," Opt. Express **30**, 27583-27592 (2022).

Dynamics of Squeezing in an Optomechanical MIM System

Priyankar Banerjee, Sampreet Kalita, Amarendra Kumar Sarma
Department of Physics, Indian Institute of Technology, Guwahati, Assam 781039, India
Author e-mail address: p.banerjee@iitg.ac.in

Abstract: We consider a membrane-in-the-middle (MIM) system driven by an amplitude-modulated laser. Due to the periodic modulation, a robust mechanical squeezing is obtained with an optimal ratio of the optomechanical coupling sidebands. We also show that the ground-state cooling of the Bogoliubov mode takes place, resulting in a competing effect between its occupancy and the quadrature variance. Finally, we infer that this scheme is quite robust against thermal occupancy of the mechanical mode.

Keywords: Optomechanical system, pump modulation, single-tone driving, mechanical squeezing.

1. Introduction

Quantum systems are being actively researched in recent years for generation of squeezed states. At a mesoscopic scale, cavity optomechanical systems [1] have been extensively used for sensing and processing information. However, its precision is limited by the zero-point fluctuations of its position or momentum quadrature. The noise present often exceed the standard quantum limit of 3 dB [2]. As a way around this, the mechanical quadrature can be squeezed beyond the SQL, while adhering to Heisenberg's uncertainty principle. Recent studies have shown that periodic modulation of the cavity driving amplitude can induce a strong mechanical squeezing [3]. For such a scheme to work, the mechanical mode must be cooled down to its ground-state.

A recent paper by Bai et. al. [4] proposes a squeezing scheme using a single driving field. In our work, we study the generation of mechanical squeezing in an optomechanical membrane-in-the-middle (MIM) system by periodic modulation of the laser amplitude.

2. Hamiltonian and Dynamics

Our set-up consists of an optomechanical system, which is driven by an amplitude-modulated field (amplitude ϵ_l, frequency ω_l). The cavity mode (frequency ω_0) interacts with the mechanical mode (frequency ω_m) quadratically via interaction of strength g. In a rotating frame of reference, the system Hamiltonian takes the form

$$H = \Delta_0 a^\dagger a + \omega_m b^\dagger b - g a^\dagger a \left(b^\dagger + b\right)^2 + i\epsilon_l \left(a^\dagger - a\right) + \eta\omega_m \left(b^\dagger + b\right),$$

We then analyze the dynamics of the quadrature fluctuations with and without using the rotating wave approximation (RWA), by plotting the Wigner Function distribution for the mechanical mode over a cycle.

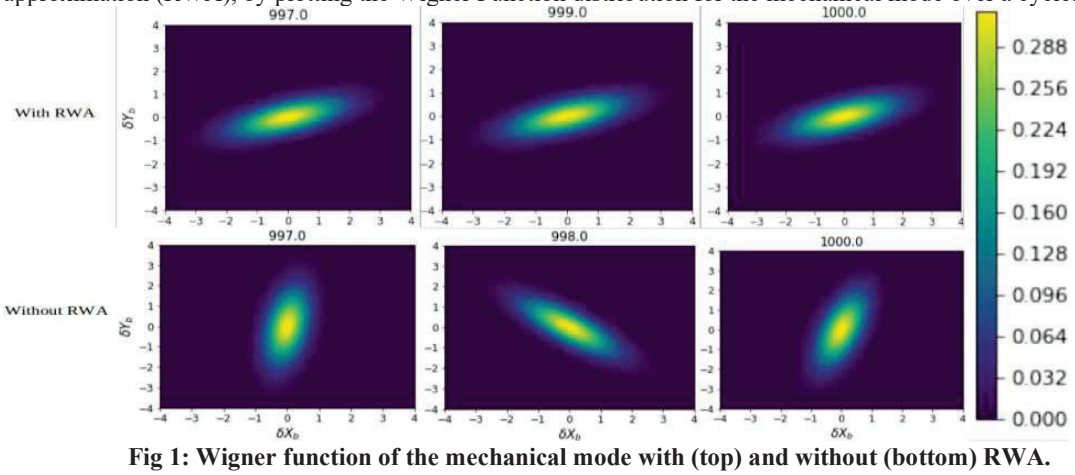

Fig 1: Wigner function of the mechanical mode with (top) and without (bottom) RWA.

We conclude that the non-resonant terms can be safely ignored under RWA for the rest of the analysis as it only contributes to the rotation of the squeezed quadrature in the phase space.

3. Squeezing Resulting from Competing Dynamics

We now calculate the steady-state squeezing generated in our system using the Bogoliubov mode operator β [5].

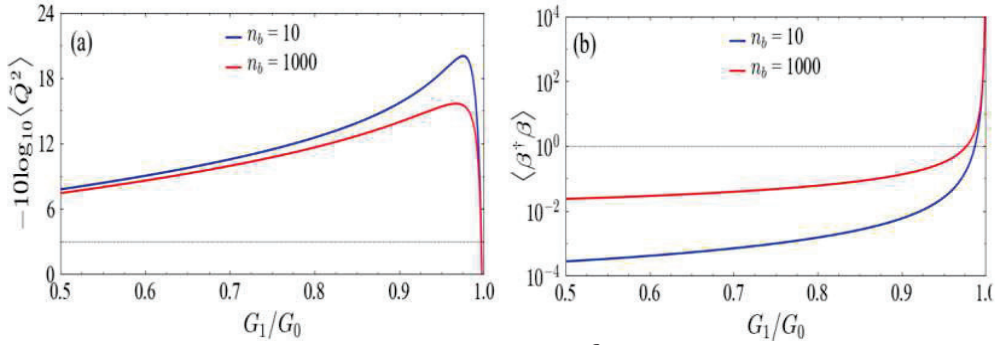

Fig 2: Behaviour of (a) variance in the position quadrature $\langle Q^2 \rangle$ and (b) occupancy of the Bogoliubov mode with variation in n_b for n_b=10 (solid blue) and n_b = 1000 (solid red).

The interaction part of the resultant Hamiltonian is in the form of a beam-splitter, which cools down the Bogoliubov mode to its ground state. The effective optomechanical coupling gradually decreases with an increase in $\frac{G_1}{G_0}$, eventually vanishing. The thermal noise plays a role in the decrease in the squeezing strength as $\frac{G_1}{G_0} \to 1$. From Fig 2 (a), we note that even a 100-fold increase in the phonon number n_b, marginally decreases the amount of squeezing obtained compared to other set-ups [4], and this qualitatively shows the robustness of this scheme.

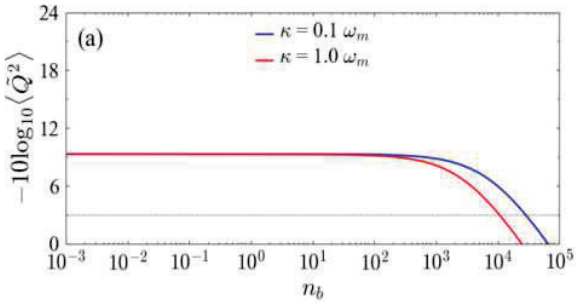

Fig 3: Magnitude of the mechanical squeezing obtained with variation in n_b

In Fig 3. we show that a strong steady-state mechanical squeezing is obtained for a low phonon number and it stays above the SQL up to a few thousands of thermal occupancies ($n_b \sim 10^4$).

4. References

[1] M. Aspelmeyer, T. J. Kippenberg, and F. Marquardt, "Cavity optomechanics", Rev. Mod. Phys. **86,** 1391 (2014).
[2] W. P. Bowen and G. J. Milburn, Quantum optomechanics (Taylor & Francis, 1995), Chap. 5.
[3] A. Mari and J. Eisert, "Gently Modulating Optomechanical Systems", Phys. Rev. Lett. **103,** 213603 (2009).
[4] C.-H. Bai et. al., "Strong mechanical squeezing in a standard optomechanical system by pump modulation", Phys. Rev. A **101,** 053836 (2020).
[5] A. Kronwald et. al., "Arbitrarily large steady-state bosonic squeezing via dissipation", Phys. Rev. A **88,** 063833 (2013)

Laser beam profile across a spatial light modulator in holographic optical tweezers

Deepak K. Gupta* and T. R. Ravindran
A Materials Science Group, Indira Gandhi Centre for Atomic Research, A CI of Homi Bhabha National Institute, Kalpakkam 603102, Tamilnadu, India
Author e-mail address: (dkg@igcar.gov.in)*

Abstract: We present a simple technique to determine the laser beam profile across a spatial light modulator (SLM) to generate structured light, in particular holographic optical traps. The optical trap generating algorithms use incident beam profile over the SLM as an input to generate optical traps or any desired pattern of light. In general the incident laser beam is assumed to be centered on the spatial area of SLM. In practice it is difficult to ensure the beam centering on the SLM with a resolution down to 10-15 μm, the pixel pitch of SLM. We present a here a method to determine the laser beam profile, the beam center location on the SLM and also demonstrate the effect of different beam center locations on various trap properties such as efficiency, uniformity and trap quality. The method allows generation of optical traps with any arbitrary laser beam profile.

Keywords: spatial light modulator, optical trapping, holographic optical tweezers, laser beam profile.

1. Introduction

A single-beam gradient trap, known as an optical tweezer, is a tightly focused laser beam capable of trapping and manipulating sub-microscopic objects in a suitable medium [1]. The ability to trap and manipulate with accuracy down to nanometers, the non-invasive and non-destructive nature of optical tweezers in probing microscopic objects have made it a valuable tool to the scientific community [2]. It finds numerous applications in the fields of material science and biological sciences because of its ability to handle mesoscopic particles to study various physical phenomena [3–5]. A tightly focused laser spot can hold either a single or multiple microscopic objects depending upon the power of the laser beam used. However, many applications require trapping and real-time manipulations of multiple particles at different locations in two or three dimensions.This brings in the use of dynamic beam shaping with the aid of a spatial light modulator in holographic optical tweezers. There are various iterative algorithms such as weighted Gerchberg Saxton, generalized adaptive additive algorithm, which generate holograms that are displayed on the SLM to generate desired patterns of light. These algorithms use the incident laser beam profile on the SLM as an input and in the iteration process as field is propagated back and forth the trapping plane and SLM plane, the input amplitude is replaced by the laser beam profile over SLM [Fig.1].The chosen beam profile, in general is assumed to be centered at the center of SLM, but in practice it becomes difficult to ensure that the laser beam center coincides with the SLM center. We present here a simple technique to determine the laser beam profile, the laser beam center across the SLM, and we also demonstrate the effect of off-centered beam on various trap properties.

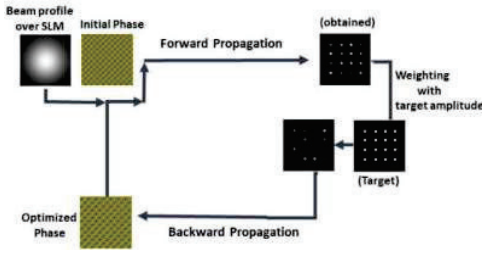

Fig. 1: Schematic diagram of iterative weighted Gerchberg Saxton Algorithm showing forward and backward propagation of fields to generate an optimized phase using laser beam profile as input.

2. Laser beam profile measurement

Fig. 2 shows a diffraction set-up which is a part of the holographic optical tweezer set-up [6] used to determine the laser beam profile across the SLM. A Nd-YAG laser beam (wavelength-1064nm) is passed through a set of polarization elements and a beam expander, and incident on SLM to fill the active area of SLM. A blazed grating displayed over the SLM produces a first order beam focused through a lens L and is measured using a power meter kept a the Fourier plane of SLM. The pinhole is used to isolate the first order beam to the detector. The SLM is divided into 64 subsections and each subsection is displayed with a blazed hologram with all other subsections kept blank. The power measured at the Fourier plane gives the contribution only due to the subsection which is displayed with the blazed hologram. The process is repeated for each of the subsections and a beam profile of the laser over the SLM is obtained. The SLM is corrected for spatially varying phase response as in [6] to ensure the correct measurement of the beam profile.

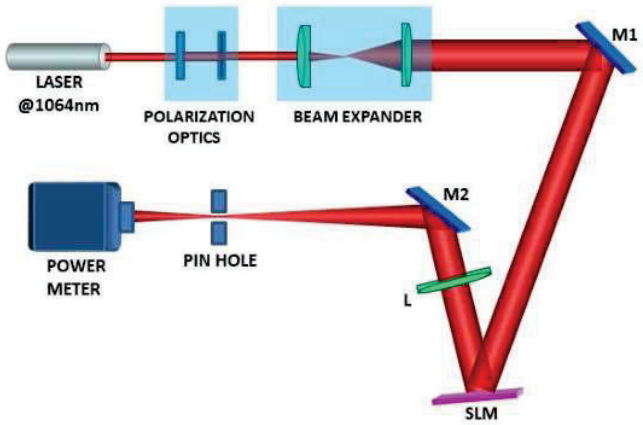

Fig. 1: Schematic diagram of the diffraction based set-up for laser beam profile measurements.

We studied the effect of off-centered beams on the SLM. There was no prominent change in diffraction efficiency in a single spot generated with displaced beam center. However, in the case of an array of trap spots there was significant deterioration in the trap properties. We generated eight spots in a circle and observed a decrease in uniformity by 15% when the beam was displaced by 130 pixels from SLM center (pixel pitch of SLM=15 μm). We further observed that the trap quality deteriorated by ~50% for beam center displacement of 130 pixels from SLM center. The trap quality was assessed by calculation of spot sharpness metric as in [6].

3. Conclusion

We measured the laser beam profile across the SLM using a diffraction based set-up and show the effect of displaced beam profile with respect to SLM center on various trap properties. We find a decrease in uniformity and trap quality by analyzing the trap spots in an array of circular traps. The method allows the use of any arbitrary laser beam profile to generate structured light instead of conventional Gaussian laser beam and allows generation of optical traps with better trap quality.

4. References

[1] A. Ashkin, J.M. Dziedzic, J.E. Bjorkholm, S. Chu, Observation of a single-beam gradient force optical trap for dielectric particles, Opt. Lett. 11 (1986) 288. https://doi.org/10.1364/OL.11.000288.

[2] K.C. Neuman, S.M. Block, Optical Trapping, Rev. Sci. 75 (2004) 2787–2809.

[3] D.K. Gupta, D. Karthickeyan, B.V.R. Tata, T.R. Ravindran, Temperature-driven volume phase transition of a single stimuli-responsive microgel particle using optical tweezers, Colloid Polym. Sci. 294 (2016) 1901–1908. https://doi.org/10.1007/s00396-016-3952-1.

[4] D. Karthickeyan, D.K. Gupta, B.V.R. Tata, Identification of volume phase transition of a single microgel particle using optical tweezers, J. Opt. 18 (2016) 105401. https://doi.org/10.1088/2040-8978/18/10/105401.

[5] Y. Ishii, A. Ishijima, T. Yanagida, Single molecule nanomanipulation of biomolecules, Trends Biotechnol. 19 (2001) 211–216.

[6] D.K. Gupta, B.V.R. Tata, T.R. Ravindran, Optimization of a spatial light modulator driven by digital video interface graphics to generate holographic optical traps, Appl. Opt. 57 (2018) 8374. https://doi.org/10.1364/AO.57.008374.

Raman spectroscopy coupled with co-labelled stable isotope probe for microbial growth monitoring

Dimple Saikia[1], Jiro Karlo[1] and S.P. Singh[1]*

[1]Department of Biosciences and Bioengineering, Indian Institute of Technology Dharwad, Karnataka, 580011, India.

Author e-mail address: ssingh@iitdh.ac.in

Abstract:
The growth phase is directly related to microbial metabolic activity. The growth of microbes is conventionally monitored using Optical density-based techniques. It is based on the cell numbers which do not provide any information regarding the biomolecules that are metabolized in the growing cells. In our work, we have used Raman spectroscopy coupled with stable isotope Deuterium for tracking the growth kinetics and metabolic activity of microbial cells at the earliest. Further, to track the de-novo synthesis of metabolites in vivo we co-labelled using D_2O and uniformly ^{13}C-labelled glucose. Our findings aid Raman-based approaches for monitoring microbial growth.

Keywords: Raman Spectroscopy, Stable isotope, Deuterium, Carbon -13, Heavy water, Microbial growth monitoring, Metabolomics.

1. Introduction

Microbial growth monitoring is an essential part to understand the microbial activity in carrying out microbiology. Real-time monitoring of microbial growth could lead to a better understanding the metabolic activity[1]. Therefore, the requirement of identifying active bacteria in a sample in a fast, sensitive, and reliable method is very important. Study has already reported that Raman spectroscopy could show the growth kinetics of bacteria at the community level[2]. Stable isotope labelling in combination with Raman microspectroscopy has become a promising approach for understanding the complex metabolic behaviour of various microorganisms. It is studied that incubation of microorganisms with stable isotopes like ^{13}C (Carbon-13), ^{15}N (Nitrogen-15), and ^{2}H (D, Deuterium) quantify growth, metabolic activity, and nutrient transfer from the cultured medium. Raman spectra are controlled by the mass of the atom involved in the molecular vibration. The addition of neutron in isotopically heavy tracer affects molecular bonds resulting in redshift in Raman spectra [1,3–6]. However, the major advantage of using Deuterium labelling with the Raman technique is that 10-50% (vol/vol) D_2O labelling enables the identification of metabolically active cells in culture because of the incorporation of D into the cell biomass. A new Carbon-Deuterium (C-D) stretching vibration band in the Raman silent region 2040-2300 cm^{-1} results from the substitution of C-H by C-D. Electrons carrying NADPH and NADH, H^+ can exchange with D^+ to form the C-D bonds to newly synthesized lipids via the fatty acid synthesis pathway which contributes 25-30% to total cellular mass. Other pathways such as amino acids and carbohydrates, D will incorporate into cells but do not contribute so much to the C-D peak region. Raman stable isotope labelling has been a widely used approach to quantify bacterial metabolism in their natural habitats such as water, soil, and colon [3,5–10].

It was already reported that Raman spectra could track the changes in physiologically active cells incubated in different labelled isotopes. In this study, we have used D_2O and D_2O coupled with uniformly ^{13}C-labelled glucose to monitor the growth along with metabolic activity in different time points of actively growing cells along temporal changes in the C-D and Phenylalanine peak. This study demonstrated how efficiently we can track the growth of metabolically active bacteria and de-novo synthesis of metabolites at the community level using ^{13}C and Deuterium labelling. This approach will bring an interdisciplinary approach for tracking microbes using stable isotope and Raman spectroscopy.

2. Methods

Escherichia coli (MCC 3109) was grown in different cultures, first at different concentrations of D_2O, second uniformly labelled ^{13}C glucose-D_2O (50%), and unlabeled *E. coli* culture. OD_{600} and Raman spectra were collected at 2,4,6,8,12,18 and 24 hours from the D_2O-culture keeping the equal volume of

cells in each time point. In a similar manner, Raman spectra were recorded at 8,12,18 and 24hrs from *E. coli* culture with ^{13}C-labelled glucose as the only carbon source and 50% D_2O. All spectral data were pre-processed using MATLAB R2021b software and plotted in Origin software.

3. Results

The suitable D_2O concentration for bacterial growth was evaluated using different concentrations of D_2O. D_2O concentration up to 50% showed no significant influence (p-value > 0.05) for the growth as shown in Fig.1(A). To understand the metabolic activity along with the growth of cells the C-D region was studied at 1800-2800 cm^{-1} of Raman spectra. It was observed that C-D peak intensity increases over time. It was found to be more intense after 6hr, this is possibly due to *E. coli* cells double in each 20 mins and during 6-8hr cells activity divides exponentially as shown in Fig.1(B). After 8 hr cells division is almost the same. Spectra after 4hr showed a very clear visible C-D band. The amount of deuterium incorporated with respect to time by generating a ratio of Raman bands specific for C-D and C-H vibrations was calculated and plotted with respect to time in Fig.1(C). The ratio of C-D/(C-H+C-D) can be used as a semi-quantitative indicator of general metabolic activity in cells [5]. Our findings are suggestive of the fact that C-D% was linearly associated with the growth of the bacteria. Further to monitor the microbial growth with the in-vivo de novo metabolite synthesis we co-labelled the cells with Carbon-13 and Deuterium. As shown in Fig.1(D) unlabelled cells show a redshift in the standard phenylalanine band and C-H band with an increase in incubation time. Thus, our finding shows the feasibility of Raman spectroscopy coupled with the stable isotope for monitoring microbial growth and de-novo metabolite synthesis simultaneously.

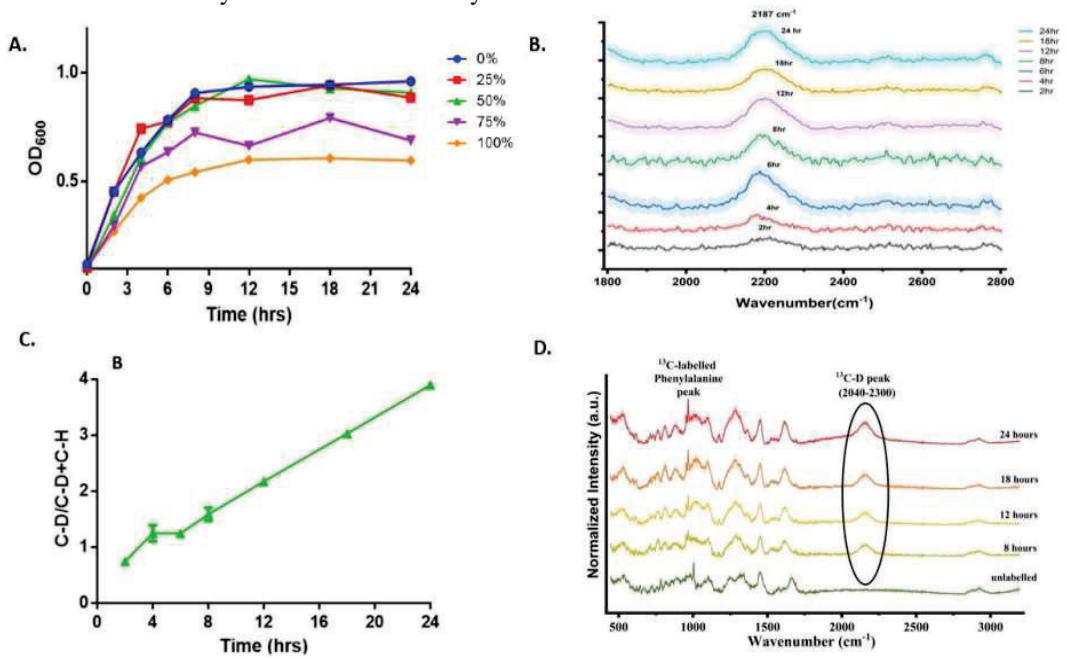

Fig. 1: 1(A) Growth curve of E. coli cells in different D_2O concentrations; 1(B) Intensity change in Carbon-deuterium peak at 2187 cm^{-1} with respect to incubation time. 1(C) C-D/(C-H+C-D) with respect to incubation time; 1(D); Average Raman spectra of unlabelled cells and ^{13}C and Deuterium labelled cells at different time points.

4. References

1. Nature Reviews Methods Primers **1**, 79 (2021).
2. D. Saikia, P. Jadhav, A. R. Hole, C. M. Krishna, and S. P. Singh, Appl Spectrosc 000370282211096 (2022).
3. Y. Song, L. Cui, J. Á. S. López, J. Xu, Y.-G. Zhu, I. P. Thompson, and W. E. Huang, Sci Rep **7**, 16648 (2017).
4. S. Radajewski, P. Ineson, N. R. Parekh, and J. C. Murrell, Nature **403**, 646 (2000).
5. Y. Wang, Y. Song, Y. Tao, H. Muhamadali, R. Goodacre, N.-Y. Zhou, G. M. Preston, J. Xu, and W. E. Huang, Anal Chem **88**, 9443 (2016).
6. H. Muhamadali, M. Chisanga, A. Subaihi, and R. Goodacre, Anal Chem **87**, 4578 (2015).
7. F. Weber, T. Zaliznyak, V. P. Edgcomb, and G. T. Taylor, Appl Environ Microbiol **87**, (2021).
8. L. Cui, K. Yang, and Y.-G. Zhu, in (2019), pp. 95–107.
9. Y. Wang, W. E. Huang, L. Cui, and M. Wagner, Curr Opin Biotechnol **41**, 34 (2016).
10. M. Li, W. E. Huang, C. M. Gibson, P. W. Fowler, and A. Jousset, Anal Chem **85**, 1642 (2013).

Sensitivity-Enhanced Surface Plasmon Resonance biosensor using Hybrid Structure of Silver with Monolayer of 2D Materials

Awadhesh Kumar[1], Anil Kumar[1], Prateek Kumar Yadav[1], S. K. Srivastava[1*]
[1]Department of Physics, Institute of Science, Banaras Hindu University, Varanasi-221005)
**Corresponding Author: S. K. Srivastava (Email: sanjay_itbhu@yahoo.com, Phone No. +919454233138).*

Abstract: This work aims to improve the sensitivity of a surface plasmon resonance (SPR) biosensor with the BK-7 prism, silver, and 2D materials mainly black phosphorous (BP) and graphene under angular interrogation techniques. The optimized thickness of the silver layer is 55nm. The proposed biosensor finds the maximum sensitivity for various sensing medium refractive indices ranging from 1.33 to 1.41. Our calculated parameters of the biosensor sensitivity of 175 deg/RIU have been obtained. This excellent performance of the proposed structure makes it suitable for detecting biomolecules and other analytes.
Keywords: surface plasmon resonance (SPR), sensitivity, graphene, biomolecules, BK-7 prism.

1. Introduction

A Surface plasmon resonance (SPR) biosensor is a very sensitive device based on optical phenomena. It is widely used for the real-time and label free detection of biomolecules. It is easy to fabricate and cost-effective and eco-friendly. Surface plasmons polaritons (SPPs) generates when the incident light wave vector matches with the surface of the metal SPs then, some incident power gets absorbed through the prism to the sensing area, resulting it gives an absorption dip. In the Kretschmann configuration angle interrogation phenomena have been used and a p-polarized light source of 633 nm wavelength. The minimum reflected light intensity is obtained known as the SPR angle. For the generated surface plasmon (SPs) at the metal-dielectric interface, used a Helium-Neon laser source. In practice, silver metal shows sharp reflectance and minimum FWHM in comparison to gold due to their special dielectric constant[1].

2. Designing and modeling of sensor

The proposed SPR biosensor is consists of three layers as depicted in Fig.1. In this proposed biosensor we arrange a BK-7 glass prism, silver-BP-graphene and sensing layers are considered. To generates surface plasmons, a monochromatic light source (He-Ne laser) at wavelength 633 nm is used. The p-polarized light is incident on metallic surface through one face of the prism and the reflected light is at another face of prism as shown in fig. 1. The silver layer is the deposited-on base of the prism. Further, the BP layer is deposited over the silver layer to enhance the performance of the SPR biosensor. The graphene layer is attached above the BP layer and its shows good performance of biosensor also used as a protective layer. Finally, in this structure, we consider it as a sensing medium above the graphene layer also assume that the refractive index (RI) changes from 1.33 to 1.41 due to presence of different concentration of biomolecules[2].

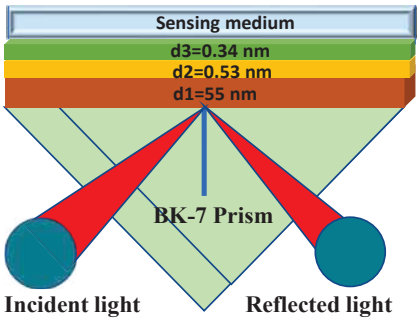

Fig. 1: Schematic diagram of proposed SPR biosensor.

Table.1 In the proposed SPR biosensor used materials with thicknesses and refractive index at 633 nm wavelength

S. N.	Materials	Thickness	Refractive Index	References
1.	Silver (Ag)	55 nm	0.056253+4.2760*1i	[3]
2.	BP	0.53 nm	3.5+0.01*	[3]
3.	graphene	0.34 nm	3+1.1491*1i	[4]

3. Modeling theory mathematical approach

Our proposed SPR biosensor is based on multilayer structure and we used the transfer matrix method (TMM) and find the optical field can represent as mathematically[5]-

$$\begin{bmatrix} E_1 \\ H_1 \end{bmatrix} = M \begin{bmatrix} E_{N-1} \\ H_{N-1} \end{bmatrix} \quad (1)$$

where E_1, $E_{N-1}$and H_1, H_{N-1} show the first and last tangential components of electric and magnetic fields at the interface. Finally, the reflection coefficient of (r_p) can be written in mathematical expression as given below-

$$r = \frac{(P_{11}+P_{12}q_N)q_1-(P_{21}+P_{22}q_N)}{(P_{11}+P_{12}q_N)q_1+(P_{21}+P_{22}q_N)} \quad (2)$$

In the last calculated reflectance is as given equation-

$$r_p = |r|^2 = (r * r)$$

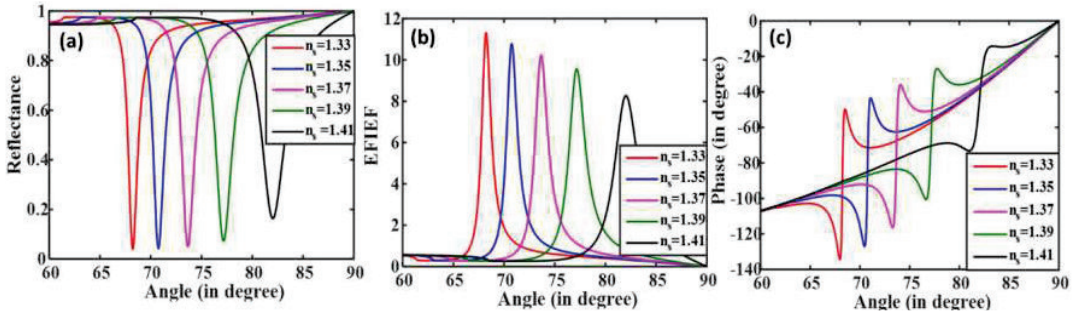

Fig. 2 Proposed SPR biosensor, (a) Incidence angle vs reflectance of SPR curve, (b) Incidence angle vs reflectance curve for phase, (c) Incidence angle vs reflectance curve for EFIEF plotted.

4. Mathematical modeling of the performance parameters

The most parameters of the SPR biosensor[4] can be calculated by the given below mathematical formula: **Sensitivity** (S) = $\Delta\theta res/\Delta n_s$, [Unit: deg./RIU^{-1}], where Δθres is change in resonance angle and Δn_s is change RI. **detection accuracy** (DA) = Δθres/FWHM, **quality factor** (QF) = S/FWHM, [Unit: (RIU-1)], Also, the resonance angle will change the phase and written as the following expression -

$$\textbf{phase } (\Phi) = \arg(r)$$

Electric field intensity enhancement factor (**EFIEF**)=$\left|\frac{E\left(\frac{L}{L-1}\right)}{E\left(\frac{1}{2}\right)}\right|^2 = \frac{\varepsilon_1}{\varepsilon_L}\left|\frac{H\left(\frac{L}{L-1}\right)}{H\left(\frac{1}{2}\right)}\right|^2 = \frac{\varepsilon_1}{\varepsilon_L}|t|^2$,where t is transmission coefficient,

5. Conclusion; In this work, our proposed SPR biosensor for the detection of biomolecules (like cancer cells or blood plasma) present in the sensing medium. The proposed structure (prism-Ag-BP-graphene-sensing medium) shows a maximum sensitivity (S) of **175 deg./RIU** with a detection accuracy (DA) of **12.39** and quality parameter (QF) **154.9 RIU-^{1}**. The proposed SPR biosensor may be used in the medical field and detection of small biomolecules.

Acknowledgement- Awadhesh Kumar says the thankful, to CSIR-HRDG for providing financial support, the physics lab of BHU, and also Prof S. K. Srivastava for supporting our work.

References

[1] R.B. Schasfoort, Handbook of surface plasmon resonance, Royal Society of Chemistry2017.
[2] B. Hossain, A.K. Paul, M.A. Islam, M.M. Rahman, A.K. Sarkar, L.F. Abdulrazak, A highly sensitive surface plasmon resonance biosensor using SnSe allotrope and heterostructure of BlueP/MoS2 for cancerous cell detection, Optik, 252 (2022) 168506.
[3] A. Kumar, A. Kumar, S. Srivastava, Silicon Nitride-BP-Based Surface Plasmon Resonance Highly Sensitive Biosensor for Virus SARS-CoV-2 Detection, Plasmonics, 17 (2022) 1065-1077.
[4] A. Kumar, A.K. Yadav, A.S. Kushwaha, S. Srivastava, A comparative study among WS2, MoS2 and graphene based surface plasmon resonance (SPR) sensor, Sensors and Actuators Reports, 2 (2020) 100015.
[5] S. Raikwar, D. Srivastava, J. Saini, Y. Prajapati, 2D-antimonene-based surface plasmon resonance sensor for improvement of sensitivity, Applied Physics A, 127 (2021) 1-8.

Laser Propagation through Overdense Magnetized Plasma

Gaurav Kumar, Hitendra K Malik

phz198682@iitd.ac.in, hkmalik@physics.iitd.ac.in

Department of Physics, Indian Institute of Technology, New Delhi, India

Abstract: Laser propagates through the underdense plasma easily as compared to the overdense plasma. While through the overdense plasma when an external magnetic field is applied then the laser imparts some part of the energy to plasma and the laser propagates through it. When the external magnetic field is further increased, a larger field of the laser propagates through the overdense Plasma. We examine 1-D and 2-D situations by Particle-in-cell (PIC) simulation using the EPOCH. In the case of the applied magnetic field due to **E**×**B** heating and the pondermotive force, the laser propagation through the overdense plasma.

Keywords: Overdense, Underdense, Particle-in-cell

Introduction

If plasma density is larger than critical density the laser is reflected at the vacuum plasma interface [1, 2] which is due to poor interaction of laser (electromagnetic wave) with unmagnetized plasma [3, 4]. While for the applied magnetic field in order of kilo Tesla the laser can propagate through overdense plasma easily. Some advanced laboratory magnetic fields of this order have now been achieved [5]. It turns out that there is a good likeliness for technological improvement to catch up in the future to have the regime of magnetized electrons available in laser-plasma interaction experiments [6, 7]. It is, therefore, crucial to realize the underlying physics of the EM wave interaction with a strongly magnetized plasma in detail.

Simulation setup

At x = 0, plasma medium starts. The laser is incident on the plasma from the left side, and the right side of the simulation box is open. The laser is assumed to propagate along the x direction, along which the external magnetic field (B) is also applied. The electric field of the laser is directed along the y direction and its magnetic field is along the z direction. The plasma simulation parameters used for 1-D and 2-D cases are given in Table 1. To reduce the computational time, we used the simulations at a reduced mass of ions, which is taken to be 25 times heavier than electrons (m_i/m_e=25). For 2-D simulation mass of ions is considered to be 1836 times heavier than the electrons (m_i/m_e=1836).

	1D simulation	Parameters			2D simulation	parameters
Parameters	Values in SI unit **Underdense**	Values in SI unit **Overdense (B=0)**	Values in SI unit **Overdense(B= 6.2kT)**	Values in SI unit **Underdense**	Values in SI unit **Overdense (B=0)**	Values in SI unit **Overdense (B=24.8kT)**
		Plasma Parameters			**Plasma Parameters**	
Density (n_0)	**$3x10^{15}$ per m^3**	**$3x10^{26}$ per m^3**	**$3x10^{26}$ per m^3**	**$3x10^{15}$ per m^3**	**$3x10^{28}$ per m^3**	**$3x10^{28}$ per m^3**
Frequency(ω_{pe})	**$5.8x10^{12}$ rad/s**	**$18.41x10^{17}$ rad/s**	**$18.41x10^{17}$ rad/s**	**$5.8x10^{12}$ rad/s**	**$18.41x10^{17}$ rad/s**	**$18.41x10^{17}$ rad/s**
(ω_{pi})	**$1.16x10^{12}$ rad/s**	**$3.68x10^{17}$ rad/s**	**$3.68x10^{17}$ rad/s**	**$1.36x10^{11}$ rad/s**	**$13.6x10^{17}$ rad/s**	**$13.6x10^{17}$ rad/s**
		Laser Parameters			**Laser Parameters**	
Intensity (I)	**$3.5x10^{19}$ Watt/m^2**	**$3.5x10^{19}$ Watt/m^2**	**$3.5x10^{19}$ Watt/m^2**	**$6.25x10^{20}$ Watt/m^2**	**$6.25x10^{17}$ Watt/m^2**	**$6.25x10^{17}$ Watt/m^2**
Frequency (ω_l)	**$2x10^{14}$ rad/s**	**$2x10^{14}$ rad/s**	**$2x10^{14}$ rad/s**	**$1.8x10^{15}$ rad/s**	**$1.8x10^{15}$ rad/s**	**$1.8x10^{15}$ rad/s**
Wavelength (λ)	**3π micron**	**3π micron**	**3π micron**	**1.06 micron**	**1.06 micron**	**1.06 micron**

Table-1. Laser and Plasma parameters in 1D simulation and 2D simulation

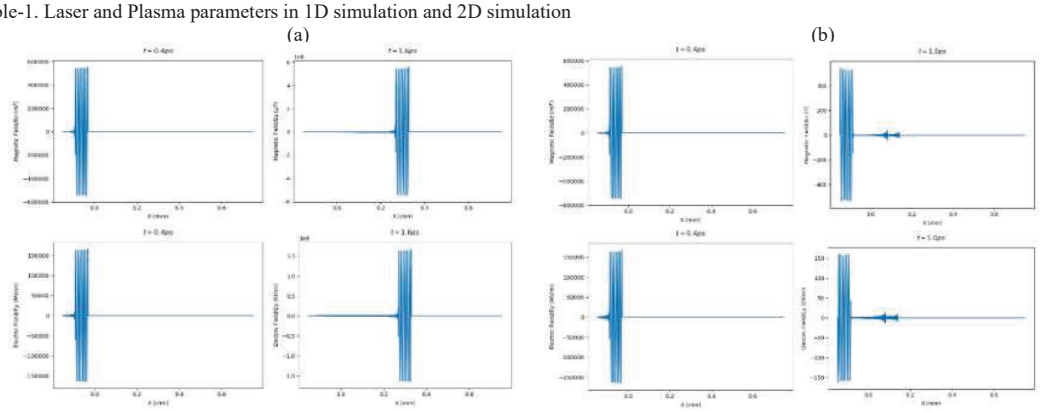

Figure1: (a)Laser electric field and magnetic field inside under-dense Plasma. (b) Laser electric field and magnetic field inside over-dense Plasma.

Results and Discussion

In an underdense case, the laser propagates through the plasma, the components of the magnetic field (B_z) and electric field (E_y) appear inside the plasma, as shown in figure 1(a). In an overdense unmagnetized case, the laser does not propagate through the plasma, which is shown in (figure 1(b)) and the laser is reflected at the boundary of the plasma (x = 0). In figure 2(a), some part of the energy is absorbed through the plasma and some part is reflected in the presence of an external magnetic field (B_0). If the external magnetic field is further increased then a larger part of the energy propagates through the overdense plasma, as shown in figure 2(b). We simulated in two dimensions also, which are shown in figures 3(a), 3(b), and 3(c). The magnetic field proves to be an important gradient in other nonlinear phenomena also [8,9].

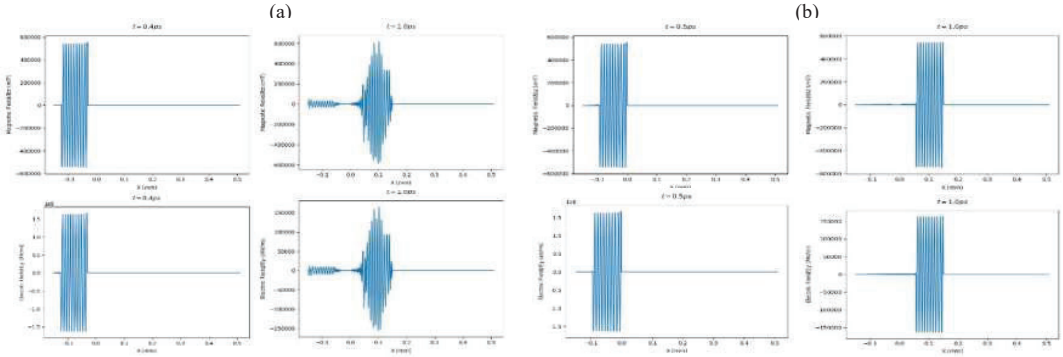

Figure2:(a) Laser electric field and magnetic field inside overdense magnetized Plasma (B0=6.2kT). (b) Laser electric field and magnetic field inside overdense magnetized Plasma (B0=707kT).

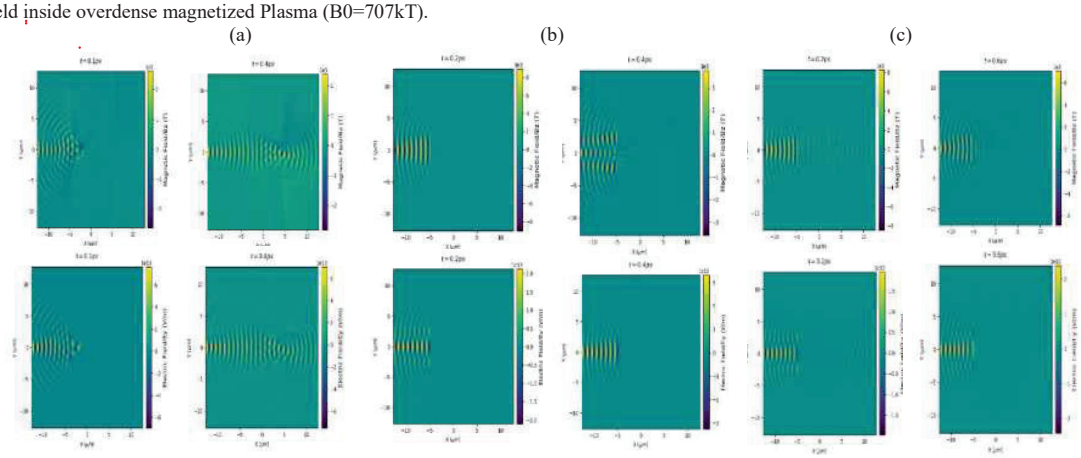

Figure3: (a) Laser electric field and magnetic field inside underdense plasma. (b) Laser electric field and magnetic field inside overdense plasma. (c) Laser electric field and magnetic field inside overdense magnetized plasma (B_0 = 24.8 kT)

Conclusion

The impact of strong magnetic field on the laser propagation in overdense plasma is simulated for 1-D and 2-D case. Unlike unmagnetized plasma, the laser can penetrate more in the case of magnetized plasma. However, a part of energy is also reflected. The results predict that heating of the plasma can be done when a stronger magnetic field is applied. The reflected part can be used for plasma diagnostics.

References

[1] H. K. Malik, Laser-Matter Interaction for Radiation and Energy, 2nd ed. (CRC Press: Taylor & Francis, 2021)
[2] P. C. Clemmow and J. P. Dougherty, Electrodynamics of Particles and Plasmas (Addison-Wesley, Reading, MA, 1969)
[3] D. Dorranian, M. Starodubtsev, H. Kawakami, H. Ito, N. Yugami, and Y. Nishida. Radiation from high-intensity ultrashort-laser-pulse and gas-jet magnetized plasma interaction. Physical Review E, 68(2):026409, 2003.
[4] V.B. Krasovitskii, V.G. Dorofeenko, V.I. Sotnikov, and B.S. Bauer. Interaction of powerful laser pulse with magnetized plasma. Physics of Plasmas, 11(2):724–742, 2004.
[5] D. Nakamura, A. Ikeda, H. Sawabe, Y.H. Matsuda, and S. Takeyama. Record indoor magnetic field of 1200 T generated by electromagnetic flux-compression. Review of Scientific Instruments, 89(9):095106, 2018.
[6] C. Federrath. Magnetic field amplification in turbulent astrophysical plasmas. Journal of Plasma Physics, 82(6), 2016.
[7] C. K. Birdsall. Particle-in-cell charged-particle simulations, plus monte Carlo collisions with neutral atoms, pic-mcc. IEEE Transactions on plasma science, 19(2):65–85, 1991.
[8] L. Malik, M. Kumar and I.V. Singh. A three-coil setup for controlled divergence in magnetic nozzle. IEEE Transactions on plasma science, 49(7):2227–2237, 2021.
[9] L. Malik. Tapered coils system for space propulsion with enhanced thrust: A concept of plasma detachment. Propulsion and Power Research 11 (2), 171-180, 2022.

Enhanced nonlinearity and effective optical limiting action of copper@graphite (Cu@C) core-shell nanostructures prepared by laser ablation

Hasana Jahan Elamkulavan, Athulya Kadeprath Satheesan, Nikhil Puthiyapurayil, Chandrasekharan Keloth*

Laser and Nonlinear Optics Laboratory, Department of Physics, National Institute of Technology, Calicut- 673601

*E-mail address: csk@nitc.ac.in

Abstract: Herein, we communicate the enhancement of optical nonlinearity of copper nanoparticles as a consequence of carbon encapsulation of copper, forming a core-shell nanostructure. Pulsed laser ablation experiments were carried out by ablating a Cu target immersed in three solvents (Ethylene glycol, Toluene and Benzonitrile)**.** The quenching of surface plasmon resonance of the Cu@graphite core-shell structures in Benzene-based solvents was verified by UV-Visible spectroscopy. The nonlinear and optical limiting analysis was done by Z-scan setup and found that the effective incorporation of graphite with copper significantly enhances its optical limiting behaviour which makes it an excellent candidate for laser safety applications.

Keywords: Pulsed Laser Ablation, Z-Scan, Nanoparticles, Core-shell nanostructure, Optical Limiting

1. Introduction

Carbonaceous materials are showing promising applications in the area of biomedicine, catalysis, sensing and optoelectronics etc. because of their physical, chemical, electronic and thermal properties [1]. They have been widely used to substitute many known materials in our day-to-day life. Among them, metal@carbon core-shell structures play a vital role in enhancing the optical properties of metal nanoparticles because they exhibit dual physical properties of the core as well as shell materials [2]. Immense research is going on to find the best applications of such materials in linear and non-linear optics.

The damages caused to sensitive optical devices by powerful laser systems can be reduced by utilizing the optical limiting (OL) properties of non-linear optical materials. Optical limiters can maintain the output power below a limiting threshold (LT) even at high power input. Unfortunately, it is hard to find naturally available nonlinear optical (NLO) materials with competent nonlinearities, especially OL properties. Therefore, it is high time to work on novel materials capable of withstanding high input powers. Here, we are exploiting the NLO response of copper@graphite (Cu@C) core-shell nanostructures to improve their optical limiting applications.

2. Experimental Techniques

Pulsed Laser Ablation in Liquids (PLAL) is one among the simplest, versatile, and adaptable routes for producing nanoparticles in liquids, which has a lot of exciting features over many other nanoparticles preparing methods used so far [3]. We used a Q-switched Nd: YAG laser of 532 nm wavelength, with a pulse width of 7 ns and a repetition rate of 10 Hz to synthesize the required samples. Cu plate (>99%) of 1.5 mm thickness was used as the target in 1.5 ml ethylene glycol, toluene and benzonitrile solvents. A convex lens of focal length 10 cm was employed to concentrate the laser beam having a pulse energy of 30 mJ/cm^2. The ablation was performed for 10 minutes. The target was translated manually after every 3 minutes to reduce the effect due to crater formation in the metal plate. As a result, the ethylene glycol solution changed its colour to pale yellow, and the solution of toluene and benzonitrile became brownish yellow and dark brown respectively.

The formation of the structures was established by taking absorption spectra of the samples (250 to 800 nm) using a 'Shimadzu-UV 2450' UV-Visible spectrometer. We utilized the same Z- scan setup to analyze the NLO characteristics of the samples. We selected an average of 80% linear transmittance to perform the Z-scan (open aperture (OA)) analysis of the as-synthesized samples. The OL characteristics were analyzed by plotting the values of normalized transmittance against input fluence.

3. Result and Discussion

The plots in Fig. 1a indicate the UV-Visible absorption of the samples prepared by ablation. The absorption spectra of colloidal Cu in ethylene glycol show an absorption maxima at 583 nm which confirms the existence of surface plasmon resonance (SPR) absorption associated with the nano-sized nature of Cu particles [4]. Cu@C nanoparticles in toluene and benzonitrile show similarity in absorption maxima, with the graphitic peak near 286 nm which dominates the expecting SPR peak of Cu. This confirms the quenching of SPR due to the graphitic layer in the samples prepared in Benzene derivative solvents like toluene and benzonitrile [5].

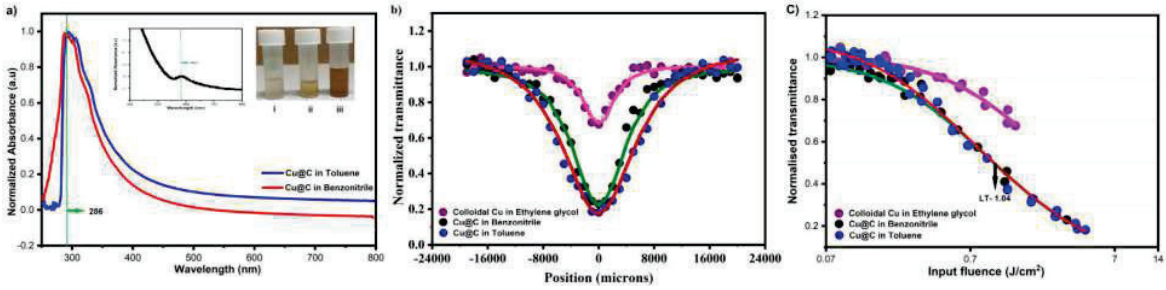

Fig. 1: a) UV-Visible absorption spectra of samples prepared (Inset shows the absorption spectrum of colloidal copper in ethylene glycol and the appearance of samples indicating the colour change of i) colloidal copper in ethylene glycol, ii) Cu@C in toluene and iii) Cu@C in benzonitrile), b) Plots of OA Z-scan data of the samples prepared, c) OL plots of the samples at 0.26 GW/cm^2 on-axis intensity.

The smooth and valley-shaped OA Z-scan plots at 0.26 GW/cm^2 on-axis intensity indicate that all the prepared samples are having reverse saturable absorption (RSA) leading to NLA characteristics as shown in Fig. 1b. Comparing the graphs, it is clear that the non-linearity of Cu@C core-shell structures in toluene and benzonitrile are dominating significantly at lower pulse energies itself. It is already reported that carbonaceous materials have enhanced nonlinearity [6]. From the graph in Fig. 1c, the LT values of the as-prepared Cu@C core-shell structures were found to be 1.04 J/cm^2, which is a fair value compared to optical limiters yet reported [7]. This extraordinary enhancement in NLO properties could be observed as a consequence of the interactivity between the modified intermediate energy levels in Cu@C core-shell nanostructures.

4. Conclusion

PLAL technique was used to synthesize Cu@C nanostructures having enhanced optical nonlinearity. The quenching of SPR of Cu by Benzene derivative solvents like toluene and benzonitrile was confirmed. The brilliant incorporation of copper with carbon results in enhanced OL properties which is much useful in efficient laser safety applications.

5. References

[1] O. A. Shenderova, V. V. Zhirnov, and D. W. Brenner, "Carbon nanostructures," *Crit. Rev. Solid State Mater. Sci.*, vol. 27, no. 3–4, pp. 227–356, 2002, doi: 10.1080/10408430208500497.

[2] F. M. Galogahi, Y. Zhu, H. An, and N. T. Nguyen, "Core-shell microparticles: Generation approaches and applications," *J. Sci. Adv. Mater. Devices*, vol. 5, no. 4, pp. 417–435, 2020, doi: 10.1016/j.jsamd.2020.09.001.

[3] N. G. Semaltianos, "Nanoparticles by laser ablation," *Crit. Rev. Solid State Mater. Sci.*, vol. 35, no. 2, pp. 105–124, 2010, doi: 10.1080/10408431003788233.

[4] S. Moniri, M. Ghoranneviss, M. R. Hantehzadeh, and M. A. Asadabad, "Synthesis and optical characterization of copper nanoparticles prepared by laser ablation," *Bull. Mater. Sci.*, vol. 40, no. 1, pp. 37–43, 2017, doi: 10.1007/s12034-016-1348-y.

[5] V. Amendola, G. A. Rizzi, S. Polizzi, and M. Meneghetti, "Synthesis of gold nanoparticles by laser ablation in toluene: Quenching and recovery of the surface plasmon absorption," *J. Phys. Chem. B*, vol. 109, no. 49, pp. 23125–23128, 2005, doi: 10.1021/jp055783v.

[6] S. Perumbilavil, A. López-Ortega, G. K. Tiwari, J. Nogués, T. Endo, and R. Philip, "Enhanced Ultrafast Nonlinear Optical Response in Ferrite Core/Shell Nanostructures with Excellent Optical Limiting Performance," *Small*, vol. 14, no. 6, 2018, doi: 10.1002/smll.201701001.

[7] S. Biswas, A. K. Kole, C. S. Tiwary, and P. Kumbhakar, "Enhanced nonlinear optical properties of graphene oxide-silver nanocomposites measured by Z-scan technique," *RSC Adv.*, vol. 6, no. 13, pp. 10319–10325, 2016, doi: 10.1039/c5ra21000c.

Ab-initio simulation of electron dynamics of anatase TiO_2 under an intense laser field

Sruthil Lal S. B[a†], Mani Lokamani[b], Devaraj Murali[c], Matthias Posselt[b], Assa Aravindh Sasikala Devi[d], Alok Sharan[a*]

[a]*Department of Physics, Pondicherry University, R. V. Nagar, Kalapet, Puducherry, India*
[b]*Helmholtz-Zentrum Dresden-Rossendorf, Bautzner Landstraße 400, 01328 Dresden, Germany*
[c]*Indian Institute of Information Technology Design and Manufacturing (IIITDM), Kurnool, Andhra Pradesh, India*
[d]*Nano and molecular systems research unit, P.O.Box 8000, FI-90014, University of Oulu, Oulu, Finland*
**alok.phy@pondiuni.edu.in, †getsruthil@gmail.com*

Abstract: Microscopic electron dynamics of anatase TiO_2 modulated by an ultrashort and intense laser field is investigated ab-initio using the real-time time-dependent density functional theory (TDDFT). We study the electron dynamics in response to 30 fs laser pulses of 800 nm and 400 nm wavelengths and peak intensities ranging from 10^7 W/cm^2 to 10^{16} W/cm^2. We identify that for 800 nm pulse, nonlinearity is perturbative, and two-photon absorption is the dominant ionization mechanism below 5×10^{11} W/cm^2. Above this value, tunneling ionization becomes dominant. The induced currents undergo a highly reversible phase shift in the perturbative regime, typically associated with the optical Kerr effect.

Keywords: Ultrashort Pulse, Nonlinear Optics, TDDFT, TiO_2, Kerr-effect, Laser-induced Damage

1. Introduction

Ultrashort laser technologies have enabled us to induce, drive and measure nonlinear polarization in crystalline solids in time resolutions less than a period of optical pulses [1]. It would ultimately lead us to achieve information processing at petahertz clock rates. Wide bandgap dielectric materials ($0.1\ eV\ < \Delta E_g < 4\ eV$) offer potential avenues for exploring sub-fs control of electron dynamics. TiO_2, widely used as a saturable absorber in passively Q-switched fiber lasers, is one of the potential candidates for nonlinear photonics applications. Optical switching capabilities of TiO_2 waveguides have already been demonstrated at 800 nm and 1550 nm wavelengths [2].

Theoretical investigations of intense ultrashort light-matter interaction are quite significant to understand the microscopic mechanism of the phenomena. We report ab-initio simulations based on the Time-dependent density functional theory (TDDFT) to describe the electron dynamics of TiO_2 induced by intense ultrashort laser pulses [3]. In TDDFT, the time evolution of Bloch orbitals $u_{nk}(\boldsymbol{r},t)$ is determined by the time-dependent Kohn-Sham equation (TDKS). The average induced current density is evaluated over the unit cell volume Ω by

$$J(t) = -\frac{e}{m\Omega}\sum_{n\boldsymbol{k}}^{occ}\int u_{nk}^{*}(\boldsymbol{r},t)\left(\boldsymbol{p}+\hbar\boldsymbol{k}+\frac{e}{c}\boldsymbol{A}(t)\right)u_{nk}(\boldsymbol{r},t)\ +\ J_{NL}(t) \qquad (1)$$

$\boldsymbol{A}(t)$ is the vector potential representing the external laser field. We use a Gaussian pulse of total duration of 30 fs. The time-resolved energy density $W(t)$ transferred between the field and the material is evaluated using the nonlinear polarization P_{NL} by $W(t) = \int_{-\infty}^{t} E(t')\frac{dP_{NL}(t')}{dt'}\,dt'$. Further, the number of excited electrons $n_{ex}(t)$ per unit cell was calculated using $n_{ex}(t) = \sum_{nn'\boldsymbol{k}}(\delta_{nn'\boldsymbol{k}} - |\langle\psi_{nk}(0)|\psi_{n'k}(t)\rangle|^2)$, where n and n' are band indices, $\boldsymbol{k}$ indexes the electron wave vectors, $|\psi_{nk}(0)\rangle$ is the KS wavefunction of the ground state, $|\psi_{n'k}(t)\rangle$ is the KS time-dependent wavefunction. For practical simulations of laser excited anatase TiO_2, we have used TDDFT as implemented in real-space, real-time code Octopus [4]. The orbital wavefunctions are represented on a three-dimensional spatial grid the in unit cell of the crystal. To express the Bloch orbitals, the real space grid is discretized with $\Delta x, \Delta y = 0.12$ Å and $\Delta z\ = 0.20$ Å. For the time evolution, we use a time step of $\Delta t\ =\ 0.02$ au.

2. Results and Discussion

The time-resolved energy $W(t)$ exchanged between anatase TiO_2 unit cell and 30 fs pulse for 400 nm, and 800 nm is shown in Figure 1. The excitation at 800 nm (1.55 eV) is forbidden as the incident photon energy is smaller than the band gap of anatase TiO_2 (2.15 eV at the GGA level). For intensities up to 10^{11} W/cm^2, the temporal energy transfer has a similar profile as the field intensity, and the energy transferred to the material is entirely reversible. This sub-

cycle energy oscillation results from virtual excitations at 800 nm. It defines the perturbative regime of optical nonlinearities. In the perturbative regime, the nonlinear induced currents undergo a highly reversible phase shift associated with the optical Kerr effect. The linear dependence of phase shift on peak intensities provides an estimate of the nonlinear refractive index 3×10^{11} cm^2/W for TiO_2

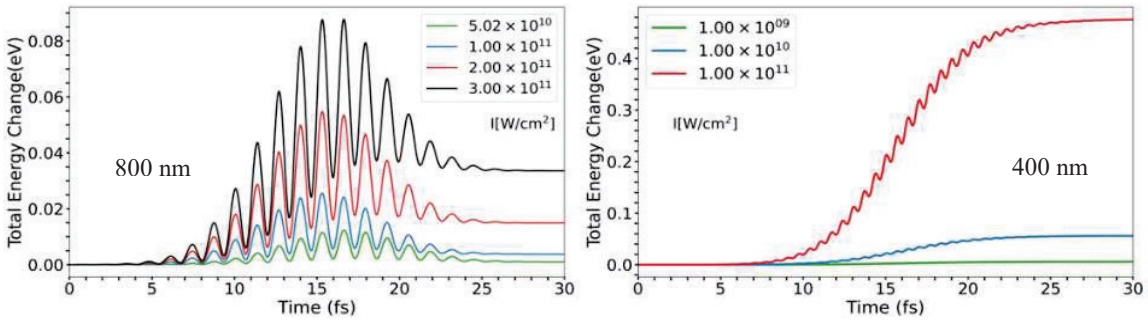

Figure 1: Energy transfer dynamics of anatase TiO_2 interacting with 30 fs laser pulse of 800 nm and 400 nm wavelengths

When the intensity increases above 1×10^{11} W/cm^2, the system absorbs energy by two-photon absorption. The amount of energy transfer accurately follows the quadratic dependence on the intensity. Population transfer to the conduction band via two-photon absorption results in an irreversible energy component indicated by the saturation of total energy towards the tail end of the pulse. However, when the incident energy is larger than the material's bandgap (400 nm i.e., 3.10 eV), single photon absorption is the dominant energy transfer mechanism.

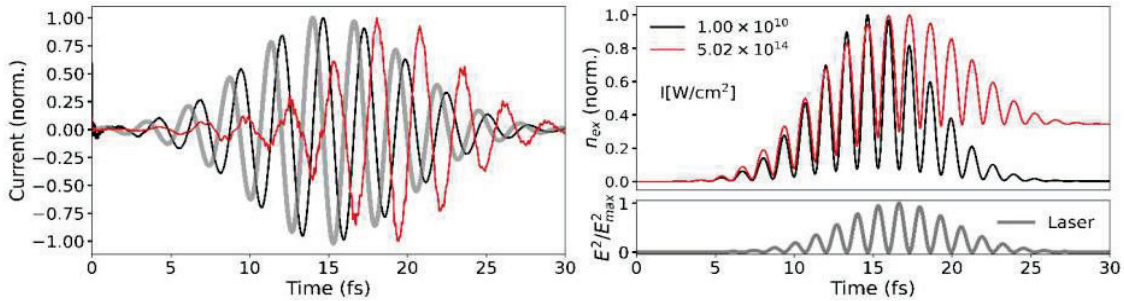

Figure 2: Laser induced current, number of excited electrons for weak and strong field regime, indicating the onset of material damage

Next, we investigate the processes that eventually lead to laser-induced materials damage. Figure 2 compares the time-dependence of induced current and the number of excited electrons for 10^{10} W/cm^2 and 5×10^{14} W/cm^2 peak intensities. The response is dielectric at the initial stage of the laser pulse, where the applied electric field is weak. The number of excited electrons and the excitation energy rapidly increase around 12 fs, indicating the ionization of electrons by tunneling. Simultaneously, the total current gradually goes out of phase with the applied electric field, signaling a large energy transfer. By about 18 fs, the applied and total electric fields are entirely out of phase. At this point, the number of excited electrons and the excitation energy reach their saturation values. The oscillation in the total induced current after the applied laser pulse ends is plasma oscillation of the electrons excited into a conduction band. Plasma formation will be followed by thermalization by carrier-carrier and carrier-phonon scattering, eventually leading to permanent structural changes in the material.

3. References

[1] Sommer, Annkatrin, et al. "Attosecond nonlinear polarization and light–matter energy transfer in solids." Nature **534**, 7605 (2016)

[2] Evans, Christopher C., et al. "Ultrafast all-optical switching in TiO_2." Nano-Optics for Enhancing Light-Matter Interactions on a Molecular Scale. Springer, Dordrecht, 377-377 (2013)

[3] Yabana, Kazuhiro, et al. "Time-dependent density functional theory for strong electromagnetic fields in crystalline solids." Physical Review B **85**.4, 045134 (2012)

[4] Tancogne-Dejean, Nicolas, et al. "Octopus, a computational framework for exploring light-driven phenomena and quantum dynamics in extended and finite systems." The Journal of chemical physics **152**.12 (2020)

Ca-Eu:Y_2O_3@SiO_2core-shell nanoparticles for the visualization of latent fingerprints and anti-counterfeiting applications

Arpita Dwivedi[1], Sanjay Kumar Srivastava
Department of Physics, Banaras Hindu University, Varanasi-221005
joinarpit@gmail.com[1], Sanjay_itbhu@yahoo.com*

Abstract: This work reports, the synthesis of divalent (Ca^{2+}) doped Eu:Y_2O_3@SiO_2 for core-shell nanomaterial first time as a fluorescent labeling agent for anti-counterfeiting applications, and visualization of LPF and solid-state lighting. The structure, morphology, and optical properties, with the thermal stability of phosphor material studied in detail. The optimal fluorescence intensity has been obtained for the 10 vol % of SiO2 (TEOS) coating and the enhancement of intensity is approximately 36 % of that uncoated sample. The synthesized core-shell phosphor material can be effetely used for security ink and latent fingerprint for forensic uses.
Keywords: core-shell, photoluminescence, Anti-counterfeiting ink, Latent fingerprint

1. Introduction

Nowadays, the lanthanoid doped core shell structure have high scientific interest due to its interesting properties by tuning the experimental conditions [1]. Core shell structure formed when one type of particle encapsulated over the other, which modifies the material properties. Modification of material properties as core shell help us to get various advantageous application in the field of photonics, electronic, spintronics and various over filed [2-4]. Till the date huge number of soft and hard templet has been used for the synthesis of various type of core shell structure. Among all of them the silica has been studied widely and frequently used for the synthesis of core-shell structured. As silica coated structure has special properties such as biocompatibility, high thermal and chemical stability, optical transparency, and harmless and tunable sizes which results efficient use of silica as core shell material [1, 5, 6]. With this silica also reduce scattering of light, improve brightness and resolution as compared to the traditional commercial materials which is very suitable for the display devise, biomedical and imaging, anti-counterfeiting applications [1, 2, 7]. Nowadays, Ln^{3+} doped nanomaterial has drawn more attention for the surface-based research specially for latent fingerprints (LFP) recognition and anti-counterfeiting applications over the traditional martials iodine fuming, cyanoacrylate fuming, and ninhydrin etc. [1, 2, 6]. As these materials are associated with various limitation such as high background interference, less detection sensitivity, harmful nature and complex working method. Thus, it is important to develop a material have which can overcome these limitations [1, 2, 6]. Various researchers' groups have reported Ln^{3+} doped core shell material for the visualization of LPF [1, 2, 5, 6]. However, the level of visualization with their material are still not slandered due to their poor imaging ability of these phosphor materials. Hence, it is necessary to synthesize new phosphor material with good qualities. Herein, we have synthesized divalent (Ca^{2+}) doped Eu:Y_2O_3@SiO_2 core-shell nanomaterial first time as fluorescent labelling agent for the anti-counterfeiting applications and visualization of LPF and solid-state lighting.

2. Results and Discussion:

In order to understand shape, sizes, morphology and composition of synthesised phosphor materials high-resolution transmission electron microscopy (HTEM) of Ca-Eu:Y_2O_3@SiO_2 phosphor has be recorded and given in **Fig 1.**

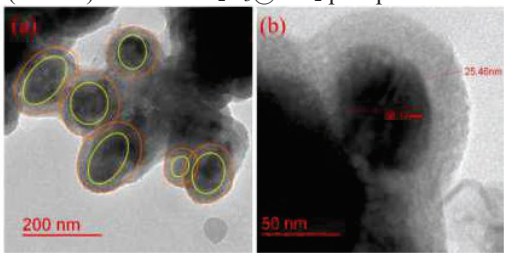

Fig 1.(a and b) TEM image of of Ca-Eu:Y_2O_3@SiO_2 core-shell phosphor material

From the **Fig 1 (a)**, TEM image it is clearly visible that a dense layer of silica has been successfully coated on the surface of the nanoparticle. With the coating of SiO_2, size of nanophosphor has been also increased. The thickness of the Silica layer over the nanoparticle in case of 10 vol. % of TEOS is approximately 26 nm (**Fig 1 (b)**). The synthesised core-shell material is also show high aggregation, this might be due to formation of surface silanol (OH-Si) group which connect particle through Vanda wall force by hydrogen bonding produce agglomeration [8].

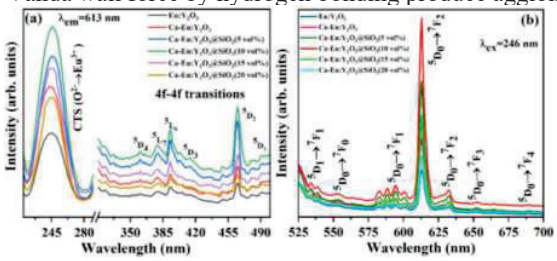

Fig. 2. (a) PL excitation spectra for λ_{ex}= 613 nm and PL emission spectra for **(b)** λ_{em}= 246 nm for Eu:Y_2O_3, Ca-Eu:Y_2O_3, Ca-Eu:Y_2O_3@SiO_2 (5, 10, 15, 20 vol%) nanophosphors

Fig 1(a-d) displays the photoluminescence excitation spectra (PEL) and photoluminescence emission spectra (PL) of Eu:Y_2O_3, Ca-Eu:Y_2O_3, Ca-Eu:Y_2O_3@SiO_2 (5, 10, 15, 20 vol%) nanophosphors respectively. In PL excitation spectra **(Fig 2 (a)),** a broad band of high energy has been observed which lie near UV range 215-280 nm with peak maxima at 246 nm. This broad raises due to charge transfer state (CTS) from O^{2-} to Eu^{3+} (2p orbit of O^{2-} to 4f orbit of Eu^{3+} ion) inside the host [7, 9]. Beside CTS band, there are other weak peak lie in longer wavelength range 310-500 nm, correspond to 4f-4f transition of Eu^{3+} ions within $4f^6$ electronic configuration [5, 6]

The emission spectra recorded for the 525-700 nm range which contain several emission peaks, theses peaks are associated with the transition from $^5D_0$ excited state to ^7F_J (J= 0-4) and $^5D_1$ to $^7F_1$ state respectively, of Eu^{3+} ion [5, 6]. These peaks arise due to the magnetic dipole (MD) and electric dipole (ED) transition of Eu^{3+} ions in Y_2O_3 host lattice[1, 2, 6]. There is approximately 36% increase of PL intensity has been observed as compared to Ca-Eu:Y_2O_3 phosphor for 246 nm excitation. SiO_2 coating could significantly affect the luminescence response in two ways [10]. One way is the SiO_2 coating significantly reduce the surface defect by improving unevenness of phosphor particle, which increase the light gathering properties by reduce light scatting effect and hydroxyl group on the surface [9, 10].

3. Applications of Ca-Eu:Y_2O_3@SiO_2 core- shell (10 vol% TEOS) Visualization of Latent finger print and security ink using:

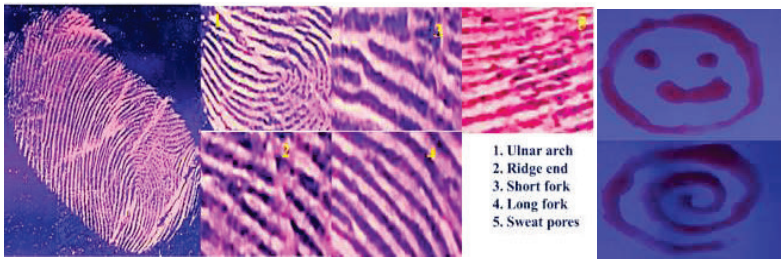

Fig. 3. Visualization of various Latent finger print, and its microstructures on the glass surface, and security ink by Ca-Eu:Y_2O_3@SiO_2 core- shell phosphor

4. References

[1] C. Suresh, H. Nagabhushana, R. Basavaraj, G. Darshan, D. Kavyashree, B.D. Prasad, S. Sharma, R. Vanithamani, SiO2@ LaOF: Eu3+ core-shell functional nanomaterials for sensitive visualization of latent fingerprints and WLED applications, Journal of colloid and interface science 518 (2018) 200-215.

[2] D. Muniswamy, H. Nagabhushana, R. Basavaraj, G.P. Darshan, D. Prasad B, Surfactant-assisted BaTiO3: Eu3+@ SiO2 core–shell superstructures obtained by ultrasonication method: Dormant fingerprint visualization and red component of white light-emitting diode applications, ACS Sustainable Chemistry & Engineering 6(4) (2018) 5214-5226.

[3] M. Dhanalakshmi, R. Basavaraj, G. Darshan, S. Sharma, H. Nagabhushana, Pivotal role of fluxes in BaTiO3: Eu3+ nano probes for visualization of latent fingerprints on multifaceted substrates and anti-counterfeiting applications, Microchemical Journal 145 (2019) 226-234.

[4] A. Sandhyarani, R. Basavaraj, G. Darshan, H. Nagabhushana, M. Kokila, Influence of surface modification on enhancement of luminescent properties of SiO2@ SrTiO3: Dy3+ nanopowders: Probe for visualization of sweat pores present in latent fingerprints, Optik 181 (2019) 1139-1157.
[5] K.N. Venkatachalaiah, H. Nagabhushana, G.P. Darshan, R.B. Basavaraj, B.D. Prasad, Novel and highly efficient red luminescent sensor based SiO2@Y2O3:Eu3+, M+ (M+=Li, Na, K) composite core–shell fluorescent markers for latent fingerprint recognition, security ink and solid state lightning applications, Sensors and Actuators B: Chemical 251 (2017) 310-325.
[6] A. Sandhyarani, M. Kokila, G. Darshan, R. Basavaraj, B.D. Prasad, S. Sharma, T. Lakshmi, H. Nagabhushana, Versatile core–shell SiO2@ SrTiO3: Eu3+, Li+ nanopowders as fluorescent label for the visualization of latent fingerprints and anti-counterfeiting applications, Chemical Engineering Journal 327 (2017) 1135-1150.
[7] H. Wang, M. Yu, C. Lin, X. Liu, J. Lin, Synthesis and Luminescence Properties of Monodisperse Spherical Y2O3: Eu3+@ SiO2 Particles with Core− shell Structure, The Journal of Physical Chemistry C 111(30) (2007) 11223-11230.
[8] A.A. Ansari, J.P. Labis, M.A. Manthrammel, Designing of luminescent GdPO4: Eu@ LaPO4@ SiO2 core/shell nanorods: synthesis, structural and luminescence properties, Solid State Sciences 71 (2017) 117-122.
[9] U. Rambabu, S.-D. Han, Enhanced luminescence intensity and color purity of the red emitting LnVO4: Eu3+@ SiO2 (Ln= Gd, Y and Gd/Y) powder phosphors, Materials Research Bulletin 48(2) (2013) 512-520.
[10] Y.-X. Fu, Y.-H. Sun, Comparative study of synthesis and characterization of monodispersed SiO2@ Y2O3: Eu3+ and SiO2@ Y2O3: Eu3+@ SiO2 core–shell structure phosphor particles, Journal of alloys and compounds 471(1-2) (2009) 190-196.

Polarization length of a coherent random light

Sourav Chandra*, Rajeev Singh, and Rakesh Kumar Singh
Laboratory of Information Photonics and Optical Metrology, Department of Physics, Indian Institute of Technology (Banaras Hindu University), Varanasi-221005, India
**Author e-mail address: souravchandra.rs.phy19@itbhu.ac.in*

Abstract: The concept of polarization length is introduced and analyzed by using normalized Stokes correlation of the random field. In order to measure the polarization length, we use Stokes parameters of the random field and then estimated two-point Stokes correlations to determine polarization length.
Keywords: Polarization, Speckle, Stokes parameters

1. Introduction

When a coherent light travels through a scattering medium, interference of scrambled wavefront of light produces complex coherent random field i.e. speckle. Compared to random spatial intensity distribution for a scalar random field, vector coherent random light field exhibit fluctuations in the state of polarization due to inherent source structure or propagation through a scattering medium. The concept of polarization length specifies the polarization states fluctuation of vector coherent light field and provides useful information about polarization dynamics of coherent light propagating through scattering medium [1], and also used to characterize spatial polarization fluctuation of the coherent random light field [2]. Two-point normalized Stokes correlation function captures the spatial variation of the state of polarization fluctuation and is used to examine the polarization length of spatially varying random light fields. The experimental investigation of source size on the correlation function as well as on the polarization length of the random light field is presented in this paper.

2. Theory

The conventional Stokes parameters (SPs) without time or space averaging are represented in terms of four Pauli matrices as

$$S_n(r,t) = \sum_{a,b} \sigma_{ab}^{n} E_a^{*}(r,t) E_b(r,t), \qquad n=0\text{-}3, \quad a,b=x,y \tag{1}$$

where, σ^0, σ^1, σ^2, σ^3 are the 2×2 identity matrix and the 2×2 three Pauli spin matrices, respectively. The spatial variations of SPs are estimated using the two-point normalized Stokes correlation function as

$$\gamma_p(\Delta r) = \frac{\langle S_1(r) S_1(r+\Delta r)\rangle + \langle S_2(r) S_2(r+\Delta r)\rangle + \langle S_3(r) S_3(r+\Delta r)\rangle}{\langle S_0(r) S_0(r+\Delta r)\rangle} \tag{2}$$

where $\langle\ \rangle$ represents ensemble average, which in practice, is replaced by spatial average assuming spatial stationarity and ergodicity such that SPs correlation depends only on the difference of spatial coordinate Δr. We define the polarization length as the length at which $\gamma_p(\Delta r)$ reduces to 15% of its maximum value as polarization fluctuation is very slow for a fully polarized speckle.

3. Experimental setup and results

The schematic of the experimental setup is demonstrated in fig. 1. A spatially filtered vertically polarized light beam of wavelength 632.8 nm from a He-Ne laser is oriented 45° with respect to the vertical direction using a half-wave plate (HWP). A circular aperture (CA) is utilized to control the source size. The light beam passes through a ground glass (GG), placed at the front focal plane of a bi-convex lens, and creates a vector coherent random field at the back focal plane of L, which is recorded by a CCD camera. The quarter-wave plate (QWP) and polarizer (P) are used to compute the Stokes parameters (SPs), which describe the state of polarization of the generated vector coherent random field. SPs, shown in fig. 1, are determined from different intensity measurements using the following equations [3]:

$$S_0(r)=I(0^\circ,0^\circ)+I(90^\circ,90^\circ),\ S_1(r)=I(0^\circ,0^\circ)-I(90^\circ,90^\circ),$$
$$S_2(r)=I(45^\circ,45^\circ)-I(135^\circ,135^\circ),\ S_3(r)=I(0^\circ,45^\circ)-I(0^\circ,135^\circ). \quad (3)$$

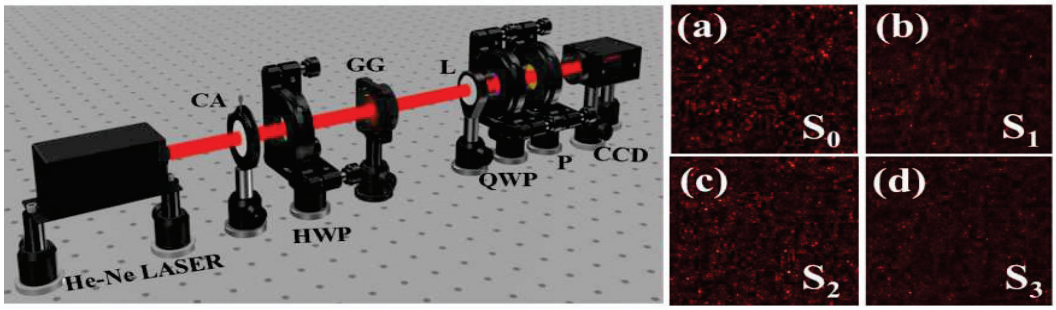

Fig.1: (Left) experimental setup to study the effect of source size on the polarization length of polarization speckle, (a) - (d) are the experimentally measured Stokes parameters

The correlations of SPs are determined from the experimentally obtained SPs from Eq. (3) and the two-point normalized Stokes correlation function, $\gamma_p(\Delta r)$, is calculated using Eq. (2), for the illuminating beam sizes of 3.5mm and 7mm, and their profiles are shown in fig. 2.

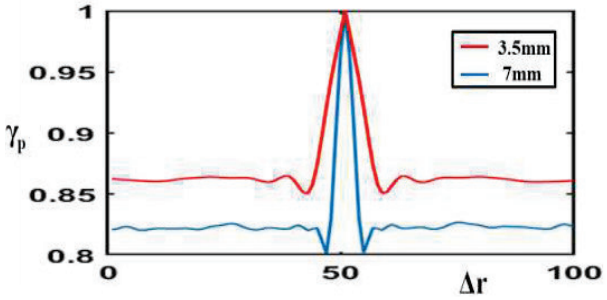

Fig.2: Profiles of $\gamma_p(\Delta r)$ for vector coherent light field with source sizes of 3.5mm and 7mm.

We see that polarization correlation drops to 15% for Δr equal to 103µm and 32µm for source sizes of 3.5mm and 7mm respectively. So with increasing source size, $\gamma_p(\Delta r)$ becomes narrower.

4. Conclusion

We have illustrated the effect of source size on the spatial variation of polarization states fluctuation of polarization speckle through the two-point normalized Stokes correlation function $\gamma_p(\Delta r)$. It is observed that the function $\gamma_p(\Delta r)$, depends upon the illuminating beam size. Therefore, it can be inferred that polarization length change depends on the source size of the beam used to generate polarization speckle. This work may be useful to characterize the polarization dynamics of random fields.

5. Acknowledgment

Sourav Chandra acknowledges the financial support from IIT (BHU).

6. References

[1] T. Setala, A. Shevchenko, M. Kaivola, A.T. Friberg, "Polarization time and length for random optical beams," Phys. Rev. A, 78, 033817 (2008)

[2] R. K. Singh, D. N. Naik, H. Itou, Y. Miyamoto, and M. Takeda, "Characterization of spatial polarization fluctuations in scattered field," J. Opt. 16, 105010 (2014).

[3] D. H. Goldstein, "Polarized Light," (CRC Press, 2011).

Generation of cylindrical vector beam using non-interferometric dual phase modulation

Mansi Baliyan and Naveen K. Nishchal*

Department of physics, Indian Institute of Technology Patna, Bihar-801 106

*nkn@iitp.ac.in

Abstract: In this paper, vector beam embedded with spatially varying polarization distribution is generated using non-interferometric arrangement and dual phase modulation approach. A single reflective type liquid crystal spatial light modulator (SLM) has been used. V-point and C-point polarization singularities embedded in cylindrical vector beam has been generated by modulating suitable phase value distributions in both orthogonal polarization components of light field.

Keywords: Orbital angular momentum, Cylindrical vector beam, Spatial light modulator, Polarization singularity

1. Introduction

Techniques to tailor the light wavefront by controlling its properties like amplitude, phase, polarization result into a structured light whose wavefront is found spiral around propagation direction due to its dependence on azimuth $e^{il\phi}$. Therefore, such light fields carry orbital angular momentum (OAM) as ± $lh/2\pi$, where l and h denote topological charge (TC) and Planck's constant, respectively. TCs denote number of rotations of phase of light per wavelength [1-8]. This study comes under the singular optics branch where we find singularities occurring in light field in any of its measurable parameters like phase and polarization.

In phase singularity, phase at the centre or along propagation direction of light field is not-defined and has dark intensity centre called vortex. Around vortex point the phase gradient circulates from 0 to $2\pi l$. The light field holding phase singularity is found with spatially not varying polarization distribution within its cross-section whereas in polarization singularity, azimuth or ellipticity angle is not-defined and light holding different polarization singularities consist of spatially varying polarization distribution within its cross-section [6] which is determined using stokes parameters with different orientation of polarizer.

2. Principle

A vector beam is generated as a superposition of two orthogonal scalar fields associated with opposite TC in circular polarization basis as [2],

$$U = \frac{1}{\sqrt{2}}\left[\psi_{p_1}^{l_1}\hat{e}_L + \psi_{p_2}^{l_2}e^{i\delta}\hat{e}_R\right] \tag{1}$$

Unitary vectors $\hat{e}_L$ and $\hat{e}_R$ represent left and right light field polarizations in circular basis and each one having corresponding orthogonal scalar fields as $\psi_{p_1}^{l_1}$, $\psi_{p_2}^{l_2}$. Selecting appropriate phase values like TCs l_1, l_2 and additional phase delay δ in one of the polarization components result into different polarization singularity like V-points singularity, in which l_1 and l_2 have equal magnitude but opposite sign and C-points singularity, in which one of the TCs, l_1 or l_2 remain zero. The spatially varying polarization within vector light is obtained using Stoke's polarimetry. Figure 1 represents the schematic diagram of proposed experimental set-up.

3. Simulation results and discussion

Spatially varying polarization distribution within cross-section of vector beam consisting of different types of polarization singularities is found by modulating different phase profiles $(e^{il_1\phi_x})$ in x-component and $(e^{il_2\phi_y+\delta})$ in y-component of light.

V-type polarization singularities are obtained as azimuthal, radial, spiral with phase delay values substituted in one of polarization components as $\delta = 3\pi/2$, $\pi/2$, π respectively and l_1=- l_2 as TC value in both orthogonal components. C-point polarization singularities are found as star, lemon by substituting zero TC in one of polarization component $l_1 = 0$, l_2 or $l_2 = 0$, l_1 and $\delta = 3\pi/2$. C-point left-handed and right-handed singularities in star are found by substituting $l_1 = 0$, $l_2 = 1$ and $l_1 = -1$, $l_2 = 0$ and in lemon are found by substituting $l_1 = 0$, $l_2 = -1$ and $l_1 = 1$, $l_2 = 0$, respectively as shown in Figs. 2 and 3, respectively.

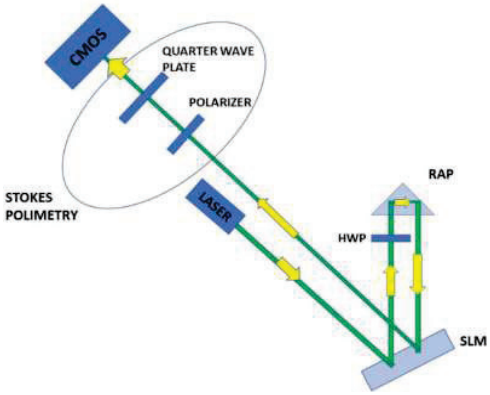

Fig. 1 Schematic of the proposed experimental set-up.

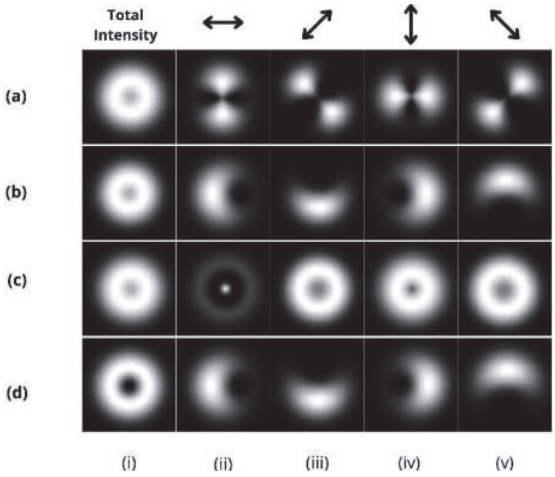

Fig. 2 Simulation results of vector beam embedded with C-point. Rows represent (a) Lemon left-handed (LH), (b) Lemon right-handed (RH), (c) Star LH, (d) Star RH distribution and column (i) represents total intensity, (ii)-(v) represent field intensity at different orientation of polarizer

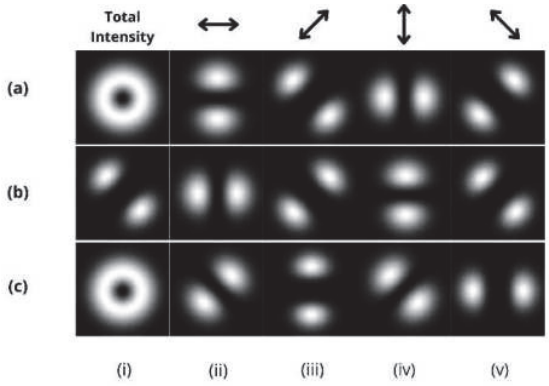

Fig. 3 Simulation results of vector beam embedded with V-point. Rows represent (a) azimuthal, (b) radial, (c) spiral polarization distributions and column (i) represent total intensity, (ii)-(v) represent field intensity at different orientation of polarizer

4. Conclusion

Generation of vector beam through numerical simulation following non-interferometric technique and dual phase modulation approach is presented. Further, work on optical implementation of the approach is being carried out.

Acknowledgement

The authors acknowledge the financial support from the SERB, Department of Science and Technology, Government of India (CRG/2021/001763).

References

[1] P. Kumar, S. K. Pal, N. K.Nishchal, and P. Senthikumaran, "Non-interferometric technique to realize vector beams embedded with polarization singularities," J. Opt. Soc. Am. A 37, 1043-1052 (2020).
[2] C. R. Guzman, B. Ndagano, and A. Forbes, "A review of complex vector light fields and their applications," J. Opt. 20, 123001 (2018).
[3] H. Rubinsztein-Dunlop *et al*. "Roadmap on structured light," J. Opt. 19, 013001 (2017).
[4] Y. Shen *et al*. "Optical vortices 30 years on: OAM manipulation from topological charge to multiple singularities," Light Sci. Appl. 8, 90 (2019).
[5] C. Rosalez-Guzman and A. Forbes, *How to Shape Light with Spatial Light Modulators*, SPIE Press (2017).
[6] Ruchi, P. Senthikumaran, and S.K. Pal, "Phase singularities to polarization singularities," Int. J. Opt. 2020, 33 (2020).
[7] C. R. Guzmán, N.Bhebhe, and A. Forbes "Simultaneous generation of multiple vector beams on a single SLM," Opt. Express 25, 25697-25706 (2017).
[8] L. Guo, Z. Feng, Y. Fu, and C. Min, "Generation of vector beams array with a single spatial light modulator," Opt. Commun. 491, 126915 (2021).

Impact of Solar Noise on Free-space Optical Wireless Communication Link: Experimental Investigations

Saroj K. Mahapatra, Sanjib K. Roy, Manotosh Hawlader, and Shailendra K. Varshney
Dept. of Electronics & Electrical Communication Engg.,
Indian Institute of Technology, Kharagpur, West Bengal, India, 721302
Author e-mail address: sarojmahapatra80@gmail.com

Abstract: Free space optical (FSO) communication offers large bandwidth, high data rate, license-free spectrum, and quick deployability. This technology will be an alternative to a next-generation wireless communication backbone network. The presence of solar light for the whole day in the atmosphere limits the FSO system potential. In this paper, we experimentally demonstrate solar light noise interference to the FSO system when its receiver (Rx) faces different orientations. The experiment outcomes confirm that the same FSO system behaves differently when its Rx keeps changing its face in various orientations.
Keywords: Optical wireless communication, Free-space optical wireless communication, Orientation-based solar light noise.

1. Introduction

The performance of the FSO communication system is limited by various atmospheric adverse effects, i.e., absorption, scattering, turbulence, and background light noise. In the background noise category, the solar light is robust as it exists for the whole of the day. V. G. Sidorovich et al. [1] have theoretically discussed on directed, reflected, and scattered sunlight effect over a horizontal FSO communication system link. M. A. Khalighi et al. [2] have reported a theoretical approach to mitigate the solar noise interference over FSO system based horizontal link. D. Rollins et al. [3] have demonstrated experimentally the solar noise effect over terrestrial horizontal FSO link in sunny and partly cloudy day concerning with the optical filter bandwidth and Rx field of view (FoV). In free space, we will be uncomfortable looking upward if the sun is positioned at the zenith. In a horizontal direction parallel to the earth's surface, we feel comfortable and most comfortable when we look downward. It happens due to variations in solar light intensity at different orientations. In some of our previous works [4-6], the theoretical performance evaluation model of optical wireless communication systems in the presence of undersea orientation-based solar light noise has been presented and concluded with significant system performance variation at different orientations. To the best of our knowledge, no theoretical and experimental model has been presented so far for FSO system performance evaluation in the presence of orientation-based solar light noise. In this paper, we have investigated the impact of solar light noise on the FSO communication system experimentally by facing its Rx to three different orientations, e.g., vertically upward (VU), horizontally leftward (HL), and vertically downward (VD).

2. Experimental Setup

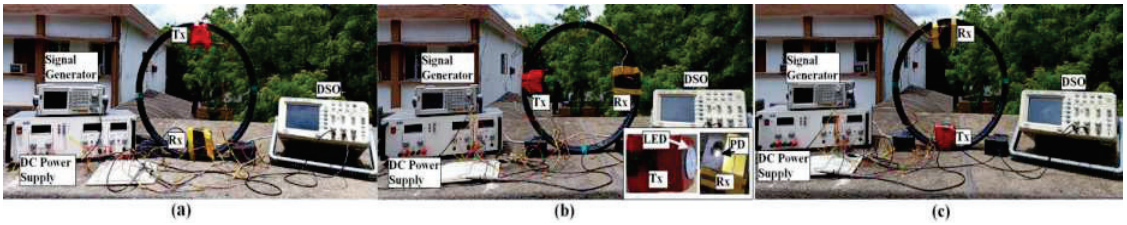

Fig.1: Schematic of a FSO communication system, the Rx faces three different orientations in (a) vertically upward (VU), (b) horizontally leftward (HL), and (c) vertically downward (VD).

The white LED has been used as a Tx light source, emitting light at a power of 0.5 watts with 115 lumen brightness in the spectral range of 400-700 nm. Intensity modulation (IM) with on-off keying (OOK) format is carried out using a signal generator, generating pulse waves at 6 kHz. The transmitted signal is detected directly using a photodetector (PD) at the Rx end. The experiment was conducted on a partly cloudy day. Ambient solar noise interferes with the light signal during the reception at the PD. Tx and Rx have been mounted over a metal ring to

keep the link distance of 22 cm unchanged during movement in various orientations. The output of the PD is processed using a trans-impedance amplifier, voltage amplifier, and threshold circuit. Both time and frequency domain analysis has been carried out over the processed signal using a digital storage oscilloscope (DSO). The DC power supply provides operating voltage to the transceiver circuits.

3. Experimental Results and discussion

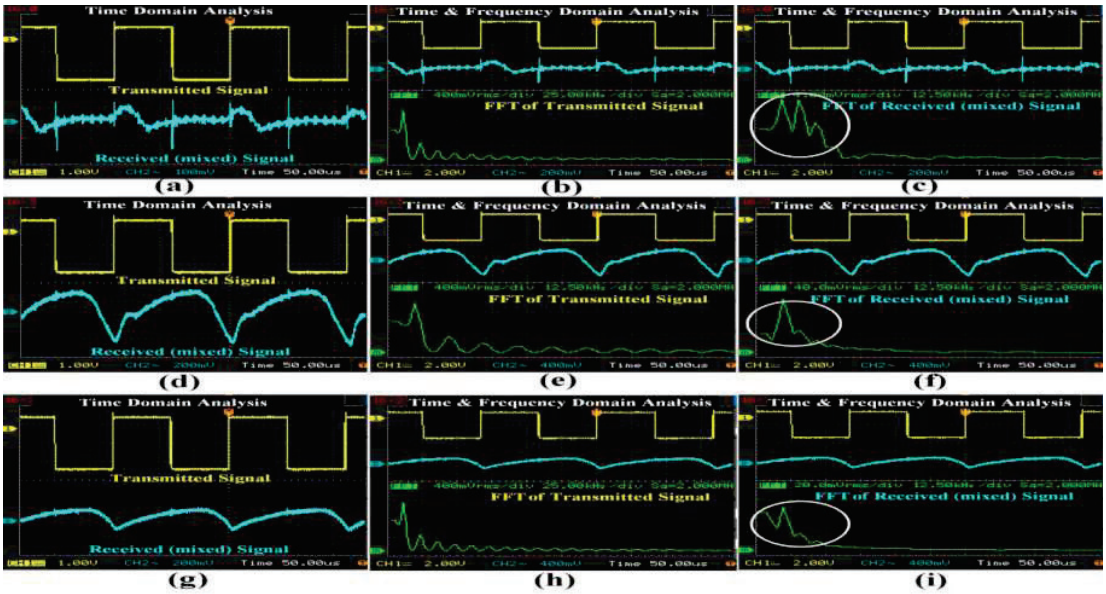

Fig.2: Time and frequency domain (FFT using Blackman window) analysis of the transmitted and received signal when system Rx faces vertically upward in (a), (b), (c), horizontally leftward in (d), (e), (f), and vertically downward in (g), (h), (i).

Based on the time and frequency domain analysis shown in Figs. 2 (a) - (i), the received signal has been corrupted mostly due to reception of highest intensity solar noise with system Rx facing vertically upward orientation and least when facing vertically downward orientation. In Fig. 2 (c), FFT analysis of the received signal, side lobes have been formed beside the main lobe due to reception of the highest intensity solar noise. In Fig. 2 (f), more spectral leakage has been noticed with an adequate roll-off rate when Rx faces horizontally leftward. In Fig. 2 (i), spectral leakage has been observed with a vertically downward facing Rx. Figs 2 (b), (e), and (h) represent the FFT analysis of the transmitted signal (directly fed to the DSO from the signal generator), used as a reference signal during the investigation.

4. Conclusion

The effect of solar noise on the free-space optical wireless communication system is investigated experimentally for various orientations.

5. References

[1] V. G. Sidorovich, “Solar background effects in wireless optical communication,” in Proc. SPIE 4873, Optical Wireless Communications V, (2002), pp. 133-142.

[2] M. A. Khalighi, F. Xu, Y. Jaafar, and S. Bourennane, "Double-Laser Differential Signaling for Reducing the Effect of Background Radiation in Free-Space Optical Systems," J. Opt. Commun. Netw., **3**, 145-154 (2011).

[3] D. Rollins, J. Baars, D. P. Bajorins, C. S. Cornish, K. W. Fischer, and T. Wiltsey, "Background light environment for free-space optical terrestrial communications links," in Proc. SPIE 4873, Optical Wireless Communications V, (2002), PP. 99-110 .

[4] S. K. Mahapatra, S. K. Varshney, “Impact of orientation-based solar light noise on the performance of underwater optical wireless communication system and noise cancellation,” Results in Optics**, 14,** 100214 (2022).

[5] S. K. Mahapatra, S. K. Varshney, “Theoretical study on the effectiveness of optical filters to suppress orientation-based solar light noise,” Applied Optics**, 60 (27),** 8600-8608 (2021).

[6] S. K. Mahapatra, S. K. Varshney, “Performance of the Reed-Solomon-coded underwater optical wireless communication system with orientation-based solar light noise,” JOSA A**, 39 (7),** 1236-1245 (2022).

Holography vs Edge Point Referencing

Surya Kumar Gautam[1], Dinesh N Naik[2]
[1]*National Physical Laboratory, (CSIR-NPL)*
New Delhi, Delhi 110012, India
[2]*Applied and Adaptive Optics Laboratory, Department of Physics, Indian Institute of Space Science and Technology (IIST), Trivandrum, Kerala 695547, India*
suryagautam89@gmail.com

Abstract: In this paper, we are pointing out the differences between the holography and edge point referencing (EPR) techniques. Additionally, common path setups are designed and proposed for generating the beams used for EPR.
Keywords: Holography, Edge point referencing (EPR), 3D complex object reconstruction.

1. Introduction

In holography [1], the reference field is generally independent and kept separately from the object. Considering the fact that one cannot isolate the optical system completely from the external vibration, the reference field can vibrate slightly with respect to the object field, this can cause repeatability problems in the reconstruction from the holography. Whereas in edge point referencing (EPR) method [2] where additional beam is used to illuminate the object edge point, even if object field oscillates due to the vibration, reference field which is scattered from the object edge point also oscillates in a similar manner. In order to reduce vibrational effects further, simple, common path and robust optical setups are designed and developed for generating the beams used for illuminating the object.

2. Holography vs Edge Point Referencing

Holography

Ideal condition, holography equation can be written as

$$I = |O|^2 + |R|^2 + R^*O + O^*R \quad (1)$$

Where O and R represent the object and reference fields.

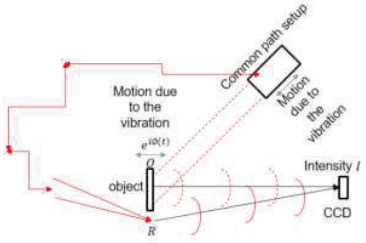

Fig. 1: A common path setup for capturing far-field intensity using off-axis hologram,

Under the vibration condition, according to the setup shown in figure 1, since object and reference fields are independent from each other, object can oscillate independently from the reference. This introduces a random phase $e^{i\phi(t)}$ in the object field which depends on the time t, by considering this factor interference equation in the holography can be written as follow

$$I = |O|^2 + |R|^2 + R^*e^{i\phi(t)}O + O^*Re^{-i\phi(t)} \quad (2)$$

One can see that in the reconstruction or 3rd term $R^*e^{i\phi(t)}O$, extra phase factor appears which produces a constant phase distribution over the object phase in the

Edge point referencing

Ideal condition, EPR equation can be written as

$$I = |O|^2 + |O_R|^2 + OO_R^* + O^*O_R \quad (3)$$

O and O_R represent the object and object edge point.

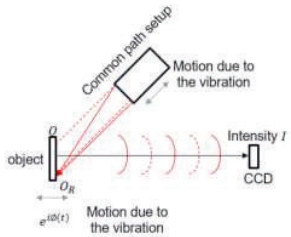

Fig. 2: A common path setup for capturing far-field intensity using edge point referencing

Under the vibration condition, according to the figure 2, since edge point of the object is acting as a reference field, due to the vibration, when object moves reference field also moves in the similar manner. This vibration introduces a random phase $e^{i\phi(t)}$ in the reference field as well in the object field, which depends on the time t, interference equation can be written as follow

$$I \approx |O|^2 + |O_R|^2 + Oe^{i\phi}O_R^*e^{-i\phi} + O^*e^{-i\phi}O_Re^{i\phi} \quad (4)$$

Rewriting $I \approx |O|^2 + |O_R|^2 + OO_R^* + O^*O_R$

One can see that in the 3rd term OO_R^*, extra phase factor does not appear, which confirms the immunity against

reconstruction. On top of that, this random factor depends on the time, hence, reconstructions of the phase of the same object in different trails retrieve different phases, results in repeatability problem in holography. Besides, if object is located far from physical reach to put a reference point near the object is not possible. Moreover, when object is located far from reach, matching the coherence length between the reference and object fields is also difficult.

the external vibration. Additionally, a common path setup is utilized for the generation of the beams; therefore, even if entire common path setup moves, it introduces almost identical phases in both the beams. Objects which are located far-from reach can also be measured. Due to the common path setup and edge point referencing, object and reference fields are located at the same plane; therefore, coherence length is matched.

3. Common Path Setups

There are several ways to generate the beams for the edge point referencing. One way is to utilize a neutral density (ND) filter which has a uniform coating throughout its region except near the periphery. By placing this ND filter in front of a collimated laser beam, one can reduce the beam intensity throughout the beam except at the location where the coating is absence then 4f geometry can be utilized for imaging the ND filter onto the object plane as shown in figure 3 (a). Second way is to place a spatial light modulator (SLM) in front of a collimated laser beam. SLM is generally sensitive to one polarization; therefore, it can only modulate certain type of polarization let say x polarization. By illuminating it with 45 degree polarized light; which has both x and y polarization states, one can generate two beams one is modulated or diffracted (x polarized) and other one is unmodulated i.e., undiffracted (y polarized). Unmodulated beam reflects from the SLM as it is, while the modulated beam can be modified according to our need by creating a phase pattern and loading it onto the SLM screen. For the edge point referencing, these two beams can be made collimated and converging respectively as illustrated in figure 3 (b).

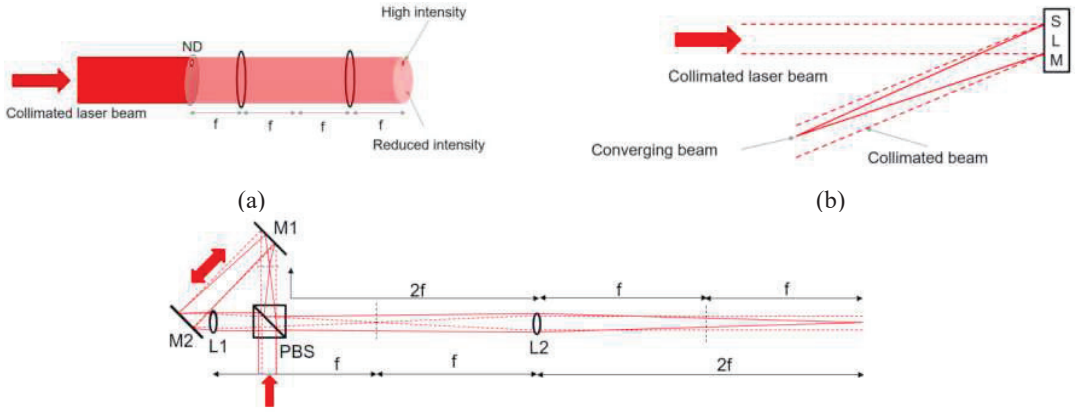

Fig. 3: Common path setup for generating edge point referencing (a) using a ND filter, (b) using a spatial light modulator and (c) using optical components.

The above two methods is limited only if one has the access of ND filter or the SLM. In figure 3 (c), a simple approach is presented to generate the beams suitable for EPR using optical components. By employing a common path Sagnac and 4f geometry using two lenses L1 and L2 and arranging the components shown in figure 3 (c), one can generate such beams. The beam transmitted from the PBS shown in figure 3 (c) follows the path shown by dotted line and the path taken by the reflected beam is shown by the solid line. Since both the beams encounter same number of optical elements, even if all the components oscillate due to the vibration the relative phase between the two beams remain stable.

4. References

[1] Emmett N. Leith and Juris Upatnieks, "Reconstructed Wavefronts and Communication Theory*," J. Opt. Soc. Am. 52, 1123-1130 (1962).
[2] Surya Kumar Gautam, R. Kumar Singh, C. S. Narayanamurthy, and D. N. Naik, "Reconstruction of complex-object using edge point referencing," J. Opt. 22, 055601 (2020).

Continuous Wave Optical Parametric Oscillator Dispersion Compensation Studies

Dadi Kamalesh[1,*] **and Kavita Devi**[1]
[1]*Department of Physics, Indian Institute of Technology Dharwad, Dharwad, Karnataka, India, 580011*
**kamalesh.dadi@iitdh.ac.in*

Abstract: We present a theoretical analysis of the effect of dispersion compensation on the mode structure of a cw DRO cavity and a comparison with that of a conventional cw DRO cavity. The analysis shows that dispersion compensation eliminates DRO instabilities like cluster hops and mode hops and provides a continuous wavelength tuning. The results also indicate that the dispersion compensated cw DROs at degeneracy can be exploited for development of devices that provide multiaxial-mode output in a cost-effective manner.
Keywords: Optical Parametric Oscillator, Doubly Resonant Oscillator, Dispersion Compensation.

Continuous-wave (cw) optical parametric oscillators (OPOs) in doubly resonant oscillator (DRO) configuration offer substantially lower pump power threshold than singly resonant oscillators (SROs). OPOs in DRO configuration should satisfy the condition of energy conservation, phase-matching and simultaneous resonance of both signal and idler. Because of the simultaneous resonance condition, the DRO configuration offers low pumping thresholds. However, the same simultaneous resonance condition also gives rise to output instabilities like mode hops and cluster hops, tuning discontinuities and other challenges [1,2]. As such it is challenging to realize stable DRO operation and continuous and monotonous tuning. There have been earlier reports on stable operation of DRO where active stabilization schemes like FM sideband-locking technique and simultaneous multiparameter control have been exploited [3,4]. In this work, we explore the passive technique of cavity dispersion control to overcome these challenges. The dispersion-compensated OPO cavity has been realized earlier, where chirped cavity mirrors have been exploited to reach near zero net cavity group-delay dispersion (GDD) [5]. Here, we studied and analyzed the effect of dispersion compensation on the above-mentioned features of the DRO theoretically.

A DRO's mode structure and its operating mechanism is very different from that of a singly resonant OPO, in part because of the presence of multiple distinct operating points across the frequency range, called cluster frequencies, where the deviation of both the signal and idler frequencies from their nearest cavity resonances are minimum and around which the OPO is most likely to oscillate. To understand mode structure, output instabilities and tuning behaviour of a DRO and to study the effect of dispersion compensation on these DRO features, the technique of using the cavity axial mode numbers as continuous variables is very useful. These variables take integer values at cavity resonances. Axial mode number 'm' is defined as $m = (2L_{opt}/\lambda) = (\omega L_{opt}/\pi c)$, where L_{opt} is total optical length of the cavity, λ and ω are the free space wavelength and the angular frequency of the respective mode, and c is the speed of light in free space. In a dispersion-compensated OPO cavity, using the continuous axial mode number, we found out a general expression for free spectral range (FSR) dispersion in the cavity

$$2\pi\left(\frac{\partial}{\partial\omega}\left(\frac{1}{FSR}\right)\right) = 4\pi(Net\ GDD) \qquad (1).$$

This expression depicts that when the net cavity GDD is zero across the gain bandwidth of the OPO, FSR is no longer a function of the frequency. This eliminates the DRO instabilities that arise from the difference in FSR of the two resonating waves, signal and idler. Two sets of axial mode number variables, each for signal and idler are crucial for the analysis of the DRO operation. Let *'m_s'* and *'m_i'* be the signal and idler mode number variables respectively. Then, the parameter *'m_{cl}'* defined as $m_{cl} = m_s + m_i$ is indicative of the position of the cluster frequencies inside the DRO mode structure. Further, let us take a parameter Δm defined as

$$\Delta m = |m_{cl} - M(m_{cl})| \qquad (2)$$

where $M(m_{cl})$ is the integer closest to m_{cl}. At signal and idler frequencies that correspond to the cluster frequency pair, the value of Δm is a local minimum in that frequency region. Also, Δm is directly proportional to the separation between the nearest signal and nearest idler axial modes on a combined signal-idler frequency scale described in [3,5]. Therefore, Δm variation with respect to signal/idler frequency is a very good map of the DRO mode structure.

In order to study the mode structure in real-time device, we considered a 532 nm pumped, 29 mm long MgO:sPPLT crystal based standing wave DRO [6] for our theoretical calculations. The grating period of the crystal is fixed at 8.01 μm and the cold cavity FSR of the OPO is taken as 211.5 MHz. With change in any parameter that changes the values of m_s and m_i with respect to corresponding frequencies, the resulting Δm value changes, denoting a shift in the position of cluster frequency pairs in the DRO mode structure. This gives rise to gradual change in the cluster frequency positions with continuous change in the tuning parameter. We have studied this particular behavior for the clusters present across the gain bandwidth in a conventional DRO (CDRO) and dispersion-compensated DRO (DCDRO). For DCDRO, a zero net cavity GDD has been considered across the full spectral range. Here, in CDRO, in both degenerate (Fig. 1a) and non-degenerate (Fig. 1b) operating points, a number of distinct cluster frequency curves (white curves) are present across the gain bandwidth. This indicates the possibility of OPO oscillating on any of these cluster frequencies, giving rise to cluster hops when subjected to fluctuations. However, we found that there is no sign of distinct cluster frequency curves when the DCDRO is operating at degeneracy (Fig. 1c) and also away from degeneracy (Fig. 1d). The DCDRO mode structure is uniform across the gain bandwidth for all values of the tuning parameters. The same kind of behavior is observed in pump frequency detuning simulations.

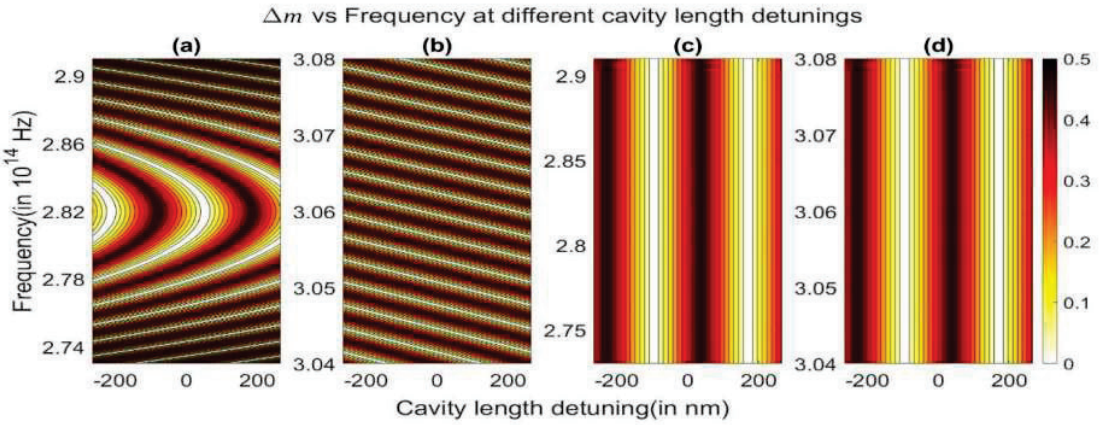

Fig. 1: CDRO and DCDRO mode structure tuning across the gain bandwidth. (a) CDRO at degeneracy; (b) CDRO away from degeneracy; (c) DCDRO at degeneracy; (d) DCDRO away from degeneracy.

Further, the simulations of the operating threshold for different cavity length detuning values showed that, at an appropriate cavity length, a large number of modes inside the cavity can have enough parametric gain to build up from noise and oscillate simultaneously, giving rise to multiaxial-mode output. We also calculated the oscillation frequency values, the frequency values at which the threshold is lowest, and plotted these for different cavity length detuning and pump detuning values for an OPO operating away from degeneracy. We have observed that the oscillation frequency tuning behaviour of a DCDRO operating away from degeneracy is void of any discontinuities unlike the CDRO where there are characteristic cluster hops and mode hops.

In conclusion, we have carried out a theoretical analysis of the effect of dispersion compensation on DRO mode structure and tuning and found out that dispersion compensation eliminates DRO instabilities like cluster hops and mode hops and provides a continuous wavelength tuning. It is also evident from the results that, at degeneracy, this kind of a system can be used to generate multiaxial-mode output in a cost-effective manner. Further detailed discussion and analysis of DCDRO operating threshold simulations and cavity length tuning and pump tuning of DCDRO's oscillation frequency will be presented.

References

[1] A.J. Henderson, M.J. Padgett, F.G. Colville, J. Zhang, M.H. Dunn, "Doubly-resonant optical parametric oscillators: tuning behaviour and stability requirements", Optics Communications, Vol. 119, Issues 1–2, 1995, pp. 256-264

[2] J. Falk, "Instabilities in the doubly resonant parametric oscillator: A theoretical analysis," in *IEEE Journal of Quantum Electronics*, vol. 7, no. 6, pp. 230-235, June 1971

[3] Robert C. Eckardt, C. D. Nabors, William J. Kozlovsky, and Robert L. Byer, "Optical parametric oscillator frequency tuning and control," J. Opt. Soc. Am. B 8, 646-667 (1991)

[4] M Bode, P K. Lam, I Freitag, A Tünnermann, H.-A Bachor, H Welling, "Continuously-tunable doubly resonant optical parametric oscillator", Optics Communications, Vol. 148, Issues 1–3, 1998, pp. 117-121

[5] K. Devi, S. Chaitanya Kumar, and M. Ebrahim-Zadeh, "Frequency Comb Based on Continuous-Wave Optical Parametric Oscillator," in *Laser Congress 2017 (ASSL, LAC)*, OSA Technical Digest (online) (Optica Publishing Group, 2017), paper ATu6A.2.

Propagation of Slow Light in Photonic Crystal Circular Ring Resonator

Puja Sharma, Nilaksha Ghosh and Sarang Medhekar*,
Department of Physics, Central University of Jharkhand, Ranchi, 835222
Author e-mail address: sarang.medhekar@cuj.ac.in

Abstract: We have investigated propagation of slow light in 2D rod type photonic crystal circular ring resonator. The plane-wave expansion method (PWEM) and the finite-difference time-domain (FDTD) method is used to conduct the analysis. Fig. 1 shows guided mode dispersion diagram of the considered basic structure obtained using PWEM. The portion of the allowed modes shown by the solid line is the slow light region. Fig. 2 shows proposed circular ring resonator (RR) created in the photonic crystal that resonates at 1553nm. Fig. 3 shows pulse delay and broadening as observed in our simulations based on FDTD. The red line curve shows the pulse output through one reference waveguide (not shown here) and the black line curve shows the same through the RR. Minimum group velocity of $4.2 * 10^{-6} ms^{-1}$ and a high group index of 70.3 is obtained in our proposed structure. Further, maximum delay of $320 fs$ with acceptable broadening is seen. The proposed device can have potential applications in nonlinear optics, optical buffers and delay lines.

Keywords: Photonic Crystals, Photonic band gap, FDTD method, PWE method, Slow light, Photonic Crystal Ring Resonator

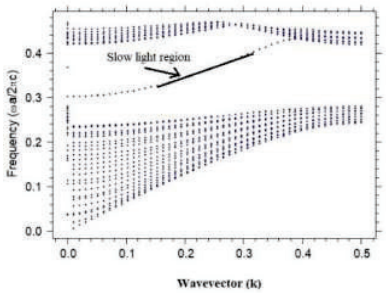

Fig(1)

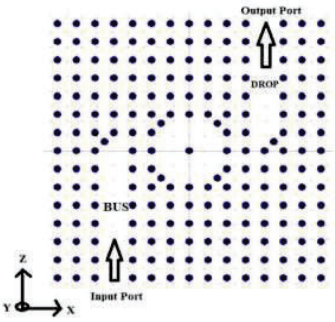

Fig(2)

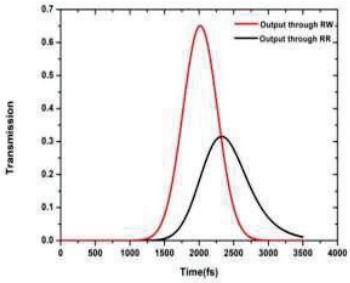

Fig(3)

Fig.1: Guided mode dispersion diagram, the flat region shows the slow light region. Fig.(2): Schematic diagram of circular ring resonator that resonates at $1553nm$. Fig.(3): Pulse delay and broadening, the red line curve shows the pulse output through reference waveguide (not shown here) and the black line curve shows the pulse output through the ring resonator.

Table1:Results

SN.	Parameters	Value
1	Resonance wavelength($\boldsymbol{\lambda}$)	$1553nm$
2	FWHM($\Delta\boldsymbol{\lambda}$)	$1.1nm$
3	Quality factor	1411
4	Group index (n_g)	70.3
5	Delay (Δt)	$320fs$

Reference

[1] S. A. Schulz, L. O'Faolain, D. M. Beggs, T. P. White, A. Melloni, and T. F. Krauss, "Dispersion engineered slow light in photonic crystals: A comparison," J. Opt., **12**, (2010).

[2] S. G. Johnson, A. Mekis, S. Fan, and J. D. Joannopoulos, "Molding the flow of light," Comput. Sci. Eng., **3**, 38–47, (2001),

[3] M. Notomi, "Manipulating light with strongly modulated photonic crystals," Reports Prog. Phys.,**73**, (2010),

[4] Y. N. Zhang, Y. Zhao, J. Li, and R. Lv, "High-sensitive refractive index sensor based on slow light engineered photonic crystal cavity," Proc. IEEE Sensors, 358–361, (2014).

[5] P. Sharma, M. Mohan, N. Ghosh, and S. Medhekar, "Materials Today : Proceedings 2D photonic crystal based all-optical add-drop filter consisting of square ring resonator," Mater. Today Proc., 1–5, (2022).

[6] P. Sharma, M. M. Gupta, N. Ghosh, and S. Medhekar, "Optical add-drop filter based on square ring resonator consisting of octagon shape core." 2021 IEEE International Conference on Technology, Research, and Innovation for Betterment of Society (TRIBES), (2021).

[7] T. Baba, "Slow light in photonic crystals," Nat. Photonics, **2**, 465–473, (2008).

[8] T. F. Krauss, "Slow light in photonic crystal waveguides," J. Phys. D. Appl. Phys., **40**, 2666–2670, (2007).

Simulation of Transform optics and Dispersive element to achieve high power diffraction limited mortal beam

Shivangi Dubey, Debasish Mishra, Renuka Sehgal, Ravinder Reddy M, Charu S Tripathi

Electro-Optics and Lasers, Product Development and Innovation Center

Centre Of Excellence, Bharat Electronics Limited

Bangalore, India.

Email: shivangidubey058@gmail.com

Abstract: Realization of high-power diffraction limited laser beam is a challenge. Beam combining techniques provide commutable approach of power scaling while retaining beam quality. An array of gain element is established to obtain power scaling. Transform optics is incorporated to attain beam separation in a compact way at the focal plane, instead of free space propagation. Spatial overlapping of beams of different wavelengths is achieved through parallel (Open loop wavelength mixing) approach. This paper delineates Multi-Wavelength power Mixing(MWPM) architecture along with the footprint analysis of the transform optics on to the combining element.

Keywords: Diffraction Grating, Transform Optics, Power Combining, Laser Array

1. Introduction

MWPM involves the mechanism of combining multiple laser beams having slightly different wavelengths using a dispersive element which acts as a combining element. The power and brightness of the output combined beam increases as the number of combining lasers increases. This mechanism suffers from the threshold power limitation of the combining element. In recent times generating very high-power laser beam by coherent combination of multiple narrow linewidth lasers have gained a lot of interest and research. But this intriguing technique demands precise control of both polarization and phase of the combining lasers to result in high brightness and high-power laser beam at far field which makes the combining scheme very challenging. Number of laser channels and the power of individual laser emitter are two of the influencing factors for deciding the final combined output power of the MWPM beam, where the beam quality of the combined beam is determined by the beam quality of single laser emitter. Beam quality in this case is greatly affected by the distortion in grating due to thermal load, beam deviation of laser array and optical aberrations present in the transform lens [1].

2. Simulation and Theoretical modelling of beam propagation and Transform Optics

Laser beam emanating from the linear fiber array is partially collimated and spatially overlapped over the surface of the diffraction grating with the help of a transform mirror. The wavelengths and angle of incidence of individual laser channels with the help of transform optics are chosen so as to satisfy the grating equation.

Multi-Wavelength power mixing can be achieved through Serial as well as Parallel approach. Figure 1 shows open loop multi-wavelength power mixing architecture (Parallel approach), unlike closed loop; no output coupler forms a laser cavity and gain elements are used as amplifier. The laser beams coming from fiber array comprising of five laser channels having wavelength separation of 2.5nm are collimated and spatially overlapped on grating plane which combines all the individual laser beams into a single combined beam. In the fiber laser array, each laser beam has an appropriate different wavelength which go through the transform optics (Lens or Mirror) and overlap on to grating with period d lines/mm which is placed at Littrow angle (for -1st order $\phi_L = \sin^{-1}(\lambda/2d)$)[2]. Beams fully overlap after diffraction from grating as they propagate to the far field.

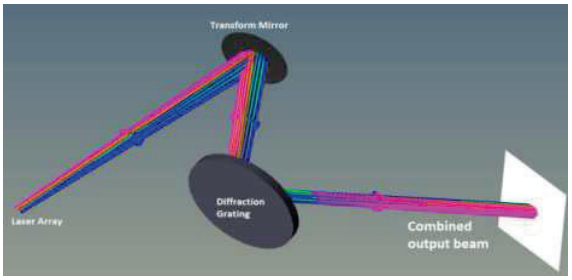

Fig 1. Simulation on shaded model of Multi-wavelength power mixing employing transform mirror & diffraction grating

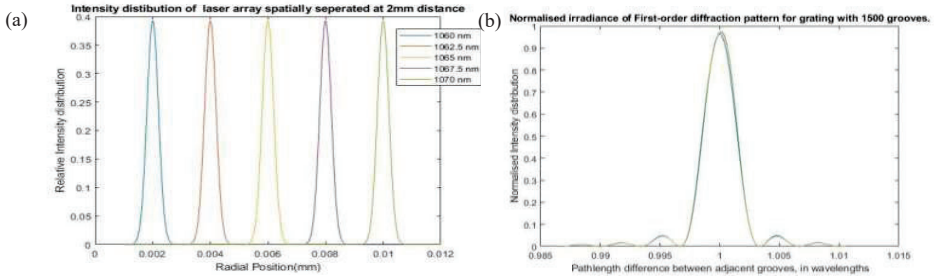

Fig.2. Intensity distribution is described in the figure (a) shows the relative intensity distribution of the fiber arrays of beam waist 0.35mm separated by 2mm distance with discrete wavelength (1060 – 1070 nm in the gap of 2.5 nm) (b) Normalized first order intensity pattern of the combined diffracted beam from the grating with 1500 grooves.

Beam propagation model of the MWPM system can be analyzed by observing the field distribution of n[th] individual gaussian beam with beam waist w_o emitted from the array of gain element with E_0 as the central electric filed component and a_m as the displacement between adjacent lasers as shown in the figure 2(a) : $E_n = E_0 \exp(-\frac{(x-a_m)^2}{w_0^2})$ ……(1). Electric field distribution of the beam traversing through transform lens and incident on the multi-layer diffraction grating[3] can be expressed as $E_n' = \sqrt{1/i\lambda_n B}\exp(ik_n z)\int_{-\infty}^{\infty} E_n \exp\left(\left(\frac{ik_n}{2B}\right)(Ax^2 - 2xx' + Dx'^2)\right) dx$ ……(2) where $k_n = \frac{2\pi}{\lambda_n}$, λ_n is the wavelength of the n[th] emitter and A,B,C,D are the propagation matrix. $E_n'' = ifft[fft(E_n' . \exp(i\theta) . h(f_x))$ ..... (3), where $h(f_x)$ is the transfer function of the grating.

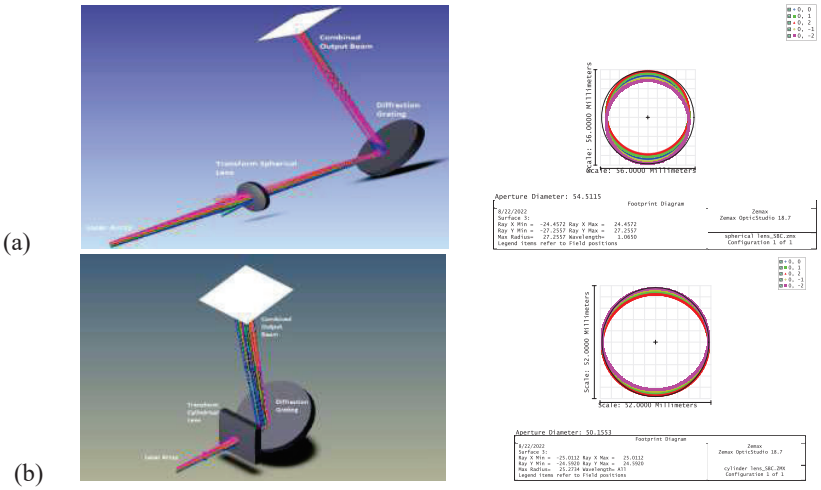

Fig 3. Shaded model of multi-wavelength power mixing using transform lens along with its footprint diagram on their respective right(a) spherical lens, (b) Cylindrical lens

Usage of transform lens in place of mirror as transform optics has been seen in many instances for multi-wavelength power mixing. In this context practically the advantage of using cylindrical lens as compared to spherical lens for generating collimating and spatially overlapping laser beam spot on the grating plane is realized. Compact design with shorter focal length can be achieved by cylindrical optics as compared to spherical optics. It is seen from the footprint diagram in fig 3 that same amount of overlapping among beams is achieved at smaller focal length using cylinder lens. Increase in the cost of lens fabrication being the major demerit of the approach.

3. Reference

[1] Eric Honea, Robert S. Afzal, Matthias Savage-Leuchs, Jason Henrie, Khush Brar, Nathan Kurz, Don Jander, Neil Gitkind, Dan Hu, Craig Robin, Andrew M. Jones, Ravi Kasinadhuni and Richard Humphreys; "Advances in Fiber Laser Spectral Beam Combining for Power Scaling";Proc. Of SPIE Vol. 9730, 97300Y SPIE; 10.1117/12.2214237;(2015)

[2] Gang Bai, Hui Shen, Yifeng Yang, Xiang Zhao, Jingpu Zhang, Haibo Zhang, Yunfeng Qi, Bing He, Jun Zhou; "Theoretical analysis of beam quality degradation in spectral beam combining of fiber laser array with beam deviation"; 10.1016, j.optlastec;(2018).

[3] Aeri Jung, Sanggwon Song, Seokjin Kim, And Kyunghwan Oh; "Numerical analyses of a spectral beam combining multiple Yb-doped fiber lasers for optimal beam quality and combining efficiency"; Vol. 30, No. 8 Optics Express 13305; 10.1364/OE.455728;(2022)

GO-ZnO nanocomposite-based optical fiber Relative humidity (RH) sensor

Sunil Mohan[1], Sunil K Khijwania[2, *]
[1,2]Indian Institute of Technology Guwahati, Guwahati-781039 Assam, INDIA
sunil.mohan@iitg.ac.in[1], skhijwania@iitg.ernet.in[2]

Abstract: An optical fiber Relative Humidity employing GO-ZnO diffused silica is reported. The developed shows a sensitivity of 33.6mV/%RH over the dynamic range 17-91%RH, which is 5.75-times more compared to the sensor based on pure silica nanostructured sensing film.

1. Introduction

Relative humidity (RH) is a critically essential parameter for various scientific and industrial areas such as the electronic instrumentation industry, automated systems, agriculture, and structural health monitoring. Due to such widespread applications, numerous efforts have been made to develop humidity sensors. Over the last few decades application of optical fiber in the sensing region has become most admired due to its remarkable inherent advantages such as high sensitivity, immunity to electromagnetic interference, small size, multiplexing, duplicability in corrosive environments, and remote sensing. From last few years, several optical fiber humidity sensors have been reported employing various sensing techniques [1]. However, observed dynamic range, nonlinear response and the sensitivity led a scope for optimizing the sensor performance. Here, we propose an evanescent wave based optical fiber RH sensor with possible simplest fiber geometry using GO-ZnO nanocomposite with an objective to increase the sensitivity manifold.

2. Experiment

Graphene oxide (GO) was synthesized via modified Hummer's method [2], and Zinc oxide (ZnO) was prepared by the co-precipitation method [3]. Finally, we prepared GO-ZnO composites by hydrothermal method. FETEM and XRD of synthesized GO-ZnO are shown in Fig.1(a) and Fig.1(b). For the development of the RH sensor, PCS fiber (200 µm core diameter) of length 50cm is used. Fiber ends were prepared (to couple maximum light form source to sensor and sensor to detector) and then about 5 cm of the cladding was removed from the central portion of the fiber. A GO-ZnO diffused silica film was chemically synthesized over a centrally decladded portion of the fiber via the sol-gel method [4]. Prepared sensing probe was dried for 48 hrs at room temperature, which was further annealed for 2 hrs at 110°C to. After drying developed sensor was characterized in humidity chamber shown in Fig 2(a) having the provision to precisely control humidity of mixing dry and humid air. Light from a He-Ne laser is coupled from one end of the fiber, whereas the other end of the sensor is connected to a photodetector. Humidity level was first reduced to the minimum possible value by injecting the dry air inside the chamber. Afterwards, the humidity was slowly increased in suitable steps to the maximum possible value by injecting humid air inside the chamber. Responses of both commercial as well fiber sensors were recorded as a function of time with a resolution of 1s using a DAQ card only after the stabilization of humidity at the desired value.

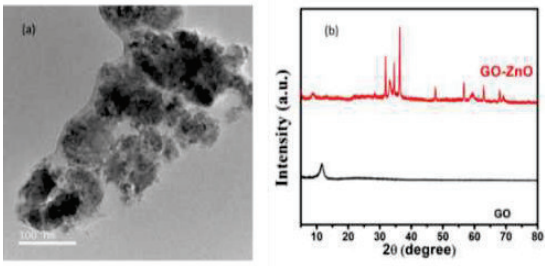

Fig 1. ***(a) FETEM of GO-ZnO nanocomposite (b) XRD of GO-ZnO nanocomposite***

3. Result and discussion

The developed sensor is based on intensity modulation through Evanescent wave (EW) absorption via GO-ZnO diffused silica matrix. The typical response of the developed sensor is depicted in Fig.2(b) during ascending humidity.

It can be observed from the plot intensity of fiber sensor output decreases with increased humidity. Similar response was observed while decreasing the humidity. This can be physically understood as following: water molecules being diffused into the nano-scaled pores of the silica matrix get adsorbed in these pores. The rate of adsorption of water molecules that infiltrates into the nano-scaled pores of the silica matrix is stimulated (greatly enhanced) owing to the presence of the GO-ZnO. Hence increase in the humidity increases adsorption of water vapors and the condensation

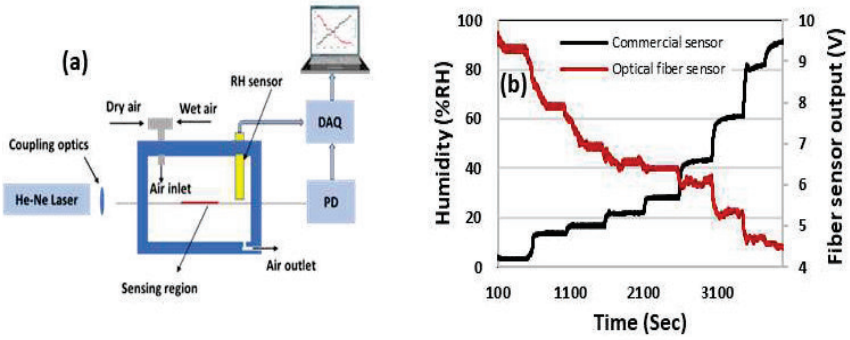

Fig.2: (a) Setup for the sensor characterization. (b) Experimental response of the developed RH sensor.

in the pores of the sensing film. This leads to a change of refractive index in the sensing region carrying GO-ZnO silica sensing film. Corresponding leakage of the guided power to the cladding modes results in a comparatively intense intensity modulation. In order to get a deeper insight, the fiber sensor's output is plotted against %RH in Fig.3 (blue color). Proposed sensor shows a throughout linear response over the dynamic range of 3−70%RH with a sensitivity of 33.6 mV/%RH. For comparative analysis, the response of the sensors having pure silica matrix (violet color), GO diffused silica matrix (red color) and ZnO diffused silica matrix (black color) are also plotted in the Fig.3. The sensitivities of pure silica matrix-based sensor, GO diffused silica matrix-based and ZnO diffused silica matrix-based are 5.9mV/%RH, 12.6mV/%RH, and 18.2mV/%RH, respectively. The proposed sensor exhibits highest sensitivity, which is 10 times, 1.8 times and over 2.9 times higher in comparison to the sensitivities observed for pure silica, pure GO diffused silica and pure ZnO nanoparticle diffused silica based optical fiber RH sensors, respectively. Similar sensitivity was observed for the proposed sensor during dehumidification. Further, under the quick cyclic test, proposed sensor observed to be highly reversible.

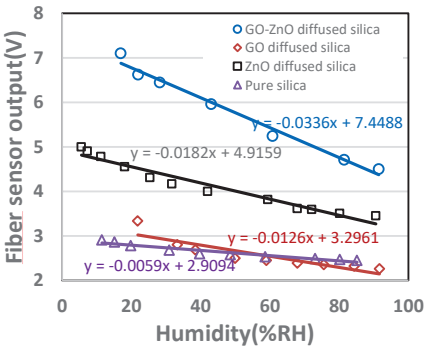

Fig.3: Fiber sensors response

4. Conclusion

An optical fiber RH sensor is reported that employs GO-ZnO diffused silica nanostructured sensing. Importantly, an excellent sensitivity enhancement is achieved in comparison to the pure GO as well as pure ZnO nanoparticle-based optical fiber RH sensors.

5. References

[1] T. L. Yeo, T. Sun, and K. T. V. Grattan, "Fibre-optic sensor technologies for humidity and moisture measurement," *Sensors and Actuators, A: Physical*, vol. 144, no. 2, pp. 280–295, 2008.

[2] W. S. Hummers and R. E. Offeman, "Preparation of Graphitic Oxide," *Journal of the American Chemical Society*, vol. 80, no. 6, p. 1339, 1958.

[3] D. Sahoo, A. Mandal, T. Mitra, K. Chakraborty, M. Bardhan, and A. K. Dasgupta, "Nanosensing of Pesticides by Zinc Oxide Quantum Dot: An Optical and Electrochemical Approach for the Detection of Pesticides in Water," *Journal of Agricultural and Food Chemistry*, vol. 66, no. 2, pp. 414–423, 2018.

[4] R. Aneesh and S. K. Khijwania, "Zinc oxide nanoparticle based optical fiber humidity sensor having linear response throughout a large dynamic range," *Applied Optics*, vol. 50, no. 27, pp. 5310–5314, 2011.

Correlation imaging with structured light

Tanushree Karmakar*, Aditya Chandra Mandal, Rajeev Singh, and Rakesh Kumar Singh
Laboratory of Information Photonics and Optical Metrology, Department of Physics, Indian Institute of Technology (Banaras Hindu University), Varanasi, 221005, Uttar Pradesh, India
*Author e-mail address: *tanushreekarmakar.rs.phy20@itbhu.ac.in*

Abstract: This paper presents a correlation imaging technique with structured light illumination. An advantage of the structured light illumination in the correlation imaging is demonstrated by recovering complex field of the light by single pixel detector (SPD). The enormous numbers of illumination patterns required are the main obstacle in developing correlation imaging by SPD. Therefore, an attempt is made to reduce the number of illumination patterns by applying the three step phase shift approach in the structured illumination rather than a four phase shifting approach. Result of this technique is presented by reconstructing the complex field in the correlation holography.
Keywords: Correlation imaging, structured light, three-step phase shift.

1. Introduction

In correlation imaging, an object is recovered as the distribution of complex coherence function by measuring the autocorrelation or cross-correlation function of the random field. One of the holographic techniques based on correlation is the coherence holography. In coherence holography, an incoherent light illuminates the hologram for the reconstruction of the complex coherence function [1-2]. Coherence holography needs an interferometry based set up and pixelated detectors for measurement of the complex coherence. In this work, we propose a technique for reconstruction of complex coherence function without any interferometry using structured light along with three step phase shift approach using single pixel detector [3]. Structured light illuminates an object, and single pixel detector measures the far-field spectrum [4]. A complex Fourier spectrum determined by intensities is acquired from the three step phase shifting in the structured light patterns. Three step Fourier single pixel imaging suppresses noise [5]. Measurement is reduced by 25 percent in three step phase shifting compared to four phase shifting [5-6]. Visibility as well as reconstruction efficiency are increased by using three step phase shifting compared to four step phase shifting.

2. Theory

In the correlation imaging technique, an object is illuminated with sinusoidal structured light, which is represented by

$$P_\theta (x,y ; k_x,k_y)= c+ d.\cos (k_x x+k_y y+ \theta) \quad (1)$$

where k_x, k_y are spatial frequencies and θ is the initial phase angle. In equation (1) c is a constant term of the light pattern and d is the contrast. Through spatial light modulator (SLM) these sinusoidal patterns can be displayed and this light pattern falls on rotating ground glass (RGG) to imitate an incoherent light source. A hologram H(x,y) is placed just after the RGG. Therefore, the complex amplitude just after the H(x,y) is represented as

$$E_\theta (x,y ; k_x.k_y) = H (x,y) \exp(i\alpha(x,y)) (c+d.\cos (k_x x+k_y y+ \theta)) \quad (2)$$

where α is the random phase generated by rotating ground glass. The complex amplitude at the single pixel detector (at far field) is denoted as

$$E_\theta (k_x, k_y) = E_b + s\iint_\Omega E_\theta(x, y ; k_x x, k_y y)dxdy \quad (3)$$

where Ω is the illuminated area and s is a scale factor which is determined by the size and the place of the detector, E_b represents background illumination. Then the random intensity is computed by the single pixel detector

$$I_\theta (k_x, k_y) = |E_\theta (k_x,k_y)|^2 \quad (4)$$

Then from mean intensity, the random intensity variation is calculated as,

$$\Delta I_\theta (k_x, k_y) = I_\theta (k_x,k_y) - < I_\theta (k_x, k_y)> \quad (5)$$

Three step phase shifting method is implemented to compute complex Fourier coefficient $F(k_x,k_y)$ for every three illumination patterns i.e. P_0, $P_{2pi/3}$, $P_{4pi/3}$. From the corresponding responses R_θ (R_0, $R_{2\pi/3}$, $R_{4\pi/3}$), the Fourier spectrum of H is obtained as

$$F(k_x,k_y) = (2R_0 - R_{2\pi/3} - R_{4\pi/3}) + (\sqrt{3}i)\,(R_{2\pi/3} - R_{4\pi/3})$$
$$= 2ds \iint_\Omega H(x,y).\exp\left[-i\left(k_x x + k_y y\right)\right] dxdy \quad (6)$$

For entire sets of spatial frequency complex Fourier coefficient is retrieved. Thus the desired complex field distribution of the object can be retrieved by applying three step phase shift approach in sinusoidal structure light. We implemented this idea using MATLAB algorithm.

3. Results

The number of random phase masks (M) created by rotating ground glass determines the quality of reconstruction. With increasing the number of phase masks reconstruction efficiency and visibility are increased. We have used here M=500 for the reconstruction of a hologram of number "7". Simulation results using MATLAB are shown below. For reconstruction of complex fields of size 100 × 100 from hologram of size 200× 200, structured light patterns are used in accordance with Eq. 1, where c = 0.5, d = 0.5, span of spatial frequency is $-2.5 \leq (k_x, k_y) \leq 2.5$ at increments of 0.0505. Fig 1.(a) and fig 1.(b) represent amplitude and phase distribution for M= 500 respectively. Central DC terms arise because of using off-axis hologram as input object. Central DC terms are suppressed digitally in fig 1.(a) and fig 1.(b) to highlight the object.

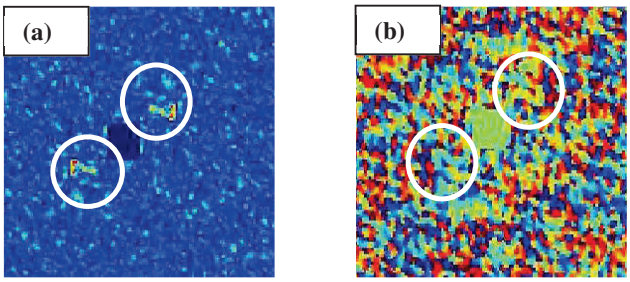

Figure 1. Reconstruction of complex field of hologram "7" for M =500 : (a) amplitude distribution; (b) phase distribution

4. Conclusion

In summary, a new unconventional holography with structured light illumination is presented for the reconstruction of the complex coherence field. This is realized by combining three step phase shifting in the structured illumination with the correlation measurement by a single pixel detector. This three step phase shift approach reduces measurement to 1.5 times the counts of pixels of the illumination patterns. So, with fewer illuminations object can be reconstructed with higher reconstruction quality and greater visibility. Computational simulation supports our ideas. The proposed technique gives new direction in correlation holography as well as in single pixel imaging with less illumination.

5. Acknowledgment

Tanushree Karmakar would like to acknowledge support from DST-INSPIRE (IF190840).

6. References

[1] Goodman, J. W. " Statistical optics" (John Wiley & Sons, 2015).
[2] Takeda, M., Wang, W., Duan, Z. & Miyamoto, Y. "Coherence holography", Opt. express 13, 9629–9635 (2005).
[3] Mandal, A.C., Sarkar, T., Zalevsky, Z. *et al.* Structured transmittance illumination coherence holography. *Sci Rep* **12,** 4564 (2022).
[4] Zhang, Z., Ma, X. & Zhong, J. "Single-pixel imaging by means of Fourier spectrum acquisition", Nat Commun 6, 6225 (2015).
[5] Zhang, Z., Wang, X., Zheng, G. & Zhong, J. "Hadamard single-pixel imaging versus Fourier single-pixel imaging", Opt. Express 25, 19619-19639 (2017).
[6] Deng, H., Gao, X., Ma, M., Yao, P., Guan, Q., Zhong, X. & Zhang, J. "Fourier single-pixel imaging using fewer illumination patterns", Appl. Phys. Lett. 114, 221906 (2019).

Temperature dependent transmission spectral studies of a one-dimensional photonic crystal

Agape Mary Mammen and Alok Sharan
Department of Physics, Pondicherry University, Kalapet, Puducherry, India-605014
agapemary6@gmail.com, aloksharan@gmail.com

Abstract: A one-dimensional photonic crystal with Cadmium Sulphide (CdS) and Silicon dioxide (SiO_2) as bilayers and water as the defect layer has been taken as the system to carry out the transmission spectral studies. Transfer Matrix Method has been employed to study the proposed structure. The defect layer's refractive index is taken as a function of temperature and wavelength. The defect mode is blue shifted as the refractive index decreases with increase in temperature. The smallest change or shift in central wavelength of the defect mode is found to be 0.0495 nm/K.
Keywords: Photonic crystal, temperature tuning, Transfer Matrix Method, defect states, Q-factor.

1. Introduction

The one dimensional dielectric photonic crystals are the artificial structures which are formed from placing dielectric layers periodically with different refractive indices in a single direction.Its also called a dielectric mirror or Bragg reflector. It helps us in the control and emission of light.The variation of the refractive indices create a range of forbidden frequencies called a photonic bandgap (PBG). PBG is due the multiple bragg scattering of incident electromagnetic waved at different media. When a defect is introduced into the structure, defect modes will be formed inside the PBG which can be used as filters, waveguides, sensors etc.

2. Theory

In this paper, a bilayer which consists of Cadmium Sulphide (CdS) and Silicon dioxide (SiO_2) and water as the defect layer has been taken to study the variation in the transmission spectrum with respect to temperature. CdS is taken as the high index layer(H) and SiO_2 is taken as the low index layer(L) with layer thicknesses satisfying the bragg condition: $n_H d_H = n_L d_L = \lambda/4$, λ is the reference wavelength, n and d being the refractive index and thickness of H and L layers. The design of the proposed structure is $(CdS/SiO_2)^5$/ water/ $(SiO_2/CdS)^5$ as shown in Fig. 1. The defect layer is taken to be $n_D d_D = \lambda$. For λ= 589nm, n_H, n_L and n_D are 2.42, 1.45 and 1.33[1-3], and their corresponding thicknesses d_H, d_L and d_D are 60.84nm, 101.55nm and 441.42nm respectively.
Transfer Matrix Method (TMM) has been employed for the transmission spectral simulations. The characteristic matrix of the entire system is the resultant of product of 2X2 matrices ie.

$M_{sys} = (M_A M_B)^5 M_D (M_B M_A)^5 = \begin{bmatrix} m_{11} & m_{12} \\ m_{21} & m_{22} \end{bmatrix}$ where $M_j = \begin{bmatrix} \cos\left(\frac{2\pi p_j d_j}{\lambda}\right) & (i/p_j)\sin\left(\frac{2\pi p_j d_j}{\lambda}\right) \\ i p_j \sin\left(\frac{2\pi p_j d_j}{\lambda}\right) & \cos\left(\frac{2\pi p_j d_j}{\lambda}\right) \end{bmatrix}$

Transmittance of the multilayer stack is given by $T_{PC} = \left| \frac{2p_a}{p_a M_{11} + p_a p_s M_{12} + M_{21} + p_s M_{22}} \right|^2$

$p_j = n_j \cos\theta_j$; j=(A,B or D), θ is the angle of incidence and p_a and p_s represent air and substrate.

Temperature tuning occurs due to two factors: thermal expansion where the thickness of the layers expand wrt temperature[$d(T) = d_o(1+ \alpha\Delta T)$] and the other one being thermal optic effect where the refractive index changes wrt temperature [$n(T) = n_o(1+ \beta\Delta T)$], where α and β are thermal expansion coefficient and thermal optic coefficient respectively. α for CdS and SiO_2 are 4.2×10^{-6} / °C and 5.5×10^{-7} / °C, [4,5], respectively. β for CdS and SiO_2 are 2.5×10^{-4} and 1×10^{-5} / °C, [6,7], respectively. The defect layer's refractive index is taken as a function of temperature and wavelength and the refractive indices of water is taken from [3].

3. Results and Discussion

The PBG of the photonic crystal with defect mode at 0°C is 209.04nm. The resonance peak(λ_{peak}) is at 589.04nm and the transmission spectra of water as the defect layer at 0°C with refractive index as 1.33432 is shown in Fig.2 with

99.5% transmittance. Fig. 3 represents the transmission spectra at temperatures 0 ºC, 50 ºC,80 ºC and 100 ºC with λ_{peak} decreasing with decrease in refractive index and increase in temperature. The λ_{peak} is said to be blue shifted.
The smallest change or shift in central wavelength of the defect mode is found to be 0.0495 nm/K. Table 1 tells us how Full Width Half Maximum (FWHM) and Q-factor changes with temperature tuning of water cavity.

$$\text{Q-factor} = \lambda_{peak} / \text{FWHM}$$

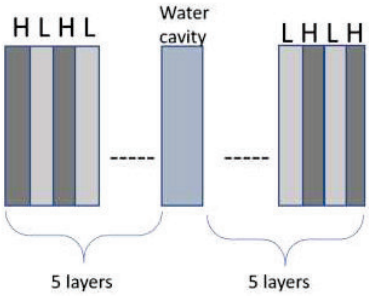

Fig. 1: Geometry of water cavity containing photonic crystal

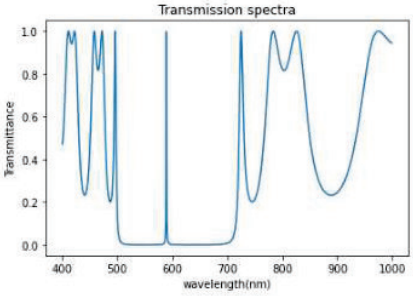

Fig. 2: Transmission spectra of Photonic crystal with defect mode

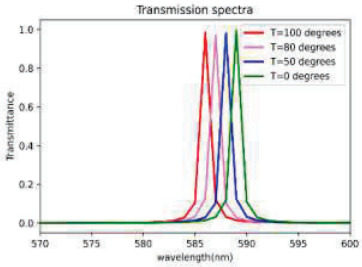

Fig. 3: Transmission spectra of Temperature tuning of water cavity

Table 1: Temperature tuning of water cavity

Temperature(ºC)	Refractive index (n)	Peak Position(nm)	FWHM (nm)	Q-factor
0	1.33432	589.04	1.00	589.04
50	1.32937	588.02	1.12	525.01
80	1.32342	587.00	1.10	533.63
100	1.31861	586.01	1.14	514.04

4. Conclusion

One dimensional photonic crystal has been simulated by Transfer Matrix Method with CdS and SiO_2 as bilayers stacked simultaneously and water cavity as defect layer in the middle of the photonic crystal with number of periods as 5 on both sides. The λ_{peak} of the defect mode is centered at 589.04nm at 0ºC. As temperature increases, λ_{peak} tends to be blue shifted as the n also decreases. The smallest change or shift in central wavelength of the defect mode is found to be 0.0495 nm/K. The shift in the central peak position can be used to determine the temperature of the water flowing. This is the demonstration of how PBG structures can be used as liquid sensors.

5. References

[1]. R E Treharne, A Seymour-Pierce, K Durose, K Hutchings, S Roncallo and D Lane, "Optical Design and Fabrication of Fully Sputtered CdTe/CdS Solar Cells," *J. Phys.: Conf. Ser.* **286** 012038(2011).

[2]. I. H. MALITSON, "Interspecimen Comparison of the Refractive Index of Fused Silica", Journal of the optical society of India, Volume **55,** number 10(1965)

[3]. Marvin J. Weber, "Water" in Index of refraction of water/ handbook of Chemistry and Physics, Eds.Lide D.R.,CRC Press LLC(2001).

[4]. P. Vinotha Boorana Lakshmi and K. Ramachandran, " On the thermal expansion of CdS by experiment and simulation ", Cryst. Res. Technol. 41, No. 5, 498 – 504 (2006

[5]. S.P. Singh, K. Pal, A. Tarafder,M. Das, K. Annapurna, B. Karmakar," Effects of SiO2 and TiO2 fillers on thermal and dielectric properties of eco-friendly bismuth glass microcomposites of plasma display panels " Bull. Mater. Sci. 33 (2010)

[6]. M. P. LISITSA, I,. F. GUDYMENKOV,.N. MALIINKOa, nd *S* F. TEREKHOVA, "Dispersion of the Refractive Indices and Birefringence of CdS,Se,$_{1}$-x, Single Crystals", phys. stat. sol. **31, 389** (1969)

[7]. W.N. Ye, R. Sun, J. Michel, L. Eldada, D. Pant, L.C. Kimerling, 5th IEEE International Conference on Group IV Photonics, Sorrento, Italy, 401(2008) pp-401.

Design Method of a Geometric Waveguide Based Optical-See-through Display System for Near-eye Applications

Naresh Kumar[1, 2], Rahul Rohilla[1, 2], Vinod Mishra[1, 2], Harry Garg[1, 2]
[1] *Academy of Scientific and Innovative Research (AcSIR), Ghaziabad, Uttar Pradesh 201002, India*
[2] *CSIR-Central Scientific Instruments Organisation, Sector 30C, Chandigarh 160030, India*
naresh.kumar@csio.res.in, rahul.csio19@acsir.res.in, vnd.mshr@csio.res.in, harry.garg@csio.res.in

Abstract: The concept of optical see-through (OST) displays is to present the combined information from a virtual scene and a real scene. A waveguide combiner and coupling elements for coupling the light in and out of the system are the main constituents of such displays. A geometric waveguide is used where light is injected into the waveguide using a prism and light is extracted using microstructures to deflect the light towards the exit pupil. The design method and analysis of parameters used in the development of an OST display are discussed.

Keywords: Optical see-through displays, Augmented reality (AR), Waveguide technology, Coupling efficiency, Geometric waveguide, Microstructures.

1. Introduction

1.1. Background

An optical see-through display systems overlaps computer generated images with the physical environment. To obtain this unique visual experience with wearable comfort, the near-eye display systems need to possess high transmittance, sufficient FOV and a compact form factor. The first system which resembled an augmented reality display was reported by Ivan Sutherland in 1962 [1]. The notion of using the terms augmented reality, virtual reality first appeared in literature when Paul Miligram and Fumio Kishino introduced a reality-virtuality continuum [2]. The distinction is also based on the ability of a particular system to have ability to interact with the user's surrounding. For example, in an AR-based display system, a user can observe the virtual symbols, text etc. and based on this this information, is able to take decisions. Cockpit head-up displays, and AR applications in manufacturing industry are popular examples for AR/VR technologies. This paper discusses the design method for see-through aspect of the augmented reality concept which comes under the head-attached category of AR technology[3].

1.2. Waveguide Concept & OST displays

One of the key technologies for see-through displays is waveguide optics, which guides light from the image source and superimposes an image in front of the viewer's eye. Waveguide technology is a less complex way of manipulating the light by means of an optically transparent substrate having two parallel-sided faces that guides the light within the substrate. It offers a cost-effective and easily installable solution contrary to conventional applications where complex lens assemblies are used to control light. The main advantage of using a waveguide substrate is the capability to expand the exit pupil which results in a large eyebox without adding complex elements to the systems.

Waveguide technology relies on planar imaging optical systems where all the optical components lies on a single substrate and results in fewer aberrations [4]. The concept of using waveguide in near-eye applications was first introduced by Y. Amitai [5,6]. In the first system [5], two holographic elements were used on the same substrate: one is used to trap the light inside a planar waveguide substrate and the second one diffracts the light rays into an observer's eye. Although the field of view was larger compared to the size of the reflecting surface element yet it wasn't sufficient considering the requirements of larger eye movements. The simplest and most basic form of a waveguide-based optical see-through display system consists of collimating optics for collimating light from display source, an optical grade substrate and light coupling elements shown in Fig. 1.

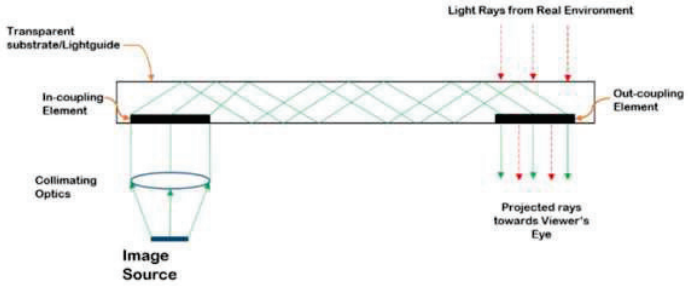

Fig. 1: Layout of an optical see-through display where light is trapped inside the waveguide structure by total internal reflection (TIR). Injection and extraction of light is controlled using the coupling elements.

2. Design Method and Analysis

Numerical analysis for a starting point design of the system is carried out. The corresponding model is shown in Fig. 2. For a ray trace simulation, rays normal to the surface (collimated) are taken in the model. A prism is used for coupling the light into a transparent substrate. Fig 3 shows a periodic, geometric microstructure profile is chosen for carrying out starting point analysis. System specifications are given in Table 1.

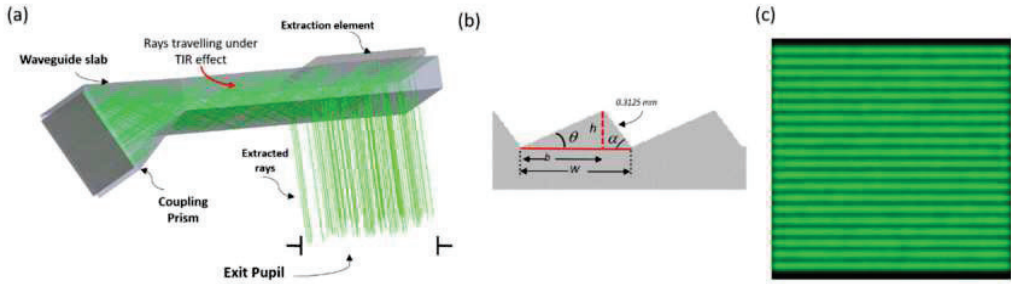

Fig. 2: (a) System components of the waveguide display system and CAD model (b) Geometry and parameters of the extraction feature (c) Light distribution in the exit pupil at an eye relief of 16mm

Light distribution at an eye relief of 16mm is shown in Fig. 2 (c). An optical efficiency of 49% is simulated. Optimization is needed to improve illuminance uniformity and optical efficiency. The aim of this work is to design a simple, cost-effective, monochrome near-eye display with high optical efficiency.

3. References

[1] Sutherland I E 1968, "A Head-Mounted Three Dimensional Display," *Proceedings of the December 9-11, 1968, Fall Joint Computer Conference, Part I* AFIPS '68 (Fall, part I) (New York, NY, USA: Association for Computing Machinery) pp 757–764

[2] Milgram P "Taxonomy of Mixed Reality Visual Displays" *Ind. Eng.* 1–14, (2011)

[3] Giunta L, Dekoninck E, Gopsill J and O'Hare J, "A review of augmented reality research for design practice: Looking to the future," *Proc. Nord. Des. Era Digit. Nord. (2018)*

[4] Jahns J and Walker S J "Imaging with planar optical systems" *Opt. Commun.* **76** 313–7, 1990

[5] Amitai Y, Reinhorn S and Friesem A A, "Visor-display design based on planar holographic optics," *Appl. Opt.* **34** 1352–6, 1995

[6] Amitai Y, "Extremely Compact High-Performance HMDs Based on Substrate-Guided Optical Element," *SID Symp. Dig. Tech. Pap.* **35** 310, P-21, (2004)

Third order nonlinearities associated with thermo-optical effects in WSe_2 thin film

Km. Surbhi and Ritwick Das
School of Physical Sciences, National Institute of Science Education and Research,
An OCC of Homi Bhabha National Institute, Jatni, Odisha - 752050, India
ritwick.das@niser.ac.in

Abstract: We present an investigation on the thermo-optical nonlinearities in WSe_2 thin-film using Z-scan technique. Our study reveals that WSe_2 thin-film exhibits strong saturable absorption behavior induced by Pauli-blocking effect and negative nonlinear refractive index attributed to self-defocusing effect in the visible spectrum.
Keywords: *Z*-scan, WSe_2 thin film, Pauli-blocking effect.

Two dimensional (2D) materials are the center of great research due to their unique properties. Over the past few years, transition metal dichalcogenides (TMDs) have received significant attention due to their versatile physical and chemical properties [1]. TMDs have been explored for a broad area of applications such as gas sensors, energy storage devices, transistors and photoswitches [2]. Moreover, TMDs include layered structure with strong in plane bonding and weak out of plane interactions. The electronic bandstructure of semiconducting TMDs depends upon the number of layers and undergoes a transition from indirect to direct as thickness tends to reduce [3]. The thickness dependence of bandgap in TMDs could induce significant variation in hyperpolarizability which is extremely important from the perspective of nonlinear optical (NLO) properties. TMDs have been explored for a broad range of photonic applications such as optical limiting, Q-switching, mode-locking, data storage, and optical-switching [4,5]. Furthermore, from the application viewpoint, it is important to study the impact of thermal effects on the nonlinearity. At high repetition rate, thermal diffusion effects come into play [6], which can substantially alter the optical nonlinear behaviour of materials. Therefore, we study the impact of high repetition rate on the third order nonlinear properties in WSe_2 thin films. In this work, we present the nonlinear optical properties of the WSe_2 thin-films using single-beam *Z*-scan technique. The investigations reveal that the nonlinear absorption in WSe_2 thin films exhibit saturable absorption behaviour at 515 nm excitation wavelength which is essentially a consequence of strong Pauli-blocking effect and a negative nonlinear refractive index attributed to self-defocusing effect.

A RF magnetron sputtering system was used to prepare the WSe_2 thin film using a WSe_2 (99.9% pure) target in an Argon environment at room temperature onto a 1 cm×1 cm glass substrate. The characterization of the RF-sputtered WSe_2 thin-film is carried out using field-emission scanning electron microscope (FESEM), X-ray diffractometer and Raman spectroscopy. The thickness of 98 nm was measured for the deposited WSe_2 thin-film using a cross-sectional FESEM image. The linear absorption spectrum of the WSe_2 thin film was recorded using a UV-VIS spectrometer. The nonlinear optical response of WSe_2 thin-film was carried out using single-beam *Z*-scan technique in an open-aperture (OA) as well as closed-aperture (CA) configuration for estimating nonlinear absorption (β) and nonlinear refractive index (n_2) respectively. The measurements were carried out using ultrashort pulses (pulse width ≈ 370 f s) at repetition rates of 1 kHz and 100 kHz. The ultrashort pulses are centered at a central wavelength of 515 nm.

The linear absorption spectrum of WSe_2 thin film is shown in Fig.1(a) and the inset shows that the bandgap is indirect which has been obtained using Tauc plot [7]. The bandgap is estimated to be 1.3 eV . The nonlinear optical properties were studied using OA and CA measurements. In order to estimate β and n_2, the measured normalized OA and CA transmittance curves were theoretically fitted using the analytical expressions given below [7],

$$T\,(z, S=1) = 1 - \frac{\beta_{\text{eff}}\, I_0\, L_{\text{eff}}}{2^{3/2}\,(1+x^2)} \qquad (1)$$

$$T\,(z, \Delta\Phi_0) = 1 - \frac{4\Delta\Phi_0 x}{(x^2+9)(1+x^2)} - \frac{2\Delta\psi_0(x^2+3)}{(x^2+9)\,(1+x^2)} \qquad (2)$$

where L_{eff} is the effective length of the sample which is defined as $L_{eff} = (1 - e^{-\alpha L})/\alpha$, L is the thickness of the films, α is the linear absorption of the film, $x = z/z_0$ where z_0 is Rayleigh length for the laser beam, $\Delta\varphi_0 = kn_2I_0L_{eff}$ is the phase change due to nonlinear refraction at the focus, $k=2\pi/\lambda$ is propagation wavevector and $\Delta\Psi_0 = \beta I_0 L_{eff}/2$ is phase change due to nonlinear absorption. Using Eq.(1), the experimental measurements in Fig. 1(b) (red dotted curve) were theoretically fitted to obtain β at 1 kHz repetition rate. As expected, the dominant single photon absorption at 515 nm excitation wavelength, manifests into Pauli-blocking effect induced saturable absorption behaviour in the WSe_2 thin

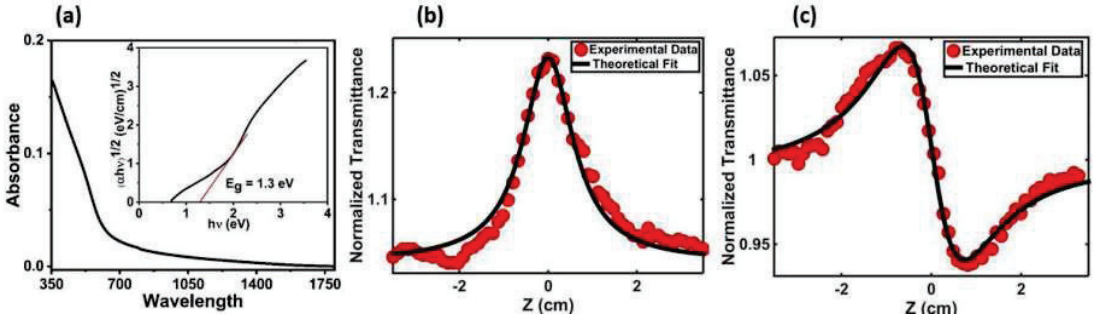

Fig. 1: (a) Linear absorption spectrum of WSe_2 thin film. Inset shows the Tauc plot for estimating bandgap. (b) Open aperture (OA) Z-scan measurement @ 1kHz. (c) Closed aperture (CA) Z-scan measurement @ 1kHz. Black solid lines depict the theoretical fitting.

Table 1: Nonlinear Absorption and Nonlinear Refraction Coefficients of the WSe_2 Samples at 515 nm Excitation Wavelength.

Repetition rate	I_0(W/cm^2)	β(cm/W)	n_2(cm^2/W)
1 kHz	6.4×10^{12}	-1.74×10^{-8}	-1.15×10^{-13}
100 kHz	3.16×10^{10}	-1.15×10^{-6}	-3.53×10^{-11}

film [7]. Using Eq.(2), the experimental measurements in Fig. 1(c) (red dotted curve) were theoretically fitted to obtain n_2. The CA *Z*-scan measurements consist of a pre-focal maxima followed by a post-focal minima which is the signature of the self-defocusing effect and corresponds to a negative value of the nonlinear refractive index. Being a semiconductor, *WSe_2* will show a negative nonlinear refractive index, since the excitation energy is above $0.7E_g$ [8]. The calculated nonlinear optical parameters for *WSe_2* thin-film are tabulated in Table.1. As we have discussed earlier that the thermal effects can alter the nonlinear optical response of the material. In order to elucidate this point, we carried out the *Z*-scan measurements at 100 kHz repetition rate and estimated the same parameters (see Table 1). The thermal diffusion effects comes into play when time-difference between the incidence of two adjacent pulses is shorter than the thermal lifetime ($t_c = w^2_0/4D$) for the medium where w_0 is beam-spot size and D is thermal diffusion coefficient for the thin-film. In case of *WSe_2* thin-films $D \sim 1 \times 10^{-3}$ cm^2/sec which results in $t_c \approx 1.4$ ms. This implies that the NLO measurements using ultrashort pulsed lasers with $R \gg$ 1kHz are inevitably accompanied by thermal effect induced manifestations. In other words, the *WSe_2* film does not return to the equilibrium state (or temperature) within the time-period between the incidence of two pulses at 100 kHz repetition rate. This results in the onset of diffusion induced accumulated thermal effect (ATE). The contribution of ATE is apparent from the values of n_2 and β in Table-1 which shows about two-orders of magnitude enhancement for 100 kHz repetition rate. This investigation suggests that the electronic contribution to NLO properties maximizes at low pulse repetition rates, preferably at time-scales lesser than the thermal lifetime.

In summary, the third order nonlinear optical response of *WSe_2* thin film was carried out using single beam *Z*-scan technique. The *WSe_2* thin film exhibits a saturable absorption behaviour with a negative value of β and a peak followed by valley signature with a negative n_2 value. The nonlinear parameters tends to increase at high repetition rate owing to thermal diffusion effect. The investigation provides a basis for the choice of *WSe_2* thin-films in Q-switching, mode-locking and optical switching applications.

References

[1] Wilson, J. A., and A. D. Yoffe. "The transition metal dichalcogenides discussion and interpretation of the observed optical, electrical and structural properties." Adv. Phys. 18, no. 73 (1969): 193-335.
[2] Chi, Dongzhi, KE Johnson Goh, and Andrew TS Wee, eds. "2D Semiconductor Materials and Devices". Elsevier, 2019.
[3] Yun, Won Seok, S. W. Han, Soon Cheol Hong, In Gee Kim, and J. D. Lee. "Thickness and strain effects on electronic structures of transition metal dichalcogenides: 2H-MX_2 semiconductors (M= Mo, W; X= S, Se, Te)." Phys. Rev. B 85, no. 3 (2012): 033305.
[4] Boyd, Robert W. "Nonlinear Optics". Academic press, 2020.
[5] You, J. W., S. R. Bongu, Q. Bao, and N. C. Panoiu. "Nonlinear optical properties and applications of 2D materials: theoretical and experimental aspects." Nanophotonics 8, no. 1 (2019): 63-97.
[6] Falconieri, Mauro. "Thermo-optical effects in Z-scan measurements using high-repetition-rate lasers." J. Opt. A: Pure Appl. Opt. 1, no. 6 (1999): 662.
[7] Surbhi, Km, Sourav Bhakta, Anupa Kumari, Utkalika P. Sahoo, Pratap K. Sahoo, and Ritwick Das. "Impact of pauli-blocking effect on optical limiting properties of *WSe_2* thin films." Opt. Mater. 129 (2022): 112479.
[8] Sheik-Bahae, Mansoor, Ali A. Said, and Eric W. Van Stryland. "High-sensitivity, single-beam n_2 measurements." Opt. Lett. 14, no. 17 (1989): 955-957.

Spectroscopic study of Λ-type doublets of nitric oxide using cavity ring-down spectroscopy

Ardhendu Pal*, Soumyadipta Chakraborty, Biswajit Panda and Manik Pradhan

Department of Chemical and Biological Sciences, S. N. Bose National Centre for Basic Sciences, Salt Lake, JD Block, Sector III, Kolkata 700106, India

**Correspondence to: ar.pal391@gmail.com*

Abstract

The spectroscopic features of nitric oxide (NO) are interesting to study due to its paramagnetic nature. Study of Λ-type doublet [1] of nitric oxide is very important as it would reveal various spectroscopic parameters. Here, we have explored various spectroscopic features that are influenced by the Λ-type doubling of the fine structure lines of nitric oxide in $(^2\prod_{1/2}, 1)\leftarrow(^2\prod_{1/2}, 0)$ and $(^2\prod_{3/2}, 1)\leftarrow(^2\prod_{3/2}, 0)$ vibrational transitions in the mid-IR figure-print region. High-resolution continuous-wave external-cavity quantum cascade laser (cw-EC-QCL) working in the 5.2 μm region coupled with cavity ring-down spectroscopy (CRDS) technique was employed for the measurement of rotationally resolved Λ-type doublet involving parity sub-states e and f of NO corresponding to $^2\prod_{1/2}$ and $^2\prod_{3/2}$ states [2]. Spectroscopic parameters such as Λ-type doublet splitting and Λ-type doubling constants were determined for these two states in the R-branch. We have investigated the pressure broadening effect on Λ-type doublets along with the dependency of pressure broadening coefficients on the rotational quantum number J of nitric oxide with three perturbing gases. Finally, we have determined the vibrational transition dipole moment value and Herman-Wallis coefficients from our experimental data. All these experimentally obtained spectroscopic parameters help us to understand this diatomic molecule more fundamentally.

Keywords

Spectroscopy, doublets, ro-vibration, nitric oxide, mid-IR, high-resolution.

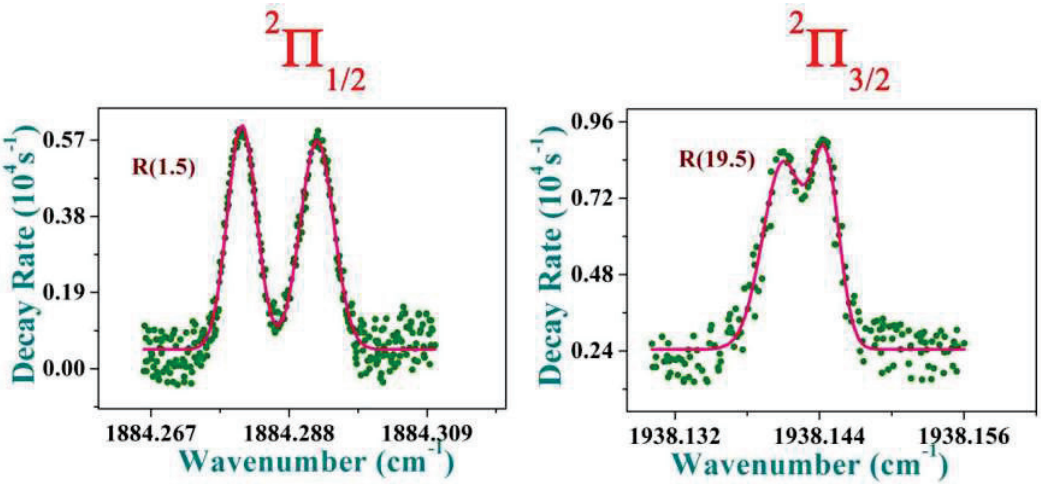

Fig. 1 *Λ-doublet spectra of NO for respective state.*

References

[1] Hinkley, R. K., J. A. Hall, T. E. H. Walker, and W. G. Richards. "Λ doubling in 2Π states of diatomic molecules." Journal of Physics B: Atomic and Molecular Physics (1968-1987) 5, no. 2 (1972): 204.

[2] Geuzebroek, F. H., M. G. Tenner, A. W. Kleyn, H. Zacharias, and S. Stotle. "Parity assignment of Λ-doublets in NO X 2Π12." Chemical physics letters 187, no. 5 (1991): 520-526.

Controlled induced Transparency in a double cavity Optomechanical system: Slow light

Anjan Samanta[1*] Kousik Mukherjee[1] Paresh Chandra Jana[1]
[1]Dept. of Physics, Vidyasagar University Medinipur, Paschim Medinipur, 721102. India
*Corresponding to: anjan.samanta744@gmail.com

We have explored the induced transparency of the transmission of a probe light in a double cavity optomechanical system with non-reciprocal coupling for different system parameters. Transparency profile shows the Fano resonance which may have potential utility for telecommunication applications. We have also shown that the group velocity of the probe field is both positive and negative which indicates the slow and fast light effect. The fast to slow light conversion may be tuned via system parameters. This may have been used for smooth pulse communication and fast signal processing.

Keywords: Slow Light, Induced Transparency, Fano Resonance.

Introduction:

In recent, it is more applicable to control the velocity of propagation of light pulse in a different material system and this can be explained via slow and fast propagation of light. Slow light propagation has fundamental insights and also has a lot of potential utilities [1]. The generation of slow light is extensively studied in the context of Electro-magnetically induced transparency (EIT) and optomechanically Induced transparency (OIT) profiles [2]. The group delay i.e., slow light and fast light effects of the optical field have been observed in solid state material at room temperature [3, 4]. Slow light propagation has different applications for data control devices [5].

The Model System:

To study the transmission of the probe field and slow light effect we consider a double cavity system with nonreciprocal coupling and the system Hamiltonian is given by [6]

$H = \Delta_a a^\dagger a + \Delta_c c^\dagger c + \omega_m b^\dagger b + \lambda_1 a^\dagger c + \lambda_2 ac^\dagger - g a^\dagger a\,(b^\dagger + b) + \mathrm{E}_p(c^\dagger e^{i\omega_p t} + c e^{-i\omega_p t})$ (1)

Here $\Delta_j = \omega_j - \omega_l$(j = a, c) are the corresponding cavity- laser detuning, ω_j and $\omega_m$are resonance frequencies of the corresponding optical cavity and mechanical resonator. Here$\lambda_j$is non-reciprocal tunneling strength from cavity a to c, and g is the coupling parameter for cavity c to mechanical mode. Here a($a^\dagger$), b($b^\dagger$), c($c^\dagger$)are annihilation (creation) operators for the cavity field modes & E_p is the input laser amplitude. Solving the Heisenberg equation of motion of different field modes, we calculate the Forward transmission profile. The transmission rate of the probe beam, defined by the ratio of the output to input field amplitudes at the probe frequency is then given by $\zeta(\omega_p) = 1 - \frac{\tau k_a A_+}{\varepsilon_p}$ The forward transmission rate $T_F = |\zeta(\omega_p)|^2$ of the probe, where $A_+ = \frac{-i\varepsilon_p(F_2 + i\Delta_p)}{(R - \Delta_p^2 Q) + i\Delta_p(P - \Delta_p^2) + i\,\lambda_1\,\lambda_2(\Upsilon - \omega_m)}$

Results & Discussions:

In this section, we have discussed the possibility of the tunable fast light to slow light and vice-versa. From the study, it is clear that on the variation of refractive index in the transparency window the above conversation occurs smoothly. Under the different system parameters, this effect is observed when the phase of the probe field varies. The mathematical expression for the phase is given by $\theta_T = Arg\{\zeta(\omega_p)\}$. Figure 1a describes the variation of phase concerning cavity detuning parameters normalized by k_a and Figure (1b) represents the Fano line shape profile. The decay constant is related by $k_c = 2k_a$, and nonreciprocal coupling defined by $\lambda_2 = 2\,\lambda_1$. The fast and slow light refers to the group velocity of a light wave i.e., group delay. The group delay is defined by the relation $\varphi_T = \frac{\partial}{\partial \omega_p}\{\theta_T(\omega_p)\}$. The value $\varphi_T < 0$ indicates negative group delay i.e., fast light and $\varphi_T > 0$ refers to positive group

delay i.e., Slow light. This is shown in the inset picture of figure 1a-1c. This is because due to the frequency dependence of the refractive index based on resonance or near resonance response. The variation of group delay is shown in figure (1c). The fast light and slow light occur due to absorption resonance and different types of nonlinear interaction in the cavity field.

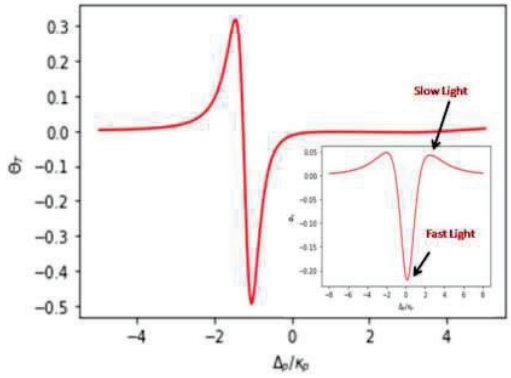

(1a)

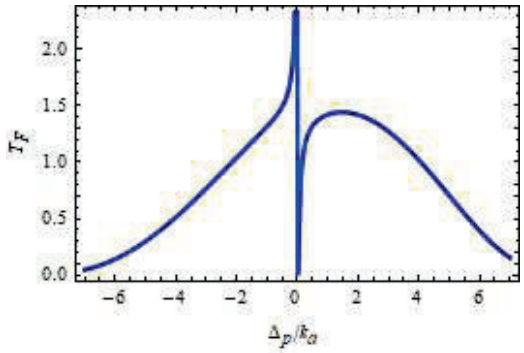

(1b)

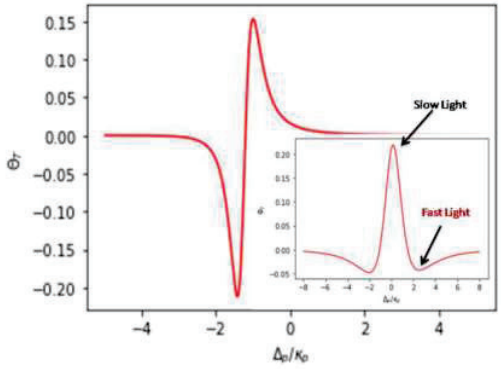

(1c)

$\Sigma = 1, , \gamma = 0.3, a_s = 0.06, \omega_m = 0.35, \Delta_a = 0.01, k_a = 1, k_c = 2.0, (1a)\Delta_c = 3.5, (1b)\Delta_c = -3, (1c)\Delta_c = 10.5$

Conclusion:

We theoretically investigate the transparency profile and Fano line shape property in a double cavity nonreciprocal system via Forward transmission profile. This result shows the sharp asymmetric Fano Resonance and tunable transparency which apply to designing different types of optical switches. Finally, to study the phase variation we achieve a slow to fast light conversation mechanism. This has many more applications to generate photonic devices, optical signal processing, optical networks on chips, etc.

Reference:

1. R. W. Boyed, "Slow and fast light: fundamentals and applications", Journal of Modern Optics, 56: 18, 1908-1915. (2009).
2. S.E. Harris, J.E. Field, A. Imamoglu., "Nonlinear optical processes using electromagneticaaly induced transparency", Phys. Rev. Lett. 64, 1107-1110, (1990) doi: 10.1103/PhysRevLett.64.1107.
3. M. S. Bigelow, N. N. Lepeshkin, R. W. Boyed, " Observation of ultraslow light propagation in a Ruby Crystal at Room Temperature", Phys. Rev. Lett. 90, 113903 (2003).
4. Y. Okawachi, M. S. Bigelow, J. E. Sharping, Z. Zhu, A. Schweinsberg, D. J. Gauthier, R. W. Boyed, A. L. Gaeta, "Tunable optical displays via Brillouin slow light in an optical fiber",Phys. Rev. Lett. 94, 153902 (2005).
5. R. W. Boyd, D. J. Gauthier, "Slow and fast light" Opt. 43, 497 (2002)
6. A. Samanta, K. Mukherjee, P. C. Jana, "Tunable induced transparency and Fano-resonance in double cavity optomechanical system" Int J Phys Res Appl. 4: 019-025, (2021)

Depolarization effect in a focused beam of vertically polarized light

Athira A and Alok Sharan
Department of Physics, Pondicherry University, Puducherry 605014
athira7rythm@gmail.com, aloksharan@gmail.com

Abstract: We studied the effect of depolarization in the weak focusing of vertically polarized light using the circular analyzer. The presence of diagonally and circularly polarized states in the Stokes parameters for the incident vertical polarized light accounts for depolarization near the focal region.
Keywords: Stokes parameter, vertically polarized light, focused beam

1. Introduction:

According to Richards and Wolf (1959), under the illumination of a monochromatic linearly polarized plane wave, the field components near the focus are nonzero in directions perpendicular to the polarization of the incident field. This knowledge is significant for many applications. For example, the longitudinal field component can be used in particle acceleration, second harmonic generation, fluorescent imaging, etc [1-3]. The formalism of the Stokes parameters offers a very convenient tool for light-matter interactions. To determine the state of polarization of an arbitrary beam of electromagnetic radiation measurement is done on the following four criteria.

(1) Total intensity of the beam (S_0).
(2) The degree of polarization with respect to horizontal/ vertical polarized states (S_1).
(3) The degree of plane polarization with respect to the diagonal axis oriented at $\pm 45^0$ to the vertical polarization (S_2).
(4) The degree of circular polarization (S_3).

1.1. Experimental Setup:

In this work, a 5 mW He-Ne laser (632.8 nm) was used as an optical source. A polarizer whose transmission axis is oriented in its vertical direction is placed parallel to the source for generating vertically polarized light. For analyzing this we use a circular analyzer method. The combined polarizer rotated through an angle of 0^0, 45^0, 90^0, and the corresponding intensities are noted as $I_c(0)$, $I_c(45)$ and, $I_c(90)$. For analyzing the linear part, flip the polarizer to the reverse order. This combination will act as a linear polarizer and the intensity measurements are noted as $I_L(0)$, $I_L(45)$, and $I_L(90)$ [4]. For studying the effect of depolarization using a focused beam, the analyzer is placed at the focus of the lens having focal length 10 cm without disturbing the alignment.

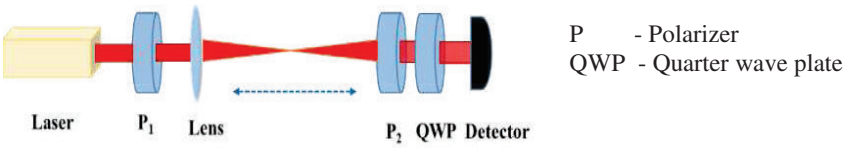

Fig. 1: Experimental setup for measuring the stokes parameters using a circular analyzer method

Stokes parameters can be found from the equations,

$$S_0 = I_c(0^0) + I_c(90^0)$$
$$S_1 = S_0 - 2I_c(45^0)$$
$$S_2 = I_c - I_c(90^0)$$
$$S_3 = -S_0 + 2I_L(0^0)$$

The measured intensities of S_0, S_1, S_2, and S_3 are normalized with respect to S_0 for constructing the Stokes vector.

2. Results and Discussions

The Stokes parameters of incident vertically polarized light and the focused beam is tabulated in *Table 1*. We observed that within the estimated error of 4% the Stokes parameters of incident light define it to be vertically polarized light. At the focus, we observe that S_2 and S_3 are nonzero, which could be due to depolarization. The deviation of S_1 component from -1.02 $\pm$ 0.04 to -0.61 $\pm$ 0.04 and the nonzero elements of S_2 and S_3 from 0.01$\pm$ 0.04 to 0.07$\pm$ 0.04 and from -0.05 $\pm$ 0.04 to -0.26 $\pm$ 0.04 shows how the vertically polarized light is depolarized near the focus. The presence of circular and diagonal polarization states in the case of focused vertically polarized light is seen. For visualizing this change, the intensity distribution of the Stokes parameters is captured using a PCO Pixelfy CCD camera of pixel resolution 6.45 μm *X* 6.45 μm (horizontal X vertical). The Images are recorded using camware 64 software, set to an exposure time of 130 µs and the images correspond to the Stokes parameters obtained using MATLAB R2013a, and it is shown in *Fig. 2.* On comparing to the intensity distribution of its vertically polarized state and its focusing, some more light is originated in the S_2 and S_3 contribution in the weakly focused beam indicates the contribution of diagonal and circular polarization states.

Table 1: Stokes parameters of the vertically polarized light with and without focusing

Polarization state	Stokes Parameter		
		Without focusing	With focusing
Vertical Polarization	S_0	1 $\pm$ 0.04	1$\pm$ 0.04
	S_1	-1.02$\pm$ 0.04	-0.61$\pm$ 0.04
	S_2	0.01$\pm$ 0.04	0.07$\pm$ 0.04
	S_3	-0.05$\pm$ 0.04	-0.26$\pm$ 0.04

Vertically polarized light

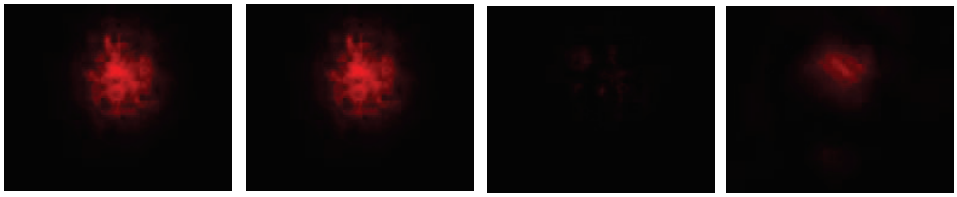

Vertically polarized light using focused beam near to the focus

Fig. 2: Intensity distribution of the S_0, S_1, S_2 and S_3 components of the Stokes parameters

3. Conclusion

In our study, we performed and compared the Stokes parameter of the vertically polarized state and the depolarization effect due to focusing. The nonzero elements in the Stokes parameters of the focused beam indicate a significant amount of depolarization in the vertically polarized state at the focus. It is also confirmed from the images of the intensity distribution of the Stokes parameters.

4. References

[1] Bouhelier,A, "Near-field second-harmonic generation induced by local field enhancement," Physical Review Letters,90, 013903.
[2] Cicchitelli,L, "Longitudinal field components for laser beams in vacuum" Physical Review A, 41,3727.
[3] Hayazawa,N,"Detection and characterization of longitudinal field for tip-enhanced Raman spectroscopy. Applied Physics Letters, 85, 6239.
[4] Edward COLLET, "Measurement of the four Stokes polarization parameters with a single circular polarizer", Optics Communications, Volume 52.

Holographic Waveguide Coupler for AR/MR with FOV expansion

Shivani, Rishabh, Abhishek Tiwari, Ravinder Reddy M, Charu S Tripathi
Electro-Optics and Lasers, Product Development and Innovation Center
Centre Of Excellence, Bharat Electronics Limited
Bangalore, India
Email: shivani@bel.co.in

Abstract: In this work, we are presenting the optical simulations and experimental proof of expansion in field of view (FOV) using plane waveguide coupler. This approach can be utilized in the booming technology trends of augmented (AR) and mixed reality (MR) systems. This approach carries an edge in the sense that it uses holographic optical elements (HOE) for in coupling and out coupling of information. The waveguide coupler presented has dimension of 80mmx200mmx20mm with output FOV 40^0(H) x40^0(V) and 22^0(H) x74^0(V) for power 6.5D and 10D power respectively with source kept at 114mm and detector at a viewing distance of 100mm.

Keywords: Waveguide coupler, Augmented reality (AR), Holographic optical elements (HOE), Field of view (FOV).

1. Introduction

Augmented reality (AR) and mixed reality (MR) are both considered immersive technologies. AR is the modification of real time environment by addition of visual elements or other sensory incentives whereas MR is an extension of augmented reality that allows real and virtual elements to interact in an environment. Waveguide couplers have found to be efficient technology for AR and MR systems compared to other types [1]. These couplers need to be compact, manageable and inclusive for their adequate use. Holographic optical elements on the other hand can be molded to perform various functionalities depending on its angular and wavelength requirements [2]. These requirements can be optimized using Kogelnik's coupled wave theory [3]. HOEs are found to be the best possible candidates in see through displays in place of bulky conventional optics. Holographic optical elements along with the planar waveguide coupler helps in achieving a larger FOV in a very small factor without the use of any conventional optics. This results in reduced encircled footprint of the AR/MR system. Because of the use of zero number of conventional optics like mirrors, lenses etc., aberrations in the image only depends on the holographic optical elements and the surface quality of the waveguide coupler in these kinds of systems which can easily be minimized by optimizing the recording process of the HOEs and ensuring a good surface quality of the waveguide coupler [4].

2. Figures

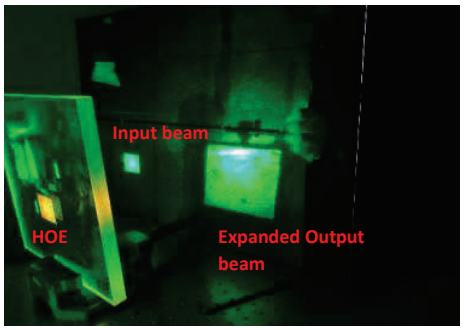

Fig. 1: Experimental results showing an input beam of 15mmX15mm expanded to a square of size 50mmX50mm at a distance of 100 mm from the HOE surface. The input beam is incident onto the HOE which then follows the Kogelnik's coupled wave theory [3], to give the expanded output beam. Here the HOE is recorded using a 532nm monochromatic beam for maximum diffraction efficiency [3].

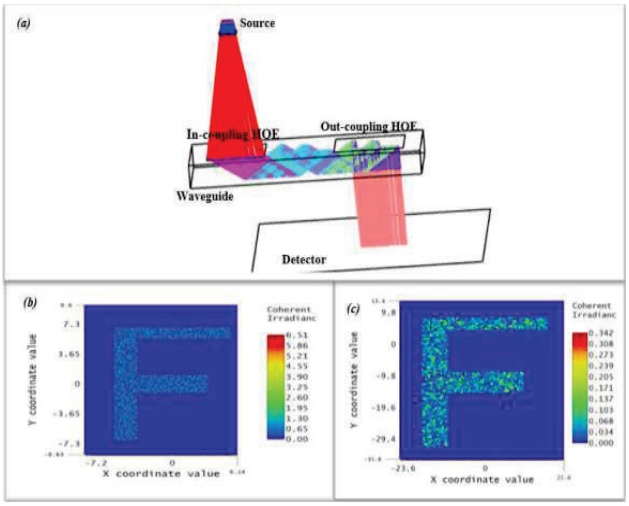

Fig. 2: (a) Depicts the waveguide coupler with two HOEs-In and out coupling HOE as shown. The image from the source follows TIR path until it is coupled out of the coupler at the out-coupling HOE. (b)& (c) shows the input and output. The input has FOV of 12^0(H)X12^0(V) and the output is expanded using the in-coupling HOE having power 6.5D with output FOV as 40^0(H)X40^0(V) at distance of 100mm from the waveguide coupler.

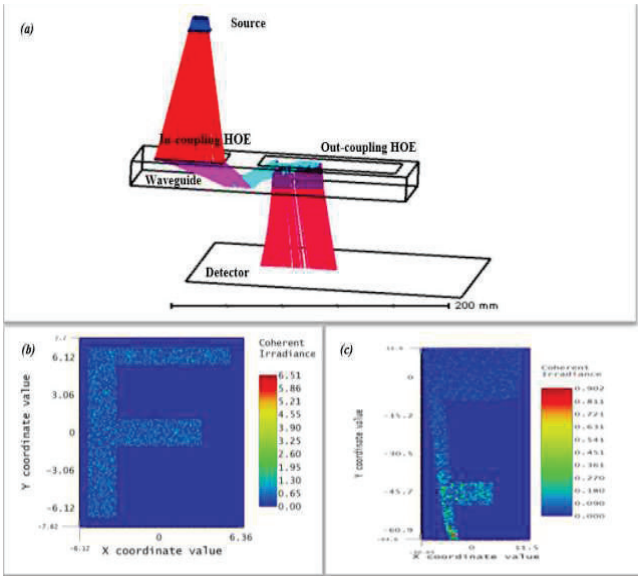

Fig. 2:(a) Depicts the waveguide coupler with two HOEs-In and out coupling HOE as shown. The image from the source follows TIR path until it is coupled out of the coupler at the out-coupling HOE. (b)& (c) shows the input and output. The input has FOV of 12^0(H)X12^0(V) and the output is expanded using the in-coupling HOE having power 10D with output FOV as 22^0(H)X74^0(V) at distance of 100mm from the waveguide coupler. The output image is aberrated because of the excess power in the in-coupling HOE. This can be compensated by optimizing the recording process of HOE [3, 5].

References

[1] Understanding waveguides: the key technology for augmented reality near-eye display (part I &II), Virtual Reality Pop, Jun18, 2019.

[2] Close, D.H., “Holographic Optical Elements”, Optical design problems in laser systems, 1975, vol. 69, pp. 118-121.

[3] H. Kogelnik, “Coupled Wave theory for thick hologram gratings,” Bell Syst. J. 48, 2909-2947 (1969).

[4] Kuang, Y., Liu, J., and Shi, X., “Effect of surface roughness of optical waveguide on imaging quality and a formula of RSE tolerance and incident angle.” Optics Express, Vol 28 (2): 1103-1113, 2020.

[5] N. Kim, Y. Piao and H. Wu, “Holographic Optical Elements and Application”, in Holographic materials and optical systems.

Designed Mie scattering expansion coefficients by nanoparticles in a tight focusing condition

Sarita*, and Rakesh Kumar Singh
Laboratory of Information Photonics & Optical Metrology, Department of Physics, Indian Institute of Technology (Banaras Hindu University), Varanasi, 221005, India
Author E-mail address: sarita.rs.phy19@itbhu.ac.in*

Abstract: We present the weightage of Mie scattering expansion coefficient in a tight focusing condition. This is implemented by considering linearly polarized light with a variable numerical aperture and a fixed obstruction ratio. The study is implemented by MATLAB algorithm to study the interaction of tight focused light with nanoparticle. The simulation results showing the significant contribution of multipoles are presented.
Keywords: Tight focusing, Mie Theory, Multipole expansion

1. Introduction

Nanoparticles (NP) have gained a lot of attention in past few decades with their use in different areas and their interaction with tight-focused incident beam has attracted considerable interest with an increasing number of applications in microscopy, data storage, particle trapping, optical levitation, sensing, and Raman scattering diagnostics. The structure of an Electromagnetic (EM) field through an aplanatic lens system in the vicinity of the focal region using vector diffraction formula has been provided by Richards and Wolf [1]. The linearly polarized Plane wave (PW) interacting with spherical NP of size comparable to the wavelength of incident light has been explained using Mie Theory [2], by introducing multipole expansion approach which is advantageous in decomposing the field to its constructing modes. Each of these modes has specific properties such as directivity, confinement, etc. The EM field at the focus due to strong focusing of the incident beam is determined using a Generalized Mie theory and the contribution of multipole order has been studied [3]. Illumination through an annular aperture in an optical system increases the depth of focus [4], narrows down the point spread function, provides a huge impact in microscopy and imaging by showing the improved quality of resolution. In this paper, we investigate the weightage of multipole orders for annular aperture and how the contribution of modes takes place when we increase the numerical aperture (NA).

2. Theory

According to Mie theory, the incident and scattered field of a high NA optical system can be written in terms of vector spherical harmonics, expansion, and scattering coefficients as follows [3],

$$E_i = \sum_{n=1}^{\infty} A_n (M_{o1n}^{(1)} - iN_{e1n}^{(1)}) \quad (1)$$

$$E_s = \sum_{n=1}^{\infty} A_n (ia_n N_{e1n}^{(3)} - b_n M_{o1n}^{(3)}) \quad (2)$$

where, n is the multipole order, N_{e1n}, M_{o1n} are the vector spherical harmonics, with superscripts $^{(1)}$ and $^{(3)}$ denoting the spherical Bessel function $(j_n(\rho))$ and spherical Hankel function of the first kind $(h_n^{(1)}(\rho))$ respectively, a_n and b_n are the scattering coefficients. The contribution of modes can be analyzed using the expansion coefficient which is given by

$$A_n = (-i)^n E_0 kf \frac{2n+1}{2n^2(n+1)^2} \int_{\theta_{min}}^{\theta_{max}} a(\theta) \left[\frac{P_n^1(\cos\theta)}{\sin\theta} + \frac{dP_n^1(cos\theta)}{d\theta} \right] sin\theta d\theta \quad (3)$$

where E_0 is the plane wave amplitude, f is the focal length of the lens, and k is the wave vector. θ is the polar angle with $\theta_{max} = \alpha$, where alpha (α) is the semi-aperture angle of the lens and calculated using the formula of numerical aperture, NA= $n_b sin\alpha$, where n_b is the refractive index of the surrounding medium, $a(\theta) = (cos\theta)^{1/2}$ is the illumination weighing factor, $P_n^{(1)}(cos\theta)$ is the associated Legendre polynomial.

The field expansion in the case of PW is same as in the case of tight focused beam except for the expansion coefficient which takes up the form, $A_n = E_0(i)^n\,(2n+1)/n(n+1)$, [2]. For the limiting case of $\alpha \to 0$ tight focused beam becomes identical to PW.

3. High-NA Optical system and Results:

We have considered the interaction of NP in free space with a tight focused incident beam linearly polarized along x direction for different cases of NA such as for α =30°, 45°, 60°, 90°. The relative contribution of different modes is determined by calculating the relative strength which is defined as $|A_n/A_1|$. The MATLAB simulation has been done for investigating the involvement of multipole orders, and we have also compared these results with PW illumination. Fig.1(a) is the recreated result in which the field expansion for multipole order, n=10 has been plotted, showing that the more the beam is tightly focused the lesser the dependence on the higher order multipoles [3]. The selected range $0° \leq \theta \leq 90°$ in eq.(3) is not restricted to its lower limit to be 0°. We introduced an obstruction ratio of θ_{min} =30° and performed a simulation for this annular aperture optical system. The results in Fig.1(b) shows the contribution of different modes, which is varying for different value of NA, although for a high NA system (such as α=90°) the dependency of higher order multipoles is still less relevant in comparison with a low-NA system.

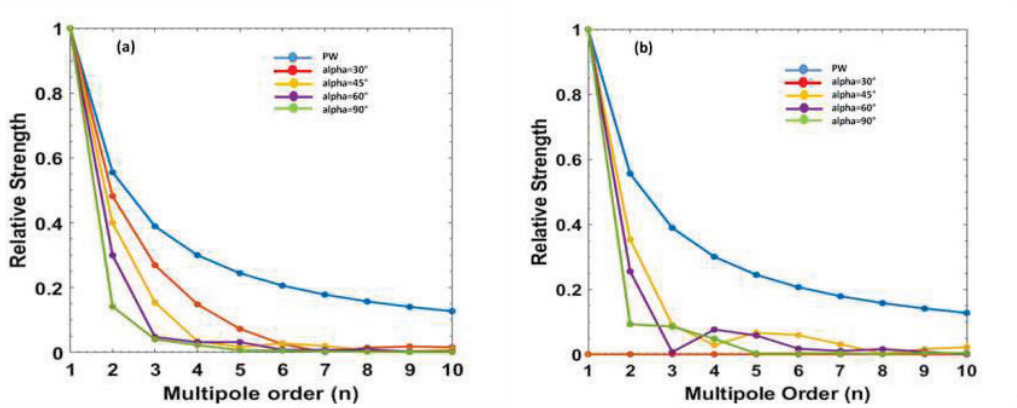

Fig.1: (a) Relative strength of the multipole expansion coefficient for tight focused condition, (b) for a tight focused beam under annular aperture condition, for PW and high-NA beam for α =30°, 45°, 60°, 90°.

4. Conclusion:

We illustrated the contribution of multipole order of incident beam for the case of tight focused condition and also for the case of the beam in similar conditions passing through an annular aperture optical system and compared results with PW illumination condition.

5. Acknowledgement:

Sarita acknowledges support from my institute IIT-BHU, and UGC (JRF) scholarship.

6. References:

[1] B. Richards and E. Wolf, "Electromagnetic diffraction in optical systems II. Structure of the image field in an aplanatic system," Proc. R. Soc. London, Ser. A **253**, 358–379 (1959)
[2] C. F. Bohren and D. R. Huffman, Absorption and Scattering of Light by Small Particles (Wiley, 1983).
[3] N. M. Mojarad, V. Sandoghdar, and M. Agio, "Plasmon spectra of nanospheres under a tightly focused beam,".Opt.Soc. Am. B **25**, 651-658 (2008).
[4] G. B. Airy, "I. On the diffraction of an annular aperture," London Edinburgh Dub. Philos. Mag. J. Sci. 18(114), 1–10 (1841).

Vibrational strong coupling in a hybrid molecular-plasmonic system

Govind Dayal Singh
Banaras Hindu University, Varanasi 221005, India
Author e-mail address: dayal@bhu.ac.in

Abstract: We report on the realization of strong coupling of infrared-active molecules embedded in a subwavelength size plasmonic nanocavity. Our hybrid system shows a clear signature of strong coupling via normal mode splitting with an extremely small number of molecules that leads to new ways of ultrasensitive molecular detection.

Keywords: Strong coupling, plasmonic cavity, molecular detection.

Vibrational strong coupling (VSC) is emerging as a powerful platform for chemical reaction control, molecular sensing and cavity quantum electrodynamics. Strong coupling occurs when the energy exchange rate between the vibrational transition of a molecule and the photon confined in an optical cavity is larger than any dissipation in the system. A particularly common approach is to use photonic environments such as high-Q optical microcavities that are unsuitable for nanoscale experiment at infrared frequencies. In this work, we demonstrate VSC between the C=O stretching mode of PMMA and the gap plasmon mode of a nanoscale plasmonic cavity. Our subwavelength size cavity consists of a gold thin film perforated with periodically placed nanoslits and stood off above a reflective ground plane separated by an ultrathin PMMA film. For a spectrally tuned system, the energy exchange rate obtained from the experimental and simulated spectra is found to be higher than the damping rates of the system which suggests that our system operates in a strong coupling regime. We observed a vacuum Rabi splitting of 128 cm^{-1} which can further be improved by the design optimization. The ultrasmall mode volume of our cavity paves the wave for ultrasensitive linear and nonlinear vibrational sensing experiments and new platforms for implementing cavity QED at room temperature.

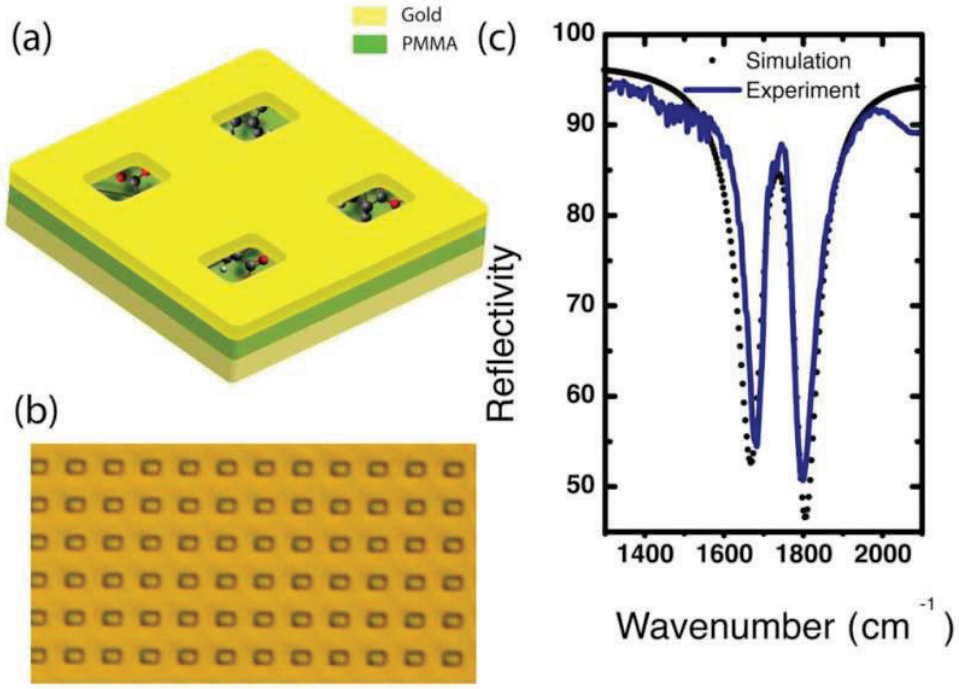

Orbital angular momentum mode identification of vortex beam using optical correlation

Rahul Kumar[1], Allarakha Shikder[1], Naveen K. Nishchal[1]*, and Ayman AlFalou[2]
[1]*Department of Physics, Indian Institute of Technology Patna, Bihta, Patna 801 106, Bihar, India*
[2]*LSL Teams, L@bISEN, Yncrea Ouest, 20 rue Cuirasse Bretagne, CEDEX 2, 29228 Brest, France*
**E-mail: nkn@iitp.ac.in*

Abstract: In recent years, considerable attention has been made on the light beams which contain orbital angular momentum because of its application in several fields. Topological charge is a property which determines the amount of angular momentum contained in the beam. In this paper, we demonstrate a method to determine the topological charge of such beams using binary differential joint transform correlation approach.

Keywords: Orbital angular momentum; Vortex beam; Topological charge; Joint transform correlator

1. Introduction

Light beams containing orbital angular momentum (OAM) have donut looking intensity distributions. Those beam have a spiral phase front expressed by $exp(il\varphi)$, where l denotes the topological charge (TC) and φ is the azimuthal angle. OAM beams are used in many applications including optical twister, optical trapping, optical encryption, communication system [1-3]. In literature, several methods for TC measurement have been reported like interferometric [4], diffractive, machine learning [5] etc. Experimental technique based on interferometric geometry has limitation in measuring higher order TCs [6]. Techniques based on diffractive element have problems in real-time applications [7]. Machine learning requires high configuration system [8].

In this study, we propose a method to identify TC of an OAM beam using binary differential joint transform correlation (BDJTC) approach [9]. Optical pattern recognition and picture identification are two of the most important applications of optical information processing. The approaches are known as joint transform correlator (JTC) and VanderLugt Correlator (VLC) [9]. The JTC does not require the establishment of *apriori* filters, whereas the VLC does. Therefore, it is evident that JTC has many advantages over VLC, but one of the primary issues with classical JTC is the existence of strong zero order dc in the output plane. Many attempts have been made to remove the dc. BDJTC performs better in case of dc removal. Through numerical simulations, we demonstrate the feasibility of the proposed approach.

2. Theory

Let $f(x,y)$ be the input image into a JTC, consisting reference image $r(x-a, y)$ and the target image $t(x+a, y)$ separated by a distance $2a$:

$$f(x, y) = t(x + a, y) + r(x - a, y) \tag{1}$$

The Fourier transform of $f(x, y)$:

$$F(x, y) = T(u, v)\exp(-idv) + M(u, v)\exp(idv) \tag{2}$$

An intensity-sensing device, a charge-coupled device camera captures the join power spectrum (JPS):

$$I(u, v) = \left|F(u, v\right|^2 = T^2(u, v) + R^2(u, v) + R(u, v)T^*(u, v)\exp(-j2au) + R^*(u, v)T(u, v)\exp(j2au) \tag{3}$$

Taking inverse Fourier transform to Eq. (3), we obtain the correlation output:

$$C(x, y) = t(x, y) \otimes t(x, y) + r(x, y) \otimes r(x, y) + r(x - 2a, y) \otimes t(x - 2a, y) + t(x + 2a, y) + t(x + 2a, y) \tag{4}$$

where $\otimes$ represents correlation operator. The JPS is differentiated first and then binarized setting a suitable threshold value. The threshold value for each subset is given by median of that segment.

$$T_{mn} = median\ [C_{nm}(u, v)] \tag{5}$$

where $C_{nm}(u, v)$ is the segmented JPS. The BDJTC can be obtained after binarizing the bipolar differential JPS,

$$E(u, v) = \begin{cases} +1, & \mathrm{C_u}(u, v) > \mathrm{T_{nm}} \\ -1, & \mathrm{C_u}(u, v) \le T_{nm} \end{cases} \tag{6}$$

3. Simulation Results

A MATLAB-based computer simulation has been carried out to test the feasibility of BDJTC in determining the TC of OAM beams. For simulation, we used 150 × 150 pixels OAM image of different TCs that are combined and zero-padded to form a 256 × 256 pixels join input image. When the target picture and reference image both contain TC (l = 5), as shown in Figure1(a), the output plane displays autocorrelation peak, as shown in Fig. 1(b), but in Fig. 1(d) no correlation output is clearly visible when the target image and reference image contain different TCs, as shown in Fig. 1(c). Finally, we trained our system by correlating each image individually for TC values l = 1 to 100. When we display any new OMA beam image for any TC value after training, it immediately correlates with our trained reference images. With the use of BDJTC, we can quickly identify the unknown image if the target and reference images are identical. The TC value of the unknown image is the same as the reference. This is evident from results shown Fig. 2(e-h).

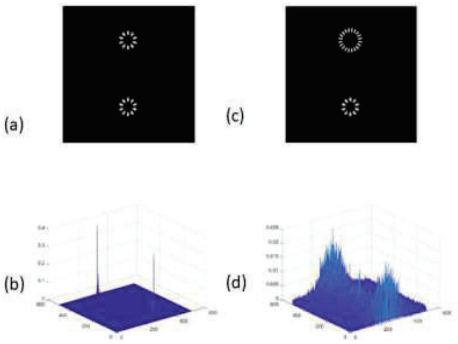

Fig. 1 simulation results (a) &(c) input images; (b) & (c) correlation output

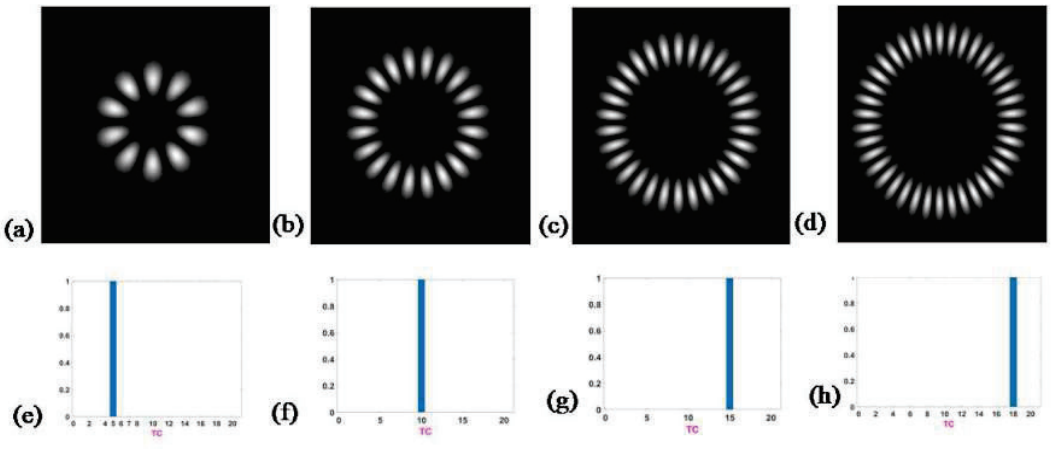

Fig. 2(a)-(d) Interference patterns of vortex beam corresponding to TC values 5, 10, 15, and 18, respectively. (e)-(h) Test results of TC measurement for corresponding TC values.

4. Conclusion

In this paper, we propose a technique to identify the TC values of OAM beams by using BDJTC method. From the obtained results, we can easily find the value of l. Such technique may find applications in real-time identification.

Acknowledgement

The authors acknowledge the support of the SERB, Department of Science and Technology, Government of India (CRG/2021/001763).

References

[1] J. E. Curtis, B. A. Koss, and D. G. Grier, "Dynamic holographic optical tweezers," Opt. Commun. 207, 169-175 (2002).
[2] V. R. Daria, P. J. Rodrigo, and J. Glückstad, "Dynamic array of dark optical traps," Appl. Phys. Lett. 84, 323-325 (2004).
[3] P. Kumar, N. K. Nishchal, and A. AlFalou, "Controllable optical vortex array for image encoding," IEEE Photon. Technol. Lett. 34, 521-524 (2022).
[4] P. Kumar and N. K. Nishchal, "Self-referenced spiral interferogram using modified lateral shearing Mach-Zehnder interferometer," Appl. Opt. 58, 6827-6833 (2019).
[5] B. Gong, S. Cai, Z. Xiao, X. Wang, L. Li, and Z. Zhang, "Recognition of OAM state using CCN based deep learning for OAM shift keying FSO system with pointing error and limited receiving aperture," IEEE Conference on Laser and Electro-Optics (CLEO), May 9-14, 2021, San Jose (2021).
[6] P. Kumar and N. K. Nishchal, "Determining orbital angular momentum of light by analyzing interferogram with conjoined fork-like structures," Workshop on Recent Advances in Photonics (WRAP), Dec. 13-14, 2019, Guwahati (2019).
[7] D. Fu, D. Chen, R. Liu, Y. Wang, H. Gao, F. Li, and P. Zhang, "Probing the topological charge of a vortex beam with dynamic angular double slits," Opt. Lett. 40, 788-791 (2015).
[8] Z. Liu, S. Yan, H Liu, and X. Chen, "Superhigh-resolution recognition of optical vortex modes assisted by a deep-learning method," Phys. Rev. Lett. 123, 183902 (2019).
[9] N. K. Nishchal, S. Goyal, A. Aran, V. K. Beri, and A. K. Gupta, "Binary differential joint-transform correlator based on a ferroelectric-liquid-crystal electrically addressed spatial light modulator," Opt. Eng. 45, 026401 (2006).

Spectral Narrowing of Amplified Spontaneous Emission in One-Dimensional Photonic Crystal Super Tamm Structure

Sudha Maria Lis S, Somnath Pandit, Someprosad Patra, Debamalya Banerjee, and Shivakiran Bhaktha B N*

Department of Physics, Indian Institute of Technology Kharagpur, Kharagpur - 721302, India
**kiranbhaktha@phy.iitkgp.ac.in*

Abstract: In this work, studies on the optical Tamm mode of a super Tamm structure consisting of a silver (Ag) thin film deposited on dye-doped polyvinyl alcohol (PVA) thin film coated on a SiO_2/ TiO_2 one-dimensional photonic crystal (1DPhC) structure are presented. The spectral narrowing of the Tamm state aided amplified spontaneous emission from the structure is attributed to the strong confinement of Tamm mode at the interface of 1DPhC and Ag thin film.

Keywords: Optical Tamm state, one-dimensional photonic crystal, amplified spontaneous emission.

1. Introduction

The fabrication of efficient and more compact laser sources is in demand for various integrated optoelectronic devices and other applications. For providing the optical feedback necessary for the lasing emission to occur, different geometries are developed such as distributed feedback structures [1], vertical cavity surface emitting lasers [2], and photonic crystals [3]. Recently, Tamm modes are getting the attention for being a good candidate as laser source. The Tamm modes appear at the interface between a metallic film and a distributed Bragg reflector (DBR) or one-dimensional photonic crystal (1DPhC) and exhibit properties of both cavity modes and plasmons [4]. Tamm mode can be visualized like a cavity mode in a zero-thickness cavity (metal-1DPhC structure or Tamm structure), or like a surface mode, with electric field intensity decreases when moving away from the metal/ dielectric spacer layer interface (metal-dielectric spacer- 1DPhC structure or super Tamm structure). The metal film deposited on 1DPhC structure with a dielectric spacer, resulting in the reduction of mode volume of Tamm mode, leading to the enhanced spontaneous emission rate of the emitters doped in the spacer layer or in the 1DPhC and even to form a threshold-less laser [5]. Herein, we demonstrate the efficient coupling between Tamm mode and the fluorophore (DCM dye) in a super Tamm structure with enhanced directional spontaneous emission under end-fire coupling excitation geometry.

2. Fabrication details

The super Tamm structure discussed in this work consists of a silver (Ag) film deposited on to a 4-(dicyanomethylene)-2-methyl-6-(4-dimethylaminostyryl)-H-pyran (DCM) dye doped polyvinyl alcohol(PVA) thin film (DCM-PVA thin film) coated on to a SiO_2/ TiO_2 1DPhC structure. The 1DPhC structure consists of eight bi-layers of quarter-wave thick alternating layers of silicon dioxide (SiO_2) and titanium dioxide (TiO_2) on a SiO_2 coated (buffer layer ~ 2 μm) silicon substrate deposited using the sol−gel synthesis route and the dip-coating technique. In order to obtain the suitable thickness of different layers, we have used quarter-wavelength stack condition being satisfied at λ_B = 600 nm.

The detailed descriptions of silica and titania sol preparation and 1DPhC fabrication are given here [6]. For fabricating the spacer layer, PVA was dissolved in dimethyl sulfoxide (DMSO) at 90°C with the concentration of 250 mg/ ml, and the DCM dye was mixed with DMSO solution with 2 mM concentration. 0.008% DCM-PVA solution was prepared and spin coated onto 1DPhC at 3000 RPM for 30 seconds. The Ag film was deposited on to the DCM-PVA coated 1DPhC by using the thermal evaporation technique under 5×10^{-6} mbar vacuum pressure.

3. Experimental results

Our results include the structural and optical characterization of the fabricated super Tamm structure. The thickness of the individual layers of the fabricated structure was obtained using field emission scanning electron microscope (FESEM) image as shown in Fig. 1(a). Average layer thicknesses of 90 (± 4) nm and 60 (± 4) nm were obtained for SiO_2 and TiO_2 layers respectively. The thicknesses

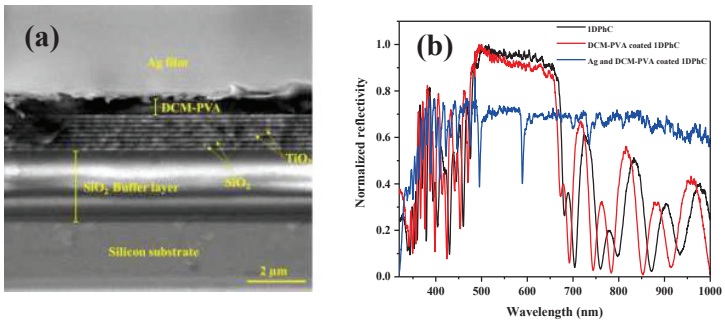

Fig. 1: (a) Field emission scanning electron microscope (FESEM) cross-section image of super Tamm structure on silicon substrate. (b)Experimentally obtained reflectance spectra of 1DPhC, DCM-PVA coated 1DPhC and Ag and DCM-PVA coated 1DPhC or super Tamm structure under normal incidence.

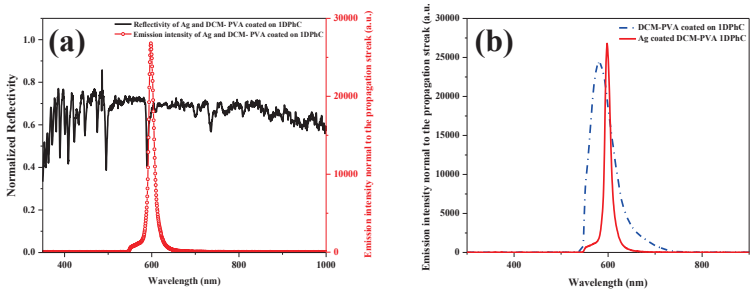

Fig. 2: (a) Emission spectrum of a super Tamm structure with DCM dye doped PVA spacer layer recorded normal to the direction of excitation overlaid on corresponding reflection spectrum at normal incidence. (b) Emission spectrum of a super Tamm structure (Ag and DCM-PVA coated on 1DPhC) and DCM-PVA coated on 1DPhC recorded normal to the direction of excitation.

of DCM doped PVA and Ag thin film is found to be 600 nm and 40 nm respectively. The normal incidence reflection spectrum of 1DPhC, DCM –PVA coated 1DPhC and Ag and DCM-PVA coated 1DPhC shown in Fig. 1(b) is recorded using fiber coupled Avantes spectrometer using a reflection probe. A broad photonic stopband (PSB) is observed in the visible region from ~ 460 nm to 680 nm, centred at λ_B = 590 nm. The Ag and DCM-PVA coated 1DPhC exhibits a sharp resonance within the PSB at 589 nm, which corresponds to the Tamm mode of the structure.

The super Tamm structure was optically pumped in waveguiding configuration using a diode pumped solid state (DPSS) laser (λ = 532 nm) and the emission spectrum for different pump powers were recorded using the light scattered out of the plane of the structure using a fiber coupled spectrometer (Avaspec-ULS2048L-EVO). The emission spectrum of a super Tamm structure with DCM dye doped PVA spacer layer recorded normal to the direction of excitation is overlaid on the corresponding reflection spectrum at normal incidence in Fig. 2(a). The emission maximum of the DCM dye at 600 nm is found to be in resonance with the Tamm mode. Also, the emission spectrum of a super Tamm structure (Ag and DCM-PVA coated on 1DPhc) and DCM-PVA coated on 1DPhC recorded using end-fire coupling set-up normal to the direction of excitation shows the narrowing of a peak at 600 nm for a pump power of 14 mW in Fig. 2(b). This spectral narrowing may be associated with the amplified spontaneous emission (ASE) of the DCM dye doped in PVA spacer layer and the strong field confinement achieved in the cavity formed by 1DPhC and Ag thin film. Further details of the emission characteristics of the super Tamm structure will be presented in the conference.

4. References

[1] T. Numai, *Fundamentals of Semiconductor Lasers*, (Springer: New York, 2004).

[2] H. Li and K. Iga, *Vertical-Cavity Surface-Emitting Laser Devices*, (Springer: New York, 2002).

[3] O. Painter et al., "Two-Dimensional Photonic Band-Gap Defect Mode Laser", Science **284**, 1819(1999).

[4] M. Kaliteevski et al., "Tamm plasmon-polaritons: Possible electromagnetic states at the interface of a metal and a dielectric Bragg mirror," Phys. Rev. B **76**, 165415(2007).

[5] M. Khajavikhan et al., "Thresholdless nanoscale coaxial Lasers", Nature **482**, 204(2012).

[6] Sudha Maria Lis S et al., "Femtosecond laser micromachined one-dimensional photonic crystal channel waveguides ", Optical Materials **126**, 112114(2022).

Fano resonance based refractive index sensing in Photonic crystal waveguide-cavity system

Nilaksha Ghosh, Puja Sharma, Sarang Medhekar
Department of Physics, Central University of Jharkhand, Ranchi-835222
Author e-mail address: sarang.medhekar@cuj.ac.in

Abstract- In the present work we have designed and simulated a Fano resonance based photonic-crystal sensor. The proposed device consists of waveguide-cavity system created in dielectric rods in air type photonic crystal (as shown in figure 1). The band structure of the device is calculated using the plane wave expansion method (figure 2). By injecting a broad-spectrum pulse at the input, spectral response of the proposed device is obtained as shown in figure 3. The propagation of the light wave in the device has been analysed using the 2D-Finite difference time domain method. The chosen operating wavelength for this purpose is the off resonant wavelength at $n = 1$ which is $1.727\mu m$. It is obvious in the table 1 that the proposed structure shows significant change in transmission when there is a change in the background refractive-index as small as 0.005.

Keywords: Fano Resonance, Band Pass, Filtration, FDTD, PWE, Photonic crystal

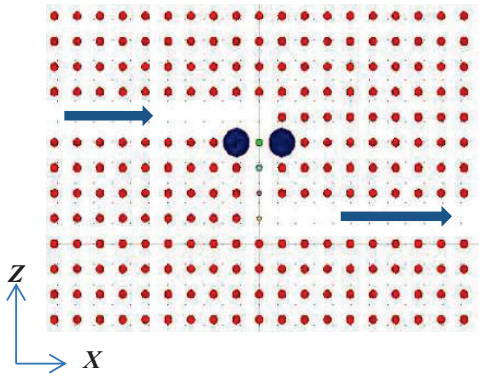

Fig.1: Schematic diagram of the device

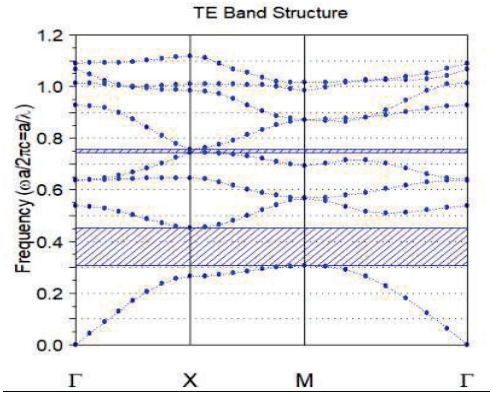

Fig.2: Band structure of the device

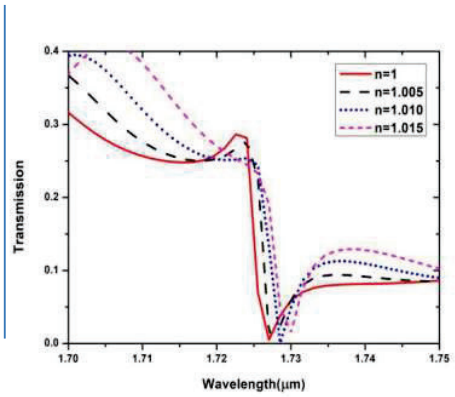

Fig.3: Spectral response of the device at different refractive indices of background

Table1.Variation of Transmission with refractive index

Refractive index(n)	Transmission
1	0%(Off state)
1.005	27.4%
1.01	25.06%
1.015	23.4%

References

[1] J.D Jonnopoulos, S.G Jhonson, J.N Winn, R.D Made, " Photonic Crystal: Modeling the Flow of Light,(Princeton University Press,2008).
[2] A. Goodrazi and M.Ghanaatshor, "Controlling Light by light: Photonic Crystal- based coherent all-optical transistor" JoSA B 33, 1594-1599(2016).
[3] Puja Sharma, Man Mohan Gupta, Nilaksha Ghosh, Sarange Medhekar, "Optical add drop Filters based onsqure ring resonator consisting of octagon shaped core," in 2021 IEEE International Conference on Technology , Research, and Innovation for Betterment of Society (Institutute of Electrical and Electronics Engineers, New York, 1900).
[4] Mindy Lee, Phillipe Fauchet, "Two-dimensional silicon photonic-crystal cavity based biosensing platform for protein detection" Optics Express 5, 1594-1599 (2016).
[5] W.Zhou, D.Zhou, Yi-Chen Shuai, H.yang, S.Chuwongin, A.Chandha, Jung –Hun Seo, Ken. X.Wang, V.Liu, Z.Ma, S.Fan, "Progress in 2D Photonic Crystal fano resonance photonics," Progress in Quantum Electronics 38,1-74(2014).
[6] Yan Deng, Guantao Cao, Hui Yang, Guanhai Li, Xiaoshuang Chen, Wei Lu, "Tunable and high-sensitivity sensing based on Fano resonance with coupled plasmonic cavity" Scientific reports 7,(2017).
[7] Yi Yu, Mikkel Heuck, Hao Hu, Weiqi Xue, Christophe peucheret, yaohui Chen, Leif Oxenlowe, Kresten Yvind, Jesper Monk, " Fano resonance control in a photonic crystal structure and its application to ultrafast switching," Applied Physics Letters,105(2014).
[8] Bing Chen, De-Yuan Chen, Yu Xia, Yan Zhang, Meng-fan Li, "Sharp fano resonance in 2D photoni crystal and its applications," Optoelectronic Letters 16, 349-354,(2020).
[9] Xiong Yeu Chew, Guangya Zhou, Hongbin Zhou, Hongbin Yu, Fook Siong Chau, " Fano resonance phenomenon utilizing photonic crystal rods for tunable filter applications," in 2008 IEEE\LEOS International Conference on Optical MEMs and Nanophotonics (Institutute of Electrical and Electronics Engineers, New York, 1900).
[10] Yuhao Zhang, ZhongZhu Liang, Dejia Meng, Zheng Qin, Yandong Fan, Xiaoyan Shi, David R.Smith, Enzhu Hou, "All-dielectric refractive index sensor based on Fano respnance with high sensitivity in mid-infrared region," results in Physics 27, 104508(2021).

Optomechanical measurement of tensile properties of silk in vacuum

Shivali Sokhi and K.P. Singh
Department of Physical Sciences, Indian Institute of Science Education and Research Mohali, Sector 81, Mohali 140306, India
E-mail: ph17046@iisermohali.ac.in, kpsingh@iisermohali.ac.in

Abstract: Spider silk is a protein based material well known for its extensive mechanical properties. Here, we present a direct measurement of the mechanical response of spider silk subjected to stress in high vacuum conditions using an optically readable cantilever setup calibrated for force measurement. A comparative study of different types of silk i.e. dragline, capture and egg case silk is made in both air and vacuum. Understanding the fundamental changes in structure, mechanical properties and function would serve as a prelude to its future utility in vacuum or space environment related applications.

Keywords: Spider silk, vacuum, stress, strain, cantilever.

Introduction

Spider silk fibers are known to have extraordinary mechanical properties, such as a combination of tensile strength and extensibility which make it a material specifically different from most manmade or naturally occurring fibers[1]. It is biocompatible, biodegradable, has high tensile strength, and great elasticity[2]. Many experimental studies have been conducted to explain the mechanical properties based on the molecular structural organization of spider silk[3,6].The properties of tensile materials are often investigated using stress-strain tests which have been well-reported for spider silk[1]. However the changes in the mechanical properties of spider silk in vacuum have not yet been fully explored and quantified. Here, we present a direct comparison of the mechanical response of spider silk subjected to stress in air and high vacuum conditions using an optically readable cantilever setup calibrated for force measurement. A comparison is drawn between dragline, capture and egg case silk indicating different behavior in vacuum. The aim of this study is to explain the changes associated with introducing the material in vacuum. We thereby quantify the changes in the mechanical properties based on the stress-strain analysis to draw one to one comparison with the behavior in ambient conditions.

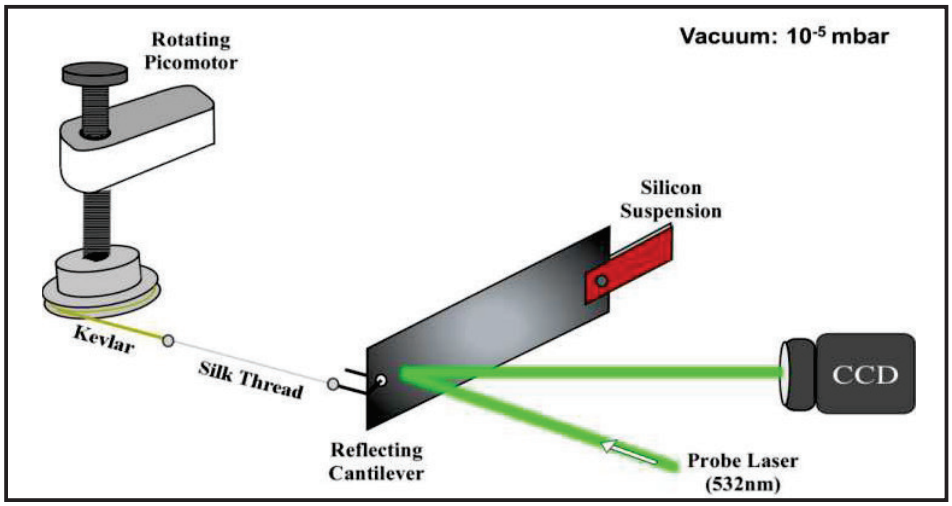

Fig. 1: Schematic of experimental setup

We customized the setup for the stress-strain measurement of spider silk which can be conveniently operated both in air and vacuum. An optically readable cantilever with spider silk connected to its edge via a hook gets deflected when the silk is pulled using a rotating picomotor. A sensitive and flexible steel sheet is used as the cantilever and is calibrated for force measurement. A non extensible kevlar thread is used with the picomotor and glued to the silk to ensure constant pulling. The setup was validated in air and then tested in vacuum. The cantilever motion is probed using a laser beam (532nm) that is reflected off the edge of reflecting cantilever.
The stress- strain measurements are performed for 3 different types of spider silk – dragline, capture and egg case silk in both air and vacuum. Using the measured curves, we compare the mechanical properties of spider silk threads in ambient conditions and vacuum. It is found that these changes are reversible to a certain extent.
Considering the extensive use of this material in recent technology[4] and its potential applications, the impact of high vacuum on spider silk in machinery or in space environment[5] must be investigated for future utility in vacuum or space environment related applications.

References

[1] Gosline, J. M., DeMont, M. E., & Denny, M. W. (1986). The structure and properties of spider silk. *Endeavour*, *10*(1), 37-43.
[2] Vollrath, F., & Porter, D. (2006). Spider silk as a model biomaterial. *Applied Physics A*, *82*(2), 205-212.
[3] Hu, X., et al. "Molecular mechanisms of spider silk." *Cellular and Molecular Life Sciences CMLS* 63.17 (2006): 1986-1999.
[4] Basu, A. (Ed.). (2015). *Advances in silk science and technology*. Woodhead Publishing.
[5] Hu, X., Raja, W. K., An, B., Tokareva, O., Cebe, P., & Kaplan, D. L. (2013). Stability of silk and collagen protein materials in space. *Scientific reports*, *3*(1), 1-8.
[6] Vollrath, F. (1999). Biology of spider silk. *International Journal of Biological Macromolecules*, *24*(2-3), 81-88.

Intensity Noise Characterization of a Tm-Fiber Oscillator Pumped by an Er/Yb-Fiber MOPA

Arathi P, Sourav Das Chowdhury*, Atasi Pal
Fiber Optics & Photonics Division, CSIR-Central Glass and Ceramic Research Institute, Kolkata - 700032 India
**Author e-mail address: sdaschoudhury6@gmail.com*

Abstract: In this work, intensity noise characterization of a thulium (Tm)-doped fiber oscillator pumped by an erbium/ytterbium (Er/Yb)-doped fiber master oscillator power (MOPA) has been carried out by frequency domain analysis obtained through Fourier transform of the temporal waveform.
Keywords: Fiber Laser, Intensity Noise, Relaxation Oscillation.

1. Introduction

Noise is a critically important parameter for any laser system including fiber lasers which are used in sensing and detection or metrology applications. One such application is gravitational wave detection where in addition to the laser linewidth, low laser intensity noise is a mandatory criterion [1] and recently fiber lasers are being employed in this field replacing the bulk solid state lasers [2]. The origin of laser noise can be manifold arising from thermal instability, environmental perturbations, spontaneous emission, mechanical vibrations etc. which manifest in the form of intensity, frequency or phase noise. In that context, this work presents preliminary results in noise characterization of a Tm-fiber laser (TmFL) at around 2 µm wavelength targeting a narrow linewidth, low noise laser source which is a next-generation requirement for gravitational wave detection [3].

2. Experimental Setup

The schematic diagram of the experimental setup consisting of an Er-Yb-doped fiber (EYDF) laser pumping a TmFL is illustrated in Fig 1. The EYDF laser contains a hybrid-ring seed (unidirectional ring cavity containing a bi-directional segment) and an EYDF amplifier. Both active fibers are cladding pumped with 976 nm multimode pump diodes through (2+1)×1 pump-signal combiners and the excess cladding pump power is removed using a cladding mode strippers (CMS). In the seed, a high-reflecting fiber Bragg grating (HR-FBG; reflectivity 99%; λ_C = 1583 nm; $\Delta\lambda_{3dB}$ = 0.56 nm) is connected via a circulator and a 90/10 splitter acts as an output coupler with 90% feedback. The output power of the seed oscillator is limited to 30 mW restricting the intra-cavity power below 300 mW to protect the single mode components. An isolator (ISO) protects the EYDF seed from any back reflection from the amplifier. The seed power is further amplified to 300 mW in the amplifier segment which pumps a TmFL consisting of a 99.5% reflective FBG (λ_C = 1940 nm; $\Delta\lambda_{3dB}$ = 2 nm), a Tm-doped fiber (TDF) and a 50% reflective FBG (λ_C = 1940 nm; $\Delta\lambda_{3dB}$ = 0.5 nm). Due to the short length of the TDF (to shift the gain in the shorter 1940 nm region), a portion of the 1583 nm pump remains excess which is separated from the 1940 nm signal using a wavelength division multiplexer (WDM). The output from EYDF laser seed and TmFL output is characterized using an optical spectrum analyzer (OSA), a photodiode (PD) and an oscilloscope (OSC) for spectral and temporal domains respectively.

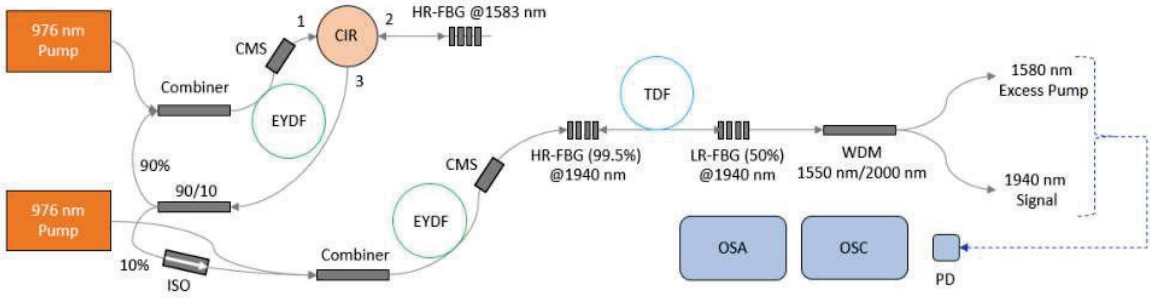

Fig. 1: Schematic Diagram of the Experimental Setup

3. Results and Discussion

Fig. 2(a) shows the 1583 nm pump and 1940 nm signal spectra obtained at the WDM ports. No prominent ASE noise in the 1900 nm – 2000 nm region, but an up-conversion component in the 1500 nm – 1560 nm wavelength region is visible. Fig. 2(b) shows the temporal trace (inset) recorded near the threshold of the TmFL and the corresponding frequency content with respect to the photodiode base noise in the time and frequency domain. The frequency content is obtained by taking the Fourier transform of the temporal waveform with suitable sampling frequency and record length, resulting in a frequency resolution of 20 Hz in the span of 20 Hz to 10 MHz. Near the threshold, due to multiple

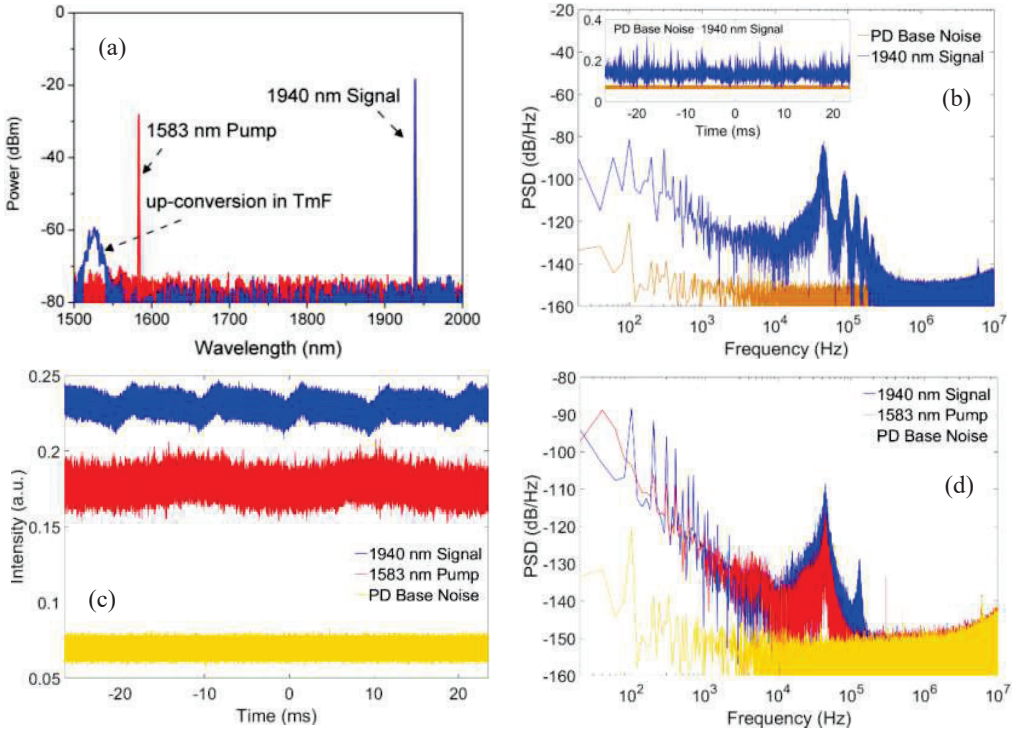

Fig. 2 (a) Pump and Signal Spectra at the WDM output ports; (b) 1940 nm signal temporal waveform and frequency content near laser threshold; (c) temporal waveform of pump and signal in stable state; (d) frequency content in the stable CW state.

sporadic relaxation oscillations and random interactions of out-of-phase cavity longitudinal modes, multiple peaks are observed in the frequency response in the frequency range of 10 kHz – 300 kHz. As the pump power is increased, the temporal waveform stabilizes which is shown in Fig. 2(c). The corresponding pump waveform is also shown in the figure. Frequency domain analysis of the stable state reveals that the 1583 nm pump itself contains a broad noise peak at 45 kHz originating from relaxation oscillation of the EYDF seed oscillator which induces a noise peak in the 1940 nm signal. There is another peak at 127 kHz originating from the TmFL oscillator relaxation oscillation. Both pump and signal noise spectrum corresponding to the temporal waveforms in Fig. 2(c) are presented in Fig. 2(d). Due to the smaller cavity length of the TmFL, the corresponding relaxation oscillation peak in the continuous wave (CW) background is at a higher frequency than the pump relaxation peak.

4. Conclusion

Here, preliminary results on noise characterization of a TmFL pumped by an EYDF laser has been presented. Intensity noise peak in the frequency domain spectrum originating in the pump laser and final laser due to relaxation oscillation in CW operation mode has been identified through experimental analysis.

5. References

[1] D. P. Kapasi et. al. "Tunable narrow-linewidth laser at 2 µm wavelength for gravitational wave detector research," Opt. Express 28, 3280-3288 (2020).

[2] P. Wessels et. al. "Single-Frequency Lasers for Gravitational Wave Detection," in *Lasers Congress 2016 (ASSL, LSC, LAC)*, OSA Technical Digest (online) (Optica Publishing Group, 2016), paper ATh5A.1.

[3] Vinicius Wagner, "Stabilization of a 2µm Laser using an all-fiber Delay Line Mach-Zehnder Interferometer" LIGO-T1800238–v1 (2018)

Study of Surface Enhanced Fluorescence of CdSeS/ZnS Alloyed Quantum Dots

Tania Mahata and Venkata Ramanaiah Dantham*

Department of Physics, Indian Institute of Technology Patna, Bihar 801103, India

**Corresponding author: dantham@iitp.ac.in*

Abstract: Herein, we report the surface-enhanced fluorescence (SEF) spectra of CdSeS/ZnS alloyed quantum dots (QDs) dispersed over cytop-coated plasmon active substrates (PASs). The PASs are fabricated by direct current sputtering of Au followed by thermal annealing and characterized using different tools. A drop-casting method is adopted for depositing cytop layers on the PASs and dispersing the QDs on the substrates. For comparison, the spectra of QDs dispersed directly on PAS, bare glass substrate, and cytop layer deposited on glass substrate are also recorded. The enhancement factor is found to vary from one to two orders of magnitude. Since the SEF enhancement depends on the electric field intensity enhancement (EFIE) in the PASs, Finite Element Method (FEM) simulations are performed to estimate the EFIE.

Keywords: Surface-enhanced fluorescence, Quantum dots, Plasmon-active substrates, Au nanoparticles

1. Introduction

Nowadays, surface-enhanced fluorescence is rapidly becoming a valuable tool to enhance the fluorescence of molecules with the help of plasmon-active substrates (PASs) [1]. According to SEF theory, when a fluorescent molecule is placed in the vicinity of the PASs, their excitation, radiative, and non-radiative rates are expected to be modified [2]. The researchers are trying to improve the electric field intensity enhancement(EFIE) using different nanoparticles [3-5]. In the PASs, when the nanoparticles are kept close to each other, it will improve the EFIE further due to the efficient plasmon-plasmon coupling (or constructive coupling) at the nanogaps [6,7].

As per the electromagnetic theory of SEF, the non-radiative rate is more predominant than the radiative rate when the separation between the fluorescent molecules and nanoplasmonic particles is typically 0 to 5 nm [2]. Some researchers have used DNA and polymers to separate the molecules away from the nanoplasmonic particles. However, the disadvantage of using DNA and polymers as spacers is that due to their flexibility, these structures don't allow complete control of the separation between nanoparticles and fluorescent molecules and can even fail to prevent physical contact, leading to fluorescence quenching rather than enhancement. To overcome this problem, silica material is used as a spacer by coating nanoplasmonic structures with silica material using suitable wet chemistry methods.

On the other hand, some researchers performed SEF-related experiments by depositing the polymer/polyelectrolyte layers on the PASs and making sandwich-type nanoplasmonic structures. These materials are expensive and adopted commercial methods for depositing the layers on the PASs. However, in the present study, we have demonstrated the significant SEF enhancement in the case of CdSeS/ZnS alloyed QDs using the thin cytop layer as a dielectric spacer formed by a simple drop-casting method. These QDs have high photostability, less toxicity, and high biocompatibility. These are found useful for labeling and imaging for cancer diagnostics. These QDs can be synthesized using various wet chemistry methods [8].

2. Experimental details

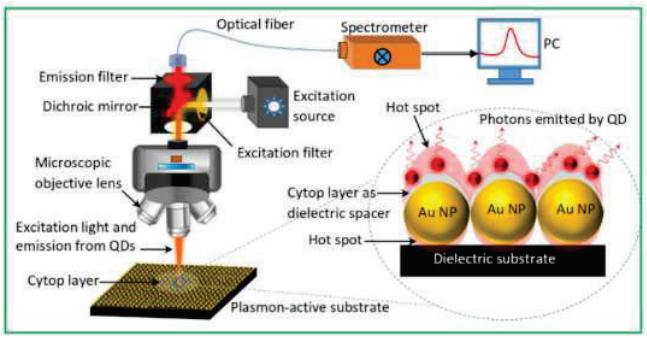

Fig. 1. *Illustration of an experimental setup for obtaining the SEF spectra of QDs using cytop layer as a dielectric spacer. The zoomed portion shows the emitted photons by the QDs adsorbed on the cytop layer deposited on the Au nanoparticles (Au NPs).*

For fabricating the PASs, first, we deposited the gold thin films using the sputtering technique (Hitachi EM-100). Then these PASs were characterized by a field emission scanning electron microscope [FE-SEM] (Carl Zeiss, Gemini SEM 500) and UV-Visible spectrophotometer (ASCO, V770). The cytop CTX-109AE and the solvent Cytop 100 E were purchased from AGC Chemicals Americas. Here cytop which is a fluoropolymer acts as a dielectric spacer. The diluted cytop solution is used to get the absorption spectra using a UV-Visible spectrophotometer. The raw CdSeS/ZnS quantum dot solution (concentration: 1mg/mL) was purchased from Sigma Aldrich, USA., and characterized using a fluorimeter(FLUOROMAX-4) and a darkfield microscope (ECLIPSE Ni-U). Then the PASs are characterized by the field emission scanning electron microscope (FE-SEM) with different magnifications. After

purchasing the cytop solution from the company, its transparency was tested by recording the absorption spectra of the cytop solution using the UV-Visible spectrophotometer.

An illustration of an experimental setup for capturing the SEF spectra of QDs is shown in Fig. 1. Here, the excitation light of wavelength range 580-630 nm was focused directly on the QDs dispersed on cytop-coated PASs with the help of an objective lens attached to the fluorescence microscope (Olympus, BX53). The incident light excites the localized surface plasmons and generates significant EFIE at the nanogaps between the nanoparticles in the PASs. Therefore, the QDs adsorbed at the nanogaps are expected to emit more photons. The emitted photons are collected in the backscattering geometry using a spectrometer (Ocean Optics, QE Pro). The same setup was used to record the spectra of QDs dispersed on bare and cytop-coated glass slides and bare PASs.

3. Results and discussions

For recording the conventional and SEF spectra, the QDs were dispersed by drop-casting 5 µl of quantum dot solution (of concentration 500 ng/µl) on bare glass slides and cytop coated glass slides, bare PASs, and cytop coated PASs. The spectrum with maximum intensity is chosen and shown in Fig. 2. The SEF intensity is maximum in the case of QDs adsorbed on the cytop coated PAS due to the significant enhancement in the radiative than the non-radiative rate and the enhancement in the excitation rate. Because in this arrangement, the cytop layer acts as a dielectric spacer between the QDs and gold nanoparticles. The SEF intensity is maximum when the QDs are dispersed on the cytop-coated PAS, and the intensity is minimum in the case of bare PAS. The reproducibility has been tested by performing the experiments using substrates fabricated at different times. Interestingly, the order of the SEF enhancement is found to be nearly the same. Fig. 2 shows the spectrum of QDs dispersed over different substrates by drop-casting of 5 µl QDs solution of concentration of 1 ng/µl. The maximum enhancement of the fluorescence signal of QDs in the presence of dielectric spacers is found one to two orders of magnitude.

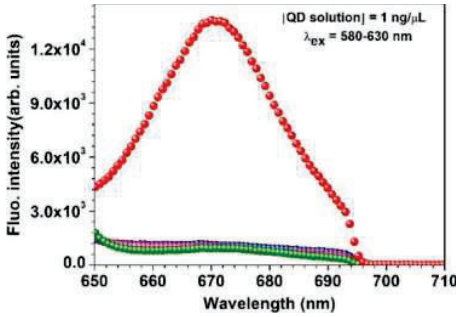

Fig. 2. *Spectra of QDs dispersed over different substrates by drop-casting of 5 µl QDs solution of concentration of 1 ng/µl. The blue, pink, green, and red dotted curves represent the spectra of QDs dispersed over (i) bare glass slide, (ii) cytop layer deposited on glass slide, (iii) PAS, and (iv) cytop layer deposited on PAS, respectively. In all cases,* λ_{ex} *=580-630 nm.*

4. Conclusions

The SEF of CdSeS/ZnS alloyed QDs has been demonstrated using thin cytop layers as dielectric spacers. The PASs are fabricated by direct current sputtering of Au followed by thermal annealing. A simple drop-casting method is adopted for forming the dielectric spacers between QDs and Au nanospheres-based PASs. The maximum enhancement of the fluorescence signal of QDs in the presence of dielectric spacers is found one to two orders of magnitude, and the experimental enhancement has been cross-checked with the FEM simulation. We strongly believe that the simple approach reported here would be helpful for the SEF community in enhancing the fluorescence signal of various fluorophores with ease.

5. References

[1] A. Saha, S. K Basiruddin, N. R Jana, "Plasmonic-fluorescent and magnetic-fluorescent composite nanoparticle as multifunctional cellular probe", John Wiley and sons (2017).

[2] S. Priya, A. Mandal, V. R Dantham, "Indium nanoparticle-based surface enhanced fluorescence from deep ultraviolet to near-infrared: A theoretical study", Spectrochim. Acta A Mol. Biomol. Spectrosc. **267**, 120603 (2021).

[3] T. Mahata, A. Mandal, V. R. Dantham, "Role of composition and size-dependent damping due to electron-surface scattering on plasmonic properties of gold-silver alloy nanoparticles: A theoretical study", J. Quant. Spectrosc. Radiat. Transf., **276** 107940 (2021).

[4] G. M. Das, R. V. William, V. R. Dantham, "Study on SERS activity of Au-Ag bimetallic nanostructures synthesized using different reducing agents", Phys. E: Low-Dimens. Syst. Nanostructures **129**,114656 (2021).

[5] T. Mahata, G. M. Das, V. R. Dantham, "Study of surface enhanced Raman scattering of IR-780 Iodide molecules using Au-Ag bimetallic nanostructures with blunt and sharp sprouts", Spectrochim. Acta A Mol. Biomol. Spectrosc. **249**,119262 (2021).

[6] S. Priya, V. R Dantham, "Effect of size-dependent damping on plasmon-hybridized modes of asymmetric nanosphere dimers: The role of nanogap, size ratio, surrounding medium, and substrate", Plasmonics **15**, 2033-2042 (2020).

[7] G. M Das, V. R. Dantham, A. Arya, "Plasmonic properties of nano-and microscale dielectric substrates-supported nanoshell dimers: effects of type and propagation direction of excitation light", IEEE Photonics J. **11**, 1-8 (2019).

[8] A. G. Martínez, J. P. Juste, L.M. L. Marzán, "Recent progress on silica coating of nanoparticles and related nanomaterials", Adv. Mater. **22**, 1182–1195 (2010).

Wet chemical route to synthesis of $Ce_3Al_5O_{12}$ Garnet structure at high temperature

ANU BALA[1] and SUMAN RANI[2]

Department of Physics, School of Chemical Engineering & Physical Sciences, Lovely Professional University, Punjab-144411, India

**suman.rani@lpu.co.in*

Abstract:

Phosphors are composed of an inert host lattice and an optically excited activator, typically a 3d or 4f electron metal. The study examined the potential of Cerium Aluminum Garnet (CAG) for improving the photonic devices efficiency. Samples of cerium aluminum garnet $Ce_3Al_5O_{12}$ were fabricated by using sol-gel method then sintered at various temperatures 500^0C, 700^0C, 900^0C, 1100^0C and 1350^0C but at 1350^0C phase of garnet found that was recognized by X-ray Diffraction. XRD pattern of CAG confirm the cubic phase. FTIR analyses were coordinated with XRD results to confirm the phase formation of CAG at 1350^oC. Luminescence properties were examined by some characterizations like FTIR, UV-Vis spectroscopy and Fluorescence spectroscopy. Emission spectra determined for three excitations i.e. 278 nm, 294 nm and 370 nm and show mixed color component on the chromaticity diagram.

Keyword : XRD, Cerium Aluminum Garnet, Phosphors and Optical.

COPaQ-2022 Manuscript No.:

Tunable Multistability and OMIT-Fano resonance in a Hybrid Optomechanical Photonic Crystal Nanocavity

Sajia Yeasmin*, Sabur A Barbhuiya, Souri Banerjee, and Aranya B Bhattacherjee
Department of Physics, Birla Institute of Technology and Science Pilani, Hyderabad Campus, Telangana-500078, India
**E-mail address: sajiayeasmin97@gmail.com*

Abstract: We theoretically present an investigation of the optical response of a hybrid optomechanical cavity quantum electrodynamics (CQED) system coupled to an auxiliary cavity via a waveguide. The possibility of tunable optical multistability like bistability, double-bistability and tristability can be seen in this hybrid system. We also report the existence of optomechanically induced transparency superimposed on the Fano resonance (OMIT-Fano). The transparency window occurs exactly at a point where the probe field detuning is equal to the resonant frequency of the mechanical oscillator.
Keywords: optomechanics, quantum dot, CQED, photonic crystal.

1. Introduction

The light-matter interaction inside a resonator has seen great progress at a fast rate due to the development of optical cavities with high quality (Q) factors which gives a potential application of quantum information processing [1]. Cavity quantum electrodynamics (C-QED) studies the physics behind the enhanced interaction between a photon and a single quantum emitter which is confined within a small volume. In C-QED the photon-quantum emitter interaction focuses on the strong coupling regime manifested by a remarkable quantum phenomenon called the vacuum Rabi splitting (VRS) [2], which has been observed experimentally in different QD-CQED systems. In cavity optomechanical systems, an interesting and useful quantum phenomenon called Optomechanically Induced Transparency (OMIT) [3] is observed which is similar to Electromagnetically Induced Transparency (EIT) exhibited in quantum optics. Therefore in this work, we aim to analyze the influence of optomechanical interaction on the optical response (steady state and OMIT-Fano resonance) of a coupled QD-optomechanical C-QED system assisted by an auxiliary cavity. Here, we have particularly analyzed the optical multistability, switching behavior, and OMIT-Fano resonance.

2. Model and Hamiltonian

Our proposed model is based on a single quantum dot embedded in an optomechanical photonic crystal (PhC) nanocavity coupled to a PhC auxiliary cavity via a single mode waveguide as shown in Figure 1(a). Small regions of disorder (artificial defects) in the photonic crystal (PhC) can serve as high-Q factor resonant optical cavities. The coupling between the primary cavity 'X' and the auxiliary cavity 'Y' is via exchange of energy with strength 'V'. The coupling strength V can be tuned by varying the distance between the two cavities. In a frame rotating at pump frequency ω_u, the total Hamiltonian is written as,

$$H_{total} = \hbar\Delta_x x^\dagger x + \hbar\Delta_y y^\dagger y + \hbar\omega_m m^\dagger m + \frac{\hbar\omega_q}{2}\sigma^z + \hbar g\left(\sigma^\dagger x + x^\dagger\sigma^-\right) + \hbar V\left(x^\dagger y + y^\dagger x\right) - \hbar g_{om}\, x^\dagger x\left(m^\dagger + m\right) + \hbar E_u\left(x^\dagger + x\right) + \hbar E_r\left(x^\dagger e^{-i\delta t} + x e^{i\delta t}\right) \quad (1)$$

where, $\Delta_x = \omega_x - \omega_u$ is the primary cavity-pump field detuning, $\Delta_y = \omega_y - \omega_u$ is the auxiliary cavity-pump field detuning, $\Delta_q = \frac{\omega_q - \omega_u}{2}$ is the exciton-pump detuning, and $\delta = \omega_r - \omega_u$ is the probe- pump detuning. ω_m is the mechanical frequency. Here, x, y, and m are the annihilation operators of primary cavity mode, auxiliary cavity mode and mechanical mode respectively. E_u and E_r are the slowly varying envelope of the pump and probe field respectively.

3. Results and discussions

Using $\frac{d}{dt}<\hat{O}> = \frac{1}{i\hbar}<[\hat{O},\hat{H}]>$ ($\hat{O}$is any operator), Heisenberg's equation of motion for the various degrees of freedom is obtained. We then analyze the steady state solutions by equating the time derivatives of the different degrees of freedom to understand the conditions under which the hybrid system exhibits multi-stable behavior. Finally, we obtain the mean number of photons described by the following equation,

$$S_5 a^5 + S_4 a^4 + S_3 a^3 + S_2 a^2 + S_1 a = S \quad (2)$$

where $S_5, S_4, S_3, S_2, S_1, S$ terms are functions of $\Delta_x, \Delta_y, \Delta_e, \omega_m, g, V,\ g_{om}, \kappa_u, \kappa_r, \kappa_m, \Gamma_1, \Gamma_2$.

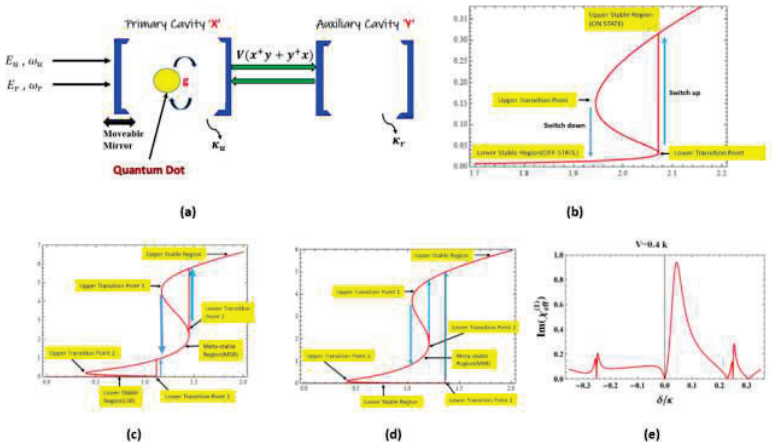

Figure 1: *(a) Schematic of the hybrid optomechanical photonic crystal system coupled to an auxiliary cavity. (b) Optical bistability. (c) Double bistability. (d) Tristability. (e) Absorption spectra of the probe field as a function of probe detuning* δ *at* $V = 0.4\kappa$.

Figure 1(b) illustrates the optical bistability curve obtained by solving Equation (2) numerically. It is a plot of intracavity photon number as a function of incident pumping rate (E_u). It shows a typical hysteresis loop that the intracavity photon number follows as the incident pumping rate is increased or decreased. Both the off-state and on-state are the stable solutions of Equation (2). Figure 1(c) and 1(d) illustrates two different tristabilities that can be generated in our hybrid system. In figure 1(c), the system shows double bistability with a switching behaviour of the form, Lower Stable Region (LSR) ⟷ Meta Stable Region (MSR) ⟷ Upper Stable Region (USR) has been observed. A tristable switching behaviour is observed in Figure 1(d) where the switching behaviour in this case is of the form LSR → USR ⇌ MSR → LSR. This interesting tristability behaviour demonstrated by our proposed hybrid system opens new possibilities to develop advanced quantum devices for multi-valued logic circuits. A high degree of nonlinearity prevails in our proposed system due to the optomechanical interaction and this may result in the possibility of optical multistability system parameters being tuned properly.

Since the probe field is weaker than the pump field, the Heisenberg's operators can be re-written as,

$O = O_s + \delta O\ ; (O = x, y, m, \sigma^z, \sigma^-)$ where O_s is the steady state mean value of O and δO is the corresponding small fluctuation with zero mean value. In order to explore the dynamics of quantum fluctuations, we neglect the small nonlinear fluctuation terms and make the ansatz $< \delta O > \ = O_+ \, e^{-i\delta t} + O_- e^{i\delta t}$.

Solving ten sets of equations analytically and working to the lowest order in E_s (probe field) we obtain the linear susceptibility as, $\chi_{eff}{}^{(1)}(\omega_s) = \frac{K_1 + iK_2}{P_1 + iP_2}$ (3)

where K_1, K_2, P_1, P_2 are functions of $\Delta_x, \Delta_y, \Delta_q, \omega_m, g, V,\ g_{om}, \kappa_u, \kappa_r, \kappa_m, \Gamma_1, \Gamma_2$.

Figure 1(e) illustrates the absorption spectra $Im\ \chi_{eff}{}^{(1)}(\omega_s)$, as a function of probe detuning δ. A typical Mollow tripet along with Fano resonance modified by OMIT (OMIT-Fano resonance) is observed. A Mollow triplet is observed only in the strong coupling regime [4]. The central peak is slightly shifted from $\delta = 0$ which may be attributed to an optomechanical effect.

4. Conclusion

The steady state mean-field analysis shows the existence of tunable multistability (optical bistability, double-bistability, and tristability) paving the way for designing novel multi-switching photonic devices. The probe absorption spectra of the fluctuations, reveal a Mollow triplet along with an OMIT modified asymmetric Fano resonances. Therefore, altogether the auxiliary cavity, the QD, and the mechanically compliant DBR offer three different quantum channels to influence and control the optical response of the system.

5. References

[1] Chen HJ. Auxiliary-cavity-assisted vacuum Rabi splitting of a semiconductor quantum dot in a photonic crystal nanocavity. Photonics Res. 2018; 6: 1171.

[2] Strauf S. Lasing under strong coupling. Nat Phys. 2010; 6:244–245.

[3] Weis S, Rivière R, Deléglise S, et al. Optomechanically induced transparency. Science. 2010; 330:1520– 1523.

[4] Del Valle E, Laussy FP. Mollow triplet under incoherent pumping. Phys Rev Lett. 2010; 105:233601.

Wavefront splitting white light interferometer for determining coherence properties of ultrabroadband sources

Akansha Tyagi, Sunil Dahiya, Ankur Mandal, Kamal P. Singh
Department of physical sciences, IISER Mohali, Punjab
akanshatyagi@iisermohali.ac.in, kpsingh@iisermohali.ac.in

Abstract: A theoretical simulation is performed for complete spatial profile of white light fringes and interferogram with wavefront split geometry. The fringe evolution is tracked and the interferogram is generated for broadband white light source-Tungsten theoretically and experimentally. Fraunhofer diffraction formulation is used for white light propagation and fringe formation. It also provides the coherence length of ultrabroadband white light source.

Keywords: White light interferometry, Diffraction theory

1. Introduction

White light interferometry is an important tool to study space or surface profile of micrometer to nanometer objects without any phase ambiguity. It uses broadband white light sources having very low temporal coherence and partial spatial coherence. Many interferometric configurations such as Mach Zehnder, Michelson and Sagnac etc. have been used with amplitude and wavefront splitting of initial spatial profile [1].

Here, we have presented a theoretical simulation for white light fringe spatial profile and corresponding interferogram using Diffraction theory. The theoretical simulation is important to study and validate surface profile change at nanometer scale while providing spatial and spectral information with high resolution.

2. Results and discussion

In the wavefront split configuration, a gaussian profile of white light source is spatially split vertically in two parts having a 50 to 100 μm gap between them. Both spatially split diffracted parts propagate in z-direction and interfere at focus. A horizontal straight-line fringe is formed at center of both split parts which evolve with Optical path difference (OPD) provided in either upper or lower part while keeping the other split part fixed. The x-y spatial profile of complete fringe and diffraction pattern at a particular distance z is simulated using Fraunhofer diffraction theory using ABCD matrix formulation [2]. The experimentally measured spectrum (S_λ) is directly used for fringe formulation by first converting the intensity in their respective RGB values ($S_{R\lambda}$, $S_{G\lambda}$, $S_{B\lambda}$) over complete wavelength span. The simulated results are verified experimentally by realizing the same concept in wavefront split delay line [3]. The interferogram is generated by tracking the intensity of central fringe over OPD which provides the temporal coherence length of the source.

The synthesized total electric field at observation plane (at focus) is defined as

$$E(x,y,z) = U_1(x,y,z) + U_2(x,y,z)\exp(ik\Delta z) \qquad (1)$$

Where, (x, y) are the coordinates of observation plane near focus at z. $U_1(x,y,z)$ and $U_2(x,y,z)$ are the spatial electric profiles of both upper and lower split parts. The split electric field at focus is defined by Fraunhofer diffraction theory, which is expressed as

$$U_{(i=1,2)}(x,y,z) = \frac{i}{\lambda B}\exp(-ikz)\iint_{y_0=\pm\delta/2}^{\pm y_0} exp\frac{(-2i\pi)\left(A\left(x_0^2+y_0^2\right)+D\left(x^2+y^2\right)-2x_0x-2y_0y\right)}{\lambda B}U(x_0,y_0)$$

A, B, C, D are matrix elements for beam path propagation through various optics and free space, (x_0, y_0) are input plane coordinates, $U(x_0, y_0)$ is input gaussian beam and δ is the gap between both split parts.

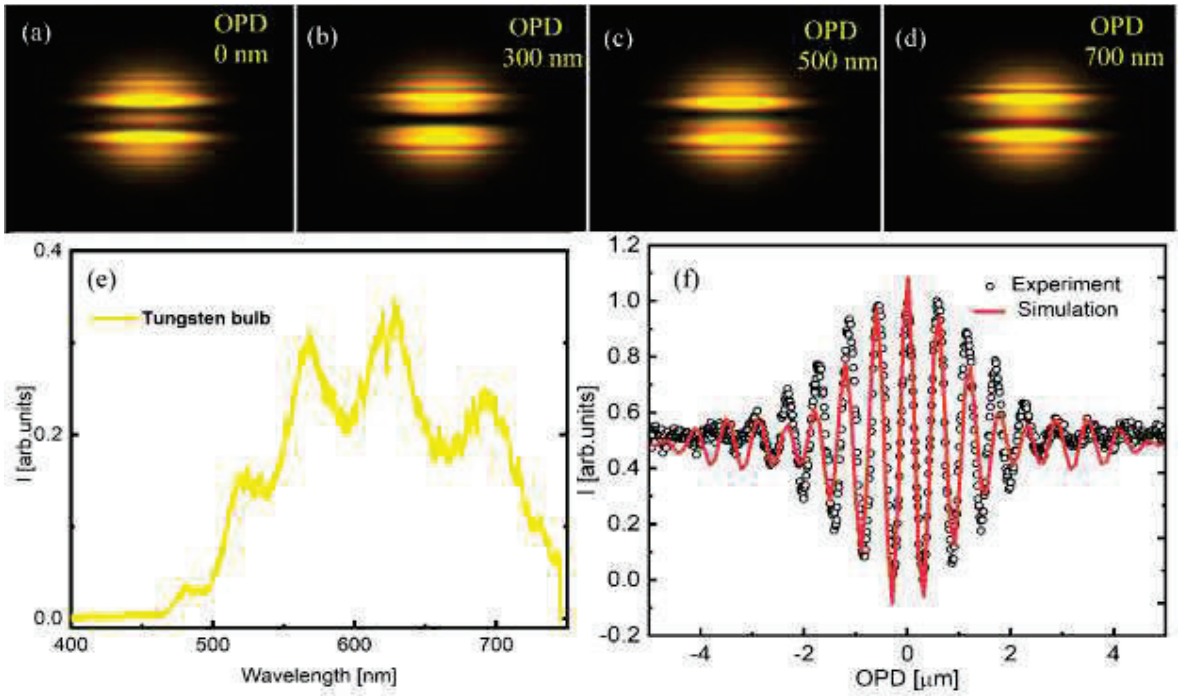

Figure 1: Tungsten fringe evolution (a) 0 OPD, (b) 300 nm, (c) 500 nm, (d) 700 nm, (e) Tungsten measured spectrum, (f) Tungsten Interferogram by tracking central fringe intensity, red line (simulation)and black dots (experiment)

Using equation (1) and (2) the simulated results are shown in fig.1. Figure 1(a)-(d) shows the Fringe evolution of Tungsten source with varying Optical path difference (OPD) starting from fig. 1(a) 0 OPD *i.e.* when both split parts covers equal distance and RGB components overlaps at this point. Fig 1 (b)-(d) shows spatial fringe pattern at 300 nm, 500 nm and at 700 nm OPD, these patterns are calculated at near focus at observation plane. Figure 1(e) shows the measured spectrum and the experimentally and simulated interferogram are shown in fig. 1(f).The coherence length of source can be estimated by the interferogram as 1/e of maximum intensity value. For tungsten, the coherence length is approx. 1.9 μm.

3. Conclusion

In conclusion, we have simulated the spatial-spectral fringe pattern and interferogram for broadband source Tungsten with spatially split Tungsten beam. The spatial-spectral pattern changes with OPD between two interferometer arms and consequently provide temporal coherence and visibility or spatial coherence of the source.

4. References

[1] S.-W Kim. & G.-H Kim, "Thickness-profile measurement of transparent thin-film layers by white-light scanning interferometry". *Appl. Opt.* **38**, 5968–5973 (1999).
[2] M. Born & E. Wolf, "*Principles of Optics: Electromagnetic Theory of Propagation, Interference and Diffraction of Light"* (Elsevier, 2013).
[3] S.Dahiya, A.Tyagi, A.Mandal, T. Pfifier, K.P. Singh, " Ultrathin picoscale white light interferometer", Sci. Rep.**12** (2022)

Experimental Study of Optical Pumping in Semiconductor Optical Amplifier Under Transparency

Nithin V*, Animesh Raj and M. R. Shenoy
Department of Physics, Indian Institute of Technology Delhi, Hauz Khas, New Delhi - 110016
**Email: v.nithin@physics.iitd.ac.in*

Abstract: In this paper, we experimentally study the optical pumping in a SOA under transparency in co-propagating and counter-propagating pumping schemes using a 1310 nm pump; the latter pumping scheme provided higher gain than the former pumping scheme. Further, the absorption spectrum of SOA was studied for different currents below the transparency.

Keywords: Semiconductor optical amplifier, optical pumping, absorption spectrum

1. Introduction

Recently, there is a huge demand for all optical signal processing for pushing the limit of high-speed optical networks. The signal processing done entirely in optical domain eliminates the requirement of optical to electrical conversion devices and thus reducing the cost of the network and conversion delay. This also reduces the overall power consumption of the network making it much reliable in performance [1,2]. SOAs are key devices employed in various optical signal processing applications such as logic gates, wavelength conversion, etc. The conventional method of injecting carriers in a semiconductor optical amplifier (SOA) is by electrical biasing. Alternatively, a light source of suitable wavelength can be employed to produce population inversion inside the active medium. This technique of pumping an SOA with a light beam (pump signal) to generate carriers is called optical pumping [3] . In the present work, we study the absorption spectrum of SOA under various currents below transparency. At transparency, we investigate the SOA gain under co-propagating and counter-propagating pumping schemes.

2. Experimental Setup and Results

Figure 1 (a) and 1 (b) shows the block diagram of the setup used to perform the experiment for the co-propagation and counter propagation pumping scheme. In Fig. 1 (a), 95:5 tap coupler is used to input both the pump and signal into the SOA. In Fig. 1 (b) 95:5 tap coupler is used to feed pump at the output end (95% arm) and take the SOA output from the 5% arm. An isolator in the pump arm is used to safeguard the pump laser from the reflections coming from coupler and SOA junctions. A transparency bias current of 16 mA is applied to the SOA through laser driver. The pump laser is kept at 1310 nm wavelength.

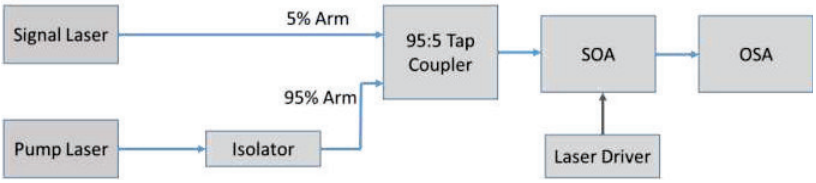

Fig. 1(a): Schematic of the experimental setup for co-propagation pumping of SOA

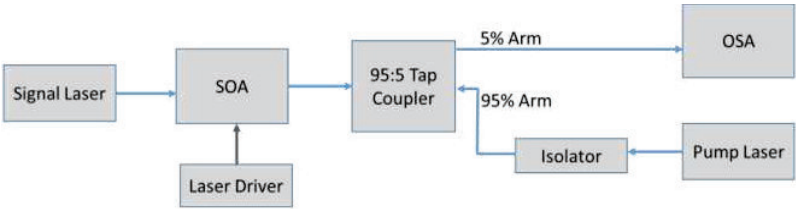

Fig. 1(b): Schematic of the experimental setup for counter-propagation pumping of SOA

Figure 2 shows the variation of fiber-to-fiber gain with the input pump power for both the pumping schemes. It can be seen that counter-propagating pump gives higher gain than co-propagating pump. As the signal gets amplified along the length of SOA, progressively higher number of carriers are depleted near the output end of SOA. Therefore, by providing higher pump power near the output end (as in counter-propagating scheme), the carrier depletion is compensated and thus, results in higher gain.

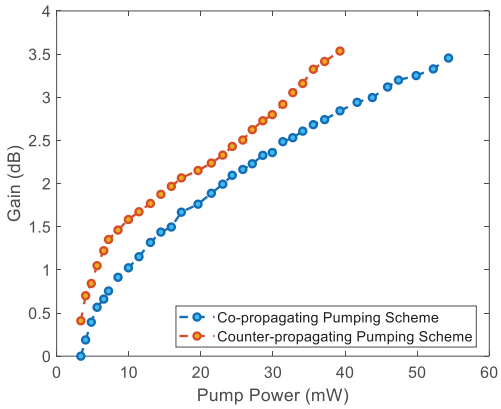

Fig. 2: Variation of fiber-to-fiber gain of SOA with optical pump power in co- and counter-propagating pumping scheme. The signal is at a wavelength of 1550 nm with an input power of 54 µW.

Figure 3 shows the absorption spectrum of SOA for different bias currents below the transparency. As expected, the absorption decreases as bias current increases. At higher bias currents (say I = 10 mA), the shape of the curve matches with the prediction made by the Connelly's numerical model [4]. At lower bias current (say I = 0), a sort of sinusoidal shape of the curve is seen at the lower wavelengths. This deviation of the curve nature was not predicted by the Connelly's model. The experiment was carefully repeated and the results are reproduced. We believe that when the injected carrier density is very less, the reflections at the SOA fiber pigtail ends will dominate over semiconductor active material absorption spectra. The amplitude of the variation in absorption spectra decreases as the bias current is increased. This leads us to infer that oscillations observed are due to the SOA waveguide geometry and not due to the semiconductor active material.

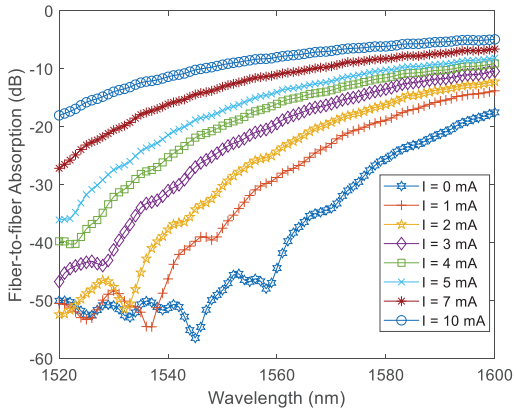

Fig. 3: Absorption spectra of SOA for different bias currents below the transparency.

3. References

[1] N. K. Dutta and Q. Wang, *Semiconductor Optical Amplifiers*, 2nd ed. (World Scientific, 2006).

[2] A. E. Willner, S. Khaleghi, M. R. Chitgarha, and O. F. Yilmaz, "All-Optical Signal Processing," Journal of Lightwave Technology **32**, 660–680 (2014).

[3] N. Vogirala, M. Shenoy, and Y. Kumar, "Efficient Optically-Pumped Semiconductor Optical Amplifier in a Coupled-Waveguide Configuration: A Novel Proposal," IEEE Photonics J **13**, 1–6 (2021).

[4] M. J. Connelly, "Wideband semiconductor optical amplifier steady-state numerical model," IEEE J Quantum Electron **37**, 439–447 (2001).

Image encryption through structured light

Praveen Kumar and Naveen K. Nishchal*
Department of Physics, Indian Institute of Technology Patna, Bihta, Patna 801 106, Bihar, India
**E-mail: nkn@iitp.ac.in*

Abstract: With the technological advancement enormous amount of information/data is being generated, stored, and disseminated, which requires efficient cryptosystem. Digital techniques of security are being further researched for improvement in terms of fast processing and robustness. Optical technologies for information security are being developed as an alternative tool with ultra-high speed. Further, desired light fields as structured beams are being considered for security applications by controlling the parameters amplitude, phase, and polarization. Image encryption through structured light has several features including intensity-based measurement that makes it suitable for storage and transmission. This paper reviews image encryption techniques employing controllable properties of light beam. © Author

Keywords: Structured light, Optical vortex, Orbital angular momentum, Image encryption

1. Introduction

Light fields having complex wavefront structures with spatial inhomogeneity give rise to unique features. One of the features is the formation of optical vortices [1]. Due to the spiral phase front of the optical field, optical vortex is created at the phase singularity, where phase becomes indeterminate and intensity is zero. Light beams with spiral phase front are expressed as $exp(il\varphi)$, which contain orbital angular momentum (OAM). The symbol φ and l denote the azimuthal angle and topological charge (TC), respectively. Theoretically, light beams can have more orthogonal modes associated with OAM than polarization, which makes optical vortices an attractive solution for optical communications, high-dimensional data encoding and processing [2].

With the pioneering work first reported in 1995, a large number of algorithms and architectures for optical image encryption have been proposed and implemented exploiting the inherent features of light [3,4]. Optical logic gates such as exclusive-OR operation which plays an important role in computing applications have been implemented through light field propagation and optical modulation. Though logic states are often expressed either by amplitude or polarization of light, the development of encryption approaches is obstructed by difficulty in high-dimensional encoding. Sincere efforts have been reported for improving the performance by expressing the logic variables through orthogonal bases of light such as OAM modes [5-7]. Various modes of OAM correspond to different orders of optical vortices assigned with integral azimuthal indices.

Optical cryptosystems are designed to prevent unauthorized information access during their distribution [3,8-11]. Polarization encoding is one of the preferred approaches [4]. It is performed with a pair of liquid crystal spatial light modulators (SLMs) for input arguments to modify the polarization. Further, encryption of quick-response (QR) codes has been demonstrated using this approach. Beyond polarization, optical vortices open up new possibilities to progress with enhanced degrees of freedom. Recent works have shown the formation of multiple vortices in an optical beam, commonly known as an optical vortex array [10,11]. Controlled realization of such array creates an opportunity to utilize the spatial degrees of freedom for parallel-processing of data using orthogonal states of light.

2. Theory

The approach of double-phase modulation of light has been implemented for two-dimensional exclusive OR operation through optical vortices. In the double-phase modulation method, the incident light is transmitted through two different phase masks, expressed as A and B. These masks are designed to create optical vortices in the light beam that transmits through it. Figure 1 depicts the illustration of two-dimensional exclusive OR operation using optical vortices for $|l| = 1$. Similarly for other TC values, the process can be followed.

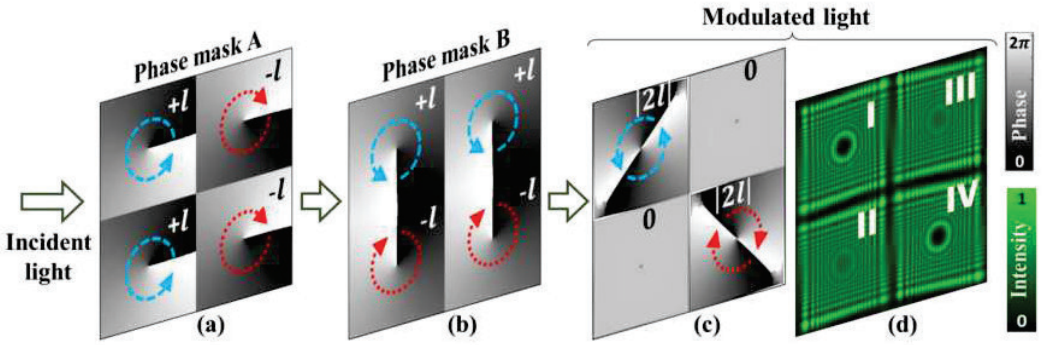

Fig. 1 Illustration of two-dimensional exclusive OR operation using optical vortices for $|l| = 1$ [Ref. 11].

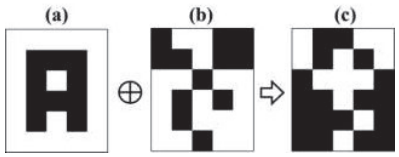

Fig. 2 Encryption using two-dimensional exclusive OR operation. (a) Input image, (b) key, and (c) encrypted image [Ref. 11].

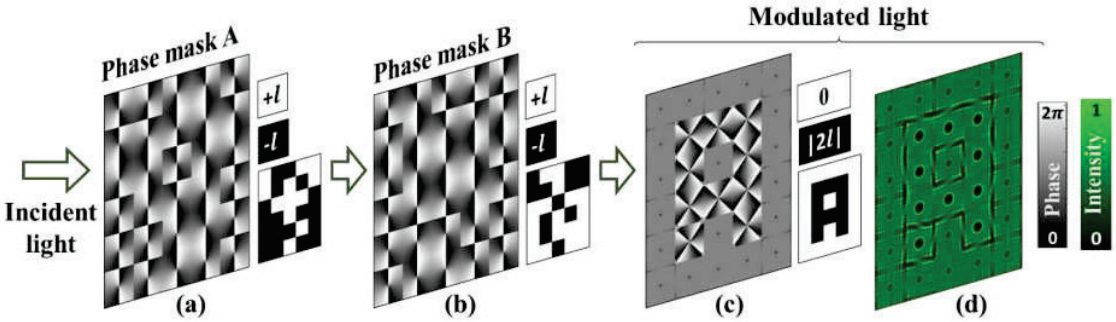

Fig. 3 Decryption through optical vortex array-based exclusive OR operation. (a) Encrypted image as a phase mask, (b) key as a phase mask, (c) exclusive OR-operated phase profile of modulated light, and (d) intensity profile [Ref. 11].

Figure 2 presents the encryption approach through exclusive OR operation and the decryption process is shown in Figs. 3(a-d). The decryption process can be carried out using exclusive OR operation with encrypted image and key phase mask as input. The input logic from each element of the encrypted image and key phase mask are encoded as azimuthal index $+l$ and $-l$ through phase masks [11].

3. Conclusion

The paper presents one of the aspects of structured light in the form of optical vortex array for image encryption and decryption. The presented method opens up new dimension in the field of optical security. Such schemes offer high level of security and can be suitable for practical systems.

Acknowledgement

The financial support from the Science and Engineering Research Board, Dept. of Science and Technology, Govt. of India through grant No. CRG/2021/001763 is duly acknowledged.

References

[1] H. Rubinsztein-Dunlop *et al*., "Roadmap on structured light," J. Opt. 19, 013001 (2017).
[2] A. M. Yao and M. J. Padgett, "Orbital angular momentum: origins, behavior and applications," Adv. Opt. Photon. 3, 161-204 (2011).
[3] N. K. Nishchal, *Optical Cryptosystems*, IOP Publs. Ltd., Bristol, UK (2019).
[4] A. AlFalou and C. Brosseau, "Dual encryption scheme of images using polarized light," Opt. Lett. 35, 2185-2187 (2010).
[5] X. Li, T. H. Lan, C. H. Tien, and M. Gu, "Three-dimensional orientation-unlimited polarization encryption by a single optically configured vectorial beam," Nat. Commun. **3**, 998 (2012).
[6] L. Liu, Y. Gao, and X. Liu, "High-dimensional vortex beam encoding/decoding for high-speed free-space optical communication," Opt. Commun. 452, 40-47 (2019).
[7] X. Fang, H. Ren, and M. Gu, "Orbital angular momentum holography for high-security encryption," Nat. Photonics 14, 102-108 (2020).
[8] P. Kumar, A. Fatima, and N. K. Nishchal, "Arbitrary vector beam encoding using single modulation for information security for information security applications," IEEE Photon. Technol. Lett. 33, 243-246 (2021).
[9] P. Kumar, N. K. Nishchal, and A. AlFalou, "Controllable Optical vortex array for image encoding," IEEE Photon. Technol. Lett. 34, 521-524 (2022).
[10] P. Kumar, N. K. Nishchal, and A. AlFalou, "Color image encryption using vectorial field through a compact optical set-up," J. Opt. 24, 064017 (2022).
[11] P. Kumar, N. K. Nishchal, T. Omatsu, and A. S. Rao, "Optical vortex array for two-dimensional exclusive-OR operation," Appl. Phys. B: Lasers Opt. 128, 98 (2022).

Structural Dependent Exciton Features in Primary Cyclic Ammonium Based Inorganic-Organic Hybrid Semiconductors Series

Mohammad Akram, Kshetramohan Dehury, G. Vijaya Prakash*
Nanophotonics Lab, Department of Physics, Indian institute of Technology Delhi, New Delhi 110016, India
prakash@physics.iitd.ac.in

Abstract: These naturally self-assembled IO hybrid semiconductors form multiple quantum well (MQW) structure due to quantum width limit of both organic moiety (quantum barrier) and extended inorganic network structure (quantum well). The quantum confinement and dielectric screening effects are mainly responsible for the formation of stable room-temperature Mott-type excitons which enhance the exciton binding energy (200 meV~300 meV) with high oscillator strength. Here we present linear and nonlinear optical probing of the structural dependent exciton in primary cyclic ammonium ($C_nH_{2n-1}NH_2$, n=3-8) based Inorganic-Organic hybrid semiconductors series.
Keywords: Inorganic-Organic hybrid semiconductors, multiple quantum well (MQW) structure, crystal structure packing, one- and two-photon excitation.

1. Introduction

Inorganic-organic hybrid semiconductors attract much more attention due to their unique characteristics of the formation of different dimensionalities of crystal structure packing and tunable optical excitonic features [1-3]. The self-assembled two-dimensional (2D) IO hybrids having general formula $(R\text{-}NH_3)_2MX_4$ are derived from the fundamental AMX_3 perovskite-type structure, where R is the organic moiety, M is the divalent metal (Pb^{2+}, Sn^{2+}, Ge^{2+}, etc.), and X is the halide ion (Cl^-, Br^-, I^-) [1-5]. Weak van der Waals interaction and hydrogen bonding between organic ammonium cations $(R\text{-}NH_3)^+$ and terminal halide of MX_6 part will determine the conformation and orientation of organic ammonium cation within the extended inorganic layered structure which further decides the formation of different dimensionalities (0D, 1D, 2D and 3D) of crystal structural packing [1-3]. The quantum confinement and reduced dielectric screening effects are mainly responsible for the formation of room temperature Mott-type exciton which enhance the exciton binding energy (200-300 meV) [6,7]. One-photon induced photoluminescence (1PA-PL, $\hbar\omega \geq E_g$) provide information about the surface excitons wherein the crystal packing of IO hybrid is perfectly aligned, however nonlinear optical pumping such as two-photon excitation (2PA-PL, $2\hbar\omega \geq E_g$) provide comprehensive understanding of crumpled excitons present inside the interior regions of crystalline thin films and single crystal platelets due to the larger penetration depth [7-9]. The unique crystal structure packing and structural dependent optical properties of self-assembled Inorganic-Organic hybrid semiconductors provide a new avenue for different optoelectronic device applications [10].

2. Results and Discussion

The 2D crystal structure packing (barrier/well width) and multiple quantum well (MQW) structure of IO hybrid semiconductors are shown in Figure 1(a). The multiple quantum well structure is formed due to quantum width limit of both organic moiety (quantum barrier) and extended inorganic (quantum well) layered structure. The schematic of exciton formation in IO hybrid semiconductor is shown in Figure 1(b).

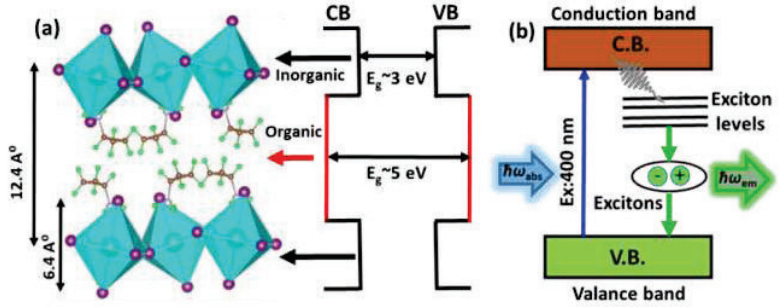

Fig. 1. (a) 2D crystal structure packing along with multiple quantum well (MQW) structure and (b) is the schematic of exciton formation in IO hybrid semiconductors.

The optical properties of self-assembled IO hybrid semiconductors depend upon the nature of the organic moiety (shape, size and position of NH_2 functional group) and structural organization of organic ammonium cation $(R\text{-}NH_3)^+$ within the extended MX_6 inorganic layered structure [3,4,9]. The conventional exciton absorption spectra of all primary cyclic ammonium based IO hybrid semiconductors are shown in Figure 2(a). The strong exciton absorption peak is due to the confinement of excitons in the lowest band gap of extended MX_6 inorganic network structure. The charge transfer peak arises due to the transfer of charge carriers from valance band of inorganic component to the HOMO of the organic moiety. The one-photon (1PA-PL, $\hbar\omega \geq E_g$) induced photoluminescence spectra of all primary cyclic ammonium based IO hybrid semiconductors are shown in Figure 2 (b). The origin of one-photon induced photoluminescence is predominantly from the optical excitons of top few perfectly aligned layered structure which is attributed to smaller penetration depth [7-9]. Similarly the nonlinear two-photon (2PA-PL, $2\hbar\omega \geq E_g$) induced photoluminescence spectra of all IO hybrid semiconductors are shown in Figure 2 (c). The nonlinear optical pumping such as two-photon excitation (2PA-PL, $2\hbar\omega \geq E_g$) gives comprehensive understanding of exciton which are present inside the interior regions of the crystalline thin films and single crystal due to larger penetration depth [7-9]. The optical properties of IO hybrid semiconductors are very much sensitive to thickness dependent, after a certain optimum thickness (~120 nm) the more distorted *Pb-I-Pb* plane bending angles changes towards more planar and more strain [5,7].

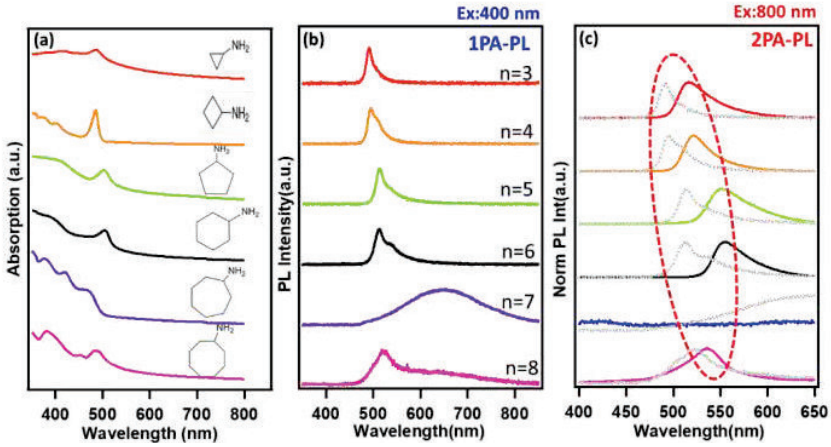

Fig. 2. (a) Conventional exciton absorption spectra and (b) is one-photon induced photoluminescence spectra and (c) is the two-photon induced photoluminescence spectra of all primary cyclic ammonium ($C_nH_{2n-1}NH_2$; n=3-8) based IO hybrid semiconductors. 1PA-PL spectra (figure 1b) have also been added as gray dotted line for comparison. For 1PA-PL (λ_{ex}~400 nm CW) and for 2PA-PL (λ_{ex}~800 nm, 120 fs, 84 MHz).

3. References

[1] D. B. Mitzi, "Introduction: perovskites," Chem. Rev. **119**, 3033-3035 (2019).
[2] D. B. Mitzi, "Thin-Film Deposition of Organic-Inorganic Hybrid Materials," Chem. Mater. **13**, 3283-3298 (2001).
[3] D. G. Billing and A. Lemmerer, "Inorganic-Organic Hybrid Materials Incorporating Primary Cyclic Ammonium Cations: The Lead Iodide Series," CrystEngComm., **9**, 236-244 (2007).
[4] K. Pradeesh, K. Nageswara Rao and G. Vijaya Prakash, "Synthesis, Structural, Thermal and Optical Studies of Inorganic-Organic Hybrid Semiconductors," R-PbI_4. J. Appl. Phys. **113**, 083523 (2013).
[5] K. Pradeesh, J. J. Baumberg and G. Vijaya Prakash, Exciton switching and Peierls transitions in hybrid inorganic-organic self-assembled quantum wells. Appl. Phys. Lett. **95**, 283 (2009).
[6] T. Ishihara, X. Hong, J. Ding and A. Nurmikko, "Dielectric Confinement Effect for Exciton and Biexciton States in PbI_4-based Two-Dimensional Semiconductor Structures,'' Surf. Sci. **267**, 323-326 (1992).
[7] M. Adnan, J. J. Baumberg and G. Vijaya Prakash, "Linear and Nonlinear Optical Probing of Various Excitons in 2D Inorganic-Organic Hybrid Structures," Sci. Rep. **10**, 2615 (2020).
[8] B. Wu, H. T. Nguyen, Z. Ku, G. Han, D. Giovanni, N. Mathews, H.J. Fan, T. C. Sum, "Discerning the surface and bulk recombination kinetics of organic-inorganic halide perovskite single crystals," Adv. Energy Mater. **6**, 1600551(2016).
[9] M. Adnan, K. N. Rao, J. N. Acharyya, D. Kumar, K. M. Dehury and G. Vijaya Prakash, "Synthesis, Structural, Linear, and Nonlinear Optical Studies of Inorganic-Organic Hybrid Semiconductors (R-$C_6H_4CHCH_3NH_3$) $2PbI_4$,(R=CH_3, Cl)," ACS omega, **4**, 19565-19572 (2019).
[10] S. Parveen, K. K. Paul and P. K. Giri, "Precise tuning of the thickness and optical properties of highly stable 2D organometal halide perovskite nanosheets through a solvothermal process and their applications as a white LED and a fast photodetector,''ACS Appl. Mater. Interfaces, **12**, 6283-6297 (2020).

Compact and portable near-IR and mid-IR wavelength modulation spectroscopy systems for real-time measurements of water vapour and carbon dioxide

Shruti De[1], Durlav Paul[1], Kenneth T V Grattan[2] and Arup Lal Chakraborty[1]

[1]*Electrical Engineering, IIT Gandhinagar, Gandhinagar 382055, Gujarat, India*

[2]*School of Science and Technology, City, University of London, London EC1V 0HB, United Kingdom*

de_shruti@iitgn.ac.in

Abstract: We report the development of two compact and portable near-IR and mid-IR sensor systems for ambient water vapour and carbon dioxide measurements. The measurements were carried out at Chandkheda, Ahmedabad and IIT Gandhinagar. A recent calibration-free $R_{1f}/\Delta I_1$ wavelength modulation spectroscopy technique was used for reliable and accurate estimation of mole fraction over extended periods of time. The detection limit for carbon dioxide (4.2 cm path length) is 0.18 ppm for an integration time of 42 s and for water vapour is 32.6 ppm (10.3 cm path length) for an integration time of 68 s.

Keywords: Quantum cascade laser, wavelength modulation spectroscopy (WMS), carbon dioxide measurement, water vapour measurement.

1. Introduction

Water vapour and carbon dioxide are important long-lived greenhouse gases in the earth's atmosphere. Gas sensing systems placed at fixed locations are not suitable for environmental monitoring over large areas. This paper demonstrates two compact and portable near-infrared and mid-infrared tunable diode laser absorption spectroscopy (TDLAS) sensor systems to monitor the variation of mole fractions of these gases. In high-resolution TDLAS, the emission wavelength of a narrow linewidth (~ MHz) laser is tuned across an absorption line of a gas (several GHz) by applying a low frequency ramp signal to the injection current to perform direct detection. Wavelength modulation spectroscopy (WMS) [1] uses an additional high-frequency sinusoidal modulation of the laser's injection current and harmonic signal components are recovered for analysis. In-field measurement systems (as opposed to laboratory systems) must contend with the inevitable variations in the received light intensity, and operate without frequent recalibration. Calibration-free WMS techniques have therefore received much attention [2,3]. This paper used a recently demonstrated $R_{1f}/\Delta I_1$ WMS method [4], in which the magnitude of the first harmonic signal (R_{1f}) was normalized by the laser's linear intensity modulation (ΔI_1) to achieve calibration-free measurements.

2. Measurement system and Experimental Results

The ambient water vapor measurement system shown in Fig 1a used a 12 mW near infrared 1392 nm DFB (distributed feedback) laser (EP1392-5-DM-B01-FM) driven by a current controller (Thorlabs, MLD203CHBE) and a temperature stabilization (Thorlabs, MTD415TE). A 3-D printed adjustable alignment stage held the collimator and the photodetector (PD) (Thorlabs, PDA10DT-EC) separated by 10.3 cm. The dimension and weight of the system is 25.5 x 20.5 x 12.8 cm and 3.86 kg respectively. The water vapour system consumes 25.5 W. The carbon dioxide measurement system shown in Fig 1b was designed with a 10 mW mid-infrared 4320 nm quantum cascade laser (QCL) (Alpes Laser, HHL-513) driven by a Thorlabs ITC4002QCL controller. The QCL and the PD (Vigo, PVI-4TE-6) separated by 4.2 cm were placed inside a 42.5 x 25 x 20 cm acrylate box with inlet and outlet valves. A Raspberry Pi and Picoscope 2406B together performed data acquisition and signal processing. Importantly, the system is remotely accessible over a wifi connection, which makes it suitable for deployment in the field..

Figure 1c and Fig 1d shows the simulated absorption spectra of 1% water vapour and 400 ppm carbon dioxide at 1 bar and 0.75 bar in the wavelength range of 4310 - 4325 nm and 1390.3 - 1394.6 nm respectively. The absorption transition at 1391.672 nm (red box in Fig 1c) with line strength 5.984 x 10^{-22} $cm^{-1}/(mol\ cm^2)$ was selected for the water vapour measurement from the wavelength range of 4.3 nm (1390.3 nm - 1394.6 nm) that can be accessed by temperature tuning (10-45 ℃) the 1392 nm laser. Five strong carbon dioxide absorption lines as shown in Fig 1d can be accessed within the 20 nm range by temperature tuning (10 - 45 ℃) of the QCL. The absorption line at 4319.30

nm (red box in Fig 1d) with line strength 7.945 x 10^{-19} $cm^{-1}/(mol\ cm^2)$ was selected for carbon dioxide measurements to avoid cross-sensitivity. The stronger lines were not used to avoid detector saturation for high mole fractions.

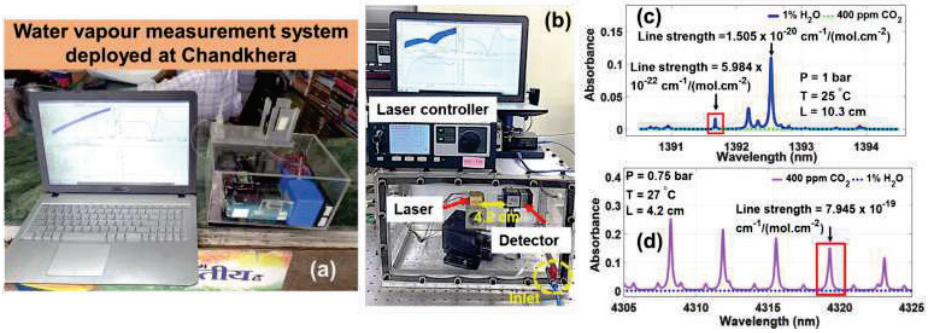

Fig. 1: Images of compact and portable (a) water vapor measurement system deployed at Chandkheda, Ahmedabad and (b) carbon dioxide measurement system. Simulated absorption spectra of (c) 1 % water vapour and 400 ppm carbon dioxide at 1 bar and (d) 400 ppm carbon dioxide and 1 % water vapour at 0.75 bar.

The variation of ambient water vapour mole fraction over 6 h at intervals of 1.5 min at Shree Umiya Book Store, Chandkheda is shown in Fig 2a. The maximum and minimum mole fractions recorded during this time were 1.85% and 1.6% respectively. Figure 2c shows the experimental and simulated $R_1/\Delta I_1$ terms for 1.74 % water vapour for a pathlength of 10.3 cm obtained at 14:25 h on 17 Aug 2022. The results of 19 h of continuous real-time measurement of indoor carbon dioxide variation inside in the lab on 23-24 June 2022 from 18:46-14:13 h are shown in Fig 2b. During this time the maximum and minimum mole fraction of carbon dioxide were 763 ppm and 533 ppm respectively. The carbon dioxide concentration level exceeded 700 ppm between 17:00 h to 22:00 h when four people were present in the lab, and then it gradually decreased once people had left. Similarly, a steep increase in mole fraction from around 10 am coincides with the time when people enter the lab. The experimental and simulated $R_1/\Delta I_1$ terms for 667 ppm carbon dioxide for a pathlength of 4.2 cm obtained at 12:18 h on 24 June 2022 are shown in Fig 2d. The low residuals indicate good agreement between the experimental and simulated $R_1/\Delta I_1$ terms and demonstrate that the extraction of gas parameters is reliable [3]. The systems showed excellent long-term stability and repeatability and are therefore suitable for long-term, time-resolved measurements in open and closed spaces.

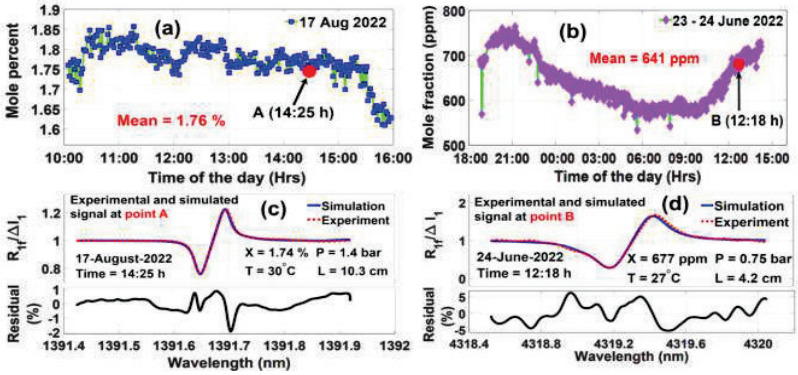

Fig. 2: Variation in (a) water vapour mole fraction over 6 h on 17 Aug 2022 and (b) carbon dioxide mole fraction over 19 h from 23 June (18:46 h) to 24 June (14:13 h) 2022. Experimental and simulated $R_1/\Delta I_1$ terms for (c) water vapour measurement obtained on 17 Aug 2022 and (d) carbon dioxide measurement obtained on 24 June 2022.

3. References

[1] S. Schilt, L. Thevenaz, and P. Robert," Wavelength modulation spectroscopy: combined frequency and intensity laser modulation", *Applied Optics*, vol. *42*, no.33, pp. 6728-6738, 2003.

[2] K. Sun, X. Chao, R. Sur, C. S. Goldenstein, J. B. Jeffries and R. K. Hanson, "Analysis of calibration-free wavelength-scanned wavelength modulation spectroscopy for practical gas sensing using tunable diode lasers", *Measurement Science and Technology*, vol. *24*, no. 12, pp. 125203, 2013.

[3] G. Wang, J. Mei, X. Tian, K. Liu, T. Tan, W. Chen and X. Gao," Laser frequency locking and intensity normalization in wavelength modulation spectroscopy for sensitive gas sensing", *Optics Express*, vol. *27*, no. 4, pp. 4878-4885, 2019.

[4] A. Roy and A. L. Chakraborty, "Intensity modulation-normalized calibration-free 1f and 2f wavelength modulation spectroscopy", IEEE Sensors Journal, vol. 20, no. 21, pp. 12691-12701, 2020.

Detection of pathogens in Water using field portable Microscopy and Spectroscopy device

Anjika Kumari[a], Anand Kumar[a], Meenakshi [b], Sachin Dhawan[c], Dalip Singh Mehta[a,b,*],

[a] Centre for Sensors, INstrumentation and Cyber-physical System Engineering, IIT Delhi; [b] Department of Physics, IIT Delhi; [c] School of Interdisciplinary Research, IIT Delhi

[*] mehtads@physics.iitd.ac.in

Abstract: In this present paper we propose a novel method to detect contamination in water. The present method is based on bright field (BF) microscopy and fluorescence spectroscopy. The presence of pathogens in water is a leading cause of water-borne diseases. At present there is no real-time technology available for the detection of different pathogens in water for the determination of the quality of water. The contaminants such as pathogens could be determined based on the shape of fluorescence spectra and bright field images.

Keywords: Autofluorescence, fluorescence spectroscopy, and microscopy

1. Introduction:

At present, one of the major challenges before world is availability safe drinking water. All the life forms require water for different metabolic activities and for regulating the body temperature, normalizing electrolytic balance, helps in digestion and prevent from health issues. Standards for microbial quality of drinking water or discharge of treated water uses presence of E. coli or any other indicator organism as surrogate for the water quality parameter [1]. Contaminated water and poor sanitation are connected to transmission of diseases such as Cholera, Diarrhea, Dysentery and Typhoid etc. Diarrhea is the most widely known water-borne diseases connected to contaminated food and water. Source water is vulnerable to contamination from many origins such as anthropogenic and biogenic sources of faecal contamination. In the present manuscript, we propose the detection of pathogen. There are so many methods to check the water contamination but most of them are time consuming and costly. We propose an idea of field portable low-cost system based on fluorescence microscopy. Basically, fluorescence is a dual stage process which involves absorption at shorter wavelength and emission at longer wavelength and is red shifted relative to the absorbed light. Fluorescence typically occur from aromatic molecules and fluorophores are the major components which leads to fluorescence. Auto fluorescence is the natural emission of light by biological structures and is used to distinguish between light which is originating from artificial addends.

2. Experimental setup:

Experimental setup for fluorescence spectroscopy and microscopy is shown below in figure 1 and figure 2, respectively. It comprises, a laser diode of 488nm (5mW, 3V, cyan blue dot laser, two lens (L1, L2) having focal lengths 3cm and 5 cm respectively, a microscopic objective (MO 100X ,0.86NA)), CCD camera (lumenera Infinity 2), Spectrometer (Avantes 200-1100nm) and a 3D mounted sample stage. The detector for the experimental setup has been different; for spectroscopy, spectrometer has been used as a detector, whereas, for microscopy CCD camera has been used. We have successfully recorded the BF images of E-coli bacteria and 1951 USAF resolution chart with the developed system. The spectra of the same samples can be recorded with the same experimental set-up with the replacement of the CCD detector with spectrometer. Table 1 shows the results of emission and excitation spectra of different bacteria in water.

Table 1: Average Emission Wavelength and Excitation Wavelength of the particles in sampled water

Name	Average emission wavelength (nm)	Excitation wavelength (nm)
E Coli	450nm	360nm
Salmonella	340nm	280nm

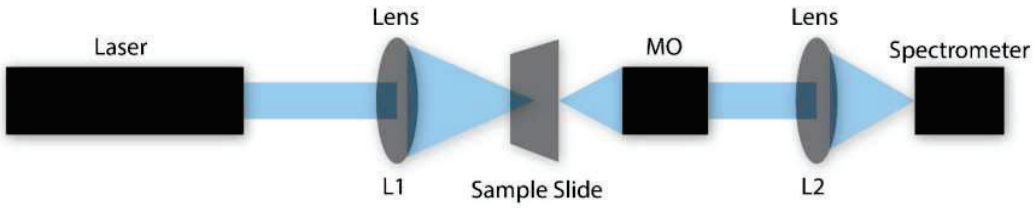

Figure 1: The schematic diagram proposed system of fluorescence spectroscope

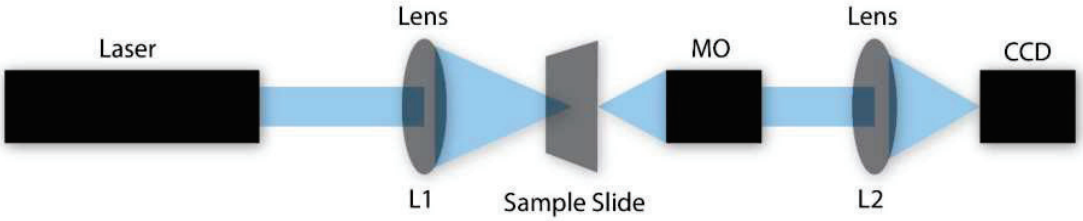

Figure 2: The schematic diagram proposed system of bright field microscopy

3. Result and Discussion:

The proposed technique employing the use of different technologies such as spectroscopy and microscopy is used for identifying the pollutants such as E. coli and salmonella etc. in water. The technology successfully detects the different fluorescence spectra of the different pollutants present in the water. This technology gives the insights on the use of microscopy and spectroscopy for the detection of contaminants in water.

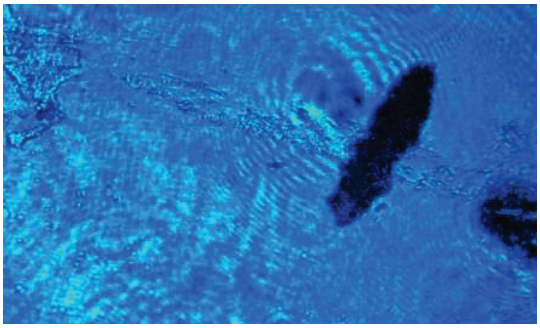

Figure 3: Recorded bright field image of E-coli bacteria

References:

[1] Amini, K. and Kraatz, H.B., 2015. Recent developments in biosensor technologies for pathogen detection in water. JSM Environ. Sci. Ecol, 3(1), pp.1-9.

[2] Tracy B, Gaida S, Papoutsakis E. 2010. Flow cytometry for bacteria: enabling metabolic engineering, synthetic biology and the elucidation of complex phenotypes. Curr. Opin. Biotechnol. 21:85–99.

[3] Renggli, S., Keck, W., Jenal, U. and Ritz, D., 2013. Role of autofluorescence in flow cytometric analysis of Escherichia coli treated with bactericidal antibiotics. *Journal of bacteriology*, *195*(18), pp.4067-4073.

Temperature-dependent light diffusion performance of nematic liquid crystal and cellulose acetate-based PDLC film

Rishikesh Kushawaha[1], Aloka Sinha[1]

[1]Department of Physics, Indian Institute of Technology Delhi, Hauz Khas, New Delhi, India 110016
Author e-mail address: rishikesh.kushawaha@physics.iitd.ac.in, aloka@physics.iitd.ac.in

Abstract: Herein, we have developed a light-diffusing film made up of 5CB nematic liquid crystal and cellulose acetate polymer. It is based on a technique that employs solvent-induced phase separation and sub-micron-sized liquid crystal droplets encapsulated in a polymer matrix that acts as a light scattering film. The film has potential applications in smart windows and optoelectronic devices.
Keywords: Liquid Crystal, Light-diffusing film, Polymer, Smart window

1. Introduction

Polymer dispersed liquid crystal (PDLC) is mainly used to fabricate smart windows [1], optical diffusers [2], and light scattering switches [3]. In PDLC, LC droplets are embedded in a continuous network of polymers as small spherical or quasi-spherical droplets. The droplets orient in a specific configuration due to their interaction with the polymer walls [1]. The film acts as a highly scattered media for incident light and diffuses light evenly and uniformly. In PDLC, LC droplets are dispersed in a continuous polymer network, which prevents light scattering particles from aggregating together [4]. The thickness of films is 27 micrometers, and they show that it diffuses light evenly and uniformly.

2. Material and fabrication

The films are made with 5CB liquid crystal and cellulose acetate (Mn~30000). A common solvent for mixing LC and CA is N, N-dimethylformamide (DMF). The films are fabricated using solvent-induced phase separation (SIPS). For PDLC film LC is in the 45 wt%, and CA acetate is the remaining part. The homogenous solution is prepared by magnetic stirring the mixture for 2 hours. It is then transferred to a petri dish and kept at 70°C for 90 minutes in a hot-air oven before being allowed to rest for 24 hours. The studies are performed on films that have a nearly uniform thickness of around 27 microns.

3. Experimental Details

The size of LC droplet or pore formation in the films is investigated using Zeiss Evo 50 Scanning electron microscope (SEM). For this LC/CA film was dipped in methanol for 48 hours, dried, and coated with gold. The light diffusion of the incident laser beam from films on a glossy paper screen is captured using the CCD camera. The Laser and hot stage are at a distance of 30 cm from each other, with the lens 5 cm away from the hot stage and the screen 16 cm from the lens. The CCD camera is at an angle of 30° from the initial direction of incident light at 35 cm.

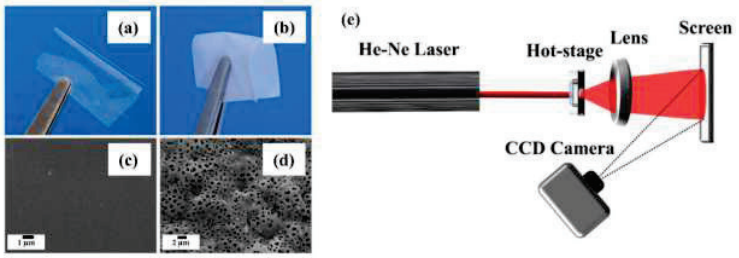

Figure 1. (a). CA film, **(b).** 45 wt % LC/CA film, **(c).** SEM image of CA film, **(d).** SEM image of 45 wt % LC/CA film**, (e).** Schematic diagram of the experimental set-up.

4. Results and Discussion

Figure 1(c) and (d) shows the SEM image of the films, and it reveals that CA films do not contain pores, but 45 wt% LC/CA films produce pores in the solid polymer matrix because of phase separation during polymerization. The LC/CA film has an average pore size of about 470 nm. The nematic to isotropic transition temperature (Tn-iso) for

the 45 wt % LC film is 31.2 °C. In CA film, the light is mostly directly transmitted, and most of the light intensity is confined around the laser spot see the color map in figure 2 (a_1-a_3). When LC is in the nematic phase, the film scatters the incident light, resulting in a nearly uniform diffused light for 45 wt % LC/CA film (see b_1-b_3 in figure 2). As LC approaches the isotropic phase, the film's capacity to diffuse light decreases, and there is a directly transmitted laser spot observed (see c_1-c_3 in figure 2). The average refractive index of LC droplets is given by $< n > = \left({}^{n_e}/_3 + {}^{2n_o}/_3\right)$, where n_o and n_e are the ordinary and extraordinary refractive index of LC molecules. In the nematic phase, LC droplets act as anisotropic scattering particles, and the optical birefringence is also high compared to the isotropic phase of LC [5]. As temperature increases, the n_e start to decrease and n_o start to increase; as a result, the birefringence starts to decrease with temperature [6]. After the clearing point, LC reaches in isotropic phase and acts as an isotropic medium with only one refractive index (n_{iso}). The film's scattering efficiency also decreases as a result of the reduced birefringence in the isotropic phase of LC, as a result the light power is confined near the laser spot.

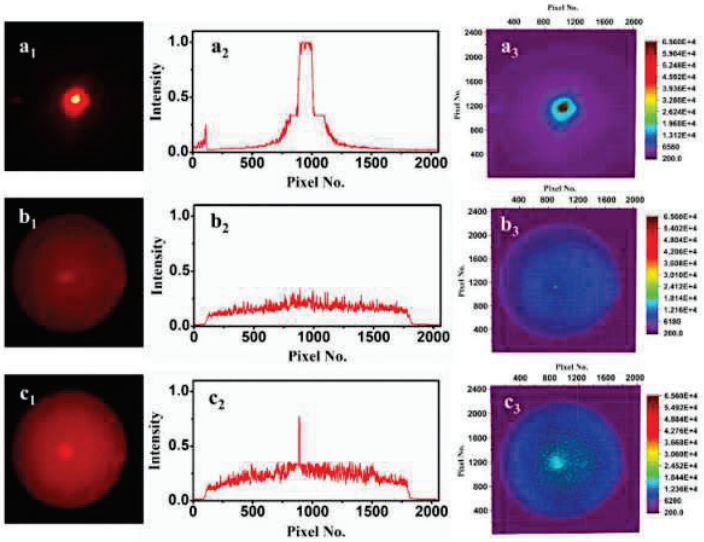

Figure 2. The CCD image of diffused light on the screen **(a_1-c_1)**, line profile across horizontal line passing centrally through laser spot **(a_2-c_2)**, and color map of the diffused light **(a_3-c_3)**. In figure, **(a_1-a_3).** CA film at 27 ºC, **(b_1- b_3).** 45 wt % LC CA film at 27 ºC, and **(c_1- c_3).** 45 wt % LC CA film at 35 ºC.

5. Conclusion

The temperature-dependent light diffusion properties of the CA and 45 wt % LC/CA-based free-standing films are investigated. The temperature-dependent scattering properties reveal that as temperature changes from the nematic phase to the isotropic phase of LC, the light diffusion property decreases, and diffuse transmitted light localization occurs near the beam spot.

Acknowledgments

Ministry of Education, Government of India, IIT Delhi, and DRDO, New Delhi (DFTM/03/3203/P/01/JATC-P2QP-01) for the research funding.

References

[1] L. Bouteiller and P Barny Le, "Polymer-dispersed liquid crystals: preparation, operation and application," Liq. Cryst. **21**, 157–174 (1996).

[2] R. Kushawaha and A. Sinha, "A facile fabrication of ultrahigh haze optical diffuser using nematic liquid crystal encapsulated by cellulose acetate biopolymer," J. Phys. D: Appl. Phys. **55**, 285303 (2022).

[3] A. Kumari et al., "Pseudopeptidic polymer microsphere-filled liquid crystals as high performance light-scattering switches," ACS Appl. Polym. Mater. **4**, 64–73 (2022).

[4] H. Ma et al., "The fabrication of novel optical diffusers based on UV-cured polymer dispersed liquid crystals," Liq. Cryst. **46**, 138–44 (2019).

[5] J. Li, S. Gauza and S. T. Wu, "Temperature effect on liquid crystal refractive indices," J. Appl. Phys. **96**, 19-24 (2004).

[6] S. Chakraborty, R. Panchal, and A. Sinha, "Determination of refractive indices for liquid crystals using a double transmission technique," Appl. Opt. **61**, 3804-3810 (2022).

Yb_2O_3-Lu_2O_3 Co-doped Nanoparticle: A Potential Candidate for High Power Fiber Laser Application

Dipanjan Karmakar[1,2*], Mukul Chandra Paul[1], Anirban Dhar[1]

[1]Fiber Optics & Photonics Division, CSIR-Central Glass & Ceramic Research Institute, 196, Raja S. C. Mullick Road, Jadavpur, Kolkata-700032, India

[2]Department of Chemistry, Jadavpur University, 188, Raja S. C. Mullick Road, Jadavpur, Kolkata-700032, India

**Author e-mail address: karmakardeep40@gmail.com*

Abstract: Yb_2O_3-Lu_2O_3 nanoparticle of optimum size (~45 nm) has been synthesized using a simple homogeneous co-precipitation method followed by thermal annealing. The different material/optical characterizations of the synthesized nanoparticles were carried out to optimize the particle size. The optimized nanoparticle is employed to fabricate optical preform using the Modified Chemical Vapour Deposition (MCVD) method coupled with solution doping technique followed by drawing of optical fiber from such preform to enhance the photodarkening resistivity suitable for high power laser application.

Keywords: Yb_2O_3-Lu_2O_3 nanoparticle, material/optical characterization, MCVD-solution doping technique, fiber laser, photodarkening.

1. Introduction:

Presently, rare-earth (RE) doped fiber lasers attract special attention due to their plentiful applications viz. material processing, medical surgery, strategic sectors [1], etc. because of their excellent beam quality, superior heat management, and compact structure [1]. Double-clad fiber design with suitable laser architecture helps to achieve laser output power up to several KW in a continuous wave regime. However, in order to improve laser performance, researchers are working to overcome several bottlenecks like nonlinear effects (SRS, SBS), thermal loading issues, as well as Photodarkening (PD) effect. Accordingly, researchers are looking for a solution through novel fiber design or the selection of new glass compositions. In this respect, search for suitable co-dopants that can enhance RE-solubility along with enhanced thermal conductivity which in turn leads to enhanced photodarkening resistivity is continuing. Lutetium oxide possesses excellent thermal conductivity along with many other advantages [2,3], and as a result Lu_2O_3 is considered as a potential co-dopant for the development of high-power fiber laser. Accordingly, the present study reports the preparation of optimized Yb_2O_3-Lu_2O_3 co-doped nanoparticles via a homogeneous co-precipitation route along with different material/optical characterizations. The synthesized nanoparticle is then doped into core of an optical fiber preform using MCVD coupled with solution doping technique followed by fiber drawing to improve photodarkening resistivity towards the development of laser fiber.

2. Experimental and result:

The Yb_2O_3 doped Lu_2O_3 nanoparticles were synthesized using room temperature homogeneous co-precipitation method using requisite amount of halide precursor to maintain Lu to Yb ratio [20:1] in aqueous solution followed by dropwise addition of NH_4OH keeping a fixed P^H. In order to obtain the desired particle size suitable amount of surfactant viz. Cetyl-Trimethyl Ammonium Bromide (CTAB) was added maintaining a particular concentration [0.15M] in presence of Al-halide salt to achieve doping of Al_2O_3 keeping a 1:20 molar ratio of Yb to Lu into Yb_2O_3 doped Lu_2O_3 nanoparticles. A sample of similar composition without alumina is also prepared for comparison to understand the effect of particle size and optical performance. The precipitate obtained was then calcined at different temperatures in the range of 800-1400°C for a fixed time span. The obtained particle was then analyzed using XRD which reveals that all Yb_2O_3 doped Lu_2O_3 nanoparticles belong to the cubic fluorite structure of Lu_2O_3 with

corresponding COD no 96-153-1488 (*Fig. 1a*), along with a phase of $Yb_3Al_5O_{12}$ with corresponding COD no 96-210-3618 in presence of the alumina-doped sample. The average crystalline size of alumina doped nanoparticles was found to be around 45 nm and was comparatively smaller than the undoped material which may assign to the formation of lattice strain. The HR-TEM analysis showed that the nanoparticles are well-defined polycrystalline in nature and belong to cubic shape (*Fig. 1b*). The EDS results coupled with the FESEM microscope exhibited the negligible loss of starting precursor even at 1400˚C.

The emission spectra of the Yb_2O_3-Lu_2O_3 nanoparticle (*Fig. 1c*), were measured by excitation at 911nm wavelength. It was observed that a zero-line emission peak at 976nm along with other two intense emission peaks at 1034nm and 1080nm also appeared. The result further shows that the intensity of emission peaks increases for different calcined materials from 800˚C to 1400˚C. The exact measurements of the fluorophore's lifetime were also done and fitted with an exponential function of adjusted correlation factor of 0.998. The measured average lifetime of the Yb_2O_3-Lu_2O_3 nanoparticle sample with and without doping of Al_2O_3 calcined at 1400˚Care was found to be 802µs, and 660µs respectively. The enhanced fluorescence lifetime of excited Yb ions into such nano-material can be explained by the further statistical distribution of Yb^{+3} ions in the AlO_6 environment of sesquioxide crystal.

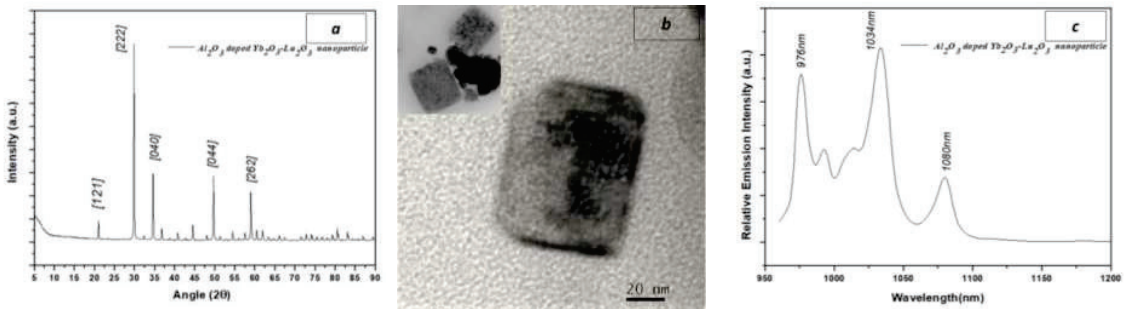

Fig.1: Al_2O_3 doped Yb_2O_3-Lu_2O_3 nanoparticle; a) XRD patterns of nanoparticle calcinated at 1400°C; b) HR-TEM images of cubic crystalline structure; c) Relative fluorescence emission spectra of nanoparticles calcinated at 1400°C

Finally, we selected Al_2O_3 doped Yb_2O_3-Lu_2O_3 nanoparticle of average particle size of 45 nm to prepare an alcoholic solution. This solution was used for soaking a porous silica soot sample deposited using the MCVD process at an appropriate temperature inside a high-quality silica tube of 1.5 mm thickness. The soaked tube was then dried and further processed to obtain collapsed preform that showed a good longitudinal uniformity of refractive index profile with a numerical aperture (NA) of ~ 0.12 and the corresponding core-clad ratio of 8:125. However, the further characterization of preform and fiber are under investigation specially its lasing performance and photodarkening resistivity.

3. Conclusion:

We have successfully synthesized Al_2O_3 doped Yb_2O_3-Lu_2O_3 nanoparticle using a homogenous co-precipitation method followed by thermal annealing to obtain an average particle size of 45 nm with a lifetime of ~802µs. This nanoparticle is used to make an alcoholic solution for the development of an optical preform using MCVD coupled with a solution doping technique that exhibits good longitudinal uniformity of refractive index profile and the fiber drawn from such nano-particles doped preform will be suitable for making high-power laser applications with enhanced photodarkening resistivity.

4. References:

[1] M. Zervas and C. Codemard, "High Power Fiber Lasers: A Review," IEEE Journal of Selected Topics in Quantum Electronics 20, 219-241 (2014).

[2] A. Pirri, G. Toci, B. Patrizi and M. Vannini, "An Overview on Yb-Doped Transparent Polycrystalline Sesquioxide Laser Ceramics," IEEE Journal of Selected Topics in Quantum Electronics 24, 1-8 (2018).

[3] R. Maksimov, V. Shitov, V. Platonov, A. Yurovskikh, G. Toci, B. Patrizi, M. Vannini and A. Pirri, "Hot isostatic pressing of transparent Yb^{3+}-doped Lu_2O_3 ceramics for laser applications," Ceramics International 47, 5168-5176 (2021).

Series Combination of Modal Interferometers for Detecting Independent Vibration Fields and Their Sequence

Kalipada Chatterjee*, Arvind Kumar Maurya, and Rajan Jha#
Nanophotonics and Plasmonics Laboratory, School of Basic Sciences, Indian Institute of Technology Bhubaneswar, Bhubaneswar-752050, Odisha, India.
*e-mail address: *rkc11@iitbbs.ac; #rjha@iitbbs.ac.in*

Abstract: In this work, series combination of modal interferometers based sensing system for detection of mechanical vibrations parameters is demonstrated. Fiber modal interferometers are realized by concatenating photonic crystal fiber (PCF) sections along single mode fiber (SMF) channel to act as in-line sensor probes. Individual PCF sections respond independently to external vibrations and produce a superposed signal that provides information about vibration components. Using a comparative computational algorithm, the frequency components about each probe is identified from single output signal. Such sensing system would be useful for monitoring structural health, industrial machinery and environmental events at different locations remotely.
Keywords: Photonic crystal fiber, Modal interferometer, Vibration sensing, Nash-Sutcliffe value.

1. Introduction

Optical waveguide based interferometry systems have been widely used for monitoring dynamic physical fields like magnetic field [1], acoustic field [2], and fluid flow [3]. However, their utility towards simultaneous monitoring of multiple dynamic fields at different locations has remained elusive. Among the various interferometry systems, specialty fiber based in-line interferometers have become more viable owing to their high sensitivity and reconfigurable features. Solid-core photonic crystal fiber modal (PCF) interferometers are one such class of specialty fiber interferometers that enable extensive dynamic field sensing and operate by wavelength interrogation method. When such fiber interferometers are subjected to oscillating fields, their response generates a dynamic optical signal that provides information about amplitude and frequency components of the field. Likewise, when multiple interferometers are concatenated along single mode fiber (SMF) channel and subjected to external field, the resultant signal is a combination of individual interferometer response. In this work, we propose a combination of identical PCF based fiber modal interferometers for sensing mechanical vibrations at different locations along single fiber channel. Further, we provide a computational algorithm for localizing the field components about each sensor probe from the single output signal which is an essential aspect of such distributed sensing systems.

2. Working Principle and Experimental Characterization

A PCF based in-line fiber interferometer enables excitation and recombination of PCF guided modes along its length. When a broad spectrum of light is coupled to such interferometer, the resultant transmitted spectrum is given by [4],

$$I_j = I_{cr} + I_{cl} + 2\sqrt{I_{cr} I_{cl}}\cos\phi \qquad (1)$$

where, $\phi = \dfrac{2\pi L(n_{cr}^{eff} - n_{cl}^{eff})}{\lambda} = \dfrac{2\pi \Delta n L}{\lambda}$ with L as interferometer length, and I_{cr} and I_{cl} as the intensities of the superposing modes. As the interferometer deforms due to vibrational field, the transmitted spectrum peak wavelengths incur dynamic spectral drift proportional to field magnitude. By tracking the spectral drift of a particular interference peak, the external field parameters can be determined. When such identical interferometers are concatenated along single fiber channel, the combined system enables detection of different vibration fields simultaneously. The individual interferometers or sensor probes (S_m) sense the external vibrations (X_m) such that the transmitted spectral drift (T_λ) is a superposition of the individual sensor response, given as,

$$T_\lambda = \sum_m \frac{\partial S_m}{\partial X_m} \qquad (2)$$

In order to characterize such a system, light from broadband source (SLED) is coupled to a series combination of PCF based fiber interferometers (S1 and S2) along SMF channel and their output is fed to a wavelength interrogator (Fig. 1(a)). Each PCF section is 1 cm long. The sensor probes are subjected to vibrational fields by placing them on

separate piezo transducers (PZTs). The PZTs are driven by a function generator to alter the field parameters over broad frequency range. The recorded signals are computationally analyzed for signal localization and sequence identification.

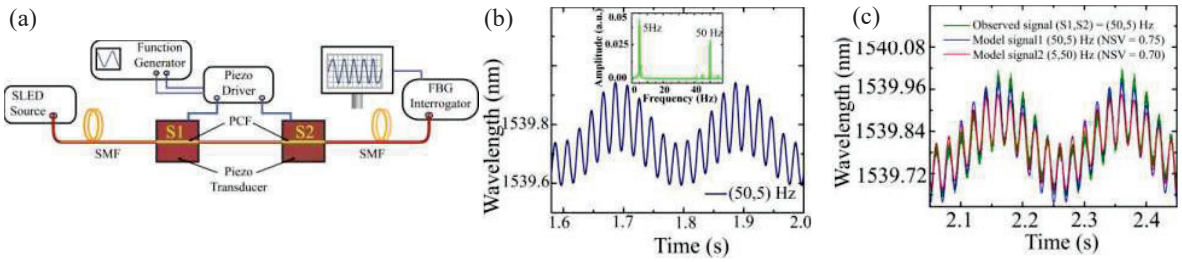

Figure 1: (a) Schematic representation of the experimental set-up used detection of vibration field at two different locations. (b) Resultant real time signal of the sensors' response showing a superposed signal. (inset) FFT of the time series signal depicting peaks at corresponding frequency components. (c) Comparison of recorded signal with modeled signals with corresponding Nash-Sutcliffe estimation for signal localization. The model signal with higher NSE predicts the position of frequency components.

3. Results and Discussions

The spectral drift due to sensors' response is recorded for various combinations of vibration field parameters applied about the probes. One such resultant output signal is shown in Fig. 1(b) where the vibration field frequencies about S1 and S2 are 50 Hz and 5 Hz respectively. The signal is linear modulation of individual fields' parameters. Fast Fourier transform (FFT) of the recorded signal provides frequency components with peak amplitude proportional to vibration field amplitude. Hence, the amplitude and frequency of vibrational fields about the sensors are identified. The system is tested to operate over frequency range of 1 Hz -1 kHz.

Now, to determine the position of frequency components about the sensors, we develop a computational algorithm. Briefly, the algorithm involves simulating model analytical signals with different frequency components and known combinations, and compare each analytical signal with observed signal. Here, the simulated model signal1 corresponds to frequency combination as (S1,S2) = (50,5) Hz while model signal2 corresponds to combination (S1,S2) = (5,50) Hz, as shown in Fig. 1(c). These signals are compared with observed signal by computing the corresponding Nash-Sutcliffe values (NSV_m), given by,

$$NSV_m = 1 - \frac{\sum_t (T_n^m - T_n^o)^2}{\sum_t (T_n^o - \overline{T_n^o})^2} \qquad (3)$$

where, T^m and T^o represent the model and observed signals respectively. Such comparative studies are widely implemented for structural and environmental monitoring [4]. The simulated model signal with higher NSV represents the observed signal. From the known combination of simulated signal, the sequence of frequency components about the sensor probes (S1 and S2) is determined from single output signal.

4. Conclusion

The proposed system enables detection of mechanical vibrations and their corresponding features about different locations using series combination of PCF based modal interferometers. Besides identifying the frequency components, the computational algorithm enables determination of fields' sequence along the sensing channel. The sensing system is compact, reconfigurable, remotely controllable and operates over broad frequency range of 1 Hz -1 kHz. Such system can be implemented for monitoring various dynamic fields such as fluid flow and acoustic fields over broad range in industrial applications and environmental surveillance.

5. References

[1] K. Chatterjee, "Reconfigurable optical magnetometer for static and dynamic fields", Adv. Opt. Mater. 9, pp. 2001574, (2021)
[2] S. Dass, "In reflection metal-coated diaphragm microphone using PCF modal interferometer", J. Light. Technol. 39, pp. 3974 (2021).
[3] V. Arumuru," Vortex shedding optical flowmeter based on photonic crystal fiber", Sci. Rep. 9, pp. 1-9, (2019).
[4] E. Olyaie, "A comparison of various artificial intelligence approaches performance for estimating suspended sediment load of river systems: a case study in United States", *Environ. Monit. Assess.* **187**, 1–22 (2015).

Acknowledgements

RJ acknowledges the support of SERB STAR Fellowship. RJ acknowledges the support from DST TDP program of Govt. of India.

Speckle-free multi-modal microscopic system for biological applications

Shilpa Tayal and Dalip Singh Mehta
Bio-photonics and green photonics laboratory, Department of Physics Indian Institute of Technology
e-mail-mehtads@physics.iitd.ac.in

Abstract: Here, we develop a single-shot multi-modal system to acquire diverse information about the biological specimen. It comprises a quantitative phase and fluorescence imaging system integrated into a single unit. The pseudo-thermal light source is synthesized from the highly coherent laser light for speckle-free illumination. The experimental results are presented.

1. Introduction

Optical microscopes are widely used to visualize the micron size object, but it fails to acquire good contrast image of transparent cells [1]. Fluorescence microscopy uses external contrast agent to tag the specimen, which provides high contrast image of the object and also provides molecular specific information [2]. But, like optical microscope, it also fails to provide the quantitative information about the specimen. Quantitative phase microscope, works on the concept of wave-front distortion, the reference beam interferes with the distorted object beam to form the interference fringe pattern, and this interferogram can be utilized to obtain various quantitative parameters like refractive index, cell thickness, cell morphology [3].
Lasers are highly coherent which are generally used to acquire the interference pattern easily, but its high coherence property leads to formation of speckles and parasitic fringes, which degrades the image quality and also leads to erroneous results.
In this paper, we have synthesized a pseudo-thermal light source for speckle-free illumination, which provides high accuracy in phase measurement. Further, we have combined oblique illumination fluorescence with the Linnik-type interferometer to acquire molecular specific as well as quantitative information at the same location of biological specimen in single-shot. The pseudo-thermal and highly coherent laser is compared by recording bright-field and interferogram using both the aforementioned sources. The MG63 osteosarcoma cells are tagged using sodium fluorescein dye and composite image is recorded which is further digitally separated to obtain interferogram and the fluorescence image.

2. Synthesis of pseudo-thermal light source

The pseudo-thermal light source is synthesized using the rotating diffuser and the Multi-mode fiber bundle to reduce the spatial coherence of highly coherent He-Ne laser. The resulting beam has low spatial and high temporal coherence, which helps in the interferometric applications. The formation of pseudo-thermal light is depicted in Fig. 1.

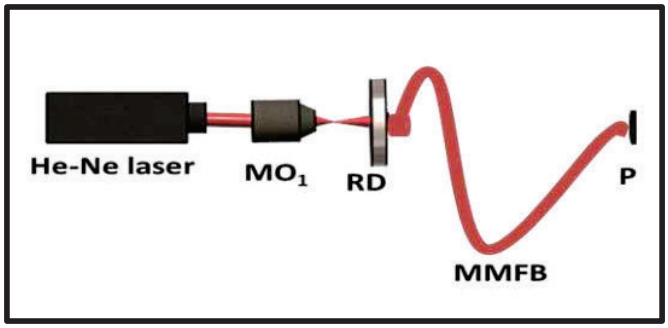

Fig. 1 Synthesis of pseudo-thermal light source from He-Ne laser

3. Results and Discussion

The Linnik type interferometer is combined with the oblique illumination fluorescence to gather multi-fold information about biological specimen. To obtain high accuracy in phase measurement, the pseudo-thermal light source is designed as explained in previous section. Here we have compared the pseudo-thermal light source with the high coherent laser light as depicted in Fig. 2(A) and (B). The MG63 osteosarcoma cells are tagged using the sodium fluorescein dye and composite image is recorded using the multi-modal system. The R-channel and G-channel is separated using the ImageJ software, as shown in Fig.3.

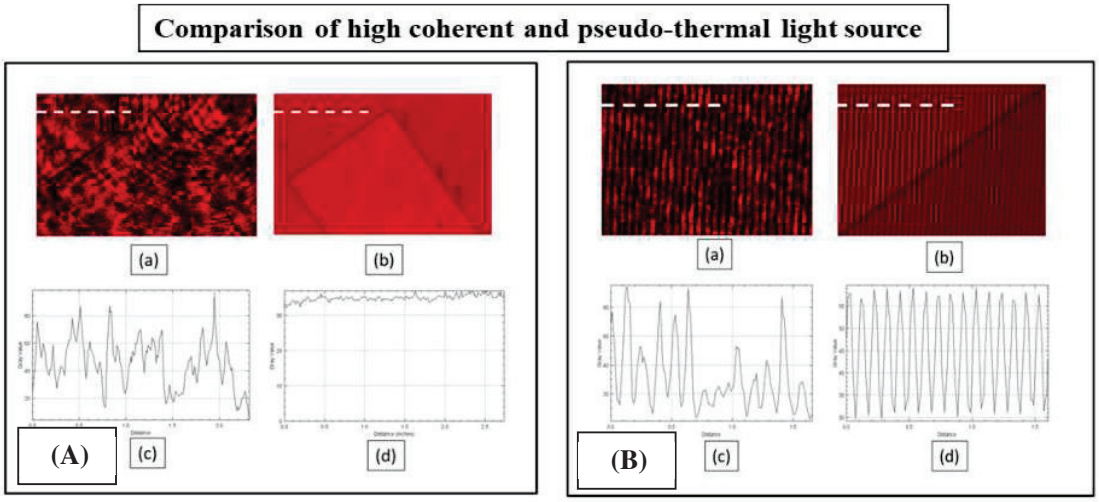

Fig. 2 (A) and (B) Demonstrating comparison between bright field image and interferogram captured using highly coherent laser and pseudo-thermal light source, respectively.

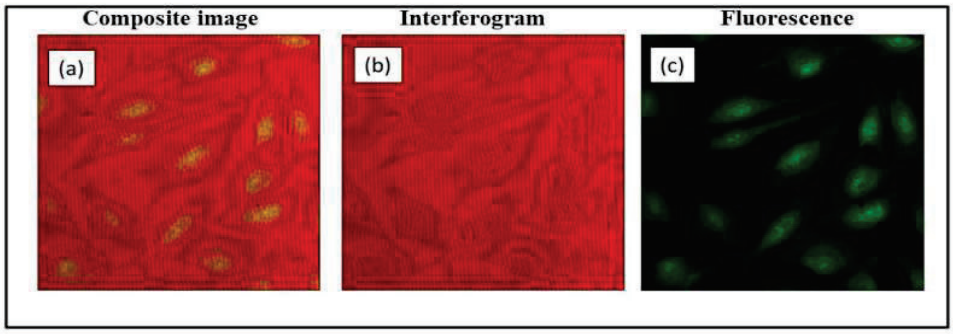

Fig. 3 (a) Composite image captured using the multi-modal system (b) R-channel representing interferogram and (c) G-channel representing fluorescence image.

4. Conclusion

We have developed a multi-modal system which can provide speckle-free interferograms that could be reconstructed to obtain quantitative parameters, and the oblique illumination fluorescence, which can be utilized to obtain molecular specific information about the object. The system is beneficial as diverse information at the same location of the object can be acquired.

5. Reference

[1] Kevin Tsia, "Understanding Biophotonics Fundamental, Advances and Application", Jenny Stanford Publishing, 2015.
[2] Hamilton N. "Quantification and its applications in fluorescent microscopy imaging." Traffic.,10(8),951-61 (2009)
[3]K. Lee, K. Kim, J. Jung, J. Heo, S. Cho, S. Lee, G. Chang, Y Jo, H. Park , Y. Park , "Quantitative Phase Imaging Techniques for the Study of Cell Pathophysiology: From Principles to Applications", *Sensors* 13, 4170–91(2013)

Spatial multiplexing of CGH for holographic displays

Lavlesh Pensia[1,2,#], Md Kamran Afroz[1,#], Bhargab Das[1], Raj Kumar[1,2,*]

[1]*CSIR-Central Scientific Instruments Organisation, Sector 30C, Chandigarh 160030, India*
[2]*Academy of Scientific and Innovative Research (AcSIR), Ghaziabad, 201002, India*
**Corresponding author: raj.optics@csio.res.in*
[#] The authors contributed equally to the work.

Abstract: We propose a methodology to enhance the amount of information displayed in the limited viewing angle of a spatial light modulator (SLM). Computer-generated hologram (CGH) is realized for a set of objects and these CGHs are combined using spatial-multiplexing method. The multiplexed CGH is reconstructed using a phase-only SLM, which results in an enhancement of amount of information projected. Our aim is to use this methodology for holographic display purpose.
Keywords: Holographic Display, Computer Generated Hologram, Spatial Light Modulator

1. Introduction

A three-dimensional holographic display is an ultimate display which can provide us with all types of 3D cues [1]. There are three fundamental elements of any 3D display. These elements are capturing, processing & displaying of information. In computer generated hologram (CGH) based 3D displays, the capturing and processing part is carried out numerically in a computer, and the optical reconstruction can be performed with the help of a spatial light modulator(SLM). But there are limitations in CGH-based 3D displays due to the relatively larger pixel size of an SLM. The viewing angle of an SLM-based display is very limited. Quantitatively, the viewing angle of most of the commercially available LCoS-based SLM is not more than 3˚ to 4˚. Various techniques have proposed in literature to enhance the viewing angle of SLM [2-3]. Also, the computation time gets increased due to the large number of pixels of an SLM. Even if the viewing angle of the SLM is less, by utilizing spatial multiplexing process on the generated CGHs, the amount of information projected within the limited viewing angle can be increased [3]. The work discussed here is focused on increasing the amount of displayed information within the limited viewing angle of SLM. Both numerical simulation and experimental demonstration is presented here.

2. Methodology

The CGHs are generated using the angular spectrum based beam propagation method and the numerical reconstruction is performed by Fresnel diffraction method [4-6], represented as

$$O_o(x,y) = \frac{\exp(-jkz)}{j\lambda z}\exp\left(\frac{-j\pi(x^2+y^2}{\lambda z}\right) * FT\left[E_h(x,y)\exp(\frac{-j\pi(x^2+y^2)}{\lambda z})\right] \quad (1)$$

where $O_o(x, y)$ and $E_h(x, y)$ are complex amplitude distributions at the CGH plane and reconstruction plane, respectively. FT represents Fourier transform, $k=2\pi/\lambda$, λ is the source wavelength, z is the propagation distance, and $j=\sqrt{-1}$.
Three different binary images of resolution 1920×1080 are taken as input objects as shown in Fig 1. Three different CGHs are generated by considering different spatial frequencies. The three CGHs are then spatially multiplexed for both numerical and optical reconstruction. For the optical reconstruction of the multiplexed CGH, an LCoS-based phase-only SLM is used having resolution of 1920×1080 with a pixel size of 6.4μm.

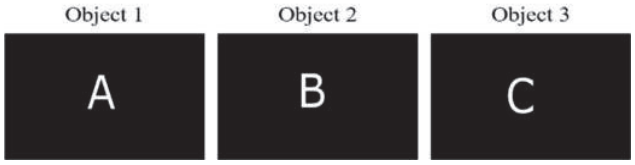

Fig.1: Three different object for CGH construction.

The schematic setup for the optical reconstruction of the numerically generated CGH is shown in Fig. 2. There are three first-order reconstruction spots, which show the presence of three different spatial frequencies in the constructed CGH.

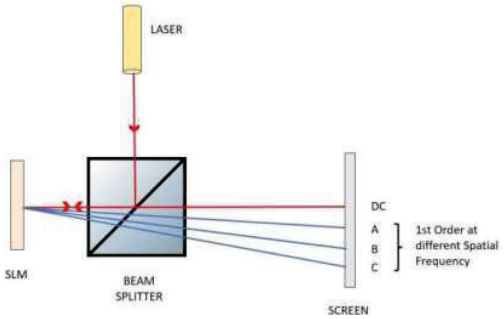

Fig.2: Schematic diagram of optical reconstruction of CGH.

The numerical reconstruction of the generated CGH by using the Fresnel diffraction method is shown in Fig. 3(a). It can be seen that all three reconstructed images of three different objects are separated. The three reconstructed images are present at different spatial and angular positions with respect to the zero-order beam. The reconstruction of the CGH can also be carried by temporal multiplexing. In the temporal multiplexing technique, all three CGHs can be display on the SLM sequentially with the frequency determined by the refresh rate of SLM.

3. Results and Discussion

The optical reconstruction of the spatially multiplexed CGH is shown in Fig. 3 which demonstrates that within the existing viewing angle of the SLM, the amount of information can be increased. In spatial multiplexing the resolution of the reconstructed image would be decreased. To maintain a good resolution, time multiplexing can be done. Hence, in the limited range of viewing angle of a holographic display, more information can be put with the help of mentioned technique.

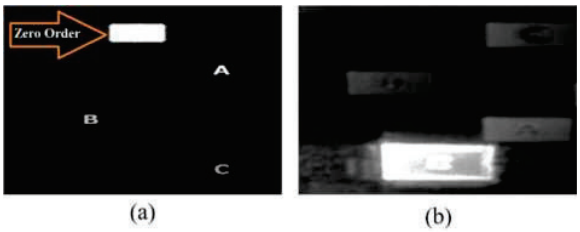

Fig.3: Three different object information reconstructions of spatially multiplexed CGH by (a) simulation and (b) optically.

In the optical reconstruction, we can see in Fig. 3 (b) that the object's information is inverted compared to the simulated results. The loaded CGHs into the SLM get data reversed in the optical reconstruction due to the reflection of the incident beam from the active region of the SLM. This technique could also be used to increase the amount of information in AR/VR eyewear displays.

4. Conclusion

In this paper, we proposed a multiplexing technique to increase the amount of information projected in the SLM's limited range of viewing angles. The proposed technique may be used in various fields of three-dimensional imaging, such as holographic displays, AR/VR near-eye displays etc.

Acknowledgement

The authors like to acknowledge CSIR, India for the financial support through a NCP project (MLP2014). Lavlesh Pensia thanks to CSIR, India for providing a fellowship to carry out this research work.

5. References

[1] G. Jason, "Three-dimensional display technologies," Advances in optics and photonics 5, 456-535 (2013).
[2] Y. Takaki, "Enlargements of Viewing Zone and Screen Size of Holographic Displays Using MEMS SLM Combined with Scanning Systems," *Applied Sciences 12*, 6495 (2022).
[3] Y. L Li, N. N. Li, D. Wang, F. Chu, S. D. Lee,Y. W. Zheng&Q. H. Wang,"Tunable liquid crystal grating based holographic 3D display system with wide viewing angle and large size," Light: Science & Applications, 11, 1-10 (2022).
[4] E. Sahin, E. Stoykova,J.Mäkinen,&A. Gotchev, "Computer-generated holograms for 3D imaging: a survey," *ACM Computing Surveys (CSUR)*, *53*, 1-35 (2020).
[5] L. Pensia, G. Dwivedi& R. Kumar,"Effect of displacement in object plane on reconstructed image in lens-based digital holography," *Engineering Research Express*, *3*, 035004 (2021).
[6] T. C. Poon & J. P. Liu, "Introduction to modern digital holography: with MATLAB,"Cambridge University Press, 2014.

Plasmon tunability of Gold Nanostar for refractive index sensor and SERS

Chhaya Sharma[1], Jyoti Katyal*[1], Deepanshi[1], Rina Singh[2]
[1]Amity Institute of Applied Science, Amity University, Noida, India; [2]CRRI-CSIR, New Delhi, India
Author e-mail address: jyoti_106@yahoo.co.in

Abstract: In this paper, we present the theoretical modelling of Gold Nanostar for localized surface plasmon resonance based sensor application and SERS over red to NIR region. Au nanostars exhibiting LSPR peak over 1400 nm were considered in isolated and multimer configuration. The refractive index sensitivity for all configurations were measured and nanostars exhibit the RIS factor upto 1175 nm/RIU. The effect of interacting nanostars on LSPR and field enhancement was studied by considering multimer configuration forming Quadrumer, rhombus, crown and closed loop nanostructure. The nanostars arranged in Quadrumer and crown shape nanostructure shows field enhancement ~ 10^9 in NIR region.
Keywords: Nanostar, Localised surface plasmon resonance, Refractive index based sensor, field enhancement.

1. Introduction

The rapid expansion of plasmonic activity in complex metal nanostructures has been aided by the development of sophisticated computational methods for investigating plasmonic activity in complicated metal nanostructures. Anisotropic shaped nanostructures have demonstrated their promise in the field of surface enhanced Raman scattering (SERS), refractive index based sensor, solar cell, photocatalysis etc [1-3]. In general, SERS is performed using a noble metal (Au or Ag) as the substrate nanomaterial. Individual metal nanoparticles have been found to have an enhancement factor (EF) of 10^3, while dimers of these nanoparticles have increased the value to 10^8-10^10, depending on the nano gap [4,5]. The development of anisotropic nanoparticles has boosted the use of SERS. Anisotropic shaped nanostructures have been synthesized using a variety of approaches. One of the shapes that has piqued the researchers' interest is the nano star, which combines a spherical centre with multiple branches of varying sharpness. It was predicted that the spherical core and individual projecting spikes would generate brilliant and dark modes based on plasmon hybridization theory. The length of the spikes, sharpness of the spikes, and inner core radius all influence the position of the peak wavelength. We present a detailed examination of the plasmonic characteristics of gold nanostar in single and multimer configurations for refractive index based sensor and SERS. The calculated extinction spectra by varying AR has extended LSPR to 1500 nm. We calculated the refractive index factor (RIS) for a single gold nanostar, which shows how the LSPR changes as the surrounding medium changes [6]. The RIS factor appears to increase as the number of arms increases for smaller sizes, while it decreases as the number of arms increases for larger sizes because of the multipolar peaks appears on larger sizes figure 1. For the 35 nm star size, the RIS factor were estimated as 519 nm/RIU, 1175 nm/RIU and 1107 nm/RIU for 4, 6, and 8 as number of arms, respectively.

It is generally known that when metal nanoparticles are placed close together, the localized surface plasmon resonances (LSPR) in each particle couple with one another, and this plasmon coupling results in a more intense plasmon resonance than that produced by the isolated particles. The electric field close to the surface of nanoparticles can be greatly amplified by the resonant stimulation of plasmons. In this study, we calculate the near- and far-field characteristics of a gold nanostar using the finite-difference time-domain (FDTD) method. The model of the nanostar shows a solid core with outwardly pointing prolate tips. Here, we discuss the possibility of understanding the physical nature of nanostar plasmons by evaluating the spatial symmetry and wavelength dependence of the numerically calculated electric field enhancements. The hybridization of plasmons linked to the core and various tips produces the plasmon resonances of the nanostar. Although the core plasmons make up a small portion of the low-energy bonding nanostar plasmons, tip plasmons make up the majority of them. In contrast to what would be produced for individual tips, the mixing in of the core plasmon mode greatly expands the cross section for the excitation of the bonding plasmons and produces extremely significant local electric field improvement which is generally referred to plasmonic hybridization theory. Further, we introduced the study of nano-star with different combinations and arrangement which is performed theoretically on the basis of FDTD to enhance electric field. The magnitude of the electromagnetic

enhancement is inversely related to the localized field strength at the SERS active surface to the fourth power. In order to design and create substrates with extraordinarily high enhancement factors, it is important to theoretically estimate the EM field enhancement for metallic nanostructures composing the SERS substrates. Figure 2 describes the measured extinction spectra of gold nanostars arranged in quadrumer shape in which tip of one nanostar come in contact with other nanostar tips such that hybridization takes place. When the light interacts with the quadrumer of gold leads to the excitation of collective plasmons in the nanostars which in turns lead to enhanced electric field enhancement factor (η) ~ 233 at 1033 nm whereas it enhances to ~ 241 at 1001 nm for crown shaped nanostructure. Table 1 summarizes the calculated max E and Max E^4 for different arrangement of Au nanostars corresponding to plasmon resonance wavelength.

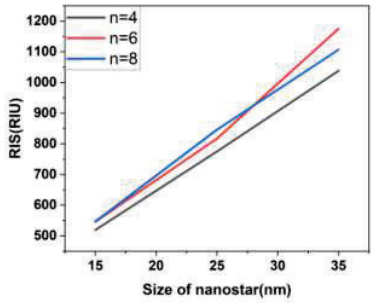

Figure 1 Refractive index sensitivity for Au nanostars. The AR is fixed as 3, 5 and 7. The number of spikes are 4, 6 and 8.

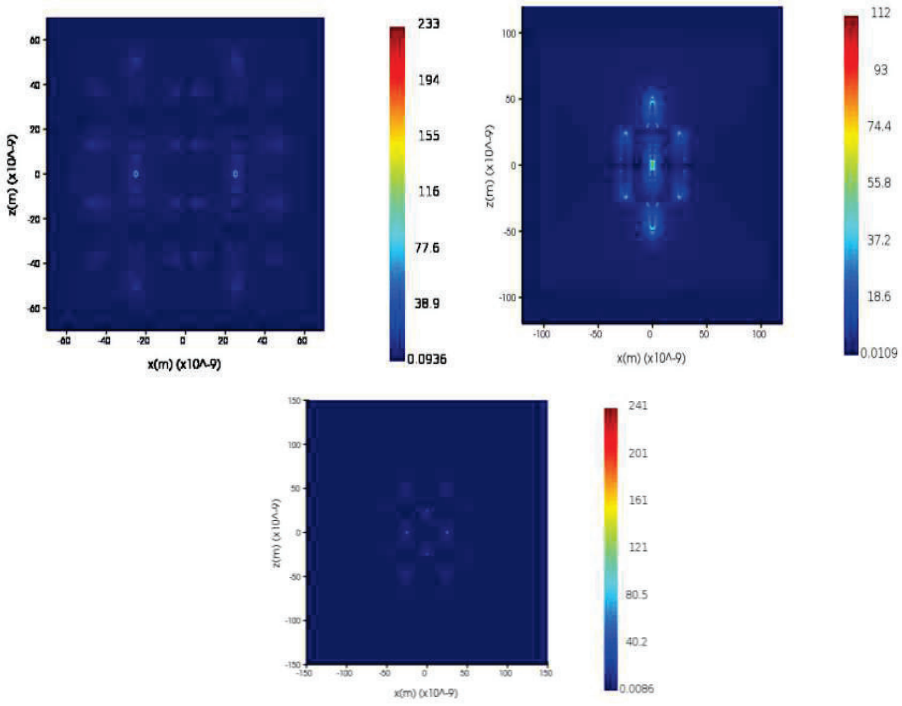

Figure 2: The Near field pattern of Au nanostars arranged in (a) quadrumer, (b) Rhombus and (c) Crown nanostructure.

Table 1: Comparison of local electromagnetic field magnitudes at the surface for multimer nanostars.

Nanostructure	No of Particle	No of Arms	Plasmon wavelength	max E	max E^4
Quadrumer	4	4	956	219	2300257521
		6	1033	233	2947295521
		8	1182	174	916636176
Rhombus	4	4	994	112	157351936
		6	1131	62.8	15553873.9
		8	1161	101	104060401
Crown	5	4	1001	241	3373402561
		6	1208	132	303595776
		8	1310	122	221533456
Cyclic	6	4	928	77	35153041
		6	1001	87	57289761
		8	1097	54	8503056

2. References

1. Bhagat, B., Mehta, K., Sinha, T.K., Baruah, P.K., Mukherjee, K. (2022). Recent Advances and Opportunities of Plasmonic Sensors. In: Yu, P., Xu, H., Wang, Z.M. (eds) Plasmon-enhanced light-matter interactions. Lecture Notes in Nanoscale Science and Technology, vol 31. Springer, Cham. https://doi.org/10.1007/978-3-030-87544-2_12
2. Liu, J.; He, H.; Xiao, D.; Yin, S.; Ji, W.; Jiang, S.; Luo, D.; Wang, B.; Liu, Y. Recent Advances of Plasmonic Nanoparticles and their Applications. Materials 2018, 11, 1833. https://doi.org/10.3390/ma11101833
3. Zhu G, Cheng L, Liu G, Zhu L. Synthesis of Gold Nanoparticle Stabilized on Silicon Nanocrystal Containing Polymer Microspheres as Effective Surface-Enhanced Raman Scattering (SERS) Substrates. Nanomaterials. 2020; 10(8):1501. https://doi.org/10.3390/nano10081501
4. ACS Nano 2019, 13, 10, 11453–11459 Publication Date:September 20, 2019 https://doi.org/10.1021/acsnano.9b04938
5. Reguera, Javier & Langer, Judith & Aberasturi, Dorleta & Liz-Marzán, Luis. (2017). Anisotropic metal nanoparticles for surface enhanced Raman scattering. Chem. Soc. Rev.. 46. 10.1039/C7CS00158D.
6. Chhaya Sharma, Jyoti Katyal,Theoretical study of Magnetic-Plasmonic Fe-Al core-shell nanostructure for sensing application,Materials Today: Proceedings,Volume 57, Part 5,2022,Pages 2148-2151,ISSN 2214-7853,https://doi.org/10.1016/j.matpr.2021.12.141.

Ultra-Broadband Visible-Telecom Photon Pairs from SiN Waveguides

Vijay[1, a], Shivani Sharma[1], Vivek Venkataraman[1,2], and Joyee Ghosh[1]
[1]*Quantum Photonics Group, Department of Physics, Indian Institute of Technology Delhi, New Delhi – 110016, India*
[2]*Department of Electrical Engineering, Indian Institute of Technology Delhi, New Delhi – 110016, India*
[a]*phz218659@physics.iitd.ac.in*

Abstract: We present silicon nitride (SiN) waveguide designs optimized for ultra-broadband phase-matching yielding photon pairs via SFWM (spontaneous four-wave mixing) over a range ~700-1650 nm, with the signal wavelengths spanning the entire telecom spectrum and the idler wavelengths covering the visible-NIR bands. SFWM bandwidths upto ~1000 nm (for pump wavelength ~981 nm) are achieved in air-clad waveguides with crossection ~ 560-nm × 1575-nm. The proposed device could be useful for multi-channel hybrid (free space + fiber) quantum key distribution (QKD) schemes, and for efficiently heralding single photons in the telecom band.
Keywords: Silicon-Nitride Photonics, Four-Wave Mixing, Quantum Key Distribution.

1. Introduction

Enhancing data rates in large-scale quantum communication relies on exploring integrated sources capable of generating single photons/photon pairs with wide bandwidths. Traditionally explored silicon-on-insulator (SOI) waveguides can yield SFWM based photon-pair sources with broad bandwidth (~500 nm) spanning the entire telecommunication spectrum (~1250-1750 nm) [1]. Silicon has a higher nonlinear index coefficient ($n_2 = 6 \times 10^{-18}$ m^2/W at 1.55 μm) than SiN [2], ($n_2 = 2.6 \times 10^{-19}$ m^2/W at 1.55 μm), but also exhibits a higher linear propagation loss (~3.5 dB/cm) [1], along with nonlinear losses like TPA (two-photon absorption) and FCA (free-carrier absorption) and a smaller transparency window (>1.1 μm). In contrast, SiN is transparent in the visible and IR ranges (> 0.4 μm) with a lower propagation loss (0.5 dB/cm) [3], and negligible nonlinear losses.

Here we present dispersion-engineered SiN waveguide designs with silica as bottom cladding (thickness ~3 μm) and air as top cladding, see schematic shown in Fig. 1(a). The optimum geometry (h × w = 560 nm × 1575 nm) is capable of yielding ultra-broadband (~1000-nm bandwidth around pump wavelength of ~981 nm) photon pairs through spontaneous four-wave mixing (SFWM) with a spectral brightness ~4×10^4 photon pairs/s/nm/mW^2 for a typical linear propagation loss of 0.5 dB/cm and waveguide length of 2.5 cm (see Fig. 2(b)).

2. Theory

Degenerate-pump SFWM involves annihilation of two pump photons at wavelength λ_p and generation of two daughter photons at wavelengths λ_s and λ_i called signal and idler, while conserving energy such that $2\omega_p = \omega_s + \omega_i$ (ω_p, ω_s and ω_i are pump, signal and idler frequencies respectively), see Fig. 1(b). Conversion efficiency from signal to idler in stimulated/classical FWM, or equivalently the generation rate of signal-idler pairs per unit bandwidth Ω_p (i.e., the photon flux) in SFWM is given by [1],

$$\Omega_p = (\gamma P_p L)^2 \, e^{-\alpha L} \left| \frac{1 - e^{-(\alpha + i\Delta\beta)L}}{(\alpha + i\Delta\beta)L} \right|^2 \quad (1)$$

where $\gamma = \frac{\omega_p n_2}{c \, A_{eff}}$ is the effective nonlinearity at pump frequency ω_p, c is the speed of light, A_{eff} is the effective modal area, P_p is the input pump power, α is the linear propagation loss of waveguide, L is the waveguide length, and Δβ is the phase-mismatch given by $\Delta\beta = 2\beta_p - \beta_s - \beta_i - 2\gamma P_p$. β_p, β_s and β_i are the propagation constants at pump, signal and idler wavelengths, respectively, and $2\gamma P_p$ is the nonlinear phase-mismatch that can be neglected for the parameters used in our work as $2\gamma P_p << 2\beta_p - \beta_s - \beta_i$. The propagation constant at a frequency ω is computed as $\beta_\omega = \frac{n_{eff}(\omega)\,\omega}{c}$ where n_{eff} is the effective index for the fundamental TE mode extracted from finite-element-method (FEM) based numerical mode simulations in COMSOL Multiphysics®, including both material and waveguide dispersion.

3. Results

Figure 1 (c) shows the variation of FWM conversion efficiency with waveguide length L for two values of the linear propagation loss (α), each for two different input pump powers (P_p). It is evident that the conversion efficiency (or equivalently the generated photon flux) first increases but eventually saturates (for L ~2.5 cm) or even starts decreasing for L ≳ 4 cm for α = 2 dB/cm. Figure 2(a) shows a continuous phase-matching bandwidth ($|\Delta\beta| < \pi/L$) of ~976-nm obtained with the optimum waveguide geometry (h = 560 nm and w = 1575 nm) for a pump wavelength of 980.7 nm. The corresponding spectral brightness of our source is computed [4], to be ~4×10^4 pairs/s/nm/mW^2, considering a typical linear propagation loss of 0.5 dB/cm and waveguide length of 2.5 cm (see Fig. 2(b)). Moreover, fabrication inaccuracies in waveguide dimensions can still be compensated by appropriately changing the input pump wavelength as shown in Fig. 2(c).

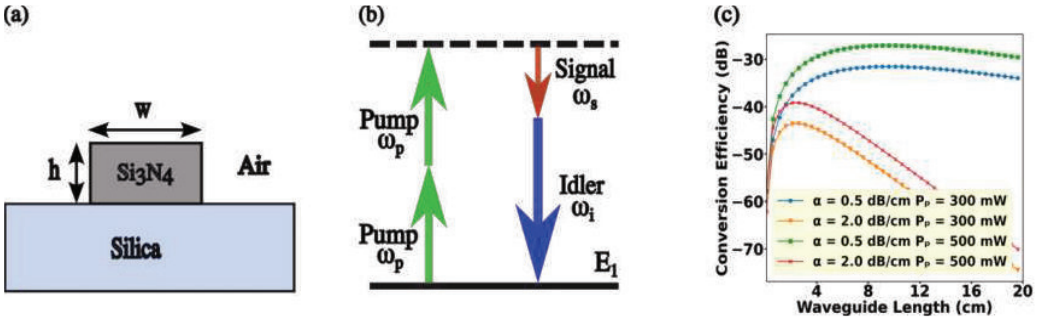

Fig. 1 (a) Schematic showing a silicon nitride (SiN) waveguide where h and w are the height and width, with air and silica as the top and bottom cladding, respectively; (b) Energy level diagram of degenerate pump FWM, annihilation of two pump photons allows creation of one signal and one idler photon; (c) FWM conversion efficiency (or equivalently photon flux) as a function of waveguide length for h = 560 nm, w = 1575 nm, λ_p = 980.7 nm, $\Delta\beta = 0$.

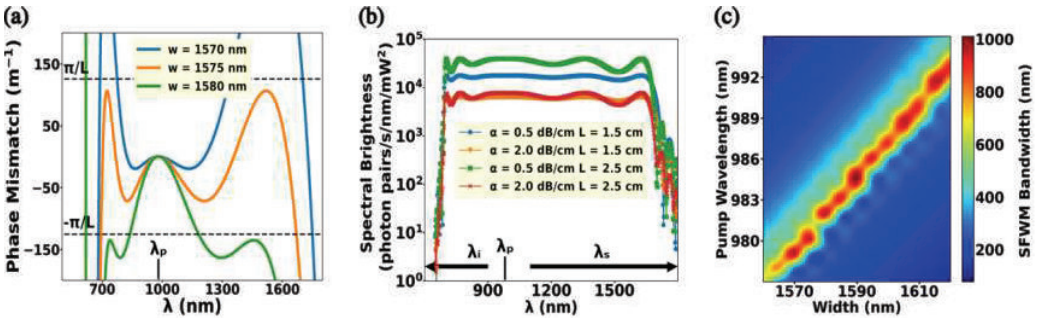

Fig. 2. (a) Phase-mismatch as a function of signal/idler wavelength for different waveguide widths (w) and height, h = 560 nm. The dashed lines denote the tolerance of phase-mismatch allowed for a waveguide of length L = 2.5 cm; (b) Spectral Brightness for h = 560 nm, w = 1575 nm at λ_p= 980.7 nm and (c) Tolerance of bandwidth towards change in waveguide width and pump wavelength for the waveguide height, h = 560 nm and length L = 2.5 cm.

4. Conclusion

We propose spectrally-bright CMOS-compatible integrated sources of photon pairs over an extremely wide wavelength range (~700-1650 nm) spanning both visible-near-infrared and telecom wavelengths based on dispersion-engineered SiN waveguides. These proposed devices could be employed in multi-channel QKD protocols utilizing the pair correlations, or heralding single photons at telecom wavelengths utilizing the high quantum efficiency detectors available in the visible spectrum.

5. References

[1] S. Sharma, V. Kumar, P. Rawat, J. Ghosh and V. Venkataraman, *"Nanowaveguide Designs in 220-nm SOI for Ultra-Broadband FWM at Telecom Wavelengths",* IEEE Journal of Quantum Electronics, vol. 56, no. 5, pp. 1-8, 2020.

[2] Hong, Yaping, Yixiao Hong, Jianxun Hong, and Guo-Wei Lu, *"Dispersion Optimization of Silicon Nitride Waveguides for Efficient Four-Wave Mixing"*, Photonics 8, no. 5: 161, 2021.

[3] J. S. Levy, A. Gondarenko, A. C. Turner-Foster, M. A. Foster, A. L. Gaeta and M. Lipson, *"Four-wave mixing in integrated silicon nitride waveguides,"* Conference on Lasers and Electro-Optics and Conference on Quantum electronics and Laser Science Conference, pp. 1-2, 2009.

[4] S. Sharma, V. Venkataraman and J. Ghosh, *"Spectrally-Pure Integrated Telecom-Band Photon Sources in Silicon", Journal of Lightwave Technology*, Journal of Lightwave Technology, doi: 10.1109/JLT.2022.3188526, 2022.

Third-order Nonlinear Optical Measurements in Natural dye extracted from Ixora coccinea

Sreeja Lakshmi.S[1], Athulya S[2], Chandrashekharan K[3], Jayaram P[4], Sudheesh P[5]

[1,4]MES Ponnani College, Ponnani, Malappuram,India

[2,3]Department of Physics, NIT Calicut, Kozhikode, India

[5]Department of Physics, NSS College Manjeri, Malappuram

sudheeshp9@gmail.com

Abstract: The role of nonlinear optical (NLO) material in the future evolution of technology and industrial application is very important. The development of applications of nonlinear optics has been still limited by the availability of materials with the required optical and environmental properties and much effort has gone into the development of superior materials for use in nonlinear optics. It has been found that the natural materials with third- order optical nonlinearity are very important for photonics and optoelectronic application. In the present study, natural dye from ixora coccinea has been extracted using cold extraction method with dimethyal formamide as solvent. The third-order NLO properties of the extracted Anthocyanin dye were measured by employing single beam Z-scan technique with nanosecond laser pulses at 532 nm. The results are quite promising for possible applications in photonic devices.

Key words: Third-order nonlinear optics, Z-scan, Anthocyanin dye

Sensing of targeted Micro-Nano Plastic pollutants in Water Bodies with Optimized Opto-Metamaterial: Surface Plasmon Resonance Approach

Mohd Mansoor Khan[1], Nilesh Sharma[2], Ramesh Kumar Sonkar[3]

[1,2] Department of Electronics and Communication Engineering
Indian Institute of Information Technology Guwahati
Guwahati-781015, Assam, India
[3] Department of Electronics and Electrical Engineering
Indian Institute of Technology Guwahati
Guwahati-781039, Assam, India
[1] mansoor@iiitg.ac.in,[2] nilesh.sharma21@iiitg.ac.in, [3] sonkar@iitg.ac.in

Abstract: This paper proposes an all-fiber micro-nano (μ-n) plastic sensing system in the water bodies utilizing the surface plasmon resonance (SPR) phenomenon. The sensing element is a tailored nanostructured Opto-metamaterial with noble metals [planer silver (Ag) and 3D-grated gold (Au)] with topmost graphite (C_{gr}) coating. The optimum thickness of combination layers is calculated as C_{gr} = 0.69 nm, Au = 6 nm, and Ag = 45 nm to maximize the absorption of the light at the SPR site. The comparative reflected intensity dip in the output SPR spectrum is 100% steeper than the planer array.

Keywords: Surface Plasmon Resonance, Micro-Nano plastics, Thin Films, Optical Fiber Sensors, Light-Matter Interaction

1. Introduction

The photoelectric effect in the form of SPR at the metal-dielectric interface produces a surface plasmon wave (SPW) [1]. The metallic electrons interact with the electromagnetic light wave to produce SPW which eventually travels parallel to the metal-dielectric surface. The incoming photons create a resonating environment resulting in the exponential increment in the electric field intensity at the interface. Employing the SPR technique, a change in the refractive index (RI) of the immediate proximal atmosphere can be sensed effectively [2,3]. The dielectric's RI in the sensor's affinity layer primarily depends on its constituents. Therefore, propagation of the SPW is strongly guided by the constituent markers of the surrounding layer. This technique has resulted in the development of ubiquitous sensing in pathogen detection of human and plant-associated diseases to the environmental monitoring of soil [2]-[5]. The appreciable sensitivities to RI changes are calibrated to the shift in reflected intensity minima of the SPR spectra concerning the corresponding angle and wavelength. Consequently, this technique can also be utilized to sense μ-n plastics, a single source of an annual 286 million tons of plastic pollution in water bodies [6]. India contributes a massive 12.8 million tons annually to plastic pollution which, due to fragmentation loop (sunlight, heat, and water/wind waves), may end up in micro (μ < 5 mm) and nano (n < 100 nm) particles with 90% and 10% contribution respectively [7,8]. Owing to the food chain, the inclusion of μ-n plastics in the human and animal (land and aquatic) bodies led to health concerns like cancer formations, organ ruptures, intestinal blockages, etc. [6,9]. Therefore, detection of these μ-n plastics should be the primary concern to avoid health disruptions.

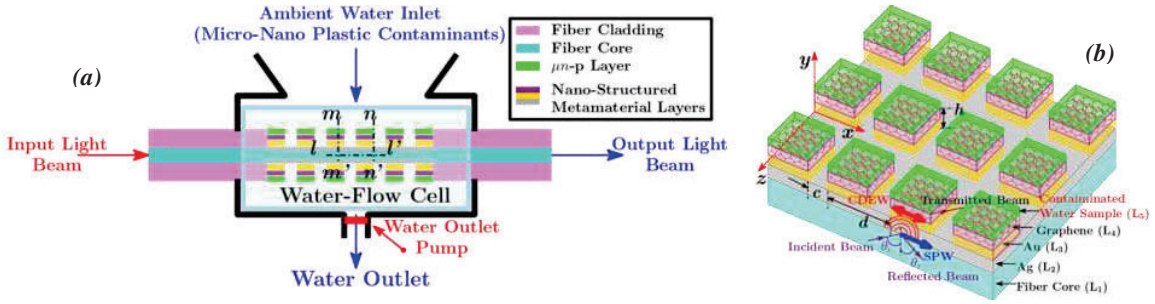

Fig. 1: (a) Proposed sensor targeted μ-n plastics detection and (b) nanostructured C_{gr} : Au: Ag metamaterial sensing element's cross sectional view sliced along l-l', m-m', and n-n'planes showing the metal-graphene nano-cuboids 3D organization and SPR mechanism on the optical fiber.

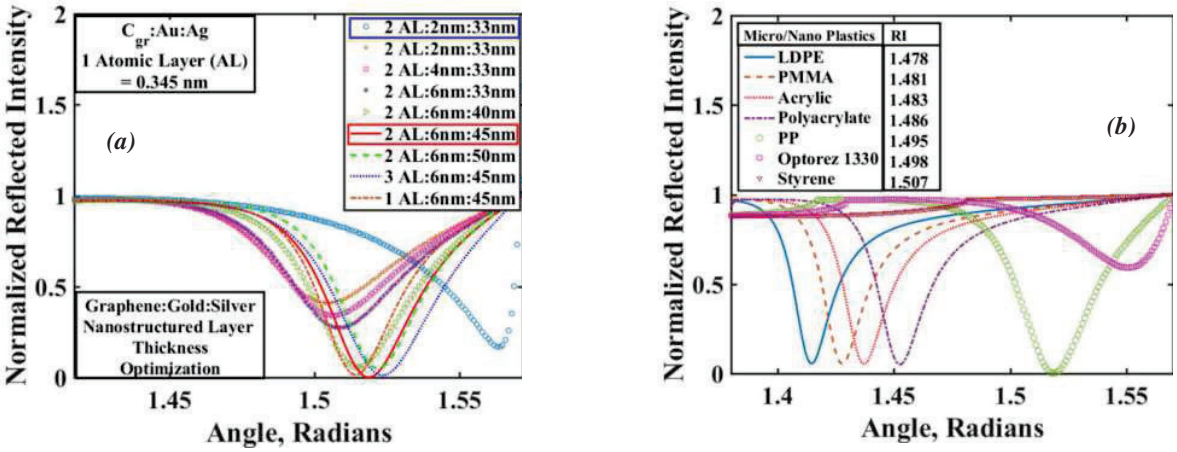

Fig. 2: (a) Planer and Nano-cuboidal thickness optimization of C_{gr} : Au: Ag layering combination highlighted in blue and red boxes. (b) Targeted μ-n plastics identification present in the affinity layer (L_5).

2. Theory, Results, and Discussions

Detection of μ-n plastics has issues due to the lesser availability of classification data sets and lack of dedicated analytical methods [6]. The technological progress in the nano-scale fabrication and thin-film coating processes resulted in the rapid transition of metamaterial manufacturing. Material sputtering processes such as atomic layer deposition (ALD) have created the possibility of single-atom thin films [10]. The proposed SPR-based nanostructured metamaterial sensor with its corresponding optimized (using transfer matrix method and finite element method) sensing element (C_{gr} = 0.69 nm, Au = 6 nm, and Ag = 45 nm) is shown in Fig. 1 (a) and (b) respectively. The comparative optimum thickness combination of different layers is shown in Fig. 2 (a). Considering the optimum nanostructured combination, the RI of the affinity layer varied from 1.478 to 1.507 for different μ-n plastics (low-density polyethylene, poly(methyl methacrylate), acrylic, polyacrylate, polypropylene, optorez 1330, and styrene) as shown in Fig. 2 (b). It can be observed that each of the mentioned μ-n plastics can be identified with its distinct SPR dip, however, the sensitivity for optorez 1330 is minimum with maximum full width at half maximum (FWHM=2.35^o and 59.5% reflected intensity).

3. Conclusions

The optimized design of μ-n plastics detection in water bodies has been proposed and simulated using optical fiber. The sensing element's combination was calculated as C_{gr} = 0.69 nm, Au = 6 nm, and Ag = 45 nm for maximum sensitivity (100% SPR dip) to various mentioned μ-n plastics at the SPR site.

4. References

[1] C.-J. Huang, G. V. Narasimha, Y.-C. Chen, J.-K. Chen, and G.-C. Dong, "Measurement of low concentration of micro-plastics by detection of bioaffinity-induced particle retention using surface plasmon resonance biosensors," Biosensors, vol. 11, no. 7, p. 219, 2021.

[2] M. M. Khan and D. A. Varma, "Surface optimization of nano-structured bimetallic metamaterial on optical fiber for multi-disease sensing through exhaled air," in 2020 IEEE Region 10 Symposium (TENSYMP). IEEE, 2020, pp. 453–456.

[3] M. G. Daher, S. A. Taya, I. Colak, S. K. Patel, M. M. Olaimat, and O. Ramahi, "Surface plasmon resonance biosensor based on graphene layer for the detection of waterborne bacteria," Journal of Biophotonics, p. e202200001, 2022

[4] B. Hossain, A. K. Paul, M. A. Islam, M. F. Hossain, and M. M. Rahman, "Design and analysis of highly sensitive prism based surface plasmon resonance optical salinity sensor," Results in Optics, p. 100217, 2022

[5] S. Oh, H. Hur, Y. Kim, S. Shin, H. Woo, J. Choi, and H. H. Lee, "Peptide specific nanoplastic detection based on sandwich typed localized surface plasmon resonance," Nanomaterials, vol. 11, no. 11, p. 2887, 2021.

[6] K.-E. Peiponen, J. R¨aty, U. Ishaq, S. P´elisset, and R. Ali, "Outlook on optical identification of micro-and nanoplastics in aquatic environments," Chemosphere, vol. 214, pp. 424–429, 2019.

[7] M. Eriksen, N. Maximenko, M. Thiel, A. Cummins, G. Lattin, S. Wilson, J. Hafner, A. Zellers, and S. Rifman, "Plastic pollution in the south pacific subtropical gyre," Marine pollution bulletin, vol. 68, no. 1-2, pp. 71–76, 2013

[8] T. M. Baynes, S. Kapur-Bakshi, N. Emami, S. Bhattacharja, S. Tap-suwan, J. Joseph, K. Locock, M. Kapur, R. Sinha, N. Bajpai et al., "A material flow analysis of polymers and plastics in india," 2021.

[9] K.-E. Peiponen, B. O. Asamoah, B. Kanyathare, J. R¨aty, and M. Roussey, "Detecting microplastics with optics," Optics and Photonics News, vol. 31, no. 11, pp. 24–31, 2020.

[10] S. Lim, S. Kwon, and H. Kim, "Zno thin films prepared by atomic layer deposition and rf sputtering as an active layer for thin film transistor," Thin Solid Films, vol. 516, no. 7, pp. 1523–1528, 2008.

Broadband Nonlinear Spectral Broadening in 1D Metal-Dielectric Photonic Crystal

Mohd Shanu, Jitendra Nath Acharyya, G. Vijaya Prakash*

Nanophotonics Lab, Department of Physics, Indian Institute of Technology Delhi, New Delhi-110016, India
**Corresponding Authors: prakash@physics.iitd.ac.in*

Abstract: A giant femtosecond supercontinuum generation (SCG) is observed from a thin (~1 μm) one-dimensional (1D) metal-dielectric (MD) photonic structure composed of 4 bilayers of silver (Ag) and silica (SiO_2) on glass substrate. The huge spectral broadening arises from the enhanced third- and high-order optical nonlinearities by the coupled Fabry-Perot resonators (-(Ag-SiO_2-Ag)-). The generated supercontinuum for four bilayer structure $(Ag/SiO_2)_4$ is compared with the single bilayer (Ag/SiO_2) and bare Ag thin film. The present results establish the strong applicability of the photonic architecture in compact on-chip supercontinuum source for ultrafast photonic applications.
Keywords: Metal-dielectric, Supercontinuum generation, Third-order nonlinearity.

1. Introduction

The immense spectral broadening of ultrashort laser pulse during the propagation through a bulk medium is known as supercontinuum generation (SCG). A huge amount of research has been carried out to investigate the origin of the spectral broadening in waveguides and bulk media [1,2]. Several factors such as nonlinear absorption, self-steepening, Kerr nonlinearity, stimulated Raman scattering, four-wave mixing play crucial role in achieving spectral broadening [1,2]. The complex interplay between the various orders of dispersion in addition with optical nonlinearities leads to the strong spectral broadening of the femtosecond laser pulse. There is a huge surge in achieving ultrafast broadband supercontinuum generation in various media and architectures due to its enormous applications in ultrafast optics and photonics.

The 1D photonic crystals (distributed Bragg reflectors (DBR) and microcavities) are another class of optical media which enable to conveniently control and manipulate the propagation of the photons on a subwavelength scale [3-7]. Among them metal-dielectric (MD) photonic crystals are special due to the appearance of optical transparency in the visible and near-infrared regions which offers accessibility of ultrafast and very high optical nonlinearities of metal [3-5]. In general, the supercontinuum generation is more noticeable in the photonic crystal fibers wherein the periodic spatial arrangements and smaller modal area result in strong optical field confinement and the enhancement of nonlinearities which help in spectral broadening [1, 2]. However, to the best of our knowledge, the femtosecond supercontinuum generation in 1D MD photonic structures is not explored so far.

In this paper, the experimental observation of broadband supercontinuum generation is demonstrated in 1D MD photonic crystal composed of four bilayers of silver (Ag) and silica (SiO_2) as $(Ag/SiO_2)_4$. The study has been extended to compare the SCG with various other structures and pure glass substrate. The findings of the present study may significantly lead to a great implication in the field of supercontinuum generation.

2. Results and Discussions

The 1D metal-dielectric photonic crystal is realized from four bilayers of silver (Ag/38 nm) and silica (SiO_2/179 nm) fabricated from DC and RF sputtering, respectively. The detailed fabrication can be found in the previous communications [3, 4]. The spectral broadening measurements have been performed using an 800 nm (120 fs, 1 kHz) laser pulse with varying peak power and the generated supercontinuum was recorded using a fiber coupled spectrometer [8]. Figure 1a represents the schematic of the $(Ag/SiO_2)_4$ 1D MD photonic structure. The transmission spectral plot of the MD structure is depicted in Fig. 1b which shows a prominent photonic bandgap in the wavelength regions from 400 to 600 nm. The transmissive regions on both sides of the photonic bandgap are the photonic minibands emerged from the coupled Fabry–Pérot cavities (Ag-SiO_2-Ag) [3, 4].

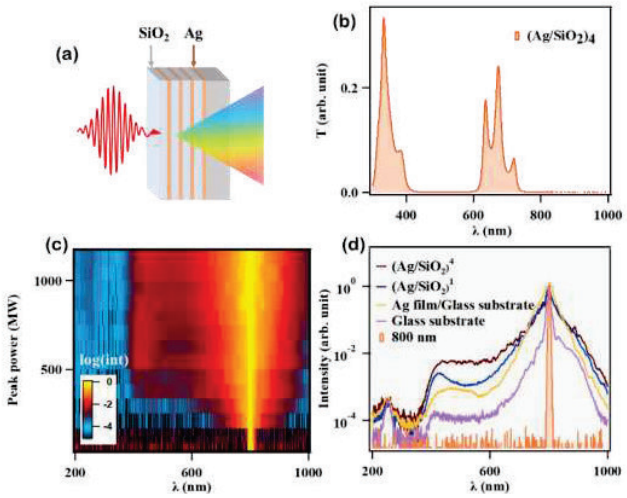

Fig. 1: (a) Schematic representation, (b) transmission spectra and (c) generated supercontinuum spectral intensity map at varying laser peak power (Pump laser: 800 nm, 120 fs, 1 kHz) of $(Ag/SiO_2)_4$ metal-dielectric 1D photonic structure. (d) A comparative plot of normalized supercontinuum spectra recorded at 1160 MW pump peak power for $(Ag/SiO_2)_4$, $(Ag/SiO_2)_1$, Ag film, and bare glass substrate.

A laser peak power-dependent (40 MW to 1160 MW) spectral intensity map of the generated supercontinuum is shown in Fig. 1c at 800 nm (120 fs, 1 kHz). Fig. 1(d) illustrates a comparative plot (in logarithmic scale) of the normalized supercontinuum spectra for $(Ag/SiO_2)_4$, $(Ag/SiO_2)_1$, Ag film, and bare glass substrate at fixed laser peak power (1160 MW). The spectral evolution illustrates a prominent spectral broadening for $(Ag/SiO_2)_4$ MD structure compared to other structures. The huge spectral broadening in case of $(Ag/SiO_2)_4$ structure can be attributed to the large Kerr nonlinearity associated with extremely high third- and higher-order optical nonlinearities originating from the manifold enhanced field confinement by the coupled Fabry–Pérot cavities (Ag-SiO_2-Ag) [8].

3. Conclusion

In conclusion, an unprecedented femtosecond spectral broadening is reported in $(Ag/SiO_2)_4$ 1D MD photonic structure. The generated supercontinuum is energetically stable. The generation of femtosecond spectral broadening can be attributed to the combined effect of self-phase modulation and the coupled Fabry-Perot resonator induced optical nonlinearity of the MD photonic structure. The present observations can be envisaged in realization of compact stable femtosecond supercontinuum sources.

4. Acknowledgements

The authors are thankful to Prof. D. Narayana Rao, Dr. Akhilesh Kumar Mishra, and Dr. R.B. Gangineni for providing insightful suggestions and experimental facilities. The central facilities of the University of Hyderabad and IIT Delhi are highly acknowledged. MS and JNA acknowledge UGC and DST-INSPIRE for the research fellowships, respectively.

5. References

[1] R. R. Alfano and S. L. Shapiro, "Emission in the region 4000 to 7000 Å via four-photon coupling in glass," Phys. Rev. Lett. **24**, 584 (1970).
[2] J. K. Ranka, R. S. Windeler, and A. J. Stentz, "Visible continuum generation in air–silica microstructure optical fibers with anomalous dispersion at 800 nm," Opt. Lett. **25**, 25-27 (2000).
[3] J. N. Acharyya, D. N. Rao, M. Adnan, C. Raghavendar, R. B. Gangineni, and G. Vijaya Prakash, "Giant Optical Nonlinearities of Photonic Minibands in Metal–Dielectric Multilayers," Adv. Mater. Interfaces **7**, 2000035 (2020).
[4] J. N. Acharyya, A. K. Mishra, D. N. Rao, A. Kumar, and G. Vijaya Prakash, "Ultrafast Nonlinear Pulse Propagation Dynamics in Metal–Dielectric Periodic Photonic Architectures," Adv. Mater. Interfaces **8**, 2100757 (2021).
[5] S. Suresh, O. Reshef, M. Z. Alam, J. Upham, M. Karimi, R. W. Boyd, "Enhanced nonlinear optical responses of layered epsilon-near-zero metamaterials at visible frequencies," ACS Photonics **8**, 125-129 (2021).
[6] J. N. Acharyya, N. R. Desai, R. B. Gangineni, and G. Vijaya Prakash, "Photonic Cavity-Mediated Tunable Ultrafast Absorption Dynamics in $BaTiO_3$-Based One-Dimensional Photonic Crystal," ACS Appl. Electron. Mater. **3**, 1904-1911 (2021).
[7] J.N. Acharyya, N.R. Desai, R.B. Gangineni, and G. Vijaya Prakash, "Effect of Photonic Cavity Interactions on Femtosecond Multiphoton Optical Nonlinear Absorptions from Bi_2O_3-Based One-Dimensional Photonic Crystal," ACS Photonics **9**, 2092–2100 (2022).
[8] J.N. Acharyya, S. Singh, M. Shanu, G. Vijaya Prakash, and A.K. Mishra, "Ultrafast pulse propagation and spectral broadening in metal-dielectric 1D photonic crystal," Opt. Mater. 131, 112688 (2022).

Whispering Gallery Mode Splitting in Microresonator Integrated in Deep Seated Negative Axicon

Jasleen Kaur[1,2], Kaushal Vairagi[1,2], Samir K Mondal[2]

[1]Academy of Scientific and Innovative Research (AcSIR), Ghaziabad 201002, India [2]CSIR-Central Scientific Instruments Organisation, Chandigarh 160030, India

Author e-mail address: jasleenkt@yahoo.in

Abstract: We study mode splitting in an integrated Optical Fiber based Whispering Gallery Mode resonator in reflection mode. The design is Barium Titanate resonator embedded in Deep Seated Negative Axicon showing Q-factor ~$4.5x10^3$.

Keywords: Whispering Gallery Mode, Microresonator, Axicon, DSNA, Mode Splitting

1. Introduction

Whispering Gallery Mode (WGM) Resonances are continuous total internal reflected light waves trapped in the periphery of curved spherical resonator. The optical properties of WGM resonator such as high Quality-factor (Q) and Low mode volume make it suitable for advanced photonics instrumentation. Several design constraints make it challenging to develop an efficient WGM resonator. We have introduced a novel in-fiber integrated WGM resonator which works in reflection mode and show mode splitting in microresonator when it is distorted from its spherical shape. The said design includes a Deep Seated Negative Axicon (DSNA) embedded with WGM resonator. The DSNA is fabricated in a photosensitive optical fiber (GF4-A) by chemical etching with 48% of Hydrofluoric acid (HF) for 40 minutes [1]. Chemical etching results in the formation of the axicon having opening close to 70µm diameter which decreases to 4µm till the apex of cone which can be seen in microscopic image of axicon in the Fig 1. Light guided through the core spreads along the cladding surfaces of cone like axicon. The evanescent field propagating on the surface of axicon surface gets coupled to the microresonator giving WGM resonances in microresonator [2] which can be seen from the simulated image in Fig.1.

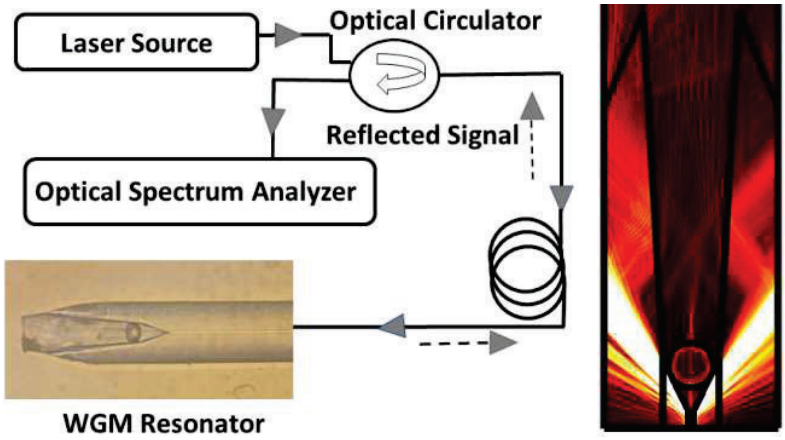

Fig 1 Schematic of WGM coupling experiment showing microscopic image of DSNA with Barium Titanate microresonator of diameter 23 µm (Left). Simulated image of DSNA with WGM microresonator (Right)

2. Result and Discussions

Light from a broadband source of wavelength 810-880nm is made to couple to an embedded Barium Titanate WGM resonator by optical circulator. The reflected signal via optical circulator is recorded in Optical Spectrum Analyzer (OSA). Barium Titanate microresonator (RI~2.0 and Density 4.25 g/cc) of diameter 23 µm is inserted inside the axicon and kept in fixed condition. The microresonator is pushed to the point where WGM characteristic peaks are observed. Fig 2 is the reflection spectrum of WGM resonator of diameter 23µm. The reflected signal indicating Q factor ~$4.5x10^3$ is achieved. The sub peaks at the Lorentzian peaks in the Fig.2 can be related to breakdown of m degeneracy due to

spheroidal shape of the resonator where m is the polar mode number of spherical resonator. It has been seen that non-sphericity introduces the mode splitting which is defined as $FSR2 = \pm FSR * \varepsilon^2/2$ where $\varepsilon = \sqrt{r_p{}^2 - r_e^2}/a$ [3]. Here, ε is eccentricity r_p and r_e are polar and equatorial radii of sphere, a is radius of sphere without distortion and FSR is Free spectral range. This expression explicitly explains that with distortion in spherical shape of microresonator, the WGM resonant wavelength shows breakdown of m degeneracy leading to different resonating wavelengths for each m value. From the geometrical parameters of resonator, we obtain $FSR2$ = 0.33 nm which is in close agreement with the experimental results obtained which can be seen in Fig 2. It has been observed that as the degree of sphericity is increased the mode splitting peaks vanish as $\varepsilon \propto {}^{1}/_{a}$

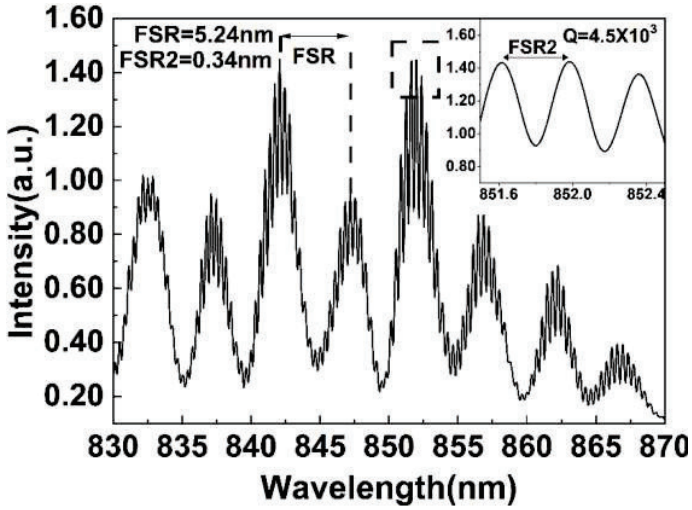

Fig 2 Reflection Spectrum of WGM resonator of diameter 23 μm.

3. Conclusions

A novel design for the excitation of Whispering Gallery resonances in microresonator is presented in this paper. The design is integrated design and doesn't require any secondary splicing element. The proposed design show Q~4.5x10^{3}and show mode splitting when the resonator is deviated from its spherical shape.

Acknowledgement

The authors gratefully acknowledge the financial support from Science and Engineering Research Board, Department of Science and Technology (SERB DST), New Delhi, under Grant CRG/2019/001215.

4. References

[1] K. Vairagi *et al.*, "Deep Seated Negative Axicon in Selective Optical Fiber Tip and Collimated Bessel Beam," *IEEE Photonics Technol. Lett.*, vol. 29, no. 10, pp. 786–789, 2017.

[2] J. Kaur, R. A. Minz, K. Vairagi, P. Gupta, and S. K. Mondal, "Excitation of Whispering Gallery Modes of a Microresonator Integrated in an Optical Fiber Axicon," *IEEE Photonics Technol. Lett.*, vol. 33, no. 24, pp. 1495–1498, 2021.

[3] H. M. Lai, P. T. Leung, P. W. Young, KBarber, and S. C. Hill, "Time- independent perturbation for leaking electromagnetic modes in open system with application to resonances in microdroplets," *Phys. Rev. A*, vol. 41, no. 9, 1990.

Laser Diode Based White Light Generation with Sunlike Full Spectrum and High CRI for General Purpose Illuminations

Dheeraj Kumar[1], Atul Kumar Dubey[2], and Dalip Singh Mehta*[1]
[1]*Green Photonics Lab, Department of Physics, IIT Delhi India, 110016*
[2]*CReST Center, Chang Gung University, Taoyuan City 33302, Taiwan*
**mehtads@physics.iitd.ac.in, dheerajastrophysics2008@gmail.com*

Abstract: A sunlike spectrum of the white light artificial source is developed for general purpose illumination by utilizing a blue laser diode (LD) (λ=447 nm, Δλ = 5 nm, and optical power (Popt.) = 600mW) and glass sheets coated using a screen-printing technique with the Ce: YAG (yellow), red and green phosphor. These phosphor-coated sheets behave as free-standing diffuser white light sources with compatible color coordinates. The experimental results are presented in form of monitoring of photoluminance spectral, and color parameters measurements.
Keywords: Laser diode, phosphor, acrylic glass, solid-state lighting, full spectrum.

1. Introduction:

Solid state lighting (SSL) currently is a highly efficient source for white light generation[1]. Since 1990, the invention of the blue light emitting diode (LED), LED-based SSL has become the most used source due to its high efficiency, long lifetime, low cost, good color rendering index (CRI), no hazardous element i.e., in mercury-based sources and fully green energy source without any greenhouse gas emissions[2–4]. There are three main methods for white light generation: (1) three color LEDs red, green, and blue (RGB) mixture (2) near ultraviolet (NUV) LED and RGB phosphors combination and, (3) a blue color LED attached with a yellow phosphor[4]. YAG: Ce, generally known as a yellow phosphor is the most common phosphor used in SSL which emits yellow light photons with a peak between (540-560nm) and under blue light excitation of the peak between (440-460 nm) known as pc-LED. Although, InGaN/GaN blue LEDs are the heart of the SSL industry, still have some constraints on their performance showing an exponential droop in efficiency under high injection current due to non-radiative transitions inside the junction region[5]. Due to the efficiency droop in LEDs, an alternative device, which can fulfil the requirement of high brightness, could be a blue laser diode (LD)[6]. The energy structure of LD is responsible for trapping the electrons and holes in junction barriers under high injection current; therefore, all the nonradiative transitions observed in LED are clamped to radiative recombination in LD. The Opto-material mechanism for white light generation in laser-driven phosphor-converted (pc-LD) sources is like pc-LED in which a blue laser diode is used to excite a down-conversion yellow phosphor for the generation of yellow photons. Further, the residual blue photons which are extracted from the phosphor layer due to scattering, combine with yellow photons to generate proper white light with the required color parameters[2]. But the spectrum of the SSL sources based on pc-LD is narrow which is not very good for white light illumination. the optimum requirement of the white light source is a full spectrum in a visible range with a high CRI value. In this paper we present Laser Diode Based White Light Generation with Sunlike Full Spectrum and High CRI for General Purpose Illumination.

2. Experimental Details:

The optical power of blue LD (λ= 447nm, Δλ = 5nm, Popt. = 600 mW) was distributed in the phosphor glass plate of size (25mm × 25mm × 1 mm), Fig.1 (a) and (f) shows the schematic representation of the proposed system. The screen-printing technique was used for developing the phosphor layer onto the glass surface. The Phosphor layer must be a uniform density of yellow phosphor 17.6 mg/cm^2 and 250 μm thick with a proper mixture of phosphor and UV adhesive prepared by mixing them in a 7:2 ratio. Similarly, $SrBaSiO_3$: Eu (515 nm- Green), and $SrAlSiN_3$: Eu (627 nm-Red) phosphor composites are coated for full spectrum. After that, the coated layer on the glass has been kept under a 405nm UV light source to dry the layer and precautionary measures have been taken during this process. The concept of an RGB-based light source in reflection mode uses to improve white light source color parameters. Fig.1. (e), and (j) shows the actual luminance of the pc-LD light source in the laboratory.

3. Results and Discussions: -

Photoluminescence spectra were recorded with the help of an LSM 6000 spectrometer to investigate the PL spectra of phosphor and UV Adhesive (7:2) matrix. We deposited different concentrations 8.8mg/cm^2, 17.6 mg/cm^2 and 26.4mg/cm^2 and optimization of phosphor concentration was monitored with the photoluminescence (PL) spectra. The optimum concentration of YAG: Ce phosphor is17.6 mg/cm^2, which shows a very high luminance with a broadband light

source emission wavelength peak at 554 nm produced without any quenching shown in Fig.1(b). The average CRI value YAG: Ce is 57 which is very low compared to the sunlight shown in Fig.1(c) and the color in CRI curves R9 (deep red), R10 (yellow), R11(green), and R12 (blue) is listed in table 1.0. Due to the absence of deep red (R9 = -93), proper white light is not generated and observed CIE 1931 color coordinates (0.4232, 0.5072) are high. The refractive index (RI) heterogeneity of medium causes scattering in the matrix layer resulting in luminance loss. LD focus on a very small area of phosphor for ultra-bright illumination, some numbers of blue photons were also transmitted from the phosphor layer due to high laser beam directionality leading to color nonuniformity and resulting in hazardous spot scattering in illumination. Therefore, we tried a reflection mode design with red and green phosphor composite to maximize luminance and utilise excessive blue photons to again interact with the phosphor, which is reflected from the metallic mirror to generate more photons, resulting broadband white light source with an optimised concentration of the composite has 85% green + 15% red phosphor in a 17.6 mg/cm^2 concentration. Still, the RI inhomogeneity causes luminance loss for a white light source. In Fig.1 (h) and (i) the CRI 88 and color coordinate (0.4054, 0.3927) respectively, shifted toward white light.

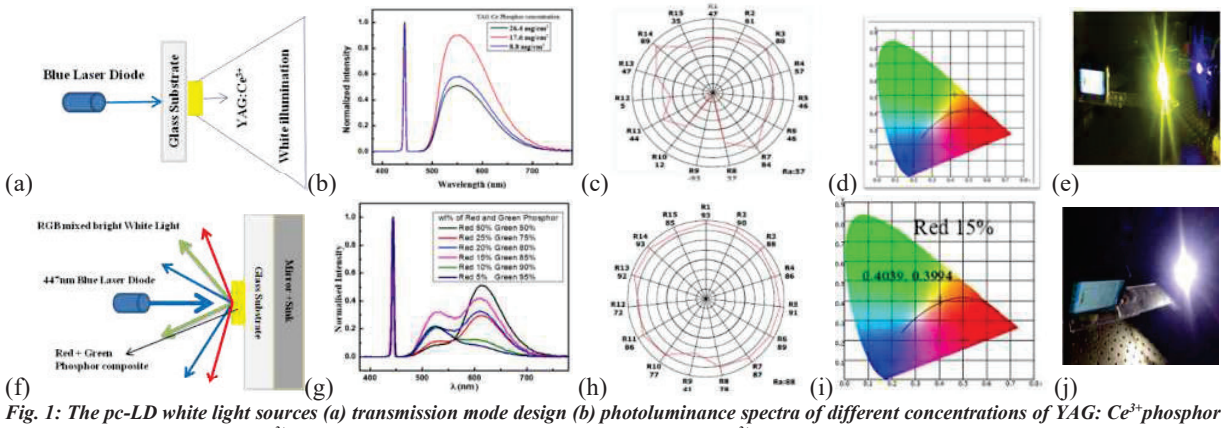

Fig. 1: The pc-LD white light sources (a) transmission mode design (b) photoluminance spectra of different concentrations of YAG: Ce^{3+}phosphor (c) CRI value chart of YAG: Ce^{3+}phosphor (d) CIE 1931 color coordinates of YAG: Ce^{3+}phosphor (e) and (j) laboratory device design setup with yellow phosphor, and 15% red-85% green phosphor composite (f) reflection mode geometry with a composite of red-green phosphor. A 15% red-85% green phosphor composite (g) photoluminance spectra (h) CRI value chart and (i) CIE 1931 color coordinates

Table: - 1.0 Comparison of color parameters, device design, and concept

Sr.No.	CRI	R9	R10	R11	R12	CIE1931 (x,y)	CCT	Device design	Concept
1.	57	-93	12	44	5	0.4232, 0.5072	3885K	Transmission	Yellow phosphor +Blue LD
2.	88	41	77	86	72	0.4054, 0.3927	3601K	Reflection	Red-green phosphor+Blue LD

4. Conclusions: -

We find an optimum concentration of Ce: YAG phosphor layer 17.6 mg/cm^2 with a thickness of 250µm. The blue laser-based pc-LD white light source with full spectrum shows broadband illumination with moderate green and deep red color components (R9 = -93). The missing color components filed with the use of multiple phosphors; therefore, the two-phosphor composite red and green considered. Composite phosphor has been developed for general illumination application using the concept of an RGB-based light source. This light source will reduce the complexity of future lighting devices. The composite phosphor light source has color coordinates (0.4039, 0.3994), with a CCT of 3601 K (cool light) and a CRI value of 88 recorded. This light source can fulfil the requirement of high CRI illumination and would be beneficial for high color quality projectors, automotive headlamps, aeroplane platform lighting, and so on.

5. References: -

[1] Khanna V K, *Fundamentals of Solid State Lighting: LEDs, OLEDs and Their Application and Displays,* vol. 33. Boca Raton FL: CRC Press.

[2] A. K. Dubey, M. Gupta, V. Kumar, V. Singh, and D. S. Mehta, "Blue laser diode-pumped Ce: YAG phosphor-coated cylindrical rod-based extended white light source with uniform illumination," *Laser Phys*, vol. 29, no. 5, p. 056203, Mar. 2019.

[3] S. Nakamura, "The invention of high efficient blue LEDs and future Solid State lighting," *Optics InfoBase Conference Papers*, p. 2020, 2014.

[4] A. K. Dubey, V. Kumar, M. Gupta, and D. S. Mehta, "Thermally stable laser-driven phosphor converted white light source using multilayer structured diffuser system," *Laser Phys Lett*, vol. 17, no. 12, Dec. 2020.

[5] A. Zabiliūtė-Karaliūnė, J. Aglinskaitė, and P. Vitta, "The reduction of the thermal quenching effect in laser-excited phosphor converters using highly thermally conductive hBN particles," *Sci Rep*, vol. 11, no. 1, pp. 1–12, 2021.

[6] J. Cho, E. F. Schubert, and J. K. Kim, "Efficiency droop in light-emitting diodes: Challenges and counter measures," *Laser and Photonics Reviews*, vol. 7, no. 3. pp. 408–421, May 2013.

Resistive heating tunable lens

Jaspal Singh*, Laxman Mandal and A R Ganesan
Applied Optics Laboratory, Department of Physics,
Indian Institute of Technology Madras, Chennai, 600036
**jassarari02@gmail.com*

Abstract: In recent years, tunable optics is on high demand. We simulate a tunable lens that can adjust the focal length without any mechanical movement and can also transform from concave to convex as the voltage is applied to the resistive heating rings. This tunable lens is polarization insensitive, broadband, and works in transmission mode. Applications of this work would be in imaging and adaptive optics.
Keywords: Tunable lens, thermal lens, PDMS polymer, wavefront, thermo optical effect.

1. Introduction

The modulation of the phase of the light is very important to transform the beam. There have been different approaches developed over time for the modulation of the phase of light. There are ways to control the wavefront of light dynamically, such as deformable mirrors and Spatial light modulators (SLM). Although they are very useful in many applications, they have some limitations on their operation. Deformable mirrors work in the reflection mode only, which limits the application in a certain domain such as endoscopic imaging. SLM is a polarization-sensitive device that modulates the phase only with certain polarized light. In recent years, there has been efforts to control the spatial phase of the light by changing optical path length. When we use conventional optics, we need mechanical movement to adjust the focal length of the lens. But with miniaturization, mechanical movement of the component is difficult. Adjusting the focal length of the optical system without mechanical movement has attracted the attention of researchers to develop methods such as electrowetting [1], strain-based tunable lens[2], thermo-pneumatic microlens[3], etc. P. Berto *et al.* [4] used resistive heating wire which can control the optical path difference depending on the voltage applied. A spiral wire grid of varying cross-sectional thickness was used to provide variation in resistance which is rather pretty difficult to fabricate and also can be used either for converging or diverging a beam. In this paper, we propose a tunable lens with a grid made of individual circular wires of constant thickness and varying diameters to provide resistive heating and can act as convex and concave by controlling the voltage in the individual wires.

2. Theory

Optical path length (δ_{opl}) is defined as the product of refractive index (n) and physical path length (L) through which the light travels.

$$\delta_{opl} = nL \tag{1}$$

$$\Delta\delta_{opl} = \left(n\frac{\partial L}{\partial T} + L\frac{\partial n}{\partial T}\right)\Delta T \tag{2}$$

$$\Delta\delta_{opl} = \delta_{opl}\left(\frac{1}{L}\frac{\partial L}{\partial T} + \frac{1}{n}\frac{\partial n}{\partial T}\right)\Delta T \tag{3}$$

$$\Delta\delta_{opl} = \delta_{opl}\left(\alpha + \frac{1}{n}\beta\right)\Delta T \tag{4}$$

where $\Delta\delta_{opl}$ is optical path difference, ΔT is change in temperature, α is the thermal expansion coefficient and β is the thermo-optical coefficient which depend on the material property. For our simulation, we have used polydimethylsiloxane (PDMS) polymer, due to its highly transparent nature in the optical frequency band and also having the property to confine heat to a certain region. The values $\alpha = 4.66 \times 10^{-4}$/ °C and $\beta = -4.5 \times 10^{-4}$/ °C for PDMS polymer available in the literature have been used [5]. We have neglected the thermal expansion as heat would be confined in a certain small region in our design.

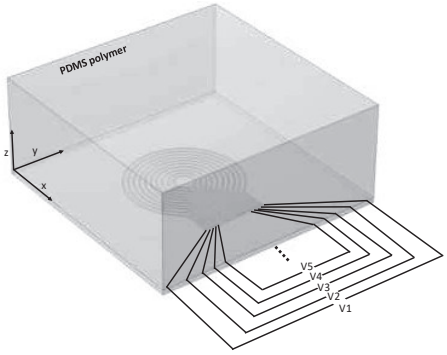

Fig. 1: Model representation of resistively heating tunable lens.

3. System design

For design simulation, we have used use 12 concentric rings of gold wire with dimensions as follows: diameter of the outer ring 20 mm, width of the wire 0.14 mm and the spacing between each wire as 0.5 mm. Each of these individual ring shaped wires have end terminals to which appropriate voltages can be applied. A 1 mm layer of PDMS polymer is deposited on the ring structure. This arrangement is stuck to a glass slab to provide strength. Figure 1 shows the design of the arrangement.

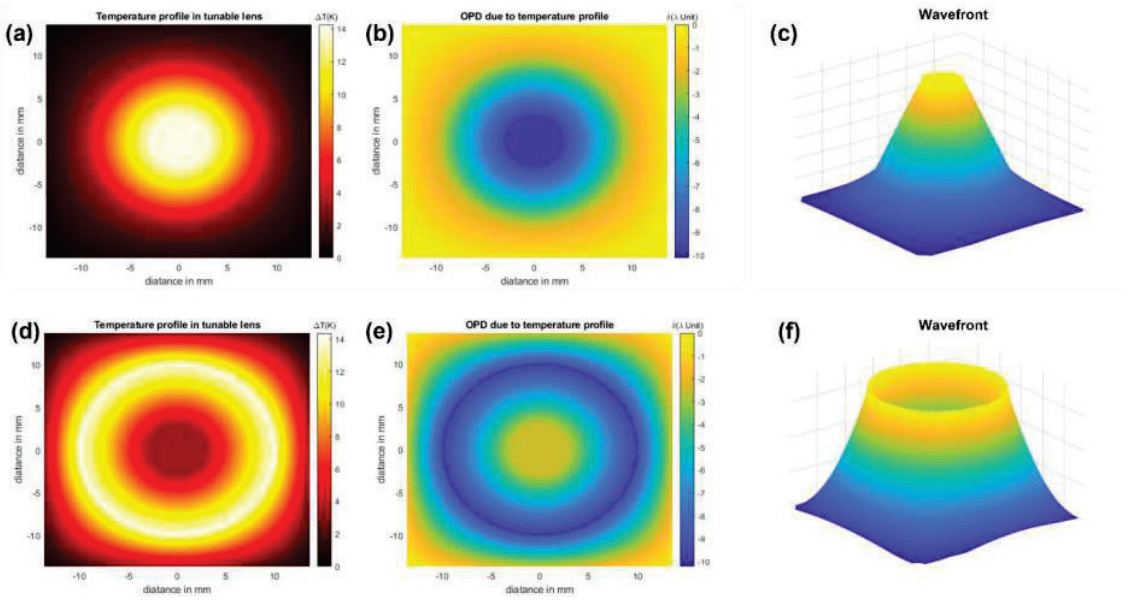

Figure 2 (a) and (d) Temperature Profile in tunable lens, (b) and (e) Optical path difference (OPD) due to temperature, (c) and (f) Wavefront.

4. Results and Discussion

We have simulated the results for an electrically tunable lens wherein we can control the voltage given to the individual rings and the corresponding temperature change to provide modification of the wavefront. An incident plane wavefront passing through the tunable lens arrangement gets converged or diverged as shown in the results presented in Fig.2. Figures 2 (a) and (d) show the temperature profile in the tunable lens, figures 2 (b) and (e) the corresponding optical path difference generated and figures 2 (c) and (f) the output wavefronts after transmission through the tunable lens. Simulation results shows the concave and convex wavefront generated from the same structure. Further work is on for the actual fabrication and testing of the simulated tunable lens and also to increase the transmission and reduce diffraction effects by using indium tin oxide (ITO) transparent conductive wires.

5. References

[1] Berge, B., Peseux, J. Variable focal lens controlled by an external voltage: An application of electrowetting. *Eur. Phys. J. E* 3, 159–163 (2000).

[2] She, Alan; Zhang, Shuyan; Shian, Samuel; Clarke, David R.; Capasso, Federico Adaptive metalenses with simultaneous electrical control of focal length, astigmatism, and shift. Science Advances, 4(2), eaap9957 (2018).

[3] Zhang, Wei & Zappe, Hans & Seifert, Andreas. Wafer-scale fabricated thermo-pneumatically tunable microlenses. Light: Science & Applications. 3. e145 (2014).

[4] Berto, P., Philippet, L., Osmond, J. *et al.* Tunable and free-form planar optics. *Nat. Photonics* 13, 649–656 (2019).

[5] Dnyandeo Pawar, Ajay Kumar, Rajesh Kanawade, Samir Mondal, and Ravindra K. Sinha, "Negative axicon tip micro-cavity with a polymer incorporated optical fiber temperature sensor," OSA Continuum 2, 2353-2361 (2019).

High resolution quantitative phase imaging using deconvolved white light phase shifting interferometry

Shubham Tiwari[1,2], Shilpa Tayal[2], Dalip Singh Mehta[1,2,*]
[1]*SeNSE, Indian institute of Technology Delhi, Hauz-Khas, New-Delhi-110016*
[2]*Bio-photonics and Green photonics laboratory, department of physics, Indian Institute of Technology Delhi, Hauz-Khas, New-Delhi-110016*
[*]*mehtads@physics.iitd.ac.in*

Abstract: We present a quantitative phase imaging method using white light phase shifting interferometry combined with a deconvolution algorithm to obtain phase map of the samples with improved resolution. The obtained phase map from the white light phase shifting interferometry can be converted to a complex image field and an iterative deconvolution algorithm with a total-variation regularizer improves the resolution. This method can prove very useful for studying various biological samples and modalities working with complex image fields. The method of improvement of spatial resolution presented in this paper is a very simple one as we do not require complicated superresolution techniques like Structure illumination microscopy(SIM).

1. Introduction

Most biological objects are optically thin transparent specimens(phase objects) and hardly scatter any light. Today histopathology involves staining them with fluorescent dyes so they can be imaged on a microscope. This poses certain limitations as dyes may alter the cell physiology and cause photobleaching, phototoxicity limiting their use in live cell imaging. Quatitative phase imaging(QPI) provides a measure of pathlength variation of light after passing through the specimen and the idea is to create a spatially resolved phase map φ(x,y) using interference with a known reference wave. [1]. The phase map can provide quantitative information related to cells and tissues, e.g. sample thickness, average refractive index, dry mass density associated with a cell(or a live cell), cell growth parameters and many statistical parameters[2].
Deconvolution is a commonly used technique used for intensity images as a post-processing tool. It inverts the process of blurring of images due to the diffraction limited point spread function(psf) of the microscope objective. Not much has been reported for deconvolution of complex image fields. In this paper we apply a Richardson-Lucy(RL) based iterative algorithm on the phase map obtained from a white light phase shifting interometer(WL-PSI) to get phase maps with improved resolution. In section 2 we provide an overview of the WL-PSI set-up. In section 3 we discuss the RL based iterative deconvolution algorithm along with some results.

2. White light phase shifting interferometry

In our lab we use a highly sensitive white light phase shifting interferometer(WL-PSI) with white light source and a Mirau objective. This offers many advantages over other modalities such as it offers speckle free measurements since it uses low coherence white light source, it has high temporal phase stability because of an on-axis nearly common path configuration, it provides phase information in multiple wavelengths. Figure 1a. shows the overall WL-PSI set-up, fig 1b. shows the working of the Mirau interferometric objective fitted with reference mirror and beam splitter. The set-up generates 5 phase shifted interferograms with the PZT producing π/2 phase shift for a wavelength of 540nm for each interferogram. The interferogram is given by the following equation[3]:

$$I_n(x,y) = I_0(x,y)[1 + V\gamma(z)\cos\{\varphi(x,y) + (n-1)\delta\}] \quad (1)$$

Where n = 1,2..5, V is the fringe contrast, γ is the coherence envelope and $\varphi(x,y,z)$ is the required phase map, δ = π/2 for λ=540nm. The 5 interferograms are solved using a 5-step phase shifting algorithm and the phase map for λ=540nm(green) is given as:

$$\varphi_i(x,y) = tan^{-1}\left[\frac{2\{I_2(x,y)-I_4(x,y)\}}{I_1(x,y)-2I_3(x,y)+I_5(x,y)}\right] \quad (2)$$

3. Result and discussion

Let U(x,y) = $|U(x,y)|e^{-\varphi(x,y)}$ be the complex image field then,

$$O(x,y) = U(x,y) \otimes h(x,y) + \eta \quad (3)$$

is the image field given by convolution of the original complex field with the system point spread function(PSF) h(x,y), η is the noise. Both magnitude and phase of the field is blurred by the PSF of the system. For thin samples we can assume the magnitude of the field to be constant and almost all information is contained in the phase. Let φ(x,y) be the initial phase obtained from WL-PSI set-up then, $I(x,y) = \exp(j\varphi(x,y))$ is the initial complex image field, the system PSF is obtained by the FIJI software providing the parameters of the microscope objective and the CCD. A total variation(TV) regularization based iterative Richardson-Lucy(RL) deconvolution algorithm[4], is applied to the initial complex image field $I(x,y)$, created using the phase map. The phase maps of 200nm beads before and after deconvolution are shown in fig.1. The figure shows the phase of the beads with improved resolution.

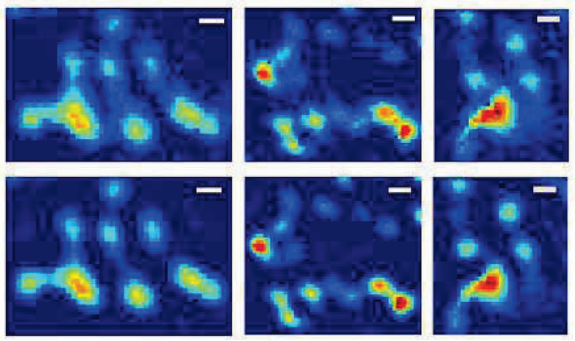

Fig.3 200nm beads before(top row) and after(bottom row) deconvolution.(Scale bar = 500nm in each case)

Thus we are able to improve the resolution of the system using deconvolution of the complex image field. This can be useful for biological samples as they are mostly phase objects.

4. References

[1] Popescu, G. Quantitative Phase Imaging of Cells and Tissues (McGraw Hill Professional, 2011).

[2] K. Lee, K. Kim, J. Jung, J. Heo, S. Cho, S. Lee, G. Chang, Y. Jo, H. Park, and Y. Park, "Quantitative phase imaging techniques for the study of cell pathophysiology: from principles to applications," Sensors 13, 4170–4191 (2013).

[3] Dalip Singh Mehta, Vishal Srivastava Quantitative phase imaging of human red blood cells using phase-shifting white light interference microscopy with colour fringe analysis Appl. Phys. Lett., 101 (20) (2012), p. 203701, 10.1063/1.4767519

[4] Dey, Nicolas, et al. "Richardson–Lucy algorithm with total variation regularization for 3D confocal microscope deconvolution." Microscopy research and technique 69.4 (2006): 260-266.

HOE based out-of-plane beam re-direction for waveguide displays

Narmada Joshi[1], Rajveer Kaur[1,2], Navreen Kaur[1], Bhargab Das[1], Raj Kumar [1,2,*],

[1]*CSIR-Central Scientific Instruments Organisation, Sector 30C, Chandigarh 160030, India*

[2]*Academy of Scientific and Innovative Research (AcSIR), Ghaziabad 201002, India*

**Corresponding author: raj.optics@csio.res.in*

Abstract: Beam re-orientation is a key technique that is required in large area waveguide displays such for head up display (HUD), head mounted display (HMD) etc. We present a ray tracing model of our optical design and propose an experimental recording geometry in which out of plane beam re-orientation is possible through holographic optical elements.

Keywords: Holographic Optical Element, Waveguide Optics, Holographic Displays, Augmented reality

1. Introduction

Holographic optical elements(HOE) are widely used because they have the capacity to make a complex system compact in design which reduces the footprint of a system [1]. HOEs are transparent and thin, thus have been employed in many instruments for developing augmented reality (AR) and see-through displays. Augmented reality is a potential display technology which can connect the real world with the data produced by computers [2]. This new generation of displays face the challenge of scaling of their physical size. In this paper, we provide an optical design simulation model as well as experimentally demonstrate out of plane beam re-orientation. The reconstructed beam changes its plane of propagation when diffracted by a suitably designed HOE. The proposed geometry may be helpful to increase the size of eye-box and the active area of display, which is critical for applications in large area displays [3].

2. Theory and working principle

The prime advantage of an HOE is that, it offers to incorporate various features in it replacing the traditional optical elements, in addition to being transparent and thin. HOE works on the basic principle of holography, where two beams interfere to record the HOE and diffraction phenomenon is used in reconstruction process. The diffraction efficiency of volume holographic grating is affected by several factors, including the angle of incidence, angle of diffraction, wavelengths of the recording & reconstruction beams, refractive index modulation, grating period. The grating period of reflection volume grating can be calculated as [4]:

$$\frac{\lambda_{rec}}{n} = 2\Delta \sin\left(\frac{\theta_{rec}}{2}\right) \tag{1}$$

λ_{rec} is wavelength of the recording beam, $\theta_{rec}$is the angle formed by two recording beams in a material with refractive index n, and Δ is the grating period of reflection volume grating.

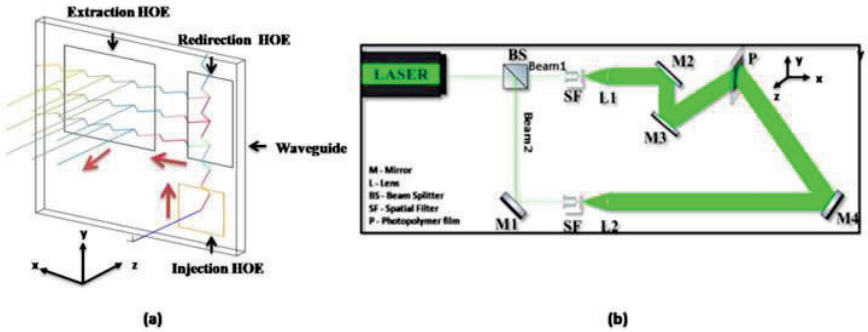

Fig. 1 (a) Isometric view of the Zemax model with each ray interaction colored differently (b) Schematic diagram of the experimental set up for the volume reflection grating

3. Computer Modeling

The model of this optical design as shown in Fig. 1(a) has been realized in Zemax Optic Studio (Student Version). The design comprises of a waveguide of dimensions 400mm×400mm×25.4mm. For injection HOE, a hologram lens is used to couple the light of 532nm wavelength inside the waveguide at an angle of 45° with respect to the surface normal, which is greater than the critical angle. It is designed to receive collimated beam from an extended source placed at 100mm and diffract it at 45° inside the waveguide to further undergo total internal reflection.

This angle is chosen to be more than critical angle (40.9°) for the BK-7 glass. The redirection HOE is placed at 20mm from the injection HOE and is designed as a reflection grating wherein the two construction beams approach from the opposite sides of the recording material. It is constructed in a way that it redirects the light towards extraction hologram which is also at 20mm distance from the redirection HOE. With each redirection, some of light is reflected and rest of it continues to undergo TIR to allow pupil expansion in one direction. The extraction HOE is made to out-couple the redirected light many times towards the observer further expanding pupil in second direction. These multiple extractions allow for the pupil to be expanded in 2-D.

4. Experimental set-up

In experimental set up as shown in Fig. 1(b), in order to demonstrate the principle of beam re-orientation, we have fabricated reflection volume holographic grating by using a green laser (532 nm, 100mW). Reflection geometry is used to record interference fringes on volume holographic gratings. Beam splitter divides the beam intensity in equal ratio. Beam 1, through the spatial filter assembly made up of a microscopic objective and pinhole gets enlarged from thin beam and further collimates through a lens, L1. The Beam1 is incident on Mirror M2 normally in x-z plane which is placed at an angle of 45º. After reflection from M2, the beam changes its path and propagate along y –axis and is incident on mirror M3. After striking in mirror M3, the beam is incident on photopolymer film at an angle of 45º with y-axis in x-y plane. The second beam, i.e., Beam 2, follows the arrangement of mirror M1, spatial filter, lens L2 and mirror M4. The beam 2 is incident from the opposite side of photopolymer film placed in x-z plane at an angle of 45^0 with x-axis as presented in Fig. 2(a). Both of the beams finally meet on the photopolymer film placed on the waveguide slab and results in the recording of the HOE.

5. Results and discussion

In the work presented here, we have successfully designed an optical ray trace model to make a design prototype and to optimize its geometrical parameters for different HOEs. But experimentally as shown in Fig. 2(b), when beam is incident in x-z plane at 45^0angles on HOE then diffracted beam is obtained in x-y plane at an angle of 45^0 with the surface normal. Similarly, when the beam is incident in x-y plane, then diffracted beam is obtained in x-z plane. Diffraction efficiency of 45% is achieved at the specified wavelength. Thus, the diffracted beam direction is rotated by an angle of 90° with respect to the plane of incidence, which is realized with volume reflection grating in the form of an HOE.

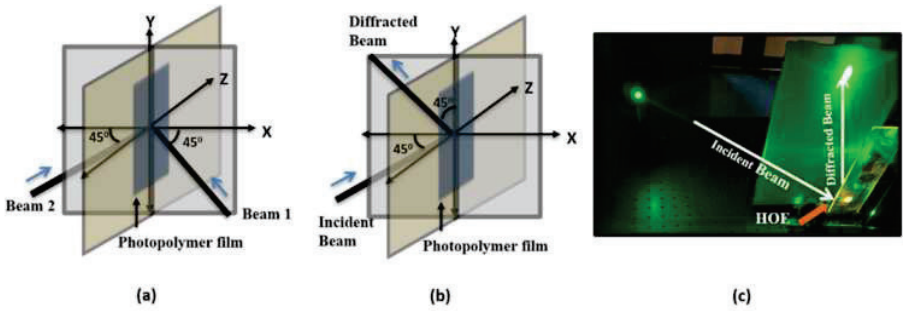

Fig.2 (a) Recording geometry, (b) Reconstruction geometry, and (c) Photograph of optical reconstruction.

Acknowledgement

Authors acknowledge CSIR, India for providing financial support under CSIR-NCP project (MLP2014) to carry out this research work. Authors like to thank Mr. Lavlesh Pensia for fruitful discussions.

6. References

[1]. D. H. Close, "Holographic optical elements," Opt. Eng. 14(5), 145408(1975).

[2]. S.Lee, B.Lee, J. Cho, C. Jang, J. Kim, and B.Lee, "Analysis and Implementation of Hologram Lenses for See-Through Head-MountedDisplay,"IEEE Photonics Technology letters 29(1), 82-85(2017).

[3]. C.T. Draper, C.M. Bigler, M.S. Mann, K. Sarma and P.A. Blanche, "Holographic waveguide head-up display with 2-D pupil expansion and longitudinal image magnification," Applied Optics 58(5), A251-A257(2019).

[4]. G. Bianco, M. A. Ferrara, F. Borbone, A. Roviello, V. Pagliarulo, S. Grilli, P. Ferraro, V. Striano, and G. Coppola, "Volume holographic gratings: fabrication and characterization,"Proc. SPIE 9508, Holography: Advances and Modern Trends IV, 950807(2015).

Calibration of Tunable wavelength Holographic Profilometer

Harikrishnan P, Athira T S, Dinesh N Naik
Applied and Adaptive optics Laboratory, Department of Physics,
Indian Institute of Space Science and Technology, Thiruvananthapuram, Kerala
Corresponding author: harikrishnanp.21@res.iist.ac.in

Abstract: The tunable wavelength laser sources provide capabilities to record multiple holograms and then reconstruct the surface profile. To implement tunable wavelength profilometry the corrections for scaling due to changes in wavelength during the recording process need to be considered and compensated, in addition, the optical elements used in the experimental setup can suffer from unknown chromatic aberrations which require a specific calibration process. We propose to record wavelength-tuned holograms of a point object and computationally obtain the correction parameters for the implementation of surface profilometry.
Keywords: Wavelength Tuning, Off axis digital holography, Fourier transform.

1. Introduction

Single wavelength laser interferometers when applied to surface profile measurement suffers from 2 π phase ambiguities [1]. To overcome this problem low coherence interferometers with coherence gating are employed. In time domain interferometers the path length needs to be scanned for mapping of the surface profile. As an alternative, the spectral domain interferometers have the capabilities to resolve the depth information from a single spectral measurement without any moving parts [2]. However, for the reconstruction of a 2-D surface profile, it requires a point or line scanning of the surface as the spectrometers can work only for a point or a line of the sample at a time. The holography provides a recording of 3D object information in a single shot. However, using a hologram recorded with a single wavelength the depth information beyond the wavelength range cannot be resolved due to the inherent 2 π phase ambiguities. The tunable wavelength laser sources provide capabilities to record multiple holograms and then reconstruct the surface profile. To implement tunable wavelength profilometry the corrections for scaling due to changes in wavelength during the recording process need to be considered and compensated, in addition, the optical elements used in the experimental setup can suffer from unknown chromatic aberrations which require a specific calibration process. We propose to record wavelength-tuned holograms of a point object and computationally obtain the correction parameters for the implementation of surface profilometry.

2. Theory and Experiment

In a normal off-axis holographic technique, the phase information of the object cannot be retrieved from the Fourier transform of the recorded holograms because of the 2π ambiguity. To retrieve object information, the hologram can be propagated. In off axis holographic technique using tunable laser, the coherence gating is possible if the interference happens at the same point for different wavelengths. Due to the chromatic aberration, the position of the focused beam in the Fourier domain changes as the wavelength changes. In order to make the position of the focusing field same for all the wavelengths, a scaling should be done. The following steps explain this.

A computational Fresnel Propagation method is applied to obtain The Fresnel propagation is given by the equation [3]

$$U(x,y) = \frac{e^{jkz}}{jkz}\; e^{j\frac{k}{2z}(x^2+y^2)} \iint_{-\infty}^{\infty} \left\{ U(\xi,п) e^{j\frac{k}{2z}\left(\xi^2+п^2\right)} \right\} e^{-j\frac{2\pi}{\lambda z}(x\xi+yп)} \mathrm{d}\,\xi\, d\,п \qquad (1)$$

Since there is a wavelength dependence for the Fourier transform kernel with each wavelength, the focus occurs at different coordinates, so scaling is done for each hologram with respect to the mean wavelength in order to do a correction in the focusing position. The scaling factor is given by $\alpha = \frac{\lambda_{(i)}}{\lambda_{mean}}$ (2) . To preserve the position of the focused field in the Fourier plane, scaling and padding techniques has to be done. The scaling and technique of padding is applied in the recorded holograms obtained from the experimental setup shown in figure 1(a). The light from the tunable laser diode is expanded using microscopic objective. The beam splitter splits the beam into reference and object beam. Using the lenses L1 and L2, the beams are focused at a particular z plane. They interfere

at the camera plane. The laser is tuned for different wavelengths from $895nm$ to $925nm$ in steps of $0.25nm$. The figures 1(b)-(d) shows holograms recorded at wavelengths $895nm, 910nm$ and $925nm$.

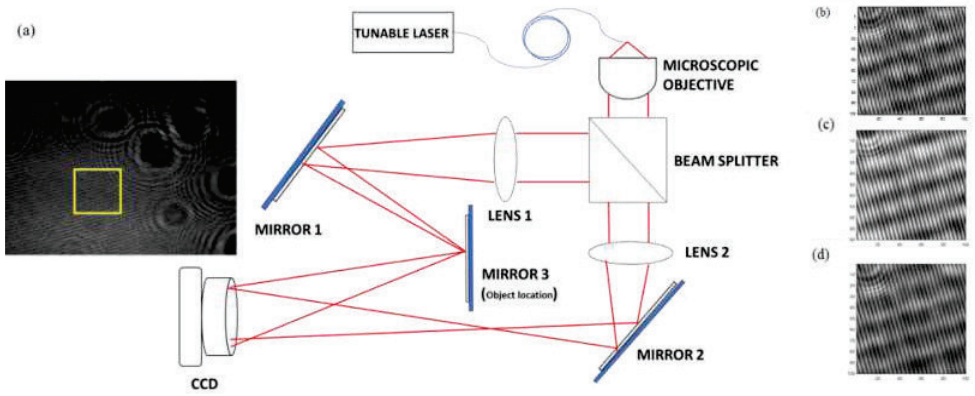

Figure 1(a) Schematic setup for wavelength calibration (b)-(d) Recorded holograms at different wavelengths 895nm,910nm,925nm

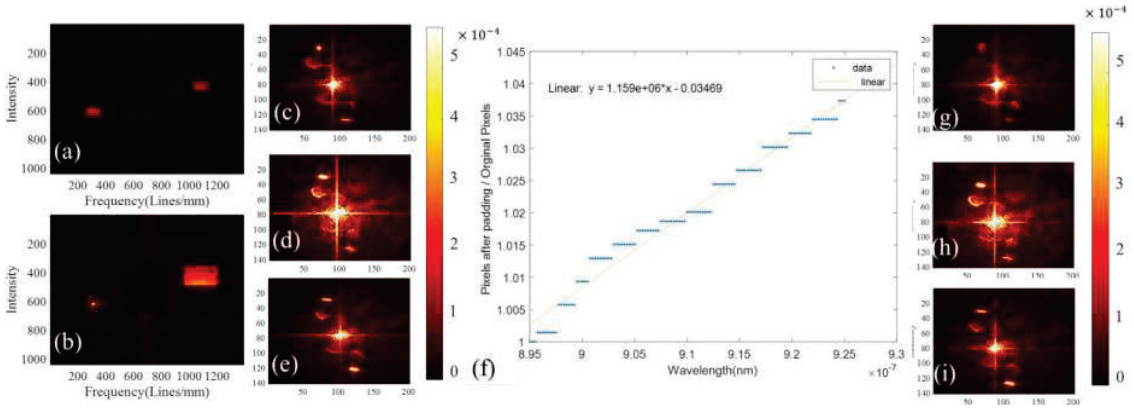

Figure 2 (a) holograms before propagation (b) after propagation (c)-(e) focusing of fields (d) The graph showing ratio of pixels after padding to original pixels to wavelength(g)-(h) focusing of fields after padding

Figure 2(a) and 2(b) shows before holograms before and after propagation.Figure (c)-(d) focussing of the fields at different pixels during wavelength tuning. Figure 2(f) shows the nonlinearity in the scaling due to achromatic behaviour. Figure 2(g)-(i) shows the focusing after padding at 895 nm,910nm and 925nm. It is also observed that there is a nonlinear relation between the wavelength and padding parameters. This could be potentially due to the aberrations present in the optical components.

3. Conclusions

Using the off axis holography setup with tunable laser as the source, the corrections for scaling due to changes in wavelength during the recording process is resolved. This way the effect of wavelength dependence of the components in an experimental setup on the recorded holograms can be avoided. Hence off axis holography with tunable laser source can have potential applications in surface profile measurement.

4. Acknowledgement

Harikrishnan P acknowledges Council of scientific and industrial India for the research fellowship.

5. Reference

[1] Etienne Cuche, Pierre Marquet, and Christian Depeursinge, "Simultaneous amplitude-contrast and quantitative phase-contrast microscopy by numerical reconstruction of Fresnel off-axis holograms," Appl. Opt. 38, 6994-7001 (1999)

[2] F. Lexer, C. K. Hitzenberger, A. F. Fercher, and M. Kulhavy, "Wavelength-tuning interferometry of intraocular distances," Appl. Opt. 36, 6548-6553 (1997)

[3] Goodman, Joseph W. *Introduction to Fourier Optics. Goodman*. McGraw-Hill, (1968).

Effect of recording angle of volume holographic gratings for Bragg degenerate diffraction in waveguide based AR/VR displays

Rajveer Kaur[1,2], Raj Kumar[1,2]*

[1]*CSIR-Central Scientific Instruments Organisation, Sector 30C, Chandigarh 160030, India*

[2]*Academy of Scientific and Innovative Research (AcSIR), Ghaziabad 201002, India*

**Corresponding author: raj.optics@csio.res.in*

Abstract: We propose a recording geometry using the Bragg degenerate case for normal incidence of reconstruction beam. We derived a relation for the angles of incidence of recording beams used in recording geometry with the propagation angle in the waveguide. The theoretical analysis is also validated experimentally.

Keywords: Volume holographic grating, Bragg degenerate diffraction, holographic waveguide, AR/VR displays

1. Introduction

Near-eye displays (NED) are the most widely used type of augmented reality (AR) and virtual reality (VR) display technologies because of their portable design and immersive effect. NED devices are beneficial for providing the visual instructions during manual tasks in the fields of education, construction, healthcare etc. [1,2]. The waveguide technology with volume holographic gratings (VHGs) results in compact form factor and less weight of eye wear waveguide display system. In holographic waveguide display, the light beam is incident on the in-coupler VHG and propagates through the glass substrate via total internal reflection. The out-coupler VHG redirects this propagating beam to couple it out from the waveguide to free space. The recording angle in the medium must meet the total internal reflection (TIR) criteria in order to trap the light beam in the waveguide. To acquire a recording angle in the medium greater than the critical angle, the large angle in the air between the two beams is required. This geometry is not practically feasible in transmission geometry without using any optical component such as prism. The performance of the entire system can be significantly impacted by the diffraction efficiency of these VHGs. By using the phenomena of Bragg selectivity, good diffraction efficiency can be achieved in Bragg degenerate case [3]. In this paper, we present a method to generate a highly efficient holographic waveguide using transmission VHGs. The experimental results demonstrate that Bragg degenerate beam is successfully coupled in waveguide and yields strong diffraction at normal incidence.

2. Theory and Methodology

According to Bragg selectivity, when reconstruction beam is exactly matched with recording beam, the maximum diffraction efficiency is obtained. In Bragg degenerate case, angular wavelength compensation is carried out in order to achieve the high diffraction efficiency. The Bragg degenerate condition is represented as [4]:

$$\left|\vec{k}_r - \vec{k}_o\right| = \left|\vec{k}_i - \vec{k}_d\right| \tag{1}$$

Where $\vec{k}_r$ and $\vec{k}_o$ are propagation vectors of reference and object beams respectively, $\vec{k}_i$ and $\vec{k}_d$ are propagation vectors of incident and diffracted beams respectively.

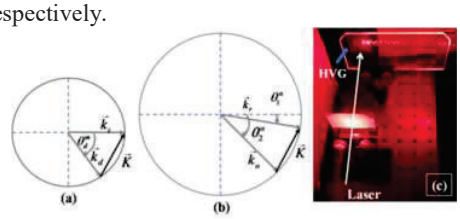

Fig.1. Ewald's sphere for(a) reconstruction geometry, (b) recording geometry, (c) Photograph of light beam trapped in glass waveguide for normal incidence

To get a large diffraction angle during the reconstruction process at a longer wavelength, the grating should be recorded with a shorter wavelength [5]. For a fixed recording and reconstruction wavelengths with desired propagation angle, the angles of incidence of both beams can be calculated as follows:

$$\theta_1^a = a\sin(n \times \sin((\theta_p^m - \theta_r^m)/2)) \qquad \theta_2^a = a\sin(n \times \sin(\theta_p^m + (\theta_p^m - \theta_r^m)/2)) \qquad (2)$$

Where θ_1^a and θ_2^a are angles of incidence of reference and object beam (measured in the air) respectively, n is refractive index of photopolymer film, θ_r^m is recording angle between two beams in the medium, θ_p^m is propagation angle. We designed our experiment to obtain diffraction angle large than critical angle. The geometries of recording and reconstruction of VHG are shown in fig.1 by using Ewald's sphere. To achieve the normal incidence of the reconstruction beam and Bragg degenerate diffraction simultaneously, the reference beam in recording geometry must impinges with a specified angle.

3. Experimental set-up

In the experimental set-up, shown in fig.2.(a), the angles of two recording beams with respect to normal of the glass plate used to fabricate the VHG are θ_1^a and θ_2^a, where 1 and 2 denotes reference beam and object beam respectively. The upper indices "a" is related to air. Two VHGs are recorded by using two collimated beams enclosing an angle of 69.98^0 in the air with a 532 nm wavelength laser. We designed a transmission geometry to guide the red light (660 nm) with normal incidence and propagate with 45^0 angles. To record a grating with these parameters the angles of beam1 and beam2 should be 6.8^0 and 76.7^0 (measured in the air) with respect to normal of the glass substrate.

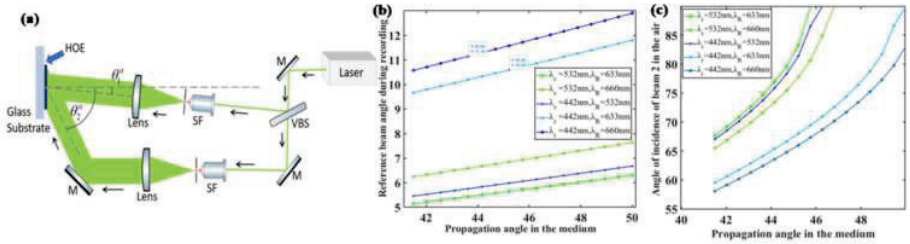

Fig.2. (a) Schematic diagram of experimental set-up, (b) variation in angle of incidence(in the air) of beam1with the propagation angle (measured in the medium), and (c) variation in angle of incidence of beam2 with the propagation angle; λ_r and λ_R are recording and reconstruction wavelengths respectively

4. Results and Discussions

The relationship between the propagation angle and the angle of incidence (Equation (2)) for both beams has been analytically calculated and obtained numerical values are shown in the plot in fig.2(b) and fig.2 (c). We experimentally demonstrated that the reconstruction beam is incident normally at 660 nm wavelength. Further, this beam propagates with 45^0 propagation angle to guide the light beam in waveguide as shown in fig.1(c). The experimental results show that Bragg degenerate beam is successfully coupled in waveguide and yields strong diffraction at normal incidence.

5. Conclusion

In this work, different recording angles are analyzed to trap the light inside the waveguide. The proposed recording geometry is analyzed theoretically and experimentally. It is an effective method for normal incidence of reconstruction beam to achieve the degenerate diffraction. The experimental findings demonstrate the successful coupling of a Bragg degenerate beam in a waveguide, which results good diffraction at normal incidence and thus may be used for AR/VR display applications.

Acknowledgement

Authors thank Mr Lavlesh Pensia and Dr Bhargab Das for fruitful discussions.
Funding: CSIR, India (Project: MLP2014 & Fellowship:31/0031(12955) /2022-EMR-I

6. References

[1] Z. He, X. Sui, G. Jin, and L. Cao, "Progress in virtual reality and augmented reality based on holographic display,"Appl Opt **58**, A74–A81 (2019).
[2] S. Choi, K. Jung, and S. D Noh,"Virtual reality applications in manufacturingindustries: past research, present findings, and future directions,"ConcurrentEng**23**, 40–63 (2015).
[3] A. Sinha, W. Sun, T. Shih, and G. Barbastathis, "Volume holographic imaging in transmission geometry," Appl Opt**43**, 1533-1551 (2004).
[4] H. Kogelnik, "Coupled wave theory for thick hologram grating," Bell Labs Tech J**48**, 2909–2947 (1969).
[5] R. Kaur, L. Pensia, O. Singh, B. Das and R. Kumar, "Study of wavelength dependency on diffraction efficiency of volume holographic gratings based couplers in waveguide displays", in Imaging and Applied Optics Congress, (Optica Publishing Group,2022), Paper JW2A.47

Characterization of a Fiber-Pigtailed MgO:ppLN Ridge Waveguide through Type II Second Harmonic Generation

Akanksha Angural,[1,#] Ramesh Kumar[1,2] and Joyee Ghosh[1,*]
Quantum Photonics Lab, Department of Physics, Indian Institute of Technology Delhi, New Delhi 110016, India
Bhaskaracharya College Of Applied Sciences, University of Delhi, New Delhi 110016, India
[#]akanksha.angural@physics.iitd.ac.in, [*]joyee@physics.iitd.ac.in

Abstract: We have characterized a fiber-pigtailed, MgO doped periodically poled lithium niobate (MgO:ppLN) ridge waveguide, type II phase-matched for an efficient second harmonic generation at 1560nm with a conversion efficiency of ~1.41%/W. The spectral variation of frequency-doubled beam power is experimentally analyzed by scanning the pump wavelength at a fixed phase matching temperature ~40˚C. The temperature tuning coefficient is also experimentally verified by scanning the phase matching temperature corresponding to the pump wavelengths. Such compact, fiber-pigtailed, type-II quasi-phase-matched MgO:ppLN ridge waveguides can be useful as photon pair sources in various applications of quantum technologies.
Keywords: Nonlinear optics, Second order nonlinearities, Quasi-phase matching, ppLN ridge waveguide

1. Introduction

Compact nonlinear optical sources are in demand for implementing nonlinear photonic circuits for commercial applications in the field of quantum technology [1]. An important application of such fiber-pigtailed sources is prominently seen for entangled photon pair generation. However, any such source is always characterized by using it in a second harmonic generation (SHG) setup as it helps us to understand the working dynamics of the source i.e., to study its behavior with respect to change in temperature or change in frequency, verifying the operating phase matching temperature etc. Lithium niobate (LN) is one of the popular $\chi^{(2)}$ materials with outstanding nonlinear optical properties (nonlinear coefficient d_{31}=4.85 pm/V for type II interaction) and a broad transparency range (0.4μm -5μm); thus, it is widely employed for frequency doubling and its reverse process-spontaneous parametric down-conversion (SPDC) in popularly used telecom band. The SHG process fulfils the conservation of energy and momentum conditions [2] and can be demonstrated in either a waveguide or a bulk crystal made of $\chi^{(2)}$ materials. The use of a waveguide over a bulk crystal offers several advantages, including strong confinement of waves leading to a generation of SHG beams in well-defined spatial modes, enhancing the degree of nonlinear interaction and hence its efficiency. These well-defined spatial modes can be efficiently coupled to single-mode optical fibers, thus aiding in compactifying such systems through fiber-pigtailing as fiber-coupling offers portability in terms of a plug-and-play device, avoiding alignment issues of a free-space optical system. In this paper, we have studied a LN ridge waveguide in which the core/ channel is doped with magnesium oxide to enhance its properties, thus making it optical damage resistant and photorefractive resistant. The ferroelectric property of LN is exploited for periodically poling the structure to quasi-phase match (QPM) the waveguide for a type II interaction (1560nm (o) +1560nm (e)→780nm (o)). The SHG signal power can be calculated using the following equation [2]:

$$P_2(L) = \frac{2\mu_o \omega^2 d_{31}^2 P_1^2 L^2}{c n_1 n_2 n_3 S} sinc^2\left(\frac{\Delta k L}{2}\right). \quad (1)$$

where n_1, n_2 are the effective refractive indices of the pump beam (o-wave, e-wave), n_3 is the effective refractive index of the output SHG beam, L is the length of the waveguide, and S is the effective mode area of the overlapping modes of the waveguide. The phase matching condition involving the phase mismatch Δk, pump propagation vectors $K_{p(o)}$, $K_{p(e)}$, signal propagation vector K_s and poling period Λ of the waveguide is given by [2]:

$$\Delta k = K_s - K_{p(o)} - K_{p(e)} - 2\pi/\Lambda \quad (2)$$

2. Experimental Setup

We have shown the schematic of the experimental setup in Fig. 1 used for frequency-doubling of 1560nm light in the fiber-pigtailed waveguide. The inset of Fig. 1 depicts a schematic of the waveguide cross-section with D=3μm, H= 5μm and W= 7.3μm as the waveguide dimensions. We used a continuous wave (CW) laser at a central wavelength of 1560nm with a power of ~15mW for pumping the 1.69 cm long ridge waveguide. Due to the type II phase matching in the waveguide (poling period ~8.9μm), a suitable polarization of the pump beam with respect to the principle axes of the waveguide is essential for efficient frequency doubling. The input coupling efficiency is ~61%, and the output coupling efficiency of the device is ~73%. The output beam is processed by employing a free-space setup comprising a fiber collimator and a dichroic mirror which transmits the remaining pump signal and reflects the SHG beam. The latter is investigated by pump wavelength tuning and measured by using a power meter at a fixed phase

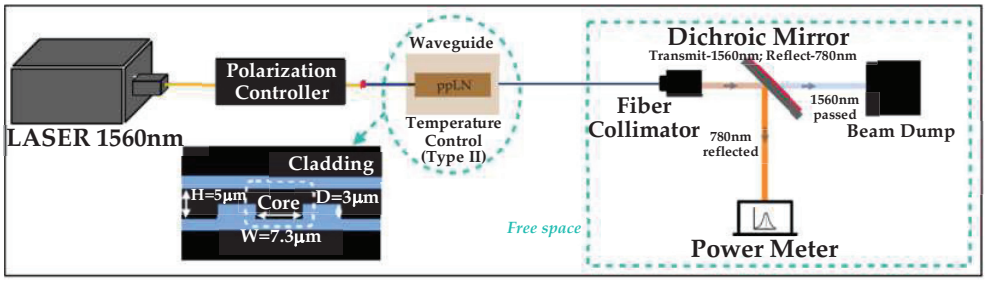

Fig. 1: Experimental setup for second harmonic generation at 1560nm pump wavelength.

matching temperature observed to be ~40˚C. A maximum SHG power of 3.43μW at 780nm is measured with an overall conversion efficiency of 1.41%/W.

3. Results

Fig. 2(a) shows the theoretical expectation (blue solid line) and experimental observation (orange dashed line with circles) of normalized SHG power with respect to the pump wavelength at the phase matching temperature ~40˚C. To characterize the waveguide theoretically, effective indices of the pump (o-wave and e-wave) are first simulated using the finite element method (FEM) in COMSOL software. A spectral broadening and non-uniform side peaks are observed in experimental SHG data and are manifested as a result of the effective index variation caused by inhomogeneous doping in the core and/or variation in the channel width along the length of the waveguide [3]. For this, we theoretically analyzed the bandwidth of the SHG beam by scaling the $sinc^2$ function (Eqn. (1)) with a suitable factor, such that the variation in effective indices and poling period is incorporated. The experimentally observed bandwidth of the beam is 0.6nm (FWHM). Fig. 2(b) shows the experimentally observed phase matching temperatures by tuning the pump wavelength. The experimentally observed temperature tuning coefficient of the waveguide is ~ −6.6˚C/nm. Fig. 2 also depicts that the waveguide is suitable for the narrowband operation in the telecom wavelengths (~1558nm to ~1562nm) for the temperature range 30˚C-50˚C.

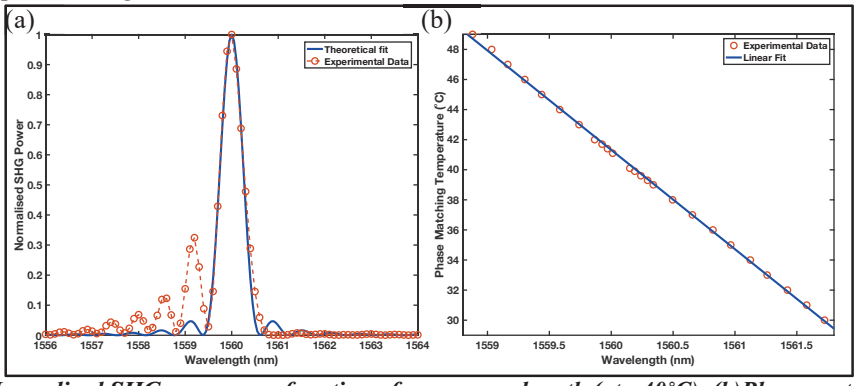

Fig. 2: (a) Normalized SHG power as a function of pump wavelength (at ~40˚C), (b)Phase-matching temperature corresponding to different pump wavelengths.

4. Conclusion

We have studied the SHG process in a compact type II quasi-phase-matched, fiber-pigtailed, MgO:ppLN ridge waveguide with a nonlinear conversion efficiency of 1.41%/W. Based on this characterization, we conclude that the behaviour of the SHG beam can be predicted by either fixing the phase matching temperature and sweeping the pump wavelength or vice versa. The shape of the SHG beam can be directly correlated to the behaviour that is displayed by generated single photons if this device is used for SPDC. Hence, such waveguide sources are promising for applications which require compact fiber- integrated modules for SHG and SPDC processes.

The authors acknowledge the Department of Science Technology, India, for the project research grant (DST/ICPS/QuST/Theme-1/2019/Q-62).

5. References

[1] Vergyris, P., Kaiser, F., Gouzien, E., Sauder, G., Lunghi, T., & Tanzilli, S. “Fully guided-wave photon pair source for quantum applications,” Quantum Science and Technology, 2(2), 024007 (2017).

[2] Robert W Boyd. Nonlinear optics. 2nd ed. Academic press, 2020.

[3] Lewis G. Carpenter, Sam A. Berry, Rex H. S. Bannerman, Alan C. Gray, and Corin B. E. Gawith, "ZnO indiffused MgO:PPLN ridge waveguides," Opt. Express 27, 24538-24544 (2019).

Modified Michelson Interferometer for tilt angle measurement with increased sensitivity

Laxman Mandal*, Jaspal Singh and A R Ganesan
Applied Optics Laboratory, Department of Physics,
Indian Institute of Technology Madras,
Chennai,600036, India.
**laxman1995mandal@gmail.com*

Abstract: Tilt monitoring is often a challenging task at nano radian scale in many engineering applications. Autocollimators and some interferometric methods with gear system have their own limitations with regard to their accuracy. A new modified Michelson Interferometer has been developed for tilt angle measurement which gives double sensitivity than the conventional Michelson Interferometer. This new kind of configuration is suitable to measure nano radian tilt angle with high accuracy.
Keywords: Michelson interferometer, Autocollimator, angle amplification, Interferometer, tilt angle measurement.

1. Introduction

Interferometry is a very sensitive optical technique for measurement. Michelson Interferometer is widly used to measure change in length and tilt angle. Marco Pisani introduced multiple reflections in one arm of the interferometer using wedge shaped mirrors arrangement to measure picometer resolution so that one can also measure tilt angle with the same setup [1]. The problem is that this setup will not give the symmetric change in fringe width due to change in tilt angle. Youn introduced multiple reflections in both arms of Michelson Interferometer using a gear system and wedge shaped mirrors arrangement in which when one mirror is tilted by nano drive, due to gear system both beams will deflect [2]. However the limitation of this gear system is that we cannot give nano scale tilts. Autocollimators are used for the long term monitoring of angles [3]. Autocollimator is a non interferometric technique in which only one beam of light is used and reflected by a plane mirror and record the position of the beam by a CCD array detector. The tilt is given to the mirror and the deflection of the beam is measured. Again, this method is not suitable for measurement of very small tilts. Pretheesh *et al.* used a multiple reflection cyclic interferometer for amplifying the tilt [4].

In this paper, we propose a modified Michelson Interferometer for tilt angle measurement which gives double the sensitivity of normal Michelson Interferometer. The system has a perfect symmetry and accuracy in the tilt introduced in both arms of the interferometer.

2. Tilt measurement using a modified Michelson Interferometer.

Figure 1 shows the schematic of the modified Michelson interferometer set up for tilt measurement. The collimated laser beam is split into two beams by the beam splitter (BS) and reflected by mirrors M1 and M2. These two beams are reflected by a right angled prism (P) in which the sides containing the right angle are reflection coated as shown in the figure 1. The prism is mounted on a precision tilt stage controlled by a nanodrive. The reflected beams interfere on the CCD to produce the fringe pattern. When a tilt is applied to the prism P by PZT tilt stage then both the beams will deflect in opposite directions and produce straight line fringes. The relation between tilt angle (α) and fringe width (d) is given by

$$\alpha = \tan^{-1}\frac{\lambda}{2*d} \qquad (1)$$

where λ is the wavelength of laser light. For zero tilt, the fringe width is infinity and we cannot distinguish between a fringe of infinite width and a fringe of width greater than the beam size. Hence it is practically impossible to set the initial tilt as zero. For this reason, we initially keep a tilt so as to get a few fringes and calculate the tilt α_1 from the obtained fringe width d_1. Now a tilt $\Delta\alpha$ is given to the prism, and the new fringe width d_2 is calculated.
The given tilt $\Delta\alpha$ is calculated as

$$\Delta\alpha = \alpha_2 - \alpha_1 \qquad (2)$$

$$\Delta\alpha = \tan^{-1}\frac{\lambda}{2*d_2} - \tan^{-1}\frac{\lambda}{2*d_1} \qquad (3)$$

where d_1 and d_2 are the initial and final fringe widths, α_1 and α_2 are the initial and final tilt angles calculated from fringe pattern.

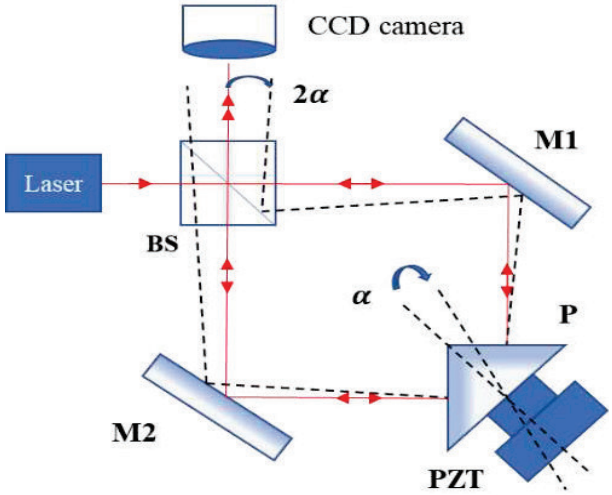

Figure 1. Schematic diagram of experimental set up of modified Michelson Interferometer for tilt measurement.

3. Results

Figure 2 shows the plot of the incremental tilt $\Delta\alpha$ given and the experimentally measured tilt for a standard Michelson and the modified Michelson interferometers. As can be seen from the graph, the modified Michelson Interferometer gives double the sensitivity compared to conventional Michelson Interferometer.

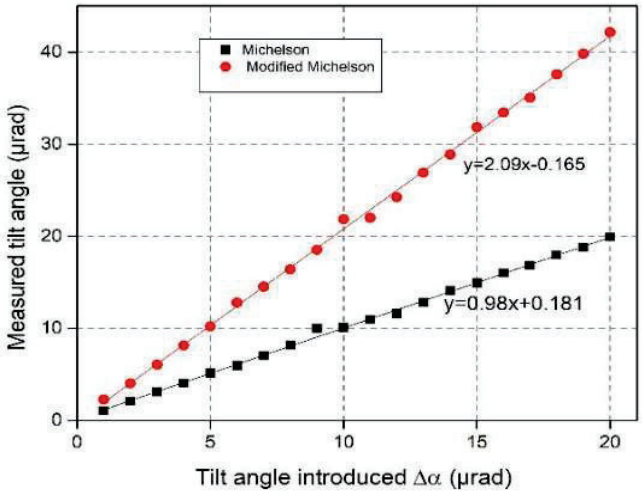

Figure 2. Plot of the measured tilt against the given tilt for both Michelson and Modified Michelson interferometer.

The advantage of the setup is that both the beams are tilted in opposite directions exactly by the same amount when compared to the earlier methods of rotating two individual mirrors with gears apart from simplicity of the present setup.

4. References

[1] Pisani, Marco. "Multiple reflection Michelson interferometer with picometer resolution." Optics Express 16 (26), 21558-21563 (2008).

[2] Youn, Woonghee. Increasing the Sensitivity of the Michelson Interferometer through Multiple Reflection. Rose Hulman Institute of Technology, 2015.

[3] R. D. Geckeler, A. Just, M. Krause, and V. V. Yashchuk, “Autocollimators for deflectometry: Current status and future progress,” Nucl. Instruments Methods Phys. Res. Sect. A Accel. Spectrometers, Detect. Assoc. Equip., vol. 616 (2–3), 140–146, 2010.

[4] Valiyaparambil Chacko Pretheesh, Charles Joenathan, Angarai Ganesan, and Umapathy Somasundram, "Increasing the sensitivity for tilt measurement using a cyclic interferometer with multiple reflections", Optical Engineering 55 (8), 084103 (2016).

Plasmonic Nanoparticles Coated U- bent Polymeric Fiber Optics Sensors

Ratan Kumar Chaudhary[1], Krishna Swain[1], Narayanan Madaboosi[2], V. V. R. Sai[1]*

[1]Department of Applied Mechanics, Indian Institute of Technology Madras, Chennai, India- 600036

[2] Department of Biotechnology, Indian Institute of Technology Madras, Chennai, India- 600036

vvrsai@iitm.ac.in

Abstract: Polymethyl methacrylate (PMMA) based polymeric optical fiber (POF) has gained considerable attention due to its robustness, cost-effectiveness, ease of handling, optical coupling, and machinability in comparison to silica optic fiber. This study shows the development of a highly sensitive localized surface plasmon resonance (LSPR) based fiber optic sensor probe by a facile one-step technique for the coating of gold nanoparticles layer on a PMMA surface without any surface modification. LSPR probes show~ 5.3 - fold improvement in refractive index sensitivity as compared to bare U- bent POF probes.

Keywords: U-bent polymeric optical fiber, gold nanoparticles, refractive index sensitivity, evanescent wave absorbance

1. Introduction

Plasmonic sensors that demonstrate the measurement of small refractive index changes have various applications in chemical, food processing, automobile drug discovery, clinical diagnosis, and environmental monitoring fields. Optical fiber-based plasmonic sensors are preferred for many applications due to their compactness, remote and real-time monitoring, and multiplexing [1]-[3]. In addition, an efficient evanescent wave (EW) based excitation of the plasmonic nanostructures on the fiber allows monitoring of their spectral properties using the light passing through the fiber and the changes in the refractive index (RI) in their microenvironment.

In recent years, polymeric optical fiber (POF) has gained considerable importance due to its ease in handling and machinability, and low cost [4] in comparison to silica fiber. In particular, U-bent POF sensor probes are known for the enhanced evanescent fields and depth of penetration [5]. They also offer several advantages, mainly ease in fabrication, robustness, compactness, low sample volume, and ergonomic design for dip-type sensing. Reports on the development of LSPR-based U-bent POF sensors involved PMMA core surface hydroxylation and amine functionalization in order to decorate the U-bent region with AuNP. In addition, the POF probes are also plagued by surface functionalization issues, which is evident from the poor bio-assay response [6].

In this work, we present a facile technique to adsorb AuNP on the decladded POF surface without any surface modification to develop the LSPR sensor probes. The stability and RI sensitivity of the AuNP-coated U-bent POF probes was evaluated.

2. Experimental Methods

2.1. Fabrication of U- bent POF probes

A 21 cm long POF (SK20, 0.5 mm diameter, Mitsubishi Rayon Ltd, Japan) was cut, bent in the middle, and then inserted into the glass capillary. The glass capillary was kept in the oven at 100 °C for 10 min. After that, the U-bent region of the POF probe was decladded by dipping in ethyl acetate followed by cleaning of the probes using isopropanol and lint-free tissue paper, sonication in DI water, and 10% ethanol twice each for 5 min.

2.2. AuNP coating on the POF probe

The clean decladded U- bent probe was incubated in AuNP (~ 40 nm size) to obtain LSPR sensor probes. AuNP binding to the fiber probe was monitored in real-time by means of evanescent wave-based absorption spectral response using the optical setup shown in Figure 1, using a halogen lamp (HL 2000) and spectrometer (USB 4000 XR1 ES, Ocean Optics) observed a red shift in peak. This occurs due to plasmonic coupling between AuNP bound to the fiber

probe surface. AuNP were bound to probe surfaces up to ~1.3 absorbance units. While the peak absorbance of AuNP was observed at 530 nm initially, it has red-shifted by 10 nm by the end of deposition; peak wavelength red-shifted to ~540 nm on bare probes as shown in figure 2. (a) and AuNP binding kinetics inserted in figure 2 (a). Then probes were washed with DI water to remove the loosely bound AuNP and incubated in a hot air oven at 55 °C for 30 min condensation and probes were used to realize refractive index sensitivity.

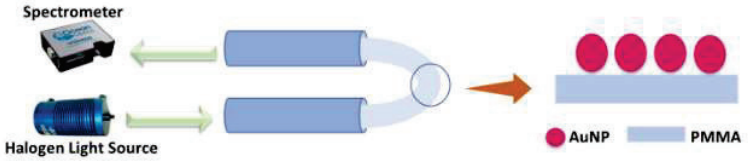

Figure 1. Schematic representation of optical setup and AuNP binding

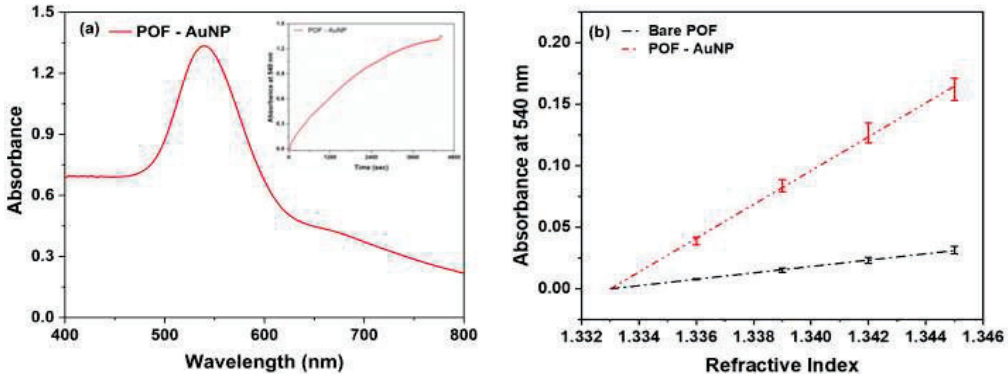

Figure 2. (a) Absorbance spectrum obtained from the AuNP binding with POF probes and (inset) Temporal response showing AuNP binding kinetics on the POF probes. (b) A linear fit of the absorbance obtained for the bare, AuNP coated on the bare U- bent POF probes sensitivity is 2.59 and 13.73 respectively

2.3. RI sensitivity of U- bent plasmonic sensor probes

The RI sensitivity was evaluated by dipping the LSPR probe sequentially in increasing sucrose solution concentrations ranging from 1.333 to 1.345 in steps of 3 milli RIU. The RI sensitivity of bare and LSPR probes are 2.59 ($\Delta A_{540\ nm}/\Delta$RIU) and 13.71 ($\Delta A_{540\ nm}/\Delta$RIU) respectively. LSPR probes show approximately 5.3- fold improvement in absorbance response as compared to the probes without AuNP as shown in Fig 3.

2.4. Conclusion

In this work, we have presented a simple, inexpensive method to fabricate the AuNP-coated U- bent LSPR POF probe for RI sensing. RI sensitivity of AuNP-coated U-bent POF probes was found to be 13.71 $\Delta A_{540\ nm}/\Delta$RIU. Further experiments are in progress to improve the RI sensitivity for biosensing applications.

3. References

[1] M. Mitsushio, K. Miyashita, and M. Higo, "Sensor properties and surface characterization of the metal-deposited SPR optical fiber sensors with Au, Ag, Cu, and Al," *Sensors and Actuators, A: Physical*, 125, 296–303 (2006).
[2] P. Nath, "Non-intrusive refractometer sensor," *Pramana - Journal of Physics*, 74, 661–668 (2010).
[3] A. Gowri and V. V. R. Sai, "Development of LSPR based U-bent plastic optical fiber sensors," *Sensors and Actuators, B: Chemical*, 230, 536–543 (2016).
[4] C. Christina, A. Subrahmanyam, and V. V. R. Sai. "Gold sputtered U-bent plastic optical fiber probes as SPR-and LSPR- based compact plasmonic sensors." Plasmonics 13, 493-502 (2018).
[5] V. V. R. Sai, T. Kundu, and S. Mukherji, "Novel U-bent fiber optic probe for localized surface plasmon resonance - based biosensor," Biosensors and Bioelectronics, 24, 2804–2809 (2009).
[6] Divagar, M., Gayathri, R., Rasool, R., Shamlee, J. K., Bhatia, H., Satija, J., & Sai, V. V. R., "Plasmonic Fiberoptic Absorbance Biosensor (P-FAB) for Rapid Detection of SARS-CoV-2 Nucleocapsid Protein", IEEE sensors journal, 21, 22758-22766, (2021).

Unidirectional Coupling of Single Photon in Optical Nanofiber with Inline Cavity

Subrat Sahu, and Rajan Jha*
Nanophotonics and Plasmonics Laboratory, IIT Bhubaneswar, Odisha-752050, India
*Author e-mail address: ss99@iitbbs.ac.in, rjha@iitbbs.ac.in**

Abstract: In this work, an optical nanofiber with an inline grating-based unidirectional single-photon coupling system is reported. The proposed structure enhances the coupling of photons into the fiber-guided modes using an inline fiber cavity mobilized with a single quantum emitter. The optimized structure has a low mode volume of 0.6 μm^3 and a Q-factor of ~ 640. The system has a unidirectional coupling efficiency of ~ 90% to the guided modes from a single quantum emitter.
Keywords: Single Photon, Single Quantum Emitter, cQED.

1. Introduction

The increasing demand for quantum communication and quantum computation has inspired significant research in the field of quantum optics [1]. The necessary technology to establish compact quantum systems is being realized using a nanostructured waveguide that offers efficient advantages over free space-based systems. Light-matter interaction (LMI) with nanostructures has become a platform for various modern research fields, mostly in quantum nanophotonics. Among all the nanostructured waveguide systems, optical nanofibers (ONFs) are a promising platform for LMI due to their ability to channel emissions from a single quantum emitter (SQE) to a single-mode fiber (SMF) system. ONFs are adiabatic tapered optical fibers with a sub-wavelength diameter (waist region) that is comparable to the wavelength of the emissions from an SQE. Due to the ability of tight transverse confinement of mode in the ONF, strong-light-matter interaction can be realized by placing an SQE on the nanofiber surface resulting in a significant amount (~22%) of photons coupled in the guided mode of the ONF [2,3]. For practical applications based on single photon sources, a single-sided cavity is essential to channel all the emitted photons in one direction [4,5].

2. Proposed structure and Results

In this work, the spontaneous emissions from the SQE are enhanced by making grating in the nanofiber to facilitate longitudinal confinement. Cavity formation on the waist region of ONF is essential for enhancing the interaction strength of SQE in accordance with cavity quantum electrodynamics (cQED) [6]. Another interest of the ONF-based cavity is that the guided field can be transmitted over long distances for the communication scheme [7], and the single photons emitted from SQEs have a high degree of polarization due to the cavity.

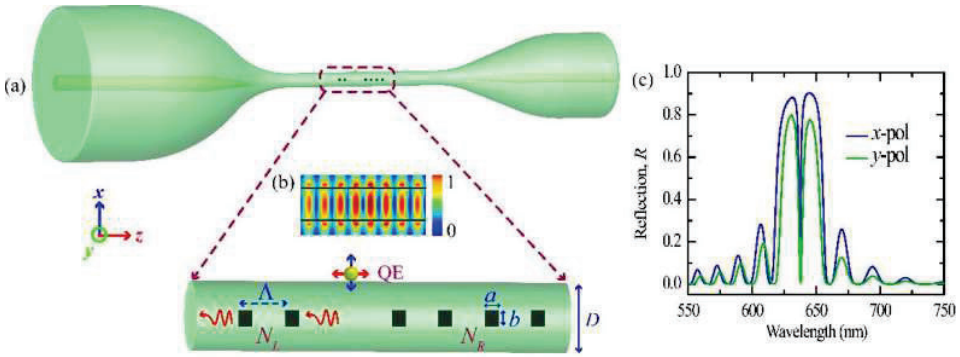

Fig. 1. (a) Schematic diagram of the device. An enlarged portion of the waist region is integrated with an SQE. N_L and N_R denote the number of gratings on the left side and right side of the cavity region, respectively. Here, $N_L \neq N_R$ (b) Electric field enhancement at the cavity region. (c) Normalized reflection spectra of x- and y- polarized light.

Figure 1(a) shows the schematic diagram of the asymmetric inline cavity on the waist region of ONF. The enlarged portion shows different optimized values and SQE integrated into it. ONF diameter and grating parameters are conscripted by doing the finite-difference time-domain (FDTD) method for a range of physical parameters to determine the optimized value that supports the fundamental mode with maximum coupling efficiency from the SQE [8]. Figure 1(b) shows the distributed electric field enhancement in the cavity region, where maximum light is confined at the center of the grating structure. Further, Fig. 1(c) shows the normalized reflection spectra for two orthogonally polarized, i.e., *x*-, and *y*- polarized modes. There is a sharp resonance peak at the middle of the photonic stop band which means the proposed cavity supports a single mode around 640 nm. The resonance peak of *x*- polarized light is sharper than *y*- polarized light because the *x*-polarized mode experiences large index modulation due to grating. The simulated *x*- and *y*- polarized have *Q*-factor of ~ 640 and ~ 215, respectively, with a low mode volume of 0.6 μm^3.

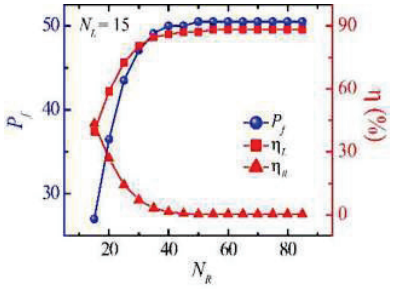

Fig. 2. Variation of Purcell factor (P_f) and coupling efficiency (η) with N_R by keeping $N_L = 15$.

When an SQE is positioned on this resonant cavity structure and emits about the wavelength of the resonant peak, then resonance occurs. As a result, the emission from the SQE enhances and increases the spontaneous emission rate. Here, N_L and N_R denote the number of gratings on the left side and right side of the cavity region, respectively. However, when $N_L = N_R = 15$, then there is equal channeling of single photons on both sides. Then, by setting $N_L = 15$, and sweeping the $N_R = 15$ to 85; the Purcell factor (P_f), coupling efficiency on the left side (η_L) increases, and coupling efficiency on the right side (η_R) decreases. The maximum $P_f = 50$ and $\eta_L \sim 90\%$ are achieved with the proposed structure at the antinode (maximum intensity) of the electric field distribution. This shows the channeling of a single photon largely in one direction. And, 10% photon losses due to the increased grating loss.

3. Conclusion

In conclusion, we propose an optimized structure of asymmetric inline grating on an ONF for enhanced light-matter interaction. Different polarization-dependent studies are carried out using the FDTD method. This cavity structure can be used to enhance the spontaneous emission rate of an SQE and maximize unidirectional coupling in the nanofiber-guided mode. The system offers a medium for developing efficient single-photon-based quantum communication with fiber networks.

4. Acknowledgment

RJ acknowledges the support from SERB STAR Fellowship (Physical Sciences).

5. References

1. H. J. Kimble, "The quantum internet," Nature **453**(7198), 1023–1030 (2008).
2. F. Le Kien, S. Dutta Gupta, V. I. Balykin, and K. Hakuta, "Spontaneous emission of a cesium atom near a nanofiber: Efficient coupling of light to guided modes," Phys. Rev. A - At. Mol. Opt. Phys. **72**(3), 1–7 (2005).
3. R. Yalla, F. Le Kien, M. Morinaga, and K. Hakuta, "Efficient channeling of fluorescence photons from single quantum dots into guided modes of optical nanofiber," Phys. Rev. Lett. **109**(6), 1–5 (2012).
4. R. Yalla, K. Muhammed Shafi, K. P. Nayak, and K. Hakuta, "One-sided composite cavity on an optical nanofiber for cavity QED," Appl. Phys. Lett. **120**(7), 071108 (2022).
5. S. Murmu, A. Kumar, and R. Jha, "Unidirectional Photon Coupling Using Asymmetric Diamond Emitters with Enhanced Spontaneous Emission," Adv. Quantum Technol. **2100160**, 1–6 (2022).
6. K. P. Nayak, J. Wang, and J. Keloth, "Real-Time Observation of Single Atoms Trapped and Interfaced to a Nanofiber Cavity," Phys. Rev. Lett. **123**(21), (2019).
7. F. Le Kien and K. Hakuta, "Cavity-enhanced channeling of emission from an atom into a nanofiber," Phys. Rev. A **80**(5), 1–15 (2009).
8. R. Yalla, M. Sadgrove, K. P. Nayak, and K. Hakuta, "Cavity quantum electrodynamics on a nanofiber using a composite photonic crystal cavity," Phys. Rev. Lett. **113**(14), 1–5 (2014).

Multi-spectral Quantitative Phase Imaging using Phase Contrast Microscopy with Transport of Intensity Equation

[1]Himanshu Joshi, [1]Priyanka Mann, [1]Pramila Thapa, [1]Bhanu Pratap Singh, [1]Dibya Jyoti Sarangi, [*1]Dalip Singh Mehta,

[1]Bio-Photonics Laboratory, Department of Physics, Indian Institute of Technology Delhi, Hauz-Khas, New Delhi-110016, India

[*]Corresponding author: mehtads@physics.iitd.ac.in

Abstract: Multi-wavelength Phase map of RBC is evaluated to verify the solution of Transport of Intensity Equation. Phase map of the cancer cell is then evaluated using the same solution of TIE. For quantitative phase imaging generally an interferometric microscope such as Michelson or Mach-Zehnder type interferometric microscopes are required. These systems are bulky and sensitive to external vibrations. Phase contrast microscopy on the other hand is a non-interferometric microscope, which is highly stable. But phase contrast microscopy can be used only for visualization of contrast. In this paper we describe **Quantitative Phase imaging using phase contrast microscopy with Transport of Intensity Equation.** Experimental results of QPI of Red blood cells and Cancer cells are presented.

Keywords: Transport of intensity equation, Multi-wavelength QPI.

1. Introduction

Most of the biological samples are transparent, which means that they absorb very small amount of light. This limits the contrast of the image under normal bright field microscope. There are various techniques to increase the contrast of such samples, which include phase contrast microscopy, Dark field microscopy, Differential phase contrast microscopy, etc. But these techniques do not provide any information about the subcellular morphology and quantitative parameters about the sample. Any optical field can be represented in terms of the amplitude and a complex exponential part, whose argument represents the phase of the sample. Amplitude part of the field is easy to comprehend in comparison to the phase, because square of amplitude represents intensity. All our sensors including human eyes are sensitive only to the intensity of the light. So, the phase information is not accessible directly. Phase of any field have a dense information about the samples, which can help to interpret the morphology and other quantitative parameters of the sample like refractive index of the sample.

Quantitative phase microscopy (QPI) is a technique to evaluate the phase map of the biological samples. However, QPI is considered to be associated with Interference of a sample and reference beams derived from monochromatic and highly coherent laser sources. These interferometric methods correspond to various limitations when considered for optical imaging and microscopy which include environmental instabilities of the fringes and associated laser speckle noise which limit their applications in optical imaging microscopy. There are various non-interferometric methods which can evaluate the phase map of the samples. Transport of intensity equation (TIE) is a non-interferometric method in which gradient of intensity in different defocused planes is used to evaluate the phase map.

2. Experimental Details and Results

TIE is a partial differential equation which establishes a relation between the axial intensity gradient and optical phase. For any Electric field, Conservation of energy is satisfied in the form of Poynting Theorem. TIE is a modification of Poynting Theorem under certain conditions. The thickness and refractive index variations in the sample are delivered in the form of wavefront distortion of the scattered wave. The concept of TIE is to recover the quantitative phase information by measuring the intensity variation induced by phase object at a defocused plane. Mathematically it is written as

$$-k\left[\frac{\partial I(\boldsymbol{x},z)}{\partial \mathrm{z}}\right] = \nabla\cdot[\mathrm{I(x,y)}\nabla\varphi(\mathbf{x})] \tag{1}$$

Here, term on the left side represents intensity gradient, k is the wave number, $\varphi(\mathbf{x})$ represents the phase of the sample, $\mathbf{x}$ is the transverse coordinates $\mathbf{x}$ = (x, y). Under the assumption of small defocus distance Δz, the above equation is simplified as,

$$-k\left[\frac{I_{+\Delta z}(\boldsymbol{x}, z) - I_{-\Delta z}(\boldsymbol{x}, z)}{2\Delta z}\right] = \left[\mathrm{I}(\mathrm{x}, \mathrm{y}) \cdot \nabla^2 \varphi(\mathbf{x})\right] \tag{2}$$

Above equation can be solved under appropriate boundary conditions to evaluate the phase map of the sample. Simple phase contrast microscope (40x) is used to capture the focused and defocused images of the RBC samples. TIE is solved using these images to evaluate the phase map of the sample.

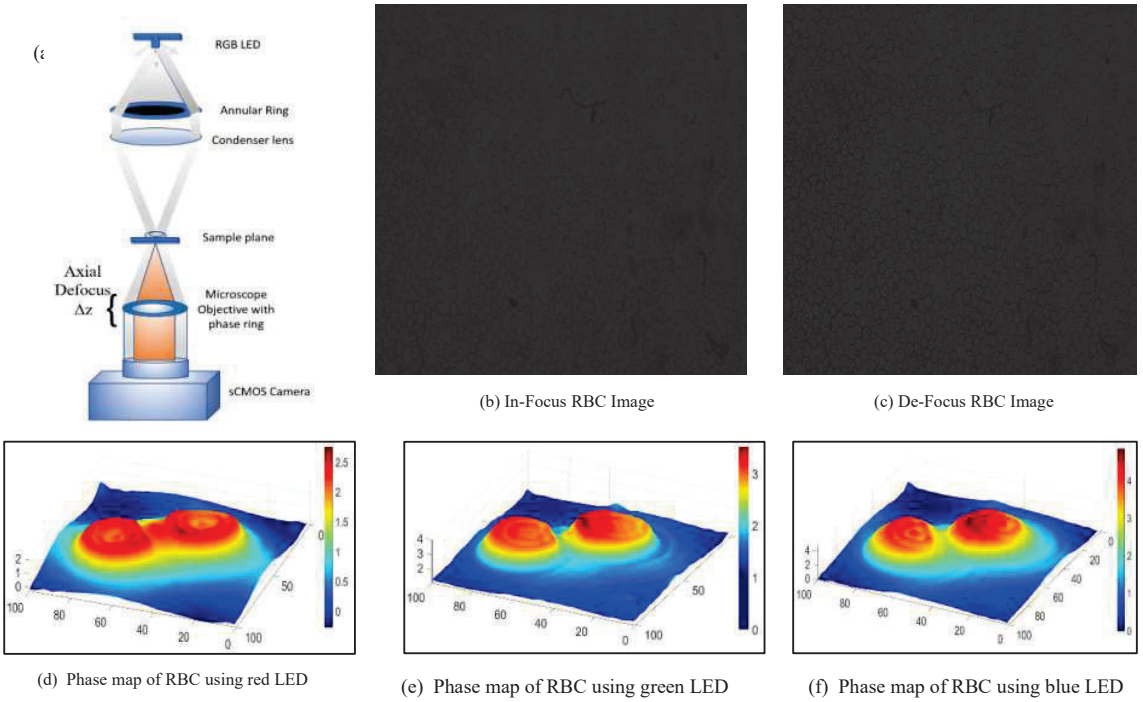

(b) In-Focus RBC Image

(c) De-Focus RBC Image

(d) Phase map of RBC using red LED

(e) Phase map of RBC using green LED

(f) Phase map of RBC using blue LED

Fig. 1: Phase map of RBC using TIE (a) schematic showing the experimental setup for acquisition of the RAW intensity images. (b) In-Focus RBC Image (c) De-Focus RBC Image (d) Phase map using red LED (e) Phase map using green LED (f) Phase map using blue LED

3. Conclusion

Phase of any biological sample has a strict dependence on the wavelength. Phase is inversely proportional to the wavelength of light used. Fig. 1 (d), (e), (f) shows multispectral phase map for three different channels evaluated using TIE.

4. References

[1] Zuo, Chao, Jiaji Li, Jiasong Sun, Yao Fan, Jialin Zhang, Linpeng Lu, Runnan Zhang, Bowen Wang, Lei Huang, and Qian Chen. "Transport of intensity equation: a tutorial." *Optics and Lasers in Engineering* 135 (2020): 106187. [2] David F. Edwards, "Silicon (Si)" in *Handbook of optical constants of solids,* E.D. Palik, ed. (Academic, Orlando, Fla. 1985).

[2] Waller L , Tian L , Barbastathis G . Transport of intensity phase-amplitude imaging with higher order intensity derivatives. Opt Express 2010a;18(12):12552–61.

[3] Waller L , Luo Y , Yang SY , Barbastathis G . Transport of intensity phase imaging in a volume holographic microscope. Opt Lett 2010b;35(17):2961–3.

[4] Kou SS , Waller L , Barbastathis G , Sheppard CJR . Transport-of-intensity approach to differential interference contrast (TI-DIC) microscopy for quantitative phase imag- ing. Opt Lett 2010;35(3):447–9.

Terahertz-Time Domain Spectroscopy (THz-TDS) for Biomedical Applications

Rajat Kumar[1, a], Ayan Gope[2, b], Shubhadeep Mondal[2, a], Subhamoy Mandal[c], Prasanta Kumar Datta[1*, a]

[a]Department of Physics, Indian Institute of Technology Kharagpur, Kharagpur, West Bengal-721302, India

[c]Advanced Technology Development Center, Indian Institute of Technology Kharagpur, Kharagpur, West Bengal-721302, India

[c]School of Medical Science and Technology, Indian Institute of Technology Kharagpur, Kharagpur, West Bengal-721302, India

**Corresponding Author Email: pkdatta@phy.iitkgp.ac.in,*

Abstract: This study summarizes the terahertz time-domain spectroscopy as a potential candidate for the replacement of other techniques used to study cancer and wound healing detection for biomedical applications. THz radiation has very low photon energy and doesn't interact with biological materials. In this study, the absorbance spectra of different rat skin tissue were obtained using Terahertz time-domain spectroscopy. We reported that the different tissue has different absorbance in the terahertz range of 0.5-3 THz due to different refractive indices of the tissues. Thus, we can detect the early stages of wound healing and malignant cancer tissues.

Keywords: Spectroscopy, Terahertz, Refractive Index, Skin Tissue

1. **Introduction:** In the electromagnetic spectrum terahertz range corresponds to 0.1 to 10 THz. In Terahertz Time Domain Spectroscopy (THz-TDS) we get both the amplitude and phase information of transmitted wave due to coherent detection which we can't get in any other kind of spectroscopy [1]. Because of this advantage of terahertz time-domain spectroscopy, we can use this technique for detecting various early stages of wound healing and oral cancer which is much important for patient treatment and recovery. Currently, non-invasive optical imaging assesses wound severity, and healing potential through interaction between light and tissue. Ultrasound, Computed Tomography (CT), and Magnetic Resonance imaging (MRI) are conventional imaging techniques to detect tissue structural differences such as heterogeneity, the density of cells, and cell apoptosis related to cancer cells [2]. For the last two decades with the emergence of ultrafast laser sources terahertz spectroscopy techniques are growing rapidly. Due to the rapid progress of terahertz spectroscopy, the applications of terahertz technology in biological and biomedicine have made potential progress in recent years. The study of wound healing in rat tissue is demonstrated by THz spectroscopy [3]. For cancer tissue detection, THz spectroscopy can distinguish peritumoral and cancerous tissue from normal tissue. The various studies reported in recent years are given.

THz System	Target	Results
THz time-domain spectroscopy reflection mode [4]	Tissues from rat glioma Fresh and paraffin-embedded	Different absorption and refractive index between glioma and normal tissue in the range (0.8-1.5 THz)
THz Imaging and Spectroscopy [5]	Freshly excised breast cancer tissue	Accuracy of 80% compared with pathological results
THz Imaging in Reflection mode [6]	Breast cancer tissue	Spatial resolution reached to millimeter range
THz Imaging in Reflection mode [7]	Paraffin-embedded malignant lung tissues	The infected tissue showed a lower refractive index and absorption

2. **Experimental Methodology:** The experimental setup for Terahertz Time Domain Spectroscopy (THz-TDS) in transmission mode developed by us in UFS Lab at IIT Kharagpur, consists of a Ti: Sapphire mode-locked ultrafast laser of pulse width 50fs having a repetition rate of 1kHz at an output beam of 808 nm. This beam was divided in a 70/30 ratio by a beam splitter 70% beam was used to generate the THz radiation and 30% was used to detect the THz beam. For the generation and detection of THz radiation, we have used <110> plane cut ZnTe crystals. THz radiation is generated by *optical rectification* and detected by the *electro-optic sampling* method both of which are second-order non-linear $\chi^{(2)}$ effects. The Schematic of the experimental setup can be found in the literature [8]. The time domain data is obtained by mapping the probe beam in the time with the motorized delay stage which was controlled by LabView Software. The time domain data were then converted into the frequency domain by FFT (Fast Fourier Transform). From FFT data we computed various optical coefficients such as refractive index, and absorption coefficient of biomedical samples under investigation [9]. For biomedical applications, we are mainly interested in refractive index and absorption coefficients. From absorption data, we can extract the various vibrational modes that could correspond to hydrogen bonds and intermolecular vibrations of biological samples.

3. Preliminary Results. We carried out THz-TDS of samples consisting of rat skin tissue in which the wound was created by peeling off the skin from the targeted area. Rat Tissue 1, Rat Tissue 2, and Rat Tissue 3 were the wound tissue, wound tissue with treatment, and wound tissue with different treatments obtained on a quartz substrate of a thickness of 1mm. The time domain data, Refractive index, and absorption coefficient of samples are shown in figures (a), (b), and (c). We can clearly distinguish between the various stages of wound healing of rat tissue because of their different THz absorption.

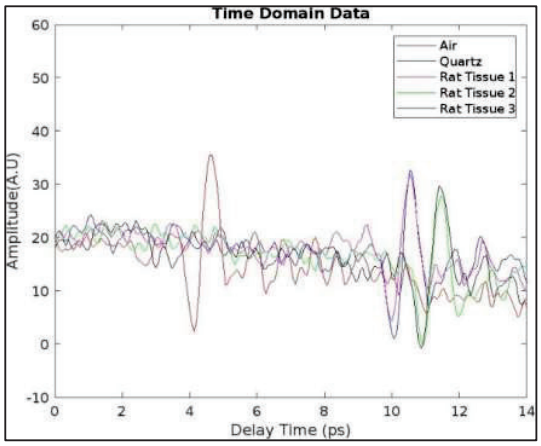

(a)

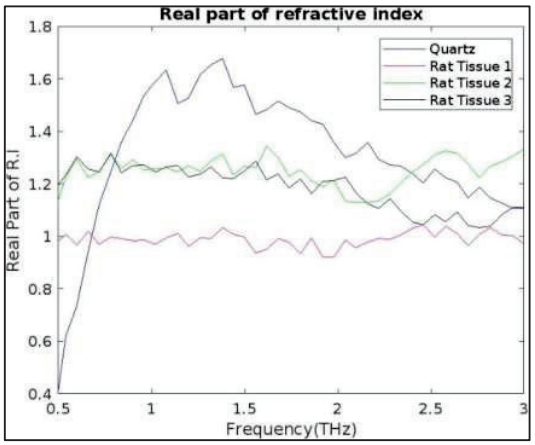

(b)

Figure (a) and (b) represents the time domain data and the real part of the refractive index of various samples as well as quartz.

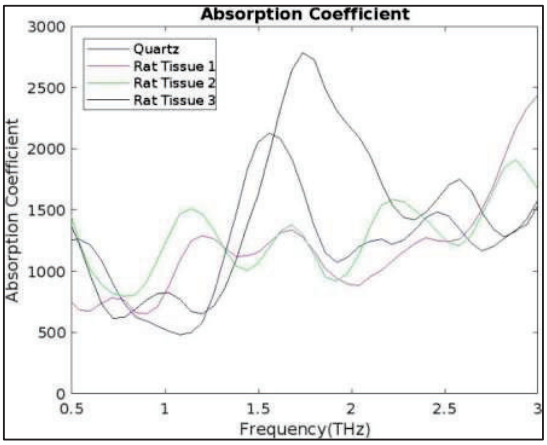

(c)

Figure (c) represents the absorption coefficients of various samples.

4. References

[1]. Das, A. C., Bhattacharya, S., Jewariya, M., Prabhu, S. S., Mandal, K. C., Ozaki, T., & Datta, P. K. (2017). Identification of combination phonon modes in pure and doped GaSe crystals by THz spectroscopy. *IEEE Journal of Selected Topics in Quantum Electronics*, *23*(4), 1-7.

[2]. García-Figueiras, R., Baleato-González, S., Padhani, A. R., Luna-Alcalá, A., Vallejo-Casas, J. A., Sala, E., ... & Vargas, H. A. (2019). How clinical imaging can assess cancer biology. *Insights into imaging*, *10*(1), 1-35.

[3]. Zuhayri, H., Knyazkova, A. I., Nikolaev, V. V., Borisov, A. V., Kistenev, Y. V., Zakharova, O. A., ... & Tuchin, V. V. (2020, November). Study of wound healing by terahertz spectroscopy. In *Fourth International Conference on Terahertz and Microwave Radiation: Generation, Detection, and Applications* (Vol. 11582, pp. 289-293). SPIE.Deka, G., Chu, S. W., & Kao, F. J. (2016). Skin wound healing revealed by multimodal optical microscopies. *Microscopy and Analysis*, *16*(10.5772), 64088.

[4]. Yamaguchi, S., Fukushi, Y., Kubota, O., Itsuji, T., Ouchi, T., & Yamamoto, S. (2016). Origin and quantification of differences between normal and tumor tissues observed by terahertz spectroscopy. *Physics in Medicine & Biology*, *61*(18), 6808.

[5]. Bowman, T., Chavez, T., Khan, K., Wu, J., Chakraborty, A., Rajaram, N., ... & El-Shenawee, M. O. (2018). Pulsed terahertz imaging of breast cancer in freshly excised murine tumors. *Journal of biomedical optics*, *23*(2), 026004.

[6]. Cassar, Q., Al-Ibadi, A., Mavarani, L., Hillger, P., Grzyb, J., MacGrogan, G., ... & Mounaix, P. (2018). Pilot study of freshly excised breast tissue response in the 300–600 GHz range. *Biomedical optics express*, *9*(7), 2930-2942.

[7]. Yeo, W. G., Gurel, O., Hitchcock, C. L., Park, S., Sertel, K., & Nahar, N. K. (2019). Evaluation of cancer tissue morphology via THz spectroscopic imaging: human lung and small intestine malignancies. *Infrared Physics & Technology*, *97*, 411-416.

[8]. Sindhu, P. S., Prasad, D., Peli, S., Mitra, N., & Datta, P. K. (2019). Terahertz spectroscopy of diglycidylether of bisphenol A: Experimental investigations and density functional theory-based simulations. *Journal of Molecular Structure*, *1184*, 114-122.

[9]. Punjal, A., Choudhary, S., Narayanan, M., Kulkarni, R., Thamizhavel, A., Bhattacharya, A., & Prabhu, S. (2022). Terahertz Optical Properties and Birefringence in Single Crystal Vanadium doped [100]\b {eta}-Ga2O3. *arXiv preprint arXiv:2201.10*

Study of Nonlinear effect and Controllable transparency in a hybrid optomechanical system with quantum dot molecules in presence of quadratic coupling

Madhav K Singh[a], Sonam Mahajan[b], Neha Aggarwal[c] and Aranya B. Bhattacherjee[d]

[a] *Department of Physics, Swami Sahjanand College, Jehanabad, (Magadh University,Bodh Gaya)Bihar-804408,*
[b]*Department of physics, DIT University, Dehradun, Uttarakhand-248009,*
[c]*Department of Physics, Government College for Women, Faridabad Haryana-121002,*
[d]*Department of Physics, Birla Institute of Technology and Science, Pilani, Hyderabad Campus, Telangana State – 570078.*
[a]*madhavkrsingh89@gmail.com*

Abstract: Multistability and Optomechanically induced transparency (OMIT) investigated in a hybrid optomechanical system embedded with quantum dot molecules (QDMs). The optical multistability and absorption and dispersion spectrum are analyzed and can be adjusted by tunning the amplitude of the strong pump field. The result obtained in this article may be used to design all-optical switching devices.

Keywords: Optomechanical System, Optomechanical induced transparency , Quantum Dot Molecule

1. Introduction

The optomechanical system (OMS) has been studied vastly due to its potential applications in entanglement, optomechanically induced transparency (OMIT), Fano resonance, ground state cooling, squeezing, and so on[1-3]. Recently, a lot of attention given to hybrid optomechanical systems because it possesses the feature of the versatility to integrate different fantastic physical systems with the bare optomechanical setups [4]. Optomechanical induced transparency (OMIT) is a phenomenon observed on the appearance of a dip in the absorption spectrum of a weak probe field when multilevel atoms or molecules significantly couple to an applied strong control field. The phenomenon of OMIT occurs due to destructive interference of electronic pathways [5]. It has been shown that OMIT can also arise in quadratically coupled optomechanical systems [6-8].

In the present article, we concentrate on the impact of the quadratically coupled optomechanical systems on multistability and OMIT in hybrid optomechanical systems embedded with quantum dot molecules. A pump and a probe field are applied to the cavity. An expression of the output field was derived by solving Heisenberg-Langevin equations using the input-output theory. Based on this, we analyzed the hybrid optomechanical system's multistability, absorption and dispersion spectrum.

2. The Model and Hamiltonian

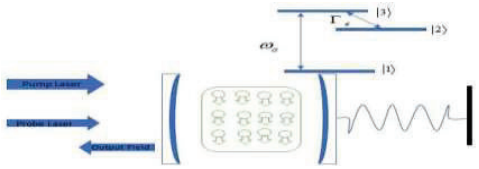

Figure 1: Schematic figure of a hybrid optomechanical system with QDMs located in the middle of the cavity.

The hybrid optomechanical system under consideration is sketched in figure 1. This system consists of an optomechanical cavity with a one-end oscillating mirror that interacts with a traditional cavity. The cavity is also embedded with quantum dot molecules (QDMs). The hybrid system on the left is exposed to a strong pump laser and a weak probe laser. On the right, through radiation pressure cavity couples the mechanical resonator linearly as well as quadratically. QDMs in the cavity is driven by cavity mode and an external electric field. By applying a gate electrode in the sample, interdot tunneling between QDs can be controlled. The Hamiltonian describing the system is given by

$$H = \hbar\omega_a a^\dagger a + \hbar\frac{\omega_m}{2}\left(Q^2+P^2\right) + \hbar\sum_{j=1}^{N}\left(\omega_{21}\sigma_{22}^j + \omega_{31}\sigma_{33}^j\right) - \hbar\left(G_1 Q + G_2 Q^2\right)a^\dagger a +$$

$$\hbar\Gamma_e\sum_{j=1}^{N}\left(\sigma_{23}^j + \sigma_{32}^j\right) + \hbar g_a\sum_{j=1}^{N}\left(a\sigma_{21}^j + a^\dagger\sigma_{12}^j\right) + i\hbar\varepsilon_l\left(a^\dagger e^{-i\omega_l t} - a e^{i\omega_l t}\right) + i\hbar\varepsilon_p\left(a^\dagger e^{-i\omega_p t} - a e^{i\omega p t}\right)$$

Utilizing the nonlinear Heisenberg-Langevin equations and input-output theory, we get an expression of intracavity photon number and transmitted probe light field.

3. Result and Discussion

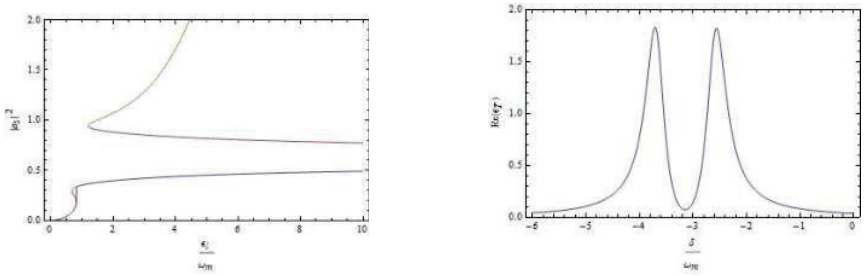

(a) (b)

The intracavity photon number versus intensity of pump laser plotted in figure (a) for the parameters $\Gamma_e = 4\omega_m$, $G_1 = 1.6\omega_m, G_2 = 0.8\omega_m, \kappa = 0.4\omega_m, \Delta_a = 2\omega_m, \Delta_1 = 3\omega_m, \Delta_2 = 4\omega_m$. The graph for intracavity photon number shows multistability in presence of quadratic optomechanical coupling while in absence of quadratic optomechanical coupling the graph shows bistability behavior (not shown here). We also studied the output probe field based on the input-output relation of the system. The absorption spectrum $\left(\mathrm{Re}\left(\varepsilon_T\right)\right)$ versus detuning of the hybrid system is plotted in figure (b) for the parameters $\Gamma_e = 5.5\omega_m$, $G_1 = 1.6\omega_m$, $G_2 = 1.4\omega_m, \kappa = 0.4\omega_m$, $\Delta_a = -3.5\omega_m$, $\Delta_1 = 2.2\omega_m, \Delta_2 = 2.5\omega_m$. The appearance of a dip in absorption spectra validates the phenomena of optomechanically-induced transparency in the system. The phenomenon of OMIT arises from destructive interference of electronic pathways, which further enhances the optical nonlinearity.

Therefore, it is demonstrated that by adjusting the quadratic optical coupling, the bistability behavior of intracavity photon number can be converted to multistability behaviour. Also, we observed the transparency window with chosen set of parameters. The application of this model can be used in controllable all-optical switching devices.

4. References

[1] Qing He, Fazal Badshah, Thamer Alharbi, Liping Li, and Linfeng Yang, "Normal-mode splitting in a linear and quadratic optomechanical system with an ensemble of two-level atoms," J. Opt. Soc. Am. B 37, 148-156 (2020**).**

[2] Yu, C., Yang, W., Sun, L. *et al.* Controllable transparency and slow light in a hybrid optomechanical system with quantum dot molecules. *Opt Quant Electron* **52,** 267 (2020).

[3] Madhav Kumar Singh, Pradip Kumar Jha and Aranya Bhattacherjee, "Optical switching and normal mode splitting in hybrid semiconductor microcavity containing quantum well and Kerr medium driven by amplitude-modulated field" Journal of Modern Optics, 67:8, 692-703, (2020).

[4] Xiaotian Zhang, Jiteng Sheng, and Haibin Wu "Temporal rocking in a nonlinear hybrid optomechanical system" Vol. 26, No. 5, Optics Express 6285, (2018).

[5] H. Xiong and Y. Wu, Fundamentals and applications of optomechanically induced transparency, Appl. Phys. Rev. 5, 031305 (2018).

[6] S. Huang and G. S. Agarwal," Electromagnetically induced transparency from two-phonon processes in quadratically coupled membranes" Phys. Rev. A 83, 023823 (2011).

[7] She, Y., Zheng, X., Wang, D., et al.: Controllable double tunneling induced transparency and solitons formation in a quantum dot molecule. Opt. Express **21**(14), 17392–17403 (2013).

[8] T. Holstein and H. Primakoff, "Field dependence of the intrinsic domain magnetization of a ferromagnet," Phys. Rev. 58, 1098–1113 (1940).

Gyrator Transform with Double Random Phase Encoding Encrypted Image Classification with Deep Learning on Cloud Computing

Poonam Yadav[1], Hukum Singh[2]

[1]*CSE Department. The North Cap University, Gurugram, India*

[2]*Applied Science Department, The North Cap University, Gurugram, India*

**Corresponding author: poonam17csd011@ncuindia.edu*

Abstrat Large amounts of private data are stored and processed in the cloud. On the other hand, data security is the biggest huddle of the wide adoption of cloud computing. Therefore, data owners store encrypted data in the cloud, such as Google Cloud, Microsoft Azure and Amazon Web Service. The decryption of big data such as images and videos require enormous computation resources, which is unsuitable for energy-constrained devices like computer vision and Internet of Things (IoT) devices, if encrypted images can be directly classified on the cloud or IoT devices without decryption then we can achieve data privacy. This paper proposes a Gyrator transform with a double random phase encoding (DRPE) technique for encrypting images and then uploaded and stored in the cloud. Encrypted images without being decrypted are classified using deep convolutional neural networks. The proposed approach simulation results indicated the feasibility and good performance.

Key Word: Double random phase encoding, Image encryption, Deep learning, Convolution Neural Network.

1. Introduction

The rapid growth of the internet and application led to the imminent creation of image and video data. The development of contemporary image cryptosystems became crucial because of the increasing need for better security relevant to applications in different fields like network communications, business, and defence mechanisms. Transform-based image encryption has been very popular in the field of image encryption. The image is transformed from spatial domain to frequency domain by using a suitable transform model. To achieve security, various transforms are used which rely on two methods.

Quadratic phase-based encryption techniques: It includes double random phase encoding (DRPE)-based techniques [1] in Fourier Transform (FT), Fractional Fourier Transform (FrFT), Fresnel Transform (FrT), or any linear canonical transformation domains.

Pixel Scrambling/permutation techniques: It includes technique or algorithms which scrambles the pixel-like Arnold transform, Jigsaw transform, logistic map, Affine transform, etc.

In this study, all images were encrypted via Gyrator Transform with DRPE algorithms. Deep learning model extract the useful feature from encrypted image, both real and imaginary parts of complex value of encrypted image are used as inputs in training a DL model. That we can use for identification and classification to preserve the privacy of user.

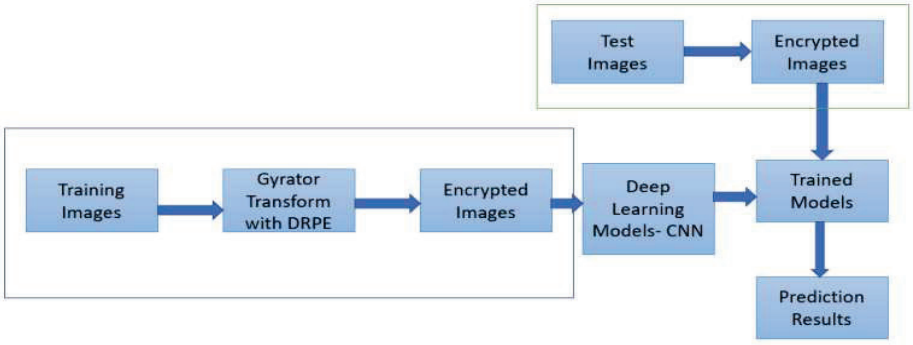

Fig 1. Procedure of encrypted image classification

2. Gyrator Transform with Double Random Phase Encoding for Image Encryption

Gyrator Transform (GT) is one of the canonical transforms proposed by Rodrigo in the field of image processing and it uses three lenses with a fixed distance between them. The 2-D function f (x, y) for GT can be mathematically expressed as

$$GT\ (u,v) = GT^{\alpha}\{\mathrm{f}\ (\mathrm{x_i}\ \mathrm{y_i})\}(u,v) = \oint_{-\infty}^{\infty}\int_{-\infty}^{\infty}\mathrm{f}\ (\mathrm{x_i}\ \mathrm{y_i})\ \mathrm{K}_{\alpha}(\mathrm{x_i}\ , \mathrm{y_i}, u, v)\ \mathrm{dx_i}\ \mathrm{dy_i} \quad (1)$$

Let input image $I(x,y)$ is diffused with Random phase key $R1(x,y)$ in the input plane and propagates a rotation angle α in the GT domain.

$$G(u,v)\ = GT^{\alpha}\ [I(x,y)\ x\ R1(x,y)] \quad (2)$$

Then the output obtained $G(u,v)$ is diffused with second phase RPM $R2(x,y)$ and propagates a rotation angle ϭ in the GT domain to get the encrypted image.

$$E(\mu,v)\ = GT^{-\mathfrak{b}}\ [G(u,v)\ x\ R2(u,v)] \quad (3)$$

The number of parameters for the key domain is R1, R2 (Random phase mask) α, and ϭ (rotation angle) which is large as compared to conventional DRPE that enhances the security [2][3].

3. Classification of Encrypted Image

This paper used fully connected CNN with an auxiliary branch for encrypted image classification as FCNAux. In this CNN, the input image size is 32 ×32× 2. As Shown in Fig.2 Conv 3 × 3 is a convolutional operation with a kernel size of 3 × 3[4].

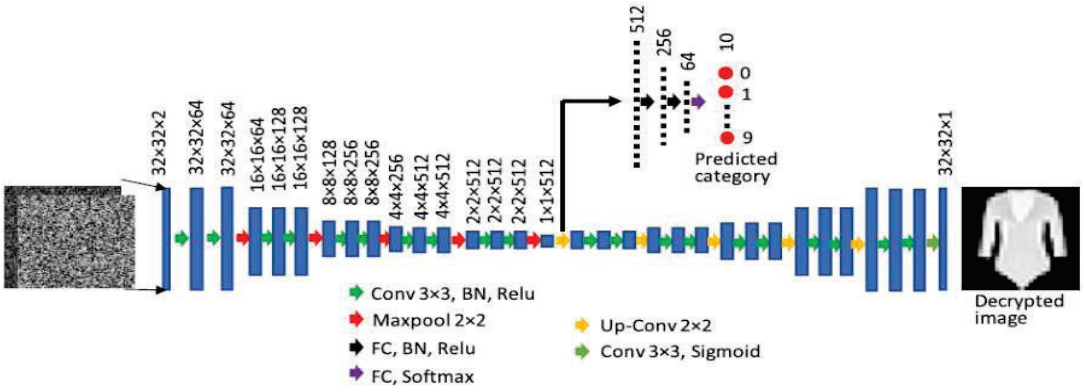

Fig 2. FCNAux architecture for Encrypted Image Classification[4]

BN: Batch normalization, ReLu: Rectified linear unit activation function, Max Pooling: means max-pooling operation with a stride value of 2, FC denotes the fully connected operation, Soft- max is a normalized exponential function, Up-Conv 2 × 2 means an up-pooling operation, that increase the feature map resolution by a factor of 2×2. The Sigmoid function is an activation function that can scale the output values to a range of 0–1 [5][6].

4. Results

The Fashion-MNIST dataset is used with proposed method it contained 2,000 images, of which 1500 are used for training and 500, for testing. The DL algorithms were implemented with PyTorch, a Python Deep Learning framework. An accuracy of 0.9098 was obtained.

Reference

[1] Refregier P, Javidi B. Optical image encryption based on input plane and Fourier plane random encoding. Opt Lett 1995;20(7):767–9.
[2] Khurana, Mehak, and Hukum Singh. "Asymmetric optical image triple masking encryption based on Gyrator and Fresnel transforms to remove silhouette problem." 3D Research 9, no. 3 (2018): 1-17.
[3] Z. Liu, L. Xu, C. Lin, J. Dai, and S. Liu, ‘‘Image encryption scheme by using iterative random phase encoding in gyrator transform domains,’’ Opt. Lasers Eng., vol. 49, no. 4, pp. 542–546, Apr. 2011.
[4] Yi, F., Jeong, O. and Moon, I., 2021. Privacy-Preserving Image Classification with Deep Learning and Double Random Phase Encoding. IEEE Access, 9, pp.136126-136134.
[5] C. F. Higham and D. J. Higham, ‘‘Deep learning: An introduction for applied mathematicians,’’ SIAM Rev., vol. 61, no. 3, pp. 860–891, Jan. 2019.
[6] L. Deng, ‘‘The MNIST database of handwritten digit images for machine learning research [best of the web],’’ IEEE Signal Process. Mag., vol. 29, no. 6, pp. 141–142, Nov. 2012.

Influence of Temporal Coherence on the Stokes Scintillations

Gaytri Arya*, Hemant Kumar Singh and Bhaskar Kanseri
Experimental Quantum Interferometry and Polarization (EQUIP), Department of Physics, Indian Institute of Technology Delhi, Hauz Khas, New Delhi, 110016, India
**phz168378@iitd.ac.in*

Abstract: The four normalized Stokes scintillations are deduced for the orthogonally polarized light field. The experimentally determined scintillation coefficients agree with the theory that validates the modulation of Stokes scintillations through temporal coherence. The study of time-based polarization fluctuation finds application in light-matter interaction, tracing the evolution of polarization state, etc.
Keywords: Stokes scintillations, temporal coherence, and Stokes parameters.

1. Introduction

The intensity-intensity correlation coefficient determined from the Hanbury-Brown Twiss interferometer is useful in many areas such as nuclear physics, atomic physics, astronomy, and classical and quantum optics. Later, this intensity correlation is extended to polarization fluctuation correlation in [1], and the effect of the Gaussian-Schell model beam on the Stokes correlations is investigated [2]. We have determined the correlations in the fluctuations of Stokes parameters at two-time points and studied the role of temporal coherence in modulating the Stokes scintillations, theoretically and experimentally. The information of variation of Stokes correlations with time is helpful to trace the evolution of polarization state, improvising signal to noise ratio and can also be useful in light-matter interactions and semiconductor lasers.
The coefficient of correlation of Stokes parameters at two-time points is defined as

$$C_{nm}(\tau) = \langle \Delta S_n(t_1)\, \Delta S_m(t_2) \rangle; \;\; \tau = t_2 - t_1. \tag{1}$$

The fluctuations in the Stokes parameters ($\Delta S(t)$) at some time t are defined as the difference between instantaneous Stokes parameters and their average values, i.e., $S(t) - \langle S(t) \rangle$. Using the advantage of Gaussian moment theorem, the higher-order moments can be decomposed into second-order moments [3], hence Stokes fluctuation correlations can be simplified as

$$C_{nm}(\tau) = \sum_{ab} \sum_{cd} \sigma_{ab}^{n}\, \sigma_{cd}^{m}\, \Gamma_{ad}(\tau)\, \Gamma_{bc}^{*}(\tau); \tag{2}$$

where *(a,b,c,d)* = (*x,y*). For zero-time difference (τ = 0), the 16 elements of Stokes fluctuations in Eq. (2) reduce to Stokes scintillations. Consider a scheme shown in Fig. (1), where the input field is split into orthogonal components using the polarizing beam splitter (PBS). The y-polarized component has travelled τ time difference greater than the x- component and combined at some time t'.

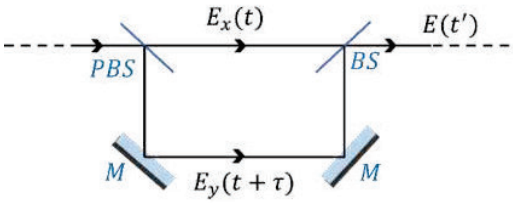

Fig. 1 Schematic view for the superposition of differently travelled orthogonally polarized fields.

The four scintillation coefficients obtained at the time t' are

$$t_{00} = \frac{1+\left|\gamma_{xy}^{(i)}(\tau)\right|^2}{2}; \quad t_{11} = \frac{1-\left|\gamma_{xy}^{(i)}(\tau)\right|^2}{2}, \quad t_{22} = \frac{1+\left|\gamma_{xy}^{(i)}(\tau)\right|^2 \cos(2\phi_{xy})}{2}; \quad t_{33} = \frac{1+\left|\gamma_{xy}^{(i)}(\tau)\right|^2 \cos(2\phi_{xy})}{2}. \tag{3}$$

The normalized coherence matrix element is denoted by $\gamma_{xy}^{(i)}(\tau)$ and the corresponding phase is given by ϕ_{xy}.

2. Experimental method and results

Initially, the variation of the coherence matrix element is measured with the longitudinal shift between the orthogonal fields [4], and experimentally validates the theoretical assumption of Gaussian statistics. In the experimental scheme shown in Fig. 1, the light field from the laser gets 45° polarized, and PBS splits the light field into *x*-pol. and *y*-pol. The *y*-component travelled extra path difference gets recombined with the *x*-component, and afterwards, the Stokes polarimetry consists of a quarter wave plate, and a polarizer is placed. The Stokes parameters are measured at intervals of 5 cm path difference, and Stokes scintillations are determined from these Stokes parameters using the relations

$$t_{00} = \frac{\langle S_0\rangle^2 + \langle S_1\rangle^2 + \langle S_2\rangle^2 + \langle S_3\rangle^2}{\langle S_0\rangle^2}; \quad t_{11} = \frac{\langle S_0\rangle^2 + \langle S_1\rangle^2 - \langle S_2\rangle^2 - \langle S_3\rangle^2}{\langle S_0\rangle^2}, \quad t_{22} = \frac{\langle S_0\rangle^2 - \langle S_1\rangle^2 + \langle S_2\rangle^2 - \langle S_3\rangle^2}{\langle S_0\rangle^2}; \quad t_{33} = \frac{\langle S_0\rangle^2 - \langle S_1\rangle^2 - \langle S_2\rangle^2 + \langle S_3\rangle^2}{\langle S_0\rangle^2}. \tag{4}$$

The experimentally obtained Stokes scintillations from Eq. (4) are plotted in Fig. (2) and fitted with the theoretical findings of Eq. (3). The close agreement of experimental data points with the theory in Fig. (2) validates the theoretical findings.

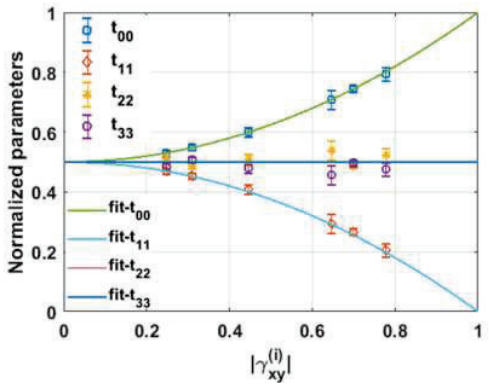

Fig 2: Experimental variation of Stokes scintillations fitted with theoretical Eq. (3).

3. Conclusion

The Stokes scintillations are derived for a scheme and illustrate the effect of temporal coherence on the scintillation coefficients. The experimental results substantiate the theoretical findings. Such studies are useful in the areas where polarization fluctuations are used to probe such as light-matter interactions.

4. Acknowledgement

The authors acknowledge the financial support received from the funding agencies DST for grant DST/ICPS/QUEST/Theme-I/2019.

References

[1] D. Kuebel and T. D. Visser,, "Generalized Hanbury Brown-Twiss effect for Stokes parameters," JOSA A **36,** 362-367 (2019).
[2] G. Wu, D. Kuebel, and T. D. Visser, "Generalized Hanbury Brown–Twiss effect in partially coherent electromagnetic beams," Phys. Rev. A 99, 033846 (2019).
[3] E. Wolf, *Introduction to the Theory of Coherence and Polarization of Light* (Cambridge University Press, 2007).
[4] R. Joshi, N. K. Pathak, and B. Kanseri, "Relationship between degree of polarization and two-time degree of coherence of electromagnetic fields," Appl. Phys. B **127**, 1–7 (2021).

Silicon Nanophotonics for Space Laser Beam Pointing

Alessandro R. Santos[a,b], Willer G. Santos[a] and Vilson R. Almeida[a,c]
[a]*Aeronautics Institute of Technology, Sao Jose dos Campos, Brazil*
[b]*Brazilian Navy Coordination Study Center in Sao Paulo, Sao Paulo, Brazil*
[c]*Brazil University, Scientific and Technological Institute, Sao Paulo, Brazil*
vilsonra@ita.br

Abstract: Silicon nanophotonics is contributing to the development of devices with small dimensions and low energy consumption. In optical systems for space applications, whether in large or small satellites, the interest for integrated photonic devices is continuously increasing, specially for the communication subsystem, since it allows for the construction of an optical beam pointing system without moving parts, such as optical phased array antennas. We propose a silicon photonic integrated approach, including a non-resonant all-optical modulator topology based on thermos-optical effect, for achieving efficient space laser beam pointing functionality. Thermal and photonics computational simulation results are presented and discussed.
Keywords: all-optical modulator; silicon nanophotonics; thermo-optical effect; integrated photonics.

1. Introduction

Optical Phased Array (OPA) Antennas have been applied for Laser Beam Pointing in several applications and environments, being a promising candidate for space applications as well, considering silicon photonics based on silicon-on-insulator as its technological platform [1]. Optical phase modulators/shifters have been used in several nanophotonic devices used in quantum optics, optical neural networks and optical phased arrays. Among several types of phase modulation schemes in silicon photonics, the thermo-optical effect is the most used [2], usually with the use of metal plates powered by electrical energy, called heater, which convert energy into heat for attaining modulation results. In addition to heater, there are other ways to heating up the waveguide, such as by causing absorption of photons in the device material, which can be seen as an indirect all-optical modulation scheme. This method consists of controlling the propagation of light signal in the waveguide by means of a second beam of light applied to and absorbed by the waveguide material [3], leading to a high modulation speed and efficiency. Such an approach finds applications in remote or harsh environment sensing and communications, as well as for space systems, where it may be relevant for the communication subsystems of a CubeSat [4]. The waveguide geometry can significantly impact the device performance, and an Archimedean spiral structure can improve it. This geometry allows the phase modulator to attain a better performance as compared to straight waveguide modulators, since their compactness requires a much smaller heating surface area1. This paper presents our current and previous works in this research field [1,5], related to OPA based on Archimedean spiral waveguides as all-optical phase modulators driven by thermo-optical effect.

2. Design, Results and Analysis

Figure 1 schematically depicts a proposed architecture for an Optical Phased Array (OPA) Antenna applied for Laser Beam Pointing functionality, whereas Figure 2 schematically depicts the cross section and top view of an Archimedean spiral waveguide, used as a building block of optical phase modulation. In order to obtain high heat concentration and rapid heat dissipation, it was necessary to build a compact thermo-optical phase modulator with a small footprint and short total waveguide length [1,5]. We performed an iterative set of photonics and thermal computational simulations, intercalated with thermo-optical calculations, until we converged to the device topology, which allows to achieve an optical phase modulation amplitude of around π radians by applying realistic optical pump power levels. The optical phase variation (shift), $\Delta\phi$, is calculated by equation (1) [1,5].

$$\Delta\phi = \frac{2\pi}{\lambda}\frac{\partial n_{eff}}{\partial T}\Delta T.L \quad (1)$$

where $\Delta\phi$ is the optical phase shift, $\partial n_{eff}/\partial T$ is the thermo-optical coefficient, ΔT is the temperature variation, λ is the optical signal wavelength, and L is the total length of the spiral waveguide. From the iterative set of computational

simulations and calculations, we obtained the device footprint dimensions of 25 µm x 25 µm with a total length of the spiral waveguide of 360 µm; the waveguide core, made of Si, has a height (h_{core}) of 310 nm and two distinct widths (w_{guide}) of 0.5 µm and 0.6 µm, in each spiral arm direction (clockwise and counterclockwise, respectively), laterally separated by a distance between the core center of two subjacent waveguides (pitch) of 1.0 µm, which leads to a lateral SiO_2 gap of 450 nm. The choice of waveguides widths and pitch arose from preliminary optimization, taking into account several parameters of interest, such as: low propagation losses, low propagation coupling, compactness and efficient optical phase modulation.

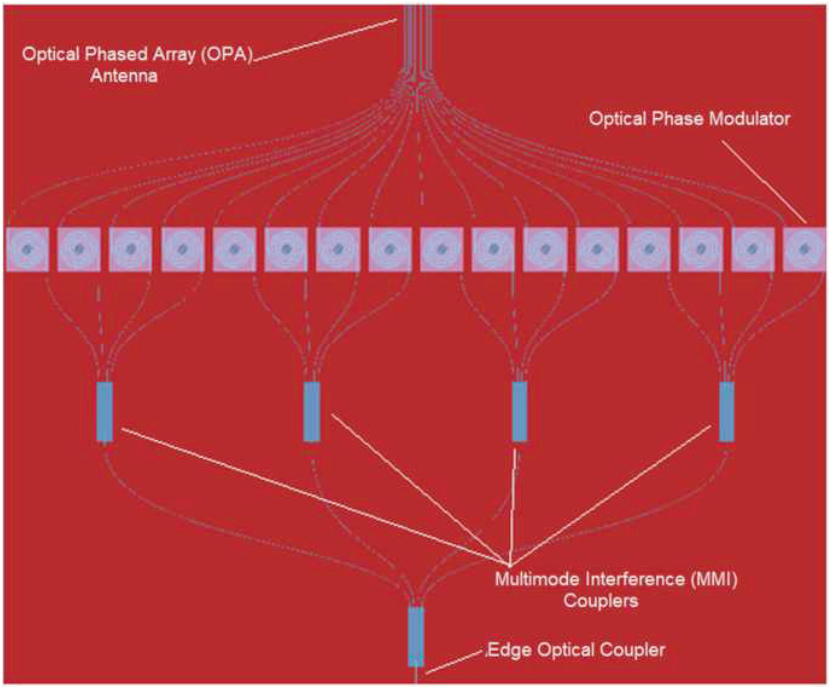

Fig. 1: Schematic of an Optical Phased Array (OPA) Antenna for Laser Beam Pointing.

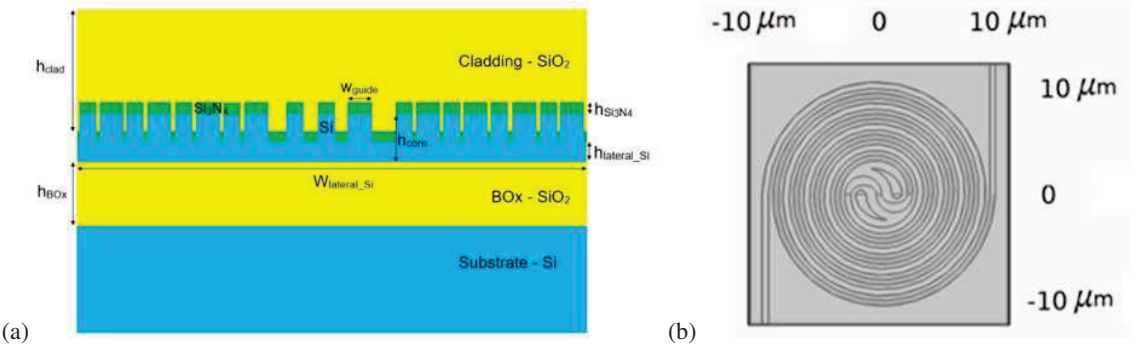

(a) (b)

Fig. 2: Schematic of an Archimedean spiral waveguide: (a) cross section and (b) top view [4,5].

Photonics computational simulations were performed with LUMERICAL software package and thermal computational simulations were carried out with COMSOL software package.

Optical heating is achieved by using visible or UV light as out-of-plane optical pump excitation (λ_p = 400 nm in this study), which is absorbed in Si core and lateral layers of the Archimedean spiral waveguide topology used as optical

phase modulators. Thermo-optical effect acts towards translating heat into optical phase modulation for optical signal carriers at C-band telecommunication wavelengths (around λ_s = 1550 nm).

We have assessed the effect of absorption of pump light by Si, by using the Transfer Method Matrix (TMM) approach; the absorption coefficient shows a peak for a 60 nm thickness of top Si_3N_4 layer, which provides an optical pump absorption rate of 88% in the waveguide core and 64% in the lateral Si layers.

The temperature distribution obtained from the simulation of stationary (steady state) heat condition mode is shown in Fig. 3, for out-of-plane optical pump excitation of P_p = 1 mW.

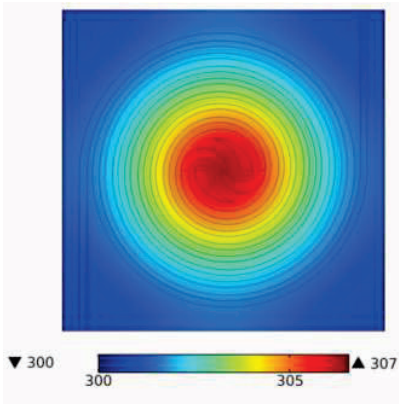

Fig. 3: Temperature distribution on the Archimedean spiral waveguide for P_p = 1 mW [1].

We observe a double temporal thermal response behavior, stemming from the fact that pump light is absorbed both by Si waveguide core and by other Si parts of the overall structure, with fast and slow thermal components showing approximate response times of only 1.4 and 10.3 μs, respectively. The steady state average temperature variation is 2.87 K. Figure 4 shows both transient and (asymptotically) steady state thermal behaviors.

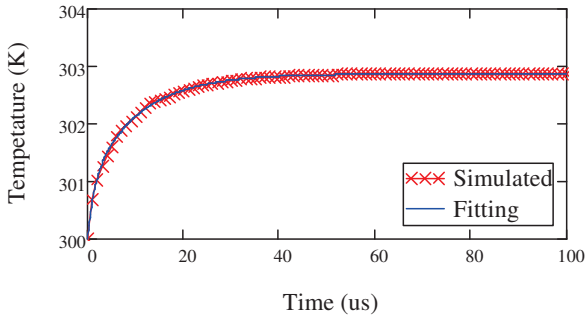

Fig. 4: Average temperature variation across the entire spiral waveguide - transient heat transfer [5].

The optical transmittance of the guided (signal) beam after propagating throughout each Archimedean spiral waveguide is found to be of 72%. This structure is still being optimized, and higher transmission efficiencies are foreseen.

From our photonics simulations, we estimate that an optical phase variation of $\Delta\phi = \pi$ in the optical signal will demand about P_p = 2.71 mW near λ_s = 1500 nm, and P_p = 2.90 mW near λ_s = 1550 nm. Comparing these results with state-of-the-art integrated optical phase modulators (phase shifters), shows that the power absorbed (or consumed) by this phase shifter, in order to attain $\Delta\phi = \pi$, is lower than those presented in references [6-9] and it is similar to the one in reference [2].

3. Conclusion

In summary, this work proposes an architecture for Optical Phased Array (OPA) Antennas related with Laser Beam Pointing functionality, based on silicon nanophotonics for compatibility with space applications; this approach includes an integrated thermo-optical phase shifter based on Archimedean spiral waveguide topology, and makes use of an all-optical modulation scheme, with out-of-plane optical pump excitation ($\lambda_p = 400$ nm) and guided optical signal (C-band) traveling inside the integrated spiral waveguide. Computational results show that such a compact device helps reduce the optical pump power consumption, allowing high non-optimized optical signal transmittance of 72%, and efficient optical signal phase shift; optical pump power below 3 mW was demanded for achieving optical signal phase shift of $\Delta\phi = \pi$ at wavelengths in the C-band. The proposed all-optical phase modulator has potential application in Optical Phased Array devices for space subsystems, remote or harsh environment sensors and communications, among others.

4. Acknowledgment

Vilson R. Almeida acknowledges Brazilian National Council for Scientific and Technological Development (CNPq) for research grants (306389/2021-5, 310855/2016-0 and 403031/2019-2).

5. References

[1] A. R. Santos, V. R. Almeida, and W. G. Santos, "Archimedean spiral waveguide as efficient all-optical phase modulator for space laser beam pointing", SPIE-OE **61**(8), 087102 (2022).
[2] H. Qiu *et al*., "Energy-efficient thermo-optic silicon phase shifter with well-balanced overall performance," Opt. Lett. **45**(17), 4806 (2020).
[3] V. R. Almeida *et al.*, "All-optical control of light on a silicon chip," Nature **431**(7012), 1081–1084 (2004).
[4] J. He *et al.*, "Review of Photonic Integrated Optical Phased Arrays for Space Optical Communication," IEEE Access **8**, 188284 (2020).
[5] A. R. Santos, W. G. Santos, and V. R. Almeida, "Archimedean spiral waveguide as a phase shifter for Optical Phased Arrays," in 2021 SBMO/IEEE MTT-S International Microwave and Optoelectronics Conference (IMOC), pp. 1–3 (2021).
[6] H. Nejadriahi *et al.* "Efficient and compact thermo-optic phase shifter in silicon-rich silicon nitride", Opt. Lett. **46**(18), 4646, (2021).
[7] S. Sabouri *et al.*, "Thermo Optical Phase Shifter with Low Thermal Crosstalk for SOI Strip Waveguide" IEEE Phot. J. **13**(2), 6600112 (2021).
[8] S. De*et al.*, "CMOS-Compatible Photonic Phase Shifters with Extremely Low Thermal Crosstalk Performance," J. Light. Technol. **39**(7), 2113–2122 (2021).
[9] J. Parra *et al.*, "Ultra-low loss hybrid ITO/Si thermo-optic phase shifter with optimized power consumption" Opt. Express **28**(7), 9393 (2020).

Micro-Endo-Spectroscopy of Oral Cancer Tissue: Simultaneous Fluorescence Polarization, Imaging and Spectroscopy

Pramila Thapa[1#], Dibya Jyoti Sarangi[1], Sunil Bhatt[1], Priyanka Mann[1], Deepika Mishra [2] and Dalip Singh Mehta[1*]

[1]Bio-photonics and Green-Photonics Laboratory, Department of Physics, Indian Institute of Technology Delhi, Hauz-Khas, New Delhi 110016, India.

[2]Oral Pathology, Centre for Dental Education & Research (CDER), AIIMS New Delhi, India

Email- #pramilathapa643@gmail.com

**mehtads@physics.iitd.ac.in*

Abstract: Utilization of multi-modality for investigation of cancerous tissues can reduce fatality-rate and increase diagnostic accuracy. In this paper multi-modal device for oral cancer screening is developed using fluorescence-imaging, fluorescence-polarization and fluorescence-spectroscopy simultaneously, named as micro-endo-spectroscopy. The device is in-house developed and oral cancer tissues are provided by AIIMS Hospital.

Keywords: multi-modal, micro-endoscope, fluorescence polarization, fluorescence spectroscopy, oral squamous cell carcinoma

1. Introduction

Fluorescence polarization (FP) imaging is a powerful technique in oral cancer detection as it probes orientation of emitted photon's electric field and directly deals with molecular level changes [1]. Microenvironment of oral cancer tissue holds the change in intracellular elements and extracellular matrices like collagen matrix, nicotinamide adenine dinucleotide, flavin adenine dinucleotide etc. compared to normal tissue [2]. FP is able to investigate these changes within the oral cancerous tissue. When the polarized light is incident on the oral cancer tissue the multiple scattering phenomenon occurs and provide information regarding scatterers within tissue and can be gathered by intensity variation in different polarization states [1]. Fluorescence spectroscopy (FS) of tissue shows the changes in chemical composition of oral cancerous tissue and normal tissue [3]. FP imaging can provide morphological changes of the cancerous tissue and fluorescence spectroscopy can give idea about the molecular formation during oral cancer progression. Integration of these three techniques within a single unit can give more accuracy and sensitivity for oral cancer detection.

In this paper a multi-modal device is used for oral cancer screening using three modalities, FP, fluorescence imaging and spectroscopy simultaneously. Linear polarization, cross polarization intensities and simultaneous fluorescence imaging and spectroscopy are calculated for the onion epithelial layers and oral cancer tissues. FP and anisotropy of these biological specimen are calculated as [1]:

$$FP = \frac{F\| - F^{\perp}}{F\| + F^{\perp}} \quad (1)$$

$$Anistropy = \frac{F\| - F^{\perp}}{F\| + 2F^{\perp}} \quad (2)$$

Where F‖ is linear polarization and $F^{\perp}$ is cross polarization state of the biological specimens.

2. Experimental Setup

Experimental system for the fluorescence polarization and spectroscopic device is shown in Fig. 1. It consists of 488nm laser, illumination optical fibre, GRIN rod lens, band pass filter F_1 and F_2 (510nm-560nm), sodium salt of fluorescein dye (488nm excitation and 520 nm emission; 1:70 with distilled water), polarizer, analyser, CCD camera and a spectrometer. The whole device is assembled in lab. With 3D printed mounts. Illumination optical fibre couples the laser light and travel through a polarizing annular ring and illuminates the sample with polarized light at 45^0. GRIN

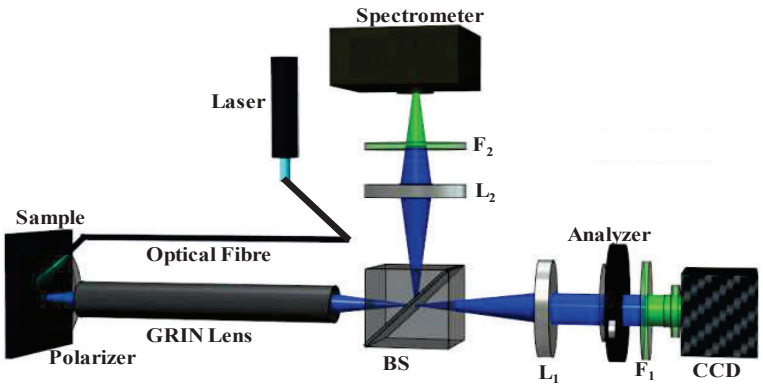

Fig: 1 Experimental setup for fluorescence polarization and spectroscopic system.

lens collects the fluorescence from sample and Beam Splitter divide the information in 50-50. In one arm of BS, L_1 collimates fluorescence signal and filter F_1 filters it which is captured by CCD camera. An analyser is used after L_1 for collecting linear FP ($F\|$) and cross FP ($F^{\perp}$). In another arm of BS L2 focuses the light after filtration from F2 to spectrometer and record the fluorescence spectrum simultaneously.

3. Results and Discussion

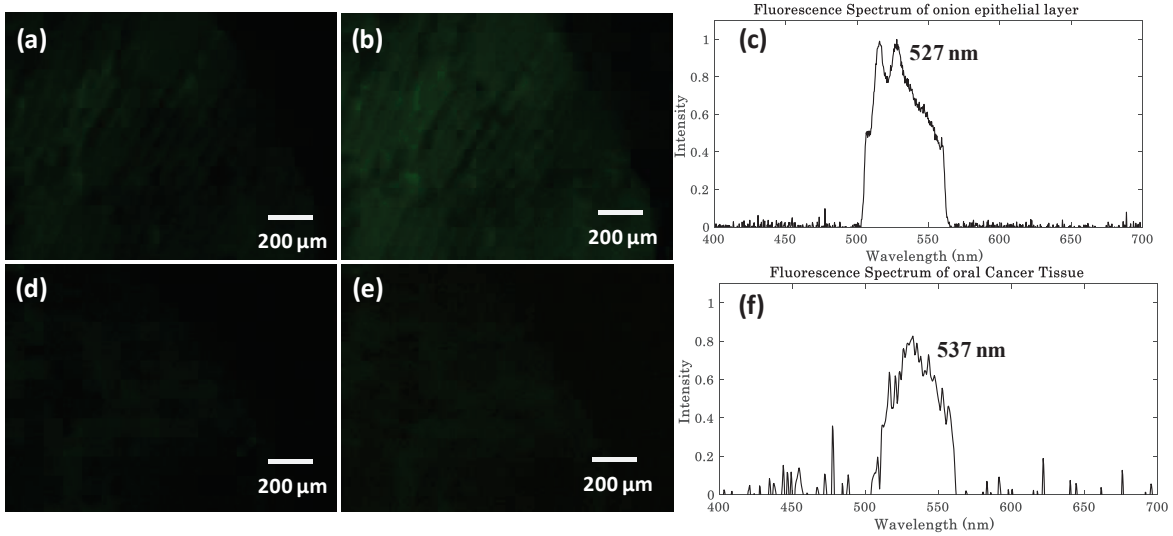

Fig. 2: Fluorescence polarization images and fluorescence spectroscopy of biological samples.

Figure 2 is showing experimental results for biological specimens. At first experiments are performed with onion epithelial layers for validation of the device and after successful adaption we performed the experiment for the oral cancer tissues and fluorescence polarization, imaging and fluorescence spectra are recorded. Oral cancer tissues are taken from the AIIMS hospital New Delhi, India and sliced in thickness of 10 µm with microtome and prepared on optically flat standard microscopic slides. Fig.2 (a)-(c) are $F^{\perp}$ image, $F\|$ image and fluorescence spectra of onion epithelial layer respectively. Fig. 2 (d)-(e) are $F^{\perp}$ image, $F\|$ image and fluorescence spectra of oral cancer tissue.

Sodium salt of fluorescein dye is used as an exogenous agent for experiments. Table 1 is indicating quantitative parameters for onion epithelial layers and oral cancer tissue. Mean fluorescence intensity indicates the tagging of dye within the specimen and due to angiogenesis in cancer tissue, mean intensity will be higher [3]. Fluorescence polarization and anisotropy deals with the fluorescein tagged molecules in cancer tissues giving morphological information and is different compared to normal tissues [1]. Peak wavelength, full width half maximum (FWHM),

area under the curve (AUC) are calculated with fluorescence spectroscopy and shows different behavior for cancerous tissues due to the increased heterogeneity and increased index of refraction [3].

Table 1: Quantitative parameters for biological specimen

Sample	Mean fluorescence intensity	Fluorescence polarization	Anisotropy	Peak wavelength	FWHM	AUC
Onion	190±1.2	$9.26 \times 10^{-2} \pm 1.4 \times 10^{-2}$	$6.37 \times 10^{-2} \pm 1.0 \times 10^{-2}$	525±1.15	50.5± 1.55	$\sim 2.7 \times 10^{6}$
Oral Cancer	163±1.14	$6.0 \times 10^{-2} \pm 1.3 \times 10^{-2}$	$4.08 \times 10^{-2} \pm 0.9 \times 10^{-2}$	535±1.14	62.22± 1.37	$\sim 4.7 \times 10^{6}$

4. Conclusion

We demonstrated a simultaneous micro-endoscopic fluorescence polarization and fluorescence spectroscopic system for the oral cancer screening. Morphological changes in cancerous tissues are probed with FP and anisotropy, and molecular level changes and chemical composition of cancerous tissues are calculated with fluorescence spectroscopy which further offers progression state of the cancer.

5. References

[1] Yaroslavsky Anna N., et al. "Fluorescence polarization of methylene blue as a quantitative marker of breast cancer at the cellular level." *Scientific reports* 9.1 (2019): 1-10.

[2] Skala, Melissa C., et al. "In vivo multiphoton microscopy of NADH and FAD redox states, fluorescence lifetimes, and cellular morphology in precancerous epithelia." *Proceedings of the National Academy of Sciences* 104.49 (2007): 19494-19499.

[3] Thapa, Pramila, et al. "Development of multimodal micro-endoscopic system with oblique illumination for simultaneous fluorescence imaging and spectroscopy of oral cancer." *Journal of Biophotonics* (2022): e202100284.

A Review of the Effect of Abrasive Slurry Characteristics during Chemical Mechanical Polishing of Fused Silica Optical Glass

[1,2,a)]Aparajita Parashar, [1,2,b)] Raj Kumar Pal, [1,2,c)]Vinod Karar

[1]*Academy of Scientific and Innovative Research(AcSIR), Ghaziabad,201002, India*

[2]*CSIR-Central Scientific Instruments Organisation (CSIR-CSIO), Sector-30,Chandigarh, 160030, India*

[a)]aparajita.csio21j@acsir.res.in [b)]rajkpal@csio.res.in [c)]vinodkarar@csio.res.in

Abstract: Due to the intensive use of fused silica, precision polishing is highly demanded for applications like astronomy, aerospace, laser systems, optical systems, etc. Various input parameters such as applied pressure, velocity, abrasives, and etc. plays important role in the polishing process. Material removal rate (MRR), surface roughness (Ra) and flatness are some parameters that depends on the characteristics of abrasive slurry used in the CMP process. Effect of various slurry properties like size and type of abrasives, pH and concentration of slurry, and morphological & chemical conditions and their effect on material removal and surface roughness have been reviewed in this article.

Keywords: CMP; MRR; Abrasive; pH; polishing; Optical glass

1. Introduction

Fused silica is compatible to work in large number of applications due to its properties of working on high temperature, transmission region includes visible, ultra-violet and infra-red, high hardness. Fused silica being used in applications like laser systems requires high precision surface accuracy. Chemical mechanical polishing (CMP) is one of the processes to generate the desired surface accuracies. Optical fabrication process generally manufactures components from glass used in the optical applications due to its properties of light transmission in different spectrum and minimum scattering of light. Optical fabrication process includes number of steps: 1). Shaping 2). Grinding 3). Polishing and 4). Sub-aperture polishing (used sometimes). This article predominantly discusses about the effect of abrasive & slurry conditions on the material removal and surface roughness of the optical fused silica glass. It delivers the inclusive knowledge of various aspects related to abrasives and slurry during the chemical mechanical polishing of an optical fused silica glass.

2. Review of Characteristics of Abrasive Slurry

Various characteristics of abrasive slurry and their effects have been described in this section. Morphological conditions refers to the shape, form and structure of the abrasives, pH tells the acidic and basic behavior of the slurry, concentration means the weight percentage of the abrasive particles present in the slurry.

2.1 *Morphological and Chemical Conditions of Abrasives*

Cook, L.M. *et al.*, [1] presented the material removal at molecular level due to chemical actions. The cerium oxide based slurry reacts with the surface of glass and form new bonds, these new bond formed are high in strength, and preferred over the primary bond and thus, the material starts getting removed chemically from the workpiece.

$$Ce - OH + HO - Si \rightarrow Ce - O - Si + H_2O$$

N. Belkhir *et al.*, [2] showed the wear behavior of the abrasive CeO_2 particles during polishing. Partial wear behavior of abrasive grains occurs due to process parameters but morphological conditions remain same.

T.S. Sreeremya *et al.*, [3] investigated the polishing efficiency of the nano-abrasives (CeO_2) in terms of the material removal and surface roughness achieved on glass substrate. Surface characteristics of the abrasives are important in polishing process, as revealed by X-ray photoelectron spectroscopy.

2.2 *pH and Concentration of slurry*

C. Kang *et al.*, [4] talked about the crucial role of slurry during CMP of fused silica. It shows that during increase of recycling time, pH decreases and increase of solid content in slurry are two main factors affecting MRR.

Liangyong Wang, *et al.*, [5] found that the rate of material removal increased, with the decrease in concentration of ceria from 1 to 0.25 weight percentage during CMP of optical glass using ceria as slurry, which is abnormal phenomenon from the conventional theories. It is because of the uniform particle size in a lower concentration and a better quantum process occurred at the ceria surface in aultra- lower concentration.

J.T. Abiade et al., [6] studied the effect of pH of ceria slurry on the removal of silica and surface morphology. Result shows that the silica removal due to ceria slurry is mainly depend on pH of slurry. The maximum amount of silica removal is found near the isoelectric point of the slurry.

2.3 *Size of abrasives*

Z. Zhang, *et al.*, [7] explored the effect of abrasive size and surfactant using colloidal silica based slurry. Founded that with the variation in size of the abrasives the mechanism of material removal can be changed from indentation of particles to surface area mechanism. Introduction of surfactants effects glass substrate due to different charge type, which causes different values for removal rate and rms roughness.

G. B. Basim *et al.*, [8] presented the effect of large sized particle in chemical mechanical polishing (CMP). It was observed that the presence of large sized particles not only affects the material removal but also causes surface damage. Polishing mechanism is discussed as a particle size and concentration of the abrasive particles.

Yan Zhou et al., [9] showed that the average size of silica particle in the slurry varies with the polishing time. With prolonging recycling polishing time, gradual increase in the average particle size of the silica was observed due to aggregation.

3. Conclusion

This article reviews the effect of various characteristics of abrasive slurry such as size of abrasives, pH & concentration of slurry, and morphological & chemical conditions of the slurry, on the material removal and surface roughness of an optical glass during the process of chemical mechanical polishing. Size of the abrasive play an important role in the material removal, large size abrasive cause's large material removal but surface roughness achieved is less and surface damage is more. Material removal generally decreases with the decrease in concentration of slurry but sometimes also increases with the ultra-low concentration of ceria slurry which is abnormal phenomenon. Morphological conditions are also an important characteristic, as the amount of surface in contact effects the material removal and surface roughness.

4. References

[1]L.M. Cook, "Chemical processes in glass polishing" Journal of Non-Crystalline Solids,(1990).
[2]N. Belkhir, "Wear behavior of the abrasive grains used in optical glass polishing", Journal of Materials Processing Technology 209(2009).
[3]T.S. Sreeremya, "Tailoring the surface properties of cerium oxide nano-abrasives through morphology control for glass CMP",Royal Society of Chemistry (2015).
[4]Chengxi Kang, "The Cycle Characteristics of Slurries in Chemical Mechanical Polishing (CMP) of Fused Silica", Chemistry Select (2020).
[5]L. Wang, "Ceria concentration effect on chemical mechanical polishing of optical glass", Applied Surface Science (2007).
[6]J.T. Abiade, "Effect of pH on ceria–silica interactions during chemical mechanical polishing", Journal of Materials Research Society, (2005).
[7]Z. Zhang, "Particle size and Surfactant Effects on CMP of Glass using Silica based Slurry", Optical Society of America (2010).
[8]G.B. Basim,"Effect of Particle Size of CMP Slurries for Enhanced Polishing with Minimal Defect",Journal of Electrochemical Society (2000).
[9]Yan Zhou, "Characteristics of Slurry Recycling in Chemical Mechanical Polishing (CMP) of Fused Silica (FS)", ECS Journal of Solid State Science and Technology, (2019).

Comparison of quantum and quasi-classical transmission in absence of bulk dissipation

Kuldeep Kumar Shrivastava*, Rajeev Singh**
/ Department of Physics, Indian Institute of Technology, Banaras Hindu University, Varanasi-221005, INDIA .*
**Kuldeep224@gmail.com*

Abstract: Our system is one-dimensional open QED lattice when the qubits are directly coupled and we are studying the non-linear optical transport of light through the 1-d chain when the chain is connected to radiation fields at the boundaries. In the absence of optical confinement (cavity) along the light propagation direction in particular we perform a comparison of quantum and quasi-classical transmission in absence of bulk dissipation when the intensity is somewhat high.
Keywords: Quantum optics, Light-matter interaction, Open quantum systems

When light is propagating through an open QED lattice here the chain of qubits in one-dimension with direct nearest neighbors coupling we are comparing quantum transport of light when the system is connected to radiation fields at the boundaries. one example of the system is putting nano-diamonds (qubits) in a photonic crystal (line-defect waveguide) and letting it to operate into optical domain.

The system shows photon blockade phenomena. Till now different theoretical approaches, including analytical and numerical methods already have been explored. The main challenge in applying these theoretical approaches is the scaling of the system sizes when we are going from single/ multiple qubits to a mesoscopic collection of qubits.

We compare two theoretical approaches first the Truncated Heisenberg Langevin equation (THLE), After truncating the quantum Heisenberg Langevin equation (QHLE) we get the truncated Heisenberg Langevin equation (THLE). Solution of this is same as master equation as we increase the system sizes the number of THLEs/QHLEs grows exponentially which tends to reach the computational limit even after large truncation.

The second approach is the quasi-classical analysis (QCA), Equations increase linearly with system size and hence enables us to analyze inelastic scattering of the photons for hundreds of qubits. However, with increasing intensity, the QCA fails to capture any effects of inelastic scattering of the photons effects as of THLE analysis.

As we are comparing the two approaches it is clear that if intensity is somewhat high and bulk dissipation is absent then the standard quasi-classical analysis (QCA) is not taking into account the photon-photon effective interaction therefore missing the phenomenon of reduction in light transmission. It is common for experiment papers to use the quasi-classical analysis to study the systems but there are limitations to what quasi-classical analysis can capture with reasonable accuracy. It can be used with good accuracy for some properties for another set of properties it can be used moderately but after a certain range where nonlinear effects cannot be neglected they shows a departure from quantum behavior.

We consider a medium to which bath are attached on both sides. Hamiltonian of the system is given below,

$$H_{Medium} = \sum_{n=1}^{N} \hbar\omega_{qn} b_n^\dagger b_n + \hbar U b_n^\dagger b_n (b_n^\dagger b_n - 1) + \sum_{n=1}^{N-1} 2\hbar J_x \left(b_n^\dagger b_{n+1} + b_{n+1}^\dagger b_n\right)$$

our system is attached to bath from left side (laser) and right side (detector) which we are model as collection of harmonic oscillators. n is the number of qubits in the system, ω_{qn} is the nth qubit frequency of the system $b_n^\dagger(b_n)$ is bosonic creation (annihilation) operator for the nth qubit of the system. U determines strength of onsite interaction, $2J_x$ is the coupling strength between neighbouring qubits. We shine Laser from left side of the qubit system with frequency ω_p.

At low intensity and in bulk dissipation the quasi-classical analysis matches the Heisenberg Langevin analysis (QHLE/THLE) but when we go to higher intensity QCA fails to matches the analysis of Heisenberg Langevin theory. By the time

the input intensity is 0.0003 the differences between both the predictions are clear and we show a comparison for the coupling strength J_x=0.01 and 0.02 for the system of two qubits.

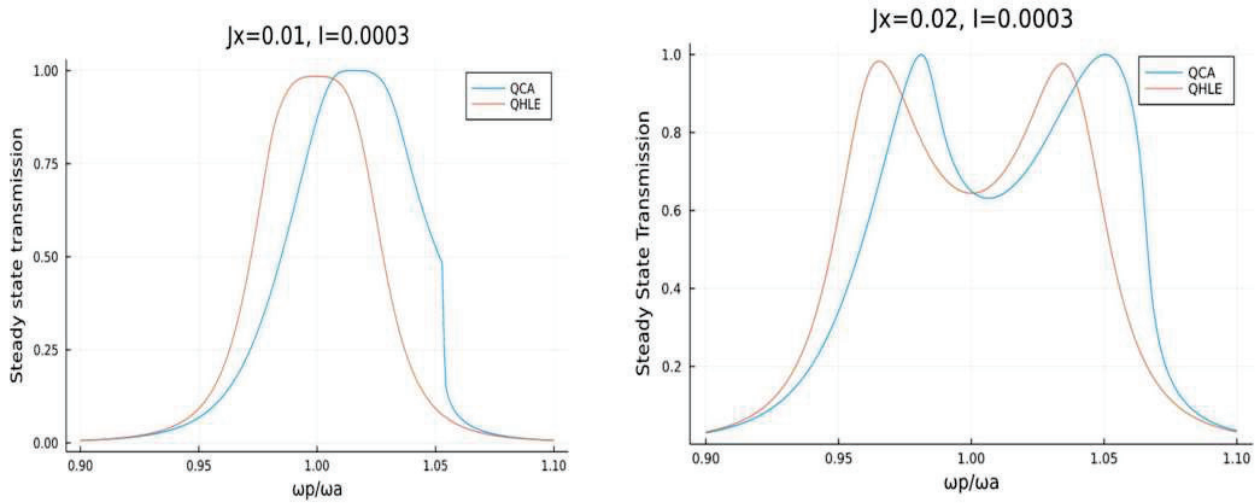

Comparison of steady state transmission as a function of input frequency using QCA and QHLE for J_X=0.01(left) and 0.02 (right)

Left figure: Here the QCA is blue one which is the quasi-classical analysis and at the resonance when qubit frequency matches the laser frequency the peak of QCA is shifted rightward from the resonance with transmission value 1 this is incorrect the correct behavior is shown by red curve which having maximum transmission at resonance and the value is also slightly lower than the QCA. also the THLE/QHLE graph is symmetric about resonance which is the correct behavior of the system.

Right figure: Here the QCA is blue one which is the quasi classical analysis and at the resonance when qubit frequency matches the laser frequency the peak of QCA is shifted rightward from the resonance which is not the correct quantum behavior. when we are increasing the coupling strength between neighboring qubits that creates effective interactions amongst the photons that is mediated by excitation of the qubit's. This effective interactions or say optical nonlinearities cause photon blockade resulting in reduction of transport of photons and also causes the splitting of transmission profile in two lobes at the top that is obvious as maximum transmission in the THLE transmission profile is getting decreased. But QCA is only showing shifting of the transmission profile also the two lobes are not symmetrical this is incorrect. The correct behavior is shown by red curve the THLE/QHLE graph is symmetric about resonance which is the correct behavior of the system.

1. References

[1] D. Roy, C. M. Wilson, and O. Firstenberg, Rev. Mod. Phys. **89**, 021001 (2017).
[2] F. M. Fitzpatrick, N. M. Sundaresan, A. C. Y. Li, J. Koch, and A. A. Houck, Phys. Rev. X **7**, 011016 (2017).
[3] P. Manasi and D.Roy, Phys. Rev. A 98, 023802(2018)
[4] M. O. Scully and M. S. Zubairy, Quantum Optics (Cambridge University Press, 1997).
[5] D. Plankensteiner, C. Hotter, and H. Ritsch, "QuantumCumulants.jl: A Julia framework for generalized mean-field equations in open quantum systems," Quantum 6, 617 (2022).

Evaluation of Wide field Telecentric, Band to Band Registered Multispectral Lens Assemblies for Ocean Color Monitor

K.Sathyanarayana Raju, M.G.Rajeesh, , Bijoy Raha , Arunita Kumari, A.Lekshmi, R.Chetan Kumar, T.E.Pramod, Ramajagol R.Rajkumar, U.R.Subrahmanyam, U.V.Sreeram Kumar, R.Venkateswaran

Sci./Engr. 'SE', Laboratory for Electro-Optics Systems (LEOS), ISRO, DOS,
1st Cross, 1st Stage, Peenya. Indl. Estate, Bangalore-560013.
ksraju@leos.gov.in

Abstract: OCM-3 is a multi-spectral camera consists of 13 spectral bands in the region of 0.402 to 1.030 microns covering a wide swath of 1440 kms through a large field of view of 87 Degrees with a resolution of 360m. In order to cater wide swath, an aspheric element based telecentric lens design is realized. Criticality of multi-spectral imagery is the geometric accuracy and band-to-band registration. It is essential to have matched image formats and distortion profiles for all the lens assemblies over the entire field of view. The absolute image formats of all lens assemblies are within ±0.015 % and distortion matching within ±0.02 %. Additionally, Collinearity (optical axis stability) is within 2 µm radius circle. The current paper presents the achieved results, namely MTF, EFL, Distortion over the entire FOV and Collinearity of all 13 lens assemblies.

Keywords: Multi spectral camera, telecentric lens, Band to Band registration, MTF, EFL, Collinearity.

1. Introduction

Ocean Color Monitor-3 (OCM-3) an improvement over OCM-1 and 2[1] having 13 spectral bands and fine spectral resolution in the region of 0.402 to 1.030 microns to cater to new ocean studies requirements. Each spectral band uses separate imaging to image the scene on to the CCD. The spectral band selection is carried out with a band-pass filter. Thus the 13-band camera consists of thirteen separate lens assemblies, each assembly having its own band-pass filter and CCD. The critical requirement of wide field coverage is achieved using an aspheric based telecentric lens design covering the FOV of 87 degrees. The challenges faced in the realization of lens assemblies are to match the image formats within 6 microns range for all 13 bands and achieving distortion within ±0.05% over entire field. Also, the relative distortion among the lens assemblies is within ±0.02%. The thermal expansion of materials is considered for having interference fit for the lens assemblies which plays an important role in the crucial image format matching and stability during environmental tests. All the lens assemblies are optimized for required performance and evaluated as per Space qualification requirements of temperature and vibration.

2. Specifications

A set of 13 matched lens assemblies are tested and qualified for space usage for OCM-3 covering spectral bands in the region of 0.402 to 1.030 microns [2]. Apart from the crucial image format and distortion matching, each of the telecentric lens assembly is realized with acceptable relative illumination, high mechanical stability [3], minimum veiling glare and high optical transmission meeting the overall SNR requirement.

The critical optical parameter specifications are given in the Table below.

Sl. No.	Optical Parameter	Specification
1.	Equivalent Focal Length (EFL) (mm)	20 ± 0.1
2.	Tolerance on EFL for a set of 13 (B1 to B13) matched lens assemblies (one for each band) (% EFL)	≤ ± 0.015

3.	Distortion (%)	≤ ± 0.05
4.	Variation in distortion for a set of matched lens assemblies (%)	≤ ± 0.02
5.	Transmission (T) (%)	≥ 60 for B1, ≥ 65 for B2, ≥ 68 for B3 to B7, ≥ 70 for B8 to B13
6.	Veiling Glare (%)	≤ 2.0
7.	Non-uniformity of Illumination in the image format (%)	≤ 22
8.	The change in collinearity during and/or after environmental tests (microns) (radius circle)	≤ ± 2.0
9.	MTF (%) @ 50 lp/mm for B1-B10 @ 17 lp/mm for B11-B13	≥ 50 for B1, ≥ 55 for B2-B10, ≥ 70 for B11-B13

3. Results

Successfully realized and qualified 13 lens assemblies complying to the stringent specifications. All lenses have undergone space qualification environmental tests. The deviations were well within the tolerances. The results of distortion, MTF, collinearity measurements and EFL variations carried out during the test and evaluation are listed in Fig. 1 to 4.

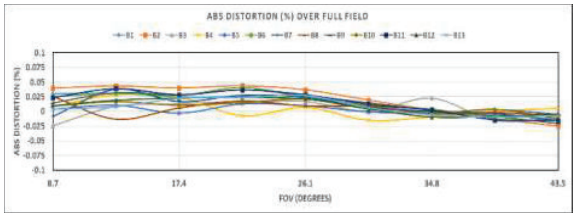

Fig. 1.Distortion

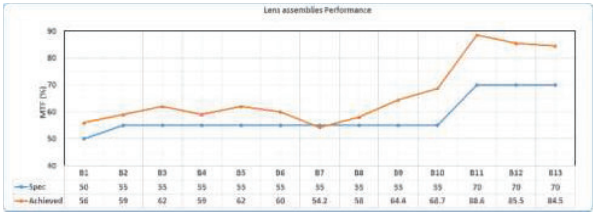

Fig.2 MTF

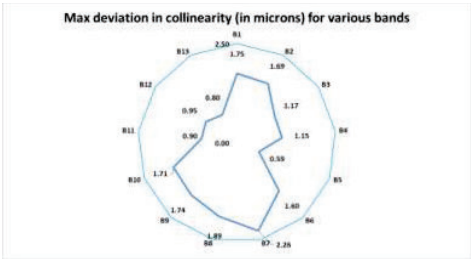

Fig. 3: Collinearity

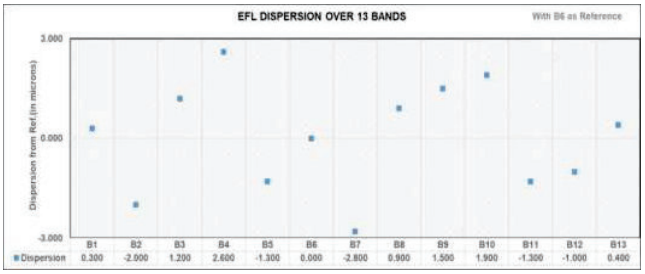

Fig. 4: EFL dispersion over 13 bands

4. Acknowledgement:

The authors express their deep gratitude and thanks to Director, LEOS for the constant encouragement and guidance given throughout the project for the realization of such challenging lens assemblies.

5. References:

[1] Ranganath R. Navalgund "Ocean Color Monitor on board-OCEANSAT-2" 13th IOCCG Committee meeting Paris, France (13-14 Feb 2008)
[2] Luc Thépaut "Fabrication and test of high performance wide angle lens assemblies for ocean colour monitor" Part of the EUROPTO Conference on Optical Fabrication and Testing • Berlin, Germany • May 1999
[3] U V Sreeram Kumar, "Characterization of Image format and Collinearity of multi-element lens optics using a high Accuracy Registration and Collinearity Test Bench," XXXVI OSI Symposium on Contemporary Optics and Opto-electronics ,IIST Thiruvananthapuram (2011).

Blue-LED Array Based Total Internal Reflection Fluorescence Microscopy and Its Applications

Shivam Trivedi, Anuj Saxena, Shilpa Tayal, D.S. Mehta

Green Photonics Laboratory, Department of Physics Indian Institute of Technology Delhi, Hauz Khas New Delhi-110016.

Author's e-mail address: Shivam.Trivedi@physics.iitd.ac.in

Abstract: We have design and developed a blue-LED array based total internal reflection fluorescence microscope, named TIRFM unit and recorded the image of chicken tissue image, for scaling we have used polystyrene bead of size 7μm. TIRFM microscopy is important for large area imaging and high signal to noise ratio. In addition, the actual axial resolution of TIRFM is high because of the limited depth of penetration of evanescent field. In most of the TIRFM system a laser light is used which is costly and cumbersome in this paper we resent a simple LED array based TIRFM microscope using special type of beam profile of LEDS is used.

Keywords: Green fluorescent protein, Polystyrene, Total internal reflection.

1. Introduction

Microscopy is one of the oldest fields of research dating back to 17th century. It has application in almost every discipline of science and industry such as medical sciences and automobile industry. Modern day microscope is capable of imaging down to the scale of nanometer using computer algorithms, but the reduction in the resolution increases the complexity of the instrument that also increases the cost of the microscope. Most of the biological samples are Transparent in nature therefore difficult to obtained high contrast images using bright field microscopy. Fluorescence microscopy was developed to improve the contrast of the image. Epifluorescence and confocal microscopy are most widely used techniques. In epifluorescence microscopy lase beam is directly focused to the sample and leads to poor SNR. In confocal microscopy the SNR can be improved by point-by-point scanning but in both these techniques direct laser beam illumination is used which may cause degradation to the sample, unwanted produce speckle pattern and also cause affect such as photo bleaching etc. That may alter the resultant image features.

TIRFM is one of the famous techniques for large area imaging and high signal to noise ratio. In addition, the actual axial resolution of TIRFM is high because of the limited depth of penetration of evanescent field. In most of the TIRFM system a laser light is used which is costly and cumbersome. in this paper we resent a simple LED array based TIRFM microscope using special type of beam shape of LED. Experimental result of biological sample will be presented.

2. Methodology

Total internal reflection fluorescence microscopy allows us to miniaturization and easy to incorporate with other modalities of microscopic techniques, it offers enhance depth of resolution. It has novel application on single molecule imaging.

When a light propagating through a medium of refractive index n_1(e.g. glass) meets an interface, medium of refractive index n_2<n_1(e.g. biological sample). Total internal reflection occurs at all angle of incident Θ that are greater than the critical angle $\theta_c = \sin^{-1}(\frac{n_2}{n_1})$.

Despite being totally reflected a part of incident beam becomes evanescent electromagnetic field that penetrate into the second medium.

Figure 1.1 Experimental setup

Penetration depth in the second medium is given by the following equation that decreases exponentially with z.

$$d = \frac{\lambda}{4\Pi.\sqrt{(n_1^2 sin^2(\Theta) - n_2^2)}}$$

The intensity as a function of z distance is given as $I = I_0 e^{(-z/d)}$.This evanescent field can be used to improve SNR in TIRFM based microscopy setups, since the light is confine in a narrow region. We have designed and developed a blue-LED array based Total internal reflection illumination unit (TIRF) for whole slide illumination, we have tagged our sample with fluorescence dye for fluorescence and used blue LED array to excite the dye, which leads to the reemission of green light. The light is being collected with low magnification (5X) objective from the sample for image recording we have used Lumera Infinity2 CCD camera.

3. Conclusion and Results

We have used a standard 1inch X 3inch cover glass slide as a multimodal waveguide for the wavelength 445nm the critical angle for BK7/glass approximately 42°, the rays that are greater than critical angle will be guided inside the coverslip.

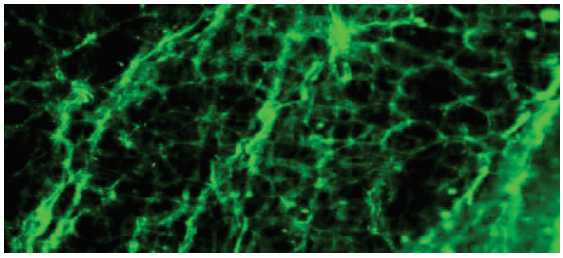

Figure 3.1 Chicken Tissue image

The image of chicken tissue was being taken from the TIRFM microscope and for scaling we have used industrial polystyrene microbead of 7μm as shown in the figure 3.2 below.

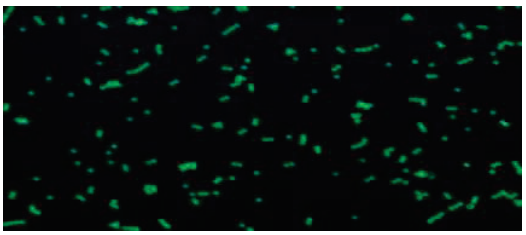

Figure 3.2 Polystyrene Microspheres

While taking these two images no expertise is needed, we just insert the sample mounted coverslip into the TIRFM unit and captured the images. This type of setup can be used by hobbyist microscopist and in schools where most of the children are unaware of how to use microscope. There is a lot to improve in terms of resolution since this microscope does not improve lateral resolution in but easy to handle and needs no expertise to operate.

[1] *Schneckenburger, Herbert. "Total internal reflection fluorescence microscopy: technical innovations and novel applications." Current opinion in biotechnology 16.1 (2005): 13-18.*

[2] Schmoranzer, Jan, et al. "Imaging constitutive exocytosis with total internal reflection fluorescence microscopy." *The Journal of cell biology* 149.1 (2000): 23-32.

[3] Mathur, Anshu Bagga, George A. Truskey, and W. Monty Reichert. "Total internal reflection microscopy and atomic force microscopy (TIRFM-AFM) to study stress transduction mechanisms in endothelial cells." Critical Reviews™ in Biomedical Engineering 28.1&2 (2000)

[4] Reck-Peterson, Samara L., Nathan D. Derr, and Nico Stuurman. "Imaging single molecules using total internal reflection fluorescence microscopy (TIRFM)." Cold Spring Harbor Protocols 2010.3 (2010): pdb-top73.

[5] Burmeister, Jeffrey S., et al. "Application of total internal reflection fluorescence microscopy to study cell adhesion to biomaterials." Biomaterials 19.4-5 (1998): 307-325.

Analytical formulation of Schmidt decomposition in SPDC

Vikash Kumar Yadav[1*], Vivek Venkataraman[1,2], and Joyee Ghosh[1]
[1]*Department of Physics, Indian Institute of Technology Delhi, New Delhi 110016, India*
[2]*Department of Electrical Engineering, Indian Institute of Technology Delhi, New Delhi 110016, India*
**phz188434@physics.iitd.ac.in*

Abstract: We outline an explicit procedure to perform Schmidt decomposition to compute the spectral correlation between photon pairs generated in a spontaneous parametric down-conversion (SPDC) process. Hermite-Gaussian functions are used as the basis to decompose the biphoton state and simple analytical formulae for the Schmidt mode coefficients (eigenvalues) are derived. The accuracy of our analytical formulation is verified against two separate sets of published values.
Keywords: Nonlinear optics, SPDC, Schmidt decomposition, Spectral correlation

1. Introduction

Spectral correlation is an important property exhibited by the photon pairs generated through the SPDC process as a direct consequence of energy conservation. A detailed knowledge of such frequency correlation between biphotons is important for applications such as quantum key distribution [1]. This correlation or entanglement can be characterized using the Schmidt decomposition metric, where a preferred orthonormal basis is constructed to measure the correlation [2]. However, for a heralded single-photon source, typically, no spectral correlation is desired between the biphotons, which can be satisfied under certain conditions. Here we derive those specific conditions for photon pairs generated via the SPDC process, and find an analytic expression that measures the degree of spectral correlation.

2. Schmidt decomposition

The biphoton output state of a SPDC source is given as [3]

$$|\psi\rangle = \mathrm{S} \iint d\omega_s \, d\omega_i \, f(\omega_s, \omega_i) \hat{a}^\dagger(\omega_s) \hat{a}^\dagger(\omega_i) |0\rangle_s |0\rangle_i \tag{1}$$

where S is the spatial overlap of pump, signal, and idler modes, $\hat{a}^\dagger(\omega_{s,i})$ are the creation operators, and $\omega_{s,i}$ are the frequencies of signal and idler, respectively. The function $f(\omega_s, \omega_i)$ is the biphoton amplitude or joint spectral amplitude (JSA) defined as

$$f(\omega_s, \omega_i) = e^{-\left(\frac{\omega_s + \omega_i - \omega_p}{\sigma_p}\right)^2} \operatorname{sinc}\left(\frac{\Delta k L}{2}\right) \tag{2}$$

where $\omega_p$and $\sigma_p$are the pump frequency and bandwidth, respectively, and Δk is the phase-mismatch. In general, the JSA is not factorable i.e., $f(\omega_s, \omega_i) \neq \psi(\omega_s)\phi(\omega_i)$, which means that the state is not separable in frequency signifying spectral correlations. One can quantify the degree of factorizability of the biphoton state produced via SPDC by performing Schmidt decomposition in the frequency basis. To characterize the degree of separability of the photon pairs, we expand the JSA in an eigenbasis such that it can be written as [3]

$$f(\omega_s, \omega_i) = \sum_n \sqrt{\lambda_n} \, \psi_n(\omega_s) \phi_n(\omega_i) \tag{3}$$

where $\sum_n \lambda_n = 1$, and $\psi_n(\omega_s)$, $\phi_n(\omega_i)$ are the solutions of eigenvalue equations given by

$$\int k_1(\omega_s, \omega) \psi_n(\omega) d\omega = \lambda_n \psi_n(\omega_s) \tag{4}$$

$$\int k_2(\omega_i, \omega) \phi_n(\omega) d\omega = \lambda_n \phi_n(\omega_i) \tag{5}$$

with $k_1(\omega_s, \omega) = \int f(\omega_s, \omega_i) f^*(\omega, \omega_i) d\omega_i$ and $k_2(\omega_i, \omega) = \int f(\omega_s, \omega_i) f^*(\omega_s, \omega) d\omega_s$ [3]. For the biphoton state with no frequency correlation, $f(\omega_s, \omega_i)$ is completely factorable i.e., only the first term (n = 0) on the right-hand side of Eq. (3) is non-zero, and all other terms (n > 0) are zero. The degree of factorizability of the state is quantified by Schmidt number (K) [4,5].

$$\mathrm{K} = \frac{1}{\sum_n \lambda_n^2} \tag{6}$$

High values of K indicate a large spectral correlation between the signal and idler photons. Specifically, for a non-factorable two-photon state with a finite spectral correlation between signal and idler photons, K > 1, whereas for a factorable state (no spectral correlation between signal and idler photons), K=1 [4,5].

The phase-mismatch (Δk) in a SPDC process is given by

$$\Delta k = k_p(\omega_s + \omega_i) - k_s(\omega_s) - k_i(\omega_i) - \frac{2\pi}{\Lambda} \tag{7}$$

where $k_p(\omega_s + \omega_i), k_s(\omega_s)$ and $k_i(\omega_i)$ are the propagation vectors corresponding to pump, signal, and idler; Λ is the poling period of the waveguide. Let $\overline{\omega_p}$, $\overline{\omega_s}$ and $\overline{\omega_i}$ be the phase-matched or central frequencies of the pump, signal,

and idler, respectively, such that $\overline{\omega_s} + \overline{\omega_i} = \overline{\omega_p}$. Considering the Taylor series expansion up to the first order of the propagation vectors about their respective central frequencies., Eq. (7) becomes

$$\Delta k = k_p(\overline{\omega_p}) - k_s(\overline{\omega_s}) - k_i(\overline{\omega_i}) - \frac{2\pi}{\Lambda} + (\omega_s + \omega_i - \overline{\omega_p})k_p' - (\omega_s - \overline{\omega_s})k_s' - (\omega_i - \overline{\omega_i})k_i' \quad (8)$$

where $k_\mu' = \frac{dk_\mu(\omega)}{d\omega}|_{\{\omega=\overline{\omega_\mu}\}}, \mu = p, s, i$. Now $k_p(\overline{\omega_p}) - k_s(\overline{\omega_s}) - k_i(\overline{\omega_i}) - \frac{2\pi}{\Lambda} = 0$ since phase matching is perfectly satisfied for the central frequencies. Therefore

$$\Delta k = (\omega_s - \overline{\omega_s})(k_p' - k_s') + (\omega_i - \overline{\omega_i})(k_p' - k_i') \quad (9)$$

To seek an analytical solution, the sinc function in Eq. (2) is approximated with a Gaussian function by neglecting the contribution from side lobes ($\text{sinc}\left(\frac{\Delta kL}{2}\right) \approx e^{-\gamma(\Delta kL)^2}$). The factor $\gamma = 0.04822$ is chosen such that full width at half maxima of sinc and Gaussian functions are equal [3,4]. Using this approximation and Δk from Eq. (9), we get

$$f(\omega_s, \omega_i) = e^{-A(\omega_s - \overline{\omega_s})^2 - B(\omega_i - \overline{\omega_i})^2 - 2C(\omega_s - \overline{\omega_s})(\omega_i - \overline{\omega_i})} \quad (10)$$

with $A = \frac{1}{\sigma_p^2} + \gamma(k_p' - k_s')^2 L^2$, $B = \frac{1}{\sigma_p^2} + \gamma(k_p' - k_i')^2 L^2$ and $C = \frac{1}{\sigma_p^2} + \gamma(k_p' - k_s')(k_p' - k_i')L^2$. As is evident, the two-photon state or $f(\omega_s, \omega_i)$ is factorable if $C = 0$ i.e. if $\frac{1}{\sigma_p^2} = -\gamma(k_p' - k_s')(k_p' - k_i')L^2$ which is possible only if $k_s' < k_p' < k_i'$ or $k_i' < k_p' < k_s'$. This inequality implies that the group velocity of the pump should lie between the group velocities of signal and idler. Equation (4) and (5) can be solved analytically by using equation (10) and choosing appropriate $\psi_n(\omega)$ and $\phi_n(\omega)$ basis functions. Hermite-Gaussian (HG) functions are a suitable choice for $\psi_n(\omega)$ and $\phi_n(\omega)$ [3,5] with the Gaussian part of the HG function having a standard deviation $\sigma = \left(\frac{B}{A^2B - AC^2}\right)^{\frac{1}{4}}$. Thus, the corresponding eigenvalues λ_n can then be computed as

$$\lambda_n = \frac{2C^{2n}\sqrt{AB - C^2}}{\left(2AB - C^2 + \frac{2B}{\sigma^2}\right)^{n+\frac{1}{2}}} \quad (11)$$

Figure 1(a) and 1(b) show the reproduced Schmidt decomposition results from literature using our formula above (Eq. (11)) for spectrally uncorrelated and spectrally correlated biphoton states, respectively.

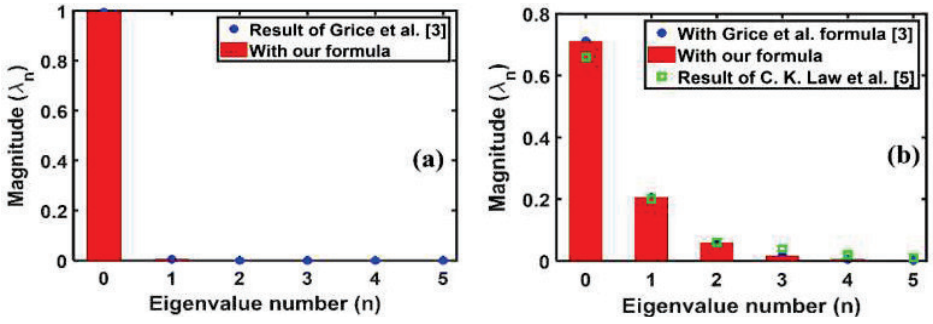

Fig. 1: Reproduced Schmidt decomposition results of (a) Ref. [3] (degenerate type-II SPDC in BBO with pump wavelength = 800 nm, L = 2.6 mm and σ_p = 15 nm) (b) Ref. [5] ($(k_p' - k_s')L$ = 0.061 ps, $(k_p' - k_i')$ = 0.213 ps and L = 0.8 mm, σ_p = 35 ps^{-1}.

3. Conclusion

We present a comprehensible derivation of analytical formulae that can be used to find the Schmidt mode coefficients (λ_n) obtained by performing Schmidt decomposition of the output biphoton state generated in a SPDC process. We have reproduced the numerical results of [3] and [5] to validate our formula for the Schmidt coefficients. Our simple expression (Eq. (11)) satisfies all the required conditions of Schmidt decomposition and can be used to find the spectral correlation between photon pairs generated in any SPDC process.

4. References

[1] T. Lutz, P. Kolenderski, and T. Jennewein, "*Demonstration of spectral correlation control in a source of polarization-entangled photon pairs at telecom wavelength*," Opt. Lett. 39, 1481-1484 (2014).

[2] A. Ekert and P. L. Knight, "*Entangled quantum systems and the Schmidt decomposition*," American Journal of Physics, 63, 415–423 (1995).

[3] W. P. Grice, A. B. U'Ren, and I. A. Walmsley, "*Eliminating frequency and space-time correlations in multiphoton states*," Physical Review A, 64, 063815 (2001).

[4] Z. Levine, J. Chen, A. Ling, J. Fan, and A. Migdall, "*Heralded, pure-state single-photon source based on a KTP waveguide*," in CLEO/QELS: 2010 Laser Science to Photonic Applications, IEEE, 1-2 (2010).

[5] C. K. Law, I. A. Walmsley, and J. H. Eberly, "*Continuous frequency entanglement: Effective finite hilbert space and entropy control*," Physical Review Letters, 84, 5304 (2000).

Non-conventional Transmission and Reflection in Asymmetric Diamond Nanowire

Satyajit Murmu*[1], Avijit kumar[2], and Rajan Jha*[1]

[1]Nanophotonics and Plasmonics Laboratory School of Basic Sciences IIT Bhubaneswar Khurda, Odisha 752050, India, [2]Low dimensional Laboratory School of Basic Sciences IIT Bhubaneswar Khurda, Odisha 752050, India

Author e-mail address: sm73@iitbbs.ac.in, avijitkumar@iitbbs.ac.in_;rjha@iitbbs.ac.in**

Abstract: In photonics, diamond nanostructures play significant role in providing nano waveguide, integration of quantum emitters with waveguides, quantum computations, qubit propagation. The feasible interface of diamond nanostructures exhibit a remarkable quantum mechanical feature in nano scale. Here, we explore light propagation characteristics in an asymmetric structure of elliptically-faceted (ELFA) diamond nanowire parallelly coupled to an optical nanofiber. Here, we report a new phenomena in the transmission spectrum beyond conventional Mach-Zehnder interference theory. This phenomena can find its applications in various fields such as multi-scale quantum photonics devices including quantum nonlinearity.

Keywords: Diamond nanowire, Supermode, phase, interference

1. Introduction

In order to address challenges in the field of photonics, more particularly related to optical communication, sensing applications, various types of waveguides have been proposed and realized. These waveguides not only provide efficient transmission of light but also causes generation of nonlinear modification in photon behavior. Recently, nano waveguides have been demonstrated to exhibit crucial role in single photon coupling, qubit propagation, and nanoscale-sized quantum sensors [1,2]. Here we present non-conventional mode generation in a hybrid structure consisting of asymmetric structure of elliptically-faceted (ELFA) diamond nanowire parallelly coupled to an optical nanofiber. This phenomenon has led to an excellent integration of quantum emitter (like NV^- center) for efficient unidirectional photon collection into optical nanofiber [3].

2. Device System Description

Figure 1(a) illustrates a three-dimensional schematic diagram of ELFA structure parallelly coupled to an optical nanofiber. Asymmetric ELFA diamond nanowire contains an elliptical facet on one side and a circular facet on the other side. The diamond nanowire can be realized using reactive ion etching and template processes [4]. The elliptical facet can be experimentally fabricated using well-optimized e-beam lithography [5]. For achieving the desired etching angle in diamond nanowires, focused ion-beam processing can also be used[6,7]. In Figure 1(b), the physical parameters of ELFA diamond nanowire are defined such as diameter of nanodiamond as D_{nd}, etched length of elliptical facet as L_e, and free length (length of cylindrical part) as L_f. D_{nf} is the diameter of optical nanofiber. The parallel coupling of optical nanofiber with asymmetric ELFA diamond nanowire allows coupling of light through diabatic to the adiabatic transfer process depending upon the value of L_e [8] [9]. Using FDTD this structure has been numerically simulated with refractive indices for optical and diamond nanowire as 1.450 and 2.410, respectively.

3. Result and disscussuion

Figure 1(b) indicates various components of light propagating inside a hybrid ELFA structure. After launching light from the elliptical side, total input intensity gets distributed into two supermodes of the hybrid structure, i.e. 1st and 2nd order supermode. After successive reflection on both sides of the diamond nanowire for two times, it exits from the hybrid ELFA structure through reflection and transmission. In Mach-Zehnder interferometer, the output spectra (i.e. both transmission and reflection spectra) will be modulated according to change in the wavelength or structural parameter of the interferometer (resulting in to phase change between the two supermodes power). Here, we observe

additional intensity spikes with the periodicity different than the phase modulation of supermodes as shown in Fig. 1(c). We have investigated the effect of structural parameter on position of the spikes and found period of spikes depending on structural parameter. Further, we have plotted the field intensity profile at xy plane (at z=0 as in figure 1(b)) corresponding to intensity spike and non-spike in Fig. 1(d) and (e), respectively. This plot shows a field shift happening for intensity spike cases.

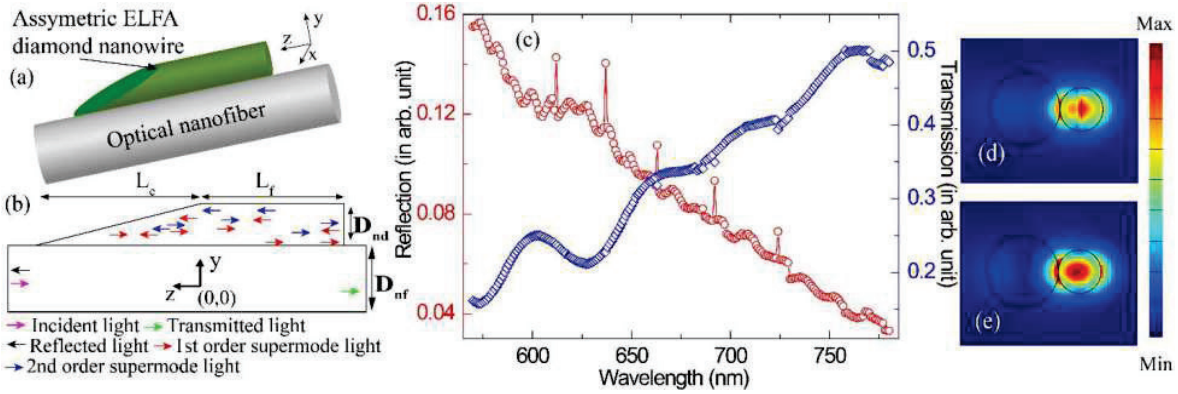

Fig. 1: (a) schematic illustration of asymmetrically hybrid ELFA structure coupled with optical nanowire. (b) light propagation of various supermode. (c) Transmission and reflection spectrum of light for different wavelengths. (d) and (e) are Electric field intensity plots for wavelength corresponding to spike and non-spike in the reflection spectrum at z=0 (xy plane).

4. Conclusion

In this article, we present a new phenomenon of light propagation through the hybrid ELFA structure and outcome behavior in spectra. This concept can be used for nanoscale interferometers for sensing purposes which may contribute to significant quantum emission coupling into the waveguide.

5. Aknowledgement

This work is supported by SERB-STAR Fellowship, Govt. of India. This work is also partially supported by STR/2020/000069.

6. References

[1] Y. Qi, F. Yang, Y. Lin, W. Jin, and H. L. Ho, "Nanowaveguide Enhanced Photothermal Interferometry Spectroscopy," J. Light. Technol. 35, 5267–5275 (2017).
[2] M. Davanco, J. Liu, L. Sapienza, C.-Z. Zhang, J. V. De Miranda Cardoso, V. Verma, R. Mirin, S. W. Nam, L. Liu, and K. Srinivasan, "Heterogeneous integration for on-chip quantum photonic circuits with single quantum dot devices," Nat. Commun. 8, 889 (2017).
[3] S. Murmu, A. Kumar, and R. Jha, "Unidirectional Photon Coupling Using Asymmetric Diamond Emitters with Enhanced Spontaneous Emission," Adv. Quantum Technol. **5**, 2100160 (2022).
[4] O. A. Shenderova, C. W. Padgett, Z. Hu, and D. W. Brenner, "Diamond nanorods," J. Vac. Sci. Technol. B Microelectron. Nanom. Struct. Process. Meas. Phenom. **23**, 2457–2464 (2005).
[5] R. N. Patel, T. Schröder, N. Wan, L. Li, S. L. Mouradian, E. H. Chen, and D. R. Englund, "Efficient photon coupling from a diamond nitrogen vacancy center by integration with silica fiber," Light Sci. Appl. 5, e16032–e16032 (2016).
[6] N. Das, A. Karar, M. Vasiliev, C. L. Tan, K. Alameh, and Y. T. Lee, "Analysis of nano-grating-assisted light absorption enhancement in metal–semiconductor–metal photodetectors patterned using focused ion-beam lithography," Opt. Commun. **284**, 1694–1700 (2011).
[7] T. Nagase, T. Kubota, and S. Mashiko, "Fabrication of nano-gap electrodes for measuring electrical properties of organic molecules using a focused ion beam," Thin Solid Films **438**–**439**, 374–377 (2003).
[8] S. Murmu, A. Kumar, and R. Jha, "Bidirectional coupling of diamond emitters to optical nanowire: tunable and efficient," J. Opt. Soc. Am. B **38**, F170–F177 (2021).
[9] S. Gröblacher, J. T. Hill, A. H. Safavi-Naeini, J. Chan, and O. Painter, "Highly efficient coupling from an optical fiber to a nanoscale silicon optomechanical cavity," Appl. Phys. Lett. **103**, 181104 (2013).

Fabrication of wavy nanograting substrate with enhanced SERS activity for trace pesticide detection

Anindita Das[1] and Rakesh S. Moirangthem[1*]
[1]Nanophotonics Lab, Department of Physics, Indian Institute of Technology (Indian School of Mines), Dhanbad 826004, JH, India
Email: rakeshap@iitism.ac.in

Abstract: In this work, we demonstrated an ultrasensitive Surface Enhanced Raman Spectroscopy (SERS) sensor on flexible lamination plastic substrate with Ag/Au bimetallic wavy nanograting structure. The flexible SERS sensor detected Rhodamine 6G dye molecules at auto molar concentrations and showed promising potential in detecting thiram, a trace pesticide.
Keywords: Plasmonics, Flexible, Surface enhanced Raman Scattering, Wavy nanograting.

1. Introduction

Pesticides have hazardous effects on the environment and living organisms. Thiram (TRM) is a fungicide and is mainly used in the rubber industry and agriculture, and its excessive use can cause damaging effects on humans and other living systems [1]. Hence, creating a platform to detect such analytes at ultralow concentrations with high sensitivity and specificity remains challenging. In this study, unlike traditional square grooves, a wavy nanograting surface is designed. The developed fabrication method allows us to produce a set of regularly spaced sinusoidal line elements. In future, the fabricated wavy nanograting substrates using the thermal nanoimprinting lithography (T-NIL) technique will be tested to develop low-cost SERS platforms for the detection of hazardous toxic chemical compounds such as trace dye and pesticides at a very ultra-low concentration in practical applications.

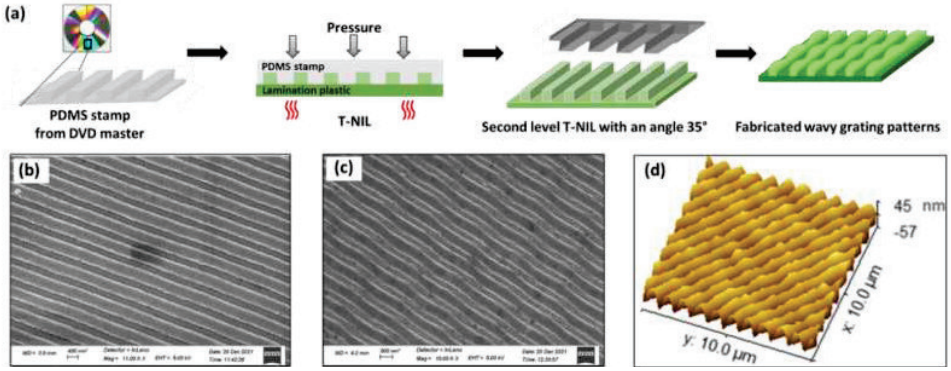

Fig. 1: (a) Schematic of wavy nanograting SERS substrate fabrication using T-NIL via sequential patterning figure with preferred style for labeling parts. SEM micrographs (top view) (b-c) images of 1D gratings and wavy grating pattern on lamination plastic substrate respectively, (d) 3dimentional (3D) AFM topography of Ag/Au wany grating substrate.

2. Experimental details

The fabrication of wavy nanograting plastic SERS substrate was done by nanoimprinting lithography technique, and the involved fabrication steps are presented in Fig 1 (a). Initially, the DVD disc (Moser Baer DVD-R, 4.7 GB; with 450 nm line width, 730 nm Periodicity and 160 nm Groove depth) was cut into small pieces and used as a master mould. The nanograting pattern was transferred onto the PDMS substrate by curing the PDMS polymer at 80° C for two hour after degassing of air bubbles. The resulting PDMS stamp, which had negative replica of the DVD nanograting structures, was used further as a master mould. Next, in the T-NIL process, a clean PET substrate with a PEVA polymer layer was placed under the PDMS master and pressed at a temperature of $90°C$ (set above the PEVA polymer's glass transition temperature) for 20 minutes. Thereafter, the PDMS master was carefully peeled off from the lamination plastic substrate and was rotated at about an angle 30°, followed by the second level T-NIL over the linear grating pattern area at a temperature of $70°C$ for 15 minutes. It is important to maintain a relatively low temperature in the second level T-NIL process than the first one to successfully fabricate wavy nanograting pattern on flexible lamination plastic substrate. Finally, 45 nm of Ag and 5 nm of Au were deposited over 2D wavy grating substrates using the e-beam evaporation technique.

3. Results and Discussion

The surface morphology and topography of imprinted nanopatterns were analysed with field emission scanning electron microscopy (FESEM; Zeiss Supra 55) and atomic force135 microscopy (AFM; Bruker-Icon). Fig 1 (b) shows SEM micrograph (top view) of the fabricated 1D gratings imprinted on lamination plastic after first level T-NIL. The smooth and defect-free uniform nanograting over a large area was seen in the FESEM images with 433.5 nm line width and 260.1 nm gap. Fig 1 (c) shows the SEM micrograph (top view) of the fabricated wavey nano gratings resulted after second level T-NIL and measured two different line widths (525 nm and 353.4 nm) and gaps (190.3 nm and 158.8 nm), confirming the change in line grating patterns (inset of Fig 1(c)). Further, the AFM topographical analysis confirms the formation of wavy grating patterns. Fig 1(d) shows the substrate's 3D AFM image over (10×10 µm2). The 3D topographical image confirms the change in the square groove pattern and height profile of the individual grating lines.

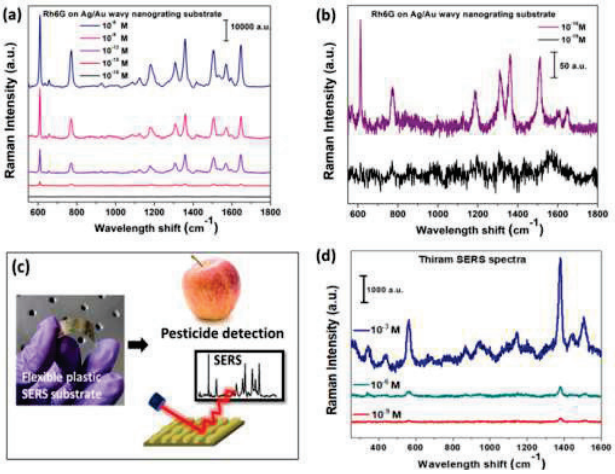

Fig. 2: (a) SERS spectra of Rh6G of 10-6 to 10-18 M concentrations on Ag/Au wavy grating substrate, (b) The Rh6G detection limit plot showing the detectable concentrations up to 10^{-18} M. (c) Fully fabricated SERS substrate flexibility and its potential to detect pesticide residues in foods, (d) SERS detection of trace level thiram up to 10^{-9} M concentration on Ag/Au wavy grating substrate.

To evaluate the SERS activity of our fabricated wavy nanograting patterns, traditional Rhodamine 6G (Rh6G) as a target analyte was used. The Rhodamine 6G (Rh6G) in ethanol solvent with different concentrations (10^{-6} to 10^{-19} M) were prepared, and a drop of 1µl of each concentration was cast on the fabricated wavy nanograting substrate and dried under ambient conditions before measurements. The SERS signal was recorded using LabRAM HR Evolution: Raman Microscope (HORIBA Scientific, France) with 532 nm laser excitation. The laser power was set at 0.1 mW. The integration time for the SERS signals' collection is 20 s. The obtained Raman peaks are matched with previously reported Raman bands for R6G molecules [3]. Quantitative SERS detection by changing analyte concentration is depicted in Fig 2(a). Notable SERS signals of Rh6G molecules at 10^{-18} M concentration were observed (Fig 2(b)). Further, the feasibility of the fabricated SERS substrate for TRM detection was investigated in the concentration range of 10^{-3} to 10^{-9} M (Fig. 2 (d)), and the intense Raman bands at 561 cm^{-1} for ν(S–S) and 1385 cm^{-1} for ν(C–N) [4] confirms the effective detection of TRM molecules down to nanomolar concentrations. However, signal homogeneity, reproducibility, and stability play a crucial role in potential SERS-based applications and can be explore further.

4. Conclusions

Detection of target analytes with high sensitivity and specificity at low concentrations is important to SERS spectroscopy. The fabricated bimetallic wavey nanograting substrate achieved excellent structural reproducibility and SERS signalling ability at auto-molar level, which can be a promising platform for SERS-based sensing applications.

5. References

[1] A. Lorena Picone, "Stamplike flexible SERS substrate for in-situ rapid detection of thiram residues in fruits and vegetables Visual system-response functions and estimating reflectance," *Food Chem.* **373,** 131570 (2022).
[2] He XN, "Surface-enhanced Raman spectroscopy using gold-coated horizontally aligned carbon nanotubes. *Nanotechnology* **20**, 23 (2012).
[3] Tran Cao Dao, "High-sensitive SERS detection of thiram with silver nanodendrites substrate," *Adv. Nat. Sci: Nanosci. Nanotechnol.* **10** 025012 (2019).

Single Photon Squeezed Cat State

Arman and Prasanta K. Panigrahi
Department of Physical Sciences, Indian Institute of Science Education
and Research Kolkata, Mohanpur-741246, West Bengal, India
a19rs004@iiserkol.ac.in

Abstract: We study the properties of the non-classical state in comparison to that of compass state. We propose a state, the superposition of the squeezed and displaced single photon state, showing closeness with the properties of the compass state for the variation in the parameters. The state is analytical investigated in the context of phase space structure, number distribution and fidelity. For the appropriate choice of squeezing and the displacement parameter, fidelity is found more than 0.99 with the compass state for the coherent amplitude $|\beta| > 0.5$. Formation of sub-Planck structures and corelation with the compass state will allow alternate preparation of such states and find their uses on optical platform for the quantum metrology and sensing, and in microwave regime for quantum error correction.
Keywords: Compass State, Squeezed State, Quantum Metrology, Quantum Error Correction.

1. Introduction

1.1. Overview

The superposition of four different coherent states [1], is known as Zurek's compass state (description of compass and kitten state is same) or kitten state (KS). The kitten state possesses sub-Planck scale structures in the phase space with oscillatory distribution as a function of small quadrature phase space shift (δx, δp). The interferometric phase space structure makes the KS state sensitive to quadrature fluctuation, therefore allowing detection of weak external forces [2–4] as well as quadrature fluctuation [5]. There have been many proposal and experimental reports for generation of low amplitude cat state in either microwave or optical platform, yet preparation for large amplitude and higher order superposition of the coherent states remain challenging because of their high sensitivity against external small fluctuation. For the production of KS in optical as well as microwave platform, we propose a state comprised of squeezing and displacement operator.

In this paper, the investigation of non-classical properties such as photon number distribution (PND), the Wigner function (W(x,p)) and fidelity (F) is performed for the large overlap of the our proposed state with the KS.

1.2. Squeezed Displaced Single Photon State

For studying various properties, we write the form of superposition of squeezed and displaced number state such that $|\psi\rangle = NS[r](D[\alpha]+D[-\alpha])|1\rangle$, where N, D[α] and S[r] are the normalization, the displacement operator with α being real and squeeze operator for r>0 respectively. We calculate Fock number distribution ($P_m=\langle m|\psi\rangle$) with help of x-projected wave vector as $\langle x|S[r]D[\alpha]|1\rangle$,$=(d/ds)(\langle x|S[r]D[\alpha+s]|0\rangle)|_{s=0}$ and generating function [6] of the Hermite Polynomial. Comparative analysis of PND is performed for appropriate superposition of coherent states ($|\psi_{KS}\rangle = |\beta\rangle - |-\beta\rangle + |i\beta\rangle - |-i\beta\rangle$) with squeezed displaced single photon state.

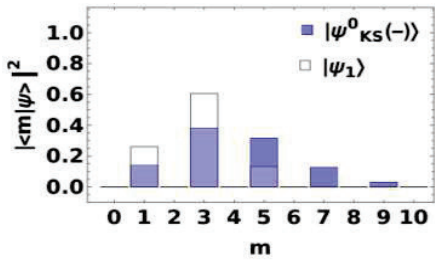

Fig. 1: PND for both states ψ_1 and ψ_{KS} shows non-zero overlap at same Fock number m, which can be maximized with help of tuning of parameter squeezing (r=0.3) and displacement (α=1.8), respectively.

Further, the Wigner distribution, a quasi-probability distribution whose negativity in phase space being the measure of non-classicality of the state, is calculated to identify the proposed state's interferometric pattern and its similarity with KS.

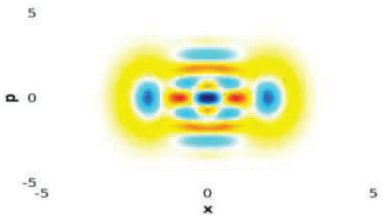

Fig. 2: The Wigner distribution of N S[r](D[α]+D[−α])\|1> for r=0.45 and α=2.

The phase space distribution showing central interference is clearly evident from the Fig.2, leading to the indication of close overlap with KS. Fig.2 depicts similar distribution and coherent states along the quadrature diagonals. Further, to quantify its distance from the KS ($|\psi_{KS}\rangle$), we use overlap measure of both our concerning states, also known as fidelity (F). This fidelity has value larger than 99% (see Table:1) for two different set of parameters i.e. squeezing (r) and displacement (α) of the proposed state to obtain coherent amplitude $|\beta|>0.5$.

Table 1: Fidelity for KS and proposed state

Squeezing (r)	Displacement (α)	Coherent amplitude (β)	Fidelity (F)
0.15	0.61	0.7(1+i)	0.9995
0.2	0.7	0.85(1+i)	0.9960

To provide the generation setup, we make use of Rabi model in the presence of two photon driving field ($G\,(a_+^2 e^{-2i\omega t} + a^2 e^{2i\omega t})$) with G driving strength [7]. This model is applicable in both optical as well as circuit-QED platforms. This can be diagonalized with the help of the squeezing and the displacement operator. Diagonalization of this model is complete with the condition that qubit has very small energy gap i.e. close to degeneracy. This condition allows to take away the effect of σ_z population in the qubit. Evident from diagonalization, system leads to eigen-spectrum of harmonic oscillator, with the superposed squeezed displaced number eigen-states.

2. Conclusion

We have investigated the PND, phase space structure and fidelity for the superposition of squeezed displaced single photon state as compared to these features of KS. The PND of our proposed state, shows potential of larger overlap with KS, which further becomes evident from evaluation of the fidelity (F) being greater than 99% (see Table:1). We discuss at last, preparation of the proposed state in the cavity with Rabi model interaction in presence of two photon drive.

3. References

[1] W. Zurek, Sub-planck structure in phase space and its relevance for quantum decoherence, Nature 412, 712 (2001).
[2] D. Dalvit, R. de Matos Filho, and F. Toscano, Quantum metrology at the heisenberg limit with ion trap motional compass states, New Journal of Physics 8, 276 (2006).
[3] J. R. Bhatt, P. K. Panigrahi, and M. Vyas, Entanglement-induced sub-planck phase-space structures, Phys. Rev. A 78, 034101 (2008).
[4] P. K. Panigrahi, A. Kumar, U. Roy, and S. Ghosh, Sub-planck structures and quantum metrology, in AIP Conference Proceedings, Vol. 1384 (American Institute of Physics, 2011) pp. 84–90
[5] F. Toscano, D. A. R. Dalvit, L. Davidovich, and W. H. Zurek, Sub-planck phase-space structures and heisenberg-limited measurements, Phys.Rev. A 73, 023803 (2006).
[6] A. W¨unsche, Hermite and laguerre 2d polynomials, Journal of computational and applied mathematics 133, 665 (2001).

[7] R. Guti´errez-J´auregui and G. S. Agarwal, Probing the spectrum of the jaynes-cummings-rabi model by its isomorphism to an atom inside a parametric amplifier cavity, Phys. Rev. A 103, 023714 (2021).

Scalar and vector Pearcey and Airy vortex beams through weak atmospheric turbulence

Shakti Singh[1], Sanjay Kumar Mishra[2], Akhilesh Kumar Mishra[1, *]
[1]*Department of Physics, Indian Institute of Technology Roorkee, Roorkee-247667, India*
[2]*Photonics Division, Instruments Research and Development Establishment, Dehradun-248008, India*
[*]*Corresponding author: akhilesh.mishra@ph.iitr.ac.in*

Abstract: We present a comparative propagation study of scalar and vector formats of Airy and Pearcey vortex beams in weak atmospheric turbulence using the multiple random phase screen method. The beams vector format's performance is found superior.
Keywords: Airy vortex beam Pearcey vortex beam atmospheric turbulence OAM of light

1. Introduction:

In last few decades abruptly autofocusing (AAF) beams have witnessed a lot of research interest and found applications in different areas of physics such as free space propagation, optical trapping, sensing and quantum communication [1]. Propagation of AAF beams with orbital angular momentum (OAM) through atmospheric turbulence have gained added advantage due to their unique nondiffracting and self-healing properties [2]. An OAM beam with uniform polarization distribution is known as scalar vortex beam [3]. Vector vortex beam is a type of beam, which carries non-uniform polarization and OAM. Radially polarized and azimuthally polarized beam are examples of vector vortex beam [4]. Due to randomly varying refractive index of turbulent atmosphere, the beam faces intensity fluctuations and beam wander. Intensity fluctuation in optical beams is characterized by a parameter known as scintillation index (SI) [5].

2. Theory and Model:

Optical beam propagation through turbulent atmosphere is modeled by stochastic Helmholtz equation. Random varying nature of atmosphere is characterized by power spectral density (PSD) . The turbulent eddy size and its statistical distribution are also characterized by PSD. Different types of PSD have been proposed for the atmospheric turbulence modeling. Here we have used the widely accepted Von Karman type PSD, whose mathematical expression is given by [6]

$$\phi_n(\kappa) = 0.033 c_n^2 (\kappa^2 + \kappa_0^2)^{-11/6} \exp\left(\frac{-\kappa^2}{\kappa_m^2}\right), \tag{1}$$

where $\kappa_0 = \frac{2\pi}{L_0}$, $\kappa_m = \frac{5.92}{l_0}$, and c_n^2 represents the strength of atmospheric turbulence. l_0 represents the inner scale and L_0 represents the outer scale of the atmospheric turbulence. To understand the propagation through turbulent atmosphere, we generated random phase screen by taking N× N array of complex Gaussian random numbers $a + ib$ of size $N \times N$. Phase spectrum of PSD is defined as

$$\phi_\theta(\kappa) = 2\pi k^2 \delta z \phi_n(\kappa). \tag{2}$$

Next, we took the square of phase spectrum and then multiplied it with complex Gaussian random number. Now we multiplied the final expression by Δ_K^{-1} where $\Delta_K^{-1} = \frac{2\pi}{N\Delta}$, wherein Δ is the spatial sampling interval and N is the number of sampling points. After taking the inverse Fourier transform of the final expression, we got random phase $\theta_1 + i\theta_2$. In our numerical model, we have taken θ_1 as random phase screen. Input field profile of Pearcey vortex beam (PVB) is given by [7]

$$E(r, \phi, 0) = Pe\left(\frac{-r}{w_0}, \zeta_0\right) exp\left[b\left(\frac{-r}{w_0}\right)\right] \exp(il\phi) \tag{3}$$

where Pe is the Pearcey function, which is defined by an integral representation as given by

$$Pe(x, y) = \int_{-\infty}^{\infty} \exp(is^4 + is^2 x + isy)\, ds \tag{4}$$

Here x and y are dimensionless variables, w_0 is the width of the beam, b is the truncation factor, ζ_0 denotes a constant and l is the value of topological charge.
Input field profile of ring Airy vortex beam (AVB) is given by

$$E(r,\phi,0) = Ai\left(\frac{R_0-r}{w_0}\right) exp\left[b\left(\frac{R_0-r}{w_0}\right)\right] \exp(il\phi), \quad (5)$$

where l is the topological charge, R_0 is radius of the primary ring and w_0 is the width of the primary ring. A vector beam can be written as linear superpositions of two scalar beams with orthogonal polarization. Hence, for vector version of Airy and Pearcey beams, we have superposed $l = 0$ and $l = 1$ beams.

3. Results and Discussion:

In this numerical investigation we have taken $w_0 = 3\ cm$, $N = 512$, $\zeta_0 = 0$, wavelength $\lambda = 2\ \mu m$, $l_0 = 1\ cm$, $R_0 = 0.07, L_0 = 3\ m$ and $b = 0.15$. We have used 20 random phase screens throughout the numerical study. 500 independent realizations have been considered to provide the sufficient statistics. We have calculated apertured average SI using formula [6]

$$SI(z) = \frac{\langle\left(\int_{-R}^{R}\int_{-R}^{R} I(x,y,z)dxdy\right)^2\rangle}{\langle\int_{-R}^{R}\int_{-R}^{R} I(x,y,z)dxdy\rangle^2} - 1 \quad (5)$$

where I is the intensity of the beam and we have considered the radius of receiving aperture $R = 5$ cm.

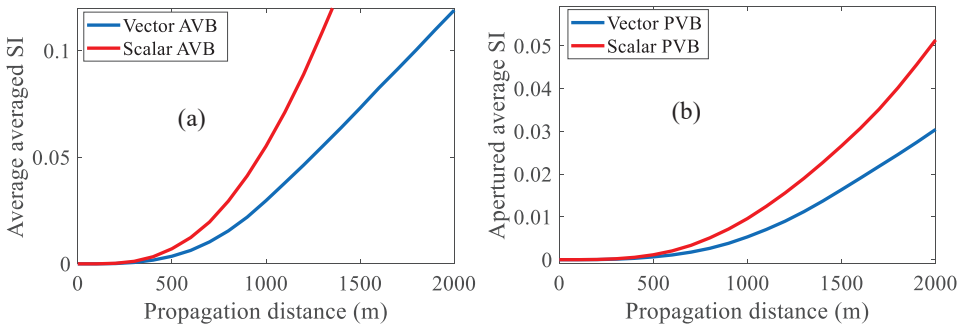

Fig. 1. Apertured average SI for $C_n^2 = 10^{-14}m^{-2/3}$ **(a)** scalar AVB and vector AVB for l=1 **(b)** scalar PVB and vector PVB for l=1

In figure 1(a) we observe that in weak turbulence vector AVB performed better than scalar vortex beam. Similarly in figure 1(b) shows that vector PVB performed better than scalar PVB beam. Out of the two vector beams, vector PVB is better suited for long distance propagation.

4. Conclusion:

We have numerically studied the propagation of scalar and vector version of AVB and PVB in weak turbulence and found that vector beams performed better in atmospheric turbulence. Moreover, as compare to vector AVB, vector PVB gave smaller SI.

5. References:

[1] A. E. Willner, K. Pang and H. Song, "Orbital angular momentum of light for communications" Appl. Phys. Rev. 8, 041312 (2021).

[2] D. G. Papazoglou, N. K. Efremidis, D. N. Christodoulides, and S. Tzortzakis, "Observation of abruptly autofocusing waves," Opt. Lett. 36(10), 1842–1844 (2011).

[3] S Singh and A K Mishra, "Spatio–temporal evolution dynamics of ultrashort Laguerre–Gauss vortices in a dispersive and nonlinear medium" J. Opt. 24, 075501 (2022).

[4] Q. Zhan, "Cylindrical vector beams: from mathematical concepts to applications," Adv. Opt. Photonics **1**, 1–57 (2009).

[5] K. Khare, P. Lochab and P. Senthilkumaran, "Orbital Angular Momentum States of Light Propagation through atmospheric turbulence" IOP Publishing (2020).

[6] S. Singh, S.K. Mishra, and A. K. Mishra, "Pearcey vortex beam dynamics through atmospheric turbulence" Preprint arXiv. 2205.10771 (2022).

Fast point-based CGH generation for holographic displays

Anuj Gupta[1*], Pardeep Bhanot[1], Bhargab Das[1], and Raj Kumar[1]
[1]CSIR-Central Scientific Instruments Organisation, Chandigarh - 160030
[*]Corresponding Author e-mail address: anujgupta@csio.res.in

Abstract: Computer Generated Hologram (CGH) generation involves huge computations which makes it hard to display the respective object information in real time. This necessitates the optimization of a CGH algorithm in order to reduce the involved intensive calculations and hence the computational time. This work includes a comparative analysis of three different optimization methods to generate a CGH using point-based method. The computational time is reduced by optimization of the sequential code which is achieved by using the Numba compiler and CuPy library that uses the CUDA cores.
Keywords: Computer-generated hologram; Holographic displays, Hardware accelerator; Point-based method.

1. Introduction

Holography accumulates all the information of a 3D physical object into a 2D complex valued hologram in terms of intensity and phase. When a digitally modeled object is used instead of a physical object, the resulting hologram is called Computer Generated Hologram (CGH) [1]. CGH generation involves huge computational cost which further increases with the increase in size of the modeled object. Thus, it calls for an optimization of this CGH generation process. The optimization is achieved by execution of the working of hardware as well as software parts in synergy. There are several hardware accelerator platforms like Central Processing Units (CPU), Graphics Processing Units (GPU), Field Programmable Gate Arrays (FPGA) etc. that can be used to accelerate the process of CGH generation [2]. Every accelerator has its own strengths and weaknesses. For instance, CPUs are good for sequential programming, whereas GPUs are good for parallel programming. The selection of an appropriate hardware accelerator, as per the availability, is the first decision to be made. Subsequently, algorithms should be designed effectively to use the available hardware resources to their maximum capacity. In sequential programming, only a single core executes the set of instructions one by one which is a time consuming process. On the other hand, parallel programming can do so in much lesser time using all the available cores simultaneously. Further, optimization with graphics card in GPU is found to be even more effective in reducing the computational time. This work is an effort to speed up the process of CGH generation for holographic displays.

2. Methodology

There are primarily four techniques to generate the CGH viz. point cloud method, polygon based method, layer based method and light field method [3]. In the present work, we have used the point based method to generate CGH. In this technique, every point on the object plane is propagated to the hologram plane considered at some distance. The hologram of the object is constructed by taking the superposition of the spherical wave fronts of all the object points on the hologram plane. For a single object point, the optical wave it casts on the hologram plane is calculated by the spatial impulse response of propagation [1] as:

$$F(m,n,z_0) = \exp\left[\frac{i2\pi\sqrt{(m\delta)^2 + (n\delta)^2 + z_0^2}}{\lambda}\right] \qquad (1)$$

Here, the intensity of the object point is taken to be one. Also, each point is considered to be a pixel in the object plane. λ is the wavelength of the light and z_o is the distance between the object plane and the hologram plane. 'm', 'n' and δ represent the indices of the discrete horizontal position, vertical position and the sampling distance between adjacent pixels on the hologram plane respectively. The object size is an important parameter that significantly affects the execution time of the program. The larger the resolution, the more will be the execution time. The optimization of the code can be done by solving the equations analytically as much as possible, making proper use of available libraries or inbuilt functions, and minimizing the redundancy of the code etc. Because all the modules of the program do not involve intensive calculations, only the time-consuming part is to be accelerated. Further, the computational cost can be reduced by parallelizing the algorithm and making use of the Numba compiler. Numba is a jit (just-in-time) compiler for 'Python' which speeds up all or part of the Python program by

compiling it at native machine code speed. It significantly increases the compiling speed of the program particularly for numpy arrays, functions, and loops. Furthermore, the use of CuPy array library, which is used for GPU-accelerated computing, also helps in enhancing the speed of the code.

3. Results and Discussion

Firstly, we have developed a basic algorithm which gives a CGH based upon a point cloud method in a sequential manner. The implementation of underlying physics was verified by developing the code for CGH generation from a planer object at a smaller resolution and reconstructing it numerically as well as optically. Subsequently, the computational cost of the code is reduced by working on a specific time-consuming section of the algorithm. The specific module of the sequential code is optimized and subsequently parallelized using Numba compiler. In order to speed it up further, the code is developed for the CUDA cores and thereafter executed on the GPU. The algorithm is realized for the dimension of x = 1920, and y = 1080, where x and y are the number of pixels of the object plane. These dimensions are chosen to match the Spatial Light Modulator (SLM) resolution, viz., 1980 × 1080 for actual experimental optical reconstruction. For the same reason, the wavelength of the light (λ) is taken to be 632.8 nm. Furthermore, the object is also numerically reconstructed. The distance between the object and the hologram/CGH plane (z_o) is considered to be 20 cm. This distance is optimized by analyzing the simulation results of the reconstruction. The numerical reconstruction of the CGH is done using angular spectrum method [4]. Fig. 1(a)-(d) shows the original object, corresponding computed CGH, the numerically reconstructed result and the optically reconstructed result, respectively. Here, we have shown the result of one model only because the results in all the different simulation models are completely consistent with each other.

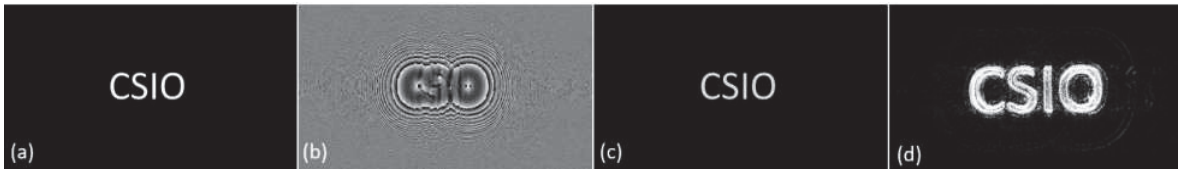

Fig. 1: (a) Original object, (b) CGH (c) Numerically reconstructed result and (d) Optically reconstructed result

The results of the optimization in CGH generation using point cloud method are compared in Table 1. The significant reduction in computation time can be seen. In addition, we have also extended the code to multi-planar problem and obtained similar results at the preliminary stage.

Table 1: Execution time in different optimizations methods

Parameter	Sequential (Optimized)	Numba (Serial)	Numba (Parallel)	CuPy (CUDA Cores)
Execution time	~ 5892 seconds	~ 2426 seconds	~ 342 seconds	~ 216 seconds

4. Conclusion

It is a computationally expensive process to generate CGH because of the involved intensive calculations. The results discussed above conclude that the computational time can be reduced significantly using Numba compiler and parallel processing in GPU. In future work, we will further extend the algorithm to a large-scale object and optimize the execution time by using a combination of Numba and CuPy.

5. Acknowledgement

Authors acknowledge CSIR, India for providing financial support under project number MLP2014 to carry out this research work. Authors thank Ms Monika Rani and Mr Lavlesh Pensia for their help in experimental setup.

6. References

[1]. P.W.M. Tsang, T.-C. Poon, and Y. M. Wu, "Review of fast methods for point-based computer-generated holography [Invited]", Photonics Research **6**, 837-846 (2018).
[2]. Y. Wang, D. Dong, P.J. Christopher, A. Kadis, R. Mouthaan, F. Yang, and T.D. Wilkinson, "Hardware implementations of computer-generated holography: a review", Optical Engineering **59**, 1-30 (2020).
[3]. T. Shimobaba, D. Blinder, T. Birnbaum, I. Hoshi, H. Shiomi, P. Schelkens, and T. Ito, "Deep-Learning Computational Holography: A Review (Invited)", Frontiers in Photonics, **3**, [854391] (2022).
[4]. T.-C. Poon, and J.-P. Liu, "Introduction to Modern Digital Holography with MATLAB", (Cambridge University, 2014).

Refractive Index Measurement of Fused Silica by Total Internal Reflection Digital Holographic Microscopy

Jagroop[1*], DakshinTillo[2], C S Narayanamurthy[2] and D Sam Dayala Dev[1]

[1]Vikram Sarabhai Space Center, Thiruvananthapuram, Kerala-695013- India, [2]Indian Institute of Space Science and Technology, Thiruvananthapuram, Kerala-695547-India

**jagroopastro5@gmail.com*

Abstract: A dual wavelength Total Internal Reflection Digital Holographic Microscopy is demonstrated for accurate measurement of RI and dispersion of polished fused silica sample. A precision Right Angle Prism (RAP) made of Sital material is realized and sample is optically contacted to achieve a perfect solid to solid interface on TIR surface. Refractive index of fused silica is measured to be matching with the reference values in few hundreds of ppm.

Keywords: Optical Contact, Total Internal Reflection Digital Holographic Microscopy (TIRDHM), Refractive Index

1. Introduction

Fused Silica glass is the first-choice material for the fabrication of precision optics because of its unique optical and mechanical properties. It is commonly used in high-end applications like Ring Laser Gyroscope (RLG), Hemispherical Resonator Gyroscopes (HRG), UV windows in Laser Ignition systems in fusion reactors, and ultra-precision optics in advanced optical instruments for ground and space applications. Refractive Index (RI) is the key property used for design of an optical instrument or experiment. Hence accurate and sensitive measurement of refractive index is essential part of photonics industry. The different available techniques of RI measurements of glasses along with dispersion are explained in ASTM standard C1648-12 [1].In the present work, an experimental setup based dual wavelength Total Internal Reflection Digital Holographic Microscopy (TIRDHM) [2, 3] is demonstrated for measurement of RI and dispersion of polished fused silica (Corning 7980). A Right Angle Prism (RAP) made of Sital material is realized based on simulations for higher sensitivity and lower errors for RI measurement of fused silica. The fused silica sample is optically contacted to TIR surface of RAP to achieve a perfect solid to solid interface. The setup is calibrated with a mixture of water and glycerol of different ratios [3]. The measured values have measurement inaccuracies (Δn) of approximately 400 ppm [3] for both wavelengths and the measured values are matching within 200 ppm to the reference values given in the datasheet of Corning 7980.

2. Theory

Ash and Kim [2] explained the basic theory of TIRDHM. The basic principle of RI measurement of sample is based on the fact that at TIR interface between two medium n_1 and n_2 ($n_1 > n_2$) and fixed angle of incidence, the TIR reflection phase depend on the n_2. The reflection phase is recorded and reconstructed through Digital holography. Hence for fixed n_1 and θ, there is a range of RI 1 to n_2 that can be measured. Jhang et.al.[3] shown the sensitivity of measurement is higher and inaccuracies (Δn) is lower for a material (n_1) whose measurement range nearly matches with n_2. Hence from simulation, a RAP made of Sital ($n_{546.2\ nm} = 1.538$ and $n_{632.9\ nm} = 1.534$) is selected with corresponding θ values 72.37^0 and 72.44^0 respectively. The RI measurement range for Sital RAP is 1-1.4658, which closely matches with reference values of RI of fused silica. The refractive index n_2 can be written in terms of n_1, θ and reflection phase is given by equation 1[3

$$n_2 = n_1\sqrt{sin^2\theta - cos^2\theta\ tan^2\tau} \qquad \tau = \tan^{-1}\left(\sqrt{n_1^2 sin^2\theta - 1}/n_1 cos\theta\right) \tag{1}$$

Where $\Delta\Phi$ is the phase difference between n_1 to air interface and n_1 to n_2 interface.

3. Experimental Configuration

The schematic of dual wavelength TIRDHM setup as shown in figure 1 is self explanatory. The polarization states of the two linearly polarized cylindrical lasers is set to p polarization by using a polarizer (Thorlabs: LPVIS050-MP2) in front of red laser and by precise mounting of green laser. The states of polarizations are verified by

Polarimeter (Thorlabs: PAX1000). The precisely fabricated Sital RAP with the surface flatness of better than λ/6 (PV), Roughness (< 2 nm rms) and Right angle accuracy (< 20 arcsec) is mounted on a six axis stage for accurate alignment and minimize the experimental error. The RAP is precisely aligned with the help of Beam Profiler (Thorlabs: BC106N-VIS/M). The setup is calibrated with a mixture of water and glycerol of different ratios [3]. The polished fused silica sample is optically contacted on the TIR surface of RAP covering the beam partially as shown in figure 1. The holograms are recorded in 5 M monochrome CMOS camera (SENtec: STC- MBS500U3V 2448(H) X 2048(V) pixels with 3.45 (H) X 3.45 (V) μ) sequentially with red and green laser, with and without sample to eliminate the setup related error. Angular Spectrum Method (ASM) for digital reconstruction and Variance based digital autofocus method [4] is used for hologram processing. Phase holograms are reconstructed in best focus plane and phase jump is calculated between air and sample interfaces by taking average phase of 400 pixels for each interface excluding 100 pixels on either side of boundary between sample and air.

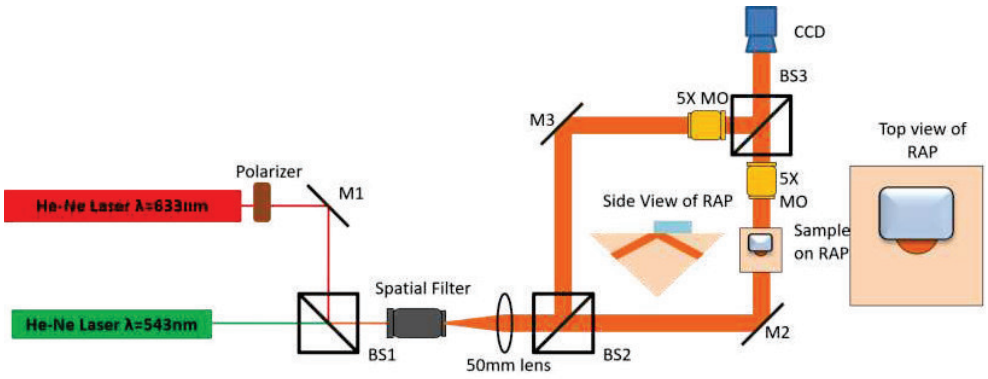

Figure 1 Schematic of Dual Wavelength TIRDHM Experimental Setup

4. Results and Conclusion

The recorded hologram for 633 nm and reconstructed phase images in best focus planes for 543 nm and 633 nm are shown in figure 2. The experimentally measured refractive index of the sample was found to be 1.4572 for 633 nm and 1.4602 for the 543 nm with an accuracy of ±400 ppm along with dispersion of 0.003. The reference values for the corresponding RI from data sheet of Corning 4980 are $n_{632.9\ nm} = 1.457016$ and $n_{546.2\ nm} = 1.460076$ with dispersion value of 0.00306. The measured RI values are closely matching with reference values.

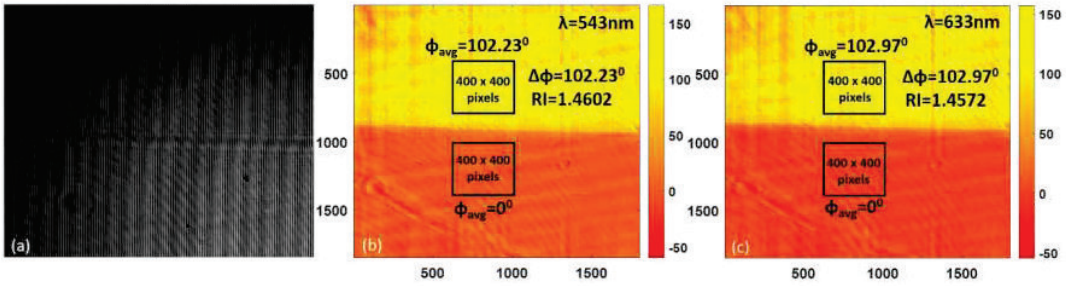

Figure 2 (a) Recorded hologram of Sample (λ=633nm). (b) Phase image of the recorded hologram for 543 nm. (c) Phase image of the recorded hologram for 633 nm

5. References

[1] ASTM standard C1648 − 12 (Reapproved 2018).
[2] W. Ash III and M. Kim, "Digital holography of total internal reflection," Opt. Express **16**, 9811-9820 (2008).
[3] J. Zhang, J. Di, Y. Li, T. Xi, and J. Zhao, "Dynamical measurement of refractive index distribution using digital holographic interferometry based on total internal reflection," Opt. Express **23**, 27328-27334 (2015)
[4] Hazar A. İlhan, Mert Doğar, Meric Özcan, "Autofocusing in digital holography," Proc. SPIE **8644**, 86440C (2013)

Numerical simulation of refractive index-based tunable metamaterial absorber

Nikita Choudhary, Mukul Jaiswal, Anjani Kumar Tiwari*
Department of Physics, Indian Institute of Technology Roorkee, 247 667, India
Author's e-mail address: anjani@ph.iitr.ac.in

Abstract: We present a numerical study of a tunable metamaterial absorber comprising of metal-dielectric-metal nanodisk array on a dielectric-metal substrate. The simulation predicts a shift in the resonant absorption peak of the metamaterial absorber by changing the refractive index of the dielectric layers. By interchanging the refractive index of the dielectric layers, the selective frequency response can be achieved, which can be applicable for color filters and transparency windows.

Keywords: Metamaterial absorber, tunable metamaterials, resonance.

Metamaterials have promising applications in sensors, solar cells, thermal emitters, invisible cloaking, wireless communications, energy harvesting, spatial light modulators, and perfect absorber [1]. A metamaterial absorber effectively absorbs electromagnetic radiation, exhibiting both narrow and broadband absorption. A simple metamaterial absorber is based on impedance-matched metal-dielectric-metal tri-layer resonators [2,3]. When the impedance of the metamaterials $Z = \sqrt{(\mu(\omega)/\varepsilon(\omega))}$ matches with the free space impedance ($Z = 1$), the reflection vanishes. At the same time, the continuous metallic layer at the bottom blocks any transmission, leading to a perfect absorption at the resonant wavelength. Most of the metamaterial absorbers are realized by periodically patterning subwavelength-sized resonant structures. Once fabricated, the arrangements of the unit cell cannot be changed or adjusted. Therefore, their spectral response is also fixed. However, it is desirable to have a tunable spectral response for various applications. This can be achieved by changing the dimension of the unit cells and the refractive index of the constituting entities [4,5,6].

We performed a computer simulation of a Metamaterial absorber based on a metal-dielectric-metal nanodisk array on a dielectric-metal substrate using a finite element method, COMSOL. The schematic of the unit cell is shown in Figure 1 (a), it has the following geometric parameters, unit cell size $a = 2\ \mu m$, $h = 200\ nm$, $d = 150\ nm$, $2r = 1\ \mu m$, $t_1 = 80\ nm$, $t_2 = 50\ nm$, and $t_3 = 100\ nm$. The substrate was taken to be germanium, and gold was chosen to be the metallic element due to better chemical stability and low Ohmic losses. Its dielectric permittivity was modeled using the Lorentz Drude expression $\epsilon(\omega) = 1 - [\omega_p^2/\omega(\omega + i\gamma)]$, with a plasma frequency of $^{\omega_p}/_{2\pi} = 2176\ THz$ and a damping frequency of $^{\gamma}/_{2\pi} = 6.5\ THz$. The refractive indices of the dielectric-1 and dielectric-2 are represented by n_1 and n_2, respectively. In our study, the refractive indices of both the dielectric layers (n_1 and n_2) are varied from 1.5 to 17. We consider a three-dimensional unit cell with periodic boundary conditions along the X–Z directions so that the structure can be regarded as an infinite two-dimensional array. The radiation was assumed to be incident along the Y-direction. The frequency-dependent reflectance ($R(\omega)$) was calculated using S-parameters, and absorbance ($A(\omega)$) was calculated using $A(\omega) = 1 - R(\omega) - T(\omega)$. Figure 1 (b) depicts the simulated absorbance of the proposed metamaterial absorber at three different refractive indices of dielectric layers. The black curve shows the absorbance when both the dielectric layers (dielectric-1 & dielectric-2) have a refractive index of 1.5. In the spectral region between $2.5\ \mu m$ to $4.5\ \mu m$, the absorption spectrum has two peaks centered at $2.73\ \mu m$ and $2.85\ \mu m$ showing absorption of 95% and 99%, respectively.

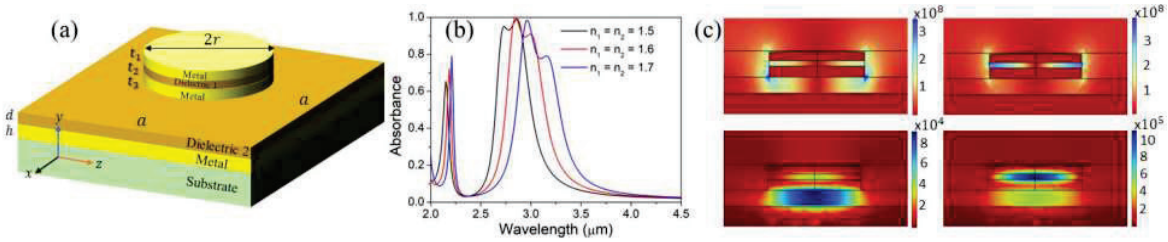

Figure1. (a) Schematic diagram of the unit cell comprising of metal-dielectric-metal nanodisk array on a dielectric-metal substrate. *(b) Calculated absorbance for* $n_1 = n_2 = 1.5$ *(black curve),* $n_1 = n_2 = 1.6$ *(red curve), and* $n_1 = n_2 = 1.7$ *(blue curve). (c) The electric (top panel) and magnetic (bottom panel) field distributions for* $n_1 = n_2 = 1.6$. *The left and right panels depict the field profiles at 2.84 μm and 3.00 μm, respectively.*

The red and blue curve depicts the absorbance when both the dielectrics have refractive indices of 1.6 and 1.7, respectively. For $n_1 = n_2 = 1.6$, the first peak and the second peak shift to *2.84* µm (absorbance 99.9%) and 3.00 µm (absorbance 92%). Similarly, for $n_1 = n_2 = 1.7$, these peaks further get red-shifted to 2.96 µm (absorbance 98%) and 3.15 µm (absorbance 79%), respectively. For $n_1 = n_2 = 1.6$, the electric and magnetic field distributions at the first resonance (2.84 µm) and at the second resonance (3.00 µm) are shown in figure 1(c). Clearly, a larger electric field is concentrated in the dielectric region. At 2.84 µm, the field is more intense on the edge of metals in the dielectric-1 region, and at 3.00 µm, it is more intense in the dielectric-2 region. The magnetic field profile depicted in the bottom panels also confirms the localization of the magnetic field in the middle of dielectric-1 and dielectric -2 regions at these resonant wavelengths.

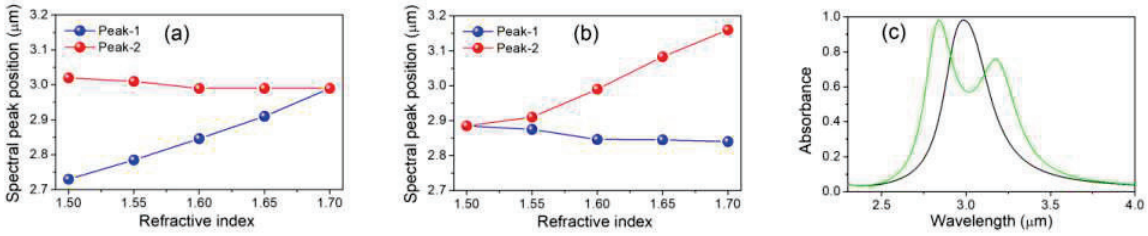

Figure 2(a) Variation of spectral peak position versus n_1 with a fixed value of $n_2 = 1.6$. (b) Variation of spectral peak position versus n_2 with a fixed value of $n_1 = 1.6$. (c) Absorbance of tunable metamaterial absorber, the black curve for $n_1 = 1.7$ and $n_2 = 1.6$ and the green curve for $n_1 = 1.6$ and $n_2 = 1.7$.

In Figure 2 (a), we plot the peak wavelength as a function of the refractive index of the dielectric-1 region, keeping a fixed value of $n_2 = 1.6$. The figure shows that as the refractive index increases, the two peaks come closer and merge when n1 reaches *1.7*. We observe that the shift in peak 1 is more prominent than in peak 2. On the hand, as we increase the refractive index of the dielectric-2 region, keeping n_1 fixed at *1.6* (Figure 2 (b)), the two peaks separate, and, in this case, the spectral shift of peak-2 is more sensitive to the change in n_2. These observations are consistent with the field profiles shown in Figure 1 (c). The green curve in figure 2 (c) is the calculated absorption spectrum for $n_1 = 1.7$ and $n_2 = 1.6$. The spectrum contains only one peak at 2.98 µm. At this resonant wavelength, both the resonances of the dielectric-1 and dielectric-2 regions overlap. When we swap the refractive indices of the dielectric-1 and dielectric-2 regions (*for $n_1 = 1.6$ and $n_2 = 1.7$*), the spectrum shows two prominent peaks at 2.83 and 3.17 µm. Moreover, a dip appears at *2.98* µm, where we had a peak earlier.

In conclusion, we have investigated a tunable metamaterial absorber based on a metal-dielectric-metal nanodisk array on a dielectric-metal substrate, wherein the absorption properties depend on the refractive indices of the dielectric materials. By interchanging the refractive index of the dielectric layers, the resonance wavelength of the absorption peak can be tuned. The proposed metamaterial can further be applicable for color filters, solar cells, and transparency windows.

Acknowledgment: N C and M J thank IIT Roorkee for the fellowship and for providing COMSOL Multiphysics simulation facilities. AKT acknowledges IIT Roorkee for the IITR-FIG grant.

References

[1] F. Capolino, "*Theory and Phenomena of Metamaterials*," CRC Press (2009).
[2] J. Hao, et al., "High performance optical absorber based on a plasmonic metamaterial," Appl. Phys. Lett. **96**, 251104 (2010).
[3] G. Dayal and S. A. Ramakrishna, "Design of highly absorbing metamaterials for infrared frequencies," Optics Express **20**, 17503 (2012).
[4] D. Shrekenhamer, W.-C. Chen, and W. J. Padilla, "Liquid crystal tunable metamaterial absorber," Phys. Rev. Lett. 110, 177403 (2013).
[5] F. Zhang, et al., "Mechanically stretchable and tunable metamaterial absorber," Appl. Phys. Lett. **106**, 091907 (2015).
[6] A. K. Tiwari, D. Biswal, and S. A. Ramakrishna, "Tunable metamaterial absorber based on liquid crystal elastomer," ISBN: 978-93-88653-41-1, International Conference on Fiber Optics and Photonics (2018).

Design and Fabrication of Microlens Array for Confocal Laser Scanning Microscopy

Sonam Berwal [1,2], Bharpoor Singh [1], K Manjunath [1,2], Neha Khatri [1,2*]
[1] *CSIR-Central scientific Instruments Organisation, Chandigarh 160030, India*
[2] *Academy of Scientific & Innovative Research (AcSIR), Ghaziabad 201002, India*
[*] *Email: nehakhatri@csio.res.in*

Abstract: Confocal microscopy is an established optical imaging method with a sub micrometer resolution, which have numerous biomedical applications. However, the slow scanning speed that extends the scan period limits the performance of microscopy. The optical design and fabrication of a plano-convex microlens array is presented for deployment in confocal laser scanning microscopy to overcome the scanning time. The microlens array of PMMA is designed with Zemax OpticStudio and fabricated via ultraprecision machining that allows splitting of the laser beam into the beamlets and focusing onto the sample. The different images from laser spots would stitch together to obtain the final image.
Keywords: Microlens array, confocal laser scanning microscopy, PMMA, single point diamond turning.

1. Introduction

Confocal laser scanning microscopy, in today's world, is the most popular imaging technique required for various applications, like industrial and biomedical imaging [1]. Having a superior optical sectioning capability that acquires advanced resolution as well as improved contrast for images of volumetric samples, the confocal microscope is also utilized for label-free and fluorescent imaging in both reflective and transmissive modes [2, 3]. In order to deliver the benefits of better spatial and temporal resolutions and improved SNR, the confocal microscope has been added with several cutting-edge features while preserving the conventional technique as a standard [4]. However, the slow scanning speed limits the scanning time that moderates the application range. Hence, homogenized illumination is a prominent method to increase imaging speed in confocal microscopy. In this study, a PMMA (Polymethyl methacrylate) microlens array (MLA) is designed and fabricated for confocal microscopy. The MLA is introduced to split the incident laser beam into a grid of beamlets that reduce the scanning time significantly. An (11 × 11) plano-convex MLA is designed with Zemax OpticStudio and fabricated by using a single-point diamond turning machine.

2. Design of 11 × 11 Microlens Array

PMMA is a widely used optical material with good optical characteristics, including high transparency, high transmittance, and low refractive index dispersion [5]. Additionally, it is often used in optical devices due to its low cost and strong mechanical processability. The design of rectangular MLA is based on the lens diameter, height and width of the microlens, radius of curvature, and refractive index of the material. The 11 × 11 plano-convex MLA ray diagram and microlens profile with design parameters are illustrated in Fig. 1. The light source of confocal microscopy is a laser with a working wavelength of 532 nm. The designed microlens of the array split the beam into a grid of beamlets. All the lenslet in the array has an identical focal length to collimate the beamlets. After that, the beams from MLA is focused on the sample. The final image is obtained by stitching the numerous laser spots together.

3. Fabrication of Microlens Array

A Single Point Diamond Turning machine (Nanoform-200) with Slow Tool Servo (STS) configuration is used to fabricate the PMMA lenslet array. STS configuration is used for the fabrication of components which are not rotationally symmetric, like toric surfaces, microlens arrays and freeform surfaces. As a promising technique, STS diamond turning is widely applied for the generation of microstructure surfaces with nanometric surface finish and profile integrity. In STS configuration, the Spindle speed and feed motion are interrelated where X & Z axis positions are defined concerning a particular angular parameter of the C-axis (Configuration as shown in figure 2a).
In the case of MLA, spindle speed mainly depends upon these factors: a) the number of X & Z axis travelling within a single rotation of the spindle, b) the magnitude of the sag value, when the parametric value of these factors is large, the spindle speed reduces and vice-versa. It is also to be noted that Spindle speed depends on the design data, the controllable parameters are C-axis angle increment and X-axis increment per revolution, as shown in figure 2b. In order to achieve optimized cutting speed, selection of these parameters plays a major role. For fabrication, aluminium fixturing is used for holding and alignment of the PMMA workpiece. Because of miniature component size, a Contour make diamond tool of 0° rake angle with a tool nose radius of 0.2 mm is used in machining. Using the design parameters, a tool path is generated in the form of a polar coordinate system (CXZ data points) using Diffsys® software. Keeping the C-axis angular increment at 3 degrees and X-axis increment per revolution at 1 µm, the machining operation is performed. The total sag value for MLA is 1.238 µm calculated from design data. During

machining, the depth of cut is kept at 2 µm keeping all other cutting parameters like tool overhang and mist selection as suggested in literature [6] . A spindle speed of 22 RPM is maintained at the combined feed of the CXZ axis.

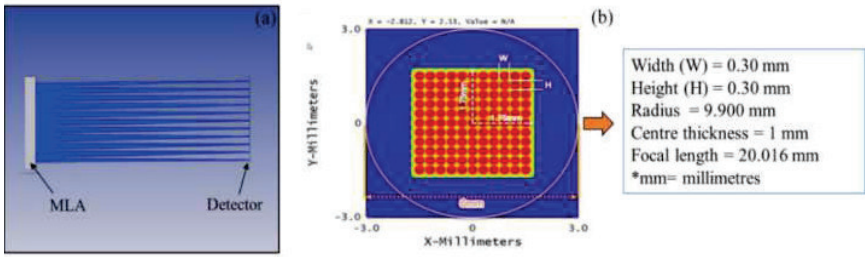

Fig. 1: Plano-convex microlens array (a) ray diagram, (b) profile of microlens with design parameters.

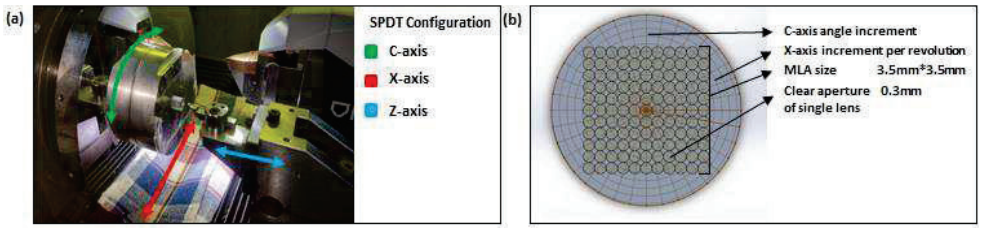

Fig. 2: (a) Slow Tool Servo axis configuration, (b) representative view of controllable parameters.

4. Results and Discussion

After fabrication, for characterization Coherence Correlation Interferometer (CCI) is used with a 5X objective. The measured 3D plot is shown in figure.3(a), and the value of sag obtained is 0.2476 µm. The total height error is 0.9904 µm as the designed value is 1.238 µm. The results concluded that the component went through overcutting due to high C-axis angle increment value. Another trial is performed by reducing the C-axis angle increment to 1 degree without altering the value of the X-axis increment where the spindle speed is maintained at 14 RPM. The fabricated surface is again measured with CCI (See fig.3b) which depicts the value of sag as 1.233µm and height error of 5 nm which is within the tolerance limit.

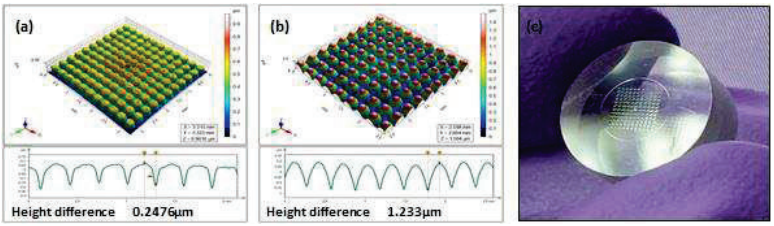

Fig. 3: CCI Results of (a) Profile after Trail, (b) Profile after later Trail, (c) Image of MLA after fabrication.

5. Conclusion

In this paper, we proposed the use of MLA for beam homogenization to increase scanning lead time in confocal microscopy, and its STS fabrication technique is optimized. With the feedback method, the profile error is reduced from 0.2476 µm to 1.233µm.

6. References

[1] M. Minsky, "Memoir on inventing the confocal scanning microscope," *Scanning,* vol. 10, no. 4, pp. 128-138, 1988.

[2] L. Novotny and B. Hecht, *Principles of nano-optics*. Cambridge university press, 2012.

[3] J.-A. Conchello and J. W. Lichtman, "Optical sectioning microscopy," *Nature methods,* vol. 2, no. 12, pp. 920-931, 2005.

[4] Y. Yu, X. Ye, and M. D. McCluskey, "Confocal microscopy with a microlens array," *Applied Optics,* vol. 59, no. 10, pp. 3058-3063, 2020.

[5] Y. Li, K. Li, and F. Gong, "Fabrication and Optical Characterization of Polymeric Aspherical Microlens Array Using Hot Embossing Technology," *Applied Sciences,* vol. 11, no. 2, p. 882, 2021.

[6] N. Khatri, V. Mishra, M. Kumar, V. Karar, and R. V. Sarepaka, "Design & development of plastics tele microscope visual aids for vision impaired using state-of-art aspheric technology," in *2017 IEEE Region 10 Humanitarian Technology Conference (R10-HTC)*, 2017: IEEE, pp. 113-116.

Calibration of nano-positioning stage using spectrally resolved white light interferometry

Pardeep Bhanot[1,2], Sanjit K. Debnath[1,2,*]

[1]*Micro and Nano Optics Centre, CSIR-Central Scientific Instruments Organisation, Sector 30C, Chandigarh, India-160030*

[2]*Academy of Scientific and Innovative Research (AcSIR), Ghaziabad 201002, India*

[*]*Corresponding author's email id: sanjit.debnath@csio.res.in*

Abstract: Optical metrology uses multiple interferograms to measure phase. Multiple phase shifted interferograms are obtained by deliberately changing the path difference between the interfering beams using a nano-positioning stage. The accuracy of the nano-positioning stage directly impacts the accuracy of the phase measurement. Thus, it is crucial to know the step size of the nano-positioning stage for better accuracy. In this work, we calibrate the nano-positioning stage by using spectrally resolved white light interferometry (SRWLI).

Keywords: Phase shifting interferometry, Phase shifter, Phase distribution, Fourier transformation, SRWLI.

1. Introduction

Interferometry is a widely used technique to determine the phase map of the test sample from recorded phase shifted interferograms. These multiple interferograms are recorded by moving an arm of the interferometer in a controlled manner using a nano-positioning stage. This movement induces a phase shift between the reference and the test beam. The induced phase shift between the consecutive interferograms may be non-constant depending on the behavior of the nano-positioner which affects the resulting phase measurement. Hence, it is very essential to accurately calibrate the step size of the nano-positoner to remove the random errors [1,2]. This work presents the calibration of the step size of the nano-positioner using the SRWLI technique.

2. Theory and Experimental setup

A white light interferogram is a superposition of several monochromatic interferograms [3]. It can be resolved into its individual spectral components using a spectrometer. In spectral domain, this decomposed beam with different spectral components is used to extract the phase of the test sample and this technique is called SRWLI [4,5].

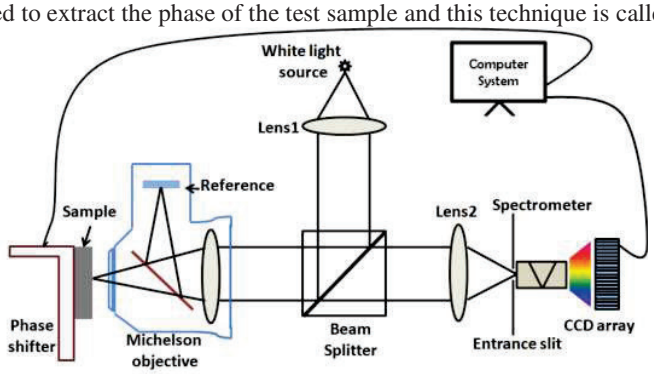

Fig. 1: The experimental setup of SRWLI

Fig. 1 shows the schematic of the experimental arrangement. A white light beam is collimated by Lens1 and is incident on a beam splitter which reflects the beam towards the Michelson interference objective. The beam is divided into reference and test beam by the beam splitter in the Michelson objective. After reflection from the reference and the sample arm, a white light interference pattern is formed which is imaged on a slit using Lens2. The nano-positioner stage to be calibrated is attached to the sample and operated by a computer. The entrance slit selects a line from the interference pattern which is fed into the spectrometer to disperse it perpendicular to the slit which is known as chromaticity axis. Each monochromatic interferogram is recorded by a CCD array which is connected to a computer. Such a spectral domain interferogram is characterized by its horizontal and vertical axis representing the optical path difference axis and the chromaticity axis respectively. The intensity distribution of a spectrally resolved white light interferogram is mathematically represented as follows:

$$I(z,\sigma) = g(\sigma)[I_r + I_t + 2I_r I_t \cos(\phi(z,\sigma) + \varphi_o)] \quad (1)$$

where σ = 1/λ is the wavenumber, I_r, I_t, $\phi(z,\sigma)$ and $g(\sigma)$ are the reference beam intensity, test beam intensity, phase difference and the source spectrum or the power spectral density of the white light source respectively. φ_o represents the phase difference produced by the shift in nano-positioner stage attached to the sample arm. The phase is given by,

$$\phi(x,\sigma) = 4\pi\sigma z(x) \quad (2)$$

which is a linear equation with respect to the wavenumber σ with x being the position coordinate of the test sample, $2z(x)$ being the optical path difference between the reference beam and the test beam. Thus, if $\phi(z,\sigma)$ is known for various σ, the slope $4\pi z(x)$ of phase (ϕ) versus wavenumber (σ) curve can be easily obtained.

In order to record the consecutive phase shifted interferograms, we deliberately move the test arm of the interferometer using the nano-positioner attached to the sample. For each interferogram, the slope of phase versus wavenumber curve is obtained using Eq. (2). This slope value for each interferogram represents the absolute optical path difference (2z) induced by the nano-positioner. By subtracting the consecutive slope values, the step size of the nano-positioner is obtained. We use Fourier transformation (FT) method to find the phase from each interferogram [3].

3. Results and discussion

Figure 2(a) shows a spectral domain interferogram recorded by the setup shown in Fig. 1. Here, x-axis represents the optical path difference axis and y-axis represents the chromaticity axis respectively. The phase map shown in Fig. 2(b) is obtained using FT method. Figure 3(a) shows the unwrapped phase versus wavenumber plot at column number 1920 in Fig. 2(b). By giving a linear fit to this curve, z value is obtained using Eq. (2). Since, we recorded multiple interferograms, such phase versus wavenumber plot is obtained for each interferogram. The difference of z of all the consecutive interferograms with respect to the first interferogram is plotted in Fig. 3(b) which shows an almost linear behavior. Also, from the difference of z value for consecutive interferograms, the step size of the nano-positioner was found to be approximately 600 nm.

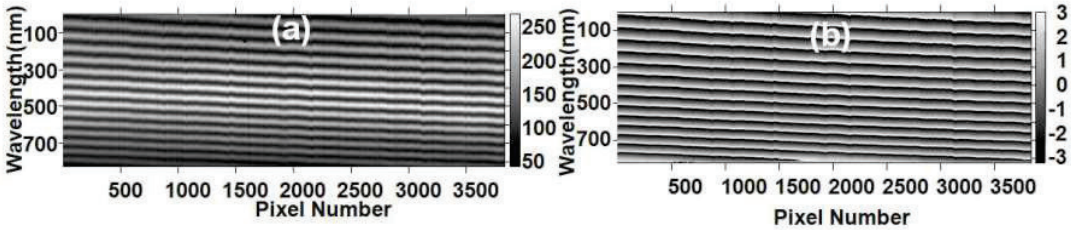

Fig. 2: (a) Spectrally resolved white light interferogram (b) Phase calculated from (a) using FT method

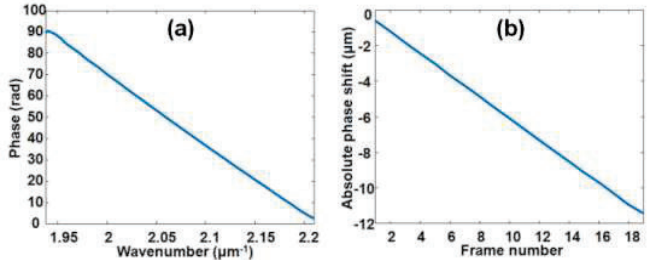

Fig. 3: (a) Phase versus wavenumber at a column (b) Absolute phase shift curve from consecutive interferograms

4. References

[1] Bernd Gutmann and Herbert Weber, "Phase-shifter calibration and error detection in phase-shifting applications: a new method," Appl. Opt. 37, 7624-7631, 1998.

[2]Balashov, E.V., Korotkov, A.S. & Rumyancev, I.A. Calibration of Phase Shifters on Basis of Vector-Sum Signals. *Radioelectron.Commun.Syst.* **61**, 515–521, 2018.

[3] J. Schwider and L. Zhou, "Dispersive interferometric profilometer," Optics letters, vol. 19, no. 13, pp. 995–997, 1994.

[4] J. Calatroni, A. L. Guerrero, C. Sainz, and R. Escalona, "Spectrally-resolved white-light interferometry as a profilometry tool," Optics & Laser Technology, vol. 28, no. 7, pp. 485–489, 1996.

[5] S. K. Debnath and M. P. Kothiyal, "Optical profiler based on spectrally resolved white light interferometry," Optical Engineering, vol. 44, no. 1, p. 013606, 2005.

Acknowledgement

Authors would like to thank Dr. Raj Kumar for providing the nano-positioner to perform experiment.

All-optical 1 × 3 switch using photonic crystal ring resonator based on Kerr effect

Priyanka Kumari Gupta
Department of Physics
IIIT Naya Raipur
Chhattisgarh, India
priyanka@iiitnr.edu.in

Shrivishal Tripathi
Department of ECE
IIIT Naya Raipur
Chhattisgarh, India
shrivishal@iiitnr.edu.in

Punya Prasanna Paltani
Department of Physics
IIIT Naya Raipur
Chattisgarh, India
punya@iiitnr.edu.in

Abstract: A novel 1 × 3 all-optical switch design is proposed using a nonlinear photonic crystal ring resonator is proposed. It works on low optical pump power which can be used for designing all-optical devices such as optical logic gates, optical add/drop multiplexers, etc.
Keywords: Photonic crystal, All-optical switch, Ring resonator, Kerr effect

1. Introduction

Over the past few years, the data communication and telecommunication fields has experienced a tremendous growth. All-optical networks belong to the third generation of networks that avoids electronic bottleneck [1-2]. Optical switches are vital components in optical networks. Photonic crystal (PC) has become the new frontier in the field of optics for proposing optical components and devices because of their unique ability of controlling and manipulating the light propagation [3-4]. Photonic crystal ring resonator (PCRR) based all-optical switches allows possibilities of low bending losses, fast operation and is almost fully scalable [5-7].
In this paper, a novel 1 × 3 all-optical switch based on a PCRR is proposed using nonlinear Kerr effect. The proposed structure is simple and operates at low operational optical pump power. The device is scalable and therefore is suitable for proposing various all-optical devices such as optical logic gates, add/drop multiplexers etc.

2. Proposed design structure

The photonic crystal ring resonator (PCRR) structure consists of square lattice of chalcogenide glass dielectric rods having ($\epsilon_r = 9.61$) in an air medium ($\epsilon_r = 1$) with an array size of 31 × 35. The radius and lattice constant of the rods are 114.27 nm and 586 nm respectively. The proposed structure consists of two waveguides namely bus and drop. The resonant ring with its core section is also an octagonal shape as shown in Fig.1(a). Optical light beam enters the structure through port A and exists from port B, C and D respectively at different optical power intensities.

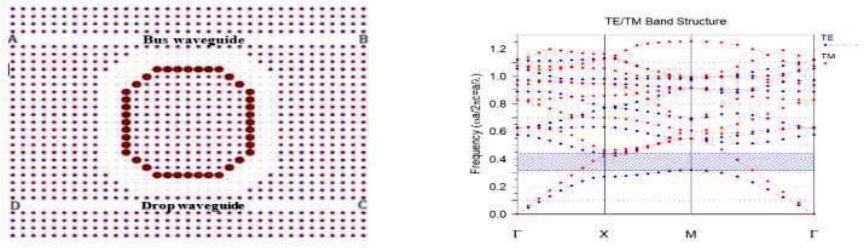

(a) (b)

Fig.1. (a) The schematic diagram of the proposed nonlinear PCRR structure in 2-D view and (b the dispersion diagram

This happens because of the application of the Kerr effect that changes the refractive index of the dielectric rods by applying high-intensity optical pump signal. The big brown rods present in the resonator core has a high nonlinear Kerr coefficient ($n_2 = 9 \times 10^{-17}\ m^2/W$). The dispersion diagram of the photonic crystal in TE/TM mode is obtained by the finite element method, a wide photonic bandgap (PBG) exists for TE mode in the range $0.316 < a/\lambda < 0.441$ which corresponds to the wavelength range of $1331\text{ nm} < \lambda < 1890\text{ nm}$ as shown in Fig.1. (b).

3. Simulation results and discussion

An electromagnetic excitation (CW Gaussian light) is introduced at port A and then observed at ports B, C, and D respectively. By comparing the incident wave to the waves at B, C, and D ports the transmission spectra are obtained. The electromagnetic excitation varied from 1548nm to 1558 nm at intensity values of $60\,W/\mu m^2, 373\,W/\mu m^2$ *and* $690\,W/\mu m^2$. The electric field distribution for the incident light and optical power spectra for different intensity values are shown in Fig. 2 and Fig.3 respectively.

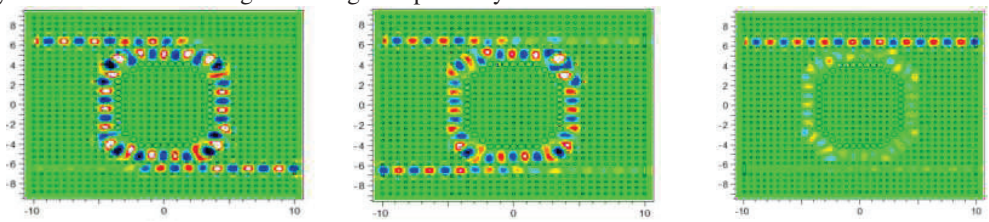

(a) (b) (c)

Fig.2. The electric field distribution for optical power intensity values of (a) $60\,W/\mu m^2$***, (b)*** $373\,W/\mu m^2$ ***and (c)*** $690\,W/\mu m^2$.

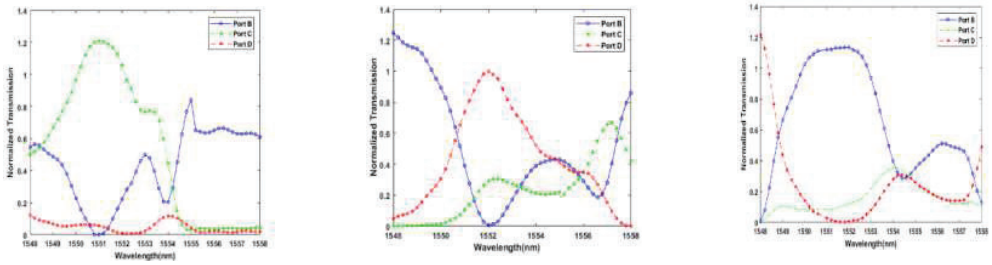

(a) (b) (c)

Fig.3. The output for the proposed PCRR shown as a function of intensities of (a) $60\,W/\mu m^2$***, (b)*** $373\,W/\mu m^2$ ***and (c)*** $690\,W/\mu m^2$.

4. Conclusion

A nonlinear photonic crystal octagonal shape ring resonator is used to propose a novel 1 x 3 all-optical switch. The proposed device works as an intensity dependent switch. The resonance wavelength is within the PBG range. The structure is simple and operates at low optical pump power which is very much essential for the integration of all-optical devices. This design structure is scalable and is suitable for designing all-optical logic gates, all-optical add/drop multiplexers.

5. Acknowledgement

Priyanka Kumari Gupta acknowledges the institute fellowship of IIIT Naya Raipur, Chhattisgarh, India.

6. References

[1] Carvalho, Joel Pedro, “Optical switching techniques: device development and implementation in fibre optic technology” (2007).

[2] Bregni, Stefano & Guerra, Giacomo & Pattavina, Achille. (2001). “State of the Art of Optical Switching Technology for All-Optical Networks”.

[3] John, S. (1987), “Strong localization of photons in certain disordered dielectric superlattices”, Physical Review Letters, 58(23), 2486–2489. doi:10.1103/physrevlett.58.2486.

[4] J. D. Joannopoulos, Steven G., J. N. Winn, and R. D. Meade, “Photonic Crystal: Modeling the Flow of Light”, Princeton University Press, P. Copyright (2008).

[5] Rajasekar, R., Kumar, K. V., Ayyanar, N., & Raja, G. T. (2020),”High Speed Optical Switch Based on Photonic Crystal Resonator”, 2020 IEEE 20th International Conference on Nanotechnology (IEEE-NANO). doi:10.1109/nano47656.2020.9183668.

[6] Shirdel, M., & Mansouri-Birjandi, M. A. (2016), “Photonic crystal all-optical switch based on a nonlinear cavity”, Optik - International Journal for Light and Electron Optics, 127(8), 3955–3958. doi: 10.1016/j.ijleo.2016.01.114

[7] Ghadrdan, M., & Mansouri-Birjandi, M. A. (2016), “Implementation of all-optical switch based on nonlinear photonic crystal ring resonator with embedding metallic nanowires in the ring resonators”, Optical and Quantum Electronics, 48(5). doi:10.1007/s11082-016-0552-8

Effect of Spectral Bandwidth of Pump on Biphotons Generated in Guided Wave Medium

Akriti Raj* and Bhaskar Kanseri

Experimental Quantum Interferometry and Polarization (EQUIP), Department of Physics, Indian Institute of Technology Delhi, Hauz Khas, New Delhi 110016, India

**akriti.raj@iitd.ac.in*

Abstract: We have theoretically studied the effect of spectral bandwidth of pulsed pump on the properties of biphotons generated in collinear type 0 spontaneous parametric down conversion (SPDC) process at telecommunication wavelength. The effect of pump broadening on the SPDC output spectrum has been experimentally demonstrated. Generation of pure single photons at high rate is an integral part of all the recent developments in the field of quantum technologies. The study can be used to generate broader SPDC spectrum in non-degenerate processes to effectively select signal and idler photons.

Keywords: SPDC, SHG, PPLN Waveguide.

1. Introduction

Spontaneous parametric down-conversion (SPDC) is a probabilistic technique for generation of twin photons in which a high energy pump photon is down converted into two lower energy photons by interaction through a nonlinear medium ($\chi^{(2)} \neq 0$). The down conversion always takes place in accordance with energy and momentum conservation laws [1]. Heralding the presence of one photon (idler) marks the presence of its counterpart (signal). The use of PPLN as a nonlinear medium in waveguide geometry strongly enhances efficiency. Also, periodic poling enables the use of highest nonlinear coefficient. Further increasing the length of the device can lead to high conversion efficiency with low pump power [2]. We have used a fiber-based scheme for generation of single photons and state of the art detection scheme for their characterization. One of the ways to increase the rate of single photons in such a scheme is to use a high repetition rate pump [3]. The property of pulsed pump strongly affects the properties of biphotons. The effect of increasing pump bandwidth on the bandwidth of SPDC output has been reported. This study will be useful in analyzing SPDC process in PPLN waveguides using a broad pump. The bandwidth of the pump can be tuned to get a broad SPDC output which will be helpful while selecting signal and idlers photons in a non-degenerate process.

2. Theoretical study

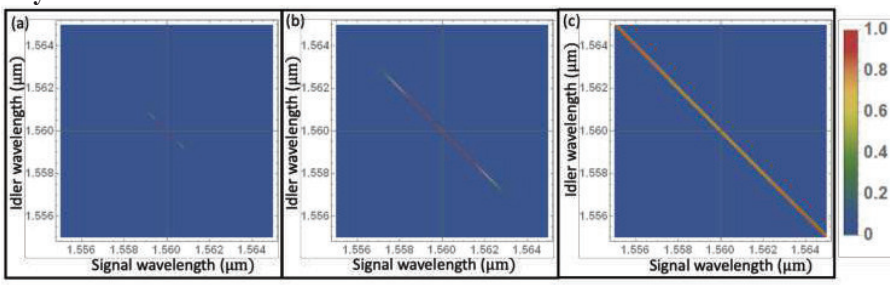

Fig 1: Joint spectral intensity of biphotons (a) 1 nm spectral width of pump (b) 10 nm spectral width of pump (c) 100 nm spectral width of pump.

The effect of pulse width spectral properties of biphotons generated in collinear type 0 SPDC process in PPLN waveguide were theoretically studied. The pump envelop function with σ_{pump} as the spectral bandwidth, ω_s, ω_i and ω_p as angular frequencies of signal, idler and pump respectively, is expressed as $\alpha_{\text{pump}} = e^{-\left(\frac{\omega_s+\omega_i-\omega_p}{\sigma_{\text{pump}}}\right)^2}$. The product of pump envelop function and the phase matching function (ϕ_{pm}) is known as joint photon spectrum or two photon spectrum $\psi(\omega_s, \omega_i) = \alpha_{\text{pump}}\phi_{\text{pm}}$ [4]. It signifies the probability amplitude for the output photon pairs. The joint photon intensity or joint probability can be calculated using modulus square of joint photon spectrum. The density plot of joint photon intensity in terms of wavelength gives information about the correlations in the wavelength of the twin photons which satisfy the phase matching conditions. From figure 1, following

observations were drawn: (1) The signal and idler are spectrally anticorrelated. (2) The bandwidth of joint photon spectrum increases with increment in spectral width of the pump.

3. Experimental study

The experimental setup is shown in figure 2(a). The SHG source consists of a 1560 nm output pulsed laser operated at different repetition rate. The 780nm pulsed output was generated using a type 0 PPLN waveguide. This process was necessary as spectrally pure laser with high repetition rate is not available at 780 nm wavelength. Polarization controllers are placed before each polarization sensitive device. The output spectra of SHG process was recorded using an optical spectrum analyser, as shown in figure 2(b). The filtered 780 nm output was then fed into another type 0 PPLN waveguide for SPDC process, that leads to the generation of biphotons at 1560 nm. The bandwidth of SPDC output was measured using a wavelength tuneable filter having fixed bandwidth of approximate 1nm. Filtered wavelength output was connected to the single photon detectors. Superconducting nanowire single-photon detector (SNSPD) having quantum efficiency approximately 85% was used for the detection. The electrical pulse generated from the detector was fed into time to digital coveter for counting the generated photons. SHG process was repeated at different repetition rate as the pulses at each rate have slightly different spectral width, which will in turn generate different bandwidth in SHG spectrum. It was observed that SPDC spectrum has bandwidth of 121.98nm, 116.3nm, and 121.78nm at 1GHz, 5GHz and 10GHz respectively. Thus in order to produce high bandwidth SPDC output the spectral width of the pump can be accordingly selected.

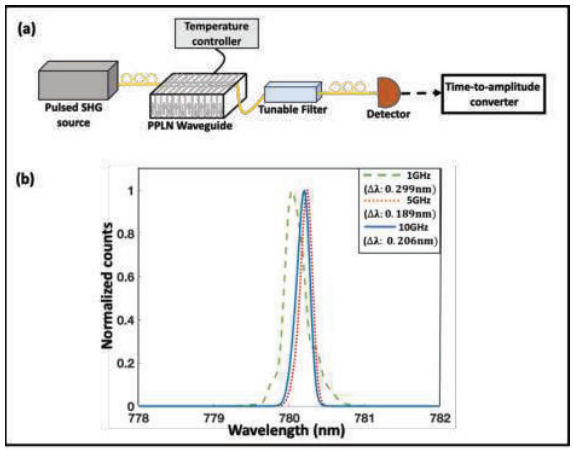

Fig 2: (a) Experimental setup (b) Bandwidth of SHG output.

4. Conclusion

One way of increasing the spectral bandwidth of SPDC can be changing the bandwidth of input pump. Since the entire setup is fiber based, all the factors are same at all rates. So, it can be concluded that the SPDC bandwidth increases with increase in pulsed pump bandwidth.

5. Acknowledgement

Author AR acknowledge financial support from Ministry of Human Resource Development (MHRD), Government of India for Prime Minister Research Fellowship (PMRF) and IIT Delhi for Institute of Eminence (IoE) project grant.

6. References

[1] Boyd RW. Nonlinear optics. Academic press; 2020 Mar 30.
[2] Tanzilli, S., et al. "PPLN waveguide for quantum communication." *The European Physical Journal D-Atomic, Molecular, Optical and Plasma Physics* 18.2 (2002): 155-160.
[3] Zhang, Qiang, et al. "Correlated photon-pair generation in reverse-proton-exchange PPLN waveguides with integrated mode demultiplexer at 10 GHz clock." *Optics Express* 15.16 (2007): 10288-10293.
[4] Kim, Ilhwan, Donghwa Lee, and Kwang Jo Lee. "Study of type II SPDC in lithium niobate for high spectral purity photon pair generation." *Crystals* 11.4 (2021): 406.

Accurate Laser Phase Noise Measurement Using Coherent Self-Heterodyne Detection Technique

Arjun Kurur, Balaji Srinivasan, Deepa Venkitesh
Dept. of Electrical Engineering, Indian Institute of Technology Madras, Chennai, 600036, India
Author e-mail address: ee20s137@smail.iitm.ac.in, deepa@ee.iitm.ac.in

Abstract: Using the Coherent Self-Heterodyne (CSHD) method, we accurately measure the FM noise of an External Cavity Diode Laser (ECDL). The In-Phase and Quadrature components are extracted using a lock-In amplifier method, which also eliminates RF driver noise from the retrieved signal. The predicted linewidth agrees with the value from the datasheet.
Keywords: Laser FM noise, CSHD.

1. Introduction

Narrow linewidth lasers find applications in varied fields such as optical communication, LIDAR, atomic clocks[1], and gravitational wave sensing[2]. The measurement of kHz or sub kHz laser linewidth is a challenging task by itself. In addition to linewidth, some of these applications require an accurate knowledge of the FM noise spectrum. The conventional technique of the delayed self-heterodyne method, where the laser output is allowed to beat with a delayed version of itself, fails for linewidths < 25 kHz. The pink noise in such lasers becomes predominant and hence, complete decorrelation of the laser requires impractical fiber lengths. There have been reports of using a recirculating loop for this purpose [3], or mathematically extract the linewidth from the lineshape function of the beat of correlated lines [4] The ideal Lorentzian spectrum would be widened to Gaussian by this long delay fiber and will also reduce the optical power reaching the photodiode. Moreover, the delayed self-heterodyne method can only measure the linewidth and cannot extract the frequency spectrum of the 1/f noise. The other alternative is to carry out a coherent self-homodyne method where the frequency fluctuations are discriminated to intensity fluctuations through an interferometer configuration [5]. However, this technique is extremely sensitive to the environmental acoustic fluctuations and hence requires acoustic isolation.

In this paper, we experimentally demonstrate a coherent self heterodyne technique that enables us to measure the frequency spectrum of phase noise fluctuations in a self-heterodyne technique, where the phase fluctuations are shifted to an IF frequency in order to avoid the influence of environmental perturbations. The phase fluctuations at a wide range of frequencies can be accurately determined using this method.

2. Coherent Self-Heterodyne Technique

In the coherent self-heterodyne (CSHD) approach, a Mach-Zehnder interferometer-based discriminator is used to measure the phase noise characteristics of a laser. The discriminator converts the signal's phase variations into amplitude variations, which are then measured on the photodetector. Schematic of the experimental setup is shown in Fig. 1a. An ECDL in Littman configuration at 1550 nm is the laser source and is expected to have a narrow linewidth (~ 10 kHz). The two 50:50 couplers and the delay fiber (shorter than the coherence length) make the all fiber Mach-Zehnder Interferometer (MZI). An Acousto-Optic Modulator (AOM) introduced in one of the arms is used to frequency shift the lasing frequency by 150 MHz. A small fraction of the power from the RF source that drives the AOM is used for lock-in detection of the output power from the photodetector. The relative electric field polarizations in the two arms and the interfering optical powers are adjusted to achieve a good signal noise ratio at the photodiode. The acquired ESA spectrum is shown in Fig. 1b. Due to the laser linewidth, this spectrum exhibits the characteristic feature shown in Fig 1b, and sub-coherence delay causes a periodic modulation. The narrow peak riding over a pedestal indicates that the light in the two arms of the interferometer is correlated. The periodic function is more prominent when the fiber length is shorter; conversely, the narrow peak evolves to a Lorentzian characteristic when the fiber length is much longer than the correlation length[5]. The AC part of the received photodiode signal is

$$V_{ac}(t) = \frac{KRP}{2} cos\left[\omega_{RF} t + \omega_0 \tau + \Delta\phi(t,\tau)\right] \qquad (1)$$

where K is the transimpedance gain, R is the responsivity of the photodiode, P is the incident optical power, $_{RF}$ is

the AOM shift frequency, $_0$ is the laser frequency and $\Delta\phi(t, \tau)$ is the useful phase term which has the phase noise information.

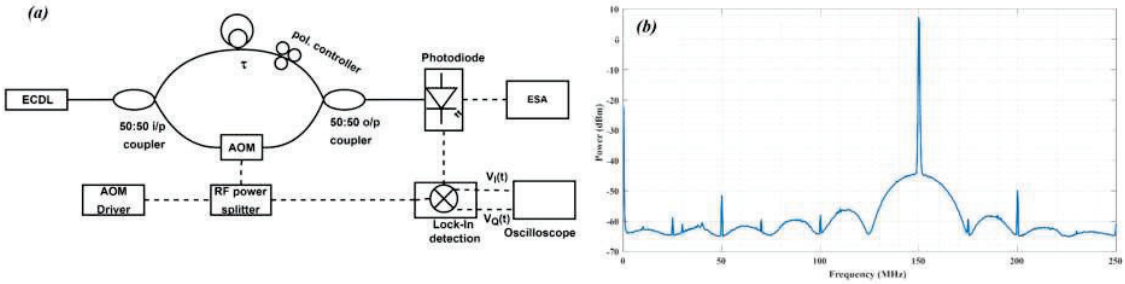

Figure 1:(a) Experimental schematic of the Coherent Self-Heterodyne technique. (b) Obtained electrical spectrum around AOM frequency of 150 MHz . RBW : 300 kHz , 100 trace average

By mixing $V_{ac}(t)$ with the RF carrier frequency produced from the same RF driver, one may extract the phase-noise information from the signal. The in-phase $V_I(t)$ and quadrature $V_Q(t)$ components can be estimated as,

$$V_I(t) = \frac{KRP}{4} cos[\Delta\phi(t,\tau) + \omega_0\tau] \qquad V_Q(t) = \frac{KRP}{4} sin[\Delta\phi(t,\tau) + \omega_0\tau] \qquad (2)$$

from which the instantaneous phase and the noise spectrum are extracted. Note that the mixing of photodiode signal with the driver signal has effectively eliminated the RF driver noise from the acquired In-Phase and Quadrature terms, thus the detected phase noise will be immune to the RF driver noise. These In-Phase and Quadrature components can be used to recreate the signal and in turn its phase noise spectrum.

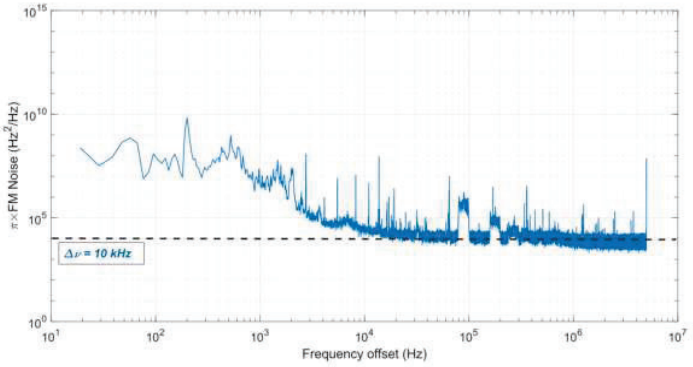

Figure 2 Measured frequency noise. Note that the white noise floor suggests a linewidth of 10 kHz

Figure 2 shows the measured FM noise PSD which suggests a laser linewidth of 10 kHz which matches the datasheet value provided by the manufacturer. This method can now be extended to compare the phase noise spectrum after linewidth reduction of such lasers.

3. Conclusion

The laser linewidth is measured using the Coherent Self-Heterodyne technique. This technique accurately measures the white noise and the 1/f noise spectrum of laser phase. Lock-in detection effectively removes the contribution of RF driver noise in the measurements. The arrangement does not require any specific acoustic isolation of the fiber interferometer and can be effectively used to measure the noise at different frequency offset values.

Acknowledgment

Funding from the LIGO India Scientific Consortium and Samsung Pravartak Fellowship is gratefully acknowledged.

Reference

[1] Bai, Z.; Zhao et al". Micro. Opt. Technol. Lett. 2021, 1–12.(2021)
[2]B. P. Abbott et al., Phys. Rev. Lett.116,061102 (2016).
[3] Hidemi Tsuchida, "Laser frequency modulation noise measurement by recirculating delayed self-heterodyne method," Opt. Lett. 36, 681-683
[4]Mo Chen,et al., "Ultra-narrow linewidth measurement based on Voigt profile fitting," Opt. Express 23, 6803-6808 (2015)
[5] D.J.Derickson.,"Fiber optic test and measurement" (1998)

Two photon lasing: Coherently and incoherently pumped two quantum dots-photonic crystal cavity system

Lavakumar Addepalli and Pradyumna K Pathak
School of Physical Sciences, Indian Institute of technology Mandi, Kamand, Himachal Pradesh, 175005, India
Author e-mail address: (ppathak@iitmandi.ac.in)

Abstract: In this paper we consider two quantum dots coupled to single mode photonic crystal cavity driven coherently and incoherently using external pump. We numerically solve the master equation to obtain the steady-state properties of the system. Exciton-phonon interactions are studied by making polaron transformation and a simplified master equation is constructed to obtain single photon and two-photon emission, absorption rates and excessive stimulated emission into cavity mode.
Keywords: Quantum dots, photonic crystal cavity, polaron transformation, Born-Markov approximation.

1. Introduction

Lasing phenomenon in quantum systems can be realised if the emission rate is greater than absorption rates. Quantum dots (QDs) coupled to photonic crystal (PhC) microcavities show a great deal in quantum information processing [1]. Strong confinement of electrons and holes results in discrete energy levels in QDs and are also called artificial atoms. Recent significant progress in lithographic techniques allow us to grow QDs at desired location in microcavities allowing for ultra-strong coupling [2]. In these systems exciton-phonon coupling plays very important role resulting in phonon mediated processes such as off-resonant cavity mode feeding, exciton dephasing, population inversion etc.

In this paper we considered two QDs coupled to single mode PhC cavity which is pumped incoherently and coherently using external pump. We obtained steady-state (SS) populations, cavity photon statistics such as average cavity photon number, zero-time delay second order photon correlation function, $g^2(0) = (\langle n^2\rangle - \langle n\rangle)/\langle n\rangle^2$ to see the bunching behavior of the cavity field and Fano factor, $F = (\langle n^2\rangle - \langle n\rangle)/\langle n\rangle$ for cavity field statistics. We calculated the single photon emission (SPE), single photon absorption (SPA), two-photon emission (TPE) and two-photon absorption (TPA) rates of the system, thereby obtained the excessive stimulated emission into the cavity mode due to single and two-photon processes. Lasing can be observed when there is population inversion exists between the excited, ground states of the system and the emission rates are larger than absorption rates. The exciton-phonon interactions present in the system are treated by making polaron transformation [3] and using Born-Markov approximation to derive the master equation, similar procedure is used in earlier works [4,5]. The master equation is numerically solved using quantum optics toolbox [6]. A simplified master equation (SME) is constructed by considering cavity coupling strengths are smaller than detuning which provides a clear picture of the processes involved in the system.

We consider two separate QDs coupled to single mode PhC cavity. The Hamiltonian for the system in rotating wave approximation (RWA) of cavity mode frequency is given by

$$\widehat{H} = \hbar\Delta_1\sigma_1^+\sigma_1^- + \hbar\Delta_2\sigma_2^+\sigma_2^- + \hbar(g_1\sigma_1^+ a + g_2\sigma_2^+ a + H.C.) + \widehat{H_{ph}}. \quad (1)$$

Here, the detuning $\Delta_i = \omega_i - \omega_c$ and ω_i, ω_c are the transition frequency between ground state, $|g_i\rangle$ and excitonic state, $|e_i\rangle$ for the i^{th} QD, cavity mode frequency respectively. The lowering and raising operators for QDs are given by $\sigma_i^+ = |e_i\rangle\langle g_i|$, $\sigma_i^- = |g_i\rangle\langle e_i|$, g_i is the exciton-cavity mode coupling constant and a is the cavity field annihilation operator. The last term in (1) represents the exciton and longitudinal acoustic (LA) phonon interaction, $\widehat{H_{ph}} = \hbar\Sigma_k\omega_k b_k^\dagger b_k + \hbar\Sigma_i\lambda_i^k\sigma_i^+\sigma_i^-(b_k + b_k^\dagger)$. Here, $b_k(b_k^\dagger)$ is the annihilation(creation) operator of k^{th} phonon bath mode of frequency, ω_k and λ_i^k is the coupling strength of exciton $|e_i\rangle$ to the k^{th} mode of phonon bath. We perform polaron transformation, $\widehat{H'} = e^S H e^{-S}$, where $S = \Sigma_i\sigma_i^+\sigma_i^-\Sigma_k\lambda_i^k(b_k^\dagger - b_k)$ and make Born-Markov approximation to derive the master equation. The incoherent processes present in the system are written in Lindblad super-operator form, $L[\hat{O}]\rho = \widehat{O^\dagger}\hat{O}\rho - 2\hat{O}\rho\widehat{O^\dagger} + \rho\widehat{O^\dagger}\hat{O}$.

Fig. 1(a) & (b) shows the steady-state populations in the collective QD states, $|e_1, e_2\rangle$ (black), $|e_1, g_2\rangle$ (blue), $|g_1, e_2\rangle$ (green), $|g_1, g_2\rangle$ (red) and cavity photon statistics by varying Δ_2 when both the QDs are coupled equally to cavity mode, $g_2 = g_1$ with cavity decay rate, κ, spontaneous emission rates, γ_i , pure dephasing rates, γ_i' at

temperature, T=5K. It can be seen the population inversion between levels $|e_1, e_2\rangle$ and $|g_1, g_2\rangle$ exists for the range of detuning considered and set of operating parameters considered and for $\Delta_2 = 0.0g_1$ there is peak in $\langle n\rangle$ (black), dip in *F* (green) implying cavity field became less noisy and decrease in $g^2(0)$ (blue) suggests cavity field departing from bunching behavior. These phenomena can be due to increase in TPE into the cavity mode and is the case as TPE dominates other processes (not shown in figures). Fig. 1 (c) & (d) shows the behavior of the system with incoherent pump rate, $\eta_1 = \eta_2 = \eta$. With increase in pump rate, $|e_1, e_2\rangle$ population increases, and the onset of population inversion can be seen for $\eta > 0.4g_1$. The SS populations of $|e_1, g_2\rangle$, $|g_1, e_2\rangle$ change equally with η, blue and green curves overlap. Fig. 1(d) shows *F* and $g^2(0)$ decrease with increase in η and it is observed that the TPE rate increases. Similar behavior of the system is observed for T=20K with decrease in values of TPE rates compared to T=5K case and this is due to increase in incoherent scattering processes.

For the case of coherently driven two QDs-PhC cavity system, the Hamiltonian in RWA of pump frequency is given by,

$$\hat{H} = \hbar\Delta_{cp}a^{\dagger}a + \hbar\Delta_{1p}\sigma_1^{+}\sigma_1^{-} + \hbar\Delta_{2p}\sigma_2^{+}\sigma_2^{-} + \hbar(g_1\sigma_1^{+}a + g_2\sigma_2^{+}a + H.C.) + \hbar\big(\eta_1(\sigma_1^{+} + \sigma_1^{-}) + \eta_2(\sigma_2^{+} + \sigma_2^{-})\big) + \widehat{H_{ph}} \quad (2)$$

Here, $\Delta_{cp} = \omega_c - \omega_p, \Delta_{1p} = \omega_1 - \omega_p, \Delta_{2p} = \omega_2 - \omega_p$, ω_p is the coherent pump frequency and η_i is the i^{th} QD pumping rate. Fig. 2 shows the steady-state population and cavity photon statistics of the coherently driven system with both the QDs coupled equally with cavity mode, $g_2 = g_1$ for T=5K. From Fig. 2(a), we can see when there is population inversion between the levels $|e_1, e_2\rangle$ and $|g_1, g_2\rangle$ and for $\Delta_{2p} = -16.1g_1$ i.e., when both QDs are equally detuned w.r.t pump frequency there is decrease in population of $|e_1, e_2\rangle, |g_1, g_2\rangle$ and Fig. 2(b) shows there is dip in $\langle n\rangle$ and peaks in *F* and $g^2(0)$. This behavior of the system at this operating point can be attributed to the decrease in TPE rate of the system and is observed that is in fact the case (not shown in figures). Fig. 2 (c) & (d) show the SS populations and cavity photon statistics of the system upon varying coherent pumping rate, $\eta_1 = \eta_2 = \eta$. The population inversion takes place for $\eta > 2.0g_1$, Fig. 2(d) shows *F* and $g^2(0)$ slightly decrease around $\eta = 4.1g_1$ and increase in TPE is observed.

2. Figures

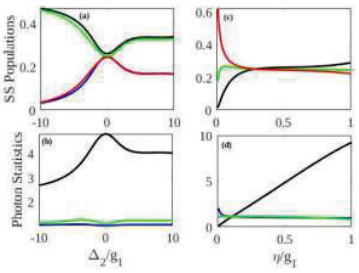

Fig. 1: Incoherently pumped two QDs-PhC cavity system (a) & (b) varying Δ_2 with $\kappa = 0.1g_1, \Delta_1 = 0.0g_1, \eta = 0.5g_1, \gamma_1 = \gamma_2 = 0.01g_1, \gamma_1' = \gamma_2' = 0.01g_1$ and (c) & (d) varying η for $\Delta_2 = 0.0g_1$ at T=5K.

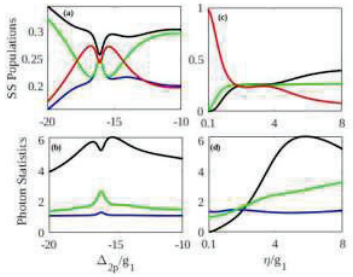

Fig. 2: Coherently pumped two QDs-PhC cavity system (a) & (b) varying Δ_{2p} with $\kappa = 0.3g_1, \Delta_{cp} = -18.0g_1, \Delta_{1p} = -16.1g_1, \gamma_1 = \gamma_2 = 0.01g_1, \gamma_1' = \gamma_2' = 0.01g_1$ and (c) & (d) varying η for $\Delta_{2p} = -16.1g_1$ at T=5K.

3. References

[1] Wei, H. R., & Deng, F. G. (2014). Scalable quantum computing based on stationary spin qubits in coupled quantum dots inside double-sided optical microcavities. *Scientific reports*, *4*(1), 1-8.

[2] Song, B. S. et.al., (2005). Ultra-high-Q photonic double-heterostructure nanocavity. *Nature materials*, *4*(3), 207-210.

[3] Xu, D., & Cao, J. (2016). Non-canonical distribution and non-equilibrium transport beyond weak system-bath coupling regime: A polaron transformation approach. *Frontiers of Physics*, *11*(4), 1-17

[4] Roy, C., & Hughes, S. (2011). Influence of electron–acoustic-phonon scattering on intensity power broadening in a coherently driven quantum-dot–cavity system. *Physical Review X*, *1*(2), 021009.

[5] Verma, J. K., Singh, H., & Pathak, P. K. (2018). Effect of phonon coupling on the cooperative two-photon emission from two quantum dots. *Physical Review B*, *98*(12), 125305.

[6] Tan, S. M. (1999). A quantum optics toolbox for Matlab 5. J. Opt. B: Quantum Semiclass. Opt, 1, 161.

Determination of Scattering Parameters of a Turbid Medium Comprising Absorbing Microspheres

Kalpak Gupta and M R Shenoy
Department of Physics, Indian Institute of Technology Delhi, Hauz Khas, New Delhi 110016, India
Author e-mail address: kalpakgupta@gmail.com

Abstract: We propose a method to determine the scattering parameters of a turbid medium through the comparison of the measured scattered power at three photodetectors, which are placed off-axis, with the simulated scattered powers for various combinations of scattering parameters. In the proposed method, calibration curves relating the scattered powers to the scattering parameters are obtained using Monte Carlo simulations. We assume a set of *test* scattering parameters for spherical particles, for which the scattered powers are simulated in lieu of experiment, and show that the scattering parameters obtained from the calibration curves are the same as the *test* parameters, thus verifying the method.
Keywords: Turbidity, Scattering parameters, Optical properties, Monte Carlo

1. Introduction

When light is incident on the suspended particles of a turbid medium, it undergoes scattering and absorption. The properties of the scattered light depend on the scattering parameters of the turbid medium—the interaction coefficient μ_t, the anisotropy parameter g, and the albedo b [1,2]. μ_t dictates the probability of an interaction event while light propagates inside the turbid medium; it is the sum of scattering coefficient μ_s and absorption coefficient μ_a, which are defined similarly. g is a measure of the angular anisotropy of the scattered light, and b defines the strength of scattering relative to the total interaction strength of the medium, i.e. $b = \mu_s/\mu_t$. The scattered light in turn can be used to determine the scattering parameters, which contain information about the particles in a turbid medium. In a previous work [1], we have shown that for a non-absorbing turbid sample, the scattered light measured at an off-axis detector can be compared with the simulated scattered power for different values of g, which gives two possible values of g; the simulations were performed using the Monte Carlo method [1,2]. Subsequently, we reported that two off-axis measurements of the scattered light gives a unique value of the particle size for turbid media comprising non-absorbing microspheres [3]—the particle size was used in lieu of g. In this work, we explore the use of three off-axis detectors to estimate the scattering parameters, and show that for a scattering system involving spherical particles, the albedo b and the particle size can be uniquely determined using three off-axis measurements.

2. Methodology

The light scattering system is shown in Fig. 1. The turbid medium comprising absorbing microspheres is contained in a quartz cuvette, and light from a He-Ne laser is incident on it. The undeviated transmitted light is measured at a detector placed far (~1 m) from the sample to determine μ_t by using the Beer-Lambert law [1,2], and the scattered light is measured at three off-axis detectors. We simulate the scattering system using Monte Carlo simulations [1,3]: 10 million photon packets are incident on the medium; the packets propagate independently, getting randomly scattered and absorbed at various locations (of the suspended particles) inside the medium in accordance with the scattering parameters. Each packet is launched with weight $w = 1$, which decreases to b times w after each interaction. After all the packets are launched, the total weight of the packets at a detector divided by the total number of initial packets is equivalent to the normalized scattered power which would be measured at the detector in an actual

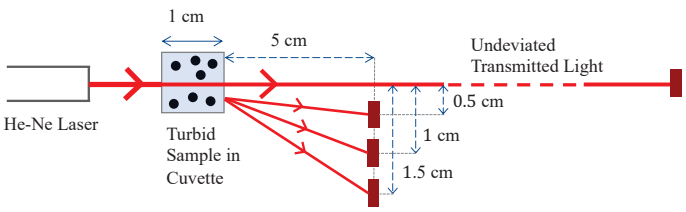

Fig. 1: Schematic of proposed setup to measure scattered power at three off-axis detectors.

experiment [2,3]. Given a turbid sample, we first determine μ_t, and then simulate the scattered power at the three off-axis detectors for various combinations of b and particle size to obtain calibration curves. The pair of b and particle size for which the measured scattered powers at the detectors are equal to the simulated scattered powers are identified as the actual scattering parameters of the given sample.

3. Results and Discussion

To test the proposed methodology, we consider a test sample with particle size = 1000 nm and b = 0.6, and $\mu_t = 1$ cm^{-1}. For this μ_t, we simulate the scattered powers at the three off-axis detectors, and assume them to be equal to the measured scattered powers at the respective detectors; this is justified since the accuracy of the simulations has been validated in our previous work [3]. Therefore, hereon we refer to these simulated powers corresponding to our *test* set of scattering parameters as the *measured* powers. We now apply the methodology discussed in Sec. 2 to determine the scattering parameters corresponding to the *measured* powers.

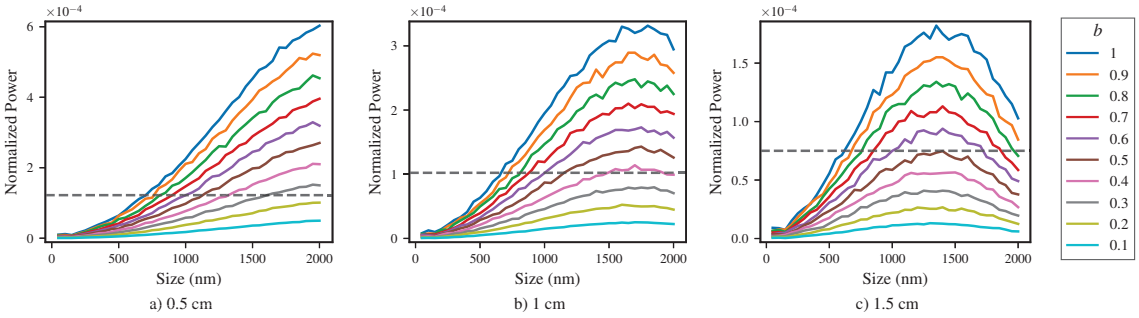

Fig. 2: Calibration curves relating the scattered power to the particle size (diameter) for different values of albedo b, for the three off-axis detectors with lateral displacements a) 0.5 cm, b) 1 cm, and c) 1.5 cm. The dotted horizontal lines indicate the* measured *scattered powers at the detectors (simulated in this case) for a given sample.

The calibration curves corresponding to the three off-axis detectors are shown in Fig. 2. There are several possible combinations of particle size and b which could correspond to the *measured* power at each detector; these are shown in Fig. 3. The parameters for which the three curves intersect, i.e., for which the simulated powers at all three detectors match with their respective *measured* powers, are found to be the same as the *test* parameters we had assumed to arrive at the *measured* powers. This validates the proposed method.

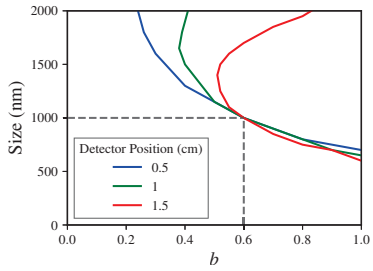

Fig. 3: Combinations of b and particle size for which the scattered power matches with the* measured *power at each detector. It can be seen that the point of intersection of the curves correctly corresponds to the scattering parameters of our* test *sample (dotted lines).

In conclusion, we have proposed a method to determine the scattering parameters of a turbid medium comprising absorbing spherical particles. The method involves measurement of the scattered power at three off-axis detectors in conjunction with calibration curves obtained using Monte Carlo simulations, and is verified numerically as well. Since the particles were spherical, the Mie phase functions were used for the simulations [1,3]. In the case of non-spherical scatterers, the appropriate phase functions have to be used, and the particle size can be replaced by g, which presents a scope of further study.

4. References

[1] K. Gupta and M. R. Shenoy, "Method to determine the anisotropy parameter *g* of a turbid medium," Appl. Opt. **57**, 7559–7563 (2018).
[2] Prerana, M. R. Shenoy, and B. P. Pal, "Method to determine the optical properties of turbid media," Appl. Opt. **47**, 3216–3220 (2008).
[3] K. Gupta and M. R. Shenoy, "Compact setup to determine size and concentration of spherical particles in a turbid medium," Appl. Opt. **60**, 8174–8180 (2021).

Characterization of Swept-Source using AOTF with Continuous Wavelength Scanning from Visible to Infrared Range for Biological Applications

Bhanu Pratap Singh[1], Himanshu Joshi[1], Pramila Thapa[1], Priyanka Mann[1], Dibya Jyoti Sarangi[1] and Dalip Singh Mehta[1*]

Bio-photonics and Green-photonics Laboratory, Indian Institute of Technology Delhi, Hauz Khas, New Delhi-110016, India.

Corresponding Author:[*] mehtads@physics.iitd.ac.in

Abstract: Characterization of broadband supercontinuum source is employed using Acousto-optic Tunable Filter (AOTF) at 5 nanometer scanning range from visible to near infrared region for multi-spectral broadband off-axis digital holographic microscopy. Intensity value, full width at half maximum (FWHM) and coherence length is calculated for each sampled wavelength. The source will be further utilized for phase microscopy and determination of refractive index of various biological samples with respect to wavelength.

Keywords: broadband supercontinuum source, acousto-optic tunable filter refractive index, FWHM.

1. Introduction

Invention of lasers sparked interest in non-linear optics as it has properties of spectral broadening and generating new frequencies due to high intensity of laser beam. Generation of supercontinuum is occasionally done by using photonic crystal fiber along with ultrafast laser pulses, of the order of nanosecond, of milliwatt Power and at repetition rate of kHz. Nanosecond pulses induces Raman scattering and four-wave mixing phenomenon in photonic crystal fibers which is the main cause of super continuum generation. The supercontinuum light sources are often used for Optical Coherence Tomography (OCT) and Optical Metrology. In addition to this, by means of integrating a wavelength scanning unit one can also use this light source for wavelength scanning Digital Holographic Microscopy.

In this paper, we report properties of a supercontinuum source as a swept-source and recorded spectral data of supercontinuum source at 5 nm scanning range of wavelength. Peak intensity values, full width at half maximum (FWHM) and gaussian adjusted coherence length at each recorded wavelength are calculated. This system will be further utilized for swept-source digital holographic microscopy.

2. Experimental Setup and Working

Figure 1 shows the block diagram of Experimental Setup for Supercontinuum Characterization. For characterization of Supercontinuum source, we have used AOTF (acousto-optic tuneable filter) to select a particular wavelength and recorded the spectrum using Avantes spectrometer. FWHM (Full width at half maximum) and coherence length of the source at that specific wavelength are calculated considering the gaussian spectrum of the selected wavelength.

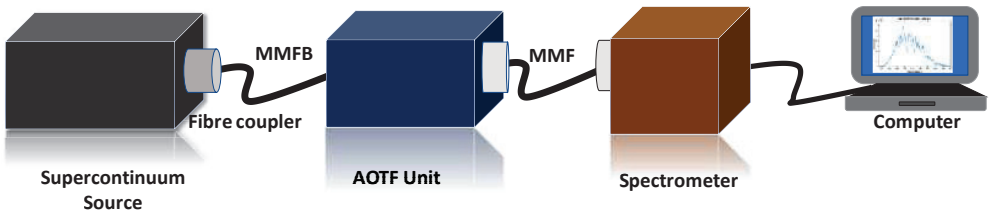

Fig 1: Block Diagram of Experimental Setup for Supercontinuum Characterization.

As supercontinuum source provides a broadband spectrum, a specific wavelength is selected by AOTF and output from AOTF is recorded in spectrometer. Spectrometer records intensity values for the corresponding wavelengths. Peak intensity wavelength and full width at half maximum is calculated from wavelength versus intensity data in

MATLAB and further coherence length is calculated by formula given below where λ_0 is peak wavelength value and $\triangle\lambda$ is FWHM.

$$Lc = \frac{2ln2}{\pi}\frac{(\lambda_0)^2}{\triangle\lambda} \quad (1)$$

3. Results and Discussion

Recorded spectrum of supercontinuum source along with normalized intensity spectrum are shown in the plots given below as shown in Figure 2. Supercontinuum source has a broadband band spectrum from which we have utilized only that part of spectrum which has significantly high intensity.

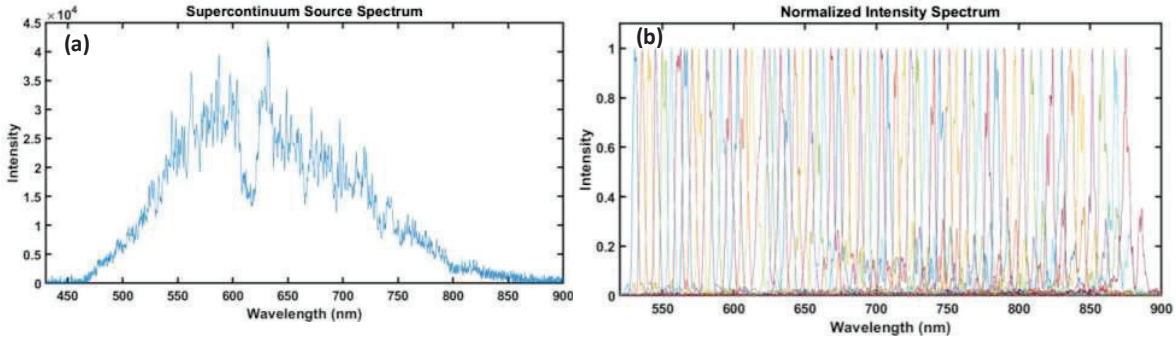

Fig 2: (a) Broadband Spectrum of Supercontinuum Source. (b) Normalized Intensity spectra of sampled wavelengths.

Table 1: This table shows coherence length, FWHM and relative intensity values at specific wavelengths.

Wavelength (nm)	Relative Intensity Values	FWHM (nm)	Coherence Length (μm)
530	44741	3.341	37.055
540	54396	3.671	32.766
550	52552	4.334	30.689
…..		……	……
640	30842	4.289	42.377
650	37694	3.295	57.041
660	36663	2.962	65.256

4. Conclusion

The study of spectrum of supercontinuum source provides some useful results. The source has sufficient coherence length and intensity at specific wavelengths. This indicates that this source can be used to generate interferograms in swept-source digital holographic microscopy. Intensity is enough to get high contrast interferograms which can be processed to develop corresponding phase maps and retrieve refractive indices with respect to wavelength.

5. References

[1] John M. Dudley Supercontinuum generation in photonic crystal fiber REVIEWS OF MODERN PHYSICS, VOLUME 78, OCTOBER–DECEMBER 2006

[2] Myung K. Kim," Principles and techniques of digital holographic microscopy," SPIE Rev. 1(1) 018005(1 April 2010) https://doi.org/10.1117/6.0000006

[3] Bj¨orn Kemper and Gert von Bally," Digital holographic microscopy for live cell applications and technical inspection," Appl. Opt. 47, A52-A61 (2008)

[4] Mustafa Mir, Gabriel Popescue et.al.," Quantitative Phase Imaging", Optics, Volume 57, ISSN 0079-6638.

[Quantum synchronization and entanglement of two mechanical oscillators, using parametric interactions, in coupled optomechanical systems]

Manju, Asoka Biswas and Shubhrangshu Dasgupta
Department of Physics, Indian Institute of Technology Ropar, Rupnagar, Punjab 140001, India
2018phz0009@iitrpr.ac.in

Abstract: We investigated the quantum synchronization and entanglement of two mechanical oscillators in a double-cavity optomechanical system with optical parametric amplifiers (OPAs) inside each cavity, which can interact mutually through an optical fiber and phonon tunneling. Here, we show that in the presence of OPAs, the degree of quantum synchronization is greatly improved and the mechanical oscillators become entangled as well at the same time. Precisely speaking, comparing with the case without OPAs, a well selected parametric gain can help to improve the quantum synchronization effect and to achieve the quantum entanglement simultaneously.
Keywords: Quantum Synchronization, Quantum Entanglement, Optical Parametric Amplifier.

1. Introduction

Spontaneous synchronization between two coupled pendula is one of the most intriguing phenomena in classical physics [1]. It has been explored in many fields with intense interest. In the last decade, many efforts have been devoted to explore synchronization to quantum regime [2]. Two coupled harmonic oscillators, described by the displacements $q_j(t)$ from their respective equilibrium positions and the linear momenta $p_j(t)$, where $j \in 1,2$, are said to be synchronized, if they maintain $q_-(t) = (q_1(t) - q_2(t))/\sqrt{2} \to \overline{0}$ and $p_-(t) = (p_1(t) - p_2(t))/\sqrt{2} \to \overline{0}$, at long times. This corresponds to complete classical synchronization. In quantum systems, however, such synchronization is inherently not possible due to uncertainty principle, $< q_-(t)^2 >< p_-(t)^2 > \geq \frac{1}{4}$. In such case. Mari *et al*. developed an effective measurement scheme and proposed a figure of merit to measure the degree of quantum synchronization in continuous variable system [2]: $S_c(t) = [\langle q_-(t)^2 + p_-(t)^2 \rangle]^{-1} \leq$ $[2\sqrt{\langle q_-(t)^2 \rangle \langle p_-(t)^2 \rangle}]^{-1} \leq 1$. The complete quantum synchronization refers to $S_c(t) = 1$. In the limit of associated classical synchronization, the $S_c(t)$ can be rewritten, in terms of δq_- and δp_-, as $S_q(t) = [\langle \square q_-(t)^2 + \square p_-(t)^2 \rangle]^{-1}$, where δq_- and δp_- are the fluctuations of position difference operator $\hat{q}_-$ and the momentum difference operator $\hat{p}_-$, respectively, about their respective expectation values. Several experiments have further followed to investigate quantum synchronization [3,4].

Synchronization is a signature of correlations between the oscillators. In quantum systems, such correlations are expected to be of quantum nature. So, we expect that there should be certain interconnection between quantum synchronization and other quantum correlations like entanglement [5] and the mutual information [6]. For a coupled bosonic system (like that of two harmonic oscillators), the joint variables q_- and p_- (which are used to demonstrate synchronization) satisfy the following uncertainty relation: $< (\delta q_-)^2 > + < (\delta p_-)^2 > \geq 1$. A stronger criterion for separability has further been proposed by Mancini [7]: $E_D = 4 \langle (\delta q_-)^2 \rangle \langle (\delta p_+)^2 \rangle \geq 1$, where the transformation $p_- \to p_+$ is made using partial transposition. This means that violation of above inequality refers to inseparability. As both quantum synchronization and inseparability have a quantum correlation in common and both measures can be understood in terms of second order moments of a set of conjugate quadrature, it is natural to explore the interconnection between these two.

In this work, we introduced an optical parametric amplifier (OPAs) inside each cavity of double cavity coupled optomechanical system and investigated the effect of OPAs on quantum synchronization and entanglement of two mechanical oscillators. The Hamiltonian of the system takes the following form($\hbar = 1$):

$$H = \sum_{j=1,2} \Delta_j a_j^\dagger a_j + \frac{\omega_{mj}}{2}\left(q_j^2 + p_j^2\right) - g a_j^\dagger a_j q_j + iE\left(a_j^\dagger - a_j\right) + iG\left(a_j^{\dagger 2} e^{-i\theta} - a_j^2 e^{i\theta}\right) - \mu q_1 q_2 - \lambda\left(a_1^\dagger a_2 + a_2^\dagger a_1\right) \quad [\ ]$$

2. Results and Discussion

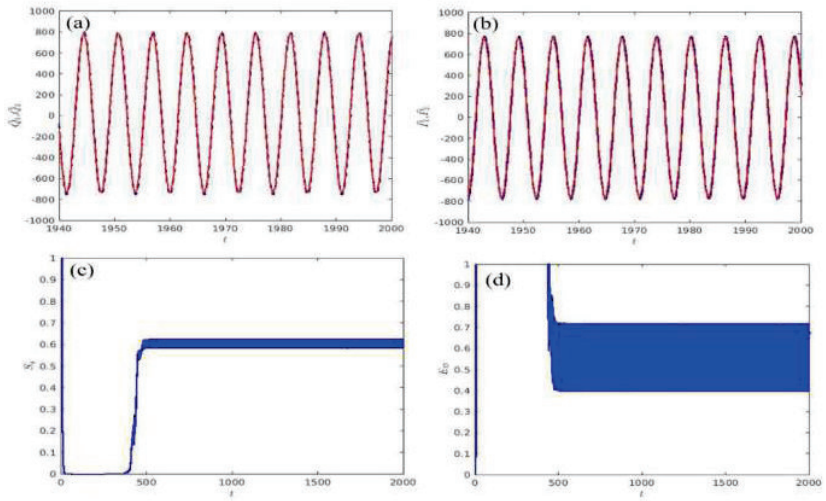

Figure 1. Time evolution of (a) mean values of $q_1(red)$ and q_2(blue), (b) mean values of p_1(red) and p_2(blue), (c) quantum synchronization S_q, (d) entanglement E_D. The parameters chosen are $\omega_{m1} = 1$, $\omega_{m2} = 1.005$,$\Delta_j = -\omega_{mj}$,$g = 0.005$,$\gamma_{mj} = 0.005, \kappa_j = 0.15, G = 0.14, \Theta = \frac{\pi}{2}, \lambda = 0.07, \mu = 0, E = 90$.

We have observed that for *G=0*, quantum synchronization is very poor and inseparability inequality is satisfied. When we switch on the OPA in our simulations, the quantum synchronization becomes much larger as compared to the case of absence of OPAs. Figures 1(a) and 1(b) illustrate the relevant classical limit cycles. Even for a small value of *G=0.14*, synchronization increases to a large value. The optimal value of S_q is 0.6 (in case of indirect coupling: (□=0, □□0) and 0.87 (in case of direct coupling: (□□0, □=0). More importantly, the entanglement between the mechanical oscillators starts appearing with *G=0.14*. The system also violates the standard inseparability criterion, as E_D becomes less than unity for both types of coupling. We noted that the quantum synchronization remain stable for large range of λ, while there is a finite window of μ to observe synchronization. The results for $G \neq 0$ suggest that with the assistance of OPAs, enhancement of quantum synchronization and appearance of entanglement can be achieved simultaneously between mechanical oscillators. Note that there exist a specific range of G and coupling coefficients (λ and μ) to see these effects at steady state. We also examined the robustness of $\bar{S}_{\bar{q}}(t)$ against T and we found that the case of indirect coupling is more appealing in achieving a preferable quantum synchronization behavior than the case of direct coupling. Here, we have shown the results for indirect coupling. We got the similar results for direct coupling.

In conclusion, we have systematically explored the quantum synchronization and entanglement between two mechanical oscillators in a double-cavity coupled optomechanical system by using OPAs. We found that the system with OPAs has better degree of quantum synchronization and mechanical oscillators become entangled simultaneously for both coupling ways. Our work attempts to find an inherent relation between the two correlations, based on the same set of quadrature fluctuations.

.

3. References

[1] C. Huygens, Oeuvres completes, vol. 7. M. Nijhoff, 1897.

[2] A. Mari, A. Farace, N. Didier, V. Giovannetti, and R. Fazio, “Measure of quantum synchronization in continuous variable systems,” Physical Review Letters, vol. 111, no. 10, p. 103605, 2013.

[3] M. Zhang, G. S. Wiederhecker, S. Manipatruni, A. Barnard, P. McEuen, and M. Lipson, “Synchronization of micromechanical oscillators using light,” Physical Review Letters, vol. 109, no. 23, p. 233906, 2012.

[4] M. Bagheri, M. Poot, L. Fan, F. Marquardt, and H. X. Tang, “Photonic cavity synchronization of nanomechanical oscillators,” Physical Review Letters, vol. 111, no. 21, p. 213902, 2013.

[5] C.-G. Liao, R.-X. Chen, H. Xie, M.-Y. He, and X.-M. Lin, Quantum synchronization and Correlations of two mechanical resonators in a dissipative optomechanical system, Phys. Rev. A 99, 033818 (2019).

[6] G. L. Giorgi, F. Galve, G. Manzano, P. Colet, and R. Zambrini, Quantum correlations and mutual synchronization, Phys. Rev. A 85, 052101 (2012).

[7] S. Mancini, V. Giovannetti, D. Vitali, and P. Tombesi, Phys. Rev. Lett. 88, 120401 (2002)

Double Aperture Speckle Interferometer using Single Hololens Imaging Configuration

Rahul Mandal[1], Mayukh Mandal[1], Abhijit Ghosh[1*] and A. K. Nirala[2]

[1]Department of Physics, National Institute of Technology Durgapur- 713209, West Bengal, India

[2]Biomedical Optics Lab, Department of Physics, Indian Institute of Technology (Indian School of Mines) Dhanbad-826004, Jharkhand, India

**Corresponding author: abhi.photonics@gmail.com*

Abstract: In present work, a double aperture speckle interferometer using a single hololens imaging configuration has been proposed and developed for measuring in-plane displacement component.

Keywords: Speckle interferometry, Young's fringes, in-plane displacement, Hololens.

1. Introduction

When a diffuse object is illuminated with coherent beam of light, dark and bright interference patterns are formed, known as speckles, distributed randomly in space [1]. Among speckle-based measurement techniques, speckle photography and speckle interferometry [1] are generally used. Leendertz [2] was the first to measure in-plane displacement precisely using a two-beam interferometry method. Later, Duffy [3] suggested replacing the two-beam illumination with two equal apertures placed side by side over the imaging lens. According to his assessment, in this imaging, the imaging lens need to be diffraction limited only over the two apertures, not over the whole area of the lens. When light passed through these two apertures, periodic grid like structure is formed within each speckle. For in-plane displacement component measurement, double exposure specklegrams are recorded in a single recording medium. For analysis of the recorded specklegram several techniques are being used- point wise filtering, whole field filtering etc. Yadav et al. [4] utilized four hololenses in designing Duffy's double aperture speckle interferometer. Jayaswal et al. [5] used a compact two hololens imaging system for measurement of in-plane displacement component.

In the present study, we have applied a single hololens imaging system for designing double aperture speckle interferometer for measuring in-plane displacement component.

2. Experimental

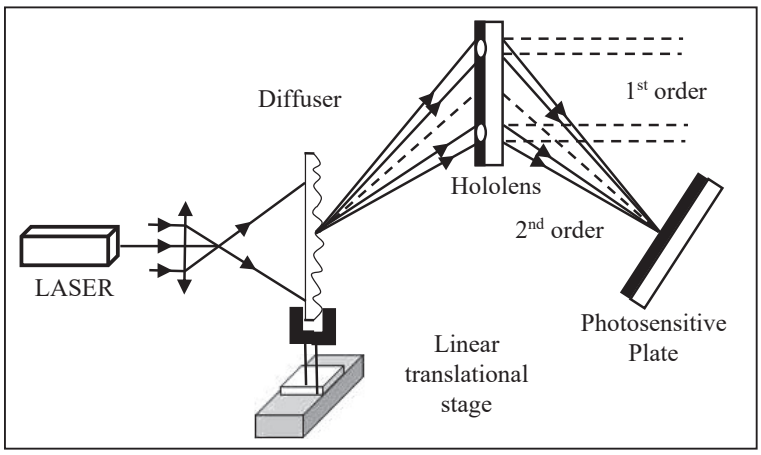

Fig.1: Schematic of experimental setup for in-plane displacement component measurement using double aperture speckle interferometer consisting of single hololens.

Hololens is interferogram recording of a diverging spherical wave with a planar wave. Here hololens was recorded on a silver halide plate having focal length is 23 cm and at the time of recording the angle between plane wave and spherical wave was 17°. Details of the hololens recording geometry and imaging characteristics was reported in our previous communication [6,7]. For generalized zone plate, higher order foci are at position $f/2$, $f/3$, $f/4$, f

/5,…… in addition to principal focus *f*. If the object is kept at $u = f$, and for 2nd order imaging $f2 = f / 2$, image distance will become $v = f$. Hence, second order focal point fulfills the criterion for one-to-one imaging [6,7].

In this experiment, an expanded laser beam was allowed to illuminate a diffuse object and imaged with the help of a double aperture speckle interferometer consisting of single hololens. Double exposure specklegram was recorded in a silver halide plate, first before giving any displacement to the diffuse object and then after giving some in-plane displacement parallel to the line joining the two apertures using a linear translational stage. Measurement of in-plane displacement was done by analyzing the double exposure specklegrams using point-wise filtering method at ±1st order diffraction halo.

3. Results and Discussion

Young's fringes are obtained by point wise filtering in zero order and ±1st order diffraction halo for different in-plane displacement values 20μm, 60μm and 100μm are shown in Fig. 2 (a-c).

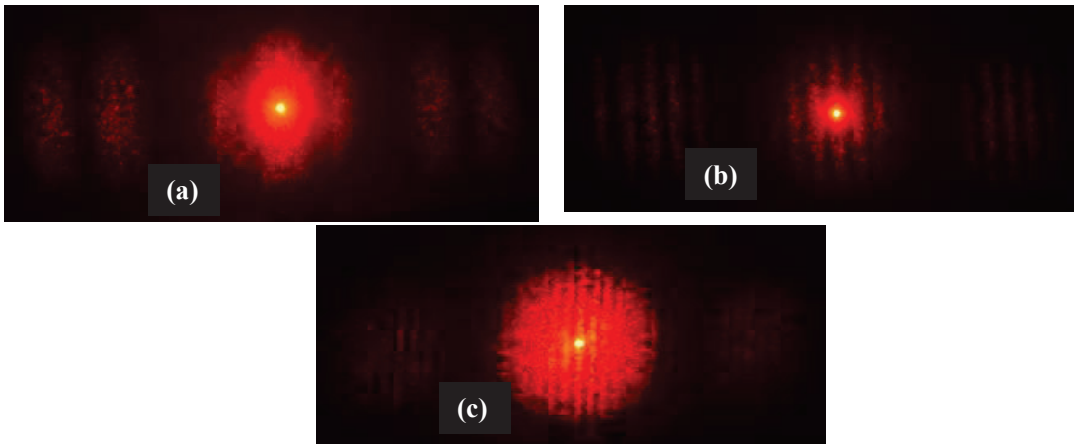

Fig.2: Photographs of the Young's fringes obtained by point wise filtering for different in-plane displacements (a) 20 μm (b) 60 μm (c) 100 μm

Table 1: Measured values of in-plane displacement corresponding to different given values of in-plane displacement

In-plane displacement given to the object (in μm)	Measured values of in-plane displacement (analyzing Young's fringes in ±1st order) (in μm)	Error (in %)
20	20.84	4.2
60	60.34	0.57
100	101.10	1.1

4. Summary and Conclusion

We have discussed the use of low cost, light weight single hololens imaging system in laser speckle interferometry, its alignment process is as simple as that of a conventional lens imaging system. Experimental results presented in the Table 1, nearly matches with the actual displacement given to the object.

5. References

[1] R. S. Sirohi, *Speckle metrology* (Marcel Decker, Inc. Ny, 1993).
[2] J. A. Leendertz, "Interferrometric displacement measurement on scattering surfaces utilizing speckle effect," J. Phys. E **3,** 214 (1970).
[3] D. E. Duffy, "Moiré gauging of in-plane displacement using double aperture imaging," Appl. Opt. **11,** 1778-1781 (1972).
[4] H.L. Yadav, et al., "Fabrication of double-aperture hololens imaging system:application to mechanics," Opt. Laser Eng. **41**, 869–877 (2004).
[5] R. K. Jayaswal, H. L. Yadav and P. K. Barhai, "Design and analysis of modified version of double aperture speckle interferometer consisting of holographic optical element: Application to measurement of in plane displacement component," Optik **126**, 1700-1704 (2015).
[6] A. Ghosh and A. K. Nirala, "One to one imagery using single hololens configuration," Opt. Rev, **21**, 765–768 (2014).
[7] A. Ghosh, N. Kumar and A. K. Nirala, "Single hololens imaging configuration in laser speckle photography for in-plane displacement measurement," Asian Journal of Physics **31**(1), 107-113 (2022).

Focusing the radially polarized light into a subwavelength focal spot

Bhavesh Pant, Ram Kalyan and Brijesh Kumar Singh
Central University of Rajasthan, Bandarsindri, Ajmer, Rajasthan, 305817
brijeshsingh@curaj.ac.in

Abstract: Focusing the doughnut-shaped radially polarized light into a subwavelength focal spot is studied using the concept of a phase mask. A structured subwavelength focal spot is generated, which is smaller than the standard diffraction limit and much smaller than the spot obtained without a mask. This method also works as a filter for the radial component in focus and has potential applications in optical systems.
Keywords: radial polarization, subwavelength, standard diffraction limit.

1. Introduction

It is interesting to study the tight focusing (focusing with a high numerical aperture (NA) lens) of a radially polarized light having wide potential applications in high resolution microscopy, optical tweezers, and data storage. The spot size of the radially polarized light under the tight focusing condition is smaller than the focal spot of other linearly polarized and circularly polarized light. And this focal spot of the tightly focused radially polarized light consists of a longitudinal field component along the optical axis and a transverse (radial) component of doughnut shape. However, the focal spot of a focusing system is restricted to a diffraction limit of 0.5λ /NA due to the diffractive nature of the light, where λ is the wavelength of the light. Therefore, many applications require the optical beams to be tailored. The tailored beam thus increases the utility of the beam. Several theoretical and experimental optical methods have been proposed to focus the light beyond this diffraction limit [1]. Super-oscillation is another approach for focusing and imaging beyond the diffraction limit. The super-oscillation can be realized by superimposing different light modes like the Bessel and Airy modes, but complicated mathematics is involved in these methods. The more suitable technique for realizing subwavelength focal spot depends on designing an optical amplitude or a phase mask. Recently, a fabricated planar binary phase lens consisting of concentric dielectric rings is used to focus radially polarized light beyond the diffraction limit [2]. However, the subwavelength size of the mask creates challenge in fabricating these lenses because they require complicated lithography techniques.

In our work, we numerically generate a subwavelength focal spot beyond the standard diffraction limit by tightly focusing a radially polarized light. For this purpose, we utilize a systematic approach in which an annular phase mask, consisting of only two regions with opposite phase, is inserted at the entrance pupil of a high NA objective lens [3]. A structured subwavelength focal spot, beyond the standard diffraction limit is generated for some specific ratio between the two regions of the mask.

2. Method

For an infinitely thin radially polarized light, the rigorous intensity profile at the focus of an objective lens of NA = 0.8 in free space is calculated using vector diffraction theory. This gives a spot of size 0.388λ (in units of wavelength), which is the standard diffraction limit for our present study. Adopting the expression from the vector diffraction theory, the field components of a radially polarized light in the vicinity of the focus can be written as [4]:

$$e_\rho(\rho,\ z) = A\int_0^\beta cos^{1/2}\theta \sin(2\theta)\, p_0(\theta)\, J_1(k\rho\sin\theta)\, e^{ikz\cos\theta}\, d\theta \tag{1}$$

$$e_z(\rho,\ z) = 2iA\int_0^\beta cos^{1/2}\theta\, sin^2\theta\, p_0(\theta)\, J_0(k\rho\sin\theta) e^{ikz\cos\theta}\, d\theta \tag{2}$$

where e_ρ and e_z are the amplitudes of the transverse and longitudinal components of the radially polarized beam respectively, $J_n(k\rho\sin\theta)$ denotes a Bessel function of the first kind of order n, $p_0(\theta)$ is the pupil apodization function, k is the wave number, and β is the maximal angle determined by the numerical aperture of the lens. In this paper, we choose $p_0(\theta) = 1$. The wavelength is set to be 532 nm, and the unit of the length is normalized to wavelength. The total field in the vicinity of the focus is defined by the vector sum of these two components. Using the Eq. (1) and (2),

the intensity distribution of a tightly focused radially polarized beam in the focus is shown in the first row of the fig. 1. The spot size at focus is defined by the full width at half maxima (FWHM) of the total intensity profile, which is 1.22λ in case no mask is used. For realizing the structured subwavelength focal spot of incident radially polarized beam, we consider the mask function expressed in the form [3]:

$$\varphi_{mask}(\theta) \propto \begin{cases} -1 & \theta \leq \varepsilon.\beta \\ 1 & \varepsilon.\beta \leq \theta \leq \beta \end{cases} \quad (3)$$

where $0 < \varepsilon.\beta < \beta$, β is the maximum angle of focus defined by NA of the lens and θ is the angular co-ordinate. ε is a variable that takes value between 0-1. We then multiply Eq. (1) and (2) by the mask function {Eq. (3)}, and calculate the modified intensity distribution in the focal plane using MATLAB software.

3. Results & Discussion

Second row of fig. 1 shows the simulation results, where the subwavelength focal spot is generated at the center of the focus. For comparison, in the first-row we show the results when no mask is used. The results in the second row corresponds to mask function with ε value 0.69. The first-column figures {Fig. 1(a, d)} represent the phase maps, the second-column figures {Fig. 1(b, e)} shows the 2D intensity profile of the tightly focused beam in the focal plane, and the third column figures {Fig. 1(c, f)} shows the cross-sectional intensity profiles of different components of the beam in the focal plane. For $\varepsilon = 0.69$, the measured FWHM of the subwavelength focal spot is 0.362λ {Fig. 1(e, f)}; which is about 3.37 times smaller than the spot in case of no mask {Fig. 1(b, c)}, and about 1.1 times smaller than the standard diffraction limit for our present study. We observe that, as the size of the focal spot reduces, the energy of the subwavelength focal spot decreases, and the contribution of the radial (transverse) component also becomes less in the central spot {Fig. 1(b, c, e, f)}. In this way, the mask works as a filter for the radial component.

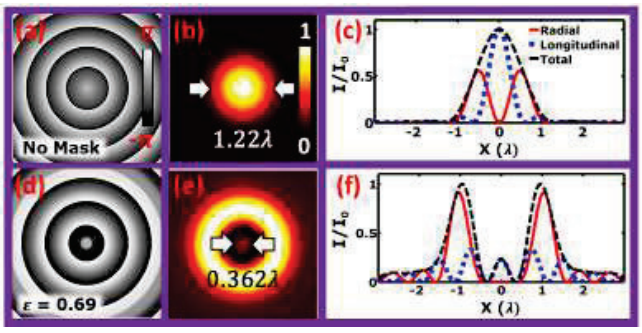

Fig. 1. Simulation results of tightly focused radially polarized beam with and without mask.

In conclusion, we introduced an efficient method for generating a structured subwavelength focal spot in a controlled manner beyond the standard diffraction limit. An extremely small spot can be obtained but with weak intensity. Despite its weak intensity, this spot may be applicable in trapping and manipulating particles due to its smaller subwavelength size. Finally, we envisage that the structured spot will be applicable in super-resolution microscopy, and optical tweezers as well.

4. References

[1] K. Kitamura, K. Sakai, and S. Noda, "Sub-wavelength focal spot with long depth of focus generated by radially polarized, narrow-width annular beam," Opt. Express **18**, 4518-4525 (2010).
[2] A. Yu, G. Chen, Zh. Zhang, and Z. Wen, "Creation of Sub-diffraction Longitudinally Polarized Spot by Focusing Radially Polarized Light with Binary Phase Lens," Sci Rep **6**, 38859 (2016).
[3] B. K. Singh, H. Nagar, Y. Roichman, and A. Arie, "Particle manipulation beyond the diffraction limit using structured super-oscillating light beams," Light. Sci. Appl. **6**, e17050 (2017).
[4] K. S. Youngworth and T. G. Brown, "Focusing of High Numerical Aperture Cylindrical-Vector Beams," Opt. Express **7**, 77-87 (2000).

Investigating the Efficiency of Photophoretic trapping with structured intensity profiles created using optical fiber

Anita Pahi* , **Souvik Sil and Ayan Banerjee[1]**
Indian Institute of Science Education and Research Kolkata, Mohanpur, District – Nadia, Pin- 741246
Author e-mail address: anita.pahi1@gmail.com, ayanban7@gmail.com[1]*

Abstract: We have shown the correlation between the efficiency of photophoretic trapping and the structure in intensity profiles present in the trapping beam. Photophoretic trapping which has a thermal origin has provided an alternative pathway for trapping mesoscopic absorbing particles in the air. The various intensity profiles are generated using different optical fibres. We have used a single, dual and four-mode optical fibre for our experiment. Here, we show that trapping efficiency increases with increase in the number of modes of optical fibre. Trapping efficiency was measured using two parameters, threshold power and radial trapping force.
Keywords: Photophoretic force, mesoscopic, Optical fiber , Viscous drag

1. Introduction

Photophoretic forces occur due to the inhomogeneous heating of an absorbing particle in a gaseous medium by a focused laser beam. It has introduced a new paradigm in optical trapping and manipulation of absorbing particles[1-3]. The photophoretic force[4] are broadly divided into two types of forces, FΔT and FΔα. The former arises from an inhomogeneous temperature distribution across an absorbing particle's surface due to laser heating of that particle and directed from the hotter side to the colder side of the particle, while the later results from a difference in the accommodation coefficient of the particle, and measures the efficiency of heat exchange between the heated particle and ambient molecules of the medium[4]. Though it is clear that the magnitude of photophoretic forces depends on the intensity of light, it is still an unanswered question whether the magnitude of photophoretic force only depends on intensity or the gradient of intensity while using structured light. In our earlier works[5-7], we showed that particles confine in at least one dimension due to the photophoretic forces balancing the gravitational force and in the other dimension, there exists a restoring force possibly generated due to the complex motion of the particle in the light field. Thus, due to the force balance, particles of a certain mass can be trapped with the appropriate intensity of the trapping light[8], with higher and lower intensities leading to particles escaping the trap[6, 8]. But in the presence of a structured intensity profile, i.e., adjacent patterns of light and dark regions - there could be opposite forces on a particle as it moves in the intensity profile. This would result in a complex restoring force on the particle even in the direction of gravity, and not merely a force balance. Although various other works[1,2,8] have used structured light for photophoretic trapping but a systematic study investigating the role of the number of dark and bright spots is not available. In this work, we have shown a definite dependence of the trapping efficiency on the intensity profile of the trapping beam.

2. Results and Discussion

From the measurement of both threshold power and radial trapping force, it is clear that four-mode fibre leads to the most efficient traps requiring the lowest threshold power to trap particles, while the single-mode fibre results in the highest threshold power. Threshold power is defined as the minimum power required for the particle to remain trapped. The threshold power reduces with an increasing number of transverse modes present in the fibre output, as is seen in the way it behaves for the dual and four-mode fibres. Also, the four mode and dual mode fibre need 3 times and 1.2 times respectively less power than single mode. The viscous drag method is used to measure the radial trapping force. When the motorized stage is moved, the trapped particle is also accelerated. As it gains velocity the drag force will also increase, at a point the drag force will equal the radial trapping force and the particle will fall. The velocity at which the particle falls can simply be calculated by $V_{escape} = \sqrt{2ad}$, where 'a' is the acceleration of the motorized stage, and d is the distance covered by the particle before falling. The force on the particle can be calculated from simple Stokes' law $F_{trap} = 6\pi\eta Rv$, where R is the particle radius, v is the particle velocity, and η is the viscosity of the air.

We observed the radial trapping force gradually increases as we increase the number of modes of the fibre.
We have also calculated the average intensity per speckle which is highest for four modes compared to dual mode.

3. Tables and Figures

(a) (b)

Fig. 1: (a) Schematic representation of the experimental set up. M1 and M2: plane mirrors TL: trapping laser (640 nm); WLS: white light source; A: aperture; CL1, CL2: plano convex lenses; AL: aspheric lens; FC: fiber coupler; SMF: Single mode fiber; MO1 and MO2: 10× objective lenses; SC: sample chamber; TS: translation stage; TP: toner particles; C1, C2 and C3: cameras. The left top inset shows a zoomed-in image of the sample chamber with a trapped particle and a measuring scale at the background for determining the axial position, while the bottom right inset depicts the actual image of the home-built mount for collimating the fiber output using AL and focusing into SC using CL1. ***(b) Output beam profiles of different fiber, from left: single mode, dual mode and four mode***

Table 1: Threshold power for different fiber

Fiber Type	Threshold Power (mW)	Lowest power	Highest Power
Single Mode Fiber	47.34(1.81)	38.84mW	61.16mW
980nm Dual mode fiber	38.98(3.79)	33.92mW	53.12mW
1260-1650nm optical fiber	29.0(3.90)	12.64mW	52mW

4. Conclusion

The work here shows that as we increase the number of modes, the dark region in the output intensity profile increases. It enhances the radial trapping force and reduces the threshold power. This work indicates using multimode fibre in future for a more efficient trap. Using optical fibre for photophoretic trapping provides simplicity in setup and alignment. Our work creates a new path for numerous applications with photophoretic trapping in spectroscopic and aerosol studies.

5. References

[1] V. G. Shvedov, A. S. Desyatnikov, A. V. Rode, W. Krolikowski, Y. S. Kivshar, Optics Express 2009, 17, 7 5743.
[2] A. S. Desyatnikov, V. G. Shvedov, A. V. Rode, W. Krolikowski, Y. S. Kivshar, Optics Express 2009, 17, 10 8201.
[3] V. G. Shvedov, A. V. Rode, Y. V. Izdebskaya, A. S. Desyatnikov, W. Krolikowski, Y. S. Kivshar, Physical review letters 2010, 105
[4] H. Horvath, KONA Powder and Particle Journal 2014, 31 181.
[5] S. K. Bera, A. Kumar, S. Sil, T. K. Saha, T. Saha, A. Banerjee, Optics letters 2016, 41, 18 4356.
[6] S. Sil, T. K. Saha, A. Kumar, S. K. Bera, A. Banerjee, Journal of Optics 2017, 19, 12 12LT02.
[7] S. Sil, P. Basak, A. Pahi, A. Banerjee, Applied Physics Letters 2020, 117, 22 221106.
[8] Porfirev, A.P., Skidanov, R.V., "Optical trapping and manipulation of light-absorbing particles by means a Hermite-Gaussian laser beam," J. Opt. Technol. 82(9), 587-591 (2015)

Phase-Switchable GST Metasurface Perfect Reflector and Partial Absorber in 7-9 μm Wavelength Window

Sridhar Singhal, Shubhanshi Sharma, and Shailendra K. Varshney
Dept. of E&ECE, Indian Institute Technology Kharagpur
sridhar.singhal@iitkgp.ac.in

Abstract: We report perfect reflector and partial absorber in GST metasurface whose material phase can be switched between amorphous and crystalline through proper thermal bias. Finite element method simulations reveal greater than 90% of reflection over 2 μm bandwidth with a peak reflectance of 98.8% whereas 40% of absorption can be achieved for crystalline phase of GST.
Keywords: GST, metasurface, long-wave mid IR

1. Introduction

$Ge_2Sb_2Te_5$ (GST) material exists in two phases, amorphous and crystalline [1]. The phase change can be realized through proper thermal bias. It is known that the GST switch from amorphous phase to crystalline at around 100-150 ℃ [2]. Correspondingly the optical properties also change. It was noticed from experimental data in [3] that the extinction coefficient of GST is drastically large for the crystalline phase in mid-IR range as compared to amorphous phase, which is loss less. This motivated us to explore the possibility to achieve simultaneously switchable reflector-absorber behavior in a single material metasurface. The target window for the device is 7.5 - 9 μm. This segment of the atmospheric transmission window is especially useful as it contains strong absorption lines for important gases like Methane and Hydrogen Peroxide [4].

2. Design of GST metasurface and results

The unit cell of the proposed metasurface design is shown in Fig. 1(a). A nanosphere made of GST with radius ***r*** rests on substrate CaF_2. The structure is repeated periodically at a period ***P*** along the x and y directions to generate two-dimensional metasurface. The structure is optimized to obtain perfect reflection at 8 μm. Due to the symmetry of spherical resonators, the structure is polarization independent. Scattering due to the spherical nanoparticles can be obtained through the Mie Scattering theory [5,6]. Since in the mid-IR region, the refractive index of GST is very high ($n > 4$), only the a_1 (electric dipole) and b_1 (magnetic dipole) terms of the Mie expansion are dominant [7], the first Kerker condition for zero backward scattering ($a_1 = b_1$) should be reasonably accurate. Considering isolated amorphous GST spheres in air alone, the scattering parameters a_1 and b_1 were calculated and radius of GST nanospheres was obtained. The geometrical dimensions were further fine-tuned for complete structure including substrate (CaF_2) to obtain perfect reflection using Finite Element Method (FEM) simulations (COMSOL Multiphysics). Experimental data from [3,8] is used for the refractive index of both GST and CaF_2. The optimal radius for the GST nanosphere is 1.18 μm and the periodicity 2.65 μm. Fig. 1(b) plots the Magnetic field distribution at resonance wavelength $\lambda = 8.1$ μm. The arrow surface is electric field. The rotating electric field implies presence of strong magnetic dipole moment component. The absorptance, transmission and reflection characteristics obtained through FEM simulations for the case of GST in amorphous and crystalline phases are illustrated in Fig. 1(c) and 1(d), respectively. The device shows greater than 90% of reflectance in the 7.42 μm to 9.06 μm wavelength band, with a peak reflectance of 98.8% at 8.1 μm. The absorptance is less than 1% in the concerned wavelength range. The absorptance, reflection and transmission of the metasurface when the GST is in crystalline phase is depicted in Fig. 1(d). Due to high extinction coefficient of crystalline GST in the mid-IR region, high absorptance, greater than 38.8% for 90% bandwidth of the reflector is observed. The absorptance is maximum at 7.42 μm (43.6%) and reduces as the wavelength increases. While the structure is not a perfect absorber, the reflection from the metasurface is lower than 36.5% in the bandwidth and acts as a tunable mirror switch.

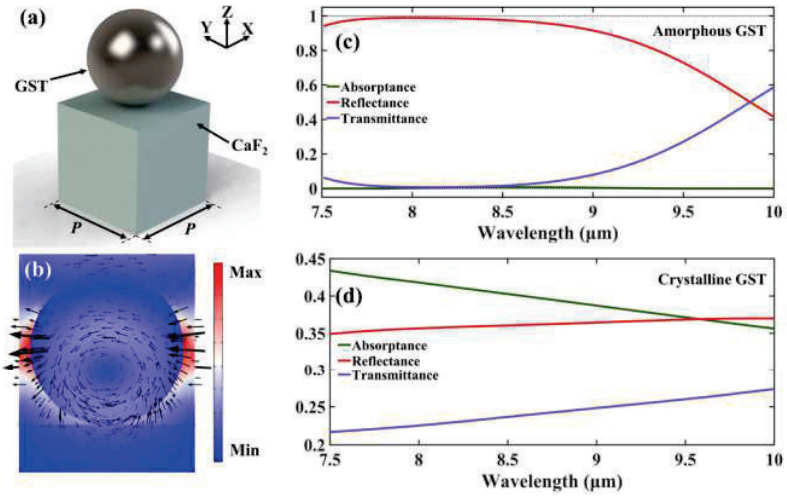

Fig. 1: (a). Unit cell of the proposed metasurface structure, consisting of GST nanosphere of radius r = 1180 nm on CaF_2 substrate repeated at cell period P = 2650 nm, (b). Magnetic field distribution at resonance wavelength λ = 8.1 μm, the arrow surface is electric field, (c). Absorptance, Reflectance and Transmittance of structure when GST is in amorphous state, and (d) in crystalline state.

3. Conclusion

We have numerically simulated a GST metasurface which exhibit perfect reflection and about ~ 40% absorption in 7-9 μm wavelength window when the material phase is switched from amorphous to crystalline owing to high extinction ratio possessed by the GST material. The proposed metasurface can provide a unique solution to trace gases such as methane and hydrogen peroxide.

References

[1] Park, Jeongwoo, et al. "Characterization of amorphous phases of Ge2Sb2Te5 phase-change optical recording material on their crystallization behavior." *Japanese journal of applied physics* 38.8R (1999): 4775.
[2]Morales-Sanchez, Eduardo, et al. "Determination of the glass transition and nucleation temperatures in Ge 2 Sb 2 Te 5 sputtered films." *Journal of applied physics* 91.2 (2002): 697-702.
[3] Kim, Hyun Jung, et al. "PCM-net: a refractive index database of chalcogenide phase change materials for tunable nanophotonic device modelling." *Journal of Physics: Photonics* 3.2 (2021): 024008.
[4] Ferreira, Mário F S et al. "Roadmap on optical sensors." *Journal of optics (2010)* vol. 19,8 (2017): 083001.
[5] Kerker, Milton, D-S. Wang, and C. L. Giles. "Electromagnetic scattering by magnetic spheres." *JOSA* 73.6 (1983): 765-767.
[6] Huang, Yali, et al. "All-dielectric metasurface for achieving perfect reflection at visible wavelengths." *The Journal of Physical Chemistry C* 122.5 (2018): 2990-2996.
[7] Li, Yan, et al. "Broadband zero-backward and near-zero-forward scattering by metallo-dielectric core-shell nanoparticles." *Scientific reports* 5.1 (2015): 1-12.
[8] Malitson, Irving H. "A redetermination of some optical properties of calcium fluoride." *Applied Optics* 2.11 (1963): 1103-1107.

Mechanical tunability of three-dimensional photonic crystal inverse opal based structures

Rina Mudi[1], Shivakiran Bhaktha B.N[2]., Kapil Debnath[3]

[1] *Advanced Technology Development Centre, IIT Kharagpur, West Bengal, 721302, India.*

[2]*Department of Physics, IIT Kharagpur, West Bengal, 721302, India.*

[3]*Department of Electronics and Electrical Communication Engineering, IIT Kharagpur, West Bengal, 721302, India.*

Author(s) e-mail address: rina.mudi08@iitkgp.ac.in

Abstract: In this work, we present a mechanically tunable inverse opal 3D photonic crystal structure. To achieve mechanical tenability we used polydimethylsiloxane (PDMS), which is an elastomer. As the PDMS thin film with inverse opal structure is stretched, causing a change in the periodicity, we observe a blue shift in the reflection spectra.

Keywords: 3D photonic crystal, PDMS inverse opal, mechanical tuning, optical sensing.

Introduction:

Photon crystals (PhC) are periodically arranged dielectric structures that have a photonic bandgap (PBG) that forbids propagation of a certain frequency range of light and allows frequencies in the allowed band to propagate without scattering[1]. One of the most popular 3D PhCs is self-assembled opals. Inspite of the unique optical properties of opal-based PhC, it is a discontinuous structure with air filled in the interspace of spheres, thus, it cannot be used as a standalone device due to fragility and lack of robustness. Several approaches were developed to make the opals-based PhC robust [2-4], but are not cost-effective. In this work, we have developed a method of realizing robust inverse opal structure in polydimethylsiloxane (PDMS). Using our fabricated device, we demonstrated tuning of the reflection spectra under mechanical stress.

Device Fabrication:

To fabricate our proposed device, we first self-assembled polystyrene (PS) opals with average diameter of 460 nm. We started by diluting 0.06ml of the aqueous solution in 3ml of DI water and sonicating for 30 mins so that the PS opals gets dispersed well. After that, a cleaned glass subsrate is placed at an angle of 45° in the solution. The solution is kept at 60°C for 24 hours so that the water evaporates. The PS opals self-assembles in face-centered cubic (FCC) lattice on the glass substrate by evaporation-assisted self-deposition. An SEM image of the fabricated self-assembled opal structure is shown in Fig. 1a. To realize PDMS inverse opal, we first mixed PDMS with the curing agent with 10:1 ratio. The mixture was degassed to remove any air bubbles before pouring over the self-assembled PS opals. After that the sample was kept in the vacuum so that the PDMS solution could properly infiltrate into the voids of the self-assembled PS opal structure by capillary action. The sample was then cured at 90°C for 48 hours.

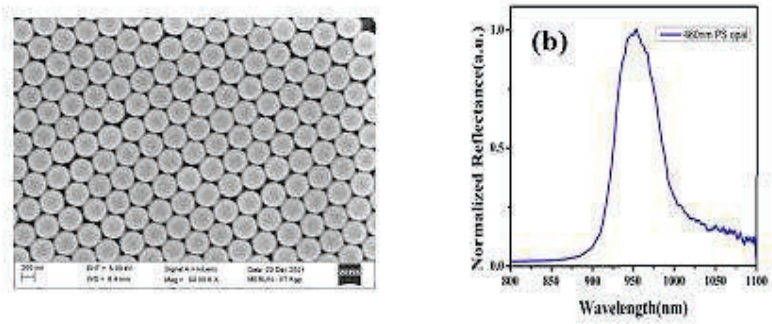

Fig.1: (a) Top-view SEM image of fabricated polystyrene opals PhC. (b)Normal incidence reflection spectra from self-assembled PS opal with average diameter of 460nm.

To remove the PS opals, the sample was then kept in acetone for 24 hours. During this process the PDMS thin film with inverse opal structure gets detached from the glass substrate.

Measurement and Discussion:

The reflection spectra of our fabricated devices were taken using a fiber-coupled light source deuterium-halogen in UV-visible range using Avantes spectrometer at normal incidence. Figure 1b shows the reflection spectra of the PS opal structure before the inverse. The peak resonance of the opals occurs at 953 nm of wavelength and the FWHM is approximately 55nm.

We have used the same setup to measure the inverse opal structure. A schematic of the PDMS inverse opal structure is shown in Fig. 2a. Figure 2b, shows the reflection spectra of the inverse opal structure with and without mechanical stress. The blue curve shows the reflection spectra of the inverse opal without any stress, which has a reflection peak at 595 nm and the FWHM is approximately 40 nm. As mechanical stress is applied, we expect a reduction in periodicity along the vertical direction, causing a blue shift in the reflection spectra. As the red curve indicates, when mechanical stress is applied the reflection spectra takes a blue shift with a peak around 512 nm and FWHM is approximately 90 nm.

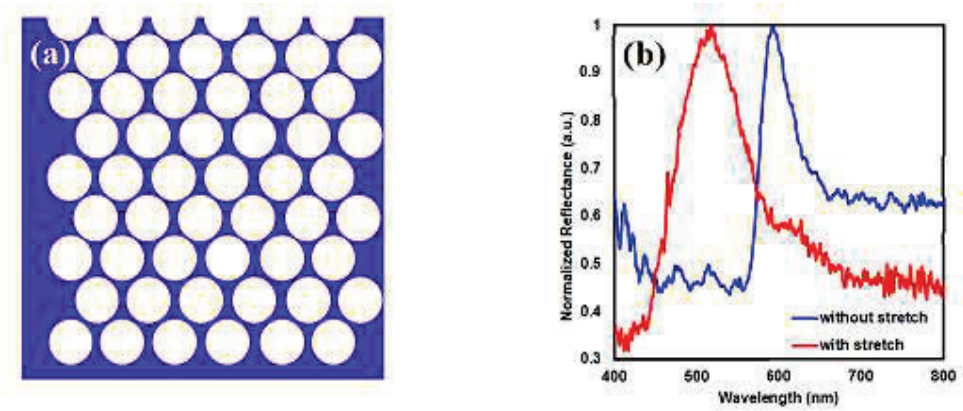

Fig. 2: (a) Schematic diagram of fabricated free-standing PDMS inverse opal structure. (b) Normal incidence reflection spectra from the PDMS based inverse opal structure with and without mechanically stretching.

Conclusion:

In summary, we experimentally demonstrated simple and practical method of fabrication of mechanically tunable inverse opal in a stretchable material, PDMS. By using reflection spectra measurement we demonstrate that such structure can be mechanically tunable without losing the photonic crystal property. Such system will find wide applications in optical sensing and imaging.

References

[1]] J.D. Joannopoulos, "Photonic Crystal: Molding the flow of light", second edition, Princeton University Press, (2008).
[2] M. Muldarisnur et al., "Structure and optical properties of opal films made by an out-of-plane electric field-assisted capillary deposition method", ACS omega, 7,8084-8090, (2022).
[3] Y. Zhang et al., "Tough and hydrophilic photonic crystal obtained from direct UV irrdiation", Macromol. Rapid Commun,31, 2115-2120, (2010)
[4] P Liu et al., "Bio-inspired robust non-iridescent structural color with self-adhesive amorphous colloidal particle arrays", Nanoscale,10,3673-3679,(2018).
[5] J-Hun et al., "Large-area printed broadband membrane reflectors by laser interference lithography", IEEE photonics journal, 5,1,2200106,(2013)
[6] J. Li et al., "Ion-beam sculpting at nanometer length scales" Nature,412, 166-169, (2001).

Emission enhancement of nitrogen-vacancy centers using metal-dielectric structure

Nitesh Singh and Rajesh V. Nair
Laboratory for Nano-scale Optics and Meta-materials (LaNOM), Department of Physics, Indian Institute of Technology Ropar, Rupnagar, Punjab 140001, India
E-mail: nitesh.19phz0007@iitrpr.ac.in

Abstract: The light emission manipulation of quantum emitters using photonic and plasmonic structures has been an intense topic of research which finds applications in spectroscopy, sensing, quantum information processing. Here, we have studied the one-dimensional metal-dielectric metasurface known as Tamm structure, coupled with NV- center as a quantum emitter. The structure is optimized to obtain Tamm plasmon resonance (TPR) at 640 nm coinciding to zero phonon line of NV- center. We observed 20 times field intensity enhancement near the metal-dielectric interface. The Green function method is utilized to calculate the LDOS for coupled single NV- centre with Tamm Plasmon. The coupling increases the Purcell factor by 4 times at the resonance wavelength.
Keywords: Metal-dielectric metasurface, Tamm plasmon, NV center, LDOS.

1. Introduction

The metal-dielectric metasurfaces gained extensive attention in the past few years due to their exceptional capability to enhance light-matter interactions. The light emission manipulation of quantum emitters using photonic and plasmonic structures has been the subject of various applications in spectroscopy, sensing, quantum information processing, lasers, and optoelectronic devices [1-4]. Controlling the light-matter interaction by framing the structural parameters of metamaterials allows modification in the emission rate of quantum emitters (QE) such as nitrogen-vacancy (NV-) centers in nanodiamonds. The NV- center is formed by a substitutional nitrogen atom adjacent to a carbon vacancy in a diamond crystal. The emission spectrum of NV- center consists of a pure electronic transition at 640 nm called zero phonon line (ZPL) assisted with broad phonon sideband (PSB) emission spanning up to 750 nm. It is observed that nearly 3-4% of transitions go into zero phonon line (ZPL), and most of them goes into phonon side bands (PSBs). Thus, at room temperature, the ZPL emission is quite feeble. According to Fermi's golden rule, the decay rate is proportional to an available number of states into which emission can take place, called local density of optical states (LDOS). Thus, altering the local environment of the emitter using metamaterials can induce modification in the ZPL emission. Therefore, it is an ongoing effort to enhance emission intensity and the rate at the ZPL with simultaneous PSB inhibition for the efficient use of NV- center in single photon generation, indistinguishable photons, optical spin readout, and quantum sensing. The search for low-cost easy fabrication of the sub-wavelength cavity structure with moderate *Q*-values is a contemporary topic of research.

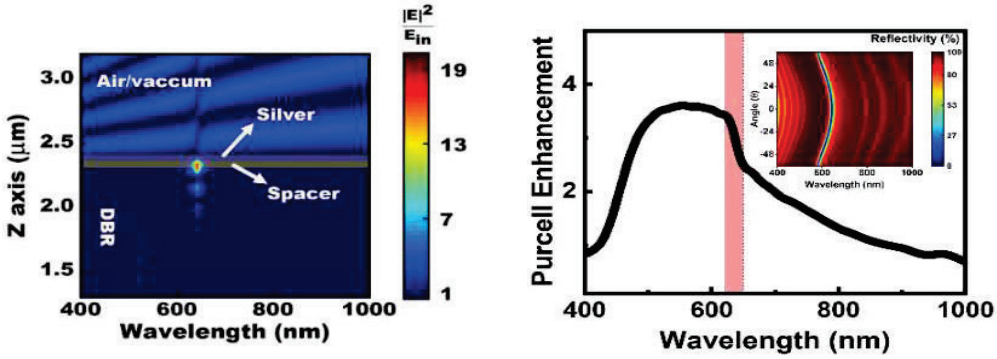

Fig. 1: (a) The electric field intensity profile in the structure at different wavelengths along growth direction (Z-axis), a large field confined between the Ag film (silver region) and spacer layer (brown region). (b) The wavelength-dependent Purcell enhancement for NV- center; (inset) reflectivity for the various angle of incidence (θ) of an incident plane wave.

We have studied a one-dimensional metal-dielectric stacked metasurface known as Tamm structure which is coupled to NV- center as a quantum emitter[5]. The structure is optimized using structural parameters like spacer thickness, metal thickness and index of dielectric bilayers forming Tamm structure to obtain Tamm plasmon resonance (TPR) at 640 nm coinciding to zero phonon line of NV- center. The transfer matrix method and the finite domain time difference (FDTD) method are used to calculate the resonance wavelength and field confinement at various wavelengths. We observed that at resonance wavelength, the field intensity enhancement is about 20 times near the metal-dielectric interface compared to the incident plane wave source intensity, see Fig. 1. The Green function method is employed to calculate the LDOS for coupled single NV- centre with plasmons. The coupling of Tamm plasmons with emitter increases the Purcell factor by 4 times at a resonance wavelength of 640 nm as seen in Fig. 1. Such Purcell enhancement is useful for generating an on-demand bright single photon source with a high emission rate.

2. Reference

[1] A.D. Rakić, A.B. Djurišić, J.M. Elazar and M.L. Majewski, "Optical properties of metallic films for vertical-cavity optoelectronic devices", *Appl. Opt.* **37**, 5271-5283,(1998).

[2] P. Neumann, R. Kolesov, B. Naydenov, J. Beck, F. Rempp, M. Steiner, V. Jacques, G. Balasubramanian, M.L. Markham, D.J. Twitchen, S. Pezzagna, J. Meijer, J. Twamley, F. Jelezko and J. Wrachtrup, "Quantum register based on coupled electron spins in a room-temperature solid", *Nature Physics* **6**,(2010).

[3] G. Balasubramanian, I.Y. Chan, R. Kolesov, M. Al-Hmoud, J. Tisler, C. Shin, C. Kim, A. Wojcik, P.R. Hemmer, A. Krueger, T. Hanke, A. Leitenstorfer, R. Bratschitsch, F. Jelezko and J. Wrachtrup, "Nanoscale imaging magnetometry with diamond spins under ambient conditions", *Nature* **455**, 648-651,(2008).

[4] E. Togan, Y. Chu, A.S. Trifonov, L. Jiang, J. Maze, L. Childress, M.V.G. Dutt, A.S. Sørensen, P.R. Hemmer, A.S. Zibrov and M.D. Lukin,"Quantum entanglement between an optical photon and a solid-state spin qubit. *Nature* **466**, 730-734,(2010).

[5] M. Khokhar, N. Singh and R.V. Nair,"Stacked metasurfaces for enhancing the emission and extraction rate of single nitrogen-vacancy centers in nanodiamond", *Journal of Optics* **24**, 024008,(2022).

Oxidized Ultrathin Metal Film as Inexpensive Transport Layer in Perovskite Solar Cells

Arun Kumar*, Sonia Rani, Dhriti Sundar Ghosh

Thin-film and Photovoltaics Laboratory, Department of Physics, Indian Institute of Technology Bhilai, Raipur

**arunbagga@iitbhilai.ac.in*

Abstract: Inorganic charge transport layers are considered a prerequisite for the fabrication of inexpensive and highly stable perovskite solar cells (PvSCs). Here we have demonstrated a thermally oxidized ultrathin copper film as a hole transporting layer in PvSCs. Optical, electrical, structural, and morphological studies have been done for better optimization of the device. A power conversion efficiency of 11.44% on an active area of 0.25 cm^2 has been achieved by the incorporation of an oxidized metal film.

Keywords: Inorganic-HTL, Oxidized Copper, Ultrathin Metal Film, Perovskite Solar Cells.

1. Introduction

Organic polymers such as PEDOT:PSS, PTAA, Spiro-OMeTAD, etc. are the most commonly used as hole transport layers (HTLs) in perovskite solar cells (PSCs) owing to their tunable conductivity and mobility resulting in high power conversion efficiencies (PCEs). However, the use of such material along with hygroscopic dopants can lead to poor device stability, and also the high cost of these materials can increase overall device fabrication costs hindering large-scale fabrication and commercialization[1]–[3]. The use of inorganic materials as transport layers can serve as a low-cost, stable, and efficient alternative to organic polymers. NiO, Cu_2O, CuI, CuSCN, etc. are being used as inorganic HTLs in PSCs and are showing similar device performance and better device stability[4], [5]. In this work, we have used a thermally oxidized ultrathin copper film (Cu_Oxd) as HTL in PSC. A device architecture of Glass/ITO/Cu_Oxd/$CH_3NH_3PbI_3$/PCBM/BCP/Ag has been utilized for the investigation of the Cu_Oxd as HTL. A PCE of 11.44% and 6.70% with 5 nm and 1 nm thickness of Cu_Oxd film respectively, the thinnest HTL to our knowledge has been obtained. The low material cost of HTL itself and incorporation of *p-i-n* architecture offering the use of low-cost back metal contact can help in the reduction of the overall device cost.

2. Device Fabrication and Characterization

ITO coated glass substrates were thoroughly cleaned with DI water, Acetone, and IPA in an ultrasonication bath for 15 minutes each. The substrates were then treated with argon plasma and placed into the sputtering chamber and evacuated to a vacuum better than 5×10^{-7} mbar. The ultrathin copper (Cu) film was deposited at a working pressure of 3×10^{-3} mbar and DC power of 48 W in an argon atmosphere. Three different thicknesses (1,5, and 10 nm) of Cu film have been deposited and then oxidized in air at 250 ºC for an hour. For deposition of the photoactive layer, 461 mg PbI_2, 159 mg MAI, 71 µL DMSO, and 640 µL DMF were mixed together and spin-coated (4000 RPM for 30 sec) over glass/ITO/Cu_2O[6]. PCBM in combination with BCP has been used as electron transport layer and was deposited using spin coating. Silver as back metal contact was deposited by thermal evaporation in a vacuum better than 5×10^{-6} mbar.

UV-Vis spectrophotometer (Shimadzu UV-2600 ISR) was used to measure optical properties of ITO/Cu_Oxd films with different Cu thicknesses. Transmittance spectra has been recorded to determine how much light is reaching the photoactive layer. AFM measurements were taken over an area of 20µm × 20µm using Bruker Dimension Icon to measure surface roughness of ITO/Cu_Oxd samples. To confirm the oxidation of Cu film and the formation of $MAPbI_3$ active layer on different thicknesses of Cu_Oxd, the GIXRD was done using Bruker D8 Advance XRD. Carl Zeiss Gemini SEM 500 scanning electron microscope was used to investigate surface morphology of the $MAPbI_3$ films deposited over ITO/Cu_2O. the photovoltaics characterizations of the fabricated devices were done using Enlitech SS-F5 class AAA Solar simulator

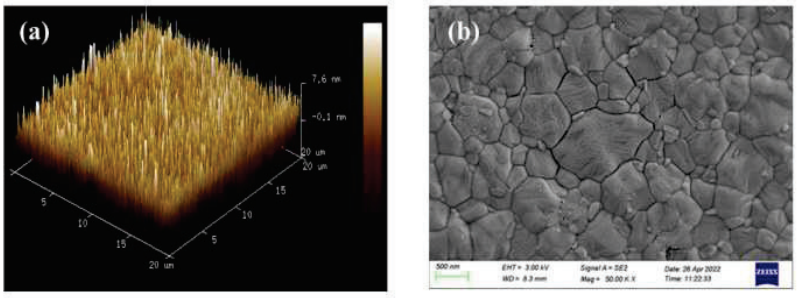

Fig. 1: *(a) 3D AFM image of ITO/Cu_Oxd (5nm) and (b) SEM image of $MAPbI_3$ film on ITO/Cu_Oxd (5nm).*

along with Keithley source meter 2450 at an illumination of 1 Sun (AM 1.5G). External quantum efficiency of the fabricated devices was measured using Enlitech EQE-R.

3. Results and Discussion

From optical transmittance measurements, it has been observed that the transmittance of ITO/Cu_Oxd films is decreasing with an increase in Cu thickness which is governed by Beer Lambert's law as the absorption in the layer is proportional to its thickness. The transmittance spectra of ITO/Cu_Oxd for different thicknesses of Cu has been shown in figure 2(a). Considering the role of surface roughness in adhesion and wettability for upcoming layers, surface roughness measurements for ITO/Cu_Oxd was done and the values of RMS roughness were found to be below 3 nm. The AFM figure for ITO/Cu_Oxd (5 nm) has been shown in figure 1 (a). The surface morphology of $MAPbI_3$ films deposited over ITO/Cu_Oxd can be seen in figure 1(b). The XRD studies to confirm the oxidation of Cu film and that for formation of $MAPbI_3$ film has also been done and the same has been shown in figure 2(b). The JV characteristics of PvSCs with different thicknesses of Cu_Oxd have been shown in figure 2(c) and the corresponding values for different electrical parameters of the devices have been given in Table 1. It has been found that at lower thickness (1 nm) of Cu_Oxd in the device the device shows lower V_{OC} values due to poor coverage of ITO and direct contact between $MAPbI_3$ layer and ITO and at higher thickness (10 nm) the device shows poor J_{SC} due to lower transmittance of 10 nm thick Cu_Oxd and hence lower photocurrent generation. EQE spectra of these devices also support the similar trend and has been shown in figure 2(d).

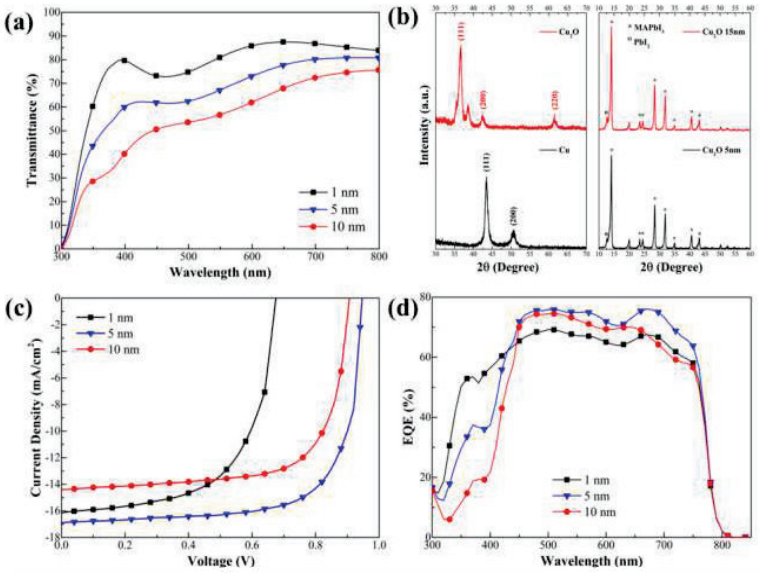

Fig. 2: *(a) Transmittance spectra of ITO/Cu_Oxd with different thicknesses of Cu_Oxd, (b) XRD plots for Cu before and after thermal treatment (left) and that for $MAPbI_3$ film fabricated over Cu_Oxd (right), (c) JV curves of the fabricated devices with different Cu_Oxd thickness, and (d) EQE spectra for the same devices.*

Table 1: **Electrical Characteristics of fabricated devices with different thicknesses of Cu_Oxd.**

Cu thickness (nm)	V_{OC} (V)	J_{SC} (mA/cm^2)	FF (%)	PCE (%)	R_S (Ω cm^2)	R_{Sh} (Ω cm^2)
1	0.675	16.14	61.47	6.70	6.97	330.79
5	0.946	16.88	71.62	11.44	5.95	817.70
10	0.906	14.39	70.00	9.13	7.49	720.43

4. References

[1] Z. Yu and L. Sun, "Recent Progress on Hole-Transporting Materials for Emerging Organometal Halide Perovskite Solar Cells," *Adv. Energy Mater.*, vol. 5, no. 12, p. 1500213, Jun. 2015, doi: https://doi.org/10.1002/aenm.201500213.

[2] Y. Han *et al.*, "Degradation observations of encapsulated planar CH3NH3PbI3 perovskite solar cells at high temperatures and humidity," *J. Mater. Chem. A*, vol. 3, no. 15, pp. 8139–8147, 2015, doi: 10.1039/C5TA00358J.

[3] G. Niu, X. Guo, and L. Wang, "Review of recent progress in chemical stability of perovskite solar cells," *J. Mater. Chem. A*, vol. 3, no. 17, pp. 8970–8980, 2015, doi: 10.1039/C4TA04994B.

[4] P. K. Kung *et al.*, "A Review of Inorganic Hole Transport Materials for Perovskite Solar Cells," *Adv. Mater. Interfaces*, vol. 5, no. 22, pp. 1–35, 2018, doi: 10.1002/admi.201800882.

[5] W. Yu *et al.*, "Ultrathin Cu2O as an efficient inorganic hole transporting material for perovskite solar cells," *Nanoscale*, vol. 8, no. 11, pp. 6173–6179, 2016, doi: 10.1039/c5nr07758c.

[6] N. Ahn, D. Y. Son, I. H. Jang, S. M. Kang, M. Choi, and N. G. Park, "Highly Reproducible Perovskite Solar Cells with Average Efficiency of 18.3% and Best Efficiency of 19.7% Fabricated via Lewis Base Adduct of Lead(II) Iodide," *J. Am. Chem. Soc.*, vol. 137, no. 27, pp. 8696–8699, 2015, doi: 10.1021/jacs.5b04930.

Entangling laser beams using optomechanics

Greeshma Gopinath and Sankar Davuluri
Department of Physics, Birla Institute of Technology and Science-Pilani, Hyderabad Campus, Hyderabad 500078.
sankar@hyderabad.bits-pilani.ac.in

Abstract: We propose a new method to create entanglement between two spatially separated laser beams by using optomechanics. The cross-correlations between the phase and amplitude quadratures of the field inside an optomechanical cavity are manipulated by the radiation pressure force coupling and the detuning between input laser and the cavity eigen frequency. The optomechanical coupling is exploited to create quantum correlations between two spatially separated laser beams such that they are entangled.
Keywords: Entanglement, Optomechanics, Quantum back-action.

1. Introduction

Entanglement is the fundamental requirement of all the quantum technologies and optomechanics provides a reliable way to create entanglement [1]. By using radiation pressure noise suppression techniques [2,3] we create entanglement between two spatially separated laser beams in this work.

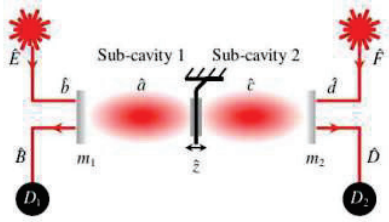

Fig. 1: Optomechanical cavity with perfectly reflective mechanical mirror in the middle. The mirrors m_1 and m_2 are rigidly fixed while the optomechanical mirror (OMM) in the centre can oscillate. The OMM leads to quantum correlations which can be engineered to create entanglement between $\hat{B}$ and $\hat{D}$. D_1 and D_2 are the photodetectors.

2. Theoretical Model

Consider the system shown in Fig. 1. The mirrors m_1 and m_2 are rigidly fixed while the optomechanical mirror (OMM), whose instantaneous position is given by $\hat{z}$, in the middle can oscillate simple harmonically. The OMM divides the cavity into two sub-cavities (see Fig. 1) of equal length l and eigen frequency ω_e. The OMM has mass m, eigen frequency ω_m, and decay rate γ. We assume that the OMM is perfectly reflective so the field from sub-cavity-1 (SC1) is not mixed with the field in sub-cavity-2 (SC2) and vice-versa. The SC1 and SC2 are driven by two independent lasers whose annihilation operators are given by $\hat{b}$ and $\hat{d}$, respectively. The $\hat{b}$ and $\hat{d}$ are normalized such that $\hbar\omega_d\langle\hat{b}^\dagger\hat{b}\rangle$ and $\hbar\omega_d\langle\hat{d}^\dagger\hat{d}\rangle$ gives the corresponding laser powers, respectively, where ω_d is input laser frequency and $\hbar$ is reduced Planck constant. The output field from the SC1 and SC2 is represented by the annihilation operators $\hat{B}$ and $\hat{D}$, respectively. The quantum fluctuations in the output field and input field are related in the Fourier frequency ω space as

$$\hat{Y}_B(\omega) - \hat{Y}_D(\omega) = e_1[\hat{Y}_b(\omega) - \hat{Y}_d(\omega)] - e_2\left[\hat{X}_b(\omega) - \hat{X}_d(\omega)\right] + \hat{\varpi}(\omega)e_3, \quad (1)$$

$$\hat{X}_B(\omega) + \hat{X}_D(\omega) = e_4[\hat{X}_b(\omega) + \hat{X}_d(\omega)] - e_4[Y_b(\omega) + \hat{Y}_d(\omega)], \quad (2)$$

where, $\hat{X}_O = \hat{\delta}_O + \hat{\delta}_O^\dagger$ and $\hat{Y}_O = i(\hat{\delta}_O^\dagger - \hat{\delta}_O)$ with $\hat{\delta}_O$ as the quantum fluctuation for operator $O = B, D, b, d$, $e_1 = 1 + \frac{\zeta(i\omega-\zeta/2)}{(i\omega-\zeta/2)^2-[\alpha(\omega)-\Delta]\Delta}$, $e_2 = \frac{[\alpha(\omega)-\Delta]\zeta}{(i\omega-\zeta/2)^2-[\alpha(\omega)-\Delta]\Delta}$, $e_3 = \frac{2g\bar{x}\sqrt{\zeta}/[m(\omega_m^2-\omega^2-i\gamma\omega)]}{(i\omega-\zeta/2)\left(1-\frac{\Delta[\alpha(\omega)-\Delta]}{(i\omega-\zeta/2)^2}\right)}$, $e_4 = 1 + \frac{(i\omega-\zeta/2)\zeta}{(i\omega-\zeta)^2+\Delta^2}$, $e_5 = \frac{\zeta\Delta}{(i\omega-\zeta/2)^2+\Delta^2}$, and $\alpha(\omega) = \frac{\hbar g\bar{x}^2}{m(\omega_m^2-\omega^2-i\gamma\omega)}$ with $g = \frac{\omega_e}{l}$ as the optomechanical coupling, $\Delta = \omega_e - \omega_d$, $\bar{x}$ is mean amplitude of sub-cavity field, ζ is the sub cavity field decay rate and $\hat{\varpi}$ is the thermal noise operator. The

input and output fields are continuous, but the measurement on these fields lasts for a finite time. Thus, we need to consider finite bandwidth of measurement [4]. According to Duan criteria [5], $\hat{B}$ and $\hat{D}$ are entangled if

$$\left\langle \left(\hat{X}_{B_f} + \hat{X}_{D_f}\right)^2 \right\rangle + \left\langle \left(\hat{Y}_{B_f} - \hat{Y}_{D_f}\right)^2 \right\rangle = 2i \,, \tag{3}$$

and $[\hat{X}_{B_f}, \hat{Y}_{B_f}]$=$[\hat{X}_{D_f}, \hat{Y}_{D_f}]$=2i, where the dimensionless operators $\hat{X}_{B_f}, \hat{X}_{D_f}, \hat{Y}_{B_f}$ and $\hat{Y}_{D_f}$ are obtained after considering the finite measurement bandwidth on $\hat{X}_B, \hat{X}_D, \hat{Y}_B$, and $\hat{Y}_D$, respectively.

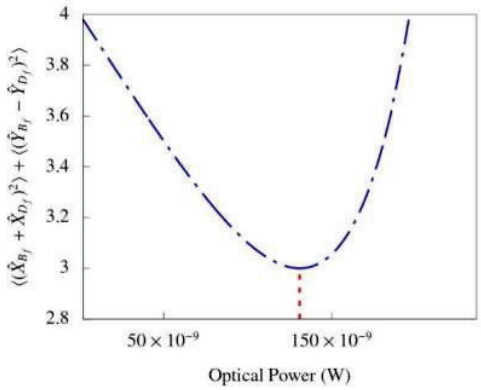

Fig. 2: Entanglement as a function of input laser power. The red line shows the optical power corresponding to P_1. For simulation, we used the optomechanical parameters $\zeta = 10^5$ Hz, $\Delta = \zeta/2, \omega_m = 10^5$ Hz, g=10^{18} Hz/m, $\lambda = 600nm, \gamma = 100Hz, T = 10^{-8}K$.

As $\left(\hat{X}_{B_f}, \hat{Y}_{B_f}\right)$ and $\left(\hat{X}_{D_f}, \hat{Y}_{D_f}\right)$ are canonically conjugate variables, decreasing $\left\langle \hat{X}_{B_f}{}^2 \right\rangle$ and $\left\langle \hat{X}_{D_f}{}^2 \right\rangle$ increases $\left\langle \hat{Y}_{B_f}{}^2 \right\rangle$ and $\left\langle \hat{Y}_{D_f}{}^2 \right\rangle$, respectively, and vice-versa. Hence Eq. (3) cannot be satisfied unless $\hat{B}$ and $\hat{D}$ are entangled. We use the radiation pressure coupling to tune the $\alpha(\omega) - \Delta$ term such that the cross-correlation between the $\hat{X}_{b_f}, \hat{Y}_{b_f}$ and $\hat{X}_{d_f}, \hat{Y}_{d_f}$ quadratures lead to entanglement. We minimize the $|e_1|^2$ and $|e_2|^2$ as a function of $\alpha(\omega) - \Delta$, as Eq. (1) is the only equation with radiation pressure coupling in it. Analytical result shows that the RHS of Eq. (1) is lowest when $\alpha(0) = 2\Delta/3$ and the possible minimum value of $\left\langle \left(\hat{Y}_{B_f} - \hat{Y}_{D_f}\right)^2 \right\rangle$ is 1 for coherent input state. The optical power P_1 corresponding to $\alpha(0) = 2\Delta/3$ is given as,

$$P_1 = \frac{2}{3}\frac{m\omega_m^2\Delta}{4\hbar g^2\zeta}(\Delta^2 + \zeta^2/4)\hbar\omega_e.$$

A plot of Eq. (3) for different input power around P_1 is shown in Fig. (2). The Y-axis in Fig. (2) is Duan inequality and $\hat{B}$ and $\hat{D}$ are entangled for Y-axis value less than 4. The laser power corresponding to the lowest value of Y-axis in Fig. (2) is 130 nW. The lowest value of Duan inequality is 3 at $\alpha(0) = 2\Delta/3$.

3. Simulation parameters

For simulation, we used the optomechanical parameters $\zeta = 10^5$ Hz, $\Delta = \zeta/2, \omega_m = 10^5\ Hz$, g=$10^{18}$ Hz/m, $\lambda = 600nm, \gamma = 100Hz, T = 10^{-8}K$

Acknowledgement

This work is supported by the Science and Engineering Research Board of India under the Grant no:SRG/2020/001167.

4. References

[1]Wang, Ying-Dan and Clerk, Aashish A. "Reservoir-Engineered Entanglement in Optomechanical Systems." *Phys. Rev. Lett* (2013): 253601.

[2]Davuluri, Sankar and Li, Yong. "Light as quantum back-action nullifying meter." *arXiv preprint arXiv:2202.06030* (2022).

[3]Davuluri, Sankar. "Quantum optomechanics without the radiation pressure force noise." *Optics Letters* (2021): 904--907.

[4]Zippilli, Stefano and Di Giuseppe, Giovanni and Vitali, David. "Entanglement and squeezing of continuous-wave stationary light." *New Journal of Physics* (2015): 043025.

[5]Duan, Lu-Ming and Giedke, G. and Cirac, J. I. and Zoller, P. "Inseparability Criterion for Continuous Variable Systems." *Phys. Rev. Lett.* (2000): 2722--2725.

Autocorrelation signatures at various regimes of incoherent optical feedback to a semiconductor laser

R .Nivedha and S .Sivaprakasam
Department of Physics, Pondicherry University, Puducherry – 605014, India.
nivedharamadoss09@gmail.com, siva@pondiuni.ac.in

Abstract: We numerically study autocorrelation character of a semiconductor laser subject to incoherent optical feedback with a time delay. The Lang-Kobayashi rate equations for incoherent optical feedback are numerically solved. The first secondary autocorrelation peak (FSP) provides information about the signature of the external cavity time delay and its understanding can help in improving the security information exchange / transmission in a diode laser based secure communication system. We find that the time of occurrence of FSP to have a direct correspondence with the identified four regimes of operation viz.: stable, chaotic, pulsed and two-state based on ascending feedback strengths.
Keywords: Incoherent optical feedback , semiconductor laser, chaotic dynamics

1. Introduction

Semiconductor lasers subject to optical feedback are known to exhibit a rich variety of complex dynamics. We know that all lasers have a finite coherence length. When the external cavity mirror is placed at a distance longer than the coherence length of the laser, then, the light that is fed back is incoherent in nature. The dynamics of such a system can be understood by way of photonic addition instead of electric field interaction. The two rate equations are coupled with each other by a delay differential term and thus we can expect instabilities and chaos in semiconductor lasers [1] when subjected to optical feedback. Dynamics arising due to incoherent feedback has been associated with four regimes of feedback strength [2]. In our work we study the autocorrelation signatures at various regimes of incoherent optical feedback to a semiconductor laser. The First secondary autocorrelation peak (FSP) provides information about the signature of the time delay, i.e., the round trip time between the laser and the external mirror, which if known can be misused by an eavesdropper. To ensure security it is important to either shift the position of FSP or to suppress the amplitude of FSP. So, this study will benefit in realizing the suitable regime for operation to suit secure optical communication based on chaotic diode lasers.

2. Theory

Fig 1:Schematic of a incoherent optical feedback system

The dynamics of a semiconductor laser subject to incoherent optical feedback can be modeled by the following rate equations [2]

$$\frac{dS}{dt} = \left[\Gamma\, G(N) - \frac{1}{\tau_p}\right] S(t) + R_{sp} \tag{1}$$

$$\frac{dN}{dt} = \frac{I}{eV} - \frac{N}{\tau_s} - G(N)S(t) - \kappa\, G(N)S(t - \tau_{ext}) \tag{2}$$

Where

$$G(N) = G_n (N - N_0) \tag{3}$$

$$\kappa = [(1 - r_2^2)\frac{r_3}{r_2}]^2 \tag{4}$$

S(t) and N(t) are time dependent photon density and carrier density respectively. Γ is confinement factor, G(N) is the gain parameter, τ_p is photon lifetime, τ_s is carrier lifetime, κ is the coupling coefficient, I is the bias current, V is the active region volume and R_{sp} is the spontaneous emission coefficient. The rate equations are solved using fourth-order Runge - Kutta algorithm. The external cavity round trip time is given by $\tau_{ext} = L_{ext}/c$, where L_{ext} is the optical path length between the laser and the mirror and c is speed of light in free space. The autocorrelation signatures are observed for different external cavity lengths viz.: 1.5m, 2.25m and 3m.

3. Results and Discussion

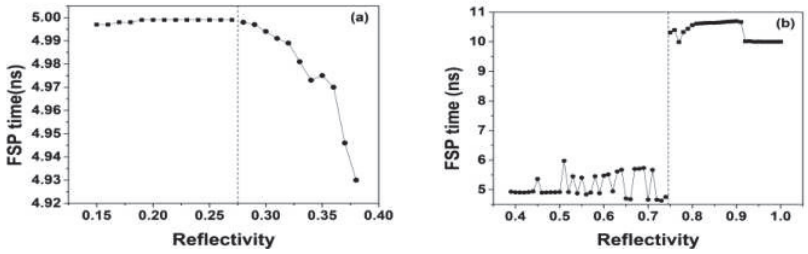

Fig 2. The time of occurrence of the first secondary autocorrelation peak verses the reflectivity for round trip time τ = 5 ns , I = 22 mA

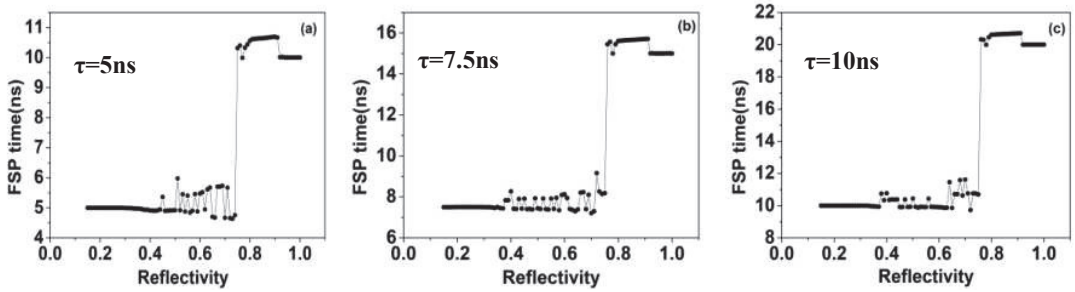

Fig 3. The time of occurrence of the first secondary autocorrelation peak verses the external mirror reflectivity for various external cavity delay times.

The time of occurrence of the first secondary autocorrelation peak (FSP) for different feedback strengths is shown in figures 2(a) and 2(b) for an external cavity delay time of 5 ns. It is seen from fig. 2(a), the FSP occurs at a time close to 5 ns but has a dependence on the external cavity reflectivity. In the first (stable) regime, the position of the first secondary autocorrelation peak is found to be stable whereas in the second (chaotic) regime, the position of the FSP decreases with increasing feedback. This is true for different bias conditions as well. In the third regime (pulsed regime), the position of the FSP is oscillatory with an increase in feedback and the oscillatory behavior increases with an increase in current .In the fourth regime (two-state regime) with an increase in feedback, there is a sudden increase at first and then a fall in the position of the FSP. Fig.(2b) shows the behavior of FSP in the pulsed and the two-state regime for τ = 5ns, I = 22 mA. Fig.(3) shows at different external cavity lengths, the position of FSP for different feedback strengths. With an increase in external cavity length, the position of the first secondary autocorrelation peak was found to increase. With an increase in external cavity length from 1.5m to 2.25m the oscillatory behavior in the pulsed regime was found for lower feedback strengths also. Whereas further increase in external cavity length to 3m does not bring any difference in the oscillatory behavior in the pulsed regime. In conclusion, we are able to find a direct correspondence of autocorrelation character with the feedback regimes of a diode laser subjected to incoherent optical feedback.

4. References

[1] J.Ohtsubo, "Semiconductor lasers Stability, Instability and Chaos," Springer second edition (2007)
[2] Rui Ju and Paul S. Spencer, "Dynamic Regimes in Semiconductor Lasers Subject to Incoherent Optical Feedback,"Journal of Lightwave Technology, vol. 23, 2513-2523 (2005)

Bessel beam optical interferometry for temperature-independent refractive index measurement

Amit Pandey[a,b] Samir K Mondal[a,b]
[a]*Academy of Scientific &Innovative Research, Ghaziabad, Uttar Pradesh, 201 002*
[b]*CSIR- Central Scientific Instruments Organization, Chandigarh, 160030, India*
Author e-mail address: samirmondal01@gmail.com

Abstract: In this paper, we have demonstrated a common path Bessel beam optical interferometry-based optical fiber refractometer for temperature-independent refractive index measurement of deionized (DI) water.

Keywords: Bessel beam, Interferometer, Temperature, Refractometer

1. Introduction

Refractometers are instruments that determine the refractive index of a sample. The refractometer plays a key role in a variety of industrial and scientific applications for material characteristics in terms of refractive index (RI). Commercial refractometers are prism-based and measure the refractive index using the total internal reflection principle. However, for temperature-independent RI measurement, they employ numerous optomechanical components that make the system bulky. [1,2].

In recent years, fiber-optic sensors for RI measurement have been explored considering their unique advantages, such as immunity to electromagnetic interference, compact size, potentially low cost, and the possibility of distributed measurement over a long distance etc. Various technology such as fiber Bragg grating (FBG) [3], long-period grating (LPG), surface plasmon resonance (SPR), and optical fiber interferometers are reported for RI measurement with each having a different operating principle for RI measurement and sensing. Here we demonstrate an interferometry base refractive index measurement that is temperature-independent.

2. Working Principle and Experimental setup

This work proposes a packaged optical fiber DSNA (deep-seated negative axicon) probe that uses Bessel beam interferometry in a common path configuration to solve the Fresnel equation and calculate the liquid solution's RI [4].

$$R = \frac{P_{ref}}{P_{in}} = \left(\frac{n_g - n_g}{n_g + n_l}\right)^2 \quad \ldots\ldots\ldots\ldots 1$$

where P_{ref} and P_{in} are reflected and incident power respectively, R represents the reflectance of the interface between glass and liquid sample with refractive index n_g and n_l respectively. The schematic of the experimental setup of RI measurement is shown in Fig. 1.

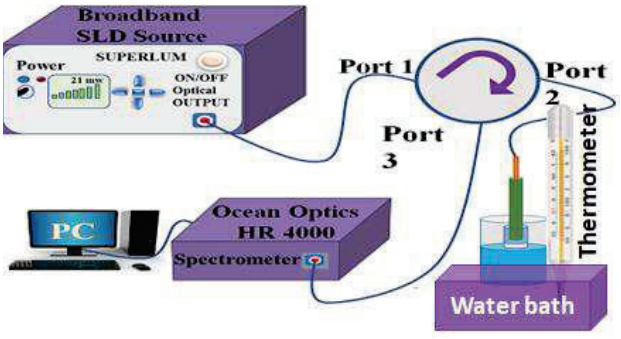

Fig. 1 Schematic of the experimental setup

The packaged probe consists of an optical fiber negative axicon sealed in a needle with a glass lid at one end [5]. Here we have used a Superluminescent diode (SLD) source having a central wavelength of 840 nm and a bandwidth of 80 nm. The output light from the low coherence SLD source is guided into the optical circulator's port 1 to the negative axicon packaged probe at port 2. The negative axicon optical fiber probe converts the Gaussian beam into a Bessel beam, which experiences partial reflection and partial transmission at the glass liquid interface. The reflected lights from the air-glass and glass-liquid interfaces interfere with the reference beam generated at the air-glass interface of the axicon. The interference spectrum is recorded in the spectrometer and processed by applying the fast Fourier transform (FFT) to obtain the corresponding reflected power spectrum. The reflected power spectrum gives well-defined power peaks for air-glass, and glass-liquid interfaces as shown in fig.2. The RI of glass (ng=1.5) helps to calculate the reflected power from the air-glass interface considering the 4% reflection of the incident power from the interface.

This reflected power is utilized to estimate the incident power at the glass-liquid interface which is 96% of the incident power at the air-glass interface. The transmitted and reflected power from the glass-liquid interface is used to calculate reflectance and solve Fresnel Eqn. 1 for RI measurement of the DI water sample at a different temperature.

3. Results

In this study, we exploited our probe to measure the RI of DI water for increasing and decreasing temperature conditions with 5ºC intervals for temperatures ranging from 25ºC to 60ºC. We have used a water bath for controlling the temperature of DI water. A graph between measured RI versus temperature is plotted as shown in fig.3. As we increased the temperature the RI of DI water decreased. Thus, the RI of DI water has a negative temperature coefficient.

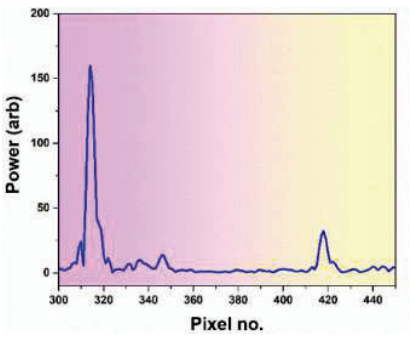

Fig.2 FFT power peaks profile

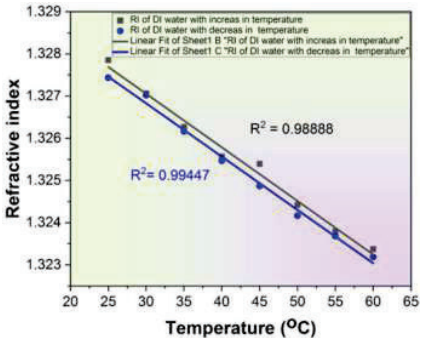

Fig. 3 Refractive index versus temperature hysteresis graph of DI water

Linear fitting of graph results in the deterministic coefficient (R^2) 0.98888 and 0.99447 for increasing and decreasing temperature respectively. The slopes of the graph (dn/dT) are -1.27046×10^{-4} °C^{-1} and 1.26301×10^{-4} °C^{-1} respectively. The refractive measurements measurement precision of the refractometer is the order of 10^{-4} and the temperature gradient are not so high. Therefore, the proposed refractometers here can be used for temperature-independent RI measurement. This follows similar trends as reported in the literature [6].

References

[1.] J. Rheims, J. K¨oser, T. Wriedt, Refractive-index measurements in the near-IR using an Abbe refractometer, Measure. Sci. Technol. 8 (1997) 601–605.

[2.] J.E. Saunders, C. Sanders, H. Chen, H.-P. Loock, Refractive indices of common solvents and solutions at 1550 nm, Appl. Opt. 55 (2016) 947–953.

[3.] B. Jiang, K. Zhou, C. Wang, Y. Zhao, J. Zhao, L. Zhang, Temperature-calibrated high-precision refractometer using a tilted fiber Bragg grating, Opt Express 25(2017) 25910–25918.

[4.] P. Gupta, A. Pandey, K. Vairagi, and S. K. Mondal, "Solving Fresnel equation for refractive index using reflected optical power obtained from Bessel beam interferometry," Review of Scientific Instruments, vol. 90, p. 015110, 2019.

[5.] Pandey, Amit, Pooja Gupta, Kaushal Vairagi, and Samir K. Mondal. "Packaged Negative Axicon Optical Fiber Probe and Bessel Beam Interferometry for Refractive Index Measurement of Hazardous Liquid Samples." Journal of Lightwave Technology (2019).

[6.] Flores-Bravo, J. A., M. A. Illarramendi, Joseba Zubia, and Joel Villatoro. "Optical fiber interferometer for temperature-independent refractive index measuring over a broad range." Optics & Laser Technology 139 (2021): 106977.

Pump-driven ultrafast adiabatic second harmonic generation

Soumik Nandi[1, 2] and Ritwick Das[1, 2]

[1]*School of Physical Sciences, National Institute of Science Education and Research, Jatni, Khurda 752050, Odisha, India*

[2]*Homi Bhabha National Institute, Training School Complex, Anushaktinagar, Mumbai 400094, India*

E-mail: soumik.nandi@niser.ac.in, ritwick.das@niser.ac.in

Abstract: Phase matching is the key to observe nonlinear optical phenomena. Recently, instead of satisfying exact phase matching condition, an adiabatic phase matching scheme is proposed for efficiently carrying out broadband second harmonic generation (SHG) in long nonlinear crystals. We report SHG invoking adiabatic constraints in a periodically poled stoichiometric lithium tantalate (PPSLT) crystal pumped by a femtosecond laser source. The impact of temperature is extensively studied in frequency conversion efficiency and in peak wavelength shift.

Keywords: Ultrashort pulses, second harmonic generation, adiabatic processes

1. Introduction

Using a high intensity light beam, a broad variety of nonlinear optical phenomena could be explored. Amongst them, second harmonic generation (SHG) is an elementary nonlinear optical process where a frequency ω is converted to its second harmonic frequency 2ω in a suitable medium. In order to ensure efficient SHG, a few techniques such as birefringent phase matching and quasi phase matching (QPM) is used to satisfy phase matching (PM) (conservation of momentum) of interacting waves [1]. For ultrashort pulses, the group velocity matching (GVM) needs to be satisfied in conjunction with PM so as to achieve desirable conversion efficiency. This is conventionally realized by using a short length crystal which adversely affects the SHG conversion efficiency [2]. In order to circumvent this problem, a new technique called adiabatic frequency conversion has emerged in recent years. In this process, instead of using periodically poled QPM crystal, an aperiodically poled QPM crystal is employed [3,4]. The phase mismatch Δk varies from a high negative to a high positive value or vice versa along the propagation direction of light inside the crystal. However, creating a suitable aperiodic poling in crystals is quite complex and expensive. In the present work, we adopted a different approach where refractive index change brought about by increase in crystal temperature facilitates a sweep in Δk. This rise in crystal temperature is essentially a consequence of high light absorption by the nonlinear crystal. Here, we report an adiabatic second harmonic generation in periodically-poled stoichiometric lithium tantalate (PPSLT) crystal by creating a suitable longitudinal temperature gradient through a focused beam inside the medium.

2. Experimental Setup

We have used an ultrashort pulsed Yb-fiber laser delivering sech^2 shaped Fourier-transform limited pulses of width ≅250 fs at a central wavelength of 1064 nm and a maximum output power of 3.6 W. This beam is linearly polarized TEM_{00} Gaussian beam having repetition rate of 84 MHz. A combination of a half-wave plate (HWP) and a polarizing-beam-splitter is used to control the power of the pump beam. Another HWP is utilized to obtain the correct polarization for the phase-matching in the PPSLT crystal. A combination of concave and convex lens is used to achieve the required beam waist at focal point. We choose 0.5 mol% MgO-doped PPSLT crystal of 30 mm length, 2.2 mm width and 1 mm thick for our experiment. This crystal has a single grating period of 7.97 μm and it is housed in an oven whose temperature could be controlled from room temperature to 200 ºC with a sensitivity of 0.1 ºC. Finally, a dichroic mirror is used to separate the pump beam (1064 nm) from the second harmonic one (532 nm).

3. Result and Discussion

From theoretical calculations, the phase matching temperature (T_{PM}) for SHG from a 1064 nm laser beam is found out to be T_{PM} = 57.2ºC for the PPSLT crystal (7.97 μm grating period). The pump beam waist was fixed at 30 μm at the crystal center. For a 30 mm long PPSLT crystal, it is expected that the SHG conversion efficiency would be < 10% as the GVM is not realized. However,

we observed that the second-harmonic (SH) power of 560 mW is generated at pump power of 2 W when the oven temperature (T_{ov}) is 40˚C. In fact, the SH power remained > 400 mW (for 2 W of pump power) when T_{ov} changed from room temperature to 90°C. It was observed that the SHG conversion efficiency maximizes at T_{ov} = 40˚C which is significantly smaller than the theoretical estimate (T_{PM}). This essentially points towards the impact of thermo-optic effects on the PM characteristics of the SHG process. It is worth pointing out that SH power generated scales in a similar manner with the pump power for all oven temperatures (see Fig. 1(a)). This essentially implies that there is no differential impact of thermo-optic effect on the growth of SH power which is quite unusual. In Fig. 1(b), we present the recorded SH spectrum at different T_{ov} (for pump power = 2 W) where we observed spectral shift in peak SH wavelength as a function of T_{ov} with spectral width remaining almost unchanged.

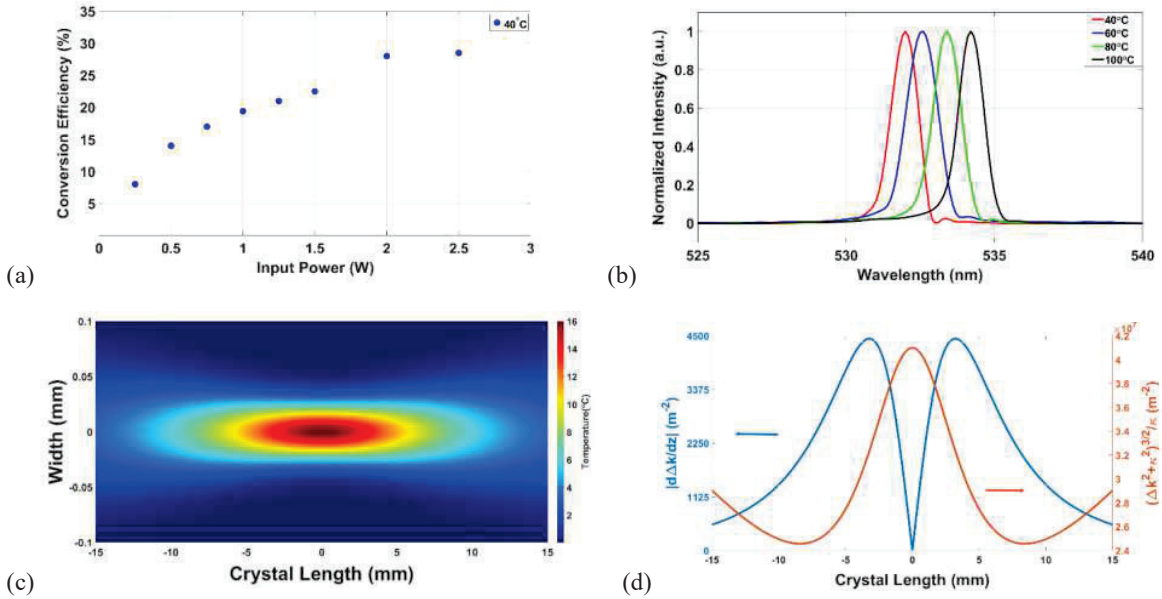

Figure 1: (a) SHG conversion efficiency variation with input pump power at 40˚C, (b) Shift in peak SH wavelength with change in oven temperature, (c) Temperature rise inside PPSLT crystal due to absorption for 2 W input power, (d) Variation of slope of Δk and coupling (κ) along the length of crystal at 40˚C

The observations could be explained through the following argument. The change in crystal temperature along the propagation direction due to absorption of the pump laser is expressed as

$$\Delta T = \frac{\alpha I(z)}{\rho C_v} \qquad (1)$$

where, α, ρ and C_v denotes absorption, density and heat capacity of the PPSLT crystal respectively and $I(z)$ is the local intensity of light inside the crystal. The estimated rise in temperature (with respect to the T_{ov}) for an incident pump power of 2 W is shown in Fig. 1(c). Since, the actual temperature is higher than T_{ov} along propagation direction (z), this rise in temperature accounts for the difference between estimated and measured value of T_{PM}. In Fig. 1(d), we plotted the variation in slope of Δk along the crystal length which shows that constraints imposed by adiabatic condition i.e. $\left|\frac{d\Delta k}{dz}\right| \ll \frac{(\Delta k^2+\kappa^2)^{3/2}}{\kappa}$ is obeyed throughout the crystal length. Here, κ is the coupling factor between the two interacting waves. The shift in peak wavelength could be attributed to the constraint imposed by the pump-induced adiabatic phase-matching condition.

4. References

[1] J. A. Armstrong, N. Bloembergen, J. Ducuing, and P. S. Pershan, "Interactions between Light Waves in a Nonlinear Dielectric," Phys. Rev. **127**, 1918 (1962)

[2] R. Eckardt and J. Reintjes, "Phase matching limitations of high efficiency second harmonic generation," in *IEEE Journal of Quantum Electronics*, **20**(10), 1178-1187 (1984)

[3] A. Dahan, A. Levanon, M. Katz, and H. Suchowski, "Ultrafast adiabatic second harmonic generation," J. Phys. Condens. Matter **29**(8), 084004 (2017)

[4] Anat Leshem, Guilia Meshulam, Gil Porat, and Ady Arie, "Adiabatic second-harmonic generation," Opt. Lett. **41**, 1229-1232 (2016)

Ultrathin autocorrelator

Sunil Dahiya, Akansha Tyagi, Ankur Mandal and Kamal P. Singh[1]

[1]*Department of Physical Sciences, Indian Institute of Science Education and Research Mohali, Sector 81, Mohali 140306, India*

Email: sun28dahiya@gmail.com, kpsingh@iisermohali.ac.in

Abstract: We present a compact ultrathin autocorrelator to characterize femtosecond (fs) pulses in near-IR range with negligible dispersion in the measuring pulse. Its performance is validated by the measurement of sub 30 fs pulses by interferometric autocorrelation technique via second harmonic generation in non-linear crystal. This in-line ultrathin autocorrelator is compact, alignment-free, robust and dispersion balanced with the capability of measuring a few cycles fs pulses and applications in ultrafast metrology.

Keywords: Autocorrelator, Interferometric autocorrelation (IAC), Second harmonic generation (SHG).

1. Introduction

The characterization of ultrafast pulses in time domain is an important and necessary task in ultrafast experiments. Interferometric autocorrelation (IAC) is a simple and widely used technique for ultrashort pulse characterization from few cycle femtosecond up to a higher time scale [1,2]. It includes the superposition of an ultrafast pulse with its replica in the collinear geometry [2]. Second harmonic generation (SHG) in nonlinear crystals [2] and two photon absorption photodiodes [3] are commonly employed for obtaining frequency resolved autocorrelation (FRAC) signal or interferometric autocorrelation (IAC). Conventional autocorrelators based on Michelson and Mach-Zehnder interferometers are commonly used in this technique for such temporal measurements having thick glass beam splitters that add dispersion in the measuring pulse giving inaccurate results [4]. Such temporal measurements with ultrashort pulses require precise alignment of autocorrelators, minimum distortion or dispersion in the measuring pulse, high temporal resolution of the interferometer and high stability against external vibrations/fluctuations.

To avoid dispersion, all reflective configurations such as Michelson type transmission grating [5], split mirror based delay line [6] and reflective prism based delayline [7] are reported earlier for long to few cycle femtosecond pulse characterization. Most of them require specialized optics and a complex setup that includes alignment difficulties. It becomes important as well as challenging to design a compact, alignment and highly stable dispersion free autocorrelator.

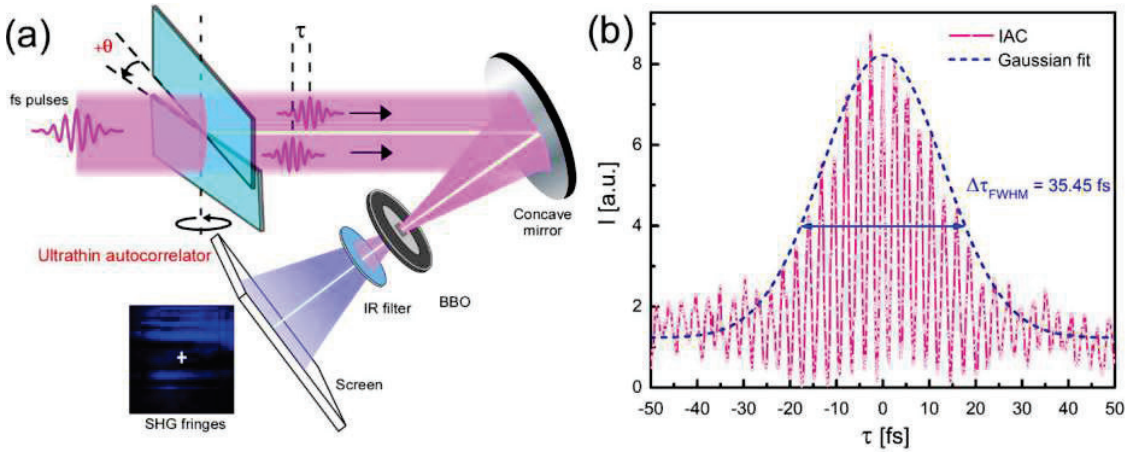

Fig1. (a) Schematic of ultrathin autocorrelator. The FRAC signal is obtained through fringe intensity evolution of second harmonic generated (SHG) from BBO (β-barium borate) non-linear crystal. SHG blue color fringes and white tracking point is shown here. **(b)** Experimentally obtained second order interferometric autocorrelation (IAC) of fs pulses (800 nm) and signal FWHM (full width at half maximum).

Our ultrathin autocorrelator is based on wavefront division of input pulse beam through a pair of ultrathin glasses (t ~140 μm) which adds negligible dispersion in the measuring fs pulses [8]. It is compact, alignment free (parallel configuration of ultrathin glasses directly results in interference fringes) and provides high stability due to common path configuration. The precise rotation of the lower glass plate via motorized stage provides a high resolution in time delay between the two interferometric arms.

2. Results

The second harmonic interference fringes are easily obtained with our ultrathin autocorrelator due to its quasi-collinear geometry. The resulted blue color interference fringes are tracked and a corresponding signal is obtained using setup in Fig.1 (a). The lower glass plate is rotated with 0.2º/s angular velocity and the corresponding variation in blue signal has been traced. Then the delayline is calibrated which relates rotation angle to time delay between the two replicas of fs pulses [8]. IAC signal obtained via ultrathin autocorrelator is shown in Fig.1.(b). The signal is symmetrical and background to peak ratio is nearly approaching 1: 7.4 showing the good alignment of our ultrathin autocorrelator. A slight variation in the ratio may be due to quasi-collinear geometry of our delayline. The central peak FWHM is calculated to be around 35.45±0.03 fs, giving fs pulse width (FWHM/$\sqrt{2}$) of 25.14 fs. The measured pulse width is within 1% error assuming 25 fs theoretical value. Here, $\sqrt{2}$ is de-convolution factor used for Gaussian shape pulses. This measurement validates the performance of our new ultrathin autocorrelator.

Further, this autocorrelator can be used for even a few cycles i.e., sub-10 fs pulses characterization due to its negligible pulse width broadening effect and high time delay resolution.

3. References

[1] J.-C. M. Diels, J. J. Fontaine, I. C. McMichael, and F. Simoni, "Control and measurement of ultrashort pulse shapes (in amplitude and phase) with femtosecond accuracy," Applied Optics **24**, 1270–1282 (1985).
[2] R. Trebino, R. Jafari, S. A. Akturk, P. Bowlan, Z. Guang, P. Zhu, E. Escoto, and G. Steinmeyer. "Highly reliable measurement of ultrashort laser pulses." Journal of Applied Physics **128**, 171103 (2020).
[3] N. F. Kleimeier, T. Haarlammert, H. Witte, U. Schühle, J.-F. Hochedez, A. BenMoussa, and H. Zacharias, "Autocorrelation and phase retrieval in the uv using two-photon absorption in diamond pin photodiodes," Optics Express **18**, 6945–6956 (2010).
[4] C. Spielmann, L. Xu, and F. Krausz, "Measurement of interferometric autocorrelations: comment," Applied Optics **36**, 2523–2525 (1997).
[5] P. V. Kolesnichenko, L. Wittenbecher, and D. Zigmantas, "Fully symmetric dispersionless stable transmission-grating Michelson interferometer," Optics Express **28**, 37752–37757 (2020).
[6] H. Mashiko, A. Suda, and K. Midorikawa, "All-reflective interferometric autocorrelator for the measurement of ultra-short optical pulses," Applied Physics B **76**, 525–530 (2003).
[7] A. Tyagi, M. S. Sidhu, A. Mandal, S. Kapoor, S. Dahiya, J. M. Rost, T. Pfeifer, and K. P. Singh, "Attosecond stable dispersion-free delay line for easy ultrafast metrology," Scientific Reports **12**, 1–7 (2022)
[8] S. Dahiya, M. S. Sidhu, A. Tyagi, A. Mandal, B. Nandy, J. M. Rost, T. Pfeifer, and K. P. Singh, "In-line ultra-thin attosecond delay line with direct absolute-zero delay reference and high stability," Optics Letters **45**, 5266–5269 (2020).

Demonstration of Enhanced Nonlinear Optical Activity in an All-Polymer Nonlinear Bragg Reflector

M. V Vijisha[1,*], Sheenu Thomas[1], K Jayakrishnan[2] and K. Chandrasekharan[3]]

[1]International School of Photonics, Cochin University of Science and Technology, Kochi, Kerala 682022
[2]Department of Physics, MES College Ponnani, Kerala, 679 586, India
[3] Department of Physics, National Institute of Technology Calicut, Kozhikode 673601, Kerala, India
Email : vijishavinu519@gmail.com

Abstract: The influence of a polymeric Bragg reflector on the nonlinear optical (NLO) characteristics of polyindole in the nanosecond regime is investigated by means of Z-scan technique. A ~3-fold enhancement in the NLO response of polyindole is achieved with the nonlinear bragg structure with respect to the reference sample. The observed enhancement in the NLO properties can be ascribed to the slow-light effects at the photonic band edge.
Keywords: Bragg reflector, nonlinear optical properties, Z-scan

1. Introduction

Photonic crystals (PCs) are artificially engineered structures, in which two or more different dielectric materials are arranged in a periodic manner[1,2]. Depending on the spatial periodicity that can be extended along one or more principal axes, PCs are categorized as one, two, and three dimensional structures. Dielectric bragg reflector (DBR), also called one dimensional PC is a multilayer structure in which layers are stacked over one another periodically. Due to this structural periodicity, DBRs exhibit photonic band gap (PBG) – a range of frequencies for which light propagation is prevented through the crystal. When used with optical nonlinearities, these structures are found to be highly promising towards the realization of all-optical signal processing[3]. Herein, we study the impact of a polymer DBR on the nonlinear optical (NLO) properties of polyindole abbreviated as 'PIN', using Z-scan method.

2. Experimental methods

The polymeric nonlinear bragg reflector is fabricated by means of spin coating technique. Here, cellulose acetate (CA) is used as the low refractive index layer and Poly(vinyl carbazole (PVK) doped with PIN make both high refractive index as well as the nonlinear layer. For the linear optical response of the DBR as well as the PIN sample, a UV-Vis double beam Spectrophotometer (UV-2450 Schimadzu) is used. Nonlinear optical transmission measurements for the PIN compound and the DBR samples are conducted using single beam Z-scan method[4,5]. A Q-switched Nd:YAG laser delivering 7 ns pulses at 532 nm is used as the excitation source in all Z-scan studies. The absorptive as well as refractive contributions to optical nonlinearity were isolated by means of open aperture (OA) and closed aperture (CA) Z-scan configurations.

3. Results and Discussions

Using theoretical simulations based on transfer matrix method, the DBR was designed to have its longer wavelength band edge at 532 nm. Fig.1 shows the reflectance spectra of the fabricated PIN doped DBR and it can be seen that the structure possesses ~93 % reflection at its bandgap center wavelength and its longer wavelength band edge is located at ~532 nm at normal incidence.

To examine the NLO properties, Z-scan studies were performed on the nonlinear DBR as well as on the bare PIN:PVK thin film sample. Open Z-scan studies were carried out at 0.27 GW/cm^2 and it is observed that PIN didn't reveal any signature of absorptive nonlinearity whereas significant reverse saturable absorption (RSA) type nonlinear absorption behaviour was recognized for the nonlinear DBR (Fig.2). The nonlinear absorption coefficient recorded for NLPC at 0.27 GW/cm^2 is 11.45x10^{-8} m/W. At an intensity of 0.83 GW/cm^2, the reference sample exhibits a value of 10.9 x 10-8 m/W for the nonlinear absorption coefficient. This implies that enhancement in the NLO response of PIN is ~3-fold

with the nonlinear DBR and the enhancement can be considered as the consequence of low group velocity at the photonic band edges. Closed Z-scan studies were also conducted for both the sample, however none of them revealed any trace of refractive nonlinearity.

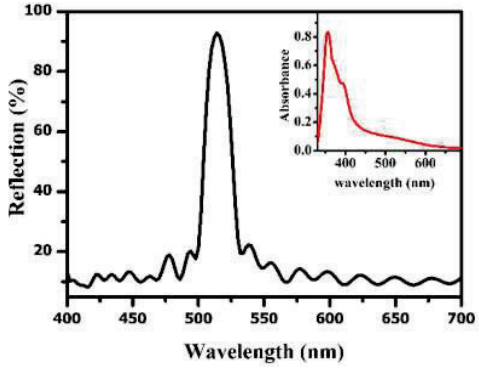

Fig. 1: Reflectance spectra of nonlinear DBR. Absorption spectrum of polyindole is shown in the inset.

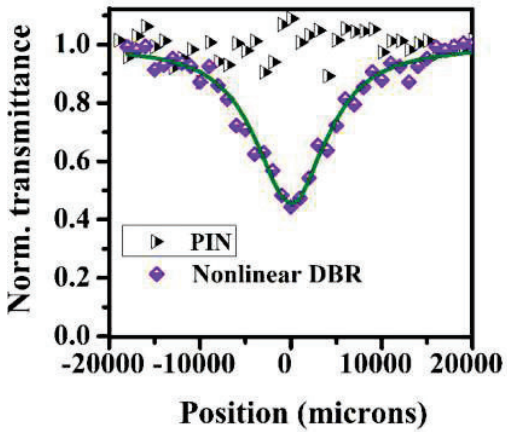

Fig. 2: Open Z-scan traces of PIN thin film and nonlinear DBR at 0.27 GW/cm²

4. Conclusion

The nonlinear optical properties of polyindole by means of a nonlinear DBR was investigated. The NLO activities of the sample PIN were found to be enhanced with the nonlinear DBR and the enhancement factor was estimated as ~3 compared to the bare sample. Band edge effects of the DBR are found to be responsible for the improved nonlinear absorption of the PIN sample.

5. References

[1] E. Yablonovitch, "Inhibited Spontaneous Emission in Solid-State Physics and Electronics", Phys. Rev.Lett., 58, 2059 (1987).
[2] S. John, "Strong localization of photons in certain disordered dielectric superlattices", Phys. Rev.Lett., 58, 2486 (1987).
[3] T. Hattori, N. Tsurumachi, H. Nakatsuka, "Analysis of optical nonlinearity by defect states in one-dimensional photonic crystals", JOSA B, 14, 348 (1997).
[4] M. Sheik-Bahae, A. A. Said, E. W. Van Stryland, "High-sensitivity, single-beam n_2 measurements"Opt. Lett., 14, 955 (1989).
[5] M. S. Bahae, A.A. Said, T. H. Wei, D. J. Hagan, E. W. Van Stryland, "Sensitive measurement of optical nonlinearities using a single beam", IEEE J. Quantum Electron., 26, 760 (1990).

Studies on the Polarization Properties of the Modes of Optofluidic Random Laser

Renu Yadav, Maruthi M. Brundavanam,[#] and Shivakiran Bhaktha B. N.[*]
Department of Physics, Indian Institute of Technology Kharagpur, Kharagpur 721302, India
[#] *bmmanoj@phy.iitkgp.ac.in* and [*] *kiranbhaktha@phy.iitkgp.ac.in*

Abstract: Random lasing in a structured two-dimensional on–average periodic dye infiltrated optofluidic device has been investigated. The threshold characteristics and multimode emission indicate random lasing action in optofluidic device due to multiple scattering from the inherent disorder in the structure. The polarization characteristics of laser emission for different optical pump polarizations have been studied. It is observed that the polar nature of gain medium and the pump configuration leads to confinement of emission polarization in a plane normal to the axis of scatterers for different pump polarization.
Keywords: Optofluidic random laser, multiple scattering, polarization

1. Introduction

Random laser (RL) is an optical device that utilizes the disorder induced multiple scattering for optical feedback [1]. Unlike conventional lasers, absence of well-defined cavities in RLs lead to a multidirectional and random emission spectrum [2]. Spatial light modulators have been utilized to control the directionality and wavelength of emission by tailoring the pump profile intensity in 1-D RLs [3], whereas in 2-D RLs such control has not been yet achieved experimentally. Optofluidic random lasers (ORLs) utilize multiple scattering by inherent randomness and are an attractive system to investigate various properties of RL due to inexpensive fabrication, mechanical stability and easier control of scattering strength by manipulation of fluids [4]. The multiple scattering in RLs can scramble the state of polarization of incident light, however, linearly polarized emission has been achieved in a RL in organic dye solution by restricting the reorientation of dye molecules and pumping the system with a linearly polarized light [5]. The emission polarization from conventional lasers is commonly controlled by polarizing elements such as Brewster windows or Lyot filters but in RLs interplay of multiple scattering and optical gain influences the spectro-polarimetric properties of lasing modes. Thus, it is interesting to study the factors that can control the emission polarization of RLs. In this work, the effect of pump polarization (PP) on the lasing from an ORL has been studied. It is observed that due to the polar nature of dye, the emission is polarized in a plane perpendicular to the axis of cylindrical scatterers for different pump polarizations.

2. Fabrication details

The microfluidic channel was fabricated by soft-lithography method described by Xia et al. [6]. The master structure was fabricated using a positive photoresist AZ 4562 by UV-photolithography. The master structure was replicated on polydimethylsiloxane (PDMS) surface. A 10:1 PDMS: cross-linker mixture (Sylgard 184) was poured on the master and then degassed for 15 minutes at a few mm Hg vacuum pressure and cured at 70 °C for 1 hour and 30 minutes. After peeling off the PDMS, the holes for inlet and outlet were created and structure was plasma bonded to a glass slide. A Rhodamine 6G dye solution of concentration 2.5 mM in methanol was infiltrated through the tubes connected to the inlets. A continuous flow of the dye was maintained to prevent the bleaching of the dye. The device consists of cylindrical pillars of PDMS of an average diameter of 17 µm and height 5 µm arranged in a square lattice pattern with an average periodicity of 20 µm in a circular microfluidic channel of diameter 3 mm. The optical microscope image of dye filled channel, optically pumped under stripe-excitation geometry is shown in Fig. 1(a).

3. Experimental details and results

The ORL was pumped with the second harmonic of a Q switched Nd:YAG laser (with 10 ns pulse width, 20 Hz repetition rate, and λ= 532 nm). The pump beam was shaped into a 12 mm long and 30 µm thick stripe by a cylindrical lens of f = 50 mm. The stripe was aligned along an array of scatterers to force the dye emission along the length of stripe as shown in Fig. 1(a). The system is pumped in transverse configuration as shown in Fig. 1(b). The emission spectrum was recorded with a CCD-based fiber probe

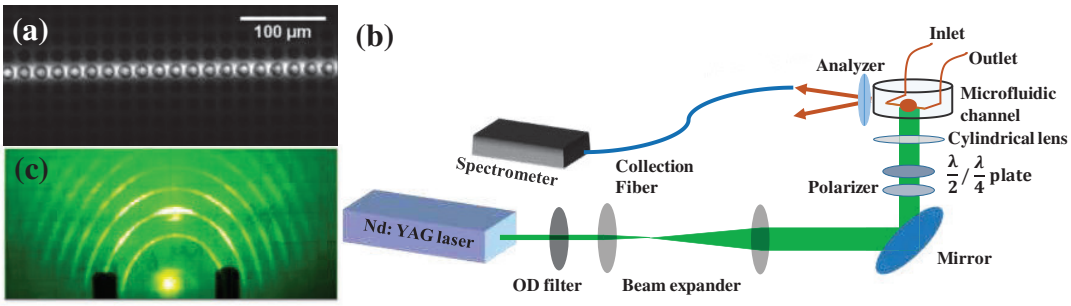

Fig. 1: (a) Optical microscope image of ORL pumped with a stripe shaped beam. (b) Schematic of experimental setup used to study the emission polarization of ORL. (c) Photograph of diffraction fringes formed on a screen kept at 7.5 cm from ORL.

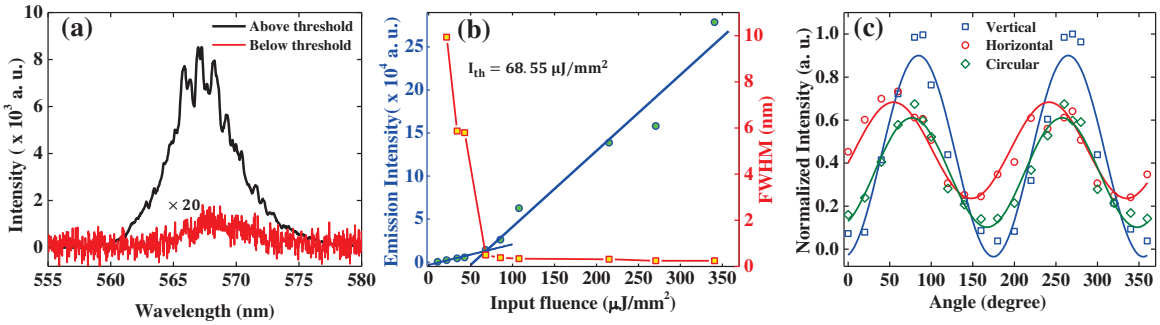

Fig. 2: (a) Emission spectrum of ORL below and above the lasing threshold. (b) Input fluence vs average output intensity plot with a threshold of $I_{th} = 68.55\ \mu J/mm^2$. The FWHM for corresponding input fluence is also shown. (c) Averaged intensity of ORL normalized with respect to emission with vertical PP, recorded at different orientations of pass axis of polarizer with respect to a plane normal to the axis of scatterers for different PPs.

Avantes spectrometer with a spectral resolution 0.04 nm, coupled with a collection fiber of diameter 1mm. Due to the on-average periodicity of scatterers elliptical diffraction fringes were observed as shown in Fig. 1(c). The emission spectrum collected at one of the diffraction fringes is shown in Fig. 2(a). The random positioned peaks denote a multimode emission. The integrated output intensity and FWHM of ORL emission vs input fluence are shown Fig. 2(b). The threshold characteristic typical of a laser is observed with a threshold value of 68.55 μJ/mm^2. The emission of ORL is stable and reproducible and does not change with time for a particular pumping configuration and flow rate of dye. The emission spectrum changes for different locations of pumping due to different disorder at different locations in the system.

The polarization characteristics of emission from ORL were studied by changing the pump polarization using a half-wave/quarter-wave plate. A sheet polarizer was placed between the edge of ORL and collection fiber to study the polarization characteristics of laser emission as shown in Fig. 1(b). Fig. 2(c) shows the intensity of an ORL mode recorded at different orientations of pass axis of analyzer with respect to a plane normal to the axis of scatterers for different PPs. It is observed that the emission is polarized normal to the axis of cylindrical scatterers. This behavior is observed due to anisotropic nature of dye molecules which forces the laser emission in the direction of PP. In the transverse pump configuration, the different PPs provide an electric field always normal to the axis of pillars thus similar results are obtained for all PPs. The emission intensity for horizontal PP is less as it leads to oscillation of dipole moment of dye molecules along the direction of emission, hence the dye dipoles can emit in the direction of collection only after reorientation. Hence, lower emission intensity is obtained for horizontal PP. A detailed discussion on the polarization properties of the modes of a random laser will be discussed in the conference.

4. References

[1] Diederik S.Wiersma, "The physics and applications of random lasers", Nature physics 4(5), 359-367 (2008).
[2] Hui Cao et al., "Random laser action in semiconductor powder", Phys. Rev. Lett. 82, 2278 (1999).
[3] Nicolas Bachelard et al., "Adaptive pumping for spectral control of random lasers", Nature physics, 10(6), 426-431 (2014).
[4] Shivakiran Bhaktha B. N., et al. "Optofluidic random laser", Applied Physics Letters 101(15), 151101 (2012).
[5] Sebastian Knitter et al., "Emission polarization of random lasers in organic dye solutions", Optics letters 37(17) ,3621-3623 (2012).
[6] Younan Xia and George M. Whitesides. "Soft lithography", Angewandte Chemie International Edition 37(5), 550-575 (1998).

Circular Dichroism of the array of C shape Gold Nanostructure

Sushant Sharma[1], Parinda Vasa[2]
Department of Physics, Indian Institute of Technology Bombay, 400076 Mumbai India
Author e-mail address: parinda@iitb.ac.in

Abstract: We study the circular dichroism of the array of gold nanostructure using COMSOL Multiphysics. It has wide application in pharmaceuticals; these arrays have enantioselective capabilities. They could also be used for chiral light detection, making broadband circular polarizers. We study the array of simple "C" shape structures with significantly fewer fabrication difficulties. These achiral planar nanostructure arrays' circular dichroism (CD) varies as we change the illumination direction. It behaves differently in the two orthogonal illuminations, theta and phi; for a better understanding of the origin of CD in plasmonic structure, we discuss the surface charge distribution.
Keywords: Circular Dichroism, Biosensing, Nanostructures Array.

1. Introduction

If an object cannot be superimposed onto its mirror image, it is said to be chiral, like our hand. This property is known as chirality [1]. Chiral objects are everywhere, for example, most protein, DNA, many organic compounds, drugs for medical use, and the list goes on. For instance, in chemistry, substances made out of chiral molecules exhibit the same physical properties like colour, mass density, molar mass, etc. However, behave differently when probed with the chiral light, as described later in this document. For starters Dopa drug is chiral, one of its enantiomers is being used to cure Parkinson's disease [2], but the other one can cause Granulocytopenia which is a dangerous disease. Identifying a particular isomer of these chiral drugs with precision require robust sensing technology. Chiral plasmonics is promising in that regard

Chiral molecules or compounds interact differently with circularly polarized light [3]. For example, sugar has chiral enantiomers, one is called levorotatory, and the other is dextrorotatory. We can dissolve one of the enantiomers in water and put it in a cuvette. Now, if we illuminate one side of the cuvette with a linearly polarized light, the polarization angle of the linearly polarized light changes to some angle to its initial polarization in the clockwise direction when it comes out from the other side of the cuvette. This property is called optical rotatory dispersion (ORD). We can repeat the experiment with another enantiomer; this time, the polarization angles change to theta, but in the opposite direction, which means in an anticlockwise direction. In contrast, a racemic mixture (50% one and 50% other) of the two enantiomers does not change the polarization angle. The media with such property are called Pasture chiral media [4]. Chirality can be quantified by the chirality parameter kappa (κ). In general, the κ can be complex for a given media. The ORD can be explained with the help of the real part of the κ,

Apart from ORD, one more important phenomenon exhibited by the chiral media is Circular Dichroism (CD). CD [3], is defined as differential absorption of left circularly polarized light (LCPL) and right circularly polarized light (RCPL). CD spectroscopy has been used to characterize chiral media for hundreds of years. Like ORD, the CD also depends upon the chirality parameter (κ). However, unlike ORD, which depends upon the real part of the κ, the CD manifestation of the imaginary part of the κ.

Using the above-described spectroscopic techniques, people have characterized the two enantiomers. Generally, the signal is too weak and difficult to record using conventional techniques such as ORD and CD. Adding more complexity to it, the need of the hour is to detect even a single molecule of such enantiomers. As we mentioned, using the plasmonics properties of metal nanostructures could give us a possible solution to this challenging problem. Hendry et al. [5] have shown how the CD of the plasmonic nanostructures can be used for ultrasensitive detection of the chiral media. Hence exploring new plasmonic structure is the need of the hour. The CD of the such plasmonic structure plays a key role in such a kind of enantioselective approach.

2. Tables and Figures

Like chiral media, an array of gold nanostructures could also be used as an effective chiral media. It could give rise to circular dichroism and optical rotary dispersion. Generally, the nanostructure which shows CD are chiral [1]. Here we study the circular dichroism of achiral nanostructure arrays using COMSOL Multiphysics. The array of C shape nanostructure is chosen because the

structure is easy to fabricate. The CD is not observed when the structure is illuminated in normal incidence. However, it becomes nonzero as the angle of incidence "theta" increases. We chose the illumination direction as per the scheme given in the figure 1(a). The observed CD enhances orders of magnitude as we go for steeper angle theta, while keeping angle phi constant at 90 degrees shown in figure 1(b).

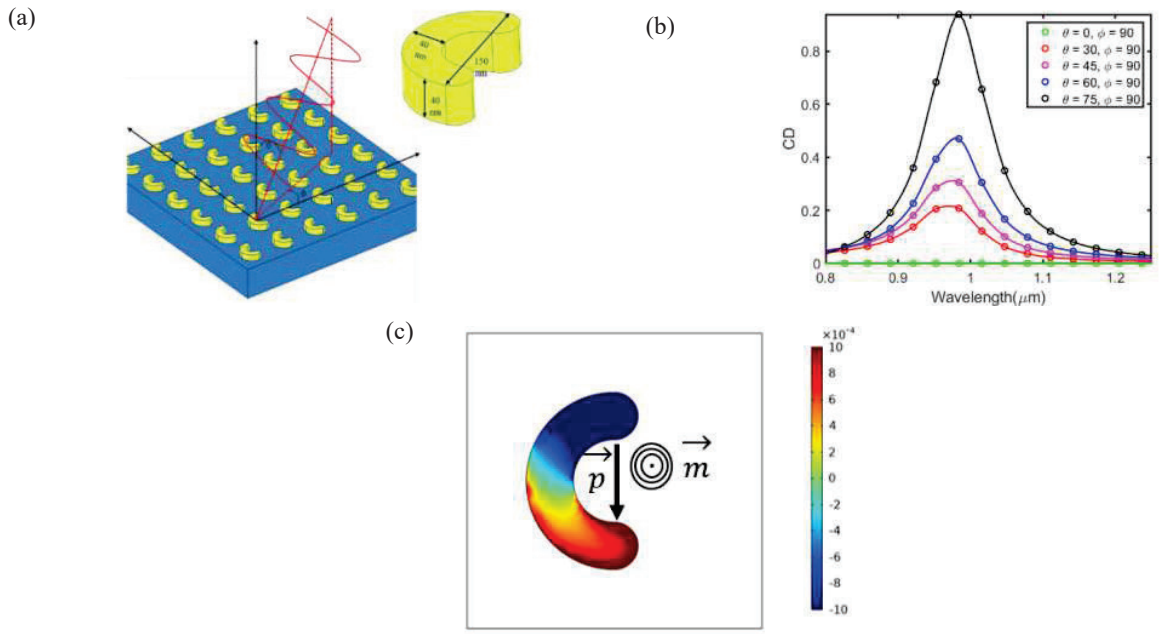

Figure 1 C Shape nanostructure is simulated using Wave Optics Module of COMSOL Multiphysics (a) Array of C shape gold nanostructure with the direction of illumination theta and phi is shown. (b) Circular Dichroism is gets enhance as we increase the θ keeping φ constant at 90 degrees. (c) The charge density (C/m^2) under the illumination of LCP light on the surface of the nanostructure at the resonance (0.995 μm) when theta is 0 and phi is 90 degrees, shows the resonance in CD is due to the electric dipole-magnetic dipole interaction.

The CD of such a plasmonic structure is the manifestation of the imaginary part of the dot product of the built-in electric dipole and magnetic dipole moment in the plasmonic structure. In figure 1(c), the surface charge density at the surface of the nanostructure is polarized as a dipole. Because of the orthogonal nature of the two dipoles, the CD goes to zero in normal incidence. The scenario changes when we move to a steeper angle, and some components of the p and m align, which gives rise to a multiple CD. As shown in figure 1(c), the charges separate upon illumination in the normal incidence. The units are in the C/m^2.

The dipole direction reverses as we change the illumination polarization from LCP to RCP. We have demonstrated that the CD of the plasmonic achiral gold nanostructure can have nonzero CD, provided we illuminate the structure at some angle. Additionally, the strength of the CD can be tuned with the angle of incidence. The profile of the surface charges can be used to identify the mode of the resonance and can provide more information about the origin of the CD resonance.

3. References

[1] M. Hentschel, M. Schäferling, X. Duan, H. Giessen, and N. Liu, "Chiral plasmonics," *Sci. Adv.*, vol. 3, no. 5, p. e1602735, 2017.

[2] J. Kumar and L. M. Liz-Marzán, "Recent advances in chiral plasmonics—towards biomedical applications," *Bull. Chem. Soc. Jpn.*, vol. 92, no. 1, pp. 30–37, 2019.

[3] M. Schäferling, "Chiral nanophotonics," *Springer Ser. Opt. Sci.*, vol. 205, 2017.

[4] I. Lindell, A. Sihvola, S. Tretyakov, and A. J. Viitanen, *Electromagnetic waves in chiral and bi-isotropic media*. Artech House, 1994.

[5] E. Hendry *et al.*, "Ultrasensitive detection and characterization of biomolecules using superchiral fields," *Nat. Nanotechnol.*, vol. 5, no. 11, pp. 783–787, 2010.

Effect of magnetic field and laser power on dual electromagnetically induced resonances in D_2 line of ^{87}Rb

Ranjit Kumar Singh*, Nayan Sharma*, Souvik Chatterjee#, Ajay Tripathi*
*Department of Physics, Sikkim University,6th mile Samdur East Sikkim, Sikkim-737102
#Department of Chemistry, Sikkim University,6th mile Samdur East Sikkim, Sikkim-737102
ranjit.edward48@gmail.com

Abstract: In this work, we have studied the effect of magnetic field and laser power on dual electromagnetically induced resonances. The experiments are carried out in the D_2 line of ^{87}Rb. Two EIT peaks are seen for very low probe power in presence of two strong lasers. However, with slight increases in probe power, one of the transmission peaks converts to absorption. The same changes are also seen by varying magnetic field. For higher magnetic field we have also observed how overlapped resonances can generate a new enhanced peak. The observations are understood by identifying the possible systems. The numerical solution validates our experimental observation.
Keywords: dual electromagnetically induced transparency, electromagnetically induced absorption, double Lambda system, tripod system, magnetic field, optical switching.

1. Introduction

Modifying optical properties of an atomic medium by laser induced coherence between atomic states is a great topic of interest in field of atomic spectroscopy. Out of many techniques, electromagnetically induced transparency (EIT) [1] and electromagnetically induced absorption (EIA) [2] has been studied widely. Switching between these phenomenon finds application in optical switching [3]. Understanding these phenomena in magnetic field have significant importance in optical magnetometry [4]. Identifying various systems possible with magnetic field can help in controlling the atoms behavior with lasers.

2. Results and discussions

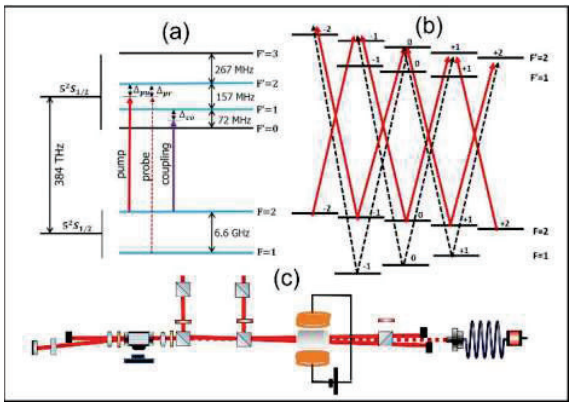

Figure 1 : (a) Energy level diagram showing the involved transitions for our experiment. (b) The transitions that are active with longitudinal magnetic field. (c) The experimental setup used in the experiments

The probe laser is scanned from F=1 to F'=2 transitions. The pump laser is locked from F=2 to F'=2 transitions. The coupling laser is locked midway between F'=1 and F'=2 transition. With magnetic field, the magnetic sublevels degeneracy is uplifted. Also, the selection rule for both the three lasers are redefined. For longitudinal field, all the three lasers will have $\sigma^{+/-}$ polarization. The energy level diagrams are shown in figure 1. The schematic of the experimental setup is shown in figure 1 (c). More information about the components can be found in [5].
The experimental results are shown in figure 2.

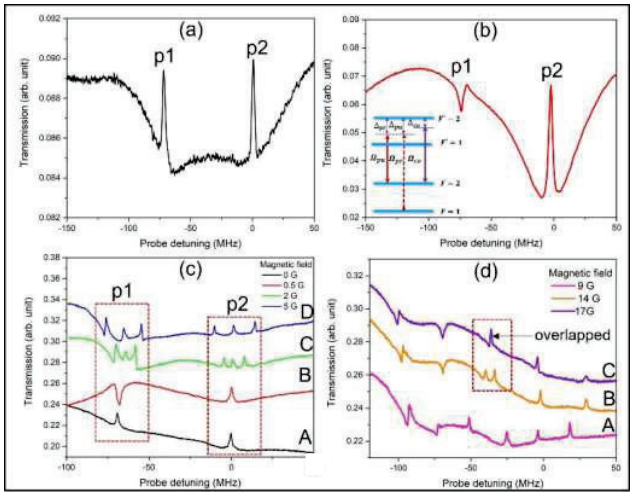

Figure 2: Probe detuning plotted as a function of transmission (a) Experimental results when probe power is 0.01 mW. (b) probe power is 0.5 mW. The power for pump and coupling laser is fixed at 4.5 mW. (c, d) Variation of magnetic field for the same configuration

For low value of probe power, two transmission peaks are seen [6]. It is due to the formation of two different Lambda systems. For a probe power of 0.5 mW, the peak *(p2)* remains transmission. However, peak *(p1)* converts to absorption. For this power, we cannot treat the two systems as individual three level system. Instead, a four-level N-type system [7] is formed. The absorption peak is generated for the system in which probe is locked at midway between F'=1 and F'=2 excited hyperfine level. It is because of the involvement of both these levels that results in absorption. For the case when pump is locked near the resonant transition (F'=2), absorption is not seen since the other hyperfine level is very far away from F'=2.

Keeping the pump and coupling laser locked, the magnetic field is varied from 0 G to 17 G. In absence of magnetic field two transmission peaks are seen. With increase in magnetic field, one of the peak converts to absorption. For magnetic field above 2 G, the degeneracy is completely uplifted. This results in six transmission peaks as seen is figure 2 (c) (spectrum D). For higher magnetic field, for the detuned system, instead of three transparency peaks, two absorption and one transmission peaks are seen. This is because of the formation of four level double Lambda systems [8]. The three transmission peaks for the detuned system retains for higher magnetic field. With magnetic field of 17 G, two peaks are overlapped, each from the resonant systems and the detuned systems. This results in enhancement of the transmission peak. It is therefore by finely tuning the probe power and also the magnetic field, different systems can be formed with same lasers. These different systems will result in switching from absorption to transmission or vice-versa.

The results are replicated by numerically solving the density matrix equations. The numerical results validate the experimental observations (not shown here).

3. References

[1] Fleischhauer, M., Imamoglu, A. and Marangos, J.P., 2005. Electromagnetically induced transparency: Optics in coherent media. *Reviews of modern physics*, *77*(2), p.633.

[2] Lezama, A., Barreiro, S. and Akulshin, A.M., 1999. Electromagnetically induced absorption. *Physical Review A*, *59*(6), p.4732.

[3] Clarke, J., Chen, H. and van Wijngaarden, W.A., 2001. Electromagnetically induced transparency and optical switching in a rubidium cascade system. *Applied Optics*, *40*(12), pp.2047-2051.

[4] Budker, D. and Romalis, M., 2007. Optical magnetometry. *Nature physics*, *3*(4), pp.227-234.

[5] Subba, I.H. and Tripathi, A., 2018. Observation of electromagnetically induced absorption in 87Rb D2 line in strong transverse magnetic field. *Journal of Physics B: Atomic, Molecular and Optical Physics*, *51*(15), p.155001.

[6] Li, S., Yang, X., Cao, X., Xie, C. and Wang, H., 2007. Two electromagnetically induced transparency windows and an enhanced electromagnetically induced transparency signal in a four-level tripod atomic system. *Journal of Physics B: Atomic, Molecular and Optical Physics*, *40*(16), p.3211.

[7] Li, J.H., Lü, X.Y., Luo, J.M. and Huang, Q.J., 2006. Optical bistability and multistability via atomic coherence in an N-type atomic medium. *Physical Review A*, *74*(3), p.035801.

[8] Singh, R.K., Sharma, N., Subba, I.H., Chatterjee, S. and Tripathi, A., 2021. Competition between off-resonant and on-resonant processes in electromagnetically induced transparency in presence of magnetic field. *Physics Letters A*, *416*, p.127673.

Optical Design of compact wide field of view Digital Micromirror Device based LED projector

Arjun Rao Gadiparthi and Krishnendu Roy
Electro-optics & Lasers, Centre of Excellence, PDIC, Bengaluru, India
Email: arjunrao@bel.co.in

Abstract: A DMD based WFOV compact LED projector system has been designed with very short throw ratio. The projector system is divided into two modules known as illumination and projector modules. Illumination module is consisting of LED, LED collimator with Fly Eye Array (FEA) homogenizer, relay optics and coupling TIR prism. The projector lens is 70° WFOV objective with distortion less than one percent.
Keywords: DMD, LED projector, WFOV, optics design, Lens design, DMD display

1. Introduction

A compact LED projector system is designed with short throw ratio. The present system is designed as a replacement of a CRT display system for a legacy Head Up Display (HUD). The short throw ratio is a necessary requirement to meet the physical sizes of the existing HUD system.

The LED based system utilizes Digital Micro-Mirror Device (DMD) as the image generation device. Due to DMD's unique micro mirror reflective property, optics design is complex. The system follows the standard TIR prism coupled illumination and projection modules [1][2][3].

Fly eye array homogenizer is used to generate the required uniform distribution [3]. In this paper, we presented the complete projector optics design with high FOV projector optics with short throw ratio.

2. Design targets and methodology

Texas instruments DMD automotive grade chip DLP5530-Q1 is selected for our application. The CRT display in the existing HUD system limits the image size and projector dimensions. The first order specification of the complete projector system is given in table-1.

Table 1: Design Considerations

Item	Parameter	Specification
1	DMD size	0.55 inch
2	DMD aspect ratio	2:1
3	Resolution	1152x576
4	f/#	2.4
5	Projected Image size	85 to 90mm
6	Exit pupil position	<70mm
7	BRIGHTNESS	3000 FL
8	Maximum allowed size	180x150x150mm

The optical system design approach of our projector is shown in figure-1. The Projector system design is divided into two parts: an illumination module from the light source to the DMD and a projection module from the light reflected by the DMD through the lens to the screen. The former is a non-imaging optical system that focuses on the illumination uniformity and efficiency, while the latter is to eliminate aberration and chromatic aberration of the lenses.

The detailed parameters of the final illumination and projection modules are given in table-2 and table-3 respectively. The illumination module and projection modules are designed separately and combined using RTIR prism mechanism to generate the complete projection system.

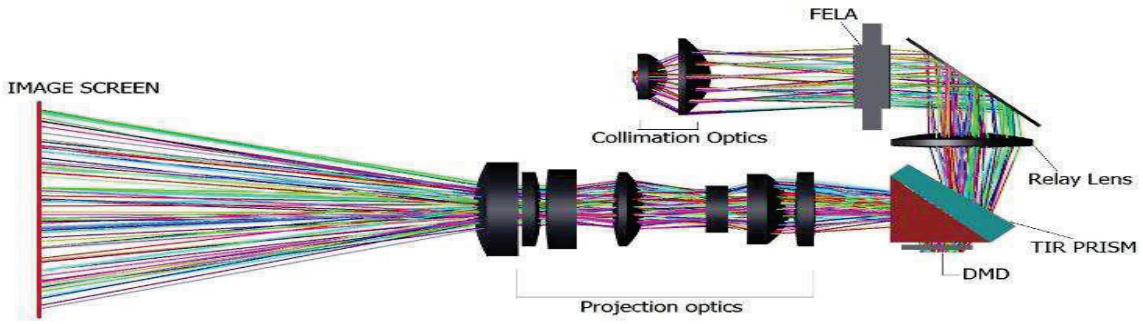

Figure 1: Optical layout of the complete projection system

Table 2: Illumination module parameters

Item	Parameter	Specification
1	Led source	OSRAM LE CG Q8WP
2	Collimation lens 1	f-11.3 mm meniscus lens
3	Collimation lens 2	f-10 mm, aspheric lens
4	Relay lens	f-22.5, aspheric lens
5	FELA	Polycarbonate; 9x17 numbers

Table-3: Projection lens parameters

Item	Parameter	Specification
1	Aspect Ratio	2:1
2	F/#	2.4
3	Field of view (FOV)	70 degrees
4	Focal length	9.975 mm
5	Wavelength	F,d and C
6	Distortion	<1%
7	Screen distance	64mm
8	Off-set	No-offset
9	No. of elements	7
10	No. of aspherics	2

3. Projection Module performance evaluation:

The complete system is designed and simulated in Zemax optics studio. The system Modulation Transfer Function (MTF) value is more than 0.55 at 67 lp /mm in all fields and spot sizes in all fields are optimized close to diffraction limited performance. The optical distortion of the system is maintained less than one percent. The MTF and Field curvature & distortion plots are shown in figure-3.

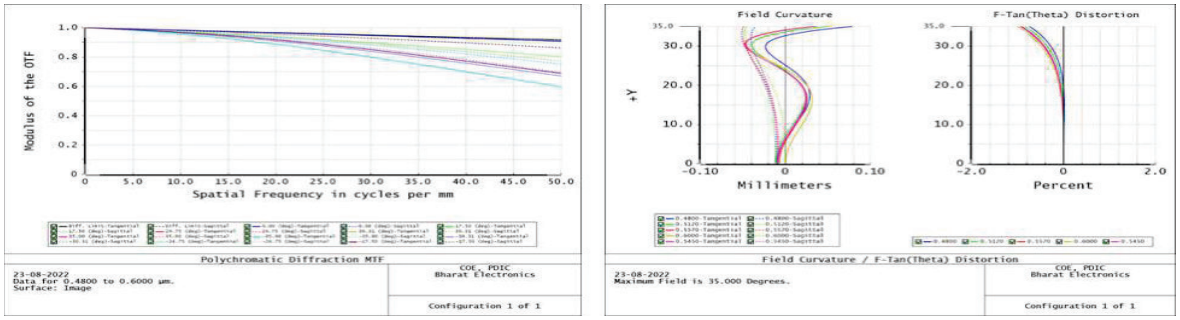

Figure 3: Optical performance of the projection lens

4. References

[1] Wen-Shing Sun, Wen-Shing Sun, Chuen-Lin Tien, Chao-Hui Ma, and Jui-Wen Pan "Compact LED projector design with high uniformity and efficiency" Applied Optics 59, 210-969 (2014)

[2] Chong-Min Chang and Han-Ping D. Shieh "Design of illumination and projection optics for projectors with single digital micromirror devices", APPLIED OPTICS 39 (2000)

[3] XUEQIONG BAI, XIAOLI JING, NINGFANG LIAO "Design method for the high optical efficiency and uniformity illumination system of the projector", Optics Express 29 421-332 (2021)

[4] Wen-Shing Sun, Yen-Chen Chiang, and Chih-Hsuan Tsuei "Optical design for the DLP pocket projector using LED light source " ICOPEN 2011

Purcell Enhancement of a Quantum emitter placed inside the Plasmonic Cavity

Arjun Upadhyay, Parinda Vasa
Department of Physics, Indian Institute of Technology Bombay, 400076 Mumbai, India
Author e-mail address: parinda@iitb.ac.in

Abstract: Nanoparticle on mirror (NPoM) plasmonic cavity can be utilized to enhance the spontaneous decay rate of a quantum emitter to a great extent. Here we calculated the Purcell factor of a quantum emitter placed in such a cavity using COMSOL Multiphysics software. We first simulated the extinction cross-section of a nanorod placed on top of a metal film separated by a small gap and then calculated the Purcell factor for a varying gap. We observed that the Purcell factor is greatly enhanced when the gap between the nanorod and the metal film is sufficiently low (<4nm).
Keywords: Plasmonic cavity, Purcell factor, NPoM, Extinction cross-section.

1. Introduction

The property of the metal nanoparticles to confine light at a subwavelength scale make them suitable for studying strong light-matter interaction. This strong field confinement is attributed to Localized surface plasmons (LSPs) and allows to study of various optical phenomena such as surface-enhanced Raman spectroscopy (SERS) [1], enhanced fluorescence [2], etc. Apart from this, the plasmonic cavity made by these nanoparticles also greatly alters the spontaneous decay rate of a quantum emitter [3]. Cavities made out of dimers and trimers nanostructures showed great enhancement in spontaneous decay rate because of their narrower gap than monomers. However, precise control over the gap is a challenging task, and further, the minimum gap between them is limited by fabrication techniques.

On the other hand, a plasmonic cavity made by placing a nanoparticle on top of a metal film, known as nanoparticle on mirror (NPoM) geometry, provides precise control over the gap. In NPoM geometry, a metal nanoparticle is separated from the metal film by a dielectric layer. By varying the thickness of the dielectric layer, the gap between nanoparticle and metal film can be controlled very precisely. Using NPoM geometry, structures having a gap of less than 1nm have been made successfully [4]. This NPoM geometry also provides an attractive platform to achieve a large enhancement in spontaneous decay rate because it confines light to an extremely small volume. It also has the flexibility to tune the resonance position of the cavity to a wide range of energies.

We simulated an Au nanorod placed on top of an Au film separated by an air gap. We use finite element based commercially available software COMSOL Multiphysics to carry out the simulations. First, we calculated the extinction cross-section of the nanorod on top of a metal film and compared it with the extinction cross-section of the nanorod in air. After that, an oscillating point electric dipole is placed between the nanoparticle and the film. We varied the separation d between the nanoparticle and metal film from 10nm to 1nm and calculated the Purcell factor for each value of d corresponding to the resonance position of the cavity.

2. Tables and Figures

Figure 1(a) shows the schematic diagram of nanoparticle on mirror (NPoM) geometry. A gold nanorod of aspect ratio 2.5 and radius 15nm is placed on top of a 45nm thin Au film. Nanorod is separated by a distance d from the metal film by a dielectric layer. An electric field having polarization along the x-axis is incident normally from the top, and the extinction cross-section is calculated under scattered field configuration. Figure 1(b) shows the extinction cross-section of a nanorod in NPoM configuration compared with the nanorod in air. The resonance peak corresponding to NPoM geometry is 1.74 eV for d=2nm, and the nanorod in the air is 2.12 eV. The extinction cross-section shifted toward the red region as the distance d between nanorod and metal film decreased. To precisely know the resonance position and linewidth, the obtained data is fitted with Fano line shapes. Figure 1(c) shows the Purcell factor as a function of distance d b/w nanorod and metal film. To incorporate the quantum emitter in COMSOL,

we consider an oscillating point electric dipole. This point electric dipole is placed inside the gap between nanorod and metal film. Purcell factor increases rapidly as the distance d decreases. Its value becomes 16,424 for a gap equal to 1nm.

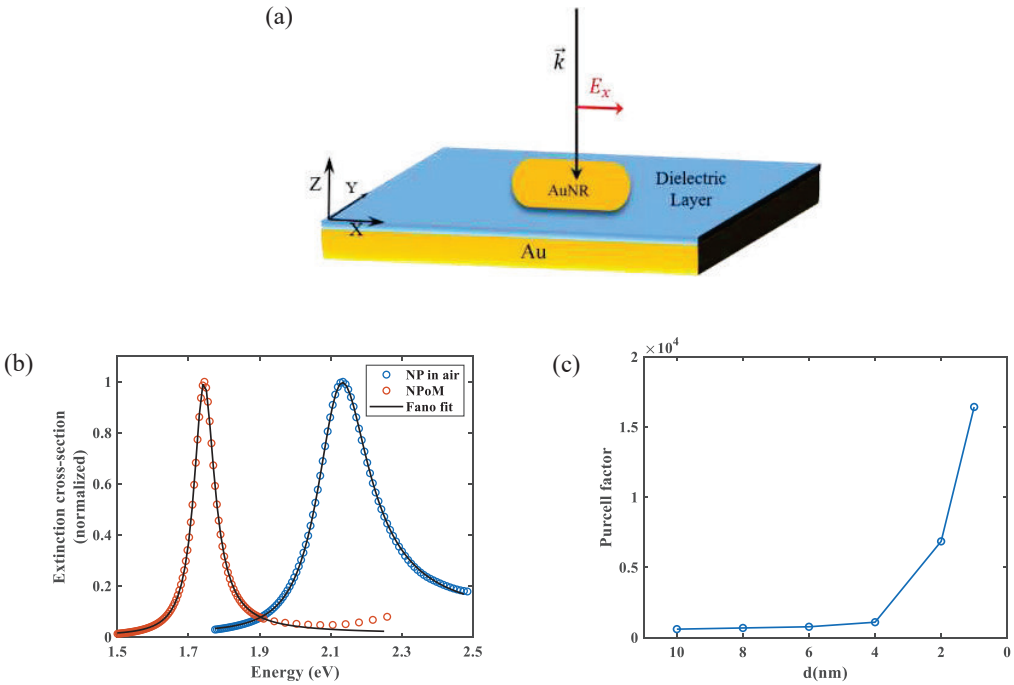

Fig. 1: (a) Schematic of the Nanoparticle on mirror (NPoM) geometry. Au nanorod is separated from the Au film by a dielectric layer (n=1) of thickness d. (b) Normalized extinction cross-section (ECS) of Au nanorod without the metal film in blue and on top of an Au metal film separated by a dielectric layer (d=2nm) in orange. Black solid lines represent the Fano fitting to ECS data. (c) Purcell factor of a quantum emitter (point dipole) as a function of separation b/w the nanorod and metal film.

By calculating the Purcell factor, we have observed that NPoM geometry shows a high modification in spontaneous emission. High Purcell factor in such geometry, evident from simulations, can be observed experimentally by simply coating the quantum emitter between the nanoparticle and metal film. However, preliminary results obtained from the simulation would help to optimize the problem efficiently.

3. References

[1] Felix Benz, "SERS of Individual Nanoparticles on a Mirror: Size Does Matter, but so does Shape" J. Phys. Chem. Lett. 2016,7,12,2264-2269.
[1] MB Mohamed, "The 'lightning' gold nanorods: fluorescence enhancement of over a million compared to gold metal" Chem Phys Lett 2000;317:517-23.
[3] Yi-Yu Cai, "Photoluminescence of gold nanorods: Purcell effect enhanced emission from hot carrier" ACS Nano 2018,12,2,976-985.
[4] Ryan T. Hill, "Plasmon Ruler with Angstrom Length Resolution" ACS Nano 2012,6,10,9237-9246.

Cardiac Monitoring With Modal Interferometer Based Wearable System

Pratik Mishra[1, 2], Kalipada Chatterjee[1, 2], Hemant Kumar[2], and Rajan Jha[1, 2]
[1]Nanophotonics and Plasmonics Laboratory, School of Basic Sciences, IIT Bhubaneswar, Odisha-752050, India
[2]School of Basic Sciences, IIT Bhubaneswar, Odisha-752050, India
Email: pm43@iitbbs.ac.in, rjha@iitbbs.ac.in

Abstract: Sensitive wearable systems for vital physiological parameters monitoring, such as pulse rate, have gained significance for personalized and public healthcare. Here, we propose and demonstrate a flexible and wearable modal interferometer based on photonic crystal fiber (PCF) embedded in a polydimethylsiloxane (PDMS) membrane for accurate pulse rate monitoring. The stretching sensitivity of the proposed sensor is observed to be 2.6 pm/μm over a range of 0 – 2000 μm. The proposed system facilitates pulse rate detection with high accuracy and repeatability. This system has the potential to act as a wearable device for extensive bio-medical applications.

Keywords: Photonic crystal fiber, Modal interferometer, Wearable sensor, Pulse wave detection.

1. Introduction

Since the rise in demand for efficient healthcare devices, flexible and wearable sensors for accurate monitoring of pulse rate have gained significance. Conventional electronic flexible sensors are user-friendly, but their response to hostile conditions is nonlinear. In recent years, optical fiber-based flexible sensors have become viable, with embedded microfibers [1, 2] and fiber Bragg grating structures [3] serving as wearable pulse wave sensing probes. However, these optical sensors have a limited operating range and involve complex fabrication. In this paper, we present a compact, sensitive, highly adaptable and biocompatible modal interferometer (MI) embedded in flexible membrane for the detection of pulse waveform in human subjects. By accurate detection of pulse waveform, an individual's cardiac health can be assessed for personalized diagnostics.

2. Working Principle and Experimental Section:

The sensing probe comprises of a fiber MI fabricated by splicing a 1.2 cm section of solid core photonic crystal fiber (PCF) along a single mode fiber (SMF) channel. The splicing technique creates regions of uniform refractive index known as collapsed zones at the splicing locations. When light from a broad-band source is coupled to the interferometer channel, it diffracts about the collapsed zones, which excites the fundamental core-type and higher order cladding-type modes (p^{th} mode) along the PCF length. These distinct effective modes interfere with one another, resulting in a consistent interference pattern over the source spectrum. The coupling of these higher order modes is affected by the wavelength-dependent mode coupling coefficient (κ^p) calculated to be [4].

$$\kappa^p(\Delta n, \lambda) = \frac{2\pi\eta^p \Delta n}{\lambda} \quad \text{(i)}$$

where, $\Delta n = n_{cr} - n_p$, is the effective modal indices difference, λ is the wavelength, and η^p is the overlap integral of the core and cladding modes. When $\kappa(\lambda)$ values satisfy the condition $\kappa L = 2m\pi$ (constructive) the spectral components are coupled to the fundamental core mode. While, for the destructive condition $\kappa L = m\pi$ the spectral components get coupled to the higher-order mode and become lossy. Here, m takes positive integer values. In the presence of perturbing external field, the value of Δn or L changes, resulting in a shift in the position of the interference dip wavelengths providing a signature of the external field. This MI is encapsulated in a polydimethylsiloxane (PDMS) membrane to create a bendable optical sensing probe. As indicated in Figure 1(a), the SCPCF portion is positioned along the diagonal of the PDMS membrane. When the PDMS membrane is stretched, due to the orientation of the PCF section, it incurs a shearing stress along its length leading to shift in spectrum dip wavelength values. This orientation can be optimized to alter the sensitivity and operating range of the sensing system.

The sensor probe is characterized by coupling light from a broadband super luminescent light emitting diode (SLED) source and recording the resulting transmitted interference spectrum with an optical spectrum analyzer (OSA). To investigate the stretching sensitivity of the sensor, it is affixed with the scotch tape on two micro-parallel displacement

stages and the sensing system is pulled along with the stage in a controlled way. The transmission spectrum is recorded as the system is stretched over 0 to 2000 μm. Furthermore, to monitor the pulse rate of a human subject, the sensor is placed on the wrist of a volunteer, and real-time wavelength shift is recorded with an interrogation monitor (IMON).

3. Results and Discussions:

The flexibility of the proposed system enables the measurement of mechanical strain caused by PDMS sheet stretching. As the sheet is extended horizontally, a shearing strain operates along the interferometer length that increases the interferometer's effective length proportionally. As a result of stretching, the κL value for constructive mode coupling condition shifts for longer wavelength values causing a red shift in interference spectrum as shown in figure 1(b). The magnitude of wavelength provides estimate of the extent of stretching. Such response can be used for monitoring joint and muscle motion of the body.

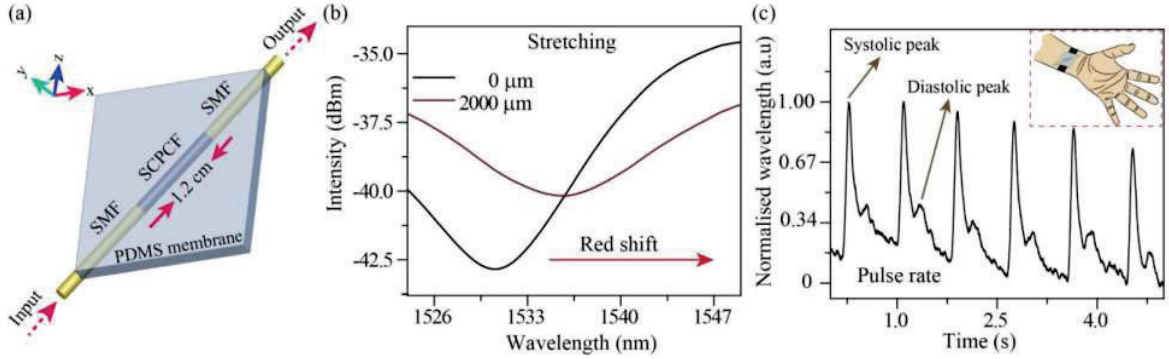

Figure 1: (a) Schematic representation of modal interferometer based wearable system (b) Spectral responses of the sensor for stretching from 0 to 2000 μm. (c) Real time wrist pulse detection by the system. Inset: pulse detector as a wrist watch type.

The flexibility and sensitivity of the proposed system permit the detection of low physical forces applied to the interferometer region. The property of detecting minute physical force is utilized to monitor human wrist pulse. The sensing system is attached on the wrist of a volunteer to monitor the pulse rate as shown in inset of the figure 1(c). Figure 1(c) depicts 6 cycles of the wrist pulse for 5 seconds. Here, the peak wavelength shift caused by the periodic physical force created by pulse beats is indicative of a healthy heart rate of roughly 75 beats per minute (bpm). The high sensitivity enables mapping the pulse waveform and identify the nature and duration of systolic and diastolic peaks of pulse wave. These crucial parameters can be used to assess the health of heart and arteries of human body for predictive medical diagnosis.

4. Conclusions:

The proposed flexible sensor enables efficient detection of stretching over a considerable range. The system's sensitivity and operational range can be altered by adjusting the interferometer length and width of the PDMS membrane. In addition, the flexible nature of PDMS makes it robust and skin-mountable. The sensor accurately identifies the human pulse wave. Therefore, the proposed system could be utilized to construct an all-optical system for comprehensive physiological monitoring.

5. Acknowledgement:

RJ acknowledges the support from SERB STAR and BRNS Fellowship.

6. References:

[1] H. Zhu, L. Zhan, Q. Dai, B. Xu, Y. Chen, Y. Lu, and F. Xu, "Self-Assembled Wavy Optical Microfiber for Stretchable Wearable Sensor", Adv. Opt. Mater. **9**, (2021).
[2] P. Mishra, H. Kumar, S. Sahu and R. Jha,"Flexible and wearable optical system based on U-shaped cascaded microfiber interferometer", Adv. Mater. Technol. **2200661**, (2022).
[3] C. Tavares, C. Leitao, D. Aniela, L. Presti, M. F. Domingues, N. Alberto, 2 H Silva, and P. Antunes,"Respiratory and heart rate monitoring using an FBG 3D-printed wearable system", Biomed. Opt. Express **13**, 2299 – 2311 (2022).
[4] Z. He, Y. Zhu, J. Kaňka, and H. Du, "Core-cladding mode coupling and recoupling in photonic crystal fiber for enhanced overlap of evanescent field using long-period gratings", Opt. Express **18**, 507 (2010).

Theoretical Analysis of Time Delay Echoes in Multimode Semiconductor Diode Laser with Optical Feedback

Neethu K and S. Sivaprakasam[1]
Department of Physics, Pondicherry University, Kalapet, Puducherry, India
[1]siva@pondiuni.ac.in

Abstract: Investigations on the time delay echoes (TDE) of a multimode semiconductor diode laser subjected to external optical feedback (EOF) is reported. Multimode Lang-Kobayashi rate equations are adopted to solve the problem. Autocorrelation and mutual information techniques are used for the analysis. The shift in the position of time delay echoes with external cavity reflectivity, cavity length, and multimode character are analyzed and it is found that the TDE are significantly influenced by the laser operating parameters.
Keywords: Multimode semiconductor laser, Time delay echoes, Autocorrelation, Mutual information

1. Introduction

Chaotic secure communication, cryptography, random number generation and other emerging applications demand intense research on semiconductor diode lasers with optical feedback [1]. The external cavity generates the optical chaos, but, at the same time, analysis such as auto-correlation function (ACF), could reveal time delay information and hence compromise security. ACF of the laser intensity output has significant peaks around the position of external cavity round trip time and its multiples and are called time delay echoes (TDE) [2]. Suppression or concealment of the TDE, thus became a focal point in research. Methods were suggested to conceal the TDE in single mode laser system, but the practical implementation is difficult in most cases [3]. This work aims to analyze the behavior of TDE in a multimode semiconductor laser with external optical feedback, as most practical diode lasers are multimode in nature. Solving multimode Lang-Kobayashi (L-K) rate equations, the temporal evolutions of laser field is generated and analyzed using ACF and mutual information (MI) techniques. This paper studies the effect of multimodeness, external cavity reflectivity (r_{ext}) and external cavity delay time (τ_{ext}) control the behavior of TDE.

2. Theoretical model

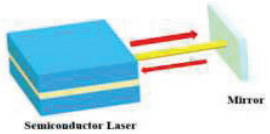

Fig. 1. Schematic Diagram of semiconductor diode laser subjected to external optical feedback.

The configuration of the semiconductor diode laser with optical feedback is shown in Fig.1. L-K rate [4] equations are modified to suit multimodeness [5]. The rate equations for $E_m(t)$, the slowly varying complex electric field of m_{th} longitudinal mode, and N(t), which is the corresponding carrier density, are given by equations (1) and (2), respectively. Here mode-dependent gain coefficient $G_m(N)$ has a parabolic profile, and its maximum is centered at central mode (m_c) .

$$\frac{dE_m(t)}{dt} = \frac{1}{2}(1+i\alpha)(G_m(N) - \frac{1}{\tau_p})E_m(t) + \kappa E_m(t-\tau_{ext})\exp(-i\omega_{0m}\tau_{ext}) + \sqrt{2\beta N(t)}\xi(t) \quad (1)$$

$$\frac{dN}{dt} = \frac{J}{e} - \frac{N(t)}{\tau_n} - \sum_m G_m(N)\left|E_m(t)\right|^2 \quad (2)$$

where J is the injection current density. $\alpha = 3.8$ is the line-width enhancement factor. $\tau_p = 2$ps is the photon lifetime, and $\tau_n = 2$ ns is the carrier lifetime. $\tau_{in} = 8$ ps is the internal cavity round trip time. κ is the feedback rate. $\beta = 10^{-10}$ is the spontaneous emission rate, and ξ is the Gaussian noise term with a zero mean. Nominal frequency of the m^{th} mode ω_{0m}.

3. Results and Discussion

The fingerprint of time delay is an accessible property of ACF, which describes how much a signal relates to its own time-delayed version. MI quantifies the information shared by two variables, such as a function and its own delayed version. We analyzed the field evolutions of single and 15-mode lasers with EOF and generated ACF and MI function.

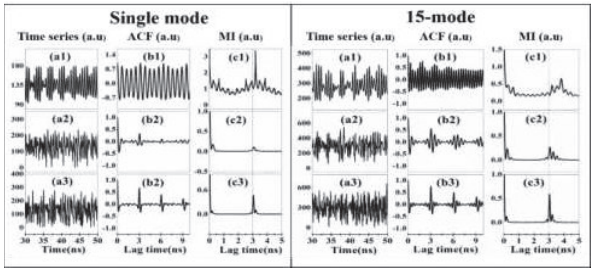

Fig. 2. ***Single mode and 15-mode semiconductor laser with EOF in which, plots ((a1),(a2)and (a3)) represents intensity time series, ((b1),(b2)and (b3))represents ACF and ((c1),(c2)and (c3)) represents MI for increasing value of external cavity reflectivity (r_{ext}=0.01(first row) 0.05(second row) and 0.1 (third row).***

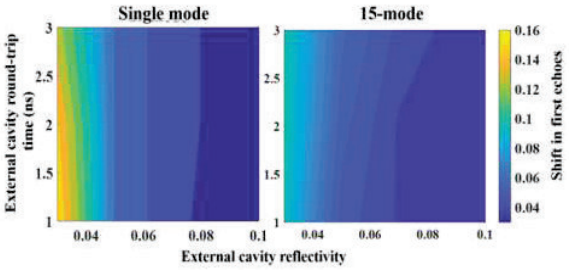

Fig. 3. Contour plot indicating Shift in the position of first echoes as a function of cavity length and external cavity reflectivity for single mode and 15- mode cases.

In Fig.2., temporal evolutions, ACF and MI are shown for single and 15 mode lasers subjected to different feedback -strengths at a fixed external cavity delay of τ_{ext} = 3ns. Plots ((a1), (a2) and (a3)) are intensity time series, plots ((b1),(b2)and (b3)) represents ACF and plots ((c1),(c2)and (c3)) represents MI for increasing value of external cavity reflectivity. Time series gradually evolve from periodic to chaotic states on increasing feedback rate. Correspondingly, the ACF and MI peaks are becoming sharper and more intense. For less feedback strength, ACF has multiple peaks around the external cavity delay time, and those peaks have a high intensity, making it difficult to predict the exact peak thereby reducing the vulnerability to an eavesdropper. MI peaks confirms these results. For higher feedback, the peak of the time delay echoes further intensifies in amplitude [6]. Fig. 3 shows the contour of shift in TDE with respect to the feedback strength and external cavity delay time. Comparison is made for the shift in first TDE position for variation in feedback, τ_{ext} and multimodeness. On investigating the modal effect, it is seen that the shift of the delayed peak from the exact value of the delay timing is more for a single mode laser at a lower feedback level. On increasing the number of modes, the ACF renders a non-uniform signature of time delay with multiple peaks near τ_{ext}, rendering a near impossible situation for extracting the time delay information. It can be seen for example, from Fig.2 (b1), the multimode effects are seen to be dominant and hence high frequency peaks are seen be present for multimode system than that of a single mode case. In the contour plot (Fig. 3) the first occurring peak of ACF, is shown for both the single mode and multimode lasers. It can be seen that the effect of feedback is dominant in shifting the ACF peak positions. The cavity length effect is more pronounced in the single mode case, and a lesser cavity length gives more shifts at a lesser feedback level.

We studied TDEs for single and multimode semiconductor laser subjected to external optical feedback. Careful parametric choices of feedback strength, external cavity delay time and multimodeness can improve security of information by not revealing the information about the cavity delay time. Multimode lasers exhibit multiple peaks in ACF arising from modal effects and thus providing relatively better concealment of cavity delay time. Future studies would involve higher order modes and encryption of a signal and its effect on TDE and hence enable to find suitable modal choice of a diode laser for secure optical information exchange

4. References

[1] M. Sciamanna and K. A. Shore, "Physics and applications of laser diode chaos," Nature photonics **9**, 151-162 (2015).
[2] X. Porte, O. D'Huys, T. Ju¨ngling, D. Brunner, M. C. Soriano, and I. Fischer, "Autocorrelation properties of chaotic delay dynamical systems: A study on semiconductor lasers," Physical Review E **90**, 052911 (2014).
[3] J.-G. Wu, G.-Q. Xia, and Z.-M. Wu, Suppression of time delay signatures of chaotic output in a semiconductor laser with double optical feedback, Optics express **17**, 20124-20133 (2009).
[4] R. Lang and K. Kobayashi, "External optical feedback effects on semiconductor injection laser properties," IEEE journal of Quantum Electronics **16**, 347-355 (1980).
[5] F. Rogister, P. M´egret, O. Deparis, and M. Blondel," Coexistence of in-phase and out-of-phase dynamics in a multimode external-cavity laser diode operating in the lowfrequency fluctuations regime," Physical Review A **62**, 061803 (2000).
[6] D. Rontani, A. Locquet, M. Sciamanna, D. S. Citrin, and S. Ortin, "Time-delay identification in a chaotic semiconductor laser with optical feedback: a dynamical point of view," IEEE Journal of Quantum Electronics **45**, 879-891 (2009).

Effect of Anisotropy on the Spin-Hall effect of Light: A Near-normal Incidence Case

Upasana Baishya† and Nirmal K. Viswanathan
School of Physics, University of Hyderabad, Hyderabad, Telangana – 500046, India
† upasanabaishya@gmail.com

Abstract: As an example case of the spin-orbit interaction (SOI) of light, we investigate the spin-Hall effect of light (SHEL), a transverse shift in the beam centroid due to its interaction with an anisotropic medium. The resulting inhomogeneous state of polarization of light of the output beam is understood as due to the SOI. The SHEL investigation of the anisotropic medium is carried out in the dark-field region of the cross-polarization component.
Keywords: Spin-Hall effect of light, Spin-orbit interaction, Weak measurement, Polarization.

1. Introduction

Spin-orbit interaction (SOI) of light leading to the mutual influence of the state of polarization (SoP) and the spatial characteristics of a transversely confined beam of light is already an emerging branch of research in optical physics [1]. Changes in the SoP during free-space propagation of a paraxial [2] or a non-paraxial [3] beam of light have been understood based on the SOI. It is also well known that anisotropic and inhomogeneous media are enablers of the SOI in a beam of light propagating through or reflected from it [4 – 6]. Among the many manifestations of the SOI, a significant and widely investigated aspect is the spin-Hall effect of light (SHEL), a polarization-dependent transverse shift in the centroid of the optical beam trajectory [7]. The SHEL has been shown to depend on the spatial distribution of the longitudinal field component of a polarized beam of light [2, 8]. The spatial distribution of the longitudinal field component gets significantly modified depending on the medium with which the focused beam of polarized light interacts and which should non-trivially affect the measured SHEL.

Among several other aspects, reflecting a beam of light at the interface of an optical crystal is one of the most widely investigated to understand the effect of crystal anisotropy on a paraxial beam of light. Almost all the measurements reported so far have used large (~ 45°) angle of incidences for the investigation and have not taken into account the polarization changes (in the beam cross-section) of the focused beam of light and, most significantly have not considered the effect of longitudinal field component in their analysis. In all these investigations, the effects arising due to the SOI of the focused beam of light and of the crystal medium are convolved in a not-so-straight forward way that makes the understanding of the effects quite complex [9]. Strong dependence on the angle of incidence, optic-axis orientation with respect to the SoP of the incident beam [10], and the wavelength dependence of the effect make the understanding of the various effects quite challenging to be resolved. One possible way to minimize the complexity is to understand the SOI arising due to light and, upon its interaction with the crystal is to work at near-normal incidence [11]. Nulling the normal incidence effect, the anisotropy effects at very small (< 1°) angles of incidence and arising due to the orientation of the OA of the crystal allows us to understand the intricacies of the effect more clearly.

2. Results and discussion

To this effect, we implement a simple and novel methodology developed by us recently, known as the dark-field SHEL [12, 13], to probe the SHEL at near-normal incidence at an air-dielectric crystal interface. A schematic of the experimental setup is shown in Fig. 1 (a). Apart from using the air-glass interface as the reference substrate, we probe the SHEL for different types of uniaxial crystals with linear and circular birefringence independently and together. Using a calcite crystal with its optic-axis perpendicular to the interface as the sample Fig. 1 (b) – (d) shows respectively the experimentally measured cross-polarization component, S3 Stokes parameter and, the SHEL shift at positions marked by 'white' colour squares (1,0) and (0,1) in Fig. 1 (b). The near-normal incidence measurements show a clear distinction between the different effects and the role played by the SOI due to light, crystal and, together. Details of which will be presented at the conference.

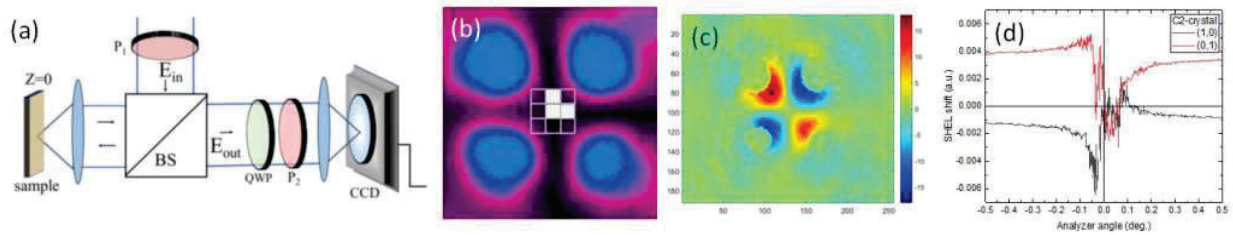

Figure 1 (a) Schematic of the experimental setup. With calcite crystal as the sample, (b) experimentally measured cross-polarization component, (c) S3 Stokes parameter and (d) the SHEL shift (at positions marked by white coloured squares in (b)) as a function of analyser angle.

3. Acknowledgements:

The authors acknowledge Science and Engineering Research Board (SERB) for financial support to this work.

4. References

[1] K. Y. Bliokh, F. J. Rodríguez-Fortuño, F. Nori, A. V. Zayats, Nat. Photonics 9, 796 (2015).
[2] A. Y. Bekshaev, Ukr. J. Phys. Opt. 12, 10 (2011).
[3] Y. Zhao et al., Phys. Rev. Lett. 99, 073901 (2007).
[4] E. Brasselet *et al.,* Opt. Lett., 34, 1021 (2009).
[5] C. T. Samlan, D. N. Naik and N. K. Viswanathan, Sci. Reports 6, 33141 (2016).
[6] T. P. Chakravarthy and N. K. Viswanathan, OSA Continuum 2, 1576 (2019).
[7] X. Ling *et al.,* Rep. Prog. in Physics 80, 066401 (2017).
[8] A. Y. Bekshaev, Phys. Rev. A 85, 023842 (2012).
[9] W. Zhu, H. Zheng, Y. Zhong, J. Yu, and Z. Chen, Phys. Rev. Lett., 126, 083901 (2021).
[10] M. Mazanov, O. Yermakov, I. Deriy, O. Takayama, A. Bogdanov and A. V. Lavrinenko, Quantum Rep. 2, 489 (2020).
[11] M. Mazanov, O. Yermakov, A. Bogdanov, and A. Lavrinenko, arXiv:2107.09738v1 (2021).
[12] N. Kumar, U. Baishya, N. K. Viswanathan, Proc. SPIE 12017, Complex Light and Optical Forces XVI, 120170A (2 March 2022); doi: 10.1117/12.2608245.
[13] U. Baishya, N. Kumar, and N. K. Viswanathan, Opt. Lett., (to appear Sept. 2022).

A study on surface plasmon resonance sensor for the improvement of sensitivity using nickel, silver and WS_2

Anil Kumar[1], Awadhesh Kumar[1] and S. K. Srivastava[1*]
Department of Physics, Banaras Hindu University, Varanasi-221005
[*]Corresponding author: sanjay_itbhu@yahoo.com

Abstract: In this work we have theoretically designed a surface plasmon resonance based (SPR) sensor using bimetallic layer (nickel and silver) with transition metal dichalcogenide (WS_2) for the sensitivity improvement. It is found that due to the inclusion of 2D materials sensitivity drastically improved. The present SPR sensor shows maximum sensitivity 180 deg./RIU with detection accuracy 5.35 for bilayer WS_2. The electric field intensity enhancement factor (EFIEF) also analyzed for the proposed SPR sensor. This sensor may be used in different field of sensing like chemical sensing, biomolecular sensing, food analysis etc.
Keywords: Surface plasmons, Silver, Nickel, Sensitivity.

1. Introduction

Surface plasmons polaritons (SPP) are charge density wave that resides at the metal-dielectric interface. These waves are very sensitive to change in the dielectric medium. So, these waves are monitored for the sensing applications. The surface plasmons resonance (SPR) is a phenomenon in which incident light wavevector matched with SPP wavevector. During excitation of surface plasmons a sharp resonance dip is observed at the reflectance curve in Kretschmann configuration. The SPR has promising application in field of environmental monitoring, food safety control, biomedical analysis etc.[1]

Silver based SPR shows very sharp dip in the reflectance curve this shows lower sensitivity as compare to gold. Gold layer shows inert nature which limits their performance. Also, it shows very poor adhesion property with the glass substrate. Nickel works as adhesion layer between silver and glass slide also improved the performance of sensor.

In recent years 2D TMDCs has considerable attention in SPR biosensor designing. As these are layered materials which have large value of dielectric constant. Single layer WS_2 absorbs ~6 % of incident light and this value increases with the no. of layers. In the present work we have designed a SPR sensor using nickel, silver and WS2 for the sensitivity enhancement analysis. Also, analysis the EFIEF variations at different RI of sensing medium.

2. Basic Principle and Mathematical Modeling-

The proposed SPR sensor consists multilayer structure on top of one face of the BK-7 glass prism with nickel, silver and WS_2 layer as shown in fig 1. A p-polarized light at wavelength 633 nm is incident on metallic-prism interface through one face of the prism and the reflected light is collected by the photodetector present at another face as shown in schematic Fig.1.

To find the reflectance of multilayer structure we have used transfer matrix method (TMM) [2]. The TMM for N-layer model relates the tangential component of electric field and magnetic field of one interface to another interface is related as -

$$\begin{bmatrix} E_1 \\ H_1 \end{bmatrix} = M \begin{bmatrix} E_{N-1} \\ H_{N-1} \end{bmatrix} \quad (1)$$

where, E_1 and H_1 represent the tangential components of electric and magnetic fields at the first layer interface. E_{N-1} and H_{N-1} represents the tangential components of electric and magnetic fields at the final layer interface. M is the characteristic matrix with elements m_{ij}, defined as-

$$M = \begin{bmatrix} m_{11} & m_{12} \\ m_{21} & m_{22} \end{bmatrix} = \prod_{k=2}^{N-1} M_k \quad (2)$$

$$\text{with} \quad M_K = \begin{bmatrix} \cos\beta_k & \frac{-i}{q_k}\sin\beta_k \\ -iq_k \sin\beta_k & \cos\beta_k \end{bmatrix} \quad (3)$$

where, k represents an arbitrary number, β_k represents phase thickness and q_k represents refractive indices of the corresponding layers, which are explained by-

$$\beta_k = \frac{2\pi d_k}{\lambda}\sqrt{(\epsilon_k - n_0^2 \sin^2\theta_0)} \quad (4)$$

$$q_k = \sqrt{(\epsilon_k - n_0^2 \sin^2\theta_0)}/\epsilon_k \quad (5)$$

where, θ_0 is angle of incidence, λ as wavelength of incident light and n_0 is the refractive index of the glass prism.

The reflection coefficient for transverse magnetic wave is given by the following relation-

$$r = \frac{(m_{11}+m_{12}q_N)q_1 - (m_{21}+m_{22}q_N)}{(m_{11}+m_{12}q_N)q_1 + (m_{21}+m_{22}q_N)}$$

Finally, the reflectance intensity for the p- polarized light is expressed as-

$$R = |r|^2$$

The optimized thicknesses and the corresponding refractive index of used materials are shown in table-

***Table 1**: Used materials and their refractive index (RI) at 633 nm*

Material	RI	Reference
Nickel (2 nm)	0.032+2.96i	[3]
Silver (50 nm)	0.056+4.27i	[4]
WS_2(0.80nm)	4.90+0.312i	[5]

Performance parameters of SPR biosensor:

Sensitivity (S) = $\Delta\theta_{res} / \Delta n_s$, where Δn_s= change in RI of sensing medium.

Detection accuracy (DA) = $\Delta\theta_{res}$ /FWHM

Phase (Φ) = arg(r)

where $\Delta\theta_{res}$ is change in resonance angle.

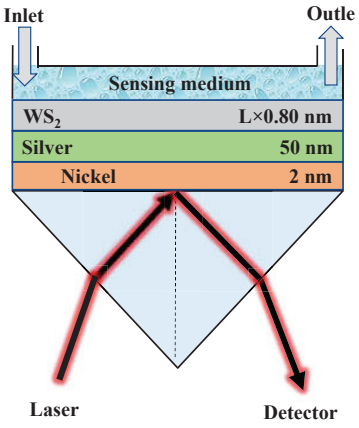

Fig. 1: Schematic Design of proposed SPR Sensor

3. Results and discussions-

For the analysis of proposed SPR biosensor first we have optimized the thickness silver layer with nickel (2nm) layer. In this work we have taken water as sensing medium in whole analysis and considered that due to addition of analyte in this its refractive index changes from 1.33 to 1.39. From the reflectance curve of three-layer structure (i.e. BK-7 glass, Ni and silver) we have found the silver with thickness 50 nm layer shows the minimum reflectance at resonance angle 68.50 deg. with minimum reflectance 3.8×10^{-4}. Above the optimized thickness of silver (50 nm), monolayer WS_2 is attached to analysis the performance. Fig. 2(a) shows the reflectance curve with WS2 monolayer and it is found that due to the addition of WS_2 layer resonance angle shifts at higher angle with broadening in reflectance curve. Furthermore, with the change in the refractive index of sensing medium from 1.33 to 1.39 the corresponding resonance angle also shifts at higher angle side. The maximum sensitivity for the proposed sensor is 180 deg./RIU with detection accuracy 5.35 for two-layer WS_2. It is also found that the corresponding phase also change at the respective resonance angles as shown in fig 2(b). The field intensity enhancement factor (EFIEF) also defines the ration of square of fields at sensing interface to the glass-metallic prism interface. The variation of EFIEF also shown in fig 2(c). This shows that maximum value of EFIEF occurs at the resonance angle.

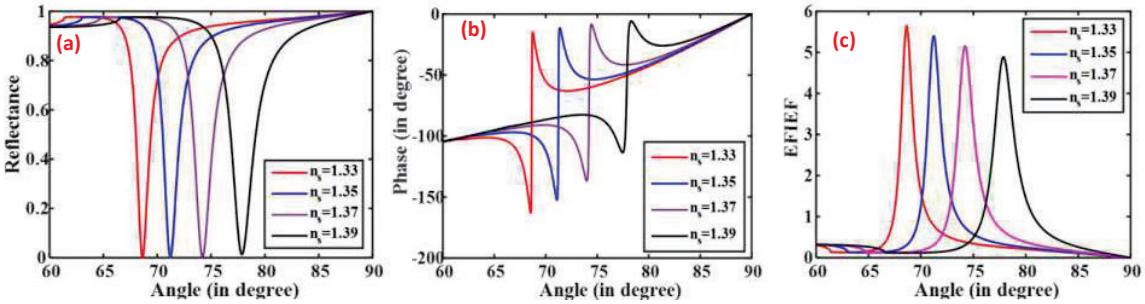

Fig. 2: For the proposed design (a) reflectance curve (b) phase sensitivity (c) electric field intensity enhancement factor (EFIEF)

4. References

[1] J. Homola, "Surface plasmon resonance sensors for detection of chemical and biological species," *Chemical reviews,* vol. 108, no. 2, pp. 462-493, 2008.

[2] Y. Singh and S. K. Raghuwanshi, "Titanium dioxide (TiO2) coated optical fiber-based SPR sensor in near-infrared region with bimetallic structure for enhanced sensitivity," *Optik,* vol. 226, p. 165842, 2021.

[3] G. AlaguVibisha *et al.*, "Sensitivity enhancement of surface plasmon resonance sensor using hybrid configuration of 2D materials over bimetallic layer of Cu–Ni," *Optics Communications,* vol. 463, p. 125337, 2020.

[4] A. Kumar, A. Kumar, and S. Srivastava, "Silicon Nitride-BP-Based Surface Plasmon Resonance Highly Sensitive Biosensor for Virus SARS-CoV-2 Detection," *Plasmonics,* vol. 17, no. 3, pp. 1065-1077, 2022.

[5] Q. Ouyang *et al.*, "Sensitivity enhancement of transition metal dichalcogenides/silicon nanostructure-based surface plasmon resonance biosensor," *Scientific reports,* vol. 6, no. 1, pp. 1-13, 2016.

Hot Electron Mediated Plasmonic Catalysis monitored by Surface-Enhanced Raman Spectroscopy employing Ag Nanorods Array

Shashank Gahlaut, Ilko Bald
Institute of Chemistry, University of Potsdam-Golm, Germany 14476
gahlaut@uni-potsdam.de

Abstract: Here, plasmonic hot electron induced dimerization of 4-Nitrothiophenol (4-NTP) is demonstrated on Ag and Au nanoarray substrates. Surface-enhanced Raman spectroscopy has been employed for in-situ monitoring of the chemical reaction (reactant and product).

Keywords: Plasmonic catalysis, Silver, Gold, SERS

1. Introduction

Plasmonic materials have found their promising applications in most of the research domains in natural sciences and engineering. The metallic nanoparticles interact with the electromagnetic radiation through the collective electronic oscillations.[1] Under some specific conditions, these oscillations resonate and generate very high intensity electromagnetic modes called surface plasmon resonance. After a series of events, these plasmons decay and the energy is transferred to the surrounding in the form of heat or highly energetic electrons. This energy is enough to induce various chemical reactions. The non-radiative decay leads to the generation of hot electrons in the metallic nanoparticles. We study the plasmonically induced chemical reactions like dimerization of molecules e.g., 4-Nitrothiophenol (4-NTP) and 4-Aminothiophenol (4-ATP) along with the dehalogenation in radiosensitizers e.g., Bromo-Adenine and Bromo-Guanine.[1-5] SERS has been employed for in-situ monitoring the chemical reactions on the hot-spots in fabricated Au/Ag nanoarray substrates.

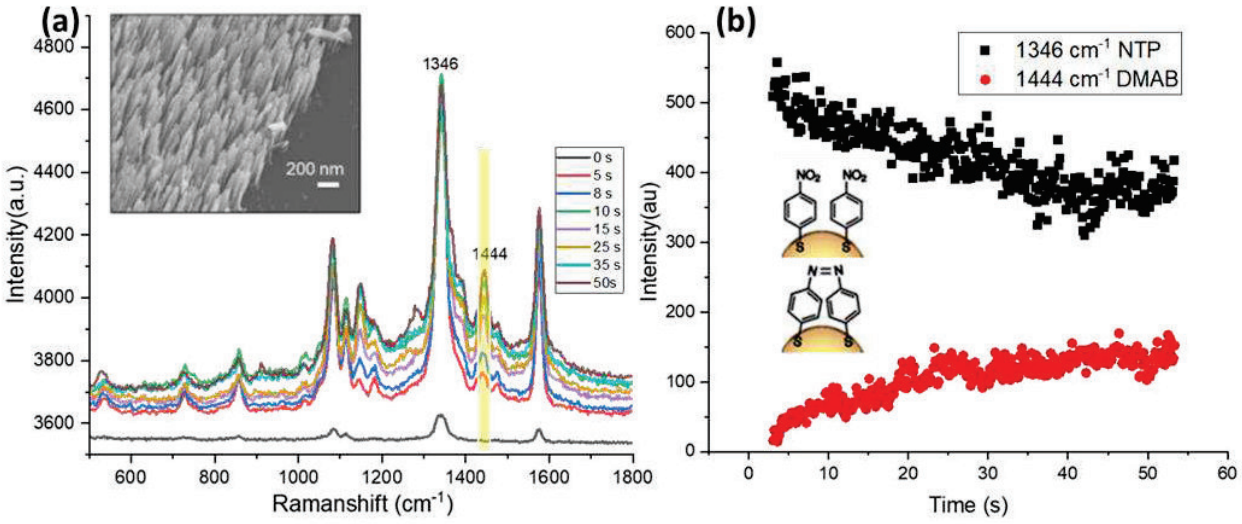

Fig. 1: Dimerization of 4-Nitrothiophenol (NTP) on the silver nanorods array fabricated on glass slide (SEM image shown in inset) (a) SERS spectra of 4-NTP after 50 sec of exposure under the laser 633 nm (1 mW

power). (b) Time-series measurements showing the decay in 4-NTP SERS peak at 1346 cm-1 and rise in the 1444 cm-1 peak corresponding to the DMAB.

Being an ultrasensitive detection tool, SERS not only investigates the reactions but also gives the information of the structural alteration of adsorbed molecules and the identification of the reaction product. For example, the plasmon induced dimerization of 4-NTP molecule on the silver nanorods array is monitored by time-dependent SERS as shown in the figure 1.

The decay in the SERS band at 1346 cm^{-1} (NO_2 stretching vibrations in NTP) and increment in the 1444 cm^{-1} band corresponds to *4-4 dimercaptoazobenzene* (DMAB) have been used to track the reaction.[5] Moreover, the reactions were studied on gold nanoparticles array and the excitation wavelength and power dependent reaction kinetics is also elucidated.[3]

In addition, we are developing a suitable heterogeneous catalyst combining plasmonic metal (core) and semiconductor (shell) to enhance the catalytic activity of catalyst by supplying the hot carriers from the metal. This was demonstrated by the enhanced degradation rate of various dyes e.g., methylene blue, methyl orange etc. in presence of nanoheterostructures.[6]

2. References

[1] Schürmann, R., Nagel, A., Juergensen, S., Pathak, A., Reich, S., Pacholski, C., & Bald, I. (2022). Microscopic Understanding of Reaction Rates Observed in Plasmon Chemistry of Nanoparticle–Ligand Systems. The Journal of Physical Chemistry C, 126(11), 5333-5342.

[2] Kogikoski Jr, S., Dutta, A., & Bald, I. (2021). Spatial Separation of Plasmonic Hot-Electron Generation and a Hydrodehalogenation Reaction Center Using a DNA Wire. ACS nano, 15(12), 20562-20573.

[3] Schürmann, R., Ebel, K., Nicolas, C., Milosavljević, A. R., & Bald, I. (2019). Role of valence band states and plasmonic enhancement in electron-transfer-induced transformation of nitrothiophenol. The journal of physical chemistry letters, 10(11), 3153-3158.

[4] Dutta, A., Schürmann, R., Kogikoski Jr, S., Mueller, N. S., Reich, S., & Bald, I. (2021). Kinetics and Mechanism of Plasmon-Driven Dehalogenation Reaction of Brominated Purine Nucleobases on Ag and Au. ACS catalysis, 11(13), 8370-8381.

[5] Koopman, W., Titov, E., Sarhan, R. M., Gaebel, T., Schürmann, R., Mostafa, A., ... & Bargheer, M. (2021). The Role of Structural Flexibility in Plasmon-Driven Coupling Reactions: Kinetic Limitations in the Dimerization of Nitro-Benzenes. Advanced Materials Interfaces, 8(22), 2101344.

[6] Gahlaut, S. K., Devi, P., & Singh, J. P. (2020). Self-sustainable and recyclable Ag nanorods for developing Ag-Ag2S nano heterostructures using sewage gas: Applications in photocatalytic water purification, hydrogen evolution, SERS and antibacterial activity. Applied Surface Science, 528, 147037.

Digitally transferring optical energy for tailoring coherent light-matter interactions and coupling photons

Amit Kumar, Sarvesh Thakur, Abhishek Paul, Himanshu Jain and S. K. Biswas*

Bio-NanoPhotonics Laboratory, Department of Physical Sciences, Indian Institute of Science Education and Research Mohali, Knowledge City, Sector 81, SAS Nagar, Manauli PO 140306, India.

**skbiswas@iisermohali.ac.in*

Abstract: Digitally transferring optical energy for coherent light-matter interactions in a controlled manner inside or through disordered crystals and meta-materials for precision excitation and event generation is currently an active research area in all optics communities. In order to detect typically weak non-linear effects at small photon numbers, one either needs to optimize the nonlinearity of the medium or tailor the coherence light fields at the target location so that it can enhance the medium's non-linearity. In this work, we digitally transfer coherent photons of light and control the number of photon intensity at a target location inside a disordered crystal as per the need for event generation. The method can be used for precession excitation, event generation and high precision measurements in quantum principle based experiments.

Keywords: coherent light, spatial light modulator, light-matter interaction, Digital optical energy transfer, non-linear effects

1. Introduction

Photons of light do not interact in freespace [1]. Manipulating coherent interaction between optical fields and quantum systems is essential for quantum technologies. Strong interactions between individual photons through nonlinear materials with weak light fields has been the goal of quantum-optics research for several decades. Nonlinear interaction between light field and nonlinear materials on a single atom/molecule and few-photon level is a fundamental and very practical interest [2-4]. In order to detect the typically weak nonlinear effects at low photon numbers, one either needs to optimize the non-linearity of the medium, or tailor the coherence light fields at the target location so that it can enhance the medium's nonlinearity [5]. Several useful concepts have been introduced in the context of coherent Rydberg excitations and interactions [6]. A detailed discussion on the coherent light-matter interactions with solid-state quantum emitters coupled to nanophotonic waveguides has been done [6]. The biggest challenges in coherent light-matter interactions are due to disorder, non-uniform refractive index distribution in the nonlinear media, scattering of light and breakdown of the focusing efficiency, which hinder the coupling of phonons.

In our current work, with waveform shaping methods, we have shown that digitally transferring the optical coherence field to the target location with controlled manner inside a nonlinear disordered crystal or metamaterials or through it can be formulated with precession for manipulating quantum coherent light-matter interactions on a single atom/molecule and few-photon level and the interactions can be enabled by coherently coupling the photons.

2. Materials and methods

The schematic of the experimental setup is shown in Fig. 2. He-Ne 633 nm laser with vertical polarization is used as a coherent light source. The modulated wavefront from the SLM is projected on the disordered non-linear disordered media. The disordered non-linear media is placed at an angle of 45 degrees to the incident light. Two objectives (10x 0.25 NA) are used to collect photons of light which are captured by the camera. The cameras are triggered to synchronize with the spatial light modulator. Genetic algorithm was used to find the optimum phase mask to control photons of light at the desired location.

3. Results

It has been demonstrated that the genetic algorithm can control the photons of the light field at the target location as per the requirement. Fig. 1 shows the change in photons of light at the target location as the algorithm progresses.

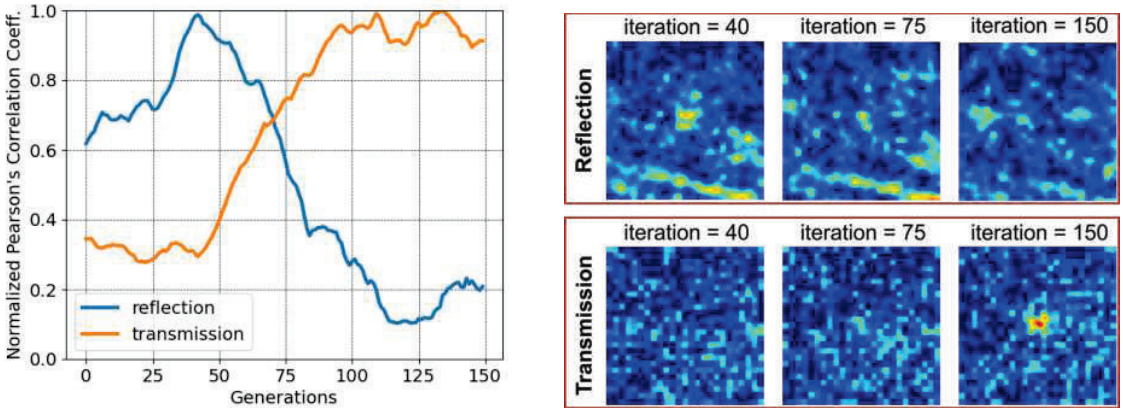

Fig. 1: Digital control of optical field at the targeted location inside a disorder media by wavefront shaping. Graph on the left side shows the fitness function used by GA plotted against the generation number. Figure on the right side shows the output camera images in the reflection and transmission modes.

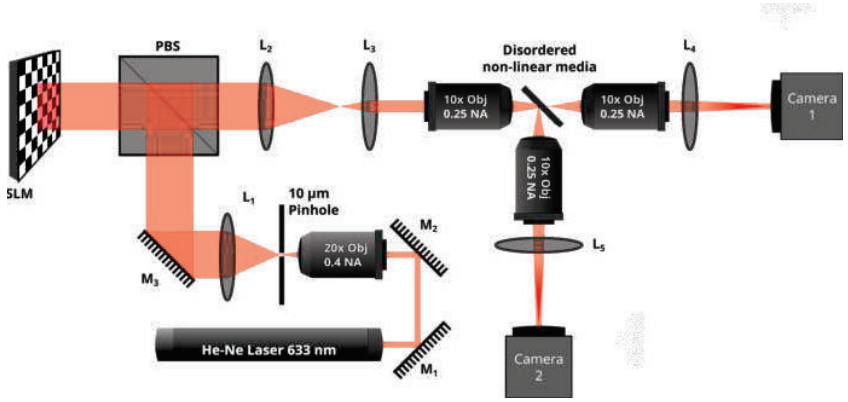

Fig. 2: Schematic setup for digitally controlling the optical field in reflection and transmission. Where M_1, M_2 and M_3 are flat mirrors. L_1, L_2, L_3, L_4 and L_5 are lenses of focal length 250mm, 200mm, 50mm, 50mm and 50mm respectively.

4. References

[1] D. Chang, V. Vuletić & M. Lukin, "Quantum nonlinear optics — photon by photo,". *Nature Photon* **8**, 685–694 (2014).

[2] M. Pototschnig, Y. Chassagneux, J. Hwang, G. Zumofen, A. Renn, and V. Sandoghdar, "Controlling the phase of a light beam with a single molecule" *Phys. Rev. Lett.*, **107** 063001 (2011).

[3] Y. L. A. Rezus, S. G. Walt, R. Lettow, A. Renn, G. Zumofen, S. Götzinger, and V. Sandoghdar, "Single-Photon spectroscopy of a single molecule" *Phys. Rev. Lett.,* **108**, 093601 (2012).

[4] Sanli Faez, Pierre Türschmann, Harald R. Haakh, Stephan Götzinger, and Vahid Sandoghdar, "Coherent interaction of light and single molecules in a dielectric nanoguide" *Phys. Rev. Lett.,* **113,** 213601 (2014).

[5] E. Garmire, *Overview of Nonlinear Optics,* Nonlinear Optics, edited by Natalia Kamanina, (IntechOpen, 2012).

[6] Pierre Türschmann, Hanna Le Jeannic, Signe F. Simonsen, Harald R. Haakh, Stephan Götzinger, Vahid Sandoghdar, Peter Lodahl and Nir Rotenberg "Coherent nonlinear optics of quantum emitters in nanophotonic waveguides" *Nanophotonics*, vol. 8, no. 10, 1641-1657 (2019).

Detection of acetone using chemo-mechanical polymer incorporated fiber Fabry-Perot interferometer

Karvan Kaushal[1,*] and Bhargab Das[2]

[1]*Academy of Scientific and Innovative Research (AcSIR), Ghaziabad, India 201002*

[2] *CSIR - Central Scientific Instruments Organization, Sector 30-C, Chandigarh – 160030, India*

**Corresponding author's e-mail address: karvan@csio.res.in*

Abstract: A fiber Fabry–Perot interferometer (FPI) based on polymethyl methacrylate (PMMA) polymer cavity is proposed and experimentally demonstrated for acetone vapor sensing. The optical properties of PMMA cavity indicate reversible optical path difference change because of absorption and desorption of acetone gas molecules, thereby shifting the phase matching conditions of the resonating modes. The proposed fiber-FPI sensor is sensitive to the changes in the concentration of acetone gas molecules.

Keywords: Optical sensor, Fiber Fabry- Perot interferometer, VOC, Acetone

1. Introduction

Gas sensors have many applications in industrial production, human health monitoring for exhaled VOC, environmental monitoring etc. Fiber optic-based gas sensors have attracted researcher's attentions because of high sensitivity, fast response and good stability [1]. Polymethyl methacrylate (PMMA), also known as acrylic or acrylic glass, being rigid thermoplastic material and also optically transparent can be employed to make a semi-transparent optical cavity [2]. In this paper, we propose an FPI sensing mechanism with PMMA cavity casted on optical fiber. Coating polymer at the end facet of the SMF fiber, go along with the advantages of being very compact size, low cost, simple fabrication and fast response. Sensitivity of the sensor is 19.84 *pm/(µl/l)* in concentration range of 20 – 70 µl, which makes it a good candidate for acetone vapor sensing.

2. Fabry-Perot Cavity Fabrication and Sensing Principle

The end facet of an optical fiber (SMF-28) is cleaned with isopropanol and is dipped inside polymer solution with dip coater. The developed FPI cavity generates partial reflecting interface through which light gets transmitted and reflected back multiple times, Fig.1(a).

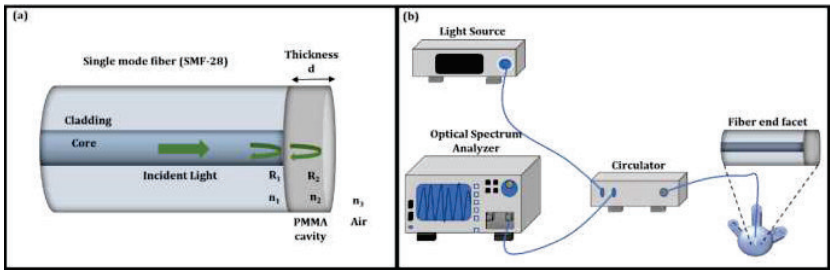

Fig.1: (a) Schematic diagram of the Fabry–Perot cavity, and (b) Experimental setup

Higher modes of reflections are ignored due to low reflectance from mirror interfaces [3]. Two beam interference is thus obtained in FPI cavity and intensity of resultant signal $I(\lambda)$ is given by:

$$I(\lambda) = I_1(\lambda) + I_2(\lambda) + 2\sqrt{I_1(\lambda)I_2(\lambda)}\cos\left(\frac{4\pi d n_2}{\lambda} + \phi\right) \quad (1)$$

Where, $I_1(\lambda)$ and $I_2(\lambda)$ are reflected intensities from R_1 and R_2 interfaces of the cavity, d is length of cavity; Φ is the initial phase of the interference; λ being operating wavelength; n_2 is the refractive index of coated material. The reflection from R_1 and R_2 interfaces is given by Fresnel's reflection coefficients:

$$r_1 = \left(\frac{n_2 - n_1}{n_2 + n_1}\right)^2, r_2 = \left(\frac{n_3 - n_2}{n_3 + n_2}\right)^2 \quad (2)$$

The experimental setup used to detect and analyze the response of the PMMA-based FPI sensor to acetone vapors is shown in Fig.1(b). It consists of a broadband light source, optical circulator and optical spectrum analyzer (OSA), a detector, which collect and analyze the reflected light from the sensor head. The developed FPI sensor was placed inside a glass chamber to create isolate conditions (100 *ml* capacity, Borosil, India).

3. Results and discussions

Initial interference spectrum of the FPI sensor was stored and set as a reference as shown in Fig.2 (a). Acetone, being an analyte was gradually interacted with the sensor from 20μl to 70μl. A shift in reflection spectra in its dip-position towards shorter wavelength is observed and spectrum shift for first dip is shown in Fig.2(b). Argon purging restores the spectrum to its original position. Fig.2(c) shows the wavelength shift as a function of concentration, which behaves linearly with a slope of 19.84 *pm/(µl/l)*. The mean response time of sensor is up to 5 seconds. The response time mentioned here is not solely of acetone interaction but include factors like acetone diffusion time, pressure, temperature and size of glass chamber.

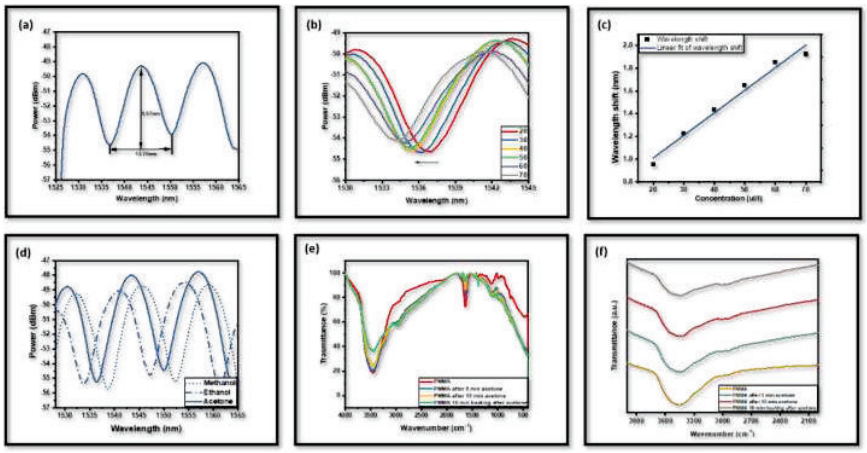

Fig.2: (a) Initial interference spectrum before interaction with acetone, (b) Resonant dip wavelength position on increasing acetone concentration, (c) Linearly fitted curve between concentration and wavelength shift, (d) Cross-sensitivity of developed sensor towards methanol, ethanol and acetone, (e) FTIR spectrum of acetone and (f) is enlarged view of same FT-IR spectrum

In Fig.2(d), Cross sensitivity study of developed sensor with same ketone group molecule was conducted. For 50µl of acetone, methanol and ethanol, the spectrum shows different amount of shift due to variation in the refractive index of interacting analyte. FT - IR study was conducted to find the interaction between the acetone and polymer as shown in Fig.2(e). The enlarged view of dips in FT- IR is shown in Fig.2 (f). Only FT-IR dips of PMMA were observed in both absence and presence of acetone and no new dip in spectrum was observed, indicating no new bond formation between PMMA and acetone molecules. This indicates PMMA and acetone molecules interactions were not correlated with any critical energy barriers to absorption or evaporation. The data reported shows the fabricated sensor operates at room-temperature with excellent sensitivity and short sensing time for detection of acetone vapors.

Acknowledgment

Ms. Karvan Kaushal acknowledges the financial support from Department of Science and Technology (DST, India) INSPIRE Programme. Ms. Karvan Kaushal also like to thank Dr. Rajesh V. Kanawade (CSIR-NCL, Pune) for helpful discussions.

4. References

[1]. C.B. Yu, Y. Wu, L. Chen, W. Fan, Z. Jin-Hao, G. Yuan, R. Yun-Jiang, and C. Yuan-Fu, "Highly sensitive and selective fiber-optic Fabry-Perot volatile organic compounds sensor based on a PMMA film," Optical Materials Express 7(6), 2111-2116 (2017).

[2]. A. Lalova, R. Todorov, A.J. Malinowski, "Optical properties of thin PMMA films for sensor application," Bulg. Chem. Commun. 47, 29-34 (2015)

[3]. Y.W. Huang, J. Tao, and X. J. Huang "Research progress on FP interference—based fiber-optic sensors," Sensors 16(9), 1424 (2016)

Axisymmetric Metallic Grating Based Self-Referenced Fiber Optic Refractive Index (RI) Sensor

Anupam Kushwaha[a], Roli Verma[a*]
[a]*Department of Physics, University of Lucknow, Lucknow 226007, India*
*roliverma10@gmail.com

Abstract: We have theoretically simulated a surface plasmons resonance (SPR) sensor for self-referencing purpose. The proposed sensor is comprised of Ag layer and Cu-MgO grating layer on top of it. Dual SPs mode found in the transmission spectra. One mode shows remarkable shift in resonance wavelength, while other remains unchanged with variation of RI of sensing medium. Characterization of sensor is done in terms of sensitivity and detection accuracy (DA). The maximum sensitivity is found to be 3690 nm/RIU. Detection accuracy of the sensor is inversely proportional to the concentration of the sensing medium.
Keywords: Surface Plasmons Resonance, Self-Reference, Fiber optic, RI.

1. Introduction

Refractive index (RI) sensors are being widely used in disease diagnostics, biological and environmental monitoring, and in chemical detection as well. SPR based RI sensors have gained significant attraction due to its advantages of no label detection, high-throughput capacity, real-time monitoring, and accurate measurement [1,2]. SPR is nothing but collective oscillation of electrons in metal at the interface of metal and dielectric. Incident photons excites these surface plasmons (SPs). SPs are very sensitive to any variation that occurs in the RI of materials of metal and dielectrics. But SPs cannot be excited by direct incident photons due to their high wave vector. Therefore, prism, optical fibers, waveguide and grating are used to match the wave vectors of SPs and incident light [3].

In recent years, self-referenced SPR sensors are being used because these sensors provide reliability in ambient conditions where parameters like temperature, pressure, humidity, and impurity have effect on the sensing capability of the sensors. Here we design self-referenced SPR sensor by using metal-metal oxide gratings layer over plasmonic metal (Ag).

2. Design and Methodology

In present study, a fiber optic based Self-reference SPR sensor has been presented. Probe design is shown in Fig. 1. To obtain self-referencing, probe is designed using an axisymmetric metal-metal oxide grating of uniform thickness placed alternatively above a metal layer preceded by bare fiber core. Axisymmetric grating design is proposed by Youqiao Ma and his group in 2014 [4]. In recent years researchers have proposed single mode fiber using the same design [4,5]. In this study, dual mode is obtained, one mode work as sensing mode and another mode work as self-reference mode. Sensing medium refractive index is varied and the transmittance curve is obtained. DA has also been calculated.

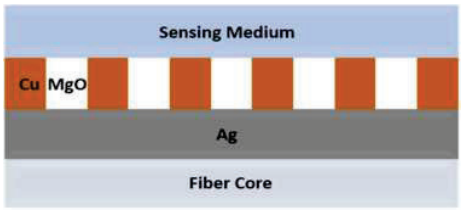

Fig. 1: Probe design

For the design of the probe, step-index multimode plastic clad silica fiber of 600 µm diameter has been used. Sensing region is formed by uncladding 1 cm region from the middle of the fiber. Over which Ag layer of thickness 15 nm was coated. On top of metal layer grating layer consisting of Cu and MgO having uniform thickness of 36 nm was formed. Period of the grating is 6 nm. Water of RI varied from 1.33 to 1.37 is used as sensing medium. For N-layer transfer matrix method (TMM) is used. Assuming that collimated incident light is used, the power distribution of the collimated light into the fiber is given as-

$$p(\theta) \alpha \frac{{n_0}^2 \sin\theta\cos\theta}{(1-{n_0}^2\cos^2\theta)^2}$$

Here, RI of the core is denoted by n_0 and θ is the angle of the incident light perpendicular to interface between core-metal [6].

3. Results and Discussions

Self-Referenced characteristics of the proposed sensor is shown in Fig. 2, where in left side plot it is clearly seen that two modes are present. One mode is present at the lower wavelength and doesn't show any variation while varying RI of sensing medium. This mode works self-referenced mode. Mode present at higher wavelength side shows shift is resonance wavelength when RI of sensing medium is varied and is termed as surface plasmons (SP) mode. To achieve high self-referencing, ratio of the grating element is optimized to 2nm and 4nm.

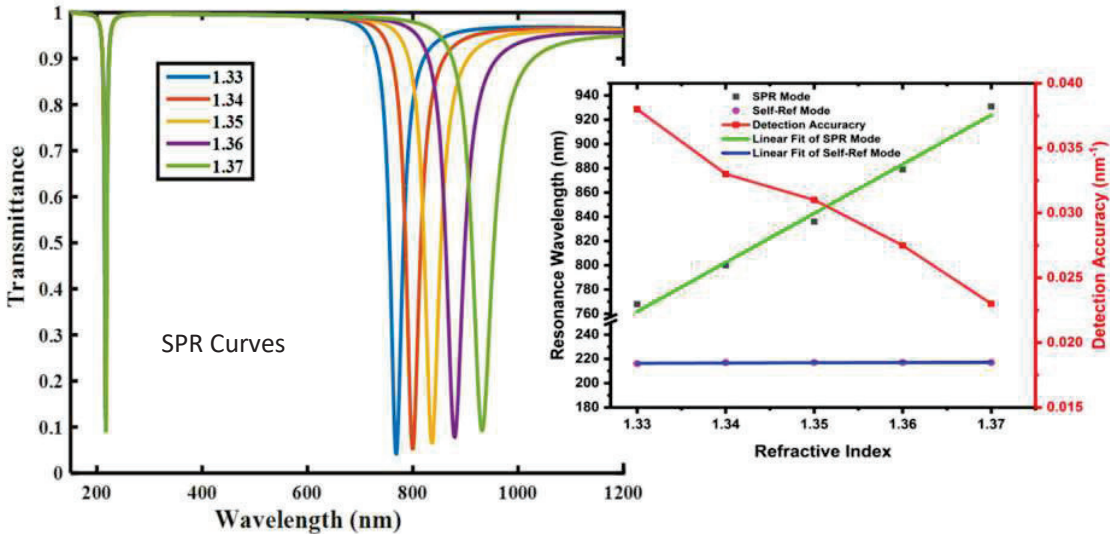

Fig. 2: SPR curves and Characteristics plot of SPR curves

Characteristic plots are shown in right side of Fig. 2. When the RI of sensing medium is varied from 1.33 to 1.37, self-referenced mode shows negligible shift of 1 nm from 216 nm to 217 nm while SP mode shows significant shift from 768 nm to 931nm. Sensitivity of the proposed sensor is calculated from the slope of the linearly fitted resonance wavelength curve plot and comes out to be 3690 nm/RIU. Detection accuracy of the sensor decreases when the concentration of the sensing medium is increased as shown (in red) at right Y axis of the plot.

In a nutshell, we have achieved self-referencing capacity using axisymmetric metal-metal oxide grating over plasmonic metal layer. It shows promising sensitivity as well as accuracy.

Dr. Roli Verma is thankful to UGC, India for the UGC-BSR Start-Up Grant.

4. References

[1] Peng Sun, "Self-referenced refractive index sensor based on hybrid mode resonances in 2D metal-dielectric grating", J. of Physics D Applied Physics **53(14),** 145101 (2020).
[2] Xiaobin Ren, "Self-reference refractive index sensor based on independently controlled double resonances in side-coupled u-shaped resonators," Sensors **18(5)**, 1376 (2018).
[3] Cem Odacı, "The surface plasmon resonance-based fiber optic sensors: A theoretical comparative study with 2D TMDC materials," RIO **3**, 100063 (2021).
[4] Youqiao Ma, "Sensitivity enhancement for a multimode fiber sensor with an axisymmetric metal grating layer." Photonics Nanostructures: Fundam. Appl **12(1),** 69-74 (2014).
[5] Satyendra K. Mishra, "Metallic grating-assisted fiber optic SPR sensor with extreme sensitivity in IR region." Plasmonics **17(2)**, 575-579 (2022).
[6] Anuj K Sharma, "Fibre optic sensor based on long-range surface plasmon resonance: a theoretical analysis." J. of Optics A: Pure and Applied Optics **9(7)**, 682 (2007).

Optical Beam Deflection based cantilever displacement sensor for Atomic Force Microscopy

Vikash Chandra[1, 2], Pankaj[1*], Ekansh Garg[1], Bhargab Das[1], Goutam Sheet[3]

[1]*CSIR-Central Scientific Instruments Organisation, Sector 30C, Chandigarh, 160030, India*

[2]*Academy of Scientific and Innovative Research (AcSIR), Ghaziabad 201002, India*

[3]*Department of Physical Sciences, Indian Institute of Science Education and Research, Knowledge city, Sector 81, SAS Nagar, Manauli PO 140306, Mohali, Punjab, India*

**Author e-mail address:pankajpec22@gmail.com*

Abstract: Optical beam deflection (OBD) based cantilever deflection system is widely used in Atomic Force Microscopy (AFM). The noise level of the deflection sensor limits the overall force sensitivity of the sensor. We have developed a low-noise OBD system with easy alignment mechanism of the optical systems. We have also designed a low noise detector electronics which is one of the major sources of noise in the system. The performance of the OBD system has been demonstrated with the help of an in-house developed AFM and a scan of standard grating sample was analyzed.

Keywords: Optical Beam Deflection, Atomic force microscope, Scanning Probe Microscope,

1. Introduction

The optical beam deflection technique introduced by "Meyer and Amer" has become one of the most preferred technique due to its simple design, low cost and high sensitivity [1-2]. Today, most of the commercial AFMs use OBD based detection scheme. The AFM has emerged as a versatile tool in nanotechnology to measure mechanical and electrical properties [3]. The measurement methodology in AFM is based on the optical beam deflection system, wherein a collimated laser beam is reflected from the sensing probe to the position sensitive detector (PSD). The researchers have used various optical systems in AFM to enhance the efficacy, scanning range and resolution of the system [4].

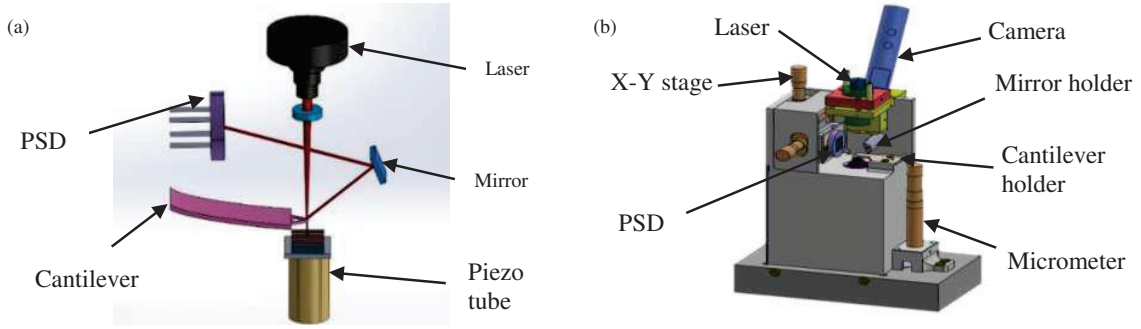

Fig. 1. (a) Basic schematic of optical beam deflection (OBD) based sensing scheme (b) OBD system incorporated in AFM head

The present research work was focused on detecting the motion of the AFM cantilever through efficient design of the optical deflection system. The schematic diagram of the optical deflection sensor and CAD model of AFM is shown in Fig 1. The collimated beam of laser light was focused with a lens to make a fine spot on the backside of the cantilever. The laser spot was optimized with various focusing lenses and the final was selected on the basis of design requirements. The laser spot was measured with an optical beam profiler from Thorlabs. The focused laser beam falls on the backside of the cantilever. The reflected laser beam was allowed to fall orthogonally on the PSD by using a front reflecting mirror. The cantilever interacts with the sample surface and a respective change in cantilever deflection is detected on the PSD in terms of voltage variation. This voltage signal is further used as a data acquisition to plot the 3D images of the sample surface.

2. Opto -Mechanical Design

The optical beam deflection (OBD) based sensing scheme as depicted in the Figure 1 integrates a collimated laser diode source coupled to an aspheric focusing lens, a four-quadrant photodiode with its electronics, a laser beam guiding mirror and a digital microscope. The laser diode source (5mW, 635nm Coherent) is focused on the backside of the free end of the cantilever using an aspheric focusing lens (Melles Griot, 12.5 mm dia, 48 mm focal length). The long working distance of the focusing lens provided enough room for integrating a digital camera, a focusing tube and a mirror. The digital camera (Basler 82440) assisted in real-time fine focusing of the laser beam on the cantilever with the help of a focusing tube to achieve smallest laser spot size. An 8X video zoom lens (Edmund, 35X Microscope) with an optical filter placed before the camera sensor provided a clear, magnified image of the cantilever. The reflected laser from the cantilever is made to fall on the quadrant photodiode almost orthogonally using a mirror. A four-quadrant Si p-i-n photodiode (S6695–01: Hamamatsu) was used as the PSD. The photo-induced current at each element of the PSPD is converted to a voltage signal by the current-to-voltage converter and the difference in voltage signals between the upper and lower segments of a four-quadrant photodiode provides a measurement of the cantilever deflection.

3. Results and Discussions

We have evaluated the performance of the developed OBD system by integrating it with our in-house developed AFM. The AFM system was used to scan a standard grating sample (Mikromasch, TGZ 01) having a step height 606 nm and pitch of 3 µm as shown in Fig 2 (a). The scan results were obtained in contact mode imaging with the help of a cantilever (Mikromasch, CS11/Si3N4) as shown in Fig 2. The laser and focusing lens were calibrated and optimized with the help of beam profiler and a laser spot size was observed as18 µm.

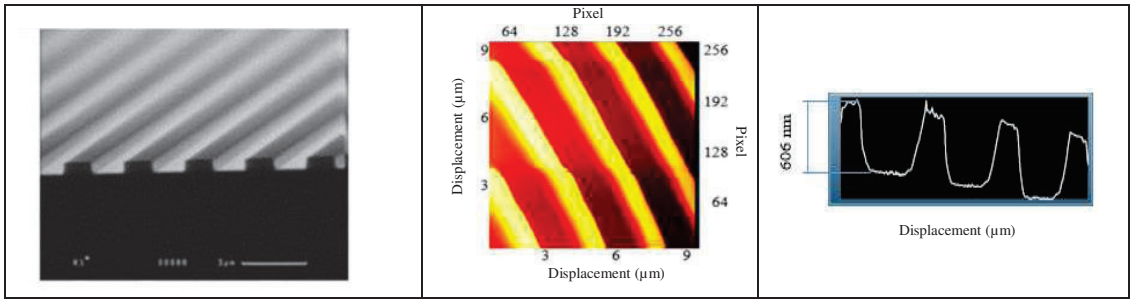

Fig. 2. Images of the standard grating sample (a) Provided by the manufacturer (b) Two-dimensional topography scanned through developed OBD sensor using AFM (c) Line scan showing the step height

4. Conclusions

We have presented a comprehensive description of the design and development of an OBD based cantilever displacement sensor scan head which can be used in AFM. We believe that the developed OBD system can easily incorporate different types of cantilevers. The mechanical design of the system has been kept simple and robust for easy fabrication and simple alignment of optics during operation. The experimental results have demonstrated that the developed OBD sensor when incorporated into the AFM set-up has been able to clearly image a standard grating of step height 606 nm and pitch of 3 µm.

5. References

1. G, Meyer and N.M, Amer, "Optical-beam-deflection atomic force microscopy: The NaCl (001) surface," Applied Physics Letters **56**, 2100-2101 (1990).
2. J, Zhang, "An investigation of the adsorption of xanthate on bornite in aqueous solutions using an atomic force microscope" Minerals, 906 (2021).
3. Y, Zhu., Z. Tan and W. Hong, "Simultaneous Electrical and Mechanical Characterization of Single-Molecule Junctions Using AFM-BJ Technique" ACS omega 6, 30873-30888 (2021).
4. T. Fukuma, 2009, "Wideband low-noise optical beam deflection sensor with photothermal excitation for liquid-environment atomic force microscopy" Review of Scientific Instruments, **80**, 023707 (2009).

In vivo monitoring of microbial protein turnover dynamics using Raman Spectroscopy and Carbon-13 isotope probe

Jiro Karlo[1], Ashish Kumar Dhillon[2], Soumik Siddhanta[2] and S.P. Singh[1]*

[1]Department of Biosciences and Bioengineering, Indian Institute of Technology Dharwad, Karnataka, 580011, India.

[2] Department of Chemistry, Indian Institute of Technology, Delhi, Hauz Khas, New Delhi, 110016, India.

Author e-mail address: ssingh@iitdh.ac.in

Abstract:

The life of proteins is very short and dynamic. A precise understanding of protein dynamics and turnover is essential for developing diagnostic or therapeutic tools to monitor these changes. We are reporting the utility of Raman isotope probing (RIsP) for monitoring proteome dynamics at the community level. We have used ^{13}C- labelled glucose and verified its incorporation in the microbial biomass in a time-dependent manner. Observed redshift and temporal changes in band intensity demonstrate the feasibility of protein turnover monitoring *in-vivo*. Findings suggest RIsP can be an adjunct tool for monitoring proteome level changes.

Keywords: Raman Spectroscopy, Carbon-13, Stable isotope, microbial proteomics, protein turnover

1. Introduction

The microbial proteome is involved in various biological processes such as host-pathogen interaction, antimicrobial resistance, and production of microbial-derived products. The challenge of dealing with the complex and dynamic nature of the proteome requires diverse analytical techniques. Mass Spectrometry (MS), Nuclear Magnetic Resonance (NMR) spectroscopy are known to be sensitive techniques widely used for proteomics and other 'omics' study[1,2]. Furthermore, understanding the protein turnover dynamics and metabolism can help us to tweak the production of various important metabolic cycles involved in the synthesis of other important microbial products. Most of these techniques involve static measurements which are a change in result of dynamic flux, so they lack any clinical translation[3]. The proteome of an organism is never constant. Different proteins are involved in diverse biochemical processes such as catalysis, transport, homeostasis, etc. The conventional technique such as MS is inherently destructive in nature. Therefore, it is not feasible for monitoring dynamic changes in protein metabolism in its native environment. The spectroscopic techniques are based on light-matter interaction and provide information about the biomolecule composition and behavior[4,5]. The working principle behind Raman spectroscopy is the inelastic light scattering of monochromatic laser radiation by molecules. Raman spectroscopy has various advantages such as: (i) label-free and non-destructive analysis of multiple molecular vibrations of different biomolecules simultaneously giving rise to a molecular fingerprint; (ii) is capable of imaging multiple molecular species simultaneously at the sub-micron resolution. The application of Raman imaging as an emerging tool for diagnosis, phenotyping, and antibiotic sensitivity has been studied and reported [2]. Our comprehensive goal is to develop a non-invasive and non-destructive approach for monitoring microbial proteome dynamics.

2. Methodology

Escherichia coli (MCC 3109) was grown in M9 minimal broth media in two cultures with glucose as the only carbon source. The first culture media contained unlabelled glucose whereas the second culture medium contained uniformly ^{13}C - labelled glucose. OD_{600} was recorded at different time points, post-inoculation. Raman spectra were recorded on nearly air-dried cells collected at 8, 12, 18, and 24 hours from both cultures. Inhibition assay was done by treating Kanamycin, at 8 hours of incubation time. All spectral data were Pre-processed using MATLAB R2021b software. The spectral intensity bar plot was generated using GraphPad and Unpaired Student's t-test was performed to assess the significance of difference.

3. Results

The feasibility of M9 minimal media with ^{13}C labeled/unlabelled glucose as the only carbon source for the viability of *E. coli* cells was evaluated and established by the OD_{600} growth curve plot as shown in Fig. 1(I). *In vivo* tracking of ^{13}C incorporation in the microbial proteome was successfully observed by studying the Redshift of different biomolecular band positions (cm^{-1}) on Raman spectra such as nucleic acids (782→769), phenylalanine (1004→966, 1033→985), tyrosine (641→620, 828→802), amide-I ((1661→1624), amide-III (1250→1234) [6–12]. No shift was observed at the di-sulfide band position (550 cm^{-1}) which is acting as our internal control as shown in Fig 2(II). Further ^{13}C incorporation and protein turnover were temporally monitored by studying four spectral bands specific to proteins monitored. Band intensity of ^{13}C-labelled biomolecules increases and unlabelled decreases with time as shown in Fig. 1(III). Furthermore, to monitor the *de-novo* protein synthesis we performed an inhibition assay using Kanamycin, a protein synthesis inhibitor at 8 hours of incubation as at this time cells are metabolically active. Mean growth curve cells can be seen in Fig1(IV). We observed a decrease in spectral intensity of standard protein bands such as phenylalanine (966,985 cm^{-1}), amide-I (1624 cm^{-1}), and amide-III (1234 cm^{-1}) at 8, 12, 18, and 24 hours as shown in Fig 1(V). Unpaired student 't-test' coupled with Welch's correction was performed to verify the statistical significance of spectral intensity difference of protein standard Raman bands of control vs treated group. Overall findings suggest that, RIsP can help in quasi-quantitatively monitoring of *in-vivo* protein turnover and dynamics.

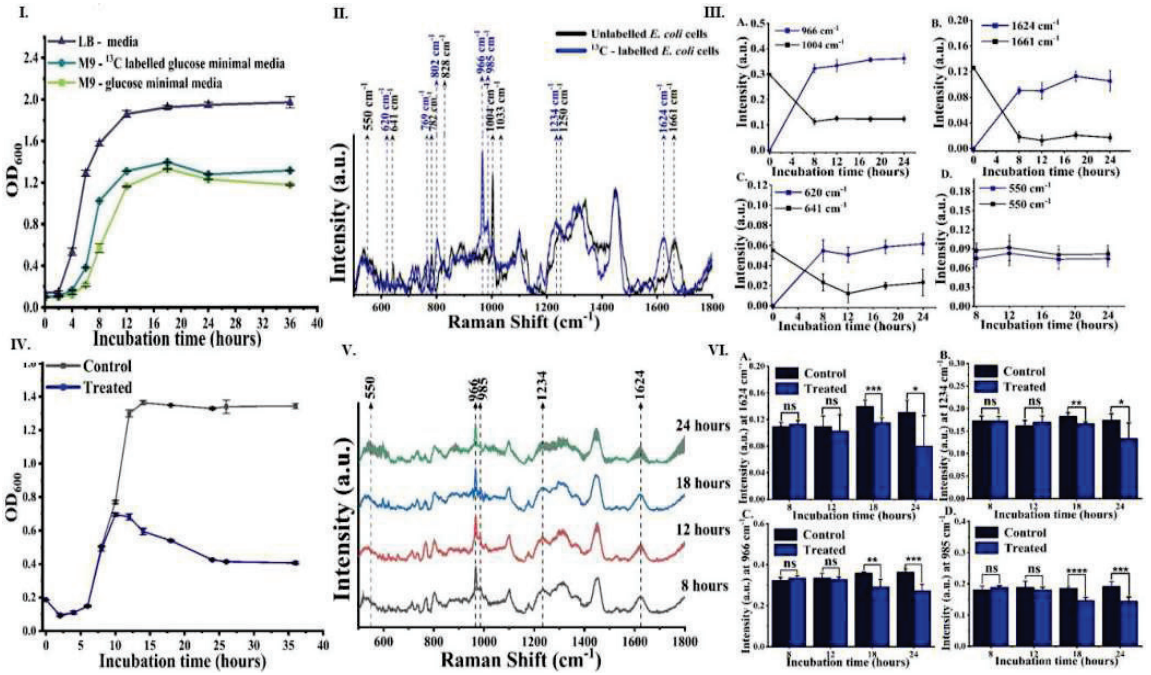

Fig. 1: 1(I) Growth curve of E. coli cells in different culture media; 1(II) Shift in Raman spectra of ^{13}C labelled and unlabelled E.coli cells at 18 hour; 1(III) Intensity plot to check ^{13}C incorporation dynamics; 1(IV) Growth curve of Control cells and Kanamycin treated cells; 1(V); Raman spectra of treated cells at different time points; 1(VI) Bar plots of different protein band intensity at different time points of control vs treated groups.

4. References

1. R. Hatzenpichler, V. Krukenberg, R. L. Spietz, and Z. J. Jay, Nat Rev Microbiol **18**, 241 (2020).
2. C. Lima, H. Muhamadali, and R. Goodacre, Annual Review of Analytical Chemistry **14**, 323 (2021).
3. N. C. VerBerkmoes, V. J. Denef, R. L. Hettich, and J. F. Banfield, Nature Reviews Microbiology **7**, 196 (2009).
4. D. Buhrke and P. Hildebrandt, Chemical Reviews **120**, 3577 (2020).
5. C. Fang and L. Tang, Annual Review of Physical Chemistry **71**, 239 (2020).
6. H. Muhamadali, M. Chisanga, A. Subaihi, and R. Goodacre, Analytical Chemistry **87**, 4578 (2015).
7. M. Li, W. E. Huang, C. M. Gibson, P. W. Fowler, and A. Jousset, Analytical Chemistry **85**, 1642 (2013).
8. Y. Wang, Y. Song, Y. Tao, H. Muhamadali, R. Goodacre, N.-Y. Zhou, G. M. Preston, J. Xu, and W. E. Huang, Analytical Chemistry **88**, 9443 (2016).
9. C. Fan, Z. Hu, A. Mustapha, and M. Lin, Applied Microbiology and Biotechnology **92**, 1053 (2011).
10. S. Sil, R. Mukherjee, N. S. Kumar, A. S., J. Kingston, and U. K. Singh, Defence Life Science Journal **2**, 435 (2017).
11. H. Muhamadali, M. Chisanga, A. Subaihi, and R. Goodacre, Analytical Chemistry **87**, 4578 (2015).
12. Y. Wang, W. E. Huang, L. Cui, and M. Wagner, Current Opinion in Biotechnology **41**, 34 (2016).

Excited State Dynamics and Multiphoton Absorption of Triphenyl Imidazole Thiophene Substituted Zinc Phthalocyanine

Md Soif Ahmed,[a] K.S Srivishnu,[b] Dipanjan Banerjee,[c] Lingamallu Giribabu,[b] Venugopal Rao Soma,[c] Sai Santosh Kumar Raavi[a]*

[a]*Ultrafast Photo-physics and Photonics Laboratory, Department of Physics, Indian Institute of Technology Hyderabad, Kandi 502285, Telangana, India*

[b]*Polymers & Functional Materials Division, CSIR-Indian Institute of Chemical Technology, Tarnaka, Hyderabad-500007, India*

[c]*Advanced Centre of Research in High Energy Materials (ACRHEM), University of Hyderabad, Hyderabad 500046, Telangana, India*

Corresponding author e-mail address: sskraavi@phy.iith.ac.in

Abstract: The ultrafast excited state dynamics of metal (Zn(II)) phthalocyanine has been studied using femtosecond transient absorption measurements upon 400 nm excitation. We have also measured the nonlinear optical responses and obtained the second hyperpolarizability value of ~10^{-31} esu.
Keywords: Ultrafast phenomena, transient absorption spectroscopy, Z-scan.

1. Introduction

Tremendous success of perovskite solar cells (PSCs) as the emerging next generation photovoltaic systems have provided impetus into search for new hole transporting materials (HTMs) to overcome the disadvantage of most commonly used hole transporting material (HTM), Spiro-OMeTAD [1]. In this regard, recent efforts are focused to design other possible HTMs highlighted the application of metal organic complexes based on phthalocyanines as HTM with planar structure owing to their excellent hole motility and thermal stability [1]. Understanding the excited state properties of the molecules provide useful information on the charge transport characteristics. In the present work, we focus our attention towards understanding the photophysical properties of a newly synthesized HTM, namely, triphenyl imidazole thiophene substituted metal (Zn(II)) phthalocyanine (ZnPc) implying femtosecond pump-probe spectroscopy [2] . Additionally, to explore the nonlinear optical (NLO) properties of this molecule we have carried out the open aperture (OA) and the close aperture (CA) femtosecond Z-scan study.

2. Experiment Section

The chemical structures of newly synthesized ZnPc molecule is shown in Figure 1 (a). The fs transient absorption spectroscopy (fs-TAS) and Z-scan measurements of ZnPc solution were carried using DCM solvent. The discussion and experimental set-up used for these experiments were discussed elsewhere [2-4].

3. Results and Discussion

Figure 1(c) depict spectral evolution at probe delay times ranging from 290 fs to 4.9 ns. The spectral feature consists of a positive difference absorption (ΔA) due to excited-state absorption (ESA) or photo-induced absorption (PIA) from 430 to 625 nm with a peak maximum around 535 nm and a negative ΔA due to ground state photo-bleach (PB) from the wavelength range 625 to 745 nm. Further examination of the TAS data reveals that the intensity of both ESA and GSB bands are decreasing with increasing the delay time. We have noticed the Q-band (near to 700 nm) for this molecule in UV-vis absorption study (Figure 1(b)). The PB band correspond to the Q-band. There is a possibility of overlapping between Q-band PB and stimulated emission (SE) bands. Dipole coupling of lowest excited levels with vibronically excited ground states is correlated with SE bands. Figure 1(d) show the kinetic profile for the GSB band and ESA band. We have noticed that the spectral features were very long lived and showed very minimal decay within 4.9 ns delay time for this metal phthalocyanine. This is an indication of long-lived triplet state formation in ZnPc. The

kinetics were fitted with biexponential decay components. The time constants by fitting the PB kinetic were 27 ps and 2300 ps. From the OA Z-scan study (Figure 1(e)) we observed that the total transmittance decreased as the intensity of the incoming beam increased which was a reverse saturable absorption process and the experimental data were best fitted using the three-photon absorption (3PA) equation [4]. The obtained 3PA coefficient is $3.7 \times 10^{-5}\ cm^3/GW^2$. The positive nonlinear refractive index (n_2) value ($2 \times 10^{-16}\ cm^2/W$) was confirmed by the obtained valley-peak structure from the CA Z-scan. Finally, we calculated the second hyperpolarizability (γ) values of ~ 10^{-31} esu.

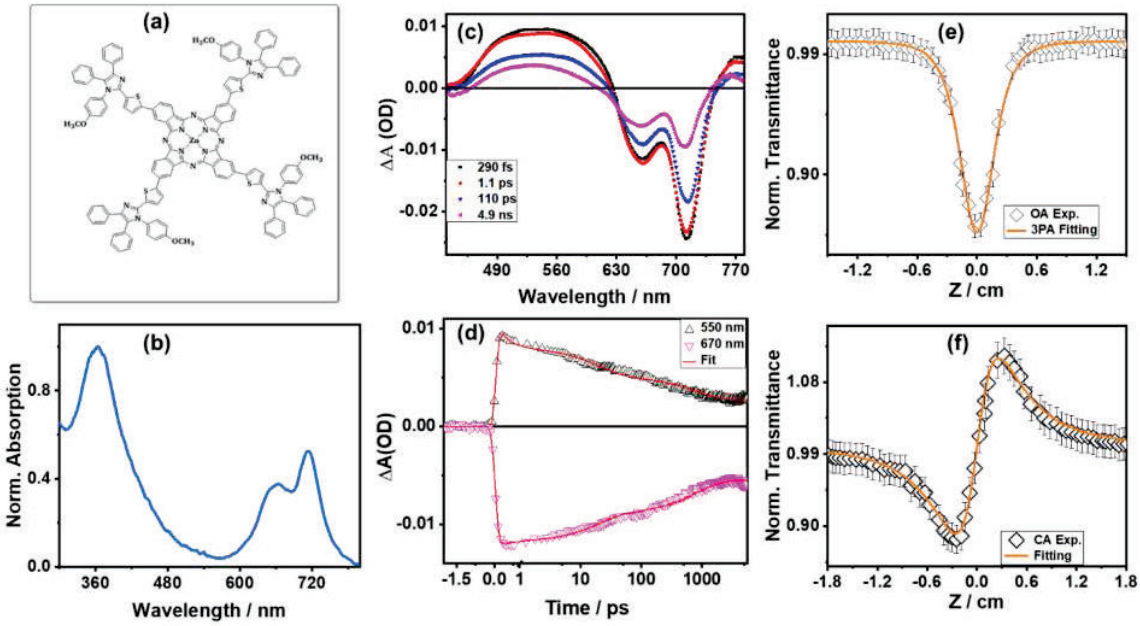

Figure 1: (a) Molecular structure of ZnPc; (b) UV-Visible absorption spectra of ZnPc; (c) and (d)- respectively are TAS spectra and kinetic profiles of ZnPc; (e) and (f)- respective are open aperture (OA) and close aperture (CA) Z-scan curves of ZnPc. Open scattered symbols are experimental data and solid lines are fitted data.

4. Conclusions

The ultrafast excited state dynamics of a metal phthalocyanine (ZnPc) have been investigated employing fs-TAS in visible spectral domain. From the kinetics of GSB band, we observed that there was an indication of long-lived triplet state formation. The long-lived component (2300 ps) of ZnPc molecule suggests a sluggish ground state recovery which is advantageous for reducing charge recombination. Additionally, the calculated second hyperpolarizability value was significantly higher than many of the similar kind of molecules.

5. Acknowledgements

For the financial support MSA acknowledge MoE, IIT Hyderabad **and** SSK**R** acknowledges the following project numbers BRICS/PilotCall2/IEEE-OSC/2018 (G) and CRG.

6. References

[1] Nouri E, Krishna JVS, Kumar CV, Dracopoulos V, Giribabu L, Mohammadi MR, et al. Soluble tetratriphenylamine Zn phthalocyanine as hole transporting material for perovskite solar cells. Electrochimica Acta 2016;222:875-80.
[2] Ahmed MS, Biswas C, Miranda PB, Raavi SSK. Nonlinear optical techniques for characterization of organic electronic and photonic devices. The European Physical Journal Special Topics 2021:1-17.
[3] Biswas C, Rao Soma V, Chetti P, Santosh Kumar Raavi S. Ultrafast Excited State Relaxation Dynamics of New Fuchsine-a Triphenylmethane Derivative Dye. ChemPhysChem 2021;22:2562-72.
[4] Ahmed MS, Biswas C, Banerjee D, Chetti P, Yang J-S, Soma VR, et al. Femtosecond Third-Order Non-Linear Optical Properties of Unconstrained Green Fluorescence Protein Chromophores. Frontiers in Physics 2022:549.

Detection of High Concentration of Metribuzin by using Graphene Oxide-Capped Gold Nanocomposite

[1]Pratiksha Maurya, *[1]Roli Verma
[1]Department of Physics, University of Lucknow, Lucknow, 226007, India
**roliverma10@gmail.com*

Abstract: We report an experimental Surface Plasmon Resonance (SPR) based biosensor for the detection of metribuzin (MB). We used Graphene Oxide (GO)-capped gold nanocomposite for the detection of MB. For MB sensing, we have used the probe SF-11 glass/Ag (47 nm)/nanocomposite. The proposed SPR-based MB sensor has the highest processing concentration range of (200 µg/ml - 300 µg/ml). The shift in resonance wavelength from lower to higher concentration is found to be 44 nm. The sensitivity and resonance wavelength increase with MB concentration. Therefore, the present sensor is useful for the high concentration detection of MB.
Keywords: SPR, GO-capped gold nanocomposite, MB

1. Introduction

At present time, the major target for scientists and researchers is to provide a healthy and disease-free environment. However, the critical use of metribuzin causes cancer, liver damage, and many more diseases. Therefore, researchers need to design a sensitive, selective, and high-performance sensor. Various studies have been done on the detection of MB by using different methods like voltammetric sensors, spectrophotometric methods, and optical sensors, etc [1,2]. MB could be present in soybeans, tomato, potato, pea, carrot, sugarcane, asparagus, and pineapple, etc. Here, we are presenting an SPR-based biosensor for the detection of high-concentration MB. For this study, we have prepared a GO-capped gold nanocomposite by the chemical synthesis which detects the MB molecules. Graphene is a 2D material and has various applications for the design of optical and electrical sensors for hazardous gasses, and pesticide detection, etc. due to it's higher conductivity, thermal stability, large surface-to-volume ratio. Moreover, heavy metal ions like copper, gold, and silver have coordinated with metribuzin [3]. Therefore, in this proposed sensor we used the interaction capabilities of GO and heavy metal ions with MB and synthesized GO-capped gold nanocomposite for MB detection. Further, SPR based technique is used for sensing [4].

2. Methodology

For the synthesis of the nanocomposite, we have purchased all chemicals from a local vendor. The GO was dispersed in DI water by sonicating. Then 0.02M of $HAuCl_4.3H_2O$ were added into ethylene glycol with the help of a magnetic stirrer. This prepared solution was mixed with GO and put in an oil bath for 6 hours at a high temperature with continuous stirring. The prepared nanocomposite was separated from ethylene glycol by centrifugation. The Composite was washed several times with DI water and dried [5]. Further, the treated SF-11 glass slide was coated with a plasmonic Ag metal layer by using the thermal evaporation coating

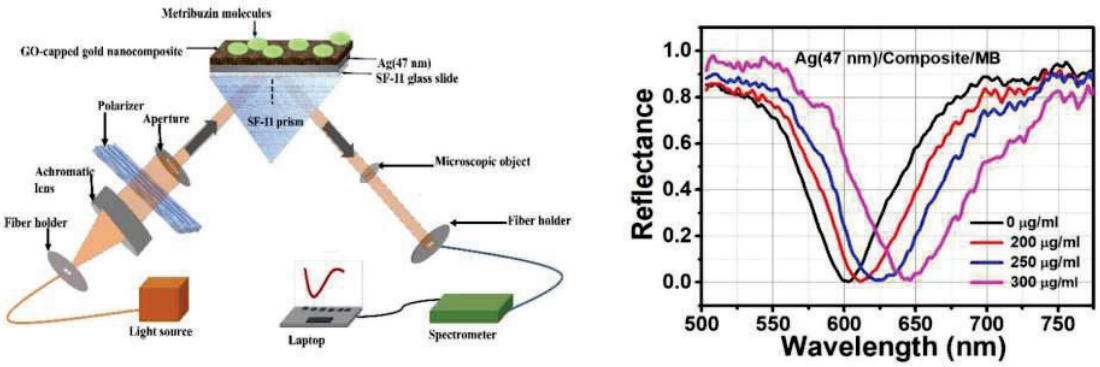

Figure 1(a). Schematic of SPR-based experimental setup for MB Sensor (b) SPR curves for variation of concentration of MB

technique. The silver-coated SF-11 glass slide was washed and dipped in prepared GO-capped nanocomposite. The GO-capped nanocomposite over layer was formed as a sensing surface over the silver-coated glass. The geometry of the proposed probe is shown in fig.1(a). The different samples of MB concentrations of 200 µg/ml, 250 µg/ml, and 300 µg/ml in DI water were prepared for study.

3. Results and Discussions

The SPR curves of different concentrations of MB have been recorded by the experimental set-up and shown in fig.1(b). The SPR curves shift towards the higher wavelength as we increase the concentration of MB. These SPR curves were recorded one by one after washing the sensing region for every concentration. The SPR curve dip position shows the resonance wavelength for corresponding MB concentrations so that the resonance wavelength for all concentrations was calculated and is shown in fig. 2(a). The total shift in resonance wavelength from lower to higher concentration was calculated and found to be 44 nm. Further, the sensitivity of the proposed sensor for the MB concentrations were calculated for 200 µg/ml, 250 µg/ml, 300 µg/ml are 0.05 nm/µg/ml, 0.3 nm/µg/ml, 0.38 nm/µg/ml respectively. These sensitivities are plotted in fig. 2 (b) in the inset which shows that the sensitivity increases with the increasing concentration of MB. The reason for the enhancement of sensitivity is the change in the dielectric properties of the sensing region.

Although, different concentrations of MB do not show much variation in refractive indices (RI). Thus, it can be said that GO-capped gold nanocomposite interacts with MB molecules and changes the dielectric properties in the vicinity of the sensing region so that SPR curves are different for different MB concentrations. Because SPR curves are highly dependent on the dielectric properties of each metal and the dielectric layer. There may be the formation of weak bonds occur between GO-capped gold nanocomposite and MB molecules. Hence, the proposed sensor is capable to detect MB.

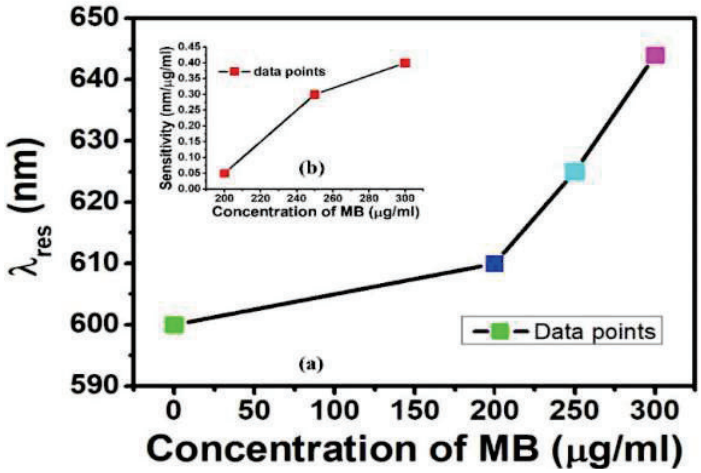

Figure 2(a).Characteristics graph of resonance wavelength vs concentraion of MB, (b) Sensitivity plot of MB concentraion

Moreover, resonance wavelength and sensitivity are higher for higher concentrations of MB and both are showing the almost same behaviour. Hence it can be concluded that the proposed SPR-based biosensor is capable to detect the higher concentration of MB ranging from (200 µg/ml - 300 µg/ml) rather than a lower permissible range of MB.

Dr. Roli Verma is thankful to UGC for providing the BSR-Start-up grant.

4. References

[1] Li, Huimin, Yapan Shi, and Yudong Gao. "A simple but highly sensitive electropolymerization of L-citrulline and β-cyclodextrin based voltammetric sensor for metribuzin." International J. Environmental Analytical Chem **102.8**,1784-1792 (2022).

[2] J. Shah, M. R. Jan, B. Ara, & M. Mohammad, "Extractive spectrophotometric method for determination of metribuzin herbicide and application of factorial design in optimization of various factors" J. Of hazardous materials, **164**, 918-922 (2009).

[3] S.M.Saleh, F.M. Alminderej, R.Lli, Abdallah, "Optical sensor film for metribuzin pesticide detection." Spectrochimica Acta Part A: Molecular and Biomolecular Spectroscopy **229**,117971 (2020).

[4] P.maurya, S.maurya, and R. Verma,"Sensitivity enhancement of SPR based refractive index sensor in VIS-NIR region by using ZnS and PVP", RIO **8**, 100246 (2022).

[5] C.Xu, X.Wang., &, J. Zhu. (2008) "Graphene− metal particle nanocomposites". J. Phys. Chem *C*, **112**, 19841-19845 (2008).

Development of Polarization Shift Keying Signal with multi-passing technique of light in Lithium Niobate Based Pockels Cell

Minakshi Mandal* and Sourangshu Mukhopadhyay
Department of Physics, The University of Burdwan, Golapbag, Burdwan, West Bengal, India, 713104
**email: minakshi.bcc@gmail.com*

Abstract: Electro-optic materials play important role in optical modulation for its wide non-linear property in the domain of optical communication techniques. In this paper, the authors propose a scheme, where digital optical communication is performed with polarization shift keying using the multi-passing technique in lithium niobate ($LiNbO_3$) based Pockels cell. By using the multi-passing of light the operation is performed at very low voltage which is easily attainable.
Keywords: Polarization Shift Keying, Optical Phase Modulation, Lithium Niobate Crystal.

1. Introduction

Optical communication technique proves its advantages due to its data security, high speed data transmission rate, large storage capacity, low power consumption etc. Amplitude, phase, frequency, polarization modulations of the carrier signal are implemented by using the non-linear property of the electro-optic Pockels and Kerr materials. An analytical investigation is done how phase difference between two orthogonally polarized signals can be increased by using the $LiNbO_3$ crystal [1]. This phase modulation plays an important role in optical modulation process [2]. All optical quantum SRCZ gate, phase shift gate, programmable one qubit gate are implemented using the phase and intensity encoding of the carrier light signal by M. Mandal et al [3-5]. In this paper the authors proposed a scheme where the polarization shift keying with multi-passing technique of light is developed by using Lithium Niobate based Pockels cell. By using the multi-passing of light the operation is performed at very low voltage which is easily attainable in electronic domain. The change of the polarization states are used to understand the ON and OFF states of the digital system. Here two orthogonal states of light are used to represent the bits '1' and '0' of a byte.

2. Phase Shift Keying

Phase shift keying is a digital phase modulation process where the occurred phase change is encoded with the digital bit. In case of optical phase shift keying when zero phase difference is occurred with respect to a reference signal in the modulation process it is encoded as '0' state or OFF state and when the phase difference is 180^o then it is encoded as '1' state or ON state.

3. Use of PSK in Polarization Shift Keying

The polarization shift keying can be generated from the phase shift keying. In case of polarization shift keying, when the phase change is zero which leads to the vertical polarization state or OFF state and when the phase difference is 180^o it leads to the horizontal polarization state or ON state.

4. Use of electro-optic material for derive the Polarization shift keying Signal

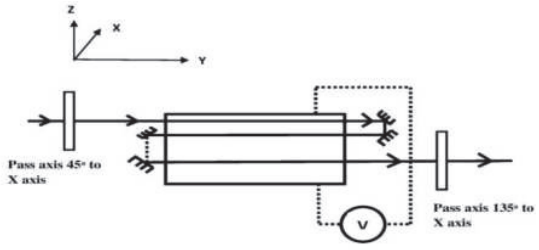

Fig. 1: Generation of Polarization Shift Keying Signal

The light signal passes through a polarizer whose pass axis is 45° to X axis in the X-Z plane, propagating through the $LiNbO_3$ based electro-optic material of length 'l' along Y direction (Fig. 1). An external biasing signal of Voltage V_z is applied parallel to Z direction of the material of width 'd'. The light signal is propagating through the material multiple times, and then the output is taken from another polarizer whose pass axis is 135° to the X axis. When the light signal is propagating through the material then a change in refractive index occurs here which leads to the phase modulation of the output light signal. When the V_π voltage is applied to the electro-optic modulator then a phase change of π is occurred at the output terminal which is considered as the horizontal polarized state. When no phase change is occurred at the output then this state is considered as vertical polarization state. By using the multi-passing technique of the carrier light signal the modulation process is done at very low voltage.

5. Result

When the light signal polarized at 45° to both X and Z axis and propagating through the Y direction, then the expression of the output signal in terms of electric field in X direction is

$$E_x(y=l) = E_0 \exp i[\omega t - kn_x l]$$
$$= E_0 \exp i[\omega t - kn_0 l + \frac{1}{2}kn_0^3 r_{13} E_z l] \quad (1)$$

The expression of the output signal in terms of electric field in Z direction is

$$E_x(y=l) = E_0 \exp i[\omega t - kn_z l]$$
$$= E_0 \exp i[\omega t - kn_e l + \frac{1}{2}kn_e^3 r_{33} E_z l] \quad (2)$$

Now, from Eq^n (1) and Eq^n (2) the phase retardation at the output can be written as,

$$\gamma = k(n_e - n_0)l + \frac{1}{2}k(n_e^3 r_{33} - n_0^3 r_{13})E_z l \quad (3)$$

So, from Eq^n (3), the phase difference occurred at the output is,

$$\emptyset = \frac{1}{2}k(n_e^3 r_{33} - n_0^3 r_{13})E_z l$$
$$\emptyset = \frac{1}{2}k(n_e^3 r_{33} - n_0^3 r_{13})V_z(\frac{l}{d}) \quad (4)$$

Here n_0 and n_e are the constant refractive index of the material, $r_{13}$and $r_{33}$are the electro-optic coefficient of the material.
This phase change (Eq^n (4)) is controlled by the applied biasing voltage and encoded as the vertical and horizontal polarization state [6,7].

6. Conclusion

The polarization shift keying is developed by using the $LiNbO_3$ crystal with the multi-passing technique. The main advantages of the polarization shift keying are uniform average byte power, highest signal to noise (SNR) ratio, low bit error rate issue, easily detectable facilities. Again, as the $LiNbO_3$ based Pockels cells are used to generate the Polarized shift keying signal, the speed of operation is very high (beyond THz range). Also, the method of generation of polarization shift keying signal at the operating voltage which is easily attainable and any electronic digital signal can be converted to the polarization keying signals very nicely.

7. Acknowledgement

The authors acknowledge University Grants Commission (UGC), Govt. of India for extending a research fellowship to Minakshi Mandal.

8. Reference

[1] M. Mandal and S Mukhopadhyay, "Analytical investigation to achieve the highest phase difference between two orthogonal components of light in lithium niobate based electro-optic system," Optoelectronics Letters **16**(5), 0338-0342 (2020).
[2] M. Mandal, R Maji and S Mukhopadhyay, "Increase of Side Band Powers in Parallel Phase Modulation by Lithium Niobate based electro-optic Crystal. Brazilian Journal of Physics," **51**(3), 738-745 (2021).
[3] M . Mandal, S. Mukhopadhyay, "Photonic scheme for implementing quantum square root controlled Z gate using phase and intensity encoding of light," IET Optoelectronics **15**, 52-60 (2021).
[4] M. Mandal, S. Mukhopadhyay, "Implementation of Quantum Optical Phase Shift Gate Adopting Multi-passing Technique in Lithium Niobate Based Electro-Optic Crystal," In: K. Singh, A. K. Gupta, S. Khare, N. Dixit, K. Pant, (eds) ICOL-2019. Springer Proceedings in Physics, vol 258, 687-690. Springer, Singapore. https://doi.org/10.1007/978-981-15-9259-1_158.
[5] M. Mandal, I. Goswami, S. Mukhopadhyay, "Implementation of programmable photonic one qubit quantum gates using intensity and phase encoding jointly," Journal of Optics. (2022).
[6] A. Ghatak and K. Thyagarajan, Optical Electronics. (New Delhi: Cambridge University Press, 1989).
[7] A. Yariv and P. Yeh, Electro-Optic Modulation in LASER Beams, Photonics-Optical Electronics in Modern Communications. (New York: Oxford University Press, 2007).

Quantum Computing: A brief Review

K. Yadav
Ahir college Rewari, Haryana India 123401
kavitayiitr@gmail.com

Abstract: Quantum mechanics can be employed as a powerful resource to speed up important computational tasks leading to intense research efforts to find adequate physical systems for quantum computation.
Keywords: Quantum computing, Superposition , Entanglement, Qubits

Introduction

Quantum mechanics, a branch of physics emerged in the early 1900's to elucidate nature on the atomic scale. Later, the idea of amalgamation of quantum mechanics and information theory emerged to exploit the quantum properties of light in various ways. The objective was to use the laws of quantum mechanics to enhance the ability of data transfer and manipulation in quantum cryptography, quantum teleportation and quantum computing [1,2].

In early 90's interest in quantum computing rose dramatically when mathematician Peter Shor developed a quantum algorithm to find the prime factors of large numbers efficiently [3]. After few years, the world's first quantum computer, D-Wave Systems was made out of superconductors. Quantum computer introduces the idea to solve certain problems much more quickly than classical computers. The concept of quantum computing is based on the coherent manipulation of quantum bits (qubits), which carry the information in a superposition of two quantum mechanical states 0 and 1.

The two important quantum mechanics properties make quantum computers unique for their operation, superposition and entanglement. Superposition is the erratic ability of a quantum particle, such as an electron, to simultaneously exist in multiple "states". If an electron is prepared in a superposition of two states (ground state and excited state), it has some probability of being in the lower state and some probability of being in the upper state. Understanding the principle of superposition makes it possible to understand the idea of qubit or quantum bits in quantum computing. In classical computing, bits corresponds to the states 0 and 1. Qubits are distinguished from classical bits, by their ability to be in superposition of states with varying probabilities that can be manipulated by quantum operations during computations. Entanglement is a phenomenon of creating or manipulating quantum entities in such a way that none of them can be illustrated without referencing the others. The quantum particles no longer exist in individual states. So far by 2021, IBM has developed 127 qubits processor.

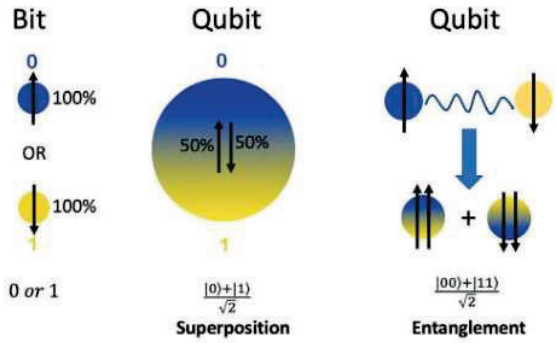

Fig. Properties of qubits

References

[1] R. P. Feynman, "Simulating physics with computers," International Journal of Theoretical Physics **21**, 467–488 (1982).
[2] M.A. Nielsen and I.L. Chuang, *Quantum Computation and Quantum Information.* (Cambridge University Press, 2000).
[3] P. W. Shor, "Polynomial-time algorithms for prime factorization and discrete logarithms on a quantum computer," SIAM J. Comput. **26**, 1484–1509 (1997).

Nonlinear Phase Accumulation for a Linear Path Delay using Three Beam Spectral Interference

Athira T S, Dinesh N Naik
Applied and Adaptive Optics Laboratory, Department of Physics,
Indian Institute of Space Science and Technology, Thiruvananthapuram, Kerala
**Corresponding author: athirats.18@res.iist.ac.in*

Abstract: In spectral interferometry, a path delay introduced between the two arms of an interferometer results in spectral modulation in the superposed fields. The Fourier transform of the modulated spectra recovers the path delay leading to applications in profilometry and tomography. A linear path delay is usually reflected as a linear shift in the position of secondary peak in the Fourier domain of the spectral signal. A method to map the linear path delay to highly nonlinear phase accumulation is proposed and experimentally demonstrated using three beam spectral interference. Proposed scheme has the potential to enhance the sensitivity of phase measurements.
Keywords: Spectral interference, Nonlinearity, Fourier fringe analysis.

1. Introduction

Low coherence interferometry is one of the robust techniques used in optical metrology for precise measurement of optical path difference in micron range [1,2]. In situations where the spatial coherence is lost or cannot be controlled, low coherence interferometry is favoured, which is capable of giving spatial and spectral information. Here the fields interfere with each other, to give spectral modulations as a function of path delay between them. The spectral interferometry along with techniques like Fourier Fringe analysis, SPIDER makes one of the easiest ways to retrieve phase information from the spectral modulations [3]. Using two beam spectral interference, researchers have found various methods to enhance the sensitivity in measurement of the phase difference between the fields. The phase accumulated by the superposition of two fields is having a nonlinear variation that can enhance the sensitivity of phase difference. Here we are proposing a technique to retrieve the phase information of the superposed field with the aid of an additional field through three beam spectral interference. This is achieved by the use of Fourier transform method of fringe analysis [4].

2. Theory and Simulation

Consider the superposition of two electric fields $E_1(t)$ and $E_2(t)$ delayed by a time $\tau = \frac{d}{c}$. In spectral domain, the interference between these two fields is obtained as $S_s(\omega) = \left|\tilde{E}_1(\omega)\exp(i\phi_1) + \tilde{E}_2(\omega)\exp(i\phi_2)\right|^2$, where $\phi_1 - \phi_2 = \frac{\omega d}{c}$. The intensity of superposed field is given by,

$$S_s(\omega) = |E_S(\omega)|^2 = \left|\tilde{E}_1(\omega)\right|^2 + \left|\tilde{E}_1(\omega)\right|^2 + \tilde{E}_1(\omega)\tilde{E}_2(\omega)^* \exp\left(\frac{i\omega d}{c}\right) + \tilde{E}_1(\omega)^*\tilde{E}_2(\omega)\exp\left(-\frac{i\omega d}{c}\right)$$

Phase of the superposed field is obtained as;

$$\phi_S(\lambda, d) = \tan^{-1}\left(\frac{\alpha\sin\left(\phi_1(\lambda,d)\right) + \sin(\phi_2(\lambda,d))}{\alpha\cos\left(\phi_1(\lambda,d)\right) + \cos(\phi_2(\lambda,d))}\right)$$

Where $\alpha = |E_2(\omega)|/|E_1(\omega)|$, the ratio of amplitudes of interfering fields. The path delay d gives linear phase between the interfering fields. It controls the number of fringes in the output spectrum. Figure 1 (a) shows the spectral intensity when the delay $d = 100\ \mu m$. If the delay, $d = \frac{\lambda}{2}$ the interference pattern results in a two Gaussian profile with a dip at the center as shown in figure 1(b). Now the third field $\widetilde{E_3}(\omega)$ is allowed to interfere with superposed field $E_s(\omega)$. The intensity of the resultant field, $\left|\widetilde{E_3}(\omega) + E_s(\omega)\right|^2$, is depicted in the figure 1(c). The Fourier transform of the field results in three peaks as shown figure 1 (d). It contains non-interfering peak $\mathcal{F}(|E_s(\omega)|^2 + \left|\widetilde{E_3}(\omega)\right|^2)$, interfering peaks $\mathcal{F}(E_s(\omega)\widetilde{E_3}(\omega)^*\exp(i\omega\tau_{s3}))$ and its conjugate. Here the delay τ_{s3} determines the delay between the superposed field $E_S(\omega)$ and the third field $\widetilde{E_3(\omega)}$.The full information about the superposed field $E_S(\omega)$, the amplitude and phase of the same, is obtained through the inverse transform of one of the interfering peaks. Hence the third/ additional field is considered as a tool to obtain the information about the interference between two fields.

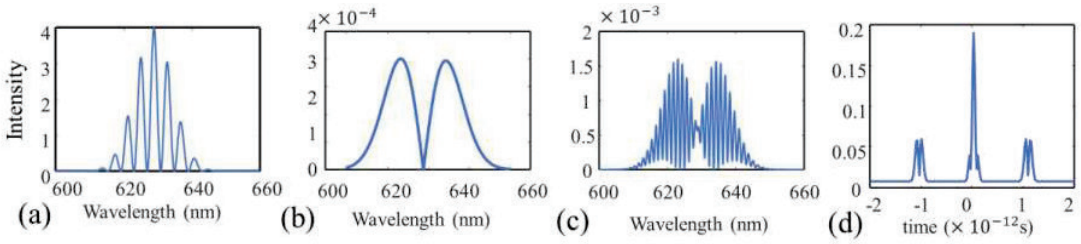

Figure 1: (a) Intensity of $E_s(\omega)$ when $d = 100\ \mu m$ (b) Intensity of $E_s(\omega)$ when $d = \lambda/2\ nm$, $\lambda = 632nm$ (c) Intensity of $E_s(\omega) + E_3(\omega)$ (d) Fourier transform of intensity $E_s(\omega) + E_3(\omega)$

3. Experiment and Results

To verify the above results, an experiment as shown in figure 2(a) is set. A light from a LED source having Gaussian spectrum centered at wavelength of 632 nm and width 10.98 nm, is imaged onto a pinhole of size 50 μm using lens L1. The lens L2 collimates the field and feeds it into a Michelson in Michelson interferometer. The fields reflected from the mirrors M1 and M2, combines at the PBS1. This field is considered as superposed field $E_s(\omega)$. The field reflected from mirror M3 is additional/ third field $E_3(\omega)$, combines with field $E_s(\omega)$ at the beam splitter BS. The half wave plate HWP, polarizing beam splitter PBS1 are used to adjust the intensity of interfering beams. To compensate the dispersion effect, another polarizing beam splitter PBS2 is used near to the mirror M3. The Polarizers P1 and P2, is kept at 45 degree orientation, to observe interference fringes at the output. To study the variation of phase with path delay between the interfering fields, one of the mirror M2 is mounted on the Piezo electric transducer device. Spectrometer records the output field for every step the mirror M2 makes. By adjusting the path delay between the mirrors, the modulation in the intensity similar to that of figure 1(c) is obtained. Using the technique of Fourier fringe analysis, the amplitude and phase are reconstructed. The mirror M2 is moved in steps of 10nm and the phase accumulated by the third field for the central wavelength is plotted as shown in the figure 2(b) and 2(c) for $\alpha = 0.88$ and $\alpha = 1.05$. Accumulated phase shows non linearity at the zero path delay. This shows a path delay near to zero path delay can be amplified through the phase of the superposed field with the help of an additional field.

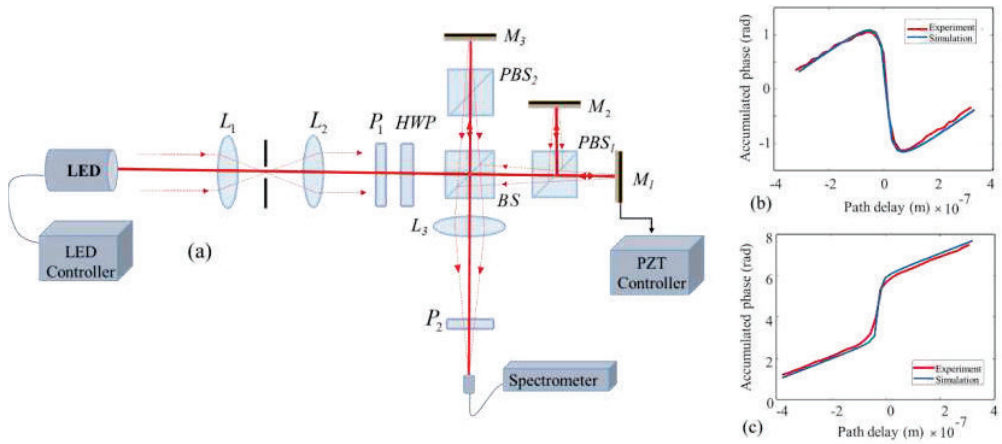

Figure 2 : (a) Experimental setup (b) & (c) The variation of phase accumulated by the superposed field with path delay for central wavelength for (b) α=0.88 and (b) for α=1.05

4. Conclusion

With the help of an additional field in spectral interference, the amplitude and phase information of the superposition of two fields are studied using simulation as well as through experiment. The phase of the superposed field accumulated through the additional reference field, shows highly nonlinear behavior near zero path delay. This property can have potential applications in enhancing phase measurement sensitivity.

5. References

[1] P. A. Flournoy, R. W. McClure, and G. Wyntjes, "White-Light Interferometric Thickness Gauge," Appl. Opt **11**(9), p. 1907-1915, (1972)
[2] B. L. Danielson and C. Y. Boisrobert, "Absolute optical ranging using low coherence interferometry," Appl. Opt. **30** 2975 (1991).
[3] L. Lepetit, G. Chériaux, and M. Joffre, "Linear techniques of phase measurement by femtosecond spectral interferometry for applications in spectroscopy,"J. Opt. Soc. Am. B **12**, p. 2467 (1995),
[4] C. Dorrer, N. Belabas, J. P. Likforman, and M. Joffre, "Experimental implementation of Fourier-transform spectral interferometry and its application to the study of spectrometers," Appl. Phys. B Lasers Opt **70**,. 99–107 (2000)

Enhancement of Kerr Nonlinearity in Asymmetric Quantum Dot Molecules

Rohit Mukherjee[1], S. Konar[2]
[1]*Department of Physics, Sarala Birla University, Ranchi, Jharkhand-835103*
[2]*Department of Physics, Birla Institute of Technology Mesra, Ranchi, Jharkhand-835215*
[1]*Author e-mail address: rohitmukherjee670@gmail.com*

Abstract: A unique approach to enhance Kerr nonlinearity in quantum dot molecules has been investigated. In such systems, the transparency of a probe could be tuned utilizing tunneling between two quantum dots. The Kerr nonlinearity of the system can be enhanced by an order of 10^6 as compared to other quantum dot molecules.
Keywords: Tunneling induced transparency, semiconductor quantum dots, quantum dot molecules, Kerr nonlinearity.

1. Introduction

Recently, a large number of phenomena associated with quantum coherence and interference in semiconductor nanostructures has drawn tremendous attention [1-3]. One such coherent optical phenomenon is the tunneling induced transparency (TIT), which might minimize linear absorption and simultaneously enhance Kerr as well as higher-order nonlinearities in quantum dot molecules (QDMs). In view of this, we investigate linear and nonlinear optical properties owing to TIT in quantum dot molecules.

2. Model and Governing Equations

As shown in figure 1, we consider asymmetric double quantum dot molecules with different energy subbands coupled by inter-dot tunneling via applied gate voltage [2]. In order to study linear and nonlinear properties of the system, we apply a weak probe field of frequency ω_p between energy levels $|1\rangle \rightarrow |2\rangle$, simultaneously a control field of frequency ω_c is applied between energy levels $|3\rangle \rightarrow |4\rangle$, and interdot tunneling coupling T_e is applied between energy levels $|2\rangle \rightarrow |4\rangle$. The linear and Kerr nonlinearity of the probe are calculated as

$$\chi^{(1)} = -\frac{2c\kappa}{\omega_p}\cdot\frac{D_p(0)}{D(0)}, \quad \text{and} \quad \chi^{(3)} = \frac{2c\kappa}{\omega_p}\cdot\frac{|\mu_{21}|^2}{\hbar^2}\cdot\frac{(|D_p(0)|^2+|\Omega_c^* T_e|^2+|d_{31}T_e|^2)}{|D(0)|^2}\cdot\frac{D_p(0)}{D(0)}. \tag{1}$$

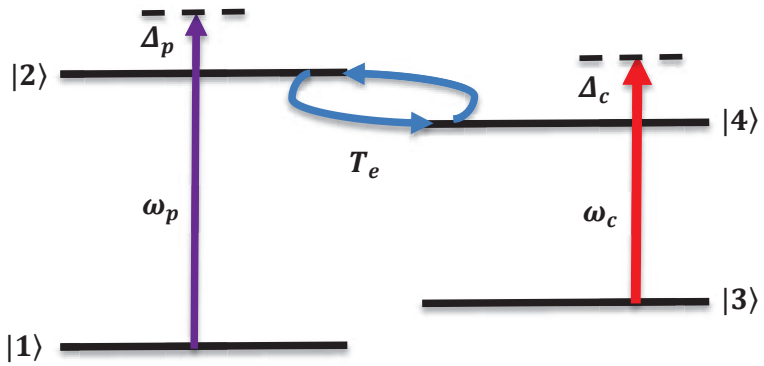

Fig. 1: Schematic energy level diagram for an asymmetric quantum dot molecules (AQDMs) with interacting probe (ω_p) and control (ω_c) fields.

3. Results

In figure 2, we have demonstrated the variation of linear absorption and dispersion of the probe as a function of probe detuning Δ_p/Γ_1 for various tunneling strength T_e. From subplot (a) it is seen that when $T_e = 0$, the probe field exhibits anomalous dispersion and largely absorbed around $\Delta_p = 0$. However, when $T_e = 5\ meV$, the transparency window is created around resonance with steep positive dispersion owing to TIT. Figure 3, shows variation of the Kerr nonlinearity with Δ_p/Γ_1 for different T_e. Figure implies that the values of $\chi^{(3)}$ can be controlled with the suitable choice of interdot tunneling T_e, and control field Ω_c within $-2.5\Gamma_1$ to $2.5\Gamma_1$ and its magnitude is quite large as compared with other double and triple quantum dot molecules.

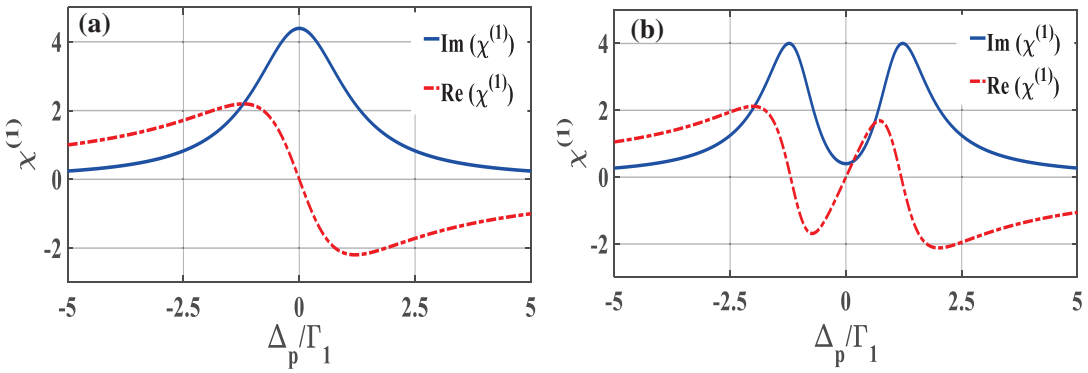

Fig. 2: Variations of the real and imaginary part of the $\chi^{(1)}$ with normalized probe detuning for different interdot tunneling. (a) $T_e = 0$, (b) $5\ meV$.

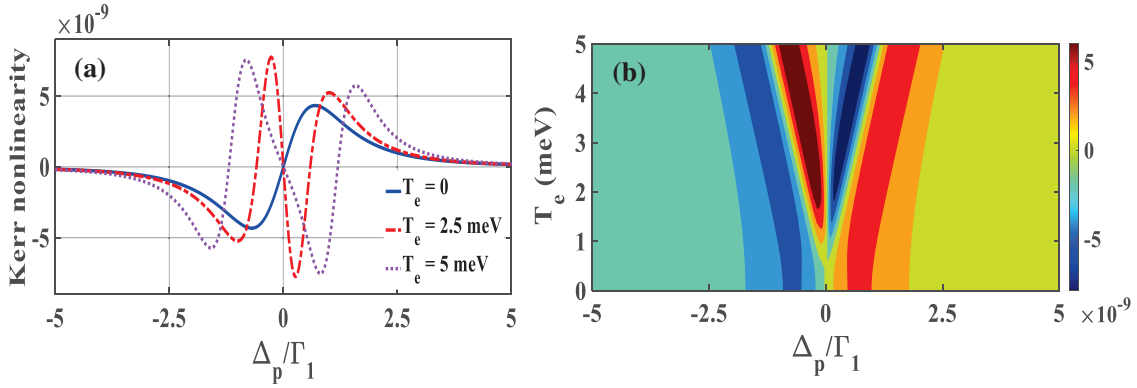

Fig. 3: (a) Variations of the Kerr nonlinearity $\chi^{(3)}$ with normalized probe detuning (Δ_p/Γ_1), (b) corresponding density plot.

4. Conclusion

In summary, we have investigated linear absorption and Kerr nonlinearity of the probe field via tunneling mechanism. The results show that linear absorption of the probe can be modified for finite values of the inter-dot tunneling T_e and at the same time Kerr nonlinearity also enhanced under TIT.

5. References

[1] J. M. V-Boas, A. O. Govorov, and S. E. Ulloa, "Coherent control of tunneling in a quantum dot molecule," Phys. Rev. B **69,** 125342 (2004).

[2] Y. She, X. Zheng, D. Wang, and W. Zhang, "Controllable double tunneling induced transparency and solitons formation in quantum dot molecule," Opt. Exp. **21**, 17394 (2013).

[3] D. Sun, H. Zhang, H. Sun, X. Li, and G. Wang, "Tunneling induced ultraslow solitons in triangular quantum dot molecules," Phys. Lett. A **383**, 148-152 (2019).

Sucrose Sensor by using Absorption of Rhodamine and Polymer

Akanksha Mishra[a], Roli Verma[a*]
[a]Department of Physics, University of Lucknow, Lucknow 226007, India
[*]roliverma10@gmail.com

Abstract: Here, we report the probe solution that is prepared with dye and polymer combination to detect the amount of sucrose intake. In this work, we have measured the absorption spectra of sucrose of different molar concentration range from 10^{-1}M to 10^{-4}M mix with Rhodamine 6G-polyvinylpyrrolidone (PVPRH) probe solution. A UV-visible spectrometer operating in the range of 300-1100 nm was used to detect the optical properties of samples. The result obtained from the experiment shows the aggregation behavior of Rhodamine 6G (Rh6G) and detection of organic compound "sucrose".
Keywords Rhodamine 6G- polyvinylpyrrolidone (PVPRH), sucrose, DI

1. Introduction

Blood sugar, heart diseases, weight gain, cavities and other dental issues become more likely by sugar consumption. So the detection of sucrose ($C_{12}H_{22}O_{11}$) is essential. When describing the interaction between photons and absorbing species in absorption spectroscopy, the term "absorption" is used. Absorption spectroscopy has wide applicability because it provides high detection limit up to 10^{-4}M and is easy and convenient to process. In recent decades, xanthene dye mix with polymer has gained a lot of attention due to the advantages of cost-effective price and compatibility between dye and polymer [1]. Rh6G ($C_{12}H_{31}CIN_2O_7$) is a cationic dye shows ferocious absorption in the visible region of the electromagnetic spectrum. The spectral properties of dyes are significantly influenced by external disturbances. That is why Polyvinylpyrrolidone (PVP) can include dye molecule to make them colorful, functional and shielding from them [2].

2. Methodology

For the study, Rh6G and sucrose were dissolved separately in de ionized (DI) water. PVP was also dissolved in DI water by using stirrer for of 20 min. Then the solution of Rh6G and PVP were mixed in appropriate amount; thus the mixed solution of Rh6G and PVP were obtained as a probe solution. After then, dilute the stock solution of sucrose into different molar concentrations (10^{-1}M, 10^{-2}M, 10^{-3}M, $5X10^{-4}$M). All the samples were stored in dark place to prevent dye-fading. We recorded absorption spectra of different molar concentrations of sucrose mixed with PVPRH probe solution using single beam spectrometer and polychromatic light source. The experimental set-up used for data collection is shown schematically in Fig. 1. Optical fibers are used as the connecting cables to couple the light between systems.

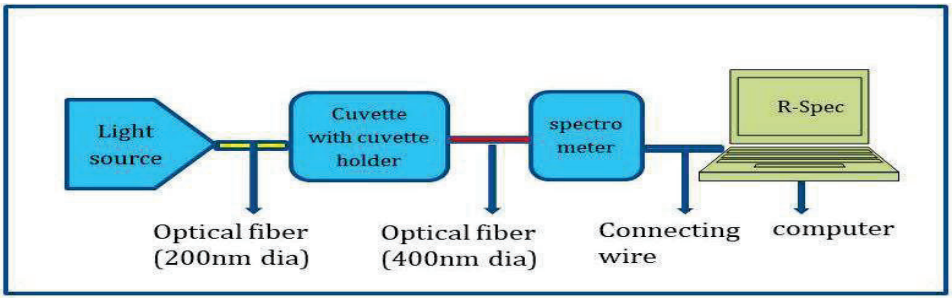

Fig.1: The schematic of experimental set-up for absorption sensor

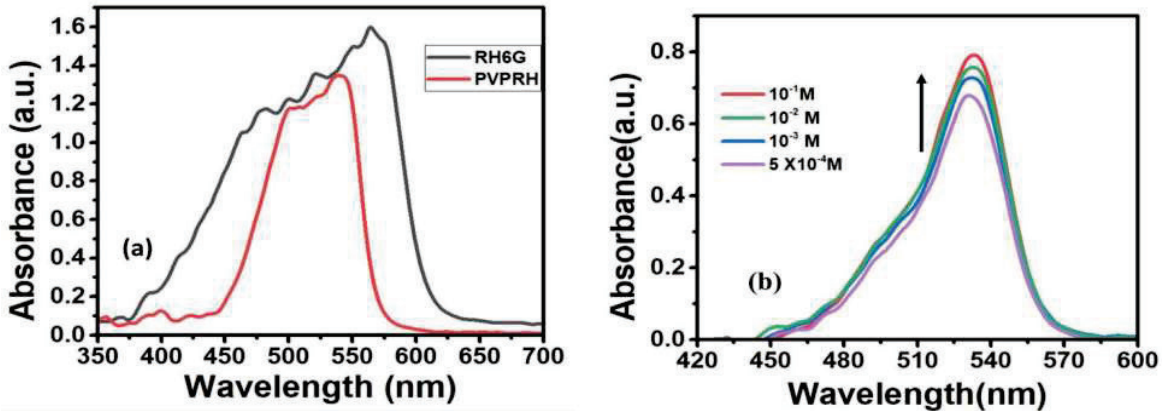

Fig.2 (a) The absorption spectra of pure Rh6G and PVPRH probe solution. (b)The absorption spectra of different molar concentration of sucrose with PVPRH probe solution.

3. Results and Discussion

The absorption spectra of pure Rh6G of 10^{-3}M and PVPRH probe solution (mixture of 10^{-3}M and 10^{-5}M of Rh6G and PVP respectively) are unwavering in fig.2 (a). This fig shows Rh6G solution exhibits a distinct absorption peak at 566nm with an intensity of 1.61 and a shoulder at 475 nm, but when mixed with PVP, causes the absorption peak to shift to 541nm with an intensity of 1.35. It reduces the spectral width of the curve also. That means there is a shift towards shorter wavelength of about 25nm and the intensity decreases up to 80%. The formation of aggregation in Rh6G is responsible for this outcome in the presence of PVP. Further the absorption spectra of sucrose at different concentrations in PVPRH probe solution were taken and shown in fig. 2. It can be seen that the spectra of the highest concentration of sucrose has an intensity peak at 532nm and a small shoulder in the range 486-508 nm. It is clearly seen that the absorption intensity increased as the sucrose concentration increased. The absorption intensity is increased from 0.67 to 0.79 A.U. while moving from lower to higher concentration of sucrose. Moreover peak wavelength slightly right shifted about 3 nm with the concentrations. This is in agreement with Beer-Lambert's law [3]. This change in absorption spectra may be because of aggregation in Rh6G molecules and the interaction of sucrose with probe solution.

4. Conclusion

The PVPRH solution provides an easy method for the determination of sucrose via absorption intensity peak. Under optimum conditions, sucrose concentrations between 10^{-1}M to $5X10^{-4}$M have an increasing effect on the absorption's intensity. In comparison to several reports, our results suggest that there is a change in both the intensity peak and line width of PVPRH after mixing the different molarity of sucrose. This method of detection provides online monitoring and is cost-effective and easy to handle.

Dr. Roli Verma is thankful to UGC, India for the UGC-BSR startup Grant.

5. References

[1]Mahasin F. Hadi Al-Kadhemy *et al.,* "Physical Properties of Rhodamine 6G Laser Dye Combined in Polyvinyl Alcohol films as Heat Sensor," IOP *Conf. Ser.: Mater. Sci. Eng.* **928** 072126 (2020)
[2] Basil Ali Abdullah, "Optical Properties of RhB dye mixed with PVP as a matrix" in JOURNAL OF KUFA-PHYSICS, **9, (2)** (2017)
[3]F. M. Zehentbauer et al., Fluorescent spectroscopy of Rh6G: Concentration and solvents effect (Spectrochim Acta-Part A, 2014)

DNA origami assisted gold dimers as SERS substrates on optical fiber tips for direct miRNA detection using hairpin probes

Anisha Pathak[1], Anushree Dutta[1] and Ilko Bald[1]
Instiute of Chemistry, Physical Chemistry, University of Potsdam, Germany
pathak@uni-potsdam.de

Abstract: A DNA origami based SERS sensor for miRNA detection is realized on an optical fiber. Hairpin DNA probes will be attached to the origami to design a OFF-ON working scheme in the presence of miRNAs. The study will provide a proof of concept for the design of miRNA sensors on optical fibers.
Keywords: SERS, optical fibers, miRNA, DNA origami, sensor.

1. Introduction

MicroRNAs (miRNAs) serve an important regulatory role in various diseases and are emerging as novel class of biomarkers for early informative diagnostics of cancer, neurological and genetic disorders. However their intrinsic properties like low abundance and short length limits their use in clinical diagnostic processes. Hence it is crucial to develop new diagnostic strategies for miRNAs which overcome the limitations of conventional techniques like Northern blotting and quantitative reverse transcriptase PCR (qRT-PCR). SERS has emerged as an exciting biodiagnostic tool over the past decade with the fast advances in nanotechnology offering the detection limits up to single molecule regime. However the single molecule sensitivity is limited to the placement of target molecule in well-defined gaps between the plasmonic (gold, silver) nanotags refereed as hotspots. A strong enhancement in Raman signal of a molecule is observed when it is precisely located in these hotspots. This precise placement of a target molecule in the hotspots still remains a challenge and require meticulously engineered nanofabrication schemes.

DNA origami offers a reliable strategy for self-assembly of nanostructures due to rich chemical functionalization possibilities. Just like electronic chips, various molecules and nanomaterials can be positioned on origami with nanometers precision to achieve predesigned structures for numerous applications. Our group have designed a versatile DNA origami termed as DNA origami nanofork antenna (DONA) with plasmonic dimers optimized for single molecule SERS detection. The gap size between the nanostructures in the dimer may be varied to accommodate differently sized analytes like dye molecules and proteins in the hotspot volume. A schematic view of DONA structure and AFM image of prepared nanoforks is shown in figure 1.

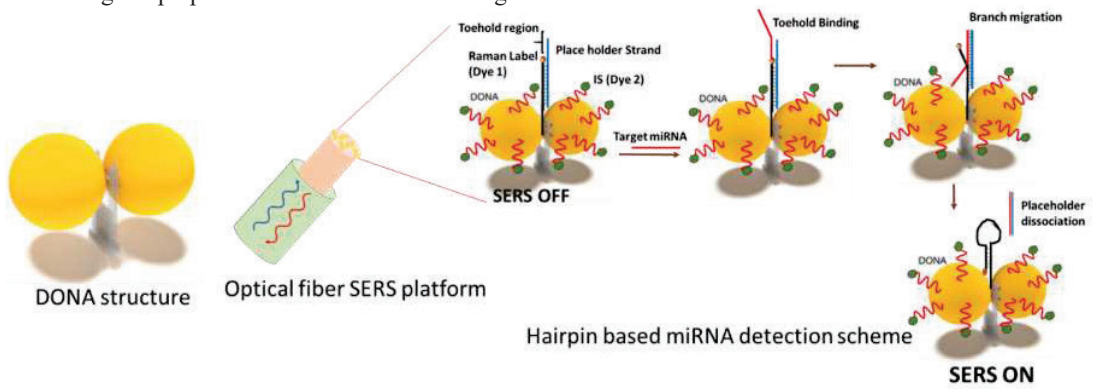

Figure 1. Schematic of DNA origami assisted gold dimers (DONA) and miRNA detection on optical fiber SERS platform

Based on this inventive DNA origami, we investigated a sensitive and specific ON-OFF SERS scheme for miRNA detection using this DONA structure integrated with hairpin DNA probes on optical fibers. The proposed scheme utilizes gold nanoflowers and DNA nanoforks integrated in DONA structure as SERS substrates. The biosensor is

designed employing a stem-loop/hairpin DNA probe with Raman label at one end, attached at the DONA hotspot, as a target identification switch. The switch is initially kept OFF by a placeholder DNA strand which hybridize to the hairpin probe through a specific region. In the presence of target miRNA, the placeholder strand is displaced initiated by a toehold binding and branch migration mechanism. This process finally releases the placeholder strand and the hairpin probe is closed bringing the Raman label in the SERS hotspot of the DONA structure enabling the switch ON with a strong SERS signal from the label dye. Thus, essentially the SERS signal of the Raman label turns OFF to ON in the presence of target miRNA enabling the direct detection of these biomarkers as shown schematically in figure 1(b). To avoid the false signals, the gold nanoflowers are coated with an internal standard (IS) molecule to record a ratiometric SERS signal between the Raman label and IS. The scheme is realized on the tip of an optical fiber to further enhance the feasibility of the system for in-situ clinical biodiagnostics. Thus, the integration of DONA structure with hairpin probe on an optical fiber SERS platform can provide a versatile strategy for the detection of miRNAs and many other biologically relevant anaytes with advantages like high sensitivity, miniaturised dimensions and feasibility of on-site continuous monitoring.

2. References

[1] C. Strobbia, P.; Ran, Y.; Crawford, B. M.; Garcia, V. C.; Zentella, R.; Wang, H. N.; Sun, T. P.; Vo-Dinh, T. Inverse Molecular Sentinel-Integrated Fiberoptic Sensor for Direct and in Situ Detection of miRNA Targets. Anal. Chem.**,** *91*, 6345-6352 (2019).
[2] Tapio, K.; Mostafa, A.; Kanehira, Y.; Suma, A.; Dutta, A.; Bald, I. A Versatile DNA Origami-Based Plasmonic Nanoantenna for Label-Free Single-Molecule Surface-Enhanced Raman Spectroscopy. ACS Nano *15*, 7065−7077 (2021).
[3] Wang, H. N.; Crawford, B. M.; Fales, A. M.; Bowie, M. L.; Seewaldt, V. L.; Vo-Dinh, T. Multiplexed Detection of MicroRNA Biomarkers Using SERS-Based Inverse Molecular Sentinel (iMS) Nanoprobes. J. Phys. Chem. *C 120*, 21047−21055 (2016).

Geometrical beam shaping by electrically tunable thermal lensing

Ashwanth P[1], Pritam P Shetty[1], Jayachandra Bingi[1*]
[1]*Bio-inspired Research and Development (BiRD) Laboratory, Photonic Devices and Sensors (PDS) Laboratory, Indian Institute of Information Technology Design and Manufacturing (IIITDM), Kancheepuram, Chennai-600127, Tamil Nadu, India.*
**Corresponding author: bingi@iiitdm.ac.in*

Abstract: An electrically tunable thermal lens in fluid medium is demonstrated. A graded refractive index(GRIN) lens is generated within a fluid medium. The geometrically shaped heater elements allowed precise laser beam shaping with tunable size.
Keywords: Thermal lens, beam shaping, Tunable lens, GRIN lens.

1. Introduction

Numerous research on the design of tunable lenses has been conducted in the past decades[1]. Spatial light modulators(SLM) are widely used for imparting spatial modulation by using transparent electrodes and liquid crystals to control the amplitude, phase and polarization of structured light[2]. The practical application of using an SLM is to produce structured lights. SLM can produce a high dynamic resolution which allows for representing phase shifts with higher fully functional control. However, the drawbacks of SLM includes the high cost, slower response time, reduction in diffraction efficiency, and dependence on wavelength and polarization. In contrast, Digital micromirror device (DMD) is a micro-opto-electro-mechanical system that can be opted for wavefront corrections. But they are comparatively more expensive than SLM. In order to overcome these drawbacks of the conventional methods, an electrically tunable system based on thermal effect have been engineered and developed. An experiment is conducted to show the spatial modulation of light with electrically tunable thermal system.

In this research an alternative system with a heater element which generates geometrically shaped Graded refractive index (GRIN)[3, 4] distribution within a fluid is proposed.

2. Experimental Setup

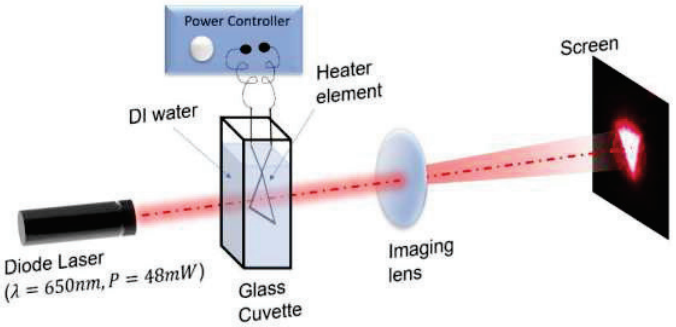

Fig. 1: Experimental setup for beam shaping using thermal lens induced by a geometrically shaped heater element.

Fig 1 shows complete experimental setup. Nichrome wire of radius 0.1mm is selected as a heating element due to its properties such as high malleability, high melting point, high resistance to corrosion and oxidation. This element is cut and made into the desired shape for the requirement of our experiment. Then the heater element is put into a custom-made glass cuvette of dimensions 25mm x 75mm. The cuvette is filled with 70ml of de-ionized water and it is ensured that there is no formation of bubbles or foreign particles, both inside and outside of the cuvette. then the terminals of the wire are connected to a power supply unit which gives a pulse width modulation (PWM) output. A

diode laser with a gaussian beam profile of 650nm wavelength and 50mW power is arranged on the optic table behind the cuvette at a distance of 180mm from screen. An optical power and energy meter from Thorlabs (PM320E) is set up on the table with the photodiode sensor connected to the system to measure laser power density with time.

3. Results and Discussion

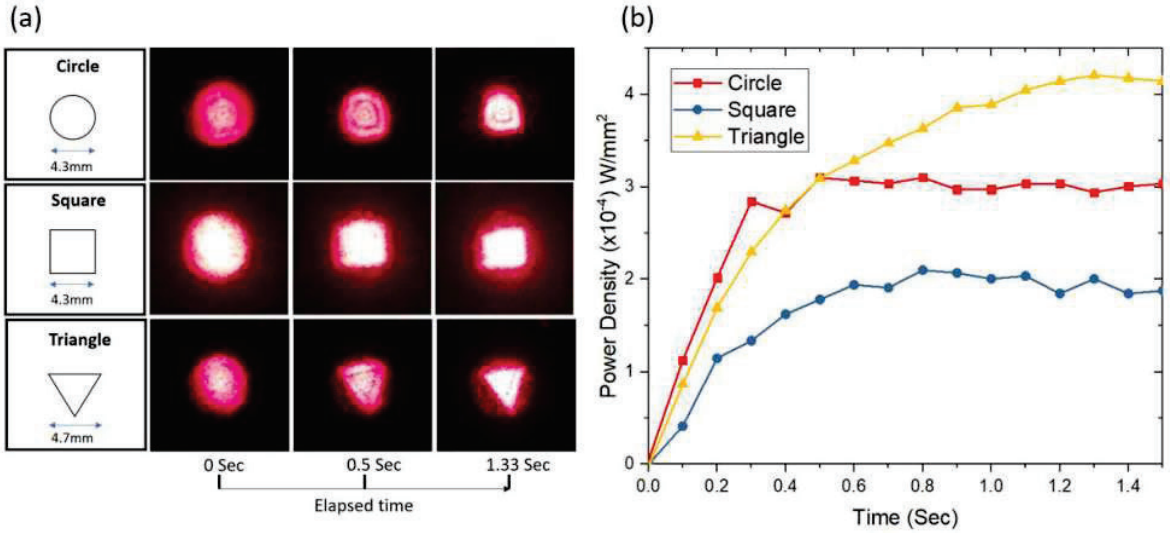

Fig. 2: (a) The first column shows shape and size of a heating element and the other columns shows time evolution of laser beam profile after powering the heater element. (b) Laser power density after passing through thermal lens versus time.

The heater element consumed ~10W of power during the operation. This power can be controlled by changing the duty cycle of PWM from the power source. By controlling the heat flux from the heater element the strength i.e. focal length of the thermal lens within de-ionized water can be controlled. Fig 2. (a) shows beam profile transformation after passing through thermal lens generated by geometrically shaped heating elements respectively. Diffraction effects seen in the beam profile is due to the use of imaging lens for capturing profiles on the screen. A circularly shaped heater element resulted in a conventional lens like behavior with variable focal length. Similarly for shapes like square and triangle its size increased or decreased by changing power input to the heater element. Fig 2. (b) shows a plot of laser power density vs time, from this graph it is clear that the generated thermal lens acts like a converging lens. Since power density increases when heater element is powered.

4. Conclusion

In this research an electrically tunable thermal lens of different geometrical shape is demonstrated. The graded refractive index distribution within fluid medium also allowed beam shaping into triangular and square geometry. The setup is simple and easy to use. Tunable beam shapers as demonstrated here are useful in the optical micro manipulation, fluorescence microscopy and bio-medical imaging.

5. References

[1] L. Chen, M. Ghilardi, J. J. C. Busfield, and F. Carpi, "Electrically Tunable Lenses: A Review," *Front. Robot. AI*, vol. 8, no. June, pp. 1–20, 2021, doi: 10.3389/frobt.2021.678046.

[2] S. Li, Z. Lu, P. Du, Y. Wang, L. Ding, and X. Yan, "Beam shaping by using small-aperture SLM and DM in a high power laser," *https://doi.org/10.1117/12.2317534*, vol. 10710, pp. 903–918, Mar. 2018, doi: 10.1117/12.2317534.

[3] W. Liu, H. Hu, F. Liu, and H. Zhao, "Manipulating light trace in a gradient-refractive-index medium: a Lagrangian optics method," *Opt. Express*, vol. 27, no. 4, p. 4714, 2019, doi: 10.1364/oe.27.004714.

[4] J. N. Mait, G. Beadie, R. A. Flynn, and P. Milojkovic, "Dispersion design in gradient index elements using ternary blends," *Opt. Express*, vol. 24, no. 25, p. 29295, 2016, doi: 10.1364/oe.24.029295.

Longitudinal-Field Component and the Spin-Hall Effect of Light

Nitish Kumar* **and Nirmal K. Viswanathan**

School of Physics, University of Hyderabad, Hyderabad, Telangana – 500046, India

*nitish.phy1@gmail.com

Abstract: High numerical-aperture (NA) focusing of a paraxial uniformly-polarized Gaussian beam transforms into spatially varying inhomogeneous polarization in the focal region. The superposition of longitudinal- and transverse-field components in the focal region leads to the appearance of complex but structured light field, which can be understood as due to spin-orbit interaction of light. We investigate here the spin-Hall effect of light in off-axis positions of cross-polarization component for different NA of the lens to understand the role played by the longitudinal component.

Keywords: Longitudinal-field, Spin-Hall effect of light, Centroid shift, Weak measurement.

1. Introduction

Stemming from the fact that the most widely used solution to the Maxwell equations and the Helmholtz wave equation correspond to ideal transverse plane-wave [1], the longitudinal component is one of the least investigated and hence understood part of the electromagnetic field. A more realistic, simple and approximate solution to the Maxwell and Helmholtz equations corresponds to the one that describes Gaussian profile laser beam, which diverges upon free-space propagation and hence possess a non-zero, and often ignored longitudinal-field component [2]. Recent theoretical calculations by Bekshaev have clearly demonstrated the central role played by the longitudinal-field component in the widely investigated *spin-Hall effect of light* (SHEL) [3 – 5]. The SHEL is a polarization-dependent transverse shift of the centroid of an optical beam. Widely investigated in the reflection / transmission geometry, the SHEL exists even in free-space propagating paraxial beam of light [3, 4]. The SHEL is thus shown to play a fundamental role in the *spin-orbit interaction* (SOI) of light, due to the role of the geometric phase and the conservation of optical angular momentum [6].

Despite being an actively researched area of optical physics, to the best of our knowledge there is not been an experimental investigation that will directly link the role played by the longitudinal-field component with the SHEL. We address this fundamental connection by measuring the SHEL in the dark-field region, at near-normal incidence of a linearly-polarized focused Gaussian beam, reflected at a dielectric interface and recollimated [7, 8]. The dark-field region appears in the cross-polarization component of the focused-reflected beam of light around normal incidence, corresponding to small wavevector variation of $\left(k_0 \pm \Delta k\right)$. The near-dark background allows us to measure the polarization dependent beam shift with high sensitivity. Measuring the beam shift in the off-axis region of the reflected beam provides us direct evidence of the role played by the longitudinal component on the SHEL. The strength of the longitudinal component is varied via the numerical aperture (NA) of the lens used to focus-collimate the beam of light. Simulation of the effect based on Richards-Wolf formalism [1,2,7,8] and polarimetry and weak measurement methods allows us to understand and quantify the SHEL as a function of the NA of the lens (from paraxial to non-paraxial) and hence the strength of longitudinal component of the field.

2. Results and discussion

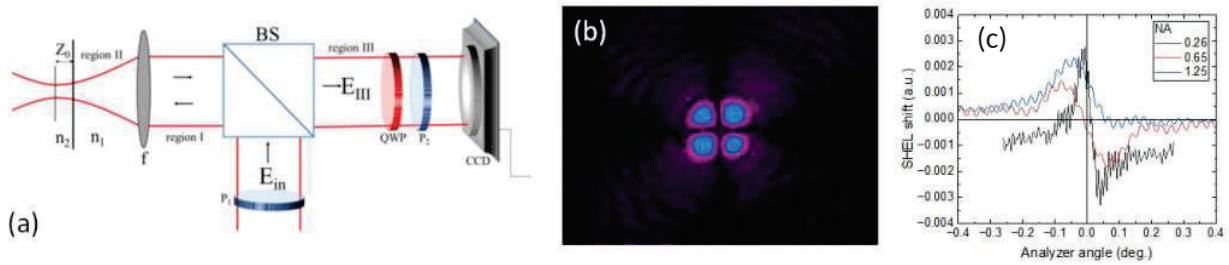

Fig. 1: (a) Schematic of the experimental setup used to measure the NA-dependent SHEL, (b) experimentally measured cross-polarized image of output beam, (c) experimentally measured NA-dependent SHEL shift at near-normal incidence.

Schematic of the experimental setup is shown in Fig. 1 (a). A linearly polarized beam of light (E_{in}), reflected by a 50-50 (R/T) beam splitter is focused using a lens of focal length *f*. A glass substrate kept at the focal plane reflects the beam and the collimated beam of light is transmitted through the beam splitter to the measurement plane (region III). The polarization characteristics of the focused-reflected beam is measured using Stokes parameters and the SHEL measurement is carried out using a rotating quarter wave plate (QWP) – analyser (P_2) combination. The spatial characteristics of beam's intensity, phase and polarization are captured using a CCD camera kept at the Fourier plane. Figure 1 (b) shows the output beam measured under cross-polarization condition using which the changes in the beam characteristics are measured, by rotating the QWP-P_2 combination for different NA of the lens. From the measured characteristics of the output beam at near-normal incidence, the SHEL shift is calculated and shown in Fig. 1 (c) for different NA of the lens. As can be seen, the behaviour of the SHEL shift shows a strong and measurable NA and hence the longitudinal-field component dependence. The difference in the analyser angle and the shift magnitude for different NA conditions are being investigated more thoroughly and will be reported.

Acknowledgements: The authors acknowledge SERB for financial support to carry out this research.

3. References

1. M. Born and E. Wolf, Principles of Optics, 7th edition, Cambridge University Press (2013).
2. A. Zangwill, Modern Electrodynamics, Cambridge University Press (2013).
3. A. Y. Bekshaev, Ukr. J. Phys. Opt. 12, 10 (2011).
4. A. Y. Bekshaev, Phys. Rev. A 85, 023842 (2012).
5. A. Y. Bekshaev, J. Opt. 19 085602 (2017).
6. K. Y. Bliokh, F. J. Rodrıguez-Fortuno, F. Nori and A. V. Zayats, Nat. Photonics 9, 796 (2015).
7. N. Kumar, U. Baishya, N. K. Viswanathan, Proc. SPIE 12017, Complex Light and Optical Forces XVI, 120170A (2 March 2022); doi: 10.1117/12.2608245.
8. U. Baishya, N. Kumar and N.K. Viswanathan, Opt. Lett., (accepted, Aug. 2022).

Near field coupled hybrid Metacavities

Sukhvinder Kaur[1], Subhajit Karmakar[1], Arun Jana[2], Shreeya Rane[2], Ravendra Kumar Varshney[1,*], Dibakar Roy Chowdhury[2]

[1] Department of Physics, Indian Institute of Technology Delhi, Hauz Khas, New Delhi, 110016, India
[2]Department of Physics, Ecole Centrale School of Engineering - Mahindra University, Jeedimetla, Hyderabad, Telangana, 500043, India
*Author e-mail address: * R.K.Varshney@physics.iitd.ac.in*

Abstract: Resonance in dipole cavities depends upon the surface plasmon excitation at specific phase-matching conditions controlled by substrate material and periodicity. In order to increase the degree of freedom for phase tunability, we have demonstrated near-field coupling of the dipole cavity with a split ring resonator.
Keywords: Terahertz, Metasurfaces, Near field coupling, Dipole cavities.

1. Introduction

Phase engineering is very important to investigate the phase-dependent physical and chemical properties of the metasurfaces and their applications. Phase engineering in various metasurfaces is reported in the literature [1-4]. One of these metasurfaces is the dipole cavity exhibiting sharp resonance at phase matching conditions. The phase matching condition for these dipole cavities is given by [5]

$$\lambda_{\mathrm{SP}} = \frac{P}{\sqrt{i^2 + j^2}} \sqrt{\frac{\varepsilon_{\mathrm{d}}\varepsilon_{\mathrm{m}}\mu_{\mathrm{d}}\mu_{\mathrm{m}}}{\varepsilon_{\mathrm{d}}\mu_{\mathrm{d}} + \varepsilon_{\mathrm{m}}\mu_{\mathrm{m}}}} \qquad (1)$$

P being the periodicity of the structure, i and j are integers representing the order of the resonance, and ε_m and ε_d ($\mu_m$and μ_d) are the electric (magnetic) permittivity of metal and substrate, respectively. It is evident from the above equation that the resonance frequency depends upon the periodicity of the unit cell and the dielectric properties of the substrate material. The change in periodicity varies the inter-unit cell coupling and an increase in periodicity may result in decreased inter-unit cell coupling. In order to tune the phase matching condition without compromising the inter-unit cell coupling, we have coupled the dipole cavities with the split ring resonators [6]. The resonance response of the split ring resonator depends on the geometric parameters of the resonator and hence providing a suitable platform to tune the phase-matching condition.

2. Proposed structure

The metastructure for the present study is shown in Figures 1(a) and (b). Figure 1(a) depicts the terahertz interaction with the hybrid resonant cavity. Figure 1(b) shows the unit cell having periodicity (P) = 83 μm. The cavity length (l) is 40 μm and the split ring length (a) is 20 μm. The width (w) and the split gap (g) of the split ring resonator are 5 μm and 6 μm, respectively. The hybrid resonant cavity is made of aluminum and is fabricated on a highly resistive intrinsic silicon wafer. The metastructure is studied experimentally as well as numerically. Commercially available CST microwave studio under unit cell boundary conditions in x- and y-direction and open boundary conditions in the z-direction is used for the numerical calculation.

3. Results and discussion

In order to study the effect of near field coupling, we have studied the coupled as well as uncoupled dipole cavities. Figure 1(c) shows the transmission spectra for the uncoupled dipole cavity for the *y*-polarized incident radiation. Both the experimental and the numerical data are plotted and they are in good agreement. The uncoupled dipole cavity shows enhanced transmission (f = 1.048 THz) at phase matching conditions. Similarly, figure 1(d) shows the transmission spectra for the uncoupled split ring resonator showing a resonance dip around 1.12 THz. With the background of the behavior of the uncoupled structure, we further investigate the near field coupling of the dipole cavity and split ring resonator. Figure 1(e) shows the transmission spectra for the coupled hybrid resonant cavity. It is evident from the figure that coupling of the dipole cavity and SRR results in the excitation of a new resonant mode. The electric field distribution corresponding to these two peaks is shown in Figures 1(f) and (g). It is evident from the field distribution that the first peak (f = 1.048 THz) is excited due to the dipole cavity as the field is concentrated more into the cavity whereas the second peak (f = 1.08 THz) has more contribution from the split ring resonator and hence

this peak is excited due to the SRR. The resonance frequency of this new resonance mode depends upon the geometrical parameters of the split ring resonator. The amplitude transmission spectra for the coupled structure on different split gap values of the SRR are shown in figure 1(h). It is clear from the figure that there is a blue shift of the resonance on increasing the split gap of the SRR. This blue shift can be explained by the modification in the effective capacitance [7]. The effective capacitance of the SRR decreases on increasing the split gap and hence results in a resonance blue shift. Thus, the coupling with the split ring resonator provides another degree of freedom for phase engineering.

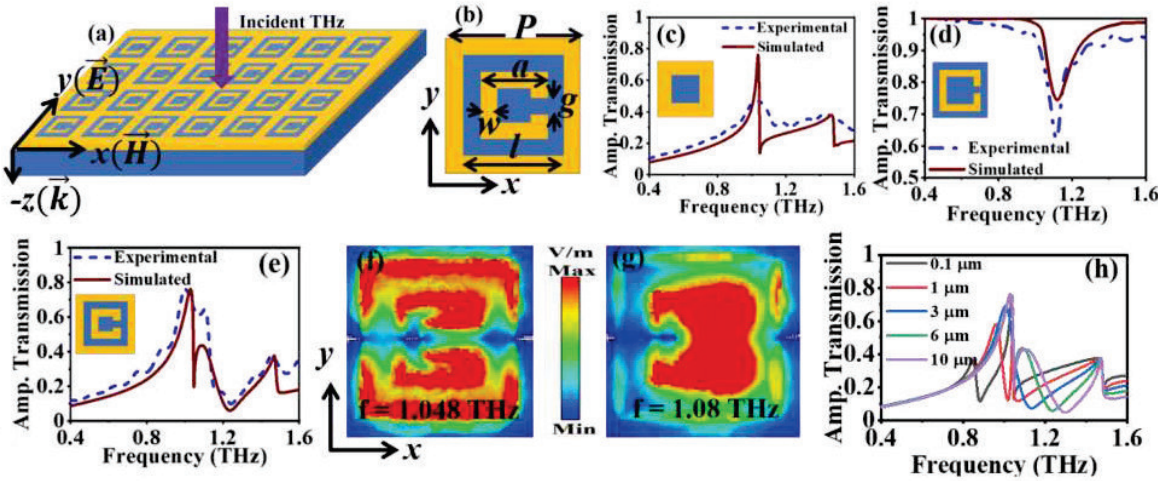

Fig. 1. (a) Schematic for the terahertz interaction with the proposed metastructure; (b) hybrid resonant cavity unit cell with periodicity (P)= 83 μm, length (l) = 40 μm, a = 20 μm, width (w) = 5 μm, and split gap (g) = 6 μm; Transmission spectra for (c) uncoupled dipole cavity, (d) uncoupled split ring resonator, and (e) coupled hybrid resonant cavity; electric filed distribution at (f) f = 1.048 THz, and (g) f = 1.08 THz; (h) Transmission spectra for varying split gap of the SRR.

4. Conclusion

In conclusion, we have demonstrated phase engineering through near-field coupling in dipole cavity and split ring resonator. Phase engineering is achieved in such a hybrid resonant cavity by varying the split gap of the split ring resonator and the resonance blue shift is observed on increasing the split gap. The proposed metastructure may have potential applications in effective phase engineering, sensing, frequency filtering, and communications-related fields.

5. References

[1] Yu, N., Genevet, P., Kats, M.A., Aieta, F., Tetienne, J.P., Capasso, F. and Gaburro, Z., "Light propagation with phase discontinuities: generalized laws of reflection and refraction" science, 334(6054), pp.333-337, 2011.

[2] Mueller, J.B., Rubin, N.A., Devlin, R.C., Groever, B. and Capasso, F., "Metasurface polarization optics: independent phase control of arbitrary orthogonal states of polarization" Physical Review Letters, 118(11), p.113901, 2017.

[3] Wang, Q., Rogers, E.T., Gholipour, B., Wang, C.M., Yuan, G., Teng, J. and Zheludev, N.I., "Optically reconfigurable metasurfaces and photonic devices based on phase change materials" Nature Photonics, 10(1), pp.60-65, 2016.

[4] Grady, N.K., Heyes, J.E., Chowdhury, D.R., Zeng, Y., Reiten, M.T., Azad, A.K., Taylor, A.J., Dalvit, D.A. and Chen, H.T., "Terahertz metamaterials for linear polarization conversion and anomalous refraction" Science, 340(6138), pp.1304-1307, 2013.

[5] Jiang, Y.W., Tzuang, L.D.C., Ye, Y.H., Wu, Y.T., Tsai, M.W., Chen, C.Y. and Lee, S.C., "Effect of Wood's anomalies on the profile of extraordinary transmission spectra through metal periodic arrays of rectangular subwavelength holes with different aspect ratio" Optics Express, 17(4), pp.2631-2637, 2009.

[6] Kaur, S., Karmakar, S., Jana, A., Rane, S., Varshney, R.K. and Chowdhury, D.R., "Hybrid resonant cavities: A route towards phase engineered THz metasurfaces" Iscience, 25(4), p.104024, 2022.

[7] Roy Chowdhury, D., Xu, N., Zhang, W. and Singh, R., "Resonance tuning due to Coulomb interaction in strong near-field coupled metamaterials" Journal of Applied Physics, 118(2), p.023104, 2015.

Generation of higher order array of vortices through in-line wavefront shaping using spatial light modulator

Allarakha Shikder and Naveen K. Nishchal*
Department of Physics, Indian Institute of Technology Patna, Bihta, Patna 801 106, Bihar, India
**nkn@iitp.ac.in*

Abstract: Array of vortices have gained remarkable attention in the field of optics because of its applications in different fields. This paper demonstrates a method to generate an array of higher order vortices using a spatial light modulator through in-line configuration. © Author(s)

Keywords: Optical vortex, Orbital angular momentum, Spatial light modulator

1. Introduction

Light beams having spiral phase front expressed by exp($il\varphi$) contain orbital angular momentum (OAM), where φ is the azimuthal angle and l is the helical mode index also referred to as topological charge (TC) [1]. Such beams have a phase singular point at the center of the beam known as vortex and the intensity at that point is zero. It is possible to make multiple vortices in the transverse plane of the beam by the proper modulation of phase. This type of beam is known as an optical vortex (OV) array or lattice [2,3]. Off late, the array of OVs has gained considerable attention because of its wide applications in metrology, micro-particle trapping and manipulation, optical encryption, etc. [3-6]. Therefore, the development of efficient technique for the generation of array of vortices is a vital topic in optics.

Many instruments and methods have been reported in literature for the generation of array of vortices such as the transformation of Laguerre-Gaussian modes [7], interferometric techniques [2], and diffractive optical elements [8]. Interferometric approaches need a complicated optical set-up as compared to diffractive optical elements. The spatial light modulator (SLM) is a digital diffractive optical element that can modulate the phase of the light beam transmitting or reflecting through it. SLMs can produce array of vortices in higher diffraction orders in an off-axis configuration with the help of a phase-only function of the array vortices and a phase carrier function. To further simplify the optical set-up, in this study, we demonstrate a method to generate an array of higher order vortices using in-line phase modulation with the help of an SLM. The SLM's phase response is calibrated to ensure a linear relationship between the gray level (within range 0 to 255) and the induced phase delay (from 0 to 2π). While obtaining CGH for this case no-additional grating phase function is used along with the phase distribution of the light beam.

2. Theory

Mathematically, an optical vortex can be expressed as,

$$U(\ell; x, y) = U_0(x, y)\exp(i\ell\phi) \tag{1}$$

where $A(x,y)$ is the intensity distribution in the transverse plane and ℓ is the TC. The phase value distribution (PVD) for an optical vortex is evaluated as,

$$P(\ell; x, y) = \mathrm{Im}[\log\{U(\ell; x, y)\}] \tag{2}$$

where 'Im' denotes the imaginary part of the complex function. Now the PVD for generating array of vortices can be achieved by appropriate distribution of the phase-only function of the single vortex. The PVD for generating array of vortices of m rows and m columns can be mathematically represented as,

$$PVD(x, y) = \begin{bmatrix} P(\ell_{11}) & P(\ell_{12}) & \cdots & P(\ell_{1m}) \\ P(\ell_{21}) & P(\ell_{22}) & \cdots & P(\ell_{2m}) \\ \vdots & \vdots & \ddots & \vdots \\ P(\ell_{m1}) & P(\ell_{m2}) & \cdots & P(\ell_{mm}) \end{bmatrix} \tag{3}$$

which contain $m \times m$ number of phase singular point.

3. Experimental Results

Figure 1(a) presents the schematic of the experimental set-up used for the generation of array of vortices in in-line phase modulation method. A phase-only SLM (Pluto Holoeye) is used for phase modulation having 1920 × 1080 pixels with a pixel pitch of 8.0 μm. A DPSS laser of 100 mW of wavelength 532 nm is used for the experiment which is polarized in the horizontal direction of the laboratory. The beam intensity in the traverse plane is recorded by a metal-oxide-semiconductor (CMOS) camera of 1280 × 1024 pixels with a pixel pitch of 5.2 μm. Figures 1(b) and (c) show the phase-only function and experimentally obtained intensity of the array of vortices of radial node 4 and helical mode index 1, respectively. Figures 2(a)-(c) show the phase-only function, experimentally obtained intensity, and interference patterns of the array of vortices of helical mode index 50, respectively.

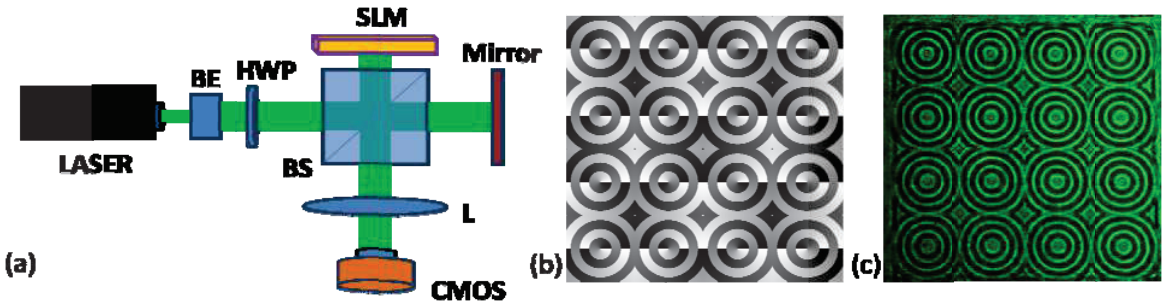

Fig. 1(a) Schematic of the experimental set-up. BE: beam expander, HWP: half-wave plate PBS: Beam splitter, L: lens. (b) Phase-only function of an array of vortex beam of radial mode index 4 and helical mode index 1. (c) Experimentally obtained intensity of an array of vortex beam of radial mode index 4 and helical mode index 1.

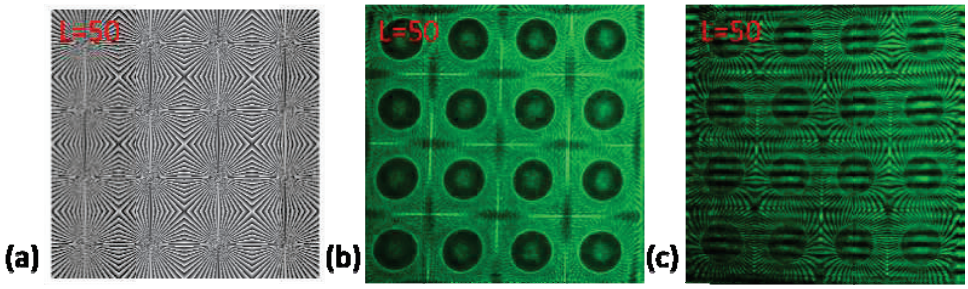

Fig. 2(a) Phase-only function of an array of vortices of l = 50. (b) experimentally obtained intensity of an array of vortices of l = 50, and (c) interference patterns of an array of vortices of l = 50.

4. Conclusion

Generation of an array of higher order vortices has been demonstrated using a phase modulation approach through in-line configuration. The approach simplifies the experimental set-up and is useful in the efficient generation of higher order array of vortices.

5. Acknowledgement

The authors acknowledge the support of the SERB, Department of Science and Technology, Government of India (CRG/2021/001763). Mr. Allarakha Shikder wishes to acknowledge the PMRF No. 701807.

6. REFERENCES

[1] *A. M. Yao and M. J. Padgett, "Orbital angular momentum: origins, behavior and applications," Adv. Opt. Photon. 3, 161-204 (2011).*
[2] *P. Kumar and N. K. Nishchal, "Array formation of optical vortices using in-line phase modulation," Opt. Commun. 493, 127020 (2021).*
[3] *X. Wang, Z. Nie, Y. Liang, J. Wang, T. Li, and B. Jia," Recent advances on optical vortex generation," Nanophotonics 7, 1533-1556 (2018).*
[4] *J. E. Curtis, B.A. Koss, and D. G. Grier, "Dynamic holographic optical tweezers," Opt. Commun. 207, 169-175 (2002).*
[5] *V. R. Daria, P.J. Rodrigo, and J. Glückstad, "Dynamic array of dark optical traps," Appl. Phys. Lett. 84, 323-325 (2004).*
[6] *P. Kumar, N. K. Nishchal, and A. AlFalou, "Controllable Optical vortex array for image encoding," IEEE Photon. Technol. Lett. 34, 521-524 (2022).*
[7] *Y. Gao, Z. Wen, J. Shan, L. Zhao, and L. Zheng, "Generation of the compound optical vortex array wave field," Optik 131, 41-48 (2017).*
[8] *R. Barboza, U. Bortolozzo, G. Assanto, E. Vidal-Henriquez, M. G. Clerc, and S. Residori, "Harnessing optical vortex lattices in nematic liquid crystals," Phys. Rev. Lett. 111, 093902 (2013).*

Use of electro-optic Pockels cell for generation of the product of two electronic biasing signals

Suranjan Lakshan *and Sourangshu Mukhopadhyay
Dept. of Physics, The University of Burdwan, Golapbag, Burdwan-713104, W.B.(India)
*laxmansur21@gmail.com

Abstract: Electro-optic Pockels cell are found very suitable for doing the analog operations among the multiple number of electronic biasing signals. Several all-optical operations are suggested to perform addition /substruction between the electronic biasing signals applied to the electro-optic Pockels cell. Here in this communication the Authors propose a new scheme of developing the product of two biasing signals by the active use of electro-optic Pockels cell.
Keywords: Electro-optic modulator (EOM), Amplitude modulation (AM), Potassium dihydrogen phosphate (KDP).

1. Introduction

High-speed communication with light is most advantageous in current days. Due to the photon as an intermediate particle for optical communication, there is very low chance of cross-talk. Overall, a lot of analog operations are done with the help of light as they support the parallelism. In this context it is told that Electro-optic modulators are an important device used as optical switch. Amplitude modulation and phase modulation can be done successfully with the help of electro-optic Pockels material. An electro-optic Pockels material changes its refractive indices in the presence of an induced electronic biasing signal. This birefringes property of the linear electro-optic crystals plays an important role in developing a phase difference between two components of an incident polarized light wave having two mutually orthogonal polarizations. Different analog operations are done with the help of the Pockels material at a very high-speed device with a small response time. Potassium dihydrogen phosphate (KDP) is the most commonly used Pockels material for its very fast switching as well as many other advantages. Different applications in optical communication, computation and data processing are found with the active use of the electro-optic modulator [1-7]. Researchers have already proposed different ideas on the basis of the different kinds of modulation with the help of an electro-optic modulator. Here in this paper, the authors propose a scheme, how one can do the product of two electronic biasing signals by proper use of electro-optic Pockels cells. The advantage of using light for conducting the product is fully utilized here.

2. Our Proposed Scheme

For the product of the two electronic signals, we used two KDP crystals successively in series. The geometrical configuration of the two KDP crystals is the same. Here, the two similar crystals are also biased by two different external biasing electronic signals. Initially, an unpolarized light wave is passing through a polarizer along the pass axis. The polarized light wave is also passing through an KDP material in the presence of an induced electronic signal. The modulated light beam is again passes through another KDP crystal with the same geometrical configuration, also biased by another electronic signal. Finally, it also passes through a polarizer, a photo-diode and also two selective filters for choosing two particular combinations of frequencies. These two frequencies are added or subtracted for doing the different analog operations. Here, we are only focused for conducting the product of two externally applied biasing signals.

3. The operation

An incident light wave with an electric field $E_0 e^{i\omega t}$is incident on a polarizer having a polarization axis in the x-y plane. Two Polarized light beams having two mutually perpendicular polarizations are now passing through a KDP crystal in presence of an external biasing voltages $V = V_a sin\omega_a t$. The emitted light beams from the output terminal are also passed through another KDP crystal connected in series having the same geometrical configuration but also biased by another external electronic signal $V = V_b sin\omega_b t$. Then the final output light beams again passes through an analyser. Thus, a modulated output light wave carries the information of the two electronic signals applied successively through the two KDP crystals. Thus, an amplitude modulation is obtained at the output of the second Pockels cell. Now the amplitude modulated light beam contains the different combinations of the frequencies. We also used a photo-diode to get the electric signal with two suitable angular frequencies in the proper choice of two active filters. Here, we are taking the frequency components $(\omega_a - \omega_b)$ and $(\omega_a + \omega_b)$. After that, by using the above frequencies are selected by filtering and adding them in proper way one can get product of two electronic biasing signal as an output directly.

4. Conclusion

An electro-optic Pockels material is a useful device as an optical switch. Different types modulations are successfully implemented by the active use of the Pockels material. Very high-speed operation is possible as photons are used as intermediate particles. As there is no crosstalk, different logical operations are performed smoothly with less error. Different types of analog operations are to be done on the order of the tbps range. As the speed of operation of the Pockels cell is beyond GHz rate, so one can conduct the multiplication scheme of two analog signal with a superfast speed. Again, proceeding in such a way one can conduct the product of three or higher numbers of analog electronic signals. This is the main advantage of the scheme.

5. Acknowledgement

One of the Authors acknowledge to the Govt. of West Bengal for the financial support.

6. References

[1] S. Lakshan, D. Saha and S. Mukhopadhyay, "Optical Scheme of Obtaining Highest Transmission Factor in Case of KDP Based Electro-Optic Crystal by the Adjustment of Suitable Biasing Voltage and Number of Feedback Passing", Journal of Optical Communication, https://doi.org/10.1515/joc-2019-0112(2019).
[2] S. Lakshan and S. Mukhopadhyay, "Pockels cells-based intensity modulation using multiple biasing signals on a single-carrier light beam", Journal of Optics (India) 51(2), pp. 283-288(2022)
[3] S. Lakshan and S. Mukhopadhyay, "An alternating approach of using multi-passing technique for development of massive phase difference between two orthogonal components of light in an electro-optic Pockels cell", Journal of Optics (India), DOI: 10.1007/s12596-022-00903-2(2022).
[4] S. Lakshan and S. Mukhopadhyay, "All-optical method for measuring the electrical parameters of passive electronic elements with active use of Pockels cells", Journal of Optics (India),DOI:10.1007/s12596-022-00858-4(2022).
[5] S. Lakshan and S. Mukhopadhyay, "Intensity and Voltage Controlled Phase Switching of Light by Joint Effort of Kerr and Pockels Material", Springer proceeding in Physics, 258, pp. 691-694(2021).
[6] A. Yariv and P. Yeh, "Photonics", New York: Oxford University Press, 2007.
[7] A. Ghatak and K. Thyagarajan, "Optical Electronics", New Delhi: Cambridge University Press, 1989.

Effect of Polaron in Electroabsorption Spectrum of PPDT2FBT: PCBM blend

Subhamoy Sahoo[1], Dhruvajyoti Barah[2], Soumya Dutta[2], Debdutta Ray[2], Jayeeta Bhattacharyya[1*]

1. *Department of Physics, Indian Institute of Technology Madras, Chennai 600036*
2. *Department of Electrical Engineering, Indian Institute of Technology Madras, Chennai 600036*

jayeeta@iitm.ac.in

Abstract: In organic solar cells, donor-acceptor blends are used as active layer for efficient carrier generation and collection. The generated carriers from polarons due to polarization of the surroundings. Polaron energy levels are located below the band edge of the semiconductors. Being a weak signature, it is generally not detected in absorption measurement. In this study, we used electroabsorption spectroscopy to calculate the polaron absorption in PPDT2FBT: PCBM blend. We estimated the order of polaron absorption in the blend from the EA spectrum at the first and second harmonic of the modulation frequency.

Keywords: Polaron, Electroabsorption, Blend, Organic Solar Cell

1. Introduction

In organic solar cells, the charge carriers are generated upon photoexcitation by various mechanisms from excitons [1]. While moving through the organic layer, the generated carriers distort the surroundings by polarization. The charge carrier moves with the distortion, called polaron since the residence time is more than the polarization time. The polarons are of two kinds, positive and negative polarons. The polarons are created in an organic blend after the creation of the charge transfer state at the donor-acceptor interface before dissociation as an intermediated step [1]. Polarons in an organic system can also be created by doping [2]. The energy levels of the polarons are located within the HOMO-LUMO gap. Therefore, polaron absorption, which is observed below the band edge energy, is generally very weak (a few orders less than the absorption in the visible region) to be detected by absorption spectroscopy in an undoped system. However, field modulation spectroscopy can be used to measure the polaron absorption due to its high sensitivity [3].

In this report, we used electroabsorption (EA) spectroscopy, where the change in the absorption coefficient of material in the presence of an externally applied field was measured to determine the polaron absorption in the PPDT2FBT: PCBM (1: 1) blend. PPDT2FBT, which is used as the active layer of the organic solar cell, has a band gap of 1.76 eV (~ 705 nm) [4]. The polaron absorption was obtained from the EA spectrum of the blend, measured at the first and second harmonic of the modulation frequency.

2. Experimental Details

A blend of PPDT2FBT and PCBM (1:1 weight %, 15 mg/ml) was prepared in dichlorobenzene solvent. The thin film of the blend was fabricated on a cleaned glass substrate by spin coating the solution at 1000 rpm, followed by thermal annealing at 130 ^{0}C for 10 minutes. The thickness of the film was 54 nm as obtained from spectroscopic ellipsometry. For EA measurement, the PPDT2FBT: PCBM film was fabricated on PEDOT: PSS coated patterned ITO-glass substrate followed by a semitransparent Al (~ 11 nm) deposition through a 2 mm shadow mask.

The EA measurement was done in transmission mode using an in-house assembled setup, where a relative change in transmittance ($\Delta T/T$) was measured. The details of the experimental setup are given elsewhere [4].

3. Results and Discussion

The pronounced peak of the EA spectrum of pristine PPDT2FBT near the band edge was at 680 nm, and the spectrum was extended to 730 nm [Fig. 1a]. In PPDT2FBT: PCBM blend, the EA spectrum had similar features at shorter wavelengths. However, the band around 680 nm was narrowed, and blue shifted compared to the pristine PPDT2FBT. Additionally, a dip was observed at 716 nm, and above 730 nm, a non-zero EA signal was obtained [Fig. 1a]. Since PCBM, which has maximum absorption in the UV region, did not show any significant EA signal in the visible and near-infrared regions, the new feature in the EA spectrum was not arising from PCBM. Some earlier reports suggested the presence of charge transfer (CT) states below the band edge in some of the organic blends [5]. The EA signal, arising due to the CT states, would vary linearly with the applied DC bias voltage while measured at the first harmonic of the modulation frequency. In contrast, we observed that the EA signal below the band edge decreased

while applying reverse bias. Whereas with forward bias, the EA signal increased. This confirmed that the EA signal below the band edge did not arise from the CT state in PPDT2FBT: PCBM blend. Therefore, the EA signature below the band edge can be assigned to be polaron absorption. Below 730 nm, the EA signal had contribution from both polaron absorption and the change in the absorption coefficient of the blend due to electric field. The second harmonic spectrum did not show any polaron signature since it depended only on AC bias (Fig. 1b). Hence, polaron absorption can be calculated from the EA spectrum at the first and second harmonic of the modulation frequency. EA signal at first harmonic with polaron contribution and second harmonic is given by

$$\left(\frac{\Delta T(\lambda)}{T(\lambda)}\right)_{1\omega} = \left(\frac{\pi d}{2}\right) \times [C(\lambda)|2F_{AC}F_{DC}| + P(\lambda)] \dots\dots\dots (1)$$

$$\left(\frac{\Delta T(\lambda)}{T(\lambda)}\right)_{2\omega} = \left(\frac{\pi d}{2}\right) \times \left[C(\lambda)\left|\frac{1}{2}F_{AC}^2\right|\right] \dots\dots\dots (2)$$

Where $C(\lambda)$, F_{AC}, F_{DC}, $P(\lambda)$ and d are a constant at wavelength λ, AC field, DC field, contribution of polaron absorption in EA signal and thickness of the device. Combining equation (1) and (2), we get

$$P(\lambda) = \left(\frac{2}{\pi d}\right) \times \left[\frac{\left(\frac{\Delta T(\lambda)}{T(\lambda)}\right)_{1\omega}}{|2F_{AC}F_{DC}|} - \frac{\left(\frac{\Delta T(\lambda)}{T(\lambda)}\right)_{2\omega}}{\left|\frac{1}{2}F_{AC}^2\right|}\right] \times |2F_{AC}F_{DC}| \dots\dots\dots (3)$$

The contribution of polaron absorption in EA is calculated using equation 3 (Fig. 1c). The strength of the absorption was found to be ~10^5 times less than the absorption associated with band gap.

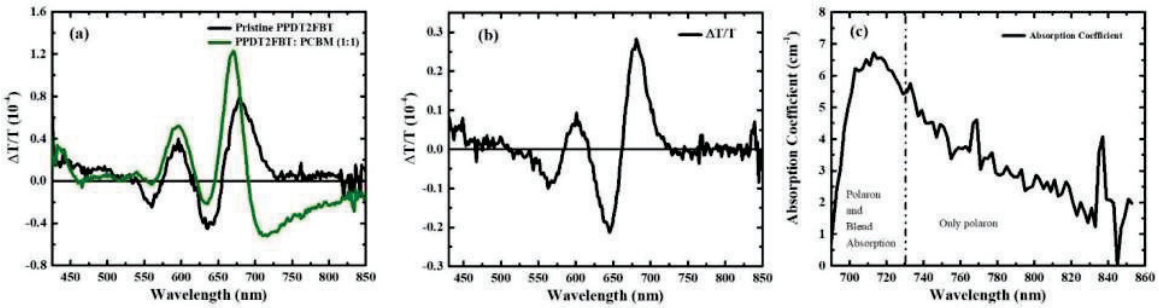

Fig. 1: (a) EA of pristine PPDT2FBT and PPDT2FBT: PCBM blend at first harmonic of modulation frequency at 0 V and 1 V DC and AC bias voltage, respectively (b) EA spectrum of PPDT2FBT: PCBM blend at second harmonic of modulation frequency at 2 V AC bias voltage, (c) polaron absorption spectrum below band edge.

4. Conclusion

We demonstrated that the EA signal of PPDT2FBT: PCBM blend at longer wavelength was arising from polaron absorption, and estimated its contribution in EA spectrum the blend. The blend showed polaron absorption under photoexcitation at 0 V DC bias. The EA signal above 730 nm was arising only from polaron absorption. The presence of polarons indicates the efficient dissociation of the carriers in the blend.

5. References

[1] Jens Niklas, Tianyue Zheng, Andriy Neshchadin, Kristy L. Mardis, Luping Yu, and Oleg G. Poluektov "Polaron and Exciton Delocalization in Oligomers of High-Performance Polymer PTB7," J. Am. Chem. Soc. **142,** 3, 1359–1366 (2020).

[2] Jun Yamamoto and Yukio Furukawa, "Electronic and Vibrational Spectra of Positive Polarons and Bipolarons in Regioregular Poly(3-hexylthiophene) Doped with Ferric Chloride," J. Phys. Chem. B, **119**, 13, 4788–4794 (2015)

[3] Naresh Chandrasekaran, Cheng Li, Shivam Singh, Anil Kumar, Christopher R. McNeill, Sven Huettner, and Dinesh Kabra, "*Role of Molecular and Interchain Ordering in the Formation of a δ-Hole-Transporting Layer in Organic Solar Cells,"* ACS Appl. Mater. Interfaces, **12**, 3806−3814 (2020).

[4] Subhamoy Sahoo, Dhruvajyoti Barah, Rajdeep Dhar, Soumya Dutta, Debdutta Ray, and Jayeeta Bhattacharyya " Investigation of nature of excitons in PPDT2FBT and effect of optical interference," J. Appl. Phys. **131**, 085702 (2022)

[5] Peng Wan, Xingtong Chen, Qi Liu, Sudhi Mahadevan, Mingxuan Guo, Jinjing Qiu, Xiaojuan Sun, Sai-Wing Tsang, Maojie Zhang, Yongfang Li, and Song Chen, " Direct Observation of the Charge Transfer States from a Non-Fullerene Organic Solar Cell with a Small Driving Force" J. Phys. Chem. Lett., **12**, 10595−10602 (2021)

Beam Waist Effect on Second Harmonic Generation Conversion Efficiency

Madhu, *Prashant Povel Dwivedi
Department of Electronics and Communication Engineering, Manipal University Jaipur, Jaipur 303 007, Rajasthan India
*ppovel28@gmail.com

Abstract: In this paper**,** we have analyzed the beam waist effect on second harmonic generation (SHG) at phase matching condition. From the simulation results (in 3-Dimension) we observed that, when increasing the beam waist of interacting beam with nonlinear crystal above the 60 µm the conversion efficiency of SHG dramatically increases at small crystal length as compare to below 60 µm beam waist.
Keywords: Beam Waist, Gaussian beam, Second-Harmonic Generation.

1. Introduction

The region along the propagation path where the beam radius is minimum, is known as the beam waist of a Gaussian beam. The determination of the waist location for the Gaussian beam was studied at the very beginning of the laser era, in the 1960s and 1970s of the last century. The key parameters of the Gaussian beam are the waist size, the waist location, and the beam divergence angle, especially the waist location and the waist size who can determine transmission characteristics of the Gaussian beam [1]. Gaussian beam is very important in various branch of physics; application include optics; radio wave etc. [2]. In ref [3, 4], several important issues related to the propagation and scattering of Gaussian beam have been solved. The SHG by quasi-phase-matching (QPM) is an attractive method to obtain compact and high power lasers emitting visible spectrum regions [5]. Here we are considering that the fundamental wave as Gaussian wave will be incident on a nonlinear crystal to generate a second harmonic wave, in this paper we compute SHG-intensity profile with Gaussian wave as fundamental wave, the parameters which we consider for our simulation analysis are converting 1560 nm laser light into 780 nm, having length 20 mm, effective nonlinear coefficient 3 *p*m/v.

2. Equations of SHG

For the process of second harmonic generation (SHG) . The well-known coupled-wave equations for SHG,

$$\frac{\partial A_2}{\partial z} = i\frac{\omega d_{eff}}{cn_2}A_1^2 e^{-i\Delta kz} \qquad \text{(Up-Conversion process)} \qquad (1)$$

$$\frac{\partial A_1}{\partial z} = i\frac{\omega d_{eff}}{cn_1}A_2 A_1^* e^{i\Delta kz} \qquad \text{(Down-Conversion process)} \qquad (2)$$

where A_1 and A_2 are the field amplitudes of the fundamental and second harmonic waves, respectively, d_{eff} is the nonlinear coefficient, n_1 and n_2 are the refractive indices of the fundamental and second harmonic waves respectively. $\Delta k = k_2 - 2k_1$ is wave vector mismatch and ω represents the angular frequency.

3. Results and discussion

We estimated SHG conversion efficiency of above equation (1) and (2) with the help of MATLAB programming. We found that when the beam waist of Gaussian beam having 60 µm incident on nonlinear crystal with a phase matching condition generate SHG about the 90% of energy conversion at 1.7 mm of crystal length as shown in fig.1 (b). when beam waist is having 110 µm as shown in fig. 2 (b) we get same energy conversion (90%) from fundamental wave to second harmonic wave starts at 0.5 mm of the crystal length. It means that increasing the beam waist size and decreasing the crystal length.

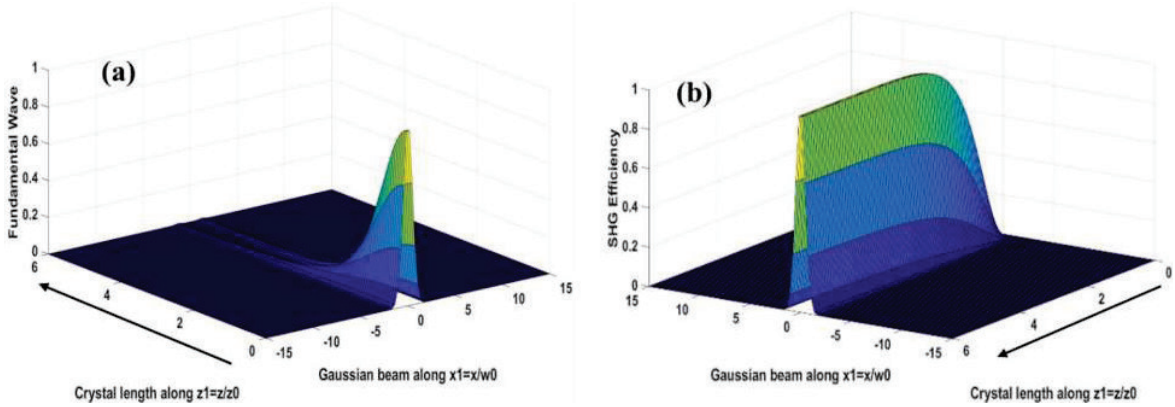

Fig. 1: Calculated SHG Conversion Efficiency from Eq. (1) and (2) at beam waist 60 µm

(a) Fundamental (b) SHG Wave

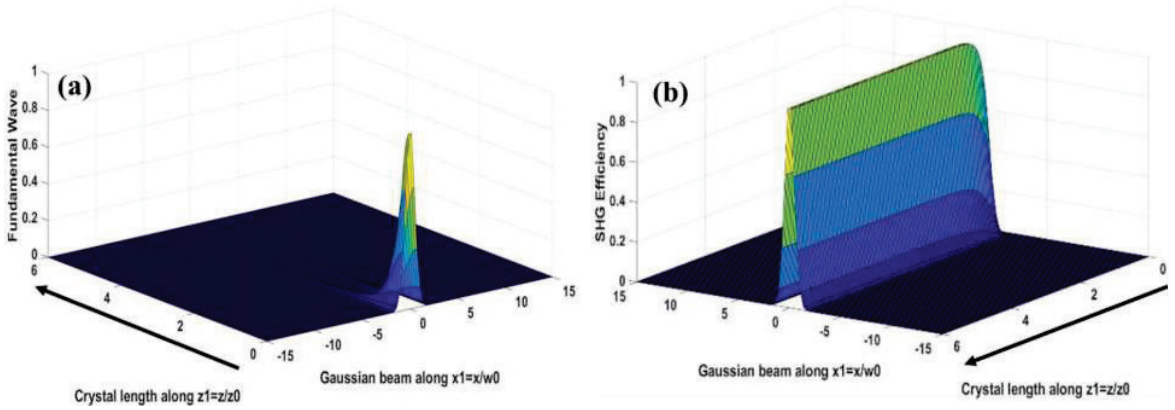

Fig. 2: Calculated SHG Conversion Efficiency from Eq. (1) and (2) at beam waist 110 µm

(a) Fundamental (b) SHG

4. Conclusion

The simulation results of the SHG efficiency vs normalized length of crystal vs Gaussian beam (3-Dimensional) are determined by using the concept of the coupled wave equation of SHG. When the beam waist increases from 60 to 110 µm it means the cross sectional area of beam increases inside the crystal, that's the reason for improving the SHG conversion efficiency at smaller crystal length as compare to the 60 µm.

5. References

[1] Jianhua Zeng, Shanyu Du, Zhiwen Sang, Shan Chang, Penghao He, and Qiu Tu, "Determination of the waist location for the Gaussian beam based on second harmonic generation of monolayer MoS2," IOP Conf. Series: Materials Science and Engineering 490 (2019) 022059.
[2] Vlastislav Cerveny, "Expansion of plane Wave into Gaussian Beam," Studia geoph. et geod. Special issue (2002), 43-54.
[3] L. B. Felsen: Complex-Source-Point Solution of the Field Equation and their Relation to the Propagation and Scattering of Gaussian beams. Ist. Naz. di Alta Matem., Sympos.
[4] L. B. Felsen, N. Marcuvitz: Radiation and Scattering of wave. Prentice-Hall, Englewood Clifffs, N. J. 1973.
[5] Tetsuro Mizushima, Hiroyuki Furuya, Shinichi Shikii, Koichi Kusukame, Kiminori Mizuuchi, and Kazuhisa Yamamoto "Second Harmonic Generation with High Conversion Efficiency and Wide Temperature Tolerance by Multi-Pass Scheme," Applied Physics Express 1 (2008) 032003.

Towards a Single Photon Source Based on a Cavity QED Platform for the Development of Scalable Quantum Networks

Abhijit Kundu[1], Sumit Achar[1], Rashtrapriya Kumar Kapri[1] & Arijit Sharma[1,2]

[1]*Department of Physics, Indian Institute of Technology Tirupati, Yerpedu-517619, Andhra Pradesh, India*

[2]*Center for Atomic, Molecular, and Optical Sciences and Technologies, Indian Institute of Technology Tirupati, Yerpedu-517619, Andhra Pradesh, India*

Author e-mail address: ph21d501@iittp.ac.in, ph21d502@iittp.ac.in, rp.kapri@iittp.ac.in, arijit@iittp.ac.in

Abstract: The development of secure communication protocols and technologies holds the key for a secure communication network. Such a network may be realized through the development of quantum networks leading to the quantum internet [1]. In this aspect, the development of networked quantum repeaters or quantum memories is of extreme importance. Such entities shall act as futuristic quantum nodes and enable the storage or creation of information in the form of single photons. In our group, we are working towards the development of a cavity qed-based node using a trapped calcium ion ($^{40}Ca^{+}$) inside a high finesse cavity [2].

Keywords: Quantum network, Cavity QED, Qubit, High Finesse Cavity, Single Photon.

1. Introduction

Classical communication networks suffer from inherent insecurities due to hacking, eavesdropping, spoofing, etc. There have been ongoing efforts to develop secure quantum networks through inter-connected quantum nodes using the principles of superposition, entanglement, and the no-cloning theorem in quantum mechanics. Such networked quantum nodes shall pave the way for secure, long-distance quantum communication and the realization of a quantum internet. Some of the key issues plaguing the practical realization of quantum computers and the development of a robust quantum information network is scalability, long distance entanglement, minimizing decoherence, reducing bit error rate, low cost and operation at ambient (non-cryogenic) temperatures [3]. Till date, the most versatile technologies that have made a critical impact in the development of quantum information processing nodes, are either solid state-based devices such as SQUIDS (super-conducting quantum interference devices), or atomic platforms based on trapped cooled atoms and ions.

Although the quantum nodes of such identical quantum networks communicate (quantum state transfer) with each other via single photons, there is still a major debate over which platform is the best since each has its own merits and demerits. The development of hybrid quantum networks [Figure 1] has thus been a new pathway that aims to combine the best of both worlds: easy storage and rapid readout of qubits.

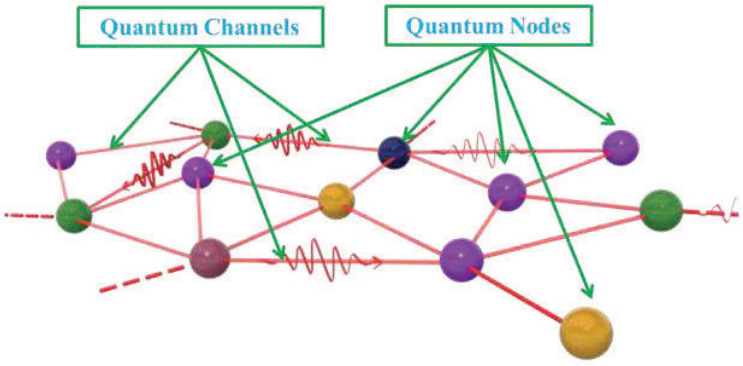

Fig. 1: Quantum network with different quantum nodes connected by quantum channel.

Central to the idea of developing a quantum network is the deterministic generation of single photons with high fidelity [4]. Single photon sources are in huge demand globally due to the following key applications:

- Quantum key distribution – multiple photons in a pulse is not desirable for QKD
- Quantum metrology – low noise light source ensures sensitive optical measurements
- Quantum computing with photons – use photons as "flying" qubits

Despite the fact that each platform has its own distinct benefits and drawbacks, a cavity-based strategy, such as a trapped ion or atom inside an optical cavity [Figure 2], appears to be promising as a deterministic single-photon source due to its long decoherence time and high likelihood of interaction with a single mode electromagnetic field. In addition, a cavity QED (cqed) platform also enables the study of other fundamental aspects of quantum information science, from the basics of initialisation, manipulation, and readout up to advanced algorithms like teleportation, quantum memory and quantum repeaters [5].

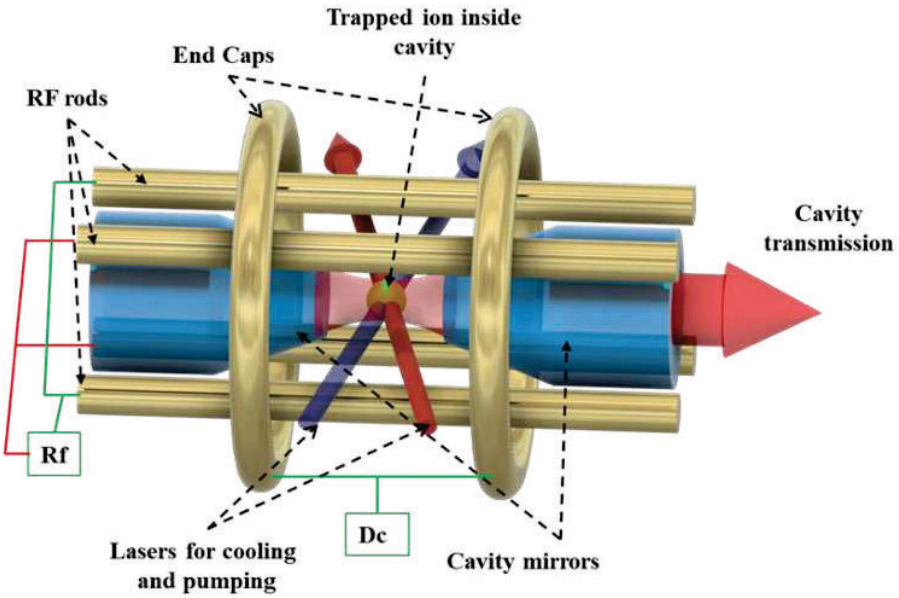

Fig. 2: Structure of cavity QED based quantum node with trapped ion.

In this paper we shall present our ongoing efforts towards the the development of a trapped ion cavity qed system for realizing an on-demand single photon generation scheme suitable for use as a quantum node in an extended scalable quantum network. We shall also highlight and discuss the ongoing efforts in our group towards the development of indigenous quantum technology for use in quantum communication schemes.

We acknowledge financial support from CAMOST and IIT Tirupati. R. K. Kapri gratefully acknowledges financial support from the I-Hub Quantum Technology Foundation, IISER Pune through the Chanakya Postdoctoral Fellowship. S. Achar gratefully acknowledges financial support from CSIR (GoI) through a Junior Research Fellowship (JRF). The authors acknowledge stimulating discussions with other scientists during the TAMIONS II Discussion Meeting supported and hosted by the International Center for Theoretical Sciences (ICTS) on 9-13 May 2022.

References

[1] H. J. Kimble, "The quantum internet," Nature **453**, 1023-1030 (2008).
[2] K. Heshami, D. G. England, P. J. Bustard, V. M. Acosta, J. Nunn & B. J. Sussman, "Quantum memories: emerging applications and recent advances," Journal of Modern Optics, **63**, 2005-2028 (2016).
[3] S. H. Wei, B. Jing, X. Y. Zhang, J. Y. Liao, C. Z. Yuan, Bo-Yu Fan, et.al, "Towards Real-World Quantum Networks: A Review," Laser Photonics Review **16**, 21002191-21002229 (2022).
[4] A. Kuhn, M. Hennrich, & G. Rempe, "Deterministic Single-Photon Source for Distributed Quantum Networking," Physical Review Letters 89, 067901-067905 (2002).
[5]H. J. Kimble, "Strong interactions of single atoms and photons in cavity QED," Physica Scripta **1998**, 127-137 (1998).

PDMS coated Fiber optic Tip sensor for Temperature measurement

Maya Chauhan [(1)] and Vinod K. Singh [(2)]
Optical Fiber Laboratory
Department of Physics, Indian Institute of Technology (ISM) Dhanbad
Author e-mail address: [(1)]maya.18dr0077@ap.iitism.ac.in, [(2)]vksingh@iitism.ac.in

Abstract: An intensity-modulated no-core fiber (NCF) based temperature sensor is experimentally demonstrated here. The sensor configuration consists of a section of NCF with a silver mirror coated tip and is covered with a temperature-sensitive PDMS layer. The sensitivity was found 0.056 dB/^{0}C for temperature range 25- 55 ^{0}C with excellent linear response and good reversibility behavior.
Keywords: Intensity modulation, NCF, PDMS, Temperature sensor, Sensitivity

1. Introduction

The temperature is an important parameter related to chemical and physical characteristics of the materials and devices. The measurement and control of temperature level is essential in environmental monitoring, medical diagnosis, manufacturing industries, and defense systems [1]. Optical fiber-based temperature sensor exhibits a set of advantages such as cheap cost, compact size, high sensitivity, quick response, immunity to light interference, and remote sensing capability [2]. It is influential in developing temperature sensors by merely coating the sensing region with a temperature-sensitive material having a high thermo-optic coefficient (TOC), when material undergoes significant temperature variation, subsequently the refractive index (RI) of the material/region changes [3]. PDMS (Polydimethylsiloxane) is an elastomeric polymer that is an inert, optically clear, non-flammable and non-toxic polymer that belongs to the silicone group. This material can adopt any shape with various molds due tohigh Poisson ratio and low elastic modulus [4]. It has many advantages, such as chemical resistance, transparency,biocompatibility, and ease of fabrication. The PDMS has a high thermal expansion coefficient (TEC) and a largeTOC, so that with the increase in degree of temperature, the PDMS RI decreases [5].

2. Sensor preparation

A cleanly cleaved 10 mm NCF sensing head was spliced with 2x1 FC/PC fiber optic coupler of the same diameter using fusion splicer in order to fabricate the sensor. The silver mirror is deposited over the free end of NCF to get back the proper reflection of light for significant output power detection after interaction with the sensing medium. The sensor head was coated with PDMS polymer via the dip-coating method [4], then it was baked at 80 ^{0}C for two hours before sensor characterization to make the coating robust. Fig. 1 depicts the schematic diagram and FESEM images of the fabricated sensor head. The experimental setup consists of a laser light source operating at wavelength 1310 nm, the prepared sensor witha 2x1 fiber coupler, and a power meter. Coupler sends and receives light signals as both the entry and exit paths are same, where one arm sends the input signal, and another component directs the back-reflected light from the sensor head to the power meter. The sensing region was dipped into deionized water to examine the sensor performance,whose temperature was monitored by a magnetic hot plate; then, the modified output powers were recorded after every five ^{0}C successive variations in the temperature.

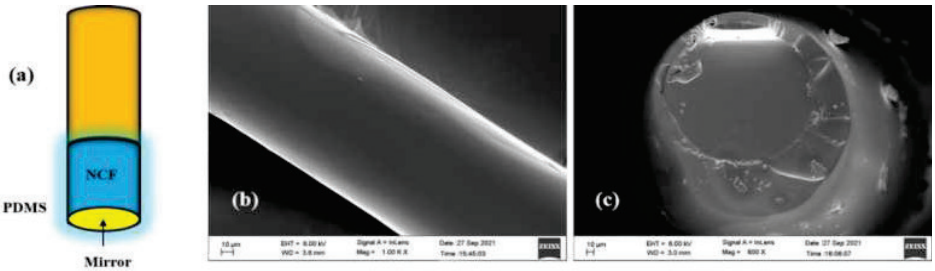

Fig. 1: (a) Probe schematic, FESEM images of PDMS coated (b) NCF, (c) Tip cross-sectional view.

3. Results and discussion

The light launched from coupler propagates through the NCF, where light leakage occurs and the evanescent field of light interacts with the surrounding medium. Spread light suffers back reflection from mirror coated at NCF tip and then couples back into the fiber coupler, hence propagating light interacts twice with the sensing medium and finally reaches the receiving end. The output power subsequently modifies according to the change in RI of the PDMS layer surrounding the sensing head. Due to high TEC and TOC of the PDMS layer, the RI will decrease with an increase in temperature, and the dimension of the PDMS layer will expand [3,5]. Hence, we got increasing nature of power with an increase in the surrounding temperature as the response clearly shown in Fig. 2(a).

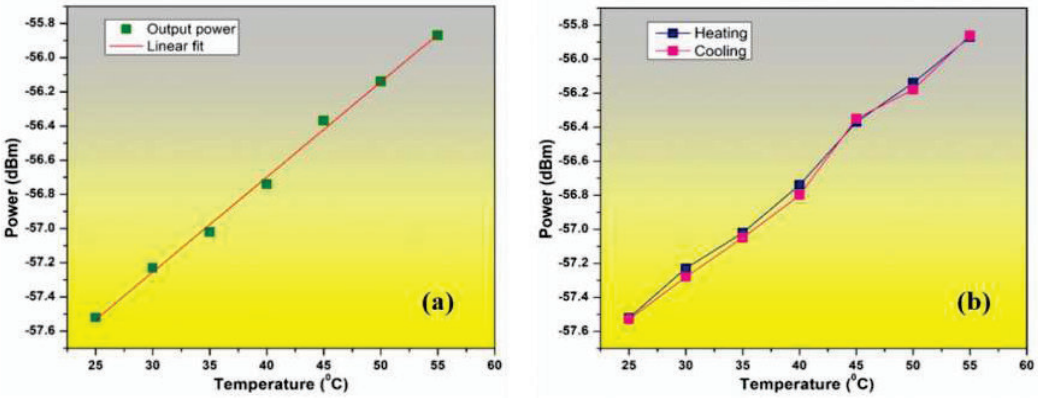

Fig. 2: Response plot of the fabricated sensor (a) sensitivity and (b) reversibility.

The linear regression equation of the response plot can be written as

$$P\,(dBm) = \ 0.056 \times T\ - 58.92 \qquad (1)$$

where, P is the output power in dBm, T is temperature in ^{0}C, and the slope gives the sensitivity of the fabricated sensor. The reverse sensing characteristic is also fundamental in temperature sensing, which also manifests the hysteresis behavior of the sensor. Fig. 2(b) shows the reversibility plot, which was measured in the sensing medium's increasing and decreasing temperature sequence. The hysteresis % can be calculated by the equation given below, we got 0.04 % hysteresis loss for the fabricated sensor, which is quite acceptable. Hence, the temperature measurement can be greatly performed reversibly in either ascending or descending order of operation.

$$\text{Hysteresis } \% = \left|\frac{Y_{md} - Y_{ma}}{Y_{max} - Y_{min}}\right| \qquad (2)$$

where $Y_{md,}$ $Y_{ma,}$ Y_{max} and Y_{min} are the middle point value of reversibility curve for descending, ascending order and maximum, minimum value of power at the curve, respectively.

4. Conclusion

We have successfully fabricated and demonstrated a robust fiber optic temperature sensor based on a sensitive outer coating layer. The sensing principle is depended on swelling/shrinkage characteristics of the PDMS layer with an increase/decrease of the temperature state, which results in alteration of RI of the outer medium. The excellent sensitivity with good reversibility behavior and considerable hysteresis loss were found. Proposed sensor owns compact size, high sensitivity, and possesses easy alignment due to reflection mode operation, which makes it useful for temperature control in the microenvironments.

5. References

[1] Liu C, Wang F, Lv J, Sun T, Liu Q, Fu C, Mu H and Chu P K 2016 A highly temperature-sensitive photonic crystal fiber based on surface plasmon resonance Gold film *Opt. Commun.* **359** 378–82

[2] Chauhan M and Singh V K 2022 ZnO coated evanescent field based fiber optic fuel adulteration sensor *Work. Recent Adv. Photonics*

[3] Wang Z, Chen D L, Yang X C, Liang S X and Sun X H 2022 Temperature sensor of single-mode-no-core-single-mode fiber structure coated with PDMS *Opt. Fiber Technol.* **68** 102793

[4] Chauhan M, Khanikar T and Singh V K 2022 PDMS coated fiber optic sensor for efficient detection of fuel adulteration *Appl. Phys. B Lasers Opt.* **128** 1–9

[5] Wang Q, Du C, Zhang J, Lv R and Zhao Y 2016 Sensitivity-enhanced temperature sensor based on PDMS-coated long period fiber grating *Opt. Commun.* **377** 89–93

Study of Different Stages of Wound Healing in Mice Skin by Terahertz Time Domain Spectroscopy

Rajat Kumar[1, a], Ayan Gope[2, b], Shubhadeep Mondal[2, a], Sayan Prodhan[2, a], Anurup Mukhopadhyay[2, c], Debnath Das[2, c], Subhamoy Mandal[c], Prasanta Kumar Datta[*, a]

[a]Department of Physics, Indian Institute of Technology Kharagpur, Kharagpur, West Bengal-721302, India

[c]Advanced Technology Development Center, Indian Institute of Technology Kharagpur, Kharagpur, West Bengal-721302, India

[c]School of Medical Science and Technology, Indian Institute of Technology Kharagpur, Kharagpur, West Bengal-721302, India

**Corresponding Author Email: pkdatta@phy.iitkgp.ac.in,*

Abstract: The current study involves exposure of mice skin to Terahertz Time Domain Spectroscopy (THz-TDS) system to mark the difference in absorption spectra before inflicting a wound and post-healing skin. The absorption spectra of normal and wound-healed skin have been measured in 0.5-3 THz. We have marked different refractive indices and absorption spectra of normal and healed skin. In addition, the absorption spectra of obtained from the above said tissues were corroborated with gold standard Hematoxylin and Eosin as well as Van Gieson's Stain and observed under a bright field microscope to establish structural and compositional differences.

Keywords: Terahertz, Wound Healing, Absorption spectra

1. **Introduction:** Healing of wounds is a complex procedure involving four distinct stages- homeostasis, inflammation, proliferation, and remodeling. Each of these phases is characterized by overlapping involvement of a wide variety of cells, growth factors, and cellular and molecular mechanisms. [1]. The evaluation of wounds through the use of non-invasive techniques is important and can aid in the diagnosis, and monitoring response to treatment, especially in the case of non-healing and chronic wounds. Several techniques and devices have been in profound use by researchers and medical professionals for evaluating different stages of healing such as Laser Doppler Flowmetry, Optical Coherence Tomography, Laser Microscopy, etc. We tend to explore a new horizon in this field by using Terahertz spectroscopy for diagnostic and monitoring applications of wound healing progression [2]. The terahertz range corresponds to 0.1 to 10 THz in the electromagnetic spectrum. THz radiation is biologically safe and has been shown to have strong absorption with water content in tissues. The water content of biological tissues varies distinctly, so their terahertz signatures are also different [3]. The high sensitivity to water makes terahertz radiation a potential interest in the medical field as it can be used to detect delicate changes in tissue composition and wound healing. [4]

2. **Sample Preparation and Experimental Methodology:** A full-thickness dorsal cutaneous wound of 1cm diameter was inflicted in mice and was allowed to heal without any external intervention. After 21 days, tissue was biopsied from the same wounded region and both, the initial skin collected on day 0 and on day 21 were subjected to THz spectroscopy. These tissues were later dehydrated, and embedded in paraffin, 5-micron sections from these tissues were stained using H&E as well as using VG stain and observed under a bright field microscope to elucidate structural and compositional differences between normal and healed tissue sections, which were later corroborated against obtained THz absorbances. A mode-locked Ti:Sapphire laser amplifier (Coherent Libra) of pulse duration 50fs, having a repetition rate of 1 kHz at a central wavelength of 800 nm was used to generate and detect the THz radiation. For generation and detection, two identical <110> plane cut ZnTe crystals of thickness 0.5 mm were used. The THz signal was generated by optical rectification and detected by the electro-optic sampling method. The detailed setup of Terahertz Time Domain Spectroscopy (THz-TDS) can be found in the literature [5].

3. **Preliminary Results.** For the initial establishment of Terahertz spectroscopy as a diagnostic tool for wound healing, it seemed important to consolidate the absorbance spectrum of the tissues obtained from THz against existing gold standard methods. The time domain data of the samples were obtained. The frequency domain data was obtained from FFT data of time domain data.

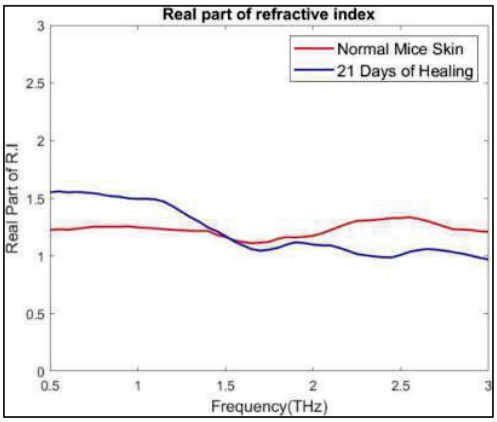

(a)

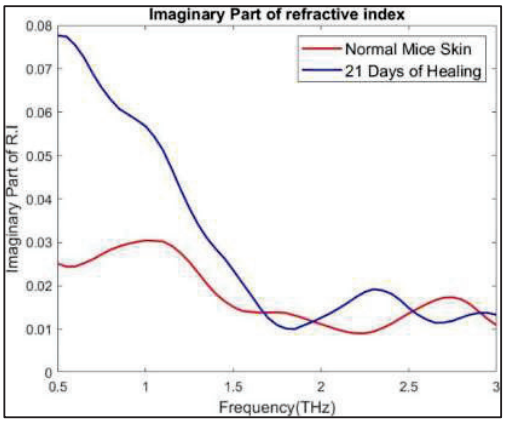

(b)

Figure (a) and (b) represents the real and imaginary part of the refractive index of normal mice skin and healed mice skin

From FFT data we computed the real and imaginary parts of the refractive indices and absorption coefficients of samples from equations that can be found in the literature [6]. We have reported the different refractive indices of Normal skin and Healed skin due to different absorbance of THz radiation which may be due to different deposition of different cell tissue and collagen protein in normal and healed mice skin.

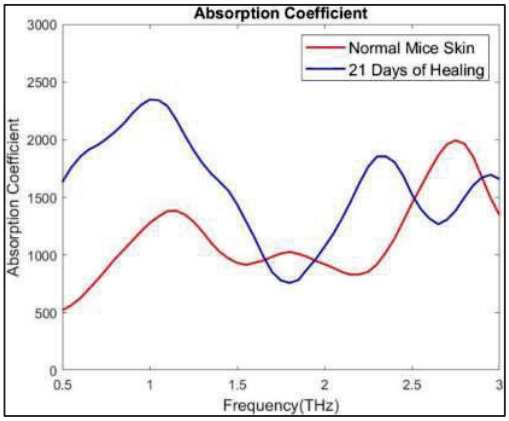

(c)

Figure (c) represents the real and imaginary part of the refractive index of normal mice skin and healed mice skin respectively

To establish the above observation the comparison of absorption spectra of mice skins with Hematoxylin and Eosin as well as Van Gieson's Stain is still undergoing.

4. References

[1]. Gonzalez, A. C. D. O., Costa, T. F., Andrade, Z. D. A., & Medrado, A. R. A. P. (2016). Wound healing-A literature review. *Anais brasileiros de dermatologia*, *91*, 614-620.

[2]. Ud-Din, S., & Bayat, A. (2016). Non-invasive objective devices for monitoring the inflammatory, proliferative and remodelling phases of cutaneous wound healing and skin scarring. *Experimental Dermatology*, *25*(8), 579-585.

[3]. Deka, G., Chu, S. W., & Kao, F. J. (2016). Skin wound healing revealed by multimodal optical microscopies. *Microscopy and Analysis*, *16*(10.5772), 64088.

[4]. Peng, Y., Shi, C., Wu, X., Zhu, Y., & Zhuang, S. (2020). Terahertz imaging and spectroscopy in cancer diagnostics: a technical review. *BME Frontiers*, *2020*.

[5]. Sindhu, P. S., Prasad, D., Peli, S., Mitra, N., & Datta, P. K. (2019). Terahertz spectroscopy of diglycidylether of bisphenol A: Experimental investigations and density functional theory based simulations. *Journal of Molecular Structure*, *1184*, 114-122.

[6]. Das, A. C., Bhattacharya, S., Jewariya, M., Prabhu, S. S., Mandal, K. C., Ozaki, T., & Datta, P. K. (2017). Identification of combination phonon modes in pure and doped GaSe crystals by THz spectroscopy. *IEEE Journal of Selected Topics in Quantum Electronics*, *23*(4), 1-7.

Nonlinearity-Dependence on Nonreciprocal Light Transmission Around Two Conjugate Exceptional Points

Arnab Laha,[1] R. K. Varshney,[1] Somnath Ghosh[2, *]

[1] *Department of Physics, Indian Institute of Technology Delhi, New Delhi-110016, India*
[2] *Department of Physics, Indian Institute of Technology Jodhpur, Rajasthan-342037, India*
*Author e-mail address: *somiit@rediffmail.com*

Abstract: We report the occurrence of two conjugate EPs in two time-symmetric variants of a gain-loss assisted planar waveguide with local Kerr-type nonlinearity, which exhibits nonreciprocal light transmission enriched with asymmetric switching of modes. The explicit dependence of nonlinearity-level on the nonreciprocal ratio for both the waveguide variants is reported.

Keywords: Exceptional Points, Gain-loss, Waveguide, Nonreciprocity, Nonlinearity, Open Systems

1. Introduction

The non-Hermitian Hamiltonian of an open system exhibits some spectral singularities as topological defects, which are called Exceptional Points (EPs). The occurrence of an EP in the system's parameter plane yields the simultaneous coalescence of corresponding coupled eigenvalues and the eigenvectors [1]. Lately, the gain-loss engineering in different photonic systems has presented EPs as nontrivial tools to control light-matter interactions that have facilitated a range of enticing applications such as lasing and antilasing, asymmetric mode-switching, achieving extreme sensitivity and giant-nonreciprocity [1-4]. A dynamic variation of gain-loss enclosing an EP allows the asymmetric transfer of modes, which results in the conversion of light into a particular dominating mode based on device chirality (in the sense of propagation direction). EP-induced relative-gain factors play a key role in transferring two different modes in two opposite directions (for a two-port device) [2-4]. Here, the reciprocity in such an EP-induced bidirectional light guidance mechanism can be broken with the onset of nonlinearity. Upon enabling the nonreciprocity at a certain nonlinearity threshold, the device can transmit a selective mode in a particular direction with a high nonreciprocal ratio; however, it blocks light in the opposite direction [3]. Now, the notion of conjugate EPs can be conceived by considering a Hamiltonian $H(\delta)$, where the presence of an EP can be realized based on the complex parameter $\delta = u + iv$. Here, two scenarios based on $v < 0$ and $v > 0$ analytically define two correlative time (T)-symmetric variants of $H(\delta)$ [provided that $T: \{i, t, x\} \rightarrow \{-i, -t, x\}$]. Such two T-symmetric variants exhibit two conjugate EPs at two complex conjugate critical points $\delta_c = u_c + iv_c$ and $\delta_c^* = u_c - iv_c$ (say EP and EP*, respectively) in their respective parameter spaces [2]. This paper investigates the nonreciprocal light transmission around two conjugate EPs in two complementary nonlinear waveguide variants based on T-symmetric gain-loss (active) profiles. With the onset of local Kerr-type nonlinearity, the correlative nonreciprocal response of two waveguide variants in terms of asymmetric transfer of modes is analyzed, where the explicit dependence of isolation ratios on nonlinearity level is reported.

2. Results and Discussions

We design a planar step-indexed waveguide distributed in xy-plane within $-w/2 \le x \le w/2$ and $0 \le z \le l$ (x and z define transverse and propagation axes along width and length, respectively), where the refractive indices of core (n_1) and cladding (n_2) are considered as $n_1 = 1.5$ and $n_2 = 1.46$. Here, w and l are chosen in terms of wavelength λ associated with a normalized wave vector, where $w = 20\lambda/\pi$ and $l = (5\lambda/\pi) \times 10^3$. The chosen operating conditions allow the guidance of only the passive fundamental and first-higher-order modes (say, ψ_1 and ψ_2). Now, with the onset of non-Hermiticity in terms of a customized gain-loss profile, two T-symmetric variants (say, WG_1 and WG_2) of the designed waveguide [as shown in Fig. 1(a)] can be represented by the complex index profiles

$$n(x)|_{\text{for WG}_1} = \begin{cases} n_1 - i\gamma, & -w/6 \le x \le 0 \\ n_1 + i\tau\gamma, & 0 \le x \le w/6 \\ n_2 + i\gamma, & w/6 \le |x| \le w/2 \end{cases} \quad \text{and} \quad n(x)|_{\text{for WG}_2} = \begin{cases} n_1 + i\gamma, & -w/6 \le x \le 0 \\ n_1 - i\tau\gamma, & 0 \le x \le w/6 \\ n_2 - i\gamma, & w/6 \le |x| \le w/2 \end{cases} \tag{1}$$

Under T-symmetry, WG_1 and WG_2 maintain two perfectly opposite active profiles along x-axis throughout the operation. Now, we investigate the trajectories of complex β_1 and β_2 (propagation constants of ψ_1 and ψ_2, respectively) for an increasing γ at different chosen τ-values. For an optimized $\tau = 3.161$, we observe the coalescence of β_1 and β_2 in Fig. 1(b) at $\gamma = 0.0082$ for both the variants, which refers to the occurrence of two EPs at $(0.0082, 3.161)$ in the (γ, τ)-plane. Based on Im(β)-axis, these two EPs (distinguishable by the reddish plane) can be called conjugate EPs [as shown by EP and EP*]. We judiciously consider a specific length-dependent gain-loss distribution to implement a closed dynamical encirclement around EP and EP* in the parameter spaces

of WG_1 and WG_2. Owing to the quantum-optical analogy $t \equiv l$, a particular encirclement direction around EP and EP* can be realized by considering light propagation in two opposite directions through WG_1 and WG_2.

Now, we investigate the propagation of ψ_1 and ψ_2 through WG_1 and WG_2 in the presence of intensity (I)-dependent local Kerr-type nonlinearity given by $\Delta n_{NL}(x,z) = n_2 I$. A chosen nonlinearity level is quantified as $(\Delta n_{NL}/\Delta n) \times 100\%$ with $\Delta n = (n_1 - n_2)$. In Figs. 1(c) and (d), the modal propagations around EP and EP* in WG_1 and WG_2 (separately) are shown for a chosen 6.75% local nonlinearity. We interestingly observe a correlation that two T-symmetric WG_1 and WG_2 are passing light in opposite active directions. Here, the dynamically encircled EP and EP* result in the asymmetric conversions $\{\psi_1, \psi_2\} \rightarrow \psi_2$ and $\{\psi_1, \psi_2\} \rightarrow \psi_1$ in WG_1 (active along $z = 0 \rightarrow l$) and WG_2 (active along $z = l \rightarrow 0$), respectively. The normalized input intensities of ψ_1 and ψ_2 are shown in Fig. 1(e), where Fig. 1(f) shows the relative output intensities for WG_1, while considering the propagation in both active ($z = 0 \rightarrow l$) and inactive ($z = l \rightarrow 0$) directions, separately (relative in terms of normalized output in the active direction). Here, we observe $\approx 98.6\%$ reduction of output intensity at $z = 0$ in comparison to the intensity at $z = L$. Similarly, $\approx 93.3\%$ intensity reduction can be observed for WG_2 in Fig. 1(g), while comparing the outputs during propagations in inactive ($z = 0 \rightarrow l$) and active ($z = l \rightarrow 0$) directions. Hence, WG_1 and WG_2 allow the nonreciprocal transmission of ψ_2 and ψ_1 in two opposite directions. We analyze the asymmetric scattering (S) matrices for different nonlinearity levels (from 2% to 8.5%) and calculate the nonreciprocal ratios (NR) as $10\log_{10}(T_a/T_i)$ (T_a and T_i are the transmissions in active and inactive directions; as obtained from associated S-matrices). Fig. 1(h) shows the dependence of nonlinearity levels on NRs for both the variants, where a maximum of ~18.6 dB and ~11.75 dB NRs are achieved for WG_1 and WG_2, respectively, at the same 6.75% nonlinearity [hence, chosen to show the propagations in Figs. 1(c, d)].

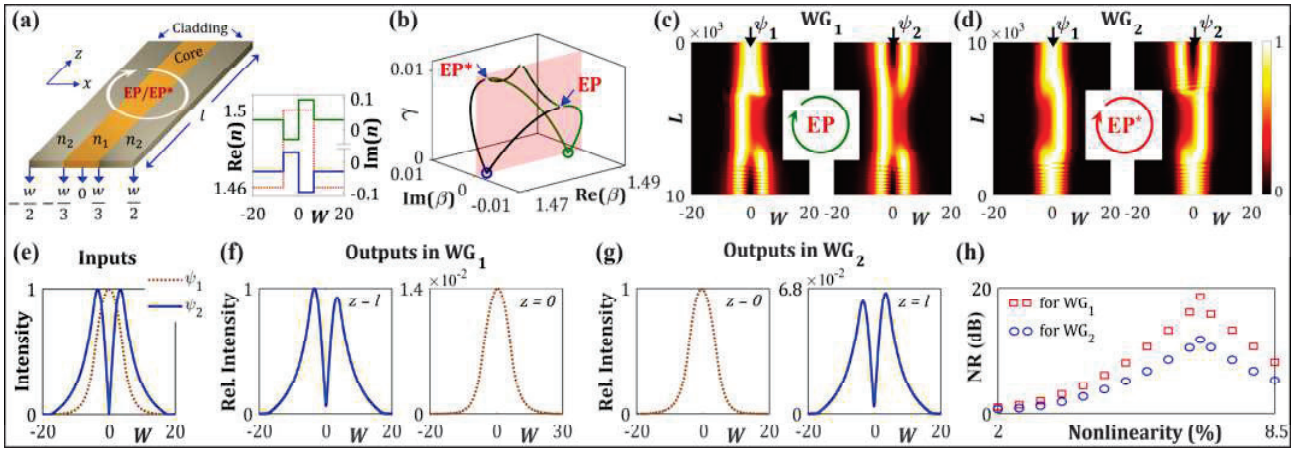

Fig. 1: (a) Schematic waveguide design along with complex $n(x)$-profiles for two chosen T-symmetric variants [solid green and blue lines represent Im(n) profiles (labelled on right y-axis) of WG_1 and WG_2 with the same Re(n) profile (labelled on left y-axis) shown by dotted red line]. **(b)** Formation of conjugate EP and EP* via coalescence between β_1 (dotted green) and β_2 (dotted black) in both WG_1 and WG_2. Nonreciprocal transmission of selective modes (in the presence of 6.75% nonlinearity) in **(c)** WG_1 from $z = 0 \rightarrow l$ (active in forward direction), assisted by the EP-induced asymmetric conversion $\{\psi_1, \psi_2\} \rightarrow \psi_2$; **(d)** WG_2 from $z = l \rightarrow 0$ (active in backward direction), assisted by the EP*-induced asymmetric conversion $\{\psi_1, \psi_2\} \rightarrow \psi_1$. **(e)** Normalized input field intensities and the associated relative difference in output fields in **(f)** WG_1, where intensity reduces $\approx 98.6\%$ at $z = 0$ during backward propagation in comparison to $z = l$ during propagation in active forward direction; **(g)** WG_2, where intensity reduces $\approx 93.3\%$ at $z = l$ during forward propagation in comparison to $z = 0$ during propagation in active backward direction. **(h)** Dependence of nonlinearity-level on NRs for both WG_1 and WG_2, where they exhibit their maximum NRs at 6.75% local nonlinearity.

3. Conclusion

Using a gain-loss assisted waveguide, we have reported the explicit dependence of nonlinearity-level of Kerr type on NRs in two T-symmetric variants, exhibiting two conjugate encircled EPs, which allows nonreciprocal transmission of two different modes in opposite directions. Both the variants exhibit their maximum NRs for the same amount of local nonlinearities. Our findings enriched with the nonlinearity-induced functionalities of conjugate EPs would facilitate the technologies for all-optical nonreciprocal devices such as isolators and circulators for integrated photonic operations.

Funding. Science and Engineering Research Board (SERB) [Grant No. PDF/2021/001322, under National Postdoctoral Fellowship], India.

4. References

[1] M.-A. Miri, and A. Alù, "Exceptional points in optics and photonics," Science **363**, eaar7709 (2019).
[2] A. Laha, S. Dey, and S. Ghosh, "Reverse-chiral response of two T-symmetric optical systems hosting conjugate exceptional points," Phys. Rev. A **105**, 022203 (2022).
[3] A. Laha, S. Dey, H. K. Gandhi, A. Biswas, and S. Ghosh, "Exceptional point and toward mode selective optical isolation" ACS Photonics **7**, 967 (2020).
[4] X-L. Zhang and C. T. Chan, "Dynamically encircling exceptional points in a three-mode waveguide system," Commun Phys. **2**, 63 (2019).

On the Toroidal Effect in $\mathbb{R}^3$ World by Photon Electromagnetic Field

Vineet Kumar
Dept. of Surface and Plasma Science, Faculty of Mathematics and Physics
Charles University, 18000 Prague -8, Czech Republic
vineet05k@gmail.com

Abstract. In this paper, based on earlier propositions, the dynamical effect of photon qubit in $\mathbb{R}^3$ world in terms of associated electromagnetic field is obtained. The effect is periodically toroidal. It is due to assumed hyperspherical coordinates of $\boldsymbol{S^3}$ −sphere in term of spatial-temporal variables by which photon qubit is dynamic. Using same it is shown that qubit and qubit-elemental actional corresponds energy content of electromagnetic field and induced metric respectively. It is also concluded that it is resultant electric field which determines the distance from the centre of tube to the centre of torus while the radius of tube by both electric and magnetic fields.
Keywords: Photon electromagnetic wave, Photon frame, Qubit, Stereographic projection, Torus.

Introduction

With ref [1] a photon qubit $|\phi\rangle$ does not hold the complex coefficients $\boldsymbol{\alpha} = cos(\vartheta_o/2)e^{i\vartheta_1}$ and $\boldsymbol{\beta} = sin(\vartheta_o/2)e^{i\vartheta_2}$ constant but functions over spacetime through hyperspherical coordinates ϑ_l for $l = 0,1,2$ with $\vartheta_2 - \vartheta_1 = \varphi$. $\vartheta_0(\varphi)$ are polar (azimuthal) angles of Bloch sphere. With $\boldsymbol{rt}$ for $\vartheta_0(\varphi)$ as $\vartheta_0 = \vartheta_0(\boldsymbol{r})$ and $\varphi = \varphi(t)$ from ref [2] a photon qubit define by eq_n (1) with phase factor $e^{i\vartheta_1}$ as $|\phi\rangle = e^{i\vartheta_1}|\phi'\rangle$ indicate homogeneous harmonic electromagnetic plane waves in transparent medium. $\boldsymbol{E}_+ + \boldsymbol{E}_-$ and $\boldsymbol{H}_+ + \boldsymbol{H}_-$ are associated fields in positive-negative directions with $\boldsymbol{\alpha}(\boldsymbol{rt}, y_l)$ and $\boldsymbol{\beta}(\boldsymbol{rt}, y_l)$ respectively. The involved electromagnetic waves of photon qubit now support Dirac statement "Each photon then interferes only with itself" but in modified way that "each photon interferes with itself" and not the other stated by Dirac as "Interference between two different photons can never occur" [3] which Glauber in ref [4] mentioned to put the dictum in rest. i is imaginary symbol. $q_0 = 0,1,\ldots$ and κ is constant.

$$|\phi'(\boldsymbol{rt}, y_l)\rangle = \left[cos\frac{\vartheta_0(\boldsymbol{r})}{2}|0\rangle + e^{i\varphi(t)}sin\frac{\vartheta_0(\boldsymbol{r})}{2}|1\rangle\right] = \left[cos\left(\boldsymbol{k}.\boldsymbol{r} - \frac{q_0\pi}{2}\right)|0\rangle + e^{i(2\omega t+\kappa\pi)}sin\left(\boldsymbol{k}.\boldsymbol{r} - \frac{q_0\pi}{2}\right)|1\rangle\right] \quad (1)$$

y_l corresponds $\boldsymbol{k}$, ω. Eq_n (1) over first and second differentials are given by eq_ns (2.1) and (2.2) respectively. Similarly $|\phi(\boldsymbol{rt}, y_l)\rangle$ as well such that inner product of $|d\phi(\boldsymbol{rt}, y_l)\rangle$ show induced metric [5] as $\langle d\phi|d\phi\rangle = \frac{1}{4}d\vartheta_0^2(\boldsymbol{r}) + cos^2\frac{\vartheta_0(\boldsymbol{r})}{2}d\vartheta_1^2(t) + sin^2\frac{\vartheta_0(\boldsymbol{r})}{2}d\vartheta_2^2(t)$. Based on different points of action in Bloch sphere it is found that $|d^k\phi'(\boldsymbol{rt}, y_l)\rangle$ for $k = 0,1,2$ holds $|d^k\phi'(\boldsymbol{rt}, y_l)\rangle_{\vartheta_0(\boldsymbol{r})=\frac{\pi}{2}} = \left[\frac{1}{\sqrt{2}}|d^k\phi'(\boldsymbol{rt}, y_l)\rangle_{\vartheta_0(\boldsymbol{r})=0} + \frac{1}{\sqrt{2}}|d^k\phi'(\boldsymbol{rt}, y_l)\rangle_{\vartheta_0(\boldsymbol{r})=\pi}\right]$ which shows equatorial points $\vartheta_0(\boldsymbol{r}) = \pi/2$ satisfaction with north and south poles. $\vartheta_0(\boldsymbol{r}) = 0, \pi$ are poles.

$$|d\phi'(\boldsymbol{rt}, y_l)\rangle = -sin\frac{\vartheta_0(\boldsymbol{r})}{2}.\frac{d\vartheta_0(\boldsymbol{r})}{2}|0\rangle + e^{i\varphi(t)}\left(cos\frac{\vartheta_0(\boldsymbol{r})}{2}.\frac{d\vartheta_0(\boldsymbol{r})}{2} + i\,sin\frac{\vartheta_0(\boldsymbol{r})}{2}.d\varphi(t)\right)|1\rangle \quad (2.1)$$

$$|d^2\phi'(\boldsymbol{rt}, y_l)\rangle = \left[-\left(cos\frac{\vartheta_0(\boldsymbol{r})}{2}.\frac{d{\vartheta_0}^2(\boldsymbol{r})}{4} + sin\frac{\vartheta_0(\boldsymbol{r})}{2}.\frac{d^2\vartheta_0(\boldsymbol{r})}{2}\right)|0\rangle + \left\{-sin\frac{\vartheta_0(\boldsymbol{r})}{2}\left(\frac{d{\vartheta_0}^2(\boldsymbol{r})}{4} + d\varphi^2(t)\right)\right.$$
$$\left. + \left(cos\frac{\vartheta_0(\boldsymbol{r})}{2}.\frac{d^2\vartheta_0(\boldsymbol{r})}{2} + i\,sin\frac{\vartheta_0(\boldsymbol{r})}{2}.d^2\varphi(t)\right) + i\,cos\frac{\vartheta_0(\boldsymbol{r})}{2}d\vartheta_0(\boldsymbol{r})d\varphi(t)\right\}e^{i\varphi(t)}|1\rangle\Bigg] \quad (2.2)$$

In term of electromagnetic waves qubit $|\phi(\boldsymbol{rt}, y_l)\rangle$ now describe by eq_n (3). $\boldsymbol{E}_\pm$ and $\boldsymbol{E}'_\pm$ are real electric and $\boldsymbol{H}'_\pm$ and $\boldsymbol{H}_\pm$ magnetic fields. $l_\pm\boldsymbol{L}_\pm = l_+\boldsymbol{L}_+ + l_-\boldsymbol{L}_-$ for $l = \mathfrak{d}, \mathfrak{h}'$ and $\boldsymbol{L} = \boldsymbol{E}, \boldsymbol{H}'$ holds. Also $m_\pm\boldsymbol{M}_\pm = m_+\boldsymbol{M}_+ - m_-\boldsymbol{M}_-$ for $l = \mathfrak{d}', \mathfrak{h}$ and $\boldsymbol{M} = \boldsymbol{E}', \boldsymbol{H}$ holds. $\epsilon_o(\mu_o)$ is permittivity (permeability) of free space.

$$|\phi(\boldsymbol{r}t,y_l)\rangle = \sqrt{\frac{\epsilon_o}{8}}\left(\mathfrak{d}_{\pm}\boldsymbol{E}_{\pm}(\boldsymbol{r}t,y_l) + i\mathfrak{d}'_{\pm}\boldsymbol{E}'_{\pm}(\boldsymbol{r}t,y_l)\right)|0\rangle + \sqrt{\frac{1}{8\mu_o}}\left(\mathfrak{h}'_{\pm}\boldsymbol{H}'_{\pm}(\boldsymbol{r}t,y_l) + i\mathfrak{h}_{\pm}\boldsymbol{H}_{\pm}(\boldsymbol{r}t,y_l)\right)|1\rangle \quad (3)$$

Eq_n (3) by $|\phi\rangle = |\phi_+\rangle + |\phi_-\rangle$ determine forward-backward propagation with $|\phi_{\pm}\rangle = \sqrt{\epsilon_o/2}\,\boldsymbol{E}_{\pm}|0\rangle + \sqrt{1/2\mu_o}\,\boldsymbol{H}_{\pm}|1\rangle$. $\boldsymbol{E}_{\pm}(\boldsymbol{r}t,y_l) = \left(\mathfrak{d}_{\pm}\boldsymbol{E}_{\pm} \pm i\mathfrak{d}'_{\pm}\boldsymbol{E}'_{\pm}\right)/2$ and $\boldsymbol{H}_{\pm}(\boldsymbol{r}t,y_l) = \left(\mathfrak{h}'_{\pm}\boldsymbol{H}'_{\pm} + i\mathfrak{h}_{\pm}\boldsymbol{H}_{\pm}\right)/2$ are complex fields. The space normalization of eq_n (3) gives eq_n (4) which remark energy in volume $\iiint d^3\boldsymbol{r}$ about position vector $\boldsymbol{r}$.

$$\iiint \phi(\boldsymbol{r}t,y_l)\phi^*(\boldsymbol{r}t,y_l)d^3\boldsymbol{r} = \left(\frac{\epsilon_o}{8}\underline{\boldsymbol{E}}^2(\boldsymbol{r}t,y_l) + \frac{1}{8\mu_o}\underline{\boldsymbol{H}}^2(\boldsymbol{r}t,y_l)\right) = \left(\frac{\epsilon_o}{2}|\mathcal{E}(\boldsymbol{r}t,y_l)|^2 + \frac{1}{2\mu_o}|\mathcal{H}(\boldsymbol{r}t,y_l)|^2\right) = 1 \quad (4)$$

$\mathcal{E}(\boldsymbol{r}t,y_l) = \boldsymbol{E}_+ + \boldsymbol{E}_-$ and $\mathcal{H}(\boldsymbol{r}t,y_l) = \boldsymbol{H}_+ + \boldsymbol{H}_-$. $\underline{\boldsymbol{E}}^2 = (\mathfrak{d}_{\pm}\boldsymbol{E}_{\pm})^2 + \left(\mathfrak{d}'_{\pm}\boldsymbol{E}'_{\pm}\right)^2$ and $\underline{\boldsymbol{H}}^2 = \left(\mathfrak{h}'_{\pm}\boldsymbol{H}'_{\pm}\right)^2 + (\mathfrak{h}_{\pm}\boldsymbol{H}_{\pm})^2$. Using stereographic projection over arbitrary points $\bigvee_{l=1}^4 \mathfrak{B}_l \in \mathbb{R}^4$ and $\bigvee_{l=1}^3 r_l \in \mathbb{R}^3$ with $\mathfrak{B}_1; \mathfrak{B}_2 = \sqrt{\epsilon_o/8}\left(\mathfrak{d}_{\pm}\boldsymbol{E}_{\pm}; \mathfrak{d}'_{\pm}\boldsymbol{E}'_{\pm}\right)$ and $\mathfrak{B}_3; \mathfrak{B}_4 = \sqrt{1/8\mu_o}\left(\mathfrak{h}'_{\pm}\boldsymbol{H}'_{\pm}; \mathfrak{h}_{\pm}\boldsymbol{H}_{\pm}\right)$ for $\langle 0|\phi(\boldsymbol{r}t,y_l)\rangle$ it determine torus in quartic form given by eq_n (5). $\bigvee_{l=1}^4 \mathfrak{B}_l$ is such that it hold $\sum_{l=1}^4 \mathfrak{B}_l^2 = 1$. The distance from the centre of tube to the centre of torus obtained is $\sqrt{8/\epsilon_o}\,.\,1/\underline{\boldsymbol{E}}(\boldsymbol{r}t,y_l)$ and the radius of tube is $1/c\,.\,\underline{\boldsymbol{H}}(\boldsymbol{r}t,y_l)/\underline{\boldsymbol{E}}(\boldsymbol{r}t,y_l)$.

$$\frac{32}{\epsilon_o}\cdot\frac{1}{\underline{\boldsymbol{E}}^2(\boldsymbol{r}t,y_l)}\sum_{j=1}^{2} r_j^{\,2} = \left(\sum_{j=1}^{3} r_j^{\,2} + \frac{8}{\epsilon_o}\cdot\frac{1}{\underline{\boldsymbol{E}}^2(\boldsymbol{r}t,y_l)} - \frac{1}{c^2}\cdot\frac{\underline{\boldsymbol{H}}^2(\boldsymbol{r}t,y_l)}{\underline{\boldsymbol{E}}^2(\boldsymbol{r}t,y_l)}\right)^2 \quad (5)$$

Using Toroidal/Poloidal coordinates $\vartheta_1(\vartheta_2)$ the Cartesian coordinate r_l in inertial frame of reference $\mathbb{I}'$ with origin O' at $\boldsymbol{r}t$ in inertial frame $\mathbb{I}$ which describes eq_n (5) hold the parametrical eq_n (6). $\kappa_1(\kappa_2)$ are constant and it's modulus hold the value in range of 0 to 1. The plane r_1r_2 is perpendicular to the travel line of photon and the axis of rotation r_3 is along the travel line.

$$\begin{aligned} r_3 = \frac{\underline{\boldsymbol{H}}(\boldsymbol{r}t,y_l)}{c\underline{\boldsymbol{E}}(\boldsymbol{r}t,y_l)}sin(2\kappa_2\pi + \omega t);\; r_2 &= \left[\sqrt{\frac{8}{\epsilon_o}}\frac{1}{\underline{\boldsymbol{E}}(\boldsymbol{r}t,y_l)} + \frac{\underline{\boldsymbol{H}}(\boldsymbol{r}t,y_l)}{c\underline{\boldsymbol{E}}(\boldsymbol{r}t,y_l)}cos(2\kappa_2\pi + \omega t)\right]sin(2\kappa_1\pi - \omega t); \\ r_1 &= \left[\sqrt{\frac{8}{\epsilon_o}}\frac{1}{\underline{\boldsymbol{E}}(\boldsymbol{r}t,y_l)} + \frac{\underline{\boldsymbol{H}}(\boldsymbol{r}t,y_l)}{c\underline{\boldsymbol{E}}(\boldsymbol{r}t,y_l)}cos(2\kappa_2\pi + \omega t)\right]cos(2\kappa_1\pi - \omega t) \end{aligned} \quad (6)$$

The coordinate set consisting of r_o, ϑ_1 and ϑ_2 is called elementary toroidal system with $r_o = \underline{\boldsymbol{H}}(\boldsymbol{r}t,y_l)/c\underline{\boldsymbol{E}}(\boldsymbol{r}t,y_l)$ and $\vartheta_j = \left[2\kappa_j\pi + (-1)^j\omega t\right]$ for $j = 1,2$. As $\underline{\boldsymbol{E}}(\boldsymbol{r}t,y_l)$ and $\underline{\boldsymbol{H}}(\boldsymbol{r}t,y_l)$ are changing at each spacetime in inertial frame $\mathbb{I}$ therefore torus also change such that it tend to a circle about r_3 axis when $\underline{\boldsymbol{E}}(\boldsymbol{r}t,y_l) \to max.$ and $\underline{\boldsymbol{H}}(\boldsymbol{r}t,y_l) \to 0$ achieve. The circle $r_1^{\,2} + r_2^{\,2} = 1$ correspond the nodes of a string wave and thus remark the basis state $|0\rangle$ of $|\phi(\boldsymbol{r}t,y_l)\rangle$ with amplitude $|\langle 0|\phi(\boldsymbol{r}t,y_l)\rangle|^2 = 1$. In case $\underline{\boldsymbol{E}}(\boldsymbol{r}t,y_l) \to 0$ and $\underline{\boldsymbol{H}}(\boldsymbol{r}t,y_l) \to max.$ the tori are nested within each other with all centered around r_3 axis. This nested condition $r_1 = r_2 = 0$ correspond the antinode of string wave and thus remark the basis state $|1\rangle$ of $|\phi(\boldsymbol{r}t,y_l)\rangle$ with measuring amplitude of $|\langle 1|\phi(\boldsymbol{r}t,y_l)\rangle|^2 = 1$.

References

[1] V. Kumar, "Intro-Extrovert World-Connectedness of a Photon in between $S^3 \subset \mathbb{R}^4$ and S^2 & $\mathbb{R}^3$," in Third International Conference on Advances in Physical Sciences and Materials 2022, of AIP Proceedings Series (American Institute of Physics., Tamil Nadu, 2022), (accepted).

[2] V. Kumar, "On the Photon Qubit Harmonic Wave," in Third International Conference on Advances in Physical Sciences and Materials 2022, of AIP Proceedings Series (American Institute of Physics., Tamil Nadu, 2022), (accepted).

[3] P. A. M. Dirac, "The Principles of Quantum Mechanics", p. 15 Oxford (1930), 4th Edition (1958).

[4] R. J. Glauber, "Dirac's famous dictum on interference: one photon or two?", *Am. J. Phys.* 63, 12 (1995).

[5] V. Kumar, "On the induced metric of photon qubit for different points of action in Bloch sphere", *J. Phys.: Conf. Ser.*, Vol. 2070 (1) IOP Publishing (2021).

Deep learning framework for automated diagnosis of diffuse large B-cell lymphoma

Vishal Srivastava, Sautami Basu, and Ravinder Aggarwal
Department of Electrical and Instrumentation Engineering
Thapar Institute of Engineering and Technology, Patiala 147004, Punjab, India
vsrivastava@thapar.edu

Abstract: Blood cancer disrupts the production and function of blood cells. It includes cancers of the bone marrow, blood, and lymphatic system. Blood cell development is hampered by abnormal blood cell growth. Hematopoietic cancers are best detected through histopathology. Examining H&E histopathological images manually is time-consuming and difficult. Histopathological images must be processed automatically. Convolutional Neural Networks (CNNs) are incapable of distinguishing complex histopathological images. Keeping this in mind, the authors proposed a unified framework for detecting diffuse large B-cell lymphoma (DLBCL) from histopathological images. CNN architecture with two channels that combines input image and attention map feature transformer (AMFT). Optimizing a new objective function that takes into account centre and cross-entropy loss reduces both inter-class dispersion and within-class variance. For training and validation, 1000 sparsely annotated images were used. The proposed model had 96% accuracy, 94.67% recall, 97.26% precision, and 97.33% specificity on the validation set. As a result, the proposed framework will expedite diagnostics.

Keywords: Diffuse large B-cell lymphoma, Deep learning, and Convolutional neural network (CNNs)

Introduction

Globally, one in six deaths are caused by cancer, which is characterized by rapidly dividing cells that spread uncontrollably to other organs and tissues. The global cancer burden is projected to reach 27.5 million new cases and 16.2 million deaths by the year 2040 [1]. A tumor of the hematopoietic and lymphoid malignancies (thymus cells (T cells) or bone marrow (B cells) is one of these types. Lymphomas are generally categorized as Hodgkin lymphoma (HL) or non-Hodgkin lymphoma (NHL) (NHL). In HL, cancer originates from lymphocytes, a specific type of white blood cells, whereas NHL (3% worldwide and the seventh most commonly diagnosed cancer in the US) encompasses all other lymphomas. Currently, pathologists examine histopathology sections under varying magnifications to determine the presence of hematopoietic malignancies. Detecting growth patterns and cytologic properties in Haemotoxylin and Eosin (H&E) stained tissue makes diagnosis laborious, time-consuming, expensive, and prone to error. In addition, an experienced oncology pathologist is necessary, which further delays the diagnosis and treatment. In addition, slide preparation and staining variations may contribute to inter-reader variability among pathologists. Due to the limitations of manual analysis of high-throughput image data, an automated diagnostic system or artificial intelligence-based system would be of great assistance in reducing pathologists' mounting workloads.

In this paper, we proposed a deep discriminative learning with a calibrated attention map (DDLM-CAM) for the classification of diffuse large B-cell lymphoma. The calibrated attention map is input to the Attention Map feature transformer (AMFT) network, and the original histopathological images are fed to the densely connected CNN (DensNet-201) (DensNet-201). The final layers of DenseNet-201 and AMFT include high-level semantic features that were merged/fused. In addition, we applied the center loss function and cross-entropy loss function to increase the separation of similar classes and decrease intra-class distance.

Dataset: The pathologic tissue slide images of DLBCL and non-DLBCL shown in Figure 1 were captured using microscope-based cameras at 40X original magnification and saved in .jpeg format for analysis. Each category contains 500 images (one pathological image per subject).

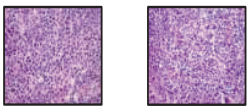

Fig. 1: Histopathological Images

The 1000- image dataset were first resized to 224 x 224pixels image size and had judiciously been divided into training and validation sets, 700 images for training and 300 images for the validation.

Network Architecture:

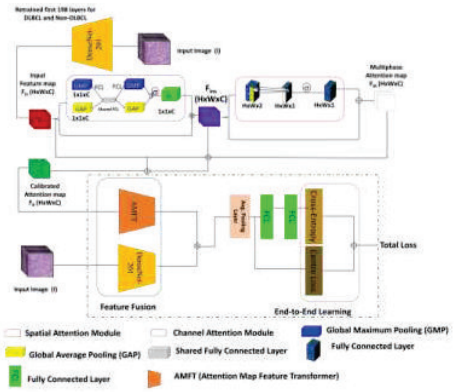

Fig. 2: Architecture of deep discriminative learning model with calibrated attention map (DDLM-CAM).

Results:

Table 1: Performance metrics for other ratios of training & validation dataset for the DDLM-CAM

Dataset ratio	Accuracy (%)	Recall (%)	Precision (%)	Specificity (%)
Training: 80	98.25	98.5	98	98
Validation:20	97.5	97	97.97	98
Training: 90	99.56	99.33	99.78	99.78
Validation:10	100	100	100	100

Conclusion: The proposed algorithm DDLM-CAM and addressed class ambiguity by learning more discriminative features for the diagnosis of diffuse large B-cell lymphoma (DLBCL) from histopathology images. Our strategy is focused on two fundamental objectives: (1) Constructing a two-stream architecture for fusing the semantic features of the calibrated attention map with the original image; (2) Training DDLM-CAM with a center-loss to acquire discriminative features for histopathological images. Combining the centre loss and the SoftMax loss increases the discriminative power of the deeply learned features obtained from the DDLM-CAM. The main benefit of the proposed framework is its ability to accurately predict DLBCL and non-DLBCL, which can assist pathologists in providing accurate and timely diagnoses.

Acknowledgements: *The authors are thankful to SERB for providing funding in project no.* ***CRG/2021/006488****.*

Light Emitting Diode Based Solar Simulator with Broad Band Spectra

Puspita Chanda[1], Vikas Kumar[1], Dheeraj Kumar[1], Kanchan Saxena[2], and D.S Mehta[1*]

1.Bio-photonics and Green photonics laboratory, Department of Physics, Indian Institute of Technology Delhi,
2. Amity Institute of Renewable and Alternative Energy, Amity University, Sector 125, Noida, UP, India
*mehtads@physics.iitd.ac.in

Abstract: Xenon arc lamp based solar simulators are generally used for characterizing solar cells in the laboratory environment. But they are costly, inefficient and short lifetime. White LED based systems are becoming popular now, because they are efficient, low cost and have long lifetime, but their spectrum is narrow. We propose the development of LED based solar simulator with broad band spectra. Broadband illumination, CCT (4500 K - 5500 K), and CRI (90-100) were obtained by means of using multiple phosphors-based white LED systems. Experimental set-ups with three combinations were studied.

Keywords: Solar Simulator, Solid-state lighting, Phosphors

1. Introduction

Solar Simulator provides a controllable spectrum similar to Sunlight in the visible range (380-780 nm). Solar simulators help in developing, testing, and rating solar collectors and solar panels [1]. Recent advances in this field offer a financial opportunity in the commercial lighting industry, where indoor light sources can precisely duplicate natural sunlight's color and atmosphere. Xenon arc lamps are commonly used in solar simulators despite their sharp spikes, energy inefficiency, short lifetime, and bulky size [2]. Now a days LEDs are being used to make solar simulators. Phosphor converted White LED (pc-WLED) lights are popular presently because they are less expensive, long life-time and more efficient [3]. Generally, for making WLED a blue LED and yellow phosphor (YAG: Ce^{+3}) is used to generate yellow fluorescence photons by absorbing blue photons [4]. Transmitted primary blue photons and secondary yellow photons create white light after getting mixed. A typical pc-WLED can have a maximum CRI around 80, which is inadequate for accurate color reproduction. To use the pc-WLEDs for artificial illumination, all of the CRI points (R1 – R15) must be more than 95. CCT of pc-WLEDs is around 6000K which is cooler color. Warm colors are soothing for the eye which means low CCT light. Sunlight in the visible range has high CRI (95-100) and warm CCT (4500K-5500K). To achieve color parameters like sunlight three kinds of multiple phosphors based experimental setups have been analyzed to achieve broad-band white light. They are – 1) Illuminating Red ($SrAlSiN_3: Eu^{+2}$), Green ($SrBaSiO_4:Eu^{+2}$), and Yellow ($Y_3Al_5O_{12}:Ce^{+3}$) phosphors separately by a blue LED, 2) Mix Phosphor layer have been illuminated by blue LED & 3) Different kind of pixel size color phosphor chip arrangement have been illuminated by blue LED.

2. Experimental Setup

Three glass slides coated with different-colored phosphors (Red, Green, Yellow) are lit with separate blue LEDs(λ =452 nm , $\Delta\lambda$ =30 nm and P=20W). One LED had phosphor-coated glasses attached. Each blue LED is attached to an aluminium heat sink to dissipate heat. The three heat sinks are joined at an acute angle. A diffuser in front of the system diffuses the color from each phosphor layer so they can mix and produce white. The Red ,Green and Yellow phosphors mixed film produced on a glass sheet have been excited by a blue LED. Three kinds of phosphors were mixed at different ratios. After analyzing the spectrum of each mixture and keeping the R.I value of these phosphors in mind, the result has been tried to improve by changing the ratio of phosphors. Pixel size (5 mm $\times$5 mm $\times$1 mm) Red, Green, and Yellow phosphor glass slides are produced by cutting (25 mm $\times$25 mm $\times$1 mm) size phosphor-coated glass by CO_2 LASER. A blue LED have been utilized to illuminate each pixel arrangement. CCT and CRI variation of these setups have been observed from $+60^0$ to -60^0 (from right to left) in front of the system.

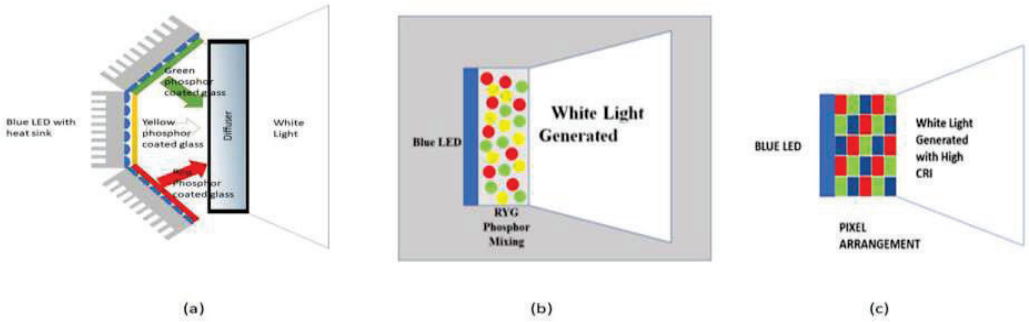

Figure 1-(a)Schematic diagram of first setup,(b)Schematic diagram of second setup & (c)Schematic diagram of third setup

3. Results and Discussions

First, three phosphor layers was illuminated with three separate blue LEDs. From this arrangement best CRI 96 has been achieved and a low CCT value. But the system was bulky for general illumination. To reduce the size of the arrangement all three phosphors have been mixed at equal concentrations first and the spectrum was analyzed. By observing the color parameter of the spectrum and keeping in mind the refractive index difference of three phosphors concentration has been changed according to that. The best result has been achieved for the concentration of red, green, and yellow phosphors was 1:3:1 in this sample. The phosphor to UV adhesive ratio was 10:3. But the CRI of that sample is 88.6 which was very low to sunlight. Luminance quenching and photoluminescence degradation were also observed in the mixed phosphor spectrum due to self-absorption. The Refractive index of red, green, and yellow phosphors is 2.69,1.67 and 1.84 respectively. Due to different refractive indexes high internal reflection happens between three phosphor molecules leading to absorption in the mixed phosphor layer causing less luminance. To overcome the problem pixel size phosphor-coated glass slides are prepared and various arrangements have been tried. Best CRI 93 has been achieved from one arrangement. Self-absorption loss was not there for the pixel arrangement spectrum as there was no internal reflection in the phosphor layer. Some pixel arrangement spectrum exhibited quenching due to the fact blue light intensity was high as transparent glass slides were used. All three system has shown low CCT but pixel size color phosphor coated glass slide has uniform CCT variation.

Figure 2 (a) shows the spectra of three types of LED sources, followed by CCT (Fig. 2 (b)), and CRI for all the three combinations (Fig. 2 (c)).

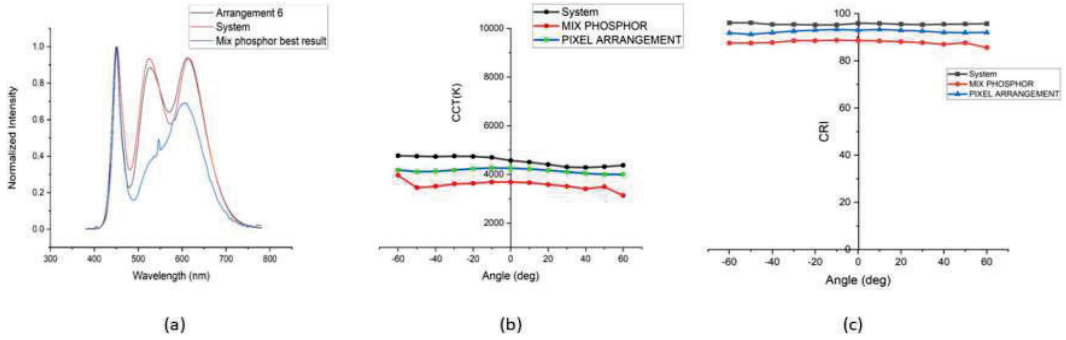

Figure 2–(a) the comparison of the spectrum of the system, best mix phosphor sample & best color pixel chip arrangement. (b) Comparison of variation of CCT of best color pixel chip arrangement, best mixed sample & system(c) Comparison of variation of CRI of best color pixel chip arrangement ,best mixed sample & system .

4. Conclusion

We conclude that pixel size color phosphor arrangement shows best CRI and CCT variation although its CRI is not good as bulky system, but it is compact than earlier.

5. References

[1] "New methods for solar cells measurement by LED solar simulator | IEEE Conference Publication | IEEE Xplore," (n.d.).
[2] E. Sofronova, "An Introduction To Solar Simulator Devices," McMaster J. Eng. Phys. 2, 481–491 (2017)
[3] C. P. Mrinalini, J. Pavithran, K. L. Osten, A. Jinumon, and M. V. A. Mohan, "LED Based Solar Simulator," IEEE 1–6 (2014).

Blind Super Resolution Strategy for Multi-modal Structured Illumination Microscopy

Krishnendu Samanta[1,*] and Joby Joseph[2]
[1]*Department of Physics, Indian Institute of Technology Delhi, New Delhi 110016, India*
[2]*Optics and Photonics Centre, Indian Institute of Technology Delhi, New Delhi 110016, India*
Author e-mail address: ksphy93@gmail.com

Abstract: Multi-modal structured illumination microscopy is demonstrated where illumination pattern contains multiple spatial frequencies. A blind reconstruction approach is implemented to bypass the reconstruction complications appeared from the multi-frequency excitation. The resolution enhancement capability of blind reconstruction for the multi-modal illumination is described through the simulation analysis.
Keywords: Fluorescence Microscopy, Structured Illumination, Super Resolution.

1. Introduction

The standard fluorescent microscopy suffers from an inherent limit of resolution due to the effect of diffraction. Non-uniform illumination significantly improves the resolution limit of the fluorescence microscope. Conventional structured illumination microscopy (SIM) [1,2] utilizes sinusoidal excitation pattern to overcomes the diffraction limited resolution by folding higher spatial frequencies into the passband (OTF) of the imaging system, which has maximal capability to provide 2-fold resolution enhancement in reflection-based system. Multi-fold resolution enhancement in SIM is achieved by implementing several nonlinear effects [3,4]. We present an alternative approach in transmission microscopy system [5] where illumination path is decoupled from the collection path to deliver full flexibility to play with illumination optics. The fluorescent sample is illuminated with a non-sinusoidal multi-periodic pattern having wide range of spatial frequencies; hence higher sample frequencies are folded within the OTF and eventually leads to superior resolution than conventional SIM. The resolution enhancement capability of blind reconstruction for the multi-modal illumination is described through the simulation analysis.

2. Theory and Results

We present a scheme where the sample is illuminated with multi-modal one dimensional structured pattern [6,7]. The pattern is generated by mutual interference of four coplanar beams with same state of polarization. The wave vector of the u[th] beam, $u \in \{-2,-1,+1,+2\}$ beam is represented by the equation $\boldsymbol{k_u} = \frac{2\pi}{\lambda}[sin\theta_u cos\varphi, sin\theta_u sin\varphi, cos\theta_u]$ where θ_u is the polar angle, φ is the azimuthal angle of the uth beam, λ is the wavelength of illumination. The mutual interference occurs in a common volumetric region where all the four coplanar overlap with each other. The resultant irradiance profile is represented by the expression,

$$I(x,y) = \sum_{u=-2}^{+2} |\boldsymbol{E_u}|^2 + \sum_{u}\sum_{\substack{v \\ u\neq v}} \boldsymbol{E_u}\cdot\boldsymbol{E_v^*}\, e^{i[(\boldsymbol{k_u}-\boldsymbol{k_v})\cdot\boldsymbol{r}+(\psi_u-\psi_v)]} \quad (1)$$

where $\boldsymbol{E_u}$ is electric field of the u[th] beam and $\delta\psi = (\psi_u - \psi_v)$ is phase difference between the interfering beams. When such structured pattern $I(x,y)$ illuminates the sample $S(x,y)$, the moiré frame is represented by the equation,

$$M(x,y) = [S(x,y)I(x,y)] \otimes h(x,y) + n(x,y) \quad (2)$$

where $h(x,y)$ is the point spread function of the imaging system and $n(x,y)$ is the noise. The graphic of the illumination scheme for the multi-periodic pattern is shown in Fig. 1(a); magnified perspective view of the region of interest is shown in Fig. 1(b), inset displays volumetric irradiance profile. Fig. 1(c) displays the spatial frequency spectra of the multi-periodic illumination pattern and Fig. 1(d) represents isotropy of the illumination in three different planes (R_1, R_2, R_3) corresponding to three different planes of incidence $\varphi_1 = 0^o, \varphi_2 = 60^o, \varphi_3 = 120^o$. The first and second order beam pairs interfere at angles $\theta_1 = 20^o, \theta_2 = 40^o$ respectively w.r.t. the optic (z) axis. The intensity expression in Eq. 1 represents the multi-periodic illumination pattern; the phase offset $\delta\psi$ is modified in such a way that that it delivers $\frac{2\pi}{N}$ phase steps to the multi-periodic structured illumination where N is the number of phase steps. In our simulation, we have chosen $N = 10$ acquisitions in each of the three orientations. Each lattice illumination pattern consists of four different spatial frequencies, $\frac{(f_2-f_1)}{2} = 0.3\lambda^{-1}, f_1 = 0.68\lambda^{-1}, \frac{(f_2+f_1)}{2} = 0.98\lambda^{-1}, f_2 = 1.28\lambda^{-1}$ in increasing order, respectively, shown in Fig. 1(c). There are two fundamental frequencies and two sum frequencies obtained from the

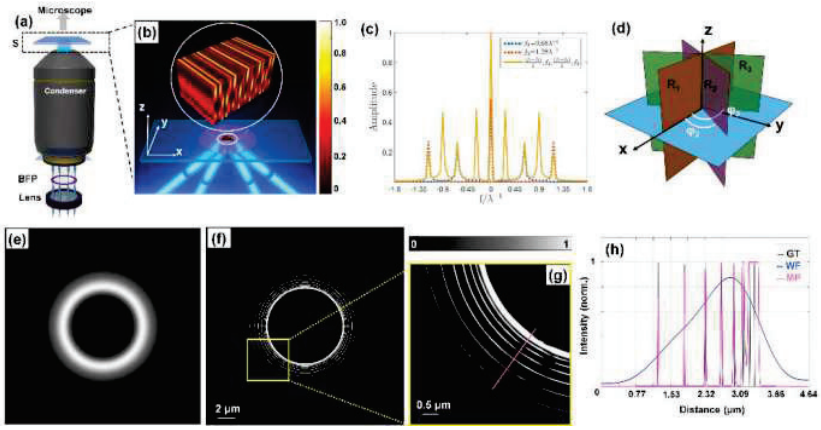

Figure 1: (a) Graphic of multi-modal structured illumination; (b) magnified view of the region of interest around the sample, inset shows volumetric intensity distribution; (c) spatial frequency spectra of the multi-modal illumination pattern; (d) isotropy of the illumination in three planes R_1, R_2, R_3 corresponding to three planes of incidence $\varphi_1 = 0^o, \varphi_2 = 60^o, \varphi_3 = 120^o$ respectively; (f) MUSICAL reconstructed image for multi-periodic illumination pattern; (g) magnified view of a small portion of the reconstructed image; (h) intensity profile along the radial direction for ground-truth, widefield and MUSICAL images.

Fourier transform of the multi-periodic pattern. The illumination pattern enables a quite broad range of spatial frequency space collected by the imaging system. This approach contributes toward the enhancement of image resolution due to multiply folding high-frequency information within the passband limit of the microscope. The simulation parameters are chosen as: objective lens NA=0.3, excitation/emission wavelength=400/450 nm, camera with square pixel size 6.5 μm. The ground-truth synthetic object chosen for the simulation representing the fluorescent sample is concentric circular rings with varying separations of 580, 450, 340, 250, 180, 130, and 100 nm from outside toward the center, respectively. As the number of illumination frequencies are higher than conventional SIM, we consider blind reconstruction to avoid reconstruction complications. The raw frames over the entire acquisition are processed via multiple signal classical algorithm (MUSICAL) [6] to achieve a super-resolved image, where MUSICAL exploits the systematic variation in illumination distribution for super-resolution. The results shown in Fig. 1 are for the multi-periodic lattice illumination with MUSICAL reconstruction, where Fig. 1(e) is the diffraction-limited widefield image of the sample, Fig. 1(f) is the reconstructed final image using MUSICAL, Fig. 1(g) represents the magnified view of a small portion of reconstructed final image, and Fig. 1(h) radial line-scan of ground-truth, widefield, and final super-resolved image of the fluorescent sample. From the result, we conclude that the rings with separation as small as 130 nm are nicely resolved using multi-periodic lattice illumination.

3. Conclusion

In conclusion, the utility of multi-periodic structured illumination is envisaged and a super-resolution imaging scheme is proposed without the prior knowledge about the illumination patterns. The illumination scheme of multi-periodic pattern is described, which contains both spatial and axial periodicities and might offer applications in 3D imaging and light sheet microscopy. The multi-modal pattern illumination microscopy delivers resolution improvement better than the conventional SIM. The higher the number of spatial frequencies in illumination the higher is the achievable resolution, which dictates that patterns with more spatial frequencies would definitely offer super-resolution.

4. References

[1] M. G. L. Gustafsson, "Surpassing the lateral resolution limit by a factor of two using structured illumination microscopy" J. Microsc. **198**, 82-87 (2000).
[2] K. Samanta and J. Joseph, "An overview of structured illumination microscopy: recent advances and perspectives", J. Opt. **23**, 123002 (2021).
[3] M. G. L. Gustafsson, "Nonlinear structured illumination microscopy: widefield fluorescence microscopy with theoretically unlimited resolution", Proc. Natl. Acad. Sci. **102**, 13081-13086 (2005).
[4] K. Samanta, A. Tiwari, S. Joseph and J. Joseph, "Saturable absorption assisted nonlinear structured illumination microscopy", Opt. Lett. **47**, 2702-2705 (2022).
[5] K. Samanta and J. Joseph, "Image reconstruction approach for a high space bandwidth product structured illumination microscopy system", J. Opt. Soc. Am. A **38**, 1744-1751 (2021).
[6] K. Samanta, S. Sarkar and J. Joseph, "Resolution enhancement in multi-periodic pattern illumination microscopy", FiO/LS, FTu8b.7 (2020).
[7] K. Samanta, S. Sarkar, S. Acuña, J. Joseph, B. S. Ahluwalia, and K. Agarwal, "Blind super-resolution approach for exploiting illumination variety in optical lattice illumination microscopy", ACS Photonics **8**, 2626-2634 (2021).

Photonic time-stretch front-end assisted instantaneous frequency measurement

Karamdeep Singh, Sreeraj S J and Deepa Venkitesh
Department of Electrical Engineering, Indian Institute of Technology Madras, Chennai, Tamil Nadu, India
Author e-mail address: karamdeep1989@gmail.com, deepa@ee.iitm.ac.in

Abstract: We demonstrate the impact of choice of repetition rate of mode-locked laser (MLL) on overall frequency measurement resolution of a photonic time-stretch front end assisted ultra-wideband instantaneous frequency measurement (IFM) scheme using numerical simulations.
Keywords: Radio frequency photonics, instantaneous frequency measurement, analog optical signal processing, time-stretching.

1. Introduction

In modern electronic warfare, RADAR warning systems, electronic intelligence and anti-stealth defense systems, instantaneous frequency measurement (IFM) of the unknown intercepted signals is of imminence importance. Traditionally, this task has been carried using electronic methods which are very slow, power hungry, prone to electro-magnetic interference (EMI) and are usually very narrowband. In order to convert narrowband electronic IFM system to work for a broadband detection scheme, usually an electronic channelization process is deployed, which is bulky and increases the complexity of overall IFM system [1-3]. Microwave photonic assisted IFM systems are envisioned as potential solutions to the limitations posed by traditional electronic IFM systems which offer faster measurement speeds, immunity to EMI, wideband operation and less operating power requirement [1-3]. J. Zhou et al. [1] and Zou & Yao [4] have proposed an IFM scheme based on microwave power monitoring induced due to dispersive fading effect experienced by frequency being measured. Y. Ma et al. [1] and X. Zhang et al. [5] have developed a photonic assisted IFM scheme which involves carrying out band pass sampling of RF signal at multiple rates using optical samplers operating at slightly different rates. However, the microwave power monitoring scheme proposed by J. Zhou et al. [1] and Zou & Yao [4], has measurement ambiguity problem for some frequencies, whereas, the other approach based on multiple optical band pass samplers proposed by J. Zhou et al. [1] and Zou & Yao [4] is fairly complex in structural terms and require optical samplers to operate at similar rates, which are locked using an atomic clock in order to guarantee measurement accuracy. In this article, we present a simulation study of a photonic time-stretch assisted IFM scheme which is very simple structurally, is truly wideband and free from measurement ambiguity problem. We acknowledge that D. Lam et al. [7] have proposed photonic time-stretch assisted IFM scheme, however, they have not highlighted the impact of MLL repetition rate on the overall frequency resolution of the time-stretch assisted IFM system. We demonstrate the impact of MLL repetition rate on the overall frequency resolution of the time-stretch assisted IFM system for following three MLL rates: 5 MHz, 20 MHz and 80 MHz.

2. Principle of operation and simulation setup

In time-stretch assisted IFM system, the instantaneous frequency (RF_{in}) to be measured is mapped on top of slightly optical chirped envelope, which is further stretched after modulation by stretch factor ($S = (L_1 + L_2)/L_1$), where L_1 and L_2 are lengths of first and second time-stretching (TS) mediums. The stretched version of RF_{in} which is modulated on stretched optical carrier is photo-detected and digitized using a low rate electronic analog-digital converter (ADC). Benefit of using time-stretch front end assisted scheme, is in the form of stretch factor, which brings down overall bandwidth/frequency of RF_{in}, enables use of low-rate electronics for measurement of truly wideband signals instantaneously. The simulation setup used in order to demonstrate the impact of MLL repetition rate on frequency measurement resolution of a photonic time-stretch front end assisted IFM scheme is shown in Fig. 1.

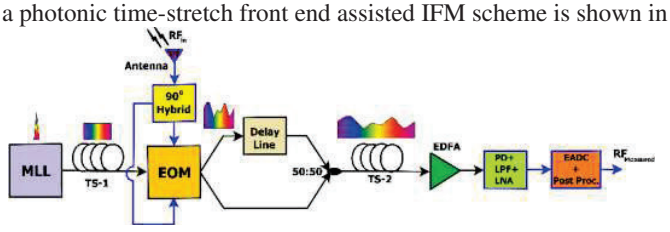

Fig. 1: Simulation setup of photonic time-stretch assisted IFM scheme.

As shown in Fig. 1, 200 fs wide pulses are generated by MLL at following considered repetition rates (rep. rates): 80 MHz, 20 MHz and 5 MHz. The inter-pulse durations between consecutive pulses for considered rep. rates are follows:

12.5 ns, 50 ns and 200 ns, respectively. The MLL pulses are then pre-stretched using TS-1 consisting of SMF links, the lengths of TS-1 used for considered rep. rates are follows: 0.25 km, 1 km and 4 km, respectively. These pulses are then imprinted with the frequency of the signal to be measured (RF_{in}), which is intercepted by antenna shown in the system and is the split using a 90° hybrid and is applied to dual-drive dual complementary output electro-optic modulator in order (Fig. 1) to perform single-sideband (SSB) modulation. Both complementary outputs of EOM are delayed with respect to each other by half of repetition rate of MLL used and are then recombined using a 50:50 coupler shown in Fig. 1. This time-multiplexed output is then passed through TS-2 consisting of SMF links, the lengths of TS-2 used for considered rep. rates are follows: 7.5 km, 30 km and 120 km, respectively. The choice of TS-1 and TS-2, for all considered MLL rep. rates yields a stretch factor (S) = 31, which is intentionally kept same, in order to demonstrate impact of MLL rep. rate on frequency resolution of TS assisted IFM scheme. As shown in Fig. 1, the stretched signal from TS-2 is amplified using erbium doped fiber amplifier (EDFA) is then photo detected and is passed through a low pass filter (LPF) with bandwidth = 2.5 GHz. A RF amplifier amplifies the output of LPF to full-scale of 5 GSa./sec. backend electronic ADC. The measured RF frequency (RF_{measured}) is related to input RF_{in} via following relation: $RF_{measured} = RF_{in}/S$.

3. Results and discussions

In order to demonstrate the choice of MLL rep. rate on overall frequency resolution of TS assisted IFM scheme, all there MLL rep. rates (80 MHz, 20 MHz and 5 MHz) TS-IFM systems are simulated for various single-tone RF_{in} signals ranging from 3.569 GHz (C-band) to 72.672 GHz (V-band). The frequency spectra of simulated time-stretched signals for considered RF_{in} signals: 3.569 GHz to 72.672 GHz for three MLL rep. rate (80 MHz, 20 MHz and 5 MHz) TS-IFM systems are shown in Fig. 2 (a-c), respectively.

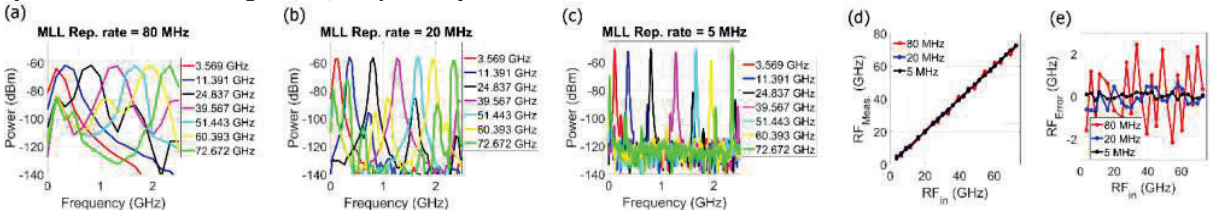

Fig. 2: Frequency spectra of TS signals for considered RF_{in} signals and for MLL rep. rate of (a) 80 MHz, (b) 20 MHz, (c) 5 MHz, (d) $RF_{measured}$ Vs. RF_{in} (e) RF_{Error} Vs. RF_{in}

It is clearly observed from Fig. 2 (a-c) that better frequency resolution is attained for MLL rep. rate = 5 MHz owing to longer inter pulse duration between consecutive MLL pulses which enables capture of more number of samples, which in turn improves the frequency resolution. Further, in order to assess the measurement frequency accuracy of TS assisted IFM scheme for various considered rep. rate TS-IFM systems, the RF_{measured} is compared to RF_{in} which is shown in Fig. 2 (d). The measured frequency error (RF_{Error}) which is calculated as per following relation: $RF_{Error} = RF_{Measured} - RF_{in} = S \times RF_{stretched} - RF_{in}$ for various considered rep. rate TS-IFM systems is shown in Fig. 2 (e). It can be clearly assessed from Fig. 2 (e) that TS assisted IFM scheme with 5 MHz rep. rate has considerably lesser error (< ±0.25 GHz) as compared to TS assisted IFM scheme with 20 MHz (< ±0.6 GHz) and 80 MHz (< ± 2.5 GHz) rep. rates. In practice, lower rep. rate pulses can be realized through a pulse picking process, external to the MLL cavity.

4. Conclusions

We have analyzed impact of choice of MLL rep. rate on the frequency resolution of TS assisted IFM system for C-band to V-band microwave single-tone signals using numerical simulations. We show that frequency accuracy of the TS assisted IFM systems, when operating at low MLL rep. rates 5 MHz (< ±0.25 GHz) is considerably better as compared to systems operating at higher MLL rep. rates 20 MHz (< ±0.6 GHz) and 80 MHz (< ± 2.5 GHz).

5. Acknowledgements

Authors acknowledge the Science and Engineering Research Board (SERB), India under IMPRINT-IIC scheme for funding this work.

6. References

[1] Y. Ma, Yangxue, D. Liang, D. Peng, Z. Zhang, Y. Zhang, S. Zhang, and Y. Liu, Optics Express **25**, 2355-2368 (2017).
[2] J. Zhou, S. Fu, S. Aditya, P. P. Shum, and C. Lin. IEEE Photonics Technology Letters, **21**, 1069-1071 (2009).
[3] S. Pan, and J. Yao. Journal of Lightwave Technology **35**, 3498-3513 (2017).
[4] X. Zou, and J. Yao. IEEE photonics technology letters, **20**, 1989-1991 (2008).
[5] X. Zhang, D. Peng, Y. Ma, B. Wang, M. Wang, Z. Li, Z. Zhang, S. Zhang, H. Li, and Y. Liu. Applied Optics **59**, 8056-8065 (2020).
[6] D. Lam, B. W. Buckley, C. K. Lonappan, A. M. Madni, and B. Jalali. IEEE Instrumentation & Measurement Magazine, **18**, 26-30 (2015).

Analyzing differential phase shift quantum key distribution with practical imperfections

Sumit Chaudhary*, Nishant Kumar Pathak, Bhaskar Kanseri
Department of Physics, Indian Institute of Technology Delhi, Hauz Khas, New Delhi, 110016, India
**schaudhary@ce.iitr.ac.in*

Abstract: Noise arising from practical imperfections limits the performance of Quantum Key Distribution (QKD) systems. Here, we analyze the performance of differential phase shift (DPS) QKD considering practical imperfections of source, channel, Mach-Zehnder interferometer (MZI) and detectors. We categorize Quantum bit error rate (QBER) into three categories and by examining the behavior of these noises we discuss the ways to improve QBER by suitable means to a possible extent. In this work, we perform the simulations incorporating realistic device performance and optimizing the performance of the QKD protocol. Our analysis helps realize high clock speed and large distance phase encoded QKD.
Keywords: Quantum Key distribution, Differential Phase Shift, Quantum bit error rate

1. Introduction

Quantum key distribution (QKD) is an unconditional secure way to share a secret key between two authentic parties Alice and Bob. The idea of quantum cryptography was first suggested in 1984 [1]; since then, enormous progress has been made in demonstrating realistic QKD systems and efforts are being made to scale these systems for larger distances [2,3,4,5]. Since a single photon source is difficult to implement [6], experimentally highly attenuated laser pulses are used in many QKD protocols. In addition to the use of attenuated laser pulses, device imperfections add noise to the QKD system, which drastically downturns QKD's performance and puts in security loopholes [7]. To develop realistic high key rate, long distance and secure QKD, understanding the behavior of noise arising from imperfect devices is essential and is the focus of this paper. Here, we present our work for the case of DPS QKD which is known for its simplicity, resistance to PNS attack and ability to produce a high key rate [7].

2. DPS QKD protocol

Alice prepares a train of attenuated coherent laser pulses (N pulses) with a mean photon number (μ) less than one and encodes each pulse with a random phase sequence of 0 or π. Then, she sends these phase-modulated pulses to Bob via fiber link. Bob receives the pulses at the fiber end and performs measurements using one pulse-delayed Mach-Zehnder interferometer. The coherent laser pulse interferes with the previous pulse and the outcome of the MZI depends on the relative phase between two adjacent pulses. Bob registers photons in either of the two single-photon detectors which are connected to the output port of MZI. Depending upon which detector clicked, Bob knows the key bit sent by Alice and through an authentic classical communication Bob reveals the timestamp of the registered photon to Alice but does not leak the information of which detector clicked. Alice and Bob only keep those events that caused click in the detector for key generation. Alice and Bob choose a fraction of their raw key bits to estimate the key rate and QBER and then perform Error Correction (EC) and Privacy Amplification (PA) to distill a secret key.

3. Device Imperfections

Intensity-modulated coherent laser pulses have a particular pulse shape in terms of pulse width and offset from zero intensity level. At high clock speed (in GHz regime), generating an ideal pulse is practically difficult and the spectral width of the source causes chromatic dispersion in the fiber channel. Further, the timing jitter of a single photon detector adds a shift to photon timing. Hence, the pulse distortion in the time domain gives rise to QBER when photons are detected in their nearby pulse slot instead of their pulse slot are categorized as $QBER_{pulse}$. Mach-Zehnder interferometer has insertion losses, extinction ratios and polarization-dependent losses for two arms that cause the transmittance of two output channels to be imperfect. The free spectral range of MZI and finite source spectral width leads photons to leak into the wrong output port. This noise is categorized as $QBER_{MZI}$. In the detector, thermal photons give rise to dark counts that increase the noise is denoted by $QBER_{darkcounts}$. Additionally, the coherence time of the source, dead time, detection efficiency and after-pulsing probability of a single photon

detector are other practical imperfections. In the approximation when $QBER_{pulse}$, $QBER_{MZI}$ and $QBER_{darkcounts}$ is small, the total QBER of the protocol in the asymptotic limit can be approximated as:

$$QBER \approx QBER_{pulse} + QBER_{MZI} + QBER_{darkcounts} \quad (1)$$

4. Results and discussion

In the simulation, we model the DPS protocol by considering all the above-mentioned imperfections and determining the probability of occurring $QBER_{pulse}$, $QBER_{MZI}$ and $QBER_{darkcounts}$. Here, we present the results when four source spectral widths 0.1MHz, 1MHz, 10MHz and 100MHz are used with single photon avalanche diode (SPAD) and superconducting nanowire single photon detector (SNPSD). We consider 2.5 GHz clock speed and 150ps laser pulse width. All parameters are chosen from the specification sheets of devices.

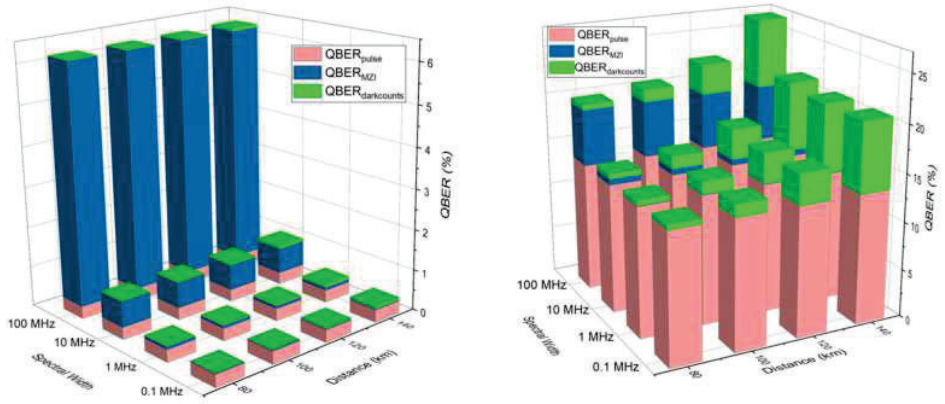

Fig. 1: $QBER_{pulse}$, $QBER_{MZI}$ and $QBER_{darkcounts}$ when using SNSPD (left) and SPAD (right) with source spectral width and length of the channel.

$QBER_{pulse}$ and $QBER_{darkcounts}$ in SPAD are more due to large timing jitter and dark counts respectively. Whereas $QBER_{MZI}$ mainly depends on source spectral width. By calculating QBER in these three categories for any choice of devices, the performance of DPS QKD could be optimized. By knowing the dependency $QBER_{pulse}$, $QBER_{MZI}$ and $QBER_{darkcounts}$ on device parameters, performance could be maximized by ameliorating the limiting QBER factor of the protocol. Thus, our simulation technique characterizes the noise to have better control on QBER.

5. Acknowledgement

We acknowledge the funding received from Defense Research and Development Organization (DRDO), Government of India.

6. References

[1] C. H. Bennett and G. Brassard, "Quantum cryptography: Public-key distribution and coin tossing," in *Proceeding of IEEE International Conference on Computers, Systems, and Signal Processing* (IEEE, 1984), pp. 175–179.
[2] T. Honjo, K. Inoue, and H. Takahashi, "Differential-phase-shift quantum key distribution experiment with a planar light-wave circuit Mach–Zehnder interferometer," Opt. Lett. **29**, 2797–2799 (2004).
[3] H. Takesue, S. W. Nam, Q. Zhang, R. H. Hadfield, T. Honjo, K. Tamaki, and Y. Yamamoto, "Quantum key distribution over a 40 dB channel loss using superconducting single-photon detectors," Nat. Photonics **1**, 343–348 (2007).
[4] Q. Zhang, H. Takesue, T. Honjo, K. Wen, T. Hirohata, M. Suyama, Y. Takiguchi, H. Kamada, Y. Tokura, O. Tadanaga, Y. Nishida, M. Asobe, and Y. Yamamoto, "Megabits secure key rate quantum key distribution," New J. Phys. **11**, 045010 (2009).
[5] K. Inoue and Y. Iwai, "Differential-quadrature-phase-shift quantum key distribution," Phys. Rev. A **79**, 022319 (2009).
[6] N. Gisin, G. Ribordy, W. Tittel, and H. Zbinden, "Quantum cryptography," Reviews of modern physics, vol. 74, no. 1, p. 145, 2002.
[7] K. Inoue, "Differential phase-shift quantum key distribution systems," IEEE Journal of Selected Topics in Quantum Electronics, vol. 21, no. 3, pp. 109–115, 2014.

Observation of Multiple Accidental BICs in Hafnium-oxide Metasurfaces

Shubhanshi Sharma[1, *], Monica Pradhan[2], Basudev Lahiri[1], Shailendra Kumar Varshney[1]
[1]Department of Electronics and Electrical Communication Engg., [2]School of Nanoscience and Technology
Indian Institute of Technology Kharagpur, Kharagpur, West Bengal, India-721302
[*]shubhanshi07@iitkgp.ac.in

Abstract: Here, we report polarization-independent multiple accidental electromagnetic bound states in the continuum in Hafnium oxide disk metasurfaces. Numerical simulations reveal that BICs manifest themselves as quasi-BICs when the vertical symmetry is broken. The resonances at a disk resonator height of 370 nm have high-quality factors of 1330 and 186.
Keywords: Metasurfaces, Mie resonances, Bound state in the continuum

1. Introduction

Non-radiating states, corresponding to strong localization of electromagnetic fields of high intensity field in a small volume of dielectric nanostructures, have gained significant research interest recently due to vast applications from physics to biology. Such non-radiating states refer to either bound states in continuum (BICs) or optical anapoles. These novel states can help to overcome the losses in metals and also confine light in low refractive index resonators [1]. BICs are the localized states that are embedded in the radiation continuum and does not couple with it [2]. These modes start to couple with the continuum of radiating modes as the symmetry of the resonator is broken or through the destructive interference between the various leaky resonances. Ideally these modes have an infinite quality factor (Q) with vanishing linewidth. When the structure's vertical symmetry is broken, the discrete modes couple with the radiation continuum and become leaky resonance that converts the ideal BIC to quasi-BIC [3]. These modes have finite linewidth and the reasonably high Q factor. These modes have wide application in nonlinear harmonic generation, wavefront shaping and manipulation, imaging, and quantum optics [4]. In this numerical study, we report the observation of polarization-independent accidental quasi-BICs in HfO_2 hollow disk resonator due to the destructive interference between the bound modes of the resonator and the modes propagating in the array of the resonator, that manifests as high-quality factor Fano resonances.

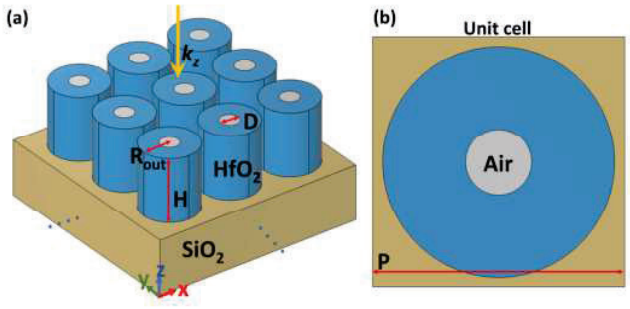

Fig.1. (a) Schematic of an array of metasurfaces showing HfO_2 disk resonator with hollow air channel in the center and (b) the top view of the unit cell. The resonator has an outer radius R_{out}, hollow air channel has a diameter D and H is the height of disk resonator. The unit cell has periodicity as P.

2. Design and Simulation results

The unit cell of the structure consists of a circular disk made of Hafnium oxide (HfO_2) with a concentric circular hollow channel of air in the center that is placed over the silica (SiO_2) substrate, as shown in Fig.1 (b). The unit cell has a period of P = 380 nm, and the radius of the outer disk is R_{out} = 175 nm. The diameter of the hollow air channel is taken as D = 35 nm. The refractive index of HfO_2 is taken as dispersive and refractive index of SiO_2 is 1.46 [5]. It

is ensured that the given design doesn't break the in-plane inversion symmetry, but the vertical mirror symmetry is broken by introducing a substrate. To numerically analyze the structure, the commercial FEM solver (COMSOL Multiphysics) is used. Here, periodic boundary conditions are used along the x- and y-axes, and perfectly matched layer is used along the z direction.

In order to attain accidental BICs, E_x polarized plane wave is incident normally on the metasurface where the height (H) of the resonator is varied while other parameters are kept constant. Since, the resonator is placed over the substrate the vertical symmetry is broken leading to the observation of quasi-BICs. From Fig. 2 (a), it is observed that the resonances experience red-shift with the increase in the disk resonator height (H= 100 nm to 1500 nm). For H = 370 nm, two resonances appear at λ_1 = 563.33 nm and λ_2 = 611.60 nm, as shown in Fig. 2 (b). These resonances exhibit magnetic toroidal quadrupolar and magnetic toroidal dipole characteristics which we confirm through Cartesian multipolar decomposition (Fig. 2 (c)) and also evident from the field distribution plot given in Fig. 2 (d) and 2(e). These resonances possess high-Q factor of 1330 and 186, respectively. We observe that for selected resonator heights, viz., H = 576 nm, 996 nm, and 1444 nm, accidental BICs at 632.7 nm, 651.1 nm and, 656.5 nm wavelengths appear, marked as I, II, and III in Fig. 2 (a). It is also noticed that as the height of the disk resonator increases the resonances almost vanish and transmission spectra becomes highly asymmetric leading to high-Q factor. These are the quasi-BICs resonances that exhibit Fano resonance characteristic in the transmission spectrum due to the modal interference.

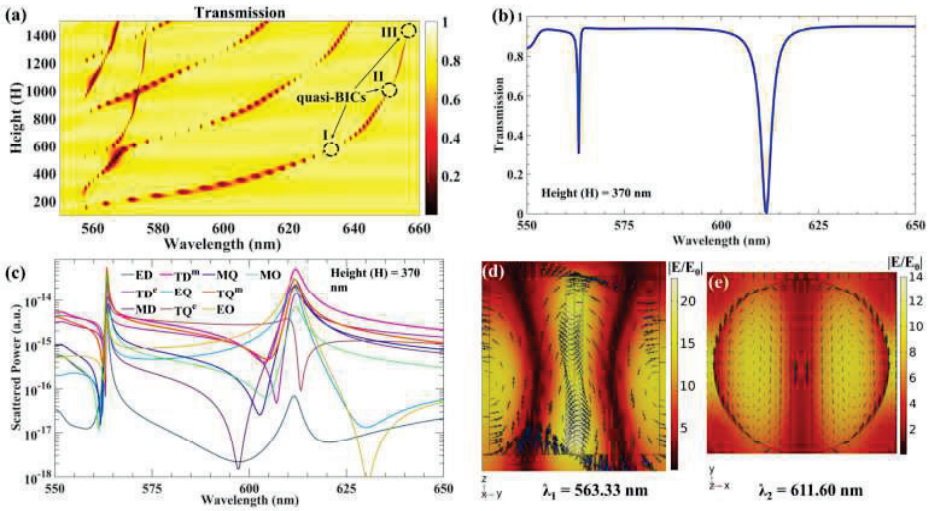

Fig.2. Simulation results illustrating accidental BICs (a) for various height of disk resonator, the dashed circles mark the quasi-BIC resonances, (b) Transmission spectrum at H =370 nm, depicting resonances at 563.33 nm and 611.60 nm, (c) Scattered power plot for H =370 nm, dictating TQ^m and TD^m nature of resonances, here ED = electric dipole, TD^e = electric toroidal dipole, MD = magnetic dipole, TD^m = magnetic toroidal dipole, EQ = electric quadrupole, TQ^e = electric toroidal quadrupole, MQ = magnetic quadrupole, TQ^m = magnetic toroidal quadrupole, EO = electric octupole, and MO = magnetic octupole. Normalized electric field distribution and magnetic field arrow plot at H =370 nm under E_x polarization at wavelength (d) λ_1 = 563.33 nm in y plane and, (e) λ_2 = 611.60 nm in xy plane.

3. Conclusion

In this work, we have studied the polarization-independent accidental BICs in HfO_2 disk resonator with an air-channel metasurface. The accidental BICs manifest as high-quality factor quasi-BIC resonances in transmission spectra. The obtained results can be utilized to develop highly efficient and multifunctional optical devices.

4. References

[1] K. Koshelev, G. Favraud, A. Bogdanov, Y. Kivshar, and A. Fratalocchi, "Nonradiating photonics with resonant dielectric nanostructures," *Nanophotonics* 8, 725–745, (2019)

[2] C. W. Hsu, B. Zhen, A. D. Stone, J. D. Joannopoulos, and M. Soljacic, "Bound states in the continuum," *Nat. Rev. Mater.*1, (2016).

[3] W. Wang, and X. Ma, "Achieving extreme light confinement in low-index dielectric resonators through quasi-bound states in the continuum," *Opt. Lett.*, *46*, 6087-6090, (2021)

[4] S. I. Azzam and A. V. Kildishev, "Photonic Bound States in the Continuum: From Basics to Applications," *Adv. Opt. Mater.*, 2001469, 2001469, (2020)

[5] M. F. Al-Kuhaili, "Optical properties of hafnium oxide thin films and their application in energy-efficient windows," *Opt. Mat.* **27**, 383-387 (2004)

Suppression of Stimulated Brillouin Scattering in a Narrow Line-Width Fiber Amplifier using Sinusoidal Phase Modulation

C N Siva Subramaniyam, Yusuf Panbiharwala, and Balaji Srinivasan*

Department of Electrical Engineering, Indian Institute of Technology Madras, Chennai 600036, India

** Author e-mail: balajis@ee.iitm.ac.in*

Abstract: In this paper, we experimentally demonstrate the suppression of Stimulated Brillouin Scattering (SBS) in a narrow line-width continuous wave (CW) fiber amplifier using sinusoidal phase modulation and achieve a 1.42 % increase in the SBS threshold (limited by pump power) for 20 MHz sinusoidal phase modulation.

Keywords: Fiber Lasers, Master Oscillator Power Amplifier, Stimulated Brillouin Scattering

1. Motivation

Narrow line-width high power laser sources are fundamental to several cutting-edge applications such as directed energy applications [1], nonlinear frequency conversion [2] and coherent beam combining [3]. SBS act as a constraint for power scaling through fiber amplifiers. There are several methods to suppress SBS in a fiber amplifier such as strain variation [4], temperature variation [5] and increasing the core diameter of gain fiber. However, strain and temperature variation techniques provide only limited improvement in the SBS threshold, and large core area fiber gives rise to transverse mode instability at high powers. Line-width broadening through phase modulation is an effective approach to suppress SBS in fiber amplifiers. The optical line-width can be increased with modulation frequency and modulation depth. Larger modulation bandwidth and depth result in better SBS threshold enhancement. However, lesser SBS enhancement is achieved as the modulation frequency reaches Brillouin gain bandwidth due to a smaller overlap between Brillouin gain and optical sidebands. The maximum modulation depth is decided by the phase modulator RF port damage threshold. Compared to noise [6] and PRBS phase modulation [7], sinusoidal phase modulation [8] can be easily performed using low-cost and compact electronic oscillators. In this paper, we experimentally demonstrate the suppression of Stimulated Brillouin Scattering (SBS) in a narrow line-width fiber amplifier through sinusoidal phase modulation.

2. Experimental Setup

A schematic diagram of the experimental setup is shown in Fig. 1. A distributed feedback (DFB) semiconductor laser diode emitting at 1064 nm with an FWHM line-width of ~100 kHz and CW output power of 40 mW is used as a seed source for the fiber amplifier. The laser output line-width is broadened using a phase modulator (EOspace, PM-0S5-10-PFA-PFA -106-SRF1W, $V\pi$= 2.9 V) and isolator before it is fed to fiber amplifier stage 1 (FA 1). Line-width broadening is performed by driving the modulator using a sinusoidal waveform at a different frequency with a modulation depth of π from an RF signal generator (Tektronix TSG 4106 A, DC – 6 GHz). The FA 1 consist of 5.8 mts of Yb-doped double-clad fiber (Nufern fiber LMA-YDF-10/130-VIII, core/clad diameter – 10/130 µm) which is cladding-pumped at 915 nm with 2.31 W optical power. The output of FA 1 is 0.5 W which is further amplified to 10.3 W (limited by SBS) by fiber amplifier stage 2 (FA 2). The FA 2 consists of 8.4 mts of Yb-doped double-clad fiber (Nufern fiber LMA-YDF-10/130-VIII, core/clad diameter – 10/130 µm) and cladding-pumped at 915 nm with 21 W optical power. Isolators are incorporated at the output of each stage to minimize back-reflection from the subsequent stage. The forward propagating signal power and backward propagating Stokes power are measured using a 2x2 95:5 tap coupler placed at the output of FA 1 and FA 2. The onset of SBS in FA 2 is detected and monitored from the 5% tap port of the coupler. The output port of the coupler is angle-cleaved at ~12^0 to reduce back-reflection coupling back into the fiber.

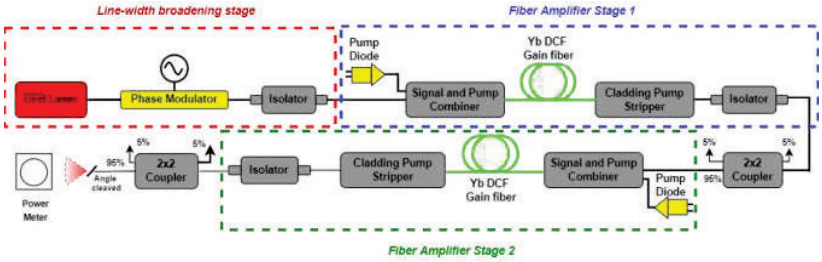

Fig. 1. Schematic diagram of the line-width broadening stage, fiber amplifier stage 1 and stage 2.

3. Results and Discussion

Fig. 2 (a) shows the FA 2 output power and the reflectivity at different FA 2 pump powers for the unmodulated case i.e., the phase modulator is not driven by any RF signal. The reflectivity is defined as the backward propagating Stokes power to output signal power ratio. The SBS threshold is the output signal power at which the reflectivity reaches 0.1%. For the unmodulated case, the SBS threshold is reached for an output signal power of 8.73 W. Later, the experiment is performed by driving the phase modulator with a sinusoidal signal of frequency 10 MHz, 15 MHz and 20 MHz with a modulation depth of π for each case. For the case of 20 MHz sinusoidal phase modulation, FA 2 output power of 13.3 W is achieved for a pump power of 27.31 W as shown in Fig. 2 (b). The reflectivity reaches 0.1 % for FA 2 output power of 12.4 W with a 20 MHz sinusoidal phase modulation as shown in Fig. 2(c). Further amplification is possible in FA 2 with higher pump power.

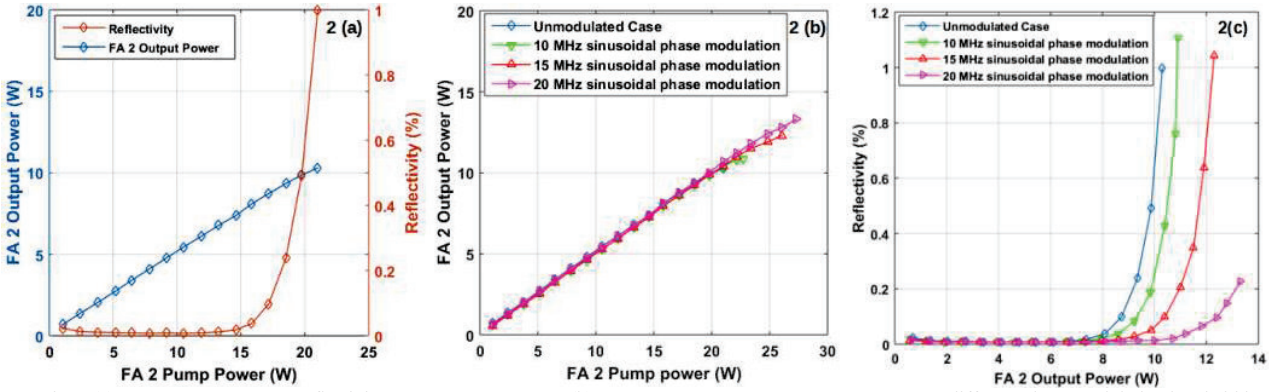

Fig. 2 (a) FA 2 output power & reflectivity vs FA 2 pump power, (b) FA 2 output power vs FA 2 pump power at different phase modulation bandwidth (c) Reflectivity vs. FA 2 output power for different phase modulation bandwidth illustrating the enhancement in SBS threshold for larger modulation bandwidth

4.Conclusion

In summary, we have experimentally demonstrated the suppression of SBS in a narrow line-width fiber amplifier and achieved a 1.42 % increase in the SBS threshold (limited by pump power) for 20 MHz sinusoidal phase modulation. In the spectral broadening method, the temporal coherence of the source is reduced, which is undesirable for coherent beam combining experiments. Hence, phase modulation formats that offer maximum SBS suppression per unit optical bandwidth are required for such applications which will be addressed in future works.

5.Acknowledgement

This research work is supported by Scheme for Promotion of Academic and Research Collaboration (SPARC/2018-22019/P942/SL). The authors would like to acknowledge Prof. Johan Nilsson, University of Southampton for technical discussions. Siva subramaniyam C N would like to acknowledge SAMSUNG India and IITM PRAVARTAK for fellowship Support. Prakash R and Umashankar are acknowledged for their technical support.

5. References

[1]. Mikhail A et al.,"High-power lasers for directed-energy applications: comment," Appl. Opt. 55, 9950-9953 (2016)
[2]. Ekaterina A et al."Tunable CW all-fiber optical parametric oscillator operating below 1 μm," Opt. Express 21, 6777-6782 (2013)
[3]. C. L. Linslal et al., "Investigation of Line Broadening Scheme Dependence on Coherent Beam Combination Efficiency," in Laser Congress 2019 (ASSL, LAC, LS&C), OSA Technical Digest (Optica Publishing Group, 2019), paper JW2A.31
[4]. N. Yoshizawa and T. Imai, "Stimulated Brillouin scattering suppression by means of applying strain distribution to fiber with cabling," J. Lightw. Technol., vol. 11, no. 10, pp. 1518–1522, Oct. 1993
[5]. A. Liu, "Suppressing stimulated Brillouin scattering in fiber amplifiers using nonuniform fiber and temperature gradient," Opt. Express, vol. 15, no. 3, pp. 977–984, 2007.
[6]. V. R. Supradeepa, "Stimulated Brillouin scattering thresholds in optical fibers for lasers linewidth broadened with noise," Opt. Express 21, 4677-4687 (2013)
[7]. Angel Flores et al., "Pseudo-random binary sequence phase modulation for narrow linewidth, kilowatt, monolithic fiber amplifiers," Opt. Express 22, 17735-17744 (2014)
[8]. Angel Flores et al., "Experimental and theoretical studies of phase modulation in Yb-doped fiber amplifiers," Proc. SPIE 8381, Laser Technology for Defense and Security VIII, 83811B (21 May 2012)

Optimization of exposure energy of holographic gratings in LLPF465 photopolymer for 447 nm wavelength

Sumedha[1], Bhargab Das[1], Raj Kumar[1]
[1]*CSIR-Central Scientific Instruments Organisation, Sector 30C, Chandigarh 160030, India*
**Corresponding author: raj.optics@csio.res.in*

Abstract: The exposure energy is optimized to achieve maximum diffraction efficiency of the holographic gratings recorded in LLPF465 photopolymer material (Light Logics) for 447 nm wavelength. The blue diode laser (447 nm) is used to record transmission gratings at a recording angle of 20^0 which corresponds to the grating period of 1.3 μm. For p-polarized light, the maximum diffraction efficiency is achieved at an exposure energy of 50 mJ/cm^2.

Keywords: Holographic Grating, Diffraction Efficiency, Photopolymer

1. Introduction

Photopolymer materials are commonly used as holographic recording media because of its unique features such as no wet processing, good resolution, large refractive index modulation, acceptable energetic sensitivity, high diffraction efficiency, and low cost [1]. Environmental and thermal stability are important parameters of recorded grating in photopolymer materials. The main components of photopolymers used for holographic applications are binder, monomer, photoinitiator, sensitized dye, and crosslinker [2]. The recording mechanism in photopolymer includes the diffusion of one or more components. When the light of a particular wavelength is incident on the photopolymer material, the photopolymerization process occurs inside the material and monomer molecules diffuse from dark region to bright region causing a change in density that forms refractive index modulation, thus the holographic grating is recorded in the material [2-3]. Dyes are used to make photopolymer material sensitive to a certain wavelength of light [3]. In this study, we optimized the exposure energy to get maximum diffraction efficiency of the recorded grating for 447 nm wavelength light source.

2. Experimental details

In this work, commercial LLPF465 photopolymer (Light Logic Holography and Optics Pvt. Ltd) is used for recording transmission holographic grating using a 447 nm laser (MDL III-447L, CNI) with 30 mW power. This material shows very good sensitivity in the red, green and blue region of the spectrum. The reported emulsion thickness and refractive index modulation of the photopolymer are 15 μm and 0.029 respectively. The LLPF465 photopolymer material shows less energy sensitivity in the lower range of wavelength. To record the transmission grating, the intensity of both the recording beams is made equal using a 50:50 beam splitter. Laser beam is passed through the spatial filter which expands the beam which is then collimated. These two beams fall on the plane mirrors which steer the beams to enclose inter beam angle of 20^0 and these beams interfere in the photopolymer material. Thus, transmission grating is recorded inside the material and the recorded grating is reconstructed using the same light source. Diffracted power in 1st order is measured using a power meter (Thorlabs, PM16-121). In this experiment, P- polarized laser beam is used so the electric vectors of the two interfering beams make an angle θ with each other, due to this visibility of interference fringes is less. The resultant diffraction efficiency of the interference fringes decreases. The visibility of interference fringes is expressed as [4]:

$$V_\theta = V \cos\theta \text{ , when } \theta > 0;\ V \text{ (visibility)} < 1$$

$$\text{when } \theta = 0;\ V \text{ (visibility)} = 1 \quad (1)$$

The value of diffracted power is calculated by the ratio of diffracted intensity in the first order to the incident intensity of the laser beam. Diffraction efficiency is expressed as:

$$DE = \frac{I_d}{I_{in}} \quad (2)$$

Where, I_d is 1st order diffracted intensity and I_{in} is the intensity of the incident beam.

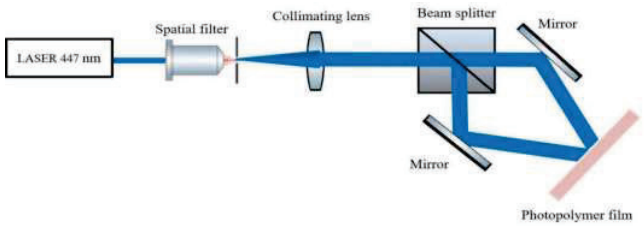

Figure 1. Schematic diagram of holographic grating recording setup

3. Results and Discussion

Transmission grating is recorded in the photopolymer film by changing the exposure energies from 20 mJ/cm^2 to 80 mJ/cm^2 to get maximum value of diffraction efficiency. Total incident power of both interfering beams is 5.12 mW/cm^2 at the recording position. Diffraction efficiency of grating increases upto exposure energy of 50 mJ/cm^2 then it decreases continuously with higher exposure energy (Fig. 2).

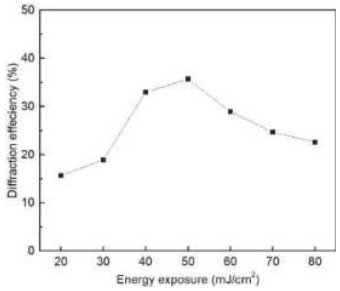

Figure 2. Measured diffraction efficiency Vs exposure energy

4. Conclusion

In this work, LLP465 photopolymer is studied to see the variation in diffraction efficiency at different exposure energy. The transmission grating is recorded into this photopolymer using p-polarized 447 nm laser. Maximum diffraction efficiency of 35.7 % of the recorded grating is obtained at 50 mJ/cm^2.

Acknowledgement

Authors thank CSIR, India for providing financial support under project number MLP2014 to carry out this research work. Authors thank Dr Kamlesh Kumar, Mr. Lavlesh Pensia and Ms. Rajveer Kaur for fruitful discussions.

5. References

[1]. M. S. Mahmud, I. Naydenova, N. Pandey, T. Babeva, R. Jallapuram, S. Martin, and V. Toal, "Holographic recording in acrylamide photopolymers: thickness limitations," Appl. Opt. 48, 2642-2648 (2009).

[2]. J. R. Lawrence, F.T. O'Neill, and J. T. Sheridan, "Photopolymer holographic recording material," Optik 112, 449-463 (2001).

[3]. A. Zanutta, A. Bianco, and F.M. Zerbi, "Photopolymer - based volume phase holographic grating for astronomical instrumentations," Proc. of SPIE 8450, 845041-1 (2012).

[4]. P. Hariharan, *Basics of holography* (Cambridge University Press,2002), Chap. 4.

Digital and photonics based Ising machines

Nistala Krishna Vamsi*, **Nitin Chandrachoodan** and **Anil Prabhakar**

Department of Electrical Engineering, Indian Institute of Technology Madras, Chennai, India
*Corresponding author: ee20s025@smail.iitm.ac.in

Abstract: Unconventional computing devices are useful for solving combinatorial optimization problems in routing, logistics, and scheduling. We present two different implementations of Ising machines using photonics and using a graphical processing unit (GPU). We discuss the advantages of each implementation and perform a comparative analysis with commercial optimizers like DWave's QPU and Gurobi, for the maxcut and number partitioning problems.

1 Introduction

Ising machines are used extensively for solving quadratic integer problems [1]. The Ising model describes interactions between magnetic spins arranged on a lattice. The spins are aligned along either +z or -z, represented by +1 or -1 respectively, and interact with each other via an exchange interaction that defines the Hamiltonian energy of the system. We discuss our implementations of a digital and a photonic Ising machine, and compare their performance against commercial optimizers from DWave, and Gurobi

2 GPU based Ising machine: digital annealer

The Ising model is an idealised description of a magnetic material where the exchange energy between spins reduces the lattice to its ground state energy. We have implemented a Markov chain Monte Carlo simulation to model this spin exchange interaction in magnetic materials. Researchers have shown that the spin configuration of the ground state of an Ising model is also the solution to NP-hard problems like maxcut and number partitioning.

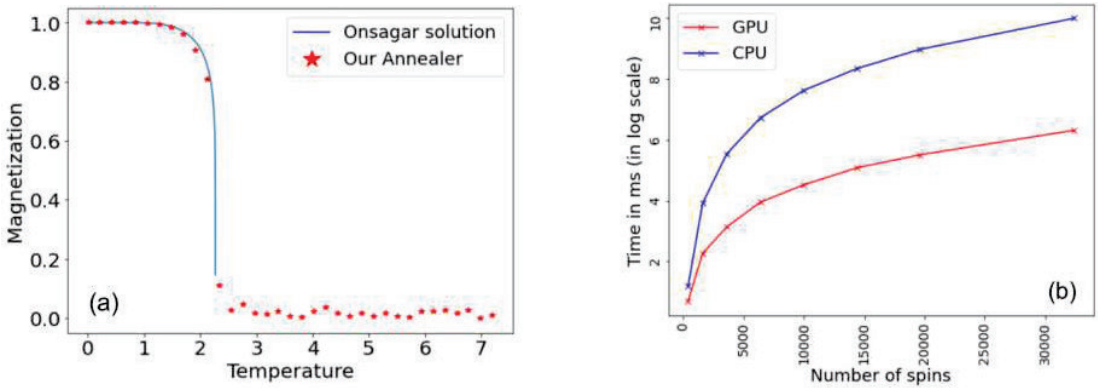

Figure 1: Comparison of a) solutions obtained on the digital annealer against Onsagar's analytic formula for a 2D lattice (b) execution time on a GPU and a CPU

We have solved the 2D-nearest neighbor Ising model on an NVidia GTX 1050 Ti GPU and validated our solution against Onsagar's analytic solutions at different temperatures, as shown in Fig 1(a). The improved performance of the Ising solver on a GPU verse a CPU is shown in Fig 1(b). We also got comparable accuracy and timing values with respect to Gurobi, a commercial optimizer for the maxcut problem, as shown in Table 1.

Graphs(V, E)	Gurobi cut (Timing in secs)	GPU cut (Timing)	Accuracy
Graph (400, 31920)	17439 (23.0 secs)	17476 (15.1 secs)	100.21%
Graph (700, 97860)	52265 (56.3 secs)	52395 (26.6 secs)	100.24%
Graph (900, 161820)	85807 (17.9 secs)	85936 (7.9 secs)	100.15%
Graph (1000, 499500)	158563 (33.0 secs)	159619 (40.3 secs)	100.66%

Table 1: Maxcut solutions for different graphs. Our GPU implementation is faster than Gurobi for small graphs (V = vertices, E = edges)

3 Spatial photonic Ising machine

A spatial photonic Ising machine (SPIM) uses the principles of photonic and Fourier optics to find the minimum energy state of a specific form of the Ising model, a fully connected graph with self-loops, called the Mattis model [2]. The SPIM uses a spatial light modulator (SLM) to embed the values of Ising spins. A Fourier lens couples each spin with every other spin allowing us to quickly calculate the Ising Hamiltonian.

Given a multiset S of positive integers, we must partition them into two subsets A and B such that the sum of the numbers in set A is as close as the sum of the numbers in set B. Fidelity for number partitioning problem is defined as difference between number set A and B over sum of all numbers.

We compare the accuracy of the solutions offered by the SPIM, digital annealer (DA), DWave's quantum annealer (DWA), and Gurobi optimizer by solving number partitioning problem. The SPIM can solve much larger problems, and is comparable to the DA, as shown in Table 2. This data was collected using these hardware configurations, (i) digital annealer on a NVidia V100 GPU processor, and (ii) Gurobi optimizer on an Intel Xeon Gold 6248 20-core, 2.5 GHz processor.

Solvers	Max. Problem Size	Avg. Fidelity for 64 spins	Max. Runtime
DA	22500	3.0E-04	90 min
SPIM	16384	4.1E-04	13 min
DWA	121	3.5E-04	6 min**
Gurobi	4900	6.2E-05	$\sim$ 20 min

Table 2: Benchmarking the SPIM, DA with Gurobi, and DWA. Fidelity is the normalized difference between the 2 number partitioned sets. **The DWA runtime indicated includes the embedding time for 121 spins.

4 Summary

NVidia GPU's massive core count, huge dedicated DRAM, and CUDA parallel programming makes the DA a good contender for solving large Ising models better than a CPU-based annealer or commerical optimizers like DWave, and Gurobi optimizer. The SPIM with its limitation of solving only the Mattis model, does converge to the solution faster than rest of the solvers even for a large problem.

References

[1] A. Lucas, "Ising formulations of many NP problems," *Frontiers in Physics*, vol. 2, p. 5, 2014.

[2] D. Pierangeli, G. Marcucci, and C. Conti, "Large-scale photonic Ising machine by spatial light modulation," *Phys. Rev. Lett.*, vol. 122, p. 213 902, 2019.

Experimental Setup for the Real-Time Detection and Sizing of Single Protein Molecules

Pranabjyoti Patar, Pragya Tiwari and Venkata Ramanaiah Dantham*
Department of Physics, Indian Institute of Technology Patna, Bihar 801103, India
*Corresponding author: dantham@iitp.ac.in

Abstract: Herein, we report a few details of a developed experimental setup for efficient coupling of laser light into nanoplasmonic-whispering gallery mode (WGM) hybrid microresonators (HMRs) and for demonstrating real-time detection and sizing of single protein molecules. Moreover, with the help of the reactive sensing principle (RSP), the theoretical simulations are performed for estimating the WGM wavelength shift of bare microresonators and HMRs upon adsorbing single protein molecules at the active sites.
Keywords: Whispering gallery mode, hybrid microresonators, real-time detection, protein molecules, reactive sensing principle

1. Introduction:

In the field of biosensing**,** the label-free or real-time detection of single protein markers has tremendous demand. Because protein markers (at extremely low concentrations) flow all around the body during the early stage of infection and disease and may act as a signal of infection or the reoccurrence of the disease. As a result, early detection of infection or disease would be accomplished by identifying single protein markers (protein molecules) in bodily fluids. Unfortunately, most of the protein molecules have masses typically less than 6 attograms (size < 30 nm). Therefore, this detection is only achievable with the use of biosensors with ultimate sensitivity and resolution. Recently, a nanoplasmonic-whispering gallery mode (WGM) hybrid microresonator (HMR) has been found useful for the real-time detection and sizing of single protein molecules [1,2]. The detection was demonstrated by monitoring the change in the WGM wavelength due to the adsorption of protein markers at the active sites on the nanoplasmonic particle of the HMR. The WGMs inside the microresonators are excited through the evanescent coupling achieved with the help of a tapered fiber. However, mechanical vibrations of the fiber taper cause problems in this configuration, leading to research into minimizing these and other noise sources. The random and nonspecific attachment of nanoparticles to the fiber tapered area may disrupt the sensory signal and quickly deteriorate transmission. Consequently, the repeatability of lengthy measurements may be affected. Additionally, the delicate taper needs to get substituted routinely, which might be a challenging task if the taper is inserted into a microfluidic channel. To overcome these problems, there is a need for another geometry to excite the WGMs. Therefore, we have developed HMR biosensor platform based on prism coupling, which has high mechanical stability and reproducibility where we excite the WGMs of nanoparticle-modified fused silica microsphere by the evanescent field generated on the prism surface due to the total internal reflection of a laser beam focused onto a prism's surface (Fig.1)

2. Experimental details:

In the setup shown in Fig. 1, the phase matching excitation of equatorial WGM of dielectric microsphere is achievable with the help of evanescent coupling using a glass prim. The evanescent field of the WGM excites the localized surface plasmons inside the metal nanoparticle anchored on the surface of the microresonator. This results in the formation of hot spots on the surface of the metal nanoparticle functionalized with suitable antibodies. The mode of the HMR placed in the aqueous medium encapsulated by the PDMS microfluidic channel can be visualized as a dip in the transmission spectrum. Once we observe the dip, the protein sample will be injected with the help of a microsyringe pump and monitor the shift in the WGM wavelength or dip minimum. As per the reactive sensing principle (RSP), the shift will be observed when the protein adsorbs at any of the hot spots of the metal nanoparticle. The size, mass, molecular weight, and number of amino acids contained inside a protein can calculate from the experimental signals.

3. Theoretical Analysis:

Based on the RSP, the fractional WGM wavelength shift due to the adsorption of a single protein to the surface of a bare microresonator [3],

$$\frac{\delta\omega_{bare}}{\omega_r} = -\frac{\frac{1}{4}Re[\alpha_{ex}]E_0^2(r_p)}{\frac{1}{2}\int \varepsilon_r(r)|E_0(r)|^2 dV} = D\frac{a_p^3}{R^{5/2}\lambda_r^{1/2}}e^{-a_p/L} \quad (1)$$

Here $\delta\omega_{bare}$ is the frequency shift, ω_r is the resonance frequency, $Re[\alpha_{ex}]$ is the real part of excess polarizability of the protein. $E_0(r_p)$ is the electric field amplitude of the mode at the location of protein, ε_r is the electric permittivity inside the microresonator, $E_0(r)$ is the electric field of the resonance mode inside the microresonator $a_p$is the radius of the protein molecule, R is the radius of the microsphere, D is the dielectric factor and L is the evanescent decay length.
The frequency shift of the mode of an HMR [4], can be defined as

$$\delta\omega = \delta\omega_{HMR} + \delta\omega_{\Delta\Omega} + \delta\omega_{\Delta T} \quad (2)$$

where $\delta\omega_{HMR}$ is the frequency shift due to the binding of the analyte (protein molecule) at the hot spot of the nanoparticle attached to the surface of HMR, $\delta\omega_{\Delta\Omega}$ is the frequency shift due to fluctuation in laser frequency and $\delta\omega_{\Delta T}$ is the frequency shift due to thermal fluctuations. Also

$$\delta\omega_{HMR} = \xi(R) * \delta\omega_{bare} \tag{3}$$

Where $\xi(R)$ is the enhancement in $\delta\omega_{bare}$ after attaching the nanoparticle to the bare microresonator, which is defined as the ratio of frequency shift due to adsorption of analyte on the nanoplasmonic particle to that just outside a bare portion of the microresonator [1].i. e.

$$\xi(R) = \frac{\delta\omega_{HMR}}{\delta\omega_{bare}} = \frac{\int \Delta\varepsilon(E_b \cdot E_a^*)_{with\ nanoparticle} dV_{potein}}{\int \Delta\varepsilon(E_b \cdot E_a^*)_{with\ nanoparticle} dV_{protein}} \tag{4}$$

where, $\Delta\varepsilon = \varepsilon_d - \varepsilon_m$; ε_d is the electric permittivity of the protein, ε_m is the electric permittivity of the medium, $E_b \cdot E_a^*$ is the product of the field before and after analyte adsorption, and $V_{protein}$ is the volume of the analyte.

Figure 2 represents the wavelength shift of the mode of HMR made by metal nanoparticles of three different shapes. From this figure, we can conclude the following points. The bare and Au nanosphere-based HMR are not useful for the detection of single BSA protein molecules because the estimated wavelength shifts are significantly lower than the experimental noise. Similarly, it is observed that Au nanoshell-based HMR is also found not useful for the same. However, Au nanospheroid-based HMR is found efficient for the detection of BSA protein molecules. This means the elongated nanoparticles are useful for improving the sensitivity of the HMR.

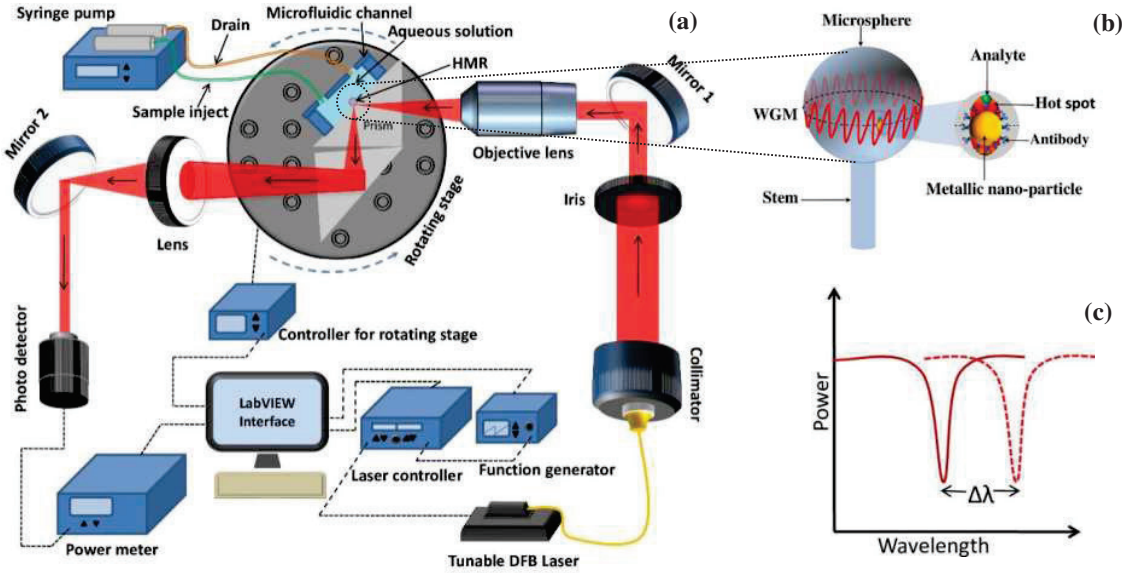

Fig.1: Panel (a) represents the illustration of an experimental set-up of nanoplasmonic WGM HMR biosensing platform. The binding of a specific protein marker at the hot spot of the nanoparticle (functionalised with suitable antibodies) excited by the evanescent field of the WGM of the microsphere (Panel (b)). Panel (c) represents the WGM wavelength shift due to the binding of a single protein molecule at the active site of the HMR.

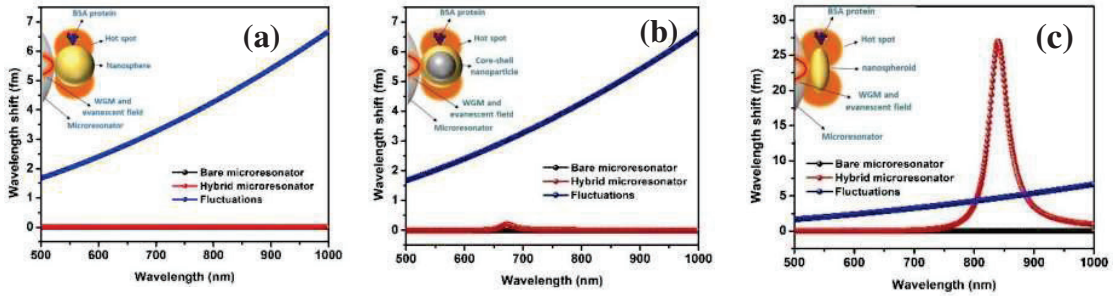

Fig.2: Theoretically estimated WGM wavelength shifts for (a)Au nanosphere (b) silica core Au nanoshell (c) Au nanospheroid-WGM HMR in the presence of a single BSA protein.

4. Conclusion:

The experimental details and merits of the developed setup are given. From the theoretical simulations based on the RSP, it is proved that the HMRs are efficient for the real-time detection of single protein molecules as compared with the bare microresonators.

5. References:

1. V. R. Dantham, S. Holler, C. Barbre, D. Keng, V. Kolchenko, S. Arnold, Nano letters 13 (7), 3347-3351 (2013).
2. V. R. Dantham, S. Holler, V. Kolchenko, Z. Wan and S. Arnold, Applied Physics Letters, 101, 043704 (2012).
3. F. Vollmer, S. Arnold and D. Keng, PNAS, 105(52), 20701-20704 (2008).
4. J. D. Swaim, J. Knittel and W. P. Bown, Applied Physics Letters, 99(24), 243109 (2011).

Facile synthesis and characterization of gC_3N_4/ZrO_2 nanocomposite with different pH of ZrO_2 nanoparticle for emissive material of OLEDs application

Jayanta Bauri, Ram Bilash Choudhary, Gobind Mandal, Debasish Nayak, Sanjeev Kumar, Sarfaraz Ansari

Nanostructured Composite Materials Laboratory (NCML), Department of Physics, Indian Institute of Technology (Indian School of Mines), Dhanbad 826004, INDIA.
***Corresponding Author:** Ram Bilash Choudhary, rbcism@gmail.com*

Abstract:
In this work, we synthesized gC_3N_4/ZrO_2 nanocomposite via ultrasonication method by varying the pH (pH2, pH4, and pH6) value of the ZrO_2 by adjusting neutral water and concentrated sulfuric acid. The X-ray diffraction technique was used to know the crystalline phase, determine the average particle size (8.48 nm). FESEM characterizations were carried out to analyse the surface morphology. UV-Visible revealed the absorbance range, refractive index (n = 2.09), and optical binding energy (E_g = 2.98 eV) of the nanocomposite. The photoluminescence technique was carried out to know the photon emission range (450 nm – 530 nm) and inform the color purity.
Keywords: pH value, Excitons, refractive Index, Photoluminescence

Introduction:
Today, the organic light emitting device became an emerging area for industrial and academic purposes with respect to other electronics devices. OLED has been used in both field lighting and modern display device purposes such as decorate of hotels, schools, wrist watches, smartphones and TV displays and also used large scale display devices. gC3N4 is promising candidate in the files of optoelectronics applications due its optical, electrical properties and higher thermal stability. ZrO2 is p type semiconducting materials, it has high electrical conductivity, wide optical band gap energy (3.26 -5.21 eV), higher thermal stability[1-2].

Experimental methodology:

Synthesis of gC3N4/ZrO2 nanocomposites:
At first gC3N4 and ZrO2 nanomaterials were synthesized via thermal polyconsasion hydrothermal methods. the ultrasonic wave treatment approach was used to create three different resulting solutions according to their pH value (pH2, pH4 and pH6) of gC_3N_4/ZrO_2 (GZ) nanocomposites. Previously prepared ZrO_2(Z) and gC_3N_4(G) powder were mixed into DI- water. After that, the two aqueous solutions were thoroughly mixed using a magnetic stirrer and then kept in an ultrasonic bath for two hours. By finishing the ultrasonication process, put them in a vacuum oven for dry. The dried solid was ground in a mortar to create fine powder.

Structure and Morphological structure analysis:

XRD and FESEM analysis:
Powder X-ray diffraction spectra of the pure gC3N4, ZrO2 (pH2, pH4, and pH6), and pH dependence gC3N4/ZrO2 nanocomposites have been shown in figure- 1(a). X-ray diffracted at position 2θ = 17.5°, 2θ = 24.1°, 2θ = 28.0°, 2θ = 30.°, 2θ = 31.26°,2θ = 34.24°,2θ = 34.24°, 2θ = 38.60°, 2θ = 40.51°, 2θ = 50.01° from the corresponding planes are (100), (110), (-111), (111), (020), (120), (102), and (221) indexes for the low pH2 of ZrO2 nanoparticles. ZrO2 has coexisted in two mixed phases, monoclinic and tetragonal for pH2 [3]. Crystal plane and diffracted peak positions of mixed-phase ZrO2 (pH2) were well matched with the JCPDS card no 00-001-0750The crystalline nature of gC3N4 has been confirmed by the sharp, intense peak at positions 2θ = 12.98° and 27.47°, diffracting from the plane (100) and (002). Miller index (100) and (002) represent the periodic arrangements of heptazine ring and layer staking with interplanar distances of 6.788 Å , 3.73 Å, respectively. No extra peaks were generated in case of gC3N4/ZrO2 nanocomposite; only peak intensity and broadening increased due superposition of gC3N4 and ZrO2 XRD peaks. Debye Scherrer formula was used to estimate the pure and composite materials' average particles or crystallite size. The Debye Scherrer formula is as follows [4],

$$D = \frac{k\lambda}{\beta\cos(\theta)} \qquad (1)$$

Where k - Scherrer constant (=0.94), which depends on the crystalline shape, λ (=0.154 Å) - wavelength of the CuK_α Radiation, β – full width and half maxima of a peak, and θ- the diffracted angle of the X-ray.
The average crystallite size of the pure ZrO2 nanoparticle is 31.58 nm.
Fig.1(b-e) shows the FESEM images of pure gC3N4, ZrO2 and gC3N4/ZrO2 nanocomposites. Fig.1(b) shows irregular arrangements of gC3N4 nanosheet and the FESEM image in Fig.1(d) shows the particles-like structure of pure ZrO2. Both phases are clearly observed in the case of gC3N4/ZrO2 nanocomposite. In FiG.1(c) has been shown that ZrO2 nanoparticles are nonuniformly agglomerate on the gC3N4 sheets [5].

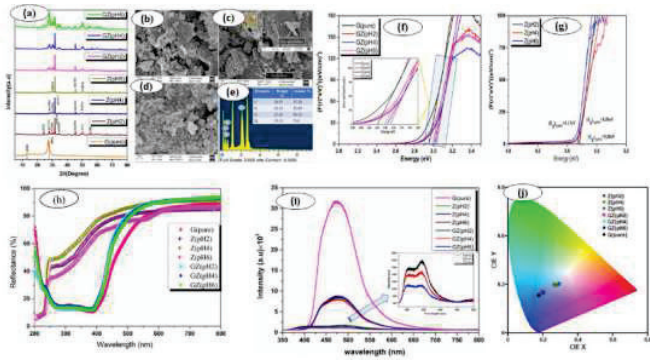

Fig. 1. (a) XRD spectra of pure gC3N4 (G), ZrO2 (Z)and pH dependents gC3N4/ZrO2 nanocomposite, FESEM images (b,d) pure gC3N4 and ZrO2 (c) gC3N4/ZrO2 nanocomposite (d) EDS spectra of gC3N4/ZrO2 nanocomposite.

Optical properties

UV Visible Photoluminescence spectra analysis:

UV Visible DRS spectra taucs plots of pure gC3N4 and ZrO2 (pH2, pH4 and pH6) nanofiller into gC3N4 matrix have showed in Fig.1 (f-h). Kubelka Munk equation was used to estimate the optical bandgap energy of the pure and nanocomposite. Kubelka Munk function used in taucs equation in place of absorbance coefficient, Kubelka Munk equation is given below [6]

$$(F(r)h\nu)^{\frac{1}{\gamma}} = B(h\nu - E_g) \quad (1)$$

Where F(r) represent the Kubelka Munk function, h planks constant, ν frequency of wavelength, B constant, E_g band gap energy of material. The exponential term γ- constant, which corresponding to the nature of the electronics transition. For direct allowed transition γ =0.5. In fig. 2 (b,c) have showed the taucs plot of the pure and nanocomposite materials. Refractive index (n) of the as obtained materials were determinate by the following equation,

$$\frac{n^2-1}{n^2+1} = 1 - \sqrt{\frac{E_g}{20}} \quad (2)$$

Refractive index and optical band gap energy of the materials have been given in tabulated form table-1.

The PL spectra of as-synthesized pure gC3N4, ZrO2, and increasing pH value (pH2, pH4, and pH6) of ZrO2 in gC3N4/ZrO2 nanocomposite materials were recorded as showed in Fig. (f). Two peaks at 414 nm and 493 nm are present in pure ZrO2(pH2) nanoparticles. As increases the pH value of ZrO2, the blue shift has been seen in PL spectra in intensity decreasing order. PL emission at the positions 414 nm and 493 nm appeared due to the transition from the oxygen vacancy level to the valence band and two oxygen vacancy levels. PL emission at 475 nm of pure gC3N4 nanosheets has been recorded due to $\pi^* \rightarrow$ LP (lone pair) transition. [7]

Materials	Optical band gap energy (eV)	Refractive index
ZrO2(pH2)	5.20	1.71
ZrO2(pH4)	5.19	1.70
ZrO2(pH6)	5.17	1.75
gC3N4	2.95	2.04
gC3N4/ZrO2(pH2)	3.03	2.02
gC3N4/ZrO2(pH2)	3.01	2.06
gC3N4/ZrO2(pH2)	2.99	1.52

Table-1. Bandgap energy and refractive index of the pure gC3N4, ZrO2 and gC3N4/ZrO2 nanocomposite.

Conclusion:

Thermal polycondensation and hydrothermal method successfully synthesized the pristine gC3N4 and ZrO2 nanoparticles, and gC3N4/ZrO2 nanocomposite was synthesized via ultrasonication method. XRD spectra of the pure ZrO2 (pH2) show a monoclinic phase, as the increased pH value (pH4 and pH6) of the ZrO2 phase has shifted monoclinic to tetragonal. Average particles size was estimated with the help of FWHM values of the peaks. The average particles size of the samples ZrO2 (pH2, ZpH4 and pH6) are 31.5 nm, 30 nm and 25.34 nm. Reduced optical bandgap energy and refractive index of composites (GZ2, GZ4 and GZ6) are 3.03 eV, 3.01 eV, 2.99 eV and 2.02, 2.06 and 1.52 respectively. PL emission in the broad spectral range 415 nm to 550 nm of composite materials.

Acknowledgments:

The authors are expressing sincere thanks to the Director of IIT (ISM) Dhanbad for providing a research facility and continuous support in this communication.

References:

[1]. Xu, Yingxi, Yafang Zhou, Jianyu Guo, Siyong Zhang, and Yan Lu. "Preparation of the poly (3, 4-ethylenedioxythiophene): poly (styrenesulfonate)@ g-C3N4 composite by a simple direct mixing method for supercapacitor." *Electrochimica Acta* 283 (2018): 1468-1474.

[2]. Wang, Yuxiong, Lei Rao, Peifang Wang, Yong Guo, Zhenyu Shi, Xiang Guo, and Lixin Zhang. "Synthesis of nitrogen vacancies g-C3N4 with increased crystallinity under the controlling of oxalyl dihydrazide: Visible-light-driven photocatalytic activity." *Applied Surface Science* 505 (2020): 144576.

[3] Kanade, K. G., J. O. Baeg, S. K. Apte, T. L. Prakash, and B. B. Kale. "Synthesis and characterization of nanocrystallined zirconia by hydrothermal method." *Materials Research Bulletin* 43, no. 3 (2008): 723-729.

[4] Alaei, Mahshad, Ali Morad Rashidi, and Iida Bakhtiari. "Preparation of high surface area ZrO2 nanoparticles." *Iranian Journal of Chemistry and Chemical Engineering (IJCCE)* 33, no. 2 (2014): 47-53.

[5] Kumari, Latha, G. H. Du, W. Z. Li, R. Selva Vennila, S. K. Saxena, and D. Z. Wang. "Synthesis, microstructure and optical characterization of zirconium oxide nanostructures." *Ceramics International* 35, no. 6 (2009): 2401-2408.

[6] Reyes, R., C. Legnani, P. M. Ribeiro Pinto, M. Cremona, P. J. G. De Araújo, and C. A. Achete. "Room-temperature low-voltage electroluminescence in amorphous carbon nitride thin films." *Applied physics letters* 82, no. 23 (2003): 4017-4019.

[7]. Hong, Yuanzhi, Yinhua Jiang, Changsheng Li, Weiqiang Fan, Xu Yan, Ming Yan, and Weidong Shi. "In-situ synthesis of direct solid-state Z-scheme V2O5/g-C3N4 heterojunctions with enhanced visible light efficiency in photocatalytic degradation of pollutants." *Applied Catalysis B: Environmental* 180 (2016): 663-673.

Sunlight Concentrating System Based on Fresnel lens and Compound Parabolic Concentrator for Water Heating and Daylighting

Krishana Ballabh Kumar, Mayank Gupta, Dalip Singh Mehta*

Green Photonics Laboratory, Department of Physics, Indian Institute of Technology Delhi, Hauz-Khas, New Delhi, India 110016

*mehtads@physics.iitd.ac.in

Abstract: We report an efficient non-tracking sunlight concentrating system with increased light collection aperture vertically based on a large Fresnel lens, reflecting mirrors, and a segmented compound parabolic concentrator (SCPC) for daylighting applications. A low-cost SCPC is designed and fabricated from a reflecting aluminium sheet, which works efficiently comparable to the ideal CPC. The application of reflecting mirrors has significantly increased the efficiency of the system as it increases the collection aperture. When incident radiation is 2000 W/m^2, SCPC's exit aperture records maximum irradiance of 6053 W/m^2. The results we obtained for this system is quite convincing and can be applied to various sunlight harvesting system.

Keywords: Fresnel lens, Compound parabolic concentrator, Daylighting, solar concentrator

1. Introduction

Sunlight being a perpetual source of energy and a viable alternative to conventional energy sources, can be utilized in many ways from water heating, cooking, and thermal storage to a daylighting system [1]. Several tracking and non-tracking solar concentrating systems have been reported based on Fresnel lens and parabolic trough or dish for thermal applications and daylight illumination but still aren't so feasible because of their high cost [1]. We report a low-cost and highly efficient non-tracking-based solar concentrating system with a combination of two concentrators Fresnel lens as a primary concentrator and SCPC as a secondary concentrator. Fresnel lens is coupled to the SCPC through highly polished segmented aluminium reflecting mirrors, resulting in a three-stage collection of light, first, the direct sunlight entering the SCPC, second, the sunlight reflected from the mirrors and third is the concentrated light from the Fresnel lens [2]. All three-stage collections are redirected to the exit aperture of SCPC as shown in fig. 1.

2. Design and development of the system

All the components of the system, Fresnel lens, Mirrors, and the SCPC are mounted on a single structure, hence increasing the vertical collection of light while taking a small horizontal area. The system shown in fig. 1 is south-facing. Sunlight first incident on Fresnel lens then concentrated spot from Fresnel lens is redirected to the SCPC. The mirrors are adjusted in such a way that the focused spot from the Fresnel lens will be redirected to SCPC from morning to evening as the azimuth and the altitude of the sun vary throughout the day.

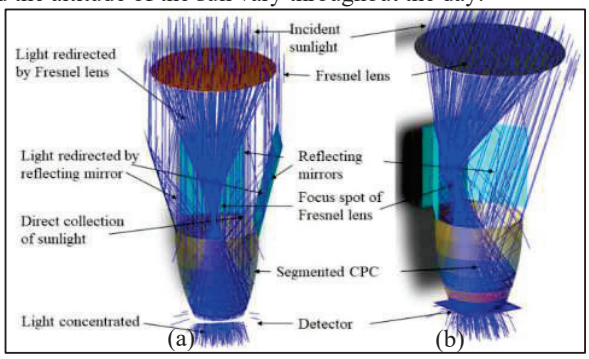

Figure 1: Optical ray simulation of the three- stage collection of sunlight for the designed system. (a)front view of the system (b) side view of the system.

The Fresnel lens used in this experiment is the spot Fresnel lens and has a diameter of 1m and a focal length of 140cm. All the design and simulation is carried out on ZEMAX and TracePro software.

3. Design and fabrication of SCPC

Fabricating an ideal CPC is a complex task as the moulding process requires extreme precision and accuracy, which results in a very high cost. However, it can be made by joining various axial or circumferential subdivisions made from reflecting sheets [3]. We have designed and developed a segmented compound parabolic concentrator (SCPC) using highly polished reflecting aluminium sheets of a thickness of 0.5mm. The CPC is divided into six segments axially and each of them is connected to get the desired SCPC as shown in fig. 2. Based on edge ray principle, overall length (l) of the CPC is related to its entry aperture, exit aperture, and the angle of acceptance as [4]:

$$l = (a + a')cot\theta_c \quad (1)$$

Where a is the semi-entry aperture, a' is the semi-exit aperture and θ_c is the acceptance angle. We have successfully fabricated and tested the SCPC designed on ZEMAX with acceptance angle 35˚ as shown in fig.2

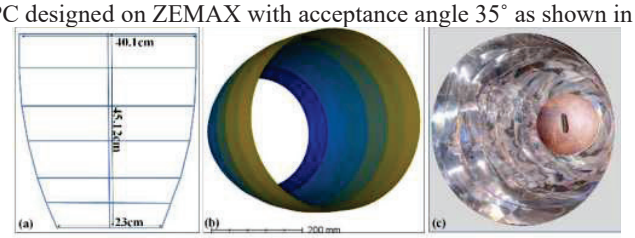

Figure 2:(a) Side view with dimension of SCPC, (b) Front view of SCPC designed on ZEMAX, (c) Fabricated SCPC

4. Results and Discussion

The optical simulation result is obtained using TracePro for two cases, with or without the segmented mirrors. Considering the concentration from Fresnel lens, the initial irradiance value for the incident rays on SCPC is taken to be 2000 W/m^2 and the total number of incident rays are 1000. Irradiance at the exit aperture of SCPC is increased significantly when light is redirected by the segmented mirrors. As we can see in the plot in fig. 3 the irradiance, as well as the total no. of rays incident, are increased up to 20˚ of incidence when the light is redirected by the mirrors and goes to a maximum value of 6053 W/m^2. But in another case when there is light collection only by SCPC the maximum irradiance value is 4927 W/m^2 and it continues to decrease from 0˚ of incidence to 35˚.

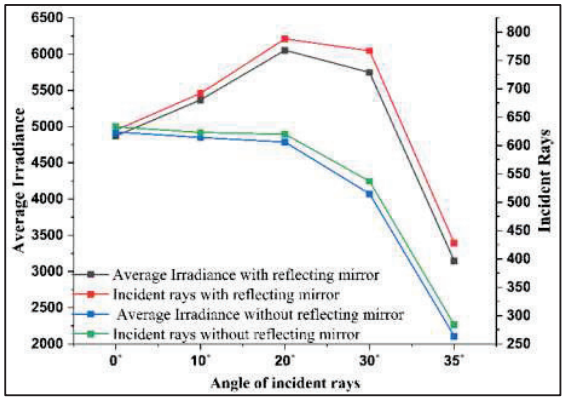

Figure 3: Optical simulation results at the exit aperture of the SCPC with and without reflecting mirror

Experimentally, the irradiance value at the exit aperture of SCPC is measured using the irradiance meter TENMARS-207. The developed SCPC is accepting the light incident up to 30˚ and the concentration level goes beyond 2000W/m^2 for the light incident along the axis of SCPC, when the input solar radiation is 830W/m^2. The concentration results we are getting for this are very promising and can be used for various sunlight harvesting purposes such as water heating, thermal oil heating, cooking as well as daylight illumination.

5. References

1. M. Gupta, A. Kumar Dubey, V. Kumar, and D. Singh Mehta, "Indoor daylighting using Fresnel lens solar-concentrator-based hybrid cylindrical luminaire for illumination and water heating," Appl. Opt. **59**, 5358 (2020).
2. M. Gupta, A. Bhatnagar, A. K. Dubey, V. Kumar, and D. S. Mehta, "Dual Fresnel lens and segmented mirrors based efficient solar concentration system without tracking sun for solar thermal energy generation," Energy Sustain. Dev. **66**, 201–208 (2022).
3. A. Timinger, A. Kribus, P. Doron, and H. Ries, "Faceted concentrators optimized for homogeneous radiation," Appl. Opt. **39**, 1152 (2000).
4. R. Winston, J. C. Miñano, and P. G. Benitez, *Nonimaging Optics* (Elsevier, 2005).

Zeeman EIT with transit-time decay in Doppler-broadened Λ-atomic system

Bharti[1] and Joyee Ghosh

Quantum Photonic lab, Department of Physics, Indian Institute of Technology, New Delhi, 110016
[1]phz198008@iitd.ac.in

Abstract: We have theoretically investigated Zeeman Electromagnetically Induced Transparency (EIT) using the density-matrix formulation in thermal ^{87}Rb vapor and obtained narrow EIT widths ~ 71 KHz with high peak transmissions >85% at control power ($P_c = 2mW$) at room temperature.
Keywords: Electromagnetically Induced Transparency (EIT), Zeeman levels, EIT Width, Peak Transmission

Electromagnetically Induced Transparency (EIT) is a quantum interference phenomenon of two coherent laser beams: a strong control and a weak probe, driving two optical transitions in a Λ atomic level system that create a quantum coherence leading to a decrease in the probe absorption and an increase in nonlinear susceptibility within the EIT window. We have studied a closed 3-level Λ-configuration in Rb-87 involving two degenerate Zeeman hyperfine ground states coupled to an excited state Zeeman sublevel via the $\sigma^{\pm}$ −polarized control and probe beams. A Zeeman EIT is advantageous over a traditional EIT for obtaining lower EIT widths with higher peak transmissions, all starting from a single laser. For this we have considered one of the closed hyperfine transitions of the D_2-line in ^{87}Rb: $F_g = 1 \rightarrow F_e = 0$ having transition strength factor, $S = 0.166$ [1] and resonance frequency of $\omega_0 = 2\pi \times 384.2344\, THz$.

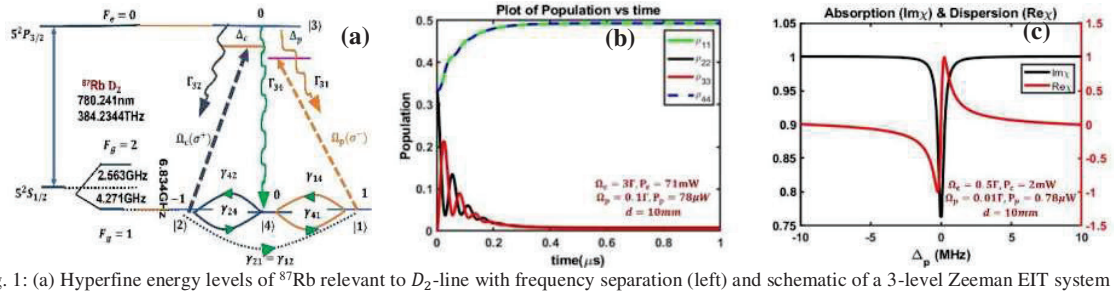

Fig. 1: (a) Hyperfine energy levels of ^{87}Rb relevant to D_2-line with frequency separation (left) and schematic of a 3-level Zeeman EIT system in Λ-configuration (right). Zeeman magnetic sublevels involved in the hyperfine transitions from ($F_g = 1 \rightarrow m_{Fg} = -1, +1$) → ($F_e = 0 \rightarrow m_{Fe} = 0$), where, transitions $m_{Fg} = -1\ and\ +1 \rightarrow m_{F_e} = 0$ are coupled via circularly polarized, (σ^+) control and (σ^-) probe beams, respectively, (b) Time variation of population in the relevant atomic levels and (c) Im[χ] (absorption 'Black') & Re[χ] (dispersion 'Red') of the probe in presence of a strong control beam rabi frequencies ($\Omega_c = 0.5\Gamma$) and probe beam ($\Omega_p = 0.01\Gamma$) for beam diameter of d=10 mm.

Fig.1. shows the spontaneous decay rates $\Gamma_{31} = \Gamma_{32} = \Gamma_{34} = \frac{\Gamma}{3}$(overall from excited state $F_e = 0 \rightarrow m_{Fe} = 0 \equiv |3\rangle$ is equally likely to all dipole allowed ground states) where $\Gamma = 2\pi \times 6.067\, MHz$ is the overall spontaneous decay rate from excited state $|3\rangle\ (\equiv F_e = 0, m_{F_e} = 0)$ to all dipole allowed degenerate ground states $|1\rangle$, $|2\rangle$ and $|4\rangle$ (corresponding to $m_{Fg} = +1, -1, 0$, respectively) of the ground state manifold $F_g = 1$. $\gamma_{12} = \gamma_{14} = \gamma_{24} = \Gamma_t \approx 10^{-3}\Gamma$ corresponding to the nonradiative decay rates between degenerate ground states. By following a semi-classical approach and considering a Hamiltonian (matrix 4×4) we obtain 16 optical Bloch equations using the electric dipole and rotating wave approximation:

$$\chi(\omega) = \chi'(\omega) + i\chi''(\omega) = \frac{N_{87}|d_{31}^2|}{\hbar\epsilon_o}(Re[\rho_{31}] + iIm[\rho_{31}]) \qquad (1)$$

Where $N_{87} = 3.2 \times 10^{15}$ is the atomic density of ^{87}Rb at T=300k and $d_{31} = \frac{4.2272ea_0}{\sqrt{6}}$ is the interaction dipole moment for the hyperfine transition: $F_g = 1 \rightarrow F_e = 0$ where, $\frac{1}{\sqrt{6}}$ is the dipole matrix element $C_{mf} = \left((-1)^{F_e - 1 + m_{Fg}}(-1)^{F_e + J + I + 1}\sqrt{(2F+1)}\begin{pmatrix} F_e & 1 & F_g \\ m_{F_e} & -q & -m_{F_g} \end{pmatrix}\sqrt{(2F_e+1)(2J_g+1)}\right)$ [1], expressed as multiples of

$\langle J_g = \frac{1}{2}||er||J_e = 3/2\rangle$ and $a_0 = 5.29 \times 10^{-11}$ m is the Bohr radius. In a setup, both probe and control beams are co-propagating for observing EIT. Considering Doppler broadening due to the moving atoms, the susceptibility in Eq-(1) is integrated over the Maxwell-Boltzmann velocity distribution resulting in

$$\chi(\omega) = \frac{N_{87}|d_{31}^2|}{2\hbar\epsilon_o}\sqrt{\pi\, ln\, 2}\; \frac{i\Gamma_t + \Delta_p}{(\Gamma_t - i\Delta_p)\left[\frac{\Gamma}{2} + \Delta\omega_D - i(\Delta_p + \Delta_c)\right] + \frac{\Omega_c^2}{4}} \tag{2}$$

where Γ_t is transit relaxation rate: $\Gamma_t = \left(\frac{d}{\sqrt{\frac{8kT}{\pi m}}}\right)^{-1} = 2\pi \times 26.976kHz$ [2] for a probe beam diameter $d = 10$mm and $2\Delta\omega_D = \sqrt{\frac{8k_B T ln2}{mc^2}\omega_0^2} = 0.5$GHz $(T = 300k)$ is the Doppler-broadened full width at half maxima (FWHM). Fig.1(b) shows the time variation of population in all the levels under the constraint with initial condition is $\rho_{11} + \rho_{22} + \rho_{33} + \rho_{44} = 1$. The populations in $|1\rangle$ and $|4\rangle$ attain a steady state value of 0.5 as a result of the optical pumping due to the control beam. Thus, in this closed configuration in ^{87}Rb, only 50% of the ground state population contributes to the dark state required for EIT condition. Fig.1(c) shows the EIT features (absorption & dispersion) near the atomic resonance corresponding to control and probe power $P_c = 2$mW and $P_p = 0.78\mu$W respectively.

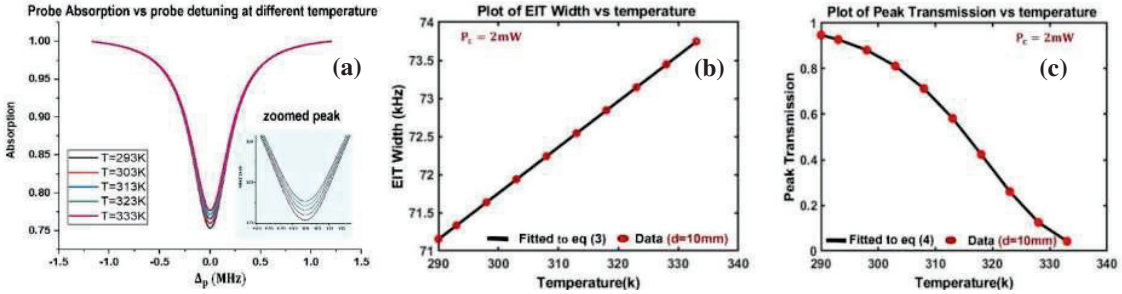

Fig. 2: (a) Absorption versus probe detuning at different cell temperatures variation of (b) EIT widths (Γ_{EIT}) and (c) Peak transmission (T_{PEAK}) versus vapor cell temperature

In addition, we investigated the EIT width and peak transmission with respect to different Rb vapor cell temperature for fixed control and probe beam power $P_c = 2$mW and $P_p = 0.78\mu$W respectively, using the following expression of EIT width (Γ_{EIT}) and Transmission (T_{PEAK}):

$$\Gamma_{EIT} = 2\Gamma_t + \frac{\Omega_c^2}{\Gamma + 2\Delta\omega_D} = 2\left[\frac{8k_B T}{\pi md}\right] + \frac{\Omega_c^2}{\Gamma + \sqrt{\frac{8k_B ln(2) T\omega_0^2}{mc^2}}} = \alpha T + \frac{\Omega_c^2}{\Gamma + \beta\sqrt{T}} \tag{3}$$

$$ln(T_{PEAK}) = \frac{ln\, T_0}{\left[1 + \frac{\frac{\Omega_c^2}{2}}{\Gamma_t(\Gamma + 2\Delta\omega_D)}\right]} = \frac{ln[\,T_0]}{\left[1 + \frac{\frac{\Omega_c^2}{2}}{\frac{8k_B T}{\pi md}(\Gamma + \beta\sqrt{T})}\right]} \tag{4}$$

where $\Omega_c^2 = \frac{d_{31}^2}{\hbar^2}\left(\frac{2P_c}{c\epsilon_0 A}\right)$, $\Omega_c^2 \propto P_c$ and T_0 is transmission in the absence of EIT. While keeping Ω_c fixed and adjusting temperature, two parameters $2\Delta\omega_D$ and Γ_t vary accordingly. From the expression of Γ_{EIT}, with increasing temperature, $2\Delta\omega_D$ and Γ_t increases which in turn increase the EIT width shown in Fig. 2(b) verified for different temperature. The atomic density of Rb vapors increases with temperature which means a significant fraction of atoms is available for probe absorption, hence absorption increases, transmission decreases as shown in Fig. 2(c).

Conclusion: We have theoretically calculated Zeeman EIT considering ^{87}Rb at varying temperature and obtained an EIT width ≈71 kHz for $d = 10$mm and relatively higher peak transmissions > 85% at room temperature.

Acknowledgement: The first author acknowledges the Council of Scientific and Industrial Research, India for her fellowship.

References

[1] D. A. Steck, Quantum and atom optics, **47**, 2007

[2] Joyee Ghosh and R. Ghosh, "*Analysis of electromagnetically induced transparency and slow light in a hot vapor of atoms undergoing collisions*," Phys. Rev. A **80**, 023817 (2009); F. Goldfarb, J. Ghosh et al., "*Observation of ultra-narrow electromagnetically induced transparency and slow light using purely electronic spins in a hot atomic vapor*," EPL (Europhysics Letters) **82**.5 (2008): 54002

Broadband Visible Light Absorber Based on Perovskite and Multilayered Metal-Dielectric-Metal Array

Rashmi Kumari[1], Shubhanshi Sharma[1], Shailendra Kumar Varshney[1], Basudev Lahiri[1]
[1]*Department of Electronics and Electrical Communication Engineering, IIT Kharagpur, West Bengal, 721302, India*
rashmi.k@iitkgp.ac.in

Abstract: We propose a broadband visible absorber with average absorption efficiency greater than 90%. The absorber consists of multilayered metal-dielectric-metal structure with perovskite film on top. The light absorbed in perovskite film for this broad range of visible wavelength can be effectively used for harvesting solar energy.
Keywords: Broadband visible absorber, metal-dielectric-metal, perovskite, solar energy.

1. Introduction

Broadband visible absorbers are highly desired for improving the utilization of solar energy for applications such as thermal emitters, photodetectors, solar cells [1]. Metamaterials, due to its property of manipulating light matter interaction have been extensively used for designing perfect absorbers. Metamaterials can be made to absorb incident light tunable from visible to microwaves regime with near-unity efficiency, simply by engineering these nanostructures[2]. Metal-dielectric-metal (MDM) nanostructures have been shown to achieve perfect absorption over a wide range of electromagnetic spectrum using plasmonic mode excitations[3].

However, these nanostructures suffer from poor charge carrier mobility. Further, to enhance the performance of visible light harvesting devices methyl ammonium lead halide perovskites ($CH_3NH_3PbI_3$) is used. These perovskites possess high charge carrier mobility, effective light absorption in broadband range (300 nm- 800 nm) and low fabrication cost [4]. Light absorption can be effectively enhanced by engineering metamaterials within the perovskite film [5]. Thus, more light absorbed in the perovskite leads to a greater number of electrons generated and thus useful in high performance photovoltaic cells [6]. In this work, we have proposed a multilayered metal-dielectric metal nanostructure covered with perovskite film to providing average absorption of 90% in broad range of 400nm-780nm.

2. Designing of Absorber

The schematic of the proposed absorber is as shown in Fig, 1(a). First, we consider single layer of metal-dielectric-metal film (Au/SiO_2/Au) films, with one-dimensional gold grating on the top. The plasmonic nanostructure is then covered by thin layer of perovskite film. Light is incident in z direction, with its electric field polarized in x- direction.

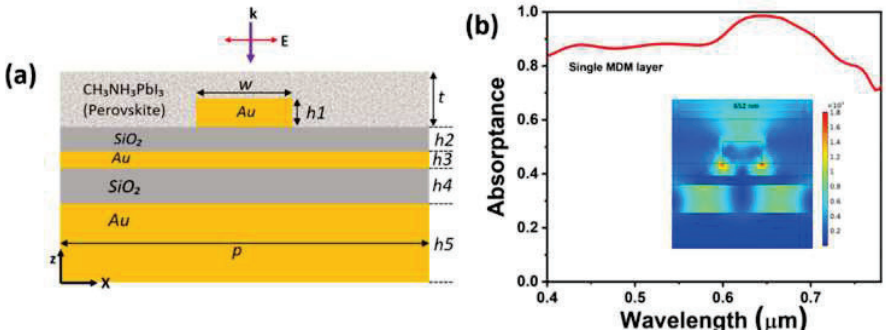

Fig. 1: (a) Schematic of the single layer MDM absorber with the geometric parameters as: p=320 nm, w= 90 nm, h_1=50 nm, h_2=28 nm, h_3=20 nm, h_4=65 nm, h_5=200 nm, t= 100 nm. (b) Absorptance spectrum showing broad absorption in the visible region (inset showing electric field distribution at wavelength of 652 nm).

The corresponding broadband absorption in the visible region is as shown in Fig. 1(b). The inset shows the electric field distribution at 652 nm, where it can be seen that the light is mostly confined in silica and perovskite layer. This high absorptance in perovskite is responsible for large carrier generation.

Multiple of these resonances can be achieved by designing the multilayered Au/SiO_2/Au structure as shown in Fig. 2(a). This multilayered structure enhances the absorption efficiency as can be shown in Fig. 2(b). The multilayered design is arranged such that the height of silica layer increases from h_4 (top) to h_4 + (N-1) d (bottom) with d=8 nm. The Schematic and enhanced absorption is shown with N=6. It can be seen that the average absorption is enhanced i.e, greater than 90% for the broad range of visible wavelength.

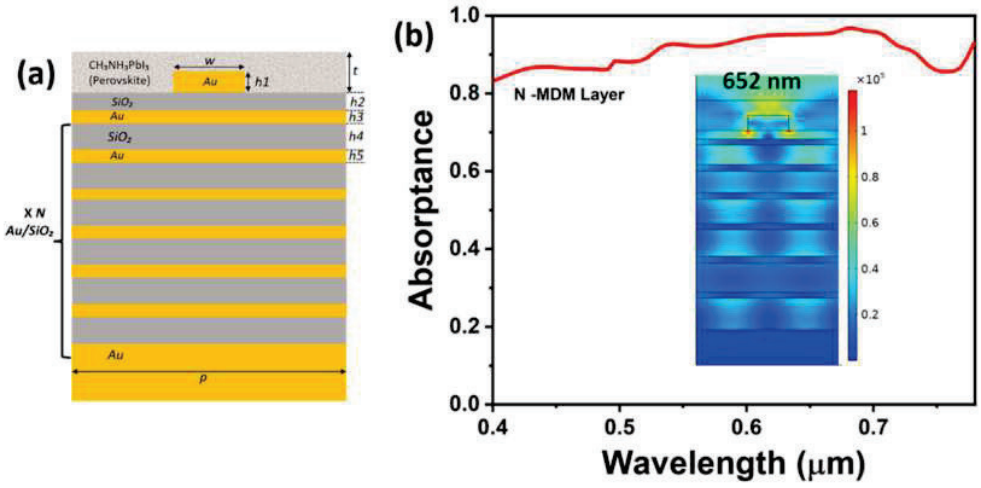

Fig. 2(a) Schematic of multilayered MDM absorber structure with N=6 (b) Corresponding enhanced absorptance spectrum with average absorption greater than 90% (inset showing electric field distribution at 652 nm).

3. Conclusion

We have numerically proposed a broadband absorber with average absorption efficiency greater than 90%. The absorber consists of multilayered Au/SiO_2/Au films with Au gold grating on the top. Perovskite film is then used to cover the nanostructure to generate large number of charge carriers. The proposed structure finds its application in efficiently harvesting solar energy such as in high performance photodetectors.

4. References

[1] P. Yu *et al.*, "Broadband Metamaterial Absorbers," *Adv. Opt. Mater.*, vol. 7, no. 3, pp. 1–32, 2019, doi: 10.1002/adom.201800995.

[2] L. J. Huang, J. Q. Li, M. Y. Lu, Y. Q. Chen, H. J. Zhu, and H. Y. Liu, "Broadband visible light absorber based on ultrathin semiconductor nanostructures," *Chinese Phys. B*, vol. 29, no. 1, 2020

[3] J. Cong *et al.*, "Broadband visible-light absorber via hybridization of propagating surface plasmon," *Opt. Lett.*, vol. 41, no. 9, p. 1965, 2016

[4] H. Wang and D. H. Kim, "Perovskite-based photodetectors: Materials and devices," *Chem. Soc. Rev.*, vol. 46, no. 17, pp. 5204–5236, 2017

[5] I. L. Gomes de Souza and V. F. Rodriguez-Esquerre, "Omnidirectional broadband absorber for visible light based on a modulated plasmonic multistack grating," *Opt. Laser Technol.*, vol. 124, no. May 2019, p. 105981, 2020

[6] N. Alwadai *et al.*, "High-Performance Ultraviolet-to-Infrared Broadband Perovskite Photodetectors Achieved via Inter-/Intraband Transitions," *ACS Appl. Mater. Interfaces*, vol. 9, no. 43, pp. 37832–37838, 2017

Tunable photodetector using a phase change material

Ram Prakash S, Rajesh Kumar, Anirban Mitra
Department of Physics, Indian Institute of Technology Roorkee, Roorkee, 247667, India
Author e-mail address: rprakashs@ph.iitr.ac.in

Abstract: In this work, we report a tunable planer photodetector based on a phase change material, $Ge_2Sb_2Te_5$ (GST), in Fabry- Perot perfect absorber. At 1550 nm a maximum absorption of 99.7% is achieved in amorphous phase of GST and can be tuned to a longer wavelength by switching to crystalline phase. Further, we achieved a maximum responsivity of 58.26 mA/W at 1620 nm in the amorphous phase of GST. Thus, the proposed design shows good photodetection property at the optical communication wavelength with tunability to a longer wavelength upon phase transformation.

Keywords: Phase change material, Ge_2SbTe_5, Perfect absorber, photodetector.

1. Introduction

Hot carrier-based devices are recently studied extensively due to their application in the field of photodetection [1], photovoltaics [2], and optical modulations [3]. Tunability in these kinds of devices can be achieved by incorporating active materials. Phase change material is one such type of active material which changes its phase with temperature. Recently $Ge_2Sb_2Te_5$ has been explored for use in active photonic devices due to its significant refractive index change upon phase transformation [4]. Due to its simplicity of fabrication, Fabry-Perot (FP) cavity-based metal-dielctric-metal structures are being researched for perfect absorption. The FP cavity consists of a dielectric spacer layer sandwiched between two metal layers. The transmittance is suppressed by using thick bottom metal acting as a mirror.

In FP based hot carrier photodetector, the light falls on the top metal film, generating hot carriers. Because of the high kinetic energy of the hot carriers, they cross the Schottky barrier formed between the metal semiconductor interface and get injected into the semiconductor, and finally produce photocurrent. Thus, photons with less energy than the bandgap of the semiconductor and energy higher than the Schottky barrier can be detected. The bandgap of GST in amorphous and crystalline phases are 0.7 eV and 0.5 eV, respectively. Hence this offers a tunable hot carrier-based photodetector by changing the phase of GST.

In this paper, we designed and simulated a tunable hot carrier photodetector using GST as the active material. The absorption spectrum for different crystallization fractions of GST is calculated. The responsivity due to the generation of hot carriers in the top metal when GST is in amorphous phase is calculated. The results show a route to achieve tunable photodetection using phase change materials.

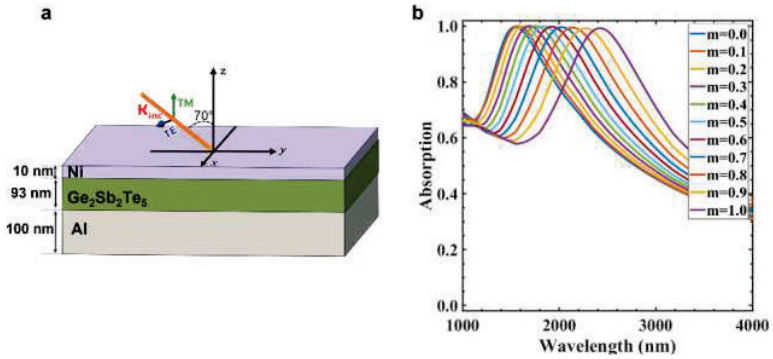

Figure 1: a) Schematic diagram of the proposed tunable photodetector. (b) The absorption spectrum for various crystallization fraction.

2. Design and Results

The schematic diagram of the tunable photodetector is shown in Figure 1(a). The structure consists of three layers, with GST sandwiched between the top layer of nickel and the bottom thick layer of aluminum, which serves as a mirror. The electric fields and absorption spectrum are solved using a self-developed MATLAB code of transfer matrix method using the scattering matrix approach [5]. The refractive index of GST in both phases is obtained from previous experimental results [6]. The effective permittivity of GST in the intermediate phase is given as [4]

$$\frac{\epsilon_{eff}(\lambda)-1}{\epsilon_{eff}(\lambda)+2} = m \times \frac{\epsilon_c(\lambda)-1}{\epsilon_c(\lambda)+2} + (1-m) \times \frac{\epsilon_a(\lambda)-1}{\epsilon_a(\lambda)+2} \qquad (1)$$

Here m is the crystallization fraction of GST in the range 0 to 1, $\epsilon_a(\lambda)$ and $\epsilon_c(\lambda)$ is the permittivity of GST in the amorphous and crystalline phases, respectively. Figure 1(b) shows the absorption spectrum of proposed structure at different crystallization fractions. It is seen that maximum absorption of 99.7% at 1550 nm and 99.2% at 2416 nm when GST is in amorphous (m=0) and crystalline (m=1) phase, respectively. It is also observed that the absorption spectrum can be tuned between 1550 to 2416 nm by controlling the crystallization fraction of GST.

To understand the possible reason for photodetection, we plotted the absorption spectrum of each layer in the proposed device when GST is in amorphous phase, and the same is shown in figure 2(a). It is observed that most of the light is absorbed by the top metal layer, and the GST layer does not contribute much to the absorption in the device. Hence, we can assume that the photo responsivity of the structure would be because of the hot carriers generated in the top metallic film.

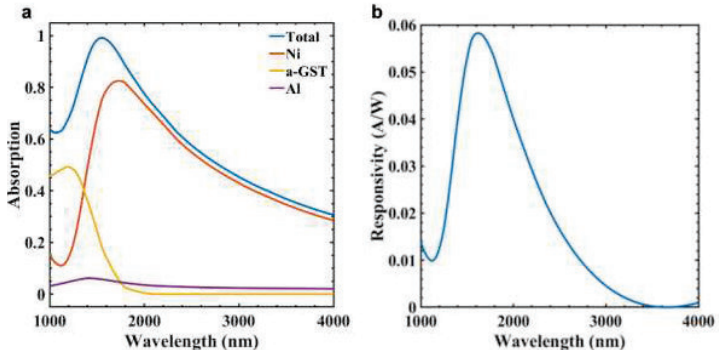

Figure 2: (a) Absorption spectra for each layer in the proposed device. (b) Spectra-dependent responsivity in amorphous phase of GST.

The photodetection in the proposed device occurs through the collection of hot carriers in GST via internal photoemission process (IPE). IPE requires that the incident photon energy exceed the Schottky barrier energy, Φ_{SB}. The Schottky barrier between Ni/a-GST is found using $\Phi_{SB} = E_g\text{-}(W\text{-}\chi)$. Here, E_g is the bandgap of GST, W is the work function of Ni and χ is the electron affinity of a-GST (χ=4.99 eV). The Schottky barrier between a-GST and Ni interface is calculated as 0.34 eV. The photoresponsivity using the Flower model is given as $R(\omega) = \frac{qA(\omega)\eta_i}{h\nu}$ [7]. Here, A is absorption in the top metal, q is the elementary charge and η_i is the internal quantum efficiency of the Schottky barrier photodetector and is given as

$$\eta_i = \frac{1}{2}\left(1 - \sqrt{\frac{\phi_{SB}}{h\nu}}\right) \qquad (2)$$

By using the above model, the calculated responsivity of the proposed photodetector is shown in Figure 2(b). It is observed that we obtain a maximum responsivity of 58.26 mA/W at 1620 nm.

3. Conclusion

In conclusion, the proposed tunable photodetector shows a tunable perfect absorption by varying the crystallization fraction of GST. The tuning range is around 866 nm, and the maximum absorption is kept over 99% across the whole tuning range. The device exhibits photoresponsivity in the optical communication wavelength and could find applications as a tunable photodetector that can detect light in the 1550 nm communication window as well as the upcoming 2 μm optical communication window.

4. References

[1] S. Chaoudhary *et al.*, "Broadband self-powered photodetection with p-NiO/n-Si heterojunctions enhanced with plasmonic Ag nanoparticles deposited with pulsed laser ablation," *J. Mater. Sci. Mater. Electron.*, vol. 33, no. 14, pp. 10761–10773, May 2022.

[2] C. Clavero, "Plasmon-induced hot-electron generation at nanoparticle/metal-oxide interfaces for photovoltaic and photocatalytic devices," *Nat. Photonics*, vol. 8, no. 2, pp. 95–103, Feb. 2014.

[3] M. Taghinejad *et al.*, "Hot-Electron-Assisted Femtosecond All-Optical Modulation in Plasmonics," *Adv. Mater.*, vol. 30, no. 9, p. 1704915, Mar. 2018.

[4] R. Prakash S, R. Kumar, and A. Mitra, "Reconfigurable and spectrally switchable perfect absorber based on a phase-change material," *Appl. Opt.*, vol. 61, no. 10, p. 2888, Apr. 2022.

[5] R. C. Rumpf, "Improved formulation of scattering matrices for semi-analytical methods that is consistent with convention," *Prog. Electromagn. Res. B*, vol. 35, no. 35, pp. 241–261, 2011.

[6] K. Shportko, S. Kremers, M. Woda, D. Lencer, J. Robertson, and M. Wuttig, "Resonant bonding in crystalline phase-change materials," *Nat. Mater.*, vol. 7, no. 8, pp. 653–658, Aug. 2008.

[7] Y. Zhu *et al.*, "Planar hot-electron photodetector utilizing high refractive index MoS2 in Fabry-Pérot perfect absorber," *Nanotechnology*, vol. 31, no. 27, 2020.

Effect of weak measurement on the amplitude-squared squeezing of superposition of Schrödinger's cat state with vacuum state

Dhiraj Yadav[1], Gaurav Shukla, Krishna Mohan Mishra and Devendra Kumar Mishra[2]
Department of Physics, Institute of Science, Banaras Hindu University, Varanasi-221005, U. P., India
E-mail address: [1]dheerajau14@gmail.com, [2]kndmishra@gmail.com

Abstract: We study the effect of post-selected von Neumann measurement on the 'amplitude-squared squeezing (ASS)' of 'superposition of Schrödinger's cat state with vacuum state (SCVS)'. By using weak measurement technique we have shown the variation of ASS with the photon number for superposition of Schrödinger's cat state with vacuum state.

Keywords: Amplitude-squared squeezing, Schrödinger cat-like state, weak measurement.

1. Introduction.

Squeezing of light, a non-classical phenomenon, plays an essential role in the framework of quantum technology. Squeezed states of light have reduced quantum noise in one quadrature component and, correspondingly, increased quantum noise in other conjugate quadrature component to satisfy the Heisenberg uncertainty relation. There are different types of squeezing such as Hong & Mandel squeezing, amplitude-squared squeezing (ASS), photon number squeezing, etc. Superposition of $|\boldsymbol{\alpha}\rangle$ and $|-\boldsymbol{\alpha}\rangle$ is the well-known Schrödinger cat state having a number of applications in quantum optics. Here, we consider the superposition of 'Schrödinger's cat state with the vacuum state (SCVS)' which exhibit different non-classicalities [1] and applications in quantum sensing [2].

In 1988, Aharonov *et al.* proposed the weak measurement [3] by a typical conditional measurement characterized by postselection and a weak value. The weak-measurement theory has various applications in quantum technology [4]. Most recently, effects of postselected von Neumann measurement on the non-classical properities of single-mode radiation field [5, 6] have been studied. It was found that postselected von Neumann measurement can affect the photon statistics and squeezing of radiation fields for different anomalous weak values and coupling strengths. ASS, a higher-order version of squeezing proposed by Hillery [7, 8], of Schrödinger's cat states via postselected von Neumann measurement has been studied [9]. As generalization, here we investigate the effect of weak measurement on the ASS exhibited by the SCVS.

2. Amplitude-squared Squeezing (ASS)

Hillery [7, 8] defined the ASS, a higher-order version of single-mode squeezing. We consider the single-mode of electromagnetic field with creation and annihilation operator $\hat{a}^\dagger$ and $\hat{a}$. The real and imaginary parts of the squared amplitude can be expressed as $\hat{X}_1 = (\hat{a}^{\dagger 2} + \hat{a}^2)/2$, $\hat{X}_2 = i\,(\hat{a}^{\dagger 2} - \hat{a}^2)/2$, satisfying the commutation relation $[\hat{X}_1, \hat{X}_2] = i(2\hat{N} + 1)$, $\hat{N} = \hat{a}^\dagger \hat{a}$ is the photon number operator. The corresponding uncertainty relation is $\Delta X_1\, \Delta X_2 \geq \langle \hat{N} + \frac{1}{2} \rangle$, where ΔX_1 denotes the variance of $\hat{X}_1$ under an arbitrary state. The state is said to exhibit ASS if it satisfies $(\Delta X_i) < \langle \hat{N} + 1/2 \rangle$.

3. Weak Measurement and its effect on the ASS exhibited by SCVS

In the quantum measurement theory, the von Neumann Hamiltonian [3] can be written as $\hat{H} = g\,\delta(t - t_0)\hat{\sigma}_x \otimes \hat{P}$. Here g is a coupling constant, $\hat{P}$ is the conjugate momentum operator to the position operator $\hat{X}$. In quantum weak measurement scenario, the interaction time between the measuring device (pointer) and measured system (meter) must be as short as possible. The time evolution of operator, $\exp\left(-\frac{i}{\hbar}\int \hat{H}\, d\tau\right)$, for the total system become $\exp\left(-\frac{i}{\hbar} g\hat{\sigma}_x \otimes \hat{P}\right)$. Here, we use the natural system of units, $\hbar = 1$. Weak measurement is characterized by using pre- and post-selection of state. For this purpose, we opt the initial state, $|\psi_i\rangle$, of the measuring device. After evolution, we take post-selection state, $|\psi_f\rangle$. By using pre- and post-selected state, we obtain the information about a physical quantity $\hat{\sigma}_x$ which is defined as $\langle \hat{\sigma}_x \rangle_w = \langle \psi_f | \hat{\sigma}_x | \psi_i \rangle / \langle \psi_f | \psi_i \rangle$. This is the weak value of system observable, pre- and post-selected state being almost orthogonal. The unitary evolution operator $e^{-\frac{i}{\hbar} g\hat{\sigma}_x \otimes P}$ can now be written as

$$e^{-\frac{i}{\hbar} g\hat{\sigma}_x \otimes \hat{P}} = \frac{1}{2}\left(\hat{I} + \hat{\sigma}_x\right) \otimes \hat{D}\left(\frac{\gamma}{2}\right) + \frac{1}{2}(\hat{I} - \hat{\sigma}_x) \otimes \hat{D}(-\frac{\gamma}{2})$$

Since the operator $\hat{\sigma}_x$ satisfies the condition $\hat{\sigma}_x^2 = \hat{I}$, where $y = \frac{g}{\sigma}$ and displacement operator with complex quantity μ is defined as $\widehat{D}(\mu) = \exp(\mu\ \hat{a}^\dagger - \mu\ \hat{a})$. The value of y characterizes the measurement strength. If $y < 1$, the coupling between system and pointer is weak and, if $y > 1$, the coupling between system and pointer is strong.

We consider the 'superposition of Schrödinger's cat state with vacuum state (SCVS)' as $|\psi\rangle = N(|\alpha\rangle + |e^{i\theta}\alpha\rangle + \gamma|0\rangle)$. Here γ is superposition constant having value $\gamma = |\gamma|\ e^{i\varphi}$ and N is normalization constant with $N^2 = \left[2 + 2\exp[|\alpha|^2(\cos\theta - 1)]\cos(|\alpha|^2\sin\theta) + 4|\gamma|\exp\left(-\frac{1}{2}|\alpha|^2\right)\cos\varphi\right]^{-1}$. We use this SCVS state as the pointer-state and we study the effect of weak measurement on the ASS exhibited by the state $|\psi\rangle$ as pointer state. After using the transformation, normalized state of the pointer state $|\psi\rangle$ can be written as

$$|\psi_1\rangle = \frac{K}{2}\left[(1 + \langle\hat{\sigma}_x\rangle)\ \widehat{D}\left(\frac{y}{2}\right) + (1 - \langle\hat{\sigma}_x\rangle)\ \widehat{D}\left(-\frac{y}{2}\right)\right]|\psi\rangle,$$

where k is normalization constant of this state.

4. Results and Discussions

To investigate the ASS of SCVS as pointer state, we have followed the condition of ASS as mention in section (2), by using some simple algebra, the condition of existence of ASS is written as

$$R = \frac{1}{2}\ Re[\langle\hat{a}^4\rangle] + \frac{1}{2}\langle\hat{a}^{\dagger 2}\hat{a}^2\rangle - (Re[\langle\hat{a}^2\rangle])^2 < 0,$$

where R represent the amplitude-squared squeezing parameter. For state $|\psi_1\rangle$ we have calculated the R and plot R as function of $|\alpha|$ as shown in Fig. 1.

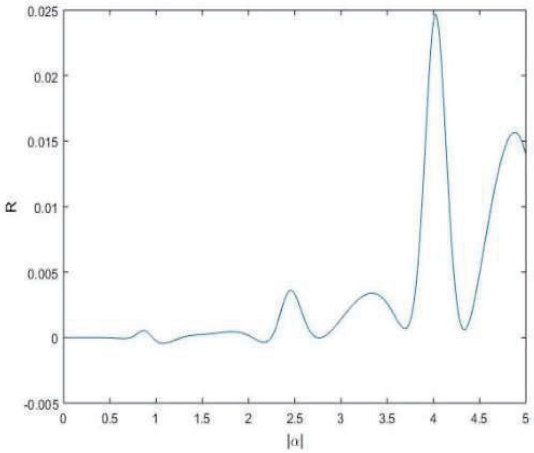

Fig. 1. Plot shows the variation of amplitude squared squeezing parameter, R, with $|\alpha|$ by taking $\theta = \frac{\pi}{2}, \varphi = \frac{7\pi}{9}, y = 2$ and $\gamma = 0$.

From Fig. 1, we can see that in weak measurement technique for some values of $|\alpha|$ variation in ASS is very small but for large values of $|\alpha|$ it changes dramatically and shows the periodic change in R having values below the zero for some values of $|\alpha|$. In addition, we have many situations with variation of different parameters, associated with the state, in which ASS increases in weak measurement method.

Acknowledgement

DY, GS acknowledges UGC for the UGC Research Fellowship and DKM acknowledge financial support from the Science & Engineering Research Board (SERB), New Delhi.

References

[1] K. K. Mishra, D. Yadav, G. Shukla and D. K. Mishra, *Phys. Scr.* **96**, 045102(2021).
[2] G. Shukla, K. K. Mishra, D. Yadav, R. K. Pandey, and D. K. Mishra, J. Opt. Soc. Am. B **39**, 59-68 (2022).
[3] Y. Aharonov, D. Z. Albert, and L. Vaidman, Phys. Rev. Lett. **60**, 1351 (1988).
[4] J. Dressel, M. Malik, F. M. Miatto, A. N. Jordan, and R. W. Boyd, Rev. Mod. Phys. **86**, 307 (2014).
[5] Y. Turek, H. Kobayashi, T. Akutsu, C.-P. Sun, and Y. Shikano, New J. Phys. **17**, 083029 (2015).
[6] Y. Turek, W. Maimaiti, Y. Shikano, C.-P. Sun, and M. Al-Amri, Phys. Rev. A **92**, 022109 (2015).
[7] M. Hillery, Opt. Commun. **62**, 135 (1987).
[8] M. Hillery, Phys. Rev. A **36**, 3796 (1987).
[9] N. Aishan, T. Yusuf and Y. Turek, Eur. Phys. J. Plus **137**, 221(2022)

Optical PAM-4 generation using Fiber Bragg Gratings

Naveenkumar M[1], V. S. Ch. Swamy Vaddadi[2], and E. S. Shivaleela[3]

ECE, Indian Institute of Science, Bangalore, India

[1]naveenkumarm@iisc.ac.in, [2]vsvaddadi@iisc.ac.in, and [3]lila@iisc.ac.in

Abstract: A 4-level optical pulse amplitude modulation (PAM-4) signal is generated, as a proof-of-concept, using Fiber Bragg Gratings (FBG) for short-reach communications. Optical generation of PAM signal offers the advantage of operating the optical source at its maximum power, which otherwise would be limited to linear region thereby tapping lower optical power. The signal can be used readily to test optical PAM-4 receiver.
Keywords: Optical PAM-4, optical generation of signal, Short reach communications.

1 Introduction

The demand for high bandwidth and throughput increased because of the increase in usage of internet services driven from high bandwidth applications. Different types of modulation schemes suitable for long and short distance communications are proposed. A multilevel PAM-4 modulation technique is a simple, spectrally efficient than on-off keying (OOK) and economical for short-reach applications. Two bits are encoded as one symbol (amplitude level), PAM-4 will have 4 distinct amplitude levels, thus twice the spectral efficiency of that of OOK. PAM-4 can be detected by direct detection of optical intensity signals. Oskars Ozolins et al., in [1] transmitted 56 Gbaud per wavelength PAM-4 signal over 81 km single core single mode fiber (SMF) and 33.6 km 7-core SMF with continuous-FBG based chromatic dispersion compensators. The authors of [2] considered next generation optical data communication standards and the types of suitable modulation formats were discussed. Duy Tien Le et al. [3] proposed a new architecture to implement a PAM-4 signaling system by using only one 2×4 multimode interference (MMI) coupler. Optical PAM-4 signal is obtained by using on-off-keying signals with Mach–Zehnder modulators (MZM) in [4]. PAM-4 is also used in optical interconnects in data centers. In this paper, we report optical generation of PAM4 signal experimentally using passive optical components.

The paper is organized as follows: In section 2, experimental setup for optical PAM4 generation is explained, experimental and simulation results are discussed in section 3, and last section 4 is about the conclusions.

2 Experimental setup

The schematic for generating optical PAM-4 signal using FBGs is shown in the Fig. 1. A Laser source with wavelength 1550 nm is modulated using Non-Return-Zero (NRZ) On-Off-Keying (OOK) PRBS 2^7-1 signal. The modulated signal is passed through port 1 of the optical circulator and the signal at port 2 of the circulator acts as an input to the SMF 1×2 splitter/combiner. The FBG of reflectivity 60 % with center wavelength of 1550 nm is connected to the branch $b1$ of the splitter and the second branch $b2$ is connected to another FBG of same wavelength and reflectivity through a variable optical attenuator (VOA) and an optical delay line which is calculated

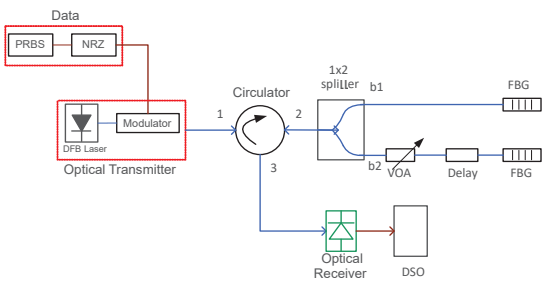

Fig. 1: Schematic of optical PAM-4 signal generation.

Fig. 2: Experimental setup for optical generation of PAM-4 signal.

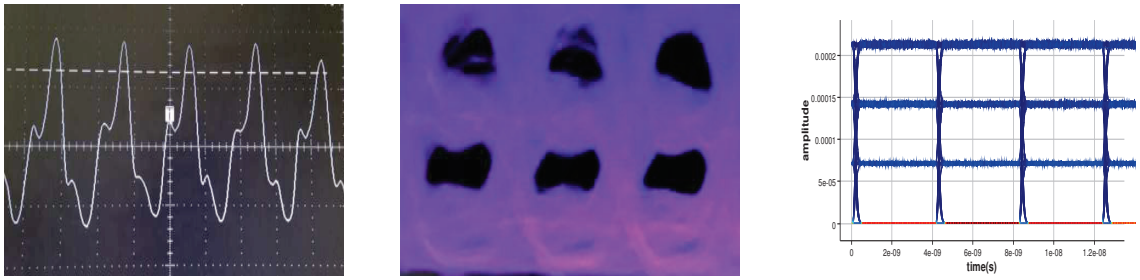

(a) ***PAM-4 signal:Experimental*** (b) ***Eye diagram: Experimental*** (c) ***Eye diagram: Simulation***

Fig. 3: Results obtained for 486 Mb/s bit rate PAM-4 signals.

depending on the baud rate. The reflected signal from one FBG in $b1$ is unprocessed and the other FBG signal in $b2$ is delayed and attenuated using VOA, and these reflected signals are combined using 2×1 SMF fiber combiner. The optical PAM-4 signal is obtained at the combiner output, which is input to port 2 of the circulator, and optical receiver at port 3 of the circulator detects the signal and analyzed using an oscilloscope. The experimental set up for the generation of optical PAM-4 signal is shown in the Fig.2.

3 Experimental Results and Simulations

The optical generation of PAM-4 signal is obtained at bit rate of 486 Mb/s and baud rate 243 Mb/s, in back-to-back configuration. PAM-4 signal obtained, when clock signal of bit rate of 486 Mb/s modulates the Laser, is shown in the Fig. 3 (a). Eye diagram, for PRBS 2^7-1 NRZ OOK modulates the Laser, acquired using digital real-time oscilloscope is shown in the Fig. 3 (b). For PAM-4 signal 3 eyes are seen vertically overlapped, but the lower eye opening is small compared to the other two eyes. This will be improved in our future work. The average received power at the detector is -25 dBm for the input power of -1 dBm at port1 of the circulator, at bit rate of 486 Mb/s. The value of BER will be measured/computed for the PAM-4 signal, using error analyzer in our future work. We have carried out the simulation for the same configuration using Ansys Lumerical INTERCONNECT tool and we are able to decode the intensity levels of the received data. The PRBS is used to modulate the laser and the PAM-4 signal generated using the optical components described earlier. The parameters considered for simulations are: transmitter power of -1 dBm, sample rate of 1.6×10^{11} Hz, with path delay of 1 ns, which is chosen at bit rate of 486 Mb/s and assumed standard insertion loss for each passive component. The simulation result eye diagram is shown in the Fig. 3 (c), achieved good performance with BER in the range of 10^{-9} order. In future work, we will transmit PAM-4 signal at higher bit rates through fiber spools of 80 km, and study the performance.

4 Conclusions

We have experimentally generated optical PAM-4 signal, as a proof-of-concept, using passive optical components and FBGs. Also carried out the simulations for the same configuration, achieved good performance with BER in the range of 10^{-9} order. PAM-4 signal is suitable for short-reach applications, as it is more susceptible to noise. For high bit rate PAM-4 signal generation Integrated-Optics approach can be explored.

References

[1] O. Ozolins, A. Udalcovs, X. Pang, R. Lin, A. Djupsjöbacka, J. Mårtensson, K. Fröjdh, L. Gan, M. Tang, S. Fu, R. Schatz, U. Westergren, D. Liu, W. Tong, J. Chen, S. Popov, and G. Jacobsen, "112 Gbps per wavelength PAM4 Inter-DCI with Continuous-Fiber Bragg Grating based Dispersion Compensators," in Advanced Photonics 2018 (BGPP, IPR, NP, NOMA, Sensors, Networks, SPPCom, SOF), OSA Technical Digest (online) (Optica Publishing Group, 2018), NeTh3F.3.

[2] J. D. Ingham, R. V. Penty and I. H. White, "Modulation formats for next-generation optical datacommunications," International Conference on Transparent Optical Networks, 2011, pp. 1-4.

[3] Duy Tien Le, Ngoc Minh Nguyen, and Trung Thanh Le, "Generation of PAM-4 Signals Based on a 2x4 MMI Coupler for Optical Interconnect Systems and Data Center Networks", In 2021 4th International Conference on Signal Processing and Machine Learning (SPML 2021).

[4] Samani A, Patel D, Chagnon M, El-Fiky E, Plant DV. Experimental parametric study of 128 Gb/s PAM-4 transmission system using a multi-electrode silicon photonic Mach Zehnder modulator. Opt Express 2017;25(12):13252–62.

Thermo-optically tuned silicon slab waveguide based on photonic crystal structure with temperature sensing applications

Varnam Sherawat[a], Yogita Kalra[a], Renuka Bokolia[a], Ravindra Kumar Sinha*[a,b]

[a] *TIFAC-Center of Relevance and Excellence in Fiber Optics and Optical Communication*
Department of Applied Physics, Delhi Technological University,
Bawana Road, Shahbad Daulatpur Village, Rohini, Delhi-110042, India
[b]*Gautam Buddha University, Greater Noida, Gautam Budh Nagar, UP-201312, India*
**Corresponding author: dr_rk_sinha@yahoo.com*

Abstract: This research presents the design of a silicon slab waveguide made using photonic crystal (PC) geometry with a hexagonal lattice arrangement. The PC's band structure, obtained using the plane-wave expansion method, shows a bandgap for the TE mode. This paper investigates the variation in the band-edge wavelengths of the PC waveguide with temperature by utilising the thermo-optic effect seen in silicon. The temperature variation is seen to cause a linear shift in the band edges of the structure for TE mode, which suggests possible temperature-sensing applications. The TE bandgap, however, shows negligible variation with temperature.
Keywords: refractive index, temperature, photonic crystal (PC), band-edge wavelength, thermo-optic effect

1. Introduction

Silicon photonic crystal waveguides find appeal in research due to various applications like second harmonic generation, slow light, wavelength filters, optical sensors, and tunable light sources [1-3].

This paper presents the design of a silicon slab PC waveguide in which air holes are placed in a hexagonal lattice geometry. The temperature values have been varied from 300 K to 400 K to analyse the effect of temperature on the band-edge wavelengths and the photonic bandgap (PBG) of the proposed PC waveguide. The PBG is determined using the plane-wave expansion method. The values of eigen-frequencies and wavelengths at various temperatures are evaluated by employing simulations in the MIT Photonic-Band (MPB) software package.

2. Temperature Dependence of Refractive Index

Silicon's refractive index in the infrared region [4], in accordance with the New Semiconductor Materials (NSM) archive [5], varies with temperature as follows:

$$\mu = 3.38(1 + 3.9\times10^{-5}\times t) \qquad 77\ K < t < 400\ K \qquad (1)$$

Equation (1) is used to determine the silicon slab's refractive index 'μ' and hence its dielectric constant at different values of temperature 't' varying from 300 K to 400 K. The eigen-frequencies of the PC waveguide are then calculated, through the MPB simulation codes, using the values of the dielectric constant at different temperatures. These frequencies yield band-edge wavelengths for various values of temperature.

3. Design and Geometry

The structure's design consists of a silicon slab with air holes in a hexagonal lattice arrangement. The radius (r) of the air holes is optimized to 0.25a where 'a' denotes the lattice constant and is taken as 259 nm. The waveguide is created by removing a row of air holes which forms the defect width. The structure parameters have been optimized to obtain a midgap wavelength of approximately 1310 nm corresponding to the band-edges at room temperature (~300 K) [4]. The schematic of the proposed PC waveguide is shown in Fig. 1.

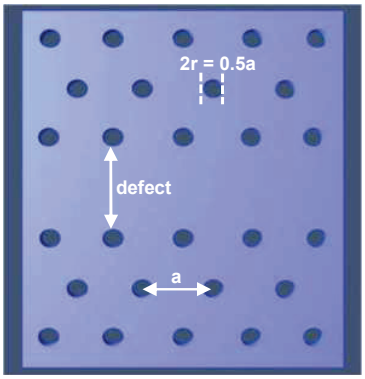

Fig. 1: Proposed PC waveguide structure.

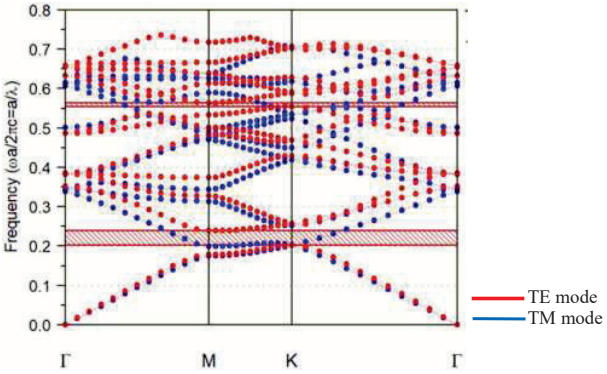

Fig. 2: Photonic band structure of the PC waveguide at 300 K.

4. Discussion and Results

The photonic band structure of the proposed PC waveguide, in Fig. 2, indicates the existence of a bandgap for the TE polarization mode (shaded red). The calculations, as per the plane-wave expansion method, show that the TE bandgap exists between bands 7 and 8. Hence, the band-edge wavelength for these bands has been computed at various temperatures.

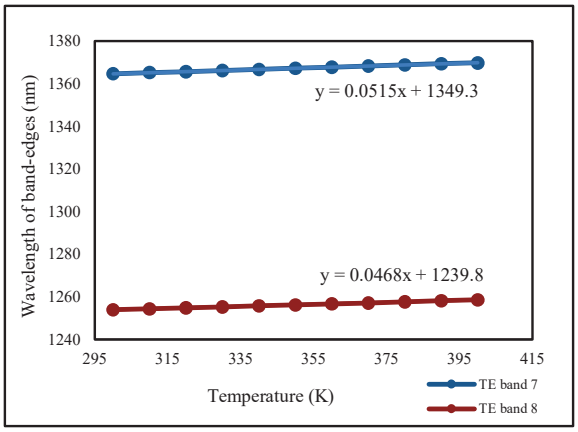

Fig. 3: Variation of the TE mode band-edge wavelengths with temperature.

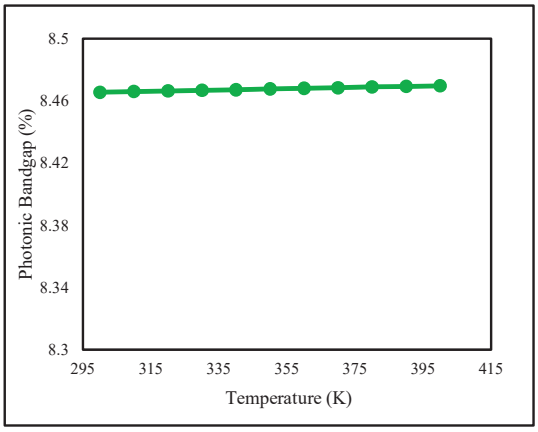

Fig. 4: Variation of the TE photonic bandgap with temperature.

The change in band-edge wavelengths with temperature is shown in Fig. 3. The shift in band-edges with temperature is linear. This linear variation indicates that the presented PC waveguide can be used as a temperature sensor with an average sensitivity of 0.04915 nm/K for the TE mode. As seen in Fig. 4, the photonic bandgap is found to be nearly constant with temperature change. This can be attributed to bands 7 and 8 shifting at nearly the same rate with temperature.

5. References

[1] Baba, T., "Slow light in photonic crystals," Nat. Photonics **2**(8), 465–473 (2008).
[2] Velazquez-Ibarra, L., Diez, A., Silvestre, E. and Andres, M. V., "Tunable Four-Wave Mixing Light Source Based on Photonic Crystal Fibers With Variable Chromatic Dispersion," J. Light. Technol. **37**(22), 5722–5726 (2019).
[3] Monat, C., Corcoran, B., Pudo, D., Ebnali-Heidari, M., Grillet, C., Pelusi, M. D., Moss, D. J., Eggleton, B. J., White, T. P., O'Faolain, L. and Krauss, T. F., "Slow Light Enhanced Nonlinear Optics in Silicon Photonic Crystal Waveguides," IEEE J. Sel. Top. Quantum Electron. **16**(1), 344–356 (2010).
[4] Sherawat, V., Bokolia, R. and Sinha, R. K., "Impact of thermal and refractive index tuning on the bandgap and band-edges of a silicon photonic crystal waveguide with sensing applications," Opt. Commun. **518**(December 2021), 128348 (2022).
[5] M.E. Levinstein, S. R. and M. S., "New Semiconductors Materials. Optical properties of Silicon," <http://matprop.ru/Si_optic>.

Optical Studies of Polymer Doped Liquid Crystals in a Tamm Plasmon Nanocavity

Nikhil Puthiya Purayil, Athulya Kadeprath Satheesan, Hasana Jahan Elamkulavan, Chandrasekharan Keloth*

[a]*Laser and Nonlinear Optics Laboratory, Department of Physics, National Institute of Technology Calicut, Kozhikkode, Kerala, India, 673601*

Corresponding Author email: csk@nitc.ac.in

Abstract: Applications of light confinement structures are intriguing in many fields where intense light-matter interactions are important. Photonic crystals and plasmonic structures are often used as a template for such applications. In this regard, Tamm plasmons (TP) formed at the metal-Bragg mirror interface are gaining new insights. Herein, we experimentally demonstrate the enhancement in the nonlinear absorption (NLA) of a nematic liquid crystal by employing TP of hybrid metal-dielectric interface. The z-scan experiments on bare sample and TP structure reveal a giant enhancement in the NLA coefficient, due to light confinement and resonant coupling of TP mode with the excitation wavelength.

Keywords: Tamm plasmon polaritons, Bragg mirror, nonlinear optics, liquid crystals

1. Introduction

The Tamm Plasmon Polaritons (TP) are electromagnetic defect states created at the interface of Distributive Bragg Reflector (DBR) and a thin metallic layer[1]. The optical field intensity of these surface modes can be confined to a spacer layer situated between the DBR and metal, subjected to certain phase-matching conditions[2]. Such structures offer high field enhancement factors, spectral tunability and easy implementation[3]. The field confinement at the metal-DBR interface arises fundamentally due to photonic band-gap (PBG) of the DBR and large extinction coefficients in metals. Unlike surface plasmon polaritons, TP modes can be excited by any polarization state and any angle of incidence without using any external dispersion-matching coupling structures as in the case for conventional surface plasmon polaritons. When compared to surface plasmon modes, the freedom in customizing the dispersion parameters of optical Tamm Plasmon modes is far greater. Hence, TP structures have gained much research interest in variety of fields, ranging from optical sensing to nonlinear devices[4][5].

In the present study, we report the giant enhancement in the nonlinear optical absorption (NLA) of polymer dispersed liquid crystal (PDLC) incorporated in the TP cavity (TPC) formed between a one-dimensional photonic crystal and a thin layer of gold.

2. Experimental Techniques

The sol-gel approach and spin coating techniques were adopted for the fabrication of DBR structure. The precursors titanium butoxide (TBOT) and tetraethyl orthosilicate (TEOS) were chosen as the precursors for TiO_2 and SiO_2 respectively. Initially, a 1.2 ml of TBOT is dissolved in 20 ml methanol and 1.7 ml of glacial acetic acid under constant stirring. A 1.5 ml of TEOS in 20 ml ethanol and 2.3 ml glacial acetic acid were prepared separately. 100 µL of each solution were spin coated sequentially on an ultra-cleaned glass substrate with spin speed ranges from 2500-2700 rpm, to get the required thickness for the DBR. The band-gap is designed at 532 nm, and quarter-wave stacks of each individual layers forms the DBR. A 30-minute annealing at 150°C was introduced after each layer deposition in order to achieve uniform films and crack-free multilayer structure. The final structure consists of 5.5 bilayers of TiO_2 and SiO_2.

The nematic 4-cyano-4′-pentylbi- phenyl (5CB) in poly-9-vinyl carbazole (PVK)/chlorobenzene solution with 3 vol % was prepared. The solution was spin coated on the top of the DBR to get an approximate solid film having a thickness of 120 nm. The thickness optimizations were done by trial-and-error method, with varying spin speeds. After the deposition of PDLC, a thin gold layer was coated on the top of the structure using RF/Magnetron sputtering. The optical transmittance of the fabricated TP structure was recorded using a UV-VIS spectrometer (Shimadzu 2450). The nonlinear optical (NLO) studies were carried out using a conventional z-scan experiment with a nanosecond pulsed Nd:YAG laser (7 ns, 532 nm) to investigate the impact of light localization effects on the PDLC. The z-scan signatures of reference PDLC film and TPC were compared at identical experimental conditions to study the enhancement in the nonlinear absorption.

3. Results and Discussion

The schematic representation of the final structure is shown in Figure 1(a). The designed thickness of TiO_2 and SiO_2 were 67 nm and 93 nm respectively. The PDLC layer thickness is chosen as 120 nm. The required thickness of top

gold layer is 10 nm. These parameters were optimized by transfer matrix simulations in such way to obtain the TP mode exactly at the excitation wavelength used for the NLO studies. The photographic image of the DBR, after the deposition of PDLC on DBR structure, and TPC against a white surface is shown in figure 1(b). The normal incidence transmission measurements on DBR and TPC is shown in Figure 1c. The fabricated DBR shows transmission dip centered at 540 nm with ~ 22% of transmission. After introducing the PDLC layer and gold coating on DBR, the transmission of the overall structure significantly reduced, which is due to the strong attenuation of metallic gold. In TPC structure, the sharp transmission peak in the bandgap region of the DBR indicates the formation of Tamm plasmon mode. The transmittance of the TP mode is 35% and is located at ~529 nm. The electric field simulations at 500-550 nm range revels a 5-fold enhancement of light intensity at the PDLC layer for ~532 nm (Figure 1d).

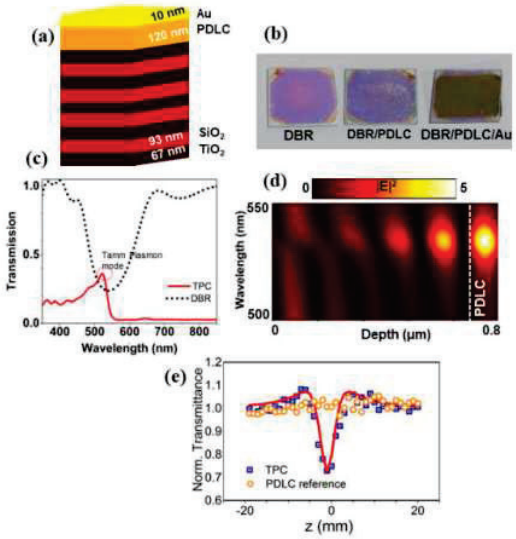

Figure 1 (a) The schematic of the fabricated TP structure (b) Photographic images of the samples (c) The transmission spectra of the DBR and TP cavity (d) Simulated electric field distribution of TP cavity (d) open aperture z-scan data of reference PDLC film and TP cavity at peak excitation intensity 0.27 GW/cm^2

The z-scan experiments were carried out on PDLC reference film and TPC for comparison. The reference sample has the exact thickness and concentration of the spacer layer. At peak excitation intensity 0.27 GW/cm^2, the reference sample exhibited negligible NLA whereas the TP structure showed considerable reduction in the transmission, which is referred to as reverse saturable absorption. The symmetrical peaks on either side of the focus in the z-scan data indicates the presence of absorption saturation at modest input powers, which is mainly due to the resonant absorption of gold layer. The giant absorption coefficient of 6.6x10^4 cm/GW is obtained for the PDLC film, which is attributed to the optical field confinement due to excitation of the TP mode.

4. Conclusions

A one-dimensional photonic crystal terminated by a metallic layer containing a nematic polymer doped liquid crystal is fabricated. The nonlinear optical absorption studies were conducted to study the light localization due to resonant excitation of Tamm plasmon mode. The enhanced-light matter interaction results in the enhancement of absorptive nonlinearity and a giant nonlinear absorption coefficient of 6.6x10^4 cm/GW is obtained for the PDLC film. The enhanced nonlinearity at low excitation power confirms the ability of our structure to use as a nonlinear optical element in nanophotonic devices.

5. References

[1] M. Kaliteevski *et al.*, "Tamm plasmon-polaritons: Possible electromagnetic states at the interface of a metal and a dielectric Bragg mirror," *Phys. Rev. B - Condens. Matter Mater. Phys.*, vol. 76, no. 16, pp. 1–5, 2007, doi: 10.1103/PhysRevB.76.165415.

[2] P. S. Maji and R. Das, "Absorption enhancement in monolayer graphene using Tamm plasmon polaritons," *OSA Contin.*, vol. 1, no. 2, p. 392, 2018, doi: 10.1364/osac.1.000392.

[3] C. Symonds *et al.*, "High quality factor confined Tamm modes," *Sci. Rep.*, vol. 7, no. 1, pp. 1–7, 2017, doi: 10.1038/s41598-017-04227-1.

[4] B. Auguié, M. C. Fuertes, P. C. Angelomé, N. L. Abdala, G. J. A. A. Soler Illia, and A. Fainstein, "Tamm Plasmon Resonance in Mesoporous Multilayers: Toward a Sensing Application," *ACS Photonics*, vol. 1, no. 9, pp. 775–780, 2014, doi: 10.1021/ph5001549.

[5] M. V. Vijisha, J. Ramesh, C. Arunkumar, and K. Chandrasekharan, "Impressive nonlinear optical responses of a cationic porphyrin derivative in a flexible all-polymer Bragg stack on optical Tamm mode coupling," *J. Mater. Chem. C*, vol. 8, no. 36, pp. 12689–12697, 2020, doi: 10.1039/d0tc01874k.

A Numerical Study on the Impact of Purcell Effect and Spontaneous Emission Factor in Lower-Dimension Semiconductor Nanolasers

Parya Reyhanian[1], Charlene J. Lobo[2], Christopher G. Poulton[2], Arti Agrawal[1]
[1] *School of Electrical and Data Engineering, University of Technology Sydney, NSW 2007, Australia*
[2] *School of Mathematical, and Physical Sciences, University of Technology Sydney, NSW 2007, Australia.*
Parya.reyhanian@student.uts.edu.au

Abstract: This paper presents a numerical approach to estimating the spontaneous emission coupling efficiency in semiconductor lasers with lower-dimension gain mediums. Also, the impact of the Purcell effect F and spontaneous emission factor β on the threshold and the height of the kink in the L-L curves is studied. Our theoretical calculations provide more insights into the laser behavior and help to optimize the laser cavity to achieve a lower threshold and higher coupling efficiency before fabrication.
Keywords: Semiconductor laser, Spontaneous emission, Purcell effect, Threshold, Gain, Laser rate equations.

1. Introduction

Semiconductor lasers are useful due to their small size, strong optical mode confinement, and high efficiency. When the size of the cavity is comparable with the emission wavelength, the Purcell effect becomes more apparent as it can significantly impact the spontaneous emission lifetime and the stimulated emission rate [1]. E. M. Purcell proved that when a system couples to a resonator, spontaneous emission lifetime is decreased by the Purcell factor [2]:

$$F = \frac{3}{4\pi^2}\left(\frac{\lambda}{n}\right)^3\left(\frac{Q}{V}\right), \qquad (1)$$

where Q is the quality factor, λ is the wavelength, n is the refractive index, and V is the volume of the cavity. Optimizing the Purcell factor is one of the fundamental techniques for achieving an ideal thresholdless nanocavity laser in which almost all spontaneous emissions couple to the lasing mode [3]. However, observing a thresholdless nanolaser is still experimentally challenging due to the imperfect fabrication processes [4]. Therefore, it is crucial to understand the relation between the Purcell factor and the spontaneous emission coupling efficiency (β) in quantum-well, nanowire, and quantum-dot nanolasers.

2. Results and Discussions

We first introduce the carrier (N) and photon (S) density rate equations for single-mode nanocavities in which the Purcell and spontaneous emission factors are studied separately:

$$\frac{dN}{dt} = \frac{\eta P}{hfV} - \frac{(1-\beta_0)N}{t_{sp}} - \frac{F\beta_0 N}{t_{sp}} - \Gamma g S, \qquad (2)$$

$$\frac{dS}{dt} = \Gamma\frac{F\beta_0 N}{t_{sp}} + \Gamma g S - \frac{S}{t_p}, \qquad (3)$$

where η is the pump efficiency, hf is the energy of a photon, V is the effective mode volume, Γ is the confinement factor, g is the gain, t_{sp} is the spontaneous emission lifetime, F is the Purcell factor, and β_0 is the spontaneous emission factor without the Purcell effect. The total spontaneous emission coupling efficiency β in a laser determines the ratio of the spontaneous emissions that couple into the lasing mode and is related to the Purcell factor as:

$$\beta = \frac{F\beta_0}{(1+(F-1)\beta_0)}. \qquad (4)$$

The parameter β is usually treated as a fitting parameter shaping the height of the kink in the L-L curves. However, for a conventional bulk semiconductor laser, β is obtained from the spontaneous emission rate into the lasing mode divided by the total spontaneous emission rate. When the emission wavelength equals the gain center, β can be estimated as $\beta_{Bulk} \sim \frac{\lambda^4}{4\pi^2 V \Delta\lambda n^3}$ [5]. Moreover, λ is the wavelength, V is the volume of the gain medium, $\Delta\lambda$ is the spontaneous emission linewidth, and n is the refractive index. Using the same approach as [5], we calculate the spontaneous emission factor (β) for quantum-well (*2D*), nanowire (*1D*), and quantum-dot (*0D*) as follows:

$$\beta_{Quantum-well} \sim \frac{\lambda^3 L_z}{2\pi^2 V \Delta\lambda n^2}, \qquad (5)$$

$$\beta_{Quantum-wire} \sim \frac{\lambda^2 L_y L_z}{2\pi n \Delta\lambda V}, \qquad (6)$$

$$\beta_{Quantum-dot} \sim \frac{\lambda^2}{\pi c \Delta\lambda}. \qquad (7)$$

In (5), it is assumed that L_z is the confined length of the gain material along the z-axis. Similarly L_y, and L_z are the confined lengths along the y and z-axis, respectively, in (6).

To examine the impact of the Purcell factor on the threshold and the height of the kink, we use the nanowire laser structure in [6]. For ten quantum disks embedded in a $2.2\mu m$ height nanowire, we calculated $F_{max} \sim 26.17$ and $\beta \sim 0.1$. This agrees with the experimental results [6]. Solving (2) and (3) for different Purcell factor values ranging from 1 to 26 shows that smaller nanowires result in higher *F,* which decreases the threshold non-linearly as shown in Figure 1a. Higher values of F lead to shorter spontaneous emission lifetimes. Therefore, more spontaneous emissions will be inside the cavity to couple into the lasing mode, creating less pronounced kinks as presented in Figure 1b. It is evident from figure 1b that for higher values of F, β gets closer to unity representing a thresholdless laser.

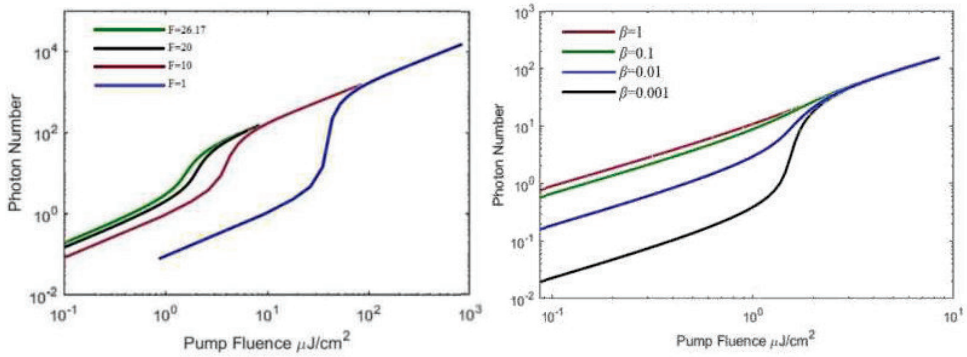

Figure 1. a) Impact of the Purcell factor, b) Impact of spontaneous emission factor on L-L curves

3. Conclusion

We proposed here how β can be obtained numerically in lower-dimension semiconductor nanolasers. Then, we showed that the Purcell factor can non-linearly decrease the threshold of the laser by shortening the spontaneous emission lifetime. Higher spontaneous coupling efficiency results in a less pronounced kink in the L-L curves.

4. References

[1] Tatebayashi, J., Kako, S., Ho, J., Ota, Y., Iwamoto, S. and Arakawa, Y., "*Room-temperature lasing in a single nanowire with quantum dots*," (*Nature Photonics*, *9*(8), 2015), pp.501-505.

[2] Purcell, E.M., *"Spontaneous emission probabilities at radio frequencies,"* (In *Confined Electrons and Photons,* Springer, Boston, MA, 1995), pp. 839-839.

[3] Yamamoto, Y., Machida, S. and Björk, G., *"Micro-cavity semiconductor lasers with controlled spontaneous emission,"* (Optical and quantum electronics, 24(2), 1992), pp.S215-S243.

[4] Romeira, B. and Fiore, A., *"Purcell effect in the stimulated and spontaneous emission rates of nanoscale semiconductor lasers,"* (*IEEE Journal of Quantum Electronics*, *54*(2), 2018), pp.1-12.

[5] Yamamoto, Y., Machida, S. and Björk, G., *"Microcavity semiconductor laser with enhanced spontaneous emission,"* (*Physical Review A*, *44*(1), 1991), p.657.

[6] Zhang, X., Yi, R., Gagrani, N., Li, Z., Zhang, F., Gan, X., Yao, X., Yuan, X., Wang, N., Zhao, J. and Chen, P., *" Ultralow threshold, single-mode InGaAs/GaAs multiquantum disk nanowire lasers,"* (*ACS nano*, *15*(5), 2021), pp.9126-9133.

Microwave synthesized Ag nanoparticles deposited on PDMS film for SERS based instant detection of pesticides from fruit peels

Sathi Das[#a], Kanchan Saxena[b] and Dalip Singh Mehta[*a]

[a]*Bio-photonics and Green Photonics Laboratory, Department of Physics, Indian Institute of Technology Delhi, Hauz-Khas, New Delhi-110016, India,*

[b]*Amity Institute of Renewable and Alternative Energy, Amity University, Sector 125, Noida, Uttar Pradesh, India*

*mehtads@physics.iitd.ac.in

#dassat123@gmail.com

Abstract: We developed a facile method of silver (Ag) nanoparticle (NP) synthesis using a microwave synthesizer technique. The synthesized AgNP solution dried on PDMS film was explored to detect toxic molecules like rhodamine 6G and thiram using the surface-enhanced Raman spectroscopy (SERS) technique. The flexible SERS substrate offers the advantage of bending over the curved surface, and transparency allows for both forward and backward collection methods. Using a portable Raman spectrometer, the substrate detects rhodamine 6G, and thiram with ultralow concentration. Thus, the flexible SERS film is perfect for instantly detecting any traces of harmful pesticides on fruits and vegetables.

Keywords: Surface enhanced Raman spectroscopy (SERS), Microwave Synthesis of Ag colloids, Transparent flexible SERS, Detection of pesticides

1. Introduction

Pesticides and various hazardous dyes are widely used in food items in recent years to preserve their freshness [1]. Long-term exposure to these hazardous substances poses a major health risk. It is vital to immediately detect poisonous and harmful compounds to prevent serious disease to humans. Raman spectroscopy can be used as a real-time screening method since it can identify molecules by their vibrational energy levels [2]. Surface enhanced Raman spectroscopy (SERS) is an efficient technique to enhance the traditionally weak Raman signal using metal nanostructures since the silver (Ag) or gold (Au) nanoparticles show plasmonic property in the visible region [3]. However, the conventional rigid SERS substrates are inconvenient to handle, fragile, and cannot be applied directly to the curve surfaces. The flexible SERS substrate is simple to use, user-friendly, and may be applied directly to the curved surfaces of fruits, leaves, and other food products [4].

In this paper, microwave-produced Ag nanoparticles are coated on a transparent, flexible Polydimethylsiloxane (PDMS) film. The microwave synthesizer enables the production of pure silver nanoparticles with controlled pressure, temperature, and reaction time [5]. For SERS activity the fabricated film was further tested considering micromolar (10^{-6}M) concentrations of toxic molecules like rhodamine 6g and thiram. R6G is commonly used in food and textile industries. Thiram (tetramethyl thiuram disulfide) is a pesticide that is frequently used to kill insects in food crops and vegetables. The developed SERS film can detect thiram concentrations of up to 1 micromolar, which is less than the usual residual limit (MRL).

2. Materials

The following materials were used for the proposed research work; Silver nitrate solution, Trisodium citrate, Rhodamine 6G, Tetramethyl thiuram disulfide.

3. Fabrication of flexible SERS

The synthesis of colloidal silver nanoparticles was done by microwave irradiation. Silver nitrate (2 ml) and citrate (1 ml) solutions were heated at 150 °C at 130-watt power for 2 minutes. The as synthesized Ag colloids were centrifuged at 20,000 rpm for 10 mins and the supernatant was removed and the pure solution was drop casted on the clean flexible PDMS film.

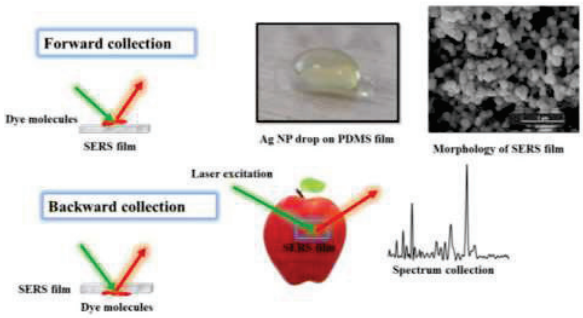

Fig. 1. Schematic diagram of spectrum acuisition of pesticides using flexible SERS substrate.

4. Morphology of Flexible film

The morphology of Ag film on PDMS film is captured by field emission scanning electron microscope (FESEM). The Ag nanoparticles having an average diameter of 50 nm, are interconnected with each other and forms porous network.

5. Collection of SERS spectra

The SERS spectra were collected using a portable Raman spectrometer having 785 nm laser source. Fig. 2 (a) exhibits the SERS spectrum of R6G for various concentrations from 10^{-3} M to 10^{-9} M. The Raman shift at 606 cm^{-1} gives in-plane bending of C-C-C ring. The shift at 1356, 1503 and 1641 cm^{-1} denote the aromatic C-C stretching [6]. Fig 2 (b) shows the spectra of SERS substrate and thiram molecules. The Raman peak at 564 cm^{-1} is assigned to ν(S–S), Raman peak at 1143 and 1379 cm^{-1} are attributed to δ (CH_3) and 1507 cm^{-1} to ν(C–N) [7].

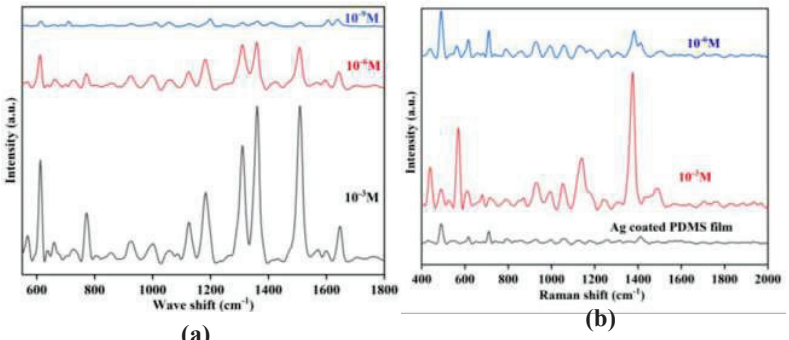

Fig. 2 (a) SERS spectra of R6G for various concentrations, (b) Ag coated PDMS film, and thiram having 10^{-3} M and 10^{-6} M concentrations

6. Conclusion

In conclusion, a transparent flexible Ag NP coated PDMS films were fabricated and used to detect toxic molecules. The fabricated SERS substrate can detect various toxic dye like R6G and pesticide like thiram at a trace level (10^{-6} M) using a field portable Raman spectrometer. Thus, the substrate can be used for the screening of food constituents regularly. Detailed experimental results will be presented.

7. References

[1] P. Nicolopoulou-Stamati, S. Maipas, C. Kotampasi, P. Stamatis, L. Hens, "Chemical Pesticides and human health: The urgent need for a new concept in agriculture," Frontiers in Public Health 4, 148 (2016).
[2] S. Das, L.P. Goswami, J. Gayathri, S. Tiwari, K. Saxena, and D. S. Mehta, "Fabrication of low cost highly structured silver capped aluminium nanorods as SERS substrate for the detection of biological pathogens." *Nanotechnology* 32, no. 49,495301(2021)
[3] S. Jain, "*Surface Enhanced Raman Spectroscopy: Biosensing and Diagnostic Technique for Healthcare Applications*." Bentham Science Publishers (2021).
[4] Yang, F., L Chen, Li, D., Xu, Y., Li, S., L. Wang, "Printer-assisted array flexible surface-enhanced Raman spectroscopy chip preparation for rapid and label-free detection of bacteria," Journal of Raman Spectroscopy **51**(6), 932–940 (2020).
[5] B. He, J. J. Tan, K. Y. Liew, and H. Liu. "Synthesis of size controlled Ag nanoparticles." *Journal of Molecular Catalysis A: Chemical* 221, no. 1-2 (2004): 121-126.
[6] Das, S., Saxena, K., D. S., Mehta, "A highly sensitive SERS substrate based on a mesoporous Ag–TiO_2 thin film for the detection of Dye Molecules," Materials Advances, 3, 5337-5343 (2022).
[7] Bhavya, M. B., Prabhu B., R., Shenoy, B. M., Bhol, P., Swain, S., Saxena, M., John, N. S., G. Hegde, A. K., Samal, "Femtomolar detection of thiram *via* SERS using silver nanocubes as an efficient substrate," Environmental Science: Nano **7**(12), 3999–4009 (2020).

Simulation studies for Optical elastography using Finite element method

Mridul Verma, Amandeep Singh, Renu John*
Medical Optics and Sensors Laboratory, Department of Biomedical Engineering,
Indian Institute of Technology Hyderabad, Kandi, Telangana-502284, India
renujohn@bme.iith.ac.in

Abstract: The quantification of biomechanical properties is very effective in examining the abnormalities in biological tissues. We demonstrate the simulation studies for optical elastography by generating surface acoustic waves on tissue phantoms using the Finite element approach. These preliminary results are very promising to design an optical elastographic platform for tissue characterization.
Keywords: Surface acoustic wave, phantom, finite element, elastography, tissue

1. Introduction

The biomechanical properties of human tissue, such as stiffness, and viscosity, can be interlinked with pathological conditions for investigating the abnormalities [1]. The changes in the mechanical properties of biological tissue provide insight into disease diagnoses such as cancer, chronic bronchitis, and neurodegeneration [2]. Elastography is an emerging medical imaging technique that is used to map local mechanical properties of tissue to measure the structural changes in response to mechanical loading [3]. It results in contrast images, known as Elastogram, that give information about biomechanical properties [4]. The traditional elastography techniques involve magnetic resonance elastography (MRE) and ultrasound elastography (US). However, both of them have a low spatial resolution that limits their application in detecting minute variations in cancerous regions [5]. Optical coherence elastography (OCE) is very effective because of its high resolution and high displacement sensitivity. The optical coherence tomography (OCT) combines with tissue excitation methods (actuator, air-puff, acoustic radiation force) in quantifying the elastic properties of tissue such as elastic modulus, Young's modulus, and shear modulus [6-8]

In the current study, we have demonstrated finite element simulations for generating surface acoustic waves on tissue-mimicking phantoms by defining the material and geometrical properties using COMSOL Multiphysics. The sinusoidal force at variable frequencies is used to induce surface waves on the rectangular block with well-defined boundary conditions. Furthermore, challenges and future scope are addressed and discussed for carrying out elastography experiments.

2. Methodology

Finite element (FE) simulations were performed in COMSOL Multiphysics using the Acoustic module. Fig. 1 represents the geometry type, force direction, and loading plane used for performing Finite elements simulations in the current work.

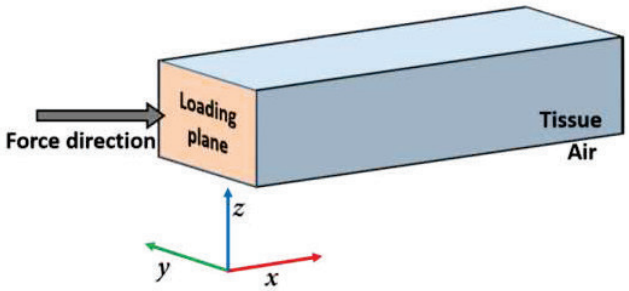

Fig. 1: Schematic representation of biological tissue model

A rectangular cuboid (linear elastic material) model with dimensions 70 x 200 x 20 cm was made to define the biological tissue model. The values for density (ρ), Young's modulus (E), and Poisson's ratio (ν) were fixed to 970 kg/m^3, 75 kPa, and 0.49 respectively. The sinusoidal loading force was defined with an amplitude of 0.1N and a frequency 250Hz on a loading plane (Fig. 1). The bottom and lateral surfaces were fixed while the top surface had a free boundary to observe the surface acoustic wave. The model had 12029 tetrahedral elements, 2052 triangular elements, 168 edge elements, and 8 vertex elements having meshing type extra fine size. A time-dependent solver (Generalized-alpha) was used with a maximum computational time of T_{max}=3sec with the time step Δt = 0.05sec.

3. Results and discussion

FE simulated surface acoustic wave (SAW) on the tissue phantom is shown in Fig. 2. The color bar represents stress values on the surface of phantom due to the applied sinusoidal loading force. It is observed that stress level and SAW amplitude profile decrease as the distance from the loading plane increases. This simulation study has been conducted for different force amplitudes and frequencies to explore the response. The preliminary results can be validated by optical elastography experiments for further studies.

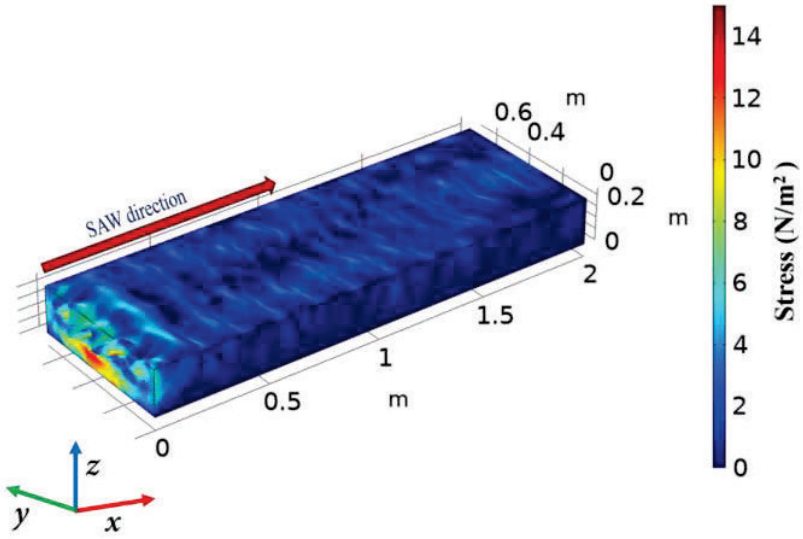

Fig. 2: The propagation of surface acoustic wave on tissue phantom

In conclusion of the current study, simulation study of SAW propagation has great potential to offer guidance for designing better optical elastography platforms for detailed tissue characterizations of different samples having varying physical and biomechanical properties.

4. References

[1] B. F. Kennedy, K. M. Kennedy, and D. D. Sampson, "A review of optical coherence elastography: fundamentals, techniques and prospects," IEEE J. Sel. Top. Quantum Electron. **20**, 272-288 (2014).
[2] B. F. Kennedy, P. Wijesinghe, and D. D. Sampson, "The emergence of optical elastography in biomedicine," Nat. Photonics **11**, 215-221 (2017).
[3] K. J. Parker, M. M. Doyley, and D. J. Rubens, "Imaging the elastic properties of tissue: the 20-year perspective," Phys. Med. Biol. **56**, R1-R29 (2011).
[4] A. Singh and R. John, "Elastography measurement for soft material using digital holography," in Fourth International Seminar on Photonics, Optics, and Its Applications (Society of Photo-Optical Instrumentation Engineers, 2020), pp. 9-16.
[5] A. Singh, P. Kumar, S. Yeleswarapu, F. Pati, and R. John, "Surface wave elastography using high speed full-field optical interferometry," Biomed. Phys. Eng. Express **8**, 025013 (2022).
[6] R. K. Wang, S. Kirkpatrick, and M. Hinds, "Phase-sensitive optical coherence elastography for mapping tissue microstrains in real time," Appl. Phys. Lett. **90**, 164105 (2007).
[7] S. G. Adie, X. Liang, B. F.Kennedy, R. John, D. D. Sampson, and S. A. Boppart, "Spectroscopic optical coherence elastography, Opt. Express 18, 25519-25534 (2010).
[8] D. Zhang, J. Wang, C. Li, and Z. Huang, "Optimal stimulation frequency for vibrational optical coherence elastography," J. Biophotonics **13**, e201960066 (2020).

A Theoretical Approach to Develop a Multilayer Plasmonic Sensor for the Potential Detection of Biochemical Analytes

Natasha Mandal[1], Anindita Das[1], Rakesh S. Moirangthem[1]*

[1]*Nanophotonics Lab, Department of Physics,*
Indian Institute of Technology (Indian School of Mines) Dhanbad, Jharkhand-826004, India
Corresponding Author e-mail address: rakeshap@iitism.ac.in

Abstract: The present work reports a theoretical model to develop a plasmonic biosensor. Our proposed sensor chip is composed of a sandwich assay of metal/dielectric multilayer Au/BaTiO3/Ag/MgF2/Au. The sensitivity of our proposed sensor was found as 3242 nm/RIU approximately with an excellent linear response of 0.958 which is higher than the conventional single-layer Au SPR sensor. The sensor chip could be utilized for the detection of lower concentrations (0-15g/dl) of glucose in human blood and urine. Our proposed SPR sensor has the potential for implementation as a biochemical sensor.
Keywords: Biosensor, surface plasmon resonance, diabetes, Glucose.

1. Introduction

The abnormality of glucose labels is the major cause of diabetes which becomes a life-threatening disease worldwide [1]. Hence monitoring the glucose level in body fluid is important for leading a healthy lifestyle. The present work reports theoretical modelling and simulation to develop a plasmonic biosensor. This study is based on the surface plasmon resonance (SPR) sensor application which is a well-established, highly sensitive, label-free, rapid optical sensing tool [2]. Here we have introduced a sandwich assay of two dielectric spacer layers of BaTiO3 (Barium Titanate) and MgF2 (Magnesium Fluoride) which gives better performance compared to commonly used SiO2 [3] and TiO2 [4] dielectric spacers due to their low dielectric loss and higher refractive index. . BaTiO3 is used in between metal layers as its advantage in low dielectric loss, higher refractive index and higher dielectric constant which enhances the sensor's performance with a small variation of refractive indices in the sensing medium. Hence, our proposed SPR sensor has the potential for the detection of glucose concentration in blood and urine with enhanced sensitivity, and high affinity, and could be utilized as a reliable platform for optical biosensing.

Theoretical modelling

A multilayer SPR sensor was modelled using Complete Ease software (version 6.51a) which is illustrated in fig.b. The sensor was designed by a coating of 30 nm Au on a BK7 glass substrate followed by a coating of 22nm BaTiO3, 15nm Ag, MgF2 85nm and 10 nm Au layer (illustrated in fig. 1b) over Au as this model gives the minimum reflectance. Here, we adopted the prism-coupling technique under the Kretschmann configuration to build the model and the experiment could be implemented by using the setup depicted in fig. 1a.

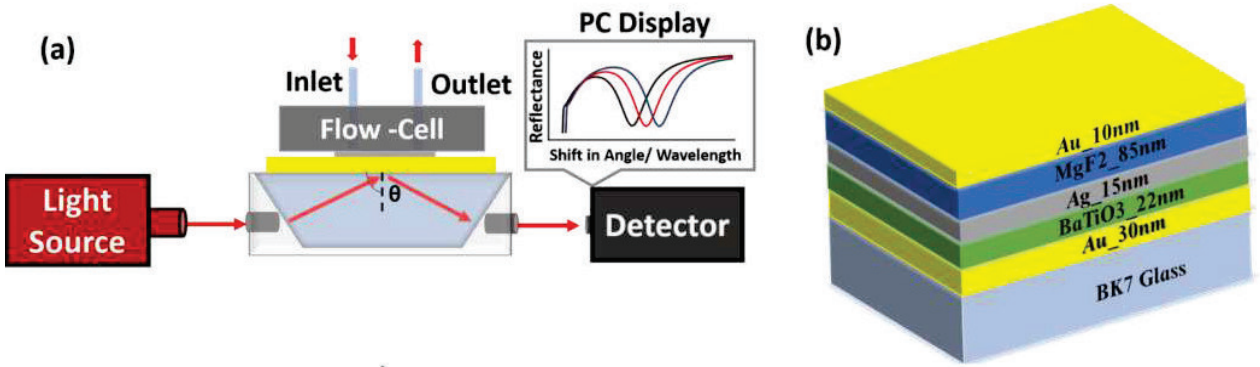

Figure 1. (a) Schematic illustration of the experimental setup for the SPR sensing using the proposed sensor chip. (b) Schematic for the designed sensor chip composed of metal/dielectric multilayer.

2. Results and Discussions

The sensitivity ($S = \frac{\Delta\lambda}{\Delta n}$) of the proposed sensor chip has been evaluated by varying the refractive indices (R.I) of analyte concentrations in the ranges from 1.333 to 1.385 (0-40) and obtained as 3241 nm/RIU (with an excellent linear response of 0.958) which is higher than conventional single layer Au sensor (3056 nm/RIU). Thus, our sensor chip has the potential to detect very low concentrations (0-15gm/dl) of glucose in human blood and urine samples which have a similar refractive index [1] in this simulated range.

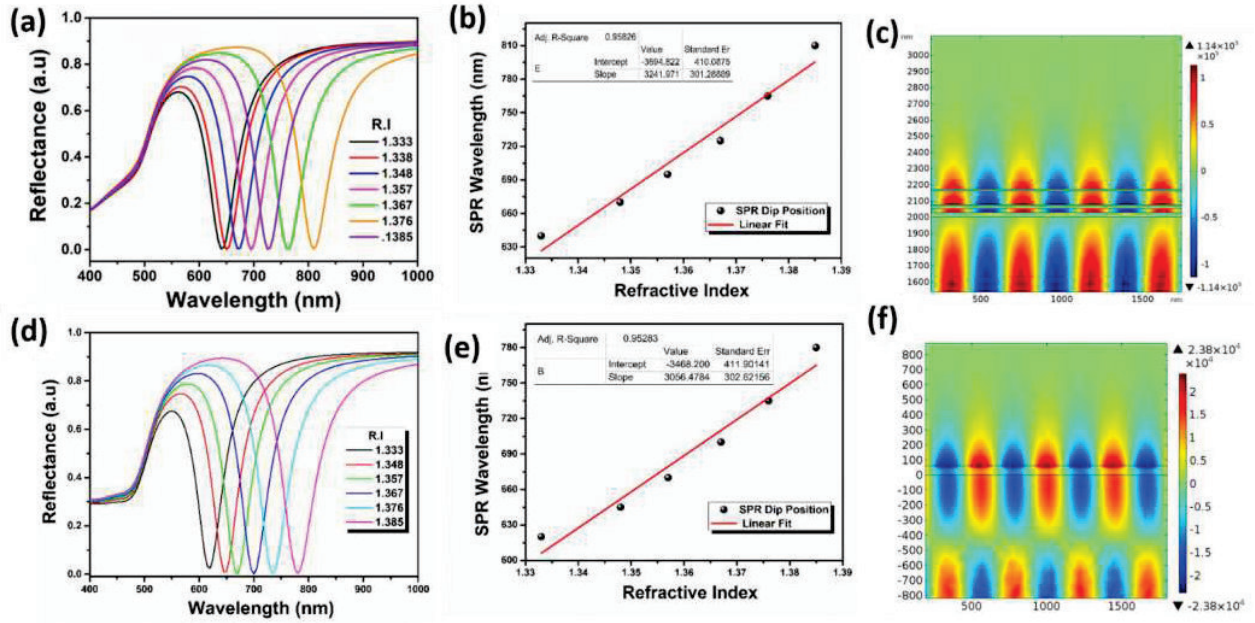

Figure 2. (a),(d) The SPR reflectance spectra as a function of wavelength for R.I variation from 1.333 (water) to 1.385 (b),(e) corresponding sensitivity plot, and (c),(f) associated evanescent field profile (normal to the surface) with penetration depth for the proposed multilayer sensor chip (Au/BaTiO3/Ag/MgF2/Au) and single layer Au respectively.

The SPR simulation results,i.e., reflectance spectra and the corresponding sensitivity plot, and the evanescent field confinement for the proposed sensor chip and single layer Au sensor has shown in fig. 2. It is observed that the evanescent field is enhanced (from COMSOL simulation) by one order (2.38×10^4 V/m for a single Au layer (50nm) and $1.14 \times 10^5\ V/m$ for multilayer) after the multilayer formation and 300 nm of penetration depth is obtained for the analyte (water-1.333) at a resonant wavelength of 645 nm where the evanescent field is guided by the metal/dielectric/metal multilayer.

3. Conclusion

A multilayer SPR chip has been designed by using Complete Ease software and the electric field profile and the penetration depth towards the analyte are obtained. Providing the dielectric spacer layer of BaTiO3 in between Au and Ag layers leads to the increment of the evanescent field strength of the surface plasmons. Adding a 15 nm Ag film in between the spacer layers gives a sharp SPR dip with minimum reflectivity.

References

[1] N. Mudgal, A. Saharia, A. Agarwal, J. Ali, P. Yupapin, and G. Singh, "Modeling of highly sensitive surface plasmon resonance (SPR) sensor for urine glucose detection," *Opt. Quantum Electron.*, vol. 52, no. 6, pp. 1–14, 2020, doi: 10.1007/s11082-020-02427-0.

[2] Y. Chen and H. Ming, "Photonic Sensors Review of Surface Plasmon Resonance and Localized Surface Plasmon Resonance Sensor ㄱ," vol. 2, no. 1, pp. 37–49, 2012, doi: 10.1007/s13320-011-0051-2.

[3] A. Omidniaee, S. Karimi, and A. Farmani, "Surface Plasmon Resonance-Based SiO2 Kretschmann Configuration Biosensor for the Detection of Blood Glucose," *Silicon*, vol. 14, no. 6, pp. 3081–3090, 2022, doi: 10.1007/s12633-021-01081-9.

[4] Z. Jin *et al.*, "A stable and high resolution optical waveguide biosensor based on dense TiO 2 /Ag multilayer film," *Appl. Surf. Sci.*, vol. 377, pp. 207–212, 2016, doi: 10.1016/j.apsusc.2016.03.123.

Dispersion Compensation in Stimulated Brillouin Scattering Based Microwave Photonic Bandpass Filter

Varun M K and Ravi Pant

Laboratory for Phoxonics and Nonlinear Optics in Nanostructures (PHONON), School of Physics, Indian Institute of Science Education and Research (IISER), Thiruvananthapuram, Kerala, 695551, India.

email: varun1818@iisertvm.ac.in, rpant@iisertvm.ac.in

Abstract: Interference-based microwave photonic filters are highly prone to dispersion effects. Here we theoretically and experimentally demonstrate dynamic dispersion compensation in Brillouin-based RF bandpass filter exploiting the bias-dependent phase shift of a z-cut intensity modulator.

Keywords: Microwave photonic filter, Dispersion compensation, Stimulated Brillouin scattering

Interference-based microwave photonic bandpass filters (MPBFs) are key components of modern RF communication systems due to their high-frequency selectivity and large out-of-band rejection [1]. Since the phase shift between the interfering signals plays a significant role in deciding the overall performance, any deviation from the optimum phase shift may lead to a significant reduction in the out-of-band rejection and asymmetric filter response. The interference-based MPBFs are, therefore, highly prone to dispersion which introduces an extra phase shift due to various dispersive components used in the filter design. Mitigation of dispersion effects in interference-based MPBFs is, therefore, important to achieve optimum performance.

In this paper, we demonstrate a MPBF with dynamic dispersion compensation. We exploit the bias-controlled phase shift in a z-cut intensity modulator to compensate the dispersion-induced impairment[2]. The MPBF is based on the RF cancellation between orthogonal polarization components of Brillouin gain processed single modulation sideband [3]. To demonstrate dispersion compensation at different dispersion values, we varied the dispersion in the filter setup by introducing fibers of different lengths. By tuning the bias voltage, the dispersion-induced phase shift has been theoretically and experimentally demonstrated. Also, we compare our results with MPBF based on phase modulation where two sidebands with a fixed π phase difference are used [4].

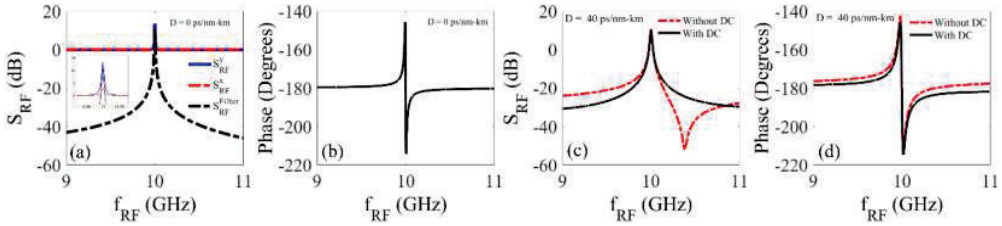

Figure 1: Simulation results showing dynamic dispersion compensation in SBS-based MPBF. (a) and (b) the concept of the filter when dispersion effects are not considered. (c) Filter response when a dispersion corresponding to D =40ps/nm-km is introduced (dashed red line) and with dispersion compensation (solid black). (d) Phase response corresponds to (c).

Here we use single sideband modulation, where equal RF power is obtained for the beat signals generated by orthogonally polarized probe components. The phase difference between the interfering RF beat signal is made π by tuning the bias voltage of the intensity modulator. By introducing different Brillouin gains in different polarizations, an amplitude imbalance is created at the desired filter frequency. On photodetection, outside the Brillouin gain resonance, the RF signals will cancel out and generate large out-of-band rejection, whereas, at Brillouin frequency, the signal remains intact. The RF power at the photodetector is given by [],

$$S_{RF}^{Filter} = K_x|G_x|^2 + K_y|G_y|^2 + 2\sqrt{K_xK_y}|G_x||G_y|\, cos\, cos\left(tani^{-1}\alpha_x - tani^{-1}\alpha_y - \varphi_x^{SBS} + \varphi_y^{SBS} + \varphi_D\right) \quad (1)$$

Here $K_{x,y}$ is dependent on modulation parameters, the load impedance of the detector, and detector responsivity. $G_{x,y}$, $\varphi_{x,y}^{SBS}$, and $tan^{-1}\alpha_{x,y}$ are the SBS gains, SBS induced phase responses and bias dependent phases and respective polarizations. φ_D is the dispersion-induced phase shift which is given by $\varphi_D = -(DL\lambda_c^2\omega_{RF}^2)/4\pi c$, where D, L, λ_c, $and\ \omega_{RF}$ are the dispersion coefficient, fiber length, carrier frequency, and modulation frequency respectively. The

phase difference between interfering orthogonal components can be tuned by changing $tan^{-1}\alpha_{x,y}$ values by tuning the modulator bias voltage. Figures 1a and 1b show the simulation results for the concept of the MPBF by considering the dispersion effects are negligible (D = 0 ps/nm-km). Solid blue and dashed red lines represent the RF powers at different orthogonal polarizations. Inset of fig. 1a shows the zoomed version around Brillouin resonance. The values of $tan^{-1}\alpha_{x,y}$ are chosen in such a way that the phase difference between two polarizations is π, which results in a large out-of-band rejection (dashed black line). Figure 1b shows the phase response of the filter. To study the effect of the dispersion-induced phase, we introduced the dispersion, where D = 40 ps/nm-km. As a result, the symmetry of the filter response is broken, and a 6 dB reduction in the out-of-band rejection is observed (fig. 1c, dashed red line). The phase difference shifted by ~ 4 degrees from the optimum condition, as shown in fig. 1d (dotted red line). Further, the effect of the dispersion is compensated by changing the $tan^{-1}\alpha_{x,y}$values. On dispersion compensation (DC), the filter gets back to its initial state, as shown in fig. 1c (solid black line), and the corresponding phase shift is shown in fig. 1d (solid black line).

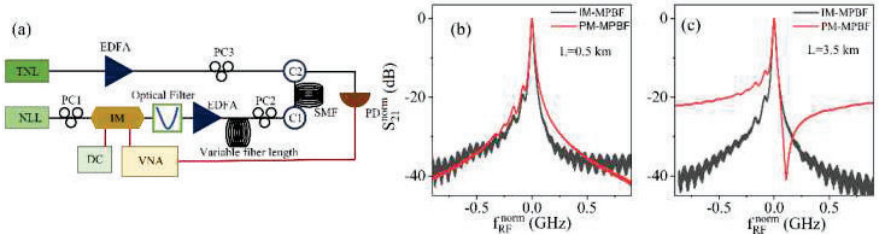

Figure 2: (a) Filter setup. (b) Intensity modulator based (IM-MPBF) and phase modulator-based (PM-MPBF) filter responses when there is no extra fiber added. (c) Filter responses after adding 3 km SMF and compensating dispersion induced phase shift using bias voltage.

Figure 2a shows the experimental setup. Light from a narrow linewidth laser (NLL) is modulated using a z-cut intensity modulator (IM), and one of the modulation sidebands is filtered out using a narrowband optical filter to generate a probe signal. By changing the polarization controller (PC2) in the probe arm, the power distribution in the orthogonal polarization components is varied to make the RF signal generated by orthogonally polarized probe components equal. Light from a tunable narrow linewidth laser (TNL)is amplified using an erbium-doped fiber amplifier (EDFA) and used as the Brillouin pump. The SBS gain in each polarization can be controlled by adjusting the polarization controller (PC3) in the arm. A 500m single-mode fiber (SMF) is used as the SBS gain medium. A constant DC voltage source is connected to the bias port of the modulator. After the interaction between pump and probe signals in 500 m SMF the back-scattered signal is collected at the third port of the circulator (C2). The filter response is observed using an ultrafast photodetector (PD) connected to a vector network analyzer (VNA). The dispersion compensation is demonstrated by changing the length of the fiber in the probe arm and by varying the modulator bias voltage. We compare our filter response at the same frequency with a phase modulator-based MPBF scheme, in which out-of-phase upper and lower modulation sidebands are used. In the case of a phase modulator-based MPBF, one of the sidebands is processed with SBS gain, and there is no bias control.

Figure 2b shows the filter responses when there is no extra fiber added to the probe arm other than the SBS medium. Using ~17 dB of SBS gain, we were able to achieve an out-of-band reject of ~40 dB for both cases. A 3 km SMF is then introduced in the probe arm in order to increase the dispersion present in the filter system. The effect of dispersion-induced phase shift will add up existing pi phase differences between interfering signals. As a result, there is a ~ 20 dB reduction in the out-of-band rejection of PM-based MPBF (fig. 2c solid red line). But in the case of IM-based MPBF, by tuning the bias voltage of the modulator, we compensate for the dispersion-induced phase contribution of a 3 km SMF and maintain an out-of-band rejection of ~ 40 dB (fig 2c solid black line).

In conclusion, we theoretically and experimentally demonstrate dynamic dispersion compensation in SBS-based MPBF exploiting bias-dependent phase shifts in a z-cut intensity modulator. Since all components used to demonstrate the MPBF are demonstrated on chip-level platforms, this technique can be implemented on-chip.

[1] Varun, M. K., *et al.* "Microwave photonics applications of stimulated Brillouin scattering." *Journal of Optics* 24.6 (2022): 063002.

[2] T. Dennis and P. A. Williams, "Chirp Characterization of External Modulators With Finite Extinction Ratio Using Linear Optical Sampling," in *IEEE Photonics Technology Letters*, vol. 22, no. 9, pp. 646-648, May1, 2010.

[3] Varun M K and Ravi Pant, "Efficient Microwave Photonic Bandpass Filter With Large Out-of-Band Rejection, High-Resolution and Low Loss up to 40 GHz," *J. Lightwave Technol.* 39, 6724-6732 (2021)

[4] R. Tao, X. Feng, Y. Cao, Z. Li and B. -o. Guan, "Widely Tunable Single Bandpass Microwave Photonic Filter Based on Phase Modulation and Stimulated Brillouin Scattering," in *IEEE Photonics Technology Letters*, vol. 24, no. 13, pp. 1097-1099, July1, 2012.

Efficient Optical Trapping of Metal-dielectric-metal Type of Nanoparticles

Sumit Yadav[a], Anita Devi[a §], and Arijit K. De[b]*

Condensed phase dynamics group, [a]Department of Physical Sciences and [b]Department of Chemical Sciences, Indian Institute of Science Education and Research (IISER) Mohali, Knowledge City, Sector 81, SAS Nagar, Punjab 140306, India.

[§]Present affiliation: Department of Physics, University of Alberta, Edmonton, AB T6G 2R3, Canada.

**akde@iisermohali.ac.in*

Abstract: Using dipole approximation, we present comparative numerical studies of optical trapping force/potential acting on different types of bare metal, dielectric-metal, and metal-dielectric-metal hybrid nanoparticles. Since the dominating scattering force for large-sized metallic particles limits the trapping, we show that metal-dielectric-metal nanoparticles can extend the size limit of trapping. The optical trapping of such nanoparticles can also be contemplated as the trapping of nano-capacitors.

Keywords: Optical trapping, hybrid nanoparticles, metal-dielectric-metal nanoparticles, nano-capacitors, dipole approximation.

Introduction

Controlled optical trapping and manipulation at the nanoscale level are desired for diverse applications. For metallic nanoparticles, the high scattering and absorption forces limit the stable trapping of large-sized nanoparticles. The trapping force/potential was shown up to a limit of 27 nm for silver nanoparticles using dipole approximation [1]. However, an enhanced trapping efficiency was shown for hybrid dielectric-metal nanoparticles. A further enhancement was shown owing to the effect of optical nonlinearity under high repetition rate femtosecond pulsed excitation [2]. Here, we present the numerical results of trapping force/potential for the metal-dielectric-metal multilayered type of nanoparticles using dipole approximation under continuous-wave (CW) excitation. We compare the trapping force/potential for bare metal, dielectric-metal, and metal-dielectric-metal types of nanoparticles.

Results and Discussion

The polarizability for the metal (silver) nanoparticle is calculated using the corrected Drude-Lorentz model [3]. Depending on the thickness of the layer and material refractive indices, the effective polarizability is calculated for the dielectric-metal (polystyrene-silver) and metal-dielectric-metal (silver-polystyrene-silver) hybrid nanoparticles [4]. The scattering, absorption, and gradient forces are calculated from the contribution of real and imaginary parts of the effective polarizability.

Figure 1 shows the trapping forces and potential for bare silver, hybrid (polystyrene-silver), and multilayered (silver-polystyrene-silver) nanoparticles suspended in water at 800 nm excitation, 100 mW laser power with focusing NA = 1.4. The overall particle size was kept as 40 nm. Due to the dominating high scattering and absorption forces over gradient force, the total force (red curve) is positive, and the potential is unbound for 40 nm silver nanoparticles, as shown in figure 1 (first column). Even for embedding a 39 nm polystyrene in a 1 nm silver shell, the total force is positive, and the potential is unbound, as shown in figure 1 (second column). However, for the gradient force, a transitions to a repulsive force due to the negative real part of effective polarizability. The absorption force is high compared to scattering and gradient forces due to the large imaginary part of effective polarizability. Earlier the transition in gradient force from attractive to repulsive was shown for other overall sizes of polystyrene-silver nanoparticles [3]. Here, an interesting result is observed for the silver-polystyrene-silver type of nanoparticles; the attractive gradient force dominates over scattering and absorption forces which contributed to a bound potential well, as shown in figure 1 (third column). Hence, a 40 nm-sized silver nanoparticle can be trapped by embedding a 20 nm silver core and a thickness of 19 nm of polystyrene as an inner shell in a 1 nm silver shell. The absolute depth (U_{abs}) of the potential well and escape potential (U_{esc}; height of the potential barrier along the beam propagation direction, which quantifies the trapping efficiency [5]) are marked by the double-sided arrow in figure 1.

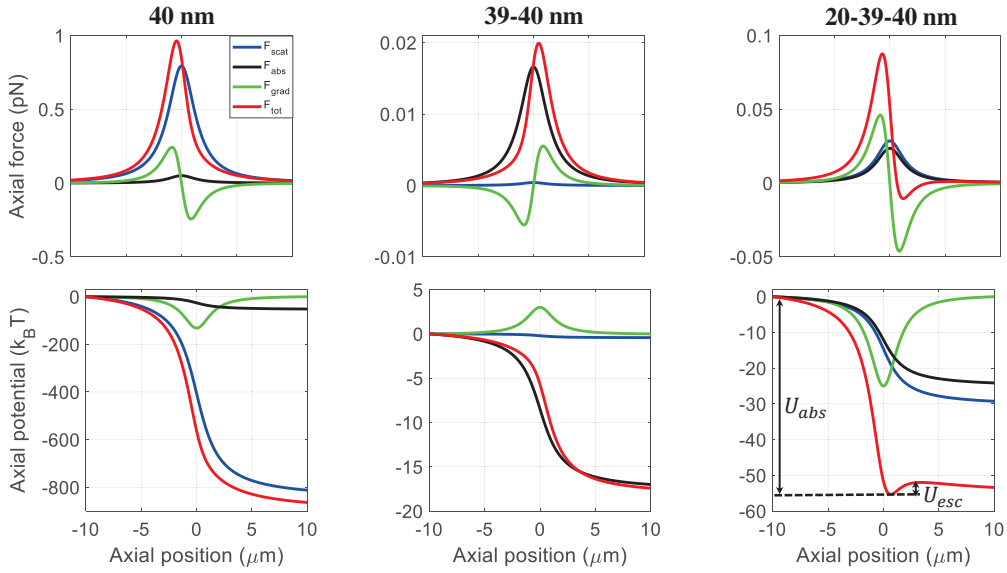

Fig. 1. Plots of trapping forces and potentials for 40 nm silver nanoparticle, 39-40 nm polystyrene-silver nanoparticle, and 20-39-40 nm silver-polystyrene-silver nanoparticle. Colors; blue, black, green, and red correspond to the scattering, absorption, gradient, and total force/potential, respectively.

Further, we extend the work to explore the effect of optical nonlinearity under femtosecond pulsed excitation [5] (not presented here). It was shown that pulsed excitation gives better trapping efficiency as compared to CW excitation for bare metallic nanoparticles [1] and dielectric–metal hybrid nanoparticles [2] because, under pulsed excitation, the nonlinear effect significantly modulates the trapping stability.

In summary, the results presented here show that the metal-dielectric-metal type nanoparticles can be trapped for an extended size limit of metal nanoparticles compared with conventional metal nanoparticles for facile nanoscale optical manipulation.

References:

[1] A. Devi, S. S. Nair, and A. K. De, "Disappearance and reappearance of optical trap for silver nanoparticles under femtosecond pulsed excitation: A theoretical investigation," EPL (Europhysics Letters) **126**, 28002 (1-7), (2019).

[2] A. Devi, S. S. Nair, S. Yadav, and A. K. De, "Controlling optical trapping of metal–dielectric hybrid nanoparticles under ultrafast pulsed excitation: a theoretical investigation," Nanoscale Adv. **3**(11), 3288-3297, (2021).

[3] M. Dienerowitz, "Plasmonic effects upon optical trapping of metal nanoparticles," Thesis Doctor of Philosophy, University of St. Andrews, UK, (2010).

[4] S. Yadav, A. Devi, and A. K. De, "Enhanced optical force on multilayered dielectric nanoparticles by tuning material properties and nature of excitation: a theoretical investigation," Nanoscale Adv. **4**, 2979 - 2987, (2022).

[5] A. Devi, and A. K. De, "Theoretical investigation on nonlinear optical effect in laser trapping of dielectric nanoparticles with ultrafast pulsed excitation," Opt. Express **24**, 21485-21496 (2016).

Optical design of microneedle array with an improved light intensity distribution on epidermal tissue layer

Diptayan Dasgupta [1], Sonam Berwal [2,3], Neha Khatri [2,3*]

[1]*Department of Applied Optics and Photonics, University of Calcutta, Kolkata 700106, India*
[2]*Academy of Scientific & Innovative Research (AcSIR), CSIR-CSIO, Chandigarh 160030, India*
[3] *Department of Manufacturing Science & Instrumentation, CSIR-CSIO, Chandigarh 160030, India*
[*]*Email: nehakhatri@csio.res.in*

Abstract: In this study, a type of microlens array integrated on a microneedle array is designed for localization of light onto the skin tissue. A light distribution of 12.69 percent of the input intensity was achieved at the fixed distance of 2.5 mm using a laser source of 20mW power. Engineering such light delivery based in-vivo biomedical device is of extreme importance for photodynamic therapy of skin cancer on and beyond the epidermal tissue layer.

Keywords: Microneedle array, optical design, microlens array, epidermal tissue layer.

1. Introduction

The microneedle arrays have the powerful potential for the delivery of light in biomedical applications [1]. Such micro-sized arrays are utilized for various applications, including vaccination, cosmetic skin treatment, cancer therapy, drug delivery and many more. New optical designs of microneedle arrays to achieve transportation distances of different lights for different purposes, such as psoralen plus ultraviolet-A radiation (PUVA) for vitiligo, long wave ultraviolet (UVA) for Sclerotic skin diseases etc., [2], has been of extreme importance in the advancement of medical science and technology. When light rays enter the skin, their functionality is mainly limited by biological tissue's scattering and absorbing properties. Without any external support, blue light can usually penetrate around 1mm in the 300-500 nm wavelength range, and near-infrared can penetrate around 2-3 mm in the 700-1300 nm wavelength range [4]. The penetration of light at different distances is known as optical penetration depth. Until date, several methods of light penetration have been recorded for drugs in vivo and in vitro applications [5]. Traditional therapeutic methods referring to radiotherapy, chemotherapy, photodynamic therapy and immunotherapy have various side effects and disadvantages, thus restraining their medical benefits. Transdermal microneedles have the ability to penetrate through the epidermal layer of the skin to deliver substantial therapeutic drugs. This avoids gastrointestinal indigestion hence reducing disadvantages phenomenally. Engineering micro-optical needles for drug delivery have been explored where a near-infrared light-responsive nanoparticle has been designed and then integrated with a dissolvable microneedle system for cancer cells such as melanoma and epidermoid [3]. In this work, an attempt has been made to explore the light delivery methodology via an optical microneedle array. A micro-lens integrated micro-needle array design in visible light wavelength range is presented for in-vivo biomedical applications. The concept of this work is to make sure more light can reach through the needle into the tissue layer than using conventional optics. The microlens array focuses the light on the microneedle array, reducing insertion loss and propagating into the skin.

2. Design of Microneedle Arrays

The microneedle array consists of a microlens array integrated at the front of its base, which focuses the light onto the needlepoint. Each individual microlens has a corresponding microneedle. An 11x11 array of the microlens is designed and optimized by using ray-tracing software (Zemax). The 11x11-microneedle array is initially designed in solid works and then imported into Zemax to evaluate the light transfer properties. Figure1 illustrates the shaded model of the micro-sized lens with the microneedle array. The selected light source is a laser with 491 nm of wavelength and 20 mW power. The designed microlens and microneedle array could be fabricated as one single optical element made of transparent, sturdy materials that should have no side effects on the skin when applied. Therefore, to meet this requirement, poly-lactic acid has a refractive index of 1.47 with an absorption coefficient of 0.014 mm-1 for wavelengths greater than 400 nm. Figure 2 shows the (a) the design parameters of the microneedle array, and (b) delivery of light into human skin.

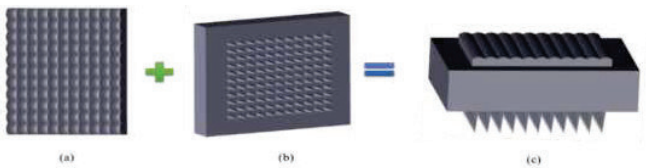

Fig. 1: Shaded model of (a) microlens array, (b) microneedle array, (c) combined system.

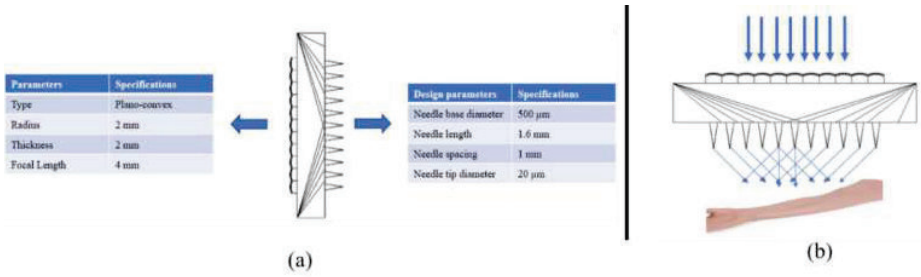

Fig. 2: (a) Design parameters of the microneedle array, (b) light distribution into human skin from microneedle array.

3. Numerical Simulation

In order to optimize the current design, the multiparameter optimization method is used. The skin model is made for tissue analysis with 7 layers from the epidermis to subcutaneous fat. Some of these layers are structured with different blood content values. The needle tip doesn't make a sharp focus inside the tissue layer, which prevents photo-damaging at the focus. The target depth is kept at 2.5 mm, right below the tissue surface for optimized results. Usually, this extended focal depth enhances the light delivery by increasing the adequate depth. The optical intensity at the tissue surface of depth 2.5 mm was around 12.69% of the input intensity. This gradually decreases as light penetrates deeper into the skin tissue. Alternatively, it can be concluded that this optical simulation has shown improved light delivery into skin fold models.

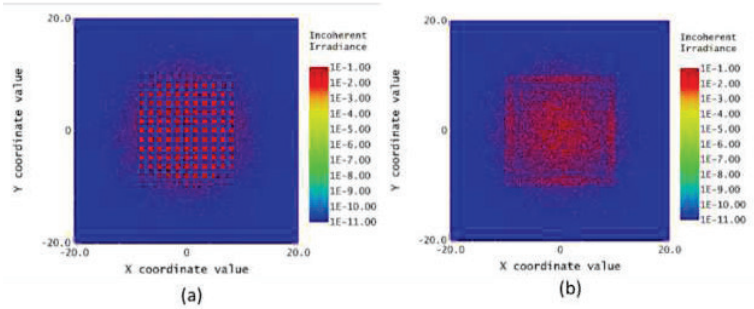

Fig. 3: Detector analysis of light penetration inside the tissue (a) at the target depth (2.5mm) and (b) away from the target depth (20mm).

4. Conclusion

In this study, investigations have been made to designed an optimized micro-needle array for better focusing at a target depth of 2.5 mm distance and analyzed its penetration inside a skin tissue. The entire ray tracing simulation is done with the Zemax non-sequential ray-tracing software. With the help of any state-of-the-art fabrication techniques, the implementation of such a scheme would give enhanced optical performance for modern biomedical applications in light delivery systems.

5. References

1. Kim M, An J, Kim KS, Choi M, Humar M, Kwok SJ, Dai T, Yun SH. Optical lens-microneedle array for percutaneous light delivery. Biomed Opt Express. 2016 Sep 21;7(10):4220-4227. doi: 10.1364/BOE.7.004220. PMID: 27867727; PMCID: PMC5102534.
2. Wu, Xiaobin, et al. "Development of Optical Microlens-Microneedle Array for Phototherapy." Proceedings of JSPE Semestrial Meeting 2019 JSPE Spring Conference. The Japan Society for Precision Engineering, 2019.
3. Ying Hao, YuWen Chen, XinLong He, Fan Yang, RuXia Han, ChengLi Yang, Wei Li, ZhiYong Qian, Near-infrared responsive 5-fluorouracil and indocyanine green loaded MPEG-PCL nanoparticle integrated with dissolvable microneedle for skin cancer therapy, Bioactive Materials,Volume 5, Issue 3, 2020.
4. Gonzalez-Romero, R.; Garcia-Torales, G.; Strojnik, M. Numerical Analysis of Micro-Lens Array to the Mid-IR Range. Eng. Proc. 2021, 8, 11. https://doi.org/10.3390/engproc2021008011
5. Dugam, S., Tade, R., Dhole, R. et al. Emerging era of microneedle array for pharmaceutical and biomedical applications: recent advances and toxicological perspectives. Futur J Pharm Sci 7, 19 (2021). https://doi.org/10.1186/s43094-020-00176-1.

Improvement in phase-sensitivity of a Mach-Zehnder interferometer with the superposition of Schrödinger's cat-like state and vacuum state as inputs under parity measurement

Gaurav Shukla[1], Krishna Mohan Mishra, Aviral Pandey, Taj Kumar, Devendra Kumar Mishra[2]

Department of Physics, Institute of Science, Banaras Hindu University, Varanasi-221005, India

Email: [1]gaurav.shukla18@bhu.ac.in, [2]kndmishra@gmail.com

Abstract: We study the improvement in the phase sensitivity of a Mach–Zehnder interferometer using the superposition of Schrödinger's cat-like state with the vacuum state (SCVS) and the vacuum state as inputs. With this setup, we examine the effect of phase sensitivity of the interferometer using a parity detection scheme. We find better phase sensitivity under some conditions for this setup having potential application in quantum sensing.

Keywords: Schrödinger's cat-like state, Fock state, phase sensitivity, parity detection, nonclassical light.

1. Introduction

Quantum interferometry is the field in which we measure the physical parameters by optical interferometers with an extremely precise value called precision measurement [1]. In order to improve the measurement sensitivity of an optical interferometer, usually, two main factors are important: the first is the input light source and the second is the detection scheme. In input light signal, we consider the best combination of input light sources, like, coherent and vacuum state, coherent and squeezed vacuum state, Schrödinger cat with vacuum state, etc. On the other hand, in the detection scheme, one can use parity detection, single intensity detection, intensity difference detection, homodyne detection, etc. In article [2], Shukla *et al* showed that by using the optimal combination of output signal detection scheme one can obtain the maximum phase sensitivity for a broad phase range. Recently, Mishra *et al.* [3] studied the non-classical properties of SCVS state and also propose the state generation plan. Shukla *et al* [4] showed that the combination of the superposition of Schrödinger's cat-like state with the Fock state (SCFS) and the coherent state as input gives better phase sensitivity as compared to other known combinations of inputs such as squeezed vacuum state and coherent state, coherent state and Fock state, vacuum state and coherent state, etc, under some conditions. Motivated by this, here, we study the phase sensitivity of MZI by using parity detection [5,6] for the combination of SCVS and the vacuum state as inputs.

2. Interferometry of MZI with SCVS using parity detection

Fig. 1 shows the block diagram of the MZI. In which, $\hat{a}_0$ and $\hat{a}_1$ are the annihilation operators for the input ports and $\hat{a}_2$ and $\hat{a}_3$ are the annihilation operators for the output ports. Two signals are entered and mixed (probe preparation) by a beam splitter (BS) and after mixing probe evolves inside the interferometer after that both probes are recombined via another BS and with the help of detectors, we analyze the results. With the help of the standard error propagation formula, $\Delta\phi = \frac{\Delta\hat{O}(\phi)}{\left|\frac{\partial\langle\hat{O}(\phi)\rangle}{\partial\phi}\right|}$, where $\hat{O}(\phi)$ is the observable and $\Delta\hat{O}(\phi)$ is the standard deviation and defined as $\Delta\hat{O}(\phi) = \sqrt{\langle\hat{O}^2\rangle - \langle\hat{O}\rangle^2}$, we calculate the phase sensitivity of the system. For observable $\hat{O}(\phi)$, we consider the parity operator denoted and defined as [7, 8]

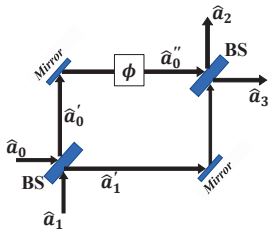

Fig. 1. Block diagram of MZI.

$$\hat{\Pi} = (-1)^{\hat{a}^\dagger\hat{a}} = \int \frac{d^2\beta}{\pi} |\beta\rangle\langle-\beta|,$$

where $|\beta\rangle$ is the coherent state. Now, we consider SCVS state, denoted and defined as $|\psi\rangle = N(|\alpha\rangle + e^{i\gamma}|e^{i\theta}\alpha\rangle + \boldsymbol{A}|0\rangle)$, where N is the normalization constant, $|\alpha\rangle$ is the coherent state, γ and θ are the phases and A is the real coefficient of the vacuum state $|0\rangle$ and vacuum state, $|0\rangle$, as the input states. After the evolution inside the interferometer, the output state becomes $|\Psi\rangle = \hat{T}|\psi\rangle$, where $\hat{T}$ is the state transformation operator of the MZI and $\hat{T} =$

$e^{-i\phi \hat{J}_y}$, with $\hat{J}_y = \frac{1}{2i}(\hat{a}_1^\dagger \hat{a}_0 - \hat{a}_1 \hat{a}_0^\dagger)$. By using the parity detection scheme, we find the phase sensitivity for different cases as mentioned in Fig. 2.

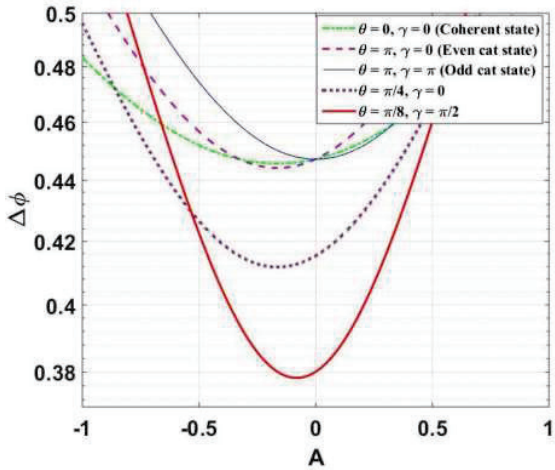

Fig. 2. Plots between phase sensitivity ($\Delta\phi$) and vacuum state coefficient **A** *for* $|\alpha|^2 = 5$ *and* $\phi = 3.14$*, by taking different values of the parameters as mentioned in the diagram.*

3. Conclusions

So, from Fig. 2 we find that for the case parity detection, phase sensitivity for $\theta = \frac{\pi}{4}, \gamma = 0$ and $\theta = \frac{\pi}{8}, \gamma = \frac{\pi}{2}$ is better than the even and odd cat state as well as the coherent state. Superposition of vacuum state (nonzero values of A) with Schrödinger's cat-like state enhances the phase sensitivity resolution (Fig. 2). Note that in other input port we use the vacuum. So, we expect that the SCVS may be an alternative nonclassical resource for enhancing the phase super-sensitivity of a Mach–Zehnder interferometer and having potential application in quantum metrology and quantum sensing.

Acknowledgement

GS acknowledge UGC for the UGC Research Fellowship. AP and DKM acknowledge financial support from the Science & Engineering Research Board (SERB), New Delhi for the CRG Grant (CRG/2021/005917). DKM acknowledges financial support under the Incentive Grant of Institution of Eminence (IoE), Banaras Hindu University, Varanasi, India.

4. References

[1] C. W. Helstrom, *"Quantum Detection and Estimation Theory"* (Academic Press, San Diego, CA, 1976).

[2] G. Shukla, D. Salykina, G. Frascella, D. K. Mishra, M. V. Chekhova, and F. Y. Khalili, "Broadening the high sensitivity range of squeezing-assisted interferometers by means of two-channel detection", Opt. Express **29**, 95 (2021).

[3] K. K. Mishra, D. Yadav, G. Shukla, and D. K. Mishra, "Non-classicalities exhibited by the superposition of Schrödinger's cat state with the vacuum of the optical field", Physica Scripta **96**, 045102 (2021).

[4] G. Shukla, K. K. Mishra, D. Yadav, R. K. Pandey, and D. K. Mishra, "Quantum-enhanced super-sensitivity of a Mach–Zehnder interferometer with superposition of Schrödinger's cat-like state and Fock state as inputs using a two-channel detection", J. Opt. Soc. Am. B **39**, 59 (2022).

[5] K. P. Seshadreesan, S. Kim, J. P. Dowling, and H. Lee, "Phase estimation at the quantum Cramér-Rao bound via parity detection," Phys. Rev. A **87**, 043833 (2013).

[6] B. T. C. Gard, D. K. Mishra, R. Singh, H. Lee, T. R. Corbitt, and J. P. Dowling, "Nearly optimal measurement schemes in a noisy Mach-Zehnder interferometer with coherent and squeezed vacuum," EPJ Quantum Technol. **4**, 4–4 (2017).

[7] William N Plick, Petr M Anisimov, Jonathan P Dowling, Hwang Lee and Girish S Agarwal, "Parity detection in quantum optical metrology without number-resolving detectors", New J. Phys. **12**, 113025 (2010).

[8] R. J. Birrittella, P. M. Alsing, and C. C. Gerry, "The parity operator: Applications in quantum metrology", AVS Quantum Sci. **3**, 014701 (2021).

Two-parameter Control of Self-Similar Rogue waves in Tapered Graded-Index Fiber

Sanjana Bhatia,[1,*] Neetu Maan [1], and C N Kumar[1,†]

[1] *Department of Physics, Panjab University, Chandigarh-160014, India*

[*] *sanjana.bhatia577@gmail.com,* [†] *cnkumar@pu.ac.in*

Abstract: We demonstrate analytical manipulation of self-similar rogue waves in a tapered graded-index nonlinear optical fiber. Our exact analysis leads us to a wide class of tapering profiles and the corresponding gain functions, which are allowed by the dynamical equations governing the tapered graded-index nonlinear fiber.

Keywords: Rogue waves, NLSE, Similaritons.

1. Introduction

"Rogue waves", "freak waves" and "killer waves", refer to giant isolated waves that appear from nowhere, having amplitudes significantly larger than the background waves. Firstly observed in the oceans as extreme water waves, rogue waves (RWs) are ubiquitous in nature and appear in a variety of different contexts such as nonlinear optical systems, Bose-Einstein condensates, microwave cavities, etc. In particular, the study of rogue waves has gained fundamental significance in nonlinear optical fiber systems, because of its potential applications in producing high-intensity optical pulses. Optical rogue solitons were first observed in nonlinear-optical-fiber-based systems by Solli et al. in 2007 [1]. Several models have been developed to study the dynamics of RWs, the nonlinear Schrödinger equation (NLSE) being the most studied one [2].

A significant aspect of the implementation of RWs in optical communication industry is the manipulation of features like amplitude, speed etc. Recently, Dai and his collaborators have studied the dynamics of controllable rogue waves, modeled by variable coefficient NLSE, through dispersion and nonlinearity management [3]. Authors in [4] have shown that the equation governing rogue wave dynamics admits a wide class of self-similar solutions, whose amplitudes can be exactly controlled by tailoring gain and tapering profiles in optical fibers through a free parameter. In the present work, we extend this class of solutions, to control the amplitude by tailoring the gain and tapering profiles through two free parameters. In the paraxial regime, the beam propagation is governed by the inhomogeneous NLSE given by

$$i\frac{\partial U}{\partial Z}+\frac{1}{2}\frac{\partial^2 U}{\partial X^2}+F(Z)\frac{X^2}{2}U-\frac{i}{2}G(Z)U+|U|^2U=0, \tag{1}$$

where $U(X,Z)$ represents the dimensionless complex field envelope, $F(Z)$ is the graded-index profile, and $G(Z)$ is the linear gain/loss function. It has been shown in [5], that Eq. (1) can be brought to a standard NLSE

$$i\frac{\partial \Psi}{\partial \zeta}+\frac{1}{2}\frac{\partial^2 \Psi}{\partial \chi^2}+|\Psi|^2=0 \tag{2}$$

through similarity transformations,

$$U(X,Z)=\frac{1}{W(Z)}\Psi\left[\frac{X-X_C(Z)}{W(Z)},\zeta(Z)\right]e^{i\Phi(X,Z)},\quad \text{where}\quad \Phi(X,Z)=C_1(Z)\frac{X^2}{2}+C_2(Z)X+C_3(Z) \tag{3}$$

Along with the well-known bright and dark soliton solutions, NLSE admits first-order rogue wave solutions with intensity given by

$$I_R=|U(X,Z)|^2=\frac{1}{W(Z)^2}\left[1+8\frac{1+4\zeta^2-4\chi^2}{(1+4\zeta^2+4\chi^2)^2}\right]. \tag{4}$$

During the course of self-similarity transformation [5], we get a set of consistency conditions among $\zeta(Z), X_C(Z), \Phi(Z), W(Z), F(Z)$and $G(Z)$, of which one corresponding to the similariton-width $W(Z)$ is a second-order ODE

$$\frac{d^2W(Z)}{dZ^2}+F(Z)W(Z)=0, \tag{5}$$

whose mathematical structure resembles the Schrödinger equation of quantum mechanics (QM). On identifying $F(Z)$ as shifted potential $(V-E_n)$ and $W(Z)$ as corresponding wave functions (χ_n), one can obtain self-similar

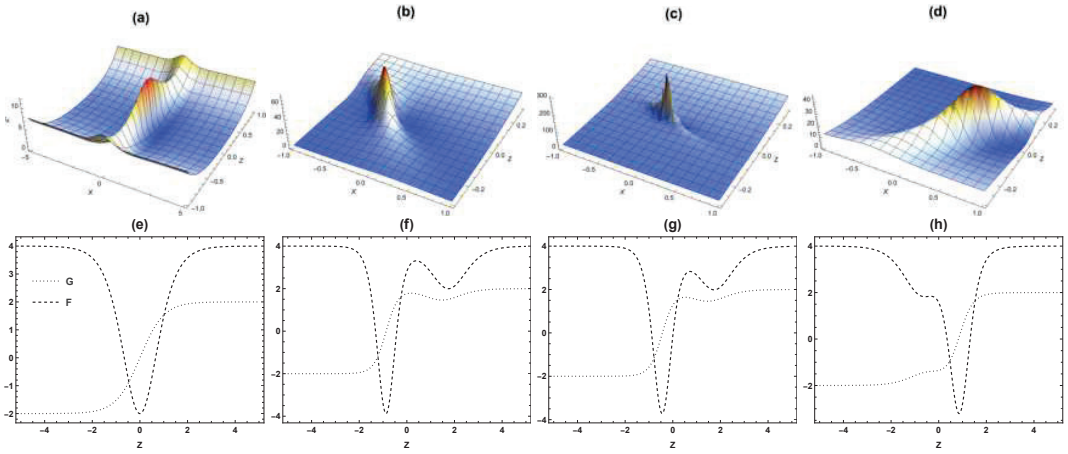

Fig. 1. (a) Rogue wave intensity corresponding to (e) tapering profile (dashed) and gain/loss function (dotted). Rogue wave intensity for (b) $\lambda_1, \lambda_2 = (0.1, -1.1)$ (c) $\lambda_1, \lambda_2 = (1, -1.1)$, and (d) $\lambda_1, \lambda_2 = (-1.1, 2.1)$, and their respective tapering profile (dashed) and gain/loss function (dotted) profiles.

solutions to Eq. (1) for every solvable QM potential. We choose tapering profile $F(Z) = 2(2 - 3\,\mathrm{sech}^2(Z))$ with width and gain/loss profile given by $W(Z) = \sqrt{3}/2\,\mathrm{sech}^2(Z)$ and $G(Z) = 2\tanh(Z)$ respectively. The RW intensity is shown in Fig. 1(a) and the corresponding tapering (dashed) and gain/loss (dotted) functions in Fig. 1(e).

2. Controlling RW dynamics

From supersymmetric QM, given n-bound state wave functions, and their respective energies, isospectral deformation of the Hamiltonian can always be performed by introducing n Riccati parameters $(\lambda_1, \lambda_2, ...) \notin (-1, 0)$ which allows the construction of new Hamiltonians with the same eigenvalue spectrum as that of the original one [6]. Thus, a n-dimensional family of potentials and hence wavefunctions can be constructed for a given problem, allowing one to tune any wavefunction dependent quantity [7], through n-free parameters. Exploiting this feature, we have generated a class of tapering profiles and width functions corresponding to $F(Z) = 2(2 - 3\,\mathrm{sech}^2(Z))$ [8], with two controlling parameters (λ_1, λ_2). Fig. 1(b),(c),(d) demonstrates the effect of Riccati parameters (λ_1, λ_2) on intensity of the RW. It can be observed that the height of the RW can be effectively controlled through judicious combination of (λ_1, λ_2). As the deformation of the tapering profile increases (Fig. 1(g)), the intensity peak of the RW increases (upto 30 times).

References

1. D. R. Solli, C. Ropers, P. Koonath, and B. Jalali, "Optical rogue waves", Nature (London) **450**, 1054 (2007).
2. N. Akhmediev, A. Ankiewicz, and M. Taki, " Waves that appear from nowhere and disappear without a trace", Phys. Lett. A **373**, 675 (2009).
3. C. Q. Dai, Y. Y. Wang, Q. Tian, and J. F. Zhang, " The management and containment of self-similar rogue waves in the inhomogeneous nonlinear Schrödinger equation", Ann. Phys. **327**, 512 (2012).
4. C. N. Kumar, R. Gupta, A. Goyal, and S. Loomba, " Controlled giant rogue waves in nonlinear fiber optics", Phys. Rev. A **86**, 025802 (2012).
5. S. A. Ponomarenko and G. P. Agrawal, "Optical similaritons in nonlinear waveguides". Opt. Letts, **32**, 1659-1661 (2007).
6. F. Cooper, A. Khare and U. Sukhatme, *Supersymmetry in quantum mechanics* (World Scientific, 2001).
7. C. N. Kumar, "Isospectral Hamiltonians: generation of the soliton profile", J. Phys. A **20**, 5397 (1987).
8. A. Goyal, R. Gupta, S. Loomba and C. N. Kumar, "Riccati parameterized self-similar waves in tapered graded-index waveguides", Phys. Lett. A **376**, 3454-3457 (2012).

S.B. acknowledges the support of Department of Science and Technology, Government of India, through INSPIRE-SRF (IF190338).

Tunable Graphene-Integrated Cascaded Silicon Microring Resonators

Prasanna Paithankar[1], Sridhar Singhal[2], Sauradeep Kar[2], Shailendra Kr. Varshney[2]
[1]*Department of Computer Science and Engineering,*
[2]*Department of Electronics and Electrical Communications Engineering,*
Indian Institute of Technology Kharagpur, West Bengal, India-721302
Author e-mail address: paithankarprasanna@kgpian.iitkgp.ac.in

Abstract: We theoretically and numerically demonstrate a tunable graphene-integrated cascaded tapered racetrack microring resonator (TRMRR) system. We have derived transmission field amplitudes of such cascaded system without graphene. The deposition of graphene on the PNF region produces an opto-electronically tunable transmission with an appreciable extinction by harnessing the unique advantages of graphene and cascaded resonator system. The proposed device can be potentially used for sensing and modulator applications.
Keywords: Silicon resonator, Graphene, Photonic Integrated Circuit

1. Introduction

On-chip, CMOS compatible microring resonators (MRRs) being an essential component in integrated photonic circuits have been explored for a plethora of applications ranging from laser cavities, wavelength filters, wavelength-division multiplexers, delay lines, optical switches, sensing and many more [1]. A basic MRR consists of a straight waveguide (bus) which is evanescently coupled to the bent waveguide (ring). The coupling gap between the bus and the ring plays a critical role in dictating the strength of coupled field in the ring and hence the quality of resonance. The coupling gap is crucially dependant on the fabrication process. The usage of multiple cascaded MRRs instead of a single MRR is a viable method by which the stringent coupling gap dependency can be lifted [2]. In addition, a cascaded MRR system provides improved extinction ratio in the resonant dips than a single resonator. In this work a cascaded racetrack MRR configuration is proposed where graphene, a two-dimensional material has been placed on top of the straight non-coupled arm of the resonator. The waveguide in the non-coupled arm of the MRR has been adiabatically tapered down, which is referred as a photonic nanofence (PNF) region. It has been reported that the usage of a PNF region can dramatically improve the sensing capability of a conventional MRR [3]. In this work, 0.34 nm thick layer of graphene been placed in the tapered region. The change in chemical potential of graphene yields a wavelength tunable resonance spectrum of the proposed device.

2. Proposed Design, Results and Discussion

The proposed cascaded TRMRR system has been shown in Fig.1. The device consists of a single bus waveguide which is evanescently coupled to two tapered racetrack microring resonators in parallel configuration, marked as *I* and *II*. The resonators have radii of R_I = 5 µm and R_{II} = 3 µm, respectively, with a straight arm length of 10 µm. For both resonators, the waveguide width (W) and height (H) for the non-tapered section are 600 nm and 220 nm respectively. The waveguide has been adiabatically tapered down to a PNF region having a width W_1 = 350 nm in the non-coupled arm of both resonators. The resonator geometry for the parallelly cascaded configuration is adiabatically tapered for the racetracks at the region away from the bus waveguide

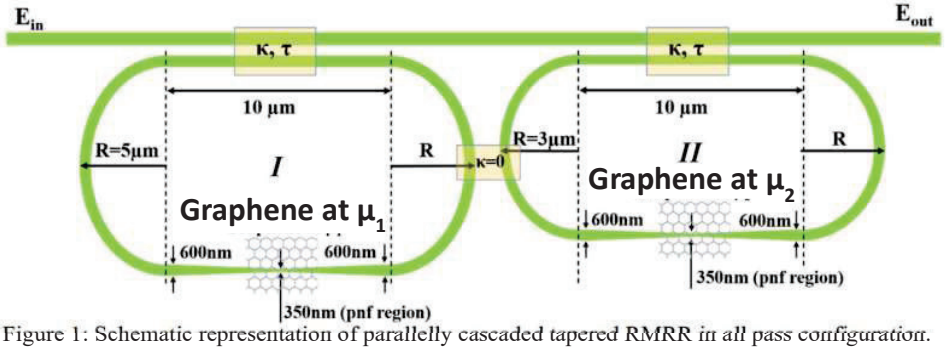

Figure 1: Schematic representation of parallelly cascaded tapered RMRR in all pass configuration.

(of thickness 600nm) to a thickness of 350nm. The region between the down-tapered region corresponding to the photonic nanofence (pnf) is where the scatter is loaded. The pnf length (l) is 3.5μm and that of adiabatically tapered transition region (l_a) is 3.25μm.

Using Transfer Matrix Method, for a single tapered racetrack, the field amplitudes can be obtained as,

$$\frac{E_{out}}{E_{in}} = \frac{M_{21} + M_{22}e^{i\frac{2\pi}{\lambda}n''l}}{M_{11} + M_{12}e^{i\frac{2\pi}{\lambda}n''l}} = e^{-i\frac{2\pi}{\lambda}n_c l_c}\left[\frac{\tau - ae^{-i\frac{2\pi}{\lambda}\sum n_k l_k}}{1 - \tau a e^{-i\frac{2\pi}{\lambda}\sum n_k l_k}}\right]$$

where $a = e^{-\alpha d}$ is the loss due to bending or scattering with α being amplitude attenuation coefficient [4]. τ is the self-coupling coefficient, n_k is the effective refractive index in region k of length l_k. The square of absolute value of E_{out}/E_{in} is taken as transmittance. The effective index of Graphene that has been placed in the pnf region has been calculated through finite element

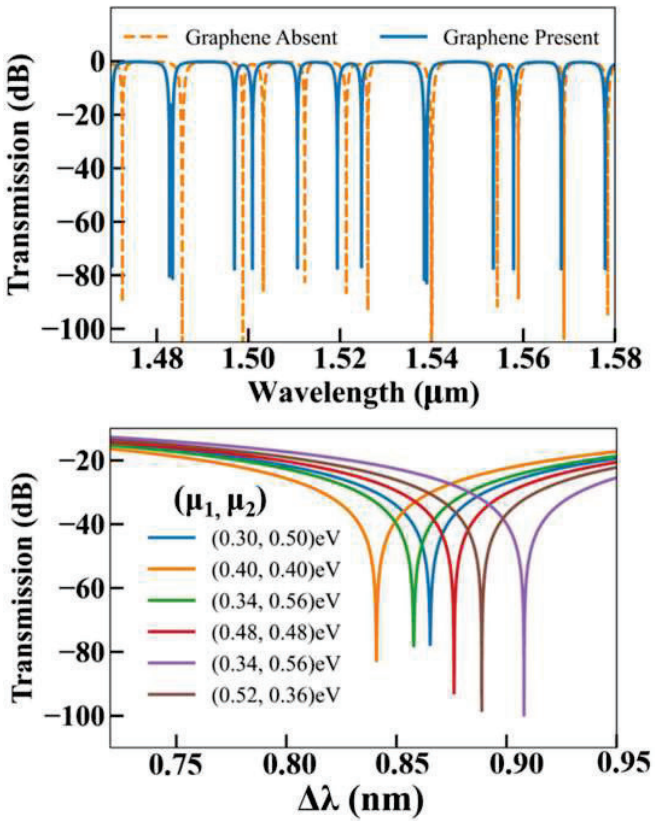

Figure 2: (a) Transmission spectrum for the proposed resonator with and without Graphene at pnf. (b) Tuning of spectra in presence of Graphene at chemical potential μ_1 and μ_2 in the pnf region of ring I and II respectively.

simulation. The cross coupling hasn't been considered in current simulations. A blueshift in resonance spectrum is observed upon presence of Graphene at different chemical potentials in the photonic nano fence region.

3. Conclusion

We observe the tuning of the spectra due to opto-electronic properties of Graphene in a cascaded configuration of tapered racetrack microring resonator making it useful for various sensing applications.

4. References

[1] Wim Bogaerts et al., "Silicon Microring Resonators" Laser Photonics Rev., vol. 6, No.1, 47-73 (2012).
[2] Jiayang et al., "Nested Configuration of Silicon Microring Resonator With Multiple Coupling Regimes" IEEE Photonics Technology Letters, vol. 25, No. 6 (2013).
[3] Sawan K Bag et al., "Tapered racetrack microring resonator for single nanoparticle detection" J. Phys. D:Appl. Phys. vol. 54 (2021).
[4] Amnon Yariv, Pochi Yeh, "Photonics: Optical Electronics In Modern Communications" Oxford University Press (2007).

Imprinted Polymer Functionalized PCF Based Sensor for Water Pollutant: Hypersensitive and Selective

Pintu Gorai, and Rajan Jha
Nanophotonics and Plasmonics Laboratory, School of Basic Sciences, IIT Bhubaneswar, Odisha, Pin-752050
Author e-mail address: pg27@iitbbs.ac.in; rjha@iitbbs.ac.in

Abstract: Detection of toxic water pollutants in natural water resources has significant importance for researchers due to dwindling marine biodiversity. In this regard, we report a compact, and highly sensitive biochemical sensor through successful integration of interferometry and molecular imprinted polymer for precise detection of the water pollutant named p-cresol. The system shows sensitivity towards p-cresol of 1.86×10^8 nm/M over dynamic operating range from 10^{-8} M to 10^{-3} M. The system is potentially suitable for medical and environmental monitoring applications due to its easy, accurate, fast responsive, selective and high-resolution performance.

Keywords: Water Pollutant, Imprinted Polymer, modal interferometer, Optical biochemical sensor

1. Introduction

Water pollution has emerged as a severe environmental issue in recent decade. One major cause of water pollution is different phenolic compounds contained in effluents of industrial wastage [1,2]. Among such compounds, the most common toxic phenolic compound discharged into water bodies is 4-methyl phenol, also known as p-cresol (para-cresol) [3]. The massive production of p-cresol for industrial applications makes this one of the primary health risks. The conventional techniques of p-cresol detection are complex, expensive, time consuming, less sensitive and less selective [4,5]. These shortcomings can be resolved by utilizing successful integration of fiber optic interferometry and molecular imprinting polymer (MIP) as an artificial recognizing element. The interferometry technique acts as high resolution, sensitive, and fast responsive sensing platform. This sensitive interferometric platform is functionalized with MIP for achieving high selectivity of desired analyte with significant accuracy. In this work, a biochemical sensor is fabricated by developing a Photonic Crystal Fiber (PCF) based interferometer with MIP to detect the toxic pollutant p-cresol precisely. Highly sensitive and broad detection range features of this combined approach make it appropiate for the development of biochemical detection and water resource monitoring applications.

2. Sensing mechanism

The sensing process of the proposed sensor is based on the variation of effective refractive index (RI) of the sensing region due to specific binding of p-cresol molecules with MIP nanoparticles layer [6]. The interferometric transducer is fabricated by splicing a small PCF segment having a length of 2 cm along single mode fiber (SMF) channel, forming a one of the stable SMF-PCF-SMF structure. This hetero fiber structure produces a stable interference pattern due to interference between core and higher order cladding modes of the PCF. On the other hand, the MIP, that acts as an artificial molecular receptor, is synthesized through polymerization of target analyte and functional monomer. The elution of target analyte from the polymeric structure creates imprinted binding sites having complementary structure in terms of shape, size and functionality of p-cresol. These complementary sites allow only the target analyte to rebind. As the p-cresol sample solution comes in contact with functionalized MIP-NPs, the complementary binding sites allow only p-cresol molecules to bind selectively through the formation of hydrogen bonds inside the polymer structure as shown schematically in fig. 1(a). As a result of such interaction, the effective RI of the functionalized hetero fiber structure or sensing region changes. Such modification alters the light signal propagation through the fiber structure. Hence, the transmitted interference pattern changes in terms of wavelength and intensity. This change is calibrated with the concentration of p-cresol samples. Thus, by measuring the shift in wavelength or intensity through spectrum analyser, the presence of p-cresol can be measured.

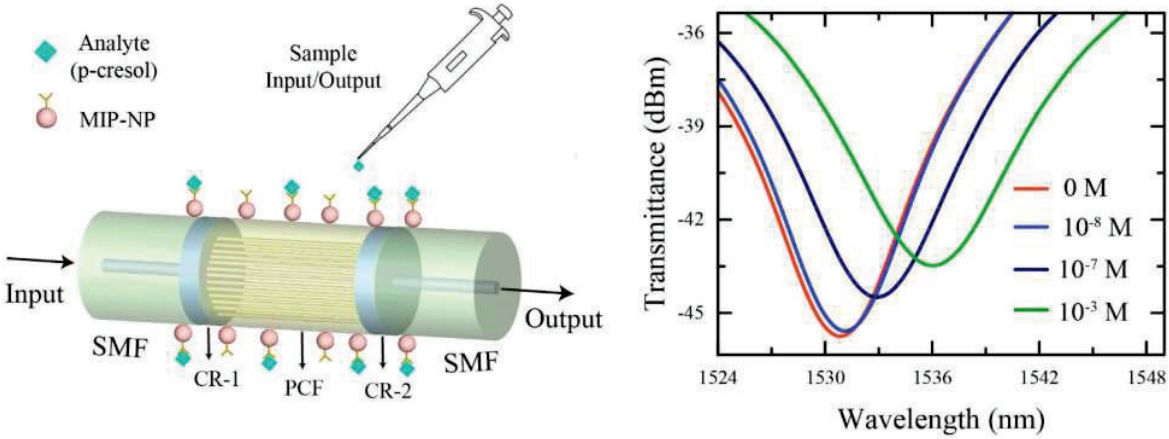

Figure 1: (a) Schematic illustration of modal interferometry-based bio-chemical detection system. (b) Concentration characterization of proposed sensor

3. Results and Discussions

The sensing probe is characterized using wavelength interrogation method for different concentration of p-cresol in aqueous medium. The samples are injected into the customized flow-cell via a microfluidic injector. The transmitted spectra for these sample are recorded in optical spectrum analyzer (OSA). Here, in this experiment the reference sample is taken as 0 M concentration. The spectral shifts for all sample solutions are measured with respect to this reference sample. The interference spectra are plotted in fig. 1(b) showing a red shift for enhancing p-cresol sample concentration. Here, only a few spectra are plotted for the sake of clarity. The wavelength shift is calibrated in terms of increasing concentration. The sensitivity is calculated using the derivative of the calibrated equation. The sensor shows wide dynamic detection range with an unprecedented sensitivity of 1.86×10^8 nm/M. It holds a minimum detection ability of 5.37 pM concentration in aqueous medium.

4. Conclusion

The proposed system is a novel approach for the detection of toxic water pollutant p-cresol utilizing combined method of modal interferometry and molecular imprinting polymer. The transducing platform is functionalized with MIP-NPs to fabricate the sensing platform. The nano sized MIP possesses improved binding cavities for attachments of target analyte p-cresol. This increases the sensitivity of the sensor. The system is compact, tailorable, label-free, inline biochemical sensor with broad operational range. Such system will have wide application in water quality monitoring and in bio-medical industries.

5. Acknowledgement

RJ acknowledges the support from SERB STAR and BRNS Fellowship.

6. References

[1] R. Altenburger, S. Ait-Aissa, P. Antczak, T. Backhaus, D. Barceló, T.-B. Seiler, F. Brion, W. Busch, K. Chipman, and M. L. de Alda, "Future water quality monitoring—Adapting tools to deal with mixtures of pollutants in water resource management," Sci. Total Environ. **512**, 540–551 (2015).
[2] A. Waheed, N. Baig, N. Ullah, and W. Falath, "Removal of hazardous dyes, toxic metal ions and organic pollutants from wastewater by using porous hyper-cross-linked polymeric materials: A review of recent advances," J. Environ. Manage. **287**, 112360 (2021).
[3] W. E. Gomes, A. A. Corrêa, T. G. Beatto, A. Etchegaray, A. B. Nogueira, and R. K. Mendes, "Removal of p-cresol using wash waters from lipopeptide production," Environ. Technol. 1–8 (2021).
[4] E. Nandini, B. Arunraj, N. Rajesh, and V. Rajesh, "Improvised method for urinary p-cresol detection and measurement using high performance liquid chromatography/mass spectrometry," Heliyon **5**, e02978 (2019).
[5] D. Bergé-Lefranc, M. Eyraud, and O. Schäf, "Electrochemical determination of p-cresol concentration using zeolite-modified electrodes," Comptes Rendus Chim. **11**, 1063–1073 (2008).
[6] P. Gorai and R. Jha, "Artificial Receptor-Based Optical Sensors (AROS): Ultra-Sensitive Detection of Urea," Adv. Photonics Res. **2**, 2100044 (2021).

Effect of Atomic Ensemble Position on the Dynamics of Cold Atoms in an Optical Cavity: Normal-Mode Splitting

Sonam Mahajan[1], Neha Aggarwal[2] and Aranya B. Bhattacherjee[3]
[1]*Department of Physics, DIT University, Dehradun, Uttrakhand-248009, India*
[2]*Department of Physics, Government College for Women, Faridabad, Haryana-121002, India*
[3]*Department of Physics, Birla Institute of Technology and Science, Pilani, Hyderabad Campus, Telangana State-500078, India*
E-mail address: sonammahajan1987@gmail.com

Abstract: We consider the dynamics of cold atoms coupled to the light field via radiation pressure within a Fabry-Perot cavity. We observe the effects of changing the effective positioning of the atomic ensemble on the effective mechanical frequency and the damping rate of cold atoms. We further study the displacement spectrum of atomic oscillator and analyze the occurrence of normal mode splitting into two modes. We mainly analyze how the position of the ensemble acts as an additional tool in significantly altering the atomic and cavity field interaction strength. The present scheme enables further studies of coherently controlling the dynamics of the cold atoms.
Keywords: optical cavity, cold atoms, normal-mode splitting, ensemble position.

1. Introduction

The experimental realizations of quantum cavity optomechanics have served as paradigms for understanding optical cooling [1–6], squeezing [7,8], optical nonlinearity [9, 10] and phonon number measurement [11] in recent years. An atom-chip-based realization of cavity optomechanics involving cold atoms embedded within a Fabry-Perot cavity [12] has also been proposed recently [12].

Motivated by such exciting developments in this research field, we propose a model comprising of an ensemble of cold atoms localized within a Fabry-Perot optical cavity. Here, we observe the effects of changing the position of the ensemble on effective mechanical frequency, effective mechanical damping rate and Normal-mode splitting (NMS) of cold atoms.

2. Figures

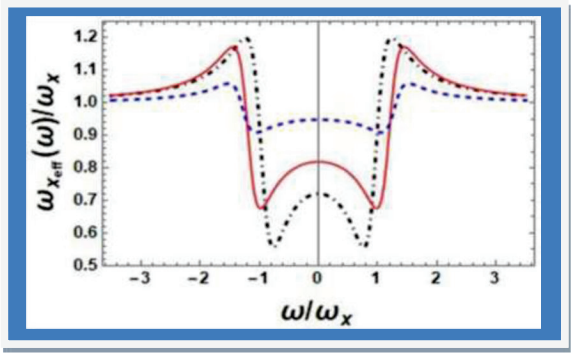

Fig. 1: Plot of normalized effective mechanical frequency ($\omega_{x_{eff}}/\omega_x$) as a function of dimensionless frequency (ω/ω_x) for three different values of θ_0 with $\theta_0 = 0$ (black dot-dashed line), $\theta_0 = 0.8$ (red solid line) and $\theta_0 = 1.2$ (blue dashed line). Other parameters used are $\Gamma_m = 10^{-5}\omega_x$, $\kappa = 0.23\omega_x$, $\Delta_c = -\omega_x$, $U_0 = 0.0001\omega_x$, $\alpha = 0.006\omega_x$, $n_b = 10^3$, $N = 1000$, $m = 87amu$ and $k = 2\pi/780nm$).

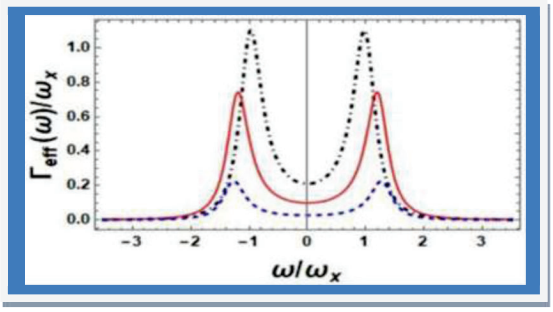

Fig. 2: Plot of normalized effective mechanical damping rate (Γ_{eff}/ω_x) as a function of dimensionless frequency (ω/ω_x) for three different values of θ_0 with $\theta_0 = 0$ (black dot-dashed line), $\theta_0 = 0.8$ (red solid line) and $\theta_0 = 1.2$ (blue dashed line). Other parameters chosen are the same as in Fig.2(a).

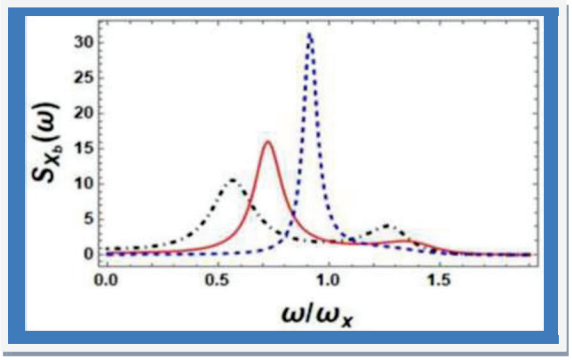

Fig. 3: Plot of displacement spectrum as a function of dimensionless frequency (ω/ω_x) for three different values of θ_0 with $\theta_0 = 0$ (black dot-dashed line), $\theta_0 = 0.8$ (red solid line) and $\theta_0 = 1.2$ (blue dashed line). Other parameters chosen are the same as in Fig.2(a).

Fig. 1 and 2 illustrate the variation of normalized effective mechanical frequency and normalized effective damping rate of the atomic oscillator respectively as a function of dimensionless frequency (ω/ω_x) for different values of θ_0, $\theta_0 = 0$ (black dot-dashed line), $\theta_0 = 0.8$ (red solid line) and $\theta_0 = 1.2$ (blue dashed line). It can be seen clearly from fig.1 that the significant deviation from the bare frequency ω_x is observed around $\omega = \pm\omega_x$. Moreover, the deviation of the mechanical frequency of the atomic oscillator from its resonance frequency ω_x decreases with the increase in the value of θ_0. Fig.2 further illustrates that the effective mechanical damping gets significantly decreased with an increase in θ_0. Thus, the effective mechanical frequency and the damping rate of the atomic ensemble can be significantly controlled by changing its position along the cavity axis. Fig. 3 shows the plot of displacement spectrum $S_{X_b}(\omega)$ as a function of dimensionless frequency (ω/ω_x), with $\theta_0 = 0$ (black dot-dashed line), $\theta_0 = 0.8$ (red solid line) and $\theta_0 = 1.2$ (blue dashed line). Here, we observe the NMS in two modes. Furthermore, the figure depicts that the amplitude of the first peak of the displacement spectrum increases whereas the amplitude of its second peak decreases with the increase in value of θ_0. This represents the coherent energy exchange between the two modes (cavity mode and the mechanical mode) of the system. We further notice that the spectrum shifts towards the right as the ensemble is shifted from the center towards the walls of the optical cavity along the cavity axis. Hence, we can conclude that the atomic-cavity field interaction strength can be controlled significantly by altering the position of the ensemble along the axis of the optical cavity.

3. References

[1] V. B. Braginsky, A. B. Manukin, "Pondermotive Effects of Electromagnetic Radiation," Sov. Phys. JETP **52**, 986-989 (1967).
[2] T. J. Kippenberg et al., "Analysis of Radiation-Pressure Induced Mechanical Oscillation of an Optical Microcavity," Phys. Rev. Lett. **95**, 033901 (2005).
[3] O. Arcizet et al., "Radiation-pressure cooling and optomechanical instability of a micromirror," Nature (London) **444**, 71-74 (2006).
[4] S. Gigan et al., "Self-cooling of a micromirror by radiation pressure," Nature (London) **444**, 67-70 (2006).
[5] Sonam Mahajan, Tarun Kumar, Aranya B. Bhattacherjee, ManMohan, "Ground-state cooling of a mechanical oscillator and detection of a weak force using a Bose-Einstein condensate," Phys. Rev. A **87**, 013621 (2013).
[6] Sonam Mahajan, Neha Aggarwal, Aranya B Bhattacherjee, ManMohan, "Achieving the quantum ground state of a mechanical oscillator using a Bose-Einstein condensate with back-action and cold damping feedback schemes," J. Phys. B: At. Mol. Opt. Phys. **46**, 085301 (2013).
[7] S. Mancini, P. Tombesi, "Quantum noise reduction by radiation pressure," Phys. Rev. A **49**, 4055 (1994).
[8] C. Fabre et al., "Quantum-noise reduction using a cavity with a movable mirror," Phys. Rev. A **49**, 1337 (1994).
[9] A. Dorsel et al., "Optical Bistability and Mirror Confinement Induced by Radiation Pressure," Phys. Rev. Lett. **51**, 1550 (1983).
[10] S. Gupta, K. L. Moore, K.W. Murch, D. M. Stamper-Kurn, "Cavity Nonlinear Optics at Low Photon Numbers from Collective Atomic Motion," Phys. Rev. Lett. **99**, 213601 (2007).
[11] A. A. Clerk, F. Marquardt, J. G. E. Harris, "Quantum Measurement of Phonon Shot Noise," Phys. Rev. Lett. **104**, 213603 (2010).
[12] T. P. Purdy et al., "Tunable Cavity Optomechanics with Ultracold Atoms," Phys. Rev. Lett. **105**, 133602 (2010).
[13] C. Maschler, H. Ritsch, "Cold Atom Dynamics in a Quantum Optical Lattice Potential," Phys. Rev. Lett. **95**, 260401 (2005).

Multimodal Endo-Spectroscopic Device: Diffuse Reflectance, Auto-fluorescence, Fluorescence Imaging and Spectroscopy of oral cancer tissues

Dibya Jyoti Sarangi[1#], Pramila Thapa[1], Shrishti Dewangan[1], Priyanka Mann[1], Bhanu Pratap Singh[1], Himanshu Joshi[1], Deepika Mishra[2] and Dalip Singh Mehta[1*]

[1]Bio-photonics and Green-photonics Laboratory, Department of Physics, Indian Institute of Technology Delhi, Hauz-Khas, New Delhi 110016, India.

[2]Oral Pathology, Centre for Dental Education & Research (CDER), AIIMS New Delhi, India

Email- #dsarangi7@gmail.com

**mehtads@physics.iitd.ac.in*

Abstract: Fatality rate of cancer can be reduced by fast-screening and early diagnosis which can be accomplished via optical techniques. Integration of more than one modality in single unit enhances system's sensitivity and accuracy. Present manuscript deals with integration of four modalities in single unit with simultaneous diffuse reflectance, autofluorescence, fluorescence polarization imaging and spectroscopy of biological specimen. Device is validated with the chicken tissue and ex-vivo oral cancer tissue and after the successful adaptation, real time in-vivo data is recorded at AIIMS hospital. Developed device is field-portable and easy to use and successfully demonstrated for oral cancer tissue.

Keywords: multimodality, endoscope, spectroscopy, fluorescence, autofluorescence, diffuse reflectance spectroscopy, polarization, oral cancer

1. Introduction

Oral Cancer is most common cancer for both sexes [1]. Generally oral cancer starts from the altered epithelial cells then it turns out to hyperplasia and then dysplasia and at last it converts into Oral Squamous Cell Carcinoma (OSCC) which is malignant in nature and very common. The survival rate for the oral cancer patients in 5 years after various treatment comes around 50% [2]. This survival rate can be increased with the help of early diagnosis and awareness among common people, and early diagnosis can be done with the help of optical techniques which must be non–contact, non-invasive, fast and accurate. In the current healthcare scenario, early and accurate diagnosis are the two most essential and foremost requirements for the fast treatment and prevention of cancer. Because of the large number of patients, fast and dependable screening methods, such as multimodal non-invasive optical technologies are required. Present manuscript deals with four modalities; diffuse reflectance (DRS), autofluorescence (AF), fluorescence (FL), polarization imaging and spectroscopy. AF probes the intracellular components of the OSCC like nicotinamide adenine dinucleotide (NADH), flavin adenine dinucleotide (FAD) etc., DRS deals with epithelial layers of OSCC, polarization can tell about the morphological changes within the cancer tissue by intensity variation [3,4,5]. Integration of these modalities in single unit enhances the diagnostic accuracy of the oral cancer.
Fluorescence polarization (pol) and anisotropy (an) of the oral cancer tissue can be calculated as:

$$pol = \frac{p\| - p^{\perp}}{p\| + p^{\perp}} \quad (1)$$

$$an = \frac{p\| - p^{\perp}}{p\| + 2p^{\perp}} \quad (2)$$

Where p‖ is linear polarization and $p^{\perp}$ is cross polarization state of the biological specimens.

2. Experimental Setup

Developed system consists of two diode lasers (488nm, <1mw, 405nm, <1mw;), endoscopic camera white LEDs embedded in endoscopic camera, optical fibres (1.2m long silica, step-index multi-mode, 0.37± 0.02 NA, ~800 um core, ~900 um cladding, 300-2400nm wavelength range), two filters (band-pass, 510-560 nm; long pass, >430nm), spectrometer 350-950 nm, 0.1 nm resolution, fluorescein dye, annular polarizer, analyzer and a smartphone.

Al2O3 Abrasive 300 (25-30 μm) and Al2O3 Abrasive 302 (15-20 μm) are employed for fibre polishing. A total 8 fibres are mounted on the periphery of endoscopic camera. Light is excited and collected from these fibres in alternative fashion. A ring-shaped polarizer was positioned directly in front of the illuminating fibre such that the light falling on the oral cancer tissue is polarized and reflected light is gathered at the endoscope, in front of which a rotatable circular analyzer is mounted. Excitation fibres are coupled with the laser and endoscopic camera and collection fibres captures and collected the scattered light from the biological specimen. Figure 1 (a) is showing the complete schematic diagram of the experimental setup and inset shows fibres geometry with endoscopic camera. Figure 1 (b) is showing the polarizer and analyzer's position in the developed system.

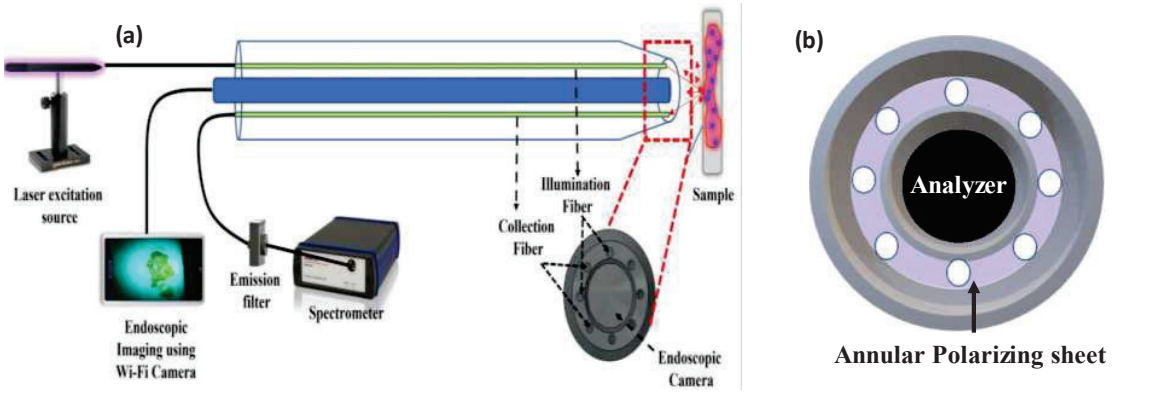

Fig: 1 Experimental setup for autofluorescence, diffuse reflectance, fluorescence and polarization imaging and spectroscopy.

3. Results and Discussion

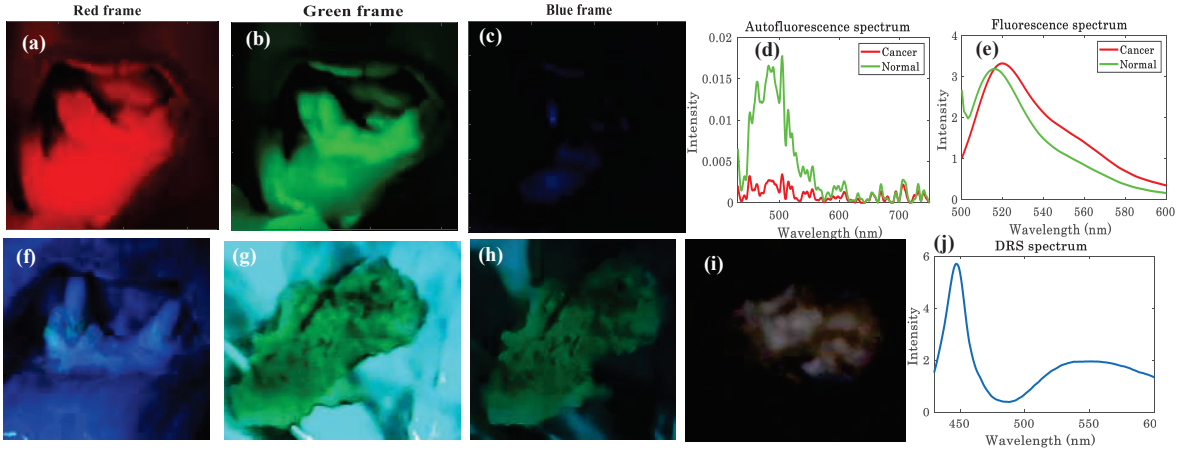

Fig. 2: Autofluorescence, fluorescence, diffuse reflectance and polarization images and spectroscopy of oral cancer tissues.

Figure 2 is showing experimental results for oral cancer tissues. Figure 2. (a)-(c) are AF images of OSCC tissue showing AF for red, green and blue frame respectively and probing indigenous fluorophores in OSCC tissue [4]. Figure 2 (d) and (e) shows AF spectra and FL spectra of oral cancer and normal tissue indicating loss in AF due to the loss in NADH in cancerous environment and a red-shift of 4nm in FL due to the increased refractive index [4,5]. Figure 2. (f) is showing FL image of OSCC patient and indicates tagging of the fluorescein dye only in cancerous area due to angiogenesis. Figure 2. (g) and (h) are $p_{\parallel}$ and $p^{\perp}$ images showing intensity variation in both images and giving fluorescence polarization of 41.60 $\times 10^{-2}$ and anisotropy of 24.36 $\times 10^{-2}$ [4]. Figure 2. (i) and (j) are DRS image and DRS spectra of the OSCC tissue respectively. DRS image gives mean of 3.6296 and spectra shows the reflectance from the upper layer of the OSCC tissue.

4. Conclusion

A multimodal endo-spectroscopic device is developed and successfully validated for ex-vivo and in-vivo procedure for the OSCC tissue screening. FL imaging and spectroscopy offers molecular level changes in OSCC tissue while AF probes progression of the cancer in OSCC tissue. DRS indicates the reflection from upper epithelial layers of OSCC tissue and polarization shows the morphological changes within OSCC tissue.

Acknowledgement

PT and DJS contributed equally in this manuscript. PT acknowledges CSIR for Senior Research Fellowship.

References

[1]V.Borse, A.N. Konwar, P. Buragohain,Oral Cancer Diagnosis and Perspective in India,Sensors International (2020)

[2]S.B. Thavarool, G. Muttath, S. Nayanar, Improved survival among oral cancer pateints:findings from a retrospective study at a tertiary care cancer centre in rural Kerla India, World J Surgery Ocology (2019)

[3] Yaroslavsky Anna N., et al. "Fluorescence polarization of methylene blue as a quantitative marker of breast cancer at the cellular level." *Scientific reports* 9.1 (2019): 1-10.

[4] Skala, Melissa C., et al. "In vivo multiphoton microscopy of NADH and FAD redox states, fluorescence lifetimes, and cellular morphology in precancerous epithelia." *Proceedings of the National Academy of Sciences* 104.49 (2007): 19494-19499.

[5] Thapa, Pramila, et al. "Development of multimodal micro-endoscopic system with oblique illumination for simultaneous fluorescence imaging and spectroscopy of oral cancer." *Journal of Biophotonics* (2022): e202100284.

Performance evaluation of DLMI for optical metrology using phase analysis

Monika Rani[1,2], Ajay Shankar[2], Raj Kumar[1,*]
[1]*CSIR-Central Scientific Instruments Organisation, Sector 30C, Chandigarh 160030, India*
[2]*Guru Jambheshwar University of Science and Technology, Hisar 125001, India*
**Corresponding author: raj.optics@csio.res.in*

Abstract: In this work studies are reported on the diffraction Lloyd's mirror interferometer to access its suitability to perform quantitative measurement on test objects. The phase information from the interferograms obtained by this interferometer is retrieved and analyzed. From the phase profiles in direct illuminated and shadow regions, it is observed that this interferometer is capable to perform optical metrology of large area objects.

1. Introduction

Interferometry has always been an important tool in optical metrology because of its ability to record and measure phase in terms of modulation of intensity in the resulting interferogram. In a two beam interferometer, a beam of light is split into two and subsequently recombined to yield an interferogram [1]. The test and reference beams follow different paths and hence they are differently affected by mechanical vibrations, air disturbance and temperature fluctuations causing instability of the fringes. The common-path interferometers naturally terminate these shortcomings. In the case, both of beams travel along the same path and interact with same elements in their way and hence are equally affected by ambient perturbations and system aberrations [2]. The reference beam and object beam both follow the same path in the diffraction Lloyd's mirror interferometer (DLMI) [3, 4], which is one of the common path interferometers. The interference fringes formed by DLMI in comparison to conventional Lloyd's mirror interferometer cover a large region [5]. This is a distinctive characteristic of DLMI. In the present study, the experimental analysis is done to assess the applicability of this interferometer in optical metrology.

2. Methodology

As compared to conventional Lloyd's mirror, there will be two sets of interference fringes in the case of DLMI. The first set of fringes is caused by the superposition of two portions of the geometrical wave, while the second set of fringes is generated by the superposition of two portions of the boundary diffraction wave. The overall intensity distribution at the sensor plane may be calculated as follows [3]:

$$\begin{aligned} I &= U(P) \times U(P)^{*} \\ &= \left| U^{(g)}(P) + U^{(g')}(P) + U^{(d)}(P) + U^{(d')}(P) \right|^{2} \end{aligned} \tag{1}$$

Here $U^{(g)}$ and $U^{(g')}$ are geometrical waves starting from focus and its virtual image formed by the Lloyd's mirror respectively, while $U^{(d)}$ and $U^{(d')}$ are boundary diffraction waves starting from the knife-edge and its virtual image respectively. According to equation (1), the interference fringes caused by the interference of two boundary diffraction waves change the intensity distribution of the fringes produced by the geometric Lloyd mirror interferometer in the region that is directly illuminated. On the other hand, in the geometrically shadowed area, only the fringes produced by the superposition of two boundary diffraction waves are produced.

3. Experimental Set-up

In the experimental set-up as shown in Fig.1, we used a coherent light source (He-Ne laser, wavelength 632.8nm, power 35mw). The light is expanded by a spatial filter assembly (microscopic objective of 40x, and a pinhole of 5 μm diameter). Further, this expanded light beam is collimated and focused to a point by using two biconvex lenses (with diameters of 100mm and focal lengths of 400mm). A knife-edge (high-quality razor blade) is positioned at the focus. To obtain the interference fringes, a front surface aluminium-coated plane mirror (Lloyd's mirror: 20mm X 50mm X 1mm) is placed at an appropriate distance and angle from the knife-edge and optical axis of the system. A CMOS sensor (resolution 1280×1024 pixels, 3.1μm ×3.1μm pixel pitch) is used to record the interferograms. The photograph of experimental setup is shown in Fig. 1 with a magnified view of the arrangement of knife-edge and Lloyd's mirror is presented in inset.

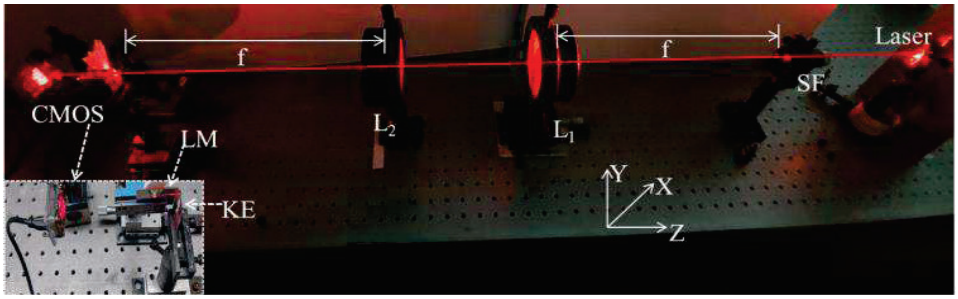

Fig.1 Photograph of experimental setup.

4. Results

We captured interferogram by placing knife-edge vertically, as illustrated in Figs. 1(inset). The knife-edge is positioned at the focal plane of L_2. Further, the Fourier transform method is used to analyse the phase of both interferograms that were captured digitally [6]. Using Goldstein's branch cut approach [2], the wrapped phase is unwrapped, and the unwrapped phase distribution is depicted in Fig. 2(c). The 3D map and 2D line profile represented in Figs. 2 (d) and 2 (e) are obtained using unwrapped phase distributions. These observations suggest that DLMI is suitable for testing of large objects as the interference fringes are present in geometrical direct and geometrical shadow region.

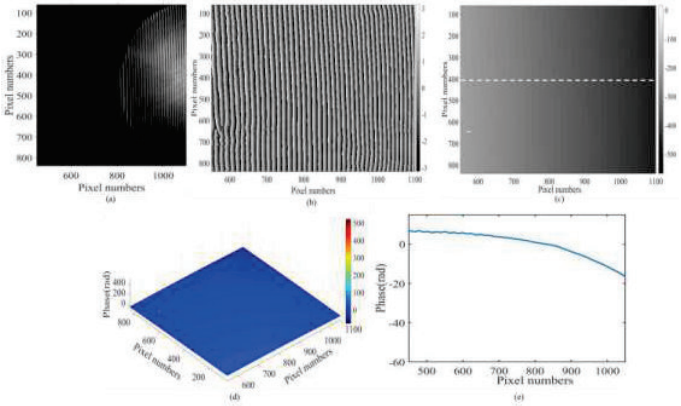

Fig.2 (a) Recorded interferogram when knife-edge is placed vertically at focus, and digitally obtained results: (b) wrapped phase distribution after using Fourier transform on recorded interferogram given in (a), (c) unwrapped phase distribution after applying Goldstein branch cut method on wrapped phase distribution, (d) 3-D map of unwrapped phase distribution, and (e) 2-D line profile along the dotted line given in (c)

5. Conclusion

In this work, we evaluated suitability of the common path "Diffraction Lloyd's mirror interferometer" for optical metrology of large objects. From the retrieved phase in the two-dimension as well as three-dimension, it is observed that both regions (direct illuminated and shadow regions) can be utilized to test large area.

Funding: This research work is financially supported by the CSIR, India under the project MLP-2014.

References

[1] P. Hariharan, Optical interferometry, (Academic Press, New York, 2003).
[2] D. Malacara, M. Servin, and Z. Malacara, Interferogram analysis for optical testing (CRC Press, Florida, 2005).
[3] R. Kumar, "Diffraction Lloyd mirror interferometer," J Opt **39**, 90-101(2010).
[4] M. Rani, A. Shankar, and R. Kumar, "Effect of quality of opto-mechanical components on fringes of diffraction Lloyd mirror interferometer," Results in Optics **8**, 100265 (2022).
[5] R. Kumar, "Straight, conic and circular fringes in single interferogram," Eur J Phys **36**, 025019(2015).
[6] M. Takeda, H. Ina, S. Kobayashi, "Fourier-transform method of fringe-pattern analysis for computer-based topography and interferometry," JOSA A **72**, 156(1982).

Dual stimuli control of Phonon Polaritons in α-MoO_3

Anjali Yadav[1,2,*], Shailendra K Varshney[2] and Basudev Lahiri[1]

[1]Nano Bio Photonics Group, [2]Fiber Optics, Nano & Quantum Photonics (FONQP) Group, Advance Photonics Laboratory, Department of Electronics and Electrical Communication Engineering, IIT Kharagpur, West Bengal,721302, India

**blahiri@ece.iitkgp.ac.in*

Abstract: We propose a van der Waals (vdWs) heterostructure to control in-plane anisotropic phonon polaritons of Molybdenum Trioxide by dual stimuli *i.e.* temperature and electrostatic potential.

Keywords: Phonon Polaritons, Tunable, Vanadium Dioxide, Graphene

1. Introduction

Newly discovered two-dimensional (2-D) materials have opened new paradigms in photonics research -- either alone or in conjugation with other materials forming vdWs heterostructures. Orthorhombic phase Molybdenum Trioxide (α-MoO_3) has gained much popularity amongst other 2-D polar materials simply because of its in-plane anisotropic response resulting from its different Mo-O bond length along the three crystalline direction ([100]-x, [001]-y and [010]-z) [1]. It supports Phonon Polaritons (PhPs), quasiparticles formed by the coupling of incident photons with lattice vibrations of MoO_3. Extreme subwavelength confinement, lossless high-wavevector (high-κ) modes and longer propagation distances are some of the key advantages of PhPs that allows their usage in emerging fields of mid-IR molecular sensing [2], thermal imaging [3] to name a few. However, these PhPs polaritons are intrinsic properties of specific material and can only exist in limited frequency range bounded by longitudinal and transverse optical frequency, often known as Reststrahlen Bands (RBs). Active tuning of such phononic response is highly desired for active polarization manipulation, directional control of light and other applications requiring frequency tuning. Various efforts for tuning hyperbolic response of MoO_3 has been demonstrated theoretically as well as experimentally by incorporating twists [4], air inclusions [5] and active materials like graphene [6], [7]. Also, phase change materials like Vanadium Dioxide (VO_2) have also been employed for achieving intensity and frequency tuning with changing temperature [8]. However, till date, a dual stimuli controlled propagation of MoO_3, has not been reported. Here, we show dynamic control of phonon polaritons in a vdWs heterostructure consisting of thin MoO_3 slab withVO_2 inclusions and graphene. By tuning the intrinsic hyperbolic response of MoO_3 to exhibit elliptical iso-frequency curves, we achieve temperature and electrostatically controlled propagation of anisotropic PhPs.

2. Design and Simulation Results

The proposed structure under study consists of MoO_3 slab of thickness 500 nm placed on a loss less substrate having refractive index (RI) of 1.5. To excite PhPs in MoO_3 slab, we use a vertically oriented dipole source placed 50 nm apart from the slab and all fields are collected at the top surface of MoO_3. Finite difference time domain (FDTD) simulation are carried out using Lumerical FDTD. We consider three different scenarios viz., MoO_3 slab only, VO_2 nanoparticles (NP) embedded in MoO_3, and single layer graphene on MoO_3 slab only. Refractive index of MoO_3 and VO_2 is taken from references [1], [9] and effective permittivity calculated from modified effective medium theory is then used for modelling MoO_3 with VO_2 NPs inclusions. VO_2 is assumed to be in form of spherical NPs and a filling

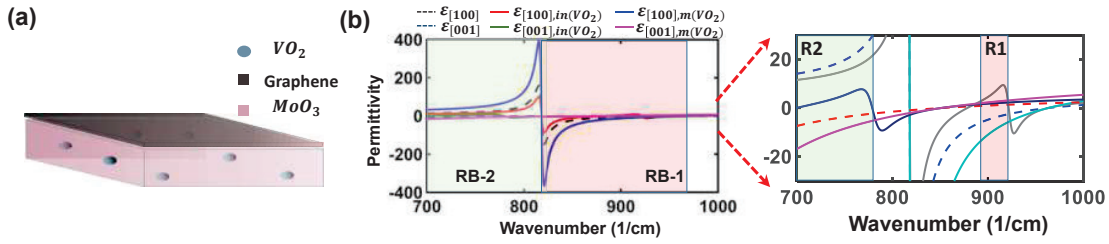

Fig. 1.(a) Schematic of the proposed structure, (b) permittivity of MoO_3 for various planes. Right side inset shows the shift in the RB band when VO2 NPs are embedded in the MoO_3

fraction (f) of 0.3. These values are chosen based on the fact that modified effective medium theory can be easily applied for $f \leq 0.3$ for polar materials [5]. Graphene being a 2D material is modelled as a conductive sheet whose response is tuned by varying Fermi potential. Figure 1(a) shows the schematic of MoO_3 slab with VO_2 NPs and graphene layer on top, excited by a dipole source. The real part of effective permittivity for in-plane crystalline direction ([100] and [001]) is plotted in Fig. 1(b) with VO_2 in insulating (in-VO_2) and metallic (m-VO_2) phase states along with permittivity of MoO_3 (alone, plotted with dashed line). It is observed that for in-VO_2, two regions (R1 and R2, marked by shaded region in inset of figure 1(b)) appears, which shows clear transition of the effective permittivity from being negative (for case of MoO_3 alone and with VO_2 metallic phase) to positive. Since, PhPs can propagate only when permittivity is negative, thus they confine or no longer propagates when VO_2 is in insulating phase. Figure 2 shows Electric field (E_Z) plots at the surface of slab for various cases, where the upper pane is dedicated to [100]

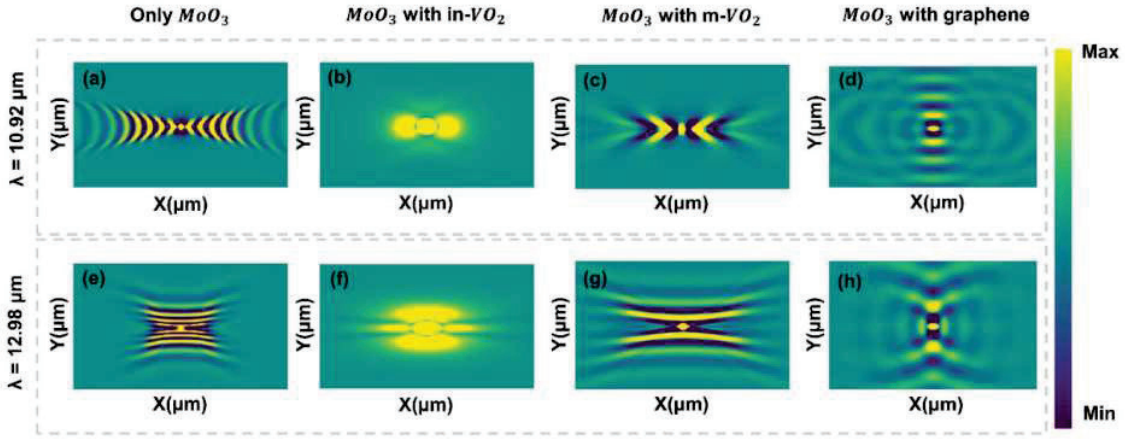

Fig. 2 Electric field plot E_Z (x-y plane) for various cases. (i) only MoO_3, (ii) MoO_3 with in-VO_2, (iii) MoO_3 with m-VO_2, and, (iv) MoO_3 with graphene at E_F=0.5Ev. Here, upper pane is for [100]-x and lower pane for [001]-y direction respectively.

and lower pane to [001] crystalline direction. It is seen that for MoO_3 alone and MoO_3 with m-VO_2, where the permittivity is negative PhPs propagates along their respective crystalline direction whereas for MoO_3 with in-VO_2, where permittivity is positive, PhPs are greatly confined at the center. Next, we include effect of graphene layer by taking its Fermi potential (E_F) equal to 0.5eV and find that PhPs can also be controlled by varying E_F (fig. 2(d) and (h)). It is seen that phonon polaritons propagate with elliptical wavefronts and thereby allowing wavefront tuning [6] as E_F increases. E_Z plots similar to MoO_3 (figure 2(a) and (d)) are obtained for E_F = 0eV.

To conclude, we have achieved dual stimuli control of phonon polaritons by utilizing phase transition of Vanadium Dioxide NPs embedded in the MoO_3 matrix when the temperature and electrostatic potential of a single layer graphene is varied.

3. References

[1] Z. Zheng *et al.*, "A mid-infrared biaxial hyperbolic van der Waals crystal," *Sci. Adv.*, vol. 5, p. eaav8690, May 2019, doi: 10.1126/sciadv.aav8690.

[2] B. Lahiri, A. Z. Khokhar, R. M. D. La Rue, S. G. McMeekin, and N. P. Johnson, "Asymmetric split ring resonators for optical sensing of organic materials," *Opt. Express*, vol. 17, no. 2, pp. 1107–1115, Jan. 2009, doi: 10.1364/OE.17.001107.

[3] P. Li *et al.*, "Hyperbolic phonon-polaritons in boron nitride for near-field optical imaging and focusing," *Nat. Commun.*, vol. 6, no. 1, p. 7507, 2015, doi: 10.1038/ncomms8507.

[4] M. Chen *et al.*, "Configurable phonon polaritons in twisted α-MoO3," *Nat. Mater.*, vol. 19, no. 12, pp. 1307–1311, 2020, doi: 10.1038/s41563-020-0732-6.

[5] M. C. Larciprete, S. A. Dereshgi, M. Centini, and K. Aydin, "Tuning and hybridization of surface phonon polaritons in \&\#x03B1;-MoO3 based metamaterials," *Opt. Express*, vol. 30, no. 8, pp. 12788–12796, Apr. 2022, doi: 10.1364/OE.453726.

[6] G. Álvarez-Pérez *et al.*, "Active Tuning of Highly Anisotropic Phonon Polaritons in Van der Waals Crystal Slabs by Gated Graphene," *ACS Photonics*, vol. 9, no. 2, pp. 383–390, 2022, doi: 10.1021/acsphotonics.1c01549.

[7] A. Yadav, R. Kumari, S. K. Varshney, and B. Lahiri, "Tunable phonon-plasmon hybridization in α-MoO3-graphene based van der Waals heterostructures," *Opt. Express*, vol. 29, no. 21, pp. 33171–33183, Oct. 2021, doi: 10.1364/OE.434993.

[8] S. Abedini Dereshgi *et al.*, "Tuning of Optical Phonons in α-MoO3–VO2 Multilayers," *ACS Appl. Mater. \& Interfaces*, vol. 13, no. 41, pp. 48981–48987, 2021, doi: 10.1021/acsami.1c12320.

[9] C. Wan *et al.*, "On the Optical Properties of Thin-Film Vanadium Dioxide from the Visible to the Far Infrared," *Ann. Phys.*, vol. 531, no. 10, p. 1900188, 2019, doi: https://doi.org/10.1002/andp.201900188.

Submicron Crack Detection on Thin Film using Digital Holographic Microscopy

Atul Kumar[1] and Anil Kumar Nirala[1*]

[1]Laser and Holographic Laboratory, Department of Physics,
Indian Institute of Technology, Dhanbad 826004, Jharkhand, India
**Corresponding author - aknirala@iitism.ac.in*

Abstract: Studies are being reported on digital holographic microscopy for submicron crack detection on cobalt ferrite ($CoFe_2O_4$) thin film. The proposed system can also measure the thickness of the thin film and the three-dimensional profile of the unwrapped phase of micro crack.

Keywords: Digital Holographic Microscopy, Thin film, micro crack, thickness

1. Introduction

Cobalt ferrite ($CoFe_2O_4$) thin film plays a significant role in the astounding development of solid-state electronics. It is suitable for various applications, including solar cells, energy storage devices, supercapacitors [1], and light-emitting diodes (LEDs). It can collect solar radiation called solar absorbers, which absorb and convert it into electrical energy. Sometimes thin film cracks affect the device's working, and these submicron size cracks may not be detected easily. Here, we have used the digital holographic microscopy (DHM) tool to detect these damages. DHM captures the amplitude and phase information simultaneously from the complex wavefront diffracted by an object [2]. One of the crucial advantages of the DHM is that it gives submicron range resolution and 3D phase information about the object. We can reconstruct the digital holograms using mathematical algorithms after recording the holograms [3].

2. Theory and reconstruction of digital holograms

The digital hologram $I(x,y)$ simultaneously collects the information of the object wave $E_O(x,y)$, and reference wave $E_R(x,y)$, which can be mathematically represented as,

$$I(x,y) = |E_O(x,y) + E_R(x,y)|^2,$$
$$I(x,y) = |E_O(x,y)|^2 + |E_R(x,y)|^2 + E_o^*(x,y)E_R(x,y) + E_O(x,y)E_R^*(x,y), \quad (1)$$

E_o^* and E_R^* are the complex conjugate of the E_O and E_R, respectively and (x,y) is the coordinate of the hologram plane.

Suppose (ξ,η), (x,y) and (ξ',η') are the coordinate system of the object plane, hologram plane and image plane, respectively. Thus, the reconstructed wavefield at the image plane (ξ',η') is obtained using Fresnel-Kirchhoff [4] integration as follows,

$$\Gamma(\xi',\eta') = \frac{i}{\lambda}\int_{-\infty}^{\infty}\int_{-\infty}^{\infty} E_R(x,y)h(x,y)\frac{\exp(-ik\rho')}{\rho'}\,dxdy, \quad (2)$$

where, λ is the wavelength of the laser, $k = \frac{2\pi}{\lambda}$, is the wave number.

Using the square of the wavefield, we can calculate the intensity,

$$I(\xi,\eta) = |\Gamma(\xi,\eta)|^2, \quad (3)$$

The phase profile can be obtained through complex amplitude and is given by,

$$\varphi(\xi,\eta) = \arctan\frac{\mathrm{Im}[\Gamma(\xi,\eta)]}{\mathrm{Re}[\Gamma(\xi,\eta)]}, \quad (4)$$

where, "Re" is the real part and "Im" is the imaginary part of the wave.

The height map h of the thin film can be obtained through its phase map φ and is given by,

$$h = \frac{\lambda\varphi}{2\pi n}, \quad (5)$$

where, λ is the wavelength of the laser beam and n is the thin film's refractive index.

3. Experimental setup

The schematic of the DHM system is shown in Fig. 1. A laser beam is divided by a beam splitter into the object beam (***O***) and reference beam (***R***). The reference beam enters into the microscope objective MO_2 resulting in a diverging wavefront. The object beam passes through the sample; then, it is collected by MO_1 and creates a diverging wavefront like the reference wavefront. The object and reference beam are re-combined at BS to form the interference pattern (hologram) and is recorded by the CCD camera. We have recorded the digital holograms with and without the thin film sample and reconstructed them in MATLAB to calculate the phase and amplitude values using the Fresnel-Kirchhoff method.

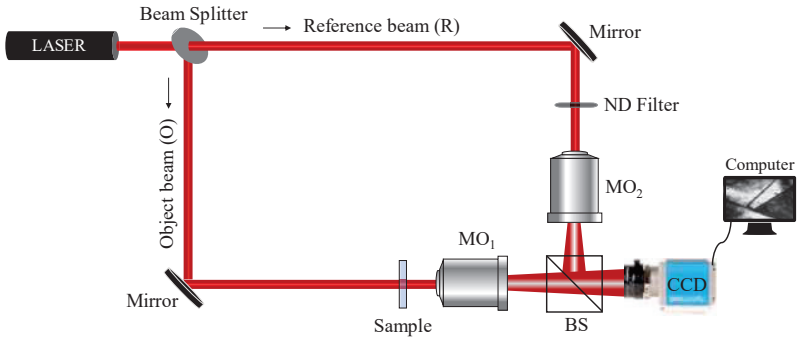

Fig. 1. Schematic representation of the off-axis DHM. *O*-object beam, *R*-reference beam, ND- neutral density filter, MO_1, MO_2 - microscope objectives, BS-beam splitter, CCD- charge-coupled device and PC- personal computer.

4. Results

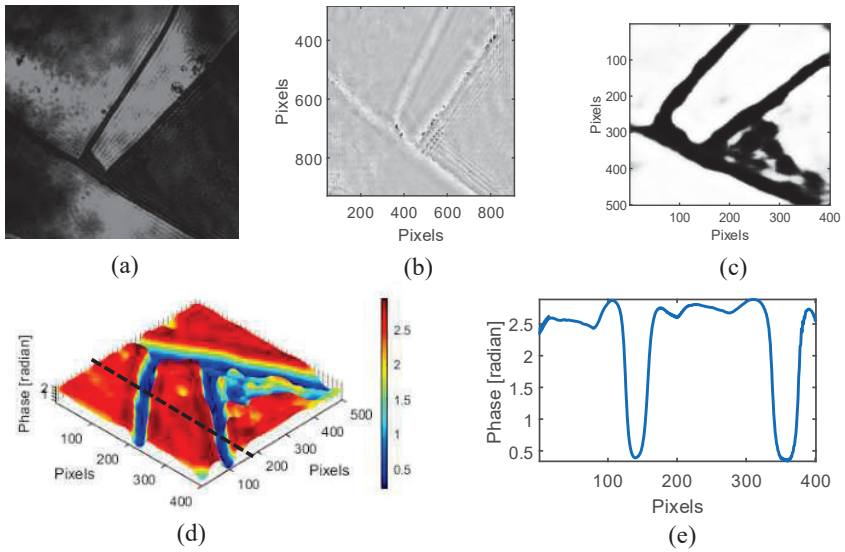

Fig. 2. (a) hologram of cracked region, (b) phase image, (c) subtract phase, (d) 3D plot of unwrapped phase and (e) line profile along the dotted line in (d)

The width of the crack is ~1 μm and thickness of thin film is ~250 nm. The cracks' width is mapped with the help of a USAF resolution microscope target and confirmed by FESEM measurement.

5. Conclusion

In this work, we have demonstrated a fast and non-contact DHM technique for detecting the submicron cracks on $CoFe_2O_4$ thin film and measured its thickness.

References

[1] He P, Yang K, Wang W, Dong F, Du L, Deng Y. Reduced graphene oxide-CoFe2O4 composites for supercapacitor electrode. Russian Journal of Electrochemistry 2013;49:359–64. https://doi.org/10.1134/S1023193513040101.

[2] Cuche E, Marquet P, Depeursinge C. Simultaneous amplitude-contrast and quantitative phase-contrast microscopy by numerical reconstruction of Fresnel off-axis holograms. Appl Opt 1999;38:6994. https://doi.org/10.1364/AO.38.006994.

[3] Kim MK. Principles and techniques of digital holographic microscopy. J Photonics Energy 2010:018005. https://doi.org/10.1117/6.0000006.

[4] Schnars U, Falldorf C, Watson J, Jüptner W. Digital Holography and Wavefront Sensing. Berlin, Heidelberg: Springer Berlin Heidelberg; 2015. https://doi.org/10.1007/978-3-662-44693-5.

Switchable higher order mode generation using a standard step-index fiber-based mode selective coupler

P. Sampathi*[1], S. Pidishety[2] and D. Karuna Sagar[1]

1. *Department of Physics, University College of Science, Osmania University, Hyderabad, Telngana-500 007, India*
2. *Optoelectronics Research Centre, University of Southampton, Southampton, SO171BJ, United Kingdom*

**Author e-mail address: sampath.pd@gmail.com*

Abstract: We present our experimental results on design and characterization of an all-fiber mode selective coupler using a standard step-index single mode and 4-mode fiber for generation of HOMs (TE_{01}, HE_{21}, TM_{01}). The special cascaded-coupler design not only simplifies the fabrication but also enables the wavelength modulated switchable generation of HOMs with ~96% coupling efficiency with negligible insertion loss.

OCIS codes: (060.2310) Fiber optics; (230.1150) All-optical devices

1. Introduction

Exploitation of the higher order modes (HOMs) in fiber has been great interest for last more than three decades due to their promising abilities for numerous applications [1–3]. Most of these applications, for instance optical communication, require the all-fiber means of switchable HOMs generating methods. Mode selective coupler (MSC) mechanism has been the only way forward to efficiently generate of HOMs via all-fiber methods as demonstrated in [4,5]. Most of these previous MSCs were designed using special fibers with complex index profiles to ensure not only generation of different type of HOMs but also propagate them with high modal purity [4,6,7]. However, fabrication of MSCs using such fiber is highly difficult and are efficiency limited. MSCs design with standard commercial fibers, yet with outstanding performance and switchable generation of HOMs is worth exploring and highly desired for the various application [1,2].

Here, we present our experimental results on design and characterization of a MSC using a standard step-index single mode (SMF) and 4-mode fiber (4MF) for generation of HOMs (TE_{01}, HE_{21}, TM_{01}). Further, we demonstrate a wavelength modulated switchable excitation of HOMs via a special cascaded-coupler design. The selection of 4MF fiber not only simplifies the fabrication complexity, but also generates stable HOMs with high coupling efficiency of ~96% and with negligible insertion loss. The spatial polarization of generated HOMs measured via Stokes measurements, further confirms the mode switching ability of the device.

2. Mode selective coupler (MSC) fabrication

A standard step-index fiber (25 /125 µm, NA 0.12, FS Inc. call no. 35275) that supports 4-modes, including HE_{11} and TE_{01}, HE_{21}, TM_{01} HOMs, and a standard SMF-28 (Thorlabs Inc.) at 1550 nm wavelength were used to fabricate a MSC and optimize the coupler parameters to excite switchable HOMs. The index profile (shown in Fig. (b)) of selected 4MF possesses the sufficient index separation (in the order of $\Delta n_{eff} \sim 10^{-4}$) between the supporting HOMs so that modes do not couple each other after they get excited. Since the degeneracy between the different polarized modes is removed, selective excitation and stability of generated HOMS can be achieved.

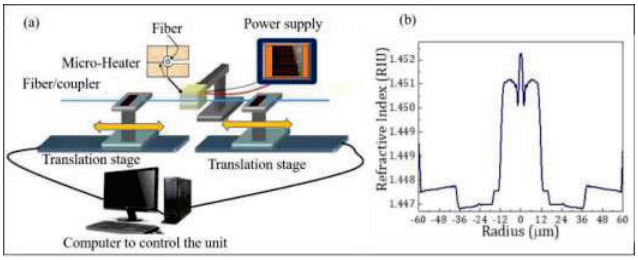

Figure 1: (a): Schematic representation of coupler fabrication tapering-rig. (b): Refractive index profile of selected 4MF.

The effective index (n_{eff}) of the HE_{11} in the SMF is different from that of HOMs in the 4MF fiber. Thus, selected modes must be phase matched, which is studied using COMSOL Multiphysics® eigenmode solver and found out the tapering ratio ($\rho = r_{SMF}/r_{4MF}$) of selected fibers [4,6]. First, SMF was adiabatically pre-tapered at ~1400°C to a radius that is calculated based on the simulations, using the tapering rig shown in Fig.1 (a). The pre-tapered SMF

was longitudinally aligned with the un-tapered, straight 4MF fiber without any twists, as previously reported in [4,6]. The degree of fusion is optimized to obtain a multi-cascaded fused coupler and the HE_{11} mode in the SMF couples into a selected HOMs in the 4MF to which it is phase matched [4,6]. The tapering and fusing was stopped when the power measured out of the 4MF fiber was maximized, which is measured to be ~96%. The fabricated coupler was carefully packed and characterized further as explained below.

3. Results and discussion

Unpolarized light from a tunable 1550-nm laser source was launched into the SMF input port of the coupler (Fig. 2(a)). The SMF was subjected to circular bends to strip out if any higher order mode present before the fused region of the device. The output beam from the 4MF fiber was collimated using an appropriate lens and the field patterns were imaged using a CCD camera. Fig. 2(b) shows a clear doughnut pattern out of the 4MF fiber port, as a function of tuned wavelength, when the polarizer is not present in the beam path before the camera. The doughnut intensity distribution qualitatively suggests that the input HE11 mode substantially coupled to the target HOMs. Further ,the wavelength of the source has been turned to three (1550, 1552.5 and 1555 nm) different wavelengths and the polarization of the output beam is analyzed as reported in [6].

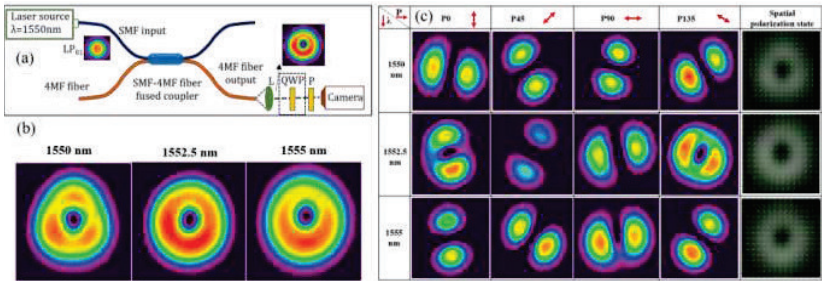

Figure 2: (a): Experimental setup for characterizing the coupler. Intensity profile of different modes out of the mode selective coupler (b), and corresponding characteristic profiles for different analyzer angles (c), as a function of tuned wavelength: The measured spatial polarization of generated modes is shown in the end column (c).

A polarization analyzer was inserted in the path of the free-space collimated beam to analyze its polarization state. The appearance of the dark line across the beam cross section, after passing through the polarizer suggests that the polarization state of the generated beams is inhomogeneous. Further rotation of analyzer axis through 0-135$_o$ at selected discrete angles, the two-lobed field pattern on the CCD also rotated along the same rotation direction. The intensity patterns as a function of different polarization azimuth, as a function of wavelength have been shown in Fig. 2 (c). The observed intensity CCD image profiles confirms that the generated beams possess different polarization at different wavelengths, as the lobe pattern is different for different polarizer axis for all the selected wavelengths. Further, rigorous polarization analysis through the Stokes polarization measurements reveals that the polarization of generated HOMs of TE_{01}, HE_{21}, TM_{01} kind, as shown in end column-Fig. 2 (c). moreover, the changing structure of spatial polarization of the modes as a function of input tuned wavelength, further confirms the switching of the generated modes. Further analysis on the purity of polarization and tunable limit is in progress and will be presented during the conference and reported elsewhere.

A switchable generation of HOMs (TE_{01}, HE_{21}, TM_{01}) via a simple mode-selective coupler design using a standard step-index single mode (SMF) and 4-mode fiber (4MF) is demonstrated. The special cascaded-coupler design enables the wavelength modulated switchable generation of HOMs with ~96% efficiency while keeping the fabrication simple. Such simple and highly efficient, yet with outstanding performance, all-fiber based devices are highly potential for various application such as optical communication, particle manipulation and modes switching.

3. References

1. S. Ramachandran and P. Kristensen, "Optical vortices in fiber," nanoph **2**(5–6), 455–474 (2013).
2. Y. Shen, S. Pidishety, I. Nape, and A. Dudley, "Self-healing of structured light: a review," J. Opt. **24**(10), 103001 (2022).
3. S. Zhu, S. Pidishety, Y. Feng, S. Hong, J. Demas, R. Sidharthan, S. Yoo, S. Ramachandran, B. Srinivasan, and J. Nilsson, "Multimode-pumped Raman amplification of a higher order mode in a large mode area fiber," Opt. Express, OE **26**(18), 23295–23304 (2018).
4. S. Pidishety, S. Pachava, P. Gregg, S. Ramachandran, G. Brambilla, and B. Srinivasan, "Orbital angular momentum beam excitation using an all-fiber weakly fused mode selective coupler," Opt. Lett., OL **42**(21), 4347–4350 (2017).
5. R. Ismaeel, T. Lee, B. Oduro, Y. Jung, and G. Brambilla, "All-fiber fused directional coupler for highly efficient spatial mode conversion," Optics Express **22**(10), 11610 (2014).
6. S. Pidishety, B. Srinivasan, and G. Brambilla, "All-Fiber Fused Coupler for Stable Generation of Radially and Azimuthally Polarized Beams," IEEE Photonics Technology Letters **29**(1), 31–34 (2017).
7. P. Gregg, P. Kristensen, and S. Ramachandran, "Conservation of orbital angular momentum in air-core optical fibers," Optica, OPTICA **2**(3), 267–270 (2015).

Optical nonreciprocity in a rotating microcavity

Kousik Mukherjee, Anjan Samanta, Paresh Chandra Jana
Department of Physics, Vidyasagar University, Midnapore, 721101, India
e-mail:kousikmukherjee89@gmail.com

Abstract: Optical nonreciprocity in a two-mode rotating semiconductor micro-cavity with second order nonlinearity is analyzed in detail. The probe response is studied when the cavity is driven from its left and right sides. The transmission spectra exhibit nonreciprocal behavior. The absorption profile shows double transparency window symmetrically placed around zero probe detuning when the cavity is driven from its right. The dispersion profiles reveal both anomalous and normal behavior. The non-reciprocity is also explained by delay time-bandwidth product according to Lorentz reciprocity theorem. The figure-of-merit strongly depends on cavity quality factor and hopping strength. Our study may offer applications in ultrafast signal processing and motion sensing.

Keywords: Non-reciprocity, Sagnac-Fizeau shift, Induced transparency.

1. Introduction

Nonreciprocal optical devices have acquired a lot of attention due to their wide range of potential applications in communication and signal processing, optical isolators and circulators [1]. These are allowing the light from one side and blocking it from the other. Here, we consider a rotating semiconductor microcavity. A rotating cavity experiences a Sagnac-Fizeau shift as a result the input light introducing from one side is on resonance and the light field introducing from other side is off resonance. Hence there is a possibility of nonreciprocal transmission of the optical field in present system.

2. The system Hamiltonian

Consider a rotating cavity system where the optical cavity consists with second order nonlinearity. The model Hamiltonian is given by $H = H_o + H_I$ where $H_o = \omega_a a^\dagger a + \omega_b b^\dagger b$ denotes the free evolution of the optical system with bosonic lowering operators a and b. a mode is related to the fundamental mode with field mode frequency ω_a and b mode is the second harmonic mode with field mode frequency ω_b, respectively. The second part of the Hamiltonian H_I indicates the interaction between the cavity field modes, which can be expressed as $H_I = g(ba^{\dagger 2} + b^\dagger a^2)$, where g denotes the photon hopping strength. The hopping strength related to nonlinear term $g = \sqrt{\frac{\hbar\omega_a}{2\epsilon_0 n_a^2 V_a}}\frac{\omega_b}{2n_b^2 V_b}\int dv\ \chi^{(2)}_{ijk}(r)E^i_a(r)E^j_b(r)E^k_b(r)$ where $\chi^{(2)}_{ijk}(r)$ denotes the second-order nonlinear susceptibility tensor, $E_{a,b}(r)$ is the spatial part of the optical field mode and satisfies the normalization condition $\int dr\left|E_{a,b}(r)\right|^2 = 1$ and $n_{a,b}$ are number of photons of the field modes. Second order nonlinearity provides the conversion of a photon of the field mode a to two photons of the field mode b or vice-versa. The optical cavity with second order nonlinearity composed of III-V semiconductors. These III-V semiconductors are basically non centro-symmetric materials. The materials are such as AlGaAs, AlGaN, GaAs, GaN, BN and AlN. The hopping strength between the field modes depends on the used III-V semiconductor material in the optical cavity. The typical value of the resonance frequency of the fundamental mode $\omega_a = 2\pi \times 163.195$ THz and the quality factors of the field modes are $Q_a = 1.6 \times 10^4$ and $Q_b = 3.2 \times 10^4$, respectively. The value of hopping strength is $\hbar g \approx 0.02$ mev [2, 3].

If a cavity rotates at a rotational speed ω_r , the light circulating in the resonator experiences a frequency shift termed as Sagnac-Fizeau shift and the cavity resonance frequency modifies as $\omega_k \rightarrow \omega_k + \Delta_{SF_k}$. The amount of shift is expressed as $\Delta_{SF_k} = \pm\frac{nr\omega_k\omega_r}{c}\left(1 - \frac{1}{n^2} - \frac{\lambda}{n}\frac{dn}{d\lambda}\right)$ where $k = a, b$; n denotes the refractive index, r indicates the radius of the cavity [4]. The rotational speed of the rotation of the optical cavity may vary from few Hz to several GHz, as reported in different experimental works [5]. The amount of shift directly depends on the rotational speed of

the cavity and also the direction of driving. The shift is negative or positive according to the external input light propagating along or against the direction of rotation i.e. the optical cavity is driven from its right and left, respectively. The eigenvalue equation of the Hamiltonian is written as $H|\Psi_i\rangle = E_i|\Psi_i\rangle$, where $i = 0, 1, 2, \ldots$. E_i denotes the eigen energy of ith state for the non-rotating cavity system. The eigenstates are $|\Psi_i\rangle$ and can be written in terms of Fock state $|n_a, n_b\rangle$, n_a and n_b represent the number of photons in the field modes a and b, respectively. The eigenenergies are modified by the term $\pm i\hbar|\Delta_{SF}|$ due to rotation of the cavity, where $\pm$ denotes to upper and lower shift of the energy w.r.t. E_i , respectively. The angular speed of rotation of the cavity follows the condition $|\Delta_{SF}| = g/2\sqrt{2}$.

The cavity is driven by a moderate control field and a weaker probe field. In presence of driving and considering the Sagnac-Fizeau shift, the system Hamiltonian [1, 3] can be written as

$$H_r = (\Delta + \Delta_F)a^\dagger a + 2(\Delta + \Delta_F)b^\dagger b + \xi(a^{\dagger 2}b + b^\dagger a^2) + i\Omega(a^\dagger - a) + i\Omega_p\left(a^\dagger e^{-i\Delta_p t} - ae^{i\Delta_p t}\right) \quad (1)$$

where $\Delta = \omega_a - \omega_L$ is the frequency detuning of a mode and $\Delta_p = \omega_p - \omega_L$ is probe detuning. According to second harmonic generation $\omega_b = 2\omega_a$, we consider $\Delta_{SF_a} = \Delta_F$ then $\Delta_{SF_b} = 2\Delta_F$. The system Hamiltonian is solved by using Heisenberg-Lagevin equation of motion and also using standard input-output relation, we calculate the amplitude of the output field with respect to the input probe field, transmission rate of the probe field, phase of the transmitted field and group delay. All these are studied under different experimentally achievable system parameters and discussed the results.

3. Results and Discussions

In this section, we have discussed the nonreciprocal transmission in a rotating micro-cavity. The absorption and dispersion properties of the amplitude of the output field are illustrated in detail using experimentally realizable parameters. Figure 1 (a) depicts the variation of the transmission rate as a function of normalized probe detuning and which indicates that complete transmission of the probe field when the cavity is driven from its right. No transmission of the probe field is occurred when the cavity is driven from its left. This confirms the transmission is nonreciprocal. This is also explained via energy level diagram. The phase variation of the probe pulse is shown in figure (b), this confirms that the possibility of both the anomalous and normal dispersion around zero probe detuning. To illustrate the group delay of the probe pulse, we plot the delay time as a function of probe detuning as depicted in figure (c). It is interesting to analyze the nonreciprocity by delay time-bandwidth product according to Lorentz reciprocity theorem [6]. Our representation successfully satisfies this theorem and the transmission is nonreciprocal. The delay time-bandwidth product and hence the figure-of-merit strongly depends on hopping strength and cavity quality factor.

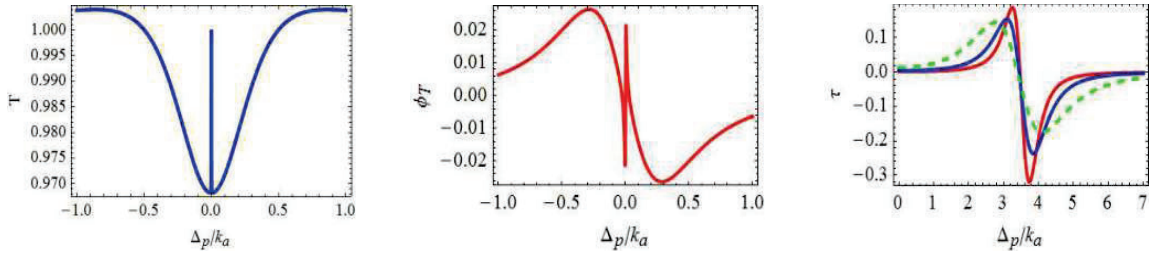

Fig. 1: Plot of transmission rate (T), phase (φ_T) and delay time (τ) as a function of probe detuning.

In conclusions, our study confirms that the present system shows that the transmission is nonreciprocal which may be used to steer optical transmission in quantum information processing. The phase variation indicates that the dispersion-enhanced light drag can be controlled by frequency detuning. This is useful for motion sensing.

4. References

[1] W. T. M. Irvine et al, "Strong coupling between single photons in semiconductor microcavities", Phys. Rev. Lett. 96, 057405 (2006).

[2] N. A. Sanford et al, "Measurement of second order susceptibilities of GaN and AlGaN", J. App. Phys. 97, 053512 (2005).

[3] K. wang, Q. Wu, Y. F. Yu, Z. M. Zhang, "Nonreciprocal photon blockade in a two-mode cavity with second-order nonlinearity", Phys. Rev. A 100, 053832 (2019).

[4] G. B. Malykin, The Sagnac effect: correct and incorrect explanations, Phys. Usp. 43, 1229 (2000).

[5] K. Mukherjee and P. C. Jana, "Probe response of a two-mode cavity with $x^{(2)}$ nonlinearity, non-reciprocity and slow and fast light", App. Phys. B 127, 168 (2021).

[6] K. L. Tsakmakidis et al, "Breaking Lorentz reciprocity to overcome the time-bandwidth limit in physics and engineering", Science 356, 1260-1264 (2017).

Rapid detection of microplastics in water using Raman Spectroscopy

Meenakshi[#a], Sathi Das[a], Anjika[a], Kanchan Saxena[b] and Dalip Singh Mehta[*a]

[a]*Bio-photonics and Green Photonics Laboratory, Department of Physics, Indian Institute of Technology Delhi, Hauz-Khas, New Delhi-110016, India.*

[b]*Amity Institute of Renewable and Alternative Energy, Amity University, Sector 125, Noida, UP, India*

*mehtads@physics.iitd.ac.in, #meenakshisingh2997@gmail.com

Abstract: Plastics are one of the most widely used materials in human life. Due to their rigorous use in daily life, the proliferation of tiny plastic particles, called microplastics, has become an emerging pollutant, causing significant concern worldwide. Microplastics severely threaten the environment, including flora, fauna, and human health. Raman Spectroscopy is a molecular fingerprinting and sensitive technique for distinguishing microplastics, their polymers, and any other form of toxic contaminants. We have detected different microplastics considering two different excitation lasers using Raman spectroscopy. A comprehensive study shows the dependance of specific strength and weakness for a particular bond length on excitation laser.

Keywords: Microplastics, Raman Spectroscopy, Water.

1. Introduction:

Over the last few decades, global awareness of plastic pollution in marine life has rapidly increased. Plastics in the environment result from various sources, including improperly managed plastic waste, plastic pellets, personal care products, microbeads, and commercial activities. Plastics are degraded into smaller particles as microplastics start to accumulate in the marine environment [1]. Microplastics are defined as plastic particles that are less than 5 mm but greater than 0.1mm. They can directly originate from primary sources, like microbeads, or from secondary sources by breaking down larger plastic particles into smaller ones at micron and nanoscale levels [2]. Their size is their primary concern. Because of their tiny size, they have a greater negative impact on the environment, are transported throughout the oceans, including the deep sea, and are exceptionally simple to incorporate into the food chain of other organisms. Seven types of microplastics are commonly found: Polyethylene (PE), Polypropylene (PP), Polyethylene terephthalate (PET), Polyvinyl chloride (PVC), low-density polyethylene (LDPE), high-density polyethylene (HDPE), and there are several other microplastics that can also be found in sediments and marine environments, such as PMMA, Polyamide, Nylon, polyester, and acrylic [2].

Raman spectroscopy has been successfully used to identify microplastic particles in different sections of the marine environment due to its high spatial resolution, wider spectral coverage, high sensitivity towards non-polar functional groups, and lower water interference [3]. The Raman spectra of two distinct microplastics, PVC (polyvinyl chloride) and PMMA (polymethyl methacrylate), were obtained in this study utilizing two different excitation lasers with wavelengths of 532 nm and 785 nm. The stability of the spectra was checked by varying incident laser power.

2. Methodology:

The Raman spectrometer of Renishaw in Via (50X MO) confocal Raman microscope was used to collect the spectra. PVC (Polyvinyl chloride) and PMMA (polymethyl methacrylate) are two different types of microplastics which are found in water. We have taken PVC and PMMA in powdered form and make a solution of 0.1g of sample into 20 mL of DI water and kept it overnight. After 24 hours a drop of solution is dropped on the glass slide and Raman Spectrum was taken using two different excitation laser wavelengths of 532 nm and 785 nm, respectively.

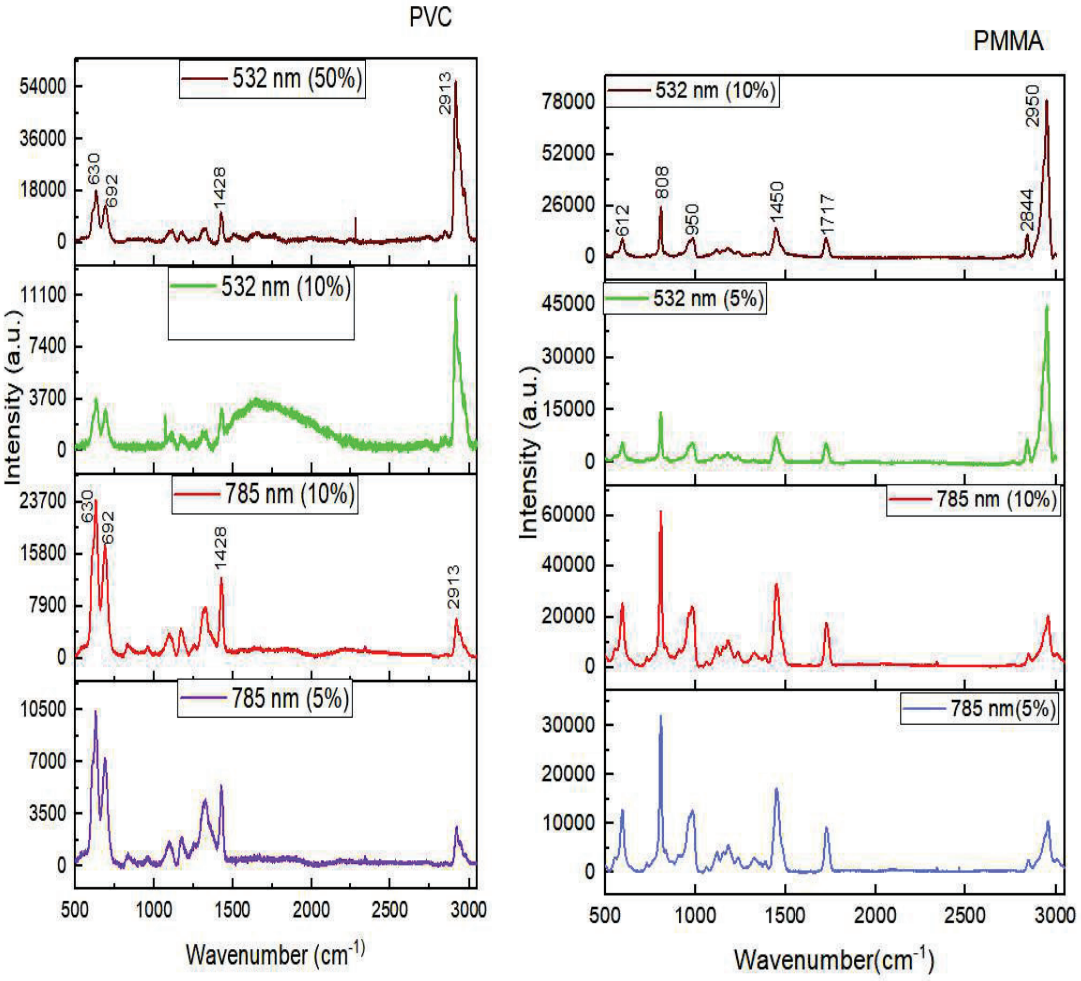

Figure 1: (a) and (b) are the Raman Spectra of PVC and PMMA with different laser source and laser power.

3. Results and discussion:

The Raman spectra of PVC and PMMA are shown in Figure 1 (a), and Figure 1(b), respectively. For PVC, CH_2 stretching shows Raman active bond at 2914 cm^{-1} and C-Cl stretching is attributed at 638 and 694 cm^{-1}. For PMMA, The Raman peak at 1081 cm^{-1} is due to C-C stretching, peaks at 2848 and 2957 cm^{-1} are attributed to O-CH_3, Raman peaks at 602, 1264 and 1736 cm^{-1} show the stretching of C=O and its overtones. The several other small peaks are due to additives, dyes and plasticizers added into the sample.

References:

[1] Nava, V., Frezzotti, M.L. and Leoni, B., 2021. Raman spectroscopy for the analysis of microplastics in aquatic systems. *Applied Spectroscopy*, *75*(11), pp.1341-1357.

[2] Schymanski, D., Goldbeck, C., Humpf, H.U. and Fürst, P., 2018. Analysis of microplastics in water by micro-Raman spectroscopy: release of plastic particles from different packaging into mineral water. *Water research*, *129*, pp.154-162.

[3] Hilbk-Kortenbruck, F., Noll, R., Wintjens, P., Falk, H. and Becker, C., 2001. Analysis of heavy metals in soils using laser-induced breakdown spectrometry combined with laser-induced fluorescence. *Spectrochimica Acta Part B: Atomic Spectroscopy*, *56*(6), pp.933-945.

Optical Characterization of Single Sprouted Potato-shaped Au-Ag Bimetallic Nanoparticles Using a Dark-field Microscope

Sibanisankar Sahoo and Venkata Ramanaiah Dantham*

Department of Physics, Indian Institute of Technology Patna, Bihar 801103, India

**Corresponding author: dantham@iitp.ac.in*

1. Abstract

Recently, sprouted potato-shaped Au-Ag bimetallic nanoparticles are found to be efficient for single molecule SERS. To optimize the SERS enhancement, there is a necessity to know the localized surface plasmon resonance wavelength of single bimetallic nanoparticles, and it can be extracted by recording their scattering spectra using a dark field microscope. Herein, we report the scattering spectra and images of the single sprouted potato-shaped Au-Ag bimetallic nanoparticles synthesized using the wet-chemistry method.

Keywords: Au-Ag nanoparticles, Localized surface plasmon resonance, Dark-field microscope, SERS

2. Introduction

In the last decade, metal nanoparticles are found useful for several applications such as surface-enhanced fluorescence and Raman scattering, label-free biosensing, non-linear optics, light harvesting, photodetection, photocatalysis, high-density data storage, optoelectronics, optical tweezers, etc [1,2]. In all these applications, the local field enhancement (field enhancement at hotspots) of the nanoparticles plays an important role, and the enhancement is expected to be optimum when the excitation wavelength of the light matches with the localized surface plasmon resonance (LSPR) wavelength [3]. Therefore, to optimize the signal-to-noise ratio (S/N) in the above-mentioned applications, there is a necessity to find the LSPR wavelength of the metal nanoparticles. In general, the quasi-static theory [4], Lorenz-Mie theory [5], and Aden-Kerker theory [6] can be used to estimate the LSPR wavelength of symmetric nanoparticles such as nanospheres, nanoshells, and nanoellipsoids. On the other hand, some numerical methods such as FDTD, DDA, and FEM can be used for asymmetric nanoparticles [7]. It is important to note that it is not feasible to model and performs the simulations on complex-shaped nanoparticles. However, the LSPR wavelength of complex-shaped nanoparticles can be estimated by recording either absorption or scattering spectra of these nanoparticles experimentally.

The dark field microscope helps us study the optical properties of single metal nanoparticles. Recently, we have found that sprouted potato-shaped Au-Ag bimetallic nanoparticles are found efficient for single molecule surface-enhanced Raman scattering (SERS). The SERS enhancement achieved using these nanoparticles is estimated as 10^9 [8]. In order to optimize the enhancement, we have studied the scattering properties of single bimetallic nanoparticles for the first time using a dark field microscope. In addition, the scattering properties of single monometallic nanoparticles are studied for comparison.

3. Synthesis and characterization of Au-Ag bimetallic nanoparticles

The Au-Ag bimetallic nanoparticles were prepared with the wet chemistry method reported by William et al [8]. A brief description of the synthesis procedure used in the present study is given below. The gold chloride ($HAuCl_4$) and silver nitrate ($AgNO_3$) solutions were prepared separately at 10 mM concentration each. At first, these solutions were added together in 1 ml of de-ionized water in the 10:7 ratio. After this, 4 µl of ascorbic acid of 100 mM was added quickly and kept the solution stable for nucleation growth. Within a few seconds, the colorless solution was converted into intense blue, indicating the formation of Au-Ag bimetallic nanostructures. During the reaction, Au^+ ions were first reduced to Au due to its higher reduction potential than Ag. Then Ag^+ gets reduced and gets deposited over the surface of Au and sorts active sites for the growth process. Therefore, the variation in thereafter synthesizing the nanoparticles, their morphology was studied using a field-emission scanning electron microscope, and most of the bimetallic nanoparticles were found to have the sprouted potato shape.

4. Scattering images and spectra of single mono and bimetallic nanoparticles

First, the commercial Au nanoparticle solution was drop-casted on the clean microscopic glass slide and focused the white light from the Halogen lamp tightly using a dark field condenser. Several elastic scattering images and spectra were recorded using a color CCD camera and high sensitivity spectrometer. Panel (a) of Figure 1 shows scattering images of Au nanoparticles. From this figure, it is clear that most of the nanoparticles appear in greenish yellow. Panel (b) shows the scattering images of several Au-Ag nanoparticles. From this figure, it is apparent that the color of nanoparticles is changed significantly. This could be due to the change in the shape and dielectric function in the presence of Ag. Panel (a) of Figure 2 shows the scattering spectrum of a single Au nanoparticle. In this spectrum, only dipole mode is observed at around 582 nm, and it is probably due to the small size of the nanoparticle. The spectrum shown in the inset of Panel (a) of Figure 2 has two peaks that represent the dipole and quadrupole modes. Panel (b) of Figure 2 shows the typical scattering spectrum of single Au-Ag bimetallic nanoparticles. In this image, only dipole mode is observed at around 674 nm, and it is probably due to the small size of the nanoparticle. The spectrum shown in the inset of Panel (b) of Figure 2 has two peaks that represent the dipole and quadrupole modes. From these two panels, we can conclude that (i) LSPR wavelength and (ii) full width at half maximum (FWHM) of the resonance peaks are significantly different in the case of small monometallic and bimetallic nanoparticles.

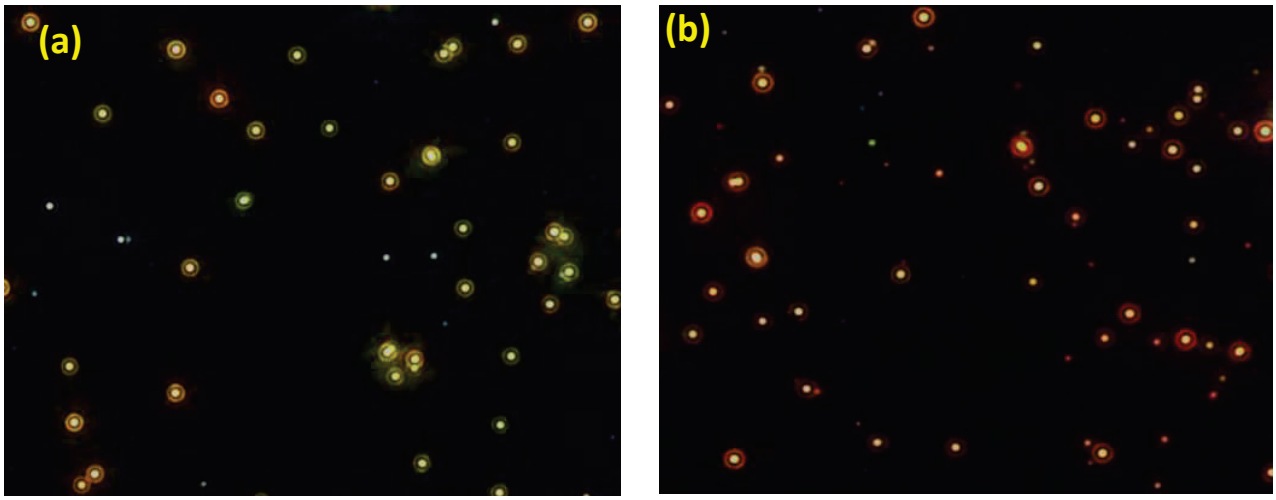

Figure 1. *Panels (a) and (b) represent the dark field microscopic images of Au nanoparticles and Au-Ag bimetallic nanoparticles, respectively.*

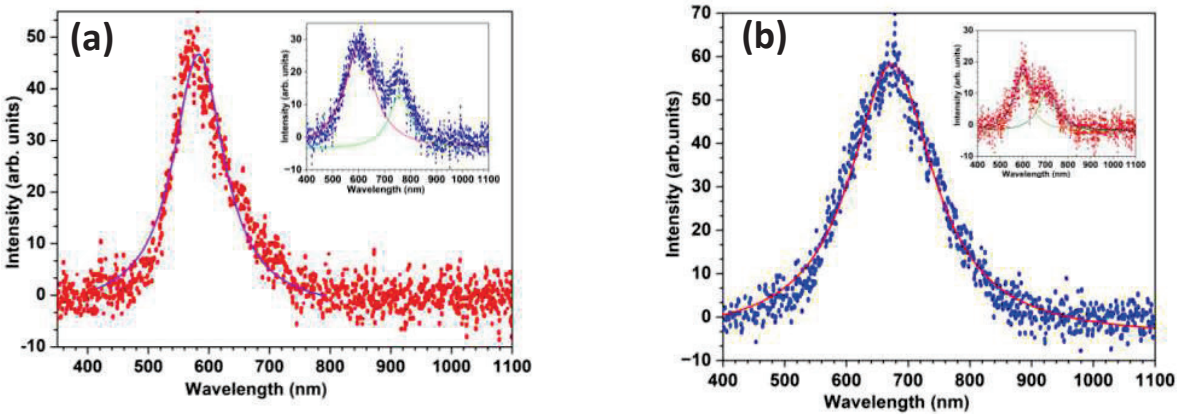

Figure 2. *Panels (a) and (b) show the scattering spectra of a single Au nanoparticle and Au-Ag bimetallic nanoparticle, respectively. Insets in these panels represent the spectra of larger nanoparticles.*

5. Conclusions

The sprouted potato-shaped Au-Ag bimetallic nanoparticles are synthesized and characterized using appropriate tools. The scattering spectra and images of these nanoparticles are recorded using a dark-field microscope. It is observed that the LSPR wavelength and FWHM of the scattering spectra are found different in the case of bimetallic nanoparticles as compared with Au nanoparticles.

6. References

[1] V. Klimov, Nanoplasmonics, Jenny Stanford Publishing, (2014).

[2] H. Masuhara, S. Kawata, Nanoplasmonics: From fundamentals to applications, Elsevier, (2006).

[3] P. Tiwari, G. M. Das, V. R. Dantham, "Optical Properties of Au-Ag Bimetallic Nanoparticles of Different Shapes for Making Efficient Bimetallic-Photonic Whispering Gallery Mode Hybrid Microresonators", Plasmonics **15**, 1251–1260 (2020). https://doi.org/10.1007/s11468-020-01141-7

[4] S. Priya, A. Mandal, V. R Dantham, "Indium nanoparticle-based surface enhanced fluorescence from deep ultraviolet to near-infrared: A theoretical study", Spectrochim. Acta A Mol. Biomol. Spectrosc. **267**, 120603 (2021).

[5] J.R.Frisvad, N. J. Christensen, H. W. Jensen, "Computing the Scattering Properties of Participating Media Using Lorenz-Mie Theory", SIGGRAPH (2007).

[6] A. Mandal, V. R. Dantham, "Short and elongated photonic nanojets emerged from single solid/hollow core-shell microparticles illuminated by focused Gaussian beams and plane wave", J. Quant. Spectrosc. RA **257**, 10735 (2020).

[7] S. Sheikholeslami, Y. W. Jun, P.K.Jain, A.P.Alivisatos, "Coupling of optical resonances in a compositionally asymmetric plasmonic nanoparticle dimer". *Nano Lett*., **10**, 2655–2660 (2010).

[8] T. Mahata, G. M. Das, V. R. Dantham, "Study of surface enhanced Raman scattering of IR-780 Iodide molecules using Au-Ag bimetallic nanostructures with blunt and sharp sprouts", Spectrochim. Acta A Mol. Biomol. Spectrosc. **249**,119262 (2021).

A Study of Methods to Find Non-Hermitian Exceptional Points in Photonics

Mukund B.[*], Balasubramanian M.[#] and Prasant Kumar Pattnaik
Department of Electrical and Electronics Engineering,
Birla Institute of Technology & Science, Hyderabad Campus, Hyderabad, India.
Author E-mail addresses:
(h20211240068@hyderabad.bits-pilani.ac.in)[*],(balasubramanian@hyderabad.bits-pilani.ac.in)[#]
,(pkpattnaik@hyderabad.bits-pilani.ac.in)

Abstract: In this paper, we investigate the implementation of non-Hermitian eigensolvers for photonic structures using MATLAB without having to consider the availability of stable electromagnetic eigensolvers in commercially available simulation software or specialized optimisers. Special eigenvalue solutions characterized by the coalescence of two repulsive energy levels results in a special degeneracy called Exceptional Point, which gives desirable characteristics such as improved sensitivity and a real-valued spectral response for a non-Hermitian sensing system. Several numerical approaches have been proposed to solve the problem of Non-Hermitian eigenvalues and each of their costs and benefits are analyzed here when implemented for practical photonics structures.
Keywords: Exceptional points, non-Hermitian eigensolver, PT-symmetry, FEAST , Schur decomposition

1. Introduction

In quantum mechanics, systems are modeled around Hermitian observables and are often solved using a characteristic equation of a linear operator known as the Hamiltonian H, represented in matrix form as given by equation (1). The solution for δ gives the eigenvalues of the system.

$$|\delta I - H| = 0 \qquad (1)$$

However, real physical structures consist of dispersive and lossy materials whose perturbation effects have to be accounted for, involving structuring the system as non-Hermitian. In the analysis of these systems, the behavior of degeneracies such as exceptional points is of particular interest as they often correspond to an extremum in the behavior of the system. We seek to take advantage of the results of such applications such as sensing, where best system sensitivity can be observed at degeneracies known as exceptional points. Exceptional points are singularities in a system that are degeneracies at the coalescence of two repulsive levels or eigenmodes. They are complex in nature, especially a pair of complex conjugates in the case of a system represented with a 2D Hermitian Hamiltonian. In photonics engineering, they are characterized by specific eigenvalues of systems which are parameterised in terms of optical gain, coupling, losses, attenuation or distribution of an optical index. These eigenvalues can be represented as solutions of a system $H = H_0 + \lambda H_1$, where H_0 represents a diagonalisable, undisturbed component of the system, while H_1 accounts for the effects of non-Hermitian perturbations in accordance with strength parameter λ. Correspondingly, the points of coalescence of repulsive levels at near coincident eigenvalues in the complex λ-plane [1] can be given by solutions of equation (2).

$$\frac{d}{d\delta}|\delta I - H| = \frac{d}{d\delta}\left|\delta I - H_0 - \lambda H_1\right| = 0 \qquad (2)$$

However, in a non-Hermitian system, the eigenpoint pair at which the exceptional point is formed - (1) and (2) satisfied simultaneously - has a real value, thus giving a real spectrum, which is conducive to real-world applications such as sensing using photonic MEMS. When a surface of exceptional points can be created, it can be protected in higher dimensions by symmetries such as parity-time (PT) symmetry [2]. This symmetry reduces the number of constraints required to produce real exceptional points from the complex points in the non-Hermitian space. In photonics , PT symmetry is important in the generation of 3D exceptional surfaces as it allows a 2D contour to protect it, since in non-Hermitian generalizations of the system , only 1D, 2D degeneracies are symmetry protected, while zero dimensional exceptional points [2] are robust in general Hermitian systems.Creating an Exceptional Surface is important to utilize the sensitivity enhancement that arises at exceptional points in photonic structures such as optical resonators. They are generated in this structure by coupling two counter-propagating modes in the same optical cavity and help avoid unwanted perturbation effects either externally or due to fabrication effects. Additionally, Exceptional Surfaces are also topological structures that give rise to exotic effects used to design Lasers and topological phase-based control circuits.

Another feature of a non-Hermitian exceptional point is that the coalescence of two levels doesn't just correspond to the eigenvalues when branch points start to disappear, but also to the eigenmodes, thus leaving only one eigenfunction rather than having separate left and right eigenfunctions corresponding to the repeating eigenvalues at the degeneracy. However, this still corresponds to the local behavior of exceptional points in Hermitian systems and is a truer degeneracy in a sense. The difference lies in the coalescence of eigenfunctions at the exceptional point between the energy levels. While designing an optical accelerometer using physical, lossy components such as gratings, interferometers, couplers and resonators [3], the observation of the system output at exceptional points is beneficial as not only is the spectral response real when the system has non-Hermitian coupling parameters in the system Hamiltonian, the sensitivity of the device is also greater at the eigenfrequency splitting observed in exceptional points than what is observed at diabolic points, another system singularity which has linear dependency on perturbation. Such a sensor can be modeled in 2D with two coupled-modes at a resonator or oscillator component.

2. Methods

Solving a general non-Hermitian case is more challenging than a Hermitian case. It is more computationally complex as the solution of eigenvalues at degeneracies such as exceptional points cannot be found traditionally, using methods such as employing a matrix pseudo-inverse. This is because these matrices do not have an orthogonal basis and are not diagonalisable. Traditional solvers that implement the spatially discretized Finite Element method and the iterative Finite Difference Time Domain employ the Finite Element Analysis and Solution Tools (FEAST) algorithm for solving general linear, Hermitian eigenvalue problems. Some methods that have been theoretically formulated to implement a non-Hermitian FEAST algorithm. In this paper, we try to use a direct implementation on higher level software such as MATLAB with minimum involvement of more advanced optimisation tools. The most fundamental part of solving a non-Hermitian eigenvalue problem is finding an orthonormal basis for eigenvectors from the appropriate subspace of the system. The most basic implementation involves numerically computing the Schur decomposition of the system matrices.

$$A = QTZ^{*} \qquad (3)$$

For matrix A, the equation (3) gives its factorisation into two unitary matrices Q and Z and an upper-triangular matrix T that contains the eigenvalues in the diagonal elements. In the Hermitian case, $Z = Q$. Several numerical techniques seek to implement such an eigensolver using common matrix operations such as shifting , inversion and more complex operations such as matrix balancing and reduction. There have been several such numerical techniques that have been formulated for solving a non-Hermitian eigenvalue problem [4,5]. Given in brief in *Table 1* is a summary of their benefits and drawbacks in solving a large photonics problem.

Table 1: Numerical techniques and their benefits and drawbacks for large photonic problems

METHOD	ADVANTAGES	DISADVANTAGES
Direct Method using QR algorithm	The QR algorithm always converges in a finite number of iterations and is backwards stable.	Costs $O(n^3)$ in floating point operations and can only offer limited reduction in computational cost by Hessenberg reduction.
Krylov Matrix Balancing	On setting an experimentally optimized number of iterations and convergence cutoff, number of matrix-vector multiplications can be limited to as few as 10 with lower relative error than without balancing	Only finds the first few largest eigenvalues with significant relative accuracy, making it less effective when trying to find small, sensitive degeneracies like exceptional points.
Arnoldi Method	Has many variants based on reorthogonalization, eigenvalues give best convergence properties. Very reliable as it is associated with the implicitly shifted QR algorithm.	Difficult to maintain numerical orthogonality. It has intensive storage requirements.
Contour Integral-based [5]	More efficiently tackles highly clustered eigenvalues, avoiding large Null space with a good preconditioning scheme.	Lack of smoothness in contours in physical components and boundary effects

References

[1] W D Heiss,"Exceptional Points of Non-Hermitian Operators", in *J. Phys. A: Math. Gen.* **37** 2455 (2004).
[2] Hengyun Zhou, Jong Yeon Lee, Shang Liu, and Bo Zhen, "Exceptional surfaces in PT-symmetric non-Hermitian photonic systems," in *Optica* **6** 190-193 (2019).
[3] M. De Carlo, F. De Leonardis, R. A. Soref and V. M. N. Passaro, "Design of an Exceptional-Surface-Enhanced Silicon-On-Insulator Optical Accelerometer," in Journal of Lightwave Technology vol. **39**, no. 18, pp. 5954-5961, (Sept.15, 2021).
[4] Chen, T., et al. "Non-Hermitian eigenvalue problems." in *Templates for the Solution of Algebraic Eigenvalue Problems: A Practical Guide,* Society for Industrial and Applied Mathematics,. 149-231 (2000).
[5] Huang, Tsung-Ming, et al. "An efficient contour integral based eigensolver for 3D dispersive photonic crystal." in *Journal of Computational and Applied Mathematics* **395** 113581 (2021).

Polarization Rotation Measurements for Fiber Health Monitoring

Jonaq Niveer Sarma, Karamdeep Singh, Deepa Venkitesh
Department of Electrical Engineering, Indian Institute Technology Madras, Chennai, Tamil Nadu, India
Author email address: ee21m062@smail.iitm.ac.in

Abstract: Polarization states in a single mode fiber are seen to change as the fiber undergoes stress. The temporal change in polarization states due to applied mechanical stress are observed by measuring the optical power at each orthogonal polarization mode. This method can help detect stress events before a potential break.
Keywords: Polarization, Fiber Cut Prediction, Optical Communication

1. Introduction

Fiber health monitoring for installed links is of interest to the telecom sector. Predictions about fiber health can allow rerouting of data traffic to minimise disruption of service and allow proactive maintenance of a link. In DWDM systems, data is multiplexed onto the two orthogonal polarization modes of a single mode fiber and transmitted. Due to built-in birefringence of a fiber, or temporal changes of stress and temperature along it, the polarization mode mixing may change. Polarization tracking using polarimeters can be expensive, and may not be practical to deploy across all fiber links. We explore a cheaper alternative by tracking optical power in each polarization. This approach has been proven to be able to track strikes on a fiber [1], track when a train passed through a bridge along which a fiber was laid [2], as well as track the slow change in birefringence due to the daily temperature changes [2]. We explain the details of how the polarisation rotation rates can be estimated and experimentally demonstrate detection of a strike to a fiber spool based on polarization diverse measurements.

2. Theory

Polarization of a propagating electromagnetic wave is the time evolution of the electric field [3]. For propagation through a single mode optical fiber, assuming propagation along z-axis, the mutually perpendicular electric field components can be described as,

$$\boldsymbol{E_x}(x,y,z,t) = A_x \boldsymbol{E_x}(x,y) e^{j(\omega t - \beta z - \delta_x)} \quad (1)$$

$$\boldsymbol{E_y}(x,y,z,t) = A_y \boldsymbol{E_y}(x,y) e^{j(\omega t - \beta z - \delta_y)} \quad (2)$$

where, $\boldsymbol{E_x}(x,y)$ and $\boldsymbol{E_y}(x,y)$ represent the electric fields corresponding to two orthogonal polarization modes, LP_{01x} and LP_{01y}, ω is the angular frequency, β is the propagation constant. Using this description, the polarization states can be described in Stokes space using parameters,

$$S_0 = A_x^2 + A_y^2,\ S_1 = A_x^2 - A_y^2,\ S_2 = 2A_xA_y\cos(\delta_y - \delta_x),\ S_3 = 2A_xA_y\sin(\delta_y - \delta_x) \quad (3)$$

Polarization state changes can be described with polarization rotation rate ($\Delta\sigma$) in Stokes space as,

$$\Delta\sigma = \frac{2}{\tau_p}\sin^{-1}\left(\frac{1}{2}\sqrt{\Delta S_1^2 + \Delta S_2^2 + \Delta S_3^2}\right) \quad (4)$$

where, τ_p is the measurement interval. As shown in [1] and [2], polarization rotation events can be captured using only the optical power measurements at each polarization using a proxy $\Delta\sigma_{PBS}$ defined as,

$$\Delta\sigma_{PBS} = \frac{2}{\tau_p}\sin^{-1}\left(\frac{1}{2}\Delta\left|\frac{V_x - V_y}{V_x + V_y}\right|\right) \quad (5)$$

where, V_x, V_y are the photodetector output voltages, assumed to be proportional to A_x^2 and A_y^2 respectively. On average, $\Delta\sigma_{PBS}$ values were found to be 40% smaller than $\Delta\sigma$ [1]. $\Delta\sigma_{PBS}$ depends only on the Stokes parameter S_1, and may not be able to detect all polarization state changes. However, this information is sufficient to detect and classify events.

3. Experiment and Results

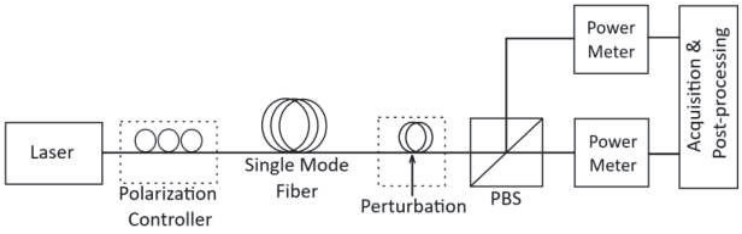

Fig. 1: Experimental setup

As shown in Fig. 1, a continuous wave (CW) laser source operating at 1550 nm is used as the optical source. To control the power at each polarization, a polarization controller (PC) is connected to the laser source. The output of the polarization controller is fed to the optical fiber under test. Our interest is in the output of the optical fiber. In order to separate the polarizations, a polarization beam splitter (PBS) is used and the power at each of the polarization are recorded through a computer-controlled acquisition, every second and the data is subsequently post-processed. When the fiber under test is perturbed by striking it, corresponding to each strike, a change in power at each polarization is observed. Fig. 2 shows the evolution of $\Delta\sigma_{PBS}$ values with and without disturbance to the fiber. Power at each polarization can be balanced using the PC, but it was not seen to be necessary for detection of disturbance events.

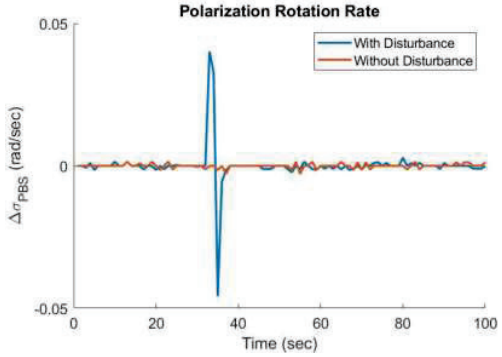

Fig. 2: $\Delta\sigma_{PBS}$ evolution with time

Fig. 2 clearly indicates the possibility of detection of polarisation rotation rate due to an external perturbation. This method needs to be further quantified with controlled acoustic perturbations, and the data obtained by this method can feed a reinforcement learning algorithm to identify potential faults.

4. Conclusions

Polarization tracking for predictive detection of mechanical disturbances to a single mode optical fiber is investigated. We establish that simple power meter measurements can provide a signature for polarisation rotation rate, which could be further used to estimate the health of a deployed fiber network. Future work includes the detection of acoustic disturbances to the fiber using faster data acquisition techniques. In a live link, the equalizer taps for polarization demultiplexing could also provide complete information to calculate the polarization rotation rate, $\Delta\sigma$.

5. References

[1] Simsarian, Jesse E., and Peter J. Winzer. "Shake before break: Per-span fiber sensing with in-line polarization monitoring." *Optical Fiber Communication Conference*. Optical Society of America, 2017.

[2] Barcik, Peter, and Petr Munster. "Measurement of slow and fast polarization transients on a fiber-optic testbed." *Optics Express* 28.10 (2020): 15250-15257.

[3] Sadiku, Matthew NO. *Elements of electromagnetics*. Oxford University Press, USA, 2007.

A differential optical absorption spectroscopy-based system for SO_2 and NO monitoring in industrial environments

Anirban Roy, Poonam Pingale, Yashwant Rajeshirke and Chayan Mitra
Research & Development Division, Forbes Marshall Pvt. Ltd., Kasarwadi, Pune, India - 411034
anirbanroy@forbesmarshall.com

Abstract: We report the development and validation of a highly sensitive differential optical absorption spectroscopy-based system for hot extractive measurement of sulphur dioxide (SO_2) and nitric oxide (NO) concentration in flue gas. The system is validated through measurement of calibrated gas samples. The error in measurement remains below 2% for all concentration values of SO_2 and NO in the test range. The detection limit of the system is 400 ppb for SO_2 and 800 ppb for NO. These were deduced from an Allan variance analysis.

Keywords: Flue gas, air pollutants, continuous emission monitoring, differential optical absorption spectroscopy.

1. Introduction

Continuous monitoring of gaseous emissions is essential for industries in India as well as in other developing countries. The Central Pollution Control Board (CPCB), a statutory organization under the Ministry of Environment, Forest and Climate Change, Government of India, issued directives for monitoring of industrial emissions in 2014. The guidelines for continuous emission monitoring [1] were later released by the CPCB in 2017. As per the directives, the industries have to install robust systems to monitor gaseous emissions and make the data available to the CPCB and respective state pollution control board (SPCB) servers. Therefore, the demand for affordable and rugged continuous emission monitoring (CEM) systems has increased significantly in recent years. Although several optical techniques are available for measurement of gaseous emissions, only a few of them can be used to build affordable and rugged CEM systems for industrial environments. One of the techniques that is widely used for flue gas monitoring is Differential Optical Absorption Spectroscopy (DOAS) [2]. In this paper, we report the development and validation of a hot extractive DOAS-based system for accurate long-term measurement of SO_2 and NO at ppm levels. The hot extractive approach was chosen because it retains the stoichiometry of the flue gas better than the cold extractive approach. The primary advantages of using the DOAS-based sensing approach are - (i) hot extraction enables accurate measurement of individual species without interconversion between gases, and (ii) negligible interference from water vapour in the operating wavelength regime. The performance of the system is evaluated through measurement of calibrated gas samples and an Allan variance analysis.

2. System Design

The measurement system consists of a 2-channel gas cell as shown in Fig. 1(a). One channel is for measurement of SO_2 and NO at ultraviolet (UV) wavelengths while the other is for water vapour measurement at near-infrared (NIR) wavelengths. For the UV channel, the optical source is a Deuterium lamp (Heraeus, SD 3651-06 TJ) while the detection part is performed by a UV spectrometer (Oto Photonics, SE1030-025-FUV7). SO_2 and NO absorb the light at specific wavelengths in the UV spectrum. The spectra are processed and gas concentrations are calculated every second using DOAS. The SO_2 concentration is extracted using the first differential method and the NO concentration is extracted using the point slope method [3]. The water vapour measurement is carried out in the second channel using absorption spectroscopy. In this case, a NIR light emitting diode (LED) and a NIR photodiode are used. The CEM system is shown in Fig. 1(b). It is necessary to maintain the gas temperature above dew point during the measurements. Heaters are therefore placed on both the measurement channels to maintain the gas temperature at 180ºC. The brain of the CEM system is a 32-bit, 120 MHz microcontroller (Texas Instruments, TM4C1294NCPDT). The communication is based on MODBUS RTU protocol (with programmable baud rate) as well as MODBUS TCP/IP (1Mbps) protocol. Zero calibration is performed automatically by the system once in a day and can also be done manually through MODBUS commands. PT100 sensors are used for heater temperature measurement and temperature control is performed using a Proportional Integral Differential (PID) algorithm to maintain the heater temperature at 180ºC. A Programmable Logic Controller (PLC) takes care of the external controls and interlocks. A Human Machine Interface (HMI) is provided for the user and it communicates with the system through the PLC.

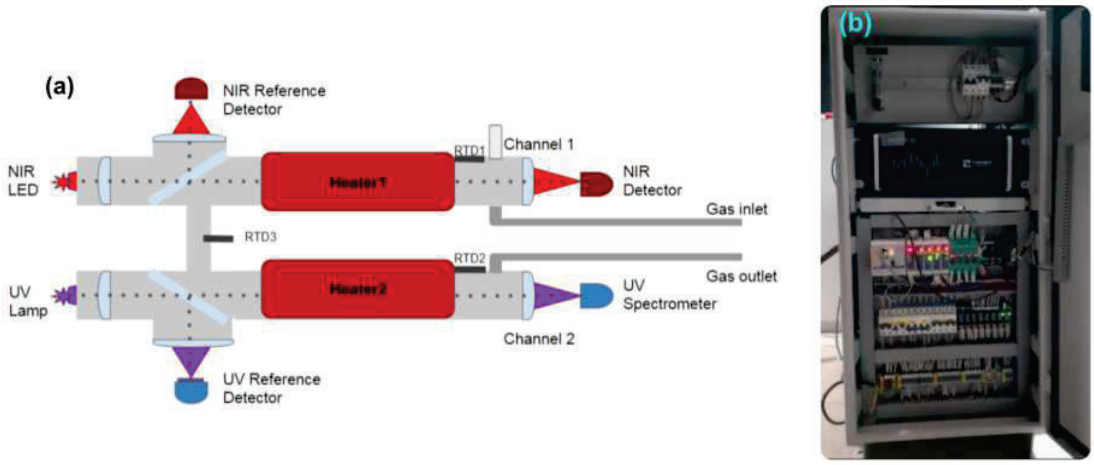

Fig. 1: (a) Schematic of the 2-channel measurement system, (b) Picture of the CEM system.

3. Performance of the System

The CEM system was validated through measurement of calibrated gas samples. Various concentrations of SO_2 and NO (balanced with N_2) were used in the experiments. The gas was passed through two preheaters to raise the gas temperature to 180ºC. The gas was then transferred to the analyser through a heated sample line. The detection limits were established by an Allan variance analysis. Figure 2(a) shows the excellent agreement between the actual and measured concentration values of SO_2. The inset shows the Allan deviation plot for SO_2. Figure 2(b) shows the very good agreement between the actual and measured concentration values of NO while the inset shows the Allan deviation plot for NO. The measurement error is below 2% for all concentration values of SO_2 and NO in the test range. Detection limits of 400 ppb for SO_2 and 800 ppb for NO were deduced from the Allan deviation plots.

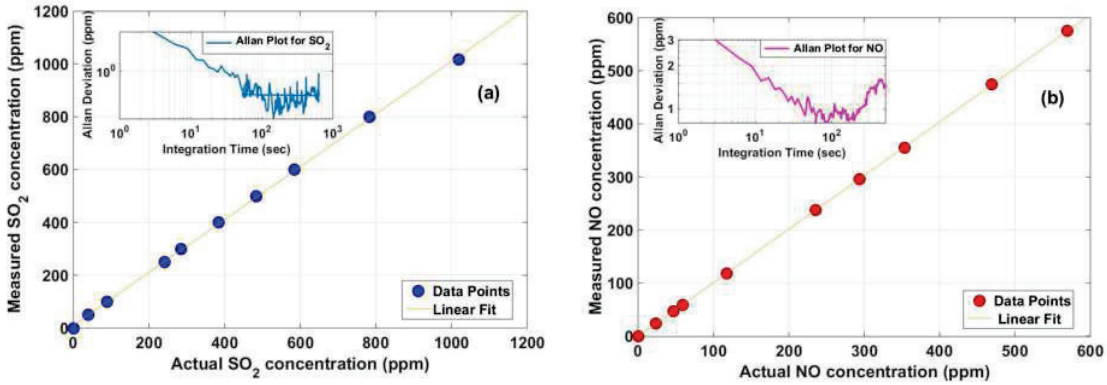

Fig. 2: Comparison of actual and measured values of (a) SO_2 and (b) NO, which shows excellent agreement between them. The insets show the Allan deviation plots for SO_2 and NO respectively.

4. Conclusion

We have demonstrated a highly sensitive CEM system for real-time monitoring of SO_2 and NO using DOAS. The use of a UV lamp of low cost (approximately INR 23,000) makes this an economically viable solution for industrial emission monitoring. The system is rugged enough for long-term deployment in hostile environments.

5. References

[1] Guidelines for Continuous Emission Monitoring Systems, 2017 (https://cpcb.nic.in/upload/thrust-area/Guidelines_on_CEMS_02.08.2017.pdf)
[2] U. Platt, "Air Monitoring by Differential Optical Absorption Spectroscopy" in *Encyclopedia of Analytical Chemistry* (Wiley, 2017).
[3] B. G. Balsubramaniam, A. Bekal, Y. Rajeshirke and C. Mitra, "Ultraviolet Absorption Spectral data analysis for Flue Gas Detection," in *Applied Industrial Optics* (2021).

Electro-Optical investigations of polymer dispersed liquid crystals incorporated with functionalized silver nanoparticles

Mudit Sahai[1*], Shivaraja S J[1], R K Gupta[1] and Manjuladevi V[1]
[1]Department of Physics, Birla Institute of Technology and Science, Pilani (BITS Pilani), India
Author e-mail address: p20200448@pilani.bits-pilani.ac.in

Abstract: Polymer dispersed liquid crystals (PDLCs) forms an interesting sub-set of liquid crystal systems which have recently attracted a lot of scientific interest for its possible use in smart windows and optical sensors. In the present work, we have studied the morphological and electro-optical properties of pure and functionalized silver nanoparticles (f-AgNPs) doped PDLCs. It was found that doping 0.2 wt% f-AgNPs in PDLC sample improves its properties, like improved transmittance value, smaller LC droplet size and reduced threshold voltage.
Keywords: Polymer dispersed liquid crystals (PDLCs), Electro-optical properties, Switchable smart window.

1. Introduction

For a long time now Liquid Crystals (LCs) have been effectively used in display devices, but the last few decades have seen a steady rise in LC based devices finding new applicational avenues in the research domains of switchable smart windows, projection systems, lasers and optical sensors [1]. Polymer dispersed liquid crystals (PDLCs) with an easier fabrication process, wider operational temperature range and better contrast ratio forms one such subset of LC systems which has recently been explored by lot of researchers across various scientific domains for a number of possible applications. PDLCs generally consists of micron-sized LC droplets embedded in the host polymer matrix. The PDLC films are fabricated using either the encapsulation or phase separation method [2], with the later being more favored as it provides greater control over the LC droplet morphology which in turn effects the switching properties of the device. In this work, an experimental investigation is carried out on electro-optical properties of PDLC cells prepared using room temperature nematic liquid crystal 4-heptyl-4-biphenylcarbonitrile (7CB) and commercially available acrylate-based UV curable monomer. The effect of hexane thiol functionalized silver nanoparticles (f-AgNPs) on electro-optical properties of PDLC are investigated by fabricating f-AgNPs incorporated PDLC cells. The PDLC cells prepared with 0.2 wt% f-AgNPs shows improved transmittance and low threshold voltage compared to the PDLC prepared with pure 7CB.

2. Experimental Setup

The nematic LC compound 7CB, purchased from TCI Chemicals (India), Pvt. Ltd. and an acrylate-based UV–Vis light-curable resin containing Pentaerythritol tetrakis (3-mercaptopropionate) 2-Carboxyethyl acrylate Diphenyl (2,4,6-trimethylbenzoyl) phosphine oxide Hydroquinone (PCDH) (product number: 900163, n_p =1.54) procured from Sigma Aldrich (India) were used without further purification. Functionalized silver nanoparticles (f-AgNPs) of average diameter 3–5 nm [3] are used as nanoparticle (NP) dopants. The nanocomposites of f-AgNPs with 7CB are prepared by dispersing them in chloroform solvent by ultrasonication. After evaporating chloroform, the f-AgNPs nanocomposites of 7CB is mixed with monomer PCDH in the ratio 60:40. These samples are filled into the LC cells (cell thickness 6 ± 0.2μm) prepared using indium tin oxide (ITO) coated glass plates with no pre-alignment treatment. For polymerization, PDLC cells were kept under UV light for about 1hr. Textural LC droplet morphology of PDLC cells was observed using a polarizing optical microscope (POM; OLYMPUS BX53M). An unpolarized He-Ne laser of wavelength 632 nm was made to incident normally on the PDLC samples which is later detected using a photodiode setup to study the electro-optical properties using a method as mentioned in our previous work [4]. Furthermore, the dielectric permittivity of the PDLC cells was measured as a function of applied voltage at 1 kHz frequency.

3. Results and discussions

The optical texture for the three PDLC cells under crossed polarizer is shown in Figure 1(a-c). As seen in Figure 1a, pure PDLC sample exhibit irregular and contorted LC droplet shapes while 0.2 wt% f-AgNPs doped sample (Figure

1b) showed ordered and spherical LC droplets. Interestingly, on further increasing the doping concentration to 0.5 wt% a prominent phase separation between LC molecules and polymer matrix occurs which is seen as dark spaces in the POM texture (Figure 1c).

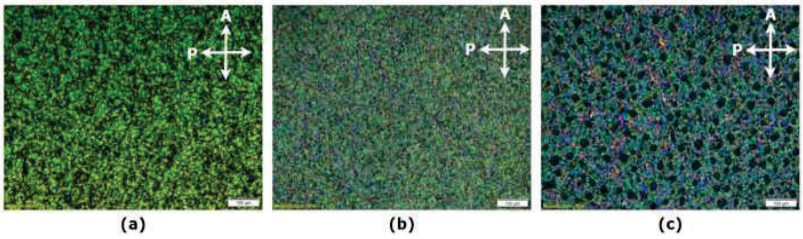

Figure 1: POM images for (a) – Pure PDLC, (b) – 0.2 wt % of f-AgNPs doped, (c) – 0.5 wt % of f-AgNPs doped under crossed polarizers. The scale bar denotes 100μm.

The Voltage-Transmittance (*V-T*) curve (Figure 2a) indicates that in the absence of external voltage all three PDLC cells exhibit an opaque state with least transmittance, but as the voltage is increased the transmittance value also increases. The rise in transmittance value with an increase in voltage though common among all cells, the 0.2 wt% f-AgNPs doped sample exhibits the highest transmittance value as the voltage is increased (transparent state). This variation of the optical difference between the three samples in ON (transparent) and OFF (opaque) states is of fundamental importance in fabricating smart windows with better contrast ratios. To further study the effect of NP doping on the PDLC characteristics the threshold voltage (V_{th}) (Figure 2b) and dielectric permittivity measurement (Figure 2c) was carried out. Here the threshold voltage refers to the voltage at which LC molecules inside the LC droplet starts to reorient along the direction of applied electric field E. The V_{th} value is the voltage at which the transmitted intensity starts changing from the constant value in the V-T curve. The value of V_{th} is reduced by 20.65% and 30.43% for PDLC prepared with 0.2 wt% and 0.5 wt% f-AgNPs respectively as compared to PDLC prepared with pure 7CB. The reduction in V_{th} value might be due to the decrease of $K/\Delta\varepsilon$ ratio (where K is elastic constant and Δε is dielectric anisotropy of LC). The value of dielectric permittivity (Figure 2c) increased in PDLC cells prepared with f-AgNPs compared to PDLC cell prepared with pure 7CB and follows the same trend as V-T graph.

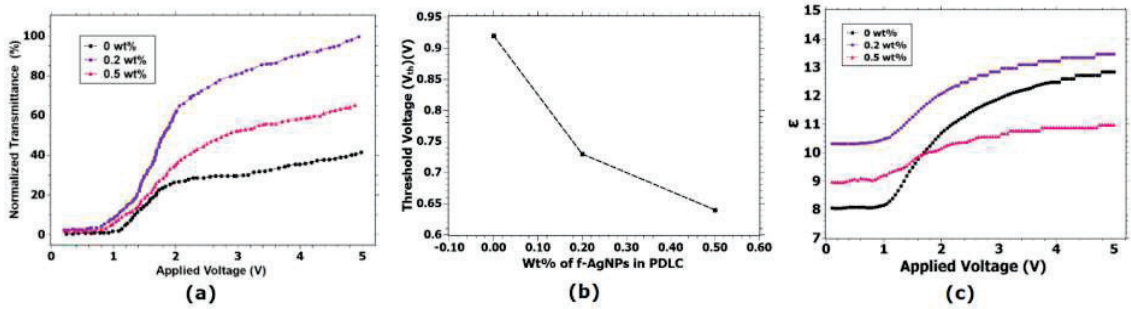

Figure 2: (a) The V-T curve of PDLC cells for all three doping concentrations. (b) Variation in threshold voltage of PDLC samples with increasing doping concentration. (c) Variation of dielectric permittivity as a function of applied voltage for pure and doped PDLC.

4. Conclusions

In the current work, the effect of doping f-AgNPs on the morphology and electro-optical properties of PDLC sample was studied. It was observed that a doping of 0.2 wt% f-AgNPs in PDLC sample results in decrease of the LC droplet size, threshold voltage and an appreciable increase in transmittance value in the ON state of V-T curve giving much better contrast ratio between the ON and OFF state of PDLC sample, this variation is of fundamental importance when considering a possible smart window application and hence needs to be explored further.

5. References

[1] S. Bronnikov, S. Kostromin, V. Zuev, "Polymer-dispersed liquid crystals: Progress in preparation, investigation, and application", *J. Macromol. Sci. Part B Phys.* **52,** (2013) 1718–1735.

[2] M.H. Saeed, H. Yang, et al, "Recent advances in the polymer dispersed liquid crystal composite and its applications", *Molecules* **25,** (2020),1–22.

[3] Varshney S, Kumar M et al. "Soft discotic matrix with 0-D silver nanoparticles: Impact on molecular ordering and conductivity", *J Mol Liq.* **238**, (2017), 290–295.

[4] SJ. Shivaraja, RK Gupta, V. Manjuladevi, "Faster switching polymer dispersed liquid crystal devices incorporated with functionalized SWCNTs", *J Mol Liq.* **354**, (2022), 118905.

Fabrication and optical studies of Silicon Nitride based 1D photonic structures

Albin Kuriakose, Pariksha Malik, G. Vijaya Prakash*
Nanophotonics Laboratory, Department of Physics, Indian Institute of Technology Delhi, New Delhi 110016 INDIA
**Author e-mail address: prakash@physics.iitd.ac.in*

Abstract: Tunable 1D photonic crystals from mono to multi-layered SiN_x films are fabricated using plasma enhanced chemical vapor deposition technique. The reflection spectrum of the multi-stacked SiN_x films showed the formation of distributed Bragg reflectors (DBR) with the increase in number of layers. Rigorous transfer matrix simulations are utilized to correlate various optical properties of the thin films. The slight deviation between the experimental and the simulations can be attributed to the non-uniformity, interfacial defects, and imprecision in thickness during fabrication. The tunable optical properties of the 1D photonic crystal can find applicability in various optical coating and optoelectronic devices.
Keywords: Photonics structures, Distributed Bragg Reflector, Silicon nitride

1. Introduction

The simplest form of 1-D photonic crystal consists of two alternate layers of dielectric material having a low and high refractive index (n_1, and n_2; $n_1 > n_2$) known as Distributed Bragg Reflector (DBR). The combination of a low and high refractive index layer of thickness in wavelength-order is called a dielectric stack which follows the relation $n_L d_L = n_H d_H = \lambda/4$ where, *n* is the refractive index (L and H stands for low and high refractive index) and *d* is thickness of the layer [1,2]. A series of dielectric stack can block (stop band) a particular range of electromagnetic radiation due to multiple interferences. The formation of top band in such photonic architecture plays an important role in optical laser damage threshold coatings, optical limiters, and various optoelectronic applications. A lot of research has been carried out in search for the proper choice of dielectric media suitable for the fabrication of such photonic structures.

The present reports the fabrication and optical characterization of 1D photonic crystals based on multi-layered SiN_x using plasma enhanced chemical vapor deposition technique. The stoichiometric-Si_3N_4/ non-stoichiometric (SiN_x) thin films have been extensively studied because of its promising electronic and mechanical properties [3]. Silicon nitride has many advantageous characteristics such as low mechanical stress, high melting point, large electronic bandgap, and a high dielectric constant that makes it as preferred candidate for various optoelectronic and microelectronic applications. The tunability of optical constants over a wide range makes SiN_x ideal for various optical applications[4].

2. Results and Discussions

The schematic representation of the 1D layered photonic structure is shown in Fig1. a. The photonic structures are fabricated by deposition of SiNx at ~200° C using the PECVD technique. The stoichiometry of the silicon nitride can be customized by controlling the flow of the precursor gases during the deposition process [5] while the thickness of the films can be varied by controlling the time of deposition. For the present structures the low and high refractive indices are found to be n_L=1.9 and n_H=2.9. The refractive index and thickness of each layer is determined by using null-ellipsometry on single layer samples with same parameters. The deposition parameters for high and low refractive index layers are given in Table 1. The amount of N and/or Si in the SiN_x-H films have a significant role in deciding the optical properties like refractive index and bandgap [6]. The main objective is to obtain the stop band maxima at the central wavelength (λ) with minimum losses. The various multilayers (2,4,6,8 layers) were deposited using PECVD and their reflectance spectra are shown in Fig.1b. The TMM simulation of the reflection spectra are shown in Fig. 1c. The slight deviation between the experimental and simulations can be attributed to the non-uniformity, interfacial defects, and imprecision in thickness during fabrication.

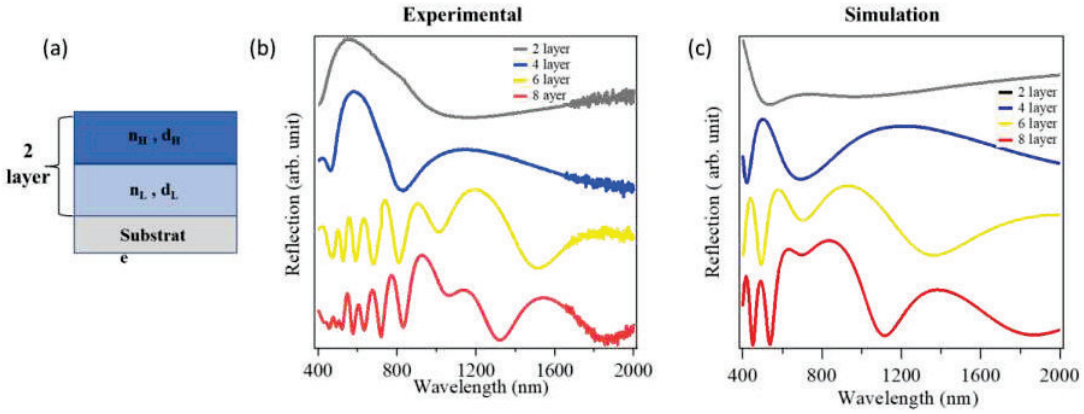

Fig. 1(a) Schematic of single stack of SiN_x (b) Experimental and (c) simulated reflectance spectra of various multilayers.

3. Conclusion

In conclusion the tunable 1D photonic crystals based on SiN_x have been fabricated for two different stoichiometric ratios. The reflection spectrum of the multilayered SiNx exhibited reflective DBR formation in the visible region with the increase in the number of layers. The reflection spectrum shows a slight deviation between experimental and simulation which can be improvised by optimizing the fabrication parameters for obtaining better uniformity and defect free layers.

4. References

[1] L. Liu, W. guo Liu, N. Cao, and C. long Cai, "*Study on The Performance of PECVD Silicon Nitride Thin Films*", Def. Technol. **9**, 121 (2013).

[2] A. E. Kaloyeros, Y. Pan, J. Goff, and B. Arkles, *Review* – "*Silicon Nitride and Silicon Nitride-Rich Thin Film Technologies: State-of-the-Art* Processing Technologies, Properties, and Applications", ECS J. Solid State Sci. Technol. **9**, 063006 (2020).

[3] F. L. Riley, "*Silicon Nitride and Related Materials"*, J. Am. Ceram. Soc. 83, **245** (2000).

[4] R. K. Bommali, S. P. Singh, G. V. Prakash, S. Ghosh, and P. Srivastava, "*Growth and Tailoring of Physical Properties of Si Quantum Dots in A-SiNx:H Matrix"*, Energy Procedia **41**, 50 (2013).

[5] O. Applicata, "*Reflectance Study of S I02 / Si3N4 Dielectric Bragg Reflectors"*, **XXXII**, (2002).

[6] X. Wang, H. Masumoto, Y. Someno, and T. Hirai, "*Optical Properties of Titania/Silica Multilayer Filters Prepared by Helicon PlasmaSputtering"*, J. Vac. Sci. Technol. A Vacuum, Surfaces, Film. **16**, 2926 (1998)

Silver nanotriangles as highly efficient SERS active substrate: Design, Optimization, and Insights using FDTD simulation

Onima Bisht[#], Sathi Das, and Dalip Singh Mehta*

Bio-photonics and Green Photonics Laboratory, Department of Physics, Indian Institute of Technology Delhi, Hauz Khas, New Delhi, 110016, India

mehtads@physics.itd.ac.in, [#]onimabisht1998@gmail.com,

Abstract: Surface enhanced Raman Spectroscopy (SERS) technique offer a rapid, sensitive detection method of molecules exploiting its vibrational energy levels. In this work, a numerical design of a robust SERS-active substrate has been proposed. The substrate is made up of silver nanotriangles that have been arranged in a circle with a specific periodicity. The nanostructure parameters were optimized using standard laser source of 633 nm wavelength and the variations in enhancements were observed by changing height and separation. Thus, the detailed finite difference time domain (FDTD) computation study with realistic nanostructure configurations provides a solid foundation for comprehending and designing optimal SERS substrates.

Keywords: SERS, Finite Difference Time Domain, localized surface plasmon resonance, electromagnetic enhancement factor

Introduction:

Surface Enhanced Raman Spectroscopy (SERS) is used to detect low concentration analytes where the efficiency of Raman spectroscopy fails. When the target molecule/analyte is placed on rough corrugated metal surfaces, as was discovered by Fleishmann et al., a high enhancement in the Raman signal was observed [1]. The two most widely accepted theories to explain this phenomenon are the (a) Electromagnetic Enhancement (EM) theory and the (b) Chemical Enhancement (CE) theory. The electromagnetic enhancement theory is based on the phenomenon of localized surface plasmon resonance (LSPR). When a laser is incident on metallic nanoparticles, the nanostructure oscillates. If the nanostructure oscillation frequency matches the incident laser frequency, an enormous amount of electric field is trapped in a minimal volume (hotspot), providing the LSPR condition [2]. The chemical enhancement occurs when a molecule is adsorbed on nanostructures, and the metal-molecule complexes are formed between the substrate and the analytes. The popularity and applicability of the SERS substrates depend on the reproducibility, stability, and scalability of the substrate. The existing state-of-the-art simulation techniques, like the finite difference time domain (FDTD) computation tool, provide a detailed understanding of the amount of local field enhancement and the distribution of hotspots.

In this paper, a realistic nanostructure of silver nanotriangles with defined periodicity has been designed to optimize its plasmonic efficiency for standard lasers. The simulations were also performed considering air, and water as a background material. The optimal parameters lead to an incredible plasmonic enhancement approaching 10^9 orders of magnitude for the 633 nm excitation laser wavelength. The detailed simulation study is discussed and thoroughly analyzed in subsequent sections.

Numerical design:

A commercially available software Ansys Lumerical software was used for the simulations. The material parameters of the triangular nanoparticle were given by the Palik database [3,4]. The triangle nanostructures were arranged in a circular manner. The length of the side of the nanostructure is 50nm. The height and the separation between these nanoparticles are varied in order to obtain the best enhancement factors. In addition to this, the two types of surrounding materials, air and water (n = 1.33) are taken in order to analyze the enhancements in these two media. The mesh size was kept to 1.2nm for all simulations. Figure 1 shows the schematic representation of the design. In Figure 1(a), a and g represent the side length and the height of the triangle whereas h represents the spacing between the two consecutive triangles. The expression of electromagnetic enhancement factor (EF) is given by [2]:

$$\mathrm{EF} = L_I(\omega_I)\, L_I(\omega_R) \approx L_I(\omega_I)^2 = L_E(\omega_I)^4 \quad (1)$$

where L_I, L_E are the local field intensity enhancement and the local field enhancement. ω_I is the source frequency and ω_R is the stokes or anti-stokes frequency.

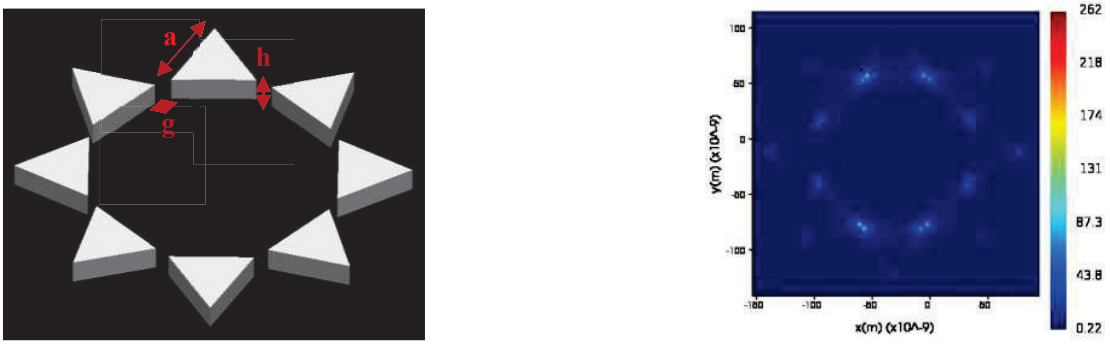

(a) (b)

Fig 1: Schematic of triangular nano structures in a circular pattern. (b) Ratio of electric field strength (E/E_0) of optimized structure (a = 50nm, g = 5nm, h = 25nm) at Raman shift = 703 nm, when it was illuminated by a laser of λ = 632 ± 2 nm.

Results and discussion:

Table 1 shows a comparison of enhancements for different media and with different height and separation between the nanoparticles.

Table 1: Analysis of the proposed substrate with respect to different design parameters with incident radiation 633 ± 2 nm.

Constant parameters (nm)	Varied parameters (nm)	Enhancement $(E/E_0)^4$ (In water)	Enhancement $(E/E_0)^4$ (In air)
a = 50, g = 5	h = 10	10^8	3.6×10^8
	h = 20	6.4×10^8	2.1×10^6
	h = 25	4.7×10^9	6.7×10^6
a = 50, g = 10	h = 10	2.5×10^8	1.2×10^8
	h = 20	9.6×10^8	3.6×10^6
	h = 25	7.8×10^8	2.3×10^6
a = 50, g = 10	h = 10	2.8×10^7	1.8×10^8
	h = 20	4.4×10^8	6.6×10^5
	h = 25	10^9	3.9×10^5

We found the highest enhancement ~ 4.7 x 10^9 , with water as the background when the separation was 5 nm, and the height of the nanostructure is 25 nm. The study gives insights plasmonic enhancement and distribution of hotspots for optimised parameters with different background. With mature fabrication technologies, it can be manufactured and can be used in biphotonic applications like the margin detection of cancer.

References:

[1] F. W. King, R. P. Van Duyne, & G. C. Schatz, (1978). Theory of Raman scattering by molecules adsorbed on electrode surfaces. *The Journal of Chemical Physics*, *69*(10), 4472-4481.
[2] R. Pilot, R. Signorini, C. Durante, L. Orian, M. Bhamidipati, , & L. Fabris, (2019). A review on surface-enhanced Raman scattering. *Biosensors*, *9*(2), 57.
[3] S. Das, K. Saxena, & D. S. Mehta, (2022). A highly sensitive SERS substrate based on a mesoporous Ag–TiO 2 thin film for the detection of dye molecules. Materials Advances.
[4] S. Chakraborty, V. Awasthi, R. Goel, & S.K. Dubey (2021). Numerical design of SERS-active substrate for analyte detection using gold-hexagonal patterns. Vibrational Spectroscopy, 117, 103312.

Intensity correlations in a photonic Su-Schrieffer–Heeger lattice

Rishav Hui[1], Trideb Shit[1], Sebabrata Mukherjee[1,*]
[1]*Department of Physics, Indian Institute of Science, Bangalore 560012, India*
[*]*mukherjee@iisc.ac.in*

Abstract: We report on the experimental investigation of Hanbury Brown-Twiss intensity correlations on the edge of a femtosecond laser-fabricated Su–Schrieffer–Heeger (SSH) photonic lattice. Using coherent states of light, we experimentally emulate photon number correlations and observe a relatively large probability of finding a two-photon paired state on the topological edge of the SSH lattice.
Keywords: Waveguide arrays, Topological photonics, Intensity correlations, Quantum optics.

1. Introduction

The propagation of light waves in engineered waveguide arrays (i.e., photonic lattices) reveals a wide variety of intriguing phenomena, including recent discoveries in topological photonics [1]. It is of great interest to understand how non-classical states of light behave in topological materials, and how topological protection can be utilized to design novel quantum-optical devices. In this work, we consider a one-dimensional photonic topological SSH lattice [2] and numerically study the evolution of two indistinguishable photons [3-6]. Following a protocol described in Ref. [3], we experimentally obtain Hanbury Brown-Twiss (HBT) intensity correlations [7] that mimic the photon number correlation $\Gamma_{m,n}$ – i.e., the probability of finding one photon at the m-th site and the other one at the n-th site. In our experiments with coherent states of light, we prepared a two-site initial state with a tunable relative phase and measured the intensity patterns at the output of the photonic lattice. We can then construct the correlation matrix $\Gamma_{m,n}$ from a phase averaged measurement. For an input state launched at the edge and separated by one site, we observe a relatively large probability $\Gamma_{1,1}$ of finding both photons on the edge site. Importantly, $\Gamma_{1,1}$ remains finite for the topological edge and goes to zero for a trivial edge. In other words, the underlining topology of the SSH lattice dictates a finite $\Gamma_{1,1}$ for the above-mentioned input state.

2. Classical and Quantum Correlations

Consider a photonic lattice made of evanescently coupled identical single-mode waveguides at the operational wavelength. In the nearest-neighbour coupled-mode approximation, the evolution of the photon creation operator at the m-th site is governed by the following Heisenberg equation [3]

$$i\frac{\partial a_m^\dagger}{\partial z} = \beta a_m^\dagger + J_{m,m+1}a_{m+1}^\dagger + J_{m,m-1}a_{m-1}^\dagger \tag{1}$$

where z is the propagation distance, β is the propagation constant, and J is the coupling between two neighbouring waveguides. Integrating Eq. (1), one obtains $a_m^\dagger = e^{i\beta z}\sum_p U_{m,p}(z)a_p^\dagger(z=0)$, where $U_{m,p}(z) = (e^{izH})_{m,p}$, and H is the coupling matrix. For a two-photon input state $a_p^\dagger a_q^\dagger|0\rangle$ launched at waveguide p and q, $p \neq q$, the quantum mechanical photon number correlation is given by [3]

$$\Gamma_{m,n}^{(Q)}(z) = \langle a_m^\dagger(z)a_n^\dagger(z)a_n(z)a_m(z)\rangle = |U_{m,p}U_{n,q} + U_{m,q}U_{n,p}|^2 \tag{2}$$

which physically signifies the probability of finding one photon at m-th site and the other one at the n-th site. On the other hand, the classical HBT intensity correlation is obtained by launching coherent states of light at waveguide p and q with a relative phase θ. The classical correlation is given by $\Gamma_{m,n}^{(C)} = \langle I_m I_n\rangle$ where $\langle . \rangle$ indicates phase averaging for $\theta \in [0, 2\pi]$. It can be shown that

$$\Gamma_{m,n}^{(C)} = |U_{m,p}U_{n,q} + U_{m,q}U_{n,p}|^2 + |U_{m,p}U_{n,p}|^2 + |U_{m,q}U_{n,q}|^2 = \Gamma_{m,n}^{(Q)} + I_m^p I_n^p + I_m^q I_n^q \tag{3}$$

where I_m^p is the intensity at the m-the site for the initial excitation of a single p-th site. Comparing Eqs. (2) and (3), it is evident that classical intensity correlation has two additional terms, which can be measured using single site excitations and then deducted to obtain the quantum correlation.

3. Results

In our experiments, photonic lattices were fabricated in a 76.2 mm-long borosilicate glass substrate using femtosecond laser-writing [8]. The photonic SSH lattice in Fig. 1(a) (with dimerized couplings $J_1 = 0.095$ mm^{-1} and $J_2 = 0.16$ mm^{-1}) supports topologically protected edge states at zero energy. We first show the existence of the edge states by launching light on a single edge site (site 1) In this case, the input state has 64% overlap with the edge states. An initial state launched at site 3 has a relatively lower overlap (22%) with the edge states, and hence, a significant amount of light penetrates the bulk. On the second set of experiments, we probed the edge

physics in a 1D integer lattice [Fig. 1(d)] made of equally spaced waveguides ($J_x = 0.075$ mm^{-1}), and no edge states were detected, as would be expected.

To obtain the HBT intensity correlations, we launch 1064 nm light at site 1 and 3 with a relative phase θ that was controlled by changing the relative path length. Figs. 1 (b) and (c) present the calculated quantum correlation and measured HBT correlation, respectively, for the SSH lattice. The peak, indicating the maximal value of $\Gamma_{1,1}$, suggests that the probability of finding the two-photon paired state is maximal at the edge site. We note that $\Gamma_{1,1}$ fluctuates initially as a function of z and then saturates to a value determined by J_1/J_2. For a long propagation, our numerical calculation suggests that a finite $\Gamma_{1,1}$ can only be found in the topological phase (i.e., $J_1/J_2 < 1$). There is also a finite probability of finding one photon at the edge and the other one in the bulk, but this probability decreases rapidly as a function of distance. On the other hand, in the equally spaced trivial lattice (Fig. 1e-f), the probability of finding the photons near/at the edge decreases as a function of z. In this case, we also observe paired state evolving into the bulk, which is absent in SSH case.

We note that the quantum interference of photons depends on the initially launched state. In Ref. [6], considering a different initial state, i.e., $a^{\dagger}_{p=1}a^{\dagger}_{q=2}|0\rangle$, it was shown that only one of the photons remains close to the topological edge of the SSH lattice whereas the other photon penetrates the bulk.

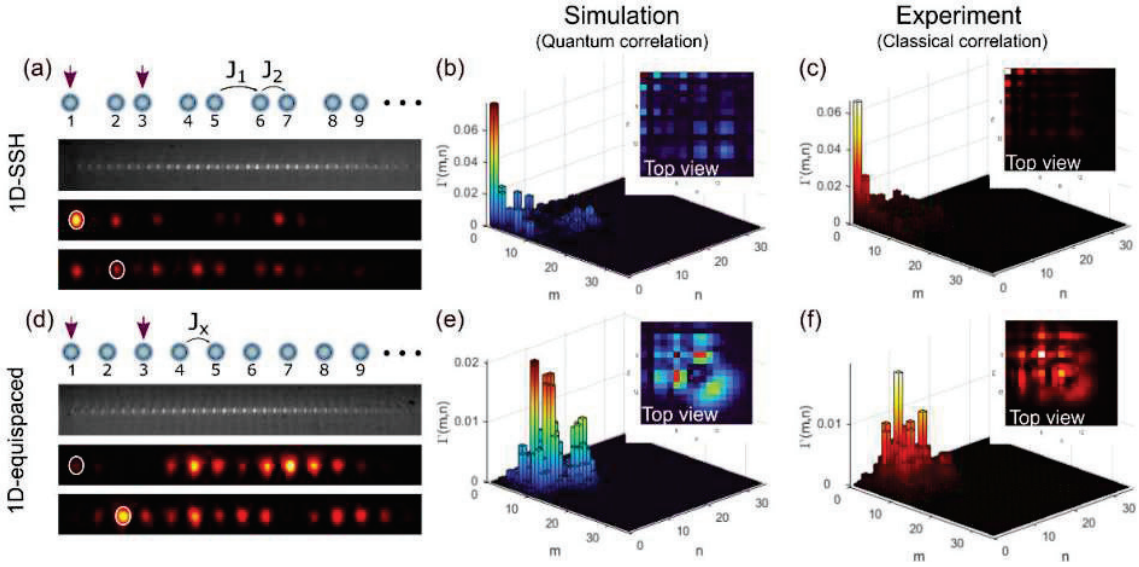

Fig 1. (a)Top-bottom: Sketch of a photonic SSH lattice with dimerized couplings; input facet image of the laser-written SSH lattice; experimentally measured output intensity distributions at $z = 76.2$ mm for initial excitation at input site 1 and 3, respectively. The excitation sites are indicated by circles. (b) Numerically calculated quantum correlation in the SSH lattice, showing a relatively large photon pairing at the topological edge. (c) Experimentally obtained HBT intensity correlation using coherent states of light. (b) and (c) are in good agreement. (d-f) Same as (a-c) for a 1D equispaced lattice. No photon pairing at the edge site was observed in (f).

4. Conclusions

Considering a topological SSH lattice, we have experimentally emulated the propagation of a two-photon input state and observed a large probability of finding a paired state on the topological edge. Along with precise state preparation, laser-written waveguide arrays can prove to be a powerful experimental setting for predicting and studying quantum topological photonics. In future work, we plan to exploit modulated two-dimensional arrays and understand the behaviour of true quantum states of light generated by spontaneous parametric down-conversion.

Acknowledgements: SM gratefully acknowledges funding from IISc startup grant and ISRO (Project No. ISTC/PPH/SM/465). The photonic lattices were fabricated by SM in Mikael Rechtsman's group at Penn State University, USA.

5. References

1. T. Ozawa, et al., "Topological photonics," Rev. Mod. Phys. **91**(1), 015006 (2019).
2. W. Su, J. Schrieffer, and A. J. Heeger, "Solitons in polyacetylene," Phys. Rev. Lett. **42**, 1698 (1979).
3. Y. Bromberg, et al., "Quantum and classical correlations in waveguide lattices," Phys. Rev. Lett. **102**, 253904 (2009).
4. A. Peruzzoet, et al., "Quantum Walks of Correlated Photons", Science 329, 1500 (2010).
5. R. Keil, et al., "Photon correlations in two-dimensional waveguide arrays and their classical estimate," Phys. Rev. A **81**, 023834 (2010).
6. F. Klauck, et al., "Photonic two-particle quantum walks in Su–Schrieffer–Heeger lattices", Photon. Res. **9**, A1 (2021)
7. R. Brown and R. Twiss., "Correlation between Photons in two Coherent Beams of Light", Nature **177**, 27 (1956).
8. S. Mukherjee, "Experimental simulation of solid-state phenomena using photonic lattices", PhD Thesis, Heriot-Watt University, (2016).

Reinforcement Learning Based Phase Control for Hexagonal Tiled Aperture Beam Combining

V.Sankar, S.Maji, C. L. Linslal, M. S. Sooraj and B. Srinivasan*
Department of Electrical Engineering, Indian Institute of Technology Madras, Chennai 600036 Tamil Nadu, India
**Email id: balajis@ee.iitm.ac.in*

Abstract: We report a new algorithm for phase synchronization for a seven-channel tiled aperture combining based on hexagonal geometry using Reinforcement Learning. Unlike previous attempts which use the phase difference of each channel as a cost function to optimize, we use the combination of power in the side-lobes and the main-lobe as the cost function. The six-fold symmetry in the hexagonal geometry gives the opportunity to easily scale the algorithm to higher number of combining elements. We achieve 7.1% improvement in the closed-loop performance for a seven-channel target in loop beam combining system.
Keywords: Reinforcement Learning, Coherent Beam Combining, Phase Synchronization.

1. Introduction

Coherent combining of multiple fiber lasers is a promising technique to achieve high power (hundreds of kW) laser beams with high efficiency and beam quality. Coherent beam combining (CBC) has several applications, including directed energy, light detection and ranging (LIDAR), and material processing [1]. Phase synchronization is a crucial step to achieve maximum combination efficiency. With the advancement in Artificial Intelligence and Machine Learning, studies have shown that machine learning-based control strategy, specifically Reinforcement Learning (RL), has been promising and can perform robust control in various real-time complex environments. This approach has been investigated for CBC application using the Deep Deterministic Policy Gradient (DDPG) algorithm which estimates actions based on phase difference between combining beams [2]. This technique is susceptible to hyperparameter tuning, which is essential for good performance. In this paper, we propose a Soft Actor-Critic (SAC) based phase control algorithm which is robust to change in hyperparameters and uses only the power in the main-lobe and side-lobes to estimate the control action.

2. Phase Control Algorithm

We evaluate the algorithm only in the presence of piston phase error. The phase noise is generated using experimental data as demonstrated in our previous work [3]. For efficient and robust RL phase control algorithms the state and reward definitions are very important. Previously, Tunnerman *et.al.* used image of the beam-profile as the state information to the policy network [2]. Capturing beam profile and processing is very difficult and expensive because of limited frame rate of the image sensor. To overcome this limitation, we propose a phase control algorithm which only needs the power in the side-lobes and main-lobe which can be easily obtained at faster rates.

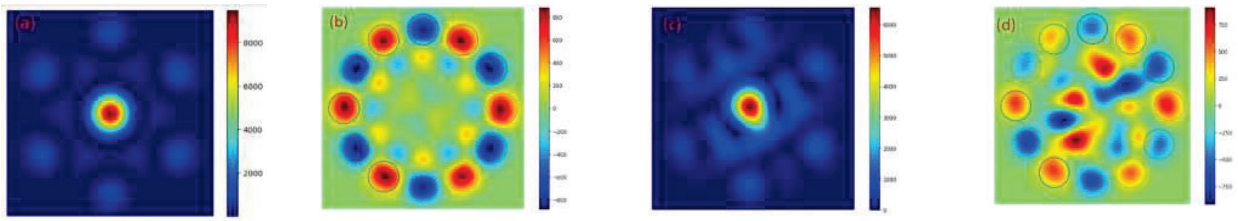

Fig 1. (a)Ideally combined beam in the far-field, (b) difference image in an ideal combined situation, (c) combined image in far-filed in the presence of piston phase noise (d) corresponding difference image.

At each time-step we observe the far-field beam profile, and construct the difference image by subtracting the 30^{o} rotated version from the original image as shown in Fig 1(b) and 1(d). The power in the side-lobes from the difference image is extracted to estimate the control signals. To ensure the Markovian nature, the state is represented as the collection of power values and actions performed in the last five time steps. Due to hexagonal symmetry, if the beams combine ideally, then the power in side-lobes will all be

uniform and power in the main lobe of the difference image would be close to zero (Fig. 1(b)). In the presence of piston phase error, this condition will not be maintained as shown in Fig 1(d). The target of the phase synchronization algorithm is to maximize the reward function which is a function of current state (s_t) and action (a_t) mentioned in Eq.1, where PIB represents power-in-bucket [4]. Here the bucket size is taken as the diffraction limited spot size.

$$r_t(s_t, a_t) = PIB^{diff}_{side-lobe} - PIB^{diff}_{main-lobe} \quad (1)$$

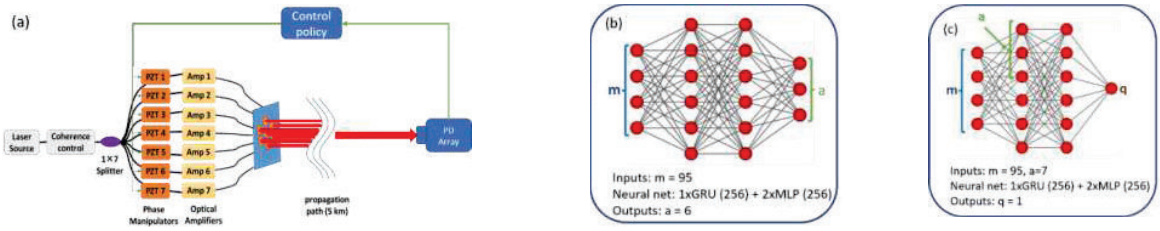

Fig 2. (a) Schematic of 7-channel target in loop (TIL) hexagonal array, (b) Control Policy Network, (c) Critic (policy evaluation) Network

For phase control we use SAC which is a variation of Actor-Critic algorithm [5]. Fig 2. shows a potential target in loop schematic, the policy network and the evaluation network architectures. Both the policy and critic network process the state through a Gated Recurrent Unit (GRU) to utilize the temporal nature of state. The policy network outputs six action voltages for phase modulation of six channels other than the center one since phase noise is applied to all the other channels keeping the center beam as reference. As the six-fold symmetry is maintained, this algorithm can be applied to even higher number of channels which would require only seven photodetectors.

3. Results & Discussion

Fig 4a. shows performance of the agent during training (dark-green and light-green shows the mean and rms value of the reward respectively). The dashed black line in Fig 4a shows the ideal reward at each time-step. Fig 4b shows the normalized open-loop fluctuation. Fig 4c. shows combined power in the central beam normalized with respect to maximum achievable power in closed-loop. The algorithm is able to maintain the closed loop power with a mean of 75.1% (black dashed-line in Fig. 4c). The algorithm has improved the mean PIB by 7.1%.

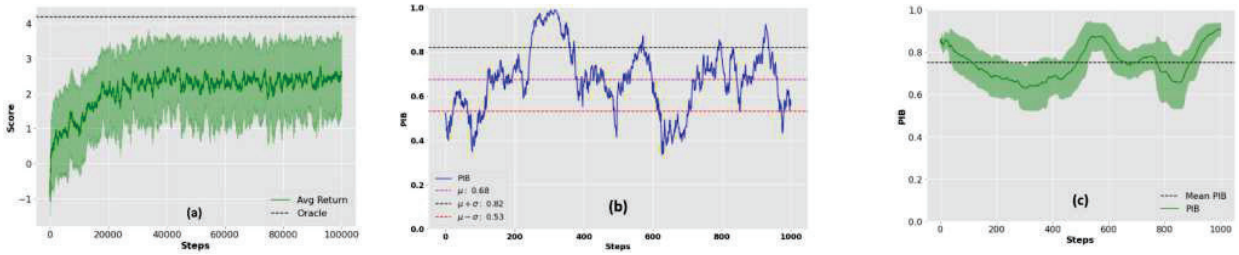

Fig 3. (a) Reward vs. no. of steps in training phase (b) Open loop fluctuation in PIB (normalized) (c) Normalized PIB in testing phase

4. Conclusion

In summary we have simulated a Reinforcement Learning based phase synchronization algorithm which uses only the power of the main-lobe and side-lobes on a seven-channel. We achieved 7.1% improvement in combined power compared to open-loop power. The robustness of the state and reward formulation is yet to be tested in the presence of transverse phase noise which will be addressed in the future work.

5. References

[1] Linslal, C.L,. et al. Challenges in coherent beam combining of high power fiber amplifiers: a review. ISSS J Micro Smart Syst 11, 277–293 (2022).
[2] Henrik Tünnermann and Akira Shirakawa 2021 J. Phys. Photonics 3 015004
[3] P. Ayyaswamy, *et.al.*, "Data-Driven Modeling of Phase Noise Sources in Coherent Beam Combining," in Laser Congress 2021 (ASSL,LAC), OSA Technical Digest (Optica Publishing Group, 2021), paper JTu1A.42.
[4] Bastien Rouzé, *et.al.* , "Coherent beam combination of seven 1.5 µm fiber amplifiers through up to 1 km atmospheric turbulence: near- and far-field experimental analysis," Appl. Opt. 60, 8524-8533 (2021)
[5] Haarnoja T, Zhou A, Abbeel P, Levine S. Soft actor-critic: Off-policy maximum entropy deep reinforcement learning with a stochastic actor. International conference on machine learning 2018 Jul 3 (pp. 1861-1870). PMLR.

Enhancement of Evanescent Field Ratio in a Slot Waveguide by Incorporating a Metal Layer in Substrate

Kanchan Gehlot, Megha Mangal, Karishma Joshi, and Bharat Lal Meena
University of Rajasthan, Jaipur-302004, Rajasthan, India
gehlot.kanchan@gmail.com

Abstract: A novel silicon-on-sapphire slot waveguide incorporating a thin layer of gold is analyzed to obtain a high evanescent field ratio (EFR) in the mid-IR. A high EFR of 56 % is obtained for a slot waveguide with a gold layer operating at the wavelength of 2.76 μm which corresponds to the absorption band of CO_2. A significantly higher EFR is obtained for a slot waveguide with a metal layer in comparison to a slot waveguide formed without a metal layer, thus making it suitable for potential application in developing trace gas sensors based on the absorption of the evanescent field.

Keywords: Trace gas sensor, Evanescent field, Slot waveguide, Silicon-on-sapphire

1. Introduction

The detection and monitoring of the levels of trace gases present in the air is crucial for human health and a healthy ecosystem [1, 2]. The high sensitivity of the optical devices and the availability of low-cost CMOS-compatible fabrication processes have led to the development of sensing devices based on planar optical waveguides, such as channel, rib, ridge, and slot waveguides [3, 4]. The trace gases, such as H_2O, CO, CO_2, CH_4, NO, N_2O and NO_2 have their rotational-vibrational absorption bands in the mid-infrared region of the electromagnetic spectrum [2]. Therefore, the sensing of the trace gases by the absorption of the optical power in the mid-IR requires an optical waveguide that shows low material losses and high overlap of the evanescent field of the guided mode with the sensing media [5]. A high-index contrast slot waveguide based on silicon-on-sapphire has low loss in the mid-IR [6] and the waveguide structure can be optimized to have a large evanescent field ratio (EFR) with strong confinement of optical power resulting in an optical waveguide suitable for sensing of trace gases by absorption of evanescent field of the guided mode [4, 7]. The EFR, defined as the ratio of optical power confined in the sensing region, which consists of the air cladding and the air slot region, to the total power confined in the slot waveguide, is an important parameter that needs to be maximized in order to design a high sensitivity optical sensor based on the absorption of the evanescent field by the sensing media [8].

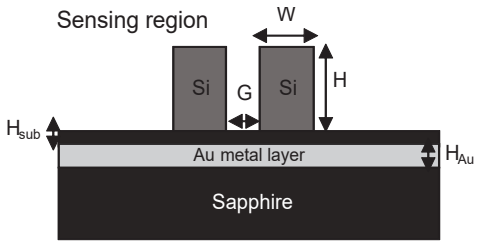

Fig 1. A 2D schematic diagram of a silicon-on-sapphire slot waveguide incorporating a thin gold layer buried in the substrate.

In the present work, a further significant enhancement in the evanescent field of the guided mode of a slot waveguide is achieved by introducing a thin layer of metal in the substrate region. As an example, the slot waveguide with a thin layer of gold in the substrate is analyzed at the operating wavelength of 2.76 μm, which coincides with the absorption band of CO_2 in mid-IR region of the electromagnetic spectrum. The modal analysis is carried out using the full-vector finite element method tool from COMSOL Multiphysics 6.0. The EFR is observed to enhance significantly when a thin gold layer of 50 nm is introduced in the substrate. An enhancement in the EFR of 6 % is observed for the slot waveguide with a gold layer buried in the substrate in comparison to the slot waveguide without any metal layer. A high EFR of the metal loaded slot waveguide makes it a suitable waveguide for sensing applications.

2. Results and Discussions

The Schematic diagram of a symmetric slot waveguide incorporating a thin layer of gold within the substrate is shown in Fig. 1. The waveguide design consists of a thin layer of gold laid over the sapphire substrate. Another layer of sapphire of thickness H_{sub} is deposited over the gold layer which is followed by the deposition of two cores of a high refractive index of Si, separated by a narrow slot region. The thickness of the gold layer is kept fixed at 50 nm. The widths and the heights of the two symmetric Si cores are denoted by W and H and the width of the gap forming the slot region is denoted by G. The refractive indices of Si and sapphire are taken as 3.4699 and 1.7193 at the operating wavelength of 2.76 μm. The slot and the cladding regions are formed of air which provides the sensing region for detecting trace gases.

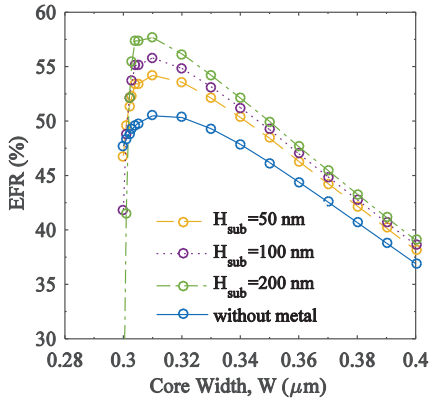

Fig.2 Variation of the EFR with core widths, W and the height of the sapphire layer, H_{sub} laid above the gold layer buried in the sapphire substrate. The other waveguide parameters are kept at the optimized values of H = 1.2 μm, W_{slot} = 60 nm to obtain high EFR.

The modal analysis of a slot waveguide with and without a metal layer embedded in the substrate is carried out using COMSOL Multiphysics 6.0. The EFR of the slot waveguide is optimized by varying the waveguide design parameters and a high EFR of 50% is obtained for a slot waveguide without any metal layer. For the optimized slot waveguide height of H = 1.4 μm and the slot width of G = 60 nm, the variation of the EFR with core widths W is shown with a solid curve in Fig. 2. The effect of the metal layer on EFR is observed by plotting the variation of EFR with core width W, for H_{sub} = 50, 100 and 200 nm. As the depth of the gold layer is increased, the peak value of the EFR increases, and an enhancement of 7% is observed for the optimized value of EFR, which occurs at H = 1.4 μm, G = 60 nm and W = 310 nm. This can provide a useful technique to enhance the EFR and hence the sensitivity of the optical waveguide sensors based on evanescent field absorption.

3. Acknowledgment

The authors acknowledge the Indian Science, Technology and Engineering facilities Map (I-STEM) program, Govt. of India for providing MATLAB and COMSOL Multiphysics 5.6. One of the authors, Ms. Megha Mangal also thanks the Council of Scientific & Industrial Research (CSIR), Govt. of India, for providing the Senior Research fellowship.

4. References

[1] J. Jauhiainen et al., "Reviews and syntheses: Greenhouse gas exchange data from drained organic forest soils–a review of current approaches and recommendations for future research," Biogeosciences **16**, 4687-4703 (2019).
[2] Korotcenkov Ghenadii. "Handbook of gas sensor materials-Conventional approaches," vol.-1 (Springer, New York, 2013).
[3] R. Soref, "The past, present, and future of silicon photonics," IEEE Journal of selected topics in quantum electronics **12,** 1678-1687 (2006).
[4] Q. Xu, V. R. Almeida, R. R. Panepucci, and M. Lipson, "Experimental demonstration of guiding and confining light in nanometer-size low-refractive-index material," Optics letters **29**, 1626-1628 (2004).
[5] G. Stewart, W. Jin, and B. Culshaw, "Prospects for fibre-optic evanescent-field gas sensors using absorption in the near-infrared," Sensors and Actuators B: Chemical **38**, 42-47 (1997).
[6] M. A. Butt, S. N. Khonina, and N. L. Kazanskiy, "Modelling of Rib channel waveguides based on silicon-on-sapphire at 4.67 μm wavelength for evanescent field gas absorption sensor," Optik **168**, 692-697 (2018).
[7] K. Gehlot and A. Sharma, "Optimization of Si slot waveguide using approximate semi-analytical method," Opt. Express **24**, 4722-4729 (2016).
[8] M. A. Butt, S. A. Degtyarev, S. N. Khonina, N. L. Kazanskiy, "An evanescent field absorption gas sensor at mid-IR 3.39 μm wavelength," Journal of Modern Optics **64**, 1892-1897 (2017).

Design and Fabrication of Meta-optics for Light Manipulation: Challenges and Prospects

Jerin Geogy George, Susan Thomas, and Shanti Bhattacharya
Department of Electrical Engineering, Indian Institute of Technology Madras, Chennai, India
shanti@ee.iitm.ac.in

Abstract: Meta-optics have been explored extensively in the past decade and have the potential to replace bulky refractive optics. These flat optical elements can also realise unique functionalities that are not possible using conventional optics. In this work, we discuss the design and fabrication of metasurfaces for light manipulation. The challenges in determining the 'meta-atom' geometries and accurately realising these structures through fabrication is presented. We also discuss using these metasurfaces for aberration correction in microlenses with the help of the design tool: ZEMAX.
Keywords: flat optics, meta-optics, dielectric metasurface, aberration correction, Zemax design

1. Meta-optics

Meta-optical elements are sub-wavelength scatterers arranged laterally to realise a desired functionality [1]. Compared to binary diffractive optical elements, meta-optical elements can provide higher efficiency as several phase levels can be realised inspite have structures of only one height. The sub-wavelength scatterers in these elements impart an abrupt phase shift to the incoming field. This phase shift can be varied by changing the lateral dimensions of the scatterers. By suitable arranging different 'meta-atom' geometries, a wavefront can be engineered or shaped. The first part in designing such elements is to create a lookup map of the meta-atoms with the imparted phase shift. Numerical simulation techniques like FEM/FDTD can be used for this purpose. For single wavelength applications, cylindrical pillars are the most commonly used geometry because of their simplicity and polarisation-independent nature [2]. The conventional approach while designing a metasurface for light manipulation is given below:

The designed metasurface is then fabricated using standard CMOS compatible processes. However, while these are well-established, there are many challenges in the design step as well as in the fabrication process, which are discussed next.

1.1. Limitations of the unit cell approximation

The popular design approach simulates meta-atoms with periodic boundary conditions to evaluate its electromagnetic (EM) response. This model assumes an infinite periodic structure and does not consider the spatial variation in the actual metasurface. Models that simulate meta-atoms as single isolated scatterers are also not accurate as they ignore the lateral scattering from neighbouring meta-atoms. A full-wave simulation of the entire metasurface can be done to obtain an accurate EM response, but it requires enormous computational power. The accuracy of the unit cell simulation is also dependent on the size of the meta-atoms. If the meta-atoms are well separated, then the lateral scattering from nearby cells can be ignored and the meta-atom can be considered an isolated scatterer. Meta-atoms that are closely spaced having local periodicity can be modeled with the periodic boundary condition [3].

1.2. The choice of meta-atom material: variations in the simulation and experiment data

The material for structuring the meta-atoms are chosen by considering its bulk optical parameters in the desired wavelength. Standard refractive index data imported or already available in the numerical simulation software are used while generating the meta-atom lookup map. The height of the meta-atoms are kept constant and the lateral dimensions are varied for generating the lookup map. This allows to complete the fabrication process with a single lithography step. A thin film of the chosen material with the designed thickness is coated on top of a substrate using a standard deposition technique. The meta-atom structure can then be defined by a substractive process. The material deposited during the fabrication process may have variations in the optical parameters compared to the simulated data. The deposition thickness may also have a tolerance, and there will be surface roughness. This will result in a slightly different EM response than the designed one.

The lookup map of the meta-atoms can be modified based on the optical parameters and thickness of the deposited material. A spectroscopic ellipsometer may be used for this purpose.

1.3. Challenges during patterning and post-processing

The most commonly used patterning technique for metasurface is e-beam lithography. The patterning is done by focusing accelerated electrons on a resist whose chemical properties change upon exposure. The patterns can then be developed using a suitable developer. E-beam lithography has excellent patterning accuracy, and while features less than 10 nm can be patterned, typical sizes are usually in the order of 100nm. The lateral resolution in e-beam lithography is mainly determined by the resist thickness and the e-beam acceleration voltage. Its' major drawback is its throughput compared to optical lithography.

Once the resist is patterned and developed, the next step is to transfer this pattern to the material. Pattern transfer techniques like lift-off/etching or both can be used for this purpose. Lift-off is normally done after metallisation and for proper lift-off, resist thickness should be much higher than the metal thickness. This limits the lateral resolution which can be achieved, as the greater the thickness of the resist, the lower the pattern resolution. Etching after metallisation or directly using resist as a mask for etching is used to define the meta-atoms. Mostly dry etching is employed as it has good anisotropy and selectivity. While wet etching causes undercuts, the sidewalls after dry etching will be corrugated [4]. This will cause undesired light scattering and deviation from predicted EM response.

Despite variations in the simulated and experimental results, metasurfaces are revolutionizing the field of optics. In the next section we discuss the use of metasurfaces for aberration correction in microlenses.

2. Aberration correction in microlenses using metasurfaces

Microlenses employed in miniaturized imaging systems such as microendoscopes suffer from optical aberrations leading to poor image quality. The conventional aberration-corrected lenses are complex in structure and challenging to realize due to their complicated phase profile. Such lenses are bulky and not suitable for endoscopic imaging systems. Metasurfaces is a flat optic solution to such optical designs with size constraints. Adding metasurface to an existing optical system imparts an additional change in the wavefront phase. The phase profile of this surface can be designed to correct the off-axis and on-axis aberrations simultaneously[5].

The optical system consisting of microlenses along with a phase element can be designed in ray tracing software such as Zemax Optic studio. The phase element is modeled as a binary optic surface in Zemax with a phase profile as given in the following equation,

$$\phi(\rho) = \sum_{i=1}^{N} a_i \left(\frac{\rho}{R}\right)^{2i}$$

where a_i is the phase coefficients, N is the number of radial polynomial coefficients, ρ is the radial aperture coordinate and R is the radius of the metasurface. The radial polynomials represent the variation in phase across the optical surface. The phase coefficients are set as variables to optimize for the best spot quality. The surface phase profile of the phase element is extracted for further design of the metasurface.

3. Conclusions

In this paper, the design and fabrication processes of meta-surfaces are discussed and means of optimising them for specific applications are presented.

4. References

[1] Brener, Igal, Sheng Liu, Isabelle Staude, Jason Valentine, and Christopher Holloway, eds. *Dielectric metamaterials: fundamentals, designs and applications*. Woodhead publishing, 2019.

[2] Dharmavarapu, Raghu, Soon Hock Ng, Fatima Eftekhari, Saulius Juodkazis, and Shanti Bhattacharya. "MetaOptics: Opensource software for designing metasurface optical element GDSII layouts." *Optics express* 28, no. 3 (2020): 3505-3516.

[3] Ciarella, Luca, et al. "Finite-Size and Illumination Conditions Effects in All-Dielectric Metasurfaces." *Electronics* 11.7 (2022): 1017

[4] Bazylenko, M. V., M. Gross, and M. Faith. "Effect of reactive ion etching–generated sidewall roughness on propagation loss of buried-channel silica waveguides." *Applied physics letters* 69, no. 15 (1996): 2178-2180.

[5] Yan Liu, "Metaobjective with submicrometer resolution for microendoscopes," Photonics Research 9:2, 106-115 (2021).

Significant Amplification of Optical Pulses in Photonic Time Crystals within Momentum-gap

Snehashis Sadhukhan, Somnath Ghosh*
Department of Physics, Indian Institute of Technology Jodhpur, NH 65 Karwar, Rajasthan, India 342037.
**somiit@rediffmail.com*

Abstract: Exclusive light dynamics in photonic time crystals is reported within the momentum gap that exhibits the profound amplification of the propagating pulses with momentum lying within several momentum-gap ranges.
Keywords: Photonic time crystal, momentum gaps, amplification.

1. Introduction

The study of time-varying media has brought about a significant paradigm shift in wave manipulation methods in photonic systems. The photonic time crystals (PTCs) where the refractive index (n) varies as a periodic function of time [1] exhibit novel physical effects such as momentum gaps [1, 2], topological aspects [3], parity-time symmetry, localization via temporal disorder and others [4, 5]. These systems resemble photonic crystals (PC), which show periodic changes of n in space. The PTCs and PCs have a separate existence from one another due to the intrinsic temporal periodicity in the PTC's display of momentum (k) gaps in the dispersion diagram whereas PCs reveals gaps in frequency. In PTCs a sudden shift in n over a femtosecond time period is an essential requirement to see the distinctive momentum gaps in the visible range. Furthermore, independent of their frequencies, all waves travelling through such a system with k within the bandgap are amplified. In this work, we aim to study the wave amplification specific k gaps.

2. Results and Discussion

We take into account a binary PTC system whose permittivity (ε) fluctuates abruptly and repeatedly over time with periodicity T (Fig. 1(a)),

$$\epsilon(t) = \begin{cases} \epsilon_1, & 0 < t < t_1 \\ \epsilon_2, & t_1 < t < T \end{cases} \tag{1}$$

with such step-like variation over time, the propagating pulse experiences time reflections occurring in a periodic manner that produce a forward propagating wave along with its time-reversed counterpart, both with the same momentum. Depending on the propagation medium, their frequency ($= kc/n$) gets modified. The displacement field for such a periodically fluctuating system may be expressed as in Eq. 2,

$$D(t,z) = \begin{cases} a_p\, e^{i\omega_1\left(t+\frac{t_1}{2}-pT\right)} + b_p\, e^{i\omega_1\left(t+\frac{t_1}{2}-pT\right)}, & 0 < t < t_1 \\ c_p\, e^{i\omega_2\left(t+\frac{t_2}{2}-pT\right)} + d_p\, e^{i\omega_2\left(t+\frac{t_2}{2}-pT\right)}, & t_1 < t < T \end{cases} \tag{2}$$

where p is for the p^{th} unit cell in time and a_p, b_p, c_p and d_p are the complex amplitudes in each temporal segments. The dispersion relation links the Floquet frequency (Ω) as a function of k in PTC that is derived by tracking the complex amplitudes of the D in such a time-varying system using the transfer matrix technique and Floquet theorem ($D = D_\Omega(t)e^{-i\Omega t}$) (Eq. 3).

$$\Omega(k) = \frac{1}{T}\cos^{-1}\{e^{i\omega_2 t_2}\left[\cos(\omega_1 t_1) + \frac{i}{2}\left(\frac{\omega_1}{\omega_2}+\frac{\omega_2}{\omega_1}\right)\sin(\omega_1 t_1)\right] + e^{-i\omega_2 t_2}\left[\cos(\omega_1 t_1) - \frac{i}{2}\left(\frac{\omega_1}{\omega_2}+\frac{\omega_2}{\omega_1}\right)\sin(\omega_1 t_1)\right]\} \tag{3}$$

The dispersion diagram reveals bands for real Ω and gaps where Ω is complex [Fig. 1(b)]. We have studied the PTC system utilizing numerical simulations. To explore the pulse dynamics in such a linear system, we simulate the propagation of different pulses inside the PTC. All pulses have the same FWHM (full width at half maxima) of 45 fs. In our simulation environment, the pulse enters the system at t=100 fs and propagates in free space ($\epsilon = 1$) until the PTC starts at t= 220 fs. The time variation stops at t=290 fs, completing N (= 35) periods in time. FDTD simulations show that the propagating pulse splits into forward and time reversed pairs at the start and end of the PTC, producing four pulses [Fig. 1(c)]. Such observations are obtained when the pulse's k lies within the band and [2]. When the pulse's momentum is inside the bandgap at the start of PTC, in that case, the pulse becomes localized in space, and its intensity increases exponentially until the PTC ends [Fig. 1(d)]. And under such

circumstances, the pules split into two. The modes with both $\pm\Omega$ are omnipresent in time. Those eventually generate an envelope of $\sim \cosh t + \sinh t$, which is responsible for the exponential growth in amplitude [4]. At first the amplification in first bandgap which falls within a range of $0.53 < k/k_0 < 0.73$ [see Fig. 1(b)] has been studied. The output and input pulse intensity ratio for *N*= 10 shows that the amplification attained a maximum value near the middle of the gap (i.e. the gap center) which in this case turns out to be $I_{out}/I_{in} \approx 890$ [as shown in Fig. 1(e)]. Moreover, the degree of amplification at the center of various bandgaps has also been investigated as shown in Fig. (f). The study has been performed over the first six bandgaps, which reveals that the pulses experience different amount of amplifications at different bandgaps.

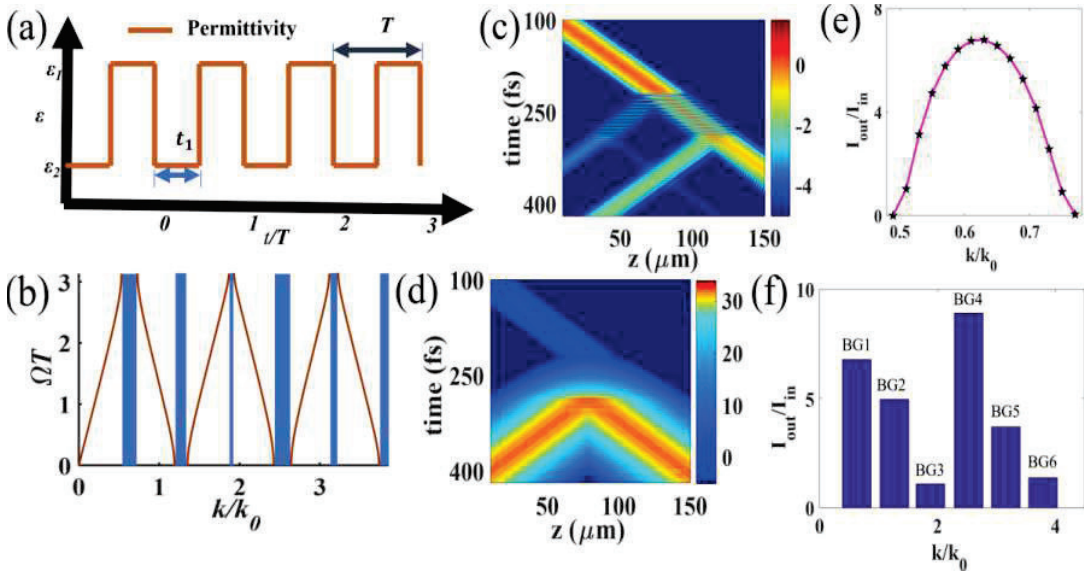

Fig. 1 (a) Schematic of a binary photonic time crystal (PTC), dielectric constant (ε) changing periodically with time where, t_1 and t_2 $(= T - t_1)$ are the duration of ε_1 and ε_2, respectively. **(b)** PTC's band diagram shows bands (brown) separated by gaps (blue) in normalized momentum ($k_0 = 2\pi/Tc$). FDTD simulation showing intensity variation (color bar in log scale) of a pulse propagating under the influence of PTC when *k* falls within the **(c)** band, and **(d)** bandgap (BG) respectively**. (e)** Amplification (in log scale) of the propagating pulse for different values of *k* within the first bandgap (BG1). **(f)** Amplification (in log scale) of the propagating pulse for *k* values at the middle of the BGs.

3. Conclusion

The *k*-gap occurs in a PTC system due to broken continuous time translation symmetry, and the time periodicity results in the discrete-time translation symmetry, which leads to the Floquet states. The propagating pulse periodically splits into a wave travelling in the forward direction and another as a time-reversed pair at the temporal interfaces, keeping the momentum constant. In PTC systems, these two pulses substantially interact, resulting in Floquet modes and dispersion bands gapped in *k*. Within the gap, Ω becomes complex and an exponential increase in the energy of the wave is observed. Within the bandgap, the amplification attains a maximum value at the gap center. Additionally, different bandgaps are equipped with different amount of amplifications. Such amplifications turn out to be a frequency independent amplification and has a huge potential to be implemented in several optical devices.

4. Acknowledgement

SS acknowledges financial support from Prime Minister's Research Fellows (*PMRF*) Scheme (PMRF ID: 2201322), India and Suman Dey for discussion.

5. References

[1] L. Zeng, J. Xu, C. Wang, J. Zhang, Y. Zhao, J. Zeng, and R. Song, "Photonic time crystals," Sci. Rep. **7**, 17165 (2017).
[2] A. M. Shaltout, J. Fang, A. V. Kildishev, and V. M. Shalaev, "Photonic Time-Crystals and Momentum Band-Gaps," CLEO, OSA Technical Digest (online), FM1D.4 (2016).
[3 E. Lustig, Y. Sharabi, and M. Segev, "Topological aspects of photonic time crystals,"Optica **5**, 1390 (2018).
[4] Y. Sharabi, E. Lustig, and M. Segev, "Disordered photonic time crystals," Phys. Rev. Lett. **126**, 163902 (2021).
[5] Y. Sharabi, A. Dikopoltsev, E. Lustig, Y. Lumer, and M. Segev, "Spatiotemporal photonic crystals," Optica **9**, 585 (2022).

ZnO nanoparticles assisted Polymer optical fibre random lasers for Speckle free Imaging

Anugop Balachandran, Vipin Balan, Manju Joseph, Kailasnath Madanan
International School of Photonics, Cochin University of Science and Technology, Kochi, Kerala-682022
Author e-mail address: anugopb@cusat.ac.in

Abstract: Here we analysed the effect of nanoparticle size on the random lasing behaviour of a polymer optical fibre. Polymer optical fibre random lasers were fabricated using ZnO nanoparticles with two different diameters as the scattering centers and Rh-640 perchlorate as the gain material. Coherent random lasing was observed for both systems. With the same number density, larger particles offered a lower threshold random lasing. Also, speckle-free imaging using the polymer optical fibre random laser as the illuminating source is also demonstrated.

Keywords: Polymer optical fibres, Random lasers, ZnO nanoparticles, Speckle-free imaging.

1. Introduction

Lasing from micro and nanodevices without a conventional mirror cavity has gained wide attention in the research field nowadays [1,2]. Owing to the ease of fabrication and low spatial and temporal coherence random lasers have promising applications in certain fields. In random lasers, the conventional mirror cavity is replaced by disorder-induced scattering. Random lasers require an active medium and a pumping scheme but optical feedback is achieved by the multiple scattering offered by the scattering centers within the gain medium. The photons generated in the gain medium encounter multiple scattering before it leaves the medium and is amplified due to stimulated emission. Different from a conventional laser, a random laser will not give directional output because of the random scattering. But in certain applications, a directional output is important and certain confinement components were introduced in the random laser system. Optical fibre structure offers a highly directional random lasing [3]. The random fibre lasers have several advantages such as low lasing threshold, low-cost of fabrication, and offer directional output. Dye-doped polymer optical fibres play an important role in the development of flexible directional random lasers and with their ability to produce speckle-free images [4], they open a new window in the field of flexible directional random lasers. In the present study, we have analysed the effect of the nanoparticle size on the random lasing threshold of polymer optical fibre doped with Rh-640 perchlorate and ZnO nanoparticles with two different diameters. Coherent random laser emission was observed in both cases and the lasing threshold was reduced when larger nanoparticles were used. Also, we demonstrate speckle-free imaging using the polymer optical fibre random laser as the illuminating source.

2. Experiment

PMMA-based polymer optical fibre random laser (POFRL) was fabricated as follows. First, a hollow polymer optical fibre preform was fabricated using Teflon method and was then heat drawn using a custom-made fibre drawing tower. A mixture of PMMA, 0.5mM gain material (Rh640 perchlorate), and $1x10^{12}/cm^3$ scattering particles (ZnO nanoparticles with an average diameter of 70nm and 130nm) in anisole was carefully filled in the hollow fibre. The fibre sample was transversely pumped using a Q-switched Nd: YAG laser (Q-smart 450) at 532 nm and random laser emission was collected using a CCD spectrometer (Acton spectrapro 500i).

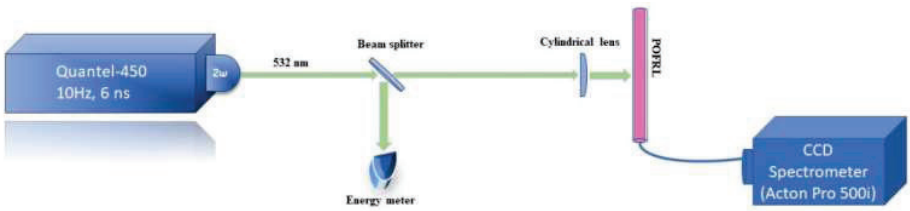

Fig. 1: Experimental set-up for the random lasing

3. Results and Discussions

The random lasing emission spectra at a pump pulse energy of 2.79mJ and the threshold behaviour of the fibres are shown in Fig.2. From the figures it is clear that the lasing threshold was reduced from 0.83mJ to 0.48mJ when the size of the ZnO nanoparticles increased from 70nm to 130nm. When the random laser system was excited with a pump laser photons will generate in the gain medium and due to the presence of ZnO nanoparticles, it will experience multi-scattering and their path length will increase and enhance the possibility of stimulated emission. One important physical parameter which determines the behaviour of a random laser is the scattering mean free path and is given by $l_s = \frac{1}{\sigma_s \rho}$, where σ_s is the scattering cross-section and ρ is the number density of the nanoparticles [5]. Here we used ZnO nanoparticles with two different diameters 70nm and 130nm which offer a scattering mean free path of 0.43cm and 0.03cm respectively. The small value of l_s provided by the large ZnO nanoparticles offers a low threshold random lasing.

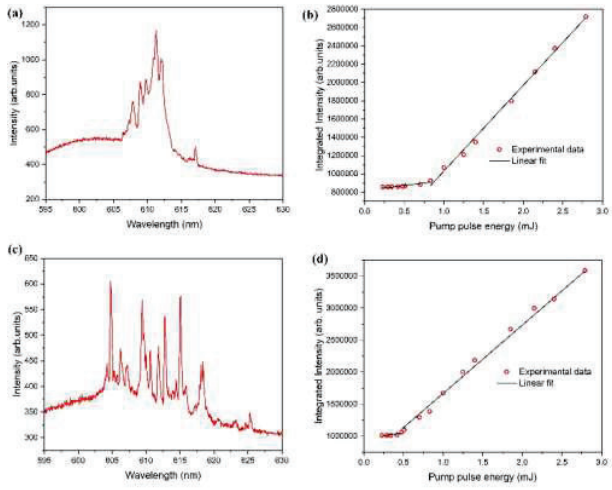

Fig. 2: Random lasing spectra (a&c) at a PPE of 2.79mJ and threshold behaviour (b&d) of POFRL

Table 1: Comparison of random lasing parameters of POFRL

Sample code	No. density of ZnO nanoparticles (cm^{-3})	Size of ZnO Nanoparticles (nm)	Scattering mean free path (mm)	Random lasing threshold (mJ)
1	$1x10^{12}$	70	0.43	0.83
2	$1x10^{12}$	130	0.03	0.48

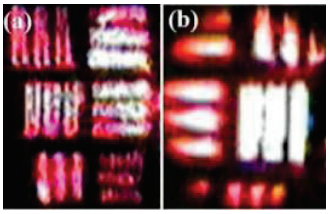

Fig. 3: Optical images of AF resolution test chart under the illumination of (a) He-Ne laser and (b) POFRL

4. References

[1] F. Luan, B. Gu, A.S.L. Gomes, K. Yong, S. Wen, P.N. Prasad, "Lasing in nanocomposite random media", Nano Today. 1–25 (2015).

[2] Z. Wang, X. Meng, A. V Kildishev, A. Boltasseva, V.M. Shalaev, "Nanolasers Enabled by Metallic Nanoparticles : From Spasers to Random Lasers", Laser Photonics Rev. 1700212 1–15 (2017).

[3] C.J.S. De Matos, L. De S. Menezes, A.M. Brito-Silva, M.A. Martinez Gámez, A.S.L. Gomes, C.B. De Araújo, "Random fiber laser", Phys. Rev. Lett. 99 1–4 (2007).

[4] B. Redding, M.A. Choma, H. Cao, "Speckle-free laser imaging using random laser illumination", Nat. Photonics. 6 355–359 (2012).

[5] J. Kitur, G. Zhu, M. Bahoura, M.A. Noginov, Dependence of the random laser behavior on the concentrations of dye and scatterers, 024009 2–7 (2010).

Laboratory Calibration of Bright Field Microscopy-Based Air Quality Monitoring System

Anand Kumar[a], Sachin Dhawan[b], Mukesh Khare[c], Dalip Singh Mehta[a,d,*],

[a] Centre for Sensors, INstrumentation and Cyber-physical System Engineering, IIT Delhi; [b] School of Interdisciplinary Research, IIT Delhi; [c] Department of Civil Engineering, IIT Delhi; d Department of Physics, IIT Delhi

[*] mehtads@physics.iitd.ac.in

`

Abstract: The present work proposes, bright-field microscopy-based air quality monitoring system that monitors the concentration of particulate matter in ambient conditions. The system provides the concentration, size, and shape of particles present in the ambient air. The intended use of the system is to augment the continuous ambient air quality monitoring systems installed across the country for particulate matter monitoring in ambient conditions.

Keywords: PM Sensor, Bright-field Imaging, Air Pollution, Environment

1. Introduction

Air pollution is one of the leading reasons of premature deaths all around the world, it contributes to about 9% deaths globally, it varies from 2% to 15% by country. In South and East Asia, the deaths due to air pollution is 15% globally. The deep inhalation of fine particulate matter (particle size smaller than 2.5 μm) and ultrafine particulate matter (particle size smaller than 1 μm) into the lungs and respiratory system; the small size with respect to the aerodynamic diameter as well as greater surface area provides a larger concentrations of adsorbed air toxicants per unit mass [1-3] The PM data has very low spatial and temporal resolution due to limited number of stations installed across the country. The action plans for the reduction of PM are based upon the concentration of PM at different micro-environments. The regulatory systems are very expensive to buy and operate, this inherent characteristic of the regulatory systems makes it difficult to install across the country. The proposed solution is to use the sensor-based systems to augment the established monitoring network.

Presently, some low-cost sensors for PM2.5 are mostly available in the western international markets. These low-cost sensors used in different countries are generally light scattering based [4-5] The accuracy of the data from the low-cost sensors are not good as regulatory instruments [5-6]. The inherent constraints of these sensors are with respect to their applicability in tropical climatic condition like India. These sensors are calibrated according to the requirements of country specifics which are different than Indian environmental conditions. The long-term stability of the sensor materials and devices depends upon the temperature, humidity and climatic conditions.

2. Material and Methods

2.1 Principle

The present system is a combination of PM sampler and PM analyzer in which air sampling and its analysis are performed one by one. Ambient air is sampled through a vacuum pump. At present, air sampling is performed at a remote place and the collected sample is brought to the laboratory for microscopic analysis under the supervision of a trained professional. The proposed system is based on the principle of bright field microscopy (BFM) based air pollution monitoring system (APMS). In the proposed APMS we employed a vacuum pump with a flow rate of 13 lpm to collect the air sample from the ambient environment on the collection media (Air-O-Cell by Zefon international). Therefore, Particulate matter (PM) in the air gets deposited on the collection media which is subsequently imaged by the BFM unit. Recorded images of the PM are analyzed, and the results are exhibited on the raspberry pi display. Analysis of the PM is performed on the image processing-based algorithm which provides the particle size.

2.2 Laboratory Calibration Procedure

A 1951 USAF resolution test chart is a microscopic optical resolution test device used for the calibration of microscopic systems. It is widely used in optical engineering laboratory work to analyze and validate imaging systems

such as microscopes, cameras, and image scanners. It is a gold standard technique to calibrate the optical systems. The resolution of the Imaging unit of the proposed system has been tested with 1951 USAF resolution chart.

3. Results and Discussions

3.1 System Calibration

The imaging of 1951 USAF resolution test chart with the proposed microscopic unit was done for resolution test; the 3rd element of 7th group of resolution test chart was successfully resolved. The length of 3rd element and found to be 15.50 µm in size (shown in figure 1). Measurement of number of pixels enclosed in 15.50 µm length which was found to be 177 pixels. Hence, we calculated the size of 1 pixel which was equal to 87.5 nm and this pixel size has been used to determine the size of Particulate matter (PM). Hence the calibrated pixel size of this system has been used for particle sizing and measurement of ambient concentration of particulate matter. After calibration, the resolution of the system was found out to be 0.35 µm.

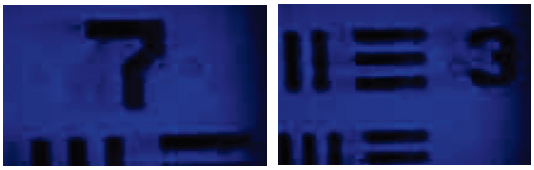

Figure 1: Laboratory calibration of microscopic unit with USAF 1951 resolution chart

3.2 Ambient Particulate Matter – Sampling and Analysis

The calibrated system is used for the sampling and analysis of the ambient particulate matter using the proposed device. The device samples the ambient air at the rate of 13 LPM (litres per minute). The sampling media used (Air-O-cell) is exposed to the sampled air. After the sampling of the ambient particulate matter on the sampling media, analysis of the particulate matter concentration is done by microscopy imaging of the sampled ambient air. The device captures the image in real time and processes with the developed algorithm to give the concentration, particle count and shape as the output of the device. The analyzed image of sampled ambient particulate matter is given in figure 2. It shows the different particles present in the samples air and the shape of the particles. The Particulate Matter count was found out to be 306 particles and the concentration is 65 µg/m^3.

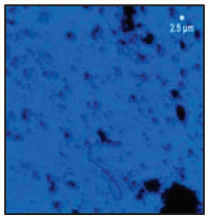

Figure 2: Image of Particulate Matter using the proposed system showing the particles and shapes of the particles.

References:

[1] Rundell, K.W. and Caviston, R., 2008. Ultrafine and fine particulate matter inhalation decreases exercise performance in healthy subjects. The Journal of Strength & Conditioning Research, 22(1), pp.2-5.

[2] Xing, Y.F., Xu, Y.H., Shi, M.H. and Lian, Y.X., 2016. The impact of PM2. 5 on the human respiratory system. Journal of thoracic disease, 8(1), p.E69.

[3] Ansari, M. and Ehrampoush, M.H., 2019. Meteorological correlates and AirQ+ health risk assessment of ambient fine particulate matter in Tehran, Iran. Environmental research, 170, pp.141-150.

[4] Sayahi, T., Butterfield, A. and Kelly, K.E., 2019. Long-term field evaluation of the Plantower PMS lowcost particulate matter sensors. Environmental Pollution, 245, pp.932-940.

[5] Sayahi, T., Kaufman, D., Becnel, T., Kaur, K., Butterfield, A.E., Collingwood, S., Zhang, Y., Gaillardon, P.E. and Kelly, K.E., 2019. Development of a calibration chamber to evaluate the performance of lowcost particulate matter sensors. Environmental Pollution, 255, p.113131.

[6] Zheng, T., Bergin, M.H., Johnson, K.K., Tripathi, S.N., Shirodkar, S., Landis, M.S., Sutaria, R. and Carlson, D.E., 2018. Field evaluation of low-cost particulate matter sensors in high-and low concentration environments. Atmospheric Measurement Techniques, 11(8), pp.4823-4846.

Exploiting the Polarimetric Features of Spatial Light Modulator for Coded Aperture Imaging

Vipin Tiwari[1], Nandan S. Bisht[2]

[1] *Applied Optics & Spectroscopy Laboratory, Department of Physics, Kumaun University, SSJ Campus Almora, Uttarakhand 263601, India*

[2] *Department of Physics, Soban Singh Jeena University, Almora, 263601, Uttarakhand, India*

Author e-mail address: vipint92@gmail.com

bisht.nandan@gmail.com

Abstract: We exploit the polarimetric characteristics of Liquid crystal spatial light modulator (LC-SLM) to construct the polarization coded apertures (PCAs) aiming to obtain improved imaging characteristics of an imaging system. Numerical simulations are carried out and demonstrated for PCA enabled imaging system. It is shown that the resulting imaging system enables enhanced depth of field (DOF) without scarifying the total light throughput.

Keywords: Spatial light modulator, polarization, coded apertures, point spread function, depth of field.

1. Introduction

LC-SLMs are regarded as key components in modern imaging applications due to their dynamic amplitude and phase modulation characteristics of light. However, polarization modulation characteristics are another crucial aspect of SLMs and have been gained substantial interest during last few decades. The polarization modulation characteristics of SLMs enable to achieve complex field modulation (both amplitude and phase) of light and hence can be utilized in various advanced imaging fields, i.e., beam shaping [1], quantum optics [2], coded aperture imaging (CAI) [3], etc. Recently, several studies have been carried out, where SLMs have been employed to import customized holograms, phase masks, structured light patterns, etc. in order to develop the advanced imaging modalities [4, 5]. The overall objective of these techniques is to achieve enhanced imaging characteristics of an imaging system, which is generally obscured by the diffraction limit [6]. The conventional method to extend the DOF is to reduce the numerical aperture but it is a major constraint under low light illumination. Therefore, techniques are required to be developed for accommodating the said issue. In this paper, we present SLM based PCAs by utilizing their pixel-voltage (grayvalues) dependent polarization modulation characteristics. The PCAs are then demonstrated for the extended DOF of diffraction limited lens using point spread function (PSF) analysis.

2. Method and Results

Fig. 1 (a) shows the schematic of the experimental configuration of the PCA enabled imaging system. The PCAs are designed by splitting a full circular aperture of radius 'R' into two regime of the equal-area i.e. the central circular region with a radius of 'r' and the outer circular region with $R = \sqrt{2}r$. It is reported earlier that the LC-SLM (Holoeye LC-R720) can modulate the states of polarization of light depending on its various grayvalues. For instance, it rotates the SOP of light by 90^0 at gray value 180 [7]. Utilizing this SOP modulation characteristic of the SLM, the inner region is provided SOP, i.e., x-polarized, while the SOP of outer annular ring is rotated by 90^0 (y-polarized). Therefore, the conventional annular aperture in polarization encoded by encrypting orthogonal SOPs across its two regions (inset of fig.1 (a)). In this manner, PCAs enable to utilize entire region of full aperture without reducing its size. Since, DOF of diffraction limited lens is inversely proportional to the NA of the aperture. Therefore, PCA enabled imaging system is expected to exhibit enhanced DOF as compared to the conventional aperture.

The point spread function of PCA imaging system is given as [8]

$$I_{PCA}(\rho) = \left| \int_0^r r' J_0\left(2\pi r' \frac{\rho}{\lambda z}\right) exp\left[i \frac{2\pi W}{\lambda} \left(\frac{r'}{R}\right)^2 \right] dr' \right|^2 + \left| \int_r^R r' J_0\left(2\pi r' \frac{\rho}{\lambda z}\right) exp\left[i \frac{2\pi W}{\lambda} \left(\frac{r'}{R}\right)^2 \right] dr' \right|^2 \quad (1)$$

Here, 'ρ' is the radial coordinate of the IPSF, 'λ' is the wavelength of incident light, 'W' is the defocus coefficient in the unit of the number of wavelengths. 'J_0' denotes the Bessel function of first type order zero and 'z' is the propagation distance i.e., the distance between PCA and image plane.

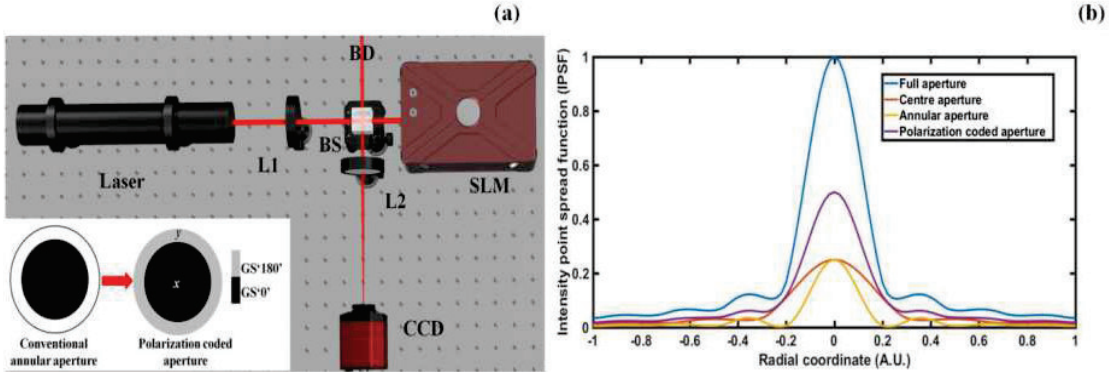

Fig.1 (a) Schematic of PCA based imaging system,. Inset represents schematic of the SLM based PCA (grayscale mapping on SLM). (b) Simulation results for IPSF for apertures with different size.[L_1, and L_2: lenses, BS: beam splitter, CCD: charge coupled device, SLM: spatial light modulator, BD: beam dumped].

Fig. 1 (b) represents the simulation result for intensity point spread function (IPSF) of diffraction limited lens corresponding to apertures with different sizes. It is evident from the fig. 1 (b) that IPSF corresponding to PCA yields similar DOF as compared to aperture with reduced size (centre aperture). However, it can restore up to two times of total intensity (50% of total intensity) as compared to the central aperture (25% of total intensity).

3. Conclusion

We have numerically analyzed the LC- SLM based PCAs by exploiting their pixel-voltage (grayvalues) dependent polarization modulation characteristics. The designed PCAs are demonstrated for the extended DOF of diffraction limited lens. The simulation results indicate the PCA enabled imaging system exhibit extended DOF as compared to conventional apertures without scarifying the total light illumination and are expected to be of great interest for further development of advanced diffraction limited imaging techniques.

Acknowledgments

Vipin Tiwari would like to acknowledge support from DST-INSPIRE (IF-170861).

References

1. Burger, L., Litvin, I., Ngcobo, S., Forbes, A.: Implementation of a spatial light modulator for intracavity beam shaping. J. Opt. (United Kingdom). (2015). https://doi.org/10.1088/2040-8978/17/1/015604
2. Andersen, J.M., Alperin, S.N., Voitiv, A.A., Holtzmann, W.G., Gopinath, J.T., Siemens, M.E.: Characterizing vortex beams from a spatial light modulator with collinear phase-shifting holography. Appl. Opt. 58, 404 (2019). https://doi.org/10.1364/ao.58.000404
3. Vijayakumar, A., Rosen, J., Rai, M.R., Ogura, Y.: Resolution enhancement in nonlinear interferenceless COACH with point response of subdiffraction limit patterns. Opt. Express, Vol. 27, Issue 2, pp. 391-403. 27, 391–403 (2019). https://doi.org/10.1364/OE.27.000391
4. Yu, X., Wang, K., Xiao, J., Li, X., Sun, Y., Chen, H.: Recording point spread functions by wavefront modulation for interferenceless coded aperture correlation holography. Opt. Lett. 47, 409 (2022). https://doi.org/10.1364/ol.439615
5. Sarkar, T., Tiwari, V., Chandra, S., Bisht, N.S., Singh, R.K.: Holography with higher-order Stokes correlation. Phys. Rev. A. 106, 13508 (2022). https://doi.org/10.1103/PhysRevA.106.013508
6. Vijayakumar, A., Rosen, J., Rai, M.R.: Superresolution beyond the diffraction limit using phase spatial light modulator between incoherently illuminated objects and the entrance of an imaging system. Opt. Lett. Vol. 44, Issue 7, pp. 1572-1575. 44, 1572–1575 (2019). https://doi.org/10.1364/OL.44.001572
7. Tiwari, V., Gautam, S.K., Naik, D.N., Singh, R.K., Bisht, N.S.: Characterization of a spatial light modulator using polarization-sensitive digital holography. Appl. Opt. (2020). https://doi.org/10.1364/ao.380572
8. Chi, W., Chu, K., George, N.: Polarization coded aperture. Opt. Express. (2006). https://doi.org/10.1364/oe.14.006634

Design and Comparative Analysis of Catadioptric Cassegrain Telescope based on Spherical and Aspherical Thin Corrector Plate

Parag Varma[1], Sonam Berwal[1, 2], Mukesh Kumar*[1, 2], Neha Khatri[1, 2]
[1]*CSIR-Central Scientific Instruments Organisation, Chandigarh-160030, India*
[2]*Academy of Scientific and Innovative Research (AcSIR), Ghaziabad- 201002, India*
paragvarma07@gmail.com, *mukeshk@csio.res.in

Abstract: To design and develop an improved reflecting telescope for various astronomical or geological applications, optical designers have long been exploring new ways to control aberrations in optical systems. In the present study, a 0.9 m Catadioptric Cassegrain telescope of 1400 mm focal length for space applications in visible-NIR (400- 1500 nm) wavelength range with 0.1° FOV has been designed. A comparative study on the use of spherical and aspherical corrector plate has also been carried out. The performance analysis was carried out with respect to various parameters such as the spot size, rms wavefront error vs. field and percentage of distortion.
Keywords: Catadioptric, Corrector plate, Aspheric, Spherical aberration.

1. Introduction

Over the past few decades, there have been extensive design and simulation studies of reflecting telescopes and this knowledge source is still looked upon for further advancements. This is because, at larger dimensions, it is easier to manufacture and handle a mirror over a lens. Apart from this, they have superiority over refracting telescopes due to minimal chromatic aberrations. Even though reflecting telescopes have very low aberrations as compared to the refractive ones, further improvement in reflecting telescope can be achieved by introducing a corrector plate. It can be a thin corrector plate placed at the front of the primary mirror as in the case of Schmidt-Cassegrain or, a thick plate which can be seen in Maksutov-Cassegrain system [1]. Sometimes this corrector plate can be placed before the secondary mirror in which case it is called as the sub-aperture corrector [1].

In this paper, a 0.9 m Catadioptric Cassegrain telescope for visible-NIR (400- 1500nm) region is designed and optimized. Later, an analysis on the effect of spherical and aspherical thin corrector plates is also included to minimize rms wavefront error and spot size.

2. Optical Design

The proposed design consists of a primary mirror which is a paraboloid whereas, the secondary mirror is a hyperboloid. The mirrors are designed and placed such that they are confocal in nature. Focal length of the system was about 1400 mm and a 0.1° FOV. Fig. 1 shows the ray-tracing diagram of the reflective telescope. The mathematical explanations, used to calculate the radius of the primary and secondary mirrors, can be found in **[2].** Once the system was optimized, the corrector plates were introduced in front of the mirror as in the case of Schmidt-Cassegrain. The corrector plate (3 mm thickness), used for aberration correction, was placed at the focus of the primary mirror. After introducing the corrector plate, both the mirror parameters remained constant and only the corrector plate were optimized to obtain a better result for a given configuration.

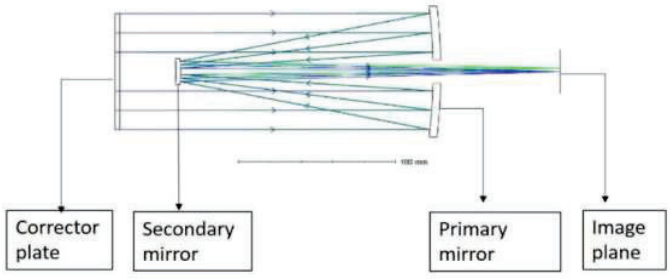

Fig. 1: Ray tracing diagram of the Catadioptric Cassegrain Telescope

3. Result & Discussion:

At first, a spherical plate (plano-convex) was placed at the above mentioned position and was optimized to gain the best possible result. Table 1 represents the maximum spot radius and rms spot value obtained at the image plane for 0° and full field value. Fig. 2(a) shows the field curve and distortion for the spherical plate. Maximum distortion was observed to be 0.001071%. Fig. 3(a) shows RMS wavefront error vs. Field plot for the spherical plate. The rms wavefront error for max. field at 555 nm is 0.7890 whereas for 1050 nm it was 0.0042. The maximum value was 0.1238 for max. field at 485nm.

Later, this Spherical corrector plate was replaced by the aspherical (hyperbolic) corrector plate and the system was optimized again, keeping the mirror parameters constant. Table 1 reveals the rms and maximum spot value at both 0° and 0.1°. Field curve and Distortion at the image plane is shown in Fig. 2(b). Maximum distortion was estimated to be 0.001065% at maximum field i.e., 0.1°. Fig. 3(b) reveals the RMS wavefront error vs. Field plot for the aspheric corrector plate. At 555 nm wavelength, the rms value at max. field is 0.0123 and at 1.050 nm, it was 0.0038. It too shows its max value at 0.1° i.e., 0.0157 at 485 nm. From Table

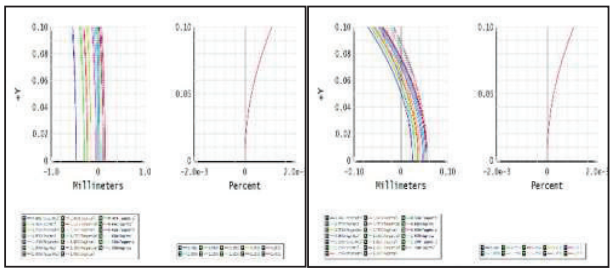

Fig. 2: Field curve and % Distortion for (a) Spherical corrector plate, (b) Aspheric corrector plate

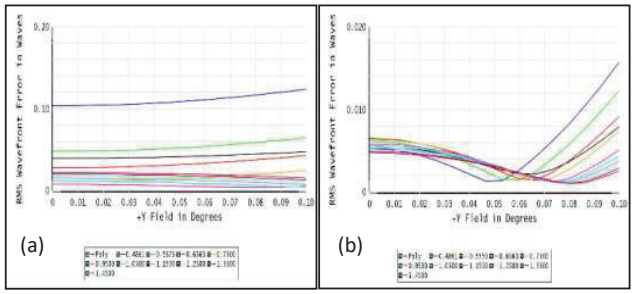

Fig. 3: RMS wavefront error in waves vs. Field in degrees for (a) Spherical corrector plate, (b) Aspherical corrector plate

1, a decrease in the rms as well as the maximum spot radius of about 80% was observed on replacing spherical corrector plate with an aspheric corrector plate. Thus, the application of aspherical corrector plate produces a sharper point than the spherical ones, thereby indicating a decrease in the spherical aberration of the system by the mirrors [3].

Table 1: RMS and maximum spot radius for a spherical and an aspherical corrector plate for 0° and 0.1° on the image plane

	Spherical corrector plate (a)		Aspherical corrector plate (b)		% change [(b-a)*100/a]	
Field (in deg)	0	0.1	0	0.1	0	0.1
RMS spot radius (μm)	4.8432	4.6902	1.0039	0.9953	-79.2725	-78.7787
Maximum spot radius (μm)	9.9926	12.2774	1.6301	2.6210	-83.6872	-78.6521

The rms wavefront error is reduced by 98.44% in the case of aspherical corrector plate case at 555 nm comparatively in the visible range, resulting in a more intense spot [4]. A very low change was observed at 1050 nm (9.52%) between the spherical and aspheric plates. Also the maximum error in the case of spherical plates at 485 nm was reduced by 87.32% when it was replaced by an aspheric plate. However, not much change was observed in the case of distortion between both the plates.

4. Conclusion:

A Catadioptric Cassegrain telescope was designed for the space applications in the visible and NIR region with 0.1° FOV. The application of the two different corrector plate's viz., spherical and aspherical corrector plates separately using Zemax OpticStudio. We can determine from the above observations that the use of an Aspherical corrector plate helps in achieving much better performance parameters such as a smaller spot radius at the image plane & low rms wavefront error vs. field, as compared to that of the Spherical corrector plate, thereby reducing the overall aberration of the system to a much lower magnitude.

References

1. https://wiki.nus.edu.sg/display/TEL/Optics(Jiahui, 21)
2. (Basic formulas for Cassegrain Telescope, n.d.)(P.Privitera, 1998)
3. The Schmidt telescope with corrector plate, G.Matthiae and P.Privitera, Universita di Roma II, Tor Vergata, and Sezione INFN di Roma II, Roma, Italy.
4. H. Ottevaere, H. Thienpont,OPTICAL MICROLENSES,Editor(s): Robert D. Guenther,Encyclopedia of Modern Optics,Elsevier,2005, Pages 21-43, ISBN 9780123693952,https://doi.org/10.1016/B0-12-369395-0/00923-4.(H. Ottevaere, 2005)

Dispersion Tailoring of a Cross Slot Waveguide for Efficient Supercontinuum Generation

Megha Mangal, Kanchan Gehlot, and Bharat Lal Meena
University of Rajasthan, Jaipur-302004, Rajasthan, India
gehlot.kanchan@gmail.com

Abstract: The novel cross-slot waveguide is tailored to have a flat group velocity dispersion (GVD) curve over a broad band of spectrum and multiple zero dispersion wavelengths (ZDWs) for efficient generation of supercontinua. The dispersion profile is tailored by tuning the structure parameters of the waveguide using the vector finite element method. A low and nearly flat dispersion profile over a broadband of wavelength with three ZDWs at 1.9 μm, 3.11 μm, and 4.39 μm is obtained.
Keywords: Group velocity dispersion, Cross slot waveguide, Supercontinuum generation

1. Introduction

The development of the chalcogenide-based optical waveguides for achieving supercontinuum generation (SCG) in on-chip photonic devices has gained considerable interest in the past couple of decades owing to the large nonlinearity, low transmission loss, and wide transparency window of chalcogenide glasses in the mid-infrared (IR) region of electromagnetic spectrum [1, 2]. The group-velocity dispersion (GVD) of the guided mode of an optical waveguide has a significant role as a flat and low dispersion with multiple zero dispersion wavelengths (ZDWs) is required for efficient SCG [3]. The chalcogenide-based slot waveguide has an inherent advantage for non-linear applications in all-optical devices as it provides confinement of a large fraction of guided optical power in a low-index slot of a few tens of nanometer wide region sandwiched between two high-index cores, which allows strong optical field confinement and hence a high nonlinearity [4].

In the present paper, a novel cross-slot waveguide is analysed for obtaining a low and flat anomalous dispersion over a broad range of spectrum in mid-IR with multiple ZDWs. A cross slot waveguide offers higher confinement of optical field and lower scattering losses than the vertical, and the horizontal slot waveguides [5]. The cross-slot waveguide is designed by combining vertical and horizontal slot waveguides in such a manner that the waveguide can confine both the quasi-TE and the quasi-TM modes [7]. A cross-slot waveguide has a larger number of geometrical parameters that allow for more flexibility in tailoring the dispersion profile than a vertical or horizontal slot waveguide. The modal and propagation characteristics of a chalcogenide-based cross slot waveguide is investigated and multiple parameters optimization is carried out with respect to all structure parameters to find the waveguide geometry that provides flat and low dispersion over a wide range of wavelengths with three ZDWs.

2. Chalcogenide based cross-slot waveguide

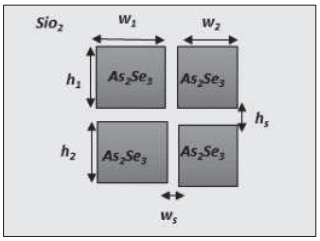

Fig 1. A 2D schematic diagram of a cross-slot waveguide consisting of four rectangular cores of As_2Se_3 embedded in SiO_2.

The investigated cross-slot waveguide consists of four rectangular cores arranged as shown in Fig.1. A vertical slot of width w_s and a horizontal slot of height h_s separates the four cores as depicted in Fig. 1. All the four rectangular cores are made of the same chalcogenide material of As_2Se_3, and silica is used in the surrounding region that consists of the two slots, substrate, and the cladding region. The refractive indices of SiO_2 and As_2Se_3 are obtained using Sellmeier equations [8]. The full vectorial finite element method is employed to calculate the propagation constant (β), and the

modal field profiles of the fundamental quasi-TE mode of the cross-slot waveguide by using COMSOL Multiphysics 6.0. The propagation constant ($\beta = k_0 n_{\text{eff}}$) is used to calculate the group velocity dispersion, which is defined as follows:

$$D = -\frac{\lambda}{c}\frac{d^2 Re(n_{eff})}{d\lambda^2} \quad (1)$$

where, λ is the wavelength of the excitation light pulse, c is the velocity of light in free space and $Re(n_{\text{eff}})$ is the real part of the effective index of the fundamental mode of the slot waveguide.

3. Result and Discussion

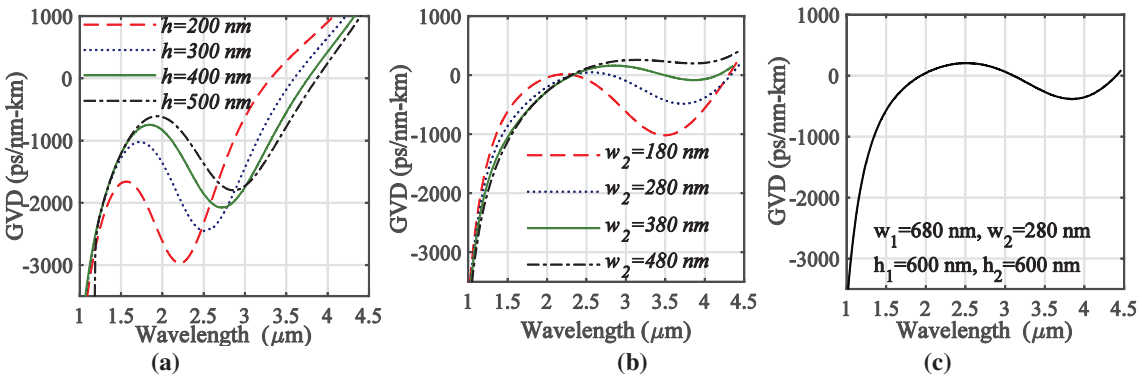

Fig. 2: For w_s = 40 nm and h_s = 50 nm, the variation in the GVD with change in (a) the height of the cores ($h_1 = h_2 = h$), for the fixed values of w_1 = 380 nm, w_2 = 180 nm, (b) the width of the right core w_2, for fixed values of $h_1 = h_2$ = 180 nm, and w_1 = 580 nm, and (c) the optimized dispersion profile of the cross-slot waveguide.

A cross-slot waveguide has six structure parameters, namely the widths w_1, w_2, w_s, and the heights h_1, h_2 and h_s as depicted in Fig. 1. Therefore, the cross-slot waveguide provides more flexibility in tailoring the dispersion profile, which is highly dependent of the waveguide design parameters. An extensive modal analysis is carried out for the cross-slot waveguide by varying all the structure parameters and a typical variation of the GVD for symmetric core heights $h_1 = h_2 = h$ is shown in Fig. 2 (a) with other structure parameters taken as w_1 = 380 nm and w_2 = 180 nm. The variation of the GVD with the width of right cores, w_2 is shown in Fig. 2 (b), where the other waveguide parameters are kept constant at $h_1 = h_2$ = 500 nm, w_1 = 580 nm, h_s = 50 nm, and w_s = 40 nm. The Fig. 2 (c) shows the optimized dispersion profile having a low and nearly flat dispersion over a broad range of wavelength with three ZDWs at 1.9 μm, 3.11 μm, and 4.39 μm.

4. Acknowledgment

The authors acknowledge the Indian Science, Technology, and Engineering facilities Map (I-STEM) for providing MATLAB and COMSOL Multiphysics 6.0. One of the authors Ms. Megha Mangal also acknowledges the Council of Scientific and Industrial Research (CSIR), Government of India for providing Senior Research Fellowship.

5. References

[1] S. Piran, M. Noori, S.A.S. Hashemi, and H. Baghban, "Super-Continuum Generation in Graphene-Based Chalcogenide Slot Waveguide" Annalen der Physik, **534**(1), p.2100226 (2022).

[2] D. Xia, Y. Huang, B. Zhang, Z. Yang, P. Zeng, H. Shang, L. Liu, M. Zhang, Y. Zhu, and Z. Li, Z., "On-Chip Broadband Mid-Infrared Supercontinuum Generation Based on Highly Nonlinear Chalcogenide Glass Waveguides", Frontiers in Physics, **9**, 598091(2021).

[3] L. Zhang, Q. Lin, Y. Yue, Y. Yan, R. G. Beausoleil, and A. E. Willner, "Silicon waveguide with four zero-dispersion wavelengths and its application in on-chip octave-spanning supercontinuum generation," Opt. Express 20, 1685–1690(2012).

[4] M. Komatsu, K. Saitoh, and M. Koshiba, "Design of highly-nonlinear horizontal slot waveguide with low and flat dispersion," Opt. Commun. 298, 180–184 (2013).

[6] J. V. Galan, P. Sanchis, J. Garcia, J. Blasco, A. Martinez, and J. Marti, "Study of asymmetric silicon cross-slot waveguides for polarization diversity schemes," Appl. Opt. 48, 2693–2696 (2009).

[7] Pan, Chao, and B. M. A. Rahman. "High-sensitivity polarization-independent biochemical sensor based on silicon-on-insulator cross-slot waveguide." IEEE Journal of Selected Topics in Quantum Electronics 23, no. 2 (2016): 64-71.

[8] B. Tatian, "Fitting refractive-index data with the Sellmeier dispersion formula," Appl. Opt. **23** 4477–4485 (1984).

Thermo-optic studies of water dispersed off-stochiometric $CuInS_2$/ZnS core-shell quantum dots

V Syammohan, M Ramya, M Kailasnath
International School of Photonics, Cochin University of Science and Technology, Chochin-682022
syammohan1300190@cusat.ac.in

Abstract: Here we report the thermo-optical studies of off-stochiometric $CuInS_2$/ZnS core-shell quantum dots (QDs) with Cu to In ratio of 1:4 using mode-mismatched dual-beam thermal lens technique. Here 4 nm sized core-shell QD were synthesized using aqueous method. Thermal diffusivity of samples found to be decreasing with increasing QD concentration; though thermal diffusivity of all the samples were found to be higher than the base fluid.
Keywords: Thermal lens, Thermal diffusivity, Copper indium sulfide/ Zinc sulfide QDs

1. Introduction

Unlike binary QDs, CIS QDs are free from toxic elements; though the presence of large amount of surface defects reduces their fluorescence intensity. However, these surface defects can be overcome by growing ZnS shell over bare CIS QDs. Which made these ternary QDs to receive more attention nowadays and enabled them to use in wide variety of applications [1]. Thermal diffusivity is a property of a material based on which we can use them as coolants or thermal insulators [2]. Although there are several techniques to measure the thermal diffusivity of materials, thermal lens technique has gained more importance since it has ultra-sensitivity in measuring liquid samples [3]. Here we report variation in thermal diffusivity of CIS/ZnS QDs dispersed in aqueous medium with varying concentration. To best of our knowledge, there are no previous studies that reports thermal diffusivity of CIS/ZnS core-shell QDs.

2. Experimental section

CIS/ZnS QDs with Cu to In ratio of 1:4 is prepared by aqueous synthesis. Thermal diffusivity (D) of samples is measured using dual beam mode mismatched thermal lens setup with 403 nm diode-pumped solid state (DPSS) laser as pump source and He-Ne laser (JDS Uniphase) operating at 632.8 nm wavelength as the probe beam.

3. Result and Discussion

Fig 1 (a) shows TEM image of the sample having average size of about 4 nm. Fig 1 (b) shows absorption spectra of samples with different concentrations labelled as S1,S2,S3 & S4.

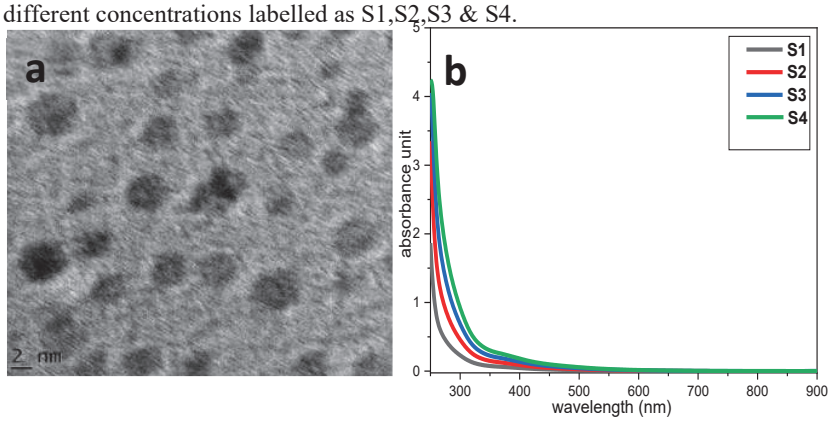

Fig 1 (a) shows TEM image of the sample having average size of about 4 nm. Fig 1 (b) shows absorption spectra of samples with different concentrations labelled as S1,S2,S3 & S4.

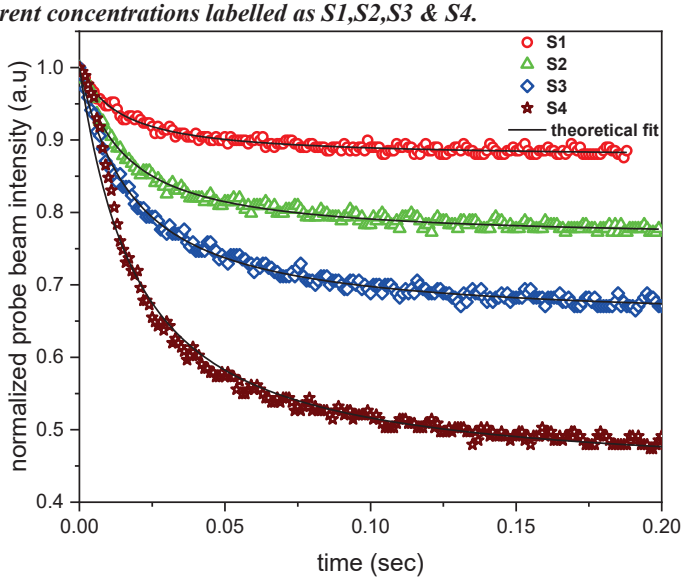

Fig. 2: Thermal lens output signal of samples

Table 1: concentration dependent variation in thermal responsetime (t_c) and thermal diffusivity (D)

Sample	Concentration (μg per 3 mL)	Time constant, t_c (sec)	Thermal diffusivity,D ($x10^{-7}$ m^2/s)
S1	200	0.00174	21.001
S2	400	0.002	18.271
S3	600	0.00246	14.854
S4	800	0.00285	12.821

As shown in table 1, thermal diffusivity of samples decreases with increase in concentration; although thermal diffusivity of all the samples are higher than that of base fluid (water).

4. Conclusion

CIS/ZnS QDs with Cu to In ratio of 1:4 is synthesized using aqueous method, and thermal diffusivity of samples with different concentration are estimated using dual beam thermal lens technique and tabulated in Table 1.

5. Reference

[1] Giacomo Morselli, Marco Villa, Andrea Fermi, Kevin Critchley and Paola Ceroni, "Luminescent copper indium sulfide (CIS) quantum dots for bioimaging applications", Nanoscale Horiz, 6, 676 (2021)
[2] T.K Nideep, M Ramya, V.P.N. Nampoori, and M Kailasnath, "The size dependent thermal diffusivity of water soluble CdTe quantum dots using dual beam thermal lens spectroscopy" Physica E: Low-dimensional Systems and Nanostructures, 116, p.113724 (2020)
[3] K.R Vijesh, U Sony, M Ramya, S Mathew., V.P.N Nampoori, and S Thomas, "Concentration dependent variation of thermal diffusivity in highly fluorescent carbon dots using dual beam thermal lens technique", International Journal of Thermal Sciences, 126, pp.137-142, (2018)

Excitation of Whispering Gallery Modes in a Microbottle Resonator

Suresh Chejarla[1], Rahul Vasanth[1], Aneesh V Veluthandath[2], Ganapathy Senthil Murugan[2] and Balaji Srinivasan[1]

[1]*Department of Electrical Engineering, Indian Institute of Technology, Madras, Chennai-600036.*
[2] *Optoelectronics Research Centre,University of Southampton, Southampton, UK - SO17 1BJ*
balajis@ee.iitm.ac.in

Abstract: We report simulation results corresponding to the excitation of Whispering Gallery Modes (WGMs) in a Microbottle Resonator (MBR). We define an axi-symmetric MBR with a mesh accuracy of $\lambda/10$ at 1.55 μm wavelength regime and use a finite element model (FEM) to analyse the same. We observe that the electric field associated with the WGM oscillates in a manner similar to simple harmonic motion within the caustics in the axial direction and it forms an annular ring structure in the transverse direction. We analyse the transverse field profile for an azimuthal mode number of 85 (m = 85) in a MBR of 20 μm radius obtained through simulations and compare it with analytical results. We extend such analysis as well as comparison to the electric field of different axial orders as well.

Keywords: microbottle resonator, whispering gallery mode and microresonator

1. Motivation

Whispering gallery modes (WGMs) are specific resonances (or modes) of a wave field that are confined at the periphery of a rotationally symmetric cavity structure. WGMs excited in optical resonators are capable of providing strong confinement of optical radiation resulting in quality factor of the order of 10^6[1,2]. Such WGMs could potentially be used for sensing applications by trapping the analytes on to the surface of the microcavity resonators [3]. Standard WGM microresonators like dielectric microspheres and microdisks typically confine the light in a narrow ring along the circumference of the resonator [4]. But these microresonators typically exhibit a large frequency spacing between resonances and a limited tunability. The microbottle resonator (MBR) has recently got attention [5-7] because it promises a customizable mode structure while maintaining a favorable Q/V ratio and good confinement as well. With two stems, instead of one, as with the conventional fiber-based microsphere, we can tune the micro bottle resonator by stretching it as demonstrated in [8]. In this work, we discuss the results obtained through simulations of the MBR in Comsol Multiphysics. Specifically we compare the simulation results with the analytical results and compare the relative results.

2. Analytical and Simulation results

We use highly prolate dielectric resonator with cylindrical symmetry and with parabolic radial profile using adiabatic tapering to analyze the WGMs. Due to the cylindrical symmetry, the azimuthal part of the wave equation can be separated with solutions proportional to $e^{im\phi}$ where m is the azimuthal mode number. The solution can thus be written $\psi(\rho, z)\ e^{im\phi}$ using the adiabatic approximation. The radial order number p will be fixed to its minimum value 1, corresponding to modes located at the periphery of the resonator. Now, using the adiabatic approximation along the z axis, $\psi(\rho, z)$ can be separated in a product of two functions namely radial wave function $\varphi_m(\rho, z)$ and axial wave function *Z(z)* and expressed as

$$\psi(\rho, \phi, z) = \varphi_m(\rho, z)\, Z_{m,q}(z)\ e^{im\phi} \qquad (1)$$

The wave equation in radial direction can be written as a combination of Bessel and modified Bessel (Hankel) functions [6]

$$\varphi_m(\rho, z) = A\, J_m\big(k_\phi(z), \rho\big), \qquad \rho < R(z) \qquad (2.a)$$

$$B\, H_m\big(k_\phi(z), \rho\big), \qquad \rho > R(z) \qquad (2.b)$$

The solution of the axial wave function along the z-direction is similar to the simple harmonic oscillator and it is given by the combination of Hermite and Gaussian functions [6] as represented in

$$Z_{m,q}(z) = \mathrm{C}\, H_q\left(\sqrt{\frac{\Delta E_m}{2}}.z\right) e^{-\frac{\Delta E_m z^2}{4}} \qquad (3)$$

where H_q is the Hermite polynomial; $\Delta E_m$is a function of profile parameter (Δk) given by $\Delta E_m = 2m\Delta k\, R_0$, q:Axial quantum number and the maximum radius of the bottle (R_0) at $z=0$.

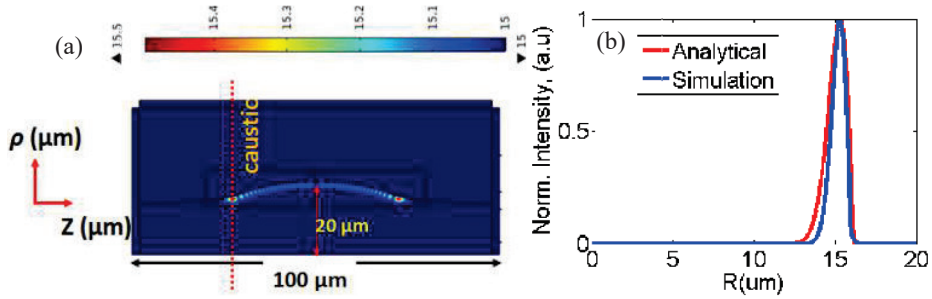

Fig. 1 (a) EM field intensity of MBR at 1.55 μm for m = 85 (b) Comparison of radial mode field profile of the MBR at one of its caustics.

A MBR of 20 μm radius with a profile parameter Δk=0.03 μm^{-1} was simulated in Comsol Multiphysics software for an azimuthal mode number which actually interacts at the tapered region and we found that at 1.55 μm for an azimuthal mode number of 85. The resulting axial standing wave structure exhibits a significantly enhanced intensity at the so-called ‘‘caustics’’ of the bottle modes and forms an intensity pattern as shown in Fig. 1 (a). The radial (transverse) field profile of the WGM has been plotted at one of the caustics of the axi-symmetric structure as shown in Figure 1(b). The axial field profiles along the axial direction (z) for different values of axial quantum number (q) were plotted in Fig. 2.

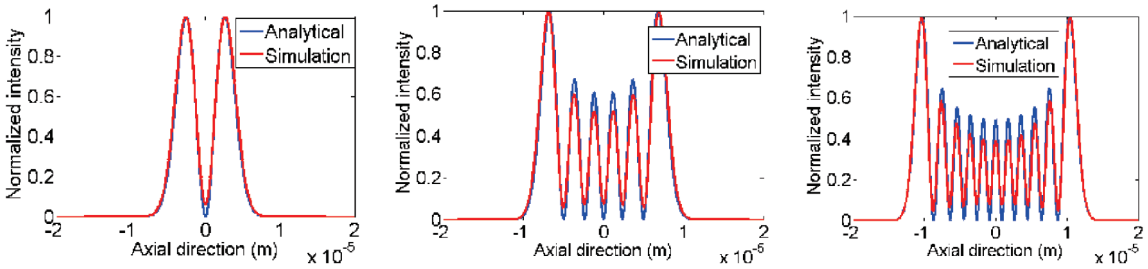

Fig. 2 Axial mode field profile *(Z(z))* for q = 1, 5, 10

The simulation results are compared with the analytical results and are found to be roughly consistent, especially at the caustics (since they are both normalized with respect to the peak values there). The inconsistency in the values near the center of the MBR is primarily attributed to the fact that the analytical results correspond to only the axial field variation Z(z) as in Equ. (3), whereas the Comsol simulations correspond to the overall field profile expressed in Equ. (1) that also includes the radially dependent $\varphi_m(\rho, z)$. Ongoing work is focused on investigating a robust mechanism to excite such modes of the MBR.

3. References

[1] Vahala, K. J., “Optical microcavities,” Nature 424 (2003).
[2] G. C. Righini, Y. Dumeige, P. F. M. F. G. N. C. D. R. and Soria, S., “Whispering gallery mode microresonators: Fundamentals and applications,” RIVISTA DEL NUOVO CIMENTO 34 (2011).
[3] Matthew R. Foreman, J. D. S. and Vollmer, F., “Whispering gallery mode sensors,” Advances in Optics and Photonics 7, 168–240 (2015).
[4] Gorajoobi, S. B., Murugan, G. S., and Zervas, M. N., “A general model for taper coupling of multiple modes of whispering gallery resonators and application to analysis of coupling-induced fano interference in a single cavity,” Optics express 27(18), 25493–25501 (2019).
[5] Sumetsky, M., “Whispering-gallery-bottle microcavities:the three-dimensional etalon,” Opt. Lett. 29, 8–10 (Jan 2004).
[6] Louyer, Y., Meschede, D., and Rauschenbeutel, A., “Tunable whispering-gallery-mode resonators for cavity quantum electrodynamics,” Phys. Rev. A 72, 031801 (Sep 2005).
[7] G. S. Murugan, J. Wilkinson, and M. Zervas, "Optical excitation and probing of whispering gallery modes in bottle microresonators: potential for all-fiber add-drop filters," Opt. Lett. 35, 1893-1895 (2010).
[8] Nasir, M. N. M., Murugan, G. S., and Zervas, M. N., “Tunable “shallow” microbottle resonators,” IEEE Photonics Technology Letters 31(11), 849–852 (2019).

Passive Synchronization of Kerr Frequency Combs in Dual Silicon Microring Resonators

Sauradeep Kar and Shailendra K. Varshney
Department of Electronics and Electrical Communication Engineering,
Indian Institute of Technology Kharagpur, Kharagpur- 721302, India.
Author e-mail address: dhruba12@iitkgp.ac.in

Abstract: The passive synchronization of frequency combs using two silicon microring resonators is proposed and studied numerically at low temperatures. Numerical simulations suggest that the phase locking between dissipative Kerr soliton result into spectral fringes in the envelope of frequency comb.
Keywords: Silicon microring resonator, Kerr frequency comb, Synchronization.

1. Introduction:

Kerr frequency comb (KFC) generated from circulating single Dissipative Kerr Soliton (DKS) in microresonators are inherently robust. Synchronization of such KFCs and hence DKSs in coupled microresonators enforces efficient frequency and temporal locking which is useful for diverse applications [1]. Recently, it has been demonstrated through numerical simulations and theoretical analysis that the KFC bandwidth as well as stability of single DKS states enhances at low temperatures [2]. In this work, the passive synchronization of two coupled silicon racetrack microring resonators (RMRR) based KFCs has been reported at low temperature when the pump is ~ 2 μm, thus avoiding the notable two-photon absorption (TPA) which is significant at 1.55 μm wavelength. The KFCs are inherently stable at the chosen temperature [2] and the proposed scheme obeys the universal Kuramoto model for the synchronization [1].

2. Design, Results and Discussion

The proposed synchronization scheme has been illustrated for two unsynchronized and synchronized KFCs in Fig. 1(a) and (b) respectively. The scheme follows the basic experimental setup used in [1]. The waveguide width and height are 2.2 μm and 2 μm, respectively. The RMRRs marked as Master (**M**) and Slave (**S**) have radius, R = 50 μm and straight arm length L_{st} = 120 μm. Both RMRRs are pumped individually using separate continuous wave (CW) driving fields. The KFCs are synchronized by feeding the output of **M** to the input of **S** through a 20 m long single-mode optical fiber [1]. Numerical simulations of the KFCs at the room (ΔT= 0K) and lower temperatures (ΔT= -18K, -21K) for the individual RMRRs have been carried out using Lugiato Lefever equation (LLE), according to the procedure described in [2]. The pump wavelength is 2.1 μm at which TPA coefficient of Si (β_{2PA}) is 1×10^{-12} m/W [3]. Note that, the wavelength dependency of the TPA is ignored presently in carrying out numerical simulations. The synchronization phenomena has been studied at a temperature gradient, ΔT= -18K at which the KFC of the individual RMRR has the maximum bandwidth. In absence of coupling between **M** and **S**, the individual KFCs are almost identical and remain unsynchronized as shown in Fig. 1(c). The comb output from the through port of the master is fed into the slave resonator along with the CW pump of the slave. The total field now drives the slave RMRR. Due to inter-coupling through the fiber link, the slave RMRR receives a time dependant modulation of its circulating intra-cavity field. The dependence of the phase profile of the single DKS on the fast time scale (τ) plays a crucial role in realizing the synchronisation phenomenon. On account of the modulation, the DKS in **S** experiences a group delay upon each round-trip within the resonator, which is dictated by the slope of the phase of the DKS which is circulating in **M**. As a result of coupling, the DKS in the slave RMRR is located in the time frame, given as,

$$\tau_S = \tau - \left(\Delta\beta_1 - \beta_{2,2}\varphi'\right)L\frac{t}{t_R} \tag{1}$$

Here τ is the fast time axis, $\Delta\beta_1$ is the group velocity mismatch between **M** and **S**, $\beta_{2,2}$ is the second-order group velocity dispersion of **S**, $\varphi' = d\varphi/d\tau$ is the slope of the intra-cavity phase of the DKS in **M**, L is the total length of the resonator, t is the slow time of evolution and t_R is the round trip time of the resonator. Based on the above transformation the LLE in the slave RMRR is modified from the traditional form as follows:

$$t_R\,\partial E/\partial t = \left[-\alpha - i\delta_{0,2} - \left(\Delta\beta_1 - \beta_{2,2}\varphi'\right)L\,\partial/\partial\tau - i\left(\beta_{2,2}/2\right)L\,\partial^2/\partial\tau^2 + i\gamma L|E|^2\right]E + \sqrt{\kappa}\,E_{in}(t,\tau) \tag{2}$$

where, E is the intracavity field of the circulating DKS, α is the roundtrip loss, $\delta_{0,2}$ is the detuning of the slave RMRR with respect to the pump, γ is the nonlinear coefficient, κ is the coupling coefficient between the bus and ring waveguide of the slave resonator and $E_{in}(t,\tau)$ is the input field of the slave resonator, which encompasses the combined effect of the CW field and the intracavity field of the master DKS fed into the input of S. The synchronized temporal profile of the **M** and **S** RMRRs at different temperatures is shown in Fig. 1(d). The two DKS states of **M** and **S** synchronize when the moving time frame τ_S of **S** appears stationary. Upon synchronization, the two DKSs are locked at specific temporal position with a fixed $\Delta\tau$ as shown in Fig. 1(d). The synchronized KFC exhibits spectral fringes over its envelope due to interference between the synchronized comb lines of **M** and **S** as shown in Fig. 1(e).

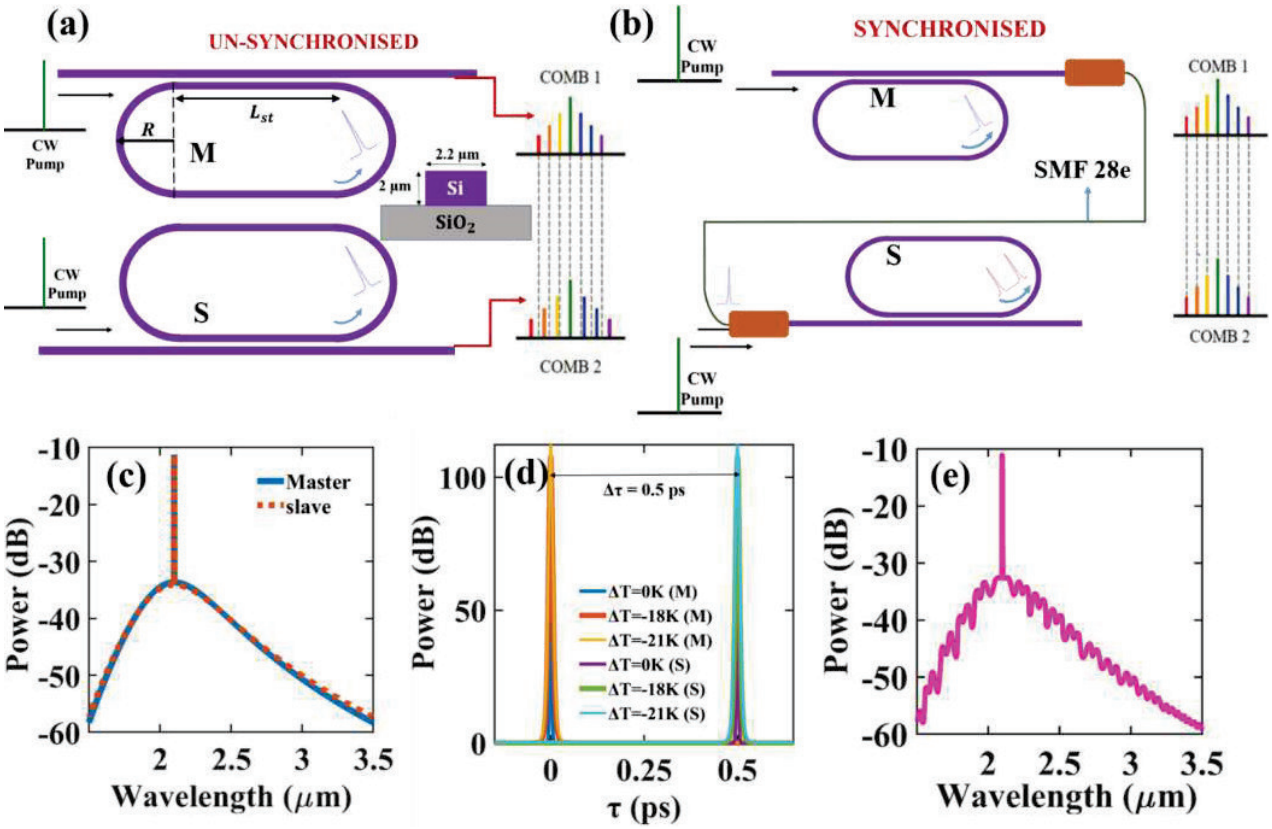

Fig. 1: Silicon RMRR for (a) unsynchronized and (b) synchronized configurations, **M** and **S** denotes Master and Slave RMRR, respectively. (c) Unsynchronized KFC of Master and Slave at ΔT = -18K (d) synchronized DKS at different temperatures for **M** and **S**, (e) synchronized comb at ΔT = -18K.

3. Conclusion:

In conclusion, passive synchronization route to achieve stable KFC and DKS state of two inter-coupled RMRRs is proposed and studied at low temperatures. The single DKS state of an individual RMRR undergoes a temporal locking and exhibit spectral fringes in the comb envelope upon synchronization.

4. References:

[1] Jae K. Jang et al., "Synchronization of Coupled optical microresonators" Nature Photonics **12,** 688-693 (2018).
[2] Kar, Sauradeep et al. "Cold-resonance-mediated self-stabilization of Kerr frequency combs in a Si_3N_4 microring resonator." Physical Review A **106**, 013517 (2022).
[3] Bristow, Alan D et al. "Two-photon absorption and Kerr coefficients of silicon for 850-2200nm." Applied Physics Letters **90**, 191104 (2007).

Optical Absorbance-Based Device for Measurement of Hemoglobin Concentration from a Drop of Blood

Neelam Verma†, Biplab Nath†, Sai Siva Gorthi*

Optics and Microfluidics Instrumentation Laboratory, Department of Instrumentation and Applied Physics, Indian Institute of Science, Bangalore, Karnataka – 560012

† These authors contributed equally to this work

**Corresponding Author e-mail address: saisiva@iisc.ac.in*

Abstract: Hemoglobin is an important hematological parameter for screening of anemia, which is predominant globally in rural areas. Hematology analyzers, and few point-of-care devices are used for hemoglobin estimation, but they face challenges in simultaneously meeting the criterion for affordability, accessibility, and accuracy. This paper reports the development of a low-cost optical hemoglobinometer which uses only a drop of blood (8 µL) and Sodium Lauryl Sulfate reagent and gives the result within 1 minute. The microcontroller-based prototype uses a 525 nm LED source and works with a standard 12V power supply. The measurement range of the device is 4-20 g/dL with a maximum estimation error of 1.3%.

Keywords: Hemoglobin, anemia, SLS, hemoglobinometer, optical absorbance.

1. Introduction

Anemia is a condition when the hemoglobin (Hb) concentration is lower than normal (11 g/dL). It is classified in three categories depending upon the concentrations of hemoglobin, which are severe (< 7.0 g/dL), moderate (7.0-9.9 g/dL) and mild (10.0-10.9 g/dL) [1]. It is a severe global health issue that disproportionately affects children and pregnant women. According to the WHO, 42% of children under the age of five and 40% of pregnant women globally are anemic [2]. The common symptoms of anemia are fatigue, shortness of breath, and feeling cold, and leaving it untreated can lead to deterioration in cardiovascular health. Thus, accurate estimation of hemoglobin is of utmost importance for early diagnosis of anemia.

Several established invasive and non-invasive techniques are present to estimate Hb. Conventional lab based invasive techniques like copper-sulfate gravimetric method, hemoglobin color scale, Sahli technique, cyanmethemoglobin method and automated hematology analyzers, use venous or capillary blood for estimation. TrueHb and HemoCue are two of the invasive Point-of-Care (PoC) digital hemoglobinometers used in India. Non-invasive devices like AJO Spectroscopic Test, and Masimo rainbow SET are also available in the market, but their sensitivity and specificity are relatively poor as compared to invasive devices [1].

The gold standard method for hemoglobin estimation is cyanmethemoglobin method, in which a solution containing potassium cyanide (KCN) and potassium ferricyanide reacts with hemoglobin, and the absorbance at 540 nm is measured to estimate Hb. However, the disadvantage of this method is the use of KCN, which is toxic and an environmental hazard [3]. Sodium Lauryl Sulfate (SLS) is a nontoxic anion surfactant which produces SLS-methemoglobin complex without hemolytic agents, is a safer alternative to KCN, and has similar absorbance vs concentration characteristics as obtained in the cyanmethemoglobin method [3].

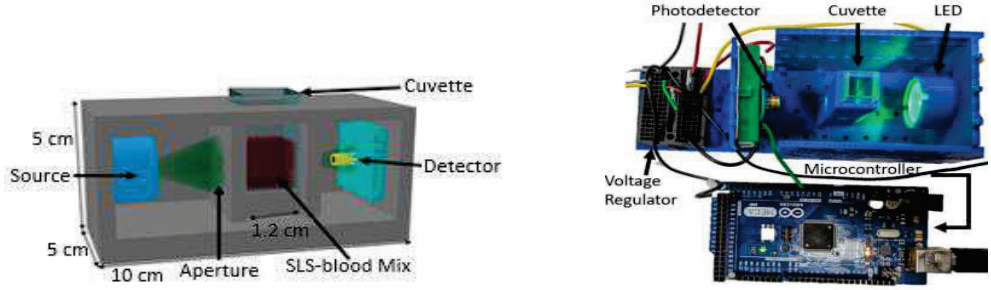

(a) (b)

Fig. 1: (a) Schematic of the optical setup used for measurement of Hb, and (b) top view of the 3D printed prototype.

In the present work, SLS is used to lyse the red blood cells and form an SLS- methemoglobin complex, and a low-cost setup (Fig.1) has been developed to measure the solution's optical absorbance in the Q-band region at 525 nm. The setup consists of a green LED as the source, with peak spectral emission at around 525 nm, a 10 mm pathlength glass cuvette, and a photodiode with an active sensing area of 2.29 mm x 2.29 mm. 2.5 mM SLS reagent was prepared using Sodium Dodecyl Sulphate, Triton X-100, and PBS buffer tablet as reported by Arcot et al. [4]. Venous blood was collected in anticoagulant coated collection tubes from healthy human volunteers after collecting their informed consent in accordance with the approval by the institutional ethics committee (IHEC No: 12/3.12.2021). The samples were stored at 2°C - 8°C until tests were performed.

Sysmex XP-100 hematology analyzer was used for measuring the actual hemoglobin concentration of the collected blood samples, and the sample with the highest hemoglobin concentration was serially diluted using PBS. 8 µL of each sample was pipetted to a cuvette containing SLS reagent in 1:250 ratio, and the solution was gently mixed. The intensity of transmitted light was recorded. The standard curve of hemoglobin concentration vs intensity was then plotted (Fig.2a). Absorbance of blood samples with unknown hemoglobin concentrations was estimated similarly as described above, and the concentration of hemoglobin was estimated by curve-fitting using the standard plot. The performance of the setup was analyzed by comparing the estimated vs actual concentrations of Hb (Fig.2b).

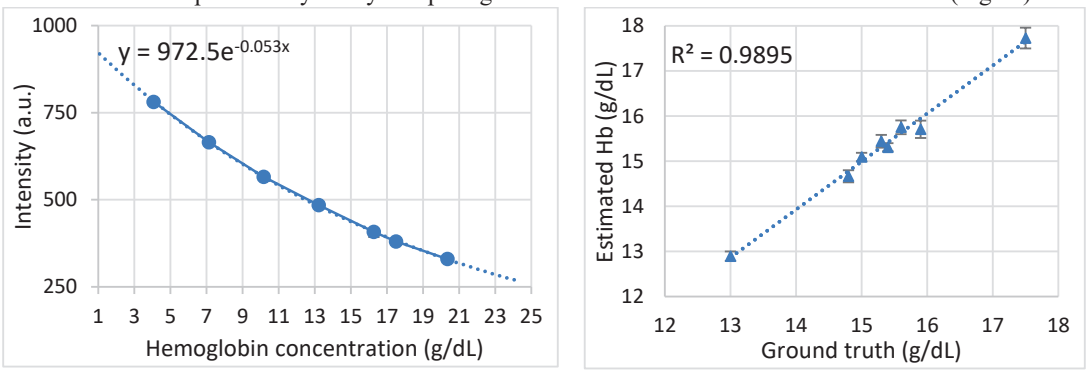

(a) (b)

Fig. 2: (a) Calibration curve generated by using known concentrations of hemoglobin, and (b) correlation between Hb determined using developed hemoglobinometer and Hb concentration measured using Sysmex XP-100.

The developed device measured hemoglobin concentrations in the range of 4-20 g/dl. The standard curve was plotted using data generated from samples prepared by serial dilution. The device was tested in a blind study with 8 clinical samples of different hemoglobin concentrations, and the coefficient of linear correlation (R^2) was calculated to be 0.9895. The maximum error in Hb estimation was calculated to be 1.3%, which is well within the Clinical Laboratory Improvement Amendments (CLIA) recommended tolerance of ±4%. The mean difference in Hb compared to gold standard of our device is 0.14 g/dL, which is better than the reported mean difference of HemoCue (0.18 g/dL) and TrueHb (0.22 g/dL) [1]. The dimension of the developed prototype is 10 cm x 5 cm x 5 cm, and the cost per test for reagents is less than ₹1, which makes it a highly economical technology for detection of hemoglobin.

Upon further development, this device has the scope to be developed into a Point-of-Care diagnostic device, yet offering the clinical performance comparable to that of conventional laboratory-based methods.

2. References

[1] All India Institute of Medical Sciences, "Diagnostic efficacy of digital hemoglobinometer (TrueHb), HemoCue and non-invasive devices for screening patients for anemia in the field settings," 2019. [Online]. Available: https://htain.icmr.org.in/images/pdf/outcome_r.pdf.

[2] WHO, "Anaemia," 2022. https://www.who.int/health-topics/anaemia#tab=tab_1 (accessed Aug. 25, 2022).

[3] I. Oshiro, T. Takenaka, and J. Maeda, "New method for hemoglobin determination by using sodium lauryl sulfate (SLS)," *Clin. Biochem.*, vol. 15, no. 2, pp. 83–88, Apr. 1982, doi: 10.1016/S0009-9120(82)91069-4.

[4] L. Arcot, S. Kandaswamy, A. Modali, S. S. Gorthi, and T. Rai Dastidar, "Developing microscopy based microfluidic SLS assay for on-chip hemoglobin estimation," *AIP Adv.*, vol. 11, no. 2, p. 025337, Feb. 2021, doi: 10.1063/5.0036446.

Symbol Rate Tolerance of Geometric Parameter Extraction-based Receiver IQ imbalance correction for mQAM systems

Sameer Ahmad Mir[1], Chuang Xu[2], Qirui Fan[2], Lakshmi Narayanan Venkatasubramani[3], Alan Pak Tao Lau[2], *Deepa Venkitesh[1]

[1] *Department of Electrical Engineering, Indian Institute of Technology Madras,Chennai, India.*
[2] *Department of Electrical Engineering, The Hong Kong Polytechnic University, Hung Hom, Kowloon, HKSAR, China.*
[3] *School of Electronic Engineering, Dublin City University, Dublin, Ireland.*
**deepa@ee.iitm.ac.in*

Abstract: In this paper, we demonstrate the symbol rate tolerance of Geometric Parameter Extraction-based Receiver IQ imbalance correction for PM-16QAM signals. We, through experiments show that the algorithm can tolerate a wide range of imbalance values for data rates upto 640 Gbps efficiently.

With the advancement in technologies, the demand for the capacity in the optical backbone network is increasing drastically. Higher order modulation formats along with the higher symbol rates are the potential solutions to meet thse increasing capacity demands. As we scale the modulation order or the symbol rates, the transmission system becomes susceptible to non-idealities due to reduction in the phase margin. Distortions due to these non-idealities are corrected using digital signal processing (DSP) at the receiver side before demodulation. One of the dominant receiver impairments which become critical especially for higher order modulation at higher baud rates is receiver gain and phase imbalance. The receiver gain imbalance arises because of the different gains introduced by the transimpedance amplifiers to I and Q arms, and the receiver phase imbalance arises because of the non ideal $\pi/2-$phase shifter of the optical hybrids in the coherent receiver, which phase deviates the I and Q arm by $\pi/2$ and thereby breaking the orthogonality. The receiver IQ imbalance needs to be corrected in the front end in the DSP sequence to avoid degradation in the performance. The popular algorithms to correct for the receiver IQ imbalance includes Gram-Schmidt orthogonalization process (GSOP) [1] and the convex hull assisted ellipse correction (EC) algorithm [2]. We recently demonstrated geometric parameter extraction (GPE) based method for correcting the Rx-IQ imbalance for higher-order modulation formats by extracting the conic section parameters from the statistics of the received signal [3].

In this paper, we experimentally demonstrate the symbol rate tolerance of (GPE) based method for correcting the Rx-IQ imbalance for higher-order modulation formats. We demonstrate the efficacy of the algorithm upto 80 GBaud PM-16QAM data which translates to the data rate of 640 Gbps. We model the effect of Rx-IQ imbalance on the received signal [2] as $g^2I^2(t) + 2g\ sin(\theta)I(t)Q(t) + Q^2(t) - 1 = 0$, where g is the gain imbalance and θ represents the phase imbalance and $I(t)$ and $Q(t)$ represent the in-phase and quadrature components, respectively. The general conic equation of the ellipse is expressed as $aI^2(t) + 2bI(t)Q(t) + cQ^2(t) + dI(t) + eQ(t) + \Delta = 0$. The values g and θ can be obtained as $g = \sqrt{(a/c)}$ and $\theta = sin^{-1}(b/2gc)$ by comparing the signal representation with that of an ellipse. The geometric parameters a, b and c are obtained from the distorted signal by the following procedure. First we define a vector containing the elements a', b' and c' as follows $[a' \quad b' \quad c'] = [(I(t) \times I(t)) \quad (I(t) \times Q(t)) \quad Q(t) \times Q(t)]$. The geometric parameters a, b and c are then extracted by normalizing the obtained elements a', b' and c' as follows $a = \frac{\sum_i a'_i}{\sum_{i,j} a'_{i,j}}$, $b = \frac{\sum_i b'_i}{\sum_{i,j} b'_{i,j}}$, $c = \frac{\sum_i c'_i}{\sum_{i,j} c'_{i,j}}$. After obtaining these geometric parameters and hence the imbalance values, the signal is then corrected using inverse transformations.

The schematic for the setup used for the transmission of PM-16QAM modulation is shown in Fig. 1(a). At the transmitter side, pseudo-random bit sequence (PRBS) is generated and mapped to 16QAM modulation. After mapping the signal is then spectral shaped using a root raised cosine (RRC) filter with a roll-off factor of 0.1. The signal is then loaded into arbitrary waveform generator operating at sampling rate of 120-GS/s. The output electrical signal from the AWG drives the IQ modulator, which encodes the information on the optical carrier centered at 1550 nm. The polarization multiplexed data is then directly fed to polarization diverse coherent receiver. The detected electrical signals are then sampled using a high-speed real-time scope operating at 256 GS/s. The receiver gain and phase imbalance is introduced to the signal digitally. The received signal is re-sampled to 2 Samples/symbol and then processed by using offline DSP, as shown in Fig. 1(a).

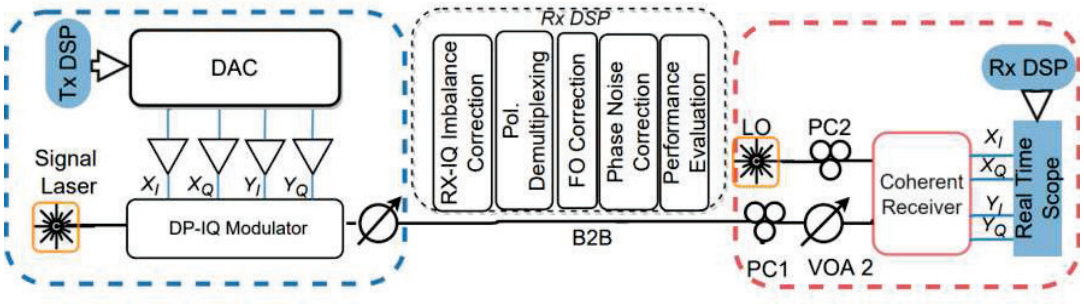

Fig. 1. Schematic of the experimental setup for PM-16QAM data transmission along with associated receiver side DSP

The RX-IQ imbalance is corrected at the front end using the GPE algorithm. Polarization demultiplexing is performed using the multi-tap Radius-Directed Equalization (RDE) algorithm. The equalizer is locked to the even samples; thus the signal is downsampled to 1 sample/symbol after polarization demultiplexing. Fourth power periodogram technique and decision directed least mean squares (DD-LMS) algorithm are used to correct for frequency offset and phase noise respectively. The experimental results are shown in Figure 2.

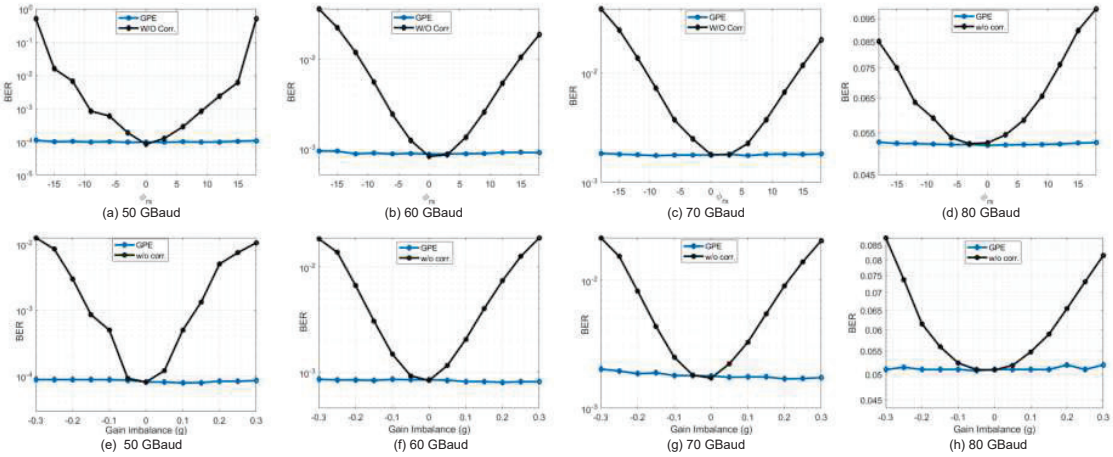

Fig. 2. Experimental results with BER performance as a function of (a-d) phase imbalance for 50-80 GBaud (e-h) gain imbalance for 50-80 GBaud PM-16QAM data.

Figure 2(a-d) shows the plot of BER as a function of phase imbalance values for 50-80 GBaud PM-16QAM data when the phase imbalance (θ) was varied from -18^0 to $+18^0$. It can be observed that the GPE algorithm can tolerate a wide range of phase imbalance values without any degradation in performance also the BER performance degrades at higher imbalance values when no explicit correction is performed. Figure 2(e-h) shows the Ber as a function of gain imbalance when the gain imbalance (g) was varied from -0.3 to $+0.3$. Here also it can be observed that a wide range of gain imbalance values are also tolerated for the higher symbol rate data.

In summary, we show the symbol rate tolerance of the GPE algorithm for Rx-IQ imbalance correction for PM-16QAM signals. The efficacy of the algorithm was evaluated for data rates upto 640 Gbps and the phase imbalance upto 18^0 and gain imbalance upto 0.3 were tolerated efficiently without any degradation in the performance. Since GPE algorithm is blind and modulation format transparent, it can be used for any mQAM system without any penalty in spectral efficiency.

The authors would like to acknowledge funding from Govt. of India agencies: MHRD, SERB and the Office of the PSA and funding from FOCS Project, IIT Madras

References

1. Seb J. Savory and David Ives,IEEE Photonics Technol. Lett., VOL. 20, NO. 20, Oct 15, 2008.
2. Qun Zhang, et al., J. Light. Technol., VOL. 37, NO. 10, May 15, 2019.
3. S. A. Mir, et al., Conference on Lasers and Electro-Optics, Technical Digest Series (Optica Publishing Group, 2022), paper SF3M.8.

Multifunctional Rare-Earth Doped Optical Nanoprobes for Huh-7 Liver Cancer Cell Line Imaging

Ib Singh Deo, Mohini Gupta, G. Vijaya Prakash*
Nanophotonics Lab, Department of Physics, Indian Institute of Technology Delhi, New Delhi, 110016 INDIA
prakash@physics.iitd.ac.in

Abstract: The research centers around the synthesis of multifunctional, biocompatible β-$KLa_{(0.95-x)}Gd_xF_4:Eu^{3+}$ nanoparticles for biomedical applications. The nanoprobes exhibit dyad property of intense red emission and strong paramagnetism. The co-precipitation method using the lanthanide precursors has been used to synthesize the nanoparticles. Silica capping enables the paramagnetic/luminescent nanoparticles for biological applications due to its colloidal stability, optical transparency in visible region, and reduced cytotoxicity. A confocal microscope with laser excitation of 460 nm is used for imaging cellular localization of liver cancer cells tagged with as-synthesized nanoparticles. Thus, these nanoparticles serve as a potent luminescent probe for accomplishing high contrast bioimaging.
Keywords: Downconversion, surface passivation, confocal microscopy, bioimaging

1. Introduction

Rapid antigen detection, efficient drug delivery, multi-modal labelling, and treatment of cancerous cells are among the fascinating possibilities that could revolutionize the research in the biological domain [1]. The advances in imaging techniques offer a great opportunity to overcome the difficulties in deep tissue/cell imaging and other biological characterization. Optical contrast techniques such as photoluminescence and variations in reflection and transmission can be employed to gather information about disease progression and pathophysiology [2,3]. Downconversion/upconversion photoluminescence has proved to be one of the most efficient imaging techniques due to its special features of site selectivity, high sensitivity, and reduced signal to noise ratio [4]. Fluoride-based highly emitting nanocrystals are superior due to their photochemical stability, reduced autofluorescence background, and optical transparency in the first biological window [5]. Highly photoluminescent, stable, biocompatible, and chemical-resistant nanoparticles are needed for biological applications such as cancer cell imaging and usage in artificial body fluids [6]. Therefore, there arises a need for rare-earth doped, uniformly dispersed, luminescent biological probes for *in vitro* and *in vivo* bioimaging.

2. Results and Discussions

The morphology, crystallinity, and phase purity of β - $KLa_{(0.95-x)}Gd_xF_4:Eu^{3+}$ (x = 0 - 0.4 mol%) nanoparticles were first determined from the Powder-X-ray Diffraction and High-Resolution Transmission Electron Microscopy as represented in Fig. 1(a). The results revealed that with the increase in the Gd^{3+} doping content the hexagonal phase became prominent thus giving rise to monophasic hexagonal nanoparticles. The paramagnetic behavior of the sample was confirmed from the magnetic measurements as shown in Fig. 1(b). The nanoparticles exhibited super-paramagnetic behavior at 5 K, making these nanoparticles a suitable candidate for MRI spectroscopy.

It is well known that Eu^{3+} plays the role of an efficient spectroscopic agent giving rise to two intense peaks at 590 nm and 613 nm that can be attributed to magnetic and electric dipole transition, respectively. In the absence of Gd^{3+} dopant, the Red/Orange (R/O) ratio was nearly 0.9, while with an increase in Gd^{3+} content, the R/O ratio varies from 1.3 to 2.8 as depicted in Fig. 1(c). This rise in R/O indicates an energy transfer from Gd^{3+} to Eu^{3+} ions, a proportionate increase in the covalent bonds strength and asymmetric occupancy of Eu^{3+} ions in the local environment.

The long-term stability of the silica passivated β- $KLa_{(0.95-x)}Gd_xF_4:Eu^{3+}$ nanoparticles in water was established by photoluminescence under 405 nm laser excitation and dynamic light scattering measurements. The aggregation and fragmentation processes were interpreted with theoretically modified Smoluchowski equations.

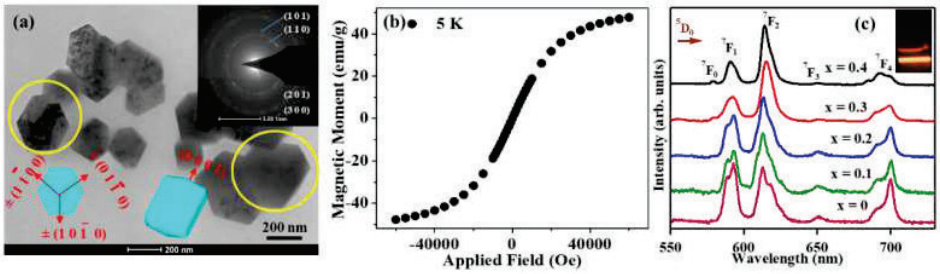

Fig. 1: (a) TEM image and SAED inset (b) Super-paramagnetic behavior of nanoparticle at 5K (c) Downconversion emission under 405 nm laser excitation of β - $KLa_{(0.95-x)}Gd_xF_4:Eu^{3+}$ where x represents the molar % of Gd^{3+} ion.

The cytotoxicity and uptake of nanoparticles into Huh-7 liver cancer cell line were investigated by MTT assay as shown in Fig. 2(a). The nanoparticles were tagged and incubated for 24 - 48 hours to Huh-7 cells and observed using a confocal PL microscope thus, establishing the potentiality of the nanoparticles for cellular internalization and localization of cancerous cells. Fig. 2(b, c) represents the photoluminescent image and confocal image of the tagged nanoprobe onto the liver cancer cell line. The nanoparticles were able to infiltrate the cytoplasm, where they emitted bright red color. Thus, the results imply that these potentially multifunctional nanoprobes can be employed for *in vitro* and *in vivo* imaging in addition to targeted medication administration.

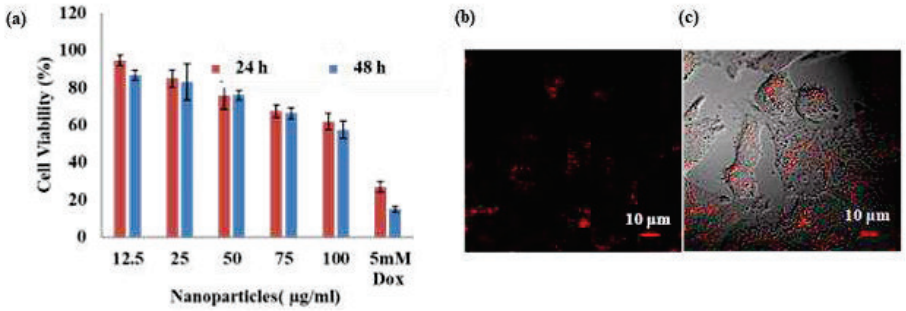

Fig. 2: (a) Cytotoxicity measurements of the nanoprobes (b) Photoluminescence image (c) Confocal image of the nanoprobe tagged to cancer cell.

3. References

[1] X. Li Xingjun, S. Lu, D. Tu, W. Zheng, X. Chen, "Luminescent lanthanide metal–organic framework nanoprobes: from fundamentals to bioapplications," Nanoscale **12**, 15021-15035 (2020).

[2] Q. Liu, Y. Zhang, C. S. Peng, T. Yang, L. M. Joubert, S. Chu, "Single upconversion nanoparticle imaging at sub-10 W cm− 2 irradiance", Nat. photonics **12**, 548-553 (2018).

[3] R. Xu, H. Cao, D. Lin, B. Yu, J. Qu, "Lanthanide-doped upconversion nanoparticles for biological super-resolution fluorescence imaging," Cell Rept. Phys. Sci. **3**, 100922 (2022).

[4] Y. Min, J. Li, F. Liu, P. Padmanabhan, E.K.L. Yeow, B. Xing, "Recent advance of biological molecular imaging based on lanthanide-doped upconversion-luminescent nanomaterials," Nanomater. **4**, 129-154 (2014).

[5] M. Gupta, M. Adnan, R. Nagarajan, G. Vijaya Prakash, "Color-tunable upconversion in Er3+/Yb3+- codoped KLaF4 nanophosphors by incorporation of Tm3+ ions for biological applications," ACS omega **4**, 2275-2282 (2019).

[6] D. Stefanakis, D. F. Ghanotakis, "Rare earth fluorescent nanoparticles for specific cancer cell targeting," J. Nanopart. Res. **18**, 1-11 (2016).

Generation of Bessel Beam Using Spatial Light Modulator and its Propagation Characteristics

Sumit Yadav[a], Abdul Alim[a], Aishwarya Kumar Priye[b], and Arijit K. De[b]*

Condensed phase dynamics group, [a]Department of Physical Sciences and [b]Department of Chemical Sciences, Indian Institute of Science Education and Research (IISER) Mohali, Knowledge City, Sector 81, SAS Nagar, Punjab 140306, India.

**akde@iisermohali.ac.in*

Abstract: In this work, we transformed a Gaussian beam into a Bessel beam using a liquid crystal spatial light modulator. The propagation properties, for example, the Gouy phase shift, of generated Bessel beam are studied. Different approaches are used in generating the Bessel beam with two types of computer-generated holograms, and the propagation properties are compared with and without interferometry.

Keywords: beam shaping, spatial light modulator, Bessel beam, Gouy phase, interference

Introduction

Beam shaping, the phenomenon of redistributing an optical beam's intensity and phase profile to achieve desired beam shape, has been used in various sectors of scientific, technical, and industrial research and development in recent years for various applications. Bessel beam, also called the non-diffracting beam, is represented by an exact solution of the Helmholtz equation in the cylindrical coordinate system [1]. The term "non-diffracting" is the property of an ideal Bessel beam, which represents an infinitely propagating light field without diffraction. Due to the unique properties of "self-healing", Bessel beams have found applications in several areas, including optical coherence tomography, optical metrology, and particle trapping in micromanipulation. A lobe-type intensity distribution was shown in the interference pattern between the Bessel beam and the Gaussian reference beam. The rotation of the lobe, independent of the beam order, was observed in the propagation due to the Gouy phase shift of the Bessel beam [2]. Here, we generated the Bessel beam using two types of computer generated hologram (CGH) on reflective SLM using spiral phase and Axicon phase with/without diffraction grating. We studied the propagation of generated Bessel beam from both types of CGH. We compared the lobe intensity profile with and without the interference of generated Bessel beam and reference Gaussian beam. Then we compared the Gouy phase shift (rotation of lobe pattern in propagation) of the Bessel beam (generated with and without diffraction grating in CGHs) by the Michelson interferometer setup.

Results and Discussion

The electric field of an l^{th}-order Bessel beam is given by

$$E_{Bessel}(\rho, \varphi, z) = J_l(\alpha\rho)\exp(-i\beta z)\exp(il\varphi)\exp(i\omega t),$$

where J_l is an l^{th}-order Bessel function of the first kind, ρ is radial coordinate, and φ is an azimuthal phase. To generate the Bessel beam, we used a CGH on SLM. The mode of the reference input Gaussian beam on SLM is cleaned up using lens and pinhole combination and expanded to fill the active region of the SLM. The hologram having a spiral phase and Axicon phase is generated using the phase transmission function,

$$T(\rho, \rho_0) = \begin{cases} \exp(il\varphi)\exp\left(-2\pi\dfrac{\rho}{\rho_0}\right) & \rho \le R \\ 0 & \rho > R \end{cases}$$

ρ_0 is a characteristic length representing a scale factor of the beam size, and R is the aperture radius of the Axicon. Using this type of CGH, the generated beam has both modulated Bessel and an unmodulated Gaussian beam; both propagate collinearly and interfere. The intensity profile of this generated beam is shown in figure 1 (lower panel), and the simulated interference pattern of the Bessel and Gaussian beam is shown in figure 1 (upper panel). Due to the interference of modulated and unmodulated beams, a lobe type of pattern is observed. The single lobe represents the first order of generated Bessel beam. It can be observed that the lobes in rings of the Bessel beam are π-phase shifted, which also rotates during propagation. Two and three lobes are observed for the second and third order of the Bessel beam, respectively. The rotation of the lobe pattern was observed in the propagation of

the beam. Figure 1e shows the π-rotation of the lobe at ~5 cm distance of propagation, and figure 1f shows the complete 2π-rotation of the lobe at ~8.5 cm distance of propagation. We also studied the rotation of lobe patterns for the higher orders of Bessel beams in the propagation.

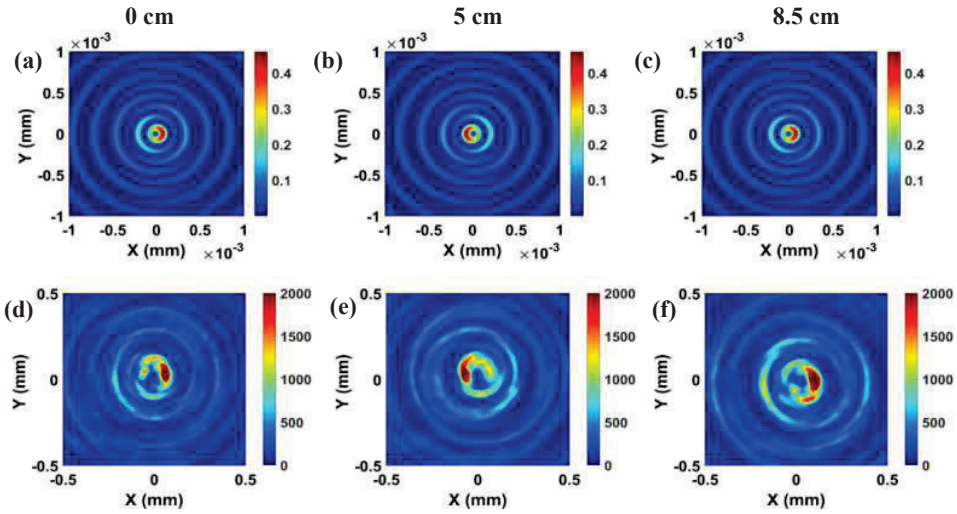

Fig. 1. Plots of a-c) simulated interference intensity pattern of Bessel beam and Gaussian beam at different propagation distances, d-f) intensity profile of experimentally generated Bessel beam at different propagation distances.

Further, we confirmed the rotation of these lobe patterns in the propagation of the beam generated with the second type of CGH (with diffraction grating), where a pure Bessel beam is generated in the first order of diffraction. Then the generated beam interfered with the reference Gaussian beam in an interferometry setup (results not shown here).

In summary, we generated the Bessel beam using SLM by applying two types of CGHs and compared their propagation characteristics. We observed the rotation of the lobe intensity pattern during propagation of the beam, and the distance required for a complete 2π-rotation depends on the order of the beam.

References:

[1] J. Durnin, "Exact solutions for nondiffracting beams. I. The scalar theory," J. Opt. Soc. Am. A **4**(4), 651–654 (1987).

[2] P. Martelli, M. Tacca, A. Gatto, G. Moneta, and M. Martinelli, "Gouy phase shift in nondiffracting Bessel beams," Opt. Express **18**, 7109 (2010).

Quantum Control of Quantum Dot Qubits using Gradient Ascent Pulse Engineering

Yash Tiwari, Vishvendra Singh Poonia
Department of Electronics and Communication, Indian Institute of Technology, Roorkee, 247667, India
vishvendra@ece.iitr.ac.in

Abstract: The gradient ascent pulse engineering (GRAPE) is a quantum control algorithm used to design the pulse sequence for a spin-based resonant system. Initially proposed for nuclear magnetic resonance system (NMR), we use the algorithm to attain a desirable state from an initial state in the quantum dot-based qubits and achieve single qubit gate operation. This will help in the engineering of the magnetic pulses which are used in electron paramagnetic resonance to perform gate operation. Further, this technique may be extended to design low noise quantum gates.

Keywords: Quantum dots, quantum control, GRAPE

1. Introduction

Quantum dots qubits are one of the most promising candidates that are being explored for realizing quantum computers. A quantum dot qubit uses a combination of hetero-structure and metallic contacts to isolate a single electron. The hetero-structure provides 2-dimensional electron gas, thereby confining electrons in a 2D plane whereby the electrons are further confined by negative potential on these metallic gates. The spin of the confined electrons can be measured using the Elzerman method [2]. The isolated electron is confined in a quantum dot and is exposed to a static magnetic field and a control magnetic field. The control magnetic field can be a single periodic pulse or a composite pulse and is used to change the spin of the isolated electron.

The GRAPE or gradient ascent pulse engineering was initially proposed for the NMR system by Naveen Khaneja et. al. [1]. It was used to calculate the weights of the control Hamiltonian to engineer a quantum state transition. The practicality of this algorithm is immense and can be used to maximize coherence and minimize relaxation and dephasing effects. The focus of this paper is to apply GRAPE for a quantum dot qubit implementation and identify its merits and demerits.

2. Simulation Methodology

The Hamiltonian of a single isolated electron under a static and a control magnetic field can be written as:

$$H(t) = H_0 + \sum_{m=1}^{m=M} u_m H_{control} \quad (1)$$

In quantum dot-based qubits, Eq.1, $H_0 = g.\mu.B_{static}\sigma_z$,where g is the gyromagnetic ratio, μ is the magnetic moment of the electron and σ_z is Pauli matrices in +z direction. The static magnetic field B_{static} is applied in +z direction. The H_0 remains constant throughout the evolution of the state. The control Hamiltonian $H_{control}$ is taken in form $g.\mu(\sigma_y - \sigma_x)$. The objective of the GRAPE algorithm would be to identify a set of {u} values for which an initial state $\rho(0)$ can be guided to $\rho(T)$ following the Liouville-von Neuman Equation (c.f. Eq.2):

$$\frac{d\rho(t)}{dt} = -i\frac{[H(t),\rho(t)]}{\hbar} \quad (2)$$

The GRAPE algorithm breaks the time scale (0, T) into smaller units $\Delta t = \frac{T}{M}$ where M is the number of time steps into which we need to break the time scale. Hence the time scale is divided into $\Delta t,\ 2\Delta t,\ 3\Delta t, \dots, m\Delta t$. Each value of u_k is constant in the time scale Δt. The set of $\{u_k\}$ values identified will take $\rho(0)$ to $\rho(T)$. For this purpose, a performance index $\varphi = tr\{C^+\rho(T)\}$ is defined which quantifies how close we are to the desired operation. Here *tr* corresponds to the trace operation, and C is the desired output we require. We start with a random set of values of {u} for each Δt. At the end of this evolution, in most cases, C $\neq\rho(T)$. These set of u values are updated in the next iteration l based on Eq. 3-7. This has been summarized in Fig. 1.

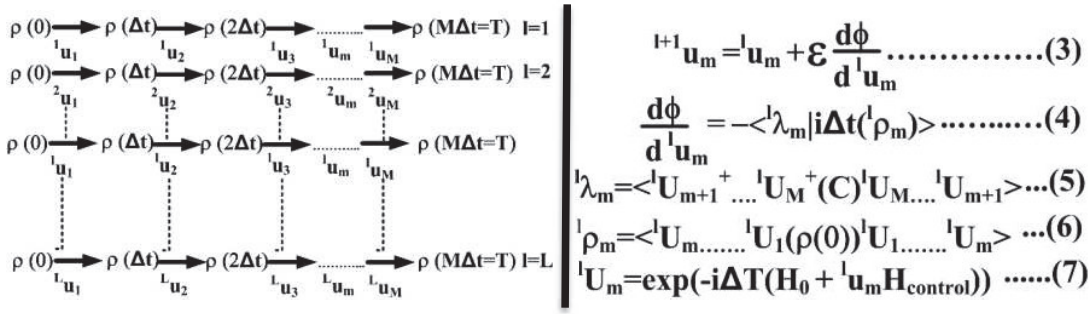

Fig. 1: [Left] Summary of grape where role of each weight $^{l}u_m$ correspond to weight of m^{th} time division for l^{th} iteration. [Right]: Equation (3) -(7) is followed to update value of $^{l}u_m$ for each iteration of l.

3. Results and Conclusion

We plot the performance index φ with respect to iteration. In Fig. 2, we have plotted seven cases in which each set of initial values was taken at random. With a set of initial random values of $^{0}u_m$ we observe that the φ start with some random value between 0-1. This depicts that for first iteration (l=1), the evolution $\rho(0)$ to time T= $M\Delta t$ result in $\rho(T)$ not equal to the desired output that we required (C). As the iteration increase, the $^{l}u_m$ values are updated in accordance with Eq.3. resulting in the new value of $\rho(T)$ for the next iteration being closer to the desired operation C.

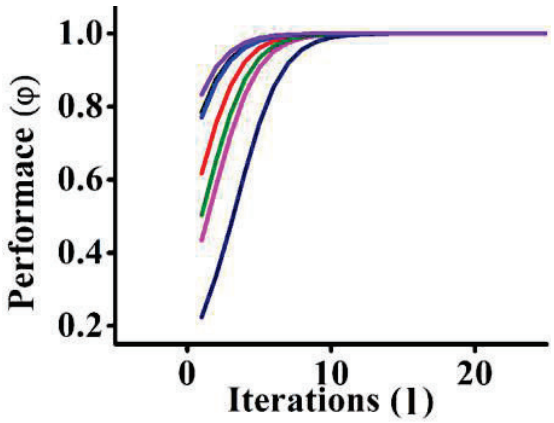

Fig. 2: Performance Index φ vs Iteration (k) for seven cases. In each of this cases the initial set of $\{u_k\}$ values are taken randomly between 0 and 1.

In Fig. 2 the algorithm ran for seven initial random set of $^{0}u_m$ values, and each time the φ value converges to the desired value. The real challenge in implementing the algorithm is the time scale of the spin system. In NMR systems, the spin state of nuclei is changed, having the time scales in ms, but for electrons, these time scales are low. This is circumvented by a high number of time divisions ($M = 10^3$) and a low value of step size ($\varepsilon = 10^{-3}$).

In this work, we have successfully implemented the GRAPE algorithm for quantum dot-based qubits to achieve the quantum control task of taking a given state to a specified final state of the qubit. The optimization of the algorithm shows that about 15 iterations are enough to reach the desired state, although we require a high division of time scale and an appropriate value of step size. In our future work, we will try to include decoherence into the GRAPE formalism to give us a pulse scheme to mitigate relaxation and decoherence noise components.

4. References

[1] N. Khaneja, T. Reiss, C. Kehlet, T. S. Herbruggen and S. J. Glasser, "Optimal control of coupled spin dynamics: design of NMR pulse sequences by gradient ascent algorithm," in Journal of Magnetic Resoance *172*(2), 296-305 (2005).

[2] J. M. Elzerman, R. Hanson, L.H. Willems van Beveren, B. Witkamp., L. M. K Vandersypen, and L. P. Kouwenhoven, Single-shot read-out of an individual electron spin in a quantum dot. *nature*, *430*(6998), 431-435 (2004).

3-D Scalar and Vector Finite Difference based Modal and Propagation Methods for Rectangular Waveguides

Pratiksha Choudhary[a] and Anurag Sharma[b]

[a, b] *Department of Physics, Indian Institute of Technology Delhi, New Delhi-110016, India*

[b] *Optics and Photonics Centre, Indian Institute of Technology Delhi, New Delhi-110016, India*

e-mail- phz188425@iitd.ac.in; asharma@iitd.ac.in

Abstract: A split-step non-paraxial finite difference method is used for the analysis of the three-dimension scalar wave equation. The method can be used to obtain modes as well as propagation of an incident field. We have presented a method based on split-step non-paraxial (SSNP) finite difference method to compute the 3-D scalar wave propagation. We have also extended the SSNP method for the vector wave propagation for large index contrast waveguide and this method can be used to obtain the modes and the propagation field in high contrast waveguides such as silicon waveguides.

Keywords: Bidirectional Beam propagation method, 3-D propagation, Finite difference method, Split-step method.

1. Introduction

We have developed a scheme for non-paraxial propagation by using the finite difference split-step nonparaxial (FDSSNP) method. The method is completely nonparaxial and the propagation operator are calculated analytically and it reduces the computational efforts. A non-paraxial bidirectional technique for scalar wave propagation is applicable for low index contrast waveguide [1,2]. For silicon photonics' high index contrast waveguide, vector approaches are important. In these waveguides, computations are often carried out using either FEM or FDTD. These processes are computational intensive. To get reflection in a guiding structure, the FDTD propagation method is typically used. The approaches for vector propagation that are now in use are generally paraxial formulations [3-5]. Here, we developed a 3-D finite-difference framework for non-paraxial propagation of vector waves. This technique can be used to compute wave propagation as well as to obtain modes.

We present here the results for the modes and propagation filed of a rectangular waveguide for scalar beam propagation method and we also present here the results for the modes of a silicon waveguide for vector method. We are working on the propagation method and the results will be presented at the conference.

2. Full Vector Formulations

Vector wave equations are derived from Maxwell's equations for the transverse component of electric fields are given by

$$(\nabla^2 + n^2k^2)E_x = -J_{xx}E_x - J_{xy}E_y \quad (1)$$

$$(\nabla^2 + n^2k^2)E_y = -J_{yx}E_x - J_{yy}E_y \quad (2)$$

where $J_{xx} = \left[\frac{\partial^2 lnn^2}{\partial x^2} + \frac{\partial lnn^2}{\partial x}\frac{\partial}{\partial x}\right]$, $J_{xy} = \left[\frac{\partial^2 lnn^2}{\partial x \partial y} + \frac{\partial lnn^2}{\partial y}\frac{\partial}{\partial x}\right]$, $J_{yx} = \left[\frac{\partial^2 lnn^2}{\partial y \partial x} + \frac{\partial lnn^2}{\partial x}\frac{\partial}{\partial y}\right]$, $J_{yy} = \left[\frac{\partial^2 lnn^2}{\partial y^2} + \frac{\partial lnn^2}{\partial y}\frac{\partial}{\partial y}\right]$ and $n(x, y, z)$ is the refractive index distribution. These equations are solved using the finite difference (FD) approximation. If J's term is not taken into account in the equations above, scalar approximation is obtained.

3. Split-step Non-paraxial Procedure (SSNP)

Using the FD formalism the equations for the transverse electric field components can be represented in terms of matrices as

$$\frac{d\phi}{dz} = H\phi \tag{3}$$

where

$$H=\begin{bmatrix} 0 & 0 & 1 & 0 \\ 0 & 0 & 0 & 1 \\ S-J_{xx} & -J_{xy} & 0 & 0 \\ -J_{yx} & -S-J_{yy} & 0 & 0 \end{bmatrix} \quad \text{and} \quad \phi = \begin{bmatrix} E_x \\ E_y \\ F_x \\ F_y \end{bmatrix} \tag{4}$$

and $F_x = \frac{\partial E_x}{\partial z}$, $F_y = \frac{\partial E_y}{\partial z}$. The matrix for the scalar technique will be obtained if the J's term in equation (4) is ignored.

4. Results

We present here the scalar mode and propagated field. The waveguide has a $5\mu m \times 2.5\mu m$ cross section and the refractive indices of the core and cladding, are $n_{co} = 1.45$ and $n_{cl} = 1.446$ and wavelength used is 1 μm. Vector modes for a silicon waveguide of height 240nm and width 440nm surrounded by air and the wavelength of propagation is 1550nm. The results are given in figure 1. Incident field and propagated field for scalar method is shown in figure 1(a) and vector modes are also shown here in figure 1(b),(c)and we are now working on the vector propagation method.

(a) (b) (c)

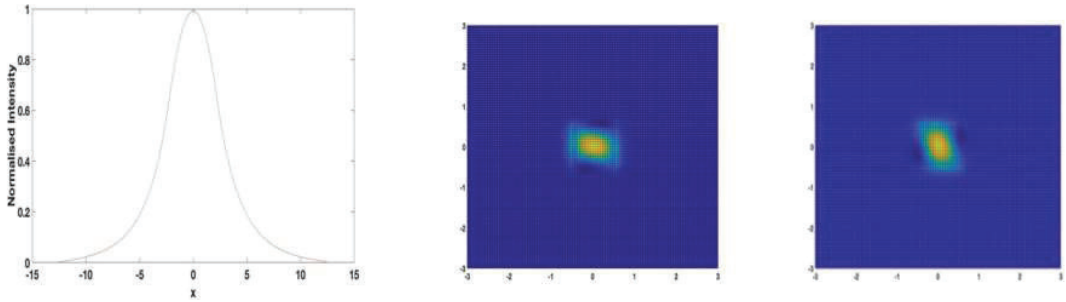

Fig.1.(a) Intensity plot for TE_0 mode of the square waveguide. The incident field at z=0 and the field after 100μm propagation are shown. Field profiles for the fundamental TE-like (b) and TM-like (c) modes in a square waveguide.

Funding. The work was partially supported by a fellowship from UGC-CSIR(Government of India) to Pratiksha Choudhary and a J.C. Bose fellowship from SERB (Government of India) to Anurag Sharma.

References

1. Sharma A. and Agrawal A. , "Non-paraxial split-step finite-difference method for beam propagation," *Opt. Quantum Electron.,* Vol. 38, pp. 19-34 (2006a).
2. D. Bhattacharya and A. Sharma, "simulation of multiple reflecting structures using a nonparaxial bidirectional split-step finite difference method," J. Light. Technol, vol. 31, no. 13, pp. 2106–2112, Jul. (2013).
3. Chung Y. and Dagli N. , "Explicit finite difference vectorial beam propagation method," *Electron Lett.*, Vol. 27, pp. 2119-2121 (1991).
4. W.P. Huang, C.L. Xu, and **S.K.** Chaudhuri , "**A** Finite-Difference Vector Beam Propagation Method for Three-Dimensional Waveguide structures (1992).
5. Huang W.P. and Xu C.L. , "Simulation of three dimensional optical waveguides by a full-vector beam propagation method," *IEEE J. Quantum Electron.*, Vol. 29, pp. 2639-2649 (1993).

Rapid Thermal Annealing of RF Sputtered Indium Tin Oxide Films

Abhimanyu[1, 2], Mukesh Kumar*[1, 2,] and Neelam Kumari[1]
[1]*CSIR-Central Scientific Instruments Organisation, Chandigarh-160030, India*
[2]*Academy of Scientific and Innovative Research (AcSIR), Ghaziabad- 201002, India*
abhimanyunirania@gmail.com, *mukeshk@csio.res.in

Abstract: A radio frequency (RF) magnetron sputtering system was used for the deposition of indium tin oxide (ITO) films. The deposited films were annealed rapidly at 300 °C for a duration of 10 to 60 seconds. The structure of the film changed to cubic polycrystalline after RTA from the amorphous structure of as-deposited films. The crystallite size of the films increased with the increase in annealing time. An increase in the resistivity was found in the ITO films from 2.79×10^{-3} Ω-cm to 3.85×10^{-3} Ω-cm with average visible transparency of 80%.
Keywords: Indium tin oxide (ITO), Radio frequency magnetron sputtering, Rapid thermal annealing (RTA).

1. Introduction

Indium tin oxide (ITO) thin films have applications in many optoelectronics instruments like solar cells, transparent heaters [1, 2], etc. as a transparent and conducting electrodes due to their high visible transparency and electrical conductivity [3]. Various approaches were applied for the deposition of ITO films like electron beam deposition, atomic layer deposition, sputtering [4-6], etc. Among these, sputtering systems are extensively used on an industrial scale due to the high control of the deposition parameters and high directionality of the system. The properties of ITO films can be controlled by controlling the various deposition parameters of the sputtering system like gas flow rate, applied power, substrate temperature, deposition pressure, etc. [7]. Rapid thermal annealing (RTA) is also an emerging post-deposition technique utilized for the enhancement of the various properties of the deposited films [8]. In this research, the ITO films were deposited on a glass substrate in an argon atmosphere. The effect of RTA for 10 to 60 seconds on the different properties of the room temperature deposited ITO films was studied in this research.

2. Materials and Methods

ITO thin films were deposited on 2.5 ×2.5 cm^2 glass substrates. The customized RF magnetron sputtering system (HHV Bangalore, India) was used for the film deposition. The sputtering target of diameter 6-inch and 6 mm thickness was used. The base pressure of the chamber was achieved to 1.8×10^{-6} mbar. The films were deposited with the RF power of 450 W and the argon gas flow of 42 sccm. The films were deposited at 1.4×10^{-2} mbar of working pressure for 30 minutes. The ITO target was pre-sputtered for 10 minutes before the deposition. The source to substrate distance was 195 mm and the substrates were rotated with a constant speed of 20 rounds per minute for thickness uniformity of films. XRD of ITO films was carried out with Bruker D8 Advance. The diffraction patterns were recorded with the Cu Kα line (0.154 nm) with the anode current of 40 A and the applied accelerating voltage of 40 kV. Optical characterization of the films was done with a UV-Vis-NIR spectrophotometer (Carry 7000, Agilent Tech, USA). The measurements of the electrical properties were performed with a four-point probe system (Indosaw, Ambala). A thin film analyzer system (Make: Filmetrics, Model: FT-10RT) was used for the measurement of the thickness of the film after deposition. The approximate thickness of the films was 180 nm. For RTA, first, the chamber was set to 300°C. When the chamber temperature of 300°C was reached, then the sample was kept in it. After a specified time, the sample was extracted out at 300°C and brought to room temperature of 25°C.

3. Results and Discussion

3.1. Structural properties

The XRD plot of the ITO films is displayed in Fig 1. The main peaks of RTA samples were well matched to the peaks reported in ICDD PDF 00-065-0688. As-deposited ITO films showed a halo pattern around 2θ = 31.54° which is characteristic of amorphous material. Up to RTA for 20 seconds, amorphous behavior was observed. But for the 30 seconds of annealing, the structure of the films started to convert into crystalline with the shift in peak towards a lower angle of 30.61°. With the further increase in annealing time, the crystallinity of the ITO films increased with the preferential peak (222) at about 30.60°. The crystallite size was increased from 1.44 nm to 61.9 nm as the annealing time increased.

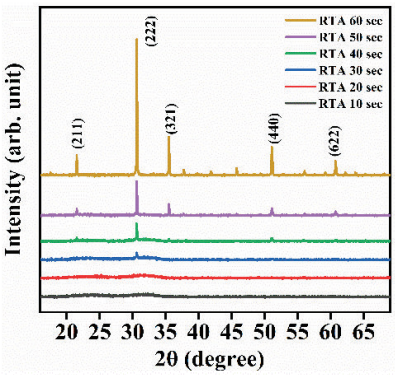

Fig. 1: XRD pattern of rapid thermal annealed ITO films

3.2. Electrical properties

The electrical properties of the samples were measured in terms of sheet resistance (R_s) as shown in Fig. 2. It was found that R_s of as-deposited samples were 155 Ω/sq. With the rapid thermal annealing, the R_s of the samples primarily increased to 2910 Ω/sq and then decreased to 214 Ω/sq. The increase in R_s was due to a decrease in oxygen vacancies [9, 10] which is the prime source of carrier concentration in as-deposited metal-doped oxide films. After 50 seconds, the decrease in R_s of the film was due to an increase in crystallinity with saturation of oxygen vacancies. The increase in crystallinity ultimately increased the mean free path since the crystallite size was increased [11]. In terms of the resistivity, the resistivity of the as-deposited ITO films was 2.79 × 10^{-3} Ω-cm. The resistivity of annealed films increased up to 52.38 × 10^{-3} Ω-cm and then decreased to 3.85 × 10^{-3} Ω-cm.

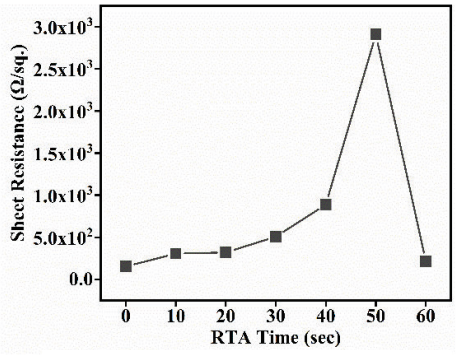

Fig. 2 Sheet Resistance of annealed films

3.3. Optical properties

Fig. 3 shows the transmittance spectra of the as-deposited and annealed films from ultraviolet (UV) to near-infrared (NIR) regions. The as-deposited ITO films were showed high transparency. The average visible transmittance of all the films was about 80%. The NIR transmittance remained nearly the same for the films annealed up to 30 seconds. After that, NIR transmittance decreased as the RTA time increased. The comparison with the XRD pattern showed a relation between the crystallinity and the NIR transmittance. It was found that as the crystallinity of the film increased, the NIR transmittance decreased. The decrease in transmittance may be due to an increase in grain boundaries on annealing. The optical band gap of the annealed ITO films was decreased from the as-deposited films up to 50 seconds due to a decrease in carrier concentration [11]. But for the 60 seconds annealed film, the band gap showed a slight increase than as-deposited films.

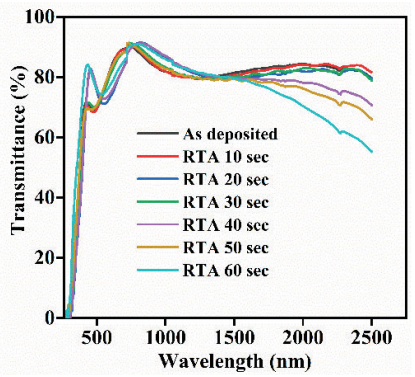

Fig. 3:Transmittance spectra of as deposited and RTA films

4. Conclusions

In conclusion, we report an RTA process applied on the room temperature deposited ITO films. The crystallinity of the films enhanced on the application of RTA process. The ITO films were converted into cubic structures after annealing from the as-deposited amorphous film. The electrical conductivity of the films decreased with the annealing up to 50 sec and then decreased. An optical study showed that the as-deposited, as well as annealed films, were transparent in nature. All the films had nearly 80% average visible transmittance. But the NIR transmittance of the films decreased with an increase in annealing time which we related to the increase in the crystallinity of the film.

Acknowledgements

The authors are thankful to the University Grants Commission (UGC), New Delhi-110002, India for providing financial support as a JRF during this research work.

5. References

1. Txintxurreta, J., et al., *Indium tin oxide thin film deposition by magnetron sputtering at room temperature for the manufacturing of efficient transparent heaters.* Coatings, 2021. **11**(1): p. 92.
2. Lu, Y., et al., *Comparative study of AZO and ITO thin film sputtered at different temperatures and their application in Cu 2 ZnSnS 4 solar cells.* Journal of Materials Science: Materials in Electronics, 2018. **29**(20): p. 17525-17532.
3. Mohamed, H., *Effect of substrate temperature on physical properties of In2O3: Sn films deposited by e-beam technique.* International Journal of Physical Sciences, 2012. **7**(13): p. 2102-2109.
4. Rozati, S.M. and T. Ganj, *Transparent conductive Sn-doped indium oxide thin films deposited by spray pyrolysis technique.* Renewable Energy, 2004. **29**(10): p. 1671-1676.
5. Ghamari, F., D. Raoufi, and J. Arjomandi, *Influence of thickness on crystallographic, stereometric, optoelectronic, and electrochemical characteristics of electron-beam deposited indium tin oxide thin films.* Materials Chemistry and Physics, 2021. **260**: p. 124051.
6. Lacroix, B., et al., *Nanostructure and physical properties control of indium tin oxide films prepared at room temperature through ion beam sputtering deposition at oblique angles.* The Journal of Physical Chemistry C, 2019. **123**(22): p. 14036-14046.
7. Kim, Y.J., et al., *Effect of oxygen flow rate on ITO thin films deposited by facing targets sputtering.* Thin Solid Films, 2010. **518**: p. 6241-6244.
8. Daoudi, K., et al., *Rapid thermal annealing procedure for densification of sol-gel indium tin oxide thin films.* Crystal engineering, 2002. **5**(3-4): p. 187-193.
9. Goncalves, G., et al., *Influence of post-annealing temperature on the properties exhibited by ITO, IZO and GZO thin films.* Thin Solid Films, 2007. **515**(24): p. 8562-8566.
10. Chan, S.H., et al., *The Effect of Annealing on Nanothick Indium Tin Oxide Transparent Conductive Films for Touch Sensors.* Journal of Nanomaterials, 2015. **2015**.
11. Kim, Y., et al., *Effect of Annealing in ITO Film Prepared at Various Argon-and-Oxygen-Mixture Ratios via Facing-Target Sputtering for Transparent Electrode of Perovskite Solar Cells.* Coatings, 2022. **12**(2).

Optical Characterization of Fast Steering Mirror

Vikash Porwal, J. S. Rawat, and S.K. Mishra[#]
Adaptive Optics Group, Instruments R&D Establishment, Dehradun-248008
e-mail:[#]skmishra.irde@gov.in

Abstract: Fast steering mirrors are used extensively in military and aerospace applications. They are being used for various imaging and laser applications such as LIDAR, High Power Laser, Laser communication, Wide-area scanning camera, IRST, Periscope for Submarine, etc. A test setup is rigged up to characterize Fast steering mirror, in terms linearity, tilt resolution and tilt range using QD and Interferometer, for its optimum utilization.
Keywords: Fast steering mirror, deblurring, scanning, interferometry, quadrant detector

Introduction

Fast steering mirror(FSM) are being used for precision active optical applications. Optical motion deblurring is one of the applications being perused in various projects at IRDE. A steering imaging system, consisting of optical relay and visible/IR camera, provides blurred imagery. Scanning of landscape can be achieved by a rotating mirror with certain angular speed, resulting in motion blur. The FSM can be inserted in the optical relay of imaging system so as to provide counter scan to the optical rays forming the image at the sensor within the exposure time of the camera[1]. This process will result into motion deblurred frames. The additional applications include, LIDAR, Laser pointing and Line of Sight stabilization, free-space and underwater laser communication, and high power laser beam delivery.

The FSM under investigation involves mirror, actuator stage, drive electronics and amplifier. Development of FSM requires rigorous suitable mirror fixing at actuator stage, testing and precision opto-mechanical assembly in the targeted applications. The FSM provides dynamic X and Y tilts through a combination of a set of piezo electric actuators.

It is imperative to characterize the FSM before using it in as a motion deblurring device or in any other application. The physical parameters for the FSM include linearity, tilt resolution, accuracy, repeatability, and tilt range. The linearity of FSM operation can be thought as voltage to tilt response, i.e. operational range where tilt is directly proportional to applied actuator voltages. The tilt resolution is the minimum tilt that can be produced in response of applied voltage; the value will be affected if axes coupling are present. The tilt range is the maximum achievable tilt for its linear operation.

Experimental Schematic

The linearity and tilt range for the FSM are estimated with a high resolution Quadrant Detector (QD) based tip-tilt sensor [3]. The schematic is shown in figure 1(a). A laser beam is allowed to fall on FSM, which is allowed to steer by applying a set of voltages over the bias voltage of 50 V. The corresponding shifts on sensor are used to predict linearity and tilt range of the FSM.

The tilt resolution is estimated with the help of interferometric analysis performed over recorded interferograms. A plane wavefront (@532 nm) from the interferometer falls on the FSM, and gets reflected back to interfere with the reference wavefront. The schematic is shown in figure 1(b).

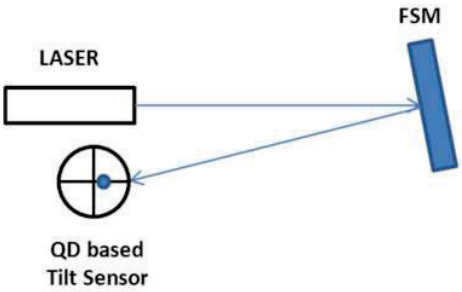

Fig 1(a): Linearity and range measurement

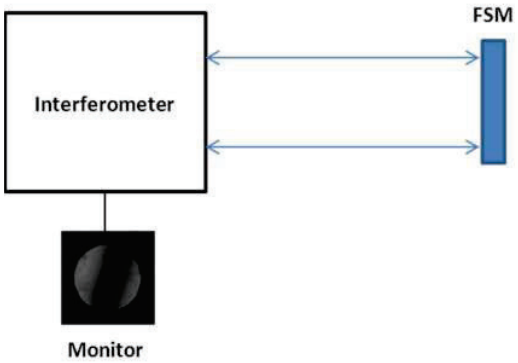

Fig. 2(b): Estimation of tilt resolution

The FSM is actuated in variety of voltage conditions and corresponding interferograms are recorded for further analysis. Interferogram of unpowered mirror surface is shown in figure 3(a), whereas null fringe is achieved at voltages 57.75 V and 56.41 V on X axis and Y axis, respectively (figure 3 b). Further, the voltages are increased in equal steps on X axis and Y axis and the typical interferograms are shown in Fig. 4. Interferograms in Fig. 4(a-c) show the increasing voltages on X axis, whereas the fig.4(d) shows the increased value of voltage on Y axis.

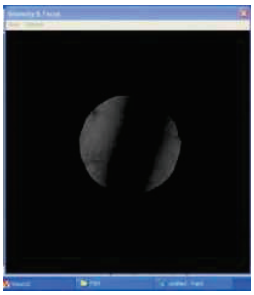

Fig. 3(a): Unpowered surface

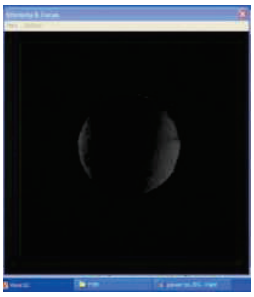

Fig. 3(b): Null fringe

Fig. 4(a): X tilt

Fig. 4(b): X tilt

Fig. 4(c): X tilt

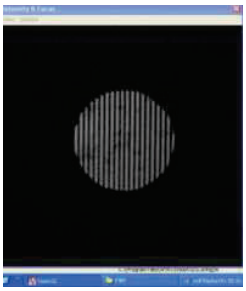

Fig. 4(d): Y tilt

Results and discussion

The FSM can linearly operate in the 0-100 V around 50 V bias with the tilt range 2 mrad (+/- 1 mrad). The Optical Path Difference (OPD) for 1 fringe is estimated as 316.4 nm with the corresponding tilt 12.64 µrad. The 1V step size of the voltage corresponds to 1.5 fringes, hence the tilt resolution is approximately 20 µrad ($1/1000^{th}$ part of 1 degree). Thus the setup is capable of measuring ≤20 µrad resolutions. A small coupling and a little difference between the response in X and Y direction are also observed, while investigating the physical properties of the FSM.

References

[1] R K Tyson, "*Principle of Adaptive Optics"* (Academic, Press 1991)

[2] G A Tyler and D L Fried, "Image Position Error associated with Quadrant Detector," JOSA, vol. 72(6) pp. 804-808 (1982)

[3] Awakash Dixit, Vikash Porwal, Aditya K. Mamgain and S. K. Mishra, "High Resolution Quadrant Detector Based Tip-tilt Sensor for Adaptive Optics", in Physics of Semiconductor Devices, Environmental Science and Engineering, (Springer International Publishing, Switzerland, 2014) pp.503-504. ***DOI*** 10.1007/978-3-319-03002-9_126.

[4] S. K. Mishra, Vikash Porwal, Sushil Chaukiyal, J. S. Rawat, and Ajay Kumar, "Real-time debluring of known motion blurs using optical means," in Proc. of Int. Conference on Optics and Photonics, (University of Kolkata, Feb. 2015), pp.

.

Modal and Propagation Analysis of Solid Core Bragg Fibers

Ajay Kumar [a], Anurag Sharma [b]
[a, b] *Department of Physics, Indian Institute of Technology Delhi, New Delhi, 110016*
[b] *Optics and Photonics Centre, Indian Institute of Technology Delhi, New Delhi, 110016*
e-mail: ajaykumargainpura@gmail.com; asharma@physics.iitd.ac.in

Abstract: We describe a method for the numerical computation of the mode of Bragg's fiber using the collocation method under the weakly guiding linearly polarized (LP) approximation. For the propagation of waves through the Bragg fiber, we used the collocation method thereby reducing the computation time significantly. The ABC boundary condition can be easily implemented for reducing the reflection from the boundary with only a small increase in computational effort.
Keywords: Bragg fiber, Periodic refractive index, Collocation method.

1. Introduction

Bragg fiber consists of a low-index core and high index low and high index alternating layers. The thickness of layers is determined by the roots of transcendental equation involving the Bessel function [1]. For, a finite number of layers, the thickness is taken uniformly for high and low index alternating layers, as an approximation. Bragg fibers have a large photonic bandgap and omnidirectional reflectivity and hence are used in infrared energy transmission, optical detection external reflection from omnidirectional with large bandwidth and negligible propagation loss [2,3].

Here, we use the collocation method, to obtain the mode as well as to propagate the beam through solid core Bragg fiber multiple bilayers of alternating high and low refractive index layers. In the collocation method, we use associated Laguerre-Gauss functions for cylindrically symmetric like Bragg fiber and investigate the model field distribution, propagation of Bragg-fiber's mode through the Bragg's fiber, and power confinement in core with wavelength.

By using the collocation method, we reduce the three-dimensional problem to two-dimensional problem as in Bragg fiber refractive index distribution is only in the radial direction. Hence, the problem is reduced to two-dimensional and computational time reduce effectively.

2. Collocation method

The scalar Helmholtz equation, under weakly guiding approximation in polar coordinates for Bragg fiber, is given as

$$\frac{d^2\psi(r)}{dr^2}+\frac{1}{r}\frac{d\psi(r)}{dr}+\left(k_0^2n^2(r)-\beta^2-\frac{m^2}{r^2}\right)\psi(r)=0 \tag{1}$$

where $k_0=2\pi/\lambda_0$, β is propagation constant and $n^2(r)$ periodic refractive index. The total field $\psi(r)$ is represented as a linear combination of the associated Laguerre-Gauss orthogonal basis function.

$$\psi(r,z)=\sum_{n=1}^{N}a_n(z)\phi_n^l(r) \tag{2}$$

where $\phi_n^l(r)=\sqrt{\frac{2(n-1)!}{(l+n-1)!}}\alpha^{l+1}r^l L_{n-1}^l(\alpha^2r^2)e^{\frac{-1}{2}\alpha^2r^2}$ and α is a scaling parameter. The expansion coefficients $a_n(z)$ are obtained from the collocation points at which the Helmholtz equation is exactly satisfied and we take the roots of $L_N^l(\alpha^2r^2)=0$ as the collocation points. Now using general procedure [4], we obtain the collocation equation

$$\frac{d^2\Psi}{dz^2}+[S+R(z)]\Psi(z)=0 \tag{3}$$

By defining $\Psi=[\psi_1\ \psi_2\ \ldots\psi_N]$ and $R(z)=diag[\beta_1^2\ \beta_2^2\ \ldots\ \beta_N^2]$ for $\beta_i^2=k_0^2n^2(r_i)$. Here **S** is a differential operator and **R(r)** is the ***r***-dependent matrix. The eigenvalues and eigenvector of matric $[S+R(z)]$ give the mode and propagation constant.

3. Propagation

For solving the above equation, let the field is evolving in propagation direction in a constant reference medium as

$$\Psi(z) = \chi(z)e^{-ik_0 n_0 z} \tag{4}$$

so that $\chi(z)$ is a slowly varying function of 'z'. Hence, neglecting the second derivative we obtained

$$\frac{d\chi}{dz} = [BA^{-1} + R(z) - k^2 I]\chi(z)/2ik$$
$$\frac{d\chi}{dz} = H(z)\,\chi(z) \tag{5}$$

which is a unidirectional beam propagation equation. This equation is solved under the paraxial approximation as

$$\chi(z + \Delta z) = e^{\frac{-1}{2}H_2\Delta z} e^{H_1\Delta z} e^{\frac{-1}{2}H_2\Delta z}\chi(z)$$
$$\chi(z + \Delta z) = PQ(z)P\chi(z) \tag{6}$$

By successive application of the above steps, we obtained the field at *L* length. By analyzing the field at length *L,* we obtained propagated field at length *L* [6].

4. Result and Discussion

The index distribution for Bragg fiber for nine bilayers of an alternating low and high index is given as

$$n(r) = \begin{cases} n_{core} & r \le r_{core} \\ n_{clad} & r \ge r_{core} + 12 * \Lambda \\ n_{high} & r_{core} + N_P\Lambda < r < r_{core} + N_P\Lambda + d_{high} \\ n_{low} & otherwise \end{cases} \tag{7}$$

where $\Lambda = d_{high} + d_{low} = 1.2\mu m + 2.4\mu m$, $N_P = 0,1,2,\ldots 9$, $r_{core} = 6.7\mu m, n_{core} = 1.446, n_{high} = 1.459, n_{low} = 1.450, n_{clad} = 1.443$. For wavelength $\lambda_b = 1.064\mu m$, propagation of mode of Bragg's fiber and Gaussian beam through *10cm* is shown. For Gaussian beam propagation, fractional power in the core is also shown with wavelength.

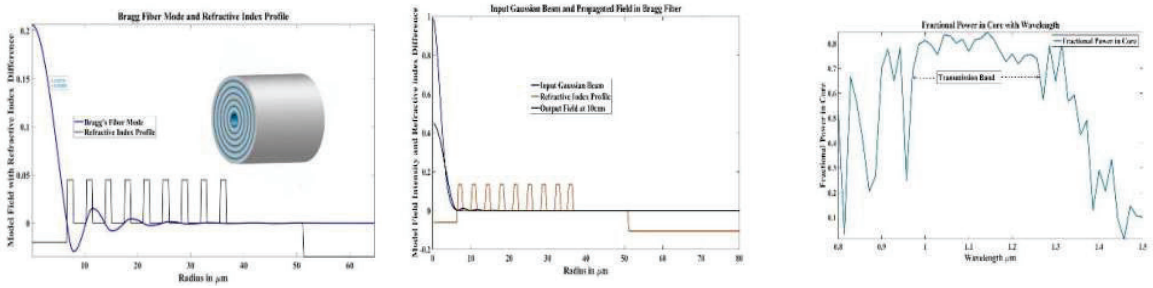

5. Conclusion

In conclusion, we have developed a scalar approach based on the collocation method to solve the Helmholtz equation in cylindrical symmetric fiber with periodic refractive index profile, including the structure like Bragg fiber. From this mathematical modeling, we obtained the mode supported by the Bragg fiber and this mode is propagated through a distance of *10 cm*. At this distance, the power of the mode remains unchanged, and hence mode propagates negligible loss. When we launch the Gaussian beam, then it starts exciting the modes of the structure. Finally, at a distance of *10 cm*, only Bragg mode sustains, and all other higher-order modes are leaked out.

Funding. The work was supported by a fellowship from CSIR (Govt. of India) to Ajay Kumar and a J.C. Bose fellowship from SERB (Govt. of India) to Anurag Sharma.

References

[1] Pochi Yeh, Amnon Yariv, and Emanuel Marom, "Theory of Bragg fiber*," J. Opt. Soc. Am. 68, 1196-1201 (1978).
[2] Fink Y, Winn JN, Fan S, Chen C, Michel J, Joannopoulos JD, Thomas EL. A dielectric omnidirectional reflector. Science. 1998 Nov 27;282(5394):1679-82. doi: 10.1126/science.282.5394.1679. PMID: 9831553.
[3] Hart SD, Maskaly GR, Temelkuran B, Prideaux PH, Joannopoulos JD, Fink Y. External reflection from omnidirectional dielectric mirror fibers. Science. 2002 Apr 19;296(5567):510-3. doi: 10.1126/science.1070050. PMID: 11964473.
[4] A. Sharma, "Collocation method for wave propagation through optical waveguiding structure," Prog. Electromagn. Res. 11, 143-198 (1995).
[5] Kliros, George. (2009). Analysis of complex refractive index solid-core Bragg fibers. Optoelectronics and Advanced Materials, Rapid Communications. 3. 309-312
[6] A. Sharma, A. Agrawal, New method for nonparaxial beam propagation, J. Opt. Soc. Am. A 21 (2004) 1082–1087.

Electrically tunable Directional Coupler using Long-Period waveguide Gratings

R. Chauhan[a], U. S. Tripathi[b] ,V. Rastogi[a,c]
[a]*Department of Physics, Indian Institute of Technology Roorkee,247667, India*
[b] *Instruments Research & Development Establishment, Dehradun, India*
[c] *Center of Photonics and Quantum Communication Technology, Indian Institute of Technology Roorkee,247667, India*
*,*rchauhan1@ph.iitr.ac.in*

Abstract: We present the design of an electrically tunable directional coupler on silicon nitride on insulator platform. Long-period waveguide gratings on sidewalls of asymmetric rib waveguide structure have been studied for coupling between the modes of structure. Liquid crystal cladding has been used to achieve tunability in resonance wavelength of the coupler.
Keywords: Liquid crystals, Directional coupler, Long period gratings

Introduction

Silicon photonics is an emerging area that has the capability to integrate both electronic and photonic circuits on the same substrate. To achieve tunability in the Photonics circuit, use of Liquid crystals (LCs) is one of the solutions. Use of liquid crystals is promising in photonics applications because of their unique electro-optic properties [1-3].

Device design

The proposed structure is shown in Fig. 1. Where two parallel asymmetric rib waveguides A and B have been formed on silicon nitride on insulator substrate. The width (W) and height (H) of both the ribs are 2.5 µm and 1.2 µm, respectively. Separation between the ribs is 5 µm. Etch depth in the side regions of both the ribs is 0.6 µm and in mid regions between ribs is 0.4 µm.

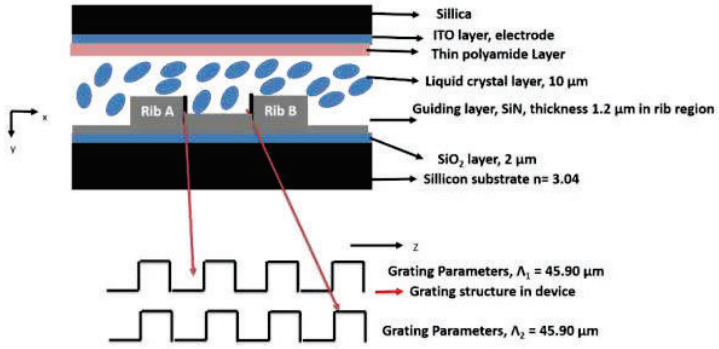

Fig. 1 Design of the simulated device

Refractive indices of silicon and silicon nitride are 3.4 and 1.99, respectively. Therefore, a 2.0 µm thick SiO_2 layer on Silicon substrate has been taken as an isolation layer between the silicon and silicon nitride layer. MLC-9200-000 liquid crystal has been taken as a cladding layer, and its refractive index can be varied from 1.46 (n_o) to 1.54 (n_e) by applying an electric field across the LC cell. ITO-coated fused silica substrate has been taken as the top electrode. A thin polyimide layer has been considered on the top substrate for anchoring Liquid crystal molecules along x-direction.

Corrugated long-period gratings are designed in core regions on sidewalls of both the ribs. The period of the gratings in both the ribs is Λ=45.90 µm. The etch depth of corrugation Δh in both the grating regions is 40 nm. Gratings in both ribs are parallel to each other. Length of the gratings is 7.3 mm. Here we assume that two ribs are sufficiently far apart, and grating is very weak which can be treated as a perturbation to the rib waveguide structure.

Methodology

The Mode coupling can be described by conventional coupled mode theory [4].

$$\frac{dA}{dZ} = -jkB\, exp(j\delta_1 z) \qquad (1)$$

$$\frac{dB}{dZ} = -jkA\,exp(-j\delta_1 z) - jk\bar{A}\,exp(-j\delta_2 z) \qquad (2)$$

$$\frac{d\bar{A}}{dZ} = -jkB\,exp(j\delta_2 z) \qquad (3)$$

Here $A(z)$ and $\bar{A}(z)$ are amplitudes of the fundamental mode in rib A and rib B. $B(z)$ is the amplitude of composite mode of the structure. δ_1 and δ_2 are the phase mismatch at a particular wavelength in two gratings. k is the coupling coefficient of gratings which is given by [5].

$$k = \frac{k_0 \Delta n_0^2}{8c\mu_0} \iint_{\substack{Grating \\ Region}} E_{00}\, E_{mn}\, dxdy$$

Here k_0 is the free space wavenumber, c is the speed of light in vacuum, and μ_0 is the permeability of medium in free space. $\Delta n_0^2 = n_{core}^2 - n_{cl}^2$ Where n_{core} and n_{cl} and core and cladding refractive indices respectively. E_{00} and E_{mn} are the field profiles of fundamental TE mode of ribs and higher order composite modes of structure.

Results

Modal analysis of this structure has been done using the Film Mode Matching (FMM) method. The coupled mode equations have been solved using the fourth order Runge-Kutta method. Light is launched into the fundamental mode of rib-A. The grating on the sidewalls of rib-A couples it to the higher order composite slab mode of structure. The Grating on sidewalls of Rib-B couples power from higher order slab mode to fundamental mode of rib-B. Figure 2 shows the variation of fractional power in rib-B with wavelength at two different values of cladding refractive index, n_{cl} = 1.54 and n_{cl} = 1.535. At zero voltage across LC cell, all the LC molecules are aligned along the x-direction, therefore cladding refractive index is n_{cl} =1.54 for TE mode. At zero voltage, the coupling of power from Rib-A to Rib-B is maximum at 1580 nm wavelength (Fig. 2 (a)), as voltage is increased to 1.75 V and refractive index of cladding LC layer changes to 1.535 and the resonance coupling wavelength of coupler changes to 1550 nm. Such a structure can be used as a tunable switch and wavelength filter.

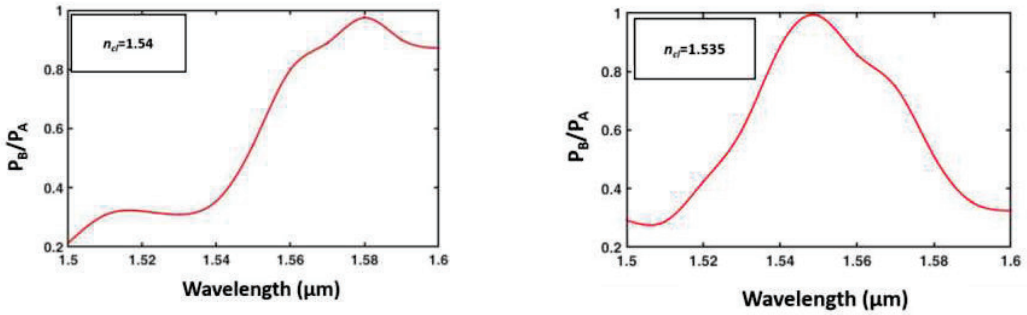

Fig. 2 Variation of coupled output power from Rib A to Rib B at (a) V= 0 V (b) V=1.75 V

Conclusion:

In this work tunable directional coupler has been achieved on silicon nitride on insulator substrate. We have shown that the resonance wavelength of the coupler can be tuned from 1580 nm to 1550 nm by applying a voltage of 1.75 V across the LC cell.

References:

[1] I. C. Khoo, "Liquid crystals", John Wiley and Sons,2007.
[2] G. T. Reed, A. P. Knights, "Silicon Photonics-An Introduction", John Wiley and Sons, 2004
[3] U. S. Tripathi, V. Rastogi,"liquid crystal based widely tunable integrated optic wavelength filters", J. Opt. Soc. Am. B **36**, 1883 (2019).
[4] Y. Bai, K. S. Chiang,"Analysis and design of Long-period waveguide grating couplers", J. Lightwave Technol. **23**, 4363 (2005).
[5] Q. Liu, K. S. Chiang, V. Rastogi,"long period gratings in planer optical waveguides", J. Lightwave Technol. **21,** 3399 (2003)

Graphene-Metal Hybrid FSS for Dual-mode Characteristics

Sambit Kumar Ghosh [(1)], Nikhil Kumar [(2)] and Somak Bhattacharyya* [(3)]
[(1, 2, 3)] *Department of Electronics Engineering, Indian Institute of Technology (BHU), Varanasi, India.*
[1]sambitkrghosh.rs.ece17@iitbhu.ac.in, [2]nikhil.jrf.ece22@itbhu.ac.in, [3]somakbhattacharyya.ece@iitbhu.ac.in

Abstract: A hybrid combination of graphene-metal FSS structure to simultaneously operate as bandpass and bandstop filter has been discussed in this report. The unit cell comprises specifically-patterned gold layers on two opposite faces of silicon dioxide layers deposited on a foam block. A graphene pattern has also been deposited along the slots of the top gold layer. The FSS structure has been optimized such that it can provide broadband bandpass filtering characteristics in between 7 THz and 11 THz in terms of a 3-dB fractional transmission bandwidth of 34.55%. The proposed device can also produce stop band response from the same configuration under the exposure of a distinct electric field (*E*). The prototype has a periodicity of λ/2.14 and its thickness λ/3.76. The reflection response is dominant when the value of *E* has been increased to a certain level. The transmission response will be significantly large when the graphene layer is in unbiased condition. The prototype is polarization independent and it provides angular stability up to 40º while EM wave will interact obliquely with the top face of the FSS. This structure can find applications in THz imaging, spectroscopy and THz communication systems.

1. Introduction

Frequency selective surfaces (FSSs) remain unique over the decades because of their capability to control the magnitude and phase of the electromagnetic (EM) wave from the microwave to optical domain [1]. FSS based spatial filter concept has been explored earlier [2]. A transmission line based approach in terms of FSS has been studied as a bandpass filter [3]. Planar configuration with slots assembled with metal strips has also been introduced as filter [4]. Metallic metasurface-based configurations have also been reported earlier for filtering applications operating in the terahertz (THz) region [5]. Pass band filters have also been realized with the stacked metallic configurations as discussed in [5]. Graphene is favorable for THz electronics applications [1] as its surface conductivity can be modulated under the exposure of the external factors, viz., external doping, mechanical stretching and electrical biasing etc. Graphene FSS has already been used for achieving variable radiation pattern from a dipole antenna at THz [1].

In this communication, we have presented a stacked configuration of metal-graphene hybrid structures to operate as simultaneous reflecting and transmitting surfaces without any structural deformations. The proposed FSS structure has been designed in such a way that it can work as a bandpass filter in between 7 THz and 11 THz with a 3-dB fractional transmission bandwidth of 34.55% under the unbiased condition (chemical potential, $\mu_c = 0$ eV). The same device can generate bandstop filtering response under the exposure of an external electric field corresponding to μc of 1 eV. Metallic FSSs [5] have already been studied earlier for filter applications but their function is bounded to particular frequency band. They also offer narrowband transmission characteristics. This proposed FSS may be very effective for upcoming 6G applications because dual performances can be achieved from a single device. This type of duality in reflection and transmission characteristics can be realized by applying a DC bias between the graphene FSS and the bottom gold surface. The unit cell of the proposed FSS comprises of a stacking of six layers. Two specifically-slotted metallic layers have been placed on two thin films (0.2 μm) made of silicon dioxide (SiO_2) separated by a foam substrate (9 μm). The thickness of the slotted metallic layers are considered as 1 μm and the effective permittivity of the foam substrate is close to unity. The SiO_2 layers have been selected as lossy material ($tan\delta = 0.001$) with a dielectric permittivity of 3.9. The top and bottom layers are made of gold ($\sigma = 4.56 \times 10^7\ S/m$). The top layer, top layer with graphene pattern, perspective view and side views of the proposed FSS have been graphically represented in Fig. 1(a), Fig. 1(b), Fig. 1(c) and Fig. 1(d), in accordingly. All the dimensions are included in Fig. 1. The EM analysis of the proposed hybrid FSS has been executed by using the finite integration technique (FIT) to compute the reflection and transmission characteristics within the band of interest. The reflection and transmission coefficient characteristics of the FSS have been presented in Fig. 2. The chemical potential (μ_c) of the top graphene pattern is taken to be 0 eV where it acts as an insulator, as shown in Fig. 2(a). Thereafter, the FSS structure has been placed under the influence of distinct electric field (*E*) so that the μ_c reaches to 1.4 eV; implying the top periodic graphene FSS surface will behave as a metal. The device will act as a partial reflector and the transmission response gets

deteriorated as depicted in Fig. 2(a). This determines the fact that the proposed graphene-metal hybrid FSS structure can provide simultaneous reflection and transmission characteristics under two different conditions.

2. Figures

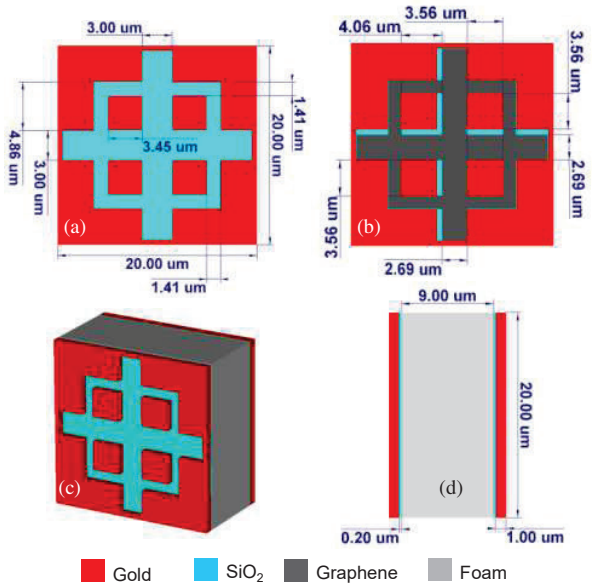

Fig. 1: (a) Top layer, (b) Top layer with graphene pattern (c).perspective view and (c) side view of the unit cell of the graphene-metal hybrid FSS.

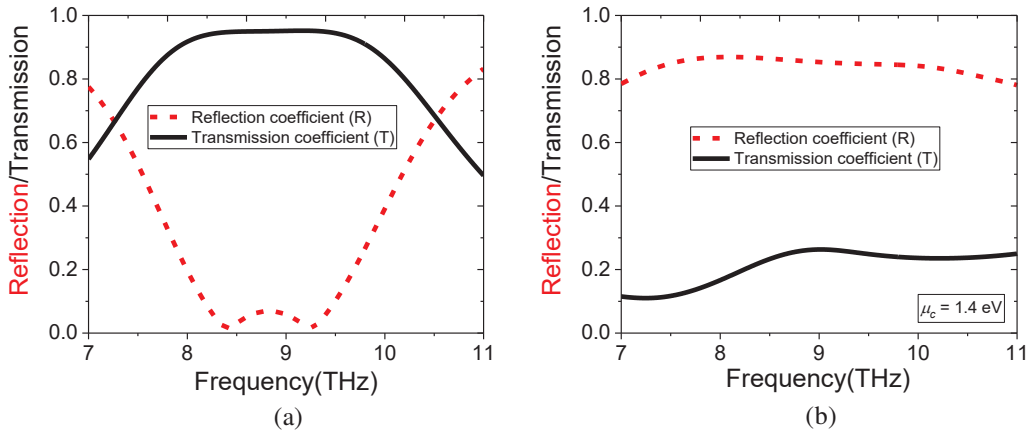

Fig. 2: Frequency responses of the reflection (R) and transmission (T) coefficients* (a) *when* $\mu_c = 0$ *eV and* (b) *when* $\mu_c = 1.4$ *eV.

3. References

[1] S. K. Ghosh, S. Das and S. Bhattacharyya, "Graphene-Based Metasurface for Tunable Absorption and Transmission Characteristics in the Near Mid-Infrared Region," *IEEE Transactions on Antennas and Propagation*, **70(6)**, 4600-4612, (2022).

[2] F. Debarros, P. Lemaître-Auger, A. De Menezes, R. Siragusa, T. Vuong, G. Tourtollet, & G. Fontgalland, ''Characterization of frequency-selective surface spatial filters in a rectangular waveguide.'' *International Journal of Microwave and Wireless Technologies*, **4(1)**, 59-69 (2012).

[3] J. D. Ortiz, J. D. Baena, V. Losada and F. Medina, "Metasurfaces made of transmission lines: A way to spatial filtering," *2013 USNC-URSI Radio Science Meeting (Joint with AP-S Symposium)*, 137-137, (2013)

[4] E. Simbolon and A. Munir, "FSS-based planar bandpass filter using strip slotted-lines," *2014 6th International Conference on Information Technology and Electrical Engineering (ICITEE)*, 1-5, (2014).

[5] B. Yang, Q. Li, M. Jia, S. Xiao and L. Zhou, "Terahertz metasurface for flexible band-pass filter," *2018 International Applied Computational Electromagnetics Society Symposium - China (ACES)*, 1-2 (2018).

Optimization of Tapered Fiber Bundle Fabrication Maintaining Adiabaticity at Low Taper Ratio

Debparna Majumder[1,2,*], Sourav Das Chowdhury[1], Atasi Pal[1,2]
1 CSIR-Central Glass & Ceramic Research Institute, Kolkata, 700032, India
2 Academy of Scientific & Innovative Research (AcSIR), Ghaziabad, Uttar Pradesh 201002, India
**Corresponding author: dmdeb66@gmail.com*

Abstract: The process of fabricating tapered fiber bundles by two-step-tapering have been optimized to achieve suitable taper ratio (TR) for low brightness loss and adiabatic transmission. Taper lengths in both the steps have been optimized so that the taper angle remains uniform. Optimized taper length of 6 mm and 9 mm in the tapering steps helps to achieve a maximum 95% transmission efficiency for the fabricated pump combiners with output fiber cladding of 125 µm.
Keywords: tapered fiber bundle, adiabatic tapering, taper ratio, pump combiners

1. Introduction

Fiber combiners are one of the essential technologies which through power combination technique helped to scale the laser average power from mW to kW in all-fiber lasers and amplifiers [1]. Pump fiber combiner fabrication through tapered fiber bundle (TFB) technique is an all-fiber based end-pumping method which combines powers from different pump sources to generate hundreds' Watts of pump power in a single double clad fiber. While fabricating the TFB, an adiabatic taper along with maintaining low taper ratio-TR (initial fiber bundle/ tapered fiber bundle diameter) are key in obtaining high transmission efficiency together with low brightness loss in pump combiners [1]. In order to maintain adiabaticity for multimode pump combiner, taper length should be determined over which transmission efficiency is maximum along with maintaining a uniform taper angle throughout the taper. In 2013, report has shown optimization of the taper length in TFB of 7x1 pump combiner[2]. In 2020, another report also explained adiabatic condition must be satisfied for high transmission efficiency for TFBs [3]. Recently, we have also shown the effect of TR, interstitial gaps and splicing optimization effect on transmission efficiency of 7x1 pump combiners [4]. In this paper, five TFBs have been fabricated by two-step-tapering to maintain a TR < 2 and determining adiabatic condition in terms of taper length along with taper angle for developing the pump combiners. In the two-step-tapering process, the taper length for both the tapers has been optimized for an overall uniformity in taper angle to achieve maximum transmission efficiency.

2. Fabrication process

The 7x1 pump combiners have been fabricated using 7 numbers of input pump fibers having cladding diameter of 125 µm, NA of 0.22 and an output fiber having cladding diameter of 125 µm, NA of 0.46. In the fabrication process, initially the fused fiber bundle is prepared by bundling the seven pump fibers inside a pre-tapered low OH silica capillary followed by multiple fusing steps to remove the interstitial gaps. In order to match the output fiber cladding, the fused fiber bundle with outer diameter (silica capillary)/inner fiber bundle diameter (OD/ID) of 520/350 µm is tapered down to OD/ID of 177/120 µm by two-step-tapering. However, to optimize the tapering process, five TFBs have been prepared with different taper lengths in both steps. In the first taper step, OD/ID of 520/350 µm is tapered

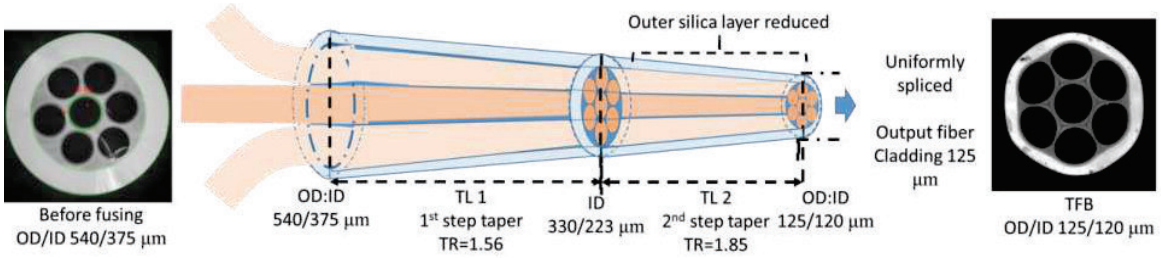

Fig. 1: Fabrication process of tapered fiber bundle by two-step-tapering process

down to 330/223 μm with taper length 'TL1' maintaining TR of 1.56. In second taper step, it is again tapered down to 178/120 μm with taper length 'TL2' maintaining TR of 1.85. The TL1 has been set in between 4 to 10 mm and TL2 has been set in between 4 to 13 mm as given in Table 1. Finally, the outer silica layer thickness of the five TFBs are reduced through chemical etching from OD/ID of 177/120 μm to 125/120 μm and finally spliced with matched diameter with the output fiber cladding of 125 μm. The schematic diagram of the fabrication process of the pump combiners with the cross-sectional image before fusing the fiber bundle (OD/ID: 540/375 μm) and after processing the TFB (OD/ID 125/120 μm) is shown in Fig. 1.

3. Result and Discussions

The fabricated pump combiners are characterized using commercial under-filled pump laser diodes whose 95% of power confined within an NA of 0.15. Significant loss in transmission efficiency would happen if 100% pump power is distributed over the NA of 0.22. Theoretically, for conserving the brightness of the 7x1 pump combiners using the aforementioned input and output fibers, the TR should be maintained below 2.09. But, in direct tapering of the fused fiber bundle to ID of 120 μm, TR should be 2.9 and such large TR can affect power loss due to distorted tapering. Thus, two-step-tapering is done to maintain TR < 2 at both the tapering steps. This has been done in such a way where the taper angle change along the whole taper length remains constant, without any sudden transition. Experimentally, we have observed for TFB 5 with TL1 and TL2 of 4 mm each, transmission efficiency is 85% due to non-adiabatic taper length and non-uniformity in the taper angle change. But in TFB 1, where TL1 and TL 2 is 10 mm and 13 mm respectively, the taper lengths are long enough to maintain the adiabatic condition. But the taper angle change is still non-uniform over the tapered region and transmission efficiency obtained is 89%. In two-step-tapering, taper angle change with sudden transition affects the adiabaticity resulting in low transmission efficiency. However, after setting the TL1 to 6 mm and TL2 to 9 mm, the taper angle is uniform over the TL which helps to achieve the highest transmission efficiency of 95%. The detailed results for five TFBs are shown in Table 1. More the uniformity in taper angle throughout the tapering can be obtained more transmission efficiency can be achieved. Tapering the fused fiber bundle in two step of tapering helps to achieve undistorted tapering along the TL along with maintaining TR below 2 at both the tapering step.

Table 1: Tapered fiber bundles with different taper parameters

TFB	TR1	TR2	TL1(mm)	TL 2(mm)	Transmission efficiency (%)
TFB 1	1.56	1.85	10	13	89
TFB 2			6	12	92
TFB 3			6	9	95
TFB 4			6	6	91
TFB 5			4	4	85

4. Conclusion

In conclusion, TFBs have been fabricated for pump combiners with 125 μm output fiber in two-step-tapering process for adiabaticity and low TR (< 2). From the fabricated five TFBs it has been observed, non-adiabatic taper length or non-uniformity in taper angle change both affects the adiabatic condition. The TFB with TL1 and TL2 of 6 mm and 9 mm in both the tapers helps to maintain uniformity in taper change over the tapering, and we have achieved maximum transmission efficiency of 95% for the pump combiner with 125 μm cladding output fiber.

5. References

[1] A. Kosterin et.al. "Tapered fiber bundles for combining high-power diode lasers," Appl. Opt. 43, 3893-3900 (2004)
[2] Q. Xiao et.al. "Tapered Fiber Bundle 7 × 1 End-Pumping Coupler Capable of High Power CW Operation," in IEEE Photonics Technology Letters, 25, no. 24, 2442-2445 (2013)
[3] Y. Shamir et.al. "Beam quality analysis and optimization in an adiabatic low mode tapered fiber beam combiner," J. Opt. Soc. Am. B vol. 27, pp. 2669-2676 (2010)
[4] D. Majumder et.al. "Design and fabrication of a tapered fiber bundle for a pump combiner with a uniform splicing region," J. Opt. Soc. Am. B vol. 39, pp. 1871-1878 (2022)

Visible Light Communication (VLC) Using Blue LED and Phosphor Converted (pc-LED) White Light Source Using Solar Panel as Detector

Aayushi Soni[1,2], Harpreet Kaur[1,2], Dheeraj Kumar[2], Shivam Trivedi[2], Dalip Singh Mehta[1,2*]

[1]SeNSE, Indian Institute of Technology, Delhi, Hauz Khas New Delhi-110016

[2]Green Photonics Laboratory, Department of Physics, Indian Institute of Technology, Delhi, Hauz Khas, New Delhi, 110016-India.

*Author e-mail address: *mehtads@physics.iitd.ac.in*

Abstract: Visible light communication (VLC) is future technology for free space communication as well as underwater communication. This is due to the fact that the frequency spectrum of light in the visible range is useful for high-speed communication as well as large bandwidth**.** We demonstrate On-Off keying (OOK) modulation and demodulation of signal using blue LED and phosphor converted LED (pc-LED) in Visible Light Communication (VLC). And their performance is computed in terms of SNR, pulse width and bit rate. Solar panel was used as detector in order to ease alignment related complexities.

Keywords: VLC, Li-fi, LED, solar cell

1. Introduction

Wireless traffic is increasing due to 5G/6G applications, artificial Intelligence and internet of things which is heavily loading the RF spectrum [1]. Optical wireless communication and VLC provides a wide range of license free spectrum along with more data security [2]. To achieve simultaneous illumination along with communication in hybrid mode, white light source is designed using conversion of blue light into broad spectrum of light using phosphors as wavelength convertors [3]. Blue LEDs are solid state lighting sources which are highly efficient, long lifetime, compact and low cost. They can be easily integrated with the electronic circuitry required for VLC/Li-Fi. In this paper we present Visible light communication (VLC) using blue LED and phosphor converted (pc-LED) white light source using Solar panel as detector. Ce doped YAG phosphor is used for down-conversion of light for achieving broad band spectrum. The experimental details of VLC circuit design and development along with various modulation schemes will be presented.

2. Experimental Setup:

2.1 Transmitter Circuit

On- off keying signal generated with carrier wave 0.5MHz pulses with 50% duty cycle and message wave as square wave with frequency of 80 Hz is sent via blue LED (1 Watt). Message signal frequency is chosen such that that eye cannot detect flickering which is troublesome in case of illumination. Spectrum is recorded using Lisun-6000 spectroradiometer at 5 cm from the source. It records a peak wavelength at 456.7 nm, FWHM of 19.6 nm while carrying signal through it in the form of direct modulation. This modulated signal is allowed to reach monocrystalline solar cell via ambient air as medium placed at 5 cm apart as detector in line of sight having diameter of 80 mm. Furthermore, to generate illumination simultaneously with communication, a phosphor film on glass substrate is inserted between source and detector in order to convert wavelength into broad spectrum. Solar panel was used as a detector because it is low cost and easily available. In addition, the solar panels can also be used for charging the battery simultaneously while using it for communication.

2.2 Design of Phosphor Film

Inorganic polycrystalline yttrium aluminum garnet doped with cerium (YAG: Ce) with average diameter of 15µm is well-mixed with UV adhesive glue. The mixture is then transferred onto glass substrate using screen printing technique and then dried in 405nm UV lamp. This film is placed at 1 cm from the blue LED. It acts as a wavelength convertor as when exited with blue photons, some of the photons is converted into yellow photons. Yellow photons mixed with residual blue photons generate white light. The light

hence obtained is characterized by Color Rendering Index (CRI), Correlated Color Temperature (CCT), CIE 1931 parameters in this paper.

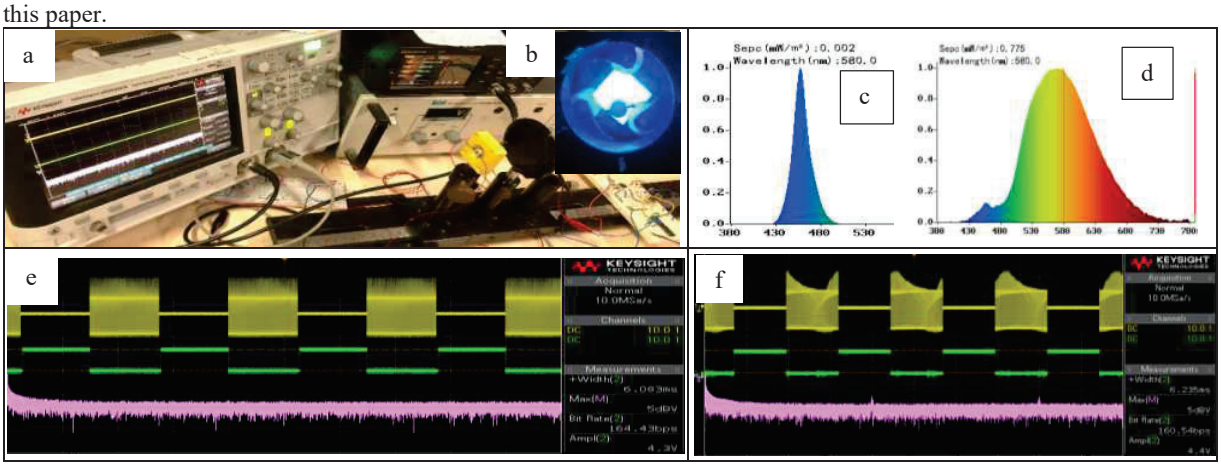

Fig. 1: a) Experimental setup b) Phosphor excitation with LED c) Spectrum of blue LED d) Spectrum of phosphor converted white light source e) Recovered signal without phosphor layer f) Recovered signal with phosphor converted LED as light source.

Table 1: Sample Table

Source	Bit Rate	Pulse Width (ms)	V_{pp} at detector (V)	SNR
Blue LED	164.43	6.083	4.3	~64 dB
pc-WLED	160.54	6.235	4.4	~64 dB

2.3 Receiver Circuit:

The signal is demodulated at the receiver end non-coherently and output waveform is displayed on oscilloscope (Keysight, Bandwidth 200 MHz). Expected value of bit rate received is 160 bits per second (bps) as 1 Hz corresponds to 2 bps. The output of Solar Panel is amplified using amplifier of gain 10 using general Op-amp. It is Followed by coupling capacitor to filter dc component of solar panel. It is followed by diode for rectification and power transistor MJE3055T for envelope detection. The waveform is then conditioned using Schmitt trigger at its inverting terminal.

3. Results and Discussion

As compared with blue LED, demodulated signal using pc-LED as light source carries has more pulse width which signifies that bandwidth is reduced. As bandwidth is inversely proportional to pulse width. Pulse broadening is due to slow component that is yellow phosphor. In ASK/OOK data rate is equal to bandwidth which signifies that more bandwidth in case of blue LED carries more data rate [4]. Hence both the trends are in same favor. However, data rate in case of pc-led is more accurate than Blue led as solar panel area is well illuminated in case of pc-LED. Signal is to noise ratio was found to nearly same i.e. 64 dB calculated by taking fast Fourier transform of demodulated wave having noise floor at -35 dBV and peak signal at 5dBV. CRI, CCT, CIE1931 of designed source is 61.1, 3724, (0.43,0.50) respectively.

4. References

[1] Chang, Yun-Han, et al. "High-bandwidth InGaN/GaN semipolar micro-LED acting as a fast photodetector for visible light communications." Optics Express 29.23 (2021): 37245-37252.
[2] Retamal, José Ramón Durán, et al. "4-Gbit/s visible light communication link based on 16-QAM OFDM transmission over remote phosphor-film converted white light by using blue laser diode." Optics express 23.26 (2015): 33656-33666.
[3] Jargus, Jan, et al. "Effect of selected luminescent Layers on CCT, CRI, and response times." Materials 12.13 (2019): 2095.
[4] Yao, Chengji, et al. "Performance Comparison among ASK, FSK and DPSK in visible light communication." Opt. Photonics J 6.8B (2016): 150-154.

1-D Waveguide System Design for AR/VR Displays

Shashank Shekhar [1], Sonam Berwal [1,2], Neha Khatri [1,2*]
[1]*Department of Manufacturing Science & Instrumentation, CSIR-CSIO, Chandigarh 160030, India*
[2]*Academy of Scientific & Innovative Research (AcSIR), CSIR-CSIO, Chandigarh 160030, India*
[*]*Email: nehakhatri@csio.res.in*

Abstract: The goal of the design is to achieve larger FOV for AR/VR display system. The HOE element is used for injection and extraction of light into waveguide. Light from source is coupled into waveguide using injection hologram and decoupled using extraction hologram. Hologram is created using object beam and reference beam. The system is designed using Zemax non sequential mode.
Keywords: HOE(Holographic optical Element), FOV(Field of View), TIR(Total Internal Reflection)

1. Introduction

Massive demand for deeper human-digital interactions beyond conventional flat panel displays has increased due to recent developments in high-speed connectivity and small mobile computing platforms. AR (augmented reality) and VR (virtual reality) displays have great potential for next-generation interactive displays to provide vivid visual experiences [1, 2]. The AR/VR displays have various applications, including education, engineering, healthcare, gaming and many more [3]. However, there is a slight difference between AR and VR. AR encourages interaction between the user, digital content and the real world, while VR is a virtual world that simulates the real-world using devices such as the headset, eyewear etc. The optical performance of AR and VR is evaluated based on numerous factors such as angular resolution, field of view (FoV), eye box, dynamic range, etc. Besides obtaining superior optical performance, AR and VR should give a user-friendly wearing experience with lightweight, compactness, and glasses-like form factor [4].

In this study, a 1-D waveguide-based AR/VR system is designed to enhance the performance of displays in respect of increased FoV. The designed system consists of the waveguide (BK-7) with holographic optical elements (HoE) as the injection and extraction holograms. The obtained FoV from the designed AR/VR system is 3.2°×3.2° to 7.0°×13.0°.

2. Optical Design

Ray tracing for the AR/VR optical system is designed using Zemax nonsequential mode shown in Fig.1. The waveguide of dimension shown in Table 1 is used for TIR and a transparent medium for the visible region. The point source is used at a distance of 800 m from the waveguide. The grid of lines is used as an object. Injection and extraction hologram is constructed using Hologram lens features in Zemax. FOV of input and output beam is calculated from detector view object in Zemax, and 532 nm wavelength is used for the design. An object and reference beam is required for injection and extraction hologram construction. These beams create holographic grating, and when rays after injection hologram diffract at an angle greater than the critical angle, it undergoes TIR. After rays travel a few distances under TIR, it interacts with the extraction hologram, which redirects rays toward the detector. The layout is shown in Fig.2.

3. Numerical Simulations

The waveguide basically acts as medium to transfer rays from injection hologram to extraction hologram. The values given in Table 1 is used for simulation. Reference beam and object beam position is chosen such that the rays fall under TIR.

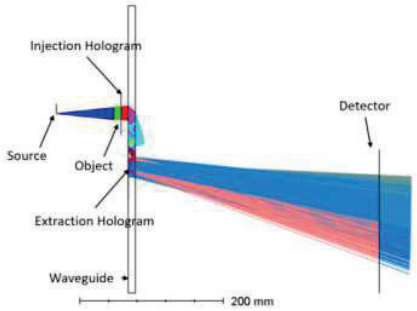

Fig. 1: Optical system design layout

Table 1: Design parameters used in Zemax optic studio

Design Parameters	Specifications (mm)
Waveguide	400×400×10
Source	1 watt at the distance of 800 from waveguide
Injection Hologram	45×45×0.2
Extraction Hologram	70×70×0.2
Detector	50×50 (at distance of 100 from waveguide)
FOV	Input: 3.2°×3.2° , Output: 7.0°×13.0°

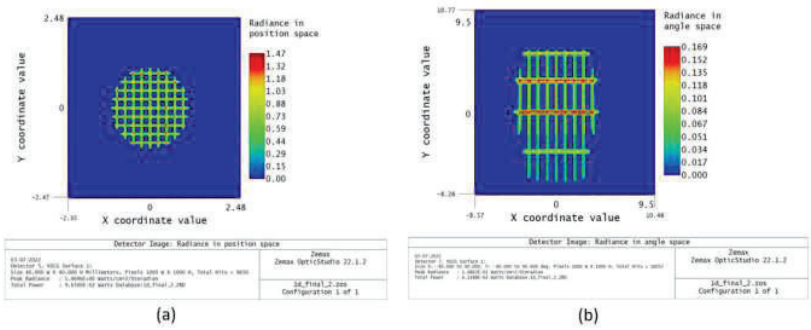

Fig. 2: (a) Rays before injection hologram (b) Rays incident on detector after extraction hologram

4. Conclusion

The design of 1-D waveguide system for AR/VR displays is simulated in Zemax using ray tracing non-sequential mode. Using the proposed method, the FOV is increase from 3.2°×3.2° to 7.0°×13.0°. The FOV is measured using radiance in angle space. For AR/VR application the larger FoV has greater significance as it can be projected on larger area.

5. References

[1] Cakmakci, O. & Rolland, J. Head-worn displays: a review. J. Disp. Technol. 2, 199–216 (2006).
[2] Zhan, T. et al. Augmented reality and virtual reality displays: perspectives and challenges. iScience 23, 101397 (2020).
[3] Xiong, J., Hsiang, EL., He, Z. et al. Augmented reality and virtual reality displays: emerging technologies and future perspectives. Light Sci Appl 10, 216 (2021). https://doi.org/10.1038/s41377-021-00658-8
[4] C. Draper, C. Bigler, M. Mann, K. Sarma, and P. Blanche, "Holographic waveguide head-up display with 2-D pupil expansion and longitudinal image magnification," Appl. Opt. 58, A251-A257 (2019).

Encryption of Images Constructed On Digital Hologram in Various Optical Domains

R. Girija*[1], H. Singh[2], G.Abirami[3]

[1]*Associate Professor, Department of Computer Science and Technology, Manav Rachna University, Faridabad.*
[2]*Associate Professor, Department of Applied Sciences, The NorthCap University, Faridabad.*
[3]*Assistant Professor, Department of Computer Science and Engineering, SRMIST, Faridabad.*
[1]Girija.srikanth09@gmail.com,
[2]hukumsingh@ncuindia.edu,
[3]abiramig@srmist.edu.in

Abstract: The use of digital hologram (DH) in optical medical images is analyzed in this paper. These analyses are done in various domains of double random phase encoding and it has been proposed. The domains are fractional Fourier, Gyrator, Fractional Hartley and Fresnel. In order to use in real time scheming, this proposal are used many medical images such as MRI Scan, X-ray and mammograms. These medical images are optically explored with the various domains of double random phase encoding. At that time, various encryption areas in double random phase encoding (DRPE) are considered with boosted confidence of security. The encryption and decryption process in various domains makes the complete chart analysis for all kind of medical images which can be used for real time processing. Simulation analysis and results shows the legitimacy and efficiency of proposed scheme.

Keywords: Digital Hologram, DRPE, Medical images, PSNR, MSE

1. Introduction

The fast and quick propagation of optical medical image handling schemes delivers numerous gradations of self-determination for safeguarding records, data, or imageries. These can be done for two dimensional (2D) imaging aptitudes, in elevation rapidity, and the parallelisms [1][2]. Researchers deeply analyzed about double random phase encoding. Javidi [3] initiated this system using Fourier transforms. Many of the researchers started to perform in various transforms such as Fresnel[5-8], gyrator transforms[9-11], fractional Fourier transform [12-15]. But all these transforms renovates input information into dissimilar mixed space-frequency domains. But most of the designed cryptosystems are symmetric and they are vulnerable to chosen plaintext attacks, chosen cipher text attacks and known plaintext attacks. In order to overcome these attacks, asymmetric cryptosystem [16-22] has been designed. Moreover digital holographic [23-24] methods uses a charge coupled device (CCD) camera for straight footage of a hologram must develop obtainable due to the growth of the imaging machinery. Popular the residence of old-fashioned random phase masks, many researchers developed different masks such as SPM(structured phase masks)[25-27] and it delivers additional benefit of consuming extra encryption secrets for enlarged confidence. It is usually whole after a Fresnel zone plate (FZP) and a spiral phase plate (SPP). Barrera et al. [27, 28] presented a structure phase masks named Toroidal zone plate (TZP). Some other phase masks are Deterministic phase masks [28-30]. One another masks is also generated which is called as chaotic structured phase masks can be used in double random phase encoding. Many simulations are performed with respect to real time medical images. All these analysis are based upon digital hologram and it is done in numerous domains which is categorized as Fresnel, fractional Fourier and gyrator transforms.

2. PROPOSED MODULE

2.1. Mathematical Principle

Figure 1 discusses about the optical experiment set up in Fourier transform domains. d_1 *and* d_2 are

distances. Interference outlines among an objective wave and position wave as holograms can stand verified as follows:

$$h(x,y) = |B(x,y)|^2 + |E(x,y)|^2 + B^*(x,y)E(x,y) + B^*(x,y)E(x,y) + B(x,y)E^*(x,y) \quad (1)$$

Where B and E is the object wave field and reference field respectively. Complex conjugate is denoted by *. The holograms remain essentially a two dimensional intensity distribution. Supplementary, it is also called as two dimensional or three dimensional distributions can be scrambled by means of visual systems such as double random phase encryption and other direct and indirect optical encrypting procedures. Equation 1 completely denotes the interference patterns at the hologram plane. Now, this can be promoted and administered in numerous Optical transforms (OPT). Some of the OPTs are Fractional Fourier Transforms (FrFT), Fresnel Transforms (FrT) and Gyrator Transforms (GT) to encrypt holograms. The encryption of all hologram created on double random phase encoding will be applied by double consecutive OPTs [4,12,13–18]. Process of doing encryption is given in below equation. $RPM1$ and $RPM2$ are the statistically independent two random phase mask, (ξ,η) and (u,v) are the coordinates. Many domains such as FrFT, FrT and GT can be implemented in equation 2.

$$E(\xi,\eta) = OPT2\{OPT1[h(x,y) \times RPM1(x,y)] \times RPM2(u,v)\} \quad (2)$$

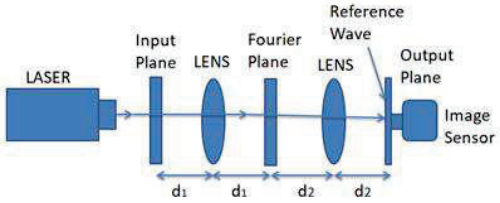

Fig.2. Optical set up of DRPE in FrFT domain.

3. Encryption and Decryption

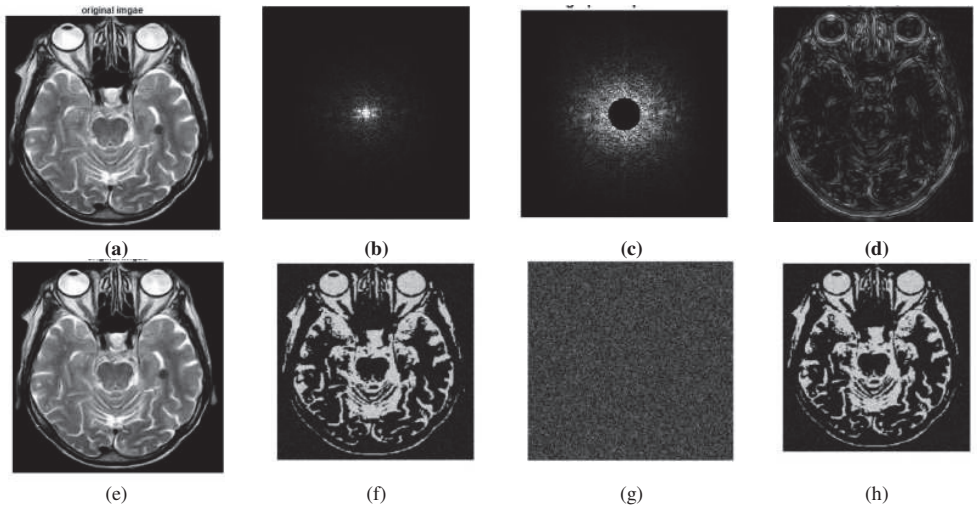

If the input image is MRI Scan, Skin cancer and Breast cancer, the MSE's are 9.515 x$10^{-26,}$ 8.045x10^{-27} ·9. 400 x10^{-26}

References:

[1] Chen, W., Javidi, B., & Chen, X. (2014). Advances in optical security systems. *Advances in Optics and Photonics*, *6*(2), 120-155.

[2] S. Liu, C. Guo, and J.T. Sheridan, "A review of optical image encryption techniques," Opt. Laser. Technol.

[3] Refregier, P., & Javidi, B. (1995). Optical image encryption based on input plane and Fourier plane random encoding. *Optics letters*, *20*(7), 767-769.

[4] Javidi, B., & Nomura, T. (2000). Securing information by use of digital holography. *Optics letters*, *25*(1), 28-30.

[5] Situ, G., & Zhang, J.: Double random-phase encoding in the Fresnel domain. Opt. Lett., 29(14), 1584-1586 (2004).

[6] Rajput, S. K., & Nishchal, N. K.: Image encryption using polarized light encoding and amplitude and phase truncation in the Fresnel domain. Appl. Opt., 52, 4343-4352 (2013).

[7] Singh, H., Yadav, A. K., Vashisth, S., & Singh, K.: Optical image encryption using devil's vortex toroidal lens in the Fresnel transform domain. Intl. J. of Opt. (2015).

[8] Vilardy, J. M., Millán, M. S., & Pérez-Cabré, E.: Nonlinear optical security system based on a joint transform correlator in the Fresnel domain. Appl. Opt., 53, 1674-1682 (2014).

[9] Rodrigo, J. A., Alieva, T., & Calvo, M. L.: Applications of gyrator transform for image processing. Opt. Commun., 278, 279-284 (2007).

[10] Singh, H., Yadav, A. K., Vashisth, S., & Singh, K.: Fully phase image encryption using double random-structured phase masks in gyrator domain. Appl. Opt., 53, 6472-6481 (2014).

[11] Singh, H., Yadav, A. K., Vashisth, S., & Singh, K.: Double phase-image encryption using gyrator transforms, and structured phase mask in the frequency plane. Opt. and Lasers in Engg., 67, 145-156 (2015).

[12] Unnikrishnan, G., & Singh, K.: Double random fractional Fourier-domain encoding for optical security. Opt. Engg., 39, 2853-2859 (2000).

[13] Unnikrishnan, G., Joseph, J., & Singh, K.: Optical encryption by double-random phase encoding in the fractional Fourier domain. Opt. lett., 25, 887-889 (2000).

[14] Garcia, J., Mas, D., & Dorsch, R. G.: Fractional-Fourier-transform calculation through the fast-Fourier-transform algorithm. Applied optics, 35, 7013-7018 (1996).

[15] Hennelly, B. M., & Sheridan, J. T.: Image encryption and the fractional Fourier transform. Optik-Intl. J. for light and Electron opt., 114, 251-265 (2003).

[16] W. Qin X. Peng.: Asymmetric cryptosystem based on phase-truncated Fourier transform, Opt. Lett. 35,118-120 (2010)

[17] W. Qin, X . Peng X. Meng B. Gao.: Universal and special keys based on phase-truncated Fourier transform, Opt. Eng., 50, 080501 (2011)

[18] S. K. Rajput N.K. Nishchal.: Asymmetric color cryptosystem using polarization selective diffractive optical element and structured phase mask, Appl. Opt., 51, 5377-5786 (2012)

[19] S. Vashisth, A.K.Yadav H. Singh K. Singh.: Watermarking in gyrator domain using an asymmetric cryptosystem, Proc. of SPIE , 9654 96542E-1/8 (2015)

[20] Ding, X., Deng, X., Song, K., & Chen, G.: Security improvement for asymmetric cryptosystem based on spherical wave illumination. Appl. Opt., 52, 467-473. (2013)

[21] Deng, X., & Zhao, D. Single-channel color image encryption based on asymmetric cryptosystem. Opt. & Laser Technol., 44, 136-140 (2012).

[22] Mehra, I., Rajput, S. K., & Nishchal, N. K.: Collision in Fresnel domain asymmetric cryptosystem using phase truncation and authentication verification. Opt. Engg., 52, 028202-028202 (2013).

[23] Javidi, B., & Nomura, T. (2000). Securing information by use of digital holography. *Optics letters*, *25*(1), 28-30.

[24] Osamu Matoba and Bahram Javidi, "Optical retrieval of encrypted digital holograms for secure real-time display," Opt. Lett. **27**, 321-323 (2002)

[25] Vashisth, S., Singh, H., Yadav, A. K., & Singh, K.: Image encryption using fractional Mellin transform, structured phase filters, and phase retrieval. Optik-Intl. J. for Light and Electron Opt., 125, 5309-5315 (2014).

[26] Vashisth, S., Singh, H., Yadav, A. K., & Singh, K.: Devil's vortex phase structure as frequency plane mask for image encryption using the fractional Mellin transform. Intl. J. of Opt. (2014)

[27] Barrera, J. F., Henao, R., & Torroba, R.: Optical encryption method using toroidal zone plates. Opt. commn., 248, 35-40 (2005).

[28] Zamrani, W., Ahouzi, E., Lizana, A., Campos, J., & Yzuel, M. J.: Optical image encryption technique based on deterministic phase masks. Optl. Engg., 55, 103108-103108 (2016).

[29] Girija, R., Singh, H. A cryptosystem based on deterministic phase masks and fractional Fourier transform deploying singular value decomposition. *Opt Quant Electron* **50,** 210 (2018). https://doi.org/10.1007/s11082-018-1472-6

[30] Girija, R., & Singh, H. (2019). Triple-level cryptosystem using deterministic masks and modified gerchberg-saxton iterative algorithm in fractional Hartley domain by positioning singular value decomposition. *Optik*, *187*, 238-257.

System for dust concentration measurement for wet stacks using optical scattering

Vinay Swakul, Karthick Somangili, Atique Shaikh, Chayan Mitra
Research & Development, Forbes Marshall Pvt. Ltd., Mumbai-Pune Rd., Kasarwadi, Pune-411034
vswakul@forbesmarshall.com

Abstract: This paper presents a hot extractive dust monitor for wet stack applications where the flue gas is below dew point temperature. The heated swirl chamber and forward scattering principle can give satisfactory results in applications where the relative humidity is 100% and dust concentration as low as 0.5 mg/m^3. The system shows a linear response for dust load ranging from 0.5 mg/m^3 to 100 mg/m^{3}and is found to be suitable for particle sizes between 0.02 µm to 4 µm.
Keywords: Dust concentration measurement, continuous emission monitoring, hot wet extractive system.

1. Introduction

Industrial stacks are categorized into two types according to the water content in the flue gases. In traditional stacks, where the flue gas is released into the atmosphere without using devices to reduce the pollutant content in the exhaust gases, the stack temperature is significantly above the dew point of the gases and water vapour present in the flue gas. The gas temperature is a critical parameter that affects the concentration of condensed droplets of water or acid in the stack, which can interfere with the in-situ type of particle monitors which work on the principle of light scatter and light attenuation. In processes where the SO_2 concentration is reduced by using a flue-gas desulphurization which uses wet scrubbers, the flue gas temperature is typically between 45℃ to 55℃ and contains droplets of water or acid as the gas temperature goes below the dew point. In these wet stacks, it becomes difficult to measure the dust concentration using in-situ dust monitors. For such a wet stack application, a hot extractive system is used, in which, the flue gas is extracted either through a heated hose or passed through a heated chamber to eliminate the interference of droplets, and the dust concentration is measured by using methods of light scatter or light attenuation. This paper focuses on a hot extractive dust monitoring system for wet stack applications by using the light scatter method.

2. System design

The dust measurement system as shown in Fig. 1(a) consists of a suction hose connected to a heated swirl chamber. The outlet of the swirl chamber is connected to the dust sensor, and an orifice plate is embedded in the connecting pipeline to measure the flow rate of the gas.

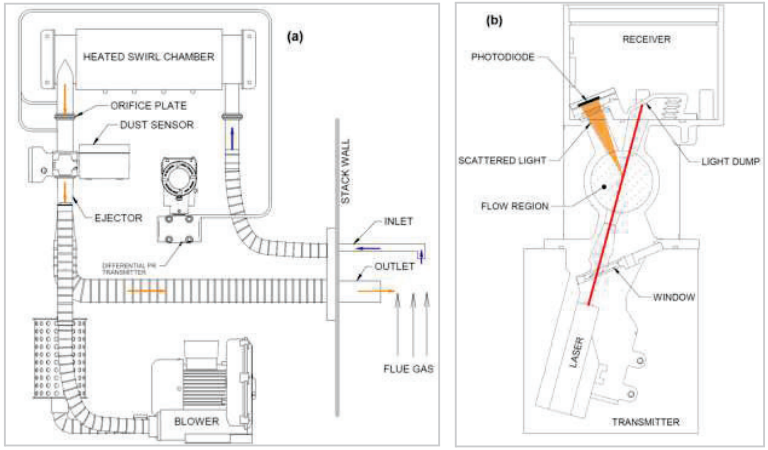

Fig. 1: (a) Components of the dust measurement system, (b) internal components in the dust sensor.

The dust sensor consists of three parts - transmitter, flow region, and receiver. As shown in Fig. 1(b), the transmitter houses the laser and window assembly, whereas, the gas flows in the flow region where the light interacts with dust

particles and scatters in all directions. A portion of this scattered light is captured by the photodiode placed in the receiver. As the particle size of dust released into the atmosphere after a wet scrubber typically ranges from 0.1 µm to 10 µm [1], the intensity of scattered light is highest between 50 ° to 90 ° forward angle [2]. The gas suction is created by an ejector powered by a blower. To avoid dilution of incoming dust, the ejector is placed after the dust sensor. The laser module (FLEXPOINT, T85 series) has a wavelength ranging from 655 nm at 25 ℃ to 668 nm at 85 ℃. The photodiode (Thorlabs, FSD10X10) has a wavelength range of 340 nm to 1100 nm and an active area of 100 mm^2. The amplifier PCB amplifies the photodiode signal and the 16-bit analog to digital converter converts it to counts ranging from 0 to 65535. The correlation between ADC counts and the dust concentration in mg/m^3 has been found experimentally using a reference sensor. For this, a particulate matter sensor (Sensirion, SPS30) is used as a reference.

3. Experimentation and system performance

To check the hardware and optical noise, the zero-check test was conducted by stopping the suction through the ejector. This ensured that there was no dust flow through the system and the ADC counts corresponding to this scenario show the zero offset of the system. The candlestick chart in Fig. 2(a) shows the zero offset of the system. Next, the dust monitor sensitivity tests were conducted using the reference sensor, and smoke was generated by burning pine wood matchsticks, which typically generates smoke with particle sizes ranging from 0.02 µm to 4 µm [3]. The test assembly is as shown in Fig. 2(b) where the smoke of burnt matchstick is circulated with a 5V fan in a closed loop arrangement by attaching SPS30 in series with the dust sensor. The correlation between ADC counts and the dust concentration as measured by SPS30 is shown in Fig. 2(c). It can be seen that the system response is linear over a wide range of dust concentrations ranging from 0.5 mg/m^3 to 100 mg/m^3, with R^2 of 0.986. The slope and intercept of the dust concentration vs ADC counts depend on the hardware and software gain and the optical design of the dust sensor. The heater response was found also satisfactory. This was tested by flowing dust-free mist with 100% RH through the heated swirl chamber, the corresponding ADC counts were equal to zero offset which implies that the interference of droplets is eliminated. Also, at a steady state, the system response time was found to be less than 1 second.

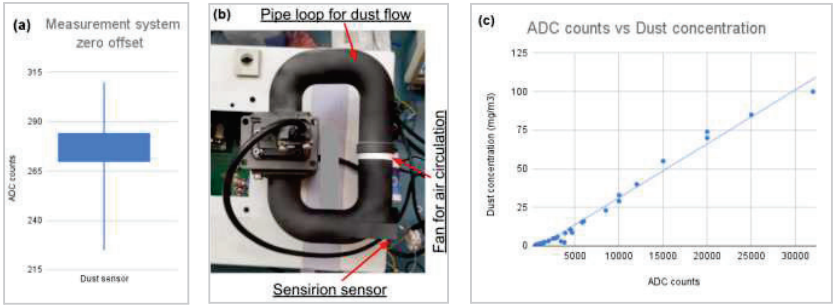

Fig. 2: (a) Candlestick chart of zero offset of the system, (b) photo of test setup of dust sensor with SPS30 and (c) correlation between ADC counts and dust concentration.

4. Conclusion

Dust measurement for below dew point application using a hot extractive system is demonstrated with linear system response over a dust load of 0.5 mg/m^3 to 100 mg/m^3. The sensitivity of the system can be further improved by finding the optimum angle at which the intensity of scattered light is maximum for given particle size. The system works fine for flue gas with very high moisture content and dust concentration as low as 1 mg/m^3.

5. References

[1] Daniel Mussatti, Paula Hemmer, **"**Wet scrubbers for particulate matter" (2002), Chap. 2, Section 6.
[2] Jeffrey M., Listak Gregory J., Chekan Jay F., Colinet James P. Rider, "Performance of a light scattering dust monitor at various air velocities: results of sampling in the active versus the passive mode" (https://www.cdc.gov/niosh/mining/UserFiles/works/pdfs/poalsd.pdf).
[3] Mustafa BG, Mat Kiah MH, Andrews GE, Phylaktou H. N., Li H *Smoke Particle Size Distribution in Pine Wood Fires*(2019).

Optical properties of gold nanoparticle embedded tissue phantoms for plasmonic photothermal therapeutics

Vikas[1,2,*], Sanjeev Soni[1,2,#] and Raj Kumar[1,2,$]
[1]Academy of Scientific and Innovative Research (AcSIR), Ghaziabad-201002, India
[2]CSIR-Central Scientific Instruments Organisation, Chandigarh-160030, India
Email id. – *vikas5293@gmail.com, #ssoni@csio.res.in, $raj.optics@csio.res.in

Abstract: The analysis of spectral variation in optical properties of tissue in presence of nanoparticles is needed for the pre-treatment planning of plasmonic photothermal therapeutics. Here, the spectral variation in total transmittance and diffuse reflectance of gold nanospheres embedded tissue phantom was measured by using an in-house prepared double integrating sphere setup. Further, the reduced scattering and absorption coefficient of the phantom was determined by using the inverse adding doubling method for the wavelength range of 450-950 nm. The results show that the absorption and reduced scattering coefficients of the medium increased by 2-3 times and 8-10 times respectively (within the wavelength range of 500-575 nm) due to the presence of 40 nm gold nanospheres suspension of concentrations of 10 µg/ml, 20 µg/ml, and 45 µg/ml within the phantom. The discussed results are useful for the selection of a nanoparticle dose for the plasmonic photothermal therapeutics.
Keywords: Gold nanospheres, absorption coefficients, reduced scattering coefficients, double integrating sphere setup, tissue phantom

1. Introduction

The interaction of the gold nanoparticles and suitable electromagnetic radiation leads to localized heat generation within a tumor within a short duration [1,2]. The generated localized heat has a high potential for the treatment of solid tumors as compared to conventional cancer treatment methods [3,4]. The optical properties such as absorption and scattering coefficients of tissue are highly affected due to the inclusion of nanoparticles such as gold nanospheres and nanorods etc. [5,6]. However, in literature scantly measured data is available for the optical properties of tissue in presence of GNSs of varying concentrations. In this study, the spectral variation in absorption and reduced scattering coefficients of tissue phantom in presence of GNSs of concentration 10 µg/ml, 20 µg/ml, and 45 µg/ml are determined by using measured values of diffuse reflectance and total transmittance of light from the tissue phantom.

2. Materials and methods

Here, a bilayer tissue phantom of ~1.0 mm thick epidermis layer and ~2 mm thick dermis layer was prepared by using agarose (A9539, Sigma Aldrich, USA), intralipid solution (Intralipid 20%, Fresenius Kabi), and coffee powder soluble in deionized (DI) water. The epidermis layer was prepared by using 1% agarose, 0.3% intralipid solution, and 0.1% coffee powder mixed in deionized (DI) water and 40 nm GNS suspension (741981, Sigma Aldrich, USA) respectively. The dermis layer was prepared by using 1% agarose, and 1% intralipid solution mixed in deionized (DI) water and 40 nm GNS suspension respectively. The mixture was poured into a cylindrical mould of Ø12×5 mm and allowed to solidify. The prepared bilayer phantom was held between two BK7 glass slides for the measurement of diffuse reflectance and transmittance. An in-house prepared double integrating sphere setup was used for simultaneous measurement of the spectral variation in diffuse reflectance and total transmittance of light from phantoms. Further, the inverse adding-doubling (IAD) method was used to calculate the absorption (μ_a) and reduced scattering (μ'_s) coefficients of tissue phantom embedded with GNSs by using the measured value of diffuse reflectance and total transmittance [7].

3. Results and discussion

The measured spectral variation in diffuse reflectance and total transmittance of tissue phantom without nanoparticles and with GNSs of concentrations of 10 µg/ml, 20 µg/ml, and 45 µg/ml is shown in Figures 1(a) and 1(b) respectively. From Figure 1(a), it is seen that the values of measured diffuse reflectance of tissue phantom increase due to the presence of GNSs as compared to the phantom without nanoparticles. Also, it is observed that due to an increase in GNS concentration from 10 µg/ml to 45 µg/ml the values of diffuse reflectance are increased by ~18% within the wavelength range of 650-950 nm. Further, from Figure 1(b), it is observed that the measured values of total transmittance are decreased due to the incorporation of GNS in phantoms as compared to the phantoms without nanoparticles. The spectral variation in absorption and reduced scattering coefficients of phantoms, calculated by using the IAD method, is shown in Figures 2(a) & 2(b).

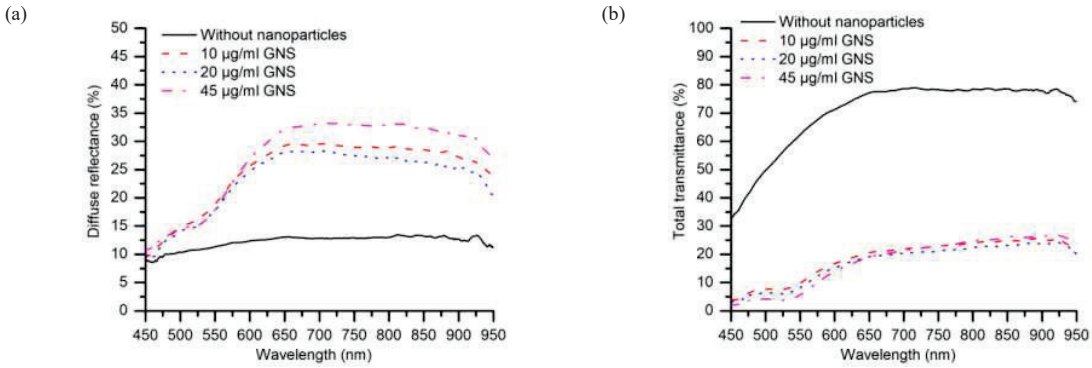

Fig. 1: Measured spectral variation in (a) diffuse reflectance, and (b) total transmittance of bilayer tissue phantom without GNS and embedded with GNSs of concentration 10 µg/ml, 20 µg/ml, and 45 µg/ml.

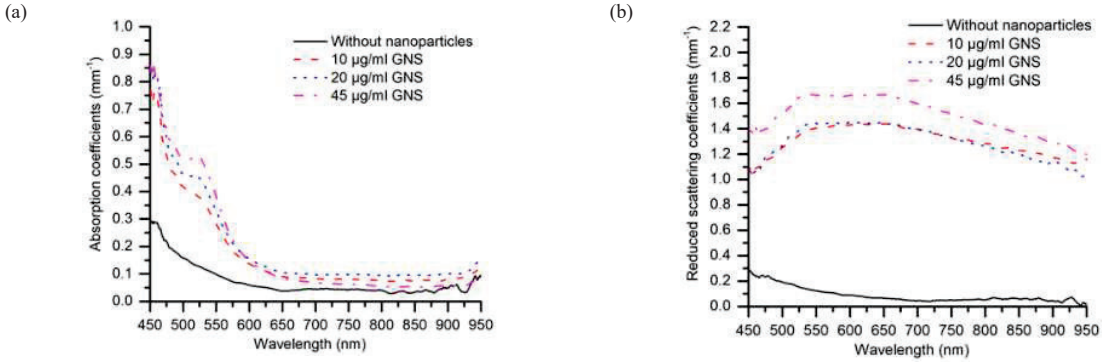

Fig. 2: Wavelength dependent (a) absorption coefficient, and (b) reduced scattering coefficient of bilayer tissue phantom without GNS and with GNSs of concentrations of 10 µg/ml, 20 µg/ml, and 45 µg/ml calculated by using inverse adding doubling method.

From Figure 2(a), it is seen that the absorption coefficient of tissue phantom is increased by ~3-fold (at the wavelength of 520 nm) due to the incorporation of GNS as compared to without nanoparticles. Further, it is observed that with an increase in GNS concentration from 10 µg/ml to 45 µg/ml the absorption coefficients of the phantoms are enhanced by 36% within the wavelength range of 500-575 nm. Also, it is observed that the reduced scattering coefficients of the phantom increased by 8-10 times due to the incorporation of GNS in the phantom as seen in Figure 2(b). Overall, it is observed the GNS in phantoms significantly influences the optical properties.

4. Conclusion

This study reports the absorption and scattering coefficients of tissue phantom in presence of gold nanospheres of different concentrations. The absorption and scattering coefficients of the phantom significantly increased on increasing the GNS concentration from 10 µg/ml to 45 µg/ml. The determined optical properties are useful for pre-treatment planning of plasmonic photothermal cancer therapeutics.

5. References

[1] X. Huang, P. K. Jain, I. H. El-Sayed, and M. A. El-Sayed, "Plasmonic photothermal therapy (PPTT) using gold nanoparticles," Lasers Med Sci **23**, 217–228 (2008).

[2] M. R. K. Ali, Y. Wu, and M. A. El-Sayed, "Gold-Nanoparticle-Assisted Plasmonic Photothermal Therapy Advances Toward Clinical Application," J. Phys. Chem. C **123**, 15375–15393 (2019).

[3] A. F. Bagley, S. Hill, G. S. Rogers, and S. N. Bhatia, "Plasmonic Photothermal Heating of Intraperitoneal Tumors through the Use of an Implanted Near-Infrared Source," ACS Nano **7**, 8089–8097 (2013).

[4] S. Soni, H. Tyagi, R. A. Taylor, and A. Kumar, "Role of optical coefficients and healthy tissue-sparing characteristics in gold nanorod-assisted thermal therapy," International Journal of Hyperthermia **29**, 87–97 (2013).

[5] A. T. Diallo, M. Tlemçani, M. Khan, J. Spadavecchia, and N. Djaker, "Size, Shape, and Wavelength Effect on Photothermal Heat Elevation of Gold Nanoparticles: Absorption Coefficient Experimental Measurement," Part. Part. Syst. Charact. **37**, 2000255 (2020).

[6] Vikas, R. Kumar, and S. Soni, "Quantitative study of concentration-dependent optical characteristics of nanoparticle-embedded tumor," Appl Nanosci **11**, 2589–2597 (2021).

[7] S. A. Prahl, "Everything I think you should know about Inverse Adding-Doubling," Oregon Medical Laser Center, St. Vincent Hospital **1344**, 1–74 (2011).

Experimental Determination of Topological Order in Photonic Stopbands

Nitish Kumar Gupta[1,*], Mukesh Kumar[2], Anjani Kumar Tiwari[3], Sudipta Sarkar Pal[2], Harshawardhan Wanare[4], S. Anantha Ramakrishna[2,4]

[1]*Centre for Lasers & Photonics, Indian Institute of Technology Kanpur, 208016, India*
[2]*CSIR-Central Scientific Instruments Organisation, Chandigarh, 160030, India*
[3]*Department of Physics, Indian Institute of Technology Roorkee, 247 667, India*
[4]*Department of Physics, Indian Institute of Technology Kanpur, 208016, India*
Author's e-mail address: nitishkg@iitk.ac.in

Abstract: We report a method for direct determination of bandgap topological character in one-dimensional photonic crystals. Our method is based on parametric ellispometric phase angle measurements where we demonstrate that in a two-dimensional parameter space, band-edges selectively proclaim zeros of the complex reflection ratio, leading to a selective emergence of phase singularities with integer (unity) topological charge. Endowed with topological robustness, the location of these phase singularities proves to be a conspicuous envoy of distinct topological character.

Keywords: Ellipsometry, photonic bandgap, topological photonics.

The momentum space global properties of a topologically non-trivial bulk bandstructure can be encapsulated in quantized topological invariants, such as Chern number and Z2 invariants in two-dimensional (2D) systems and topological Zak Phase or winding number in the case of one-dimensional (1D) systems, which are extracted from the geometric Berry phases associated with the bulk bandstructure [1]. Having dug out the latent topological aspects becomes immensely helpful in manifesting unconventional surface or edge states by combining structures of different topological orders [2]. These topological surface states offer access to additional degrees of design freedom, and consequently have garnered significant research interest in the last decade facilitating the dawn of topological photonics.

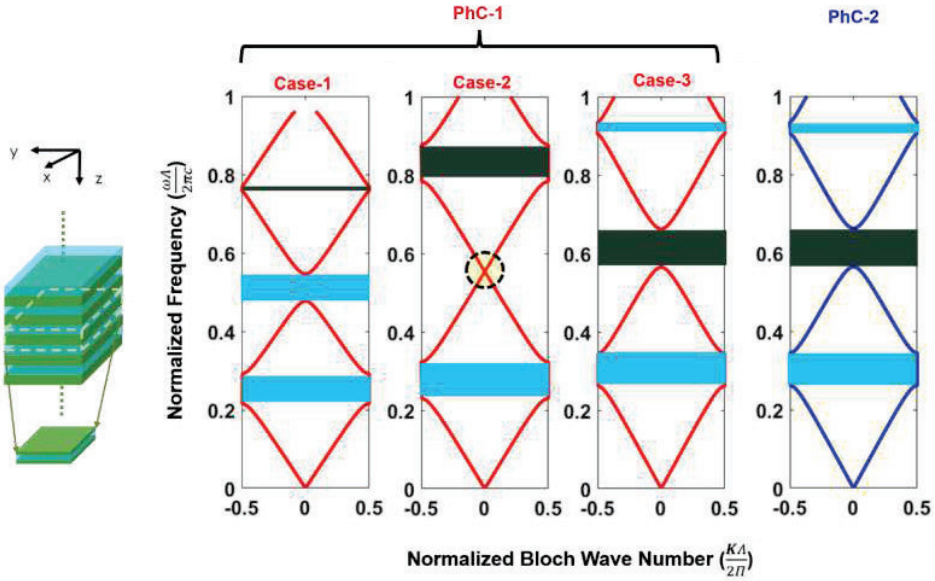

Fig.1: Calculated topological bandstructures for two representative one-dimensional photonic crystals (three topologically distinct cases are depicted for PhC-1).

A crucial step in investigating topologically non-trivial system is concerned with the determination of topological invariants or bandgap topological character. Although the methods of their theoretical determination are fairly developed (Fig.1 depicts the Zak phase-based methodology of determining the bandgap character) [3], when it comes to their experimental determination, almost invariably we refer to the bulk-boundary correspondence principle. This

has some serious drawbacks in photonic realizations: firstly, the application of this principle requires two photonic bandgap materials to be concatenated which is a wasteful affair in photonic systems; secondly the application of this principle merely establishes the equivalence/non-equivalence of bandgaps and is incapable of providing any more information regarding their topological character.

In an attempt to surmount these inherent limitations associated with the experimental investigations of photonic topological insulators, we have devised a method based on standard spectroscopic ellipsometric measurements. The method allows us to discern the topological character of the bandgaps in terms of the sign information of ellipsometric phase angle inside the bandgaps. More importantly, by performing parametric ellipsometric measurements with the angle of incidence, we find a more exciting signature where we find that the bandg-edges selectively proclaim the zeros of complex reflection ratio and leads to selective emergence of topologically robust phase singularities on either band-edge of the photonic stopband. A glimpse of the obtained experimental results is being provided in Fig.2 where we clearly observe the selective emergence of topological phase singularities on either the red or the blue band-edge.

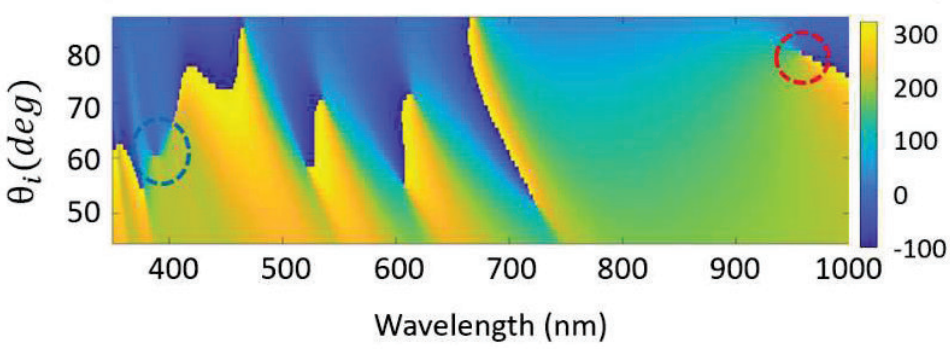

Fig. 2: Measured ellipsometric phase angle dispersion plots for the Fig.1 bandstructure corresponding to PhC-1 Case-3.

In this work, we will systematically establish the connections between the bulk properties and the surface characteristics and present our recent simulations and experimental results based on these connections.

References

[1] Ling Lu, John D. Joannopoulos, and Marin Soljačić, "Topological photonics," Nature photonics **8**, no. 11, 821-829 (2014).
[2] Nitish Kumar Gupta, Sapireddy Srinivasu, Anjani Kumar Tiwari, Harshawardhan Wanare, and S. Anantha Ramakrishna, "Realizing quasi-monochromatic switchable thermal emission from electro-optically induced topological phase transitions." Scientific reports **12**, no. 1, 1-10, (2022).
[3] Xiao, Meng, Z. Q. Zhang, and Che Ting Chan, "Surface impedance and bulk band geometric phases in one-dimensional systems," Physical review X **4**, no. 2, 021017, (2014).

Determination of time-dependent shape deformation of polishing pitch lap using digital holography

Monika Rani, Vinod Mishra, Abhinav Kaushal, Omendra Singh, Raj Kumar*
CSIR-Central Scientific Instruments Organisation, Sector 30C, Chandigarh 160030, India
**Corresponding author e-mail address: raj.optics@csio.res.in*

Abstract: The present work describes use of double exposure holography for determination of shape deformation of polishing pitch with respect to time. Digital image processing is applied on numerically reconstructed wavefronts of the pitch lap for the quantitative analysis of results. Experimental studies demonstrate deformation in shape of polishing pitch lap at micro scale with time.
Keywords: Polishing Pitch Lap, Shape Deformation, Digital holography.

1. Introduction

Many applications, including high-power laser systems, glass mirrors for astronomical reflecting telescopes, folding mirrors for avionics displays, display covers, and substrates for biomedical imaging and sensing, etc., have placed a high demand on precision optical surfaces. The close surface tolerances in terms of form and finish offer many challenges for manufacturing of such components. However, the property of pitch to flow under load and with respect to the time is the main issue with pitch polishing which restrict the form accuracies [1,2]. Hence, to obtain the desired optical surface properties, it is important to study the behavior of pitch with respect to the time. Different methods like displacement sensor [3-4], needle viscosimeter [5], and etc. are used to characterize the polishing pitch flow behavior. In this paper, the double exposure digital holographic interferometry technique is implemented with a portable digital holographic camera (DHC) [6] for characterization of changes in pitch lap shape with time.

2. Methodology

DHC is used to record holograms of polishing pitch lap at different times. Digital holographic interferometry is applied to compare the reconstructed wavefronts of the holograms. The wavefront of light scattered from the pitch lap is recorded in digital hologram, which further numerically reconstructed by using Fresnel diffraction method. The amplitude and phase values are calculated individually for each reconstructed wavefront. The phase unwrapping is applied in order to obtain the continuous phase by using Goldstein branch cut method. In order to analyse the change in shape of pitch lap, two and three dimensional profiles are plotted from the recovered phase.

3. Experimental Set-up

In experimental set-up, a portable digital holographic camera (DHC) [6], shown in Fig.1(b), is used to record the digital hologram. DHC consists of diode laser of 660nm as light source, a beam expander to expand the beam, and a non-polarizing 50:50 cube beam splitter to divide the laser beam into two parts. The interference pattern, called the digital hologram is recorded by a charge-coupled device (CCD) sensor (3376 x 2704, 3.1μm). Further, this digital hologram is stored and numerical reconstruction is applied on it to reconstruct the wavefront of the light scattered from test object.

4. Results and discussion

The pitch lap is mounted in a holder vertically in front of the DHC as shown Fig. 1(b). Due to its intrinsic property of flow, the shape of pitch is changed due to gravity with time. To analyze these changes, we recorded three digital holograms of the pitch lap at three different times (0min, 2min, and 4min). The complex amplitudes are subtracted (2 min and 4 min reconstructed wavefronts are subtracted from 0min reconstructed wavefront) which shows variation in interference fringes according to time variations on sample as shown in Figs. 2(a&b). The wrapped phase as shown in Figs. 2(c&d) are unwrapped using Goldstein's branch cut method and are shown in Figs. 2(e&f). 3D map and 2D profile are created from unwrapped phase as shown in Figs. 2(g&h) and 2(i&j) respectively. The 2D profile in Fig. 2(e) shows deformations in the shape of pitch lap when scanned along y-axis. The obtained results for recorded holograms at 2 min and 4min are shown in Fig.2.

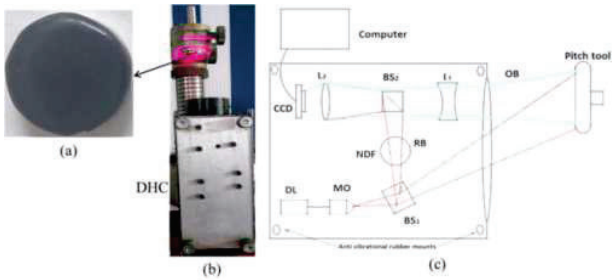

Fig. 1: (a) Photograph of polishing pitch lap, (b) photograph of experimental set-up, and(c) schematic representation of DHC; DL: diode laser, MO: microscopic objective, BS_1 and BS_2: cube beam splitters, NDF: neutral density filter, L_1: concave lens, L_2: convex lens, OB: object beam, and RB: reference beam

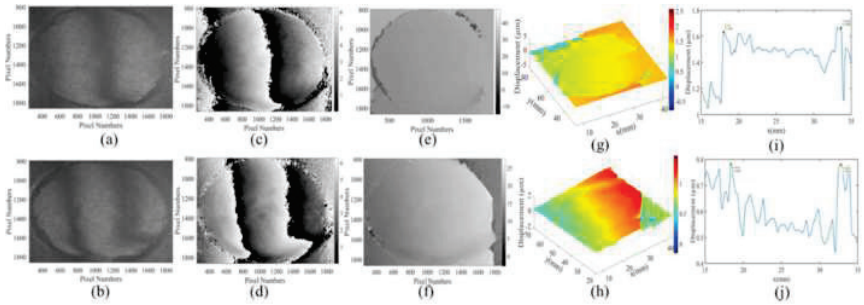

Fig. 2: Retrieved information from recorded hologram for 2min (1) and 4 min (2): (a&b) Complex amplitude after subtraction of two reconstructed wavefronts at different times i.e. 0min and 2 min, (c&d) wrapped phase distribution extracted from (a&b), (d&e) unwrapped phase distribution, (g&h) 3D map of unwrapped phase distribution, and (i&j) 2D line profile along the center of unwrapped phase distribution, respectively

At the position of abrupt change in surface of the sample, discontinuity in the fringes can be observed as shown in Fig. 2(b). From 2D profiles given in Figs. 2 (i&j) and, it is observed that the shape of pitch lap is varied at micro scale with time.

4. Conclusion

In this work, the digital holographic interferometric technique is reported to detect the shape deformation of pitch lap with time. The shape deformation is presented in the form of 2D profile and 3D map. The shape of pitch lap varies at micro scale with time that will affect the surface being polished. In future, we will study the effect of other parameters like temperature, and position of holding on pitch lap.

Acknowledgement: The authors are grateful to Dr. Shravana Kumar RR from CSIR-CSIO, Chandigarh for fruitful discussions.

Funding: This research work is financially supported by the CSIR, New Delhi under the project MLP-2014 and DST/TSG/NTS/2015/59.

5. References

[1] B. Gillman, and F. Tinker, "Fun facts about pitch and the pitfalls of ignorance," Proc SPIE **3782**, (SPIE, 1999), pp. 72-79.
[2] H. Schott, "Dependence of activation energy for viscous flow of polyhydrocarbons on bulk of substituents," J Appl Polym Sci **6**, S29-S30(1962).
[3] R. Varshneya, J.E. DeGroote, L.L. Gregg, and S.D. Jacobs, "Characterizing optical polishing pitch", Optifab (SPIE, 2003), pp. 87-89.
[4] D. Liao, R. Xie, R. Sun, S. Zhao, L. Ren, F. Zhang, J. Wang, and Q. Xu, "Improvement of the surface shape error of the pitch lap to a deterministic continuous polishing process," J Manuf Process **36**, 565-70(2018).
[5] DeGroote, Jessica E., Stephen D. Jacobs, Leslie L. Gregg, Anne E. Marino, and Jennifer C. Hayes, "Quantitative characterization of optical polishing pitch," Optical Manufacturing and Testing IV,(SPIE, 2001) pp. 209-221.
[6] R. Kumar, G. Dwivedi, and O. Singh, "Portable digital holographic camera featuring enhanced field of view and reduced exposure time," Opt Lasers Eng **137**, 106359(2021).

An inspection of Single-photon based QKD protocols under free-space losses

Mitali Sisodia, Omshankar, Joyee Ghosh
Quantum Photonics Lab, Department of Physics, Indian Institute of Technology Delhi, New Delhi 110016, India.
E-mail address: mitalisisodiyadc@gmail.com

Abstract: In this paper, we have compared the performance of prepare-and-measure based (BB84 and six-state) QKD protocols for 5km free-space channel link considering different free-space losses, such as geometrical losses, atmospheric losses by evaluating the quantum bit error rate and secure key rate. In the results, we showed channel loss tolerance of ~32 dB and ~38 dB for BB84 and six-state protocols, respectively with the consideration of specific values for 5km channel length.

Keywords: BB84, Six-state, geometrical losses, atmospheric losses, quantum bit error rate, secure key rate.

1. Introduction

Quantum key distribution (QKD) is a technique to establish a secret key between two parties through a quantum channel. Several QKD protocols have been proposed such as BB84, E91, BBM92, etc. [1]. Quantum communication schemes can be performed using optical fiber, terrestrial free-space optical (FSO), and satellite-based FSO, etc. Numerous QKD protocols have been implemented using optical fibers only for few hundred kilometer of fiber length due to the limitation of exponential increase of fiber losses with length. A FSO (terrestrial and satellite) link has proved to be a promising quantum channel providing secure quantum communication for longer distance (globally) and overcoming the problem of limited distant quantum communication through fiber. The main challenge of implementing QKD protocols over free-space link is free-space losses. Some of the QKD protocols using FSO channel has already been implemented [2]. In this paper, we have theoretically compared the performance of prepare-and-measure based (single-photon based) BB84 and six-state protocols for a 5km free-space quantum channel and studied the effect of geometrical and atmospheric losses on quantum bit error rate (QBER) and secure key rate (SKR).

2. Theory and calculation

BB84 is a four non-orthogonal state-based protocol in which Alice (sender) prepares a string of single photons in one of the four polarization states ($|H\rangle, |V\rangle, |+\rangle, |-\rangle$) and send it to Bob (receiver) who randomly performs the measurement in the rectilinear ($|H\rangle, |V\rangle$) or diagonal ($|+\rangle, |-\rangle$) bases. An extended version of BB84 i.e., Six-state protocol has been proposed with more tolerance to noise and enhances the security rate compared to BB84 [3]. In this protocol, six-states ($|H\rangle, |V\rangle, |+\rangle, |-\rangle, |+_+\rangle, |-_-\rangle$)[1] in three bases ($\{|H\rangle, |V\rangle\}, \{|+\rangle, |-\rangle\}, \{|+_+\rangle, |-_-\rangle\}$) is used. The extra choice of basis creates an obstacle on Eve's measurement path and produces higher error rate. Consequently, Alice and Bob can easily detect the Eve's presence. In both the protocols, Alice and Bob keep the photons which are measured in the same basis and discarded the remaining photons. They randomly select ~10% photons (sifted key) to calculate the quantum bit error rate (QBER). If the obtained error (ideally 0; lower the value of QBER, higher the security of the protocol or vice versa) is higher than the threshold value (vary for different QKD protocols; 11% for the BB84 and 12.6% six-state protocol [1]) that determines the security of the QKD protocol then they discard the protocol and repeat the QKD protocol. The non-zero value of QBER is due to free-space losses, Eve's presence, noises, imperfections in the physical devices, etc. The unconditional security proof of BB84 and Six-state protocol has already been reported [4, 5].

We have considered an attenuated coherent pulsed laser in the visible optical range with a mean photon number (μ) of 0.1 and repetition rate (ν) of 1 MHz to compare the performance of BB84 and Six-state protocols**.** The sifted key from the raw key can be calculated as $R_{sift} = n_{sift}.R_{raw} = n_{sift}.\mu.\nu.\eta.T_{link}$, where n_{sift} is the basis reconciliation factor (1/2 and 1/3 for BB84 and six-state, respectively) η (60%) is the detector efficiency and T_{link} is the link transmittance.

[1] Where $|\pm\rangle = \frac{|H\rangle \pm |V\rangle}{\sqrt{2}}, |\pm_\pm\rangle = \frac{|H\rangle \pm i|V\rangle}{\sqrt{2}}$

The free-space losses can broadly be classified into geometrical and atmospheric losses [6] which is calculated as $T_{link} = \frac{{D_r}^2}{(D_s+\theta L)^2} . \exp(-\alpha . L)$, where D_r (15mm) and D_s (12mm) are the receiver and transmitter apertures, respectively, θ (0.2 mrad) is the beam divergence, L (5km) is the channel length and α (0.1 dB/km) is the atmospheric attenuation factor [7]. Fig. 1 shows the QBER of the security protocol (BB84 and six-state) as a function of channel losses calculated using [6]

$$Q = P_{opt} + \frac{P_{dark} n\, k}{\boldsymbol{T_{link}}\, \eta \mu}$$

where P_{opt} (0.001) is the probability of wrong polarization detection of photon, P_{dark} (0.000001) is the dark count probability, n is the number of detectors used, and k (0.5 for BB84 and 0.66 for six-state protocol) is a constant.
The secret key rate (SKR) for BB84 and six-state protocol is calculated as

$$SKR_{BB84} = \frac{1}{2}[1 + 2Q log_2 Q + 2(1-Q) log_2 (1-Q)],$$

$$SKR_{Six-state} = \frac{1}{3}\left[1 + \frac{3Q}{2} log_2 \frac{Q}{2} + (1 - \frac{3Q}{2}) log_2 \left(1 - \frac{3Q}{2}\right)\right],$$

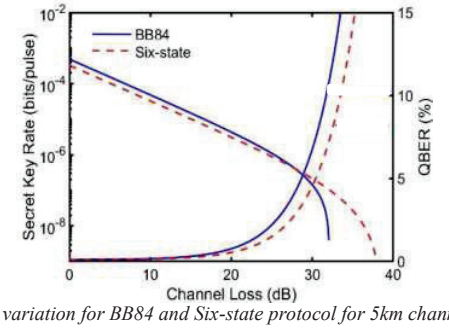

Fig. 1: QBER and SKR variation for BB84 and Six-state protocol for 5km channel length under free-space losses.

From Fig. 1, it is shown that BB84 achieve the highest key rate per pulse compared to six-state protocol because of the high (50%) probability (33% for six-state protocol) of measuring the photons in the same polarization state, thus allowing a higher number of photons to generate the sifted key. It is also evident that six-state protocol tolerate the highest channel losses (~38 dB) compared to BB84. Thus, we have observed that there is trade-off between high secure key rate generation and high channel loss tolerance.

3. Conclusion

In conclusion, we have compared the performance of BB84 and Six-state protocol under free-space losses for 5km free-space quantum channel. We have shown that with the selected values secret key generation rate is possible for considered length. We have also concluded that Six-state protocol tolerates higher channel loss compared to BB84 protocol.

Acknowledgements: We thank the funding agency, Defence Research and Development Organization (DRDO), Government of India for a project grant: DFTM/03/3203/P/07/JATC-P2QP-07/463/D (R & D).

4. References

[1] S. Pirandola, U.L. Andersen, et al., "Advances in quantum cryptography. Advances in optics and photonics" **12**, 1012-1236, (2020)
[2] N. Hosseinidehaj, Z. Babar, R. Malaney, S.X. Ng, L. Hanzo, "Satellite-based continuous-variable quantum communications: State-of-the-art and a predictive outlook" IEEE Communications Surveys & Tutorials, **21**, 881-919, 2018
[3] D. Bruÿ, "Optimal eavesdropping in quantum cryptography with six states" Phys. Rev. Lett., **81** 3018 (1998)
[4] P.W. Shor, J. Preskill, "Simple proof of security of the BB84 quantum key distribution Protocol, Phys. Rev. Lett. **85** 441 (2000)
[5] H.K. Lo, "Proof of unconditional security of six-state quantum key distribution Scheme" Quant. Inf. Comput. **1**, 81 (2001)
[6] N. Gisin, G. Ribordy, W. Tittel, H. Zbinden, "Quantum cryptography" Rev. Mod. Phys. **74** 145-195 (2002).
[7] M.T. Mushtaq, S.M. Yasir, et al., "Analysis of internal design parameters to minimize geometrical losses in free-space optical communication link" Acta Phys. Polonica A, **134**, 275-277, (2018)

Solvent Dependent Studies on Spatial Self Phase Modulation of Pyrromethene 567 Dye

Titu Thomas, Jayaprasad K V, Priya Mary N J, Manu Vaishakh
International School of Photonics, Cochin University of Science and Technology, Cochin - 682022
Author e-mail address: manu.vaishakh@cusat.ac.in

Abstract: Spatial self-phase modulation (SSPM) was observed when a continuous wave laser with sufficient energy propagated through a cell containing pyrromethene 567 dye. Temperature-dependent refractive index distribution induces a phase shift leading to the formation of diffraction patterns in the far-field. SSPM patterns were observed in pyrromethene 567 dissolved in different solvents. The nonlinear refractive index, n_2 of pyrromethene 567 dye in different solvents, were calculated.
Keywords: Spatial self-phase modulation, Pyrromethene 567, nonlinear refractive index

1. Introduction

Spatial Self-Phase Modulation (SSPM) is referred to a phenomenon in which a high-intensity laser beam propagating through a medium interacts with the medium and imposes a phase modulation on itself [1-3]. As a result, diffracted patterns of beam divergence characterized by an intensity-dependent refractive index are observed in the far field. By analyzing the SSPM patterns, the nonlinear response of novel materials can be directly and quantitively obtained [3,4].

Pyrromethene 567 (PM 567) belongs to a class of laser dyes showing fascinating and encouraging photo-physical properties. They show prominent laser action. They emit in the green-yellow region. In this experiment, we investigate spatial self-phase modulation of Pyrromethene 567 in different solvents to analyze the nonlinear optical properties.

2. Experiment

A 532 nm continuous wave laser was focused vertically into a cuvette containing 50 μM pyrromethene 567 dye dissolved in different solvents. A lens with a focal length of 15 cm was used to focus the beam, and the cuvette containing the sample was placed 5 cm before the focus of the laser beam. The diffraction patterns were recorded on a screen in the far field using a digital camera. The input power of the laser beam was varied, and the corresponding diffraction patterns were recorded. The schematic representation of the experimental setup is shown in figure 1.

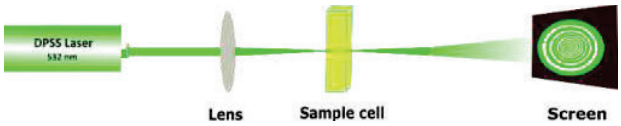

Fig. 1: Experimental setup of SSPM.

3. Result and discussion

The absorption spectrum of pyrromethene 567 shows a strong characteristic peak around 517 nm. Localized absorption of a focused beam propagating through an absorbing dye medium produces a spatial temperature distribution in the sample and, consequently, a spatial variation in the refractive index, resulting in the severe phase change of the propagating beam. The phase shift thus produced results in the diffraction of the propagating beam in the far-field.

The on axis nonlinear phase shift, $\Delta\phi$ can be related to the number of rings and the nonlinear refractive index n_2 is given by [3,4]

$$n_2 = \frac{\lambda}{L_{eff}} \frac{N}{I} \qquad (1)$$

Where λ is the laser wavelength, L_{eff} is the path length, I is the input intensity, and N is the number of rings.

Experimentally observed SSPM patterns of PM 567 in different solvents at 40 mW input power are shown in figure 2. It can be seen that for a particular input power, the number of rings obtained for PM 567 in different solvents varies. At 40 mW input power, PM 567 in DMSO exhibits the most number of rings.

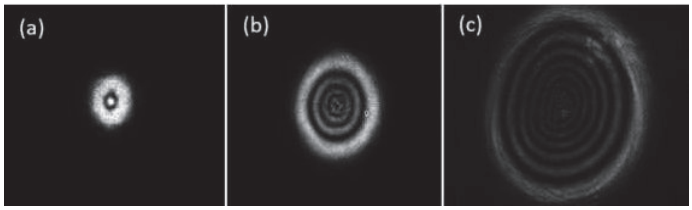

Fig. 2: SSPM patterns of pyrromethene 567 at 40mW power in (a) Methanol (b) DMF (c) DMSO

The various cases of SSPM patterns with different incident power for a particular solvent are also studied. The input power of the laser beam is varied and the corresponding patterns are recorded. The nonlinear refractive index n_2 is calculated by estimating the $\frac{N}{I}$ values from the intensity vs number of rings plot in figure 3. It can also be noted that the number of rings per each pattern increases linearly with the input power. The intensity of the outermost ring of each patterns is brighter than the inner ones. The nonlinear refractive index for different solvents are calculated and tabulated in table 1.

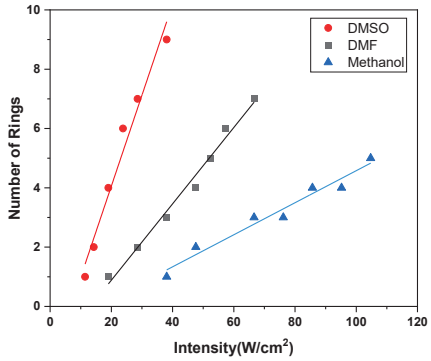

Fig. 3: Intensity vs Number of rings with different concentrations

Table 1: Nonlinear refractive index, n_2 values of PM 567 in different solvents

Solvent	n_2 (cm^2/W) X 10^{-6}
DMSO	16.31
DMF	6.40
Methanol	2.87

4. Conclusion

Spatial Self Phase Modulation was observed in pyrromethene 567 dye dissolved in different solvents. The number of rings observed in different solvents varied. The nonlinear refractive index n_2 of pyrromethene 567 in different solvents were estimated.

5. References

[1] Ogusu Kazuhiko, Yoshiaki Kohtani, and H. Shao. Laser-Induced Diffraction Rings from an Absorbing Solution. **3**, 232–234 (1996).
[2] Shabeeb, G. M., Emshary, C. A., Hassan, Q. M. A. & Sultan, H. A. Investigating the nonlinear optical properties of poly eosin-Y phthalate solution under irradiation with low power visible CW laser light. Physica B: Condensed Matter 578, 411847 (2020).
[3] Hassan, Q. M. A., Badran, H. A., Al-Ahmad, A. Y. & Emshary, C. A. Physical origin of observed nonlinearities in Poly (1-naphthyl methacrylate): Using a single transistor - Transistor logic modulated laser beam. *Chinese Physics B* **22**, 1–6 (2013).
[4] Zidan, M. D., EL-Daher, M. S., Al-Ktaifani, M. M., Allahham, A. & Ghanem, A. Spatial phase modulation and all-optical switching of tris(2 ',2-bipyridyl)iron(II) tetrafluoroborate. *Optik (Stuttg)* **219**, 165275 (2020).

Demonstration of High-Power Pulsed Thulium Doped Fiber Laser with Emission at 2 μm

Anjali. P.S, Balaji Srinivasan, Deepa Venkitesh
Department of Electrical Engineering, Indian Institute of Technology Madras, Chennai, 600036, India
deepa@ee.iitm.ac.in

Abstract: We experimentally demonstrate a pulsed Thulium doped fiber laser with tunable repetition rate through external modulation using an acousto-optic modulator. Power scaling of upto 335 W of peak power is achieved through multiple amplifier stages in master oscillator power amplifier configuration.
Keywords: TDFRL, MOPA, AOM

1. Introduction

Thulium doped fiber lasers have received significant attention in the recent past due to their versatile applications in various fields such as medicine, material processing, sensing and for infra-red counter measures [1,2]. For directional infrared counter measure applications, a high-power modulated source at 2 μm is used as a jammer in order to obscure the seeker missile and jam them so that the seeker fails to identify and track the target. High power fiber laser sources with precise control of pulse width and repetition rate are an optimal choice for such applications.

In this paper, we experimentally demonstrate pulsed operation of a thulium doped fiber ring laser through external modulation using acousto-optic modulator (AOM) and the subsequent pulse amplification through multiple amplifier stages, to achieve hundreds of watts of peak power, in master oscillator power amplifier (MOPA) configuration.

2. Experimental setup

The schematic of the thulium doped fiber ring laser (TDFRL, the seed laser) is shown in Fig. 1 (a). It consists of 2 m length of thulium doped double clad fiber as the gain medium, which is pumped at 790 nm using high power multimode semiconductor laser diode with maximum output power of 4 W. Pumping at this wavelength is very effective because of the "two for one'' cross relaxation mechanism associated with it, despite the large quantum defect.

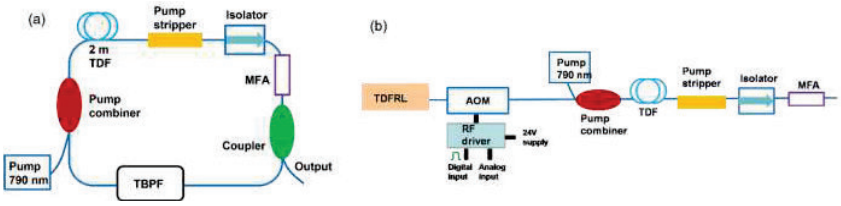

Fig.1: Schematic of experimental setup of (a) seed laser (b) fiber amplifier for pulse amplification

Pump stripper is used to eliminate any residual pump power after the gain medium. Isolator ensures unidirectional propagation of light and mode field adaptor (MFA) enables efficient coupling of light from a double clad geometry to a single clad geometry. Feedback is given through a 3 dB coupler and multimode pump combiner (MPC). Seed laser has a tunable bandpass filter (TBPF) in the cavity, with which the output lasing wavelength can be tuned from 1955 nm to 2045 nm. Figure 2 (b) shows the schematic of the experimental setup for pulse amplification, where an AOM is introduced in the path for external modulation and thus to pulse the seed laser with desired pulse widths and repetition rates. Modulating the RF signal to the AOM controls the pulse width and the repetition rate of the output. The minimum achievable pulse widths are limited only by the AOM switching time, which is about 33 ns. The pulses at the output of the AOM are amplified through three amplifier stages, one of which is shown in Fig.1 (b). The length of gain medium used in the first, second and third amplifier stages are respectively 2 m, 2 m and 4.3 m. Additionally, the first, second, and third amplifier stages, respectively, are pumped with 4W, 8 W and 12 W respectively to achieve the desired output power levels. The lengths of the fiber and the pump power required are estimated by numerically

simulating the rate equations corresponding to the propagation of pump and signal in a double clad thulium doped fiber, including the cross relaxation parameters.

3. Experimental results

Pulse amplification experiment is initially performed at a wavelength of 2040 nm. All the amplifier stages are characterized at repetition rate of 200 kHz and 50 kHz with duty cycle of 4 % and 1 % respectively. A thermal power meter is used to measure the average power after each amplifier stages and the time domain characterization is done using a photodetector of bandwidth 10 GHz and an oscilloscope.

Table 1 : Output characteristics of different amplifier stages

Amplifier Stage	Repetition rate (kHz)	Duty cycle (%)	S_{in} (W)	P_{avg} (W)	Gain (dB)	Peak (W)
First Amplifier	200	4	3.6×10^{-3}	0.25	18.4	6.25
	50	1	0.9×10^{-3}	0.14	22	13.6
Second Amplifier	200	4	0.192	2.1	10.4	52
	50	1	0.108	1.84	12.3	184
Third Amplifier	200	4	1.67	3.73	3.5	93
	50	1	1.44	3.35	3.7	335

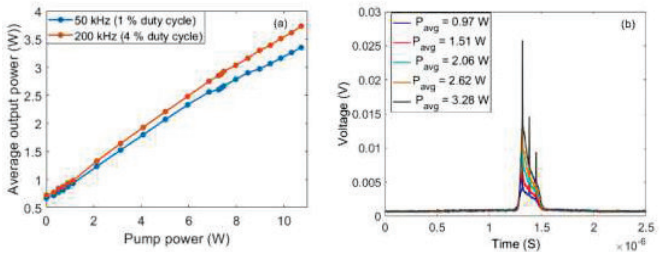

Fig.2: Output of third amplifier stage (a) Average output power vs input pump power (b) Output pulse at 50 kHz with 1 % duty cycle

The characteristics of different amplifier stages, average output power (P_{avg}), gain, pulse peak power, signal input power (S_{in}), at different repetition rate and duty cycle are summarized in Table 1. Figure 2 (a) shows the average output power from the third amplifier stage at different operating conditions. At 200 kHz with 4 % duty cycle, the maximum average power measured is about 3.73 W. This corresponds to a gain of 3.5 dB (S_{in} = 1.67 W) and peak power of 93 W. At 200 kHz with 1 % duty cycle, the maximum average power measured is about 3.35 W. This corresponds to a gain of 3.7 dB (S_{in} = 1.44 W), peak power of 335 W and pulse energy of 32 μJ. A change in the slope is observed in the plot of output average power vs pump input power when exactly the third pump diode connected to the third amplifier stage is turned on. This could potentially be due to the shift in the pump wavelength with respect to the input current to the pump diode. Figure 2 (b) shows the output pulse from the third amplifier stage at 50 kHz with duty cycle of 1 %. The pulse shape appears to be distorted because of gain saturation due to large peak power. The pulse deformation could be avoided by modifying the shape of the seed pulse such that it will allow pre-compensation of pulse deformation due to saturation [3]. On top of the normal pulse, some extra peaks could be seen. These pulses are a consequence of the self mode-locking characteristics of the seed laser as reported in [4]. Pulse amplification experiments are repeated at wavelength of 2000 nm as well. Compared to 2040 nm, 2000 nm has a larger emission cross-section, and thus resulted in a comparatively higher output average power of 4.17 W at 200 kHz with 1 % duty cycle.

4. Conclusion

We experimentally demonstrate pulsed high-power operation of thulium doped fiber laser of desired repetition rate and duty cycle through external modulation using AOM. Maximum output average power of 3.35 W and peak power of 337 W is attained at 2040 nm, at repetition rate of 50 kHz with duty cycle of 1 %.

5. References

[1] Jackson, Stuart D, “Towards high-power mid infra red emission from a fiber laser,” Nature Photonics 6, 423-431 (2012)
[2] Moulton, Peter F., et al, "Tm-doped fiber lasers: fundamentals and power scaling," IEEE J. of Sel. Top. Quantum Electron.,15. 85-92 (2009)
[3] Schimpf, Damian N., et al. "Compensation of pulse-distortion in saturated laser amplifiers." Optics Express 16.22 (2008): 17637-17646.
[4] Anjali, P. S., et al. "Investigation of Passive Mode Locking Characteristics of Thulium Doped Fiber Ring Laser." Asia Communications and Photonics Conference. Optical Society of America, 2016.

Numerical Simulation of Conical Intraoral Probe Tip for Multispectral Uniform Illumination within Region of Interest

Uttam M. Pal[1,*], Pushkraj A. Janwadkar[2], Sree T. Sucharita[3], I. Kannan[4], Hardik J. Pandya[2]

1. Biomedical Engineering, Department of Sciences and Humanities, Indian Institute of Information Technology, Design and Manufacturing, Kancheepuram-Chennai
2. Department of Electronic Systems Engineering, Indian Institute of Science Bangalore
3. Department of Research, Panimalar Medical College Hospital & Research Institute, Chennai
4. Department of Microbiology, Tagore Medical College and Hospital, Chennai, Tamil Nadu, India

**Corresponding author e-mail address: uttampal@iiitdm.ac.in*

Abstract: A right circular conical geometry-based optical probe tip is numerically designed, simulated, and optimize to establish uniform illumination on the region of interest (10 mm-30 mm diameter) within the oral cavity.

Keywords: Intraoral, oral cancer, ray optics, numerical simulation, COMSOL Multiphysics.

1. Introduction

The commercially available intraoral cameras are now becoming a norm for evaluating oral cavity health. These imaging tools perform only white light imaging, which provides information about the morphology of the blood vessels within the oral cavity. However, there is no information about the oxygenated (HbO_2) and deoxygenated (Hb) blood within the blood vessels. Multispectral imaging-based intraoral cameras have been developed recently to quantify the composition of HbO_2 and Hb [1-3]. These imaging tools use LEDs operating at 545 nm and 575 nm to target the two absorption peaks of HbO_2. It has been observed that the diffused reflectance intensity at 545 nm and 575 nm are substantially lower in the lesion compared to normal tissues due to various reasons such as thickening epithelium, neovascularization, and high collagen content in the diseased region. The tool working on autofluorescence modality uses LED operating at 410 nm for fluorescence and white light for visualization. One of the challenges in intraoral imaging is to illuminate the tissue surface uniformly. The current imaging tools have a planar configuration, where the LEDs and camera lie on the same horizontal plane. The planar configuration creates an offset between the center of illumination and the center of the image captured by the camera, which may result in an error while quantifying the composition of HbO_2 and Hb. Hence there is a critical need for a right circular conical configuration where the LEDs are placed on the inclined surface, and the camera is placed at the vertex, which is numerically studied in this work using COMSOL Multiphysics®.

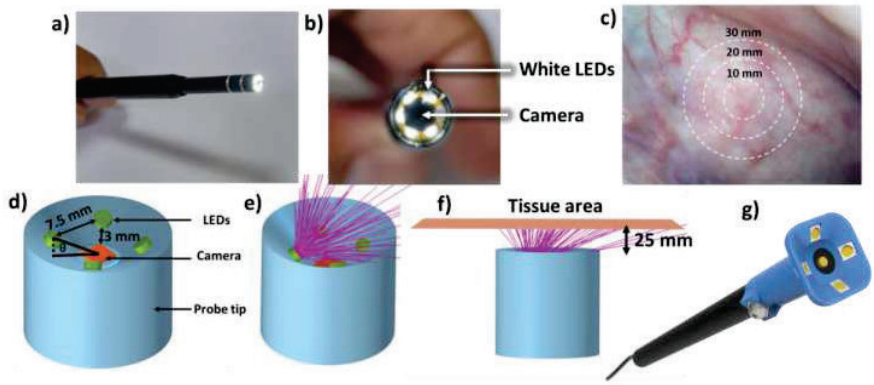

Fig.1: a) Commercially available endoscope camera, b) Configuration of six white light LEDs surrounding the camera at the center, c) White light image captured using the endoscope camera showcasing the blood vessels in the sublingual and submandibular glands in the floor of the mouth (white dashed circles representing Region of Interest of 10 mm, 20 mm, and 30 mm diameter), d) Probe tip with angle of inclination as 30° e) Ray propagating from a single LED, with angle of inclination as 35°, f) Side view of the rays from optic probe interacting with tissue, with angle of inclination as 30°, and g) Proposed design of the conical probe tip attachment to the commercially endoscope camera.

2. Design and Methodology

The currently commercially available While Light Imaging (WLI) optic probe uses six sub-miniaturized white light LEDs surrounding the camera, as shown in Fig. 1a-b. The white light image can resolve the blood vessels of the sublingual and submandibular region of the oral cavity, as shown in Fig. 1c. Performing multispectral imaging requires LEDs of 545 nm, 575 nm, 415 nm, and 680 nm on the outer periphery of the optic probe as shown in the Fig.1d. The cone angle or angle of inclination (θ) of the optic probe governs the effective intensity of light incident on the tissue area. A numerical design and analysis were performed using the Ray Optics Module of COMSOL Multiphysics ®. The ray trajectories were evaluated by varying the inclination angle (θ) between 0° and 55° with a step of 2.5°, as shown in Fig. 1e. A rectangular tissue area with dimension 50 mm x 50 mm was placed 25 mm above the probe tip as shown in Fig. 1f, to quantify the effective tissue illumination area. The effective area was characterized as a region of interest (ROI) with a varying diameters of 10 mm, 20 mm, and 30 mm. A total of 25,000 rays were launched in a normal direction from a single LED in this simulation which took about 1 minute 30 seconds for the parametric sweep of θ. The proposed design of the probe tip attachment to the commercially available endoscope camera is shown in Fig. 1g.

3. Results and Discussion

The normalized incident intensity of light on the tissue area is shown in Fig. 2a. When the angle of inclination (θ) is 0°, the incident intensity is focused away from the center of the region of interest. As θ increases, the incident intensity is shifted diagonally to the top-right corner and expands radially outwards. The effective tissue illumination area can be defined as the tissue surface area (mm^2) with an incident intensity higher than a threshold value (Th) of 0.5. This effective tissue area would be responsible for the back-scattered reflected light from the tissue area acquired by the camera. The effective tissue illumination area plot is shown in Fig. 2b. The solid line represents the actual data, and the dotted line represents the five-point adjacent averaged data (Arrow representing peaks). It can be observed that considering the circular ROI at the center with a 10 mm diameter, the effective tissue area linearly increases to about θ = 45° and then significantly drops. For ROI of 20 mm, the effective tissue area slowly increases to the peak value of about θ = 30°, then significantly declines. For ROI of 30 mm, the effective tissue area plateaus around θ = 20°, then slowly decreases till θ = 40°, following which decays drastically. A significant effective tissue illumination for the ROI with a diameter of 10 mm, 20 mm, and 30 mm can be hence achieved with the angle of inclination θ as 42.5°, 30°, and 20° respectively, as shown in the table in Fig. 2c. As the threshold value is increased from 0.5 to 0.1, the effective area also increases towards the total tissue surface area. The future work involves designing and developing a polarimetric intraoral optical probe for oral cancer diagnosis, an extension of the previous earlier works in breast cancer [4,5] and myocardial disease diagnosis [6].

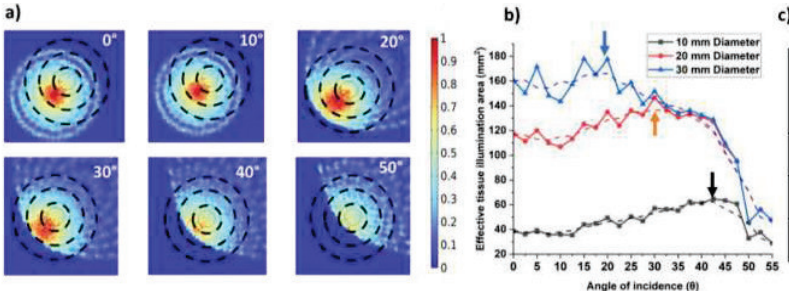

ROI (ϕ)	θ	Effective area (mm²)			Total ROI area (mm²)
		Th = 0.5	Th = 0.3	Th = 0.1	
10 mm	42.5	64.81	78.50	78.50	78.50
20 mm	30	146.57	238.65	314.15	314.15
30 mm	20	177.75	329.32	613.70	706.85

Fig.2: a) Illumination with varying angle of inclination (0°, 10°, 20°, 30°, 40°, and 50°), b) Effective tissue illumination area for varying region of interest with diameter of 10 mm, 20 mm, and 30 mm (arrow representing peaks), considering threshold (Th) as 0.5, and c)Table representing the effective area for respective ROI, considering the threshold value (Th) as 0.5, 0.3, and 0.1.

4. References

[1] Bhowmik A et al., "Portable, handheld, and affordable blood perfusion imager for screening of subsurface cancer in resource-limited settings", Proceedings of the National Academy of Sciences of the United States of America.;119(2):e2026201119, 2022.

[2] N, Praveen Birur et al., "mHealth-Based Point-Of-Care Diagnostic Tool for Early Detection of Oral Cancer and Pre-Cancer Lesions in a Low-Resource Setting", The Lancet, 2021 (Preprint).

[3] Narayanan S et al., "Bimodal multispectral imaging system with cloud-based machine learning algorithm for real-time screening and detection of oral potentially malignant lesions and biopsy guidance", 26(8):086003, J Biomed Opt. 2021.

[4] Arif Mohd. Kamal et al., "Towards the development of a portable LED-based polarization spectroscopy tool for breast cancer diagnosis", J. Biophotonics, 15(3), e202100282, 2022.

[5] UM Pal et al., "Hybrid spectral-IRDx: near-IR and ultrasound attenuation system for differentiating breast cancer from adjacent normal tissue", IEEE Transactions on Biomedical Engineering 68 (12), 3554-3563, 2021.

[6] Twinkle Bagha et al., "Toward the development of a polarimetric tool to diagnose the fibrotic human ventricular myocardium," J. Biomed. Opt. 27(5) 055001, 2022.

LFOV: Pap-smear Imaging with Deep Learning based Single-shot Lensless Holography

Ashwini S Galande, Aswathy Vijay, Nikhil Prakash, Renu John*

Medical Optics and Sensors Laboratory, Department of Biomedical Engineering, Indian Institute of Technology, Hyderabad, India.

**Author e-mail address: renujohn@bme.iith.ac.in*

Abstract: Quantitative phase information about the cervical cells obtained using the inline holographic microscope is a value addition for disease diagnosis. The end-to-end deep learning methods can reconstruct complex object wavefront directly from the single hologram with acceptable reconstruction precision. However, the massive training data pairs are required with environmental and system stability which is very difficult to achieve. To overcome this problem, we propose the physics aware deep neural network to reconstruct a large field-of-view (LFOV) lensless hologram without any prior training required. We prove that the quantitative phase information about cervical cells improves risk prediction as compared to the intensity-only images.

Keywords: Lensless holography, deep learning, cervical cancer.

1. Introduction

Cervical cancer is the fourth most common cancer in women according to World Health Organization. India contributes a quarter of the total burden of cervical cancer cases worldwide, yet proper attention is not given to proper health care and diagnostics [1]. 80% of the women affected by cervical cancer belong to rural areas due to a lack of resources and awareness, fostering the need for a low-cost and portable solution for cancer diagnosis [2,3]. One of the very common cytology procedures for early diagnosis of cervical cancer is the Pap test. There are various methods to prepare Pap slides to observe changes in the cell nuclei and the number of qualitative characteristics used by clinicians. Hence, the Pap test is subjective and observer-dependent and that contributes to the reasons for low early detection. Quantitative phase imaging modalities are meant to improve cytology procedures by providing quantitative phase profiles of the cells along with the intensity images. It has been proved in the literature that the phase profile of the cell along with the intensity image improves classification accuracy considerably [5]. However, these imaging modalities are based on interferometric procedures to retrieve phase information of the sample and they are bulky, expensive, and hungry for highly coherent light sources (Laser). This limits their use beyond well-equipped laboratories. Single-shot, label-free, noninvasive nature of quantitative imaging techniques like inline holographic microscopy makes it fit for cellular imaging.

Digital inline holographic microscopy (DIHM) is inherently affected by twin image artifacts and interference related noise. However, the end-to-end deep learning methods can reconstruct object wavefront directly from the single hologram with acceptable reconstruction precision. The massive training data pairs are required with environmental and system stability which is very difficult to achieve. Apart from that, in many practical applications, it is highly challenging to obtain sufficient ground-truth images for training. Deep learning based end-to-end solutions for hologram reconstruction have emerged as a promising method for twin image-free phase retrieval. However, the requirement of massive one-to-one training pairs with all possible variations in recording conditions is difficult to achieve. Also, the trained network is application-specific and requires separate training for different applications. To alleviate this data requirement problem, physics aware deep learning (Deep Image Prior (DIP)) is proposed for different applications [6-8] aiming to reduce training time and achieve better accuracy. Phase reconstruction using DIP is achieved by incorporating a physical model (forward propagation) that represents the image formation process into conventional deep learning. Network parameter optimization and phase reconstruction happen through the interplay between the deep network and the physical model. This method can achieve considerable improvement over conventional phase reconstruction methods without extensive training. Also, the single-shot holography will simplify the set-up complexities and can be used in live and moving cell imaging and will create new opportunities for cell imaging in resource constrained environments.

2. Methods

In the proposed DIHM set-up a partially coherent LED light source of wavelength 627nm illuminates the sample kept at distance $z_1 \sim 3-5cm$ and the interference pattern is captured at the detector. The distance between the sample and the detector, z_2, is usually in the range of millimeters (~1mm), which results in a FOV equal to the active area of the detector. The captured hologram intensity I is given as an input to the U-net (R_θ) which then reconstruct the complex object u_o. The new hologram is generated using forward model as given in Eq. 2 and Eq. 3. The error between the captured and the measured hologram is given back to the network to update the parameters. The interplay between the network (R_θ) and the forward model ($H(u_o)$) results in the learned network parameters (θ) which will search the amplitude and phase of the object most consistent with the input hologram.

$$R_{\theta^*} = \text{argmin}_{u_{o,\theta}}\{\|HR_\theta(z) - I\|_2^2\} \qquad s.t.\ \ u_o = R_\theta(z) \tag{1}$$

$$I = |U_o + U_R|^2 = |U_o|^2 + |U_R|^2 + U_o^* U_R + U_o U_R^* \tag{2}$$

The effect of $|U_R|^2$ is eliminated by normalizing the hologram and the self-interference term, $|U_o|^2$ is considered as system noise, e. Eq. (2) can be written as:

$$I = U_o^* U_R + U_o U_R^* + e = H(u_o) \tag{3}$$

where, $H(.)$ is the function that maps the object field to the hologram intensity with the known reference wave. The workflow diagram of the proposed method is given in Fig. 1.

We have segmented the nucleus and cytoplasm to calculate area and volume ratios. The cytology procedures generally require large data to conclude the prognosis of a patient. The large FOV helps in scanning large data in a short period.

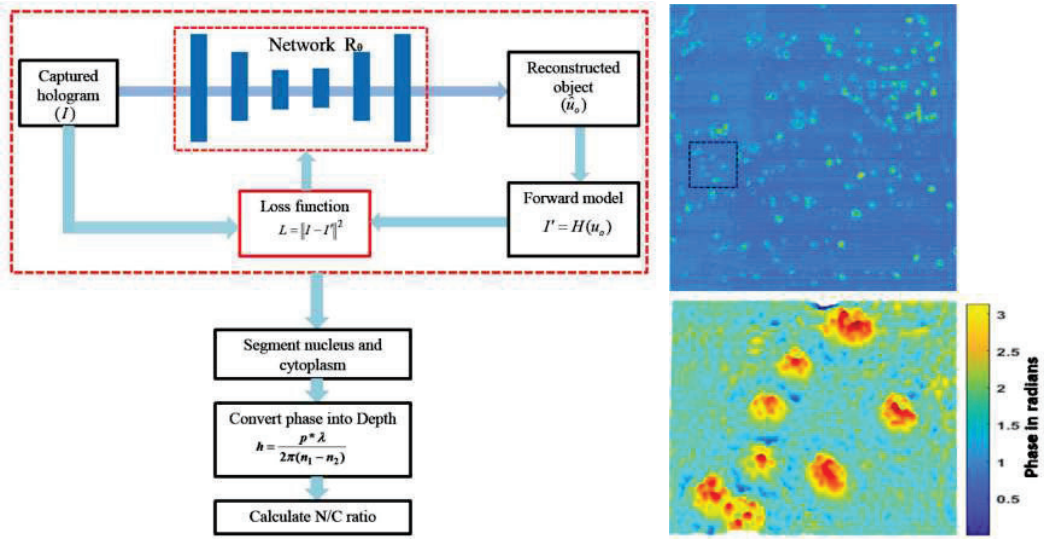

(a) (b)

Fig. 1: (a) Workflow diagram of the proposed method. (b) LFOV phase of cervical sample reconstructed by the proposed method

3. Conclusion

The DIP based phase retrieval does not require a large data set for training and it is suitable for single-shot phase retrieval. Further, the use of this low-cost, portable microscope for cervical cancer diagnosis in remote areas will promote regular screening and early detection of cancer and hence, is expected to reduce the fatality rate significantly. The large FOV helps in scanning large data in a short period. Thus, apart from the low-cost advantage of the lensless microscope, it also reduces the burden of complex scanning systems in collecting large data.

4. References

[1] N. Benzerdjeb, C. Garbar, P. Camparo,"Digital holographic microscopy as screening tool for cervical cancer preliminary study,"Cancer Cytopathol.,**124**(8), 573-580 (2016).

[2] D Pathania, C Landeros, L. Rohrer, V. D'Agostino, S. Hong, I. Degani, M. Avila-Wallace, M. Pivovarov, T. Randall, R. Weissleder, H. Lee, H. Im and C. M. Castro,"Point-of-care cervical cancer screening using deep learning-based microholography," Theranostics, **9** (26), 8438 (2019).
[3] A. N. Srivastava, J. S. Misra, S. Srivastava, B. C. Das, S. Gupta,"Cervical cancer screening in rural India: Status & current concepts,"*Indian J Med Res*., **148**(6), 687(2018)
[4] L.Denny, R.Herrero, C.Levin, J.J.Kim, "Cervical cancer," Cancer: Disease Control Priorities, Third Edition (Volume 3) (2015).
[5] J. Mangal, R. Monga, S. R. Mathur, A. K. Dinda, J. Joseph, S. Ahlawat, K. Khare, "Unsupervised organization of cervical cells using bright-field and single-shot digital holographic microscopy," J. Biophotonics **12**(8), (2019).
[6] Y.Yao , H.Chan, S.Sankaranarayanan, P. Balaprakash , R. J.Harder, M. J. Cherukara,"AutoPhaseNN: Unsupervised Physics-aware Deep Learning of 3D Nanoscale Coherent Imaging," arXiv preprint arXiv:2109.14053 (2021).
[7] S. Kumar, "Phase retrieval with physics informed zero-shot network," Opt. Lett. **46**, 5942-5945 (2021).
[8] H. Li, X. Chen, H. Wu, Z. Chi, C. Mann, and A. Razi, "Deep DIH: Statistically Inferred Reconstruction of Digital In-Line Holography by Deep Learning," IEEE Access, (2020).

Atomic Vapor Based Radio-frequency Magnetometer

Soumya R. Mishra,[1,*] Sushree S. Sahoo,[1,2] G. Rajalakshmi,[2] Ashok K. Mohapatra[1,#]

[1]*National Institute of Science Education and Research Bhubaneswar, Jatni 752050, HBNI, India*

[2]*TIFR Centre for Interdisciplinary Sciences, Tata Institute of Fundamental Research, Hyderabad 500046, India*

* *soumya.ranjan.mishra@niser.ac.in* [#]*a.mohapatra@niser.ac.in*

Abstract: We present a radio-frequency(rf) atomic magnetometer based on the nonlinear magnetoelectric (ME) effect in atomic vapor. First, we demonstrate the ME effect in atomic vapor for a linearly polarized input optical field which couples to an rf magnetic field leading to the generation of new optical fields. By varying the polarization states of the input linear optical field we study the polarization dependence of the generated field amplitude. We could achieve the rf-field sensitivity of 70 $fT/\sqrt{Hz}$ at 1kHz for zero static fields in an unshielded environment. The dynamic range is estimated to be up to 10^{12} using our system.

Keywords: Magnetoelectric effect, Sensitivity, Dynamic range, Magnetometry

1. Introduction

The parametric interaction of electric and magnetic fields in a medium result in the magnetoelectric (ME) effect that leads to the enhancement of electric polarization by magnetic fields and magnetization enhanced by electric fields. ME effects have been demonstrated in some heterostructures like multiferroics [1,2], due to their diverse applications in memories and magnetic sensors fabrication. But we are the first to demonstrate the nonlinear ME effect in an atomic vapor medium where the coupling of optical electric fields and rf-magnetic fields leads to the generation of new optical electric fields [3]. This nonlinear ME effect has a significant application in precision rf magnetometry where the rf magnetic field-dependent generated optical field has the key role in magnetic field sensing. So far atomic vapor rf-magnetometers are based on the polarization rotation of input linearly polarized light [4-6]. However, in this work using the ME effect we could achieve the minimum rf-field sensitivity of 70 $fT/\sqrt{Hz}$ at 1kHz in an unshielded environment [3].

2. Experimental Methods and Results

The atomic energy levels coupling to the input optical electric and rf-magnetic fields are depicted in Fig.1(a). We apply a dc magnetic field to split the Zeeman sub-levels of the ground state (^{87}Rb, $F = 1$) and a transverse rf-magnetic field(ω_{rf}) to induce the coherence between those sub-levels. A linearly polarized optical field(ω_p) couples one of the ground states to the excited state (^{87}Rb, $F = 0$), and finally, the mixing of the optical field with the rf-magnetic field creates the coherence between the excited state and other ground states that lead to the generation of new optical fields of frequencies ($\omega_p \pm \omega_{rf}$) [3]. Angular momentum conservation decides the polarization states of the generated optical fields. The generated optical field is detected using the optical heterodyne detection technique by interaction with a local oscillator.

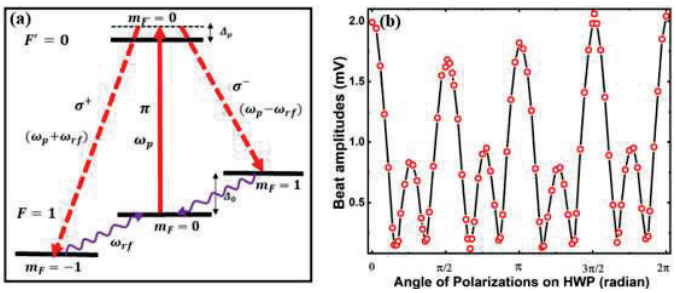

Fig.1. (a) Depiction of ME effect in the energy level diagram (b) Polarization-dependence of the mixing process.

We keep the input light at any arbitrary linear polarization of the form $a|\sigma^+\rangle + b|\sigma^-\rangle + c|\pi\rangle$, where a, b and c determine the magnitude of respective polarization components and can be adjusted by a $\lambda/2$ plate before the medium.

Another $\lambda/2$ plate is put after the medium to convert back to any orthogonal linear polarization. By varying the angle of the 1st $\lambda/2$ plate the beat amplitude of generated optical field with the local oscillator for each input polarization state is plotted in Fig. 1(b). In the figure, the first maxima correspond to the input light polarization of form $1/\sqrt{2}\,(|\sigma^+\rangle + |\sigma^-\rangle)$, where the generated optical field is π polarized so we can filter it to the maximum amount by the 2nd $\lambda/2$ plate hence, we have a larger signal amplitude. Whereas, in the case of second maxima, the input light is π polarized and the generated optical fields are of $\sigma^+$and σ^- polarizations so we cannot filter it all through the $\lambda/2$ plate hence, the smaller signal amplitude. The minima correspond to the state with equal polarization components which destroy the ground state coherence since there would be no population difference among the ground states and hence the absence of any mixing process.

3. rf-Magnetometry using ME effect

We study the variation of the beat amplitude between the input pump field (ω_p) and generated optical fields ($\omega_p \pm \omega_{rf}$) with rf-field frequencies for both zero and nonzero static fields. In the case of a zero bias field, the optical generation is more efficient at lower rf frequencies, whereas the strength of generated field amplitude decreases with increasing rf-field frequency as shown by blue open squares in Fig. 2(a) and for a finite field, resonance behavior in the signal implies the optical generation to be efficient at some Zeeman resonance frequency as shown by red open circles in that figure.

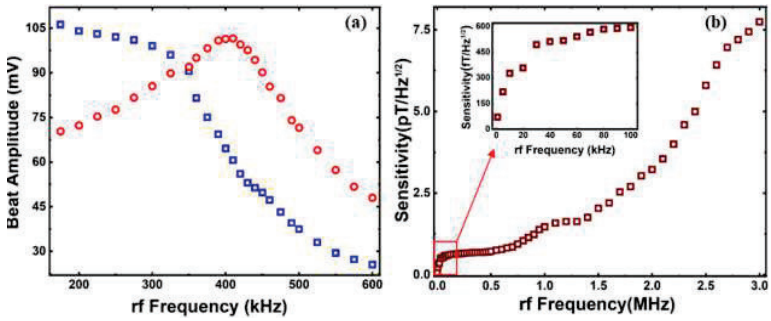

Fig. 2. (a) Variation of beat amplitude with rf frequencies (b) rf-field sensitivity plot of the system.

For a given input rf magnetic field (B_{rf}), we keep the input light polarization at larger maxima (Fig. 1(b)) and measure the signal-to-noise ratio (SNR) of the system experimentally and calculate the rf magnetic field sensitivity (δB) by using the expression, $\delta B = B_{rf}/SNR$. For zero biasing field, at lower rf frequencies the contribution from multiple nonlinear phenomena enhances the signal amplitude hence we have better sensitivity in that regime. Experimental data of δB variation with rf-field frequencies are depicted in Fig. 2(b), where using our system we could achieve a best rf-field sensitivity of $70fT/\sqrt{Hz}$ at 1kHz to $7.5pT/\sqrt{Hz}$ at 3MHz in an unshielded environment and the theoretical model explaining our system calculates the dynamic range to be up to 10^{12} [3].

4. Conclusion

This work briefly explains the ME effect in atomic vapor and the system could be treated as a suitable candidate for rf magnetic field sensing due to its significant features like high dynamic range and arbitrary frequency resolution.

5. Acknowledgment

The authors are grateful to acknowledge the financial support from NISER Bhubaneswar and TIFR, Hyderabad, Department of Atomic Energy, Government of India.

6. References

[1] D. A. Filippov, V. M. Laletin and T. O. Firsova, Phys. Solid State 56, 980–984 (2014).
[2] L Y Fetisov et al J. Phys. D: Appl. Phys. 51 154003 (2018).
[3] Sushree S. Sahoo, Soumya R. Mishra, G. Rajalakshmi, and Ashok K. Mohapatra, Phys. Rev. A 105, 063509 (2022).
[4] M. Savukov, S. J. Seltzer, M. V. Romalis, and K. L. Sauer, Phys. Rev. Lett. 95, 063004 (2005).
[5] D. Budker and M. Romalis, Nat. Phys. 3, 227–234 (2007).
[6] W. chalupczak, R. M. Godun, S. Pustelny, and W. Gawlik, Appl. Phys. Lett. 100, 242401 (2012).

Fiber-optic Sensor for Detecting Food Spoilage

Shwinky [a, b], Sudipta Sarkar [a, b], Girish C. Mohanta[a, b*]

[a] *CSIR- Central Scientific Instruments Organization (CSIR-CSIO), Chandigarh-160030, India*

[b] *Academy of Scientific and Innovative Research (AcSIR-CSIO), CSIR- Human Resource Development Centre, Ghaziabad, Uttar Pradesh, India (201002).*

E-mail address: gmohanta@csio.res.in

Abstract: Spoilage of food is one of the biggest threats to global food security. It is also responsible for foodborne illness resulting into loss of life and economic activities. Animal origin foods are particularly at risk of spoilage due to microbial contamination during storage and transportation. Therefore, early detection of spoilage is necessary for preventing disease outbreaks and economic losses. Volatile organic compounds (VOCs) like biogenic amines are major indicator of food spoilage. In this work, we report a rapid, cost-effective and highly sensitive fiber-optic sensor for VOC detection. Detection of as low as 500 ppb has been achieved.

Keywords: Fiber-optic sensor, Biogenic amines, Food quality, VOC

1. Introduction

Animal origin foods such as meat, fish, and poultry constitute a major portion of global food trade. In fact, it is expected to cross over 1 trillion USD businesses by 2022. The hygiene and freshness of food are important quality indicators for acceptance. Therefore, any spoilage of food, particularly by microbial contamination is a major public health concern [1]. Thus, sensors which could detect spoilage of food are increasingly sought after by the regulatory authorities and food industries globally.

Microbial spoilage produces several metabolites with undesirable flavor and pungent odor [2]. In particular, biogenic amines which are very pungent, reactive and highly volatile has been accepted as quality indicators for spoilage [3]. These amines are collectively called as total volatile basic nitrogen (TVB-N) and mainly consists of trimethylamine (TMA), dimethylamine (DMA), and ammonia (NH_3). They are emitted from food as VOCs. The conventional detection techniques like gas chromatography (GC) are too complex, expensive, and are limited to large scale setups. Consequently, several low cost, electrochemical and optical sensors have been explored. In particular, optical sensors based on fluorescent dyes are best suited due to their sensitive and robust nature. These sensors respond to TVB-N by either fluorescence quenching or turn-on phenomenon. Recently, sensor integration on fiber-optic platforms has been increasingly reported due to their ease of fabrication, robust nature, miniaturization, and capability of remote sensing. Furthermore, optical signals are immune to conditions like humidity, temperature and electromagnetic interferences. In these contexts, we fabricated a fibre-optic (FO) sensor based fluorescent sensor for on-field detection of ammonia (NH_3). The sensor was fabricated from a polymer-fluorescent dye composite coated at one end of the fiber and then exposed to ppm levels of ammonia.

2. Experiment Details

The FO sensor was fabricated by integrating polymer- fluorescent dye composite on 600 µm multimode optical fiber through dip coating. The coating solution was prepared by mixing 10 mg mL^{-1} solution of fluorescein (free acid) with PVP (MW 40000) to a final concentration of 20% (w/v) polymer. For efficient coupling of the fluorescence signal, the core of the optical fiber was exposed prior by first removing the plastic jacket and then HF (48%) etching for 10 min followed by washing. The fabricated sensor was then fixed in sensing setup (Figure 1) which has a provision for gas flow and excitation source at orthogonal position. The sensor was exposed to different concentration of ammonia in gas phase.

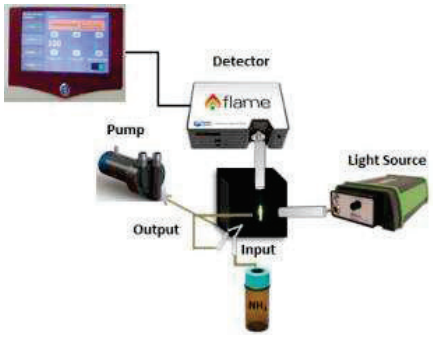

3. Results and discussion

The fluorescein (free acid) is a pH responsive dye with emission maxima around 550 nm in its deprotonated form (basic pH). At low pH fluorescein is non-fluorescent. Since ammonia is chemically a lewis base, therefore pH responsive property of fluorescein has been exploited to create a fluorescence turn-on type ammonia sensor. Accordingly, the sensor was first exposed to hydrochloric acid fumes which significantly quenched the sensor fluorescence (figure 2a). However, on exposure to ammonia (NH_3) in gas phase, the fluorescence of the dye was quickly and quantitatively recovered (figure 2b). The emission peak around at 550 nm increases with increase in the ammonia exposure along with slight wavelength red shift.

During fabrication, we found out that polymeric binder plays a crucial role in sensing capability and stability of FO sensor. Best results were obtained with hydrophilic polymers such as Polyvinylpyrollodine (PVP). Whereas, hydrophobic polymer like PDMS failed to generate any response. This could be attributed to the fact that hydrophilic polymers could retain moisture which in-turn facilitates acid-base chemistry of dye and ammonia exposure. The FO sensor produced considerable signal change within 30 seconds of ammonia exposure. Increasing the exposure time further produced smaller changes and reached saturation. Therefore, 30s was considered as ideal response time of the FO sensor. In contrast to literature for substrate based fluorescent detection platforms [4], FO sensors have higher sensitivity due to optical signals. This is also evident in our Figure 2(a), wherein we could sensitively detect NH_3 concentration as low as 500ppb. The sensitivity response curve Figure 2(d) of the FO sensor exhibited a polynomial function which could be attributed to enhancement factor with varying the concentration of ammonia from 500ppb to 5ppm range. Nonetheless, the fabricated FO sensor performed well at lower concentrations. The sensor shows repeatable fluorescence on exposure to ammonia which is represented as bar graph in Figure 2 (e). These results conclusively show potential of developed FO sensor for sensitive detection of TVB-N for monitoring spoilage.

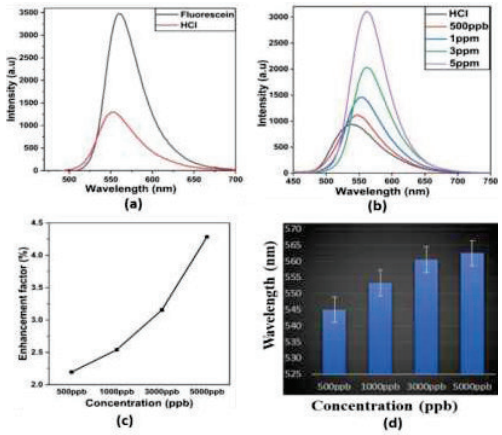

Figure 2: (a) Shows the fluorescence signal with quenching effect with HCl, (b) emission spectra of fluorescein composite with ammonia exposure, (c) Sensitivity response curve of NH_3, (d) Represents bar graph of ammonia sensing with fluorescein dye.

4. References

[1] Chun, Hae-Na, et.al." Food science and biotechnology 23.5, 1719-1725(2014).

[2] Getu et.al "Post-harvesting and major related problems of fish production." Fisheries and Aquaculture Journal 6.4 (2015)

[3] Jairath, Gauri, et al. "Biogenic amines in meat and meat products and its public health significance: A review." Journal of Food Science and Technology 52.11, 6835-6846 (2015).

[4] Lei, Jincan, et al. "Detection of ammonia based on a novel fluorescent artificial nose and pattern recognition." Atmospheric Pollution Research 7.3, 431-437 (2016).

[5] Staneva, et.al. "Optical sensor for aliphatic amines based on the simultaneous colorimetric and fluorescence responses of smart textile." Journal of applied polymer science 106.3, 1950-1956 (2007).

Micropatterning of Semi-Conducting Polymer Using Microbubble Lithography

Anand Dev Ranjan[1], Rakesh Sen[2], Basudev Roy[3], Soumyajit Roy[2], Goutam Dev Mukherjee[1], Ayan Banerjee[1]*

[1]Department of Physics, IISER Kolkata, Nadia, West Bengal, 741246
[2]Department of Chemistry, IISER Kolkata, Nadia, West Bengal, 741246
[3]Department of Physics, IIT Madras, Chennai, India, 600036
Author's Email: ayan@iiserkol.ac.in

Abstract: The development of plastic electronics requires the patterning of organic polymers in micro dimensions. Traditional top-down lithography is expensive economically and wastes a lot of materials. Here, we present an in-situ patterning technique called microbubble lithography (MBL) [1] for patterning dispersed organic polymers in micro dimensions. We selected poly(3,4-ethylenedioxythiophene) polystyrene sulfonate (PEDOT:PSS) [2], a well studied semiconducting organic polymer, for the proof of concept despite the method's broad application. EDAX and IV characteristics are used to confirm the elemental composition and continuity of the PEDOT:PSS patterns. This paves the way for the development of microelectronics devices using MBL.

Keywords: Micropatterning, Optical tweezers, Semi-conducting polymer, Microbubble lithography, PEDOT:PSS.

1. Introduction

One of the current generation's most pressing interests is the development of transparent and plastic electronics. For this development, the conventional metal presents a challenge because it is neither transparent nor flexible in smaller dimensions. Organic polymers can be formed into thin films that are transparent and flexible since they are available in solution form. These thin films can be used to create micropatterns by employing top-down approaches. The typical top-down technique is used to etch out the desired designs, but it causes significant material waste [1]. In addition, developer solutions used in top-down fabrication contain harsh chemicals that are harmful to the environment and are therefore less suitable for use in biomedical applications. Therefore, we require a technique that produces micropatterns of organic polymers in their solution state without the use of additional doping agents or harsh chemicals. This will lower their price, broaden their biological applications, and make it possible to pattern them in smaller dimensions, which is required for the production of electronic chips. To solve these problems, we employed a bottom-up technique called microbubble lithography (MBL).

MBL, a distinctive, affordable, and yet widely applicable technique, relies on the formation of a microbubble upon optical illumination to fabricate patterns over very small dimensions ranging from 2 μm to 100 μm on transparent substrates [1]. Metal nanoparticles [3], polymers [4], and soft oxometalates (SOM) [5] have all been patterned using MBL. Even though conducting patterns could already be seen with this technique, the substance that was deposited wasn't entirely organic. We discovered that organic polymers like PEDOT:PSS can be patterned using the MBL in the form of micro dimensional patterns. This opens up great opportunities for the creation of flexible electronics and heterostructures that could one day be used to create electrical devices using conducting polymers.

2. Results and Conclusion

The patterning experiment using MBL is conducted using an optical tweezer. A 10 μl sample of PEDOT:PSS purchased from Sigma Aldrich is placed inside the sample chamber of the optical tweezers. When the laser is focused on the sample plane where PEDOT:PSS dispersion is present, a microbubble nucleates as a result of the high absorptivity of the PEDOT:PSS. The translation of this microbubble leads to the deposition of the dispersed material at the base of the bubble [1]. This translation process can be continued as long as a pattern of desired shape and size is obtained on the substrate. The size and width of the patterns can be easily controlled by varying the laser

power and exposure time of the laser. As the laser is passed through a high numerical aperture objective where the typical focal spot width is in um's. This um spot eventually leads to formation of patterns in that dimension. In order to minimise the heating effect changes to the PEDOT:PSS low laser power has been used for the patterning experiment. The typical laser power varies from 10 mW to as low as 3 mW at the focal plane of the sample chamber. The patterned PEDOT:PSS with laser power 20 mW is shown in Fig 1(a).

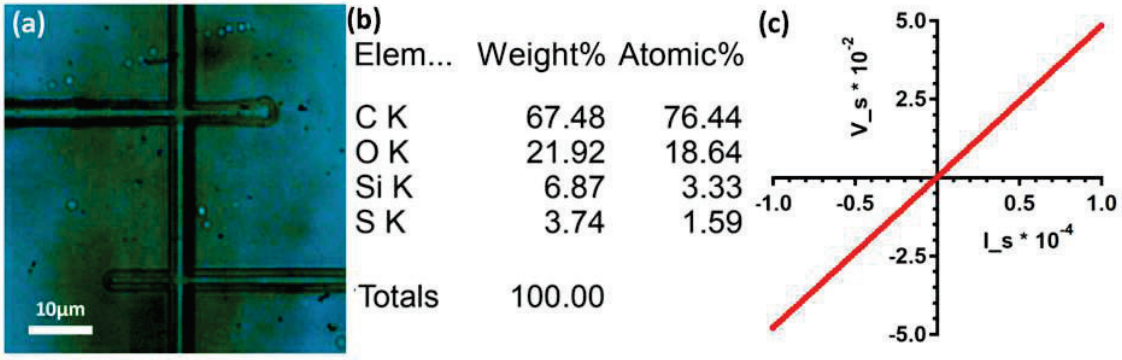

Fig. 1: (a) PEDOT:PSS pattern formed using MBL (b) the elemental composition of the patterned PEDOT:PSS using EDAX (c) the IV characteristic of the patterns proving the patterns to be continuous

Now in order to confirm if the patterned material is indeed PEDOT:PSS, we performed energy dispersive x-ray spectroscopy (EDAX) to check for the elemental composition of the patterns. As shown in Fig 1 (b), the patterned PEDOT:PSS contains all three of the elements found in the PEDOT:PSS, namely Carbon, Oxygen, and Sulphur. The Silicon present in the EDAX is due to the glass substrate where the patterns are formed.

The continuity of the circuit is among the most crucial factors to take into account while designing a circuit. Therefore, it is essential to confirm the pattern's continuity if we intend to use them for any electronic application. As a result, we also performed an IV measurement on the PEDOT;PSS patterns formed in the Hall-bar configuration as shown in Fig. 1 (a) to determine if the patterns are continuous. A four probe configuration is created by connecting two of the pattern's terminals to a continuous current source and measuring the potential difference at the pattern's other two arms. The linear IV characteristics, as illustrated in Fig. 1(c) confirms the continuous nature of the patterns.

We successfully demonstrate the patterning of a semiconducting organic polymer PEDOT:PSS using a bottom-up self-assembly technique (MBL). The EDAX and IV characteristics further confirm the elemental composition and the continuity of the patterns. Because the patterns are continuous and in micron dimensions, they can be easily employed for the development of microcircuits. They are particularly appropriate for bio electronics applications because the procedure doesn't include etching or doping with any harsh chemicals.

3. References

[1] Ghosh S, Ranjan AD, Das S, Sen R, Roy B, Roy S, Banerjee A., "*Directed self-assembly driven mesoscale lithography using laser-induced and manipulated microbubbles: complex architectures and diverse applications*", Nano letters 21.1 (2020)

[2] Fan X, Nie W, Tsai H, Wang N, Huang H, Cheng Y, Wen R, Ma L, Yan F, Xia Y. "*PEDOT: PSS for flexible and stretchable electronics: modifications, strategies, and applications*", Advanced Science. 2019 Oct;6(19):1900813.

[3] Jin CM, Lee W, Kim D, Kang T, Choi ,"*Photothermal convection lithography for rapid and direct assembly of colloidal plasmonic nanoparticles on generic substrates"*, Small. 2018 Nov;14(45):180305.

[4] Ghosh S, Das S, Paul S, Thomas P, Roy B, Mitra P, Roy S, Banerjee A. "*In situ self-assembly and photopolymerization for hetero-phase synthesis and patterning of conducting materials using soft oxometalates in thermo-optical tweezers*", Journal of Materials Chemistry C. 2017;5(27):6718-28.

[5] Roy B, Arya M, Thomas P, Jürgschat JK, Venkata Rao K, Banerjee A, Malla Reddy C, Roy S," *Self-assembly of mesoscopic materials to form controlled and continuous patterns by thermo-optically manipulated laser induced microbubbles",* Langmuir. 2013 Nov 26;29(47):14733-42.

Electromagnetic focusing through a tilted stratified medium

Sauvik Roy
Department of Physical Sciences, IISER-Kolkata, Mohanpur 741246, India
sauvikroy3388@gmail.com
Nirmalya Ghosh
Department of Physical Sciences, IISER-Kolkata, Mohanpur 741246, India
nghosh@iiserkol.ac.in
Ayan Banerjee
Department of Physical Sciences, IISER-Kolkata, Mohanpur 741246, India
ayan@iiserkol.ac.in
Subhasish Dutta Gupta
School of Physics, Hyderabad Central University, India
sdghyderabad@gmail.com

Abstract: In the recent past optical tweezers incorporating a stratified medium have been exploited to manipulate the translation and rotation of mesoscopic particles. In this paper we study the other aspect of fundamental interest, namely, the interplay of the spin and orbital angular momentum (SAM and OAM, respectively) densities to reveal an enhanced spin-orbit coupling originating from tight focusing due to high NA objective and the medium stratification. Furthermore we consider a tilted system with a broken axial symmetry to reveal additional control on transverse spin and Belinfante momentum.
Keywords: Electrmagnetic focusing, broken symmetry, titlted stratified medium, transverse SAM .

1. Introduction

It has been known for decades that free space propgation of light is accompanied by intrinsic spin and orbital angular momentum [1] [2], classically associated with the circular polarization state and the evolution of the wave vector, respectively. Although the presence of SAM and OAM in any electromagnetic field is general in nature, their separate manifestations - both experimentally and analytically - for arbitrary field configurations is very difficult. For an elliptically polarized plane wave or a paraxial Gaussian beam, the spin angular momentum (SAM) is determined by the helicity $\sigma(-1 \leq \sigma \leq 1)$of the beam. However, higher order paraxial beams, having complex amplitude and phase structure, carry orbital angular momentum - that can have both intrinsic and extrinsic nature [3] [4]. Interactions between these two types of optical momenta with drastically different physical connotations and properties is referred to as Spin-Orbit interactions (SOIs) of light. SOI can be widely

Recent studies on the SAM and OAM for fields at the nano- and mesoscopic scale with high nonparaxiality [5] [6] and/or inhomogeneity reveal that there exists a component of SAM that is surprisingly independent of the helicity of the input light and is also non-collinear with the wave vector. This extraordinary SAM in evanescent waves produced due to transverse modes confined in waveguides has already found applications in futuristic devices. Recent studies also predict the presence of transverse SAM (TSAM) in other non-evanescent, structured wavefields, such as tightly focused light beams in free space. TSAM is a consequence of the presence of a longitudinal component of the light field that leads to transverse components in the total momen- tum of light - both canonical and spin [1]. Understandably, TSAM is enhanced when the longitudinal component is increased - which is the case for the generation of evanescent waves or tight focusing and scattering. However, to the best of our knowledge, the dependence of the TSAM on processes that break geometrical symmetry while the light propagates in an optical medium has not been studied. Such a breaking of symmetry may be simply realized by inserting a refractive index (RI) stratified medium in the path of tightly focused light and tilting the medium with respect to the beam propagation direction. In this paper, we present an in-depth theoretical analysis and simulations on the generation of TSAM in such a system, where a tightly focused paraxial Gaussian laser beam is incident on a RI stratified mediumobliquely, this breaking the axial symmetry for all input field distributions.

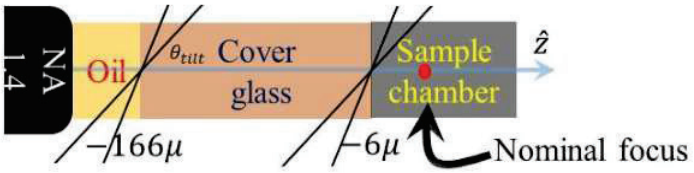

Fig. 1: Schematic diagram of tilted stratified medium used for simulation..

2. References

[1] K. Y. Bliokh, A. Y. Bekshaev, and F. Nori, Extraordinary momentum and spin in evanescent waves, Nature Communications **5**, 1 (2014).
[2] M. V. Berry, Optical currents, Journal of Optics A: Pure and Applied Optics **11**, 094001 (2009).
[3] A. T. O'Neil, I. MacVicar, L. Allen, and M. J. Padgett, Intrinsic and extrinsic nature of the orbital angular momentum of a light beam, Phys. Rev. Lett. **88**, 053601 (2002).
[4] S. Saha, N. Ghosh, and S. D. Gupta, Transverse spin and transverse momentum in structured optical fields, In digital Encyclopedia of Applied Physics, Wiley-VCH Verlag GmbH & Co. KGaA (Ed.). https://doi.org/10.1002/3527600434.eap818 (2019).
[5] A. Aiello, P. Banzer, M. Neugebauer, and G. Leuchs, From transverse angular momentum to photonic wheels, Nature Photonics **9**, 789 (2015).
[6] D. Pal, S. D. Gupta, N. Ghosh, and A. Banerjee, Direct observation of the effects of spin dependent momentum of light in optical tweezers, APL Photonics **5**, 086106 (2020).

Study of Hybrid Optomechanical System containing Multiple Quantum Dots

Vijay Bhatt[1], Surabhi Yadav[2], Pradip K. Jha[3*], Aranya B. Bhattacherjee[2]

1 Department of Physics and Astrophysics, University of Delhi, New Delhi 110009, India

2 Department of Physics, Birla Institute of Technology and Science, Pilani, Hyderabad Campus, Hyderabad - 500078, India

3 Department of Physics, DDU College, University of Delhi, New Delhi 110078, India

corresponding *author mail: pkjha.physics@gmail.com*

Abstract: To analyse the hybrid optomechanical system made up of an ensemble of N quantum dots, a theoretical model is proposed (QDs). We investigate the bistability in a hybrid $\chi^{(3)}$ third order nonlinear optomechanical system. We further show that the bistability phenomena can be modified by tuning the system's parameters.

Keywords: Optomechanical; quantum dots; bistability;,absorption

1. Introduction

Cavity optomechanics has recently become a fast expanding field at the interface of quantum optics and nanoscience. Numerous studies have been conducted on the optomechanical system's (OMS) characteristics and uses [1-3]. In addition, a fascinating phenomena known as optical bistability has been researched in a number of optomechanical systems [4-8] which was experimentally seen in semiconductor microcavities [9]. A traditional approach to solving the situation with several quantum dots is described in ref. [10]. According to earlier studies, OB may be observed using just one QD [11-12] when the QD is directly stimulated or pumped by an external laser, causing the system to enter bistability. We do not directly pump the QDs into our system. A kerr nonlinear medium is also additionally placed within the cavity. When a $\chi^{(3)}$ medium is positioned inside a cavity, a lot of photons are created. There is a considerable nonlinear interaction between photons as a result of the $\chi^{(3)}$ medium. Additionally, a different investigation into the bistability of coupled double quantum dot systems (CDQDs) [13-14] discovered that the cavity field is bistable for high levels of cavity-dot coupling. The goal of this work is to compute bistability, and then it should be feasible to modify it by altering system parameters in order to improve switching performance.

2. Model and Hamiltonian

Figure 1 depicts the paradigm we covered in this paper. Microcavities are created using a set of Distributed Bragg mirrors (DBR). Between the cavity is a two-level QD system ensemble. As an added bonus, the cavity contains a nonlinear $\chi^{(3)}$ medium, which interacts with the QD ensemble by generating photons. In the rotating-wave approximation, the interaction Hamiltonian of the entire system, which consists of the quantum-dot ensemble and the $\chi^{(3)}$ medium is given as,

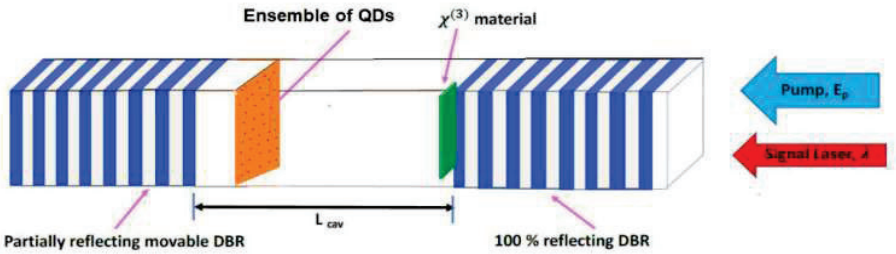

Fig. 1: The system, which consists of an ensemble of N quantum dots that are strongly linked inside the cavity, is shown schematically. Cavity mode is generated by DBR mirrors.

$$H = \sum_{i=1}^{N}[\Delta_{d_i}\sigma_+^i\sigma_-^i + \Omega_i(a^+\sigma_-^i + a\sigma_+^i)] + \Delta_c a^+a + \frac{\omega_m}{2}(p^2+q^2) + \varepsilon_p(a^+ + a) + \lambda(a^+e^{-i\delta t} + ae^{i\delta t}) - Ga^+aq + \alpha a^+a^+aa \quad (1)$$

The first term of the above Hamiltonian denotes the energy of QDs. Second term shows the interaction between cavity and dots. Third term shows the energy of the cavity mode. Fourth term is energy for the harmonic oscillator. Fifth and sixth term shows the interaction of pump laser and probe laser with cavity mode respectively. Seventh term shows the optomechanical coupling. The last term shows the Kerr nonlinear interaction with cavity photons.

3. Results and Discussion

Solving the Hamiltonian (1) described above in the steady-state condition, we get the bistability.

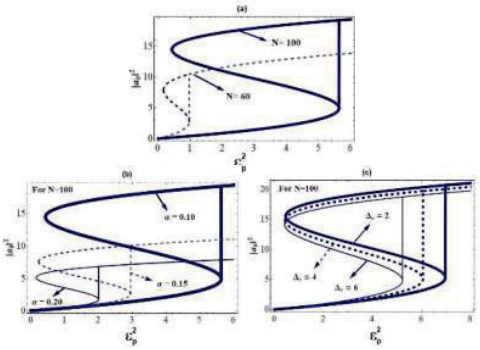

Fig. 2: The number of photons as a function of input pump power. (a)- For different number of QDs. (b)- For different values of kerr-nonlinear strength with fix N=100. (c)- For different values of cavity detuning with fix N=100

Figure 2(a) illustrates bistable behaviour in the quantity of photons as a function of input pump power. (With N = 100 and 60) (i.e., number of QDs). We see that the bistability window shrinks as the number of QDs decreases. Figure 2(b) displays the number of photons as a function of the input pump power for various third order nonlinear medium strength α values. We can see that for a fixed value of N=100, the number of photons reduces as the value of α grows, and the amount of pump power for which bistability occurs likewise lowers. For fix N=50, we note that on increasing the value of Δ_c, the input filed strength for which bistability occurs shift towards lower value. In figure 2(c), for fix N=100, we observe that the input field strength for which bistability occurs shifts towards a lower value as the value of Δ_c is increased. In order to achieve optical bistability with a reasonable value for $|a_0|^2$, we must choose an optimal value for α and Δ_c.

As a result, we are able to understand how various system parameters impact the system's optical switching characteristics and infer that careful attention to these factors is necessary for the system to effectively serve as a "all-optical switch".

References

[1] T. J. Kippenberg and K. J. Vahala, "Cavity optomechanics: backaction at the mesoscale," Science **321**, 1172–1176 (2008).
[2] P. Meystre, "A short walk through quantum optomechanics," Ann. Phys. **525**, 215–233 (2013).
[3] J. Kippenberg and K. J. Vahala, "Cavity opto-mechanics," Opt. Express **15**, 17172–17205 (2007).
[4] C. Jiang, H. Liu, Y. Cui, X. Li, G. Chen and X. Shuai Phys. Rev. A **88** 055801 (2013)
[5] E. A. Sete and H. Eleuch Phys. Rev. A **85** 043824 (2012).
[6] B. Sarma and A. K. Sarma J. Opt. Soc. Am. B **33** 7 (2016).
[7] V. Bhatt, Sabur A. Barbhuiya, Pradip K. Jha and Aranya B. Bhattacherjee, J. Phys. B: At. Mol. Opt. Phys. **53** 155402 (2020).
[8] V. Bhatt, Surabhi Yadav, Pradip K. Jha and Aranya B. Bhattacherjee, J. Phys.: Condens. Matter **33** 365302 (7pp) (2021)
[9] A. Bass, J. P. Karr, H. Eleuch and E. Giacobino Phys. Rev. **69** 023809 (2004).
[10] Y. Peng, Z. Yu, Y. Liu, W. Zhang, H. Ye, Optics communications **324**, 172-177 (2014).
[11] J. Li, R. Yu, J. Liu, P. Huang, and X. Yang, Physica E **41**, 70 (2008).
[12] A. Majumdar et.al., Proceedings of SPIE - The International Society for Optical Engineering 7611 (2010)
[13] A. Mitra and R. Vyas Phys. Rev. A **81**, 012329 (2010)
[14] V. Bhatt, S. Yadav, Pradip K. Jha and Aranya B. Bhattacherjee, Photonics and Nanostructures - Fundamentals and Applications **51**(4) (2022) 101043.

CGH generation of 3D object from a single RGB image using Deep Learning

Arvind Kumar, Virendra Kumar, Bhargab Das, Raj Kumar*

CSIR-Central Scientific Instruments Organisation, Sector 30C, Chandigarh 160030, India
Corresponding author: raj.optics@csio.res.in

Abstract: Computer generated hologram (CGH) is a popular technique to represent three dimensional objects due to its advantages over conventional holography. Acquiring accurate 3D information and its processing is still a challenging task in CGH generation. Use of depth camera can resolve this but it increases setup complexity and processing time. In this paper, we propose Deep learning approach to generate CGH from a single RGB image. Use of Deep learning method for depth map calculation is cost effective and avoids limitations related with system calibration and camera range.
Keywords: Computer Generated Holography, Depth Map, Point-based Method, Deep Learning.

1. Introduction

CGH is a method of computationally calculating complex valued holograms that can reconstruct the same wave field as of real objects. CGH is preferred over conventional holography as it removes the necessity of complex optical setup and recording material. Due to these advantages, CGH has potential to be used in various applications such as augmented reality/virtual reality (AR/VR), 3D imaging, and Data storage. CGH modeling is the process of producing and processing point cloud by retrieving 3D information from any form such as depth map [1,2]. Processing of point cloud includes rotation, translation and transformation by removing noise or decreasing density of point cloud. Most common way of acquiring 3D information of a real world scene is through a depth camera [3]. Limitations of Depth camera for 3D depth map includes complex setup, limited range and increment in processing time. Deep Learning, whose performance has improved in recent years, is another method to calculate CGH [4]. In this paper we explore the use of Deep learning approach to generate CGH from a single RGB image.

2. Methodology

This study is focused on CGH generation of 3D objects using point based methods. CGH is generated using a single RGB image and the camera parameters. First step is to capture 3D information of objects. We used the Middlebury Stereo Dataset for RGB images [5]. 3D information is obtained from the depth map, which contains the distance of each pixel in grayscale value. A Deep Learning model named Midas is used to calculate the Depth map [6]. Depth map is further used to calculate real world coordinates of image points. This calculation requires a camera intrinsic matrix and parameters to map image points into real world points. Camera intrinsic matrix, K is as given below [7]:

$$K = \begin{bmatrix} f_x & 0 & c_x \\ 0 & f_y & c_y \\ 0 & 0 & 1 \end{bmatrix}$$

where f_x and f_y are focal lengths of the camera and c_x and c_y are optical centers in respective directions.
After calculating real world coordinates, a point cloud is created by placing all points together in a common coordinate system. Point cloud is a nice way to visualize the object and remove extra or unnecessary points from the objects. We removed points from the point cloud by two methods: uniform down sampling and statistical outlier. Uniform down sample function reduces total number of points by choosing every k^{th} point and discards rest points. Statistical outlier is used for removing noise in point cloud. It removes points having less neighbors than threshold value. We used point based approach to generate CGH due to its simplicity [8]. Point based method assumes that each point of the object acts as a spherical light source. Let there are *m* points with amplitude A_i in the object, which emits light towards the hologram plane at z = 0, the wave field of single object point $i(x_o, y_o, z_o)$ at hologram plane H (x, y) can be calculated as follows-

$$H(x,y) = \sum_{i=0}^{m} A_i \; exp\left(\frac{2\pi j}{\lambda}\sqrt{(x-x_0)^2 + (y-y_o)^2 + z_o^2}\right)$$

3. Results and Discussion

Reconstruction of objects from the generated CGH has been done numerically. Wavelength and pixel pitch used for CGH generation are 632 nm and 6.4 micron respectively. An object (Dice) is reconstructed at a distance of 50 cm and another object (Toy flower) is reconstructed at a distance of 45 cm from the hologram plane. The obtained results are shown in figure 1. Deep Learning based Depth map worked well in modeling of objects. Proper 3D modeling and preprocessing (including noise removal) of point cloud has been performed. Point cloud with a higher number of points leads to a clearer image but increases computation time drastically.

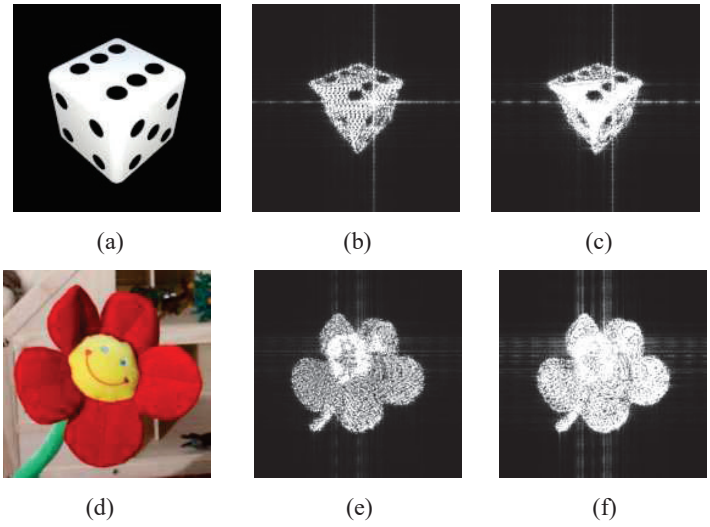

Fig. 1: (a) Original Dice object, (b) Dice reconstruction with 4862 points, (c) Dice reconstruction with 9015 points, (d)Original Flower toy, (e) Flower toy reconstruction with 12k points, (f) Flower toy reconstruction with 25 k points

4. Conclusion

In this paper, we report the use of Deep learning approach for calculation of CGH from a single RGB image. Techniques are used to reduce the number of calculation points in the depth map of the object's point cloud. Calculated CGHs are numerically reconstructed and the effect of number of calculation points is studied. The proposed technique may be used in various fields of three-dimensional imaging, such as holographic displays, AR/VR near-eye displays etc.

Acknowledgement: Authors thank Dr Sanjit Debnath, Dr Anuj Gupta and Ms Pradeep Bhanot for useful discussions.
Funding: CSIR, India (Project No.: MLP2014-CSIO).

5. References

[1]. Kazempourradi, Seyedmahdi, Erdem Ulusoy, and Hakan Urey. "Fast computer-generated hologram computation using rendered depth map image." Practical Holography XXXI: Materials and Applications. Vol. 10127. SPIE, 2017.

[2]. Zhao, Yu, et al. "Depth-layer weighted prediction method for a full-color polygon-based holographic system with real objects." Optics Letters 42.13 (2017): 2599-2602.

[3]. Marrugo, Andres G., Feng Gao, and Song Zhang. "State-of-the-art active optical techniques for three-dimensional surface metrology: a review." JOSA A 37.9 (2020): B60-B77.

[4]. Chenliang Chang, Dongchen Zhu, Jiamao Li, Di Wang, Jun Xia, and Xiaolin Zhang, "Three-dimensional computer holography enabled from a single 2D image," Opt. Lett. 47, 2202-2205 (2022)

[5]. Scharstein, Daniel, et al. "High-Resolution Stereo Datasets with Subpixel-Accurate Ground Truth." *German Conference on Pattern Recognition (GCPR 2014)*, 2014.

[6]. Ranftl, R., et al. "Towards Robust Monocular Depth Estimation: Mixing Datasets for Zero-shot Cross-dataset Transfer." *IEEE Transactions on Pattern Analysis and Machine Intelligence (TPAMI)*, 2020.

[7]. Joongseok Song, Changseob Kim, Hanhoon Park, and Jong-Il Park, "Practical system for generating digital mixed reality video holograms," Appl. Opt. 55, 5362-5371 (2016)

[8]. Waters, James P. "Holographic image synthesis utilizing theoretical methods." *Applied physics letters*, vol. 9, no. 11, 1966, pp. 405-407.

Filtering Techniques for Flame Temperature Measurement using Digital Holographic Interferometry

Nusrat Jabeen[1]*, Anil Kumar Nirala[1]
[1]*Biomedical Optics Lab, Department of Physics, Indian Institute of Technology (ISM) Dhanbad, Dhanbad 826004, Jharkhand, India*
*e-mail address: *nusratjabeen99@gmail.com*

Abstract: Digital holographic interferometry is a potential technique for the study of the flame temperature. However, the presence of noise in the interference phase map affects the measurement procedure adversely. In the present work, we are operating the interference phase map with two types of filters (isotropic and anisotropic median filter) for reduction of noise of phase map. Anisotropic median filtering is observed to reduce noise more efficiently in the phase map as compared with the isotropic median filtering. The temperature calculated by these techniques are found to be lying close to the temperature measured by the thermocouple.
Keywords: Digital holographic interferometry, flame, median filtering.

1. Introduction

Recent upsurge in the number of the fire catastrophes throughout the globe has drawn attention towards the study of flame. The temperature is a crucial thermodynamic parameter which can play a pivotal role in fire risk assessments and designing of fire safety equipment. Various contact and non-contact methods have been reported for measurement of flame temperature [1]. Optical techniques are non-invasive and have high accuracy and hence used widely for investigation of the flame temperature. Digital holographic interferometry (DHI) has been employed as a potential modality for flame temperature measurement [2]. However, the presence of noise in the interference phase map may hamper the accuracy of the measurement procedure. Phase maps are filtered through various filtering techniques to mitigate the noise. In the present work, we have used isotropic and anisotropic median filtering for noise reduction and the temperature is calculated subsequently.

2. Theory

A hologram contains the amplitude as well as phase information of the wave. The complex amplitude [3] of the reconstructed wave is given by eqn. (1)

$$A(m,n) = \frac{i}{\lambda d}\exp\left[-i\pi\lambda d\left(\frac{m^2}{N^2{\Delta x_1}^2}+\frac{n^2}{N^2{\Delta y_1}^2}\right)\right] X \sum_{p=1}^{N}\sum_{q=1}^{N} R(p,q)h(p,q)\exp\left[-i\frac{\pi}{\lambda d}(p^2{\Delta x_1}^2 + q^2{\Delta y_1}^2)X\exp\left[i2\pi\left(\frac{pm}{N}+\frac{qn}{N}\right)\right]\right] \quad (1)$$

where A (m, n) is the complex amplitude of the reconstructed wave for a point coordinate (m, n) in the plane of reconstruction, λ is the wavelength of the reconstruction beam, d is the distance of the object from the CCD sensor, $h(p,q)$ is the hologram function,(p,q) and (m,n) are the corresponding coordinates of a point in the hologram and image plane, respectively. The size of the hologram is N X N. The phase value can be extracted from the real and imaginary parts of the complex amplitude [3]. When a light ray enters a flame, it bends as a consequence of non-uniform refractive index of the medium. The phase change in the path of the light ray is used to measure temperature. We calculate the temperature T corresponding to refractive index n_r at a point r in the flame using Lorentz-Lorenz eqn. given by eqn. (2).

$$T = \frac{T_o}{\left[\frac{n_r - n_o}{n_o}\right]\left[1+\frac{2RT_o}{3PA}\right]+1} \quad (2)$$

T_o and P are the ambient temperature and pressure, respectively. R is the gas constant and A is the molar refractivity of air. The interference phase map is invaded by noise. In the present work, we are applying two types of median filtering on the phase map:

(a) Isotropic median filtering: In this technique, we use a kernel size of 3X3 for median filtering of the sine and cosine components of phase map.
(b) Anisotropic median filtering: Here, we use a kernel size of 7X3 for median filtering because the density of fringes is higher in the horizontal direction than in the vertical direction for the sample under investigation (flame).

3. Method

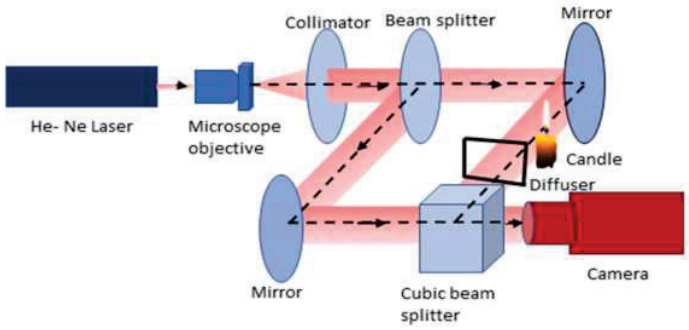

Fig. 1. Schematic of the experimental set up for recording a hologram

The schematic of the experimental set up used for the recording of a hologram is shown in the Fig. 1. In the present investigation, we record two holograms one in the presence and another in the absence of the flame.

4. Result

The phase difference between the phases of two holograms is calculated. The phase map is operated with isotropic and anisotropic median filtering techniques with same number of iterations. The speckle noise is observed to be reduced in the anisotropic filtered phase map. We extract line profile of phase map at a height of 1.0 cm above the base of the flame. Positions of minima in the line profile are located. The fringes are numbered from edge to the center of the flame [2]. The temperature is calculated for both of the isotropically and anisotropically filtered phase maps. Plot of temperature vs distance is shown in Fig. 2(c). The temperature profiles measured for both of the phase maps are found to lie in close vicinity to that of the temperature procured through the thermocouple.

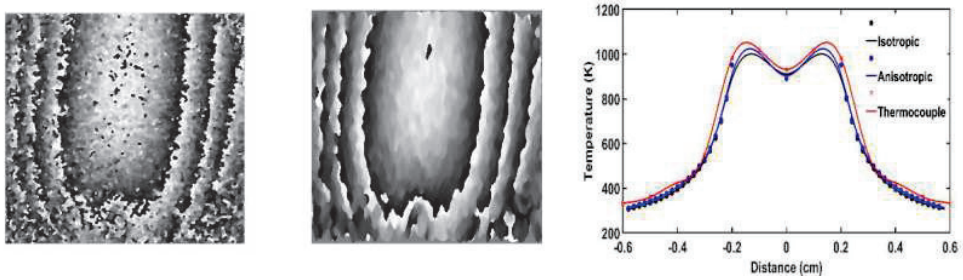

(a) (b) (c)

Fig. 2. (a) Isotropic filtered phase map (b) Anisotropic filtered phase map (c) Plot of temperature vs distance

5. Conclusion

The present investigation suggests that the phase map filtered with the anisotropic median filtering technique has evidently lesser noise than that of the phase map operated with isotropic filtering technique. Temperature measured through both the phase maps are in good agreement with the thermocouple.

6. References

[1] P. R. N. Childs, J. R. Greenwood, *and* C. A. Long**, "**Review of temperature measurement," Rev. Sci. Inst. **71**, 2959-2978 (2000).
[2] N. Jabeen and A. K. Nirala, "Digital holographic interferometry for temperature measurement of oil lamp flames with different wick thicknesses," Sust. Energy Tech. and Assessm.**52,** 101964, 2022.
[3] U. Schnars and W.P.U. Juptner, "Digital recording and numerical reconstruction of holograms," Meas. Sc. And Tech. **13**, R85-101 (2002)

Engineering the angular momentum dynamics of birefringent particles by spin-orbit interaction effects in a structured vector beam in optical tweezers

Ram Nandan Kumar,[1] Subhasish Dutta Gupta,[1, 2, 3] Nirmalya Ghosh,[1, *] and Ayan Banerjee[1, †]

[1]*Department of Physical Sciences, Indian Institute of Science Education and Research Kolkata, Mohanpur-741246, West Bengal, India*

[2]*School of Physics, Hyderabad Central University, India*

[3]*Tata Institute of Fundamental Research Hyderabad, India*

[*] nghosh@iiserkol.ac.in [†] ayan@iiserkol.ac.in

Keywords: Angular momentum, Transverse spin angular momentum of light, SOI

Abstract: The effects of spin-orbit interaction (SOI) - which couples the spin and orbital degrees of freedom of light - are not visible macroscopically, but lead to several exotic phenomena in scattering, imaging, and tight focusing of light - often giving rise to interesting and unprecedented applications at mesoscopic length scales. The SOI has been particularly useful in inducing intriguing rotational dynamics in particles confined under optical tweezers, with both spin motion around the particle axis and orbital motion around the beam axis being generated rather routinely. Here, we use SOI of light generated by tight focusing in optical tweezers has been extensively used in inducing rotational motion in trapped mesoscopic particles both about the particle axis (spin), and the beam axis (orbital rotation). However, generating both at different spatial regions in an optical trap remains a challenge. Here, we present a design where we employ structured vector beams with no intrinsic angular momentum to generate both orbital motion and the experimentally elusive transverse spin at spatially separated regions in an optical trap. Thus, the large longitudinal field component generated by tight focusing of the radially polarized vector beam leads to a significant extrinsic orbital angular momentum off axis - which we utilize in an optical trap developed using a refractive index stratified medium in the light path to trap and rotate multiple birefringent particles around the beam axis. In addition, the longitudinal field component at the beam center generates transverse spin angular momentum, whose effects we unambiguously observe on a birefringent particle trapped at the beam center, since the longitudinal spin angular momentum is zero in that region. Our experiments demonstrate the effectiveness of SOI in engineering spatially separated spin dynamics of mesoscopic.

The spin motion can be induced using tightly focused spin-polarized (left or right circular polarization) Gaussian beams which exchange their longitudinal spin angular momentum with birefringent micro-particles, while orbital motion is typically induced using beams that carry intrinsic angular momentum (OAM). Recently, such OAM-carrying beams have also been used to demonstrate very high rotation speeds in trapped particles [1], particle cooling [2], and in measuring the angular velocity of spinning objects. Other than these standard techniques, interesting manifestations of SOI - such as the spin-Hall effect - have also been used to induce spin motion using a linearly polarized Gaussian beam passing through a refractive index (RI) stratified medium [3], while orbital motion has been observed by tightly focusing a circularly polarized Gaussian beam – again through a RI stratified medium - to generate large transverse momentum which even carried signatures of the elusive Belinfante spin [4]. Recently, experimental evidence of transverse spin angular momentum - a direct consequence of the generation of a longitudinal

component of the electric field - has been obtained in the case of evanescent fields in the form of rotation of dielectric particles. In addition, the subtle effects of spin-orbit interaction that the transverse spin angular momentum generates in vortex fields have also been demonstrated [5], thus promising even more interesting and subtle applications of these exotic properties of light. However, obtaining signatures of both spin and orbital motion in spatially separated regions in an optical trap are difficult to obtain experimentally. Structured beams hold special significance in optics due to their wide applications in lossless propagation, near-field microscopy [6], and even in metrology [1]. Such beams are also rather useful in studies of SOI due to the intrinsic orbital angular momentum (OAM) they usually carry, which couples with the spin polarization states of the beams to lead to large effects of SOI, which have been probed using optical tweezers typically in the form of rotation of trapped mesoscopic particles. However, vortex beams of finite topological charge possess a phase singularity on the beam axis leading to zero field intensity. Thus, interesting dynamics are observed for particles confined in the high-intensity lobes around the beam axis in optical tweezers.

[1] M. P. Lavery, F. C. Speirits, S. M. Barnett, and M. J. Padgett, Science 341, 537 (2013).
[2] Y. Arita, M. Mazilu, and K. Dholakia, Nature communications 4, 1 (2013).
[3] B. Roy, N. Ghosh, A. Banerjee, S. D. Gupta, and S. Roy, New Journal of Physics 16, 083037 (2014).
[4] D. Pal, S. D. Gupta, N. Ghosh, and A. Banerjee, APL Photonics 5, 086106 (2020).
[5] Z. Shao, J. Zhu, Y. Chen, Y. Zhang, and S. Yu, Nature communications 9, 1 (2018).
[6] B. Sick, B. Hecht, and L. Novotny, Physical Review Letters 85, 4482 (2000).

Comparison of LIBS and laser-induced fluorescence assisted LIBS for phosphorus quantification in soil

Shweta Soni[1, 2], Jan Viljanen[2], Pavel Veis[1]
[1]*Comenius University, FMPH, Mlynska dolina F2, 842 48 Bratislava, Slovakia*
[2]*Photonics Laboratory, Physics Unit, Tampere University, FI-33101 Tampere, Finland*
shweta.soni@fmph.uniba.sk

Abstract: Precise quantification of phosphorus in soil plays critical role in development and growth of plants. Deficiency of phosphorus in soil slows down the plant's growth and, on the other hand, excess phosphorus in soil will lead to problems. Therefore, constant monitoring and quantification of phosphorus in soil is essential. In this work, the two analytical approaches; laser-induced breakdown spectroscopy (LIBS) and laser-induced fluorescence assisted LIBS is compared for precise quantification of phosphorus in soil. The calibration curves are plotted to evaluate the detection limit. Compared results demonstrate improvement in sensitivity and S/N ratio in the signal originated from LIF-LIBS measurements.

Keywords: LIBS, LIF-LIBS, soil, phosphorus quantification

1. Introduction

Soil is the fundamental component of ecosystem and plays important role in plant's growth [1,2]. Clay soil holds water more efficiently than any other types of soil and therefore, is very beneficial for plants growth. Soil contain many minerals and elements among which phosphorus is responsible for plants growth [3]. Laser-induced breakdown spectroscopy (LIBS) is a micro-destructive, contactless, rapid analytical tool and can be a suitable candidate for such analysis. LIBS utilizes a pulsed laser to ablate the sample and to create plasma. The electromagnetic plasma emission contain elemental information about the sample and can be collected for spectral analysis. However, LIBS quantification of phosphorus in natural resources is very difficult due to its weak spectral emission [3-5]. To improve LIBS emission for phosphorus detection, laser-induced fluorescence (LIF) can be used for excitation of atomic phosphorus emission in LIBS signal [5]. Laser-induced fluorescence is considered as a individual elemental detection technique with high sensitivity. In LIF technique, atom or molecule gets excited to a higher energy level by the absorption of a specific wavelength of laser light. After few nanoseconds, the excited species de-excite resulting in the spontaneous emission of light classified as fluorescence.

2. Materials and methodology

2.1. Samples

Eight different clay soil samples with different phosphorus content collected from different places in Finland were analyzed. For calibration curve, the phosphorus concentration in samples was already measured by chemical analysis. The sample was pressed into pellets to obtain smooth and regular surface for the ablation.

2.2. Experimental Setup

The LIBS measurements were performed by an standard Q-switched Nd:YAG laser, operating at third harmonic frequency (355 nm, Quantel) with repetition rate of 10 Hz, for sample ablation and plasma creation while for LIF-LIBS analysis, the laser induced plasma is spatially synchronized with another laser pulse generated by a tunable OPO laser operating at 253.6 nm for the LIF-excitation of phosphorus line at 213.5 nm. The plasma emission is transmitted via an optical fiber to the spectrometer for analysis. The spectrometer is equipped with an iCCD camera for signal detection. The LIBS spectrum was recorded at 300 ns gate delay and 2µs of gate width while the LIF-LIBS spectrum is acquired at 57 ns of gate delay in addition to the inter-pulse delay of 2µs and with 200 ns of gate width. Detailed schematic diagram of experimental setup is illustrated in Fig. 1.

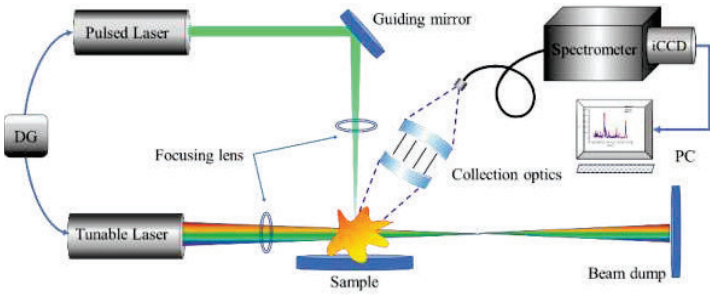

Fig 1. Schematic diagram of laser-induced fluorescence assisted LIBS

3. Preliminary results and conclusion

A significant improvement in signal to noise ratio (S/N) and sensitivity of LIBS was observed when used in combination with tunable OPO laser operating at 253.6 nm for laser-induced fluorescence assisted LIBS. The variation in intensity of phosphorus line at 213.55 nm with different excitation wavelength is demonstrated in Fig. 2 (a) while a typical compared spectrums are illustrated in Fig. 2 (b). In addition, quantitative analysis of phosphorus in soil will be performed using LIBS and LIF assisted LIBS. The limits of detection are evaluated from the calibration curves plotted for phosphorus line at 213.55 nm with a set of eight known samples.

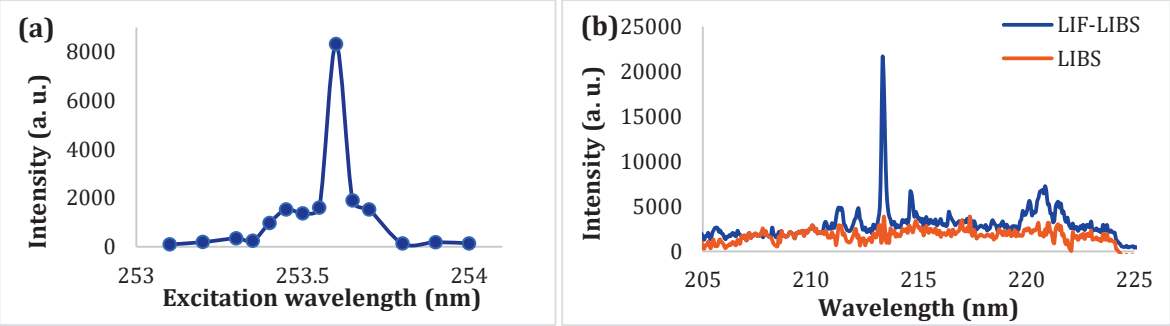

Fig 2. (a) variation in intensity of 213.55 nm line with different λexc **(b)** Comparison of LIBS and LIF-LIBS spectrum at gate delay of 2µs

4. Acknowledgement

The authors acknowledge the financial support from SRDA (APVV-16-0612, APVV-20-0111) and VEGA (1/0803/21, 2/0144/21). SS would like to acknowledge Comenius University grant (UK/95/2022, FMFI) and JV would like to acknowledge Academy of Finland (decision 338338).

5. References

[1] R. Prasad, & D. Chakraborty, D. "Phosphorus basics: Understanding phosphorus forms and their cycling in the soil, Alabama Coop. Ext. Syst. (2019).
[2] Saha, Jayanta K., Rajendiran Selladurai, M. Vassanda Coumar, M. L. Dotaniya, Samaresh Kundu, and Ashok K. Patra. "Soil and its role in the ecosystem." In Soil pollution-an emerging threat to agriculture, pp. 11-36. Springer, Singapore, 2017.
[3]Sánchez-Esteva, Sara, Maria Knadel, Rodrigo Labouriau, H. Rubæk Gitte, and Goswin Heckrath. "Total phosphorus determination in soils using laser-induced breakdown spectroscopy: evaluating different sources of matrix effects." Applied Spectroscopy 75, no. 1 (2021): 22-33.
[4] P.R. Villas-Boas, M.A. de Menezes Franco, L. Martin-Neto, H.T. Gollany, D.M.B.P. Milori. ''Applications of Laser-Induced Breakdown Spectroscopy for Soil Characterization, Part II: Review of Elemental Analysis and Soil Classification''. Eur. J. Soil Sci. 2019. 1–16
[5] Shen, X. K., H. Wang, Z. Q. Xie, Y. Gao, H. Ling, and Y. F. Lu. "Detection of trace phosphorus in steel using laser-induced breakdown spectroscopy combined with laser-induced fluorescence," Applied optics, 48(13), 2551-2558 (2009).

Dynamic holographic display using a portable digital holographic camera

Sonali Chakraborty[1], Raj Kumar[1,*]
[1]*CSIR-Central Scientific Instruments Organization, Sector 30C, Chandigarh-160030, India*
**Corresponding author: raj.optics@csio.res.in*

Abstract: A three-dimensional (3D) holographic video display is developed with a portable digital holographic camera incorporated with a reflective-phase-SLM which captures different perspective of an object to generate quasi-real-time dynamic holograms. Some reconstructed images are presented.
Keywords: Digital holographic camera, Holographic display, Fresnel propagation, Dynamic hologram.

1. Introduction

Holography generates realistic 3D scenes which are visible without aid of any special eyewear. Conventional holographic materials like silver halide, photopolymers have sufficiently small grain size for recording object information with sub-wavelength density which consequently generates large image area with high resolution. Nanophotonic phased array [1], metasurfaces [2,3] are also presently used as holographic materials. But these media are non-updatable and not capable of producing dynamic holograms. Photorefractive materials are being used these days to generate dynamic holograms [4] but with limited updating frequency resulting in a quasi-real-time video display. Wavefront modulators such as spatial light modulators (SLMs) can update holographic patterns for real-time 3D video generation but their space-bandwidth product (SBP), which determines the image area and the viewing angle, is limited by the pixel-pitch and pixel-number. Pixels of electronic media for recording and display of holograms couldn't be fabricated as small as the grain-size of conventional holographic media to till date with the present status of technology. Hence even ultra-high resolution SLMs are capable of producing only a small image area (a few tens of mm in maximum) with a narrow viewing angle (a few degrees only). The issues of small SBP have been resolved to some extent through pupil tracking [5], using holographic diffuser screen [6], use of a steering backlight unit to illuminate the display [7] etc. SBP of the display device may be increased by increasing number of pixels in large amount but then the size of the computer generated hologram (CGH) has to be increased accordingly which increases the amount of computation. Several algorithms are developed [8] to increase the computation speed but high-performance clustered processors are still required which causes huge computation cost and real-time CGH generation only feasible up to a certain extent.

In present work, a video is made with holographic frames acquired with a portable digital holographic camera [9] from a real and dynamic object. Hence the requirement of CGH generation is eliminated here. The phase distributions of the frames are displayed on a reflective-phase-SLM sequentially and illuminated with a s-polarized laser beam to implement reconstruction through Fresnel propagation for generating the 3D dynamic image.

2. Recording setup

The off-axis holographic setup inside the digital holographic camera (DHC) has a special lens arrangement comprised of a pair of concave and convex lens (as illustrated in Fig.1) which facilitates an effective field-of-view (FoV) beyond the constraint set by pixel-pitch of the recording media and wavelength of the light source. When there is no object inside the FoV of the camera, only reference beam is incident on the sensor. Whenever a diffuse object is placed inside the FoV, a Fresnel hologram is synthesized on the digital sensor of the camera. The light diffused by the object is collected by a concave lens to form a demagnified virtual image and a following convex lens collects the rays diffracting from the virtual image and forms a real image onto the sensor (CCD, Lumenera, Lt1265RM with 3376 (H) × 2704 (V) array of pixels and 3.1µm × 3.1 µm pixel-pitch). So the spatial frequencies generated on the hologram plane are less than spatial frequencies would have generated if the hologram has been captured directly from the object. This allows the sensor to record larger objects beyond the constraint of dimensions set by laboratory parameters. The FoV of the camera is thus enhanced than conventional holographic setup and the camera is capable of recording object of up to 90 mm of length. Therefore, there is no need to incorporate multiple CCD cameras and spatial multiplexing up to a considerable size of object [10].

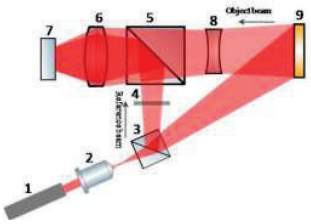

Fig.1. Schematic diagram of the DHC; the numbers in the figure denote:: 1: diode laser, 2: microscope objective, 3: beam-splitter -1, 4: neutral density filter, 5: beam-splitter-2, 6: convex lens, 7: sensor, 8: concave lens, 9: object.

3. Results and discussions

A bust in the FoV of the camera is given mechanical rotations using a rotatable stage and Fresnel holograms are captured at different orientations of the bust. After capture, holographic frames are numerically matched with the resolution of the SLM (1920 (H) x 1080 (V), pixel-pitch: 6.4 μm). Some still shots of the 3D video are given in Fig.2. The camera can also be rotated around an object with a movable stage in order to capture different perspectives. Presently we are working to increase the FoV of the camera and viewing angle of the SLM without increasing number of pixels.

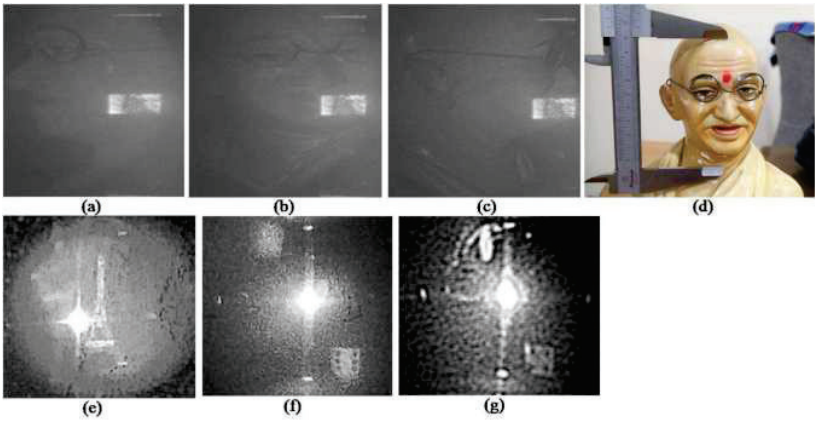

Fig.2.(a)-(c) Reconstructed images of different perspectives of the bust, (d)dimension of the bust is measured to be ≈ 90 mm, (e)-(f) reconstructions of a tower model and a dice through the SLM display.

4. Conclusion

We reported a technique, which could lead to development of a cost-efficient holographic display for dynamic objects and eliminates the computation cost and use of multiple CCDs or SLMs. Recording of dynamic holograms from real object instead of CGH generation makes the model feasible to develop a real-time display.

Funding: This research work is financially supported by the CSIR, India under the project MLP-2014.

5. References

[1] J. Sun, E. Timurdogan, A. Yaacobi, E. S. Hosseini, M. R. Watts , "Large-scale nanophotonic phased array" Nature 493, 195-199 (2013).
[2] X. Ni, A.V. Kildishev, V. M. Shalaev, "Metasurface holograms for visible light", Nature Communications 4, 2807 (2013).
[3] L. Huang et. al, "Three-dimensional optical holography using a plasmonic metasurface", Nature Communications, 4, 2808 (2013).
[4] P. A. Blanche et. al, "Holographic three-dimensional telepresence using large-area photorefractive polymer" Nature, 468, 80-83 (2010).
[5] R. Häussler, A. Schwerdtner, N. Leister, "Large holographic displays as an alternative to stereoscopic displays", in Proc. SPIE 6803 (2008).
[6] X. Sang et al., "Demonstration of a large-size real-time full-color three-dimensional display", Optics Letters, 34 (24), 3803-3805 (2009).
[7] J. An et. al, "Slim-panel holographic video display", Nature Communications, 11:5568 (2020).
[8] T. Shimobaba, T. Kakue, T. Ito, "Review of fast algorithms and hardware implementations on computer holography", IEEE Transactions on Industrial Informatics, 12, 1611-1622 (2016).
[9] R. Kumar, G. Dwivedi, O. Singh, "Portable digital holographic camera featuring enhanced field of view and reduced exposure time", Optics and Lasers in Engineering, 137, 106359 (2021).
[10] M. Kujawinska, et al., "Multiwavefront digital holographic television." Optics Express 22, 2324-2336 (2014).

All-solid-state, Tunable, Narrowband Laser for Spectroscopic Applications

Siba Prasad Sahoo[1, 2, a)], Swarupananda Pradhan[1, 2], Jaya Mukherjee[1,2], V. S. Rawat[1, 2]
[1]*Homi Bhabha National Institute, Anushaktinagar, Mumbai 400094*
[2]*Beam Technology Development Group, Bhabha Atomic Research Centre, Trombay, Mumbai 400085*
[a)] Corresponding author: *sibaps@barc.gov.in*

Abstract: An all-solid-state, widely tunable, narrowband visible laser was developed using Cr:forsterite and BBO crystal. A wide tuning range of 580 nm to 662 nm was achieved with a laser linewidth of 0.8 nm. The laser linewidth was further narrowed down to ~ 250 fm using intracavity etalons in which single longitudinal mode (SLM) oscillation was established. Wavelength and linewidth stability of ~ 100 MHz of ~ 67 MHz were achieved respectively. The spatial profile of SLM laser output closely matches the Gaussian Profile (> 90%). This laser has potential applications in various spectroscopic as well as the laser-based process.

Keywords: All-solid-state laser, Single longitudinal mode (SLM), Cr:forsterite, Second harmonic generation (SHG)

1. Introduction

All-solid-state, tunable, pulsed, narrowband laser in the visible region has immense applications in the field of spectroscopy, laser isotope separation, biomedicine, photolithography, and remote sensing. Cr:forsterite is a widely tunable solid-state laser in the near-infrared (NIR) region having a tuning range from 1130 to 1370 nm. A major part of the visible spectrum can be generated from this crystal through its second harmonic generation (SHG). The SHG of the Cr:forsterite laser bridges the wavelength gap between the second harmonic and fundamental wavelength of the Ti:sapphire laser. Hence, by combing these two crystals an all-solid-state laser system can be developed which can generate a wide wavelength range from near UV to NIR. The narrowband, tunable operation of Ti:sapphire laser system along with its SHG is well studied and developed [1-3]. However, there is limited literature available on narrowband, pulsed tunable Cr:forsterite laser in the visible region [4-7]. In this paper, we have reported the development of an all-solid-state laser in the visible region that can be tuned from 580 to 662 nm. The linewidth of the laser was narrowed down and single longitudinal mode (SLM) oscillation was established having a linewidth of ~ 250 fm.

2. Experimental Setup

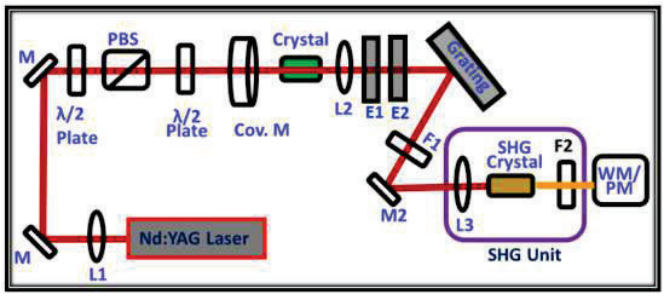

Fig 1: Schematic of the experimental setup of Cr:forsterite laser cavity.

The schematic of the experimental setup of the narrowband tunable Cr:forsterite laser cavity is shown in Fig. 1 in which a Cr:forsterite crystal having a dimension of 5 mm x 5 mm x 12 mm was used as a gain medium. The crystal has an absorption coefficient of 1.47 cm-1 at 1064 nm for polarization along the b-axis (E∥b) and a figure of merit (FOM) of 17. A Nd:YAG laser beam of 8 mm diameter, 10 ns pulse width, and 10 Hz pulse repetition rate was used to pump the crystal. The narrowband tunable cavity was set up using a concave mirror of 100 mm radius of curvature, and a 600 lines/mm grating in Littrow configuration. The concave mirror has a reflectivity of ~ 99% at 1150 -1350 nm and a transmission of 98% at 1064 nm. For SLM generation two Fabry Perot etalons (E1 and E2) were used inside the Littrow cavity. Etalon E1 has a free spectral range (FSR) of 300 GHz and a Finesse of 28 at 1130-1370 nm, whereas etalon E2 has an FSR of 15 GHz and Finesse of ~ 30 at 650 nm. The SHG of the tunable Cr:forsterite laser was carried out using a non-linear BBO crystal having a dimension of 4 mm x 4mm x 10 mm. The crystal is cut at $\theta = 210$, $\Phi = 900$ for type I phase matching. The beam coming from the SHG unit is characterized in terms of its energy, spectral, temporal, and spatial characteristics.

3. Results and Discussion

The tuning range of the SHG Cr:forsterite laser is shown in Fig. 2 (a) which shows the laser can be tuned from 580 nm to 662 nm with a peak wavelength of 622 nm. At the peak wavelength maximum output energy of 38 μJ is obtained which gives the second harmonic conversion efficiency of ~ 10 %. The maximum output energy 46.5 μJ was obtained for an absorbed pump pulse energy of 8.5 mJ. The FWHM linewidth of the laser was measured using a laser spectrum analyzer (LSA) and found to be 0.8 nm. The SLM output was monitored through a wavelength meter (WS-7) as shown in Fig.2 (b) which gives a linewidth of ~ 250 MHz (250 fm at 605.34 nm). The SLM behavior is observed to be stable for more than 40 minutes in free running mode (without any active feedback). The wavelength and linewidth stability of the laser was measured to be ~ 100 MHz, and 67 MHz respectively.

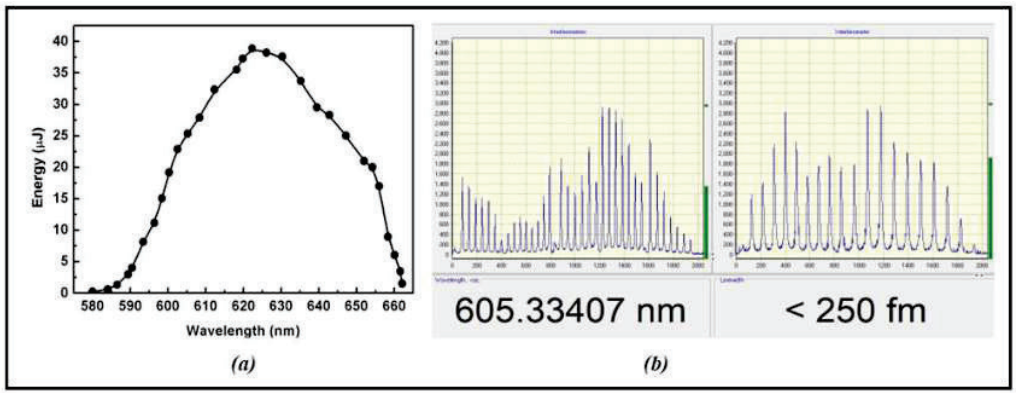

Fig 2: (a) Tunning range of SHG Cr:forsterite laser (b) Wavelength and linewidth of SLM Cr:forsterite laser

The spatial beam profile and temporal pulse profile of the SLM Cr:forsterite laser is shown in Fig. 3 (a) and Fig. 3 (b) respectively. The spatial beam profile closely matches the Gaussian beam profile (> 90%). The temporal pulse profile shows that the laser has pulse width (FWHM) of 8.5ns.

The above attributes of the laser make it a potential candidate that can be used in various spectroscopic applications as well as in different laser-based process.

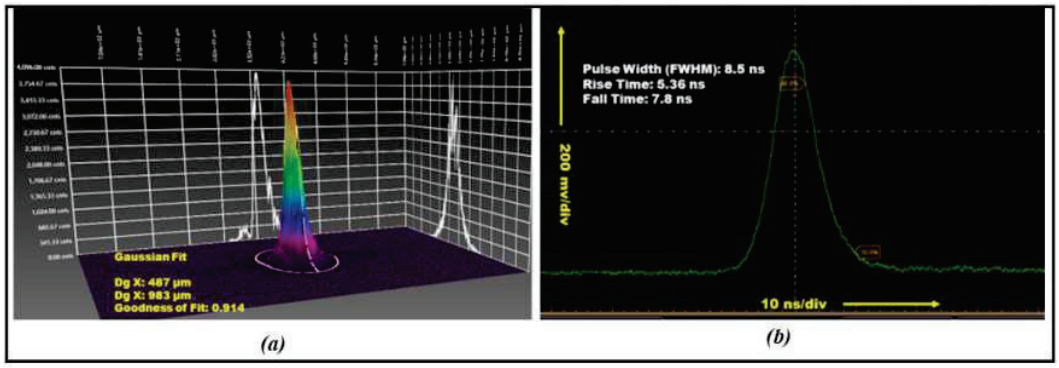

Fig.3: Spatial beam profile and temporal pulse profile of SLM Cr:forsterite laser

4. References

1. P. F. Moulton, "Spectroscopic and laser characteristics of Ti:Al_2O_3", J. Opt. Soc. Am. B, **3**, 125-133 (1986).
2. K. W. Kangas, D. D. Lowenthal, and C. H. Muller, "Single-longitudinal-mode, tunable, pulsed Ti:sapphire laser oscillator", Opt. Lett. **14**, 21-23 (1989).
3. Nebel and R. Beigang, "External frequency conversion of cw mode-locked Ti:Al2O3 laser radiation", Opt. Lett. **16**, 1729-1731 (1991).
4. V. Petricevic, S.K. Gayen, and R.R. Alfano, "Laser action in chromium-doped forsterite", Appl. Phy. Lett. **52**, 1040-1042 (1988).
5. J. C. Diettrich, I. T. Mckinnie, and D.M. Warrington, "Tunable high-repetition-rate visible solid-state lasers based on intracavity frequency doubling of Cr:forsterite", IEEE J. of Quant. Electr. **35**, 1718-1713 (1999).
6. I. T. Mckinnie, and A. L. Oien, "Narrow linewidth 578 nm light generation using frequency-doubling with a waveguide PPLN pumped by an optical injection-locked diode laser", Opt. Comm. **141**, 157-161 (1997).
7. Siba Prasad Sahoo, V.S. Rawat, Jaya Mukherjee, S. Pradhan, "Investigation of a polarization-based Cr:forstrite laser, Journal of Modern Optics", Journal of Modern Optics, 68 (2021) 707-716., (2021).

Highly uniform coatings of photopolymer using digital film applicator for holographic applications

Heena, Kamlesh Kumar, Bhargab Das, Raj Kumar*
CSIR-Central Scientific Instruments Organisation, Sector 30C, Chandigarh 160030, India
Corresponding author: raj.optics@csio.res.in

Abstract: In the present study, a red sensitive dye consisting photopolymer based on polyvinyl alcohol/acrylamide is fabricated for the holographic applications. The work focuses on the fabrication of a uniform photopolymer films of different sizes. The films are prepared using digital film applicator at different coating speed. It is observed that the obtained film thickness depends on the coating speed. Thicker films are obtained at the lower speed of the coater. The film prepared using this method have good uniform surface and thickness that can contribute to better diffraction efficiency values.
Keywords: Photopolymer, diffraction efficiency, automatic digital film applicator.

1. Introduction

Photopolymers are fast becoming one of the most popular recording media for holographic applications for a variety of reasons; they have excellent holographic characteristics such as high refractive index modulation, large dynamic range, good light sensitivity, real time image development, high optical quality, and low cost [1]. The photopolymer consists of a binding polymer, monomer, photosensitizing dye and initiator. The performance of the film depends on the composition of the components [2]. A good optical quality is the most important requirement of a holographic recording medium, therefore, a reliable and repeatable method is needed to form a uniform coating of the photosensitive solution onto glass substrate in order to obtain high optical quality layers. Different coating methods such as dip coater, spin coating, drop casting, etc., have been used for the preparation of good quality of photopolymer films [3]. The present work deals with the fabrication of AA/PVA based red sensitive photopolymer films using digital film applicator based on principle of bar coating in order to yield uniformly homogeneous films of the photosensitive mixture.

2. Methodology

Materials and coating of film

The material used in this study is an acrylamide-based water-soluble photopolymer. The composition consists of acrylamide (0.6 g), methylene bisacrylamide (0.2 g) as monomer, methylene blue (2 mL 0.11 % w/v) as sensitizer, triethanolamine (2 mL) as photoinitiator, and PVA (20 mL 10 %wt.) as a binder [4]. All the chemicals in stated concentration are dissolved in deionized water to prepare the solution and put at constant stirring for 30 minutes. A definite amount of photopolymer solution is poured on clean microscopic glass slides to prepare photopolymer films. The coating technique used in this work is a digital film applicator based on the principle of bar coating to yield uniform layers of solution on substrates of different dimensions. The cylindrical bar moves onto the substrate with solution on one side of bar at constant speed. The speed and direction of coating can be adjusted using controller provided in the applicator. The instrument with necessary accessories shown in Fig.1. is used to coat the glass slides of dimensions 7.6 cm×2.6 cm and 5 cm ×5 cm at various speeds (15 mm/s – 100 mm/s). The coated surfaces are dried for 72 hours in dark under normal laboratory conditions (room temperature 28-30˚C, RH 50-60 %). Finally, thickness of the dried films is measured using contact type profilometer.

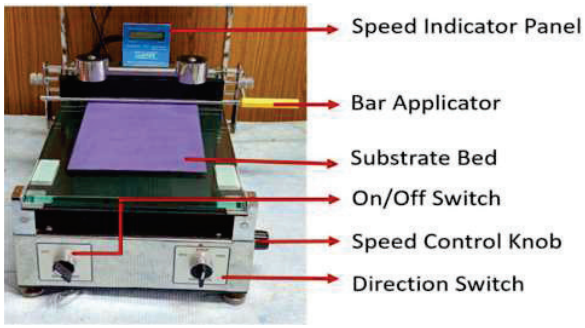

Fig. 1: Photograph of the Digital film applicator

.

3. Results and Discussion

Glass substrates exhibits uniform coating of photopolymer solution using digital film applicator with two different dimensions (2.6 cm×7.6 cm, (b) 5 cm×5 cm) as shown in Fig. 2 (a). Characteristically, the UV-VIS spectra of prepared photopolymer show absorption maxima ranging from 630-670 nm that confirms its sensitivity towards red wavelength Fig.3 (a). It is experimentally observed that the coated film thickness is influenced by the speed of coating which is graphically represented in Fig. 3 (b). The lower speed leads to thicker films and vice versa.

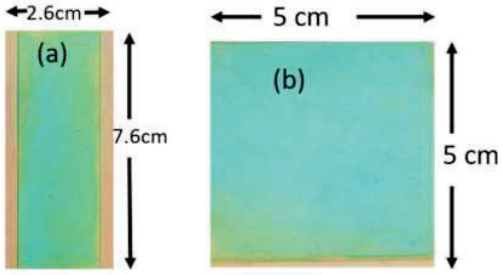

Fig. 2: Photograph of coated photopolymer films

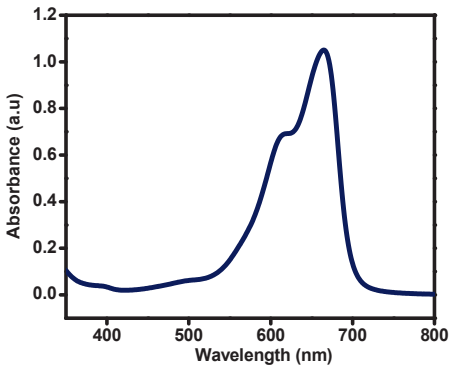

Fig. 3: (a) Absorption spectra of photopolymer solution

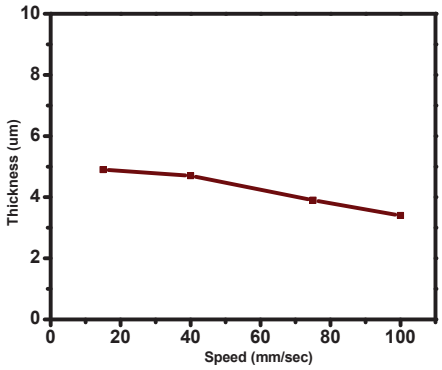

Fig. 3: (b) Experimental variation of thickness vs speed.

Conclusion

In this work, it has been analyzed that using digital film coater uniform layer of photopolymer solution is obtained irrespective of dimensions of substrate that is not possible with the spin coating and gravity settling method. Moreover, film thickness can be tuned by speed of the coater.

Acknowledgement

Authors thank Sachin Goyal, Abhinav Kaushal, Sumedha, Omendra Singh for fruitful discussions.

Funding: This research work is financially supported by the CSIR, India under the project MLP-2014.

References

[1] H. Akbari, I. Naydenova, "Diffractive optical elements with a large angle of operation recorded in acrylamide based photopolymer on flexible substrates," International Journal of Polymer Science, **2014**, 918285 (2014).

[2] D. Kim, Y. Kim, S. Nam, J. Lim, "Effects of modifying PVA/AA photopolymer film with SeO_2 crystals on diffraction efficiencies for holographic recording," J. Ind. Eng. Chem., **12**, 762-768 (2006).

[3] S. Martin, V. Toal, "Self developing dry photopolymer layers for holographic applications," 1993 Fourth International Conference on Holographic Systems, Components and Applications, 1993, pp. 71-75.

[4] S. Martin, C. A. Feely, V. Toal, 'Holographic recording characteristics of an acrylamide- based photopolymer," Applied Optics, **36**, 5757-5768 (1997).

Self-healing of optical beams

Baby Komal,[1] Gauri Arora,[1] Sunil Kumar,[2] and P. Senthilkumaran[3]

[1] *Singular Optics Laboratory, Department of Physics, Indian Institute of Technology Delhi, Hauz Khas, New Delhi 110016, India*

[2] *Femtosecond Spectroscopy and Nonlinear Photonics Laboratory, Department of Physics, Indian Institute of Technology Delhi, Hauz Khas, New Delhi 110016, India*

[3] *Optics and Photonics Center, Indian Institute of Technology Delhi, Hauz Khas, New Delhi 110016, India*

[*] *bkomal2015@gmail.com*

Abstract: Self-healing refers to the reconstruction of the optical beam characteristics upon propagation. It is an interesting property that makes them suitable for applications like efficient optical communication and microscopy. We discuss here the healing of one of the most commonly obtained optical beams in labs, i.e. elliptical beams. Interestingly, elliptical beam heals its intensity but with a rotation of 90° in the far-field.

1. Introduction

Recovery of the light beam characteristics after getting disturbed by different obstacles is termed self-healing. Most commonly, Bessel beams are known to self-heal [1]. There are other optical beams like Gaussian beams [2], vortex beams (LG beams) [**?**], conical beams [4], Airy beams [5], etc., which also self-heal in the far-field. Different reasoning have been provided for their self-healing like caustic, ray, wave and ray-wave explanations [6]. Here, we discuss the healing of one of the commonly generated form of optical beams i.e. elliptical beams.

2. Healing of optical beams

The Fraunhofer diffraction pattern of the blocked beam in the far-field can be used to study the impact of the obstruction in the beam after propagation. Let T represent the obstacle's transmittance function. The beam in the far-field can be represented as,

$$\psi_f = \mathscr{F}[\psi \times T] = \mathscr{F}[\psi] \otimes \mathscr{F}[T]. \tag{1}$$

Here, ψ represents different input optical beam.
A Gaussian beam is given by,

$$\psi_G = \exp((-x^2)/w_1^2. \tag{2}$$

The Fourier transform of this Gaussian beam is given by,

$$\mathscr{F}[\psi_G] = \frac{1}{\sqrt{2}} w_1 e^{(-w_1^2 f_x^2)/4} \tag{3}$$

Therefore, the Fourier transform of a Gaussian beam remains Gaussian in nature with some scaling factors. The obstruction perturbs the input beam and their effect can be obtained by convolution of the Fourier transform of obstacle as given by Eq. 1. It can be seen in the figure that the Gaussian beam self-heals maintaing its form after getting obstructed by different obstacles. Therefore, diffraction plays an important role in smoothing out the wavefront after propagation. The vortex (LG) beam is also reported to self-heal. The rotation of the azimuthal component of Poynting vector is responsible for its self-healing [8]. The Fourier transform of a vortex beam is also a vortex beam, which makes the form of the beam propagation invariant even after perturbation [9]. The obstructed elliptical beam is similarly studied to obtain the beam pattern in the far-field. It is given by,

$$\psi = \exp((-x^2)./{w_1.}^2 + (-y^2)./{w_2.}^2);\ w_1 \neq w_2 \tag{4}$$

where, w_1 and w_2 represents the beam waist in x and y directions. For, $w_1 < w_2$, i.e. the beam waist in x-axis lesser than in y-axis, i.e. the elliptical axis has major axis in y-direction.

$$\mathscr{F}[\psi] = \frac{1}{\sqrt{2}}[w_1 e^{(-w_1^2 f_x^2)/4} + w_2 e^{(-w_2^2 f_y^2)/4}] \tag{5}$$

Due to the scaling property of the Fourier transform [7], the elliptical beam undergoes a rotation in the far-field. The ellipse now has its major axis in x-direction. This is now convoluted with the Fourier transform of different obstacles. We, here show three different obstacles: circular, triangular and rectangular. It can be observed from the figure that although the elliptical beam's intensity is regained but a rotation of 90° is obtained.

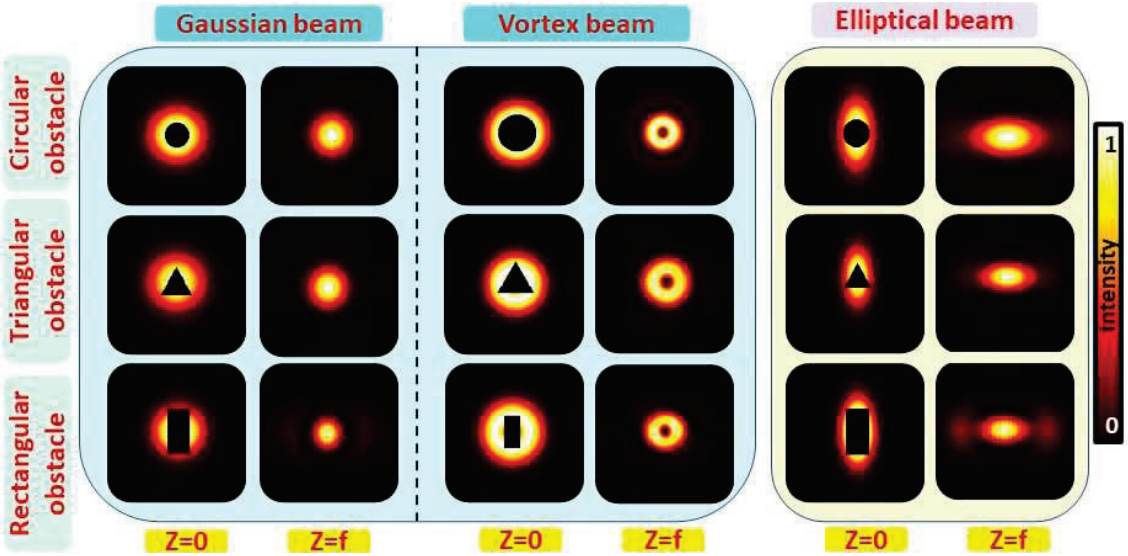

Fig. 1. Convolution of a circular symmetric function shown in (A) with different types of symmetrical and asymmetrical functions shown in (B). (C) shows the resultant amplitude profile from the convolution and (D) shows the amplitude contour.

3. Conclusion

The self-healing of an elliptical beam is studied in the far-field. It is observed that although the intensity of the input unobstructed beam is regained but the rotation of the beam pattern is obtained by 90°. This is due o the scaling property of the Fourier transform.

References

1. Chu, X. Analytical study on the self-healing property of Bessel beam. Eur. Phys. J. D 66, 259 (2012).
2. A. Aiello, G. S. Agarwal, M. Paúr, B. Stoklasa, Z. Hradil, J. Řeháček, P. de la Hoz, G. Leuchs and L. L. Sánchez-Soto, Unraveling beam self-healing, Opt. Express 25(16), 19147 (2017) .
3. M.V. Vasnetsov, I.G. Marienko, M.S. Soskin, Self- reconstruction of an optical vortex, JETP Letters 71(4), 130 (2000)
4. B.K. Singh, D.S. Mehta, P. Senthilkumaran, Conical light sword optical beam and its healing property, Opt. Lett. 39(7), 2064 (2014).
5. J. Broky, G.A. Siviloglou, A. Dogariu, D.N. Christodoulides, Self-healing properties of optical Airy beams, Opt. Express 16(17), 12880 (2008).
6. Y. Shen, S. Pidishety, I.M. Nape, A. Dudley, Self-healing of structured light: a review, Journal of Optics (2022).
7. E. Kreyszig, Advanced Engineering Mathematics (John Wiley and Sons, 2010).
8. B. Komal, G. Arora, S. Kumar, P. Senthilkumaran, Self- healing of vector field singularities, Optics Communica- tions 524, 128796 (2022).
9. M.V. Berry, Optical vortices evolving from helicoidal in- teger and fractional phase steps, Journal of Optics A: Pure and Applied Optics 6(2), 259 (2004).

Surface Plasmon Resonance Based Sensor using Ga-doped ZnO and $MoSe_2$ for Glucose Sensing

[1]Mohd Uwais*, [2]Ashish Bijalwan, [1,3]Vipul Rastogi

[1]Department of Physics, Indian Institute of Technology Roorkee 247667, Uttarakhand, INDIA

[2]Department of Physics, Pt. Shiv Ram Govt. Degree College, Tyuni, Deharadun 248199, Uttarakhand, INDIA

[3]Center for Photonics and Quantum Communication Technology, Indian Institute of Technology Roorkee, INDIA

**muwais@ph.iitr.ac.in*

Abstract: In this paper, we propose a surface plasmon resonance (SPR) based sensor for detection of glucose in urine sample at 633 nm wavelength. The structure of the sensor is based on Kretschman configuration, using Ga-dopped ZnO, 2D material $MoSe_2$ with Au layer over the glass prism. The numerical simulations show a maximum sensitivity of 260 deg./RIU corresponding the 1.33-1.335 refractive indices. The proposed sensor could be utilized for glucose detection in urine sample with maximum sensitivity of 260 deg./RIU.

Keywords: Surface plasmon resonance (SPR), glucose, 2D material $MoSe_2$, Ga-doped ZnO

1. Introduction

Glucose level monitoring is very important for diagnosis and treatment of several diseases related to heart, kidney and eyes. Nowadays, diabetes is a very common disease, which arises due to the high concentration of the glucose in human blood. Although blood glucose monitoring is widespread, urine glucose monitoring is just as important since it allows us to assess kidney function. High level of glucose in urine leads to the renal glycosuria, in this situation, glucose level in blood remain normal but urine glucose could be higher [1]. Among several biosensors, surface plasmon resonance based sensors offer high sensitivity and label free detection. SPR based biosensors have applications in sensing of anti-bodies, antigens, enzymes, nucleic acids, drugs, cells and viruses [2]. When the p polarized light incidents on the metal and dielectric interface, the energy of the photons is transferred to collective oscillation of free electrons at metal surface, known as surface plasmons. The condition at which the wave vector of incident light and surface plasmon become equal is referred to as surface plasmon resonance, and it leads to a resonance dip in reflectance spectrum [3]. Kretschman configuration is commonly used for setup the SPR condition, where a metal layer is deposited on the glass prism. The SPR condition is highly sensitive towards the small changes in the refractive index, which results in the shifting of the resonance dip in SPR reflectance spectrum [4].

In this work, we present an SPR-based sensor using the Kretschman configuration for glucose detection in urine sample. Here a dielectric layer of Ga-doped ZnO and 2D material $MoSe_2$ monolayer are incorporated above the Au metal layer to enhance the performance of the proposed sensor. Numerical simulations have been carried out to analyze the performance of the sensor at 633 nm wavelength. The maximum sensitivity of the sensor has been reported as 260 deg./RIU in the refractive index range 1.33-1.335. In the case of glucose detection, the maximum sensitivity is also observed to be 260 deg./RIU.

2. Structure and Results

The structure of the 5-layers SPR based sensor is depicted in Fig.1 (a). where, an SPR active material

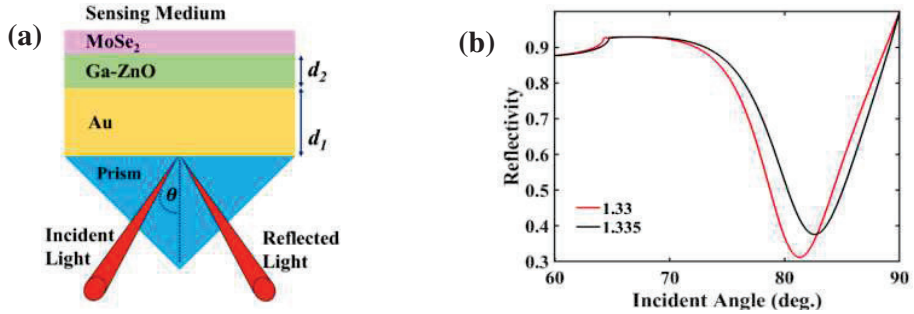

Fig.1: (a) The schematic diagram of the proposed SPR based sensor. (b) SPR response of the sensor over the 1.33-1.335 refractive index.

Au layer of thickness d_1 is deposited on the glass prism. Between the Au layer and $MoSe_2$ monolayer (0.70 nm) lies a 3 nm thick (d_2) dielectric layer of Ga-doped ZnO, which shows the high refractive index and considerable shift in SPR angle [5]. The dichalcogenides (TMDCs) as $MoSe_2$ are used to enhance the performance of the conventional SPR sensor [6]. The light of 633 nm wavelength is incident at an angle θ through the glass prism. In Kretschmann scheme, surface plasmons are excited by the attenuated total reflection (ATR), and the prism

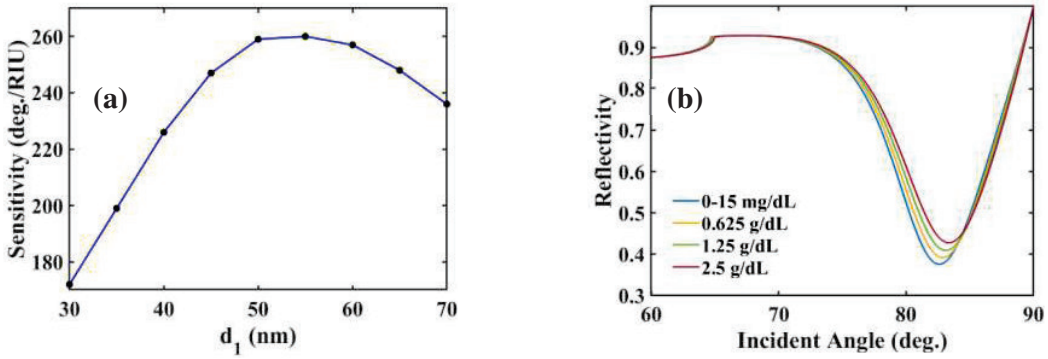

Fig.2: (a) The variation of the sensitivity with Au layer thickness (d_1). (b) The SPR response of the sensor corresponding to different concentrations of the glucose.

levels the wave vector of the incident photons (K) with that of surface plasmons (K_{SP}), the enhance wave vector of the incident photons along metal-dielectric interface, is given as [7],

$$K = n_p k_o \sin\theta$$

where k_o is the incident light wave vector, n_p is the refractive indices of the prism .

The sensitivity of the sensor is defined as the ratio of the shift in the resonance angle ($\Delta\theta_{SPR}$) with the change in the refractive index (Δn) of the sensing medium. In Fig.2(a), we have shown the variation of sensitivity of the sensor with the Au layer thickness (d_1). From here we can conclude that at 55 nm thickness of the Au, we achieved the maximum sensitivity of 260 deg./RIU corresponding the 1.33-1.335 refractive indices. The SPR response of the sensor is shown in Fig.1(b).

We have extended this study for the detection of glucose in urine sample. The refractive indices corresponding to the different concentrations of the glucose in urine sample have been adopted from ref [8]. The SPR response of the sensor for the different concentrations of the glucose is represented in Fig. 2(b). Here, we can see that the resonance angle shifting takes place due to the change in the refractive index, and this change in the refractive indices arises because of the variation of the glucose concentration in urine sample. The resonance angles are observed to be 82.605 deg., 82.865 deg., 83.115 deg. and 83.36 deg. corresponding the 0-15 mg/dL, 0.625 g/dL, 1.25 g/dL, and 2.5 g/dL concentrations of the glucose respectively. We have obtained the maximum sensitivity of 260 deg./RIU for the glucose concentration detection in urine sample. Thus, the proposed sensor could be a good candidate of the glucose sensing.

3. References

[1] M.N. Karim, S.R. Anderson, S. Singh, R. Ramanathan, and V. Bansal, "Nanostructured silver fabric as a free-standing NanoZyme for colorimetric detection of glucose in urine," Biosens. Bioelectron **110**, 8-15 (2018).

[2] R. Karlsson, "SPR for molecular interaction analysis: a review of emerging application areas," J. Mol. Recognit. **17(3)**, 151-161 (2004).

[3] I. Abdulhalim, M. Zourob, and A. Lakhtakia, "Surface plasmon resonance for biosensing: a mini-review," Electromagnetics **28(3)**, 214-242 (2008).

[4] A. Bijalwan, B.K. Singh, and V. Rastogi, "Surface plasmon resonance-based sensors using nano-ribbons of graphene and WSe2," Plasmonics **15(4)**, 1015-1023 (2020).

[5] L. Hsu, C.S. Yeh, C.C. Kuo, B.R. Huang, and S. Dhar, "Optical and transport properties of undoped and Al-, Ga-and In-doped ZnO thin films," J. Optoelectron. Adv. Mater. **7(6)**, 3039 (2005).

[6] Q. Ouyang, S. Zeng, L. Jiang, J. Qu, X.Q. Dinh, J. Qian, S. He, P. Coquet, and K.T. Yong, "Two-dimensional transition metal dichalcogenide enhanced phase-sensitive plasmonic biosensors: theoretical insight," J. Phys. Chem. C, **121(11)**, 6282-6289 (2017).

[7] A. Verma, A. Prakash, and R. Tripathi, "Sensitivity enhancement of surface plasmon resonance biosensor using graphene and air gap," Opt. commun. **357**, 106-112 (2015).

[8] S. Mostufa, A.K. Paul, and K. Chakrabarti, "Detection of hemoglobin in blood and urine glucose level samples using a graphene-coated SPR based biosensor," OSA Contin. **4(8)**, 2164-2176 (2021).

Random Laser Spectroscopy

Priyanka S. Choubey,[1] Renu Yadav,[2] Anirban Sarkar,[3] Shivakiran Bhaktha B.N.[1,2,*]

[1] *School of Nano-Science and Technology, Indian Institute of Technology Kharagpur, Kharagpur - 721302, India*

[2] *Department of Physics, Indian Institute of Technology Kharagpur, Kharagpur - 721302, India*

[3] *Department of Physics, National Institute of Technology Calicut, Kozhikode 673601, India*

[*]kiranbhaktha@phy.iitkgp.ac.in

Abstract: Random laser emission spectra strongly depend on the properties of the scatterers embedded gain media. Here, statistical analysis of random laser intensity fluctuations is presented in a dye-doped polymer thin film waveguide subjected to a constant heat treatment. The changes occurring in the density of the polymer thin film during the various stages of solvent evaporation are studied using the changes in the statistics of random laser emission intensities. The statistical analyses of the random laser emission intensity fluctuations help us to develop a novel spectroscopic tool to probe material properties.

Keywords: random laser, replica symmetry breaking, dye-doped polymer waveguides, photoluminescence spectroscopy

1. Introduction

Polymer based waveguides have attracted considerable attention over silicates as well as semiconductor-based technologies for the development of photonic devices due to their low-cost, ease of fabrication, low-temperature and low-pressure processing ability [1,2]. Polymer waveguides have great potential for the fabrication of all-optical devices as they are good host materials for organic dye molecules, and also due to their optical transparency in the visible as well as near infrared region. Incorporation of dye molecules in polymer waveguides has driven the development of solid-state dye lasers and optical amplifiers [3,4] leading to the growth of cost-effective photonic technologies.

Dye-doped polymers, though very attractive, also give rise to scattering of light due to inhomogeneities created by polymer density variations or dye aggregate formation. The phenomenon of random laser (RL) emission has been studied in the past in many optically active dye-doped polymer waveguides (DDPWs) [5,6]. Furthermore, in recent years, the ease of fabrication of DDPWs using spin-coating or dip-coating techniques have led to their interesting applications and mass production. In these devices, the evaporation of solvent can tailor the morphology of the film by creating polymer density fluctuations, and thus play a vital role in attaining desired optical quality. Hence, it is essential to understand the behavior of the DDPWs during the solvent evaporation process. However, there are scarce experimental tools available to track the formation of these microscopic inhomogeneities in real-time. Here, we propose RL as a probe to track microscopic changes in polymers via monitoring the statistics of RL emission intensity fluctuations and replica symmetry breaking (RSB) phase transitions [7]. The changes occurring at the microscopic level in the polymer due to the solvent evaporation process leads to fluctuations in DDPW RL emission intensities as shown in Fig. 1. The effect of microscopic changes, in the polymer thin film, on the RL modes are being studied in a controlled manner by selective excitation of the modes under various experimental configurations (scattering strengths, solvent evaporation rates and optical pump profile). The RL emission intensity statistics [8] is used to model the microscopic changes in the polymer thin film during the solvent evaporation process. This novel RL tool opens up a new avenue to RL spectroscopy that can monitor real-time microscopic changes in various materials.

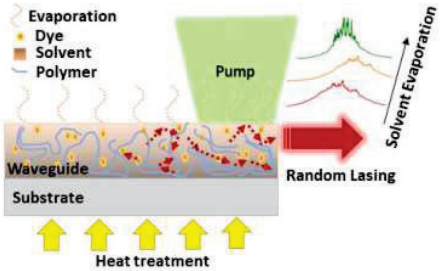

Fig. 1. Schematic representation of solvent-evaporation and corresponding changes in RL emission.

2. Experiments and Results

In this work, we study both wet (wet-DDPW) and heated thin films (HT-DDPW). The threshold characteristic of the HT-DDPW is shown in Fig. 2(a), with its lasing threshold at 0.01 mJ. The full width at half maximum (FWHM) of the emission spectrum is found to reduce drastically at the RL emission threshold. When the pump pulse energy exceeds the lasing threshold, discrete narrow

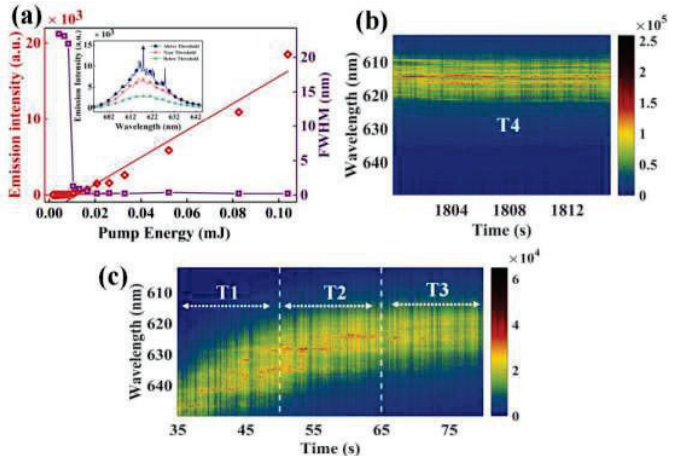

Fig. 2. (a) RL threshold plot for HT-DDPW. Insert shows the RL emission spectra recorded below and above the lasing threshold for HT-DDPW. RL emission spectra I(λ,t) recorded for the wet-DDPW in windows: (b) T4 (from 1800 to 1815 s) and (c) T1 (from 35 to 50 s), T2 (from 50 to 65 s) and T3 (from 65 to 80 s).

lasing peaks appear in the emission spectrum as shown in the insert of Fig. 2(a), which is a characteristic behaviour of a RL. Figure 2(b) shows the series of emission spectra recorded for HT-DDPW, referred to as window T4 (from 1800 to 1815 s). For the studies on wet-DDPW, a constant heating was maintained at 65 ˚C throughout the experiment. To ensure the observation of narrow lasing peaks throughout the duration of the experiment, an optimum incident pump pulse fluence was chosen. Single-pulse emission spectra I(λ,t) were recorded over a large number of pulses at a fixed pump energy as shown in Fig. 2(c). The series of recorded spectra were divided into several windows for analysis. In Fig. 2(c) three windows are considered, T1 (from 35 to 50 s), T2 (from 50 to 65 s) and T3 (from 65 to 80 s), of $\Delta T = 15$ s duration each (300 pulses), for the sake of statistical analysis. The choice of ΔT is based on the fact that the spectra change drastically during the initial 15 s, and change gradually in the next 15 s, before reaching a quasi-steady behaviour, as evident in Fig. 2(c). In windows T1 to T4, sharp peaks are observed in the emission spectra confirming the lasing behaviour of the wet-DDPW and HT-DDPW samples.

Overall, as the solvent dries from the wet-DDPW the random lasing characteristics evolve. A detailed discussion on the statistical properties of the lasing modes observed during the drying process of the wet thin film will be discussed in the conference. The modal interactions will be quantified in terms of correlation, survival function and RSB analysis.

3. References

[1] L. Sznitko, J. Mysliwiec and A. Miniewicz, "The role of polymers in random lasing," *J. Polym. Sci. Part B Polym. Phys.* **53,** 951–74 (2015).

[2] S. V. Frolov, Z. V. Vardeny, K. Yoshino, A. Zakhidov and R. H. Baughman, "Stimulated emission in high-gain organic media," *Phys. Rev. B* **59,** R5284–7 (1999).

[3] A. Costela, O. García, L. Cerdán, I. García-Moreno and R. Sastre, "Amplified spontaneous emission and optical gain measurements from pyrromethene 567-doped polymer waveguides and quasi-waveguides," *Opt. Express* **16,** 7023–36 (2008).

[4] T. Grossmann, S. Schleede, M. Hauser, M. B. Christiansen, C. Vannahme, C. Eschenbaum, S. Klinkhammer, T. Beck, J. Fuchs, G. U. Nienhaus, U. Lemmer, A. Kristensen, T. Mappes and H. Kalt, "Low-threshold conical microcavity dye lasers," *Appl. Phys. Lett.* **97,** 1–3 (2010).

[5] A. Tulek and Z. V. Vardeny, "Studies of random laser action in π-conjugated polymers," *J. Opt. A Pure Appl. Opt.* **12,** 024008 (2010).

[6] A. Sarkar, N. N. S. Ojha and B. N. S. Bhaktha, "Effect of photonic stop-band on the modes of a weakly scattering DCM-PVA waveguide random laser," *Appl. Phys. Lett.* **110,** 25110 (2017).

[7] A. Sarkar, B. N. Shivakiran Bhaktha and J. Andreasen, "Replica Symmetry Breaking in a Weakly Scattering Optofluidic Random Laser," *Sci. Rep.* **10,** 1–12 (2020).

[8] R. Uppu, A. K. Tiwari, and S. Mujumdar, "Identification of statistical regimes and crossovers in coherent random laser emission," *Opt. Lett.* **37**, 662 (2012).

Broadband metamaterial absorber based on *TiN* hollow cylinders

Mukul Jaiswal, Nikita Choudhary, Anjani Kumar Tiwari*
Department of Physics, Indian Institute of Technology Roorkee, Roorkee, India 247 667
Author e-mail address: anjani@ph.iitr.ac.in

Abstract. We systematically investigate a metamaterial absorber consisting of *a TiN* hollow cylinder on the *ZnS-TiN* platform. The absorption spectrum of the metamaterial shows a sharp peak at 2025 nm, which can be utilized for refractive index sensing. Including another concentric hollow cylinder results in a broadband absorption (>85%, between 0.76 μm to 2.5 μm), the absorber's performance is also lenient to the height of the cylinders.
Keywords: Metamaterial, metamaterial absorber, refractive index sensor.

Metamaterials are artificially engineered composite structures comprising of a periodic array of sub-wavelength entities. The performance of the metamaterials strongly depends on the structural parameters of these entities. By manipulating the properties of its constituting entities, these materials demonstrate various unconventional phenomena like negative refractive index, superlensing, cloaking, perfect absorption, etc. Metamaterial-based perfect absorber has been exploited for energy storage devices, sensors, and photodetectors [1,2]. A simple tri-layer-based metal/dielectric/metal metamaterial absorbers were limited to absorb a selective range of the electromagnetic spectrum [3,4]. For most practical applications, an absorber should be broadband, polarization-independent, and able to absorb over wide angles. For this purpose, many efficient metamaterial structures have been proposed and realized.

Here, in this work, we systematically investigate a metamaterial absorber consisting of two concentric cylindrical structures on a thin metal-dielectric platform. The absorption properties are investigated using the COMSOL Multiphysics software. The unit cell of the first structure (only one cylinder) is shown in Figure 1(a), it comprises of a hollow *TiN* cylinder on the *ZnS-TiN* platform. The geometrical parameters of the structure are *a* (size of the unit cell) = *2 μm*, *h (*height of the cylinder*) = 400 nm, t = 100 nm, d = 70 nm,* r_1 *= 200 nm* and R_1 *= 300 nm*. Periodic boundary conditions are set in the X-Y direction; thus, the system can be considered as an infinite 2D array of nanocylinders. For the simulation, the radiation is incident along the Z axis, and the absorbance of the metamaterial structure is calculated using $A(\omega) = 1 - |S_{11}|^2 - |S_{12}|^2$ where, $|S_{11}|^2$ is the reflectance, and $|S_{12}|^2$ is the transmittance.

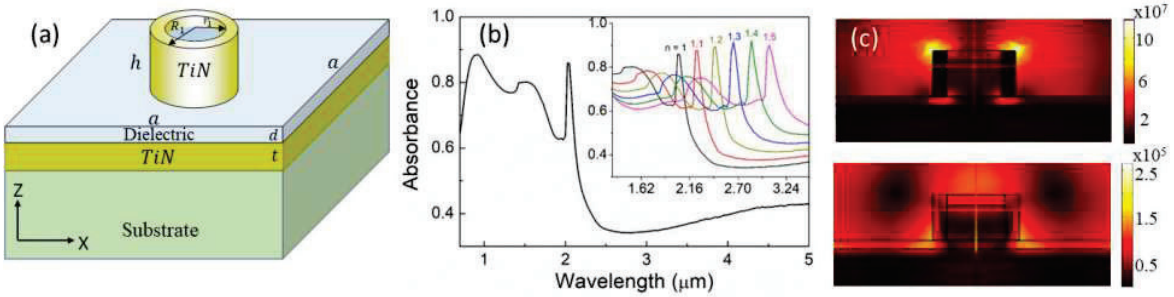

Figure 1 (a) Schematic diagram of the unit cell comprising of a TiN hollow cylinder on *the ZnS-TiN* platform. *(b) Simulated absorption spectrum. Inset shows the effect of the refractive index of the surrounding medium. (c) Electric (top panel) and magnetic (bottom panel) field profiles at λ = 2025 nm.*

Figure 1 (b) depicts the simulated absorbance of this structure in the spectral range between 0.6 μm to 5 μm. Air (n = 1) is taken as a surrounding medium. The absorbance is more than 70% between 0.64 μm and 1.75 μm. The absorption spectrum shows a sharp peak at 2025 nm. As shown in the inset, this absorption peak shifts as we vary the environment's refractive index. The refractive index sensitivity (δλ/δn) of this peak is 2050 nm/RIU, and the figure of merit is 30/RIU. Therefore, this structure can be utilized for the refractive index sensor. To understand the origin of the peak at 2025 nm, we simulate the electric and magnetic field distribution, and the results are depicted in Figure

which is Mie type, dominates confining magnetic field in the center of each Si strip, whereas in the second resonance the confinement of the magnetic field in each Si strip is due to the energy exchange between the Si and Au film. Due to the confinement of field within the Si strip leads to the high-quality factor in each case. The resonances at λ_1= 2.74 μm and λ_2= 4.52μm have Q factor as 390 and 227 respectively.

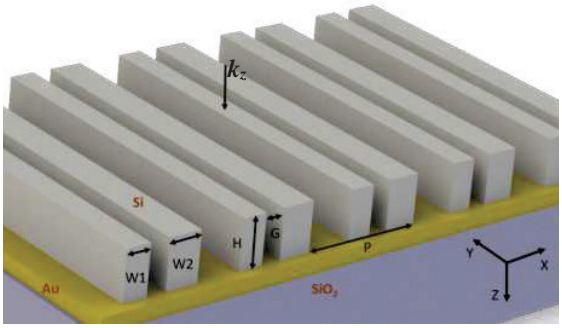

Fig. 1: 3D Schematic of proposed periodic design, Dimensions: W_1= 650 nm, W_2= 675 nm, H= 690 nm, G= 400 nm, P= 2.5 μm

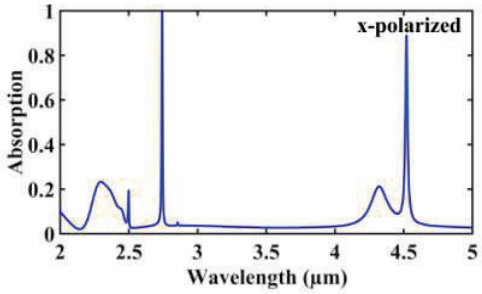

Fig. 2: Absorption response for x polarized incident light

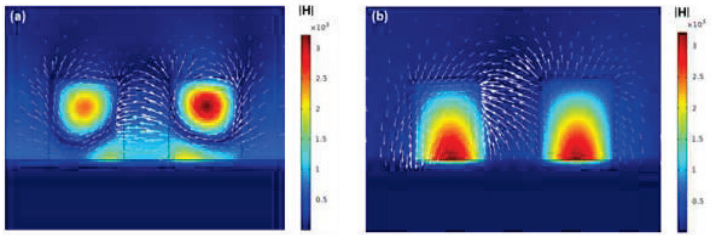

Fig. 3: Magnetic field distribution and electric field arrow plot of resonances (a) at λ_1 = 2.74 μm, and (b) λ_2 = 4.52 μm

4. Conclusion

We have numerically simulated a narrow dual band perfect absorber based on asymmetric silicon grating structure on gold film in mid-infrared wavelength range.

5. References

[1] N. I. Landy et al. "Perfect metamaterial absorber," Phys. Rev. Lett. 100, 207402 (2008).
[2] K. Aydin et al. "Broadband polarization-independent resonant light absorption using ultrathin plasmonic super absorbers," Nat. Commun. 2, 1-7 (2011).
[3] E. Buhara et al. "An all-dielectric metasurface coupled with two-dimensional semiconductors for thermally tunable ultra-narrowband light absorption," Plasmonics 16, 687-694 (2021).
[4] X. Liu et al. "Isotropic Mie resonance-based metamaterial perfect absorber," App. Phys. Lett. 103, 031910 (2013).
[5] D. F. Edwards, “Silicon (Si)” in Handbook of optical constants of solids, E.D. Palik, ed. (Academic, Orlando, Fla. 1985).

Advantage of Non-isotropic Correlations for Partially Coherent V-point Singularity Detection

Manisha,[1,*] Saba N Khan,[2] Stuti Joshi,[3] Bhaskar Kanseri,[1] and P Senthilkumaran[1,3]

[1] *Department of Physics, Indian Institute of Technology Delhi, Hauz Khas, New Delhi 110016, India*
[2] *School of Physics and Astronomy, University of St Andrews, North Haugh, St Andrews KY16 9SS, UK*
[3] *Optics and Photonics Center, Indian Institute of Technology Delhi, Hauz Khas, New Delhi-110016, India*

[*] *manisha12101994@gmail.com*

Abstract: We utilize here the advantage of non-isotropic correlation states for the detection of partially coherent V-point singularities (PCVS). Non-isotropic correlation state refer to the interdependence of correlations between parallel and orthogonal electric field components. Such differences in the correlation parameters leads to the azimuthal asymmetry in the intensity distribution of PCVS, that determines the index of these beams. This study foresees potential application in free space optical (FSO) communication, detecting and imaging atmospheric lidar and so on.

Keywords: V-point Singularity; Non-isotropic correlation; Statistical optics;

1. Introduction

It is well known, the unified theory explored the electromagnetic (EM) fields in both scalar and vector domains, where both the polarization, correlation features and their interdependence plays a vital role [1]. The statistical properties of EM fields in partially coherent fields with isotropic ($\delta_{xx} = \delta_{yy} = \delta_{xy}$) and non-isotropic ($\delta_{xx} \neq \delta_{yy} \neq \delta_{xy}$) correlation states are more advantageous over fully coherent beams in some applications due to speckle reduction and robustness through turbulence. Recently, these partially coherent field have attracted much attention, when explored with singularities in scalar (phase singularity) and vector (polarization singularity) domain. V-point polarization singularities are of specific use due to their application in optical trapping, FSO communication and so on [2]. The embedded V-point singularity is characterized by the Poincaré–Hopf index (PHI), $\eta = \frac{1}{2\pi}\oint \Delta\psi dl$. Also, partially coherent V-point singularities (PCVS) are more robust to longer distances for FSO communication than partially coherent phase singular beams. Recently, PCVS are explored with both isotropic and non-isotropic correlation states [3,4]. In this work, We present a method for the detection of PCVS by utilizing the non-isotropic nature of correlation states.

2. Theoretical Analysis

Based on the unified theory [1], the statistical properties of PCVS with non-isotropic correlation states can be characterized using cross spectral density (CSD) matrix at two spatial points $\mathbf{r}_1(r_1,\theta_1))$ and $\mathbf{r}_2(r_2,\theta_2))$ in the source with elements,

$$W_{0\alpha\beta}(\mathbf{r}_1,\mathbf{r}_2) = 4\alpha\beta \exp\left[-\frac{\mathbf{r}_1^2}{4\sigma^2} - \frac{\mathbf{r}_2^2}{4\sigma^2} - \frac{(\mathbf{r}_2-\mathbf{r}_1)^2}{2\delta_{\alpha\beta}^2}\right], (\alpha = x,y; \beta = x,y), \tag{1}$$

here σ, $\delta_{\alpha\beta}$ are beam waist and correlation parameter respectively, that satisfy some realizability conditions [5],

$$\max(\delta_{xx},\ \delta_{yy}) \neq \delta_{xy} \neq \min\Big(\frac{\delta_{xx}}{\sqrt{|B_{xy}|}}, \frac{\delta_{yy}}{\sqrt{|B_{xy}|}}\Big) \quad \text{And} \quad \frac{1}{4\sigma^2} + \frac{1}{\delta_{\alpha\beta}^2} << \frac{2\pi^2}{\lambda^2} \tag{2}$$

here, λ is the wavelength. Within the paraxial approximations, the CSD elements at the observation plane can be obtained using generalized Collin's formula [6],

$$\begin{aligned} W_{\alpha\beta}(\rho_1,\rho_2,z) = \frac{1}{\lambda^2 B^2}\int_0^\infty\int_0^\infty\int_0^{2\pi}\int_0^{2\pi} W_{0\alpha\beta}(\mathbf{r}_1,\mathbf{r}_2)\exp\left[\frac{ikD}{2B}(\rho_2^2-\rho_1^2) - \frac{ikA}{2B}(\mathbf{r}_1^2-\mathbf{r}_2^2)\right] \\ \times \exp\left[\frac{ik}{B}(\mathbf{r}_1.\rho_1 - \mathbf{r}_2.\rho_2)\right] r_1 r_2 \mathrm{d}r_1 \mathrm{d}r_2 \mathrm{d}\theta_1 \mathrm{d}\theta_2, \end{aligned} \tag{3}$$

where, $k = \frac{2\pi}{\lambda}$, $\rho_1(\rho_1,\phi_1)$ and $\rho_2(\rho_2,\phi_2)$ are two spatial points in the observation plane. $A = D = 0, B = f$ and $C = -1/f$ are the transfer matrix elements of the optical system between source and observation plane.

2.1. *The Intensity Distribution*

The intensity of PCVS with non-isotropic correlation states at observation plane can be obtained as,

$$I(\rho,z) = Tr[\mathbf{W}(\rho,\rho,z)] = W_{xx}(\rho,\rho,z) + W_{yy}(\rho,\rho,z) \tag{4}$$

The intensity distributions for various index ($|\eta| = 1,2,3$) PCVS with non-isotropic correlation states are shown

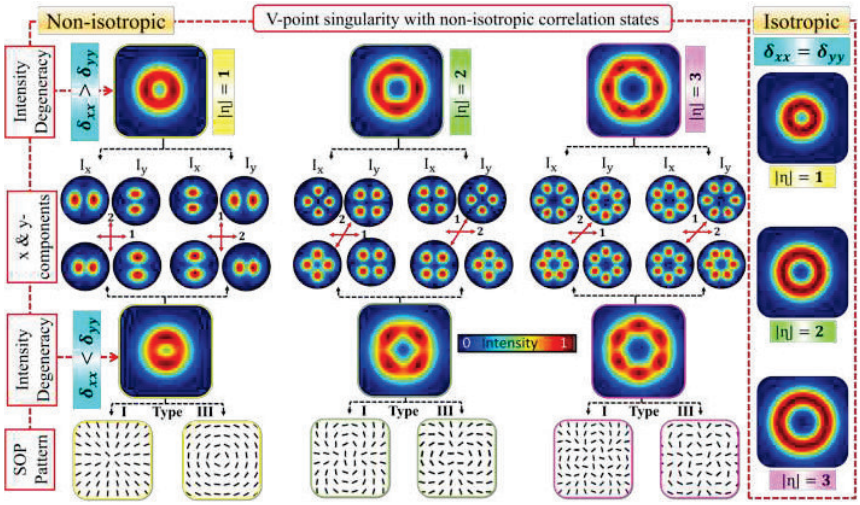

Fig. 1. The intensity distribution for various index ($|\eta| = 1,2,3$) PCVS with non-isotropic correlation states along with x & y- intensity components (I_x & I_y). The arrow lines 1 and 2 show the rotation of I_x and I_y with respect to horizontal axis respectively, differentiate type I and type III PCVS. The intensity distributions of PCVS with isotropic correlation states are shown for comparison.

in Fig. 1. For a particular $|\eta|$, there are four types (I, II, III, IV) of polarization distributions and all are intensity degenerate. Here, we discussed two types (I, III) with positive index and rest of two types (II, IV) with negative index will have same distribution respectively. Due to the degeneracy associated with these beams, the fully coherent V-point singularity and isotropic PCVS can not be detected directly from intensity distributions. For instance, one can see the intensity distributions for isotropic PCVS within red dashed box in Fig. 1, that possesses circular symmetry [3]. In contrast, for non-isotropic PCVS (see Fig.1), the distribution is no more circularly symmetric but aquired an azimuthal asymmetry [4]. The asymmetry appears in the form of a particular no. (N) of maximum intensity regions around the core such that $|\eta| = N/2$. The two non-isotropic cases $\delta_{xx} > \delta_{yy}$ and $\delta_{xx} < \delta_{yy}$ are shown here with intensity components I_x and I_y. These components differentiate the two types from each other and the arrow lines 1 and 2 are shown for easy understanding of their respective rotations. Also the switching between $\delta_{xx} > \delta_{yy}$ and $\delta_{xx} < \delta_{yy}$ results the rotation of intensity distributions by some particular angles for example; $\pi/2$, $\pi/4$, $\pi/6$... for $|\eta| = 1,2,3,...$ respectively. This aspect can be used in the directional measurements.

3. Conclusion

We discussed here the detection approach for partially coherent V-point singularities (PCVS), which is based upon the utilization of non-isotropic nature of correlation sates. The intensity distribution of such beams directly gives the magnitude of PHI of PCVS. Additionally, the rotational characteristic of PCVS under non-isotropic correlations discussed briefly. This method will unquestionably offer a simple way to detect such beams in FSO communication and other applications.

References

1. E. Wolf, *Introduction to the Theory of Coherence and Polarization of Light*, Cambridge university press, (2007)
2. P. Senthilkumaran, *Singularities in Physics and Engineering*, IOP Publishing, (2018)
3. Stuti Joshi and Saba N Khan and P Senthilkumaran and Bhaskar Kanseri, Physical Review A, **103**, 053502, (2021)
4. Manisha, Stuti Joshi and Saba N Khan and P Senthilkumaran and Bhaskar Kanseri , Optics Express, **30**, 32230–32243, (2022)
5. Hema Roychowdhury and Olga Korotkova , Optics Communications, **249**, 379-385, (2005)
6. Qiang Lin and Yangjian Cai, Optics letters, **27**, 216–218, (2002)

Thermally Switchable Frequency Selective Surface for Single to Dual Band Transmission in Terahertz Gap

Nikhil Kumar, Sambit Kumar Ghosh, Somak Bhattacharyya
Department of Electronics Engineering, Indian Institute of Technology (BHU), Varanasi, U.P., India

Abstract: This paper presents a frequency selective surface (FSS) providing single to dual transmission frequency bands under different thermal excitations. Vanadium dioxide (VO_2) has been incorporated into metallic FSS to produce switching characteristics. The proposed FSS offers single band transmission response at 1.41 THz when the VO_2 layer is acting as a metal under high temperature condition (above 340 K). The same FSS exhibits dual band transmission response at 1.41 THz and 2.66 THz when temperature drops below than 340 K. This type of device can be applicable for THz communication systems, radome applications, shielding purposes etc.

1. Introduction:

Research on FSSs is an interesting topic to the community due to their potential applications in different fields, viz. satellite communication, radomes, electromagnetic shielding, performance enhancement of antennas and many other areas [1]. Advancements in terahertz domain shows its versatility for achieving multifunctional tunable characteristics without any structural modifications. Works based on materials which have the ability to change their properties under external factors, such as external voltage, light and thermal excitations [2]. Vanadium dioxide (VO_2) is well known for its unique property to switch from insulator to conductive metallic state at 340 K, based on the Joule heating principle [3]. Reconfigurable FSSs received wide attention among researchers owing to their tunable frequency responses.

In this work, reconfigurability has been achieved in terms of transmission frequency bands. A single unit of the proposed FSS structure is composed of a square ring shape slot and a plus shape slotted silver sheet ($\sigma = 6.3012 \times 10^7$ S/m) deposited on silicon dioxide (SiO_2) substrate which has relative permittivity 3.9 and a loss tangent of 0.001 [4]. The plus shaped slot is filled with an identical VO_2 layer deposited on the SiO_2 substrate. The top view, side view and bottom view of proposed FSS unit-cell have been illustrated in Fig.1 with the optimized dimensions. VO_2 is used in the plus slot which acts as an insulator below 340 K and becomes conductive above this temperature. Electromagnetic (EM) simulations have been performed on CST Microwave studio platform to characterize the spectral responses of the FSS. When the temperature is greater than 340K, VO_2 is in conducting state with the conductivity of 2×10^5 S/m [5]. In this condition, the FSS is allowing only one band to pass through it as shown in Fig. 2(a). The reflection and transmission coefficients at 1.41 THz are -20.7l dB and -0.75 dB respectively; thereby exhibiting transmission at 1.41 THz. When the temperature drops below 340 K, the VO_2 layer becomes insulator in nature with a dielectric constant value of 9 [4]. At this temperature, the FSS becomes electromagnetically transparent for two distinct frequency bands i.e., 1.41 THz and 2.66 THz. In these two bands, the values of the reflection coefficient minima are -21.3 dB and -14.5 dB respectively while the respective transmission coefficients are -0.474 dB and -0.693 dB as seen from Fig. 2(b). It can be concluded that the transmission at 1.41 THz is switched to dual bands at 1.41 THz and 2.66 THz when the temperature goes below 340 K. Hence, the designed FSS offers switchable characteristics by means of thermal excitations.

2. Figures

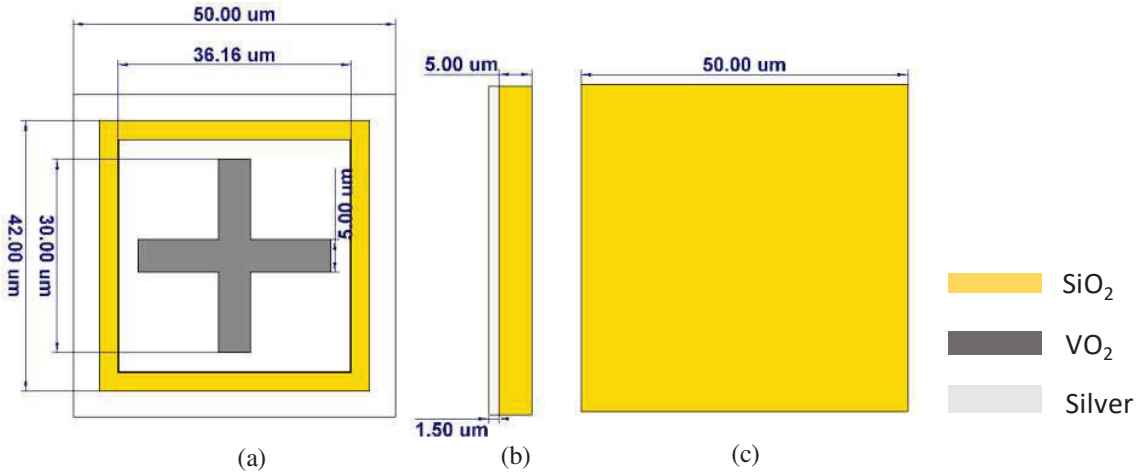

(a) (b) (c)

Fig. 1: (a) Front view (b) side view (c) back view of proposed frequency selective surface unit-cell

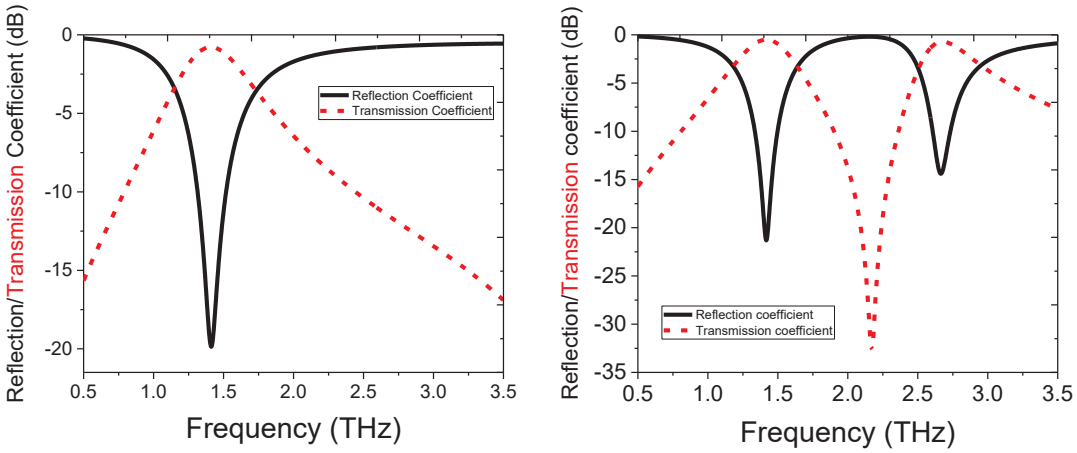

(a) (b)

Fig. 2: (a) Reflection and transmission coefficients when temperature is above 340 K, (b) Reflection and transmission coefficients when temperature is below 340 K.

3. References:

[1] Anwar, Rana & Mao, Ling-Feng & Ning, Huansheng. (2018). Frequency Selective Surfaces: A Review. Applied Sciences. 8. 1689. 10.3390/app8091689.

[2] Ghosh Sambit, Das Santanu, Bhattacharyya Somak. Graphene-Based Metasurface for Tunable Absorption and Transmission Characteristics in the Near Mid-Infrared Region. IEEE Transactions on Antennas and Propagation. (2022) 70. 1-1. 10.1109/TAP.2022.3140904.

[3] H.S. Choi, J.S. Ahn, J.H. Jung, T.W. Noh, D.H. Kim, Mid-infrared properties of a VO_2 film near the metal–insulator transition, Phys. Rev. B 54 (1996) 4621–4628.

[4] H. Liu, Y.-X. Fan, H.-G. Chen, L. Li, Z.-Y. Tao, Active tunable terahertz resonators based on hybrid vanadium oxide metasurface, Opt. Commun. 445 (2019) 277–283.

[5] M. Sun, T. Lv, Z. Liu, F. Wang, W. Li, Y. Zhang, Z. Zhu, C. Guan, and J. Shi, "VO2-enabled transmission-reflection switchable coding terahertz metamaterials," Opt. Express 30, 28829-28839 (2022).

Multispectral Polarization Microscopy and Stokes mapping of Oral benign tissue

[1]Priyanka Mann, [1]Pramila Thapa, [1]Himanshu Joshi, [1]Bhanu Pratap Singh and [1*]Dalip Singh Mehta

[1]Bio-photonics Laboratory, Department of Physics, Indian Institute of Technology Delhi, Hauz-Khas, New Delhi-110016, India.
**Corresponding author: mehtads@physics.iitd.ac.in*

Abstract: Most of the biological specimens are intrinsically birefringent although they are weakly, but this parameter can be used as an important tool in diagnostic process. We propose Multispectral Polarization Microscopy and Stokes imaging of biological specimens. Experiments were performed on oral benign tissue which can be further utilized in classification of benign and malignant oral cancer tissues. We found significant changes in the statistical parameters of stokes components at multiple wavelengths.

Keywords: Polarization, diagnosis, tissue, Stokes parameter.

1. Introduction

Polarization characterizes the wave nature of electromagnetic radiations and provides the correlation between its electric and magnetic counterparts [1]. Early-stage detection is the most important concern of modern healthcare systems. In literature a lot of interferometric, non-interferometric and many other optical modalities have been exploited to analyze the optical properties of biological specimens. Birefringence is one of the intrinsic optical properties of most of the biological samples although they are weakly optically active, but this can be used as an important approach for diagnostic process [2].

Cancer is a global concern and major cause of deaths worldwide and in 2020 nearly 10 million deaths or one in six deaths are reported as per the World Health Organization (WHO) statistics [3]. Hence there is a primary requirement for early-stage cancer detection techniques which is affordable to each section of our society especially for developing countries like India. In this paper we employed a basic Polarization microscope for multispectral Stokes mapping of biological specimens. Experiments were performed on oral benign tissue. During experimentation a set of six intensity images (I_0, I_{45}, I_{90}, I_{135}, I_{RCP}, I_{LCP}) of oral benign tissue are captured by rotating the plane of polarization of polarizer, analyzer, and retarder plate as per the requirements [4,5]. Multispectral stokes mapping is achieved by separating the respective RGB components from a single white light intensity information computationally.

2. Experimental setup

The schematic view of the experimental setup is shown in Fig 1. It comprises of a broadband white light source. The light from the source is focused to the sample stage using lens L_1 and the scattered frequency components are then collected using Microscope objective (MO) lens.

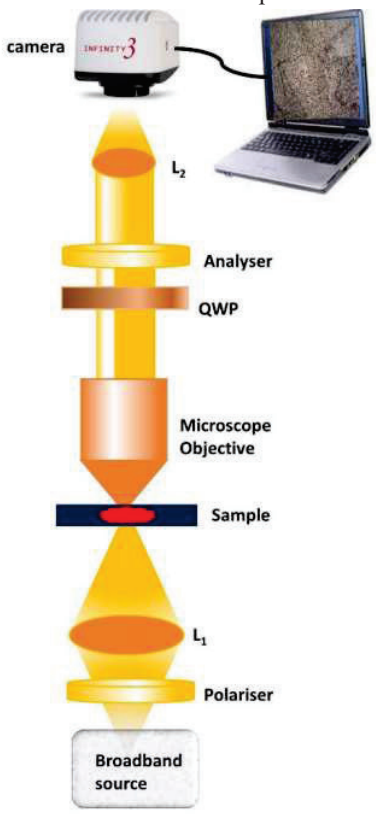

Fig. 1: Schematic diagram of white light polarizing microscope; L_1 and L_2 are the lenses, MO is the microscope objective lens and QWP is the Quarter wave plate

The sample information is then imaged at the CCD camera plane using lens L_2 after passing through the Quarter wave plate and the analyzer. The state of polarization of the incoming light can be re-oriented by rotating the plane of polarization of polarizer, quarter wave plate and analyzer respectively and a set of intensity images ($I_{0,}$ I_{45}, I_{90}, I_{135}, I_{RCP}, I_{LCP}) are recorded which can be further processed in MATLAB to achieve Multispectral stokes mapping of oral benign tissue.

3. Results and Discussion

Here we are reporting the Multispectral stokes mapping of oral benign tissue by recording a set of intensity images ($I_{0,}$ I_{45}, I_{90}, I_{135}, I_{RCP}, I_{LCP}). As discussed in section 1 stokes parameters can be calculated using the following equations:

$$S_0 = I_0 + I_{90} \quad (1)$$

$$S_1 = I_0 - I_{90} \quad (2)$$

$$S_2 = I_{45} - I_{135} \quad (3)$$

$$S_3 = I_{RCP} - I_{LCP} \quad (4)$$

Where $I_{0,}$ I_{45}, I_{90}, I_{135} are the intensity measurements at 0^0, 45^0 ,90^0, 135^0 and I_{RCP}, I_{LCP} are the right and left circularly polarized components and S_0, S_1, S_2, S_3 are the stokes vector components. The single white light intensity information can be distributed in its respective RGB components digitally in MATLAB and the respective stokes mapping is evaluated.

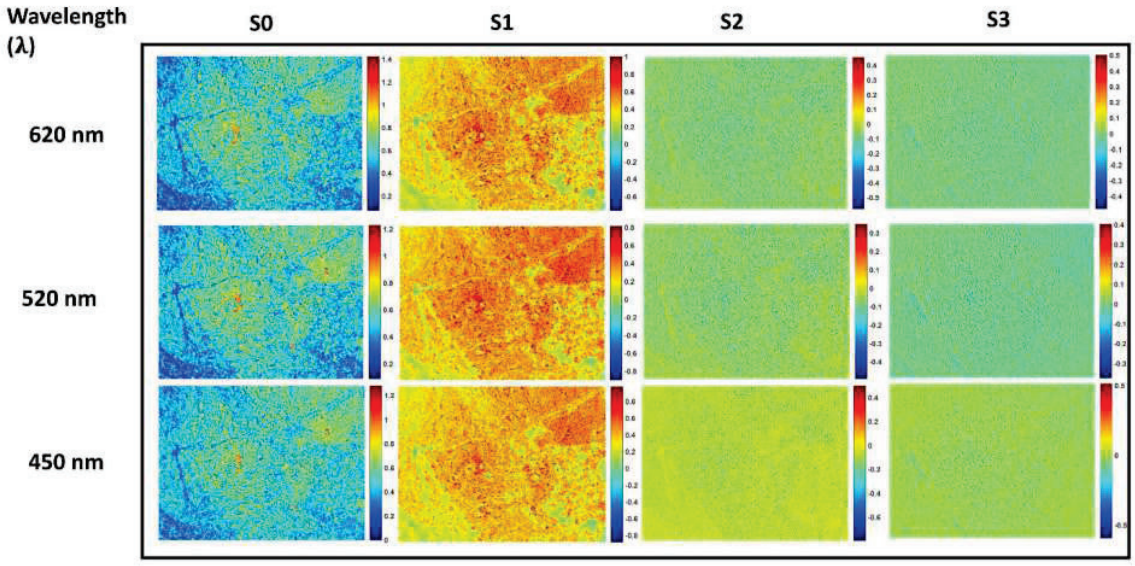

Fig. 2: Stokes imaging of oral benign tissue corresponding to red, green and blue wavelengths respectively.

Figure 2 shows the stokes imaging of oral benign tissue at multiple wavelengths corresponding to red, green and blue wavelengths respectively

Table 1: Mean value of Stokes parameters

Stokes Parameter	620 nm	520 nm	450 nm
S_0	0.5811	0.5315	0.4950
S_1	0.4387	0.3947	0.3781
S_2	-0.0720	-0.0691	-0.0682
S_3	-0.0132	-0.0106	-0.0100

Further we calculated the mean value of stoke components at each wavelength and observed a significant change in the mean values of stokes parameters as we go from red to blue as shown in Table 1 and the negative value of S_3 depicts the presence of more left-handed circularly polarized component in the sample.

4. Conclusions

We conclude that the proposed method provides multispectral stokes mapping of biological specimens which can be further employed for classification problems. The broadband source has low spatial and temporal coherence which offers speckle free imaging as compared to lasers. The proposed system is compact, easy to align and can be utilized in various biomedical applications

References

[1] J. Wang, L. Dong, H. Chen et al.," Birefringence measurement of biological tissue based on polarization- sensitive digital holographic microscopy", Appl. Phys. B **124,** 240 (2018).

[2] R.H. Newton, J. Haffegee, M.-W. Ho, "Polarized light microscopy of weakly birefringent biological specimens", Journal of microscopy, 180(20):127-130 (2011)

[3] https://www.who.int/news-room/fact-sheets/detail/cancer

[4] H. G. Berry, G. Gabrielse, and A. E. Livingston, "Measurement of the Stokes parameters of light", Applied optics, Vol. 16, Issue 12, 3200-3205 (1977)

[5] W. H. McMaster , "Polarization and the Stokes Parameters", American Journal of Physics 22, 351 (1954)

Image Quality Analysis of Astronomical Telescopes using Python Modules

Kishan Malaviya[1,a] **, Anwesh Kumar Mishra**[2,b] **, Shashikiran Ganesh**[2,c]

[1]*St. Xavier's College (Autonomous), Ahmedabad,* [2]*Physical Research Laboratory, Ahmedabad*

[a]*kishanmalaviya35@gmail.com,* [b]*anwesh@prl.res.in,* [c]*shashi@prl.res.in*

Abstract: Optical simulations are presented using python modules for the image quality analysis of astronomical telescopes. We have modelled the 1.2M telescope of Mount Abu Infrared Observatory (MIRO) in *POPPY* to understand the effects of diffraction on the resolution of the telescope. The PSFs at different wavelengths, encircled energy profiles & radial profiles are obtained. To analyze the contributions of the optical aberrations, we've used the *RAYOPTICS* module. The optical parameters of the 1.2M telescope are utilized to produce raytracing diagrams, spot and aberration plots. The methods used are general in nature and may be adapted to other telescopes as well as different optical systems.

Keywords: python, optical simulation,point spread function, RAYOPTICS, POPPY,

Image quality at the focus of an astronomical telescope is affected by various factors such as atmospheric turbulence, optical aberrations within the telescope with the ultimate coming from the diffraction limit. In this work we have produced optical simulations using free/open-source software – *POPPY* and *RAYOPTICS* python modules – for estimating diffraction and optical aberration related effects. Free/opensource software are important for scientific research as they generate results that can be reproduced and verified by others. POPPY (Physical Optics Propagation through PYthon) is developed primarily by a team of astronomers at the Space Telescope Science Institute(STScI). *POPPY* was originally developed for the James Webb Space Telescope project (Perrin, 2012)[1,2] but is general enough to be useful in many different kinds of imaging simulations. Here, we have modeled the 1.2M Telescope, MIRO (Mount Abu InfraRed Observatory) [3]in *POPPY*. The PSF resulting from the finite nature of the primary mirror and the obstruction due to secondary mirror and mirror support structures is simulated. The simulated entrance pupil, PSF and created encircled energy profile of the telescope are shown in figure 1. This analysis is important as it puts quantitative constraints on the effects of diffraction which can be non-negligible for upcoming near-infrared instruments such as NISP[4].

For simulating optical aberrations the choice of software is not as straight forward. There exist various commercial software such as ZEMAX and CODE V which can perform these tasks but these are not free/opensource and are expensive (typically with cumbersome subscription schemes). Although raytracing software itself is not a new concept[5] and there exist some free/open-source software (e.g. BEAM4[6]), they have not enjoyed widespread use. In this context, the *RAYOPTICS* module[7], which is completely based on the general purpose Python language is a promising development. *RAYOPTICS* is a geometrical optics and image forming optics library which provides a geometric ray tracing foundation for the analysis of image forming and coherent optical systems. For illustration purposes, we have modeled the 1.2M Telescope at MIRO in *RAYOPTICS*. We initiated the sequentially created model of the 1.2M telescope to obtain its optical layout depicting the arrangement of the different optical elements of the telescope and an aberration plot showing Seidel aberration coefficients (shown in figure 2). We have also produced Spot diagrams for different field points as shown in figure 3. As both of these modules are written in Python, it is possible to combine functionalities of each into one single script so as to simulate practical real world performance of optical systems.

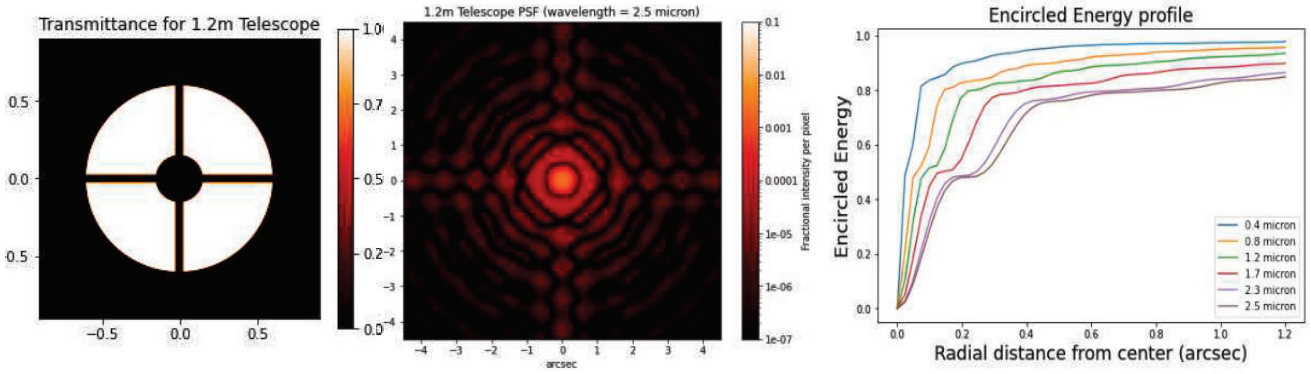

Fig. 1: (a) Entrance Pupil, (b) PSF at 2.5 µm wavelength & (c) Encircled energy profile of 1.2M Telescope

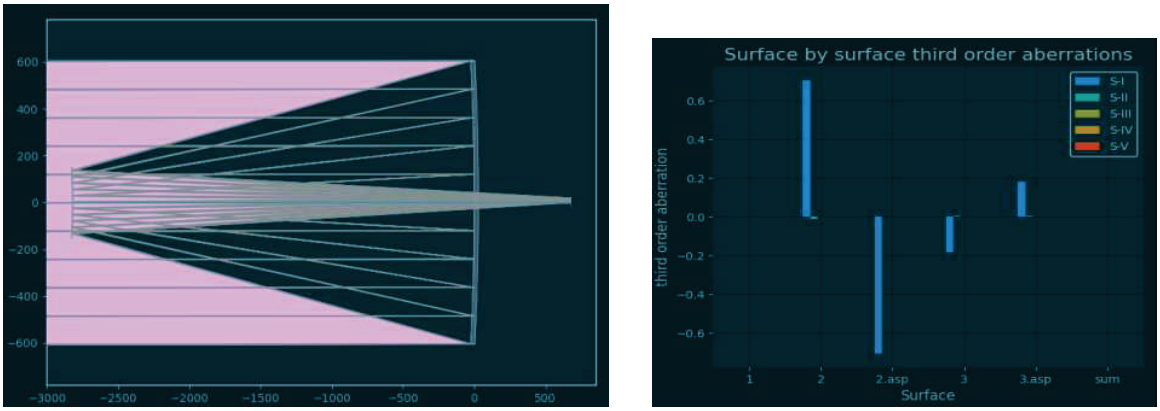

Fig. 2: (a) The Optical Layout (b) Seidel Aberration plot for 1.2 M Telescope

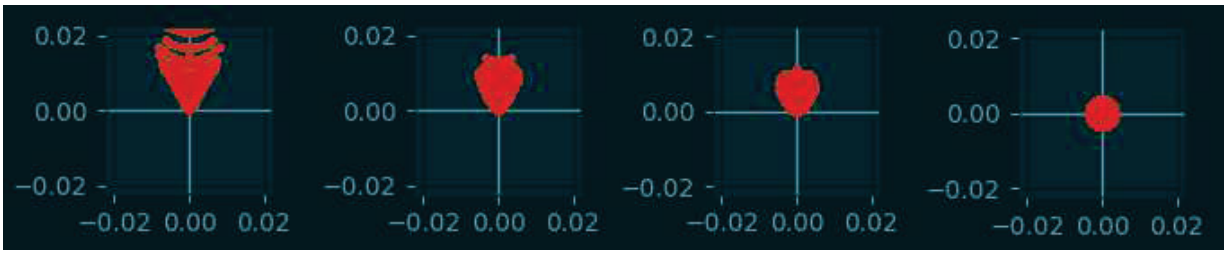

Fig. 3: Spot diagrams (in mm x mm scale) for field point values 10', 5',2.5',0' (arcminutes) respectively

References

[1] Perrin, Marshall D., et al. "Simulating point spread functions for the James Webb Space Telescope with WebbPSF." *Space Telescopes and Instrumentation 2012: Optical, Infrared, and Millimeter Wave*. Vol. 8442. SPIE, 2012.

[2] POPPY module – documentation - https://poppy-optics.readthedocs.io/en/latest/about.html

[3] MIRO Website- *https://www.prl.res.in/~miro/*

[4] Rai, Archita, et al. "Optical aspects of Near-Infrared Imager Spectrometer and Polarimeter instrument (NISP)." *Ground-based and Airborne Instrumentation for Astronomy VIII*. Vol. 11447. SPIE, 2020.

[5] Brixner, Berlyn. "Automatic lens design for nonexperts." *Applied Optics* 2.12 (1963): 1281-1286.

[6] BEAM FOUR by Stellar Software -https://www.stellarsoftware.com/about-us

[7] *RAYOPTICS* module - documentation- https://ray-optics.readthedocs.io/en/latest/

Gyro-Sensor and Spectral Interferometry

Shouvik Sadhukhan[1], Saikat Sadhukhan[2], Maruthi M Brundavanam[3] and C S Narayanamurthy[4]
[1,4]*Department of Physics, Indian Institute of Space Science and Technology (IIST), P.O: Valiamala, Trivandrum - 695547, State: Kerala; India*
[2]*Department of Mining Engineering, Indian Institute of Engineering Science and Technology, Shibpur, Howrah-711 103, West Bengal, India.*
[3]*Department of Physics, Indian Institute of Technology, Kharagpur-721302, West Bengal, India.*
Corresponding Email: shouvikphysics1996@gmail.com[1]

Abstract: We have discussed the spectral switch shift around spectral anomalies in this present work. Our main motivation is to incorporate the gyro sensing technology with the spectral switch shift which is efficient to give the nano scale measurements using polychromatic waves. In our designed gyro-sensor we have shown the calibration of spectral switch shift around spectral anomalies with angular momentum and radius of gyroscopic interferometer.

Keywords: Spectral anomalies, Temporal Coherence, Spectral switch, Sagnac Interferometer, Gaussian polychromatic Beam, Galilean Frame, Doppler shift

1. Introduction

In recent times, the spectral shifts around spectral switches are used to measure the Nano-displacement technique that is done with broad band polychromatic source in spectral interferometers. This Nano-displacement technique has not been used in the measurements of angular momentum of optical gyroscope. Also, the application of optical gyroscopic motion with white light can provide the results for Doppler shift. Hence, it is necessary to find the relation between the spectral shift around spectral switch and Doppler shift. Several experiments have been reported in literature using spectral shifts around spectral switches, for example, phase singularity in the complex analytic signal of a speckle pattern as indicators of displacement in nanometer scales, an interferometric phasemeter based on attenuated total internal reflection as nanoscale linear sensor and spectral-domain phase microscopy for detection of nanometer-scale motions in living cells.
In this paper, the spectral shifts around spectral switches are used to measure the angular momentum of the gyroscope based on modified Spectral Sagnac interferometer. The calibration curves for the measurements of angular momentum, radius and angular velocity of the gyroscope are obtained using analytical calculations and computer simulations. The results obtained in this paper will be useful in aircraft velocity measurements and Gravitational wave detection [1,2,3].

2. Design of the proposed method

The work starts from the following experimental diagram. The experimental set up contains a gyroscopic stage, a square type three mirror Sagnac interferometer with non-polarizing beam splitter and computer operated rotor motor. The diagram can be attached as follows.

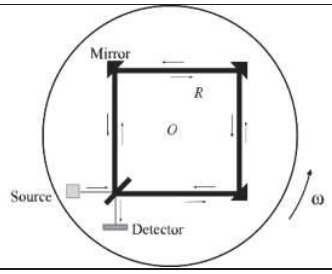

Fig.1 Block Diagram of Gyro Sensor

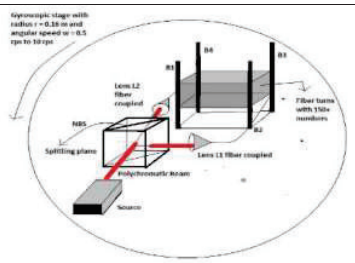

Fig. 2 Realistic Engineering Diagram of Gyro Sensor

The engineering diagram contains four optical stands with 150+ turns of polychromatic optical fiber. The set-up is in a compact form on a gyroscopic stage with a diameter of maximum 0.33 meter. The gyroscopic stage is connected with a special computer-controlled motors. The fundamental theories applicable on this sensor technique can be given as follows. The mathematical form of the polychromatic intensity output can be given as follows.

$$I(\lambda) = H_0 \exp\left(-\frac{1}{2}\left(\frac{\lambda-\lambda_0}{\Delta\lambda}\right)^2\right)(1+\cos\theta) \quad (1)$$

Here, in equation (1) we have used polychromatic source with peak wavelength λ_0. The gyroscope provides the phase difference θ where, we can write the phase difference as follows relation. We have used the gyroscopic stage with radius R and angular speed as ω.

$$\theta = \frac{8\pi^2}{c}\frac{R^2\omega}{\lambda} \quad (2)$$

With changing the rotation and radius of the stage we can find the first spectral switch point. The change of the calibrated switch points can bring a shift in the spectral switch. The spectral switch must come with the relation as follows.

$$\frac{8\pi^2}{c}\frac{R^2\omega}{\lambda_0} = \pi \quad (3)$$

We can show the calibrated results of our sensor as follows in next section. This spectral switch shift measurement technique basically increases the sensitivity of the gyro sensor. Now the sensor is capable to measure 0.001 rps speed very easily. Even, smaller measurements can be done here. The turbulent medium average density can also be measured with this sensor. The phenomena can also incorporate the doppler shift (z) with the following equation.

$$z = \frac{\Delta\lambda}{\lambda} = \frac{\omega R}{c} \quad (4)$$

The calibration of doppler shift has also been given in the result section.

3. Figures and Results

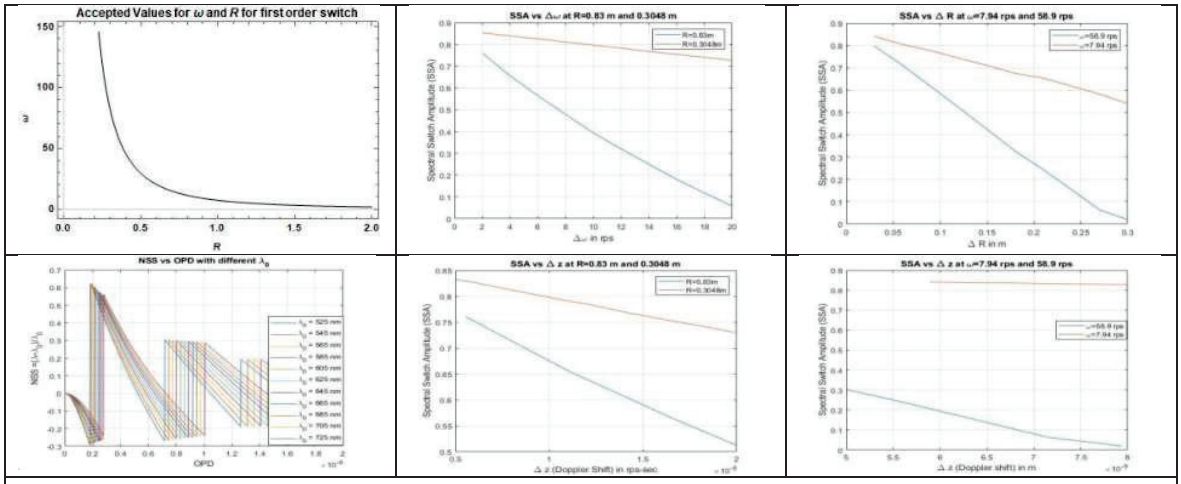

Fig. 3. The results of our work with NSS and SSA of Spectral switch shift and Doppler shift calibration

Those results are useful in the study of turbulence medium with spectral switch interferometry and gyro sensor.

4. References

[1] Sadhukhan, S., Sadhukhan, S., Brundavanam, M.M. and Narayanamurthy, C.S., 2022. Spectral Switch Anomalies in Sagnac Interferometer with respect to Galilean Frame. *arXiv preprint arXiv:2204.06190*.

[2] Brundavanam, M.M., Viswanathan, N.K. and Desai, N.R., 2007. Spectral anomalies due to temporal correlation in a white-light interferometer. Optics letters, 32(16), pp.2279-2281.

[3] Brundavanam, M.M., Viswanathan, N.K. and Rao, D.N., 2008. Nanodisplacement measurement using spectral shifts in a white-light interferometer. Applied optics, 47(34), pp.6334-6339

[4] Brundavanam, M.M., Viswanathan, N.K. and Rao, D.N., 2009. Effect of input spectrum on the spectral switch characteristics in a white-light Michelson interferometer. JOSA A, 26(12), pp.2592-2599.

Time-frequency of single photons as quantum continuous variables

Nicolas Fabre
Departamento de Óptica, Facultad de Física, Universidad Complutense, 28040 Madrid, Spain
nfabre@ucm.es

Abstract: Various discrete degrees of freedom of single photons have been used in quantum protocols. We consider the time and the frequency not only as discrete but as continuous variables, and tackle all the hypotheses to consider them as so. We study the universal set of gates for this new encoding, and how such a set can be implemented experimentally. Finally, we will discuss a direct application of photon pairs in quantum sensing protocols for the estimation of time and frequency shifts.
Keywords: Continuous variables, single photons, quantum optics, time-frequency estimation protocols

In this talk, I will present why we can consider the time and the frequency degree of freedom of single photons as continuous quantum variables. Such a degree of freedom is generally discretized into modes for experimental reasons, but it is not a physical requirement. The origin of the quantumness of the time and frequency variables can be explained because of the non-commutativity of time and frequency operators - which can be defined properly- when restricted to the one photon per mode subspace. As a consequence, I will show that frequency and time operators can be used to define a universal set of gates in this particular subspace [1].

We discuss the physical implementation of these gates as well as their effect on single photon states, and show that frequency and time variables can also be used to implement continuous variables quantum information protocols, in the same way that polarization is currently used as a two-dimensional quantum variable. In particular, I will discuss the recent experimental implementation of a frequency shifter [2], which is an essential operation for any quantum protocols using time and frequency degree of freedom, and how it can be used for performing the tomography of single photon fields.

Finally, I will explain the importance of time-frequency grid biphoton states in temporal error correction and how they can be generated with integrated optical waveguides [3]. These time-frequency grid states can also be used in time and frequency shift-estimation protocols using the Hong-Ou-Mandel interferometer [4]. I will explain how we can compare the performance of various time-frequency biphoton states in such sensing protocols. I will show that time-frequency grid states can provide a resolution under the attosecond.

[1] N. Fabre, A. Keller, and P. Milman, Time and Frequency as Quantum Continuous Variables, Phys. Rev. A **105**, 052429 (2022).
[2] S. Kurzyna, M. Jastrzębski, N. Fabre, W. Wasilewski, M. Lipka, and M. Parniak, Variable Electro-Optic Shearing Interferometry for Ultrafast Single-Photon-Level Pulse Characterization, arXiv:2207.14049 (to be accepted in Optics Letters).
[3] N. Fabre et al., *Generation of a Time-Frequency Grid State with Integrated Biphoton Frequency Combs*, Phys. Rev. A **102**, 012607 (2020).
[4] N. Fabre and S. Felicetti, Parameter Estimation of Time and Frequency Shifts with Generalized Hong-Ou-Mandel Interferometry, Phys. Rev. A **104**, 022208 (2021).

Line-Field Time-Domain Optical Coherence Tomography of Fish Eye

Harpreet Kaur[1,2], Pitambar Mukherjee[2], Dibakar Borah[2], Sunil Bhatt[2], and Dalip Singh Mehta[1,2,*]

[1]*SeNSE, Indian Institute of Technology Delhi, New Delhi- 110016*

[2] *Bio-photonics and Green-photonics Laboratory, Department of Physics, Indian Institute of Technology Delhi, Hauz-Khas, New Delhi 110016, India.*

[*]mehtads@physics.iitd.ac.in

Abstract: We proposed a line-field time-domain optical coherence tomography (LF-TD-OCT) for the sectioning of the biological samples by utilizing the longitudinal spatial coherence (LSC) property of the light source. Here, we have used an NIR laser light ($\lambda = 808$ nm) as a partially spatially coherent (PSC) source by passing it through the microscope objective (MO), rotating diffuser (RD) and multi multimode fiber bundle (MMFB). We illuminate the sample with line of light illumination by passing the PSC light through the cylindrical lens. Further, the z-scanned dataset with a constant step size is recorded and used for the sectioning of the fish eye. We successfully reconstructed the multiple layers of the fish eye with improved signal-to-noise ratio (SNR) employing the proposed LF-TD-OCT. Thus, the proposed approach can be further utilized for the multilayer sectioning of biological samples with improved SNR.

Keywords: optical coherence tomography, longitudinal spatial coherence, fisheye imaging, coherence

1. Introduction

Optical coherence tomography (OCT) is a cutting-edge technique with wide applications because of its non-contact, non-invasive, real-time, cross-sectional imaging capabilities with micrometer-scale resolution. OCT is one of the most well-known methods in biomedical imaging. When compared to microscopy, OCT creates cross-sectional images of interior structures with 100 times greater depth of penetration than confocal microscopy [1]. Time domain optical coherence tomography (TD-OCT) is the most oftenly used technique for the cross-sectional imaging [2]. In this paper, LF-TD-OCT has been introduced, which provides better SNR as compare to full-field OCT due to its line illumination reduces the background noise comparatively in layer-to-layer detection of biological and non-biological samples. Using line illumination of NIR laser light, multiple A-scans are acquired with light source having LSC which produce high axial resolution. In general, OCT is performed using low temporal coherence of the light source. Here, we exploit the LSC property of a monochromatic light source which result same order of axial resolution.

2. Methodology

The study is performed on biological sample i.e., fish eye using the experimental setup as shown in Fig. 1. In this experiment, Linnik interferometer is used that has two microscope objectives (MO_2 and MO_3), one at the sample arm and one at the reference arm, respectively.

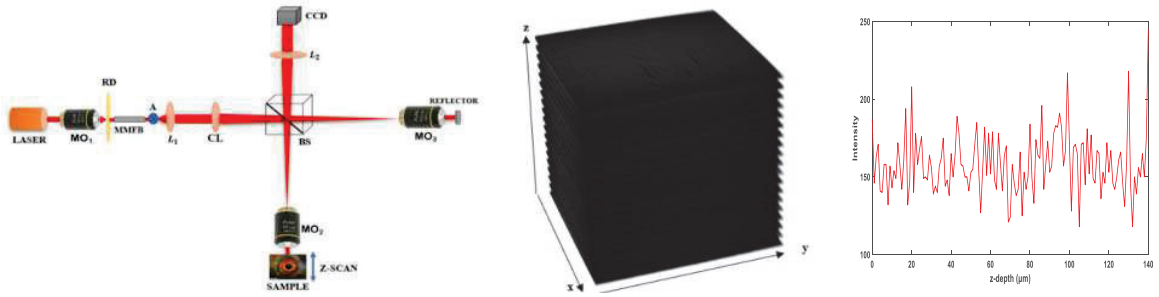

Fig. 1. (a) Experimental set-up of LF-OCT system. MO: microscope objectives; BS: beam splitter; L: lenses; CL: cylindrical lens, RD: rotating diffuser; MMFB: multi multimode fiber bundle; A-aperture; and CCD-charge coupled device**.** ***(b) Stack of recorded 20 interferograms obtained by scanning the sample along vertical direction. (c) Intensity variation at a particular pixel of interferogram's stack along z direction.***

A direct laser is avoided in imaging due to its high spatial coherence property which generates speckles reduces the image quality. Hence, an NIR laser (808 nm) is passed through a MO, RD, and a MMFB to eliminate speckles and noise due to angular, spatial and temporal diversity. The output of MMFB is treated as an extended light source with high temporal but low spatial coherence property i.e., PSC light source. Thus, a PSC light is input into the Linnik interferometer where lens L_1 collects and collimate the input light and transformed into line by passing through a cylindrical lens (CL) and focused it into the back focal plane of the identical MO's: MO_2 and MO_3 in sample and reference arm are for the uniform illumination in the front focal plane of the objectives [3]. The back reflected light from the sample and reference got interfered at BS plane which further projected on the camera plane using a tube lens L_2. We placed the sample onto the sample stage and scanned axially with a constant step size of 1 µm to record the interferograms from -z to +z respectively, thus, total 142 interferograms are recorded. All the interferograms are then stacked along the z direction. The intensity of the interferogram becomes maximum, when optical path difference (OPD) is zero. As the OPD increases, the intensity of the interferogram decreases [4].

In MATLAB (R2021b), FFT is used to reconstruct the interferograms. Then, we stack all the interferogram as shown in fig 1(b). Following that, we took a scan along one pixel. Fig 1(c) shows the intensity variation along the z-depth at a particular pixel in interferogram's stack, and after removing interferograms noise by gaussian filter and normalization, layers of fish eye is found with high SNR.

3. Result and Discussion

The interferograms made from biological samples may contain a variety of noise and fluctuations that skew the signal. As a result, we processed interferograms, first normalizing the signal by dividing each interferogram by its greatest intensity. Then, using the gaussian filter in convolution, we attempted to smooth the signal [5]. Following that, we obtain the result depicted below by performing the FFT and IFFT. Fig 2(a) shows the noise reduced FFT signal obtained from the intensity profile for a single pixel (661,81). Fig 2(b) shows the interferogram peaks at different positions which may be used to interpret the fish eye's layer interfaces.

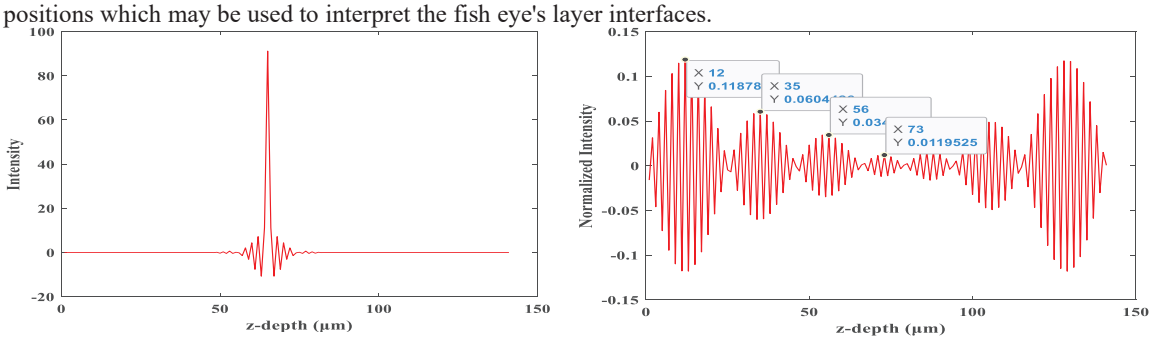

Fig.2. (a) Result obtained using FFT method (b) Interferogram signal acquired by line illumination at pixel (661,88) showing layer interfaces

4. Conclusion

We proposed an idea of LF-TD-OCT for the tomography of biological samples. In order to obtain a speckle-free interferogram at the output of the CCD camera, we transformed a direct NIR laser into a PSC light source by reducing its spatial coherence. The interferograms are stacked and then reconstructed to provide the high-quality cross-sectional imaging.

5. References

[1]. Drexler, W., & Fujimoto, J. G. (Eds.). (2015). Optical coherence tomography: technology and applications (Vol. 2). Berlin: Springer.

[2]. Dubois, A., Levecq, O., Azimani, H., Davis, A., Ogien, J., Siret, D., & Barut, A. (2018). Line-field confocal time-domain optical coherence tomography with dynamic focusing. Optics express, 26(26), 33534-33542.

[3]. Ahmad, A., Mahanty, T., Dubey, V., Butola, A., Ahluwalia, B. S., & Mehta, D. S. (2019). Effect on the longitudinal coherence properties of a pseudothermal light source as a function of source size and temporal coherence. Optics letters, 44(7), 1817-1820.

[4]. Srivastava, V., Nandy, S., & Singh Mehta, D. (2013). High-resolution corneal topography and tomography of fish eye using wide-field white light interference microscopy. Applied Physics Letters, 102(15), 153701.

[5]. Sokolovsky, J., Yitzhaky, Y., & Abdulhalim, I. (2012). Analysis of interferograms of multi-layered biological samples obtained from full field optical coherence tomography systems. Applied Optics, 51(35), 8390-8400.

A purview into highly sensitive magnetic SERS detection of hemozoin biomarker for rapid malaria diagnosis

Sarjana Yadav[a], Rizwin Khanam[a], J.P. Singh[a]*

a. Department of Physics, Indian Institute of Technology Delhi, HauzKhas, New Delhi-110016, India

Email: jpsingh@physics.iitd.ac.in

Abstract

Here, we report detection of hemozoin, a metabolic byproduct of malaria parasite exhibiting paramagnetic properties using magnetic surface enhanced Raman spectroscopy (M-SERS). The SERS active silver nanorods were deposited over neodymium magnetic substrates (0.3 T) kept at 120K temperature using glancing angle deposition technique. Magnetic field augmented SERS measurements were performed for hemozoin on these M-SERS substrates and AgNRs deposited over glass (conventional SERS) substrates in presence of an external magnetic field (0.3 T). The SERS signal intensity was found to be enhanced by ten-fold compared to the measurements performed on the conventional SERS substrates in the absence of any magnetic field. The presence of high spin trivalent iron in hemozoin structure led the magnetic field induced agglomeration of these molecules in vicinity of the electromagnetic 'hotspots' available on the SERS substrates which was confirmed by running RCWA based simulations. These interactions lead to higher enhancement of vibrational modes of the porphine group directly linked to iron. The limit of detection of hemozoin for M-SERS was obtained as low as 10^{-11} M (< 10 parasites/µl) which can be employed for early stage malaria detection.

Keywords: Hemozoin, Malaria, Hemoglobin, Surface enhanced Raman spectroscopy, Glancing angle deposition, magnetic substrates

1. Introduction

According to the world malaria report for the year 2020 by the World Health Organization (WHO), nearly half of the world's population is at risk of malaria.[1] Malaria is a disease caused by the Plasmodium parasite, a single-celled protozoan that spreads through the biting

of an infected female Anopheles mosquito. Hemoglobin in our blood constitutes the major protein part in the red blood cells (RBCs), and these parasites feed and digest around 70 -75% of the cell's hemoglobin during the invasion of erythrocytes. This process involves a series of enzymatic events leading to formation of peptides and subsequently releasing several free heme moieties as byproducts.[2] Free heme being very toxic in nature for parasites causes cellular oxidative damage and cell rupture. Therefore, it is neutralized by the parasite and gets converted into an insoluble "malaria pigment" hemozoin as a distinct attribute of malaria.[3] The early-stage detection of malaria is crucial for its proper treatment. More efforts are needed in the direction of enhancing the detection of minute hemozoin concentration in the infected RBC's. Also, reproducibility and sensitivity are the significant issues in these SERS based malarial detection. It has been reported that hemozoin displays an unusual super paramagnetic behavior. An external magnetic field can magnetize these nanostructures if they are paramagnetic. The advantage of using a super paramagnetic material is that the materials saturate with a relatively high magnetization at low applied fields. When held below the material's Curie temperature, the magnetic moments inside a magnetic domain align parallel to the applied field to produce the high magnetization. This specific property can enhance the SERS spectra of hemozoin, increasing the specificity of the malaria diagnosis.

In this work, we report a novel method of magnetic field augmented SERS detection of hemozoin by fabricating silver nanorods (AgNRs) directly on neodymium magnetic substrates and also by using an external magnetic field. A comparative study has been done for conventional SERS detection of hemozoin using AgNRs over glass substrates and its magnetic field based SERS detection.

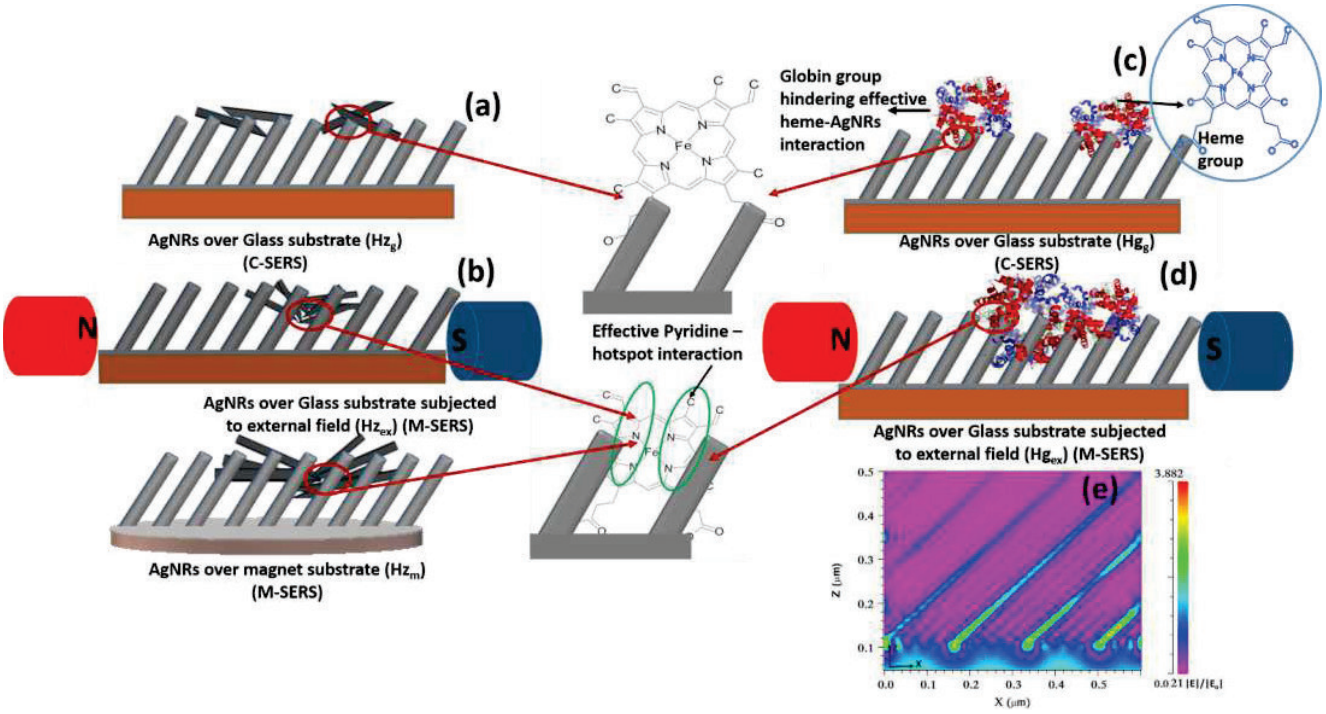

Figure 1: : Schematic diagram showing (a) pyridine- AgNRs interaction for unmagnetized Hz over AgNRs SERS substrate (c-SERS) (b) effective pyridine – AgNRs interaction for Hz in the vicinity of magnetic field (M-SERS). (c) pyridine- AgNRs interaction for unmagnetized Hg over AgNRs SERS substrate (c-SERS) (d) effective pyridine – AgNRs interaction for Hg in the vicinity of magnetic field (M-SERS). (e) RCWA modelling to show localized hotspots in the nanorods gap for effective hotspot-analyte interaction

References

[1] W. Health Organization, World malaria report 2020: 20 years of global progress and challenges, 2020. https://www.wipo.int/amc/en/ (accessed April 5, 2021).

[2] Hemoglobin - an overview | ScienceDirect Topics, (n.d.). https://www.sciencedirect.com/topics/chemistry/hemoglobin (accessed May 2, 2021).

[3] A.K. Tripathi, B.L. Tekwani, S.K. Garg, A physiochemical mechanism of hemozoin (β-hematin) synthesis by malaria parasite, Biochem. Biophys. Res. Commun. 290 (2002) 595–601. https://doi.org/10.1006/bbrc.2001.6231.

[4] S. Kumar, P. Goel, J.P. Singh, Flexible and robust SERS active substrates for conformal rapid detection of pesticide residues from fruits, Sensors Actuators, B Chem. 241 (2017) 577–583. https://doi.org/10.1016/j.snb.2016.10.106.

[5] A. Rajput, S. Kumar, J.P. Singh, Vertically standing nanoporous Al-Ag zig-zag silver nanorod arrays for highly active SERS substrates, Analyst. 142 (2017) 3959–3966. https://doi.org/10.1039/c7an00851a.

Tunable Optical Frequency Comb

Vikas, Soumendu Jana*

SPMS, Thapar Institute of Engineering & Technology, Patiala,147004

*soumendu.jana@thapar.edu

Abstract

Scientific and technological studies are useless without accuracy and precision. The optical frequency comb has increased the accuracy in the performance of an experiment. In this article, we present the optical frequency comb in a microresonator with different saturable absorbers, namely, graphene saturable absorber, semiconductor saturable absorber mirror and graphene flakes saturable absorber. The optical frequency comb has been generated via cavity solitons. The intracavity field, given by a CGLE has been numerically solved. Using the split-step Fourier method to achieve the optical frequency comb for a range of system parameters.

Keywords: optical frequency comb, saturable absorber, cavity soliton.

Introduction

The optical frequency comb[1] (OFC) is a spectrum of equispaced lines that represent different frequencies. It has become a gadget for high precision and accuracy in an experimental set-up. In the last part of the twentieth century, the production of OFC has become one of the top trend among scientists. There are different kinds of OFC depending upon the generating methods and characteristics of OFC such as by mode-locked laser, by four-wave mixing, by optical parametric oscillation, from second harmonic generation, by phase modulation, from solitons[2,3] etc. Here we are generating the OFC via cavity soliton and checking the effects of the input of chirping on it. Chirping is the instantaneous change in the frequency of a pulse when it passes through a nonlinear medium. For e.g. squeezing or broadening. Chirping can be generated in a pulse during propagation due to chromatic dispersion and /or nonlinearities of the medium.

In this article, we have produced OFC in a microresonator with the help of different saturable absorbers (SAs) namely, graphene saturable absorber (GSA), semiconductor saturable absorber mirror[5] (SESAM) and graphene flakes saturable absorber (GFSA). Also, different chirps of the input field have been used. For the different values of the cavity parameters, different structures of OFC are formed.

System Equation

The proposed investigation will be on the generation and dynamics of OFC via cavity soliton. The governing equation for the intracavity field is usually a modified complex Ginzburg Landau equation[6] (CGLE).

$$\frac{\partial E}{\partial t} = [-(1 - i\theta) + \frac{(1 - i\alpha)}{1 + g_1 I}\mu(1 - i\beta) - \gamma\frac{(1 - i\beta)}{1 + s g_2 I} + \alpha_{ns} + i\Delta]E + (a - i\,b)E \quad \ldots.(1)$$

Where, $a = \frac{\sigma\lambda^2}{\lambda^2 + \Omega_0^2}$ and $b = \frac{\sigma\lambda\,\Omega_0}{\lambda^2 + \Omega_0^2}$.

In this above modified CGLE, E is slowly varying cavity field amplitude, I is instantaneous intensity, t is cavity round trip time, θ is cavity detuning parameter that measures the mismatch between feedback field and the cavity field, α and β are linewidth enhancement factors for active and passive medium respectively. α_{ns} is the amount of non-saturable absorption coefficient. μ is the pump parameter, s is the saturation strength, g_1 and g_2 are the enhancement factors of saturation strength of GSA/GFSA with respect to SESAM for active

and passive media respectively. λ is the bandwidth of the feedback field. $\mathbf{\Omega}_0$ is the resonance frequency of the feedback field and σ is the feedback strength (coupling strength) of the feedback field. .

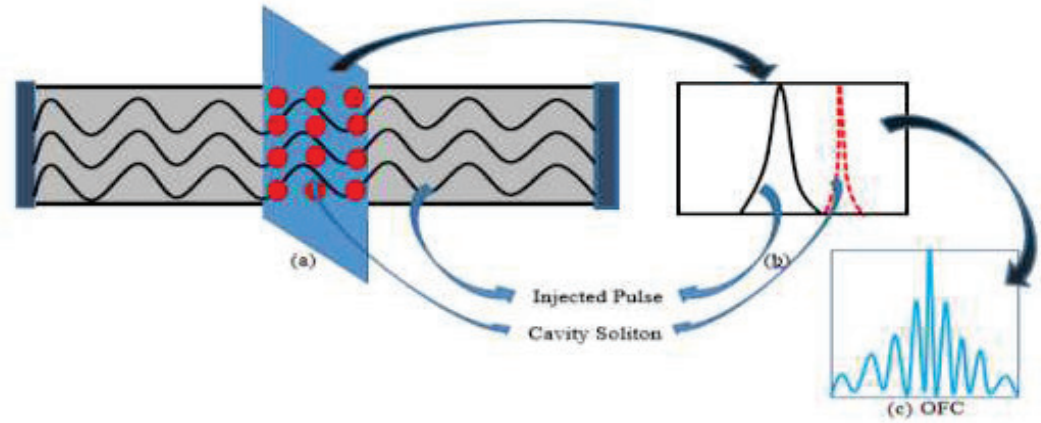

Figure 1: Schematic diagram for generation of OFC via cavity soliton

Generation and Tuning of OFC

The governing CGLE (1) is solved by the split-step Fourier method. For numerical simulations, we consider the system parameters as follows (unless mentioned otherwise).

$g_1 = g_2 = 1$ (SESAM), $g_1 \neq g_2 \neq 1$ (GSA/ GFSA), $\mu = 1.37$, $\alpha = 5$, $\gamma = 0.5$, $\beta = 0.5$, s = 10, $\lambda = 0.5$, $\sigma = 0.3$, $\mathbf{\Omega}_0 = 1.6$

For certain range of system parameters cavity soliton can be generated (fig.1 (b)). The Fourier transform of that cavity soliton leads to OFC (fig. 1(c)). Since spatial structure, the generated OFC is basically a spatial frequency comb. OFC for different SAs and different chirps "c" of the input beam are demonstrated in figs 2, 3 and 4.

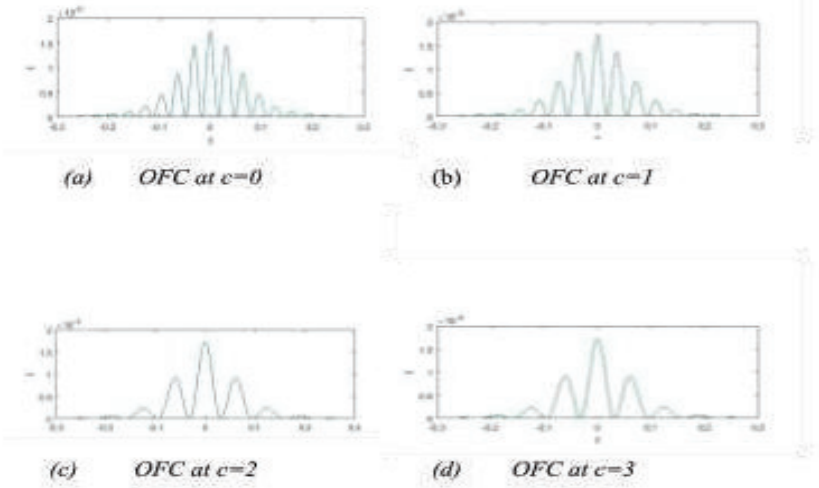

Figure 2: OFC profiles for different chirp "c" in case of SESAM

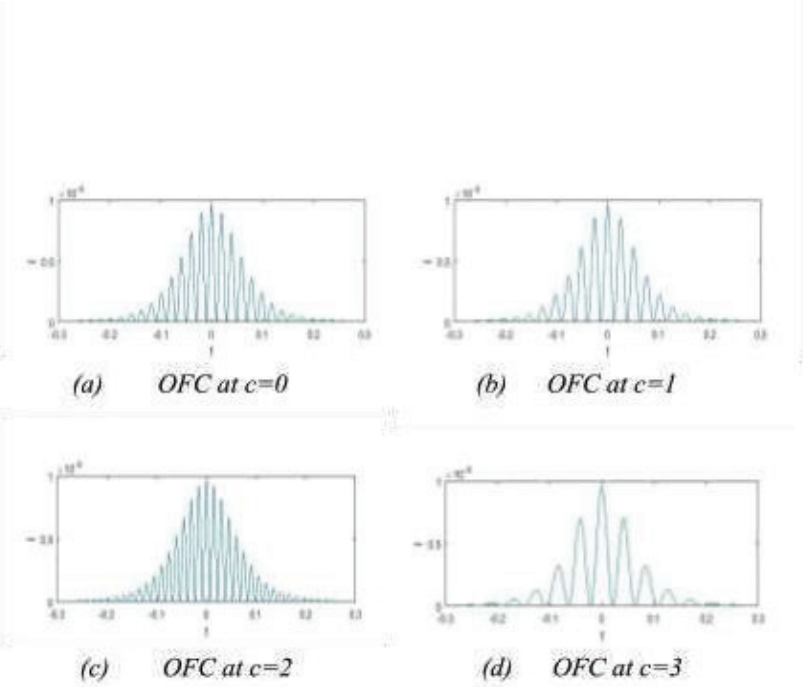

Figure 3: OFC profiles for different chirp "c " of the input beam in case of GSA

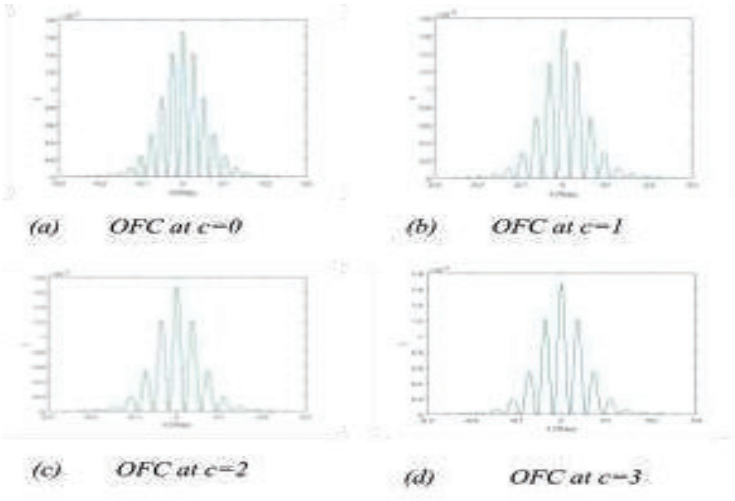

Figure 4: OFC profiles for different chirp "c" of the input beam in case of GFSA

Figure 2, 3, and 4 shows that the chirp of the input beam and SA parameters significantly influence the OFC structure. Other system parameters can also do the same for a certain selected range. Thus tunable OFC is possible.

Conclusion

Different OFC has been generated via cavity soliton in a microresonator with different SAs and selective frequency feedback. By changing the SAs parameters and the chirping of the input beam the OFC can be tuned. Other system parameters can also be varied to tune the OFC. The results presented here can be applied for further experimental verification and construction of tunable OFC devices.

Acknowledgment

S. Jana acknowledges the financial help of SERB, Govt. of India, through the Core Research Grants (File Number: CRG/2019/005073 & TIET/CEEMS/Regular/2021/021/6.9.2021).

References:-

1. Udem, Th, Ronald Holzwarth, and Theodor W. Hänsch, *Nature.* **416**, 233 (2002).
2. Yi, Xu, Qi-Fan Yang, Ki Youl Yang, Myoung-Gyun Suh, and Kerry Vahala, *Optica.* **2**, 1078 (2015).
3. Fortier, Tara, and Esther Baumann, *Communications Physics.* **2**, 1 (2019)
4. Chen, Shihua, Yi Zhou, Lili Bu, Fabio Baronio, Jose M. Soto-Crespo, and Dumitru Mihalache, *Optics express.* **27**, 11370 (2019).
5. Torizuka, Kenji, Zhigang Zhang, Taro Itatani, Katsuyuki Kobayashi, Takeyoshi Sugaya, and Tadashi Nakagawa, *Femtosecond Technology*. 284 (1999).
6. Nagi, Jaspreet Kaur, and Soumendu Jana, *Chaos, Solitons & Fractals.***158** (2022).

Fast layer-based CGH generation for large matrix dimensions

Anuj Gupta*, Raj Kumar and Bhargab Das
CSIR-Central Scientific Instruments Organisation, Chandigarh - 160030
**Corresponding Author: anujgupta@csio.res.in*

Abstract: The generation of a computer generated hologram (CGH) involves intensive calculations making the display of object information hard to achieve. The object size, number of pixels, and resolution significantly affect the computational cost of CGH generation. Therefore, it becomes very important to optimize the CGH generation algorithm for large matrix dimensions in order to use it in several practical applications, such as holographic printers. This work includes the comparative analysis of CGH generation for various resolutions in two different programming languages, viz., MATLAB and Python.
Keywords: Computer-generated hologram; Holographic displays, Layer-based method.

1. Introduction

Holography represents the formation of a two dimensional complex pattern which contains the amplitude as well as the phase information of a three dimensional (3D) scene. This information is used to optically reconstruct the object from the recorded hologram. Computer generated hologram (CGH) is a hologram which can be generated by numerical methods even in the absence of any physical object [1]. CGH generation is very useful but it is a computationally expensive process. It involves the intensive calculations which depends upon several factors such as size of the modeled object, pixel size in the object plane, the resolution of the CGH or hologram plane etc. The huge computational cost which significantly increases with the increase in any of the above mentioned factors necessitates the optimization of the CGH generation process. This work is an effort to optimize the process of CGH generation for holographic displays at higher resolutions. The optimization of this process can be achieved by executing the working of hardware as well as software parts in synergy. In order to accelerate the process of CGH generation, several hardware accelerator platforms like CPU, GPU, FPGA etc. are used [2]. Along with this, algorithms should be designed in an optimized way to get the maximum output from the available sources. This work is an effort to work on the efficiency of the algorithm so as to speed up the process of CGH generation for higher resolutions.

2. Methodology

Point cloud based, polygon based, layer based, and light field method are the four major categories in which CGH generation is divided [3]. In the present work, the layer based method is implemented to generate the CGH. The method can also be called as plane based method because of the implementation of only a single plane in the algorithm. The pixel size and the number of pixels in the object plane significantly affect the execution time of the algorithm. The larger the resolution, the higher will be the execution time. We started with the lower resolution of 1024×1024 and generated the CGH for this. Subsequently, the resolution of the object model is increased to 2048×2048, 4096×4096 and 8192×8192. The pixel pitch is kept to be 6.4 μm, wavelength 632.8 nm and distance between object plane and CGH plane is $1m$.

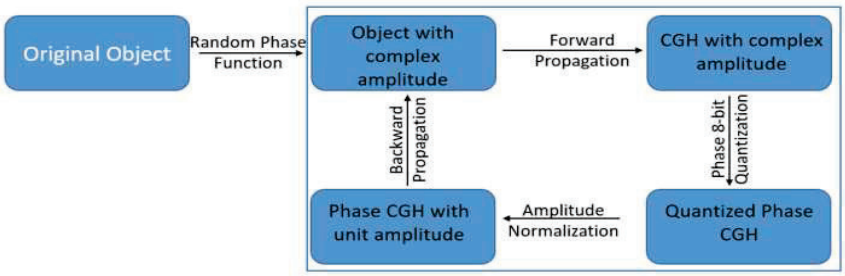

Fig. 1: Flow chart of the plane-based CGH generation with iterative beam propagation method

Initially, the original object is combined with a diffusive function implemented by a random phase pattern. Afterwards, the object plane is propagated in the forward direction using FFT based algorithm. The propagated field

is a complex amplitude function consisting of phase as well as amplitude information. In this CGH plane, the phase part is retained and amplitude part is reduced to unit value. Subsequently, phase of the CGH is 8-bit quantized. This unit amplitude phase-CGH is propagated back to the object plane wherein the amplitude information is replaced by the original object information. Multiple iterations are carried and the generated phase-CGH is used for both numerical and optical reconstruction.

3. Results and Discussion

Firstly, we developed a basic algorithm in MATLAB as well as in Python which generated a CGH using a plane based technique in a sequential manner. The implementation of underlying physics is cross verified by developing the algorithms for an object at a smaller resolution and reconstructing its output CGH numerically as well as optically. The resolution of generated CGH is matched with that of spatial light modulator (SLM) resolution viz. 1920×1080. This is achieved with the use of zero padding of the CGH. Subsequently, the phase CGH is quantized to 8 bit and loaded into the SLM in order to reconstruct the object optically. In addition to this, object models are also reconstructed numerically with the basic technique of backward propagation to the object plane. Fig. 2(a)-(c) shows the original object, corresponding computed CGH zero padded to match SLM resolution, and the numerically reconstructed result, respectively.

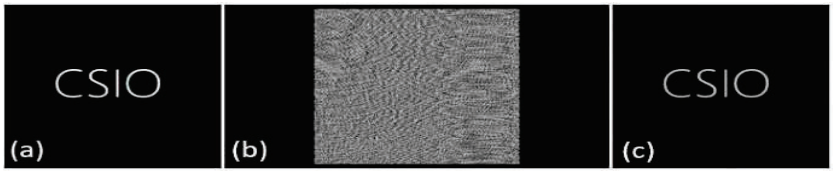

Fig. 2: (a) Original object of resolution 1024 × 1024, (b) CGH padded to SLM resolution of 1920 × 1080 (c) Numerically reconstructed result

Here, we have shown the results of only one model because the results in all the different simulation models are completely consistent with each other. After the successful benchmarking of the algorithm, the object models are run at higher resolutions and execution times for the same are observed.

Table 1: Execution time for different resolutions

Resolution Execution time	1024 × 1024	2048 × 2048	4096 × 4096	8192 × 8192
MATLAB	~ 3 seconds	~ 18 seconds	~ 1.2 minutes	~ 6.76 minutes
Python	~ 7 seconds	~ 24 seconds	~ 1.6 minutes	~ 7.06 minutes

The results of different resolutions of object model in this CGH generation by two different programming languages are compared in Table 1. It can be seen that MATLAB and Python produces the results almost at same speed for higher matrix dimensions. It is a computationally expensive process to generate CGH because of the involved intensive calculations. In the future work, we will further extend the algorithm to higher dimension and optimize the algorithm by parallelizing it or by using the available hardware accelerators like GPU.

4. Acknowledgement

Authors acknowledge CSIR, India for providing financial support under project number MLP2014. Authors thank Ms Pardeep Bhanot and Ms Monika Rani for their help.

5. References

[1]. E. Sahin, E. Stoykova, J. Makinen, and A. Gotchev, "Computer-generated holograms for 3D imaging: A survey", ACM Comput. Surv. **1**, 1 (2019)

[2]. Y. Wang, D. Dong, P.J. Christopher, A. Kadis, R. Mouthaan, F. Yang, and T.D. Wilkinson, "Hardware implementations of computer-generated holography: a review", Optical Engineering **59**, 1-30 (2020).

[3]. T. Shimobaba, D. Blinder, T. Birnbaum, I. Hoshi, H. Shiomi, P. Schelkens, and T. Ito, "Deep-Learning Computational Holography: A Review (Invited)", Frontiers in Photonics, **3**, [854391] (2022).

Temperature Dependent Raman Spectro-microscopy to Investigate Fermi Level Position in Degenerate Silicon

Chanchal Rani, Rajesh Kumar*

Materials And Device Laboratory, Department of Physics, Indian Institute of Technology Indore, Simrol-453552, India

*Email: rajeshkumar@iiti.ac.in

Abstract: Temperature dependent Raman spectro-microscopy[1,2] has been performed here to investigate the information about temperature dependent Fermi level position in heavily doped Silicon e.g., p and n type[3]. Information about the position of Fermi-energy in an extrinsic semiconductor and its relative position with respect to the intrinsic counterpart is of great interest. Typical asymmetrically broadened Raman spectral line-shape from sufficiently doped n- and p-type silicon has been analyzed here to get the associated latent information about the Fermi level position. Consequently, a simple formula, developed based on existing established theoretical frameworks, has been proposed that can be used to calculate the position of Fermi level in doped silicon. This proposed Raman spectro-microscopy based formulation was found suitable for n- and p-type silicon. Calculated Fermi level position and its temperature dependent variation are consistent with the existing reports. In brief, temperature dependent Raman spectro-microscopy proves to be a simpler yet powerful tool for estimating Fermi-energy.

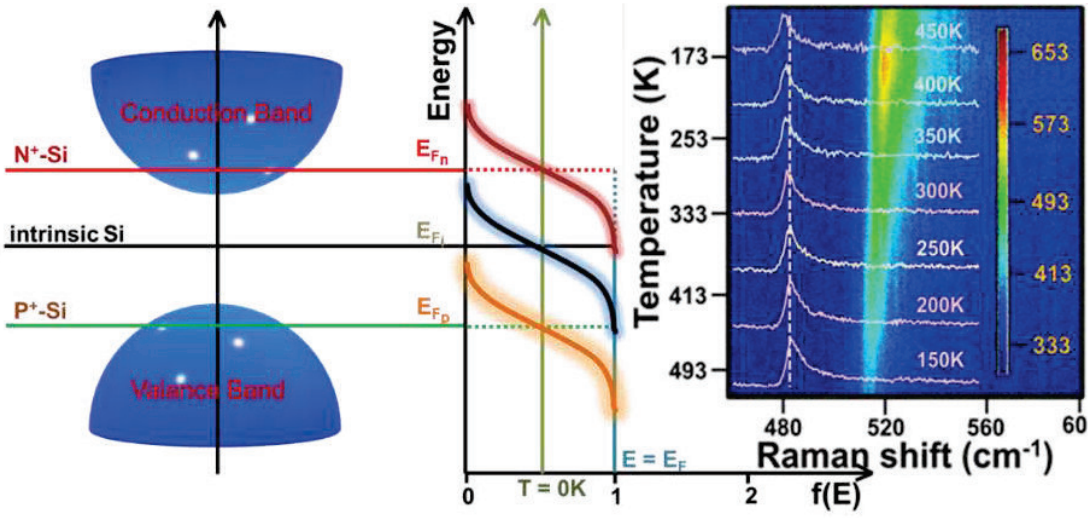

Keywords: *Temperature dependent Raman spectromicroscopy, Fano interaction, Fermi level position, Heavily doped semiconductor*

Acknowledgement: Author acknowledges financial support from science and engineering board, Govt. of India (Grant No. CRG/2019/000371). Facilities received from Department of Science and Technology DST, Govt. of India under FIST scheme (Grant no. SR/FST/PSI-225/2016) is highly acknowledged.

References:

(1) Hart, T. R.; Aggarwal, R. L.; Lax, B. Temperature Dependence of Raman Scattering in Silicon. *Phys. Rev. B* **1970**, *1* (2), 638–642. https://doi.org/10.1103/PhysRevB.1.638.
(2) Balkanski, M.; Wallis, R. F.; Haro, E. Anharmonic Effects in Light Scattering Due to Optical Phonons in Silicon. *Phys. Rev. B* **1983**, *28* (4), 1928–1934. https://doi.org/10.1103/PhysRevB.28.1928.
(3) Huang, K. M.; Wang, K. L.; Wang, D. P.; Huang, K. F.; Huang, T. C.; Chu, A. K. Temperature Dependence of Fermi Level Obtained by Electroreflectance Spectroscopy of Undoped N+-Type Doped GaAs. *Appl. Phys. Lett.* **1997**, *71* (26), 3889–3891. https://doi.org/10.1063/1.120535.

A Narrow Band Perfect Absorber with the Largest Q Value for Near Infrared Regime

Sagar Kumar Verma[1], Sachin Kumar Srivastava[1,2]
[1]*Department of Physics, Indian Institute of Technology Roorkee, Roorkee, Haridwar, Uttarakhand 247667, India*
[2]*Centre for Photonics and Quantum Communication Technology, Indian Institute of Technology Roorkee, India*
sachin.srivastava@ph.iitr.ac.in

Abstract: Simulation and optimization of a plasmonic metagrating was performed near-infrared spectral range and utilized as narrow band perfect absorber with 99.33% maximum absorbance value at resonance wavelength 1612.72 nm. This absorber possesses the largest quality factor (Q) 1697.603. Because of the very narrow full-width half maxima (FWHM) value of .95 nm, the simulated plasmonic metagrating can be used in various photonic applications such as wavelength selective absorbers, filters, mode locking, and Q switching for NIR lasers, smart windows, photodetectors, etc.
Keywords: Plasmonic metagrating, Absorber, Quality factor

1. Introduction

Metagrating is a one-dimensional (1D) periodic sub-wavelength plasmonic nanostructure, which can control the phase, polarization, etc. properties of light incident on the meta structure itself [1]. In the past decade, near-infrared (NIR) absorbers are considered to be one of the most promising photonic devices because they are used as the key device of photodetectors [2]. It was reported that the absorbers have diverse metallic nanostructures of metal–insulator–metal (MIM) multilayer [3], insulator-metal bilayer [4], or their analogs. The excitation of surface plasmons (SPs) in metallic nanostructures plays a crucial role in high optical absorptions in metal-dielectric hybrid meta structure. Metagrating based perfect NIR absorber behaves such as a meta cavity bounded by metallic metagrating and reflecting metal film. The perfect absorption is governed by the Fabry-Perot cavity resonance via multiple reflections between the "quasi-open" boundary of resonator and the "close" boundary of reflector [5]. In this study, a 1D plasmonic metagrating consisting of MIM multilayers by sandwiching a thin SiO_2 layer as a spacer medium between Ag grating and a continuous Ag layer is used as a narrow band perfect NIR absorber. The SPs modes supported by the periodic nanostructure results in the confinement or absorption of light in the spacer medium and the selection of specific geometrical parameters decide the performance of the NIR absorber whether it is a narrow band or wide band absorber.

2. Metagrating Design and Simulation

A schematic of the perfect absorber is shown in Fig. 1(a). In the proposed meta-structure, 'Λ' is the period, 'W' is the width of meta grating, 'a' is the groove width in meta-structure, 'H' is the thickness of the reflecting Ag layer, 'd' is the thickness of SiO_2 spacer layer between upper Ag grating and bottom Ag layer, 's' is the thickness of Ag grating and fill factor '*f*' (=W/ Λ). Substrate and superstrate medium were considered to be SiO_2 and air respectively. The metagrating was simulated by rigorous coupled wave analysis (RCWA) under the normal incidence of TM polarized light for the near infra-red (NIR) range of the electromagnetic spectrum from the top side of the structure, and 0^{th} order of diffraction of the light reflected and transmitted through the plasmonic meta structure were analyzed.

3. Result and Discussion

First, the plasmonic metagrating was optimized for the maximum absorbance value and the largest Q value. The optimized parameters were Λ (1600nm), W (1000nm), H (100nm), d (20nm), s (10nm), and f (0.625). In Fig. 1(b), it has been plotted the spectrum for the light reflected, transmitted, and absorbed at resonance wavelength ($\boldsymbol{\lambda}_{res}$) 1612.723 nm for the optimal structure. At $\boldsymbol{\lambda}_{res,}$ a sharp resonance dip in the reflectance curve can be observed with 0.67% reflectivity which is because of the 99.33% absorbance of the light with zero transmittance at same $\boldsymbol{\lambda}_{res}$ and the resonance peak in absorption spectrum with the smallest FWHM value 0.95 nm and largest Q value 1697.603 has been achieved. In Fig. 1(c) to (e), simulations were performed to study the fabrication tolerance of the device. In Fig. 1(c), Absorption spectrum has been plotted for different 's' values from 6-14 nm and it can be observed very small

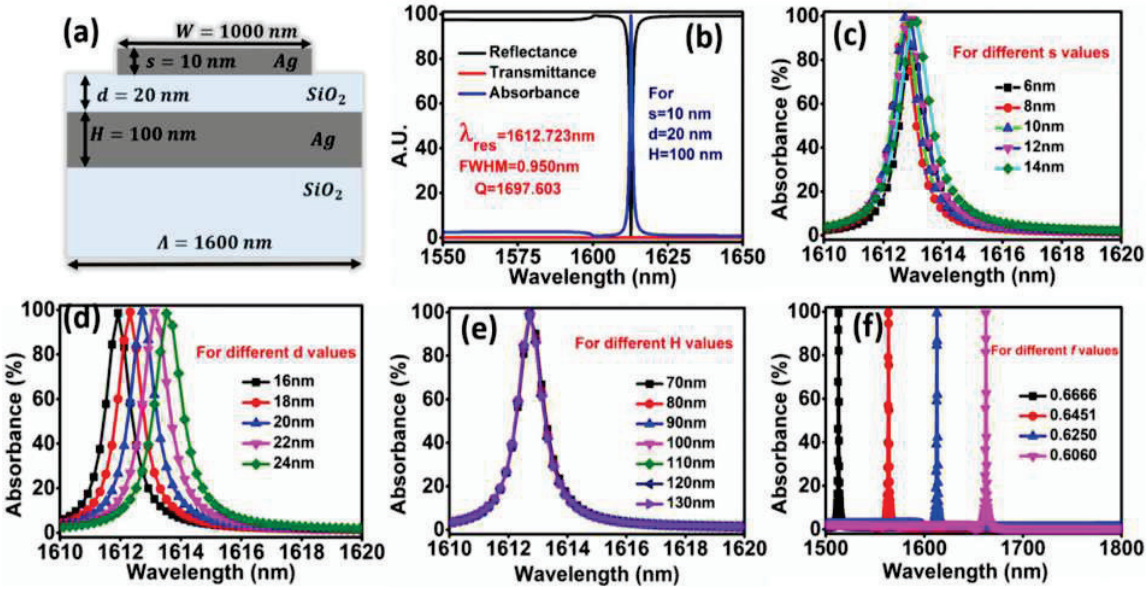

Fig.1: (a) Schematic of the perfect absorber, (b) Spectrum of the reflected, transmitted and absorbed light at resonance wavelength for the optimized meta structure, and absorption spectrum for (c) different 's' values, (d) different 'd' values, (e) different 'H' values, (f) different 'f' values

variation resonance wavelength corresponding to different 's' values as well as ±1% variation in maximum absorbance which do not affect the device performance too much. In Fig. 1(d), Absorption spectrum has been plotted for 'd' values from 16-24 nm and a continuous redshift can be observed with increasing 'd' values without any variation in maximum absorbance and FWHM values. It provides the flexibility to tune $\boldsymbol{\lambda}_{res}$ by varying 'd' values without affecting the device performance. Similarly, the absorption spectrum for different 'H' values has been plotted in Fig. 1 (e) and it can be observed that the change in 'H' values from 70-130 nm does not affect the device performance. In Fig. 1(f), Absorption spectrum has been plotted for different fill factors with a constant value of W (1000nm) and changing Λ from 1500-1650 nm and a continuous redshift can be observed for 'Λ' values without any variation in maximum absorbance and FWHM values. It also provides the flexibility to tune $\boldsymbol{\lambda}_{res}$ by varying 'Λ' values as per the application requirements.

4. Conclusions

In summary, we have designed, simulated, and optimized a plasmonic metagrating to utilize as a narrow band perfect absorber in NIR spectral region of the electromagnetic spectrum with 99.33% maximum absorbance value at resonance wavelength 1612.72 nm and the largest Q value of 1697.603. The resonance wavelength of the proposed perfect absorber can be tuned by tuning the geometrical parameters as per the application requirements. The simulated plasmonic metagrating can be used in various photonic applications such as wavelength selective absorbers, filters, mode locking, and Q switching for NIR lasers, smart windows, photodetectors, etc.

5. Acknowledgments

Funding from IITR-FIG, INSPIRE Faculty Grant, MoE-STARS, SERB-SRG, DST: Indo-Korea JNC, and DST-BDTDgrants are thankfully acknowledged. Sagar Kumar Verma thanks IITR and MoE for the Ph.D. fellowship.

6. References

[1] Sagar K. Verma, Sachin K. Srivastava, "Giant extra-ordinary near infrared transmission from seemingly opaque plasmonic metasurface: Sensing applications.," Plasmonics, **17**,653-663, (2021).
[2] Jurgen Michel, Jifeng Liu, Lionel C. Kimerling. "High-performance Ge-on-Si photodetectors.". Nat Photonics, **4**,527–34, (2010).
[3] Koray Aydin, Vivian E. Ferry, Ryan M. Briggs and Harry A. Atwater "Broadband polarization-independent resonant light absorption using ultrathin plasmonic super absorbers." Nat Commun., **2**,1–7, (2011).
[4] Mikhail A. Kats, Romain Blanchard, Patrice Genevet, Federico Capasso, "Nanometre optical coatings based on strong interference effects in highly absorbing media." Nature Mater., **12**, 20–4, (2013).
[5] Khagendra Bhattarai, Sinhara Silva, Kun Song, Augustine Urbas, Sang Jun Lee, Zahyun Ku and Jiangfeng Zho, "Metamaterial Perfect Absorber Analyzed by a Meta-cavity Model Consisting of Multilayer Metasurfaces" Sci. Rep., **7**,10569 (2017).

Investigation of the structural and optical properties of the Bi_2O_3 incorporated g-C_3N_4 composite as an emissive layer application

Sanjeev kumar, Ram Bilash Choudhary, Debashish Nayak, Jayanta Bauri

Nano structured Composite Materials Laboratory (NCML), Department of Physics
Indian Institute of Technology (Indian School of Mines), Dhanbad, Jharkhand-826004, India
Author email address: sanjeeviitism95@gmail.com

Abstract: Herein, g-C_3N_4/Bi_2O_3 composite was synthesized by one step calcination method. Crystallite sizes were calculated as 8, 70 and 37 nm for g-C_3N_4, Bi_2O_3 and g-C_3N_4/Bi_2O_3 composites by the X-ray diffraction (XRD) analysis. UV-Vis and photoluminescence (PL) spectra were recorded to study the optical properties of the composites. Direct optical band gap was estimated as ~ 2.94 eV for g-C_3N_4/Bi_2O_3 composite by using Tauc's plot. Enhanced photoluminescence intensity has been recorded for g-C_3N_4/Bi_2O_3 as compare to pure g-C_3N_4 suggested that this material could be used as emissive layer application in optoelectronic devices.

Key words: Composites**;** Graphitic carbon nitride; Photoluminescence; Emissive layer

1. Introduction:

In recent years, composite materials based on the graphitic carbon nitride (g-C_3N_4) and inorganic oxides have attracted the scientists and researchers due to its emerging applications in OLEDs, photovoltaics and thin film-based transistors [1]. g-C_3N_4 composite proven that it could be used to increase the flexibility of the optoelectronic devices [2]. Previously, Zhang et. al [3] and Ragupathi et. al [4] studied g-C_3N_4 for optoelectronic applications. In this article, we proposed g-C_3N_4/Bi_2O_3 as an emissive layer material for optoelectronic devices due to its excellent photoluminescence properties.

2. XRD and FE-SEM analysis:

The characteristic peak of g-C_3N_4 was found at 27.53° in the XRD spectra depicted in Fig. 1(a). The XRD spectra of the Bi_2O_3 showed the main diffraction peaks located at angle (2θ) = 16.72°, 26.82°, 27.33°, 35.40°, 46.34°, 52.39° and 61.49° corresponding to the hkl planes (011), (111), (120), (031), (041), (-321) and (231) respectively which was well matched with standard JCPDS Card No. 00-041-1449 as shown in Fig 1(a). In the XRD spectra of g-Bi_2O_3, diffraction peaks of both the g-C_3N_4 and Bi_2O_3 were present which confirmed successfully formation of the composite. Crystallite sizes (D) of the samples were calculated by Debye Scherrer's equation (1).

$$D = \frac{0.89\lambda}{\beta \cos\theta} \quad (1)$$

Where λ is the wavelength of the X-ray used in the XRD instrument, θ is the diffraction angle and β is defined as FWHM (full width at half maxima) [5].Calculated crystallite sizes were 8, 70 and 37 nm for g-C_3N_4, Bi_2O_3 and g-Bi_2O_3 samples. The g-C_3N_4 depicted the agglomerated sheet like morphology and Bi_2O_3 particles showed the micro-rod type structure which were clearly seen in the FESEM image of the g-Bi_2O_3 in Fig. 1(i). EDX study revealed the presence of C, N, Bi and O elements in the EDX spectra as Shown in Fig. (j) Which supported the result obtained by XRD.

2. Optical study

2. (a) UV-Vis and PL analysis

UV-Vis diffuse reflectance spectroscopy is broadly used technique to investigate the optical properties of the materials. Absorption edge for g-C_3N_4 was found at 425 nm and for g- Bi_2O_3 absorption edge was red shifted as depicted in Fig. 1(b)[6]. Direct optical band gap was estimated by tauc's plot based on the Kubelka Munk theory and Kubelka Munk function F(R) is defined by the following equation (2)

$$F(R) = (1-R)^2/2R = k/S = \alpha \quad (2)$$

Where k is the function of absorption, s is the scattering constant, R is the absolute reflectance considering sample is enormously thick and α is the absorption coefficient [7]. Tauc equation (3) is illustrated by the following formula.

$$\alpha h\nu = A(h\nu - E_g)^{1/2} \quad (3)$$

Where h is Planck's constant, A is proportionality constant. ν is the frequency and Eg is the direct optical band gap of the samples [8]. Direct optical band gap is calculated as 2.88, 2.95 and 2.90 eV for the g-C_3N_4, Bi_2O_3 and g- Bi_2O_3 respectively shown in Fig 1(d), Fig 1(e) and Fig 1(f). In PL spectra of the g-C_3N_4, emission peak was found at 487 nm which laid in the greenish blue region. PL intensity was heavily enhanced after insertion of the Bi_2O_3 in the g-C_3N_4 to form the g-Bi_2O_3 composite illustrated in Fig. 1(c). The main region of enhancement of the PL intensity was synergetic interaction between g-C_3N_4 and Bi_2O_3. In this interaction, rate of recombination of electron-hole charges were increased due to the charge transfer between the g-C_3N_4 and Bi_2O_3. This enhanced PL intensity insisted that g-Bi_2O_3 could be used as emissive layer material in Optoelectronic devices [9, 10].

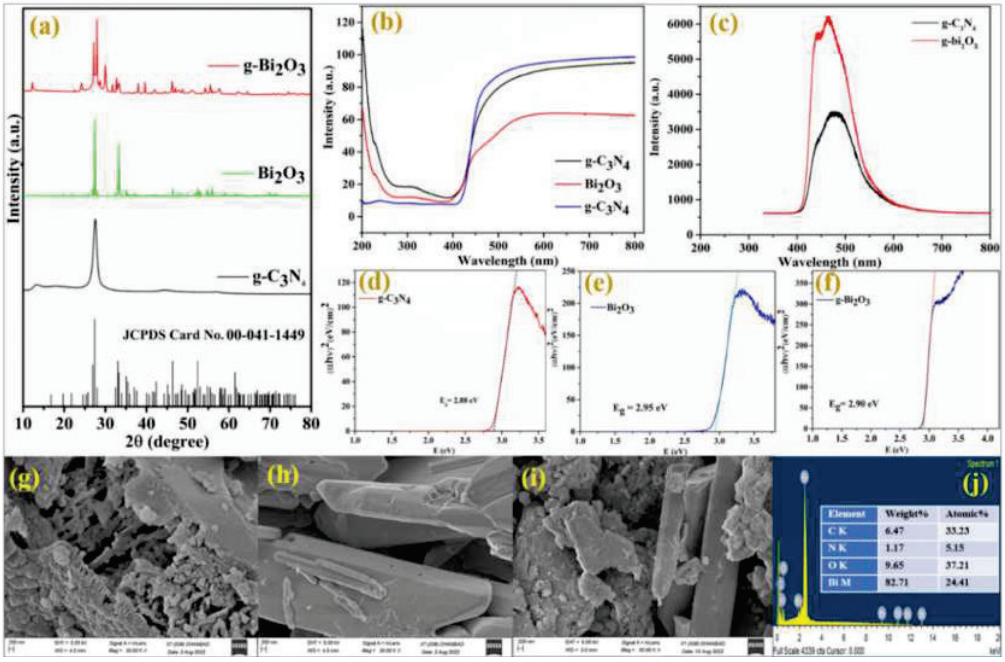

Fig. 1 Represents the (a) XRD spectra (b) UV-Vis spectra (c) PL spectra of the composites and (d), (e) and (f) show the Tauc's plots of g-C_3N_4, Bi_2O_3 and g-Bi_2O_3 composites. Fig 1. (g), (h) and (i) represent the FESEM image of the g-C_3N_4, Bi_2O_3 and g-Bi_2O_3 composite and Fig. 1 (j) shows EDX spectra of the g-Bi_2O_3 composite.

3. Conclusion:

g-Bi_2O_3 composite was synthesized by calcination of the melamine monomer in the presence of the Bi_2O_3. XRD and FESEM analysis revealed the successful inhibition of the Bi_2O_3 particles into g-C_3N_4. UV-Vis spectra of g-Bi_2O_3 exhibited that absorption edge was red shifted after the insertion of Bi_2O_3 and optical band gap was calculated as 2.90 eV. PL intensity of g-Bi_2O_3 was enhanced which suggested that it could be used as emissive layer application in optoelectronic devices.

References:

1. Bano, N., et al., Hybrid nanocomposites for organic light-emitting diodes. Results in Optics, 2022. **8**: p. 100258.
2. Yang, Y.H., et al., Graphitic Carbon Nitride/Polyvinylpyrrolidone Composite Dielectric for Low-Voltage Flexible InZnO Thin Film Transistor Grown on a Polyethylene Terephthalate Substrate. IEEE Electron Device Letters, 2020. **41**(3): p. 381-384.
3. Hoh, H.Y., et al., Harnessing the Potential of Graphitic Carbon Nitride for Optoelectronic Applications. Advanced Optical Materials, 2021. **9**(16): p. 2100146.
4. Ragupathi, V., et al., Scalable fabrication of graphitic-carbon nitride thin film for optoelectronic application. Materials Today: Proceedings, 2021.
5. Kumar, S. and R.B. Choudhary, Influence of MnO2 nanoparticles on the optical properties of polypyrrole matrix. Materials Science in Semiconductor Processing, 2022. **139**: p. 106322.
6. Hernández-Uresti, D., et al., Performance of the polymeric g-C3N4 photocatalyst through the degradation of pharmaceutical pollutants under UV–vis irradiation. Journal of Photochemistry and Photobiology A: Chemistry, 2016. **324**: p. 47-52.
7. Choudhary, R.B. and S. Kumar, Optimum chemical states and localized electronic states of SnO2 integrated PTh–SnO2 nanocomposites as excelling emissive layer (EML). Optical Materials, 2022. **131**: p. 112736.
8. Mishra, N.K., R. Kripal, and K. Kumar, Emission and EPR studies on green and red color emitting gallate phosphor containing manganese/chromium ions. Optical Materials, 2022. **128**: p. 112443.
9. Beltran-Huarac, J., Mn-based nanostructured building blocks, synthesis, characterization and applications. 2014.
10. Kandulna, R., et al., PMMA–TiO2 based polymeric nanocomposite material for electron transport layer in OLED application. Journal of Materials Science: Materials in Electronics, 2018. **29**(7): p. 5893-5907.

Patterning of Dielectrophoretic force in the presence of Gaussian and two interfering beams

Lwithwsa Swargiary and Alika Khare
Laser and Photonics Lab, Department of Physics, IIT Guwahati, Guwahati 781039, India
Author e-mail address: lswargiary@iitg.ac.in

Abstract: Dielectrophoretic force is computed for the Gaussian beam and two beam interference patterns. It is observed that with the Gaussian beam the maximum in dielectrophoretic force is around full width at half maximum. With two beam interference periodic structure is observed for dielectrophoretic force. The results can be applied for manipulating the neutral particle for trapping.
Keywords: Dielectrophoretic force, Gaussian beam, Two beam interference.

1. Introduction

The light induced space charge phenomenon is well known in photorefractive material (PR). This space charge generates the evanescent field in the vicinity of PR material. This evanescent field gives rise a force on the nanoparticles in its vicinity and hence particles can be manipulated and trapped. This force is known as dielectrophoretic (DEP) force. In this technique trapping of neutral particle depends on polarization property of particles under the influence of the evanescent field. The DEP force that the neutral charge particles experience is expressed as [1]

$$\boldsymbol{F}_{DEP} = -\boldsymbol{\nabla}(-\boldsymbol{p}.\boldsymbol{E}) \tag{1}$$

Where $\boldsymbol{p}$ represents the induced dipole moment of the neutral charge particles in the presence of evanescent field $\boldsymbol{E}$. The crystalline/geometrical anisotropy of the particle makes the induced dipole moment to be tensor and expressed as [1]

$$p_i = \varepsilon_0 \alpha_{ij} E_j \tag{2}$$

Where, α_{ij} is the second order polarizability tensor of the neutral particles and ε_0 being the permittivity of the free space. For the spherical isotropic particles, the polarizability (α_{ij}) becomes a scaler form and given by [1]

$$\alpha_p = 6V\varepsilon_m \frac{\varepsilon_p - \varepsilon_m}{\varepsilon_p + \varepsilon_m} \tag{3}$$

The ε_p and ε_m are the dielectric permittivity of neutral particles and the host medium respectively. V is the volume of the spherical isotropic particles. From the equation (1) and (2), the DEP force acting on the spherical isotropic can be expressed as,

$$\boldsymbol{F}_{DEP} = -\boldsymbol{\nabla}(-\boldsymbol{p}.\boldsymbol{E}) = \boldsymbol{\nabla}(\varepsilon_0 \alpha_p E^2) = \varepsilon_0 \alpha_p \boldsymbol{\nabla} I \tag{4}$$

The equation (4) shows that the DEP force acting on neutral charge particles depends on the gradient of the intensity profile of the light incident. Therefore, different patterning profile can be generated by different light configurations such as single gaussian beam, two beam interference etc. In this paper, Gaussian beam and two beam interference patterns of light beam is implemented to compute the pattern of nanoparticles in PR material.

In single gaussian beam configuration, the intensity distribution profile of the beam propagating in z direction can be expressed as [2],

$$I(x,y) = I_0 e^{-2(x^2+y^2)/w(z)^2} \tag{5}$$

Where, I_0 is the intensity at $x = 0,\ y = 0$. $w(z)$ is the beam spot size at a location z along the beam propagation direction (z).

$$w(z) = w_0 \left[1 + \left(\frac{z}{z_0}\right)^2\right]^{1/2} \tag{6}$$

Where, $w_0 = \frac{\lambda z_0}{\pi}$ and λ is the wavelength of the light used having the Rayleigh length z_0.

In two beam configurations, the intensity profile of interference of two lasers beam of intensities I_1 and I_2 can be expressed as [3]

$$I(x) = I_0(1 + m cos Kx) \tag{7}$$

Where, $I(x)$ represents the sinusoidal intensity pattern along x direction and $I_0\ (= I_1 + I_2)$ is the intensity addition of two light beams. K defines the spatial frequency and $m\left(= 2\frac{\sqrt{I_1 I_2}}{\sqrt{I_1 + I_2}}\right)$ represents the modulation index of the light.

2. Results and Discussion

The simulated result of DEP force profile calculated using the equations (4) for single gaussian beam as well as two interfering beams are shown in the figure 1 (a) and 1 (b) respectively along with normalized intensity profile. For the Gaussian beam, the simulation of DEP force is compiled at a location $z = 3$ meters away from the beam waist along the beam propagation direction.

He-Ne laser of wavelength $\lambda = 633$ nm having the beam waist of 0.5 millimeter is incorporated for the simulation. In figure 1(a), the result shows that the DEP force of Gaussian beam consists of two loops having two peaks at two different positions. At the peak position of the intensity of the Gaussian beam the DEP force experience a less force due to less gradient in the intensity profile. However, the DEP forces experience a maximum force around the Full width at half maximum of the Gaussian beam due to highest gradient for the intensity of the Gaussian beam. The 2-dimensional DEP force profile for Gaussian beam is also shown in insect in figure 1(a).

The plotting of intensity profile of two beam interference and its corresponding DEP force pattern for coinciding angle at $\theta = 60°$ is shown in figure 1(b) over a range of 0-70 μm. The 633 nm (He-Ne laser) wavelength is considered for the simulation along with the modulation index $m = 1$. The DEP force shows the maximum at the maximum gradient in sinusoidal intensity pattern and less at the position of less gradient in the sinusoidal intensity profile. The results can be applied for manipulating the neutral particles as well as the charged particles in periodic structure.

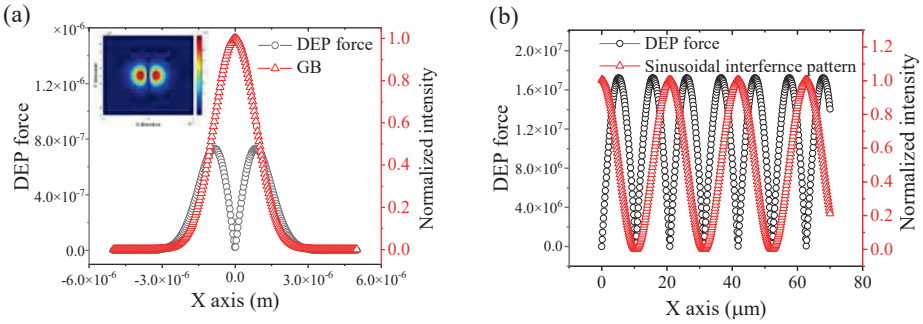

Fig. 1: (a) Gaussian beam (GB) intensity pattern and its DEP force profile, 1 (b) Sinusoidal interference pattern and its DEP force profile for the coinciding angle between the beams at $\theta = 60°$.

3. References

[1] M. Carrascosa, A. García-Cabañes, M. Jubera, J. B. Ramiro, and F. Agulló-López, "LiNbO3: A photovoltaic substrate for massive parallel manipulation and patterning of nano-objects," *Applied Physics Reviews*, vol. 2, no. 4. American Institute of Physics Inc., Dec. 01, 2015. doi: 10.1063/1.4929374.

[2] G. L. Coté, L. H. v. Wang, and S. Rastegar, "Biomedical optics and lasers," *Introduction to Biomedical Engineering*, pp. 977–1043, 2005, doi: 10.1016/B978-0-12-238662-6.50019-7.

[3] J. Villarroel, H. Burgos, Á. García-Cabañes, M. Carrascosa, A. Blázquez-Castro, and F. Agulló-López, "Photovoltaic versus optical tweezers," *Optics Express*, vol. 19, no. 24, p. 24320- 24330, 2011, doi.org/10.1364/OE.19.024320 2011.

Study of Propagation Behaviour of Lorentz Gaussian Laser Beam in Isotropic Plasma

P.T. Takale[1,2], K.Y. Khandale[1], T.U. Urunkar[1], S.S. Patil[3], S.D. Patil[3*], M.V. Takale[1*]

1. Department of Physics, Shivaji University, Kolhapur, Maharashtra – 416004 India

2. Department of Physics, Shivraj College, Gadhinglaj, Kolhapur, Maharashtra – 416502 India

3. Department of Physics, Devchand College, Arjunnagar, Kolhapur, Maharashtra – 591237 India

e-mail: mvtphyunishivaji@gmail.com, sdpatilphy@gmail.com

Abstract: It is quite known that critical beam radius and critical beam power plays significant role in propagation behaviour of laser beam. In this paper author studied the effect of critical beam power by keeping critical beam radius constant on propagation behaviour of Lorentz Gaussian beam in collisionless plasma. Coupled differential equations of beam width parameters are obtained using Akhmanov's parabolic approach under WKB, Paraxial approach. Differential equations are solved numerically and results are shown graphically.

1. Introduction :

Interaction of laser and plasma has many applications such as laser particle accelerations, Inertial Confinement fusion, high harmonic generation. In nonlinear optic phenomena, self-focusing plays important role. In recent history, Lorentz beam and Lorentz Gaussian beam are proposed by Gawhary and Severini [1]. Some Laser sources like double heterojunction $Ga_{1-x}Al_x$ As produces highly divergent fields. In such sources, Lorentz Gaussian profile is more suitable model for beam profile. Propagation of Lorentz beam and Lorentz Gaussian beam in uniaxial crystal is studied by Zhao and Cai. [2]. It is quite interesting to study propagation behaviour of Lorentz Gaussian beam in isotropic collisionless plasma. So variation in beam width parameters is studied in isotropic collisionless plasma.

2. Theoretical Formulation:

The behaviour of electric field in collisionless plasma under consideration of slowly varying envelope approximation is given as

$$-2ik\frac{\partial E}{\partial z}+\frac{\partial^2 E}{\partial z^2}+\left(\frac{\partial^2 E}{\partial x^2}+\frac{\partial^2 E}{\partial y^2}\right)+\frac{\omega^2}{c^2}(\epsilon-\epsilon_0)E=0 \ldots\ldots\ldots\ldots\ldots\ldots (1)$$

Consider Lorentz Gaussian beam propagating through isotropic collisionless plasma. Field distribution of Lorentz Gaussian in plasma is given as[1-3]

$$A=\frac{E_0}{r_0\sqrt{f_1 f_2}}\frac{1}{\left[1+\left(\frac{x}{r_0 f_1}\right)^2\right]}\frac{1}{\left[1+\left(\frac{y}{r_0 f_2}\right)^2\right]}Exp[-\left(\frac{x}{r_0 f_1}\right)^2]\,Exp[-\left(\frac{y}{r_0 f_2}\right)^2] \ldots\ldots (2)$$

Where E_0 is constant, r_0 is beam waist, f_1, f_2 are dimensionless beam width parameters along x , y directions respectively.

Effective dielectric constant of isotropic collisionless plasma is given as [4]

$$\epsilon=\epsilon_0+\phi(EE^*) \ldots\ldots\ldots . (3)$$

Where ϵ_0 and ϕ are linear and nonlinear parts of dielectric constant of isotropic collisionless plasma and can be given as

$$\epsilon_0=1-\left(\frac{\omega_p}{\omega}\right)^2 \ldots\ldots.(4)$$

$$\phi(EE^*)=\left(\frac{\omega_p}{\omega}\right)^2[1-Exp(-\alpha EE^*)] \ldots\ldots (5)$$

Where $\omega_p=\sqrt{\left(\frac{4\Pi N_0 e^2}{m}\right)}$ is plasma frequency, $\alpha=\frac{3m\alpha_0}{4M}$, $\alpha_0=\frac{e^2}{6m\omega^2 k_B T_0}$, N_0 is density of plasma, m is mass of electron, ω is angular frequency of laser, $k_B$is Boltzmann's constant, T_0 equilibrium plasma temperature.

By using equations (2), (3), (4), (5) and following Akhmanov's approach et al [5] and its extension by Sodha [6], differential equations of f_1 and f_2 are obtained as

$$\frac{\partial^2 f_1}{\partial \zeta^2} = \frac{22}{f_1^3} - \frac{4\,Exp[-\left(\frac{P}{r_0^2}\right)P\rho^2]}{f_1^2 f_2^1 r_0^4} \quad \ldots\ldots (6)$$

$$\frac{\partial^2 f_2}{\partial \zeta^2} = \frac{22}{f_2^3} - \frac{4\,Exp[-\left(\frac{P}{r_0^2}\right)P\rho^2]}{f_2^2 f_1^1 r_0^4} \quad \ldots\ldots\ldots (7)$$

Where $\zeta = \frac{z}{kr_0^2}$ is dimensionless distance of propagation, $P = \frac{\alpha E_0^2}{f_1 f_2}$, $\rho = \frac{r_0 \omega_p}{c}$

3. Result, Discussion, Conclusion :

Equations (6) and (7) are second order, nonlinear, coupled ordinary differential equations which represents behaviour of $f_1$and f_2 in plasma. Equations (6) and (7) can be solved numerically using following parameters $\lambda = 1.06\mu m, r_0 = 0.02cm, N_0 = 10^{18}$. Under critical conditions at $\zeta = 0$, $f_1 = f_2 = 1$, $\frac{\partial f_1}{\partial \zeta} = \frac{\partial f_2}{\partial \zeta} = 0$, equations (6) and (7) ,modifies as

$$\rho^2 = \frac{11\, r_0^4\, Exp\left(\frac{P_0}{r_0^2}\right)}{2P_0} \quad \ldots\ldots\ldots (8).$$

Where $P_0 = \alpha E_0^2$

Figure (1) gives critical curve which is graphical representation of relation of critical beam power (P_0) and critical beam radius (ρ). It divides graph into two regions i.e Region I and Region II. Choice of point (P_0, ρ) determines propagation behaviour of Lorentz Gaussian beam in plasma. Figure (2) shows variation of f_1, f_2 along dimensionless distance of propagation ζ for $\rho = 1$ and taking $P_0 = 0.002$ from region I, $P_0 = 0.004$ from region II. Choice of $P_0 = 0.002$, $\rho = 1$ and $P_0 = 0.004$, $\rho = 1$ is evident from figure (1). In figure (2), oscillatory self-focusing of beam is observed for (P_0, ρ) in region I while oscillatory defocusing is observed for (P_0, ρ) in region II. In present study, propagation of Lorentz Gaussian in isotropic plasma is studied theoretically using paraxial approximation. Critical curve is plotted in order to determine nature of propagation of beam in plasma. Oscillatory self-focusing and oscillatory defocusing of beam is observed. Our studies may be useful in a variety of laser plasma interaction applications.

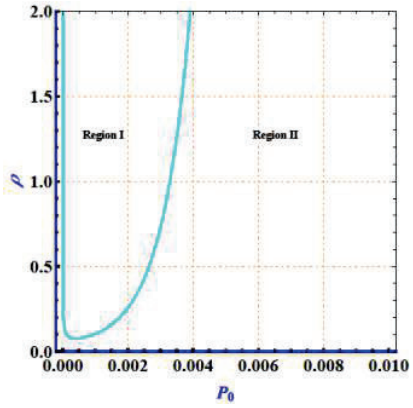

Fig. 1 Critical Curve (ρ vs P_0)

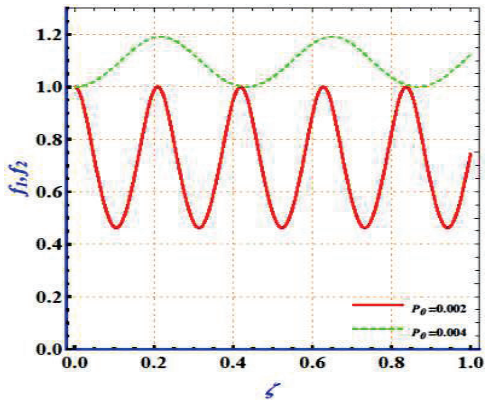

Fig. 2 Variation of f_1, f_2 along ζ for $P_0 = 0.002, 0.004$

4. References :

[1] O. Gawhary and S. Severini, J. Opt. A, Pure Appl. Opt., **8,** 409-414 (2006)
[2]C. Zhao and Y. Cai, J. Mod. Opt., **57**, 375-384 (2010)
[3] L. Song, X. Jiang, Z. Yang, X. Li and S. Zhang, J. Nonlinear Opt. Phys. Mater., **27**, 1850041 (2018)
[4] M.V. Takale, S.T. Navare, S.D. Patil, V.J. Fulari and M.B. Dongare, Opt. Commun., **282**, 3157–3162 (2009)
[5] S. A. Akhmanov, A. P. Sukhorukov and R. V. Khokhlov, Sov. Phy. Usp. **10,** 609-636 (1968)
[6] M. S .Sodha, A. K. Ghatak and V. K. Tripathi, Progress in Optics, **13**, 169-265 (1976)

Dielectric environment sensing using MMI in tapered optical fiber and dynamic dispersion tuning using ENZ conditions in ITO

Arun Mambra, Ravi Pant and Joy Mitra
School of Physics, Indian Institute of Science Education and Research, Thiruvananthapuram – 695551, India
itsmearun18@iisertvm.ac.in

Abstract: The non-trivial optical properties of indium tin oxide (ITO) near its epsilon-near-zero (ENZ) regime, like field confinement, field enhancement, and perfect absorption makes it amenable for electro-optic modulation and sensing applications. Here, we showcase an optical device in which electrostatic gating is used to dynamically tune the ENZ regime. The change in optical properties is sensed by a tapered optical fiber placed in contact with the thin film. Evanescent fields of the tapered fiber couple to the environment, which changes the modal dispersion of the fiber and is measured using multi-modal-interference (MMI), observed in the transmitted light intensity.
Keywords: epsilon-near-zero, optical modulation, modal interference.

1. Introduction

Optical fiber based sensing has been explored since the development of modern low-loss fibers [1]. Tapered fibers, where "leaky" guided modes have been used to sense the dielectric environment via evanescent field coupling, have expanded the scope of optical sensing [2]. Recently, tapered optical fiber based devices have attracted huge interest for practical applications in the fields of optical telecommunications, lasers, nonlinear optics, sensing, high Q resonators, etc. Tapered optical fibers have unique features including large evanescent fields, strong optical coupling, mechanical flexibility and ease of fabrication. Utilizing the concept of Multimodal Interference (MMI) in tapered optical fibers gives added advantage in sensing the environment parameters like humidity, refractive index, and bio-sensing [3], within the vicinity of the tapered region.

Here, we utilize a single-mode fiber (SMF28e), in which the incident energy is confined within the fundamental HE11 mode with a Gaussian profile, for all the MMI experiments. Depending on the wavelength of operation, tapering the fiber allows excitation of multiple modes in the tapered region, dominant among which is the non-Gaussian HE12 mode with substantial evanescent field extending beyond the taper boundary. Coupling this mode to a gated indium tin oxide (ITO) film then allows further modulation of the modal dispersion via externally controlled electrostatic gating. ITO is an exciting material which has already attracted interest due to its ease of fabrication and diverse applications in plasmonics, optoelectronics, and photonics [4,5]. ITO exhibit dielectric to metal transition in the near-infrared (NIR) regime, at the ENZ wavelength (λ_{ENZ}). The real part of dielectric function ($Re(\epsilon)$) is positive for $\lambda < \lambda_{ENZ}$ and becomes negative for $\lambda > \lambda_{ENZ}$, thus showing metal like optical properties and $Re(\epsilon) = 0$ for $\lambda = \lambda_{ENZ}$ [6]. In this work, we have used commercially available ITO coated glass slides with a sheet resistance of 10-100 Ω/sq. Importantly, the origin of doping in ITO i.e., the Sn^{4+}/Sn^{2+} ratio controlled by the oxygen stoichiometry and it's magnitude allow for both static and dynamic control of n_e, which directly changes λ_{ENZ} [6]. In the ENZ regime, ITO exhibits remarkable properties like field enhancement, perfect absorption, enhancement of nonlinear properties etc., [6]. The ability to actively tune λ_{ENZ} opens new avenues to exploit the fascinating properties at desirable wavelengths. In this work, we display a dispersion sensing setup using MMI in a tapered optical fiber and effectively tuning the dispersion of the fiber by dynamically modulating the ENZ region in ITO using the electrostatic gating mechanism.

2. Results and Discussion

The schematic of the experimental setup is shown in figure 1a. Figure 1b shows experimental results of channel modulation with respect to gate voltage and the corresponding change in the ITO's number density. A consistent shift of MMI is recorded in the transmitted spectra of the sensing system when the tapered fiber is evanescently

coupled with ITOs of different λ_{ENZ} (figure 1c). Theoretical simulations using finite element method (FEM) provide qualitative agreement to the experimental result observed. Figure 1d, shows the evolution of the HE12 mode as ITOs with different λ_{ENZ} evanescently coupled with the tapered optical fiber, simulated using FEM. The evolution of these HE12 modes show a qualitative agreement with the actual refractive index of ITOs with different λ_{ENZ}. These results verify that the MMI technique works as an efficient sensor. In parallel, ITO coupled with a tapered optical fiber system actively tunes the dispersion of the fiber as the ENZ region of ITO is modulated.

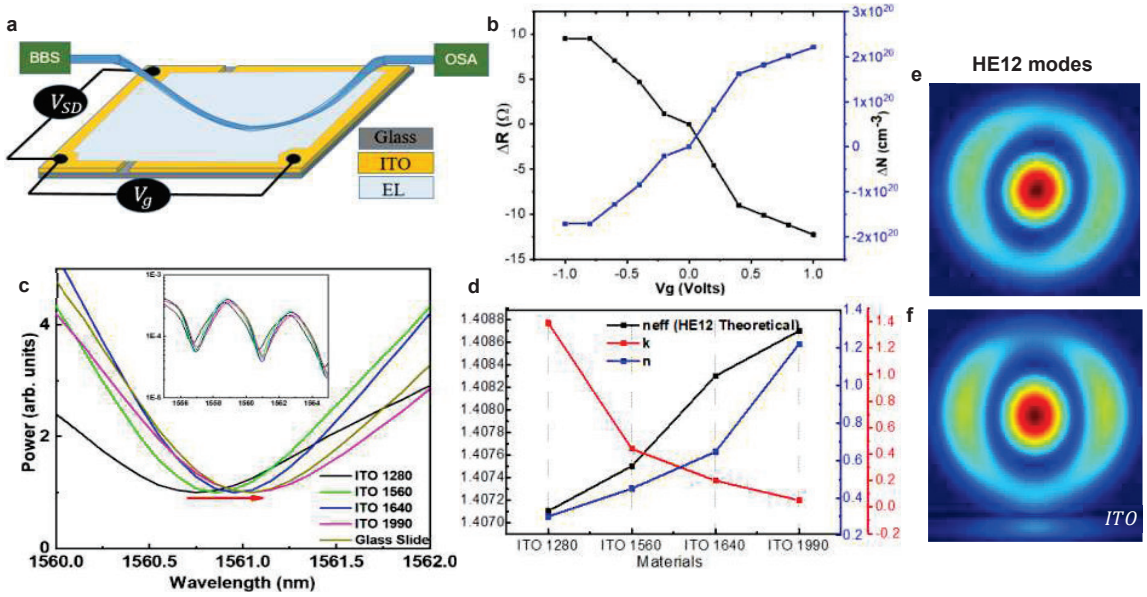

Fig. 1: (a) Experimental setup for MMI sensing along with dynamic dispersion tuning. (b) Gating effect on channel resistance and carrier density. (c) Experimental shift in the interference patterns observed in the transmitted spectra, when coupled with ITO sample of different λ_{ENZ}, the red arrow shows the increase in refractive index. (d) Change in effective index of HE12 mode as ITO of different λ_{ENZ} is coupled with the tapered fiber. (e) HE12 modes of tapered fiber in air and (f) HE12 modes of a tapered fiber in air with ITO coated glass below it; simulated used FEM.

Furthermore, ITO exhibits huge field enhancement within its ENZ regime, which brings in an added advantage in sensing an interstitial material of single or few layer atoms between the ITO and the tapered fiber. Finally, we demonstrate a flexible platform that can actively detect dielectric environments with decent precision and a dynamic system with an optical response that can be modulated using an electrostatic gate.

3. References

[1] Grattan, K. T. V., and T. Sun. "Fiber optic sensor technology: an overview." Sensors and Actuators A: Physical 82(1-3), 40-61 (2000).
[2] Wang, Pengfei, Haiyan Zhao, Xianfan Wang, Gerald Farrell, and Gilberto Brambilla. "A re-view of multimode interference in tapered optical fibers and related applica-tions." Sensors 18(3), 858 (2018).
[3] Wang, Pengfei, Haiyan Zhao, Xianfan Wang, Gerald Farrell, and Gilberto Brambilla. "A review of multimode interference in tapered optical fibers and related applications." Sensors 18, no. 3 (2018): 858.
[4] Kinsey, N., C. DeVault, J. Kim, M. Ferrera, V. M. Shalaev, and A. Boltasseva. "Epsilon-near-zero Al-doped ZnO for ultrafast switching at telecom wavelengths." Optica 2(7), 616-622 (2015).
[5] Naik, Gururaj V., Vladimir M. Shalaev, and Alexandra Boltasseva. "Alternative plasmonic materials: beyond gold and silver." Advanced Materials 25(24), 3264-3294 (2013).
[6] Johns, Ben, Navas Meleth Puthoor, Harikrishnan Gopalakrishnan, Akhileshwar Mishra, Ravi Pant, and J. Mitra. "Epsilon-near-zero response in indium tin oxide thin films: Octave span tuning and IR plasmonics." Journal of Applied Physics 127, no. 4 (2020): 043102.

Extensive Qualification and Mechanical Studies on CVD SiC Cladded Sintered Silicon Carbide Mirrors for Space Optical Applications

Tayaramma D.P.V. Jalluri*, B.Vishweshwara Rao, K.Sathyanarayana Raju, Bijoy Raha
S.Bhaskar Raju, Venkateswaran andK.V.Sriram

Laboratory for Electro-Optics Systems (LEOS), Indian Space Research Organization,
Peenya, Bangalore- 560058, India
**** pushpavalli4@gmail.com***

Abstract

Silicon Carbide (SiC) is a novel material for space optical (reflective) applications. Although Sintered SiC (SSiC) exhibits superior mechanical and thermalproperties, it can't be used as such. Therefore, surface modification is carried out onSSiC using SiC by CVD. The CVD SiC coated sintered SiC is subjected to griding and polishing process and achieved optical polishablity i.e 50 nm PTV surface accuracy with the surface finish 10Å micro-roughness. These polished mirrors have been subjected to the space qualification tests humidity, thermal shock cycling and thermo-vacuum cycling. The mirror surface coating characteristics and mechanical properties were evaluated before and after the tests.

Key words: Sintered silicon carbide, chemical vapour deposition, telescope optics, surface figure, surface roughness, space qualification tests, Nano hardness and Modulus.

Introduction: Silicon Carbide (SiC) is a non-oxide ceramic and it has been used as advanced reflective material for space optics application. Although sintered silicon carbide exhibits superior mechanical, thermal and radiation resistant properties, its use in high surface quality performance optical systems has been very limited due to its inherent porosity and microstructural defects [1,2]. The front surfaces of sintered SiC blanks are ground to either flat or curved shape. In the present study, a thick layer of SiC is deposited on ground sintered silicon carbide substrate by chemical vapour deposited method which are highly dense and facilitates good optical polishability [3,4]. In order to fabricate optical polished mirror surfaces with good surface accuracy and micro-roughness from these coated blanks, a technology has been developed at LEOS which involves several processes such as grinding, polishing and figuring.

The phase pure crystalline SiC CVD coatings on SSiC exibits adequate mechanical properties (Nano hardness- 34.766 ± 3.14 and modulus 478.58± 21.49) at a microstructurallength scale. Optical polishing yielded 50 nm PTV surface accuracy over the clear aperture with a surface finish 10Å micro-roughness consistently for all the processed samples. In orderto qualify these processes and employ these SiC mirrors in space, test mirror flats having sizes 100mm diameter (5 No.s) and 50 mm (5 No.s) have been realized. These mirrors havebeen subjected to the space qualification tests comprising of environmental tests such as humidity, thermal shock cycling and thermo-vacuum cycling. The mirror surface coating characteristics and mechanical were evaluated before and after the tests. Nano mechanical Properties on CVD SiC cladded sintered silicon carbide substrate have been measured using Berkovich inventor.

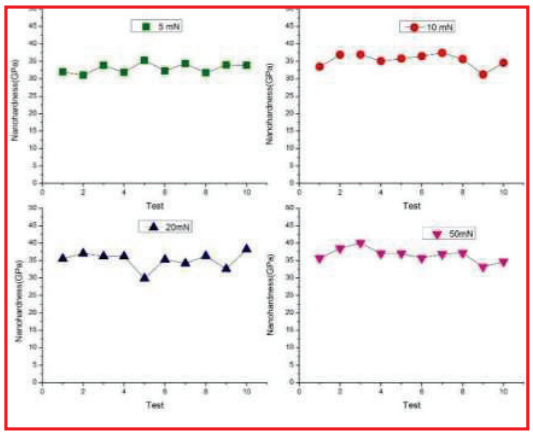

Figure1: Nao hardnessmeasured with applied load 5mN, 10mN, 20 mN and 50 mN.

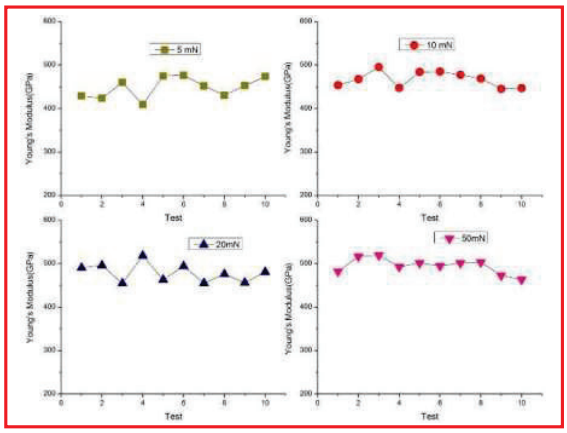

Figure2: Young's modulus measured with applied load 5mN, 10mN, 20 mN and 50 mN.

The measured nano hardness on CVD SiC is 34.766 ± 3.14 and modulus 478.58± 21.49

Table 1: Space Qualification tests conducted on CVD SiC sintered silicon carbide mirror samples

• **Humidity test:** Humidity test at 95% RH/50 ^{0}C for 48 hours	• **Thermo Vacuum Cycling Test:** Hot: 125 ^{0}C / 2 hrs soak Cold: - 50 ^{0}C / 2 hrs soak Vacuum: 10 $^{-5}$ m bar for 10 cycles
• **Thermal shock cycling test** Hot: 125 ^{0}C / 5 min. soak Cold: - 50 ^{0}C / 5 min. soak No. of cycles: 1500 cycles.	• **Thermal Storage test:** Hot: +125 ^{0}C / 24 hrs soak Cold: - 50 ^{0}C / 24 hrs soak No. of cycles: 1 cycle

Conclusions: A ductile-regime procedure for grinding of CVD clad sintered SiC blanks is demonstrated and found to be well suited for polishing small sized optics. The grinding process and the polishing recipe based on diamond slurry is effective in achieving high- quality optical finish. This could be evidenced from the attainment of surface figure accuracyof the order of 50nm (PTV), 12nm (RMS) and micro-roughness in the order of 10Å for several flat samples. Further, space qualification tests have been carried out on CVD SiC mirrors as per international standards and samples have passed all the tests successfully. The mechanical properties of CVD SiC have been measured and those are well matching with literature values[5].

References:

[1]. Jalluri TDPV, Somashekar S, et al. Characterization of thermal sprayed Si on sintered SiC for space optical applications. Surf Eng. 37(5), 1-14, (2020).

[2]. Jalluri TDP V, Gouda GM et al. Development and characterization of silicon dioxide clad silicon carbide optics for terrestrial and space applications, Ceram Int. 48(1),96-110 (2022).

[3]. D. E. Lencioni, D. R. Hearn et al. Advanced Land Imager calibration and performance overview, Earth Obs. Syst. IV 3750, 89 (1999).

[4]. Y. Ling et al. Low-Damage Grinding / Polishing of Silicon Carbide Surfaces. (2001).

[5]. G. Subhash, P. Hittepole, S. Maiti, Mechanical properties of PECVD thin ceramic films, J. Eur. Ceram. Soc. 30 (2010) 689–697.

Spin Orbit interaction of light in plasmonic metamaterials

Jeeban K Nayak[1], Shyamal Guchhait[1], Niladri Modak[1], Sayantan Das[1], Ayan Banerjee[1], Subhasish Dutta Gupta[2] and Nirmalya Ghosh[1*],

[1]Department of Physical Sciences, IISER Kolkata , [2] School of Physics, Hyderabad Central University
**Author e-mail address: nghosh@iiserkol.ac.in*

Abstract: Spin orbit interaction (SOI) of light has led to the observation of a number of non-trivial optical effects in various light-matter interactions. Controlled enhancement of various exotic SOI effects is demonstrated in spatially tailored hybridized plasmonic metamaterials and the prospect of development of novel spin-orbit photonic meta-devices are discussed.

Keywords: Angular momentum of light, Polarization, Spin orbit interaction, Plasmonics, Nano optics.

The terminology spin orbit interaction (SOI) refers to interaction and coupling of spin and orbital degree of freedom of spinning particles such as electrons or other quantum particles. The universal nature of such interaction has led to its manifestation in diverse fields of physics, ranging from atomic, condensed matter to optical systems. In wave optics, the angular momentum (AM) of light is related to the circular (elliptical) polarization of light wave or helical phase fronts (vortex) of optical beams [1-3]. The former is associated with the rotation of the electric field vector around the propagation axis and is referred to as the spin angular momentum (SAM); while the latter is associated with rotation of the phase structure of a light beam and is known as orbital angular momentum (OAM) [1-3]. From a fundamental point of view, coupling and inter-conversion between the spin and orbital AM degrees of freedom of light is thus expected under certain circumstances, and accordingly the evolution of polarized light in a trajectory should mimic the SOI effect of a mass-less spin 1 particle (photon) (ala the SOI effects exhibited by spin ½ electrons while evolving under an external field). A number non-trivial spin-orbit optical phenomena like spin and orbital Hall effect of light, optical Rashba effect, photonic Aharonov–Bohm effect, rotational Doppler effect, transverse spin, Belinfante's spin-momentum and spin-momentum locking in optical fields etc. have recently been observed in diverse mico and nano scale optical system [2-8]. These have created a new area in photonics, namely, the spin orbit photonics that not only deals fundamental light-matter interaction effects but have also opened up possibility of development of a new generation of miniaturized and on-chip integrable multifunctional photonic devices based on the angular momentum and geometrical phase of light.

Experimental methods to controllably enhance and desirably tailor the SOI effects in nanostructured metamaterials and to gain new insights on the various intertwined SOI effects are highly sought after in this regard. We have recently studied SOI of light and observed a number of intricate and intriguing spin (polarization) optical effects in various processes involving light-matter interactions. Specifically, we have demonstrated controlled enhancement of SOI and the resulting spin Hall effect of light in metal nanostructures exhibiting surface plasmon resonance, giant photonic spin Hall effect in spatially tailored inhomogeneous anisotropic medium, optimized weak measurements on photonic spin Hall effect, resonant enhancement of some of the rather illusive fundamental entities of light, namely, the helicity-independent transverse spin angular momentum and the polarization-dependent transverse momentum (the so-called Belinfante's spin momentum) in spatially tailored plasmonic nanostructures, and so forth [9-19]. In this regard, we have introduced quantitative polarization Mueller matrix (a 4×4 polarization transfer matrix that contains complete information about the polarization properties of a medium) studies in the domain of nano plasmonics [20,21]. For this purpose, we have developed a unique dark field polarization spectroscopic microscopy system capable of recording complete polarization spectroscopic Mueller matrix from single isolated nanostructure or nanoparticle. This custom-designed system was used to demonstrate a novel concept of weak value amplification (WVA) using asymmetric spectral response of Fano resonance as the pointer arising naturally in precisely designed metamaterials, namely, waveguided plasmonic crystals [13, 14]. Further studies on SOI of light in spatially tailored plasmonic metamaterials have opened up novel route towards development of spin-photonic meta-devices. In this regard, we have demonstrated two interesting concepts on geometrical phase of light. (a) Specially designed metamaterials, namely, geometric phase gradient plasmonic metasurface has been used for spin polarization-based control and manipulation of light at nanometer length scale [15], (b) a new class of polarization measurement has been introduced, namely, 'geometric phase polarimeter' that enables single-shot measurement of space varying polarization state of light through

interferometric quantification of geometric phase [16]. A novel type of spin Hall effect of light was also observed in random medium. Specifically, an extraordinary spin asymmetric random scattering mode were observed in a disordered anisotropic medium with synchronous geometric and dynamical phase distribution [18]. We have also demonstrated micro-beam deflector using SOI of light in linear polarizer [22].

This talk will cover some of the aforementioned recent work in the area on spin orbit interaction of light in spatially tailored plasmonic systems and other hybridized metamaterials. In this regard, this new field of spin orbit photonics will be introduced and fundamental issues related to different SOI effects originating from various light-matter interactions will be discussed. The practical implications of the observed effects and the prospect of development of spin-orbit nanophotonics meta-devices and their numerous potential applications will be highlighted.

References

1. Optical Angular Momentum, edited by L. Allen, S. M. Barnett, and M. J. Padgett (Taylor & Francis, London, 2003).
2. The Angular momentum of Light, edited by D.L. Andrews and M. Babiker, (Cambridge University Press, 2013) (Chapter 8, "Spin orbit interaction of light" by K.Y. Bliokh, A. Aeillo and M.A. Alonso).
3. S. D. Gupta, N. Ghosh, and A. Banerjee, *Wave Optics: Basic Concepts and Contemporary Trends* (CRC Press, Boca Raton, FL, 2015).
4. K. Y. Bliokh, A. Niv, V. Kleiner and E. Hasman, Nature Photonics, 2, 748 – 753 (2008).
5. O. Hosten and P. Kwiat, Science **319**, 787 (2008).
6. K. Y. Bliokh, F. J. Rodríguez-Fortuño, F. Nori, and A. V. Zayats, Nat. Photonics **9**, 796 (2015).
7. N. Shitrit, I. Yulevich, E. Maguid, D. Ozeri, D. Veksler, V. Kleiner, and E. Hasman, Science **340**, 724 (2013).
8. E. Maguid, M. Yannai, A. Faerman, I. Yulevich, V. Kleiner, and E. Hasman, Science **358**, 1411 (2017).
9. S. Goswami, S. Dhara, M. Pal, A. Nandi, P. K. Panigrahi, and N. Ghosh, Optics Express, 24, 6041 (2016).
10. Ankit Kumar Singh, Sudipta Saha, Subhasish Dutta Gupta, Nirmalya Ghosh, Physical Review A, 97, 043823 (2018).
11. Mandira Pal, Chitram Banerjee, ShubhamChandel, Ankan Bag, Shovan K. Majumder & Nirmalya Ghosh, Scientific Reports, 6, 39582 (2016).
12. Mandira Pal, Sudipta Saha, Athira B S, Subhasish Dutta Gupta, and Nirmalya Ghosh, Phys. Rev. A, 99, 032123 (2019).
13. Subir Kumar Ray, Shubham Chandel, Ankit Kumar Singh, Abhishek Kumar, ArpitaMandal,SubhradeepMisra, ParthaMitra, and Nirmalya Ghosh, ACS Nano, 11, 1641-1648 (2017).
14. Ankit Kumar Singh, Subir Kumar Ray, Shubham Chandel, Angad Gupta, Semanty Pal, Partha Mitra, and Nirmalya Ghosh, Physical Review A, 97, 053801 (2018).
15. SK Ray, AK Singh, S Chandel, P Mitra, N Ghosh, Physical Review A 100 (3), 033805 (2019).
16. BS Athira, M Pal, S Mukherjee, J Mishra, D Nandy, N Ghosh, Physical Review A 101 (1), 013836 (2020).
17. Niladri Modak, Athira B S, Ankit Kumar Singh, and Nirmalya Ghosh, Phys. Rev. A 103, 053518 (2021).
18. AK Singh, A Das, S Das, N Ghosh, Physical Review A 102 (3), 033518 (2020).
19. S Guchhait, BS Athira, N Modak, JK Nayak, A Panda, M Pal, N Ghosh, Scientific reports 10 (1), 1-9 (2020).
20. Shubham Chandel, JalpaSoni, Subirkumar Ray, Anwesh Das, AnirudhaGhosh, Satyabrata Raj and Nirmalya Ghosh, Scientific Reports, **6**, 26466 (2016).
21. Soumitra Satapathi, Jalpa Soni, and Nirmalya Ghosh, Applied Physics Letters, 104, 131902 (2014).
22. Niladri Modak, Sayantan Das, Priyanuj Bordoloi, and Nirmalya Ghosh, Tunable giant two-dimensional optical beam shift from a tilted linear polarizer, Phys. Rev. A 105, 033713 (2022).

Unzipping of Single Wall Carbon Nanotubes and its potential in Optical Switching Devices

Gayatri Sharma, Mayank Agarwal, Sudhisht Kumar, Manmohan Singh Shishodia*

Department of Applied Physics, Gautam Buddha University, Greater Noida-201312, India

**Corresponding Author: manmohan@gbu.ac.in*

Abstract: Carbon Nanotubes (CNTs) exhibit outstanding optical properties and high potential for integration with photonic devices. Moreover CNTs are emerging as potential quantum light source. Considering wide ranging functionality of CNTs, the present study discuss an effective method for unzipping single-walled carbon nanotubes (SWCNTs) through chemical route. The raw SWCNTs are treated with KNO_3 and H_2SO_4 for two hours with constant stirring for unzipping the SWCNTs. The unzipped-SWCNTs produced from SWCNTs were characterized using Raman spectroscopy. The current-voltage (I-V) measurements shows an important aspect of resistive-switching which is likely to play a pivotal role in the area of memory devices and the switching properties can be furter explored for its potential applications in optical switching in plasmonic waveguides. Unzipped graphene is a promising element for building such high-performance memories with an unconventional form factor because of its exceptional electrical conductivity, outstanding mechanical properties, and processing versatility as desirable for hybrid integration.

Keywords: Quantum Light Source, Graphene Nanoribbon, Unzipping, SWCNTs.

1. Introduction

The Single Wall Carbon Nanotubes (SWCNTs) consist of a hollow graphene cylinder. Unzipping is a process for forming graphene by cleaving single wall carbon nanotubes (SWCNTs) longitudinally. Recent reports suggest that GNRs are superior materials for many applications such as energy storage and memory devices, chemical and biosensors, catalysis, nano-composites, and nano-electronics. Despite their advantages for many applications [1], it is still challenging to synthesize GNRs efficiently in bulk quantity. Consequently, the development of a facile, large-scale, and high-yield production of GNRs will lead to important advances in both fundamental study and innovative applications [2].

The CNT longitudinal is done using a mixture of strong acids like KNO_3, and H_2SO_4 and a strong oxidizing agent like $KMnO_4$ has been demonstrated to produce a large yield [3].In this method, the crucial step is to decrease the strong van der waal interaction between the walls of CNTs by interacting with SO^4 ions. Hence, the nanotube is unzipped with the oxidant attaching to one of the internal C-C bond by stretching and breaking the CNT bonds to produce nanoribbon structures. In our method, we have done Raman characterization to produce a high yield to study the electrical properties of unzipped single-walled carbon graphene nanotubes. The pretreatment of KNO_3 and H_2SO_4 provides an important role in the unzipping process [4].

2. Methodology

The first footstep towards the unzipping CNTs is to use a pretreatment of raw SWCNTs with KNO_3 and $H2SO_4$ under proper conditions, it gives K+, NO_3^- and SO_4^{2-} ion to peeling the bundled CNTs into coaxial walls of CNTs. The second step is to use the $KMnO_4$ as the oxidant to unzip longitudinally SWCNTs [3]. Overall, it is possible to decrease the Van der Waals interaction between individual nanotubes and the coaxial wall of CNTs. Additionally, by using the proper amount of H_2SO_4 to produce graphene nanoribbons from CNTs with a high yield and reduce the usage of strong acid during the nanotube zipping [5].

3. Results and Discussion

Raman spectroscopy is a useful technique for determining the properties of thin film of carbon-based materials. The untreated CNTs and modified CNTs' Raman spectra are shown in figure 1. The Raman spectrum curve shows three

fundamental graphene bands, which is " D-band at 1355 cm-1 (defect), a G band at 1582 cm-1 (graphite band), and a 2D-band at 2696 cm-1 (D overtone)" [3]. As shown in figure 1 unzipped CNTs have a stronger D band which implies larger defect concentrations in unzipped CNTs as compared to untreated CNTs.

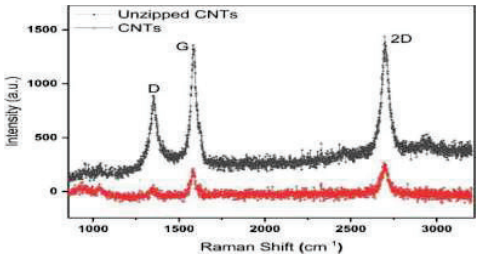

Figure 1. Raman Spectra of Unzipped CNTs

Electrical hysteresis behavior in the Current-voltage (I-V) characteristics is an important aspect of a resistive-switching memory device, as shown in Figure 2 I-V measurements can be used to explore the electrical characteristics of non-volatile memory. In a cycle, the applied voltage across the device is changed from negative bias to positive bias and then back to negative bias. The I-V curve shows the rectification nature or we can say that it shows the two separate conducting states, the ON state and the OFF state, which correspond to the high-current and low-current states, respectively.

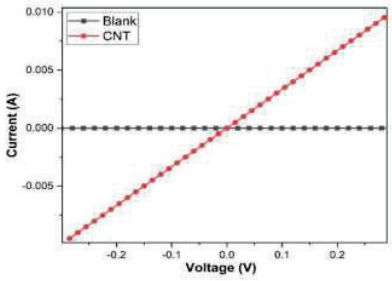

Figure 2 I-V characteristics of without CNTs

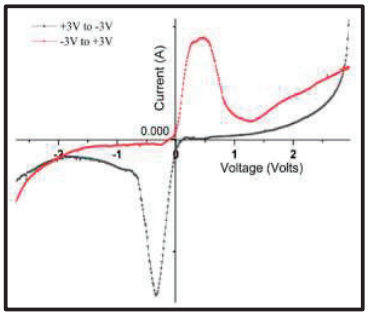

Figure 3 I-V characteristics of Unzipped CNTS

In figure 3 CNTs show linearity in I-V characteristics which states that they cannot be used in memory storage devices. For the memory device applications the switching in current from high to low resistive modes from positive to negative bias and then again going back to negative to positive bias, which is an important required aspect of a resistive switching memory device. Unzipped CNTs show excellent switching behavior in I-V characteristics shown in the figure 3.

4. Conclusion

In conclusion, we report the oxidative process to produce grpahene nanoribbions CNTs longitudinal unzipping and the sample has been analyzed through Raman spectra. The I-V characteristics show excellent switching behavior which gives it potential for its application in memory devices.

References

[1] Ma, L., Wang, J. & Ding, F. Recent Progress and Challenges in Graphene Nanoribbon Synthesis. *Chem. Phys. Chem*. **14,** 47–54 (2013).

[2] Davis, D. J. *et al.* Silver-Graphene Nanoribbon Composite Catalyst for the Oxygen Reduction Reaction in Alkaline Electrolyte. *Electroanal*. **26,** 164–170 (2014).

[3] Li, YS., Liao, JL., Wang, SY. *et al.* Intercalation-assisted longitudinal unzipping of carbon nanotubes for green and scalable synthesis of graphene nanoribbons. *Sci Rep* **6**, 22755 (2016).

[4] Kosynkin, D. V. *et al.* Longitudinal unzipping of carbon nanotubes to form graphene nanoribbons. *Nature* **458,** 872–876 (2009).

[5] Shinde, D. B., Majumder, M. & Pillai, V. K. Counter-ion dependent, longitudinal unzipping of multi-walled carbon nanotubes to highly conductive and transparent graphene nanoribbons. *Sci. Rep.* **4,** 4363.

Optimization of a 10 W Tm-Fiber MOPA with Low ASE and Intensity Noise

Shubhranil Maity[1,2,*], Sourav Das Chowdhury[1], Vincent Akash Gomes[1,3], Atasi Pal[1,3]
[1]*Fiber Optics & Photonics Division, CSIR-Central Glass and Ceramic Research Institute, Kolkata - 700032*
[2]*Department of Physics, Jadavpur University, Jadavpur, Kolkata-700032, India*
[3]*Academy of Scientific & Innovative Research (AcSIR), Ghaziabad, Uttar Pradesh 201002*
**Author e-mail address: 2013shubhranil@gmail.com*

Abstract: In this work, a high-power all-fiber thulium-doped fiber laser (TDFL) in a master oscillator power amplifier (MOPA) configuration providing output power up to 10 W is demonstrated. The slope efficiency of the power amplifier is about 40%. The center wavelength of this laser is located at 1999.2 nm and the 3-dB spectral width is 0.24 nm. High SNR from the amplified spontaneous emission (ASE) noise is obtained in the experiment.
Keywords: Fiber Laser, Fiber Amplifier, Thulium Fiber Laser, Signal to Noise Ratio

1. Introduction

Thulium-doped fiber lasers (TDFL) and amplifiers (TDFA) have attracted much attention due to their numerous applications in the 2 μm wavelength band during past decades, such as gas sensing, clinical surgery, and optical communication, and coherent LIDAR [1-2]. Narrow linewidth single-frequency TDFLs with long coherent length are in great demand for remote atmospheric sensing to improve the resolution, sensitivity, and sensing distance [3]. Another most recent requirement of low noise, narrow linewidth TDFL or TDFA at 2 μm has arisen from the development of next generation gravitational wave detection [4]. To achieve high average power with low noise and narrow linewidth; amplification is an effective method using a suitable seed source. In that context, here we report on the optimization of an all-fiber Tm-doped fiber master oscillator power amplifier (MOPA) with low-intensity noise and high optical signal-to-noise ratio (OSNR) with respect to amplified spontaneous emission (ASE) noise.

2. Experimental Setup

The all-fiber TDFL in MOPA architecture consists of a stable low-power fiber oscillator and single-stage cladding-pumped thulium-doped fiber amplifier. The master oscillator (MO), as shown in Fig. 1 consists of a section of Tm-doped double-clad fiber (TDF), a pump laser diode (PLD) at 793 nm, a (6+1)×1 pump and signal combiner, and a pair of fiber Bragg gratings (FBGs) which have a central wavelength at 1999.2 nm with a reflectivity and 3-dB bandwidth of 99%, 50% and 2 nm, 0.5 nm respectively. The performance of the MO has been studied using two different LR-FBGs with reflectivity 10% and 50% respectively. The Tm-doped fiber has a core diameter of 10 μm and an inner-cladding diameter of 130 μm. The corresponding numerical apertures (N.A.) of the core and inner cladding are 0.15 and 0.46, respectively. The absorption coefficient of the active fiber

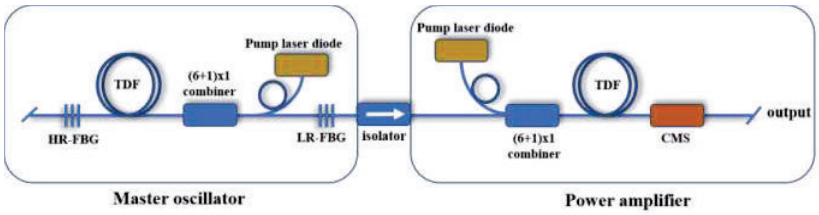

Fig.1 Schematic setup of thulium-doped all-fiber MOPA

is about 3 dB/m at 793 nm and a length of 0.5 m is employed in the experiment. In the main power amplification configuration, a (6+1)×1 pump and signal combiner and a section of TDF are employed. An isolator is inserted between the output of the MO and the input signal port of the (6+1)×1 pump and signal combiner to prevent any back reflection. One PLD of 793 nm is connected with one of the pump port of (6+1)×1 pump and signal combiner. A cladding mode stripper (CMS) is connected with TDF to remove the unabsorbed cladding pump power.

3. Result and Discussion

Temporal measurements of the pulse train were carried out using a photodiode (PD: Thorlabs PDA10D-EC, 15 MHz) and an oscilloscope (OSC: Tektronix DPO7254C, 2.5 GHz, 40 GS/s). As shown in Fig. 2(a)(i) when 10% LR-FBG was used, there was significant temporal fluctuations in the MO output though operating in

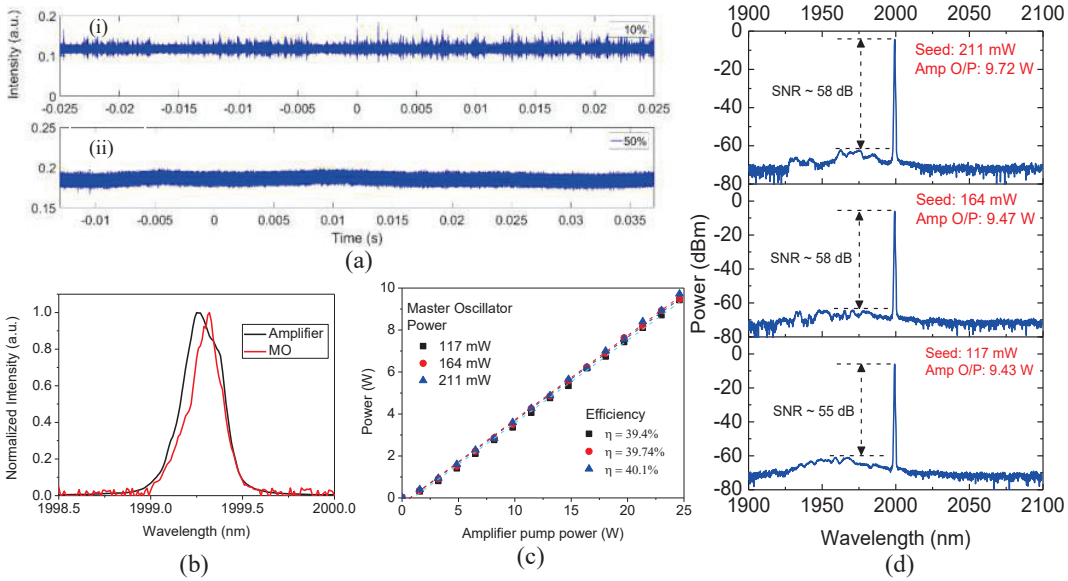

Fig 2: (a) oscilloscope trace with 10% and 50% reflectivity of LR-FBG (b) spectrum of MO and amplifier (c) output power of the amplifier vs launched pump power (d) spectrum of the laser amplifier at highest power level for different seed power

continuous wave (CW) mode. The temporal instability arose due to gain competition among multiple longitudinal modes within the FBG bandwidth under low cavity feedback. When the feedback was increased by using 50% reflectivity LR-FBG, the temporal instability reduced significantly for the same pump power level as shown in Fig. 2(a)(ii). For 50% LR-FBG which provided stronger feedback, gain competition among the longitudinal modes reduced resulting alleviation the temporal instability issue. Accordingly, for further amplification, LR-FBG of reflectivity 50% was chosen. In such a configuration the 3-dB linewidth of the MO was measured to be 0.21 nm as shown in Fig. 2(b). The experimental results from the amplifier are summarized in Table 1.

Table 1: Summary of experimental results

MO power (mW)	Amplifier output Power (W)	Amplifier Efficiency (%)	Amplifier OSNR (dB)	Amplifier gain (dB)
117	9.43	39.40	55	19.06
164	9.47	39.74	58	17.61
211	9.72	40.10	58	16.63

Fig.2(c) shows the amplified laser output power as a function of the pump power of the amplifier. Fig. 2(d) shows the spectrum of the amplifier at maximum output power with three different MO powers, which was measured by an optical spectrum analyzer (OSA: Yokogawa AQ6375) with a resolution of 0.05 nm. The center wavelength of this laser is located at 1999.2 nm, corresponding to the central wavelength of the HR-FBG. The linewidth (3-dB) of the amplifier output is 0.24 nm implying no significant broadening of linewidth after amplification. As shown in Table 1, slope efficiency of the amplifier can be further increased by length optimization of the TDF and by implementing better thermal management. From Fig. 2(c) it is evident further power scaling is possible with an increase in pump power. The future work includes further power scaling beyond 10 W with high OSNR, increased efficiency, and minimal linewidth broadening. Also, mechanical vibration isolated system assembly is to be employed for low environmental noise operation.

4. References:

[1] S. D. Jackson, "Towards high-power mid-infrared emission from a fiber laser," Nat. Photonics **6(7)**, 423–431 (2012)

[2] P. F. Moulton, G. A. Rines, E. V. Slobodtchikov, K. F. Wall, G. Frith, B. Samson, and A. L. G. Carter, "TmDoped Fiber Lasers: Fundamentals and Power Scaling," IEEE J. Sel. Top. Quantum Electron. **15(1)**, 85–92 (2009)

[3] T. M. Taczak and D. K. Killinger, "Development of a tunable, narrow-linewidth, cw 2.066-μm Ho:YLF laser for remote sensing of atmospheric CO_2 and H_2O," Appl. Opt. **37(36)**, 8460–8476 (1998).

[4] LIGO Scientific Collaboration, "Instrument Science White Paper 2018", LIGO-T1800133–v3 (2018)

Bifunctional Application of Viologen-MoS_2-CNT/Polythiophene Device as Electrochromic Diode and Half-Wave Rectifier

Suchita Kandpal[1], Rajesh Kumar[1,2] *

[1]*Materials and Device Laboratory, Department of Physics, Indian Institute of Technology Indore, Simrol-453552, India.*
[2]*Centre for Indian Scientific Knowledge Systems, Indian Institute of Technology Indore, Simrol-453552, India.*

** Corresponding Author: rajeshkumar@iiti.ac.in (Rajesh Kumar)*

ABSTRACT

A dual-purpose solid state electrochromic device has been fabricated using polythiophene (P3HT) and ethyl Viologen (EV), pre-doped with multiwalled carbon nanotubes (MWCNTs) and MoS_2. The MoS_2 nanoflower and MWCNTs are synthesized by one-step hydrothermal and pyrolysis techniques and well characterized by SEM, XRD and Raman spectroscopy. The charge holding properties of MoS_2 & MWCNTs gives the asymmetric diodic I-V characteristic to the device which has been exploited to use the electrochromic device for rectification application. Electrochromic properties of the device reveal its improved performance in terms of faster switching speed (0.47s/0.8s) between two colored states (Magenta & Blue), high coloration efficiency (642cm^2/C) and good color contrast (46% at 515nm). Along with electrochromic property, it has been realized as a half-wave rectifier which rectifies an AC voltage of frequency 1Hz or less making it suitable for low frequency operation. This study opens a new possibility to design and fabricate multipurpose frequency selective electrochromic rectifiers.

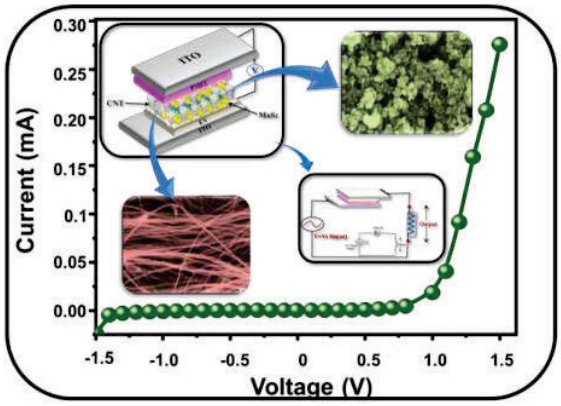

Acknowledgment:
The authors acknowledge financial support from Science and Engineering Research Board, Government of India (Grant CRG/2019/000371), UGC (Ref. 1304-JUNE-2018-513215), Govt. of India, Department of Science and Technology (DST), Government of India, under FIST scheme (Grant SR/FST/PSI-225/2016) for providing facilities and fellowship.

A Novel Birefringent Holey Photonic Crystal Fiber for Terahertz Wave Applications

Kandaswamy Renuka Rani[1,3], Krishnan Chitra[2,4]
[1]*School of Advanced Sciences, Vellore Institute of Technology, Vandalur – Kelambakkam Road, Chennai – 600127, India*
[2]*School of Electronics Engineering, Vellore Institute of Technology, Vandalur – Kelambakkam Road, Chennai – 600127, India*
[3]*renukarani.k2020@vitstudent.ac.in*
[4]*chitra.krishnan@vit.ac.in*

Abstract: A novel hexagonal photonic crystal fiber (PCF) is realized for the localization of electromagnetic modes in terahertz (THz) regime. The proposed holey fiber is numerically analyzed using Finite Element Method (FEM) based COMSOL Multiphysics software. The optical properties of the PCF such as birefringence, effective mode area and confinement loss were determined for various core diameter. From the simulation, birefringence is found to be in the order of 10^{-5} and it is noted that effective mode area increases when the core diameter is increased whereas confinement loss decreases. Hence, this PCF can be used for several THz applications.
Keywords: holey photonic crystal fiber; terahertz; hollow core; birefringence; confinement loss; effective mode area

1. Introduction

In the past few years terahertz photonic crystal fiber have become remarkable among the researchers due to its prominent optical characteristics and applications. THz based PCF have drawn great attention from the scientific community for the application in medical imaging [1], sensing [2], communication [3], etc. PCF can be productive in imminent fields of optical communication like parametric amplification [4], supercontinuum generation [5] and so on. Based on the guiding mechanism, PCFs are classified into photonic bandgap (PBG) PCF and index-guiding PCF. In PBG-PCF, the effective refractive index of cladding is higher than core and hence light propagates by PBG effect. As the effective refractive index of core is higher than cladding, light propagates by total internal reflection (TIR) in index-guiding PCF. The proposed holey PCF guides light through PBG mechanism and the optical characteristics are determined using FEM. Confinement loss develops in the PCF as the cladding possess finite number of air holes and this loss can be found using the following equation [6].

$$\alpha_{CL}\left(\frac{dB}{m}\right) = 8.686\ \frac{2\pi f}{c}\ Im\left(n_{eff}\right) \qquad (1)$$

where; f is the frequency of e-m radiation, c is the velocity of light and $Im\left(n_{eff}\right)$ represents the imaginary part of the effective refractive index respectively.

2. Results and discussion

The holey fiber is designed using hexagonal lattice of circular shaped air holes with lattice constant, a = 840 µm and radius of the air holes, r = 0.25a in polyimide background. This fiber contains six rings of air holes with similar radii as shown in fig. 1 and the geometry has been modeled using COMSOL Multiphysics.

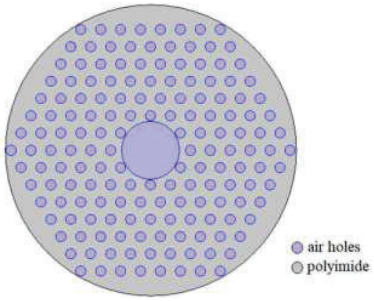

Fig. 1: Geometry of hexagonal lattice holey fiber (a = 840 µm and r = 0.25a).

The diameter of the core is varied from 1.15*a* to 1.35*a* for which THz wave confinement is feasible. Confinement loss as a function of core diameter has been plotted in fig. 2 for three different electromagnetic modes - monopole, dipole and quadrupole localized in the fiber at 0.094 THz, 0.16 THz and 0.21 THz.

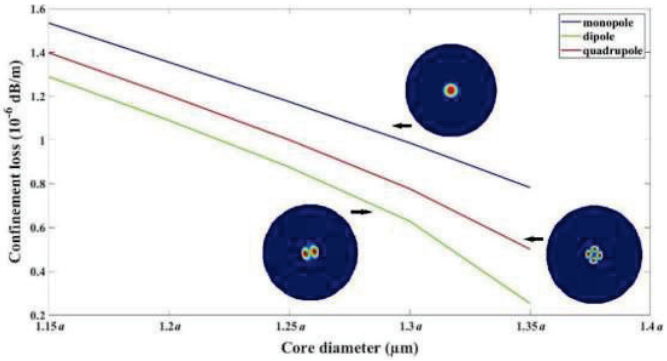

Fig. 2: Confinement loss for different core diameter (1.15a to 1.35a).

From this plot, it is seen that confinement loss decreases as the core diameter is increased and the value of this loss is found using equation (1) mentioned in section 1. The simulation results provide larger effective mode area for higher core diameter as given in table 1 and birefringence is found to be in the order of 10^{-5} for the analyzed PCF.

Table 1: The values of effective mode area for different core diameter (1.15a to 1.35a)

Electromagnetic modes	Core diameter (μm)	Effective mode area (10^{-6} m^2)
monopole	1.15*a*	1.3972
	1.2*a*	1.5213
	125*a*	1.6507
	1.3*a*	1.7854
	1.35*a*	1.9254
dipole	1.15*a*	1.26
	1.2*a*	1.3718
	125*a*	1.4885
	1.3*a*	1.6099
	1.35*a*	1.7358
quadrupole	1.15*a*	1.2773
	1.2*a*	1.3907
	125*a*	1.509
	1.3*a*	1.632
	1.35*a*	1.7597

3. Conclusion

A holey PCF designed using hexagonal lattice of air holes arranged in polyimide background is realized. Due to PBG effect, the loss is minimized and electromagnetic modes such as monopole, dipole and quadrupole were confined in the core of the PCF at 0.094 THz, 0.16 THz and 0.21 THz respectively. By increasing the core diameter, it is found that effective mode area increases, whereas confinement loss decreases. From the analysis, birefringence of this holey fiber is found to be in the order of 10^{-5}. We anticipate that the modeled PCF with low loss and large effective area would be utilized for various THz applications like communication, sensing, medical imaging, spectroscopy, etc.

4. References

[1] F. Begum and Y. Namihira, Nat Sci (Irvine) **03**, 401 (2011).
[2] M. S. Islam, J. Sultana, A. A. Rifat, A. Dinovitser, B. Wai-Him Ng, and D. Abbott, IEEE Sens J **18**, 4073 (2018).
[3] M. Abdullah-Al-Shafi, N. Akter, S. Sen, and M. S. Hossain, Optik (Stuttg) **243**, (2021).
[4] N. Cao, H. Zhu, P. Li, S. Taccheo, Y. Zhu, X. Gao, and Z. Wang, Opt Rev **25**, 316 (2018).
[5] L. C. Van, V. T. Hoang, V. C. Long, K. Borzycki, K. D. Xuan, V. T. Quoc, M. Trippenbach, R. Buczyński, and J. Pniewski, Laser Phys **30**, (2020).

Caloric Study of The Bulk Chalcogenide Quaternary Alloy System

Parul Kaushik[1*], Hukum Singh[1], Ambika Devi[2]

[1]*Department of Applied Sciences, The NorthCap University, Gurugram, India.*
[2]*Department of Applied Sciences, Amity University, Gurugram, India.*

**Corresponding author: pkaushik520@gmail.com*

Abstract: Bulk glasses of the composition $Bi_1Te_{15}Se_{84-x}$ Pb_x ($0 \leq x \leq 8$) has been prepared using melt quenching technique. The crystallization kinetics of the chalcogenide system is obtained using the DSC (differential Scanning Calorimetry) technique. From the heating rate dependence of glass transition temperature T_p, the activation energy of glass transition E_g, the activation energy of crystallization E_c, and other parameters are obtained via models like Kissinger, Augis-Bennett. Some kinetic parameters are studies as functions of heating rates and compositions.

Keywords: Differential thermal analysis, Glass activation energy, Stability Parameter, Chalcogenide glasses

1. Introduction

Chalcogenide glasses have been studied extensively because they are good glass formers and possess good thermal stability [1-5]. Chalcogenide glasses exhibit optical transparency from visible to infrared regions making them suitable for use in optical magnifiers, infrared imaging and optoelectronic applications. In the recent years, work has been done on ternary and binary nanostructured glasses but work on quaternary nanostructured glasses is still in its early stages. There are two methods can be used to study the crystallization kinetics in chalcogenide glasses: isothermal and non-isothermal methods. In the isothermal method, the sample is brought near to the crystallization temperature very quickly and then any physical quantity change drastically is measured as a function of time. In the non-isothermal method, the sample heated at a fixed rate and physical parameter recorded as a function of temperature. We use the non-isothermal method because the measurements made in a relatively rapid and precise manner. The aim of the present work is to analyse the glass transition and crystallization kinetics of the composition by means of non-isothermal differential thermal analysis (DTA) measurements at different heating rates using three different methods of analysis namely, Kissinger's relation [6], Matusita-Sakka theory [7] and Augis-Bennett approximation [8].

2. Experimental Techniques

$Bi_1Te_{15}Se_{84-x}$ Pb_x ($0 \leq x \leq 8$) chalcogenide bulk sample is prepared using the conventional melt quenching technique. High purity materials (99.999% purity) were weighed according to their atomic weight percentage and sealed in quartz ampoules in a vacuum of 10^{-4} torr. The ampoules were placed inside a furnace that is heated at a rate of 2-3 degrees Celsius per minute until the temperature 1000 degrees Celsius is attained. In order to make the sample homogeneous, the process of shaking the samples at regular interval is done. Ice-cold water is used to quench the bulk sample. In this composition Se is used as major constituent because of its extensive applications in electronic and optoelectronic device materials. The composition $Bi_1Te_{15}Se_{84-x}$ Pb_x is selected as base composition as it possesses appreciable optical, electrical and thermal properties. The addition of a metallic additive, like lead, to a ternary chalcogenide changes the population of positively and negatively charged valence alteration pairs, which then affects the properties of this composition.

3. Results

DTA thermogram of the bulk sample has been represented in Fig (1) and (2) respectively. The DTA traces show two characteristic phenomena. The first one is an endothermic region while the second one is the exothermic phenomenon manifesting the crystallization process.

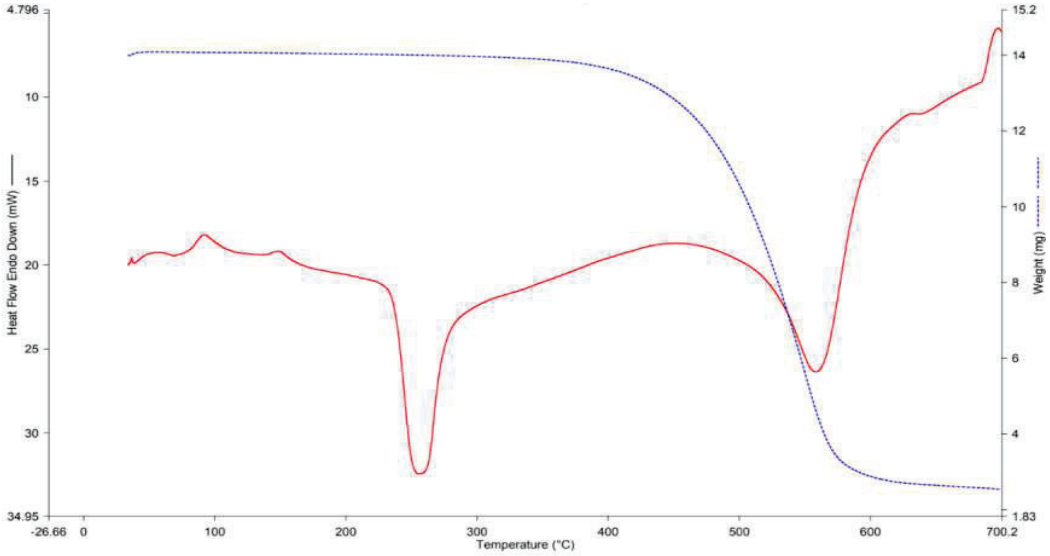

Fig 1. Endothermic and Exothermic graph for the bulk composition when X=2

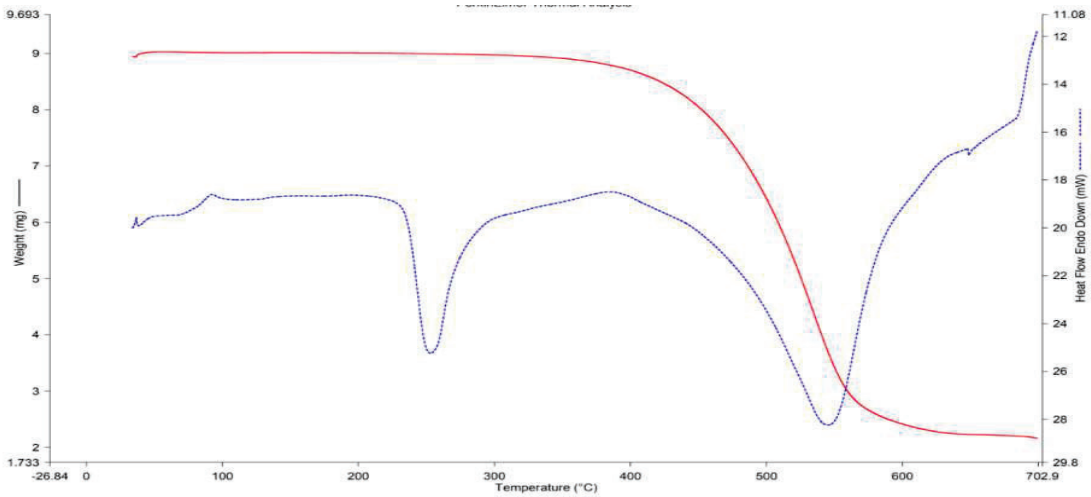

Fig 2. Endothermic and Exothermic graph for the bulk composition when X=4

4. Acknowledgement

Parul Kaushik is thankful to Amity University, Manesar (India) for lending out the DTA instrument.

References

[1] M.A. Majeed Khan, M. Wasi Khan, Mansour Alhoshan,"Structural, optical and electrical characterization of selenium sulphide nanostructured thin film," J.Materials Letters ;**64**:1929- 1932(2010).

[2] Deepika, Hukum Singh"Structural and optical study of nanostructured Se 80 − x Te 20 Sb x (0 ≤ x ≤ 12) thin films, J. Infrared Physics & Technology;**85**:39-43(2017).

[3] M. S. Kamboj, R. Thangaraj, "Calorimetric studies of bulk Se-Te-Pb glassy system. Eur. Phys. J. Appl.Phys **24**: 33-36. (2003).

[4] N.B. Maharjan, D. Bhandari, N.S. Saxena," Study of electrical conduction in nanostructured $Se_{2.5}Ge_{1-x}Sn_x$ (x=0, 0.3, 0.5) thin films" J. Material Sci.;**23**:369-376(2000).

[5] S.B. Bhanu Prashanth, S. Asokan," Effect of antimony addition on the thermal and electrical-switching behavior of bulk Se–Te glasses", J. Non-Cryst. Solids **355**:164–168(2009).

[6] R.M. Mehra, A. Ganjoo, P.C. Mathur,"Electrical and optical properties of (Se0.7 Te0.3)100-x lnx system," J. Applied Physics, **75**: 7339–7334, (1994).

[7] V. Sharma, A. Thakur, N. Goyal, G.S.S. Saini, S.K. Tripathi, "Effect of In Additive on the Electrical Properties of Se–Te Alloy," J. Semiconductor Science and Technology, **20,** 103–107, (2005).

[8] M.A. Imran, D. Bhandari, N.S. Saxena, "Glass Transition Phenomena, Crystallization Kinetics and Thermodynamic Properties of Ternary Se80Te20−x nx (x=2, 4, 6, 8 and 10) Semiconducting Glasses: Theoretical and Experimental Aspects," J. Materials Science and Engineering: A,**292**, 56, (2000).

Monitoring Leaf Bio-activity with Laser Speckle Imaging Techniques Under Different Intensity Conditions

A. K. Sooraj Viswam, A. Mujeeb

International School of Photonics, Cochin University of Science and technology, Kochi, Kerala, India, 682022
Author e-mail address: soorajviswam@cusat.ac.in

Abstract: Photosynthesis and respiration are two of the fundamental biological activities occurring in plants. While Photosynthesis is found to vary with the intensity of light radiation, respiration occurs throughout the plant's life cycle. In this paper we try use laser speckle technique to qualitatively and quantitatively analyze the rate of plant metabolism in a non-destructive manner. With the help of various speckle image processing algorithms, we try to compare the plant bio activity rates for different light intensities.
Keywords: laser speckle, plant metabolism, NDT, photosynthesis

1. Introduction

Plant Metabolism consists of mainly two activities: Photosynthesis and Respiration. While Photosynthesis occurs in the presence of light, only respiration exists in the absence of light. The speed of photosynthesis changes depending on the environmental light intensity, carbon dioxide and water availability, temperature and the amount of chlorophyll present in an organism.

1.1. Photosynthesis

Photosynthesis is the process used by plants and chlorophyll containing organisms to turn inorganic molecules and light energy into sugars to fuel cellular function. The required inputs are sufficient carbon dioxide, water and light. These raw ingredients are funneled into organelles within the cells called *chloroplasts*, which converts them into usable glucose and oxygen as a byproduct. In 1934, E.C.C. Baley et al. observed that the main factors determining the rate of photosynthesis where temperature, intensity of irradiation and Carbon di-oxide content in the surrounding medium.

1.2. Laser Speckle Imaging Techniques

Laser Speckle is nothing but an intensity distribution of dark and bright dots arising due to the interference of coherent light reflected by/passing through an optically rough surface. This intensity distribution called the Specklegram is the signature of the reflecting surface and the propogating medium. Any variation in the medium or the surface reflects in the Specklegram. Here the optically rough surface is the leaf of the plant under observation and the light reflected from it is modulated by the plant activity. We create the Time History Speckle Pattern (THSP) matrix by choosing a particular column from the specklegram and then we calculate the covariance matrix from which we get a qualitative picture about the activity of the column under observation[1]. Then we calculate the Inertia Moment [2] value for the covariance matrix which is given by

$$IM = \sum_{ij} M_{ij}(i-j)^2$$

the IM value is treated as a quantitative figure representing the dynamic activity of the pixel column through time.

Experimental Setup

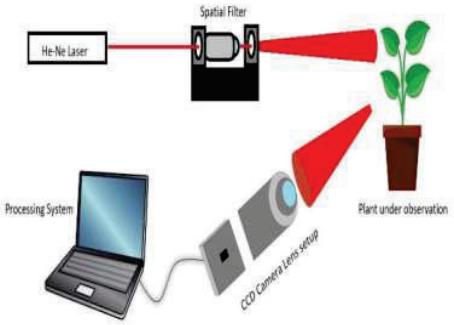

Fig. 1: Experimental Setup

A 632.8 nm (Red) 5 mW He-Ne laser is used as the non destructive probe source. The laser beam is filtered and expanded using a spatial filter. An expanded beam of uniform intensity is made to fall on the leaf of the specimen plant. The plant is exposed to high, medium, low, darkness, low, medium and high intensities of light respectively each for 1 minute and the speckle images are grabbed for 20 second durations after each exposure. The plant was kept in high brightness followed by medium and low brightness and then in darkness, the light intensities were provided by an led white light source.

2. Results

The THSP is calculated for 4 different columns in 4 different regions and both co occurrence matrix and IM values are calculated for these columns. The IM values are obtained for different light intensity conditions and are compared. The plant bio activity values observed from the leaf for different intensity conditions are shown in figure 2.

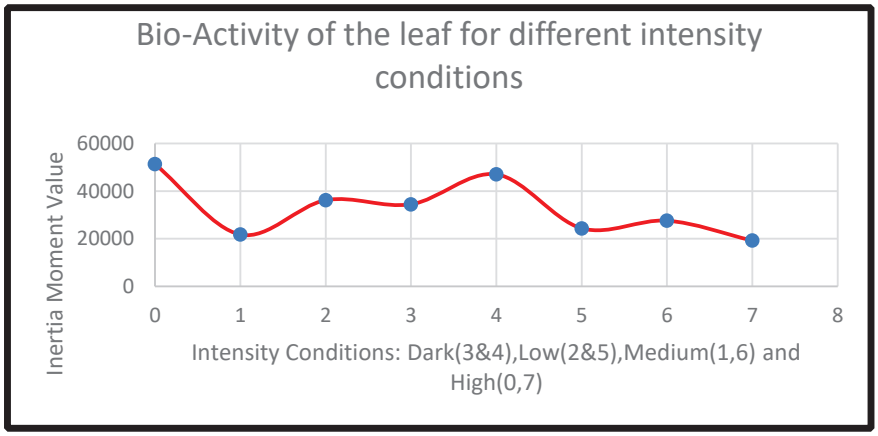

Figure 2: Average Inertia Moment values for different light intensities

References

[1] Arizaga, Ricardo, Marcelo Trivi, and Héctor Rabal. "Speckle time evolution characterization by the co-occurrence matrix analysis." *Optics & Laser Technology* 31.2 (1999): 163-169.

[2] Goodman, Joseph W. "Statistical properties of laser speckle patterns." *Laser speckle and related phenomena*. Springer, Berlin, Heidelberg, 1975. 9-75.

Analysis of Failure Mechanisms in High Power Semiconductor Lasers

Abhishek Sharma[1,2], D.S. Rawal[1], G. Vijaya Prakash[2]

1. *Solid State Physics Laboratory, Timarpur, Delhi (India)*
2. *Indian Institute of Technology, Hauz Khas, Delhi (India)*

Author e-mail address: abhijiphy@gmail.com

Abstract: High power semiconductor lasers are essential components of various defence systems. A complete understanding of various failure mechanisms is required to make semiconductor lasers and associated systems reliable and long lasting. Testing of high power laser diodes is carried out and analysis of various failure mechanisms is presented along with possible cause of failures.

Keywords: Semiconductor lasers, Catastrophic optical mirror damage (COMD), Failure modes

1. Introduction

High power semiconductor lasers are being used for pumping of fiber and solid state lasers as well as for initiation of explosive detonation, laser range finders, laser dazzlers, underwater communication & sensing etc [1-3]. As the output power of an edge emitting semiconductor laser diode increases, load on laser facet keeps on increasing and leads to catastrophic optical mirror damage (COMD). Once COMD happens laser cavity is destroyed and laser action is stopped. Apart from COMD, there are various other failure modes in high power laser diodes like thermal runaway, creeping of solder material to epitaxial region, imperfect facets, degradation of contacts, dark line defects etc[2,3]. Edge emitting high power semiconductor lasers have been fabricated, packaged and tested. Some of the devices did not perform as per expected behavior and failed during the testing procedure. Possible causes of their failures were analyzed along with solutions and presented in the work.

2. Device fabrication

Edge emitting single quantum well (QW) semiconductor laser diodes emitting at 976 nm wavelengths were fabricated in mesa stripe geometry configuration using GaAs/InGaAs/AlGaAs based material system. Photolithography, mesa etching, dielectric deposition and etching using photolithography, formation of p Ohmic contacts, backside wafer thinning, n Ohmic contacts, cleaving for laser bar formation, facet coating for anti reflection (AR) and high reflection (HR), single element formation were carried out for device fabrication. After device fabrication these devices were packaged on F-mount laser diode packages as shown in Fig, 1.

Fig.1: Single emitter laser diode in F-mount configuration

3. Device testing and analysis

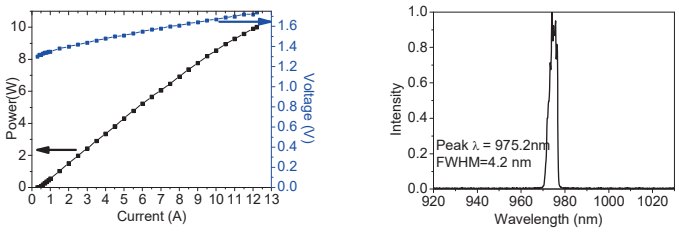

Fig.2: L-I-V and spectral characteristic of F mount packaged single emitter laser diode

Packaged devices were tested in terms of power-current, current-voltage, and spectral characteristics. Maximum power of 10 W was achieved in CW mode. Spectral and LIV characteristics of packaged laser device are shown in Fig. 2. Few devices were failed during the testing procedure. Possible reasons for device failure were analyzed in detail and presented below.

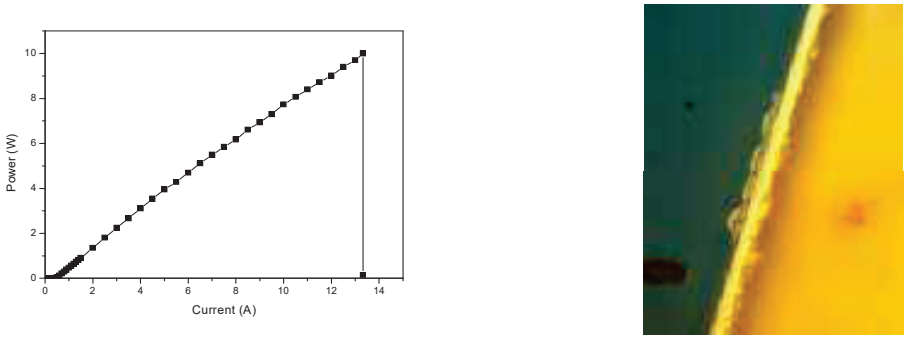

Fig.3: L-I characteristic of the failed device and laser facet after failure

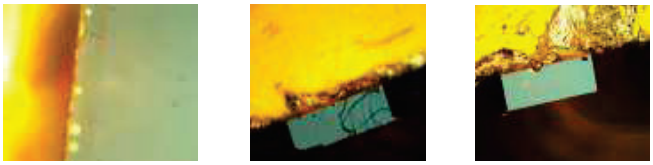

Fig.4: Laser facet before testing (a) damage points, (b)imperfect facets, (c) Creeping of solder material

Fig. 3 shows L-I characteristic and laser facet after the device failure. Laser facet after failure shows small spots of damages due to intensive optical load on the facet known as COMD. Fig 4(a, b) shows laser device facets before operation, having few damage spots. These damage spots were created during the laser bar formation process. During the device testing, these damage spots acts as major absorption centers and microscopically temperature rises at these points, which lead to increase in refractive index followed by more absorption of light and temperature rise. This cyclic process leads to thermal runaway of the temperature and output power falls and sometimes it also leads to COMD. Fig. 4 (c) shows creeping of solder material in the epitaxial region which obstructs the laser light and often it sorts the p and n junction of the epitaxial layers. Another failure mechanism for high power laser diodes is issues in mounting of laser diode on the laser package. Fig. 5 shows that there is small gap (~ 2 μm) between laser device and carrier. As these devices are operated at very high CW current, a huge amount of heat is also generated. If heat is not dissipated efficiently device temperature rises and performance of the laser device degrades and device fails.

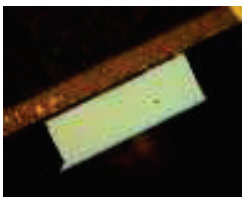

Fig. 5: Gap between laser device and carrier (Packaging issue)

4. References

[1] R. Diehl, High Power Diode Lasers, Fundamentals, Technology and Applications, Springer, Germany, 2000.
[2] M. Fukuda, Reliability and Degradation of Semiconductor Lasers and LEDs, Artech House, Boston, 1991.
[3] A. Knauer et al., Semiconductor Science and Technology, Vol 20, No 6, (2005).

Low-Cost Hydrothermally Synthesized Highly Crystalline 2D-SnS Nanoflakes for Optoelectronic Applications

Prashant Kumar Gupta, Amritanshu Pandey
Department of Electronics Engineering, IIT (BHU), Varanasi 221005, India
prashantkrgupta.rs.ece19@itbhu.ac.in, apandey.ece@iitbhu.ac.in

Abstract: This article reports the improved, low-cost, and facile hydrothermal method for synthesizing the highly crystalline 2D-SnS nanoflakes. A good percentage crystallinity of 87.172 % of SnS nanoflakes was achieved. XRD analysis and TEM images with SAED pattern in in-set also confirm their highly crystalline nature. UV-visible spectra of 2D-SnS nanoflakes reveal their potential use in UV-Visible optoelectronic applications.
Keywords: good crystallinity, SnS nanoflakes, UV-visible.

1. Introduction

2D-transition metal dichalcogenides (2D-TMDs) have appeared as an active area of research and gained special attention in the scientific community because of their remarkable electrical, mechanical, chemical, and optoelectronic properties [1]. The 2D-TMDs are strongly connected by a covalent bond in the lateral direction in a layer while weekly connected between interlayers [2] such as MoS_2, $MoSe_2$, WS_2, WSe_2, SnS, etc. Among all, low-cost solution-processed, highly crystalline 2D-SnS nanoflakes are not much explored due to the difficulty in optimization of the synthesis process. SnS offer a direct bandgap of 1.3 eV [3] in its monolayer form with a high absorption coefficient of 10^4 cm^{-1} [4], respectively. Since their bandgaps lie in the range of the solar spectrum so these materials are a promising candidate for developing efficient optoelectronic devices to convert optical energy into electrical energy or vice versa. Thus, we are proposing a 2D-SnS nanoflakes-based MSM photodetector structure [5] (Al/2D-SnS Nanoflakes/Al) for UV-visible optoelectronic application.

2. Experimental Details

Synthesis of 2D-SnS Nanoflakes

Initially, 4.5126 gm tin dichloride dihydrate ($SnCl_2.2H_2O$) was dissolved into 60 ml distilled water by continuous stirring until a uniformly dispersed solution is achieved. Then, 1.3701 gm thiourea ($CH_4.N_2S$) was added to it and again stirred for 45 min. Further, the homogeneous solution was transited into a 100 ml stainless steel autoclave, sealed, and then heated at 200°C for 24 hours. After natural cooling, the black precipitate was washed with DI water and ethanol several times to remove the residuals. Finally, the products were dried at 60°C for 24 hours.

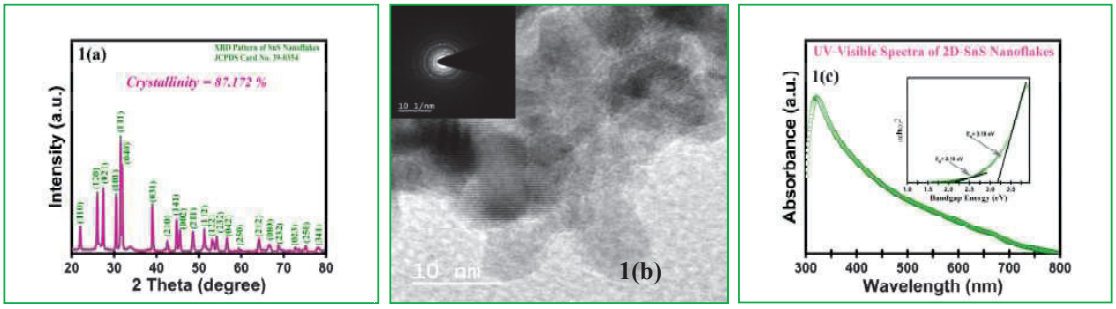

Fig. 1 (a) shows the XRD pattern of 2D-SnS nanoflakes. Fig. 1(b) shows the transmission electron microscope (TEM) image of 2D-SnS nanoflakes with selected area diffraction pattern (SAED) in in-set. Fig. 1 (c) shows the UV-visible spectra2D-SnS nanoflakes with tauc-plot in in-set

3. Structural Characterization

Rigaku smart laboratory 9 kW with a 1.5405 Å Cu K-a radiation source equipment was used for X-ray diffraction (XRD) analysis of as-synthesized 2D-SnS nanoflakes. This successfully reveals their good crystalline nature. The XRD spectra of 2D-SnS nanoflakes with their proper crystalline phases are shown in Fig. 1 (a) well matched with the JCPDS card Number 39-0354 [6]. A good percentage crystallinity of 87.172 % of SnS nanoflakes was achieved.

Transmission electron microscope (TEM), Tecnai G2 20 Twin, FEI, USA equipment was used to investigate the as-synthesized 2D-SnS nanoflakes. TEM images of as synthesized 2D-SnS nanoflakes are shown in Fig. 1 (b) with their respective selected area diffraction pattern (SAED) pattern in-set. The TEM images and their SAED patterns also confirm the successful synthesis of highly crystalline 2D-SnS nanoflakes.

UV-visible spectra of 2D-SnS nanoflakes are shown in Fig. 1(c) with tauc-plot in in-set, revealing their potential use in UV-Visible optoelectronic application.

4. Proposed 2D-SnS Nanoflakes Based MSM Photodetector

We are proposing 2D-SnS nanoflakes-based MSM photodetector structure [5] (Al/2D-SnS Nanoflakes/Al) for UV-visible application. Since the contact between Al metal and 2D-SnS Nanoflakes (act as p-type semiconductor) is Schottky in nature. So this kind of assembly among metal, semiconductor, and metal forms a back-to-back double Schottky MSM type photodetector structure. Which is suitable for achieving low dark current and fast time response with adequate responsivity.

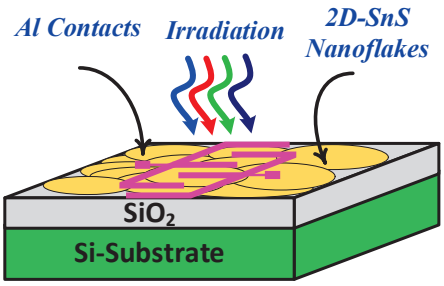

Fig. 2 Schematic diagram of proposed 2D-nanoflakes based MSM photodetector

5. Conclusion

This article demonstrates the improved facile hydrothermal processes for synthesizing the highly crystalline 2D-SnS nanoflakes. The XRD analysis successfully confirms their good crystalline nature with adequate percentage crystallinity of 87.172 %. The TEM images and their SAED patterns also confirm the successful synthesis of highly crystalline 2D-SnS nanoflakes. Thus as-synthesized 2D-SnS nanoflakes may be a promising candidate for developing efficient optoelectronic devices. We have also proposed a 2D-SnS nanoflakes-based MSM photodetector structure (Al/2D-SnS Nanoflakes/Al) for UV-visible application, which should give low dark current, fast time response with adequate responsivity.

6. References

[1] S. Manzeli, D. Ovchinnikov, D. Pasquier, O. V. Yazyev, and A. Kis, "2D transition metal dichalcogenides," Nat. Rev. Mater., vol. 2, 2017, doi: 10.1038/natrevmats.2017.33.

[2] W. Choi, N. Choudhary, G. H. Han, J. Park, D. Akinwande, and Y. H. Lee, "Recent development of two-dimensional transition metal dichalcogenides and their applications," Mater. Today, vol. 20, no. 3, pp. 116–130, 2017, doi: 10.1016/j.mattod.2016.10.002.

[3] S. S. Hegde and K. Ramesh, "Advances in low-cost and nontoxic materials based solar cell devices," J. Phys. Conf. Ser., vol. 2070, no. 1, 2021, doi: 10.1088/1742-6596/2070/1/012043.

[4] M. S. Mahdi, N. M. Ahmed, A. Hmood, K. Ibrahim, and M. Bououdina, "Comprehensive photoresponse study on high performance and flexible π-SnS photodetector with near-infrared response," Mater. Sci. Semicond. Process., vol. 100, no. May, pp. 270–274, 2019, doi: 10.1016/j.mssp.2019.05.019.

[5] F. F. Masouleh and N. Das, "Application of Metal-Semiconductor-Metal Photodetector in High-Speed Optical Communication Systems," in Advances in Optical Communication, N. Das, Ed. Rijeka: IntechOpen, 2014. doi: 10.5772/58997.

[6] J. Chao, Z. Wang, X. Xu, Q. Xiang, W. Song, G. Chen, J. Hu, and D. Chen, "Tin sulfide nanoribbons as high performance photoelectrochemical cells, flexible photodetectors and visible-light-driven photocatalysts," RSC Adv., vol. 3, no. 8, pp. 2746–2753, 2013, doi: 10.1039/c2ra22092j.

.

Tunable Refractive Index and Band Gap of TiO_2 Thin Film Grown on Si Substrate by Employing Sol-gel Spin Coating

Soham Lodh[1,2], Rajib Chakraborty[1*]

[1]*Department of Applied Optics and Photonics, University of Calcutta, JD-2, Sector-III, Salt Lake, Kolkata-700106, INDIA*

[2]*Department of Electronics & Communication Engineering, MCKV Institute of Engineering, Liluah, Howrah-711204, INDIA*

**Author e-mail address: rcaop@caluniv.ac.in*

Abstract: Titanium dioxide thin film with tunable refractive index and band gap is grown on Si substrate by using sol-gel spin coating process at different revolutions per minute (rpm). It is observed that the refractive index decrease with increase in rpm. Band gap of the thickest film is smallest and it increases with decrease in film thickness.

Keywords: Sol-gel TiO_2 thin film, high refractive index TiO_2 film, TiO_2 band-gap

1. Introduction

Titanium dioxide (TiO_2) has become an attractive research material in the recent times owing to its easy availability, high refractive index, good transmittance in the near infrared and visible region, excellent physical, thermal and chemical stability [1, 2]. TiO_2 is used for antireflective coating, solar cells, gas sensors, photocatalyst, multilayer optical applications etc [1]. Nowadays organic light emitting diodes (OLEDs) are very popular in lightning and displays for its very attractive and promising characteristics. But the main drawback of bottom-emitting OLEDs is the light extraction efficiency (LEE), which is about 20% whereas the internal quantum efficiency has reached almost 100%. To overcome this problem, high refractive index transparent TiO_2 thin film can be used to increase the LEE of bottom-emitting OLEDs [2].

In the present work TiO_2 thin films are deposited on Si substrate at 2000, 3000 and 4000 rpm. Thicknesses along with optical characterization of the deposited films are studied with spectroscopic ellipsometry (SE) measurement.

2. Tables and Figures

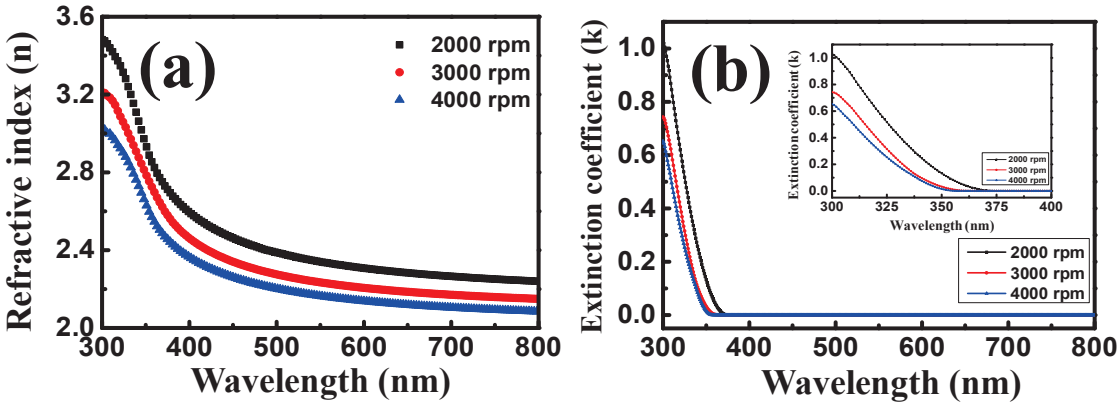

Fig. 1: (a) Refractive index and (b) extinction coefficient vs. wavelength

In the present work 0.92 mol of ethanol is mixed with 0.118 mol of acetic acid inside of a confined glass beaker for 10 minutes, later titanium (IV) iso-propoxide (TTIP) of 0.024 mol is added drop wise under continuous stirring for another 3 hours. The prepared solution is further aged for 24 hours, and then spin coated (30 µL for 15s) on precleaned Si substrates at three different revolutions per minute (2000, 3000 and 4000 rpm). All the prepared

samples are dried under N_2 gas flow for 10 minutes followed by annealing at 300°C for 30 minutes. Spectroscopic Ellipsometry (SE) is used to measure the thickness, refractive index and extinction coefficient of the TiO_2 films on Si substrate. Tauc and Menth [1] method is used to calculate the band gaps.

Thickness measured with SE reveals 198.32, 136.19 and 97.49 nm for 2000, 3000 and 4000 rpm samples respectively. Refractive index (RI) and extinction coefficient plot for all the three samples are shown in figure 1. It can be observed from figure 1 that the 2000 rpm sample exhibits highest RI of 2.34 at 550 nm, which reduces to 2.23 and 2.16 for 3000 and 4000 rpm samples respectively. Decrease in RI with decrease in thickness may be due to the packing density [3], where higher packing density attributes to higher RI. Extinction coefficient plots (figure 1b) reveal that all the three TiO_2 films are highly transparent in the visible and near infrared region, whereas sharp decrease in light transmission is observed in the ultra-violet (UV) region owing to fundamental light absorption [1].

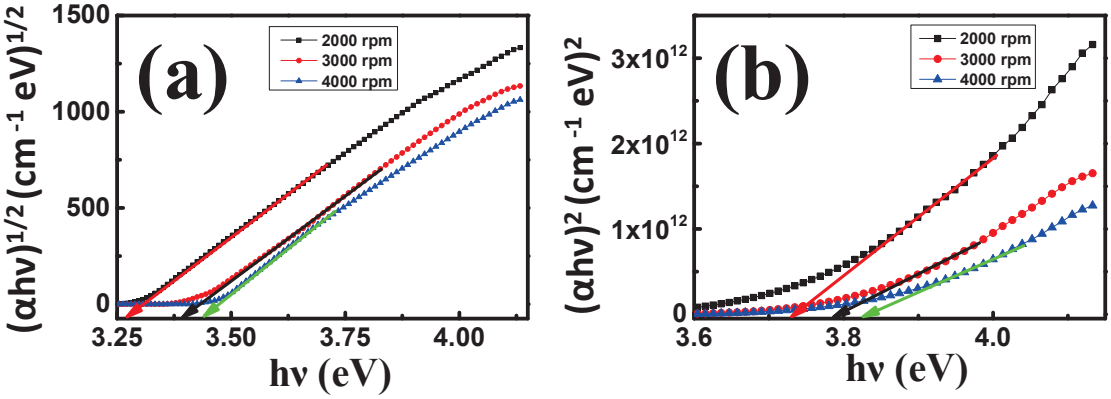

Fig. 2: Plot of hγ vs. $(\alpha h\gamma)^j$ indicating (a) indirect (for j=1/2) (b) direct (for j=2) band gap

Band-gap study by employing Tauc and Menth method [1] is shown in figure 2 for both indirect and direct band-gap. Sample with highest thickness exhibits lowest indirect as well as direct band-gap of 3.27 and 3.73 eV respectively. Both indirect and direct band-gap increases with decrease in thickness further establish the fact that 2000 rpm sample has the highest packing density [1,3], which reduces with increase in rpm.

It can be concluded that high transmittance, tunable RI and band-gap TiO_2 thin film can be grown on Si substrate by using low cost sol-gel spin coating method, which could be used as antireflective coating, UV range photo detector, solar cell, enhancement of the LEE of OLEDs and other optical applications.

Table 1: Refractive index (RI), thickness, direct and indirect band gap

Sample rpm	Thickness (nm)	Refractive index (550 nm)	Indirect band-gap (eV)	Direct band-gap (eV)
2000	198.32	2.34	3.27	3.73
3000	136.19	2.23	3.39	3.78
4000	97.49	2.16	3.44	3.82

3. References

[1] Soham Lodh and Rajib Chakraborty, "Bandgap Engineering of Sol–Gel Spin-Coated TiO2 Thin Film on Glass Substrate," in Photonics, Plasmonics and Information Optics (CRC Press, 2021), pp. 13-30.

[2] Soham Lodh, Rajib Ghosh, and Rajib Chakraborty, "Studies on high refractive index amorphous TiO2 thin film for possible improvement of light extraction efficiency in organic light emitting diodes," Optical Engineering 59(10), 107104 (2020).

[3] Mohammed Hadi. Shinen et al, "Preparation of high transmittance TiO2 thin films by sol-gel technique as antireflection coating," J. Phys.: Conf. Ser. 1032 012018 (2018).

Fabrication of microlens array using thermal reflow technique and ICP RIE dry etching

Mukund Kumar Singh, M Srinivasa Raju, Hriday Patel, K Biju Kumar, Prashant Varma
Space Applications Centre-ISRO, Ahmedabad, India 380015
mukundsingh@sac.isro.gov.in

Abstract: A three step process is developed for microfabrication of fused silica Microlens Array (MLA) by combining Photolithography, Thermal reflow of resist and Reactive Ion Etching (RIE). The process allows patterning of resist cylinders using Laser Direct Writing, creation of polymeric lens structure using thermal reflow and pattern transfer into the fused silica substrate using RIE. Fabricated MLA has smooth lens structures with surface roughness better than 3.5nm, microlens pitch of 300µm, sag height of 3µm and Numerical Aperture (NA) of 0.018. Pattern transfer accuracy better than 95% in lateral as well as vertical directions has been successfully achieved. Fabricated MLA is tested in an in-house Shack-Hartmann Wavefront Sensor (SHWFS), achieving 80% encircled energy in 66 µm diameter of the Point Spread Function (PSF).
Keywords: Microlens array, shack-hartmann wavefront sensor, thermal reflow, dry etching

1. Introduction

Space-borne high resolution telescopes require large monolithic primary mirror or sparse aperture segmented mirror and deployable arrangements to minimize launch envelopes. The image quality of such telescopes is mainly affected by wavefront error at the focal plane. The wavefront errors are introduced by optical component fabrication, alignment & assembly errors, launch loads and post launch thermomechanical stresses under orbital conditions. Active optics systems are utilized to measure wavefront error and correct it in closed loop to achieve desired image quality. This correction chain includes two primary components, wavefront sensor for wavefront measurements and deformable mirror for wavefront correction [1]. MLA samples incoming wavefront and convert phase variation to the intensity variation at detector. MLA fabricated in this work will be used in an In-house developed Shack-Hartmann Wavefront Sensor (SHWS) with a commercial of-the-shelf detector. The targeted MLA has a pitch of 300µm and sag height 3 µm to provide wavefront measurement over large dynamic range. The incoming light is sampled using MLA and light is focused on to the CMOS camera. The off-the-shelf camera has a pixel pitch of 5.5µm with 2048 x 2048 format.

2. Fabrication of MLA

2.1. LASER Direct Write Lithography

In this step, cylindrical resist structures of height 7-8µm are created on top of substrate as shown in fig-1. To achieve this, AZ4620 photoresist by Microchemicals GmbH is spin coated onto the substrate at 3800rpm. This is followed by Laser Direct Write exposer of polymer using µPG101 by Heidelberg Instruments Mikrotechnik GmbH. Exposed patterns are then resolved using the development process by agitating the exposed substrate inside AZ400K developer for 2-3 minutes to get the desired cylindrical structures. The exposure dose and defocus parameters are crucial for the sharp pattern generation in laser direct write system, especially for such thicker resist films.

2.2. Thermal Reflow

Thermal reflow is an inherent characteristics of the photoresists which do not cross-link. Almost all the positive photoresists do not crosslink and undergo thermal reflow when heated beyond a specific temperature called as softening temperature [2]. For thermal reflow, the developed resist cylinders as shown in fig-2(a), are melted at a temperature of 140-180°C on a hot plate. Above the glass transition temperature, the surface tension acts on the melting resist and rearranges it to minimize its surface area into a drop like structure, which gives the spherical lens shape as shown in fig-2(b) and 2(c). Height of the lens structure increased after thermal reflow by approximately 40%, which is carefully considered in the dry etching process.

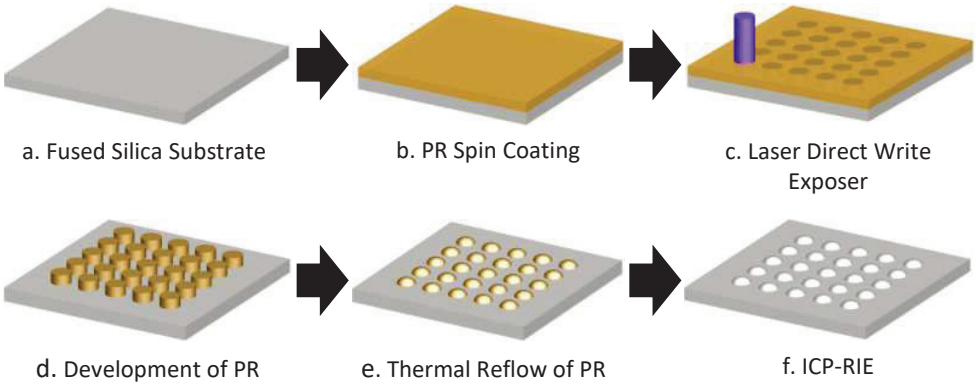

Fig. 1 Microlithography Process Flow for Fabrication of MLA

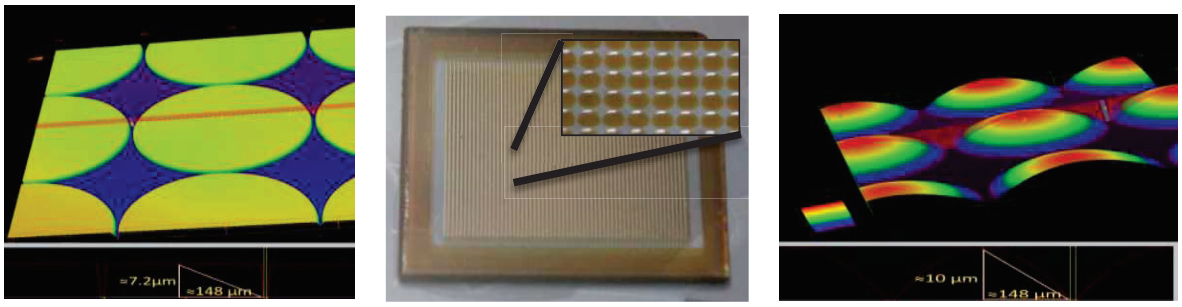

Fig. 2: (a) 3D profile of thick cylindrical structures after resist development, (b) Microlens structure on resist after thermal reflow, Inset Image- Zoomed view of the resist microlens, (c) Smooth resist profile after thermal reflow with sag height 10µm

2.3. ICP-RIE based dry etching

Dry etching process is used to transfer the thermally reflowed polymeric MLAs into an optical substrate. SF6 + O2 is used as the process gas in a high vacuum chamber while maintain ICP power and RF bias power at 450W and 350W respectively. The etching process is performed in multiple steps of etch runs to maintain the etch rate and etch selectivity to 200nm/min and 1:3.3 respectively. Due to high anisotropy and low etch selectivity, the diameter remains unchanged while the sag height reduces to 3µm in the etched microlens as shown in fig-4. The optimized RIE process allows etching of polymeric microlens with high NA of 0.083 to get fused silica microlens with low NA of 0.018 without changing the microlens diameter.

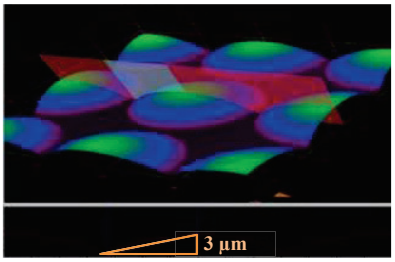

Fig-3: Lens profile on fused quartz after dry etching

3. References

[1] G. Y. Yoon, T. Jitsuno, M. Nakatsuka, and S. Nakai, "Shack Hartmann wave-front measurement with a large F-number plastic microlens array," Appl. Opt. 35, 188–192 (1996).
[2] Philippe Nussbaum and Hans Peter Herzig, "Low numerical aperture refractive microlenses in fused silica," Optical Engineering 40, 1412–1414 (2001).
[3] Www.Microchemicals.Com/Downloads Application_notes.Html (Microchemicals, 2013), p. 2.

On Exploration of Effect of q-Parameter and Initial Beam power on propagation dynamics of q-Gaussian Laser Beam

K.Y. Khandale[1], P.T. Takale[1], S.S. Patil[2], P.P. Nikam[2], M.B. Mane[2], V.S. Pawar[2], T.U. Urunkar[1], S.D. Patil[2*], M.V. Takale[1*]

1. Department of Physics, Shivaji University, Kolhapur, Maharashtra – 416004 India
2. Department of Physics, Devchand College, Arjunnagar, Kolhapur, Maharashtra – 591237 India
e-mail: mvtphyunishivaji@gmail.com, sdpatilphy@gmail.com

Abstract: The beam-width parameter (BWP) differential equation is reduced to two variables as q parameter and initial beam power (p_0) which govern the propagation dynamics of q-Gaussian laser beam. In current study, intervals of p_0 of a q-Gaussian laser beam have been investigated theoretically. The nonlinearity in dielectric function used herein is collisional plasma. The effect of intervals of p_0 and q is further used to explore propagation dynamics of q-Gaussian laser beam in underdense collisional plasma. The Akhmanov's parabolic equation method under paraxial and WKB (Wentzel-Kramers-Brillouin) approximations are used in current work. Results have been found interesting, are revealed graphically and discussed.

Keywords: Initial beam radius, Underdense collisional plasma, Self-focusing/defocusing, q-Gaussian.

1. Introduction

An intense laser beam can shrink when propagating in a material medium through the influence of self-focusing was first proposed by Askar'yan in 1962 [1]. Self-focusing/defocusing of laser beams in nonlinear media has been studied by Akhmanov *et al.* [2] and Sodha *et al.* [3] did its pedagogical straight forward extension to plasmas. When the laser beam incidents on plasma, it modifies the dielectric constant results in modification of the refractive index of plasma and hence laser beam self-focuses/defocuses. Self-focusing of laser beams has wide range of applications such as ICF, higher harmonic generation, X-ray lasers etc., [4-6]. Most of the studies on the interaction of laser-plasma have been conducted by assuming Gaussian distribution of laser beam [7-10]. But Patel *et al.* [11], have reported in their investigation that the intensity profile of the laser beam deviated from the Gaussian distribution known as q-Gauussian in the case of Vulcan Peta watt laser. Additionally, M. Nakatsutsumi *et al.* [12], have recommended that the beam intensity distribution, can be rigorously featured by an q-Gaussian distribution of the form of $I(r) = I(0)\left(1 + \frac{r^2}{q{r_0}^2}\right)^{-q}$. Afterwards the significant interest has been shown by many researchers towards q-Gaussian laser beam. One should note that in all above beams Gaussian remains intact. However, in most of the cases amplitude attenuation is obtained through associated functions like Cosh, Hermite and Hermite-cosh etc. Here we changed the values of q and in the limit $q \to \infty$, the beam becomes Gaussian. Thus freedom of exploring q in underdense collisional plasma is our prime interest for current theoretical investigations.

2. Basic Theoretical Formulation

Consider the q-Gaussian laser beam propagating in collisional plasma along z-axis, the initial electric field distribution of laser beam at $z = 0$, is

$$E = A(r,z)\exp[i(\omega t - k_0 z)] \quad (1)$$

In the cylindrical co-ordinate system, wave equation describing electric field E of laser beam in the plasmas along with effective dielectric constant ε [3], is given as,

$$\frac{\partial^2 \bar{E}}{\partial z^2} + \frac{\partial^2 \bar{E}}{\partial r^2} + \frac{1}{r}\frac{\partial \bar{E}}{\partial r} + \frac{\omega^2}{c^2}\varepsilon\,\bar{E} = 0 \quad (2)$$

$$\varepsilon = \varepsilon_0 + \phi\,(EE^*) \quad (3)$$

where, ε_0 is linear part and the $\phi(EE^*)$ is nonlinear part of dielectric constant for collisional plasma [3, 10] given

$$\phi\,(EE^*) = \frac{{\omega_p}^2}{\omega^2}\left(\frac{\alpha EE^*}{2 + \alpha EE^*}\right), \quad (4)$$

Substituting equations (1) and (3) in equation (2), one can obtain parabolic wave equation as,

$$\frac{\partial^2 A}{\partial r^2} + \frac{1}{r}\frac{\partial A}{\partial r} + \frac{\omega^2}{c^2}\phi(\,EE^*)\,A = 2ik_0\,\frac{\partial A}{\partial z} \quad (5)$$

with, $A = A_0(r,z)\exp[-ikS(r,z)]$, (6)

where, S is eikonal of wave. By following Akhmanov *et al.* [2] and Sodha *et al.* [3], we get

$$S = \frac{r^2}{2}\beta(z) + \phi(z)\,, \quad (7)$$

$$A_0^2(r,z\,) = \frac{E_0^2}{f^2(z)}\left(1 + \frac{r^2}{f^2(z)\,q\,r_0^2}\right)^{-q}, \quad (8)$$

$$\frac{d^2 f}{d\xi^2} = \left[\frac{(4+q)}{q\,f^3}\right] - \left[\frac{2\,\alpha{E_0}^2 f\,\omega_p^2\,r_0^2}{\left(\alpha{E_0}^2 + 2\,f^2\right)^2 c^2}\right] \quad (9)$$

where, $\xi = z/R_d$, and $R_d = k\,r_0^2$ is Rayleigh length.

3. Result, Discussion and Conclusion

The nonlinear second order, differential equation (9) governs propagation dynamics of q-Gaussian laser beam and is solved under critical conditions f=1, $d^2f/d\xi^2 = 0$ &numerically using the parameters: ω_p= 1.7760×10^{15} rad/s, r_0 = 20×10^{-4} cm, c = 3×10^{10} cm/s, n_0 =10^{18} cm^{-3}, ξ is dimensionless propagation distance, R.H.S. of equation (9) reduces

$$F(p_0) = \left(\frac{4+q}{q}\right) - \left(\frac{280.3712\ p_0}{(p_0+2)^2}\right) \qquad (10)$$

where, p_0 and ρ_0 are initial beam power and critical beam radius, respectively. Equation (10) shows dependence of $F(p_0)$ on p_0. Figure 1 shows 3 distinct regions of propagation dynamics as mentioned in table I. From Figure 1, it has been seen that the interval of p_0 for self focusing and defocusing increases with increase in the values of q.

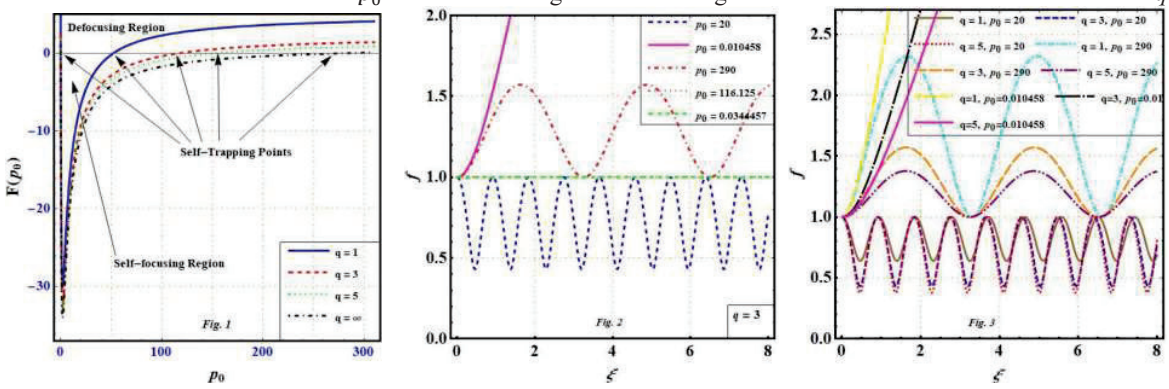

Fig. 1: Dependence of $F(p_0)$ with respect to initial beam power p_0 for various values for q (q = 1, 3, 5, ∞)
Fig. 2: BWP f versus ξ in underdense collisional plasma for various values p_0 for q = 3
Fig. 3: BWP f versus ξ in underdense collisional plasma for various values for q = 1, 3, 5 and fixed p_0
Table 1: Analytical investigation of Self-focusing, Defocusing, and Self-trapping for various values for q

q	Self-focusing region $F(p_0) < 0$	Defocusing region $F(p_0) > 0$	Self-trapping points $F(p_0) = 0$
1	0.0769271 < p_0 < 51.9973	51.9973 < p_0 < 0.0769271	p_0 = 0.0769271 and p_0 = 51.9973
3	0.0344457 < p_0 < 116.125	116.125 < p_0 < 0.0344457	p_0 = 0.0344457 and p_0 = 116.125
5	0.0263617 < p_0 < 151.735	151.735 < p_0 < 0.0263617	p_0 = 0.0263617 and p_0 = 151.735
∞	0.014474 < p_0 < 276.357	276.357 < p_0 < 0.0144740	p_0 = 0.014474 and p_0 = 276.357

From Fig. 2, the oscillatory self-focusing is noticed within the self-focusing interval of p_0 as mentioned in table I, and within the defocusing interval of p_0, for smaller values of p_0 (p_0 < 0.0344457) for q = 3, the steady defocusing is observed while for large values of p_0 (p_0 > 116.125) for q = 3 the oscillatory defocusing is observed also the similar behaviour is observed for q = 1 and 5. From Fig. 3, within the self-focusing region as q increases (q = 1, 3, 5) the oscillatory and enhanced self-focusing is observed for fixed value of p_0 = 20, while within the defocusing interval of p_0, for smaller and fixed value of p_0= 0.010458, steady defocusing and for large values of p_0 > 290 oscillatory defocusing is observed. And for the both case as q increases the rate of defocusing is also decreases. Finally, in conclusion current analysis represents that propagation dynamics of q-Gaussian laser beam in underdense collisional plasma can be explored effectively, under the pre-conditioning of q parameter and initial beam power p_0.

4. References

[1] G. A. Askar'yan, Sov. Phys. – JETP, **15**, 1088 (1962)
[2] S. A. Akhmanov, A. P. Sukhorukov and R. V. Khokhlov, Sov. Phy. Usp. **10,** 609-636 (1968)
[3] M. S .Sodha, A. K. Ghatak and V. K. Tripathi, Progress in Optics, **13**, 169-265 (1976)
[4] M. Tabak, J. Hammer, Glinsky, M. E., *et al.*, Phys. Plasmas, **1**, 1626 (1994)
[5] J. Rajput, N. Kant, H. Singh and V. Nanda, Opt. Commun. **282**, 4614-4617 (2009)
[6] S. Suckewer and C. H. Skinner, Science, **247**, 1553-1557 (1990)
[7] M. V. Takale, S. T. Navare, S. D. Patil, V. J. Fulari and M. B. Dongare, Opt. Commun. **282**, 3157–3162 (2009)
[8] S. D. Patil and M. V. Takale, Phys. Plasmas **20**, 072703 (2013)
[9] M. Aggarwal, S. Vij and N. Kant, Optik, **125**, 5081-5084 (2014)
[10] A. T. Valkunde, S. D. Patil, B. D. Vhanmore, et. al., Phys. Plasmas **25**, 033103 (2018)
[11] P. K. Patel, M. H. Key, A. J. Mackinnon, et. al., Plasma Phys. Control. Fusion **47**, B833-B840 (2005)
[12] M. Nakatsutsumi, J. R. Davies, R. Kodama, et. al., New J. Phys. **10**, 043046 (2008)

Realization of All Optical Diode Action from a Nonlinear Photonic Crystal/ Au Hybrid configuration

Shiju E[a], Jaismon Francis[b], Sheenu Thomas[a]

[a]*International School of Photonics, Cochin University of Science and Technology, Kalamassery, Kochi 682 022, Kerala, India*

[b]*Department of Physics, National Institute of Technology Calicut, India*

Abstract: *We report all-optical diode action from two axially asymmetric nonlinear optical medium by juxtaposing a saturable absorber (SA) and reverse saturable absorber (RSA) in tandem. The asymmetry in nonlinear absorption leads to non-reciprocity in light transmission which makes the out transmittance from the nonlinear medium direction dependent. A nonlinear photonic crystal consisting ZnSe as defect fabricated by spin coating polyvinyl carbazole/cellulose acetate quarter-wave stacks with a photonic bandgap around 532 nm and a thin layer of Au deposited on the photonic crystal by thermal evaporation form the diode structure. Forward and reverse direction action of the diode was demonstrated by varying the input fluence of a Q switched Nd: YAG laser operating at 532 nm*

Keywords: Nonlinear optics, photonic crystal, optical diode, Z scan

Introduction

Intense research is going on in photonics to replace the traditional electronic device with integrated photonic system, which offers enhances performances. Hence it is mandatory to develop an optical analogue of the electronic diode, which is the basic component of electronic circuit. Non-reciprocal light transmission is crucial for realizing optical diode action. Similar to normal diode action, optical diode exhibits directional dependent transmission behavior, where it blocks light in one direction (reverse direction condition) and letting in the other direction (forward direction). A number of different structures and configurations were proposed for non-reciprocal light transmission, but practical demonstration of these structures was still challenging due to complex structure and/or relatively large size. Moreover, these approaches demand high cost, low scalability and limited probability of device fabrication though they are conceptually smart. The proposed optical diode is based on axially asymmetric light transmission from an orderly placed thin saturable absorber (SA) and reverse saturable absorption (RSA). A Saturable Absorber (SA) and Reverse saturable absorber (RSA) is juxtaposed in the beam direction causes axially asymmetric transmission of light. Besides the effortlessness in fabrication, these structures have scalable low-cost design that makes them suitable choice for the integrated device [1-3]. The diode action in forward and reverse direction were investigated by varying the fluence of a Q switched Nd:YAG laser operating at 532 nm. This optical diode offers high non-reciprocity factor with low input threshold, with good chemical and mechanical stability, making it a potential candidate towards realizing all-optical analogous of electronic devices.

Materials and Methods

1-D Photonic with photonic band gap located around 532 nm crystal comprising 20 bilayers of two polymers polyvinyl carbazole (PVK,Sigma Aldrich, Mw=1,100,000) and Cellulose acetate (CA, Mw=100,000,Acros Organics) with refractive index 1.68 and 1.47 respectively were spin coated on glass substrate with quarter wave optical thickness. A defect layer of ZnSe NPs at 532 nm forms resonant cavity for light. ZnSe NPs were synthesized pulsed laser ablation using a Q-Switched Nd:YAG laser, having 7ns pulse width, 532 nm wavelength and the obtained TEM image and absorption spectra is shown in figure 1 (a) and (b). A thin layer of gold vacuum coated on the photonic crystal acts as SA medium The individual Z scan studies and optical diode actions were investigated by Z scan technique using above mentioned laser system. The structure of fabricated NL-PhC is given in Figure 1(c).

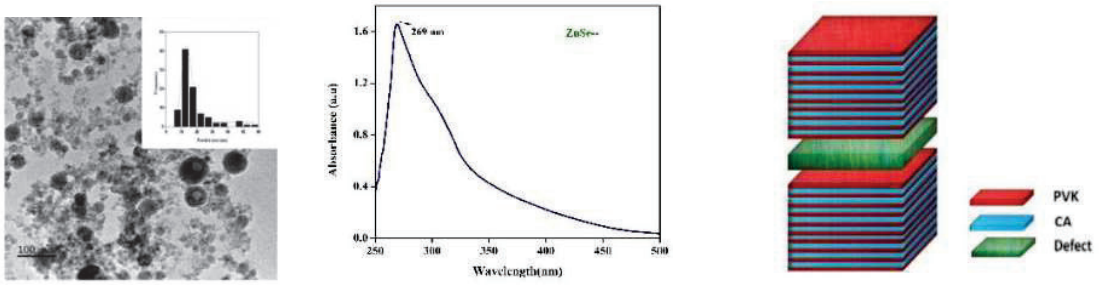

(a) (b) (c)

Figure 1: (a) TEM image, (b)absorption spectra of synthesized ZnSe NPs and (c) structure of fabricated NL-PhC

Results and Discussion

Prior to the realization of the diode action, individual NLA activity of ZnSe NPs doped CA film, nonlinear PhC and Au thin film were done using Z scan technique. with a Q-switched Nd:YAG laser(pulse width 7 ns, wavelength 532 nm). The input energy is fixed at 10 μJ and focal length of the lens is 15 cm.. From transmittance vs fluence plot it is clear that the NLA activity of reference film is negligible, whereas that nonlinear PhC exhibit strong NLA and it is atributed to the intense optical field cofinement in photonic cavity, which is clearly understanable from simlatin studies carried out using transfer matrix method. Au thin film shows SA activity, due to the bleaching of ground state population.

For the SA/RSA hybrid system, the sharp discontinuity in the NLA behavior results in non-reciprocal transmission of light. When the laser beam first interacts with SA medium, there will be a gradual increasing transmittance and it is interacted with the RSA medium leads to the reduction in transmittance. Since, the role of SA is more effective here than RSA, the resultant output will be an increasing transmittance, which is analogues to the forward bias operation of an electronic diode. On the other hand, when light first interact with a RSA medium followed by SA, output transmittance gets attenuated due to strong RSA effect. Here the transmitted intensity from RSA medium is not enough to evoke the NLA in SA medium.

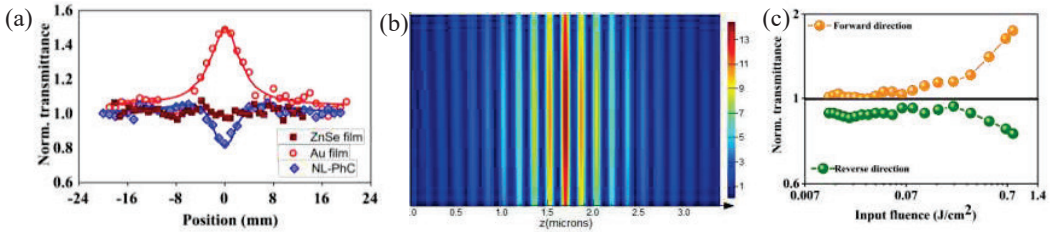

Figure 2: (a) Open aperture z scan data of ZnSe bare film, Au film and NL-PhC, (b)Simulated electric field distribution in the NL-PhC (c) Optical diode action of of NL-PhC/Au hybrid system.

Conclusion

In summary, all optical diode action realized from a nonlinear PhC/Au thin film hybrid structure. The intense photon confinement in PhC leads to strong NLA and Au thin film displayed strong SA activity. Axial asymmetry in NLA activity of NL-PhC and gold layer leads to the non-reciprocal transmission of light. Optical diode action is verified using a Q switched ns laser at 532 nm. The proposed structure can play crucial role in various applications in nanophotonics and for realizing all-optical devices with better on-chip integrability

References

1 R. Philip, M. Anija, C. S. Yelleswarapu and D. V. G. L. N. Rao, , DOI:10.1063/1.2794015.

2 B. Anand, R. Podila, K. Lingam, S. R. Krishnan, S. Siva Sankara Sai, R. Philip and A. M. Rao, *Nano Lett.*, 2013, **13**, 5771–5776.

3 E. Shiju, M. Bharat, N. K. Siji Narendran, D. Narayana Rao and K. Chandrasekharan, *Opt. Mater. (Amst).*, 2020, **99**, 10955

Highly Sensitive Plexcitonic Refractometer

Triranjita Srivastava[1] and Rajan Jha[2,*]

[1]*Department of Physics, University of Allahabad, Prayagraj, Uttar Pradesh, India*

[2]*Nanophotonics and Plasmonics Laboratory, School of Basic Sciences, Indian Institute of Technology Bhubaneswar, Argul, Odisha, India*

**Corresponding author: rjha@iitbbs.ac.in; rajaniitd@gmail.com*

Abstract: A highly sensitive plexcitonic sensor based on hybrid mode arising due to coupling between surface plasmon polariton and surface exciton polariton has been studied for gaseous environment. It is observed that the plexcitonic sensor exhibits better performance as compared to the pure plasmonic counterpart. In this paper, we proposed to sandwich a thin layer of Silicon between organic semiconductor; J-aggregate cyanine dye (5,5′,6,6′-tetrachloro-1,10-diethyl-3, 30-di(4-sulfobutyl) benzimidazolo-carbocyanine (TDBC)) and plasmonic active Silver coated SF11 prism. The sensitivity of the proposed sensor is found to be 36% more than that of plexcitonic sensor. We believe that the present study shall open a window for sensing application.

Keywords: Surface Plasmon Polariton, Excitons, Plexcitons, Sensors

1. Introduction

Since past half century the study of surface plasmon polaritons (SPPs) has led to a new branch of applied physics, namely; plasmonics and has attained an important status in the biochemical sensing industry. The SPPs are *p*-polarized electromagnetic (em) waves, which arises due to the interaction of em waves with the coherent oscillations in the metal known as plasmons. These are one of the basic categories of surface waves, which are exponentially decaying in nature and propagate along the metal-dielectric interface, provided the dielectric constant of the metal and dielectric media are of opposite signs [1]. Therefore, they are highly sensitive to the environmental conditions, and leading to sensing applications.

Another form of surface waves is surface exciton polariton (SEP) which arises due to the interaction of em waves with excitons (electron-hole pair) present in the organic/inorganic semiconductor. The study of SEP in sensing applications was limited, because initially Wannier–Mott excitons were realized only at low temperatures. However, in 2017, Takatori et al. proposed SEP excitation at an organic semiconductor; J-aggregate cyanine dye (5,5′,6,6′-tetrachloro-1,10-diethyl-3, 30-di(4-sulfobutyl) benzimidazolo-carbocyanine (TDBC)) and air interface. Such J-aggregate possess Frenkel excitons and has been experimentally realized at room temperature [2]. Recently, we proposed a plexcitonic nose comprising of thin layer of TDBC deposited over Silver coated prism [3], which showed high performance, as compared to the pure plasmonic counterpart. In this paper, we propose to apply a thin Silicon layer (thickness d_s) sandwiched between Ag (thickness d_m) and TDBC (thickness d_t) (see fig. 1). It is observed that the proposed structure exhibits 36% enhanced sensitivity as that of plexcitonic nose. Therefore, the present study shall provide a new platform for gaseous sensing applications.

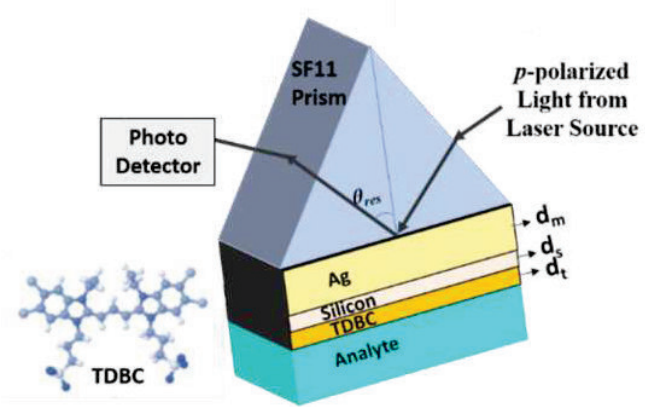

Fig. 1: Schematic diagram of the proposed structure

2. Results and discussion

In this paper, we employed standard transfer matrix method [4] to study the performance of the proposed structure. Figure 2(a) illustrates the variation of reflectance curve with respect to angle of incidence for conventional SPP (SF11 prism/Ag/Air) and plexcitonic (SF11 prism/Ag/TDBC/Air) sensor at 532 nm wavelength. The thicknesses of Ag and TDBC are considered as 50 nm and 5 nm respectively. It is observed that the shift in the resonance angle (thereby sensitivity (=shift/RIU)) for plexcitonic sensor is more as compared to that in conventional pure plasmonic sensor. To enhance the sensitivity, we propose to employ a thin layer of Silicon in between Ag and TDBC. The variation of sensitivity with respect to analyte refractive index for different thicknesses of Silicon is shown in Fig. 2(b). It is observed that the application of 5 nm silicon, has resulted into ~36% (for n_a = 1.100) sensitivity enhancement as compared to the plexciton sensor. Also, the sensitivity linearly increases with increasing analyte refractive index over a wide range. Therefore, the modified plexcitonic sensor can be utilized for the detection of wide range of harmful and toxic gases.

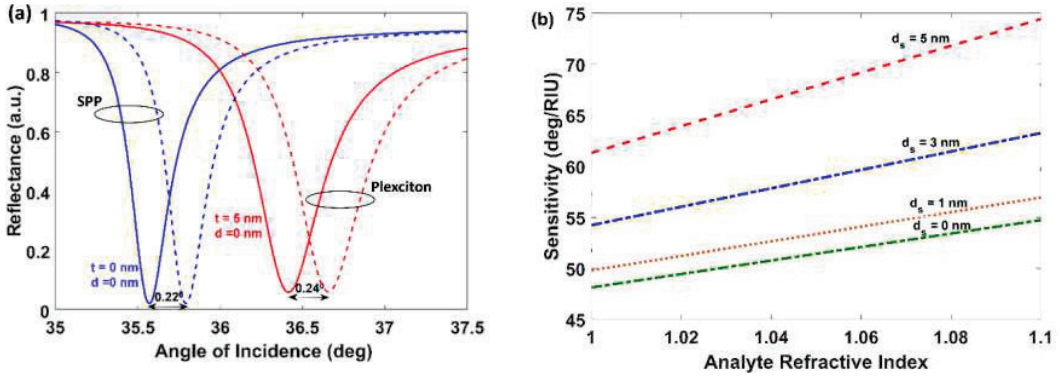

Fig. 2 (a): Variation of reflectance with respect to angle of incidence for conventional SPP sensor (t=0 nm; blue curve) and Si based plexcitonic sensor (5 nm TDBC layer; red curve) for anayte refractive index; n_a = 1.000 (solid line) and 1.005 (dashed line). (b) Variation of sensitivity with respect to analyte refractive index, for the proposed Silicon based plexcitonic sensor comprising of 5 nm TDBC and different thicknesses of Silicon, ranging from d_s = 0, 1, 3 and 5 nm, at λ = 532 nm.

3. Conclusion

In this paper, hybrid SPP, and SEP based plexcitonic sensor is studied. To enhance the sensitivity over a wide range of harmful gaseous environment, we proposed to implement a thin layer of Silicon between Ag and TDBC. It is observed that the sensitivity for proposed structure increases upto 36 % as compared to that of conventional plexcitonic sensor. We believe that the study shall provide a new insight in sensing applications.

4. References

[1]. Ha, D. T., Thuy, D. T., Hoa, V. T., Thanh Van, T. T., and Viet, N. A., "On the theory of three types of polaritons (phonon, exciton and plasmon polaritons)", Journal of Physics Conference Series, vol. 865, (2017).

[2]. Kentaro Takatori, Takayuki Okamoto, Koji Ishibashi, and Ruggero Micheletto, "Surface exciton polaritons supported by a J-aggregate-dye/air interface at room temperature," Optics Letters 42, 3876-3879 (2017).

[3]. Triranjita Srivastava and Rajan Jha , "Plexcitonic nose based on an organic semiconductor", Applied Physics Letters 117, 093301 (2020)

[4]. Atef Shalabney, Ibrahim Abdulhalim, "Electromagnetic fields distribution in multilayer thin film structures and the origin of sensitivity enhancement in surface plasmon resonance sensors," Sensors and Actuators A: Physical, vol. 159, Issue 1, Pages 24-32, (2010)

Effect of Self-focusing, Diffraction Length on Propagation of Laser Beam in Non-Degenerate Germanium having Space Charge Neutrality with Linear Absorption

S.S. Patil[1], K.Y. Khandale[2], P.T. Takale[2], P.P. Nikam[1], M.B. Mane[1], T.U. Urunkar[2], S.D. Patil[1*], M.V. Takale[2*]

1. Department of Physics, Devchand College, Arjunnagar, Kolhapur, Maharashtra – 591237 India
2. Department of Physics, Shivaji University, Kolhapur, Maharashtra – 416004 India
e-mail: sdpatilphy@gmail.com, mvtphyunishivaji@gmail.com

Abstract: The effect of self-focusing length R_n and diffraction length R_d in propagation dynamics of Gaussian laser beam in non-degenerate germanium having space charge neutrality under ponderomotive nonlinearity is investigated. The key interest of present theoretical investigation is to study effect of interval of R = R_d /R_n and light absorption to sustain the competition between phenomena of diffraction and self-focusing during beam propagation. The differential equation governing the beam width parameter *f* is set up by using Wentzel–Kramers–Brillouin (WKB) and paraxial approximations and solved numerically. To explain it further plot between *F(R)* against *R* is studied in depth. Results are presented graphically and discussed.
Keywords: Gaussian, germanium, self-focusing/defocusing, self-trapping.

1. Introduction

There are wide range of applications for interactions of high intensity laser beam with plasma such as laser particle acceleration[1], inertial confinement fusion [2]. For these applications laser must have to propagate through plasma medium without any divergence (Self-focusing or defocusing). Self-focusing is a third order nonlinear phenomena. In present paper authors have adopted the theoretical approach given by Akhmanov *et al.* [3] and developed by Sodha *et al.* [4] called WKB and Paraxial approximation. This paper confers the propagation of Gaussian laser beam in non-degenerate germanium having space charge neutrality. In present medium the nonlinearity is induced because of the non-uniform heating and consequent redistribution of carriers in the presence of an electromagnetic beam.

2. Theoretical Framework

Consider a field distribution of Gaussian laser beam of the following form propagating along z axis

$$A_0^2 = \frac{E_0^2}{f^2} exp\left(\frac{-r^2}{r_0^2 f^2} - 2k_i z\right) \quad (1)$$

where E_0 is an initial amplitude of Gaussian laser beam with initial beam-width r_0 and *f* is the dimensionless beam width parameter. The effective dielectric constant of nonlinear medium is

$$\varepsilon = \varepsilon_0 + \Phi\,(A_0^2) \quad (2)$$

where, ε_0 and Φ(EE*) are the linear and nonlinear terms of the dielectric constant. For non-degenerate germanium the nonlinear term of the dielectric constant is given by [5]

$$\Phi(EE^*) = \frac{\omega_p^2}{\omega^2}\alpha_e\left(1 + \frac{m_e}{m_h}\right)A_0^2 \quad (3)$$

with $\alpha_e = (e^2 M/6\, k_B T_0 \omega^2 m^2)$, where, k_B, *M*, *m*, T_0 are Boltzmann constant, mass of ion, electron mass, temperature of the plasma, respectively. Following approach given by Akhmanov *et al.*[3] and developed by Sodha et al. [4], we have obtained the dimensionless beam-width parameter (BWP) *f*

$$\frac{d^2 f}{d\xi^2} = \frac{4}{f^3} - \frac{4}{f^3}\frac{R_d^2}{R_n^2} e^{4k_i'} \quad (4)$$

where, $\xi = \frac{z}{R_d}, R_d = kr_0^2, R_n = (2\varepsilon_0 r_0^2/\varepsilon_2 E^2)^{1/2}$, $k_i' = k_i R_d$, R_d, R_n, k_i' and ξ are diffraction, self-focusing lengths, absorption coefficient and dimensionless distance of propagation respectively. The below necessary numerical parameters are used in the present theoretical investigation:
$m_e \approx 1\times10^{-28}$ g, $m_h \approx 3\times10^{-28}$ g, $N_{oe} \approx 1.5\times10^{15}$ cm^{-3}, $N_{oh} \approx 1.4\times10^{16}$ cm^{-3}, $\omega = 2\times10^{14}$ rad/s, $r_0 = 500$ μm, $\varepsilon_2 = 1.2\times10^{-7}$ esu, $E_0 = 15$ esu, $T_0 = 77$ K.

3. Result, Discussion and Conclusion

Equation (4) is second order nonlinear differential equation which gives evolution of a laser beam during propagation to non-degenerate germanium. The first term on right-hand side of this equation gives to the diffraction divergence of the beam while second term gives the convergence resulting from the ponderomotive nonlinearity. Under initial condition ($f = 1$, $\xi = 0$) the right hand side of equation (4) becomes,

$F(R) = 4\,(1 - R^2\, e^{4k_i'})$, where, $R = R_d/R_n$.

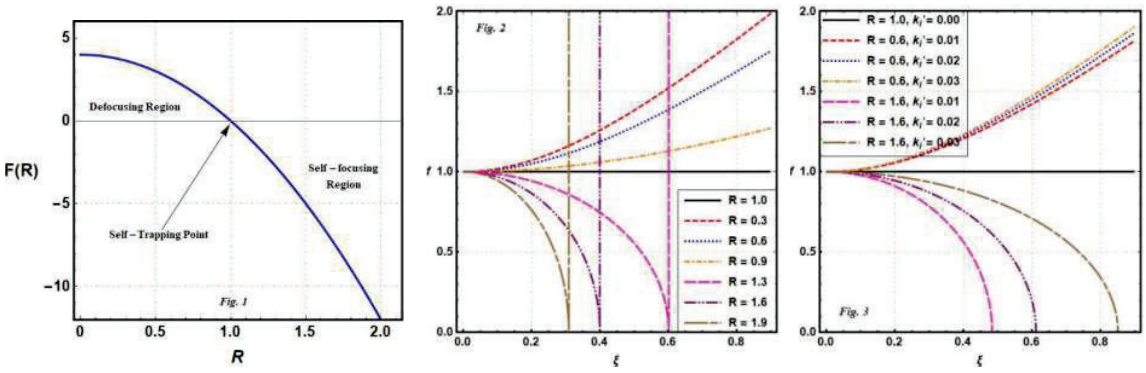

Fig. 1: Variation of F(R) as a function of R.
Fig. 2: Dependence of BWP f with respect to normalized propagation distance ξ.
Fig. 3: Dependence of BWP f with respect to normalized propagation distance ξ with $\mathbf{k_i' = 0.01, 0.02, 0.03}$.

To explore the effect of R right at the beginning one has to pay little attention to plot shown in Fig.1.The plot can be conveniently studied for three distinct conditions.

Self-trapping region:

$F(R) = 0$ for $R = 1$ *i.e.* $R_d = R_n$

Self-focusing region:

$F(R) < 0$ for $R > 1$ *i.e.* $R_d > R_n$

Defocusing region:

$F(R) > 0$ for $R < 1$ *i.e.* $R_d < R_n$

The simple analytical approach leads to following limits for R is depicted in Fig.1. The limits of R investigated in above conditions can support the graph of beam width parameter f versus normalized propagation distance ξ as shown in Fig.2. From Fig.2 the steady state defocusing of beam is observed for $R<1$ the beam undergoes defocusing. Again as R increases from 0 to 1 rate of defocusing decreases. The beam propagates without convergence or divergence (self-trapped mode) at exact value $R = 1$. It is also evident from Fig.2 that self-focusing is observed for $R>1$ and as R increases from 1 self-focusing length decreases. Such self-focusing character of Gaussian beam in beam in non-degenerate germanium having space charge neutrality has been already reported in earlier studies [5]. From Fig. 3, it is observed that as absorption increases $k_i' = 0.01, 0.02, 0.03$ the self-focusing as well as defocusing increases. It is observed that our investigation shows that pre-conditioning of self-focusing and diffraction length at the beginning of propagation can determine propagation dynamics effectively.

4. References

[1] V. Malka, Phys. Plasmas **19**, 055501 (2012)
[2] S. Atzeni, Eur.Phys.Lett. **109**, 45001 (2015).
[3] S. A. Akhmanov, A. P. Sukhorukov and R. V. Khokhlov, Sov. Phy. Usp. **10,** 609-636 (1968)
[4] M. S .Sodha, A. K. Ghatak and V. K. Tripathi, Progress in Optics, **13**, 169-265 (1976)
[5] S. Patil, M. Takale, V. Fulari, M. Dongare, *J. Mod. Opt.* **55**, 3527–3533 (2008).

Real frequency splitting in triple coupled PT-symmetric micro ring resonator

Priyanka Chaudhary* **and Akhilesh Kumar Mishra**
Department of Physics, IIT Roorkee, Roorkee-247667, Uttarakhand, India.
**e-mail address: pchaudhary@ph.iitr.ac.in*

Abstract: Exceptional points (EPs) in parity-time (PT)-symmetric systems (i.e., degeneracies in non-Hermitian system) have gained a lot of research attention in recent years. The effect of perturbation on output function near EP has been studied for a system with two micro rings, which leads to complex splitting. In present work, we indirectly couple two rings with equal amount of gain and loss via an intermediate neutral ring to provide real splitting in output transfer function.

Keywords: Exceptional point, PT-symmetry, micro ring resonator, sensitivity.

1. Introduction

The field of PT-symmetry is witnessing a lot of research activities due to its exquisite property of exhibiting completely real eigen spectra even with non-Hermitian Hamiltonians. PT-symmetric systems show a phase transition (often known as EP) beyond which the eigenvalues become complex [1]. These EPs can be utilized as an optimal condition for sensing applications [2].

Real frequency splitting has been realized in an indirectly coupled anti-PT-symmetric sensor at micro- and nano-scales [3, 4]. In recent years, many studies have been performed for two coupled PT- and anti-PT-symmetric micro cavities near EP for different sensing applications [4, 5].

In the present work, we address PT-symmetric optical device based on three coupled micro ring resonators, which experiences real splitting in output function with perturbation in micro rings.

2. Mathematical Model

We numerically model a system that consists of three identical micro rings as shown schematically in Fig.1. We have neglected any direct coupling between ring 1 and ring 3. Ring 1 and bus waveguide at the input end and ring 3 and the bus waveguide at output end of the system are coupled directly, as shown in Fig. 1.

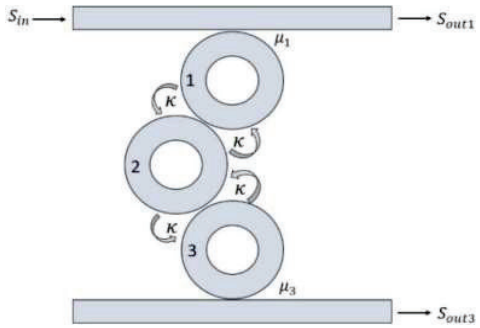

Fig. 1: **Schematic diagram of three coupled micro ring resonator.**

The Hamiltonian matrix for unperturbed coupled system can be given by

$$H = \begin{bmatrix} \omega_1 - i\gamma_1 & \kappa & 0 \\ \kappa & \omega_2 - i\gamma_2 & \kappa \\ 0 & \kappa & \omega_3 - i\gamma_3 \end{bmatrix}, \quad (1)$$

where $\omega_{1,2,3}$ is the angular frequencies of the three rings, $\gamma_{1,2,3}$ are the respective gain (if positive, neutral if zero and loss if negative) in the rings, κ is the coupling strength between rings.

The resonant eigenfrequencies $\omega_{PT_{c,u,l}}$ (central, upper, lower frequency) of the PT-symmetric system (with almost identical rings) evaluated using above matrix are

$$\omega_{PT_{c,u,l}} = \omega_0, \omega_0 \pm \sqrt{2\kappa^2 - \gamma_0^2}. \quad (2)$$

$\omega_{PT} = \omega_0$ for central frequency (ω_{PT_c}), $\omega_{PT} > \omega_0$ for upper frequency (ω_{PT_u}), and $\omega_{PT} < \omega_0$ for lower frequency (ω_{PT_l}) respectively. We can reach EP, if the expression in square root vanishes i.e.,

$$2\kappa^2 - \gamma_0^2 = 0, \quad (3)$$

and this point can be used to enhance sensitivity of the system towards an external perturbation. A small change in cladding index of any ring would affect the resonance and we have the expression for perturbation as $\delta_\omega = -\frac{\Delta\lambda_R}{\lambda_R}\omega_R$ [5]. Now, let us apply a perturbation δ_ω to first ring ($\omega_1 \to \omega_1' + \delta_\omega$) of the system. The eigen values of such system are the roots of the following characteristic equation

$$\Omega(\omega) = (\omega_1' + \delta_\omega - i\gamma_1 - \omega)(\omega_2 - i\gamma_2 - \omega)(\omega_3 - i\gamma_3 - \omega) - \kappa^2(\omega_1' + \delta_\omega - i\gamma_1 - \omega) - \kappa^2(\omega_3 - i\gamma_3 - \omega) = 0 \quad (4)$$

We can find the eigenfrequencies $\omega_{PT_{c,u,l}}$ for perturbed PT-symmetric systems by solving the above equation.

3. Results

In our analysis, only first ring is perturbed, and rest of the system is kept isolated. To see the behavior of output function with applied perturbation, the normalized transmitted power at the end of output bus waveguide $\left|\frac{S_{out3}}{S_{in}}\right|^2$ is plotted in Fig. 2(a). We observe that the PT-symmetric system exhibits real splitting and provides splitting for both negative and positive perturbations. The output of PT-symmetric system with positive and negative perturbations are the inverted mirror images of each other as depicted in Fig. 2(a). In Fig. 2(b) the difference between real frequency and incident frequency is plotted against the difference between imaginary frequency and the excited frequency. The space generated by these two frequencies represents the phase-space of eigenvalues of the system. This phase diagram talks about the eigenfrequencies splitting.

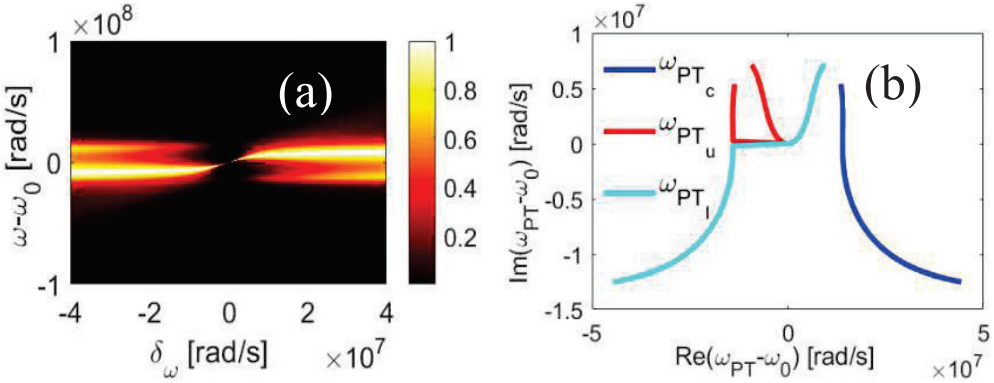

Fig. 2: **(a) Variation of normalized output transmittance at output bus waveguide with perturbation ($\omega_1 = \omega_1' + \delta_\omega$) in first ring, and (b) real vs imaginary frequency difference plot.**

4. Conclusion

It is noticed that even PT-symmetric micro ring-based system can offer real frequency splitting which is directly detectable. Hence, such a system can be used for sensing applications.

References

[1] Bender, Carl M., and Stefan Boettcher. "Real spectra in non-Hermitian Hamiltonians having PT symmetry." *Physical review letters* 80.24 (1998): 5243.

[2] Xing, Tong, et al. "Ultrahigh sensitivity stress sensing method near the exceptional point of parity-time symmetric systems." *Journal of Physics D: Applied Physics* 53.20 (2020): 205102.

[3] Li, Wenxiu, et al. "Real frequency splitting indirectly coupled anti-parity-time symmetric nanoparticle sensor." *Journal of Applied Physics* 128.13 (2020): 134503.

[4] De Carlo, Martino, et al. "High-sensitivity real-splitting anti-PT-symmetric microscale optical gyroscope." *Optics letters* 44.16 (2019): 3956-3959.

[5] De Carlo, Martino. "Exceptional points of parity-time-and anti-parity-time-symmetric devices for refractive index and absorption-based sensing." *Results in Optics* 2 (2021): 100052.

Angular spectrum-based Classification of Laguerre-Gaussian Modes Using Machine Learning

Parul Jain[1], Shreya Garg[2], Vijay Kumar[3]

[1]Department of Physics, Indian Institute of Technology, Guwahati, Assam-781039, India

[2]Department of Physics and Astronomy, Katholieke Universiteit Leuven, Celestijnenlaan 200D, 3001 Leuven, Belgium

[3]Department of Physics, National Institute of Technology, Warangal, Telangana-506004, India

Email: [1]paruljain@iitg.ac.in, [2]shreya.garg@student.kuleuven.be, [3]vijay@nitw.ac.in

Abstract: A comparative study for the efficient classification of Laguerre-Gaussian modes has been performed using standard machine learning algorithms. The angular spectrum-based Random Forest Classifier yields $> 99\%$ accuracy for as low as 50 images per class.
Keywords: Machine Learning, optical communication, Optical angular momentum, Speckle

1. Introduction

The Laguerre-Gaussian (LG) beams are the set of beams that carry orbital angular momentum with a helical phase $e^{il\Phi}$. The mutual orthogonality among various modes of LG beams makes them exploitable for applications in optical communication [1]. The conventional algorithms to classify LG modes are laborious and prone to experimental errors. However, in the past few years, machine learning methods have gained reverence for their modesty, accurate predictions, and time effectiveness [2, 3]. These methods required the whole modal field for the classification. LG beam scattered off the rough surface results in a speckle pattern. Speckle-learned convolutional neural networks are used to classify LG modes just by capturing a small part of the whole speckle field [4-6]. In this paper, we have undertaken a study to classify LG modes with traditional machine learning algorithms. The standard machine learning algorithms such as the Random Forest classifier (RFC), k-Nearest Neighbour (k-NN), and Support Vector Classifier (SVC) have been utilized to classify eight LG beams, namely, LG_{01} to LG_{08}. To improve the classification accuracy with minimum possible data, feature extraction has been performed using three different techniques: Principal Component Analysis (PCA), Discrete Wavelet transform (DWT), and Angular spectrum (AS) representation. The lowest training time and the best prediction accuracy have been achieved with AS-based RFC. We achieved an accuracy of $> 99\%$ for as low as 50 images per class.

2. Concept and Methodology

Applying LG modes in optical communication using conventional methods becomes extremely difficult due to their distortion in free space while propagating. The challenges posed by this cannot be overcome even using machine learning algorithms. In our approach, LG_{pl} modes are subjected to random phases ($e^{il\phi_R}$) to generate the far-field speckle pattern $\mathcal{F}(LG_{pl}e^{il\phi_R})$, where $\mathcal{F}$ represents Fourier transform. Our study has been performed on different random phases to ensure the robustness of the model. The novelty of our scheme is exhibited by the fact that to identify the LG modes from its speckle data, a small region randomly picked from the whole speckle field would suffice. A region of 256×256 pixels has been randomly selected for the machine learning analysis using RFC, k-NN & SVC.

Machine learning algorithms perform better after pre-processing the data and applying feature extraction or dimensionality reduction techniques. We have done a comparative study focused on improving the accuracy and decreasing the train-test time and the computation load by experimenting with different machine learning techniques while incorporating data pre-processing. Our dataset consists of speckle images of the corresponding LG modes ($LG_{01} - LG_{08}$). We vary the number of images from 20 to 300 per class to study its effect on the accuracy and train-test time. The training and testing of the model are performed on 70% and 30% of the dataset, respectively. To tune our model to the speckle data, a technique, Randomized Search CV, is utilized to find the optimum parameters of

the machine learning algorithms (RFC, *k*-NN, SVC). The model's evaluation metrics are the accuracy, precision rate, recall rate, and the F1 score. We train our model on the original speckle images to serve as the base for further comparison.

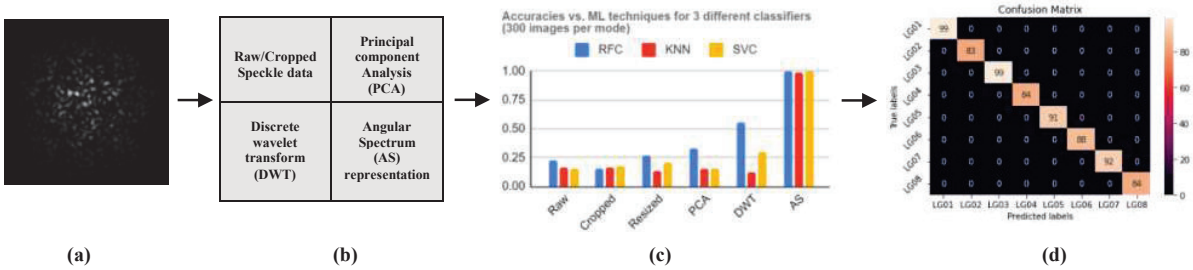

Fig 1: (a) Raw data (b) Pre-processing and Feature Extraction (c) Machine Learning models (d) Confusion matrix for AS-based RFC

Fig 2: (a) Raw speckle data; (b) Cropped speckle data. Feature Extraction: (c) PCA (d) DWT (e) AS representation

The dimensionality reduction and feature extraction techniques: PCA, DWT, and AS are performed on the original speckle data and used as input data to the machine learning algorithms. The classification accuracy of $> 99\%$ has been achieved using an angular spectrum-based Random Forest Classifier.

3. Summary

We have presented a comparative study for classifying LG modes using standard machine learning algorithms: RFC, *k*-NN, and SVC. The extensive study infers that feature extraction from the original data and feeding those images to the machine learning classifier will yield the desired results, instead of directly providing the data to machine learning classifiers. The feature extraction and dimensionality reduction techniques, PCA, DWT, and AS representation are used to enhance the learning process on the classifiers. We have observed that the "Angular spectrum representation" of the original data fed to the "Random Forest Classifier" provides the most suitable classifying algorithm for our dataset by yielding the highest classification accuracy $> 99\%$. The parameters such as precision, recall, and F1-score have been evaluated, all of which are one. Another advantage of our model is that only a portion of the speckle pattern containing a sufficient number of speckles is required. Hence, there is no need to capture the whole speckle pattern or whole mode image and to focus much on the optical alignment. The proposed model has potential application in optical communication systems utilizing space division multiplexing.

4. Acknowledgement: V.K. acknowledges the SERB grant (SRG/2021/001375).

5. References

[1] A. E. Willner, H. Huang, Y. Yan, Y. Ren, N. Ahmed, G. Xie, C. Bao, L. Li, Y. Cao, Z. Zhao, J. Wang, M. P. J. Lavery, M. Tur, S Ramachandran, A. F. Molisch, N. Ashrafi, and S. Ashrafi, "Optical communications using orbital angular momentum beams," Advances in Optics and Photonics, **7**, 66–106 (2015).

[2] M. Krenna, J. Handsteinera, M. Finkb, R. Ficklerd, R. Ursinb, M. Malika, and A. Zeilingera, "Twisted light transmission over 143 km," Proceedings of the National Academy of Sciences, **113,** 13648-13653 (2016).

[3] Mitchell G. Schiworski, Daniel D. Brown and David J. Ottaway, "Modal decomposition of complex optical fields using convolutional neural networks", JOSA A, 38, 1603-1610 (2021).

[4] V. Raskatla and V. Kumar, "Deep Learning Assisted Classification of Noisy Laguerre Gaussian Modes," in *Front. Opt. Laser Sci. 2021*, (OSA, Washington, DC, 2021).

[5] V. Raskatla, B. P. Singh, S. Patil, V. Kumar, and R. P. Singh, “Speckle-based deep learning approach for classification of orbital angular momentum modes,” *J. Opt. Soc. Am. A* **39**, 759 (2022).
[6] V. Raskatla & V. Kumar, "Deep Learning Assisted Classification of Noisy Laguerre Gaussian Modes," Frontiers in Optics, JTu1A.16 (2021).

An electrically tunable liquid crystal waveguide-based continuous polarization rotator

Rahul Panchal* and Aloka Sinha
Department of Physics, Indian Institute of Technology Delhi, New Delhi, India- 110016.
**rahulpanchal212@gmail.com, aloka@physics.iitd.ac.in*

Abstract: We proposed an electrically controlled liquid crystal (LC) optical waveguide-based continuous polarization rotator (PR). The waveguide is fabricated on glass substrates, and the nematic 4-cyano-4'-pentylbiphenyl (5CB) LC is used as the propagation medium. A strip of ITO electrode is used to apply an electric field across the LC waveguide. We experimentally demonstrate a continuous polarization rotation up to 27º at a low operating voltage of 7 V_{pp}. The device is presented with a faster response of 9.8 ms as rise time and 40 ms as fall time.
Keywords: Liquid crystal, Optical waveguide, Polarization rotator, Electro-optic device.

1. Introduction

Polarization rotator (PR) devices rotate the plane of polarization of the incident beam to the desired angle [1]. The plane-polarized light has significant applications in biosensing and polarization microscopy [2,3]. Therefore, it is quite essential to control the plane of polarization. Generally, mechanical-controlled waveplates are used to rotate the plane of polarization, but these devices encounter significant disadvantages due to mechanical errors with slower responses. To avoid mechanical limitations, it is required to develop a PR that can be controlled using external stimuli. Liquid crystal (LC) is a material with several attractive features like high electro-optic coefficient, polarization sensitivity, and high birefringence that make it promising for fabricating tunable PR devices [4]. Previously, LC was extensively used in twisted configurations to rotate the plane of polarization which has application in display technologies. Twisted nematic LC (TNLC) devices are well-established electrically controlled PR devices that can rotate the plane of polarization to a given angle [5]. But this technology could deliver only two polarization states corresponding to on and off voltage. In this work, we propose a simple LC core optical waveguide-based electrically controlled PR. When a horizontal linearly polarized light is coupled in the waveguide, the electric vector of polarization follows the long axis of the LC molecule, which is controlled using applied voltages.

2. Design and principle of the device

The proposed device comprises a 5 mm long and 6 µm thick LC-layer (nematic 5CB) sandwiched between glass substrates. Figure 1(a) shows the cross-sectional view of the proposed device. The LC molecules are homogeneously aligned in the waveguide perpendicular to the direction of propagation, as shown in Figure 1(b). Both the substrates consist of a strip of ITO electrode of 1 mm width at the end of the waveguide, as shown in Figure 1(b). When voltage is applied, the molecules under the electrodes get reoriented in the direction of the electric field and get homeotropically aligned, while the molecules in the electrode-free zone remain homogeneously aligned. There is a gradient change of the orientational angle of LC molecules at the boundary of the electrode, which increases in a gradient manner from 0˚ to 90˚ when we move from homogeneous to homeotropic region.

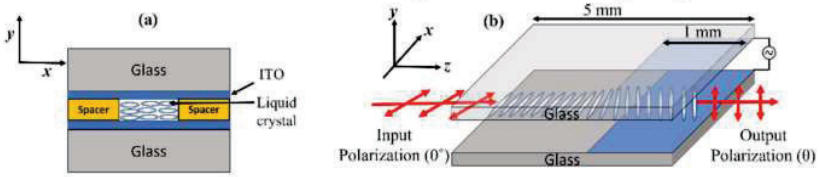

Figure 1. (a) Schematic cross-sectional view of the proposed device (b) Three-dimensional schematic design of the proposed liquid crystal waveguide-based polarization rotator.

The horizontal polarization (i.e., at 0˚) is launched in the waveguide. The polarization of light follows the long axis of the LC molecule as in the case of TNLC [5]. When the horizontally polarized light beam passes through the electrode boundary region, it faces a gradient rotation of the LC director. Hence, the electric vector of the polarized light beam also rotates according to the LC director and rotation in the polarization occurs. A standardized experimental setup with a laser of wavelength 633 nm is utilized to characterize the LC waveguide [6].

3. Results and discussion

The output polarization state of the waveguide is measured using Stoke's polarimetry. In order to determine the state of the polarization of light, four sets of output power (P_0, P_1, P_2, and P_3) are measured. The output power P_0, P_1, and P_2 are measured by keeping a linear polarizer at 0˚, 90˚, and 45˚, respectively, at the output. The fourth power set, P_3, is determined by introducing a quarter waveplate (0˚) just before the analyzer (45˚).

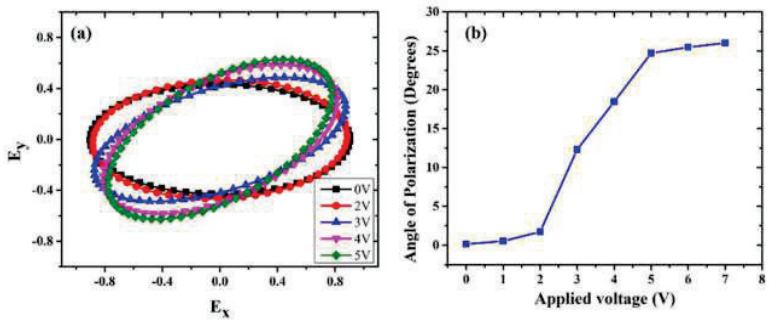

Figure 2. (a) The output state of polarization measured using Stoke's polarimetry, (b) Variation of the angle of the plane of polarization with applied voltages.

Four Stoke's parameters (S_0, S_1, S_2 and S_3) are evaluated corresponding to these measured powers (P_0, P_1, P_2 and P_3) as: $S_0 = P_0 + P_1$, $S_1 = P_0 - P_1$, $S_2 = 2P_2 - S_0$ *and* $S_3 = 2P_3 - S_0$. The output state of polarization is determined by using these four Stoke's parameters and plotted using the MATLAB platform. The input linear polarization appears as a slightly elliptical polarization when propagated through the waveguide, which is due the scattered components of the light[7]. When a voltage greater than Freedericksz transition voltage is applied, the LC molecules under the electrodes reorients. Accordingly, the ellipse's major axis rotates, as shown in Figure 2(a). The variation of rotation angle with applied voltage is shown in Figure 2(b). A continuous polarization rotation angle of 27˚ is obtained at an applied voltage of 7 V_{pp}. We have measured the response time of the waveguide using the conventional optical transmission method. An analyzer (at 90º) is placed at the output of the waveguide, and the time response of output power with voltage is recorded. The rise time of the device is calculated as 9.8 ms and the fall time as 40 ms at an applied voltage of 10 V_{pp}.

4. Conclusion

We demonstrate a continuous polarization rotation in a liquid crystal-based optical waveguide. The waveguide delivers a continuous rotation of polarization from 0º to 27º at an operating voltage of 0-7 V_{pp}. The device exhibits a good rise time of 9.8 ms and fall time of 40 ms. A faster response time and electrically controllable features make the device promising in polarization-dependent applications such as polarization microscopy and medical imaging.

Acknowledgment

The authors acknowledge IIT Delhi, DRDO India (grant no. DFTM/03/3203/P/01/JATC-P2QP-01) for resources and CSIR-HRDG Government of India for senior research fellowship under Grant no. - 09/086(1330)/2018-EMR-I.

References

[1]. C. Ye, "Construction of an optical rotator using quarter-wave plates and an optical retarder," Opt. Eng. **34,** 3031-3035 (1995).
[2]. I. Meglinski, C. Macdonald, A. Doronin, B. Kunnen and M. Eccles, "Polarized Light Biosensing," Asia Commun. Photonics Conf. ACP (2014).
[3]. K. Zhanghao, J. Gao, D. Jin, X. Zhang and P. Xi, "Super-resolution fluorescence polarization microscopy," J. Innov. Opt. Health Sci. **11** (2018)
[4]. I. C. Khoo, "Liquid Crystals," Second ed. (John Wiley & Sons 2007).
[5]. P. Fiala, C. Dorrer and K. L. Marshall, "Twisted-Nematic Liquid Crystal Polarization Rotators for Broadband Laser Applications," Conf. Lasers Electro-Opt. CLEO (2015).
[6]. R. Panchal and A. Sinha, "Low threshold optical attenuator based on electrically tunable liquid crystal cladding waveguide," Opt. Commun., **513**, 128089 (2022).
[7]. A. A. Egorov, "Study and Analysis of Light Scattering Loss in Irregular Integrated Optical Waveguides," Phys. Wave Phenom., **27**, 217-228 (2019).

Generation of Non-Collinear Type-0 Spontaneous Parametric Down Conversion using Collinear Type-2 PPKTP Crystal

Sohan Singh Bisht*, Rajeev Dwivedi and Bhaskar Kanseri
Experimental Quantum Interferometry and Polarization (EQUIP), Department of Physics, Indian Institute of Technology Delhi, Delhi, India
**sohansinghbisht134@gmail.com*

Abstract: We demonstrate a non-collinear degenerate type-0 SPDC process in a periodically poled KTiOPO4 (KTP) crystal with poling period 10.00 μm. We observe SPDC ring images due to the non-collinear propagation of the signal/idler satisfying type-0 phase matching conditions. The observed results are consistent with the calculated results based on Sellmeier's formulas and phase matching conditions. Results help to generate entangled multiphotons in a single crystal by changing the polarization of the pump and the temperature of the crystal.
Keywords: SPDC, KTP, QPM

1. Introduction

Spontaneous parametric down-conversion (SPDC) is the $\chi^{(2)}$ three-wave mixing process, in which the pump photon splits into the daughter photons known as signal and idler photons. SPDC is the quantum process that relies on vacuum fluctuations; therefore, the generation of twin photon are random following Poissonian distribution. Energy and momentum conservation laws must be satisfied for the SPDC process. Increasing the length of the crystal improves the efficiency of generated SPDC photons. The pump and signal/idler waves will become out of phase after coherence length, reducing conversion efficiency. We are using periodically poled crystals based on a quasi-phase matching condition in which ferroelectric poles of the crystal are periodically inverted at the poling period Λ to compensate for the extra phase due to birefringence. Quasi-phase matching (QPM) is a technique of engineering the crystal to be periodically poled that allows to overcome the dispersion effects for long crystals and gives higher conversion and narrow bandwidths. The periodic poling allows generating different wavelengths by selecting the proper poling period. The modified phase matching equation includes the poling period term [1].

$$\frac{n(\lambda_p,\ T)}{\lambda_p} = \frac{n(\lambda_S,\ T)}{\lambda_S} + \frac{n(\lambda_i,\ T)}{\lambda_i} + \frac{m}{\Lambda}, \qquad (1)$$

Where m is the poling order, $n(\lambda_p, T)$, $n(\lambda_S, T)$, and $n(\lambda_i, T)$ are the refractive indices for pump, signal, and idler, respectively.

2. Theoretical study

The quasi-phase matching must be satisfied for SPDC photon generation in periodically poled crystal. Several experiments are related to multiple nonlinear effects in the same crystal [2,3]. We theoretically studied the type-0 SPDC process in type- 2 crystal of poling period 10 microns. By tuning the wavelength of the pump, we generate SPDC by 3rd (m=3) order type-0 QPM. The pump at 403 nm produces degenerate collinear down-converted photons at T = 67.1˚C (threshold temperature). The figure below plots the effect of varying the pump wavelength for the given poling period. Figure (1. b) shows the half cone angle of the signal/idler photons for different pump wavelengths by solving equation (3) along axial and perpendicular directions and putting the Sellmeier equation in the above equation [4,5].

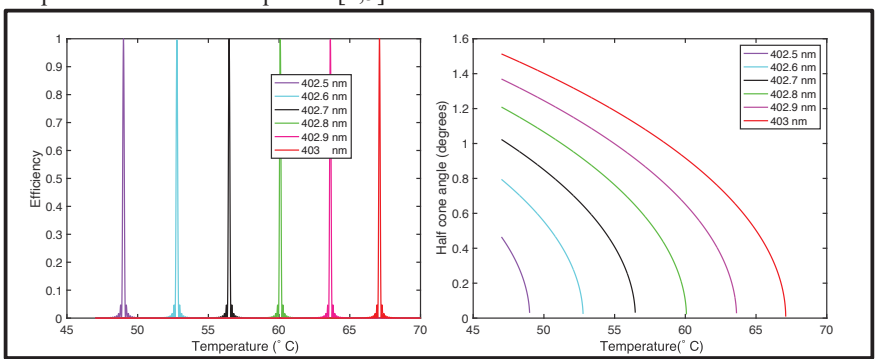

Figure 1: (a) Plot of efficiency vs temperature for different pump wavelengths in degenerate collinear SPDC; (b) Dependence of cone angle on temperature for different pump wavelengths.

3. Experimental scheme

The pump beam of 403 nm and power of 1.5 mW is incident on the crystal of poling period 10 microns. Lens L_1 focuses the beam at the centre of the ppKTP crystal, mounted on the oven, and the temperature controller is used to vary the temperature of the crystal. The polarization of the pump is adjusted using a half waveplate (HWP) parallel to the z-axis of the crystal. The SPDC photons are collimated using the lens L_2 placed at a focal length distance. The dichroic mirror (DM) reflects the pump power, and interference filters (IF) are used to select specific photons. Electron Multiplying Charge-Coupled Device (EMCCD) collected the spatial profile of the rings. The type of SPDC photons generated is examined by changing the temperature of the crystal and observing the spatial profile of the SPDC rings. Figure (2. b) shows the effects of changing temperature on the spatial profile, the size of the ring increases with a decrease in temperature, which confirms the SPDC is type 0 phase matched. The signal and idler are polarized parallel to the pump polarization direction, confirming the type-0 SPDC process.

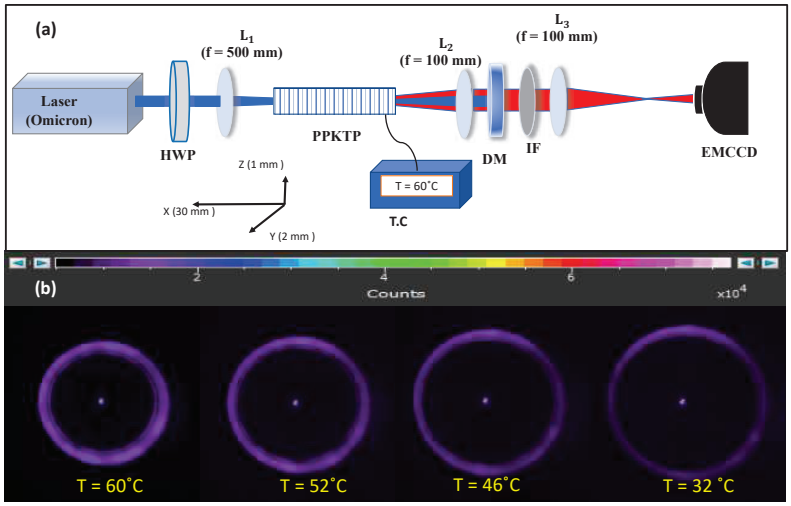

Figure 2 : (a) Experimental scheme for investigation of type-0 degenerate SPDC; L1, L2 and L3 lenses, PPKTP periodically poled potassium titanyl phosphate, DM dichroic mirror, IF interference filter, HWP half-waveplate, EMCCD Electron Multiplying Charge Coupled Device, T.C temperature controller. The pump polarization is along the z-axis, and corresponding SPDC photons are also z polarized. (b) The spatial profile of SPDC rings at different oven temperatures.

4. Conclusion

We demonstrated the generation of the type -0 SPDC in a type- 2 PPKTP crystal of poling period 10 microns. The type-0 SPDC were generated via 3rd-order type-0 QPM when the pump beam was incident on the crystal. We observed ring images of the non-collinear type-0 SPDC signals in the visible region polarized parallel to the z-axis of the crystal. The SPDC rings size increases with decreasing temperature, which is peculiar behaviour of the type- 0 SPDC process. Using the phase matching equation and Sellmeier equation of the ppKTP crystal, we have calculated the threshold temperature (The temperature point where SPDC become collinear). The results will help generate entangled multiphoton in a single crystal by changing the polarization of the pump and the temperature of the crystal.

5. Acknowledgement

Research leading to these results has received funding from Defense Research and Development Organization (DRDO), Government of India.

6. References

[1] Wang, S., Pasiskevicius, V., Hellström, J., Laurell, F., & Karlsson, H. (1999). First-order type II quasi-phase-matched UV generation in periodically poled KTP. Optics letters, 24(14), 978-980.
[2] Lee, H. J., Kim, H., Cha, M., & Moon, H. S. (2012). Simultaneous type-0 and type-II spontaneous parametric down-conversions in a single periodically poled KTiOPO4 crystal. Applied Physics B, 108(3), 585-589.
[3] Jabir, M. V., & Samanta, G. K. (2017). Robust, high brightness, degenerate entangled photon source at room temperature. Scientific reports, 7(1), 1-8.
[4] Ramelow, S., Fedrizzi, A., Poppe, A., Langford, N. K., & Zeilinger, A. (2012). Polarization-entanglement-conserving frequency conversion of photons. Physical Review A, 85(1), 013845.
[5] Kato, K., & Takaoka, E. (2002). Sellmeier and thermo-optic dispersion formulas for KTP. Applied optics, 41(24), 5040-5044.

Structural and Optical properties of ZnSe Nanostructure with two different morphology

Alveera Sohel[a], Sarika Singh[a*]

[a]Department of Chemistry, Manipal University Jaipur, Jaipur, Rajasthan 303007, India;

*Email ID: sarika.singh@jaipur.manipal.edu

Abstract: Zinc Selenide nanoparticles were synthesized by hydrothermal method to form two different morphologies by varying the time duration. The flower like structure of ZnSe is obtained at 180^0 C for 3 hours. At short time duration, these flower like structure of ZnSe are transformed to nanoassembly with increasing the time duration from 3 to 7 hours of pressure applied during the hydrothermal synthesis. The structural analysis of synthesized nanoparticles were characterized by using X-Ray diffraction (XRD), Scanning electron microscope (SEM), Fourier transform infrared spectrophotometer (FT-IR). The morphological dependant optical properties of these nanostructure were studied. These two nanostructures were investigated for photocatalytic degradation application.

Keywords; Hydrothermal, Nanoassembly, Morphology, optical, Nanoparticles.

Introduction; Water is the basic necessity of every human being, but water scarcity is a major and serious issue that is very rapidly increasing day by day. A wide variety of substances including dye, pathogens, heavy metal ions toxic chemicals and radioactive substances are the major pollutants that causes various harmful effects on human beings. And, also the presence of these pollutants in the environments reduces the efficiency of oxygen in water that leaves adverse effect on the aquatic lives. The industries like textile, pharmaceutical or dye intermediates discharges dye, heavy metals containing effluents that is hazardous due to their color which generates toxic products through hydrolysis, oxidation and other chemical reactions. Thus in order to protect our environment from the harmful pollutants, it is necessary to develop simple, cost-effective and environmentally friendly materials which is efficient and remove broad range of contaminants from water. Photocatalytic decomposition/degradation is an excellent route for the removal of organic pollutants from waste water. Various nanomaterials with different type of nanostructure have already been synthesized for the photocatalytic degradation of dye pollutants. Zinc Selenide (ZnSe) is an n-type semiconductor with wide band-gap which is efficient for the photocatalytic dye degradation. In the present work we synthesized a novel shape of ZnSe with flower like nanostructure and nanoassemblies and further studied its optical and photocatalytic properties.

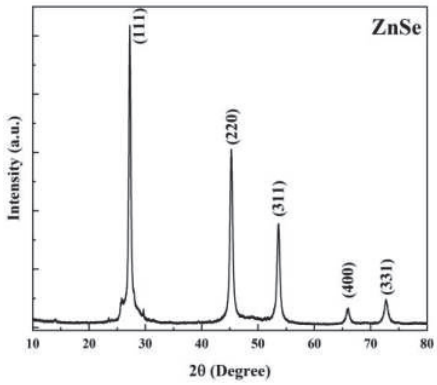

Figure 1; X-ray diffraction pattern of ZnSe nanostructure.

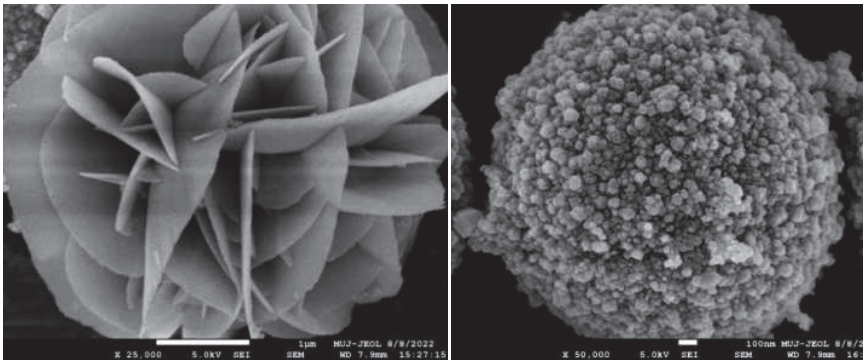

Figure 2: SEM images of ZnSe flower and assembly synthesized at 180 ^{0}C for 3 h and 7 h, respectively.

References;

[1] N. M. Flores, "Effects of morphology, surface area, and defect content on the photocatalytic dye degradation performance of ZnO nanostructures," RSC Adv. 4, 41099–41110(2014).

[2] M. Saranya, "A template-free facile approach for the synthesis of CuS–rGO nanocomposites towards enhanced photocatalytic reduction of organic contaminants and textile effluents," RSC Adv. 5, 15831–15840(2015).

[3] D. Wu, "Fabrication of pit-structured ZnO nanorods and their enhanced photocatalytic performance," RSC Adv 3, 20054–20059(2013).

[4] E. Prabakaran, "Synthesis of N-doped ZnO nanoparticles with cabbage morphology as a catalyst for the efficient photocatalytic degradation of methylene blue under UV and visible light," RSC Adv 9, 7509(2019).

[5] S. Mosleh, "Bi2WO6/Ag2S/ZnS Z-scheme heterojunction photocatalyst with enhanced visible-light photoactivity towards the degradation of multiple dye pollutants," RSC Adv 9, 30100-30111(2019).

[6] J. Antony, "Enhancing the visible light induced photocatalytic properties of WO3 nanoparticles by doping with vanadium," J Phys Chem Solids 157, 110169(2021).

[7] M. Mahanthappa, "Enhanced Photocatalytic degradation of methylene blue dye using CuS-CdS nanocomposite under visible light irradiation," J Appl Sci12, 178(2018).

[8] G. Liu, "Ag2O nanoparticles decorated TiO2 nanofibers as a p-n heterojunction for enhanced photocatalytic decomposition of RhB under visible light irradiation," Appl Surf Sci 9, 216(2018).

[9] S. Alkaykh, " Simultaneous remediation of methylene blue and Cr(VI) by mesoporous BiVO4 photocatalyst under visible-light illumination," Heliyon 6, (2020).

Super-Resolution via Two-Photon Interference

Jerin A Thachil, B Ramanan, and Ashok Kumar
Department of Physics, Indian Institute of Space Science and Technology (IIST),
Valiamala (PO), Thiruvananthapuram– 695547, India
Email:jerinthachil@gmail.com

Abstract: The multi-parameter estimation theory allows us to explore super-resolution imaging techniques, i.e., obtaining imaging resolution beyond the limit defined by the Rayleigh criterion. In this work, we exploit the multi-parameter estimation theory to estimate simultaneously and optimally the centroid and object separation with two-photon interference techniques. Using quantum metrology tools, we compute the Fisher information for estimating the centroid and object separation for a pair of objects, probed by Gaussian and secant hyperbolic spatially shaped pulses. We show that the secant hyperbolic pulses lead to enhanced precision in simultaneous estimation of the centroid and object separation compared to the Gaussian pulses.
Keywords: Two-photon interference, super-resolution, secant hyperbolic pulses

1. Introduction

Rayleigh criterion is a widely accepted benchmark and specifies the minimum resolvable distance between two incoherent sources [1]. Since the derivation of the criterion is heuristic, we can consider Fisher information (FI) and the associated Cramer-Rao bound [2] as a quantitative measure for resolution limit. For any set of unbiased estimators, the Cramer-Rao bound sets a lower bound on the covariance matrix of the estimators as,

$$\mathrm{Cov}[\lambda_i\, \lambda_j] \geq \frac{1}{NF(\lambda)}, \qquad (1)$$

Here $F(\lambda)$ is the Fisher information which quantifies the amount of information gained per single photon about the unknown parameter and N is the number of photons used to probe the object. The FI can be given by the following expression,

$$F_{ij} = \int_{-\infty}^{\infty} \frac{\partial_{\theta_i} P_\theta(x) \partial_{\theta_j} P_\theta(x)}{P_\theta(x)} dx \qquad (2)$$

where $\theta = (\theta_i, \theta_j)$ are the parameters to be estimated and $P_\theta(x)$ is the probability for obtaining an output result x for a given parameter θ. We can define the precision in measurements as the reciprocal of the corresponding variances. In direct detection methods, it was observed that the FI drops to zero for object separations below the Rayleigh limit, resulting in a divergent uncertainty [3]. Fig. 1(a) depicts a direct detection scenario where the light pulses reflected/transmitted from the objects are directly detected with a camera. Tsang and coworkers [3,4] used quantum Cramer-Rao bound (qCRB) to estimate the fundamental lower bound and showed that the qCRB showed no dependence on the separation between the objects. Thus, the Rayleigh limit is not a fundamental limit and can be circumvented using phase-sensitive measurements, allowing super-resolution.

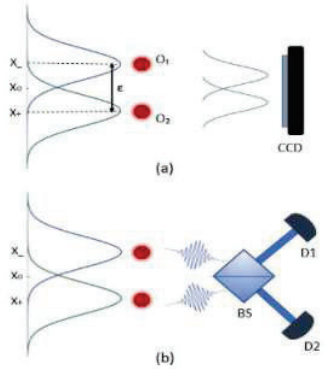

Fig.1. Two-point objects (O_1 and O_2) centered at x_- and x_+ are illuminated by two photonic wavefunctions. The separation and centroid of the objects are denoted by ϵ and x_0, respectively. Schematic for (a) direct imaging with a CCD, (b) two-photon interference technique.

Most super-resolution techniques deal with single parameter estimation and require prior information about the centroid of the two objects that are to be resolved. In this work, we exploit the multi-parameter estimation theory to estimate simultaneously and optimally the centroid x_o and object separation ϵ. The incompatibility in the measurement of different parameters can be removed by performing collective measurement on photons.

Parniak et.al [5] used a two-photon interference scheme followed by spatially resolved detection to achieve super-resolution in imaging two-point sources. Fig.1(b) shows such a scheme where two photons emitted by a composite source arrive simultaneously at the input ports of the beam splitter BS and are detected by spatially resolving detectors D1 and D2. In this method, the number of cross-coincidences increases with the distinguishability of the photons and hence, conveys information about the separation ϵ. Here, we extend the theoretical analysis as done in Ref [5] and model the pulses with a secant hyperbolic amplitude profile of the form

$$\psi(x) = \sqrt{\frac{1}{2} sech(\frac{\pi}{2}x)}. \qquad (3)$$

2. Results

We compute the FI for the estimation of centroid x_o and object separation ϵ, both analytically and numerically. The precision bound is then obtained by using the Cramer-Rao inequality. We evaluate the FI for both finite visibility ($V \neq 1$) and perfect visibility case ($V = 1$). The analytical expression is obtained by approximating the terms inside the integral up to the second order. As a result, the precision in the estimation of centroid and object separation per single photon takes the following form,

$$(\Delta^2\epsilon)^{-1} = \frac{\pi^2}{64}(1 + \frac{23\pi^2}{512}\epsilon^2) \quad \text{for V =1} \qquad (4)$$

$$(\Delta^2\epsilon)^{-1} = \frac{\pi^4}{8192}\frac{(7V^2-16)}{(V^2-1)}\epsilon^2 \quad \text{for V}\neq 1. \qquad (5)$$

The numerical results for estimation precision of object separation for both Gaussian and secant hyperbolic function are plotted in Fig. 2. We have also plotted results for the direct detection method in the same figure.

The enhancement in precision using secant hyperbolic profile over Gaussian profile is seen in case of both finite and perfect visibility and for all values of separation ϵ. The advantage with secant hyperbolic amplitude over the Gaussian profile is also seen in the case of direct detection. Thus, by using such engineered secant hyperbolic profiles one can improve the resolution limits and measure closely separated point objects in various applications like imaging and microscopy.

This work is supported by DST-SERB under Grant SRG/2019/001631.

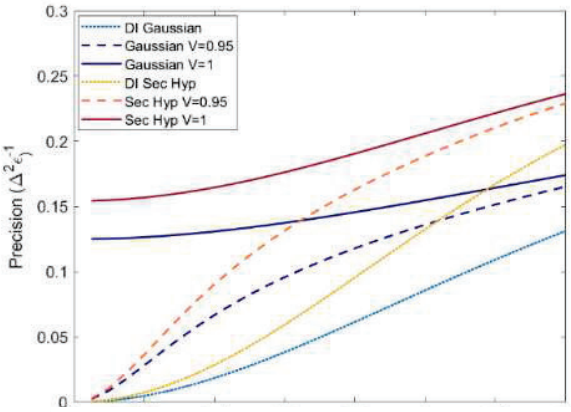

Fig.2. The numerical results for the estimated precision of ϵ against the separation ϵ between the point objects

3. References

[1] L. Rayleigh, Investigations in optics, with special reference to the spectroscope, Philos. Mag. 8, 261 (1879).
[2] C. W. Helstrom, Quantum detection and estimation theory,J. Stat. Phys. 1, 231 (1969).
[3] M. Tsang, R. Nair, and X.-M. Lu, Quantum theory of super resolution for two incoherent optical point sources, Phys. Rev. X 6, 031033(2016).
[4] R. Nair and M. Tsang, Far-field superresolution of thermal electromagnetic sources at the quantum limit, Phys.Rev. Lett. 117, 190801 (2016).
[5] M. Parniak, S. Bor´owka, K. Boroszko, W. Wasilewski, K.Banaszek, and R. Demkowicz-Dobrza´nnski, Beating the rayleigh limit using two-photon interference, Phys. Rev.Lett. 121, 250503 (2018)

Implementation of a super-resolution microscope based on structured illumination

S S Goutam Buddha*, Simran Rawal and Tamal Das
Tata Institute of Fundamental Research, Hyderabad, India
** Email: sgbuddha@tifrh.res.in*

Abstract: Structured illumination microscopy (SIM) is a super-resolution imaging technique for imaging various live biological specimens. SIM enables a two-fold enhancement in lateral resolution compared to conventional optical microscopy and captures dynamic intracellular organization in live cells. In this work, we have implemented a SIM setup by incorporating several essential components.
Keywords: Structured illumination microscopy, super-resolution imaging, optical instrumentation.

1. Introduction

Over the last decade, super-resolution optical microscopy techniques have become an essential tool for imaging biological specimens with a resolution surpassing the optical diffraction limit. One of the most popular super-resolution microscopy techniques is structured illumination microscopy (SIM) due to its simple experimental arrangements, minimal sample preparation steps, fast imaging speed, and minimal invasion [1-3]. SIM is a widefield microscopy technique in which structured illumination patterns with a periodicity of approximately half of the excitation wavelength are incident on the sample. The high-frequency components of the sample superimpose with the structured illumination pattern to form Moiré patterns. The structured light pattern is rotated by several angles (0°, 60° and 120°), and at each angular position is further phase shifted by several phase shifts (0, $\pi/3$ and $2\pi/3$), producing nine composite Moiré patterns. The super-resolved image of the sample is then calculated from those nine images with an optimal lateral resolution of about 100 nm, which is a two-fold enhancement in lateral resolution compared to conventional optical microscopy [1, 4].

2. Methods and Experiment

The most important part of implementing the SIM setup is generating structured illumination patterns. To do so, gratings patterns are numerically constructed for each orientation by using Matlab. The physical grating can be realized by sending the numerically constructed grating patterns to a ferroelectric spatial light modulator (SLM) with a sub-millisecond pattern switching time. The SLM consist of 1280 × 1024 pixels, and each pixel can be digitally set to an *on* or *off* state. The *on* state corresponds to the transparent portion of the grating, whereas the *off* state corresponds to the opaque. To realize the illumination pattern at the sample plane, the resulting diffracted orders from the gratings are filtered and relayed by using combinations of lenses.

The basic experimental arrangement of the SIM setup is shown in Fig. 1. A polarized laser beam from a solid-state diode laser is expanded and collimated using L_1 and L_2 and incident to a polarizing beam splitter (PBS). The *s*-polarized component of the beam is reflected by the PBS and passes through a half wave plate (HWP) inclined at 45° to ensure the *p*-polarization before incident onto the SLM. Here the SLM acts as a half wave plate with its fast axis rotated at an angle of 45°, thus the diffracted beams just after the SLM are *s*-polarized. The diffracted beams are transmitted through the PBS and focused by lens L_3. The polarization of the diffracted beams is changed to circular polarization by a quarter-wave plate (QWP). Here we used a Fourier mask, *i.e.* a matte black aluminium foil with six holes at the positions of the first diffraction orders to isolate the ±1 orders for three grating directions. To get maximum modulation depth of the illumination pattern at the sample plane, the polarization of the beam at the back focal plane of the objective lens should be *s*-polarized. A customized patterned polarizer (azimuthal polarizer) comprised of six identical angular polarizers with the transmission axis of each individual section is employed to obtain the s-polarization at the back focal plane of the objective lens. Then the two diffraction order beams superpose, forming an illumination grating with a period close to the diffraction limit. The fluorescent light from the sample is then collected by the objective lens and detected by an sCMOS camera.

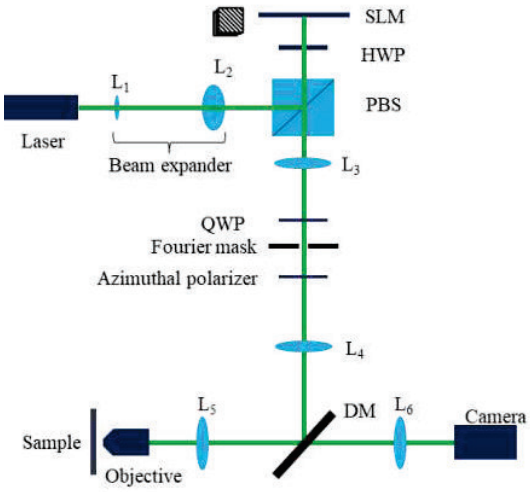

Fig. 1: Schematic diagram of the experimental setup

3. Result and Discussion

After recording all the raw images corresponding to each grating pattern, a super-resolved image is constructed by combining the frequency components of each image. Here we have used FairSIM, an opensource ImageJ plugin for the reconstruction of the super-resolve image from the raw data acquired from the microscope [5]. We have imaged actin filaments of MDCK cells, and the widefield and reconstructed super-resolved image is shown in Fig. 2. The line plot in the figure shows the resolution enhancement in the SIM setup.

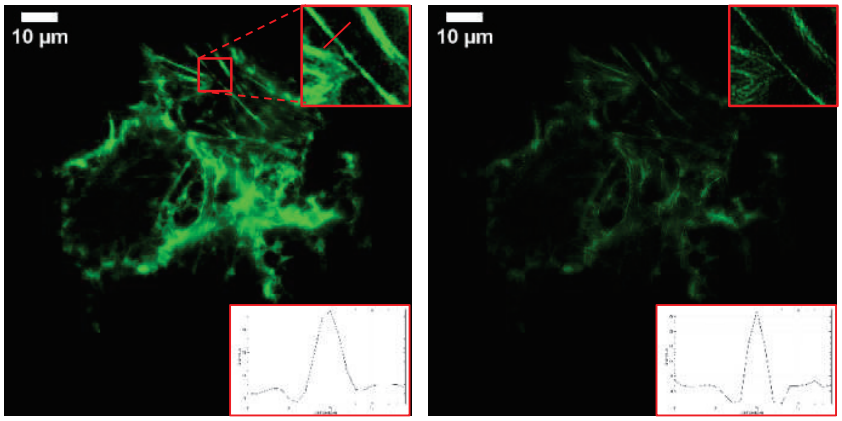

Fig. 2: Widefield (left) and super-resolved (right) image of actin filaments stained with Alexa fluor 568. Aline plot (inset fig) of an actin filament shows the resolution enhancement in case of the super-resolved image.

4. References

[1] Gustafsson, Mats GL. "Surpassing the lateral resolution limit by a factor of two using structured illumination microscopy." Journal of microscopy 198.2 (2000): 82-87.
[2] Lu-Walther, Hui-Wen, et al. "fastSIM: a practical implementation of fast structured illumination microscopy." Methods and Applications in Fluorescence 3.1 (2015): 014001.
[3] Kner, Peter, et al. "Super-resolution video microscopy of live cells by structured illumination." Nature methods 6.5 (2009): 339-342.
[4] Young, Laurence J., Florian Ströhl, and Clemens F. Kaminski. "A guide to structured illumination TIRF microscopy at high speed with multiple colors." *JoVE (Journal of Visualized Experiments)* 111 (2016): e53988.
[5] Müller, Marcel, et al. "Open-source image reconstruction of super-resolution structured illumination microscopy data in ImageJ." Nature communications 7.1 (2016): 1-6.

Emission studies of few color centers in diamonds

Ashish and Rajesh V. Nair

Laboratory for Nano-scale Optics and Meta-materials (LaNOM), Department of Physics,
Indian Institute of Technology Ropar, Rupnagar, Punjab 140001, India
E-mail address: ashish.20phz0011@iitrpr.ac.in

Abstract: The practical implication of quantum science applications like quantum computing and quantum key distribution requires a stable single photon source. To efficiently use a single photon source for such applications it should be bright, having high emission rate, with good collection efficiency and indistinguishability. The nitrogen vacancy is a better single photon candidate for quantum applications along with its excellent spin properties. In this study we would characterize the emission properties of nitrogen vacancy centers in diamond. We observe an overall decrease in emission lifetime with an increase in emission wavelengths.

Keywords: Nitrogen vacancy; single photons.

1. Introduction

In recent years, quantum technologies have been gaining popularity due to their applications in optical quantum processing, quantum key distribution, entangled state generation, and quantum sensing. However, these applications' practical implications require a bright, indistinguishable, and deterministic single photon source [1,2]. Single photon sources are the optical sources that emit only one photon at a time with quantum characteristics like photon antibunching. Additionally, such a source should be stable for photo blinking and bleaching at room temperature. Various defects in the solid state have been studied in recent years. The nitrogen vacancy (NV) defect centers in diamonds are perhaps the most suitable candidate for such technologies due to their photostability at room temperature and excellent spin properties [3]. NV is a spin triplet system that initializes after a few optical pumping cycles into one of its ground sublevels. Subsequent application of microwave pulse can generate the superposition state and its long coherence time adhere the system into that state before applying the quantum protocols [4]. In this study, we discuss the emission properties of few NVs in the diamonds so that we can use them more efficiently for integrated photonics and quantum science.

2. Results and Analysis

To characterize the NVs, we isolated the nanodiamonds onto a glass coverslip. The commercially available nanodiamonds containing a few and an ensemble of NVs were diluted and drop-casted onto the coverslip. The amount of dilution depends upon the mutual interaction of nanoparticles and substrate.

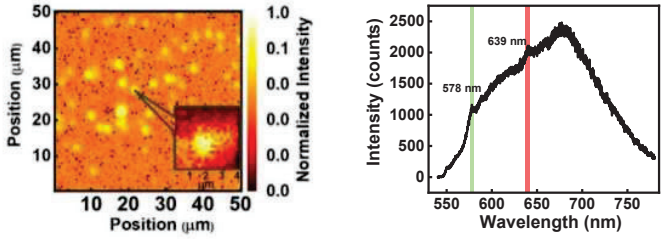

Fig. 1: (left) Confocal scan of nanodiamonds containing NVs drop casted on a glass substrate. (right) PL spectra of the emitter as identified and shown in the inset of fig.1. The vertical green line and red correspond to the zero phonon lines of NV at 578 nm and 639 nm.

The confocal study of the sample gives us the precise location of emitters in a plane transverse to the excitation beam. We were able to locate the emitters onto the glass coverslip as shown in fig. 1 (left) and thereafter, the emission spectra is measured followed by spectral-dependent decay rate measurements. We clearly observe the zero phonon lines of NV at 640 nm and the broad phonon side band induced emission extending up to 750 nm, as shown in fig. 1 (right). The decay rate measurements were done on the same emitter with the help of time correlated single photon counting module. We measured the spontaneous emission decay rate of NV with bandwidth of about 10nm centered at wavelengths 600nm, 660nm, and 700nm. We observed a decrease in the lifetime with an increase in the emission wavelength.

3 References

[1] Aharonovich, I., Englund, D. & Toth, M. "Solid-state single-photon emitters," *Nature Photon* **10**, 631–641 (2016).
[2] Tim Schröder, Sara L. Mouradian, Jiabao Zheng, Matthew E. Trusheim, Michael Walsh, Edward H. Chen, Luozhou Li, Igal Bayn, and Dirk Englund, "Quantum nanophotonics in diamond," J. Opt. Soc. Am. B **33**, B65-B83 (2016).
[3] Marcus W. Doherty, Neil B. Manson, Paul Delaney, Fedor Jelezko, Jörg Wrachtrup, Lloyd C.L. Hollenberg, "The nitrogen-vacancy colour centre in diamond," Physics Reports **528**, 1-43 (2013).
[4] B. D. Wood, G. A. Stimpson, J. E. March, Y. N. D. Lekhai, C. J. Stephen, B. L. Green, A. C. Frangeskou, L. Ginés, S. Mandal, O. A. Williams, and G. W. Morley, "Long spin coherence times of nitrogen vacancy centers in milled nanodiamonds," Phys. Rev. B 105, 205401 (2022).

Modeling Length and Angular Sensing and Control Techniques in a Three-Mirror Coupled Cavity

Parivesh Choudhary[1], Manasadevi P Thirugnanasambandam[2]

1. *Indian Institute of Technology Kanpur, Kanpur, India*
parivesh@iitk.ac.in
2. *Inter-University Centre for Astronomy and Astrophysics, Pune, India*
manasa@iucaa.in

Abstract: A three-mirror coupled cavity system is the simplest optical system that resembles the multiple coupled cavities of an interferometric gravitational wave detector in dual-recycled Fabry Perot Michelson configuration. In this paper, we present the results pertaining to system design parameters for implementing fool-proof length and angular sensing and control schemes in a 5m three-mirror coupled cavity using frequency-domain interferometer simulation software, *Finesse*.
Keywords: Coupled resonators, Interferometry, Fabry-Perot, Precision measurement, Length sensing, Angular sensing

1. Introduction

The sensitivity of interferometric gravitational wave (GW) detectors is significantly improved by modifying the simple Michelson interferometer into a dual-recycled Fabry-Perot Michelson configuration. This modified optical configuration introduces several coupled optical cavities. The uptime of the interferometric GW detectors depends greatly on the stability of sensing and control schemes that hold the multiple coupled cavities of the interferometer at resonance. When the GW detector is maintained to have a dark fringe output in the power recycled Fabry-Perot Michelson (PRFPMI) configuration, the optical setup can be simply represented as a three-mirror coupled cavity. The two length degrees of freedom for such a coupled cavity system are the power recycling cavity length (PRCL) and the arm cavity length (ARM), while the six angular degrees of freedom come from the pitch and yaw motion of each mirror. Interferometer length sensing and control techniques have been investigated for three-mirror coupled cavity systems both numerically and experimentally in the past on a 10m prototype that used the sub-carrier method to sense the length degrees of freedom[1].

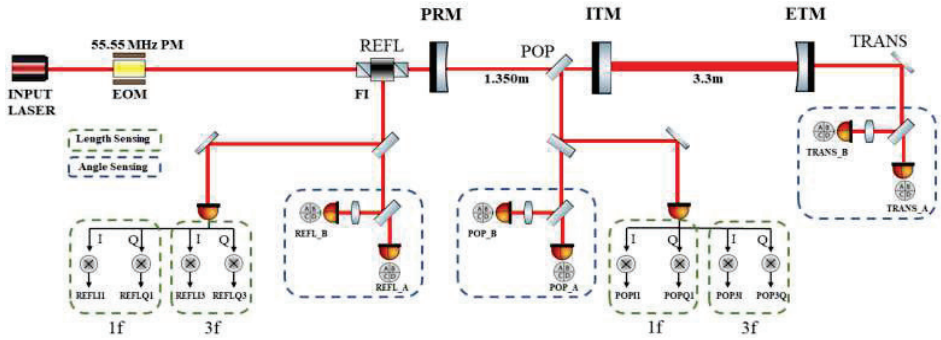

Fig 1. Length sensing and angular sensing scheme in a 5m three mirror coupled cavity system. EOM- Electro-optic modulator, FI - Faraday isolator, REFL- Reflection port, PRM - Power Recycling Mirror (R = 0.8599, T = 0.1), ITM- Input Test Mass (R = 0.98997, T = 0.01), ETM- End Test Mass (R = 0.99996, T = 0.00001), POP- Power recycling cavity pick-off port, TRANS- Transmission port.

In this work, we model a 5m prototype facility that is proposed to be set up for LIGO-India training and research (Fig. 1). We use the third harmonic demodulation technique[2] used in LIGO to sense the length degrees of freedom of the coupled cavity system. We also model angular sensing and control techniques on the coupled cavity system for the first time. The goal of this modeling effort is to obtain a diagonalised sensing matrix which allows us to relate the information about each degree of freedom to a single sensor at one of the output ports. Modeling of the optical system in *Finesse* [3] allows us to optimize the cavity lengths, modulation frequencies, demodulation phases and Gouy phases that directly affect the purity of the sensing and control scheme implemented.

2. Methodology

2.1 Three-Mirror Coupled Cavity System

The optimum cavity lengths in the three mirror coupled cavity test system are obtained by modeling for the best possible resonance condition of the fundamental mode in the arm cavity. The optimum length of the ARM cavity that renders maximum suppression of higher order modes is 3.3m with a stability factor of g=0.708. The PRC length is 1.350m and has a stability factor of g=0.935.

2.2 Length Sensing

The third harmonic demodulation technique [2] which is an extended form of the Pound-Drever-Hall scheme [4] is used to sense and control the length degrees of freedom. The modulation frequency is chosen to be 55.556MHz, such that it is resonant in the PRC and antiresonant in the ARM. Eight output signals are obtained from two ports demodulated at two different demodulation frequencies (*f*=55.56MHz and *3f*=166.68MHz) at two different demodulation phases (I and Q). Out of these, only two are used for sensing the two length degrees of freedom. The selection of a final length sensor, one each for PRCL and ARM to get maximum decoupling in length control error signals is obtained by tuning the demodulation phase to maximize the slope of the error signal. Fig 2(a) shows one such case where the demodulation phase is optimized for the sensor at the REFL port. Fig 2(b) shows the final length sensing matrix for the optical system.

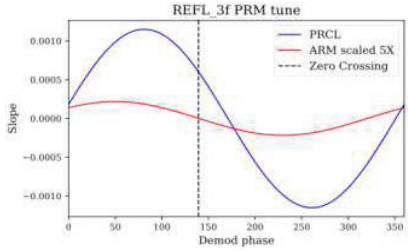

(a)

PORT	*PRCL*	*ARM*
POPI1	1	$-4.76X10^{-03}$
REFLI3	$3.16X10^{-02}$	1

(b)

Fig 2.(a) Slope of the linear range of PDH error signal for REFLI3 port demodulation phase. The black line corresponds to the phase corresponding to the maximum decoupling, 139 deg in this case. (b) The optimized sensing matrix for length sensing and control of coupled cavity.

2.3 Alignment Sensing

For the detection of angular misalignment, there are two techniques; Anderson technique[5] and Ward technique[6]. For the three mirror coupled cavity system, a combination of both of these techniques is used. The error signal for controlling the alignment of the mirrors is obtained from quadrant photodiode (QPD) sensors at the different output ports shown in Fig.1. The QPDs allow directional detection and subsequent demodulation[7]. The QPD output signals can be optimized such that the sensing matrix will provide maximum sensitivity for a particular error signal for each angular degree of freedom.

3. Conclusion

A thorough numerical modeling for sensing and controlling the length and angular degrees of freedom of a 5m three-mirror cavity was done using *Finesse*. The system design parameters obtained from this work will be used in setting up a robust coupled cavity test prototype that will demonstrate optimum performance.

4. References

[1] S H Huttner et al, “Techniques in the optimization of length sensing and control systems for a three-mirror coupled cavity” Class. Quantum Grav. 25 235003, (2008)

[2] Arai, K., Ando, M., Moriwaki, S., Kawabe, K., Tsubono, K. 2000. New signal extraction scheme with harmonic demodulation for power-recycled Fabry-PerotMichelson interferometers. Physics Letters A 273, 15–24.

[3] A Freise et al, “Frequency-domain interferometer simulation with higher-order spatial modes”, Class. Quantum Grav. 21 S1067,(2004)

[4] Eric D. Black , "An introduction to Pound–Drever–Hall laser frequency stabilization", American Journal of Physics 69, 79-87 (2001)

[5] Dana Z. Anderson, "Alignment of resonant optical cavities," Appl. Opt. 23, 2944-2949 (1984)

[6] Euan Morrison et al, "Automatic alignment of optical interferometers," Appl. Opt. 33, 5041-5049 (1994)

[7] M. Mantovani, The automatic alignment in the Virgo interferometer, Ph.D. Thesis for the Università Degli Studi di Siena

Bessel beam axicon probe using CP-OCT for malignancy identification

P. Gupta[a,b], K. Vairagi[a,b], S. Mondal*[,a], V. Sharma[c], and, K. K. Prasad[c]
[a]CSIR-Central Scientific Instruments Organisation, Chandigarh 160030, India;
[b]Academy of Scientific and Innovative Research, Uttar Pradesh 201002, India
[c] Post Graduate Institute of Medical Education & Research, Chandigarh 160012, India

ABSTRACT

The ability to detect the malignancy inside the tissue structure non-invasively have immense potential in the clinical application. In this work, a Bessel beam axicon probe based common-path optical coherence tomography system is demonstrated for detection of malignancy inside the human tissue. This probe is employed in this system having an axicon structure which is chemically etched inside the optical fiber end. This probe generates a quality Bessel beam owning a large depth-of-field, ~700µm and small central spot size. This probe effectively identifies the malignancy in the human colon tissue hence it could be a great tool as an endoscopic probe in future for either early-stage or during surgery diagnosis.

Keywords: Axicon, Bessel beam, common-path optical interferometry, malignancy, optical coherence tomography.

1. INTRODUCTION

Malignancy detection inside tissue is always a challenging task specifically at the interaction regions owing to partial resection of tissue which stimulate recurrence of abnormal tissue growth. Hence, it is imperative to implement non-invasive, cost-effective, and label-free cancer detection method for during surgery as well as early-stage diagnostic hence optical coherence tomography (OCT) [1] is best suited for such applications, OCT [2] is a non-invasive and label-free approach for cross-sectional imaging with micron-order resolution up to a few millimeter depth possessing enormous applications in the field of biomedical imaging. It is capable to visualize the abnormalities or malignancy [3] within the complex biological tissue for diagnosis. Different type of human tissues have been differentiated among normal and malignant using OCT [4–6]. Generally, these techniques [7] utilized the high numerical aperture (NA) refractive objective lens for achieving fine lateral resolution that leads to loss in the depth-of-field (DOF) of the sample beam. A typical 20x lens with 0.4 NA having only ~6µm DOF. The trade-off between DOF and lateral resolution can be compensated by using Bessel beam [8] which is having extended DOF. The DOF can be extended by free space micro-optic axicon lens, in-fiber axicon lens at the tip, and all-fiber optical probe consists gradient-index (GRIN) lens and no core fiber (NCF). Among these approaches, in-fiber probe [8] by etching probe uses simple setup and probe fabrication with maximum ~600µm DOF which can be further extended by using the recently developed fiber-based negative axicon with ~700µm DOF [9].

In this paper, a Bessel beam axicon probe based common-path OCT system is proposed for malignancy detection. The human colon tissues including both normal and malignant tissue types are differentiated which shows the promising potential of our system.

2. EXPERIMENTAL SETUP

2.1 Bessel beam Axicon Probe

The negative axicon structure is formed by etching chemically inside the photosensitive single-mode optical fiber. For etching, the fiber's end superficially dipped into the hydrofluoric acid solution for ~41 minutes as presented in Fig. 1(a). The dimensions of the axicon are measured as ~290µm long and ~63µm wide at opening that reduced gradually at the apex to ~3µm. The brief description about axicon fabrication can be found in our previous work [9]. This axicon structure converts the Gaussian beam into the Bessel beam

having a large depth-of-focus, ~700µm. A typical picture of the Bessel beam transverse profile captured through camera from Helium-neon laser (633nm) is shown in Fig. 1 (b).

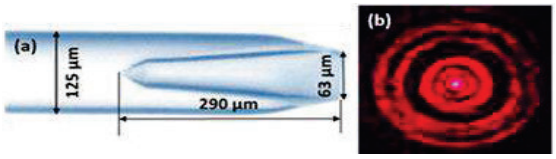

FIGURE 1. (a) Bessel-beam axicon probe. Transverse beam profile of the Bessel beam recorded at the (b) camera through a screen from 632nm Helium-neon laser source.

2.2 Common-path Optical Coherence Tomography System

Fig. 2 is the schematic of the experimental setup uses a broadband SLD source from SUPERLUM with FWHM (full width half maxima) is 45nm and center wavelength 840nm used for experiments. The axicon is coupled with the source via an optical circulator and spectrometer. The tissue sample is placed over the 3-axis stage for A-scan. The source launches the beam into the tip and the reflected beam from the sample is coupled back to the tip. This beam interferes with the reference beam generated due to the structure of the axicon, then the interference spectra are acquired at detector and stored in the computer. The data acquisition, controlling and processing are done through a customized program written on LabVIEW platform.

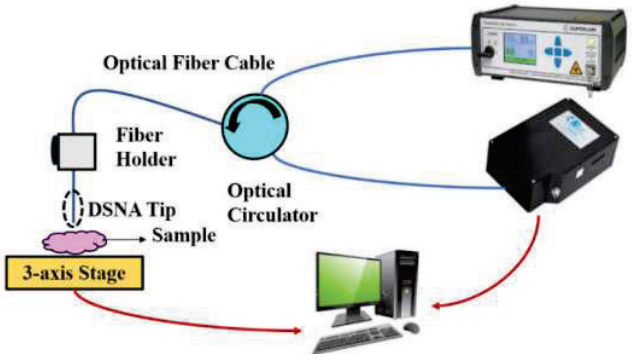

FIGURE 2. Schematic of the experimental setup of common-path optical coherence tomography.

2.3 Image Construction

As the optical fiber probe non-invasively scans the tissue sample, the interference spectra are recorded by the spectrometer. A traditional Fast Fourier Transform (FFT) based image reconstruction method has been applied on the acquired interference spectra to obtain the tissue cross-sectional image [10]. The fixed-pattern noise results into the bold horizontal lines in the constructed image which is removed by applying the mean subtraction method. To reconstruct the A-scan in terms of depth, the spectrum is re-sampled from the λ-space into the linearly sampled k-space before applying the FFT. Afterwards, the FFT is applied to the interpolated data to obtain the axial depth profile of the sample by only taking the FFT magnitude.

3. RESULTS

The cross-sectional image of human colon tissues along with the histopathological images are represented in Fig. 3. The human tissue samples are collected from the Post Graduate Institute of Medical Education & Research (PGMIER), Chandigarh within 2-3 hour after the tissue is removed from the body and kept at room temperature. Then, the sample is preserved in formalin solution after the experimentation such that the histology can be performed afterwards for ground truth. The presence of malignancy in the human colon sample is confirmed by histopathologist. The image from the OCT system of malignant human colon tissue is illustrated in Fig. 3. It is observed that the malignant region present in the image is marked by square box. Hence, our system can effectively visualize the abnormalities exist in the tissue morphology.

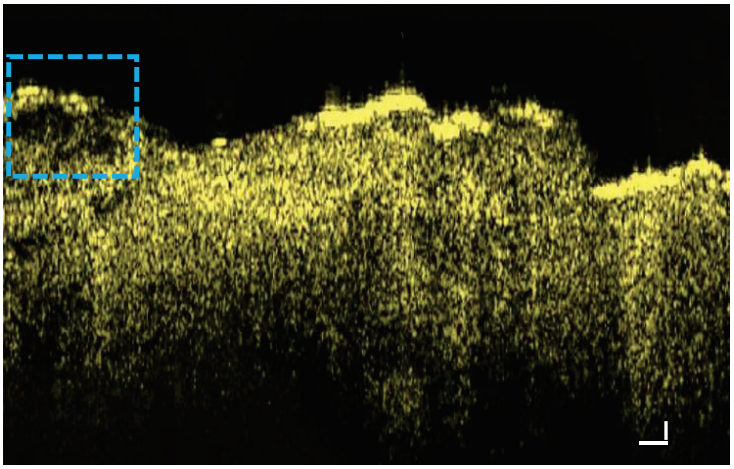

FIGURE 3. The cross-sectional histopathology images of tumour human colon tissue. Scale bar: 100μm.

4. CONCLUSION

In conclusion, we have demonstrated that the common-path optical coherence tomography system for detection of malignancy in different biological tissue using Bessel beam axicon probe. The proposed OCT system will be modified as an endoscopic probe in future for tissue malignancy detection.

REFERENCES

1. Zysk, A.M.A., Adie, S.G.S., Armstrong, J.J.J., Leigh, M.S., Paduch, A., Sampson, D.D., Nguyen, F.T., and Boppart, S.A. (2007) Needle-based refractive index measurement using low-coherence interferometry. *Opt. Lett.*, **32** (4), 385–7.
2. Leitgeb, R., Hitzenberger, C., and Fercher, A. (2010) Performance of fourier domain vs time domain optical coherence tomography. *Opt. Express*, **11** (8), 889.
3. Butola, A., Ahmad, A., Dubey, V., Srivastava, V., Qaiser, D., Srivastava, A., Senthilkumaran, P., and Mehta, D.S. (2019) Volumetric analysis of breast cancer tissues using machine learning and swept-source optical coherence tomography. *Appl. Opt.*, **58** (5), A135.
4. Muller, B.G., van Kollenburg, R.A.A., Swaan, A., Zwartkruis, E.C.H., Brandt, M.J., Wilk, L.S., Almasian, M., Schreurs, A.W., Faber, D.J., Rozendaal, L.R., Vis, A.N., Nieuwenhuijzen, J.A., van Moorselaar, J.R.J.A., de la Rosette, J.J.M.C.H., de Bruin, D.M., and van Leeuwen, T.G. (2018) Needle-based optical coherence tomography for the detection of prostate cancer: a visual and quantitative analysis in 20 patients. *J. Biomed. Opt.*, **23** (08), 1.
5. Panta, P. (2019) Oral cancer detection: Novel strategies and clinical impact. *Oral Cancer Detect. Nov. Strateg. Clin. Impact*, 1–314.
6. Fujimoto, J.G., Pitris, C., Boppart, S.A., and Brezinski, M.E. (2002) Optical Coherence Tomography: An Emerging Technology for Biomedical Imaging and Optical Biopsy. *Neoplasia*, **2** (1–2), 9–25.
7. Drexler, W., and Andersen, P.E. (2009) Optical Coherence Tomography in Biophotonics. *J. Biophotonics*, **2** (6–7), 339–341.
8. Tan, K.M., Mazilu, M., Chow, T.H., Lee, W.M., Taguchi, K., Ng, B.K., Sibbett, W., Herrington, C.S., Brown, C.T.A., Dholakia, K., Flotte, T., Gregory, K., Puliafito, C.A., Fujimoto, J.G., and Coherence, O. (2009) In-fiber common-path optical coherence tomography using a conical-tip fiber. **17** (4), 2231–2235.
9. Vairagi, K., Minz, R.A., Kaur, S., Kumbhakar, D., Paul, S., Tiwari, U., Sinha, R.K., Fick, J., and Mondal, S.K. (2017) Deep Seated Negative Axicon in Selective Optical Fiber Tip and Collimated Bessel Beam. *IEEE Photonics Technol. Lett.*, **29** (10), 786–789.
10. Ali, M., and Parlapalli, R. (2010) Signal processing overview of optical coherence tomography systems for medical imaging. *Texas Instruments Whitepapers*, (June), 1–22.

A comparative analysis of filtering performance of ring resonator with different cavity shapes & sizes

Prasenjeet Damodar Patil[1]
Associate Professor, Department of Computer Science & Engineering, School of Engineering, MIT ADT University, Rajbaug, Loni Kalbhor, Pune, Maharashtra, India.
prasenjeet.patil@mituniversity.edu.in
Gajanan Govind Sarate[2]
Head of Department, Department of Electronics Engineering, Government Polytechnic, Amravati,Maharashtra, India
ggsanshu@gmail.com
Pradip Ram Selokar[3]
Assistant Professor, Department of Electronics and Communication Engineering, Shri Ramdeobaba College of Engineering and Management, Nagpur (MS), India.
selokarpr@rknec.edu

Abstract: Optical ring resonators are passive components used as channel dropping filters in dense wavelength division multiplexing(DWDM). Filtering performance of ring resonators depends upon various parameters viz, size and shape of cavity, coupling length, and separation gap from adjacent waveguides etc. Computationally complex Maxwell's equations are solved either in time or frequency domain in order to study behavior of wave propagation inside optical components. Effect of separation gap on filtering performance is available in literature, but is less explored. In this paper, effect of separation gap on filtering performance of optical resonator with different types of cavity shapes and sizes are analyzed. Simulation results shows that with the decrease in separation gap, there is improvement in filtering performance which validates the theoretical results. This paper also investigates effect of negative separation gap on filtering performance of ring resonator

Keywords: DWDM, FDTD, BPM, FD-BPM, evanescence coupling etc

1. Introduction

Analysis of optical components requires finding solution of Maxwell's equations in time or frequency domain. Numerical methods available includes, Effective Index Method, Finite Difference Time Domain (FDTD)[7][15], Finite Element Analysis(FEM), Full Wave Analysis, Beam Propagation Method(BPM)[2][15], Eigen Value Expansion Method, Method of Lines(MoL) etc. Selection of a particular method depends upon on complexity of the problem and other parameters like computational time, efficiency, accuracy, hardware requirements etc. Commercially available software's for waveguide analysis are either expensive or limited to use of specific method.

Finite difference time domain method (FDTD) is one of the widely used method for analysis of optical components. In this method, to find the solution of E & H field components for small step change, the problem is discretized into small grids and central limit approximations are used for computing values of field components. The computational time increases with decrease in step size, which further increases memory requirements. Beam Propagation Method is oldest and easiest to implement method used for analysis of 2D and 3D structures. It is used for analysis of complex structures extending longitudinally along the propagation direction.

In this paper, Finite Difference Beam Propagation Method (FD-BPM)[8][9] is used for analysis of ring resonator with square and circular cavity with different sizes.

2. Finite Difference Beam Propagation Method

For linear, isotropic and homogeneous medium, the wave equation can be reduced to scalar Helmholtz equation represented completely in terms of either E or H-field component.

$$\frac{\partial^2 E}{\partial x^2}+\frac{\partial^2 E}{\partial y^2}+\frac{\partial^2 E}{\partial z^2}+k_0^2 n^2 E(x,y,z)=0 \qquad (1)$$

The above equation is valid for wave propagation along both directions of z-axis. For the rapidly changing field along the z-direction, equation (1) in Cartesian coordinate system can be written as

$$\frac{\partial^2\Phi}{\partial x^2}e^{(-jk_0n_0z)}+\frac{\partial^2\Phi}{\partial y^2}e^{(-jk_0n_0z)}+\frac{\partial^2\Phi}{\partial z^2}e^{(-jk_0n_0z)}-2jk_0n_0\frac{\partial\Phi}{\partial z}e^{(-jk_0n_0z)}-k_0^2n_0^2\Phi e^{(-jk_0n_0z)}+k_0^2n^2\Phi e^{(-jk_0n_0z)}=0 \tag{2}$$

Using slowly varying envelope approximation along propagation direction leads to

$$\left|\frac{\partial^2\Phi}{\partial z^2}\right|<<\left|2k_0n_0\frac{\partial\Phi}{\partial z}\right| \tag{3}$$

On further simplification, it reduces Fresnel's equation

$$2jk_0n_0\frac{\partial\Phi}{\partial z}=\frac{\partial^2\Phi}{\partial x^2}+\frac{\partial^2\Phi}{\partial y^2}+k_0^2(n^2-n_0^2)\Phi \tag{4}$$

which can be written as

$$j\frac{\partial\Phi(x,y,z)}{\partial z}=G\Phi(x,y,z) \tag{5}$$

For the small step size of Δz along z direction the solution of the above equation can be written as

$$\Phi(x,y,z+\Delta z)=e^{(-j\Delta zG)}\Phi(x,y,z) \tag{6}$$

The central difference approximation can be used to replace the partial derivatives accurate up to second order

$$\Phi_{i,m}(z+\Delta z)=\Phi_{i,m}(z-\Delta z)-\frac{2j\Delta z}{a_0\Delta x^2}\left[\Phi_{i-1,m}(z)+\Phi_{i+1,m}(z)\right]-\frac{2j\Delta z}{a_0\Delta y^2}\left[\Phi_{i,m-1}(z)+\Phi_{i,m+1}(z)\right]-\frac{2j\Delta z}{a_0}P_{i,m}\Phi_{i,m}(z) \tag{7}$$

Where i & m are discretized coordinates along x and y direction. Equation (7) is known as finite difference BPM[5][8][14]. The stability of this algorithm depends on the step size along z direction

$$\Delta z<2k_0n_0\left[\frac{4}{\Delta x^2}+\frac{4}{\Delta y^2}+k_0\left|n_{i,m}^2-n_0^2\right|_{max}\right]^{-1} \tag{8}$$

3. CAVITY RESONATOR

A ring resonator is a passive optical device consisting of two parallel adjacent straight waveguides & a cavity embedded between them. As shown in figure 1, one of the straight waveguide acts as a add port and second acts as a drop port. Wave incident at add port gets evanescently coupled in the cavity, builds up its energy by constructive interference over multiple round trips inside cavity. The wave evanescently gets coupled into the second waveguide and comes out from the drop port. The amount of energy coupled depends upon, coupling length between waveguide

and cavity, dimension of cavity and the separation gap between waveguides and cavity. A ring resonator comes with cavities of different shapes viz. circular, elliptical, square, toroidal, spherical etc.

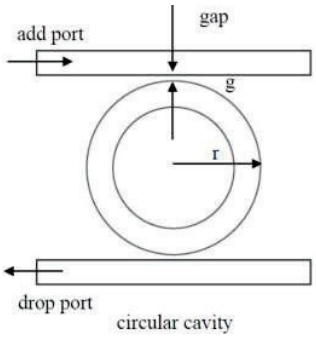

Fig. 1. Ring resonator with circular cavity

3.1 Add-drop filter with circular cavity

The ring resonator with circular cavity can be used as wavelength filter. The filtering performance of the resonator depends mainly on the coupling length, separation gap from the waveguides and radius 'R' of the ring. Figure 1 shows the details about these parameters.

The simulations are done by selecting the parallel waveguides of 10µm x 150µm and the coupling coefficients is set to 1 i.e(100%) coupling from both the sides of waveguides. For the purpose of analysis, keeping wavelength constant, for a fixed radius, the gap distance is varied to check the effect on power dropped at drop port. Observations are taken for two different cases viz positive gap distance and negative gap distance for which the ring overlaps with the waveguides. The details of these cases are present in the subsequent subsections.

Effect of coupling gap on different sizes of circular cavity resonator is investigated, for wavelength 1550nm and refractive index 2.44 constant. Since the coupling efficiency depends on the outer radius of ring, the observations are taken for the outer ring diameter.

Figure 2 shows circular cavity with 70 µm outer radius with gap of 0µm. A soft source generates, fundamental TE mode of unit amplitude and wavelength 1.550µm at add port. Observations are taken by varying the gap distance from parallel waveguide and its effect on transmitted and dropped power in secondary waveguide is averaged.

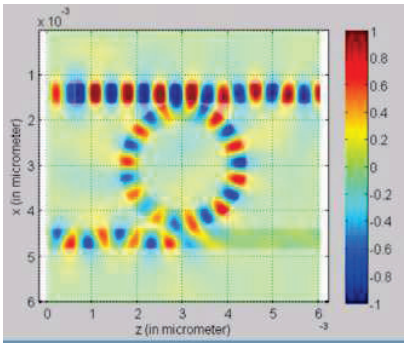

Fig. 2. Resonance condition

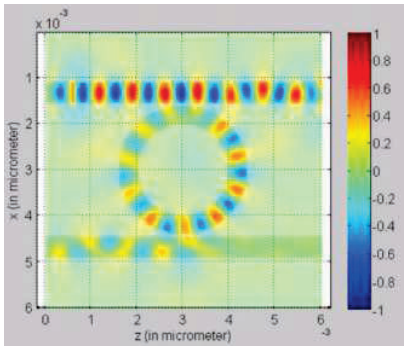

Fig. 3. Off-resonance condition

Figure 2 shows input power transmitted from port 1. With the increasing order of time steps, the power in the circular cavity builds up with each round trip of the wave adds constructively. The cavity is said to be in resonance, when it adds the power due to constructive interference during multiple round trip of the wave. Figure 2 also shows the resonance condition of the ring. At the time of resonance maximum power is coupled to the secondary waveguide. The cavity is said to be off-resonance, when destructive interference takes place inside cavity, due to phase mismatch during the round trips of the wave, causing zero power coupling in the secondary waveguide. Figure 3 shows off-resonance condition of the cavity.

Figure 4 shows, input power transmitted through primary waveguide. It reaches its maximum value of 1.3 at approximately 680 time steps. With the increasing time steps as the power coupled in the cavity increases, the input power starts dropping in the primary waveguide

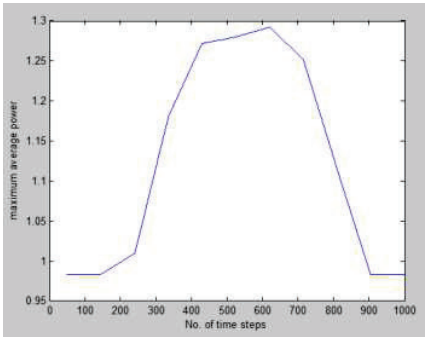

Fig. 4. Input power at port 1

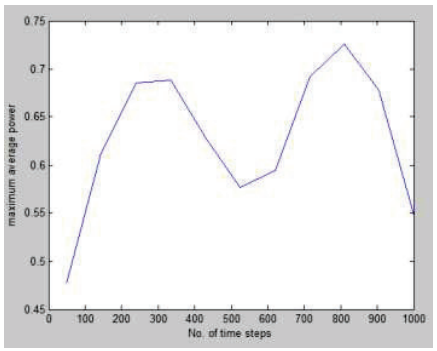

Fig. 5. Dropped power at port 1

Figure 5 shows, drop power in secondary waveguide as a function of time steps. The first peak is achieved after 220 time steps and second peak at 825 time steps where the dropped power is maximum .73 or 73%.

Each simulation takes 12 to 15 minutes (depending on the platform and computer configuration) for the time steps in between 1000 to 1200, and generates two plots for input and output power. In order to reduce the number of plots, observation results are presented in tabular form for each cavity diameter change against gap distance variation. Also, a single plot showing transmitted and dropped power is shown for each case.

Table I gives the observations obtained for transmitted power **Pi** at the input port and the dropped power **Pd** at the drop port for change in the gap distance. In this research, analysis of effect of negative gap separation of cavity has been also analyzed. In negative gap, some portion or the cavity completely overlaps with the parallel waveguides. Figure 6 shows circular cavity with negative separation gap. Figure 7 and 8, add-drop filters with circular cavity with separation gap of .5µm and 1µm.

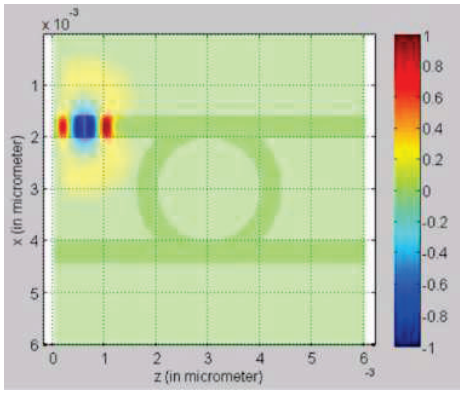

Fig. 6. Circular cavity with 70µm diameter and gap with -ve gap

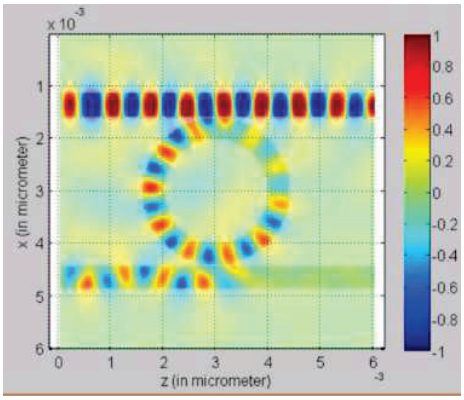

Fig. 7 Circular cavity with 70µm diameter and gap of 0.5µm

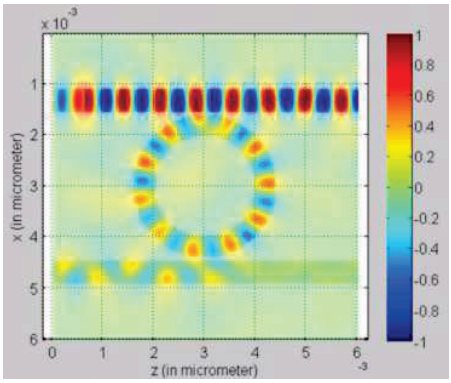

Fig. 8 Circular cavity with 70µm diameter and gap of 1µm

3.2 Circular cavity with 70µm diameter

Table I shows, summary of input power through port 1 and the power dropped through port 2 of the circular cavity with 70μm diameter for different separation gap distance.

TABLE I: Summary of Input/Dropped power for 70µm diameter cavity

-ve gap		0 gap		.5µm		1µm		1.5µm	
Pin	Pd	Pin	Pd	Pin	Pd	Pin	Pd	Pin	Pd
1.153265	0.08518	0.9002	0.609065	0.927211	0.292613	0.919168	0.101027	0.98377	0.097338
1.669677	0.090935	1.168486	0.753325	1.196211	0.355698	1.200217	0.136505	0.98377	0.123022
2.141324	0.080185	1.493872	0.802535	1.564771	0.367892	1.57035	0.160271	1.090724	0.13453
2.477429	0.057156	1.833631	0.755562	1.910626	0.329027	1.965596	0.15883	1.296946	0.130222
2.641759	0.034648	2.061295	0.62904	2.155001	0.254937	2.279641	0.134347	1.432789	0.112577
2.709283	0.022334	2.180778	0.538553	2.353915	0.21936	2.463313	0.095841	1.547673	0.093674
2.769904	0.026254	2.332807	0.741701	2.419909	0.324686	2.484855	0.08347	1.555779	0.11267
3.099639	0.054519	2.3048	0.905255	2.34063	0.399895	2.340954	0.126177	1.453319	0.140308
3.105912	0.083887	2.087165	0.972398	2.122995	0.432661	2.052912	0.157171	1.254105	0.153369
2.745882	0.097426	1.827936	0.905092	1.790654	0.42346	1.656102	0.189058	0.987358	0.146442
2.080912	0.090011	1.505278	0.714312	1.383158	0.353125	1.200079	0.193243	0.98377	0.119373

Figure 9 shows the energy transferred through port 1. It can be observed that maximum input power is for negative gap and least is for 1.5μm gap, while for other separation distance, it remains nearly same.

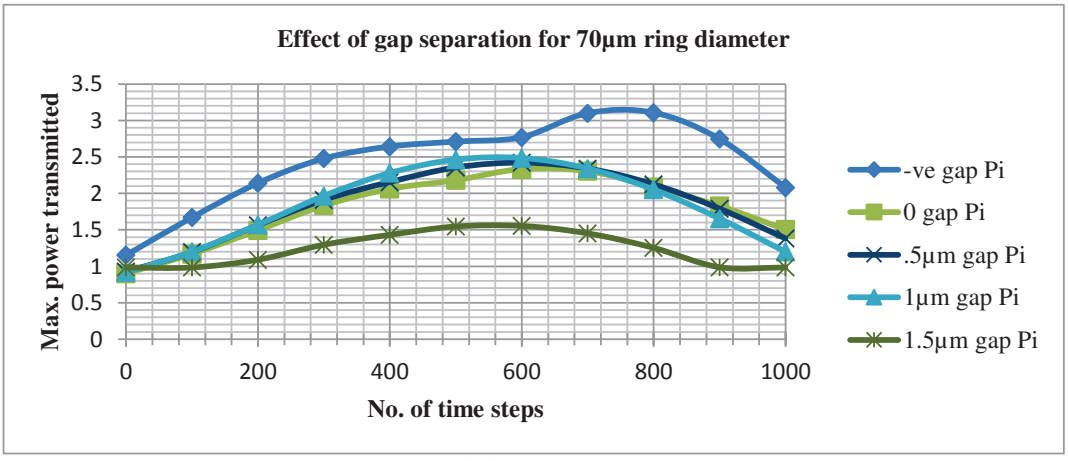

Fig. 9 Graph showing input power(Pi) at port 1

Figure 10 shows the power dropped in secondary waveguide. From the graph it is clear that, as the separation distance goes on increasing the coupling efficiency goes on decreasing so is the power drop in secondary waveguide. Maximum coupling is obtained for 0µm gap, with the average power dropped is 97% for multiple round trips of the wave. The average power obtained for 0.5µm is 43%. The minimum power dropped is for negative gap separation.

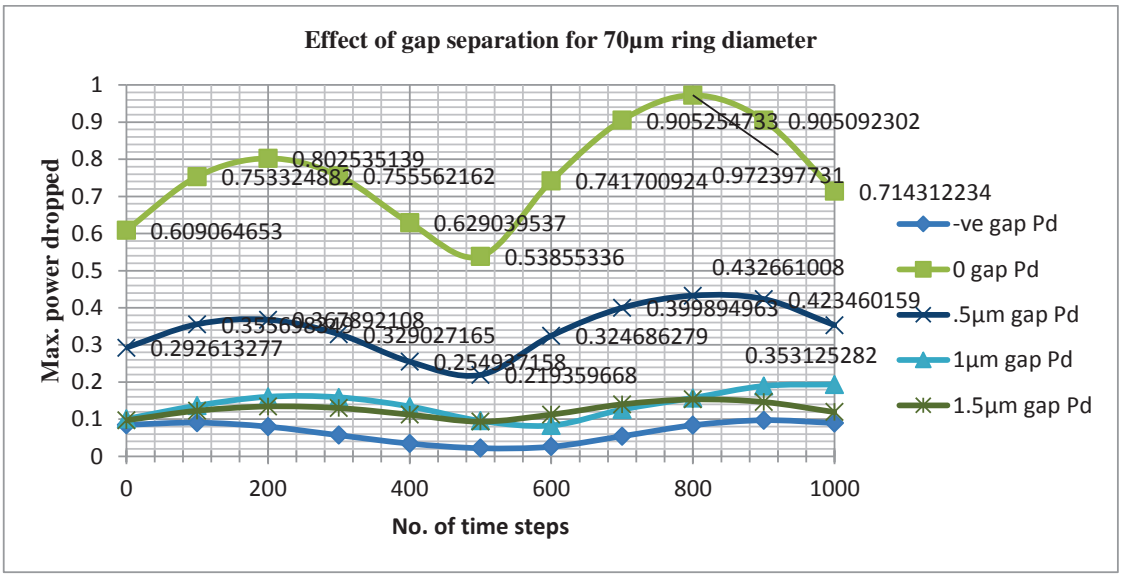

Fig. 10 Graph showing dropped power(Pd) at port 2 for 70µm diameter cavity

3.3 Circular cavity with 60µm diameter

Table II gives the observations obtained for transmitted power Pi at the input port and the dropped power Pd at the drop port for circular ring with 60μm outer diameter.

TABLE II SUMMARY OF INPUT/DROPPED POWER FOR 60µM DIAMETER CAVITY

-ve gap		0 gap		.5µm		1µm		1.5µm	
Pin	Pd	Pin	Pd	Pin	Pd	Pin	Pd	Pin	Pd
1.607702	0.039295	0.587569	0.560303	0.873278	0.207535	0.635404	0.275827	0.885543	0.091629
2.233689	0.037393	0.849515	0.611957	1.249419	0.254099	0.922482	0.292062	1.263463	0.108769
2.680261	0.030478	1.195747	0.592827	1.631932	0.268546	1.283828	0.27381	1.61183	0.111391
2.873353	0.019054	1.495064	0.523857	1.940049	0.249166	1.612585	0.229481	1.910977	0.099468
2.817007	0.008528	1.773982	0.564364	2.144313	0.204462	1.926811	0.30357	2.125525	0.07761
2.590139	0.00389	1.974206	0.695528	2.230937	0.268108	2.125997	0.387431	2.202321	0.113235
2.830395	0.010376	2.033141	0.753479	2.217851	0.327063	2.172897	0.453167	2.157528	0.166744
2.837466	0.022951	1.991832	0.72227	2.037142	0.414523	2.131508	0.487049	1.983496	0.217215
3.013771	0.035106	1.815414	0.643508	1.710129	0.457801	1.949882	0.453542	1.745067	0.241443
2.834554	0.043333	1.516969	0.502984	1.390438	0.436258	1.703459	0.361166	1.422736	0.229481
2.290556	0.042437	1.384015	0.322067	1.119993	0.353659	1.511426	0.235637	1.05448	0.184845

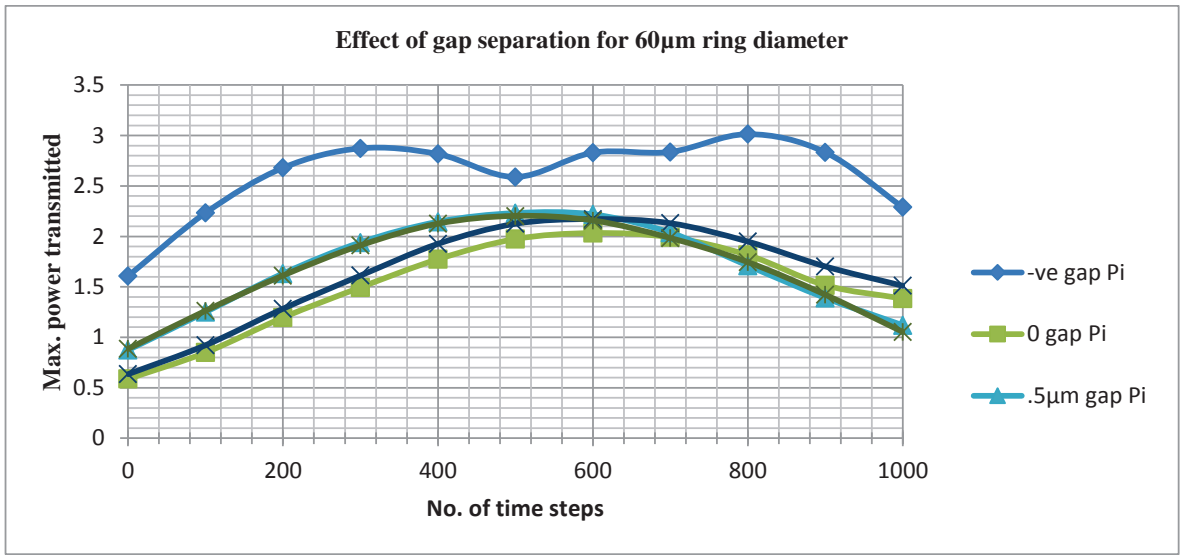

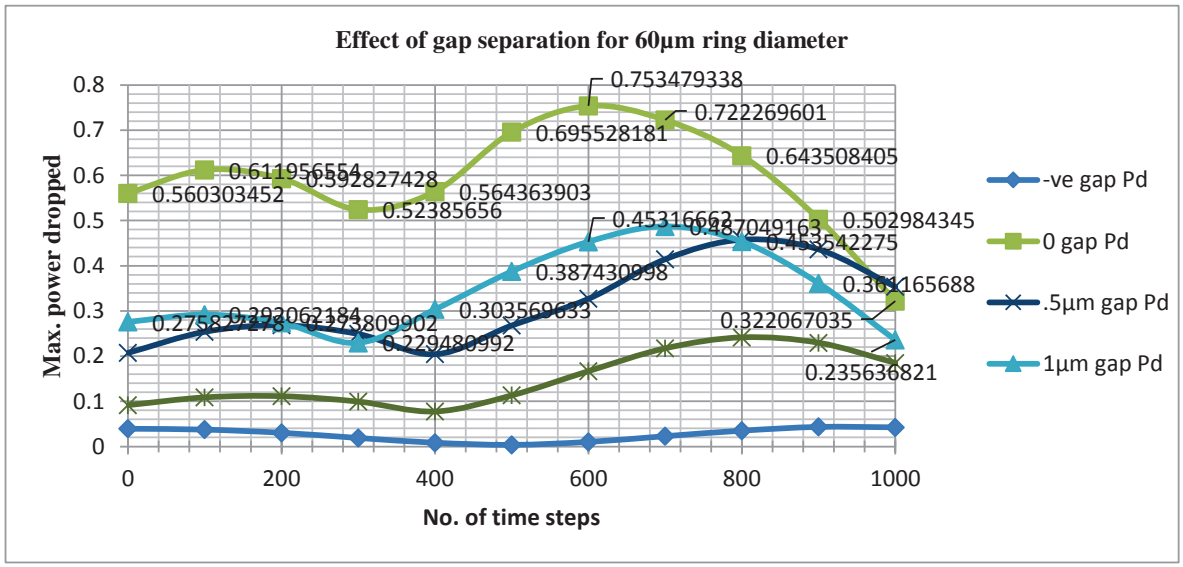

4. References

[1] K. S. Yee, "Numerical solution of initial boundary value problems involving Maxwell's equations in isotropic media ", IEEE Trans. Antennas and Propagation, vol. AP-14, pp. 302307, May 1966.

[2] Roey, J. V., Donk, J. V., Lagasse, P. E., "Beam Propagation Method: Analysis and assessment", Journal of Optics Society of America, 71,803-810,1981

[3] B.M.A. Rahman, J.B. Davies, "Finite-Element Analysis of Optical and Microwave Waveguide Problems", IEEE Transactions on Microwave Theory and Techniques, Volume: 32, Issue: 1,20-28, Jan. 1984.

[4] Chung, Y. Dagli, N., "Explicit Finite Difference Beam Propagation Method: Application to Semiconductor Rib Waveguide Y-Junction Analysis", Elect Letters., 26, 711-713, 1990.

[5] Chung, Y. Dagli, N., "Analysis of Z-Invariant and Z-Variant Semiconductor Rib Waveguides by Explicit Finite Difference Beam Propagation Method with Non-uniform Mesh Configuration", IEEE J. Quant. Elect.,27,2296-2305, 1991.

[6] R. J. Hawkins, R. McLeod, "Finite-difference time-domain simulations of linear integrated photonic devices", Antennas and Propagation Society International Symposium, AP-S. Digest, IEEE,June, 1992 .

[7] S.T. Chu , S.K. Chaudhuri , W.P. Huang, "Analysis of optical guided wave devices with the finite-difference time-domain method", Antennas

and Propagation Society International Symposium, AP-S. Digest.,IEEE,18-25 June, 1992.
[8] Haung, W. P., Xu, C. L., Chaudhari, S. K., "Application of the Finite-Difference Vector Beam Propagation Method to Directional Coupler Devices", IEEE J. Quant.Elect. ,28,1527-1532, 1992.
[9] C. L Xu and W.P. Huang, "Finite Difference Beam Propagation Method for guided wave optics", Progress in Electromagnetics Research, PIER 11,1-45, 1995.
[10] Pierre Berini, "Modeling high-speed optoelectronic components using the method of lines", Symposium on Antenna Technology and Applied Electromagnetics, ANTEM vol1 1998.
[11] J. Peng and C. A. Balanis, "A generalized reflection-free domain truncation method: transparent absorbing boundary" ,in IEEE Transactions on Antennas and Propagation, vol. 46, no. 7, pp. 1015-1022, Jul 1998.
[12] Scarmozzino R., Gopinath A.,Pregla R. Helfert S., "Numerical Techniques for Modeling Guided-Wave Photonic Devices ,IEEE J. Quantum Elect., Vol. 6, No.1, pp.150-162, 2000.
[13] Thang Q. Tran , Sangin Kim., "Stability Condition of Finite-Element Beam Propagation Methods in Lossy Waveguides",IEEE Journal of Quantum Electronics Volume: 50, Issue: 10,808 - 814, Oct. 2014.
[14] Gurinder Singh, R. S. Kshetrimayum and Thingbaijam Rajkumari Chanu, "A comparative study on Explicit and Implicit FDTD methods for Electromagnetic simulation", Asia Pacific Microw. Conf. (APMC),New Delhi, India, Dec. 2016.
[15] A. Taflove and S. C. Hagness, "Computational Electrodynamics: TheFinite-Difference

Numerical analysis of interferometric interrogation technique for π-Phase-Shifted Fiber Bragg Grating sensor

Deepa Srivastava[1,2,#], Sudipta Sarkar Pal[1], Divya Dhawan[3] and Bhargab Das[1]

[1]Micro and Nano Optics Centre, CSIR-Central Scientific Instruments Organization, Chandigarh, 160030, India

[2]Academy of Scientific and Innovative Research (AcSIR), Ghaziabad 201002, India

[3]Electronics and Communication Department, Punjab Engineering College (Deemed to be University), Chandigarh, 160012, India

[#]deepa@csio.res.in

Abstract: A theoretical analysis for sensitivity and dynamic region of interferometric interrogation technique based on π-FBG sensor with Bragg wavelength shift measurement is presented. In order to achieve the least amount of Bragg wavelength measurement uncertainty, analytical formulae for the optimal physical path length difference (PPLD) were found to be useful. The analysis findings can be used to improve the fiber interferometer's sensitivity, visibility, and other characteristics, even though our computational model used a π-FBG as a temperature/strain sensor. The sensitivity and dynamic range of the interference pattern were studied, and the interferometer's response was analyzed for a series of PPLDs.

Keywords: Interferometric interrogation, Fiber Bragg grating, Phase shifted fiber Bragg grating

1. Introduction

There has been a lot of study done on measuring the Bragg wavelength shift or interrogation technique for fiber grating-based sensors, and numerous techniques have been established over past [1]. The use of an unbalanced fiber interferometer in combination with an interrogation approach for grating sensors based on the interferometric principle has proven to be useful in obtaining absolute measurements with a wide dynamic range and high sensitivity. Unresponsive to optical power fluctuations and appropriateness for sensor multiplexing are other significant characteristics that make these systems viable for a wide range of applications. When compared to the previous edge filter-based interrogation methods, the price for these benefits is relatively precise fabrication. Interferometric based demodulation technique allows determining the measurand value through interferometric pattern analysis in spectral domain [2]. Through simulation and experimental study, we have also subsequently demonstrated a number of relevant approaches for interferometric interrogation of fiber grating sensors [3,4]. We suggested and experimentally proved a novel idea for validating a unique class of grating sensor known as π-phase shifted FBG (π-FBG). A π-FBG is formed of a phase jump in the grating structure's middle. Two identical gratings separated apart by half the grating pitch (ʌ) are the outcome of the intermediate phase shift region. The transmission/reflected spectrum of the grating exhibits a narrow spectral peak or dip at the center due to this phase gap and it is distinguished by a transmission peak with a very small linewidth in the middle. This transmission peak's FWHM (full width at half maximum) bandwidth measurement is around 10 pm. The narrow transmission peak is the only factor that matters in the case of π-FBG sensors.

A fiber-based Mach-Zehnder interferometer (F-MZI) can measure the wavelength alteration of the narrow transmission peak under the impact of external perturbation. The output intensity of an MZI can be expressed as:

$$I(\lambda_B) = A[1 + k\cos\Delta\phi(t)] \qquad (1)$$

where, A is proportional to the intensity of an envelope which is defined by the transmission central narrow peak of π-FBG and k is the interference fringe visibility. The fringe visibility can be expressed as [5]:

$$k = \operatorname{sinc}\left(\frac{\Delta\lambda * OPD}{\lambda_0^2}\right) \qquad (2)$$

Where, $OPD\ (Optical\ path\ difference) = n_{eff} * d$; n_{eff} is the effective refractive index of the optical fiber core and d is the PPLD (physical length difference between the arms of the MZI). Δλ is the FWHM of an envelope and λ_0 is the Bragg wavelength.

The optical path difference is a key parameter for this interferometric-based interrogation technique. The sensitivity of the interrogation approach is determined by this OPD. The coherence length requirements for obtaining a stable interference phenomenon at the interferometer's output determine the upper limit of OPD. The dynamic range and sensitivity characteristics of the sensing technique are likewise controlled by this OPD. Since the interferometric interrogation method using π-FBG sensors has sensitivity and dynamic range requirements, it is crucial to select an optimized OPD value. We have developed a computational model to investigate the feasibility of the interferometric interrogation concept in an effort to rationalize this.

2. Results and Discussion

Fig. 1(a) shows the intensity variation at the output of the interferometer for different PPLDs of the F-MZI considering the Lorentzian distribution as the input light from the π-FBG sensor. The values of 20 mm, 40mm, 60 mm and 80 mm are PPLD. The OPD can be obtained after multiplication with the effective refractive index of 1.45. In our analysis, the unperturbed Bragg wavelength of π-FBG is 1550 nm with FWHM 10 pm and the corresponding coherence length is 165 mm. Hence the OPDs of 29 mm, 58 mm, 87 mm and 116 mm are all within coherence length. The model also simulates the intensity variation at the output of the interferometer by assuming the π-FBG sensor to be under the influence of temperature modulation. With increase in PPLD the visibility and free spectral range of the interference signal shown in Fig. 1(b) goes down and becomes zero at the coherence length and beyond. Furthermore, the sensitivity increases with increase in PPLD of the F-MZI which is defined as the slope of the dynamic range (the range between the maxima and minima of the interference pattern). On the basis of this study, we can formulate two analytical equations for sensitivity and dynamic range.

$$Sensitivity \propto PPLD \quad (3)$$

$$Dynamic\ Range \propto PPLD^{-1} \quad (4)$$

These findings, which are described in Fig. 1(c), are comparable with the existing interreference theories. These results show the effectiveness of our computational model, which is further used to develop and optimize the interferometric based interrogation technique for various applications involving the π-FBG sensor. In the actual presentation, comprehensive results will be presented.

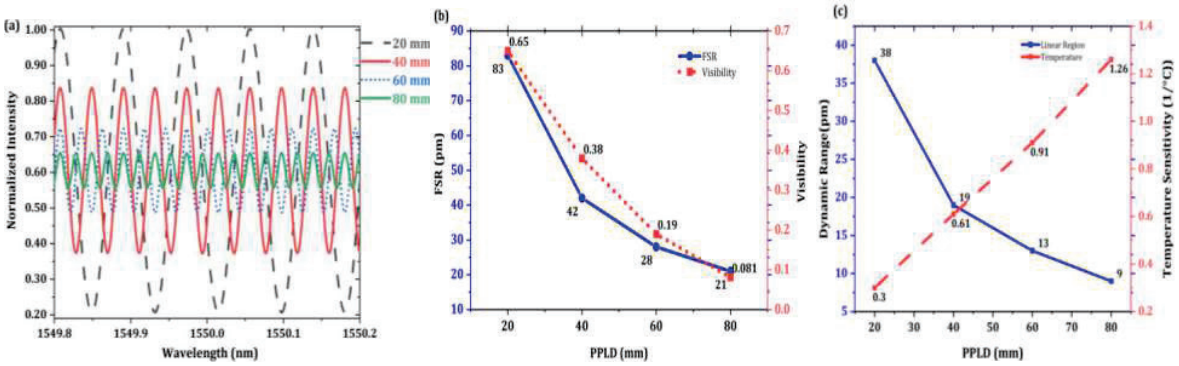

Fig. 1 (a) F-MZI output intensity with respect to π-FBG sensor Bragg wavelength modulation, (b) Free-spectral range and visibility response for different PPLDs, (c) Temperature sensitivity and dynamic range response for different PPLDs.

3. Acknowledgement

Deepa Srivastava and Bhargab Das would also like thank Director, CSIR-CSIO for an in-house project for the interferometric interrogation technique for phase-shifted fiber Bragg grating sensors.

4. References

[1] S. Yin, P. B. Ruffin, and F. T. S. Yu, Fiber Optic Sensors, (CRC Press 2008).
[2] A. D. Kersey, M. A. Davis, H. J. Patrick, M. LeBlanc, K. P. Koo, C. G. Askins, M. A. Putnam, and E. J. Friebele, "Journal of Lightwave Technology," 15, 1442-63 (1997).
[3] B. Das, D. Srivastava, U. Tiwari and B.C. Choudhary, "OSA Continuum," 1, 1172-84 (2018).
[4] D. Srivastava and B. Das, "Sensors & Actuators A: Physical," 315, 1-14 (2020).
[5] Michael Bass, Handbook of Optics: Fundamentals, Techniques, and Design, (The McGraw-Hill Companies Inc. 1995).

Eu^{3+}/Yb^{3+} Doped $NaYF_4$ Upconversion Phosphor For Latent Fingerprint Detection

Kumar Shwetabh[1a)], Neeraj K. Mishra[1], K. Kumar[1]

[1]*Optical Materials and Bio-imaging Research Laboratory, Department of Physics, Indian Institute of Technology (Indian School of Mines), Dhanbad-826004 India*

[a)] *Corresponding author E-mail: kmrshw14@gmail.com*

Abstract: This work presents a synthesis and upconversion study of $NaYF_4:Eu^{3+}/Yb^{3+}$ phosphor. The upconversion phosphor has been synthesized via a thermal decomposition reaction route. The information about crystallinity and phase purity has been obtained by X-ray diffraction experiment. The upconversion fluorescence spectroscopy experiment is performed with a laser having a wavelength of 980 nm coupled with an optical fiber and CCD. The synthesized phosphor shows strong emissions in the region from blue to red due to various transitions of Eu^{3+} ions. Moreover, CIE coordinate calculation and the application of the synthesized phosphor for fingerprint detection have been demonstrated.

Keywords: Upconversion, Thermal decomposition, CIE coordinate, Fingerprint detection.

1. Introduction

A non-linear optical phenomenon that uses low-energy photons to generate higher ones called upconversion (UC) gained significant interest in the past few decades due to its immense applicability across various fields for example lightening, security, biological labeling, medical imaging, and therapy[1,2]. This process generally uses a chemically stable, low phonon, and high refractive index inorganic crystal lattice as a host and some lanthanide ions for doping. Due to the doping of lanthanide ions, the doped crystals utilize the multiple intermediate energy levels of doped ions to produce anti-stoke-type emissions. These ions accumulate low excitation energies to promote ions to higher levels and then radiative de-excitation leads to UC emission. Commonly used some host materials are based on fluoride, oxide, molybdate, and phosphate among which fluorides are most efficient due to very low phonon energy. The benefit of using fluoride-based host materials includes the efficient suppression of nonradiative energy transfer processes and enhanced emission processes. Till now, $NaYF_4$ is proved to be the most efficient host while doped with Er^{3+} or Tm^{3+} ion codoped with Yb^{3+}. Here Yb^{3+} acts as a sensitizer ion while Er^{3+} or Tm^{3+} ions act as activator ions. This notation as a sensitizer and activator creates distinctions between two different ion species in which the former species absorbs incident light while later showing emission. Sensitizers are commonly used to increase the absorption in desired spectral range and hence increase the upconversion emission intensity.

Here we synthesized the $NaYF_4:Eu^{3+}/Yb^{3+}$ phosphor and explored its upconversion ability. Although various rare earth ion-doped $NaYF_4$ phosphors have been investigated in recent years and found to be efficient for upconversion the Eu^{3+} ion is still very less explored. Some recent studies suggest its potential candidature for upconversion-based applications[3,4]. Due to this possibility, we selected the Eu^{3+} ion for doping along with the Yb^{3+} ion in the $NaYF_4$ host, and the upconversion along with structural and optical properties has been investigated.

2. Experimental

2.1 Material synthesis

In this synthesis, the required amount of rare earth oxides was 0.80 mmol of Y_2O_3, 0.15 mmol of Yb_2O_3, and 0.05 mmol of Eu_2O_3 was dissolved in diluted acetic acid to prepare rare earth acetate as a precursor. The as-synthesized precursor was incorporated into a mixture of 8 ml oleic acid and 10 ml of octadecane in a 100 ml three-neck round bottom flask. After stirring at 150 ^{0}C for 30 minutes the transparent solution was cooled down to room temperature. At this stage, the methanol solution of 2.1 mmol NaOH and 4 mmol of NH_4F was poured into this transparent solution. After the addition of NaOH and NH_4F, the temperature of the solution was increased to 100^{0}C and kept for 20 minutes to remove the methanol from the solution. After that, the temperature is increased to 310 ^{0}C and maintained at this temperature for 50 minutes with constant nitrogen flow. After 50 minutes the solution was cooled down to room temperature and then excess ethanol was added to get the precipitate. The obtained precipitate was centrifuged and washed several times with ethanol and hexane (3:2) solution. Overnight drying at 60^{0}C yields the upconversion phosphor in form of white powder.

2.2 Characterizations

X-ray diffraction spectroscopy was performed to analyze the phase formed by the synthesized phosphor. Up-conversion spectroscopy was performed to study the various electronic transition phenomenon which leads to up-conversion emission.

3. Results and discussion

3.1 X-ray diffraction spectroscopy

X-ray diffraction spectroscopy was performed to reveal the phase information and crystalline nature of the synthesized Phosphor. The as-synthesized phosphor consists of a pure hexagonal phase with a crystallite size of ca. 39 nm. XRD spectra with reference are shown in fig. 1.

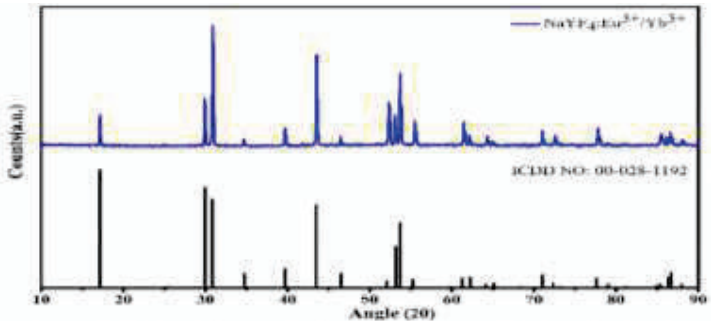

Fig 1: XRD spectra of synthesized $NaYF_4:Eu^{3+}/Yb^{3+}$ phosphor with reference pattern

3.2 Up-conversion emission spectroscopy

The up-conversion emission spectrum of the as-synthesized phosphor sample has been recorded using a 980 nm laser diode. The up-converted spectrum shows various emission peaks ranging from blue (400 nm) to red (700 nm) due to the transition of Eu^{3+} ions. Based on various emission wavelengths a possible energy level diagram is plotted and shown below in fig. 2.

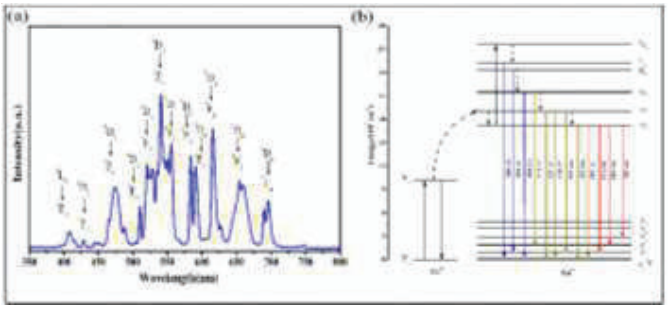

Fig. 2: (a) UC spectra and (b) a possible energy level diagram for synthesized $NaYF_4:Eu^{3+}/Yb^{3+}$ phosphor

4. Applications

The synthesized phosphor has the capability of producing white light and this can effectively be used for latent fingerprint detection. Below is fig. 3, the CIE coordinate diagram, and a demonstration for latent fingerprint detection has been shown. CIE diagram shows the coordinate (X,Y) as (0.34,0.38).

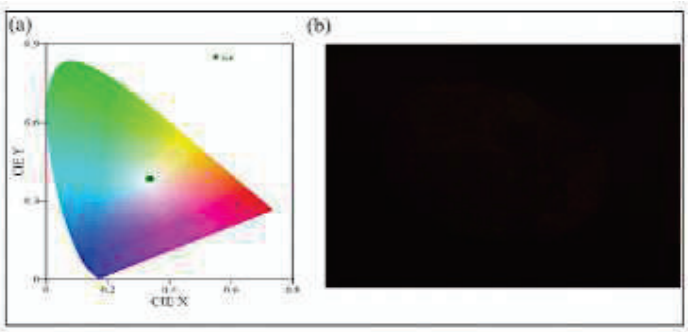

Fig. 3: (a) CIE coordinate diagram and (b) latent fingerprint detection by synthesized $NaYF_4:Eu^{3+}/Yb^{3+}$ phosphor

5. Conclusion

In summary, Eu^{3+}/Yb^{3+} ion doped $NaYF_4$ phosphor has been synthesized by thermal decomposition reaction method using oleic acid and 1-octadecane as reaction medium. The as-synthesized phosphor was characterized using an XRD experiment which revealed a hexagonal phase. UC emission study has been performed using a 980 nm diode laser and the spectrum shows various emission peaks by the phosphor. The energy level diagram and CIE diagram have been plotted to calculate its CIE coordinates resulting in the white light region. Furthermore, latent fingerprint detection has been made using the synthesized phosphor.

6. References

[1]. J. Chen and J. X. Zhao, "Upconversion Nanomaterials: Synthesis, Mechanism, and Applications in Sensing," Sensors 12, 2414 (2012).
[2]. Y. Yang," Upconversion nanophosphors for use in bioimaging, therapy, drug delivery and bioassays," Microchim Acta 181, 263 (2014).
[3]. H. Wang, C. Duan, and P. A. Tanner," Visible Upconversion Luminescence from Y2O3:Eu3+,Yb3+,"J. Phys. Chem. C 112, 16651 (2008).
[4]. T. K. Pathak, A. Kumar, L. J. B. Erasmus, A. Pandey, E. Coetsee, H. C. Swart, and R. E. Kroon, "Highly efficient infrared to visible up-conversion emission tuning from red to white in Eu/Yb co-doped NaYF4 phosphor," Spectrochimica Acta Part A: Molecular and Biomolecular Spectroscopy 207, 23 (2019).

Malaria stage classification using deep learning and spatial coherence microscopy

Gyanendra Singh*, Sarthak Jhalani, Vishal Srivastava
Department of Electrical and Instrumentation Engineering
Thapar Institute of Engineering and Technology, Patiala 147004, Punjab, India
**Corresponding Author: gyanendra.singh@thapar.edu*

Abstract: Early detection of the mosquito-borne blood disease malaria is vital to health. With limited label data, automated classifications of malaria phases remain a challenge, especially for early trophozoite and late trophozoite or schizont phases, where sensitivity is low. The study seeks to construct a rapid method for classifying malaria stages with a limited labelled data set by employing a pre-trained convolutional neural network (CNNs). Spatial Coherence microscopy (SCM) is used for recording the data sets. Our network, which has fewer layers than other standard CNNs, has comparable performance. In our opinion, this method is transferable to other, similarly under-annotated biological datasets.

Keywords: Malaria, Deep learning, Convolutional neural network (CNNs), Microscopy

1. Introduction

Malaria is a mosquito-borne disease that affects many [1]. It's a common syndrome that needs early treatment. Malaria can be prevented and cured with early detection. Early and late trophozoites infect malaria-infected RBCs. Early trophozoites have no size change and two or more chromatin dots, while late trophozoites are vacuolated and black. To investigate a promising antimalarial drug's influence on host cell invasion, parasite departure, and schizont formation [2]. Such a paradigm will promote efforts to identify new antimalarial drugs and antibodies targeting Plasmodium falciparum erythrocytic stages. Microscopy is the gold standard for diagnosing malaria due to its low cost and reputation [3]. In recent decades, quantitative phase microscopy has made great progress to overcome traditional phase microscopy's limitations [4]. Several quantitative phase imaging (QPI) approaches are utilized to quantify unstained malaria-infected RBCs [4]. All these biomedical procedures are successful, but they have drawbacks. To capture cell dynamics such as membrane fluctuations, dry mass cell density, etc. Off-axis interferometry or holography is preferable because it provides comprehensive information in a single shot [5]. Coherent noise and parasitic fringes from laser light impair image quality and phase measurement accuracy [5]. Problems like these can be put to rest by using light sources with a high temporal coherence but a low spatial coherence. Light sources with a high temporal coherence but a low spatial coherence produce a high fringe density across the whole camera's FOV and do not need dispersion adjustment. This light is preferable for working with biological samples that exhibit a highly variable or non-uniform spectral response. Absorption, emission, and scattering are all modified by the wavelength. With the use of many wavelengths, information can be gleaned more easily. Since the refractive index varies with wavelength, it has physical and biological implications. [6]. Malaria may be automatically diagnosed from stained blood cell micrographs [6] using machine learning. K-NN, Naive Bayes, ANN, and SVM are just some of the machine learning algorithms that have been used to classify malaria parasite-infected RBCs. However, their accuracy ranges from 84-95%. [7]. In this study, we showed how a customized CNN with a multi-wavelength SCM can automatically identify malaria stages with a restricted dataset.

2. Experimental Set-Up

SCM analyses malaria-infected RBCs. Fig. 1 shows the system's schematic diagram, which contains three lasers (632 nm, 532 nm, and 460 nm), More details for the experimental set-up is given in the reference [5]. Fig. 2 shows the flowchart used to detect healthy vs. infected and early vs. late trophozoite malaria-infected stages.

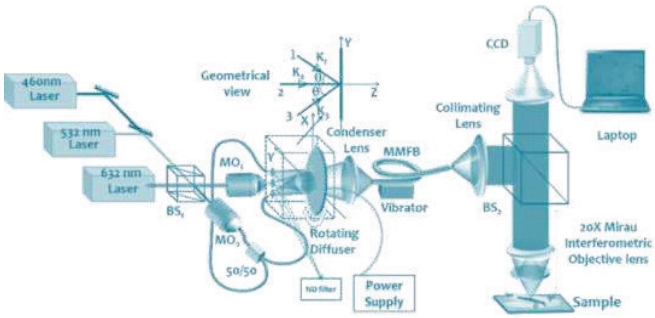

Fig. 1. Schematic diagram of SCM system

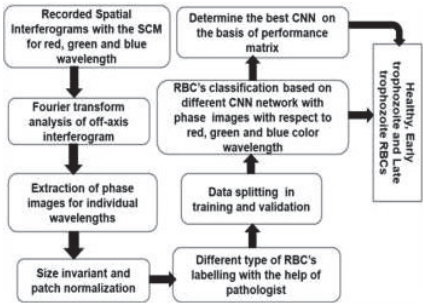

Fig. 2. Overall flowchart of our proposed training methodology for the malaria infected RBCs CNN classification model

3. Result & Discussion

In this study, we used machine learning TL models to distinguish between RBCs infected with early and late trophozoite stages of malaria and healthy RBCs. Malaria-infected red blood cells were interpreted by a seasoned pathologist. CNN's ability to distinguish between uninfected and infectious red blood cells, as well as early and late trophozoite red blood cells, has been the subject of various research. Figure 3 shows images of early and late trophozoites in red, green, and blue phases. There were a total of 29 samples examined: 8 normal, 15 early, and 13 late trophozoites. To train the network, 5 healthy, 10 early trophozoite, and 7 late trophozoite persons were used, and to test the dataset, 1 healthy, 2 early trophozoite, and 2 late trophozoite participants were used. 7 healthy, 13 early trophozoite, and 11 late trophozoite volunteers were used for training and validation. In our experiment, all the transfer learning models and custom model is trained using SGD with a momentum factor of 0.9 and the learning rate for the pre-trained network is 0.0001. All the models were trained for 15 epochs and the minibatch size for all the models is 32. In our experiment, all transfer learning and custom models were trained using SGD at 0.9 momentum and 0.0001 learning rate. All models have 15 epochs and 32 minibatches. The customized network used in paper runs faster than other models due to fewer computational layers. We attained 97% accuracy, 97% sensitivity, and 97% specificity for healthy and malaria-infected RBCs, and 88% accuracy, 90% sensitivity, and 86% specificity for early and late trophozoite stages. Less-layered tailored networks perform as well as deeper ones. In the future, a more precise segmentation algorithm will be utilized to include overlapping RBCs, and the current system will be changed to get the spectrum response of the cells, which will improve sickle cell, diabetic, and cancer cell classification.

The authors are thankful to SERB or providing funding in project no. CRGR/2021/006488

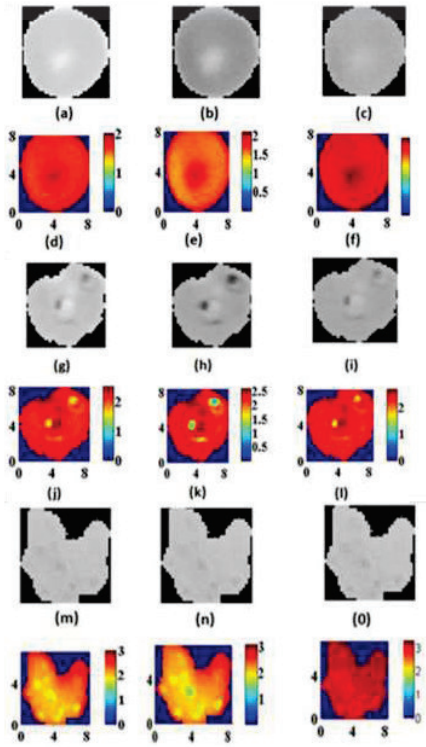

Fig. 3 (a), (b), (c), (g), (h), (i), (m), (n) and (o) are the amplitude images and (d), (e), (f) , (j), (k), (l), (p), (q) and (r) are the phase (radian) images of healthy, early trophozoite and late trophozoite malaria infected RBCs for red, green and blue

4. References

[1] World Health Organization. Accessed: Mar. 20, 2018. [Online] Available: http://www.who.int/malaria/media/world-malaria-report 2015/en/.
[2] S. Moon, S. Lee, H. Kim, L.H. Freitas-Junior, M. Kang, L. Ayong, and M.A. Hansen, "An image analysis algorithm for malaria parasite stage classification and viability quantification," PloS One **8,** e61812 (2013).
[3] C. C. Das, D. K. Das and R. Mukherjee, "Computational microscopic imaging for malaria parasite detection: a systematic review," J. Microsc. **260,** 1–19 (2015).
[4] G. Popescu, Y. Park, W. Choi, R.R. Dasari, M.S. Feld, and K. Badizadegan, "Imaging red blood cell dynamics by quantitative phase microscopy," Blood Cells, Molecules, and Diseases **41,** 10-16 (2008)
[5] A. Ahmad, V. Dubey, V. Singh, A. Butola, T. Joshi, and D.S. Mehta, "Reduction of spatial phase noise in the laser based digital holographic microscopy for the quantitative phase measurement of biological cells." Vol. **10414** of SPIE Proceedings (Optica Publishing Group, 2017).
[6] D. Bibin, M. S. Nair and P. Punitha, "Malaria Parasite Detection from Peripheral Blood Smear Images Using Deep Belief Networks," in IEEE Access **5,** 9099-9108 (2017).
[7] T. Go, J. H. Kim, H. Byeon, and S. J. Lee, "Machine learning-based in-line holographic sensing of unstained malaria-infected red blood cells," J. Biophotonics, **11,** 1–9 (2018).

Detailed Investigation of MSM Fiber Structure for Various Sensing Applications

Koustav Dey and Sourabh Roy
Department of Physics, National Institute of Technology, Warangal, TS 506 004, INDIA
physicskoustav@gmail.com , sroy@nitw.ac.in

Abstract: A detailed investigation of multi-single-multi (MSM) fiber structure for various sensing applications under varying sensing lengths of MSM has been propounded and investigated. Exceptionally high sensitivity is achieved for temperature, strain and refractive index with higher dynamic range and resolution.
Keywords: MSM fiber structure, temperature, strain, refractive index.

1. Introduction

In the last couple of decades, the sensing mechanism by employing optical fibers has become a new research hotspot owing to their higher sensitivity, high accuracy, simple fabrication, reliable measurement, low cost, ease of packaging etc. [1] Sensing arrangements like fiber Bragg grating (FBG), long-period grating (LPG), Fabry-Perot interferometers (FPI), in-fiber interferometers are the most popular and fascinating methods for monitoring the aforementioned temperature, strain and refractive index (RI) [2-4]. However, the fabrication process of FBG includes different expensive types of equipment. Wide spectral responses of LPG dips confer diverse restrictions on demodulation and multiplexing. FPI based methods offer few advantages but are restricted due to the implementation of costly components. Furthermore, controlling the precise cavity length is also quite tricky. Although in-fiber Mach-Zehnder interferometers (MZI) based sensors offer higher sensitivity, it is limited due to the employment of costly fiber such as Panda fiber and precise fabrication techniques. Higher intrinsic sensitivity is of paramount importance and an important parameter for any kind of sensing structure. Different fiber segment combinations which can simply be designed by the fusion splicing method have entrancing spectral behavior due to mode coupling between the different fiber segments. To overcome the aforementioned issues, two popular and fascinating fiber combinations, Single - multi-single-mode (SMS) fiber and multimode-singlemode-multimode (MSM) are introduced. Due to the compactness of the free spectral range (FSR) along with the higher homogeneous property, the MSM structure provides greater advantages over SMS. Although extensive scopes are there to study in detail, a small number of pieces of literature are available where MSM is employed as a sensing structure to upsurge the sensitivity [5].

In this study, first time to the best of our knowledge we propose a detailed investigation of the influence of the SMF length on different sensitivities along with characteristics of the transmission spectrum. A theoretical model has also been established for these purposes. In the meanwhile, different characteristic studies of the MSM are also reported. The MSM fiber structure exhibits the highest sensitivity of 133.25 pm/°C, - 3.41 pm/ με and - 52.10 nm/RIU for temperature, strain and refractive index, respectively for the 12 cm length of the SMF. In addition, the proposed sensor shows a higher resolution capability over a dynamic range.

2. Principle of sensor and effect of sensing fiber length

2.1 Principle of sensor

The MSM structure relies on the principle of the modal interference that occurs in the SMF section among the modes of the core and cladding. Owing to the large core diameter, MMF has the capabilities of exciting a large number of cladding modes into the SMF for the mismatching in the mode field. The effect of the field distribution could be manifested as the superposition of several modes in the sensing region and expressed as

$$\xi_S(r) = \sum_{M=1}^{M} \alpha_m \varphi_m(r) \exp\,(i\beta_m L) \quad (1)$$

where, φ_m signifies the field distribution of the eigenmodes supported in the core of the multi-mode fiber. L is the length of the fiber where the electric field can be comprised. β_m is the propagation constant of each eigenmode in the SMF section. Under external perturbation such as temperature, strain and refractive index, the effective refractive of core and cladding, length of the sensing region i.e., SMF may change which in turn change the eigenmodes of the SMF core i.e., $\varphi_m(r)$. As a result, there will be a change in the coupling coefficient i.e., α_m. Hence, we can conclude that, upon change of the SMF length, there will be a change in the coupling coefficient between the LP_{01} and LP_{0m} which causes the change in the transmission spectrum of the MSM.

2.2 Effect of sensing fiber length

If L is the SMF length, Δn_{eff} is the effective RI difference between the core and the cladding mode, then the m[th] order resonant dip of the transmission spectrum can be denoted under the phase-matching condition $\varphi = (2m + 1)\pi$, where m=0,1, 2... as

$$\frac{2\pi\Delta n_{eff}L}{\lambda} + \varphi_0 = (2m+1).\ \pi \quad (2)$$

If the external perturbation ($P_{ext.}(T, \varepsilon, n)$) in terms of temperature, strain and RI on the designed sensor probe is applied, then the shift of the resonance dip with the external perturbation could be written as

$$\frac{\partial\lambda_m}{\partial P_{ext.}} = \frac{2}{2m+1}\left[\left\{\Delta n_{eff}.\frac{\partial L}{\partial T} + L.\frac{\partial\Delta n_{eff}}{\partial T}\right\} + \left\{\Delta n_{eff}.\frac{\partial L}{\partial \varepsilon} + L.\frac{\partial\Delta n_{eff}}{\partial \varepsilon}\right\} + \left\{\Delta n_{eff}.\frac{\partial L}{\partial n} + L.\frac{\partial\Delta n_{eff}}{\partial n}\right\}\right] \quad (3)$$

The term $\Delta n_{eff}.\frac{\partial L}{\partial T}$ and $L.\frac{\partial\Delta n_{eff}}{\partial T}$ contribute to the thermal expansion coefficient and thermos-optic coefficient, respectively. The above theoretical analysis provides a clear visualisation of the wavelength of the dip shifts with the external perturbation. Furthermore, the temperature, strain and refractive index sensitivity are relevant to the length of the SMF section.

3. Results and Discussions

The proposed schematic diagram for the different sensing purposes has been depicted in Fig. 1. It comprises a super luminescence diode source (SLD, S5FC1005S, Thorlabs), the MSM segment and the Optical Spectrum analyser (OSA, Agilent 86142B). Figure 1 (b) exhibits the temperature while Fig. 1 (c) and (d) exhibits strain and refractive index characterization.

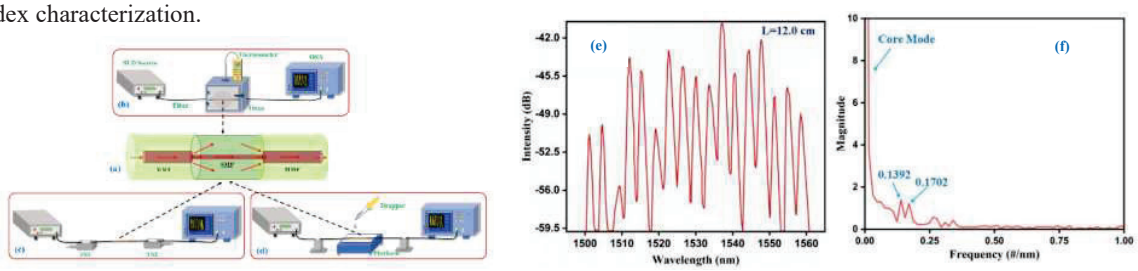

Fig. 1. Schematic of (a) the MSM structure and for (b), (c) and (d) temperature, strain and RI characterization; (e) transmission spectrum and (f)FFT of the spectrum for 12 cm length of SM fiber

Optimizing the SMF length is one of the best choices to strengthen the sensitivity of the sensor further compared to the other reported techniques. Here, for the first time, a comprehensive analysis of the impact of the SMF length on the sensitivity is analyzed thoroughly.

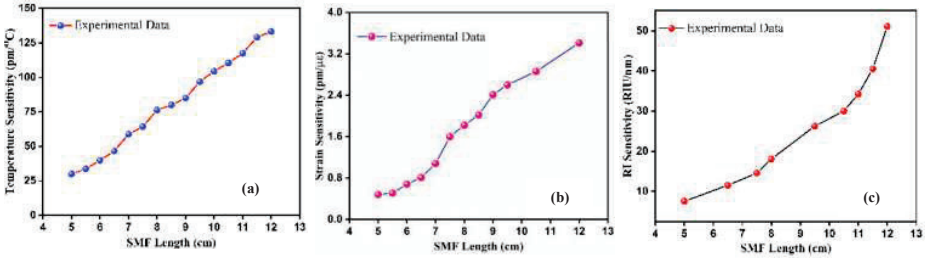

Fig. 2. Impact of SMF length on (a) temperature, (b) strain and (c) RI sensitivity

From Fig. 2 it can be depicted that as the SMF length increases, the sensitivities also increase continuously which exactly matches with our theoretical analysis and the highest sensitivities of 133.25 pm/°C, - 3.41 pm/ με and - 52.10 nm/RIU could be observed at the 12 cm length of the SMF. The employed OSA has an intrinsic wavelength resolution of 0.01 nm. Hence the designed sensor has the resolution of 0.075 °C, 2.93 με and 0.19 RIU over the range of 20-100 °C, 0-3000 με and 1.33-1.43 for temperature, strain and refractive index, respectively. These higher resolutions affirm the potential employment of the senor.

3. References

[1] Q. Zhao *et al., "Shipborne expendable all-optical fiber ocean temperature-depth profile sensor*," Appl. Opt. **61**, 2089-2095 (2022)

[2] K. Dey, V.D.R. Pavan, R. Buddu, S. Roy, "*Axial force analysis using half-etched FBG sensor*", Optical Fiber Technology, **64**, 102548, (2021).

[3] H. Zeng and T. Geng, et al., "*Combining two types of gratings for simultaneous strain and temperature measurement*", IEEE Photon. Tech. L **28**, 477–480, (2016).

[4] J. Tian, Y. Jiao, S. Ji, X. Dong, Y. Yao, "*Cascaded-cavity Fabry–Perot interferometer for simultaneous measurement of temperature and strain with cross sensitivity compensation*", Opt. Commun**. 412,** 121–126, (2018).

[5] Y. Ma et al., "*Torsion and Temperature Sensor Based on Polished MSM Structure*," IEEE Photonics Technology Letters, **32**,1117-1120, (2020).

Optical Design of Uncooled Thermal Imager using Wavefront Coding

Vikas Dua*, Manish Uniyal, Ranabir Mandal, P. K. Sharma
Instruments Research & Development Establishment, Dehradun - 248008
vikasdua.irde@gov.in

Abstract: In this paper, the optical design of uncooled thermal Imager using wavefront coding technique is presented. In certain applications there is a need of developing low cost and low weight thermal imagers. These thermal imagers are supposed to operate in a wide temperature range. Since the dn/dt of optical material in the IR range is large, the performance of the IR optical system is strongly dependent on environmental temperatures. The main thermal effect of these systems is the focus shift, so it becomes necessary to maintain invariable focus over a wide temperature range i.e Athermalized design. Many techniques have been reported to achieve the athermalization of IR optical systems, such as the mechanically active, passive and optical passive etc. We have used wavefront coding technique to control thermal defocus. It comprises of a specially designed cubic phase plate placed at the pupil plane of the system. The blurred image formed by the phase plate will then be restored by the help of digital image processing.

The f#1.2 Optics is designed for a 640 x 480 array with 17µm pitch uncooled microbolometer detector having spectral response from 8 to 12µm over a temperature range of -20°C to 50°C.

Keywords: Optical Design, Uncooled Thermal Imager, Wavefront Coding.

1. Introduction

An uncooled thermal camera is one in which the imaging sensor does not require cryogenic cooling and the detector design is based on the microbolometer. The Optics in the wavefront coded system modifies the point spread function in such a way that the image formed by the optics is degraded and appears blurred. However, these blur is constant throughout the depth of image. The Fourier transform of the point spread function produces the optical transfer function. The modulus transfer function of a traditional system changes dramatically with misfocus and temperature change. But the modulus transfer function of the wavefront coded system is almost constant with misfocus and temperature change. Moreover, it contains no regions of zero[Ref 2]. In addition, these systems increase the depth of field (DOF) with the usage of a specially designed phase mask. The digital image processing analyzes the obtained point spread function characteristics and uses complex algorithms to get the final sharp and clear image. This jointly optimized optical and digital system is called a wavefront coding system. The wavefront coded design will be used to athermalize optical system with an optimized cubic phase mask.

2. Optical Design and Layout

The designed optics is for uncooled microbolometer detector having 640 x 480 array with 17µm pixel pitch. The effective focal length is 75 mm, which covers a Field of view of 8° × 6° and the f number is kept 1.2.

In this design after considering pros and cons of many configurations and combination of materials, a system, consisting of 2 lens elements has been designed. To reduce the spherical aberration and to balance the other aberrations one aspheric surface is used. The overall length of the designed optics upto image plane is around 115 mm. Aperture Stop was placed at the first surface of a plate used for reference after first lens. Germanium material was used in the design. Design has been carried out using CodeV® Optical Design software. Optical Layout of the designed system is shown in Fig. 1 respectively.

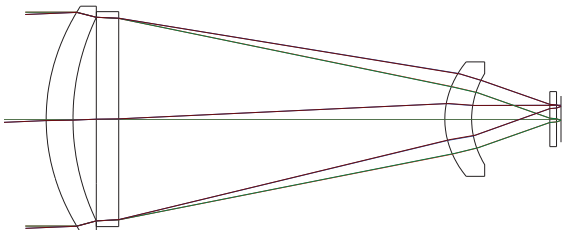

Fig. 1: Optical layout

The system was designed for the operating temperature of 20°C. The figure 2 below shows the MTF plot of the designed system at 20°C:

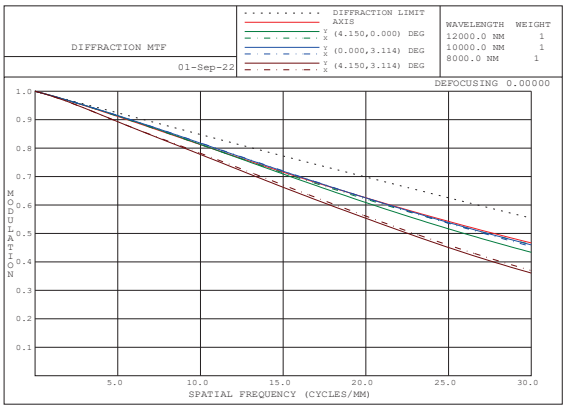

Fig. 2: MTF Plot at 20°C

The performance of the designed system was analyzed at different temperatures. The figure 3 below shows the MTF plots of the designed system at -20°C & 50°C respectively.

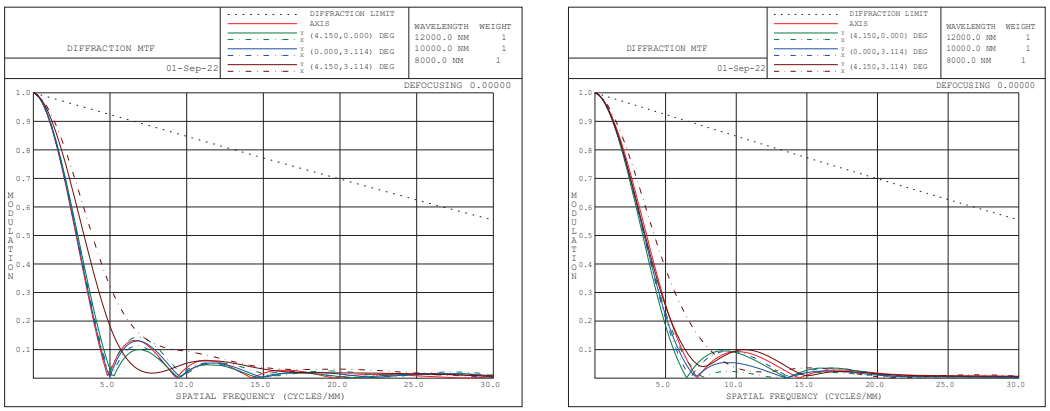

Fig. 3: MTF Plots at -20°C & 50°C

It is evident from the MTF plots shown, the system does not perform same at all temperature values. The performance severely degrades as the system deviates from the designed temperature value.

The wavefront coded design consists of phase plate introduced after 1st lens as shown in Fig.1 i.e placed at the pupil. The phase plate modifies the incoming wavefront in such a way that the PSF is insensitive to misfocus.

But this generated PSF are not similar to that of a traditional imaging system discussed above. The MTF obtained has no regions of zero values within the nyquist frequency.

In our design, we have used a cubic phase mask and is represented by

$$E_i(x, y) = \propto (x^3+y^3).$$

where (x,y) are normalized coordinates of the Aperture Stop. The design is analyzed after every optimization to get a constant MTF and spot diagram across all fields. The resultant PSF is also checked so that the in-focus and out-of-focus PSF have similar blur characteristics. The PSF will then be used for obtaining the sharp and final image through digital image processing.

The figure 4 below shows the PSF & MTF plot of the designed system with cubic phase plate at 20°C:

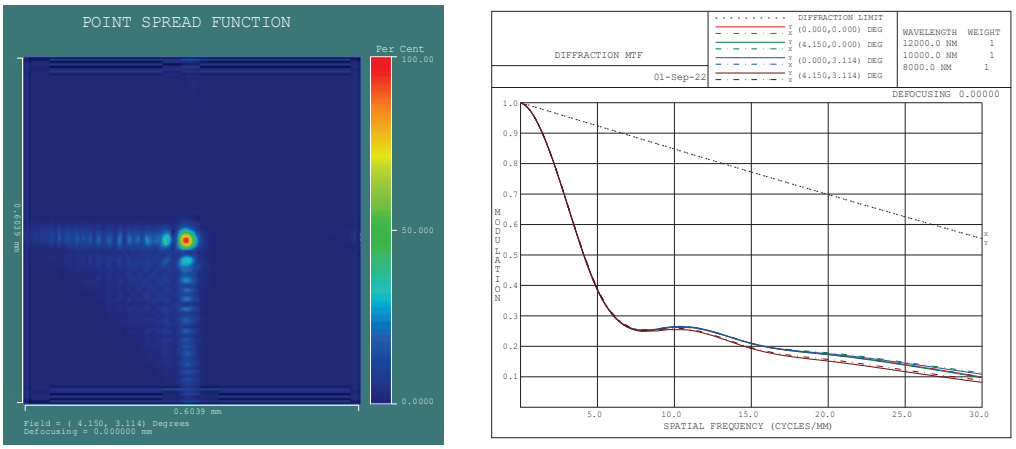

Fig. 4: PSF & MTF Plot of the Designed System with Cubic Phase Plate at 20°C.

The performance of the designed system was again analyzed at different temperatures to see the effect of cubic phase plate. The figure 5 & 6 below shows the PSF & MTF plots of the designed system at -20°C & 50°C respectively.

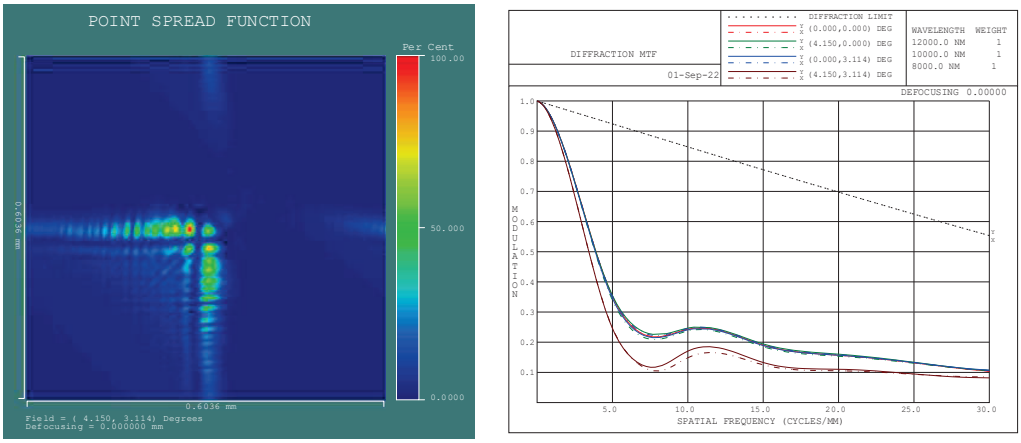

Fig. 5: PSF & MTF Plot of the Designed System with Cubic Phase Plate at -20°C.

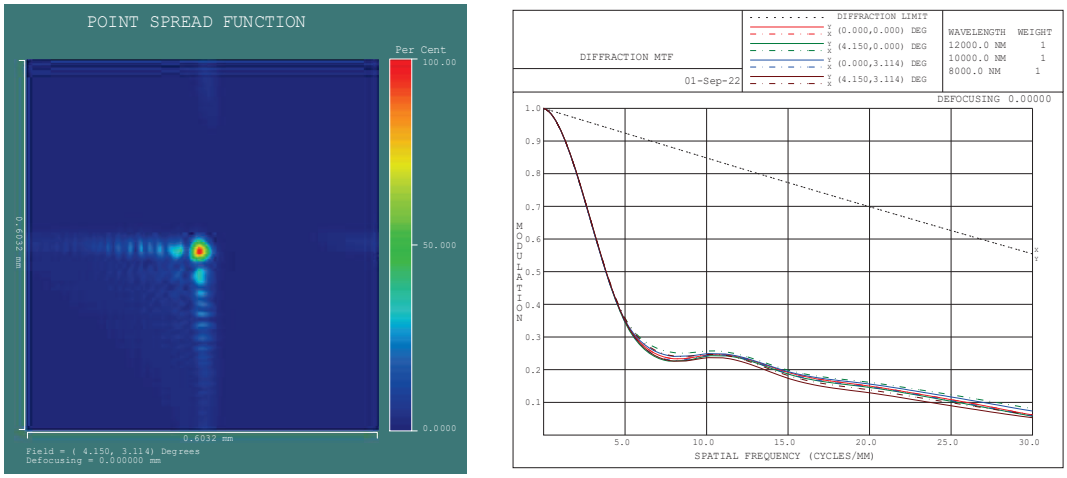

Fig.6: PSF & MTF Plot of the Designed System with Cubic Phase Plate at 50°C.

It is evident from the PSF & MTF plots shown, the designed system with cubic phase plate does almost perform similar at all temperature from -20°C to 50°C. The performance does not degrade as the system deviates from the designed temperature value.

3. Conclusion

In this paper, designs for f#1.2 Optics was discussed for a 640 x 480 array with 17µm pitch uncooled microbolometer detector having spectral response from 8 to 12µm. Design without cubic phase plate showed diffraction limited performance at nominal temperature (20°C) but performance severely degrades as the system deviates from the designed temperature value. Designed system with cubic phase plate does almost perform similar at all temperature from -20°C to 50°C.

The output of this lens i.e raw image will be processed through image processing software whose key will be based on PSF of the lens system. After post processing the image will be similar to the original image like that of a conventional lens system.

4. Acknowledgement

Authors are thankful to Director IRDE for his guidance, inspiration and encouragement.

5. References

1. Edward R Dowski Jr, Gregory E Johnson, "Wavefront Coding: A modern method of achieving high performance and/or low cost imaging systems," Proc. SPIE 3779, 137-145 (1999).
2. Gonzalo Muyo, Andrew R Harvey, "Wavefront coding for athermalization of infrared imaging systems," SPIE 25612-30 (2004).
3. Edward R Dowski Jr, Robert H Cormack, Scott D Sarama, "Wavefront Coding:jointly optimized optical and digital imaging systems," SPIE 4041-10 (2000).

Stimulated Brillouin Scattering of Cosh Gaussian Laser Beams in Axially Inhomogeneous Plasmas: Effect of Self Focusing

[1]Naveen Gupta, [1]Suman Choudhry, [2]S. B. Bhardwaj and [1]Rohit Johari

[1]Lovely Professional University Phagwara

[2]SUS Govt College, Matak-Majri, Indri, Karnal

Naveens222@rediffmail.com

Abstract: Stimulated Brillouin scattering (S.B.S) of intense Cosh-Gaussian (ChG) laser beams interacting with axially nonuniform plasmas has been investigated theoretically. The axial inhomogeneity of the plasma has been modeled by a ramp shaped density profile and the optical nonlinearity of the plasma has been considered to be originating due the ponderomotive force acting on the plasma electrons. An intense laser beam with frequency ω_0 propagating through plasma gets coupled with a preexisting ion acoustic wave (IAW) at frequency ω_{ia} and produces a back scattered wave at frequency $\omega_s = \omega_0 - \omega_{ia}$. Using variational theory semi analytical solution of the set of coupled wave equations for the pump, IAW and scattered wave has been obtained under W.K.B approximation.

1. Introduction

Stimulated scatterings are the processes in which an incident electromagnetic beam interacts nonlinearly with bosonic excitations of a medium and hence gets converted to a frequency up or down shifted scattered wave. The difference in the photon energy between the incident and scattered waves is supplied by of taken up by the nonlinear medium. In case of plasmas the role of bosonic excitations is played by the propagating plasma waves (EPWs) or IAWs. SBS involves the interaction of light with sound waves in solids, liquids, gases or with IAWs in plasmas. The crests of these IAWs act as partially reflecting mirrors for the incident laser beam and thus reflect back a significant amount of laser energy in inertial confinement fusion (ICF) and thereby reducing the efficiency of laser plasma coupling. Thus, in context of ICF it becomes vital to investigate different aspects of the phenomenon of SBS.

2. Mathematical Model

The nonlinear dielectric function of plasma for a ChG laser beam with amplitude structure

$$E_0(r,\, z) = \frac{E_{00}}{f} e^{-\frac{r^2}{2r_0^2 f^2}} \cosh\left(\frac{b}{r_0 f} r\right) \tag{1}$$

is given by

$$\phi(E_0 E_0^{\star}) = \frac{\omega_{p0}^2}{\omega_0^2}(1 + \tan(dz))\left\{1 - e^{-\frac{e^2}{8m\omega_0^2 T_0 K_0} E_0 E_0^{\star}}\right\} \tag{2}$$

Here, b is known as decentered parameter of the laser beam, r_0 is the radius of the beam and d is associated with axial inhomogeneity of plasma density and is called as slope of the density ramp. The evolution of beam width f is governed by

$$\frac{d^2 f}{d\xi^2} = \left(\frac{1 + e^{-b^2}(1 - b^2)}{2(1 + b^2)}\right)\frac{1}{f^3} - \left(\frac{e^{-b^2}}{1 + b^2}\right)\left(\frac{\omega_{p0}^2 c^2}{c^2}\right)\frac{\beta E_{00}^2}{f^3}(1 + \tan(d'\xi))(T_1 - bT_2) \tag{3}$$

where,

$$T_1 = \int_0^\infty x^3 e^{-2x^2} \cosh^4(bx) e^{--\frac{\beta E_{00}^2}{f^2} e^{-x^2} \cosh^2(bx)} dx$$

$$T_2 = \int_0^\infty x^2 e^{-2x^2} \cosh^3(bx) \sinh(bx) e^{--\frac{\beta E_{00}^2}{f^2} e^{-x^2} \cosh^2(bx)} dx$$

$$x = \frac{r}{r_0 f}$$

$$\xi = \frac{z}{k_0 r_0^2}$$

The SBS reflectivity of plasma has been obtained as

$$R = \frac{\left(\frac{\omega_{p0}^2}{c^2}\right)^2}{\left(\frac{\omega_S^2}{c^2} - k_s^2\right)^2} \frac{\int \left(\frac{n_{ia}}{n_0^0}\right)^2 E_0 E_0^\star d^2 r}{\int E_0 E_0^\star d^2 r} \qquad (4)$$

$$n_{ia} = \frac{n_{00}}{f_{ia}} e^{-\frac{r}{2r_0^2 f_{ia}^2}}$$

$$\frac{d^2 f_{ia}}{d\xi^2} = \frac{1}{f_{ia}^3} - \left(\frac{\omega_{ia}^2 r_0^2}{v_{th}^2}\right) \frac{1}{f_{ia}^3} (1 + \tan(d'\xi))(T_3 - bT_4)$$

$$T_3 = \int_0^\infty x^3 e^{-x^2} e^{-\frac{f^2}{f_{ia}^2} x} \cosh^4(bx) e^{--\frac{\beta E_{00}^2}{f^2} e^{-x^2} \cosh^2(bx)} dx$$

$$T_4 = \int_0^\infty x^2 e^{-x^2} e^{-\frac{f^2}{f_{ia}^2} x} \cosh^3(bx) \sinh(bx)\, e^{--\frac{\beta E_{00}^2}{f^2} e^{-x^2} \cosh^2(bx)} dx$$

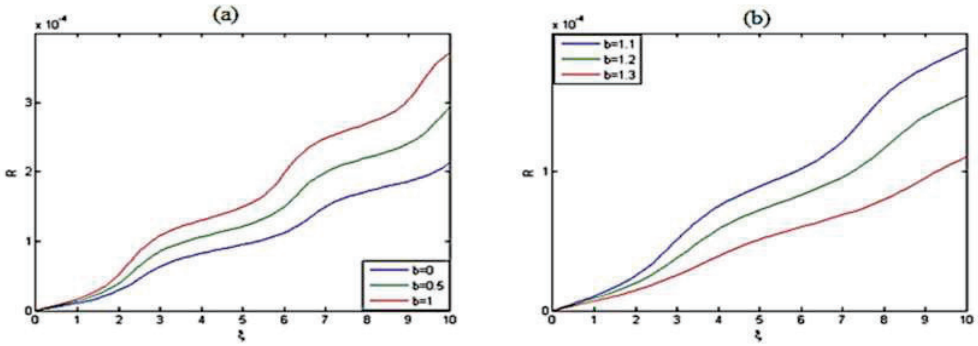

Fig: Effect of cosh factor on evolution of stimulated Brillouin reflectivity of plasma for fixed value of slope of the density ramp i.e., $d' = 0.025$.

3. References

1. D. Anderson, M. Bonnedal and M. Lisak, "Nonlinear propagation of elliptically shaped Gaussian laser beams,"**23**, 115 (1980).
2. D. Anderson and M. Bonnedal, "Variational approach to nonlinear self-focusing of Gaussian laser beams," Phys. Fluids **22**, 105 (1979).

Femtosecond Laser Patterned Silicon Decorated with Gold Nanostars as SERS platform for Pesticide Detection

M. S. S. Bharati, B. Chandu, and S. Venugopal Rao
Advanced Centre for Research in High Energy Materials (ACRHEM), University of Hyderabad, Prof. C. R. Rao Road, Hyderabad 500046, Telangana, India

Corresponding author e-mail: ***soma_venu@uohyd.ac.in*** *OR* ***soma_venu@yahoo.com***

Abstract: In this work, we developed simple and cost-effective surface-enhanced Raman scattering (SERS) substrates for the trace detection of thiram, a pesticide molecule. Surface patterns (micro/nanostructures) on silicon (Si) substrates were fabricated using femtosecond (fs) laser irradiation in ambient air. By tuning the number of laser pulses per unit area (4200, 8400, 42000, and 84000 pulses/mm^2) on Si, different surface patterns were achieved. Later, chemically synthesized gold (Au) nanostars were deposited on the laser-patterned areas of Si to achieve a plasmonic active SERS substrate (structured Si-Au nanostars). Further, the SERS activity of as-prepared Si decorated Au nanostars substrates were tested with a probe molecule of thiram. The as-prepared substrates allowed us to detect a minimum concentration of 0.1 ppm thiram using a portable Raman spectrometer. Additionally, the optimized SERS substrate has shown ~21 times higher SERS enhancement than the plain Si decorated Au nanostars substrate.
Keywords: laser ablation, nanoparticles, thiram, SERS.

1. Introduction

Surface-enhanced Raman scattering (SERS) is a broadly recognized spectroscopic tool because of its high-sensitive nature and is widely used in countless applications.[1] Over the past few decades, different sized/shaped noble metal colloids have been extensively used as SERS substrates by depositing them into the solid substrates.[2] Instead of depositing those colloids on a plain substrate such as silicon/glass, rough surfaces may further strengthen the Raman signal of the analyte molecule because of its high surface-to-volume ratio. Nanostructures can also be fabricated in many methods such as electrochemical, lithography, electrochemical etching, laser ablation, etc[3]. Ultrafast laser ablation is a versatile platform that can induce various surface patterns on solid substrates like two/three-dimensional micro/nanostructures on diverse materials (metal, semiconductor, polymers, etc.).[4, 5] Recently, nanoparticles (NPs) having star-shaped morphology attained significance as SERS substrate fabrication because of the confined field enhancement at tips which acts as excellent "hot spots" for the Raman signal enhancement. Here, in this work, we have developed efficient silicon (Si) based SERS substrates by using the approaches of laser-patterning and a chemical route. Different patterned Si substrates were fabricated by varying the number of pulses and then coated with chemically prepared Au nanostars. The as-prepared Si decorated with Au nanostars was utilized to detect thiram.

2. Experimental details

Si micro/nanostructures were fabricated using a Ti: sapphire femtosecond (fs) laser system (LIBRA, M/s Coherent) delivering ~50 fs pulses at a central wavelength of 800 nm and a repetition rate of 1 kHz. The Si wafer (99.9%, Sigma-Aldrich) with dimension 1×1 cm was placed on the holder and then mounted on the X and Y stage, controlled by a computer. The Si surface was irradiated by focusing the fs laser beam normally through the plano-convex lens of a focal length of 10 cm. Over an area of 5×5 mm^2, linear and squared array patterns were drawn by varying the stage velocities (X=5 mm/s, Y=0.5 mm/s with a line pitch of 50 µm). The estimated number of laser pulses per mm^2 on the sample as (1) 4200 for Si at 5 mm/s line pattern (denoted as Si_5L), (2) 8400 for Si at 5 mm/s cross pattern (denoted Si_5C) (3) 42000 for Si at 0.5 mm/s line pattern (denoted as Si_0.5L), and (4) 84000 for Si at 0.5 mm/s cross pattern (denoted as Si_0.5C). The fabricated NSs were named Si_5L, Si_5C, Si_0.5L, and Si_0.5C for their respective pulse numbers. The experiments were carried out at ~30 µJ of pulse energy. The laser linear and crossed patterns achieved on the Si surfaces were studied by a field emission scanning electron microscope (FESEM) and atomic force microscope (AFM). Earlier, our group had demonstrated the Au nanostars fabrication using chemical routes.[6] Briefly, PVP (2.5 mM) was dissolved in DMF mixed with NaOH (1.5mM) and $HAuCl_4 \cdot 3H_2O$ (0.27mM). Finally, SERS measurements were conducted after Au nanostars deposition on the Si micro/nanostructures by a simple drop-

costing procedure. The SERS measurements were executed with a portable Raman spectrometer (M/s B&W Tek, USA) emits a wavelength of 785 and utilized laser power was ~30 mW in all the recorded spectra.

3. Results and discussions

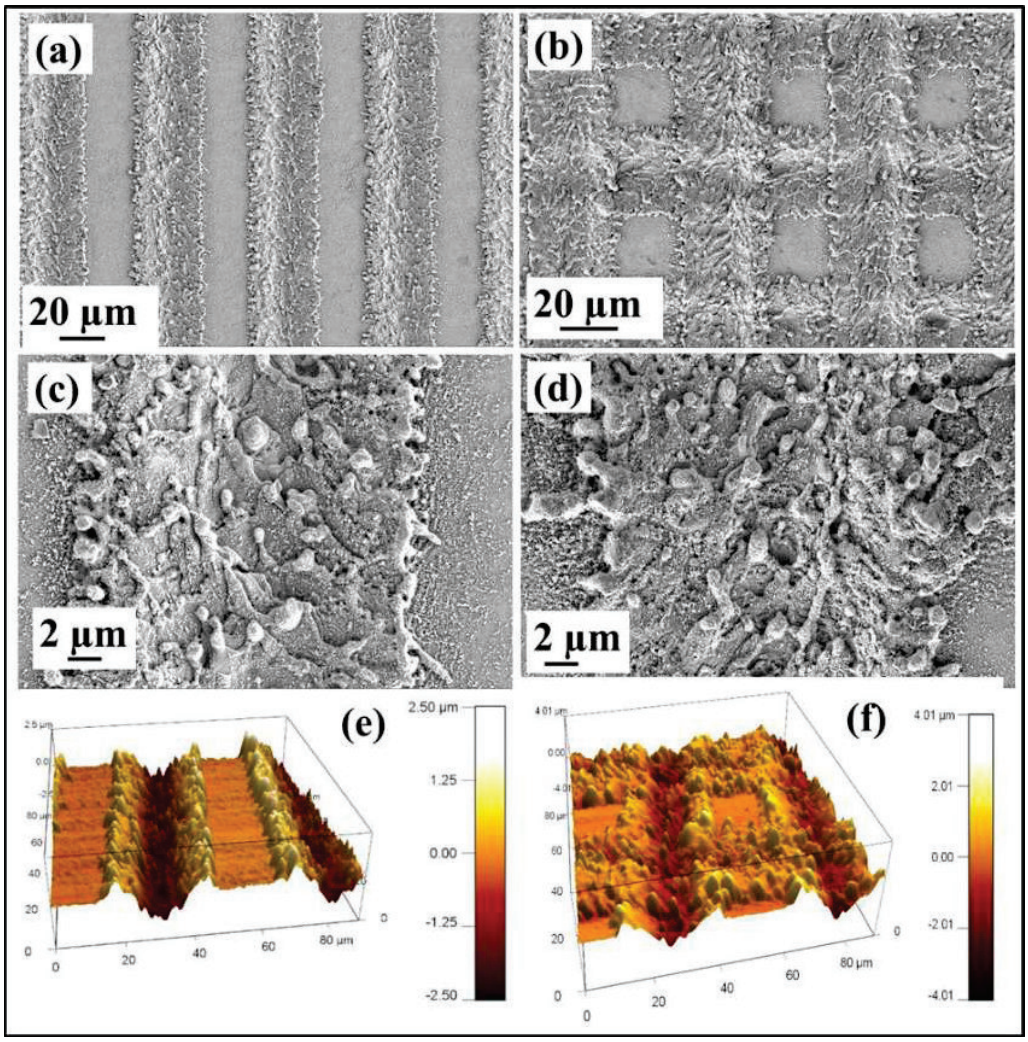

Fig. 1: (a b) and (c, d) lower and higher magnification FESEM images (e and f) AFM images of Si_5L and Si_5C, respectively.

Figures 1(a)-1(d) illustrate the FESEM micrographs recorded at lower and higher magnifications. The surface topography images collected using AFM are shown in figures 1(e) and 1(f) (donated as Si_5L and Si_5C). The micro-spikes around the nanoprotrusions/nano-holes occurred along the scan path of the laser. From figures 1(a) and 1(b), it is evident that the width of the crater was ~30 µm and the non-interacted area width was ~20 µm, while the line spacing was ~50 µm. The ablation region consisted of micro-spikes, and re-deposited Si nanoparticles were clearly noticed along the patterned laser areas. Because of intense laser interaction, the sample surface melts leading to a surface tension gradient of molten silicon, which will be dragged from hotter areas to colder areas. Thus, the melted material solidifies on the surface and leads to the formation of nano spikes/nano craters along the ablation line. In the case of crossed pattern, the large number of pulses interact with the sample leading to the formation of a number of micro-spikes with nanoclusters as compared to the linear pattern, which is evident from the FESEM images [figure 1(a)-1(d)]. Figures 1(e) and 1(f) depict the AFM images of lower scan speed linear and crossed patterned Si surface, respectively. The surface roughness of Si_5L and Si_5C were estimated from "Ra" (the arithmetic average of the

absolute value of the surface height deviations measured from the mean plane) and "Rq" (the root-mean-square average of height deviation taken from the mean image data plane). The roughness values of Si_5L were Ra = ~593.780 nm, Rq= ~593.785 nm and for that of Si_5C were Ra = ~620.228 nm, Rq= ~620.233 nm. As expected, in the case of crossed patterns, a large number of ablated particles were re-deposited onto the silicon surface compared to the linear patterned silicon surface under laser irradiation.

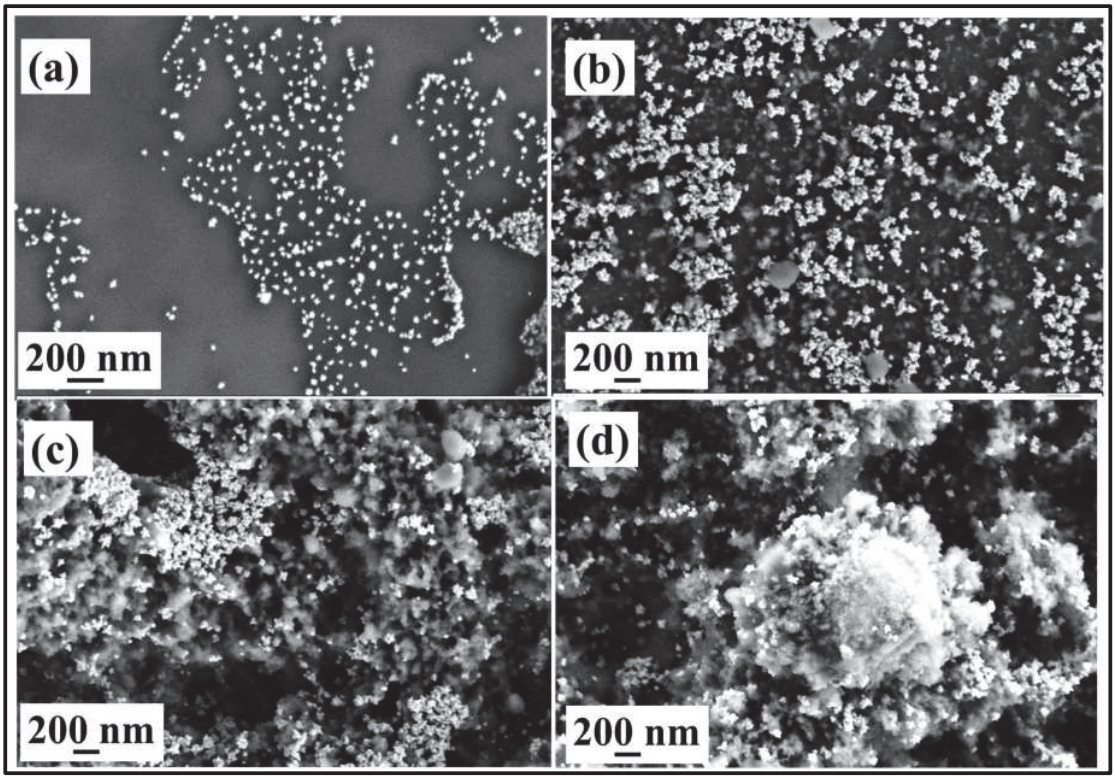

Fig. 2: Gold nanostars deposited on (a) plain Si (b-d) laser patterned Si_5C, Si_0.5L, and Si_0.5C.

Figure 2 depicts the FESEM images of Au nanostars deposited on the plain Si and laser-patterned Si surfaces. The distribution of the Au nanostars on (a) plain Si and (b)-(d) laser patterned Si micro/nanostructures. The Au nanostars were distributed randomly in the gaps of patterned laser areas of Si and we believe this might lead to the generation of multiple hot spots. The SERS efficiency of the laser patterned Si surfaces with Au nanostars was inspected with a probe molecule of thiram. Figure 3(a) shows the enhanced Raman spectra of thiram-0.1 ppm recorded from all four samples decorated with Au nanostars along with plain silicon with Au nanostars. All the samples exhibited a strong and sharp Raman scattering peak at a 1370 cm^{-1} in the case of thiram, corresponding to the CH_3 symmetric in-plane deformation and C-N stretching.[7] Unlike planar silicon substrates used in previous studies, laser-patterned surfaces exhibited an enormous enhancement due to the accommodation of Au nanostars in the micro/nondimensional areas. The larger surface area of micro spikes/nanoclusters possibly provided an outstanding density of the closely packed NPs with a large cross-section leading to the generation of a large number of hotspots, where the fields are further amplified in narrow gaps between interacting particles. To establish the reproducibility of the method, we measured relative standard deviation (RSD) for a series of 15 spectra collected on each substrate. Figure 3(b) illustrates the average intensity of the prominent peak at 1370 cm^{-1} identified on all the samples. Compared to plain Si, the laser-patterned Si surface exhibited the highest enhancement. The highest enhancement by Si_0.5C mainly originates from their morphological differences, which enables the excitation of numerous hot spots. The SERS measurements were conducted at 15 random locations on the Si_0.5C substrate, is also shown in figure 3(c). The main peak intensity values at 1370 cm^{-1} from 15 random locations from all the four samples (i) Si_5L (ii) Si_5C (iii) Si_0.5L (iv) Si_0.5C are shown as a histogram plot in figure 3(d). The obtained calculations reveal that the SERS substrates have an RSD of 7.8%, 7.1%, 10.9% and 5.6% for Si_5L, Si_5C, Si_0.5L, and Si_0.5C, respectively, indicating a good uniformity over the entire substrate.

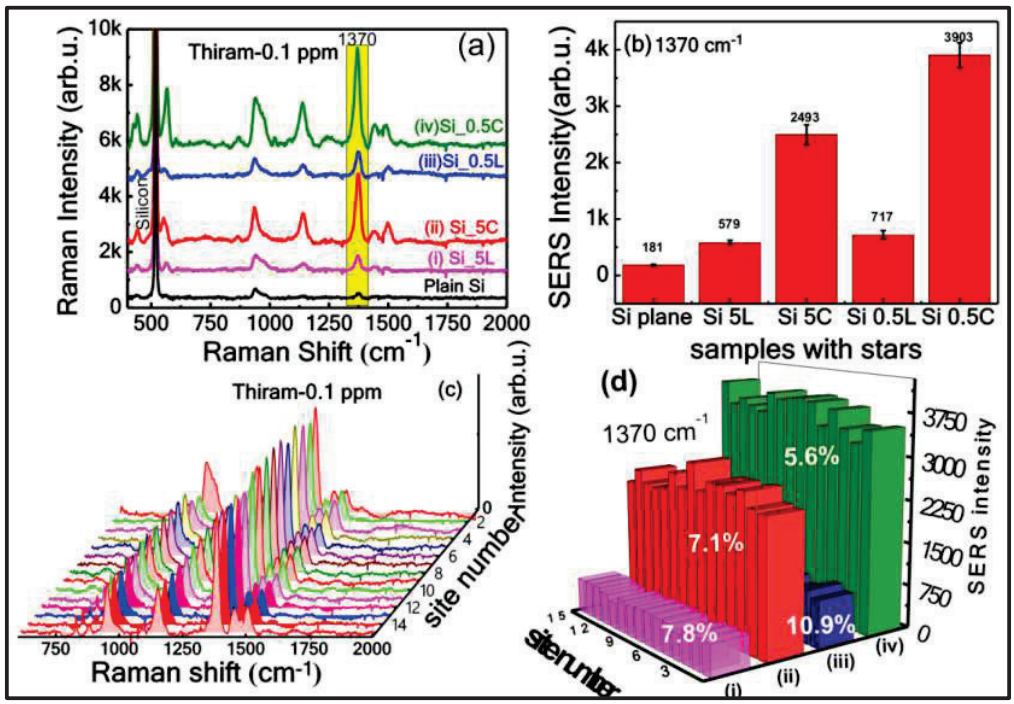

Fig. 3: (a) SERS spectra of thiram 0.1 ppm (b) Intensity of SERS signal at1370 cm^{-1} (c) reproducibility of SERS spectra from 15 different locations on Si_0.5C (d) RSD histogram of thiram from Au nanostars deposited on plain Si, (i) Si_5L (ii)Si_5C (iii)Si_0.5L (iv) Si_0.5C.

4. Conclusions

Femtosecond laser-patterned Si surface will further improve the SERS performance when it is embedded with Au nanostars compared to the plain Si decorated Au nanostars substrate. The two-order higher enhancement was attained for the Si_0.5C (1.3×10^5) SERS substrate than the plain Si (6.2×10^3) with Au nanostars substrate. Moreover, high sensitivity (0.1 ppm) and superior reproducibility (< 11%) were attributed to the Si-crossed array decorated with Au nanostars, among the others, which can be used for real-time field applications.

5. Acknowledgments

We thank the University of Hyderabad for support through the Institute of Eminence (IoE) project UOH/IOE/RC1/RC1-2016. The IoE grant was obtained vide notification F11/9/2019-U3(A) from the MHRD, India.

6. References

[1] S. Weng, X. Hu, J. Wang, L. Tang, P. Li, S. Zheng, L. Zheng, L. Huang, Z. Xin, Advanced Application of Raman Spectroscopy and Surface-Enhanced Raman Spectroscopy in Plant Disease Diagnostics: A Review, Journal of Agricultural and Food Chemistry 69(10) 2950-2964 (2021).

[2] R. Zamora Sequeira, R. Starbird Pérez, O. Rojas Carillo, S. Vargas Villalobos, What are the Main Sensor Methods for Quantifying Pesticides in Agricultural Activities? A Review, Molecules (Basel, Switzerland) 24(14) 2659 (2019).

[3] J.F. Betz, W.W. Yu, Y. Cheng, I.M. White, G.W. Rubloff, Simple SERS substrates: powerful, portable, and full of potential, Phys. Chem. Chem. Phys. 16(6) 2224-2239 (2014).

[4] D. Zhang, B. Gökce, S. Barcikowski, Laser synthesis and processing of colloids: fundamentals and applications, Chem. Rev. 117(5) 3990-4103 (2017).

[5] S.S.B. Moram, A.K. Shaik, C. Byram, S. Hamad, V.R. Soma, Instantaneous trace detection of nitro-explosives and mixtures with nanotextured silicon decorated with Ag–Au alloy nanoparticles using the SERS technique, Anal. Chim. Acta 1101 157-168 (2019).

[6] K. Nehra, S.K. Pandian, M.S.S. Bharati, V.R. Soma, Enhanced catalytic and SERS performance of shape/size controlled anisotropic gold nanostructures, New J. Chem. 43(9) 3835-3847 (2019).

[7] J. Rathod, C. Byram, R.K. Kanaka, M. Sree Satya Bharati, D. Banerjee, M. Akkanaboina, V.R. Soma, Hybrid Surface-Enhanced Raman Scattering Substrates for the Trace Detection of Ammonium Nitrate, Thiram, and Nile Blue, ACS Omega 15969–15981 (2022).

All-optical generation of spatially structured light beam via electromagnetically induced transparency

Onkar Nath Verma and Niti Kant
Department of Physics, University of Allahabad, Prayagraj-211002, U.P. India
onkarnath15verma@gmail.com

Abstract: We suggest a scheme to produce spatially structured light beams in electromagnetically induced transparency atomic vapor. The atoms are modeled as three-level system in Λ-configuration and driven by two optical fields namely a weak probe and a relatively stronger control field. An additional microwave field is applied between two ground states of Λ-system to form a closed three-level system. This results into a phase-sensitive optical response. We explore such a response to generate spatially structured beams by measuring probe transmission for various orders of Laguerre–Gaussian modes imprinted on control field.
Keywords: Electromagnetically induced transparency, Laguerre–Gaussian mode, Structured light beams.

1. Introduction

Laguerre–Gaussian (LG) modes and its nonlinear interaction with material media has fascinated researchers due to its potential applications in optical tweezing, optical trapping and manipulation and generation of structured beam [1]. An LG mode is basically a phase structured beam where phase in the field circulates around the axis of the beam resulting in a helical wavefront [2]. This helical wavefront of LG beam is responsible for an orbital angular momentum (OAM) of light field. In addition, the transverse intensity profile of LG beam has a doughnut-shaped structure. Our study is focused on the transfer of phase structure of LG control beam onto co-propagating plane-wave probe beam in an electromagnetically induced transparency (EIT) medium controlled by an auxiliary microwave field [3]. In traditional EIT systems, the optical response is phase insensitive and there is hardly any discussion on the transfer of phase information between probe and control laser beams [4]. The presence of a microwave field between two hyperfine levels of the three-level Λ-system of EIT leads to the formation of closed EIT Λ-system and resulting optical response becomes phase sensitive (see inset of Fig.1) [5]. We exploit this to transfer the phase structure into transverse intensity distribution in a gaseous medium composed of ^{87}Rb atoms.

2. Theoretical Model and Propagation Equations

We consider a homogeneously broadened gas consisting of ^{87}Rb atoms. The atoms are driven by two optical fields, namely a weak probe field and a comparatively stronger control field from two hyperfine levels |1> and |2> to the same excited level |3>, respectively. The presence of an additional microwave field between hyperfine levels $|1\rangle$ and $|2\rangle$ leads to a three-level closed Λ-system. The three fields are defined as $\vec{E}_j(\vec{r},t)=\hat{e}_j\varepsilon_j(\vec{r})e^{i(k_j z-\omega_j t+\phi_j)}$, where ε_j (r) are the slowing varying envelope functions, e_j the unit polarization vectors, ω_j the laser field frequencies and k_j is the wave numbers of fields. The master equation descrbing dynamics of atomic system is govern by a standard density matrix approach:

$$\dot{\rho}=(i\hbar)^{-1}[H,\rho]-\Gamma\rho \qquad ...(1)$$

where the matrix element of decay operator Γ is given by $\Gamma_{ij}=(\gamma_i+\gamma_j)+\gamma_{ij}$. Here $\gamma_i$is the population decay rate of the state |i>. The pure dephasing rate γ_{ij} is due to the phase relaxation. The steady state solutions to the density matrix equations Eq. (1) are obtained by setting the time derivatives of its left hand side to zero. In order to calculate the probe atomic coherence ρ_{31} analytically, we assume that the intensity of control field is much stronger than the probe and microwave fields that make most of the population to stay in the ground state |1>.

Thus, we obtain solution for probe coherence: $$\rho_{31}=\frac{i(\gamma_c+i\delta)G_p-pG_CG_\mu}{(2\gamma+i\Delta_p)(\gamma_c+i\delta)+|G_c|^2} \qquad ...(2)$$

where G_i and p (= $e^{-i\Phi}$) represents Rabi frequency and the relative phase of all three applied fields. The two-photon detuning is denoted by $\delta = (\Delta_p - \Delta_c)$. Here, Δ_i is single photon detuning. The influence of atomic response on probe beam propagation is govern by the paraxial wave equation:

$$\frac{\partial G_p}{\partial z} = \frac{i}{2k}\left(\frac{\partial}{\partial x^2} + \frac{\partial}{\partial y^2}\right) G_p + i\eta\rho_{31} \qquad ...(3)$$

where coupling constant η is given by $\eta = 3N\lambda^2/8\pi$. It should be noted that first term in parentheses on the right-hand side accounts for the diffraction, whereas the second term is responsible for the dispersion and absorption or gain of the probe beam.

3. Results and Discussion

We choose spatially dependent Rabi frequency of control beam as LG mode: $G_c(r) = G_{c0}(r/w)^{|l|} e^{-r^2/w^2} e^{-il\varphi}$. where r is the radial distance from the center axis of the beam, w is the beam radius at which the field amplitudes fall to 1/e. Here *l* is referred as topological charge and signifies the orbital angular momenta of beam along the propagation axis z and φ is the azimuthal angle. Note that the radial index is assumed to be zero for present analysis.

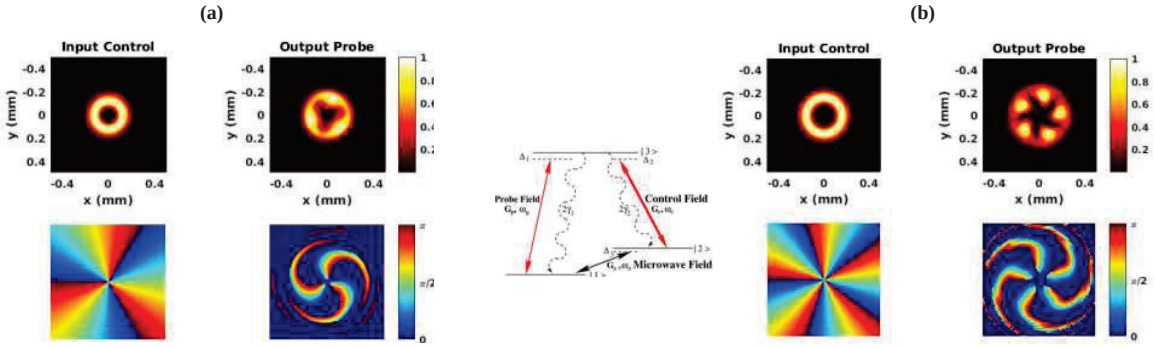

Fig. 1: Cross sectional intensity (top) and its helical phase patterns (bottom) of the input LG control beam and generated structured probe beam for (a) index l=3, (b) l=-5. The parameters used are G_{C0} = 2 γ, G_{P0} = 0.1 γ, Δ_C = 0, Δ_p = 0, γ_c = 0.001γ, Φ = 0, γ= 3π×10⁶ rad/s, λ_P = 795 nm, and N= 1 x 10^{12} atoms/cm^3. The input waist of control beam is set at w_c= 100 μm. Inset shows a three-level closed Λ-system.

Now, in order to see the effect of LG control beam on probe beam propagation, we numerically integrate the paraxial wave equation (3). Fig. 1(a). depicts the intensity distributions of the input LG control beam at the entrance and output probe beam behind 5-cm long Rb cell for topological charge *l*=3. It is evident that the spatial phase information carried by the LG mode is transformed into intensity distribution like a flower petals. This is true for any integer values of *l* and can be used to create multiple structured lights. Note that the number of bright spots in a petal gives information about OAM of input LG beam. The spiral phase profile of output probe is a result of interference between two parts of optical response in equation (2), *i.e.*, a plane wave of probe in first part and a vortex wave of control in second part. Since the topological charge *l* can have both negative and positive values and thus we try to analyze transverse phase effect for *l*=-5. This is illustrated in Fig. 1(b). The intensity distribution is again a five lobe petal pattern. This pattern does not provide any information about the sign of OAM. However, the direction of spiral phase structure is reversed in this case. We also observe a rotation of the intensity distribution for same magnitude but different sign of *l*. This is due to relative phase change occurring for two opposite values of OAM. Such a transfer of phase profile into an intensity distributions is valid for any arbitrary value *l*. Thus the present study may be useful for high capacity quantum information processing applications.

4. Acknowledgment

Financial help from UGC Gov. of India for DSK-PDF (F.4-2/2006 (BSR)/PH/20-21/0054) gratefully acknowledged.

5. References

[1] L. Allen *et al.*, "Orbital angular momentum of light and the transformation of Laguerre-Gaussian laser modes," Phys. Rev. A **45**, 8185 (1992).
[2] M. J. Padgett, "Orbital angular momentum 25 years on," Opt. Express **25**, 11266 (2017).
[3] M. Fleischhauer *et al.*, "Electromagnetically induced transparency: Optics in coherent media ," Rev. Mod. Phys. **77,** 633 (2005).
[4] O. N. Verma and T. N. Dey, "Optical cloning of arbitrary images beyond the diffraction limits," Phys. Rev. A **88**, 013810 (2013).
[5] O. N. Verma and S. Roy, "Microwave field controlled electromagnetically induced focusing," Jpn. J. Appl. Phys. **57**, 08PF01 (2018).

Design and Simulation of micro-pillar cavity based single photon source

Manish Kumar Sahu, Naresh Babu Pendyala, Prashant Varma
Microelectronics Group, Space Applications Centre, ISRO, Ahmedabad, 380015, India
manish11@sac.isro.gov.in

Abstract: High efficiency on demand single photon sources are much needed for the implementation of secured quantum communication. Semiconductor quantum dots in an optical cavity serve as excellent source of on demand, high brightness quantum light source. In this work, for 1550 nm wavelength, a quantum dot embedded in a micro-pillar cavity was simulated using finite difference time domain (FDTD) method. Design parameters of the micro-pillar structure like number of top and bottom Distributed Bragg Reflector (DBR) pairs, cavity Q-factor and DBR mirror reflectivity have been simulated. It has been demonstrated that DBR (with 24 pairs) have a reflectivity in excess of 99%, required for efficient extraction of photons from top side of micro-pillars.

Keywords: Quantum Dot, FDTD, Quantum Communication

1. Introduction

Quantum communication using telecom wavelength (1550 nm) is highly desirable for implementing daylight quantum key distribution (QKD). This telecom C-band wavelength (around 1550 nm) provides low loss propagation through atmosphere [1] as well as through optical fibers. On demand single photon source is an essential tool for implementing secure QKD. Such sources generate photons having quantum nature. This quantum nature of photons is characterized by high indistinguishability and near zero multi-photon emission probability [2].

Semiconductor quantum dots provide an excellent platform for fabricating such single photon sources [3]. InAs/InP quantum dots have been reported [4] to emit single photons at telecom wavelengths when excited by a pump beam. Quantum dots coupled to a micro cavity can lead to enhancement of spontaneous emission via the Purcell effect. Appropriate DBR mirror pairs can help to funnel out the emitted photons for coupling them efficiently to an optical fiber. In this work, we report the simulation of such QD based micro-pillar cavity structures for efficient extraction of single photons.

2. Simulation results

Fig. 1 shows the simulated micro-pillar structure in FDTD software Lumerical. Quantum dot is modelled as a electric dipole source located at the center of the cavity. The structure consists of a cavity (thickness, d_{cav}: λ/n_{GaAs}) sandwiched between top and bottom DBR reflectors. DBR reflectors consist of alternating layers of AlAs (thickness, d_{AlAs}: $\lambda/4n_{AlAs}$) and GaAs (thickness, d_{GaAs}: $\lambda/4n_{GaAs}$) where n_{AlAs}, n_{GaAs} and λ are refractive index of AlAs, GaAs and designed wavelength respectively. For the design wavelength of 1550 nm, d_{cav}: 459.4 nm, d_{AlAs}: 133.2 nm and d_{GaAs}: 114.8 nm. The refractive index data for GaAs and AlAs was imported from data available online into Lumerical's materials database and fitted across the simulation bandwidth.

FDTD simulations were performed with a broadband electric dipole source. The simulation was allowed to run for reasonable time to allow the electric fields to decay completely. The reflectivity of the DBR pairs by varying the DBR pairs number was estimated for the designed wavelength.

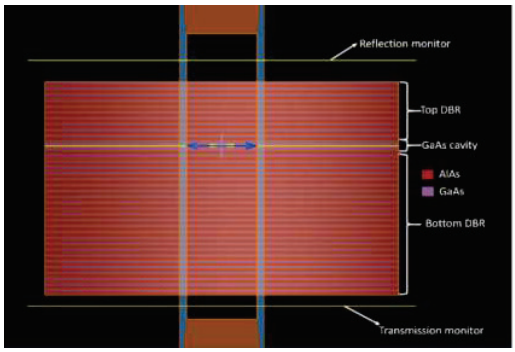

Fig. 1: X-Z plane view of simulated micro-pillar structure.

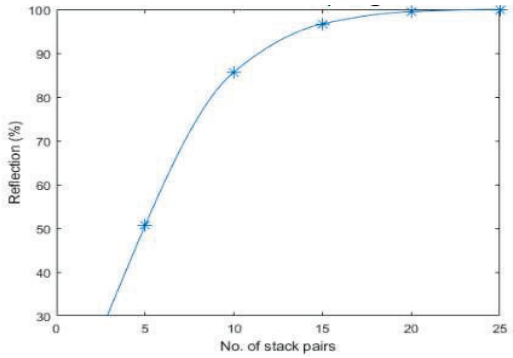

Fig. 2: Reflectivity as a function of DBR pairs for designed wavelength

Fig. 2 shows the obtained results for different number of DBR pairs. Reflectivity more than 99% was achieved. The Q-factor of the cavity was estimated using both analytic methods and from FDTD simulations (Fig. 3). The number of bottom DBR pairs (N_b) was kept constant at 24 and number of top DBR pairs (N_t) were varied. Fig. 4 shows the un-normalized transmission measured from monitor located at the top of DBR structure with different meshing conditions along the height of micro-pillar (Z-axis). For coarse meshing conditions, a red shift in peak reflectivity was observed. For 5 nm z mesh size, very high values of reflectivity were obtained (un-normalized) at the designed wavelength indicating the enhancement of photon emission rate when dipole source was placed in the cavity (Purcell enhancement).

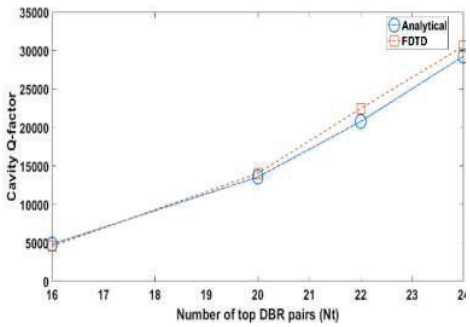

Fig. 3: Cavity Q-factor calculated from FDTD simulation and analytically with varying N_t at fixed $N_b = 24$

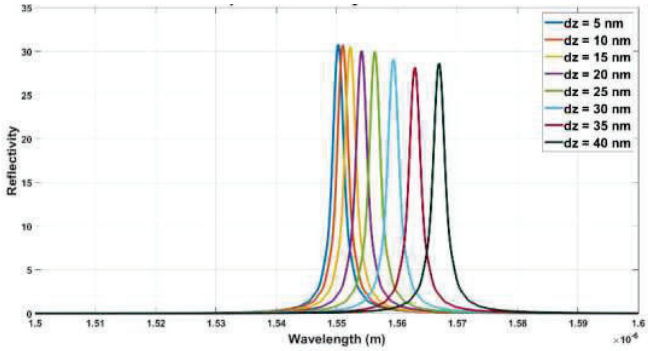

Fig. 4: Reflectivity measurement from top of micro-pillar as a function of z mesh sizes

Further optimization of micro-pillar diameter has to be performed to increase the Q-factor and photon extraction from top of the micro-pillar.

3. References

[1] Liao SK, Yong HL, Liu C, Shentu GL, Li DD, Lin J, Dai H, Zhao SQ, Li B, Guan JY, Chen W. Long-distance free-space quantum key distribution in daylight towards inter-satellite communication. Nature Photonics. 2017 Aug;11(8):509-13.
[2] Lodahl P, Ludwig A, Warburton RJ. A deterministic source of. Physics Today. 2022 Mar;75:3-44.
[3] Arakawa Y, Holmes MJ. Progress in quantum-dot single photon sources for quantum information technologies: A broad spectrum overview. Applied Physics Reviews. 2020 Jun 11;7(2):021309.
[4] Sittig R, Nawrath C, Kolatschek S, Bauer S, Schaber R, Huang J, Vijayan P, Pruy P, Portalupi SL, Jetter M, Michler P. Thin-film InGaAs metamorphic buffer for telecom C-band InAs quantum dots and optical resonators on GaAs platform. Nanophotonics. 2022 Feb 2;11(6):1109-16.

Performance of Heisenberg-coupled spins as quantum Stirling heat machine near quantum critical point

Chayan Purkait, Asoka Biswas
Indian Institute of Technology Ropar, Rupnagar, Punjab, India
Author e-mail address: 2018phz0001@iitrpr.ac.in

Abstract: We study the performance of quantum Stirling machines near the quantum critical point in two-spin working system, in which the spins are coupled by nearest neighbour interaction of Heisenberg-XX type. This system exhibits first order quantum phase transition (QPT) when the external magnetic field becomes equal to the interaction strength between the spins, corresponding to a ground state energy level crossing at very low temperature. QPT in the system is also investigated in terms of non-analyticity in the measure of entanglement and correlation. During a cycle, the working system performs either as a heat engine or a refrigerator, if the magnetic field is decreased or increased, respectively, to the critical value pertaining to the quantum phase transition. At the QCP, the efficiency of the engine and the coefficient of performance of the refrigerator attain the corresponding values of their Carnot counterparts, along with maximum work output. We analyze how such enhancement can be attributed to the nonanalytic behaviour of spin-spin correlation and the entanglement near the QCP. Further, we explore how two spins perform as a thermal machine in presence of a third spin, when all the three spins are in thermodynamic equilibrium and exhibit quantum Stirling cycle.

Keywords: Quantum heat engines and refrigerators, Quantum phase transition, Quantum thermodynamics

1. Introduction

The advent of miniaturization of technology and the ability to control the system down to the nanoscale have created renewed interest in studying the thermodynamics at quantum level. While usual classical thermodynamics deals with heat and work for a system of many particles (corresponding to the so-called thermodynamic limit), it is quite interesting to explore how heat and work are interpreted in quantum regime when a system of a few particles interacts with a thermal environment. Specifically, a major effort has been invested in quantum thermal machines, e.g., the heat engines, the refrigerators and the heat pumps made up of quantum systems, which convert either heat into work or vice versa. Quantum features of the working system and of the heat bath have been explored in details to improve the performance of these thermal machines beyond that achievable by their classical counterparts [1]. The efficiency can also be increased beyond that of a Carnot engine, even without violating the second law of thermodynamics, by exploiting the quantum property of the heat baths, namely, the quantum-coherent bath, squeezed bath, non-Markovian and quantum-correlated heat baths.

Based on the nature of the strokes, the different kinds of reciprocating quantum thermodynamic [2] cycles are the quantum Carnot cycle, quantum Otto cycle, quantum Stirling cycle etc. The purpose of studying these cycles is to gain a better understanding of the thermodynamic properties of quantum systems.

2. Model

In our work [3], we have studied the quantum Stirling cycle, which consists of four stokes, which are mainly four quantum thermodynamic processes. Two strokes are quantum isothermal processes where the working system is coupled with heat baths, and an external control parameter of the system is driven very slowly such that the system remains in thermal equilibrium with the baths at every instant. Another two strokes are quantum isochoric processes, where the external control parameter of the system remains unchanged and the system is coupled with heat baths. The system reaches thermal equilibrium with the baths at the end of the process. The schematic diagram of the quantum Stirling cycle is shown in the figure below.

The working system is a two-spin system coupled with Heisenberg-XX interaction. Although this is a few spins system, it exhibits a quantum phase transition under very low temperatures, which is measured by thermal

entanglement. Therefore, the system experiences QPT during two isothermal processes. We have studied the behaviour of the cycle in the vicinity of the QPT.

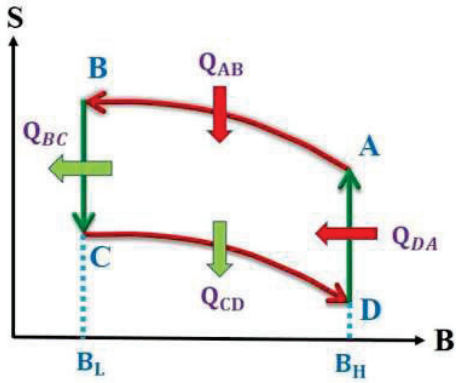

Schematic diagram of the Stirling cycle on the entropy Vs magnetic field plane. AB and CD are two isothermal processes, and BC and DA are two isochoric processes. Heat transfers between the system and the heat baths take place in all four processes, but the work done takes place in the two isothermal processes.

3. Thermodynamic quantities –

Work done in a complete cycle, heat absorption and heat release by the system and also the efficiency for engine operation or performance coefficient for refrigerator operation in the cycle are calculated [3].

4. Performance of the cycle

By plotting all these thermodynamic quantities we can find that the cycle can work as a heat engine or a refrigerator depending on all the control parameters of the cycle. Also, the heat engine or refrigerator can achieve their Carnot performance limit at the QPT point [3].

5. Theoretical Analysis

We have analyzed theoretically [3] how the engine or refrigerator can achieve their Carnot's limit of performance at the critical point.

6. Effect of a third spin

Also, we have studied how the machine (engine or refrigerator) behaves under the action of a third spin.

[1] Sai Vinjanampathy & Janet Anders, "Quantum thermodynamics", Contemporary Physics, (2016) 57:4, 545-579

[2] H. T. Quan, Yu-xi Liu, C. P. Sun, and Franco Nori, "Quantum thermodynamic cycles and quantum heat engines", Phys. Rev. E 76, 031105

[3] Chayan Purkait, Asoka Biswas, "Performance of Heisenberg-coupled spins as quantum Stirling heat machine near quantum critical point", Physics Letters A 442 (2022) 128180

Influence of Filament Temperature on the Photoluminescent Properties of SiO_xC_y Thin Films Deposited by O-Cat-CVD Technique using Silicon-based Organometallic Precursor

Manmohan Jain [(1)*], Andres Galdamez [(2)], Ateet Dutt [(2)], Yasuhiro Matsumoto [(1)]

[(1)] SEES, Electrical Engineering Department, Centro de Investigación y de Estudios Avanzados del IPN, Mexico City, 07360, Mexico

[(2)] Instituto de Investigaciones en Materiales, Universidad Nacional Autónoma de México, Coyoacán, 04510, Mexico City, Mexico

**Author e-mail address (Manmohan Jain): manmohan@cinvestav.mx*

Abstract: This work aims to evaluate the influence of filament temperature on photoluminescence properties of silicon based thin film i.e. silicon oxycarbide (SiO_xC_y) by using organic catalytic chemical vapor deposition (O-Cat-CVD) method. Tetra-ethyl orthosilicate (TEOS) liquid precursor was used to obtain thin films. The films were characterized for the study of structural, chemical and optical properties with the help of Fourier transform infrared (FTIR), X-ray Photoelectron Spectroscopy (XPS), and Photoluminescence (PL). FTIR and XPS confirmed the formation of SiOxCy thin films. Wide and intense photoluminescence emission were observed for as deposited films and emission mechanism was explained related to different mechanisms.

Keywords: O-Cat CVD, Photoluminescence, SiO_xC_y, Tetraethyl orthosilicate

Plasmonic Nano-Sculptured Thin Film based Surface Enhanced Fluorescence Platform for Enhancement of Fluorescence Signal of Rhodamine 6G

Arti Yadav[1], Sachin Kumar Srivastava[2]

[1]Department of Physics, Indian Institute of Technology, Roorkee- 247667, India
[2]Center for Photonics and Quantum communication Technology, Department of Physics, Indian Institute of Technology, Roorkee- 247667, India
**sachin.srivastava@ph.iitr.ac.in*

Abstract: Nano-sculptured thin film provides an excellent platform for plasmon enhanced fluorescence. An enhancement of 2.5 x 10^5 in the fluorescence signal of Rhodamine 6G on a plasmonic nano-sculptured thin film was achieved.

Keywords: Sculptured thin film, Enhanced spectroscopy, Plasmonics

1. Introduction

Metallic nanostructures are generally used for modifying the fluorescence signal of the molecules. Nowadays, nano-sculptured thin films are widely used in surface enhanced spectroscopic techniques (SERS, SEF, SEIRA etc.) [1]. Trace level detection and even a single molecule detection of analyte molecule is possible by surface enhanced spectroscopic techniques. Nano-sculptured thin films are fabricated by glancing angle deposition technique, where source vapor flux arrives at a larger oblique angle (>70°) with respect to the substrate surface normal to form nanocolumnar structures of various morphology [2]. Nano-sculptured thin films (nSTFs) consisting of various morphology can be fabricated by changing the inclination angle, rotation speed, and temperature of the substrates [3]. The electromagnetic field interacting with the plasmonic nanostructures produces a high local field confined near the nanostructure geometry. It is such high local field areas (hot spots), which provide the maximum enhancement of the fluorescence signals of the molecule adsorbed on the surface of the nanostructures. STFs provide a uniform, reproducible plasmonic substrate consisting of a large scale of hot spots [4,5]. The enhancement in fluorescence signal is due to high local field created near the plasmonic nanostructures, which are generated by localized surface plasmons on the metallic nanostructures. The enhancement of the fluorophore emission is maximum when fluorophore emission overlaps with plasmonic band of the nSTFs[6,7].

2. Experimental methods

Nano-sculptured thin films of silver are fabricated on a Silicon substrate. The characterization of nano-sculptured thin films is done using Scanning electron microscope. SEM image of it is shown in Figure 1(a). The porosity of the nSTF was estimated to be 42% using ImageJ software [8]. Nanocolumn array of nSTF has diameter of 68 nm, and height of 98 nm. Rhodamine 6G (R 6G) dye is excited by a wavelength of 532 nm. Fluorescence spectra of R6G adsorbed on nSTF have been shown in the Figure 1(b). The maximum emission of the R 6G is at wavelength 550 nm.

The enhancement factor is defined by the following formula [9] as,

$$Enhancement\ factor = \frac{{}^{I_{SEF}}/_{N_{ads}}}{{}^{I_{bulk}}/_{N_{bulk}}} \qquad (1)$$

Where I_{SEF} is the intensity of fluorescence signal of R 6G adsorbed on the nSTF, I_{bulk} is fluorescence intensity of a bulk chuck of R 6G over the silicon substrate, N_{ads} is number of R 6G molecules adsorbed on the nSTF and N_{bulk} is number of molecules of bulk chuck of R 6G illuminated by incident light.

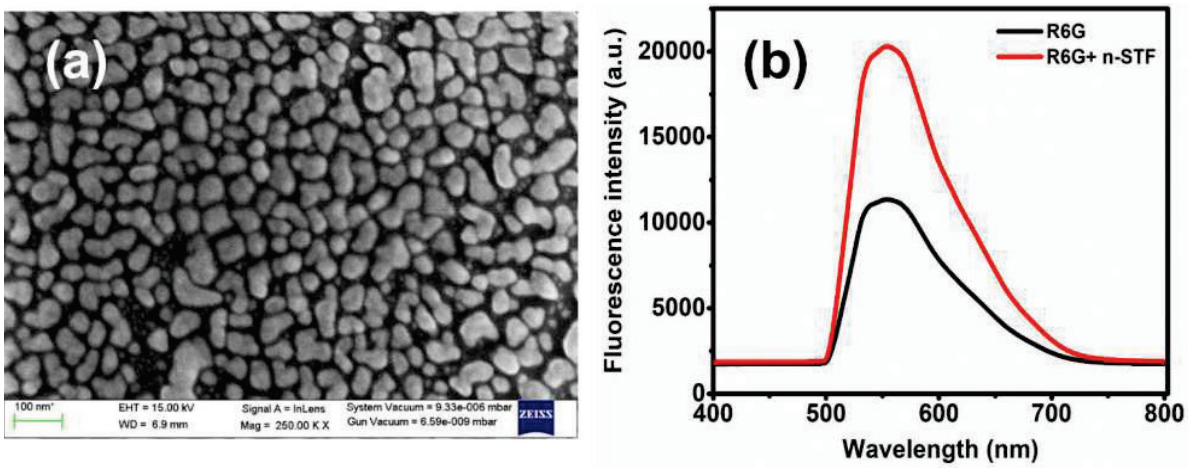

Figure 1 (a). Scanning electron microscope image of the fabricated nSTF and (b). Fluorescence spectra of R6G on silicon substrate and nSTF respectively.

The enhancement in the fluorescence signal is due to photo-induced high local electric field created in the gap the nanocolumnar array nano-sculptured thin film. The size, shape and porosity of the nanostructures play a key role in the enhancement of the fluorescence signal of R 6G. Thus, nSTF platform exhibit an enhancement factor calculated to be 2.5 x 10^5.

Conclusion: Nano-sculptured thin film provides an excellent platform for plasmon enhanced fluorescence. We report an excellent enhancement of fluorescence signal of the R 6G using a nano-sculptured thin film fabricated by glancing angle deposition method. The enhancement in fluorescence signal is due the photo-induced localized surface plasmons near the metallic nanostructure geometry. The enhancement factor achieved for R 6G is 2.5 x 10^5.

Acknowledge: Arti Yadav thanks CSIR for junior research fellowship. Financial support from IITR-FIG, INSPIRE Faculty Grant, MoE-STARS, SERB-SRG, DST: Indo-Korea JNC and DST-BDTD grants is thankfully acknowledged.

3. References

[1] Badshah MA, Koh NY, Zia AW, Abbas N, Zahra Z, Saleem MW, "Recent Developments in Plasmonic Nanostructures for Metal Enhanced Fluorescence-Based Biosensing. Nanomaterials" (Basel) 1749 (2020).
[2] Y.J. Liu,Hsiao Yun Chu, and Y.P. Zhao, "Silver Nanorod Array Substrates Fabricated by Oblique Angle Deposition: Morphological, Optical, and SERS Characterizations," J. Phys. Chem. C 114, 8176–8183 (2010).
[3] Akhilesh Lakhtakia and Russell Messier, *Sculptured thin film: nanoengineered morphology and optic,* (SPIE press, 1957).
[4] Huakang Yu, Yusi Peng, Yong Yang and Zhi-Yuan Li, "Plasmon-enhanced light–matter interactions and applications" npj Comput Mater 5, 45 (2019).
[5] Chris D. Geddes and Joseph R. Lakowicz, "Metal Enhanced fluorescence" Journal of Fluorescence volume 12, 121–129 (2002).
[6] Meiling Wang, Min Wang, Ganhong Zheng, Zhenxiang Dai and Yongqing Ma, " Recent progress in sensing application of metal nanoarchitecture-enhanced fluorescence" Nanoscale Adv. 3, 2448-2465 (2021).
[7] Shrivastav, A.M., Cvelbar, U. and Abdulhalim, "I. A comprehensive review on plasmonic-based biosensors used in viral diagnostics" Commun Biol 4, 70 (2021).
[8] Sachin K. Srivastava, Christoph Grüner, Dietmar Hirsch, Bernd Rauschenbach, and Ibrahim Abdulhalim, "Enhanced intrinsic fluorescence from carboxidized nano-sculptured thin films of silver and their application for label free dual detection of glycated hemoglobin," Opt. Express 25, 4761-4772 (2017).

Line-Field Optical Coherence Tomography of a Biological Sample

Dibakar Borah, Harpreet Kaur, Sunil Bhatt, Anand Kumar, and Dalip Singh Mehta[#]

Bio-Photonics and Green-Photonics laboratory, Department of Physics, Indian Institute of Technology, Delhi, New Delhi, Hauz Khas, 110016.

[#]*mehtads@physics.iitd.ac.in*

Abstract: We generated a partially spatially coherent (PSC) light source by using a microscope objective, rotating diffuser and a multi-multimodal fiber bundle (MMFB). We propose the idea of line-field optical coherence tomography (LF-OCT) on a multi-layered biological sample by using the longitudinal spatial coherence property of PSC light source.

Keywords: optical coherence tomography, coherence

1 Introduction

Optical techniques such as OCT, profilometry, and quantitative phase microscopy, all proposed techniques are dependent on the source's coherence properties. The biggest disadvantage of employing broadband sources in OCT is poor lateral resolution due to low NA objective and the need of a dispersion compensation mechanism which makes system bulky. This motivated us to move towards a monochromatic source that would reduce the dispersion mechanism components and provide high lateral and axial resolution. But using a laser source directly results in the generation of speckles, coherent noise, and parasitic fringe formation from optical components and sample which degrades the image quality. Thus, to avoid all these problems, we generate a PSC light source [1], i.e., highly temporal and low spatial coherence which is used for topography and tomography of different multi-layered samples.

2 Experimental Set-up

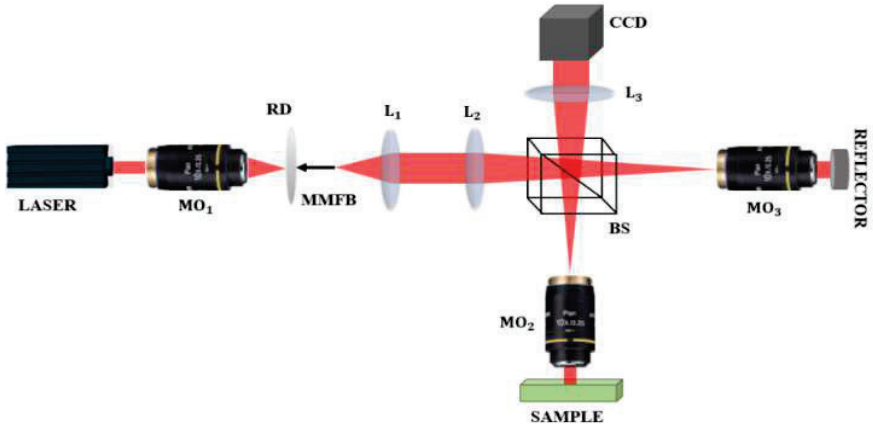

Figure 1: Schematic diagram of the proposed LF-OCT. $MO_{1\text{-}3}$: microscope objectives; $L_{1,3}$: Lenses , L_2 :cylindrical Lens, RD: rotating diffuser; BS: beam splitter; MMFB: multi multi-mode fiber bundle; CCD: charged couple device

A monochromatic light source (He-Ne laser) is made to pass through the microscopic objective (MO_1) for tight focusing at the plane of a rotating diffuser (RD). The RD produces a temporally fluctuating speckle field that progressively lowers the contrast of the speckle[1]. Photons dispersed by the diffuser plane are coupled into the MMFB, which is situated very near to the diffuser plane to maximise the amount of photons coupled into the MMFB. The output port of MMFB works as an extended light source which has high temporal but low spatial coherence property. The output, received at the end of MMFB is passed through a Linnik interferometer which is a Michelson type with additional MO at two of its arms. In this system, the light is divided by a beam splitter 'BS' into two parts which sends one portion of the light to the reference arm (reflector i.e. a mirror) and the other to the sample arm. Now at the 'BS' plane, the backscattered light from both the sample and the reference arm interferes and is sent back into the camera plane by using a tube lens L_3. This interference signal is recorded and is further used for tomographic and topographic information of the samples. To do the LF-OCT we use a cylindrical lens L_2 so that we are able to generate a line of light. Whenever a line of light is allowed to fall on a sample it illuminates a very small portion of the sample as a result of which the number of back reflections from

the sample is avoided and thus, we have a very high SNR. In LF-OCT [2] multiple A-scans are acquired in parallel to obtain B-scan images. To display potentiality of LF-OCT, we placed a multi-layered sample on the sample plane and have performed imaging on the sample.

3 Results and Discussions

The longitudinal spatial coherence (LSC) length(L_{lsc}) relies on the light source's angular and temporal frequency spectrums which is given by:

$$L_{lsc} = [\frac{2sin^2(\theta_z/2)}{\lambda} + \frac{\Delta\lambda}{\lambda^2}cos^2(\theta_z/2)]^{-1}, \quad (1)$$

$\Delta\lambda$ represents the width of source's temporal spectrum; the half width of angular spectrum given by θ_z; λ gives the central wavelength. But when we are using a monochromatic light source the second term of the expression is neglected for a very small $\Delta\lambda$ value and high NA, now can provide high lateral resolution which is not possible when we were using the broadband light as an source in OCT. Here the axial resolution ($L_{lsc}/2$) is solely given by the LSC length rather than the source's temporal coherence length.

We prepared a biological sample manually by placing two chicken fat tissue crossed one over other. We then z-scanned the sample and performed the LF-OCT on the sample whose results are shown below:

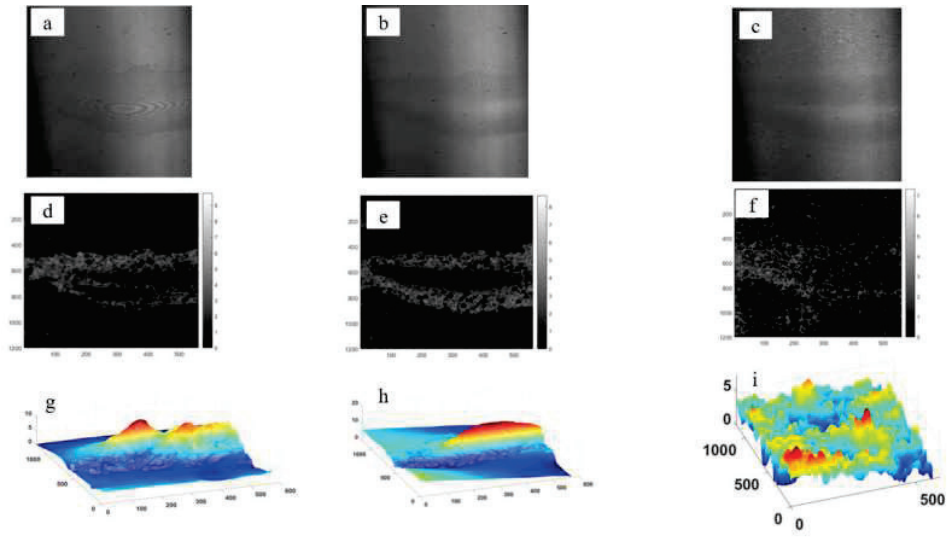

Figure 2: (a), (b) and (c) are the interferometric images sample using LF-OCT when the sample stage is at $0\mu m$, $95\mu m$, and $195\mu m$, respectively. (d), (e) and (f) are the corresponding amplitude images. (g), (h) and (i) are the phase images of the multi-layered sample at $0\mu m$, $95\mu m$, and$195\mu m$ respectively.

When we perform LF-OCT on the sample and go deep down the sample, we see that there is a change in the fringe pattern at $0\mu m$,$95\mu m$ and $195\mu m$. We have also shown the amplitude and the corresponding phase images of the first, second and the third layer respectively. We see that there is a difference in the phase map of the layers. Since we have prepared the sample using two tissue layers, but after performing LF-OCT we are able to see three distinct layers which enable us to conclude the presence of three different layers in the sample. Thus, we see that LF-OCT performs optical sectioning of biological samples and provide a better SNR with high axial (using LSC) and high lateral resolution (when we use high NA objective). Hence the potentiality of LF-OCT has been demonstrated.

4 Conclusion

We conclude that using a PSC light source in LF-OCT, we are able to do optical sectioning of multi-layered biological samples. The proposed idea can be implemented on natural biological specimen so as detect the deformation present in different layers.

5 References

[1] S. Bhatt, A. Butola, S. R. Kanade, A. Kumar, and D. S. Mehta, "High-Resolution Full-Field Optical Coherence Microscopy Using Partially Spatially Coherent Monochromatic Light Source," Imaging and Applied Optics Congress (2020), paper JTh2A.5 JTh2A.5 (2020).

[2] A. Dubois, O. Levecq, H. Azimani, D. Siret, A. Barut, M. Suppa, V. del Marmol, J. Malvehy, E. Cinotti, P. Rubegni, and J.-L. Perrot, "Line-field confocal optical coherence tomography for high-resolution noninvasive imaging of skin tumors," https://doi.org/10.1117/1.JBO.23.10.106007 **23**, 106007 (2018).

Ultrafast All-optical Logic Gates with $MoTe_2$ Nanocomposite Thin Films

Anam Saifi and Sukhdev Roy*
Department of Physics and Computer Science
Dayalbagh Educational Institute, Agra 282005, India
**sukhdevroy@dei.ac.in*

Abstract: We present a detailed theoretical analysis of ultrafast saturable absorption and reverse saturable absorption in $MoTe_2$ and $MoTe_2/MoS_2$ nanocomposite films with femtosecond laser pulses at 800 nm. Theoretical results are in good agreement with reported experimental results. The switching characteristics are sensitive to input intensity, NLA coefficient and sample thickness and have been theoretically optimized to design all-optical AND, OR logic gates with $MoTe_2$, $MoTe_2/MoS_2$ nanocomposite films and all-optical fs universal NOR and NAND logic gates using $MoTe_2$ nanofilms. $MoTe_2/MoS_2$ nanocomposite possess larger nonlinear absorption than pure MoS_2, $MoTe_2$ films and therefore show enhanced SA resulting in good switching contrast.

Keywords: Nonlinear absorption, transition metal dichalcogenides, all-optical switching, ultrafast information processing.

1. Introduction

The requirement for ultrafast and ultrahigh bandwidth information processing has provided tremendous impetus to design, synthesize and characterize the nonlinear optical (NLO) response of different molecular configurations. The wide range of materials studied for various photonic applications include, chromophores, phthalocyanines, porphyrins, rhodopsins, MXenes and transition metal dichalcogenides (TMDCs) [1-3]. The basic challenge is to design an energy-efficient all-optical switch that exhibits ultrafast response time, high contrast, low-power operation and high photo-thermal stability [4]. Heterostructures based on 2D TMDCs are important due to prospective applications as p–n junctions, field-effect transistors (FETs), optoelectronic devices and photovoltaic cells [5]. Although, all 2D TMDCs exhibit potential for optoelectronics applications, their heterostructures show remarkable properties that may not occur in their constituent layers [6]. $MoTe_2/MoS_2$ nanocomposite films are promising 2D heterostructures for nonlinear optoelectronic devices. Logic gates are the basic building block of computing circuits. The objective of this paper is to study the ultrafast nonlinear absorption in $MoTe_2$ and $MoTe_2/MoS_2$ nanocomposite thin films and to determine optimized conditions with respect to absorption cross-section, excitation intensity and sample thickness to design all-optical ultrafast logic gates.

2. Theoretical Model

Ultrafast nonlinear absorption in $MoTe_2$ thin films can be described by the four-level energy diagram as shown in inset of Fig.1 [7]. The excitation and de-excitation processes have been studied using rate equations and reported experimental parameters in [7]. Similarly, NLA dynamics in $MoTe_2$/ MoS_2 nanocomposite thin films has been studied at reported experimental parameters [8].

3. Results and Discussion

NLA has been studied through numerical simulations using rate equations for $MoTe_2$ thin films by considering reported experimental parameters [7]. We consider a laser pulse from Ti:Sapphire femtosecond laser at 800 nm to excite the sample with beam waist 30 μm. The effect of intensity on transmittance at different peak pump intensities has been studied. It is evident that the percentage modulation increases with increase in I_o, as more molecules get excited from the ground state to the higher excited-states. NLO response is also found to be sensitive to the film thickness due to the coupling of layers in the films which could influence exciton formation, relaxation and transport of charge carriers [9]. Two input all-optical OR and AND logic gates have been theoretically designed by optimising SA using fs pulses at 800 nm and $I_o = 303$ GW/cm^2, with pure $MoTe_2$, MoS_2 films and $MoTe_2/MoS_2$ nanocomposite films as shown in Fig. 2.

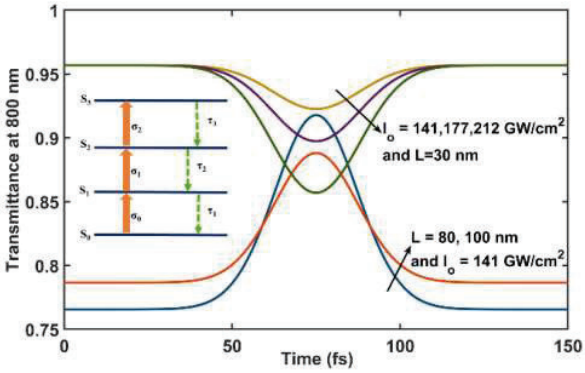

Fig. 1: Variation of transmittance with time for $MoTe_2$, 35 fs input pulse at 800 nm. Inset shows the four-level energy diagram.

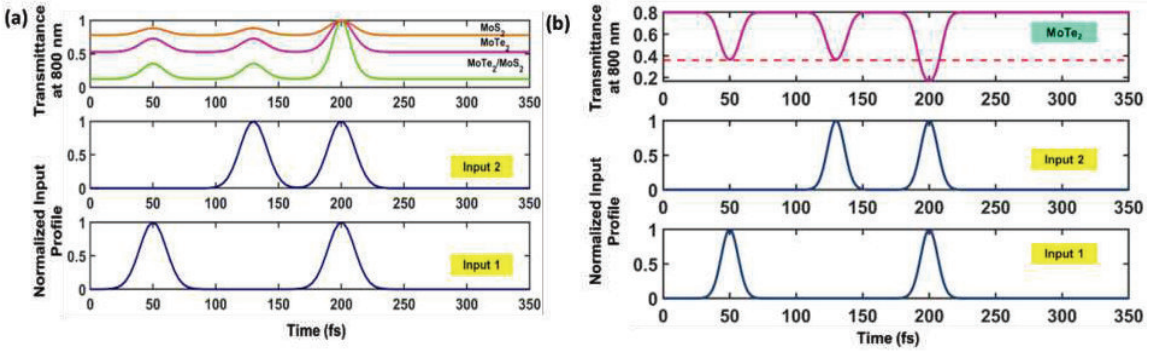

Fig. 2: Variation of transmittance with time and design of all-optical) logic gates with I_o = 303 GW/cm^2, at 800 nm and τ_P = 15 fs (a) OR (without threshold) and AND (with threshold (b) NAND (without threshold) and NOR (with threshold), (dashed line as threshold at 0.36) for $MoTe_2$ thin films and film thickness 150 nm.

NOR and NAND logic has been realised by optimising RSA of $MoTe_2$ films by considering the threshold at 0.36 (dashed line) shown in Fig. 2, NAND logic can be realised when both the inputs are high simultaneously, the output transmittance is low and above threshold it is considered to be high.

4. Conclusion

The SA and RSA behaviour of TMDCs films have been utilized to design ultrafast all-optical logic gates. Ultrafast operation at relatively low pump intensities demonstrates the applicability of transition metal dichalcogenides for ultrafast all-optical information processing.

5. References

[1] M. N. Arshad *et al.*, "Donor moieties with D–π–a framing modulated electronic and nonlinear optical properties for non-fullerene-based chromophores," *RSC advances*, vol. 12, no. 7, pp. 4209–4223, 2022.

[2] M. Yahya, Y. Nural, and Z. Seferoğlu, "Recent advances in the nonlinear optical (NLO) properties of phthalocyanines: A review," *Dyes and Pigments*, vol. 198, p. 109960, 2022.

[3] C. Yadav and S. Roy, "Optimization of ultrafast reverse saturable to saturable absorption transition in Ru dioxolene complex for all-optical logic applications," *Optical and Quantum Electronics*, vol. 49, no. 1, Art. no. 1, 2017.

[4] L. Feng, Z. Wang, W. Wang, F. Li, Y. Ren, and Y. Wang, "Constructing Urbach-Tail-Free and Low-Threshold Perovskite Heteronanowire Lasers toward All-Optical Switching," *ACS Photonics*, 2022.

[5] D. Somvanshi and S. Jit, "Transition metal dichalcogenides based two-dimensional heterostructures for optoelectronic applications," in *2D Nanoscale Heterostructured Materials*, Elsevier, 2020, pp. 125–149.

[6] M.-Y. Li, C.-H. Chen, Y. Shi, and L.-J. Li, "Heterostructures based on two-dimensional layered materials and their potential applications," *Materials Today*, vol. 19, no. 6, pp. 322–335, 2016.

[7] C. Quan *et al.*, "Transition from saturable absorption to reverse saturable absorption in $MoTe_2$ nano-films with thickness and pump intensity," *Applied Surface Science*, vol. 457, pp. 115–120, 2018.

[8] C. Quan *et al.*, "Band alignment of $MoTe_2/MoS_2$ nanocomposite films for enhanced nonlinear optical performance," *Advanced Materials Interfaces*, vol. 6, no. 5, p. 1801733, 2019.

[9] Y. Jiang, S. Chen, W. Zheng, B. Zheng, and A. Pan, "Interlayer exciton formation, relaxation, and transport in TMD van der Waals heterostructures," *Light: Science & Applications*, vol. 10, no. 1, pp. 1–29, 2021.

Computational Study of Optogenetic Pacing of Human Heart with ChRmine

Gur Pyari, Himanshu Bansal and Sukhdev Roy*
Department of Physics and Computer Science
Dayalbagh Educational Institute, Agra 282005, India
**sukhdevroy@dei.ac.in*

Abstract: A major challenge in cardiac optogenetics is deep excitation of cardiac cells at safe light powers. We present a theoretical analysis of optogenetic excitation of ChRmine expressing-human ventricular cardiomyocytes (HVCMs) at 650 nm. Excitation of ChRmine at 650 nm is another advantage for deeper excitation over earlier opsins. Action potential (AP) in ChRmine-expressing HVCMs can be triggered at 0.5 mW/mm^2 on illuminating with 10 ms light pulse, which enables deeper excitation upto ~ 8 mm from the pericardial surface at safe light irradiances. High-fidelity optical pacing of HVCMs is possible upto 2 Hz with ChRmine. The study provides insights for optimizing cardiac optogenetics experiments and highlights the potential of ChRmine for low-power and deeper control.

Keywords: Cardiac optogenetics, Cardiomyocytes, ChRmine, Computational optogenetics, Arrhythmias.

1. Introduction

Cardiac optogenetics is an alternative method for controlling electrical activity of the heart by overcoming limitations associated with electrical stimulation that include high-voltage shocks, low-specificity, non-synchronous depolarization, and myocardial tissue damage [1-2]. Optogenetics involves light-sensitive proteins, which are genetically expressed in the cardiac tissue for all-optical high-throughput contactless control and monitoring of cellular activity. It offers a therapeutic potential in cardiac electrophysiology, restoring pacemaking ability, suppression and manipulation of rotors in cardiomyocyte monolayers with unprecedented spatiotemporal resolution [1], [3-5].

In cardiac optogenetics, the key challenge is to achieve low power, deep excitation with minimal invasiveness [1], [6]. Recently, a new potent red-shifted opsin ChRmine has been discovered that exhibits larger photocurrent and high-sensitivity along with millisecond temporal kinetics [7-8]. Although, this opsin has significantly improved optogenetic excitation in the brain, its potential in the cardiac system is yet to be explored. The objective of this paper is to formulate an accurate theoretical model of optogenetic excitation of ChRmine-expressing human ventricular cardiomyocytes (HVCMs) at 650 nm and study the effect of various photostimulation conditions to achieve low-power, deep and noninvasive optogenetic control of HVCMs.

2. Theoretical Model

We consider a four-state model with two closed C_1 and C_2 and two open O_1 and O_2 and states for simulating the photocurrent in ChRmine [7-8]. The photocurrent through the ChRmine channels ($I_{ChRmine}$) can be expressed as follows,

$$I_{ChRmine} = g_{ChRmine}(O_1 + \gamma O_2)\, G(V)(V - E_{ChRmine}) \quad (1)$$

where, $g_{ChRmine}$ is the channel conductance, V is the membrane voltage, and O_1 and O_2 are the open-states populations, respectively. $\gamma = O_1/O_2$, $G(V)$ is the rectification function, and $E_{ChRmine}$ is reversal potential of opsins [7-10]. Further, the photocurrent through the opsin-channels has been integrated into the biophysical circuit model of HVCMs to simulate single cell voltage response as follows,

$$C_m \dot{V_m} = -(I_{Na} + I_{K1} + I_{to} + I_{Kr} + I_{Ks} + I_{CaL} + I_{NaCa} + I_{NaK} + I_{pCa} + I_{pK} + I_{bCa} + I_{bNa} + I_{rel} + I_{up} + I_{leak} + I_{xfer}) - I_{stim} - I_{ChRmine} \quad (2)$$

The details of different ionic currents and model parameters are as reported in the literature [5, 7-11]. The achievable tissue depth has been determined from the light attenuation model and parameters for different layers of cardiac tissue at different wavelengths [5, 7-11].

3. Results and Discussion

The effect of irradiance and pulse-width on optogenetic excitation of ChRmine-expressing HVCMs has been analyzed in detail (Figs. 1a, b). Minimum irradiance threshold (MIT) decreases on increasing pulse width and saturates onward. The minimum energy required is at 0.18 mW/mm^2 and 20 ms pulse-width (Fig. 1c). ChRmine can generate high-fidelity APs upto 2 Hz with 20 ms light pulse at 0.18 mW/mm^2 (Fig. 1d). At 3 Hz, it fails to maintain single-spike resolution. Considering 0.18 mW/mm^2 as threshold irradiance at 650 nm, deeply situated HVCMs up to 8.01 mm can be safely excited from the outer surface of the pericardium.

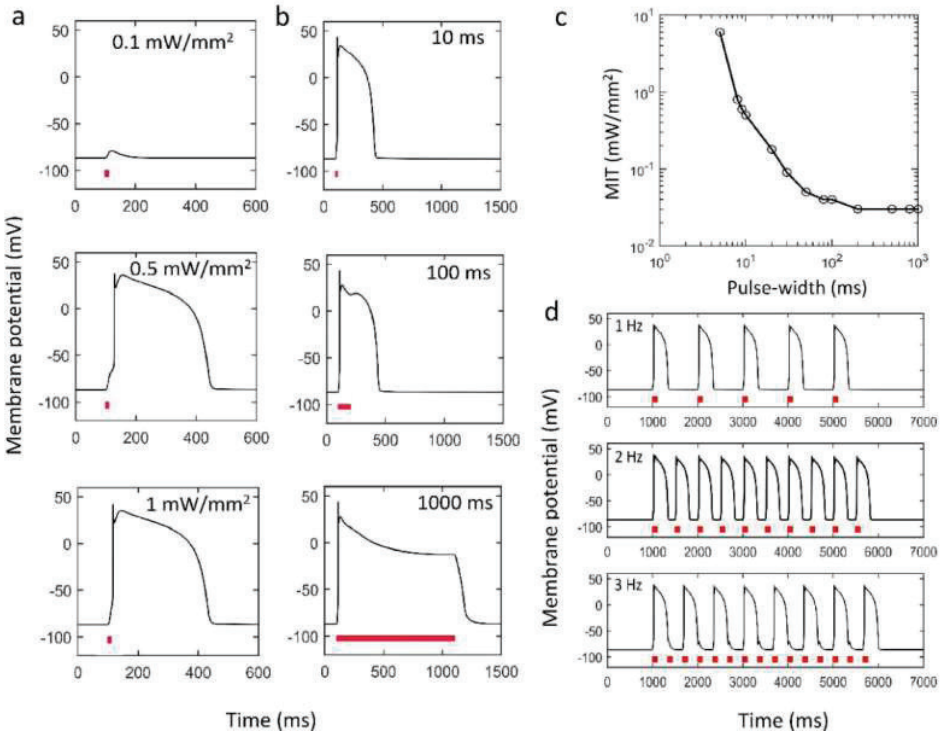

Fig. 1 Effect of irradiance and pulse-width on optogenetic excitation of ChRmine-expressing human ventricular cardiomyocytes (HVCMs) at 650 nm. Variation of membrane potential with time on illuminating with (a) 10 ms light pulse at indicated irradiances, and (b) pulses of different pulse-widths at 5 mW/mm^2. (c) Variation of minimum irradiance threshold (MIT) to evoke AP with pulse-width. (d) Optical pacing in ChRmine-expressing HVCMs on illuminating with 20 ms light pulse at 0.18 mW/mm^2 at indicated frequencies.

4. References

[1]. E. Entecheva and M. W. Kay, "Cardiac optogenetics: a decade of enlightenment," *Nat. Rev. Cardiol.* **18,** 349-367 (2021).

[2]. V. Emiliani, *et al.,* "Optogenetics for light control of biological systems," *Nat. Rev. Methods Primers* **2**, (2022).

[3]. R. A. Ochs *et al.,* "Optogenetic stimulation using anion channelrhodopsin (GtACR1) facilitates termination of reentrant arrhythmias with low light energy requirements: A computational study," *Front. Physiol.* **12,** 718622 (2021).

[4]. T. Bruegmann *et al*., "Optogenetic defibrillation terminates ventricular arrhythmia in mouse hearts and human simulations," *J. Clin. Investig.* **126,** 3894-3904 (2016).

[5]. G. Pyari., H. Bansal, S. Roy, "Ultra-low power deep sustained optogenetic excitation of human ventricular cardiomyocytes with red-shifted opsins: A computational study," *J. Physiol.* (2022). DOI: 10.1113/JP283366

[6]. S. Sridharan *et al.,* "High-performance microbial opsins for spatially and temporally precise perturbations of large neuronal networks," Neuron, **110**, pp. 1139-1155, (2022).

[7]. J. H. Marshel *et al., "*Cortical layer-specific critical dynamics triggering perception," *Science* **365,** eaaw5202 (2019).

[8]. H. Bansal, N. Gupta and S. Roy, *"*Theoretical analysis of optogenetic spiking with ChRmine, bReaChES and CsChrimson-expressing neurons for retinal prostheses," *J. Neural Eng.* **18,** 0460b8 (2021).

[9]. J. C. Williams *et al., "*Computational optogenetics: empirically-derived voltage- and light-sensitive channelrhodopsin-2 model," *PLoS Comput. Biol.* **9,** e1003220 (2013).

[10]. H. Bansal, G. Pyari and S. Roy, "Co-expressing fast channelrhodopsin with step-function opsin overcomes spike failure due to photocurrent desensitization in optogenetics: a theoretical study," *J. Neural Eng.* **19,** 026032 (2022).

[11]. K. H. W. J. ten Tusscher and A. V. Panfilov, "Alternans and spiral breakup in a human ventricular tissue model," *Am. J. Physiol. Heart Circ. Physiol.* **286,** H1088-H1100 (2006).

Detection and estimation of polarization-spatial entanglement using interference fringes

Soumya Asokan and J. Solomon Ivan
Applied and Adaptive Optics Lab, Department of Physics, Indian Institute of Space Science and Technology, Valiamala P.O., Thiruvananthapuram 695 547, India
soumyaasokan11@gmail.com

Abstract: Fringe movement upon rotation of a linear polarizer, with the light field passing through the polarizer, is shown to be a sufficient condition in detecting polarization-spatial entanglement in coherent paraxial vector light fields. Maximally entangled light fields are generated using two Gaussian light fields having slight relative tilt and orthogonal polarizations. Tunable polarization-spatial entanglement is achieved experimentally using an interferometer setup.
Keywords: Classical entanglement, Interference, Coherence.

1. Introduction

The superposition principle applies to several optical phenomena such as coherence, interference, diffraction, etc. When the problem involves two or more degrees of freedom, the notion of entanglement emerges. It was introduced by Schrödinger in the context of quantum mechanics in 1935, whose formulation mirrored classical optics, through the wave-particle duality. Numerous works have been done towards detection and estimation of entanglement in the optical context, by importing and implementing formal methods developed in quantum theory/quantum information [1-3]. Typically, this renders the experiment cumbersome in terms of the means to achieve entanglement, and also in terms of the use of additional devices in the setup. For instance, violation of Bell-type inequality (well known in quantum mechanics) towards detection of entanglement have been demonstrated in Ref. [1].

A simple consequence of the superposition principle is the formation of fringes, well observed for instance in the Newton's rings experiment. Since both fringe formation and entanglement are a consequence of the superposition principle, it is rather tempting to think that the phenomenon of entanglement, should manifest itself through the observed fringes, in an interferometry experiment. In this work [4], the movement of fringes in an interferometry experiment (see Figs.1 and 2), under some considerations, is shown to be a manifestation of the phenomenon of entanglement. Estimation of entanglement is demonstrated using polarimetry (see Fig. 3).

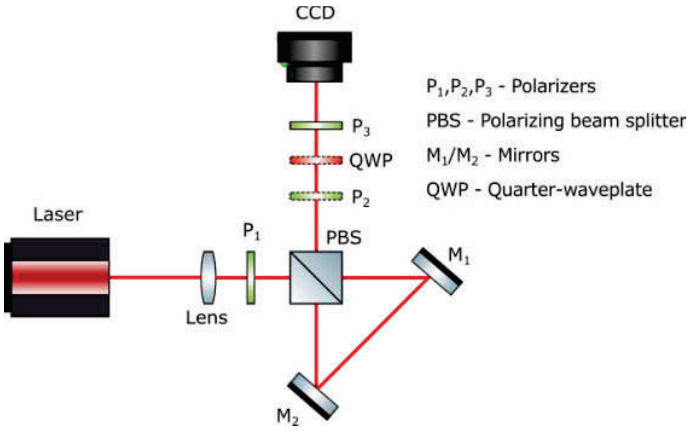

Fig. 1: Schematic diagram of a folded Mach-Zehnder interferometer setup that generates entanglement between the polarization and spatial degrees of freedom in the incoming laser light. Even the slightest misalignment in the mirrors, (relative tilt of the order of 10^{-4} radians), renders the device to be maximally entangling. Fringe movement as observed on a screen on rotation of polarizer P_3, implies polarization-spatial entanglement in the present experiment.

As understood formally from the Schmidt decomposition [5], orthogonal modes were a necessity for maximal entanglement and sophisticated experimental setups, that use devices such as spatial light modulators, dove prisms and digital micromirror devices [1-3], were required in achieving it. Nevertheless, we are able to show that two Gaussian light fields with a small relative tilt, (of the order of 10^{-4} radians), but with substantial spatial overlap, and orthogonal polarizations, can have close to 1 ebit, (≈0.99 ebit, see Fig. 3) of polarization-spatial entanglement. This is attributed to the inherent wavelength dependent scale in the problem.

A folded Mach-Zehnder interferometer setup, as shown in Fig. 1, is used to generate polarization-spatial entanglement in a coherent vectorial paraxial light field. Here, fringe movement, achieved by rotation of the linear polarizer P_3, is a sufficient condition for the detection of polarization-spatial entanglement. Note that the dotted elements in the setup and the CCD camera are not necessary for the detection of entanglement. That is, fringe movement, on rotation of polarizer P_3, observed on a white screen held at the output of P_3 is sufficient. Tunable polarization-spatial entanglement is obtained by rotating polarizer P_1. Even the slightest misalignment in the experimental setup (relative tilt of the order of 10^{-4} radians between the mirrors M_1 and M_2), renders the device to be maximally entangling. The obtained results are definitely relevant to several applications that require maximal entanglement, which we have generated without using higher-order spatial modes.

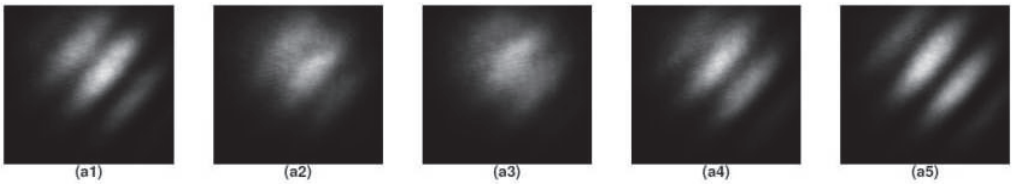

Fig. 2: (a1) - (a5) show the fringe movement as polarizer P_3 is rotated from 70° to 110° in steps of 10°. The initial polarizer P_1 is fixed at 45°. The fringe movement demonstrates entanglement.

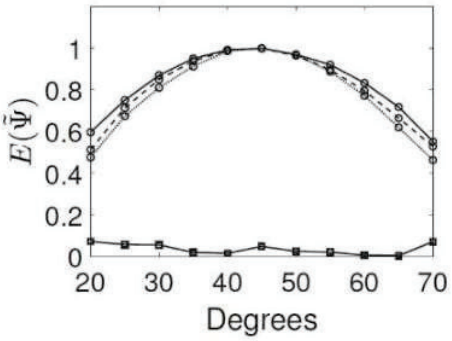

Fig. 3: The ○ plot the estimated polarization-spatial entanglement for three different tilts (shown by solid, dashed and dotted lines), for varying P_1 orientation. The □ plot the estimated polarization-spatial entanglement for a particular tilt when P_2 is inserted after the PBS (see Fig. 1). Insertion of P_2 destroys entanglement.

2. References

[1] X.-F. Qian, B. Little, J. C. Howell, and J. H. Eberly, "Shifting the quantum-classical boundary: theory and experiment for statistically classical optical fields," Optica 2, 611-615 (2015).
[2] C. Samlan and N. K. Viswanathan, "Generation of vector beams using a double-wedge depolarizer: non-quantum entanglement," Opt. Laser Eng. 82, 135-140 (2016).
[3] B. Zhao, X.-B. Hu, V. Rodríguez-Fajardo, A. Forbes, W. Gao, Z.-H. Zhu, and C. Rosales-Guzmán, "Determining the non-separability of vector modes with digital micromirror devices," Appl. Phys. Lett, 116, 091101 (2020).
[4] S. Asokan and J. Solomon Ivan, "Gaussian spatial-polarization entanglement in a folded Mach-Zehnder interferometer," J. Opt. Soc. Am. A 37, 825-832 (2020).
[5] M. A. Nielsen and I. L. Chuang, *Quantum computation and quantum information*, Cambridge University Press (2004).

Design of an Optical Antenna Using Subwavelength Grating on SOI Platform

Mayank Agrawal*, Manoranjan Minz, Soibam Aruna Chanu Ramesh Kumar Sonkar
Department of Electronics and Electrical Engineering, Indian Institute of Technology Guwahati, Guwahati
*m.agrawal@iitg.ac.in

Abstract: A subwavelength grating based highly unidirectional optical antenna is presented. The simulation result shows upward diffraction efficiency of 91.52% with a diffraction angle of 17.08°.

1. Introduction

The optical antenna has become a prominent element to couple the light from photonic integrated circuits to optical fibers. Plasmonic resonance based optical antennas have been investigated recently, which resulted in lossy coupling with lower radiation efficiency [1]. It has been observed from the literature on surface grating-based optical antennas that the two main factors which determine the overall diffraction efficiency and directionality are the scattering of light towards BOX and the refractive index mismatch between input waveguide and grating [2]. Optimized complex design structures can overcome the problem of unwanted scattering of light and apodization of the grating can be used to make the transition smoother between input waveguide and grating [3].

In this paper, a surface grating-based optical antenna is proposed on a silicon-on-insulator (SOI) platform with 220 nm silicon. The L-shaped waveguide geometries have been used to improve the directionality of the antenna. Subwavelength grating (SWG) structures have been optimized to reduce the back reflections. Finite-difference time-domain (FDTD) simulation of the optimized structure exhibits high diffraction efficiency, unidirectionality with the broadband operation. The antenna has a compact footprint of 8 μm × 4.44 μm.

2. Design Methodology

The schematic view of the proposed optical antenna is shown in Fig. 1. The design is implemented on a SOI platform with 220 nm silicon core, 1 μm buried oxide (BOX) and 2 μm silicon dioxide (SiO_2) as cladding. The structure is based on L-shaped geometries [4] with full (220 nm) and shallow (133 nm) etch trenches. This L-shaped silicon provides blazing effect to diffract most of the input power upwards. A synthesized SWG structure, consisting of periodic L-shaped silicon segments, is implemented between L-shaped elements. The complete antenna structure is constructed with an apodized and uniform section. The first unit cell is apodized to allow maximum power transfer from the input waveguide to the grating. This is followed by a periodic unit cell involving L-shaped elements and SWG structures. The dimension of the first cell L_1, L_2, L_3 and L_4 refer to the length of the un-etched SWG segment, shallow etched SWG segment, shallow etched silicon slab, un-etched silicon slab respectively as shown in Fig. 1(b). The width of the fully etched gap and L-shaped silicon segment is denoted by W_1, W_2 respectively. The pitch of the SWG section is $\Lambda_{SWG1} = W_1 + W_2$ and the duty cycle is $DC_{SWG1} = W_2/\Lambda_{SWG1}$. For the subsequent periodic unit cells, the corresponding parameters are L_5, L_6, L_7, L_8, W_3, W_4, Λ_{SWG2}, DC_{SWG2}.

All the parameters mentioned above are optimized for 220 nm silicon for maximum upward diffraction efficiency. Directionality of the antenna is calculated as the ratio of total power diffracted upwards (P_{up}) to the sum of power diffracted upwards and downwards (P_{down}).

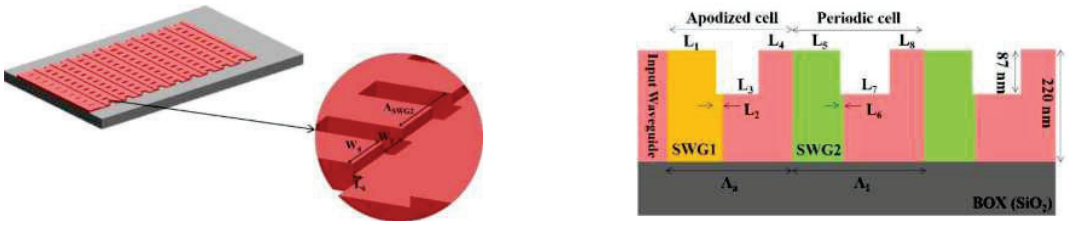

(a) (b)

Fig. 1: (a) Three-dimensional (3D) view schematics of the design (b) Two-dimensional side view schematics of the antenna with L-shaped SWG structures

3. Simulation results and discussions

To investigate the performance of the antenna, the number of periodic unit cells are varied from 4 to 19, targeting maximum diffraction efficiency at 1550 nm wavelength. The Diffraction efficiency of the antenna is defined as the part of input power diffracted upwards. It can be observed from plot shown in Fig. 2(a) that 9 periodic cells provide both compactness and high diffraction efficiency. For 9 periodic cells, the structural parameters are obtained as L_1 = 289 nm, L_2 = 40 nm, L_3 = 217 nm, L_4 = 209 nm, L_5 = 283 nm, L_6 = 40 nm, L_7 = 272 nm and L_8 = 210 nm. L-shaped SWG sections are structured with Λ_{SWG1} = 410 nm, DC_{SWG1} = 0.82 for first apodized unit cell and Λ_{SWG2} = 381 nm, DC_{SWG2} = 0.62 for periodic cells. 3D FDTD simulation is performed to evaluate the diffraction efficiency over the wavelength range from 1.4 µm to 1.7 µm for fundamental TE mode input. The diffraction efficiency and directionality at 1550 nm wavelength is obtained as 91.52% and 94.43 % respectively. Diffraction efficiency spectra having 1-dB bandwidth of 271 nm with ripple factor 0.09 is shown in Fig. 2(b).

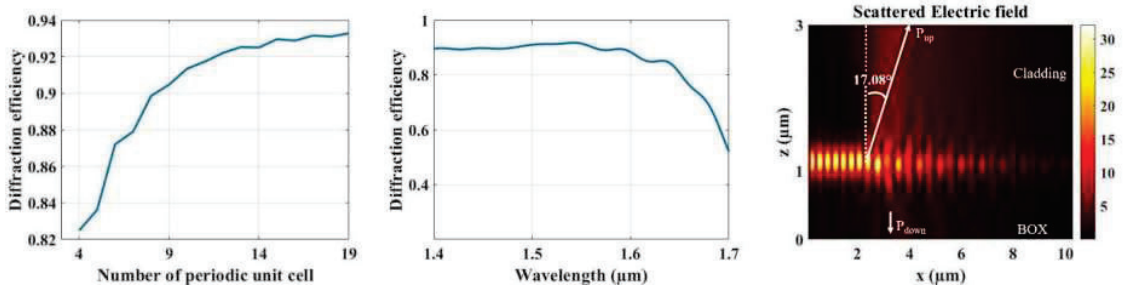

(a) (b) (c)

Fig. 2: (a) Diffraction efficiency at 1550 nm for varying number of periodic cells (b) 3D simulation result for upward diffraction efficiency as a function of wavelength (c) Electrical field distribution of the antenna

Fig. 2(c) shows the electric field distribution of the antenna. It can be observed that most of the input power is diffracted upwards, and little power is diffracted towards the BOX. The far-field distribution at 1550 nm of the designed structure is shown in Fig. 3. The diffraction angle is found to be 17.08°, and the full width at half maximum along the polar coordinate and azimuth coordinate is 6.6°, 49.2° respectively.

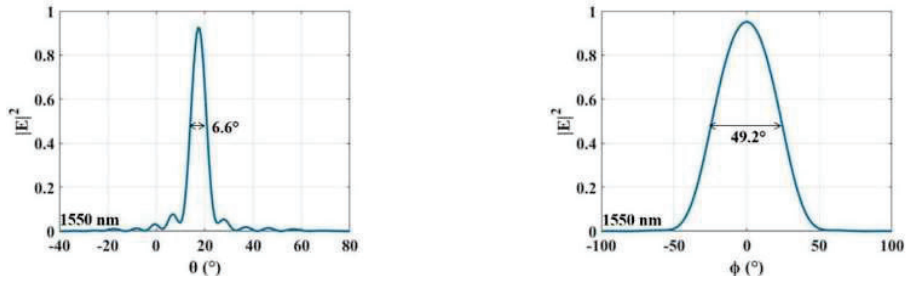

(a) (b)

Fig. 3: (a) Far field distribution as a function of polar coordinate (θ) for ϕ = 0° (b) Far-field distribution as a function of azimuth coordinate (ϕ) for θ= 17.08°

4. Conclusions

In this paper, a surface grating based optical antenna on SOI platform is presented, where SWG structures are implemented for higher diffraction efficiency. 3D FDTD simulation of the design provides a diffraction efficiency of 91.52% with a 1-dB bandwidth of 271 nm. The antenna has a directionality of 94.43% with a footprint of 8 µm × 4.44 µm to provide low loss interconnectivity between photonic integrated circuits and standard single-mode fibre. The presented compact optical antenna can be used to realise a highly dense optical phased array.

5. References

[1] G. N. Malheiros-Silveira, L. H. Gabrielli, C. J. Chang-Hasnain and H. E. Hernandez-Figueroa, "Breakthroughs in Photonics 2013: Advances in Nanoantennas", *J. IEEE Photonics Journal* vol. 6, pp. 1-6, 2014.
[2] R. Marchetti et al., "Coupling strategies for silicon photonics integrated chips", *J. Photonics Research*, vol. 7, pp. 201-239, 2019.
[3] D. Benedikovic et al., "Sub-decibel silicon grating couplers based on L-shaped waveguides and engineered subwavelength metamaterials", *J. Opt. Express* vol. 27, pp. 26239-26250, 2019.
[4] S. Khajavi et al., "Compact and highly-efficient broadband surface grating antenna on a silicon platform", *J. Opt. Express*, vol. 29, pp. 7003-7014, 2021.

Study of Diffraction of Poincare-Hopf Beams through a Sectorial Aperture

S.Deepa[1], Gauri Arora[1] and P.Senthilkumaran[2]

1.Singular Optics Lab, Department of Physics, Indian Institute of Technology Delhi, Hauz Khas, New Delhi-110016
2. Optics and Photonics Centre, Indian Institute of Technology Delhi, Hauz Khas, New Delhi-110016.
deepasathya12@gmail.com

Abstract: Polarization singularities broadly classified into ellipse and vector field singularities have proved to be promising in various different arenas. In this work, we report results observed when vector field singularities or Poincare Hopf beams are diffracted through a sectorial aperture. The intensity pattern obtained can lead to the determination of Poincare Hopf index of the vector field singularity under study. The polarization pattern of the diffracted beam shows transformation of the input vector field singularity into generic ellipse field singularities, upon diffraction. The index and sign rules are conserved in the process.

Keywords: Diffraction, vector field singularities, Poincare Hopf index.

1. Introduction

The generation, detection and characteristics studies of polarization singularities have produced many interesting publications in the recent years. The commonly studied polarization singularities are vector field singularities and ellipse field singularities. For the former, the handedness is undefined and for both types, the azimuth (γ) is undefined, and they are characterized by Poincare Hopf index (η) and C point index (I_c), respectively. Index (η) takes integer values in general whereas I_c index takes half integer values. The polarization singularities can generally expressed in the form as shown below [1,2]:

$$\vec{E}(r,\emptyset) = \left[r^{|m|}exp(im\emptyset)\widehat{e_R} + r^{|n|}exp(in\emptyset + \emptyset_0)\widehat{e_L}\right] \quad (1)$$

where, m and n are the topological charges of the right circular polarization (RCP) component and left circular polarization (LCP) component beams that superpose to give any singular beam. The eq.1 represents a V-point or vector field singularity if m = -n and a C point or an ellipse field singularity if $|m| \neq |n|$. The C points are generally categorized as lemon, star or monstar. The V points of index 1 are categorized as Type I, II, III and IV.

2. Diffraction through a sectorial aperture

In the present work we have studied diffraction of generic and higher order V points through a sectorial aperture and have shown that the intensity pattern of the diffracted beam can give the Poincare Hopf index of the input V point beam. We can generate the different V points using commercially available S waveplates and half wave plates combination, as per index requirement.

In the case of scalar beams, it has been shown that the number of bright intensity beads in the diffracted intensity pattern is equal to the magnitude of the topological charge of the constituent orbital angular momentum beam [3]. The diffracted beam unveils the characteristics of the incident light fields. From the figure 1 we see that the number of bright intensity spots divided by 2 gives $|\eta|$. This is in abidance with the fact that the diffracted intensity patterns corresponding to the degenerate set of V-point singular beams are identical [4, 5]. But the polarization distribution pattern of the diffracted beam can give information about the sign of the Poincare Hopf index of the vector beam singularity and thus lift the degeneracy. We have also noticed that V points, on small perturbation become topologically unstable, and split into lower-order C-points on diffracting through the sectorial aperture. These disintegrated C-point singular beams have been observed to be receding away from the optic axis with the propagation distance. The disintegrated C-point singular beams are separated by the L-lines (as shown in the Fig. 1). The index is conserved and the sign rule is obeyed in the diffracted polarization pattern in all the cases.

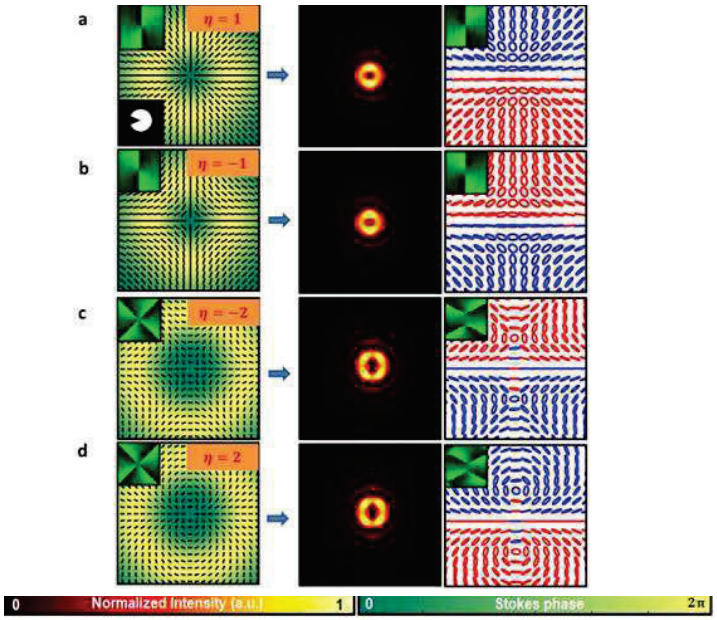

Fig. 1: Diffracted intensity and polarization distributions of different Poincare Hopf index V-points through a sectorial aperture. The corresponding Stokes phases have been shown as insets. The I column (a, b, c and d) shows the input vector field singularities, the II column shows the diffracted intensity patterns and the III column shows the polarization distribution of the diffracted beams showing the splitting into ellipse field singularities.

3. Conclusion

The diffraction of Vector field singularity through a sectorial aperture has been studied. The diffracted intensity pattern can help to determine the Poincare Hopf index of the vector field singularity under study. The polarization pattern of the diffracted beam shows transformation of the input vector field singularity into generic ellipse field singularities, conserving index in the process.

References:

[1] Maurer, C., Jesacher, A., F¨urhapter, S., Bernet, S., and Ritsch-Marte, M., "Tailoring of arbitrary optical vector beams," New. J. Phy. 9(-), 78 (2007).
[2] Pal, S. K., Ruchi, and Senthilkumaran, P., "Polarization singularity index sign inversion by half-wave plate," Appl. Opt. 56(22), 6181–6190 (2017).
[3]Ruishan Chen, Xiaoqiang Zhang, Yong Zhou, Hai Ming, Anting Wang, and Qiwen Zhan, "Detecting the topological charge of optical vortex beams using a sectorial screen", *Applied Opt.* 56, no. 16, pp. 4868-72 (2017).
[4]P. Senthilkumaran,"Singularities in Physics and Engineering", Academic Press, California (2003).
[5]B S Bhargava Ram, Anurag Sharma, and P. Senthilkumaran, "Diffraction of V-point singularities through triangular apertures", *Opt. Exp.* 25, no. 9, pp. 10270-10275 (2017).

Liquid crystal waveguide-based retarder for polarization converter and high optical path generation

Vaibhav Sharma, and Aloka Sinha*

Department of Physics, Indian Institute of Technology Delhi, New Delhi, India.

vaibhavsharma0495@gmail.com, aloka@physics.iitd.ac.in

Abstract: We have fabricated a Liquid Crystal (LC) core waveguide-based retarder and a high optical path generator on an indium tin oxide (ITO) coated glass substrate. We have experimentally demonstrated that the linearly polarized light ($+45^0$) can be converted into elliptically polarized light and depending upon the optical path difference (OPD), an externally applied voltage rotates the orientation angle of the ellipse. We have numerically shown that the applied voltage of a few volts can provide a large OPD of 1.8 mm between TE and TM polarized light. The proposed device has potential application in Fourier Transform Spectroscopy (FTS) to detect biomolecules.

Keywords: Liquid Crystal, Optical waveguide, Polarization convertor, Optical path generator

1. Introduction

Liquid crystals (LCs) are widely used in integrated optics to modulate the properties of incident light using an externally applied electric field [1-2]. Conventional LC cell-based retarders consist of an LC layer sandwiched between two transparent electrodes coated glass substrates. ITO is generally used as an electrode layer to apply the electric field in the cell and create the optical path difference (OPD) between two orthogonal polarized light [3]. There are two limitations to traditional LC cells. First, the transparent electrodes limit the total power because of the complex refractive index of the ITO layer. Second, to create a large OPD, the LC film thickness should be large. The large film thickness makes the device opaque and slow in response. To overcome this limitation, we have designed and fabricated an LC core waveguide-based retarder that converts the linearly polarized light into elliptically polarized light, and the applied voltage rotates the orientation angle of the ellipse in the clockwise direction. The proposed device provides a large OPD of 1.8 mm between two orthogonal polarized lights by just applying 12 volts of an external electric field. The proposed device can be used to replace the moving mirror arrangement (Michelson interferometer) in Fourier Transform Spectroscopy (FTS) to detect biomolecules [4].

2. Design, Fabrication and Experimental Setup

Figure. 1 (a) illustrates the schematic representation of the proposed device. It consists of an LC layer (ordinary (n_o) and extraordinary refractive index (n_e) are 1.53 and 1.71, respectively at 633 nm wavelength) sandwiched between two polyvinyl alcohol (PVA) coated glass plates. The PVA of refractive index 1.47 acts as a cladding layer and also provides homogeneous alignment to the LC molecules. The PVA layer of thickness 4 µm is spin-coated on the ITO-glass substrates. The homogeneous alignment of LC molecules is achieved by rubbing the PVA layer with a velvet cloth. Spacers of thickness 6 µm are used to form the core region. In the end, both the glass plates are assembled with the help of UV curable glue. The LC is filled in the core region by the capillary action.

Figure. 1 (b) shows the experimental setup for the characterization of the device. It comprises of a He-Ne laser of 633 nm wavelength, a polarizer, those pass axis is set at $+45^0$. The microscope objective (MO) lens is used to launch the light into the fabricated device, and the power meter measures the output power of the fabricated device. The quarter wave plate (QWP) and polarizer at the output end are used to measure the output polarization state of the fabricated device using the Stokes parameters. The function generator is used to apply the electric field.

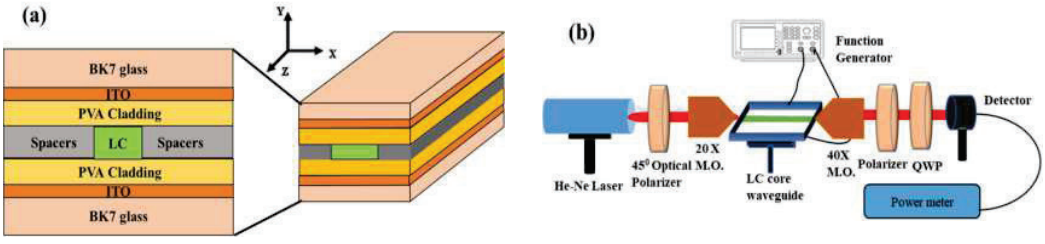

Figure. 1 (a) Schematic of the proposed device, (b) Experimental setup to characterize the waveguide.

3. Experimental and Numerical Results

The output polarization state of the fabricated device is measured by calculating the Stokes parameters [5]. After calculating the Stokes parameter, the output polarization of the fabricated device is plotted. Figure. 2 shows the output

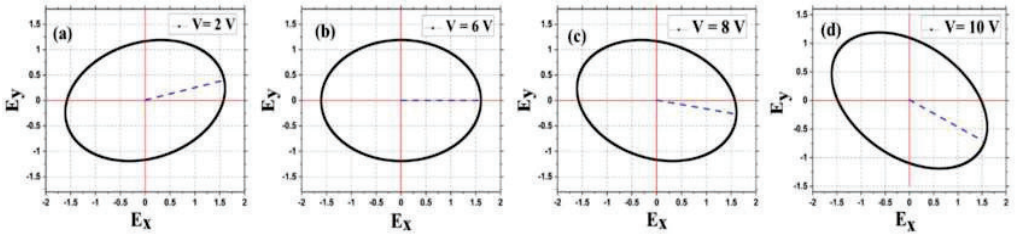

Figure. 2. Output polarization state of the waveguide at different applied voltages.

polarization of the device at different applied voltages. The applied voltage of 2 V introduces a phase difference between two orthogonal polarized light; hence it converts the linearly polarized light into elliptically polarized light (see Figure. 2(a)). Figure. 2 (b), (c), and (d) show that the further increment in voltage change the orientation angle of the ellipse.

Figure. 3 (a) shows the variation of capacitance of the fabricated device with the applied voltage. It shows that the threshold voltage to reorient the LC molecules is around 1.5 V, and because of that, the fabricated device has a low operating voltage range (from 2 to 12 volts). The OPD generated by the waveguide is numerically calculated and plotted with the applied voltage. Fig. 3 (b) represents the voltage dependent OPD of the fabricated device. At V= 12 V, the TM polarized light sees the maximum $n_e(\theta)$ (=1.71) of LC, and TE polarized light sees the n_o (=1.53). This translates to a volage tuneable OPD = $((n_e-n_o)\, l)$ of 1.8 mm for a 10 mm waveguide length (l). In the FTS, the resolution of the spectrum is inversely proportional to the OPD. Hence, the large OPD is the key requirement in this field.

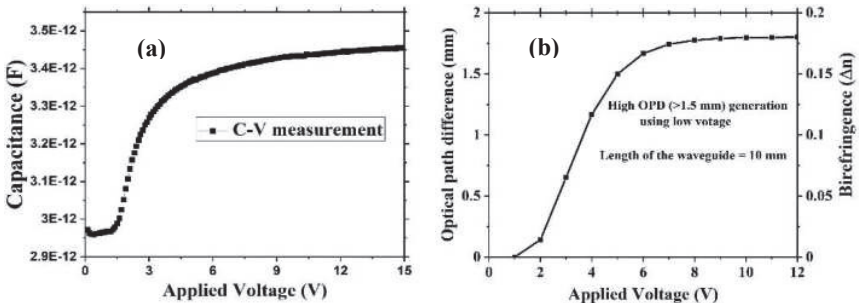

Figure. 3. (a) Variation of capacitance with the applied voltage, (b) Dependence of OPD on the applied voltage.

4. Conclusion

A voltage-controlled LC waveguide-based retarder is fabricated on the ITO-coated glass substrate. The waveguide is used to convert the linearly polarized light into elliptically polarized light by applying the external voltage. The fabricated device of length 10 mm generates a large OPD up to 1.8 mm between TE and TM polarized light in the voltage range of 2 to 12 volts. The device can be an alternative approach to the Michelson interferometer in FTS for the chemical analysis of the biomolecules.

Acknowledgments

DST Inspire (DST/INSPIRE/03/2018/000262), IIT Delhi and DRDO, New Delhi (DFTM/03/3203/P/01/JATC-P2QP-01) for the funding.

References

[1] J. Beeckman, K. Neyts, and P. J. M. Vanbrabant, "Liquid-crystal photonic applications," Opt. Eng., 50 (8), 081202 (2011).

[2] V. Sharma, A. Sinha, and M.R. Shenoy, "Mode size converter based on periodically segmented liquid crystal core waveguide", J. Lightwave Technol., 40 (14), 4728-34 (2022).

[3] J. M. López-Tellez, N. C. Bruce, and O. G. Rodríguez-Herrera, "Characterization of optical polarization properties for liquid crystal-based retarders", Appl. Opt. 55 (22), 6025-33 (2016).

[4] J. Mandon, G. Guelachvili, and N. Picque, "Fourier transform spectroscopy with a laser frequency comb", Nature Photon, 2009, 3, 99–102, (2009).

Enhanced Absorption due to the Localized Surface Plasmon Coupling in CdS – CdTe Hetero Junction Nanorods Decorated with Mg Nanoparticles

Saleem Shaik[1*], Manoranjan Minz[2], Bhaveshkumar Kamaliya[3], Rakesh G Mote[4]
*[*1,2]Electrical Engineering Department, Indian Institute of technology Bombay,400076, Powai*
[3,4]Mechanical Engineering Department, Indian Institute of technology Bombay,400076, Powai
[*]saleems.iitk@gmail.com

Abstract: Finite Difference Time Domain (FDTD) simulations were performed to find the enhancement in the absorption due to the localized surface plasmon (LSPR) coupling in CdS - CdTe heterojunction semiconductor Nano Rod (NR) structure decorated with Mg Nanoparticles (NP) in the visible wavelength range (490 nm – 670 nm) as compared to the noble (Au, and Ag) metallic NP. Propagating modes were also observed on the surface of the NR due to the LSPR coupling.
Keywords: LSPR, Au, Ag, Mg, CdTe, CdS, Nanorod, and FDTD

1.Introduction

In the recent past II–VI hetero semiconductor nanowires (NW) are most researched because of their 1D structure, where the light is confined only in one direction. Among all II–VI hetero Semiconductors NW Cd chalcogenide structure like CdTe – CdS NW were most researched p, and n type materials because of various applications in Solar cells, Light emitting diodes, Photo Detectors, and laser diodes etc[1]. In the current scenario FDTD simulations were studied on the NP decorated CdTe – CdS NR structure to understand the enhancements in the absorption for finding applications in the solar cells. CdS nano wires were considered for the Solar Cell applications because of it's increased absorption spectra from 350 – 490 nm range as compared to planar thin films, and have lower exciton binding energies 29 meV, just 4 meV above the room temperature[2]. In the FDTD modeling porous Al_2O_3 was used as a substrate as the growth of NR in flexible Nanoporous anodic alumina (NAA) flexible membrane has good absorption[4]. CdTe has high absorption of 95% within 1 μm level inside the bulk, thereby it is called as absorber layer[3]. Further the CdTe NW structures were also designed to reduce the losses in planar thin film form[4]. In the current study It was found that the penetration of the Electric fields (EF) inside NR system due to the LSPR coupling in the gap (20 nm) between the NP symmetrically arranged on the NR surface along X and Y directions was the cause for improved absorption and it is predominant in Mg NP at the peak wavelength range (490 nm – 670 nm) of solar radiation. Mg with high LSPR quality factor is suitable for the peak of the solar spectrum next to Ag, and it has very lower losses in the 380 – 520 nm range[5].

2. Lumerical FDTD Modeling

The Fig. 1(a) shows the FDTD model with EF monitors of single unit cell heterojunction CdS-CdTe NR structures decorated with NP symmetrically in X and Y directions. The plane wave was incident from the bottom of the unit cell along Z direction 200 nm below the P -N junction. The metallic NP half spheres are of 40 nm in diameter arranged periodically with the gap of 20 nm. The dimensions of the unit cell were mentioned in the Fig. 1b (left panel). In all of the simulations periodic boundary conditions were applied. So, it takes into consideration the array of unit cells.

3. Results and Discussion

The absorption of the entire unit cell with periodic boundary conditions was shown in the Fig. 1b (right panel). It is evident that the absorption in NP decorated NR system is predominant from 600 nm – 900 nm. Mg has high absorption at 630 nm, Ag, and Au NP decorated NR has the peak absorption at 750 nm, and 800 nm. In case of Mg NP at 490 nm, and 570 nm the LSPR coupling is predominant as compared to the Au, and Ag NP as it was shown in the Fig. 1c, and 1d. Most of the Solar radiation peak intensity falls in between 490 nm – 650 nm. Interestingly, in the case of Mg NP the fields are mostly concentrated at the boundaries on the surface of NR system as compared to the Au, and Ag as shown by the peaks and valley in the blue curve in Fig. 1c (λ – 490 nm), and 1d (λ – 570 nm). It was also observed that the EF modes were also absorbed inside the Au, and Ag NP as shown by the silver and orange colored curves in Fig. 1c (λ – 490 nm). As shown in Fig. 1d (λ – 570 nm) the LSPR coupling in the Ag also improved as observed by the silver curve, and in the Au still the LSPR coupling did not improve. All these measurements were taken just 5 nm

above the surface of the NR system along the Z direction (length of the NR). The penetration of these fields from the boundaries of NP inside the CdS – CdTe NR system also exists due to this the improvement in the absorption was observed. The propagating modes were formed due to the coupling of LSPR modes on the surface of the NR system. At the end of the length of the NR system the decay in the intensity of EF was observed. This decay may be due to insufficient coupling because of the absorption of the NP, trapping of the photons in the gap between the NP etc.

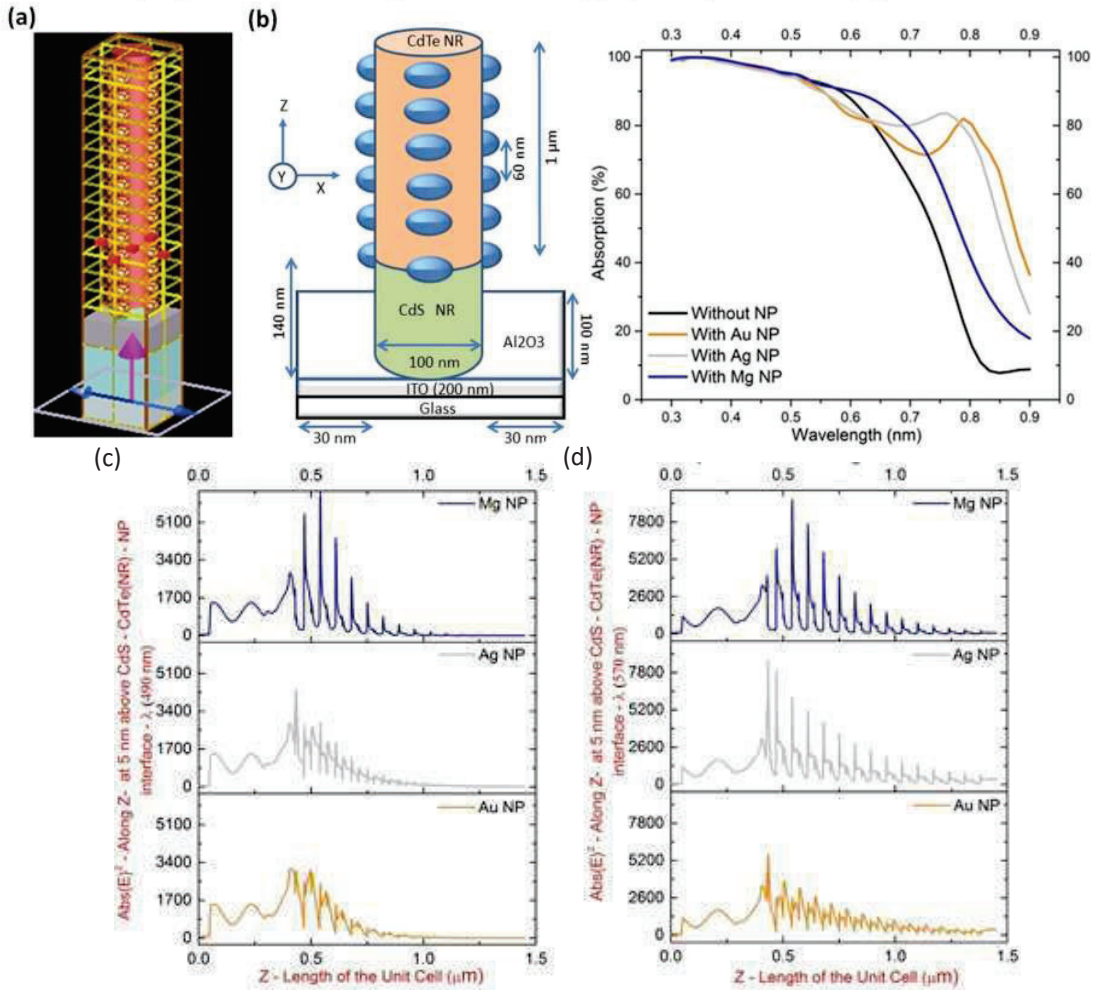

Fig. 1: (a). Unit cell (UC) for FDTD model with EF monitors, (b). UC dimensions along X, and Z directions (left panel), and the absorption spectra (right panel), (c, d). EF Intensity distribution at 5 nm above the CdTe – CdS NR surface decorated with Au, Ag., and Mg NP symmetrically along X, and Y directions at 490 nm and 570 nm wavelengths.

4. Conclusions

The enhanced absorption due to the LSPR coupling and the field penetration in the Mg NP decorated CdTe – CdS NR structure is observed in 490 nm – 670 nm range. Due to the LSPR coupling the existence of propagating modes was observed in the form of decaying EF distributions. This type of system is very suitable for Photovoltaic applications.

5. References

[1 Xiwei Zhang,, Di Wu, and Huijuan Geng," Heterojunctions Based on II-VI Compound Semiconductor One-Dimensional Nanostructures and Their Optoelectronic Applications", Crystals, 307, 7, (2017)

[2] Lilhare, D and Khare, A, "Development of chalcogenide solar cells: Importance of CdS window layer," Opto-Electronics Review **28,** (2020).

[3] Romeo, Alessandro and Artegiani, Elisa, "CdTe-based thin film solar cells: past, present and future", Energies, 1684, 14(6), (2021).

[4] Fan, Zhiyong Razavi, Haleh, Do, Jae-won, Moriwaki, Aimee and Ergen, Onur ,Chueh, YuLun,Leu, Paul W Ho, Johnny C,Takahashi, Toshitake,, Reichertz, Lothar A, Three-dimensional nanopillar-array photovoltaics on low-cost and flexible substrates, Nature Materials, 648, 8(8), 2009.

[5] Emilie Ringe, Shapes, Plasmonic Properties, and Reactivity of Magnesium Nanoparticles, J. Phys. Chem. C , 15665−15679, 124, (2020)

Angle-dependent switching in metamaterial absorber at infrared frequencies

Raghwendra Kumar [*(1)] and Pankaj Kumar[(2)]

(1) Department of Physics, B. N. College, Patna University, 800004, India

(2) Department of Computer Science and Engineering, Graphic Era Hill University, Dehradun, 248002

*Corresponding author's e-mail address: raghaviitk0@gmail.com

Abstract: We present numerical studies on an angle-dependent switchable metamaterial absorber operating at near-infrared frequencies. The absorber consists of an array of one-dimensional silicon strips on a silicon substrate followed by a thin layer of gold of a thickness of 30 nm. Computer Simulation Technology Microwave Studio was used for numerical simulations. The absorption is caused due to the Fabry–Perot (FP) cavity resonances in the system. The absorption band can be switched from single to dual with the chance in the angle of incidence. So, this absorber can be exploited for the single band and dual-band absorber as per requirement.

Keywords: Metamaterial absorber, Dual-band absorber and Fabry Perot resonance.

1. Introduction

Electromagnetic metamaterials are artificially structured materials that have attracted extensive attention in the last few decades and exhibit exotic electromagnetic responses which are not found in naturally occurring materials [1, 3]. With the development of metamaterials, a series of intriguing applications have emerged, such as complete absorption of electromagnetic radiation as a metamaterial (MM) absorber at a particular frequency, artificial optical chirality, wavefront modification, cloak of invisibility, negative refraction, perfect lenses [4]. Among these applications, MM absorbers have received considerable attention due to their importance for radar stealth at microwave and terahertz frequencies, development of sensitive and reliable infra-red detectors, micro-bolometer arrays.

Most of the reported MM absorbers exhibit only one resonance absorption band; however, absorbers with two absorption bands are desired in many applications such as detectors and chemical and biomedical sensing. Recently, several MM absorbers with more than one band have been reported by researchers using different absorption mechanisms such as impedance matching, cavity resonance, guided-mode resonance and FP mode resonance [5]. Most of the absorbers exhibit either single or double absorption bands for a particular configuration. So, the MM absorber having the capacity of switchability from single band to double band and vice versa is most desirous from the switching point of view.

Here, we propose and demonstrate an angle-dependent switchable metamaterial absorber comprising a one-dimensional silicon strip array on a silicon substrate followed by a thin layer of gold. It works under the TE (electric field parallel to the length of strip) mode excitation at IR frequencies. It has an absorptance of around 0.99 and a resonance wavelength of 1.481 um. As confirmed by the numerical simulation, the absorption is caused by the formation of double FP cavities in the system; one is in the strip, and the other is in between the two consecutive strips[6]. Due to the separate requirement of structuring and deposition, this absorber is very robust for large-area fabrication processes. As we reported in our previous work, the soft lithography technique can be used for large areas of fabrication[7]. The proposed design of a compact and efficient absorber would be greatly useful in various applications, including filters, sensors, thermal emitters, solar cells, and imaging devices.

2. Results and Discussions:

A schematic diagram of the proposed MM absorber is shown in Fig. 1. It consists of an array of one-dimensional silicon strips of height (h) and width (w) on a silicon substrate followed by a thin layer of gold of the thickness (t) on the top of strips as well as on the remaining parts of the substrate not covered by the strips. The ultra-sparse distribution of strips enables the formation of FP cavities in the strip in the vertical direction and between two consecutive strips in the horizontal direction. In a vertical strip cavity, the gold layer at the top of the strip works as a perfect reflector. In the cavity between two consecutive strips, the strips are working as a partial reflector.

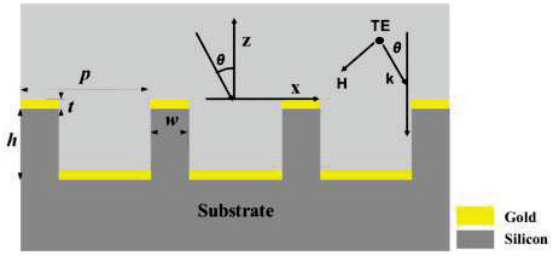

Fig. 1: Schematic diagram of the MM absorber. p, t, w and h are the periodicity of the strip array, the thickness of the top gold layer, the width of the strip and the height of the strip, respectively.

The numerical simulations of the MM absorber are performed using finite integration technique based CST Microwave Studio. The simulated transmittance, reflectance and absorptance spectra of the absorber are shown in Fig. 2(a). The optimized parameters used for simulations are as p = 1300 nm, w = 100 nm, t = 30 nm, n_s = 1, h = 1000 nm and θ = 0°. It is clear that there is an absorption peak with an absorptance of about 0.99 and at resonance wavelength 1.491 µm. The angle dependent switchability of the MM absorber is shown in Fig. 2(b). It is clear that at normal incidence and up to 3°, there is only one absorption peak. But, beyond 3°, there is an appearance of an extra peak around 1.54 um wavelength, and it is shifting towards shorter wavelengths with increasing the angle of incidence. The extra peak is being enhanced in magnitude with increasing the angle of incident, and it reached around 0.99 absorptance at 10°.

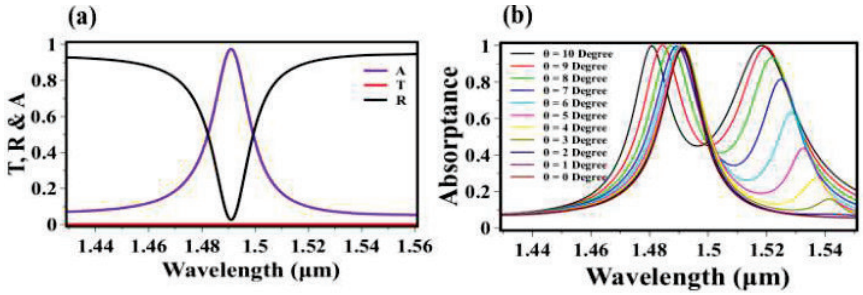

Fig. 2. (a) Simulated reflectance, transmittance and absorptance spectra of the MM absorber at normal incidence, (b) Angle dependent absorptance of the MM absorber. The parameters used for simulations: periodicity, height, width of the strip, top gold layer thickness are 1300 nm, 1000 nm, 100 nm, 30 nm, respectively.

3. References:

[1] Landy NI, Sajuyigbe S, Mock JJ, Smith DR, Padilla WJ. Perfect metamaterial absorber. Physical review letters. 2008 May 21;100 (20):207402.

[2] Watts CM, Liu X, Padilla WJ. Metamaterial electromagnetic wave absorbers. Advanced materials. 2012 Jun 19;24 (23) OP98-120.

[3] Pendry JB. Negative refraction makes a perfect lens. Physical review letters. 2000 Oct 30;85 (18):3966.

[4] Engheta, N.; Ziolkowski, R. Metamaterials: Physics and Engineering Explorations; John Wiley & Sons: New York, NY, USA, 2006; ISBN 9780471784180.

[5] B. Zhu et al., "Dual band switchable metamaterial electromagnetic absorber," Prog. Electromagn. Res. 24, 121–129 (2010).

[6] Kumar, Raghwendra, and Pankaj Kumar. "Fabry–Pérot cavity resonance based metamaterial absorber for refractive index sensor at infrared frequencies." Optics Communications 514 (2022): 128142.

[7] R. Kumar, A.K. Agarwal, S.A. Ramakrishna, Development of a metamaterial structure for large-area surfaces with specified infrared emissivity, Opt. Eng. 57 (8) (2018) 087109.

Design and Development of a Prism-Mirror Module for Single-Shot Phase Retrieval using Transport of Intensity Equation

Neeraj Pandey[a,b], M P Singh[a,b], Kedar Khare[a]

[a]*Department of Physics, Indian Institute of Technology, Delhi, New Delhi, India, 110010*
[b]*Instruments Research and Development Establishment, Dehradun, India, 248008*
Email: neerajspn@gmail.com

Abstract: Transport-of-intensity equation (TIE) is a deterministic method to estimate the transverse phase of propagating light wave by the longitudinal intensity derivative. The phase is retrieved by measuring the intensity of propagating light wave multiple planes by moving the detector in longitudinal direction and then solving the transport of intensity equation. In this article, we present a single-shot transport of intensity equation based phase retrieval using a prism-mirror based module to capture the two defocused intensity images simultaneously. The proposed method has been applied for the transmitted wavefront measurement of micro lens. The results obtained by single shot transport of intensity equation based phase retrieval have been compared with interferometry based measurements.

1. Introduction

Phase measurement is very useful in various applications including optical metrology, 3D imaging in biomedical applications and surface measurements, etc. [1]. Phase measurement is mostly carried out by interferometry, which relies on phase shifting method or Fourier transform based spatial carrier fringe analysis method. Besides the interferometric methods, other non-interferometric techniques also exist, which includes Shack-Hartman sensor, iterative phase retrieval, Fourier ptycography and transport of intensity equation based phase retrieval, etc. Transport-of-intensity equation (TIE) based phase retrieval is a deterministic non-interferometric method [3]. The TIE can be used for phase retrieval, by measuring experimentally, the intensity of an optical source measured at different planes after various amounts of Fresnel diffraction. Suppose a scalar coherent wavefront of wavelength λ is travelling in the z direction, then the intensity derivative along z-direction and phase ϕ are related by the transport of intensity equation.

$$\frac{2\pi}{\lambda}\frac{\partial I}{\partial z} = -\nabla_{xy}.I\nabla_{xy}\emptyset \qquad ...(1)$$

where I is the intensity in the focused image plane, λ is the wavelength of illumination and ∇_{xy}denotes the gradient operator in the lateral dimension (x, y) only. The intensity patterns in these defocused planes are used to calculate the longitudinal intensity derivative in the desired plane. In the case of transport of intensity equation, phase is obtained by solution of a partial differential equation, rather than by arc-tangent function, so the recovered phase is always in unwrapped form. Phase information form TIE is retrieved by intensity derivative and to get the intensity derivative, the intensity images at multiple axially displaced planes are recorded by translating camera sensor. To increase capturing efficiency and expand the applicability to dynamic objects, several approaches have been proposed to capture simultaneous various defocused intensity patterns. In this paper, we present a single-shot transport-of-intensity equation based phase retrieval using a prism-mirror based module to capture the two defocused intensity images simultaneously to get intensity derivative and subsequently, we solve the TIE using fast Fourier transform based solution to get unwrapped phase profile [5].

2. Single-Shot TIE experiment using prism-mirror module

We have designed and developed a prism-mirror module based experimental configuration to achieve single shot phase retrieval through transport of intensity equation [6]. The prism-mirror module consists of a prism beam splitter and a plane mirror. These optical components were fabricated using optical lapping and polishing methods in NBK7 optical glass. The prism-mirror module is shown in the figure 1a, where prism A is a right angled prism and prism B is a four sided prism. The prism A has 50-50 transmission and reflection beam-splitter coating on hypotenuse surface generated by multilayer dielectric thin film coating in the spectral band 500 nm to 680 nm. The hypotenuse surface of prism A is optically cemented with largest surface of prism B. The fabricated prism module is shown in figure 1b. The experimental set up for transmission mode TIE shown in figure 1c is used to measure the transmitted wavefront of micro lens of diameter 400 μm. The microlens array is shown in figure 2a. Light from a LED source is collimated by a lens of 100 mm focal length and it is spectrally

filtered through a filter having central wavelength 589.3 nm. The collimated light passes through the micro lens and it is received by an infinity corrected microscopic objective (0.25 NA, 10X). Then the propagated light is passed through the prism-mirror configuration. The reflected beam from beam splitter coating moves towards the mirror and it is reflected back towards the camera. The transmitted beam after reflections by prism B moves towards camera. Hence both the images from different planes are recorded simultaneously on camera, which are laterally displaced. Initially the optical path length of both the beams is made same, then mirror is moved axially to provide 0.5 millimetre defocus displacement. The simultaneously recorded intensity patterns are shown in figure 2b. Using the two intensity images, we get intensity derivative and on applying the TIE algorithm, we get the unwrapped phase profile as shown in figures 2c. The measured peak-to-valley of transmitted wavefront through microlens obtained by TIE method is 1.6 waves. The same lens was tested for transmitted wavefront on Fizeau interferometer using phase shifting technique. The figures 2d and 2e display one of the recorded interferogram and unwrapped phase respectively. The measured peak-to-valley of transmitted wavefront through microlens obtained by interferometric method is 1.7 waves. The obtained results by TIE are in close agreement with the results obtained by interferometry.

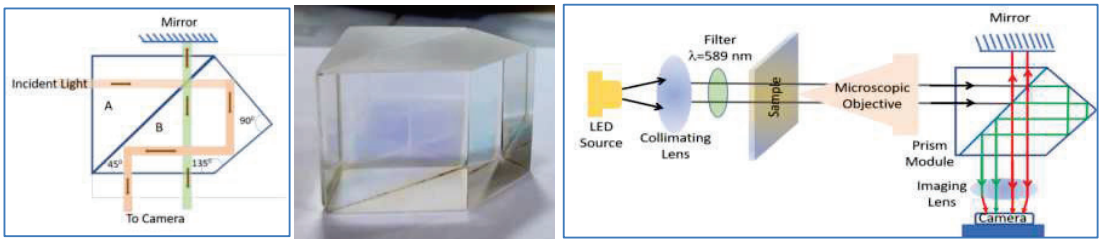

(a) (b) (c)

Fig. 1(a) Schematic of prism-mirror module (b) Fabricated prism (c) Experimental setup

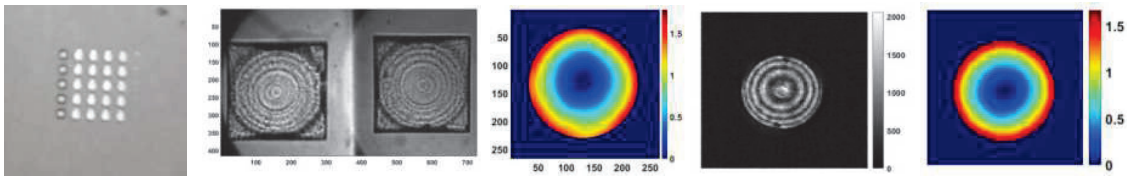

(a) (b) (c) (d) (e)

Fig: 2(a) Micro lens array (b) Simultaneous captured intensity image (c) Recovered phase by TIE (e) One of the interferogram (e) Recovered phase by interferometry

Conclusion

Transport-of-intensity equation based optical metrology is simple and cost-effective alternative measurement method in the place of interferometry and profilometry. In this article, we have shown that single shot phase measurement can be achieved using prism-mirror module based TIE configuration, which is simple, accurate and cost-effective solution. Experimental result on metrology of micro-lens has described the accuracy of this technique as it produces results comparable to interferometry with accuracy of 0.1 waves. The developed prism-mirror module can be easily integrated with any transport of intensity equation based experimental setup or any microscope.

Acknowledgments

Authors are thankful to Dr. Ajay Garg, Director IRDE, Dehradun and Sh P K Sharma, Scientist-G for encouragement of this work and their valuable suggestions.

References

1. D. Malacara, "Optical Shop Testing," 2nd ed., Wiley series in Pure and Applied Optics, Wiley, New York, 1992.
2. Kedar Khare, "Fourier Optics and Computational Imaging," Wiley, 2015.
3. M. R. Teague, "Deterministic phase retrieval: a Green's function solution," J. Opt. Soc. Am. 73, 1434-1441, 1983.
4. Paganin D and Nugent K A, "Non-interferometric phase imaging with partially coherent light," Phys. Rev. Lett. 80: 2586-2589, 1998.
5. Neeraj Pandey, Kedar Khare, "Two dimensional phase unwrapping using the transport of intensity equation", Appl. Opt. **55**, 2418-2425, 2016.
6. Neeraj Pandey, M P Singh, P K Sharma, Kedar Khare, "Single-shot phase retrieval for aspheric surface testing based on the transport of intensity equation and a prism-mirror module", Optical Engineering, Vol. 61(5), 2022.

The Resilience of Zero Order Bessel -Gaussian Beams to the Impact of Dynamic Kolmogorov Kind of Turbulence

Lekshmi SR and C S Narayanamurthy

Applied and Adaptive Optics Laboratory, Department of Physics, Indian Institute of Space Science and Technology (IIST), Valiamala (PO), Trivandrum – 695547, India

lekshmisrphy@gmail.com

Abstract: Propagation characteristics of Bessel Gaussian beams and Gaussian beams passing through a dynamic Kolmogorov kind of turbulence are analyzed at the laboratory level using simulations and experiments. The impact of rotating pseudo-random phase plates on Bessel Gaussian and Gaussian beams is quantitatively characterized by calculating scintillation index, beam wandering, and intensity line profile. Our analysis clearly shows the resilience of Bessel Gaussian beams to the impact of dynamic turbulence. This is the first time in the literature where the effect of rotating dynamic turbulence on the BG beams is experimentally investigated. These results can be effectively applied in free-space optical communication systems.

Keywords: Bessel-Gaussian beam, Kolmogorov turbulence, free-space communication.

1. Introduction

Bessel beam corresponds to an exact, propagation invariant solution to the Helmholtz equation. An ideal Bessel beam contains an infinite amount of energy which is impossible to achieve. Hence, in a practical scenario, we use approximations of Bessel beams called Bessel-Gaussian beams (BG beams). BG beams are generated using axicons, annular slits, and digital holograms using spatial light modulators. The complex amplitude of the BG beam has the form in the source plane ($z = 0$) [1,2],

$$U(r,\theta) = AJ_l(k_r r)\exp(\frac{-r^2}{\omega_0^{\,2}})\exp(il\theta) \qquad (1)$$

Where A denotes the complex amplitude, J_l is the Bessel function of the first kind of order l, k_r corresponds to the radial component of wavevector, and ω_0 denotes the beam waist of the corresponding Gaussian beam.

In our present work, we experimentally verify the impact of a dynamic, transmissive Kolmogorov kind of turbulence on the BG beams. BG beams are produced using axicons and then passed through a rotating Pseudo random phase plate (PRPP) [3] mimicking atmospheric turbulence. It has been experimentally verified that the PRPP mimics Kolmogorov-type atmospheric turbulence at a wavelength of 633 nm. Propagation characteristics of these turbulence-impacted BG beams are quantitatively evaluated by calculating the scintillation index Our study confirms the resilience of BG beams compared to Gaussian beams when passing through dynamic turbulence.

2. Experimental set-up

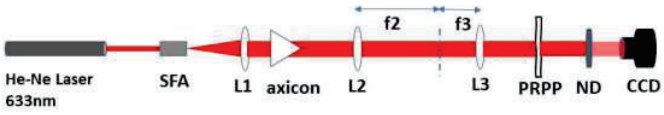

Fig. 1: shows the experimental setup for the generation of BG beams and passage through PRPP. SFA is spatial filter assembly and L is the collimating lens. Lenses L2 and L3 form a telescopic system. PRPP is the pseudo-random phase plate while ND denotes a neutral density filter. CCD is the camera used.

Fig.1 shows the experimental geometry where a laser beam is spatially filtered and collimated using a lens L of a focal length of 50mm. It is passed through an axicon of apex angle 1° to generate BG beams. BG beam formed behind the axicon is passed through a telescopic system consisting of L2 and L3 for dimensional scaling [4]. These beams are further passed through a PRPP which is the atmospheric turbulence simulator. After passing through the PRPP the beam is recorded using a CCD camera (Charge Coupled Device, PCO pixelfly USB). Neutral density filters are used

to reduce the intensity of light beams falling onto the CCD. To create a dynamic turbulence effect, PRPP, which is fixed on a rotary stage, is rotated using a stepper motor with the aid of LabVIEW software. The speed of PRPP is kept at the lowest value so that CCD sees PRPP stationary at a particular instance. The distance between PRPP and CCD is varied from 5cm to 50cm with an interval of 5cm, and in each case, turbulence-affected beams are recorded. These recorded beams are further processed in MATLAB to find the intensity line profile and scintillation index. The experiment is repeated for a conventional Gaussian beam by removing the axicon and telescopic system.

3. Results

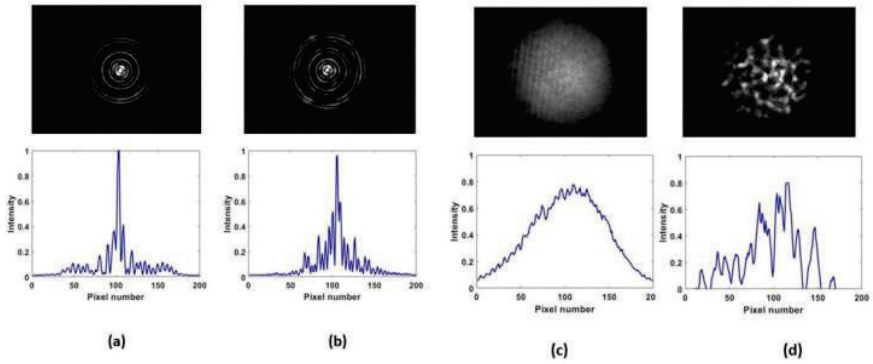

Fig. 2: shows the BG beams (a-b) and Gaussian beams (c-d) before and after the turbulence impact. The blue lines show their corresponding intensity line profiles.

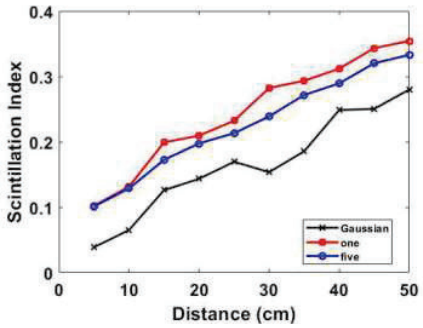

Fig. 3: shows the scintillation index corresponding to BG beams and Gaussian beams.

Fig. 2 shows the BG beams and Gaussian beams before and after the turbulence impact. The blue lines show their corresponding intensity line profiles. From the figure, it is evident that BG beams retain their shape even after passing through transparent dynamic turbulence while conventional Gaussian beam loses their shape. Fig 3 sums up the scintillation index data obtained for BG beams formed by two axicons and conventional Gaussian beams. It is clear that the variations in scintillation index corresponding to BG beams are lower than that of Gaussian beams. The main result of our experiment can be seen in figure 2 which clearly shows the ability of BG beams to retain their shape even after passing through dynamic turbulence. This is the first time in the literature the effect of dynamic turbulence on BG beams is investigated. These results find applications in free-space communications because of the resemblance of experimental conditions to the actual atmospheric turbulence.

3. References

[1] J. Durnin, J. Miceli, Jr., and J. Eberly, “Diffraction-free beams,” Phys. Rev. Lett. 58, 1499–1501 (1987).
[2] J. Durnin, “Exact solutions for nondiffracting beams. I. The scalar theory,” J. Opt. Soc. Am. A 4, 651–654 (1987).
[3] S. V. Mantravadi, T. A. Rhoadarmer, and R. S. Glas, "Simple laboratory system for generating well-controlled atmospheric-like turbulence," P Soc Photo-opt Ins 290–300 (2004).
[4] V. Kollarova, T. Medrik, R. Celechovsky, Z. Bouchal, O. Wilfert, and Z. Kolka, "Application of nondiffracting beams to wireless optical communications," P Soc Photo-opt Ins 67361C-67361C–9 (2007).

Effect of volume contraction of phase change material in a photonic binary memory cell

Mohammad Faraz Abdullah, Ram Ashish Yadav, Rajesh Kumar
Department of Physics, Indian Institute of Technology Roorkee, 247667, Roorkee, India
mfarazabdullah@ph.iitr.ac.in

Abstract: We present effect of volume contraction of $Ge_2Sb_2Te_5$ on the performance of phase change material photonic binary memory. $Ge_2Sb_2Te_5$ dimensions are optimized to get the maximal readout contrast and minimal insertion loss with an ultra low volume of $Ge_2Sb_2Te_5$. The effect of volume reduction of $Ge_2Sb_2Te_5$ during crystallization on readout contrast of the memory cell is presented.
Keywords: Phase change material, photonic memory, Germanium Antimony Telluride, silicon on insulator waveguide.

1. Introduction

We have carried out numerical investigations for an all-optical binary memory based on silicon on insulator waveguide with partially embedded phase change material ($Ge_2Sb_2Te_5$, GST [1]) for operation at 1550 nm wavelength. By optimizing GST memory cell dimensions, we obtained high readout contrast (RC), low insertion loss (IL), and a compact footprint. We define a figure of merit (FOM) as $FOM = RC/IL \cdot (Active\ volume)$ [2] to accommodate all the considered parameters in one. Moreover, we take the volume/density change ranging from approximately 5%–

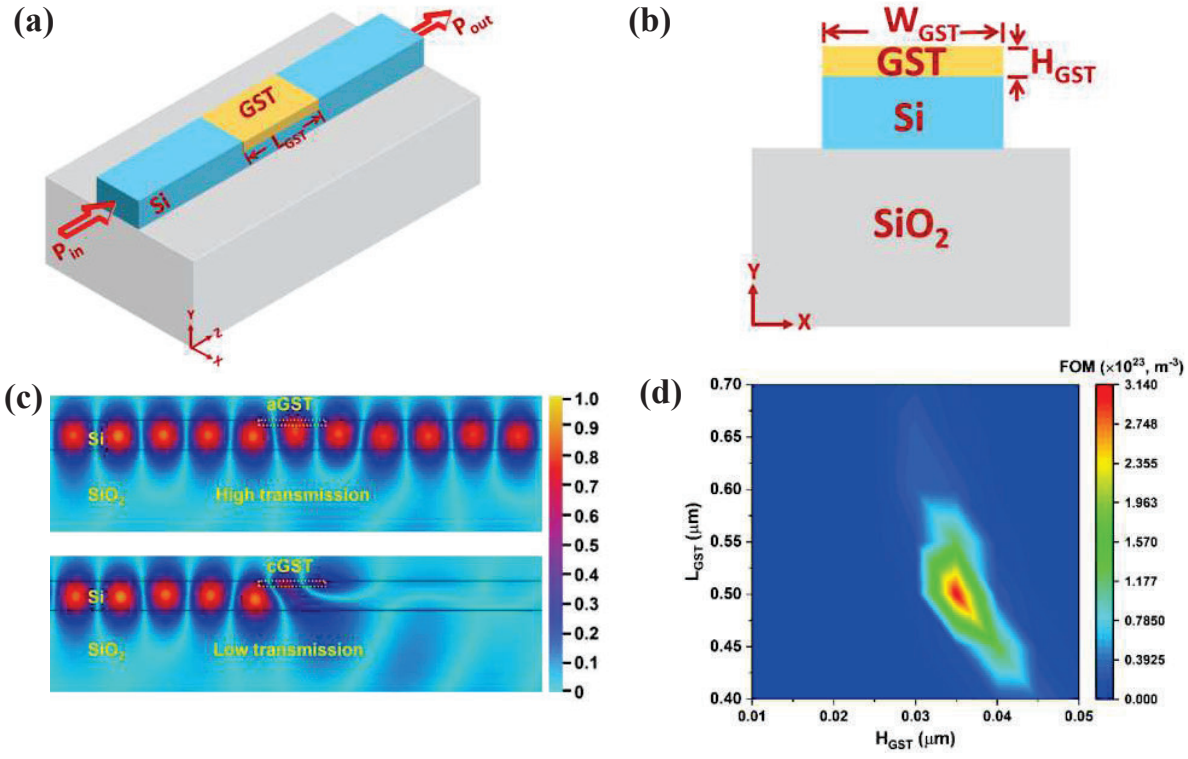

Figure 1: (a) Schematic diagram of the memory cell, (b) Cross-section view at the center, (c) A side view of field profile along the length, and (d) Figure of merit variation with length and height of GST cell.

10% [3–6] upon GST phase transformation into consideration to see how the optical performance, mainly RC, is affected in the event of volume reduction upon phase transformation from amorphous to crystalline form.

2. Resutls

The maximum RC of ~33dB was obtained for L_{GST} and H_{GST} values of 500 nm and 35 nm, respectively, the FOM attains its maximum value of 3.14×10^{23} m^{-3} (Fig. 1d). The proposed photonic memory cell exhibits a linear decrease in RC with an increase in volume contraction (Fig. 1a). The trend can be understood in terms of backreflection and absorption when GST is in the crystalline phase. When volume reduction happens, the air gaps appearing at the

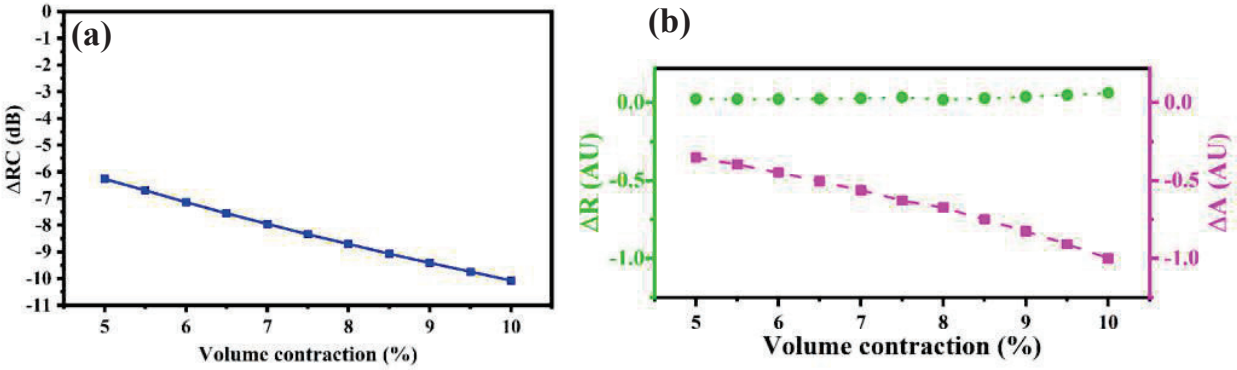

Figure 2: (a) Change in readout contrast with volume contraction, (b) Change in reflection and absorption (ΔR and ΔA) with GST volume contraction. AU, arbitrary unit.

interface of GST and Si lead to a fixed fraction of backreflected power, irrespective of the percentage of reduction in volume. However, the total power absorbed in GST depends upon the percentage of volume reduction. A change in reflection (ΔR) and a change in absorption (ΔA), with respect to zero contraction in volume, are plotted as a function of volume contraction of GST upon phase transformation from an amorphous to crystalline phase, which is shown in Fig. 2(b). From this curve, it is clear that ΔR stays constant with a change in volume, whereas it is not the case with ΔA.

3. References

[1] C. Rios, P. Hosseini, C. D. Wright, H. Bhaskaran, and W. H. Pernice, “On-chip photonic memory elements employing phase-change materials,” Adv. Mater. 26, 1372–1377 (2014)

[2] Mohammad Faraz Abdullah, Nadir Ali, Vilson R. Almeida, Roberto R. Panepucci, Yiwei Xie, Daoxin Dai, and Rajesh Kumar, "Active volume engineered waveguide embedded nonvolatile photonic memory cell," J. Opt. Soc. Am. B 39, 1419-1428 (2022)

[3] T. Nonaka, G. Ohbayashi, Y. Toriumi, Y. Mori, and H. Hashimoto, “Crystal structure of GeTe and Ge2Sb2Te5 meta-stable phase,” Thin Solid Films 370, 258–261 (2000).

[4] A. Cywar, Z. Woods, S. Kim, M. BrightSky, N. Sosa, Y. Zhu, H. S. Kim, H. K. Kim, C. Lam, A. Gokirmak, and H. Silva, “Modeling of void formation in phase change memory devices,” Solid-State Electron. 164, 107684 (2020).

[5] K. Do, D. Lee, D.-H. Ko, H. Sohn, and M.-H. Cho, “TEM study on volume changes and void formation in Ge2Sb2Te5 films, with repeated phase changes,” Electrochem. Solid-State Lett. 13, H284 (2010).

[6] W. Zhou, L. Wu, X. Zhou, F. Rao, Z. Song, D. Yao, W. Yin, S. Song, B. Liu, B. Qian, and S. Feng, “High thermal stability and low density variation of carbon-doped Ge2Sb2Te5 for phase-change memory application,” Appl. Phys. Lett. 105, 243113 (2014).

Latent Finger-mark Detection and Security Ink Application Using Tm^{3+}/Yb^{3+}: La_2O_3 Phosphor

Madan M. Upadhyay*, Minarul I. Sarkar, Kaushal Kumar

Optical Materials & Bio-imaging Research Laboratory, Department of Physics, Indian Institute of Technology (Indian School of Mines) Dhanbad-826004, India

**Corresponding author: madan.iitism@gmail.com*

Abstract: Tm^{3+}/Yb^{3+}:La_2O_3 phosphor was synthesized via solid state reaction method. Pure hexagonal phase of La_2O_3 was confirmed by X-ray diffraction (XRD) analysis.The upconversion (UC) spectrum shows bands in blue and red regions under the 980 nm laser diode excitation. Latent fingermark detection was performed by powder dusting method. Moreover, Security ink application of the synthesized phosphor was also performed by dissolving the phosphor into ethanol. These applications reveal the use of prepared phosphor as a security probe.
Keywords: Upconversion, Security ink, latent fingermark detection.

1. Introduction

Upconversion (UC) luminescence materials doped with rare earth ions have been extensively studied due to its immense applications in numerous fields. Such as lasers, optical temperature sensors, fingerprint detection, cathode ray tubes, white light emitting diodes, solar cells, medical diagnostics and so on [1].Oxides and fluorides are often selected among the several solid host materials because they have low cut-off phonon frequencies, which reduce energy loss via non-radiative relaxation channels. As a result, a low phonon energy host La_2O_3 with a phonon frequency of ~400 cm^{-1} should be ideal for the fabrication of highly efficient phosphor. Addition benefit of using this host is its good chemical and thermal stability, comparable ionic radius with most triply ionised rare earth dopants and its low cost. Since a fingermark is one of the most potent traces that may be used as proof for an individual's identification. Latent fingerprints are often the most frequent type found at crime scenes. Specifically, they are usually undetectable to investigators and can only be seen through specific emerging methods. Fingerprint scientists have explored and employed a variety of fingermark development methods such as powder dusting, silver nitrate soaking, and so on [2]. But these conventional methods continue to have significant issues with the development of latent fingermarks, such as poor detection sensitivity, significant background interference, challenging operation, and high toxicity. UC phosphors emit strong visible fluorescence upon the 980 nm laser diode excitation. So it can be used in high contrast latent fingermark development. The aim of present study is to synthesize Tm^{3+}/Yb^{3+}:La_2O_3 phosphor and perform their application in development of latent fingeremark using the 980 nm laser diode excitation.

2. Experimental

2.1. Material synthesis

0.3 mol% Tm^{3+}/5 mol% Yb^{3+} codoped La_2O_3 phosphor has been synthesized using solid state reaction method. La_2O_3, Tm_2O_3 and Yb_2O_3 were used as starting materials. The initial materials were weighed in a stoichiometric ratio and ground with the help of an agate mortar and pestle for 1 hour using acetone as the mixing media.The obtained powder was put into an alumina crucible and kept in a furnace at 1300 ^oC for 5 hours.

3. Results and discussion

The XRD pattern of 0.3 mol% Tm^{3+}/5 mol% Yb^{3+} : La_2O_3 phosphor produced at 1300 ^oC is shown in Fig.1 (a). All the diffraction peaks are well matched with the hexagonal phase of La_2O_3 (JCPDS No: 01-074-2430). The absence of secondary phases in the pattern suggests that Tm^{3+} and Yb^{3+} ions are entirely doped into the La_2O_3 host lattice. Furthermore, the sample had a high degree of crystallinity, as seen by the sharp diffraction peaks. The UC spectrum of 0.3 mol% Tm^{3+}/5 mol% Yb^{3+} : La_2O_3 phosphor under 980 nm laser diode excitation is

shown in Fig. 1(b). The spectrum consist of four UC emission bands at 476 nm, 652 nm, 670 nm and 698 nm resulted from $^1G_4 \rightarrow {}^3H_6$, $^1G_4 \rightarrow {}^3F_4$, $^3F_2 \rightarrow {}^3H_6$ and $^3F_3 \rightarrow {}^3H_6$ transitions of Tm^{3+} ion. Fig. 1(c) illustrates energy level diagram of Tm^{3+}/Yb^{3+}:La_2O_3 phosphor upon the 980 nm laser diode excitation.

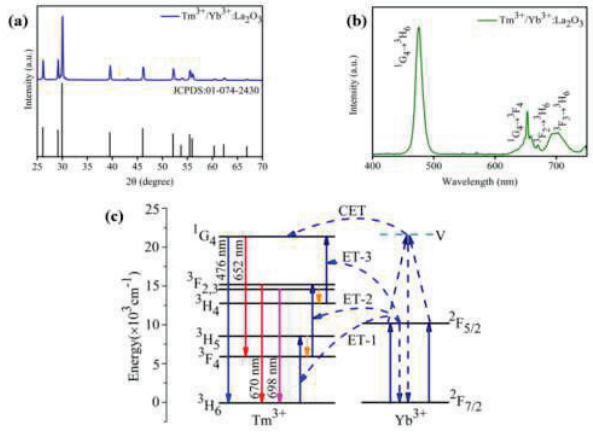

Fig.1 (a). XRD pattern of 0.3 mol% Tm^{3+}/ 5 mol% Yb^{3+} :La_2O_3 phosphor; (b) UC emission spectrum of synthesized phosphor upon 980 nm laser excitation; (c) Energy level diagram of Tm^{3+} and Yb^{3+} ions and their energy transfer process (ET-Energy transfer, CET-Cooperative energy transfer).

In application, we have shown the development of latent figure print on glass surface and security ink under the 980 nm excitation. Fig 2(a) illustrates the powder dusting of prepared phosphor on latent finguremark on glass surface and Fig. 2(a') shows same upon the 980 nm laser diode excitation. The security ink application is also performed by dissolving synthesized phosphor into ethanol and writing alphabet "M" as shown in Fig. 2(b,b').

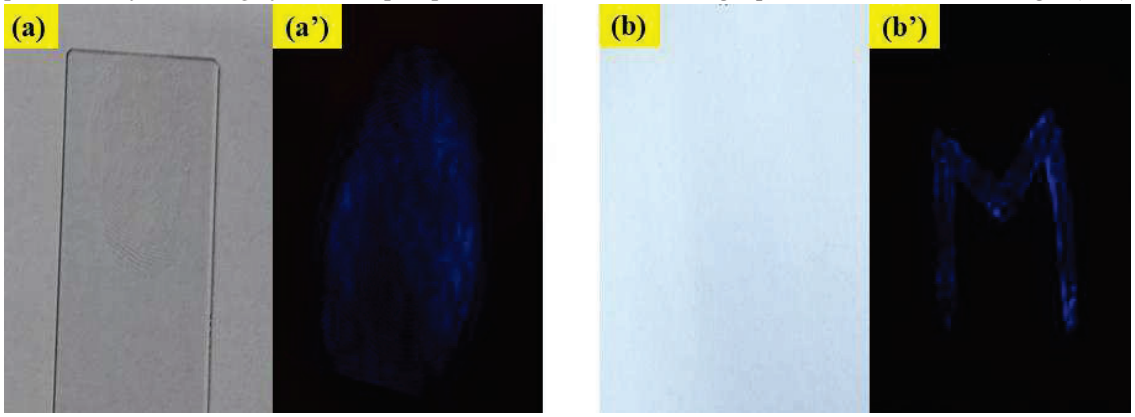

Fig.2 (a). Shows powder dusted latent fingeremark on glass substrate under daylight; (a'). Same under 980 nm laser excitation; (b) Alphabet "M" written on plain paper under daylight; (b'). Same under 980 nm illumination.

4. Conclusions

Tm^{3+}/Yb^{3+}:La_2O_3 phosphor has been successfully synthesized in pure hexagonal phase via high temperature solid state reaction technique. The UC emission shows bands in blue (476 nm) and red (652, 670, 698 nm) regions from Tm^{3+} ion transition. Fingermark and security ink application was performed using 980 nm laser excitation which shows latent fingermark and alphabet ("M") with high sensitivity and contrast.

References

[1] Xubin Tu, et. al., "Color-tunable upconversion luminescence and temperature sensing behaviour of Tm^{3+}/Yb^{3+} codoped $Y_2Ti_2O_7$ phosphors," Mater. Res. Bull.**112,** 77-83 (2019).

[2] Meng Wang, et.al., "NIR-induced highly sensitive detection of latent fingermarks by $NaYF_4$:Yb,Er upconversion nanoparticles in a dry powder state," Nano Res.**8,** 1800-1810 (2015).

Deep Learning enabled Speckle-based OAM Shift-Keying through Intensity Degenerate Modes

Venugopal Raskatla[†], Purnesh Singh Badavath[‡], and Vijay Kumar[*]
Department of Physics, National Institute of Technology, Warangal, India-506004
Author e-mail address: [†]venuraskatla@gmail.com, [‡]bpurneshsingh@gmail.com, [*]vijay@nitw.ac.in

Abstract: We present a deep learning model for speckle-based Orbital Angular Momentum Shift-Keying (OAM-SK) for optical Communication. A Convolutional Neural Network (CNN) is trained to recognize intensity degenerate OAM modes through their astigmatic transformed far-field intensity speckle patterns. For robustness, the CNN is trained with noisy OAM modes incorporated with Gaussian White Noise (GWN). This trained CNN is implemented to demonstrate an OAM-SK communication link with a GWN channel of 3dB SNR and is able to reconstruct a 4-bit grey-scale image with an accuracy of $> 99\%$.
Keywords: Orbital Angular Momentum Beams, Optical Communication, Deep Learning, Speckles.

1. Introduction

The Orbital Angular Momentum (OAM) beams with helical phase-front are the potential candidate to increase the bandwidth and information carrying capacity of communication links. OAM beams of different order have orthogonality between them hence, each beam serves as the signal carrier and multiple OAM beams can be combined to improve channel capacity [1]. But the use of only non-conjugate modes limits the utilization of multiplexing resources. Various methods are being proposed for the recognition of mutual conjugate modes to utilize the full OAM spectrum. Classically, these modes can be identified from the orientation of the pattern formed in the interference and diffraction methods. Recently, machine learning methods are also being proposed for detecting these modes by using astigmatic transformation via a cylindrical lens [2,3]. The traditional and machine learning methods utilizing the direct mode intensity images are very sensitive to alignment and need to capture the whole mode for their classification. The speckle-based Convolutional Neural Network (CNN) and Wavelet Scattering Network have been demonstrated to be more robust against noise and alignment but they are unable to distinguish the mutual conjugate modes [4–7]. Here, we demonstrate the speckle-based CNN to classify these mutual conjugate modes via their astigmatic transformed far-field speckles. These astigmatic transformed far-field speckles are generated by taking the one-dimensional Fourier Transform (1D FT) of the product of the direct OAM field and random phase mask. The Gaussian White Noise (GWN) is also added to make our model more robust. This CNN is utilized for reconstructing a 4-bit grey-scale in an OAM communication link with the GWN channel.

2. Concept and Methodology

The Laguerre–Gaussian ($LG_{p,l}$) modes possessing OAM are the solution of the paraxial Helmholtz equation in a cylindrical coordinate system where p is a radial mode index and l is an azimuthal mode index. The modes $LG_{p,l}(\boldsymbol{r})$ and $LG_{p,-l}(\boldsymbol{r})$ are the mutual conjugate modes having intensity degeneracy with complex conjugate phases. The noisy modes ($LG^{N}_{p,l}(\boldsymbol{r})$) are generated by adding GWN with SNR of N dB, where $N = -10\ to + 10$. These noisy modes are then multiplied with the random phase mask $\phi_R(\boldsymbol{r})$ of uniformly distributed phase values between 0 and 2π and 1D FT ($\mathcal{F}_{1D}$) is taken to generate an astigmatic transformed far-field speckle pattern (U_{sc}).

$$U_{sc}(\boldsymbol{r}) = \mathcal{F}_{1D}\left\{LG^{N}_{p,l}(\boldsymbol{r})e^{i\phi_R(r)}\right\} \tag{1}$$

The intensity images of these speckle patterns $I_{sc}(\boldsymbol{r}) = U_{sc}(\boldsymbol{r})U^{*}_{sc}(\boldsymbol{r})$ are used for developing the deep learning model. To build a 4-bit classifier, we have generated intensity speckle images for $LG_{p,l}$ modes with $p = 0$ and $l = \pm 1$ to ± 8 (16 modes). We have generated 1000 images for each mode with image sizes $227 \times 227 \times 3$ pixels.

The intensity speckle images (I_{sc}) is fed to an Alexnet (Fig.1 (a)), a CNN which is known for its high accuracy and low computational load. We have only modified the last layer of Alexnet to classify sixteen modes and retained its weights and biases. These weights and biases are updated during training. Utilization of the pre-trained network

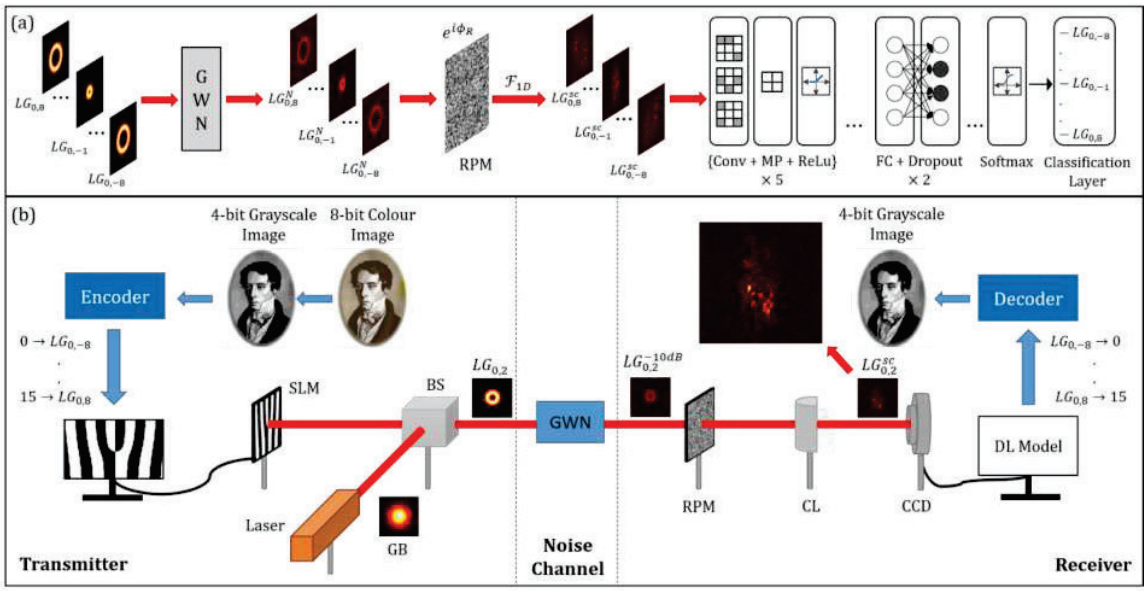

Fig. 1 (a) Workflow for training the CNN with the OAM speckles generated by passing OAM modes through RPM. **(b)** Optical communication link for demonstrating speckle-based OAM-SK using intensity degenerate modes.

reduces the training time and computational load as compared to the network trained from scratch. Among the 1000 images of each class, we used randomly selected 80% of the data to train the model and the rest to evaluate the model. We have used the "sgdm" algorithm with a learning rate of 0.0001 and momentum of 0.9 for training the model. We have achieved a classification accuracy of $> 99\%$. An optical communication link is simulated for transmitting a 4-bit grayscale Fresnel image with a resolution of 150×200 pixels where the pixel values range from 0 to 15. Here, the image is sent pixel-by-pixel where each pixel value is encoded in one of the 16 different OAM modes. We use 16 pure $LG_{p,l}$ modes with $p = 0$ and $l = -8$ to 8 except $l = 0$. Fig. 1(b) shows the OAM-based optical communication link with the GWN channel. In this numerical simulation, the image was reconstructed with a Bit Error ratio ~ 0.

3. Summary

In this paper, we have presented a novel deep learning model for speckle-based OAM-SK using intensity degenerate modes for optical communication. We have trained a CNN to identify intensity degenerate OAM modes through their astigmatic transformed far-field speckle patterns. This allowed us to utilize the full OAM spectrum and therefore, increases the bandwidth and information carrying capacity of the communication link. For robustness, we have also trained the CNN on various GWN levels quantified SNR values. Finally, to demonstrate the proof of concept for its practical application, we have simulated an optical communication link where a 4-bit grayscale image is transmitted through sixteen different OAM modes, and the image is faithfully reconstructed with the help of trained CNN.

4. Acknowledgments

V.K. acknowledges SERB grant (SRG/2021/001375)

5. References

[1] A. E. Willner, K. Pang, H. Song, K. Zou, and H. Zhou, "Orbital angular momentum of light for communications," *Appl. Phys. Rev.* **8**, 041312 (2021).
[2] B. P. da Silva, B. A. D. Marques, R. B. Rodrigues, P. H. S. Ribeiro, and A. Z. Khoury, "Machine-learning recognition of light orbital-angular-momentum superpositions," *Phys. Rev. A* **103**, 063704 (2021).
[3] P. Wang, X. Zhang, D. Fan, J. Liu, L. Sheng, Y. He, W. Xiong, Z. Huang, X. Zhou, et al., "Convolutional Neural Network-Assisted Optical Orbital Angular Momentum Recognition and Communication," *IEEE Access* **7**, 162025–162035 (2019).
[4] V. Raskatla and V. Kumar, "Deep learning assisted OAM modes demultiplexing," in *Fifteenth Int. Conf. Correl. Opt.*, O. V. Angelsky, Ed., (SPIE, Chernivtsi, Ukraine, 2021).
[5] V. Raskatla and V. Kumar, "Deep Learning Assisted Classification of Noisy Laguerre Gaussian Modes," in *Front. Opt. Laser Sci. 2021*, (OSA, Washington, DC, 2021).
[6] V. Raskatla, B. P. Singh, S. Patil, V. Kumar, and R. P. Singh, "Speckle-based deep learning approach for classification of orbital angular momentum modes," *J. Opt. Soc. Am. A* **39**, 759 (2022).
[7] V. Raskatla, P. S. Badavath, and V. Kumar, "Convolutional networks for speckle-based orbital angular momentum modes classification," *Opt. Eng.* **61** (2022).

Lasing in microfluidic chip generated linear array of droplets and twin droplets

K. Shadak Alee[1*], Aswathy Sundaresan[2], N. Soniya[2]

[1]Department of Physics and Nanotechnology, SRM Institute of Science and Technology, Kattankulathur, Chengalpattu (District), Tamilnadu-603203, India.

[2]School of Physics, IISER - Thiruvananthapuram, Maruthamala PO, Vithura, Thiruvananthapuram - 695551, Kerala, India.

**shadakk@srmist.edu.in*

Abstract: We demonstrate low threshold lasing of the acceptor dye when it is introduced in specially designed configurations of twin-droplets and linear array of microdroplets generated in a microfluidic system. Various reasons contribute to this low threshold lasing process are discussed.

Keywords: lasing, microfluidics, droplets

1. Brief details of the work

Droplet microfluidics is an emerging field of research that utilizes the unique characteristics of microdroplets and microfluidics to demonstrate novel applications [1–5]. Although microdroplets were recognized in the 1980s as potential candidates for high-quality whispering gallery mode lasers (WGM), their incorporation into lab-on-chip systems was not achieved until Xia et al. [6], developed soft lithography to manufacture microfluidic platforms. Due to their control over droplet size and shape, microfluidic systems can also produce arrays of microdroplets with unconventional shapes and study their lasing behavior [7, 8]. Even so, microfluidics is still largely unexplored in terms of its ability to create distinctively arranged microdroplets and their lasing behavior. As part of this approach, we present a novel method of generating twin droplets and a linear array of droplets. We also demonstrate experiments demonstrating low threshold lasing from them.

Following the discovery of WGMs in microdroplets, extensive research in coupled micro-resonators has been conducted, both theoretically and experimentally. A majority of these studies focus on size-matched and size-mismatched coupled resonators, as well as periodic on average random systems [9-14]. A single laser dye was doped in most of these systems in order to study the underlying mechanism for lasing. However, microfluidics offers two distinct features during the generation of twin droplets and the linear array of droplets. Firstly, in the case of twin droplets, they are characterized by the fact that one is doped with a donor dye while the other is doped with an acceptor dye. In such a case, the focusing effect of a droplet has been exploited to achieve the low threshold lasing from acceptor [15]. Further, there was a need to carefully position the acceptor droplet along the principal axis of the twin droplets in order to achieve low threshold lasing due to unequal intensities of the focused bright spots along the diameter of the droplet. Secondly, a linear array of droplets can also be generated by choosing a surrounding medium whose refractive index is higher than that of the droplet, so that they do not obey the WGM condition. In that case, the droplet system allowed us to study lasing solely in the context of one-dimensional scattering systems by eliminating the possibility of WGM lasing [16]. Additionally, this system includes alternate donor and acceptor droplets. In both droplet configurations, lasing was facilitated by the radiative energy transfer from donor to acceptor. At the time of the conference, the complete details of the work will be provided to the conference participants.

2. References

[1] M. Joanicot and A. Ajdari, "Droplet control for microfluidics," Science **309**, 887–888 (2005).
[2] S.Y. Teh, R. Lin, L.H. Hung, and A. P. Lee, "Droplet microfluidics," Lab Chip **8**, 198–220 (2008).
[3] A. B. Theberge, F. Courtois, Y. Schaerli, M. Fischlechner, C. Abell, F. Hollfelder, and W. T. S. Huck, "Microdroplets in microfluidics: an evolving platform for discoveries in chemistry and biology," Angew. Chemie Int. Ed. **49**, 5846–5868 (2010).
[4] J. Sánchez Barea, J. Lee, and D.K. Kang, "Recent advances in droplet-based microfluidic technologies for biochemistry and molecular biology," Micromachines **10**, 412 (2019).
[5] X. Fan and S.H. Yun, "The potential of optofluidic biolasers," Nat. Methods **11**, 141–147 (2014).
[6] Y. Xia and G. M. Whitesides, "Soft lithography," Annu. Rev. Mater. Sci. **28**, 153–184 (1998)

[7] S. Aswathy, N. Soniya, K. S. Alee, “Effect of Forster resonance energy transfer efficiency and pump wavelength absorption on the acceptor’s amplified spontaneous emission in an on-chip droplet system”, J. Opt. Soc. Am. B, **38**, 273 (2021)
[8] S. Aswathy, N. Soniya, K. Shadak Alee, “Wavelength tuning of amplified spontaneous emission through on chip control of the droplet size”, Optical Materials, **106**, 109966, (2020)
[9] S. V Boriskina, "Coupling of whispering-gallery modes in size-mismatched microdisk photonic molecules," Opt. Lett. **32**, 1557–1559 (2007).
[10] E. I. Smotrova and A. I. Nosich, "Optical coupling of an active microdisk to a passive one: effect on the lasing thresholds of the whispering-gallery supermodes," Opt. Lett. **38**, 2059–2061 (2013).
[11] S. P. Ashili, V. N. Astratov, and E. C. H. Sykes, "The effects of inter-cavity separation on optical coupling in dielectric bispheres," Opt. Express **14**, 9460–9466 (2006).
[12] T. Mukaiyama, K. Takeda, H. Miyazaki, Y. Jimba, and M. Kuwata-Gonokami, "Tight-binding photonic molecule modes of resonant bispheres," Phys. Rev. Lett. **82**, 4623 (1999).
[13] Y. Hara, T. Mukaiyama, K. Takeda, and M. Kuwata-Gonokami, "Photonic molecule lasing," Opt. Lett. **28**, 2437–2439 (2003).
[14] K. Shadak Alee, R. Kumar, S. Mujumdar, “Weak-disorder induced reduction of lasing threshold in periodic systems”, Phy. Rev. A., **91**, 053818 (2015)
[15] S. Aswathy and K. S. Alee, Position controlled lasing threshold of the acceptor emission in a dynamic twin droplet system made using a microfluidic chip, Accepted in J. Opt. Soc. Am. B
[16] S. Aswathy, N Soniya, K. S. Alee, On chip random lasing performance of the acceptor dye in a specially designed linear and zig zag array of microdroplets with intrinsic disorder, Scientific Reports, **12**,1-9, (2022)

Funding: KSA acknowledges SERB, India for financial support (File No. CRG/2021/00724).

Geometric Phase Shift in Michelson Interferometer with Polarizing Beam Splitter

Shouvik Sadhukhan[1], Maruthi M Brundavanam[2], Jagroop[3] and C S Narayanamurthy[4]

[1,4]*Department of Physics, Indian Institute of Space Science and Technology (IIST), P.O: Valiamala, Trivandrum - 695547, State: Kerala; India*

[2]*Department of Physics, Indian Institute of Technology, Kharagpur-721302, West Bengal, India.*

[3]*Vikram Sarabhai Space Center, Indian Space Research Organization (ISRO); India*

Corresponding Email: bmmanoj@gmail.com[1]

Abstract: In the present work the geometric phase shift scheme has been presented in Michelson interferometer set-up in presence of polarizing beam splitter. It is totally a new technique to find the geometric phase shift in MI interferometer with PBS. The technique is also efficient to produce non-linear geometric phase shift in same set up. Hence, this work can also produce a sensor on the movements of PBS as well as the polarization components. A small rotation on PBS can change the intensity distribution of the output. It is also capable to produce dispersion compensated geometric phase shift for polychromatic source.

Keywords: Geometric Phase Shift, Michelson Interferometer, Polarizing Beam Splitter, Geometric Phase Shift Generator

1. Introduction

Geometric phase is an adiabatic phase that generates in any interferometer without having any dynamical path shift between the interfering beams. This happens due to rotation of polarization state and retrieval of the initial one. When the polarization state is rotated using some polarimetric set-up and the initial state is retrieved with some similar set-up, it can be framed like this " the presented scheme is efficient in producing both linear and nonlinear geometric phase. This extra phase doesn't provide any kind of dispersion. This phase is called geometric phase. Several type of phase generators are available in literatures whereas our generator is efficient to produce both linear and non-linear geometric phase.

The geometric phase generator works as a rotor. The relative angle of rotation of the polarizing components provides the geometric phase shift on the interference output. In the present work the HWP (Half Wave Plate) behaves as the rotor. The details of the generator and interferometer have been discussed in next section. The linear geometric phase follows linear relation with the rotation angle whereas for non-linear geometric phase, it follows non-linearities. The nature of the non-linearities is dependent upon the geometric phase shift generator and the interferometric set-up we used. [1,2,3,4]

2. Design of the proposed method

Figure 1 and Figure 2 represent a schematic of designed Michelson interferometric set-up to achieve linear and nonlinear phase shifts respectively. This set-up contains a polarizing beam splitter, four linear polarizers, two quarter wave plates and a half wave plate. The geometric or dynamic path difference between those two arms with mirrors are kept zero. The source can be either polychromatic or laser. The generator kept the dispersion zero. All the polarizers are kept 45 degrees with horizontal plane. For linear geometric phase shift we kept QWP1 at 45 degrees with polarizer p3. QWP2 is kept parallel to QWP1. The HWP is rotated with angle θ with p4. Thus, the output found in detector D can show geometric phase shift with four times than the rotating angle. The John matrix for the geometric phase generator is as follows.

$$\begin{pmatrix} \exp(i\,4\theta) & 0 \\ 0 & \exp(-i\,4\theta) \end{pmatrix} \quad (1)$$

Now for unpolarized inputs and the polarizers combinations, the output intensity should become as follows which can produce a geometric phase shift with 4θ.

$$I(\lambda) = H_0 \exp\left(-\frac{1}{2}\left(\frac{\lambda-\lambda_0}{\Delta\lambda}\right)^2\right)(1+\cos(4\theta)) \quad (2)$$

QWP1 and QWP2 at any arbitrary angle must be kept at arbitrary angle α where $\alpha \neq \frac{\pi}{4}$. Hence, the geometric phase generator matrix can be written as follows.

$$\begin{pmatrix} 2i\cos(2\theta) - 2\cos(2\alpha - 2\theta) & i(\sin(2\theta) - \sin(4\alpha - 2\theta)) \\ i(\sin(2\theta) - \sin(4\alpha - 2\theta)) & 2i(\cos(4\alpha - 2\theta) - \cos(2\theta)) - 2\cos(2\alpha - 2\theta) \end{pmatrix} \quad (3)$$

Hence, the matrix in equation (3) can provide non-linear geometric phase shift with same experimental set-up.

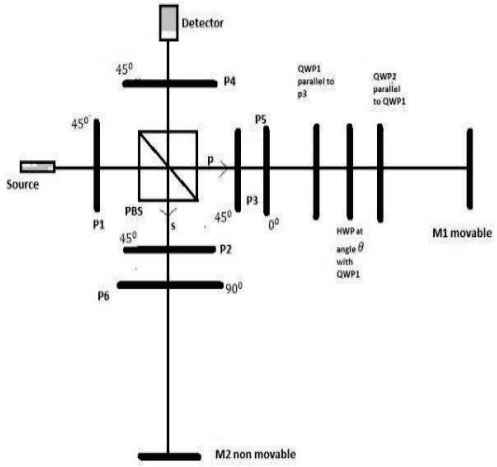

Fig.1 Block Diagram of Polarizing Beam Splitter based Michelson Interferometer and Geometric Phase for Linear case

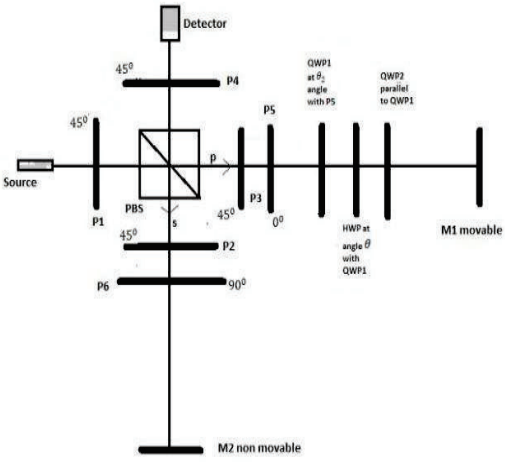

Fig.2 Block Diagram of Polarizing Beam Splitter based Michelson Interferometer and Geometric Phase For Non-Linear case

3. Figures and Results

In this section we have shown the discretized geometric phase with angle of rotation.

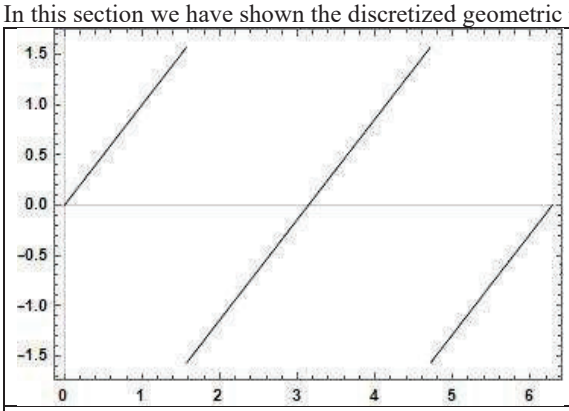

Fig. 2 Linear geometric phase with θ; Geometric phase is in Y axis and rotational angle is in X axis

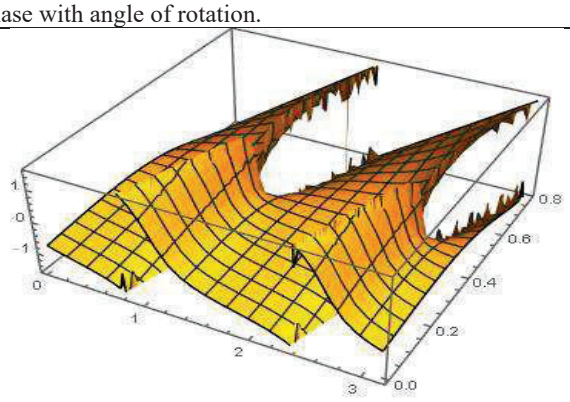

Fig. 3 Non-Linear geometric phase with θ; Geometric phase is in Y axis and rotational angle is in X axis

The results can be continuous after some modifications of the simulation tools in MATLAB or MATHEMATICA.

4. References

[1] P. Hariharan and Maitreyee Roy (1992) A Geometric-phase Interferometer,39:9, 1811-1815, DOI: 10.1080/09500349214551881

[2] P. Hariharan , Kieran G. Larkin and Maitreyee Roy (1994) The Geometric Phase: Interferometric Observations with White Light, , 41:4, 663-667, DOI: 10.1080/09500349414550681

[3] Sadhukhan, S., Sadhukhan, S., Brundavanam, M.M. and Narayanamurthy, C.S., 2022. Spectral Switch Anomalies in Sagnac Interferometer with respect to Galilean Frame. arXiv preprint arXiv:2204.06190.

[4].Jackin, B.J., Narayanamurthy, C.S. and Yatagai, T., 2016. Geometric phase shifting digital holography. *Optics Letters*, *41*(11), pp.2648-2651.

Broadband Spectral Interferometry for Characterization of Inhomogeneous Broadening

Parinda Vasa
Department of Physics, Indian Institute of Technology Bombay, Mumbai 400076, India
parinda@iitb.ac.in

Abstract: In this talk, application of broadband spectral interferometry as a simple and effective technique involving only linear optics and a broadband partially coherent light source to determine complex transmission response function of a sample will be discussed. The technique is further extended to determine the lineshape changes induced by inhomogeneous broadening.
Keywords: Spectral interferometry, Michelson interferometer, inhomogeneous broadening

1. Introduction

Lorentz-Drude or Lorentz model satisfactorily describes absorption spectra associated with a wide variety of materials. One of the limitations of this model is that it only offers effective spectral width without differentiating multiple damping mechanisms. Hence, the ensemble spectral lineshape deviates from an individual entity [1-4].

2. Results and Discussion

In this talk, we shall discuss the application of broadband spectral interferometry to determine the extent of deviation of the optical response from Lorentz model in chlorophyll-a solutions and gold nano-colloids as demonstrated by P. S. Aparna et al [1]. Using this technique, the optical phase difference between the reference and sample can be determined with high sensitivity. The obtained spectral phase is analysed further to compare the inhomogeneity of liquid samples [1]. A distinct feature of spectral interferometry is that a partially coherent broadband light source like LED or a lamp is sufficient, making it highly accessible as well as promising [1-4].

3. References

[1] P. S. Aparna, S. Schrod, B. P. Singh, and P. Vasa, White-light spectral interferometry for characterizing inhomogeneity in solutions and nano-colloids, ACS Nanoscience Au (Invited article, https://doi.org/10.1021/acsnanoscienceau.2c00014, Open Access with full third-party rights).

[2] W. Wang, P. Vasa, E. Sommer, A. De Sio, P. Gross, R. Vogelgesang, and C. Lienau, "Observation of Lorentzian lineshapes in the room temperature optical spectra of strongly coupled J-aggregate/metal hybrid nanostructures by linear two-dimensional optical spectroscopy", Journal of Optics 16, 114021, 2014.

[3] W. Wang, H. Zhang, R. Vogelgesang, P. Vasa, and C. Lienau, "Field-level characterization of the opticalresponse in J-aggregate/metal hybrid nanostructures by chirp-compensated spectral interferometry", Applied Physics Letters 110, 151101, 2017.

[4] W. Wang, P. Vasa, R. Pomraenke, R. Vogelgesang, A. De Sio, E. Sommer, M. Maiuri, C. Manzoni, G. Cerullo, and C. Lienau, "Interplay between strong coupling and radiative damping of excitons and surface plasmon polaritons in hybrid nanostructures", *ACS Nano* 8, 1056, 2014.

Image Encryption and Enhancement Using Recurrent Convolution Neural Network Model Based on Fractional Fourier Transform

Bhavana Sharma [1*], Hukum Singh[2], Mehak Khurana[1]
[1]*Department of Computer science and Engineering, The NorthCap University, Gurugram, India.*
[2] *Department of Applied science, The NorthCap University, Gurugram, India.*
**Corresponding author: bhavanasharma@ncuindia.edu*

Abstract: This paper is mainly based on ConvLSTM model of recurrent convolutional neural network for denoising the decrypted image to improve the robustness of image. In this paper, first an optical cryptosystem based on pixel scrambling along with fractional Fourier transform is proposed to secure the image from various type of attacks, the most common of which is noise attack. The deep ConvLSTM improves the resolution of the reconstructed image and secures the images from not only noise attack but also occlusion attack, blur attack. Image parameters such as structural similarity index matrix (SSIM), Peak signal to noise ratio (PSNR) are used in comparing with various existing models. The obtained simulation results demonstrate that the proposed cryptosystem outperforms the existing state-of-the-art denoising methods. The proposed method can be used in secure image transmission in healthcare, multimedia transmission etc.

Keywords: Optical image encryption, fractional Fourier transform, convolutional neural network, long short-term memory, Image denoising

1. Introduction

In today's era where multimedia is growing rapidly, there arises a high demand to protect the information from attacks. As the use of image is increasing day by day, the area of image encryption is in high demand. In recent years optical image encryption technology is being paid more attention due to its characteristics of high parallelism, high security, and vast data capacity. Further many more encryption algorithms have emerged. P. Refregier and B. Javidi proposed Double random phase encoding (DRPE) [1] technique of image encryption using 4*f* method which has been further extended to fractional transform, gyrator transform, Fresnel transform and are widely used by researchers. The fractional Fourier transform proposed by Unnikrishnan et. al [2] is widely used and based on random phase encoding has not only outstanding properties of Fourier conventional transformation but also offers added explanations, dimensional considerations & fraction orders for an encryption scheme that ensures high security. Encryption systems suffer from different threats, the most common is noise attack due to which image quality decreases at the receivers end after decryption of the image. Therefore, many solutions [3] have been proposed by researchers to this issue, like filtering bases, spare models, non-local self-similarity (NSS), or random field models from Markov. In recent years, some evolved CNN algorithms have achieved outstanding success in denoising, for example, image restoration CNN [4]. These existing methods have major issues comprising complex optimization and large testing time therefore to overcome this we propose an effective ConvLSTM and CNN based encoder and CNN based decoder using recurrent convolutional neural network [5] having extra layers in prediction of spatio temporal features.

2. The convolutional long short-term memory (ConvLSTM) model based on deep learning

The convolution block helps in learning the important features. The LSTM layers capture the temporal features. ConvLSTM layers helps in spatio-temporal prediction [5]. Its equations (1-4) are as presented follow

$$It = \sigma(Wxi * Xt + Whi * Ht - 1 + Wci \odot Ct - 1 + bi) \quad (1)$$
$$Ft = \sigma(Wxf * Xt + Whf * Ht - 1 + Wcf \odot Ct - 1 + bf) \quad (2)$$
$$Ct = ft \odot Ct - 1 + it \odot \tanh(Wxc * Xt + Whc * Ht - 1 + bc) \quad (3)$$
$$Ot = \sigma(Wxo * Xt + Who * Ht - 1 + Wco \odot Ct + bo) \quad (4)$$

However, It, Ft , Ct , Ot , Ht are the parameters used for defining the input gate, forget gate, past cell, output gate and the final state respectively, whereas "*" is used for convolution operator and ⊙ is used as the Hadamard product.The ConvLSTM finds the forthcoming state of a certain unit in a grid by the input and previous states of its local operators, this can be determined by its convolution operation in the state- state and input- state transitions.

3. Proposed Scheme

In this work, two-level encryption model has been proposed in which level one is used for image encryption to increase the protection of images and level two enhances quality of the image with noise removal via the deep-ConvLSTM that have already proven their efficiencies [5]. In this proposed work, first, the greyscale image of "cameraman" of size 512x512 pixels are collected and encrypted. It consists of 16384-pixel blocks of 2 pixels in size. In the encryption process, initially pixel scrambling is applied which is used as a private key to provide added security to the encryption. Then the scrambled image is multiplied with random phase mask generated by random function in fractional Fourier transform domain with orders α and β (0.5 each). Encrypted image is targeted artificially during the encryption phase to help mimic the actual noise attack situation on the encryption device as presented in Fig 1(a). The introduced noise is the Gaussian, Salt and Pepper, speckle, and Poisson. Decryption is inverse of encryption process. After decryption, deep ConvLSTM is utilized for denoising. The denoising is being viewed as an inverse issue to return from the noisy image pursuing a degradation model the latent clean image. PSNR and SSIM are checked as an indicator to check the quality of the image between the corresponding pixel of the original grayscale image compared with denoised extracted grayscale image as shown in Table 1

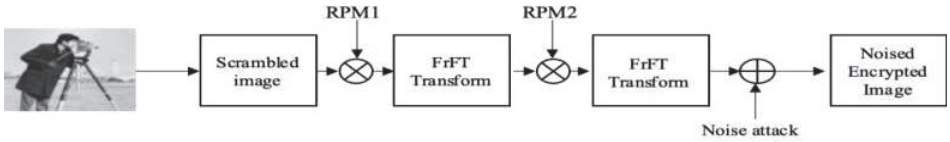

Fig.1(a) Schematic of the proposed encryption model

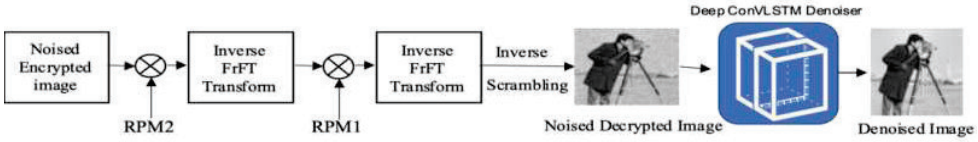

Fig.1(b) Schematic of the proposed decryption model

Fig. 2 (a) input image, (b) scrambled image, (c) encrypted image, (d) decrypted image, (e) Noised decrypted image, (f) Denoised image

Table 1. PSNR and mean SSIM values of result image from different denoising model

Image Quality Indicators	PSNR			SSIM		
Variance	0.05	0.10	0.15	0.05	0.10	0.15
Noised Decrypted image	27.52	24.65	20.15	0.2314	0.4217	0.4258
BM3D Model	28.03	25.42	26.87	0.8391	0.7862	0.7380
MLP Model	26.45	27.41	23.68	0.7011	0.6579	0.5114
CNN [6]	28.18	27.30	25.33	0.8885	0.8729	0.8135
Proposed model	**31.25**	**29.51**	22.53	**0.8971**	0.7923	**0.8895**

References

[1] P. Refregier and B. Javidi, "Optical-image encryption based on input plane and Fourier plane random encoding," Opt. Lett., **20**, 767-769, (1995).
[2] G. Unnikrishnan, J. Joseph, and K. Singh, "Optical encryption by double-random phase encoding in the fractional Fourier domain," Opt. Lett., **25**,887-889, (2000).
[3] A. Buades, B. Coll, and J.-M. Morel, "A non-local algorithm for image denoising,'' in Proc. IEEE Comput. Soc. Conf. Comput. Vis. Pattern Recognit.",**2**,60–65, (2005).
[4] K. Zhang, W. Zuo, S. Gu, and L. Zhang, "Learning deep CNN denoiser prior for image restoration," in Proc. IEEE Conf. Comput. Vis. Pattern Recognit.", 2808-2817, (2017).
[5] K. Cho, B. van Merrienboer, C. Gulcehre, F. Bougares, H. Schwenk, and Y. Bengio., "Learning phrase representations using RNN encoder-decoder for statistical machine translation". 1724– 1734, (2014).
[6] Chen, Jing, Li, Xiaowei and Wang Qiong-Hua. "Deep Learning for Improving the Robustness of Image Encryption" IEEE Access. **7**. 181083-181091, (2019).

Novel Method for Low-Power High-Fidelity and Sustained Optogenetic Control of Neural Spiking

Himanshu Bansal, Gur Pyari and Sukhdev Roy*
Department of Physics and Computer Science
Dayalbagh Educational Institute, Agra 282005, India
**sukhdevroy@dei.ac.in*

Abstract: We present a novel method of co-expressing fast and bistable opsins in neurons to overcome the challenge of sustained optogenetic spiking. A detailed theoretical study of optogenetic excitation of ChETA-SOUL-expressing hippocampal neurons has been carried out that shows that light pulses at lower irradiances can maintain spike-fidelity. Pulse irradiance reduces to ~ 90 % at g_{SOUL} = 0.4 mS/cm^2. The study is important to design and optimize new experiments with low-power, high-fidelity and long-term optogenetic control of neurons.
Keywords: Optogenetics, desensitization, spike-failure, bistable opsins, SOUL, ChETA

1. Introduction

Optogenetics has revolutionized neuroscience with its ability to control neural activity with unprecedented spatio-temporal resolution [1]. A major challenge is low-power and high-fidelity neural spiking for long duration [1-4]. ChETA, a very fast mutant of channelrhodopsin-2, can evoke spikes upto 200 Hz in fast-spiking interneurons. However, fast desensitization of its photocurrent leads to spike-failure. Recently, a new stable step-function opsin opsin with ultra-high light sensitivity (SOUL) has been discovered. SOUL enables depolarization of deeply situated neurons (~ 6 mm) in mice at safe light powers [3]. Although, SOUL and ChETA have their respective limitations, their co-expression can overcome the desensitization challenge. The objective of the paper is to theoretically study optogenetic excitation of neurons co-expressed with ChETA and SOUL. Further, a detailed analysis of the effect of expression of SOUL and photostimulation conditions for high-fidelity spiking has also been carried out.

2. Theoretical Model

We formulate an integrated optogenetic circuit model of hippocampal neurons [5-9]. The rate of change of membrane voltage of neuron in response to can be expressed as,

$$C_m\dot{V}_m = -I_{ionic} + I_{DC} + I_L + I_{ChETA} + I_{SOUL} \qquad (1)$$

where, I_{ionic} is the sum of natural ionic currents in the membrane, I_{ChETA} and I_{SOUL} are the photocurrent through ChETA and SOUL opsin molecules [5-9].

3. Results and Discussion

The photocurrent in ChETA, SOUL and SOUL-ChETA-expressing neurons on illuminating with multiple light pulses has been shown in Fig. 1. Under pulsed illumination, the peak photocurrent in ChETA decreases with number of light stimuli in the train due to fast desensitization and is reduced by 11.16 % at 20th light stimulation. In SOUL, the photocurrent increases monotonically with the light stimulus and is higher at higher expression level. In SOUL-ChETA-expressing neurons, the photocurrent in response to later stimulations increases. In these neurons, the photocurrent does not get completely inhibited before arrival of the subsequent light pulse and thus leads to non-zero photocurrent plateau, which can be quantified as return to baseline (RTB%). RTB%, an important parameter for determining spike-fidelity, decreases on increasing expression level of SOUL. The RTB % at 20th light stimulus is 88.52 %, 59.35 % and 41.23 % at g_{SOUL} = 0.04 mS/cm^2, 0.2 mS/cm^2 and 0.4 mS/cm^2, respectively (Fig. 1).

Spiking in ChETA (g_{SOUL} = 0 mS/cm^2) and SOUL-ChETA-expressing neurons has been simulated on illuminating with multiple light pulses. It is evident that ChETA fails to evoke sustained spikes in these neurons, while ChETA-SOUL-expressing neurons either exhibit spike burst or very high plateau potential (Fig. 2a). Furthermore, heating is an important issue in long-term optical stimulation, as the temperature variations during *in vivo* experiments can have both electrophysiological and behavioral consequences [10]. Thus, it would be better to change pulse-to-pulse

irradiance to evoke high-fidelity sustained spiking. Theoretical simulations clearly show that in absence of SOUL or at its lower expression, ChETA-SOUL-expressing neurons require light pulses of increasing irradiance, whereas, at higher expression of SOUL, they require light pulses at lower irradiances to maintain spike-fidelity (Fig. 2b,c). 89.47 % decrease in pulse irradiance upto 20 stimulations can evoke high-fidelity spiking in ChETA-SOUL-expressing hippocampal neurons at g_{SOUL} = 0.4 mS/cm^2 (Fig. 2b).

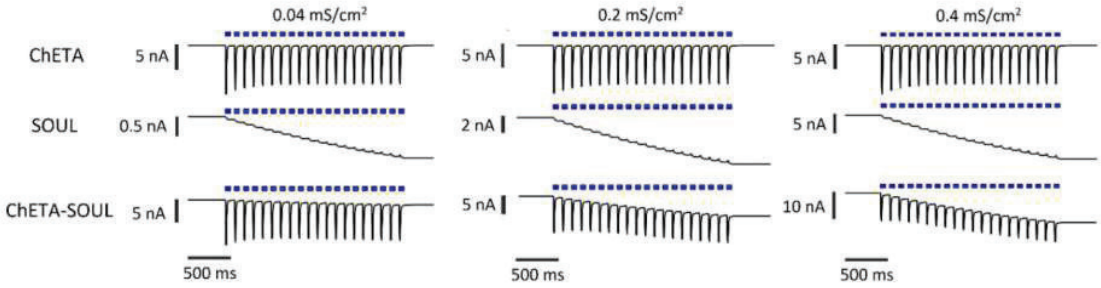

Fig.1: Photocurrent in ChETA, SOUL, ChETA-SOUL-expressing hippocampal neurons at different expression densities of SOUL. Variation of photocurrent with time on illuminating with 10 ms blue light pulse (470 nm) at 0.5 mW/ mm^2 at 10 Hz.

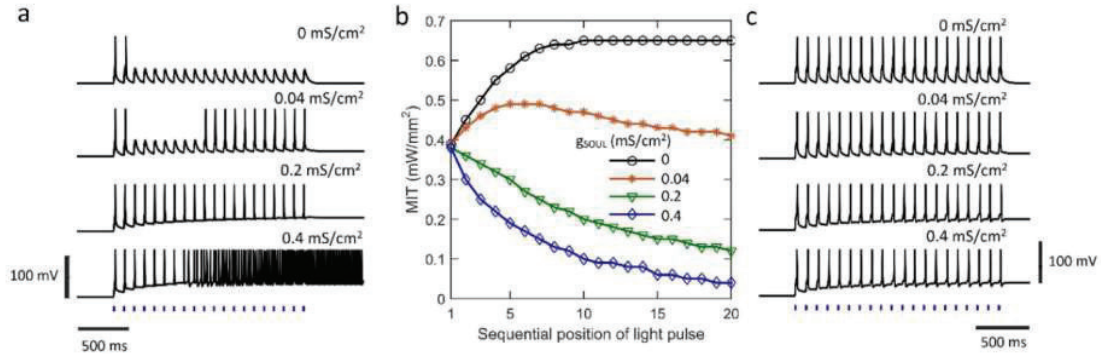

Fig. 2: Low-power and high-fidelity spiking in ChETA-SOUL-expressing hippocampal neurons at different expression densities of SOUL at 10 Hz. (a) Variation of membrane potential with time on illuminating with 20 light pulses each of 10 ms at 0.45 mW/mm^2. (b) Variation of minimum irradiance threshold to evoke each spike with sequential position of light pulse (10 ms) at indicated g_{SOUL} and (c) corresponding spiking patterns.

4. Conclusion

It has been shown that step-function opsins co-expressed with fast channelrhodopsins overcome the limitation of spike-failure due to fast desensitization of photocurrent. It is important to optimize and design new experiments for low-power, high-fidelity and long-term control of neurons with light.

5. References

[1]. V. Emiliani, E. Entcheva, R. Hadrich, P. Hegemann, "Optogenetics for light control of biological systems," Nat. Rev. Methods Primers **2** (2022).

[2]. S. Sridharan et al., "High-performance microbial opsins for spatially and temporally precise perturbations of large neuronal networks," Neuron **110**, 1139-1155 (2022).

[3]. X. Gong *et al*., "An ultra-sensitive step-function opsin for minimally invasive optogenetic stimulation in mice and macaques," Neuron 1**07**, 38-51 (2020).

[4]. J. Vierock *et. al*., "BiPOLES: a tool for bidirectional dual-color optogenetic control of neurons," Nat. Commun. **12**, 4527 (2021).

[5]. H. Bansal, N. Gupta and S. Roy, "Theoretical analysis of low-power bidirectional optogenetic control of high-frequency neural codes with single spike resolution," Neurosci. **449**, 165-188 (2020).

[6]. H. Bansal, N. Gupta and S. Roy, "Theoretical analysis of optogenetic spiking with ChRmine, bReaChES and CsChrimson-expressing neurons for retinal prostheses," J. Neural Eng. **18**, 0460b8 (2021).

[7]. H. Bansal, G. Pyari and S. Roy, "Co-expressing fast channelrhodopsin with step-function opsin overcomes spike failure due to photocurrent desensitization in optogenetics: a theoretical study," J. Neural Eng. **19**, 026032 (2022).

[8]. N. Gupta, H. Bansal and S. Roy, "Theoretical optimization of high-frequency optogenetic spiking of red-shifted very fast-Chrimson-expressing neurons," Neurophoton. **6**, 025002 (2019).

[9]. S. Saran, N. Gupta and S. Roy, "Theoretical analysis of low-power fast optogenetic control of firing of Chronos-expressing neurons," Neurophoton. **5**, 025009 (2018).

[10]. S. F. Owen, M. H. Liu, and A. C. Kreitzer, "Thermal constraints on in vivo optogenetic manipulations," Nat. Neurosci. **22**, 1061-1065 (2019).

Utilization of Poly Vinyl Alcohol as layer stabilizer in LMR based optical fiber sensors

Kavita[1] and R.K. Verma[1, Z]

[1]*Department of Physics, Central University of Rajasthan, NH-8 Bandarsindri, Ajmer 305817, Rajasthan, India*

[Z]*E-mail: rkverma@curaj.ac.in*

Abstract: From last few decades, lossy mode resonance technique based optical fiber sensors are acquiring attention due to their compact size, low-cost, real-time monitoring, high sensitivity and accuracy. A large number of techniques are available for the deposition of LMR active layer but stability and durability of the probe is still a challenge. In this study, a highly stable, durable TiO_2 bilk layer coated optical fiber probe is developed utilizing a hydrogel named poly vinyl alcohol (PVA). Uniformity of the deposited layer is confirmed by FESEM characterization. Stability of the probe is confirmed by multiple times use of the probe. PVA does not affect the chemical composition of the material used for the excitation of LMR and hence does not affect the sensitivity of the sensor. This is confirmed by the UV characterization of both the samples with and without PVA. This study may find ample consideration in the field of sensing by enhancing the accuracy, sustainability and durability of the sensor without affecting its sensitivity.

Keywords: Poly vinyl Alcohol, Lossy Mode Resonance, optical fiber sensors

1. Introduction

Hydrogels are three-dimensional hydrated networks designed by crosslinking of polymers through covalent or non-covalent interactions. There is a large number of binding agents which are used to bound the molecule of a material or a liquid. These binders can be natural and synthetic both. Best part of these binding agents is the binding the molecules of the material without changing its properties [1].

LMR based optical fiber sensors are getting popular in the field of sensing. To excite the LMR, metal oxides are used as active material. There is a numerous technique to deposit a layer of metal oxide like hydrothermal, solvothermal and thermal evaporation etc. But these techniques are available with some drawbacks for metal oxides.

In this study, we have used this concept of binding agents to fabricate the stable, durable and accurate optical fiber sensor. We have used PVA as binding agent due to its due wide availability and low cost. Poly Vinyl Alcohol (PVA) is a synthetic crystalline hydrogel like poly ethylene glycol, poly acrylamide gel and poly lectic acid. Poly vinyl alcohol is a synthetic hydrogel which is used in artificial organs, regenerative medicines, contact lens, surgical thread, wound dressing and food packaging due to its nontoxicity, biodegradability, biocompatibility, water holding capability and good mechanical properties [2].

In order to achieve the expected outcomes, we have fabricated two probes one of them is TiO_2 coated probe and the other one is TiO_2/PVA coated probe. Results are compared to see the effects of using PVA. FESEM and UV visible characterizations are done for the confirmation of uniformity of the deposited layer and variation in optical properties. This study will be very significant in the field of sensing.

2. Figures

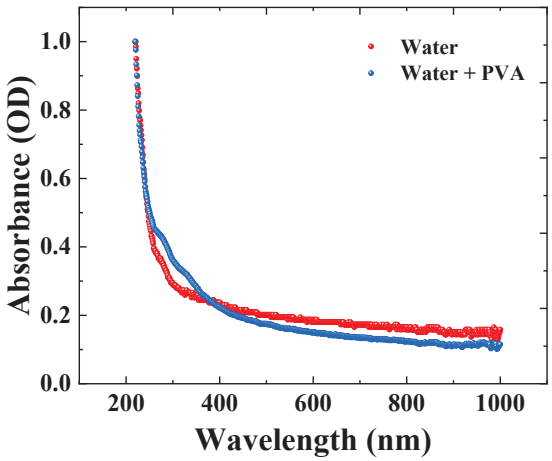

Fig. 1: UV-Vis spectra representing absorbance of the samples with and without PVA

3. References

[1] M. C. Bavya, L. George, R. Srivastava, and V. R. K, "Natural and synthetic materials in regenerative medicine : progress over the past five years," *Encycl. Smart Mater.*, vol. 1, pp. 113–144, 2019.

[2] R. Singh, S. Gautam, B. Sharma, and P. Jain, "Chapter 2 - Biopolymers and their classifications," *Biopolym. Their Ind. Appl.*, pp. 21–44, 2021.

Improved Asymmetric Cryptosystem based on TRPE with UMD in the Gyrator Domain

Kapil Shankar Gaur[1*], Hukum Singh[1], Seema Thakran[1]
[1]Department of Applied Sciences, The NorthCap University, Gurugram, India.
**Corresponding author: kapilshankar09@gmail.com*

Abstract In this paper, we proposed a scheme which is based on triple random phase encoding in the gyrator domain. To increase the security of the cryptosystem unequal modulus decomposition (UMD) is used in the gyrator domain. The security of the scheme enhances with the use of transform angle parameter in the gyrator transform. The effectiveness of the scheme is tested using MATLAB (2022a). The robustness against occlusion attacks and multiplicative gaussian noise have been analysed to check the efficiency of this scheme. Mean square error (MSE) and peak signal to noise ratio (PSNR) is also evaluated for the grayscale and binary images to check the efficiency of this scheme.
Keywords Gyrator Transform, Unequal modulus Decomposition (UMD), Random phase mask (RPM).

1. Introduction

Digital image processing for information security is most popular area in research. Over the past several years, research on security methods based on these systems are of high priority. Optoelectronic-based optical security systems can function more precisely and securely for information concealment. The double random phase encoding (DRPE), first published by Refregier and Javidi, is a very effective method for optical image encryption [1]. It is possible to perform the results of DRPE digitally and optically both. So, it has a wide range of potential applications including security verification systems, information concealment, watermarking etc. For the enhancing the security of the optical cryptosystem, DPRE is also performed in gyrator domain [2-3]. It is well reported fact symmetric DRPE is vulnerable to KPA [4], chosen plain text attack (CPA) [5]. Esmail et al. [6] introduced TPPE which is resist from KPA, CPA and CCA. Later on, Yadav and Singh [7] proposed an asymmetric cryptosystem based on TRPE, while performing the cryptoanalysis of [7] we found that RPM 3 used in this scheme has no impact while decrypted the image this weaken the cryptosystem. we proposed a cryptosystem based on the unequal modulus decomposition [8-10] which enhances the security of the proposed TRPE based cryptosystem by adding an extra key.

2. Gyrator Transform

Gyrator transform [2-3] is similar to fractional Fourier transform but the kernel used in GT is the product of hyperbolic and plane waves, while in the case of FrFT we used a kernel that is the product of spherical and planes waves. For any two-dimensional function f (x, y) the GT can be expressed as

$$G(u,v) = G^{\alpha}\{f(x,y)\}(u,v) = \iint f(x,y)K_{\alpha}(x,y;u,v)dxdy \tag{1}$$

The kernel $K_{\alpha}(x,y;u,v)$ can be written as

$$K_{\alpha}(x,y;u,v) = \frac{1}{|sin\alpha|}\exp\left[2i\pi\frac{(xy+uv)cos\alpha - xv - yu}{sin\alpha}\right] \tag{2}$$

3. Proposed Cryptosystem

For the steps of encryption, we started with image I (x, y) which is first multiply with RPM1 followed by gyrator transform with transform angle $\alpha = .4\pi$. The resultant image is now divided into two parts, phase truncation (PT) part and phase reservation (PR) part. PT is taken forward and UMD is applied to get the intermediate image $\bar{G}(u,v)$ while PR reserves as the first key of the cryptosystem. The intermediate image is again multiply with RPM2 and gyrator transform having transform angle $\beta = .5\pi$ is performed after that RPM3 is bonded with the resultant image to get to get the encrypted image. The Mathematical way to represent the encryption process as follows

$$\bar{G}(u,v) = UMD[PT\{GT^{\alpha}(I(x,y) * RPM1)\}] \tag{3}$$

$$E(x,y) = \quad [\{GT^{\beta}(\bar{G}(u,v) * RPM2)\} * RPM3] \tag{4}$$

For the decryption process, we performed the reserve step of the encryption to decrypt the image. Figure (1) shows the result of the proposed cryptosystem.

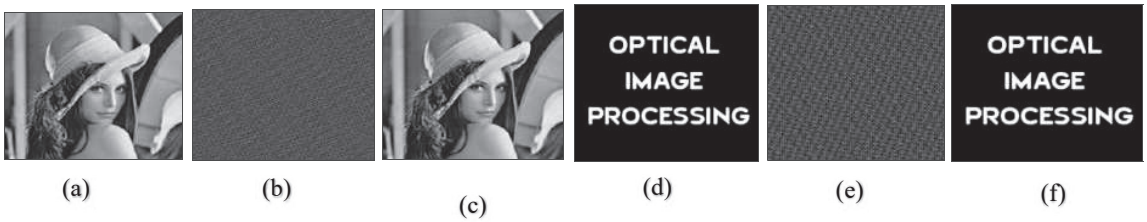

Figure 1 (a) lena grayscale image; (b) lena cipher image; (c) lena decrypted image;(d) binary image; (e) binary encrypted image; (f) binary decrypted image.

4. Results and simulation

To validate the proposed method, we compare the retrieved image to the original input image using the term commonly used as the mean square error (MSE). With the suggested method, obtained MSE values for grayscale and binary images are 9.34×10^{-24} and 1.47×10^{-22} respectively. An image's PSNR is calculated by comparing the decrypted version of an image with the original image. Input and decrypted images are compared using a PSNR formula. Obtained PSNR value for Lena and binary image are $230.29dB$ and $218.32dB$ respectively which show that scheme provide high quality of decrypted image. The plots of MSE and PSNR with the transform angle $\beta = .5\pi$ are shown in figure (2).

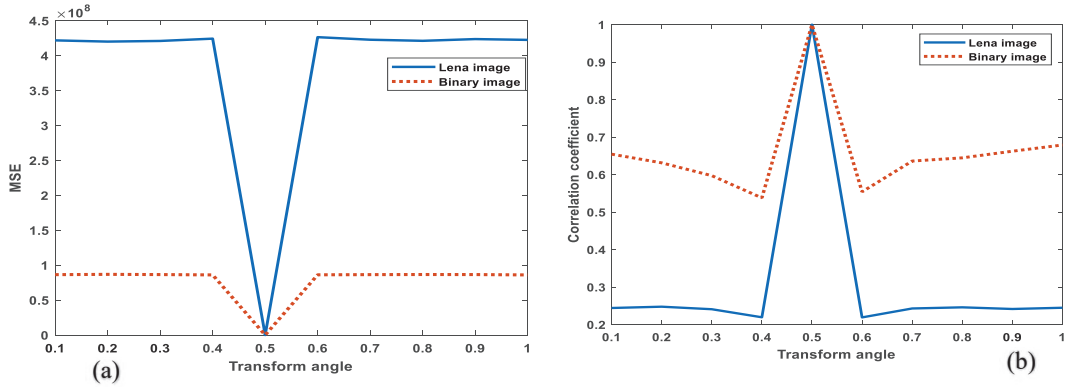

Figure 2. (a) MSE vs transform angle plot; (b) Correlation coefficient vs Transform angle plot.

5. Acknowledgement

Author Kapil Shankar Gaur is thankful to CSIR (India) for funding under grant (09/1276(0001)/2019-EMR-1.

6. References:

1. P. Refregier and B. Javidi, "Optical image encryption based on input plane and Fourier plane random encoding," Opti Letters, **20**, 767–769 (1995).
2. H. Singh, A.K. Yadav, S. Vashisth & K. Singh. "Fully-phase encryption using double random-structured phase masks in Gyrator domain". Applied Optics, **53**, 6472–6481(2014).
3. N.K Nishchal, Optical Cryptosytem(IOP,2019).
4. X. Peng, P. Zhang, H. Wei & B. Yu, "Known-plaintext attack on optical encryption based on double random phase keys," Optics Letters, **31**, 1044–1046 (2006).
5. X. Peng, H. Wei & P. Zhang, "Chosen-plaintext attack on lensless double-random phase encoding in the Fresnel domain," Optics Letters, **31**, 3261–3263 (2006).
6. E. Ahouzi, W. Zamrani, N. Azami, A. Lizana, J. Campos & M. J.Yzuel, "Optical triple random-phase encryption",Optical Engineering,56(11),113114,(2017).
7. S. Yadav and H. Singh, "Asymmetric cryptosystem based on fractional Fourier transform domain using triple random phase masks", Communication and Computing Sysytems-Prasad et al.(eds**),**105-111, (2019).
8. L. Chen, X. Gao, X. Chen, B. He, J. Liu & D. Li , "A new optical image cryptosystem based on two-beam coherent superposition and unequal modulus decomposition", Optics & Laser Technology ,**78**,167–74(2016).
9. M. Abdelfattah, SF. Hegazy, NFF. Areed & SSA. Obayya , "Compact optical asymmetric cryptosystem based on unequal modulus decomposition of multiple color images", Optics and Lasers in Engineering,**129**,106063(2020).
10. T. Archana, Sachin & P. Singh, "Cascaded unequal modulus decomposition in Fresnel domain-based cryptosystem to enhance the image security," Optics and Lasers in Engineering, **137**, 106399 (2021).

Optical System Design for Spectro-polarimetry of HAbitable Planet Earth(SHAPE)

[1]Bijoy Raha, [2]U. R. Subramanyam, [3]K. Satyanarayana Raju, [4]K. V. Srinivasa Rao, [5]U. V Sreeramkumar, [6]R. Venkateswaran, [7]K. V. Sriram, [8]Bhavesh Jaiswal

[1-7] LABORATORY FOR ELECTRO OPTICS SYSTEMS (LEOS), PEENYA, BANGALORE-560013

[8] ISRO SATTELITE INTEGRATION AND TEST ESTABLISMENT (ISITE), MARATHALLI, BANGALORE-560037

[1]bijoy_raha@leos.gov.in

Abstract: Study of spectrometry and polarimetry of Exo planets provides greater insights about its Habitability. In this regard, study of Earth will help in understanding the nature and characteristics of water-rich Exo-planets. Earth's angular size from Moon is ~ 2°, hence placing an instrument around the Moon would be an ideal place. This paper describes the Optical design (using Code-V) of a Spectro-polarimetric instrument using Acousto-Optic Tunable Filter (AOTF). Design is carried out to operate in NIR region, as the NIR band would contain most of the absorption bands of various gases as well as the Mie scattering signatures of clouds.

Keywords: Polarimetry, Exo-Planet, Mie Scattering, NIR Band, AOTF, Code-V.

1.0 Introduction

SHAPE optics is to study the exo-planet atmosphere using spectro-polarimetry with the use of AOTF i.e Acousto-optic tunable filter. It is a technology demonstration payload which will make the study of earth's atmosphere using spectro-polarimetry from the moon. Several imaging spectrometers and spectro-polarimeters [1] have been designed on a basis of acousto-optical tunable filters (AOTF) for astronomy [2-3]. The use of acousto-optics tunable filter give several advantages in designing such systems. Fast random-access wavelength tuning is one of advantages of AOTFs compared to other spectral imaging methods. The use of AOTF makes the system more compact, reliable and reduces the mass of the overall system. The criticality of using the AOTF in the present configuration produces two symmetric diffracted beams separated by twice the angle of diffraction which are bundled and focussed on to separate detector with minimum separation in order to make it compact. This paper describes the overall optical design of the SHAPE optics considering the performance parameters of the system. The AOTF is simulated in the optical design using Code-V design software including the other optical components. The Specification for the Optical design is given below in Table 1.0.

Table 1.0

Parameter	Range/Value
Spectral Range	1.0 - 1.7 μm
Spectral Resolution	< 5 nm
Field of View(FOV)	~2 Degrees
Polarisation	Linear
Telescope Aperture	Lens Type, 2 mm(Dia)
AOTF (Material)	TeO2
AOTF RF	80-160 MHz
Detector(Type)	Linear Array InGaAs
Detector Pixel	500 X 50 μm

The focal length of the instrument is derived from the detector active area and the FOV of the instrument. The instrument is designed to cater the FOV of earth's disc projection from the moon orbit. The Acousto-Optic Tunable Filter(AOTF) is used to filter and polarise the incident light. It is driven by an external RF driver to tune it for a particular wavelength. The principle of AOTF is a piezo-electric transducer attached to a birefringent crystal to generate acoustic waves that forms a spatial diffraction grating inside the crystal. Based on the principle of Bragg's diffraction inside the crystal, the crystal acts as a tunable filter, tuned by an external RF source. In the proposed design, we use one dual-beam AOTF, having a two beam output polarised in perpendicular directions to each other. One InGaAs (1D) detector is used to detect the two beams ('e' and 'o' beams).

2.0 Optics Design

The Optical design of the SHAPE optics is divided into three parts: the beam expander, the post AOTF optics and the focusing optics assembly. In order to observe 'full' Earth from Moon, the instrument is required to have a Field-of-View of ~ 2°. Since the input aperture and FOV of AOTF (used in our design) is limited to ~ 5 mm and +/-3°, it is required to have a small aperture at the front of the telescope with an acceptance angle of ~ 2°. Beam expander has been used in order to control the divergence of the input beam, by maintaining the beam dia. at the input aperture of AOTF to less than 5 mm. The output of the beam expander will be the input of the AOTF optics and the output of AOTF is two angularly separated perpendicular polarized beams. The angle of diffraction is dependent on the wavelength and the table below gives the details of the wavelength dependence with respect to the diffraction angle.

Table 2.0

Wavelength in nm	RF Frequency MHz (+/-5 MHz)	Separation Angle in deg	Spectral Resolution in nm
900	159	8.31	0.9
1000	142	8.24	1.1
1100	128	8.18	1.4
1200	117	8.15	1.7
1300	108	8.11	2.0
1400	100	8.09	2.3
1500	93	8.07	2.7
1600	87	8.06	3.1
1700	82	8.04	3.5

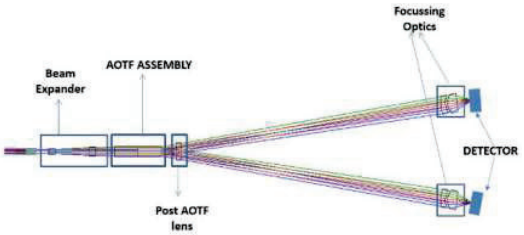

Figure 2.1 Optics Design layout of SHAPE optics

As we see from Table 2.0, for a wavelength range of 0.9 - 1.7µm, the angular separation varies from 8.31^0-8.04^0. The beam incident on the AOTF is quasi collimated for the full field. The design has been optimized for the central wavelength i.e 1.4µm so that the design remains symmetric with respect to the whole band width i.e 1.0-1.7µm.
A Post AOTF optics is used to maintain the divergence of each diffracted beam i.e the e and o-beam. This post AOTF optics is a simple plano-convex lens which is placed just after the AOTF. The diameter of the post AOTF optics is higher than the AOTF output aperture since it has to accommodate the diffracted beam for the whole bandwidth. After Post AOTF optics, the beam is diffracted into three different beams i.e the central maximum or the un-diffracted beam and two equally placed diffracted beams i.e that is the e-beam and the o-beam. A pair of Focusing Optics is placed just before the detector plane. The orientation of the focusing lens depends on the angle of diffraction of the central wavelength made by the chief ray.

3.0 Design Analysis and Results

The final design with fabrication and mechanical alignment tolerances is achieved with optimum blur diameter at 1400nm and falling systematically for wavelength at both the extremes. Figure 3.0 shows the spot diagram at 1400 nm and Table 3.0 shows the blur diameters achieved for different wavelengths.

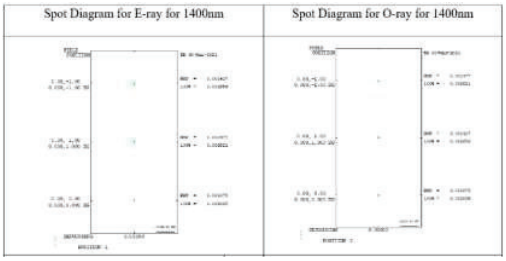

Figure 3.0 Spot diagram for Central wavelength and Full FOV

Table 3.0 Blur Dia w.r.t each Wavelength

Wavelength(nm)	Theta(Deg)	Blur Dia (um)
1100	8.18	304.5
1200	8.15	302
1300	8.11	294
1400	8.09	292
1500	8.07	315.5
1600	8.06	339
1700	8.04	366.4

4.0 References

[1] Z. P. He, B. Y. Wang, G. Lv, C. L. Li, L. Y. Yuan, R. Xu, K. Chen, and J. Y. Wang, "Visible and near-infrared imaging spectrometer and its preliminary results from the Chang'E 3 project," Rev. Sci. Instrum. **85**(8), 083104 (2014).
[2] R. B. Wattson, S. A. Rappaport, and E. E. Frederick, "Imaging spectrometer study of Jupiter and Venus," Icarus **27**, 417–423 (1976).
[3] W. H. Smith and K. M. Smith, "A polarimetric spectral imager using acousto-optic tunable filters," Exp. Astron. **1**, 329–343 (1990).

Single Particle Tuning of Localized Surface Plasmon Resonance of Gold Nanorods Immersed in Ascorbic Acid for multi-channel biosensing platform

Payel Ghosh*[a], Reha Panigrahi*[b], Saumyakanti Khatua*[b], Arup Lal Chakraborty*[a]
*[a] *Discipline of Electrical Engineering, IIT Gandhinagar, Gujarat-382055, India*
*[b] *Discipline of Chemistry, IIT Gandhinagar, Gujarat-382055, India*
ghosh_payel@iitgn.ac.in

Abstract: Plasmonic properties of gold nanoparticles are responsible for their utility in several applications such as the development of biosensors, immunoassays, and surface-enhanced Raman Spectroscopy (SERS). Controlling these properties with external stimulus after deposition on a substrate will be highly beneficial for multi-channel sensor development. Here, we report the tuning of localized surface plasmon resonance (LSPR) wavelength of a single gold nanorod deposited on glass substrate by 532 nm light in presence of Ascorbic acid. A redshift of ~70 nm, dependent on the surface properties of the nanorod is obtained.
Keywords: Plasmonic, LSPR, nanorods.

1. Introduction

Gold nanorods (AuNRs) has been a subject of research due to its ease of chemical synthesis and tunable optical properties by virtue of localized surface plasmon resonance (LSPR). Although, the LSPR wavelength of gold nanorods (AuNRs) can be tuned enormously at the time of synthesis but this do not give the flexibility of tuning the LSPR of AuNRs deposited on substrate post synthesis. This paper shows light induced tunablity of AuNRs deposited on glass substrate. Previously, LSPR tuning of AuNRs with 532 nm light has been reported in Ferric chloride and sodium dodecyl sulfate [1,2]. In this paper, similar trend of red shift is observed in presence of Ascorbic acid solution.

2. Synthesis of AuNRs and Sample Preparation

The AuNRs used in the experiments shows LSPR ~ 650 nm as in bulk spectra water medium. They are chemically synthesized using two modified seed -mediated techniques by El-Sayed and Murphy [3,4]. In one procedure the growth solution is prepared in single surfactant hexadecyltrimethylammonium bromide (CTAB) and in the other binary surfactant mixtures composed of hexadecyltrimethylammonium bromide (CTAB) and sodium oleate (NaOL) is used for the growth. Accordingly, the resulting nanorods surfaces are either CTAB coated or CTAB-NaOL coated. The characterization is done using the UV-visible spectrum of the bulk sample in water and morphology is studied using scanning electron microscope (SEM) shown in Fig.1.

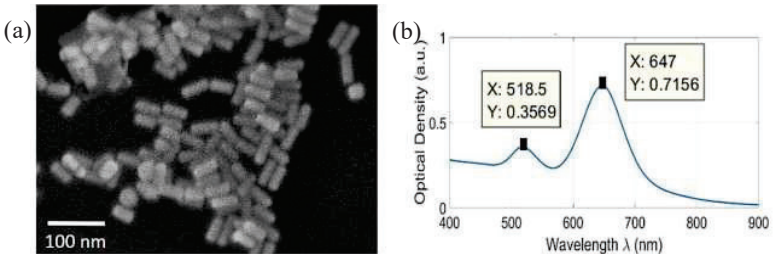

Fig. 1: a) SEM image of the CTAB coated AuNRs sample, (b) UV-vis spectrum of the bulk sample in water [Length: 43.8 ± 6 nm; Width: 18.7 ± 3; Aspect Ratio: 2.34]

Samples are prepared by spin coating a small amount of dilute solution of the gold nanorods (with optimized optical density) on glass coverslips thoroughly cleaned and treated by ozone and oxygen plasma.

3. Results and Discussions

The AuNRs coated glass coverslip is mounted on a home-built confocal microscope set up (Fig 2) on a customized flow-cell. 532 nm laser light is focused on a single gold nanorod through the microscope objective and the corresponding photoluminescence (PL) image of the sample area is captured using an avalanche photodetector (APD). Ascorbic acid is flowed to the sample and the PL emission spectrum of the single AuNR is recorded with time using a CCD spectrometer.

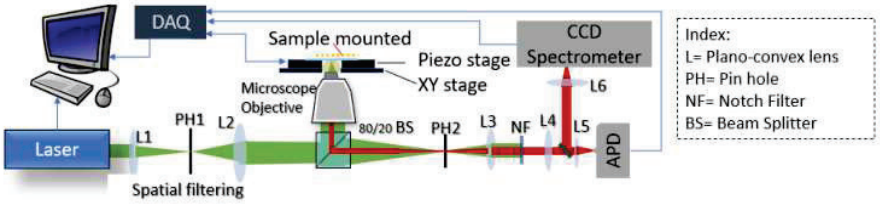

Fig. 2: Home-built confocal microscopy setup used for the experiment

The initial emission spectrum of a single CTAB coated gold nanorod on glass substrate is obtained in water showing LSPR wavelength at 641 nm. Spectral shift of 68 nm (from 641 nm -709 nm) is observed on continuous illumination with 532 nm laser light in presence of Ascorbic acid for 70 minutes (Fig 3(a)). The variation of the LSPR wavelength with time (inset plot in Fig 3(a)) shows that an initial amount of time is required for the activation of the process of spectral shift to speed up significantly. From this observation we suspect a mechanism of charge induction that needs to be investigated further. The experiment has also been conducted on AuNRs synthesized with bi-surfactant CTAB-NaOL under same experimental conditions. No spectral shift is observed in that case (Fig 2(b)). This depicts that the phenomenon of spectral shift is not only dependent on the chemical environment but also on the surface ligand properties of the particular AuNR.

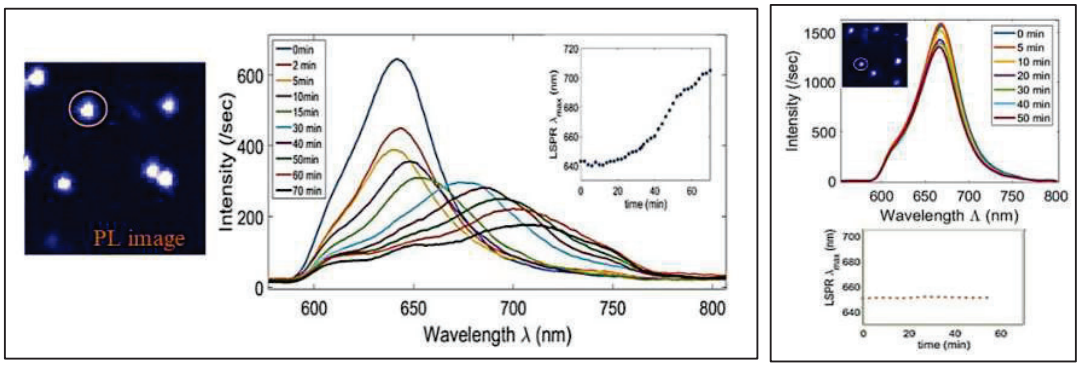

(a) (b)

Fig. 3: (a)Photoluminescence (PL) image of the single CTAB coated AuNR (encircled in PL image) in 60mM Ascorbic acid under continuous illumination with 532 nm laser (0.46 mW power at the back of the objective) and the corresponding PL spectrum at different time of the experiment showing a redshift of 68 nm over 70 minutes (shown in the inset plot). (b) Results for CTAB-NaOL coated AuNR under same experimental conditions showing no significant spectral shift after 50 minutes.

This method can be utilized to selectively tune the LSPR of the AuNRs uniformly deposited on substrate and forms multiple channels with AuNR of different LSPR values functionalized for different sensing targets.

4. References

[1] Ghosh, P., Thambi, V., Kar, A., Chakraborty, A. and Khatua, S., 2021." Light-induced in situ active tuning of the LSPR of gold nanorods over 90 nm." Optics Letters, 46(18), p.4562.

[2] Thambi, V., Kar, A., Ghosh, P. and Khatua, S., 2018." Light-Controlled in Situ Bidirectional Tuning and Monitoring of Gold Nanorod Plasmon via Oxidative Etching with FeCl3." *The Journal of Physical Chemistry C*, 122(43), pp.24885-24890.

[3] Nikoobakht, B. and El-Sayed, M., 2003. "Preparation and Growth Mechanism of Gold Nanorods (NRs) Using Seed-Mediated Growth Method." Chemistry of Materials, 15(10), pp.1957-1962.

[4] Ye, X., Zheng, C., Chen, J., Gao, Y. and Murray, C., 2013. "Using Binary Surfactant Mixtures to Simultaneously Improve the Dimensional Tunability and Monodispersity in the Seeded Growth of Gold Nanorods." *Nano Letters*, 13(2), pp.765-771

Refractive index variation of human red blood cell using transmission of polarized light

Tania Das[a], Kallol Bhattacharya[b]
[a]*Department of Electronics and Communication Engineering, Heritage Institute of Technology,Kolkata 700107*
[b]*Department of Applied Optics and Photonics, University of Calcutta, Kolkata 700106*
taniadas.physics@gmail.com

Abstract: Polarized light transmission is used to evaluate spatial variation of refractive index of human red blood corpuscles (RBC). Polarized light that is made to transmit through a glass prism is analyzed after emerging from the surface of containing the blood smear. The ratio of transmittivities for s and p polarized light is related to the refractive index of the sample through a calibration curve from which the refractive index is quantitatively evaluated for every pixel of the image. Experimental results are presented.

1. Introduction

Microscopic evaluation of optical properties of human red blood cells (RBC) has wide impact on medical research and diagnosis. The knowledge of refractive index distribution of red blood corpuscles (RBC) in human blood is important to interpret optical properties and physiological factors [1].Since Standard refractometers are not suitable to measure the spatial variation of refractive index of RBC, several interferometric based techniques are available to study the variation [2]. However, since interferometric arrangements are unable to yield refractive index distribution unless the sample thickness is known. In present work a simple in-line set up is described for quantitatively measuring refractive index distribution of RBC using normal transmission of polarized light,.

2. Theory, Results and Discussions

Following Fresnel's equation, the transmittivity for s and p polarized light beams reflected from a pair of media having refractive indices n_1 and n_2 ($n_2>n_1$) can be expressed as

$$t_s = \frac{2n_1 \cos\theta_1}{n_1 \cos\theta_1 + \sqrt{n_2^2 - n_1^2 \sin^2\theta_1}}$$

$$t_p = \frac{2n_1 \cos\theta_1}{n_2 \cos\theta_1 + \frac{n_1}{n_2}\sqrt{n_2^2 - n_1^2 \sin^2\theta_1}}$$

In this equation θ_1 is the incident angle at the interface of n_1 and n_2.Fig.1 represents experimental set up for measuring refractive index distribution of RBC using transmission technique.

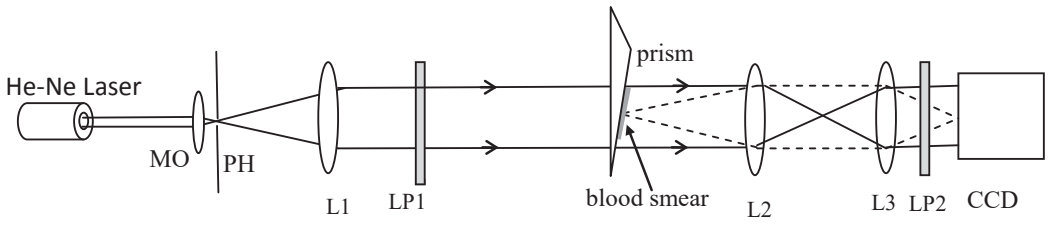

Fig 1. Experimental set up. MO=Microscopic objective, PH: pinhole, L1, L2, L3:lenses, LP1=input linear polarizer, LP2=output linear polarizer, CCD = charge couple device.

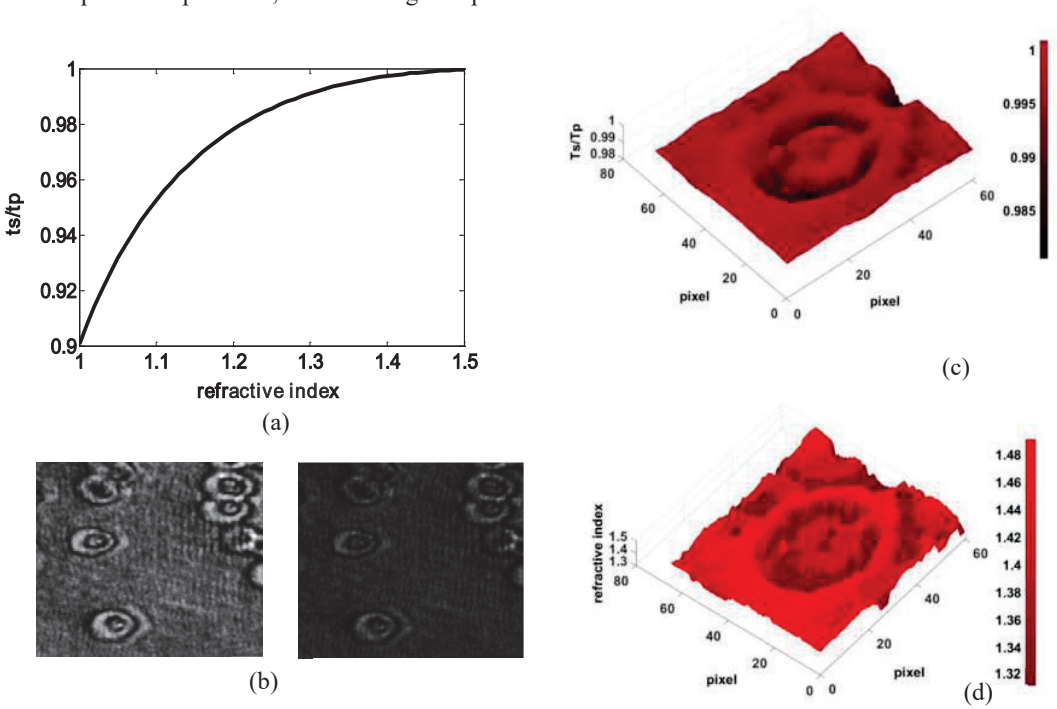

Fig.2.(a) Calibration curve: changes of the ratio Ts/Tp with respect to variation of refractive index for constant n_1=1.518 and θ_1=21.6°.(b) Two intensity data frames for I_0^o and I_{90}^o for transmitted image captured at CCD (c) T_s/T_p ratio image for a single RBC (d) 3-D refractive index distribution of a single RBC.

Fig. 2.(a) represents calibration curve, generated using Fresnel's equation for transmission mentioned in Eq (1) and Eq(2) for the said experimental parameters. Fig 2 (b)-(d) describes experimental results. Fig 2(d) represents the range of refractive index distribution.It is clear from the Fig.2(d) that spatial variation of refractive index of RBC lies in the range of 1.329-1.41 which is well matched with reported values [2].

3. References

1.N. Bosschaart, G. J. Edelman, M. C. G. Aalders, T. G. van Leeuwen, D. J. Faber, 'A literature review and novel theoretical approach on the optical properties of whole blood', Lasers in Medical Science ,vol. 29, p-p 453–479,2014.

2. Zhang, Qinnan & Zhong, Liyun & Tang, Ping & Yuan, Yingjie & Shengde, Liu & Tian, Jindong & Lu, Xiaoxu. (2017). Quantitative refractive index distribution of single cell by combining phase-shifting interferometry and AFM imaging. Scientific Reports.

Software Package for Designing Plamonics Nanoparticle based Refractive Index Sensors

Manmohan Singh Shishodia*, Alok Singh

Department of Applied Physics, Gautam Buddha University, Greater Noida-201312, India

**Corresponding Author: manmohan@gbu.ac.in*

Abstract: The development of software package for computing small particle scattering and designing refractive index sensors based on the scattering behavior of plasmonic nanoparticles is crucial for developing highly efficient optical sensors. The present work is the part of our endeavor to develop a software package capable of simulating optical properties of plasmonic nanoparticles and designing biological sensors and light harvesting systems. The tool will be further equipped to design fiber optic sensors, and the systems based on fluorescence resonance energy transfer.

Keyword: Computational techniques, nanoscale materials and structures, biosensor, refractory nitrides, graphene.

Introduction

Localized Surface Plasmon Resonance based plasmonic sensors have found wide ranging applications *e.g.,* in, biosensing, lasing, energy harvesting, fluorescence resonance energy transfer, surface enhanced Raman spectroscopy, environmental monitoring etc., to name only a few [1-2]. The present work consider nanoshell and nanomatryoshka particles comprising of metallic core, and the graphene shell. The outer shell is kept in the contact of analyte or the environment to be sensed. Such systems are extremely useful for sensing food adulteration, blood plasma monitoring, and waterborne bacteria [3]. The graphene layer is used to minimize the effect of external factors on the sensing characteristics. The plasmonic sensor discussed in this communication is based on the principle that, when light falls on the nanoparticle based system embedded in the sensing medium characterized by different refractive indices, the surface plasmon resonance peak in the scattering spectra shifts in proportion to the change in the refractive index of embedding environment. The sensitivity (S) of these sensors is defined as the rate of change of resonance wavelength (λ_R) with the refractive index (n) of sensing medium. Mie Scattering Theory (MST) is employed to calculate scattering characteristics such as scattering efficiency, extinction efficiency, and absorption efficiency, of plasmonic nanoparticles *e.g.,* sphere (Fig. 1.a), nanoshell (Fig. 1.b), and nanomatryoshka (Fig. 1.c).

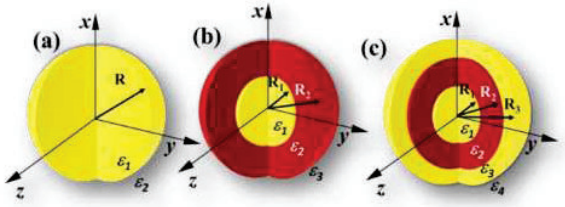

Figure 1: Schematic representation of, **(a).** Sphere (radius, R), **(b).** Nanoshell {core (radius, R_1)-shell (radius, R_2)}, and **(c).** Nanomatryoshya {core (radius, R_1)-innershell (radius, R_2)-outershell (radius, R_3)}, geometries used for calculating the optical properties in NanoSensorLab. The particles are embedded in the medium of dielectric constant ε_2 (sphere), ε_3 (nanoshell), and ε_4 (nanomatryoshya).

Subsequently, resonant wavelength, quality factor, full width at half maximum (FWHM), and the sensitivity are obtained from corresponding scattering spectra. Mie theory is based on exact analytical solutions of Maxwell equations, and it is one of the most powerful tools to calculate scattering, absorption and extinction spectra of spherically symmetric plasmonic nanosystems. In Fig. 2.a, the organization of depicting the steps followed for theoretical calculations of scattering spectra, and subsequently, the quality factor (QF), sensitivity (S), and the Figure of Merit (FOM), is presented in Fig. 2. The graphical user interface for sensor simulator is shown in Fig. 2 (b-c). The salient features of the toolbox shown in Fig. 2 may be outlined as follows:

1. **Select Modules:** Currently, the toolbox has two modules namely, Nanoscattering and Nanosensor. Nanoscattering is primarily meant to calculate Mie theory based scattering efficiency (Q_{sca}), absorption efficiency (Q_{abs}), extinction efficiency (Q_{ext}), peak wavelength, peak scattering, FWHM, and quality factor (QF). Nanosensor module in addition to scattering calculations is equipped to calculate sensitivity (S) and figure of merit (FOM) of nanoshell (NS) and nanomatryoshka (NM) based sensing structures.
2. **Select Particle Type:** The user can choose a geometry from the options of sphere, nanoshell, and nanomatryoshka.

3. **Geometrical Parameter:** User need to provide radii of different layers for example user will provide R_1 (nm) for sphere; R_1 and R_2 for nanoshell; R_1, R_2, and R_3 for nanomatryoshka.

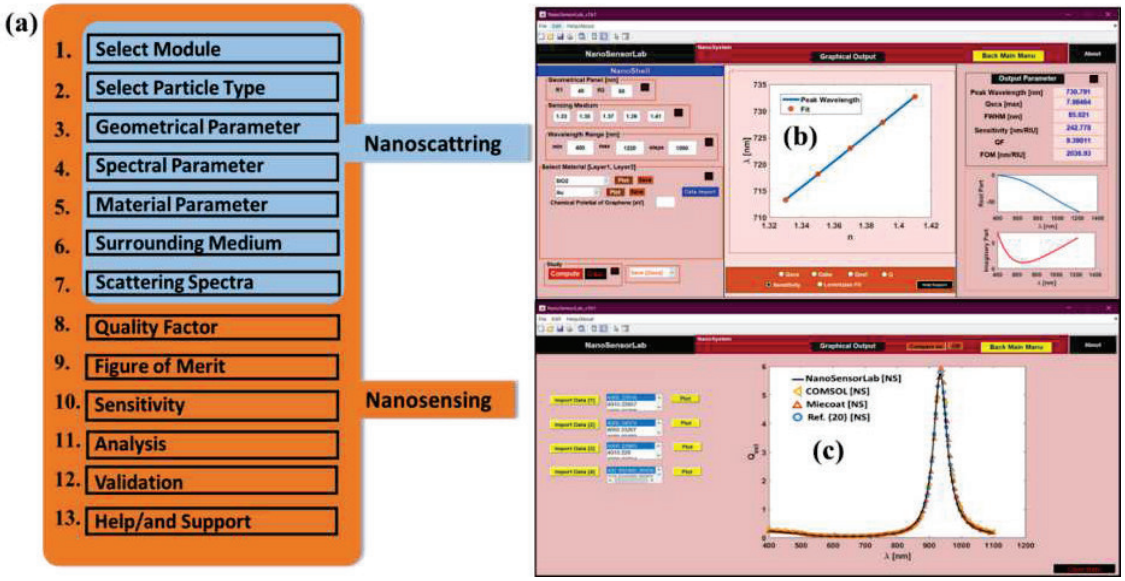

Figure 2: (a). Organization of NanoSensorLab, (b). Calculated scattering characteristics such as scattering efficiency, absorption efficiency, extinction efficiency, Sensitivity, Quality Factor and Figure of merit of the nanoshell (SiO_2/Au). (c). Benchmark and comparison for scattering spectra of Au_2S (ε_1 = 5.44)/Au (nanoshell [R_1=15 nm; R_2= 17]).

4. **Spectral Parameter:** The user can specify wavelength range and the number of steps for calculations.
5. **Material Parameter:** The user can select layer by layer materials (e.g. Au, Ag, Al, Cu, TiN, ZrN, HfN and 2-D graphene) for above chosen geometry from the built-in drop down menu. Alternatively, user can include a material of import the data for any material of his/her choice. User define Drude parameter also provided.
6. **Surrounding Medium:** The user can provide the host medium of the selected systems.
7. **Scattering Spectra:** After computing, the scattering, absorption, and extinction spectra can be calculated.
8. **Quality Factor:** Quality factor (λ_R/FWHM) is the ratio of peak wavelength and full width and half maximum. After computing, the quality factor can be calculated for the selected systems.
9. **Figure of Merit:** The figure of merit is the product of the quality factor (Q) and sensitivity (S). This can be calculated for the system under investigation.
10. **Sensitivity:** The sensitivity ($S=d\lambda/dn$) is defined as the rate of change of resonance wavelength with the refractive index. This is calculated from the slope of the graph as depicted in Fig. 2 (b).
11. **Analysis:** After computation, the scattering and sensitivity can be plotted in Nansensor module. Scattering peaks can be fitted into Lorentzian/Fano shape. Subsequently, FWHM, peak wavelength, and q-factor will be displayed. Options for zooming, data reading, and data saving are available. The calculated data can be exported to other programs for further analysis.
12. **Validation:** The scope of validation through available data by importing and plotting is provided.
13. **Help and Support:** Help and Support: Available at each step.
14. **Download:**https://drive.google.com/drive/folders/1h6IyFgoB2jvx6StOlQOb305qOApbqdE?usp=sharing

The results obtained from the package have been validated from standard literature. The final and finished product may be useful for classroom teaching, concept demonstration, device design, and advanced research.

Acknowledgment: MSS gratefully acknowledge SERB, Department of Science and Technology (DST), Government of India for providing financial support through Grant No. CRG/2019/006912.

References:

[1]. GuangQi Li, M. S. Shishodia, B. D. Fainberg,B. Apter, M.Oren, A. Nitzan, and M. A. Ratner, Nano Lett. 12, 2228 (2012).
[2]. M. S. Shishodia, and P. Pathania, Phys. of Plasmas, 25, 042101 (2018).
[3]. A. Singh, and M. S. Shishodia, Physica E Low Dimens. Syst. Nanostruct. 124, 114288 (2020).

Chirped pulse induced control of ground state coherence.

Nayan Sharma*, Ranjit Kumar Singh*, Souvik Chatterjee[#], Ajay Tripathi*.

**Department of Physics, Sikkim University, 6th Mile Samdur East Sikkim, India - 737102.*

[#]Department of Chemistry, Sikkim University, 6th Mile Samdur East Sikkim, India - 737102.

nayansharma1492@gmail.com

Abstract: In this work, we study the development of ground state coherence and population dynamics in a 3-level Λ system in presence of a continuous wave laser and frequency chirped pulse. The time evolution of the coherence and populations shows dependence upon the value of the chirping rate. The study clarifies that the one-to-one correspondence between the time evolution of coherence and population essentially breaks down at particularly higher values of the chirp rate. This loss of correspondence may not always hamper the efficiency of population transfer.

Keywords: Frequency chirped pulse, 3-level system, ground state coherence.

1. Introduction

Coherent control of population and coherence among the quantum states has numerous applications. Processes such as Stimulated Raman adiabatic passage (STIRAP)[1] and Stark-shift-chirped rapid adiabatic-passage (SCRAP)[2] are used to selectively transfer the populations into various quantum states through the use of laser pulses. In a simple 2-level system, it has been observed that the excitation probability can be controlled by the chirping rate [3, 4] and one can engineer the population amongst the states involved in the system [5]. It has been shown by Djotyan et al. [6,7] that a single frequency chirped pulse can lead to a population transfer between two ground states in a simple 3-level Λ system with controllable development of coherence amongst the ground states. Use of the chirped pulse for selective population transfer and coherent coherence creation in various other configurations can be found in the works [8, 9].

2. Numerical Results.

We consider the interaction of a continuous wave (CW) laser and a frequency chirped (FC) pulse with an ensemble of stationary atoms in a simple 3-level Λ type system as shown in figure 1.

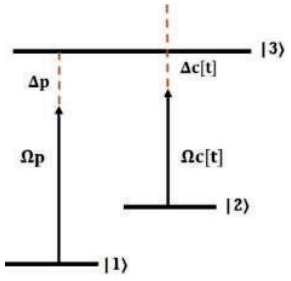

Figure 1: 3-level Λ model system. The transition |1> → |3> is coupled by a continuous wave (CW) laser and a frequency chirped (FC) pulse is applied in the |2> → |3> transition.

As typical of a Λ system, states |1> and |2> are taken to be of same parity (dipole forbidden) along with a third higher energy state |3> which is of opposite parity with respect to the states |1> and |2>. The density matrix equations were solved to study the dynamics of the system with the initial condition $\rho_{11} = 1$. In our model we neglect the phenomenological terms such as spontaneous decay and decay due to collisions as the duration of the FC pulse is taken to be short compared to these decay rates.

To understand the effect of the chirping rate α and the ratio between the Rabi frequencies Ωc and Ωp on the transfer of population (ρ_{22}) and coherence (ρ_{12}), contour was plotted for a wide range of parameters (figure 2 (a) and (b)). The

value of the Ωp is kept constant at 2 GHz for this study and the ratio Ωc/Ωp is changed by increasing the value of Ωc with τ =2ns. Figure 2 (a) shows the contour plot for ρ_{12} where the absolute value of the coherence at the end of the pulse (t=5ns) is plotted. This case for the coherence shows interesting features in which coherence follows a periodic behavior with respect to both the parameters (α and Ωc). The change in the coherence w.r.t the ratio is more prominent in the case of near resonance (up to 1 GHz/ns). For larger value of the α, the nature of the coherence changes showing different kind of periodic nature. The small thin strips represent the region where the value of the coherence remains non zero which is accompanied by the presence of region where the value of the ρ_{12} becomes zero. Figure 2 (b) shows the corresponding contour plot for ρ_{22} (at t = 5ns i.e., at the instant where the pulse finishes) in which the presence of the multiple regions where the population transfer to the state |2> is more or less robust is present. When the value of the α is kept constant at near resonance (up to 1 GHz/ns) small change in the value of the ratio Ωc/Ωp can induce a sharp change in the value of ρ_{22}. The near resonance behavior of the coherence as observed in figure 2 (a) is mapped into the population curve. The increase in the value of the ratio changes the value of the pulse area (Θ) and hence leads to such an oscillatory behavior of the population. For larger values of the α the change in the population is not much as because of the fact that the laser now is in the region of far-off resonance. The increase in the Θ in this region is compensated by the value of the α and hence the periodic sharp change is not seen as was present for low values of α (near-resonance). For far off resonance case i.e., when the value of the α is large the presence of the robust regions in the population with a periodic change in the coherence suggests that the strong correspondence between the ground state coherence ρ_{12} and population transfer (ρ_{22}) is lost.

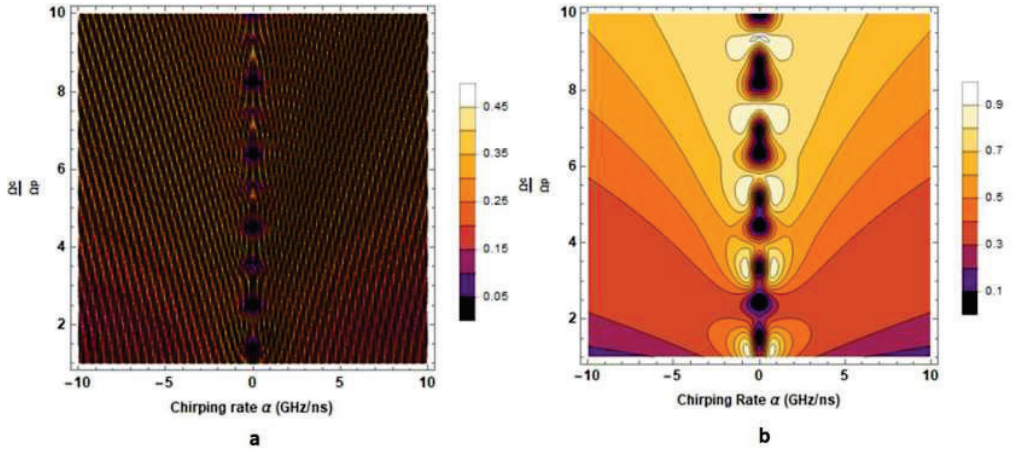

Figure 2: Contour plots for pulse width τ=2ns (a) variation in absolute value of coherence ρ_{12} and (b) variation in the population ρ_{22}.

3. References.

[1] Nikolay V Vitanov, Andon A Rangelov, Bruce W Shore, and Klaas Bergmann. Stimulated raman adiabatic passage in physics, chemistry, and beyond. Reviews of Modern Physics, 89(1):015006, 2017.

[2] Johann-Heinrich Schonfeldt, Jason Twamley, and Stojan Rebi´c. Optimized control of stark-shift chirped rapid adiabatic passage in a λ-type three-level system. Physical Review A, 80(4):043401, 2009.

[3] VA Astapenko and MS Romadanovskii. Excitation of a two-level system by a chirped laser pulse. Laser physics, 19(5):969–973, 2009.

[4] S Zhdanovich, EA Shapiro, M Shapiro, JW Hepburn, and V Milner. Population transfer between two quantum states by piecewise chirping of femtosecond pulses: theory and experiment. Physical review letters, 100(10):103004, 2008.

[5] Z Ghaedi, M Hosseini, and F Sarreshtedari. Population engineering of the cesium atom fine structure levels using linearly chirped gaussian laser pulse. Optics Communications, 431:109– 114, 2019.

[6] GP Djotyan, JS Bakos, Zs S¨orlei, and J Szigeti. Coherent control of atomic quantum states by single frequency-chirped laser pulses. Physical Review A, 70(6):063406, 2004.

[7] GP Djotyan, N Sandor, JS Bakos, and Zs S¨orlei. An extremely robust strong-field control of atomic coherence. Optics express, 19(18):17493–17499, 2011.

[8] YA Sharaby, A Joshi, and SS Hassan. Coherent population transfer in v-type atomic system. Journal of Nonlinear Optical Physics & Materials, 22(04):1350044, 2013.

[9] Nora Sandor, Joseph S Bakos, Zsuzsa S¨orlei, and Gagik P Djotyan. Creation of coherent superposition states in inhomogeneously broadened media with relaxation. JOSA B, 28(11):2785–2796, 2011.

Exploring the Effects of Terbium doping in ZnO Nanostructures

Alphin Joseph M J, Harikrishnan G, J. Mitra
School of Physics, IISER Thiruvananthapuram, Kerala-695551
Email - joseph717@iisertvm.ac.in

Abstract: Despite the fact that doping semiconductors like ZnO with rare earth elements is challenging, it has been actively pursued because of its important applications in optoelectronics as visible-wavelength emitters. In this work, Terbium (Tb), a lanthanide which emits in the green region was successfully incorporated into ZnO during its synthesis. While structural studies showed signatures of Tb incorporation, the photovoltaic and optical properties were also investigated.

Keywords: Lanthanides, photoluminescence, near band edge emission, broadband emission, collisional quenching

1. Introduction

ZnO is a wide and direct band gap (3.37 eV) semiconductor with a large exciton binding energy (60 meV) and crystallizes naturally in the wurtzite structure [1, 2]. Photoluminescence (PL) spectrum of ZnO reveals near band edge (NBE) emission located in the near UV region at ~372-387 nm, originating from excitonic recombination (a pair of excited electron and hole that are bonded together with their Coulombic attraction force) and a broadband emission in visible region originating from shallow and deep level defect states [3, 4] in the wavelength range of 420-750 nm. Light emitting semiconducting materials incorporating rare earth (RE) ions (e.g., Eu, Yb, Er, Ho, Tm, and Tb) have been investigated for applications in optoelectronics [5, 6]. Here, we demonstrate a system obtained by doping Tb in ZnO nanostructures. Light emission from Tb^{3+} ions is characterized by a stable and sharp luminescence [7, 8] associated with the transitions occurring from the excited $^5D_4$ level down to the lower levels ^7F_J (J = 3, 4, 5, 6). Hence it is expected that a sharp and intense visible luminescence will be observed due to the energy transfer mechanism from the ZnO host to Tb^{3+} ions upon UV excitation. We optimized an efficient chemical method using a terbium (III) salt for the synthesis of doped ZnO nanostructures and characterized it for further potential applications.

2. Results and Discussions

SEM images showed nanorod like structures (Fig 1(a)) and EDAX confirmed the presence of Zn and O atoms. The presence of Tb atoms was significant only for higher doping concentrations. While XRD data confirmed the formation of hexagonal wurtzite structure for pure and Tb doped ZnO (inset of Fig 1(b)), a noticeable shift in XRD peaks were observed with doping.

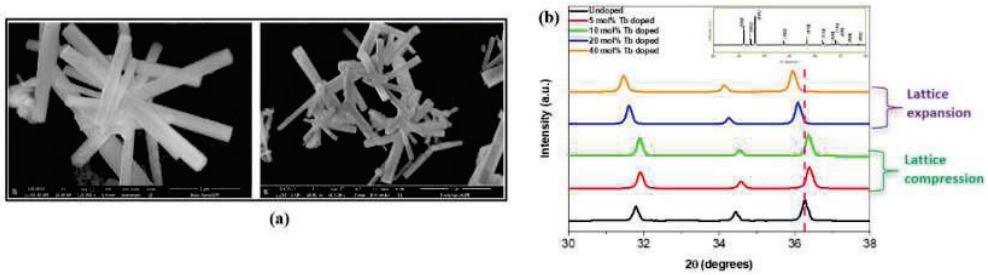

Fig. 1: (a) *SEM images of nanostructures* ***(b)*** *Shift in XRD peaks with doping and the inset shows the XRD patterns of ZnO.*

Due to the greater atomic size of Tb, substitution of Zn by Tb is expected to result in an expansion of the crystal lattice which eventually shifts the XRD peaks towards lower angles. But this was observed only at higher doping

concentrations. At lower concentrations it is rather likely that the Tb^{3+} accumulates on the surface of ZnO nanostructures which results in some compressive strain in the lattice which in turn shifts the XRD peaks towards greater angles (Fig 1(b)).

Photoluminescence measurements showed a suppression in the NBE peak of low Tb doped ZnO upon annealing and an increase in highly doped samples (Fig 2). The visible peaks showed a blue shift with increasing doping concentration (Fig 2(a)). Deconvolution of the PL data for the annealed 10%Tb doped ZnO nanostructures showed the presence of an extra peak around green region in addition to the broadband peak which can be attributed to the energy transfer from ZnO to Tb^{3+} ions.

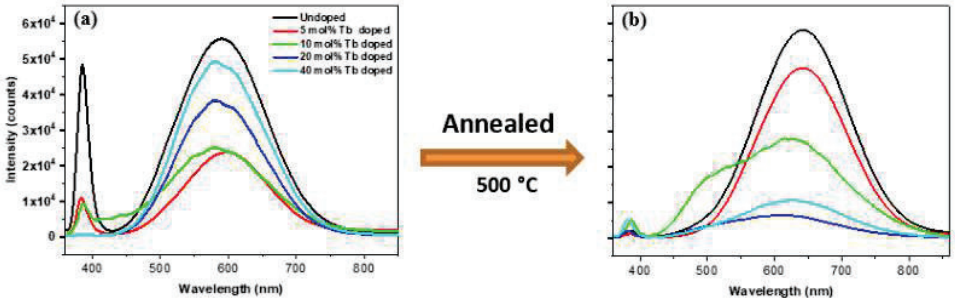

Fig. 2: *Room temperature PL spectra* ***(a)*** *before and* ***(b)*** *after annealing*

Electrical measurements of annealed samples, drop-casted on pre-patterned electrodes showed significant photo conductance, a sudden decrease in resistance upon UV irradiation. The UV response however is found to be a non-monotonic function of Tb incorporation and was observed to be highest in 5 mol% Tb doped ZnO nanostructures. The mechanism of photoconductivity enhancement and potential applications are discussed in the presentation.

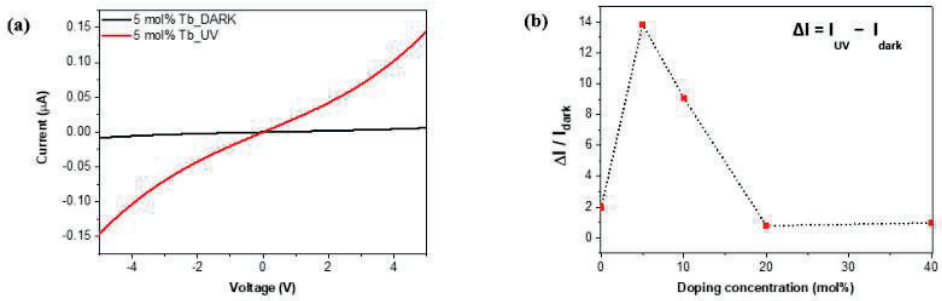

Fig. 3: ***(a)*** *I-V graph of 5 mol% Tb doped ZnO* ***(b)*** *UV response graph at -2V*

3. References

[1] Janotti, A., & Van de Walle, C. G. *Fundamentals of zinc oxide as a semiconductor*. Reports on progress in physics, 72(12), 126501 (2009).
[2] Klingshirn, C. ZnO: *From basics towards applications*. physica status solidi (b), 244(9), 3027- 3073 (2007).
[3] Bandopadhyay, K., & Mitra, J. *Zn interstitials and O vacancies responsible for n-type ZnO: what do the emission spectra reveal?*. Rsc Advances, 5(30), 23540-23547 (2015).
[4] Zeng, H., Duan, G., Li, Y., Yang, S., Xu, X., & Cai, W. *Blue Luminescence of ZnO nanoparticles based on non-equilibrium processes: defect origins and emission controls*. Advanced Functional Materials, 20(4), 561-572 (2010).
[5] Steckl, A. J., Park, J. H., & Zavada, J. M. *Prospects for rare earth doped GaN lasers on Si*. Materials Today, 10(7-8), 20-27 (2007).
[6] Yuhua, W., Ge, Z. H. U., Shuangyu, X. I. N., Qian, W. A. N. G., Yanyan, L. I., Quansheng, W. U., ... & Wanying, G. E. N. G. *Recent development in rare earth doped phosphors for white light emitting diodes*. Journal of Rare Earths, 33(1), 1-12 (2015).
[7] Kobelev, N. P., Kolyvanov, E. L., & Khonik, V. A. *An acoustic study of irreversible structural relaxation in a bulk metallic glass*. In Solid State Phenomena (Vol. 115, pp. 113-120). Trans Tech Publications Ltd (2006).
[8] Pawade, V. B., Swart, H. C., & Dhoble, S. J. *Review of rare earth activated blue emission phosphors prepared by combustion synthesis*. Renewable and Sustainable Energy Reviews, 52, 596-612 (2015).

Schrödinger Cat States in Quantum-Dot-Cavity Systems using Squeezed Light

Urmimala Dewan and Amarendra K. Sarma
Department of Physics, Indian Institute of Technology Guwahati, Guwahati – 781039, India
Author e-mail address: d.urmimala@iitg.ac.in

Abstract: We have proposed a protocol to create Schrödinger cat states in Quantum Dot cavity system (QDC) using squeezed light. The protocol exploits the internal dynamics of Jaynes Cummings model to create a state by collapse and revival of states. The paper observes the possibility of engineering a cat state in realistic conditions.

Keywords: Schrödinger cat state, coherent squeezed state, quantum dot, Wigner function

1. Introduction

Schrödinger cat states are basically superposition of macroscopically distinguishable states analogous to Schrödinger's famous thought experiment where the cat is alive and dead at the same time. Studying Schrödinger cat state can provide solution for century long controversy of quantum measurement. The creation of Schrödinger cat state may allow controlled study of quantum decoherence which is anticipated as a way of quantifying the elusive boundary between classical and quantum worlds. Coherent states are useful for the 'classical description' of radiation fields. A more general class of radiation have been introduced which is known as squeezed 'coherent states'. Squeezing is an effect that reveals the quantum properties of radiation field and cannot be explained classically. Squeezing is characterized by a field state in which variance of one of two non-commutating observables (say position x and momentum p_x) is less than one half of the absolute value of their commutator. While many platforms are suggested for generation of nonclassical states, quantum dot cavity systems are particularly interesting as they have already become an integral part for generation of nonclassical light, entangled photon pairs, quantum cryptography and many more. Using Quantum dot cavity as a source of Schrödinger cat state would be a new feather to the crown. The main difference between atomic cavity and quantum dot cavity is that in Quantum dot cavity, in addition to cavity losses, there are phonon losses present which are inevitable. Physicists have successfully engineered Schrödinger cat state in atomic cavity before [2]. Recently M. Cosacchi et al. [5] simulated Schrödinger cat state in Quantum dot cavity using coherent light based on the proposal of Gea-Banacloche [3,4], where by using a coherent state as an initial state a Schrödinger cat state can be generated exploiting the properties of Jaynes Cummings Hamiltonian. We have considered a more general approach by using squeezed coherent light in a Quantum dot to generate a Schrödinger cat state in a Quantum dot cavity system.

2. The Model

The schematic diagram of the system is shown in Fig. 1. In a microcavity we have a single quantum dot and the cavity system, irradiated either with coherent squeezed light or with squeezed light. The QDC system is comprised of a driven two level QD coupled to a single photon mode.

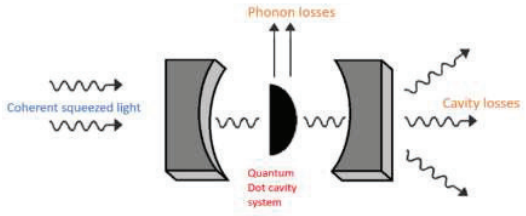

Fig 1: Schematic diagram of quantum dot cavity system.

The Hamiltonian for the system is described by: $H = H_{QDC} + H_{driving}$, where $H_{QDC} = \hbar\omega_X + \hbar\omega_c a^\dagger a + \hbar g(a\sigma_X{}^\dagger + a^\dagger\sigma_X)$ and $H_{driving} = -\frac{\hbar}{2}[f_p{}^\star(t)a + f_p(t)a^\dagger]$. Here ,$f_p(t)$ is the exciting laser pulses and are of Gaussian

form. Our initial state is a squeezed coherent state. Here $|X>$ is the exciton state at energy $\hbar\omega_X$, $\sigma_X := |G><X|$ is the transition operator between the excited state $|X>$ and the ground state $|G>$ and $a^\dagger, a$ are the creation and annihilation operators, g is the coupling coefficient.

3. Results and Discussions

One of the best ways to probe the nonclassical states of light is to study the corresponidng Wigner distrubution functions of the states. In Fig. 2 Wigner function of the final created states are depicted when coherent squeezed state and squeezed states are used as inputs. The emergence of a Schrödinger cat state could be seen clearly. Here $\hbar\omega_X = \hbar\omega_c = 1.5$ meV , taking the coupling coefficient as $g = 0.2$.

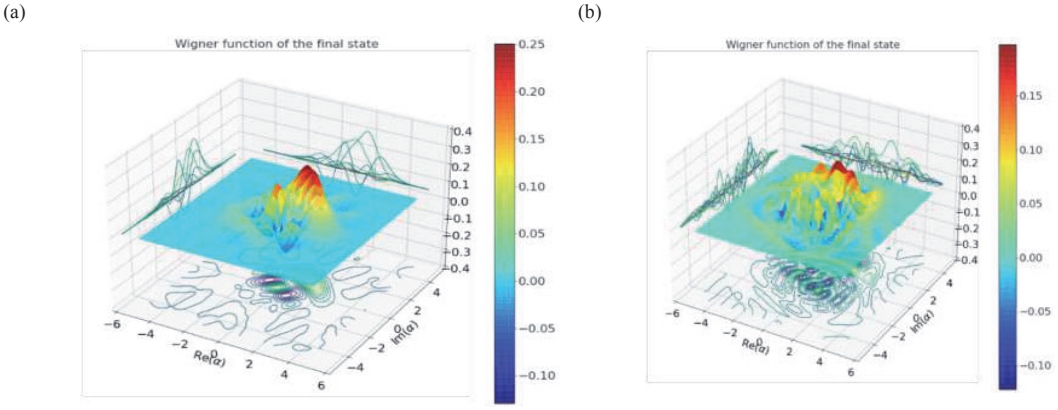

Fig 2 :Wigner function of final state created (a) using coherent squeezed state(left) (b) using squeezed state(right).

Looking at the Wigner function we get the confirmation of generation of a Schrödinger cat state in the cavity, where the Gaussians indicate the macroscopically distinct states and oscillations between them show the superpositions of those states. The negative part of the function (shown in blue in plot) shows the non classicality of the final state.

Table-I

Coupling strength (g)	Non classicality measure (δ)		
	coherent	Coherent squeezed	squeezed
0.05	0.57	0.58	1.18
0.10	0.71	0.73	1.43
0.15	0.72	0.70	1.41
0.20	0.41	0.49	1.38
0.25	0.56	0.55	1.40
0.30	0.43	0.32	1.51

Table 1 enlists the nonclassicality measure, denoted by δ [1], for coherent, coherent-squeezed and squeezed light against various coupling strengths. The finite values of δ confirms the existence of Schrödinger cat state in the cavity.

[1]A. Kenfack, K. Życzkowski , " Negativity of the Wigner function as an indicator of non-classicality", J. Opt. B: Quantum Semiclass. Opt. 6 396, 10 (2004).
[2]C. Monroe, D.M Meekhof,B.E King,D.J Wineland,"A Schrodinger cat superposition state of an atom", Science 272,5265, 6 (1996).
[3]J. Gea-Banacloche, "Collapse and Revival of the State Vector in Jaynes Cummings modell: An Example of State Preparation by a Quantum Apparatus", Phys. Rev. Lett. 65, 3385 , 4 (1990).
[4]J. Gea-Banacloche, "Atom- and field-state evolution in the Jaynes-Cummings model for large initial fields", Phys. Rev. A 44, 5913, 19 (1991).
[5]M. Cosacchi et al , "Schrödinger cat states in quantum-dot-cavity systems ", Phys. Rev. Research 3, 023088 ,11 , (2021).

Investigation of Third-Order Optical Nonlinearity in Silver Nanoparticles with thiol-containing capping agents

Aditya Kurdekar#[a,b], Prajal Chettri[a], Rajasimha K[a], V. Krishna Chaitanya[a]

a FEMTOFAB Lab, Department of Physics, Sri Sathya Sai Institute of Higher Learning, India
b OMI labs, Department of Instrumentation and Applied Physics Indian Institute of Science, India
 # Corresponding author email- adityakurdek@iisc.ac.in

Abstract: We explore the third-order non-linear properties of silver nanoparticles with thiolated capping agents. Thiolated biomolecules such as Coenzyme A, glutathione and cysteine were considered as the capping agents in this study. The third-order nonlinear susceptibilities were measured using the Degenerate Four-Wave mixing Technique (DFWM). The thiol-capped silver nanoparticles exhibited higher non-linear susceptibility than the non-thiol-capped silver nanoparticles. The highest nonlinearity was measured in Coenzyme A-capped silver nanoparticles. The enhanced nonlinearity can be attributed to the LSPR of silver nanoparticles.

Keywords: Third order nonlinearity, DFWM, silver nanoparticles, LSPR

Paper summary

The nonlinear optical characteristics of metal nanoparticles distributed in various optically transparent solid matrices have been the subject of several studies. Yet, the nonlinear optical experiments on the silver nanoparticles in the thiolated templates have not yet been reported. In this work, the Degenerate Four-Wave Mixing tests performed to examine the nonlinearity of different thiol-capped silver nanoparticles are described.

Silver nanoparticles with thiolated capping agent, Coenzyme A, glutathione and cysteine were prepared by chemically reducing silver nitrate with $NaBH_4$ and then adding the capping agent into the mixture. The majority of the nanoparticles were spherical, as revealed by transmission electron microscopy. The nanoparticles ranged in size from 5 to 15 nm. Because it falls within the range of wavelengths that corresponds to the surface plasmon resonance phenomena of nanoparticles, UV-VIS examination confirmed the presence of absorption maxima at 429 nm, which indicated the production of nanosized silver particles.[1].

Studies on degenerate four-wave mixing were done to examine the silver nanoparticles' nonlinear characteristics (Fig 1). By using carbon disulphide (CS2) as a reference ($\chi(3) = 1.75 \times 10^{-12}$ esu), it was possible to determine the thiol capped AgNPs' third-order nonlinear optical features. Table 1 presents the values for all the examined samples' refractive indices and third-order nonlinear susceptibility.

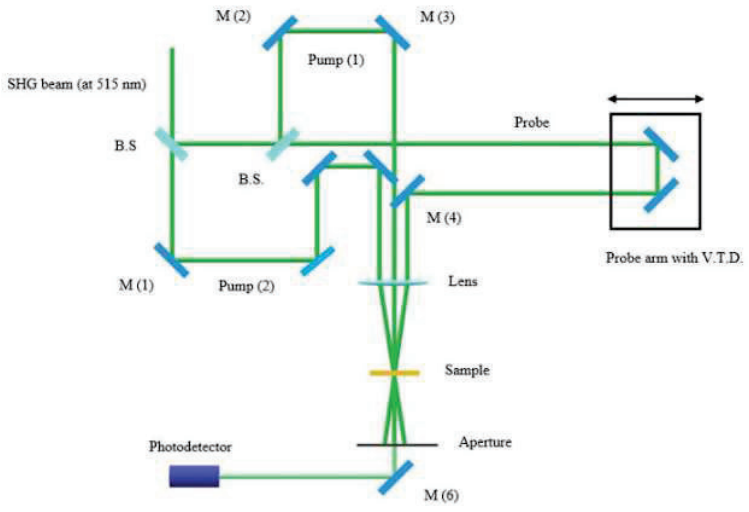

Fig 1: (Left) DFWM setup used in the study of the third-order nonlinear properties of silver nanoparticles.

The third-order nonlinear susceptibility measurements were done for the uncapped AgNP, and AgNP capped with Co-Enzyme-A, L-Glutathione, Cysteine and Trisodium citrate. The third-order nonlinear susceptibility values are listed in Table 1.

Table 1: Comparison of Third Order Nonlinear Susceptibilities measured for different capped Silver Nanoparticles systems

Sample	Third-order susceptibility (± error) (in x10 $^{-13}$ esu)
Carbon Disulphide (ref)	(17.50 ± 0.57)
CoA capped AgNPs	(1.38 ± 0.04)
Glutathione capped AgNPs	(1.17 ± 0.05)
Cysteine capped AgNPs	(1.30 ± 0.04)
Borohydride capped AgNPs	(0.82 ± 0.12)
Trisodium citrate capped	(0.41 ± 0.12)

The third-order susceptibility for CoA capped nanoparticles was measured to be 1.38 x 10^{-13} esu whereas glutathione capped and cysteine capped nanoparticles exhibited third order susceptibilities of 1.17 x 10^{-13} esu and 1.30 x 10^{-13} esu respectively.

It is also remarkable that nanoparticles with thiolated functional groups recorded higher non-linear susceptibility compared to non-thiolated functional groups. Coenzyme A, Cysteine and Glutathione are thiol-containing capping agents and their nonlinear susceptibility was 30 % higher than non-thiolated functional groups. Borohydride-capped $AgNO_3$ had a value of 0.82 x10^{-13} esu, which is 40% lower than that recorded for CoA-AgNPs. This confirmed that surface functionalization plays a major role in the nonlinear interaction of nanoparticles with light. This information can be of great use to material engineers as well as optical material designers as they can tune the non-linearity as per their requirements.

The reason we observe nonlinearity in AgNPs is due to the excitation of LSPRs in AgNPs such that absorption prevails at the site of NPs[2]. The coupling of an incident photon to surface plasmons of nanomaterials determines the amount of electric field in the vicinity of nanomaterials. To maximize these properties in an assembly, the interparticle gap between adjacent plasmonic nanoparticles needs to become sub-nanometric[3]. This results in a large local electric field enhancement on the surface of the nanoparticles, giving rise to unique optical properties.

The experimental result suggests that the thiol-capped silver nanoparticles may have future photonic applications.

References

[1] S. L. Smitha, K. M. Nissamudeen, D. Philip, and K. G. Gopchandran, "Studies on surface plasmon resonance and photoluminescence of silver nanoparticles," *Spectrochim. Acta Part A Mol. Biomol. Spectrosc.*, vol. 71, no. 1, pp. 186–190, Nov. 2008, doi: 10.1016/j.saa.2007.12.002.

[2] G. Krishna Podagatlapalli, S. Hamad, M. Ahamad Mohiddon, and S. Venugopal Rao, "Effect of oblique incidence on silver nanomaterials fabricated in water via ultrafast laser ablation for photonics and explosives detection," *Appl. Surf. Sci.*, vol. 303, pp. 217–232, Jun. 2014, doi: 10.1016/j.apsusc.2014.02.152.

[3] A. S. L. Gomes *et al.*, "Linear and third-order nonlinear optical properties of self-assembled plasmonic gold metasurfaces," *Nanophotonics*, vol. 9, no. 4, pp. 725–740, Apr. 2020, doi: 10.1515/nanoph-2019-0521.

[Quantum-accelerated Imaging of N Stars]

Fanglin Bao[1], Hyunsoo Choi[1], Vaneet Aggarwal[2], and Zubin Jacob[1]

[1] *Birck Nanotechnology Center, Elmore Family School of Electrical and Computer Engineering, Purdue University, West Lafayette, Indiana 47907, USA*

[2] *School of Industrial Engineering, and School of Electrical and Computer Engineering, Purdue University, West Lafayette, Indiana 47907, USA*

zjacob@purdue.edu

Abstract: In traditional direct imaging, estimating the characteristic like centroid and intensity of point sources within the sub-Rayleigh region usually requires prohibitively long integration time. Here, we propose quantum-accelerated imaging(QAI) to significantly reduce the measurement time and advanced estimation accuracy by adopting information-theoretic approach, maximizing the quantum Fisher information (QFI).

Keywords: Rayleigh limit, Quantum Fisher information, Adaptive mode, Quantum supremacy

Imaging point sources with low angular separation near or below the Rayleigh criterion are important in astronomy, e.g., in the search for habitable exoplanets near stars. However, the measurement time required to resolve stars in the sub-Rayleigh region via traditional direct imaging is usually prohibitive. Here, we propose quantum-accelerated imaging (QAI) for a constellation with unknown number of stars, unknown position, and unknown brightness [1]. Our approach of QAI adaptively learns modal bases from data to maximize Fisher information per detected photon. We demonstrate quantum acceleration factors of around 10~100 times compared to direct imaging for a given resolution. QAI uses an adaptive mode projector as the hardware on the image plane to selectively measure photons in a given modal basis. The adaptive mode projector could consist of a deformable mirror followed by single-photon detectors. The former projects the input optical field onto the given basis while the latter collect excited photons of corresponding modes. The key algorithm of QAI is to find optimal positive operator-valued measures (POVMs) to maximize Fisher information for given number of photons. Since the ground truth, namely, number of stars, brightness and positions are unknown, optimal POVMs are approached in an adaptive manner. We start with initial POVMs defined by projections to first 10 Zernike modes. We then approximate the ground truth with posterior estimations to adaptively find subsequent POVMs. This working procedure forms a loop of POVMs-Measurement-Estimation-POVMs, and it only exits when a pre-set criterion is met. The entire procedure is illustrated in the additional multimedia animation. Fig.1 shows the overall quantum acceleration factor of our proposed QAI against direct imaging. For given estimation accuracy, the acceleration factor is defined as the ratio of photons consumed by direct imaging over photons consumed by QAI. We analyze the statistics of the acceleration factor for 12 different scenes (6 different position configurations times 2 different brightness configurations). Each scene is tested with 12 independent runs, and the mean (curves) and standard deviation (error bars) of acceleration factor are derived from these 12 values. The acceleration effect is robust as the acceleration factor is significantly over 1.

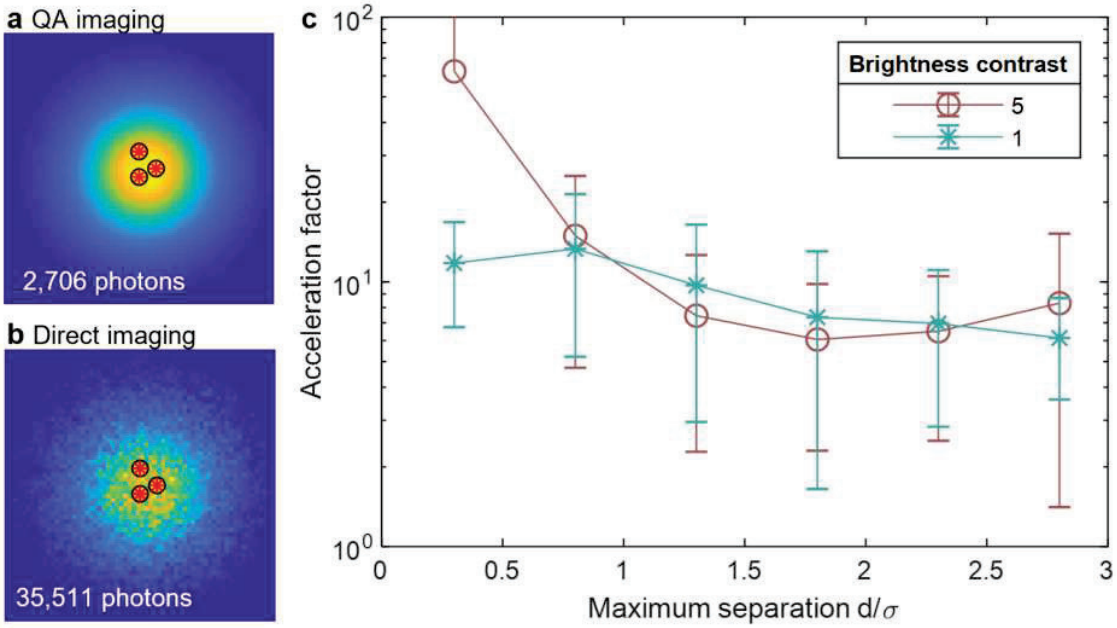

Figure 1 Demonstration of QAI for pre-set accuracy showing acceleration against direct imaging. a, QAI of 3 stars (red star) consumes 2,706 photons to hit the ground truth (black circle). b, Direct imaging of the same 3 stars consumes 35,511 photons to hit the ground truth. c, Acceleration factor for 12 different scenes shows 10~100 times universal acceleration of QAI. d is the maximum distance among 3 stars. σ is the width of the point-spread function. Brightness contrast is the ratio of the highest brightness over the lowest brightness among 3 stars.

[1] F. Bao, etc., "Quantum-accelerated imaging of N stars," Opt. Lett. 46, 3045-3048 (2021)

Unconventional Magnon Blockade in Three Mode Hybrid Ferromagnet-Qubit System

Pooja Kumari Gupta and Amarendra K. Sarma
Indian Institute of Technology Guwahati, Department of Physics, Guwahati-781039, Assam, India
pooja.kumari@iitg.ac.in

Abstract: In this work, we propose a scheme to achieve unconventional magnon blockade using a hybrid ferromagnet-qubit system containing two magnon modes and a superconducting qubit. The magnon correlation has been analyzed.

Keywords: Magnon blockade, superconducting qubit, optomagnonics.

1. Introduction

In the last few years Hybrid quantum systems have attracted considerable interest for the study of interaction between light and matter [1]. 'Cavity Optomagnonics' is a very recent development in the area of Cavity quantum electrodynamics [2]. This emerging field is a result of advancement in the quantum technologies. Some remarkable experiments in the past couple of years have motivated to explore the possibility of coupling photons to magnetic spin excitations and superconducting qubit. Cavity optomagnonics deals with the interaction between photons and magnons (the spin wave excitation). This field provides a new platform for the manipulation of quantum information and its processing, storage of information, control and measurement in microwave domain [3]. In the future, many new exciting physics are to be discovered in terms of coherent interaction between photon and magnon in the area of electronics, photonics and spintronics. Magnons are very suitable candidates for information processing and information storage as they have long life time (2 to 60 microseconds), they are tunable in frequency and we can also couple them with other degrees of freedom such as electrons and phonons. Magnons are the collective elementary excitations of a ferromagnetic system. They are quanta of spin waves in the magnetic material [4]. Owing to their high spin density and low dissipation rate, ferromagnetic system like Yttrium Iron Garnet (YIG) provides a promising platform for study of magnon coupling with other degrees of freedom. People have realized the coupling of Kittle mode in the YIG sphere with superconducting qubits, photons and phonons. There has been a significant progress in this area like generation of entanglement between two magnon modes via magnetostrictive interaction [5], simultaneous blockade of photon, phonon and magnon induced by a two-level atom [6], coherent coupling between magnon and superconducting qubit [7], tunable magnon antibunching in hybrid ferromagnet-superconductor system with two qubits [8]. The coherent coupling between magnon and superconducting qubit via virtual photon excitation cause the generation of single magnons. Similar to Coulomb blockade, photon blockade and phonon blockade, the magnon blockade also utilizes second order correlation function to show statistical properties of antibunching. In this work, we have investigated magnon blockade using a hybrid ferromagnet-qubit system containing two magnon modes and a superconducting qubit.

2. Theory, Model and Discussions

We consider a hybrid superconducting qubit-ferromagnet system consisting of one superconducting qubit and two YIG sphere placed in a microwave cavity as shown in Fig.1. Qubit and the magnon modes are coupled through virtual cavity photons. The YIG sphere are placed at the position where the magnetic field of cavity has its maximum. The two Kittle modes magnetically couples with the cavity mode. The superconducting qubit is placed where the electric field is close to the maximum. The coupling between qubit and the two magnon modes is mediated by the cavity modes.

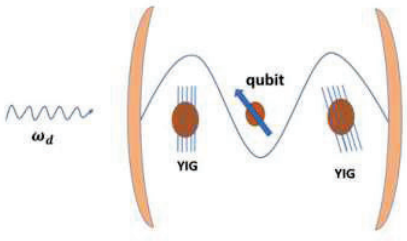

Fig. 1: Schematic diagram of the system with two YIG sphere and a qubit.

The two YIG spheres are uniformly magnetized by applying static magnetic field. In addition, they are driven by an optical field with frequency w_d. The Hamiltonian of the system is written as:

$$\widehat{H} = w_q\,\sigma^{\dagger}\sigma + w_1\,m_1^{\dagger}m_1 + w_2\,m_2^{\dagger}m_2 + g_{q1}\left(\sigma^{\dagger}m_1 + \sigma\,m_1^{\dagger}\right) + g_{q2}\left(\sigma^{\dagger}m_2 + \sigma m_2^{\dagger}\right) + \Omega_1\left(m_1^{\dagger}\,e^{-i\,w_d t} + m_1\,e^{i\,w_d t}\right) + \Omega_2\left(m_2^{\dagger}\,e^{-iw_d t} + m_2\,e^{i\,w_d t}\right) \quad (1)$$

The first term in the Hamiltonian represents qubit energy, the second and third terms represents the energy of the two magnon modes, the fourth and fifth terms describes the interaction of qubit with two magnon modes separately and the last two terms describe the driving input fields and its interaction with the two magnon modes. The resonance frequency of two magnon modes are w_1 and w_2 and w_q is the transition frequency of qubit. The coupling strength between qubit and the two magnon modes are denoted by g_{q1} and g_{q2}. $\sigma^{\dagger}(\sigma), m_1^{\dagger}(m_1), m_2^{\dagger}(m_2)$ are the creation and annihilation operator for the qubit and the two magnon modes respectively. The last two terms describe the driving input fields and its interaction with the two magnon modes. Magnon antibunching would be studied by analyzing steady state second order correlation function which is given by,

$$g^2(0) = \frac{<m_1^{\dagger}(t)\,m_1^{\dagger}(t)m_1(t)m_1(t)>}{<m_1^{\dagger}(t)m_1(t)>^2} \quad (2)$$

In the magnon blockade effect the first magnon in the system prevents the simultaneous excitation of second magnon and therefore provides a restriction to its transmission. The antibunching causes an ordered flow of magnons which is necessary for realization of single magnon source. There are mainly two types of magnon blockade, first the conventional magnon blockade (CMB) in which the strong nonlinear interaction leads to a quantum anharmonicity in the energy spectrum. If the nonlinear shift in the two magnon state is greater than the loss of the cavity, then the population of two magnon state is suppressed such that only one magnon is allowed in the system at a given time. In contrast to CMB, in a weakly nonlinear quantum system we have unconventional magnon blockade where the destructive quantum interference between two transition paths causes the magnon blockade effect. We have studied the magnon blockade effect in the system under weak nonlinear regime by evaluating the optimal parameters using analytical methods and numerically solving quantum master equation to evaluate the steady state second order correlation function $g^2(0)$. The nonclassical antibunching effect arises when $g^2(0) < 1$. The function $g^2(0) \to 0$ indicates complete magnon blockade.

3. References

[1] 1. Ö. O. Soykal and M. E. Flatté, "Strong field interactions between a nanomagnet and a photonic cavity," Phys. Rev. Lett. 104, 077202 (2010).
[2] L. Bai, M. Harder, Y.-P. Chen, X. Fan, J.-Q. Xiao, and C.-M. Hu, Spin Pumping in Electrodynamically Coupled Magnon-Photon Systems. Phys. Rev. Lett. 114, 227201 (2015)
[3] S. A. McGee, D. Meiser, C. A. Regal, K. W. Lehnert and M. J. Holland, Mechanical resonators for storage and transfer of electrical and optical quantum states. Phys. Rev. Lett. 87, 053818 (2013)
[4] A. A. Serga, A. V. Chumak, and B. Hillebrands, YIG magnonics, J. Phys. D 43, 264002 (2010)
[5] Jie Li, Shi-Yao Zhu, and G. S. Agarwal, Magnon-Photon-Phonon Entanglement in Cavity Magnomechanics. Phys. Rev. Lett. 121, 203601 (2018)
[6] Chengsong Zhao, Xun Li, Shilei Chao, Rui Peng, Chong Li and Ling Zhou, Simultaneous blockade of a photon, phonon, and magnon induced by a two-level atom. Phys. Rev. A 101, 063838 (2020)
[7] Yutaka Tabuchi, et al., Coherent coupling between a ferromagnetic magnon and a superconducting qubit. Science (2015)
[8] Xiyun Li et al. Tunable magnon antibunching in a hybrid ferromagnet-superconductor system with two qubits. Phys. Rev. B 104, 224434 (2021)

Atos is a global leader in digital transformation with 111,000 employees and annual revenue of c. € 11 billion. European number one in cyber security, cloud and high-performance computing, the Group provides tailored end-to-end solutions for all industries in 69 countries. A pioneer in decarbonization services and products, Atos is committed to a secure and decarbonized digital for its clients. Atos is a SE (Societas Europaea), listed on Euronext Paris. The Purpose of Atos is to help design the future of the information space.
Its expertise and services support the development of knowledge, education and research in a multicultural approach and contribute to the development of scientific and technological excellence. Across the world. The Group enables its customers and employees, and members of societies at large to live, work and develop sustainably, in a safe and secure information space.

Atos Global Head Office
River Ouest, 80 quai Voltaire
95877 Bezons cedex – France
+33173260000


OPTICA
Formerly OSA

Supported by

Government agencies

Telephone

Convener contact:

+919023082848, +919368588862

Travel and accommodation contact:

+919792414519, +919639936038

Email : copaq2022@iitr.ac.in

Website : https://iitr.ac.in/copaq2022